VOLUME 24 NU[illegible]
JULY 1963

THE
JOURNAL OF
PHYSICS
AND
CHEMISTRY
OF SOLIDS

AN
INTERNATIONAL
JOURNAL

Editor-in-Chief
HARVEY BROOKS
Cambridge, Mass.

Associate Editors

H. B. G. CASIMIR
Eindhoven

G. J. DIENES
Brookhaven

JACQUES FRIEDEL
Paris

E. M. LIFSHITZ
Moscow

PERGAMON PRESS
NEW YORK · OXFORD · LONDON · PARIS

THE JOURNAL OF PHYSICS AND CHEMISTRY OF SOLIDS

Editors:

Prof. Harvey Brooks (*Editor-in-Chief*), *217 Pierce Hall, Harvard University, Cambridge 38, Mass., U.S.A.*

Prof. Dr. H. B. G. Casimir, *N.V. Philips' Gloeilampenfabrieken, Eindhoven, The Netherlands*

Dr. G. J. Dienes, *Brookhaven National Laboratory, Upton, Long Island, New York, U.S.A.*

Prof. Jacques Friedel, *Service de Physique des Solides, Faculté des Sciences (Group II), B.P. No. 11, Orsay, (S. & O.) France*

Prof. E. M. Lifshitz, *Institute for Physical Problems, Vorobievshoye Chaussee, 2, Moscow, V–334, U.S.S.R.*

Editorial Advisory Board

U.S.A.

E. N. Adams, New York
D. Alpert, Illinois
L. Apker, Schenectady
J. Bardeen, Illinois
D. S. Billington, Oak Ridge
R. G. Breckenridge, Cleveland
Leo Brewer, Berkeley, Calif.
E. Burstein, Penn.
J. A. Burton, New Jersey
N. Cabrera, Virginia
G. C. Danielson, Iowa
J. C. Fisher, Schenectady
H. K. Henisch, Pennsylvania
F. Herman, Palo Alto
Conyers Herring, New Jersey
A. R. von Hippel, Cambridge, Mass.
J. H. Hollomon, Schenectady
W. V. Houston, Houston
H. B. Huntington, Troy
H. M. James, Purdue
C. Kittel, Berkeley, Calif.
W. Kohn, La Jolla, Calif.
J. A. Krumhansl, Ithaca
A. W. Lawson, Riverside, Calif.
H. W. Leverenz, Princeton
O. T. Marzke, Pittsburgh
B. T. Matthias, New Jersey
L. R. Maxwell, Silver Spring
Joseph E. Mayer, La Jolla, Calif.
J. W. Mitchell, Charlottesville
E.W. Montroll, Yorktown Heights, N.Y.
David Pines, Princeton
George T. Rado, Washington, D.C.
H. Reiss, Canoga Park, Calif.
J. R. Reitz, Cleveland
A. Rose, Princeton
R. A. Smith, Cambridge, Mass.
R. Smoluchowski, Princeton
F. H. Spedding, Iowa
D. Turnbull, Schenectady
J. H. Van Vleck, Cambridge, Mass.
B. E. Warren, Cambridge, Mass.
Eugene P. Wigner, Princeton
B. H. Zimm, La Jolla, Calif.

Canada

R. E. Burgess, Vancouver
D. K. C. MacDonald, Ottawa
W. B. Pearson, Ottawa

United Kingdom

A. Charlesby, Shrivenham, Berks.
W. J. Dunning, Bristol
I. Estermann, London
F. C. Frank, Bristol
H. Jones, London
A. B. Pippard, Cambridge
M. H. L. Pryce, Bristol
O. C. Simpson, Baldock
K. W. H. Stevens, Nottingham
F. C. Tompkins, London

France

E. F. Bertaut, Grenoble
A. Guinier, Orsay
Louis Néel, Grenoble
Louis Weil, Grenoble

Germany

M. Born, Bad Pyrmont
Ulrich Dehlinger, Stuttgart
R. Hilsch, Göttingen
G. Leibfried, Aachen
E. Mollwo, Erlangen
H. Pick, Stuttgart
H. Welker, Erlangen

Italy

F. G. Fumi, Pavia

Czechoslovakia

J. Tauc, Praha

Japan

Toshinosuke Muto, Tokyo

The Netherlands

A. Michels, Amsterdam
G. W. Rathenau, Amsterdam

Sweden

J. O. Linde, Stockholm
Per-Olov Löwdin, Uppsala

Switzerland

G. Busch, Zurich
P. Scherrer, Zurich

U.S.S.R.

G. S. Zhdanov, Moscow

Publishing Offices

American Continent: Pergamon Press, Inc., 122 *East* 55*th Street, New York* 22, *N.Y.*

Rest of the World: Pergamon Press Ltd., Headington Hill Hall, Oxford.

Issued in parts. Annual Subscription (A) for libraries, £35 (*U.S.A.* $100.00); (*B*) *for subscribers who write directly to the publisher certifying that the subscription is for their own personal use,* £5 5*s.* (*U.S.A.* $15.00), *including postage.*

Surcharge for airmail subscriptions:

U.S.A. and South America	$28.00 (£10) per annum
Far East	$40.00 (£14) per annum
European countries	£5 ($14.00) per annum

Copyright © 1963 Pergamon Press Ltd.

PERGAMON PRESS, INC.

122 EAST 55TH STREET, NEW YORK 22, N.Y.   HEADINGTON HILL HALL. OXFORD

J. Phys. Chem. Solids Pergamon Press 1963. Vol. 24, pp. 787–794. Printed in Great Britain.

TRANSITION RATES OF KNO_3 HIGH-PRESSURE POLYMORPHS*

BRIANT L. DAVIS and LEASON H. ADAMS

Institute of Geophysics, University of California, Los Angeles, California

(*Received* 10 *December* 1962; *revised* 13 *February* 1963)

Abstract—A beryllium pressure vessel mounted in an X-ray goniometer and modified for heating to 300°C has permitted the direct recording of transition rates across all of the equilibrium boundaries of the KNO_3 phase diagram.

Most transitions show rate curves that taper off near the completion of the process, but metastable persistance of phase III occurs in the phase II field and becomes greater at high pressures and low temperatures along the negative II–III phase boundary.

Several diffraction patterns of the transitions I–II and III–II revealed preferred orientation of grains in the resulting aragonite-type phase.

Cell parameters of KNO_3-I and KNO_3-III (both modified calcite-type structures) taken in their stability fields show a marked reduction in the *c*-axis length going from phase I to phase III with increasing pressure at constant temperature.

INTRODUCTION

THE KNO_3 phase diagram, Fig. 1, reveals two hexagonal (I and III) and two orthorhombic (II and IV) phases, all lying in a pressure and temperature region allowing easy study of the rates across any of the phase boundaries. From the present study something can be said about the rates across all boundaries, but more effort was put into a study of the $KNO_3\text{-I} \rightleftharpoons KNO_3\text{-II}$ and $KNO_3\text{-II} \rightleftharpoons KNO_3\text{-III}$ rates because of the similarity of these phases in structure to those of calcite and aragonite. EDWARDS(1) found that KNO_3-II had the aragonite structure and TAHVONEN(2) determined KNO_3-I to be calcite-type but with disorder present in the NO_3^- groups. FINBAK and HASSEL(3) also described KNO_3-III as calcite-type but later BARTH(4) proposed a smaller cell ($Z = 1$) for the structure. The disorder of the NO_3^- ion in KNO_3-I and the uni-directional order of the NO_3 ion in KNO_3-III, both resulting in a loss of the 113 and other lines of the normal calcite-type pseudo-cell,† might justify halving the *c*-axis of this large cell, but the structural arrangement of the cations and ionic groups are nearly identical in $CaCO_3$-I, $CaCO_3$-II, KNO_3-I, and KNO_3-III; therefore the normal calcite-type pseudo-cell (hexagonal, $Z = 6$) has been retained in this study.

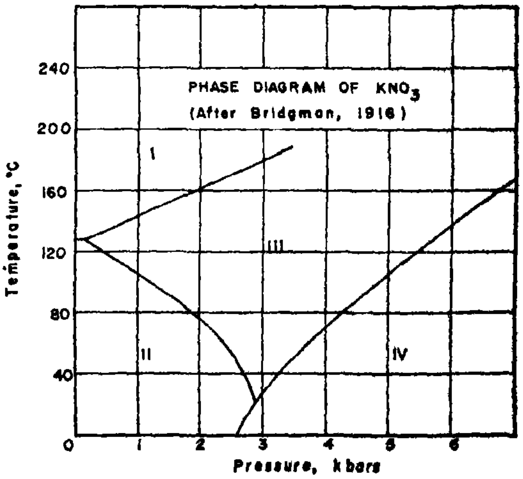

FIG. 1. Phase diagram of KNO_3 (after BRIDGMAN(5)).

---

* Publication No. 269 of the Institute of Geophysics.

† The true unit cell of calcite is a rhombohedron with $Z = 2$ formula weights per cell).

A

411

828

The rates were measured in a beryllium cylinder mounted on a Norelco X-ray goniometer, a detailed description of which has already been presented (DAVIS and ADAMS[5]). The vessel was modified for heating to 300°C by winding the cylinder with No. 22 (B. & S. gauge) Nichrome-V wire. The heating coil was separated from the vessel wall by a thin layer of Alundum cement; another layer of this cement was applied over the furnace to act as thermal insulation against heat loss to the atomsphere. The temperature was measured by means of a Chromel-alumel thermocouple placed in a hole directly beneath the lower piston. Temperatures were determined from readings on a Leeds–Northrup portable potentiometer with which one scale division corresponded to 0·02 mV.

Previously (DAVIS and ADAMS[5]) the KNO_3 was mixed with starch in an attempt to obtain better pressure distribution throughout the sample. However, since this might also affect the rate, only pure KNO_3 was used in the present study. The sample material was pressed into pellets 4·6 × 1 mm and placed at the bottom of the cylinder bore under a similar pellet of beryllium metal.

The transition rates were measured by fixing the goniometer at the 2θ value expected for a high-pressure or high-temperature line while the chart recorder is operating, then applying the pressure or temperature to start the transition. There was some difficulty experienced in boosting the temperature over the phase boundary and then being able to stop it from rising further. Since some creep of the temperature was unavoidable, an accurate record of the variation of the temperature on the sample during the progress of a transition has been included with the rate curves.

RESULTS

KNO_3-II $\rightleftharpoons$ KNO_3-IV

Forward and reverse transitions for this rate have already been described (DAVIS and ADAMS[5]). The conclusions concerning these rates are summarized as follows:

(1) The rate curve is assymetrical. In two experiments the forward change required 14–30 min for completion and the reverse change only seconds.

(2) The forward change appears to take place in steps, whereas the reverse apparently does not (possibly because of the rapidity of the rate the steps were not seen).

(3) Except for the step intervals one of the rate curves approached first-order kinetics, but it is apparent that factors, such as nucleation, strain energy, and grain growth, may affect the order of the rate.

KNO_3-III $\rightleftharpoons$ KNO_3-IV

Phase III is the high-temperature phase (see Fig. 1) and therefore the forward rate, as written in the above heading, occurs with lowering temperature. As the temperature is raised the IV–III change takes place quite slowly. At a pressure of 3000 bars and a temperature rising from 50 to 85°C, only about 20 per cent conversion took place in 15 min. Upon raising the temperature to 105°C the reaction went to completion in 10 min. It is assumed that much of the change took place in the several minutes required to raise the temperature to the 105°C value.

For the reverse (III–IV) rate no transformation had taken place after 17 min at 3000 bars and 29°C. At this pressure the temperature was not low enough to permit the formation of phase IV again. When the pressure was suddenly dropped to zero, phase II appeared leaving about 10 or 20 per cent of phase III remaining.

KNO_3-I $\rightleftharpoons$ KNO_3-II

Examination of the phase diagram, Fig. 1, shows that the stability fields of phases I, II, and III meet at a triple-point at 113 bars and 128·3°C.* The only place possible to measure the rate of the KNO_3-I $\rightleftharpoons$ KNO_3-II transition is near this point, and it has been very difficult to obtain records not showing the appearance of phase III. It is fortunate that the strong peak of phase III lies less than one degree (2θ) from the strong peak of phase I; otherwise accurate recording of the appearance of these two phases simultaneously and in closely following intervals would have been difficult. The up-temperature transformation often went to completion without the appearance of phase III. For example, at

---

* As measured by BRIDGMAN.[6]

$P = 1$ bar the temperature was very slowly raised from 124°C. The transition began at 127°C and was essentially complete in 2¼ min. No phase III was observed. Figure 2 shows the rate curve and the slight temperature shift during the transition. In one experiment, in which the piston was left out of the vessel,* the II–I transformation went to completion in about one minute. In another experiment, in which approximately 500 bars had been applied to the sample, the transition commenced at $t = 115$°C and took about 3½ min to run to completion.

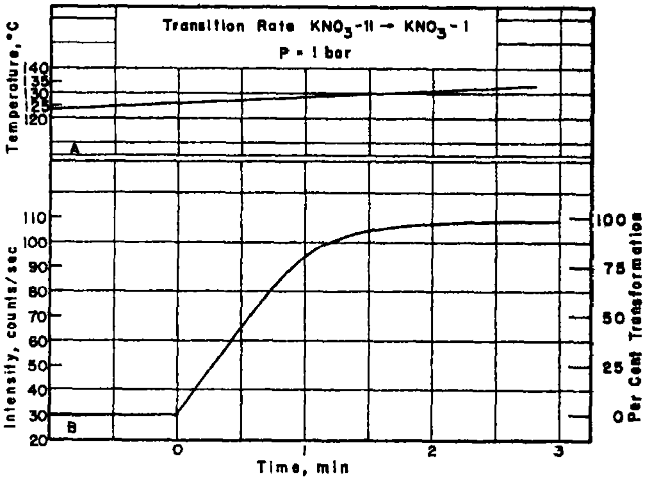

FIG. 2. Transition rate KNO_3-II → KNO_3-I at 1 bar; (a) variation of temperature during the rate, and (b) rate curve representing growth of the strong 014 peak with time. MoKα radiation.

It was not possible in any of the runs to record the I–II rate without the appearance of phase III. An example of the rate curves recorded when phase III appeared is found in Fig. 3. At a temperature slightly less than 125°C the peak representing phase I dropped off suddenly, leveled off, and then grew some again. At 120°C it dropped off again, this time permanently, while another peak, representing phase III began to grow. Actually the growth of phase III might have begun earlier, as indicated by the dashed line of Fig. 3, since a drop in intensity of the phase I peak occurred here. Phase III grew to a maximum, leveled off, and then rapidly died out as phase II appeared.

Figure 4 shows rate curves during which phase III appeared both at the beginning and at the end of the experiment. At the start, about 125°C, phases I and III both grew simultaneously at the expense of phase II, and shortly thereafter phase III disappeared. Why phase I did not grow more when phase III disappeared is not understood. This is strange when it is seen that phase III grew an additional amount at the time when phase I was diminished at the end of the experiment.

The appearance of phase III, as shown in Figs. 3 and 4, illustrates the well-known phenomenon that in a chemical or polymorphic transition the phase that first appears, as the *P–t* environment is changed, may not be the one which is most stable in that environment. The appearance of phase III at the end of the experiments mentioned took place at temperatures below that of the established phase boundary; at these temperatures phase III considered to be metastable.

KNO_3-II ⇌ KNO_3-III

At a pressure of 500 bars the transition II–III took place in less than 2 min and began at

---

* *To avoid applying even a few bars pressure on the sample.*

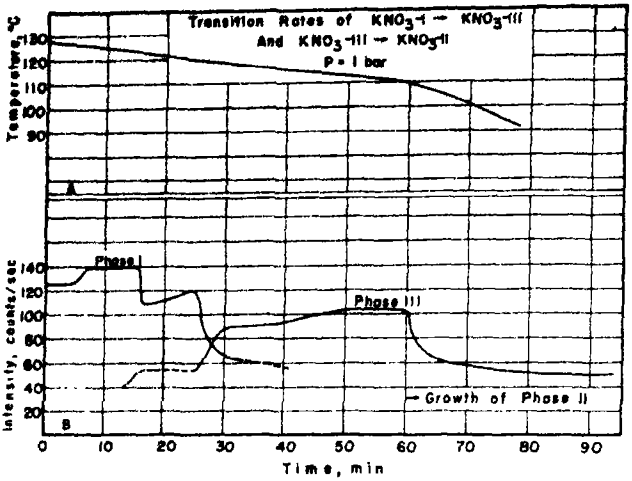

FIG. 3. Transition rate of KNO_3-I → KNO_3-III and of KNO_3-III → KNO_3-II at 1 bar; (a) variation of temperature during the rates, and (b) rate curves representing growth and diminution of the strong 014 peaks of phases I and III. MoKα radiation.

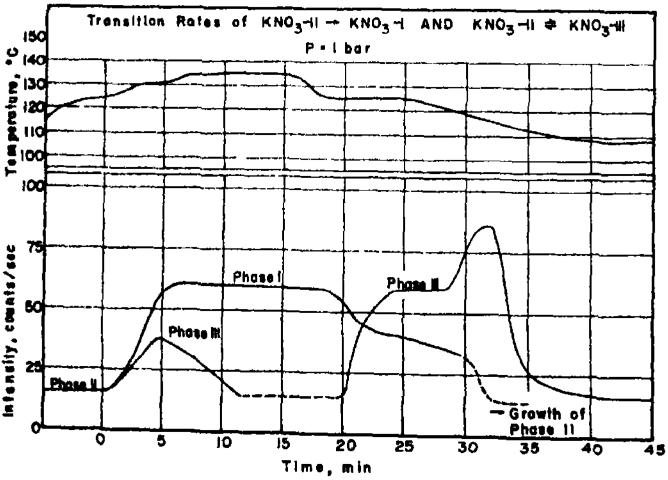

FIG. 4. Transition rate of KNO_3-II → KNO_3-I and of KNO_3-II ⇆ KNO_3-III at 1 bar; (a) variation of temperature during the rates, and (b) rate curves representing growth and diminution of the strong 014 peaks of phases I and III. MoKα radiation.

$t = 118°C$. As the temperature was increased slowly to 130°C the III–I transition took place. The temperature maximum of 143°C was attained after which the temperature was lowered slowly. At 128–130°C the reverse transition I–III took place and immediately (at about $t = 120°C$) the transition III–II began, but slowly. At this pressure the III–II transition went to completion in approximately 13 min.

Essentially the same transition sequence was observed at a pressure of 1500 bars. Here the initiation of the II–III transition took place at 113°C, the III–I transition at 145°C, the I–III transition again at 145°C, and the III–II transition somewhere near 115°C. This latter point was not accurately determined because the transition III–II proceeded so slowly that after $\frac{1}{2}$ hr only a small amount of phase II had appeared. After 10 hr there was still about 10 per cent of phase III remaining. During the 10 hr period, however, the pressure had dropped to about 500 bars due to leaks in the pressure system; had the pressure remained constant during this time, less of the transformation might have taken place.

Other similar experiments performed support the conclusion that the metastability of phase III is prolonged at low temperatures when pressure is increased and that the duration of the persistence of phase III increases with lowering temperature and increasing pressure along the negative slope of the II–III phase boundary. Because of the effect of lower temperatures in the phase II field as pressure is increased this phenomenon is not wholly unexpected. The separation of the effects of pressure and temperature on the kinetics of this transition cannot be made with certainty. The rate IV–III (with the phase boundary dt/dP positive) was also sluggish at 3000 bars and 100°C, but since the rate here is between different phases a comparison cannot be made.

One transition across the II–III boundary was studied at constant temperature. At $t = 93°C$ the pressure was abruptly raised to 3000 bars. The transition II–III took place within $1\frac{1}{2}$ min. Upon release of the pressure to zero (nominal) the reverse transition III–II went to completion in 7 min. It is interesting to note the lack, in this experiment, of the persistence of phase III that was seen under similar P–t conditions but with pressure constant and temperature variable.

GRAIN ORIENTATION RESULTING FROM TRANSFORMATION

Preferred orientation of grains in the powder pellet was very striking during the rate study of KNO_3-II $\rightleftharpoons$ KNO_3-III. With the forward rate, the pattern of phase III was quite consistent from experiment to experiment but after completing the reverse process the resulting aragonite-type phase II yielded an anomalous pattern. In two cases the 111 (relative intensity $I/I_0 = 100$, normally) and 021 ($I/I_0 = 56$, normally) peaks were completely missing. The 221 ($I/I_0 = 41$, normally) and 041 ($I/I_0 = 20$ normally) peaks were very weak. On the other hand, the unresolved lines 040 and 220 showed an intensity of 90–100 whereas usually each line should show I/I_0 less than 10. Line 211 was also unusually strong.

These results might indicate an orientation of the crystals with the 010 and 110 cleavages, or both, normal to the direction of applied load, thus indicating the lack of true hydrostatic stress conditions within the pressure vessel.

A similar orientation effect was noticed upon completion of the rate KNO_3-I → KNO_3-II. In this case, however, the strong lines were either 130, 112, or 022, or some combination of these (all are unresolved with molybdenum radiation).

Such orientation phenomena indicate that the transition of a calcite-type structure (i.e., I and III) to the aragonite-type structure (II) is not of the "single-crystal" variety, but is one involving complete breakdown of crystal units and reconstruction of those of the new phase, a concept wholly in harmony with the accepted nature of the calcite–aragonite transition.

ORDER OF TRANSITION

All of the rate curves of the study are non-linear; that is, the curves show a marked tail-off near completion of the transition.

Using a general rate theory (with the variables defined to conform to solid-state transitions) modified by PESSEN,(7) it can be concluded that the rate of transformation at any instant, for most of these transitions, is equal to a constant times the quantity of reactant phase remaining raised to a power between 1 and 2 (i.e., the transition order lies between 1 and 2).

It is suspected that such tail-off is the result of the elimination of the rate-accelerating processes of strain and nucleation toward the end of the transition. A more detailed treatment of rate theory as applied to polymorphic transitions has been presented elsewhere (Davis(8)).

CELL CONSTANTS OF KNO_3-I AND KNO_3-III

Cell constants of KNO_3-I have already been determined at 152°C and 1 bar by Tahvonen(2) and those of KNO_3-III at 120°C and 1 bar by Barth,(4) where in the latter case the KNO_3 compound was obtained in a metastable condition. The present data are justified in that the constants for phase I were obtained at conditions closer to those of the I–II boundary, and that those of phase III were obtained within the stability field of this phase. Table 1 summarizes the cell data for all known polymorphs of KNO_3, and includes the new data of this paper.

The 110 lines of both phases I and III were accurately obtained with slow scanning ($\frac{1}{4}$-deg/min) with a resulting 1-deg 2θ/in. chart scale. A diamond powder internal standard was used to correct for sample-height change and the pressure on the sample was estimated from vessel-calibration curves. For phase I the temperature was 133°C and the pressure atmospheric. For phase III, $t = 133$°C and $P = 2500 \pm 500$ bars. Excellent patterns obtained at slightly different P–t conditions provided the complete diffraction data, and the spacings were corrected to the pressures and temperatures mentioned above. Figure 5 is an X-ray diffraction pattern of KNO_3-I taken at $t = 137$°C and $P = 1$ bar, and Fig. 6 is a pattern of KNO_3-III taken at $t = 103$°C and $P = 3600 \pm 500$ bars. The radiation is MoKα with an applied power of 40 kV and 20 mA.

Final cell-constant data were obtained from a least-squares program designed for the IBM 7090 computor by W. E. Sharp of this institution. The observed and calculated spacings are summarized in Table 2. The constants are those of the calcite-type hexagonal pseudo-cell ($Z = 6$); they allow convenient comparison with dimensions of other calcite-type cells found in the nitrates and carbonates. It should be pointed out that the primitive cells of phases I and III are actually rhombohedrons with $Z = 2$ and $Z = 1$ respectively.

Although Barth(4) was able to obtain the phase III structure metastably at 120°C and room pressure, the cell constants resulting from his data

Table 1. *Cell constants of the* KNO_3 *polymorphs*

Phase	Source	P (bars)	t (°C)	Cell constants Å		Z	space group
I	Tahvonen(2)	1	152	$a_0 = 5{\cdot}396$	$c_0 = 19{\cdot}410$	6	H*
				$a = 7{\cdot}181$	$\alpha = 44° 8{\cdot}5'$	2	$R\bar{3}2/m$
I	Davis and Adams (This paper)	1	133	$a_0 = 5{\cdot}42_3$	$c_0 = 19{\cdot}33_3$	6	H*
II	Edwards(1)	1	25	$a_0 = 5{\cdot}44$	$b_0 = 9{\cdot}19$		
				$c_0 = 6{\cdot}46$		4	$Pmcn$
III	Barth(4)	1	120†	$a_0 = 5{\cdot}431$	$c_0 = 18{\cdot}222$	6	H*
				$a = 4{\cdot}365$	$\alpha = 76°53'$	1	$R3m$
III	Davis and Adams (This paper)	2500	133	$a_0 = 5{\cdot}44_0$	$c_0 = 17{\cdot}51_6$	6	H*
III	Finbak and Hassel(3)‡	1	115†	$a_0 = 5{\cdot}44_2$	$c_0 = 18{\cdot}26_5$	6	H*
				$a = 6{\cdot}849$	$\alpha = 46°48'$	2	$R\bar{3}2/m$
IV	Jamieson(9)	5000	25	$a_0 = 16{\cdot}12$	$b_0 = 10{\cdot}12$		
				$c_0 = 7{\cdot}75$		18	?
IV	Davis and Adams(5)	3000	25	$a_0 = 11{\cdot}04_8$	$b_0 = 8{\cdot}36_7$		
				$c_0 = 7{\cdot}40_2$		10	$Pmn2_1$?

* Hexagonal pseudo-cell (when ordered, space group = $R\bar{3}c$).

† Obtained metastably.

‡ Hexagonal constants calculated from a and α given by Finbak and Hassel.(3)

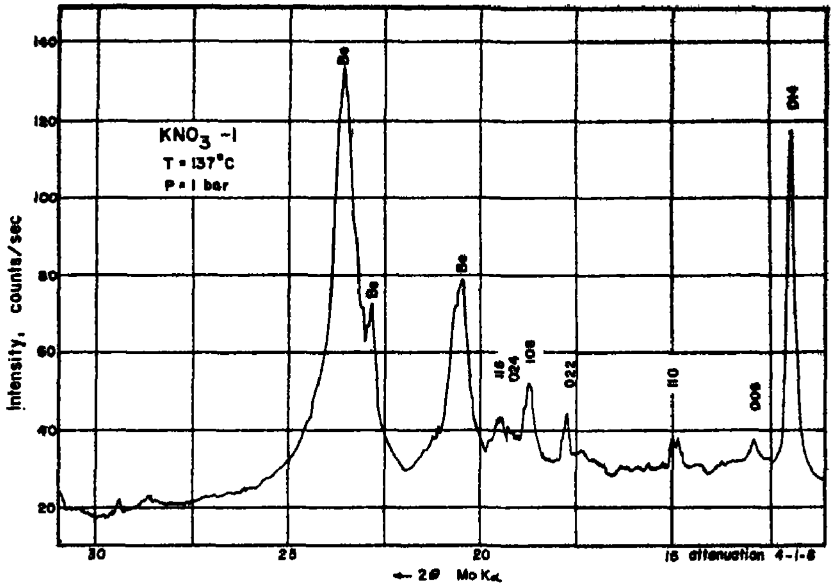

FIG. 5. X-ray diffraction pattern of KNO$_3$-I at 137°C and 1 bar. Indices based on hexagonal pseudo-cell (calcite-type). Diffraction peaks from beryllium vessel walls labeled Be. MoKα radiation.

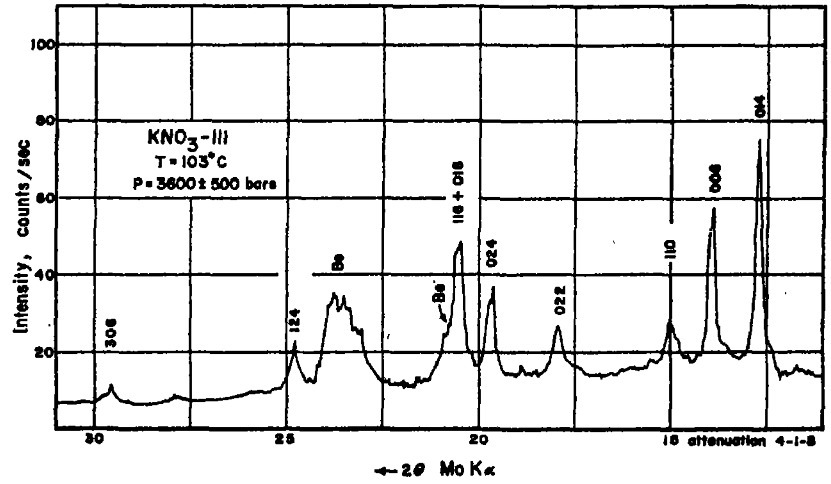

FIG. 6. X-ray diffraction pattern of KNO$_3$-III at 103°C and 3600 ± 500 bars. Indices based on hexagonal pseudo-cell (calcite-type). Diffraction peaks from beryllium vessel walls labeled Be. MoKα radiation.

Table 2. X-ray diffraction data

KNO_3-I

hkl	d_{calc} (A)	d_{obs} (A)	I/I_0*
014	3·37	3·39	100
006	3·22	3·13	5
110	2·71	2·71	9
022	2·28	2·28	13
108	2·15	2·16	22
024	2·112	2·111	7
116	2·075	2·074	10

Cell constants: $a_0 = 5{\cdot}42_3$ Å, $c_0 = 19{\cdot}33_3$ Å.
Temperature 133°C, Pressure 1 bar.

KNO_3-III

hkl	d_{calc} (A)	d_{obs} (A)	I/I_0*
102	4·15	4·10	3
014	3·21	3·20	100
006	2·92	2·92	65
110	2·72	2·73	16
022	2·27	2·28	19
024	2·074	2·074	37
108	1·986 }	2·015	58
116	1·990 }		
124	1·650	1·652	16
306	1·383	1·389	8

Cell constants: $a_0 = 5{\cdot}44_0$ Å, $c_0 = 17{\cdot}51_6$ Å.
Temperature 133°C, Pressure 2500 ± 500 bars.

* Relative peak heights.

would not be expected to represent either the same absolute dimensions or same axial ratio that the cell would have at other temperatures and pressures. The data of this paper show that there is a relatively large compression parallel to the *c*-axis of phase III in going from atmospheric pressure (Barth's data) to 2500 bars (our data). The large compression along the *c*-axis as compared to that along the *a*-axis is expected in light of previous high-pressure work with KNO_3 and $CaCO_3$ (DAVIS(8)).

The pressure existing at the equilibrium boundary I–III at 133°C is 500 bars. When the specific volumes of each phase are corrected to this point we have for phase *I*, $v = 0{\cdot}48_7$ cm³/g, and for phase III, $v = 0{\cdot}45_1$ cm³/g, giving a Δv of $0{\cdot}03_6$ cm³/g.

SUMMARY

Observations on transition rates across the boundaries of the KNO_3 phase diagram have been obtained using a beryllium pressure vessel wired for heating to moderate temperatures. The rates are determined by continuous scan by X-radiation passing through the walls of the vessel.

Most of the curves obtained show decreasing rates near completion of the transition, resulting in transition orders lying between 1 and 2. However, changes studied near the triple-point I–II–III were complicated by the metastable appearance of phase III, both with increasing temperature and decreasing temperature across the point. The persistence of phase III in the phase II field becomes greater with lowering temperature and increasing pressure.

The I–II and III–II transitions often result in preferred orientation of the aragonite-type phase (II) with the 010 or 110 cleavages, or both, lying normal to the direction of applied load.

It is suspected that the elimination of such rate-modifying factors as nucleation and strain may be responsible for the tail-off observed in nearly all of the transition curves measured.

KNO_3-I at $t = 133$°C and $P = 1$ bar has cell constants $a_0 = 5{\cdot}42_3$ Å, $c_0 = 19{\cdot}33_3$ Å $(Z = 6)$ using the hexagonal pseudo-cell of calcite. Constants for KNO_3-III at $t = 133$°C and $P = 2500 \pm 500$ bars are $a_0 = 5{\cdot}44_0$ Å, $c_0 = 17{\cdot}51_6$ Å $(Z = 6)$ referred to the same cell. The specific volume decrement, Δv, at the transition boundary ($t = 133$°C $P = 500$ bars) is $0{\cdot}03_6$ cm³/g.

Acknowledgements—The writers wish to acknolwedge the support of the National Science Foundation in this research; and wish to thank the Computing Facility of U.C.L.A., and also W. E. Sharp, Institute of Geophysics U.C.L.A., for use of the IBM 7090 computor and aid in calculation of the cell constants.

REFERENCES

1. EDWARDS D. A., *Z. Krist.* **80,** 154–163 (1931).
2. TAHVONEN P. E., *Ann. Acad. Sci. Fennicae, Ser. A, I. Math-Phys.* **44,** 20 (1947).
3. FINBAK C. and HASSEL O., *Z. phys. Chem.* **37,** 75–80 (1937).
4. BARTH T. F. W., *Z. phys. Chem.*, **B43,** 448–450 (1939).
5. DAVIS B. L. and ADAMS L. H., *Z. Krist.* in press (1962).
6. BRIDGMAN P. W., *Proc. Amer. Acad.* **51,** 581–625 (1916); *Proc. Amer. Acad.* **52,** 57–88 (1916).
7. PESSEN H., *Science* **134,** 676 (1961).
8. DAVIS B. L., High-Pressure and High-Temperature X-ray Investigation of the $CaCO_3$ Polymorphs: Unpublished PhD Dissertation, University of California, Los Angeles (1963).
9. JAMIESON J. C., *Z. Krist.* **107,** 65–71 (1956).

J. Phys. Chem. Solids Pergamon Press 1963. Vol. 24, pp. 795–822. Printed in Great Britain.

A FERROMAGNETIC–ANTIFERROMAGNETIC MODEL FOR COPPER–MANGANESE AND RELATED ALLOYS

J. S. KOUVEL

General Electric Research Laboratory, Schenectady, New York

(*Received* 4 *January* 1963)

Abstract—The microscopically inhomogeneous magnetic structure conceived for Cu–Mn, Ag–Mn and other related alloys at very low temperatures is simulated by a simple model in which the magnetic unit is a small ensemble of mutually-interacting ferromagnetic and antiferromagnetic domains. In the ground state of the hypothetical system each domain-ensemble has zero net magnetization, but when the system is cooled in a magnetic field some of its domain-ensembles are forced into a different state (with a non-zero magnetization) which is stabilized by the growth of a strong anisotropy (K_A) in the antiferromagnetic domains. In this field-cooled state, the magnetic hysteresis loops of the system are displaced asymmetrically from the origin, and its torque curves even at very high fields indicate a single easy direction of magnetization. These and related properties and their variation with field applied during cooling and with temperature, as predicted by the model, are in excellent qualitative agreement with the field-cooled behavior of Cu–Mn, Ag–Mn and other alloys.

According to this model, the temperature of maximum susceptibility for each of these alloys is to be interpreted not as a Néel temperature but as simply the point at which the anisotropy K_A disappears; the alloy does not become paramagnetic until a significantly higher temperature (T_c) is reached. It is predicted that at T_c there will be a kink in the inverse susceptibility vs. temperature curve, and this has been observed experimentally in various Cu–Mn and Ag–Mn alloys. Also consistent with this prediction is the electrical resistivity anomaly (of a type suggestive of a magnetic transition) found at this higher temperature (T_c) in each of these materials.

1. INTRODUCTION

FROM recent measurements,[(1)] we learned that certain unusual magnetic properties previously observed by us in alloys of about 25 at. % manganese in copper and in silver[(2)] are characteristic of these alloy systems over wide ranges of composition. Specifically, it was discovered that when these alloys are cooled to very low temperatures in a magnetic field, their magnetic hysteresis loops are displaced from their symmetrical positions about the origin. When the alloys are subsequently raised in temperature, this loop displacement decreases and its disappearance is accompanied by large hysteresis losses. At very low temperatures, where the hysteresis losses are low and the two branches of the displaced loops are essentially coincident, the loops have the simple form typified by curve A in Fig. 1. One of the principal features of this curve, distinguishing it from the hysteresis loop obtained by cooling in zero field (curve B in Fig. 1), is the remanent magnetization (M_R).

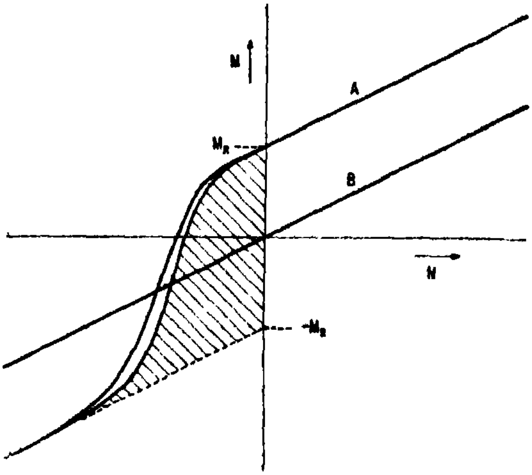

FIG. 1. Typical low-temperature hysteresis loops for Cu–Mn and Ag–Mn alloys cooled in a positive magnetic field (A) or in zero field (B). Shaded area represents unidirectional anisotropy energy.

This thermoremanence was originally observed in Cu–Mn alloys by OWEN *et al.*(3) and by SCHMITT and JACOBS(4) and was investigated more recently by LUTES and SCHMIT.(5) Although these thermoremanence studies established that a substantial ferromagnetic spin alignment can be produced in these alloys by cooling them in a magnetic field, very little could be deduced about the origin of this phenomenon.

Even the field-cooling experiments on Cu–Mn alloys by STREET and SMITH,(6) in which the magnetizations for a field parallel or antiparallel to the field applied during cooling were found to be quite different, were unable to provide an unambiguous clue to the appropriate mechanism. This clue, we believe, was provided only when the displaced hysteresis loops for Cu–Mn (and Ag–Mn) alloys were measured in their entirety.(1,2) It then became clear, as illustrated in Fig. 1, that the thermoremanence of these materials represents a ferromagnetic moment which can be reversed completely by a large enough field and which reverts back to its original polarity when the reverse field is removed. This asymmetric behavior, indicative of a single easy direction of magnetization (where the unidirectional anisotropy energy is represented by the shaded area in Fig. 1), had been observed earlier in Ni–Mn(7) and Co–Mn(8) alloys and attributed to an *exchange anisotropy* mechanism, analogous to that evoked for the Co–CoO system.(9) According to this mechanism, a unidirectional anisotropy is produced under field-cooling conditions by an exchange coupling between ferromagnetic and antiferromagnetic parts of the system. It was argued that the statistical composition fluctuations inherent to atomically disordered systems such as Ni–Mn and Co–Mn, together with a coexistence of positive and negative short-range magnetic interactions, can give rise to microscopic regions of ferromagnetic and antiferromagnetic order.

The same basic argument was applied to the Cu–Mn and Ag–Mn alloys,(1,2) for which it was assumed that the coupling between nearest-neighbor Mn atoms is antiferromagnetic and that the coupling between Mn atoms of larger separation is ferromagnetic. Hence, the regions in these alloys that for purely statistical reasons are relatively rich or poor in Mn can be expected to have antiferromagnetic or ferromagnetic spin alignment, respectively. In terms of the magnetically inhomogeneous states of such a system, it was then found possible to rationalize not only a low temperature displaced hysteresis loop behavior but also the magnetic (and associated electrical) properties of these alloys at higher temperatures as well.

Of particular interest in these alloys at higher temperatures is the peak in their magnetic susceptibility, which occurs just where the hysteresis losses (and the remanence), having risen to a maximum with increasing temperature, again disappear. The curves shown in Fig. 2 for the temperature dependence of the remanent magnetization and of the magnetization in a moderately high field (the latter being approximately proportional to the susceptibility) are typical for all the Cu–Mn and Ag–Mn alloys examined after being cooled to low temperatures in zero field.(1, 2) Although it is tempting to associate the temperature of the susceptibility maximum (T_s) with an antiferromagnetic Néel temperature, other experimental evidence also presented in Refs. 1 and 2 indicates that this association would be incorrect, except possibly for the alloys very dilute in Mn. It was found that the electrical resistivity (ρ) of each of these alloys exhibits an anomaly of the type usually attributed to a magnetic order–disorder transition but that this anomaly takes place at a temperature (T_C) considerably higher than T_s, as shown schematically in Fig. 2; the decrease of ρ above T_C presumably reflects some residual short-range magnetic order. Also shown in this figure is the distinctive kink that appears in the inverse susceptibility vs. temperature curves of the more concentrated Mn alloys at T_C. Above this kink, the $1/\chi$ vs. T curves become linear and extrapolate to negative values for the paramagnetic Curie temperature. These effects left little doubt that these alloys are in some state of magnetic order well above their susceptibility-maximum temperatures.

In discussions of these and other properties of Cu–Mn and Ag–Mn alloys,(1, 2) the concept of inhomogeneous ferromagnetic–antiferromagnetic states (mentioned above) proved to have at least qualitative validity. It is obvious that any theory based on such a concept and applied rigorously to these atomically disordered systems, especially those of fairly high Mn concentration, would be a formidable undertaking. A lesser task, but one that can ultimately provide a preliminary framework for a more rigorous theory, is the development of a suitable schematic model, to which the remainder of this paper is devoted. Many approximations have been made in order to simplify this complicated disordered alloy problem, but we believe that its most essential magnetic features have been retained.

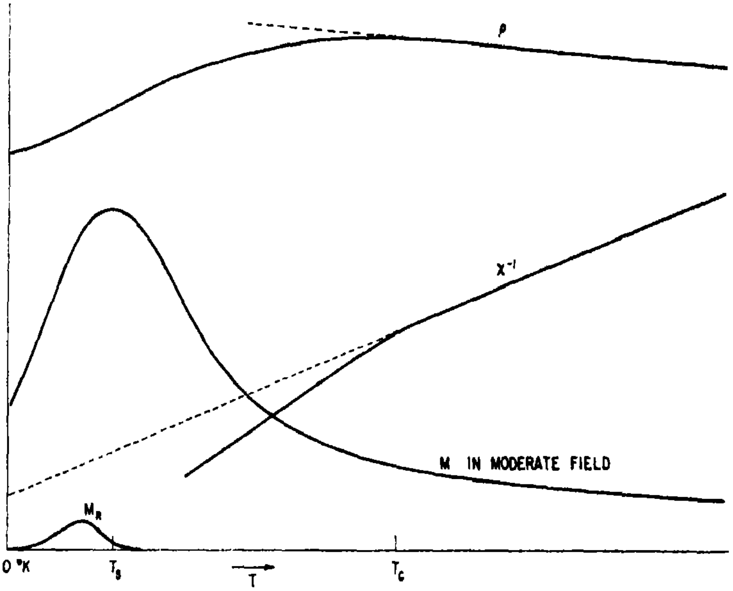

Fig. 2. Typical temperature dependences of remanent magnetization, magnetization in moderate field, inverse susceptibility and electrical resistivity for Cu–Mn and Ag–Mn alloys cooled initially in zero field. T_s is the temperature of maximum susceptibility and T_c the magnetic-disordering temperature.

In the following Section, we propose a basic model according to which the magnetic unit of the system is an ensemble of mutually-interacting ferromagnetic and antiferromagnetic domains. The system is described both in its ground state and in the metastable state achieved when cooled in a magnetic field; its magnetic properties in the latter state are studied in detail under the simplifying condition that all the domain ensembles in the system are equivalent. In the next (third) Section, this equivalence condition is relaxed for the parameter that determines the net coupling between domains within each ensemble. With the inhomogeneity of the system thus represented more realistically, we proceed to discuss the temperature dependence of the initial susceptibility and, finally, the criteria for achieving the field-cooled state manifested in the displaced hysteresis loop. At appropriate points throughout these discussions (most of whose mathematical details are relegated to various Appendices at the end), we compare the predictions of our model with the experimentally observed properties of Cu–Mn and Ag–Mn alloys.

2. THE BASIC MODEL AT LOW TEMPERATURES

As we have indicated earlier, a fundamental assumption of our phenomenological model for Cu–Mn and Ag–Mn alloys is that the sign of the magnetic interaction between neighboring Mn atoms depends critically on the distance of separation. The Ruderman–Kittel(10) type of interaction, which has this kind of critical dependence, is presumably the principal long-range coupling mechanism in the alloys extremely dilute in

Mn.(11) However, the thermoremanence results cited earlier suggest that even in the alloys with as little as one atomic percent Mn there may be very strong short-range magnetic forces of a different origin (e.g., direct exchange between neighboring Mn atoms, superexchange involving intervening Cu or Ag atoms). Our assumption applying specifically to these short-range forces is that their net effect is to couple nearest-neighbor Mn atoms antiferromagnetically and those of larger separation ferromagnetically. It then follows from the short-range nature of these interactions that there will be spatial fluctuations in the type of spin alignment corresponding closely to the statistical composition fluctuations in these atomically disordered alloys. For fairly dilute Mn alloys, the magnetic state that emerges from these considerations is that of very small ferromagnetic regions (or domains) coupled antiferromagnetically through nearest-neighbor Mn atom pairs. This state has been proposed earlier by others(12) as one of the alternatives consistent with susceptibility, magnetoresistance, and electron spin resonance results for Cu–Mn. It is also approximately the state considered for Cu–Mn by DEKKER(13) in a simple theoretical analysis of the temperature dependence of the susceptibility; however, this analysis involved very small isolated groups of interacting Mn atoms and was therefore valid only for extremely low Mn concentrations.

In the alloys somewhat richer in Mn, in which an appreciable fraction of the Mn atoms have two or more Mn nearest-neighbors, the antiferromagnetic boundaries between the ferromagnetic domains will have so thickened that they can be more properly thought of as antiferromagnetic domains. Moreover, at these compositions, the high concentration of short-range exchange couplings within the different domains will give rise to fairly well defined ferromagnetic–antiferromagnetic domain boundaries. Although the interactions across these boundaries may not significantly affect the type of moment alignment within the domains, they will however determine the relative orientation of the moments in adjacent domains. In fact, since there is an equal probability that a ferromagnetic domain will be predominantly coupled to any one of the sublattices of a neighboring antiferromagnetic domain, it follows quite generally that the total net magnetization of such a system in its ground state (and in the absence of an external field) will be zero. This general property of a system of this kind was recently pointed out by us(1, 2) and related to the zero (or near-zero) remanence exhibited by Cu–Mn and Ag–Mn alloys after being cooled to very low temperatures in zero field.

All the above features of a system of well defined and closely coupled ferromagnetic and antiferromagnetic domains are incorporated in the schematic ground-state configuration of our model shown in Fig. 3(a). In this configuration, we have an ensemble of two equivalent ferromagnetic domains, F_1 and F_2, and two equivalent antiferromagnetic domains, A_1 and A_2, the boundaries of which are indicated by the dotted lines; each ferromagnetic domain interacts with both antiferromagnetic domains, and vice versa. Each antiferromagnetic domain contains Mn atoms with two or more Mn nearest-neighbours which comprise the core of a Mn-rich region in the system, whereas each ferromagnetic domain contains Mn atoms having no more than one Mn nearest-neighbor and therefore represents a Cu(or Ag)-rich region, including the outer fringes of neighboring Mn-rich regions. As mentioned earlier, the interactions within each domain are allowed to dictate the relative alignment of all its moments, including those located at the domain boundaries. This moment alignment obviously cannot help but disobey some of the interactions across the ferromagnetic–antiferromagnetic domain boundaries. Thus, with respect to the antiferromagnetic nearest-neighbor (and presumably the strongest) interactions across the domain boundaries in Fig. 3(a), we have chosen m' and m'' to represent the numbers of these interactions that are obeyed and disobeyed, respectively, by the moment alignment at the F_1–A_1 and F_2–A_2 boundaries, and n' and n'' to represent the corresponding numbers for the F_1–A_2 and F_2–A_1 boundaries. Furthermore, since the total number of disobeyed interactions should be a minimum in the ground state configuration, we set $m' > m''$ and $n' > n''$. Conversely, by this latter stipulation, we are making certain that the configuration of Fig. 3(a), in which the two ferromagnetic domains have oppositely directed magnetizations, is indeed the ground state configuration. Since we are also assuming that the magnetizations of the two ferromagnetic domains are equal in magnitude, the net magnetization of this small ensemble of domains is zero, which is the condition that must be satisfied by the system as a whole in its ground state, as discussed earlier.

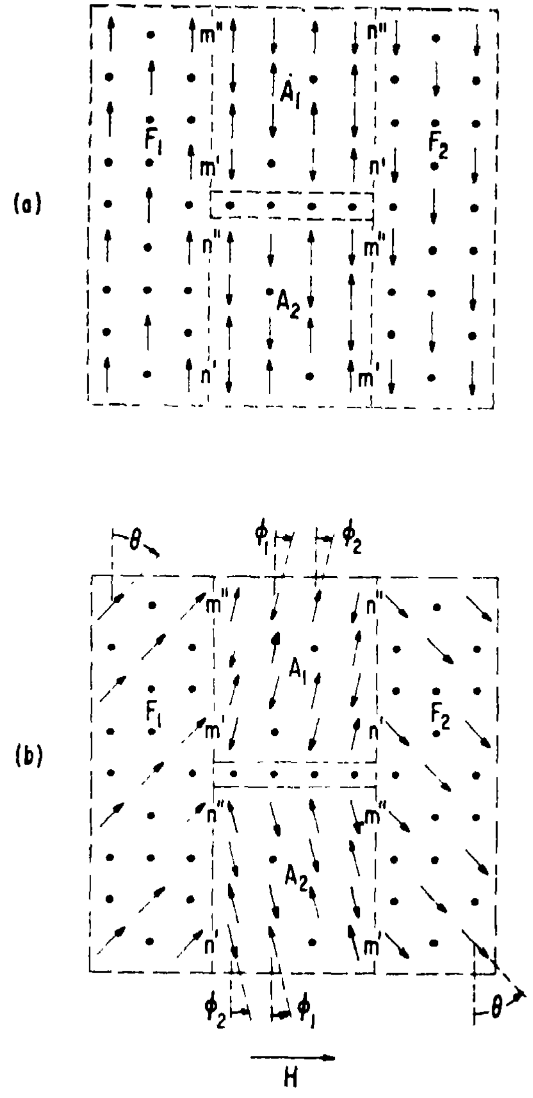

FIG. 3. Schematic spin configuration for an ensemble of ferromagnetic domains F_1, F_2 and antiferromagnetic domains A_1, A_2, in the ground state with (a) no external field or (b) a field applied as shown. Arrows represent atomic magnetic moments and heavy dots represent non-magnetic atoms. m', m'', n' and n'' signify numbers of nearest-neighbor interactions across domain boundaries (indicated by dotted lines).

Let us consider that at very low temperatures the entire system is comprised of domain ensembles having the configuration of Fig. 3(a). For simplicity, we assume that all the magnetic (Mn) atoms in the ferromagnetic domains experience the same exchange field, namely $\frac{1}{2}\lambda_F M_F$, resulting from interactions within the domains; $\frac{1}{2}M_F$ is the magnetization of each ferromagnetic domain and λ_F is the appropriate exchange coefficient. For the antiferromagnetic domains, we suppose that each has a two-sublattice magnetic structure, with each Mn atom coupled antiferromagnetically to its nearest-neighbors of the opposite sublattice, and that these interactions can be represented by an exchange field of magnitude $\frac{1}{4}\lambda_A M_A$, where $\frac{1}{4}M_A$ is the magnetization of each sublattice. Hence, the intra-domain exchange energy for each domain ensemble is

$$E' = -\tfrac{1}{4}\lambda_F M_F^2 - \tfrac{1}{8}\lambda_A M_A^2. \tag{1}$$

In addition, we must consider the coupling between adjacent domains in each ensemble. The configuration of Fig. 3(a) is such that at the boundaries of each domain there are $m'+n'$ interactions in agreement with the moment alignment and $m''+n''$ of them in opposition. Hence, if we associate an energy of strength $\lambda_{FA}\mu_F\mu_A$ with each bond between an atom of moment μ_F in a ferromagnetic domain and an atom of moment μ_A in an antiferromagnetic domain, the total inter-domain exchange energy per ensemble is $-2\lambda_{FA}\mu_F\mu_A(\Delta m+\Delta n)$, where $\Delta m \equiv m'-m''$ and $\Delta n \equiv n'-n''$ are both positive quantities. The total ground state energy for each domain ensemble may therefore be written as

$$\begin{aligned} E &= E' - 2\lambda_{FA}\mu_F\mu_A(\Delta m+\Delta n) \\ &= E' - \lambda'_{FA} M_F M_A, \end{aligned} \tag{2}$$

where λ'_{FA} the effective inter-domain coupling coefficient is defined as $2\lambda_{FA}(\Delta m+\Delta n)/N_F N_A$; $N_F(\equiv M_F/\mu_F)$ and $N_A(\equiv M_A/\mu_A)$ are the number of magnetic atoms per unit volume in the ferromagnetic and antiferromagnetic domains.

We will now examine an alternative state for the same domain ensemble after it has been cooled to low temperatures in a magnetic field. In a sufficiently strong field, not only will the magnetizations of both ferromagnetic domains be turned into the direction of the field but the moments within the antiferromagnetic domains, even if they are held rigidly antiparallel to one another, will also be changed in orientation. The latter arises from the fact that each antiferromagnetic domain is not coupled with equal strength to all its neighboring ferromagnetic domains. Specifically, in our domain ensemble we must allow that in general $\Delta m \neq \Delta n$, and throughout the following discussion we will assume arbitrarily that $\Delta m \geqslant \Delta n$. If we also suppose that at somewhat higher temperatures the magnetic anisotropy forces in the system are negligible and the weakest exchange interactions are still those across the domain boundaries, the response of the ground state configuration to a small external field will be that illustrated in Fig. 3(b). If the field equals or exceeds some characteristic value (which we will discuss later) the moments in the system will be aligned so that all the angles (θ, ϕ_1 and ϕ_2) indicated in the figure are 90°. The resulting configuration may be represented equivalently as shown in Fig. 4(a). It is readily seen that the total energy for each domain ensemble in this configuration (in the presence of the field) is

$$E = E' - 2\lambda_{FA}\mu_F\mu_A(\Delta m - \Delta n) - H_{\text{eff}}M_F, \qquad (3a)$$

where E' the intra-domain energy is still expressed by equation (1) and where H_{eff} the effective field on each domain ensemble is assumed for our present purposes to go to zero when the external field is removed. Alternatively, we may write equation (3a) as

$$E = E' - \lambda'_{FA}M_FM_A\alpha - H_{\text{eff}}M_F \qquad (3b)$$

where λ'_{FA} is defined as before and the new parameter, $\alpha \equiv (\Delta m - \Delta n)/(\Delta m + \Delta n)$. Consistent with our assumption that $\Delta m \geqslant \Delta n$, it follows that α is a positive quantity that ranges from 0 to 1. Hence in the absence of a field, the energy expressed by equation (3b) is higher than that expressed by equation (2) (except for the extreme case of $\alpha = 1$) and the system would ordinarily be expected to revert to its ground state configuration. However, let us postulate that with decreasing temperature there is a rapid increase in a magnetic anisotropy that fixes the absolute orientation of each of the moments in the antiferromagnetic domains. Under this condition, the cooling of the system in a large field will result in a retention of the configuration shown in Fig. 4(a) even when the field is subsequently removed at the lowest temperature. This configuration corresponds therefore to a metastable low-temperature state in which each domain ensemble contributes a moment M_F to the remanent magnetization of the system, in contrast to the zero remanence contribution of a domain ensemble in its ground state.

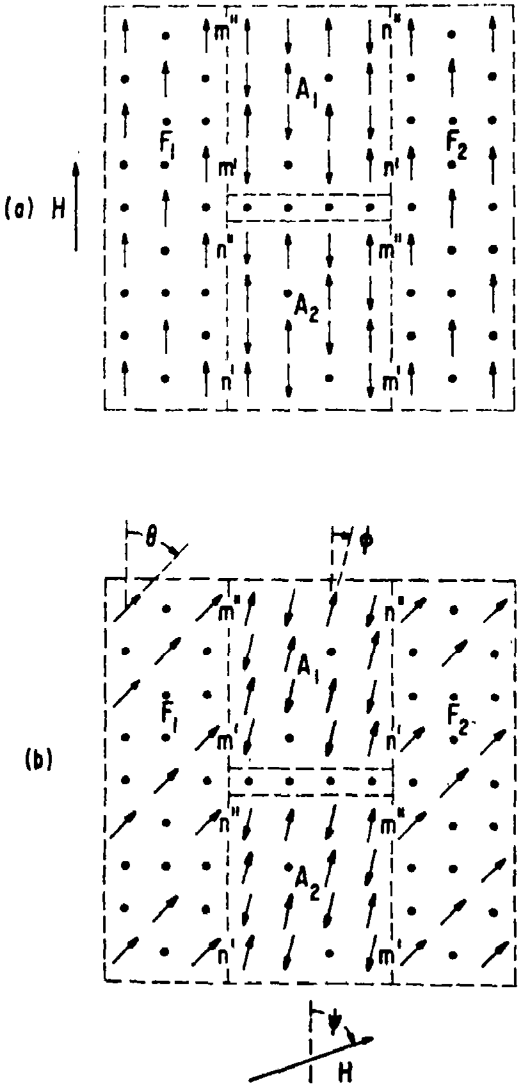

FIG. 4. Same as Fig. 3 except that domain-ensemble is in metastable state achieved by cooling in a field directed as shown in (a).

Let us first suppose for simplicity that the system consists of domain ensembles that are identical in every respect, including the α-parameter defined above, and that all the ensembles are in the field-cooled state shown in Fig. 4(a). We also assume here (and in all later discussion) that there is a coupling between different domain ensembles which can be represented by a molecular field proportional to M, the average net magnetization of the system. The total effective field on each ensemble is thus expressible as

$$H_{\text{eff}} = H+\lambda_M M, \tag{4}$$

where H is the externally applied field and λ_M is the molecular field coefficient. Hence, if we take λ_M to be large and positive, there will be a strong ferromagnetic coupling between domains in the same ensemble as well as in different ensembles, and in response to a field (in any direction other than that of the field applied during cooling) all the ferromagnetic domain moments in the system will rotate in unison from their remanence directions, as indicated in Fig. 4(b). In addition, even though the moments within each antiferromagnetic domain may be aligned rigidly antiparallel to one another and thus not be affected directly by the applied field, they will nevertheless turn as shown in the figure owing to their net coupling with adjacent ferromagnetic domains. This latter effect, however, will be opposed by the strong anisotropy forces postulated earlier which prefer that these antiparallel moments retain their original orientations in the field-cooled state.

Should these anisotropy forces be overwhelmingly large compared to the net exchange coupling between ferromagnetic and antiferromagnetic domains, the angle ϕ in Fig. 4(b) will remain fixed at zero regardless of the magnetization direction of the ferromagnetic domains. Consequently, when the system consisting of identical domain ensembles is subjected to a field opposite in direction to the field previously applied during cooling, all the ferromagnetic domain magnetizations will hold their remanence direction ($\theta = 0$) until the reverse field reaches a critical value $-H_c$, at which point they will abruptly reverse their direction (to $\theta = 180°$). Moreover, when the reverse field is reduced through the same critical value, the magnetizations will all revert discontinuously to their original orientation. It follows from previous discussion leading to equation (3b) that

$$H_e = \lambda'_{FA} M_A \alpha \equiv H_{FA}\alpha. \tag{5}$$

In effect, H_e acts like a fixed biasing field on the ferromagnetic domains (arising from their net exchange coupling with neighboring antiferromagnetic domains), and the result is a magnetic hysteresis loop that is displaced from the origin as shown by the solid curve in Fig. 5(a). It is obvious that the direction of H_e, which is fixed in the lattice by the field applied during cooling, is the easiest direction of magnetization and that the opposite direction is the hardest. This unidirectional anisotropy would be manifested not only in a displaced hysteresis loop but also, as shown in Fig. 6(a), in a sinusoidal variation of the torque on the system rotated about an axis perpendicular to the field-cooling direction in a large external field. The amplitude of this torque curve is $M_F H_{FA}\alpha$, and if we define $U_{1(H)}$ and $U_{1(L)}$ as the shaded areas indicated in Figs. 5(a) and 6(a) respectively, we find that

$$U_{1(H)} = U_{1(L)} = 2M_F H_{FA}\alpha, \tag{6}$$

which may be taken as alternative measures of the unidirectional anisotropy energy.

We will now investigate how the magnetic behavior of this field-cooled system changes as the temperature increases and the moments in the antiferromagnetic domains are no longer fixed along the axis of field-cooling but are allowed to deviate by an angle ϕ as shown in Fig. 4(b). If a uniaxial anisotropy $K_A \sin^2\phi$ is associated with each of these moments, the total energy per domain ensemble in this configuration,

$$\begin{aligned} E = E' - M_F H_{FA}\alpha \cos(\theta-\phi) - N_A K_A \sin^2\phi \\ - M_F H \cos(\psi-\theta) - \lambda_M M_F^2. \end{aligned} \tag{7}$$

Starting with this equation, we develop in Appendix A a detailed analysis of the hysteresis loop response of this system to an external field applied along the axis of field-cooling (i.e., $\psi = 0$) for increasing values of the ratio, $M_F H_{FA}\alpha/2N_A K_A \equiv \rho$. The solid curves in Fig. 5, computed from the results of this analysis, indicate that as ρ increases from zero but is less than $\frac{1}{2}$ the hysteresis loop changes in shape (the magnetization reversing less abruptly) but remains asymmetrical with respect to the origin. In fact, over this limited range of ρ, the unidirectional anisotropy energy $U_{1(H)}$ stays constant at the value given in equation (6). When $\rho = \frac{1}{2}$ and a large enough reverse field is applied, the inter-domain exchange forces are just strong enough to pull the antiferromagnetic domain moments over their diminished anisotropy energy barriers, and all the moments in the system will abruptly change to new stable directions along $\theta = \phi = 180°$. An analogous process, with the easy direction switching back to $\theta = \phi = 0$, then occurs at comparable positive fields. Thus, the hysteresis loop is no longer asymmetrical about the origin; it is also not a single-valued function but encloses an area that is a measure of the hysteresis energy loss W_H, as shown in Fig. 5(c). As ρ is increased beyond $\frac{1}{2}$, there is a gradual decrease in the magnitude of the field at which the abrupt change in magnetization takes place, the magnitude of this magnetization change increasing and eventually, for $\rho \geqslant 1{\cdot}62$, amounting to a complete discontinuous reversal (from M_F to $-M_F$ or vice versa). Hence, after its sudden appearance at $\rho = \frac{1}{2}$, W_H decreases monotonically with increasing ρ, as indicated by the hysteresis loop areas in Fig. 5(c)–(f).

Also studied in detail in Appendix A is the hysteresis loop response of this system to a field applied *perpendicular* to the axis of field-cooling (i.e., $\psi = 90°$) and is represented by the dashed curves in Fig. 5. In this case, it follows directly from the uniaxial symmetry assumed for the antiferromagnetic domain anisotropy that for any value of ρ the hysteresis loop is symmetrical about the origin and there is no hysteresis energy loss. As ρ increases, the magnetization rises and approaches saturation more rapidly with increasing field. Correspondingly, there is a monotonic decrease of the energy of magnetization $U_\perp$ defined as indicated by the area in Fig. 5(a). For $\rho = 0$, $U_\perp$ has its maximum value of $M_F H_{FA} \alpha$,

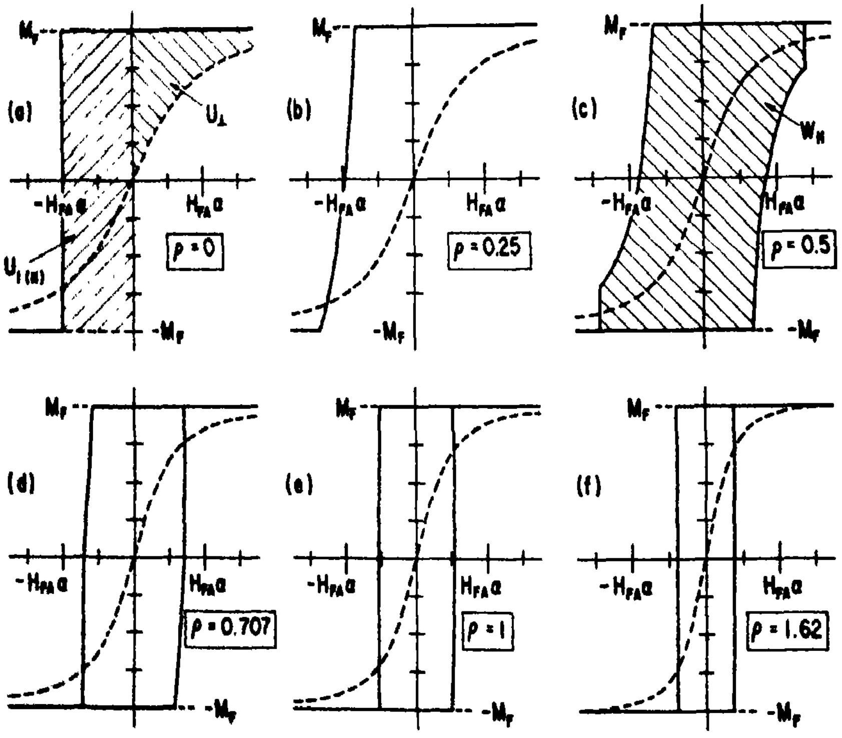

FIG. 5. Hysteresis loops of M vs. H computed for field-cooled system for increasing values of ρ. Solid and dashed curves are for H parallel and perpendicular, respectively, to field applied during cooling. Shaded areas $U_{1(H)}$, $U_\perp$ and W_H define unidirectional anisotropy energy, an energy of magnetization and hysteresis energy loss, respectively.

which according to equation (6) is exactly half the value of both $U_{1(H)}$ and $U_{1(L)}$, the unidirectional anisotropy energies determined from the displaced hysteresis loops and torque curves, respectively.

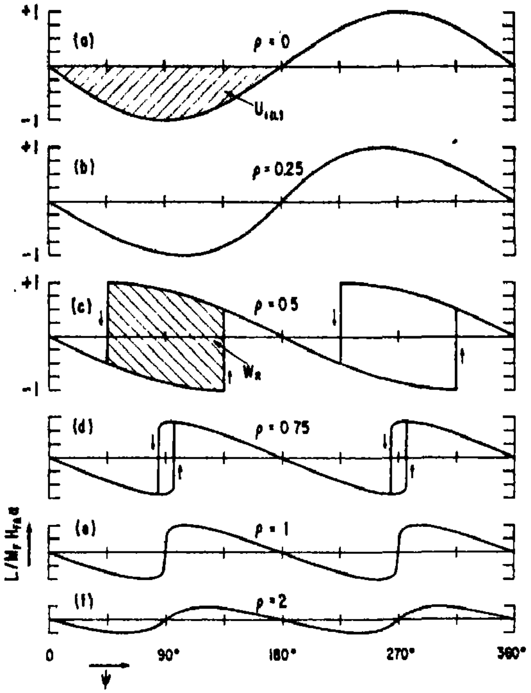

FIG. 6. Torque curves computed for field-cooled system rotated in very large field, for increasing values of ρ. $\psi = 0°$ (and 360°) corresponds to direction of field applied during cooling. Shaded areas $U_{1(L)}$ and W_R define unidirectional anisotropy energy and rotational hysteresis energy, respectively.

The torque curves for this field-cooled system at different values of ρ are derived in Appendix B. The starting point is again equation (7) except that ψ is now increased or decreased smoothly through 360°, corresponding to a complete cycle of rotation of the system with respect to the external field. Moreover, it is assumed that the external field is strong enough to align the ferromagnetic domain moments essentially parallel to its direction (i.e., $\theta \approx \psi$) yet is not strong enough to affect the antiferromagnetic domain moments directly. The results of this analysis are represented by the computed curves shown in Fig. 6, and it is evident that as ρ initially increases from zero the torque curve changes in shape (becoming less sinusoidal) but remains unidirectional in character, the one and only easy direction of magnetization always being parallel to the field-cooling direction (i.e., at $\psi = 0$). As long as $\rho < \frac{1}{2}$, the magnitude of the maximum torque and the unidirectional anisotropy energy $U_{1(L)}$ have the fixed values, $M_F H_{FA}\alpha$ and $2M_F H_{FA}\alpha$, respectively. However, when ρ reaches the value $\frac{1}{2}$, the net exchange coupling with the ferromagnetic domains is able to cause the antiferromagnetic domain moments to jump discontinuously over their relatively weaker anisotropy energy barriers. Since this abrupt transition in moment direction (and therefore in torque) repeats every half-cycle, as shown in Fig. 6(c), the direction $\psi = 180°$, as well as $\psi = 0$, is now an easy direction of magnetization. It is also clear from this figure that the abrupt transition occurs at analogous but different values of ψ when the system is rotated in opposite directions with respect to the external field. Hence, the torque curve is no longer single-valued but instead encloses the shaded area shown in Fig. 6(c), which is half the total area enclosed over a complete cycle and is therefore the usual measure of the rotational hysteresis energy W_R. It should be noted that within the context of this analysis the value of W_R is non-vanishing with increasing external field. As ρ is increased beyond $\frac{1}{2}$, W_R decreases monotonically and finally vanishes when $\rho = 1$, at which point the torque curve is once again single-valued but is uniaxial rather than unidirectional in character. With any further increase of ρ, the amplitude of the torque variation decreases continuously, as indicated by Figs. 6(e)–(f). The non-zero limiting value of W_R at high fields and its variation with ρ was recently discussed by MEIKLEJOHN[14] with reference to a simple ferromagnetic–antiferromagnetic system (corresponding to our model for the case of $\alpha = 1$).

The results obtained in Appendices A and B for the low-temperature hysteresis loop and torque properties of the field-cooled state of our model are presented in an alternative form in Fig. 7, where various energies previously defined are shown as functions of increasing ρ. A close correspondence is immediately obvious between the energies derived from high-field torque curves and those derived from hysteresis loops where the field is applied parallel to the field-cooling axis. In each case, the unidirectional anisotropy energy has a constant value $2M_F H_{FA}\alpha$ over the range

$0 \leqslant \rho \leqslant \frac{1}{2}$ and then vanishes abruptly at $\rho = \frac{1}{2}$ when simultaneously there is a sudden appearance of magnetic losses of roughly the same magnitude. As ρ is increased further, the magnetic losses decrease monotonically to zero, the decrease being much more rapid in the cause of W_R. Contrastingly, the hysteresis loop behavior when the field is applied perpendicular to the field-cooling axis is characterized by an energy of magnetization $U_\perp$ which decreases monotonically from $M_F H_{FA} \alpha$ as ρ increases from zero. In all these considerations, it is important to note that when ρ becomes very large, corresponding to a very weak anisotropy associated with the antiferromagnetic domains, the system will relax from its field-cooled state to its ground state. It will then be necessary to recool the system in a field in order to regain the properties for small ρ displayed in Figs. 5, 6 and 7.

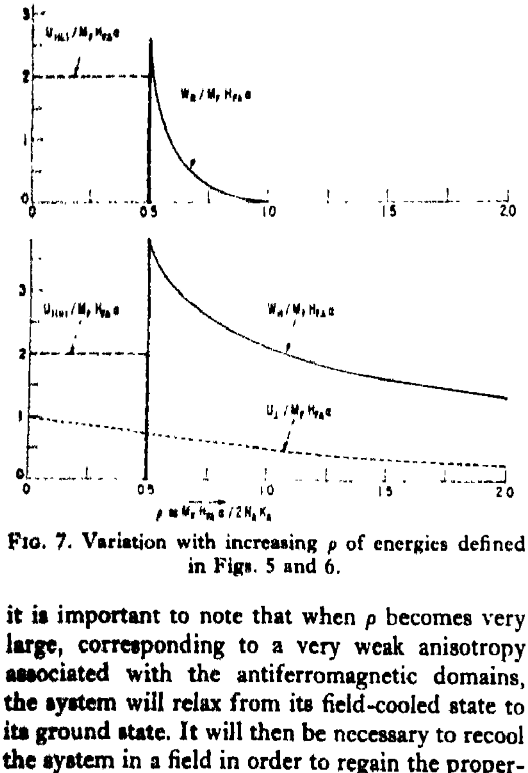

FIG. 7. Variation with increasing ρ of energies defined in Figs. 5 and 6.

We have implicitly assumed that with increasing temperature the anisotropy energy K_A associated with each antiferromagnetic domain moment decreases much more rapidly than $M_F H_{FA} \alpha$, the effective inter-domain exchange energy. Since ρ is defined as $M_F H_{FA} \alpha / 2N_A K_A$, the sequence of events for increasing ρ described in Figs. 5, 6 and 7 is appropriate for a rising temperature. When we then compare the field-cooled properties predicted by our model with those obtained experimentally in Cu–Mn and related alloys,(1, 2, 7, 15) we find a gratifying degree of agreement. For example, essentially the same value for the unidirectional anisotropy energy is derived from both displaced hysteresis loop and high-field torque measurements on a given alloy at low temperatures, and this value is almost exactly twice the energy of magnetization derived from the low-temperature hysteresis loop measured perpendicular to the field-cooling axis. Moreover, with increasing temperature both hysteresis loop and torque measurements give a monotonically decreasing unidirectional anisotropy energy whose disappearance is accompanied by a maximum in magnetic losses. In the case of the torque measurements, these losses take the form of a rotational hysteresis which approaches a constant value at very high fields (instead of diminishing rapidly to zero as in a normal ferromagnet).

It is not surprising that the abrupt changes in various properties shown in Figs. 5, 6 and 7 are much more gradual when observed experimentally in the atomically-disordered Cu–Mn alloys. In the form used in predicting these properties, our model was kept as simple as possible. Hence, all the domain ensembles of the system were characterized by physical parameters (i.e., H_{FA}, α, etc.) having the same average values, whereas it would be closer to reality if the values of these parameters were allowed to follow appropriate distributions. This over-simplification of our model becomes much more serious with respect to other parts of this problem, and in the next Section we are forced to incorporate a parameter value distribution into the model.

3. THE EFFECTS OF AN α-PARAMETER DISTRIBUTION

a. *Temperature dependence of the initial susceptibility*

Of the various parameters in our model, it would appear that the α-parameter, being extremely sensitive to the exact conditions at the domain boundaries, would have the broadest distribution in its value among different domain ensembles. Consequently, we will henceforth represent the distribution in α by the probability function P_α, which is normalized such that

$$\int_0^1 P_\alpha \, d\alpha = 1, \tag{8}$$

where the integral form of this equation is justified by the close spacings in the α value spectrum. All the other parameters will continue to be represented by their average values.

With the model modified in this way, let us first consider the effect of a small external field on the system in which all the domain ensembles are initially in the ground state configuration shown in Fig. 3(a). At very low temperatures, it is again assumed that the antiferromagnetic domain moments are rigidly fixed in orientation by a large uniaxial anisotropy. Hence, there will be essentially no response to a field applied parallel to the anisotropy axis as long as it is smaller than the inter-domain exchange field on each ferromagnetic domain, whose magnitude is $\lambda'_{FA}M_A$ (or H_{FA}) according to equation (2). However, for a field applied perpendicular to the anisotropy axis, the response will be as shown in Fig. 3(b). Except at elevated temperatures (which will be discussed later) the antiferromagnetic domain moments will be considered to be rigidly antiparallel so that $\phi_1 = \phi_2 = \phi$. The energy of this ensemble can therefore be written

$$E = E' - 2\lambda_{FA}\mu_F\mu_A\{\Delta m\cos(\theta-\phi)+\Delta n\cos(\theta+\phi)\} - N_AK_A\sin^2\phi - M_FH_{\text{eff}}\sin\theta,$$

which becomes

$$(E-E')/M_F = -H_{FA}(\cos\theta\cos\phi+\alpha\sin\theta\sin\phi) - \tfrac{1}{2}H_K\sin^2\phi - H_{\text{eff}}\sin\theta \qquad (9)$$

in terms of parameters defined in the previous section and $H_K \equiv 2N_AK_A/M_F$. It is shown in Appendix C that when the external field is very small the equilibrium value for θ derived from equation (9) is given by

$$\sin\theta = \frac{H_{\text{eff}}(H_{FA}+H_K)}{H_{FA}\{H_{FA}(1-\alpha^2)+H_K\}} \qquad (10)$$

As before, $H_{\text{eff}} = H + \lambda_M M$, where M the average magnetization of the whole system is now expressed as

$$M = \tfrac{2}{3}M_F\int_0^1 P_\alpha\sin\theta\,\mathrm{d}\alpha, \qquad (11)$$

the factor $\tfrac{2}{3}$ arising from an assumed random orientation of the anisotropy axes of different ensembles. If we also assume that at very low temperatures $H_K \gg H_{FA}$, equation (10) becomes simply $\sin\theta = (H+\lambda_M M)/H_{FA}$, which we combine with equations (8) and (11) and obtain for the initial susceptibility at or very near 0°K:

$$\chi_0 = M/H = \tfrac{2}{3}M_F/(H_{FA}-\tfrac{2}{3}\lambda_M M_F), \qquad (12)$$

which is valid as long as $\tfrac{2}{3}\lambda_M M_F < H_{FA}$.

When the temperature is increased, the antiferromagnetic domain anisotropy (and hence, H_K) is again considered to drop rapidly to zero. Under this condition, the moments of *all* the domain ensembles align themselves with respect to the field in the manner indicated in Fig. 3(b); hence, the average magnetization of the system,

$$M = M_F\int_0^1 P_\alpha\sin\theta\,\mathrm{d}\alpha. \qquad (13)$$

Moreover, equation (10) in this case reduces to $\sin\theta = (H+\lambda_M M)/H_{FA}(1-\alpha^2)$, which combined with equation (13) gives the initial susceptibility at this higher (but still fairly low) temperature:

$$\chi = p\bar{\mathbf{M}}_F/(\bar{\mathbf{H}}_{FA} - p\lambda_M\bar{\mathbf{M}}_F)$$

where

$$p \equiv \int_0^1 P_\alpha\,\mathrm{d}\alpha/(1-\alpha^2). \qquad (14)$$

In this expression (valid for $p\lambda_M\bar{\mathbf{M}}_F < \bar{\mathbf{H}}_{FA}$), we have replaced M_F and H_{FA} by their somewhat diminished time-averaged values, $\bar{\mathbf{M}}_F$ and $\bar{\mathbf{H}}_{FA}$ (i.e., $\lambda'_{FA}\bar{\mathbf{M}}_A$), appropriate for this higher temperature. Since $\bar{\mathbf{M}}_F$ can be expected to decrease more rapidly than $\bar{\mathbf{M}}_A$ with increasing temperature (as we will show later), equation (14) indicates that correspondingly there will be a decrease in susceptibility, as shown in Fig. 8 where T_1 is the temperature at which K_A (and hence, H_K) vanishes. When the temperature is decreased below T_1, the susceptibility will no longer follow equation (14) and increase as indicated by the dashed curve in Fig. 8; instead, owing to the rapid rise in K_A, χ will start decreasing towards the value χ_0 given by equation (12), as indicated by the solid curve. That χ_0 is smaller than χ at T_1 follows from the definition of p in equation (14). It is obvious that for any distribution function P_α that obeys equation (8) the value of p cannot be less than

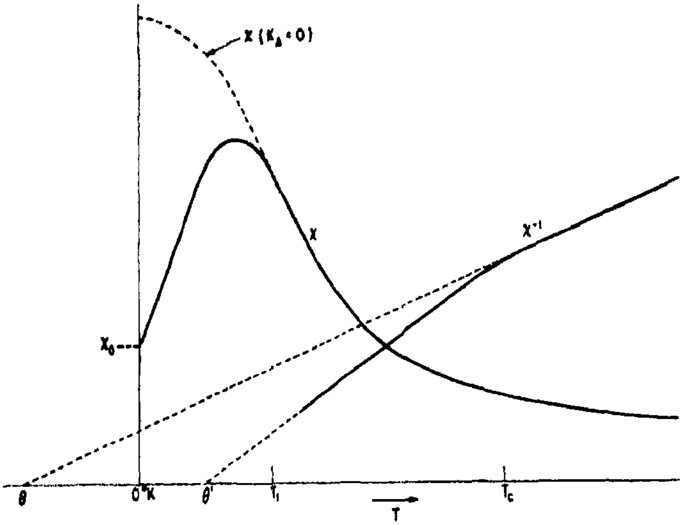

FIG. 8. Magnetic susceptibility and its reciprocal vs. temperature for hypothetical system cooled initially in zero field. T_1 is temperature at which anisotropy K_A vanishes; dashed curve gives susceptibility below T_1 for the case $K_A = 0$. T_c is the magnetic-disordering temperature; θ' and θ are the apparent and true paramagnetic Curie temperatures, respectively.

unity. In Table 1 are listed some simple possibilities for P_α which progressively emphasize small values of α, and the corresponding values of p which decrease monotonically towards unity; the case of $P_\alpha = 1$ demonstrates the general fact that p is infinite for any form of P_α having a nonzero value at $\alpha = 1$.

Table 1

P_α	p*	q*
1	∞	0·50
$\frac{3}{2}(1-\alpha)^{1/2}$	1·87	0·40
$2(1-\alpha)$	1·39	0·33
$3(1-\alpha)^2$	1·16	0·25

* p and q are the integrals defined in equations (14) and (27b) respectively.

We may therefore conclude that for any reasonable choice of the function P_α the susceptibility will have a maximum value $\chi_{\max}$ at a temperature just below T_1 and will drop to a significantly smaller value χ_0 at very low temperatures. According to equations (12) and (14), if p is large enough the ratio $\chi_{\max}/\chi_0$ can easily exceed $\frac{3}{2}$ (the value associated with a simple polycrystalline antiferromagnet), and this is consistent with the "anomalous" values of just over 2 observed in Cu-Mn alloys of high Mn concentration.(1, 2) However, a $\chi_{\max}/\chi_0$ ratio of over $\frac{3}{2}$ can also be justified within the context of an antiferromagnet of low crystal symmetry (such as the ordered alloy Au_3Mn(16)). Consequently, for a less ambiguous test of our model, we must examine the susceptibility behavior above the temperature of $\chi_{\max}$, where according to our model (in contrast to the usual theory of antiferromagnetism) the system is still in an ordered magnetic state.

At these higher temperatures, we must allow that the sublattice moments of the antiferromagnetic domains are not strictly antiparallel in the presence of an external field. Hence, with reference to Fig. 3(b), $\phi_1 \neq \phi_2$, and the energy of a given domain ensemble in the system is

$$\begin{aligned} E = & -\tfrac{1}{4}\lambda_F \bar{\mathbf{M}}_F^2 - \tfrac{1}{8}\lambda_A \bar{\mathbf{M}}_A^2 \cos(\phi_1-\phi_2) \\ & -2\lambda_{FA}\mu_F\mu_A\{m' \cos(\theta-\phi_1) - m'' \cos(\theta-\phi_2) \\ & + n' \cos(\theta+\phi_2) - n'' \cos(\theta+\phi_1)\} \\ & - \bar{\mathbf{M}}_F \bar{\mathbf{H}}_{\text{eff}} \sin\theta + \tfrac{1}{2}\bar{\mathbf{M}}_A \bar{\mathbf{H}}_{\text{eff}}(\sin\phi_1 - \sin\phi_2), \end{aligned}$$

where $\bar{\mathbf{H}}_{\text{eff}} = H+\lambda_M\bar{\mathbf{M}}$, $\bar{\mathbf{M}}$ being the average magnetization of the whole system. If we set $2\lambda_{FA}(m'+m''+n'+n'')/N_FN_A \equiv \lambda''_{FA}$ and make the simplifying assumption that $m'+m'' = n'+n''$, the above expression becomes

$$\begin{aligned} E = &-\tfrac{1}{4}\lambda_F\bar{\mathbf{M}}_F^2-\tfrac{1}{8}\lambda_A\bar{\mathbf{M}}_A^2\cos 2\epsilon \\ &-\lambda'_{FA}\bar{\mathbf{M}}_F\bar{\mathbf{M}}_A(\cos\theta\cos\phi+\alpha\sin\theta\sin\phi)\cos\epsilon \\ &-\lambda''_{FA}\bar{\mathbf{M}}_F\bar{\mathbf{M}}_A\sin\theta\cos\phi\sin\epsilon \\ &-\bar{\mathbf{H}}_{\text{eff}}(\bar{\mathbf{M}}_F\sin\theta-\bar{\mathbf{M}}_A\cos\phi\sin\epsilon), \end{aligned} \tag{15}$$

where $\phi = \frac{1}{2}(\phi_1+\phi_2)$ and $\epsilon \equiv \frac{1}{2}(\phi_1-\phi_2)$. In the detailed analysis given in Appendix C, equilibrium values for θ, ϕ and ϵ are obtained from equation (15) in the limit of small H and are then used in deriving an expression for the initial susceptibility χ in terms of $\bar{\mathbf{M}}_F$, $\bar{\mathbf{M}}_A$, and the various λ's. For the case where $\lambda_A \gg \lambda_F \gg \lambda'_{FA}, \lambda''_{FA}$ or λ_M, corresponding to a predominantly strong coupling within the antiferromagnetic domains and a relatively weak coupling between domains, it is shown that $\bar{\mathbf{M}}_F/\bar{\mathbf{M}}_F \ll \bar{\mathbf{M}}_A/M_A$ at all but very low temperatures (resulting from the more rapid disordering of the ferromagnetic domains with increasing temperature) and that the expressions for the magnetic disordering (or Curie) temperature and the initial susceptibility are simply

$$T_c \simeq \tfrac{1}{4}C_A\lambda_A \tag{16}$$

and

$$\chi \simeq \frac{1}{\frac{1}{2}\lambda_A-\lambda_M}\left\{1+\frac{\frac{1}{2}C_F(\lambda_A-4\lambda''_{FA}+2\lambda_M)p}{T-\frac{1}{2}C_F\lambda_F-C_F\lambda_Mp}\right\} \tag{17}$$

when higher order terms in λ'_{FA}, λ''_{FA} and λ_M are neglected. The constants, $C_F \equiv N_F\mu^2(S+1)/3Sk$ and $C_A \equiv N_AC_F/N_F$, where $\mu = \mu_A = \mu_F$ $(\equiv gS\mu_B)$; p is the integral defined in equation (14). At temperatures well below T_c and comparable to $C_F\lambda_F$, equation (17) reduces further to

$$\chi \simeq C'/(T-\theta') \tag{18}$$

where $\quad C' \equiv C_F\{1-4(\lambda''_{FA}-\lambda_M)/\lambda_A\}p$

and $\quad \theta' \equiv \frac{1}{2}C_F\lambda_F+C_F\lambda_Mp.$

Thus, even though the system is certainly not paramagnetic at these temperatures, a plot of χ^{-1} vs. T will approximate a straight line, in apparent conformity to a Curie–Weiss relationship with a positive or ferromagnetic interaction temperature θ', as indicated in Fig. 8.

For temperatures above T_c, a straightforward analysis in Appendix C yields a fairly complicated expression for the initial susceptibility, which, however, gives the same value of χ at T_c as equation (17) and which approaches the following Curie–Weiss relationship at very high temperatures:

$$\chi \simeq C/(T-\theta), \tag{19}$$

where $C \equiv C_A+C_F$ and $\theta = (-C_A\lambda_A+2C_F^2\lambda_F-8C_FC_A\lambda_{FA}+4C^2\lambda_M)/4C$. In contrast to θ' in equation (18) which is always positive, θ in equation (19) can be either positive or negative depending on the relative strength and number of the various ferromagnetic and antiferromagnetic interactions in the system.

Figure 8 shows the variation of the initial susceptibility (and its reciprocal) above as well as below T_c, as predicted by our model for the case where θ is negative. It is clear that while χ varies with deceptive smoothness through T_c, $1/\chi$ has an anomalous temperature dependence corresponding to a gradual but distinct transition from equation (18) to equation (19). There is a striking similarity between this behavior and that observed in Cu–Mn and Ag–Mn alloys of high Mn concentration (see Fig. 2), which is particularly significant because the theoretical curves in Fig. 8 apply specifically to a system for which θ is negative, implying a predominance of antiferromagnetically coupled moments (which we have consistently identified with the moments of nearest-neighbor Mn atoms). Furthermore, in agreement with our definition of T_c as the Curie temperature of the system, the electrical resistivity of each of these alloys is found to exhibit an anomaly indicative of magnetic ordering at the same temperature as that of the peculiar kink in its $1/\chi$ vs. T curve, as shown in Fig. 2. The maximum susceptibility of each of these alloys which occurs at a lower temperature (T_s in Fig. 2) and the Curie–Weiss-like behavior just above T_s both give the misleading impression of an antiferromagnet with a Néel temperature at T_s and with a positive paramagnetic Curie temperature. Our model, however, successfully interprets all these phenomena within the context of a more complex system with a significantly higher magnetic disordering temperature (T_c).

b. *Field-cooling criteria and displaced hysteresis loops*

The inclusion of an α-parameter distribution in our model is particularly important when we consider the effects of cooling the system in different fields. We will suppose that initially the temperature of the system is well below its Curie temperature yet high enough for the anisotropy associated with its antiferromagnetic domains (K_A) to be vanishingly small, i.e., with reference to Fig. 8, $T_1 < T < T_c$. At such a temperature and in an external field H, each domain ensemble will have the spin configuration of Fig. 3(b) with $\phi_1 = \phi_2 = \phi$. Specifically, according to a detailed analysis given in Appendix D, all the ensembles whose α-parameters equal or exceed the value α_0 defined by the equation

$$H = \bar{\mathbf{H}}_{FA}(1-\alpha_0^2)/\alpha_0 - \lambda_M \bar{\mathbf{M}}, \tag{20}$$

will be in the saturated state given by θ and $\phi = 90°$, whereas for the ensembles with $\alpha < \alpha_0$ the following conditions obtain:

$$\sin\theta = \frac{1-\alpha_0^2}{\{(1-\alpha_0^2)^2+(\alpha_0^2-\alpha^2)(1-\alpha_0^2\alpha^2)\}^{1/2}} \tag{21a}$$

and

$$\sin\phi = \frac{(1-\alpha_0^2)\alpha}{(1-\alpha^2)\alpha_0} \tag{21b}$$

Hence, the average magnetization of the entire system may be written as

$$\bar{\mathbf{M}} = \bar{\mathbf{M}}_F \int_{\alpha_0}^{1} P_\alpha \, d\alpha + \bar{\mathbf{M}}_F \int_{0}^{\alpha_0} P_\alpha \sin\theta \, d\alpha, \tag{22}$$

where $\sin\theta$ is given by equation (21a). The situation for α_0 approaching unity is equivalent to both H and $\bar{\mathbf{M}}$ being very small, and the initial susceptibility ($\bar{\mathbf{M}}/H$) obtained from equations (20), (21a) and (22) reduces properly to that expressed in equation (14). For smaller values of α_0, these equations when solved simultaneously give progressively larger values of $\bar{\mathbf{M}}$ and H, which plotted against each other result in the full magnetization curve appropriate for low temperatures just above where K_A is assumed to vanish. Choosing $P_\alpha = 2(1-\alpha)$ for illustration purposes, we have plotted in Fig. 9(a) our computed values of $\bar{\mathbf{M}}/\bar{\mathbf{M}}_F$ vs. $H/\bar{\mathbf{H}}_{FA}$ for $\lambda_M = 0$ and $\lambda_M = \bar{\mathbf{H}}_{FA}/4\bar{\mathbf{M}}_F$; the two curves serve to show that a positive λ_M makes the approach to ferromagnetic saturation more rapid.

On the basis of equation (21), we show in Appendix D that as α drops below α_0 there is a very rapid decrease of ϕ to zero from its value of 90° for $\alpha \geqslant \alpha_0$, whereas θ decreases much more

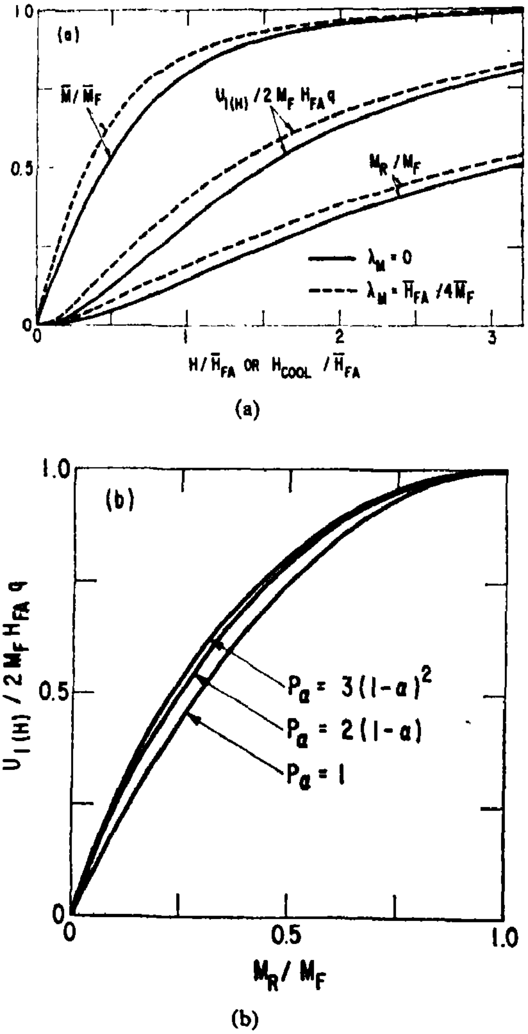

(a)

(b)

FIG. 9. (a) Variation of $\bar{\mathbf{M}}$ (with $H/\bar{\mathbf{H}}_{FA}$) and $U_{1(H)}$, M_R (with $H_{cool}/\bar{\mathbf{H}}_{FA}$), all normalized to their saturation values at temperature, computed for $P_\alpha = 2(1-\alpha)$ and different values of λ_M. (b) $U_{1(H)}$ vs. M_R, both normalized to their saturation values, computed for different P_α functions.

slowly. Moreover, when the system is cooled in a field, this fairly sharp distinction between the domain ensembles with $\alpha \geqslant \alpha_0$ and those with $\alpha < \alpha_0$, in the orientations of their antiferromagnetic domain moments, will be retained if the anisotropy K_A develops with its easy axis parallel to these moments. Consequently, when the external field is removed at very low temperatures, the remanent state of the system will be such that all the domain ensembles with $\alpha \geqslant \alpha_0$ will be stabilized in the field-cooled configuration of Fig. 4(a), whereas the ensembles with $\alpha < \alpha_0$ will be stabilized in the ground state configuration of Fig. 3(a). The value of α_0 itself is determined by equation (20) in which H should be interpreted as the external field applied during cooling (henceforth called H_{cool}) and in which $\bar{\mathbf{M}}$, the total magnetization at the temperature where K_A vanishes, is still given by equation (22). The low temperature remanent magnetization of this field-cooled system will be

$$M_R = M_F \int_{\alpha_0}^{1} P_\alpha \, \mathrm{d}\alpha \tag{23}$$

and this expression, together with equation (20), has been used to compute the curves of M_R/M_F vs. $H_{\text{cool}}/\bar{\mathbf{H}}_{FA}$ plotted in Fig. 9(a), where $P_\alpha = 2(1-\alpha)$ and $\lambda_M = 0$, $\bar{\mathbf{H}}_{FA}/4\bar{\mathbf{M}}_F$ were again chosen for illustration. The slower increase of M_R/M_F with $H_{\text{cool}}/\bar{\mathbf{H}}_{FA}$ relative to that of $\bar{\mathbf{M}}/\bar{\mathbf{M}}_F$ with $H/\bar{\mathbf{H}}_{FA}$ follows from the fact that M_R, in contrast to $\bar{\mathbf{M}}$, gets no contributions from the domain ensembles with $\alpha < \alpha_0$. Nevertheless, it is clear that M_R, like $\bar{\mathbf{M}}$, is enhanced by the presence of a positive λ_M.

For the field-cooled system described above, let us consider the low-temperature magnetization response to an external field. Since the domain ensembles with $\alpha < \alpha_0$ are stabilized in the ground state configuration, they will contribute a small magnetization essentially proportional to the field, the susceptibility being given approximately by

$$\chi_g \simeq \chi_0 \int_{0}^{\alpha_0} P_\alpha \, \mathrm{d}\alpha, \tag{24}$$

where χ_0 is the initial susceptibility of the system cooled in zero field (i.e., $\alpha_0 = 1$) expressed by equation (12), and where the integral takes into account the appropriate volume fraction. To a crude approximation, this susceptibility can be simply added to the response of the rest of the system. Keeping this in mind, we now turn our attention to the domain ensembles with $\alpha \geqslant \alpha_0$ which are stabilized in the field-cooled configuration shown in Fig. 4(a), the moments of their antiferromagnetic domains being held rigidly parallel (and antiparallel) to the field-cooling direction by the anisotropy K_A. According to a detailed discussion in Appendix D, if the external field H is applied parallel to the field-cooling direction, the equilibrium states of this part of the system are such that for

$$H > -H_{FA}\alpha_0 - \lambda_M M_R (\equiv H_1)\colon M = M_R$$

and for $H < -H_{FA} + \lambda_M M_R (\equiv H_2)\colon M = -M_R$.

Since M_R is given by equation (23), these two states obviously correspond to all the ensembles with $\alpha \geqslant \alpha_0$ having their ferromagnetic domain moments either parallel or antiparallel to the field-cooling direction. Moreover, the manner in which M decreases from M_R to $-M_R$ as H decreases from H_1 to H_2 is found to be determined by the following pair of equations:

$$M/M_F = \int_{\alpha}^{1} P_\alpha \, \mathrm{d}\alpha - \int_{\alpha_0}^{\alpha} P_\alpha \, \mathrm{d}\alpha \tag{25}$$

and

$$H + \lambda_M M + H_{FA}\alpha = 0, \tag{26}$$

where it is clear that for any given value of α between α_0 and 1 the ensembles with an α-parameter larger or smaller than this value will have their ferromagnetic domain moments parallel or antiparallel respectively, to the field-cooling direction.

It follows that the domain ensembles with $\alpha \geqslant \alpha_0$ give rise to a hysteresis loop that is displaced asymmetrically with respect to the origin. Again choosing $P_\alpha = 2(1-\alpha)$ and $\lambda_M = 0$, $\bar{\mathbf{H}}_{FA}/4\bar{\mathbf{M}}_F$ for illustration, we have used equations (25) and (26) to compute the two sets of displaced hysteresis loops drawn in the upper part of Fig. 10. For each set, we picked four successively lower values of α_0 (*corresponding to successively higher* values of H_{cool}) such that $M_R/M_F = \frac{1}{4}, \frac{1}{2}, \frac{3}{4}$ and 1. The most remarkable feature of these hysteresis loops, aside from their displacement from the origin, is the fact that the magnitude of the coercive field decreases as M_R (and the H_{cool} producing it) increases. It is readily seen by setting $M = 0$ in equations (25) and (26) that this feature obtains for any analytic form assumed for P_α and is completely independent of λ_M. Although the coercive field is invariant with λ_M, it is obvious from Fig. 10 that a non-zero (and positive) λ_M can cause a pronounced "squaring up" of the hysteresis loop; the significance of this effect is left for later discussion.

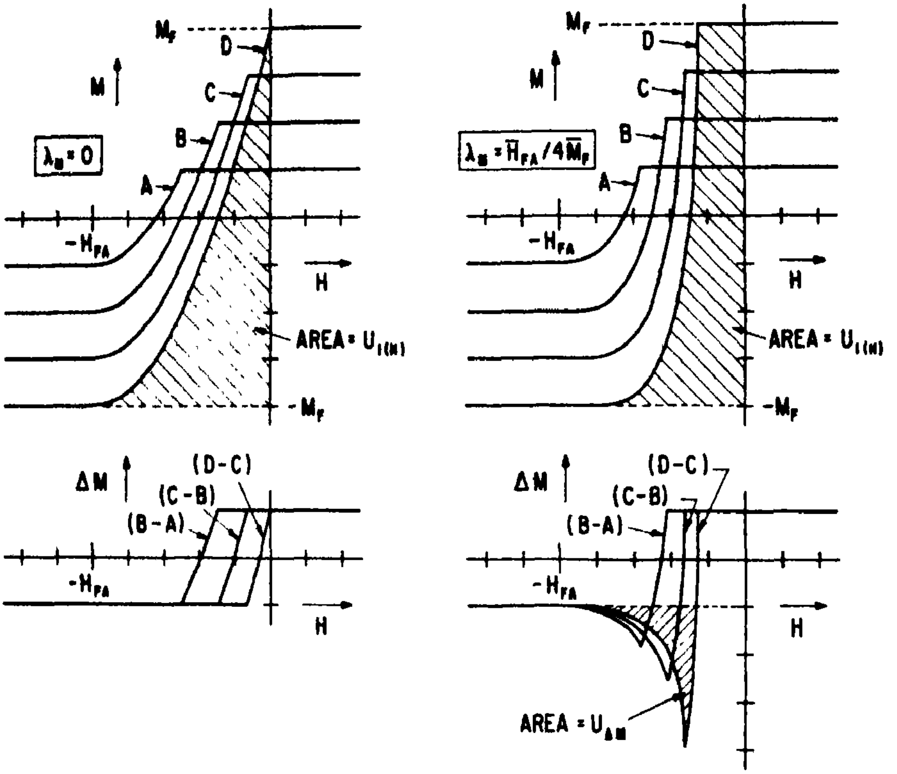

FIG. 10. Hysteresis loops and ΔM vs. H curves computed for system cooled in various fields, with $P_\alpha = 2(1-\alpha)$ and different values of λ_M.

As before, we define the unidirectional anisotropy energy $U_{1(H)}$ as the area enclosed by the displaced hysteresis loop and the M axis between the saturation magnetization limits. Applying this definition to the hysteresis loops determined by equations (25) and (26), we obtain by a fairly straightforward analysis (whose details are given in Appendix D) the following general expression:

$$U_{1(H)} = 2M_F H_{FA} \int_{\alpha_0}^{1} \alpha P_\alpha \, d\alpha. \tag{27a}$$

Thus, when H_{cool} is very large and $\alpha_0 \to 0$, $U_{1(H)}$ will approach an upper limit of $2M_F H_{FA} q$, where

$$q \equiv \int_{0}^{1} \alpha P_\alpha \, d\alpha. \tag{27b}$$

In Table 1, we have listed the values of q corresponding to several simple forms for P_α; it is clear that q gets smaller as P_α places greater emphasis on small values of α. From the combination of equations (20) and (27a), we have computed $U_{1(H)}/2M_F H_{FA} q$ as a function of $H_{cool}/\bar{H}_{FA}$, again assuming that $P_\alpha = 2(1-\alpha)$ and $\lambda_M = 0$ or $\bar{H}_{FA}/4\bar{M}_F$. From the results plotted in Fig. 9(a), we observe that with increasing H_{cool} the approach of $U_{1(H)}$ to its upper limit is considerably faster than that of M_R. This difference can be predicted qualitatively by comparing equations (23) and (27a) and recognizing that the domain ensembles with small α-parameters (which require large cooling-fields for transformation to the field-cooled state) make a relatively smaller contribution to $U_{1(H)}$ than to M_R. It also follows that this difference between $U_{1(H)}$ and M_R will become more pronounced as P_α increasingly favors the relative population of domain ensembles with small α. This is clearly borne out in Fig. 9(b) where $U_{1(H)}/2M_F H_{FA} q$ is plotted directly against M_R/M_F for a few simple forms for P_α.

The inverse relationship between the coercive field and M_R noted in Fig. 10 can now be interpreted as a direct consequence of the more rapid approach to saturation of $U_{1(H)}$ compared to M_R. Furthermore, it is clear from equation (27a) that for a given M_R corresponding to a given α_0 the value of $U_{1(H)}$ is invariant with λ_M; hence, the two sets of hysteresis loops in Fig. 10, though very different in shape, share the same values of $U_{1(H)}$ as well as the same remanences and coercive fields. However, as we will now show, the difference in shape between these two sets of curves is not trivial but contains important information on the effect of λ_M on the magnetization process in this complex system. In the lower part of Fig. 10, we have taken the difference in magnetization (ΔM) between each pair of adjacent hysteresis loops shown in the upper part of this figure and plotted it against the field at which ΔM was evaluated. For both values of λ_M, the resulting ΔM vs. H curves resemble the hysteresis loops from which they were derived, in being asymmetrical with respect to the origin. In the case of $\lambda_M = 0$, ΔM varies strictly within the limits $\pm\ \Delta M_R$, where ΔM_R is the remanence increase arising from the additional domain ensembles stabilized in the field-cooled state when the system is cooled in a larger field. It follows that in this case these ensembles contribute purely additively to the magnetization, which is a manifestation of the fact that when $\lambda_M = 0$ all the domain ensembles in the system are magnetically independent. Clearly, this will not be so when $\lambda_M > 0$, and in this case the ΔM vs. H curves in Fig. 10 exhibit a dip in ΔM to values well below $-\Delta M_R$, indicating that the domain ensembles all of which are now ferromagnetically coupled reverse their magnetizations cooperatively. This effect is discussed analytically in Appendix D where it is assumed for simplicity that the two hysteresis loops of interest are for the system cooled in slightly different fields. The expression for ΔM derived from these hysteresis loops in the region of magnetization reversal is the following:

$$\Delta M \simeq -\Delta M_R H_{FA}/(H_{FA} - 2\lambda_M M_F P_\alpha), \quad (28)$$

which clearly states that ΔM will have a minimum value lower than $-\Delta M_R$ as long as $\lambda_M > 0$. Under the same assumptions, it is also found that the shaded area indicated with respect to one of the ΔM vs. H curves in Fig. 10, which is dimensionally an energy, can be expressed as

$$U_{\Delta M} \simeq 2\lambda_M M_R \Delta M_R \quad (29)$$

and therefore is not explicitly dependent on the form of the distribution function P_α. In fact, since the quantities $U_{\Delta M}$, M_R and ΔM_R can be readily evaluated for any pair of displaced hysteresis loops that are closely related, equation (29) offers a convenient graphical method for determining λ_M.

For comparison with the theoretical curves in Fig. 10, we have chosen our recently published data[(1)] on a Cu–Mn and a Ag–Mn alloy of approximately 20 at. per cent Mn. The displaced hysteresis loops shown in the upper part of Fig. 11 were obtained by cooling the alloys to 1·8°K in a 5 or 10 kOe field and then measuring their magnetizations in a variable field parallel to the cooling-field direction. As indicated, the two branches of the hysteresis loops for the Cu–Mn alloy are essentially coincident. Allowing for the small component of magnetization proportional to field, we observe that the hysteresis loops for each of these materials exhibit an inverse relationship between remanent magnetization and coercive field, which was also a prominent feature of the theoretical curves in Fig. 10. Moreover, when the appropriate graphical integration (described earlier) is performed with respect to each hysteresis loop in Fig. 11, it is found that for both these alloys the unidirectional anisotropy energy $U_{1(H)}$ remains essentially constant (at about $3{\cdot}5 \times 10^4$ erg/cm^3) whereas the remanence M_R almost doubles when the cooling-field is increased from 5 to 10 kOe. The fact that $U_{1(H)}$ approaches a saturation limit faster than M_R agrees qualitatively with the theoretical prediction as presented in Fig. 9. However, this experimental difference between the variations of $U_{1(H)}$ and M_R is quantitatively so severe as to suggest that the distribution function P_α appropriate for these alloys is more drastic in its favoring of small values of α than any of the forms of P_α represented in Fig. 9(b), and/or that some of the other assumptions of our model (e.g., the use of average rather than distributed values for all the parameters other than α) are too oversimplified.

The small component of magnetization proportional to field exhibited by all the experimental hysteresis loops in Fig. 11, can be readily associated with the susceptibility contributed by the domain ensembles that are stabilized in the ground state configuration. Our approximate theoretical expression for this susceptibility is equation (24), which by virtue of equations (8), (12) and (23) can be written as

$$\chi_\theta \simeq \tfrac{2}{3}(M_F - M_R)/(H_{FA} - \tfrac{2}{3}\lambda_M M_F). \quad (30)$$

Hence, if M_R is rising rapidly with increasing cooling-field, indicating that it is still well below its saturation value M_F, χ_θ will remain relatively unchanged. This situation is clearly applicable to each of the alloys represented in Fig. 11. Furthermore, our published data[(1)] on Cu–Mn and Ag–Mn alloys more dilute in Mn show that with decreasing Mn concentration the remanence is increasingly closer to saturation at the maximum cooling-field of 10 kOe and, in agreement with equation (30), there is a correspondingly larger relative decrease of χ_θ.

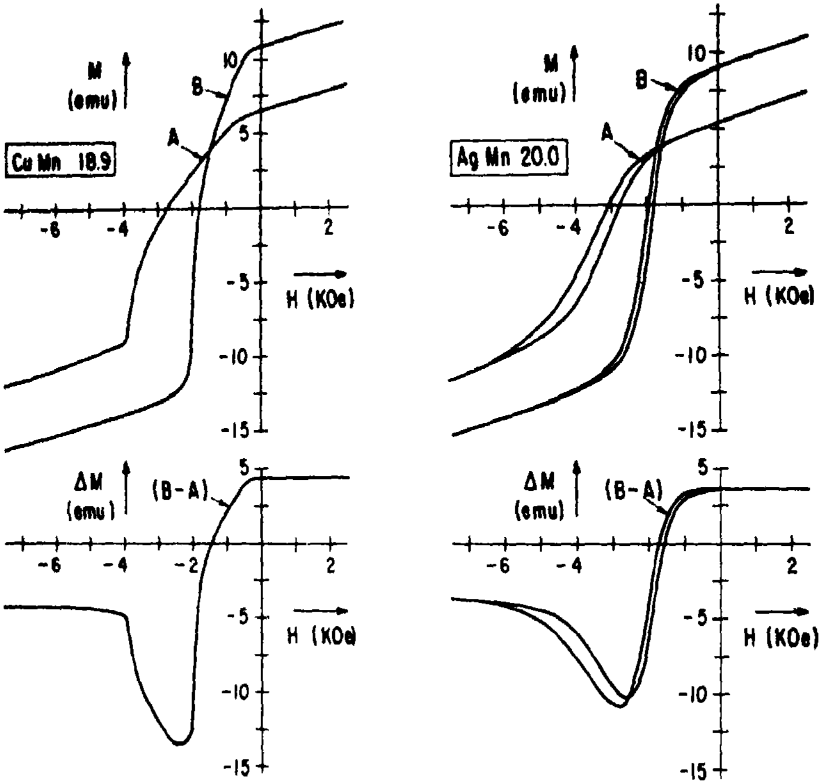

FIG. 11. Hysteresis loops and ΔM vs. H curves (derived from these loops) for Cu–Mn and Ag–Mn alloys (designated by at. per cent Mn) cooled to 1·8°K in 5 kOe (curves A) or in 10 kOe (curves B).

In the lower part of Fig. 11 are plotted the ΔM vs. H curves derived from the experimental hysteresis loops immediately above. It is quite obvious that for both materials in the region of magnetization reversal ΔM decreases to values considerably below $-\Delta M_R$. The close resemblance between this behavior and that exhibited in Fig. 10 for the theoretical case of $\lambda_M = \bar{H}_{FA}/4\bar{M}_F$, in contrast to the case of $\lambda_M = 0$, strongly suggests the presence of a positive (ferromagnetic) interaction which links adjacent magnetic units throughout each of these alloys and causes the reversal of magnetization to be a cooperative process. In applying equation (29) to the ΔM vs. H curves in Fig. 11, we take for M_R the average remanence for each pair of hysteresis loops and evaluate $U_{\Delta M}$ by the graphical method described earlier. For the Cu–Mn and Ag–Mn alloys, respectively, we find that $\lambda_M \simeq 180$ and 250 e.m.u., or in terms of the interaction field at remanence, $\lambda_M M_R \simeq 1600$ and 1800 Oe. Although equation (29) is not strictly valid for hysteresis loops that are as far apart as those in Fig. 11, these results probably give a reliable measure of the interaction field $\lambda_M M_R$ which, according to previous discussion, is responsible for the changes in the shape of the displaced hysteresis loops of these alloys for different fields applied during cooling.

4. SUMMARY

The low-temperature magnetic structure of Cu–Mn and related alloys is conceived as a microscopically inhomogeneous mixture of ferromagnetic and antiferromagnetic regions (or domains) resulting from the combined effects of statistical composition fluctuations inherent to atomically-disordered systems and a critical dependence of the short-range exchange coupling between two magnetic (Mn) atoms on the separation distance. As an attempt to simulate this structure and yet avoid many of its statistical complexities, we propose a simple model in which the magnetic unit is a small ensemble of mutually-interacting ferromagnetic and antiferromagnetic domains. The system as a whole is considered to be an aggregate of these domain ensembles, all of which are initially assumed to be equivalent. The interactions among the domains of each ensemble are so arranged that in its ground state configuration the ensemble has zero net magnetization; this ensures the zero remanence appropriate for such a system in its ground state (the state achieved by cooling the system in zero field).

When the system is cooled in a large field, a different spin configuration is produced, in which the moments of the antiferromagnetic domains, though still antiparallel to one another, have rearranged themselves consistent with their interactions with the ferromagnetic domains whose moments are now aligned parallel to the field. We then assume that during the cooling process a strong anisotropy (K_A) develops and fixes the antiferromagnetic domain moments, thus preventing the system from reverting to its ground state when the field is removed. In this metastable field-cooled state, the system has a remanent magnetization whose direction is always that of the field applied during cooling (H_{cool}), even after the magnetization has been completely reversed by a large enough reverse field. Hence, its magnetic hysteresis loop is asymmetrically displaced from the origin. Under the same conditions, the torque on the system in a large field will reveal a unidirectional anisotropy, the single easy direction of magnetization coinciding with that of H_{cool}.

As the temperature of this field-cooled system rises, we assume that ρ, the ratio of the exchange energy of interaction between adjacent domains to twice the anisotropy energy associated with K_A, increases due to the more rapid decrease of K_A. It is found that as long as $\rho < \frac{1}{2}$ the unidirectional anisotropy energy determined by hysteresis loop or torque measurements remains constant, but as soon as $\rho = \frac{1}{2}$ this reversible energy vanishes and there is a sudden appearance of magnetic energy losses. In the case of torque measurements these losses take the form of a rotational hysteresis with a non-zero limiting value at very high fields. As the temperature (and ρ) is increased further, these losses rapidly diminish, and eventually when K_A becomes very small the system relaxes to its ground state configuration. If the external field is applied perpendicular rather than parallel to H_{cool}, the magnetization curve of the field-cooled system is always symmetrical and reversible, and at the lowest temperatures it gives an energy of magnetization that is exactly half the unidirectional anisotropy energy. All these unusual properties predicted by our model for the system cooled in a field and subsequently raised in temperature (which are illustrated in Figs. 5, 6 and 7) are entirely in accord with those recently observed in Cu–Mn and Ag–Mn alloys over wide ranges of composition.(1)

For the remainder of the discussion, instead of assuming that all the domain ensembles of our hypothetical system are equivalent, we allow the α-parameter, which is a sensitive function of the moment alignment at the domain boundaries, to vary (between 0 and 1) from one ensemble to another according to an arbitrary distribution function (P_α). On this basis, we first investigate the temperature dependence of the susceptibility of the system initially cooled in zero field and therefore in its ground state configuration. Again assuming that the anisotropy K_A decreases rapidly with increasing temperature, we find that the maximum susceptibility, which occurs at about the temperature where K_A vanishes, can be many times larger than the susceptibility at 0°K, the ratio depending sensitively on the form of P_α. In order that this ratio be approximately two, as observed experimentally in various Cu–Mn and Ag–Mn alloys,$^{(1)}$ the function P_α must be chosen so as to strongly favor domain ensembles of small α.

According to our model, the magnetic-disordering or Curie temperature (T_C) is in general considerably higher than the temperature of maximum susceptibility (T_s). The linear temperature dependence of the inverse susceptibility of Cu–Mn alloys$^{(1)}$ observed just above T_s is interpreted not as paramagnetic behavior but as a consequence of a rapid yet continuous decrease of magnetic order in the ferromagnetic domains of the system with increasing temperature; this also accounts for the apparent paramagnetic Curie temperature being positive. At T_C, where both ferromagnetic and antiferromagnetic domains lose their magnetic order completely, our model predicts (again in agreement with experiment) that the alloys of high Mn concentration will have a kink in their $1/\chi$ vs. T curves and that above T_C these curves will again become linear, extrapolating to a true paramagnetic Curie temperature which is negative. The electrical resistivity anomaly characteristic of a magnetic transition that is found to occur at T_C in each of these alloys, is also consistent with the predictions of this model.

We next consider the effects of different fields applied during cooling (H_{cool}) on our hypothetical system which now includes an α-parameter distribution. For a given H_{cool}, the remanent condition of the system at very low temperatures is found to be such that all its domain ensembles with $\alpha_0 \leqslant \alpha \leqslant 1$ are in the metastable field-cooled state described above and all those with $0 \leqslant \alpha < \alpha_0$ are in the ground state. With increasing H_{cool}, the critical parameter value α_0 slowly decreases and the remanent magnetization M_R gradually rises to its maximum limit. The magnetic hysteresis loops of the system under these conditions are displaced asymmetrically with respect to the origin. Another impressive feature of these theoretical curves is that the coercive field decreases with increasing H_{cool}; this inverse relationship has been noted experimentally in Cu–Mn and Ag–Mn alloys. From the theoretical displaced hysteresis loops, we derive a unidirectional anisotropy energy $U_{1(H)}$ which rises much more rapidly than M_R to its maximum limit with increasing H_{cool}. In order that this difference between the variations of $U_{(1H)}$ and M_R with H_{cool} be as severe as that found experimentally in the alloys, it is necessary to assume a predominant population of domain ensembles with small α, which is consistent with the type of distribution function (P_α) suggested earlier by susceptibility ratio considerations. The shapes of the theoretical displaced hysteresis loops are significantly affected by the coupling between different domain ensembles, represented in our model by the molecular field $\lambda_M M$ where M is the net magnetization of the whole system and λ_M is a constant. Since this effect changes with the remanence associated with the hysteresis loop, we are able to devise a method of evaluating λ_M from any two (preferably adjacent) displaced hysteresis loops of a given system. Applying this method to experimental curves for Cu–Mn and Ag–Mn alloys of about 20 at. per cent Mn cooled in 5 and 10 kOe fields, we obtain a positive λ_M (of roughly the same magnitude for both materials) indicative of a ferromagnetic coupling.

Acknowledgements—I am extremely grateful to G. W. Rathenau whose continued interest and advice have contributed immeasurably to the development of this model, to the General Electric Company whose generosity allowed me to spend a month at the University of Amsterdam with Professor Rathenau, and to my colleagues I. S. Jacobs, W. H. Meiklejohn and R. H. Pry for many valuable discussions.

APPENDIX A

Using equation (7) and setting $\partial E/\partial\theta$ and $\partial E/\partial\phi = 0$, we find that the general equilibrium conditions for the field cooled configuration shown in Fig. 4(b) are

$$\rho \sin(\theta-\phi) = \tfrac{1}{2}\sin 2\phi = (H\rho/H_{FA}\alpha)\sin(\psi-\theta), \qquad \text{(A-1)}$$

where $\rho \equiv M_F H_{FA}\alpha/2N_A K_A$. We will first consider hysteresis loops where the magnetization M is measured parallel to the direction of field cooling along which the external field H is applied. Hence, $M = M_F \cos\theta$ and $\phi = 0$. One solution of equation (A–1) is obviously then

$$\sin\theta = 0, \quad \sin\phi = 0.$$

For the other solution, we set $\sin\phi/\rho \sin\theta \equiv \zeta$ and obtain in terms of this parameter

$$\cos\theta = H(\zeta-1)/H_{FA}\alpha\rho\zeta^2 \qquad \text{(A–2a)}$$

and

$$\cos\phi = -H/H_{FA}\alpha\zeta, \qquad \text{(A–2b)}$$

which recombined with $\rho^2\zeta^2(1-\cos^2\theta) = 1-\cos^2\phi$ give

$$H^2 = (H_{FA}\alpha)^2\zeta(\rho^2\zeta^2-1)/(\zeta-2) \qquad \text{(A–3a)}$$

$$M^2 = M_F^2\cos^2\theta = M_F^2(\zeta-1)^2(\rho^2\zeta^2-1)/\rho^2\zeta^3(\zeta-2) \qquad \text{(A3–b)}$$

and

$$\cos^2\phi = (\rho^2\zeta^2-1)/\zeta(\zeta-2). \qquad \text{(A–3c)}$$

Thus, the magnitudes of M and H (and $\cos\phi$) are related parametrically through equations (A–3), their relative signs being given by equations (A–2). For sufficiently small ρ, as ζ is increased from $\zeta_+ \equiv (1+\rho)^{-1}$ to $\zeta_- \equiv (1-\rho)^{-1}$, $\cos\theta$ (i.e., M/M_F) decreases from 1 to -1, H decreases from $H_+ \equiv -H_{FA}\alpha\zeta_+$ to $H_- \equiv -H_{FA}\alpha\zeta_-$, whereas ϕ increases and then returns to zero. When $H > H_+$ or $H < H_-$, the applicable solutions having the lowest energy are $\theta = \phi = 0$ and $\theta = \pi$, $\phi = 0$, respectively. It is clear that M is a reversible function of H that is asymmetrical with respect to the origin.

The unidirectional anisotropy energy $U_{1(H)}$ is defined as the area enclosed by the displaced hysteresis loop and the M axis for $-M_F < M < M_F$. Hence

$$U_{1(H)} = -\int_{-M_F}^{M_F} H\,\mathrm{d}M = -\frac{M_F}{2}\int_{\zeta_-}^{\zeta_+} \frac{H}{\cos\theta}\,\frac{\mathrm{d}(\cos^2\theta)}{\mathrm{d}\zeta}\,\mathrm{d}\zeta,$$

where $\zeta_\pm$ are defined above. When $H/\cos\theta$ and $\mathrm{d}(\cos^2\theta)/\mathrm{d}\zeta$ are expressed as functions of ζ by virtue of equations (A–2a) and (A–3b),

$$\begin{aligned} U_{1(H)} &= -\frac{M_F H_{FA}\alpha}{\rho^2}\int_{\zeta_-}^{\zeta_+} \frac{(1-\rho^2)\zeta^2-3\zeta+3}{\zeta^2(\zeta-2)^2}\,\mathrm{d}\zeta \\ &= M_F H_{FA}\alpha\{F_H(\zeta_+)-F_H(\zeta_-)\} \qquad \text{(A–4)} \\ &= 2M_F H_{FA}\alpha, \end{aligned}$$

since $F_H(\zeta) \equiv -(3\zeta^2+4\rho^2\zeta-10\zeta+6)/4\rho\zeta(\zeta-2)$. Thus, $U_{1(H)}$ is independent of ρ as long as equations (A–2) and (A–3) are valid for $\zeta_+ < \zeta < \zeta_-$.

In order that equations (A–2) and (A–3) represent a stable equilibrium solution, the following conditions must be satisfied:

$$\partial^2E/\partial\theta^2 > 0 \qquad \text{(A–5a)}$$

$$\partial^2E/\partial\phi^2 > 0 \qquad \text{(A–5b)}$$

and

$$\frac{\partial^2E}{\partial\theta^2}\,\frac{\partial^2E}{\partial\phi^2} > \left(\frac{\partial^2E}{\partial\theta\partial\phi}\right)^2, \qquad \text{(A–5c)}$$

where E is expressed by equation (7) with $\psi = 0$. Since $\partial^2E/\partial\theta^2 = M_F H_{FA}\alpha\rho\zeta$ and since ζ as defined is always positive, equation (A–5a) is satisfied for all values of ρ. Equation (A–5c), being more restrictive now than equation (A–5b), is the only remaining criterion for the stability of this solution and may be written as

$$(1-\rho)(\zeta_- - \zeta)(\zeta-\zeta_+)G_H(\zeta) > 0, \qquad \text{(A–6)}$$

where $\zeta_\pm = (1 \pm \rho)^{-1}$ as before, and $G_H(\zeta) \equiv \zeta^3-3\zeta^2+\rho^{-2}$. As shown in Fig. 12, $G_H(\zeta)$ vs. ζ forms a set of identically shaped curves that are displaced vertically downward with increasing ρ. The loci of points on these curves for $\zeta = \zeta_\pm$ are indicated as dotted curves (except for the negative values of ζ_- for $\rho > 1$, which are not represented). It follows immediately from equation (A–6) that the shaded area in Fig. 12, enclosed by the two dotted curves and the ζ-axis, corresponds to the region of stability for the solution given by equations (A–2) and (A–3). Thus, for $\rho < \frac{1}{2}$, the solution is stable over the entire range of $\zeta_+ < \zeta < \zeta_-$, and M as a function of H varies reversibly between its extreme values $\pm M_F$. However, for $\frac{1}{2} < \rho < \frac{1}{2}(1+\sqrt{5}) \simeq 1{\cdot}62$, a point is reached as ζ increases from ζ_+, H decreases from H_+ ($\equiv -H_{FA}\alpha\zeta_+$) and M decreases from M_F, when the $G_H(\zeta)$ vs. ζ curve intersects the ζ-axis and the solution becomes unstable. Substituting ζ_1 defined by $G_H(\zeta_1) = 0$ into equations (A–2) and (A–3), we obtain

$$H = -H_{FA}\alpha\rho\zeta_1^{3/2} \equiv H_1$$

$$M = -M_F(\zeta_1-1)\zeta_1^{-1/2} \equiv M_1 \text{ or } M_F\cos\theta_1$$

and

$$\cos\phi = \rho\zeta_1^{1/2} \equiv \cos\phi_1, \qquad \text{(A–7)}$$

and we find that at this point of instability M and $\cos\phi$ decrease discontinuously from M_1 and $\cos\phi_1$ to $-M_F$ and -1, respectively, and stay constant at these latter values when H is decreased below H_1. In this latter state, all the moments of the antiferromagnetic as well as the ferromagnetic domains are completely reversed from their original directions, and it follows that the same reversal process will repeat when the field is raised to corresponding positive values. Hence, for $\frac{1}{2} < \rho < 1{\cdot}62$, the hysteresis loops of M vs. H are symmetrical about the origin and enclose an area representing an irreversible energy loss. This is also true for $\rho > 1{\cdot}62$. In this case, however, the only valid solution is $\sin\theta = 0$, $\sin\phi = 0$. More specifically, it is found from equation (A–5c) that $\theta = \phi = 0$ for $H > H_+$ and

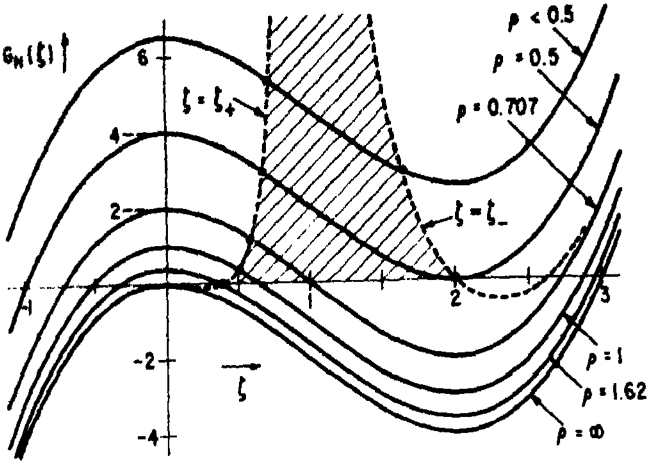

FIG. 12. $G_H(\zeta)$ vs. ζ for different values of ρ (solid curves) and loci of points for $\zeta = \zeta_\pm$ (dotted curves).

$\theta = \phi = \pi$ for $H < -H_+$, where $H_+ \equiv -H_{FA}\alpha(1+\rho)^{-1}$ as before; thus, M reverses abruptly from M_F to $-M_F$ at $H = H_+$ and then reverses abruptly back to M_F at $H = -H_+$.

In general, the hysteresis energy loss,

$$W_H = \oint H \, \mathrm{d}M,$$

where the integration is taken completely around a hysteresis cycle. From the above discussion, it follows that for $\frac{1}{2} < \rho < 1{\cdot}62$,

$$W_H = -2\int_{-M_F}^{M_F} H \, \mathrm{d}M - 2(M_1 + M_F)H_1,$$

H and M being expressed by equations (A-2) and (A-3) and H_1 and M_1 by equations (A-7). When the integral in this equation is evaluated by the procedure used in deriving equation (A-4) and when H_1 and M_1 are expressed in terms of ζ_1, we obtain

$$W_H = 2M_F H_{FA}\alpha$$
$$\times \{F_H(\zeta_+) - F_H(\zeta_1) - \rho\zeta_1(\zeta_1 - \zeta_1^{1/2} - 1)\}, \quad \text{(A-8)}$$

where ζ_+, ζ_1 and $F_H(\zeta)$ are defined as before. Equation (A-8) gives a monotonic decrease of W_H for increasing ρ. Specifically, when $\rho = \frac{1}{2}$: $\zeta_+ = \frac{2}{3}$, $F_H(\zeta_+) = \frac{3}{4}$, $\zeta_1 = 2$, and when L'Hospital's rule is used to resolve an indeterminacy, $F_H(\zeta_1) = -\frac{3}{4}$; thus, $W_H/M_F H_{FA}\alpha = 1 + 2^{3/2} \simeq 3{\cdot}82$. At the upper end of the range where $\rho = \frac{1}{2}(1+\sqrt{5}) \simeq 1{\cdot}62$: $\zeta_+ = \zeta_1 = \frac{1}{2}(3-\sqrt{5}) \simeq 0{\cdot}38$ and thus $W_H/M_F H_{FA}\alpha = 2(3-\sqrt{5}) \simeq 1{\cdot}53$. For $\rho > 1{\cdot}62$, it follows from previous discussion that

$$W_H = 4M_F H_{FA}\alpha/(1+\rho), \quad \text{(A-9)}$$

which gives the same value of W_H for $\rho = 1{\cdot}62$ and continues the monotonic decrease of W_H with increasing ρ.

We will next consider hysteresis loops where H is applied and M is measured perpendicular to the field-cooling direction, i.e., $\psi = \frac{1}{2}\pi$ and $M = M_F \sin\theta$. For the solution of equation (A-1) other than

$$\cos\theta = 0, \cos\phi = 0,$$

we find after setting $\cos\phi/\cos\theta \equiv \rho\eta$ that

$$\sin\theta = H(\eta+1)/H_{FA}\alpha\eta^2\rho \quad \text{(A-10a)}$$

and

$$\sin\phi = H/H_{FA}\alpha\eta, \quad \text{(A-10b)}$$

which we recombine with $\rho^2\eta^2(1-\sin^2\theta) = 1-\sin^2\phi$ and get

$$H^2 = (H_{FA}\alpha)^2\eta(\rho^2\eta^2-1)/(\eta+2) \quad \text{(A-11a)}$$

$$M^2 = M_F^2\sin^2\theta = M_F^2(\eta+1)^2(\rho^2\eta^2-1)/\rho^2\eta^3(\eta+2) \quad \text{(A-11b)}$$

and

$$\sin^2\phi = (\rho^2\eta^2-1)/\eta(\eta+2). \quad \text{(A-11c)}$$

If we let $\eta = \rho^{-1}$, we find that both M and $H = 0$ but that the initial susceptibility $\chi_0 \equiv (M/H)_{H\to 0} = M_F(1+\rho)/H_{FA}\alpha$. As η is increased from ρ^{-1}, equations (A-10) and (A-11) give values for M,H and $\sin\phi$ that increase monotonically. For $\rho < 1$, M reaches its saturation value M_F only as η and $H \to \infty$ (and $\sin\phi \to \rho$). However, for $\rho > 1$, saturation is achieved when $H = H_{FA}\alpha/(\rho-1)$, corresponding to $\eta = (\rho-1)^{-1} \equiv \eta_s$ (and $\sin\phi = 1$). As we expect, the hysteresis loop in this case is symmetrical with respect to the origin for all values of ρ; moreover, M is always a single-valued function of H and there is therefore no hysteresis energy loss.

Defining $U_\perp$ as the magnetic energy required for saturation perpendicular to the direction of field-cooling, we may write

$$U_\perp = \int_0^{M_F} H\,\mathrm{d}M = \frac{M_F}{2}\int_{\rho^{-1}}^{\eta_s} \frac{H}{\sin\theta}\frac{\mathrm{d}(\sin^2\theta)}{\mathrm{d}\eta}\,\mathrm{d}\eta$$

where $\eta_s = \infty$ for $\rho \leqslant 1$ and $\eta_s = (\rho-1)^{-1}$ for $\rho > 1$. Using equations (A–10a) and (A–11b) to express the integrand in terms of η, we find that

$$U_\perp = \frac{M_F H_{FA}\alpha}{\rho^2}\int_{\rho^{-1}}^{\eta_s} \frac{(1-\rho^2)\eta^2+3\eta+3}{\eta^2(\eta+2)^2}\,\mathrm{d}\eta$$

$$= M_F H_{FA}\alpha\{F_H(-\eta_s)-F_H(-\rho^{-1})\}$$

where the function F_H has been previously defined in connection with equation (A–4). This in turn reduces simply to

$$U = M_F H_{FA}\alpha(1-\tfrac{1}{2}\rho) \quad \text{for } \rho \leqslant 1$$

$$= M_F H_{FA}\alpha/2\rho \quad \text{for } \rho > 1,$$

giving a monotonic decrease of $U_\perp$ with increasing ρ.

APPENDIX B

With reference to the configuration shown in Fig. 4(b) whose energy is expressed by equation (7), the torque about an axis perpendicular to the field-cooling direction and to the direction of a uniform external field may be written as

$$L = -\frac{\mathrm{d}E}{\mathrm{d}\psi} = -\frac{\partial E}{\partial\psi} - \frac{\partial E}{\partial\theta}\frac{\mathrm{d}\theta}{\mathrm{d}\psi} - \frac{\partial E}{\partial\phi}\frac{\mathrm{d}\phi}{\mathrm{d}\psi},$$

and since $\partial E/\partial\theta$ and $\partial E/\partial\phi = 0$ at equilibrium,

$$L = -\partial E/\partial\psi = -M_F H\sin(\psi-\theta). \quad \text{(B–1)}$$

We will restrict ourselves to the case where H is so large that $\theta \to \psi$. In this case, when equation (B–1) is combined with equation (A–1) which gives the general equilibrium conditions explicitly, it is found that

$$L = -M_F H_{FA}\alpha\sin(\psi-\phi) \qquad \text{(B–2a)}$$

and

$$\rho\sin(\psi-\phi) = \tfrac{1}{2}\sin 2\phi. \qquad \text{(B–2b)}$$

From inspection, equation (B–2b) gives $\phi = \psi+n_1\pi = n_2\pi/2$ where n_1 and n_2 are integers. However, for the full range of solutions we set $\rho\cos\psi/\cos\phi \equiv \xi$ and find that equations (B–2) become:

$$L = -M_F H_{FA}\alpha\rho\sin\psi\cos\psi/\xi(\xi+1) \quad \text{(B–3a)}$$

and

$$\sin\phi = \rho\sin\psi/(\xi+1), \qquad \text{(B–3b)}$$

which recombined with $\rho^2(1-\sin^2\psi) = \xi^2(1-\sin^2\phi)$ gives

$$L^2 = (M_F H_{FA}\alpha)^2\{(\xi+1)^2-\rho^2\}(\rho^2-\xi^2)/\rho^2(2\xi+1)^2 \qquad \text{(B–4a)}$$

$$\sin^2\psi = (\xi+1)^2(\rho^2-\xi^2)/\rho^2(2\xi+1) \qquad \text{(B–4b)}$$

$$\sin^2\phi = (\rho^2-\xi^2)/(2\xi+1). \qquad \text{(B–4c)}$$

Thus, equations (B–3) and (B–4) interrelate the magnitudes and signs of L, ψ and ϕ through the parameter ξ. For sufficiently low values of ρ, these equations give continuous stable solutions as ξ is varied from ρ to $-\rho$ and ψ increases from 0 to π, while both $|L|$ and ϕ increase and then return to zero. The magnitude of the maximum torque is found to be $M_F H_{FA}\alpha$, occurring when $\sin^2\psi = \tfrac{1}{2}+\tfrac{1}{2}(1-4\rho^2)^{1/2}$, $\sin^2\phi = \tfrac{1}{2}-\tfrac{1}{2}(1-4\rho^2)^{1/2}$ and corresponding to $\xi = -\tfrac{1}{2}+\tfrac{1}{2}(1-4\rho^2)^{1/2}$. The positions of maximum torque shift from $\psi = \pm\tfrac{1}{2}\pi$ (and $\phi = 0$) when $\rho = 0$ to $\psi = \pm\tfrac{3}{4}\pi$ (and $\phi = \pm\tfrac{1}{4}\pi$) when $\rho = \tfrac{1}{2}$; higher values of ρ will be discussed later. Furthermore, at $\psi = 0$ and π where $L = 0$, the slope of the torque curve, $\mathrm{d}L/\mathrm{d}\psi = -M_F H_{FA}\alpha/(1+\rho)$ and $M_F H_{FA}\alpha/(1-\rho)$, respectively.

The unidirectional anisotropy energy $U_{1(L)}$ is defined as the area enclosed by the torque curve and the ψ axis between $\psi = 0$ and π, which correspond to the easy and hard directions of magnetization, respectively. Hence,

$$U_{1(L)} = -\int_0^{\pi} L\,\mathrm{d}\psi = -\int_{\rho}^{-\rho} \frac{L\,\mathrm{d}(\sin^2\psi)/\mathrm{d}\xi}{2\sin\psi\cos\psi}\,\mathrm{d}\xi,$$

which by virtue of equations (B–3a) and (B–4b) becomes

$$U_{1(L)} = -M_F H_{FA}\alpha\int_{\rho}^{-\rho} \frac{3\xi(\xi+1)+1-\rho^2}{(2\xi+1)^2}\,\mathrm{d}\xi$$

$$= M_F H_{FA}\alpha\{F_L(-\rho)-F_L(\rho)\}$$

$$= 2M_F H_{FA}\alpha, \qquad \text{(B–5)}$$

since $F_L(\xi) \equiv -\{6\xi(2\xi+1)-1+4\rho^2\}/8\rho(2\xi+1)$. Thus, $U_{1(L)}$ is invariant with ρ as long as eqs. (B–3) and (B–4) are valid over the range $-\rho < \xi < \rho$.

A solution given by equations (B–3) and (B–4) is valid only if it satisfies the general stability criteria expressed by equations (A–5), the total energy being given by equation (7). For such a solution, we find (again in the limit of very high fields) that $\partial^2E/\partial\theta^2 = M_F H$, which satisfies equation (A–5a), and that equations (A–5b) and (A–5c) both reduce to

$$G_L(\xi)/(2\xi+1) > 0, \qquad \text{(B–6)}$$

where $G_L(\xi) \equiv 3\xi(\xi+1)+1-\rho^2$. As shown in Fig. 13, a plot of $G_L(\xi)$ vs. ξ gives a family of identical parabolic curves that are displaced vertically downward with increasing ρ; the loci of points on these curves for $\xi = \pm\rho$

and $1-\rho$ are represented by dotted curves. The shaded area in this figure, enclosed by the $\xi = -\rho$ locus and the ξ-axis for $-\frac{1}{2} < \xi < 0$ and by the $\xi = \rho$ and $1-\rho$ loci for $\xi \geqslant 0$, lies well within the region of stability defined by equation (B–6) and represents the conditions under which the solutions of equations (B–3) and (B–4) are meaningful as well as stable. Thus, for $\rho < \frac{1}{2}$, the solution over the entire range of $-\rho < \xi < \rho$ is stable, and the torque L varies reversibly as ψ increases or decreases through a full cycle. However, for $\frac{1}{2} \leqslant \rho \leqslant 1$, a point is reached as ξ decreases from its value ρ (where L and $\phi = 0$) when the $G_L(\xi)$ vs. ξ curve intersects the ξ-axis and the solution becomes unstable. At this point, ξ changes abruptly from its value ξ_1, defined by $G_L(\xi_1) = 0$, to a new value ξ_2, determined by fixing the direction of the external field so that ψ is the same for both ξ_1 and ξ_2. From the definition of $G_L(\xi)$ and from equation (B–4b) we obtain $\xi_1 = \frac{1}{2}(a-1)$ and $\xi_2 = \frac{1}{2}(-a+2b-1)$, where $a \equiv \{(4\rho^2-1)/3\}^{1/2}$ and $b \equiv \{(\rho^2+2)/3\}^{1/2}$. For $\rho = \frac{1}{2}$; $\xi_1 = -\frac{1}{2}$ and $\xi_2 = \frac{1}{2}(\sqrt{3}-1)$, which we substitute into equations (B–3) and (B–4) and find that at $\psi = 3\pi/4$, L changes discontinuously from $-M_F H_{FA}\alpha$ to $+\frac{1}{2}M_F H_{FA}\alpha$ and ϕ jumps from $\pi/4$ to $\cos^{-1}\{-(2)^{-3/2}(\sqrt{3}+1)\} \simeq 165°$. Hence, the coupling with the ferromagnetic domain moments is just sufficient to pull the antiferromagnetic domain moments over their anisotropy energy barriers, and the $\psi = \pi$ direction becomes an easy direction of magnetization (equivalent to $\psi = 0$). The abrupt change in torque will then repeat for every half-cycle increase of ψ, and an analogous process will obtain for decreasing ψ, resulting in a L vs. ψ curve that is no longer single-valued for increasing and decreasing ψ. Furthermore, as ρ increases and approaches unity, both ξ_1 and ξ_2 converge on zero, and it follows that L and ϕ (both before and after their abrupt changes) approach the values 0 and $\frac{1}{2}\pi$, respectively, while the position of this transition gradually moves towards $\psi = \frac{1}{2}\pi$. Thus, for $\rho \geqslant 1$, L is once again a single-valued function of ψ. Specifically, from equations (B–3) and (B–4) we find that as ξ is varied between ρ and $\rho-1$, L passes through zero when both ψ and $\phi = 0$, $\frac{1}{2}\pi$, π, $\frac{3}{2}\pi$ and reaches a maximum magnitude of $M_F H_{FA}\alpha/2\rho$ at intermediate values of ψ and ϕ.

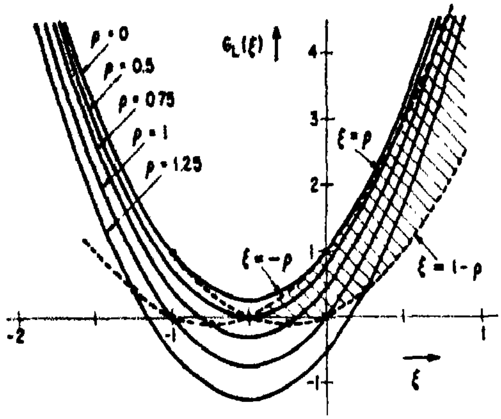

FIG. 13. $G_L(\xi)$ vs. ξ for different values of ρ (solid curves) and loci of points for $\xi = \pm\,\rho$, $1-\rho$ (dotted curves).

It follows from this discussion that when $\frac{1}{2} < \rho < 1$ there is rotational hysteresis whose energy per cycle W_R may be equated to half the area enclosed by the torque curves or increasing and decreasing ψ. Hence, from the symmetrical relationship between these curves,

$$W_R = -2\int_{\psi_2}^{\psi_1} L\,\mathrm{d}\psi,$$

where ψ_1 and ψ_2 ($= \pi-\psi_1$) are evaluated at $\xi = \xi_1$ and ξ_2, respectively and L is taken for increasing ψ. Determining the integral in this equation by the procedure used in deriving equation (B–5), we obtain

$$\begin{aligned} W_R &= 2M_F H_{FA}\alpha\{F_L(\xi_1)-F_L(\xi_2)\} \\ &= M_F H_{FA}\alpha\rho^{-1}(a+2b)(a-b)^2, \end{aligned} \qquad \text{(B–7)}$$

where the function $F_L(\xi)$ has been defined earlier and $a \equiv \{(4\rho^2-1)/3\}^{1/2}$ and $b \equiv \{(\rho^2+2)/3\}^{1/2}$ as before. For $\rho = \frac{1}{2}$, equation (B–7) gives $W_R/M_F H_{FA}\alpha = (3)^{3/2}/2 \simeq 2{\cdot}60$, and as ρ increases to unity W_R decreases monotonically to zero.

APPENDIX C

The equilibrium conditions at low temperatures for a domain ensemble in the configuration shown in Fig. 3(b) are obtained from equation (9) by setting $\partial E/\partial\theta$ and $\partial E/\partial\phi = 0$; they are as follows:

$$H_{FA}(\alpha\cos\theta\sin\phi-\sin\theta\cos\phi)+H_{\text{eff}}\cos\theta = 0$$

and

$$H_{FA}(\alpha\sin\theta\cos\phi-\cos\theta\sin\phi)-H_K\sin\phi\cos\phi = 0.$$

For H_{eff} very small, we find that

$$\sin\theta \simeq \theta = H_{\text{eff}}(H_{FA}+H_K)/H_{FA}H'$$

and

$$\sin\phi \simeq \phi = H_{\text{eff}}\alpha/H',$$

where $H' \equiv H_{FA}(1-\alpha^2)+H_K$. This expression for $\sin\theta$ is used in Section 3 in obtaining the initial susceptibility of the entire system.

At higher temperatures (but below the magnetic disordering temperature), the energy of this domain ensemble is given by equation (15). Setting $\partial E/\partial\theta$, $\partial E/\partial\phi$ and $\partial E/\partial\epsilon = 0$, we obtain equilibrium conditions which for very small $\mathbf{H}_{\text{eff}}$ reduce to

$$\lambda'_{FA}\overline{\mathbf{M}}_A\theta-\lambda'_{FA}\overline{\mathbf{M}}_A\alpha\phi-\lambda''_{FA}\overline{\mathbf{M}}_A\epsilon = \mathbf{H}_{\text{eff}}$$

$$\alpha\theta-\phi = 0$$

and

$$\lambda''_{FA}\overline{\mathbf{M}}_F\theta-(\lambda'_{FA}\overline{\mathbf{M}}_F+\tfrac{1}{2}\lambda_A\overline{\mathbf{M}}_A)\epsilon = \mathbf{H}_{\text{eff}},$$

from which it follows that

$$\theta = \frac{\phi}{\alpha} = \frac{\bar{\mathbf{H}}_{\mathrm{eff}}(1-R)}{\lambda'_{FA}\bar{\mathbf{M}}_A(1-\alpha^2)-\lambda''_{FA}\bar{\mathbf{M}}_F R}$$

and

$$\epsilon = \frac{\bar{\mathbf{H}}_{\mathrm{eff}}\{\bar{\mathbf{M}}_F/\bar{\mathbf{M}}_A-\lambda'_{FA}(1-\alpha^2)/\lambda''_{FA}\}R}{\lambda'_{FA}\bar{\mathbf{M}}_A(1-\alpha^2)-\lambda''_{FA}\bar{\mathbf{M}}_F R}, \tag{C–1}$$

where $R \equiv \lambda''_{FA}\bar{\mathbf{M}}_A/(\tfrac{1}{2}\lambda_A\bar{\mathbf{M}}_A+\lambda'_{FA}\bar{\mathbf{M}}_F)$. Since the magnetization of a given domain ensemble is $\bar{\mathbf{M}}_F\theta-\bar{\mathbf{M}}_A\epsilon$ in the limit of very small fields, the average magnetization of the whole system may be written as

$$\bar{\mathbf{M}} = \int_0^1 (\bar{\mathbf{M}}_F\theta-\bar{\mathbf{M}}_A\epsilon)P_\alpha\,\mathrm{d}\alpha. \tag{C–2}$$

Hence, by virtue of equations (C–1) and (C–2),

$$\bar{\mathbf{M}}/\bar{\mathbf{H}}_{\mathrm{eff}} = p'\bar{\mathbf{M}}_F(1-R)^2+R/\lambda''_{FA}$$

where

$$p' = \int_0^1 \frac{P_\alpha\,\mathrm{d}\alpha}{\lambda'_{FA}\bar{\mathbf{M}}_A(1-\alpha^2)-\lambda''_{FA}\bar{\mathbf{M}}_F R},$$

which combined with $\bar{\mathbf{H}}_{\mathrm{eff}} = H+\lambda_M\bar{\mathbf{M}}$ gives

$$\chi \equiv \frac{\bar{\mathbf{M}}}{H} = \frac{p'\bar{\mathbf{M}}_F(1-R)^2+R/\lambda''_{FA}}{1-\lambda_M\{p'\bar{\mathbf{M}}_F(1-R)^2+R/\lambda''_{FA}\}} \tag{C–3}$$

In the limit of very large λ_A, R becomes vanishingly small and equation (C–3) reduces properly to equation (14).

Representing the temperature dependences of $\bar{\mathbf{M}}_F$ and $\bar{\mathbf{M}}_A$ by the usual Brillouin functions, we write

$$\bar{\mathbf{M}}_F = N_F\mu B_S(\mu\bar{\mathbf{H}}_F/kT) \tag{C–4a}$$

and

$$\bar{\mathbf{M}}_A = N_A\mu B_S(\mu\bar{\mathbf{H}}_A/kT), \tag{C–4b}$$

where the atomic moment $\mu = \mu_F = \mu_A$ and the spin quantum number $S = \mu/g\mu_B$. In these equations, $\bar{\mathbf{H}}_F$ is assumed for simplicity to be the average exchange field experienced by all the moments in the ferromagnetic domains, and $\bar{\mathbf{H}}_A$ has the same meaning for the antiferromagnetic domains, Since $\bar{\mathbf{H}}_F$ and $\bar{\mathbf{H}}_A$, as well as all the moments, are aligned approximately perpendicular to the small external field, it follows that

$$\bar{\mathbf{H}}_F = \tfrac{1}{2}\lambda_F\bar{\mathbf{M}}_F+\lambda'_{FA}\bar{\mathbf{M}}_A$$

and

$$\bar{\mathbf{H}}_A = \tfrac{1}{4}\lambda_A\bar{\mathbf{M}}_A+\lambda'_{FA}\bar{\mathbf{M}}_F, \tag{C–5}$$

subject to the assumption made in connection with equation (15) that $m'+m'' = n'+n''$. At the Curie temperature T_c, the arguments of the Brillouin functions in equation (C–4) become vanishingly small, and hence,

$$\bar{\mathbf{M}}_F = C_F\bar{\mathbf{H}}_F/T_c \text{ and } \bar{\mathbf{M}}_A = C_A\bar{\mathbf{H}}_A/T_c,$$

where $C_F \equiv N_F\mu^2(S+1)/3Sk$ and $C_A \equiv N_AC_F/N_F$. From these expressions and equation (C–5) we obtain

$$T_c = \tfrac{1}{4}C_F\lambda_F+\tfrac{1}{8}C_A\lambda_A$$
$$\pm\{(\tfrac{1}{4}C_F\lambda_F-\tfrac{1}{8}C_A\lambda_A)^2+C_FC_A(\lambda'_{FA})^2\}^{1/2} \tag{C–6}$$

Restricting our concern to the case where $\lambda_A \gg \lambda_F \gg \lambda'_{FA}$ we find that equation (C–6) becomes simply

$$T_c \simeq \tfrac{1}{4}C_A\lambda_A. \tag{C–7}$$

For this case, moreover, it is clear from equations (C–5) that $\bar{\mathbf{H}}_F \ll \bar{\mathbf{H}}_A$; thus, from equation (C–4) it follows that $\bar{\mathbf{M}}_F/M_F \ll \bar{\mathbf{M}}_A/M_A$ at temperatures well below T_c. Consequently, equation (C–4a) can be approximated by

$$\bar{\mathbf{M}}_F = C_F(\tfrac{1}{2}\lambda_F\bar{\mathbf{M}}_F+\lambda'_{FA}\bar{\mathbf{M}}_A)/T, \tag{C–8}$$

which when substituted into equation (C–3) produces equation (17), an expression for the initial susceptibility valid for

$$\lambda_A \gg \lambda_F \gg \lambda'_{FA},\quad \lambda''_{FA} \text{ or } \lambda_M.$$

Above T_c, the only moments are those induced parallel to the external field. The moments in each antiferromagnetic domain can be separated into two sublattices which experience different exchange fields and therefore have different magnetizations (except at 0°K). Identifying these sublattices as those whose moment directions are set in Fig. 3(b) by the angles ϕ_1 and ϕ_2, we label their magnetizations $\tfrac{1}{2}\bar{\mathbf{M}}'_A$ and $\tfrac{1}{2}\bar{\mathbf{M}}''_A$, respectively; at low fields, the Brillouin function expressions for $\bar{\mathbf{M}}_F$, $\bar{\mathbf{M}}_A$ and $\bar{\mathbf{M}}''_A$ reduce to

$$\bar{\mathbf{M}}_F = C_F(\bar{\mathbf{H}}_{\mathrm{eff}}+\tfrac{1}{2}\lambda_F\bar{\mathbf{M}}_F-\lambda_+\bar{\mathbf{M}}'_A-\lambda_-\bar{\mathbf{M}}''_A)/T$$

$$\bar{\mathbf{M}}'_A = C_A(\bar{\mathbf{H}}_{\mathrm{eff}}-\tfrac{1}{4}\lambda_A\bar{\mathbf{M}}''_A-\lambda_+\bar{\mathbf{M}}_F)/T$$

and

$$\bar{\mathbf{M}}''_A = C_A(\bar{\mathbf{H}}_{\mathrm{eff}}-\tfrac{1}{4}\lambda_A\bar{\mathbf{M}}'_A-\lambda_-\bar{\mathbf{M}}_F)/T,$$

where C_F and C_A are defined as before and $\lambda_\pm \equiv \lambda''_{FA} \pm \lambda'_{FA}\alpha$. Again restricting ourselves to the case where $\lambda_A \gg \lambda_F \gg \lambda'_{FA}$, λ''_{FA} or λ_M, we obtain from the above equations

$$\bar{\mathbf{M}}'_A+\bar{\mathbf{M}}''_A = \frac{2C_A(H_{\mathrm{eff}}-\lambda''_{FA}\bar{\mathbf{M}}_F)}{T+\tfrac{1}{4}C_A\lambda_A} \tag{C–9a}$$

$$\bar{\mathbf{M}}_F \simeq \frac{C_F(T-\tfrac{1}{4}C_A\lambda_A)(T+\tfrac{1}{4}C_A\lambda_A-C_A\lambda'_{FA})\bar{\mathbf{H}}_{\mathrm{eff}}}{(T+\tfrac{1}{4}C_A\lambda_A)\{(T-T_c)(T-T'_c)+C_FC_A(\lambda'_{FA})^2(1-\alpha^2)\}} \tag{C–9b}$$

where T_c and T_c' are determined by alternate choice of sign in equation (C–6). Specifically,

$$T_c \simeq \tfrac{1}{4}C_A\lambda_A + 4C_F C_A(\lambda'_{FA})^2/(C_A\lambda_A - 2C_F\lambda_F)$$

$$T_c' \simeq \tfrac{1}{4}C_F\lambda_F, \qquad \text{(C–10)}$$

where the second term in the expression for T_c is now retained in order that equation (C–9a) be valid for $T \simeq T_c$. The average magnetization of the whole system,

$$\bar{\mathbf{M}} = \int_0^1 (\bar{\mathbf{M}}_F + \tfrac{1}{2}\bar{\mathbf{M}}'_A + \tfrac{1}{2}\bar{\mathbf{M}}''_A)P_\alpha \, \mathrm{d}\alpha.$$

Combining this expression with equation (C–9) and with $\bar{\mathfrak{H}}_{\mathrm{eff}} = H + \lambda_M \bar{\mathbf{M}}$, we get

$$\chi \equiv \frac{\bar{\mathbf{M}}}{H} \simeq \frac{C_A + p''C_F(T - \tfrac{1}{4}C_A\lambda_A)(T + \tfrac{1}{4}C_A\lambda_A - 2C_A\lambda''_{FA})}{T + \tfrac{1}{4}C_A\lambda_A - \lambda_M\{C_A + p''C_F(T - \tfrac{1}{4}C_A\lambda_A)(T + \tfrac{1}{4}C_A\lambda_A - 2C_A\lambda''_{FA})\}}$$

where

$$p'' \equiv \int_0^1 \frac{P_\alpha \, \mathrm{d}\alpha}{(T - T_c)(T - T_c') + C_F C_A(\lambda'_{FA})^2(1 - \alpha^2)} \qquad \text{(C–11)}$$

which for $T \simeq T_c$ (expressed by equation (C–10)) gives the same value of χ as equation (17), thus assuring first-order continuity. At very high temperatures, equation (C–11) reduces to the simple asymptotic expression given in equation (19).

APPENDIX D

In the configuration shown in Fig. 3(b), the anisotropy axis of the antiferromagnetic domains is now considered to be parallel to the external field. Hence, the total magnetic energy of this domain ensemble is expressed by equation (9) with the sign of the anisotropy term reversed. The equilibrium conditions obtained by setting $\partial E/\partial\theta$ and $\partial E/\partial\phi = 0$ are as follows:

$$\bar{\mathfrak{H}}_{FA}(\alpha \cos\theta \sin\phi - \sin\theta \cos\phi) + \bar{\mathfrak{H}}_{\mathrm{eff}} \cos\theta = 0$$

and

$$\bar{\mathfrak{H}}_{FA}(\alpha \sin\theta \cos\phi - \cos\theta \sin\phi) + \bar{\mathfrak{H}}_K \sin\phi \cos\phi = 0,$$

where time-averaged values ($\bar{\mathfrak{H}}_{FA} = \lambda'_{FA}\bar{\mathbf{M}}_A$, $\bar{\mathfrak{H}}_{\mathrm{eff}} = H + \lambda_M\bar{\mathbf{M}}$, $\bar{\mathfrak{H}}_K = 2N_A\bar{\mathfrak{K}}_A/\bar{\mathbf{M}}_F$) are used in order to extend the validity of these equations to higher temperatures. For the solution of these equations, other than $\cos\theta$ and $\cos\phi = 0$, we set $\cos\phi/\cos\theta \equiv \gamma$ and obtain

$$\sin\theta = \bar{\mathfrak{H}}_{\mathrm{eff}}\, x/\bar{\mathfrak{H}}_{FA}\gamma(x - \alpha^2) \qquad \text{(D–1a)}$$

$$\sin\phi = \bar{\mathfrak{H}}_{\mathrm{eff}}\, \alpha/\bar{\mathfrak{H}}_{FA}(x - \alpha^2) \qquad \text{(D–1b)}$$

where

$$x \equiv 1 - \bar{\mathfrak{H}}_K\gamma/\bar{\mathfrak{H}}_{FA},$$

which recombined with $1 - \sin^2\phi = \gamma^2(1 - \sin^2\theta)$ give

$$\bar{\mathfrak{H}}^2_{\mathrm{eff}} = \bar{\mathfrak{H}}^2_{FA}(\gamma^2 - 1)(x - \alpha^2)^2/(x^2 - \alpha^2) \qquad \text{(D–2a)}$$

$$\sin^2\theta = (\gamma^2 - 1)x^2/\gamma^2(x^2 - \alpha^2) \qquad \text{(D–2b)}$$

and

$$\sin^2\phi = (\gamma^2 - 1)\alpha^2/(x^2 - \alpha^2). \qquad \text{(D–2c)}$$

From these equations, we find that the saturation conditions, $\sin\theta$ and $\sin\phi = 1$, are attained when $\gamma = \bar{\mathfrak{H}}_{FA}/(\bar{\mathfrak{H}}_{FA}\alpha + \bar{\mathfrak{H}}_K)$ and

$$\bar{\mathfrak{H}}_{\mathrm{eff}} = \frac{\bar{\mathfrak{H}}^2_{FA}}{\bar{\mathfrak{H}}_{FA}\alpha + \bar{\mathfrak{H}}_K} - \bar{\mathfrak{H}}_{FA}\alpha. \qquad \text{(D–3)}$$

Thus, if $\bar{\mathfrak{H}}_K$ rises rapidly from zero with decreasing temperature, the external field required to retain these saturation conditions decreases and, in fact, goes to zero when

$$\bar{\mathfrak{H}}_K \geqslant H^2_{FA}/(\bar{\mathfrak{H}}_{FA}\alpha + \lambda_M\bar{\mathbf{M}}) - \bar{\mathfrak{H}}_{FA}\alpha.$$

It follows that if the cooling is done in a fixed external field, the minimum field required to saturate a given domain ensemble, whose α value we shall call α_0, is determined by equation (D–3) for $\bar{\mathfrak{H}}_K = 0$, i.e.,

$$\bar{\mathfrak{H}}_{\mathrm{eff}} \equiv H + \lambda_M\bar{\mathbf{M}} = \bar{\mathfrak{H}}_{FA}(1 - \alpha_0^2)/\alpha_0. \qquad \text{(D–4)}$$

It is clear from equation (D–4) that in this fixed field all the domain ensembles in the system, whose $\alpha \geqslant \alpha_0$, will be saturated, whereas those whose $\alpha < \alpha_0$ will not be. For the latter, we substitute $\bar{\mathfrak{H}}_K = 0$ and equation (D–4) into equation (D–1a), (D–1b) and (D–2a), and by eliminating γ we get

$$\sin\theta = \frac{1 - \alpha_0^2}{\{(1 - \alpha_0^2)^2 + (\alpha_0^2 - \alpha^2)(1 - \alpha_\theta^2\alpha^2)\}^{1/2}} \qquad \text{(D–5a)}$$

and

$$\sin\phi = \frac{(1 - \alpha_0^2)\alpha}{(1 - \alpha^2)\alpha_0}. \qquad \text{(D–5b)}$$

Using these equations, we compute θ and ϕ vs. α for different values of α_0, and the results are shown in Fig. 14. This figure clearly demonstrates the rapidity with which ϕ decreases from 90° to 0 as α drops below α_0, in contrast to the more gradual decrease of θ (especially when α_0 is small).

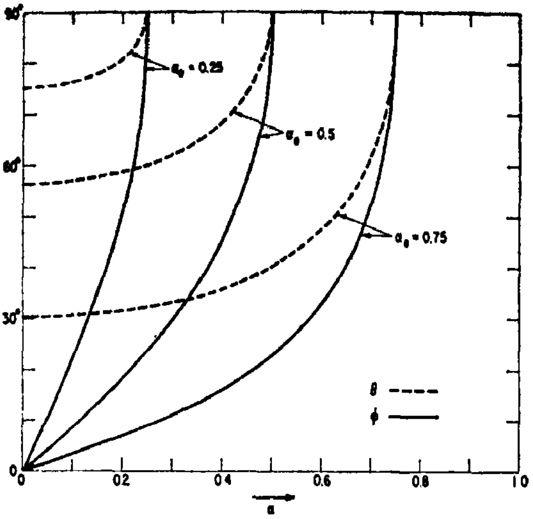

FIG. 14. θ and ϕ vs. α for different values of α_0. For $\alpha \geqslant \alpha_0$, θ and $\phi = 90°$.

Hence, without much loss in accuracy, we can ignore any partial alignment of the antiferromagnetic domain moments parallel (and antiparallel) to the field in all the domain ensembles with $\alpha < \alpha_0$, so that the growth of $\mathfrak{H}_K$ at very low temperatures will stabilize these ensembles in the ground state configuration shown in Fig. 3(a). By the same token, all the domain ensembles with $\alpha \geqslant \alpha_0$ will become stabilized in the field-cooled configuration shown in Fig. 4(a), and we will now consider the contribution of these ensembles to the low-temperature magnetization in an external field H applied parallel to the direction of field-cooling. In this direction, there will also be a fixed exchange field $H_{FA}\alpha$ on the ferromagnetic domains of each of these ensembles, resulting from the coupling with the antiferromagnetic domains whose moments are assumed to be held rigidly along the axis of $\mathfrak{H}_K$. If the effect of the coupling between different ensembles is also included, the total field on the ferromagnetic domains of a given ensemble will be $H+\lambda_M M+H_{FA}\alpha$. Moreover, the magnetizations of these domains will orient themselves parallel to this total field. It therefore follows that for a given external field, the condition

$$H+\lambda_M M+H_{FA}\alpha = 0 \qquad \text{(D–6)}$$

defines a particular value of α, whereby the ensembles with α larger or smaller than this value will have their ferromagnetic domain moments parallel or antiparallel, respectively, to the direction of the field applied during cooling. Hence, the total average magnetization in this direction will be

$$M = M_F \int_{\alpha}^{1} P_\alpha \, \mathrm{d}\alpha - M_F \int_{\alpha_0}^{\alpha} P_\alpha \, \mathrm{d}\alpha \qquad \text{(D–7)}$$

since only the ensembles with $\alpha \geqslant \alpha_0$ are involved in this process. From equations (D–6) and (D–7) we find that as α is increased from α_0 to 1, M decreases from its remanence value,

$$M_R = M_F \int_{\alpha_0}^{1} P_\alpha \, \mathrm{d}\alpha, \qquad \text{(D–8)}$$

to $-M_R$, and H decreases from $-H_{FA}\alpha_0-\lambda_M M_R$ to $-H_{FA}+\lambda_M M_R$. Since $|M|$ cannot exceed $|M_R|$, it is obvious that for $H > -H_{FA}\alpha_0-\lambda_M M_R$ and $H < -H_{FA}+\lambda_M M_R$, M is constant at M_R and $-M_R$, respectively. Thus, the curve of M vs. H is asymmetrical with respect to the origin, its shape depending sensitively on the distribution function P_α and on λ_M.

The unidirectional anisotropy energy $U_{1(H)}$ is defined as the area enclosed between the asymmetrical magnetization curve and the M axis for $-M_R < M < M_R$. Therefore, according to the above discussion,

$$U_{1(H)} = -2M_R H_1 + \int_{H_2}^{H_1} (M+M_R) \, \mathrm{d}H,$$

where $H_1 \equiv -H_{FA}\alpha_0-\lambda_M M_R$ and $H_2 \equiv -H_{FA}+\lambda_M M_R$. By means of equations (D–6)–(D–8), this expression is readily transformed to

$$\frac{U_{1(H)}}{2M_F} = H_{FA} \int_{\alpha_0}^{1} \left\{ \alpha_0 P_\alpha + \int_{\alpha}^{1} P_\alpha \, \mathrm{d}\alpha \right\} \mathrm{d}\alpha$$

$$+\lambda_M M_F \int_{\alpha_0}^{1} P_\alpha \left\{ \int_{\alpha_0}^{1} P_\alpha \, \mathrm{d}\alpha - 2\int_{\alpha}^{1} P_\alpha \, \mathrm{d}\alpha \right\} \mathrm{d}\alpha,$$

which by virtue of the general identities,

$$\alpha_0 \int_{\alpha_0}^{1} P_\alpha \, \mathrm{d}\alpha = -\left[\alpha \int_{\alpha}^{1} P_\alpha \, \mathrm{d}\alpha \right]_{\alpha_0}^{1} = \int_{\alpha_0}^{1} \alpha P_\alpha \, \mathrm{d}\alpha$$

$$- \int_{\alpha_0}^{1} \int_{\alpha}^{1} (P_\alpha \, \mathrm{d}\alpha) \, \mathrm{d}\alpha$$

and

$$\left\{ \int_{\alpha_0}^{1} P_\alpha \, \mathrm{d}\alpha \right\}^2 = -\left[\left\{ \int_{\alpha}^{1} P_\alpha \, \mathrm{d}\alpha \right\}^2 \right]_{\alpha_0}^{1}$$

$$= 2\int_{\alpha_0}^{1} P_\alpha \int_{\alpha}^{1} (P_\alpha \, \mathrm{d}\alpha) \, \mathrm{d}\alpha,$$

reduces simply to equation (27a).

Let us now consider a ΔM vs. H curve of the type shown in the lower part of Fig. 10, where for simplicity we suppose that the system has been cooled in two slightly different fields which according to equation (D-4) give rise to two slightly different values of α_0. Using equations (D-7) and (D-8), we express the difference in magnetization at a given field as

$$\Delta M = 2M_F \int_{\alpha''}^{\alpha'} P_\alpha \, \mathrm{d}\alpha - \Delta M_R.$$

Since α' and α'', which are the α values for the system under these two conditions, will be taken to be arbitrarily close, we may write

$$\int_{\alpha''}^{\alpha'} P_\alpha \, \mathrm{d}\alpha \simeq (\alpha' - \alpha'')P_\alpha.$$

Furthermore, since the field is fixed, it follows from equation (D 6) that

$$H_{FA}(\alpha' - \alpha'') = \lambda_M \Delta M,$$

which combined with the previous two expressions gives

$$\Delta M \simeq -\Delta M_R H_{FA}/(H_{FA} - 2\lambda_M M_F P_\alpha). \quad \text{(D-9)}$$

Thus, if $\lambda_M \to 0$, ΔM will have a minimum value lower than $-\Delta M_R$. The shaded area shown with respect to one of the ΔM vs. H curves in Fig. 10 corresponds dimensionally to an energy which can be written as

$$U_{\Delta M} \equiv \int_{H_2}^{H_1} (-\Delta M - \Delta M_R) \, \mathrm{d}H,$$

where again $H_1 = -H_{FA}\alpha_0 - \lambda_M M_R$ and $H_2 = -H_{FA} + \lambda_M M_R$. Using equation (D-9) and the relationship $\mathrm{d}H \simeq -(H_{FA} - 2\lambda_M M_F P_\alpha)\,\mathrm{d}\alpha$ obtained by differentiation of equations (D-6) and (D 7), we convert the above equation to

$$U_{\Delta M} \simeq 2\lambda_M M_F \Delta M_R \int_{\alpha_0}^{1} P_\alpha \, \mathrm{d}\alpha,$$

which by virtue of equation (D-8) reduces to equation (29).

REFERENCES

1. Kouvel J. S., *J. Phys. Chem. Solids* **21**, 57 (1961).
2. Kouvel J. S., *J. appl. Phys. Suppl.* **31**, 142 (1960).
3. Owen J., Browne M. E., Knight W. D. and Kittel C., *Phys. Rev.* **102**, 1501 (1956); Owen J., Browne M. E., Arp V. and Kip A. F., *J. Phys. Chem. Solids* **2**, 85 (1957).
4. Schmitt R. W. and Jacobs I. S., *Canad. J. Phys.* **34**, 1285 (1956); *J. Phys. Chem. Solids* **3**, 324 (1957); Jacobs I. S. and Schmitt R. W., *Phys. Rev.* **113**, 459 (1959).
5. Lutes O. S. and Schmit J. L., *Phys. Rev.* **125**, 433 (1962).
6. Street R. and Smith J. H., *J. Phys. Radium* **20**, 18 (1959).
7. Kouvel J. S., Graham C. D. Jr. and Jacobs I. S., *J. Phys. Radium* **20**, 198 (1959); Kouvel J. S. and Graham C. D. Jr., *J. appl Phys. Suppl.* **30**, 312 (1959); *J. Phys. Chem. Solids*, **11**, 220 (1959).
8. Kouvel J. S., *J. Phys. Chem. Solids* **16**, 107 (1960).
9. Meiklejohn W. H. and Bean C. P., *Phys. Rev.* **102**, 1413 (1956); **105**, 904 (1957).
10. Ruderman M. A. and Kittel C., *Phys. Rev.* **96**, 99 (1954).
11. Hart E. W., *Phys. Rev.* **106**, 467 (1957); Yosida K., *ibid.*, **106**, 893 (1957); **107**, 396 (1957).
12. Fisher J. C., as reported in Refs. 3 and 4.
13. Dekker A. J., *Physica* **14**, 697 (1958).
14. Meiklejohn W. H., *J. appl. Phys. Suppl.* **33**, 1328 (1962).
15. Kouvel J. S. and Graham C. D., Jr., unpublished torque data on Cu–Mn and Co–Mn alloys.
16. Jacobs I. S., Kouvel J. S. and Lawrence P. E., *J. phys. Soc. Japan* **17**, (Suppl. B-1), 157 (1962).

J. Phys. Chem. Solids Pergamon Press 1963. Vol. 24, pp. 823–834. Printed in Great Britain.

THERMOLUMINESCENCE AND THE RELATION BETWEEN THERMAL AND OPTICAL ACTIVATION ENERGIES IN DIAMOND

J. NAHUM* and A. HALPERIN

Department of Physics, The Hebrew University of Jerusalem, Jerusalem, Israel

(*Received* 13 *December* 1962)

Abstract—Glow curves were recorded for diamonds of types I and II(a) and the features characteristic to each of the types are pointed out.

Thermal activation energies were determined from the various glow peaks and were compared with the optical energies obtained from the spectral response curves for optical bleaching of the glow peaks and from the photoconductivity response curves.

For type II(a) diamonds the thermal energies were found to be equal to the optical energies (up to 1·5 eV). In the case of type I diamonds the thermal energies were comparatively lower and the ratio $E_{\text{optical}}/E_{\text{thermal}}$ varied between 1·5 and 2·5 depending on the glow peak involved.

INTRODUCTION

Diamonds were known for a long time to exhibit thermoluminescence. Only a few papers, however, were published on this subject. Chandrasekharan[1] reported that blue fluorescent diamonds emit a blue glow at 540°K. Bull and Garlick[2] have observed two glow-peaks, a weak one near 400°K and a strong peak at 520°K, with activation energies of 0·5 and 0·7 eV respectively.

Activation energies for diamonds were measured by different authors using various methods. A summary of the measured energies and the methods used was given recently by Urlau *et al.*[3] Most of the energies were measured by the indicated experimental observations and values obtained by one method could not be correlated with those obtained by other methods. Of special interest in the present work is the relation between the thermal and optical activation energies. Champion[4] has assumed an optical/thermal ratio of about 2·5 for diamond and has built an energy-level scheme based on this assumption.

Thermoluminescence measurements provide the thermal activation energies and as will be shown below also enable correlation with the optical energies. In a previous paper,[5] we have reported on some properties of semiconducting, or type II(b) diamonds,[6] in which case the thermal energies were found to be *equal* to the optical ones. It was of interest, therefore, to extend the investigation to type I and type II(a) diamonds, which was the aim of the present work. In addition to the glow curves and their characteristics, the measurements included the spectral response of the photoconductivity, optical bleaching of the glow peaks and optical absorption of the diamonds. The combination of the various observations provided a good correlation between the optical and thermal energies. For type II(a) diamonds the optical energies were found to be equal to the thermal ones, while for type I the ratio optical/thermal was found to be higher than one.

EXPERIMENTAL

Experimental arrangements were similar to those described previously.[5] In brief, glow curves were recorded with the crystal mounted in a vacuum cryostat, which served also for the photoconductivity measurements. An E.M.I. 6256B photomultiplier was used as a detector with its photocathode less than 1·0 cm away from the crystal. This set-up enabled us to record glow curves even of diamonds showing a comparatively weak glow. A rate of heating of about 15°/min was used in all the thermoluminescence experiments.

---

* Detached from the Israel Atomic Energy Commission.

The diamonds were excited by u.v. radiation. In some of the experiments this was obtained from a Hg-light-source through a u.v. transmitting filter. In most of the measurements, however, the thermoluminescence was excited with monochromatic light of about 20 Å spectral width, and still narrower spectral bands were used in some of the thermoluminescence excitation spectra to secure the high resolution needed to reveal the fine structure. The monochromatic light was obtained from a Hanovia type 507C, 800W xenon compact arc lamp in conjunction with a Beckman DU monochromator.

Absorption measurements were taken with a Beckman DK spectrophotometer. In these measurements the crystal was mounted in another vacuum cryostat designed to fit the spectrophotometer.

A Keithley model 410 electrometer with a Leeds and Northrup recorder were used for the photoconductivity measurements. Electrical contacts to the crystal were made with high temperature conducting silver paint. Both the electrodes were painted on the same side of the crystal on which the exciting radiation was incident. The u.v. excitation was obtained in the same way as for the thermoluminescence experiments. In the infrared region, a 100W zirconium arc lamp replaced the xenon source.

RESULTS

(a) *Glow curves*

Glow curves of all the examined diamonds (6 type I and 5 type II(a) specimens) exhibited a variety of peaks throughout the whole temperature range of 80–600°K. Both, type I and type II(a) diamonds, showed large variations in relative intensities of the various peaks from one specimen to another. Nevertheless, the character of the thermoluminescence was different for the different types of diamond.

Figure 1 shows a few typical examples of glow curves. The thermoluminescence in this case has been excited with Hg-light filtered with a Wratten 18a filter (transmitting 300–400 mμ with a maximum at 360 mμ). Curve a gives the glow curve of a type I diamond (specimen T1). It shows broad peaks, appearing as an almost continuous glow, weak at low temperature and growing stronger above room temperature with the main peak at 525°K. Occasionally a type I diamond had somewhat stronger peaks below room temperature.

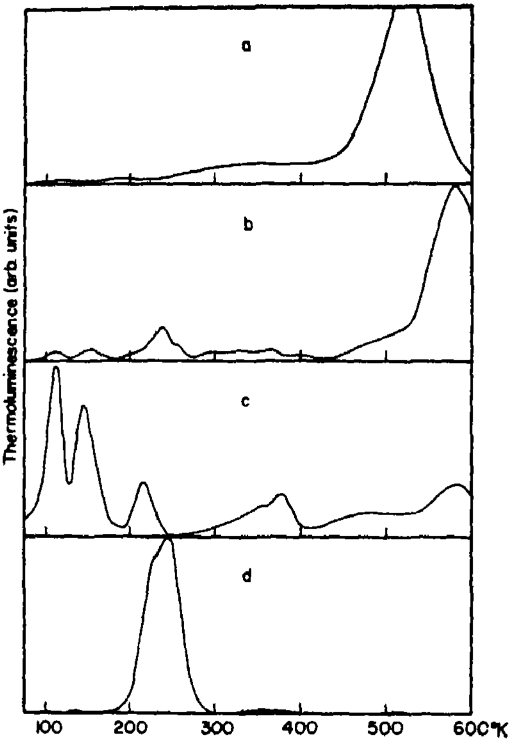

FIG. 1. Glow curves. a—type I diamond (T1), b—type II(a) (P11), c—type II(a) (T5), and d—a type (IIb) diamond.

Curves b and c are for two type II(a) diamonds, chosen to demonstrate the differences in glow curves of specimens of the same type. In spite of the large differences, all type II(a) diamonds had a few features in common by which they differed from type I. The characteristic features were as follows:

(a) The appearance of sharp and almost separated peaks in the glow curve was found to be typical to type II(a) diamonds, while broad overlapping peaks forming almost a continuous glow were observed in all the examined type I specimens. (b) The low temperature glow peaks of type II(a) were stronger compared to those of type I. For instance, specimen T5 (type IIa) showed three sharp intense peaks at low temperatures (at 113, 150 and 217°K), while the glow of T1 (type I) in the same temperature range was much weaker. (c) Type II(a) usually had a strong peak near 600°K instead of the peak at 525°K in type I. (d) The thermal activation energies of the glow peaks appearing in the same temperature region were found to be higher for the type II(a) compared to those of type I (see Fig. 6).

Curve *d* (Fig. 1) gives for comparison the glow curve of type II(b) diamonds, which was found⁽⁵⁾ to be identical for the two specimens examined, but to differ entirely from those of the other types. In this case the glow was obtained after excitation with 225mμ light.

On excitation at 80°K the glow peaks in type I diamonds below room temperature were found to saturate under exposures of only a few minutes, while the main peak at 520°K did not fully saturate even under exposures of about 4 hr. Because of the very low absorption of type II(a) in the region of the used excitation (mainly 366 mμ), even the low temperature glow peaks of these specimens were difficult to saturate.

Strong blue–green phosphorescence was observed at room temperature in those specimens which showed strong glow peaks near room temperature (300–400°K). This phosphorescence seems to be caused by thermal release of the carriers from the traps related to the glow peaks near room temperature. This view is further supported by the fact that the excitation spectrum for the phosphorescence at room temperature was found to follow exactly that of the thermoluminescence below 400°K (see Fig. 2d).

b. *Excitation spectra*

Excitation spectra for a few glow peaks are given in Fig. 2. The points in the curves were obtained separately for each wavelength, keeping the light intensity and the time constant for all wavelengths. Curve a is the excitation spectrum for the peak at 240°K of type II(b) (see Fig. 1d). It shows a sharp maximum at 225mμ with an abrupt fall towards longer wavelengths. The fall towards longer wavelengths seems to go in parallel with the u.v. absorption⁽⁵, ⁷⁾ which at 80°K showed a sharp edge at 225 mμ and no absorption at longer wavelengths near the edge.

Curve *b* describes the excitation spectrum for the peaks below room temperature (at 110, 150, and 210°K) of specimen T5 (type II(a), see Fig. 1c). The main maximum appears now at about 227 mμ with a sharp fall towards shorter wavelengths. The interesting features of curve b are the minima (or inverted maxima) at 230, 236 and 240 mμ which occur exactly at the wavelengths of the absorption bands and the main maxima in the luminescence excitation spectra⁽⁸⁾ near the absorption edge.

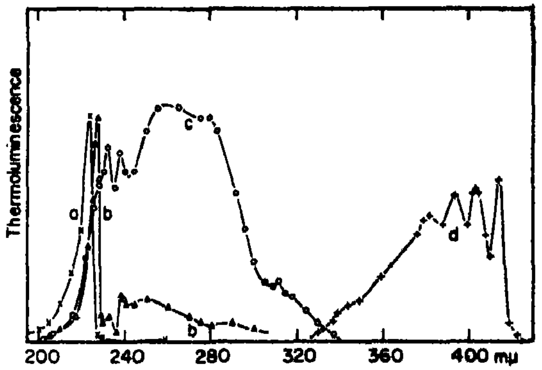

FIG. 2. Excitation spectra for different glow peaks. a—240°K peak of II(b) diamonds, b—110, 145 and 210°K peaks of T5 (IIa), c—525°K peak of T1 (I), and d—400°K peak of T1).

Changing the wavelength of the exciting light was often found to excite different glow peaks in the same specimen. Figure 3 gives two glow curves of specimen T1 (type I) excited with the same light-sum but with different wavelengths. Curve a which was excited with 415 mμ shows an almost pure peak at about 400°K, while on excitation with 330 mμ the main peak appears at 525°K (curve b). The 525°K peak becomes much stronger after excitation with still shorter wavelengths. Curves c and d of Fig. 2 give the excitation spectra for the peaks at 525 and 400°K respectively. Curve c showed a broad main maximum at about 265 mμ which seems to be associated with the nitrogen bands⁽⁹⁾ of type I diamonds. The minima which appeared in curve b near the edge were also obtained in curve c in spite of the strong secondary absorption in this region up to 290 mμ.

The excitation spectrum for the peak at 400°K (Fig. 2d) is quite different. It follows exactly the so-called 415 mμ absorption system,(4) and the steady luminescence excitation spectrum.(18) This implies that the glow peak under consideration is directly related with absorption in the 415 mμ system. Figures 2(c) and (d) were obtained on excitation at 80°K. Excitation at room temperature gave similar curves.

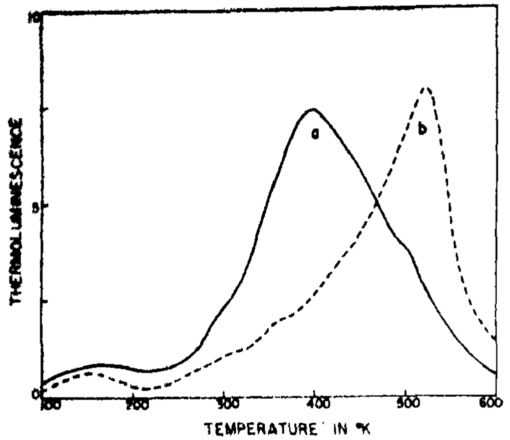

Fig. 3. Glow curves of the same diamond (type I) excited for 3 min at 80°K with light of the same intensity but different wavelengths: a—415 mμ; b—330 mμ.

As mentioned above, the excitation spectrum for the phosphorescence at room temperature was the same as that in Fig. 2(d). Qualitatively this has already been reported by Chandrasekharan,(1) who found that u.v. below 3000 Å was less effective in exciting the phosphorescence at room temperature than u.v. of longer wavelengths.

c. *Thermal activation energies*

Activation energies of various glow peaks were measured by the initial rise method(10) and also from the shape of the peaks.(10) The method of initial rise was used repeatedly on the same glow throughout the whole temperature range 80–650°K. Often, some sixty "initial rise" curves were recorded over the whole temperature range of the glow for specimens which showed an intense glow.

Results from such sets of measurements are summarized in Fig. 4 and Fig. 5 for type I and II(a) diamonds respectively. Each experimental point in these figures corresponds to an activation energy value computed from an "initial rise" curve, and different notations of the experimental points were used for different specimens. Only points obtained from 3 specimens of each type are given in Figs. 4 and 5, but similar results were obtained also with other specimens.

It can be seen in Fig. 4 that the activation energies for type I diamond are about 0·12 eV at 180°K and increase with temperature up to 1 eV above 500°K. The overlapping peaks characterizing the glow curves of type I introduced some uncertainty at temperatures near transitions from one main peak to another. Nevertheless, several values of activation energies typical to type I diamonds can be deduced. These are: 0·12 eV below 200, 0·4–0·5 at 300–400, 0·8 at 450, and about 1 eV near 520°K. For a given temperature range, the activation energies differ to some extent from one type I specimen to another.

Figure 5 shows that type II(a) diamonds are

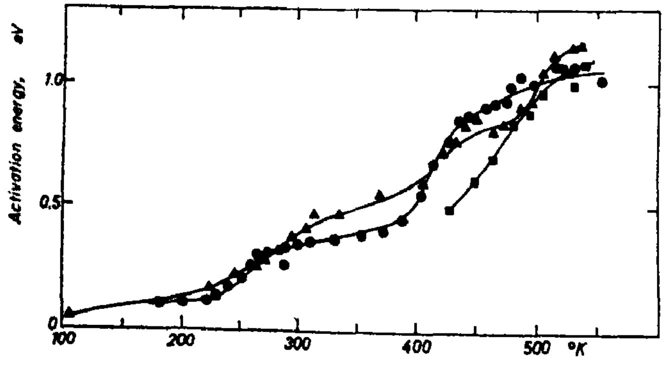

Fig. 4. Thermal activation energies for the temperature region 100–600°K for three type I diamonds: T1 (circles), T3 (triangles) and J3 (squares).

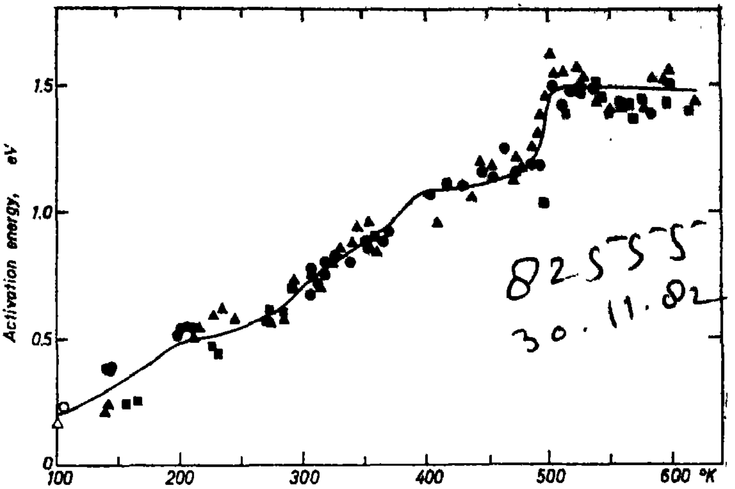

82-5-5-5
30.11.82

FIG. 5. As Fig. 4 for three type II(a) diamonds. T5 (circles), H3 (triangles) and T4 (squares).

characterized by higher thermal activation energies compared to type I. Values as high as 0·2 eV were obtained at 100°K, and the activation energies increased up to 1·5 eV at 500°K. In contrast with type I specimens the scattering in activation energies of different type II(a) diamonds was found to be small for temperatures above 200°K (see Fig. 5). The clear steps on the curve of Fig. 5 indicate the existence of discrete values of activation energies. Thus, an activation energy of about 0·55 eV is obtained at 200–300°K, about 1·2 eV is obtained at 400–480°K and a value of 1·5 eV at about 500°K. This remains nearly constant up to 620°K. Curves I, II and IIb of Fig. 6 give for comparison the activation energies throughout the temperature range of 100–600°K for type I, II(a) and II(b) diamonds respectively. The high activation energies of type II(a) compared to those of type I are evident.

For resolved and "cleaned" peaks,(10) activation energies were computed also by the method based on the shape of the glow peaks.(10) By this method activation energies for first order kinetics are given by the formula:

$$E_1 = (1{\cdot}72/\tau)\, kT_g^2(1-2{\cdot}58\Delta), \qquad (1)$$

and for second order kinetics by:

$$E_2 = (2/\tau)\, kT_g^2(1-3\Delta), \qquad (2)$$

where k is Boltzmann's constant, T_g is the peak temperature, $\tau = T_g - T_1$, with T_1 the half intensity temperature at the low temperature side of the peak, and $\Delta = 2kT_g/E$ is a correction factor usually small compared to one. Formulae (1) and (2) assume excitation into either the conduction or the valence band but not to an excited level within the forbidden band. As will be seen, photoconductivity measurements and other arguments to be discussed below justify this assumption.

Some examples of the calculated activation energies typical to type I, IIa and IIb diamonds are given in Table I. Values obtained by the

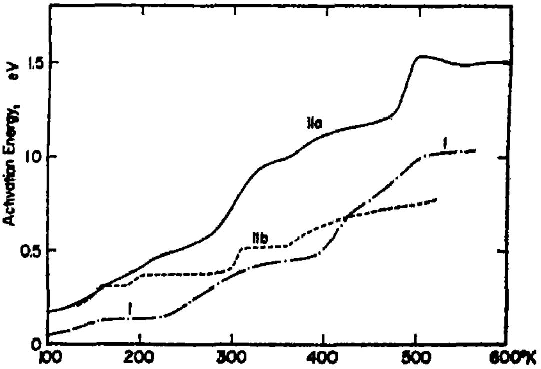

FIG. 6. Thermal activation energies for diamonds of types I, II(a) and II(b).

Table 1. Typical examples of activation energies for glow peaks of type I, *type* II(a) *and type* II(b) *diamonds as computed by the method of initial rise* (E_i), *and from formulae* (1) *and* (2), (E_1 *and* E_2 *respectively*). *For the meaning of the other parameters see text.*

Serial Number	Diamond type	T_g(°K)	μ_g	τ(°K)	Δ	E_1(eV)	E_2(eV)	E_i(eV)	Specimen
1	I	553	0·46	30	0·1	1·07	1·18	1·00	T1
2	I	559	—	33	0·1	0·91	1·01	0·92	T2
3	I	558	0·51	30	0·09	1·16	1·28	1·06	T3
4	I	564	0·43	33	0·1	1·05	1·15	0·99	J3
5	II(a)	108	0·57	9·2	0·12	0·13	0·14	0·16	H3
6	II(a)	113	0·55	8·2	0·08	0·18	0·20	0·23	T5
7	II(a)	150	0·45	11·5	0·12	0·20	0·22	0·21	H3
8	II(a)	151	0·52	9·6	0·07	0·29	0·33	0·37	T5
9	II(a)	217	0·48	11·7	0·07	0·49	0·55	0·55	T5
10	II(a)	375	0·46	19·2	0·08	0·08	0·89	0·88	H3
11	II(a)	373	0·49	19·5	0·07	0·88	0·95	0·86	T5
12	II(a)	563	0·53	29·0	0·06	1·36	1·53	1·50	T5
13	II(b)	140	—	11·6	0·11	0·17	0·19	0·21	I
14	II(b)	252	0·51	18·6	0·11	0·36	0·39	0·37	I

initial rise method (E_i) for the same glow peaks are also given for comparison. The first four lines in Table I give the values calculated for the main peak at 525°K of type I specimens. All the peak temperatures (T_g) appearing in Table I for this glow peak are above 550°K. This was caused by the effective cleaning of the peak which bleached away more than 95 per cent of the 525°K glow, leaving only a comparatively weak component above 550°K.

As already mentioned, the glow of type II(a) diamonds is characterized by the appearance of sharp peaks: their calculated activation energies are given in examples 5–12 of Table 1 for H3 and T5 specimens (type IIa). At low temperatures the activation energies of T5 are higher than those of the respective peaks of H3. Thus, 0·37 eV is obtained at 150°K for T5 compared to only 0·21 eV for the same peak for H3. These differences disappeared above 200°K for type II(a) diamonds (see Fig. 5).

The last two lines in Table 1 give for comparison the computed activation energies for the glow peaks at 140 and 240°K of type II(b) diamonds.

Comparison of E_1 and E_2 to the E_i values shows a better agreement between E_2 and E_i for type II(a) and II(b) diamonds, whereas for type I diamonds the E_1 values agree better to E_i. This seems to indicate a second order process for the glow of type II(a) and II(b) diamonds, while that of type I specimens seems to be of first order. The high values of the symmetry factor* μ_g obtained for II(a) and II(b) specimens (see Table 1) also support the bimolecular character of the process.(11) For another check of the order of the kinetics, the recorded peaks were replotted as: (a) ln I, (b) ln(I/n), and (c) ln(I/n^2) vs. $1/T$, where I is the thermoluminescence intensity and n the concentration of full traps at the temperature T. The ln(I/n) curve should form a straight line in case of first order kinetics, while ln(I/n^2) should do it when the kinetics is of second order.

A set of such curves for the glow peak of T5 at 150°K is given in Fig. 7(1), and for that of T1 at 550°K is given in Fig. 7(2). Again, the glow peak of T5 appears to be of second order, while the behavior of T1 (type I) fits a first order process.

d. *Optical bleaching of the glow peaks*

For these measurements the diamonds were first excited with u.v. light. Then, before recording the glow curve, the excited specimen was irradiated with monochromatic infrared light. Infrared of suitable wavelengths was found to reduce

---

* $\mu_g = (w-\tau)/w$, where w is the half intensity width of the glow peak; see Ref. (11).

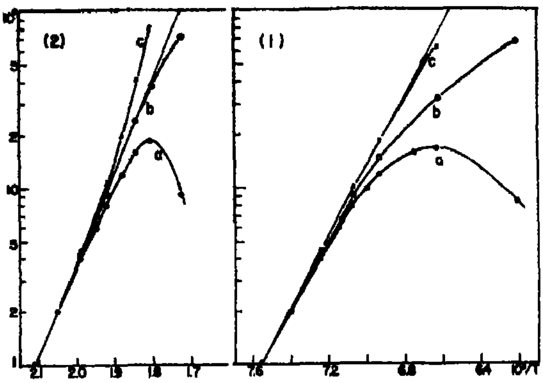

FIG. 7. Glow peaks of a type II(a) diamond at 150°K (curve 1), and of a type I diamond at 550°K (curve 2) plotted vs. 1/T with: (a) log I, (b) log (I/n), and (c) log (I/n^2) in the ordinate.

the intensity of the glow peaks compared to that obtained by the u.v. excitation alone. Repeating the measurements with the same u.v. excitation but with different infrared wavelengths gave the "bleaching spectra" for the various glow peaks. The light-sums of the infrared radiation was, of course, kept constant for all the wavelengths in a bleaching spectrum.

Curves a and b of Fig. 8 show the bleaching spectra for the glow peaks at 375 and 575°K of specimen H3 (type IIa), while that of the peak at 525°K of T1 (type I) is given by curve c. The thermal activation energy of the 375°K peak of T5 was found to be 0·92 eV (see Fig. 5). We see now that 1·35μ (0·92 eV) is just the long wavelength limit for optical bleaching of this glow peak. For the glow peak at 575°K we obtain (Fig. 8b) a wavelength limit of about 0·85μ (1·46 eV), which fits well its thermal activation energy of 1·5 eV. It is worthwhile to note that the glow peaks below room temperature were bleached entirely even by the longest wavelength used in the present experiments (2μ, 0·62 eV).

In spite of the low thermal activation energy of only 1 eV for the peak at 525°K of type I diamonds its bleaching spectrum (Fig. 8c) was found to fit that of the high temperature peak of type II(a) (Fig. 8b). The glow peaks at about 400°K and below room temperature of type I could also be bleached by infrared radiation but their exact

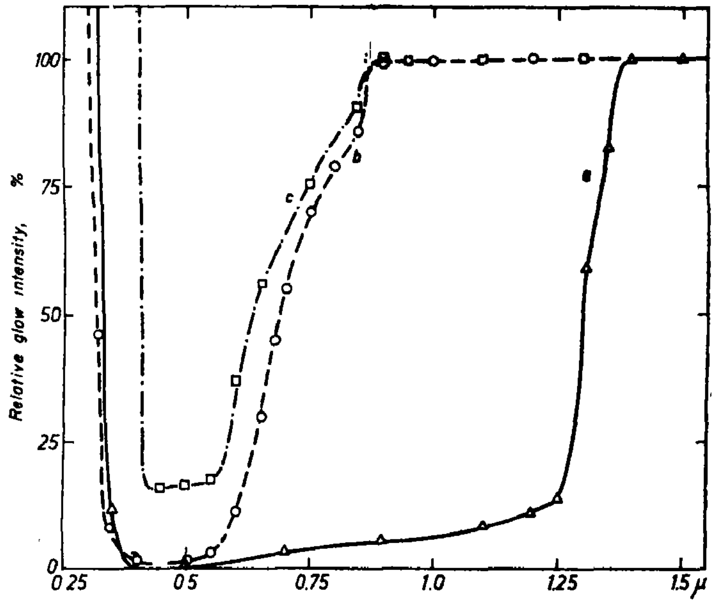

FIG. 8. Infrared bleaching spectra: (a) for the glow peak of specimen H3 (type IIa) at 375°K, excited with 280 mμ; (b) For the glow peak of the same diamond at 575°K, excited with 300 mμ; (c) For the glow peak of T1 (type I) at 525°K, excited with 290 mμ. The 100 per cent intensity corresponds to that obtained without infrared iradation.

bleaching spectra could not be determined accurately because of the comparative weakness and the complex structure of the glow (see Fig. 1a).

A common feature of the optical bleaching experiments was that all the glow peaks of diamonds, irrespective of their activation energies were effectively bleached by irradiation in the spectral range of 0·4–0·6μ ($\sim$ 3–2 eV). This is in accordance with Chandrasekharan's observation that blue fluorescent diamonds, previously excited at room temperature, gave rise to blue emission when irradiated by light of wavelength longer than 0·42μ and that 0·55μ radiation was most effective in producing this emission. We found, however, that shorter wavelengths down to 0·35 μ were still effective in bleaching the glow peaks of type II(a) specimens (curves a, and b of Fig. 8). The difference between type I and II(a) in the shorter wavelength limit results from the differences in the respective excitation spectra (see curves b and c, Fig. 2).

e. *Photoconductivity*

Excitation of photoconductivity by u.v. using the same specimens as in the present work, has been described elsewhere.(8) In the present work we shall describe some experiments on the infrared excited photoconductivity of specimens previously excited by u.v. light. In this case the infrared releases trapped carriers. One can then expect a correlation to exist between the optical energies obtained from the excitation of the photoconductivity, and the thermal energies obtained from thermoluminescence. This will be shown below.

Figure 9 gives an example of a set of measurements with specimen T5 (type IIa). In this case u.v. of 227 mμ was used for previous excitation. Starting from the longer wavelength end, 2μ in the present experiments, the photoconductivity was recorded while scanning the spectrum. The monochromator slit was kept constant during the scan, but the curves of Fig. 9 were drawn with the proper correction for the change in the intensity of the monochromatic light with wavelength. Curve a was obtained at 80°K soon after excitation with u.v. The crystal was then warmed up to 300°K and cooled back to 80°K, when curve b has been taken. A subsequent measurement at 80°K after warming to 425°K gave curve c, and another, after warming up the crystal to 575°K, resulted in curve d.

In the low energy range of the present measurements curve a indicated the presence of trapping levels with energies 0·65–0·9 eV (1·9–1·4 μ). At higher energies the curve rises nearly smoothly except for some indication of a maximum near 1·5 eV (about 0·8 μ).

A clearer correlation between the photoconductivity and the trapping levels involved is obtained from the other curves of Fig. 9. Warming up to room temperature empties all the shallow trapping levels up to those which give the thermoluminescence above room temperature. At the same time the photoconductivity for $\lambda > 1 \cdot 4\ \mu$ (0·9 eV) is completely eliminated (Fig. 9b). This fits well the thermal activation energy of nearly 0·9 eV calculated for the glow peaks of type II(a) just above room temperature (see Fig. 6). Similarly warming to 425°K (Fig. 9c) the lowest energy producing photoconductivity is 1·24 eV (1·0 μ) compared to nearly 1·2 eV of the thermal energy. Finally, warming to 575°K leaves only the glow

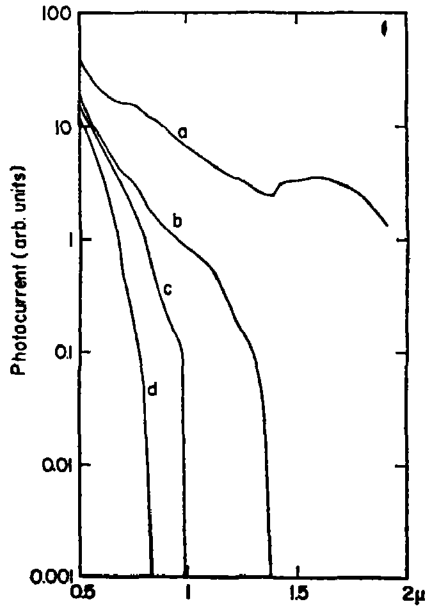

FIG. 9. Photoconductivity at 80°K of a u.v. excited type II(a) diamond (T5): a—the crystal was not warmed above 80°K after excitation, b, c, d—the crystal was annealed by warming to 300, 425, 575°K respectively.

peak at 590°K with a thermal activation energy of 1·5 eV, which fits well the limit for photoconductivity (0·83 μ), 1·5 eV) as obtained from curve d.

Similar experiments with type I diamonds gave nearly the same energy thresholds for the photoconductivity. Obviously, previous u.v. excitations at different temperatures should give rise to different limits for the photoconductivity. This is shown in Fig. 10 for specimen T3 (type I). Each curve in Fig. 10 was obtained after a separate u.v. excitation with 265 mμ at a given temperature. The photoconductivity curves were recorded continuously and corrected for the dependence of the intensity of the light on wavelength as before. Curve a was taken at 80°K after previous excitation at this temperature. In the next run the crystal was excited at room temperature and then cooled to 80°K, when curve b has been taken. Similarly, excitations at 420 and 540°K followed by subsequent cooling to 80°K resulted in curves c and d respectively. In another measurement the crystal was heated up to 640°K and cooled down to 80°K, when curve e was obtained.

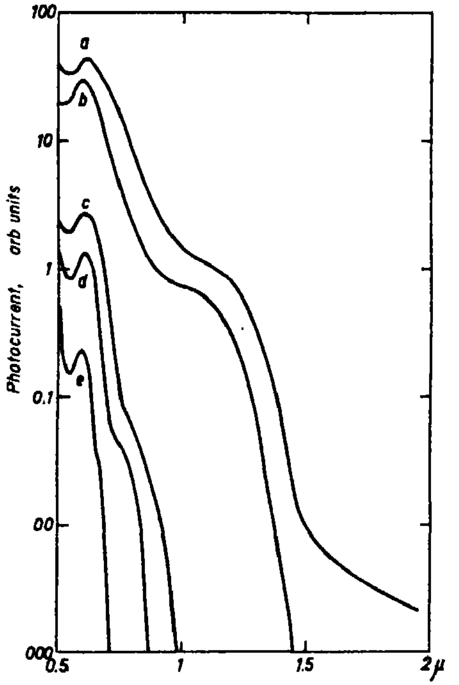

Fig. 10. Photoconductivity at 80°K of a type I diamond (T3) excited at different temperatures: (a)—80, (b)—300, (c)—420 and (d)—540°K. Curve e was obtained again at 80°K, but after annealing the crystal at 640°K.

It follows from curve a that on excitation at 80°K even shallow trapping levels with energies down to the limit of our experiments (~ 0·6 eV) are filled. Excitation at room temperature, however, filled only levels of energies above 0·86 eV and hence no photoconductivity was revealed below 1·45 μ (0·86 eV, curve b). This value is much higher than the corresponding thermal activation energy (~ 0·4 eV) of type I specimens just above room temperature (Fig. 6), but is in good agreement with the threshold energy in type II(a) (see Fig. 9b). Similarly, excitation at 420 and 540°K filled only trapping levels of higher energies as indicated by the photoconductive limits at 1 and 0·88 μ (1·2, 1·4 eV) respectively (curves c, d of Fig. 10). Again there is an agreement with the corresponding threshold energies in type II(a) diamonds (see curves c, d of Fig. 9), and again the optical thresholds are much higher compared to the respective thermal activation energies. Curve e shows that warming to 640°K eliminated the photocurrent down to 0·71 μ (1·75 eV).

Summing up, we conclude that in type I diamonds the optical energies associated with the trapping levels are higher than the corresponding thermal energies (by more than 50 per cent).

Of interest is the photoconductivity maximum at about 0·6 μ (~ 2·1 eV) shown clearly by the various curves of Fig. 10. This fits the value of 2·1 eV assigned by Urlau *et al.*[3] to an electron trapping level in diamond.

f. *Optical absorption*

All type I and II(a) diamonds examined showed a weak broad absorption band with some structure between 1·2–2·4 μ (about 1–0·5 eV). Another weak band was found at 0·8 μ (1·5 eV), and some diamonds showed also a band at 0·6 μ (2·1 eV).

Figure 11 describes these absorption bands for a type I (T1) and a type II(a) (H3) diamond. The absorption of a type II(b) diamond (C1) is given for comparison.

The origin of these absorption bands is still not clear. Their energies seem to fit well the optical energies for the release of trapped carriers as obtained in the present work. The absorption, however, did not change with the excitation of the crystal, which makes it difficult to correlate them with the trapping levels. It should be noted that absorption bands near 0·8 μ have already been reported previously.[6] It seems, however, that the bands observed in the present work between 1·2–2·4 μ have not been reported by earlier workers.

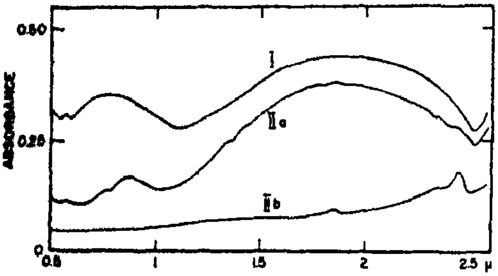

FIG. 11. Absorption spectra of type I, II(a) and II(b) diamonds (samples T1, H3 and C1 respectively) in the near infrared (0·5–2·5 μ).

DISCUSSION

The two peaks reported by BULL and GARLICK[2] were found in the present work to be the main peaks in the glow of type I diamonds. Many more peaks were observed in the present work, and for type II specimens the main glow was found to appear often below room temperature or near 600°K.

In spite of the large variations in the relative intensities of the various glow peaks when passing from one specimen to another, the thermoluminescence exhibited characteristic features by which diamonds of one type could be distinguished from those of other types.

The thermoluminescence excitation spectra (Fig. 2) warrant some discussion. The excitation spectrum for the glow peak below 400°K (curve d) was found to follow exactly the 415 mμ absorption system, which suggests that this peak is excited directly by absorption in the 415 mμ system. The same excitation spectrum was obtained also for the phosphorescence at room temperature, which indicates that the phosphorescence results from thermal release of carriers from the same trapping levels which produce the glow peak below 400°K.

The 520°K glow peak seems to involve quite different transitions as follows from its excitation spectrum (Fig. 2c). The minima which appear at 230, 236 and 240 mμ have already been discussed elsewhere.[12] Neglecting these minima there appears a broad maximum which extends from about 220 to 300 mμ. This seems to be related with the nitrogen bands characteristic to type I diamonds. It is interesting that the excitation spectrum of the typical type II(a) specimen T5 (Fig. 2b) also shows a band, though weak, in this region, which indicates that a very low concentration of nitrogen is present even in this diamond. The main excitation band in this case occurs, however, at about 225 mμ, which is typical for type II diamonds.

The optical energies were measured in the present work by two independent methods, namely from the infrared photoconductivity of excited crystals and from the bleaching of the glow peaks. Both types of measurements were carried out in such a way as to enable correlation with the thermal energies.

The action of infrared light on diamonds previously excited by u.v. has already been demonstrated by GUDDEN and POHL,[13] and was interpreted as due to the release of positive holes which became trapped during the u.v. excitation. URLAU *et al.*[3] have carried out various experiments, including measurements of the change of total charge while counting or photoconducting. From these experiments they concluded that *hole* trapping levels exist at 0·94 and 1·6 eV above the valence band. This fits fairly well our energies of 0·92 and 1·5 eV, which we assume, therefore, to be hole trapping levels above the valence band. Our experiments show clearly that the extra photocurrent in excited diamonds is directly connected with the trapping levels involved in the thermoluminescence. By partial thermal bleaching of the glow we were able to correlate directly each of the glow peaks with the photoconductivity due to the optical release of the carriers from the given trapping level.

Optical activation energies obtained from the bleaching spectra (Fig. 8) were in good agreement with those obtained from the photoconductivity of the u.v. excited diamonds (Figs. 9, 10). There is, however, some complication in the bleaching spectra for the high temperature glow peaks (Fig. 8 curves b and c). In both the curves bleaching starts at about 0·85 μ (1·46 eV). The bleaching at this wavelength is partial, and nearly full bleaching occurs only at 0·6 μ (~ 2·1 eV). It has already been suggested(3) that a trapping level for *electrons* 2·1 eV below the conduction band was present in diamond. The interpretation of the behavior of the bleaching curves (Fig. 8b and c) will then be as follows: light of about 0·8 μ has just the energy for releasing the trapped *holes* from the trapping level situated 1·5 eV above the valence band. Because of the comparatively low light-sums of the bleaching light the glow peaks were only partially bleached. On reaching the wavelength of 0·6 μ, however, the energy is enough to release *electrons* from the level at 2·1 eV below the conduction band. The free electrons help then to annihilate the still trapped positive holes, which results in a more effective bleaching.

The rise of the bleaching curves on the short wavelength end starts on approaching the energy region at which excitation occurs. The "excitation limit" for type I (Fig. 8c) appears at about 0·42 μ, while that for type II(a) diamonds which do not absorb until shorter wavelengths, appears near 0·3 μ.

One of the characteristics of type II(a) diamonds was the relative sharpness of their glow peaks compared to those of type I. Theoretically the width of a glow peak appearing at a given temperature should decrease with the reciprocal of its energy (see Ref. 11, also equations 1 and 2 in the present paper). The relative sharpness of the peaks of type II(a) is thus a good indication of their high thermal activation energies compared to those of type I, a fact which was verified by quantitative measurements of the activation energies.

While the thermal activation energies at a given temperature range were higher for type II(a) compared to type I, the optical energies were the same for both types. This indicates that the same levels are involved in both types of diamond. The lower thermal activation energies should then be attributed to smaller escape frequency factors. This is supported by the change from second to first order kinetics on passing from type II(a) to type I. From the principle of detailed balance it follows that the probability for retrapping decreases with the escape frequency factor. A large decrease in this probability may well bring it to be small compared with the probability for recombination, when the kinetics becomes of first order.(11)

CHAMPION(4) has assumed a ratio of 2·5 for the optical/thermal energies of diamond. The present work shows that this is not generally correct. For type II(b) diamonds we have already reported(5) that the thermal energies were equal to the optical ones. The present work shows that the same is true for type II(a), and in this case up to energies of 1·5 eV at least. Only for type I diamonds the ratio thermal/optical was larger than one. Still no constant ratio was found. It changed from 1·5 at 500°K to about 2 at room temperature, and only at lower temperature it reached the value of 2·5 assumed by Champion.

Optical and thermal energies were correlated to each other with success only in a few crystals. It seems that most widely investigated were germanium and silicon. For these crystals the thermal and optical energies were compared for various donor and acceptor levels introduced by different impurities.(14) The energies involved varied from 0·01 to about 0·5 eV and in most cases the optical energies were found to be nearly equal to the thermal. Of special interest is the case of zinc- and boron-doped silicon.(15) Zinc was found to introduce an acceptor level of 0·31 eV. When the zinc concentration was about 100 times that of the boron it was possible to introduce a 0·20 eV level. The optical energy, however, did not change and remained at about 0·31 eV.

This just fits our observations on diamond. The main difference between type II(a) and type I diamonds is due to the high concentration of nitrogen in the latter.(9) The high concentrations of nitrogen seem to affect the thermal activation energies without changing the optical energies in a similar way to that of the zinc in the boron doped silicon. There is no clear explanation for this effect. CARLSON(15) suggests that the complex of levels may arise from interstitial zinc donors of low solubility, or from interactions of zinc donors with boron acceptors to form ion pairs. The latter suggestion might fit our case, although it is not quite clear why the optical energies are not changed. In any case it seems that the nitrogen impurities in type I diamonds are in close association with the defects due to an unknown impurity which is responsible for the trapping levels in type II diamonds.

The difference between thermal and optical energies is usually explained(16) as due to shifts between the ground and excited states in the configuration coordinate diagram. Thermal transitions are assumed to occur over a period of several vibrations, while optical transitions are instantaneous and therefore appear as vertical transitions in the diagram (Franck–Condon principle). Another model for thermal ionization assumes instantaneous multi-phonon transitions,(17) in which case the thermal energies should be equal to the optical ones.

Our results, according to which the thermal energies were found to equal the optical up to 1·5 eV would be difficult to explain by multi-phonon ionization. Although KUBO(17) has obtained a comparatively slow decrease in the probability of multi-phonon transitions with the rise in the number of phonons involved, he still agrees that for energies above 1 eV the process is very improbable. It seems, therefore, that the equal energies in the thermal and optical transitions in type II diamonds should be attributed to the lack of a shift in the configuration curve of the excited state compared to that of the ground state.

Acknowledgement—We wish to thank Dr. J. F. H. CUSTERS, Director of Research, Diamond Research Laboratory, Johannesburg, for supplying some of the diamonds used in the present work.

REFERENCES

1. CHANDRASEKHARAN V., *Proc. Indian Acad. Sci.* **A24,** 187 (1946).
2. BULL C. and GARLICK G. F. J., *Proc. phys. Soc. Lond.* **63,** 1283 (1950).
3. URLAU R. R., LOGIE H. J. and NABARRO F. R. N., *Proc. phys. Soc. Lond.* **78,** 256 (1961).
4. CHAMPION F. C., *Proc. Roy. Soc.* **A234,** 541 (1956).
5. HALPERIN A. and NAHUM J., *J. Phys. Chem. Solids* **18,** 297 (1961).
6. For the classification of diamonds see: CLARK C. D., DITCHBURN R. W. and DYER H. B., *Proc. Roy. Soc.* **A234,** 363 (1956). In the present paper intermediate diamonds were classified as type II(a).
7. CLARK C. D., *J. Phys. Chem. Solids* **8,** 481 (1958).
8. NAHUM J. and HALPERIN A., *J. Phys. Chem. Solids* **23,** 345 (1962).
9. KAISER W. and BOND W. L., *Phys. Rev.* **115,** 857 (1959).
10. HALPERIN A., BRANER A. A., BEN-ZVI A. and KRISTIANPOLLER N., *Phys. Rev.* **117,** 416 (1960).
11. HALPERIN A. and BRANER A. A., *Phys. Rev.* **117,** 408 (1960).
12. HALPERIN A. and NAHUM J., *Luminescence of Organic and Inorganic Materials* (edited by KALLMAN H. P. and SPRUCH G. M.) p. 252. John Wiley New York (1962).
13. GUDDEN B. and POHL R. W., *Z. Phys.* **17,** 331 (1923).
14. For Tables listing the thermal and optical energies in germanium and silicon and for references see: BUBE H., *Photoconductivity of Solids*, pp. 136–7, John Wiley New York (1960).
15. CARLSON R. C., *Phys. Rev.* **108,** 1390 (1957).
16. MOTT N. F. and GURNEY R. W., *Electronic Processes in Ionic Crystals*: p. 156. University Press, Oxford (1940).
17. GOODMAN B., LAWSON A. W. and SCHIFF L. I., *Phys. Rev.* **71,** 191 (1947); KUBO R. *ibid.* **86,** 929 (1952); VASILEFF H. D., *ibid.* **96,** 603 (1954).
18. DYER H. B. and MATTHEWS I. G., *Proc. Roy. Soc.* **A243,** 320 (1958).

J. Phys. Chem. Solids Pergamon Press 1963. Vol. 24, pp. 835–850. **Printed in Great Britain.**

GALVANO-THERMOMAGNETIC EFFECTS IN SEMICONDUCTORS AND SEMIMETALS—III. THE STANDARD AND KANE BAND MODELS

T. C. HARMAN, J. M. HONIG and B. M. TARMY*

Lincoln Laboratory,† Massachusetts Institute of Technology, Lexington 73, Massachusetts

(*Received* 27 *November* 1962)

Abstract—A general theory of transport for a band of spherical symmetry in k-space was developed in a prior paper. Using three special functions for the dependence of energy on wave number vector (the parabolic band, the Kane band for energy gap small or large compared to the spin-orbit splitting), the six basic galvano-thermomagnetic transport coefficients (GTMTC) have been determined in terms of specific transport integrals which must be evaluated numerically. Simple analytic expressions for the GTMTC have been obtained in certain limiting cases. It is of special interest that the parametric dependence of the Nernst coefficient on the scattering index is sensitive to the band curvature.

1. INTRODUCTION

IN AN earlier paper,[(1)] a general theory of transport phenomena was developed for a one-band material where the dependence of the electron energy ϵ on wave number vector k is spherically symmetric but otherwise arbitrary. Six galvano-thermomagnetic transport coefficients (GTMTC) were specified in terms of the following set of transport integrals:

$$I_i = \int_0^\infty \frac{x^{i-1}k^{2r}(\partial x/\partial k)^2 e^{x-\eta}}{(1+e^{x-\eta})^2\{1+\beta^2(k^2)^{2r-3}(\partial x/\partial k)^4\}}\,\mathrm{d}x \tag{1.1a}$$

$$J_j = \int_0^\infty \frac{x^{j-1}k^{4r-3}(\partial x/\partial k)^4 e^{x-\eta}}{(1+e^{x-\eta})^2\{1+\beta^2(k^2)^{2r-3}(\partial x/\partial k)^4\}}\,\mathrm{d}x \tag{1.1b}$$

where $x \equiv \epsilon/kT$, $\eta \equiv \mu_B/kT$, μ_B being the Fermi level taken relative to the appropriate band edge energy. In the above, β represents a collection of parameters

$$\beta = (3\pi^2H_z/Zec)g \tag{1.2a}$$

with

$$g = 4e^2(kT)^2\tau_0/3h^2, \tag{1.2b}$$

where τ_0 is the proportionality constant in the expression for the relaxation time $\tau = \tau_0(k^2)^{r-1}(\mathrm{d}\epsilon/\mathrm{d}k)$, r being the so-called scattering index. The remaining symbols retain their conventional significance (see also Ref. 1).

In the present paper, we shall determine (1.1) and (1.2) explicitly after specifying $\epsilon(k)$ for several cases of interest. The six primary GTMTC can then be calculated, and the remaining 554 possible coefficients derived. The one-band results can subsequently be combined into multi-band results, using the methods of irreversible thermodynamics or transport theory.[(2, 3)]

It is generally a task of considerable magnitude to specify τ_0 from first principles. Therefore, we base the determination of g on equation (4.9a) of part II; since $\sigma(0) = gI_1(0) = ne\mu$, where n is the density of charge carriers in a single band and μ the mobility, we find

$$g = \sigma(0)/I_1(0) = e\mu n/I_1(0) \tag{1.3}$$

---

[*] Summer staff member; permanent address: University of Pennsylvania, Philadelphia, Pennsylvania.

[†] Operated with support from the U.S. Army, Navy, and Air Force.

$I_1(0)$ being the integral of equation (1.1a) with $\beta = 0$. The charge carrier density may be eliminated through the usual relation

$$n = (1/\pi^2)\int_0^\infty \{k^2/(e^{x-\eta}+1)\}\,\mathrm{d}k \tag{1.4}$$

2. THE PARABOLIC BAND SHAPE

In order to have a standard of comparison for our later results, we now consider the band of parabolic form, where

$$\epsilon = \hbar^2k^2/2m^* \text{ or } k^2 = \gamma_0 x \tag{2.1a}$$

in which

$$\gamma_0 \equiv 2m^*kT/\hbar^2 \tag{2.1b}$$

It follows that

$$\partial x/\partial k = \sqrt{(4x/\gamma_0)} \tag{2.2}$$

For this special case, equation (1.4) becomes

$$n = (1/2\pi^2)\gamma_0^{3/2}F_{1/2}(\eta) \equiv (1/2\pi^2)\gamma_0^{3/2}N_0(\eta) \tag{2.3}$$

where $F_{1/2}(\eta)$ is the Fermi–Dirac integral which has been redefined as $N_0(\eta)$ to conform better with our later generalization. Setting $\beta = 0$ in equation (1.1a), one obtains

$$I_i(0) = 4\gamma_0^{r-1}(r+i)F_{r+i-1}(\eta) = 4\gamma_0^{r-1}I_i^{(0)}(\eta;r,0) \tag{2.4a}$$

where

$$I_i^{(0)}(0) \equiv I_i^{(0)}(\eta;r,0)$$

$$= \int_0^\infty \{x^{r+i}\exp(x-\eta)/[1+\exp(x-\eta)]^2\}\,\mathrm{d}x$$

$$= (r+i)F_{r+i-1}(\eta) \tag{2.4b}$$

the latter result being obtained by integration by parts of the central expression.

On inserting these results in equations (1.3) and (1.2a), one finds

$$\beta = \beta_0\frac{\gamma_0^{5/2-r}}{4} \tag{2.5a}$$

where

$$\beta_0 \equiv \frac{3}{2}\frac{\mu H}{Zc}\frac{N_0(\eta)}{I_1^{(0)}(\eta;r,0)} \tag{2.5b}$$

We have thus succeeded in specifying β in terms of measurable quantities, and integrals that can be numerically evaluated.

Before proceeding to determine the transport integrals, we note that the term involving β^2 in the denominator (1.1) may be rewritten as

$$\beta^2(k^2)^{2r-3}(\partial x/\partial k)^4 = \beta_0^2x^{2r-1} \tag{2.6}$$

Accordingly, the transport integrals become

$$I_i = 4\gamma_0^{r-1}I_i^{(0)}(\eta;r,\beta_0) \tag{2.7a}$$

where

$$I_i^{(0)}(\eta;r,\beta_0) = \int_0^\infty \frac{x^{i+r}\exp(x-\eta)\,\mathrm{d}x}{[1+\exp(x-\eta)]^2(1+\beta_0^2x^{2r-1})} \tag{2.7b}$$

and

$$J_j = 16\gamma_0^{2r-7/2}J_j^{(0)}(\eta;r,\beta_0) \tag{2.8a}$$

where

$$J_j^{(0)}(\eta;r,\beta_0) = \int_0^\infty \frac{x^{j+2r-1/2}\exp(x-\eta)\,\mathrm{d}x}{[1+\exp(x-\eta)]^2(1+\beta_0^2x^{2r-1})} \tag{2.8b}$$

For later use, we also require the integral

$$J_j^{(0)}(0) \equiv J_j^{(0)}(\eta;r,0) = \int_0^\infty \frac{x^{j+2r-1/2}\exp(x-\eta)\,\mathrm{d}x}{[1+\exp(x-\eta)]^2}$$

$$= (j+2r-\tfrac{1}{2})F_{j+2r-3/2}(\eta) \tag{2.9}$$

3. THE KANE BAND MODEL FOR LOW GAP MATERIALS

We now consider the case where $\epsilon(k)$ is specified by the KANE function[(4)]

$$\epsilon = \hbar^2k^2/2m_0 - \mathscr{E}_G/2 + (\mathscr{E}_G^2 + 8P^2k^2/3)^{1/2}/2 \tag{3.1}$$

in which m_0 is the free electron mass, $\mathscr{E}_G$ is the energy band gap, P is a matrix element defined in the original publication. The applicability of the Kane model to III–V compounds and to certain compounds in the II–VI series has been amply demonstrated; a transport theory based on this model should therefore be of interest. In the cases investigated so far, the parameter P assumes the constant value $8{\cdot}5\times10^{-8}$ eV-cm within experimental error; EHRENREICH(5) has in fact suggested that this quantity might be regarded as a universal constant.

The above expression is applicable if the spin-orbit splitting of the valence band is much greater than the gap energy or kP. The Kane model is applicable in semiconductors with small effective masses (i.e. $m^* \ll m_0$), such as InSb, HgSe, etc.; under these conditions, the first term in (3.1) can be neglected. On solving the remaining relation for k^2, one obtains

$$k^2 = (\tfrac{3}{2})(kT/P)^2x(x+x_G) \equiv \gamma_1 x(x+x_G) \quad (3.2)$$

where $x_G \equiv \mathscr{E}_G/kT$ is the reduced gap; attention is directed to the definition γ_1. Proceeding by analogy with Section 2, we first determine

$$\partial x/\partial k = \sqrt{\{(4/\gamma_1)[x(x+x_G)]\}}/(2x+x_G) \quad (3.3)$$

and then evaluate

$$n = (1/2\pi^2)\gamma_1^{3/2}N_1 \quad (3.4a)$$

where

$$N_1 = \int_0^\infty \{[x(x+x_G)]^{1/2}(2x+x_G)/[1+\exp(x-\eta)]\}\mathrm{d}x \quad (3.4b)$$

In addition, we require for use in (1.3), the transport integral (1.1a) with $\beta = 0$; after substituting from (3.2) and (3.3), one is led to the result

$$I_l(0) = 4\gamma_1^{r-1}I_l^{(1)}(\eta,x_G;r,0) \quad (3.5a)$$

with

$$I_l^{(1)}(0) \equiv I^{(1)}(\eta,x_G;r,0) = \int_0^\infty \frac{x^{r+l}(x+x_G)^{r+1}\exp(x-\eta)\,\mathrm{d}x}{(2x+x_G)^2[1+\exp(x-\eta)]^2} \quad (3.5b)$$

Insertion of these results into equations (1.3) and (1.2a) gives

$$\beta = \beta_1\frac{\gamma_1^{5/2-r}}{4} \quad (3.6a)$$

where

$$\beta_1 \equiv \frac{3}{2}\frac{\mu H}{Zc}\frac{N_1(\eta,x_G)}{I_1^{(1)}(\eta,x_G;0,0)} \quad (3.6b)$$

Moreover, for the model under consideration, we find that

$$\beta^2(k^2)^{2r-3}(\partial x/\partial k)^4 = \beta_1^2[x(x+x_G)]^{2r-1}/(2x+x_G)^4 \quad (3.7)$$

Using these results in (1.1a) and (1.1b), we obtain

$$I_l(\eta,x_G;r,\beta) = 4\gamma_1^{r-1}I_l^{(1)}(\eta,x_G;r,\beta_1) \quad (3.8a)$$

where

$$I_l^{(1)}(\eta,x_G;r,\beta_1) = \int_0^\infty \frac{x^{l+r}(x+x_G)^{r+1}\exp(x-\eta)\,\mathrm{d}x}{(2x+x_G)^2[1+\exp(x-\eta)]^2\{1+\beta_1^2[x(x+x_G)]^{2r-1}/(2x+x_G)^4\}} \quad (3.8b)$$

and

$$J_j(\eta,x_G;r,\beta) = 16\gamma_1^{2r-7/2}J_j^{(1)}(\eta,x_G;r,\beta_1) \quad (3.9a)$$

where

$$J_j^{(1)}(\eta,x_G;r,\beta_1) = \int_0^\infty \frac{x^{2r+j-1/2}(x+x_G)^{2r+1/2}\exp(x-\eta)\,\mathrm{d}x}{(2x+x_G)^4[1+\exp(x-\eta)]^2\{1+\beta_1^2[x(x+x_G)]^{2r-1}/(2x+x_G)^4\}} \quad (3.9b)$$

A special case of (3.9b) occurs when $H_z = 0$; then

$$J_j^{(1)}(0) \equiv J_j^{(1)}(\eta,x_G;r,0) = \int_0^\infty \frac{x^{2r+j-1/2}(x+x_G)^{2r+1/2}\exp(x-\eta)\,\mathrm{d}x}{(2x+x_G)^4[1+\exp(x-\eta)]^2} \quad (3.10)$$

The limits in the above integrals require a comment. According to equation (3.2), the value $k = 0$ is consistent either with $x = 0$ or with $x = -x_G$. However, the latter possibility may be precluded on grounds that the energy as defined by equation (3.1) must remain non-negative. The upper limit is permissible because the ratio $\exp(x-\eta)/[1+\exp(x-\eta)]^2$ rapidly approaches zero as x increases.

4. THE KANE BAND MODEL FOR WIDE GAP MATERIALS

In this Section, we briefly consider another limiting expression of the KANE theory[4] which applies when the gap energy greatly exceeds the spin-orbit splitting of the valence band. The function of interest is now given by

$$\epsilon(k) = \hbar^2k^2/2m_0 - \mathscr{E}_G/2 + (\mathscr{E}_G^2 + 4P^2k^2)^{1/2}/2 \qquad (4.1)$$

Comparison with equation (3.1) shows that the two cases differ only in that the P of Section 3 is now replaced by $P\sqrt{(\frac{3}{2})}$. From equation (3.2), it is evident that if one utilizes the quantity

$$\gamma_2 \equiv (kT/P)^2 \qquad (4.2)$$

in place of $\gamma_1 \equiv (\frac{3}{2})(kT/P)^2$, then the remainder of the analysis proceeds just as in Section 3. In particular, one finds that $N_2 = N_1$, $I_i^{(2)} = I_i^{(1)}$ and $J_j^{(2)} = J_j^{(1)}$.

By analogy to equation (3.6b), we find that

$$\beta_2 = \frac{3}{2}\frac{\mu H}{Zc}\frac{N_2(\eta, x_G)}{I_1^{(2)}(\eta, x_G; 0,0)} \qquad (4.3)$$

5. GENERAL TRANSPORT THEORY

We are now ready to express the GTMTC in terms of a final set of transport integrals. For this purpose, we first rewrite the results of paper (II), utilizing equations (1.2) and (1.3) where necessary

$$\sigma_I(H_z) = [\sigma_I(0)/I_1(0)I_1]\{I_1^2+\beta^2J_1^2\} \qquad (5.1)$$

$$\mathscr{R}_I(H_z) = (3\pi^2/Zecn)\{nJ_1/(I_1^2+\beta^2J_1^2)\} \qquad (5.2)$$

$$\kappa_I(H_z) = \kappa_L + \frac{k^2T}{e^2}\sigma(0)\left\{\frac{I_3I_1^2-I_1I_2^2+\beta^2(J_1^2I_3-2J_1J_2I_2+I_1J_2^2)}{I_1(0)[I_1^2+\beta^2J_1^2]}\right\} \qquad (5.3)$$

$$\mathscr{P}_I(H_z) = (k/Ze)\{(I_1I_2+\beta^2J_1J_2)/(I_1^2+\beta^2J_1^2)-\eta\} \qquad (5.4)$$

$$\mathscr{N}_I(H_z) = (k\beta/ZeH_z)\{(J_1I_2-J_2I_1)/(I_1^2+\beta^2J_1^2)\} \qquad (5.5)$$

$$\mathscr{M}(H_z) = \frac{\beta}{H_z}\left\{\frac{J_1I_2^2-2I_1I_2J_2+I_1^2J_3-\beta^2(J_1J_2^2-J_1^2J_3)}{I_1^2I_3-I_1I_2^2+\beta^2(I_3J_1^2-2I_2J_1J_2+I_1J_2^2)+\dfrac{e^2\kappa_LI_1(0)}{\sigma(0)k^2T}(I_1^2+\beta^2J_1^2)}\right\} \qquad (5.6a)$$

or

$$\mathscr{M}(H_z) = \frac{\beta\sigma(0)k^2T}{e^2H_z\kappa_II_1(0)}\left\{\frac{J_1I_2^2-2I_1I_2J_2+I_1^2J_3-\beta^2(J_1J_2^2-J_1^2J_3)}{(I_1^2+\beta^2J_1^2)}\right\} \qquad (5.6b)$$

In equations (5.1)–(5.6), the transport properties $\sigma_I(H_z)$, $\mathscr{R}_I(H_z)$, $\kappa_I(H_z)$, $\mathscr{P}_I(H_z)$, $\mathscr{N}_I(H_z)$, and $\mathscr{M}(H_z)$ are defined as the isothermal electrical conductivity, isothermal Hall coefficient, isothermal thermal conductivity, isothermal Seebeck or isothermal Ettingshausen–Nernst coefficient, isothermal Nernst coefficient, and the Righi–Leduc coefficient, respectively.

Attention is now directed to the following fact which may be verified by direct substitution: If n, I_i and J_j are of the form indicated below

$$n = (1/2\pi^2)\gamma_\nu^{3/2}N_\nu \qquad (5.7a)$$

$$I_i = 4\gamma_\nu^{r-1}I_i^{(\nu)} \qquad (5.7b)$$

$$J_j = 16\gamma_\nu^{2r-7/2}J_j^{(\nu)}, \qquad (5.7c)$$

so that one obtains

$$\beta = \beta_\nu(\gamma_\nu^{5/2-r})/4, \qquad (5.8)$$

then, β, I_i and J_j in (5.1)–(5.6), can be replaced by β_ν, $I_i^{(\nu)}$, and $J_j^{(\nu)}$ respectively without altering the GTMTC. Specifically, one finds

$$\sigma_I(H_z) = \sigma(0)\,[I_1^{(\nu)2}+\beta_\nu^2 J_1^{(\nu)2}]/I_1^{(\nu)}(0)I_1^{(\nu)} \tag{5.9}$$

$$\mathscr{R}_I(H_z) = \frac{1}{Znec}\left\{\frac{3}{2}\,\frac{N_\nu\, J_1^{(\nu)}}{I_1^{(\nu)2}+\beta_\nu^2\, J_1^{(\nu)2}}\right\} \tag{5.10}$$

$$\kappa_I(H_z) = \kappa_L + \frac{k^2T}{e^2}\,\frac{\sigma(0)}{I_1^{(\nu)}(0)}\left\{\frac{I_3^{(\nu)}I_1^{(\nu)2}-I_1^{(\nu)}I_2^{(\nu)2}+\beta_\nu^2(J_1^{(\nu)2}I_3^{(\nu)}-2J_1^{(\nu)}J_2^{(\nu)}I_2^{(\nu)}+I_1^{(\nu)}J_2^{(\nu)2})}{I_1^{(\nu)2}+\beta_\nu^2 J_1^{(\nu)2}}\right\} \tag{5.11a}$$

$$= \kappa_L + \frac{k^2T}{e^2}\,\sigma_I(H_z)\left\{\frac{I_1^{(\nu)}I_3^{(\nu)}}{I_1^{(\nu)2}+\beta_\nu^2 J_1^{(\nu)2}} - \frac{I_1^{(\nu)2}(I_2^{(\nu)2}+\beta_\nu^2 J_2^{(\nu)2})+2\beta_\nu^2 I_1^{(\nu)}I_2^{(\nu)}J_1^{(\nu)}J_2^{(\nu)}}{(I_1^{(\nu)2}+\beta_\nu^2\, J_1^{(\nu)2})^2}\right\} \tag{5.11b}$$

$$\mathscr{P}_I(H_z) = \frac{k}{Ze}\left\{\frac{I_1^{(\nu)}I_2^{(\nu)}+\beta_\nu^2\, J_1^{(\nu)}J_2^{(\nu)}}{I_1^{(\nu)2}+\beta_\nu^2\, J_1^{(\nu)2}} - \eta\right\} \tag{5.12}$$

$$\mathscr{N}_I(H_z) = \frac{3}{2}\,\frac{k}{e}\,\frac{\mu}{c}\,\frac{N_\nu}{I_1^{(\nu)}(0)}\left\{\frac{J_1^{(\nu)}I_2^{(\nu)}-I_1^{(\nu)}J_2^{(\nu)}}{I_1^{(\nu)2}+\beta_\nu^2 J_1^{(\nu)2}}\right\} \tag{5.13}$$

$$\mathscr{M}(H_z) = \frac{\left\{\begin{array}{l}\dfrac{3}{2}\,\dfrac{\mu}{Zc}\,\dfrac{N_\nu}{I_1^{(\nu)}(0)}\,\{I_2^{(\nu)2}J_1^{(\nu)}-2I_1^{(\nu)}I_2^{(\nu)}J_2^{(\nu)}+I_1^{(\nu)2}J_3^{(\nu)}\\ \qquad -\beta_\nu^2(J_1^{(\nu)}J_2^{(\nu)2}-J_1^{(\nu)2}J_3^{(\nu)})\}\end{array}\right\}}{\left\{\begin{array}{l}I_1^{(\nu)2}I_3^{(\nu)}-I_1^{(\nu)}I_2^{(\nu)2}+\beta_\nu^2(I_3^{(\nu)}J_1^{(\nu)2}-2I_2^{(\nu)}J_1^{(\nu)}J_2^{(\nu)}+I_1^{(\nu)}J_2^{(\nu)2})\\ \qquad +\dfrac{e^2\kappa_L I_1^{(\nu)}(0)}{k^2T\sigma(0)}\,(I_1^{(\nu)2}+\beta_\nu^2\, J_1^{(\nu)2})\end{array}\right\}} \tag{5.14a}$$

$$= \frac{3}{2}\,\frac{k^2T}{e^2}\,\frac{\mu}{Zc}\,\frac{\sigma(0)}{\kappa_I(H_z)}\,\frac{N_\nu}{[I_1^{(\nu)}(0)]^2} \times\left\{\frac{I_2^{(\nu)2}J_1^{(\nu)}-2I_1^{(\nu)}I_2^{(\nu)}J_2^{(\nu)}+I_1^{(\nu)2}J_3^{(\nu)}-\beta_\nu^2(J_1^{(\nu)}J_2^{(\nu)2}-J_1^{(\nu)2}J_3^{(\nu)})}{I_1^{(\nu)2}+\beta_\nu^2 J_1^{(\nu)2}}\right\} \tag{5.14b}$$

Thus, the various GTMTC as calculated on the basis of several functions $\epsilon(k)$, differ from one another solely in that β_ν, $I_i^{(\nu)}$ and $J_j^{(\nu)}$ involve transport integrals whose numerical values depend on the $\epsilon(k)$ functions that are introduced. Since the models considered in Sections 2, 3 and 4 conform to the requirements (5.7), the transport coefficients can be calculated from equations (5.9)–(5.14) after the evaluation of β_ν, $I_i^{(\nu)}$, $J_j^{(\nu)}$ according to the model under consideration.

The following items are noteworthy: (1) The collection of constants γ_0, γ_1, or γ_2 is entirely absent from the final general equations. (2) The factor $I_1^{(\nu)2}+\beta_\nu^2\, J_1^{(\nu)2}$ in the denominators of the above relations can be eliminated using equation (5.9). (3) Equation (5.10) is of the general form $\mathscr{R}_I = A/Zenc$; once A is known, the charge carrier density in the band is determined from Hall effect measurements. (4) Equation (5.11b) is written in a form which shows that the Wiedemann–Franz law is applicable; the Lorenz number is given by the quantity in curly braces. (5) Equation (5.12) can be utilized to determine η experimentally once the transport integrals are calculated. (6) Both $\mathscr{R}_I$ and $\mathscr{P}_I$ change sign with the sign of the charge carrier. (7) The Nernst coefficient $\mathscr{N}_I$ is independent of Z; its sign is determined by that of the numerator in the curly braces of equation (5.13). (8) The mobility μ may be eliminated from

(5.13) and (5.14) by multiplying (5.10) with $\sigma(0) = ne\mu$. This leads to the result

$$\mu = c\sigma(0)[Z\mathscr{R}_I(H_z)]\left\{\frac{2}{3}\,\frac{I_1^{(\nu)2}+\beta_\nu^2 J_1^{(\nu)2}}{N_\nu J_1^{(\nu)}}\right\} \quad (5.15)$$

which may be used to rewrite both $\mathscr{N}_I(H_z)$ and $\mathscr{M}(H_z)$ in terms of the product $\sigma(0)\,(Z\mathscr{R}_I)$. One should note that the product $Z\mathscr{R}_I$ is always positive, so that $\mu \geqslant 0$.

Two specializations are of interest: In zero magnetic field, $\beta = 0$, and the following results are obtained for the Seebeck coefficient and thermal conductivity:

$$\alpha(0) = (k/Ze)[I_2^{(\nu)}(0)/I_1^{(\nu)}(0)-\eta] \quad (5.16)$$

$$\kappa(0) = \kappa_L+\frac{k^2T}{e^2}\,\sigma(0)\left\{\frac{I_3^{(\nu)}(0)}{I_1^{(\nu)}(0)}-\frac{I_2^{(\nu)2}(0)}{I_1^{(\nu)2}(0)}\right\} \quad (5.17)$$

Also, for the Corbino disk geometry, discussed in (II), one finds

$$\sigma(H_z) = gI_1(H_z) = \sigma(0)I_1^{(\nu)}(H_z)/I_1^{(\nu)}(0) \quad (5.18)$$

$$\alpha(H_z) = (k/Ze)[I_2^{(\nu)}(H_z)/I_1^{(\nu)}(H_z)-\eta] \quad (5.19)$$

$$\kappa(H_z) = \kappa_L+\frac{k^2T}{e^2}\,\sigma(0)\left\{\frac{I_3^{(\nu)}(H_z)}{I_1^{(\nu)}(0)}-\frac{I_2^{(\nu)2}(H_z)}{I_1^{(\nu)}(H_z)I_1^{(\nu)}(0)}\right\} \quad (5.20)$$

6. GTMTC FOR MATERIALS IN THE LIMIT OF CLASSICAL STATISTICS

Henceforth, we consider special cases of Section 5, for which the various GTMTC assume a simple form. We begin with the classical approximation, by regarding $\exp(x-\eta) \gg 1$ in all transport integrals. Furthermore, we restrict ourselves to the low magnetic field approximation, in which $\beta_0^2 x^{2r-1} \ll 1$ or $\beta_{1,2}^2[x(x+x_G)]^{2r-1}/(2x+x_G)^4 \ll 1$ in equations (2.7), (2.8) and (3.8), (3.9) respectively. In the range $0 \leqslant r < \frac{1}{2}$, this assumption fails at $x = 0$ unless β_ν^2 also vanishes. However, we shall prove later that the error incurred in proceeding with this approximation is small if $\beta_\nu^2 > 0$ is small.

Let us now consider the different band models in turn. (a) For $\nu = 0$ (parabolic bands) we employ the results of Section 2: In the weak field limit, the relevant transport integrals are given by equations (2.4b) and (2.9). For classical statistics, these integrals tend to the limit

$$I_i^{(0)}(0) = e^{\eta}\Gamma(r+i+1) \quad (6.1a)$$

$$J_j^{(0)}(0) = e^{\eta}\Gamma(j+2r+\tfrac{1}{2}) \quad (6.1b)$$

where the Γ are the standard gamma functions.

The electrical conductivity is found through the relation $\sigma(0) = ne\mu$ into which one may substitute equation (2.3); the result is entered in Table 1, column A. An alternate formulation is obtained by introducing the mean free path, l, related to the relaxation time by $\tau = l/v$. The expression $\tau = \tau_0(k^2)^{r-1}(\mathrm{d}\epsilon/\mathrm{d}k)$ is to be substituted on the left and the quantities $\ell = \ell_0' \;\epsilon^r \equiv \ell_0 x^r$ and $v = (1/\hbar)\,(\mathrm{d}\epsilon/\mathrm{d}k)$, on the right. The following relation between τ_0 and ℓ_0 can then be established:

$$\tau_0 = m^*\gamma_0^{1\;\;r}\ell_0/2kT\hbar \quad (6.2)$$

We now employ the relation $\sigma_I(0) = gI_1(0)$; after substituting equations (1.2b), (6.2), (2.4a) and (6.1a), one obtains

$$\sigma_I(0) = 16\pi m^* kTe^2\ell_0 e^{\eta}\Gamma(r+2)/3h^3 \quad (6.3)$$

which formulates σ in terms of ℓ_0.

The remaining GTMTC may be found systematically by setting $\beta_\nu = 0$ in equations (5.10)–(5.14) and by substituting equations (6.1) into the resulting expressions. In addition, the relations $N_0 \equiv F_{1/2}(\eta) \rightarrow e^{\eta}\Gamma(\tfrac{3}{2}) = (e^{\eta}/2)\sqrt{\pi}$ and $\Gamma(m+1) = m\Gamma(m)$ will be utilized; one then obtains the remaining results listed in Table 1, column A.

(b) Next, we consider the weak field, classical statistics approximation in conjunction with the case $\nu = 1$ (Kane band model, $x_G \rightarrow 0$ or $x_G \ll |\eta|$). Here, the transport integrals (3.5b) and (3.10) are of relevance; however, simple analytic relations are obtained only in the limit $x_G \rightarrow 0$. It is important to recognize that the combination of vanishing gaps and classical statistics leads to inconsistencies. From the viewpoint of mathematics, this situation arises because our contemplated procedure is tantamount to setting $\mathscr{E}_G = 0$ in equation (3.1); the latter then reduces to $\epsilon = Pk\sqrt{(\tfrac{2}{3})}$ on neglect of the term involving m_0. While this relation is acceptable for k sufficiently far removed from the band edge, it is known from general principles that near a nondegenerate (except for spin) band edge, ϵ must vary quadratically with k. Thus, the dependence of ϵ on k when $\mathscr{E}_G = 0$ is totally inappropriate precisely in the region of k values which are of crucial importance in the regime of classical statistics. In the physical interpretation, one should note that for materials with small $\mathscr{E}_G$, the effective mass of the carriers is likewise small. In these circumstances, ϵ rises rapidly with $|k|$, so that the Fermi level moves into the band for quite low values of n. In other words, as $x_G \to 0$, one hardly ever encounters the classical regime in cases of physical interest. For the exceptional cases, it is clearly necessary that the band form be correctly specified for the few energy states which are occupied by particles. In this event, one must resort to numerical integrations of transport integrals.

(c) Finally, we turn to the case $\nu = 2$ (Kane band model, $x_G \gg |\eta|$, large reduced gaps). To obtain simple results, we assume that x may be neglected compared to x_G in the relevant transport integrals, (3.4b), (3.5b) and (3.10). Manifestly, this approximation fails near the upper limit of these integrals. However, due to the presence, in the classical approximation, of the factor $e^{\eta - x}$ in each integrand, the failure of the approximation $x \ll x_G$ for large x occasions no difficulty. The reader can readily check that in the case considered here,

$$N_2 = x_G^{3/2}(e^{\eta}/2)\sqrt{\pi} \tag{6.4a}$$

$$I_i^{(2)}(0) = x_G^{r-1}e^{\eta}\Gamma(r+i+1) \tag{6.4b}$$

$$J_j^{(2)}(0) = x_G^{2r-7/2}e^{\eta}\Gamma(2r+j+\tfrac{1}{2}) \tag{6.4c}$$

When these results are used in equations (5.10)–(5.14), one obtains the same results as for the case $\nu = 0$; only the expression for $\sigma_I(0)$ is slightly altered, as shown in Table 1, column A. The special cases obtained on setting $r = 0$ are entered in column B.

It is conceivable that the weak field approximation could lead to serious errors when the scattering index is in the range $0 \leqslant r < \frac{1}{2}$; for, under these conditions, the quantity β_0^2/x^{1-2r} grows without limit as $x \to 0$. That this is not the case may be seen from a computation of the difference between the integrals in which the weak field approximation is not or is invoked. In the limit of classical statistics and for the transport integrals I_i, this quantity is given by

$$\Delta_i^{(0)} = e^{\eta}\int_0^{\infty}\left(\frac{x^{i+r}}{1+\beta_0^2x^{2r-1}} - x^{i+r}\right)e^{-x}\,\mathrm{d}x$$

$$= -e^{\eta}\int_0^{\infty} x^{i+r}\frac{\beta_0^2x^{2r-1}}{1+\beta_0^2x^{2r-1}}e^{-x}\,\mathrm{d}x \tag{6.5a}$$

On omitting the second term in the denominator, one arrives at the following inequality:

$$|\Delta_i^{(0)}| < e^{\eta}\beta_0^2\int_0^{\infty} x^{i+3r-1}e^{-x}\,\mathrm{d}x = e^{\eta}\beta_0^2\Gamma(i+3r) \tag{6.5b}$$

A similar operation, carried out on the integrals $J_j^{(0)}$ leads to the result

$$|\Delta_j^{(0)}| < e^{\eta}\beta_0^2\Gamma(j+4r-\tfrac{1}{2}) \tag{6.5c}$$

Thus, no matter what the value of r, the difference between the exact and approximate transport integrals will not exceed the values shown in (6.5b) and (6.5c). As expected, Δ can be made arbitrarily small by letting β_0^2 approach zero. Analogous considerations apply to the case $\nu = 2$.

7. GTMTC IN THE CLASSICAL APPROXIMATION FOR MATERIALS IN STRONG MAGNETIC FIELDS

We now extend the considerations of Section 6 to the case of strong magnetic fields. The approximation consists in neglecting unity relative to the terms $\beta_0^2\,x^{2r-1}$ or $\beta_{1,2}^2[x(x+x_G)]^{2r-1}/(2x+x_G)^4$ in the denominators of the transport integrals. Questions regarding the validity of this approximation will be dealt with at the end of the Section.

(a) For the case $\nu = 0$, the integrals of interest read

$$\lim_{\beta_0\to\infty} I_i^{(0)}(\eta;r,\beta_0)$$

$$= (1/\beta_0)^2\int_0^{\infty} x^{i-r+1}e^{\eta-x}\,\mathrm{d}x = (e^{\eta}/\beta_0^2)\Gamma(i-r+2) \tag{7.1a}$$

$$\lim_{\beta_0\to\infty} J_j^{(0)}(\eta;r,\beta_0) = (e^{\eta}/\beta_0^2)\Gamma(j+\tfrac{3}{2}) \tag{7.1b}$$

where β_0 is defined in equation (2.5). We now return to equations ([illegible]) and neglect all terms not involving β_0^2 relative to those that do; after introducing the results (7.1a) and (7.1b), as well as (6.1) and $N_0 = (e^\eta/2)\sqrt{\pi}$, the six basic GTMTC reduce to the form shown in Table 2, column A.

(b) As explained earlier, the case $\nu = 1$ with $x_G = 0$ is incompatible with the classical approximation and will not be considered further.

(c) For $\nu = 2$, simple analytic results can be obtained by neglecting x relative to x_G. Difficulties arising towards the upper limit of the transport integrals are of no consequence because of the presence in the integrands of the factor e^{-x}. For $x_G \gg x$ and in the limit of very high fields, equations (3.8b) and (3.9b) reduce to

$$\lim_{\substack{x_G\to\infty\\ \beta_2\to\infty}} I_i^{(2)}(x_G,\eta;r,\beta_2) = (x_G^{4-r}e^\eta/\beta_2^2)\Gamma(i+2-r) \tag{7.2a}$$

$$\lim_{\substack{x_G\to\infty\\ \beta_2\to\infty}} J_j^{(2)}(x_G,\eta;r,\beta_2) = (x_G^{3/2}e^\eta/\beta_2^2)\Gamma(j+\tfrac{3}{2}) \tag{7.2b}$$

If we then substitute these results as well as (6.4a) and (6.4b) into the general relations (5.9)–(5.14) and proceed as in the case $\nu = 0$, we again recover the entries listed in Table 2, column A. Results for the GTMTC with $r = 0$ are shown in column B.

It remains to investigate whether serious errors are incurred from the fact that the strong field approximation cannot remain valid over the whole range of x values. For the case $\nu = 0$, the question centers about those x for which the inequality $\beta_0^2x^{2r-1} \gg 1$ can no longer be maintained. In the range $0 \leqslant r < \frac{1}{2}$, difficulties arise at the upper limit of x; this is no problem since contributions to $I_i^{(0)}$ and $J_j^{(0)}$ are negligible in this range. For $r > \frac{1}{2}$, difficulties may arise near $x = 0$. The possible errors involved in this approximation may be ascertained by computing, as in Section 6, the difference between the exact and approximate transport integrals in the classical regime. One then finds

$$\Delta_i^{(0)} = e^\eta\int_0^\infty\left(\frac{x^{i+r}}{1+\beta_0^2x^{2r-1}}-\frac{x^{i+r}}{\beta_0^2x^{2r-1}}\right)e^{-x}\,\mathrm{d}x$$

$$= -\frac{e^\eta}{\beta_0^2}\int_0^\infty\frac{x^{i-r+1}\,e^{-x}}{1+\beta_0^2x^{2r-1}}\,\mathrm{d}x \tag{7.3a}$$

On neglecting the second term in the denominator relative to the first, one obtains the following inequality:

$$|\Delta_i^{(0)}| < (e^\eta/\beta_0^2)\int_0^\infty x^{i-r+1}e^{-x}\,\mathrm{d}x = (e^\eta/\beta_0^2)\Gamma(i-r+2) \tag{7.3b}$$

Similarly, one may prove that

$$|\Delta_j^{(0)}| < (e^\eta/\beta_0^2)\Gamma(j+\tfrac{3}{2}) \tag{7.4}$$

These results show that the Δ have an upper bound which becomes vanishingly small for sufficiently large β_0. An investigation of case $\nu = 2$ in the approximation $x_G \gg x$ leads to similar conclusions; one obtains the results

$$|\Delta_i^{(2)}| < (x_G^{4-r}\,e^\eta/\beta_2^2)\Gamma(i-r+2) \text{ and }$$
$$|\Delta_j^{(2)}| < (x_G^{3/2}\,e^\eta/\beta_2^2)\Gamma(j+\tfrac{3}{2}).$$

8. GTMTC IN THE WEAK FIELD APPROXIMATION FOR CONDITIONS OF EXTREME DEGENERACY

In this Section, we discuss the limiting case which involves the weak field approximation and the assumption of extreme degeneracy. (a) For $\nu = 0$, we utilize the integrals (2.4b) and (2.9). In the limit of extreme degeneracy, we employ the Bethe–Sommerfeld representation of the Fermi–Dirac integrals

$$\left(\frac{1}{m}\right)\int_0^\infty x^m\left(-\frac{\partial f_0}{\partial x}\right)\mathrm{d}x = F_{m-1}(\eta)$$

$$= \frac{\eta^m}{m}\{1+m(m-1)\frac{\pi^2}{6\eta^2}+\ldots\} \tag{8.1}$$

where $f_0 = [1+\exp(x-\eta)]^{-1}$. The quantities multiplied by $(\pi^2/6\eta^2)^\ell$ will be designated as being of ℓ'th order.

From equation (5.7a), the weak field electrical conductivity is found to be

$$\sigma_I(0) = (e\mu/2\pi^2)\gamma_0^{3/2}N_0 = (e\mu/3\pi^2)\gamma_0^{3/2}F_{1/2}(\eta) \tag{8.2}$$

so that on application of equation (8.1), one obtains the result listed in Table 3, column A. Alternately, one may proceed as in Section 6 to write

$$\sigma_I(0) = (16\pi m^* kT\ell_0 e^2/3h^2)(r+1)F_r(\eta)$$
$$\approx (16\pi m^* kT\ell_0 e^2/3h^2)\eta^{r+1}[1+r(r+1)\pi^2/6\eta^2] \tag{8.3}$$

The remaining transport coefficients are found from equations (5.10)–(5.14); on neglecting terms containing β_0^2, substituting (2.4b) and (2.9) in the remaining terms, and then employing (8.1), one arrives at the results listed in Table 3, column A. In this connection, it is important to note that zero and first order terms appear only in the expressions for σ_I and $\mathscr{R}_I$; for all other GTMTC, the zero order terms cancel identically. If results to higher order are desired, it is necessary to return to equation (8.1), and to include the next term in the expansion. The algebra becomes extremely lengthy and was not carried through for that reason.

(b) For the case $\nu = 1$, one may proceed in similar fashion. Inspection of Section 3 shows that the transport integrals $I_i^{(1)}$ and $J_j^{(1)}$ are of the type $L = -C\int_0^\infty h(x)\cdot(\partial f_0/\partial x)\,\mathrm{d}x$, in which f_0 is the Fermi function and $h(x)$ a function which varies slowly over the energy range where $\partial f_0/\partial x$ is sharply peaked. Accordingly, we can write

$$L \approx Ch(\eta)+\frac{\pi^2}{6}C\left[\frac{\mathrm{d}^2h}{\mathrm{d}x^2}\right]_{x=\eta}+\ldots \tag{8.4}$$

For later use, we require the integral N_1, given by equation (3.4b). Rewriting the latter as

$$N_1 = \frac{2}{3}\int_0^\infty \frac{\mathrm{d}}{\mathrm{d}x}(x^2+xx_G)^{3/2}f\,\mathrm{d}x$$
$$= -\frac{2}{3}\int_0^\infty (x^2+xx_G)^{3/2}(\partial f_0/\partial x)\,\mathrm{d}x \tag{8.5}$$

we can identify $h(x)$ with $(x^2+xx_G)^{3/2}$. On applying equation (8.4), we find

$$N_2 = N_1 = \tfrac{2}{3}(\eta^2+\eta x_G)^{3/2}+[\pi^2/12\sqrt{\{\eta(\eta+x_G)\}}]$$
$$\times\ [4\eta(\eta+x_G)+(2\eta+x_G)^2] \tag{8.6}$$

In order to obtain analytically manageable results, we assume here that $x_G \ll |\eta|$. Equation (8.6) then reduces to

$$N_1 = (2\eta^3/3)\,[1+\pi^2/\eta^2] \tag{8.7}$$

The analytical approximation to the transport integrals $I_i^{(1)}$ can be handled in similar fashion. Here, $h(x) = x^{i-1}[x(x+x_G)]^{r+1}/(2x+x_G)^2$. The determination of these integrals according to equation (8.4) is a perfectly straightforward though tedious exercise in calculus. One ultimately obtains the following general result

$$\boxed{\begin{aligned}I_i^{(1)}(\eta,x_G;\,r,0) = \frac{\eta^{i+r}(\eta+x_G)^{r+1}}{(2\eta+x_G)^2}&\left\{1+\frac{\pi^2}{6}\left[\frac{(i+r)(i+r-1)}{\eta^2}\right.\right.\\ +\frac{r(r+1)}{(\eta+x_G)^2}+\frac{24}{(2\eta+x_G)^2}+\frac{2(i+r)(r+1)}{\eta(\eta+x_G)}-\frac{8(i+r)}{\eta(2\eta+x_G)}&\left.\left.-\frac{8(r+1)}{(\eta+x_G)(2\eta+x_G)}\right]\right\}\end{aligned}} \tag{8.8}$$

In the limit $x_G \ll |\eta|$, the above reduces to

$$I_1^{(1)}(\eta;\,r,0) = (\eta^{2r}/4)\,\{1+(\pi^2/3\eta^2)r(2r-1)\} \tag{8.9a}$$
$$I_2^{(1)}(\eta;\,r,0) = (\eta^{2r+1}/4)\{1+(\pi^2/3\eta^2)r(2r+1)\} \tag{8.9b}$$
$$I_3^{(1)}(\eta;\,r,0) = (\eta^{2r+2}/4)\,\{1+(\pi^2/3\eta^2)(2r^2+3r+1)\} \tag{8.9c}$$

It remains to obtain the corresponding simplifications for the transport integrals $J_j^{(1)}$. Here,

$$h = x^{j+2r-1/2}(x+x_G)^{2r+1/2}/(2x+x_G)^4.$$

The general expression reads

$$\boxed{\begin{aligned}J_j^{(1)}(\eta,x_G;r,0) = {} & \frac{\eta^{j+2r-1/2}(\eta+x_G)^{2r+1/2}}{(2\eta+x_G)^4}\left\{1+\left(\frac{\pi^2}{6}\right)\right. \\ & \times\left[\frac{(j+2r-\frac{1}{2})(j+2r-\frac{3}{2})}{\eta^2}+\frac{(2r+\frac{1}{2})(2r-\frac{1}{2})}{(\eta+x_G)^2}+\frac{80}{(2\eta+x_G)^2}\right. \\ & \left.\left.+\frac{2(2r+\frac{1}{2})(j+2r-\frac{1}{2})}{\eta(\eta+x_G)}-\frac{16(j+2r-\frac{1}{2})}{\eta(2\eta+x_G)}-\frac{16(2r+\frac{1}{2})}{(\eta+x_G)(2\eta+x_G)}\right]\right\} \qquad (8.10)\end{aligned}}$$

For the special case $x_G \ll \eta$, we find

$$J_1^{(1)}(\eta;r,0) = (\eta^{4r-3}/16)[1+(\pi^2/3\eta^2)(8r^2-14r+6)] \qquad (8.11a)$$

$$J_2^{(1)}(\eta;r,0) = (\eta^{4r-2}/16)[1+(\pi^2/3\eta^2)(8r^2-10r+3)] \qquad (8.11b)$$

$$J_3^{(1)}(\eta;r,0) = (\eta^{4r-1}/16)[1+(\pi^2/3\eta^2)(8r^2-6r+1)] \qquad (8.11c)$$

We are now in a position to proceed as earlier in this Section. The weak field electrical conductivity is given by

$$\sigma_I(0) = e\mu\gamma_1^{3/2}N_1/2\pi^2; \qquad (8.12)$$

on inserting (8.7), one arrives at the result listed in Table 3, column B. To find the other GTMTC, from equations (5.10)–(5.14), we neglect all terms containing β_1, and introduce (8.7), (8.9) and (8.11) into the remainder. The results are cited in Table 3, column B. The zero order terms appear only in the expressions for σ_I and $\mathscr{R}_I$; to obtain results containing higher order terms, it is necessary to begin anew with the next term in the expansion (8.4). The algebraic manipulations become excessively cumbersome and have not been carried through.

(c) In taking up the case $\nu = 2$, we assume that $x_G \gg |\eta|$ in order to simplify the subsequent mathematical manipulations. The integral N_2, specified by equation (8.6), then reduces to

$$N_2 = (\tfrac{2}{3})(\eta x_G)^{3/2}\{1+\pi^2/8\eta^2\} \qquad (8.13)$$

The remaining transport integrals are found from equations (8.8) and (8.10); in our present approximation, they reduce to

$$I_1^{(2)}(\eta,x_G;r,0) = \eta^{r+1}x_G^{r-1}\{1+r(r+1)\pi^2/6\eta^2\} \qquad (8.14a)$$

$$I_2^{(2)}(\eta,x_G;r,0) = \eta^{r+2}x_G^{r-1}\{1+(r+1)(r+2)\pi^2/6\eta^2\} \qquad (8.14b)$$

$$I_3^{(2)}(\eta,x_G;r,0) = \eta^{r+3}x_G^{r-1}\{1+(r+2)(r+3)\pi^2/6\eta^2\} \qquad (8.14c)$$

and to

$$J_1^{(2)}(\eta,x_G;r,0) = \eta^{2r+1/2}x_G^{2r-7/2}\{1+(2r+\tfrac{1}{2}) \times (2r-\tfrac{1}{2})\pi^2/6\eta^2\} \qquad (8.15a)$$

$$J_2^{(2)}(\eta,x_G;r,0) = \eta^{2r+3/2}x_G^{2r-7/2}\{1+(2r+\tfrac{3}{2}) \times (2r+\tfrac{1}{2})\pi^2/6\eta^2\} \qquad (8.15b)$$

$$J_3^{(2)}(\eta,x_G;r,0) = \eta^{2r+5/2}x_G^{2r-7/2}\{1+(2r+\tfrac{5}{2}) \times (2r+\tfrac{3}{2})\pi^2/6\eta^2\} \qquad (8.15c)$$

respectively.

After introducing (8.13) in (5.7a), one obtains the expression listed in Table 3, column C for the isothermal, weak field electrical conductivity. The remaining transport coefficients are found from equations (5.10)–(5.14) after appropriate simplification and on introducing the results (8.13), (8.14) and (8.15). Again, the first order terms cancel out from the expressions for κ_I, $\mathscr{P}_I$, $\mathscr{N}_I$ and $\mathscr{M}$.

Finally, it should be noted that no difficulties arise from regions of x where the terms $\beta_0^2 x^{2r-1}$ or $_{,2}[x(x+x_G)]^{2r-1}/(2x+x_G)^4$ become large relative to unity, since in those regions $(-\partial f_0/\partial x)$, which appears as a factor in the integrand of the transport integrals, becomes negligibly small for $x \to 0$ or $x \to \infty$.

9. GTMTC FOR THE STRONG FIELD LIMIT IN THE CASE OF EXTREME DEGENERACY

It remains to obtain the limiting expressions for degenerate materials placed in extremely large magnetic fields. Here, we neglect unity relative to the terms $\beta_0^2x^{2r-1}$ or $\beta_{1,2}^2[x(x+x_G)]^{2r-1}/(2x+x_G)^4$ in the denominators of the transport integrals.

(a) For $\nu = 0$, we have, as before, $N_0 = F_{1/2}(\eta)$. Equations (2.7b) and (2.8b) reduce to the form

$$\lim_{\beta_0\to\infty} I_i^{(0)}(\eta; r,\beta_0) = (i-r+1)F_{i-r}(\eta)/\beta_0^2 \quad (9.1a)$$

$$\lim_{\beta_0\to\infty} J_j^{(0)}(\eta; r,\beta_0) = (j+\tfrac{1}{2})F_{j-1/2}(\eta)/\beta_0^2 \quad (9.1b)$$

We now return to equations (5.9)–(5.14) and neglect terms not involving β_0^2 relative to those that do. We then substitute into the resulting expressions from equations (2.4b), (2.5b) and (9.1). Subsequently, equation (8.1) is utilized to eliminate the Fermi–Dirac integrals. After simplifying and neglecting all terms of second order or higher, one obtains the results listed in Table 4, column A.

(b) The case $\nu = 1$ is handled in a manner analogous to the corresponding case in Section 8. The integral N_1 is again represented by equations (8.6), and (8.7) when the approximation $x_G \ll |\eta|$ is introduced. Further, in the strong field approximation, the transport integrals (3.8b) and (3.9b) are given by

$$\lim_{\beta_1\to\infty} I_i^{(1)}(\eta,x_G; r,\beta_1)$$

$$= (1/\beta_1^2)\int_0^\infty x^{i-r+1}(x+x_G)^{2-r}(2x+x_G)^2$$

$$\times\ (-\partial f_0/\partial x)\,\mathrm{d}x \quad (9.2a)$$

$$\lim_{\beta_1\to\infty} J_i^{(1)}(\eta,x_G; r,\beta_1) = (1/\beta_1^2)$$

$$\times\int_0^\infty x^{j+1/2}(x+x_G)^{3/2}(-\partial f_0/\partial x)\,\mathrm{d}x \quad (9.2b)$$

In the limit of extreme degeneracy, we can again represent the integrals (9.2) by equation (8.4). After carrying out the requisite mathematical manipulations, and neglecting x_G relative to η, we obtain the results

$$\lim_{\beta_1\to\infty,x_G\to 0} I_i^{(1)}(\eta,x_G; r,\beta_1) = \frac{4}{\beta_1^2}\eta^{i-2r+5}$$

$$\times\left\{1+\frac{\pi^2}{6\eta^2}(2r-i-5)(2r-i-4)\right\} \quad (9.3a)$$

$$\lim_{\beta_1\to\infty,x_G\to 0} J_j^{(1)}(\eta,x_G; r,\beta_1) = \frac{1}{\beta_1^2}\eta^{j+2}$$

$$\times\left\{1+\frac{\pi^2}{6\eta^2}(j+1)(j+2)\right\} \quad (9.3b)$$

We now return to equations (5.9)–(5.14), neglect the terms not involving β_1^2, and substitute into the resultant from equations (3.6b), (8.7), (8.9a), and (9.3) to obtain the results listed in Table 4, column B.

(c) Lastly, we consider the case $\nu = 2$; here, equation (8.13) still applies. The relevant transport integrals have the same form as (9.2); after representing them by means of the expansion (8.4) and on neglecting all second order terms in which x_G appears in the denominator, we obtain the results

$$\lim_{\beta_2,x_G\to\infty} I_i^{(2)}(\eta,x_G; r,\beta_2) = \frac{\eta^{i-r+1}x_G^{4-r}}{\beta_2^2}$$

$$\times\left\{1+\frac{\pi^2}{6\eta^2}(i+1-r)\,(1-r)\right\} \quad (9.4a)$$

$$\lim_{\beta_2,x_G\to\infty} J_j^{(2)}(\eta,x_G; r,\beta_2) = \frac{\eta^{j+1/2}x_G^{3/2}}{\beta_2^2}$$

$$\times\left\{1+\frac{\pi^2}{6\eta^2}(j+\tfrac{1}{2})\,(j-\tfrac{1}{2})\right\} \quad (9.4b)$$

The last step consists in returning to equations (5.9)–(5.14), neglecting terms not containing β_2^2 and substituting in the resultant from equations (4.3), (8.13) and (9.4). One then arrives at the GTMTC listed in Table 4, column C.

Once again, in the limit of extreme degeneracy, no problems arise from regions where the strong field approximations $\beta_0^2x^{2r-1} \gg 1$ or $\beta_{1,2}^2[x(x+x_G)]^{2r-1}/(2x+x_G)^4 \gg 1$ fail; for, at $x = 0$ or $x \to \infty$, the factor $(-\partial f_0/\partial x)$ in the integrands becomes negligibly small.

10. GENERAL DISCUSSION

In providing a general discussion of the results listed in Tables 1–4 one should note first that there are few materials whose properties can be interpreted in terms of a spherically symmetric parabolic band structure. The applicability of the simple band model is restricted to pure semiconductors at low temperatures. The smaller the energy gap, the greater is the required degree of purity for the simple band model to apply. The exact calculations to be published in a subsequent paper show that the nonparabolic characteristics of a band are reflected in some GTMTC even when classical statistics prevail. EHRENREICH(26) had already established that deviations from parabolicity did not appreciably affect the calculated α, provided the correct Fermi level, given by equation (3.4a), is used in equation (5.16) with $\nu = 0$. In agreement with this, we find that for a fixed η and r, the calculated difference in α for the parabolic and Kane band shapes is less than 10 per cent, at least for $x_G = 4{,}7$. However, for fixed $H_z \gg 0$, η, and r, the exact calculations show that the fractional change in α or ρ with band shape can exceed one order of magnitude even in the region of classical statistics. Next, it should be remembered that the formulae derived in Sections 7 and 9 fail to account for various quantum oscillatory phenomena encountered at very low temperatures. Attention is also directed to the references in the tables of earlier work on the same subject; except for minor differences due to misprints, our results agree with those of other workers. However, our relation for $\mathscr{P}_I(0)$, $\mathscr{P}_I(\infty)$ and $\kappa(\infty) - \kappa_L$ differ radically from those cited by BASS and TSIDIL'KOVSKII(7) and by TOLPYGO.(15)

Inspection of Table 1 shows that the expressions for $\mathscr{R}_I(0)$, $\mathscr{N}_I(0)$ and $\mathscr{M}_I(0)$ involve the ratio $\Gamma(2r+\frac{5}{2})/\Gamma^2(r+2)$, whereas in Table 2, the quantities $\sigma_I(\infty)$, $\kappa_I(\infty) - \kappa_L$, and $\mathscr{N}_I(\infty)$ depend on the product $\Gamma(2+r)\ \Gamma(3-r)$ in the classical limit. It is of interest that $\sigma_I(\infty)$, $\mathscr{R}_I(\infty)$ and $\mathscr{P}_I(\infty)$ do not involve the product μH and hence do not approach zero as $\mu H \rightarrow \infty$. Further, it is evident that within each of the four tables, κ_I and $\mathscr{M}_I$ are independent of the case ν; similarly, the relations for $\mathscr{R}_I$ differ from one another only within Table 3, and then only in the first order terms. In Table 4, the difference between $\sigma_I(\infty)$ and $\sigma_I(0)$ is small. For any of the cases under consideration, the isothermal Hall coefficient in strong magnetic fields is given by the quantity $1/Znec$; this relationship remains essentially valid also for $\mathscr{R}_I(0)$ under conditions of extreme degeneracy. In the classical approximation, $\kappa_I - \kappa_L$ depends on r, but is independent of the scattering index in the limit of extreme degeneracy. The Seebeck coefficient changes with r in the weak field but not in the strong field limit. For classical statistics, $\mathscr{P}_I$ is a linear function of η, whereas for degenerate materials, $\mathscr{P}_I \propto 1/\eta$. Changes in magnetic field strengths exert a much smaller effect on $\mathscr{P}_I$ than the transition from classical to quantum statistics. The Nernst coefficient is independent of the sign of the charge carrier but exhibits a dependence on the factor $\mathscr{N}_I \sim (\frac{1}{2}-r)$, except for the case $\nu = 1$ in Tables 3 and 4, where $\mathscr{N}_I \sim (\frac{3}{2}-r)$. As will be recalled, the case $\nu = 1$ cannot be treated in the limit of classical statistics. Exact calculations to be published later show that under a variety of conditions, $\mathscr{N}_I$ does not change sign in the range $0 < r < 1$. In view of these results, one cannot, as has been recommended in the literature,(18–24) use the sign of $\mathscr{N}_I$ to determine the range of r values experimentally, unless the band shape is known. Furthermore, these results definitely disprove the contention by NASLEDOV(25) that the band form is without influence on the parametric dependence of $\mathscr{N}_I$ on r. Some similar qualitative arguments concerning Nasledov's work on GaAs have recently been given by CARLSON(27) *et al.* Finally, in the approximation schemes utilized here, $\mathscr{M}$ is independent of r except for the cases covered in Table 1.

In a sequel paper, the theoretical expressions presented here will be compared with experimental data on HgSe and InSb.

REFERENCES

1. HARMAN T. C. and HONIG J. M., *J. Phys. Chem. Solids* **23**, 913 (1962). Hereafter referred to as (H).
2. CHAMBERS R. G., *Proc. Phys. Soc. Lond.* **A65**, 903 (1952).
3. PUTLEY E. H., *The Hall Effect and Related Phenomena*. Chap. 3. Butterworths, London (1960).
4. KANE E. O., *J. Phys. Chem. Solids* **1**, 249 (1957).
5. EHRENREICH H., *Phys. Rev.* **120**, 1951 (1960).
6. APPEL J., *Z. Naturf.* **9a**, 167 (1954).
7. BASS F. G. and TSIDIL'KOVSKII I. M., *Zh. eksp. teor. fiz. S.S.S.R.* **31**, 672 (1956); translation: *Sov. Phys. J.E.T.P.* **4**, 565 (1957).
8. DRABBLE J. R. and GOLDSMID J. H., *Thermal Conduction in Semiconductors*, p. 110. Pergamon Press, Oxford (1961).
9. HARMAN T. C., WILLARDSON R. K. and BEER A. C., *Phys. Rev.* **94**, 1065 (1954).
10. MADELUNG O., *Z. Naturf.* **8a**, 791 (1953).
11. RODOT M., *Ann. phys.* **5**, 1085 (1960).
12. SEITZ F., *The Modern Theory of Solids*, pp. 178, 192. McGraw-Hill, New York (1940).

13. SMITH R. A., *Semiconductors*, pp. 118, 169, 172, 173, 181, 183, 185. University Press, Cambridge (1959).
14. TAUC J., *Photo and Thermoelectric Effects in Semiconductors*, pp. 52, 54, 57, 215. Pergamon Press, Oxford (1962).
15. TOLPYGO K. B., *Trud. fiz. akad. nauk. Ukrain. S.S.R.* Sec. **3** (1952).
16. WILSON A. H., *The Theory of Metals*, pp. 220, 232, 238. University Press, Cambridge (1958).
17. ZIMAN J. M., *Electrons and Phonons*, p. 385. Clarendon Press, Oxford (1960).
18. TSIDIL'KOVSKII I. M., *Dokl. akad. nauk. S.S.S.R.* **102,** 737 (1955).
19. RODOT M., *J. phys. radium* **19,** 140 (1958).
20. ZHUZE V. P. and TSIDIL'KOVSKII I. M., *Zh. tekh. fiz. S.S.S.R.* **28,** 2372 (1958); translation: *Sov. Tech. Phys.* **3,** 2177 (1959).
21. EMEL'YANENKO O., ZOTOVA N. and NASLEDOV D., *Fiz. tverd. tela* **1,** 1868 (1959); translation: *Sov. Phys. Solid State* **1,** 1711 (1960).
22. EMEL'YANENKO O. and NASLEDOV D., *Fiz. tverd. tela* **1,** 985 (1959); translation: *Sov. Phys. Solid State* **1,** 902 (1959).
23. NASLEDOV D., *J. chim. phys.* **57,** 479 (1960).
24. EMEL'YANENKO O., NASLEDOV D. and PETROV R., *Fiz. tverd. tela* **2,** 2455 (1960); translation: *Sov. Phys. Solid State* **2,** 2188 (1961).
25. NASLEDOV D., *J. Appl. Phys.* **32,** 2140 (1961).
26. EHRENREICH H., *J. Phys. Chem. Solids* **2,** 131 (1957).
27. CARLSON R. O., SILVERMAN S. and EHRENREICH H., *J. Phys. Chem. Solids*, in press.
28. EHRENREICH H., *J. appl. Phys.* **32,** 2155 (1961), cf. Fig. 5.

APPENDIX A

Applicability of Results Listed in Tables 1–4.

1. The results presented in the subsequent tables are not applicable if

(a) more than one type of carrier plays an appreciable role in the determination of the transport property under consideration.

(b) the electronic energy surfaces are not spherically symmetric.

(c) the electric field and temperature gradient are so large that Ohm's and Fourier's laws are not obeyed.

2a. The Kane model finds its most fruitful application in polar materials. In these compounds, at least in the low temperature and lattice scattering range, the relaxation time approximation is not valid. However, EHRENREICH[28] has compared the results of the variational technique for polar scattering with those of the relaxation time approximation. For temperatures only a little greater than that corresponding to the longitudinal optical frequency, the two approaches gave the same results.

2b. The formulae cited below are valid if a relaxation time exists such that τ can be written as $\tau_0(\mathrm{d}\epsilon/\mathrm{d}k)k^{2r-2}$.

3. It is expected theoretically that the effects on observed GTMTC due to orbital or spin quantization will be small for at least the range $\hbar eH_z/m^*ckT \lesssim 1$ and $\dfrac{\mu H_z}{c} \equiv \dfrac{eH_z\tau}{m^*c} \lesssim 1$.

4. The limiting value of $\mathscr{R}_I$ in very large magnetic fields remains valid, independent of the symmetry of the energy surfaces and of the mechanism of charge carrier scattering for materials with the cubic crystal structure.

Table 1. GTMTC *in the limit of weak fields, classical statistics*

Effect	A General Formula	B Special Case; $r = 0$	References to Prior Work
$\frac{\sigma_I(0)^*}{e\mu/2\pi^2}$	$\begin{cases}\gamma_e^{3/2}(e^\eta/2)\sqrt{\pi} & (\nu = 0)\\ (\gamma_0 x_\sigma)^{3/2}(e^\eta/2)\sqrt{\pi} & (\nu = 2)\end{cases}$	—	
$\frac{\mathscr{R}_I(0)}{[Znec]^{-1}}$	$\frac{3}{4}\sqrt{\pi}\,\frac{\Gamma(2r+\frac{3}{2})}{\Gamma^2(r+2)}$	$\frac{3\pi}{8}$	3, 11, 12, 13, 14, 16
$\frac{\kappa_I(0)-\kappa_L}{k^2T\sigma(0)/e^2}$	$2+r$	2	3, 7, 8, 13, 14
$\frac{\mathscr{P}_I(0)}{k/Ze}$	$2+r-\eta$	$2-\eta$	3, 7, 8, 13, 15, 16
$\frac{\mathscr{N}_I(0)}{k\mu/ec}$	$(\frac{1}{2}-r)\,\frac{3}{4}\sqrt{\pi}\,\frac{\Gamma(2r+\frac{3}{2})}{\Gamma^2(r+2)}$	$\frac{3\pi}{16}$	3, 7, 13, 14, 15
$\frac{\mathscr{M}(0)}{\frac{k^2T\sigma(0)}{e^2\kappa_I(0)}\,\frac{\mu}{Zc}}$	$(\frac{7}{4}+r+r^2)\,\frac{3}{4}\sqrt{\pi}\,\frac{\Gamma(2r+\frac{3}{2})}{\Gamma^2(r+2)}$	$\frac{21\pi}{32}$	3, 13

* Corresponding entry in Table 3 is $\sigma_I(0) \div e\mu/3\pi^2$.

Table 2. GTMTC *in the limit of very strong fields, classical statistics*

Effect	A General Formula	B Special Case; $r = 0$	References
$\sigma_I(\infty)/\sigma_I(0)$	$\frac{9\pi}{16}\,\frac{1}{\Gamma(3-r)\Gamma(2+r)}$	$\frac{9\pi}{32}$	3, 6, 10, 16
$\frac{\mathscr{R}_I(\infty)}{[Znec]^{-1}}$	1	1	3, 6, 9, 10, 14, 16
$\frac{\kappa_I(\infty)-\kappa_L}{\frac{k^2T}{e^2}\,\sigma(0)\left(\frac{c}{\mu H_z}\right)^2}$	$\frac{16}{9\pi}(r^2-2r+\frac{13}{4})\Gamma(3-r)\Gamma(2+r)$	$\frac{104}{9\pi}$	7, 15
$\frac{\mathscr{P}_I(\infty)}{k/Ze}$	$\frac{5}{2}-\eta$	$\frac{5}{2}-\eta$	7, 15
$\frac{H_z\mathscr{N}_I(\infty)}{\frac{k}{e}\left(\frac{c}{\mu H_z}\right)}$	$\frac{16}{9\pi}(\frac{1}{2}-r)\Gamma(3-r)\Gamma(2+r)$	$\frac{16}{9\pi}$	7
$\frac{H_z\mathscr{M}(\infty)}{\frac{k^2T}{e^2}\,\frac{Zc}{\mu H_z}\,\frac{\sigma(0)}{\kappa_I(\infty)}}$	$\frac{5}{2}$	$\frac{5}{2}$	

Table 3. GTMTC *in the limit of weak fields, extreme degeneracy*

Effect	A Case $\nu = 0$	References	B Case $\nu = 1$	C Case $\nu = 2$
$\dfrac{\sigma_I(0)^*}{e\mu/3\pi^2}$	$(\gamma_0\eta)^{2/3}\left\{1+\dfrac{\pi^2}{8\eta^2}\right\}$	—	$\gamma_1^{3/2}\eta^3\left\{1+\dfrac{\pi^2}{\eta^2}\right\}$	$(x_0\gamma_2\eta)^{2/3}\left\{1+\dfrac{\pi^2}{8\eta^2}\right\}$
$\dfrac{\mathscr{R}_I(0)}{[Znec]^{-1}}$	$1+\dfrac{\pi^2}{3\eta^2}(r-\frac{1}{2})^2$	—	$1+\dfrac{\pi^2}{3\eta^2}(2r-3)^2$	$1+\dfrac{\pi^2}{3\eta^2}(r-\frac{1}{2})^2$
$\dfrac{\kappa_I(0)-\kappa_L}{k^2T\sigma(0)/e^2}$	$\dfrac{\pi^2}{3}$	8, 12, 16, 17	$\dfrac{\pi^2}{3}$	$\dfrac{\pi^2}{3}$
$\dfrac{\mathscr{P}_I(0)}{k/Ze}$	$\dfrac{\pi^2}{3\eta}(1+r)$	13, 16	$\dfrac{2}{3}\,\dfrac{\pi^2 r}{\eta}$	$\dfrac{\pi^2}{3\eta}(1+r)$
$\dfrac{\mathscr{N}_I(0)}{k\mu/ec}$	$\dfrac{\pi^2}{3\eta}(\frac{1}{2}-r)$	13	$\dfrac{2\pi^2}{3\eta}(\frac{3}{2}-r)$	$\dfrac{\pi^2}{3\eta}(\frac{1}{2}-r)$
$\dfrac{\mathscr{M}(0)}{\dfrac{k^2T}{e^2}\,\dfrac{\sigma(0)}{\kappa_I(0)}\,\dfrac{\mu}{Zc}}$	$\dfrac{\pi^2}{3}$	—	$\dfrac{\pi^2}{3}$	$\dfrac{\pi^2}{3}$

* Corresponding entry in Table 1 is $\sigma_I(0) \div e\mu/2\pi^2$.

Table 4. GTMTC *in the limit of very strong fields, extreme degeneracy*

Effect	A Case $\nu = 0$	References	B Case $\nu = 1$	C Case $\nu = 2$
$\sigma_I(\infty)/\sigma_I(0)$	$1-\dfrac{\pi^2}{3\eta^2}(r-\frac{1}{2})^2$		$1-\dfrac{\pi^2}{3\eta^2}(2r-3)^2$	$1-\dfrac{\pi^2}{3\eta^2}(r-\frac{1}{2})^2$
$\dfrac{\mathscr{R}_I(\infty)}{[Znec]^{-1}}$	1	3, 6, 9, 10, 14, 16	1	1
$\dfrac{\kappa_I(\infty)-\kappa_L}{\dfrac{k^2T}{e^2}\sigma(0)\left(\dfrac{c}{\mu H_s}\right)^2}$	$\dfrac{\pi^2}{3}$		$\dfrac{\pi^2}{3}$	$\dfrac{\pi^2}{3}$
$\dfrac{\mathscr{P}_I(\infty)}{k/Ze}$	$\dfrac{\pi^2}{2\eta}$		$\dfrac{\pi^2}{\eta}$	$\dfrac{\pi^2}{2\eta}$
$\dfrac{H_s\mathscr{N}_I(\infty)}{\dfrac{k}{e}\,\dfrac{c}{\mu H_s}}$	$\dfrac{\pi^2}{3\eta}(\frac{1}{2}-r)$		$\dfrac{2\pi^2}{3\eta}(\frac{3}{2}-r)$	$\dfrac{\pi^2}{3\eta}(\frac{1}{2}-r)$
$\dfrac{H_s\mathscr{M}(\infty)}{\dfrac{k^2T}{e^2}\,\dfrac{\sigma(0)}{\kappa_I(\infty)}\left(\dfrac{Zc}{\mu H_s}\right)}$	$\dfrac{\pi^2}{3}$		$\dfrac{\pi^2}{3}$	$\dfrac{\pi^2}{3}$

APPENDIX B

List of symbols in tables:

GTMTC	Galvano-thermomagnetic transport coefficient.
$\sigma_I(0)$, $\sigma_I(\infty)$	isothermal electrical conductivity for zero and very strong magnetic fields, respectively.
$\mathscr{R}_I(0)$, $\mathscr{R}_I(\infty)$	isothermal Hall coefficient in weak and very strong magnetic fields, respectively.
$\kappa_I(0)$, $\kappa_I(\infty)$	isothermal thermal conductivity in weak and very strong magnetic fields, respectively.
κ_L	lattice thermal conductivity.
$\mathscr{P}_I(0)$, $\mathscr{P}_I(\infty)$	isothermal Seebeck coefficient for weak and very strong magnetic fields, respectively.
$\mathscr{N}_I(0)$, $\mathscr{N}_I(\infty)$	isothermal Nernst coefficient for weak and very strong magnetic fields, respectively.
$\mathscr{M}(0)$, $\mathscr{M}(\infty)$	Righi–Leduc coefficient for weak and very strong magnetic fields, respectively.
T	temperature.
H_z	magnetic field strength.
e	absolute value of electronic charge.
k	Boltzmann constant.
h	Planck constant.
c	velocity of light.
r	carrier scattering parameter; $r = 0$ corresponds to acoustical mode scattering, $r = 1$ corresponds to optical mode scattering, and $r = 2$ corresponds to ionized impurity scattering.
μ_B	Fermi level energy with respect to the band edge energy.
$\mathscr{E}_G$	energy gap which occurs in the Kane band model.
μ	isothermal conductivity carrier mobility for $H_z = 0$.
n	carrier concentration.
m^*	effective mass of the charge carriers in parabolic band model.
P	matrix element defined in Ref. 4.
ν	index symbol specifying the case under study; $\nu = 0$ is the parabolic band model, $\nu = 1$ is the narrow gap Kane band model, and $\nu = 2$ is the wide gap Kane band model.
Z	$+1$ for holes and -1 for electrons.
$\eta = \mu_B/kT$	reduced Fermi level energy.
$x_G = \mathscr{E}_G/kT$	reduced energy gap.
$\gamma_0 = 2m^*kT/\hbar^2$	
$\gamma_1 = \frac{3}{2}(kT/P)^2$	
$\gamma_2 = (kT/P)^2$	
$\hbar = h/2\pi$	

Note added in proof: In equations (4.7a) and (4.7b) of paper II in this series, replace J_Q^x/T and J_Q^y/T by J_S^x and J_S^y, respectively, where $TJ_S = J_Q - \mu_B J$; J_S is the entropy flux vector. Then equations (4.7) satisfy the Onsager reciprocity conditions.

J. Phys. Chem. Solids Pergamon Press 1963. Vol. 24, pp. 851–862. Printed in Great Britain.

ORBITAL SUSCEPTIBILITY OF DILUTE ALLOYS

W. KOHN and **M. LUMING**

Department of Physics, University of California, San Diego, La Jolla, California

(*Received* 26 *December* 1962)

Abstract—An explicit expression is obtained for the change of the orbital (diamagnetic) susceptibility of an electron gas produced by a localized spherical perturbation. The result is applied to a study of dilute solutions of Zn, Ga, Ge and As in Cu, but does not help to account for the experimental data. Comments are made on previous theoretical interpretations.

1. INTRODUCTION

OVER the past years several measurements of temperature independent total magnetic susceptibilities of metallic alloys have been reported.(1,2,3) One expects that, at least for some simple alloys, the total susceptibility can adequately be regarded as consisting of three parts: A diamagnetic core contribution, the paramagnetic spin susceptibility and the orbital diamagnetic susceptibility of the conduction electrons. The core susceptibility can be rather simply estimated and some simplified theories for the spin susceptibility exist.(4) However, no well-founded theory for the diamagnetic contribution of the solute atoms has been available.

In the present paper we present a theory for the diamagnetic susceptibility of a simple model of a dilute alloy. We describe the effect of each solute atom by a spherical potential $V(r)$ and regard the conduction electrons as independent particles moving in this potential. In this model effects of the periodic potential of the host lattice can be included only very roughly through an appropriate choice of an effective mass of the electrons; and the electron–electron interaction enters only through the value of the effective mass and the form of $V(r)$ which should be chosen to incorporate the screening of the solute atom by the conduction electrons.

For this model we obtain an explicit expression (equation 3.31) for the contribution of each solute atom to the orbital susceptibility. It consists of a diamagnetic term, arising from the screening charge and identical in form to the diamagnetism of an atom, and an orbital paramagnetic term expressible in terms of scattering phase shifts. For an electron density characteristic of Cu, the two terms largely cancel leaving a very weak orbital diamagnetic contribution of impurities with excess valence ΔZ. It is also explicitly shown that if the perturbation due to the solute atom can be treated as weak, our expression reduces correctly to the change in diamagnetism due to the addition of ΔZ electrons to the host material.

Unfortunately, our theory does not at all agree with experiment, presumably because of the neglected band characteristics of the Cu electrons.

2. WEAK PERTURBING POTENTIAL

If the perturbation due to a solute atom can be regarded as weak, the effect of alloying on the diamagnetic susceptibility can be extremely easily determined.

Consider a gas of N non-interacting electrons in an enclosure of volume V in the presence of a magnetic field $\mathscr{H}$ and of a weak perturbing potential $\lambda V(r)$. We denote the orbital ground state energy of the system by $E^N(\mathscr{H},\lambda)$ and its uniform density, when $\lambda = 0$, by $\rho^N(\mathscr{H})$. It is evident from the spatial homogeneity of the system that, *for all values of* $\mathscr{H}$,

$$\rho^N(\mathscr{H}) \equiv \frac{N}{V}. \tag{2.1}$$

Now by first order perturbation theory in λ we find

$$\begin{aligned} E^N(\mathscr{H},\lambda) - E^N(\mathscr{H},0) &= \lambda \int V(r)\rho^N(\mathscr{H})\,\mathrm{d}\mathbf{r} \\ &= \lambda \frac{N}{V} \int V(r)\,\mathrm{d}\mathbf{r} \end{aligned} \tag{2.2}$$

independent of $\mathscr{H}$. The diamagnetic susceptibility is given by

$$\chi^N(\mathscr{H},\lambda) = -\frac{1}{V}\frac{\partial^2 E^N(\mathscr{H},\lambda)}{\partial \mathscr{H}^2}. \tag{2.3}$$

Therefore, when we differentiate (2.2) twice with respect to $\mathscr{H}$, we obtain

$$\chi^N(\mathscr{H},\lambda) = \chi^N(\mathscr{H},0), \tag{2.4}$$

to first order in λ.

We see, then, that if the perturbation due to the solute atoms can be treated as weak, the susceptibility of an alloy is the same as that of a free electron gas with the same number of electrons as the alloy. Using the standard theory of diamagnetism of free electrons, this give the following result,(5)

$$\Delta\chi = -\Delta Z\frac{1}{12c^2k_F^2}, \tag{2.5}$$

for the contribution to the volume susceptibility of one solute atom with excess valence ΔZ per unit volume. Here k_F is the Fermi momentum of the host material.

3. PERTURBING POTENTIAL OF ARBITRARY STRENGTH

We begin by considering the diamagnetic response of a free electron gas in the absence of a perturbing potential. The gas is in a spherical enclosure of radius R and the field $\mathscr{H}$ is taken to be in the z direction. We write the vector potential as

$$A = \tfrac{1}{2}\mathscr{H}\times r. \tag{3.1}$$

Then the total Hamiltonian for each electron is

$$H_T = -\tfrac{1}{2}\nabla^2+\frac{\mathscr{H}}{2ic}\left(x\frac{\partial}{\partial y}-y\frac{\partial}{\partial x}\right)+\frac{\mathscr{H}^2}{8c^2}(x^2+y^2). \tag{3.2}$$

Writing

$$L_z \equiv \frac{1}{i}\left(x\frac{\partial}{\partial y}-y\frac{\partial}{\partial x}\right) \tag{3.3}$$

we split this as follows

$$H_T = H+H', \tag{3.4}$$

where

$$H \equiv -\tfrac{1}{2}\nabla^2+\frac{\mathscr{H}}{2c}L_z, \tag{3.5}$$

and

$$H' = \frac{\mathscr{H}^2}{8c^2}(x^2+y^2). \tag{3.6}$$

We are interested in the magnetic moment M of the system which is given by

$$M = M_0+M_1, \tag{3.7}$$

where

$$M_0 \equiv -\frac{1}{2c}L_z \tag{3.8}$$

and

$$M_1 = -\frac{\mathscr{H}}{4c^2}(x^2+y^2). \tag{3.9}$$

To obtain the expectation value of M to first order in $\mathscr{H}$ one is tempted to proceed in the following manner: Treating $\mathscr{H}$ formally as a small parameter one neglects H', which is of second order in $\mathscr{H}$, in the calculation of the ground state wave function Ψ. The computation is then quite easy since the Schroedinger equation corresponding to H separates. However, a well-known difficulty of this procedure (which makes it inappropriate for the calculation of the diamagnetism of a free electron gas) is that while $\mathscr{H}$ is small, the expression $\mathscr{H}^2(x^2+y^2)$ occurring in H' is not. Nevertheless, in calculating the *change* of the diamagnetism due to a solute atom it turns out that the relevant values of x and y are of the order of the range of the potential $V(r)$, rather than R, so that this difficulty does not arise. Any doubts concerning one's right to use the method just outlined are removed in Appendices I and II where our result is shown to reduce to that obtained in Section 2 for a weak potential and is re-derived by an entirely independent but more complicated method.

We now proceed as explained. The eigenfunctions of H are

$$\phi_{k,l,m} = j_l(kr)Y_{l,m}(\theta,\phi) \tag{3.10}$$

and the corresponding energies

$$E_{k,l,m} = \tfrac{1}{2}k^2+\frac{\mathscr{H}}{2c}m. \tag{3.11}$$

The allowed values of k are determined by the boundary condition

$$j_l(kR) = 0 \tag{3.12}$$

which for values of

$$l \ll kR \tag{3.13}$$

is equivalent to

$$(kR)^{-1} \sin\left(kR - \frac{l}{2}\pi\right) = 0 \tag{3.14}$$

or

$$kR - \frac{l}{2}\pi = n\pi, \quad n = \text{integer}. \tag{3.15}$$

Let E_F be the Fermi energy in the presence of the field $\mathscr{H}$. Then all single particle states with

$$E_{k,l,m} \leqslant E_F \tag{3.16}$$

are occupied, all others empty.

Take for example $l = 1$. By (3.11) and (3.16) the maximum values of k associated with $m = 1, 0$, and -1 are given by

$$\begin{aligned} \tfrac{1}{2}k^2_{1,1} &= E_F - \frac{\mathscr{H}}{2c} \\ \tfrac{1}{2}k^2_{1,0} &= E_F \\ \tfrac{1}{2}k^2_{1,-1} &= E_F + \frac{\mathscr{H}}{2c}. \end{aligned} \tag{3.17}$$

Since, by (3.8),

$$\langle M_0 \rangle_{k,l,m} = -\frac{1}{2c} m \tag{3.18}$$

we see that the total contribution to $\langle M_0 \rangle$ from states with $l = 1$ is

$$\langle M_0 \rangle_1 = \frac{\mathscr{H}}{2c} g_1(E_F) \tag{3.19}$$

where $g_l(E_F)$ is the density of states with given l, and any compatible value of m, at $\frac{1}{2}k^2 = E_F$. As (3.19) already contains an explicit factor $\mathscr{H}$, the field can be ignored in calculating $g_l(E_F)$. From equation (3.15) one finds

$$g_l(E_F) = \frac{2R}{\pi k_F}, \tag{3.20}$$

including spin degeneracy.

Turning now to M_1, we may evaluate its expectation value in the completely unperturbed ground state ($\mathscr{H} = 0$). The contribution of states with $l = 1$ is

$$\langle M_1 \rangle_1 = -\frac{\mathscr{H}}{4c^2} \langle x^2 + y^2 \rangle_1 \tag{3.21}$$

where

$$\langle x^2 + y^2 \rangle_1 = \int (x^2 + y^2) \rho_1(r) \, d\mathbf{r}, \tag{3.22}$$

ρ_1 being the unperturbed density associated with $l = 1$. In the same way we obtain from a general value of l

$$\langle M_0 \rangle_l = \frac{\mathscr{H}}{2c^2} g_l(E_F) \frac{(2l+1)(l+1)l}{6} \tag{3.23}$$

and

$$\langle M_1 \rangle_l = -\frac{\mathscr{H}}{6c^2} \int r^2 \rho_l(r) \, d\mathbf{r}. \tag{3.24}$$

It should be noted however that (3.23) is valid only for moderate values of l, which satisfy the condition $l \ll k_F R$ (see equation (3.13)) as well as $(\mathscr{H}/2c) l \mathscr{H} E_F$, since in deriving (3.23) the magnetic energy $(\mathscr{H}/2c)m$ has been neglected compared to E_F. We shall see (equation 3.30) that only such values of l occur in our final result.

We now consider the same system except that a short range spherical potential $V(r)$ is added to the Hamiltonian and the total number of electrons is adjusted in such a way that E_F, and hence the electron density at large distances, is unchanged. The potential can be of arbitrary strength and may or may not have bound states.

The radial eigenfunctions of H with positive energies now have the asymptotic behavior

$$(kr)^{-1} \sin\left(kr - \frac{l}{2}\pi + \eta_l(k)\right) \tag{3.25}$$

where the η_l are the phase shifts associated with $V(r)$. The boundary conditions (3.15) are therefore replaced by

$$kR - \frac{l}{2}\pi + \eta_l(k) = n\pi, \quad n = \text{integer} \tag{3.26}$$

giving rise to an altered density of states

$$g_l'(E_F) = 2\left[\frac{R}{\pi k_F}+\frac{1}{\pi}\left(\frac{\mathrm{d}\eta_l}{\mathrm{d}E}\right)_{E=E_F}\right]. \tag{3.27}$$

Thus (3.23) is simply replaced by

$$\langle M_0\rangle_l' = \frac{\mathscr{H}}{2c^2}g_l'(E_F)\frac{(2l+1)(l+1)l}{6} \tag{3.28}$$

and instead of (3.24) we have

$$\langle M_1\rangle_l' = -\frac{\mathscr{H}}{6c^2}\int r^2\rho_l'(r)\,\mathrm{d}r \tag{3.29}$$

where $\rho_l'(r)$ is the electron density associated with angular momentum l, in the presence of $V(r)$ but in the absence of $\mathscr{H}$.

The additional moment due to the solute atom is found by subtracting the sum of (3.23) and (3.24) from the sum of (3.28) and (3.29) and adding up the contributions from all l-values. The result is

$$\Delta M = \frac{\mathscr{H}}{c^2}\left[\frac{1}{\pi}\sum_{l=1}^{\infty}\frac{(2l+1)(l+1)l}{6}\left(\frac{\mathrm{d}\eta_l}{\mathrm{d}E}\right)_{E=E_F} -\frac{1}{6}\int\Delta\rho(r)r^2\,\mathrm{d}r\right] \tag{3.30}$$

where $\Delta\rho$ is the change of the electron density due to the solute atom. Thus if there are N_s solute atoms per unit volume the additional magnetic susceptibility per unit volume is (with e, $\hbar$ and m restored)

$$\Delta\chi = N_s\left[\left(\frac{e\hbar}{mc}\right)^2\frac{1}{\pi}\sum_{l=1}^{\infty}\frac{(2l+1)(l+1)l}{6}\left(\frac{\mathrm{d}\eta_l}{\mathrm{d}E}\right)_{E=E_F} -\frac{e^2}{6mc^2}\int\Delta\rho(r)r^2\,\mathrm{d}r\right]. \tag{3.31}$$

This is the central result of the present paper. The second term in equation (3.31) has the same form as the diamagnetic susceptibility of isolated atoms whose charge density is $\Delta\rho(r)$. We see, however, that the correct expression contains also another term, which we shall find to have a comparable magnitude and the opposite sign.

4. APPLICATION TO A FREE ELECTRON MODEL OF DILUTE ALLOYS OF COPPER

In attempting quantitative application of our theory to an alloy one should in principle:

1. Obtain a self-consistent impurity potential $V(r)$.
2. Using this potential and corresponding electron density evaluate the phase-shifts and mean-value of r^2, as needed in equation (3.31).

Generally this is a very lengthy program, and we shall follow it completely in only one limiting case: An electron-gas, with density corresponding to copper, in which point charges of *small* magnitude ΔZ are immersed. A dilute alloy of Zn in Cu ($\Delta Z = 1$) corresponds most closely to this model.

In this model the self-consistent Hartree potential $V_H(r)$ is known.(6) It is given, to first order in ΔZ, by

$$V_{H,\mathrm{lin}} = \Delta Z\frac{1}{2\pi^2}\int\frac{4\pi W(\mathbf{p})}{p^2[4\pi W(\mathbf{p})+p^2]}e^{i\mathbf{p}\cdot\mathbf{r}}\,\mathrm{d}\mathbf{p}-\frac{\Delta Z}{r} \tag{4.1}$$

and the corresponding electron density is

$$\Delta\rho_{H,\mathrm{lin}}(r) = \Delta Z\frac{1}{(2\pi)^3}\int\frac{4\pi W(p)}{4\pi W(\mathbf{p})+p^2}e^{i\mathbf{p}\cdot\mathbf{r}}\mathrm{d}\mathbf{p}\,; \tag{4.2}$$

here

$$4\pi W(\mathbf{p}) = 0{\cdot}3317\; r_s k_F^3\left[1+\frac{k_F}{p}\left(1-\frac{p^2}{4k_F^2}\right)\times\log\left|\frac{p+2k_F}{p-2k_F}\right|\right] \tag{4.3}$$

and r_s is the Wigner–Seitz radius.

With the help of equation (Al.10) one finds directly that

$$\Delta\chi^-_{H,\mathrm{lin}} \equiv -\left[\frac{1}{6c^2}\int\Delta\rho(r)r^2\,\mathrm{d}r\right]_{H,\mathrm{lin}} = -\frac{\Delta Z}{c^2}\frac{\pi}{4k_F} \tag{4.4}$$

and similarly, from (4.1) and (A1.8)

$$\Delta\chi^+_{H,\mathrm{lin}} \equiv \left[\frac{1}{c^2\pi}\sum_{1}^{\infty}\frac{(2l+1)(l+1)l}{6}\times\left(\frac{\mathrm{d}\eta_l}{\mathrm{d}E}\right)_{E=E_F}\right]_{H,\mathrm{lin}} = \frac{\Delta Z}{c^2}\left(\frac{\pi}{4k_F}-\frac{1}{12k_F^2}\right) \tag{4.5}$$

Using these results in (3.31) gives, in atomic units,

$$\Delta\chi_{H,\text{lin}} = -\frac{\Delta Z}{12k_F^2c^2} \tag{4.6}$$

per solute atom in agreement with the linear result (2.5), which holds for arbitrary $V(r)$ and the $\Delta\rho(r)$ produced by it. The values of (4.4) and (4.5) as well as their sum which gives the additional orbital susceptibility per solute atom are given in Table 1, columns 1, 4, and 7. It will be noticed that there is a large degree of cancellation. In fact, the ratio of the final result $\Delta\chi$ to the "atomic type" result $\Delta\chi^-$ is, in the case of copper,

$$\frac{\Delta\chi}{\Delta\chi} = \frac{1}{3\pi k_F} = 0{\cdot}15. \tag{4.7}$$

This cancellation makes reliable quantitative estimates of $\Delta\chi$ very hard, particularly since both $\Delta\chi^+$ and $\Delta\chi^-$ are very sensitive to the distant parts of the screening charge.

We now attempt to do better than the linear theory, which cannot be a priori relied on since in reality ΔZ is at least equal to 1. For this purpose we make use of available solutions of the non-linear Thomas Fermi equation(7) for various values of ΔZ. But first, to check the validity of the Thomas Fermi procedure, let us compare its results for small ΔZ with the results of the self-consistent Hartree potential, equations (4.4) and (4.5). The Thomas Fermi equation gives for small ΔZ

$$\Delta\rho_{TF}(r) = \Delta Z\frac{\kappa^2}{4\pi}\frac{e^{-\kappa r}}{r} = \frac{\Delta Z\kappa^2}{(2\pi)^3}\int\frac{1}{p^2+\kappa^2}e^{i\mathbf{p}\cdot\mathbf{r}}\,d\mathbf{p} \tag{4.8}$$

where

$$\kappa^2 = \frac{4k_F}{\pi} \tag{4.9}$$

and

$$V_{TF}(r) = -\Delta Z\frac{e^{-\kappa r}}{r} = -\frac{4\pi\Delta Z}{(2\pi)^3}\int\frac{1}{p^2+\kappa^2}e^{i\mathbf{p}\cdot\mathbf{r}}\,d\mathbf{p} \tag{4.10}$$

From (4.8) we find

$$\Delta\chi_{TF}^- = -\frac{\Delta Z}{c^2}\frac{\pi}{4k_F} \tag{4.11}$$

and using $V_{TF}(r)$ in equation (A1.8) gives

$$\Delta\chi_{TF}^+ = \frac{\Delta Z}{c^2}\frac{\pi}{4k_F}, \tag{4.12}$$

leading to

$$\Delta\chi_{TF} = 0. \tag{4.13}$$

Comparison with (4.4) and (4.5) shows that, at least for small ΔZ,

$$\Delta\chi_H^- = \Delta\chi_{TF}^- \tag{4.14}$$

and

$$\Delta\chi_H^+ = \left(1-\frac{1}{3\pi k_F}\right)\Delta\chi_{TF}^+ = 0{\cdot}8525\,\Delta\chi_{TF}^+. \tag{4.15}$$

In what follows we shall calculate $\Delta\chi_{TF}^\pm$ for $\Delta Z = 1, \ldots 4$ and then estimate $\Delta\chi_H^\pm$ by assuming, as plausible, that the relations (4.14) and (4.15) continue to hold also for these finite values of ΔZ. Because of the near-cancellation between $\Delta\chi^+$ and $\Delta\chi^-$ we must be prepared for the possibility that the $\Delta\chi_H$ thus obtained may be significantly different from the true $\Delta\chi_H$, particularly at the higher values of ΔZ.

For $\Delta Z = 1, \ldots 4$, $\Delta\chi_{TF}^\pm$ have been calculated with the help of the available $\Delta\rho_{TF}^{(7)}$. $\Delta\chi_{TF}^+$ was obtained by first determining V_{TF} from $\Delta\rho_{TF}$, using Poisson's equation, then calculating the phase-shifts η_l and their derivatives $(d\eta_l/dE)$ numerically and substituting into the first term of equation (3.31). The calculated phase shifts and their derivatives are listed in Table 5, and the corresponding values of $\Delta\chi_{TF}^+$ in Table 1, column 2. $\Delta\chi_{TF}^-$ was obtained by evaluating the mean values of r^2 with the available $\Delta\rho_{TF}$. The results are given in Table 1, column 5. The sum $\Delta\chi_{TF}^+ + \Delta\chi_{TF}^-$ is given in Table 1, column 8.

In order to obtain the total change of susceptibility due to the valence electrons, we must add to the change of orbital susceptibility, that of the spin susceptibility and that of the core susceptibility.

Using the model of non-interacting electrons we have the general formula

$$\chi^{\text{spin}} = \frac{1}{4c^2}\frac{g(E_F)}{V} \tag{4.16}$$

where $g(E_F)$ is the density of states (including spin degeneracy) at the Fermi surface. Calculating the

Table 1. Contribution to orbital susceptibility of various solute atoms in Cu (*theory*)

	1	2	3	4	5	6	7	8	9
ΔZ	$\Delta\chi^{+}_{H\mathrm{IIa}}$	$\Delta\chi^{+}_{TF}$	$\Delta\chi^{+}_{H}$	$\Delta\chi_{H\mathrm{IIa}}$	$\Delta\chi^{-}_{TF}$	$\Delta\chi^{-}_{H}$	$\Delta\chi_{\mathrm{IIa}}$	$\Delta\chi_{TF}$	$\Delta\chi_{H}$
1 (Zn)	5·586	5·263	4·487	− 6·553	− 5·222	− 5·222	−0·967	+0·041	−0·735
2 (Ga)	11·172	9·510	8·107	−13·106	− 9·274	− 9·274	−1·934	+0·236	−1·167
3 (Ge)	16·758	13·245	11·291	−19·658	−12·683	−12·683	−2·900	+0·561	−1·392
4 (As)	22·344	16·687	14·226	−26·211	−15·663	−15·663	−3·867	+1·025	−1·437

The numbers give the additional volume susceptibility per solute atom in units of $(e^2/6mc^2)a_0^2 = 1{\cdot}315 \times 10^{-30}$ cm^3. Our best estimate for the change of orbital susceptibility per solute atom is given in column 9.

change of $g(E_F)$ due to an impurity as in Section 3, we find for N added impurities per unit volume

$$\Delta\chi^{\mathrm{spin}} = N\frac{1}{4c^2}\cdot\frac{2}{\pi}\sum_{0}^{\infty}(2l+1)\left(\frac{\mathrm{d}\eta_l}{\mathrm{d}E}\right)_{E=E_F} \quad (4.17)$$

The numerical results, using the phase shifts listed in Table 5, are given in Table 2, column 2.

Next we must allow for the fact that the core susceptibilities of the solute ions ($1s^2\ 2s^2 \ldots 3d^{10}$) are smaller than of the Cu ions which they replace, because of their smaller radius. For an estimate of this effect we followed the procedure of Henry and Rogers.$^{(1)}$ The results are listed in Table 2, column 3. Column 4 is the sum of columns 1, 2 and 3 and represents a preliminary theoretical estimate of $\Delta\chi$.

At this point, in preparation for comparison with experiment we convert units to change of atomic susceptibility$^{(9)}$ per atomic concentration of solute. For this purpose column 4 must be multiplied by Avogadro's number, assuming for the moment that the alloying produces no change of volume. The result is entered as $\Delta\chi_1^{-\mathrm{th}}$ in column 1 of Table 3. A final effect is due to the change of lattice parameter a, caused by the alloying. It is given by$^{(1)}$

$$\Delta\chi_2^{-\mathrm{th}} = 2\frac{\Delta a}{a}\chi^{\mathrm{cond}} \quad (4.18)$$

where χ^{cond} is the atomic susceptibility of the Cu-conduction electrons, which in our free electron model has the value $4{\cdot}6\times10^{-6}$. Values of $\Delta a/a$ were taken from Ref. 1. The results for $\Delta\chi_2^{-\mathrm{th}}$ are entered in Table 3, column 2. Our final theoretical result, shown in Table 3, column 3 will be seen to be in serious disagreement with experiment, even predicting the wrong sign.

To test the dependence of our results on the details of the assumed impurity potential, the entire calculation was repeated with a potential of the form $-(\Delta Z/r)\exp(-\lambda r)$, where for each ΔZ the value of λ was adjusted to satisfy the Friedel sum rule. The final theoretical results differed from those in Table 3, column 3 by not more than 21 per cent.

Table 2. Contributions to the magnetic susceptibility of various solute atoms in Cu

	1	2	3	4
ΔZ	$\Delta\chi^{\mathrm{orb}}$	$\Delta\chi_{\mathrm{spin}}$	$\Delta\chi^{\mathrm{core}}$	$\Delta\chi^{\mathrm{th}}$
1 (Zn)	−0·73	1·54	4·1	4·9
2 (Ga)	−1·17	2·83	7·0	8·7
3 (Ge)	−1·39	4·95	8·9	12·5
4 (As)	−1·44	6·74	10·2	15·5

Same units as in Table 1.

Table 3. Comparison of theory and experiment

	1	2	3	4
ΔZ	$\Delta\chi_1^{-\text{th}} \times 10^6$	$\Delta\chi_2^{-\text{th}} \times 10^6$	$\Delta\chi^{\text{th}} \times 10^6$	$\Delta\chi^{\text{exp}} \times 10^6$
1 (Zn)	3·9	0·5	4·4	− 7·2
2 (Ga)	6·9	0·7	7·6	−19·3
3 (Ge)	9·9	0·8	10·7	−27·4
4 (As)	12·3	1·2	13·5	−38

All susceptibility changes are in e.m.u. per g-at. per atomic concentration of the solute. Column 1 are the theoretical results neglecting lattice parameter changes; column 2 are the estimated effects of change of lattice parameter; column 3 are the sums of columns 1 and 2, our final theoretical results; and column 4 are the experimental results of Ref. 1.

We are therefore convinced that the total susceptibility change of the conduction electrons due to alloying, as calculated with the free electron model, cannot overcome the positive change due to the substitution of smaller cores. In other words, on this model, one cannot understand why the observed change of susceptibility has the opposite sign from that expected from the differences of the cores only.

We are then driven to attribute the disagreement between theory and experiment to the neglect of the crystalline potential. Unfortunately, we do not know at this time how to incorporate the effects of this potential into a theory for the orbital susceptibility.

We wish to make two further comments. Henry and Rogers in analyzing their data on dilute alloys of Zn, Ga, Ge and As with Cu, present a theory which accounts quite well for their experimental results. In the light of our present work, we would like to question two features of their analysis.

1. Looking apart from changes of the lattice parameter, they take for the change of orbital susceptibility per solute atom

$$\Delta\chi^{\text{orb}} = -\frac{e^2}{6mc^2}\int \Delta\rho(r)r^2\,\mathrm{d}r + \chi^{\text{orb}}(0)\cdot\frac{\Delta g}{g} \tag{4.19}$$

where $\Delta\rho$ is the screening charge due to ΔZ electrons, $\chi^{\text{orb}}(0)$ and g are the orbital susceptibility and density of states of pure Cu, and Δg is the change of g due to adding ΔZ electrons to the conduction band. For a parabolic band, both terms are negative. Our result, equation (3.31), agrees with this as far as the first term of (4.19) is concerned, but in place of the second term of (4.19), we obtain a term with the opposite sign. Further, as we show in Appendix 1, the full result equation (3.31) reduces, in the weak perturbation limit, to just the second term of (4.19). Thus the use of (4.19) does not have a firm theoretical foundation.

2. For the change of spin susceptibility Henry and Rogers use the expression

$$\Delta\chi^{\text{spin}} = \chi^{\text{spin}}(0)\cdot\frac{\Delta g}{g} \tag{4.20}$$

where χ^{spin} is the spin paramagnetism of Cu and $\Delta g/g$ has the same meaning as before. This expression is justified when the perturbation due to the impurities is weak (linear approximation); but in general it must be replaced by equation (4.16). In the present case the results are quite different as is shown in Table 4.

In our opinion these considerations detract considerably from the significance of the relatively good agreement between experiment and the theory of Henry and Rogers. Unfortunately we cannot offer at present any constructive theoretical considerations which would contribute to a better understanding of the data.

Acknowledgements—It is a pleasure to thank Dr. J. Appel for some stimulating conversations and Drs. W. G. Henry, J. L. Rogers and N. H. March for very helpful correspondence.

Table 4. Spin paramagnetism

ΔZ	$\Delta\chi^{\text{spin}}$ (linear approx.)	$\Delta\chi^{\text{spin}}$ (from phase shifts)
1 (Zn)	2·90	1·54
2 (Ga)	5·80	2·83
3 (Ge)	8·70	4·95
4 (As)	11·60	6·74

Same units as in Table 1.

Table 5. Phase shift calculations

	$\Delta Z = 1$ Numerical	Born Approximation		$\Delta Z = 2$ Numerical	Born Approximation
η_0	1·05504	0·66605	η_0	2·13886	1·19676
η_1	0·14291	0·12355	η_1	0·28992	0·21699
η_2	0·02937	0·02813	η_2	0·05310	0·04914
η_3	0·00701	0·00691	η_3	0·01234	0·01205
η_4	0·00177	0·00176	η_4	0·00310	0·00307
η_5	0·00046	0·00046	η_5	0·00080	0·00080
η_6	0·00012	0·00012	η_6	0·00021	0·00021
$\partial\eta_0/\partial E$	−0·71219	0·25970	$\partial\eta_0/\partial E$	−1·44221	0·50460
$\partial\eta_1/\partial E$	0·35801	0·31320	$\partial\eta_1/\partial E$	0·71740	0·55377
$\partial\eta_2/\partial E$	0·13894	0·13140	$\partial\eta_2/\partial E$	0·25459	0·22988
$\partial\eta_3/\partial E$	0·04799	0·04708	$\partial\eta_3/\partial E$	0·08494	0·08210
$\partial\eta_4/\partial E$	0·01591	0·01579	$\partial\eta_4/\partial E$	0·02781	0·02751
$\partial\eta_5/\partial E$	0·00512	0·00511	$\partial\eta_5/\partial E$	0·00894	0·00890
$\partial\eta_6/\partial E$	0·00162	0·00162	$\partial\eta_6/\partial E$	0·00282	0·00281

	$\Delta Z = 3$ Numerical	Born Approximation		$\Delta Z = 4$ Numerical	Born Approximation
η_0	2·82600	1·65427	η_0	3·40134	2·05985
η_1	0·45935	0·29369	η_1	0·67321	0·35932
η_2	0·07371	0·06613	η_2	0·09252	0·08071
η_3	0·01672	0·01619	η_3	0·02058	0·01977
η_4	0·00417	0·00413	η_4	0·00511	0·00504
η_5	0·00108	0·00108	η_5	0·00132	0·00132
η_6	0·00029	0·00029	η_6	0·00035	0·00035
$\partial\eta_0/\partial E$	−1·24198	0·74473	$\partial\eta_0/\partial E$	−1·35889	0·97769
$\partial\eta_1/\partial E$	1·10535	0·75448	$\partial\eta_1/\partial E$	1·50950	0·92598
$\partial\eta_2/\partial E$	0·35762	0·30983	$\partial\eta_2/\partial E$	0·45316	0·37803
$\partial\eta_3/\partial E$	0·11560	0·11036	$\partial\eta_3/\partial E$	0·14264	0·13471
$\partial\eta_4/\partial E$	0·03752	0·03696	$\partial\eta_4/\partial E$	0·04602	0·04515
$\partial\eta_5/\partial E$	0·01203	0·01195	$\partial\eta_5/\partial E$	0·01469	0·01461
$\partial\eta_6/\partial E$	0·00378	0·00378	$\partial\eta_6/\partial E$	0·00463	0·00462

All phase-shifts were obtained with the Thomas Fermi potential calculated by ALFRED and MARCH.(7)

REFERENCES

1. Henry W. G. and Rogers J. L., *Phil. Mag.* **1**, 237 (1956).
2. Childs B. G. and Penfold J., *Phil. Mag.* **2**, 389 (1957).
3. Henry W. G. and Rogers J. L., *Canad. J. Phys.* **38**, 908 (1960).
4. Houghton A., *J. Phys. Chem. Solids* **20**, 289 (1961).
5. Atomic units ($|e| = \hbar = m = 1$) are used.
6. Langer J. and Vosko S., *J. Phys. Chem. Solids* **12**, 196 (1959).
7. Alfred L. C. R. and March N. H., *Phil. Mag.* **46**, 759 (1955).
8. It should be remarked here that if the Schroedinger equation is solved with V_{TF} and the electron density constructed from the solutions, one does *not* obtain exactly ρ_{TF}. For example, it is well-known that the screening charge calculated with any localized potential has long range oscillations.
9. This is the susceptibility per N_0 atoms, where N_0 is Avogadro's number.

APPENDIX 1

Reduction of the general result in the case of weak perturbing potentials.

In Section 2 it was shown that if the effect of the solute atoms can be treated as a weak perturbation, their contribution to the diamagnetism may be calculated from the standard free electron result

$$\chi_0 = -\frac{k_F}{12\pi^2c^2} \qquad \text{(A1.1)}$$

by using the value of k_F corresponding to the *total* number of valence electrons. If we denote the excess valence of the solute by ΔZ this gives, for each solute atom per unit volume

$$\Delta\chi_{\text{lin}} = -\Delta Z\frac{1}{12c^2k_F^2}. \qquad \text{(A1.2)}$$

On the other hand we found in Section 3 that for a perturbation of arbitrary strength, the contribution to the diamagnetism is given by

$$\Delta\chi = \frac{1}{6c^2}\left[\frac{1}{\pi}\sum_{l=1}^{\infty}(2l+1)(l+1)l\left(\frac{d\eta_l}{dE}\right)_{E=E_F} - \int\Delta\rho r^2\,dr\right]. \qquad \text{(A1.3)}$$

In this Appendix we shall show explicitly that for weak perturbations (A1.3) reduces to A1.2)

We begin with the first term of (A1.3). We note the following two standard results for the scattering amplitude $f(\theta)$ due to a weak potential

$$f(\theta) = \frac{1}{k}\sum_l(2l+1)\eta_lP_l(\cos\theta) \qquad \text{(A1.4)}$$

and

$$f(\theta) = -\frac{1}{2\pi}\int\frac{\sin[2k\sin\theta/2\,r]}{2k\sin\theta/2\,r}V(r)\,dr, \qquad \text{(A1.5)}$$

so that

$$\sum_l(2l+1)\eta_lP_l(\cos\theta) = -\frac{k}{2\pi}\int\frac{\sin[2k\sin\theta/2\,r]}{2k\sin\theta/2\,r}V(r)\,dr. \qquad \text{(A1.6)}$$

Further $P_l(\cos\theta)$ satisfies the following differential equation

$$\frac{1}{\sin\theta}\frac{d}{d\theta}\left(\sin\theta\frac{dP_l}{d\theta}\right) + l(l+1)P_l = 0 \qquad \text{(A1.7)}$$

Hence operating on (A1.6) with the differential operator appearing in (A1.7) and taking the limit $\theta \to 0$, gives

$$\sum_l(2l+1)(l+1)l\,\eta_l = \frac{k}{2\pi}\lim_{\theta\to0}\frac{1}{\sin\theta}\frac{d}{d\theta} \times\left[\sin\theta\frac{d}{d\theta}\int\frac{\sin[2k\sin\theta/2\,r]}{2k\sin\theta/2\,r}V(r)\,dr\right] = -\frac{k^3}{3\pi}\int V(r)r^2\,dr. \qquad \text{(A1.8)}$$

By differentiation with respect to $E = k^2/2$ we then find

$$\frac{1}{\pi}\sum_{l=1}^{\infty}(2l+1)(l+1)l\left(\frac{d\eta_l}{dE}\right)_{E=E_F} = -\frac{k_F}{\pi^2}\int V(r)r^2\,dr. \qquad \text{(A1.9)}$$

We now turn to the second term in (A1.3), and note that if we write

$$\Delta\rho(r) = \frac{1}{(2\pi)^3}\int\Delta\rho_p\,e^{ip\cdot r}\,dp \qquad \text{(A1.10)}$$

then

$$\int \Delta\rho(r) r^2 \,\mathrm{d}r = -[\nabla_p^2 \Delta\rho_p]_{p=0}. \quad \text{(A1.11)}$$

Now by first order perturbation theory, the wave functions of the perturbed conduction electrons are given by

$$\psi_k(r) = \frac{1}{L^{3/2}} \mathrm{e}^{ik\cdot r} + \sum_{k'} \frac{V_{k'k}}{\frac{1}{2}(k^2-k'^2)+i\epsilon} \frac{1}{L^{3/2}} \mathrm{e}^{ik'\cdot r} \quad \text{(A1.12)}$$

where for convenience we now quantize in a large cube of volume L^3, with the solute at the center, and

$$V_{k'k} = \frac{1}{L^3} \int \mathrm{e}^{-i(k'-k)\cdot r} V(r) \,\mathrm{d}r. \quad \text{(A1.13)}$$

From (A1.12) we can compute

$$\Delta\rho(r) = 2\Delta \sum_{k<k_F} |\psi_k(r)|^2 = \frac{2L^3}{(2\pi)^6} \int \mathrm{d}k \int \mathrm{d}k' \times \frac{V_{k'k}}{\frac{1}{2}(k^2-k'^2)+i\epsilon} \mathrm{e}^{i(k'-k)\cdot r} + c.c. \quad \text{(A1.14)}$$

which gives, by (A1.10),

$$\Delta\rho_p = \frac{2}{(2\pi)^3} \left[\int \mathrm{e}^{-ip\cdot r} V(r) \,\mathrm{d}r \right] \times \left[\int_{k<k_F} \mathrm{d}k \frac{1}{-k\cdot p-(p^2/2)+i\epsilon} + c.c. \right]. \quad \text{(A1.15)}$$

Now for small p,

$$\int \mathrm{e}^{-ip\cdot r} V(r) \,\mathrm{d}r = \int V(r) \,\mathrm{d}r - \frac{p^2}{6} \int V(r) r^2 \,\mathrm{d}r. + \dots \quad \text{(A1.16)}$$

The other factor in (A1.15) gives in cylindrical coordinates

$$\int_{k<k_F} \mathrm{d}k \frac{1}{-k\cdot p-(p^2/2)+i\epsilon} + c.c.$$

$$= \pi \int_{-k_F}^{k_F} \mathrm{d}k_z \frac{k_F^2-k_z^2}{-k_z p-(p^2/2)+i\epsilon} + c.c.$$

$$= \frac{2\pi}{p} \left\{ -k_F p + \left(\frac{p^2}{4} - k_F^2 \right) \log \left| \frac{k_F+p/2}{k_F-p/2} \right| \right\}$$

$$= -4\pi k_F + \frac{\pi}{3k_F} p^2 + \dots . \quad \text{(A1.17)}$$

Combining these results gives for small p

$$\Delta\rho_p = -\frac{k_F}{\pi^2} \int V(r) \,\mathrm{d}r + p^2 \left\{ + \frac{1}{12\pi^2 k_F} \int V(r) \,\mathrm{d}r + \frac{k_F}{6} \int V(r) r^2 \,\mathrm{d}r \right\} + \dots \quad \text{(A1.18)}$$

so that by (A1.11)

$$\int \Delta\rho(r) r^2 \,\mathrm{d}r = -\frac{1}{2\pi^2 k_F} \int V(r) \,\mathrm{d}r - \frac{k_F}{\pi^2} \int V(r) r^2 \,\mathrm{d}r \quad \text{(A1.19)}$$

Substitution of (A1.9) and (A1.19) into the general formula (A1.3) gives

$$\Delta\chi = \frac{1}{6c^2} \frac{1}{2\pi^2 k_F} \int V(r) \,\mathrm{d}r. \quad \text{(A1.20)}$$

But from (A1.10) and (A1.18) we can also write

$$\Delta Z = \lim_{p\to 0} \Delta\rho_p = -\frac{k_F}{\pi^2} \int V(r) \,\mathrm{d}r \quad \text{(A1.21)}$$

so that (A1.20) is equivalent to

$$\Delta\chi = -\Delta Z \frac{1}{12c^2 k_F^2} \quad \text{(A1.22)}$$

which is the desired weak perturbation limit, equation (A1.2).

APPENDIX 2

Alternative derivation

In view of the possible doubts concerning the validity of the method used in Section 3, and discussed there, we present here an alternative derivation of our central result, equation (3.31).

The full Hamiltonian of our problem, with or without perturbing potential, would be separable in spherical coordinates, were it not for the term

$$H' = \frac{\mathscr{H}^2}{8c^2} (x^2+y^2). \quad \text{(A2.1)}$$

This difficulty can be overcome as follows.

Consider an electron gas in a spherical enclosure of radius R, in which there is present an external potential

$$U \equiv \alpha z^2 \quad \text{(A2.2)}$$

Adjust the number of electrons so that their density at the origin is independent of α. In a weak magnetic field $\mathscr{H}$, in the z-direction, this gas will have a magnetic moment linear in $\mathscr{H}$, say

$$M = K(\alpha)\mathscr{H}. \quad \text{(A2.3)}$$

Now imagine that a spherical localized perturbing potential is introduced, and the number of electrons is adjusted to keep the density far away unchanged, resulting in a total moment

$$M' = K'(\alpha)\mathscr{H} \tag{A2.4}$$

The moment due to the perturbing potential is then

$$\Delta M = \Delta K(\alpha)\mathscr{H} \tag{A2.5}$$

where

$$\Delta K(\alpha) \equiv K'(\alpha) = K(\alpha). \tag{A2.6}$$

The quantity of interest to us is $\Delta K(0)$. However, it follows on dimensional grounds that $\Delta K(\alpha) \approx \Delta K(0)$, provided that α is much smaller than k_F^4 and d^{-4}, where d is some length characteristic of the perturbing potential In particular, if we choose

$$\alpha = \frac{\mathscr{H}^2}{8c^2} \tag{A2.7}$$

which is of the order of a^{-4}, where a is the dimension of the lowest Landau state, this condition is evidently satisfied for small $\mathscr{H}$. Thus it is permissible to obtain ΔM by taking the difference of the magnetic moments of the two systems described by the Hamiltonians

$$H_T = -\tfrac{1}{2}\nabla^2 + \frac{\mathscr{H}}{2c}L_z + \frac{\mathscr{H}^2}{8c^2}(x^2+y^2) + \alpha z^2 \tag{A2.8}$$

and

$$H_T' = H_T + V(r) \tag{A2.9}$$

where α has the value (A2.7) and the expectation value of M is evaluated to first order in $\mathscr{H}$.

We turn first to the moment associated with H_T of equation (A2.8). Writing the solutions in the form

$$\phi_{n,l,m} = R(r)Y_{l,m} \tag{A2.10}$$

we find for R the equation

$$\left\{-\frac{1}{2}\frac{d^2}{dr^2} + \frac{l(l+1)}{r^2} + \frac{\mathscr{H}}{2c}m + \frac{\mathscr{H}^2}{8c^2}r^2\right\}R(r) = ER(r) \tag{A2.11}$$

whose eigenvalues are (for moderate l)

$$E_{n,l,m} = (2n+l+m+\tfrac{3}{2})\frac{\mathscr{H}}{2c}. \tag{A2.12}$$

Fixing our attention on a given value of l, we first consider the part M_0 of the magnetic moment operator:

$$\langle M_0\rangle_{n,l,m} = -\frac{1}{2c}\langle L_z\rangle_{n,l,m} = -\frac{m}{2c}. \tag{A2.13}$$

Now for a given l and m we find from (A2.12) that

$$n_{\max} = c/\mathscr{H}\, E_F - \tfrac{1}{2}(l+m+\tfrac{3}{2}).$$

Therefore, adding all contributions from m and $-m$ gives

$$\sum_n (\langle M_0\rangle_{n,l,m} + \langle M_0\rangle_{n,l,-m}) = 2\frac{m^2}{2c} \tag{A2.14}$$

where the 2 takes care of spin degeneracy. Finally, summing over m gives for the total contribution of states with given l

$$\langle M_0\rangle_l = \frac{1}{c}\sum_0^l m^2 = \frac{1}{c}\frac{(2l+1)(l+1)l}{6}. \tag{A2.15}$$

For the expectation value of M_1 we have simply

$$\langle M_1\rangle_l = -\frac{\mathscr{H}}{6c^2}\int \rho_l(r)\, r^2\, dr. \tag{A2.16}$$

Next we include the perturbing potential $V(r)$. The radial equation then becomes

$$\left\{-\frac{1}{2}\frac{d^2}{dr^2} + \frac{l(l+1)}{r^2} + \frac{\mathscr{H}}{2c}m + \frac{\mathscr{H}}{8c^2}r^2 + V(r)\right\}R'(r) = E'R'(r). \tag{A2.17}$$

We divide the positive r-axis into a near region, $r<b$ and a far region, $r>b$, where

$$d, \frac{l}{k_F} \ll b \ll \frac{k_F c}{\mathscr{H}}. \tag{A2.18}$$

In the near region the term $(\mathscr{H}^2/8c^2)r^2$ in (A2.17) may be neglected and hence we have near $r = b$

$$R'(r) = C\sin\left[Kr - \frac{l}{2}\pi + \eta_l\left(E' - \frac{\mathscr{H}}{2c}m\right)\right] \tag{A2.19}$$

where

$$K^2 \equiv \left(E' - \frac{\mathscr{H}}{2c}m\right). \tag{A2.20}$$

In the far region, the centrifugal term and $V(r)$ can be neglected so that we have

$$\left\{-\frac{1}{2}\frac{d^2}{dr^2} + \frac{\mathscr{H}^2}{8c^2}r^2\right\}R'(r) = \left(E' - \frac{\mathscr{H}}{2c}m\right)R'(r). \tag{A2.21}$$

In the limit of small $\mathscr{H}$, for energies near E_F, we may solve this by the B.W.K. approximation which gives with standard methods

$$E'_{n,l,m} = \left(2n+l+m+\frac{3}{2}-\frac{2}{\pi}\eta_l\left(E'_{n,l,m}-\frac{\mathscr{H}}{2c}\right)\right)\frac{\mathscr{H}}{2c} \tag{A2.22}$$

As in the absence of $V(r)$ we have

$$\langle M_0\rangle'_{n,l,m} = -\frac{m}{2c}. \tag{A2.23}$$

But by (A2.22) we now have, for given l and m,

$$n'_{\max} = \frac{c}{\mathscr{H}}E_F-\tfrac{1}{2}(l+m+\tfrac{3}{2})+\frac{1}{\pi}\eta_l\left(E_F-\frac{\mathscr{H}}{2c}m\right). \tag{A2.24}$$

Therefore

$$\sum_n(\langle M_0\rangle'_{n,l,m}+\langle M_0\rangle'_{n,l,-m}) = -2\frac{m}{2c}$$

$$\times\{(n'_{\max})_{l,m}-(n'_{\max})_{l,-m}\}$$

$$= -\frac{m}{c}\left\{-m+\frac{1}{\pi}\left[\eta_l\left(E_F-\frac{\mathscr{H}}{2c}m\right)\right.\right.$$

$$\left.\left.-\eta_l\left(E_F+\frac{\mathscr{H}}{2c}m\right)\right]\right\}$$

$$= \frac{m^2}{c}+\frac{m^2\mathscr{H}}{\pi c^2}\left(\frac{\mathrm{d}\eta_l}{\mathrm{d}E}\right)_{E=E_F} \tag{A2.25}$$

Summing over m gives

$$\langle M_0\rangle'_l = \left(\frac{1}{c}+\frac{\mathscr{H}}{\pi c^2}\left(\frac{\mathrm{d}\eta_l}{\mathrm{d}E}\right)_{E=E_F}\right)\frac{(2l+1)(l+1)l}{6} \tag{A2.26}$$

For M_1 we obtain simply

$$\langle M_1\rangle'_l = -\frac{\mathscr{H}}{6c}\int\rho'_l(r)\,r^2\,\mathrm{d}r. \tag{A2.27}$$

where ρ'_l is the density in the presence of $V(r)$.

The moment associated with the impurity is obtained by subtracting from the sum of (A2.27) and (A2.26) the sum of (A2.15) and (A2.16). The result is the previously obtained expression (3.30).

J. Phys. Chem. Solids Pergamon Press 1963. Vol. 24, pp. 863–870. Printed in Great Britain.

SOME ELECTRIC AND MAGNETIC PROPERTIES OF RARE EARTH MONOSULFIDES AND NITRIDES

R. DIDCHENKO and F. P. GORTSEMA
Parma Research Laboratory, Union Carbide Corporation, Parma 30, Ohio

(*Received* 8 *November* 1962)

Abstract—Lanthanon monosulfides show semimetallic conductivities with the exception of EuS and YbS, which are insulators, and of SmS, which is an *n*-type semiconductor with an energy gap of 0·24 eV. Ytterbium monosulfide becomes a *p*-type semiconductor when doped with sulfur. A new value for the susceptibility of EuS is given. Rare earth nitrides have the same crystal structure (NaCl) but are not isoelectronic with the monosulfides, except for CeN in which cerium has an oxidation state of +4. Magnetic measurements revealed that in EuN there is present Eu^{2+} in large amounts depending on the oxygen content; SmN and YbN also contain metal ions in +2 state. In all other nitrides of the series the metal is present as tripositive ion. All nitrides show semimetallic conductivity with the exception of YbN which appears to be a semiconductor.

INTRODUCTION

BEFORE EASTMAN and BREWER(1) predicted theoretically and confirmed experimentally in 1950 the existence of CeS, the only known monosulfide of the lanthanide series was EuS, first prepared by BECK and NOWACKI(2) in 1938 and later studied by KLEMM and SENFF.(3) While EuS behaved as a normal ionic compound of dipositive europium, CeS showed some unusual properties: it was a highly refractory material with the NaCl structure and a melting point of 2500°C; nevertheless, it dissolved rapidly in diluted acetic acid; it resembled brass in appearance, had a high electrical conductivity comparable with that of mercury and a high thermal conductivity. It was nearly stoichiometric, but magnetic measurements showed conclusively that cerium was present as tripositive ion. To explain these properties, Eastman and Brewer used Pauling's model of the metallic bond and proposed that there was one free electron per metal atom which participated in a resonant bond involving metallic orbitals directed along the diagonals of the unit cell.

While we were studying the preparation(4) and refractory properties of lanthanon monosulfides, it occurred to us that if the above explanation of the electrical conductivity were true, then because of the enhanced stability of the dipositive states of Sm, Eu and Yb, the concentration of conduction electrons in their monosulfides might be depleted to such an extent that they would become semiconductors or insulators. This hypothesis was confirmed by experimental work not only in these laboratories but also by parallel and independent investigation of SmS by HOUSTON.(5)

The extension of these studies to the lanthanon nitride series appeared desirable since these compounds also are known to form NaCl-lattice. Beyond the crystallographic data of KLEMM and WINKELMANN(6) and a few scattered literature references to the metallic conductivity of these materials, no pertinent information about this series was available to date. It was believed that the combination of electric measurements and magnetic susceptibility studies would shed some light on the bonding character in these compounds and also allow some meaningful comparisons of the conduction mechanism with the monosulfides based on the principle of isoelectronic configurations of the metal ions. The study was also motivated by the desire to find useful high temperature thermoelectric materials.

EXPERIMENTAL

Preparation of materials

The monosulfides were prepared via elemental synthesis. The metals were procured in the purest grade available either from Lindsay Company or from Lunex Company and used without further purification. The metallic assay was 99·9+ per cent, the major nonrare earth impurities being Ta, Mg, Zn (up to 50 p.p.m. each), Ca (up to 10 p.p.m.) and smaller amounts of Al, Fe, Ni, Si, and Zr. All metals contained 0·02–0·03 per cent of oxygen. Because of their softness, they could be converted into filings or turnings under protective atmosphere without increasing their impurity content. Sulfur of nearly spectroscopic purity was obtained by cracking H_2S gas at 600–700°C. Stoichiometric amounts of metal and sulfur weighed to the nearest 5 mg, in batches of approximately 0·1 mole, were introduced into a fused alumina crucible contained in a quartz tube. The tube was then sealed off under vacuum and heated first to 500–600°C until all sulfur vapors disappeared, then to 800–900°C for 4–6 hr. For electrical measurements, the powders were pressed into bars $0{\cdot}6 \times 0{\cdot}6 \times 4$ cm and sintered in purified argon at 1500–1600°C.

The nitrides were prepared mostly from metal ingots or sponge by first converting these into hydrides and then treating them with ammonia at 1000°C. This method works well for all metals except Sm and Yb. These were converted into filings and nitrided directly by prolonged treatment with ammonia. Ammonia was passed through a column of BaO and through UN powder kept at 750–800°C. The latter is very effective in removing traces of moisture and oxygen from the gas. The nitriding was continued until the weight gain was within a few milligrams from the calculated one and did not increase upon continued heating in ammonia. In order to achieve this, it was sometimes necessary to grind the partially nitrided material into a fine powder and continue the treatment with ammonia. All transfer and grinding operations were performed in a pressurized glove box filled with nitrogen. The nitrides are rather sensitive to air, the sensitivity decreasing as one progresses along the series up to YbN; EuN and LuN oxidize very easily. The danger of oxidation is particularly acute during the pressing of the bars for electric measurements. It was largely eliminated by pouring liquid nitrogen into the die filled with powder and keeping the die during pressing in a loose polyethylene bag containing some dry ice. The pressed bars were sintered in argon at 1500°C, except for SmN, EuN and YbN, which evaporate rapidly at temperatures above 1200°C. The sintered materials were analyzed for lanthanons compleximetrically with EDTA, for nitrogen by a modified Kjehldal method and for oxygen by the LECO combustion method. The content of lower oxidation states was determined by back titration of samples dissolved in acid $FeCl_3$ solutions. (Evolution of hydrogen was never observed.)

Electric measurements

Room temperature resistivity was measured by the four-probe method; the Seebeck coefficient was determined by means of a "thermoelectric bridge" in which the voltage from the sample was balanced against that from a thermocouple, both being in the same temperature gradient.

The resistivity and the thermoelectric power were measured simultaneously as a function of temperature by two Pt–Rh thermocouples brought in contact with the sample bars by means of heavy molybdenum pins under tension of tungsten springs. The sample was held between graphite holders acting as current leads. An auxiliary heater at the bottom of the assembly created an adjustable temperature gradient. A 12-point recorder recorded the *IR* drop and the thermoelectric voltages between the platinum and between the rhodium legs of the thermocouples as well as the direct output of both thermocouples. Whenever necessary the voltages were amplified through L and N microvoltmeter. There was an automatic switch for changing the direction of the current for *IR* drop measurement. To eliminate the thermal voltages, the samples were suspended inside an evacuated heavy wall quartz tube and the temperature raised uniformly at the rate of 225°C per hr. From the recorded data, the resistivities, temperature gradients and the thermoelectric voltages could be easily calculated as a function of temperature. The entire apparatus was calibrated with Armco iron and found to give an accuracy of $\geqslant 4$ per cent for the resistivity $\geqslant 8$ per cent for the thermoelectric power.

Magnetic measurements

Magnetic measurements were made on powders in an apparatus consisting of an electromagnet with 50 mm pole pieces (27 mm gap) and a

Mettler semimicrobalance. The current through the electromagnet was regulated by means of a G. E. Amplidyne. The field was calibrated and mapped out by means of a Rawson coil. The Gouy tube was suspended inside a double wall dewar with provision for circulating, cooling and heating solutions. The tubes were stoppered with tightly fitting "Teflon" plugs and protected from air by a slow, constant stream of helium. The entire system was calibrated with Hg[Co(CNS)$_4$] and a very good agreement with the published results[(7)] has been obtained. In order to prevent distortion of the magnetic field and attraction to the poles due to the extremely high paramagnetism of rare earth compounds, it was necessary to use small amounts of powder (0·5–1·0 g) in tubes 15 cm long with an internal diameter of about 2 mm. The results of CABRERA and DUPERIER[(8)] on Gd$_2$O$_3$ as function of temperature have been well reproduced in our apparatus.

RESULTS AND CONCLUSIONS

I. *Lanthanon sulfides*

A convenient starting point for the discussion of these materials is a plot of their lattice parameters shown in Fig. 1. Our results are in very good agreement with those of IANDELLI.[(9)] The lattice parameter of 5·86 Å reported for SmS by DOMANGE *et al.*,[(10)] seems to be therefore erroneous. These data agree very well with the lattice parameter calculated from the dipositive ionic radii for Sm, Eu, and Yb and from the tripositive ions for the remaining members of the series.

Magnetic properties. This division of the monosulfides into two groups is again reflected in their magnetic properties. Ytterbium monosulfide shows very weak paramagnetism; it probably would be diamagnetic if it were free of impurities. The molar susceptibility of SmS $\chi_m^{298} = 4480 \cdot 10^{-6}$ e.m.u. was close to IANDELLI's[(9)] value of $4717 \cdot 10^{-6}$ e.m.u. The compound showed a small dependence of the susceptibility on the temperature, typical for Sm^{2+} compounds with a Weiss constant of −195 (Iandelli: −201) extrapolated from the nearly linear plot between 77 and 372°K. Europium monosulfide does not show the paramagnetic behavior ($\theta \doteq 0$) reported by Klemm but instead follows the Curie–Weiss law with $\theta = +18$ (Fig. 2) and has the susceptibility $\chi_m^{298} = 27400 \cdot 10^{-6}$ e.m.u., i.e., considerably larger than 23,800 e.m.u. found by Klemm at 293°K. This discrepancy is probably caused by errors in extrapolation from the Honda–Owens plots made necessary by the ferromagnetic impurities in Klemm's samples. It is interesting to note that europium monosulfide is the only ferromagnetic member of the series.*[(9)]

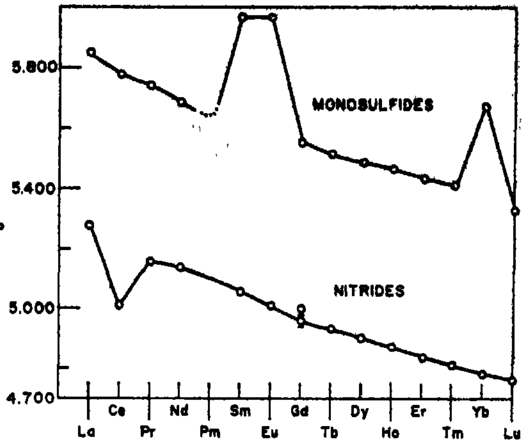

FIG. 1. Lattice parameters of lanthanon monosulfides and nitrides.

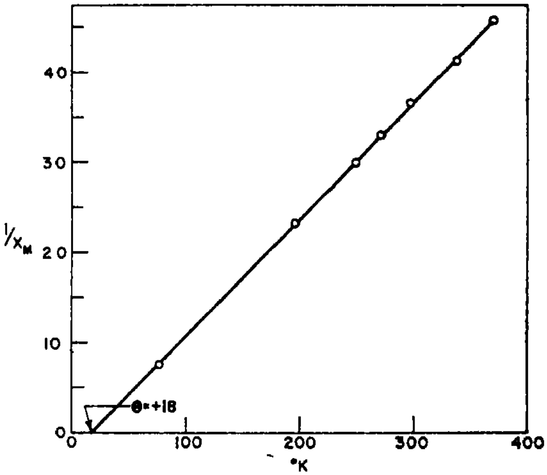

FIG. 2. Plot of $1/\chi_m$ vs temperature for EuS.

Electric properties. It is then not surprising that the monosulfides with dipositive metal ions show electrical and thermoelectric properties very different from those of the remaining members of the lanthanide series. While the latter exhibit the previously mentioned metallic behavior with the resistivities rising slightly with increasing temperature and low Seebeck coefficients (5–10μV/deg), EuS was found to be an insulator up to 1000°C, while SmS behaved like a semiconductor as shown in Figs. 3 and 4. Ytterbium monosulfide with nearly stoichiometric composition has very high resistivities in the order of 10^4–10^5 Ω-cm and is probably an insulator when truly stoichiometric. Excess of sulfur makes it a *p*-type semiconductor with an energy gap of approximately 0·33–0·36 eV. (Fig. 5). Strong doping with sulfur will reduce its resistivity to the minimum room temperature value of about 30 Ω cm at the nominal composition $YbS_{1.05}$ which still shows an X-ray pattern of pure sodium chloride. Upon further addition of sulfur, lines of the Th_3P_4 lattice appear and the resistivity increases (Fig. 6). Attempts to dope EuS with sulfur were unsuccessful.

---

* While this paper was being prepared for publication, ferromagnetic transition at 20°K for EuS has been reported by WILD R. L. and ARCHER R. D., *Bull. Amer. phys. Soc.* Ser. II, 7, 440 (1962).

The Hall effect measurement on SmS gave the number of carriers $n = 4{\cdot}30 \cdot 10^{18}\ cm^{-3}$ and the mobility $\mu = 22{\cdot}4\ cm^2/V\text{-}sec$. In the case of YbS, due to the electric noise in the samples, only limiting values could be established namely, $n > 10^{17}\ cm^{-3}$ and $\mu < 1{\cdot}3\ cm^2/V\text{-}sec$.*

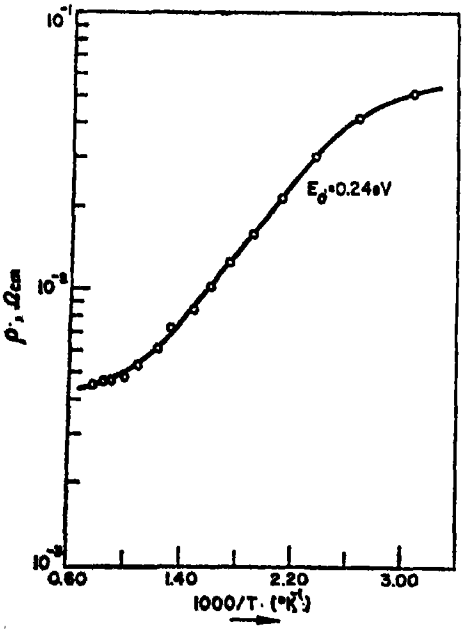

FIG. 3. Resistivity of SmS as a function of $1/T$.

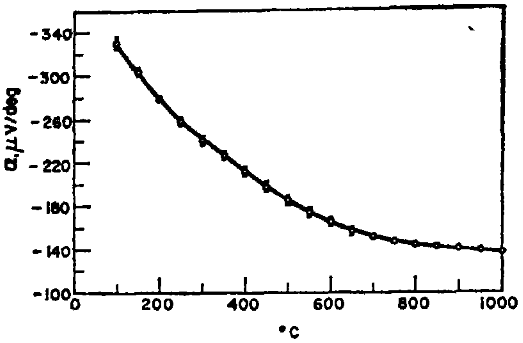

FIG. 4. Thermoelectric power of SmS as a function of temperature.

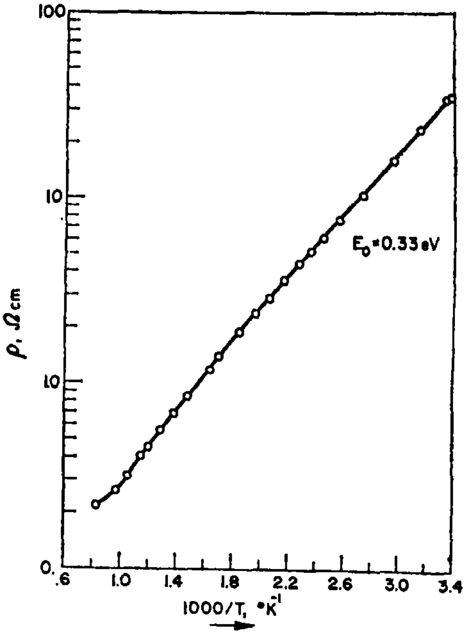

FIG. 5. Resistivity of $YbS_{1.05}$ as a function of $1/T$.

All above results are in agreement with the following qualitative band model of the electrical conductivity in the lanthanon monosulfides: The conduction band is made of the 5*d* or the 6*s* levels

---

* The authors are indebted for these results to Dr. W. S. WILLIAMS, National Carbon Research Laboratory, Div. of Union Carbide Corp, Parma Research Center.

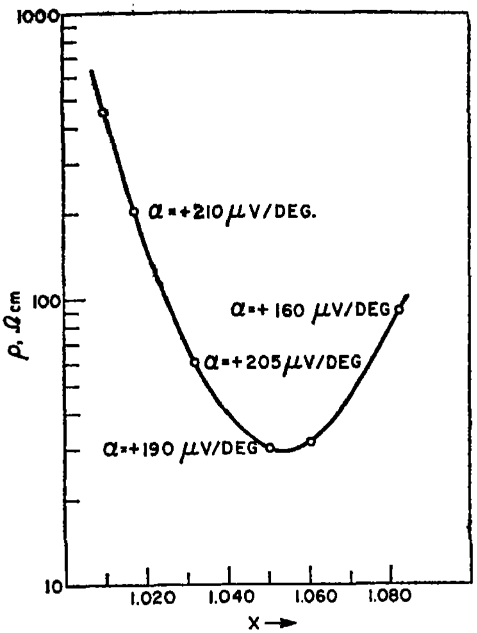

FIG. 6. Resistivity and thermoelectric power of YbS_x at 296°K.

of the metal atoms or of a mixture of both. There is approximately one electron per metal ion in this level. In the monosulfides of Ce, Pr, and Nd, the upper levels of the 4*f* shell are degenerate with the conduction band. In SmS this degeneracy is largely removed due to the well-known compression and general lowering of the 4*f* levels in the Sm^{2+} ion. The material behaves therefore as a semiconductor with low activation energy. In EuS, the stable half filled 4*f* shell is located far below the conduction band and the material is an insulator. In the second half of the series, high pairing energy of the last 4*f* electron puts it preferentially in the conduction band. Stoichiometric YbS with completely filled low lying 4*f* shell is again an insulator. When excess sulfur is present in the lattice, hole conductivity appears, probably in the 3*p* band of sulfur. A more refined treatment of this model was given by McClure. (This issue pp. 871–880.)

It is interesting to note that the lanthanon monosulfide is an ideal system for the formation of binary or even ternary solid solutions in which the electrical properties may be varied almost at will from an insulator to a metal. Some of the results obtained along these lines are given in Table 1.

Table 1. *Electrical properties of solid solutions of lanthanon monosulfides*

Composition	α(μV/deg)	$\sigma[\Omega^{-1}\ cm^{-1}]$ 25°C	1000°C
EuS·CeS	−40	200	
$(EuS)_3$·CeS	−65	50	
SmS·YbS	−442	1·0	30
$(SmS)_3$ YbS	−336	2·0	
$(YbS)_4$ GdS	−325	20	60
$(YbS·SmS)_4$ GdS	−230	5	80

II. *Lanthanon nitrides*

The lattice parameters of the nitrides series (NaCl structure), as shown in Fig. 1, were the only systematic set of data[(6)] about these materials available when the present work began. All these values were found to be very reproducible, except in the case of GdN for which we obtained consistently a slightly lower value, $a_0 = 4{\cdot}92$ Å. The lowering of the lattice parameters exhibited by CeN, also found in the case of lanthanon borides and carbides, is generally attributed to the presence of Ce^{4+} ion. The remaining members of the series show no deviations from the lanthanide contraction which, as it will be seen later, is rather deceiving.

Magnetic properties. The results of the measurements of paramagnetic susceptibility as a function of temperature between 77 and 372°K are given in Table 2.

The agreement between the experimental numbers of Bohr magnetons, and those calculated by Van Vleck for tripositive ions, is very good for the nitrides of Pr, Nd and of all elements between Gd and Yb. The agreement of our Curie points with those found by magnetic neutron scattering is also very satisfactory. The nitrides of lanthanum, lutecium and, surprisingly, cerium showed only very weak molar susceptibilities, which were practically independent of temperature. This leads us to believe that in CeN the 4*f* electron has been delocalized in the conduction band in a similar manner as in CeS. The slight paramagnetism of LaN and LuN may be due to presence of other lanthanides as impurities.

Table 2. Magnetic susceptibilities of lanthanon nitrides

Compound	$\chi_m^{298} \cdot 10^6$ e.m.u.	Θ(°K)	μ_B(exp.)	μ_B(calc. for Me^{3+})
LaN	small, temp. independent paramagnetism			
CeN	433	temp. independent		
PrN	5616	0	3·66	3·68
NdN	6180	+19	3·71	3·68
SmN	1125	See Fig. 7		
EuN	see Table 3			
GdN	35600	+60	8·2	7·9
TbN	42900	+38(42)*	9·5	9·7
DyN	48900	+22	10·6	10·6
HoN	47800	+19(20)*	10·3	10·6
ErN	36300	+ 5	9·2	9·6
TmN	23600	0	7·5	7·6
YbN	7250	−90	4·8	4·5
LuN	small, temp. independent paramagnetism			

* Determined from magnetic neutron scattering by WILKINSON *et al.*, *J. appl. Phys.*, Suppl. **31**, 358 (S) (1960).

The susceptibility of EuN varied widely from sample to sample and was sometimes much higher than could be expected from a compound of tripositive europium. The suspicion that a lower valency state may be present in this compound has been confirmed analytically. Table 3 shows the content of Eu^{2+} as per cent of total metal and the susceptibilities calculated on this basis, assuming that the susceptibility of Eu^{2+} will be similar to Gd^{3+} in its nitride and taking for Eu^{3+} the values of CABRERA and DUPERIER for Eu_2O_3 and $Eu_2(SO_4)_3$.[11] It is realized that the content of lower oxidation states determined analytically in dissolved samples is not necessarily the same that may have existed in the solid, but the excellent correlation with the magnetic data proves that this was the case in this instance.

The samples 1 and 2 were purposely oxidized during the preparation and although the agreement between the analytical oxygen content and that calculated on the basis of $EuN_{1-x}(EuO)_x$ is not very good, which may be due to a small content of Eu_2O_3, there is an obvious relation between the degree of oxidation and the percentage of Eu^{2+}. This suggests that the oxygen ion with the radius of 1·40 Å can very easily substitute for N^{-3} (1·53–1·58 Å) in the lanthanon nitrides, based on the data of TEMPLETON and DAUBEN,[12] and force an equivalent number of eruopium ions into the 2+ state. It should be noted that the X-ray pattern of all eruopium nitride samples showed only lines of pure NaCl structure and no significant variations in the lattice parameters. From 3 to 5 per cent of the 2+ ions have been

Table 3. Susceptibilities of EuN *samples*

		Eu^{2+} content as % of total Eu	$\chi_{m(calc)}^{298}$ ($\times 10^6$ e.m.u.)	$\chi_{m(found)}^{298}$ ($\times 10^6$ e.m.u.)	Oxygen at. % found
1.	EuN	32·8	15040	14710	37·2
2.	EuN	13·3	9060	9170	20·8
3.	EuN	3·9	6190	6170	6·1

also found analytically in SmN, which may account for the fact that the molar susceptibilities of Sm^{3+} in the nitrides appear to be about 20 per cent higher than in the oxides while still showing the temperature dependence typical for Sm^{3+} ion (Fig. 7). Otherwise, the temperature dependence of the magnetic susceptibility is in excellent agreement with the theoretical curve calculated by FRANK.(13) Ytterbium nitride was also found to contain small amounts of Yb^{2+} ion. It should be noted, that the nitride is the only anti-ferromagnetic member of the series. The regular decrease of the Curie temperatures from gadolinium to thulium is indicative of the weakening of the ferromagnetic interactions with the progressive filling of the 4*f* shell. The question why the ferromagnetic behavior disappears in TmN and the interaction becomes anti-ferromagnetic in YbN presents an interesting theoretical problem.

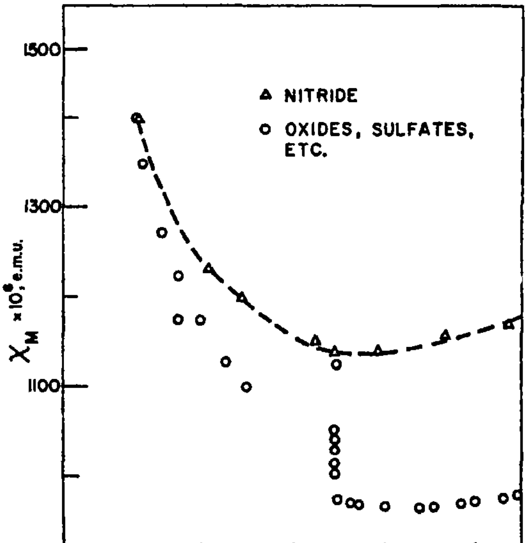

FIG. 7. Molar susceptibility of SmN as a function of temperature.

Electrical properties. The specific resistivities of rare earth nitrides at room temperature are shown in Fig. 8. These values have been corrected for density variations using the formula of RUSSELL.(14) All nitrides show electronic conductivity except CeN which is a *p*-type conductor. Some representative plots of resistivity and of thermoelectric power as a function of temperature are shown in Fig. 9. They are typical of semimetallic behavior, with the exception of YbN which shows a negative temperature coefficient of resistivity. Hall effect measurements on YbN gave number of carriers $n = 2 \cdot 10^{21}$ cm^{-3} and mobility $\mu = 0{\cdot}3$ cm^2 V^{-1} sec^{-1}.

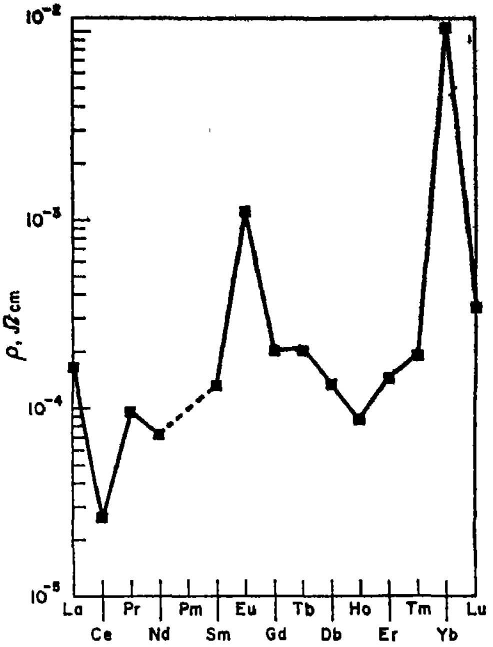

FIG. 8. Room temperature resistivity of lanthanon nitrides.

The resistivities of EuN and YbN, measured during the heating and cooling, showed pronounced hysteresis effects which decreased while the general level of resistivity increased upon repeated cycling. No explanation can be offered for this phenomenon at this time but it has been observed that the content of lower valency states in these materials decreased upon prolonged thermal cycling. This also seems to contradict the finding that the resistivity of EuN increases with the degree of oxidation.

Since the analytical data are never sufficient to prove that no electronically significant deviations from stoichiometry exist, it seemed desirable to establish by other means that the nitrides were not deficient in nitrogen. For this purpose, samples of lanthanum and gadolinium nitrides were heated for 1 hr at 1500°C under 3000 atm of nitrogen. There was no change in electrical properties of these samples before and after this treatment.

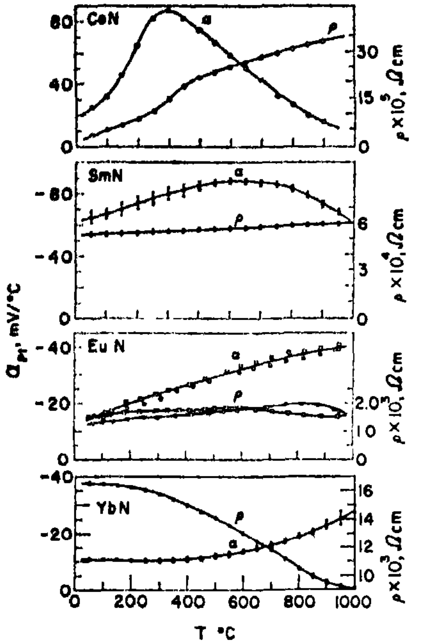

Fig. 9. Resistivity and thermoelectric power of several lanthanon nitrides as a function of temperature.

Our results are in general agreement with the theories of electrical conductivity of the "hard metals" proposed by Rundle$^{(15)}$ and Krebs$^{(16)}$ and refined by Biltz.$^{(17)}$ The magnetic susceptibilities of the lanthanon nitrides considerably reduce the room for speculation as to the degree of ionicity in these materials. The metal atoms are completely ionized (as in the metals) but since the electrons are distributed among the *s–d* "metallic" levels and the *p*-valency level of nitrogen the latter must have a formal charge less than -3, possibly close to -2. The magnetic data show convincingly that the *p*-type CeN has about one more electron in the conduction band than the *n*-type CeS. The hole conductivity of CeN could arise either from a nearly filled 6*s* or more than half filled 5*d*–6*s* band. In general, there seems to prevail in the lanthanon nitrides a rather fine balance in the competition for electrons between the 4*f* levels of the metals, the conduction band and the nitrogen ions, the total outcome of which is that the nitrides behave electrically rather like the monosulfides as evidenced by the resistivity peaks at EuN and YbN in Fig. 8.

Acknowledgements—The authors are indebted to Dr. W. S. Williams from the National Carbon Research Laboratories for the determination of Hall constants. Dr. C. R. Whitsett assisted with some of the resistivity measurements and the discussions with Dr. J. W. McClure were invaluable. Very careful analyses were made by Mr. J. Dolesch. Drs. R. G. Breckenridge and E. R. Van Artsdalen deserve credit for their support and encouragement of this work. The study was partially supported by the U.S. Bureau of Ships, whose sponsorship is gratefully acknowledged.

REFERENCES

1. Eastman E. D., Brewer L., Bromley L. A., Gilles P. W. and Lofgreen N. L., *J. Amer. chem. Soc.* **72,** 4019 (1950).
2. Beck A. and Nowacki W., *Naturwissenschaften* **26,** 495 (1938).
3. Klemm W. and Senff H., *Z. anorg. Chem.* **241,** 259 (1939).
4. Didchenko R. and Litz L. M., *J. electrochem. Soc.* **109,** 247 (1962).
5. Houston M. D., *Ceramic Age*, 50 September (1961).
6. Klemm W. and Winkelmann G. *Z. anorg. Chem.* **288,** 87 (1956).
7. Figgis B. N. and Nyholm R. S., *J. chem. Soc.* 4190 (1958).
8. Cabrera B. and Duperier A., *C.R. Acad. Sci. Paris* **188,** 1640 (1929).
9. Iandelli A., *Rare Earth Research*, p. 135. McMillan, New York (1961).
10. Domange L., Flahaut J. and Guittard M., *C.R. Acad. Sci. Paris* **249,** 697 (1959).
11. See e.g. van Vleck, J. H., *The Theory of Electric and Magnetic Susceptibilities*, p. 251. University Press Oxford (1932).
12. Templeton D. H. and Dauben C. H., *J. Amer. chem. Soc.* **76,** 5237 (1954).
13. Frank A., *Phys. Rev.* **39,** 119 (1932).
14. Russell H. W., *J. Amer. ceram. Soc.* **18,** 1 (1935).
15. Rundle R. E., *Acta. Cryst.* **1,** 180 (1948).
16. Krebs H., *Acta. Cryst.* **9,** 95 (1956).
17. Biltz H. Z., *Phys.* **153,** 338 (1958).

J. Phys. Chem. Solids Pergamon Press 1963. Vol. 24, pp. 871–880. Printed in Great Britain.

THE ELECTRONIC STRUCTURE OF RARE EARTH MONOSULFIDES

J. W. McCLURE*

Parma Research Laboratory, Union Carbide Corporation, Parma 30, Ohio

(*Received* 17 *January* 1963)

Abstract—A simple model for the electronic structure of the rare earth monosulfides, monoselenides and monotellurides is presented. The model correlates the magnetic susceptibility data with the type of electrical conductivity (metallic or *n*- or *p*-type semiconduction) observed. Rough quantitative agreement is obtained with conductivity, Hall effect, and thermoelectric power data.

I. INTRODUCTION

RECENT investigations(1, 2) have shown that the rare earth monosulfides have interesting electrical properties. This paper proposes a model for the electronic energy structure of these materials. We first show that the magnetic susceptibility data can be used to determine the number of 4*f* electrons in each compound. The resulting numbers of 4*f* electrons are consistent with the type of conduction (metallic or semiconducting) in each compound and are also in harmony with fundamental theoretical considerations. We then propose a model for the energy band structure and derive approximate values of the parameters involved from the experimental data on the Hall effect, thermoelectric power, and electrical resistivity.

II. THE NUMBER OF 4*f* ELECTRONS

The theory of the magnetic susceptibilities of the 4*f* electrons has been worked out by HUND(3) and by VAN VLECK and FRANK(4), and applied with good results to data for various rare earth salts.(5) Before applying their theory to the monosulfides, we first discuss the various effects not included in the theory. Certain of these could be corrected for, but for our purposes it is sufficient to show that the deviations are small. First is the diamagnetic correction: the diamagnetic susceptibility of the S^{2-} ion is -40×10^{-6} e.m.u./mole, and that of the xenon core is -66×10^{-6} e.m.u./mole.(6) The smallest paramagnetic susceptibility with which we are concerned here is about 2000×10^{-6} e.m.u./mole, so that the diamagnetic corrections are less than 5 per cent. For the paramagnetism of the conduction electrons we use the Pauli theory(7) which gives

$$\chi_c = \mu_B^2 \int dEN(E)(-\partial f/\partial E), \tag{2.1}$$

where

$$f = 1/\{1+\exp[(E-\zeta)/kT]\}, \tag{2.2}$$

and

$$-\partial f/\partial E = (f/kT)/\{1+\exp[(\zeta-E)/kT]\}. \tag{2.3}$$

In the above equation, μ_B is the Bohr magneton, E the energy, $N(E)$ the density of states for the conduction band, f the Fermi–Dirac distribution function, T the absolute temperature, and k Boltzmann's constant. We can use the above expressions to find an upper limit on the susceptibility of the conduction electrons. Equation (2.3) shows that

$$-\partial f/\partial E \leqslant f/kT. \tag{2.4}$$

Thus

$$\chi_c \leqslant \mu_B^2\, n/kT, \tag{2.5}$$

where

$$n = \int dEN(E)f \tag{2.6}$$

is the concentration of conduction electrons. Expression (2.5) shows that the upper limit on the paramagnetic susceptibility is the same as the classical value, or the high temperature limit. For

---

[*] Present address: Department of Physics, University of Oregon, Eugene, Oregon.

one conduction electron per rare earth atom, χ_e would be 1250×10^{-6} e.m.u./mole at room temperature. Such a value is enough to cause important deviations; however, the actual values are considerably less. For the semiconducting compounds the carrier density is about 10^{-3} less than the value used above, lowering χ_e proportionally. For the metallic compounds, the Fermi energy estimated below is of the order of an electron volt, so that degenerate statistics apply and the susceptibility is given by

$$\chi_e = 3n\mu_B^2/2\zeta \simeq 50\times 10^{-6}\ \text{e.m.u./mole.} \qquad (2.7)$$

The diamagnetism of the conduction electrons is of the order of one-third of the Pauli paramagnetism, thus it is also negligible. Finally, we must discuss the effect of crystal field splittings on the susceptibility of the $4f$ shell. The effect of the cubic crystal field on the susceptibility of the Sm^{3+} ion in Sm_2O_3 has been calculated by URYU.(8) His results show that the crystal field effects are appreciable at low temperatures but cause deviations of a little less than 10 per cent at room temperature. Though such calculations have not been applied to the monosulfides, the crystal field effects are probably of the same order of magnitude.

In using the susceptibility results to deduce the number of f electrons, we use the effective number of Bohr magnetons per rare earth atom, defined by

$$\mu_{\text{eff}} = [3\chi kT/N\mu_B^2]^{1/2} \qquad (2.8)$$

where N is the number of rare earth atoms (N is Avogadro's number when χ is the molar susceptibility). In Table 1 we list the theoretical results of Van Vleck and Frank for the values of μ_{eff} for different numbers of f electrons. In Table 2 we list the experimental μ_{eff}'s for the rare earth monosulfides, selenides, and tellurides, and the number of $4f$ electrons deduced from comparison with Table 1. All of the compounds listed in Table 2 except those with samarium follow the Curie–Weiss law rather well,

$$\chi = c/(T+\theta), \qquad (2.9)$$

and the values of θ are small (10 or 20°K). Thus, for instance, all values of μ_{eff}, except for the samarium compounds, are calculated replacing T by $T+\theta$ in equation (2.8). The temperature dependence of the susceptibility of the samarium compounds is similar to that calculated by Frank for the Eu^{3+} ion, which has six f electrons. The corrections discussed above would amount to approximately 5 per cent of μ_{eff}, or about 0·1–0·5. As this is the order of the discrepancies between theory and experiment, we believe that the assignments of numbers of f electrons in Table 2 are correct.

The above assignments are supported by the qualitative behavior of the electrical resistivity. The f electrons are highly localized and are commonly held not to contribute to the electrical

Table 1. *Theoretical results of* VAN VLECK *and* FRANK(5)

Number of $4f$ electrons	Ground state	Effective number of Bohr magnetons, μ_{eff}
0	^1S	0
1	$^2F_{5/2}$	2·56
2	$^3H_4$	3·62
3	$^4I_{9/2}$	3·68
4	$^5I_4$	2·83
5	$^6H_{5/2}$	1·55–1·65
6	$^7F_0$	3·40–3·51
7	^8S	7·94
8	$^7F_6$	9·7
9	$^6H_{15/2}$	10·6
10	$^5I_8$	10·6
11	$^4I_{15/2}$	9·6
12	$^3H_6$	7·6
13	$^2F_{7/2}$	4·5
14	^1S	0

Table 2. Experimental results for rare earth monosulfides, selenides, and tellurides

Rare earth	μ_{eff} Sulfide	μ_{eff} Selenide	μ_{eff} Telluride	Number of f electrons	Number of conduction electrons
La	0·82†	0·13‡		0	1
Ce	2·24†	2·28‡		1	1
Pr		3·32‡		2	1
Nd	3·23†	3·38‡		3	1
Pm					
Sm	3·35* 3·44† 3·30§	3·28* 3·24‡	3·20*	6	0
Eu	7·85§	7·38‡		7	0
Gd	8·01*	8·20* 7·26‡	7·63*	7	1
Tb	9·63*	9·82*	9·57*	8	1
Dy	10·4*	10·4*	10·5*	9	1
Ho	10·5*	10·6*	10·5*	10	1
Er	9·5*	9·6*	9·3*	11	1
Tm	7·4*	6·9*	7·6*	12	1
Yb	0·33§			14	0

* IANDELLI A., *Rare Earth Research*, p. 135. Macmillan, New York (1961).
† PICON M. and PATRIC M., *C.R. Acad. Sci. Paris* **242**, 1321 (1956).
‡ GUITTARD M. and BENACERRAF A., *C.R. Acad. Sci. Paris* **248**, 2589 (1959).
§ DIDCHENKO R., Ref. 1.

conductivity. Rough considerations presented in Appendix A confirm this point of view. It is also likely that the compounds are ionic so that two of the electrons from each rare earth ion are bound on the sulfur atoms. This situation is supported by the discussion in Appendix C. Thus, the remaining valence electrons (if any) are available for electrical conduction. This number is listed in the last column of Table 2. Experimentally, it is observed that the compounds of samarium, europium, and ytterbium are semiconductors, and the others are metallic.(1) This is in agreement with the assignments in Table 2 for it is the semiconducting compounds which have no conduction electrons in the ground state so that all conduction will be by thermally excited carriers.

The results seem reasonable from the theoretical point of view. As the atomic number increases, the effective nuclear charge for the f shell electrons increases so that the binding is stronger. Thus, more $4f$ electrons are accommodated in the ground state. For the completed or nearly completed half shell (SmS and EuS) and for the full shell (YbS) the exchange interaction is stronger, giving enough extra binding to rob the conduction band of its electrons.

III. THE CONDUCTION BAND AND ELECTRICAL PROPERTIES

We have already seen that perfect crystalline SmS, EuS, and YbS would have no conduction electrons in their ground states. The most likely process which gives carriers is thermal activation of electrons from the $4f$ shell to the conduction band. Such a mechanism would give n-type conductivity which is the case for SmS and EuS. However, YbS shows p-type conductivity. We suggest that this may be due to excess sulfur. In Appendix C we argue that it is not unlikely that with such an excess there may be holes in the sulfur p-bands which could then carry electrical current. The mobility in YbS is less than⁽⁹⁾ $1{\cdot}3$ cm²/V-sec which is an order of magnitude smaller than that for SmS.

It is most likely that the conduction band is based mostly on s orbitals on the rare earth atoms. The evidence for this is that the 6s levels are lower than the 5d levels in the free atoms and that the width of the 6s band should be greater than that of the 5d band. The greater band width of the 6s band is due to the greater overlap of 6s orbitals on nearest neighbor metal atoms (see Appendix B). The minimum for the s band should be in the center of the Brillouin zone, and Kramer's theorem shows that there can be no spin orbit splitting,⁽¹⁰⁾ so that the simple model of an isotropic free electron gas should work fairly well. The energy gap is then the energy needed to raise an electron from the 4f shell to the bottom of the conduction band.

We shall now make use of the measured thermoelectric power to find the Fermi level as a function of temperature. The thermoelectric power Q is given for the simple one-carrier model by⁽¹¹⁾

$$eQT = \zeta - K_{5/2}/K_{3/2}, \tag{3.1}$$

where

$$K_j = \int_0^\infty \mathrm{d}E\, E^j \tau(E)(-\partial f/\partial E). \tag{3.2}$$

Assuming that the relaxation time τ is proportional to E^p and performing a partial integration (valid if $p > -3/2$), we find

$$eQ/k = \eta - (p+5/2)\mathscr{F}_{p+3/2}/\mathscr{F}_{p+1/2}, \tag{3.3}$$

where $\eta = \zeta/kT$ and

$$\mathscr{F}_j(\eta) = (1/j!) \int_0^\infty \mathrm{d}\epsilon\, \epsilon^j/(1+e^{\epsilon-\eta}). \tag{3.4}$$

A convenient tabulation of the $\mathscr{F}$'s is given by BLAKEMORE.⁽¹²⁾ For Boltzmann statistics, all the $\mathscr{F}_j$'s are equal to $\exp \eta$, so that (3.3) becomes the familiar result

$$Q = -[\zeta - (p+5/2)kT]/Te. \tag{3.5}$$

It is a simple matter to plot eQ/k against η from equation (3.3), and then use the measured thermoelectric power to determine η (and thus ζ). We have done this for $p = -1/2$ (acoustical scattering⁽¹³⁾) and $p = 1/2$ (polar mode scattering⁽¹⁴⁾). The results for $p = -1/2$ are given in Table 3. It is seen that the Fermi level is in the neighborhood of the band edge so that the exact expression must be used instead of the non-degenerate approximation (3.5).

Knowing the Fermi level we may now calculate the change in the carrier concentration with temperature, given by⁽¹⁵⁾

$$n = A \int_0^\infty dE E^{1/2} f(E) = q\mathscr{F}_{1/2}(\eta), \tag{3.6}$$

Table 3. *Fermi level, carrier density and electron mobility in* SmS, *derived from thermoelectric and resistivity data*

T (°K)	$-Q$* (μV/°C)	σ* (mho/cm)	$p = 1/2$ η	μ (cm²/V-sec)	$p = 1/2$ η	$n \times 10^{-18}$ (cm⁻³)	μ (cm²/V-sec)
300	342	18	−0·80	19·6	−1·9	5·7	19·7
400	316	28	−0·45	15·1	−1·6	11·5	15·3
500	268	55	0·20	11·3	−0·95	29·2	11·8
600	233	87	0·80	9·0	−0·45	59·4	9·2
700	204	120	1·45	6·9	0	108	6·9
800	180	145	2·00	5·0	0·40	180	5·0
900	162	184	2·50	4·1	0·75	276	4·2
1000	149	195	2·85	3·2	1·00	381	3·2
1100	142	210	3·05	2·8	1·20	498	2·6
1200	139	215	3·15	2·4	1·25	582	2·3
1300	138	233	3·20	2·1	1·30	684	2·1

* Experimentally measured values, see Ref. 1.

where $q = BT^{3/2}$

$$B = 2(2\pi m^*k/h^2)^{3/2}. \tag{3.7}$$

In the above h is Planck's constant and m^* is the effective mass of the electron. First we use the measured room temperature Hall coefficient to find B, and thus determine m^*. The Hall coefficient measurements gave a carrier density of $4{\cdot}3\times10^{18}$ cm^{-3} and a mobility of 22·4 cm^2/V-sec on a sample with a conductivity of 15·5 mho/cm, assuming that the Hall coefficient is given by the simple expression $1/Ne$. For acoustic scattering ($p = -1/2$), the Hall coefficient is given by $(3\pi/8)/Ne$, and for polar scattering by $(45\pi/128)/Ne$. These expressions are for Boltzmann statistics, but a direct calculation for the room-temperature case shows that the Fermi level is sufficiently depressed for the expression to be valid. Thus the conductivity mobility would be 19·0 cm^2/V-sec for acoustical scattering and 20·3 cm^2/V-sec for polar scattering. For convenience we shall adopt the average value of 19·6 cm^2/V-sec. The measurements of resistivity and thermoelectric power were made on a sample whose room temperature conductivity was 18 mho/cm. We assume that the mobility is the same in the two samples, which gives a room temperature carrier density of about $5{\cdot}7\times10^{18}$ cm^{-3} in the sample whose thermoelectric power and resistivity were measured as a function of temperature. This gives $q = 4{\cdot}0\times10^{19}$ cm^{-3} and $m^* = 1{\cdot}4\, m_0$ for acoustic scattering, and $q = 1{\cdot}45\times10^{19}$ cm^{-3} and $m^* = 0{\cdot}70\, m_0$ for polar scattering. With the value of B determined, n was calculated from equation (3.6), and the results given in Table 3 for $p = -1/2$. The results for n if $p = 1/2$ are very little different.

Using the calculated carrier densities and the measured resistivity, we calculate the conductivity mobility as a function of temperature. A log-log plot of the result is given in Fig. 1. It is seen that the mobility drops a little faster than $T^{-1\cdot5}$, and goes like T^{-2} at the highest temperatures. As there are various uncertainties in the calculation of the mobility, the result is not inconsistent with the scattering being due to acoustical phonons (which gives a $T^{-1\cdot5}$ variation). However, the mobility measured by Petritz and Scanlon[16] on PbS also goes approximately like T^{-2}, and they concluded that it was due to a mixture of polar and acoustic scattering. The Debye temperature for PbS is 194°K and Callaway[17] has estimated the Debye temperature of EuS to be about 200°K, so that the comparison of the mobilities between PbS and SmS is probably reasonable. Thus at this point the question of which type of scattering is dominant is unanswered, though weak evidence in favor of acoustical scattering is given below.

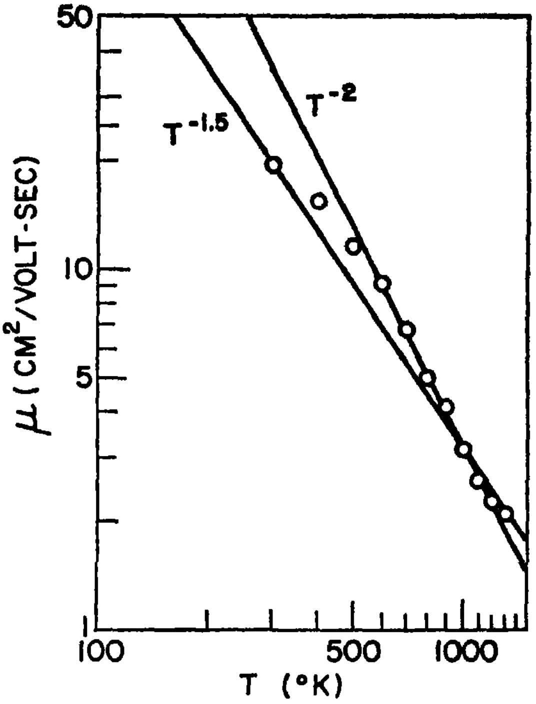

Fig. 1. The electron mobility in SmS, assuming acoustic scattering.

We now attempt to explain the observed temperature variation of the Fermi level on the basis of the simple model. To do this we shall have to introduce impurity levels, but first we shall consider the pure material. In this case the value of the Fermi level is found by setting n equal to the number of "ionized" f shells. For SmS the "normal" number of electrons in the $4f$ shell is 6 and an "ionized" $4f$ shell would have 5. The former case is sometimes referred to as Sm^{2+} and the latter as Sm^{3+}, though the actual charge on the atom is 2+ in both cases. We must also use the fundamental fact that ζ is the free energy per electron[18] (chemical potential), and require that the change in free energy of the total system is zero when an electron is promoted from the 4*f* shell to the conduction band. The "normal" 4*f* shell has several states of different energy and different degeneracies corresponding to different total angular momenta. Let E_i^0 be the energies of the states (with E increasing as i increases) and $g_i^0 = 2J_i^0+1$ be the degeneracies of the states. The partition sum for a single "normal" 4*f* shell is

$$Z_0 = \sum_i g_i^0 \exp(-E_i^0/kT). \tag{3.8}$$

Similarly, let the superscript^1 stand for the same quantities for the "ionized" 4*f* shell. Then the energy $E_0^1-E_0^0$ is the energy required to remove an electron from the "normal" 4*f* shell (in its ground state) and put it in the bottom of the conduction band (leaving the "ionized" 4*f* shell in its ground state). Let the number of atoms per unit volume be N and remember that the number of conduction electrons per unit volume n is equal to the number of "ionized" 4*f* shells per unit volume. The total free energy per unit volume of the 4*f* shells is then

$$\begin{aligned} F = -kT\{&\ln[N!/n!(N-n)!] \\ &+(N-n)\ln Z_0+n\ln Z_1\} \end{aligned} \tag{3.9}$$

The change of F when one 4*f* shell is "ionized" is $\partial F/\partial n$ and this quantity is equal to $-\zeta$. Thus, we find

$$-kT\{-\ln n+\ln(N-n)+\ln(Z_1/Z_0)\} = -\zeta, \tag{3.10}$$

which yields

$$n/(N-n) = (Z_1/Z_0)\exp(-\zeta/kT). \tag{3.11}$$

As the carrier density is small in all our applications, we shall neglect the n in the denominator so that

$$\begin{aligned} n/N = (Z_1/Z_0)\exp(-\zeta/kT) &= (q/N)\mathscr{F}_{1/2}(\zeta/kT) \\ &= C\mathscr{F}_{1/2}(\zeta/kT). \end{aligned} \tag{3.12}$$

The number of rare earth atoms in SmS is about $2{\cdot}3\times10^{22}$ cm^{-3}, so that C is about $1{\cdot}1\times10^{-3}$ at room temperature. For Boltzmann statistics, $\mathscr{F}_{1/2}(\zeta/kT) = \exp(\zeta/kT)$, and we can easily solve for ζ,

$$\zeta = \tfrac{1}{2}kT\ln(Z_1/Z_0C), \tag{3.13}$$

and

$$n/N = (CZ_1/Z_0)^{1/2}, \tag{3.14}$$

Because we have measured the energy from the bottom of the conduction band in equation (3.6), all other energies must also have that reference level. Thus, $E_0^1 = 0$.

We must also consider the effect of impurities. A very important impurity is another rare earth atom substituted for Sm. As all other rare earth sulfides (except EuS and YbS) have one electron per atom in the conduction band, we expect these impurities to act as donors which are ionized at all temperatures. The expression (3.11) gives only the number of "ionized" Sm 4*f* shells, so the equation (3.12) should now read

$$n/N = n_D+(Z_1/Z_0)\exp(-\zeta/kT) = C\mathscr{F}_{1/2}(\zeta/kT), \tag{3.15}$$

where n_D is the number of donors per rare earth atom. The expression for the Fermi level for Boltzmann statistics is now

$$\zeta = kT\ln\{(n_D/2C)+[(n_D/2C)^2+Z_1/CZ_0]^{1/2}\}, \tag{3.16}$$

and the carrier density becomes

$$n/N = n_D/2+[(n_D/2)^2+CZ_1/Z_0]^{1/2}. \tag{3.17}$$

These formulas will not hold at very low temperatures as the carrier statistics become degenerate and the approximation of $\mathscr{F}_{1/2}(\eta) = \exp\eta$ is not valid.

In this paper we will treat the energy gap $\Delta E = E_0^1-E_0^0$ as a free parameter but take the energy levels $E_i^0-E_0^0$ and $E_i^1-E_0^1$ from Van Vleck.[19] We then have approximately

$$Z_0 = \exp(\Delta E/kT)\sum_{J=0}^{6}(2J+1)\exp[-J(J+1)y], \tag{3.18}$$

$$Z_1 = \sum_{J=5/2}^{15/2}(2J+1)\exp\{[(35/4)-J(J+1)]y\}, \tag{3.19}$$

where $y = 215/T$. We write

$$Z_1/Z_0 = \beta\exp(-\Delta E/kT). \tag{3.20}$$

The quantity β is equal to 6 in the low temperature limit, to 1·35 in the high temperature limit, to 3·42 at room temperature (300°K), and to 1·71 at 900°K.

We now wish to pick values of ΔE and n_D such that equation (3.15) is satisfied. To do this we rewrite the equation as

$$\exp(-\Delta/kT) = (e^{\eta}/\beta)[(n/N)-n_D]. \tag{3.21}$$

We now guess a series of values for n_D and make a semilog plot of the right-hand side of (3.21) against $1/T$. Not only should the plot give a straight line, but it should have the value unity when $1/T = 0$. As seen in Fig. 2, the actual plots are only moderately good straight lines, the maximum deviations from the best straight line being about 20 per cent [of $\exp(-\Delta/kT)$]. The results for $p = 1/2$ came closer to giving the correct value of $1/T = 0$. In fact, a value of $p = -1$ should give the best results. Due to the error which comes from the uncertainty in β, we cannot really fix the value of p. If we assume $p = -1/2$, then the best fit gives $\Delta E = 0{\cdot}39$ eV and $n_D = 5{\cdot}5 \times 10^{18}$ cm^{-3}. This value of ΔE contrasts with the value 0·24 eV found⁽¹⁾ from the slope of the resistivity curve. The difference is mainly due to the temperature dependence of β. It would be interesting to have a direct measurement of ΔE from the infrared absorption. The values of ΔE and n_D adopted would reproduce the measured carrier density quite well up to about 800°K. Above that the calculated carrier density would be too small by as much as 50 per cent.

We may test the assumption of acoustic scattering by estimating the mobility of GdS, which according to our model is a metal with one conduction electron per atom. We assume that the effective mass, Debye temperature and scattering cross section are the same in GdS and SmS. Then the theory⁽¹³⁾ gives that the ratio of the mobility in SmS to that in GdS is $2(\zeta/\pi kT)^{1/2}$, where ζ is the Fermi level in GdS. Using the effective mass model and taking one carrier per rare earth atom, we find $\zeta = 2{\cdot}2$ eV, which gives a ratio of 10·4 so that the estimated mobility in GdS is 1·9 cm^2/V-sec. By assuming one carrier per atom and using the measured resistivity of GdS we find a mobility of 2·1 cm^2/V-sec. The close agreement is encouraging but may be fortuitous. The fact that the experimentally measured mobility in GdS is much smaller than that in SmS means that the scattering rate increases with energy if it is due to the same mechanism in both materials.

With our knowledge of the mobility and effective mass we may estimate the scattering time and mean free path in SmS. Using the approximate relation $\mu = e\tau/(300\, m^*)$ (e and m^* in cgs units, μ in practical units), we find that τ is about $0{\cdot}2 \times 10^{-13}$ sec. The thermal velocity in SmS at room temperature is about 10^7 cm/sec, so that the mean free path is about 20 Å or about five times the distance between nearest neighboring Sm atoms. Thus there is no need to mistrust standard band theory at room temperature. However, at 1300°K the mean free path is only about 5 Å so that the standard band theory may not apply.

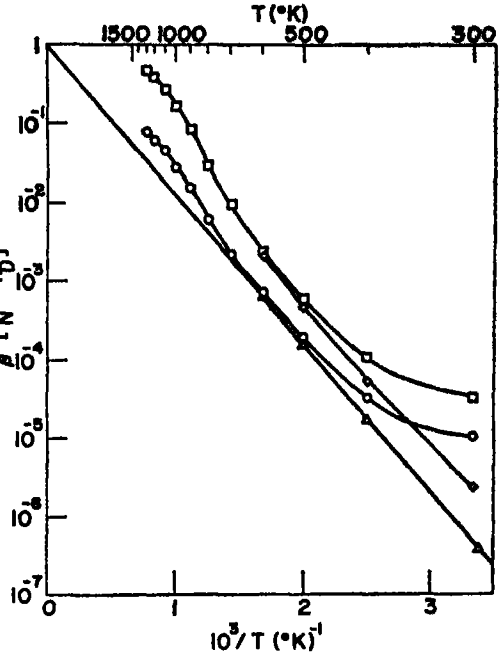

FIG. 2. Activation energy plots for the electrons in SmS:
○—Acoustical scattering, $n_D = 0$
△—Acoustical scattering, $n_D = 5{\cdot}5 \times 10^{18}$ cm^{-3}
□—Polar scattering, $n_D = 0$
◇—Polar scattering, $n_D = 5{\cdot}5 \times 10^{18}$ cm^{-3}

IV. RARE EARTH NITRIDES

Some of the same considerations may be applied to the rare earth nitrides. The magnetic susceptibility data⁽¹⁾ indicate that, with the exception of CeN, the number of $4f$ electrons is three less than the total number of electrons in the $4f$, $5d$ and $6s$ shells in the free atom. In CeN there are no $4f$ electrons. Thus, the conduction bands in the nitrides compete more successfully for electrons than in sulfides. There is some tendency for the $4f$ shell to acquire more electrons in EuN and YbN.

If the nitrogen ions could hold three extra electrons, then all the nitrides but CeN would be semiconductors. However, all except YbN are

n-type semimetallic, so that the nitrogen ions must hold less than three, which is reasonable theoretically. CeN is a p-type semimetal. If the nitrogen ions held three extra electrons, then CeN would have one conduction electron per unit cell. However, as the nitrogen ions hold less than three, there must be more than one conduction electron per unit cell. If the conduction band were based on $6s$ orbitals, it would then be more than half filled and p-type (hole) conduction would result.

Any further consideration of the nitrides should take into account their ferromagnetic and antiferromagnetic properties.

V. CONCLUSIONS

We believe that the use of the magnetic susceptibility data to determine the number of f electrons is quite valid and that it also applies to the polysulfides.(2, 20) The general model of the electronic energy structure of SmS is probably correct but the parameter values are not highly reliable. However, we feel that the presently available data do not warrant a more elaborate analysis. The results of this study may help in understanding the occurrence of ferro- and antiferromagnetism in some of these compounds.

Acknowledgements—It is a pleasure to acknowledge interesting and stimulating discussions of the present work with Dr. R. G. Breckenridge and Dr. R. Didchenko.

APPENDIX A

Localization of f electrons

The radius of the $4f$ shell is very small. The radius of maximum radial charge density(21) is about 0·3 Å. We have estimated the overlap between $4f$ orbitals on nearest neighbor samarium atoms in SmS by using the formula for overlap between $4s$ orbitals. Using the radial wave function of Freeman and Watson(21) we find that only the fourth term in their expansion gives an appreciable contribution. The value of the overlap integral so found is about 2×10^{-5}. Now the maximum value that a Y_3^0 spherical harmonic will have relative to the value of a Y_0^0 harmonic is $(2l+1)^{1/2} = 7^{1/2}$. Thus an estimate of the biggest overlap between $4f$ orbitals is seven times that calculated ignoring the angular part, giving about $1{\cdot}4 \times 10^{-4}$ for the overlap integral. The band width of the $4f$ band is approximately the overlap integral times the average value of the potential between the nearest neighbor samarium atoms. The Madelung potential in this region is small, as the center point is also halfway between two sulfur atoms. We shall guess that the potential is about 1 eV, which gives a band width of about 10^{-4} eV. This gives an average effective mass of about 10^4 times the free electron mass. The band width is so small that conservation of energy would not allow optical mode scattering in the $4f$ band. The mobility limited by acoustical mode scattering is given by the deformation potential theory.(13) If we guess that the deformation potential constant is 1 eV and that the Debye temperature is 200°K, we find a mobility of about 10^{-8} cm^2/V-sec. Assuming one carrier per samarium atom, this would give a conductivity of about 10^{-5} mho/cm at room temperature, compared to the measured value(1) of about 15 mho/cm. Our estimate could be off by an order of magnitude or two, but this would not change the conclusion that the conductivity of the $4f$ bands is negligible.

APPENDIX B

Overlap integrals for 5d and 6s electrons

The effective charge of a $5d$ or $6s$ electron on a doubly ionized rare earth atom is equal to 3. The effective radial quantum numbers are 4·0 and 4·2, respectively.(22) Thus, the radius for maximum radial charge density is about $4^2 \times 0{\cdot}53/3 \simeq 2{\cdot}8$ Å. This is very nearly equal to half the distance between the rare earth and sulfur ions, and indicates strong binding. The particular overlap integrals we require are the $5d$–$5d$ and $6s$–$6s$ on nearest neighbor rare earth ions. These have not been calculated explicitly but their value can be estimated from plots of overlap integrals which have been calculated.(23) For instance, we plotted the overlap integrals for $1s$–$1s$, $2s$–$2s$, $3s$–$3s$ $5s$–$5s$ for the value of the parameter $p = Z_{\text{eff}}r/na_0 = 6$ (r is the ion–ion distance, equal to 4 Å), and extrapolated to find a value of 0·7 for the $6s$–$6s$ overlap integral. A similar comparison of the $5s$–$5s$ and $5p$–$5p$ results leads us to an estimate of 0·5 for the $5d$–$5d$ overlap integral. These estimates are, of course, approximate but they allow us to say that the band widths of both the $5d$ and $6s$ bands are of the order of 1 eV or so.

APPENDIX C

The binding of the rare earth monosulfides

In this Appendix we shall discuss the binding as if the compounds were fully ionized.(24) We start with neutral atoms infinitely separated and then doubly ionize the rare earth atoms which requires an energy of about 5·6 eV + 11·4 eV = 17 eV per rare earth atom. The numbers 5·6 eV and 11·4 eV are the first and second ionization potentials, respectively, for europium but those for the other rare earths are very little different. We then transfer two electrons to each sulfur atom which requires an energy of about 4 eV per sulfur atom,(25) which is the negative of the electron affinity of S^{2-}. We next form the NaCl type lattice, gaining the electrostatic energy(26) of $\alpha(2e)^2/d \cong 34$ eV per pair of atoms, where d is the nearest neighbor distance ($\sim 2{\cdot}9$ Å) and $\alpha = 1{\cdot}75$ is the Madelung constant. Thus, we arrive at a binding energy of about $34-4-17 \cong 13$ eV per molecule (pair). If we regarded the compound as singly ionized, the binding energy would be $(34/4)+2{\cdot}1-5{\cdot}6 \cong 5$ eV, where the 2·1 eV is the electron affinity(27) of S^-. Thus, we agree with the general opinion that the sulfur atoms are doubly ionized.

It is interesting to calculate the energy required to remove one electron from a sulfur atom and put it on a metal atom far away. We imagine ionizing an atom of S^{2-} to S^-, gaining about 6 eV. We then transfer the electron to the vicinity of a metal atom far away. As the electrostatic potential near the sulfur is +17 V, and that near the metal is −17 eV, the transfer costs 34 eV. We then allow the electron to be bound to the metal atom, gaining about 11 eV. Thus, the creation of the electron-hole pair costs about 17 eV, so that it is a most unlikely process. If we transferred the electron to a nearest neighbor metal atom, the required energy is about 6 eV less, due to the electrostatic interaction. Even with some relaxation of the lattice around the electron-hole pair, it is very unlikely that the energy of formation could be lowered enough for the process to become important.

In this Appendix we have neglected the fact that the electrons are in bands and not localized. However, the estimated band widths are 1 or 2 eV so that the considerations presented here are still valid. The conduction bands do contribute to the binding as can be seen from the fact that the metallic rare earth sulfides generally have smaller lattice constants(1) than the semiconducting sulfides.

We also wish to consider the situation when there are rare earth vacancies, particularly for YbS. We may think initially that two electrons will be missing from the sulfur $3p$ bands. Next, we must ask if the energy is lowered if electrons are transferred from the $4f$ bands (there being none in the $6s$ or $5d$ bands of YbS) to fill the holes in the sulfur band. The experimental situation is that p-type conductivity is observed in sulfur-doped samples, with an activation energy of 0·3 eV. This indicates that the ground state is one with the holes in the $4f$ bands of the Yb atoms, but that it requires only 0·3 eV to transfer a hole to the sulfur $3p$ band. For stoichiometric YbS the activation energy is the energy required to transfer an electron from the $4f$ to $6s$ band. This energy is so high that conductivity is not observed. We first need to know the third ionization potential for Yb, which does not seem to have been measured or calculated. We shall estimate it using SLATER's rules(22) and the first two ionization potentials. According to the Slater rules, the effective charge Z_{eff} for a $6s$ electron in a neutral rare earth atom is $2{\cdot}85e$. The one-electron energy is in atomic units $-(Z_{\mathrm{eff}}/n^*)^2$, where n^* is the effective quantum number. Slater gives 4·2 for n^* for the $n = 6$ shell but we get the right first and second ionization potentials by using $n^* = 5{\cdot}1$. Thus, for the total energy of the two electrons in the 6th shell of the neutral atom, we find $-2(2{\cdot}85/5{\cdot}1)^2 = -0{\cdot}625$ a.u. = −17 eV. The effective charge for a $6s$ electron on Yb^+ is $3{\cdot}2e$, so that its energy is $1(3{\cdot}2/5{\cdot}1)^2 = -0{\cdot}39$ a.u. = 10·8 eV. Thus, the first ionization energy is 6·2 eV and the second is 10·8 eV in agreement with the experimental values(25) of 6·2 eV and 12 eV. The third electron must come from the $4f$ shell. Assuming that the $4f$ shell is outside of the $5s$ and $5d$ shells, Slater's rules give that the effective charge for a $4f$ electron is 11·45 in Yb^{2+} and 11·8 in Yb^{3+}. If we use the same n^* as above, we find for the ionization energy $14(11{\cdot}45/5{\cdot}1)^2-13(11{\cdot}8/5{\cdot}1)^2 = 1$ a.u. = 27 eV. Slater recommends $n^* = 3{\cdot}7$ for the $4f$ shell which would give a third ionization potential of 53 eV. We adopt the value of 27 eV, and show that this is in agreement with the idea given above. If we imagine that both holes were on the same sulfur atom, the energy to transfer one electron from a Yb^{2+} ion far away would be $+27-34-2$ eV $= -9$ eV. To fill the other hole with an electron taken from another Yb^{2+} ion which is far away from the first, takes $+27-34+6 = -1$ eV. With these values the ground state would consist of all holes in the $4f$ band, and the creation of a hole in the sulfur $3p$ band would require 1 eV. We have neglected the fact that the holes are not localized but are in energy bands. As the holes are the highest unfilled states in the band, the energy gained on filling a hole will be less than calculated above. The calculations presented here are quite inaccurate, but they do show that the model is not unreasonable.

REFERENCES

1. DIDCHENKO R. and GORTSEMA F. P., *J. Phys. Chem. Solids* **24**, 863 (1963).
2. HOUSTON M. D., *Ceramic Age*, p. 49 (Sept. 1961).
3. HUND F., *Z. Phys.* **33**, 855 (1925).
4. VAN VLECK J. H. and FRANK A., *Phys. Rev.* **34**, 1494 and 1625 (1929).
5. VAN VLECK J. H., *The Theory of Electric and Magnetic Susceptibilities*, Chap 9, University Press, Oxford (1932).
6. VAN VLECK J. H., *The Theory of Electric and Magnetic Susceptibilities*, p. 225. Chap. 9, University Press, Oxford (1932).
7. KITTEL C., *Introduction to Solid State Physics*, 2nd ed., p. 261. John Wiley, New York (1956).
8. URYU N., *J. phys. Soc. Japan* **15**, 2041 (1960).
9. WILLIAMS W. S., see Ref. 1.
10. HEINE V., *Group Theory in Quantum Mechanics*, p. 169. Pergamon Press, London (1960).
11. SEITZ F., *Modern Theory of Solids*, p. 180. McGraw-Hill, New York (1940).
12. BLAKEMORE J. S., *Semiconductor Statistics*, p. 346. Pergamon Press, New York (1962).
13. KITTEL C., *Introduction to Solid State Physics*, 2nd ed., p. 352. John Wiley, New York (1956).
14. HOWARTH D. and SONDHEIMER E., *Proc. Roy. Soc. Lond.* **A219**, 53 (1953).
15. KITTEL C., *Introduction to Solid State Physics*, 2nd ed., p. 255. John Wiley, New York (1956).
16. PETRITZ R. and SCANLON W., *Phys. Rev.* **97**, 1620 (1955).
17. CALLAWAY J. and STROMBERG T., *Phys. Rev. Letters* **9**, 376 (1962).
18. KITTEL C., *Introduction to Solid State Physics*, 2nd ed., p. 591. John Wiley, New York (1956).

19. Van Vleck J. H., *The Theory of Electric and Magnetic Susceptibilities*, p. 248. Chap. 9, University Press, Oxford (1932).
20. Cutler M., Fitzpatrick R. and Leavy J., *Bull. Amer. phys. Soc.* Series II, **7**, 221 (1962).
21. Freeman A. J. and Watson R. E., *Phys. Rev.* **127**, 2058 (1962).
22. Slater J. C., *Quantum Theory of Atomic Structure*, Vol. 1, Chapter 15, McGraw-Hill, New York (1960).
23. Mulliken R. S., Rieke C. A., Orloff D. and Orloff H., *J. chem. Phys.* **17**, 1248 (1949).
24. The arguments presented here are to be found in Seitz F., *Modern Theory of Solids*, Chaps. 12 and 13, McGraw-Hill, New York (1940).
25. Landolt–Bornstein, Vol. I, pt. 2, 6th ed., p. 212, Springer, Berlin (1950).
26. Kittel C., *Introduction to Solid State Physics*, 2nd ed., p. 77. John Wiley, New York (1956).
27. Branscomb L. M. and Smith S. J., *J. chem. Phys.* **25**, 598 (1956).

J. Phys. Chem. Solids Pergamon Press 1963. Vol. 24, pp. 881–884. Printed in Great Britain.

MEASUREMENT OF THE Cd–CdS LIQUIDUS*

H. H. WOODBURY

General Electric Research Laboratory, Schenectady, New York

(*Received* 14 *February* 1963)

Abstract—The Cd–CdS liquidus has been measured between 700°C and 1250°C. In the low temperature region, the liquidus rises exponentially with temperature similar to that observed in III–V semiconducting compound systems.

INTRODUCTION

It is well known that deviations from stroichiometry of the II–VI compound semiconductors can profoundly change their electrical and optical properties. However, the details of what happens when such a semiconductor is fired in one of its components are little understood. One effect on certain impurities has been shown, namely, the firing of such semiconductors in the metal component will remove or getter Cu and Ag.[1] To establish the basic ground work for such studies in CdS, a portion of the Cd–CdS liquidus has been determined. An attempt was made to determine the S–CdS liquidus but the solubility of CdS in sulfur in the temperature range accessible (up to 1000°C) was found to be very small. Only one point on the S–CdS liquidus was determined (see Fig. 1).

PROCEDURE

A weight-loss procedure was employed as follows: Single crystal pieces of high-purity CdS, ranging between 10 mg and 250 mg, were sealed in quartz tubing with 0·1–1 g of Cd. For temperatures up to 1100°C, 5 mm i.d. × 7·4 mm o.d. tubing was used; at 1150°C, 4 mm i.d. × 6 mm o.d. tubing was used; and at the highest temperatures (1200–1250°C), capillary tubing with 2–3 mm i.d. and 10 mm o.d. was used. The maximum temperature was limited by the softening and expansion of the quartz under the Cd pressure. Quartz tubing or rods were often placed inside the firing tubes which would hold the sample at one end of the tube (the bottom when firing) but would permit the Cd to separate upon inversion of the tube. This separation was necessary to prevent the freezing Cd from cracking the sample. Above 900°C, the liquid Cd would become very viscous (presumably due to the dissolved sulfur) and it was necessary to mechanically tap the tube to separate the liquid from the crystal. The Cd sticking to the samples or partly embedding them was removed in cold (< 10°C) dilute (7 per cent) HNO_3. Although this treatment would apparently reduce the dissolved CdS to free sulfur, it did not measurably attack the single crystal CdS. The weight loss of the sample could thus be determined and from the known Cd metal originally in the firing tube, the Cd–CdS liquidus could be calculated. The weight loss measurements were checked for a few samples by analyzing the sulfur which had dissolved in the Cd, using standard chemical techniques. The two methods were in agreement within 10 per cent, the reproducibility of the measurements.

The main problem encountered in the procedure was the establishment of equilibrium during the firing. It was necessary to keep the bottom end of the 2–3 cm long quartz tubes colder than the top; otherwise Cd would condense in the top. Too great a temperature gradient and worse, too great a temperature cycling, would cause material transport away from the crystal. Small crystals, separate from the original crystal, have

---

* The research reported in this paper was sponsored in part by the Air Force Cambridge Research Laboratories, Office of Aerospace Research, under contract AF19(628)-329.

been observed to grow under conditions of large temperature variations. For the liquidus measurements, the temperature gradient and cycling were kept less than 1°C. Different samples were fired for different lengths of time at each temperature to ensure that equilibrium was obtained. For example, reproducible results were obtained when the firing time was varied from 1/2 hr to 4 hr at the highest temperature (1250°C) and 16–60 hr at the lowest temperatures (700°C).

The procedure for sulfur firing was somewhat simpler since it was not necessary to separate the liquid sulfur from the samples. Also, the sulfur was easily removed from the crystals by washing them in CS_2. The maximum temperature of the sulfur firing was limited to 1000°C, above which temperature the 2 mm i.d. × 10 mm o.d. quartz tubing would explode.

RESULTS

The averages of the calculated composition values for several runs at each of the temperatures indicated are plotted in Figs. 1 and 2. Figure 1 gives the Cd–CdS liquidus on a linear temperature-composition phase diagram. The maximum melting point, $T_m = 1475 \pm 15$°C, is the value given by ADDAMIANO.[2] The dashed extrapolated portion was arbitrarily drawn. Figure 2 gives the same data on a dimensionless plot.

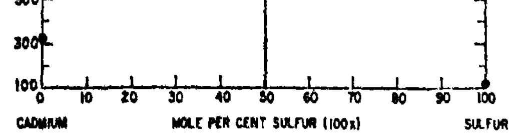

FIG. 1. Phase diagram of CdS showing portion of the Cd–CdS liquidus that has been measured. The melting point of CdS is taken from Ref. 2. The one point on the sulfur rich side at 1000°C corresponds to a Cd solubility of 0·1 ± 0·1%.

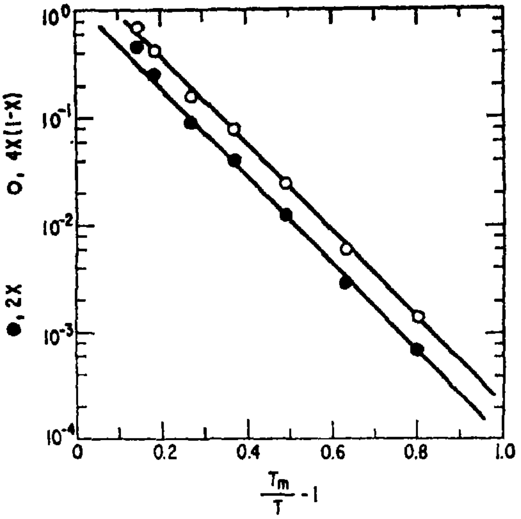

FIG. 2. Dimensionless plot of Cd–CdS liquidus where x is the sulfur composition at temperature T. T_m, the melting point of CdS, and T are in °K. See the text for a discussion of the choice of the ordinate function.

DISCUSSION

Thermodynamic considerations give the relationship between the composition variables and the temperature provided one has a model for the equilibrium reaction. The usual first assumption is an unionized, dissociated state for the liquid. That is, the solid $(AB)_s$ is assumed to melt in a liquid of composition $(1-x)A_l + xB_l$ where x is the mole fraction of the B component in the liquid. As a first approximation, the liquid is assumed to be ideal with respect to the two, noninteracting components, A_l and B_l. Equating the chemical potential of the compound in the solid state to its components in the liquid state and assuming the heat of fusion to be temperature independent, one easily derives the following relationship between the melting temperature, T, and the liquid composition, x:

$$\left(\frac{T_m}{T} - 1\right) = \left(-\frac{R}{\Delta S}\right)[\ln 4x(1-x)]. \tag{1}$$

Here T_m is the maximum melting temperature of the compound and ΔS is the entropy of fusion. The data for CdS is plotted as open circles in Fig. 2 using $\ln[4x(1-x)]$ as the ordinate. Second approximations to (1) have been derived assuming only that the solution is regular.⁽³⁾ It is noted that equation (1) still applies if the two components are assumed to be completely ionized.

It has been observed that the vapor pressure over the melt of CdS is very low compared to the vapor pressure over either component at the same temperature.⁽³⁾ This is an indication of considerable interaction between the components in the liquid state and suggests that an undissociated model for the liquid state may be a better approximation. Specifically, assume the liquid to have excess A over B and to take the form $(1-y)A_l+y(AB)_l$ where y is the mole fraction of the $(AB)_l$ component. Again, assume ideal behavior of the two components of the liquid, A_l and $(AB)_l$, and that the heat of fusion is temperature independent. One then derives the following relation for the melting temperature, T, for the equilibrium $(AB)_s \rightleftarrows (AB)_l$:

$$\left(\frac{T_m}{T}-1\right) = -\frac{R}{\Delta S}\ln(y),$$

or, in terms of the variable x used in (1),

$$\left(\frac{T_m}{T}-1\right) = -\frac{R}{\Delta S}\ln(2x), \quad x \leqslant 1/2. \tag{2}$$

The data for CdS is plotted as closed circles in Fig. 2 using $\ln(2x)$ as the ordinate. It is evident that plotted this way, the data better approximates the ideal behavior of a straight line drawn through the maximum melting point, $(T_m/T-1) = 0$, $x = 1/2$. However, no definitive conclusions can be drawn because of the lack of data near the melting point.

Combinations of all of these models, i.e. a partially ionized, partially undissociated liquid state could be formulated but the arbitrariness of such a model makes it of doubtful value even with good data near the melting point. The point to be emphasized is that even in the first approximation of an ideal liquid, considerable choice is available in the models one can consider. It is suggested that of the two simplest models for compounds like CdS, an undissociated liquid state may be the better first approximation.

It is noted that the general thermodynamic relationships on which equations (1) and (2) are based are valid over the composition range from the melting point to the A–AB (Cd–CdS) eutectic. Thus, assuming that the heat of fusion is independent of temperature, these equations give the temperature dependence of x in the limit of small sulfur composition. Viewed this way, equations (1) [or (2)] represent the temperature dependence of the solubility of sulfur in Cd [or of CdS in Cd]. The straight line portion of Fig. 2 verifies the regularity of the liquid for small x. Hence, a straight line extrapolation of the curves in Fig. 2 should be valid to the Cd–CdS eutectic. If these curves are extrapolated to the temperature corresponding to the Cd melting point as an upper limit of the eutectic temperature, a sulfur composition of the order 10^{-12} is calculated. This indicates that the Cd–CdS eutectic is immeasurably different from the Cd melting point and that the extrapolation itself is valid to any measurable composition value.

The data as presented in Fig. 2 gives a plot similar to that found for the III–V semiconducting compounds. Specifically, within the experimental errors, the value of ΔS determined from the slope of the lines drawn in Fig. 2, 18 cal deg^{-1} mole^{-1}, is identical to the value found for III–V semiconducting compounds.⁽⁴⁾ This implies that the change in randomness upon melting is the same for these types of compounds. Since the solids of these compounds are crystallographically similar (tetrahedral arrangements of atoms), this seems to imply that their liquid states are similar also.

Note added in proof: The Cd-rich liquidus has been measured for CdTe⁽⁵⁾ and CdSe⁽⁶⁾ in the region from the melting point of the compounds to approximately 95 mole per cent Cd. The qualitative behavior of the Cd-rich liquidus in the range of common measurement is similar for these related compounds; CdS, CdSe, and CdTe. It seems likely that the phase diagram curve (Fig. 1) is probably peaked at the maximum melting point in the CdS system as it is in the other two. Unless the similarity in the behavior of the liquidus between CdS and the III–V compounds in the dilute (small x) region is fortuitous, one would also expect CdSe and CdTe to follow the dimensionless plot shown in Fig. 2. Little can be said about the sulfur-rich liquidus for CdS although the very small solubility measured at 1000°C may be indicative of a behavior similar to that observed for the CdSe system.(6)

Acknowledgements—The author thanks R. N. HALL and J. S. PRENER for comments. He is particularly grateful to M. R. LORENZ for discussions on the subject of this paper. B. B. BINKOWSKI assisted in the experimental work. M. AVEN suggested ways of mechanically separating the Cd from the CdS.

REFERENCES

1. AVEN M. and WOODBURY H. H., *Appl. Phys. Letters* **1**, 53 (1962).
2. ADDAMIANO A., *J. phys. Chem.* **61**, 1253 (1957).
3. WAGNER G., *Acta Met.* **6**, 309 (1958); SCHOTTKY W. F. and BEVER M. B., *Ibid.* **6**, 320 (1958); L. J. VIELAND *Ibid.* **11**, 137 (1963).
4. HALL R. N., *J. electrochem. Soc.* May (1963).
5. DE NOBEL D., *Philips Res. Rep.* **14**, 488 (1959); LORENZ M. R., *J. Phys. Chem. Solids* **23**, 939 (1962).
6. REISMAN A., BERKENBLIT M. and WITZEN M., *J. phys. Chem.* **66**, 2210 (1962).

J. Phys. Chem. Solids Pergamon Press 1963. Vol. 24, pp. 885–897. Printed in Great Britain.

HgTe–MnTe ALLOYS—II. ELECTRICAL PROPERTIES

R. T. DELVES†

The General Electric Company Limited, Central Research Laboratories,
Hirst Research Centre, Wembley, England

(*Received* 26 *February* 1963)

Abstract—The Hall effect magnetoresistance and Seebeck effect have been measured at 77 and 300°K in sintered samples of $Hg_{1-x}Mn_xTe$ alloys which have the zinc blende type lattice. The hole mobility is about 100 cm²/V sec at 77 and 300°K and $m^*{+}/m = 0{\cdot}3$ when $x < 0{\cdot}2$. A conduction band, probably from an (000) valley with mobility $= 2\text{–}4 \times 10^4$ cm²/V sec at 77°K and $m^*{-}/m = 0{\cdot}005\text{–}0{\cdot}012$ overlaps the valence band when $x < 0{\cdot}13$. An energy gap develops when $x > 0{\cdot}13$, and another conduction band with a lower mobility replaces the (000) valley when $x > 0{\cdot}15$. Only p-type material has been obtained when $x > 0{\cdot}25$.

Most stoichiometric samples contained at least 10^{17} cm^{-3} acceptors. Some could be removed by annealing, others may be due to metallic impurities or oxygen. Excess tellurium and copper are acceptor impurities. Excess mercury is a donor when $x < 0{\cdot}05$, and has a complicated effect when $x > 0{\cdot}05$. The number of holes increases when oxygen is added and the energy gap appears to decrease as well.

1. INTRODUCTION

THIS paper gives a general survey of the electrical transport properties of HgTe–MnTe zinc blende type alloys, using sintered samples. The phase constitution of these alloys is described separately.(1) They have not been discussed before though work has been done on HgTe–HgSe and HgTe–CdTe alloys.(2)

Though sintered material is very convenient for exploratory work in an unknown semiconducting system, there are some obvious objections to its use (which are discussed in Section 3) and one must not push the analysis of the results too far. For example, the mobility at low temperatures might be limited by grain boundary scattering, and a detailed discussion of scattering mechanisms is not appropriate.

Most of the results are for alloys with 5–15% MnTe (all percentages are molar per cent). It will be shown that in most of these alloys there are both electrons and holes at 77 and 300°K. Figure 1 illustrates the band structure. As a result, the usual methods of analysis in semiconductor work (e.g. a plot of $\ln(RT^{3/2})$ against $1/T$) are not useful. The holes are found to have a low mobility $\mu_+ \sim 100$ cm²/V sec, and the electrons have a mobility μ_-, greater than about 2×10^4 cm²/V sec at 77°K. It is possible to separate the properties of each by analysing the way in which the Hall coefficient R and electrical resistivity ρ depend on magnetic field at 77°K. Some limited

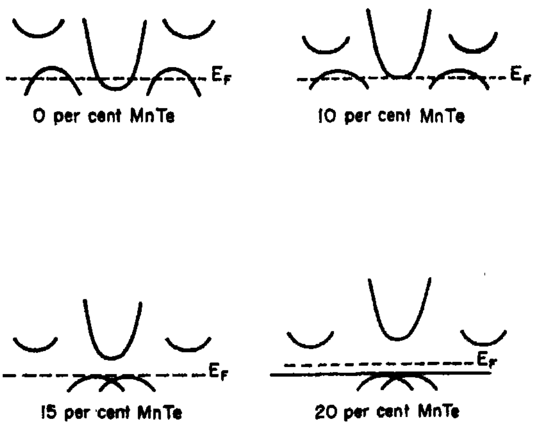

0 per cent MnTe

10 per cent MnTe

15 per cent MnTe

20 per cent MnTe

FIG. 1. Schematic band structure of (HgMn)Te alloys from the present work. The position in the Brillouin zone and shape of the valleys is not known.

---

† Now at the Royal Radar Establishment, Malvern, Worcs.

work has also been done with the Seebeck coefficient, α.

It can be assumed by analogy with PbTe and Bi_2Te_3 that the static dielectric constant of HgTe rich alloys will be of the order of 100. The impurity levels of donor or acceptor centres will overlap at quite small concentrations, and their ionization energy will be small or zero. Consequently the introduction of large numbers of acceptor centres can have three effects. The number of holes increases, the valence band is displaced towards the conduction band, and the top of the valence band can be distorted in shape. We find in HgTe–MnTe alloys good evidence for the first and second effects, and slight evidence for the third effect. More detailed measurements should allow quantitative comparison with the theories of WOLFF,(3) KELDYSH,(4) KANE(5) and others. In some of our alloys it is difficult to dope the material *n*-type, but by adding some acceptors the energy gap of the composition can be decreased sufficiently for electrons to be introduced. The properties of the electrons can then be studied, even though there is a large background of holes. We call this process of introducing electrons antidoping for want of a better name.

These alloys were originally chosen to attempt the study of scattering between the conduction electrons and the spins of the *d*-shells of the transition metal ions. These alloys, and the similar HgSe–MnSe system, are one of the few semiconducting systems that contain appreciable quantities of transition metals and have high mobilities. There is no real evidence of 'spin' scattering down to 77°K. It might be that at very low temperatures the electrons are scattered on impurity centres, dislocations, or the strain fields associated with alloying. If they did interact appreciably with the *d* shell electrons, various interesting experiments might become possible. For example, the Nernst effect could be anomalously large,(6) or simultaneous cyclotron and paramagnetic resonance be possible.

2. JUSTIFICATION FOR USING SINTERED SAMPLES

The following objections can be raised to making electrical measurements on sintered samples:

(*a*) The grains are randomly oriented.

Few measurements have been reported on single crystals of alloys between two compound semiconductors and it is usually rather difficult to prepare these single crystals. The random orientation is not a serious objection for magnetoresistance measurements in a cubic material whose conduction band is spherically symmetrical, as is believed to be the case for most of these alloys. The symmetry of the valence band is unknown, but as the hole mobility is low, the magnetoresistance effects in these alloys are due entirely to the electrons.

(*b*) The material is porous.

The density of the samples is only 85 per cent of the theoretical density. Higher densities could probably be obtained by hot pressing instead of cold pressing, but the former process is inconvenient if the alloys contain volatile components. REGEL(7) used hot pressed samples in his early work on HgTe. A correction was applied for porosity which is probably reasonably accurate for the majority of samples. The results for the few samples in which $R\sigma H > 1$, and for which the correction might be in error, seem to be reasonable. If $R\sigma H \gg 1$, it is doubtful whether any reliable correction for porosity could be applied.

(*c*) A conducting layer of free mercury might be deposited from the vapour onto the surface of the pores as the sample is cooled down after sintering.

There is no evidence for such an effect even for those samples which were sintered with an excess of mercury.

(*d*) Pressing might introduce dislocations or other defects which could scatter electrons, and could act as impurity centres.

It is difficult to comment on the importance of these effects, which would be more important at low temperatures than at high temperatures.

(*e*) The powders are easily contaminated in the various handling operations.

High purities were not expected in the present work. Finely divided tellurides and selenides are easily oxidized when they are exposed to air. All powders were handled in argon to avoid this. Some samples were accidentally contaminated with oxygen through the MnTe powder which had been used. The samples EA 1 to EA 12 were prepared with special care to avoid oxygen contamination and were found to have lower acceptor concentrations than samples which contained oxygen.

However, EA 11 for example had about 10^{17} cm^{-3} acceptors. These might be due to traces of oxygen. It might be very difficult to exclude oxygen completely from sintered samples, and be preferable to work with zone melted samples. It may be remarked that it is not a trivial problem to eliminate oxygen from zone melted HgTe alloys, and published accounts of the preparation of such alloys do not consider this point. It is also possible that oxygen diffuses into samples at room temperature, or in the process of soldering contacts. Oxygen has an interesting role as an acceptor impurity which is discussed in Section 9.

The advantages of sintered material are that the composition of the sample and the departure from stoichiometry are known and exactly controlled, and that it is easy to prepare a homogeneous single phase sample. (Zone melted alloys are prone to *microsegregation* problems.) Also, samples of various compositions can be prepared quickly from the stock powders, the samples are mechanically robust, and they require little preparation after sintering before electrical measurements can be made.

3. MEASUREMENT TECHNIQUES

The samples were prepared by methods described elsewhere.(1) Many samples were prepared in pairs from the same powder, and were sintered in the same tube. They only differed in subsequent annealing treatments or the addition of extra mercury. The properties of such pairs are compared in the discussion of the results.

Electrical measurements were made with three pressure contacts on each side of the sample as potential probes. This checked the homogeneity of the sample and the reliability of the contacts. Occasionally a contact gave spurious magnetoresistance measurements which were rejected. Geometrical effects due to the shortening of the Hall voltage by the finite length to width ratio were not important. Soldered indium contacts were used for current connections. Potentials were measured to 1 μV by a conventional d.c. potentiometer. Magnetic fields up to 6500 Oe were available. The sample was directly immersed in liquid nitrogen for measurements at 77°K. Chopped d.c. was used at 300°K for those samples in which thermoelectric effects could have been troublesome. The porosity of the sample was allowed for by the formulae(8)

$$\sigma_m/\sigma = (1-\delta)/(1+\tfrac{1}{2}\delta) \tag{1}$$

$$R_m/R = (1-\tfrac{1}{4}\delta)/(1-\delta) \tag{2}$$

The subscript m refers to the measured properties and δ is the proportion of free space in the sample.

The Seebeck coefficient was also measured for a few samples at 77°K with and without a magnetic field There was a possible error of ~ 5 per cent.

4. THEORY OF THE METHOD OF ANALYSIS

R and ρ are not directly related to the numbers and mobilities of the charge carriers, as most samples contained both holes and electrons. It is not possible to analyse the temperature dependence of R and ρ without doubtful assumptions such as that the ratio μ_-/μ_+ and the energy gap are both independent of temperature.

It is more useful to study the variation of R and ρ with magnetic field at a fixed temperature. In this work the temperature is 77°K. The electrical properties of the alloys can be explained if they are supposed to contain low mobility holes, μ_+ equal to about 100 cm²/V sec, and a smaller number of high mobility electrons. The contribution of the electrons to R and ρ decreases as H increases and in principle it is possible to separate the electron part from the hole part. The band structure of the alloys is shown schematically in Fig. 1.

After correcting for porosity, we convert the measured Hall coefficient R and magnetoresistance ρ to R_c, a kind of Hall conductivity coefficient, and magnetoconductivity σ by

$$R_c = R/(\rho^2+R^2H^2) \tag{3}$$

$$\sigma = \rho/(\rho^2+R^2H^2) \tag{4}$$

In this preliminary work we do not distinguish between Hall and conductivity mobilities. R_c and σ are now written as the sum of terms due to electrons and holes. As μ_+ is small $\mu_+H \ll 1$ in the magnetic fields that were used, and

$$R_c/e = \mu_+^2 n_+ - \mu_-^2 n_- F(2\lambda;H)/F(2\lambda;0) \tag{5}$$

$$\sigma/e = \mu_+ n_+ + \mu_- n_- F(\lambda;H)/F(\lambda;0) \tag{6}$$

where e is the electronic charge and n_+, n_- are the numbers of holes and electrons.

$$F(S,H) = \int_0^\infty \left[\frac{\partial}{\partial_x}\left(\frac{1}{1+\exp(x-\eta)}\right)\right] \times \frac{x^{(1\cdot 5+S)}\,\mathrm{d}x}{1+x^{2\lambda}p^2H^2\mu_-^2} \tag{7}$$

$x = E/kT$, η is the reduced Fermi level and it is assumed that a relaxation time exists which is proportional to E^λ and that the conduction band is spherically symmetrical and has a parabolic density of states, p, a numerical factor of the order of unity, is

$$p = F(\lambda;0)/F(2\lambda;0) \tag{8}$$

These assumptions are usually made in preliminary work on semiconductors. The assumption about a parabolic density of states is questioned later. There is no evidence from the present work about the shape of the conduction band. It has been shown that the conduction band of HgTe is spherically symmetrical and centred at $k = 0$ in the Brillouin zone.(9, 10) There is no abrupt change in electron properties as we add up to 15% MnTe to HgTe, so it is reasonable to suppose that these alloys have the same (000) minimum which is found in HgTe. There does seem to be a break in μ_- between 15 and 20% MnTe, so probably here the (000) valley is replaced by other valleys as the lowest point of the conduction band.

If the electrons are fairly degenerate, good approximations to equations (5) and (6) are

$$R_c/e = \mu_+^2 n_+ - \mu_-^2 n_-/(1+\mu_-^2 H^2) \tag{9}$$

$$\sigma/e = \mu_+ n_+ + \mu_- n_-/(1+\mu_-^2 H^2) \tag{10}$$

and these formulae fit the results for fairly degenerate samples quite well. However, in general we need to know the position of the Fermi level and the scattering mechanisms. Not only are these not known in our samples, but also the integrals needed in equation (7) have only been tabulated for non-degenerate statistics and a combination of acoustic mode and ionized impurity scattering. The best that can be done is to try to fit the values of R_c and σ in low magnetic fields to

$$R_c/e = \mu_+^2 n_+ - \mu_-^2 n_-/(1+k^2 H^2) \tag{11}$$

$$\sigma/e = \mu_+ n_+ + \mu_- n_-/(1+l^2 H^2) \tag{12}$$

by comparison with equations (5) and (6) we see that if the electrons are scattered by the acoustic mode vibrations, ($\lambda = -\frac{1}{2}$) and the electrons are non-degenerate then $k = \sqrt{2p}\ \mu_-$, $l = p\mu_-$, and $p = 2/\sqrt{\pi}$.

The values of k and l have been found and are tabulated for comparison with μ_-. p increases if the electrons become degenerate and is 2·1 when $\eta = 4kT$ and $\lambda = -\frac{1}{2}$.

In the majority of samples at 77°K R_c at low fields is predominantly due to the electrons and $\mu_-^2 n_-$ in equation (11) can be found accurately. In some samples R_c becomes positive in high fields, and $\mu_+^2 n_+$ can be found, but in many cases it cannot be separated from R_c. The conductivity σ on the other hand is usually mostly due to holes, and $\mu_+ n_+$ can be found accurately. $e\mu_- n_-$ or σ_- was found by extrapolating the measured magnetoconductivity to infinite fields. This process causes some error in the estimates of σ_-, which are only reliable to 10 per cent in most samples. The values of μ_+, n_+, σ_+; n_- and μ_- that have been derived from equations (11) and (12) are quoted in the various tables.

At room temperature the Hall coefficient of the specimens does not drop by more than 10 per cent when the magnetic field increases to 6500 Oe. The kind of analysis which was used at 77°K is not possible. Instead we use the weak field magnetoconductivity and Hall coefficient. In practically all samples, the electron contribution to R is far greater than the hole part, so

$$\mu_- = R\sigma^2/\sigma_- \tag{13}$$

$$\frac{\Delta\sigma}{H^2\sigma} = \frac{\sigma_-}{\sigma} p^2 \mu^2 \tag{14}$$

If we know p, we can calculate μ_- and σ_-. The majority of samples are non-degenerate at 300°K, but the scattering mechanism is not known. If we assume acoustic scattering we often obtain nonsensical results that $\sigma_-/\sigma > 1$. It seems that p is close to unity. This is quite likely if the electrons are scattered by a combination of acoustic and optical phonons. The results at room temperature have been analyzed assuming that $p = 1$. This should provide a reasonable estimate of μ_- and n_-. However, σ_+, usually only a small part of σ, can only be estimated roughly. As far as can be seen the rough values of σ_+ are reasonable if $\mu_+ \simeq 100$ cm²/V sec at 300°K (as in sample CY 29) and at 77°K, and there are the same number of holes at these two temperatures. The number of thermally excited holes is small compared to the extrinsic number. These remarks apply to samples with less than 13% MnTe. Samples with more than 15% MnTe appear to have an activation energy for the acceptor centres.

5. RESULTS FOR 5% MnTe ALLOYS

The results of the analysis of various samples with 5% MnTe are shown in Table 1. All the samples probably contained some oxygen. The electrons are partially degenerate at 77°K, and the measurements fitted equations (11) and (12) quite well, so the detailed curves of R and ρ as a function of magnetic field are not given. The values of μ_-, k and l are in good agreement.

It is seen from sample DH 56 that excess tellurium has some effect as an acceptor. Excess mercury in DH 51 has increased the number of electrons, and also increased σ_+. The solubility limit of excess mercury in this alloy is close to 1 at. %. Annealing sample DH 43 seems to have increased n_- by comparison with DH 44 which was made from the same powder. μ_- seems to have increased too. Similar effects have been found by BRACH[11] and RODOT[12] in HgTe.

Table 1. *Results for* 5% MnTe *alloys k and l are "mobilities" deduced from the magnetic field dependence of R and σ*

Sample	% MnTe	% dope	Annealing$^{(a)}$ time	$R(H=0)^{(b)}$	$\sigma^{(c)}$	77°K $\mu_+^{(d)}$	$n_+^{(e)}$	$\sigma_+^{(c)}$	$n_-^{(g)}$	$\mu_-^{(f)}$	$k^{(f)}$	$l^{(f)}$
DH 56	5	1·2 Te	0	− 16	23·7	60	$2·3\times10^{18}$	22·2	1·2	0·75	0·75	—
DH 44	5	0	0	− 58	20·0	—	—	17·3	1·9	0·87	0·87	1·2
DH 43	5	0	10	− 71	32·7	—	—	19·3	4·1	1·1	1·5	1·4
DH 51	5	1·0 Hg	0	−107	65·0	—	—	38	10·0	1·7	1·8	1·9
DY 4	6·5	0	10	−142	28·0	—	—	22·0	2·2	1·8	2·4	2·4

Sample	% MnTe	% dope	Annealing$^{(a)}$ time	$R^{(b)}$	$\sigma^{(c)}$	300°K $\alpha^{(h)}$	$\Delta\sigma/\sigma H^{2(J)}$	$\mu_-^{(f)}$	$n_-^{(g)}$
DH 56	5	1·2 Te	0	−55	101	−102	0·63	1·1	28
DH 44	5	0	0	−49	102	−100	0·43	0·85	44
DH 43	5	0	10	−43	210	−115	1·11	1·2	76
DH 51	5	1·0 Hg	0	−42	320	−125	2·0	1·5	120
DY 4	6·5	0	10	−93	125	−120	—	—	—

(a) In days at 240°C. (b) cm^3 C^{-1}. (c) Ω^{-1} cm^{-1}. (d) cm^2 V^{-1} sec^{-1}. (e) cm^{-3}. (f) 10^4 cm^2 V^{-1} sec^{-1}. (g) 10^{15} cm^{-3}. (h) μV deg^{-1}. (J) 10^{-8} Oe^{-2}. ( ) Quantities assumed by comparison with similar samples.

DH 51 has the most electrons at 300°K and the Seebeck coefficient should be almost entirely due to electrons. A density of states effective mass of $m^*_-/m = 0{\cdot}012$ is deduced if we assume $\lambda = 0$. If $\lambda = -\frac{1}{2}$ the value is 0·015.

6. RESULTS FOR 10% MnTe ALLOYS AT 77°K

The 10% MnTe alloys were studied in most detail. Values of R and the magnetoresistance are shown in Figs. 2 and 3 for selected samples, and the results of the analysis are given in Table 2.

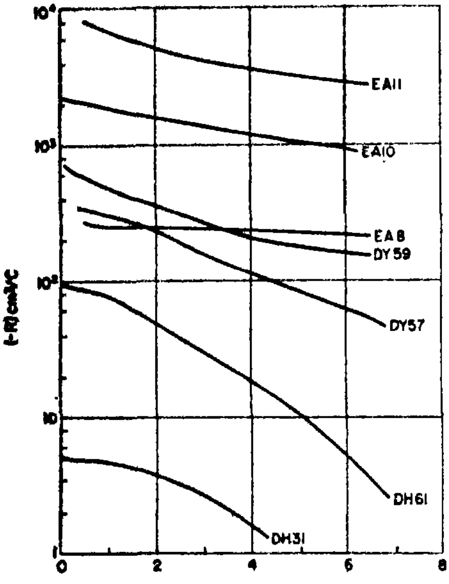

FIG. 2. Hall coefficient vs. magnetic field for 10% MnTe samples. (Results not corrected for porosity in Figs. 2 to 5.)

We discuss first sample EA 11, which has the least hole conductivity. About half the conductivity is due to holes, and using the hole mobility found in other samples, there appear to be about 7×10^{16} cm^{-3} acceptors in this sample. These might be due to residual oxygen or metallic impurities. However, if we compare EA 11 with EA 10, which was made from the same powder we see that annealing has reduced the acceptor concentration. The acceptors in EA 11 may be due to some structural disorder, for example a mercury atom occupying a tellurium site and leaving two interstitial tellurium atoms. If so, the prospects for reducing the acceptor concentration below 10^{15} cm^{-3} are not hopeful. Annealing out the acceptors seems to have reduced n_- too, so the energy overlap has decreased. Elsewhere it is also found that the energy gap increases as the acceptor concentration goes down. Possibly HgTe and all HgTe–MnTe alloys would have positive energy gaps if the acceptor and donor concentrations could be reduced to below 10^{14} cm^{-3}. Then the band structure might be similar to KANE's model for InSb.(13) HARMAN(10) has fitted the conduction band of HgSe and $\mathrm{HgSe_{0\cdot5}Te_{0\cdot5}}$ to Kane's model, but, as in this model the valence band is below the minimum of the conduction band, Harman assumes a further valence band that overlaps the conduction band to make these alloys the semimetals that they are found to be. There is no direct evidence for two sets of valence bands in HgTe and HgSe. It is suggested that in fact the valence band is basically as in Kane's model, but it has been raised in energy and presumably distorted in shape by the impurity states so that it overlaps the conduction band.

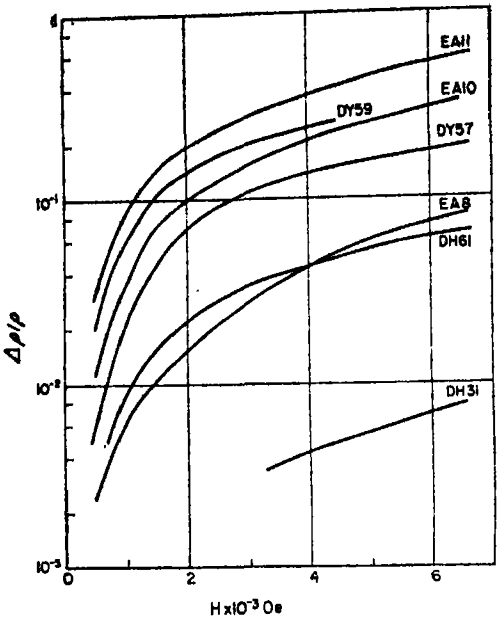

FIG. 3. Magnetoresistance vs. magnetic field for 10% MnTe samples.

It would be interesting to determine the shape

Table 2. Results for 10% MnTe *alloys*

			77°K									300°K					
Sample	Dope (%)	Annealing[a]* time	$R(H=0)$[b]	σ[c]	n_+[d]	μ_+[e]	σ_+[c]	n_-[g]	μ_-[f]	k[f]	l[f]	R[b]	σ[c]	α[h]	$\Delta\sigma/\sigma H^2$[j]	μ_-[f]	n_-[g]
EA 11	0	28	−7320	1·93	7×10^{16}	(100)	1·11	0·15	3·3	8	8	−183	40	−230	0·80	1·1	15
EA 10	0	0	−1830	4·7	—	—	3·05	0·42	2·5	6	6	−190	25	−225	0·27	0·6	23
EA 8	3 Hg	0	− 230	20	—	—	17·5	0·45	3·6	10	8	−140	29	−230	0·27	0·65	18
DH 59	0	10	− 135	27	—	—	24	0·7	3·0	4·8	4·0	−154	40	− 98	0·38	0·6	—
DH 61	0	0	− 75	14·5	7×10^{17}	120	13·4	0·45	1·6	4·2	4·0	−105	24	− 10	—	—	—
DY 49	0	10	− 170	37·5	—	—	27	2·7	2·3	3·0	2·0	− 70	200	−145	1·9	1·4	85
DH 88	1 Hg	0	−1310	13·5	—	—	7·5	0·9	4·1	4·7	4·6	−135	29	−140	0·21	0·55	24
DY 17	1 Hg	0	− 165	15	—	—	13	0·8	2·0	2·8	2·5	−130	34	− 93	0·31	0·70	19
DY 57	2 Hg	10	− 290	24	1×10^{18}	105	19	1·05	3	4·7	3·8	−145	53	−151	0·58	0·75	44
DH 6	2 Hg	0	− 525	7	—	—	5	1·3	1	1	1·5	−305	12	−230	0·19	0·50	8
DY 58	3 Hg	0	− 480	27	—	—	19	1·1	4·4	7·5	5·6	−165	44	−230	0·48	0·7	38
DY 59	3 Hg	10	− 520	32·5	—	—	21	1·5	5	10	9	−115	52	−230	—	—	—
DH 34	1 Te	0	− 21	19·3	$1{\cdot}4\times10^{18}$	85	19	0·05	~3	3	—	− 90	28	− 20	0·12	0·5	20
DH 31	2 Te	0	− 4	25·9	$1{\cdot}6\times10^{18}$	100	25·7	0·09	2	2	2	−120	37	− 13	—	—	—
DY 67	0·5 Al	10	− 260	32	—	—	21	2·9	2·4	3·0	3·0	− 85	120	−154	0·87	1·1	69
CY 29	2 Cu	0	+0·15	1200	4×10^{19}	180	1200	0·00	—	—	—	+0·11	860	+ 71	0·00	—	—

* See Table 1 for key to (a) etc.

of the valence band experimentally, but as the mobility is low, magnetoresistance measurements would be difficult. Perhaps piezoresistance measurements might help.

The Hall mobility of EA 11 is found to be $3{\cdot}3\times10^4$ cm²/V sec and this is probably a good estimate, as we can deduce from the magnetoconductivity in 6500 Oe that μ_- is certainly less than $3{\cdot}6\times10^4$ cm²/V sec. However, k and l which can be found fairly accurately in this sample are rather higher. If we assume $\lambda = -\frac{1}{2}$ we would expect $k = 5{\cdot}5\times10^4$ and $l = 4\times10^4$. A similar discrepancy is found in other 10% MnTe samples, and the difference between k, l and μ_- seems to be greater in 15% MnTe samples. Geometrical and porosity effects are unlikely to cause the discrepancy, as we find good agreement between k, l and μ_- in the 5% MnTe samples. Three obvious explanations are possible. (a) There may be electrons with low mobilities, $\mu_- \sim 2\times10^4$ cm²/V sec from minima in other parts of the Brillouin zone besides the electrons with $\mu_- \sim 8\times10^4$ cm²/V sec from the (000) minimum.

This explanation is unlikely as the analysis of k and l as function of magnetic field suggests that there are electrons with a complete range of mobilities, and not two separate groups. We find too, that the discrepancy becomes less when the number of electrons increases as in DY 67. There is some evidence for other conduction minima coming in above room temperature in 10% MnTe alloys but it seems unlikely that there are electrons from these minima at 77°K. (b) There is some form of scattering mechanism for which $\lambda < -0{\cdot}5$, or possibly for which a relaxation time does not exist.

This explanation seems unlikely as k and l are roughly equal, suggesting $\lambda \simeq 0$, and no scattering mechanism is yet known that gives $\lambda < -\frac{1}{2}$. This does not explain why the discrepancy is removed when the number of electrons increases. (c) The density of states is very nonparabolic.

This seems to the author the most likely explanation. The states at the bottom of the conduction band must have a much smaller effective mass, and consequently a higher mobility, than states higher in the band. This would give the electrons a wider spread in mobility than usual. While such nonparabolicity results from the kind of band structure discussed by Kane[13] and found in

InSb and other semiconductors, the effect seems to be too large in HgTe–MnTe alloys to be completely explained in this way. Perhaps the bottom of the conduction band has been distorted by the perturbation of the large number of impurity centres in the samples used in this work.

The remaining samples contained various amounts of oxygen which is reflected in the values of σ_+. We note that an occasional sample is found, such as DH 6, whose mobility is rather lower than the others. This we attribute to some defect in the powders or pressing technique. The Hall mobilities vary from 3 to 4×10^4 cm^2/V sec. The samples with highest mobilities also seem to have $2l > k$ and k higher than μ_-.

Aluminium was introduced into DY 67 in attempt to make it more n-type. This was only partially successful. On the other hand the sample CY 29 which was very heavily doped with copper was p-type at 77 and 300°K, and allowed the hole properties to be found directly. Here, the shift of the Fermi level into the valence band is much greater than any shift of valence band into conduction band. It is also possible to make the specimens p-type by adding excess tellurium. The samples DH 31 and DH 34 contained oxygen, and the effect of excess tellurium is to reduce n_- rather than increase n_+.

The effect of excess mercury in the 10–15% MnTe alloys is complicated. In some samples the effects are obscured by the oxygen also present, but sample EA 8 shows them most clearly. There seems to be no increase in n_- when mercury is added, nor does μ_- increase, yet σ has increased considerably. The part of σ not due to the electrons in the (000) valley is tabulated under σ_+ in Table 2 for convenience, and at first we would attribute this to an increase in the number of holes. But the Hall coefficient of these extra carriers was determined by extrapolating the Hall coefficient in 6500 Oe to infinite magnetic fields in the usual way, and was found to be about -130 cm^3/C. We would have expected a much smaller positive value. α of these extra carriers is found in the same way to be about -35 μV/°C.

Though some of the extra carriers are no doubt holes it is clear that some are electrons. It seems unlikely, for reasons similar to those already discussed, that the extra electrons come from higher valleys. It might be that the extra mercury has caused the spread in mobilities of electrons in the (000) valley to increase considerably at the low mobility end. Three at. % Hg is equivalent to 5×10^{20} atoms/cm^3 and this is a very large number. Measurements on single crystals in fields up to 20,000 Oe would be required to clarify the origin of the extra electrons.

α of EA 10 was -43 in zero field and $+21$ in 6000 Oe. (All α are in μV/deg.) Using the estimates of $\sigma_+\sigma_-$ and the measured magnetoresistance we find $\alpha_- = -230$ $\alpha_+ = 145$. Assuming $\mu_+ = 100$ cm^2/V sec and $\lambda = 0{\cdot}0$ we obtain $E_G = -0{\cdot}005$ eV (so the valence and conduction band overlap), and estimates for $m^*_-/m = 0{\cdot}004$, $m^*_+/m = 0{\cdot}2$.

In DY 58 α was -11 and $+98$ in zero field and 6000 Oe respectively. With the same assumptions we find $\alpha_- = -240$, $\alpha_+ = 125$, $E_G = -0{\cdot}007$ eV, $m^*_-/m = 0{\cdot}006$, $m^*_+/m = 0{\cdot}3$.

7. 10% MnTe SAMPLES AT 300°K

The second method of analysis described in Section 4 was used to obtain the figures that are given in Table 2, for the properties at 300°K. It was found that above 300°K the conductivity of a sample such as EA 8 increased and the Hall coefficient dropped. At the same time the Seebeck coefficient increases rapidly. These results suggest that above 300°K electrons are thermally excited into some higher minima in the conduction band. This agrees with the abrupt change in mobility found at 300°K in going from 15 to 20% MnTe, a result presumably due to a change from the (000) valley to some other valleys. There is no information from the present work as to the number, position or shape of the new minima. A plot of $\ln(RT^{3/2})$ against $1/T$ for DH 6 from 0 to 100°C was a straight line and gave apparent energy gap of 0·1 eV which should be the gap between the valence band and the higher minima. It is worth noting that an energy gap of 0·15 eV has been found in thin films of HgTe.(14) This is presumably due to transitions from the valence band to the higher valleys, and not to the (000) valley.

The Seebeck coefficient at 300°K cannot be separated in to α_- and α_+, but in EA 11 σ_+ is small and $\alpha \simeq \alpha_-$. Assuming $\lambda = 0{\cdot}0$ we find $m^*_-/m = 0{\cdot}006$. CY 29 is so heavily doped that it contains only holes. We find $m^*_+/m = 0{\cdot}5$.

8. RESULTS FOR 10–15% MnTe ALLOYS

The results for samples with 10–15% MnTe are summarized in Table 3, and *R* and the magnetoresistance effect are shown in Figs. 4 and 5 for selected samples. The electronic part of σ is small in most samples and the magnetoresistance is usually small, causing some uncertainty in ρ. The Hall coefficient usually drops rapidly with increasing magnetic field and this gives large values of *k*, which can be determined reasonably accurately. Adding iodine or aluminium did not increase n_- appreciably. Probably a pure 15% MnTe alloy would show only hole conduction at 77°K, as does CZ 21. The 14 and 15% samples which do show partially electronic conduction contained some oxygen, which introduces electrons by the 'antidoping' mechanism discussed in Section 1. The discrepancy between μ_-, *k* and *l* is more marked in these alloys than for 10% MnTe alloys.

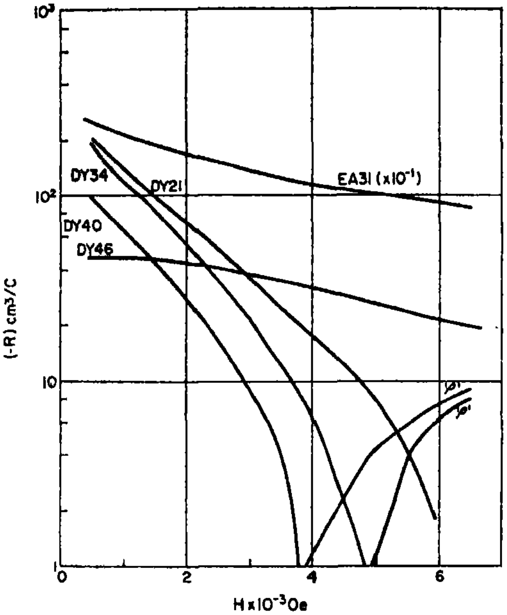

FIG. 4. Hall coefficient vs. magnetic field for 10–15% MnTe samples.

DY 23 had a rather small saturated magnetoresistance in high magnetic fields, and this results in the high value of μ_- quoted, which may be erroneous. The effects of large excesses of mercury in DY 35 and DY 46 are anomalous as in 10% alloys. DY 25 was also measured at 200°K, where there are thermally excited electrons, and μ_-, *k*, and *l* are in good agreement. The results of DY 63 could not be fitted to the accurate values of equations (5) and (6) assuming non-degenerate statistics and $\lambda = -\frac{1}{2}$, using the integrals tabulated by BEER,(15) though the agreement was better than when equations (11) and (12) were used.

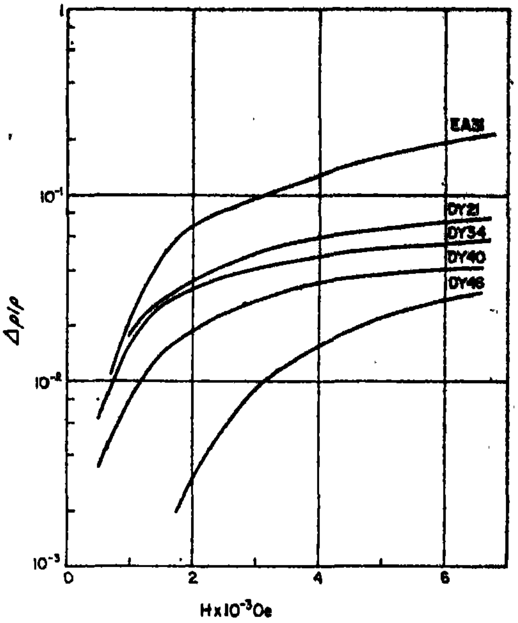

FIG. 5. Magnetoresistance vs. magnetic field for 10–15% MnTe samples.

The Seebeck coefficient of DY 40 was +160 μV/deg in zero field and +193 μV/deg in 6000 Oe. This gives $\alpha_- \simeq -485\,\mu$V/deg and $\alpha_+ = 195$ μV/deg. Assuming $\lambda = -\frac{1}{2}$, $E_G = 0{\cdot}025$ eV, $m_-^*/m = 0{\cdot}012$, $m_+^*/m = 0{\cdot}3$. These values are in reasonable agreement with what has been found in other alloys. About twice this energy gap 0·05 eV, is found if we use the increase in number, of carriers as the temperature goes from 77 to 300°K. If the energy gap is affected by impurity bands it may be rather sensitive to temperature, and this discrepancy is understandable.

It is possible to introduce electrons into a 15% MnTe sample by replacing some of the tellurium by selenium, as in EA 31. However, the

Table 3. *Results for* 10–15% MnTe *alloys*

Sample	MnTe (%)	Dope (%)	Annealing$^{(a)*}$ time	$R(H=0)^{(b)}$	$\sigma^{(c)}$	$n_+^{(g)}$	$\mu_+^{(e)}$	$\sigma_+^{(c)}$	$n_-^{(g)}$	$\mu_-^{(f)}$	$k^{(f)}$	$l^{(f)}$	$R^{(b)}$	$\sigma^{(c)}$	$\alpha^{(h)}$	$\Delta\sigma/\sigma H^2$ (j)	$\mu_-^{(f)}$	$n_-^{(g)}$
				77°K									300°K					
DY 19	11	1 Hg	0	− 215	14·9	550	140	12·3	0·85	1·9	4·4	3·2	−140	30	− 97	0·63	1·5	3·7
DY 21	12	1 Hg	0	− 200	11·2	830	75	10·0	0·35	2·2	7·5	5·5	−150	20	−125	0·20	0·7	8
DY 22	12	1 Hg	10	− 390	19·5	570	170	15·5	0·7	3·7	7·5	6	−158	34	−120	—	—	—
DY 34	12	2·5 Hg	0	− 210	8·3	330	145	7·8	0·12	2·9	9·5	9·5	−167	16·5	− 5	—	—	—
DY 35	12	∼5 Hg	0	− 27	15·3	—	—	14·5	0·65	0·8	8	4	−360	10	−115	0·22	0·6	7
DY 23	13	1 Hg	0	− 70	6·7	360	115	6·6	0·005	6·5	9·5	—	−145	13	+ 35	0·12	0·6	4
DY 42	13	1 Te	0	− 94·5	14·2	650	125	12·8	0·6	1·5	3·7	2·8	−119	25·5	− 35	0·25	0·8	7
DY 46	13	3·5 Hg	0	− 40	25·0	—	—	23·0	1·3	1·25	1·5	—	− 94	86·5	−115	0·97	1·2	30
DY 41	14	1 Te	0	− 85·5	14·5	700	120	13·3	0·95	1·5	3·2	2·8	−120	26	− 32	0·23	0·7	10
DY 25	14	1 Hg	0	∼+ 10	5·6	360	95	5·6	0·0	—	—	—	−110	11	+115	0·067	0·5	3
DY 25(m)	14	0	0	− 120	7·6	420	105	7·2	0·17	1·6	1·8	1·6						
CZ 21	15	0	0	+ 65	1·9	90	125	1·9	0·00	—	—	—	−450	3·2	+ 30	—	—	—
DY 28	15	1 Hg	10	∼−40	6·1	400	95	6·1	∼·01	∼3	—	—	−120	10·5	+105	—	—	—
DY 40	15	1 Te	0	− 100	11·0	500	130	10·5	0·11	3	8·5	5	−130	17·5	+ 20	0·13	0·6	8
DY 63	15	0·5 Al	10	− 275	7·3	300	135	6·7	0·12	2·5	9	6	−200	17	−102	0·22	0·65	9
DY 27	15	∼6 Hg	0	+ 120	0·805	50	95	0·805	0·000	—	—	—	−995	2·15	−285	0·087	0·4	1·7
EA 31	15	5 Se(n)	0	−2010	2·3	100	(100)	1·6	0·25	1·6	7	5	−230	15	−205	0·17	0·5	13

* See Table 1 for (a) etc. For Table 3 only (m) at 200°K; (n) 5 per cent Se replacing Te.

solubility of selenium is rather limited in alloys with more than 20% MnTe. (HgMn) (SeTe) alloys will be discussed in more detail elsewhere.

An interesting effect is seen in DY 27. This was prepared as +1% mercury, from the same powder as DY 28, and a quick check showed that it had similar properties. Mercury was then diffused in to saturation. We see that at 77°K there is no contribution to R or σ from the electrons, and the number of holes has diminished appreciably compared to those in DY 28. This effect was not seen in DY 35 which was similarly saturated with mercury. No doubt DY 27 first contained shallow acceptor levels from the oxygen impurity. These levels are emptied by the addition of the mercury, so probably the mercury forms some deep donor levels, and the situation is analogous to semi-insulating gallium arsenide.(16, 17) Perhaps mercury first enters both interstitially and by replacing tellurium atoms, and when present in sufficient quantities, creates vacancies in the tellurium sublattice which act as deep donors. It would appear too that the number of electrons is reduced as well as the number of holes. It is possible that adding deep donors reverses the decrease in energy gap found when shallow acceptors are added.

An attempt was made to do the same thing to EA 1 after oxidation, but possibly because there were too many acceptors, this was not sucessful. Some effect is seen in DY 61. α in DY 27 at 77°K was only 144 μV/deg. This would give an effective mass $m_+^*/m = 0{\cdot}04$, which is too low by an order of magnitude.

9. SAMPLES OXIDIZED IN STAGES

A comparison of samples DH 61 and EA 10 shows that oxygen acts as an acceptor impurity. Though the number of holes increases the number of electrons does not necessarily decrease as oxygen is added. To confirm these ideas, sample EA 1, containing 15% MnTe and believed to be relatively free from oxygen, was deliberately oxidized in stages by heating it in air. The results are given in Table 4. The original sample had only a few holes present at 77°K. At first adding oxygen increases the number of holes. Next we find electrons contributing to R and σ, and μ_-, k and l can be found in the usual way. This stage is similar to some of the other 15% samples which were accidently contaminated with oxygen.

In the final stage mercury was diffused into the sample in an attempt to reproduce the behaviour of DY 27. Judging by the results this was not successful and the main effect of the final treatment may have been to diffuse in more oxygen than was already present in the pores of the sample. After this treatment the number of electrons increased considerably, and now dominate both R and σ. μ_- has dropped considerably, probably due to contributions from higher conduction minima than the (000) valley. The Seebeck effect of the sample in this state was $-60\ \mu$V/°C at 77°K, giving $m_-^*/m = 0{\cdot}013$ if $\lambda = -\frac{1}{2}$. This value is quite close to 0·012 which was found in DY 40, a non-degenerate sample.

The sample DY 61, containing 20% MnTe, was also oxidized by heating it in a sealed tube containing a volume of air at room temperature equal to the volume of the sample. The sample contained $\frac{1}{2}$ per cent aluminium, but this should not affect the interpretation. It also contained some oxygen in its original form. The results are given in Table 5. The stage where there are only a few electrons which corresponds to the fourth stage in Table 4 was not observed in this sample. As R does not change appreciably with magnetic field the usual method of analysis is not applicable. Instead $R\sigma$ and $\Delta\sigma/(\sigma H^2)$ were used to get μ_- and n_-, assuming $p = 1$, as described in the second part of Section 4. The results seem reasonably reliable, and estimates of n_+ at 77 and 300°K agree fairly well.

We find high mobility electrons in the most heavily oxidized sample, and also that μ_- at 300°K increases considerably as the number of electrons increases. It is probable that in alloys with 20% MnTe the lowest conduction minimum is not the (000) valley but some other band below it. The electrons in this other band must have lower mobilities than electrons in the (000) valley. If the sample is doped sufficiently there is a contribution to R and σ from electrons in the (000) valley, and μ_- appears to increase.

A large excess of mercury was diffused into the sample in the final stage of treatment. The number of holes and the number of electrons seems to have been reduced, an effect seen previously in sample DY 27. The decrease in the number of

Table 4. Results for sample EA 1 (15% MnTe), *oxidized in stages*

Treatment	77°K									300°K					
	$R(H=0)^{(b)*}$	$\sigma^{(c)}$	$n_+^{(g)}$	$\mu_+^{(d)}$	$\sigma_+^{(c)}$	$n_-^{(g)}$	$\mu_-^{(f)}$	$k^{(f)}$	$l^{(f)}$	$R^{(b)}$	$\sigma^{(c)}$	$\alpha^{(h)}$	$\Delta\sigma/\sigma H^2$ (j)	$\mu_-^{(f)}$	$n_-^{(g)}$
28 days 250°C in vacuum	—	$1\cdot5\times10^{-2}$	1·8	(50)	$1\cdot5\times10^{-3}$	0·00	—	—	—	−1313	0·98	−46	0·040	0·3	0·8
2 hr 100°C in air	+893	$4\cdot9\times10^{-2}$	7	44	$4\cdot9\times10^{-2}$	0·00	—	—	—	−1300	1·07	—	0·040	0·3	0·8
2 hr 200°C in air	+227	0·77	32	175	0·77	some	—	—	—	—	—	—	—	—	—
16 hr 250°C in air	−644	2·73	—	—	2·46	0·1	1·7	8·4	5·3	− 403	5·8	−10	0·20	0·86	1·1
2 days 450°C+4% Hg in vacuum	− 71	29	—	—	∼1·3	80	·22	—	0·5	− 61	19·4	−91	0·006	0·12	100

* See Table 1 for key to (b) etc.

Table 5. Results for sample DY 61 (20% MnTe, ½ per cent Al), *oxidized in stages*

Treatment	77°K							300°K					
	$R(H=0)^{(b)*}$	$\sigma^{(c)}$	$n_+^{(g)}$	$\mu_+^{(d)}$	$\dfrac{\Delta\sigma}{\sigma H^2}^{(j)}$	$\mu_-^{(f)}$	$n_-^{(f)}$	$R^{(b)}$	$\sigma^{(c)}$	$\alpha^{(h)}$	$\dfrac{\Delta\sigma}{\sigma H^2}^{(j)}$	$\mu_-^{(f)}$	$n_-^{(g)}$
After sintering	+30	0·8	200	24	0	—	0·0	− 44	4·8	+295	∼0·003	∼0·15	∼ 3
18 hr 240°C	+15	8·4	400	120	0·007	—	some	− 64	9·1	+200	0·016	0·27	4·4
18 hr 350°C	−80	18·5	800	(120)	0·14	0·95	1·9	− 83	37	− 26	0·305	1·0	7·1
3 days 450°C	−12	27	1400	(120)	0·05	1·5	2·4	−100	62	− 82	0·845	1·35	13
3 days 450°C+7% Hg	−65	10·7	500	(120)	0·04	0·57	1·4	− 34	13	+ 98	0·018	0·40	2

* See Table 1 for key to (b) etc.

holes was attributed to the formation of deep donor centres by the excess mercury atoms, the apparent decrease in the number of electrons when mercury is added is thought to be due to an increase in energy gap as in DY 27.

10. ALLOYS WITH MORE THAN 20% MnTe

These alloys have not been studied in detail. They are all found to be *p*-type at 300°K, with Seebeck coefficients of about 600 μV/°C and conductivities 0·3 to 0·03 Ω^{-1} cm^{-1}. Hall coefficients could not be measured, except in a sample with 25% MnTe which had $\mu_+ \sim 50$ cm^2/V sec at 300°K. A plot of ln σ against $1/T$ for a 50% MnTe sample between 80 and 400°K gave an activation energy of 0·08 eV. No discontinuity in σ which might have indicated the onset of antiferromagnetic ordering was observed.

An attempt was made to dope a 50% MnTe sample by diffusing in copper. However, a mixture was formed of a mercury rich zinc blende type phase and a new metallic compound with a face centred cubic lattice (a = 4·94–4·95 Å).(18) This compound was ferromagnetic at about 100°K and was thought to be roughly (CuMn)Te$_2$.

11. CONCLUSIONS

The magnetic field dependence of the Hall coefficient and resistivity in sintered MnTe–HgTe alloys has been used to separate the electron and hole contributions to R and σ. The alloys are semimetallic when there is less than 13% MnTe, and probably the lowest conduction band changes from an (000) valley to some other set when there is more than 15% MnTe.

The mobilities, number of carriers, and effective masses of the carriers have been found. The hole mobility is low. The electron mobility is 2–4 × 10^4 cm^2/V sec at 77°K in most alloys and could be even higher in single crystals.

Most samples have a net acceptor concentration of 10^{17} cm^{-3}. The origin of the acceptors has been discussed. Copper and excess tellurium are acceptors. Oxygen is an acceptor, and when present in large quantities seems to reduce the energy gap. Excess mercury has various effects which are not fully understood. These alloys are suitable for the study of impurity band effects as the mobilities are not reduced much on heavy doping. The analysis has been pushed as far as is worthwhile with sintered samples. Further work would require more extensive measurements on single crystals.

Acknowledgement—The author is indebted to Dr. A. K. Jonscher for a discussion on impurity bands.

REFERENCES

1. Delves R. T. and Lewis B., *J. Phys. Chem. Solids* **24**, 549 (1963).
2. References given in Ref. 1 above.
3. Wolff P. A., *Phys. Rev.* **126**, 405 (1962).
4. Kane E. O., *Proceedings of the International Conference on the Physics of Semiconductors, Exeter, England* 1962. Physical Society, London (1963).
5. Keldysh L. V., *Proceedings of the International Conference on the Physics of Semiconductors, Exeter, England* 1962. Physical Society, London (1963).
6. de Vroomen A. R. and Potters M. L., *Physica*, **27** 1083 (1961).
7. Regel A. R. and Nikol'skaya E. I., *Zh. tekh. fiz.* **25**, 1352 (1956).
8. Juretschke H. J., Landauer R. and Swanson J. A., *J. appl. Phys.* **27**, 838 (1956).
9. Rodot M., Rodot H. and Triboulet R., *J. appl. Phys.* **32**, 2254 (1961).
10. Harman T. C. and Strauss A. J., *J. appl. Phys.* **32**, 2265 (1961).
11. Brach B. Ya., Zhdanova V. V. and Lev E. Ya, *Sov. Phys.—Solid State* **3**, 571 (1961).
12. Rodot H. and Triboulet R., *C.R. Acad. Sci., Paris* **254**, 852 (1962).
13. Kane E. O., *J. Phys. Chem. Solids* **1**, 249 (1957).
14. Langrenaudie J., *J. chim. Phys.* **55**, 175 (1958).
15. Beer A. C., Armstrong J. A. and Greenberg I. N., *Phys. Rev.* **107**, 1506 (1957).
16. Gooch C. H., Hilsum C. and Holemen B. R., *J. appl. Phys.* **32**, 2069 (1961).
17. Haisty R. W., Mehal R. W. and Stratton R., *J. Phys. Chem. Solids* **23**, 829 (1962).
18. Private communication from Mr. B. Lewis of these laboratories.

J. Phys. Chem. Solids Pergamon Press 1963. Vol. 24, pp. 899–907. Printed in Great Britain.

THE INFLUENCE OF TWIN STRUCTURE ON GROWTH DIRECTIONS IN DENDRITIC RIBBONS OF MATERIALS HAVING THE DIAMOND OR ZINC-BLENDE STUCTURES*

N. ALBON† **and A. E. OWEN**‡

Westinghouse Research Laboratories, Pittsburgh, 35, Pennsylvania, U.S.A.

(*Received* 31 *December* 1962)

Abstract—A procedure by which dendritic ribbons of germanium may be grown in a ⟨211⟩ direction by rapidly pulling from a melt was developed by BILLIG(1,2) and BENNETT and LONGINI(4) showed that twinning on a {111} plane was essential for growth. Later WAGNER(5) and HAMILTON and SEIDENSTICKER(6) demonstrated that at least two twin planes are required for continuous propagation.

Experiments by the authors have shown that indium antimonide may readily be grown in the ⟨321⟩ and ⟨110⟩ directions as well as ⟨211⟩. The appearance of these new growth directions depends critically upon the twin structure and supercooling. The ⟨110⟩ growth, for instance, occurs only with two twins spaced at less than 5 μ, whereas ⟨321⟩ growth has been observed only with certain multiply twinned structures.

The observations are explained by a simple model of the dendrite tip faceted with {111} planes. This model takes no account of the polarity of indium antimonide and should therefore apply equally to materials such as germanium which crystallize in the diamond lattice. Additional experimental evidence in support of this conclusion has been obtained with both silicon and germanium in which the twin spacing and structure is again found to be a most critical factor.

INTRODUCTION

THE "dendritic" growth of germanium crystals in the form of long ribbons propagated in the ⟨211⟩ directions and bounded by {111} planes has been described by BILLIG,(1,2) BILLIG and HOLMES(3) and BENNETT and LONGINI.(4) This mode of growth was shown to depend upon the presence of twinning on the {111} plane which contains the directions of growth(4) and the later work of WAGNER(5) and HAMILTON and SEIDENSTICKER(6) has demonstrated that for continuous propagation two or more twins are required.

In principle it is possible for growth to occur in any direction lying in the {111} twin plane but under the experimental conditions used only ⟨211⟩ was found. Bennett and Longini described the features of such dendritic ribbons noting that when an odd number of twins are present there are three preferred directions and for an even number of twins the six ⟨211⟩ directions are equivalent. Limited growth in a ⟨110⟩ direction from impure melts has been noted by O'HARA.(7)

FAUST, NICHOLSON and MOSS(8) investigated the growth of indium antimonide dendrites concluding that they show the same features as germanium dendrites and that the polar axis does not interfere with the growth. Recent experiments by the authors,(9) however, have revealed aspects of the growth of indium antimonide which have not been reported in germanium. It has been found that, as well as growth in the ⟨211⟩

---

* This work was supported in part by the Manufacturing Technology Laboratory, Aeronautical Systems Division, Wright-Patterson Air Force Base, Ohio, U.S.A

† Now at Battelle Memorial Institute, Columbus, Ohio, U.S.A.

‡ Now at the University of Sheffield, Sheffield, England.

directions, propagation can also occur in ⟨110⟩ and ⟨321⟩ directions. Dendrites have been grown to a length of 2–3 in. in ⟨321⟩ directions and to about 5–6 in.—limited only by the apparatus—in ⟨110⟩ directions. In this paper the experimental conditions which favor growth in a given direction are described and a simple model of a dendrite tip used to explain these observations. The polarity of the InSb lattice is not, however, invoked either in constructing the model or in the subsequent arguments and it follows therefore that the same behavior should, under the right conditions, be observed in silicon and germanium. Some experimental confirmation of this assertion will be described.

EXPERIMENTAL METHODS AND OBSERVATIONS

The experimental methods and techniques of dendritic ribbon growth have been adequately described elsewhere[1,4] and will not be elaborated on here. It will suffice to say that the apparatus used was very similar to a Czochralski crystal-pulling furnace except that there was no rotation of the crucible or seed and the pulling speeds were somewhat greater (in the range 0·05–0·5 cm/sec). The melt, about ½ in. deep, was contained in a graphite crucible approximately 2 in. in overall diameter and 2 in. high and this was supported on a graphite rod roughly 9 in. long fixed to the baseplate of the furnace. The crucible was contained inside a fused-silica furnace tube 6 in. dia. and 21 in. long and was heated inductively by an r.f. coil external to the furnace tube. The temperature was measured by means of a sapphire light-pipe inserted vertically near the edge of the crucible and focussed on a thermopile assembly located in the baseplate of the furnace. This device was calibrated immediately prior to each experiment by measuring the output voltage obtained at the melting-point of the indium antimonide. In operation the furnace was first pumped out and a flow of argon introduced before the indium antimonide was melted down. The procedure of seeding etc. was precisely the same as that developed for germanium.[4,10]

Four melts of indium antimonide have been used; in three of these the impurity concentrations at room temperature were, very approximately 10^{17}, 10^{15}, and less than 10^{14} per cm^3. The fourth had an excess of 0·1 at. per cent of indium which was added to the 10^{14} melt. Controlled growth was obtained over a range of supercooling which varied from melt to melt. The lower limit at which only slow growth of a button was observed varied from 2–4°C of supercooling. The upper limit, defined as the temperature at which growth was so fast as to become uncontrolled, varied from 10–18° of supercooling. The ⟨321⟩ growth was observed within these limits but over a much narrower temperature interval of 2–3°. These results are summarized diagrammatically in Fig. 1. The appearance of ⟨110⟩ directions depended only slightly upon supercooling within this range.

In the ⟨211⟩ directions indium antimonide shows the same general features as germanium and such differences as do exist, e.g. more pronounced faceting, may be due to differences in thermal conditions. BENNETT and LONGINI[4] observed that 3-twin germanium exhibits "favorable" [$2\bar{1}\bar{1}$] and "unfavorable" [$\bar{2}11$] growth directions but in indium antimonide there does not appear to be such a marked difference in these directions.

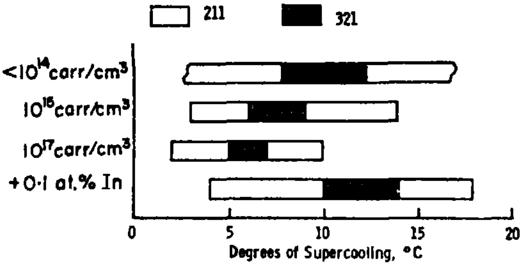

FIG. 1. Range of controlled growth in the four melts of indium antimonide.

The growth direction referred to here as ⟨321⟩ actually shows some deviation from the precise crystallographic orientation. Using a ⟨211⟩ direction as a datum line, propagation has been observed experimentally at an angle varying between 10 and 15° from this; the crystallographic angle between a ⟨211⟩ and the adjacent ⟨321⟩ directions in a {111} plane is 10·89°. Growth in ⟨321⟩ directions has been observed mainly from a seed containing seven twins and, as described above, in a very narrow range of supercooling. It is expected, however, that five twins would also show a strong tendency to propagate in this direction (see following discussion) but a seed of this structure was not obtained in these experiments. With a suitable seed oriented in a ⟨211⟩ direction it was always found that the initial growth was in the same direction, diverging into $\langle 321\rangle$ directions after 1 or 2 in.—a typical example is shown in Fig. 2. The $\langle 321\rangle$ growth has been continuously propagated for 2–3 in. after which it normally reverted to $\langle 211\rangle$ as the sides of the crucible were approached. A detailed examination of a $\langle 321\rangle$ dendrite indicates that it is, like a $\langle 211\rangle$ dendrite, bounded entirely by $\{111\}$ planes (Fig. 3). Sections through $\langle 321\rangle$ dendrites show a different geometry to those grown in a $\langle 211\rangle$ direction suggesting that the *H*-arm mechanism described by JOHN and FAUST(11) does not occur in this instance.

Growth in the $\langle 110\rangle$ directions has been observed predominantly from a seed containing two twin planes with a spacing of less than about 5 μ. It has occasionally been observed from seeds of more complex structure but on examination it proved that the excess twins had quickly grown out and the $\langle 110\rangle$ propagation continued with just two closely spaced twins. With two-twin seeds having a spacing greater than 10 μ propagation was observed only in $\langle 211\rangle$ directions under all conditions. In the intermediate region of spacings between 5 and 10 μ, $\langle 110\rangle$ and $\langle 211\rangle$ growth was found to occur equally readily. The critical effect of twin spacing on the growth direction was demonstrated in an experiment using a two-twin seed with a spacing at one edge of 11 μ and at the other of about 5 μ. It was observed that subject to the right degree of supercooling, propagation from the 5 μ side quickly diverged into $\langle 110\rangle$ directions while from the 11 μ side growth occurred exclusively in $\langle 211\rangle$ directions. Under the right conditions of twin structure and supercooling indium antimonide can readily be propagated continuously in a $\langle 110\rangle$ direction from a seed which itself is oriented in that direction. An illustration of such growth is shown in Fig. 4. There appears to be no difference in the ease of growth for the six $\langle 110\rangle$ directions in a $\{111\}$ plane. The sectional geometry of $\langle 110\rangle$ dendrites is also, like the $\langle 321\rangle$, different from the $\langle 211\rangle$ perhaps indicating the absence of the *H*-arm mechanism.

The experimental results, which have been described briefly in the preceding paragraphs, are summarized in Table 1 which represents the accumulation of several hundred observations.

DISCUSSION

As the presence of twin planes is essential for the growth of these dendrites, corresponding ridges and reentrant grooves would exist at the tip.(6) These areas would then be bounded by $\{111\}$ facets. Farther away from the faceting at the twins the dendrite surface may be rounded as, under the non-equilibrium conditions existing, growth does not proceed out to crystallographic planes. The shape of this curved surface is usually determined by thermal considerations and will not be discussed in detail.

Table 1. *Twin structures and growth directions of* InSb

No. of twins	Total twin spacing (μ)	Observed growth directions		Symmetry
		Continuous	Branching	
2	2–3·5	110 only	110 > 211	6-fold
2	5·5	110, 211	211, 110	6-fold
2	11–16	211 only	211	6-fold
3	3–3·5	211 only	211	3-fold
3	50·3	211	211	6-fold
7	9·6	211, 321	211, 321	—
9	15·4	211	211, 321	—

Notes

(1) Continuous propagation means here, for $\langle 110\rangle$ and $\langle 211\rangle$ dendrites, a length limited by the apparatus (about 5 in.) and for $\langle 321\rangle$, more than $\frac{1}{2}$ in. (longest length grown was about 2 in.).

(2) $\langle 321\rangle$ growth is only obtained over a sharply defined range of supercooling (see Fig. 1) as described in the text.

(3) Branches in the $\langle 110\rangle$ direction have been observed when using seeds containing three or more twins but in all samples so far examined these branches contained only two closely spaced twins.

Experimental observations indicated that the growth directions observed were dependent upon whether the twin spacing was greater or less than a critical value. We will describe a spacing less than this value as "close" and a greater spacing as "wide". The relation between number of twins and growth directions will be considered separately for closely and widely spaced twins. When the twins are closely spaced it is assumed that the faceted regions at the reentrant grooves will overlap and an explanation of the growth directions observed is given using a model of the tip comprised entirely of {111} facets. The resultant growth direction depends upon the number of twin reentrant grooves and their orientation. As the twin spacing is increased a point will be reached when the {111} planes forming the reentrant grooves intersect the curved surface rather than the other twin groove. The hypothesis is made that this occurs at the critical spacing. For widely spaced twins therefore the model used is that of a tip with faceted regions around each reentrant groove separated by a curved surface. An increase in tip curvature resulting from a change in growth conditions should result in an alteration in the width of the critical spacing. Thus, the parameter depends upon thermal conditions and with indium antimonide, under the experimental conditions described, the critical spacing was approximately 5 μ.

1. *Closely spaced twins*

(a) *Two-twin seeds.* The presence of two twin planes in a body bounded by {111} planes leads to a shape having sixfold symmetry (Fig. 5(a)) with a single reentrant groove and a ridge perpendicular to each ⟨211⟩ direction (Fig. 5(b)). For continuous propagation of dendrites in any given direction the growth process must preserve the tip morphology. The assumption is made that under equivalent conditions nucleation and growth occur at the same rate at each reentrant groove at the facceted tip. Overall rate of growth will of course depend upon such parameters as the supercooling. Nucleation and growth from the reentrant groove *A–B* (Figs. 5(b) and (c)) together with growth at the same rate from each of the grooves *CD* and *EF* result in a lengthening of the groove *A–B*. Thus in the ⟨211⟩ direction the tip widens and growth in this direction is not stable.

When viewed from the ⟨110⟩ direction (Fig. 6(a)) the twin grooves and ridges intersect at a corner. Growth advances this corner in the ⟨110⟩ direction without any change in shape so that continuous propagation of ⟨110⟩ dendrites is possible (Fig. 6(b)). Table 1 shows that ⟨110⟩ growth was preferred for indium antimonide when seeds having two twin planes closer than 5 μ were used.

All sides of dendrites grown in the ⟨110⟩ directions are bounded by {111} planes lying parallel to the growth direction. The "sawtooth" arrangement of {111} planes observed on ⟨211⟩ dendrites does not arise and lateral growth originating from the reentrant corners at the intersection of these {111} planes cannot occur. Widening of ⟨110⟩ dendrites usually proceeds at the twin reentrant grooves and it is observed experimentally that the twin planes almost invariably extend right across the dendrites.

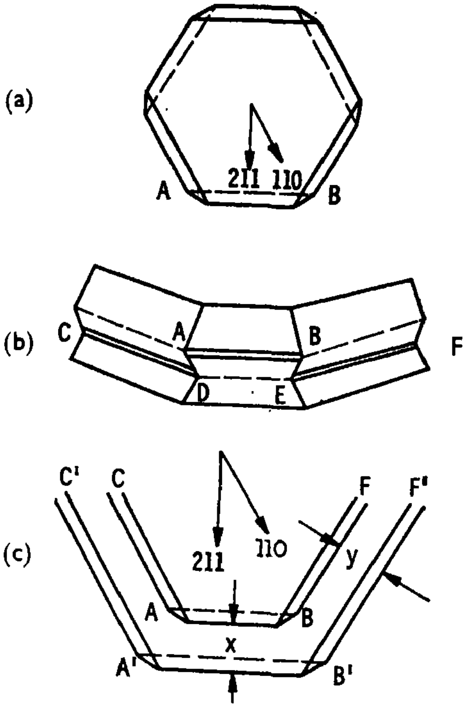

Fig. 5. Schematic diagram of dendrite with two-twin planes.
(a). Equilibrium shape of crystal bounded by {111} planes and having two twins in plane of paper. (b). The ⟨211⟩ tip of dendrite with two-twin planes. Twin Groove ═══ Twin Ridge — — —. (c). Growth occurring equally from each ⟨211⟩ facet (x/y = 1) resulting in lengthening of the groove *AB*. Twin planes in plane of paper.

(b) *Three-twin seeds.* Dendrites grown from three-twin seeds have been extensively studied especially with germanium (see Ref. 4), and will only be discussed briefly. A theoretical description of the growth of germanium dendrites in the ⟨211⟩ direction has been given by Bolling and Tiller.[12] The structure of tips bounded by

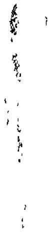

FIG. 2. A typical example of a ⟨211⟩ InSb dendrite branching into ⟨321⟩ directions.

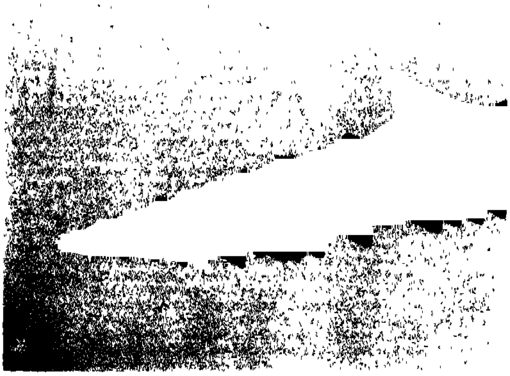

FIG. 3. Tip of a ⟨321⟩ InSb dendrite.

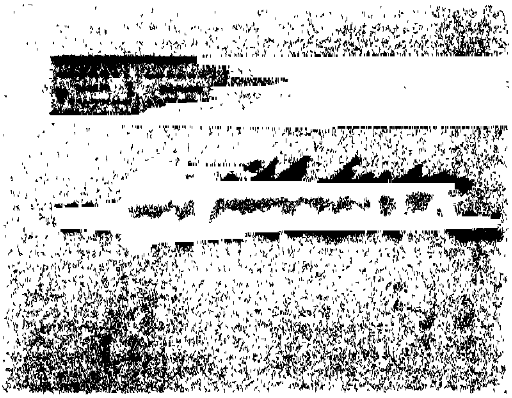

FIG. 4. Propagation of a ⟨110⟩ InSb dendrite.

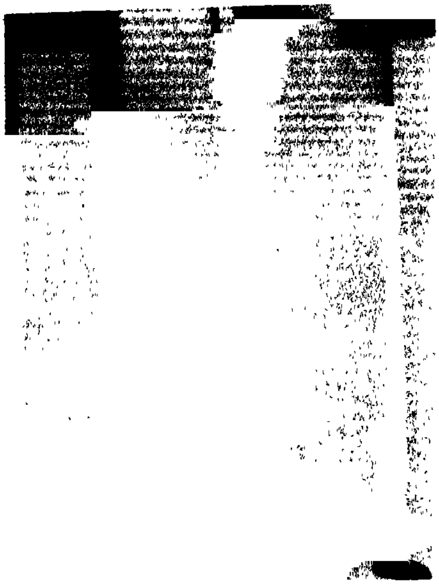

FIG. 11. ⟨110⟩ InSb growth from a very closely spaced two-twin seed.

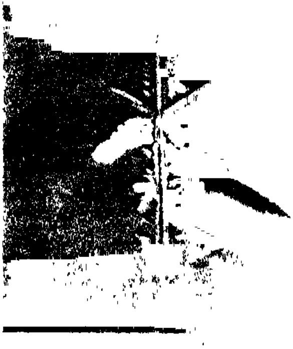

FIG. 12. A germanium dendrite showing ⟨110⟩ branches from a ⟨211⟩ stem.

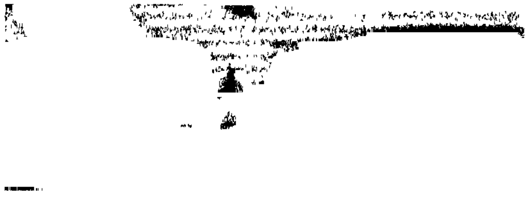

FIG. 14. Illustrating the loss of a twin in development of a ⟨110⟩ branch in the Ge dendrite of Fig. 12 (×358).

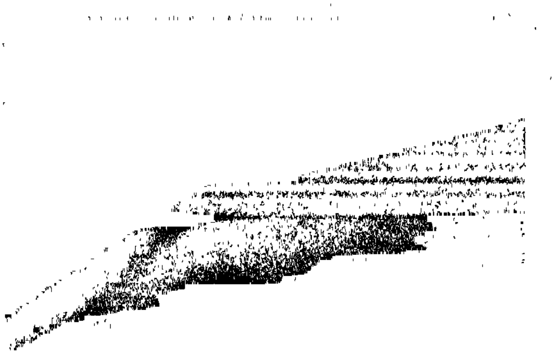

FIG. 15. A section near the tip of a ⟨211⟩ dendrite having asymmetrically placed twins (×966).

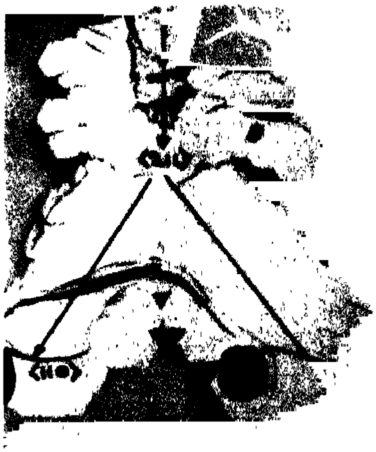

FIG. 16. ⟨110⟩ branching from a ⟨211⟩ silicon dendrite.

{111} facets and viewed from the ⟨211⟩ and ⟨110⟩ directions are shown on Figs. 7(a) and 7(b). There is one set of three ⟨211⟩ directions terminated by two reentrant grooves and one ridge and another set having one reentrant groove and two ridges. The assumption is made that growth where two reentrant grooves emerge is at approximately twice the rate for the direction where one groove emerges. Then the growth on the grooves *AB* and *GH* (Fig. 7(a)) and on the grooves *CD* and *EF* results in maintenance of the length *AB* (Fig. 7(c)). Thus continuous propagation in three ⟨211⟩ directions occurs.

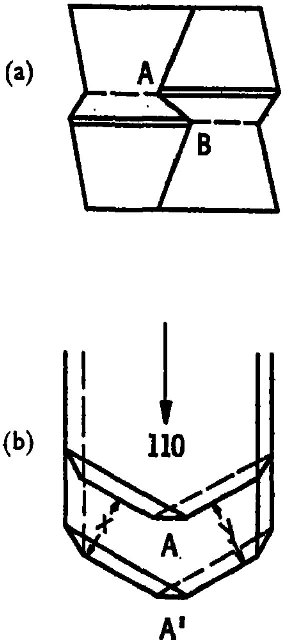

FIG. 6. Two-twin dendrite; ⟨110⟩ aspect.
(a). ⟨110⟩ tip. Twin planes perpendicular to paper. Viewed from ⟨110⟩ direction. Twin Groove ═══; Twin Ridge — — —. (b). Twin planes in plane of paper $x/y = 1$.

As the corners *A* and *B* move in a ⟨211⟩ direction continuous propagation of ⟨110⟩ dendrites having three closely spaced twins is not observed.

(c) *Multi-twin seeds.* The structure of a faceted tip of a dendrite having 7 equally spaced twin planes is shown in Fig. 8(a) as viewed from a ⟨211⟩ direction. There are four reentrant grooves perpendicular to one set of three ⟨211⟩ directions such as *AB* and three grooves perpendicular to the other set (*CD* and *EF*). Making the assumption previously used that the relative growth rate at the faceted tip in each direction depends only on the number of reentrant grooves in that direction the corners *A* and *B* will advance to *A'* and *B'* (Fig. 8(b)) and the length of *AB* will increase. There is therefore a tendency for the dendrite to divide and growth in the ⟨321⟩ direction most nearly satisfies the requirement of preserving tip morphology. These arguments will also apply when there are variations in the spacing of the twins provided that each reentrant groove contributes equally to the rate of growth. In the seven-twin seed used experimentally the spacing of the individual twins varied from approximately 1 to 3 μ and the total spacing was 9·6 μ (Table 1). Figure 3 shows the tip of a ⟨321⟩ dendrite. A corner such as *B* (Figs. 8(a) and (b)) will project furthest into the melt and the two sets of reentrant grooves will be at different

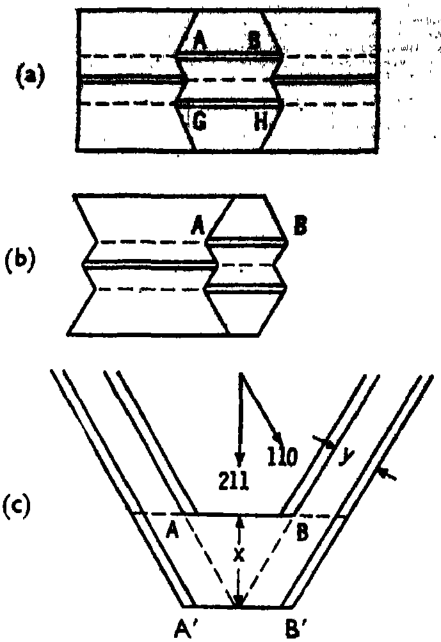

FIG. 7. Three-twin dendrite.
(a). ⟨211⟩ tip. Twin planes perpendicular to paper. Viewed from ⟨211⟩ direction. Twin Groove ═══. Twin Ridge — — —. (b). ⟨110⟩ tip. Twin planes perpendicular to paper. Viewed from ⟨110⟩ direction. (c). Twin planes in plane of paper $x/y = 2$, leading to stable propagation in vertical ⟨211⟩ direction.

angles to the ⟨321⟩ growth direction. Propagation requires a balance between the rates of growth from these two groups of grooves, and it seems likely that, as is observed, this would only occur over a narrow range of supercooling.

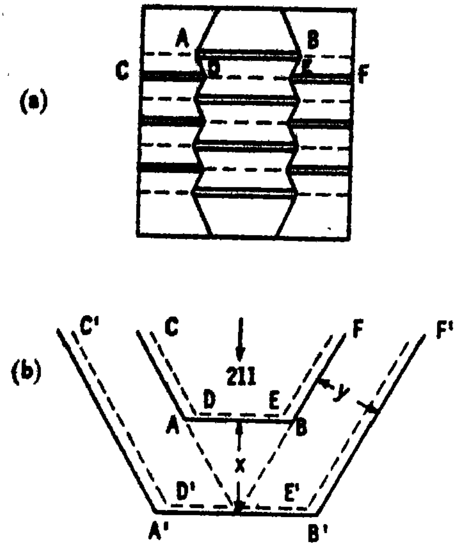

FIG. 8. Seven-twin dendrite.
(a). ⟨211⟩ tip. Twin planes perpendicular to paper viewed from ⟨211⟩ direction. Twin Groove ═══. Twin Ridge — — —. (b). Twin planes in plane of paper, $x/y = 4/3$, leading to lengthening of groove AB.

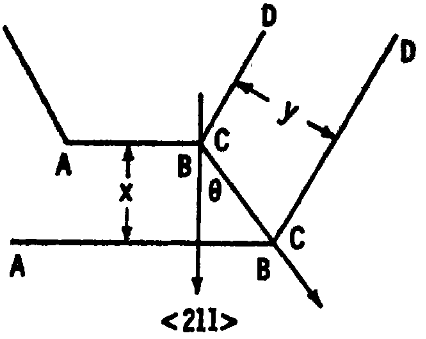

FIG. 9. Diagram to illustrate calculation of growth direction.

Table 2. Calculation of angle of growth, θ, relative to ⟨211⟩ for various twin structures

No. of twins	$r = x/y$	$\theta = \tan^{-1}(2-r)/\sqrt{3}r$
Even	1	30°
3	2	0
5	3/2	11°
7	4/3	16°
9	5/4	19°

Note

Crystallographically, the ⟨110⟩ direction makes an angle of 30° and the ⟨321⟩ direction an angle of 10·89° to the ⟨211⟩ direction.

As mentioned earlier the direction of growth of ⟨321⟩ dendrites often deviates from the exact angle. Assuming as before, that the ratio, rate of advance normal to AB/rate of advance normal to CD is equal to the ratio of the number of reentrant grooves perpendicular to these two directions, then the direction in which the corner B advances can be calculated (Fig. 9). Table 2 shows the angle θ which this direction makes with the ⟨211⟩ direction. This calculation indicates that ⟨321⟩ growth would be most favored from a closely spaced five-twin seed. Experimental confirmation of this was not possible as a suitable seed was not available.

2. *Widely spaced twins*

(a) *Two-twin seeds.* When the twin planes are widely spaced the reentrant grooves will be separated by curved regions as assumed earlier and shown diagrammatically on Fig. 10. Nucleation will still occur in the reentrant grooves and for continuous propagation the tip morphology must be maintained. This is achieved by layers originating at the reentrant grooves and advancing over the curved interface to the adjacent facets. For example, the facet A is maintained in equilibrium by a process of nucleation and growth at its reentrant groove together with widening by layers advancing from facets B and C. This is essentially similar to a mechanism proposed by HAMILTON and SEIDENSTICKER.(6) Hence the growth directions are those in which the facets advance, i.e. ⟨211⟩. The presence of two twin planes is essential for continuous propagation(6) but in contrast to the situation with closely spaced twins the second twin does not influence the direction of growth. It may be expected that growth directions resulting from this mechanism will be sensitive to the influence of thermal geometry.

(b) *Multi-twin seeds.* The same considerations apply to seeds containing a number of twins although complex details may arise from the variations in spacing which occur.

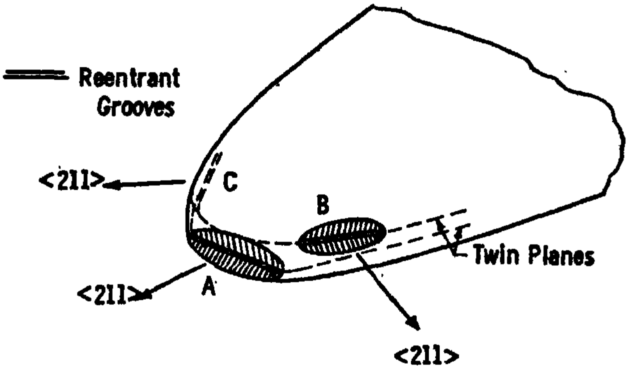

FIG. 10. Schematic drawing of facets on curved tip of dendrite having two widely spaced twin planes.

3. *Thermal conditions*

(a) *Supercooling.* Experimental observations of the effect of supercooling on the appearance of various growth directions were described earlier in this paper. This will not be discussed further here.

(b) *Thermal and solute gradients.* Growth of dendrites of indium antimonide in the ⟨110⟩ and ⟨321⟩ directions occurs readily using the experimental conditions described, indicating that the thermal gradients which exist are favorable. A low thermal gradient favors corner growth because latent heat is then dissipated more readily and this will make growth in the ⟨321⟩ and especially the ⟨110⟩ direction preferred. Referring to Fig. 6, nucleation at the reentrant grooves followed by growth will be favored near the corners *A* and *B*. These growth layers can interact and form a projection in the ⟨110⟩ direction before growth on each reentrant groove results in a projection in the ⟨211⟩ direction. Thus, low thermal gradients and narrow twin spacing both favor ⟨110⟩ growth. When a two-twin indium antimonide seed having the closest spacing available ($<2\,\mu$) was used, growth in the two ⟨110⟩ directions at 60° to the seed axis was favored over propagation in the direction of the seed. This observation was repeated using the seed rotated through 180° and occurs because this mode of growth dissipates latent heat most readily. An example is shown in Fig. 11.

During growth from a solution or from an impure melt a concentration gradient may become the controlling factor in determining dendrite shape behind the tip and the same considerations apply. The shape of the tips of ⟨110⟩ and ⟨211⟩ dendrites is such that diffusion processes can occur more readily when growth is in the ⟨110⟩ direction.

EXPERIMENTAL OBSERVATIONS ON GERMANIUM AND SILICON

Although the preceding discussion was based on experimental observations made with indium antimonide no account was taken of the polarity of this compound in postulating a mechanism. The same features should therefore apply to elements crystallizing in the diamond lattice.

When germanium dendrites are grown with similar apparatus to that used in this work for indium antimonide the thermal gradients are high and do not favor ⟨110⟩ growth. However, examination of a germanium sample grown from a pure melt under experimental conditions which reduce the imposed thermal gradients revealed branches in ⟨110⟩ directions. We are indebted to Dr. S. O'HARA for supplying this sample which is shown in Fig. 12 and diagrammatically in Fig. 13. An examination of the twin structure by fracture at the points marked on Fig. 13 showed a relation between numbers of twins, twin spacing and growth direction which is summarized in Table 3.

Threefold growth symmetry in ⟨211⟩ directions is shown by the main stem and many branches and all of those examined show three closely spaced twins. Two kinds of branches in the ⟨110⟩ direction occur and both have only two twin planes, either of the two outside twin planes of the main stem being lost. Those branches with

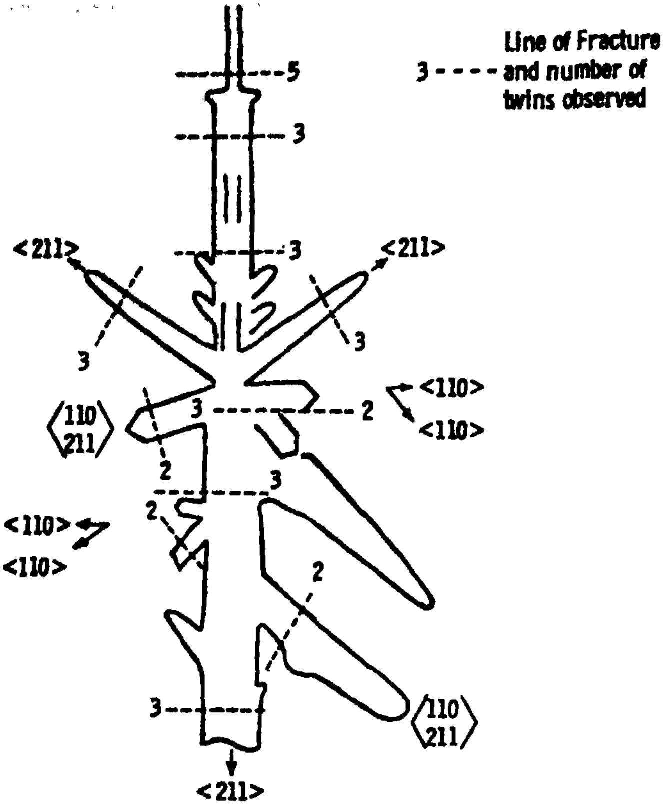

FIG. 13. Diagram of dendrite shown in Fig. 12.

two twins of 5 μ spacing show features of both ⟨211⟩ and ⟨110⟩ growth and this appears to be the critical spacing for these growth conditions. The branches having two twin planes of only 1 μ spacing show only features of ⟨110⟩ growth with sixfold symmetry.

Table 3. *Growth directions and twin structure, germanium*

Section	Direction	No. of twins	Spacing μ
Seed	211	5	1-5-7·5-15
Main Stem	211	3	1-5
Branches	211	3	1-5
Branches	110 and 211	2	5
Branches	110	2	1

These observations are similar to those made on indium antimonide. At the dendrite tip a projection in the ⟨110⟩ direction is formed at two twin planes and when the ⟨110⟩ branch grows, a twin is lost. In Fig. 14 is shown a section across the main ⟨211⟩ stem and a ⟨110⟩ branch which illustrates that the third twin jogs to the surface. Either twin can be readily lost including one of a pair with a spacing of only 1 μ. That twin may be lost which lies closest to a face of the dendrite parallel to the twin planes as suggested by SEIDENSTICKER and HAMILTON(13) who discuss the loss of twin planes when asymmetrically placed during later stages in growth. An early stage in this process is shown in Fig. 15 of a section near the tip of a 211 branch on a germanium sample. This shows the lag in growth of one twin plane.

Similar behavior can readily be observed on samples of silicon. Observations which duplicate closely those described for germanium have been made on silicon dendrites supplied by A. I. BENNETT and J. MELNGALIS. One of these samples consisted of a strip grown in the ⟨211⟩ direction which terminated in 110 branches. The sample was fractured close to the point of division as shown in Fig. 16. Examination of the fracture showed that one of the original three twins was lost at the point where ⟨110⟩ growth commenced.

The observations on silicon and germanium indicate therefore, that under certain conditions dendrites can propagate in the ⟨110⟩ directions thus confirming the model proposed on the basis of experiments with indium antimonide.

CONCLUSIONS

It has been found that InSb dendrites may be propagated in ⟨321⟩ and ⟨110⟩ directions as well as the more usual ⟨211⟩ directions. The appearance of these new directions depends critically on the twin-structure of the seed crystal and also, in the case of ⟨321⟩, on supercooling. The experimental observations are discussed in terms of a simple morphological model of the dendrite tip and it is shown that this can adequately account for the new features. The model and mechanism make no reference to the polarity of InSb and should therefore, be applicable to Si and Ge. Subsequently observations on Si and Ge have confirmed that, under suitable conditions, the same features may be found in these materials.

Acknowledgements—We are indebted to a number of colleagues at the Westinghouse Research Laboratories for discussions and assistance and wish particularly to acknowledge considerable help received from Dr. A. I. BENNETT. Thanks are also due to Drs. D. R. HAMILTON and R. L. LONGINI for critical reading of the manuscript.

REFERENCES

1. BILLIG E., *Proc. Roy. Soc.* **229**, 346 (1955).
2. BILLIG E., *Acta Met.* **5**, 54 (1957).
3. BILLIG E. and HOLMES P. J., *Acta. Met.* **5**, 53 (1957).
4. BENNETT A. I. and LONGINI R. L., *Phys. Rev.* **116**, 53 (1959).
5. WAGNER R. S., *Acta. Met.* **8**, 57 (1960).
6. HAMILTON D. R. and SEIDENSTICKER R. G., *J. appl. Phys.* **31**, 1165 (1960).
7. O'HARA S., private communications.
8. FAUST J. W., NICHOLSON H. and MOSS R., *Electrochem. Soc. electron. Div. Abs.* **9**, 165 (1960).
9. ALBON N. and OWEN A. E., *Electrochem. Soc. electron. Div. Abs.* **10**, 95 (1961).
10. FAUST J. W. and JOHN H. F., *J. electrochem. Soc.* **108**, 855 (1961).
11. FAUST J. W. and JOHN H. F., *J. electrochem. Soc.* **108**, 860 (1961).
12. BOLLING G. F. and TILLER W. A., *J. appl. Phys.* **32**, 2587 (1961).
13. SEIDENSTICKER R. G. and HAMILTON D. R., *Electrochem. Soc. electron. Div. Abs.* **10**, 60 (1961).

J. Phys. Chem. Solids Pergamon Press 1963. Vol. 24, pp. 909–917. Printed in Great Britain.

A SIMPLIFIED METHOD FOR CALCULATING THE DEBYE TEMPERATURE FROM ELASTIC CONSTANTS

ORSON L. ANDERSON

American-Standard Research Laboratories, Union, New Jersey

(*Received* 9 *July* 1962; *revised* 8 *January* 1963)

Abstract—The Reuss–Voigt approximations are well known methods whereby the isotropic polycrystalline elastic constants can be calculated from the single crystal elastic constants. It is shown here that the Reuss and the Voigt approximations can be used to estimate, accurately, the mean sound velocity of a crystal. Using this method, the Debye Temperature, which is proportioned to the mean sound velocity, can be determined without recourse to the published tables or high speed computers. This approximation is valid for all crystal classes.

I. INTRODUCTION

THE Debye temperature is an important parameter of a solid. It is found in equations describing properties which arise from atomic vibrations, and in theories involving phonons.

One of the standard methods of calculating the Debye temperature is from elastic constant data, since θ is proportional to the sound velocity (averaged) v_m by the equation

$$\theta = \frac{h}{k}\left[\frac{3q}{4\pi}\frac{N\rho}{M}\right]^{1/3} v_m \qquad (1)$$

and where h/k have the usual meanings of quantum mechanics, N is Avogadro's number, ρ is the density, M is the molecular weight of the solid and q is the number of atoms in the molecule ($q = 2$ for NaCl, 3 for CaF_2).

The use of equation (1) is often hindered by the problem of computing v_m. Since θ is a scalar, it follows that v_m must also be a scalar, and herein lies the difficulty of this method. The stress is a tensor quantity, and for each direction in a crystal, there are three velocities each of which is a complicated function of the stress components. The expression[1] for v_m is

$$v_m = \left(\frac{1}{3}\sum_{i=1}^{3}\int_{V}\frac{1}{v_i^3}\frac{d\Omega}{4\pi}\right)^{-1/3} \qquad (2)$$

This integral is solved by numerical methods as follows: the three sound velocities, v_1, v_2, v_3 are found in an arbitrary direction and then stored; the process is repeated for a large sample of directions, throughout space; and a numerical summation using Simpson's rule made in place of the volume integral.

The equation shown above is the rigorous way to find the mean sound velocity, but it is impractical to use except by means of high speed computer methods. The solution of the equation requires knowledge of the elastic constants of the crystal.

This paper will be concerned with a substitute for equation (2) to determine the mean sound velocity. Only one class of symmetry—that of isotropy—lends itself to an easy calculation of v_m, for in that case equation (2) reduces to the simple form

$$v_m = \left(\frac{1}{3}\left[\frac{2}{v_s^3}+\frac{1}{v_l^3}\right]\right)^{-1/3} \qquad (3)$$

In this case, isotropy includes truly isotropic materials like glass, and polycrystalline materials where the shear and longitudinal sound velocities, v_s and v_l are invariant with direction.

The idea presented in this paper is that the experimentally measured velocities v_s and v_l of the polycrystalline solid can be closely approximated by a simple, but well known, averaging scheme of the single crystal elastic constants, yielding $\bar{v}_s$ and $\bar{v}_l$. Further, it is proposed that the averaged velocities when used in equation (3) yield a value

$$\bar{v}_m = \left(\frac{1}{3}\left[\frac{2}{\bar{v}_s^3} + \frac{1}{\bar{v}_l^3}\right]\right)^{-1/3}, \tag{4}$$

which is little different from the value v_m calculated by the rigorous method, equation (2).

The particular averaging scheme used and recommended will be presented in Section II. A description of the detailed calculations involved in proving that $\bar{v}_m$ is a close approximation of v_m is presented in Section III. The results of several hundred crystals will be presented in Section IV. The implications and benefits to the materials scientist resulting from the use of $\bar{v}_m$ will be discussed in Section V. Numerous tables of the elastic constants used are collected in several appendices.

II. LITERATURE BACKGROUND FOR THE AVERAGING SCHEME

The recommended scheme for averaging the elastic constants and sound velocities is a synthesis of several ideas which have appeared in the literature. It will be called hereafter the VRHG approximation (Voigt, Reuss, Hill and Gilvarry).

That part of the VRHG approximation due to Voigt(1) is a simple linear relation between the isotropic shear and bulk moduli of a polycrystalline composite and the single crystal moduli (c_{ij}'s represent stiffness)

$$K_V = f_1(c_{ij}) \tag{5}$$

$$G_V = f_2(c_{ij}) \tag{6}$$

Equations (5) and (6) are expanded in Appendix I.

A different linear relation between the isotropic shear and bulk moduli and the single crystal elastic moduli was derived by Reuss(1) (s_{ij}'s represent compliance.)

$$K_R = f_3(s_{ij}) \tag{7}$$

$$G_R = f_4(s_{ij}) \tag{8}$$

Equations (7) and (8) are expanded in Appendix I.

Using energy considerations Hill(2) proved that the Voigt and Reuss equations represent upper and lower limits of the true polycrystalline constants, and he recommended that a practical estimate of the polycrystalline moduli were the arithmetic means of the extremes,

$$K_H = 1/2(K_R + K_V) \tag{9}$$

$$G_H = 1/2(G_R + G_V) \tag{10}$$

The probable values of the average sound velocities are computed from (9) and (10) as follows

$$\bar{v}_s = \sqrt{(G_H/\rho)} \tag{11}$$

$$\bar{v}_l = \sqrt{(K_H + 4/3G_H)/\rho} \tag{12}$$

Finally the approximate sound velocity is found by using the values computed from (11) and (12) in (4), and the Debye temperature then is easily computed by (1). Gilvarry used virtually the same method to approximate the Debye temperature of sodium,(3) and deserves credit for insight to the method.

The point is that the VRHG approximation (equations (4) through (12)) for computing $\bar{v}_m$ requires only about ten minutes on the slide rule and is good for any symmetry, whereas the exact method using equation (1) requires numerical methods on a high speed computer, or access to tables such as have been published by deLaunay for some of the high symmetry solids.(4)

It is the purpose of this paper to demonstrate that the VRHG approximation is not only practical but quite accurate. In fact, the VRHG approximation was applied to the data of over 200 crystals of all classes. In all but a very few cases, which will be later discussed, the error of the approximation was less than the probable error of the experimental results themselves.

There are other approximations in the literature, but these, in the author's opinion, either lack generality or accuracy. For example, a number of "mathematical" approximations to equation (1) which have been explored by Blackman(5) are sometimes accurate but cannot be applied generally—typically one technique is accurate for a certain class, but not for another. One approximation due to Post, is general to all crystal classes, but it yields results which are considerably more erroneous than the VRHG approximation.

The VRHG approximation as applied to the trigonal crystal alumina, is presented in detail in Appendix I.

III. PROVING THE VRHG APPROXIMATION

The proof consists of an analytical part and an experimental part. The analytical proof is that $\bar{v}_m$, equation (4), is close in value to v_m, equation (2), when the same elastic constant data are used in both calculations. The experimental proof is that the computed Young's modulus and Shear modulus, E_H and G_H from equations (9) and (10) which average the elastic constants of the single crystal, are close in value to the measured E and G of the highly dense polycrystalline phase which is hot pressed from the crystalline powder.

A. *Analytical proof*

A program for the IBM 7090 was written to solve equation (2) for v_m. The following is read into the computer program as input data: the elastic constants, c_{ij}, or the elastic compliances, s_{ij}; the density; the molecular weight of the crystal; the limits of integration shown in equation (1)—(for a cubic crystal the limits correspond to a one-fourth of the sphere); and the increment of angles in the numerical integration (usually 5°).

Given the elastic constants the elastic compliances are computed, or vice versa by a subroutine which inverts any reasonably sized $n \times n$ matrix.

Next the solution of the equations of motion of elastic waves is found. This involves solving the determinant for a particular direction of wave propagation. In the general case, each element of the determinant involves all elastic constants.(7) To get the velocities the eigenvalues of the determinant are obtained by a sub-routine which used double precision statistical methods.

The three velocities allow the integrand in equation (2) to be defined. The integrand is stored, and the program repeated for a new direction. The integration is replaced by a summation which sums the integrands according to Simpson's rule. The program is arranged so that any fraction of the sphere can be chosen for the integration (quadrant, octant, etc.) and the correct multiplication factor is retained. As a typical case, integrating one-fourth of a sphere at 5° intervals in the polar angles θ and ϕ takes about 10 sec on the IBM 7090.

If θ is the polar angle, and ϕ the azimuthal angle, the volume of integration is then $\sin\theta d\theta d\phi$. The limits on integration for θ is always 90°. The limits on ϕ are 30° for hexagonal crystals, 45° for tetragonal, 60° for trigonal, 90° for orthorhombic and 180° for monoclinic.

After v_m, equation (2), is computed; the Voigt and Reuss elastic moduli, equations (4) to (8), are computed and finally various sound velocities, including $\bar{v}_m$, equation (4).

The program was checked by comparing the Debye temperature θ from the computed v_m, with the Debye temperature given by others using various methods where in all cases the same elastic constants were used for the solid. (It was not always possible to ascertain whether the density was the same as that used by other authors.) This crosscheck is shown in Table 1.

Table 1. *Comparison of the value of the Debye temperature from this IBM program with values in the literature*

Element	Density	Mol. Wt.	θ (here)	θ (published)	Source of Information
Ag	10·635	107·88	226·5	226·4	Alers and Neighbors
Al	2·734	26·965	426·7	426·6	Huntington
Au	19·488	197·00	161·7	161·6	Alers and Neighbors
Cu	9·02	63·54	344·5	345·3	Overton and Gaffney
Li	0·545	6·94	326·0	335·9	Alers and Neighbors
Ni	8·968	58·71	476·2	476·2	Alers and Neighbors
Th	11·787	232·05	164·2	164·2	Armstrong Carlson, Smith
V	6·022	50·95	393·2	394·0	Bolef and Menes
Hexagonal					
Beryl	1·848	9·013	1463·5	1462.0	Smith
Cd	8·719	112·41	214·2	213·0	Garland and Silverman
Mg	1·779	24·32	386·0	385·8	Alers
Zn	7·134	65·38	328·3	328·1	Alers and Neighbors

The print out of the program is: (1) the basic information including crystal class, author and publication (source of elastic constant data), temperature of measurement, density, and instructions for the integration; (2) the elastic constants themselves in matrix form; (3) the Voigt, Reuss and Hill approximations for the isotropic moduli; (4) the final results, including the rigorous average sound velocity v_m, the approximate average sound velocity, the Debye temperature, and the approximation error.

$$\Delta = (\bar{v}_m - v_m)/v_m \tag{13}$$

The analytical proof is completed by showing that Δ is about the same order as the uncertainty in measuring elastic constants. This will be demonstrated in some detail in Section IV.

B. *Experimental proof*

When pure and finely divided crystalline powder is hot pressed, in the appropriate way, the result is a bar of the material which is uniform in density, and isotropic, which approaches the density of the single crystal, and which is large enough to make resonance measurements of the elastic moduli. If a sufficient number of these bars are prepared, with a variety of values of porosity all close to zero, the isotropic elastic constants of the polycrystalline materials at zero porosity can be obtained by extrapolation.

The experimental proof is completed by showing that the extrapolated values of the elastic moduli of the hot pressed solids (zero porosity) are close to the values obtained by the Hill mean, equations (9) and (10) from single crystal elastic constant data.

This proof has already been established for several polycrystalline metals by HILL.[6] Data on oxides are rarer. The polycrystalline elastic constants of hot pressed alumina were reported in the Master's thesis (1961) of DAE-HYUN CHUNG of Alfred University.[7] Chung's results are shown in Table 2. The values in the parenthesis are the writer's extrapolations. These results are plotted in Figs. 1 and 2. The results in the last line above are to be compared with the values predicted from the elastic constants of trigonal alumina, as shown in Appendix I.

Table 2. Measured isotropic moduli of polycrystalline alumina

Density	Porosity (%)	Young's modulus (kbars)	Shear modulus (kbars)
3·835	3·79	3571	1439
3·848	3·46	3607	1462
3·885	2·53	3702	1503
3·900	2·16	3764	1538
3·914	1·81	3784	1549
3·947	0·98	3928	1591
3·986	(0)	(4050)	(1650)

Table 3. Predicted isotropic moduli of polycrystalline alumina

	Young's modulus (kbars)	Shear modulus (kbars)
Max. (Voigt)	4083	1660
Mean (Hill)	4027	1634
Min. (Reuss)	3972	1607

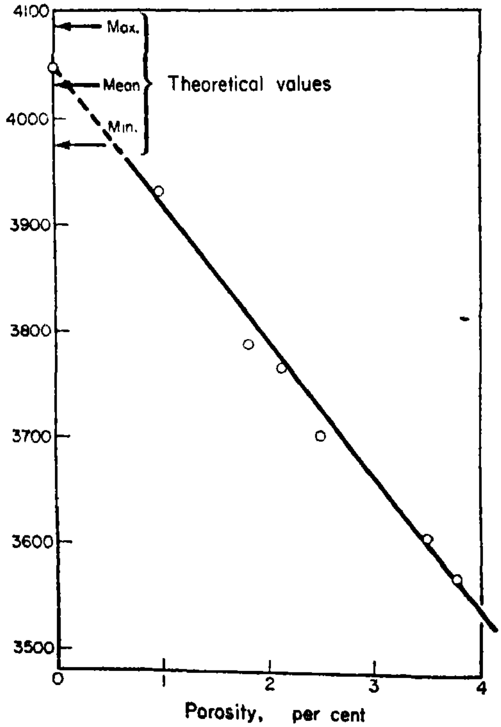

FIG. 1. Variation of Young's modulus with porosity for sintered alumina (after CHUNG[8]).

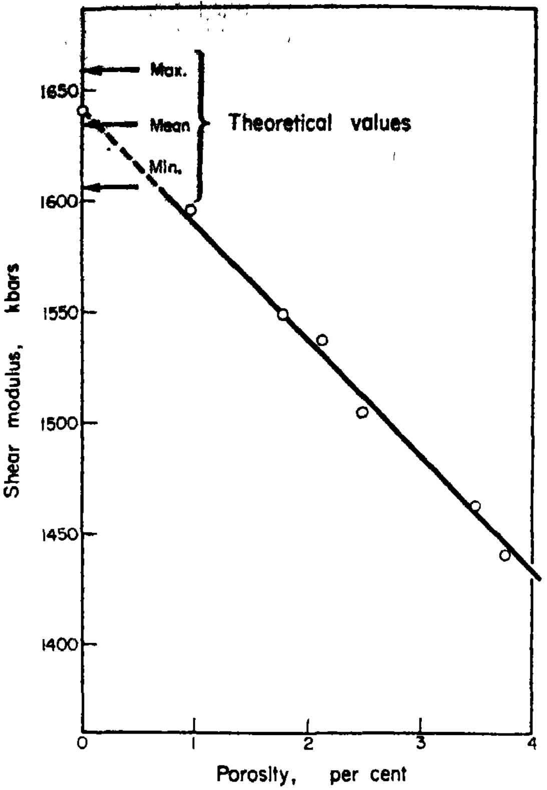

FIG. 2. Variation of shear modulus with porosity for sintered alumina (after CHUNG[8]).

The agreement between the mean values in Table 3 and the last row in Table 2 is remarkably good. Further work must, of course, be done on non-metallic polycrystalline solids, but the experimental proof can be considered as established, at least tentatively.

IV. THE VRHG APPROXIMATION FOR SIX CRYSTAL CLASSES

The IBM program for the calculation of v_m, $\bar{v}_m$, and Δ (equation (13)) was used for a number of sets of elastic constant data obtained by reading the literature, including 106 cubic crystals, 60 hexagonal crystals, 19 trigonal crystals, 18 tetragonal crystals, 19 orthorhombic crystals and one monoclinic crystal.*

A. *Cubic system*

Numerous approximations exist in the literature for the value of v_m for cubic symmetry. In the author's opinion none of the approximations are more accurate than the VRHG approximation.

It turns out that for most cubic crystals, the error Δ is less than 1 per cent. Those crystals in which it is more than 2 per cent are all highly anisotropic. A convenient method of defining anisotropy, following HILL,[2] is the spread of the computed shear modulus computed by the Reuss and Voigt limits, the degree of anisotropy is:

$$\delta = \frac{1}{2}\frac{G_v - G_R}{G_H} = \frac{G_v - G_R}{G_v + G_R}$$

$$= \frac{3[2c_{44} - (c_{11} - c_{12})]^2}{12c_{44}^2 + 38c_{44}(c_{11} - c_{12}) + 3(c_{11} - c_{12})^2} \qquad (14)$$

It turns out that whenever δ is less than 20 per cent, Δ is less than 2 per cent This is illustrated in Fig. 3. Here it is shown that the results cluster around two simple curves, the upper composed mostly of the halide crystals, the lower being elements and other compounds besides halides. This relationship between Δ and δ permits a rather exact estimate of the Debye temperature from the elastic constants of a cubic crystal. The author recommends the following procedure. Compute $\bar{v}_m$ by the VRHG method. Compute δ by equation (14). If δ is less than 20 per cent, Δ is less than 2 per cent. If δ is more than 20 per cent, the value of Δ can be estimated, it being approximately 1/10 δ and positive.

B. *Hexagonal system*

In Appendix II, typical examples of the results obtained for 60 hexagonal crystals are presented. The maximum error in Δ is 3 per cent for ice. Cadmium and zinc are fairly anisotropic, and the value of Δ is about 2-1/2 per cent. But in general, the VRHG approximation is quite good for this class, and in most cases better than the probable accuracy in measuring elastic constants.

C. *Trigonal system*

In Appendix II, typical examples of the results obtained for 19 trigonal crystals are presented. Here the elastic constant data from one author compared with another are not always in agreement, and the value of Δ takes on a

---

* The full tabular data can be obtained by writing the author.

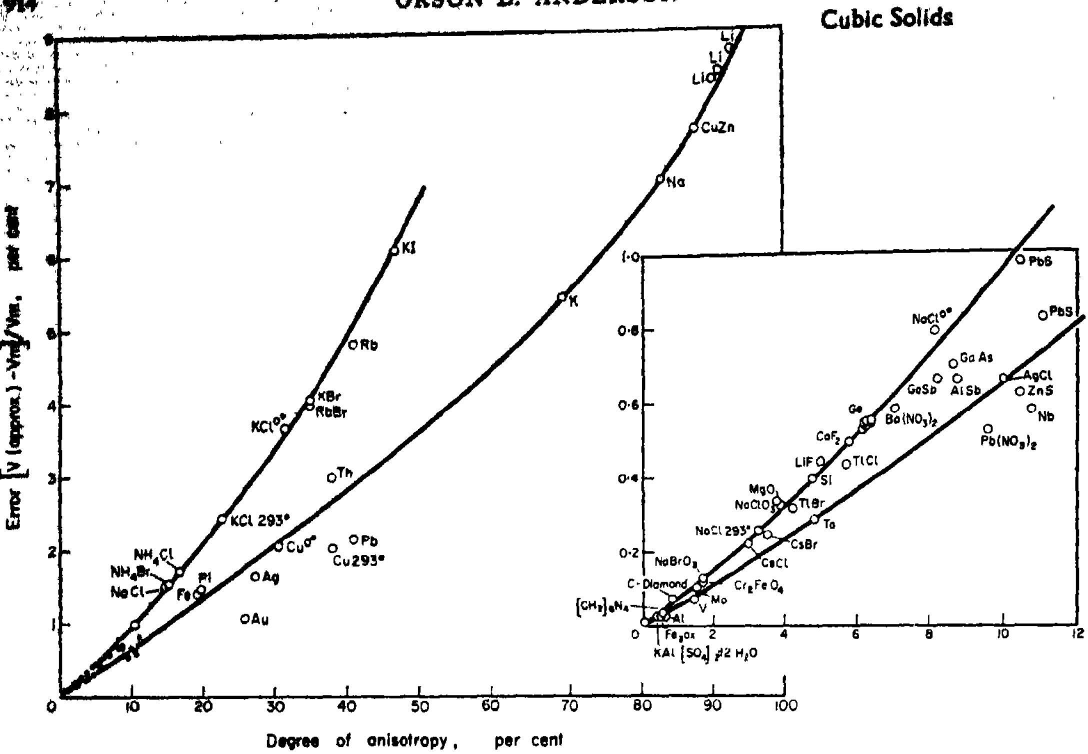

FIG. 3. Degree of anisotropy per cent.

number of values. Whenever, the elastic constant data are very good, the value of Δ is low. For instance, when the most recent measurements on alumina by Wachtmann and Teft in which the elastic constants were very carefully cross checked for internal consistency are used, Δ is only $-1{\cdot}36$ per cent. Older data for alumina shows Δ to be as much as 8·5 per cent. The elastic constant data for Koga for α-quartz is very reliable, and in this case Δ is $-2{\cdot}2$ per cent, whereas other data yields a higher error. The worst value calculated by the VRHG method is for mercury, where Δ is 25 per cent. However, these elastic constant data were reported in 1934, and should be rechecked. In the author's opinion, Δ is less than 2·5 per cent for this class whenever there has been careful cross checking of the elastic constant data by the experimenters.

D. *Tetragonal system*

In Appendix II, typical values obtained for 18 tetragonal crystals are presented. Again, whenever there is evidence of internal consistency of the elastic constants, the value of Δ is small. For instance, the values for v_m for Rutile are $5{\cdot}652 \times 10^5$ and $5{\cdot}557 \times 10^5$ from Birch, and from Joshi and Mutri respectively, revealing a discrepancy of about 2 per cent in the primary measurement data. Yet, the difference between the approximate and the rigorous values of v_m are 2 per cent, using the same data in both cases. Consequently, the approximation is about as accurate as the data itself. On the other hand, the values for the crystal KH_2PO_4 vary considerably from author to author, and correspondingly the value of Δ is somewhat higher. In the author's opinion, the VRHG approximation is reliable for this class.

E. *Orthorhombic system*

The results for the orthorhombic system are especially interesting as shown by the example in Appendix II. All values of Δ are low except for $KB_5O_8 \cdot 4H_2O$ which is 4·3 per cent. Especially interesting is the value for uranium in which Δ is below 1 per cent. The elastic constants for this solid were accurately determined and carefully checked for internal consistency. It would appear that the VRHG approximation is reliable for this class.

F. *Monoclinic system*

The data for one monoclinic crystal was found, which is presented in Appendix II.

G. *Temperature dependence of v_m*

The elastic constant data at absolute zero are needed for the determination of the Debye temperature. The elastic constant data at room temperature are more often available. There are a number of instances in the literature where the elastic constants at room temperature are accurately integrated by equation (2), to obtain a value of the Debye temperature, and this Debye temperature is then compared with the corresponding Debye temperature calculated from specific heat measurements. This value of θ thus obtained is meaningful only to the extent the v_m is independent of temperature. The temperature dependence of v_m was checked for three solids where the elastic constants were well determined from room temperature. In these three solids, Beryl, Cd, and Zn, the change of the rigorous value of v_m between room temperature and 0°, and the VRHG approximation is shown in Table 4, and in Fig. 4.

Table 4. *Comparison of Δ with temperature extrapolation error* (*velocity in* 10^5 *cm/sec*)

	Beryl	Cd	Zn
Absolute zero value of v_m	9·871	1·995	2·773
Room temp., value of v_m	9·752	1·812	2·551
Per cent change of v_m from R.T. to 0°K (in %)	1·0	0·93	0·63
Δ at absolute zero (in %)	0·088	0·248	0·22
Δ at room temp (in %)	0·082	0·254	0·241

It is evident that for most solids, especially where the anisotropy is not excessive, that the true value of the Debye temperature is off by as much when the room temperature values are used in equation (2), as when the VRHG approximation in place of equation (2).

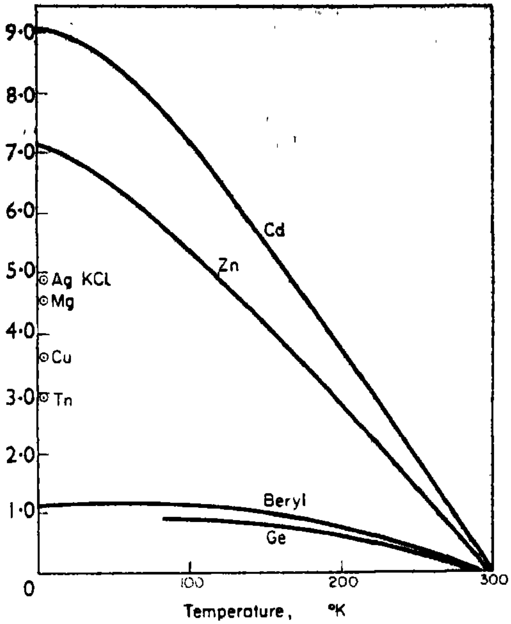

FIG. 4. Per cent change in value of mean sound velocity v_m from room temperature value.

V. DISCUSSION

It is concluded that the elastic constants of a well sintered solid can be predicted if the single crystal constants are known. The difference between predicted and observed values will result from the method of sintering.

It is also concluded that a solid does not have to be grown in the form of a single crystal in order to measure isotropic elastic parameters. The solid can be hot pressed from fine powder into a dense specimen and the appropriate experiments made. The values measured will be the integrated values of the single crystal and suitable for determining Debye θ.

Acknowledgements—The author is grateful for the help of Mrs. J. ROOT who programmed this problem for the IBM 7090, and to Professor CRANDALL and Mr. D. CHUNG of Alfred University who provided the data on polycrystalline alumina.

REFERENCES

1. Huntington H. B., *Solid State Physics* (edited by Seitz F. and Turnbull D.) Vol. 7, Chap. III. Academic Press, New York (1958).
2. Hill R., *Proc. phys. Soc. Lond.* **65**, 350 (1952).
3. Gilvarry J. J., *Phys. Rev.* **103**, 1701 (1956).
4. de Launay J., *Solid State Physics* (edited by Seitz F. and Turnbull D.) Vol. 2, p. 286. Academic Press, New York (1958).
5. Blackman M., *Theory of Specific Heats, Handb. Phys.*, **VII**, (Part I) p. 342 (1955).
6. Mason, W. P., *Physical Acoustics*, p. 369 Van Nostrand, New York (1958).
7. Crandall W. B., Chung D. H. and Gray, T. J., *Mechanical Properties of Engineering Ceramics*, Chap. 22, Interscience, New York (1961).

Note added in Proof: The VRHG approximation has been found accurately applicable to MgO at all temperatures, reported recently by Mr. D. H. Chung, (1963) *Phil. Mag.*, in press.

APPENDIX I

Computation of elastic constants of alumina

Equations for all crystal classes

Bulk Modulus (maximum) by the Voigt approximation:

$$K_V = 1/9(c_{11}+c_{22}+c_{33})+2/9(c_{12}+c_{23}+c_{13})$$

Shear Modulus (maximum) by the Voigt approximation:

$$G_V = 1/15(c_{11}+c_{22}+c_{33})-1/15(c_{12}+c_{23}+c_{31}) + 1/5(c_{44}+c_{55}+c_{66})$$

Bulk Modulus (minimum) by the Reuss approximation:

$$1/K_R = (s_{11}+s_{22}+s_{33})+2(s_{12}+s_{23}+s_{13})$$

Shear Modulus (minimum) by the Reuss approximation:

$$15/G_R = 4(s_{11}+s_{22}+s_{33})-4(s_{12}+s_{23}-s_{13}) +3(s_{44}+s_{55})+s_{66})$$

Reduced equations for trigonal class:

$$K_V = 1/9(2c_{11}+c_{33})+2/9(c_{12}+2c_{13})$$

$$G_V = 1/15(2c_{11}+c_{33})-1/15(c_{12}+2c_{13}) +1/5(2c_{44}+c_{66})$$

$$1/K_R = (2s_{11}+s_{33})+2(s_{12}+2s_{13})$$

$$15/G_R = 4(2s_{11}+s_{33})-4(s_{12}+2s_{13}) +3(2s_{44}+s_{66})$$

Data for Al_2O_3, by Wachtman and Teft, *J. Res. NBS*, **64A**, 3 (1960):

$c_{11} = 4968$ kbars	$s_{11} = 0{\cdot}235\times10^{-3}(\text{kbars})^{-1}$
$c_{33} = 4981$	$s_{33} = 0{\cdot}217$
$c_{44} = 1474$	$s_{44} = 0{\cdot}694$
$c_{66} = 1666$	$s_{66} = 0{\cdot}614$
$c_{12} = 1636$	$s_{12} = -0{\cdot}072$
$c_{13} = 1109$	$s_{13} = -0{\cdot}036$

Bulk Modulus (kbars):

Max: $K_V = 2514$

$K_R = 2509$

Mean: $K_H = 1/2(2514+2509) = 2512$

Shear Modulus (kbars):

Max: $G_V = 1660$

Min: $G_R = 1607$

Mean: $G_H = 1634$

Young's Modulus (kbars):

$$\text{Max: } E_V = \frac{9K_V\times G_V}{3K_V+G_V} = 4083$$

Min: $E_R = 3973$

Mean: $E_H = 4028$

Longitudinal Modulus (kbars):

$$M_H = K_H+\tfrac{4}{3}G_H = 4692$$

Sound Velocity ($\rho = 3{\cdot}986$):

$\bar{v}_s = 6{\cdot}41\times10^5$ cm/sec

$\bar{v}_l = 10{\cdot}91\times10^5$ cm/sec

$\bar{v}_m = 7{\cdot}09\times10^5$ cm/sec

$\theta = 1045°K$

APPENDIX II

Velocity units 10^5 cm/sec

Crystal	Accurate v_m	Approx. $\bar{v}_m$	Per cent Error
Hexagonal system			
$BaTiO_3$	3·280	3·283	0·09
Beryl, 0°K	9·870	9·879	0·08
Beryl, 300°K	9·751	9·760	0·09
Beryl	9·360	9·314	0·09
Cd, 0°K	2·000	2·04	2·50
Cd, 300°K	1·813	1·859	2·46
CaBa	2·584	2·597	0·4
CdS	2·110	2·105	0·22
Co	3·392	3·412	0·59
ice	0·761	0·785	3·07
Mg, 0°K	3·67	3·672	0·03
Mg, 293°K	3·514	3·516	0·04
SiO_2	4·457	4·462	0·1
Y, 0°K	2·774	2·775	0·03
Y, 300°K	2·640	2·641	0·02
Zn, 4·2°K	2·732	2·795	2·29
ZnO	3·188	3·187	−0·02
Trigonal system			
Al_2O_3	7·190	7·093	−1·36
$AlPO_4$	3·644	3·531	−3·10
Bi	1·302	1·261	−3·16
$CaCO_3$	4·017	3·898	−2·94
Fe_2O_3	4·729	4·674	−1·17
Hg	0·559	0·698	24·96
$(NaBr)C_6H_{12}O_6$	2·243	2·254	0·50
$(NaCl)C_6H_{12}O_6$	2·280	2·270	0·50
$NaNO_2$	3·408	3·604	5·7

Crystal	Accurate v_m	Appox. $\bar{v}_m$	Per cent Error
Trigonal system			
Sb	1·925	2·049	6·2
SiO_2	4·570	4·468	−2·22
Tourmaline	5·733	5·743	0·17
Tetragonal system			
$BaTiO_3(E)$	3·875	3·93	1·45
$BaTiO_3(D)$	3·439	3·523	2·42
In, 0°	1·12	1·03	8·7
In, 293°K	0·901	0·925	2·73
KH_2PO_4	2·758	2·860	3·73
$NH_4H_2PO_4$	2·664	2·788	4·62
$NiSO_46H_2O$	2·540	2·567	1·05
Sn	1·996	1·997	0·06
TiO_2	5·652	5·745	1·66
$ZrSiO_4$	2·216	2·267	2·29
Orthorhombic system			
$BaSO_4$	2·463	2·491	1·14
$CaCO_3$	3·942	3·991	1·26
$KB_5O_8 \cdot 4H_2O$	2·264	2·361	4·28
$MgSO_4 \cdot 7H_2O$	2·543	2·586	1·23
$SrSO_4$	1·979	2·080	5·10
S_8	1·978	2·019	2·11
Topaz	6·331	6·341	0·15
$ZnSo_4 \cdot 7H_2O$	2·758	2·794	1·33
U	7·286	7·349	0·86
Olivine	5·408	5·472	1·17
Monoclinic system			
$Li_2SO_4H_2O$	3·29	3·30	3·0

J. Phys. Chem. Solids Pergamon Press 1963. Vol. 24, pp. 919–925. Printed in Great Britain.

OXIDATION OF MAGNESIOWUSTITE SINGLE CRYSTALS—I. OPTICAL AND KINETIC DATA

W. L. SCHAEFER* and G. W. BRINDLEY

College of Mineral Industries, The Pennsylvania State University,
University Park, Pennsylvania

(*Received* 7 *January* 1963)

Abstract—The oxidation of homogeneous magnesiowustite single crystals, prepared by diffusing iron into MgO single crystals, is studied optically and by X-ray diffraction. Crystals designated *L* (low), *M* (medium) and *H* (high), containing about 20, 36, and 67 cation per cent Fe were prepared. By control of temperature and oxygen partial pressure using appropriate CO/CO_2 gas mixtures, the magnesiowustite crystals were equilibrated at or near their upper ferric iron composition, and then were oxidized to magnesioferrite in air at temperatures in the range 800–1100°C and for various periods of time. Photomicrographs showed that *L* and *M* crystals oxidized by forming magnesioferrite surface layers, with "fingers" of magnesioferrite extending into the crystals and with numerous small isolated "islands" of magnesioferrite within the crystals. The growth of the external oxidized layer was found to be linear with time and with an activation energy of about 30 kcal/mol. Photomicrographs of *H* crystals show major development of magnesioferrite on external surfaces, with small amounts of hematite on or near the original surface and also on some internal (111) planes. The growth of the external oxidized layer is proportional to $(\text{time})^{1/2}$, suggesting a diffusion controlled mechanism, and the activation energy is about 18 kcal/mol. Comparison is made with data for oxidation behavior of iron oxides.

1. INTRODUCTION

A STUDY has been made of the oxidation of single crystals of magnesiowustite (Mg, Fe)O, by optical and X-ray diffraction methods. The oxidation has been carried out at temperatures in the range 800–1100°C under normal atmospheric conditions, with three groups of crystals, designated *L*, *M*, and *H*, containing respectively low, medium and high iron contents, approximately 20–23, 35–40, and about 67 cation per cent. The crystals were prepared by diffusing iron into single crystal blocks of MgO with linear dimensions of the order of $1 \times 0{\cdot}5 \times 0{\cdot}5$ cm and homogenizing the resulting materials at appropriate temperatures and oxygen partial pressures.

Phase relations in the system $MgO–FeO–Fe_2O_3$ have received considerable attention but not all features have been fully evaluated as yet. It will suffice here to mention briefly only those aspects which are particularly relevant to the present study. The system Fe–O within which $FeO–Fe_2O_3$ occurs was studied by DARKEN and GURRY[1, 2] who established that wustite, Fe_xO, is stable within a range of oxygen partial pressures approximately 10^{-6}–10^{-26} atm. and a range of temperatures approximately 560–1370°C, and x may vary from about 0·85–0·96; see also the discussion by MUAN[3] of phase equilibria in systems involving changes in oxidation states. The pressure–temperature–composition limits within which magnesiowustites are stable seem not yet to be fully established. In normal atmospheres and with temperatures exceeding about 1000°C, the iron is principally in the ferric state and equilibrium can be considered between end members MgO and Fe_2O_3 with magnesioferrite, ideally $MgFe_2O_4$, as an intermediate phase. PHILLIPS, SOMIYA and MUAN[4] have described the phase relations under these conditions. The magnesiowustite phase can incorporate a considerable proportion of Fe^{3+} ions which increases rapidly as the temperature rises above about 1000°C. Phase relations in the ferrite region for oxygen pressures from 1·0 to 0·01 atm. have been discussed particularly by PALADINO(5) who has shown that the Mg ion content may be appreciably higher than is given by the ideal formula and may correspond to $(MgO)_xMgFe_2O_4$ with $x = 0{\cdot}092$. At low partial pressures of oxygen, iron occurs in both ferrous and ferric states and the resulting phases in the ternary system will depend on temperature and oxygen pressure. Full information is not available, but a partial treatment by BRYNESTAD and FLOOD(6) of equilibrium relations at 1400°C under various oxygen pressures has been found useful in the present work.

---

* Dow Corning Corp., Midland, Mich. This study forms part of the M. S. Thesis in Solid State Technology submitted by W.L.S.

A simple, perhaps too simple, representation of the oxidation of magnesiowustite to magnesioferrite is as follows:

$$2(Mg_{1-x}Fe_x^{2+})O + x/2O_2 \rightarrow xMgFe_2^{3+}O_4 + (2-3x)\,MgO$$

This equation neglects a fraction of ferric ions in magnesiowustite, and assumes ideal formulae for the magnesioferrite and magnesium oxide. The maximum value of x for which this equation can hold is $x = 2/3$ and the product is then wholly magnesioferrite.

From a crystallographic viewpoint, the reaction is principally one in which cations occupying octahedral sites in magnesiowustite occupy partly octahedral and partly tetrahedral sites in magnesioferrite. The oxygen anions have essentially the same configurations, a face-centered cubic arrangement, in all the solid phases. However, in wustite and probably also in magnesiowustite some ferric ions are present and some of these may occupy tetrahedral sites. ROTH(7) has studied by magnetic and by X-ray diffraction methods the defects in wustite and has shown that where Fe ions are displaced to tetrahedral sites, the resulting defects may resemble magnetite in structure. A similar situation in magnesiowustite may provide favorable nuclei for the development of magnesioferrite. By and large, however, the reaction is one involving cation redistribution within a constant framework of oxygen ions.

From a chemical viewpoint, the equation indicates the addition of $(x/2)O_2$ gas molecules, or x O^{2-} ions by a process of the following kind:

$$2Fe^{2+} + \tfrac{1}{2}O_2 \rightarrow 2Fe^{3+} + O^{2-}$$

Since the oxygen ions in the solid phases are in cubic close-packed array, the additional oxygen ions will be added *externally* to a crystal and will require outward migration of Fe ions and also of Mg ions if a uniform distribution of cations is maintained. Concomitant with this process is a decrease of the Fe/O ratio within the crystal so that *internal* oxidation also may take place, aided probably by the nature of the lattice defects discussed in the previous paragraph. The present experiments provide clear evidence for these two kinds of oxidation.

A brief reference may be made to the technological importance of the subject. Oxidation of magnesiowustite plays an important role in the behavior of basic refractories in steel plant processes, where iron (or FeO) diffusing into MgO produces magnesiowustite which subsequently may pass through oxidation–reduction cycles. MUAN and OSBORN(8) have surveyed the technical importance of these reactions from the standpoint of phase equilibria, and G. R. RIGBY(9) has emphasized particularly the volume changes involved.

2. PREPARATION OF HOMOGENEOUS MAGNESIOWUSTITE CRYSTALS

Single crystal blocks of magnesiowustite, about 10 × 4 × 2 mm in size, were prepared by diffusing iron into single crystals of magnesium oxide by packing cleaved blocks of MgO in reagent grade Fe_2O_3, or in ferrous oxide obtained by reducing the Fe_2O_3, or by attaching iron sheet (reagent grade) to the larger crystal surfaces and firing under appropriate conditions of temperature and oxygen partial pressure (usually around 1250°C and 1:4 CO/CO_2 gas mixture). After treatment, any superficial polycrystalline oxide was removed by grinding to expose the single crystal containing diffused Fe ions. The clean crystals were returned to the furnace, usually mounted on scrap MgO or (Mg,Fe)O of similar composition, and were made homogeneous by holding for several days at temperatures between 1200 and 1400°C with a 1:4 CO/CO_2 gas mixture. With these conditions, which provide an oxygen pressure of the order of $10^{-9.4}$ atm., it is to be expected from the work of BRYNESTAD and FLOOD(6) that a small but significant proportion of Fe ions will be in the ferric state, a condition which E. B. RIGBY and CUTLER(10) have shown facilitates diffusion in MgO—(Mg,Fe)O couples. Magnesiowustites with high iron concentrations were obtained by repeating this process on previously homogenized (Mg,Fe)O crystals.

Homogeneity of the prepared crystals was checked by cleaving them into numerous sections and sub-sections, and analyzing a number of them by X-ray diffraction using high-order reflections to obtain accurate lattice parameter values. Compositions were determined by reference to specially prepared lattice spacing/composition curves (see Appendix).

3. PRE-OXIDATION WITHIN THE MAGNESIOWUSTITE PHASE

In general, magnesiowustites can be oxidized in two stages, namely (i) oxidation within the magnesiowustite phase itself, and (ii) oxidation to magnesioferrite. The first stage involves no change of crystal structure but corresponds to an increasing proportion of ferric ions. The second stage involves converting the remaining ferrous ions to the ferric state with a change of cation distribution to that of the spinel structure but without major change of the oxygen anion arrangement.

Attention has been focussed principally on the second stage of oxidation, and accordingly the magnesiowustite crystals were brought (at least approximately) to the magnesiowustite/magnesioferrite phase boundary. The correct conditions were found by X-ray powder diffraction analysis of magnesiowustite compositions treated at various temperatures and oxygen partial pressures. The limit of the magnesiowustite phase was indicated by a broadening of the 333, 511 X-ray reflection from magnesiowustite and the appearance of the 400 reflection from magnesioferrite. Crystals to be oxidized were 'soaked' at an oxygen pressure on the low (magnesiowustite) side of the phase boundary at the temperature at which the subsequent oxidation would take place.

4. THE OXIDATION EXPERIMENTS

(a) *Oxidation procedure*

The magnesiowustite crystals thus prepared were cleaved into plates 0·2–0·7 mm thick, placed on a porous alundum body, and drawn into a pre-heated furnace for oxidation in normal atmospheres at various temperatures and for various times.

(b) *Optical examination*

Oxidized crystals were cleaved on their smallest cross-sections, and both freshly cleaved surfaces and also lightly ground surfaces, sometimes etched with a solution of 5 ml HF, 10 ml HNO_3, and 50 ml water, were examined optically by reflected light.

(c) *Phase identification*

Phases were identified by X-ray powder diffraction and included magnesiowustite (of various compositions), magnesioferrite, and hematite. The composition of magnesiowustite was determined by reference to calibration curves (see Appendix).

5. RESULTS

The cleaved faces of all magnesiowustite crystals prior to oxidation were smooth, shiny and black. Following oxidation, they had a dull appearance except that the *H* crystals at the highest oxidation temperature (1100°C) had an appearance almost as shiny as the initial cleavage face. Corners and edges of crystals lost their sharpness and surface irregularities were "softened" or disappeared. Microscopic examination showed that the dull appearing surfaces had irregularities with "hills" and "valleys" differing in level by about 0·003 mm.

Photomicrographs of *L*, *M*, and *H* crystals oxidized in air for various times at temperatures from 800–1100°C show that *L* and *M* crystals behave similarly, but *H* crystals behave differently and must be considered separately.

(a) *Oxidation of L and M crystals*

The only phases observed were magnesiowustite and magnesioferrite which appear as dark and light phases respectively in the micrographs. Evidence was sought for the formation of hematite transiently, but none was found. X-ray evidence showed that the magnesioferrite was formed on the surface of the magnesiowustite in parallel orientation.

In the earliest stages of oxidation, thin layers of magnesioferrite appear on the external surface together with small and randomly distributed "islands" of magnesioferrite within a zone parallel to the external surface. Figure 1(a) shows the cleavage surface of an *L* crystal after 1½ hr at 900°C. With increasing time and temperature, the surface layer thickens, the "islands" become larger, they increase in number occupying a wider zone of the magnesiowustite, and they also join together to form "fingers" extending at right angles to the external surface.

Figures 1(b) and 1(d) show *L* and *M* crystals oxidized for 13 hr at 1000°C where the thickened rim and finger formation are clearly seen. Figure 1(c) shows an *M* crystal polished to remove the surface layer; the cross sections of the fingers are seen to exhibit no particular pattern and to be of roughly constant cross-sections. Fingers are seen also developing from internal surfaces, probably cracks.

(b) *Oxidation of H crystals*

Their behavior is more complex than that of *L* and *M* crystals, and the analysis requires consideration of both the phases formed and their compositions, the latter information being derived from X-ray measurements of high-order lattice spacings. The sequence of observations for one particular *H* crystal may be briefly summarized.

After a 20 min oxidation at 850°C, single crystal reflections from the magnesiowustite cleavage surface were replaced by corresponding reflections from magnesioferrite, together with a reflection or reflections from hematite. The 400 reflection from magnesiowustite, $d = 1{\cdot}067$ Å, was replaced by the 800 reflection from magnesioferrite, $d = 1{\cdot}048$ Å, which corresponds to a 2 per cent linear decrease of the cubic close-packed oxygen arrangement. The magnesioferrite was well oriented at first with respect to the substrate but the orientation became less perfect as the process continued. The hematite phase also showed evidence for some degree of orientation; the first reflections to be observed were the combined 1,0,10–119 reflection and the 108 reflection (i.e., using hexagonal axes for the hematite lattice). These are among the weaker reflections from hematite, but they correspond to lattice planes most nearly perpendicular to the *c*-axis. The hematite tends to develop, therefore, with the *c*-axis more or less normal to the substrate. The 800 lattice spacing of the magnesioferrite varied with time showing that when first formed it had a composition corresponding to $MgFe_2O_4$ but, as oxidation continued, it became richer in iron, approaching $FeFe_2O_4$, but after about 15 hr oxidation the composition reverted to that of $MgFe_2O_4$.

Figure 1(e) shows the development of magnesioferrite (grey phase) and hematite (white phase) from magnesiowustite (dark phase) after oxidation for 2 hr at 1000°C. At this stage the hematite is confined to the surface layer, but later (c.f. Fig. 1(*f*), *H* crystal oxidized for several days at 800°C) the magnesiowustite disappears entirely, the hematite layer thickens and additional hematite is precipitated in sheets on the (111) planes of the magnesioferrite. Similarly oriented precipitations of hematite were reported previously by GRUNER.(11) In Fig. 1(*f*) the hematite lines lie at angles of about 63° and 37° to the edge of the crystal and correspond to a polished section at about 22° from a 100 cube face.

The amount of hematite forming is dependent on the temperature and from the phase diagram (PHILLIPS, SOMIYA and MUAN,(4)) the maximum amount is expected at temperatures of about 800–900°C. After heating at 1100°C, only traces of hematite were observed. An *H* crystal was oxidized for 12 hr at 1200°C followed by 12 hr at 800°C. The hematite then precipitated on the (111) planes of the magnesioferrite as shown in Fig. 1(g) where the hematite lines are at approximately 90° to each other and 45° to the outer surface; the plane of the photograph corresponds closely to a (100) cube face.

Several attempts were made to induce the crystallization of cubic γ-Fe_2O_3 which might be expected to form preferentially in the cubic environment of magnesioferrite. *H* crystals oxidized at 800°C yielded hematite in the oxidized rim. The crystal illustrated in Fig. 1(g) was examined by X-rays and the precipitated phase was found to be hematite.

One further observation may be made concerning oxidized magnesiowustite crystals, more particularly those rich in iron. Occasionally, when air-quenched after oxidation, they fractured spontaneously, more particularly when left longer in the oxidizing atmosphere. This seldom happened in the case of *L* crystals. It is clearly an indication of strains arising from the oxidizing process.

6. RATE STUDIES ON THE DEVELOPMENT OF SURFACE OXIDATION

L, *M* and *H* crystals, previously brought near the oxidation limit of the magnesiowustite phase, were oxidized in air at 800, 900, 1000, and 1100°C for various periods of time. Measurements were made of the thickness x of the oxidized surface layer from photomicrographs of cleavage surfaces, for various oxidation periods t. The results, shown in Figs. 2(a), (b) and (c) for *L*, *M* and *H* crystals respectively, were obtained from measurements on about 100 different crystals.

For *L* and *M* crystals the observations lie on straight lines through the origin within the probable experimental errors so that the process can be represented by equations

$$x_L = k_L t \text{ and } x_M = k_M t \qquad (1)$$

where k_L and k_M are rate constants for surface oxidation.

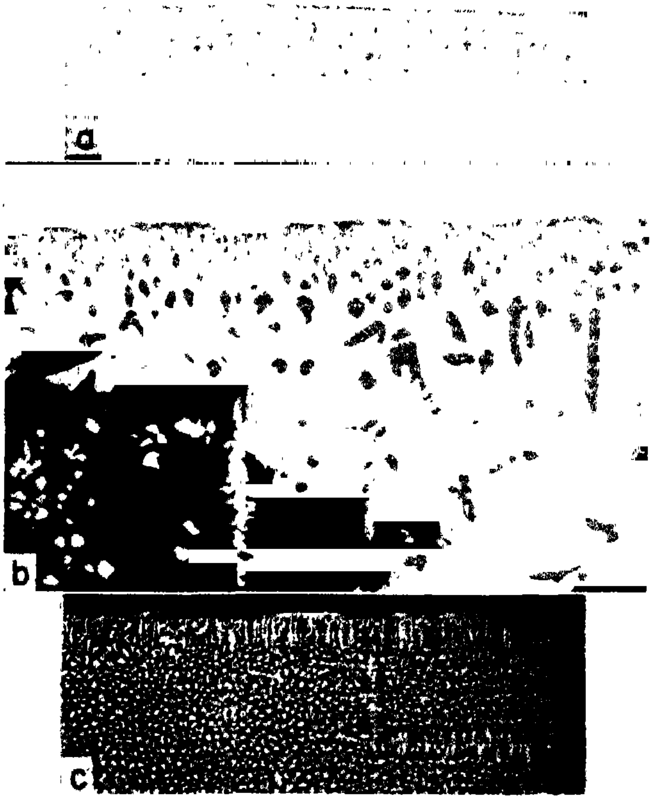

Fig. 1. Photomicrographs of magnesiowustite single crystals oxidized in air.

(a) L crystal, oxidized 1½ hr at 900°C. (400 ×).
(b) *L* crystal, oxidized 13 hr at 1000°C. (400 ×).
(c) *M* crystal, oxidized at 900°C. (100 ×).

(a) cleaved section; (b)–(g) polished sections.
Phases: (a), (b), (c), (d): white = MF; dark = MW. (e), (f), (g): white = H; grey = MF. (e) dark = MW. MW = magnewiosustite; MF = magnesioferrite; H = hematite.

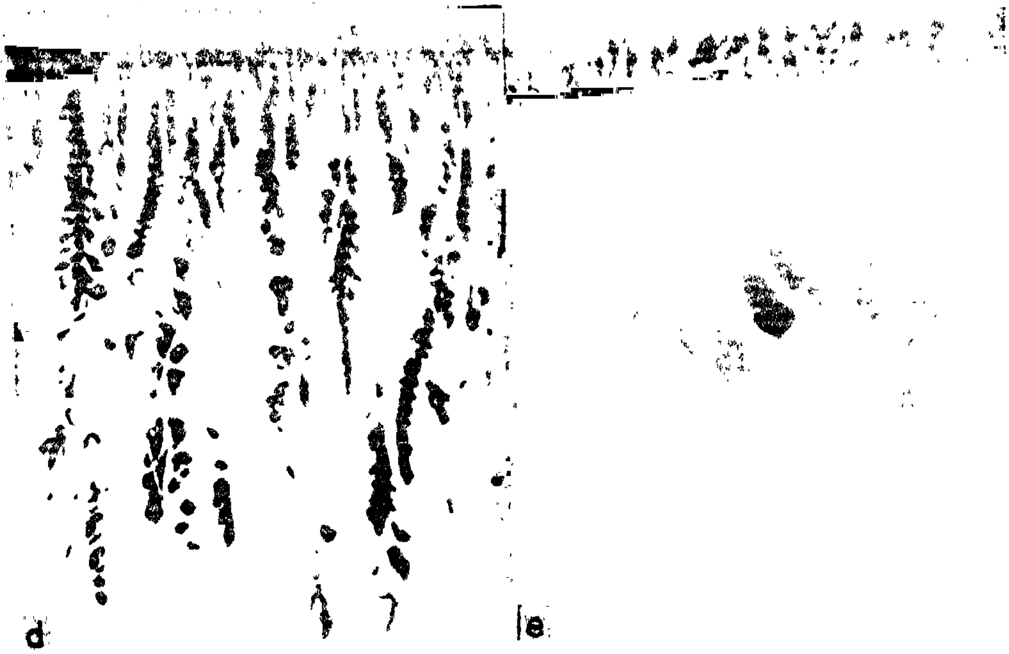

FIG. 1. Photomicrographs of magnesiowustite single crystals oxidized in air. (d) *M* crystal, oxidized 13 hr at 1000°C. (400×). (e) *H* crystal, oxidized 2 hr at 1000°C. (400×).

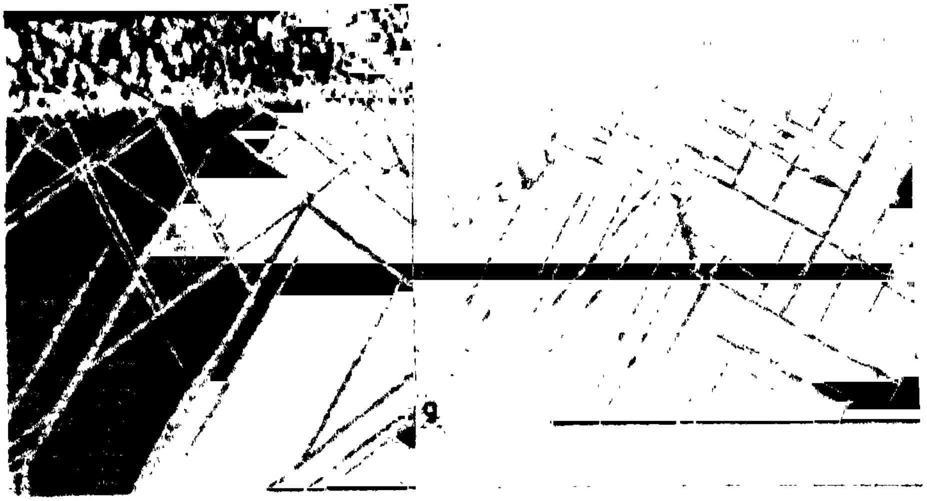

FIG. 1. Photomicrographs of magnesiowustite single crystals oxidized in air. (f) *H* crystal, oxidized several days at 800°C. (400×). (g) *H* crystal, oxidized 12 hr at 1200°C, 12 hr at 800°C (400×).

For H crystals, the observations in Fig. 2(c) do not fall on straight lines, but appear to follow parabolic curves. This is confirmed in Fig. 3 where x_H is plotted against $\sqrt{t}$ expressed in $(\text{min})^{1/2}$. An allowance of 1 min is made as an approximate correction for the time to bring a crystal to full temperature when drawn into the hot zone of the furnace. On the linear time scale used in Fig. 2, such a correction is unnecessary.

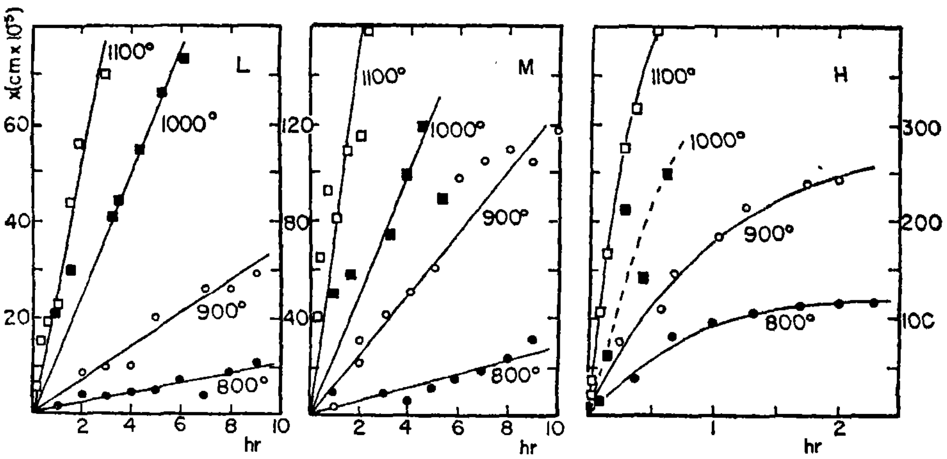

(a) (b) (c)

FIG. 2. Thickness, x, of oxidized rim vs. time of oxidation. (a) L crystals, (b) M crystals, (c) H crystals. Temperatures of oxidation in °C.

The results obtained at 1000°C were exceptionally erratic (see Fig. 2(c)) and are omitted from Fig. 3. From the gradients of the lines in Fig. 3 the rate constants k_H in the equation

$$x_H = k_H\sqrt{t} \tag{2}$$

have been determined.

If the temperature dependence of oxidation is given by a relation of the Arrhenius type,

$$k = A\exp(-E/RT) \tag{3}$$

then a plot of $\ln k$ vs. $1/T$, reciprocal of the absolute temperature, should give straight lines of slope $(-E/R)$. The results are shown in Fig. 4, and the calculated activation energies are respectively:

$$E_L \approx E_M \approx 30 \text{ kcal/mol}$$
$$E_H \approx 18 \text{ kcal/mol}$$

7. DISCUSSION OF THE KINETIC DATA

It appears that L and M magnesiowustite crystals oxidize according to a linear time variation, but H crystals follow a parabolic relation. The latter relation suggests a diffusion controlled process in which the rate of development of the surface layer of magnesioferrite, dx/dt, is inversely proportional to the thickness x of the layer, i.e., $dx/dt = k/x$ which on integration becomes

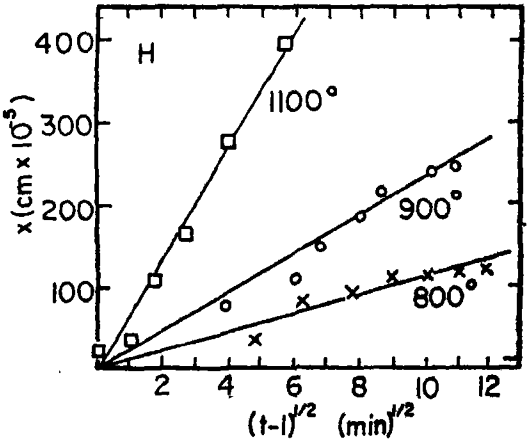

FIG. 3. Thickness, x, of oxidized rim of H crystals vs. square root of oxidation time. Temperatures of oxidation in °C.

$x = k'\sqrt{t}$. If oxidation takes place always at a constant rate, then $x = kt$ in accordance with the linear relations for *L* and *M* crystals.

The difference in oxidation behavior of *L* and *M* crystals and of *H* crystals must be sought in the cation percentages of Fe in the materials studied. *H* crystals, with approximately 67 per cent Fe cations, 33 per cent Mg cations, have the appropriate cations to form entirely magnesioferrite by oxidation. *L* and *M* crystals, with fewer Fe and more Mg cations, will form mixtures of magnesioferrite and magnesiowustite.

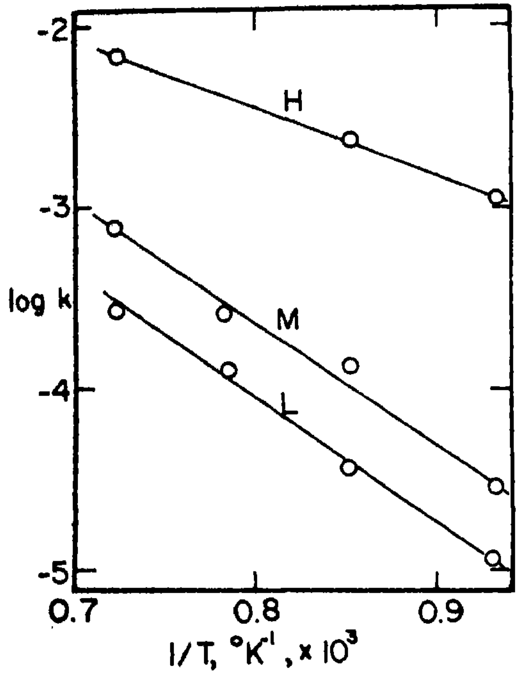

FIG. 4. Log *k* vs. reciprocal of absolute temperature for *L*, *M* and *H* crystals.

Since the lattice parameters of magnesiowustite and magnesioferrite are not exactly equal, the latter being a few per cent smaller than the former depending on precise compositions, a system of microcracks or of dislocations can be expected to develop which may facilitate migration of Fe ions to the reacting surface. The development of "fingers" of magnesioferrite in *M* and *L* crystals (see Fig. 1(b) and (d)) may reflect the formation of such microcracks. In *H* crystals, a more "solid" development of the oxidized surface appears to take place; Fig. 1(e) shows that although there is something resembling "finger" formation, the magnesioferrite near the surface has a much more homogeneous appearance (apart from the hematite) than one finds in *M* and *L* crystals. In *H* crystals a reaction interface may start at the surface and in effect move inwards. The actual process, however, is one in which oxygen ions are added externally and become bound by Fe cations diffusing outwards through the oxidized layer. Diffusion through a developing layer seems to be an essential feature of the process in *H* crystals.

The activation energies which have been determined can be compared with related data for iron oxides. HIMMEL, MEHL and BIRCHENALL(12) found for the activation energies of self diffusion of iron in wustite, magnetite, and hematite, values of about 30, 55, and 110 kcal/mol respectively. The value of 30 kcal/mol for self diffusion of iron in wustite agrees with the values found in the present study for oxidation of *L* and *M* crystals. If, as previously suggested, their oxidation depends on the formation of microcracks, then the rate-controlling process may be a diffusion of iron to these microcracks which permit easy passage of the cations by surface migration to the external surface. Both the constancy of the reaction rate (which is shown in Fig. 2(a), (b)) and the activation energy of 30 kcal/mol appear to be consequences of the constant diffusion process within the magnesiowustite phase.

As regards the activation energy of 18 kcal/mol found for oxidation of *H* crystals, it may be noted that in the work of DAVIES, SIMNAD and BIRCHENALL(13) on the oxidation of wustite to magnetite in the range 850–950°C, the oxidation was found to follow a parabolic law; from the data in their Table II an activation energy of about 18 kcal/mol has been calculated. There is consistency, then, as regards both the activation energy and the parabolic relation in these reactions.

8. CONCLUSIONS

Oxidation of magnesiowustite single crystals containing low and medium iron concentrations, approximately 20 and 35–40 cation per cent Fe, takes place by surface oxidation by addition of externally bound oxygen ions and by internal oxidation arising from the changed cation/anion ratio within the structure. The external oxidized layer of magnesioferrite develops at a constant rate with respect to time and has an activation energy of the order of 30 kcal/mol. The constant rate of surface oxidation is considered to arise from the formation of microcracks which enable ferrous ions to reach the oxidizing surface layer by energetically easy paths. The activation energy is considered to reflect a diffusion process which transports ferrous ions to the conducting cracks. High iron magnesiowustites (67 cation per cent Fe) also develop an oxidation rim but the process is proportional to $\sqrt{t}$, suggesting a diffusion-controlled reaction with diffusion taking place through an increasingly thick surface layer. The activation energy of the process, about 18 kcal/mol, and the parabolic relationship agree with data for the oxidation of wustite to magnetite.

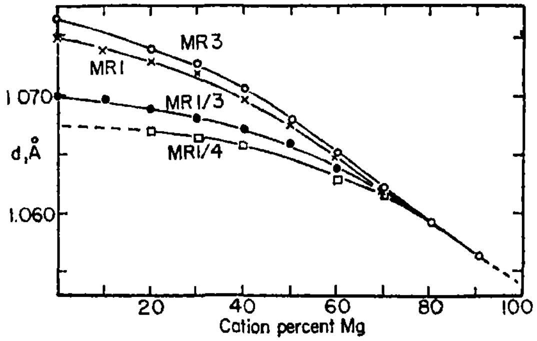

FIG. 5. Lattice spacing $d(400)$, in Å, for magnesiowustites equilibrated at 1250° in various CO:CO$_2$ gas mixtures; MR = mixing ratio CO/CO$_2$.

Acknowledgements—This investigation forms part of a program for studying the kinetics of high temperature solid state reactions supported by a grant, G5799, from the National Science Foundation to one of us (G.W.B.). It is a pleasure to acknowledge the valuable assistance given by Dr. GEORGE K. LAYDEN during the early stages of developing these experiments.

REFERENCES

1. DARKEN L. S. and GURRY R. W., *J. Amer. chem. Soc.* **67**, 1398 (1945).
2. DARKEN L. S. and GURRY R. W., *J. Amer. chem. Soc.* **68**, 798 (1946).
3. MUAN A., *Amer. J. Sci.* **256**, 171 (1958).
4. PHILLIPS B., SOMIYA S. and MUAN A., *J. Amer. ceram. Soc.* **44**, 167 (1961).
5. PALADINO A. E., *J. Amer. ceram. Soc.* **43**, 183 (1960).
6. BRYNESTAD J. and FLOOD H., *Z. Elektrochem.* **62**, 953 (1958). See also FLOOD H. and HILL D. G., *ibid.*, **61**, 18 (1957).
7. ROTH W. L., *Acta Cryst.* **13**, 140 (1960).
8. MUAN A. and OSBORN E. F., *Amer. ceram. Soc. Bull.* **41**, 450 (1962).
9. RIGBY G. R., *Amer. ceram. Soc. Bull.* **41**, 456 (1962).
10. RIGBY E. B. and CUTLER I. B., *Amer. ceram. Soc. Bull.* **41**, 584 (1962).
11. GRUNER J. W., *Amer. Mineral.* **14**, 227 (1929).
12. HIMMEL L., MEHL R. F. and BIRCHENALL C. E., *Trans. Amer. Inst. min. (metall.) Engrs.* **197**, 827 (1953).
13. DAVIES M. H., SIMNAD M. T. and BIRCHENALL C. E., *Trans. Amer. Inst. min. (metall.) Engrs.* **191** 889 (1951).
14. HAHN W. C. JR., Ph.D. Thesis, Pennsylvania State Univ. (1960). See also HAHN W. C. JR. and MUAN A., *Trans. met. Soc. Amer. Inst. min. (metall.) Engrs.* **224**, 416 (1962).

APPENDIX

Lattice spacing vs. composition curves of magnesiowustites

Calibration curves were made relating lattice spacing to composition for magnesiowustites equilibrated at 1250°C and various oxygen partial pressures obtained with flowing gas mixtures of CO and CO$_2$. Since the gas mixing ratio is known more exactly than the resulting oxygen pressures, results are expressed in terms of the CO/CO$_2$ mixtures used. Oxide mixtures at intervals of 10 cation % Fe from 10 to 90 per cent were prepared by mixing appropriate amounts of MgO and Fe$_2$O$_3$ under acetone in an agate mortar. After firing under desired conditions, the samples were removed from the furnace, crushed and small pellets prepared. These were fired at 1250°C and with the desired gas mixing ratio, air-quenched, ground under acetone, and the (400) lattice spacing determined by X-ray diffraction using Mn-filtered FeKα radiation and a scanning rate of $\frac{1}{4}°\ (2\theta)$/min with a Philips Norelco diffractometer. The (400) reflection occurs in the neighborhood of 128°(2θ) for wustite and 133·4°(2θ) for MgO. The diffractometer was calibrated with reference to a silicon standard.

The results are given in Fig. 5 where $d(400)$ in Å is plotted against Mg cation per cent for various ratios CO/CO$_2$. The upper curve, CO/CO$_2$ = 3, represents the most reducing condition employed and at 1250°C the conditions are in the vicinity of the wustite–metallic iron boundary. However, no iron was detected. The results agree closely with experimental data by HAHN[14] for magnesiowustites in equilibrium with liquid iron; his observations fall on the curve CO/CO$_2$ = 3 in Fig. 5.

From the shape of the spacing-composition curves, it is evident that X-ray data are more useful for estimating low iron concentrations (approximately less than 50%) than for estimating high iron concentration (approximately greater than 70%). It is also noteworthy that the curves depart considerably from the linear Vegard law. Finally, it is clear that lattice spacing data for such a system are useful for determining composition *only* if the oxygen partial pressure is controlled.

J. Phys. Chem. Solids Pergamon Press 1963. Vol. 24, pp. 927–931. Printed in Great Britain.

TRANSIENTS IN THERMOCHROMY OF ANILS*

A. AHARONI, H. DITKOVSKY, E. H. FREI and A. TZALMONA

Department of Electronics, The Weizmann Institute of Science, Rehovoth, Israel

(*Received* 9 *November* 1962; *revised* 15 *February* 1963)

Abstract—The time constant for color formation with temperature change was studied by applying a pulse of heat to films of thermochromic salicylidene-anilines. There is a weak absorption band formed around 5400 Å, in which the time constant for color formation is about 50 msec. For the larger absorption band, around 4800 Å, the time constant was shorter than the sensitivity of our instrument, i.e. shorter than 5 msec. This indicates the mechanisms are different for the two bands. Both are probably intramolecular processes, the 4800 Å band being caused by tautomerization to a quinoid state, while the 5400 Å band is due to another species whose exact nature is not well understood.

I. INTRODUCTION

SOME crystalline anils of salicylaldehyde are photochromic, i.e. their color deepens from yellow to red on irradiation with near u.v. light.(1) This color-deepening is due to the appearance of an absorption band extending from 4000 to 6000 Å with a maximum at about 4800 Å, and shoulder at 4900 Å. The deep color can be bleached by light absorbed in this latter band. Those crystalline anils of salicylaldehyde which are not photochromic are found to be thermochromic, i.e. their color deepens with increasing temperature. Here, again, a new absorption band in the visible is responsible; it is very similar to the band described above insofar as wavelengths of maximum absorption and shoulder are concerned. However, the absorption of the thermochromic crystals has been reported(2) to cut off sharply at about 5200 Å, so that there appears to be an additional band in photo-colored crystals at long wavelengths (5200–6000 Å).

We have investigated the speed of response of thermochromic crystals to rapid changes in temperature. The response of the main band (4000–5200 Å) has been found to be "immediate" on our time scale. However, these studies have shown that there *is* a change in absorption also in the long wavelength region, and that there is a finite time lag between application of the heat pulse and the response in this region. Thus, there is an absorption band at long wavelengths even in thermochromic crystals, although its intensity is much less than that of the photoformed one. Further, the mechanism of formation of the species absorbing at these wavelengths must be different from that of formation of the species responsible for the main absorption.

In Section II we describe the apparatus, and in Section III we report the results of our measurements.

II. EXPERIMENTAL

(a) The optical arrangement is shown schematically in Fig. 1. Light from the light source *S* (30 W 6 V incandescent) passes into a monochromator *M* (Bausch and Lomb DL 1892) and is focused by lenses and mirror arrangement, *Mi*, on the sample anil *A*. It is then reflected into the 1P21 photomultiplier tube, *P*, fed by a highly stabilized power supply. The output of the tube is fed into one of the beams of a Tektronix 502 double beam oscilloscope.

(b) The sample *A* was a thin film cast on a machined iron anular plate I, whose dimensions are given at the top of Fig. 1. The form of a ring is necessary to achieve a homogenous heating. Two current leads and two voltage leads, *L*, were silver soldered to the back of the plate and

---

* Work supported by the National Cash Register Co., Dayton, Ohio.

served to measure the resistance of the iron, as a measure of the temperature. (Initially a thermocouple was used for this purpose, but was found to lag considerably behind the temperature rise. Change in resistivity can be assumed to take place immediately.) About 5 A d.c., obtained by series connection with the incandescent lamp fed from an accumulator, was used in the current leads, and this was sufficient to give measureable and stable readings on the oscilloscope. Since the resistance of the silver-solder is unpredictable each ring iron used in these experiments was calibrated first while immersed in an oil bath whose temperature was measured directly. An arrangement (not shown in the figure) for blowing cool air on the sample, enabled us to superimpose the heat pulse on any desired ambient temperature between −70°C and room temperature.

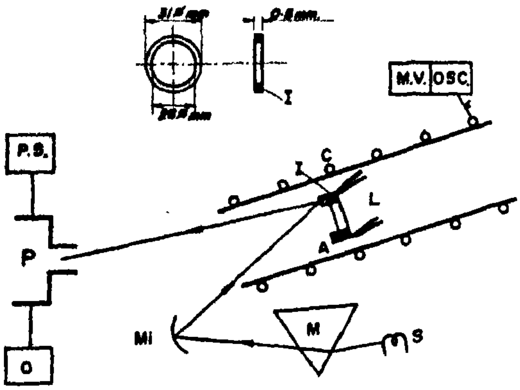

Fig. 1. Schematic representation of the apparatus described in the text.

By feeding the output of the voltage leads (i.e. the iron resistance) to one beam of the scope and the output of the photomultiplier to the other beam, one obtains simultaneously the intensity of the reflected light and of the temperature as a function of time both during the heating period and later. Because the film is very thin, it is assumed that its temperature is always the same as that of the iron. Checks on this will be discussed in the next part.

For applying a short heat pulse, dielectric heating was first tried, but proved unsatisfactory because the anils are very good insulators, with extremely low losses, at all frequencies used. We therefore introduced the method of coating the material on a flat iron ring, which was heated by an induction heater.

(c) The heating is carried out by applying a pulse of r.f. to the coil C in Fig. 1. It consisted of 15 windings on each side, of No. 14 (B. and S.) copper enameled wire, wound on a threaded 1½ in. Norton furnace core. It serves as the anode coil of a Hartley type oscillator, which supplies 100 W at 2·7 Mc/s.

The grid of the oscillator tube (805) is normally held negative by a one-shot multivibrator, thus preventing the oscillations. The multivibrator is flipped manually by a push-button switch, and is flipped back after a time determined by one of a set of condensers. The oscillator is thus switched on for a period of time which can be selected by a switch. In the final form, 2 positions of the switch were used, yielding oscillations for 50 msec and 100 msec respectively, as measured on the Tecktronix oscilloscope. The longer pulses were used around 4800 Å where a relatively large temperature change is needed to get an appreciable change in signal, because of the high absorbance of the materials in this spectral region. For the longer wavelengths, the shorter pulses were sufficient, due to the high sensitivity of the photomultiplier. The heating rate was 800°C/sec, so that the longer pulse yielded a temperature change of 80°C and the shorter pulse yielded a temperature change of 40°C.

(d) It would have been relatively simple to increase the power of the oscillator, so that shorter pulses would suffice to obtain the necessary temperature rise, with a possibility of studying shorter time-constants for color formation. This was not considered practical, however, because of severe limitations in heat transfer from the iron to the sample under study. In a poorly prepared sample, i.e. one which did not adhere well to the iron plate, a delay could be observed in the *start* of the change in light-reflection, with respect to the change in temperature. Even for carefully prepared samples, such a delay could normally be observed in certain *parts* of the film (the light-focusing arrangement allowed a choice of a small portion of the film to be studied) and it was only in certain parts that the curves started simultaneously, so that measurements could be made.

When the film was left for a day or two, parts of it started to peel off, and this was first observed for the portions in which delays were observed initially. After longer times, or after many successive heatings, even the "good" parts started to show delays, and later to, peel off. The measurements reported in the next Section were therefore carried out only on selected parts of freshly prepared films, which were cast on the iron ring, previously heated to give better adhesion. While the anil was still liquid it was pressed slightly to yield a thin enough film (normally about 0·05 mm).

These difficulties did not encourage any decrease in the time of pulse, since it seemed that the technique was in any case not applicable to shorter time constants than reported here.

III. RESULTS

In Fig. 2 typical curves are given of reflection from the sample and of temperature of the iron, as functions of time. It can be seen that the color continues to form long after the temperature has stopped rising, and even when it shows a tendency to decrease. A rather large noise is seen towards the end, but this can usually be overcome by taking several photographs and averaging the noise out.

It is seen from the figure that it is not desirable to depend on the exponential part of the curve (i.e. after the switching off of the heater) to give the time constant, because of the noise and because the heating period is comparable with the time constant. Nevertheless, this has been done in some cases, and the time constants for color formation computed in this way roughly agree with those obtained by the method described below. To get a better estimate, consider a process in which a function A of the temperature T (e.g. absorbance or reflection in our case), approaches its stationary value exponentially in time, with a time-constant τ which does not depend on temperature. If one starts with a thermal equilibrium at temperature T_0, where A has its stationary value $A(T_0)$, then at time $t = t_0$ the temperature is suddenly raised to T_1, an exponential dependence means that A is given by

$$A(t, T_1) = A(T_1) - \{A(T_1) - A(T_0)\} \times \exp\{-(t-t_0)/\tau\} \qquad (1)$$

(which has the stationary value $A(T_0)$ for $t = t_0$ and the other stationary value $A(T_1)$ when $t \to \infty$). In particular, this formula is used at the time $t = t_0 + \delta t$, when it is assumed that another jump is made to the temperature T_2. Here one does not start from thermal equilibrium, therefore at the time $t = t_0 + 2\delta t$,

$$\begin{aligned} A(t_0+2\delta t, T_2) - A(T_2) &= \{A(T_2) - A(t_0+\delta t, T_1)\} \\ &\times \exp(-\delta t/\tau) = A(T_2) - \{A(T_2) - A(T_1)\} \\ &\times \exp(-\delta t/\tau) - \{A(T_1) - A(T_0)\} \exp(-2\delta t/\tau) \end{aligned} \qquad (2)$$

etc. Consider now the case where A is a linear function of T (which is a good approximation when the total change in temperature is not large) i.e.

$$A(T) = (T - T_0)a + A(T_0) \qquad (3)$$

where a is a constant. Assume further the jumps in temperature are always by the same amount δT (which is justified in our case where the heating is linear in time), then one obtains after n such jumps:

$$A(t_0 + n\delta t, T_n) - A(T_n) = -\alpha \delta T \sum_{m=1}^{n} \exp(-m\delta t/\tau)$$

The sum of the geometric series can be easily carried out, and if one writes for the *total* heating time $\Delta t = n\delta t$, and for the total temperature change $\Delta T = n\delta T$, and passes to the limit $\delta t \to 0$, $n \to \infty$

$$1 - \frac{A(t+\Delta t, T+\Delta T)}{A(T+\Delta T)} = \frac{\tau}{\Delta t}\left(1 - \exp\left(-\frac{\Delta t}{\tau}\right)\right) \qquad (4)$$

From a graph like Fig. 2, one should therefore determine the total heating time, Δt, and the ratio between the value of reflection at the end of the heating period and its value after a long time (or, actually, its maximum, since eventually the reflection decreases again). These two when substituted in (4) suffice to yield τ by solving a transcendental equation, easily carried out using a graphical plot of (4). As can be expected. (4) is particularly useful for $\tau \approx \Delta t$, while for $\tau \ll \Delta t$ it yields no information except that the reflection curve exactly follows the temperature curve.

The results of the measurements on 5′-chloroanil* of salicyladehyde heated from room temperature, are plotted in Fig. 3. It will be seen that there is a finite time-lag for absorption at wavelengths 5100–5600 Å. Outside this region, and in particular in the main color band around 4800 Å, the reflection curve exactly follows the temperature curve with no observable time-lag, as is illustrated in Fig. 4, i.e. the time constant is zero on our scale, or less than about 5 msec. Practically the same results were obtained for the 5′-Br and 5′-Me anils, at room temperature. For 4800–5100 Å the color change below room temperature is larger than at room temperature, but a change can be observed practically up to the melting point. Nowhere in the range of −70°C to the melting point was any time-lag observed in the three anils studied, for these wavelengths.

In the longer wavelength band the signal decreases rapidly when the ambient temperature is lowered and there is evidently no absorption below 0°C. The lowest ambient temperature at which a measurable signal could be obtained was −15°C and, within the poor accuracy of ± 20 per cent possible there, due to the relatively high noise level, the time constant is the same as at room temperature.

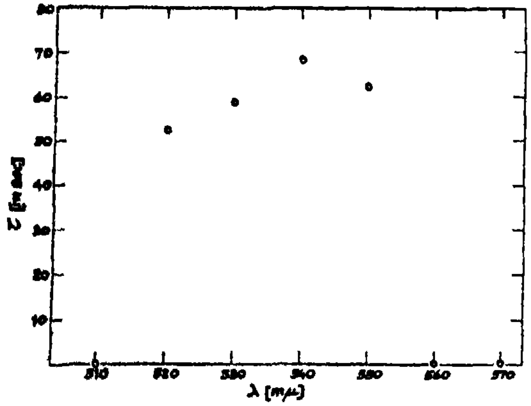

Fig. 3. The time-constant for color formation as a function of wavelength (5′ Cl at room temperature).

The fact that a time-lag is observed only in a limited wavelength range proves that this lag is actually associated with the time of formation of color, and not with the transfer of heat into the sample, since the latter can hardly be expected to depend on wavelength. To check this further, we studied with the same apparatus the color change in azobenzene, whose optical properties are very similar to those of the anils. No time-lag was observed for this material in any wavelength.

IV. DISCUSSION

It has been argued(1,2) that the color-band at 4800 Å is due to formation of the quinoid form, i.e. a displacement of a proton:

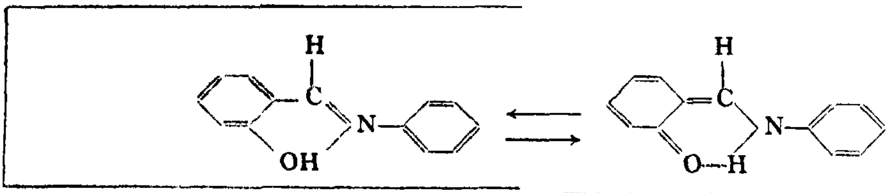

This is mainly based on the necessity of the ortho-hydroxyl group for these processes(2) but also on a more direct n.m.r. evidence for a similar material.(3) In the similar photochromic anils we have found(4) that the OH line in n.m.r. disappears on irradiation, supporting this assumption. The fact that the longer wavelength color takes a longer time to form indicates that the absorbing species is formed by a different mechanism from that of the 4800 Å absorbing one, this may be true also in the photochromic case. The fact that the 5400 Å band does not form at low temperatures evidently means that it is due to some change in the colored quinoid state rather than in the uncolored phenolic state. It is probably some rotation of the phenyl ring, which, according to the crystallographic data(2) should be easier in the photochromic than for the thermochromic crystals. This explains why the long wavelength band is much smaller for the thermochromic than for the photochromic case.

Evidence for two different processes can also be qualitatively deduced from measurements at an intermediate wavelength, e.g. 5000 Å, where the 2 bands contribute to the color change observed.

---

* The prime indicates that the substituent is in the aldehyde-ring.

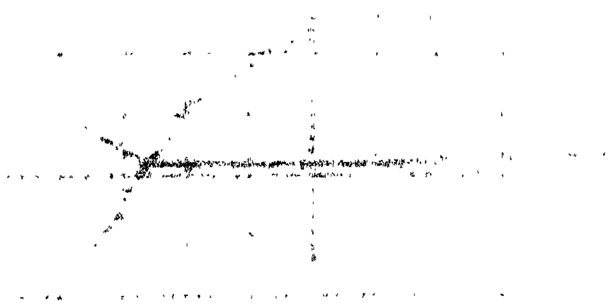

FIG. 2. The temperature (straight lines) and the output from the photomultiplier as functions of time. Time scale: 50 msec/cm. Temperature scale: 1 mV/cm. Light intensity scale: 50 mV/cm. The material was 5′ Cl anil studied at 5400 Å (room temperature).

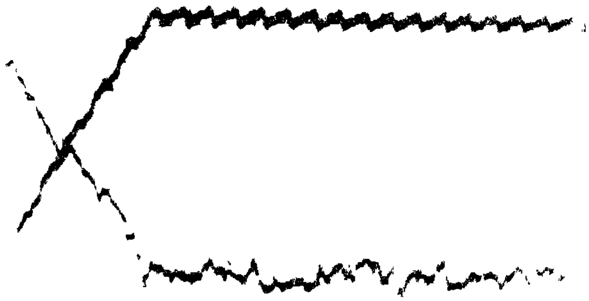

FIG. 4. A case of no-delay in the reflection of light (5′ Cl anil at 4800 Å at room temperature). Time scale: 50 msec/cm. Temperature scale 0·5 mV/cm. Light intensity scale: 50 mV/cm.

The signal from the photomultiplier at such a wavelength shows a break, going from an initial fast increase in color to a later slower increase, although there is no measurable over-all time-lag, as has been mentioned before. To show this effect clearly requires the use of thick films, as otherwise the slower process is completely dominated by the more rapid one. For thick enough films, the break could be observed at room temperature down to 4700 Å. At −70°C there was definitely no break indicating a disappearance of the slower process. Because of the noise, it was impossible to define the temperature at which this effect disappears.

Acknowledgements—The authors are much indebted to Drs. J. Bregman, M. D. Cohen and G. M. J. Schmidt of the Department of X-Ray Crystallography of this Institute, for preparing the materials, and for many valuable discussions.

REFERENCES

1. Cohen M. D., Hirshberg Y. and Schmidt G. M. J., in *Hydrogen Bonding*, pp. 293–300. Pergamon Press, London (1959).
2. Cohen M. D. and Schmidt G. M. J., *J. phys. Chem.* **66**, 2442 (1962).
3. Dudek G. O. and Holm R. H., *J. Amer. chem. Soc.* **83**, 3914 (1961).
4. Aharoni A., Ditkovsky H., Frei E. H. and Tzalmona A., to be published.

J. Phys. Chem. Solids Pergamon Press 1963. Vol. 24, pp. 933–937. Printed in Great Britain.

THE DIAMAGNETIC SUSCEPTIBILITY OF A QUANTUM PLASMA

JOHN J. QUINN

Laboratories RCA Ltd., Zurich

(*Received* 29 *January* 1963)

Abstract—*The current density induced in a degenerate electron gas in the presence of a uniform* magnetic field $\boldsymbol{B}_0$ by a small perturbing field $\boldsymbol{B}_1$ is calculated by the self-consistent field method. The field $\boldsymbol{B}_1$ can vary in space in an arbitrary way. From the Fourier transform of the induced current density one can obtain the function $\nu(\boldsymbol{q}, \boldsymbol{B}_0)$, which is the ratio of the Fourier transform of the magnetic field strength $\boldsymbol{H}_1$, to the Fourier transform of the magnetic induction $\boldsymbol{B}_1$ of the perturbing field. In the limit as the wave vector $\boldsymbol{q}$ approaches zero ($\boldsymbol{B}_1$ is independent of the spacial coordinates) ν^{-1} reduces to the usual expression for the magnetic permeability, displaying the de Haas–van Alphen oscillations.

I. INTRODUCTION

THE experimental investigation of the quantum oscillations of the diamagnetic susceptibility$^{(1)}$ has proved a very useful tool in the study of the electronic structure of solids. The explanation of the oscillatory behavior of the susceptibility was given by LANDAU$^{(2)}$ and PEIERLS,$^{(3)}$ and is based on the quantization of the energy levels of electrons in the presence of a magnetic field. The Landau treatment involves a calculation of the free energy for an electron gas in the presence of a uniform magnetic field and the differentiation of the free energy with respect to the strength of the uniform magnetic field. The present treatment represents a somewhat different approach to the problem, which yields the Landau diamagnetism as a special case. The present work is a natural by-product of the derivation of the self-consistent response of a degenerate electron gas in the presence of a uniform magnetic field to an arbitrary electromagnetic disturbance.$^{(4)}$ In the present work we calculate the response of the electron gas to an infinitesimal magnetic field, which is constant in time but can vary in an arbitrary way in space. If $\boldsymbol{B}_0$ is the magnetic induction and $\boldsymbol{H}_0$ the intensity of the constant magnetic field, the magnetic permeability μ is defined by the relation

$$\boldsymbol{B}_0 = \mu(|\boldsymbol{B}_0|)\boldsymbol{H}_0. \tag{1}$$

The magnetic permeability depends on the magnitude of $\boldsymbol{B}_0$ as indicated in equation (1). When we perturb the system by adding an infinitesimal magnetic field of induction $\boldsymbol{B}_1$ and intensity $\boldsymbol{H}_1$, we have

$$\boldsymbol{B}_0 + \boldsymbol{B}_1 = \mu(|\boldsymbol{B}_0 + \boldsymbol{B}_1|)(\boldsymbol{H}_0 + \boldsymbol{H}_1). \tag{2}$$

By subtracting equation (1) from (2) and considering the limit as $\boldsymbol{B}_1$ tends to zero we arrive at two distinct cases. If $\boldsymbol{B}_1$ is perpendicular to $\boldsymbol{B}_0$ one obtains

$$\mu(B_0) = B_1/H_1, \tag*{(2)}$$

while for $\boldsymbol{B}_1$ parallel to $\boldsymbol{B}_0$ one obtains

$$\mu(B_0) = [1 - \mu'(B_0)H_0]B_1/H_1, \tag{4}$$

where $\mu'(B_0)$ is the derivative of μ with respect to B_0. Thus it is only for the case in which $\boldsymbol{B}_1$ is perpendicular to $\boldsymbol{B}_0$ that the ratio of $\boldsymbol{B}_1$ to $\boldsymbol{H}_1$ is equal to the magnetic permeability of the system.

In the first Section of this paper, a summary of the self-consistent field method for an electron gas in a uniform magnetic field is presented. In Section II, we apply the self-consistent field approach to the problem at hand, the calculation of the magnetic susceptibility. The Landau diamagnetism is obtained as the special case in which the perturbing field $\boldsymbol{B}_1$ is constant in space.

The final Section contains a discussion of the results of the present calculation and suggests some generalizations to which the self-consistent field approach should be applicable.

II. SELF-CONSISTENT FIELD APPROACH TO AN ELECTRON GAS IN A UNIFORM MAGNETIC FIELD

The general theory of the response of an electron gas in a uniform magnetic field of induction B_0 to an arbitrary electromagnetic disturbance that varies as $\exp(i\omega t - i\boldsymbol{q}\cdot\boldsymbol{r})$ has been presented in some detail in Ref. 4, so only a brief summary is given here. We consider an electron gas consisting of N electrons in a cubic box of side L in the presence of a magnetic field of induction B_0. Let $A(\boldsymbol{r},t)$ and $\phi(\boldsymbol{r},t)$ be the vector and scalar potential for the self-consistent field produced by the disturbance, and let $A_0 = (0, B_0x, 0)$ be the vector potential of the d.c. magnetic field B_0. We have chosen a cartesian coordinate system with the z-axis parallel to B_0.

The Hamiltonian for a single electron in the presence of the self-consistent field and of B_0 is

$$\mathscr{H} = \mathscr{H}_0 + \mathscr{H}_1, \tag{5}$$

where

$$\mathscr{H}_0 = \frac{1}{2m}\left(p - \frac{e}{c}A_0\right)^2, \tag{6}$$

and

$$\mathscr{H}_1 = -\frac{e}{c}(\boldsymbol{v}\cdot\boldsymbol{A} + \boldsymbol{A}\cdot\boldsymbol{v}) + e\phi. \tag{7}$$

The operators H_0 and

$$\boldsymbol{v} = \frac{1}{m}\left(p - \frac{e}{c}A_0\right)$$

are the Hamiltonian and velocity for an electron in the field B_0. In equation (7) we have dropped the quadratic terms in A, which is justified because we are interested in infinitesimally small A. The eigenfunctions and eigenvalues of $\mathscr{H}_0$ are given by(2)

$$|\nu\rangle = |nk_yk_z\rangle = L^{-1}\exp(ik_yy + ik_zz) \times u_n(x + \hbar k_y/m\omega_0), \tag{8}$$

$$E_\nu = E_n(k_z) = \hbar\omega_0(n+\tfrac{1}{2}) + \hbar^2k_z^2/2m. \tag{9}$$

The allowed values of the wave number k_y and k_z are obtained by imposing periodic boundary conditions. The quantum number n can be any non-negative integer and $u_n(x)$ is a normalized simple-harmonic oscillator wave-function for a particle of mass m and characteristic frequency $\omega_0 = eB_0/mc$.

The electron current density induced by the self-consistent field is calculated with the aid of the single particle density matrix. The single particle density matrix ρ satisfies the equation of motion

$$i\hbar\frac{\partial}{\partial t}\rho = [\mathscr{H}, \rho]. \tag{10}$$

We set $\rho = \rho_0 + \rho_1$ where ρ_1 is a small change in the single particle density matrix from its equilibrium value ρ_0 caused by the self-consistent field. By linearizing and taking off diagonal matrix elements of the equation of motion of ρ one obtains

$$\langle\nu|\rho_1|\nu'\rangle = [f_0(E_{\nu}') - f_0(E_\nu)](E_{\nu}' - E_\nu - \hbar\omega)^{-1} \times \langle\nu|\mathscr{H}_1|\nu'\rangle. \tag{11}$$

In writing down equation (11) we have assumed ρ_1 varies in time as $\exp(i\omega t)$ and used the condition

$$\rho_0|\nu\rangle = f_0(E_\nu)|\nu\rangle, \tag{12}$$

where $f_0(E)$ is the Fermi distribution function. The induced electron current density at a position $\boldsymbol{r}_0$ and time t is

$$\boldsymbol{j}(\boldsymbol{r}_0,t) = \sum_\nu \left\langle\nu\left|\frac{e}{2}\left(\boldsymbol{v} - \frac{e}{mc}\boldsymbol{A}\right)\delta(\boldsymbol{r}-\boldsymbol{r}_0) \times \rho + h.c.\right|\nu\right\rangle, \tag{13}$$

where $h.c.$ designates the Hermitian conjugate of the preceding operator. Taking the Fourier transform of equation (13) and making use of equation (11), one obtains for the Fourier components $\boldsymbol{j}(\boldsymbol{q},\omega)$ of the electron current density.

$$\boldsymbol{j}(\boldsymbol{q},\omega) = -\frac{\omega_p^2}{4\pi c}[(1+I)A(\boldsymbol{q},\omega) - K\phi(\boldsymbol{q},\omega)], \tag{14}$$

where $A(\boldsymbol{q},\omega)$ and $\phi(\boldsymbol{q},\omega)$ are the Fourier components of the electromagnetic potentials, and the tensor $\boldsymbol{I}$ and vector $\boldsymbol{K}$ are given by

$$\boldsymbol{I}(\boldsymbol{q},\omega) = \frac{m}{N} \sum_{\nu\nu'} [f_0(E_{\nu'}) - f_0(E_\nu)](E_{\nu'} - E_\nu - \hbar\omega)^{-1} \times \langle\nu'|\boldsymbol{V}(\boldsymbol{q})|\nu\rangle\langle\nu'|\boldsymbol{V}(\boldsymbol{q})|\nu\rangle,^* \tag{15}$$

and

$$\boldsymbol{K}(\boldsymbol{q},\omega) = \frac{mc}{N} \sum_{\nu\nu'} [f_0(E_{\nu'}) - f_0(E_\nu)](E_{\nu'} - E_\nu - \hbar\omega)^{-1} \times \langle\nu'|\boldsymbol{V}(\boldsymbol{q})|\nu\rangle\langle\nu'|\exp(i\boldsymbol{q}\cdot\boldsymbol{r})|\nu\rangle.^* \tag{16}$$

The operator $\boldsymbol{V}(\boldsymbol{q})$ is defined by

$$\boldsymbol{V}(\boldsymbol{q}) = \tfrac{1}{2}\exp(i\boldsymbol{q}\cdot\boldsymbol{r})\boldsymbol{\nu} + \tfrac{1}{2}\boldsymbol{\nu}\exp(i\boldsymbol{q}\cdot\boldsymbol{r}). \tag{17}$$

In Ref. 4 a more detailed treatment of the derivation of the induced current density is presented; in particular the gauge invariance of equation (14) is established. In the present work we are interested in the effect of a small magnetic field $\boldsymbol{B}_1$ perturbing the system. We can choose $\phi = 0$ and $\boldsymbol{A}$ independent of time, i.e. we consider a zero frequency disturbance. We can also choose $\boldsymbol{q}$, the wave vector of the disturbance to lie in the y–z plane with no loss of generality. The matrix elements of the components of $\boldsymbol{V}(\boldsymbol{q})$ can be evaluated directly; they are given by

$$\langle n'k_y'k_z'|V_x(\boldsymbol{q})|nk_yk_z\rangle = \delta(k_y',k_y+q_y) \times \delta(k_z',k_z+q_z)\, i \left(\frac{\hbar\omega_0}{2m}\right)^{1/2} X^{(-)}_{n'n}(q_y), \tag{18}$$

$$\langle n'k_y'k_z'|V_y(\boldsymbol{q})|nk_yk_z\rangle = \delta(k_y',k_y+q_y)\delta(k_z',k_z+q_z) \left[\frac{\hbar q_y}{2m} f_{n'n}(q_y) + \left(\frac{\hbar\omega_0}{2m}\right)^{1/2} X^{(+)}_{n'n}(q_y)\right] \tag{19}$$

and

$$\langle n'k_y'k_z'|V_z(\boldsymbol{q})|nk_yk_z\rangle = \delta(k_y',k_y+q_y)\delta(k_z',k_z+q_z) \times \frac{\hbar}{m}(k_z+q_z/2) f_{n'n}(q_y). \tag{20}$$

The symbol $\delta(k',k)$ is zero unless $k' = k$ in which case it is unity, and $f_{n'n}(q_y)$ may be expressed as

$$f_{n'n}(q_y) = i^{n-n'} \int_{-\infty}^{\infty} u_{n'}(x)\exp(iq_yx)u_n(x)\, dx. \tag{21}$$

The symbols $X^{(\pm)}_{n'n}(q_y)$ are given by

$$X^{(\pm)}_{n'n}(q_y) = (n+1)^{1/2} f_{n',n+1}(q_y) \pm n^{1/2} f_{n',n-1}(q_y) \tag{22}$$

III. DIAMAGNETISM OF A DEGENERATE ELECTRON GAS

Equation (14) allows us to calculate the current density induced by an arbitrary electromagnetic disturbance. Maxwell's equations give us the relation

$$\nabla\times(\boldsymbol{B}-\boldsymbol{H}) + \frac{1}{c}\frac{\partial}{\partial t}(\boldsymbol{D}-\boldsymbol{E}) = \frac{4\pi}{c}\boldsymbol{j}, \tag{23}$$

where $\boldsymbol{j}$ is the induced current density. We now choose $\phi = 0$, and $\boldsymbol{A}$ proportional to $\exp(-i\boldsymbol{q}\cdot\boldsymbol{r})$ but independent of time; therefore $\boldsymbol{D} = \boldsymbol{E} = 0$. The perturbing magnetic field $\boldsymbol{B}_1$ is simply $\nabla\times\boldsymbol{A} = -i\boldsymbol{q}\times\boldsymbol{A}$. For simplicity we shall investigate separately the two cases $\boldsymbol{q}$ parallel to $\boldsymbol{B}_0$, and $\boldsymbol{q}$ perpendicular to $\boldsymbol{B}_0$.

A. *q Parallel to the field* $\boldsymbol{B}_0$

In this situation $\boldsymbol{A} = \boldsymbol{A}\exp(-iq_zz)$ and the perturbing field $\boldsymbol{B}_1 = iq_z(A_y, -A_x, 0)$ is perpendicular to the applied field $\boldsymbol{B}_0$. We define the tensor $\boldsymbol{\nu}$ by the relation

$$\boldsymbol{H}_1 = \boldsymbol{\nu}\boldsymbol{B}_1. \tag{24}$$

Taking the curl of $(\boldsymbol{B}_1 - \boldsymbol{H}_1)$ and equating it to $4\pi/c$ times the induced current density gives the relations

$$\nu_{xy} = \nu_{yx} = 0, \tag{25}$$

$$\nu_{xx}(q_z) = 1 + \frac{\omega_p^2}{c^2q_z^2}(1+I_{yy}) = 1 + \frac{\omega_p^2}{c^2q_y^2}(1+I_{zz}), \tag{26}$$

$$\nu_{yy}(q_z) = 1 + \frac{\omega_p^2}{c^2q_z^2}(1+I_{xx}). \tag{27}$$

The conditions imposed by gauge invariance, which are established in Ref. 4, are quite useful. One of these conditions, which has been used in writing down equations (25)–(27), is

$$-\boldsymbol{q} = \boldsymbol{I}\cdot\boldsymbol{q}. \tag{28}$$

The only non-vanishing components of the tensor $\boldsymbol{I}$ (in the limit of zero frequency considered in this work) are the diagonal elements and $I_{yz} = I_{zy}$.

With the aid of equation (28) I_{yy} and I_{yz} can be expressed in terms of I_{zz}, so that we can consider the tensor I to have only two independent elements I_{xx} and I_{zz}:

$$I_{yz} = I_{zy} = -(1+I_{zz})q_z/q_y, \qquad (29)$$

$$1+I_{yy} = (1+I_{zz})q_z^2/q_y^2. \qquad (30)$$

B. *q Perpendicular to the field B_0*

In this case q is in the x–y plane, and as we have stated previously we may choose the y-axis to lie in the q direction with no loss of generality. The vector potential A is then of the form $A\exp(-iq_y y)$ and the perturbing field $B_1 = iq_y(-A_z, 0, A_x)$. The use of equations (24), (23) and (14) then gives the result

$$\nu_{xz} = \nu_{zx} = 0, \qquad (31)$$

$$\nu_{xx}(q_y) = 1+\frac{\omega_p^2}{c^2q_y^2}(1+I_{zz}), \qquad (32)$$

$$\nu_{zz}(q_y) = 1+\frac{\omega_p^2}{c^2q_y^2}(1+I_{xx}). \qquad (33)$$

It should be emphasized that in equations (25)–(27), the components ν are of functions of q_z, while in equations (31)–(33) they are functions of q_y. In the former case we are interested in I_{xx} and I_{yy} in the limit that q_y tends to zero; in the latter we must know I_{xx} and I_{zz} in the limit as q_z approaches zero. ν_{xx}, ν_{yy} and ν_{zz} represent the ratio of the infinitesimal magnetic field strength H_1 to the magnetic induction B_1. From equations (3) and (4) it is clear that in the limit that B_1 is independent of the spacial coordinates (i.e. $q_y = q_z = 0$), ν_{xx} and ν_{yy} must reduce to usual Landau diamagnetism which displays De Haas–van Alphen oscillations, and ν_{zz} is related to the magnetic permeability and its derivative with respect to magnetic field strength.

For zero temperature the two independent elements I_{xx} and I_{zz} of the tensor I can be expressed as

$$I_{xx}(q_y,q_z) = -\frac{1}{N}\sum_{nk_yk_z} f_0[E_n(k_z)] \sum_{n'=0}^{\infty} X_{n'n}^{(-)2}(q_y)$$
$$\times\left[n'-n+\frac{\hbar q_z}{m\omega_0}(k_z+q_z/2)\right]^{-1}, \qquad (34)$$

and

$$I_{zz}(q_y,q_z) = \frac{-2\hbar}{m\omega_0 N}\sum_{nk_yk_z} f_0[E_n(k_z)]\sum_{n'=0}^{\infty} f_{n'n}^2(q_y)$$
$$\times (k_z+q_z/2)^2\left[n'-n+\frac{\hbar q_z}{m\omega_0}(k_z+q_z/2)\right]^{-1}. \qquad (35)$$

Using equation (21) $f_{n'n}(q_y)$ can easily be expanded in powers of q_y

$$f_{n'n}(q_y) = \sum_{r=0}^{\infty} i^{n-n'+r}\, q_y^r\langle n'|x^r|n\rangle/r! \qquad (36)$$

where $\langle n'|x^r|n\rangle$ is the matrix element of the rth power of the coordinate x between simple harmonic oscillator states n' and n. This matrix element can be evaluated in a straightforward way by expressing x in terms of creation and annihilation operators, a^+ and a, for a simple harmonic oscillator:

$$x = \left(\frac{\hbar}{2m\omega_0}\right)^{1/2}(a^+ + a). \qquad (37)$$

Equations (34) and (35) can then be expanded to any desired power of q_y and q_z. The expansion is convergent provided qv_0, the product of the vector q and the Fermi velocity v_0, is smaller than the cyclotron frequency ω_0. To order q^2 we obtain

$$\nu_{xx}(q_z) = \nu_{yy}(q_z) = 1+\frac{\omega_p^2}{mc^2\omega_0^2}\Bigg\{\langle\epsilon_{xy}\rangle - 2\langle\epsilon_z\rangle$$
$$+\frac{q_z^2}{m\omega_0^2}\left(6\langle\epsilon_{xy}\epsilon_z\rangle - 4\langle\epsilon_z^2\rangle - \frac{\hbar^2\omega_0^2}{4}\right)\Bigg\} \qquad (38)$$

$$\nu_{xx}(q_y) = 1+\frac{\omega_p^2}{mc^2\omega_0^2}\Bigg\{\langle\epsilon_{xy}\rangle - 2\langle\epsilon_z\rangle + \frac{q_y^2}{2m\omega_0^2}$$
$$\times\left(3\langle\epsilon_{xy}\epsilon_z\rangle - \tfrac{3}{4}\langle\epsilon_{xy}^2\rangle - \frac{\hbar^2\omega_0^2}{16}\right)\Bigg\}. \qquad (39)$$

The expression for ν_{zz} is found to diverge. The significance of this result will be discussed later. In equations (38) and (39) $\epsilon_{xy} = \hbar\omega_0(n+\frac{1}{2})$, $\epsilon_z = \hbar^2k_z^2/2m$ and the symbol $\langle\epsilon\rangle$ means average value of ϵ; for example

$$\langle\epsilon_{xy}\epsilon_z\rangle = \frac{1}{N}\sum_{nk_yk_z} f_0[E_n(k_z)]\hbar\omega_0(n+\tfrac{1}{2})\hbar^2k_z^2/2m. \qquad (40)$$

In the limit that q_y or q_z approaches zero, equations (38) and (39) yield the usual Landau diamagnetism as expected.

$$\mu^{-1}(B_0) = 1+\frac{\omega_p^2}{mc^2\omega_0^2}(\langle\epsilon_{xy}\rangle-2\langle\epsilon_z\rangle). \quad (41)$$

The functions $\langle\epsilon_{xy}\rangle$ and $\langle\epsilon_z\rangle$ have been evaluated in the case of a free electron gas by QUINN and RODRIGUEZ;(5) using these expressions the oscillatory behavior of $\mu^{-1}(B_0)$ is apparent

$$\mu^{-1}(B_0) = 1+\frac{3\pi\rho\omega_p^2}{2m\omega_0^2c^2}\left[\left(\frac{\hbar\omega_0}{2\rho}\right)^{1/2}\frac{kT}{\rho}\sum_{n=1}^{\infty}\frac{(-1)^n}{n^{1/2}}\right.$$
$$\left.\times\frac{\sin(2\pi n\rho/\hbar\omega_0-\pi/4)}{\sinh(2\pi^2nkT/\hbar\omega_0)}+\frac{1}{3\pi}\left(\frac{\hbar\omega_0}{2\rho}\right)^2\right], \quad (42)$$

where ρ is the Fermi energy of the free electron gas.(6) The functions $\langle\epsilon_{xy}\epsilon_z\rangle$, $\langle\epsilon_{xy}^2\rangle$ and $\langle\epsilon_z^2\rangle$ can also be expressed in oscillatory series by using the Poisson sum formula.(7) The results derived here are valid only for zero temperature, although we have included the temperature dependence of $\langle\epsilon_{xy}\rangle$ and $\langle\epsilon_z\rangle$ in equation (42).

The divergence of ν_{zz} is apparently related to the derivative of the oscillatory series with respect to magnetic field strength. Evaluating equation (42) at zero temperature and investigating the series obtained by differentiating term by term, one finds a divergent result, implying that $\mu^{-1}(B_0)$ is not a continuous function of B_0.

IV. CONCLUSION

The self-consistent field approach is a very useful method since it can be applied to a wide variety of problems which involve the response of an electron gas to an arbitrary electromagnetic disturbance. In the present work we have shown how this method can be applied to the diamagnetism of a degenerate electron gas. The response of the electron gas to a small perturbing magnetic field B_1 is calculated by the self-consistent field approach. In the special case that B_1 is independent of the spatial coordinates we obtain the Landau result for the oscillatory susceptibility. In addition we obtain the leading terms in q when the field B_1 varies in space as $\exp(-i\boldsymbol{q}\cdot\boldsymbol{r})$. As far as the author is aware this is a new result.

It is quite straightforward to generalize the problem to a multicomponent plasma since the induced current density is simply the sum of the induced current densities of each component. The resulting susceptibility contains a sum of terms, one for each component of the plasma, like the second term on the right hand side of equation (38). One should also be able to take into account the effect of a finite collision time for the electrons by introducing an appropriate small imaginary part in the energy denominator of equation (15). One would hope that such a treatment would reproduce the results of DINGLE(8) for the effect of collisions on the magnetic susceptibility.

REFERENCES

1. SCHOENBERG D., *Phil. Trans.* **A245**, 1 (1952).
2. LANDAU L., *Z. Phys.* **64**, 629 (1930).
3. PEIERLS R., *Z. Phys.* **80**, 763; **81**, 186 (1933).
4. QUINN J. J. and RODRIQUEZ S., *Phys. Rev.* (to be published).
5. QUINN J. J. and RODRIGUEZ S., *Phys. Rev.* (to be published).
6. This is the usual result for the oscillatory susceptibility; see for example WILSON A. H., *The Theory of Metals*, 2nd ed. p. 171. University Press, Cambridge (1958).
7. See for example TITCHMARSH E. C., *Introduction to the Theory of Fourier Integrals*, p. 443. University Press, Oxford (1937).
8. DINGLE R. B., *Proc. Roy. Soc.* **A211**, 517 (1952).

J. Phys. Chem. Solids Pergamon Press 1963. Vol. 24, pp. 939–495. Printed in Great Britain.

NUCLEAR MAGNETIC RESONANCE IN METAL HEXABORIDES

EDWARD J. McNIFF, Jr. and SIDNEY SHAPIRO

Arthur D. Little, Inc., Cambridge, Massachusetts

(*Received* 31 *January* 1963)

Abstract—n.m.r. investigations of a number of metal hexaborides were carried out at room temperature and a field of 5800 G. Both positive and negative Knight shifts were observed for the B^{11} resonance. Magnetic polarization of the conduction electrons by the metal ion cores provides a basic explanation for the signs and magnitudes of the shifts in the paramagnetic hexaborides. In LaB_6, CaB_6, and EuB_6 the B^{11} resonance frequency was observed to depend upon composition. These shifts were determined to be associated with alterations of the conduction electron density. However, the large diamagnetic shifts observed in metal-deficient samples of CaB_6 and EuB_6 could not be explained on the basis of any of the mechanisms suggested.

I. INTRODUCTION

METAL hexaborides have been the subject of numerous researches since the synthesis of CaB_6 by MOISSAN and WILLIAMS(1) in 1897. This continuing interest is due, in part, to the simple crystal structure of the hexaborides(2–4) which can be considered as formed of two interpenetrating simple cubic lattices, one composed of metal atoms, the other of octahedra of boron atoms. Thus the space lattice is body-centered cubic with one MB_6 group per unit cell (see Fig. 1), where M represents any one of a large number of alkaline earth or rare earth atoms.

The boron bonding in the hexaborides has been studied theoretically by several authors.(5–8) The starting point of all these studies is the treatment of the lattice as composed of linked boron octahedra with ionized metal atoms in the interstices. The role of the metal atoms is to provide the additional electrons necessary to form those boron–boron bonds which stabilize the framework of linked octahedra.

In the work of LONGUET-HIGGINS and ROBERTS,(5) electron energy bands arising from 2*s* and 2*p* boron atomic orbitals are calculated in a tight-binding approximation. It is shown that an energy gap exists in this band structure and that the valence band is filled by the electrons available from the boron atoms together with two electrons from each metal ion. Any additional electrons go into a conduction band. Thus the divalent alkaline earth metals are predicted to form insulating or semiconducting hexaborides, while the predominantly trivalent rare earth metals are predicted to form metallic hexaborides with essentially one conduction electron per metal atom.

The work of FLODMARK,(7,8) although differing in some details of the calculation, generally confirms this picture, provided only the 2*s* and 2*p*

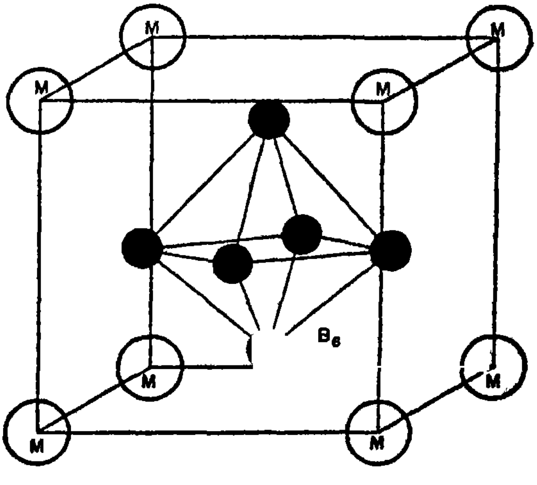

FIG. 1. Metal hexaboride crystal structure.

boron orbitals are included. He has, however, extended his analysis to include the effects of 3*s*, 3*p*, and 3*d* boron orbitals. The result is that bands arising from these orbitals overlap the bands arising from the 2*s* and 2*p* orbitals in such a way as to fill up the gap. Thus Flodmark predicts all hexaborides to be metallic.

Studies of the resistivity and Hall effect,(9) magnetic susceptibility,(10–12) and thermionic emission(12,13) have confirmed the metallic nature of the hexaborides of trivalent metals. However, work on the hexaborides of divalent metals(3,12) has been much more limited and is not conclusive as to the nature of the conductivity. It was the object of the present work to gain more knowledge of the electron energy band structure of the hexaborides, by investigation of electron-nucleus interactions via studies of nuclear magnetic resonance (n.m.r.) behavior.

The n.m.r. technique has several advantages in a study of the hexaborides. Significant information can be obtained even in the presence of considerable amounts of impurity. The B^{11} resonance is reasonably strong and readily studied. In the hexaborides, the boron framework maintains its structure not only for various metal substitutions but also for a range of nonstoichiometric, metal-deficient compositions. Further, the lattice constant is only slightly different for any two members of the series (see Table 1). Thus the boron resonance frequency should be insensitive to changes that are not accompanied by modification or re-arrangements in the occupation of the available electron energy bands. Changes in the number of conduction electrons should result in a change in the B^{11} KNIGHT shift.(14)

Table 1

Hexaboride	a_0 (Å)
CaB_6	4·145(4)
YB_6	4·113(4)
LaB_6	4·156(4)
CeB_6	4·141(4)
NdB_6	4·128(4)
EuB_6	4·163(12)
GdB_6	4·112(4)
YbB_6	4·144(4)

The situation is complicated by the quadrupolar effects associated with the spin 3/2 B^{11} nucleus and the magnetic interactions present for most of the rare earth hexaborides. The latter effects, studied extensively by GOSSARD and JACCARINO,(15) were not of primary interest in the present investigation. The quadrupolar effects, studied by KUSHIDA, LAURANCE and SILVER,(16) were accounted for by a procedure to be described later.

Most attention was concentrated on the hexaborides of La, Ca, and Eu and on the effect of variations in stoichiometry on the B^{11} Knight shift in those compounds. The B^{11} Knight shift in the hexaborides was found to depend on the metal atom, and for a given metal atom, on the stoichiometry. Where the data overlap, the results of this work agree with those of Gossard and Jaccarino in both the magnitude and sign of the Knight shift. The hexaborides exhibit shifts which are generally small. However, a large dependence on stoichiometry is found in several of them, and, in the case of the hexaborides of divalent metals, relatively large negative shifts are encountered.

Following Sections devoted to experimental details, explanation of data analysis, and presentation of results, various possible explanations for the behavior of the hexaborides are discussed with particular attention to their relationship to the theories of Longuet-Higgins and Roberts, and of Flodmark.

II. EXPERIMENTAL

The n.m.r. spectra of powder samples of a number of hexaborides were observed at room temperature with a Pound–Watkins spectrometer operating at a fixed radio frequency of 7·911 Mc/s. A field-modulation lock-in detection scheme was employed, the derivative of the absorption being recorded on a strip chart recorder. Magnetic field markers were entered manually by noting the proton resonance in a sample of mineral oil mounted in close proximity to the hexaboride sample. The proton resonance was observed with a circuit similar to one described by KNIGHT,(17) and the resonant frequency measured with a BC-221-AK frequency meter.

Both proton and hexaboride sample r.f. coils were mounted in a jig between the pole faces of a 6-in. Varian magnet to assure positional reproducibility. Data were found to be reproducible whether samples were reinserted after a day or several weeks. The proton and hexaboride coils could also be interchanged in the jig without change in the data.

Typical derivative traces are shown in Fig. 2. The top trace is the derivative of the B^{11} resonance observed in crystalline boron, and is typical of the resonances observed in the diamagnetic hexaborides. The center trace is the derivative of B^{11} in NdB_6; there is some evidence of quadrupole asymmetry in the line. The bottom trace is the B^{11} derivative in GdB_6, showing strong quadrupole asymmetry and magnetic broadening.

Analysis of these experimental traces was complicated by the width and asymmetry of the lines. The asymmetry was apparently not due to mechanical strains within the crystallites since annealing produced no detectable change in resonance characteristics. The predominant causes appear to be quadrupole coupling to the spin 3/2 B^{11} nucleus, and for some samples, magnetic interactions.

A schematic representation of the absorption in a quadrupole broadened line is shown in

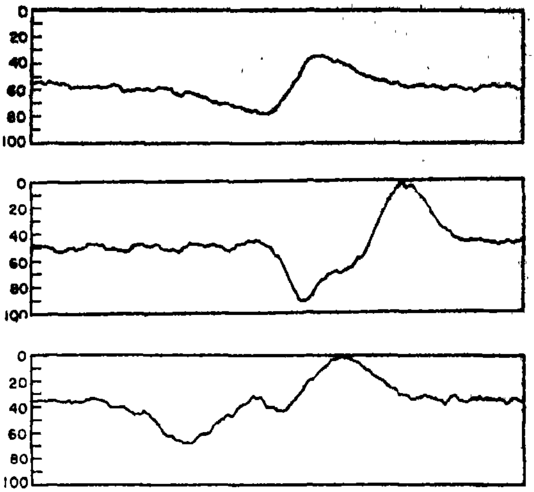

FIG. 2. B^{11} nuclear magnetic resonance absorption derivatives in boron (top), NdB_6 (center), and GdB_6 (bottom).

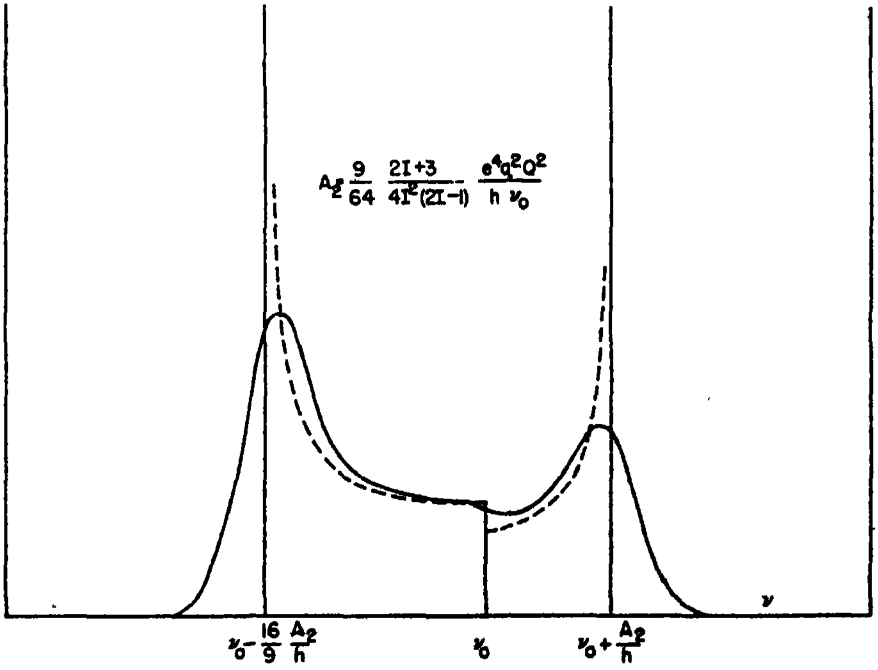

FIG. 3. Line shape of central component ($m = 1/2 \leftrightarrow -1/2$) showing asymmetric broadening produced by second-order quadrupole interaction.

Fig. 3. The unshifted resonant frequency, ν_0, should be calculable from the separation of the absorption peaks(18) given by

$$\Delta H = 25A_2/9 \tag{1}$$

where
$$A_2 = \frac{9}{64}\frac{2I+3}{4I^2(2I-1)}\frac{(e^2qQ)^2}{h\nu_0} \tag{2}$$

where the symbols have their usual meaning. It is apparent from Fig. 2, however, that in the hexaborides the derivative zero-crossings, corresponding to the absorption peaks, were not well resolved, making the application of equation (1) and (2) of dubious accuracy. To obtain the desired degree of accuracy, the method used by Gossard and Jaccarino(15) was adopted. This method involves a double integration of the derivative curves in order to locate the center of gravity of the line. The correction, Δ, given by Saha and Das(19)

$$\Delta = 8A/15h \tag{3}$$

is then applied to the center of gravity. Integration was necessary only for the asymmetric lines, for the diamagnetic samples the asymmetry was negligible and the correction was applied directly to the derivative zero-crossing.

III. SAMPLE PREPARATION

Most of the samples were obtained commercially* as powders, then ground further and passed through a 325-mesh screen. X-ray exmination indicated the presence of only the hexaboride phase for all the samples except yttrium hexaboride, which contained a small admixture of the tetraboride.

Several samples of nonstoichiometric composition were manufactured in our own laboratory. Ca_xB_6 was formed from Ca metal and high purity boron. X-ray examination detected the presence of only the hexaboride phase. An approximate composition was determined by chemical analysis, but this technique is not sensitive enough to detect small composition changes. Similarly, X-ray examination, dependent on changes in lattice parameter to detect changes in composition, cannot readily resolve the small differences produced in the stable hexaboride framework. There is, therefore, a limitation on the accuracy of absolute composition of this compound. However, several of the CaB_6 samples had compositions which varied enough to be detectable by chemical analysis, so that the sense, if not the absolute magnitude, of the composition changes was known.

LaB_6 has no metal-rich composition and changes color as it becomes progressively more metal deficient.(20) Further, the La system is more amenable to chemical analysis than the Ca or Eu systems, so that such analyses can be carried out and result in significant composition data. The sense and a good estimate of the range of composition are therefore available. Reacting stoichiometric LaB_6 with excess boron produced a compound $La_{0.77}B_6$, which is the extreme of the metal-deficient range.(20)

Reacting stoichiometric EuB_6 with excess boron produced what was assumed to be metal-deficient material, although chemical analysis could detect no difference. There was, however, a resonance shift in the direction expected for a metal-deficient sample.

IV. RESULTS

A comparison of the B^{11} Knight shifts observed for various compounds of stoichiometric composition referenced to B^{11} in a solution of sodium metaborate is shown in Fig. 4. (An alternative reference is B^{11} in triethylborate,(16) which produces a strong, narrow resonance at slightly higher field.) The results for the paramagnetic, trivalent-metal hexaborides agree with the work of Gossard and Jaccarino who propose the mechanism of conduction electron polarization by metal ion cores. The results for the diamagnetic hexaborides (LaB_6 and CaB_6) and the divalent metal paramagnetic hexaboride (EuB_6) must be treated separately, and will be considered in the following Section.

Table 2 summarizes the investigations of resonance shift as a function of composition in LaB_6, CaB_6, and Eub_6. Each sample was subjected to X-ray examination, chemical analysis, and wherever possible, metallographic examination, to insure the existence of only the hexaboride phase. The data indicates a direct correspondence between metal content and B^{11} shift, the higher

---

* Suppliers were American Potash and Chemical Corp. and Norton Company.

Table 2. Knight shifts in hexaborides of various compositions

Sample	Material	Preparation	Shift (%)
10681–15/20	CaB_6	Commercial CaB_6	−0·291
10681–15	CaB_6	10681–15/20 reacted with calcium	+0·011
10681–25	CaB_6	10681–15 reacted with boron	−0·069
10681–16	EuB_6	Commercial EuB_6	−0·059
10681–21	EuB_6	10681–16 reacted with boron	−0·133
10488–48	LaB_6	Commercial LaB_6	+0·031
10681–9	LaB_6	10488–48 reacted with boron	+0·018

metal content (greater conduction electron density) producing more paramagnetic shifts in each case.

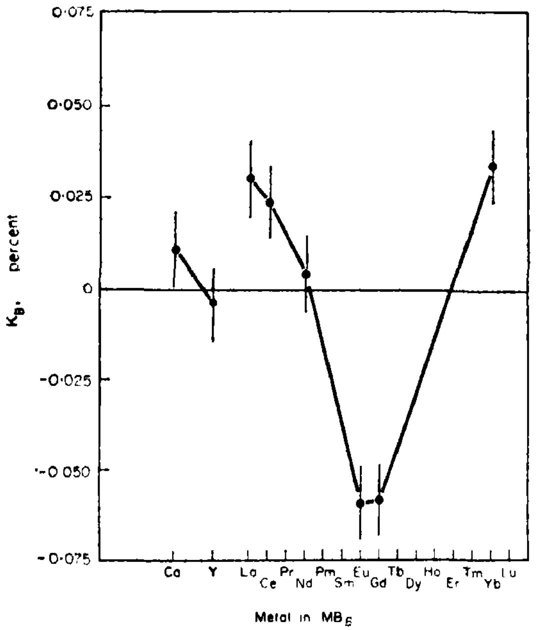

FIG. 4. Knight shifts in MB_6 compounds of stoichiometric composition.

In the course of the hexaboride work, we also investigated several other boron systems. These were the transition metal diborides, and samples of crystalline boron. In all of these materials, the observed shifts were extremely small, of the order of the shifts observed in the diamagnetic hexaborides. The latter thus appear to be typical of boron systems. Also, the diborides appear to show composition dependent shifts, similar to those observed in the hexaborides, but with a much smaller range.

V. DISCUSSION

The Knight shift dependence observed here is in sharp contrast to previous work involving variation of the conduction electron density. Semiconductors(21–24) exhibit a major change in line width and intensity, but little, if any, change in Knight shift with doping. NARATH and WALLACE(25) observe large (approximately 0·15 per cent) negative shifts for W^{183} in cubic sodium–tungsten bronzes such that larger diamagnetic shifts correspond to higher conduction electron density. The hexaboride data shown in Table 2, however, indicate larger diamagnetic shifts correspond to lower conduction electron density. JONES *et al.*(26) observe no paramagnetic Knight shifts for Na^{23} in the same compound. In the lithium–vanadium bronze system(27) only very small (approximately 0·002 per cent) diamagnetic shifts are observed for Li^7.

An approximate calculation of the Knight shift of B^{11} in LaB_6, based on a single *s*-character conduction electron indicates $\Delta H/H \sim 0{\cdot}1$ per cent, which is considerably larger than the observed value. This would indicate that either the conduction electrons have little *s*-character, or there is a diamagnetic contribution cancelling their paramagnetic effects, or both. One obvious contribution is the diamagnetic shielding due to other atomic electrons. However, for boron this correction, approximated by the free atom value of 0·02 per cent, is too small to be a major factor although it may contribute to the observed shifts.

Longuet-Higgins and Roberts, Flodmark, and Yamazaki attribute varying degrees of *s*-character to the conduction electrons, all considerably less than 100 per cent. Using the Longuet-Higgins picture of one conduction electron per LaB_6 cell, and assuming 35 per cent *s*-character, leads to a shielding-corrected resonance shift of approximately +0·03 per cent (experimental value +0·031 per cent, sample 10488–48). A change of 23 per cent in electron density ($LaB_6 \rightarrow La_{0.77}B_6$) reduces the Knight shift to +0·023 per cent (experimental value +0·018 per cent, sample 10681–9). In this picture, however, CaB_6 has no conduction electrons, so it is hard to understand the positive shift observed for stoichiometric material.

When the Flodmark picture is used with the statistical value of 1·66 electrons as the number necessary to satisfy the boron bonds,(12) then LaB_6 has 1·34 conduction electrons and CaB_6 has 0·34. Now in order to arrive at a corrected resonance shift of approximately +0·03 per cent for LaB_6 and +0·023 per cent for $La_{0.77}B_6$, approximately 25 per cent *s*-character must be assumed. On this basis, the predicted shift in CaB_6 is +0·008 per cent (experimental value +0·011 per cent, sample 10681–15). While the agreement is not always extremely good, there is a reasonable correspondence between shift and electron density, indicating that the diamagnetic hexaborides, containing either divalent or trivalent metals, do approximate behavior predictable by the Flodmark model, at least over limited ranges of composition.

CaB_6 samples having maximum metal content (e.g., sample 10681–15) showed a relatively narrow, intense B^{11} resonance. As in the LaB_6 system, this maximum metal content should correspond to a stoichiometric composition. When an attempt was made to investigate metal-deficient CaB_6 (samples 10681–15/20 and 10681–25), it was observed that the line width increased sharply, with a corresponding decrease in intensity, indicative of an increased quadrupolar interaction, probably caused by a destruction of some of the boron symmetry. (This broadening was not observed in any of the other materials, either paramagnetic or diamagnetic, possibly because the composition differences achieved were not great enough.) The relative instability of CaB_6 is consistent with a lower conduction electron density, which presumably allows the escape of fewer metal atoms before the boron structure deteriorates. Moreover, the lower boiling point of Ca (1400°C) compared to La (4515°C) and Eu (1800°C) indicates that evaporation of metal from the CaB_6 complex should be more easily accomplished.

Part of the negative shifts in these samples can be attributed to the increased quadrupole interaction, but after correcting for an assumed upper limit for the interaction, there still remains a substantial negative shift (approx. −0·20 per cent) which must be explained.

There are several mechanisms which can produce such large diamagnetic shifts. Those, such as exchange polarization(25,28) and conduction electron polarization,(15) which are magnetic in origin, are not relevant to the diamagnetic CaB_6 system. Diamagnetic "ring currents"(28) have been suggested to explain in part the Knight shift results in diborides.(29) The hexaborides do not possess the closed ring structure of the diborides, and an estimate of the effects off "ring currents" within or between the boron octahedra leads to corrections far too small to be the significant source of diamagnetism. We have had a similar lack of success in applying any of the suggested mechanisms to the CaB_6 system and arriving at shifts of the order of those observed.

The results for EuB_6 are complicated by magnetic interactions and the divalent character of the Eu ion. This divalent character, suggested by the lattice parameter(20) was confirmed by observation of the electron spin resonance arising from the $4f^7$ electron configuration.(30–32) This resonance was observed at room temperature and 77°K, but was not observable at 4·2°K, indicating a transition, probably antiferromagnetic, somewhat above 4·2°K. (For GdB_6(33) $T_N = 13$°K).

The electron density of EuB_6 is therefore similar to that of CaB_6 while the magnetic interactions should be similar to those in GdB_6. Subtraction of the GdB_6 results from those of EuB_6 indicates the effects of electron density variations alone. The composition dependence in EuB_6 is considerably greater than in LaB_6, while the fact that it is not as large as in CaB_6 may be due to differences in composition range. Presumably, the same mechanism responsible for the diamagnetic shifts in CaB_6 will explain those in EuB_6.

VI. CONCLUSION

The variation of conduction electron density appears to be the basis for all the composition dependent Knight shifts. In each case, decreased density (lower metal content) produced shifts in the diamagnetic direction. Unfortunately, the size of the shifts encountered and the limitations on accuracy preclude detailed examination of the data with a view toward developing a consistent picture of the hexaboride energy band structure and its variation. In particular, the temperature dependence of the Knight shift, which has proved to be of great value in energy band structure determination(34) would not be obtainable with sufficient accuracy to justify the effort.

The magnetic state of the material appears to be a more important parameter than the valence state of the metal ion in determining the resonance shift. However, the latter appears to be instrumental in determining the effect of composition change on the shift. In this light, it is difficult to substantiate either the theory of Flodmark or of Longuet-Higgins and Roberts, although our results seem somewhat more consistent with the former. The deterioration of the B^{11} signal in metal-deficient CaB_6 and the masking effects of the magnetic interactions make more detailed comparison difficult.

Acknowledgements—We wish to express our appreciation to G. Feick and G. Clay who expended great effort in the preparation of our samples, and to A. Gossard for an enlightening discussion.

REFERENCES

1. Moissan H. and Williams P., *C.R. Acad. Sci. Paris* **125**, 629 (1897).
2. Kiessling R., *Acta Chem. Scand.* **4**, 209 (1950).
3. v. Stackelberg M. and Neumann F., *Z. phys. Chem.* **B19**, 314 (1932).
4. Blum P. and Bertaut F., *Acta Cryst.* **7**, 81 (1954).
5. Longuet-Higgins H. C. and Roberts M. de V., *Proc. Roy. Soc.* **A224**, 336 (1954).
6. Yamazaki, M., *J. phys. Soc. Japan* **12**, 1 (1957).
7. Flodmark S., *Ark. Fys.* **9**, 357 (1955).
8. Flodmark S., *Ark. Fys.* **14**, 513 (1959).
9. Lafferty J. M., *J. appl. Phys.* **22**, 299 (1951).
10. Klemm W., Schüth W. and v. Stackelberg M., *Z. phys. Chem.* **B19**, 321 (1932).
11. Benoit R. and Blum P., *C.R. Acad. Sci. Paris* **234**, 2428 (1952).
12. Samsonev G. V., *Usp. khim.* **28**, 189 (1959). This review article contains extensive references, particularly to the Russian literature. A translation into English is available from Office of Technical Services, U.S. Department of Commerce, Washington 25, D.C.
13. Kmetko E. *Phys. Rev.* **116**, 895 (1959).
14. Knight W. D., *Solid State Physics*, Vol. 2 (edited by Seitz F., and Turnbull D.) p. 93. Academic Press, New York (1956).
15. Gossard A. and Jaccarino V., *Proc. phys. Soc., Lond.* **80**, 877 (1962).
16. Kushida T., Laurance N. and Silver A. H., *Bull. Amer. phys. Soc.* **7**, 226 (1962).
17. Knight W. D., *Rev. sci. Instrum.* **32**, 95 (1961).
18. Cohen M. H. and Reif F., *Solid State Physics*, Vol. 5 (edited by Seitz F. and Turnbull D.) p. 321. Academic Press, New York (1957).
19. Saha A. K. and Das T. P., *Theory and Applications of Nuclear Induction*, p. 227. Saha Institute of Nuclear Physics, Calcutta (1957).
20. Johnson R. W. and Daane A. H., *J. Amer. chem. Soc.* **65**, 909 (1961).
21. Weinberg I. and Calloway J., *Nuovo Cim.* **24**, 190 (1962).
22. Rhoderick E. H., *Phil. Mag.* **3**, 545 (1958).
23. Oliver D. J., *J. Phys. Chem. Solids* **11**, 257 (1959).
24. Weinberg I., *J. chem. Phys.* **37**, 1571 (1962).
25. Narath A. and Wallace D., *Phys. Rev.* **127**, 724 (1962).
26. Jones W. H., Jr., Garbaty E. A. and Barnes R. G., *J. chem. Phys.* **36**, 494 (1962).
27. Gendell J., Cotts R. M. and Sienko M. J., *J. chem. Phys.* **37**, 220 (1962).
28. Pople J. A., *J. chem. Phys.* **24**, 1111 (1956).
29. Silver A. H. and Kushida T., *Bull. Amer. phys. Soc.* **7**, 226 (1962); Silver A. H. and Kushida T., *J. chem. Phys.* **38**, 865 (1963).
30. Coles B. R., Cole T., Lambe J. and Laurance N., *Proc. phys. Soc., Lond.* **79**, 84 (1962).
31. Kip A. F., Kittel C., Portis A. M., Barton R. and Spedding F. H., *Phys. Rev.* **89**, 518 (1953).
32. Peter M. and Matthias B., *Phys. Rev. Letters* **4**, 449 (1960).
33. Coles B. R. and Griffiths D., *Proc. phys. Soc., Lond.* **77**, 217 (1961).
34. Clogston A. M. and Jaccarino V., *Phys. Rev.* **121**, 1357 (1961).

J. Phys. Chem. Solids Pergamon Press 1963. Vol. 24, pp. 947–951. Printed in Great Britain.

DEPENDENCE OF MAGNETOCRYSTALLINE ANISOTROPY ON FIELD STRENGTH

J. VEERMAN, J. J. M. FRANSE and G. W. RATHENAU

Natuurkundig Laboratorium der Universiteit van Amsterdam, Amsterdam, The Netherlands

(*Received* 4 *February* 1963)

Abstract—The constant K_1 of magnetocrystalline anisotropy of nickel depends linearly on magnetic field strength. At 30°C it is found: $(1/K_1)(\mathrm{d}K_1/\mathrm{d}H) = (0{\cdot}53 \pm 0{\cdot}05)$ per cent/kOe, at least up to fields of 33 kOe. It is shown that this effect is an intrinsic property of the pure crystal. It is found that within the experimental errors K_1 depends only on the intrinsic magnetization when varying the two independent variables field strength and temperature, at least at room temperature. The field dependence of the magnetocrystalline anisotropy is connected with the anisotropy of the intrinsic magnetization, of which a calculation could be made. The case of iron is also discussed.

1. INTRODUCTION

By the magnetocrystalline anisotropy energy $E_A(\boldsymbol{\alpha})$ for field strength H we mean: the work per unit volume which must be done by the (mechanical and magnetic) torque forces to rotate the magnetization M from a reference direction to some direction $\boldsymbol{\alpha}$ with respect to the crystal while the magnitude of the magnetic field H remains constant. For cubic crystals like those of iron and nickel we may write this energy as a power series:

$$E_A(\boldsymbol{\alpha}) = K_0 + K_1(\alpha_2^2\alpha_3^2 + \alpha_3^2\alpha_1^2 + \alpha_1^2\alpha_2^2) + K_2\alpha_1^2\alpha_2^2\alpha_3^2 + \ldots,$$

where the components α_i are taken with respect to the crystal axes. In the case that M is confined to the (001) plane, as in our measurements, the part containing the angular dependence reduces to: $E_A(\theta) = -K_1/8 \cos 4\theta + \ldots$, where θ is the angle between M and the X-axis (Fig. 1). The torque per unit volume due to the anisotropy, which is exerted on the crystal by the magnetic field, can be shown to be given by:

$$L(\theta) = -\,\mathrm{d}E_A/\mathrm{d}\theta = -(K_1/2)\sin 4\theta + \ldots.$$

It is generally assumed, as concluded from experiments, that the coefficients K_i are independent of H. So the same must hold for the function $L(\theta)$. The experimental finding that for smaller fields the $L(\theta)$ curve is somewhat lower and for increasing H seems to tend to a limit is ascribed to incomplete saturation of the magnetization in that region of H. The "true" value

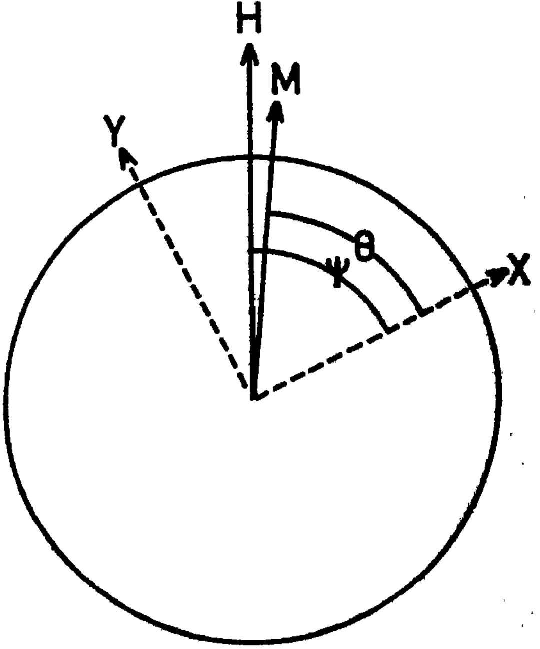

Fig. 1. Definition of the angles when measuring the torque, due to magnetic anisotropy, acting on a single crystal. The field lies in a plane containing two cubic axes *x* and *y*.

of K_1 is found by extrapolation of the "effective" values of K_1 to infinite field.(2).

2. MEASUREMENTS AND RESULT FOR NICKEL

Investigating the anisotropy of a nickel single crystal this $L(\theta)$ curve was measured. It must be remembered that the direct result of the measurement is the $L(\Psi)$ curve, where Ψ is the angle between the magnetic field H and the X-axis of the crystal. But from this curve $L(\theta)$ is easily found by calculating θ for each Ψ by means of the relation $L = -HM \sin(\Psi-\theta)$. We found that $L(\theta)$ has nearly a $\sin 4\theta$ shape: the values of K_1 computed from the slopes of L for the [100] and [110] direction, where $L = 0$, (acting as if the curve were a pure sine) differ by (0 ± 2) per cent and (-3 ± 2) per cent respectively from the one according to the peak of L. This measurement was done for $H = 10$ kOe. Also at other field strengths, peaks and slopes were measured. Our result, however, was not in accordance with the description in the introduction. After a steeper course at lower fields, the torque increased linearly with H above ~ 8 kOe, at least up to the maximum value we could reach, 33 kOe. Several measurements, described below, gave that the change of L relative to the value for 10 kOe amounted to $(0{\cdot}53 \pm 0{\cdot}05)$ per cent/kOe, at 30°C.

We have concluded that the observed effect is an intrinsic property of the pure crystal, i.e., the true or *intrinsic* K_1 *is really given by the measured* L above some minimum field of about 8 kOe, and so depends, contrary to the expectation, on H. Other more trivial sources which could give a similar effect have been excluded by varying the type of measurement and by using specimens of different origin as follows.

A nickel single crystal produced from the melt as well as a pseudo single crystal sheet with a strong cube texture were available as starting materials. Static measurements were done in which the torque due to the magnetic anisotropy was compensated by the torque of a torsion wire. Also dynamic measurements were performed in which the magnetic torque gave the restoring couple of an oscillating system. The equilibrium positions for which the dynamic measurements were done were the two [110] directions in the disk plane while the static measurements were carried out in two directions of maximum torque in a (100) plane. A sphere of 8 mm diameter and a disk of 5 mm diameter and 0·5 mm thickness manufactured from the single crystal were investigated with the static and the dynamic method respectively. From the pseudo single crystal a disk 5 mm in diameter and 0·1 mm thick, was subjected to the dynamic measurement. As has been said a magnetic field up to 33 kOe has been made use of, also more homogeneous types of field with field strengths up to 27 kOe. All measurements led to the same slope of the $K_1(H)$ line within an error of 10 per cent.

The more trivial sources which may cause a dependence of the observed anisotropy on H and the reasons why we exclude them as explanations of the effect measured by us are as follows.

(a) Parasitic torques by imperfect mounting of the sample. The sample could have been fixed eccentrically with regard to the suspension axis in an inhomogeneous field. Also the normal to the plane of the disk might not have been parallel with that axis. From the fact that the same value of $\mathrm{d}K_1/\mathrm{d}H$ is found in all measurements as well as from calculations, together with an estimation of the possible imperfections, such errors can be ruled out.

(b) Incomplete saturation connected with the shape of the specimen. KOUVEL and GRAHAM(1) have found a dependence of $L(\theta)$ on field strength for a silicon–iron alloy, though smaller than our effect for nickel and not linear with field, but approaching a limit according to

$$K_1' = K_1(1 - C/\sqrt{H}),$$

where K_1' is the effective K_1 determined by $L(\theta)$. They used fields up to 20 kOe. They explain their effect in the manner already mentioned above, namely by lack of technical saturation of the magnetization, which they are able to show at the edges of the crystal. At the edges remain domains in which the rotation of the magnetization to the net direction is still incomplete. The extent and nature of these domains, and therefore the magnitude of the net magnetization $\bar{M}$ of the crystal disk, will depend on the direction of M for a given field strength, in which case it is necessary to use a modified expression for the torque: $L = -\mathrm{d}E_A/\mathrm{d}\theta + H\cos(\Psi-\theta)\mathrm{d}\bar{M}/\mathrm{d}\theta$. It is pointed out that a small deviation from complete saturation already causes an appreciable value of torque and so accounts reasonably for the observed effects. In our experiments incomplete saturation does not play an important role as may be clear from the constant value of dK_1/dH in a large region of H, the independence of the effect on the shape of the sample and the relatively small value of M_s for nickel. Possibly only the deviation from linearity of $K_1(H)$ for lower fields may be connected with the lack of technical saturation.

(c) Imperfections of the crystalline structure. No major influence of such imperfections on the observed effect has been indicated in the comparative measurements of the single crystal and the fine grained (~ 0·1 mm) texture.

3. DISCUSSION

After all, a dependence of the intrinsic magnetocrystalline anisotropy on H could be expected. We conclude this from special theories on the temperature dependence of the anisotropy,(2,3,4) although there are large quantitative discrepancies between these theories and experiment. They consider the relations $K_1(M)$, $K_2(M)$, etc., which arise when the temperature is varied. One must conclude that the relations of this kind obtained when varying the applied field strength do not differ very much from the former, because H will, at least partly, change M in the same manner as does T, namely by varying the extent of alignment of the atomic moments. And experimentally it is found that M depends measurably on H.(5) By M we mean here the intrinsic M or the M of the pure crystal at complete technical saturation. Let us, to examine this question on the basis of the experimental values, compare the relative change of M with H (from Danan's measurements at the highest field strengths) with the relative change of K_1 with H (from our measurements), i.e., m_H in the relation $(1/K_1)(dK_1/dH) = m_H \cdot (1/M)(dM/dH)$ (if there exists a relation of the form $K_1 = C \cdot M^n$, then $n = m_H$). Danan gives curves for two specimens of nickel at 15°C, for which we find $m_H \simeq 21$ and 26, at 15°C. We can also calculate an m_T with respect to temperature variations. Making use of the most recent values for the temperature dependence of the spontaneous magnetization found by Budnick and quoted by PUGH and ARGYLE,(6) which in the temperature range 70–120°K are in good agreement with the sensitive measurements of PUGH and ARGYLE,(6) and of those of the first anisotropy constant K_1 by PUZEI,(7) we get $m_T \simeq 26$ for 15°C. Thus, we see that within the limits of experimental error the anisotropy is even completely determined by the intrinsic magnetization when varying the two independent variables of state H and T, so we can write: $K_1(M[T, H])$, at least near room temperature.

A difficulty exists when making this conclusion: According to Danan, M should be proportional to $\sqrt{H}$, while in our measurements K_1 is rather linear with H. It should be remarked that only according to the *theoretical* equation the linearity of M with $\sqrt{H}$ has been revealed, whereas *experimentally* the errors of measurement are such that at least in the region 10–25 kOe we just as well can regard M as linear with H. On the other hand the theory, being the work of HOLSTEIN and PRIMAKOFF,(8) is in very good agreement with the experiment concerning the mean value of the susceptibility.

4. TEMPERATURE DEPENDENCE

We have also measured values of $(1/K_1)(dK_1/dH)$ as a function of temperature (Fig. 2). Outside 30°C they represent only dynamic measurements on the pseudo-unicrystalline disk. The difference between the measurements along the two [110] directions in the disk plane is indicated. As magnetization measurements as a function of

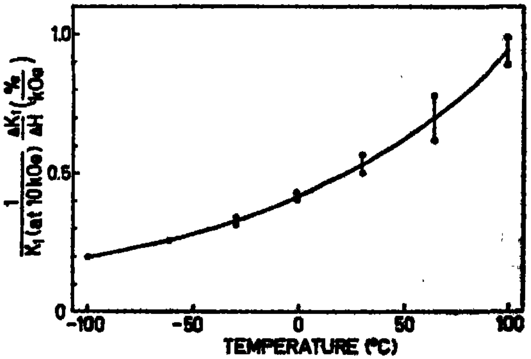

FIG. 2. Relative change of the first anisotropy constant K_1 of nickel with magnetic field H as a function of temperature.

field strength are not available for large H outside 15°C, we are not able to compare $(1/K_1)(dK_1/dH)$ with measured values of $(1/M)(dM/dH)$. The only thing we could do was to make calculations of $(1/M)(dM/dH)$ in two manners for comparison purposes, namely:

(a) Using the equation of Holstein and Primakoff, with which Danan obtained a correct dependence of M on H at room temperature (Fig. 3a). For $M(T)$ in this equation we used the values of Budnick, which are available up to 27°C.

(b) Supposing $m_T \simeq m_H$ should hold also outside room temperature. We used again the values of $M(T)$ by Budnick and those of $K_1(T)$ by Puzei to calculate $m_T(T)$, and then our measured values of $(1/K_1)(dK_1/dH)$ to get $(1/M)(dM/dH)$ (Fig. 3b).

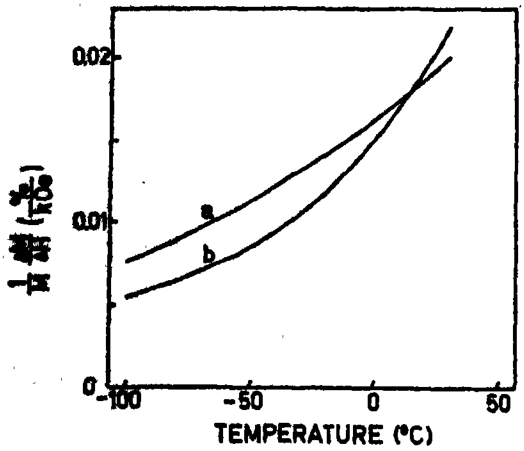

FIG. 3. Relative change of the intrinsic magnetization M of nickel with magnetic field H as a function of temperature. (a) According to the theoretical equation of Holstein and Primakoff. (b) Computed from the measured $(1/K_1)(dK_1/dH)$ curve in Fig. 1, supposing a relationship $K_1(M[T, H])$ in the temperature range involved.

5. ANISOTROPY OF MAGNETIZATION

As has been pointed out by CALLEN and CALLEN,(9) the field dependence of the magnetocrystalline anisotropy is thermodynamically related to the anisotropy of M, namely:

$$(\partial E_A/\partial H_M)_\alpha = -M(\alpha).$$

Here H_M is the component of H in the direction of M, while E_A is defined for constant H_M instead of for constant H. For practical purposes, however, we may for the fields used by us take the E_A as defined in Section 1, so replace H_M by H, because the difference introduced by this is far below the accuracy of the measurements. If we expand M in the same manner as E_A, namely:

$$M(\alpha) = M_0+M_1(\alpha_2^2\alpha_3^2+\alpha_3^2\alpha_1^2+\alpha_1^2\alpha_2^2)+ \dots,$$

it follows that $M_1 = -dK_1/dH$. According to our $K_1(H)$ curve M_1 will be independent of H in the field region used by us and

$$(M_1/M_0) = -(K_1/M_0)\cdot(1/K_1)(dK_1/dH)$$
$$\simeq 0\cdot5\times10^{-3}$$

at 30°C. This is much more than the estimation Callen and Callen give on the basis of their theory. Moreover, with the aid of the temperature dependence of $(1/K_1)(dK_1/dH)$ (Fig. 2) and that of K_1 by Puzei we find between −100° and +100°C for M_1 a temperature dependence as shown in Fig. 4, the shape of which also differs appreciably from the result of Callen and Callen.

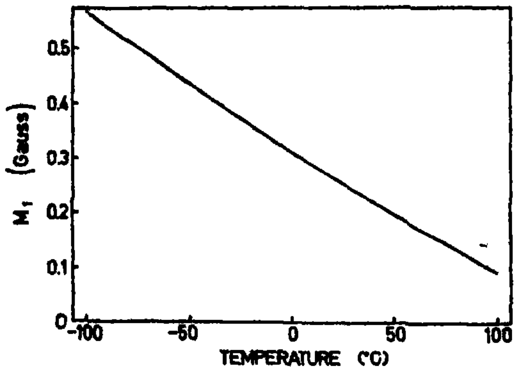

FIG. 4. M_1, defined by the expression for the intrinsic magnetization $M = M_0+M_1(\alpha_2^2\alpha_3^2+\alpha_3^2\alpha_1^2+\alpha_1^2\alpha_2^2)+\dots$, as a function of temperature. $M_1 = -dK_1/dH$ is calculated in multiplying the $K_1(T)$ values of Puzei by the $(1/K_1)(dK_1/dH)$ values in Fig. 2 measured by us. $M_0 = 484$ G at 20°C.

6. THE CASE OF AN IRON ALLOY

It may be interesting to see what a calculation of $(1/K_1)(dK_1/dH)$ will give for the silicon–iron alloy (of 3·5 wt per cent silicon) investigated by Kouvel and Graham, using again the assumption

$m_T \simeq m_K$. Making use of the result of measurements on the anisotropy of a 3 per cent silicon–iron crystal by GRAHAM,⁽¹⁰⁾ giving $m_T \simeq 6{\cdot}5$, and taking the value of the intrinsic susceptibility measured by Danan: $(1/M)(\mathrm{d}M/\mathrm{d}H) \simeq 0{\cdot}0075$ per cent/kOe for iron (by lack of information on silicon–iron) at $H = 20$ kOe, we get

$$(1/K_1)(\mathrm{d}K_1/\mathrm{d}H) \simeq 0{\cdot}05 \text{ per cent/kOe.}$$

In a report⁽¹¹⁾ being an extension of Ref. 1 KOUVEL and GRAHAM find that the value of C (as defined in our Section 2), so $(1/K_1')(\mathrm{d}K_1'/\mathrm{d}H)$ for constant H, depends on the thickness to diameter ratio of the disk specimen. Extrapolation to ratio 0, however, does not give $C \simeq 0$ as one would expect if C would be due only to lack of technical saturation, but about 4·5. This means that

$$(1/K_1')(\mathrm{d}K_1'/\mathrm{d}H) \simeq 0{\cdot}08 \text{ per cent/kOe}$$

at $H = 20$ kOe. This limiting value for the maximum field where measurements were done may approximate the intrinsic $(1/K_1)(\mathrm{d}K_1/\mathrm{d}H)$, so must be compared with the above result of 0·05 per cent/kOe.

Acknowledgements—Helpful discussion with Prof. Dr. G. DE VRIES is gratefully acknowledged. The material for the specimens has been kindly furnished by the Philips Research Laboratories, Eindhoven. This work is part of the research program of the Foundation F.O.M. and was made possible by financial support of the organizations Z.W.O. and T.N.O.

REFERENCES

1. KOUVEL J. S. and GRAHAM C. D., JR., *J. appl. Phys.* **28**, 340 (1957).
2. ZENER C., *Phys. Rev.* **96**, 1335 (1954).
3. CARR W. J., JR., *Phys. Rev.* **109**, 1971 (1958).
4. VAN VLECK J. H., *J. Phys. Radium* **20**, 124 (1959).
5. DANAN H., *C.R. Acad. Sci., Paris* **246**, 401 (1958).
6. PUGH E. W. and ARGYLE B. E., *J. appl. Phys.* **33**, 1178 (1962).
7. PUZEI I. M., *Izv. akad. nauk S.S.S.R. Ser. fiz.* **21**, 1088 (1957).
8. HOLSTEIN T. and PRIMAKOFF H., *Phys. Rev.* **58**, 1098 (1940).
9. CALLEN E. R. and CALLEN H. B., *J. Phys. Chem. Solids* **16**, 310 (1960).
10. GRAHAM C. D., JR., *J. Appl. Phys.* **30**, 391 (1959).
11. KOUVEL J. S. and GRAHAM C. D., JR., *General Electric Research Laboratory Rep.* No. 56-RL-1632, Schenectady, New York (1956).

J. Phys. Chem. Solids Pergamon Press 1963. Vol. 24, pp. 953–955. Printed in Great Britain.

ELECTRON TRANSFER IN ZINC-BLENDE III–V COMPOUNDS*

C. C. WANG† and LEO H. SPINAR‡

Department of Chemistry, Colorado State University, Fort Collins, Colorado

(*Received* 26 *October* 1962; *revised* 5 *February* 1963)

Abstract—The X-ray powder diffraction patterns for AlP, BP, GaAs, GaSb, InAs and InSb have been measured. From these and previously reported data, a correlation of the bond order, interatomic distance and electron transfer is made for intermetallic III–V compounds having a zinc-blende structure. The ionic character of the bonds is determined quantitatively in terms of electron transfer. The energy gap between the valence and conduction band decreases with increasing bond length in compounds of a similar bond character and same crystal structure. The energy gap increases with increasing ionic character in isoelectronic series.

I. INTRODUCTION

A CLASS of intermetallic compounds having the formula $A^{III}B^{V}$ are formed by elements in group III and group V. The chemical bonding in this class of compounds is largely covalent.(1) This covalency concentrates the chemical energy of the system in directed bonds between each atom and its nearest neighbors only, thus constraining the crystal to a high degree of chemical and structural perfection. Except for the nitrides, § all the compounds of this class have a face-centered cubic (zinc-blende type) structure in which each group III atom has four tetrahedrally arranged group V atoms as nearest neighbors bonded through covalent sp^3 hybrid bonds. Likewise each group V atom is bonded to 4 group III atoms.

A quantitative measurement of the effective charge of these bonds can be made by measuring the Reststrahl frequency in the far infrared. It is possible also to obtain a quantitative correlation of crystal structure and ionic character in the following manner.

Using the concept of the resonating bond, Pauling postulated and later experimentally confirmed(2) the relation between the bond length and bond order for many compounds to be:

$$D(n) = D(1) - 0{\cdot}60 \log_{10} n \tag{1}$$

$D(n)$ is the bond length for bond order, n, which is the ratio of the valence of the atom to the number of bonds. $D(1)$ is the bond length for a single bond. As Pauling has indicated, a consideration of the interatomic distances shows that electron transfer from atoms of one element takes place in many intermetallic compounds. The amount of electron transfer is related to valence changes which may result from the gain or loss of electrons, the partial ionic character of bonds between unlike atoms, or the equalization of the electronegativity differences between atoms. A purely covalent bond in the zinc-blende structure will be characterized by a bond order of $\frac{3}{4}$. In most zinc-blende compounds, there will be some electron transfer. The electron transfer per bond is equal to $(n-\frac{3}{4})$. Since there are four bonds per atom, the electron transfer per atom for compounds of this class is $4(n-\frac{3}{4})$. The value of the bond order, n, may be calculated from equation (1) using experimentally determined values of $D(n)$ and $D(1)$.

---

* Abstracted in part from a thesis submitted by C. C. Wang in partial fulfillment of the requirements for the Ph.D.

† Present Address: Department of Chemistry, University of Kansas, Lawrence, Kansas.

‡ Present Address: Department of Chemistry, University of Missouri, Columbia, Missouri.

§ Both cubic and graphitic type hexagonal forms have been reported for BN. AlN, GaN and InN have wurzite type hexagonal structure. We have observed high temperature wurzite type hexagonal BP.

II. EXPERIMENTAL PROCEDURES AND RESULTS

The X-ray powder diffraction patterns for AlP, BP, GaAs, GaSb, InAs and InSb were measured in this laboratory* using a General Electric XRD–5 diffractometer, using filtered copper radiations and a scanning speed of 1° (θ) per minute. All of the patterns show the zinc-blende structure.† The cubic parameter, a_0, was obtained by the least squares refinement of NELSON and RILEY(3) in which the minimum error in the cubic parameter occurs in the limit when $\cos^2\theta(1/\sin\theta+1/\theta)$ approaches zero. A comparison of the a_0 values determined in this work with those reported in the ASTM X-ray powder data file is shown in Table 1. Because of the geometry of the zinc-blende structure, the interatomic distance, $D(n)$, is equal to $3^{1/2}a_0/4$.

The single bond lengths, $D(1)$, are given by:

$$D(1) = r_A + r_B - c|x_A - x_B| \qquad (2)$$

where r_A and r_B are the single bond radii as given by PAULING(4) x_A and x_B are the electronegativities of the atoms as given by PAULING(5) and c is the Schomaker–Stevenson coefficient which PAULING(6) assigns a value of 0·08 for a bond with boron, 0·06 for a bond with Al, 0·04 for a bond with Ga, 0·02 for a bond with In.

The bond order, n, was calculated from equation (1) using these values of $D(n)$ and $D(1)$. Then the electron transfer per atom was calculated and the results tabulated in Table 2.

Table 1. The cubic parameter, a_0 determined in this laboratory and the value reported in the ASTM X-ray powder data file

	This Laboratory	ASTM	Card Number
BP	4·534	4·538	11–119
AlP	5·467	5·451	Ref. (11)
GaAs	5·675	5·637	12–608
GaSb	6·098	6·095	7–215
InAs	6·076	6·0584	8–387
InSb	6·481	6·4782	6–0208

Table 2. Bond numbers and electron transfer per atom for some III–V compounds

	$D(1)$ (Å)	$D(n)$ (Å)	Bond order, n	Electron transfer per atom	Structural data source
BN	1·47	1·565	0·71	−0·16	WENTORF(7)
BP	1·89	1·963	0·76	0·04	this lab
BAs	2·01	2·068	0·79	0·16	POST *et al.*(8)
AlP	2·31	2·367	0·79	0·16	this lab
AlAs	2·43	2·438	0·96	0·84	NATTA(9)
AlSb	2·62	2·656	0·87	0·48	GIESECKE(10)
GaP	2·33	2·360	0·89	0·56	ADDAMIANO(11)
GaAs	2·44	2·448	0·96	0·84	this lab
GaSb	2·63	2·640	0·96	0·84	this lab
InP	2·51	2·541	0·89	0·56	ADDAMIANO(11)
InAs	2·62	2·631	0·96	0·84	this lab
InSb	2·81	2·806	1·00	1·00	this lab

---

* The AlP and BP were prepared in this laboratory and found to be 99·9+ per cent pure by spectrographic analysis. Single crystals of InSb, InAs, GaAs, and GaSb of purity greater than 99·9 per cent were supplied by *Texas Instruments Incorporated*, Dallas, Texas.

† WENTORF(7) suggests a hexagonal structure for AlP similar to that of AlN. We have found AlP to be of the zinc-blende type.

III. DISCUSSION AND CONCLUSIONS

Table 2 clearly shows that all values of $D(n)$ except that for BN are between the value of $D(1)$ and $D(\frac{3}{4})$ which means that the bond orders, n, are between $\frac{3}{4}$ and 1·00. Thus the bonds exhibit the ionic character as indicated by the electron transfer value.

The results for BN are inconsistent with what one would predict on the basis of the electroneutrality principle whereby there would be electron transfer in order to counteract the partial ionic character of the B–N bond. The measured interatomic distance in BN (1·565 Å) is only slightly higher than the distance (1·54 Å) obtained by the addition of the covalent bond radii given by Pauling. Thus it is not necessary to make the Schomaker–Stevenson correction for the B–N bond just as it is not necessary to do so for the C–Cl bond.⁽⁶⁾ The corrections for the other boron compounds in this study are so small, due to the small differences in electronegativity, that it is difficult to determine if the correction is required for any of the other boron bonds. The "ionic character" of these bonds has not been measured by other experimental methods.

Using a value of $D(1) = 1{\cdot}54$ Å for BN, the value of the bond order is 0·91 and the electron transfer per atom is 0·64. Ignoring the Schomaker–Stevenson correction, bond orders of 0·79 are calculated for BP and BAs which is no change for BAs and a small change for BP. Further justification for the omission of the Schomaker–Stevenson correction in the B–N bond can be made on the basis of the observation that unusually large B–N distances occur in all known tetrahedrally bound B–N compounds such as pyridine-boron trifluoride and amino-boron trifluoride which have been discussed by GELLER.⁽¹²⁾

This rather large electron transfer for BN would be intuitively expected upon the large electronegativity difference. However, a closer examination of the other data shows no simple correlation between the electronegativity and the electron transfer. In fact one will observe that if there is any apparent trend, it is in the opposite direction. For a group of compounds of the same group V element, the electron transfer tends to increase with the increasing size of the group III elements. For a group of compounds of Ga and In, the same trend occurs with increasing size of the group V element.

Two qualitative correlations can be made between the energy gap of these semiconducting compounds and the bond nature and length. The energy gap decreases with increasing bond length in substances with the same crystal structure and similar degree of bond character. The energy gap increases with increasing ionic character in an isoelectric series. These correlations indicate that the less tightly bound electrons are capable of not only undergoing a greater degree of transfer in the bond but also are more easily raised to a conduction band.

Acknowledgements—The authors wish to thank Dr. LINUS PAULING for his helpful discussions. The generous support of this work by Texas Instruments Incorporated, Dallas, Texas, is gratefully acknowledged.

REFERENCES

1. WOLFF G. A. and BRODER J. D., *Acta Cryst.* **12,** 313 (1959).
2. PAULING L., *J. Amer. chem. Soc.* **69,** 542 (1947); *Proc. Nat. Acad. Sci. U.S.* **36,** 533 (1950); *Acta Cryst.* **10,** 685 (1957); *Nature, Lond.* **189,** 656 (1961).
3. NELSON J. B. and RILEY D. P., *Proc. phys. Soc. Lond.* **57,** 160 (1945).
4. PAULING L., *Nature of the Chemical Bond,* 3rd ed. p. 407. Cornell University Press, Ithaca, New York (1960).
5. PAULING L., *Nature of the Chemical Bond,* 3rd ed. p. 93. Cornell University Press, Ithaca, New York (1960).
6. PAULING L., *Nature of the Chemical Boad,* 3rd ed. p. 229. Cornell University, Press, Ithaca, New York (1960).
7. WENTORF R. H., *J. chem. Phys.* **34,** 809 (1961); *J. chem. Phys.* **26,** 956 (1957).
8. PERRI J. A., LA PLACA S. and POST B., *Acta Cryst.* **11,** 30 (1959).
9. ASTM X-ray Powder Data File Card Number 2–127h.
10. GIESECKE V. G. and PFISTER H., *Acta Cryst.* **11,** 369 (1958).
11. ADDAMIANO A., *J. Amer. Chem. Soc.* **82,** 1537 (1960).
12. GELLER S., *J. Phys. Chem. Solids* **10,** 340 (1959).

J. Phys. Chem. Solids Pergamon Press 1963. Vol. 24, pp. 957–963. Printed in Great Britain.

ABSORPTION EDGE IN FERROELECTRIC SbSI UNDER ELECTRIC FIELDS

GÜNTHER HARBEKE
RCA Laboratories, Zürich, Switzerland

(*Received* 28 *January* 1963)

Abstract—The shift of the absorption edge in SbSI caused by an applied electric field has been measured as a function of temperature and field strength. It shows a sharp maximum at the Curie temperature T_c, a linear field dependence below T_c and a quadratic field dependence above T_c. This behavior can be explained by the known dielectric and electromechanical properties.

I. INTRODUCTION

THE absorption edge in semiconductors and insulators is due to light induced transitions between states in the uppermost filled band and states in the lowest empty band. External parameters like magnetic or electric fields are mostly of weak influence on the shape and the spectral position of the edge. High electric fields of the order of 10^5–10^6 V/cm are known to shift the absorption edge to longer wavelengths by a small but in some cases detectable amount depending on the steepness of the edge and the effective masses both in the initial and final state.(1) KERN(2) has found a remarkably large shift of the absorption edge in SbSI to shorter wavelengths in fields of the order of 10^3 V/cm to 10^4 V/cm.

According to DOENGES,(3) SbSI crystallizes in the orthorhombic structure with the lattice constants $a = 8{\cdot}49$ Å, $b = 10{\cdot}10$ Å and $c = 4{\cdot}16$ Å. It tends to grow in form of thin needles along the c-axis and is red transparent since the absorption starts increasing around 6500 Å. The material is photoconducting(4) with a maximum photocurrent at 6300–6400 Å. The edge shift is produced by a d.c. field applied along the c-direction and the light direction perpendicular to c independent of the field direction and seems to be connected with an electromechanical elongation of the crystal.

In the course of further investigation of these effects SbSI was found to be a ferroelectric material(5) with the c-axis as ferroelectric axis. The Curie point is at 21°C, the spontaneous polarization is more than 7 μ C/cm^2 at 0°C. The ferroelectric properties are reported elsewhere.(5) This paper is concerned with some new features based on the correlation between ferroelectricity and the behavior of the absorption edge.

II. INSTRUMENTAL

The optical set up for the experiments is similar to the one used by KERN.(2) The monochromator slits were set at a resolution of 0·003 eV or better. The samples were measured under vacuum in a chamber thermally stabilized to a few tenths of a degree.

III. RESULTS

(a) *Absorption without an applied field*

The transmission and reflection of thin crystals with plane parallel faces was measured around the band edge with the light direction perpendicular to the c-axis. The crystals were taken as grown without any polishing or etching treatment. From these data the absorption constant K was determined. The $F = 0$ curves in Fig. 1 show K both for light polarized parallel and perpendicular to the c-axis without an applied field. A remarkable energy difference of 0·07 eV in the positions of the two edges corresponding to the two directions of polarization can be noted. These measurements are in agreement with the transmission measurements of KERN.(2) On the high photon energy

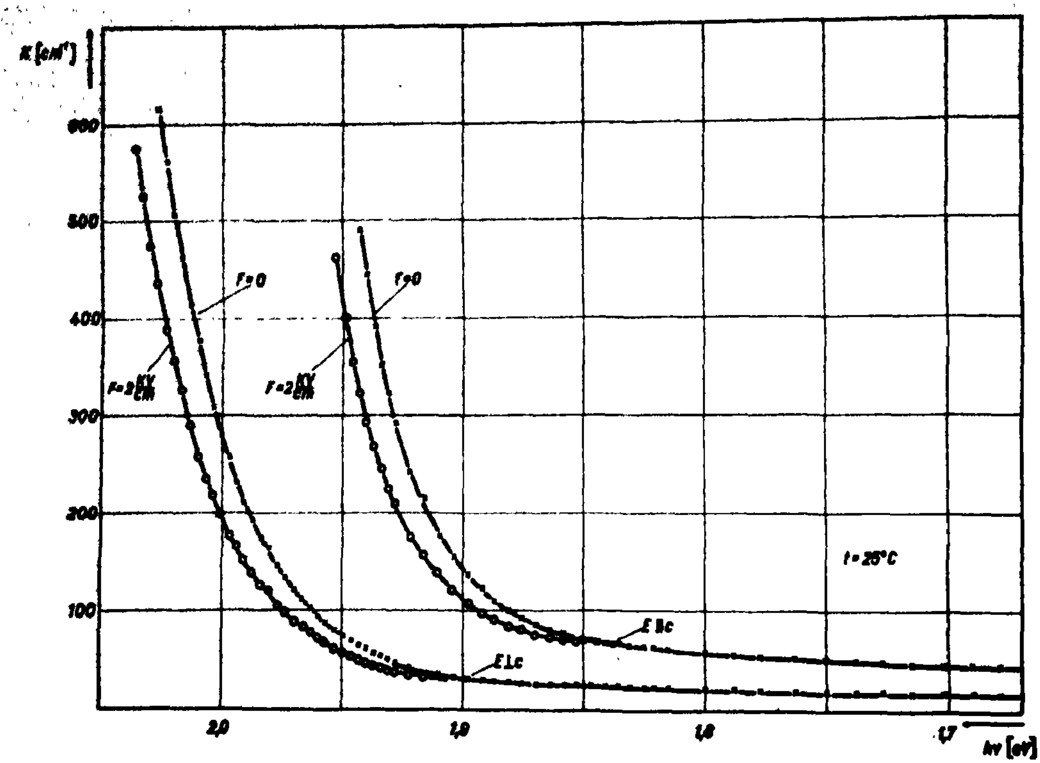

Fig. 1. Absorption constant of SbSI for polarized light $E\perp c$ and $E\parallel c$ with and without applied d.c. field as a function of incident photon energy. Light direction perpendicular to the c-axis.

side the measurement of K was terminated by the low transmission level in even the thinnest crystals available. The energy dependence of the absorption in the edge gives no information about the type of transitions causing the edge. Therefore no detailed conclusions can be drawn concerning the band structure of the compound. They only indicate band gap values of about 1·95 eV for $E\perp c$ and about 1·88 eV for $E\parallel c$.

Both edges shift with temperature without altering their shape. The energy of maximum photosensitivity is known to shift with an extraordinarily high temperature coefficient of $dE_{\max}/dT = -1{\cdot}5\times 10^{-3}$ eV/°K,(4) a value averaged between room temperature and 80°K. This value was found by Kern(2) to be identical with the averaged temperature coefficient β of the absorption edge for unpolarized light. On the other hand, the measurements through this temperature range show that the relation $E_G(T) = E_G(0)+\beta T$ with constant β does not hold. Taking β for the tangential slope of the $E_G(T)$ curve(2) one finds β changing from -1×10^{-3} eV/°K around 80°K to $-2{\cdot}3\times 10^{-3}$ eV/°K between 0 and 20°C. The shift of the edge around the Curie temperature is shown in Fig. 2 for $E\perp c$ and $K = 500$ cm^{-1}. The temperature coefficient below 20°C is $-(2{\cdot}2 \pm 0{\cdot}2)\cdot 10^{-3}$ eV/°K in perfect agreement with the value quoted above; above 22°C it is $-(0{\cdot}9 \pm 0{\cdot}2)\cdot 10^{-3}$ eV/°K. Thus, a sharp break in $E_G(T)$ occurs right at the Curie temperature. In

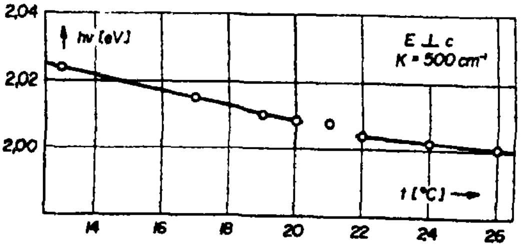

Fig. 2. Shift of absorption edge of SbSI with temperature around the Curie temperature.

very pure and tiny single crystal needles the same temperature coefficients were found. In addition to this, a reversible spontaneous jump of the absorption edge to lower energies of 0·02 eV equivalent to 60 Å was observed going across T_c with increasing temperature. It must be noted that T_c can vary from sample to sample and that there is a small temperature hysteresis in the jump.

(b) *Absorption under a d.c. field*

The effect of a d.c. field parallel to the *c* direction on the absorption edge for polarized light can be seen in Fig. 1 at 25°C. It does not depend on the sense of the field. At a mean field of 2 kV/cm the edge shifts by 0·012 eV to higher photon energies. The mean field is taken as the ratio of applied voltage and electrode distance, since by visual observation it can be seen that the change in transmission is nearly uniform over the entire crystal. This shift ΔE_G is of opposite direction and some orders of magnitude higher than the Franz effect would predict. This is in qualitative agreement with the results of KERN.(8) Since it became clear, that ΔE_G is very sensitive to small changes in temperature around T_c the measurements were performed at a constant field of 2 kV/cm under accurate temperature stabilization. The result (Fig. 3) shows a very pronounced peak right at the Curie temperature. At the maximum point the edge shift is at least 10 times larger than either 10° below T_c or 15° above it. It is an interesting feature that this curve has a striking similarity to the dielectric constant vs. temperature curve.(5)

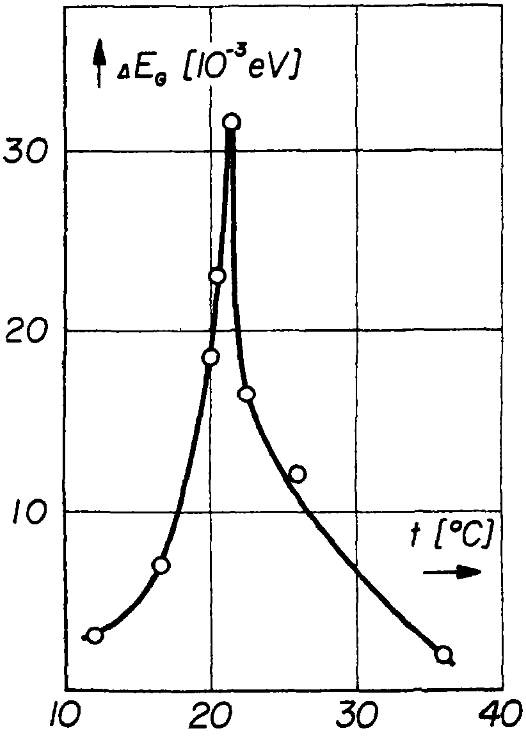

FIG. 3. Shift of absorption edge of SbSI under a d.c. field of 2 kV/cm applied along the *c*-axis vs. temperature around the Curie temperature.

Another property which depends very strongly on the temperature around T_c is the d.c. field dependence of ΔE_G. In Fig. 4, ΔE_G is plotted vs. the applied field at 16·6°C. At this temperature, well below T_c, the field dependence is linear. In Fig. 5, ΔE_G is plotted vs. the square of the applied field at 25·5°C. At this temperature, well above T_c, the field dependence is quadratic. The dependence is linear up to 20°C and quadratic above 22°C. In the intermediate temperature region, i.e. for $T_c - 1°$ to $T_c + 1°$, a mixed field dependence was observed.

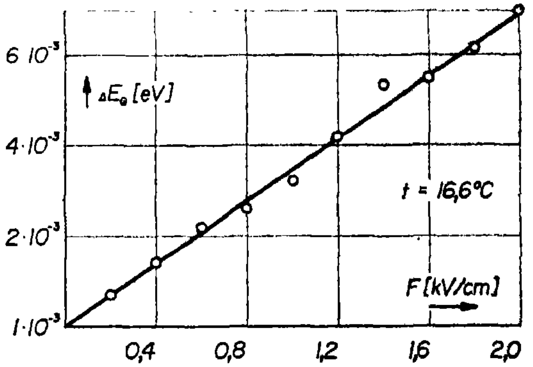

FIG. 4. D.C. field dependence of the shift of absorption edge in SbSI at 16·6°C.

Preliminary investigations of the dilatation of the crystal in a d.c. field by an electrical condenser method show a strong elongation in *c*-direction independent of the sense of the field. A typical value for the relative elongation $\Delta l/l$ is 7×10^{-4} at a field of 2 kV/cm. The field dependence is neither strictly linear nor quadratic. These measurements

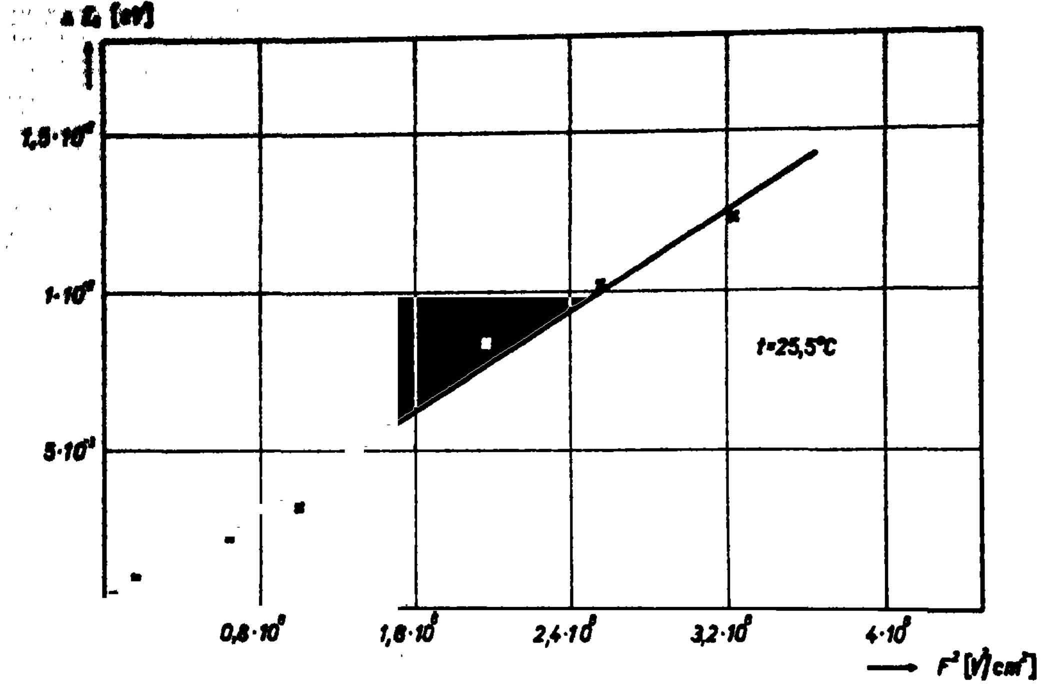

FIG. 5. D.C. field dependence of the shift of absorption edge in SbSI at 25·5°C.

were done in air at room temperature, that is, in the immediate neighbourhood of T_c. This might explain the similarity to the optical effects which is confirmed by the time dependence of the elongation. The response time consists of a fast part of less than 1m sec duration and a very slow part of a few seconds. This performance resembles the time dependence of the edge shift,(2) and in both cases the fast part corresponds to about two thirds of the whole effect.

IV. DISCUSSION

The existence of ferroelectricity in a crystal requires a lack of a center of symmetry in the structure. SbSI is reported to be of orthorhombic structure, space group D_{2h}^{16}, thus having a center of symmetry.(8) It therefore appears that all previous X-ray work in determining the crystallographic structure must have been done in the non-ferroelectric region above the Curie temperature of 21°C. The ferroelectric phase has not been determined so far. From our optical data the phase transition is indicated by the sharp change in the band gap as a function of temperature (see Fig. 2) and by the spontaneous jump of the absorption edge at T_c in some crystals. In the ferroelectric region near T_c the temperature coefficient of the band gap is nearly three times that in the non-ferroelectric region.

The temperature coefficient of an energy difference between two levels consists out of two parts, one due to the change in atomic distance with temperature and the other due to the level broadening with increasing temperature by electron–phonon interaction. For a cubic crystal this can be expressed in the following way:

$$\frac{\mathrm{d}E_G}{\mathrm{d}T} = \frac{\partial E_G}{\partial a}\cdot\frac{\mathrm{d}a}{\mathrm{d}T} + \left(\frac{\partial E_G}{\partial T}\right)_a \qquad (1)$$

The second term is negative in every case and of the order of kT, hence about 10^{-4} eV/°K. In general, temperature coefficients of semiconductors and insulators are of the order of 10^{-4}–10^{-3} eV/°K. The extraordinarily high negative value of $-2{\cdot}2\times10^{-3}$ eV/°K below T_c indicates that in

SbSI the first term is strongly negative too. It depends on the relative motion of both bands containing the initial and the final state involved in the optical transition caused by the change in atomic distance. The negative thermal expansion coefficient of SbSI along the *c*-axis, found by preliminary X-ray investigations,(6) substantiates this assumption.

The dichroism defined as the relative difference in the absorption coefficients $2(K_\parallel - K_\perp)/(K_\parallel + K_\perp)$ is very large in SbSI. Well remote from the edge on the low energy side at 1·7 eV this quantity is approximately equal to unity and increases towards the edge to 1·5 at 1·95 eV and 25°C (see $K_\parallel$ and $K_\perp$ in Fig. 1, where the reflection losses have been taken into account). Hence the dichroism in SbSI is comparatively much higher than in $BaTiO_3$(7) due to its stronger deviation from the cubic structure. The results do not contradict the selection rule $K_\perp < K_\parallel$ derived from first principles by CASELLA and KELLER(7) since this rule is valid only for crystals in the crystal classes C_{nv} and C_n, where $n = 3,4$ or 6.

The electro-optical effect in solids is the change in the refractive index ellipsoid caused by an electric field. The field can cause both a deformation and a rotation of this ellipsoid, a cubic crystal can become uniaxial and thus birefringent, an uniaxial crystal can become biaxial. One has to differentiate between the true electro-optical effect and the indirect effect as a result of the piezoelectric or electrostrictive deformation of the crystal. Theory shows that one can expect a true linear electro-optical effect when the material is piezoelectric. In this case the symmetry conditions of the electro-optical effect are the same as in the piezoelectric effect. A true quadratic electro-optic effect, Kerr effect, can be expected when the material is not piezoelectric. In this case the effect corresponds to the quadratic electrostriction. This behavior arises simply from the fact that the refractive index is equal to the square root of the dielectric constant. For this reason the temperature dependence of both quantities is the same in ferroelectrics e.g. in KH_2PO_4 and KD_2PO_4.(8)

Numerous papers are concerned with the electro-optical effects, but to our knowledge, an electro-optical band edge shift in ferroelectrics has not been reported yet. Like the electro-optical effect the edge shift behaves very similar to the dielectric properties; e.g. the temperature dependence of the edge shift (Fig. 3), is similar to the temperature dependence of the dielectric constant. The dielectric properties of SbSI are not known in detail so far. However the sharp transition from a linear field to a quadratic field dependence of the shift at the Curie temperature indicates that piezoelectricity and electrostriction are determining this optical performance.

It must be noted that there seems to exist a contradiction between the linear field dependence of the shift below T_c and its independence of the direction of the field along the *c*-axis. However, since all measurements were taken above the coercive field strength (100 V/cm at 0°C) all ferroelectric domains reverse when a field is applied in opposite direction thus restoring the previous symmetry. The parallelism between edge shift and dielectric behavior may be illustrated by the situation above the Curie temperature. Here the structure appears to be orthorhombic(8) belonging to the crystal class D_{2h} which excludes piezoelectricity. Hence no linear electro-optical effect can be expected and only a quadratic (Kerr) effect should be observable. Experimentally a purely quadratic edge shift is found.

The structure below T_c is not known but since it is ferroelectric the matrix of its piezoelectric constants must be different from zero; thus a linear dependence has to be expected. Experimentally, a purely linear behavior was found well below the Curie point. In the intermediate region $T_c - 1°C < T < T + 1°C$ the performance is affected by the transition from the paraelectric to the ferroelectric state or vice versa. It could also be affected by a field induced transition into the ferroelectric state above the Curie temperature as discussed by MERZ for $BaTiO_3$.(9)

Since a very close relationship between the band edge shift and the dielectric properties has been established the question arises, whether it is only a secondary result due to the piezoelectric and electrostrictive deformations of the crystal or whether it contains a direct effect. There is no doubt that an indirect, secondary effect occurs. After a dielectric deformation the ions are in different positions than before thus the potential distribution inside of the crystal is changed and hence also the initial and final state involved in the transition which causes the edge. Analogous to equation (1) one can write for the field dependence:

$$\frac{\mathrm{d}E_G}{\mathrm{d}F} = \frac{\partial E_G}{\partial a}\cdot\frac{\mathrm{d}a}{\mathrm{d}F} + \left(\frac{\partial E_G}{\partial F}\right)_a \qquad (2)$$

for the simplified case of a cubic crystal.

Quantitatively one can not calculate both terms from equations (1) and (2) because SbSI is not a simple cubic crystal. The orthorhombic structure consists of chains of composition $(Sb_2S_2I_2)_n$ running parallel to the c-axis. The bonding between neighbouring chains is of van der Waals type or weak anion–cation bonding between the chains. The distances between anions in adjacent chains are too long in order to form direct anion–anion bonding. From these considerations MOOSER and PEARSON(10) concluded that the conditions of the semiconducting bond are fulfilled and predicted that SbSI and compounds of the same structure should show semiconducting properties. That means that the electronic properties like the energy required to create an electron-hole pair are determined by the situation inside the chains. From dilatation measurements it is known that the crystal expands strongly in the c-direction under a d.c. field. Since one would expect that in the first approximation the volume of the crystals keeps constant this must result in a contraction perpendicular to c or at least in either the a- or b-direction. Furthermore it must be assumed that the crystal does this contraction perpendicular to c by varying the distance between neighbouring chains since the weakest bonds are there. Thus the atomic distance inside the chains which determine the electronic properties such as the energy gap should not be influenced. Due to the fact that the chains are running parallel to the c-axis the interaction with an electric light vector parallel to them is stronger than with an electric light vector perpendicular to them. For the same reason the dielectric constant parallel to c is about 1000 times larger than perpendicular to c. The result is that in contrast to the situation in other crystal structures the absorption constant K for $E\|c$ is larger than for $E\perp c$. One might think of an allowed first order transition for $E\|c$ and a first order forbidden transition for $E\perp c$. In both possible transitions the simultaneous presence of a static electric vector parallel to c which causes a small motion of certain ions from their former positions produces a comparatively small perturbation of the inner potential. This explains the observation that for both polarization directions $E\|c$ and $E\perp c$ the edge shift under an electric field is exactly the same.

In the general form of equation (2) for different atomic distances a, b, c,

$$\frac{\mathrm{d}E_G}{\mathrm{d}F} = \frac{\partial E_G}{\partial a}\cdot\frac{\mathrm{d}a}{\mathrm{d}F} + \frac{\partial E_G}{\partial b}\cdot\frac{\mathrm{d}b}{\mathrm{d}F} + \frac{\partial E_G}{\partial c}\cdot\frac{\mathrm{d}c}{\mathrm{d}F} + \left(\frac{\partial E_G}{\partial F}\right)_{a,b,c} \qquad (2a)$$

one can therefore neglect the first two terms on the right side and is left with

$$\frac{\mathrm{d}E_G}{\mathrm{d}F} = \frac{\partial E_G}{\partial c/c}\cdot\frac{\mathrm{d}c/c}{\mathrm{d}F} + \left(\frac{\partial E_G}{\partial F}\right)_c \qquad (2b)$$

The same considerations are true for equation (1); one obtains

$$\frac{\mathrm{d}E_G}{\mathrm{d}T} = \frac{\partial E_G}{\partial c/c}\cdot\frac{\mathrm{d}c/c}{\mathrm{d}T} + \left(\frac{\partial E_G}{\partial T}\right)_c \qquad (1b)$$

Both equations contain the quantity $\partial E_G/\partial c/c$. If one neglects the second term in (1b) which should be small compared to the high value of $-2{\cdot}2\times10^{-3}$ eV/°K for $\mathrm{d}E_G/\mathrm{d}T$ and puts in the preliminary value of $-5{\cdot}10^{-5}$/°K for $\mathrm{d}c/c/\mathrm{d}T$ (expansion in c-direction by cooling) one gets $\partial E_G/\partial c/c = 44$ eV. This means the absorption edge shifts to higher energies with increasing atomic distance in the c-direction. This value and $\mathrm{d}c/c/\mathrm{d}F = 3{\cdot}5\cdot10^{-7}$/V/cm (see Section IIIb) gives about $1{\cdot}4\cdot10^{-5}$ eV/V/cm for the first term in (2b). Since $\mathrm{d}E_G/\mathrm{d}F = 1{\cdot}6\cdot10^{-5}$ eV/V/cm at T_c the edge shift with electric fields comes out in the right order of magnitude from independent measurements. On the other hand, this rough estimate shows that the second term, the true effect, is small compared to the indirect effect. From the present data no more accurate conclusions can be drawn. This would be possible if one could know $\partial E_G/\partial c$ and $\mathrm{d}c/\mathrm{d}F$ more accurately. These values could be evaluated by measuring the absorption edge shift under pressure and the compressibility for $\partial E_G/\partial c$; the piezoelectric and electrostrictive constants for $\mathrm{d}c/\mathrm{d}F$.

Acknowledgements—The author wants to thank Dr. KERN and Dr. NITSCHE for preparing the crystal material. Helpful discussions with Dr. MERZ are gratefully acknowledged.

REFERENCES

1. FRANZ W., *Z. Naturf.* **13a,** 484 (1958). KELDYSH L. W., *Sov. Phys. J.E.T.P.* **7,** 788 (1958).
2. KERN R., *J. Phys. Chem. Solids* **23,** 249 (1962).
3. DOENGES E., *Z. anorg. Chem.* **263,** 112 (1950); **265,** 56 (1951).
4. NITSCHE R. and MERZ W. J., *J. Phys. Chem. Solids* **13,** 154 (1960).
5. FATUZZO E., HARBEKE G., MERZ W. J., NITSCHE R., ROETSCHI H. and RUPPEL W., *Phys. Rev.* **127,** 2036 (1962).
6. LAPPE F., private communication.
7. CASELLA R. C. and KELLER S. P., *Phys. Rev.* **116,** 1469 (1959).
8. ZWICKER B. and SCHERRER P., *Helv. Phys. Acta* **17,** 346 (1944).
9. MERZ W. J., *Phys. Rev.* **91,** 513 (1953).
10. MOOSER E. and PEARSON W. B., *J. Phys. Chem. Solids* **1,** 65 (1958).

LETTERS TO THE EDITOR

Cohesive energy of the alkali halide crystals*

(*Received* 4 *February* 1963; *revised* 1 *April* 1963)

INTEREST in Born model treatments of the cohesive energy of the alkali halide crystals at atmospheric pressure has recently been revived,(1–6) mainly for the purpose of obtaining empirical information on the Born repulsive energy. It has, on the other hand, been shown(6) that a Born-type analysis of crystal data at atmospheric pressure in a given alkali halide crystal does not allow a meaningful test of the functional dependence on the interionic distance assumed for the Born repulsive energy in the salt. It is nevertheless apparent(6) that the systematic examination of the discrepancies between the values of the cohesive energy calculated in different approximations and the experimental values, in the entire family of salts, may provide a direct criterion to discriminate among the alternative forms of the Born repulsive energy which have been extensively used in the literature. This procedure is used here to show that the Born repulsive energy in the alkali halides at atmospheric pressure is represented better by the single exponential form than by the inverse power form, and to elucidate the role of the van der Waals energy and of a proper treatment of the equation of state in the determination of the parameters entering the Born model expression for the lattice energy.

Table 1 reports the values of the cohesive energy of the alkali halide crystals at room temperature and at atmospheric pressure, calculated by the Born model in different approximations, and their deviations from the experimental values, determined by a Born–Haber cycle in these thermodynamic conditions. In the first four columns the single exponential form was adopted for the Born repulsive energy, while in the last column the inverse power form was taken. With both forms, the repulsive parameters were determined separately for each salt from data at room temperature and at atmospheric pressure, using the equation of state and its volume derivative at constant temperature. In the first column the equation of state was chosen to have the form appropriate for a static crystal, which is of course inconsistent with the use of data at room temperature, whereas the Hildebrand form of the equation of state (Ref. 7, equations (21) and (22)) was adopted in the second, third and fifth columns, and the Mie–Grüneisen form (Ref. 7 equations, (17) and (18)) was adopted in the fourth column. Finally, the van der Waals energy was also included in the last three columns, using the pertinent coefficients given by MAYER.(8) The results are somewhat sensitive to uncertainties in the various data. We are therefore mainly interested in examining the trends which are apparent in the discrepancies between the various calculated values of the cohesive energy and in their deviations from experiment.

The most simple treatment of the first column(1) yields surprisingly good results in the fluorides, but large and consistently positive deviations from experiment in the other salts, as it overestimates the Born repulsive energy. The comparison of the first and second columns shows a nearly systematic improvement of the theoretical results upon replacing the equation of state appropriate for the static crystal by the Hildebrand equation of state. Of course, the improvement is connected with the use of a correct thermodynamic treatment, which reflects itself in the contribution of the Born repulsive energy to the cohesive energy. This correction is, however, insufficient by itself, since the signs of the deviations from experiment in the second column are still mostly positive. The explicit consideration of the van der Waals energy in the third column improves further the overall agreement between theory and experiment. Practically identical results are obtained in the fourth column, confirming the essential equivalence of the Hildebrand and Mie–Grüneisen forms of the equation of state for the alkali halides in the thermodynamic conditions in question.(7) Finally, the comparison of the third and fifth columns shows that mostly positive, and frequently large, deviations from experiment reappear upon replacing the single exponential form for the Born repulsive energy by the inverse power form. This is a clear indication that the

---

* Based on work performed under the auspices of the U.S. Atomic Energy Commission.

*Table 1. Cohesive energy of the alkali halide crystals at room temperature and at atmospheric pressure** (kcal/mole)

LiF	−242·2 (0·1)	−245·4 (−3·1)	−246·1 (−3·8)	−246·4 (−4·1)	−239·3 (3·0)
LiCl	−192·9 (6·0)	−197·1 (1·8)	−198·1 (0·8)	−198·6 (0·3)	−194·0 (4·9)
LiBr	−181·0 (8·8)	−185·7 (4·1)	−186·9 (2·9)	−187·3 (2·5)	−183·3 (6·5)
LiI	−166·1 (11·6)	−168·5 (9·2)	−169·8 (7·9)	−169·5 (8·2)	−165·7 (12·0)
NaF	−215·2 (−0·8)	−214·8 (−0·4)	−215·5 (−1·1)	−214·8 (−0·4)	−210·0 (4·4)
NaCl	−178·6 (4·0)	−182·6 (0·0)	−183·7 (−1·1)	−184·0 (−1·4)	−180·9 (1·7)
NaBr	−169·2 (4·4)	−172·2 (1·4)	−173·3 (0·3)	−173·4 (0·2)	−170·5 (3·1)
NaI	−156·6 (6·6)	−158·6 (4·6)	−159·9 (3·3)	−159·9 (3·3)	−157·1 (6·1)
KF	−189·1 (0·7)	−189·9 (−0·1)	−191·1 (−1·3)	−190·9 (−1·1)	−187·1 (2·7)
KCl	−161·6 (4·2)	−164·0 (1·8)	−165·6 (0·2)	−165·6 (0·2)	−162·9 (2·9)
KBr	−154·5 (4·0)	−157·6 (0·9)	−159·3 (−0·8)	−159·3 (−0·8)	−157·0 (1·5)
KI	−144·5 (5·4)	−147·4 (2·5)	−149·2 (0·7)	−149·3 (0·6)	−147·1 (2·8)
RbF	−180·4 (1·0)	−182·6 (−1·2)	−184·4 (−3·0)	−184·4 (−3·0)	−181·1 (0·4)
RbCl	−155·4 (3·9)	−158·8 (0·5)	−160·9 (−1·6)	−161·0 (−1·7)	−158·8 (0·5)
RbBr	−148·3 (4·3)	−151·5 (1·1)	−153·6 (−1·0)	−153·7 (−1·1)	−151·5 (1·1)
RBI	−139·6 (5·3)	−143·2 (1·7)	−145·5 (−0·6)	−145·6 (−0·7)	−143·8 (1·1)
CsF	−171·2 (1·3)	−175·6 (−3·1)	−178·6 (−6·1)	−178·8 (−6·3)	−176·4 (−3·9)
CsCl	−146·6 (8·8)	−150·2 (5·2)	−153·8 (1·6)	−153·8 (1·6)	−152·0 (3·4)
CsBr	−141·1 (8·3)	−144·1 (5·3)	−147·9 (1·5)	−147·9 (1·5)	−146·1 (3·3)
CsI	−132·7 (9·7)	−136·1 (6·3)	−140·1 (2·3)	−140·1 (2·3)	−138·6 (3·8)

* The data at room temperature and at atmospheric pressure used in the Born model calculations of the cohesive energy were taken as follows: the interionic distance, the coefficient of volume thermal expansion, the isothermal compressibility of the cesium halides, and the temperature and pressure coefficients of the compressibility, mostly from Cubicciotti,(4) except that in some salts his estimated values for the two latter quantities were replaced by experimental values taken from M. L. Huggins, *J. Chem. Phys.* **5**, 143 (1937) and from P. W. Bridgman, *Proc. Amer. Acad. Arts Sci.* **74**, 21 (1940) and **77**, 187 (1949); the isothermal compressibility of the other salts, from the elastic constants data of K. Spangenberg, *Naturwissenschaften* **43**, 394 (1956). The vibrational internal energy, the heat capacity at constant volume and its temperature coefficient were estimated by the Debye model, with a Debye temperature evaluated from the preceding data by the formula of M. Blackman, *Proc. Roy. Soc.* **A181**, 58 (1942). The data for the Born–Haber cycle determination of the cohesive energy were taken as follows: the electron affinity of the fluorine atom, from T. L. Bailey, *J. chem. Phys.* **28**, 792 (1958); the electron affinity of the other halogen atoms, from J. E. Mayer *et al.*, *J. chem. Phys.* **3**, 20 (1935), **11**, 56 (1943) and **12**, 323 (1944); the other thermochemical quantities, from Cubicciotti.(4) For each salt, the difference of the two numbers reported in any column reproduces the value of the cohesive energy obtained from these thermochemical data.

dependence of the Born repulsive energy in the alkali halide crystals on the interionic separation, in the neighborhood of the equilibrium separation at atmospheric pressure, is represented better by the exponential form. The same conclusion was reached by Baughan(3) by an argument which involved, however, the comparison of derivatives of the Born repulsive energy in the crystal and in the molecule.

The sensitivity of the repulsive parameters to the procedure used in their determination is illustrated for a few representative salts in Table 2. Clearly, the thermodynamic correction and the van der Waals energy correction have large, but partly compensating, effects on the repulsive parameters.

In conclusion, the approximations leading to the results displayed in the third column of Table

*Table 2. Parameters of the single exponential form for the Born repulsive energy in a few alkali halide crystals.**

NaCl	1·05	2·39	1·99	2·02
	0·321	0·288	0·301	0·300
NaBr	1·33	2·07	1·72	1·69
	0·328	0·308	0·322	0·323
KCl	2·05	3·04	2·21	2·19
	0·326	0·309	0·330	0·330
KBr	2·30	5·40	3·34	3·36
	0·336	0·303	0·328	0·328

* For each salt, the upper line reports the values of the pre-exponential parameter (in 10^{-8} erg/molecule) and the lower line reports the values of the hardness parameter (in 10^{-8} cm). The columns correspond to the first four columns of Table 1. Complete tables of the repulsive parameters are available.

1 represent the best of the simple Born-model treatments considered here for the cohesive energy of the alkali-halide crystals at atmospheric pressure. This treatment involves the use of a single exponential form for the Born repulsive energy and of the Hildebrand equation of state, and the explicit consideration of the van der Waals energy. The deviations from experiment found in this treatment display no distinct broad regularities, and lie in most salts within the combined uncertainties of the data used in the calculations and of the experimental cohesive energy. Actually, these deviations do not compare unfavorably with the corresponding deviations found by Cubicciotti(4) with the more refined Born–Mayer form for the Born repulsive energy, except in salts such as lithium iodide and sodium iodide where the Born repulsion of like ions is strong. It is also found that the net effect of the inclusion of the van der Waals energy on the calculated cohesive energy, which involves both a change of the pre-exponential factor of the Born repulsive energy and a change of its relative slope, is much smaller (by a factor $\frac{1}{4}$ to $\frac{1}{8}$) than the actual amount of the van der Waals energy itself, confirming a qualitative argument of Born and Huang.(9) Finally, the corrections due to the use of a correct thermodynamic treatment and to the inclusion of the van der Waals energy are found to be approximately additive. Both corrections are clearly necessary to obtain good agreement with experiment, although the former correction is generally more important. Both corrections were neglected by Kapustinskii,(1) and the former correction was neglected by Ladd and Lee(2) and by Baughan.(3)

Acknowledgements—I am indebted to Prof. F. G. Fumi for a critical reading of the manuscript, and to Mr. J. T. Schnute, student aide for the summer of 1962, for programming the calculations on an IBM 1620 computer.

Argonne National Laboratory,
Argonne, Illinois.
Mario Tosi

References

1. Kapustinskii A. F., *Quart. Rev.* **10**, 283 (1956).
2. Ladd M. F. C. and Lee W. H., *Trans. Faraday Soc.* **54**, 34 (1958).
3. Baughan E. C., *Trans. Faraday Soc.* **55**, 736 (1959).
4. Cubicciotti D., *J. chem. Phys.* **31**, 1646 (1959); **33**, 1579 (1960); **34**, 2189 (1961).
5. Guggenheim E. A., McGlashan M. L. and Prue J. E., *Molec. Phys.* **4**, 433 (1961).
6. Fumi F. G. and Tosi M. P., *J. Phys. Chem. Solids* **23**, 1671 (1962).
7. Fumi F. G. and Tosi M. P., *J. Phys. Chem. Solids* **23**, 395 (1962).
8. Mayer J. E., *J. chem. Phys.* **1**, 270 (1933).
9. Born M. and Huang K., *Dynamical Theory of Crystal Lattices*, p. 28. University Press, Oxford (1954).

Absorption edge in degenerate *n*-type gallium arsenide*

(*Received* 28 *March* 1963)

Studies of degenerate semiconductors have described shifts of the absorption edge to both higher(1) and lower(2) energies with increasing carrier concentration. The experimental situation for GaAs is somewhat obscured by the difficulty in finding *n*-type impurities that are well behaved at high carrier concentrations. In a previous study(3) it was shown that at high concentrations selenium enters the GaAs lattice primarily as an unionised complex, giving rise to an absorption starting at about 0·9 eV. The measurements have been extended into the region where the principal absorption mechanism is one of band to band transitions, and the excess absorption due to selenium may be neglected, thereby providing a direct measure of the shift in band edge with electron concentration.

---

* The research reported was sponsored in part by the Manufacturing Technology Laboratory, Aeronautical Systems Division, Air Force Systems Command, U.S. Air Force under Contract No. AF33(600)–37268 and RCA Laboratories, Princeton, New Jersey.

Single-crystal specimens used for the transmission measurements were cut from ingots grown by the horizontal Bridgman technique. Hall measurements were made on adjacent slices. Sample thicknesses, of the order of 4μ, were measured interferometrically.

Table 1. The electron effective mass and Fermi level calculated from Kane's theory for the carrier concentrations listed

Sample	$N(\text{cm}^{-3})$	m^*/m_0	ζ (eV)
1	7×10^{16}	0·072	—
2	$5{\cdot}3\times10^{18}$	0·084	0·128
3	$6{\cdot}9\times10^{18}$	0·0855	0·150

Table 1 lists the samples used in this investigation. The total selenium concentration of Sample 3 is about an order of magnitude higher than the electron concentration. The room temperature absorption coefficients as a function of photon energy are shown in Fig. 1. For absorption coefficients $\geqslant 5\times10^2$/cm the absorption rises exponentially, and shifts to higher energies with increasing electron concentration.

Since the band structure of GaAs is the same as InSb, with different effective masses, a relation derived by KAISER and FAN(4) to describe the shift of the absorption edge in degenerate n-type InSb was applied to the GaAs samples investigated:

$$h\nu = Eg+\left[\zeta-kT\ln\left(\frac{\alpha_0}{\alpha}-1\right)\right]\left(1+\frac{m_e}{m_h}\right) \qquad (1)$$

Here $h\nu$ is the photon energy, Eg is the band gap, α_0 and α are the absorption coefficients of the pure and degenerate sample at the frequency ν, ζ is the Fermi energy measured from the bottom of the conduction band, and m_e and m_h are the electron and hole effective masses, respectively. Eg was taken as 1·4 eV and $m_h = 0{\cdot}50\,m_0$.(5) Values of α_0 were taken from the absorption curve of Sample 1.

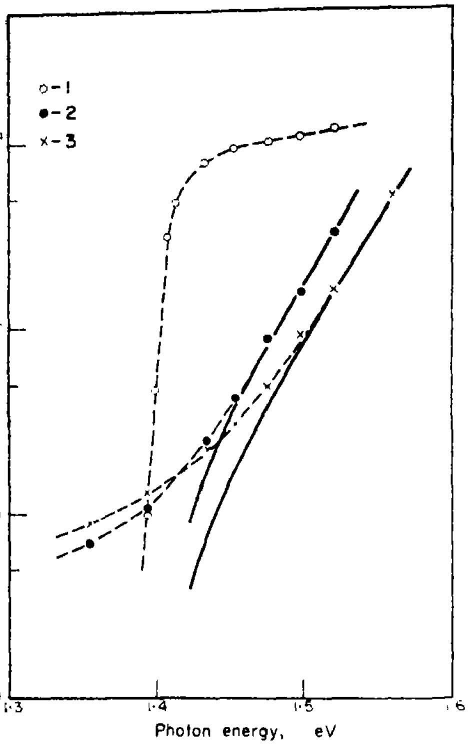

FIG. 1. Absorption coefficient as a function of photon energy at 300°K: experimental data, broken line; calculated curve, solid line.

The electron effective mass of degenerate GaAs has been determined previously.(6, 7) However, the results differ substantially, and do not extend over the entire range of interest. Values of m_e and ζ were, therefore, determined by applying KANE's(8) theory for InSb to GaAs. The E-k curve for GaAs has been computed from Kane's theory by MOSS,(9) and the same parameters were used in the present calculation. The electron effective mass and Fermi energy corresponding to the appropriate carrier concentrations are listed in Table 1. The effective mass determined by SPITZER and WHELAN(6) for a sample of $n = 5{\cdot}4\times10^{18}$ cm^{-3} agrees within experimental error with the value obtained for Sample 2.

The absorption curves calculated from equation (1) are shown as solid lines in Fig. 1. The good agreement with the data indicates that the band structure remains unchanged for these impurity concentrations; i.e., the shape of the absorption edge is determined by the shift of the fundamental absorption edge to higher energies as a result of the filling of the bottom of the band by conduction electrons (BURSTEIN shift[10]). This shift is in quantitative agreement with the conduction band model of Kane.

Radio Corporation of America,
RCA Laboratories,
Princeton, New Jersey.
I. KUDMAN
L. VIELAND

References

1. GOBELI G. and FAN H. Y., *Phys. Rev.* **119**, 613 (1960).
2. PANKOVE J., *Phys. Rev. Letters* **4**, 454 (1960).
3. VIELAND L. and KUDMAN I., *J. Phys. Chem. Solids* **24**, 437 (1963).
4. KAISER W. and FAN H. Y., *Phys. Rev.* **98**, 966 (1955).
5. EDMOND J. T., BROOM R. F. and CUNNELL F. A., *SERL Tech. J.* **6**, 123 (1956).
6. SPITZER W. G. and WHELAN J. M., *Phys. Rev.* **114**, 59 (1959).
7. CARDONA M., *Phys. Rev.* **121**, 752 (1961).
8. KANE E. O., *J. Phys. Chem. Solids* **1**, 249 (1957).
9. MOSS T. S., *J. appl. Phys. Suppl.* **32**, 2137 (1961).
10. BURSTEIN E., *Phys. Rev.* **93**, 632 (1954).

Thermodiffusion in den Hochtemperaturphasen von Zirkon und Titan

(*Received* 1 *February* 1963)

VOR einiger Zeit ist die Thermodiffusion in mehreren Kupfer-Zinn-Legierungen beschrieben worden.(1) Bei diesen Versuchen beobachtete man besonders grosse Dimensions- und Gefügeänderungen an der Phasengrenze Tieftemperatur-/Hochtemperaturphase. Dies ist eine Folge der an der Phasengrenze auftretenden sprunghaften Änderung der Beweglichkeiten. Es lag nahe, auch Reinmetalle, die bei höheren Temperaturen ihre Kristallstruktur ändern, zu untersuchen.

Bisher sind Transporterscheinungen im Temperaturgefälle von folgenden Reinmetallen bekannt: Gold,(2, 3) Platin,(3, 4) Kupfer(2, 3) Aluminium(3) und γ-Eisen.(5) Auch bei Wolfram(6) und Tantal(7) ist aus der Oberflächengestalt, die sich im Temperaturgefälle ausbildet, auf Vorhandensein und Richtung eines Materiestromes geschlossen worden.

Zur Durchführung der Versuche werden rohrförmige Proben aus Titan* und Zirkon† mit einem Aussendurchmesser von 5 mm, einem Innendurchmesser von 3 mm und einer Länge von 50 mm zwischen gekühlten Kupferbacken eingespannt und mit Wechselstrom von 50 Hz belastet. Während der Versuche wurde ein Vakuum von $< 10^{-5}$ Torr aufrechterhalten. Die Versuchsanordnung bedingt ein symmetrisches Temperaturgefälle mit nahezu parabolischer Temperaturverteilung. Im mittleren Bereich der Proben bildet sich die Hochtemperaturphase aus (Abb. 1a und 2a). Die Glühdauer der einzelnen Titan- und Zirkonproben betrug 72 bzw. 48 Stunden bei einer Maximaltemperatur in der Probenmitte von 950°C. Die Abkühlungsgeschwindigkeit nach dem Versuch betrug ca. 10° pro Minute. Im einzelnen ist die experimentelle Anordnung in einer anderen Arbeit(1) beschrieben worden.

Die Umwandlungstemperatur von Titan ist 882°C. Bei Raumtemperatur liegt Titan in der hexagonalen Kristallstruktur vor, die Hochtemperaturphase ist kubisch-raumzentriert. Die Umwandlungstemperatur des Zirkons ist 862°C. Zirkon kristallisiert unterhalb und oberhalb der Umwandlungstemperatur in den gleichen Kristallstrukturen wie Titan.

In Abb. 1(a) ist für eine Zirkonprobe der Temperaturverlauf als Funktion der Ortskoordinate dargestellt. Die Phasengrenzen sind eingezeichnet. In Abb. 1(b) sind die nach dem Versuch vorgefundenen Abstandsänderungen (punktierte Kurve, linker Masstab) ebenfalls gegen die Ortskoordinate aufgezeichnet. Bei mikroskopischer Betrachtung der angeschliffenen Fläche ist die Lage der Phasengrenzen relativ zu den in der Nähe liegenden Markierungen genau festlegbar. Man sieht bei der in Abb. 1(b) dargestellten Zirkonprobe Abstandsverkürzungen zwischen den

---

* Die Analyse des Titans ist: 450 p.p.m. Fe, 70 p.p.m. Si, 15 p.p.m. Mn, 60 p.p.m. N, 600 p.p.m.O. Rest Titan.

† Die Analyse des Zirkons lautet: 400 p.p.m. Fe, 95 p.p.m. C, 70 p.p.m. Hf, 40 p.p.m. Al, 0,2 p.p.m. B, 5 p.p.m. Co, 60 p.p.m. Sr, 20 p.p.m. Cu, 24 p.p.m. Mn, 10 p.p.m. Ni, 5 p.p.m. Pb, 60 p.p.m. Si, 20 p.p.m. Ti, 20 p.p.m. V, 10 p.p.m. Mo. Rest Zirkon.

Markierungen als Folge des Abbaus von Gitterebenen im Bereich der Tieftemperaturphase in unmittelbarer Nähe der Phasengrenzen und Abstandsvergrösserungen im Bereich zwischen den Phasengrenzen als Folge eines Zwischenbaus von Gitterebenen in Achsrichtung. Dies lässt auf eine Wanderung der Atome in Richtung zur höheren Temperatur schliessen. Der Zwischenbau von Gitterebenen innerhalb der Hochtemperaturphase wird aber nicht von einem gleichgrossen Abbau an den Phasengrenzen kompensiert, sodass insgesamt eine Verlängerung der Probe resultiert. Diese Verlängerung lässt sich bei nachträglichem Glühen nur zum Teil rückgängig machen (siehe Abb 1(c) und die Erklärung weiter unten).

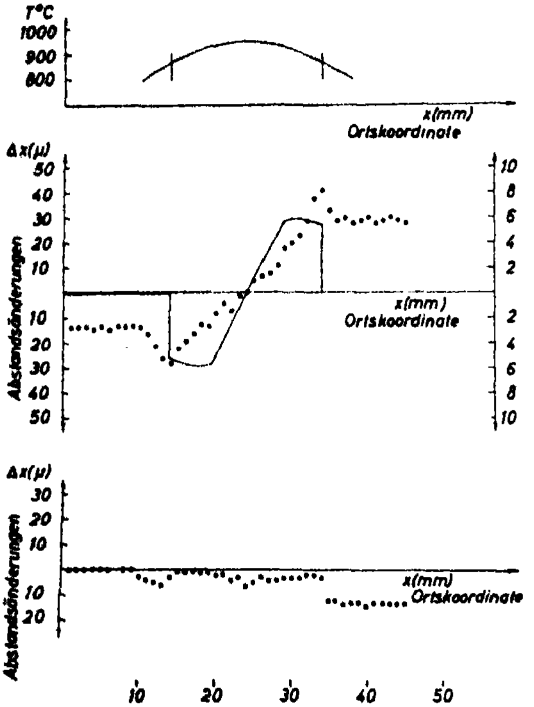

ABB. 1. Temperaturverlauf und Abstandsänderungen von Markierungen als Funktion der Ortskoordinate. (a) Temperaturverlauf längs einer Zirkonprobe. (b) Experimentelle Abstandsänderungen der Markierungen als Funktion der Ortskoordinate bei einer Zirkonprobe (punktierte Kurve, linker Masstab). Berechnete Abstandsänderungen der Markierungen (ausgezogene Kurve, rechter Masstab).

Versuchsbedingungen: Direkte Heizung mit Wechselstrom von 50 Hz, 72 h, T_{max} 950°C, Vakuum $< 10^{-5}$ Torr. (c) Abstandsänderungen der Markierungen als Funktion der Ortskoordinate beim nachträglichen Glühen bei 950°C, Glühdauer 8 h.

Bei den Versuchen ergibt sich eine lineare Abhängigkeit der Markierungswanderung von der Zeit. Die Effekte sind gut reproduzierbar.

Ob dieser unerwartet grosse Effekt bei einem Reinmetall mit den bisherigen Vorstellungen über die Thermodiffusion in Einklang zu bringen ist, lässt sich mit der Berechnung einer theoretisch zu erwartenden Kurve der Abstandsänderungen prüfen. Für eine Maximalabschätzung kann man mit Hilfe der Beziehung zwischen dem Massestrom J einer Komponente im Temperaturgefälle, dem Selbstdiffusionskoeffizienten und der Transportwärme Q^{*}(8)

$$J = \frac{D^{*}}{RT^{2}f}\,Q^{*}\,\frac{\mathrm{d}T}{\mathrm{d}x}\ \text{cm/sec} \qquad (1)$$

die Grösse der zu erwartenden Markierungswanderung berechnen. f ist in Beziehung (1) der Korrelationsfaktor,(9) der für einen Leerstellenmechanismus im kubisch-innenzentrierten Gitter 0,72 beträgt.

Für D^{*} des β-Zirkons sind mehrere unterschiedliche Werte(10, 11, 12) bekannt, von denen wir den grössten einsetzen. Q^{*} ist seinem Betrage nach vom Transportmechanismus abhängig. Die Transportwärme ergibt sich bei Vorliegen einer thermischen Fehlordnung aus der Differenz von Bildungs- und Wanderungsenergien der Leerstellen, kann aber maximal gleich der Aktivierungsenergie für die Diffusion werden. Betrachtet man den Hochtemperaturbereich, nimmt Q^{*} als temperaturunabhängig an und setzt dafür einen Maximalwert von 24 kcal und für $D^{*} = 4{,}2 \times 10^{-5} \exp(-24000/RT)$(10) an, so erhält man die in Abb. 1(b) dargestellte ausgezogene Kurve (rechter Masstab). Bei der Berechnung ist $f = 0{,}727$ gesetzt worden. Aus dem Masstabsunterschied geht hervor, dass die experimentell gefundenen Markierungswanderungen etwa um einen Faktor 5 grösser sind als die berechneten. Eine Thermodiffusion im α-Zirkon kann wegen der kleinen Beweglichkeit der Zirkonatome in der Tieftemperaturphase(12) ausgeschlossen werden.

Die Differenz zwischen beobachteter und berechneter Kurve und insbesondere die

Abstandsverkürzungen innerhalb der α-Phase können verschiedene Ursachen haben :

Einmal könnten gitteraufweitende Einlagerungselemente wie Wasserstoff, Stickstoff, Sauerstoff, Kohlenstoff und Bor eine Rolle spielen, indem sie bei der Diffusion im Temperaturgefälle in dem Volumenelement, aus dem sie herausdiffundieren eine Gitterkontraktion und in den Bereichen, in die sie hineinwandern, eine Gitteraufweitung hervorrufen. Von den erwähnten Einlagerungselementen ist nur Kohlenstoff in dem verwendeten Material vorhanden. Beim Arbeiten im Vakuum bei ca. 10^{-5} Torr können Sauerstoff und Stickstoff nicht in nennenswerten Mengen in die Probe gelangen. Sauerstoff und Stickstoff würden auch wie Rieck und Bruning(13) gezeigt haben, im Temperaturgefälle zum kalten Teil wandern und so in der heissen Mitte eine Kontraktion hervorrufen. Bekannt ist der Einfluss des Kohlenstoffs auf die Thermodiffusionserscheinungen bei γ-Eisen.(5) Hier findet in unmittelbarer Nähe der Phasengrenze α/γ im α-Bereich eine Gitterkontraktion und damit eine Abstandsverkürzung zwischen den Markierungen infolge des Abdiffundierens des Kohlenstoffs in die γ-Phase statt und in der γ-Phase tritt eine Gitteraufweitung ein. Eine weitere Möglichkeit der Erklärung der Kurve der Abstandsänderungen ist der Einfluss der Umwandlung auf Dimensionsänderungen. Bei Glühversuchen mit Zirkonproben bei 950°C und homogener Temperatur wurden jedoch keine Dimensionsänderungen festgestellt. Im Schliffbild sind Anzeichen für ein bevorzugtes Kornwachstum in Achsrichtung wie man sie bei Titan (siehe weiter unten) und Eisen(5) beobachten kann, nicht zu finden. Möglicherweise überdeckt der Zerfall der β-Körner bei der Umwandlung die Beobachtung der während des Versuchs bevorzugt in Achsrichtung gewachsenen Körner.

In Analogie zu den Dimensionsänderungen bei Thermodiffusionsversuchen an innenzentrierten Kupfer–Zinn-Phasen,(1) ist es denkbar, dass die Abbauerscheinungen in der Nähe der Phasengrenze im α-Gebiet auf das Ausheilen von Leerstellen zurückzuführen sind und einen Ausstrahlungseffekt darstellen. Nimmt man an, dass Leerstellen aus der β-phase an die Phasengrenze herandiffundieren und dort ausheilen, so ist es denkbar, dass sie auch in die α-Phase eindringen. Wenn auch von mehreren Autoren,(1, 14–17) mittlere freie Weglängen von Leerstellen bei höheren Temperaturen bis zu 1 mm gefunden wurden, so erscheint doch der hier beobachtete Wert von mehreren Millimetern sehr hoch. Beim nachträglichen Glühen bei homogener Temperatur tritt eine weitere Dimensionsänderung auf, wie Abb. 1(c) zeigt. In unmittelbarer Nähe der Phasengrenzen findet im α-Bereich eine Abstandsverkürzung der Markierungen von ca. 10 μ entsprechend einem nachträglichen Abbau von Gitterebenen statt. Dies deutet daraufhin, dass das Leerstellengleichgewicht sich während des Thermodiffusionsversuches nicht einstellt. Auch die Probenoberfläche wirkt als Leerstellensenke, sodass ein Teil der an die Phasengrenze herandiffundierenden Leerstellen an der Oberfläche in der Nähe der Phasengrenzen ausheilen kann. Dies würde die Diskrepanz zwischen dem Betrag des Abbaus an der Phasengrenze und dem Betrag des Zwischenbaus innerhalb der Phase erklären können.

Eine restlos befriedigende Erklärung für den Unterschied zwischen beobachtetem und berechnetem Thermodiffusionseffekt kann noch nicht gegeben werden. Möglicherweise gilt im vorliegenden Fall nicht der für einen Leerstellenmechanismus berechnete Korrelationsfaktor, sondern ein kleinerer Wert. Aus einigen anderen Arbeiten(z.B.4) geht hervor, dass auch die Transportwärme temperaturabhängig sein kann. Ein temperaturabhängiges Q^* könnte eine Korrektur an der berechneten Kurve ergeben.

Abb. 2(a) zeigt den Temperaturverlauf auf einer Titanprobe und in Abb. 2(b) sind die nach dem Versuch vorgefundenen Abstandsänderungen gegen die Ortskoordinate aufgetragen. Es hat den Anschein, als ob innerhalb der Tieftemperaturphase keine Dimensionsänderungen auftreten. In der Nähe der Phasengrenze innerhalb der Hochtemperaturphase ist eine Abstandsvergrösserung zwischen den Markierungen als Folge des Zwischenbaus von Gitterebenen zu beobachten. Zur heissen Mitte hin schliesst sich ein Gebiet an, in dem die Abstandsverkürzungen auf den Abbau von Gitterebenen schliessen lassen. Aus dem Diagramm entnimmt man, dass der Materiestrom in der Hochtemperaturphase des Titans zu niedrigeren Temperaturen gerichtet ist. Die Abstandsverkürzungen überwiegen die Abstandsvergrösserungen, sodass insgesamt eine Verkürzung der Probe eintritt. Diese Verkürzung wird nur zum Teil bei nachträglichem Glühen wieder rückgängig gemacht, wie Abb. 2(c) zeigt (siehe weiter unten). Der Effekt der Verkürzung (Ti) bzw. der Verlängerung (Zr) der Proben im Temperaturgefälle ist auch bei anderen Reinmetallen z.B. Fe⁽⁵⁾ und an Kupfer-Zinn-Legierungen⁽¹⁾ gefunden worden, ohne dass bisher eine befriedigende Erklärung dazu vorliegt.

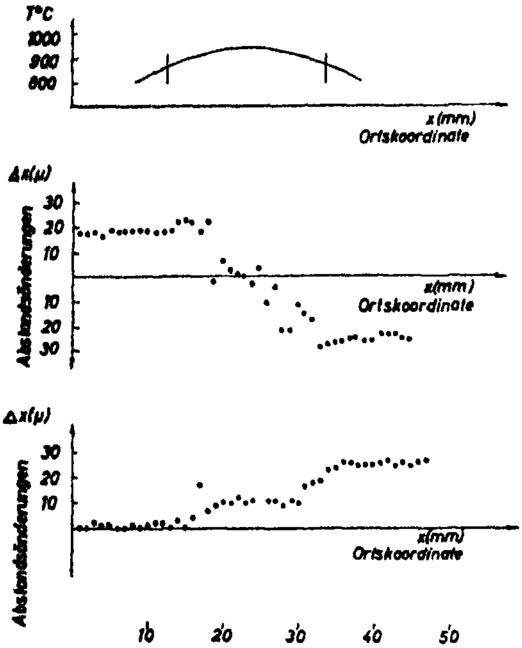

Abb. 2. Temperaturverlauf und Abstandsänderungen von Markierungen als Funktion der Ortskoordinate. (a) Temperaturverlauf längs einer Titanprobe. (b) Abstandsänderungen der Markierungen als Funktion der Ortskoordinate bei einer Titanprobe.

Versuchsbedingungen: Direkte Heizung mit Wechselstrom von 50 Hz, 48 h, T_{max} 950°C, Vakuum $< 10^{-5}$ Torr. (c) Abstandsänderungen der Markierungen als Funktion der Ortskoordinate beim nachträglichen Glühen bei 950°C, Glühdauer 8 h.

Die sprunghaften Änderungen in der Kurve der Markierungsverschiebungen sind auf das grosse Kornwachstum in der Hochtemperaturphase in der Probenmitte zurückzuführen. Das Kornwachstum scheint durch die Transporterscheinungen im Temperaturgefälle gefördert zu werden. In Abb. 3 sieht man die Phasengrenze zwischen Tief- und Hochtemperaturphase und das bevorzugte Wachstum der Körner in Achsrichtung. Über die bei diesen Versuchen durch das Zusammenwirken von Transporterscheinungen und thermischer Ätzung an Titanproben auftretende Oberflächengestalt ist in einer anderen Arbeit⁽¹⁸⁾ berichtet worden.

Wie Glühungen von unbehandelten Titanproben bei homogener Temperatur zeigen, kann man wie im Falle des Zirkons. Dimensionsänderungen keine feststellen. Dagegen ergibt sich bei Glühungen nach dem Thermodiffusionsversuch im Hochvakuum bei 950°C und homogener Temperatur an den Phasengrenzen in dem Bereich, in dem während des Thermodiffusionsversuches ein Zwischenbau erfolgte, ein weiterer Zwischenbau von ca. 12μ, wie Abb. 2(c) zeigt. Dies lässt darauf schliessen, dass sich das Gitterfehlstellengleichgewicht während des Versuchs nicht einstellt. Der nachträgliche Zwischenbau lässt einen Zwischengittermechanismus bei der Diffusion im Temperaturgefälle möglich erscheinen. Wieweit das grosse Kornwachstum die Thermodiffusionserscheinungen innerhalb der Phase geringfügig überdeckt, ist noch nicht zu übersehen.

Eine ähnliche Abschätzung der Grösse des zu erwartenden Effektes wie bei Zirkon kann noch nicht gegeben werden, da ein Selbstdiffusionskoeffizient von Titan wegen des Fehlens eines geeigneten Isotops noch nicht gemessen wurde. Man kann aber aufgrund der Arbeiten von Peart und Tomlin⁽¹⁹⁾ annehmen, dass die Aktivierungsenergie und der Frequenzfaktor für die Selbstdiffusion des β-Titans in der gleichen Grössenordnung wie für β-Zirkon liegen. Betrachtet man umgekehrt für eine Abschätzung des Selbstdiffusionskoeffizienten aus den Thermodiffusionsdaten den Bereich der Phasengrenze, setzt die Abstandsänderungen ein und nimmt den gleichen Betrag für die Transportwärme wie bei Zirkon an, so ergibt sich für den Diffusionskoeffizienten des β-Titans bei der Temperatur

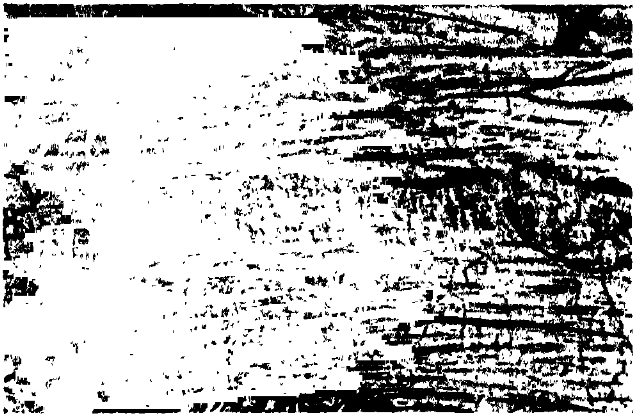

ABB. 3. Übersichtsaufnahme an der Phasengrenze Tieftemperatur-/Hochtemperaturphase. Innerhalb der Hochtemperaturphase in Achsrichtung gewachsene Körner.

der Umwandlung aufgrund der Beziehung (1)

$$D^{*}_{\mathrm{Ti}\ 882^{\circ}\mathrm{C}} \sim 5\times 10^{-10}\ \mathrm{cm}^{2}/\mathrm{sec}$$

Die Ergebnisse zeigen, dass die Transportwärme des Zirkons in der Hochtemperaturphase positiv ist. Die Transportwärme des Titans in der Hochtemperaturphase scheint dagegen negativ zu sein. Die Grösse der Transportwärmen kann noch nicht angegeben werden. Die Diffusion im Temperaturgefälle zeigt eindeutig, dass in den kubisch-innenzentrierten Gittern der Hochtemperaturphasen von Titan und Zirkon die Diffusion im Temperaturgefälle nicht über einen Ringmechanismus verläuft, wie das für das ebenfalls kubisch-innenzentrierte α-Eisen vermutet wird.⁽²⁰⁾ Während bei Titan die Diffusion im Temperaturgefälle möglicherweise über einen Zwischengittermechanismus abläuft, deuten die Ergebnisse bei Zirkon auf einen Leerstellenmechanismus hin. Die Grösse des Effekts ist mit dem normalen Leerstellenmechanismus allerdings nicht zu erklären.

Weitere Versuche sind im Gange.

Institut für Metallkunde der
Technischen Universität Berlin,
Berlin 12

H. G. Feller
H. Wever

Literatur

1. Feller H. G., Wever H., *Z. Metall.* **17**, 414 (1963).
2. Meechan C. J. und Lehmann G. W., *J. appl. Phys.* **33**, 634 (1962).
3. Huntington H. B. und Ho S.-C.: Preprint.
4. Hehenkamp Th. und Ho S.-C.: *Phys. Rev. Letters*, eingereicht.
5. Feller H. G.: *Arch. Eisenhüttenw.* eingereicht.
6. Johnson R. P., *Phys. Rev.* **54**, 459 (1938).
7. Mrowca B. A., *J. appl. Phys.* **14**, 684 (1943).
8. Wever H., *Z. Naturf.* im Druck.
9. Compaan K. und Haven Y., *Trans. Faraday Soc.* **52**, 1 (1956).
10. Volokoff D., May S. und Adda Y., *C.R. Acad. Sci. Paris* **251**, 2341 (1960).
11. Kidson G. und McGurn J., *Canad. J. Phys.* **39**, 1146 (1961).
12. Lyashenko V. S., Bykov V. N. und Pavlinov L. V. *Phys. Met. Mettallogr.* **8**, 40 (1958).
13. Rieck G. D. und Bruning H. A. C. M., *Nature, Lond.* **190**, 1181 (1961).
14. Balluffi R. W., *Acta Met.* **2**, 194 (1954).
15. Starke E., *Dissertation TU Berlin* (1962).
16. Wever H., *Habilitationsschrift TU Berlin*, 83 (1958).
17. Lee C. H. und Maddin R., *J. appl. Phys.* **32**, 1846 (1961).
18. Feller H. G. und Feller-Kniepmeier M., *Z. Metallk.* **54**, 296 (1963).
19. Peart R. F. und Tomlin D. H., *Acta Met.* **10**, 123 (1962).
20. Brammer W. G., *Acta Met.* **8**, 630 (1960).

Electrical properties of single crystal Bi_2S_3*

(*Received* 25 *March* 1963)

There has been no previous literature published on the electrical properties of single crystals of bismuth trisulfide at temperatures other than 300°K.⁽¹⁾ The electrical properties of this material, particularly in single crystal form, are important because the high Seebeck coefficient (550 μV/°C at 300°K) makes it of some interest in thermoelectric applications.

In a previous investigation several single crystals of Bi_2S_3 were produced using a modified zone melting technique.⁽¹⁾ One of these crystals was used in the present investigation. The crystal as grown was in the form of a boule about 8 cm in length and 1·5 cm in diameter. The (010) plane, which is the principal cleavage plane for this material, was inclined to about a 45° angle with the growth axis. The samples used for Hall and conductivity measurements were cleaved from the central portion of the boule. The conductivity samples had dimensions on the order of 15 × 5 × 2 mm. In the following data all measurements were made with the current flow parallel to the cleavage planes. It was found to be very difficult to prepare samples with other orientations because of the brittleness of the material.

Chemical analysis of bismuth in the central portion of the boule showed that there is an excess of sulfur on the order of 0·1 per cent over that required for stoichiometric proportions. Spectroscopic analysis indicated no impurities. The sensitivity of the analysis was about 10 p.p.m.

Electrical leads were attached to the sample by melting small drops of lead in a V of nichrome wire; when the droplet reached a temperature where the oxide film disappeared the droplet was

---

* This work supported by the U.S. Atomic Energy Commission.

touched to the sample surface. The resulting contact was ohmic, physically strong, and soldered connections could be made to it. This technique for making contact minimizes the heating of the bulk of the sample.

Conductivity measurements were made by a standard four probe method. The Hall measurements were made using an a.c. method with narrow band detection. This technique appears to be required with Bi_2S_3 because the large amount of noise inherent in the material tends to obscure the Hall signal.

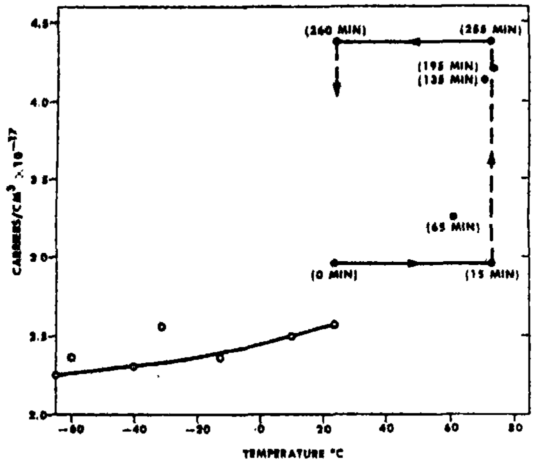

FIG. 1. Temperature dependence of carrier density taken from Hall effect measurements.

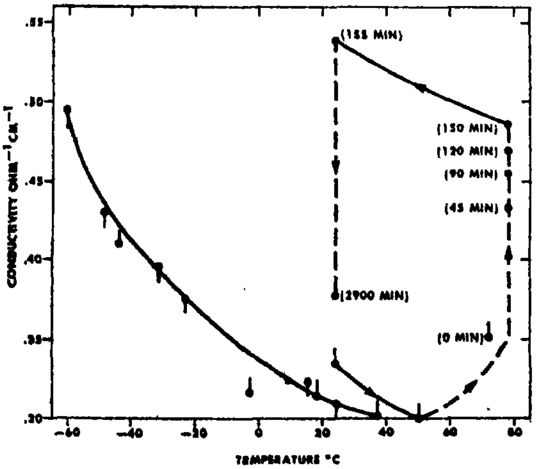

FIG. 2. Temperature dependence of conductivity.

The material exhibits certain instabilities, particularly above room temperature, which makes the conductivity and Hall data not entirely reproducible. The data in Figs. 1 and 2 have been selected to show typical behavior of our samples and they suggest that three effects are required for a consistent explanation. First, as reflected in the lower temperature Hall measurements, there is a very weak *direct* dependence of the carrier concentration on temperature. If the data below 25°C are interpreted in terms of an activated process, the activation energy is less than 0·01 eV. Second, a typical decrease in mobility with increasing temperature is observed (Fig. 3). We have found the mobility to be quite reproducible, and, unlike the other properties, to be independent of the sample's immediate history. Third, at temperatures above room temperature (e.g. 70°C) there is a slow increase in the carrier density with time at a fixed temperature. This is reflected in the conductivity as well as the Hall effect. Based on the slow rate at which the carrier density changes (see time markings on Figs. 1 and 2) and the fact that the rate is much slower at room temperature than at 70°C, we speculate that the change in carrier density is associated with a change in chemical composition which is temperature dependent and diffusion controlled.

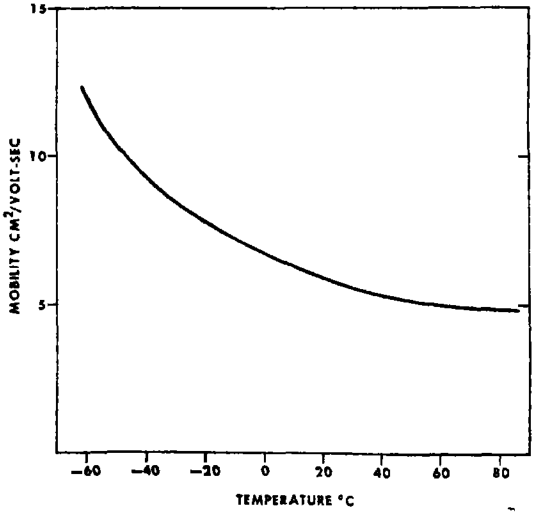

FIG. 3. Temperature dependence of mobility.

Rapid cooling from a high temperature quenches in the high temperature composition. This is seen in Fig. 1 where Hall measurements show that there is no change in carrier concentration when the sample is quenched from 73 to 24°C within a 5 min. interval. The conductivity shows a similar effect, but with a superimposed mobility change. Both carrier density and conductivity decrease toward their original values upon prolonged storage at room temperature. Below room temperature compositional changes proceed so slowly that they play no part in the measurements.

The calculation of the mobility curve in Fig. 3 is not entirely straightforward since it has not been possible to make simultaneous measurements of the conductivity and the Hall effect on the same sample. From room temperature down the calculation is made using data taken on samples which have been kept at room temperature or lower after being cleaved from the boule. Above room temperature the curve is obtained by extrapolation and then checked under the assumption that changes in conductivity upon quenching from 70 to 24°C are due entirely to mobility changes. In plotting the conductivity certain of the solid lines are curved without direct support of data points. The curvature is such as to reflect the shape of the mobility curve.

These results are at variance with those obtained from sintered, polycrystalline and thin film samples.(1–4) In all except single crystals large exponential dependences of conductivity on the temperature have been observed. BLACK *et al.*(2) report carrier concentrations of $3 \times 10^{18}/\text{cm}^3$ at 300°K for polycrystalline material, about a factor of ten larger than found here in single crystals.

Sandia Corporation,
Albuquerque,
New Mexico.

RICHARD C. HECKMAN
D. M. MATTOX

References

1. GILDART L., KLINE J. M. and MATTOX D. M., *J. Phys. Chem. Solids* **18**, 286 (1961).
2. BLACK J., CONWELL E. M., SEIGLE L. and SPENCER C. W., *J. Phys. Chem. Solids* **2**, 240 (1957).
3. KONOROV P. P., *Zh. tekh. fiz.* **26**, 1126 (1056); English translation: *Sov. Phys.—Tech. Phys.* **1**, 1100 (1957).
4. GORIUNOVA N. A., KOLOMIETS B. T. and MAL'KOVA A. A., *Zh. tekh. fiz.* **26**, 1625 (1956); English translation: *Sov. Phys.—Tech. Phys.* **1**, 1583 (1957).

BOOK REVIEWS

ALBERT DE SY and JULIEN VIDTS. **Metallurgie Structurale.** Dunod, Paris, 1962. 480 pages. 75F.

THIS book is written (in French) for students in metallurgical or mechanical engineering. The first and second chapter (about one fourth of the book) are devoted to a rapid summary of our basic knowledge on pure metals and alloys: structure of perfect crystals, imperfection in crystals, work-hardening and creep, diffusion, alloys and their phase diagrams. In the third chapter the authors describe the techniques of metallographic observation. It is to be noted that X-ray diffraction is quite ignored.

Then the authors describe in detail the main properties of current metals and alloys. This is the most useful part of the book although an index and some bibliographic references would be a great help to the reader.

G. SAADA

V. K. SEMENCHENKO: **Surface Phenomena in Metals and Alloys.** Addison–Wesley, Reading, Massachusetts (1962). 466 pp. $14.75.

THIS book was originally published in 1957 by V. K. SEMENCHENKO whose researches have contributed a great deal to what is presently known about metal surfaces. As he himself points out, his collaborators contributed about one-quarter of all the data on surface tension of metals which exists in the present world literature.

The book covers general discussions on surface tension in metallic and non-metallic systems, the thermodynamics of surface phenomena including the developments of J. WILLARD GIBBS and IRVING LANGMUIR, the molecular statistical theories, single and multiple-component systems, surface phenomena in solids, effect of impurities, and theory of surface tension. Detailed treatment is included on effect of impurities on properties of metals, including recrystallization temperatures and microstructure.

The approach used by the author emphasizes theory somewhat more than it does either experiment or experimental results, although both areas are covered.

The barriers in the way of constructing an adequate theory of surface tension apparently are great, even for pure metals. Attempts in this direction, it is stated, are mostly by Russian scientists, the first publication in this regard being by YA. FRENKEL in 1917. The calculated value in terms of electrostatic energy of the surface double layer are in good agreement with observations for mercury but not for other metals. Subsequent theoretical contributions by others are described in detail, but they also leave something to be desired insofar as agreement with experiment is concerned. However, as the author points out, this situation is not unexpected in view of the present imperfect theories of liquids and metals.

The reviewer was unable to find any mention of the determination of surface energies of solid metals by the balanced weight method described by TAMMANN, and later by UDIN *et al.* The results of these researches are of sufficient importance to have merited detailed description in a book of this kind.

On p. 17, it is pointed out that the Russian, A. BACHINSKII in 1922 was the first to show the connection between surface tension and differences in density of two phases. A similar relation was reported one year later in the *Transactions of The Faraday Society* by B. MACLEOD. Two years later, S. SUGDEN used this relation to derive the familiar "parachor". Subsequently, R. H. FOWLER attempted a theoretical derivation of the parachor, but this in SEMENCHENKO's opinion falls short of the mark and is not valid.

It may come as a surprise to find on p. 100 that presently we have neither a firmly established value for the surface tension of mercury nor do we know the form of its temperature dependence. The main difficulty is apparently one of metal purity, which greatly influences surface tension.

Al and Mn increase the surface tension of tin; the author shows that these elements must, therefore, lower the recrystallization temperature, and it is observed that they do, reaching values somewhat below room temperature. On the other hand, Na, Bi and Te are surface active and they raise the recrystallization temperature. Zn behaves anomalously, increasing both surface tension and the recrystallization temperature. Other interesting data of this kind appear throughout various chapters.

The translation is well-done. The photo off-set process used by the publisher is less than pleasing and some of the formulae are obscure and difficult to read. One hopes that the present book does not represent a trend in the mechanics of publishing specialized monographs of this kind. The location of all the tables at the back of the book is not convenient.

The monograph fills a real need in the scientific literature on a subject which is treated much less thoroughly in related treatises. It is a useful reference source to all those who are concerned with surface properties of metals including grain boundary properties.

H. H. UHLIG

J. Phys. Chem. Solids Pergamon Press 1963. Vol. 24, pp. 979–984. Printed in Great Britain.

ELECTRICAL CONDUCTIVITY IN LEAD TITANATE ZIRCONATE CERAMICS

R. GERSON* and **HANS JAFFE**

Electronic Research Division, Clevite Corporation, Cleveland, Ohio

(*Received* 14 *February* 1963; *revised* 4 *April* 1963)

Abstract—Ferroelectric lead titanate zirconate ceramics prepared by sintering in air are found to have *p*-type conductivity, believed to result from an excess of lead vacancies. Donor substituents for lead, titanium, or zirconium reduce the conductivity by electron-hole compensation, but *n*-type conductivity is not observed and is probably prevented by the formation of lead site vacancies. The data supporting this view are presented. These include observations on the effect of donor and acceptor doping and of oxygen pressure during sintering on resistivity, and measurements of thermal e.m.f. A comparison is made between effects observed in lead titanate zirconate ceramics and those in barium titanate, which can have high *n*-type conductivity at room temperature after doping, and in barium zirconate.

INTRODUCTION

In investigations of the dielectric and piezoelectric properties of perovskite lead titanate–lead zirconate ceramics,(1–6) the conductivity of these materials has in general received attention only as a secondary matter, although the 1000-fold increase in resistivity caused by additives of excess valency(7) has become of great practical significance. It is the purpose of this article to present experimental results on this conductivity and an interpretation of these results. The interpretation will be extended to consider ceramic barium titanate, a material whose conductivity behavior is less clear-cut.

The nature of the electronic processes in certain compounds consisting of an element from Group II of the Periodic Table and another from Group VI, such as the sulfides, selenides, and tellurides of cadmium and zinc, has been extensively studied. Two recent reviews contain references to much of the work in this field.(8, 9) In these compounds it was found that the stoichiometry played a major part in determining the conduction mechanism. Vacancies in the position of the Group II element were found to serve as acceptors and those of the Group VI element as donors. "Pure" single crystals of some II–VI compounds, e.g. CdS and CdSe, are *n*-type, while those of ZnTe are *p*-type conductors. It is easy to bring these crystals to a high resistivity state by adding acceptor impurities to the former and donor impurities to the latter crystal, but formation of additional vacancies makes it difficult to change the conduction type of a given compound. *n*-type conductivity due to oxygen deficiency was observed long ago in titanium dioxide and zinc oxide. Rudolph(10) has shown that *p*-type conductivity is present in several pure simple oxides, including BaO and ZrO_2, fired in air.

He explains this by a state of "over-oxidation," that is, metal site vacancies. It has been suggested that a similar situation occurs in lead titanate zirconate ceramics(11) and that excess valency substituents compensate for this deficiency.

In the present investigation it is demonstrated that the usual lead titanate zirconate ceramic fired in air is indeed a *p*-type semiconductor in the temperature range between 100 and 600°C. The *p*-type conduction is probably due to vacancies at lead sites, and the usual criteria of *p*-type conduction are present: thermal e.m.f. measurements result in a positive Seebeck coefficient, the electrical resistivity is decreased as the oxygen

---

[*] Present address: Missouri School of Mines and Metallurgy, Rolla, Missouri.

pressure used during the firing of the ceramic is increased, and an increase in electrical resistivity is found when *n*-type substituents are added to compensate the *p*-type conduction.

MEASUREMENTS

1. *Thermal e.m.f.*

One would like to measure this quantity at a temperature where the resistivity is high, in order to establish the characteristics of the ceramic in the insulating condition. The difficulty is that if the resistivity of the ceramic is much in excess of 10^6 Ω cm, the thermoelectric effect is masked by extraneous electrochemical potentials, which are invariably present in these ceramics. The samples used were typically about 1 cm dia. and 1 mm thick, and had both plane surfaces coated with a thin layer of DuPont silver frit to improve electrical and thermal contact. The silvered faces were placed between stainless steel pistons, one of which was kept about 20°C hotter than the other by an auxiliary heating coil. The measured data for a number of ceramics are given in Table 1. It is seen that, except for the one sample of barium titanate which had received a treatment in a reducing atmosphere, all of the ceramics measured were *p*-type. As quantitative results, however, it is difficult to assess the numerical accuracy of these data. Slight variations in impurity content, atmosphere during firing, or rate of cooling may be expected to affect the numerical magnitudes, but not the sign of the Seebeck coefficient.

2. *Conductivity as a function of oxygen pressure*

The conductivity of two of the ceramics was determined after firing under neutral and oxidizing conditions. The samples measured were disks about the same size as those used for thermal e.m.f. measurements and had their flat surfaces coated with DuPont silver frit. The density of the samples exceeded 96 per cent of the theoretical value calculated from X-ray determination of lattice parameters. Guard rings were not used for the measurements, because in the 150–400°C temperature range surface conductivity is negligible. The instrument used was a Bruel and Kjaer megohmmeter, which applies a d.c. potential of about 100 V. The measuring field gradient was therefore about 100 V per mm; at low fields resistivity is substantially independent of field gradient.

In the ceramic, whose resistivity temperature curves are shown in Fig. 1, the effect of increased oxygen during sintering is clearly to lower the resistivity. This is characteristic of a *p*-type oxide in which the holes are generated by ionization of metal vacancies. Increasing oxygen pressure reduces the concentration of oxygen vacancies and therefore, as a result of the Mass Action Law, the number of metal vacancies is increased and more holes are created.

Table 1. *Seebeck coefficient of ferroelectric perovskites*

Composition	Temperature of measurement (°C)	Seebeck coefficient (μV/°C)	Resistivity (Ω cm)	Conductivity type from Seebeck coefficient
$Pb_{0.94}Sr_{0.06}Zr_{0.53}Ti_{0.47}O_3$	460	500	10^4	*p*
$PbZr_{0.52}Ti_{0.48}O_3$	420	1300	2×10^7	*p*
+1 wt.% Nb_2O_5	540	900	2×10^6	*p*
$BaTiO_3$	490	600	5×10^4	*p*
$BaTiO_3$ + 1 wt.% Nb_2O_5	550	600	7×10^5	*p*
$BaTiO_3$ + ½ wt.% Nb_2O_5 Reduced in carbon at 900°C.	330	−300	4×10^4	*n*

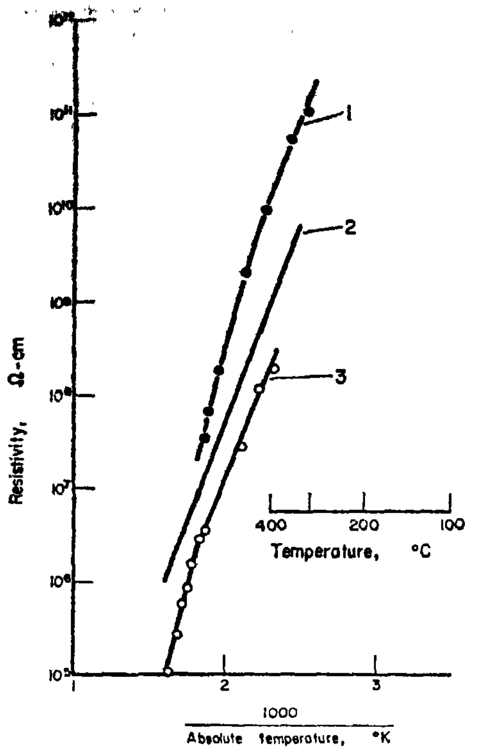

FIG. 1. Resistivity–temperature curves for $Pb_{0.94}Sr_{0.06}Zr_{0.53}Ti_{0.47}O_3$ fired in gases of varying oxygen content. Curve (1): Firing atmosphere was nitrogen with an oxygen partial pressure of approximately 1 Torr. Curve (2) Average curve for air-fired ceramic. Curve (3) Firing atmosphere was oxygen at a pressure of 8 atm.

The influence of grain boundaries on resistivity in these materials has not been fully evaluated, but does not seem to be major. When the ceramic is over 90 per cent dense, the resistivity was found independent of the exact density attained in a given atmosphere. In addition samples of undoped ceramic whose average grain sizes differed by an order of magnitude were found to have essentially the same resistivity.

3. *Effect of doping*

The doping of ceramics may be carried out with either donors or acceptors, and the effect of each depends on whether the ceramic is *n*- or *p*-type at the pressure and temperature of sintering. Figure 2 shows the resistivity as a function of temperature for air-fired lead titanate zirconate ceramics with niobium or scandium added for doping. The measurements were made as described in the previous experiment.

The substitutional site of niobium, based on its ionic radius, should be the titanium position. Since the normal valency of niobium is +5, rather than the +4 value found in titanium, niobium may be expected to function as a donor. Scandium has a valency of +3 and is expected to behave as an acceptor when substituting for titanium.

Figure 2 shows that donor additions increase the resistivity, while acceptor additions decrease it. This is added evidence that the ceramic is a *p*-type conductor whose conductivity is increased

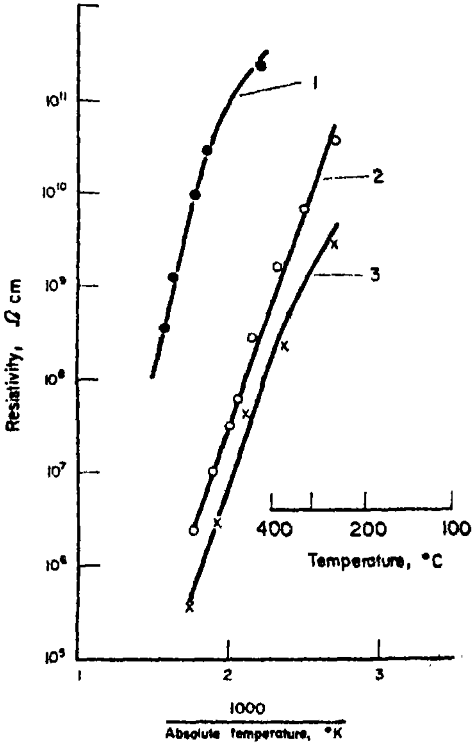

FIG. 2. Resistivity–temperature curves for lead titanate zirconate ceramics with donor and acceptor additions. Curve (1): Donor addition, ceramic composition $(PbZr_{0.52}Ti_{0.48}O_3)_{0.98}+(PbNb_2O_6)_{0.02}$. Curve (2) No addition, ceramic composition $PbZr_{0.53}Ti_{0.47}O_3$. Curve (3) Acceptor addition, ceramic composition $(PbZr_{0.53}Ti_{0.47}O_3)_{0.99}+(PbSc_2O_4)_{0.01}$.

somewhat by acceptor substituents (Sc) but reduced drastically through compensation by donor substituents (Nb).

If the above hypothesis is correct, it should follow that similar electrical behavior will be measured when other elements are added as dopants. It was found(7) that additions of one mole per cent of tantalum, neodymium, or lanthanum were equivalent to the niobium addition. Tantalum also has a valency of +5 and fits the titanium position, while neodymium and lanthanum have a valency of +3 and fit the lead position, replacing a divalent element. Potassium, an element of valency +1 and ionic radius of the right size for the lead position, behaves exactly as scandium does in increasing the conductivity and may also be classified as an acceptor.

The compensation effect is achieved with a few tenths mol per cent of donor substituent or more. In our experience with hundreds of samples it has never been found that increased amounts of donor cause the resistivity to drop again by formation of *n*-type carriers. This may be explained by the relatively easy expulsion of lead during firing of ceramics with more donor substituent than needed to overcome the electron deficiency (see Appendix).

DISCUSSION

The method of regulating the vacancy equilibria and hence the conductivity of simple oxide ceramics by varying the oxygen pressure has been explored previously.(10) The fact that titanium dioxide in its rutile modification is an *n*-type semiconductor, and that perovskite barium titanate behaves like rutile in becoming a semiconductor after reduction in hydrogen, seemed to indicate that perovskite titanates will be *n*-type. As was shown above this conclusion is not valid for lead titanate zirconate ceramics, which behave as *p*-type semiconductors. In terms of stoichiometry, lead titanate zirconate sintered in air contains excess oxygen, and therefore cation vacancies.

Two other perovskites will now be briefly considered. The first is barium zirconate, an extremely refractory oxide. Sintering temperatures for this ceramic are about 1700°C, as opposed to below 1300°C for the lead titanate zirconate ceramics. Koenig(12) has found that the resistivity of this ceramic in the temperature range between 200 and 500°C can be increased by several orders of magnitude by the addition of one mole per cent of lanthanum or niobium. The ionic radii and valency considerations are about the same as observed in the lead titanate zirconate system, and this evidence suggests that a *p*-type semiconductor, barium zirconate, is being compensated by donor addition.

The conductivity of barium titanate doped with donor additions has been investigated.(13–16) These materials were of particular interest because some of the ceramics were found to show a very strong positive temperature coefficient of resistivity in a temperature range extending upward from the tetragonal-cubic phase change, associated with the disappearance of ferroelectricity. Small amounts of donor additives (of the order of 0·1 mol per cent) cause barium titanate to be an *n*-type semiconductor whose room temperature resistivity may be as low as 10 Ω cm. However, when one mole per cent or more of these donors are added to barium titanate, it becomes a highly insulating ceramic similar to compensated lead titanate zirconate.

It is suggested that the occurrence of high conductivity in donor-doped barium titanate may be due to a lack of equilibrium at high temperature. The compensation process in these oxides consists of several steps (see Appendix), of which the first is ionization of the donor atoms, producing a surplus of electrons. To compensate and attain high resistivity the ceramic must react by producing more cation vacancies which can ionize and absorb the electrons. However, vacancy production is a relatively slow process involving interaction with the surrounding atmosphere. The interaction may be expected to be faster in compounds containing lead than in those containing barium, because of the high vapor pressure of lead at the sintering temperature. It is also plausible that the diffusion of barium out of $BaTiO_3$ containing small amounts of donor substituents should be initially slow at the firing temperature, but that at higher donor concentrations the driving force for diffusion is sufficient to initiate the formation of vacancies. These in turn speed the entire diffusion process, so that a state of equilibrium can be rapidly approached. The equilibrium state involves *p*-type conductivity of a lower magnitude than that of the undoped oxide, as in the case of the lead compounds. This hypothesis can be supported by some data presented by SAUER and FISHER,(13) who show that the room temperature resistivity of a lanthanum doped barium strontium titanate could be raised from 5×10^{3} to 10^{7} Ω.cm by increasing the high temperature sintering period.

One possible explanation for the increase in resistivity of *n*-type conductive $BaTiO_3$ near its Curie point is an increase in the donor ionization energy, or increase in the activation energy for electron hopping, caused by the drastic drop in dielectric constant. It is also worth noting that in some perovskite semiconductors having magnetic Curie points, there is a resistivity anomaly below the Curie point similar to the one observed in ferroelectric perovskites, but much smaller in magnitude.(17) MILLER, *et al.*, attributed the anomaly in magnetic materials to added scattering by disaligned *d*-shells. A more complete understanding of the conduction phenomena in barium titanate would include consideration of scattering mechanisms in the paraelectric and ferroelectric states. However, a change in conductivity type is also noted in the transition from tetragonal to cubic,(16) and the resistivity anomaly may well signal a considerable change in energy-band structure.

GOODMAN(19) observed that a donor-doped $BaTiO_3$ single crystal has even higher conductivity than a corresponding ceramic, and much less temperature dependence of conductivity than the latter. He takes this as evidence that barriers at the grain boundaries cause the anomalous resistivity. We propose another possible explanation. Diffusion of barium from single crystals is probably a very slow process as compared with diffusion from ceramics. Thus, under the usual preparation conditions the doped single crystal may be maintained for long periods in an essentially metallic state, which may not be an equilibrium state. It is felt that the evidence in this article demonstrates that vacancy equilibria are an important feature of conductivity in some perovskites and should probably be considered in all perovskites.

Acknowledgements—The authors acknowledge the contributions of the whole staff of the Clevite Electronic Research Division to the study of modified lead titanate zirconate ceramics, and especially the initiative of W. R. COOK on acceptor substituents.

REFERENCES

1. SHIRANE G., SAWAGUCHI E. and TAKAGI Y., *Phys. Rev.* **84**, 476 (1951).
2. SHIRANE G. and SUZUKI K., *J. phys. Soc. Japan* **7**, 333 (1952).
3. SAWAGUCHI E., *J. phys. Soc. Japan* **8**, 615 (1953).
4. JAFFE B., ROTH R. S. and MARZULLO S., *J. appl. Phys.* **25**, 809 (1954).
5. BERLINCOURT D. and KRUEGER H. H. A., *J. appl. Phys.* **30**, 1804 (1959).
6. GERSON R., *J. appl. Phys.* **31**, 188 (1960).
7. KULCSAR F., *J. Amer. ceram. Soc.* **42**, 343 (1959).
8. KROGER F. A. and VINK H. J., *Solid State Physics*, **Vol. 3**, p. 307 (edited by SEITZ F. and TURNBULL D.) Academic Press, New York (1956).
9. HUTSON A. R., in *Semiconductors*. Chap. 13, p. 541 (edited by HANNAY N. B.) Reinhold, New York (1959).
10. RUDOLPH J., *Z. Naturf.* **14a**, 727 (1959).
11. JAFFE H., *Proc. Inst. elect. Engrs Lond.* **109B**, Suppl. 22, 351 (1962).
12. KOENIG J., *J. Amer. ceram. Soc.*, to be published.
13. SAUER H. A. and FISHER J. R., *J. Amer. ceram. Soc.* **43**, 297 (1960).
14. SAUER H. A. and FLASCHEN S. S., *Proceedings Electronics Components Symposium*, 7th, Washington, D.C., p. 41 (1956).
15. SABURI O., *J. Amer. ceram. Soc.* **44**, 54 (1961).
16. TENNERY V. J. and COOK R. L., *J. Amer. ceram. Soc.* **44**, 187 (1961).
17. MILLER R. C., HEIKES R. R. and MAZELSKY R., *J. appl. Phys.* **32**, 2202 (1961).
18. BUSCH G., *Helv. Phys. Acta.* **21**, 212 (1948).
19. GOODMAN G. *J. Amer. ceram. Soc.* **46**, 48 (1963).

APPENDIX

Calculation of the change in resistivity of a *p*-type oxide semiconductor due to donor additives:

Assume that a typical ceramic may be presented as $M^{2+}O^{2-}$. In $PbTiO_3$ or $PbZrO_3$ this neglects the effect of Ti or Zr, but both of these metals are of substantially lower volatility than lead and may be expected to interact with the atmosphere to a lesser extent.

The holes which are the major cause of conductivity are generated by the process:

$$V_M \rightleftarrows V_M^{2-} + 2h \tag{1}$$

where

V_M is an unionized cation vacancy
V_M^{2-} is a doubly ionized cation vacancy
h is a hole.

The Law of Mass Action, applied to equation (1) yields the relationship:

$$\frac{p^2[V_M^{2-}]}{[V_M]} = K_1 \exp(-E_1/kT) \tag{2}$$

where [ ] around the quantity designates the concentration of the quantity

p is the hole concentration

K_1 is a constant

E_1 is the reaction energy for the process represented by equation (1).

Rudolph has shown that at high temperatures $[V_M]$ comes to equilibrium at a value determined by the gas partial pressures on the system. The oxygen and metal pressure are not independent, and on varying the oxygen pressure the entire vacancy equilibrium situation is shifted. (Rudoph's article treats this equilibrium quantitatively and shows the nature of the variation.) There is a temperature T_F below which the time required for establishing equilibrium becomes very long. On cooling a system at fixed oxygen pressure, $[V_M]$ and $[V_O]$ (the oxygen vacancy concentration) do not change by interaction with the atmosphere below T_F. When a cation of high volatility, such as lead, is used, T_F may be expected to be 500–600°C.

To calculate the value of p as a function of temperature it is first assumed that the hole concentration is determined solely by equation (1), so that $V_M^{2-} = p/2$, and that $[V_M^{2-}] \ll [V_M]$ at low temperatures.

Then from equation (2):

$$p = (2[V_M]_F K_1)^{1/3} \exp(-E_1/3kT) \qquad (3)$$

where $[V_M]_F$ is the metal vacancy concentration at the temperature T_F. Now suppose a normally trivalent ion N^{3+} enters the M site substitutionally. If this atom could be substituted at very low temperature, the lattice would tend to impose a divalent structure on N. At high temperature, however, N^{2+} will further ionize almost completely to N^{3+}. The electrons created by this process combine with holes formed according to equation (1), and shift the equilibrium to the right side of this equation, with formation of additional vacancies until $[V_M^{2-}]$ approaches $[N^{3+}]/2$. For doping levels near 1 mol. % $[V_M^{2-}] \gg [V_M]$.

To calculate the *resistivity* of the "doped" ceramic below T_F we again use equation (2) but now both $[V_M^{2-}] \approx [N^{3+}]/2$ and $[V_M] \approx [V_M]_F$ are nearly temperature independent because p is much smaller than either $[V_M^{2-}]$ or $[V_M]$; hence:

$$p = \left(\frac{2K_1[V_M]_F}{[N^{3+}]}\right)^{1/2} \exp(-E_1/2kT). \qquad (4)$$

Equation (4) makes two predictions:

1. The hole concentration in the doped ceramic will be considerably less than that in the undoped ceramic.

2. If logarithm p is plotted as a function of $1/T$ below T_F both equations (3) and (4) yield straight lines. The slope of equation (4) is greater than that of equation (3) by a factor of 1·5. This means that the doped ceramic drops more rapidly in conductivity than the undoped as the temperature is lowered. Both of the above predictions are borne out by the experimental data (Fig. 2).

J. Phys. Chem. Solids Pergamon Press 1963. Vol. 24, pp. 985–992. Printed in Great Britain.

AN X-RAY AND DILATOMETRIC STUDY OF ORDER AND THE "K-STATE" IN IRON–ALUMINUM ALLOYS

R. G. DAVIES

Scientific Laboratory, Ford Motor Company, Dearborn, Michigan

(*Received* 12 *October* 1962; *revised* 6 *March* 1963)

Abstract—A dilatometric and X-ray study of certain iron–aluminum solid solution alloys has shown that the FeAl order field completely surrounds the Fe_3Al order phase; this is in agreement with theoretical predictions. It has also been conclusively demonstrated that the so called "*K*-state", which is produced in certain alloys on annealing at a low temperature after quenching from a high temperature or after cold working, is an ordered structure but with a very small antiphase domain size. It is proposed that ordering on slow cooling is not observed because of kinetic difficulties. Many of the anomalous properties of iron–aluminum alloys can now be explained with the aid of this new phase boundary information, and a knowledge of the nature of the "*K*-state". It has also been shown that the production of the "*K*-state" in iron–aluminum alloys can lead to a 25 per cent increase in the flow stress.

INTRODUCTION

IN THEIR classical X-ray study,(1) BRADLEY and JAY distinguished the Fe_3Al and FeAl ordered structures in the solid solution of aluminum in iron. They found that the region of Fe_3Al order commenced at ~ 19 at. % aluminum and extended to ~ 34 at. % aluminum with a maximum of 550°C in the critical temperature for ordering at 27 at. % aluminum. The recent results of TAYLOR and JONES (lattice parameters),(2) and MCQUEEN and KUCZYNSKI (dilatometry and resistivity)(3) agree quite well with this Fe_3Al field, while LAWLEY and CAHN (high temperature diffractometry)(4) observed that Fe_3Al order commences at 23 at. % aluminum. Bradley and Jay, and Lawley and Cahn, found that FeAl order commenced at 25 at. % aluminum at temperatures above the Fe_3Al field, Taylor and Jones, and McQueen and Kuczynski place the FeAl boundary close to 20 at. % aluminum. RUDMAN,(5) using the Zeroth approximation, has proposed a diagram in which the Fe_3Al is completely surrounded by the FeAl field. To add to the complexity of the phase diagram is the observation of the "*K*-state"(6) in alloys containing less than 20 at. % aluminum.

The "*K*-state" is produced in many alloys, whose compositions are close to known or postulated order–disorder boundaries, when they are quenched from a high temperature, or cold worked, and then given a low temperature anneal. Its presence has been detected in Fe–Al,(7) Fe–Si,(7) Ni–Cr,(7–13) Fe–Al–Cr,(6,7) Ni–Al,(7) Ni–Cu–Zn,(7,14) Cu–Ni,(7) Ni–Fe,(10) Ni–Fe–Cr(10,13,15) and Ni–Fe–Mo(10,16,17) by an increase in resistivity after the above heat treatment. The theories thus far advanced as to the nature of the "*K*-state" are: (1) short-range(7,12,14,15) or a form of long range order,(8,9) (2) clustering or Guinier–Preston zones,(10) and (3) clustering of some atoms followed by ordering of the matrix.(17)

The effect of the "*K*-state" upon mechanical properties has, as far as the author is aware, only been studied in 80% nickel–20% chromium (Nichrome) alloys. NORDHEIM and GRANT,(9) and LIFSHITZ(10) observed a 20% increase in hardness, and STARIKOVA and PRESNYAKOV(18) noted an increase in the ultimate tensile strength on the formation of the "*K*-state". Lifshitz also reports that the work hardening balances the destruction of the "*K*-state", and thus there is no increase in hardness for a "*K*-state" Nichrome alloy cold-rolled 20–80 per cent reduction in area; after 80 per cent in area the "*K*-state" is completely destroyed and the hardness increases with deformation.

In view of the differences which exist between the proposed iron–aluminum equilibrium diagrams, it was decided to re-investigate the composition range 16 to 25 at. % aluminum by dilatometric and X-ray diffuse scattering methods. The effect of the "*K*-state" upon flow stress has also been studied in an iron – 16·5 at. % aluminum alloy.

EXPERIMENTAL DETAILS

(a) *Dilatometric study*

The dilatometer was of a standard pattern with all the heated parts made of silica. A Pt/Pt–Rh thermocouple was in contact with the 1 in. long specimens. A displacement transducer that could detect a change of 5×10^{-6} in. (it was normally used on a less sensitive range) measured the dilatation.

The specimens were heated to ~900°C for 1 hr *in situ*, cooled at ~ 1°C per min, which is slow enough to maintain equilibrium,(4) and every 15°C the temperature was stabilized and a reading taken. No attempt was made to measure absolute expansion coefficients. Discontinuities in the expansion-temperature curve indicated when a transformation had taken place. It was unnecessary to employ a protective atmosphere as the oxidation resistance of iron–aluminum alloys is excellent.

For a study of the "*K*-state" (which only forms under the conditions outlined above), it was necessary, for the elimination of instrumental alignment errors, to measure any dilatation due to the "*K*-state" without removing the specimen from the dilatometer. To achieve this, the quenched 17·9 at. % aluminum specimen was put into the dilatometer preheated in the range of 300–400°C and after 2 hr the reading given by the transducer was noted. (THOMAS(6) has shown by resistivity measurements that 1 hr at temperatures above 300°C is sufficient to produce the maximum value of the "*K*-state" in iron–aluminum alloys.) The transducer reading for the specimen in the slow cooled state was obtained by heating to 650°C *in situ* to destroy the "*K*-state",(6) and then cooling at ~ 1°C per min. to the original annealing temperature (300–400°C). Thus the difference in the transducer readings gives the dilatation due to the "*K*-state".

(b) X-*ray procedure*

A General Electric XRD-5 X-ray set, with a focussing lithium fluoride monochromator in the diffracted beam and pulse height analyzer to eliminate harmonic wavelengths of the cobalt radiation, was used to investigate the structure of a series of iron–aluminum alloys containing from 16 to 22 at. % Al. The method of obtaining the diffraction pattern over the range of 2θ from 15 to 45° was to count for at least 100 sec every 1/3 degree with a slit subtending 1° in 2θ at the focus; the probable counting error was less than 2 per cent. All measurements were made at room temperature.

For the study of the order–disorder boundaries solid specimens in the composition range 16–22·3 at. % aluminum, were cooled at 10°C per hr from 500°C with a 16 hr anneal at 400 and 300°C, and a 65 hr anneal at 200°C and finally quenched into water from 100°C; for comparison purposes they were also water quenched from 850°C.

The "*K*-state" formation was studied in detail in the 17·9 at. % aluminum specimen by quenching from 850°C and annealing for at least 1 hr in the temperature range 250–360°C. In addition the remaining alloys, previously quenched from 850°C, were annealed for 1 hr at 323°C.

In order to check whether the "*K*-state" formation is the same in other alloy systems, an iron – 8·7 at. % silicon alloy was given a similar series of heat treatments.

(c) *Flow stress determination*

LAWLEY, VIDOZ and CAHN(19) have shown that strains as large as 2 per cent can be completely recovered in polycrystalline iron–aluminum alloys by a 2 hr anneal at 800°C so that one specimen can be used for a whole series of tests. This procedure was adopted for this investigation of the effect of the "*K*-state" upon the flow stress.

The specimens, with gage section dimensions of $1 \cdot 5 \times 0 \cdot 08 \times 0 \cdot 04$ in., were tested in a Polanyi type machine at a strain rate of $\sim 5 \times 10^{-5}$ sec^{-1}. The alloys were prepared from super pure aluminum and iron with a carbon content of 0·03% maximum, in a high frequency induction furnace with an argon atmosphere. A typical recrystallized grain size was 0·10 mm.

The flow stress after 0·05 per cent plastic strain (a 0·05 per cent proof stress) was found for specimens in the following conditions: (1) quenched from a high temperature, 700–900°C, and annealed for 1 hr at 350°C to develop the "*K*-state" and (2) quenched from 850°C and annealed in the temperature range 200–425°C. Attention was focussed on an iron −16·5 at. % aluminum alloy but other iron–aluminum and iron–silicon alloys were used to check the generality of the results.

RESULTS

(a) *Equilibrium Diagram*

The X-ray scattering results for the alloys 22·3–16 at. % aluminum are summarized in Table 1. "Pseudo FeAl" is a state, intermediary between short-range order (S.R.O.) and FeAl order, which results in a (100) diffraction peak, or inflexion in the scattering curve, at $2\theta = 34$–$35°$ instead of at 36° for perfect FeAl order. "Imperfect FeAl" refers to FeAl having small antiphase domains as indicated by a broadened (100) diffraction peak. Thus on slow cooling the Fe_3Al–FeAl order boundary is between 20·5 and 21·85 at. % aluminum, and the FeAl-disorder boundary is between 18·8 and 20·5 at. % aluminum.

The proposed iron–aluminum equilibrium diagram, which is composed of dilatometric,⁽³⁾ specific heat⁽²⁰⁾ and resistivity data,⁽²¹⁾ Fig. 1, shows that the FeAl phase does in fact completely surround the Fe_3Al phase.

(b) "*K-state*"

The dilatometric results show that the contraction due to the "*K*-state" increases with decreasing annealing temperature after quenching from 825°C, Fig. 2, and that the contraction on annealing at 350°C, Fig. 3, increases with increasing quenching temperature until ∼ 800°C when a saturation value of the contraction is observed.

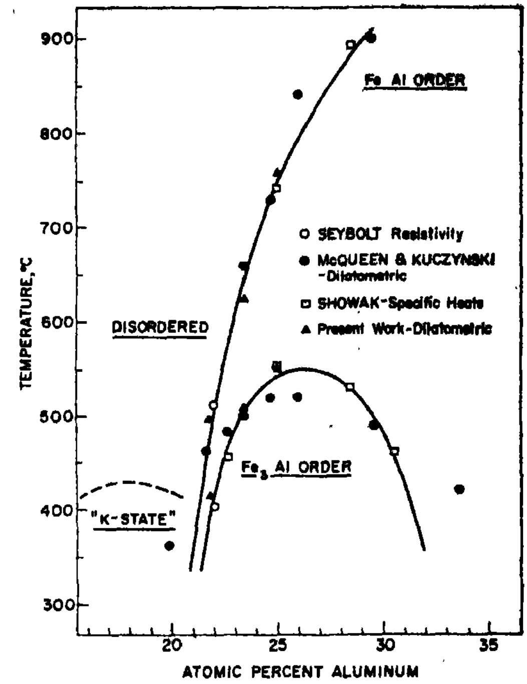

FIG. 1. Proposed equilibrium diagram for the solid solution of aluminum in iron.

Table 1. The structures produced in a series of iron–aluminum alloys after various heat treatments

At. % Al. Heat Treatment	22·3	21·85	20·5	18·8	17·9	16
Slow cool	Fe_3Al	Fe_3Al	S.R.O. + "Imperfect FeAl"	S.R.O. + "Pseudo FeAL"		
Quench from 850°C	"Imperfect FeAl"		S.R.O.	Short Range Order (S.R.O.)		
Quench from 850°C + 1 hr at 323°C	Fe_3Al	Fe_3Al	FeAl	"Imperfect FeAl"		

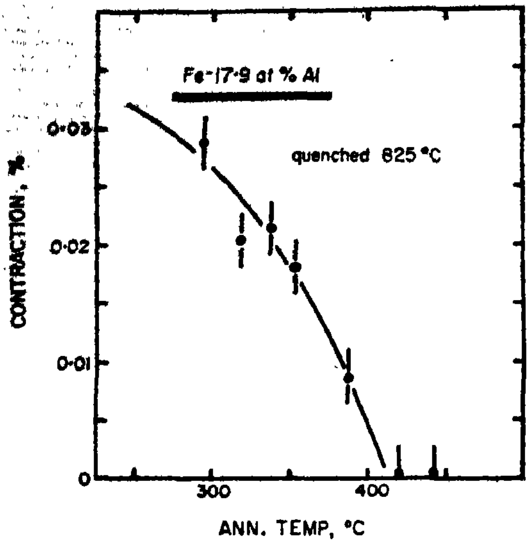

FIG. 2. Percentage contraction produced by the "*K*-state" after quenching from 825°C and annealing at lower temperatures.

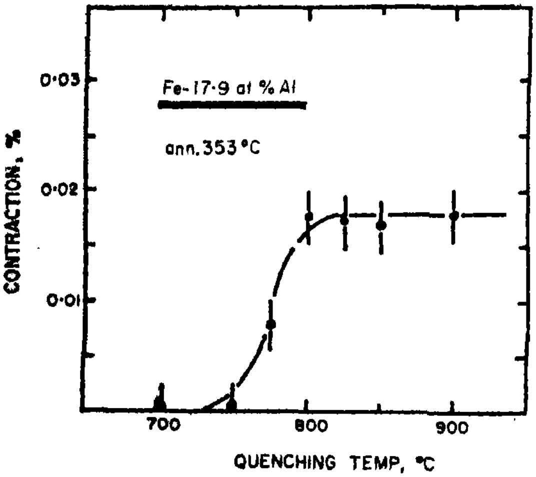

FIG. 3. Percentage contraction produced by the "*K*-state" on annealing at 350°C after quenching from the indicated temperatures.

In Fig. 4 are shown the uncorrected diffraction patterns for the 17·9 at. % aluminum alloy after the various quenching and annealing treatments. The type of long range order present is indicated by the number and position of the superlattice lines. FeAl (B2) type of order gives a (100) superlattice line at $2\theta = 36°$; $Fe_3Al(DO_3)$ type of order, which has a unit cell composed of eight body centered cubic cells, produces a (111) superlattice line at $2\theta = 31°$ as well as a (200) superlattice line at $2\theta = 36°$. If however Fe_3Al order is forming from a fully FeAl ordered lattice, only the intensity of the (111) superlattice line at $2\theta = 31°$ will change. The presence of short-range order is indicated by a very diffuse peak at $2\theta = 25$–$29°$. It is seen that the lower the annealing temperature after the 850°C quench, the greater the tendency to form Fe_3Al type of order; the 255°C anneal does in fact produce a Fe_3Al structure but with a very small domain size as indicated by the width of the superlattice lines.

The uncorrected diffraction patterns for the iron −8·7 at. % silicon alloy, Fig. 5, show that after quenching from 850°C there is only short range order present. Slow cooling produces FeSi (B2) type of order, while annealing for one

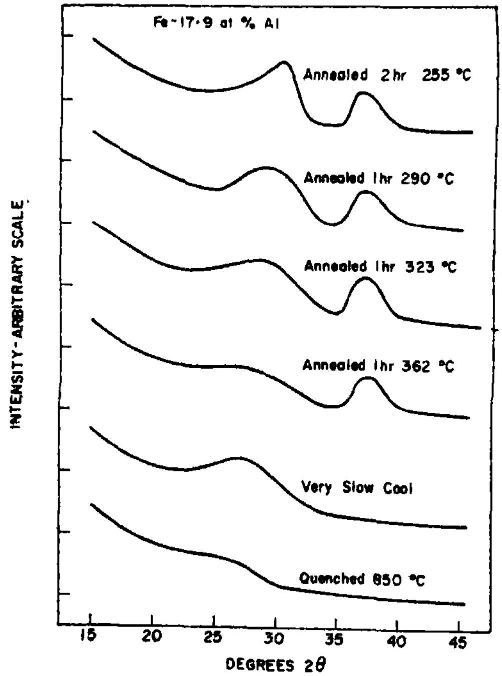

FIG. 4. Uncorrected X-ray diffraction patterns for the iron–17·9 at. % aluminum alloy after the indicated heat treatments.

hour at 323°C, after quenching from 850°C, gives $Fe_3Si(DO_3)$ type of order but, as indicated by the width of the (111) superlattice line, with a small domain size.

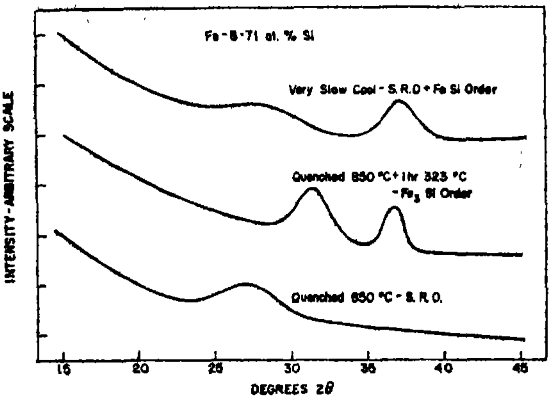

FIG. 5. Uncorrected X-ray diffraction patterns for the iron-8·7 at. % silicon alloy after various thermal treatments.

This X-ray diffraction data indicates that quenching from a high temperature followed by a low temperature anneal produces a more perfect form of order than slow cooling alone; the DO_3 order is, from the number and type of atomic bonds, a more perfect form of order than the B2 order.

(c) *Flow stress**

The results are expressed as the percentage increase in the 0·05 per cent proof stress on forming the "*K*-state" compared to the 0·05 per cent proof stress after quenching. There was no difference between the flow stress of the quenched and furnace cooled states; in agreement with previous work(22) the 0·05 per cent proof stress after quenching was 67,000 p.s.i. Figure 6 shows that there is a maximum increase of ~ 25 per cent in the flow stress on annealing for 1 hr at 300°C following a quench from 850°C. Figure 7 shows that the increase in flow stress on annealing at 350°C is dependent upon the quenching temperature in a manner very similar to the variation of contraction with quenching temperature (Fig. 3).

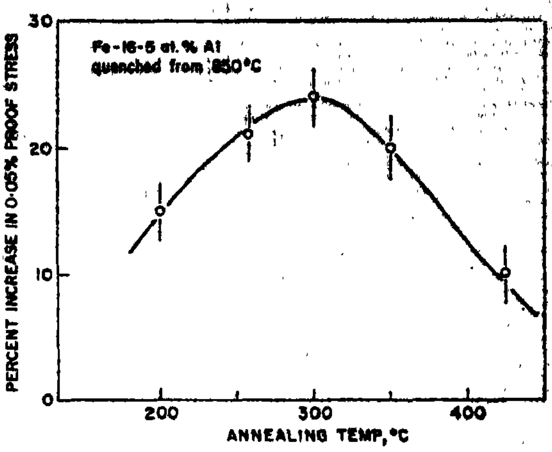

FIG. 6. Variation of 0·05 per cent proof stress with annealing temperature.

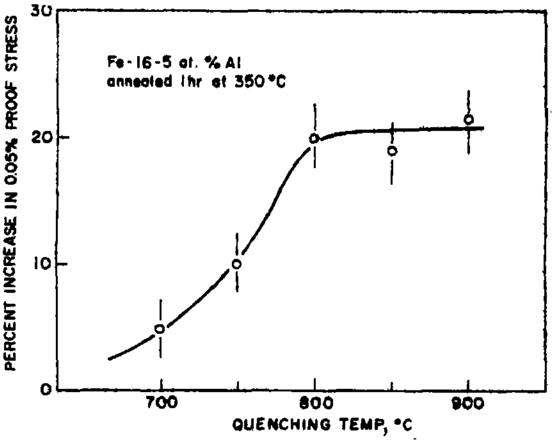

FIG. 7. Variation of 0·05 per cent proof stress with quenching temperature.

An increase in the 0·05 per cent proof stress upon forming the "*K*-state" was shown by iron -16 to 19 at. % aluminum alloys and by iron -6 to 10 at. % silicon alloys. The magnitude of the increase was dependent upon composition; the closer the alloy composition was to the order-disorder boundary the greater was the increase in proof stress upon forming the "*K*-state".

---

[*] This work was done by Lic. MAXIMO VICTORIA at the Instituto de Fisica, San Carlos de Bariloche, Argentina.

DISCUSSION

(a) *Equilibrium diagram*

The order–disorder boundaries drawn in Fig. 1 were those observed after slow cooling at a practical rate, and the agreement between the results obtained by different workers is quite good. The critical ordering temperatures in alloys containing more than 22 at.% aluminum agree very well with those obtained by TAYLOR and JONES,(2) but at lower compositions there is considerable disagreement. At the moment there is no apparent explanation for the major differences between the present diagram and those proposed by BRADLEY and JAY,(1) and LAWLEY and CAHN.(4) SEYBOLT(21) tentatively suggested that the inflexions in his resistivity–temperature curve indicated a two phase ordered plus disordered field, but, as his points fit the proposed diagram so well, it is concluded that they delineate the FeAl field.

The proposed equilibrium diagram confirms the prediction of RUDMAN(5) that the Fe_3Al phase is completely surrounded by the FeAl phase. As the FeAl structure, which has aluminum atoms at second nearest neighbor distances, is intermediary between disorder, or short-range order, and the Fe_3Al structure, where aluminum atoms are at third nearest-neighbor distances, one would expect, on slow cooling, the formation of the FeAl prior to the Fe_3Al superlattice and thus an equilibrium diagram of the form observed.

(b) "*K-state*"

Our X-ray findings provide a direct proof that the "*K*-state" is a form of order; the contraction of the lattice is also an excellent indication that ordering is taking place. On slow cooling, only short-range order is formed; quenching from a high temperature followed by a low temperature anneal produces the same type of order observed in more concentrated alloys. Therefore it is proposed that the "*K*-state" is the equilibrium state which is attained because the excess vacancies quenched in (or produced by cold work) accelerate diffusion; order does not form on slow cooling solely because of kinetic difficulties. Assuming that the activation energy for atomic migration is that of vacancy motion alone, in the presence of excess vacancies, and knowing the activation energy for vacancy formation (~ 18 kcal/mole),(23) it can be calculated that the diffusion process at 323°C is accelerated by a factor of ~ 10^5. Since after quenching it takes approximately 1 hr at 323°C for the resistance to reach a constant value,(6) the calculation indicates that it would take approximately 10 years to reach the same state with the equilibrium concentration of vacancies present. A similar enhancement of diffusion by a factor of 10^4–10^5 has been observed in a silver–zinc alloy after quenching from a high temperature.(24)

POPOV and KARPOV(12) also have shown the importance of excess vacancies in forming the *K*-state. They studied the increase in resistivity as a Ni–18·25 at.% Cr alloy was annealed at 200–300°C after quenching from 650 to 1100°C, and observed that the resistivity, and presumably the amount of the *K*-state, increased monotonically with increasing quenching temperature. Assuming that the rate of formation of the *K*-state was vacancy controlled, they calculated the activation energy for vacancy migration to be 38·7 kcal/mole. LIFSHITZ(10) observed in nichrome (80% Ni–20 Cr) an activation energy of 43 kcal/mole for the formation of the *K*-state. The activation energy for vacancy migration in pure nickel is 39 kcal/mole.(12)

The observed dilatometric saturation at quenching temperatures above 800°C, Fig. 3, is no doubt related to the quenching rate and thus the concentration of quenched in vacancies.

For iron–aluminum alloys, THOMAS(6) has detected the "*K*-state" in alloys as dilute as 10 at.% aluminum, and he observed, as have others,(25) that as the temperature is raised the "*K*-state" disappears in the range 400–450°C for alloys around 18–19 at.% aluminum. The "*K*-state" may be the $Fe_{13}Al_3$ phase proposed by TAYLOR and JONES,(2) or a continuation of the observed FeAl and Fe_3Al fields. Considering the shape of the order–disorder boundaries in Fig. 1, this latter suggestion is very unlikely. As the "*K*-state" approaches equilibrium only with the help of excess vacancies it is not certain, at a first glance, whether it belongs on an equilibrium diagram at all. One may consider this to be analogous to the θ′ phase in aluminum–4 wt.% copper alloys which is not the equilibrium phase yet is stable over a certain temperature range. Nevertheless, it is considered that the "*K*-state" should be included in an equilibrium diagram as it is attempting to form Fe_3Al (or $Fe_{13}Al_3$) type of order which is the equilibrium structure for alloys containing only slightly more aluminum.

The reason why the "*K*-state" has only been observed in the specific alloy systems mentioned previously, is probably related to the relative quenching and annealing temperatures in ordering alloy systems in general. The alloy systems listed above contain at least one transition element and so have a melting point of 1400–1500°C; to form the "*K*-state" they are usually quenched from ~800°C (0·65 T_M where T_M is the absolute melting temperature) and annealed at ~300°C (0·33 T_M). Alloys based on copper, silver or gold are also normally quenched from ~800°C (0·9 T_M) and annealed at a minimum of 200°C (0·4 T_M). Thus with the greater number of excess vacancies and the higher relative annealing temperature, diffusion will be very rapid, and the increase in resistance due to the "*K*-state" will occur too quickly to be recorded. An excellent example of this is to be found in the paper by KOREVAAR(26) on quenching and annealing Au_3Cu. When Au_3Cu was quenched from 488°C (0·64 T_M) and annealed at temperatures below 200°C an increase in resistivity, due to either short range or long range order with small antiphase domains, was observed; at 70°C (0·3 T_M) this increase remained constant with time. Upon quenching from 802°C (0·9 T_M) no resistance increase was noted but only a decrease due to long range order. SELISSKI(27) has demonstrated that there is an increase in the resistivity of a cold worked iron −25 at. % aluminum alloy upon annealing at a low temperature (~200°C); recent X-ray work(28) has shown that such a thermal treatment results in a very small antiphase domain size.

Thus it is concluded that the "*K*-state" is an ordered state but with a very small antiphase domain size which leads to an increase in resistivity. This resistivity increase is stable because domain growth is impossible at relatively low temperatures. Many of the magnetic, resistivity and mechanical(29,30) property anomalies in iron–aluminum alloys can be explained on the basis of this increased understanding of the structure produced by different heat treatments. Alloys containing less than ~ 22·5 at. % aluminum are very sensitive to thermal history.(4, 6, 23) The domain size in alloys that do order on slow cooling is still relatively small,(4) but can be increased by quenching from a high temperature and annealing at a lower temperature; this is illustrated in Table 1 by the increase in perfection in the FeAl type of order for the 20·5 at. % aluminum alloy.

(c) *Flow stress variation with "K-state"*

Since the "*K*-state" has been shown to be an ordered state with a very small domain size, the strengthening is probably due to a combination of antiphase domain size and order hardening. BIGGS and BROOM,(31) and ARDLEY(32) have demonstrated antiphase domain strengthening in Cu_3Au, and it is also thought to occur in Fe_3Al,(19) Lawley, Vidoz and Cahn have also shown that there is a maximum in the strength of Fe_3Al at an intermediate degree of order.

The maximum in the curve of increase in proof stress with annealing temperature, Fig. 6, is probably due to the small amount of the "*K*-state" that will be produced by annealing for one hour at temperatures below ~300°C.

SUMMARY

(1) An equilibrium diagram for the iron–aluminum solid solution, obtained from dilatometric and X-ray results, indicates, in accord with Rudman's theoretical predictions, that the Fe_3Al field is completely surrounded by the FeAl field.

(2) The "*K*-state" has been shown, by X-ray scattering, to be an ordered structure but with a very small antiphase domain size. This order, which only appears when excess vacancies are initially present, is not observed on slow cooling due to kinetic difficulties.

(3) The production of the "*K*-state" in an iron −16·5 at. % aluminum alloy gives a 25 per cent increase in the flow stress, which is thought to be due to a combination of antiphase domain size and order hardening.

Acknowledgements—The author would like to acknowledge the financial assistance provided by the International Atomic Energy Agency, Vienna, and the Argentine Atomic Energy Commission as part of this work was carried out at the Institute de Fisica, San Carlos de Bariloche, Rio Negro, Argentina. He would also like to thank his colleagues, Dr. W. SHOWAK, for allowing him to quote unpublished results, and Drs. T. L. JOHNSTON and R. H. RICHMAN for critically reviewing the manuscript.

REFERENCES

1. Bradley A. J. and Jay A. H., *Proc. Roy. Soc.* **A136**, 210 (1932).
2. Taylor A. and Jones R. M., *J. Phys. Chem. Solids* **6**, 16 (1958).
3. McQueen H. J. and Kuczynski G. C., *Trans. Amer. Inst. min. (metall.) Engrs* **215**, 619 (1959).
4. Lawley A. and Cahn R. W., *J. Phys. Chem. Solids* **20**, 204 (1961).
5. Rudman P. S., *Acta Met*, **8**, 321 (1960).
6. Thomas H., *Z. Metallk.* **41**, 185 (1950).
7. Thomas H., *Z. Phys.* **129**, 219 (1951).
8. Taylor A. and Hinton K. G., *J. Inst. Metals* **81**, 169 (1952).
9. Nordheim R. and Grant N., *J. Inst. Metals.* **82**, 440 (1953).
10. Lifshitz B. G., *Izv. akad. nauk. S.S.S.R.* **21**, (9), 1225 (1957).
11. Baer H. G., *Z. Metallk.* **49**, 614 (1958).
12. Popov L. E. and Karpov G. I., *Dokl. akad. nauk. S.S.S.R.* **129**, 1208 (1959).
13. Muller H. G. and Muth P., *Z. Metallk.* **50**, 217 (1959).
14. Yano Z., *Japan Nickel Rev.* **9**, 17 (1941).
15. Thomas H., *Metal* **10**, 95 (1956).
16. Assmus F. and Pfeifer F., *Z. Metallk.* **42**, 294 (1951).
17. Dekhtyar M. V., *Fiz. metal. metalloved* **3**, 55 (1956).
18. Starikova G. V. and Presnyakov A. A., *Fiz. metal. metalloved* **10**, 943 (1960).
19. Lawley A., Vidoz E. A. and Cahn R. W., *Acta Met.* **9**, 287 (1961).
20. Showak W., private communication.
21. Seybolt A. U., *Trans. Amer. Inst. min. (metall.) Engrs* **218**, 570 (1960).
22. Justusson W., Zackay V. F. and Morgan E. R., *Trans. Amer. Soc. Metals* **49**, 905 (1956).
23. Bransky J. and Rudman P. S., *Trans. Amer. Soc. Metals* **55**, 335 (1962).
24. Nowick A. S. and Sladek R. J., *Acta. Met.* **1**. 131 (1953).
25. Parsons D., Sucksmith W. and Thompson J. E., *Phil. Mag.* **3**, 1174 (1958).
26. Korevaar B. M., *Physica* **25**, 1021 (1959).
27. Selisskii Ya. P., *Fiz. metal. metalloved* **10**, 829 (1961).
28. Davies R. G., to be published.
29. Masumoto H. and Saito H., *Sci. Rep. res. Inst. Tohoko Univ.* **4A**, 321 (1952).
30. Yamamoto M. and Taniguchi S., *Sci. Rep. res. Inst. Tohoko Univ.* **8A**, 193 (1956).
31. Biggs W. D. and Broom T., *Phil. Mag.* **45**, 246 (1954).
32. Ardley G. W., *Acta Met.* **3**, 525 (1955).

J. Phys. Chem. Solids Pergamon Press 1963. Vol. 24, pp. 993–1002. Printed in Great Britain.

UNTERSUCHUNG DER NAHORDNUNG IN MAGNETISCH ISOTROPEN UND ANISOTROPENEISEN–NICKEL-LEGIERUNGEN MIT DER MÖSSBAUER-METHODE

W. ZINN

Siemens & Halske AG, Forschungslaboratorium, München.

M. KALVIUS, E. KANKELEIT und P. KIENLE

Labor für Technische Physik der Technischen Hochschule, München.

und

W. WIEDEMANN

Kommission für Tieftemperaturforschung der Bayerischen Akademie
der Wissenschaften, Herrsching.

(*Received* 16 *November* 1962)

Zusammenfassung—Mit der Mössbauer-Methode wurde die Hyperfeinstruktur des 14,4 keV-Übergangs von Fe^{57} in 75 % Ni/25 % Fe — Folien mit und ohne Ni$_3$Fe-Überstruktur und in 81 % Ni/19 % Fe-Permalloy-Aufdampfschichten mit und ohne uniaxiale magnetische Anisotropie untersucht.

Aus dem Abstand der Hyperfeinlinien wurden die am Eisenkern wirksamen Magnetfelder bestimmt. Aus den gemessenen Verbreiterungen und Verformungen der Hyperfeinlinien konnte das Schwankungsspektrum der inneren Magnetfelder ermittelt werden. Es liess sich auf Schwankungen der Zahl und Nahordnung der Eisen- und Nickelatome auf den Gitternachbarplätzen zurückführen; die Ni$_3$Fe-Überstruktur bewirkte eine merkliche Abnahme der Schwankungsbreite und eine geringe Abnahme der Hyperfein-Aufspaltung. Anhand der Messungen an magnetisch anisotropen Permalloy-Aufdampfschichten wird diskutiert, inwieweit Änderungen der magnetischen Struktur in der Nachbarschaft einzelner Eisenatome, insbesondere die Ausrichtung von Eisenpaaren als Anisotropieursache, mit der Mössbauer-Methode noch nachweisbar sind.

Abstract—The hyperfine-structure of the 14·4 keV-γ-transition in Fe^{57} was measured by the Mössbauer Effect in foils of ordered and disordered Ni$_3$Fe and in Permalloy-films (81 % Ni, 19 % Fe) with and without uniaxial magnetic anisotropy. The magnetic field at the iron nucleus was determined from the separation of the hyperfine-lines. The broadening and the asymmetrical form of the measured lines can be explained by a spectrum of hyperfine fields resulting from statistical fluctuations in the microenvironments of the iron atoms. In the ordered Ni$_3$Fe the broadening of the resonance lines was appreciably reduced.

No differences were found for the width and the form of the hyperfine-lines in Permalloy-films with and without uniaxial magnetic anisotropy; the number of directed iron-pairs in films with uniaxial magnetic anisotropy is shown to be smaller than 10^{20} pairs/cm.^{3}.

1. EINLEITUNG

DAS Mössbauer-Spektrum des 14,4 keV-Übergangs von Fe^{57} besteht in ferromagnetischen Stoffen infolge Zeeman-Aufspaltung der Kernniveaus aus sechs Hyperfeinlinien.(1) Aus ihrem Abstand und den bekannten magnetischen Momenten der Kernzustände kann das am Kern wirksame Magnetfeld bestimmt werden. Es ist antiparallel zur Magnetisierung gerichtet und wird hauptsächlich durch eine Spinpolarisation der *s*-Elektronen der inneren Schalen erzeugt.(2)

In metallischem Eisen ist das Magnetfeld am

Ort aller Eisenkerne gleich und beträgt −330 kOe.(3) Die Hyperfeinlinien sind daher scharf und lassen sich durch Lorentzkurven gleicher Breite darstellen. In Legierungen aus statistisch verteilten Atomen unterschiedlichen magnetischen Moments schwanken die inneren Felder statistisch mit der Zusammensetzung und Struktur der atomaren Nachbarschaft der einzehen Eisenkerne. Die Abstände der Hyperfeinlinien ändern sich mit der Legierungszusammensetzung ; die Linien sind in charakteristischer Weise verbreitert und deformiert.

Linienverbreiterungen und Änderungen der Hyperfeinstruktur, die auf statistische Schwankungen der Magnetfelder am Kern zurückgeführt werden konnten, wurden bisher nur an Fe–Al-Legierungen von Flinn und Ruby(4) beobachtet. Johnson u.a.(5) untersuchten die inneren Felder in Ni–Fe-Legierungen. Sie fanden systematische Änderungen der Aufspaltung mit der Legierungszusammensetzung, jedoch keine merklichen Linienverbreiterungen. Die nach Neutronenstreuungen von Shull und Wilkinson(6) um bis zu 2,5 Bohrsche Magnetonen unterschiedlichen magnetischen Momente von Eisen und Nickel einerseits, die beobachtete Änderung des mittleren Magnetfeldes am Kern mit der Legierungszusammensetzung andererseits sollten jedoch gut messbare, von der Nahordnung der Eisen- und Nickelatome abhängige Linienverbreiterungen nach sich ziehen. Wir haben daher die Hyperfeinspektren in Folien aus 75% Ni/25% Fe mit und ohne Ni$_3$Fe-Überstruktur und in 81% Ni/19% Fe-Permalloy Aufdampfschichten mit und ohne uniaxiale magnetische Anisotropie daraufhin untersucht.

2. ABSORBERHERSTELLUNG

Zur Aufnahme des Eichspektrums wurden 15μ dicke, weichgeglühte Reinsteisenfolien aus sechsmal zonengezogenem Eisen verwendet.

Die Folien aus 75% Ni 25% Fe wurden auf $5 \cdot 10^{-3}$ cm Dicke ausgewalzt und 2 Stunden bei 1000°C in gereinigtem Wasserstoff geglüht. Ein Teil davon wurde anschliessend 2 Stunden bei 600°C getempert und dann unter Wasserstoff auf Zimmertemperatur abgeschreckt ; die Gitterplätze sind dann weitgehend statistisch von Eisen- und Nickelatomen besetzt. Ein anderer Teil der Folien wurde 168 Stunden bei 450°C getempert und dann an Luft abgeschreckt ; durch Rontgenbeugungsaufnahmen konnte nachgewiesen werden, dass sich teilweise eine Ni$_3$Fe-Überstruktur gebildet hatte ; der spezifische Widerstand war 25% kleiner als bei statistisch ungeordneten Folien.*

Die Eisen- und Permalloy-Aufdampfschichten (81% Ni, 19% Fe) wurden im Hochvakuum von einigen 10^{-7} Torr aus Aluminiumoxydtiegeln senkrecht auf jeweils drei 0,1 mm dicke Glasplättchen bei Trägertemperaturen von 250°C aufgedampft. Der zu 80% mit Fe^{57} angereicherte Eisen-Absorber bestand aus drei aufeinandergepackten, etwa 700 Å dicken Aufdampfschichten, über die zum Korrosionsschutz noch dünne Nickelschichten aufgedampft waren. Bei den Permalloy-Absorben wurden je sechs Aufdampfschichten zu einer etwa $2 \cdot 10^{-4}$ cm dicken Absorberschicht zusammengepackt. Auf der Vorderseite jedes der drei Glasträgerplättchen wurden hierzu aus 2 Öfen nacheinander etwa 4000 Å dicke Schichten, auf der Rückseite anschliessend aus einem weiteren Ofen etwa 2000 Å dicke Schichten aus einer Schmelze von 82% Nickel und 18% Eisen aufgedampft ; das Eisen war zu 80% mit Fe^{57} angereichert. Der Schichtträger befand sich im Zentrum gekreuzter Helmholtzpulenpaare ; durch sie konnte während des Aufdampfens der magnetisch anisotropen Permalloy-Absorber ein homogenes magnetisches Gleichfeld, während des Aufdampfens der magnetisch isotropen Schichten ein homogenes 50-Hz-Zweiphasen-Drehfeld von 30 Oe in Schichtebene erzeugt werden. Die einzelnen Permalloyschichten hatten Koerzitivfeldstärken zwischen 0,5 und 8 Oerstedt ; die Anisotropiefeldstärken bei den magnetisch anisotropen Schichten betrugen etwa 2,5 Oe. Die im Drehfeld aufgedampften Eisenschichten hatten Koerzitivfeldstärken von etwa 10 Oe. Die Zusammensetzung und Dicke der Schichten wurde durch Röntgenfluoreszenzmessungen und interferometrisch bestimmt. Die Legierungszusammensetzung war bei den einzelnen Schichten nur um 0,2 bis 0,4% unterschiedlich.

3. MESSANORDNUNG

Es wurde die Transmission der 14,4 keV Gammastrahlung durch die Resonanzabsorber als Funktion der relativen Geschwindigkeit zwischen Quelle und Absorber gemessen. Auf Bild 1 ist die Messanordnung dargestellt. Die Quelle bestand aus 10 mC Co^{57}. Dieses wurde elektrolytisch auf einer Platinfolie abgeschieden und anschliessend etwa 10 min im Vakuum bei ca. 900°C eindiffundiert. Eine derartige Quelle emittiert eine unaufgespaltene Kernresonanzlinie nahezu natürlicher Linienbreit.(7) Durch eine Kunststoffhalterung wurde die Quelle starr mit dem elektromagnetischen Antrieb(8) verbunden. Von den beiden mechanisch gekoppelten Lautsprechersystemen diente eines zur Erzeugung und Regelung der Resonanzschwingung, während das andere eine der momentanen Geschwindigkeit der Quelle proportionale Spannung lieferte. Diese

---

* Für die Herstellung der Absorberfolien möchten wir den Herren F. Pfeifer und H. Hillmann, für die Röntgenbeugungsuntersuchung Herrn Dr. H. G. Baer von der Vacuumschmelze AG, Hanau, an dieser Stelle herzlich danken.

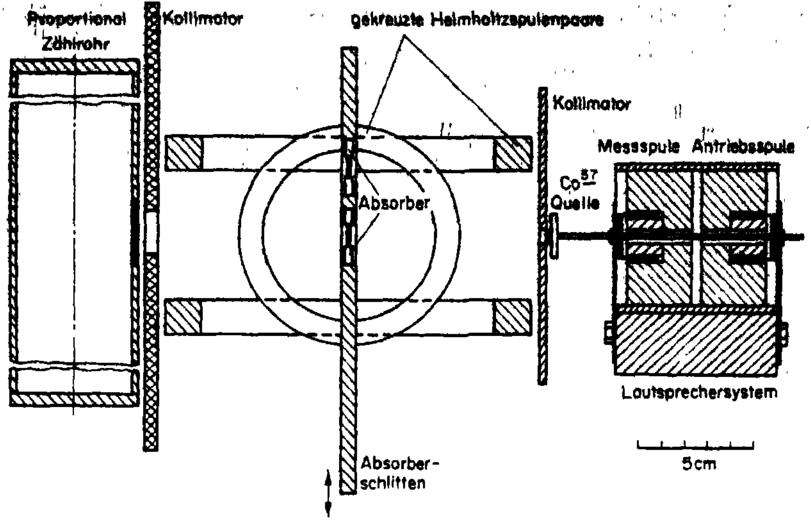

Bild 1. Messanordnung zum Vergleich der Kernresonanzabsorption von Fe^{57} in zwei verschiedenen. Absorbern und zwei in Schichtebene senkrecht aufeinanderstehenden Magnetisierungsrichtungen.

wurde als Regelgrösse mit dem sinusförmigen Spannungsverlauf (Klirrfaktor kleiner 0,1%) eines extrem stabilen RC-Generators (Krohn-Hite 440 Å) verglichen. Die Differenz wurde verstärkt und als Stellgrösse der Antriebsspule zugeführt. Man erreicht so, dass die Bewegung der Quelle beim Betrieb in der Resonanzfrequenz des Systems (13,3 Hz) um höchstens 0,05% vom Verlauf der Generatorspannung abweicht.(9)

Die vom Resonanzabsorber durchgelassene Gammastrahlung wurde mit einem Proportionalzählrohr (Xenon–Methan-Füllung) nachgewiesen, die der 14,4 keV-Linie zugehörigen Zählimpulse in einem 256-Kanal-Zähler gespeichert. Ein mit der sinusförmigen Bewegung der Quelle synchronisierter Oszillator unterteilte die Zeit für eine volle Schwingung des Antriebssystems in 256 gleiche Intervalle. Die einzelnen Kanäle wurden nacheinander durch die Oszillatorimpulse zur Speicherung geöffnet. Jedem Zählkanal entsprach ein bestimmtes Geschwindigkeitsintervall. Man erhält das gesamte Mössbauer-Spektrum über einem sinusförmig verzerrten Geschwindigkeitsmasstab. Für die vorliegenden Messungen war vorteilhaft, dass bei grossen Relativgeschwindigkeiten die Messpunkte besonders dicht lagen.

Um die Mössbauer-Spektren zweier Folien oder Schichten genau vergleichen zu können, waren die Absorber auf einem pneumatisch bewegbaren Schlitten montiert und konnten abwechselnd in den Strahlengang gebracht werden. Der gerade durchstrahlte Absorber stand in Zentrum gekreuzter Helmholtzspulenpaare; durch diese konnten Magnetfelder von etwa 15 Oe in zwei senkrechten Richtungen der Schichtebene erzeugt werden. Durch einen elektronischen Programmschalter wurden die Absorber oder ihre Magnetisierungsrichtungen automatisch in kurzen Zeitabständen gewechselt und die zu vergleichenden Spektren in entsprechenden Untergruppen des Vielkanalzählers gespeichert. Systematische Fehler durch einen Gang der Apparatur bei Langzeitmessungen konnten so vermieden werden.

4. MESSERGEBNISSE

In Bild 2 sind die gemessenen Hyperfeinspektren dargestellt. Aufgetragen sind die in Transmission pro Geschwindigkeitsintervall gezählten Impulse über der Relativgeschwindigkeit zwischen Quelle und Absorber. In Bild 2(a) ist das Spektrum der Reinsteisenfolie dargestellt; die Linien sind Lorentzkurven der Halbwertsbreite 0,32 mm/s. Das zum Vergleich eingezeichnete Spektrum der Fe^{57}-Aufdampfschicht zeigt eine geringfügige Linienverbreiterung. Beim Vergleich der Eisenspektren auf Bild 2(a) mit den Eisen-Nickel-Spektren in Bild 2(b) und (c) sind die Abnahme der Aufspaltung mit zunehmenden Nickelgehalt und die Verbreiterung der Hyperfeinlinien deutlich erkennbar. Besonders auffallend ist die asymmetrische Verformung der Linien. In Bild 3 und 4 ist dies quantitativ dargestellt.

In Bild 3 sind die Magnetfelder an den Eisenkernen in Ni/Fe-Legierungen, bezogen auf das im Reinsteisen gemessene innere Magnetfeld, über den Atomprozenten Nickel aufgetragen. Die

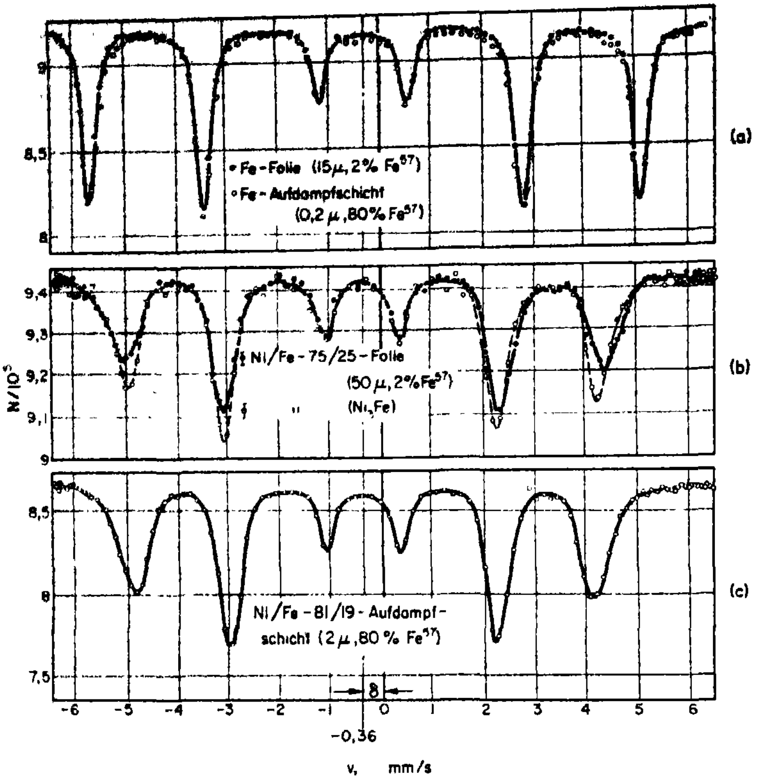

BILD 2. Hyperfeinspektren der 14,4 keV-Fe^{57}-Kernresonanzlinie (a) einer 15 μ-Reinsteisenfolie (●) und einer 0,2 μ Eisen-Aufdampfschicht (O); (b) einer 75% Ni/25% Fe-Folie ohne (⧫) und mit (Φ) Ni_3Fe-Überstruktur. (c) eines aufgedampften 81% Ni/19% Fe-Permalloy-Absorbers Bei 2a und 2c entspricht der Durchmesser der Messpunkte ihrem statistischen Fehler. δ ist die Isomerieverschiebung zwischen Emissions und Absorptionslinie. Die Absorber waren in Schichtebene magnetisiert.

bei Zimmertemperatur gemessenen inneren Felder wurden auf Sättigungsmagnetisierung bei 0°K korrigiert.

Unsere Werte stimmen im Rahmen der Messgenauigkeit gut mit dem von JOHNSON u.a.(5) gefundenen Verlauf überein. Der Vergleich mit der gestrichelt eingezeichneten Kurve für das magnetische Moment μ_{Fe} des Eisens in Ni/Fe-Legierungen(9) zeigt, dass im Gegensatz zu allen anderen bisher untersuchten kubischen Eisen-Legierungen(10) bei den Eisen–Nickel-Legierungen keine Proportionalität zwischen Magnetfeld am Kern und magnetischem Moment des Eisens besteht. Johnson u.a. haben bereits daraufhingewiesen, dass das Magnetfeld am Eisenkern offenbar von den magnetischen Momenten der Nickelnachbarn mitbeeinflusst wird; der Verlauf des Magnetfeldes am Eisenkern zeigt daher mehr Ähnlichkeit mit der Slater-Pauling-Kurve für das ebenfalls eingezeichnete mittlere magnetische Moment $\bar{\mu}$.

In Bild 4 sind die vollen Linienbreiten bei halber Linienhöhe für je eine innere, mittlere und äussere Hyperfeinlinie über der Geschwindigkeit am Linienmaximum aufgetragen.

Wie schon erwähnt, sind alle Hyperfeinlinien der Reinsteisenfolie gleich scharf; dies beweist, dass keine apparativen Linienverbreiterungen mit zunehmender Geschwindigkeit auftreten. Aus der nur geringfügigen Linienverbreiterung bei der

Fe^{57}-Aufdampfschicht wird weiterhin ersichtlich, dass eine erhöhte Zahe von Fehlstellen und Korngrenzen offenbar auch nur sehr kleine Schwankungen der Magnetfelder am Kern bewirkt.

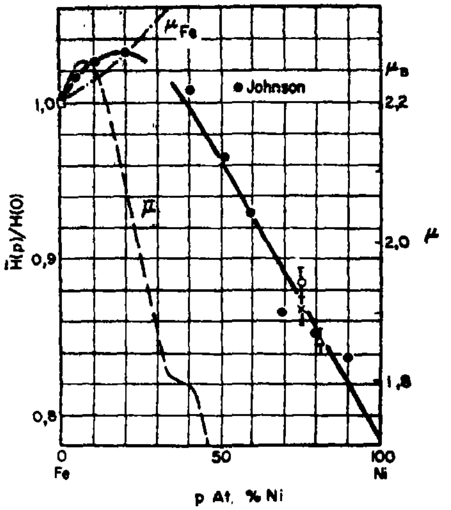

Bild 3. Mittlere Magnetfelder $\bar{H}(p)$ am Fe^{57}-Kern, mittleres magnetisches Moment $\bar{\mu}(p)$ und magnetisches Moment $\mu_{Fe}(p)$ von Eisen in Eisen–Nickel-Legierungen mit p Atomprozenten Nickel.

- ☐ Reinsteisenfolie ($H(0) = -330$ kOe).
- ○ 75% Ni/25% Fe-Folie ohne Ni_3Fe-Überstruktur
- × 75% Ni/25% Fe-Folie mit Ni_3Fe-Überstruktur
- △ 81% Ni/19% Fe-Permalloy-Aufdampfschicht
- —●— Verlauf von $\bar{H}(p)/H(0)$ nach Johnson u.a.(5)
- –·–·– Verlauf von μ_{Fe} nach Shull und Wilkinson.(6)
- - - - - $\bar{\mu} = p \cdot \mu_{Ni} + (1-p)\,\mu_{Fe}$ (in Bohrschen Magnetonen μ_B).

Die Halbwertsbreiten der Hyperfeinlinien der Ni/Fe-Legierungen nehmen dagegen in beträchtlichem Masse mit der Geschwindigkeit im Transmissionsspektrum zu. Wie die durch die Messpunkte gelegten Geraden zeigen, ist die auf die Geschwindigkeit am Linienmaximum bezogene relative Linienverbreiterung für alle Linien eines bestimmten Absorbers im Rahmen der Messgenauigkeit gleich. Sie beträgt für die Permalloy-Aufdampfschicht, etwa 8%, für die ungeordnete Ni/Fe—75/25%-Folie etwa 10%, für die teilweise geordnete Ni/Fe-Folie nur etwa 6%. Bei der äussersten Linie der ungeordneten Ni/Fe-Folie entsprichte dies einer Verbreiterung der Absorberlinie auf das Fünffache der natürlichen Linienbreite; dabei wurde entsprechend der im Reinsteisen gemessenen Halbwertsbreite die Breite der Emissionslinie zu 0,2 mm/s angenommen. Die Linienform ist bei der geordneten und ungeordneten Folie verschieden, die Aufspaltung bei der geordneten Folie etwas kleiner. Beim Vergleich der Hyperfeinspektren von magnetisch isotropen und anisotropen Permalloy-Aufdampfschichten konnte keine direkte messbare Änderung der Linienbreite und -form gefunden werden. Das gleiche negative Ergebnis ergab ein Vergleich der Hyperfeinspektren des magnetisch anisotropen Absorbers, wenn dieser einmal in leichter, einmal in schwerer Richtung magnetisiert wurde, worauf in Abschnitt 5.3 noch näher eingegangen wird.

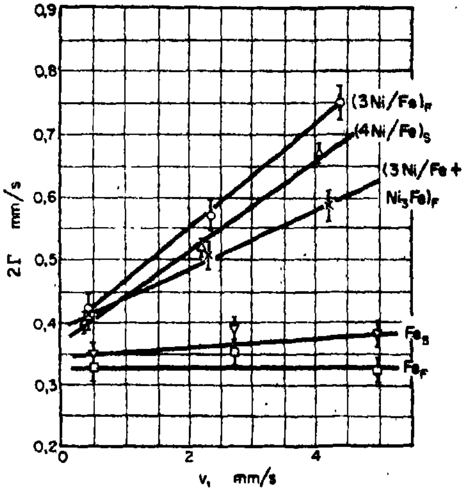

Bild 4. Halbwertsbreiten der Fe^{57}-Hyperfeinlinien in Eisen- und Nickel–Eisen-Folien (Index "F") und -Aufdampfschichten (Index "S"), aufgetragen über der Lage des Linienmaximums in Transmissionsspektrum.

- ☐ 15 μ-Reinsteisenfolie
- ▽ 0,2μ-Eisen-Aufdampfschicht
- ○ 75% Ni/25% Fe-Folie, ungeordnet
- × 75% Ni/25% Fe-Folie, mit Ni_3Fe-Überstruktur
- △ 81% Ni/19% Fe-Permalloy-Aufdampfschicht

5. SCHWANKUNGEN DER INNEREN MAGNETFELDER

Die Proportionalität der Halbwertsbreiten mit der Geschwindigkeit (Bild 4) zeigt, dass die Linienverbreiterungen offenbar durch Schwankungen der inneren Magnetfelder verursacht werden.

Eine zusätzliche Linienverbreiterung können schwankende elektrische Quadrupolwechselwirkungen hervorrufen; sie ist im Falle des Fe^{57} für alle Hyperfeinlinien gleich. Die in Bild 4 aufgetragenen Halbwertsbreiten der verschiedenen Hyperfeinlinien zeigen, dass ein solcher Beitrag für die untersuchten Absorber klein ist; er wird bei der weiteren Diskussion nicht berücksichtigt.

Bei der Diskussion der Schwankungen der Magnetfelder am Kern sollen ihrer verschiedenen Ursachen nach zwei Beiträge ΔH_1 und ΔH_2 auseinandergehalten werden.

ΔH_1 wird auf lokale Schwankungen der Legierungszusammensetzung zurückgeführt, also auf die von Eisenatom zu Eisenatom schwankende Anzahl nächster Eisen- und Nickel-Nachbarn im Gitter. Derartige Schwankungen der Magnetfelder am Kern sind nach der beobachteten Änderung der mittleren Felder mit der Legierungszusammensetzung (Bild 3) zu erwarten.

ΔH_2 kommt bei konstanter Zahl Eisen- und Nickel-Nachbarn infolge ihrer verschiedenen räumlichen Anordnungsmöglichkeiten und unterschiedlichen magnetischen Momente hinzu; dieser Beitrag entspricht also den Schwankungen des Lorentzschen Mikrofeldes am Ort des zentralen Eisenkerns. Es wird bei gleichartigen Gitternachbarn in kubischer Symmetrie bekanntlich Null. Summiert man hingegen die Dipolfelder der um 2,4 Bohrsche Magnetonen unterschiedlichen magnetischen Momente der Eisen- und Nickelnachbarn m_{Fe} und m_{Ni} in den Legierungen, dann erhält man Lorentzfelder ΔH_2, die mit der Anordnung und Richtung der n magnetischen Momente m_{Fe} der Eisenatome auf den Gitternachbarplätzen schwanken.

Wir beschreiben das Magnetfeld H an einem bestimmten Eisenkern also durch eine Summe aus dem mittleren Feld $\bar{H}$ (Bild 3) und den Schwankungen ΔH_1 und ΔH_2:

$$H(n, m_{Fe}, m_{Ni}) = \bar{H} + \Delta H_1(n) + \Delta H_2(n, m_{Fe}, m_{Ni}) \qquad (1)$$

5.1. STATISTISCHE VERTEILUNG DER LEGIERUNGSPARTNER

Bei statistischer Verteilung der Legierungspartner ist die Wahrscheinlichkeit, gerade n Eisennachbarn auf den 12 nächsten Gitternachbarplätzen eines Eisenatoms anzutreffen, durch eine Binomialverteilung

$$W(n,p) = \binom{12}{n} p^{12-n}(1-p)^n \qquad (2)$$

gegeben; p ist die Konzentration der Nickelatome in der Legierung. Ordnen wir der mittleren Zahl der Eisennachbarn $\bar{n} = 12 \cdot (1-p)$ das für p gefundene mittlere Feld $\bar{H}$ zu und vernachlässigen zunächst ΔH_2, dann erhalten wir bei einer um $(n-\bar{n})$ vom Mittelwert $\bar{n}$ abweichenden Eisennachbarnzahl n ein Feld $H(n)$, das sich entsprechend um

$$\Delta H_1(n) = (n-\bar{n})\, \mathrm{d}\bar{H}/\mathrm{d}\bar{n} \qquad (3)$$

vom Mittlewert $\bar{H}$ unterscheidet. Dabei setzen wir voraus, dass $H(n)$ sich mit der Eisennachbarnzahl n in gleicher Weise ändert wie die mittleren Felder $\bar{H}$ mit der makroskopischen Legierungszusammensetzung p bzw. $\bar{n}$; ΔH_1 wird daher proportional der aus Bild 3 entnommenen Änderung $\mathrm{d}\bar{H}/\mathrm{d}\bar{n}$ des mittleren Feldes mit der Legierungszusammensetzung angesetzt.

Die Maxima der sechs Hyperfeinlinien ($i = 1, 2, \ldots, 6$) bei Aufspaltung der Kernzustände durch das mittlere Magnetfeld $\bar{H}$ liegen im Transmissionsspektrum bei den Geschwindigkeiten v_i.

Ändert sich $\bar{H}$ um ΔH_1, so werden die Hyperfeinlinien entsprechend um $(v-v_i)$ auf benachbarte Geschwindigkeiten v verschoben.

Aus dem Zusammenhang zwischen Zeeman-Aufspaltung der Kernenergieniveaus

$$\Delta E_i = E_i - E_0 = (m_a\mu_a/I_a - m_g\mu_g/I_g)H \qquad (4)$$

und Dopplerverschiebung

$$\Delta E_i/E_0 = v_i/c \qquad (5)$$

folgt

$$(v-v_i)/v_i = \Delta H_1/\bar{H}. \qquad (6)$$

(In (4) und (5) bedeuten E, m, μ, I der Reihe nach Resonanzenergien, magnetische Quantenzahlen, magnetische Momente und Spins des Kerns im angeregten Zustand (Index "a") und Grundstand (Index "g"); für den 14,4 keV-Übergang in Fe^{57} gilt: $E_0 = E_a - E_g = 14{,}4$ keV; $\mu_a = -0{,}153\mu_k$; $\mu_g = 0{,}0903\mu_k$; $\mu_k = 3{,}14 \cdot 10^{-12}$ eV/Oe = Kernmagneton; $I_a = \frac{3}{2}$; $I_g = \frac{1}{2}$).

Nach (6) kann $(v-v_i)$ aus ΔH_1 berechnet werden. Die Wahrscheinlichkeit $W(v)$, eine Hyperfeinlinie bei der Geschwindigkeit v zu finden, ist somit durch (2), (3) und (6) gegeben, Sie ist in Bild 5 für die äusserste Hyperfeinlinie ($i = 6$) der ungeordneten 75% Ni/25% Fe-Folie gestrichelt eingezeichnet. Statt einer einzigen Hyperfeinlinie bei v_i erhalten wir also jeweils ein ganzes Spektrum von Hyperfeinlinien um v_i, das nach (6) dem Schwankungsspektrum der Magnetfelder an den Eisenkernen entspricht.

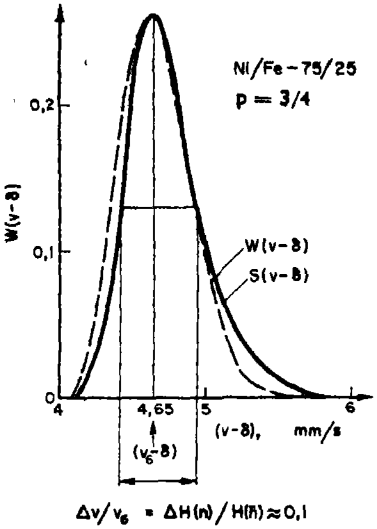

BILD 5. Häufigkeitsverteilung der äussersten Hyperfeinlinien der ungeordneten 75% Ni/25% Fe-Folie (Maximum in Transmissionsspektrum bei $(v_6 - \delta) =$ 4,65 mm/s ; $\delta = -0{,}36$ mm/s = Isomerierverschiebung zwischen Emissions und- Absorptionslinie).

- - - Aus der Binomialverteilung der Eisen–Nickel-Atome auf den 12 Gitternachbarplätzen und der Änderung der mittleren Magnetfelder $\bar{H}(p)$ mit der Legierungszusammensetzung berechnete Verteilung W.

—— Aus dem gemessenen Hyperfeinspektrum ermittelte Verteilung S.

Andererseits entstehen die gemessenen Hyperfeinspektren $M(v)$ auf Bild 2 durch eine Faltung des tatsächlichen Spektrums S der Hyperfeinlinien mit der im Reinsteisen gemessenen Lorentzkurve L als Kern der folgenden Integralgleichung

$$M(v)\,dv = dv \int_{-\infty}^{+\infty} S(u)L(v-u)\,du. \tag{7}$$

Wir haben S daraus durch ein numerisches Iterationsverfahren ermittelt, im Maximum der berechneten Häufigkeitsverteilung $W(v)$ normiert und erhalten die ausgezogene Kurve in Bild 5. Ihrer Halbwertsbreite entsprechen mittlere Schwankungen der Magnetfelder am Kern von 10%, ΔH_1 ist also von der Grössenordnung 10^4 Oe. Die Übereinstimmung von W und S zeigt, dass sich die Verbreiterungen der Hyperfeinlinien praktisch allein auf die Magnetfeldschwankungen ΔH_1 zurückführen lassen und die asymmetrische Linienform durch die Binomialverteilung der Eisenatome auf den Nachbarplätzen geprägt wird.

Weitere Linienanalysen lassen darauf schliessen, dass auch ein Einfluss der sechs übernächsten Nachbarn eines Eisenatoms auf die Schwankungen ΔH_1 der Magnetfelder am Kernort vorhanden ist.

Die Binomialverteilung ist bei 50% Eisen am breitesten und wird mit abnehmenden Eisengehalt schmäler. Daher ist verständlich, dass die Linien der Folie mit 25% Eisen breiter sind als die der Permalloyschicht mit 19% Eisen.

5.2. LEGIERUNGEN MIT ÜBERSTRUKTUR

In einer vollständig zu Ni_3Fe geordneten 75% Ni/25% Fe-Legierung haben alle Eisenatome gleiche Umgebung und nur nächste Nickel-Nachbarn ; es sind daher keine Magnetfeldschwankungen und Linienverbreiterungen zu erwarten. Die Linien müssen mit zunehmenden Ordnungsgrad schärfer werden. Dies ist in Übereinstimmung mit den beobachteten schmäleren Linien in der teilweise zu Ni_3Fe geordneten 75% Ni/25% Fe-Folie.

Aus der Form und Breite der Hyperfeinlinien kann der Ordnungsgrad für Überstrukturen in Ni/Fe-Legierungen bestimmt werden.

Die Linienform wird insbesondere davon abhängen, ob die Ni_3Fe-Phase sich ausscheidet oder ob über Nahordnungsvorgänge ein für alle Bereiche der Schicht gleichmässiger, stetiger Übergang in die geordnete Phase stattfindet. Eine Analyse des Hyperfeinspektrums der teilweise zu Ni_3Fe geordneten Legierung ergab etwa einen Ordnungsgrad von 50% ; in Übereinstimmung mit Röntgenbeugungsaufnahmen liegen geordnete und ungeordnete Bereiche nebeneinander vor.

Nach der in Abschnitt 5.1. dargelegten Anschauung sollte bei 12 nächsten Ni-Nachbarn das mittlere Magnetfeld $\bar{H}$ dem Feld im reinen Nickel entsprechen, also für die Ni_3Fe-Phase etwa 10% kleiner sein als das der ungeordneten 75% Ni/25%

Fe-Folie. Tatsächlich beobachteten wir ein Feld $\bar{H}$, das nur etwa 2% kleiner war als in der ungeordneten Legierung. Dieses Ergebnis deutet wieder auf einen Einfluss der sechs übernächsten Eisennachbarn auf das Magnetfeld am Eisenkern hin, worauf bei der Diskussion der Linienverbreiterungen bereits hingewiesen wurde.

5.3. LEGIERUNGEN MIT EINACHSIGER MAGNETISCHER ANISOTROPIE

Die bisherige Diskussion zeigte, dass die beobachteten Verbreiterungen der Hyperfeinlinien auf ΔH_1 allein zurückführbar sind. Verbreiterungen durch Schwankungen ΔH_2 der Lorentzschen Mikrofelder an Eisenkernen konnten nicht direkt aus den gemessenen Hyperfeinspektren ermittelt werden.

Wir haben jedoch versucht, Änderungen von ΔH_2 durch einen noch empfindlicheren Vergleich *der Linienform nachzuweisen.*

Dabei wurden $\bar{H}$, ΔH_1 und die übrigen Versuchsbedingungen exakt konstant gehalten und die Änderungen von ΔH_2 in ein und demselben Absorber erzeugt. Derartige Änderungen von ΔH_2 *sollten* an *ausgerichteten Eisenpaaren in magnetisch* anisotropen Permalloyschichten auftreten, wenn man sie einmal in magnetisch leichter, einmal in magnetisch schwerer Achse magnetisiert. Damit bestand zugleich Aussicht, das Vorhandensein derartiger ausgerichteter Eisenpaare als eine der vermutlichen Ursachen für die *M*-induzierte magnetische Anisotropie dünner Permalloyschichten direkt nachzuweisen.(11, 12) Nach Néel(11) entsteht beim Aufdampfen oder Tempern mit festgehaltener Magnetisierungsrichtung *M* eine magnetisch leichte Achse dadurch, dass ein Bruchteil überschüssiger Eisenpaare mit Achsen parallel zu dieser Magnetisierungsrichtung induziert wird.

Magnetisiert man einen solchen Absorber einmal in leichter, *einmal in* schwerer Richtung, dann werden die magnetischen Momente eines vollständig ausgerichteten Eisenpaares einmal in Richtung seiner Paarachse und einmal senkrecht dazu ausgerichtet. Die Lorentzfelder $(\Delta H_2)_\parallel$ und $(\Delta H_2)_\perp$ unterscheiden sich dabei je nach Zahl und Anordnung der übrigen Eisennachbarn um 10^2 bis 10^4 Oe Im Mittel erwartet man an ausgerichteten Eisenpaaren somit Unterschiede der Magnetfelder am Kern von grössenordnungsmässig 1%; dem entsprechen im Transmissionsspektrum Verschiebungen der Hyperfeinlinien für die in Néel-Paaren enthaltenen Eisenkerne von grössenordnungsmässig 10% der gemessenen Halbwertsbreiten.

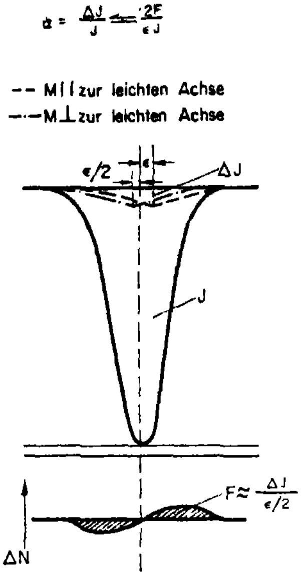

Bild 6. Modifizierung der Hyperfeinlinie eines magnetisch anisotropen Permalloy-Absorbers bei Magnetisierung in magnetisch leichter (– – –) und schwerer (–·–·–) Achse (Prinzip!).

Der Flächenanteil ΔJ, der dem Bruchteil α von Eisenkernen in ausgerichteten Paaren entspricht, wird um $3/2\ \epsilon$ verschoben. Aus der Fläche F unter der resultierenden Differenzkurve ΔN kann $\alpha \cdot \epsilon$ bestimmt werden. Die relative Verschiebung von ΔJ um $\frac{3}{2}\epsilon = \frac{3}{2}\epsilon_\parallel = \epsilon_\parallel - \epsilon_\perp = (v_l/\Gamma \cdot \bar{H})\ [\Delta H_{2_\parallel} - \Delta H_{2_\perp}]$ entspricht dabei der Änderung der Lorentzschen Mikrofelder ΔH_2 bei Magnetisierung parallel (∥) und senkrecht (⊥) zur magnetisch leichten Achse.

Wie in Bild 6 veranschaulicht ist, wird bei Ummagnetisierung in leichter und schwerer Richtung nur der den Néel-Paaren entsprechende Flächenbruchteil ΔJ jeder Hyperfeinlinie um diesen Betrag verschoben. Die darunter skizzierte Differenzkurve $\Delta N(v)$ beider Hyperfeinlinien resultiert also nur aus diesen verschobenen Anteilen. Das Verhältnis der Fläche $2F$ unter der Differenzkurve zur Gesamtfläche J unter der Hyperfeinlinie ist näherungsweise gleich dem Produkt aus der mittleren, auf die gemessene Halbwertsbreite bezogenen Verschiebung der Hyperfeinlinien

$\epsilon = \Delta v/\Gamma$ und dem Bruchteil α der in ausgerichteten Paaren enthaltenen Eisenkerne

$$\alpha \cdot \epsilon \approx 2F/J \quad (\text{für } \epsilon \ll 1). \qquad (8)$$

Wir haben versucht, das Verhältnis $2F/J$ an dem in Abschnitt 2 beschriebenen, 2μ dicken, magnetisch anisotropen Permalloy-Absorber zu messen. Bei den über mehrere Tage laufenden Messreihen wurde der Absorber durch gekreuzte Helmholtzspulenpaare nach jeder Minute automatisch von einer Achsenrichtung in die andere ummagnetisiert. Die zu vergleichenden Hyperfeinspektren wurden in die zwei Hälften eines 256-Kanal-Zählers eingespeichert. Das Ergebnis ist in Bild 7 dargestellt. Bei etwa 3 Millionen Impulsen pro Messpunkt jedes Spektrums betrug der statistische Fehler, bezogen auf das Maximum der mittleren Hyperfeinlinie, nur noch etwa 0,25%. Diese Genauigkeit war ausreichend, um ein Produkt $\alpha \cdot \epsilon$ von $5 \cdot 10^{-3}$ noch nachzuweisen ; Verschiebungen der gesamten Hyperfeinlinie ($\alpha = 1$) um 0,5% ihrer Halbwertsbreite wären also gerade noch messbar gewesen.

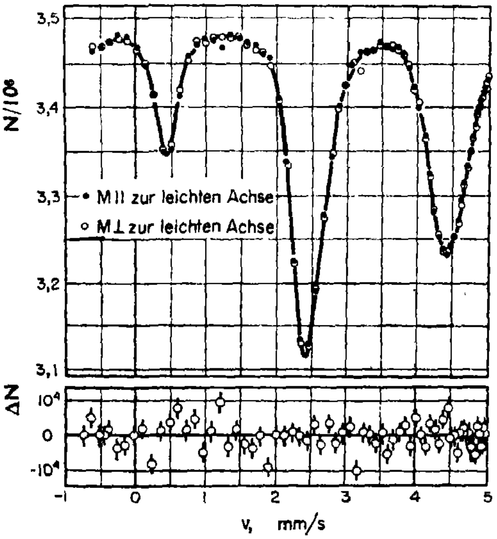

Bild 7. Transmissionsspektren $N(v)$ und ihre Differenz $\Delta N(v)$ für einen magnetisch anisotropen Permalloy-Absorber (81 %Ni/19 %Fe ; 80 %–Fe^{57}–angereichertes Fe ; Dicke $2 \cdot 10^{-3}$ cm; Anisotropiefeldstärke 2,5 Oe) bei Magnetisierung parallel (●) und senkrecht- (○) zur magnetisch leichten Achse. (Beim Transmissionsspektrum $N(v)$ entspricht der lichte Durchmesser der Messpunkte ihrem statistischen Fehler).

Die unten aufgetragene Differenzkurve zeigte jedoch keinen über den Rahmen der statistischen Fehlerbreiten hinausgehenden systematischen Verlauf ; der Bruchteil ausgerichteter Eisen-Paare liegt also unterhalb der mit der Mössbauer-Methode erreichbaren Nachweisgrenze. Bei einer mittleren Verschiebung der Hyperfeinterme um 10% der Linienbreite würden grössenordnungsmässig 10^{20} Néel-Paare pro cm^3 noch nachweisbar sein. Für die mittlere Anisotropieenergie pro ausgerichtetes Paar folgt daraus zusammen mit der gemessenen Anisotropiefeldstärke von 2,5 Oe eine untere Grenze von 10^{-17} erg. Nach Néel(11) beträgt diese Energie jedoch 10^{-15} bis 10^{-16} erg.

Um die Eisenpaar-Ausrichtung als Ursache für die M-induzierte magnetische Anisotropie dünner Permalloyschichten nachzuweisen oder auszuschliessen, müsste entweder die Nachweisgrenze oder die Zahl der Néel-Paare, also die Anisotropie, um ein bis zwei Grössenordnungen erhöht werden. Diskutabel ist nur das Letztere. Durch Tempern im Magnetfeld ist eine grössenordnungsmässige Erhöhung von α jedoch nicht mehr möglich, da das zugehörige thermische Gleichgewicht bei so tiefen Temperaturen liegen würde, dass Platzwechselvorgänge im Gitter praktisch nicht mehr stattfinden. Paulevé u.a.(18) zeigten jedoch kürzlich an einer 50%Ni/50% Fe-Probe, dass man die gewünschten Nahordnungsvorgänge dann eventuell durch Neutronenbestrahlung erzielen kann.

6. SCHLUSSWORT

Die bisherigen Untersuchungen lassen sich wie folgt zusammenfassen : Die Magnetfelder am Kernort von Eisenatomen in Eisen-Nickel-Legierungen schwanken. Das Spektrum der inneren Magnetfelder konnte mit Änderungen der Eisen-Nickel-Zusammensetzung auf den Gitternachbarplätzen in Zusammenhang gebracht werden.

Messungen an magnetisch anisotropen Permalloyschichten zeigten, dass weniger als 10^{20} ausgerichtete Eisenpaare im cm^3 enthalten sind.

Anerkennung—Herrn Prof. W. Kleen, Herrn Prof. H. Maier-Leibnitz und Herrn Prof. W. Meissner danken wir dafür, dass sie die Zusammenarbeit ermöglicht und die Arbeit stets gefördert haben.

LITERATUR

1. Hanna S. S., Heberle J., Littlejohn C., Perlow G. J., Preston R. S., und Vincent D. H., *Phys. Rev. Letters* **4**, 177 (1960).
2. Watson R. E. und Freeman A. J., *Phys. Rev.* **123**, 2027 (1961).
3. Hanna S. S., Heberle J., Perlow G. J., Preston R. S. und Vincent D. H., *Phys. Rev. Letters* **4**, 513 (1960).
4. Flinn P. A. und Ruby S. L., *Phys. Rev.* **124**, 34 (1961).
5. Johnson C. E., Ridout M. S., Cranshaw T. E. und Madsen P. E., *Phys. Rev. Letters* **6**, 450 (1961).
6. Shull C. G. und Wilkinson M. K., *Phys. Rev.* **97**, 304 (1955).
7. Kehler W. und Neuwirth W., *Z. Phys.* **167**, 176 (1962).
8. Kankeleit E., (unveröffenlicht).
9. Kankeleit E., *Z. Phys.* **164**, 442 (1961). Kalvius M., Zahn U., Kienle P. und Eicher H., *Z. Naturf.* **17a**, 494 (1962).
10. Kocher C. W. und Brown P. J., *J. appl. Phys.* **33**, 1091S (1962).
11. Néel L., *J. phys. Radium* **15**, 225 (1954).
12. Taniguchi S., *Sci. Rep. Res. Insts. Tôhoku Univ.* **A7**, 269 (1955).
13. Paulevé J., Dautreppe D., Laugier J. und Néel L., *C.R. Acad. Sci. Paris* **254**, 965 (1962).

J. Phys. Chem. Solids Pergamon Press 1963. Vol. 24, pp. 1003–1010. Printed in Great Britain.

CORRECTIONS TO THE GROUND STATE ENERGIES OF SHALLOW DONORS IN SILICON AND GERMANIUM

P. CSAVINSZKY

Texas Instruments Incorporated, Dallas, Texas

(*Received* 18 *December* 1962; *revised* 18 *February* 1963)

Abstract—The correct potential in the effective mass equation should be the difference of the potential of a donor in the solid and that of an atom of the semiconductor host crystal. In the present paper such a difference potential is constructed for the central-cell region (defined by a sphere of radius of half the nearest neighbor distance), by making use of the Thomas–Fermi statistical theory, and considered as a perturbation to the potential (a simple Coulomb potential shielded by the static dielectric constant of the semiconductor) of the uncorrected theory. Using first-order perturbation theory the energy corrections are computed and the ground state energies of P, As, Sb and Bi in Si and Ge are found to be (the minus signs are not denoted) 31, 35, 39, 45 meV and 8·9, 9·3, 9·6, 10.0 meV, respectively, representing a definite improvement over the values of 29 meV and 9·2 meV which were predicted for all donors in Si and Ge, respectively, by the uncorrected theory. The possible sources of the still remaining discrepancies between theoretical and experimental values are discussed and attributed partly to effects outside of the central-cell region and partly to approximations involved in the present treatment that resulted in obtaining a lower limit for the size of the corrections.

1. INTRODUCTION AND STATEMENT OF THE PROBLEM

It is well known from the theory of impurity levels$^{(1)}$ that it predicts the same ground state energy for all Column V (so called shallow) impurities in Si on the one hand and Ge on the other hand whereas measurements show that in both semiconductors this quantity markedly depends on the specific nature of the donor. Furthermore, it is also known that the absolute value of the predicted ground state energy is considerably smaller (especially in Si) than any one of the measured values. This defect of the theory can be traced back to an approximation, namely to the use of an incomplete potential with which the effective mass equation is solved. According to theory$^{(2)}$ the correct potential should be the difference of the potential of a donor in the solid and that of an atom of the semiconductor host crystal. Since it would be very difficult to construct such a difference potential valid for all regions of space, in practice it is approximated by its asymptotic form that is obtained from the following considerations: As a first step one imagines that out of the five valence electrons of a (Column V) donor atom one is removed and then the resulting ion and the free electron is substituted in the semiconductor lattice. In this case the ion will establish four (covalent) bonds with its four neighbors and the electron will move under the influence of the difference potential. At large distances from the impurity center the semiconductor component of the difference potential is negligibly small compared to the donor component which, as can be shown from first principles,$^{(3, 4)}$ is a simple Coulomb potential shielded by the static dielectric constant of the semiconductor. For this reason in earlier actual calculations only the asymptotic form of the donor component of the difference potential was used. It is clear, that in the vicinity of the impurity center this approximation is poor since there the semiconductor part of the difference potential might not be negligible compared to the donor part which itself might be very different there from its asymptotic form.

It is the purpose of the present paper to investigate what corrections will result to the simple theoretical ground state values$^{(1)}$ of Column V donors in Si and Ge by considering the full difference potential in the immediate vicinity of the impurity center and using the shielded Coulomb potential as an approximation for the difference potential outside of this region. It is hoped that by so doing one will be able to ascribe the discrepancies that are still expected to remain between the calculated and measured values to other factors such as the space dependence of the dielectric constant[4, 5] (i.e. the deviation of the donor potential from its asymptotic form), the modification of the conduction band edge due to the strain resulting from the replacement of an atom of the semiconductor by a donor of a different size[6] and the role the possible mixing-in of other bands might play in the effective mass formalism.

2. THEORY AND CALCULATION

In what follows the actual band structure of both Ge and Si will be ignored and a simple spherical conduction band will be assumed. While it is true that consideration of the actual band structure of Si and Ge would make a more attractive model it is pointed out that this simplification is necessary in order to arrive at manageable formulae for the energies of the donor ground states. The reason for this is that consideration of the non-sphericity of the conduction bands in Si and Ge would necessitate the inclusion of non-spherically symmetric (pancake-like) wave functions that would render the numerical computation completely unmanageable. Since, however, this idealization is important in judging the reliability of the present model an estimate will be made at a later stage of how much the computed energy corrections are expected to be modified had one been able to do the calculations in conformity with the actual band structures.

In the absence of any impurities the Hamiltonian for a conduction electron in the perfectly periodic semiconductor crystal is given[1] by

$$H_0 = -\frac{\hbar^2}{2m_0}\Delta + U(r), \tag{1}$$

where $U(r)$ is the potential energy of the electron in the effective periodic potential of the crystal and m_0 is the free electronic mass. If now one of the atoms of the lattice is replaced by a positive singly charged impurity ion then the Hamiltonian for a conduction electron is modified to

$$H = H_0 - e\eta(r), \tag{2}$$

where $\eta(r)$ is the difference potential defined by

$$\eta(r) = V_{D^+}(r) - V_S(r). \tag{3}$$

Since in the present work one is primarily interested in the form the difference potential takes near the lattice point of substitution one may assume that the potential due to a neutral atom of the semiconductor $V_S(r)$, or that due to a donor ion $V_{D^+}(r)$, is the same in the solid as in the free systems.

To obtain the atomic and ionic potentials of equation (3) use is made of the Thomas–Fermi statistical theory.[7] According to this theory the charge distribution of a neutral atom extends to infinity, whereas that of a positive ion goes to zero at a certain distance r_0 (which for the present purposes need not be specified here further) from the nucleus of the ion. As to the potential distribution it can be written[7] as

$$V_S(r) = \frac{Z_S e}{r}\phi_S(r) \tag{4}$$

for the neutral atom and

$$V_{D^+}(r) = \frac{Z_D e}{r}\phi_{D^+}(r) + V_0 \quad \text{for} \quad r < r_0 \tag{5a}$$

$$V_{D^+}(r) = \frac{(Z_D - N)e}{r} \quad \text{for} \quad r > r_0 \tag{5b}$$

for the positive ion. In equations (4) and (5a, b) $\phi_S(r)$ and $\phi_{D^+}(r)$ are appropriate solutions of the Thomas–Fermi equation; Z_D is the atomic number of the ion, Z_S is that of an atom of the semiconductor, e is the electronic charge, N is the number of electrons of the ion, and V_0 is a constant related to r_0 the radius of the ion. Since present interest centers only in a space region which is smaller than that of a sphere with the radius of the ion use will only be made of equation (5a). Such a restriction is compelling for two reasons: First, it is known[8] from comparisons with more sophisticated quantum mechanical calculations that the Thomas–Fermi potentials are not reliable at large distances from the nucleus and second, as already mentioned, the potential of an ion or atom in the solid can be taken identical with that in the free systems only in the vicinity of the nucleus where the influence of neighboring atoms of the lattice (causing deviation from spherical symmetry) is not felt.

Though the functions $\phi_S(r)$ and $\phi_{D^+}(r)$ could be inferred from available tables, for the present purposes a more comprehensive tabulation is required and for this reason analytic approximations proposed by SOMMERFELD(9) will be used. These approximations have been shown(9) to be in very good agreement with the exact solutions of the Thomas–Fermi equation and are given(10) by

$$\phi_S(r) = [(1+C_S r^{4/5})^{15/4}]^{-1} \tag{6}$$

and

$$\phi_{D^+}(r) = [(1+C_D r^{4/5})^{15/4}]^{-1} \times [1-C'_D(1+C_D r^{4/5})^{75/8}]. \tag{7}$$

The constants appearing in equations (6) and (7) are defined by

$$C_S = \frac{Z_S^{4/15}}{144^{4/15}\times 0{\cdot}8853^{4/5}a_0^{4/5}}$$

$$C_D = \frac{Z_D^{4/15}}{144^{4/15}\times 0{\cdot}8853^{4/5}\,a_0^{4/5}}$$

$$C'_D = \left(1+\frac{X_D^{4/5}}{144^{4/15}}\right)^{-75/8}$$

where a_0 is the first Bohr radius and the quantity X_D is a dimensionless constant, related to the atomic number and degree of ionization of the particular donor atom. The values of x_D, as inferred from the Thomas–Fermi theory,(11) are given below

$$X_D(P^+) = 13{\cdot}27, \quad X_D(\mathrm{As}^+) = 20{\cdot}54,$$

$$X_D(\mathrm{Sb}^+) = 24{\cdot}95, \quad X_D(\mathrm{Bi}^+) = 32{\cdot}37.$$

In terms of the X_D's the quantity V_0 in equation (5) can be expressed as

$$V_0 = \frac{eZ_D^{1/3}}{0{\cdot}8853\;X_D\,a_0}.$$

Making use of equations (3), (4) and (5a) one may rewrite the difference potential as

$$\eta(r) = \frac{Z^*(r)e}{r}\text{ for } r < r_0 \tag{9}$$

where

$$Z^*(r) = Z_D\phi_{D^+}(r) - Z_S\phi_S(r) + rV_0. \tag{10}$$

One is now in a position to write down the effective mass equation. Recalling that the difference potential is considered only in the vicinity of the impurity center one may write

$$\left[-\frac{\hbar^2}{2m^*}\nabla^2 - e\eta(r)\right]\psi = E\psi\text{ for } r < R_S \tag{11}$$

and

$$\left[-\frac{\hbar^2}{2m^*}\nabla^2 - \frac{e^2}{\kappa r}\right]\psi = E\psi\text{ for } r > R_S, \tag{12}$$

where κ is the static dielectric constant of the semiconductor ($\kappa = 12$ for Si and $\kappa = 16$ for Ge), E is the ground state energy of the donor and R_S is a parameter characterizing the region within which the difference potential is considered.

In principle one could determine E by solving the differential equation both for the interior and the exterior region and by matching ψ and its derivative at the boundary R_S. This, however, is a very complicated numerical procedure and it is much easier to proceed in a different fashion.

Before doing that, however, one must be assured that the effective mass equation is meaningful since it becomes unreliable for a potential which varies very rapidly over a unit cell. In the present case the situation is favorable since instead of a very rapidly varying potential a difference potential is used whose dependence on r is much smoother than that of either one of its components. This is especially true for P in Si and for As in Ge where the variation of the difference potential is the smoothest since in both cases the atomic number of the semiconductor differs only by unity from that of the impurity. In the former case the ratio $[Z^*(r_2)e/r_2]/[Z^*(r_1)e/r_1]$ is 0·65 when for the sake of demonstration the values of $r_2 = 2a_0$ and $r_1 = 1a_0$ are chosen, while in the latter case with the same choices of r_1 and r_2 the ratio is 0·72. For the cases of Bi in Si and Bi in Ge, where the difference in the atomic numbers is the largest among the cases considered in this paper, the difference potential is found to vary still not too rapidly since the ratios at the same values of r_1 and r_2 as above are found to be 0·16 and 0·17, respectively, that is of the same order of magnitude as before.

Returning now to equation (12) one sees that if for the moment R_S is taken to be zero then equation (12) is just the effective mass equation of the uncorrected theory[(1)] and has the well-known hydrogen-like solutions. In correcting the theory one may consider $[-e\eta(r)]$ as a perturbation that acts in the $0 \leqslant r \leqslant R_S$ region, and calculate the first order perturbation energy from

$$\epsilon_{\text{correction}} = \int_0^{R_S} \psi^*[-e\eta(r)]\,\psi\,\mathrm{d}v, \tag{13}$$

where

$$\psi = (\pi a^{*3})^{-1/2}\exp[-(r/a^*)] \tag{14}$$

and $\mathrm{d}v = 4\pi r^2\,\mathrm{d}r$. The quantity a^* in equation (14) is given by

$$a^* = \frac{\hbar^2\kappa}{m^*e^2} = a_0\frac{\kappa}{\gamma},$$

where $\gamma = m^*/m_0$ and m^* is an effective isotropic electronic mass.

It is mentioned at this point that care should be exercised in the physical interpretation of equation (13). It represents the interaction energy of an electron with a spherically symmetric potential but not the interaction of an electron with a core into which it penetrates. The donor electron moves neither in the field of the core of a semiconductor atom nor in the field of the core of the substituted impurity atom but in the difference of their fields. The view that the donor electron moves in the field of a single core would lead to difficulties since one would have two $1s$ electrons in the core and one impurity electron described by a modified $1s$ wave function all within a single system that could not be reconciled with the Pauli principle. This problem, however, does not appear here and the difference potential, as already said, might simply be looked upon as an electrostatic perturbation coming from the origin and acting only over a restricted space region.

Should one attempt a variational solution of equations (11) and (12) then further difficulties would emerge because certain orthogonality conditions must be satisfied in order to obtain a reliable energy value. These conditions are simple when an electron moves in the field of a core since they merely require that the wave function of the electron should be orthogonal to the wave functions of the core electrons. In the present case when the potential is the difference of the potentials of two different cores it is not quite clear just how the orthogonality conditions should be formulated in a variational procedure. The perturbational approach adopted in this paper is free from this difficulty because one simply has to use the unperturbed wave function ψ whose form cannot be changed by orthogonalization since that would amount to changing the unperturbed problem.

To evaluate equation (13), two quantities need to be fixed, R_S and m^*. Such a procedure unavoidably has elements of arbitrariness but within the framework of the present treatment this cannot be circumvented. As to R_S one can take half of the nearest neighbor distance which for Si is 2·22 a_0 and for Ge 2·32 a_0.[(12)] As for m^* it is taken to be 0·306 m_0 for Si and 0·173 m_0 for Ge. These values are obtained (following a suggestion of KOHN[(13)]) from the requirement that the uncorrected isotropic effective mass equation should give the same ground state energy (−29 meV for Si and −9·2 meV for Ge), as that obtained by solving the uncorrected anisotropic effective mass equation by the variational technique.

With the above choices of the parameters the integrand of equation (13) has been tabulated for the various cases and numerical integrations have been performed. The results are given in Columns II of Tables 1 and 2. Columns III show the corrected ground state energy values, $-29+\epsilon_{\text{Si}}$ and $-9{\cdot}2+\epsilon_{\text{Ge}}$, Columns IV the experimental values and Columns V the difference between the experimental and corrected values.

3. DISCUSSION AND CONCLUSIONS

It is seen from Table 1 that for all donors in Si the corrections to the ground state energies are negative. Table 2 shows that for Ge the correction to the ground state of P is positive while the corrections to the other donors are negative. The reason for this lies in the fact that for small values of r the difference potential, $\eta(r)$, is always positive for donors in Si since there $Z_D > Z_{\text{Si}}$, while in the case of Ge $Z_P < Z_{\text{Ge}}$ but $Z_D > Z_{\text{Ge}}$ for the other donors. It is also seen from the Tables that the

Table 1. Corrections to the ground state energies of shallow donors in Si. (*Uncorrected value*[1] *for all donors is* −29 meV)

Donor	$\epsilon_{\text{correction}}$ (meV)	$E^{\text{calculated}}_{\text{ground state}}$ (meV)	$E^{\text{experimental}}_{\text{ground state}}$ (meV)	Remaining discrepancy (meV)
P	−1·5	−31	−45 (a)	−14
As	−6·4	−35	−53 (a)	−18
Sb	−10	−39	−43 (a)	− 4
Bi	−16	−45	−69 (b)	−24

Values denoted by (a) were determined by optical measurements and are taken from Table 1 of Ref. 1, p. 262, while the value denoted by (b) was determined by thermal measurements and is taken from the same source.

Table 2. Corrections to the ground state energies of shallow donors in Ge. (*Uncorrected value*[1] *for all donors is* −9·2 meV)

Donor	$\epsilon_{\text{correction}}$ (meV)	$E^{\text{calculated}}_{\text{ground state}}$ (meV)	$E^{\text{experimental}}_{\text{ground state}}$ (meV)	Remaining discrepancy (meV)
P	+0·28	− 8·9	−12·8 (a)	−3·9
As	−0·11	− 9·3	−14·0 (a)	−4·7
Sb	−0·42	− 9·6	− 9·8 (a)	−0·2
Bi	−0·84	−10·0	−12·5 (a)	−2·5

Values denoted by (a) were determined by optical measurements and are taken from H. Y. Fan and P. Fisher, *J. Phys. Chem. Solids* **8**, 270 (1959).

corrections increase with increasing differences between the atomic number of the semiconductor and that of the donor in question.

One also sees from the Tables that in terms of the ground state energy values obtained from the uncorrected theory (−29 meV for Si and −9·2 meV for Ge) the present correction values range from about 5% for P in Si to 55% for Bi in Si and from about 3% for P in Ge to 9% for Bi in Ge. One may thus conclude that the perturbational approach used for the calculation of the corrections is well justified for donors in Ge and still reasonable for donors (with the possible exception of Bi) in Si. The fact that the corrections in Si are relatively much larger than in Ge is not surprising since the donor "orbits" are much smaller in Si than in Ge and, for this reason, the central-cell region is relatively more important for Si than for Ge.

Comparing the corrected energy values with the experimental ones one still finds large discrepancies. One might assume that they could be reduced by taking larger values for R_S than the ones chosen. Apart from the difficulty of reconciling such a choice with the spatial restrictions imposed by the lattice it has been ascertained that no significant gain would be had since the correction values are very insensitive to any small increase beyond the R_S values used. This is also the reason why the same R_S value has been used for all donors in a particular semiconductor. A refinement in this regard would only be justified if the calculated energy values were very close to the measured ones.

One might also argue that another choice of m^* would lead to another set of correction values. This is certainly true generally but in the perturbational approach the value of m^* cannot be changed without changing the zeroth-order Hamiltonian, $\left(\dfrac{\hbar^2}{2m^*}\nabla^2 - \dfrac{e^2}{\kappa r}\right)$, whose ground state wave function was used in the calculation of the correction values to its ground state energy value.

One might also assume that consideration of the actual band structure of Si and Ge could have led to significantly different energy corrections. A definite answer could be given for this question if one would calculate the perturbation energy from

$$\epsilon' = -e \int_0^{R_S} F^2 \eta \, \mathrm{d}v. \tag{15}$$

with the pancake-like wave function(14)

$$F = (\pi a^2 b)^{-1/2} \times \exp\left\{ -\left[\frac{x^2+y^2}{a^2} + \frac{z^2}{b^2}\right]^{1/2} \right\} \tag{16}$$

instead of from

$$\epsilon = -e \int_0^{R_S} \psi^2 \eta \, \mathrm{d}v \tag{13}$$

with

$$\psi = (\pi a^{*3})^{-1/2} \exp(-r/a^*) \tag{14}$$

as has been done in this paper. The quantity of importance is ϵ/ϵ', since it tells one how the replacement of the simple isotropic wave function, ψ, by the more exact anisotropic one, F, would modify the magnitude of the energy corrections due to a change in the probability of finding the donor electron in the central-cell. Because of the mathematical difficulties involved in evaluating ϵ' one cannot calculate ϵ/ϵ' exactly but one can estimate it in the following way. First, one assumes that one is interested in a spherical shell within the central-cell that is characterized by an inner radius of R_1 and by an outer radius of R_2 $(R_1 < R_2 < R_S)$. If the shell is sufficiently thin $(R_1 \gtrsim R_2)$ then the difference potential $\eta(r)$ can be considered as a constant over the width of the shell and consequently can be removed from under the integral sign. In this case one finds that

$$\frac{\epsilon}{\epsilon'} \cong \frac{\displaystyle\int_{R_1}^{R_2} \psi^2 \, \mathrm{d}v}{\displaystyle\int_{R_1}^{R_2} F^2 \, \mathrm{d}v}, \tag{17}$$

where the symbols in equation (17) indicate integration over the volume of the spherical shell and the numerator and denominator are simply the probabilities of finding the electron in the shell when it is associated with wave functions ψ and F, respectively.

Considering that in Ge, for instance, the central-cell is characterized by a radius R_S of about 2·3 a_0, that is small in comparison with $a^* = 48{\cdot}9$ Å and(14) $a = 64{\cdot}5$ Å, $b = 22{\cdot}7$ Å, one can expand $F^2(x,y,z)$ into a triple MacLaurin series around $x, y, z = 0$ and also $\psi^2(r)$ around $r = 0$. Keeping only linear terms in x, y, z and r and substituting the expansions into equation (17) one finds after integration that

$$\frac{\epsilon}{\epsilon'} \cong \frac{a^2 b}{a^{*3}} \left(1 - \frac{3}{2a^*} \frac{R_2^4 - R_1^4}{R_2^3 - R_1^3}\right). \tag{18}$$

For all allowed choices of R_1 and R_2 the second term in the parenthesis is negligibly small compared to the first one and therefore equation (18) can be written as

$$\frac{\epsilon}{\epsilon'} \cong \frac{a^2 b}{a^{*3}} = \frac{\psi^2(r=0)}{F^2(x,y,z=0)} = 0{\cdot}81$$

Thus, one may conclude that the treatment based on spherical wave functions underestimates the size of the central-cell corrections and that consideration of pancake-like wave functions would enlarge the energy corrections obtained by a factor of 1/0·81 = 1·2 for donors in Ge. In the same way as above, using $a^* = 20{\cdot}7$ Å and(14) $a = 25{\cdot}0$ Å, $b = 14{\cdot}2$ Å, one finds that for donors in Si the correction factor is 1·0. This result is not unexpected since the deviation of the wave function from spherical symmetry is much less in the case of Si than in the case of Ge because the ratio of the longitudinal effective mass to the transverse effective mass is only about 5 for Si while it is about 20 for Ge. One may thus conclude that the idealization of the band structures in the present model, with the choice made for the isotropic effective masses, has no serious consequences and one must look for other reasons in trying to explain the origin of the still remaining sizable discrepancies between the theoretical and experimental energy values.

Another source for the discrepancies might be suspected in the role that the possible mixing-in of bands (other than the conduction band) could play in the effective mass formalism. The reason for this is that only shallow impurity states can be represented in terms of wave functions from only the bottom of the conduction band while for deeper states the inclusion of successively more functions from the conduction band and perhaps also from other bands above the conduction band might be necessary. However, within the framework of the present model there is no room for such considerations since one has to use the unperturbed ground state wave function that was derived by considering wave functions from only the bottom of the conduction band. The mixing-in effect might possibly be important for Bi in Si, for instance, where it is questionable that one should consider the donor state (-69 meV) as a shallow state.

One might look upon the form of the difference potentials as another source of discrepancy. Since, however, they were calculated by approximations which are known to be very good it is not likely that any change in this regard would result in the improvement of the ground state values.

The region outside of the central-cell might also be responsible for part of the remaining discrepancies. In this region the potential has been considered as a Coulombic one shielded by the static dielectric constant. The deviation of the static dielectric constant from a "local dielectric constant"(4, 5) is probably a significant factor in the defectiveness of the theory. Just how important is this factor (whose consideration would certainly improve the calculated values(5)) cannot be ascertained at the present time since there is no reliable way of extracting this effect from those already mentioned.

It is mentioned that should one calculate the perturbation correction to the donor wave function ψ one would obtain different ground state wave functions for the different donors in Si and Ge. Such a modification in the wave functions might have some importance in the calculation of the mobility resulting from neutral impurity scattering(15) since its calculation is directly related to the wave function of the donor impurity. In ionized impurity scattering,(16) where the difference potential should also be used, the effect of the central-cell region on the mobility is anticipated to be small since it is mostly determined by small angle scattering which does not take part in the immediate vicinity of the scattering center.(17)

Finally, a word might be said about the corrections to the ground states of shallow acceptors which also show a dependence on the specific nature of (Column III) impurities.(1) In principle, the corrections could be computed by a similar perturbational treatment. In practice, however, this would be very complicated since the uncorrected effective mass equation is not hydrogen-like(18) because of the complicated structure of the valence bands in Si and Ge.

REFERENCES

1. For a review of the subject see Kohn W., *Solid State Physics*, **Vol. 5**, p. 257 ff. (edited by Seitz F. and Turnbull D.) Academic Press, New York (1957).
2. Kohn W. and Luttinger J. M., *Phys. Rev.* **97**, 883 (1955).
3. Kohn W., *Phys. Rev.* **105**, 509 (1957).
4. Morita A., Azuma M. and Nara H., *J. Phys. Soc. Japan* **17**, 1570 (1962).
5. Weiser K., *Bull. Amer. phys. Soc.* **6**, 156 (1961); The author is indebted to K. Weiser for a correspondence on the subject.
6. Weinreich G., *J. Phys. Chem. Solids* **8**, 216 (1959).
7. For a review of the subject see Gombás P., *Encyclopedia of Physics*, **Vol. XXXVI**, p. 109 ff. (edited by Flügge S.) Springer, Berlin (1956).
8. For a review of the subject see Gombás P., *Encyclopedia of Physics*, **Vol. XXXVI**, Sec. II, p. 132 ff. (edited by Flügge S.), Springer, Berlin (1956).
9. For a review of the subject see Gombás P., *Encyclopedia of Physics*, **Vol. XXXVI**, Sec. II, p. 125 ff. (edited by Flügge S.). Springer, Berlin (1956).
10. The formulas in equations (6) and (7) were obtained from those of Ref. (9) after some manipulation and upon replacing a constant $\lambda = 0{\cdot}8034$ by 8/10.
11. By making use of Table 2 of Ref. (7), p. 131.
12. Smith R. A., *Semiconductors*, Chap. 10, p. 346, University Press, Cambridge (1959).
13. For a review of the subject see Kohn W., *Solid State Physics*, **Vol. 5**, Sec. III, p. 291 (edited by Seitz F. and Turnbull D.) Academic Press, New York (1957).
14. For a review of the subject see Kohn W., *Solid State Physics*, **Vol. 5**, Sec. III, p. 288 (edited by Seitz F. and Turnbull D.) Academic Press, New York (1957).
15. For a review of the subject see Blatt F. J., *Solid State Physics*. **Vol. 4**, Sec. V, p. 354 ff. (edited by Seitz F. and Turnbull D.) Academic Press, New York (1957).

16. For a review of the subject see BLATT F. J., *Solid State Physics*, Vol. 4, Sec. V., p. 343 ff. (edited by SEITZ F. and TURNBULL D.) Academic Press, New York (1957).
17. MOTT N. F. and MASSEY H. S. W., *The Theory of Atomic Collisions*, 2nd ed., Chap. VII, p. 124 ff. Clarendon Press, Oxford (1949).
18. For a review of the subject see KOHN W., *Solid State Physics*, Vol. 4, Sec. IV, p. 297 ff. (edited by SEITZ F. and TURNBULL D). Academic Press, New York (1957).

J. Phys. Chem. Solids Pergamon Press 1963. Vol. 24, pp. 1011–1024. Printed in Great Britain.

SYSTEMATICS OF DEFECT STRUCTURES IN GLASSES WITH IONIC SUBSTITUTIONS

W. C. LEVENGOOD

The University of Michigan, Institute of Science and Technology, Ann Arbor, Michigan

(*Received* 4 *September* 1962; *revised* 31 *December* 1962)

Abstract—The effects of various ionic substitutions on defect structures in glass were investigated in soda–lime–silica systems. It is shown that detailed measurements of flaw characteristics provide a useful tool for investigating subtle internal energy variations in this solid. Influences of specific ions were quantitatively studied by determining the parameters of flaw length (F_l), and flaw number (F_n). Flaws produced on freshly broken surfaces under controlled loading conditions, were shown to be a direct indication of the stress response of the glass network. Relative bond strength and rigidity or brittleness of the structures varied with the ionic field strengths of added cations. Alkali ions in the form of oxides, were substituted for sodium and alkaline earth ions for calcium. Other additions and substitutional ions were also studied in detail. In general, the changes in flaw parameters were found to agree with theoretical predictions of internal energy changes based on the manner in which the ion entered the network, that is, as a lattice modifier, interstitial or network former. In specific systems, the variations in flaw length and flaw numbers were tentatively explained by changes in defect concentration and free volume as the ions were substituted.

I. INTRODUCTION

FOLLOWING the discovery of a method for quantitatively studying minute structure-sensitive flaws in glass,(1) it became apparent that this technique could be utilized to study the effect of various ionic substitutions in the network. Detailed investigations have shown that these defects have properties similar to dislocations in crystals and that the stress energies required to move or form these flaws are of the same order of magnitude as the energies necessary to move dislocations in crystalline lattices. It has been repeatedly demonstrated that the minute flaws in glass are not the same as gross bond rupture or visible cracks and the structure-sensitive characteristics of the defects have been confirmed in numerous investigations.

To a more limited degree, the influences of composition variations on the defect patterns have been quantitatively shown in soda–lime–silica systems.(2, 3) A dynamic spherical indenter technique was employed to create flaws under known, controlled loading conditions. The length of the flaws produced by this device was found to vary in a systematic manner with various ionic substitutions.

The results of more extensive experimentation pertaining to the influences of substitutional ions on defect properties are presented in this paper. Substitutions were made in three component systems, and two flaw parameters were studied; namely flaw length and number. By considering both of these parameters, the relative bond readjustment or yield was determined for a given stress condition. These quantitative flaw characteristics were compared with the ionic field strength or polarization of substituted ions. A hypothesis of changes in free volume with changes in internal ionic configuration was found to be in qualitative agreement with the experimental data. In general it is shown that the structure-sensitive defect patterns are related to internal energy variations.

II. EXPERIMENTAL

Oxide substitutions were made in a base glass containing 70 per cent silica and an initial soda–lime ratio of 1·14 (Na_2O/CaO on a weight per cent basis). The selection of this particular glass was not entirely arbitrary, as will be shown in a following Section. Reagent grade materials were used throughout these studies. The silica was pulverized (200 mesh) and was also of reagent grade. The basic raw materials were thoroughly mixed, placed in platinum–rhodium crucibles* and melted at 1400°C for 30 min. Sufficient batch was used to give 20 g of melted glass, which was poured out into a sample about ¼ in. thick and 1¼ in. in diameter. The samples were generally free of bubbles (at most only two or three "seeds") and the internal homogeneity appeared to be comparable to commercial glass. These samples were annealed with a final internal tension of around 20 p.s.i. (somewhat lower stress than in ordinary commercially annealed ware). After annealing, a test slug was diametrically scored with a glass cutter, then broken open using a fast break to give a relatively smooth test surface. The dynamic spherical indenter was applied within 30 sec after breaking. This indenter device was previously described(3) and consists of a $\frac{5}{16}$ in. steel ball provided with an axle so that it can rotate longitudinally under an applied vertical load. A 500 g load was used with a horizontal velocity of about 0·5 cm per sec. After making the ball trace, the samples were subsequently etched to develop the flaw patterns.

The flaw counts and flaw lengths were determined by microscopic examination using about 100× magnification. An ocular micrometer with a precision of about ± 0·001 mm was used to determine the flaw length. Only those flaws which were directly associated with the trace lines were included in the analyses. Under these loading conditions, at least 30 flaws were measured on all of the samples studied. The flaw length designated as F_l is the average of length of the flaws extending from the trace line and the flaw number designated as F_n is the average number of flaws nucleated per mm of trace line.

III. INTERPRETATION OF FLAW CHARACTERISTICS

The value of flaw length (F_1) is taken as an indication of the relative bond strength under the given loading conditions. The greater the F_l value, the weaker the bonds; in other words, the flaws propagate outward from a high stress region until they reach a critical zone where the elastic stress is no longer of sufficient magnitude to produce bond displacement or slip. Detailed studies have indicated(3) that the flaw lines are the edges of slip planes created by mechanical or thermal stresses. The origin or core of the slip plane lies below the surface ($\sim 12\mu$). The linear magnitude of the slip line is closely related to the internal structure of the glass. This situation has been defined by GRAY.(4) "In theory all internal imperfections occasioned by impurities, structural defects or energy changes will have related effects at the surface, modifying the surface activity."

The number (F_n) of flaws produced with a given applied stress is an indication of the bond rigidity and might be loosely termed a "brittleness factor". In a flexible network, the stress energy is dissipated by a greater bending or distortion of bonds and a few flaws are initiated. A more rigid structure nucleates more flaws, due to the fact that bonds will break before much bending occurs. The parameter of flaw number might be expected to be related to Young's modulus, and this possibility is indicated in a later Section.

If we desire to obtain information regarding the relative number of bonds broken, or the degree of slip under a given stress, it is necessary to consider the product of flaw length (F_l) and flaw number (F_n). This product is designated simply as

$$N_b = (F_l)(F_n) \qquad (1)$$

This empirical relationship, as previously mentioned, has already been critically examined and it has been shown that the parameters vary with type and composition of the glass. The relationship between stress and radial distance r from the central point of loading on the spherical indenter is given by

$$\sigma = \left[\frac{(1-2\nu)}{2\pi}\right] P/r^2 \qquad (2)$$

where P is the applied load and ν is Poisson's ratio. The critical yield stress occurs at the point where the flaws, initiated at the trace line, terminate. This stress may be found by substituting F_l for r in equation (2) which gives

$$\sigma_{\mathrm{crit}} = PK/(F_1)^2 \qquad (3)$$

---

* Materials corrosive to platinum were melted in porcelain crucibles. Impurities from these crucibles were found to produce a slight increase in the flaw parameters of the base glass. The use of porcelain did not, however, significantly alter the shapes of the flaw parameter vs. composition curves.

where

$$K = (1-2\nu)/2\pi \tag{4}$$

If we assume that the glass is isotropically uniform then σ_{crit} is a constant determined by the ratio of applied load P to flaw length squared, providing, of course, the load is high enough to exceed this critical stress and initiate flaws. The load, therefore, determines in a unique way the distance the flaw will spread before the shear forces have been attenuated to a level where they are counterbalanced by the cohesive or bond energy of the glass. By rearrangement of equations (3) and (4) we may therefore predict more precisely how the flaw length is related to the applied load by

$$F_l = (PK/\sigma_{\text{crit}})^{1/2} \tag{5}$$

Equation (5) shows that one would expect a linear relationship between the flaw length and the square root of the applied load. The data presented in Fig. 1 were obtained with a commercial sheet glass and show that this relationship is confirmed over a wide range of applied loads. Each point on this curve represents an average of over 50 flaw measurements. The form of the equation is, however,

$$F_l = aP^{1/2}+b \tag{6}$$

The constant b in equation (6) represents a threshold stress which must be introduced into the system to initiate the flaws. The form of the curve in Fig. 1 has been confirmed with different types of glasses and these data provide additional evidence that the flaws associated with the trace line are a direct indication of the response of the network to applied stress.

IV. NETWORK SUBSTITUTIONS

Before making substitutions, using the so-called network modifying ions, systematic variations were made to determine the manner in which the flaw characteristics change in three component systems. Three soda–lime–silica systems were made up for this study, and in each series the silica was held constant at 60, 65 and 70 per cent with the soda–lime ratio (based on weight percent) varied over wide limits. The results of the flaw length measurements are summarized in Fig. 2 (the 60 per cent SiO_2 curve was previously given[2] but is redrawn here for comparison). It may be seen that the flaw lengths generally increase with increasing silica content of the glass. In each series, there appears to be a maximum in the curve, and the significance of this will be discussed later.

In spite of the flaw length increase with increasing silica, one would expect that with increasing concentration of this network-forming oxide, a general increase in the strength of the structure

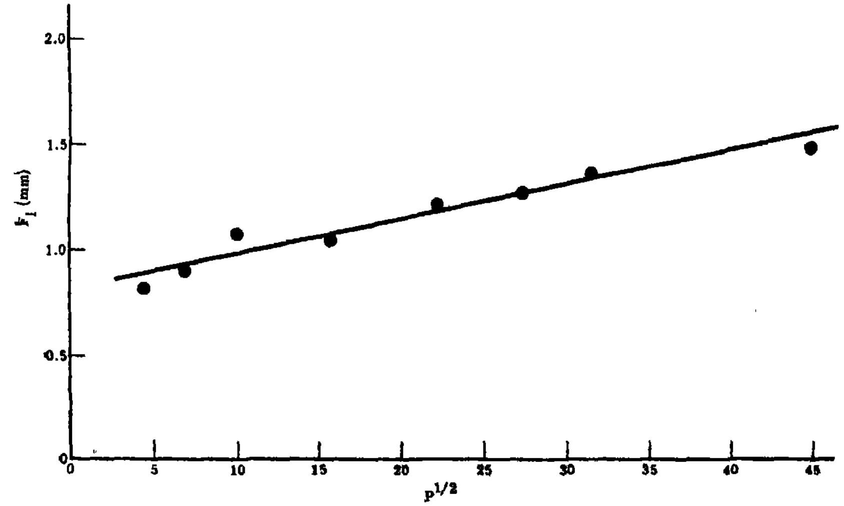

FIG. 1. Relationship between load (P) and flaw length (F_l). Indenter applied to the fresh surface of a commercial sheet glass.

or a decrease in the N_b product would occur. That this is generally true may be seen in the data representing flaw number and N_b product in Table 1.

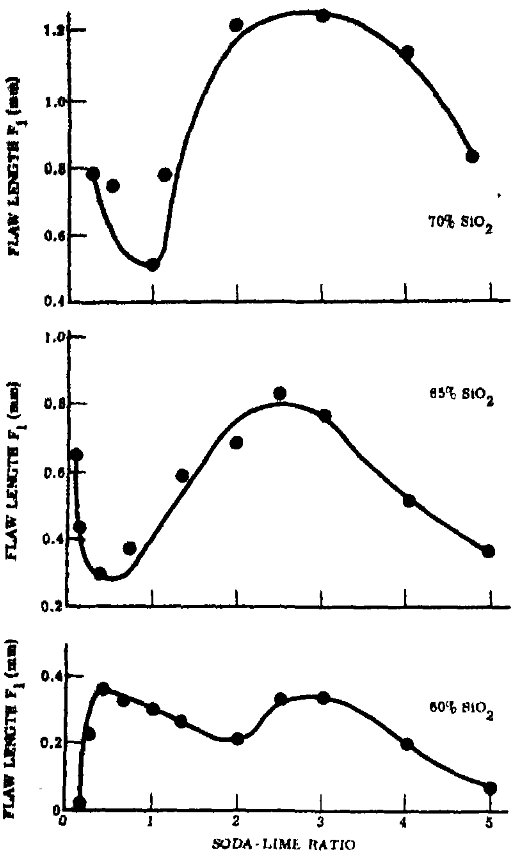

FIG. 2. Flaw length variations in three component systems with different silica bases.

The largest values of N_b are found in the 60 per cent SiO_2 series with high flaw nucleation numbers. It is also interesting to note that the spiral formations occurred in the 60 per cent SiO_2 series with soda–lime ratios from 0·5 to 2·0; also, in this same range, the F_n values are very large and the rigidity of the network is high.

The base glass chosen from this group to be used for the network modifying substitutions was the 70 per cent SiO_2 glass with a soda–lime ratio of 1·14. It may be seen in Fig. 2 that this glass is located on a steep portion of the flaw length curve. It appears that changes in the network would be readily detected by marked variations in flaw lengths. This glass is also within the range of composition used in numerous commercial soda–lime–silica systems. The calculated weight percent composition of this base glass is 70 per cent SiO_2, 16 per cent Na_2O and 14 per cent CaO.

A. *Network modifying cations*

The majority of the substitutional series were prepared with oxides of the network modifying cations. Oxides of the di- and trivalent cations were substituted for CaO and the univalent ions for Na_2O. The Fe_2O_3 and CuO additions were in small quantities and were added without substitution for an oxide. Cations in this group are of intermediate sizes and field strengths (Z/r^2) and appeared to produce similar changes in the flaw parameters as they were added into the network. However, in this series of network modifiers, it was found that the effects could be further divided into two subgroups consisting of ions of "medium" and "low" field strengths.

1. *Ions of "medium" field strength.* The ions in this subgroup are listed below along with the field strengths as calculated from the data of PAULING,(5) where r is the crystal radius of the ion and Z its charge.

Ion	Z/r^2
Sn^{2+}	3·06
Sb^{3+}	6·52
Pb^{2+}	2·53
Bi^{3+}	5·46
Zn^{2+}	3·63
Cu^{2+}	3·06
Li^{1+}	2·78
Fe^{3+}	7·32

Because of similar chemical properties, tin and antimony as well as lead and bismuth may be compared as pairs. The flaw parameters for lead and bismuth were previously given;(3) however, their curves are included since they fit into this group of ions.

The similarities in the effects of these ion pairs are shown in Figs 3 and 4 where both the flaw lengths and flaw numbers are plotted on the same

Table 1. *Flaw measurements in three component systems with varying silica bases*

R = Soda/Lime ratio

Series	R	F_l	F_n	N_b
60% SiO_2	0·20	0·000	0·00	0·00
	0·33	0·230	1·84	0·42
	0·40	0·366	2·82	1·03
	0·50	0·333	10·72	3·58
	0·66	0·314	12·00	3·86
	0·80	0·314	10·20	3·20
	1·00	0·298	10·78	3·21
	1·33	0·263	8·00	2·10
	2·00	0·204	11·65	2·38
	2·50	0·336	1·61	0·54
	3·00	0·342	2·10	0·72
	4·00	0·200	3·81	0·76
	5·00	0·068	2·30	0·16
65% SiO_2	0·13	0·658	1·52	1·02
	0·17	0·439	1·18	0·52
	0·40	0·300	1·42	0·43
	0·75	0·375	0·68	0·26
	1·33	0·590	0·94	0·55
	2·00	0·686	1·10	0·76
	2·50	0·825	1·42	1·17
	3·00	0·763	0·84	0·64
	4·00	0·511	0·76	0·39
	5·00	0·362	0·55	0·20
70% SiO_2	0·33	0·782	0·70	0·55
	0·50	0·745	0·53	0·39
	1·00	0·516	0·71	0·37
	1·14	0·792	0·76	0·60
	2·00	1·213	0·50	0·61
	3·00	1·244	0·40	0·50
	4·00	1·113	0·24	0·27
	5·00	0·815	0·12	0·10

curve as a function of the moles of oxide substituted. It should be noted that a different scale (on the right in Figs 3 and 4) was used for the F_n values due to the pronounced increase in flaw number with moles of oxide added. This method of plotting demonstrates in a direct manner the changes in flaw parameters with moles of oxide substituted into the network of the base glass. As these ions were substituted, there was a general increase in flaw length to a maximum point, followed in subsequent additions by a rapid decrease. In Figs 3 and 4 the maximum F_l value and more rapid increase in F_n occurs with fewer moles in the case of the ions with the higher field strengths. For example, bismuth oxide of high field strength produces a maximum with fewer moles than lead oxide of low field strength and antimony oxide produces a maximum with fewer moles than tin oxide. The general changes in the flaw parameter curves are similar in these two groups. The significance of the maximum point in the F_l curves in Figs 3 and 4 will be discussed presently. The remaining members in this subgroup also produced similar changes in flaw parameters as may be seen by examining the data summarized in Table 2 (the zinc oxide curve is given later).

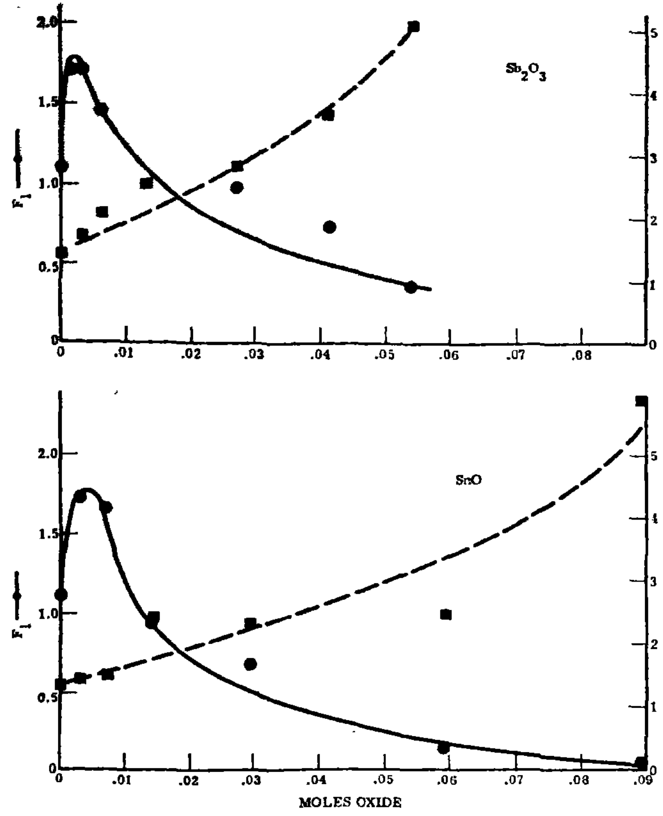

FIG. 3. Effect of substituting tin and antimony oxide for silica on flaw parameters.

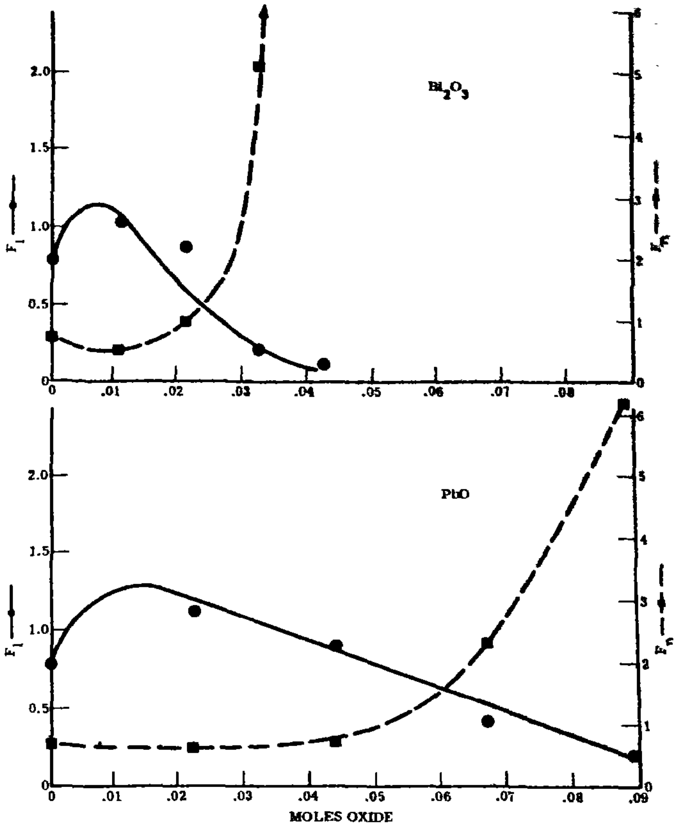

FIG. 4. Flaw parameter variation with moles of bismuth and lead oxide substituted for SiO$_2$.

Table 2. Flaw parameters in series containing ions of "medium" field strengths

Series	Moles oxide	F_l	F_n	N_b
Li_2O	0·000	0·792	0·76	0·60
	0·044	0·933	1·32	1·23
	0·174	0·550	1·48	0·81
	0·349	0·397	2·10	0·83
	0·523	0·318	2·96	0·94
	0·610	0·187	5·18	0·97
CuO	0·0000	1·108	1·39	1·54
	0·0015	1·818	1·30	2·36
	0·0030	1·629	1·61	2·62
	0·0058	1·529	1·71	2·62
	0·0121	1·601	1·90	3·04
	0·0241	1·256	2·22	2·79
	0·0390	1·178	2·39	2·81
Fe_2O_3	0·00000	0·792	0·76	0·60
	0·00019	1·058	0·66	0·70
	0·00038	1·283	0·78	1·00
	0·00063	1·286	0·82	1·06
	0·00125	1·543	0·83	1·28
	0·00250	1·457	0·90	1·31
	0·00501	1·622	1·30	2·11
	0·01002	0·741	1·83	1·36
	0·02003	0·580	2·32	1·35

Again each ion produced changes of slightly different magnitude.

2. *Ions of "low" field strengths*

Ion	Z/r^2
Sr^{2+}	1·56
Cr^{2+}	2·13
Ba^{2+}	1·06
K^+	0·56

The flaw parameter data for ZnO from subgroup 1 and SrO from the "low" field strength group are plotted in Fig. 5 to demonstrate the differences between ions in these two series. In general, the flaw length changes in the subgroup 2 ions are similar to those in the "medium" field strength subgroup. With the "low" field strength ions, a greater amount of oxide is necessary to reach the maximum in the flaw length curve. Also, the F_n curves in Fig. 5 disclose a general decrease in flaw number in the SrO glasses in contrast with the pronounced increase in flaw number in the ZnO series with the ions of "medium" field strength. The flaw data for BaO, CdO and K_2O are given in Table 3, and these ions also produce effects similar, to the SrO results; particularly the cadmium oxide with the marked increase in flaw length and decreasing flaw number. The K^+ and Ba^{2+} ions both disclose initial increases in flaw number instead of decreases; however, it was felt that they should be included in this subgroup because of the shapes of the flaw length curves. The K^+ ion behaves almost like a "pure" interstitial as will be pointed out later.

B. *Discussion of network modifying effects*

One characteristic feature of the flaw length curves in both the network modifying series is the increase to a maximum value. These general changes are shown schematically in Fig. 6 with M representing the moles of oxide substituted into the network. Conceivably the modifying cations initially fill intersticies in the network. As the holes become filled, the ions may take up lattice positions; however, these internal energy changes are not considered as being a monotonic function of the substituted cation. An example of this non

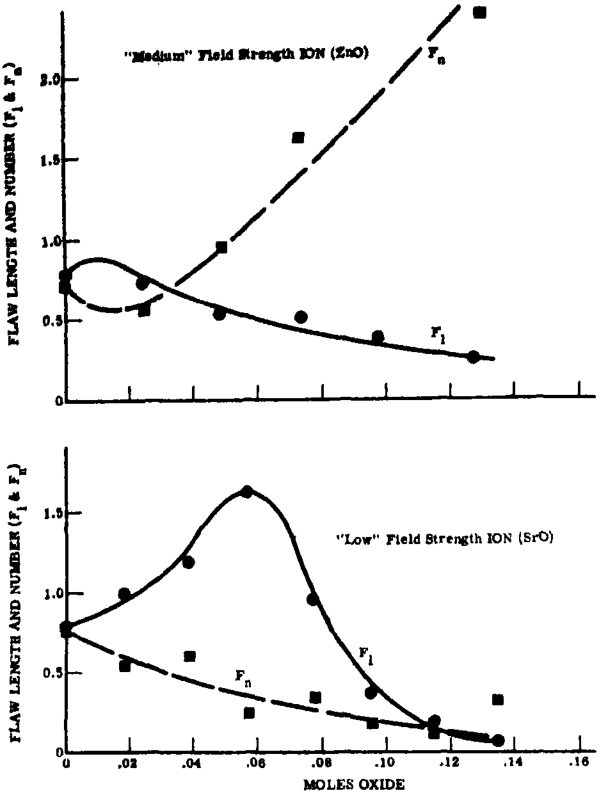

FIG. 5. Variations in flaw parameter curves using net-work modifying ions of "medium" and "low" field strength (substitutions for CaO).

uniform change in energy has been given by DIETZEL and WICKERT[6] for a binary silicate. As Na_2O was added to silica the rates of crystallization disclosed maxima and minima. The maximum rates of crystallization occurred in glasses with compositions corresponding to the di- and meta-silicates. This type of change in internal structure may occur with varying sodium and calcium ion ratios and could at least partially explain the formation of the maxima and minima observed in the curves in Fig. 2.

In the various series reported here, the cations replace either sodium or calcium (with the exception of a few cases such as bismuth and lead and where small additions were made). Replacement or addition of ions of different size creates lattice defect through misfit and bond distortion. It should be kept in mind, however, that defects are present in the base glass and the substitutions only modify the existing defect structure. As more "misfit" ions are added into the network, the defect concentration increases, until the ions no longer enter as interstitials but instead form stronger ionic or covalent associations in the network. The point of maximum flaw length (at M' in Fig. 6) is thought to represent the critical defect concentration or maximum disorder in the system. Also, in Fig. 6, N represents the number of ions necessary to produce the maximum disorder.

The free energy (F) of the system is expressed by,

$$F = \epsilon - T(S_{cf} + S_{th}) \tag{7}$$

where S_{cf} is the configurational entropy produced by N ions creating n defects and S_{th} the thermal entropy. The defects formed may be combinations of both Schottky (cation–anion vacancies) and Frenkel types. In the formation of the Frenkel disorder, the ions (cations more likely than anions) pass from lattice sites into interstitial positions with the formation of vacant lattice sites and there is less volume change as compared with the Schottky type. The Frenkel type of disorder is more likely when the lattice polarization is strong and may, therefore, predominate in these substitutional series.

It is assumed that the thermal entropy S_{th} will change with the added ions to a lesser degree than the configurational entropy. As pointed out by DEKKER[7] S_{th} may be considered to be independent of n/N. In the case shown here, the introduction of ions with different field strengths increase the disorder and the negative entropy term produces a decrease in the free energy as the ions are initially added and defects are created. Such a decrease would be thermodynamically favorable and defect formation could, therefore, more than compensate for any initial increase in (ϵ) within the network.

The point M', therefore, indicates the maximum S_{cf} influence of randomly distributed defects. The point at M' may also represent the maximum randomization of free volume (v_f) defined by TURNBULL and COHEN[8] as

$$v_f = \bar{v} - v_0 \qquad (8)$$

where $\bar{v}$ is the specific volume and v_0 is the van der Waals volume of a molecular region. These authors have suggested that molecular transport may occur by the formation of "voids" during the free volume redistribution. They further point out that the random distribution of this unoccupied volume may occur more readily in the amorphous than in the crystalline phase. Any increase in order would, therefore, tend to decrease the free volume of the system.

The application of an external stress to a system with maximum disorder would allow considerable structural yield and bond readjustment as a result of the free volume redistribution, with the maximum free volume change occurring at the point of maximum defect (void) concentration or at M' in the F_l curve. A structural yield and free volume redistribution could conceivably produce a slight decrease in the F_n curve since more bonds would bend instead of creating slip and nucleating flaws. Although the F_n data shows scatter, this predicted decrease in F_n to the point M' may be indicated experimentally, specifically in Fig. 4 and in the upper curves in Fig. 5.

With ionic additions $M > M'$, both complex ionic and covalent bonds begin to form through chemical association with the added cations. The lattice is, therefore, additionally modified by the formation of more extensively ordered groupings and a consequent reduction in energy (ϵ). With the formation of more ordered units and stronger bonds the observed decrease in F_l (beyond M') is readily explained; however, along with the formation of ordered groupings, structural yield or bending of bonds would tend to decrease and flaw nucleation under applied stress would increase. This would explain the rapid increase in F_n with additions greater than M', as observed in Figs 3 and 4. It appears that in the case of larger ions in the "low" field strength series (subgroup 2) a greater misfit of the ions produces a continuous increase in defect concentration (and free volume), which is not entirely compensated by an increase in order. The bond flexibility increases with creation of the free volume, and F_n decreases as shown in the lower curves in Fig. 5 and in Table 3.

In many of the series, the glasses crystallized with additions greater than point M_c in Fig. 6. The kinetic barrier for nucleation may rapidly decrease after the point M' and as ordered groupings form, crystal nucleation is promoted.

C. *Interstitial additions*

These same general defect hypotheses may be applied to the effects of interstitials on flaw parameters. The addition of interstitials produces steady increases in S_{cf} with increasing M; however, no rapid decrease in energy (ϵ) occurs. There are no strong bonds or ordered groupings formed between the added ions and the surrounding network. As the structure steadily weakens, both F_l and F_n increase. Carbon provides an excellent example for the interstitial effect as shown in Fig. 7. The carbon was added in low percentages without substitution for any specific oxide and the glass became smokey in appearance as additions were made. The interstitial or "insoluble" nature of carbon in non-sulfur and non-iron containing glasses is well known and an excellent discussion may be found in WEYL's book on colored glasses.[9]

Table 3. Flaw parameters in series containing ions of "low" field strengths

Series	Moles oxide	F_l	F_n	N_b
K_2O	0·000	0·792	0·76	0·60
	0·018	0·929	1·07	0·99
	0·073	0·942	1·31	1·23
	0·145	1·024	1·67	1·71
	0·218	1·000	1·60	1·60
CdO	0·000	0·792	0·76	0·60
	0·016	1·231	0·41	0·50
	0·031	1·344	0·42	0·56
	0·047	1·639	0·37	0·60
	0·062	1·907	0·14	0·27
	0·078	0·000	0·00	0·00
BaO	0·000	0·792	0·76	0·60
	0·006	1·006	1·08	1·09
	0·027	0·849	1·72	1·46
	0·052	0·602	0·63	0·38
	0·078	0·132	0·09	0·12
	0·091	0·068	0·10	0·01

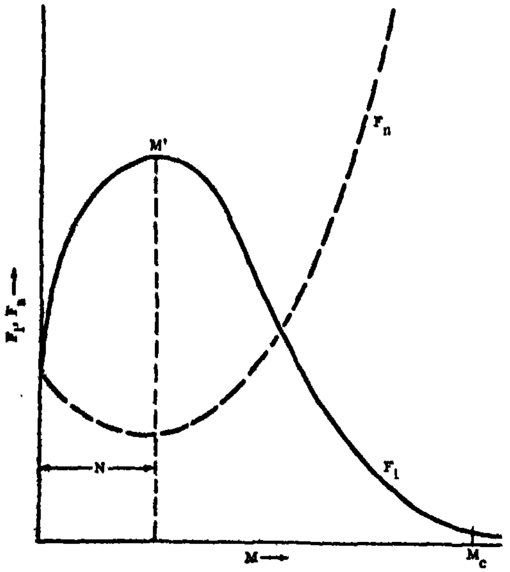

Fig. 6. Schematic diagram showing general effect of network modifying ions on flaw parameters

M —moles of oxide substituted

M' —critical defect concentration; point of maximum disorder.

N —number of ions necessary to produce maximum disorder.

M_c —point of maximum order; just preceding crystallization.

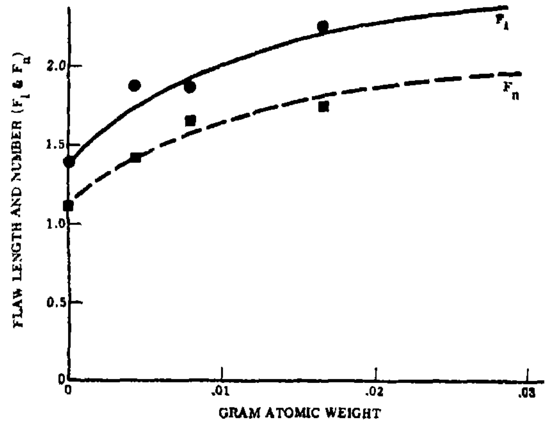

Fig. 7. Influence of carbon on flaw parameters.

In the discussion of the effect of fluorine in glass, Weyl also points out that substitution of the monovalent fluorine ion for divalent oxygen "causes a weakening of the glass structure". This weakening effect of fluorine was confirmed in a series with NaF substituted for Na_2O. The number of Na^+ ions was held constant as the additions were made. As shown in Fig. 8, both F_l and F_n initially increase as the structure weakens. With additions greater than about 0·25 moles NaF crystallization occurred. The decreasing values of F_l and F_n at higher additions of NaF may, therefore, represent a decrease in free energy as ordered groupings precede the visible, fluoride opal color. A maximum is observed in the F_1 curve as in the case of the modifying cations (point M' in Fig. 6); however, because of the pronounced initial increase in both the flaw parameters, this ion is considered as having an interstitial effect.

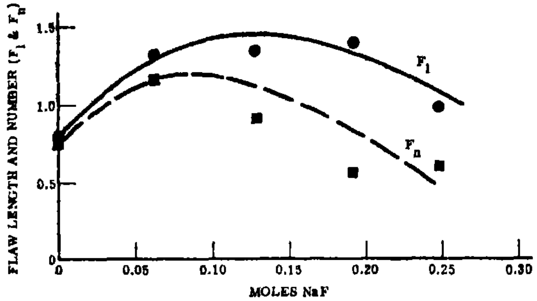

FIG. 8. Effect of the fluorine ion on flaw formation.

It is also problematical whether the results from the K$^+$ series should also be placed in the interstitial column. As a result of its low field strength potassium appears to possess both modifying and interstitial properties (see data in Section A).

D. *Network former effects*

The so-called network formers have very high field strengths and replace the strong silicon-oxygen bonds. Network formers may produce a greater effect on internal energy (ϵ) than on disorder (S_{cf}). Although the effects are more difficult to predict, one might expect less change in F_l with added ions or perhaps even a decrease in some cases if the bond strength is increased. Ordered groupings through chemical association might also be expected to be less than in the case of the modifying ions and consequently F_n would remain unchanged or perhaps decrease. The various ions which were substituted for silica are as follows

Ion	(Z/r^2)
P^{5+}	41·67
Al^{3+}	12·00
B^{3+}	75·00

The substitution of both P_2O_5 and Al_2O_3 were found to produce the effects on the flaw parameters as predicted. As shown in Table 4, both the flaw lengths and number decrease with the addition of these ions with high field strengths. Additions of Al_2O_3 greater than around 0·05 moles produced immiscibility and reliable flaw measurements could not be obtained.

In the case of B_2O_3, the results were much

Table 4. Flaw parameters in series containing ions with high field strengths

Series	Moles oxide	F_l	F_n	N_b
Al_2O_3	0·000	0·792	0·76	0·60
	0·010	0·306	0·66	0·20
	0·049	0·284	0·63	0·18
P_2O_5	0·000	1·108	1·39	1·54
	0·014	0·784	1·23	0·96
	0·035	0·594	0·83	0·49
B_2O_3	0·000	0·792	0·76	0·60
	0·072	0·917	0·42	0·38
	0·144	0·971	0·38	0·37
	0·215	1·114	0·49	0·55
	0·287	1·023	0·54	0·55
	0·359	1·006	0·56	0·56
	0·431	0·990	0·62	0·61
	0·502	0·853	0·78	0·67
	0·574	0·948	0·28	0·27
	0·646	0·681	0·40	0·27

more difficult to explain, even on a qualitative basis. The flaw results in Table 4 show the more erratic behavior of the boron ion. A B_2O_3 glass is however noted for its complex changes in structure. As the B^{3+} ion enters the network, vacancy defects may be created as it replaces the silicon–oxygen bonds. This would explain the initial increase in F_l and decrease in F_n as was observed in the case of the large modifying ions. The difference in charge and the high field strength of the B^{3+} ion may account for complex structural groupings in the network. For example, WEYL and MARBOE[10] point out that vitreous B_2O_3 may consist of molecules which have widely different molecular weights and odd shapes. Additional study of defect structures in systems containing the B^{3+} ion might shed more light on the influence of this ion on the structural changes.

E. *Anomalous behavior of* MgO

The effects produced by the substitution of MgO for CaO were difficult to categorize. In general, Fig. 9 indicates that the Mg^{2+} ion ($Z/r^2 = 4{\cdot}76$) produces effects similar to the network formers with an initial decrease in F_l and little change in F_n. An increase in F_l occurs, however, as the point of complete substitution is approached. The F_n values continue to decrease and the final structure appears to be weak with low brittleness or high bond flexibility. The anomalous behavior of the Mg^{2+} ion has also been discussed by PETZOLD, WISHMANN and KAMPTZ[11] in their studies of the microhardness of glass. It was suggested that magnesium may, as the result of oxygen coordination changes, take either network modifying or network forming positions.

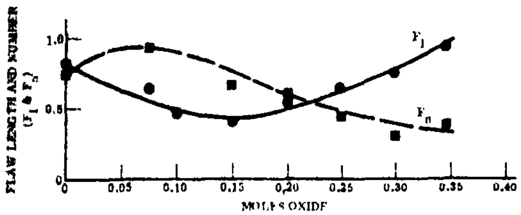

FIG. 9. Flaw variations in glass with MgO substituted for CaO.

F. *Ionic field strength of lattice modifying ions*

It was previously suggested in Section B that the number (N) of lattice modifying ions producing the maximum disorder (point M' in Fig. 6) is related to the field strength of the ions. This number (N) was determined (as g at. wt) in all of the series showing the maximum (M') and Fig. 10 shows the results of plotting with the field strength of the corresponding ion. The number of ions producing the maximum disorder change by three orders of magnitude over this limited range of field strength. The scatter of the points in Fig. 10 in many cases, is due to uncertainty in locating the point M'. In most series all the glasses were made up before the flaw parameters were determined and it was necessary to extrapolate between missing data points at low concentrations. The results in Fig. 10 indicate the influence of ionic field strength of the lattice modifying cations on the flaw parameters. These findings are also in accord with the suggestions of WEYL and MARBOE,[12] who also stressed the importance of ionic configuration in determining defect structures in glass.

V. DISCUSSION OF RESULTS

It appeared pertinent to compare the flaw parameter results with recent studies by LOEWENSTEIN[13] of glasses possessing high Young's moduli. In many cases he substituted the same ions as used in the series reported in the preceding Sections. The compositions of the glasses used by Loewenstein were not identical with those reported here; therefore, any comparisons will by necessity be qualitative in nature.

The flaw parameter most closely related to Young's modulus is the number of flaws nucleated per length of trace line (F_n). A high Young's modulus (E) indicates a rigid structure with little yield under applied stress. As discussed in Section III the F_n value would also be high in a glass with high E; this proposed relation might be expressed by,

$$E \approx CF_n \tag{9}$$

where C is a proportionality constant. There are some excellent qualitative agreements between Loewenstein's work and the changes in the F_n parameter as various ions were substituted. For example, it is pointed out that the network formers such as Si, B, P and Al lower the Young's modulus. Data in Table 1 show the decrease in F_n with increasing SiO$_2$, and Table 4 demonstrates decreasing F_n for B, P and Al cations (the boron values are more erratic as was pointed out). The network formers substantiate the relation indicated in equation (9).

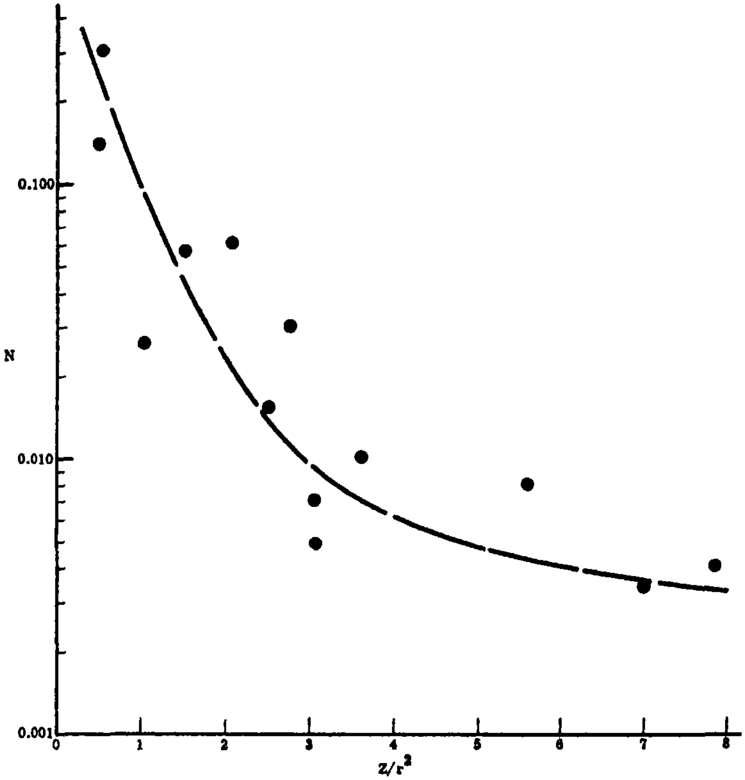

FIG. 10. Relation between the number of ions producing maximum disorder and ionic field strength. (N is given as gram atomic weight of ions in the glass.)

Loewenstein also states that "ions which do not enter the network yet increase the Young's modulus appreciably possess a low solubility in the base glass". An excellent example of this is shown by carbon which increases F_n but does not significantly enter the network. Large ions, such as Sr and Ba were reported to lower E and this also appears to be generally in agreement with the present findings. An examination of the flaw parameter curves show that initial additions of the modifying ions tend to produce decreases in F_n.

Potassium is an apparent exception in the comparison of these two different studies. It was reported by Loewenstein that K$^+$ decreased E whereas the F_n value increased with substitution of potassium for sodium. The substitution of Li$_2$ for Na$_2$O produced marked increase in F_n and an increase in E was also reported for this substitution. In this rather superficial comparison it is indicated that there is a relation between Young's modulus and the F_n parameter. By comparing E and F_n on the same glasses, the relationship could be more rigorously determined than given by equation (9).

VI. SUMMARY

Defects created under controlled loading conditions were utilized in an investigation of structural variations in glasses produced by ionic substitutions. Detailed changes in the flaw parameters were shown to be related to the manner in which an ion entered the network; that is as a modifier, interstitial or network former.

Ions of intermediate field strength, or the network modifiers, produced an initial disorder in the structure and an increase in the flaw length values. With increasing ions substituted, a maximum occurred in the flaw length curve. With additions beyond this maximum the flaw lengths rapidly decreased and the flaw number disclosed a marked increase. These variations in flaw parameters were attributed to free energy changes as the ions were substituted. Vacancies and interstitial defects are believed to be formed as ions were initially added and these promoted a free volume redistribution of voids, which was most pronounced at the maximum in the flaw length curves. With additions beyond this maximum point, the ions formed chemical associations and the internal order increased. The formation of ordered groupings increased the bond strength and the flaw length decreased. The ordered groupings also increased the brittleness and, in most cases, the flaw number (F_n) increased beyond the maximum.

These same general defect hypotheses were used to explain interstitial and network former effects. In the case of interstitial additions, such as carbon, no strong associations developed and the flaw lengths and number increased continuously with increasing concentration. The interstitials were ions of low field strengths. The network formers or ions with high-field strengths replaced Si in the network and the bond strengths generally increased with resulting decreases in flaw lengths and number.

Superficial comparisons were also made between the studies reported here and work by Loewenstein on ionic substitutions effecting Young's modulus of glass. These qualitative comparisons showed that as predicted (in Section III) the F_n values are a measure of the brittleness of the glass network. In general ions causing an increase in E also disclosed increases in F_n and those producing a decrease in E disclosed decreasing F_n values. By determining these parameters on the same glass, the relationship between E and F_n (and F_l) could be be more precisely determined.

Acknowledgements—The author would like to express his appreciation to Mr. WILLIAM WOLFE, at the University of Michigan, for his very helpful comments and to Mr. R. A. GAISER, director of research, Ball Brothers Research Corp., Muncie, Indiana for allowing portions of the experimental results to be released for publication.

REFERENCES

1. LEVENGOOD W. C., *J. appl. Phys.* **30,** 378–386 (1959).
2. LEVENGOOD W. C. and VONG T. S., *J. appl. Phys.* **31,** 1416–1421 (1960).
3. LEVENGOOD W. C., *J. appl. Phys.* **32,** 2525–2533 (1961).
4. GRAY T. J., *The Defect Solid State*, Interscience, New York (1957).
5. PAULING L., *The Nature of the Chemical Bond*, Cornell University Press, New York (1960).
6. DIETZEL A. and WICKERT H., *Glastech. Ber.* **29,** 1 (1956).
7. DEKKER A. J., *Solid State Physics*, Prentice Hall, Englewood Cliffs, N.J. (1957).
8. TURNBULL D. and COHEN M. H., *J. chem. Phys.* **34,** 120–125 (1961).
9. WEYL W. A., *Coloured Glasses*, The Society of Glass Technology, Sheffield, England (1951).
10. WEYL W. A. and MARBOE E. C., *Glass Ind.* **41,** 625 (1960).
11. PETZOLD A., WISHMANN F. G. and KAMPTZ H., *Glastech. Ber.* **34,** 56–71 (1961).
12. WEYL W. A. and MARBOE E. C., *J. Soc. Glass Tech.* **43,** 417 (1959).
13. LOEWENSTEIN K. L., *Phys. Chem. Glasses*, **2,** 69–82 (1961).

J. Phys. Chem. Solids Pergamon Press 1963. Vol. 24, pp. 1025–1028. Printed in Great Britain.

THE DIFFUSE REFLECTANCE SPECTRA OF SOME TITANIUM OXIDES

AUDREY L. COMPANION and ROBERT E. WYATT*

Department of Chemistry, Illinois Institute of Technology, Chicago 16, Illinois

(*Received* 3 *April* 1963)

Abstract—Diffuse reflectance spectra in the visible and near ultraviolet are reported for TiO, Ti_2O_3, and the anatase, rutile and natural brookite crystalline modifications of TiO_2. Results are interpreted qualitatively in the light of crystal field theory.

INTRODUCTION

WITH the advent of crystal field theory interest in the optical spectra of solids and solutions containing transition metal ions has intensified. The present report is the second(1) resulting from a program of investigation of the electronic structure of the bulk oxides of the first transition series metals, primarily through measurement of their diffuse reflectance spectra. Here we present results and tentative interpretation of the spectra of TiO, Ti_2O_3 and the anatase, brookite, and rutile modifications of TiO_2.

There is already in the literature some optical data on titanium oxides. BRECKENRIDGE and HOSLER(2) observed a sharp absorption in the transmission spectrum of a single crystal of rutile beginning at 410 mμ (3·03 eV), but no comparable studies have been reported for anatase or brookite. Single crystals of anatase have not yet been grown, and brookite occurs in nature as small blue-black crystals of dubious purity. GLEMSER and SCHWARZMANN(3) have reported synthesis of mixtures of rutile and brookite by the hydrolysis of hot alkoxytitanium, but pure brookite has not yet been synthesized in the laboratory. CROMER and HERRINGTON(4) have presented diffuse reflectance spectra of rutile and anatase pigments, terminating their measurements at 3·87 eV. VRATNY and KOKALAS(5) reported the reflectance spectrum of a TiO_2 sample, but its crystalline modification was not specified. PEARSON(6) measured the transmission spectrum of powdered Ti_2O_3 imbedded in a matrix of KBr, observing a very narrow absorption at 0·06 eV, followed by a broad band centered at 0·74 eV extending from about 0·6 to 1·9 eV. His measurements were terminated shortly after a weak shoulder at 2·7 eV. To our knowledge no optical study on TiO has been reported.

EXPERIMENTAL DETAILS

Titanium monoxide and titanium sesquoxide were prepared by the reduction of anatase TiO_2 (Baker Analyzed Reagent) with powdered titanium metal (United International Research, Incorporated, 99 per cent pure). Pellets of appropriate Ti–TiO_2 mixtures were placed in a molybdenum lined alumina crucible which was inserted into a molybdenum succeptor and then into a zirconia crucible to prevent heat loss. The whole crucible system rested in a quartz tube which was surrounded by the coils of a GE 20 kW induction heater and then evacuated to $5{\cdot}5 \times 10^{-5}$ mm Hg. The temperature was raised to 1400°C over a 3 hr period, maintained for 1·5 hr reaction time, and then lowered to 1200°C for 4·5 hr annealing. The sample was then rapidly quenched.

The TiO obtained was a dull bronze solid, metallic in appearance and quite hard. When powdered, it was dark brown. Its composition, determined by oxidation to TiO_2, was $TiO_{1{\cdot}09}$. The Ti_2O_3 was a deep purple solid, non-metallic in appearance, and an inky black color when powdered. Its composition was $Ti_2O_{3.07}$. X-ray diffraction powder patterns of our samples agreed with the results of ANDERSSON and coworkers[(7)] for Ti_2O_3 and (NaCl type) TiO.

---

* At present a graduate student in the Department of Chemistry, The Johns Hopkins University, Baltimore 18, Maryland.

The TiO_2 samples studied were the high purity anatase mentioned above, and rutile prepared from this by heating in air at 1000°C for 8 hr. Independent samples of rutile and anatase pigments were donated by the New Jersey Zinc Company of Pennsylvania. X-ray diffraction patterns of all these coincided with results of ANDERSSON and coworkers.[(7)] Samples of brookite were obtained in the form of an ore from Magnet Cove, Arkansas. The small blue-black crystals of brookite, less than 2 mm in diameter, were separated by hand from the rock matrix, washed in water and dilute H_2SO_4, and ground in a Spex Wig-L-Bug to a blue-grey powder. X-ray diffraction results agreed well with those of YOGANARASIMHAM and RAO.[(8)] When heated in oxygen, the powdered brookite took on a muddy yellow color which remained on cooling. This result, along with the analysis of RAO, FAETH and YOGANARASIMHAM,[(9)] suggests the presence of Ti^{3+} ions in brookite, despite the absence of any pronounced Ti^{3+} absorption in the reflectance spectrum.

Diffuse reflectance spectra were measured at room temperature with the ring-type reflectance attachment to the Cary Model 14 PMR Spectrophotometer, employing monochromatic radiation. A tungsten bulb served as light source from 800 to 300 mμ, and a hydrogen lamp from 400 to 210 mμ. Reagent grade Mallinkrodt MgO was used as the standard. The resulting spectra are shown in Figs 1 and 2. Reflectance data are expressed in terms of optical density, where

$$OD = \log_{10}[R_{MgO}/R_{Sample}].$$

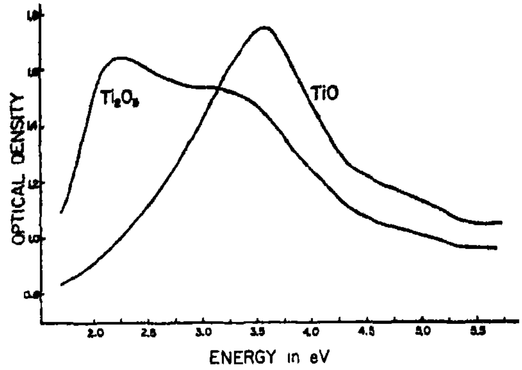

FIG. 1. Diffuse reflectance spectra of TiO and Ti_2O_3.

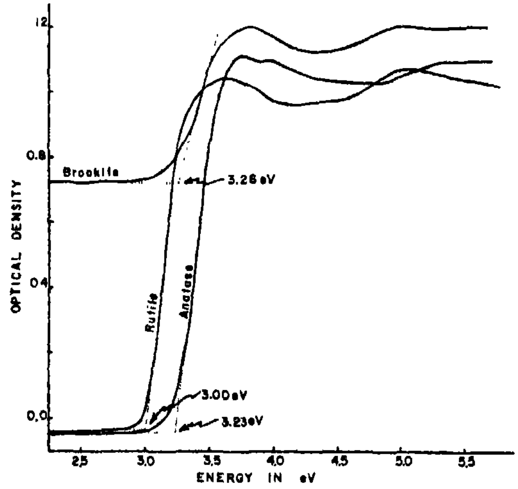

FIG. 2. Diffuse reflectance spectra of anatase, natural brookite and rutile TiO_2.

DISCUSSION

The qualitative aspects of the application of crystal field theory to transition metal oxides have already been discussed in considerable detail by MORIN[(10, 11)] and O'REILLY.[(12)] For TiO, Morin's arguments, based on conductivity and magnetic measurements, favor the existence of a partially filled *band* formed by the overlapping of (normally t_{2g}) orbitals on the Ti^{2+} ions with their 12 nearest metal neighbors in the rock salt lattice. Such a band in the many-ion solid corresponds to a t_{2g} level in a molecular orbital scheme based on the microsymmetry of the Ti^{2+} ion octahedral environment. Here, six $2p$ orbitals on the oxide ions may be appropriately combined with the $3d$, $4s$ and $4p$ orbitals on the metal ion to form the lower energy bonding *MO*'s: non-degenerate a_{1g}, triply degenerate t_{1g}, and doubly degenerate e_g,[(13)] which in TiO may be localized and filled with 12 electrons supplied by the oxide ions. The non-bonding, triply degenerate t_{2g}, next highest in energy, contains two electrons. This level, discrete within a hypothetical isolated TiO_6 unit, may broaden into a band $\frac{1}{3}$ full through overlap of t_{2g} *MO*'s with those of similar units throughout the lattice. It seems a reasonably palatable assumption that the antibonding e_g^* *MO*'s, which follow t_{2g} in increasing energy, may be similarly delocalized into a band. The absorption peak observed in our spectrum at 3·57 eV may within this model correspond to transitions between t_{2g} and e_g^* bands, with additional broadening due to distortions induced by the excess oxygen in $TiO_{1 \cdot 09}$.

In Ti_2O_3 the oxide ions form a field of distorted trigonal symmetry closely approximating the environment of a metal ion in α-Al_2O_3. McCLURE(14, 15) has observed for Ti^{3+} ions implanted in corundum transitions at 2·29 and 2·59 eV, results comparable with our observed reflectance peaks at 2·25 and 3·4 eV in Ti_2O_3. The higher energy transition may be shifted in the bulk solid due to metal–metal interactions or to distortions induced by the excess oxygen in the solid. The significance of the double peak has been discussed in detail by McCLURE and by BALLHAUSEN.(16)

The reflectance spectra of rutile and anatase TiO_2 show sharp absorptions beginning at 3·00 eV and 3·23 eV respectively. The rutile result compares favorably with that of BRECKENRIDGE and HOSLER.(2) It is difficult to evaluate the brookite results; the absorption edge appears to occur at 3·26 eV, slightly higher than that of anatase. For anatase only, the edge ends with a reproducible twin peak maximizing at 3·75 eV and 4·00 eV. For rutile, the edge peaks at 3·67 eV and for brookite at 3·82 eV. The broader ripples observed past 4·25 eV for all the dioxides appear to vary somewhat with sample preparation, and are thus probably not significant.

We propose that these absorptions correspond to electron transfer excitations from the O^{2-} $2p$ levels to empty levels on the Ti^{4+} ions. The intensity change at the absorption edge is like that commonly associated with charge transfer processes. Furthermore, we suggest that the receptor levels are those of the empty metal $3d$ orbitals with degeneracy partially or wholly removed by the distorted octahedral environment.

Corroborating evidence for this identification may be found in recent X-ray studies of K absorption edges. HANSON and KNIGHT(17) demonstrated the presence of a weak absorption near the onset of the K edge in several transition metal oxides with incomplete d levels, and identified these as $K \rightarrow 3d$ transitions, forbidden by selection rules and consequently weak. SHIRAIWA(18) observed similar pips of low intensity occurring above the beginning of the K edge of rutile and anatase, but his spectra show no evidence of the d orbital octahedral splitting. This latter detail appears in the work of VAINSHTEIN and co-workers(19) and removes any doubt about the origin of the absorption. In Fig. 3 we have reproduced the qualitative features of the shapes of the edges determined by these authors for rutile and brookite. Superimposed in dotted lines is the relative position of the $K_{\beta 5}$ emission line, observed at approximately the same energy in all three oxides and the metal itself. This emission results from $3p$ to K transitions on the titanium core and thus may be used to position the $3d$ bands relative to the core.

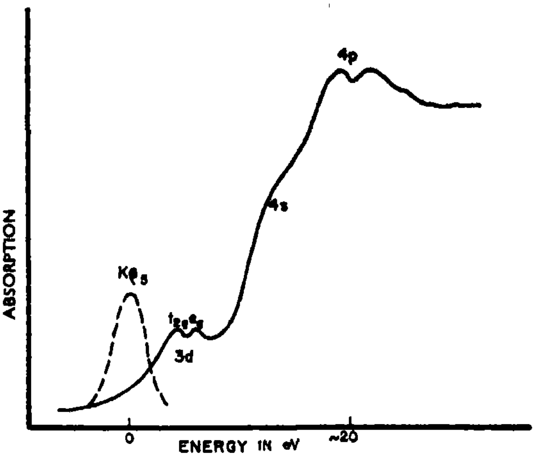

FIG. 3. Shape of the X-ray K absorption edge in rutile and brookite TiO_2 (after VAINSHTEIN and co-workers(19)).

The low energy structure of the absorption edge results from internal transitions of K electrons to the empty octahedral t_{2g} and e_g orbitals on Ti^{4+}. Further splitting due to distortion of the octahedron was not observed. Interpolation of Vainshtein's graphs yields an energy separation of about 5–6 between the $K_{\beta 5}$ and t_{2g} levels. This result, coupled with our optical data, indicates that the oxide $2p$ band is centered somewhat above the $3p$Ti^{4+} band in the oxides. The t_{2g}–e_g separation estimated from the X-ray results is 3–4 eV for both rutile and brookite, a value consistent with the generally observed increase in octahedral splitting with increase in oxidation number of the metal. No t_{2g}–e_g separation was observed by Vainshtein for anatase.

The shoulder of the X-ray edge (Fig. 3) may be due to K electron transitions to a broad $4s$ band, and the high energy absorptions to K–$4p$ transitions, as suggested by the work of COTTON and HANSON.(20) COTTON and BALLHAUSEN(21) have shown that in a field of D_{4h} symmetry the $4p$ level, normally degenerate in a perfect octahedral field, separates into two levels. Both anatase and rutile have this symmetry; brookite has even lower symmetry.

The work of CRONEMEYER(22) adds more strength to the crystal field interpretation of the energy structure of these oxides. For rutile TiO_2 this author measured photocurrent produced as a function of incident radiation, and observed at room temperature a well-defined peak at 3·05 eV, agreeing well with measurements of the optical energy gap. At low temperatures this peak split to the extent of about 0·1 eV, attributed by MORIN(11) to octahedral distortion.

CRONEMEYER's optical study of reduced rutile (containing some Ti^{3+} ions in Ti^{4+} sites) indicates possible further splitting of the t_{2g} level. The broad absorption at 1·85μ (0·67 eV) may be due to excitation of the Ti^{3+} d-electron from the lowest to the highest of the three levels comprising t_{2g}. The X-ray absorption evidence makes $t_{2g} \rightarrow e_g$ an unlikely identification for this transition. Rather, the $t_{2g} \rightarrow e_g$ excitation on Ti^{3+} should be masked by the charge transfer.

Qualitatively, much of the present optical and X-ray data for the three modifications of TiO_2 appear to be compatible with a crystal field interpretation of their energy structure, and indeed invite quantitative theoretical investigation. Some semi-empirical crystal field and ligand field treatments are in progress in this laboratory.

More X-ray absorption data would be useful, particularly in the low energy portion of the K edge. Although Vainshtein's graphs hint of interesting structure, little numerical information can be obtained from them.

Acknowledgements—The authors wish to thank the donors of the American Chemical Society Petroleum Research Fund for major support of this work, the National Science Foundation for its support of R.E.W. through its Undergraduate Research Participation Program (June 1960–August 1961), and the Graduate School of the Illinois Institute of Technology for a Faculty Research Fellowship to A.L.C. during the completion of this work.

REFERENCES

1. COMPANION A. L., *J. Phys. Chem. Solids* **23**, 1685 (1962).
2. BRECKENRIDGE R. G. and HOSLER W. R., *Phys. Rev.* **91**, 793 (1953).
3. GLEMSER O. and SCHWARZMANN E., *Angew. Chem.* **68**, 791 (1956).
4. CROMER D. T. and HERRINGTON K., *J. Amer. chem. Soc.* **77**, 4708 (1955); *ibid.* **78**, 6419 (1956).
5. VRATNY F. and KOKALAS J. J., *Appl. Spectrosc.* **16**, 176 (1962).
6. PEARSON A. D., *J. Phys. Chem. Solids* **5**, 316 (1958).
7. ANDERSSON S., COLLEN B., KRUUSE G., KUYLENSTIERNA U., MAGNELI A., PESTMALIS H. and ASBRINK S., *Acta Chem. Scand.* **11**, 1653 (1957).
8. YOGANARASIMHAM S. R. and RAO C. N. R., *Analyt. Chem.* **33**, 155 (1961).
9. RAO C. N. R., FAETH P. A. and YOGANARASIMHAM S. R., *Trans. Faraday Soc.* **57**, 504 (1961).
10. MORIN F. J., *Phys. Rev. Letters* **3**, 34 (1959).
11. MORIN F. J., *Bell Syst. tech. Journal*, **37**, 1047 (1958).
12. O'REILLY D. E., *J. Chem. Educ.* **38**, 312 (1961).
13. See for example, ORGEL L. E., *An Introduction to Transition-Metal Chemistry—Ligand Field Theory*, p. 32. Methuen, London (1960).
14. WEAKLIEM H. A. and MCCLURE D. S., *J. appl. Phys.* **33**, Suppl. 1, 347 (1962).
15. MCCLURE D. S., *J. chem. Phys.* **36**, 2757 (1962).
16. BALLHAUSEN C. J., *Introduction to Ligand Field Theory*, p. 227. McGraw-Hill, New York (1962).
17. HANSON H. P. and KNIGHT J. R., *Phys. Rev.* **102**, 632 (1956).
18. SHIRAIWA T., *J. phys. Soc. Japan* **15**, 240 (1960).
19. VAINSHTEIN E. E., STARYI I. B. and BRIL M. N., *Dokl. akad. nauk S.S.S.R.* **105**, 934 (1955); VAINSHTEIN E. E. and ZHURAKOVSKII E. A., *Bull. Acad. Sci. U.S.S.R., Div. Chem. Sci.* 1444 (1959) (in English translation); VAINSHTEIN E. E., STARYI I. B. and BRIL M. B., *Bull. Acad. Sci. U.S.S.R., Phys. Ser.* **20**, 713 (1956) (in English translation).
20. COTTON F. A. and HANSON H. P., *J. chem. Phys.* **25**, 619 (1956); *ibid.* **28**, 83 (1958).
21. COTTON F. A. and BALLHAUSEN C. J., *J. chem. Phys.* **25**, 617 (1956).
22. CRONEMEYER D. C., *Phys. Rev.* **87**, 876 (1952).

J. Phys. Chem. Solids Pergamon Press 1963. Vol. 24, pp. 1029–1032. Printed in Great Britain.

ON THE INFLUENCE OF A UNIFORM EXCHANGE FIELD ACTING ON THE SPINS OF THE CONDUCTION ELECTRONS IN A SUPERCONDUCTOR

G. SARMA

Centre d'Etudes Nucléaires de Saclay, France

(*Received* 26 *September* 1962; *revised* 21 *February* 1963)

Abstract—The effect of a uniform exchange field acting on the spins of the conduction electrons is treated within the framework of the B.C.S. theory of superconductivity. The transition from the superconducting to the normal state is shown to be of the first or second order according to the values of the field.

INTRODUCTION

A NUMBER of authors[1, 2, 3] have discussed the influence of a uniform magnetic field of strength h acting only on the spins of the conduction electrons in a superconductor, all orbital effects being neglected. Such a field may be the exchange interaction between the conduction electrons and the impurity spins in dilute superconducting alloys with magnetic impurities. In most cases a uniform field model is not suitable, owing to the random orientation of the impurity spins, and the problem with such disordered impurity spins has been studied in detail by different authors.[4, 5, 6] It seems however of interest to study the uniform field model in view of the existence of substances with both superconducting and ferromagnetic regimes.[7, 8, 9] There is unfortunately disagreement between the authors who have considered this problem, and in particular the conclusions of the paper by VONSOVSKII and SVIRSKII[2] seem to us to be incorrect. On the other hand, some strange features that occur in the treatment of this model (such as the rather peculiar shape of the curve of the critical temperature vs. h that one gets by cancelling the energy gap in the B.C.S. integral equation), have been already pointed out[3] but not completely explained, although in a simple discussion SUHL[10] has proved the existence of a first order transition. In the present paper a simplified model will be solved exactly within the framework of the B.C.S. theory,[11] and it will be shown that the transition from the superconducting to normal state is either of the second or of the first order according to the values of the field.

We shall take the following simplified Hamiltonian:

$$\mathscr{H} = \sum_{k} \epsilon_k (a_{k\uparrow}^* a_{k\uparrow} + a_{k\downarrow}^* a_{k\downarrow}) + h(a_{k\uparrow}^* a_{k\uparrow} - a_{k\downarrow}^* a_{k\downarrow})$$

$$- \sum_{k,k'} V_{kk'} a_{k'\uparrow}^* a_{-k'\downarrow}^* a_{-k\downarrow} a_{k\uparrow} \tag{1}$$

where ϵ_k is the energy, relative to the Fermi energy, of the electron. We also make the B.C.S. assumption that $V_{kk'} = V$ for $|\epsilon_k|, |\epsilon_{k'}| < \omega$ and $V_{kk'} = 0$ otherwise, ω being an average phonon frequency. The pairing approximation is equivalent to considering $a_{k'\uparrow}^* a_{-k'\downarrow}^*$ or $a_{-k\downarrow} a_{k\uparrow}$ to be approximate c-numbers, and this leads to the following equivalent Hamiltonian which can be diagonalized

$$\mathscr{H}' = \sum_{k} \epsilon_k (n_{k\uparrow} + n_{k\downarrow}) + h(n_{k\uparrow} - n_{k\downarrow})$$

$$- \sum_{kk'} V_{kk'} (\langle a_{k'\uparrow}^* a_{-k'\downarrow}^* \rangle a_{-k\downarrow} a_{k\uparrow} + a_{k'\uparrow}^* a_{-k'\downarrow}^*$$

$$\times \langle a_{-k\downarrow} a_{k\uparrow} \rangle)$$

$$+ \sum_{kk'} V_{kk'} \langle a_{k'\uparrow}^* a_{-k'\downarrow}^* \rangle \langle a_{-k\downarrow} a_{k\uparrow} \rangle$$

where $\langle \ldots \rangle$ denotes the thermal average.

Putting now

$$\Delta_k = \sum_{k'} V_{kk'} \langle a_{-k\downarrow} a_{k'\uparrow} \rangle$$

we first get

$$\Delta_k = 0 \text{ for } |\epsilon_k| > \omega$$

and

$$\Delta_k = \Delta = V \sum_{|\epsilon_{k'}| < \omega} \langle a_{-k'\downarrow} a_{k'\uparrow} \rangle \text{ for } |\epsilon_k| < \omega \quad (2)$$

and $\mathscr{H}'$ reduces to

$$\mathscr{H}' = \sum_k (n_{k\uparrow} + n_{k\downarrow}) + h(n_{k\uparrow} - n_{k\downarrow})$$

$$- \sum_k \Delta_k (a_{-k\downarrow} a_{k\uparrow} + a^*_{k\uparrow} a^*_{-k\downarrow}) + \Delta^2/V \quad (3)$$

The following well known equation for the gap Δ is readily found either by minimizing the free energy or as a self-consistency condition on Δ:

$$\frac{1}{NV} = \int_0^{\omega} \frac{1}{\sqrt{(\epsilon^2+\Delta^2)}} \left[\frac{1}{\exp\beta(h - \sqrt{[\epsilon^2+\Delta^2]}) + 1} - \frac{1}{\exp\beta(h + \sqrt{[\epsilon^2+\Delta^2]}) + 1} \right] \mathrm{d}\epsilon \quad (4)$$

where N is the density of states at the Fermi level and $\beta = (kT)^{-1}$. The expression for the free energy reads

$$\mathscr{F} = \sum_k \left[\epsilon_k - \frac{1}{\beta} L(2\mathrm{ch}\beta h + 2\mathrm{ch}\beta\sqrt{[\epsilon_k^2 + \Delta_k^2]}) \right] + \frac{\Delta^2}{V} \quad (5)$$

If one makes the assumption that the gap vanishes at the transition point from the superconducting to the normal state, then the relation between h and the critical transition temperature should be, according to (4)

$$\frac{1}{NV} = \int_0^{\omega} \frac{\mathrm{d}\epsilon}{\epsilon} \left[\frac{1}{\exp\beta(h-\epsilon)+1} - \frac{1}{\exp\beta(h+\epsilon)+1} \right] \quad (6)$$

This relation, however, takes the curious shape shown by the curve I of Fig. 3. So the question arises of a more careful investigation.

ZERO TEMPERATURE SOLUTIONS

At $T = 0$ there are three different solutions that we shall label, I, II and III.

Solution I is the well known Pauli paramagnetism of the normal metal, which is in particular the limiting form of any superconducting solution when Δ vanishes, as can be seen from equation (5) which reduces at $T = 0$ to

$$E_1 = \sum_k \epsilon_k - \sum_{|\epsilon_k| > h} |\epsilon_k| - \sum_{|\epsilon_k| < h} h \quad (7)$$

The region where $\epsilon_k < -h$ is filled with electrons with up and down spins, and the region $|\epsilon_k| < h$ is filled with only down spin electrons.

Solution II is given by equation (4) which for $\Delta > h$ reduces to

$$\frac{1}{NV} = \int_0^{\omega} \frac{\mathrm{d}\epsilon}{\sqrt{(\epsilon^2+\Delta_2^2)}}$$

This is the unpolarized B.C.S. ground state, with an energy

$$E_2 = \sum_k \epsilon_k - \sqrt{(\epsilon_k^2 + \Delta_k^2)} + \frac{\Delta_2^2}{V} \quad (8)$$

The fact is not surprising, since the total polarization commutes with the Hamiltonian (1). The gap Δ_2 is independent of h and equal to $\Delta_2 = 2\omega/\alpha$ in the weak coupling approximation, where $\alpha = \exp(NV)^{-1}$. The fact that this solution is restricted to $h < \Delta$ is related to its unstability for $h > \Delta$: the quasi particle energies being $\pm h + \sqrt{(\epsilon_k^2 + \Delta^2)}$, some of these would take negative values for $h > \Delta$.

A third solution is obtained from equation (4) which for $\Delta < h$ reduces to

$$\frac{1}{NV} = \int_{\sqrt{(h^2-\Delta^2)}}^{\omega} \frac{\mathrm{d}\epsilon}{\sqrt{(\epsilon^2+\Delta^2)}} \quad (9)$$

This equation gives an h dependent gap. In Refs 1 and 2 was found the wrong equation

$$\frac{1}{NV} = \int_h^{\omega} \frac{\mathrm{d}\epsilon}{\sqrt{(\epsilon^2+\Delta^2)}}$$

which does not minimize the energy.

For sake of simplicity we shall from now on assume the weak coupling approximation, although similar conclusions will hold in general. Equation (9) then gives the following solution

$$\Delta_3 \simeq \frac{2}{\alpha}\sqrt{[\omega(\alpha h-\omega)]} \text{ for } \frac{\omega}{\alpha} < h < \frac{2\omega}{\alpha}$$

The complete solution of equation (4) in the limit of zero temperature, which consists of Δ_2 and Δ_3 is shown in Fig. 1.

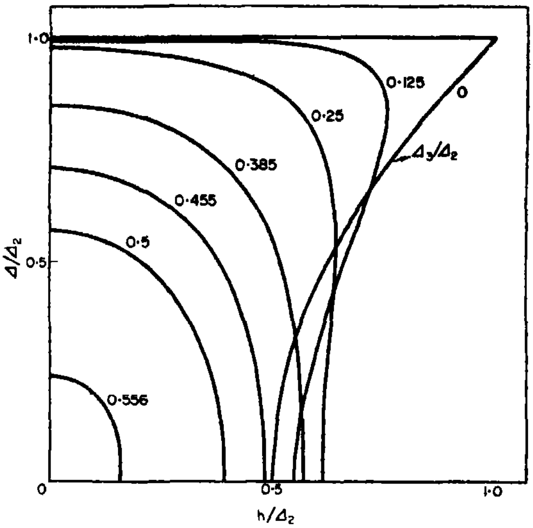

FIG. 1. Curves giving Δ/Δ_2 vs. h/Δ_2 for different values of kT/Δ_2. The values of kT/Δ_2 are indicated on the curves.

The energy of solution (III) is readily seen to be

$$E_3 = \sum_k \epsilon_k - \sum_{|\epsilon_k|<\sqrt{(h^2-\Delta_3^2)}} h - \sum_{|\epsilon_k|>\sqrt{(h^2-\Delta_k^2)}} \sqrt{(\epsilon_k^2+\Delta_k^2)} + \frac{\Delta_3^2}{V} \tag{10}$$

One can easily construct the B.C.S. type wave function corresponding to this solution. The result is that in the region $|\epsilon_k| < \sqrt{(h^2-\Delta^2)}$ around the Fermi surface, there are only electrons with spin down. The region $\sqrt{(h^2-\Delta^2)} < |\epsilon_k| < \omega$ is occupied by "Cooper" pairs. So this solution appears as a mixture of Pauli paramagnetism and B.C.S. type solution, with an h-dependent gap.

In Ref. 2 the half width of the first region was arbitrarily put equal to h. In fact it is equal to $\sqrt{(h^2-\Delta_3^2)} \sim (2\omega/\alpha)-h$. When h increases from ω/α to $2\omega/\alpha$, it goes from ω/α to zero, and correspondingly the half width of the region occupied by the pairs increases from $\omega-(\omega/\alpha)$ to ω.

In the two limiting cases, $h = \omega/\alpha$ and $h = 2\omega/\alpha$, solution III goes continuously into solutions I and II respectively.

Let us put

$$E_0 = \sum_k \epsilon_k - \sum_k |\epsilon_k|$$

which is the energy of the normal ground state. One gets from (7), (8) and (10) after some algebra

$$E_0-E_1 = Nh^2$$

$$E_0-E_2 = 2N\frac{\omega^2}{\alpha^2}$$

$$E_0-E_3 = 2N\frac{\omega^2}{\alpha^2}-N\frac{(2\omega-\alpha h)^2}{\alpha^2} \tag{11}$$

The three curves are plotted in Fig. (2). The conclusion is that at zero temperature the system is in the B.C.S. unpolarized ground state up to $h = (\omega\sqrt{2})/\alpha$. At $h = (\omega\sqrt{2})/\alpha$ the transition occurs from the superconducting to the normal paramagnetic state, even though the gap has not vanished. One can thus expect that at low enough temperatures, the situation will be similar, the transition occurring at a point where the free energy curves intersect, the energy gap being different from zero.

FINITE TEMPERATURE CALCULATIONS

Numerical calculations have been performed by solving equation (4) and computing the free energy $\mathscr{F}$ with the aid of (5).

The variation of Δ vs. h as given by (4) is shown for different temperatures in Fig. 1. The free energy of the normal paramagnetic state is practically independent of T and equal to $E_1 = E_0-Nh^2$.

At each temperature is plotted in Fig. 2 $E_0-\mathscr{F}$ where $\mathscr{F}$ is the free energy of the superconducting state. At low enough temperatures, this curve is seen to consist of two branches which join together at a singular point. The upper branch corresponds to solution II and the lower branch corresponds to the unstable solution III. The

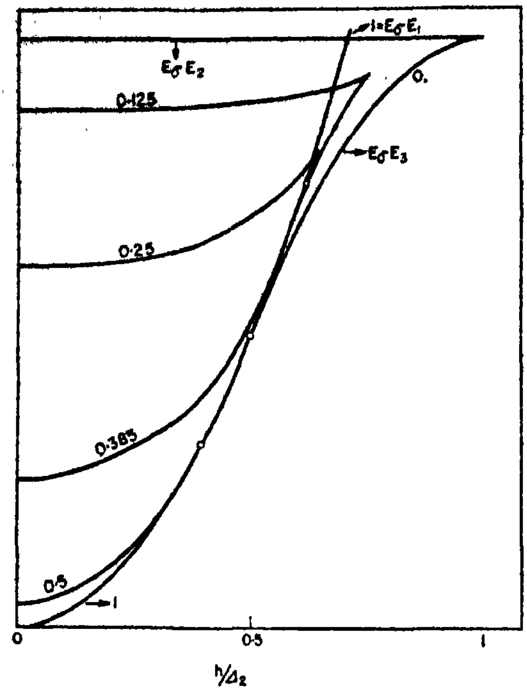

FIG. 2. The free energy curves vs. h/Δ_2 for different values of kT/Δ_2 indicated on the curves. The parabola (I) is the free energy curve for the temperature independent Pauli paramagnetism.

lower branch is tangent to the curve E_0-E_1 at a point where Δ vanishes. It should be noticed that when the temperature increases the curve $E_0-\mathscr{F}$ undergoes a continuous deformation with the result that the lower branch which corresponds to solution III becomes smaller and smaller, until it vanishes. The deformation appears clearly if one compares the curves labelled 0·125 and 0·25.

One can now see that for the transition temperature there are two different cases. Below a certain temperature T_0, the curve $E_0-\mathscr{F}$ intersects the curve E_0-E_1 for a non zero value of Δ, and the transition occurs at this point (the point where Δ vanishes is the point where these curves are tangent and belongs to the branch of free energy curve which corresponds to the unstable solution III). When the temperature is higher than T_0, the two curves have no other intersection point than the point of tangency where $\Delta = 0$. For $T < T_0$ the transition is a first order one, and for $T > T_0$ it is a second order one. So the branch of the curve of Fig. 3 which corresponds to $T > T_0$ is to be conserved, whereas for $T < T_0$ it has to be replaced by the curve of the intersection points. The result is shown in Fig. 3.

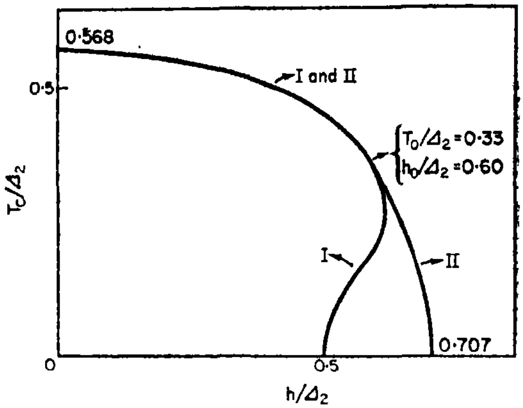

FIG. 3. The two T_c vs. h curves. Curve (I) is given by equation (6). (II) is the corrected curve. The temperature T_0 below which the transition is of the first order is indicated.

Acknowledgements—I express my thanks to Dr. P. G. DE GENNES who suggested this work and to MME D. PILLARD who performed the numerical calculations.

REFERENCES

1. MARADUDIN A. and PERETTI J., *C.R. Acad. Sci., Paris* **248**, 2856 (1959).
2. VONOVSKI S. V. and SVIRSKII M. S., *J. exp. teor. Phys. U.S.S.R.* **12**, 272 (1961).
3. BALTENSPERGER W., *Suppl. Physica* **24**, S153 (1958).
4. ABRIKOSOV A. and GORK'OV L. P., *J. exp. teor. Phys. U.S.S.R.* **12**, 1243 (1961).
5. BALTENSPERGER W., *Helv. Phys. Acta* **32**, 197 (1959).
6. SUHL H. and MATTHIAS B. T., *Phys. Rev.* **114**, 977 (1959).
7. MATTHIAS B. T., SUHL H. and CORENZWIT E., *Phys. Rev. Letters* **1**, 449 (1958).
8. PHILLIPS N. E. and MATTHIAS B. T., *Phys. Rev.* **121**, 105 (1961).
9. MATTHIAS B. T. and SUHL H., *Phys. Rev. Letters* **1**, 92 (1958).
10. SUHL H., *Lecture Notes*. Ecole d'Eté de Physique Théorique, Les Houches 1961, Gordon and Breach, New York (1961).
11. BARDEEN J., COOPER L. N. and SCHRIEFFER J. R., *Phys. Rev.* **108**, 1175 (1957).

J. Phys. Chem. Solids Pergamon Press 1963. Vol. 24, pp. 1033–1041. Printed in Great Britain.

ANNEALING OF γ-RAY IRRADIATED N-TYPE GERMANIUM*

SHIORI ISHINO, FUMIKO NAKAZAWA† and RYUKITI R. HASIGUTI

Department of Metallurgy, University of Tokyo, Bunkyo-ku, Tokyo, Japan

(*Received* 13 *August* 1962; *revised* 3 *January* 1963)

Abstract—Isochronal and isothermal annealing above room temperature has been studied in antimony and arsenic doped γ-irradiated germanium. Three annealing stages are found at 370, 430 and 530°K with activation energies of 0·7–0·8 eV, 1·2–1·3 eV and 2·2 (As-doped)–2·5 (Sb-doped) eV, respectively. Impurity dependence of annealing behavior is found in all these stages. The results are discussed in terms of electronic and elastic interactions of defect centers with impurity atoms.

I. INTRODUCTION

ALTHOUGH radiation damage in germanium has been studied by a number of workers,(1) many problems have been left unsolved about the nature and properties of lattice defects introduced by irradiation. The annealing process of radiation damage is one of such unsolved problems.

BROWN and others(2, 3) investigated the annealing of electron bombarded germanium and found a remarkable effect of doping impurities upon the annealing process above room temperature. For all their close investigation, the mechanism of the annealing process has not yet been understood satisfactorily. Isothermal annealing around room temperature after γ-ray irradiation has been studied by ASADA *et al.*(4) They obtained activation energies for the annealing processes but did not make any detailed interpretation.

The present authors have carried out experiments on annealing of radiation damage, considering how electronic states affect atomic behavior of lattice defects. In the present research annealing of radiation damage in *n*-type germanium above room temperature is investigated after Co^{60} γ-ray irradiation at about 20°C. Dependence of the annealing behavior on impurities is investigated. The study on impurity dependence proves to be useful for studying radiation damage.

II. EXPERIMENTAL PROCEDURE

Resistivity of all samples used was about 20 Ω-cm at room temperature. The samples, doped with antimony or arsenic were offered by Tokyo Shibaura Electric Co. and by Fuji Communication Apparatus Mfg. Co. They were in the form of rod, $12 \times 2 \times 1$ mm and were fixed on a mica plate by gold wire leads of 0·2 mm in diameter. Gold wire leads were welded to the samples by applying a.c. current directly, under blowing argon gas.

Hall coefficient and conductivity were measured by standard d.c. technique with a Leeds and Northrup K–3 potentiometer. Magnetic field used was about 700 G.

The samples were exposed to Co^{60} γ-rays at about 20°C at Japan Atomic Energy Research Institute (10 kc), at Institute of Physical and Chemical Research (1 kc) or at University of Tokyo (1 kc).

The samples were annealed by immersing directly in an oil bath. Shin'etsu KF–54 silicone oil was used for the bath. To avoid diffusion of impurities, especially of copper, into the samples, an oil container was made of stainless steel and the sample mount which was dipped in oil, was made of mica plate, gold and aluminum leads, and aluminum screws and nuts. No copper parts nor brass parts were used.

---

* Part of a thesis submitted in June, 1961 to the University of Tokyo, by one of the authors (S.I.) in partial fulfilment of the requirement for the degree of doctor.

† Graduate Course in Physics.

Annealing was carried out in a temperature range between 310 and 560°K. Annealing temperatures were controlled to an accuracy of ± 0·3°C.

Measurements before irradiation and at various stages of annealing were made at three temperatures between 85°K and 93°K to obtain the values at 90°K by interpolating these three data graphically.

The sample mount was put into a dark box during measurement, while annealing was performed in ambient light.

III. EXPERIMENTAL RESULTS

(a) *Isochronal Studies*

Figure 1 shows the fraction not annealed, $f = \frac{n_0 - n}{n_0 - n_t}$, after isochronal annealing obtained from measurements of Hall coefficients of antimony doped germanium, where n_0, n_t and n are the carrier concentrations before irradiation, after irradiation and after each annealing, respectively. The sample T20–7 was left 13 days at room temperature and T20–9 was annealed immediately after irradiation. The initial carrier concentration of $8{\cdot}3\times10^{13}/\text{cm}^3$ was reduced to $4{\cdot}2\times10^{13}/\text{cm}^3$ in T20–7 and to $3{\cdot}5\times10^{13}/\text{cm}^3$ in T20–9 by irradiation. The curves were derived from the values at 90°K after annealing 15 min at each temperature.

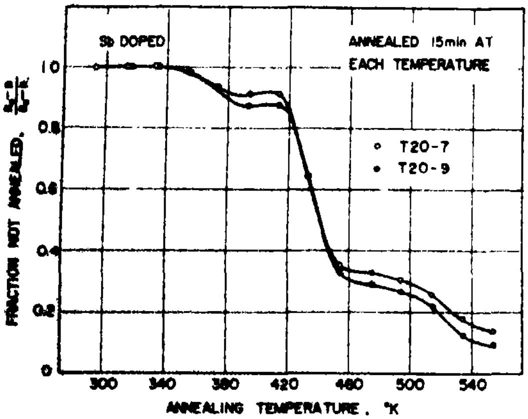

Fig. 1. Isochronal anneal of carrier concentration in antimony doped *n*-type germanium crystals. (○); T20–7, aged at room temperature for 13 days after irradiation and annealed. (●); T20–9, annealed immediately after irradiation. Annealed for 15 min at each temperature. Measured at around 90°K (see text).

Three recovery stages are observed in both samples. The first is centered at 370, the second at 430 and the third at 530°K. No remarkable difference in two curves was observed in the antimony doped samples.

Fairly similar curves were obtained from conductivity measurements. The Hall mobility at 90°K decreases by irradiation. After a sequence of isochronal annealing up to 533°K, it completely recovers or rather overshoots as compared with the mobility before irradiation.

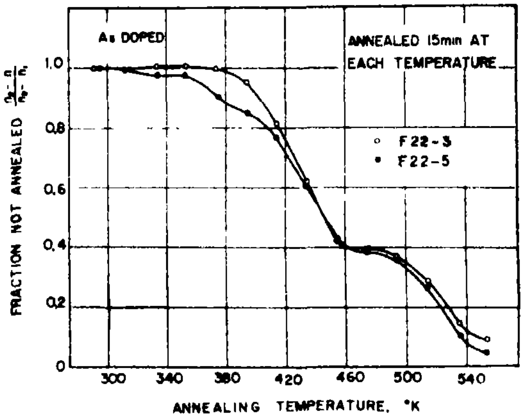

Fig. 2. Isochronal anneal of carrier concentration in arsenic doped *n*-type germanium crystals. (○); F22–3, aged at room temperature for 40 days after irradiation and annealed. (●); F22–5, annealed immediately after irradiation. Annealed for 15 min at each temperature. Measured at around 90°K (see text).

Figure 2 shows the similar curves in arsenic doped germanium. Both the samples, F22–3 and F22–5, were cut from the same ingot and initial carrier concentration was $6{\cdot}2\times10^{13}/\text{cm}^3$ at 90°K. Irradiation reduced the carrier concentration to about one third of its initial value. After irradiation the sample F22–5 was annealed immediately while F22–3 was left 40 days at room temperature.

There are remarkable differences in isochronal annealing curves between antimony and arsenic doped germanium as follows:

(1) Aging at room temperature has a pronounced effect on annealing curves in arsenic doped samples.

(2) The recovery stage centered at 430°K in arsenic doped germanium is broader than that in antimony doped germanium. This point will also be shown in Fig. 7.

(3) The Hall mobility in arsenic doped germanium does not recover completely.

Figure 3 shows temperature dependence of Hall coefficients in an arsenic doped sample after each isochronal annealing.* Annealing intervals are also 15 min. A distinct electronic energy level, which makes a step centered at 200°K in Hall coefficient curves, largely anneals out in the temperature range from 394 to 433°K but remains slightly up to 533°K. This energy level is evaluated to be located 0·24 ± 0·03 eV below the conduction band from curves of seven samples. This level position is slightly lower than that reported by other workers.[5, 6]

It seems that there is another shallower energy level evidenced by a slight slope of the curves in Fig. 3 below 100°K which becomes steeper by further annealing until about 370°K annealing and then gradually disappears as the annealing temperature goes higher.

In both 370 and 530°K recovery stages, changes in carrier concentration and in conductivity were small, so that isothermal annealing was not investigated for these stages. Analyses of the isochronal curves show that the kinetics is nearly first order and that the activation energy is 0·7–0·8 eV for the 370°K stage in antimony doped samples. As for the stage at 530°K, the kinetics is nearly second order and the activation energy is found to be 2·20 ± 0·02 eV and 2·5 ± 0·3 eV in arsenic and antimony doped samples, respectively. The method of the analysis is given in the Appendix I.

(b) *Isothermal studies*

To study the kinetics of the annealing process of the stage centered at 430°K, a number of samples were annealed isothermally.

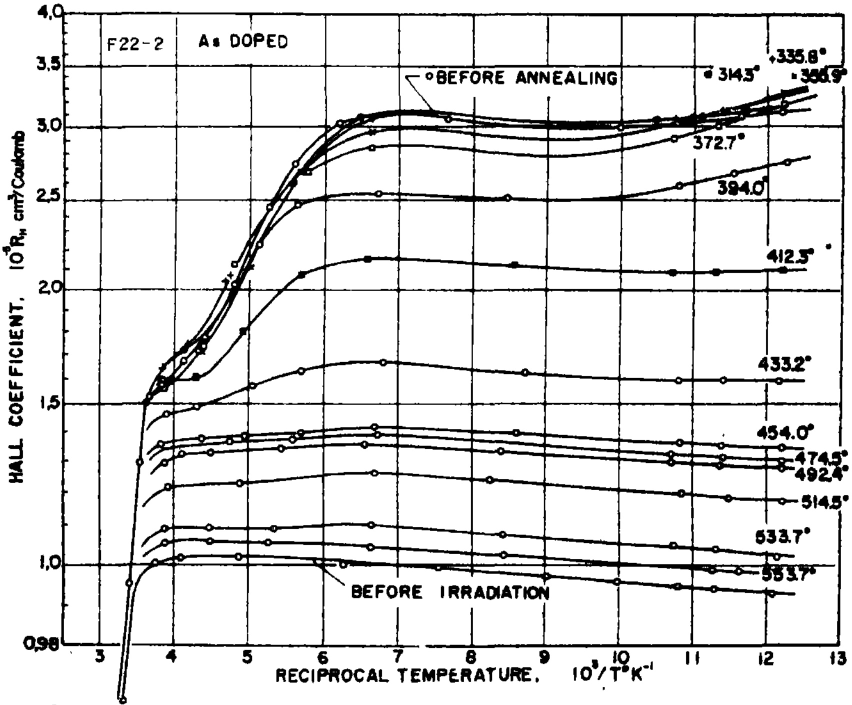

FIG. 3. Temperature dependence of Hall coefficient before and after irradiation and after successive isochronal anneals in an arsenic doped germanium crystal.

---

* Similar curves are obtained with an antimony doped sample.

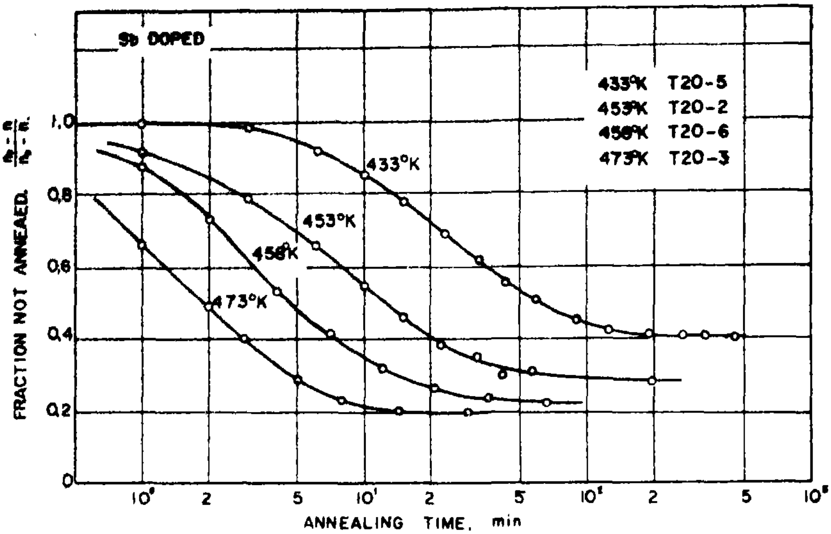

FIG. 4. Isothermal annealing of carrier concentration in antimony doped *n*-type germanium crystals. Activation energy is 1·20 ± 0·15 eV.

Figure 4 shows the results in antimony doped samples derived from Hall coefficient measurements at 90°K. Annealing temperatures are 433, 453, 458 and 473°K. The recovery curves seem to have asymptotic values, which depend on the annealing temperatures. The recovery process of fractional carrier concentration, $(n_a-n)/(n_a-n_i)$, where n_a is the asymptotic carrier concentration, is fairly well represented by first order kinetics, if we assume the asymptotic values of 0·395, 0·28, 0·215 and 0·19 corresponding to the anneals at 433, 453, 458 and 473°K, respectively. The activation energy for this recovery process is found to be 1·2 ± 0·15 eV.

Figures 5 and 6 show the results in arsenic doped samples. The curves are plotted in such a way as to normalize the recovered carrier concentration n_a-n_i to unity. The samples shown in Fig. 5 do not have the same history, that is, after irradiation the sample F22–6 was left at room temperature for 4 days, F22–4 for 43 days, F22–1 for 50 days and F22–8 for 4 days. The annealing temperatures are 443, 453, 463 and 473°K, respectively. In this case, all the curves do not coincide with each other, even if the time scale is adjusted. The time necessary for the same fractional annealing to occur is plotted in Fig. 7 for several different fractions as a function of reciprocal annealing temperature. It seems that some process with low activation energy may be mixed in at the beginning of the annealing. This agrees with the results that the isochronal annealing curves for this stage are broader in arsenic doped samples than in antimony doped samples.

All the samples shown in Fig. 6 were irradiated together and were left at room temperature for about one month intentionally, so that they have

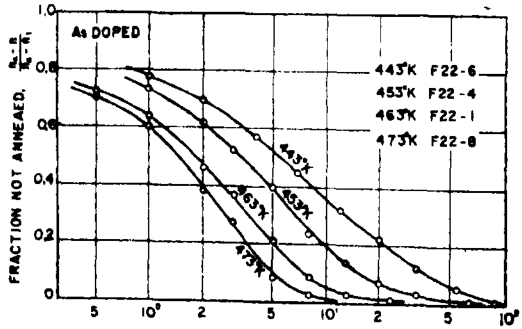

FIG. 5. Isothermal anneal of carrier concentration in arsenic doped *n*-type germanium crystals. Their histories are not identical. Total annealable amount, n_a-n, is normalized to unity.

the same history. Figure 8 shows the curves for these samples which are similar to those of Fig. 7. In this case, the process has a single activation energy of 1·31 ± 0·04 eV but its kinetics can be represented neither by first nor by second order.

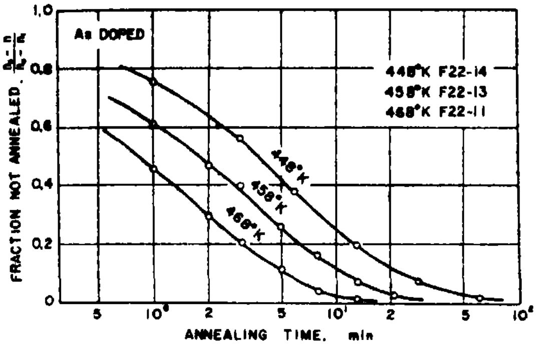

Fig. 6. Isothermal anneal of carrier concentration in arsenic doped n-type germanium crystals. The samples were intentionally aged for one month at room temperature after irradiation. Fraction not annealed is given in ordinate, total annealable amount being normalized to unity.

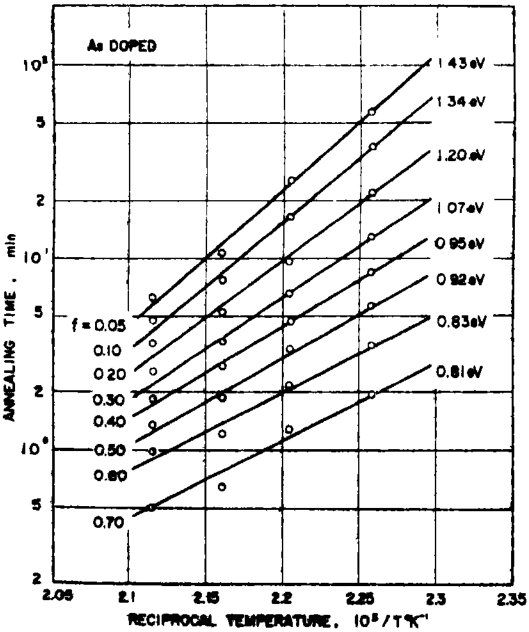

Fig. 7. Determination of activation energy from Fig. 5. A process, which has low activation energy, is mixed in the initial part of anneal.

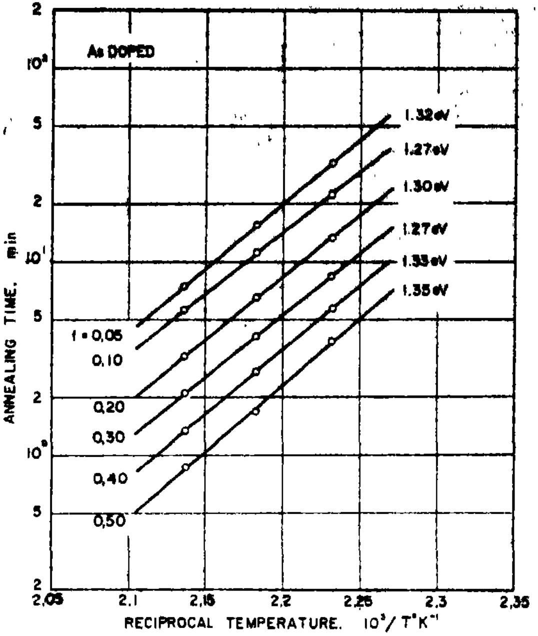

Fig. 8. Determination of activation energy from Fig. 6.

IV. DISCUSSION

A general trend of the annealing behavior of irradiated germanium is schematically shown in Fig. 9, which is constructed from data in the literature,(3, 7, 8) and from the present results. For convenience, the annealing stages will be named hereafter as shown in the figure: stages I, II, III_p, III_n, IV_p, VI_n and V_n. In this paper, we are chiefly concerned with the three stages (III_n, IV_n and V_n) above room temperature.

(a) *Stage* III_n

The characteristics of this stage are summarized as follows:

(1) The activation energy is about 0·7 ~ 0·8 eV.
(2) The kinetics of the process seems to be nearly first order.
(3) The recovery process is strongly dependent on doping impurities.
(4) The recovery of mobility is impurity-dependent.(3)

This stage may be divided into two parts: impurity-independent (III_n^A), and impurity-dependent (III_n^B) parts. Since it is almost certain that interstitials are more mobile than vacancies

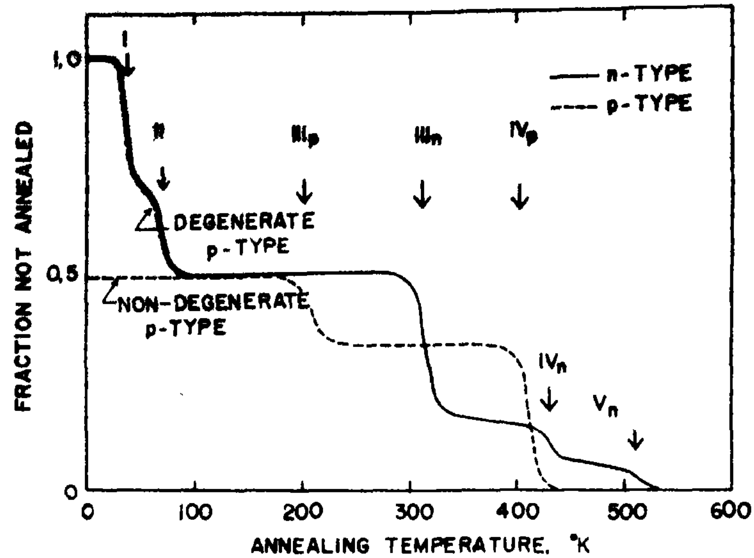

FIG. 9. Schematic representation of annealing stages of irradiated germanium. The figure is constructed from various published results and from the present experimental results.

in most metals, we assume that the same argument can be applied to germanium. It should be reminded that no annealing stage has been found between 67 and 330°K in n-type germanium.(3) Since stage II (67°K) is interpreted as annihilation of close vacancy-interstitial pairs,(8) the next stage, stage III$_n$, may be related to migration of interstitials. We tentatively assign that the impurity independent part III$_n^A$ may be due to migration of neutral or negatively charged interstitials. BARUCH's experiment(11) seems to support the neutral state. The observed activation energy of stage III$_n^A$ in antimony-doped samples may be assigned to migration energy of an interstitial.

Since the samples were irradiated at room temperature where interstitials are mobile, most of them have migrated throughout the crystal. The isochronal curves obtained in arsenic doped samples show that interstitials are already trapped in most of our experimental conditions, except in the case in which annealing was done immediately after irradiation. Thus in Fig. 2, the step at 370°K (III$_n^A$) is found only in the case of F22–5 which was annealed immediately after irradiation. Dissociation and annihilation of interstitial-donor atom pairs which is our assignment of stage III$_n^A$, seems to occur around 400°K in arsenic doped samples, causing a broadening in the appearance of stage IV$_n$. On the other hand, aging of the sample at room temperature produces no remarkable effect on annealing behavior in the case of antimony doped samples. This only reduces the fraction of stage III$_n^A$. These experimental facts lead to the conclusion that an arsenic atom may provide a deep trap for a neutral interstitial while an antimony atom may provide a shallow one or none. The binding force for trapping seems to have an elastic rather than a Coulombic nature in this case, so that an undersized impurity (such as arsenic or phosphorus) may give rise to a stronger trapping force for interstitials than an oversized one (antimony).

If we assume the charge state of the interstitial-arsenic pair as $(I^- As^+)^0$ at liquid nitrogen temperature, it seems fairly easy to explain the difference in the recovery of mobility between arsenic and antimony doped germanium obtained by BROWN *et al.*(3)*

---

* In an antimony doped sample, "the mobility and carrier concentration recover together", whereas in an arsenic doped sample, "the mobility almost recovers its preirradiation value while the carrier concentration has returned only a third of the way." (See Figs 8 and 9 in Ref. (3).)

One of the difficulties in our interpretation is that a level which 0·24 eV below the conduction band, disappears in stage III_n and IV_n as Fig. 3 shows. According to theoretical predictions,(9, 10) this level may arise from an interstitial. It might be possible that this level is due to other defects than an interstitial or alternatively that interstitial-donor pairs would be stable up to stage IV_n even in the case of antimony doped samples. This point should be investigated in more detail in future.

Another problem unsolved is the number of jumps made by an interstitial atom prior to annihilation. In the Appendix II, an attempt is made to work out this difficulty.

(b) *The stage* IV_n

A résumé of the present experimental results of this stage is listed below:

(1) The stage appears at about 430°K regardless of the kind of doping impurity.
(2) More than 50 per cent of the total change induced by γ-irradiation at room temperature recovers in this stage.
(3) The activation energy is about 1·2–1·3 eV.
(4) In antimony doped samples, kinetics of the process is nearly first order, while in arsenic doped samples, it is complex.
(5) Hall mobility recovers markedly in antimony doped samples. It becomes even larger than the preirradiation value in some cases. The recovery is less striking in arsenic doped samples.

This stage may be interpreted by vacancy migration. It is presumed from fact (1) listed above that this stage may be related to some "intrinsic" defect. As BARUCH's experiment(11) shows, the migrating species responsible for this stage is negatively charged.* On the other hand, the fact (5) shows that the species seems to form more stable pairs with antimony than with arsenic. This fact is consistent with the elastic interaction model between a vacancy and an impurity atom.

The activation energy of about 1·2–1·3 eV is in accord with that of vacancy migration as estimated from self-diffusion and quenching experiments. It is generally accepted that self-diffusion in germanium proceeds by a vacancy mechanism. Since there is evidence that thermally induced acceptors are vacancies(12) or at least vacancies plus copper atoms,(13), the observed energy for introducing an acceptor should be close to that for the formation of a vacancy. These experiments have given the activation energy of 3·0 eV for self-diffusion,(14) and of 1·7–2·0 eV for formation of a vacancy (E_f)(12, 13, 15). Therefore, the migration energy of a vacancy is given by $E_M = E_{SD} - E_f$, which yields 1·0–1·3 eV in agreement with the activation energy of the stage IV_n.

In the course of annealing in this stage, some vacancies may happen to form pairs with chemical donors. This pairing process is considered to be written as $V^- + Sb^+ \rightarrow (V^-Sb^+)^0$ in the case of antimony doped samples. Thus neutral pairs will result. The Hall mobility increases as the inherent charged scattering center of Sb^+ decreases by forming pairs, which explains the overshooting of mobility recovery. The dependence of the asymptotic values of the fraction not annealed on the annealing temperature as shown in Fig. 4 is presumably related to the pairing process.

Again in this stage, the number of jumps calculated simply from equation (A8) in Appendix II is too small for vacancies to interact with donors. The situation in this stage would be better than that in the previous stage since capture radius of the Sb^+ atom would be much larger for V^- than for I^0 because of the presence of long range Coulombic attraction.(16)

(c) *The stage* V_n

This stage may be interpreted as annihilation of vacancy-donor pairs formed in the stage IV_n. The reaction may be written as

$$(V^-Sb^+)^0 \rightleftharpoons V^- + Sb^+$$
$$V^- \rightarrow \text{annihilation}$$

in the case of antimony doped samples. Rate equations corresponding to these reactions cannot be solved analytically except in a few special cases. In the general case, machine calculations are required.(17) We can solve them approximately assuming that the concentration of vacancies is small as compared with that of donors and that $dC_v/dt \sim 0$ is satisfied where C_v denotes the concentration of negatively charged vacancies. The latter condition is valid when strong binding exists between a vacancy and a donor atom. If V^- annihilates at constant sinks, for example at dislocations or crystal surfaces, kinetics becomes nearly first order. If V^- recombines with an interstitial, nearly second order process will result. In both cases, the activation energy can be expressed approximately by $E_M + B$, where B is the binding energy. In the present research, binding energies of the vacancy-antimony and the vacancy-arsenic pairs are evaluated to be about 1·3 and 1·0 eV, respectively. They seem to be in reasonable magnitude since Coulombic energy plays a major part in the binding energy. That the binding energy of the V–Sb pair is slightly higher than that of the V–As pair is accounted for by the difference of elastic interactions which should be added to the Coulombic interactions.

---

* Baruch's results obtained in a temperature range from 40 to 70°C turn out to correspond to our stage IV_n, if his annealing time, which is 200–400 times longer compared with ours, is considered.

Second order kinetics remains still unsolved. However, it seems to be instructive to note that a slight step at 200°K in curves of temperature dependence of Hall coefficient continues to exist up to 533°K annealing as seen in Fig. 3. It follows that a part of the interstitials would exist in some form up to this stage to serve as sinks for vacancies. Formation of divacancies might also be considered. In this case, however, Coulombic repulsion between vacancies would be unfavorable to form pairs. LETAW's analysis[18] on the kinetics of the formation of divacancies does not agree with the results of the present stage. This stage should be examined in more detail.

In the course of the above discussion, one of the most troublesome problems we have encountered in almost all the stages is a problem of the number of jumps. Probably the complication arises from the charge of defects and from impurities. In this regard there is a limitation on information, which is derived from measurements of Hall coefficients and conductivities. It is hoped that experimental techniques other than electrical measurements as have been fruitfully applied to some lattice defects in silicon[19] will become applicable to germanium as well.

V. CONCLUSION

(1) There are three annealing stages above room temperature in γ-ray irradiated n-type germanium. They are named stages III_n, IV_n and V_n.

(2) Stage III_n is composed of stage III_n^A and stage III_n^B. Stage III_n^A is interpreted as migration and annihilation of neutral interstitials and the stage III_n^B as dissociation and annihilation of interstitial-donor pairs. The activation energy of stage III_n^A is found to be 0·7–0·8 eV.

(3) Stage IV_n is associated with migration and annihilation of single-negatively charged vacancies. The activation energy is found to be 1·2–1·3 eV.

(4) Stage V_n is related to decomposition and annihilation of vacancy-donor pairs. The binding energy of a vacancy with an antimony atom is about 1·3 eV and with arsenic 1·0 eV.

(5) An arsenic atom seems to form a more stable pair with a neutral interstitial than an antimony atom does. The situation is reversed with a vacancy. This fact is in agreement with the prediction from the atomic size. Data on mobility can be explained by this model.

Acknowledgements—The authors wish to express their hearty thanks to Dr. F. NAGATANI of the Toshiba Central Research Laboratory and to Dr. T. ABE of the Toshiba Transister Works for furnishing various kinds of germanium crystals. They are also indebted to Mrs. A. OHNUKI of Fuji Communication Apparatus Mfg. Co. for providing several arsenic doped germanium crystals.

APPENDIX I

The activation energy and the reaction order are obtained from isochronal studies as follows.

We shall assume a process with a single activation energy. Let C be the concentration of defect species which disappear at the stage under consideration. The rate equation will be as follows:

$$\frac{\mathrm{d}C}{\mathrm{d}t} = -K(T) \cdot f(C) \tag{A1}$$

where $K(T)$ is a rate constant and $f(C)$ is an appropriate function of the concentration of the defect. Let us assume that the i-th isochronal anneal is made at temperature T_i for the time duration Δt, and that the resultant concentration becomes C_i. During this anneal the process is controlled by the equation

$$\frac{\mathrm{d}C}{\mathrm{d}t} = -K(T_i) \cdot f(C). \tag{A2}$$

Defining

$$F^{-1}(C) = \int \frac{\mathrm{d}C}{f(C)}, \tag{A3}$$

one obtains

$$K(T_i) = \frac{1}{\Delta t}\{F^{-1}(C_{i-1}) - F^{-1}(C_i)\}. \qquad \text{(A4)}$$

If the right hand side of the equation (A4) can be calculated, the activation energy is obtained from the plot of log $K(T_i)$ vs. $1/T_i$.

Let us consider a γ-th order reaction as a simple example, that is

$$f(C) = C^{\gamma}. \qquad \text{(A5)}$$

From the equations (A3), (A4) and (A5), we obtain

$$K(T_i) = \frac{1}{\Delta t}\log(C_{i-1}/C_i) \text{ for } \gamma = 1 \qquad \text{(A6)}$$

and

$$K(T_i) = \frac{1}{\Delta t}\cdot\frac{1}{1-\gamma}(C_{i-1}^{1-\gamma} - C_i^{1-\gamma}) \text{ for } \gamma \neq 1. \qquad \text{(A7)}$$

If the C_i's are obtained from experiments, γ is the only unknown. Making suitable choice of γ so that log $K(T_i)$ vs. $1/T_i$ curve may give a straight line, one may estimate the order of the reaction.

APPENDIX II

One can evaluate the number of jumps n_j, which is simply given by

$$n_j = Az\,\nu_0 t \exp(-E/kT), \qquad \text{(A8)}$$

to be 10^4–10^5, using experimental values of the activation energy E(0·8 eV) and of the annealing time t (10^3 sec at 330°K) and appropriate values of the entropy factor A (unity), of the coordination number z (four) and of the atomic vibrational frequency ν_0(10^{13}/sec.). This value of 10^4–10^5 is smaller by a factor of the order of 10^3–10^2 for an interstitial to interact with chemical donors. Such a discrepancy will also be met in the stages IV$_n$ and V$_n$. If a barrier to recombination with a barrier height R exists, the discrepancy could be explained. In this case, the true number of jumps n_j, is given by

$$n_j' = Az\,\nu_0 t \exp(-E_M/kT) \qquad \text{(A9)}$$

where E_M is the true migration energy expressed as $E_M = E - R$. Therefore,

$$n_j' = n_j \exp(R/kT). \qquad \text{(A10)}$$

To remove the discrepancy of a factor of 10^3–10^2 at $T = 330$°K, R should be about 0·15 eV, which is not unreasonable.

REFERENCES

1. For the recent development in the field of radiation effects in semiconductors, see *J. appl. Phys.* **30**, 1117–1322 (1959). (Gatlinburg Conference issue.)
2. Brown W. L., Fletcher R. C. and Wright K. A., *Phys. Rev.* **92**, 585 (1953).
3. Brown W. L., Augustyniak W. M. and Waite T. R., *J. appl. Phys.* **30**, 1258 (1959).
4. Asada T., Saito H., Ohmura K., Oku K. and Oka M., J. *Phys. Soc. Japan* **15**, 93 (1960).
5. Cleland J. W., Crawford J. H. and Holmes D. K., *Phys. Rev.* **102**, 722 (1956).
6. Crawford J. H. and Cleland J. W., *J. appl. Phys.* **30**, 1204 (1959).
7. Gobeli G. W., *Phys. Rev.* **112**, 732 (1958); McKay J. W., Klontz E. F. and Gobeli G. W., *Phys. Rev. Letters* **2**, 146 (1959).
8. McKay J. W. and Klontz E. F., *J. appl. Phys.* **30**, 1269 (1959).
9. James H. and Lark-Horovitz K., *Z. phys. Chem.* **198**, 107 (1951).
10. Blount E. I., *Phys. Rev.* **113**, 995 (1959); *J. appl. Phys.* **30**, 1218 (1959).
11. Baruch P., *J. appl. Phys.* **32**, 653 (1961).
12. Logan R. A., *Phys. Rev.* **101**, 1455 (1956).
13. Tweet A. G., *J. appl. Phys.* **30**, 2002 (1959).
14. Letaw H., Portnoy W. M. and Slifkin L. M., *Phys. Rev.* **93**, 892 (1954).
15. Hasiguti R. R., Ishino S., Nakazawa F., Ishibachi T. and Yamaguchi S., Preprint of the 16th Annual Meeting of the *Phys. Soc. Japan* **2**, 13 (1961).
16. Reiss H., Fuller C. S. and Morin F. J., *Bell Syst. tech. J.* **35**, 535 (1956).
17. Damask A. C. and Dienes G. J., *Phys. Rev.* **120**, 99 (1960).
18. Letaw H., *J. Phys. Chem. Solids* **1**, 100 (1956).
19. Watkins G. D. and Corbett J. W., *Phys. Rev.* **121**, 1001 (1961); Corbett J. W., Watkins G. D., Chrenko R. M. and McDonald R. S., *ibid.* **121**, 1015 (1961).

J. Phys. Chem. Solids Pergamon Press 1963. Vol. 24, pp. 1043–1047. Printed in Great Britain.

ORDERING IN ALLOY Cu_3Au—III

E. NAGY and J. TÓTH

Central Research Institute for Physics, Hungarian Academy of Sciences,
Budapest, Hungary.

(*Received* 9 *January* 1963)

Abstract—Absolute thermoelectric power in the alloy Cu_3Au was investigated in various states of order and domain structure. At temperature kinetic measurement clearly distinguished between ordering proper and boundary wall movement. Ordering proper is brought about by an atomic mechanism, different from that responsible for wall movement. The activation energy for atomic ordering was found to be about 1·8 eV.

INTRODUCTION

IN FORMER communications(1, 2) we have investigated the kinetics of ordering in Cu_3Au by electrical resistance and Hall-constant measurements. In the present paper we report on a similar study using measurements of absolute thermoelectric power. It was hoped that the sensitive dependence of this quantity on Fermi-surface changes during ordering and the already established dependence on lattice imperfections would render it a suitable tool for kinetic studies. The absolute thermoelectric power of the alloy Cu_3Au has been treated theoretically by PETROVA.(3) The experimental material is somewhat scanty; we know only of SATO's work(4) and that of JAUMOT and SAWATZKY.(5) A preliminary communication on our work was included in the proceedings of the Balatonfüred Solid State Congress.(6)

SAMPLE AND EXPERIMENTAL ARRANGEMENT

The sample was taken from the same batch as used for our previous studies.(1, 2) A piece of wire was mounted in an evacuated glass bulb with a small furnace producing a temperature difference directly on the potential leads. The entire bulb was placed into an electric furnace of small thermal inertia, where the temperature could be maintained within ± 0·2°C for more than a day by means of an electronic proportional regulator. Now, as is seen from Fig. 1, V_{ab} measures the temperature at which the kinetic study is conducted. The temperature difference between points 1 and 2 was determined both from ΔV_{xa} and ΔV_{xb}. The leads *a* were of platinum, while those marked *b* were made from the standard platinum–rhodium alloy.

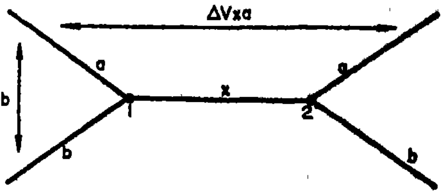

FIG. 1. Schematical thermocouple arrangement.

The entire specimen was kept at constant annealing temperature, except for the short time of the actual act of measurement, when one end of the sample was heated by the small furnace about 2° above the annealing temperature. This temperature difference, while sufficient to provide easily measurable thermoelectric voltages, is still small enough to allow the assignment of a definite temperature to the process of ordering investigated by this means. The cold points of the thermocouples were kept in a thermostat at 30°C. A low resistance compensator of type PPTN–1 was used for the voltage measurements. A detailed description of the apparatus and the assessment of the various errors has been published elsewhere.(7)

The arrangement has the advantage that it does away easily with parasitic thermoelectric voltages.

As we have learned from our own experience the plot of ΔV_{xa} or ΔV_{xb} vs. ΔT seldom passes through the coordinate origin. What is needed is the slope of the straight line $\Delta V_{xa} = S_{xa}\Delta T$, which can be determined only if more than one temperature difference is set up and the corresponding thermoelectric voltages measured.

The slope of this line is independent of any disturbing potentials only if these do not change during the time of an actual measurement, taking about 2 min. This hope was fulfilled, all our ΔV vs. ΔT plots were accurate straight lines. This circumstance had not been fully realized at the time of our earlier publication,(6) which somewhat impaired those results.

In our new arrangement the error in S_{xa} is less than 1 per cent. The absolute thermoelectric power was determined by means of an interpolation formula derived from CUSACK's data.(8) The whole series of measurements was performed on a single sample, but the results were checked on two other similar samples. The difference in absolute thermoelectric power was in all the cases well below $0{\cdot}1\mu V/°\mathrm{C}$, which could be explained by some difference in the precarious triple weldings 1 and 2.

RESULTS

The previous work of SATO,(4) JAUMOT and SAWATZKY(8) has already indicated that the absolute thermoelectric power of the alloy Cu_3Au decreases in the course of ordering. While this statement holds almost generally there are some differences in the detailed results. Jaumot and Sawatzky obtained $-1{\cdot}2\mu V/°\mathrm{C}$ at 50°C after a 24 hr heat treatment at 375°C, while our measurement gave in a similar case a value around $-3{\cdot}2\mu V/°\mathrm{C}$. A similar discrepancy was found in the values for the disordered state. Jaumot and Sawatzky found $+0{\cdot}4\mu V/°\mathrm{C}$ at 50°C after a quench from 600°C, while we found $-0{\cdot}5\mu V/°\mathrm{C}$ at 50°C after a quench from a lower temperature, 420°C. We checked our results by the traditional method of integral thermoelectric power measurement, obtaining complete agreement with our previous determinations. The absolute thermoelectric power in the disordered state is seen in Fig. 2. It appears that the absolute thermoelectric power depends linearly on the temperature. Figures 3–4 show the change in the absolute thermoelectric power during the establishment of order. The samples were kept at 415–420°C for 1 hr before each measurement then brought as fast as possible to the required ordering temperature. The cooling was accomplished in 2–5 min. The first data could be obtained at the temperature of ordering immediately thereafter. The data show clearly that the variation of absolute thermoelectric power is substantially different from the variation either of the electrical resistivity or the Hall-constant. Both of these latter properties, as found in our previous studies,(1, 2) show a monotonic change at all temperatures, while the thermoelectric power seems to show, at least above 335°C, a distinct *minimum*. This fact lends added support to our previous contention(1, 2) that the structural changes occuring after cooling below the Curie-temperature are at least twofold; the establishment of equilibrium long range order within the domains and the establishment of an equilibrium domain pattern. These data of course cannot be subjected to so thorough an analysis as the previous conductivity data, for the accuracy of the present measurements clearly does not warrant it. All that can be done is to show that the late stages of the kinetics are not in disagreement with exponential kinetics. with the time constants taken from Refs 1 and 2. This was checked and no disagreement found. Inspection of Figs 3–4 shows that the exponential behavior is less in evidence for lower temperatures. For the lowest temperature 288°C, there is no indication of a minimum even after 25 hr.

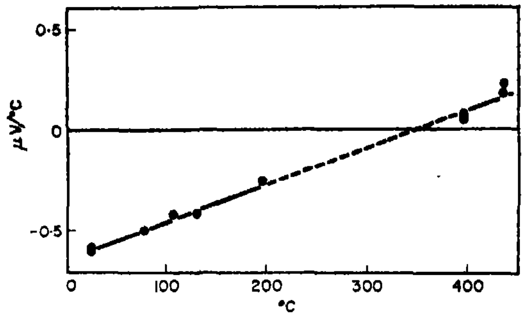

FIG. 2. The temperature dependence of the absolute thermopower of disordered Cu_3Au.

For the study of the behaviour at low ordering temperatures we had recourse to the two-step

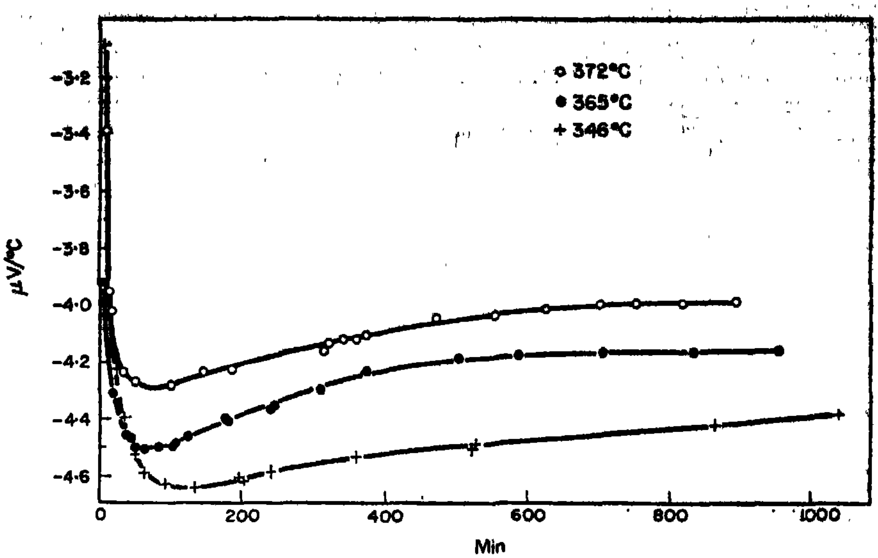

FIG. 3. The variation of the absolute thermopower of Cu_3Au during ordering at 372, 365 and 346°C.

treatments used with advantage in our previous studies.

Our experimental arrangement allowed a temperature reduction of about 100° in 3 min. These measurements brought about a more complete picture. First we found that if the higher temperature anneal, below the Curie-temperature, was long enough to lead to a substantial advancement of domain growth then the long-range order corresponding to a lower temperature was established quite rapidly. The thermoelectric power did not show any change after the first 10 min. A reheat to the higher temperature led to the same thermoelectric power as was observed there before cooling, irrespective of the duration of the low temperature anneal. The kinetics at the high temperature was followed again and was exactly the same as when no intermediate cooling had taken place.

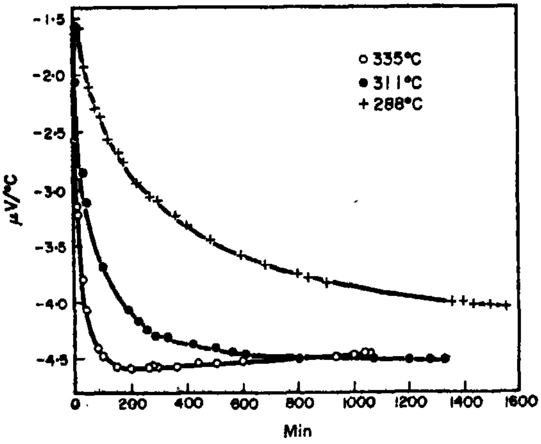

FIG. 4. The variation of the absolute thermopower of Cu_3Au during ordering at 335, 311 and 288°C.

Figure 5 shows the thermoelectric power measured at 280 and 330°C as a function of the duration of the 346°C anneal, Fig. 6, the thermoelectric power at 280, 310 and 330°C for a higher annealing temperature of 365°C. Evidence for domain growth at the higher annealing temperature is suggested by the greater and more rapid

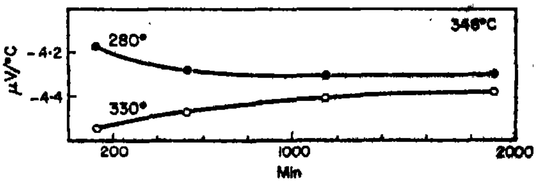

FIG. 5. The change of the absolute thermopower of Cu_3Au measured at 330 and 280°C plotted against the duration of a 346°C anneal.

change of the thermoelectric power with annealing time, especially for the measurement at 280°C. The data shown, which are merely representative of a much larger set of measurements, also indicate that domain growth causes an increase in thermoelectric power above 300°C and a decrease below 300°C.

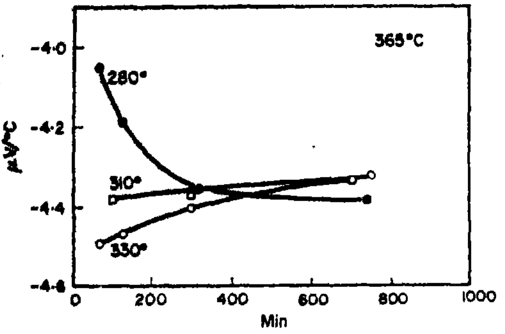

FIG. 6. The change of the absolute thermopower of Cu_3Au measured at 330, 310 and 280°C plotted against the duration of a 365°C anneal.

It is felt that our data cannot be explained in terms of simplified free electron-like models. An attempt to explain the data on the basis of a spherical Fermi surface with a parabolic E vs. k dependence and a relaxation time dependent on a power of energy only led nowhere. Nevertheless, we feel the data do throw interesting light on the mechanisms of domain growth and the atomic ordering process.

On Fig. 7 we plot the deviation of the absolute thermoelectric power from its minimum as a function of the time of ordering for various temperatures. The similarity of these curves is clear, they can be brought into coincidence by a horizontal shift. The time constants for 0·2, 0·9 and 1·35μV/°C deviations are plotted as functions of the reciprocal absolute temperature on Fig. 8. All the three curves are parallel straight lines indicating an activation energy of about 1·8 eV. One could question the validity of this method of plotting, considering that the exponential process occurring in the later stages of annealing (to the right of the minimum in Fig. 3) has not been taken into account. However, even if the exponential process of the later stages is extrapolated back to zero time and subtracted from the curves for the early stages, the correction shifts the points of Fig. 7 slightly upwards, with a greater shift for the higher temperature curves. This result in some diminution of the slopes in Fig. 8, but even this most extreme correction does not decrease the activation energy below 1·45 eV.

That is the point we want to emphasize now. The later stage process, which we have previously ascribed to domain wall movement, proceeds with an activation energy of 0·80–0·84 eV while the first process has an activation energy of about

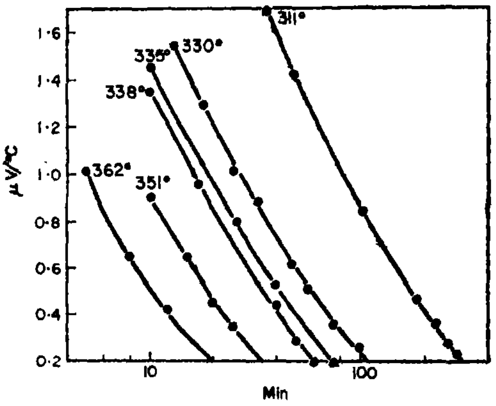

FIG. 7. The deviations from the minimum; S–S_{min}, plotted against $\log_{10}t$ for different ordering temperatures.

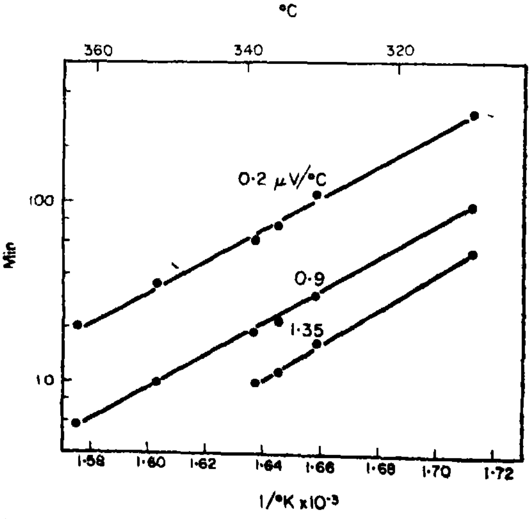

FIG. 8. $\log_{10}t$ corresponding to a given S–S_{min}, plotted against the reciprocal of the absolute temperature.

1·8 eV. This suggests that different types of atomic movement are responsible for the ordering within the domains and for the domain wall movement. The activation energy found here for the ordering proper is in substantial agreement with that found for lattice constant changes.(9)

We propose that the domain wall movement is effected by vacancies retained on the surface of ordered nuclei during cooling from the disordered state. These surfaces then eventually coalesce into domain walls. The ordering proper is brought about by vacancies in thermal equilibrium. We hope that further corroboratory evidence for this suggestion can be presented shortly.

Acknowledgements—The authors wish to express their appreciation to I. NAGY for numerous discussions of this and his unpublished works to F. TÓTH for designing the temperature regulator and I. FEKETE for expert technical assistance.

REFERENCES

1. NAGY E. and NAGY I., *J. Phys. Chem. Solids* **23**, 1605 (1962).
2. NAGY E. and ELKHOLY H., *J. Phys. Chem. Solids*. **23**, 1613 (1962).
3. PETROVA L. N., *Fiz. Metalloved.* **12**, 173 (1961).
4. SATO H., *J. phys. Soc. Japan* **5**, 268 (1950); *Metal Abstr.* **19**, 708 (1952).
5. JAUMOT F. E. and SAWATZKY A., *Acta Met.* **4**, 127 (1956).
6. *Festkörperphysik*. Akademie, Berlin, p. 157 (1961).
7. TÓTH J., *KFKI. Közl.* **10**, 357 (1961), (in Hungarian).
8. CUSACK N. and KENDALL P. *Proc. Roy. Soc.* **72**, 898 (1958).
9. NOWICK A. S. and WEISBERG L. R., *Acta Met.* **6**, 260 (1958).

J. Phys. Chem. Solids Pergamon Press 1963. Vol. 24, pp. 1049–1051. Printed in Great Britain.

ANTIFERROMAGNETIC GROUND STATE

TAKEHIKO OGUCHI*

Department of Physics, Carnegie Institute of Technology, Pittsburgh, Pennsylvania

(*Received* 22 *March* 1963)

Abstract—The calculations of the energy of the antiferromagnetic ground state by Fisher are corrected. The revised results are in good agreement with other theories for spin $\frac{1}{2}$. The apparent contradictions as to the average z component of spin on one sublattice, and the perpendicular susceptibility in several theories are clearly resolved.

I. IMPROVEMENT ON FISHER'S CALCULATIONS

IN A very interesting paper, FISHER⁽¹⁾ investigated the antiferromagnetic ground state by a variational method. His result for the energy of the ground state is

$$\lambda_0 = -\left[1+\frac{1}{2ZS-1}\right] JZNS^2/2. \tag{1}$$

Here we use the same notations as those used in Fisher's paper. If we consider a linear chain of spins with $S = \frac{1}{2}$, the above result gives $\lambda_0 = -JN/2$, which is lower than the rigorous result $-(JN/2)\times 0{\cdot}8863$ obtained by HULTHÉN.⁽²⁾ Therefore the above result is obviously doubtful. We wish to show that a more careful application of Fisher's method leads to a reasonable result in the case of $S = \frac{1}{2}$. At the same time, we shall point out limitations on the application of this method for $S \geqslant 1$.

Let us denote the spin function on the plus sublattice whose z component is S^z by $\Theta_j^{S^z}$ and the spin function on the nearest neighboring site whose z component is $-S^z$ by $\Theta_l^{-S^z}$. Then we have

$$\tfrac{1}{2}(S_j^+S_l^-+S_j^-S_l^+)\Theta_j^S\Theta_l^{-S} = S\Theta_j^{S-1}\Theta_l^{-S+1}, \tag{2}$$

$$\tfrac{1}{2}(S_j^+S_l^-+S_j^-S_l^+)\Theta_j^{S-1}\Theta_l^{-S+1} = S\{\Theta_j^S\Theta_l^{-S} +2(2S-1)\Theta_j^{S-2}\Theta_l^{-S+2}\}, \tag{3}$$

$$\tfrac{1}{2}(S_j^+S_l^-+S_j^-S_l^+)\Theta_j^S\Theta_l^{-S+1} = \{S(2S-1)\}^{1/2} \times \Theta_j^{S-1}\Theta_l^{-S+2}, \tag{4}$$

$$\tfrac{1}{2}(S_j^+S_l^-+S_j^-S_l^+)\Theta_j^{S-1}\Theta_l^{-S} = \{S(2S-1)\}^{1/2}\Theta_j^{S-2}\,\Theta_l^{-S+1}. \tag{5}$$

The number of such pairs as given in (2), (3), (4), and (5) are $(ZN/2)-(2Z-1)m$, m, $(Z-1)m$, and $(Z-1)m$, respectively. We assume that $\Theta^{\pm(S-2)}$ can be neglected. This is an exact statement when $S = \frac{1}{2}$. Therefore the case of $S = \frac{1}{2}$ will be most accurate. If we use the above assumption, we can get (a), (b), and (c) in p. 45 in Fisher's paper, except in (b), the number of pairs, $ZN/2$, which he gave, must be replaced by $(ZN/2)-(2Z-1)m$. Of course m is smaller than N, but the second term cannot be neglected. Thus the result is modified as follows,

$$\lambda_m = -\frac{ZJNS^2}{2}+J(2ZS-1)m-JS(2ZNm)^{1/2} +JS(2Z-1)m(2m/ZN)^{1/2}. \tag{6}$$

If we consider more precisely the ratios of $n_{m\pm1}$ and n_m, we get

$$\frac{n_{m+1}}{n_m} \doteqdot \frac{ZN}{2m}\left(1-\frac{2m}{ZN}\right),\quad \frac{n_{m-1}}{n_m} \doteqdot \frac{2m}{ZN}\left(1+\frac{2m}{ZN}\right) \tag{7}$$

However, (7) does not change the result if we neglect the terms of order more than $(m/N)^{3/2}$.

The solution of $\partial\lambda_m/\partial m = 0$ is

$$\left(\frac{m}{N}\right)^{1/2} = \frac{-(2ZS-1)+\{(2ZS-1)^2+6S^2(2Z-1)\}^{1/2}}{3S(2Z-1)(2/Z)^{1/2}}. \tag{8}$$

---

[*] On leave of absence from Department of Physics, Tokyo University of Education, Tokyo, Japan.

Inserting (8) into (6), we get the energy of the ground state λ_0.

The average z component of spin on the plus sublattice $\langle S^z \rangle$ is given by

$$\langle S^z \rangle = S\left(1-\frac{2m}{N}\right)+(S-1)\frac{2m}{N}. \qquad (9)$$

The numerical values of $-\lambda_0/(JN/2)$ and $\langle S^z \rangle$ for the case of $S = \frac{1}{2}$ are shown in the following Table 1.

Table 1. The values of $-\lambda_0/(JN/2)$ and $\langle S^z \rangle$ for $S = \frac{1}{2}$

	MARSHALL[8]	TAKETA–NAKAMURA[4]	KUBO[5]	DAVIS[6]	Present Result	Spin Wave[7]
Linear chain	0·816	0·816	0·698	0·868	0·846	0·863
	0	0	finite	0·241	0·325	0
Quadratic layer	1·312	1·282	1·294	1·328	1·286	1·316
	0	0	finite	0·382	0·427	0·303
Simple cubic	1·805	1·772	—	1·800	1·774	1·791
	0	0	—	0·436	0·455	0·492
Body centered cubic	2·314	2·266	2·276	2·296	2·268	2·292
	0	0	finite	0·453	0·467	0·493

The upper lines show $-\lambda_0/(JN/2)$, while the lower lines show $\langle S^z \rangle$.

Fisher has thought that his method can be applied to the case of arbitrary S. However, this is not true for the cases of $S \geqslant 1$ unless we add the vague assumption mentioned above that $\Theta^{\pm(S-2)}$ can be neglected. Therefore we need further considerations for the cases of $S \geqslant 1$ in his method as well as in the MARSHALL[3] and TAKETA-NAKAMURA[4] methods.

II. DISCUSSION

If we look at Table 1, we note that the energies of the ground state obtained by the various methods are in fairly good agreement with each other, while there are clear disagreements in the average z component of spin on the sublattice. We can divide the theories into three groups. In the first group, which includes Marshall's and Taketa–Nakamura's papers, $\langle S^z \rangle$ is zero for all lattices. In the second group, which includes Kubo's and Davis' and the present papers, $\langle S^z \rangle$ is not zero for all lattices. In the third group, which includes the spin-wave method[7] and the Green function method,[8] $\langle S^z \rangle$ is zero for the linear chain and not zero for the two and three dimensional lattices.

MARSHALL proved[3] that if the variational function of the ground state is of a certain form, the ground state is a singlet. Furthermore, PRATT[9] proved that if the ground state is a singlet, $\langle S^z \rangle$ must be zero. Therefore it is very probable that $\langle S^z \rangle$ is zero for the exact ground state. This means that the wave function of the exact ground state is impartial between the up and down orientations of the sublattice.

On the other hand, the theories in the second and third groups are based on the assumption that the Néel state is a fairly good approximation of the ground state, i.e., that another Néel state in which all spins are reversed from the original Néel state is excluded. It was pointed out by ANDERSON[10] that the system will take more than a year to switch from one Néel state to the other Néel state. In fact, O'SULLIVAN *et al.*[11] found experimentally that in $CuCl_2 2H_2O$ there was no sublattice switching within a day. Therefore from the standpoint of experimental fact, either the second or third group is appropriate.

The fact that the switching time is very long means that the resonance energy between two Néel states is negligibly small. This conclusion is the reason why the energies of the ground state in three groups are in good agreement with each other in spite of there being the apparent contradiction in $\langle S^z \rangle$.

Similar considerations can be applied to the perpendicular susceptibility, $\chi_\perp$. If the ground state is a singlet, $\chi_\perp$ must be zero at 0°K. This can be actually shown in the antiferromagnetic system with a small number of spins.(12) On the other hand, non-vanishing $\chi_\perp$ has been obtained by the theories in the second and third groups. In order to explain the observed $\chi_\perp$ we must use the theories in the second or third groups.

Acknowledgement—The author wishes to thank Professor S. A. Friedberg for reading the manuscript.

REFERENCES

1. Fisher J. C., *J. Phys. Chem. Solids* **10**, 44 (1959).
2. Hulthén L., *Arkiv. Mat. Astr. Fys.* **26A**, No. 11, 1 (1938).
3. Marshall W., *Proc. Roy. Soc.* **A232**, 48 (1955).
4. Taketa H. and Nakamura T., *J. phys. Soc. Japan* **11**, 919 (1956).
5. Kubo R., *Rev. Mod. Phys.* **25**, 344 (1953).
6. Davis H. L., *Phys. Rev.* **120**, 789 (1960).
7. Kubo R., *Phys. Rev.* **87**, 568 (1952).
8. Oguchi T. and Honma A., *J. appl. Phys.* **34**, 1153 (1963).
9. Pratt G. W. Jr., *Phys. Rev.* **122**, 489 (1961).
10. Anderson P. W., *Phys. Rev.* **86**, 694 (1952).
11. O'Sullivan W. J., Robinson W. A. and Simmons W. W., *Phys. Rev.* **124**, 1317 (1961).
12. Katsura S., *Phys. Rev.* **127**, 1508 (1962).

J. Phys. Chem. Solids Pergamon Press 1963. Vol. 24, pp. 1053–1055. Printed in Great Britain.

LATTICE THERMAL CONDUCTIVITY OF ANTI-FERROMAGNETIC MnF_2 BELOW ITS NÉEL TEMPERATURE*

B. N. MEHROTRA†

Department of Physics, Washington University, St. Louis, 30, Missouri

(*Received* 18 *December* 1962; *revised* 13 *March* 1963)

Abstract—The theoretical model of Callaway for lattice thermal conductivity at low temperatures has been used for MnF_2 to calculate the $l_{ga}(T)$ term in the reciprocal mean free path equation $l_g^{-1} = l_{ga}^{-1}+l_{gm}^{-1}$. The $l_{gm}(T)$ part has also been calculated to get $l_g(T)$. The $K_g(T)$ value calculated from these $l_g(T)$ are compared with Slack's results. For satisfactory agreement it is necessary to conclude that, at low temperatures the boundary scattering term in the relaxation time formula of Callaway is temperature dependent and diverges from Casimir's model by a factor which changes from 6 to 1·2 in the temperature range 3–10°K.

INTRODUCTION

CALLAWAY(1) in 1958 gave a phenomenological model to explain lattice thermal conductivity at low temperatures. Recently AGARAWAL and VERMA(2) made use of the theoretical model of Callaway to evaluate the lattice conductivities at low temperatures of the diamagnetic crystals ZnF_2 and CaF_2 and compared them with the experimental data of SLACK.(3)

In the present paper the Callaway model has been used to evaluate the phonon–phonon mean free path in antiferromagnetic MnF_2 below its Néel temperature. The phonon–magnon scattering mean free path has been evaluated and the reciprocal of the two combined to calculate the reciprocal total mean free path. The thermal conductivity calculated from this is compared with the experimental values of Slack.

THEORY

As pointed out by Slack, the total thermal conductivity of MnF_2 is the sum of the phonon term K_g and the magnon term K_m

$$K_{\text{tot}} = K_m + K_g \tag{1}$$

Now K_m term is given by

$$K_m = \tfrac{1}{3} l_m V_m' C_m \tag{2}$$

where l_m is the magnon mean free path. Slack further pointed out that, as a consequence of the strong magnon–magnon scattering, l_m is quite small and therefore K_m can be neglected and $K_{\text{tot}} = K_g$ itself. The K_g term is given by

$$K_g = \tfrac{1}{3} l_g C_g V_g \tag{3}$$

where l_g is the phonon mean free path determined by the following scattering mechanisms: (a) the processes which do not conserve the total crystal momentum and (b) the phonon–magnon scattering. The former processes include (i) Umklapp processes, (ii) impurity scattering and (iii) boundary scattering. Denoting the mean free path corresponding to the mechanisms (a) by l_{ga} and that corresponding to (b) by l_{gm} the value of l_g is determined by adding the reciprocal mean free paths.(4)

$$\frac{1}{l_g} = \frac{1}{l_{ga}} + \frac{1}{l_{gm}} \tag{4}$$

Use of the Callaway model to evaluate l_{ga}

The elements Mn and F have a single naturally occuring isotope and so there will be no isotope

---

* This work supported by U.S. Air Force Office of Scientific Research.

† On study leave from Gorakhpur University, Gorakhpur (U.P.) India.

scattering. The following two formulas given by CALLAWAY(1) are used:

At very low temperatures: equation (36) with $A = 0$

$$K_{ga} = \frac{2k\pi^2}{15}\frac{L}{C^2}\left(\frac{kT}{\hbar}\right)^3\left[1-\frac{20}{7}B_1T^3\left(\frac{\pi kT}{\hbar}\right)^2\frac{L}{c}\right] \tag{5}$$

At temperatures where Umklapp scatterings are important

$$K_{ga} = \frac{k^2}{6\hbar(B_1+B_2)cT^2}\left[1-\frac{3}{\pi^2}e^{-(\Theta/T)}\times\left(\frac{\Theta^2}{T^2}+\frac{2\Theta}{T}+2\right)-\frac{3\hbar}{2\pi kT^{5/2}}\left[\frac{c}{L(B_1+B_2)}\right]^{1/2}+\frac{7}{25}\frac{B_2}{B_1}\right] \tag{6}$$

Calculation of l_{gm} (T)

Since l_{gm} is inversely proportional to the fraction of disordered spins it is given by(5)

$$l_{gm} = \frac{l^0_{gm}}{[1-(M/M_0)]} \tag{7}$$

where l^0_{gm} is the temperature independent value of phonon–magnon scattering length above the Néel temperature. (M/M_0) can be determined from the work of ERICKSON.(6)

The constants used in the calculation of K_{ga} from the equations (5) and (6) are given in Table 1.

PROCEDURE

The phonon–phonon scattering length was calculated using equations (5) and (6). The basic parameters in these equations are evaluated from the experimental data of Slack. (B_1+B_2) was determined from Slack's experimental results for the conductivity at $T = 75°$K by using equation (6) and neglecting the term proportional to B_2/B_1. B_2 itself is determined to a good approximation by using equation (6) and the experimental result at $T = 300°$K, where Umklapp scattering term B_1 can be assumed to be absent. It has been pointed out by DEKKER(7) that Umklapp scattering is dominant only in the temperature range $\Theta/10$ to $\Theta/20$.

Using the calculated value of K_{ga} (T), $l_{ga}(T)$ was computed from $K_{ga} = \frac{1}{3}l_{ga}V_gC_g$. Taking $l^0_{gm} =$ 4000 Å (as estimated by Slack) $l_{gm}(T)$ was computed from equation (7). These two mean free paths when substituted in equation (4) gave $l_g(T)$ which in turn gave $K_g(T)$. There was found to be good agreement between the computed $K_g(T)$ and experimental data of Fig. 6 Slack's paper, except at very low temperatures. In the temperature range 3–10°K the calculated thermal conductivity changes from approx. 6 times the experimental result to approx. 2 times.

DISCUSSION

At very low temperatures, the present calculations imply a temperature dependent nature for the boundary scattering term cL^{-1} in the relaxation time formula (equation (17) Callaway's paper)

$$\tau_c^{-1} = CL^{-1}+(B_1+B_2)\omega^2T^3+A\omega^4 \tag{8}$$

For the good fit of the experimental and calculated conductivity, the ratio of cL^{-1} required by the experimental data and that calculated from the dimensions on CASIMIR's model,(8) changes from approximately 6 to 1·2 in the temperature range 3–10°K. The deviation, which is due to the

Table 1

Substance	Debye Temp. (°K)	v_g (cm/sec)	L (cm)	(B_1+B_2) (10^{-22} sec deg^{-3})	B_2 (10^{-23} sec deg^{-3})	$\frac{(c/L)_{\exp}}{(c/L)_{\text{cal}}}$
MnF$_2$	450(a)	3×10^5	0·25(a)	2·61	4·27	Approx. 6 to 1·2 in the temperature range 3–10°K.

(a) These constants are from SLACK's data.(3)

presence of fluctuations in the composition of the solid on microscopic scale, decreases with increasing temperature, as expected.

Acknowledgement—The author is indebted to Prof. R. E. NORBERG for his stimulating interest and helpful suggestions.

REFERENCES

1. CALLAWAY J., *Phys. Rev.* **113**, 1046 (1959).
2. AGARAWAL B. K. and VERMA G. S., *Physica* **28**, 559 (1962).
3. SLACK G. A., *Phys. Rev.* **122**, 1451 (1961).
4. KLEMENS P. G., *Solid State Physics*, Vol. 7, p. 1. (edited by SEITZ F. and TURNBULL D.) Academic Press, New York (1958).
5. NAGAMIYA T. YOSIDA K. and KUBO R., *Advanc. Phys.* (edited by MOTT N. F.) **4**, 1 (1955).
6. ERICKSON R. A., *Phys. Rev.* **90**, 779 (1953).
7. DEKKER A. J., *Solid State Physics*, Sec. 11–9. Prentice–Hall, Englewood Cliffs (1957).
8. CASIMIR H. B. G., *Physica* **5**, 495 (1938).

J. Phys. Chem. Solids Pergamon Press 1963. Vol. 24, pp. 1057–1061. Printed in Great Britain.

POWDER NEUTRON DIFFRACTION STUDY OF $LiNbO_3$

YŌICHI SHIOZAKI and TOSHIO MITSUI

Department of Physics, Faculty of Science, Hokkaido University, Sapporo, Japan

(*Received* 21 *February* 1963)

Abstract—Crystal structure of $LiNbO_3$ has been determined using powder neutron diffraction data. Refinements of the two structure models proposed by Bailey have resulted in a unique model, which suggests a disordered distribution of lithium ions in the crystal. A discussion is given of the ferroelectric effect in $LiNbO_3$.

I. INTRODUCTION

IN 1949 MATTHIAS and REMEIKA found a ferroelectric effect in $LiNbO_3$ and $LiTaO_3$.(1) The hysteresis loop observed at 200°C was a perfect rectangle.(2) The saturation polarization was as large as 25×10^{-6} C/cm^2, but it decreased with decreasing temperature(1) probably due to a large coercive field. These crystals were described as belonging to the ilmenite ($FeTiO_3$) structure in old literatures.(3) In 1952 SCHWEINLER(4) assumed that $LiTaO_3$ has the so-called ideal ilmenite structure, and discussed its ferroelectricity using the method which SLATER(5) introduced in his theory of $BaTiO_3$.

In the same year BAILEY(6,7) carried out X-ray studies of $LiNbO_3$ and found that its crystal structure is significantly different from that of ilmenite; the space group of $LiNbO_3$ is $R3c$ while that of ilmenite is $R\bar{3}$, and the sequence of cations along the triad axis (representing an empty site by X) is Nb, Li, X, Nb, Li, X, Nb, ... in $LiNbO_3$ whereas it is Fe, Ti, X, Ti, Fe, X, Fe, ... in $FeTiO_3$. $LiTaO_3$ was found isomorphous with $LiNbO_3$. Bailey, however, could not determine uniquely the position of Nb relative to those of Li and O, and proposed two possible structure models which will be illustrated later in Fig. 1. A difficulty of the X-ray study of $LiNbO_3$ seems to consist in the fact that Nb ion has a much larger atomic scattering factor than Li and O ions; the scattering factors for the forward X-ray scatterings are 36, 2, and 10 in the electron unit for Nb^{5+}, Li^+ and O^{2-}, respectively. The neutron diffraction study has the advantage in this respect because the scattering lengths for slow neutrons are 0·69, −0·18, and 0·58 in unit of 10^{-12} cm for Nb, Li and O nuclei, respectively.(8)

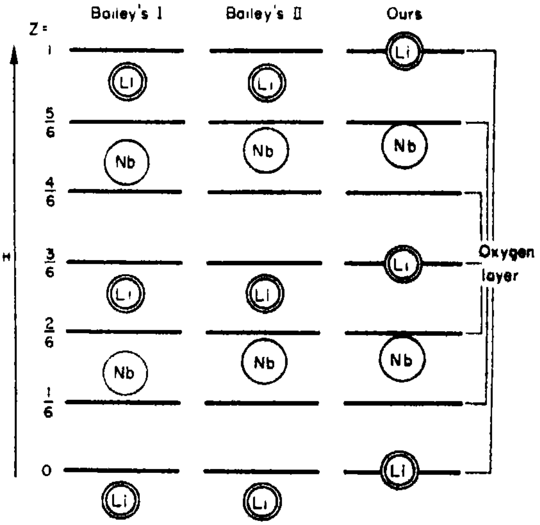

FIG. 1. Cation positions along the *c* axis of the hexagonal unit cell, for the three structure models.

II. STRUCTURE ANALYSIS

Neutron diffraction data have been furnished to us by courtesy of Dr. R. NATHANS of Brookhaven National Laboratory, U.S.A. The neutron beam used had the wavelength of 1·11 Å. Powder $LiNbO_3$ was put in a parallel-sided container, and the transmission method employed. The scanning was made from 12° to 53° in twice the Bragg angle, at room temperature. The absorption coefficient of the specimen was determined by the transmission measurement of the direct neutron beam.

On the diffraction pattern the extinction rule characteristic to the space group $R3c$[9] was recognized. There were eleven well-resolved Bragg peaks along with four peaks each of which was a superposition of two Bragg reflections. The observed structure factor $|F_0|$ was derived for the eleven reflections through the usual procedures including the absorption and Lorentz corrections. The scattering lengths mentioned above were used to obtain the calculated structure factor F_c for each structure model. The scale factor to express $|F_0|$ in unit of 10^{-12} cm was so determined that the relation

$$\sum_{hkl} |F_c| = \sum_{hkl} |F_0|$$

held.

The discrepancy factor

$$R = \sum \Big| |F_0| - |F_c| \Big| / \sum |F_0|$$

was found as high as 0·8 for the ideal ilmenite model assumed by SCHWEINLER,[4] and therefore this model was discarded.

According to BAILEY,[6] the rhombohedral unit cell of $LiNbO_3$ has the lattice parameters of $a = 5{\cdot}4920$ Å and $\alpha = 55° 53'$, and contains two formula units. The space group is $R3c$, and therefore positional parameters are given by[9] Li at (uuu) and $(\frac{1}{2}+u\ \frac{1}{2}+u\ \frac{1}{2}+u)$; Nb at (vvv) and $(\frac{1}{2}+v\ \frac{1}{2}+v\ \frac{1}{2}+v)$; O at (xyz), (zxy), (yzx), $(\frac{1}{2}+y\ \frac{1}{2}+x\ \frac{1}{2}+z)$, $(\frac{1}{2}+z\ \frac{1}{2}+y\ \frac{1}{2}+x)$ and $(\frac{1}{2}+x\ \frac{1}{2}+z\ \frac{1}{2}+y)$.

The first and the second columns of Table 1 give numerical values of these parameters for the two models proposed by Bailey. The structure of $LiNbO_3$ is most easily pictured by use of the hexagonal unit cell, of which the dimensions are $a_H = 5{\cdot}147$ Å, $c_H = 13{\cdot}856$ Å and the contents are six formula-units. The space group symmetry requires six equi-distant oxygen layers in the hexagonal unit cell. In Fig. 1 cation positions are illustrated referring to these oxygen layers.

The discrepancy factor R was fairly low for the two models of Bailey as indicated in Table 1. These two models have been refined by series of least square calculations for the five positional parameters and the scale factor. The electronic computors NEAC 2203G and HIPAC 103 were used for the calculations. The temperature factor was put equal to zero during the machine calculations. First the diagonal approximation[10] was used in the least square calculation, but this approximation turned out to be so bad that it even raised the R factor to about 0·3. This rather surprising result seems to be caused by the facts that the number of data was too few for such an approximation and that the rhombohedral cell axes are not orthogonal to each other.[10] Full matrix refinements[10] produced good results. Bailey's model II shown in Table 1 has been refined by ten cycles of least square calculations with a final R factor of 0·034. The obtained positional parameters are given on the last column of Table 1. The atomic positions are illustrated in Fig. 1 in comparison with Bailey's models. Ten cycles of refinements of Bailey's model I gave crystallographically the same structure as in the case of the model II, with the same R factor of 0·034. In the structure derived from the model I, however, the polarity of unit cell was opposite to that in the structure derived from the model II. In other words, refinements of Bailey's two models resulted in the two twin components (or domains) of $LiNbO_3$. It was tried to estimate the overall temperature factor B by plotting[11] $\log|F_c|/|F_0|$ against $(\sin\theta/\lambda)^2$, but a well defined curve could not be drawn due to scattered data points. A few trial B values did not reduce the R factor, suggesting that B is close to zero. The scanning angle seems to be too small to determine the temperature factor more exactly. In Table 2, comparison is made between the observed and calculated structure factors for $B = 0$.

Table 1. *Atomic coordinates in fraction of the rhombohedral cell edges*

		Bailey's model I	Bailey's model II	Our model
Li	u	0·43	0·43	0·5008
Nb	v	0·23	0·27	0·2788
O	x	0·378	0·378	0·3849
	y	−0·378	−0·378	−0·3557
	z	0	0	−0·0292
R		0·19	0·23	0·034

Table 2. Observed and calculated structure factors in unit of 10^{-12} cm. *Miller indices (hkl) are referred to the rhombohedral unit cell*

hkl	$\lvert F_0\rvert$	$\lvert F_c\rvert$	*hkl*	$\lvert F_0\rvert$	$\lvert F_c\rvert$
110	2·10	2·10	220	2·21	2·11
211	0·61	0·60	312	2·90	2·88
$10\bar{1}$	0·58	0·58	$2\bar{1}0$	1·20	1·37
222	2·73	2·77	302	1·49	1·37
210	2·86	2·78	422	1·11	1·19
200	1·12	1·17			

As mentioned above, on the diffraction pattern there were four peaks each of which was a superposition of two Bragg reflections. $|F_0|$'s of these eight reflections were estimated on the assumption that contribution of each reflection to the observed peak was proportional to the multiplicity factor times $|F_c|^2$, which were calculated with our atomic coordinates given in Table 1. The R factor became 0·046 when these (*hkl*)'s were taken into account in addition to the eleven (*hkl*)'s. This low value of R seems to suggest that our structure model is close to reality.

III. DISCUSSION

As seen in Fig. 1, lithium ion lies on nearly the same plane as oxygens. Figure 2 shows this O and Li plane on the hexagonal (001) plane. The figure was drawn with O^{2-} radius of 1·35 Å and Li^+ radius of 0·60 Å,(12) and demonstrates close contact among ions. There are only three different oxygen–oxygen distances on the (001) plane since the triad axes are at (000), (1/3 2/3 0) and (2/3 1/3 0). Table 3 gives these distances numerically. The oxygen ions are approximately in hexagonal close packing as shown in Fig. 3, where ion arrangement is seen along the c axis of the hexagonal unit cell. The oxygen ions at $z = 3/6$, $4/6$ and $5/6$ are related to those at $z = 0$, $1/6$ and $2/6$ by the c glide plane shown in the figure. Figure 3 was drawn by using the above-mentioned ionic radii and Nb^{5+} radius of 0·70 Å.(12) The cations are all on the (110) plane of the hexagonal unit cell as shown in Fig. 4. The shift of Nb ion from the middle point between oxygen layers (0·399 Å) and the slight deviation of Li ion from the oxygen layer (0·011 Å) are the polar deviation in $LiNbO_3$. The spontaneous polarization of $60{\cdot}7\times10^{-6}$ C/cm^2 was obtained from these shifts assuming that the ionic charges of Nb and Li ions were $+5$ and -1, respectively. It is larger than the value of 25×10^{-6} C/cm^2 observed at high temperatures.(2) It seems doubtful that the interatomic bondings are purely ionic in $LiNbO_3$, and a part of this discrepancy may come from an over-estimation of the charge of the Nb ion. It is interesting to observe the effects of these cation shifts on the oxygen–oxygen distances in Fig. 3. Along the hexagonal c axis, as seen in Fig. 4, the Nb ion lies apart from the oxygen layer at $z = 1/6$ and close to the oxygen layer at $z = 2/6$, resulting in the larger inter-oxygen distances at $z = 2/6$ than at $1/6$ as shown in Fig. 3. The bond lengths are given numerically in Table 3.

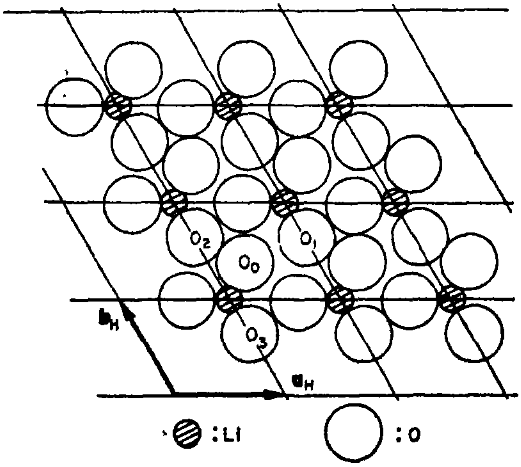

FIG. 2. O and Li layer on the (001) plane of the hexagonal lattice.

Table 3. Bond lengths in $LiNbO_3$. O_0, O_1, O_2 *and* O_3 *are as indicated in Fig.* 2. $O_{1/6}$ *and* $O_{2/6}$ *are the oxygens at* $z = 1/6$ *and* $2/6$ *in Fig.* 3

O_0-O_1	3·028 Å	O_0-Li	1·911 Å
O_0-O_2	2·618 Å	$O_{1/6}-Nb$	2·168 Å
O_0-O_3	3·309 Å	$O_{2/6}-Nb$	1·904 Å

As mentioned above, the Li ion lies approximately on the same plane as oxygen. However, it is doubtful that this position really corresponds to its stable position; there is ample space for Li ion between oxygen layers to where it may be easily squeezed out. Remembering that the

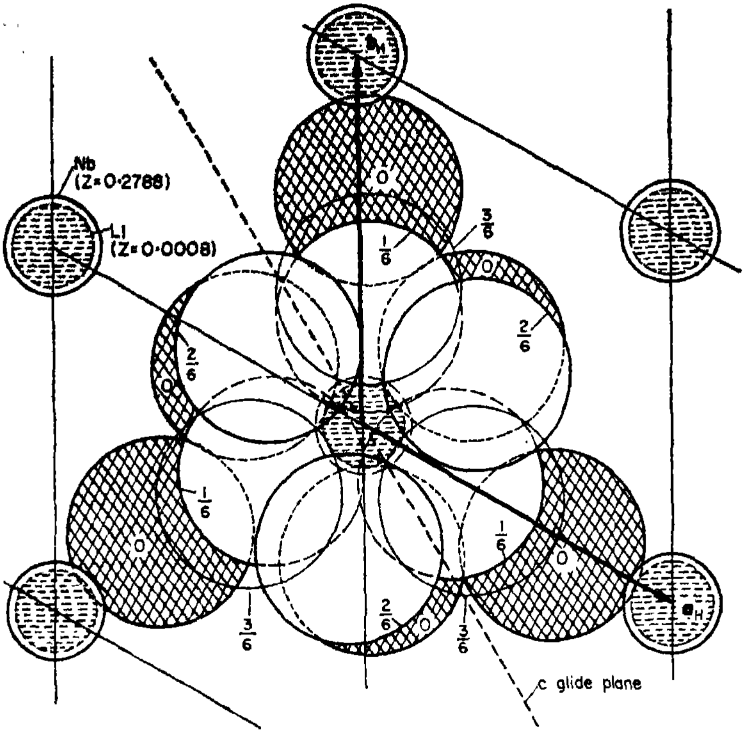

FIG. 3. Packing of oxygens (large circles). The fraction indicates the z-parameter in the hexagonal unit cell.

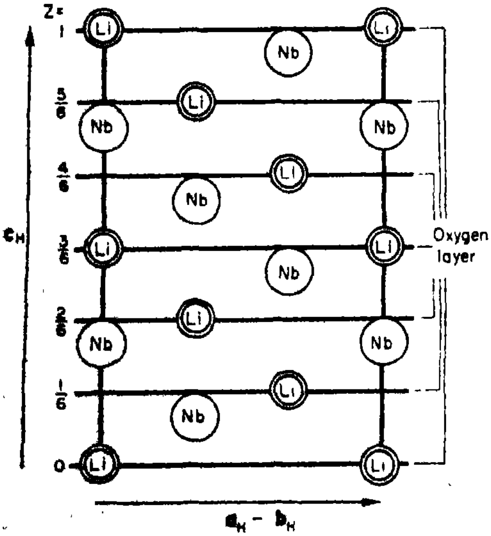

FIG. 4. Cation positions on the (110) plane of the hexagonal unit cell.

structure analysis such as the present one gives only a mean position of each ion, the real crystal structure could be a disordered one as demonstrated in Fig. 5(b), where the fraction of lithium ion means that the ion can be found at that position with the probability of about 50 per cent. Then the paraelectric structure, if it exists, could be as shown in Fig. 5(c). This speculation implies that $LiNbO_3$ has disordered structures in both paraelectric and ferroelectric phases, and that the phase transition is caused by the shifts of Nb ions.

MEGAW[7] discussed the relation of $LiNbO_3$ to $BaTiO_3$ structure on the basis of Bailey's models. She demonstrated that the $LiNbO_3$ structure can be derived geometrically from the perovskite structure by a continuous displacement of atoms. Somewhat similar argument can be made also for our structure model. It is, however, not known whether the large atomic displacement associated with the transition is physically possible. A

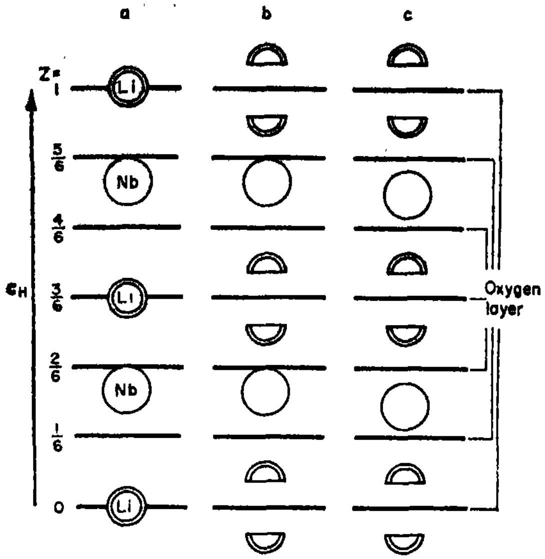

FIG. 5. Plausible disordered structures seen along the *c* axis of the hexagonal unit cell. (a) Mean cation positions in the ferroelectric phase; (b) Plausible disordered structure of the ferroelectric phase; (c) Plausible disordered structure of a paraelectric phase (if it exists).

disordered structure such as shown in Fig. 5(c) seems to be more realistic as a paraelectric LiNbO$_3$ than the perovskite structure.

Acknowledgements—A preliminary part of this work was done by one of the present authors (T.M.) at Brookhaven National Laboratory, Upton, N.Y., U.S.A. He is very grateful to Professor R. PEPINSKY and Dr. B. C. FRAZER for their stimulating discussions, and to Dr. R. NATHANS for his kindness in supplying the neutron data. Thanks are also due to Professor J. FURUICHI for his encouragement and to Mr. K. TOCHINAI for his help in programming of the least square calculations.

REFERENCES

1. MATTHIAS B. T. and REMEIKA J. P., *Phys. Rev.* **76**, 1886 (1949).
2. MATTHIAS B. T., in *Phase Transformations in Solids* (edited by SMOLUCHOWSKI R., MAYER J. E. and WEYL W. A.) p. 340. Wiley, New York (1951).
3. ZACHARIAZEN W. H., *Skr. Norske Vidensk. Akad. Oslo.* I. *Mat-Naturv.* Klasse No. 4 (1928), and WYCKOFF R. W. G., *Crystal Structures* Va5 and VA6. Interscience, New York (1951).
4. SCHWEINLER H. C., *Phys. Rev.* **87**, 5 (1952).
5. SLATER J. C., *Phys. Rev.* **78**, 748 (1950).
6. BAILEY P., Thesis, Bristol (1952), cited in Refs 7.
7. MEGAW H. D., *Acta Cryst.* **7**, 187 (1952), and *Ferroelectricity in Crystals*, p. 103. Methuen, London (1957).
8. BACON G. E., *Neutron Diffraction*, p. 28. Oxford University Press, London (1955).
9. *Internationale Tabellen zur Bestimmung von Kristallstruckturen* **I**, p. 243. Gebrüder Borntraeger, Berlin (1935).
10. For instance, CRUIKSHANK D. W. J., *et al.*, in *Computing Methods and The Phase Problem in X-Ray Crystal Analysis* (edited by PEPINSKY R., ROBERTSON J. M. and SPEAKMAN J. C.), p. 32, Pergamon Press, New York (1961).
11. For instance, LIPSON H. and COCHRAN W., *The Determination of Crystal Structures*, p. 61. Bell, London (1953).
12. PAULING L., *The Nature of The Chemical Bond*, Chap. 13. Cornell University Press, New York (1960). The O^{2-} radius of 1·35 Å was derived from the average O–O distance in crystals showing anion contact (p. 518).

LETTERS TO THE EDITOR

Transition processes in semiconductor lasers

(*Received* 22 *March* 1963)

THERE has been considerable interest in the nature of the electron transitions which occur in gallium arsenide lasers.(1, 2, 3) The three possible types of optical transitions are band-to-band, band-to-acceptor, and donor-to-acceptor. These transitions are illustrated schematically in Fig. 1. NATHAN and BURNS(4) have shown that the recombination process involves an acceptor.

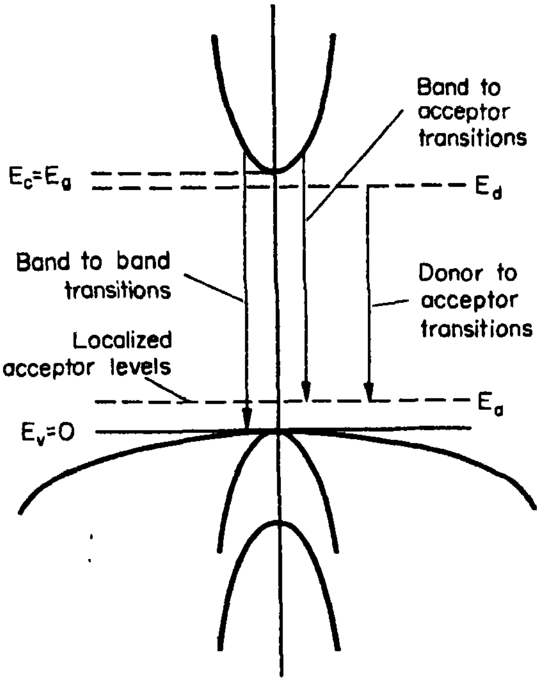
Band to acceptor transitions
$E_c = E_g$
E_d
Band to band transitions
Donor to acceptor transitions
Localized acceptor levels
E_a
$E_v = 0$

FIG. 1. Energy band structure of GaAs showing important optical transitions (not to scale)

Although the original theoretical studies which suggested the feasibility of semiconductor lasers considered only band-to-band transitions,(5) these are not likely to be important. Under normal operating conditions (77°K, $N_A \approx 3 \times 10^{18}\,\text{cm}^{-3}$, $N_D \approx 10^{17}\,\text{cm}^{-3}$), the Fermi level which at absolute zero would be located midway between the valence band and the acceptor levels is only slightly displaced toward the band, so that $\epsilon_F/KT > 2$. Hence the valence band states are occupied with high probability whereas the acceptor states are nearly empty.

In this note we report a calculation of the transition probabilities and absorption constants for the band-to-acceptor and donor-to-acceptor transitions. It is possible, fortunately, to use experimental information concerning the absorption associated with band-to-band transitions(6, 7) in order to determine an important matrix element involved in these calculations. Band-acceptor transitions have also been studied by DUMKE.(8)

The calculation follows the procedures of standard first order time dependent perturbation theory. The wave functions for donor and acceptor states are determined in principle from the theory of LUTTINGER and KOHN.(9) The formal theory of transitions involving impurity states has been given by BOWLDEN.(10) Since no calculations of the acceptor wave functions in GaAs have been reported, it is necessary to assume that these are hydrogenic with an effective Bohr-radius, a_v, determined from the observed binding energy $E_a = 0{\cdot}04$ eV.

We obtain the following absorption coefficient for acceptor-band transitions:

$$\alpha_{a-c} = \frac{32\pi a_v^3 N_a (2m^*)^{3/2} K}{[1+2m^*/\hbar^2\, a_v^2(E_a+\hbar\omega-E_g)]^4} \times \frac{\sqrt{(\hbar\omega+E_a-E_g)}}{\hbar\omega} \tag{1}$$

in which E_g is the band gap and m^* is the effective mass of electrons in the conduction band. The quantity K is given by

$$K = \frac{2e^2|\epsilon \cdot P_{cv}|^2}{\pi^2 m^2 \hbar^2 n \epsilon_0 c} \tag{2}$$

where ϵ is the polarization vector of the electromagnetic field, P_{cv} is the momentum matrix element for band-to-band transitions and n is the index of refraction. K can be determined from optical absorption in the direct transition, since this has an absorption constant.

$$\alpha_{cv} = 2^{3/2}K(\mu_1^{3/2}+\mu_1^{3/2})\frac{\sqrt{(\hbar\omega - E_g)}}{\hbar\omega} \qquad (3)$$

in which μ_1 and μ_2 are reduced effective masses of the conduction band and the heavy and light hole bands. Broadening of the acceptor levels has not been included in (1).

In the case of donor–acceptor transitions, the finite width of the donor and acceptor levels must be explicitly included. This is caused by differences in the local environment of each donor and acceptor. We will assume that this distribution is Gaussian, characterized by a width η. There is an additional parameter in this case: the average overlap integral between donor and acceptor wave functions, which we denote by S_{ad}. In the case $N_d \ll N_a$, we find

$$\alpha_{a-d} = K\frac{2\pi^{3/2}\hbar^2 N_d}{\eta\omega}S_{ad}^2 \exp\left[-\frac{(\hbar\omega + E_a - E_d)^2}{\eta^2}\right] \qquad (4)$$

The overlap integral has been computed for hydrogenic wave functions and its square averaged over a Poisson distribution of donor–acceptor distances. For N_A between 1×10^{18} cm^{-3} and 5×10^{18} cm^{-3}, $S_{ad}^2 \approx 0{\cdot}2$.

We use the experimental value for the band to band transitions[(6)]

$$\alpha_{cv} = \alpha_0\sqrt{(\hbar\omega - E_g)}$$

with

$$\alpha_0 = 3\times 10^4 \text{ cm}^{-}\text{eV}^{-1/2}. \qquad (5)$$

The level width η can be inferred from the experiment of NATHAN and BURNS[(4)] to be $\eta \approx 0{\cdot}017$ eV. We then find for the band-acceptor transitions

$$\alpha_{a-c} = \beta_0\left(\frac{N_a}{10^{18}}\right)\sqrt{(\hbar\omega + E_a - E_g)} \qquad (6)$$

where $\beta_0 = 7\times 10^3$ cm^{-1}/eV$^{1/2}$ and for the donor transitions

$$\alpha_{a-d} = 110 \text{ cm}^{-1}\left(\frac{N_d}{10^{17}}\right)\exp\left[-\frac{(\hbar\omega + E_a - E_d)^2}{\eta^2}\right]$$

The absorption coefficients calculated here seem to be adequately large to permit the operation of a laser.* Direct test of the calculated absorptions would be possible in part through the study of the optical properties of heavily compensated n-type GaAs (although in that case N_a would appear in equation 7 instead of N_d). The acceptor–band transitions discussed here would produce an absorption edge lying approximately 0·04 eV below the principal edge at 1·51 eV at low temperatures. The acceptor-donor transitions would appear as a moderately broad background.

Aeronutronic Division of
Ford Motor Co.,
Newport Beach, Calif.

JOSEPH CALLAWAY†

---

* No account has been taken of the degeneracies of the donor and acceptor states. This should be correct for transitions in which the initial state is a localized acceptor state. When the initial state is in the conduction band, or associated with a donor, the relevant formulae should be multiplied by factors of four and two, respectively.

† Permanent address, Dept. of Physics, University of California, Riverside, California.

References

1. HALL R. N., FENNER G. E., KINGSLEY J. D., SOLTYS T. J. and CARLSON R. O., *Phys. Rev. Letters* **9**, 366 (1962).
2. NATHAN M. I., DUMKE W. P., BURNS G., DILL F. H. and LASHER G., *Appl. Phys. Letters* **1**, 62 (1962).
3. QUIST T. M., REDIKER R. H., KEYES R. J., KRAG W. E., LAX B., MCWHORTER A. L. and ZEIGLER H. J., *Appl. Phys. Letters* **1**, 91 (1962).
4. NATHAN M. I. and BURNS G., *Appl. Phys. Letters* **1**, 89 (1962).
5. DUMKE W. P., *Phys. Rev.* **127**, 1559 (1962).
6. MOSS T. S., *J. appl. Phys.* **32**, 2136 (1961).
7. STURGE M. D., *Phys. Rev.* **127**, 768 (1962).
8. DUMKE W. P., *Bull. Amer. phys. Soc.* **8**, 201 (1963).
9. LUTTINGER J. M. and KOHN W., *Phys. Rev.* **97**, 869 (1955).
10. BOWLDEN H. J., *Phys. Rev.* **106**, 427 (1957).

The distribution of zinc between solid GaSb and Ga–Sb melts

(*Received* 17 *April* 1963)

IN A RECENT paper,[(1)] the distribution coefficient for zinc in the indium–antimony system was shown to depend rather sharply on zinc concentration. The present work was carried out to determine whether similar behavior would be found in the very closely related gallium–antimony system.

The experimental technique used was much the same as that described in the earlier paper. Ingots of GaSb were pulled from Ga–Sb–Zn melts held in silica crucibles under a hydrogen atmosphere. Seed crystals oriented in the ⟨111⟩ direction were used, and single crystals were obtained except at the highest zinc concentrations and for the melts in which the gallium content was less than ~40 at. % or more than ~60 at. %. The pull rate for all samples was 1·3 to 1·5 cm/hr and the rotation speed was 30 to 35 r.p.m. The distribution coefficients were determined using Zn^{65} as a tracer.

A previous determination of the distribution coefficient for zinc in gallium antimonide was reported by Hall and Racette,(2) who obtained a value of 0·3.

The results obtained in the present work for a series of crystals containing $< 1\times10^{19}$ atoms Zn/cm^3 and grown from melts of varying Ga:Sb ratio are shown in Fig. 1. It is apparent that there is a marked effect of gross melt composition on the distribution coefficient. It is known that zinc acts as an acceptor in GaSb and it is generally assumed that the zinc atoms occupy gallium sites. Thus, we might expect the chemical equation

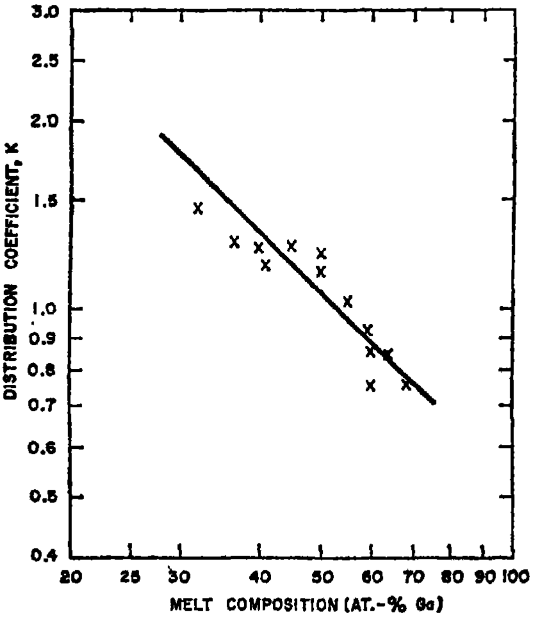

Fig. 1. Distribution coefficients for Zn in Ga–Sb alloys.

$$Zn_l + GaSb_s = ZnSb_s + Ga_l, \qquad (1)$$

where the subscripts l and s refer to the liquid and solid solutions, respectively, to describe the distribution. The equilibrium constant is, then,

$$K' = \frac{\{ZnSb_s\}\{Ga_l\}}{\{Zn_l\}}, \qquad (2)$$

where the braces denote activities and the activity of $GaSb_s$ has been assumed to be unchanged by the small $ZnSb_s$ additions of interest here.

The activity coefficient of $ZnSb_s$ is presumably independent of zinc concentration below 1×10^{19} atoms Zn/cm^3 as evidenced by the measurements described below, and if we assume that the ratio of the activity coefficients for gallium and zinc in the liquid is independent of concentration, then the activities in equation (2) may be replaced by concentrations (denoted by brackets), and we obtain for the distribution coefficient, K,

$$K = \frac{[ZnSb_s]}{[Zn_l]} = \frac{K'}{[Ga_l]}. \qquad (3)$$

The solid line of Fig. 1 has been drawn to agree with equation (3) and shows that a reasonable representation of the data is obtained by choosing $K' = 0{\cdot}55$, for $[Ga_l]$ expressed as an atom fraction. The earlier data on zinc in the In–Sb system do not fit this relationship well, which probably indicates that the necessary assumptions concerning activity coefficients were less well satisfied there than in the present case.

The results of measurements at varying zinc concentration are shown in Fig. 2. They are very similar to those reported and discussed earlier for the indium antimonide case. From the data of Liefer and Dunlap(3) we can estimate an intrinsic electron concentration of about $1\times10^{18}/cm^3$ in gallium antimonide at its melting point. Thus here, as in indium antimonide, the decline in distribution coefficient occurs at a much higher value of zinc concentration than would be expected on the basis of the known

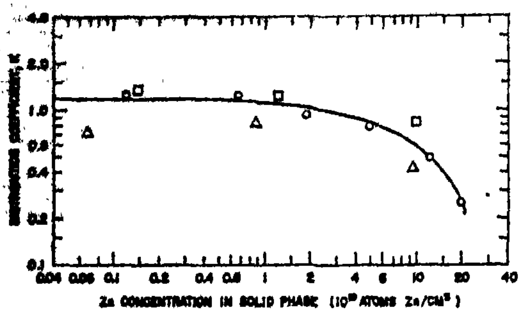

FIG. 2. Dependence of distribution coefficient on Zn concentration.

□ 40 at. % Ga.
○ 50 at. % Ga.
△ 60 at. % Ga.

properties of the pure compound, if the concentration dependence is to be attributed to a donor-electron equilibrium in the bulk solid.

General Atomic Division of General Dynamics Corporation,
John Jay Hopkins Laboratory for Pure and Applied Science,
San Diego,
California

U. MERTEN
A. P. HATCHER

References

1. MERTEN U. and HATCHER A. P., *J. Phys. Chem. Solids* **23**, 533 (1962).
2. HALL R. N. and RACETTE J. H., *J. appl. Phys.* 32, 856 (1961).
3. LIEFER H. N., and DUNLAP W. C., JR., *Phys. Rev.* **95**, 51 (1954).

Neutron diffraction by Li_2MgPb*

(*Received* 22 *April* 1963)

WE PREVIOUSLY reported,⁽¹⁾ on the basis of X-ray diffraction data, that Li_2MgPb had a face centered cubic structure ($a_0 = 6{\cdot}78_1$ Å) with one of three possible atomic arrangements. Assuming lead atoms to occupy the position (0, 0, 0), these arrangements are: Type 1, Mg at $(\frac{1}{2}, \frac{1}{2}, \frac{1}{2})$ and 2 Li at $(\frac{1}{4}, \frac{1}{4}, \frac{1}{4})$ $(\frac{3}{4}, \frac{3}{4}, \frac{3}{4})$; Type 2, Li at $(\frac{1}{2}, \frac{1}{2}, \frac{1}{2})$ and Li and Mg at $(\frac{1}{4}, \frac{1}{4}, \frac{1}{4})$ $(\frac{3}{4}, \frac{3}{4}, \frac{3}{4})$; or Type 3, $\frac{2}{3}$ Li and $\frac{1}{3}$ Mg at $(\frac{1}{2}, \frac{1}{2}, \frac{1}{2})$ and $\frac{2}{3}$ Li and $\frac{1}{3}$Mg at $(\frac{1}{4}, \frac{1}{4}, \frac{1}{4})$ $(\frac{3}{4}, \frac{3}{4}, \frac{3}{4})$. In order to determine which of the arrangements is most probable, we carried out neutron diffraction on powdered samples of the compound in a previously described⁽²⁾ apparatus.

For *h k l* of 111, 200, 220, and 311 of the three arrangements we compare calculated and observed diffracted intensities:

h k l	Calculated Relative intensities Type 1	Type 2	Type 3	Observed intensities
111	74	529	393	521
200	784	39	215	72
220	262	257	306	251
311	47	342	254	323

The formula and coherent scattering amplitudes given by SHULL and WOLLAN⁽³⁾ were used in calculating the intensities. No temperature factors or absorption were included.

These data show that the most probable structure for Li_2MgPb is Type 2. We have not looked for disordering which might lead to the Type 3 structure at higher temperatures.

University of California,
Lawrence Radiation Laboratory,
Livermore, California

WILLIAM J. RAMSEY
DONALD E. SANDS†
S. WARREN MEAD

---

* This work was performed under the auspices of the United States Atomic Energy Commission.

† Present address: Chemistry Department, University of Kentucky, Lexington, Kentucky.

References

1. RAMSEY W. J., *Acta Cryst.* **14**, 1091 (1961).
2. MEAD S. W. and SPARKS J. T., *Conference on Neutron Diffraction in Relation to Magnetism and Chemical Bonding, Gatlinburg, Tennessee*, April 20–22, 1960; abstracted in *Bull. Amer. phys. Soc.* II, **5**, 464 (1960).
3. SHULL C. G. and WOLLAN E. O., *Solid State Physics* (edited by SEITZ F. and TURNBULL D.) Vol. **2**, pp. 143–146. Academic Press, New York (1956).

A comment on the Born model treatment of the polymorphic transitions of the alkali halides*

(*Received* 27 *March* 1963)

IN A recent Born–model treatment of the pressure transition of the potassium and rubidium halides from the NaCl to the CsCl structure$^{(1)}$ it was shown that it is possible to obtain a fit of the pressure–volume relationship of the two phases of each salt around the transition point and to account for the observed values of the mechanical work accompanying the transition, only by allowing for a difference in the parameters entering the Born repulsive energy of the two phases. A subsequent paper of SCHUMACHER$^{(2)}$ seems to contradict this conclusion, insofar as it reports values of the transition pressure, and of the volume change of the NaCl phase up to the transition, in potassium chloride and rubidium iodide which are computed by assuming equal hardness of the Born repulsive energy in the two crystal structures, and are in good agreement with experiment. We should like to point out that, while we were unable to reproduce the Schumacher values for these quantities, the Schumacher choice of repulsive parameters for the CsCl structure implies a disagreement with experiment in the pressure–volume relationship of this phase, and does not account consistently for the observed values of the mechanical work involved in the transition.

Schumacher follows the early work of LÖWDIN$^{(3)}$ in writing the lattice energy of an alkali halide crystal in the form

$$W_L(r) = -\frac{\alpha e^2}{r} + MB\exp(-r/\rho) \qquad (1)$$

The parameter B is then eliminated by means of the equilibrium equation of the static crystal at zero pressure, to obtain the following expressions for the pressure and the Gibbs free energy of the static crystal as functions of the interionic distance:

$$p(r) = \frac{\alpha e^2 r}{3v}\left\{\frac{1}{r_0^2}\exp[(r_0-r)/\rho]-\frac{1}{r^2}\right\} \qquad (2)$$

$$G(r) = -\frac{\alpha e^2}{r}+\frac{\alpha e^2\rho}{r_0^2}\exp[(r_0-r)/\rho]+p(r)v \qquad (3)$$

Equations (2) and (3), which apply separately to the two crystal structures, contain as unknown parameters the interionic distance at zero pressure r_0 for the CsCl structure, and the parameter ρ for both structures. A choice of values for these three parameters allows one also to determine the transition pressure, by finding the intersection of the Gibbs free energy curves of the two structures as functions of the pressure.$^{(3)}$

LÖWDIN$^{(3)}$ assumed a common value of ρ for the two structures, and determined this value for each salt from the compressibility of the NaCl phase at atmospheric pressure. This determination implies a rather good agreement with the experimental pressure–volume relationship of this phase up to fairly high pressures. He then evaluated r_0 for the CsCl structure from the value of r_0 for the NaCl phase by assuming that the pre-exponential parameter B in equation (1) be also common to the two structures. As shown in Table 1, for the salts in question this choice of repulsive parameters for the CsCl structure yields fair agreement with the experimental pressure–volume relationship of this phase, but leads to a gross overestimate of the mechanical work $p_t\Delta v_t$ involved in the transition. In fact, an approximation in which this work is simply taken equal to the difference in lattice energy of the two structures at zero pressure$^{(4)}$ yields values of $p_t\Delta v_t$ which are only about 10 per cent larger.

SCHUMACHER$^{(2)}$ assumes also a common value of ρ for the two structures, taking for it the somewhat arbitrary value 0·345 Å. However, he chooses to determine r_0 for the CsCl structure by simply adding the amount 0·08 Å to the value of r_0 for the NaCl phase.$^{(5)}$ This choice yields values of r_0 for the CsCl structure which are too low: in the potassium and rubidium salts, they are respectively only slightly larger than, and practically equal to, the experimental values of the interionic distance of this phase at the transition point.$^{(6,7)}$ This assumption is equivalent to an underestimate of the parameter B in the CsCl structure, and involves then an overestimate of the absolute value of its Gibbs free energy. This in turn causes a considerable decrease of the computed transition pressure, accompanied by an overestimate of the volume change involved in the transition. The theoretical results for $p_t\Delta v_t$ are fortuitously somewhat improved, but the pressure–volume relation-

---

* Based on work performed under the auspices of the U.S. Atomic Energy Commission.

*Table 1. Parameters of the pressure transition of the potassium and rubidium halides**

	KCl	KBr	KI	RbCl	RbBr	RbI
$p_t \Delta v_t$ (Kcal/mole)	2·0	1·9	1·9	0·7	0·7	0·7
	3·3	3·1	2·9	3·7	3·1	2·7
	2·1	1·9	1·8	1·9	1·7	1·4
$1 - \dfrac{v(\text{NaCl})}{v_0(\text{NaCl})}$	0·085	0·088	0·105	0·030	0·033	0·035
	0·085	0·092	0·108	0·029	0·033	0·035
	0·085	0·092	0·108	0·029	0·033	0·035
$1 - \dfrac{v(\text{CsCl})}{v_0(\text{NaCl})}$	0·197	0·193	0·190	0·170	0·166	0·161
	0·207	0·213	0·228	0·166	0·167	0·177
	0·230	0·238	0·253	0·193	0·198	0·202

* For each quantity, the first row reports the experimental values, taken from BRIDGMAN,(6) and the second and third row report the values computed using respectively the choice of Löwdin and of Schumacher for r_0 in the CsCl structure. The volume changes refer to the experimental transition pressure. The theoretical results have been obtained using the values of ρ reported by Löwdin, which are 0·324, 0·335, 0·350, 0·338, 0·352 and 0·351 Å for the six salts. These agree rather closely with more recent data.

ship of the CsCl phase is misrepresented, as shown in Table 1. The results reported here have been obtained with the Löwdin values for the parameter ρ, but this does not affect the preceding discussion.

Finally, the comparison of the theoretical results reported in Table 1 with the corresponding experimental values displays clearly the opposite shifts of the computed $p_t \Delta v_t$ and of the computed pressure–volume relationship in the CsCl phase, which accompany a change in the pre-exponential parameter B when the hardness ρ of the Born repulsive energy is maintained common to the two crystal phases. These results provide then an independent proof of the fact that a proper Born-model treatment of polymorphic transitions in ionic crystals requires the use of different repulsive parameters for the two crystal structures, to be determined from data on both phases.

Acknowledgements—The author is indebted to Dr. D. P. SCHUMACHER for informative correspondence on his work, and to Dr. F. G. FUMI for helpful discussions.

Argonne National Laboratory,
Argonne, Illinois.
MARIO P. TOSI

References

1. TOSI M. P. and FUMI F. G., *J. Phys. Chem. Solids* **23**, 359 (1962).
2. SCHUMACHER D. P., *Phys. Rev.* **126**, 1679 (1962).
3. LÖWDIN P. O., *A Theoretical Investigation into Some Properties of Ionic Crystals*, pp. 99–103 and Figs 7 and 8. Uppsala (1948); *Phil. Mag. Suppl.* **5**, 140 (1956).
4. BORN M. and HUANG K., *Dynamical Theory of Crystal Lattices*, Section 13. Oxford University Press, London (1954).
5. ZACHARIASEN W. H., unpublished work reported by KITTEL C., *Introduction to Solid State Physics*, Table 3.5. Wiley, New York (1956).
6. BRIDGMAN P. W., *Proc. Amer. Acad. Arts Sci.* **76**, 1 (1945).
7. JACOBS R. B., *Phys. Rev.* **54**, 468 (1938).

BOOK REVIEW

Landolt-Börnstein. Zahlenwerte und Funktionen aus Physik, Chemie, Astronomie, Geophysik und Technik. 6th edition. Volume II: J. Bartels, H. Borchers, H. Hausen, K.-H. Hellwege, K. Schäfer and E. Schmidt (Editors): *Eigenschaften der Materie in ihren Aggregatzuständen* Part 9: *Magnetische Eigenschaften I—Magnetic Properties I.* 35 contributors, edited by K.-H. Hellwege and A. M. Hellwege. Springer, Berlin–Göttingen–Heidelberg (1962) 2256 figures, 935 pp. DM496.

With the ever increasing research activity in science, and especially such potentially useful fields as the solid state, there can be no doubt that comprehensive assemblies of experimental results are nowadays more important than ever. Some impression of the amount of information now available may be gained from the fact that the present volume, covering almost a thousand pages, constitutes only one of ten parts dealing with the bulk properties of matter. It is the first of two volumes on magnetic properties, the second still being in preparation.

The material covered in this volume is grouped into seven sections: (1) The properties of magnetic elements and alloys. (2) Magnetic compounds with definite structures (spinels, garnets, perovskites and hexagonal ferrites). (3) Inorganic compounds with one or several ions with partly filled shells (d-shells, $4f$ ions, actinides). (4) Crystals and glasses with defects (centers and impurities). Semiconductors. (6) Paramagnetic relaxation (spin-lattice and spin-spin). (7) Nuclear magnetic relaxation (gases, liquids, metals, inorganic and organic solids). In each of these fields the coverage includes, where appropriate, both static and resonance magnetic measurements, thermal properties, phase diagrams, and structural details. There are also some very welcome details of chemical purity.

In such a huge compilation of facts several important matters of principle arise, concerning the form of presentation and the detail of coverage which should be attempted. It may be argued that a volume such as this should constitute a completely self contained body of information containing *all* the available data within a given field, and in some ways the present volume attempts this. There are, for example, tables showing all known antiferromagnets with their Néel temperature, Curie–Weiss temperature, magnetic structure and direction of spin axis. A table such as this can be very concise, this particular one listing over 100 compounds in 6 pages plus four for explanatory diagrams and references. Other kinds of information, on the other hand, are very much more difficult to summarize so concisely. There are, for example, many cases in which susceptibility measurements have been reported in the literature simply as empirical results with little or no comment, and the only way this information can be reproduced in a reference volume is by means of a graph or a table of experimental values.

The question now arises whether this is worthwhile. The editors of the present series clearly think it is, and they are not deterred by the fact that this necessarily implies a very large and costly book (over $100 for this one volume). In the reviewer's opinion much of this trouble and expense is wasted. In any serious investigation based on earlier work it is almost always necessary to go back to the original reference for further details of the measurements and results, and the principal value of a reference volume such as this is to draw attention to the simple fact that some work has already been performed in the particular system. Compilations in the form of tables with full cross referencing are often quite adequate for this purpose.

It may now be argued that such abbreviated references already exist and that there is nevertheless a need for a really complete and detailed summary. This may be so, but for this purpose the present volume, in spite of its great length, is probably too *short*. If it really is the intention to provide the reader with all the essential information contained in the original papers, the considerably more text and comment are required than given in several sections of the present volume.

It is clear that the choice between conciseness and completeness is a difficult one to reach and it is one which the editors have here not imposed on their writers. In some cases, such as for example Dillon's excellent article on "Manganese iron oxides with the spinel structure" enough text is provided in the figure captions and short explanatory paragraphs to enable the enquiring reader to form a really clear picture of the present status of knowledge in this field. In contrast to this, several other sections consist mainly of a series of briefly labeled diagrams, which are left to speak entirely for themselves.

The answer to these contrasts probably lies in the fact that certain topics (such as Dillon's) have been defined with enough precision to make a coherent discussion possible, while others have to cover more motley and inconclusive sets of results. Some of these sections might have condensed without serious loss.

One vital feature of a volume such as this is the lists of references which it provides. These should be complete, accurate and easy to find. On the first two of these counts the present volume is quite satisfactory, though it is as always possible to find errors and omissions. The presentation of the references on the other hand is, in the reviewer's opinion, far from satisfactory. One annoying, though not very serious feature, is the fact that a number of different styles of abbreviations are used in different parts of the book. Thus in various sections a paper by Smith 1961 might appear in a table or caption as 61Sm, Sm61, Sm61(2), S61, Sm, or [27]. Much more seriously confusing, however, is the fact that the keys to these abbreviations, i.e., the full references, are grouped according to an equally irregular, and apparently random system. In some sections the references are all grouped into a long list at the end of the section, many pages away from the abbreviations in the text but all on one page. In other sections the references are collected in little groups interspersed into the text, though still not necessarily on the same page as the abbreviation to which they refer. Sometimes single references are scattered into the text. All this makes the finding of references unnecessarily hard. It is clearly a very difficult matter to organize the vast number of references which occur in a book of this kind, but a more unified and convenient system could surely be devised. Collecting larger groups of references on specially marked or colored pages might, for example, be one solution.

It is clearly inevitable that there should be a certain amount of overlap of subject matter (compare for example the figures on pages 3–60 and 3–66 with those on pages 3–261 and 3–266), but a more efficient cross-referencing system in the text might have helped to reduce this. The complete index of substances which forms the last section is extremely useful.

If we have criticized some of the layout of this volume rather severely, it is because this is a unique and very expensive kind of book which cannot afford to be less than perfect if it is to be bought by the individual scientist. One way of making it more attractive to the individual might be to make the different sections available separately. There must be quite a few who are interested in ferrites and not nuclear magnetic relaxation and vice-versa. In its present form it is a must mainly for libraries and institutions.

All in all this is a very workmanlike and extremely useful assembly of a vast number of facts, and we must be grateful to the many contributors who helped to collect them. The printing and reproduction of the figures is uniformly excellent.

WERNER P. WOLF

ERRATUM

G. Simkovich: The nature of point defects in solid lead chloride. *J. Phys. Chem. Solids* **24**, 213–216 (1963).

p. 213 equation (8) should read:

$$\frac{x_{\mathrm{Pb}\square''}}{x^0_{\mathrm{Pb}\square''}} = \left(\frac{x_{\mathrm{Cl}\square^{\cdot}}}{x^0_{\mathrm{Cl}\square^{\cdot}}}\right)^{-2}$$

p. 214, the 2nd line below equation (11) should read:

(11) vs. $\Delta y = y_{\mathrm{KCl}} - y_{\mathrm{LaCl_3}}$, one . . .

p. 214, the first line above equation (15) should read:

letting $x^0_{\mathrm{Cl}\square^{\cdot}} = x^0_{a'\square^{\cdot}}$ for . . .

MEETING ANNOUNCEMENT

A REVIEW of recent work on "Alloying Behavior in Concentrated Solid Solutions" will be held on Monday morning and afternoon, October 21, 1963, at the Statler Hilton Hotel, Cleveland, Ohio, during the fall meeting of the AIME. The speakers and their subjects will be M. H. COHEN, University of Chicago: "Electronic Theories of Solid Solutions;" J. A. RAYNE, Westinghouse Research Laboratories: "Some Electronic Properties of Extensive Solid Solutions;" A. BLANDIN, University of Paris: "Quantum Mechanical Calculations of Size Effects and Interaction Energies in Solid Solutions;" H. W. KING, University of London; "Atomic Volume and Size Correlations in Solid Solutions;" J. W. CHRISTIAN and P. SWANN, Oxford University and U.S. Steel Laboratories: "Stacking Faults in Solid Solutions;" P. HAASEN, University of Göttingen: "Structural Defects in Solid Solutions;" H. SATO, Ford Motor Company: "Long Period Superlattices in Solid Solutions;" and P. DUWEZ, California Institute of Technology: "Non-Equilibrium Structures in Solid Solutions." The program is sponsored by the Committees on Alloy Phases and Chemistry and Physics of Metals, Institute of Metals Division, AIME., and is open for attendance by all. Ten minute abstracts of current alloy research may be submitted to D. A. PARKS, *Secretary, I.M.D., The Metallurgical Society of AIME*, 345 *East 47th Street, New York, U.S.A.*, before June 28, 1963. For other questions concerning this meeting write Dr. T. B. MASSALSKI, *Mellon Institute*, 4400 *Fifth Avenue, Pittsburgh* 13, *Pennsylvania. U.S.A.*

J. Phys. Chem. Solids Pergamon Press 1963. Vol. 24, pp. 1073–1080. Printed in Great Britain.

SILICON HEAVILY DOPED BY ENERGETIC CESIUM IONS

J. O. McCALDIN and A. E. WIDMER

North American Aviation Science Center, Canoga Park, California

(*Received* 25 *April* 1963)

Abstract—Cesium ions of a few kilovolts energy were driven in ⟨110⟩ direction into *p*-type silicon held at 500°C. This treatment introduced donor centers at concentrations $> 4 \times 10^{19}/\text{cm}^3$, even though the solubility of cesium is estimated to be $\lesssim 10^{15}/\text{cm}^3$. This supersaturation was observed to relax very slowly at 500°C, though the damage introduced by the bombardment annealed. Consequently, the diffusivity D_{Cs} at 500°C is estimated to be $\lesssim 10^{-15}$ cm^2/sec (compared to $D_{\text{Li}} = 10^{-7}$ cm^2/sec). Field-effect transistors were fabricated with Cs-bombarded material constituting the "channel". A field-effect carrier mobility about half that of a comparable, phosphorus-diffused channel was observed. A minimum sheet donor concentration of $2 \times 10^{13}/\text{cm}^2$ was indicated in the field-effect measurements, with the likelihood that the actual concentration is appreciably larger. Tracer measurements showed the cesium sheet concentration to be $\sim 6{\cdot}8 \times 10^{14}/\text{cm}^2$. Various evidence suggests that the concentration profile for the donor centers consists of a layer of relatively slowly changing concentration near the surface followed by an exponentially decreasing "tail" at greater depths.

INTRODUCTION

IT HAS been known for many years(1) that a surface exposed to energetic ions not only will lose some of its own atoms by sputtering but will also retain some of the incident ions. Under commonly encountered conditions the retained ions amount to the equivalent of one or more atom layers(2) in the host substance and are distributed(3, 4) over depths of hundreds of atom layers. Thus the chemical concentration of the incident species commonly is of the order of 1 per cent, in a thin surface layer of the host.

The doping effect produced by the interjected specie in the case of a semiconductor host crystal has been considered by several investigators. The early studies(5, 6) of OHL showed that bombarded silicon surfaces behaved very differently in point contact diodes than did conventionally prepared surfaces. The bombarding species used were helium, argon, hydrogen, and nitrogen and, in view of present knowledge, the crystal damage effects attending the bombardment evidently predominated over the chemical effects of the interjected specie.

In 1955 CUSSINS(7) studied a wider variety of bombarding species, directed against germanium substrates. His results suggested "that the only effect of bombardment . . . is the disruption of the surface layers of the germanium lattice to produce defects which can act as acceptors . . .". These defects could be removed by a 500°C anneal in vacuum, but apparently no significant effects due to the chemical nature of the bombarding species were detected.

More recently, several investigators have shown that, under suitable experimental conditions, chemical effects could dominate over damage effects. BREDOV *et al.*(8) deduced from point contact diode measurements that the effects of energetic oxygen and nitrogen ions on germanium and silicon substrates differed due to "microchemical effects". ROURKE *et al.*(9) introduced group III and V dopants into silicon with an ion beam, obtaining doping concentrations estimated at $10^{18}/\text{cm}^3$. ALVÄGER and HANSEN(10) applied this technique to form shallow junctions for use as nuclear particle detectors; their practice of annealing after irradiation caused "appreciable diffusion of the phosphorus . . . thus producing a deeper junction than would have been expected". Junction depths of about 1μ were obtained in silicon by KING and SOLOMON,(11) using one MeV boron ions. BREDOV and NUROMSKII(12), again using point contact diode effects for evaluation, demonstrated that *p*-type silicon with $2\times 10^{15}/\text{cm}^3$ acceptors could be overdoped by 5 or 10 keV lithium ions to form an *n*-type surface layer.

The doping obtained in the investigations cited appears consistent with known solubilities(13) of the dopants. Ion beam technology, however, offers the additional possibility of producing substantial departures from equilibrium. During ion bombardment, the solubility reaction at the surface of the host crystal is driven in the forward direction by energies many magnitudes greater than the thermal energy, kT. In systems where the reverse reactions are relatively slow, strong supersaturation effects could be expected. This prospect was emphasized in the present experiments by the deliberate choice of a dopant with low solubility.

A related interest was reported by STRACK,(14) who studied the enhanced diffusivities of boron and phosphorus in silicon undergoing bombardment. The observed enhancement was presumably the result of greatly increased concentrations of point defects near the surface, probably representing a supersaturation condition for the defect species.

PENETRATION DEPTH

An important consideration for the present experiments is the concentration profile of the penetrating ions. The recent investigations of DAVIES and associates(4, 15) typically indicate a profile that is asymmetric about a most probable penetration depth, R_P. Most of the asymmetry arises from an exponential tail, which has been detected by tracer techniques to depths $\geqslant 5\ R_P$. Current efforts(16) to understand the deeply penetrating component, or "tail", are directed to computer calculations of the phenomenon of "channelling", whereby an incident particle travelling in certain favored crystal directions undergoes only glancing collisions. The calculations have established that $\langle 110\rangle$ directions are most favored in f.c.c. lattices, and a similar result seems probable for the diamond lattice of silicon.

The best estimate* that can be made for the present case of 10 keV Cs^+ ions driven into Si comes from the data of DAVIES *et al.*(4) Their results for the profiles of Cs^+ ions of various energies driven into aluminum targets can be applied directly to silicon, since the Bohr–Nielsen relation† differs by less than 2 per cent for the two target materials. Their data indicates a mean penetration depth, R_M, of 100 Å in the present case, and an exponential tail in which the concentration decreases by a factor of two every $X_{1/2} =$ 55 Å. The data on which these estimates are based come from *polycrystalline* aluminum targets, rather than oriented single crystals, as contemplated in channelling calculations.(16) Since $\langle 110\rangle$ oriented crystals were used as targets in the present experiments, channeling was thereby emphasized and the resulting "half-thickness" distance, $X_{1/2}$, was probably greater than the above estimate.

BOMBARDMENT CONDITIONS

An experimental ion propulsion engine provided the beam of cesium ions for the present experiments.‡ The engine, which was originally designed for thrust studies, operates conventionally, using a porous tungsten contact ionizer. The beam energy could be maintained within ~ 2 per cent of any setting up to 10 keV; the beam density, however, was subject to fluctuations of the order of 20 per cent probably due to electrons travelling the beam.

The engine operated inside a vacuum chamber maintained at ~ 10^{-5} torr. Before commencing a bombardment, cesium was first flowed into the system via the hot tungsten ionizer, but with no accelerating potential applied, for ~ 30 min. By flushing the system with cesium in this way, the partial pressures of other gases were probably reduced; thus, for example, it was observed that all metal surfaces in the chamber became strongly photoemissive to white light. While flushing the system, the silicon specimen was brought up to temperature; then the bombardment was begun.

Certain standard experimental conditions were employed in all the bombardments, except where specified otherwise. These conditions are listed in Table 1. Where a given variable could not be closely controlled or accurately measured, an approximate figure is indicated, or an estimate given for the uncertainty.

The surface of the silicon specimen exposed to the beam was a (110) face within an uncertainty of ~ 2°. Also the specimen was struck by the beam in a perpendicular direction, with an uncertainty of perhaps 2°, judging from shadows cast by the beam in the apparatus.

After bombardment the specimen was stored in a desiccator until just before making electrical measurements. The purpose of the standard storage procedure was to minimize the influence of the ambient gas on the field effect measurements. However, this influence was

---

* Some early measurements of BREDOV *et al.*(17, 18) are neglected here, in view of a later comparative study.(19)

† Page 1543 of Ref. (4).

‡ Courtesy of Rocketdyne, a Division of North American Aviation, Inc.

Table 1. *Standard experimental conditions*

Beam energy	10 keV
Beam density	~ 3 μA/cm^2
Vacuum	~ 10^{-5} torr
Duration of preliminary cesium flushing	~ 30 min
Duration of bombardment	30 min
Direction of bombardment	⟨110⟩, ± 4°
Specimen temperature	~ 500°C
Specimen: Czochralski-pulled Si doped with 4×10^{17}/cm^3 boron	

probably negligible, as indicated by the observation that soaking a specimen in each of several common reagents (nitric acid, hydrogen peroxide, hydrofluoric acid) produced negligible changes.

ELECTRICAL MEASUREMENTS

The bombarded surface was studied principally through its electrical properties. Type-testing with thermo-electric probes clearly showed the Cs$^+$ bombarded regions to have converted to n-type; all other regions of the 500°C silicon not directly in the beam remained p-type. The conversion to n-type was observed regardless of the bulk acceptor doping in the range, $4\times10^{17} \leqslant N_A \leqslant 4\times10^{19}$/cm^3.

To measure the number of donor centers introduced by the bombardment, field-effect transistor structures were fabricated on the specimens. A typical specimen geometry is shown in Fig. 1. Using conventional oxide masking procedures, phosphorus was diffused to form the two contacting "islands" and the field electrode. Using a second oxide masking step, a window was provided so that the Cs$^+$ beam could strike the silicon only in the "channel" region of the transistor structure, as shown in the figure. Elsewhere the Cs$^+$ beam would strike the oxide, causing various deleterious effects on the electrical measurements; these could be remedied, however, by subsequent removal of the oxide.

A four-point probe was used on this structure to measure sheet conductivity. Both the current and the voltage probes contacted the specimen on the diffused islands. Small potentials, typically less than 50 mV, were applied in order to introduce only minimal field effects in the conductivity measurement itself. When a field effect was desired, a given potential was applied to the $n+$ region labelled "field electrode". In the data presented in this paper, this applied potential is reported, rather than the actual potential existing between the bulk p-type and the transistor structure. Thus a small error, perhaps 0·1–0·2 V is present, corresponding to the forward bias at the junction between field electrode and bulk.

A more serious problem in the field effect measurements was the leakage current that flowed between the bulk and the transistor structure when the field voltage was applied. A typical leakage current is shown in Fig. 2, labelled "not guarded". This current would cause a floating potential to exist at one island (for example, the transistor "drain") when the field voltage was applied to the other island ("source"). Thus the field effect measurements had to be limited for each specimen to field voltages producing only comparatively small leakage currents.

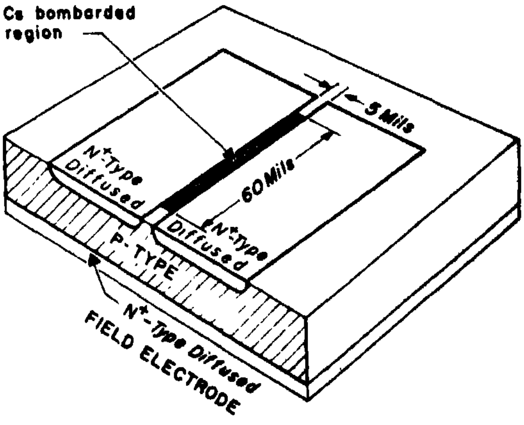

FIG. 1. Specimen geometry for measuring sheet conductivity with field effect.

The field effect on sheet conductivity provides a measure of the sheet charge density in the depleted region of a p–n junction. SHOCKLEY's original paper(19) on the field effect transistor treats the case of an abrupt junction. With minor modification, the same treatment can be applied to the present junctions; we need only replace the abrupt junction by a doping profile with a heavily-doped $n+$ surface layer and lightly p-doped bulk. In such a doping profile, nearly all the junction potential, ϕ = applied voltage$+E_g$, where E_g is the "built-in" potential due to the band gap, occurs in the lightly doped bulk. Using simple junction theory,(20) the sheet density of donor centers in the depletion region is

$$q\int_0^{x_n} N_D\,\mathrm{d}x_n \simeq (2\kappa\epsilon_0 q N_A \phi)^{0.5} \qquad (1)$$

in m.k.s. units, where N_A is the bulk acceptor concentration, N_D is the concentration of donors introduced by Cs^+ bombardment, x_n is the thickness of the depletion layer on the n-side, q is the electronic charge, κ is the dielectric constant, and $\epsilon_0 = 8{\cdot}854\times10^{-12}$ F/m. If sufficient potential could be applied to the junction to "pinch off" the channel, i.e., reduce its sheet conductivity to zero, all donor centers introduced by the bombardment would be accounted for by relation (1). Although leakage and breakdown effects prevent us from applying the full pinch-off voltage, the field effect measurements can be extrapolated to estimate the total donor concentration.

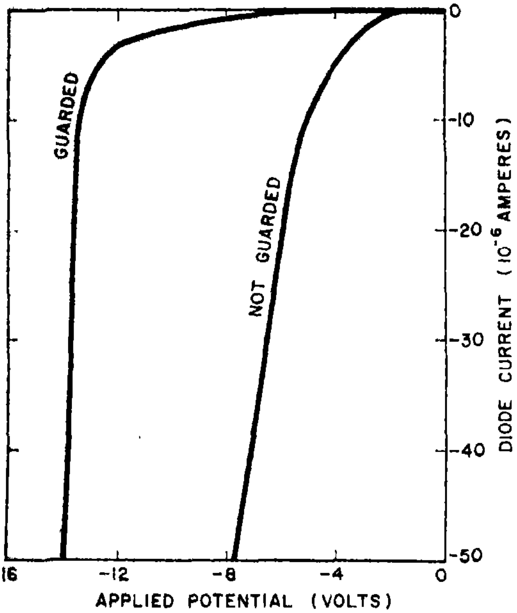

FIG. 2. Typical reverse I/V characteristics between Cs^+ bombarded regions and the p-type bulk. "Not guarded" refers to the geometry of Fig. 1; whereas "guarded" refers to a Cs^+ bombarded region completely surrounded by a phosphorous-diffused ring.

In a few instances the breakdown of these p–n junctions was studied. A guard ring structure was required to obtain the reduced leakage currents indicated in Fig. 2. This structure was fabricated using oxide mask techniques so that a circular region, typically 10^{-2} cm in diameter, of Cs^+ bombarded silicon was surrounded by phosphorus diffused regions. Rather long heat treatment was necessary to reduce the grading of the phosphorus diffusion front and raise the breakdown voltage there above its value in the region of interest.

RESULTS

Using standard experimental conditions, the sheet conductivities shown in Fig. 3 were observed. The abscissa in this figure indicates the applied field voltage and its equivalent in charge density according to relation (1). Using the latter coordinate, the slope in the plots is the so-called field effect mobility. Since the slope is approximately constant, except for very small field voltage, the mobility appears to be constant and amounts to ~ 80 cm^2/V sec; this value corresponds to the bulk mobility observed[21] in n-type silicon doped to a few times 10^{19}/cm^3.

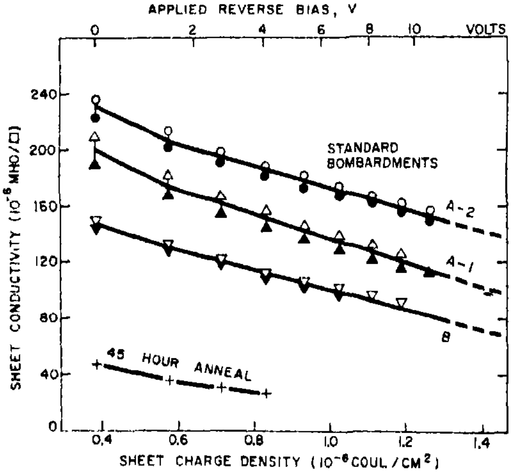

FIG. 3. Sheet conductivity vs. field voltage under standard conditions. Silicon wafer A was processed through the experiment twice; wafer B, once. For comparison, the effect of a 500°C anneal is shown.

The considerable discrepancy between the various bombardments shown in Fig. 3 is instructive. Each silicon wafer contained two complete transistor structures, the results for which are plotted as filled and open symbols in the figure.

The discrepancy between these structures is relatively small. On the other hand, the discrepancy from one bombardment to the next is large, even when the same wafer was reprocessed. Thus the bombardment conditions appear to be the least reproducible feature of the experiments. Some of the bombardment parameters were varied to explore this point. Increasing the time of bombardment to 2 hr made little difference; however, decreasing the time to 6 min reduced the agreement between the two structures on a given wafer and resulted in lower sheet conductivity. Raising the specimen temperature to 700°C had little effect. Lowering the temperature to 300°C, however, caused the sheet conductivity to fall by two to three magnitudes, whereas room temperature bombardment resulted in an apparently intrinsic surface layer. These results at low temperatures correspond to damage effects predominating over the chemical character of the bombarding ion, in agreement with CUSSINS.(7)

Possible annealing effects were also investigated. A 2 hr anneal at 500°C had no effect within the uncertainties just described. A 45 hr anneal, however, caused a fourfold decrease in sheet conductivity, as shown in Fig. 3.

The reverse bias which could be applied was limited by leakage currents and junction breakdown. If the present results are *linearly* extrapolated to pinch off ($\sigma = 0$), however, a total sheet donor concentration of $\sim 3\mu$ C/cm^2, or 2×10^{13} charges/cm^2 is indicated. Linear extrapolation assumes that the carrier mobility (i.e., the slope in Fig. 3) remains constant up to pinch-off. One could expect lower mobility carriers to be encountered when larger biases are applied, however, due to the effects on the mobility of surface scattering and of the increased Coulomb scattering in the more heavily doped layers near the surface. The presence of lower mobility carriers would cause the curves in Fig. 3 to approach the abscissa more gently, at large bias, and thus to indicate a total sheet donor concentration larger than 2×10^{13}/cm^2.

Neutron activation analysis* was used to measure the chemical concentration of cesium. A 3 hr irradiation in a thermal neutron flux of 9×10^{12} neutrons/cm^2 sec was followed by various wet chemical procedures. The gamma activity induced in a bombarded wafer was approximately 100 times greater than in a control (unbombarded) wafer. A cesium concentration of $6{\cdot}8 \times 10^{14}$/cm^2 was indicated. This amounts to nearly one atom layer of the silicon host lattice, and is about 30 times the donor concentration estimated by *linear* extrapolation in the field effect measurements.

The influence of the bulk doping, N_A, was also investigated, all other conditions remaining unchanged. The results are presented in two ways in Fig. 4. First a field effect plot, as in Fig. 3, provides some information about mobilities and charge densities. The simple analysis of relation (1), which assumes $N_D \gg N_A$, becomes increasingly less applicable as the bulk doping is raised. Nevertheless Fig. 4(a) does show clearly, if qualitatively, that less mobile carriers are involved for large values of N_A. Furthermore, extrapolation to estimate the total concentration of donor centers suggests that the latter decreases relatively slowly as N_A is increased.

The zero-bias plot of Fig. 4(b) allows some estimate of asymptotic values for σ and N_D. The maximum value of σ obtainable by decreasing the bulk doping appears to be well under 1000 μ mho/□. On the other hand, the maximum obtainable concentration N_D appears to be of the order of 10^{20}/cm^3. Experimental verification of this point by using larger values of N_A than reported here may be difficult, however, due to the thinness of the *n*-type layers.

Attempts were made to uniformly remove thin surface layers from the wafers, so that only cesium which had penetrated deeply into the wafer would remain. A boiling water/etch cycle(22) was tried, as were several etchants alone. The results were erratic, a frequent difficulty being that the wafer, or part of it, would become passivated. Occasionally, however, a structure was obtained which came close (e.g., within 10 per cent) to pinch off before large leakage currents were encountered.

A more reproducible way to obtain thinner *n*-type layers is to reduce the energy of the bombarding ions. Figure 5 shows the result of reducing the ion energy to 3 keV (with beam density × bombardment time held constant). The observed ~ threefold reduction in ion energy corresponds to ~ fivefold reduction in sheet conductivity and ~ twofold reduction in total donor concentration, as judged by linear extrapolation to pinch off. The effective mobility is lower than under standard conditions, but follows the same trends with bias.

---

* Performed by Union Carbide Nuclear Co., Tuxedo, New York.

For comparison purposes, a few structures were prepared by phosphorus diffusion instead of Cs$^+$ bombardment. The specimens were held at 800°C in P_2O_5 vapor for 5 min and typically became more conducting than the bombarded specimens. However, one phosphorus diffused specimen happened to fall in the same conductivity range as the 3 keV results just described; the two specimens are compared in Fig. 5. Evidently the effective mobility in the phosphorus-diffused specimen is about twice that in the bombarded specimen. An interesting feature of the phosphorus diffusion is the way in which the effective mobility continues to decrease with increasing bias* over the full range of measurement.

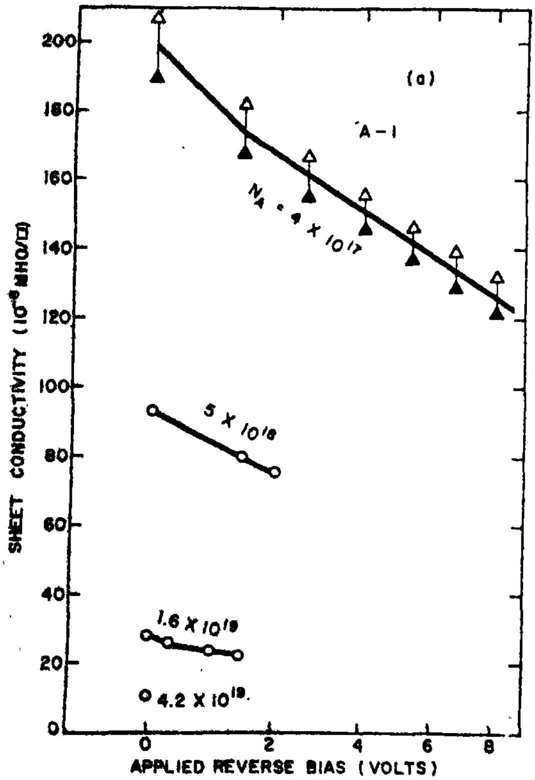

FIG. 4(a)

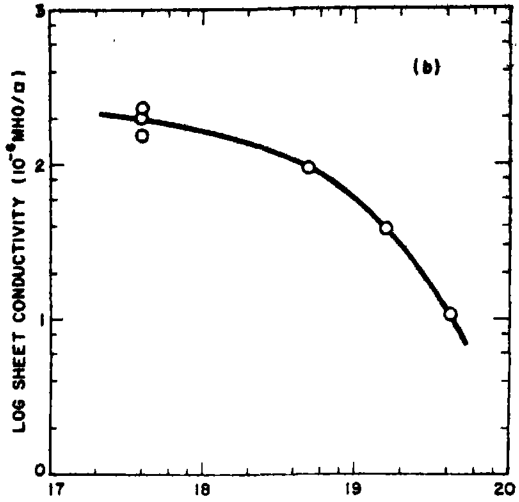

FIG. 4(b). The effect of changing the bulk doping, N_A. (a) The field-effect sheet conductivity at four values of N_A. (b) The zero-bias sheet conductivity vs. N_A.

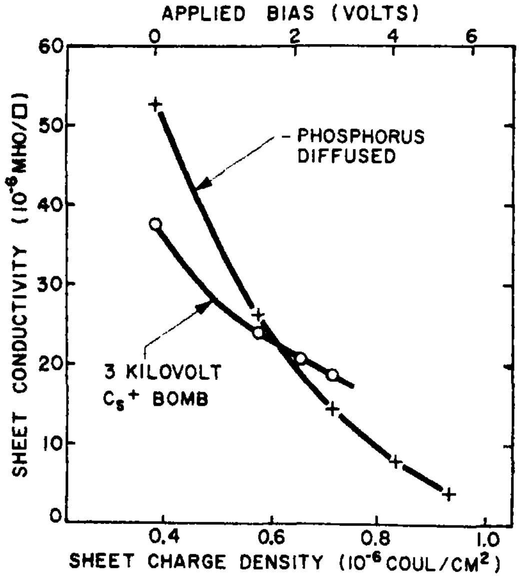

FIG. 5. The effect of lowered ion energy. For comparison the sheet conductivity of a phosphorous diffused layer is shown.

Avalanche breakdown was studied in guard ring structures prepared under standard conditions.

---

* This may be the result of diffuse scattering at the surface.(28)

The breakdown voltage estimated by extrapolating to zero breakdown current was in the range of 13–14 V as can be seen in Fig. 2. This value can be compared to the ~ 7 V breakdown reported(24) for abrupt silicon junctions between $4 \times 10^{17}/\text{cm}^3$ bulk doping and heavy surface doping. Thus the present breakdown voltage suggests a doping gradient more gentle than the abrupt case, at least in the vicinity of the junction.

DISCUSSION

The present experiments show that an alkali atom other than the much-studied lithium(25) can heavily dope silicon. This heavy doping very likely reflects not an equilibrium solubility, but a strong supersaturation. Even lithium, the smallest of the alkali atoms, has a maximum solubility(13) at this temperature of only 2×10^{18} (c.f. to ~ $10^{20}/\text{cm}^3$ reported here). Cesium, being the largest of the stable alkali atoms, is expected to have a much smaller solubility.(26, 27) Probably the best analog to cesium in terms of atom size and valency, among the elements for which solubilities are reported,(13) is gold, with a solubility less than $10^{15}/\text{cm}^3$ at 500°C. Thus, a best estimate for the degree of supersaturation in the present experiments is a factor of 10^5 or possibly more.

Such a strongly supersaturated material could be expected to nucleate precipitates. Lithium-supersaturated germanium, for example, undergoes precipitation at room temperature.(28, 29) In the present case, however, relaxation processes appear to take place only at elevated temperatures, and then rather slowly. This fact suggests that the injected cesium atoms diffuse very slowly. For example, if the effects of the 45 hr anneal corresponded to diffusion of cesium atoms to the free surface, typically less than 500 Å away, the diffusivity at 500°C would be less than 10^{-15} cm^2/sec. Other precipitation processes may be important, e.g., clustering of cesium atoms inside the crystal, but these would also imply a short diffusion length. On the other hand, defect centers created by the bombardment are evidently able to anneal out more easily, as shown by the influence of specimen temperature on sheet conductivity.

Possible structures for the donor center produced by cesium injection can be partly delineated by the present experiments. We do know, for example, that a minimum of one donor is present for ~ 30 cesium atoms injected. Also additional scattering centers are present, compared to conventionally doped silicon, as indicated by reduced carrier mobility. These facts can be fitted by several possible models ranging from that of an isolated cesium interstitial to that of a large complex containing many cesium atoms. The cesium may well be distributed over a variety of such structures, not all of which introduce donor centers under the present experimental conditions. One argument for a simple structure such as the isolated cesium interstitial, however, is the observed small diffusivity. Evidently the location of a cesium atom in the lattice is governed primarily by the original energetic events during injection, and subsequent movements due to thermal energies are rare.

Let us consider now the distribution of donor centers with depth. As a first approximation, the present results indicate an abrupt junction between a heavily doped surface layer and, under standard conditions, a more lightly doped bulk. This situation was assumed in obtaining relation (1) and, to the extent that the plots of Fig. 3 are linear, was confirmed. However, a region of steeper slope is discernible for small bias in Fig. 3, and may correspond to an exponential tail in the doping profile as it approaches the bulk doping. Similarly the breakdown voltage measurements imply that the junction is not strictly an abrupt one. Furthermore the variation in sheet conductivity with bulk doping cannot be explained simply due to compensation but rather indicates grading in the doping profile. These facts suggest a concentration profile for the donor centers like that of DAVIES *et al.*(4) for the cesium itself. Efforts to obtain a quantitative comparison between these profiles are deferred to later experiments, however.

A variety of further experiments are suggested by the present results. The supersaturation observed for cesium injected into silicon may occur in other systems as well. An interesting feature to determine in such systems is the principal mechanism tending to restore equilibrium, whether it be dissolution at the free surface, internal precipitation at impurity sites, defect sites, etc. If the restoring mechanisms are sufficiently weak, it may be possible to obtain supersaturation to macroscopic depths in the host crystal. Aside from this possibility, the surface properties of a supersaturated crystal are themselves of considerable interest. For example, when supersaturated surfaces are admitted to consideration, it should be possible to vary the work function over a wider range. The surface conductivity resulting from supersaturation also can be expected in some systems to cover a wider range than in the equilibrium case, allowing conduction processes to be studied in these systems.

CONCLUSIONS

Electrical measurements were used to characterize the surface layers of silicon suitably exposed to energetic cesium ions. Donor centers at concentrations as high as $\sim 10^{20}/\text{cm}^3$ were found to be present. The donor concentration evidently decreases with depth in the crystal, possibly in the same way as the cesium concentration is reported to do. A field-effect mobility about half that of phosphorus diffused material of comparable doping is observed.

The heavy doping obtained by ion injection represents what is probably a very strong supersaturation. Yet the metastable material produced relaxes only very slowly at temperatures as high as 500°C. Evidently cesium has a diffusivity, D, estimated to be less than 10^{-15} cm^2/sec, at 500°C in silicon.

Acknowledgements—The authors wish to thank R. Steele, whose help with the ion propulsion apparatus was essential; M. Waldner, who provided valuable advice and criticism; R. Rayburn, who assisted in some of the experiments; and H. Reiss, who encouraged us in this work.

REFERENCES

1. Dushman S., *Scientific Foundations of Vacuum Technique*, Chap. 9, 2nd ed. John Wiley, New York (1962); Koch J., *Nature, Lond.* **161**, 566 (1948).
2. DeAngelis H. M., *J. appl. Phys.* **33**, 2657 (1962).
3. Powers D. and Whaling W., *Phys. Rev.* **126**, 61 (1962).
4. Davies J. A., McIntyre J. D., Cushing R. L. and Lounsbury M., *Canad. J. Chem.* **38**, 1535 (1960).
5. Ohl Russell S., *Bell Syst. tech. J.* **31**, 104 (1952).
6. Kingsbury Edwin F. and Ohl Russell S., *Bell. Syst. Tech. J.* **31**, 802 (1952).
7. Cussins W. D., *Proc. phys. Soc. Lond.* **B68**, 213 (1955).
8. Bredov M. M., Lepilin V. A., Schestakov I. B. and Shakh-Budagov A. L., *Sov. Phys. Solid State* **3**, 195 (1961).
9. Rourke F. M., Sheffield J. C. and White F. A. *Rev. Sci. Instrum.* **32**, 455 (1961).
10. Alväger Torsten and Hansen Niels J., *Rev. sci. Instrum.* **33**, 567 (1962).
11. King W. J. and Solomon S. J., Abstract No. 58, *Electron. Div. Abstr. Electrochem. Soc.* May (1962).
12. Bredov M. M. and Nuromskii A. B., *Sov. Phys. Solid State*, **4**, 409 (1962).
13. Trumbore F. A., *Bell Syst. tech. J.* **39**, 205 (1960).
14. Strack Hans, *Bull. Amer. phys. Soc.* **7**, 543 (1962).
15. Davies J. A., McIntyre J. D. and Sims G., *Canad. J. Chem.* **40**, 1605 (1962).
16. Robinson Mark T. and Oen O. S., *Appl. Phys. Letters* **2**, 30 (1963).
17. Bredov M. M. and Okuneva N. M., *Dokl. akad. nauk. S.S.S.R.* **113**, 795 (1957).
18. Bredov M. M., Lang I. G. and Okuneva N. M., *Sov. Phys. Tech. Phys.* **3**, 228 (1958).
19. Shockley W., *Proc. Inst. Radio Engrs.* **40**, 1365 (1952).
20. Shockley W., *Electrons and Holes in Semiconductors*, Van Nostrand, Princeton (1950).
21. Irwin John C., *Bell Syst. tech. J.* **41**, 387 (1962).
22. Beck John W., *J. appl. Phys.* **33**, 2391 (1962).
23. Kingston R. H., quoted by Schrieffer J. R., *Semiconductor Surface Physics* (edited by Kingston R. H.), p. 64. University of Pennsylvania Press, Philadelphia (1957).
24. Maserjian J., *J. appl. Phys.* **30**, 1613 (1959).
25. Reiss H., Fuller C. and Morin F., *Bell Syst. tech. J.* **5**, 535 (1956).
26. Reiss Howard, *J. chem. Phys.* **25**, 681 (1956).
27. Kaus Peter E., *Phys. Rev.* **109**, 1944 (1958).
28. Morin F. and Reiss H., *J. Phys. Chem. Solids* **3**, 196 (1957).
29. Carter J. R. and Swalin R. A., *J. appl. Phys.* **31**, 1191 (1960).

J. Phys. Chem. Solids Pergamon Press 1963. Vol. 24, pp. 1081–1092. Printed in Great Britain.

KINETICS OF OXIDE FILM GROWTH ON METAL CRYSTALS—I.

FORMULATION AND NUMERICAL SOLUTIONS*

A. T. FROMHOLD, Jr.
Sandia Laboratory, Albuquerque, New Mexico

(*Received* 20 *August* 1962; *revised* 25 *March* 1963)

Abstract—A system of coupled diffusion equations can describe oxide film growth. Ideal treatment of surface processes leads to linear-type growth for surface controlled rate, and provides boundary values for the coupled equations for diffusion controlled rate. A comparison of the space charge relaxation time with the monolayer formation time, as well as direct numerical computation, justifies steady-state equations for 100 Å films with defect concentrations less than 1 per cent of the lattice sites. Fourier analysis of the fixed boundary problem provides an iterative solution for Stefan's problem. Numerical solutions for time-dependent interfacial charge densities show a parabolic-type growth for charged particles with an enhanced rate constant ξk, where k is the parabolic rate constant for the diffusion of uncharged particles. The enhancement factor ξ is determined by an electrical potential difference ϕ independent of $L(t)$ developed across the film. The parameters ξ and ϕ depend on relative values of the products of concentration C and mobility μ, increasing with increasing μC for the electronic species and decreasing with increasing μC for the ionic species. Typical values of ϕ and ξ are 0·3 V and 3. For equal values of μC, ϕ is nearly zero and ξ is approximately *one* in the small space charge limit. Non-negligible space charge relative to interfacial charge density decreases ξ. In certain cases, ϕ and ξ depend on $L(t)$, so departures from parabolic growth occur, especially in the transient stages of growth. Numerical solutions for constant external or surface charge fields yield Nth root and logarithmic growth laws. Space charge can aid or hinder growth; this is determined by the contribution of the space charge field to transport and the change in ion distribution for this field. Experimental data for growth of Cu_2O on Cu crystals at 50 and 130°C were fit assuming small space charge.

1. INTRODUCTION

Two categories of protective film growth commonly are observed: parabolic growth at high temperature and a limiting thickness (Nth root or logarithmic-type) growth at low temperature. Although bulk diffusion is recognized as a primary transport mechanism for growth, it is considered to be rate limiting only for parabolic growth, since a parabolic law is obtained from Fick's law for steady-state diffusion of either uncharged particles or neutral pairs. Consequently, attempts have been made to explain logarithmic growth by a number of other mechanisms (e.g., electron tunnelling, nucleation, adsorption kinetics, space charge, and variation of boundary concentrations with film thickness), although none of the proposed mechanisms have been quantitatively successful for large classes of experimental data. The current question seems to be whether oxide film growth is actually rate limited by so many different processes that a different one is applicable for almost any change in metal or environment, or whether most experimental data can be related to several limiting cases of some general phenomena.

Wagner(1a) recognized that growth in the thick film region at high temperatures occurs by the transport of charged species through the film. Fick's law is therefore inapplicable, since the electric field due to the charged species modifies the transport process considerably from diffusion of uncharged species. Unfortunately, the thermodynamic approach used by WAGNER(1b) to explain his experimental data also neglects the large effect on transport of the internal electric field, since each element of volume of the film is considered to be electrically neutral. An alternative derivation of the parabolic law by HOAR and PRICE(2a) and JOST(2b) is based on Ohm's law and the assumption that the free energy release due to chemical reaction at the film interface creates an electrical driving force for mass transport of the charged particles. This approach does not distinguish between a small free energy difference due to a difference in concentration along the concentration gradient and a large free energy release due to chemical reaction at the interface. Thus, a satisfactory explanation for parabolic growth has not yet been given for growth by diffusion of charged particles.

---

* This work performed under the auspices of the U.S. Atomic Energy Commission.

MOTT(3) offered two interesting hypotheses to explain logarithmic growth. These seem to be the only ones proposed which had any possibility of providing a general explanation of logarithmic growth. The first(3a,b) considers growth rate to be limited only by ion diffusion so long as electrons penetrate the film easily by the tunnel effect, but then growth rate decreases rapidly for film thicknesses large enough to limit the tunnel current. This mechanism limits the ultimate film thickness to about 50 Å and causes it to be independent of temperature, contrary to low temperature experimental data.(4) The second hypothesis(3c,d) (sometimes referred to as the MOTT–CABRERA theory) assumes ion transport can occur only by nonlinear diffusion through the film under a very large electric field created by electrons. The electrons are considered to penetrate the film by thermionic emission or the tunnel effect and set up a steady-state thickness-dependent electric field by ionizing adsorbed oxygen. At the present time this approach has not been quantitatively successful in explaining commonly observed kinetics, such as the oxidation of copper(5) at intermediate temperatures.

The present work, based on the macroscopic approach, is an attempt to explain the kinetics of oxidation phenomena in terms of rate being controlled by limiting cases of the interfacial processes and bulk diffusion of several charged species through a homogeneous oxide film in the electric field of these species. The kinetics of growth in this approach are determined somewhat by the variation of the electric field through the film, but especially by the variation of this field with film thickness. Some processes not inherent in the macroscopic approach (e.g., electron tunnelling) are included implicitly since such processes determine to a great extent the variation of the field with film thickness.

Section 2 provides a statement of the film growth problem in terms of mass and charge gradients by using a system of macroscopic diffusion equations coupled through the electric field. Limiting cases of the interfacial reactions are considered to determine rate in certain instances, but in general serve to determine the boundary conditions for the system of coupled equations. The complexity of the problem is reduced greatly by considering the diffusion of only two species and by justifying the steady-state approximation. In Section 3 numerical solutions to this simplified problem are given. The computations for diffusion of charged particles show that a fixed electrical potential difference dependent on the system parameters is established across the oxide film. This results in parabolic growth with a different rate constant ξk from the rate constant k corresponding to diffusion of uncharged particles. Whenever transport of one of the two species cannot occur by diffusion (e.g., at low temperatures), the diffusion current redistributes charge to create an electric field which is modified by the transport mechanism of the other species (e.g., field emission or electron tunnelling). Computations for the simple case of a fixed surface charge field illustrate logarithmic and Nth root behavior of growth for both large and small space charge. This approach is shown to provide a good fit to the intermediate temperature data of RHODIN(4) and of YOUNG, CATHCART and GWATHMEY(5) for the oxidation of Cu crystals. Conclusions are presented in Section 4.

2. DEVELOPMENT OF THE PROBLEM

A. *Coupled equations*

Application of the usual macroscopic diffusion equation to each species diffusing through a planar oxide film together with Poisson's equation and the equation of continuity yields a system of coupled nonlinear partial differential equations. Provided the current J_i in the x-direction of a given species i is independent of the concentration gradient $\partial C_j/\partial x$ of other species C_j $(j \neq i)$, the system of equations applicable to each species can be written as follows:

$$J_i = \mu_i C_i E - D_i \frac{\partial C_i}{\partial x} \tag{1}$$

$$\frac{\partial J_i}{\partial x} + \frac{\partial C_i}{\partial t} = 0 \tag{2}$$

$$E(x,t) = (1/\epsilon) \int_0^x \sum_{i=1}^r q_i C_i(x,t)\,\mathrm{d}x + (1/\epsilon) \sum_{i=1}^r q_i \sigma_i(0,t) \tag{3}$$

$$\sigma_i(0,t) = \sigma_i(0,0) - \int_0^t J_i(0,t)\,\mathrm{d}t \tag{4}$$

$$\sum_{i=1}^r q_i \sigma_i(0,t) + \sum_{i=1}^r q_i \sigma_i(L(t),t) + \int_0^{L(t)} \sum_{i=1}^r q_i C_i(x,t)\,\mathrm{d}x = 0 \tag{5}$$

μ_i = mobility in the oxide film in the x-direction, which is the direction normal to the crystal face.
D_i = diffusion coefficient of the ith species in the x-direction.
E = total electric field at any point in the film.
t = time.
q_i = charge per particle of the ith species.
r = total number of species.
ϵ = dielectric constant of the film.
$\sigma_i(0,t)$ = surface density of the ith species at $x = 0$.

Any externally applied field can be included in one of the terms $q_j\sigma_j$. The Einstein relation holds between the μ_i and D_i. The D_i depend on direction through the oxide and in general can be nonlinear functions of the concentrations of all species in the film.

B. *Boundary conditions*

Boundary conditions appropriate to this system of equations are the bulk concentrations of all species at the film interfaces for all time, the concentrations through the film at $t = 0$, and the interfacial surface charge densities $\sigma_i(0,0)$. Kinetic relations exist between the instantaneous interfacial surface densities and the instantaneous bulk concentrations in the film at the interfaces. The relations are specific to each system and are functions of all the σ_j and C_j at the interface in question as well as temperature, pressure, energies of formation of bulk defects from surface defects, and the number of bulk defects in the film at the interface. Thus, the set of boundary conditions for the equations for transport through the film can be formally replaced by relations involving surface interfacial concentrations.

Ideally, the surface interfacial concentrations can be considered to change with time as a result of four processes:

1. Currents $J_i(\gamma,t)$ of all species to and away from each interface γ, to be determined from the bulk transport equations.
2. Chemical reactions $m_i(\gamma,t)$ of the surface species with each other to increase the film thickness.
3. Decomposition $s_i(\gamma,t)$ of one surface species to form another, such as decomposition of adsorbed molecules into adsorbed atoms, or ionization of adsorbed atoms to form ions.
4. Deposition $p_i(\gamma,t)$ of matter on the surface from the solution (or gas) phase or onto the metal–film interface from the metal. The rate is a function of the flux of incident particles, the energy of adsorption of the particles, the interfacial concentrations, the equilibrium interfacial concentrations, t, pressure and temperature.

The growth rate $\mathrm{d}L(t)/\mathrm{d}t$ of the film is thus established by a combination of bulk diffusion and interfacial reaction rates. In the following subsections this formal treatment is reduced to the cases usually treated, in which rate is determined either by interfacial or steady-state diffusion processes. This illustrates the assumptions and limitations inherent in macroscopic theory, in addition to providing a system of equations amenable to numerical solution.

C. *Surface reaction controlled rate*

Consider the formation of a volatile oxide, or a non-volatile oxide containing macroscopic pores and cracks. Oxygen is readily accessible to the metal surface, so bulk diffusion can be neglected. For low oxygen pressures, the arrival rate p_i can be small compared to the decomposition and reaction rates, and the surface concentration of oxygen ions approaches some small steady-state value. The oxidation rate is then proportional to p_i and the metal oxidizes linearly with time at a rate determined by the temperature and pressure of the system. For higher pressures but a slow decomposition rate s_i compared to the reaction rate, the surface concentration of oxygen ions approaches a steady-state value. Oxidation is then linear in time and proportional to the decomposition rate at the given temperature and pressure. Likewise for high pressures and a rapid decomposition rate compared to the chemical reaction rate, oxidation occurs linearly with time and is proportional to the chemical reaction rate on the interface.

If all surface reactions occur at about the same rate, the sum of the above processes should cause oxidation to be approximately linear in time. Some departures from linearity are expected in the transient stages until the steady-state is reached. Qualitatively, the result of a decrease in concentration or a depletion of one of the species during the oxidation process is obvious. The above discussion applies equally well to the growth of protective oxide films for a bulk diffusion rate much greater than the slowest surface reaction rate. For example, systems in which the oxygen pressure is as low as 10^{-10} mm Hg can be rate limited by the rate of arrival of oxygen molecules at the surface. In general, then, surface controlled oxidation can be expressed

$$L(t) = k't \tag{6}$$

where k' can depend markedly on the temperature and oxygen pressure of the system.

D. *Bulk Diffusion controlled rate*

In most instances the interfacial reactions are rapid compared to bulk diffusion through the film. Then the interfacial concentrations are constant in time and can be obtained from surface equilibrium isotherms such as the one of Langmuir and $\mathrm{d}L(t)/\mathrm{d}t$ depends on the $J_i(\gamma,t)$ produced by the concentration gradients and field in the film. Even for the case where surface reactions are not rapid enough compared with bulk diffusion to be in true equilibrium, it is often a good assumption to consider them to be in some dynamc steady-state (independent of time) determined by the magnitude of the current to the interface and the ambient conditions. For these limiting cases the $C_i(\gamma,t)$ can be assumed to be constant in time (though not necessarily independent) at each interface and therefore provide the boundary conditions for the bulk transport equations.

Since the activation energy for diffusion in a given direction in a nonmetallic film varies with the species, the diffusion of one ionic species usually accounts for almost the entire growth at a given temperature. It should be remembered, however, that a change in temperature can shift the mechanism of growth from diffusion of one ionic species to the diffusion of a different ionic species as symbolized by the exponential dependence of diffusion rate on the ratio of activation energy to temperature and different values of the pre-exponential factor.

The simplest situation for diffusion controlled growth, then, consists in the diffusion of one ionic species with a corresponding electronic current. Only two D_i and two μ_i are then of interest, one relating to the diffusion of the ionic species and one relating to diffusion of the electronic species. These two defects are quite different both physically and chemically, so that the D_1 and μ_1 depend primarily on $C_1(x,t)$, and D_2 and μ_2 depend primarily on $C_2(x,t)$. To a first approximation this dependence on concentration can be neglected, as is usually done in order to obtain results not specifically limited to any one system.

Thus, the problem of diffusion controlled oxidation is reduced to solution of the set of coupled equation (1) through (5) for $i = 1, 2$, with D_i and μ_i constant parameters of the system. The film growth rate is given by

$$\frac{\mathrm{d}L(t)}{\mathrm{d}t} = R\, J_1(\gamma',t) \tag{7}$$

where γ' represents the reaction interface, J_1 is the ionic current and R is the volume of oxide formed per ion which diffuses through the film.

The initial and boundary conditions to be specified are $\sigma_i(0,0)$ and $C_i(x,0)$ [including $C_i(0,0)$ and $C_i(L(0),0)$] with $i = 1,2$.

The solution of this system of equations containing one fixed and one free boundary yields the position of the free boundary in time. This problem differs from the one of STEFAN[(6)] since it contains the nonlinear term involving the electric field which couples the equations. The problem, however, is simplified by the steady-state approximation which is discussed below.

E. *Steady-state approximation*

The total number of defects in an oxide film less than 100 Å thick is fewer than the number required to form a monolayer of the oxide, unless the defect concentration rises to within an order of magnitude or so of the atomic concentration. Essentially all particles for growth must diffuse from one boundary to the other through the entire film. Any departure from steady-state defect concentration in the film can be eliminated by this flux of particles. For the purpose of computing growth rates, then, the steady-state approximation

$$\frac{\partial J_i(x,t)}{\partial x} \simeq 0, \tag{8}$$

should be valid.

A mathematical justification of the steady-state approximation for growth by diffusion of uncharged particles can be obtained in the following manner. Solve the diffusion equation for fixed boundaries by separation of variables. The time dependent portion of the solution is composed of exponential terms, with the longest relaxation time contained in the first term of the series. The ratio of this relaxation time τ to the time T needed for the film to increase in thickness by 1/10 of a monolayer is given by

$$\tau/T \leqslant 10^{-15}\, L(t)\, [C(0,t) - C(L,t)] \tag{9}$$

(see Appendix 1). This ratio is small for thin films except for the unlikely possibility of a concentration within an order of magnitude or so of the atomic concentration. The concentration, therefore, is expected to be nearly steady-state during growth.

The above solution obtained by separation of variables can be extended to diffusion in the presence of a constant field by a simple transformation. The field has the effect of decreasing the ratio τ/T, so the steady-state approximation is better in the presence of a field (see Appendix 1). This approximation gives

$$J(t) = \mu E \left[\frac{C(L(t),t) - C(0,t)\exp(E\mu L(t)/D)}{1 - \exp(E\mu L(t)/D)}\right], \tag{10}$$

which is the current expected if the field due to surface charge (or an external applied field) dominates the contribution to the field made by the inhomogeneous space charge.

A straightforward iterative scheme (see Appendix 2) based on a Fourier series solution for the fixed boundary problem can be used to compute growth rates for the diffusion of uncharged particles in the limit of non-steady-state growth.[(7)] To illustrate the effect of non-steady-state growth, the equation for diffusion in zero field was programmed directly for computer computation. Figure 1 illustrates that the relative amount of retardation from parabolic growth resulting from a defect concentration equal to 1/10 the number of lattice sites is about 1·5 to 2 per cent, independent of film thickness. This shows that the actual amount of deviation is proportional to film thickness, in agreement with equation (9). The rate constant

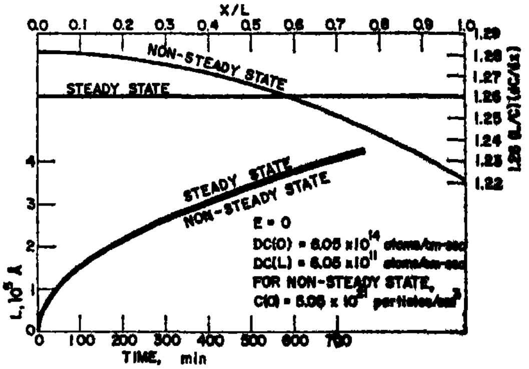

FIG. 1. Comparison of film growth and defect distribution for non-steady-state growth with steady-state (parabolic) values.

$$k = RD\,[C(L(0),0) - C(0,0)] = 1{\cdot}20 \times 10^{-8}\,\frac{\text{cm}^2}{\text{sec}} \tag{11}$$

is the same for the two curves and approximates a Cu_2O film growing at 900°C. Figure 1 shows a plot of $dC(x)/dx$ vs. x (normalized for film thickness) for both the steady-state and non-steady-state conditions. Note the departure from linearity of the concentration vs. x curve for non-steady-state growth, which is the reason that non-steady-state growth is retarded slightly from the parabolic. The normalization shows this departure to be independent of film thickness.

These computer computations confirm the results of the mathematical analysis for conditions of validity of the steady-state approximation given in Appendix 1. Although deviations from parabolic growth have been observed for films as thick as 100,000 Å on copper, the reason is probably local oxygen depletion or some other perturbing effect rather than departure from the steady-state since such effects were observed primarily for the lower oxygen pressures. Defect concentrations as large as one defect per 10 lattice sites are not expected under ordinary circumstances, so the steady-state approximation (although not the equilibrium approximation)(8) should be quite generally valid for film growth computations. At this point the problem of film growth has been reduced to the simplest form for the case of significant space charge. The primary difference between the present formulation and other diffusion treatments is the use of two coupled steady-state diffusion equations rather than a single steady-state diffusion equation to describe growth. The coupling through the electric field term precludes reducing the problem to diffusion of one species only.

3. NUMERICAL SOLUTIONS

A. *Time dependent interfacial charge densities*

Equations (1), (3), (4), (5) and (7) were used in the first series of computations.* Two diffusing species were considered with zero external field. The time-dependent interfacial charge densities were determined from an integral of the boundary values of the diffusion currents according to equation (4). The electric field (units: V/cm) is thus characteristic of the system parameters and results from the tendency of the system to approach equilibrium. Since the field can aid transport of one species and hinder transport of the other, it is self-limiting in magnitude and affects growth rate. Values used for concentrations (units: number/cm^3), mobilities (units: number/cm^2 V sec), and diffusion coefficients (units: number/cm^2 sec) approximate those of the Cu_2O system at 900°C with ϵ chosen to be 18·1 ϵ_0. The bulk concentrations at $x = 0$ and $x = L$ are denoted respectively by $C(0)$ and $C(L)$.

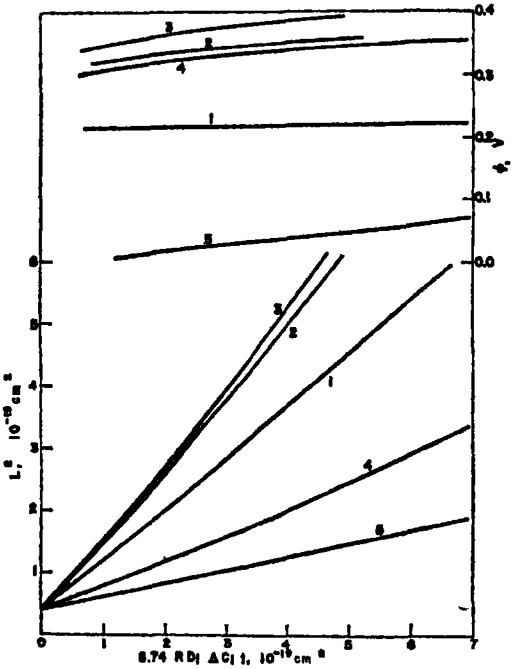

FIG. 2. Oxide film growth and potential developed across film by interfacial charge densities vs. time for different values of the system parameters.

Figure 2 shows the square of the film thickness and the potential ϕ as a function of normalized time for different values of the parameters. It is especially interesting to note that the growth curves are nearly parabolic and the potential ϕ across the film nearly independent of time (and therefore independent of film thickness). The differences in rate can be expressed in terms of an enhancement factor ξ equal to the ratio of $L(t)^2$

---

* Computations were performed on the Sandia Laboratory CDC Model 1604 Digital Computer. Both explicit and implicit methods of solution for the coupled equations were used; the agreement in the results gives us confidence in the accuracy of the solutions.

computed using the coupled equations to the corresponding square of the film thickness $\{2RD_i[C_i(0)-C_i(L)]\}$ applicable for diffusion of uncharged particles. Since the time is normalized for Fig. 2, ξ for a particular curve is proportional to the slope. For all curves shown in Fig. 2, the ratio of the ionic concentrations at the boundaries $C_i(0)/C_i(L)$ is 1000 and the product of diffusion coefficient and concentration at $x = 0$ for electrons $D_eC_e(0)$ is $3{\cdot}75\times10^{18}$.

Curves 1, 2, and 3 of Fig. 2 were obtained by using the same values of D_i, D_e, and $C_i(0)$, but different values of the ratio $C_e(0)/C_e(L)$. The values used are $D_i = 5{\cdot}55\times10^{-5}$, $D_e = 6{\cdot}47$, $D_iC_i(0) = 8{\cdot}77\times10^{13}$, and $C_e(0)/C_e(L) = 10, 100$, and 1000, respectively. The increase in $C_e(0)/C_e(L)$ thus enhances the growth rate, and the values of ξ corresponding to the three curves are 2·40, 3·35 and 3·55. The corresponding values of the electrical potential difference developed across the film also increase, and these are given also in Fig. 2. The maximum values are 0·222, 0·357, and 0·386 V, respectively. Further increases in $C_e(0)/C_e(L)$ to values of 10^4 and 10^5 with the other parameters fixed does not cause ξ and ϕ to deviate from the values corresponding to Curve 3.

Next, a study was made of the effect on growth rate of varying the parameters D_i, D_e, $C_i(0)$, and $C_e(0)$ while keeping the values of $D_iC_i(0)$, $D_eC_e(0)$, $C_i(0)/C_i(L)$, and $C_e(0)/C_e(L)$ fixed at the values used for Curve 3. Three computations were performed, and for each successive computation the values of D_i and D_e were decreased by an order of magnitude and the values of $C_i(0)$ and $C_e(0)$ were increased by an order of magnitude. In all three cases, identical growth and potential curves were obtained which were the same as Curve 3 in Fig. 2. Therefore ξ and ϕ are independent of the values of D and $C(0)$ for the two species provided the respective values of $DC(0)$ and $C(0)/C(L)$ do not change.

Curve 4 of Fig. 2 was obtained by further decreasing the values of D_i and D_e by two orders of magnitude and further increasing $C_i(0)$ and $C_e(0)$ by two orders of magnitude. The values of D_i and D_e are then $5{\cdot}55\times10^{-10}$ and $6{\cdot}47\times10^{-4}$, respectively. Again the other parameters remain fixed at the values used for Curve 3. For the first time in the computations the space charge becomes appreciable with respect to the surface charge: the space charge field (due almost entirely to ions) is about 1 per cent of the surface charge field. Note that both the growth rate and potential have decreased; ξ has the value 1·28. To see whether this effect was due to space charge field, another computation was performed with D_e further decreased by an order of magnitude and $C_e(0)$ increased by an order of magnitude, with all other parameters fixed. The space charge field, still due primarily to ions, was thus unaffected. The computation gave growth and potential curves identical to Curve 4, thereby indicating that the effect of an appreciable space charge field due to ion concentration is to decrease the enhancement factor.

Several computations were performed to study the effect on growth rate of increasing D_i, keeping the values of all other parameters fixed at the values used for Curve 4 in Fig. 2. Curve 5 in Fig. 2 is the one for which D_i was increased by a factor of 500, to the value $2{\cdot}33\times10^{-7}$. This curve is representative and shows that an increase in D_i decreases the growth rate and potential across the film.

A computation (not shown) for $D_iC_i(0) = D_eC_e(0)$ and $C_i(0)/C_i(L) = C_e(0)/C_e(L)$ in the small space charge limit yielded an almost zero potential ($0{\cdot}978\times10^{-5}$ V) and a value of 1·04 for ξ. Therefore, in the absence of an applied field, growth by charged particle diffusion under these particular circumstances is indistinguishable from the case for growth by uncharged particle diffusion.

The most important conclusion obtained from these computations is that experimental data conforming to the parabolic law observed so frequently at high temperatures (e.g., data of BENARD and TALBOT$^{(9)}$ for Cu crystals) is compatible with a growth mechanism based on diffusion of charged particles for both the small and large space charge limits. The potential and enhancement factor are interesting parameters resulting from this analysis; these parameters thus increase with increasing ratio $C_e(0)/C_e(L)$, decrease with increasing D_i, and are independent of the values D_i, D_e, $C_i(0)$, and $C_i(L)$ for fixed values of $D_iC_i(0)$, $D_eC_e(0)$, $C_i(0)/C_i(L)$, and $C_e(0)/C_e(L)$ in the small space charge limit. In the large space charge limit, the space charge field decreases ξ. Zero potential and a unity enhancement factor result for $D_iC_i(0)$

equal to $D_e C_e(0)$ and $C_i(0)/C_i(L)$ equal to $C_e(0)/C_e(L)$ in the small space charge limit.

In some instances, especially in the early stages of growth, ϕ tends to vary with $L(t)$. A steadily increasing ϕ was observed to produce growth rates (not shown) which tended to be linear in time, since the increasing potential for increasing film thickness is equivalent to a continuously increasing enhancement of the diffusion process. This tends to offset the normal decrease in diffusion current with increasing film thickness. It is not believed that this is pertinent to linear-type behavior of oxidation observed for some metals (e.g., aluminum).(10) Probably oxide films corresponding to such behavior contain macroscopic cracks, and the discussion leading to equation (1) is therefore more appropriate.

A potential independent of film thickness is expected to yield parabolic growth in the small space charge limit, as can be seen readily from equation (10), since the relation $\phi = EL$ is therefore valid. A change in rate constant is evident, which is taken into consideration above by the factor ξ. Also, the general behavior of increasing potential and growth rate with increasing ratios of the boundary values of the electron concentration and with decreasing ionic mobility can be understood easily in a qualitative manner. A larger concentration gradient of electrons implies that more electrons flow to the oxide–oxygen interface, thereby creating a larger electric field to enhance ionic transport. Similarly, a relatively larger ionic mobility or concentration gradient causes more ions to flow to the oxide–oxygen interface, which tends to keep the electric field due to electrons to lower values so that enhancement of the ionic transport is less. The decrease in ξ with ionic space charge field is also due in part to the fact that the positive field aiding ionic transport at $x = 0$ is decreased by the equivalent of the total ionic space charge due to neutrality of the total system.

Clearly, then, the factor ξ should depend on a combination of values of concentrations and mobilities of both the ionic and electronic species. This effect results from the coupling between the electron and ion diffusion equations. The correlation between ξ and ϕ is as expected, since the potential (if positive) can aid the transport of ions through the film and thereby enhance the diffusion process.

Perhaps the most feasible way to verify this analysis experimentally is to measure ξ, since a good measurement of ϕ across a growing oxide film would be difficult. A comparison of oxidation rate variations of copper as a function of temperature with the experimental self-diffusion coefficients of the copper species in cuprous oxide(11) indicates a ξ of approximately 3, which is comparable with the values computed above. A more accurate value of ξ could be obtained from such a comparison by measuring the oxidation rate on single crystals in the parabolic region and then measuring the bulk diffusivity of the oxide obtained from further oxidation of the same crystals at the same temperatures. This would eliminate some difficulties in the comparison due to impurities, defect structure, and defect concentration.

B. *Time independent interfacial charge densities*

The second series of computations is based on equations (1), (3) and (7), and this is applicable to oxidation in either an applied field(12, 13, 14) or a surface charge field maintained at a constant value by some process (e.g., field emission or electron tunnelling). The computations are discussed in terms of an applied field, although the results are equally valid for a field created by the surface charge.

Figure 3 illustrates film growth vs. time for

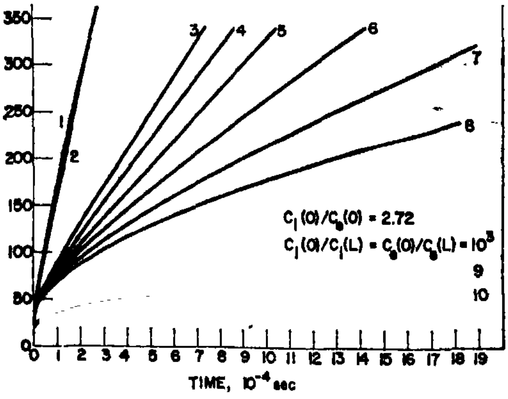

FIG. 3. Oxide growth in the thin film region as a function of defect concentration and external field.
($C_i(0) = 1{\cdot}6 \times 10^{18}$: 2, 6–8, 10;
$C_i(0) = 1{\cdot}6 \times 10^{19}$: 1, 3–5, 9;
$E = 7 \times 10^5$: 1, 2; $E = -7 \times 10^5$: 9, 10;
$E = 5 \times 10^4$: 3, 6; $E = -5 \times 10^4$: 5, 8;
$E = 0$: 4, 7)

several values of the applied field E for values of the concentration differing by an order of magnitude. For these conditions, ions and electrons diffuse from the metal–oxide interface to the oxide–oxygen interface. The net space charge is positive, and $L(0)$ is 20 Å. It can be seen that growth in the largest field (7×10^5) is not affected appreciably by the magnitude of the space charge. This positive field yields a very large growth rate, and the corresponding negative field yields a very small growth rate. For fields of zero and $\pm\ 5 \times 10^4$, however, the field due to the space charge becomes more important than the external field for growth rate. The three curves illustrating growth rates in these fields for ionic concentrations of $1{\cdot}6 \times 10^{18}$ lie below the corresponding three curves for ionic concentrations of $1{\cdot}6 \times 10^{19}$. For both concentrations, the growth rate increases in the order -5×10^4, 0, and $+5 \times 10^4$, as expected. Even in the largest fields the growth rate is somewhat greater for the larger concentration for both positive and negative fields. For films less than several hundred angstroms in thickness under these conditions, then, growth rate increases with increasing field and with increasing concentration, with concentration being the more important factor for fields less than 5×10^4. Increasing concentration would decrease the growth rate in a corresponding manner for a net space charge that is negative instead of positive. Note, however, that the form of the growth curves does not depend as much on space charge as on surface charge.

A set of curves (not shown) for the thick film region (greater than several hundred angstroms) corresponding to the above curves shows a different ordering in growth rates due to the increased effect of space charge. In addition, a redistribution of the ionic space charge in the large space charge field affects growth rate. The growth rate becomes zero for the two curves with largest opposing field and for the curve with $C_i(0) = 1{\cdot}6 \times 10^{18}$ in the opposing field -5×10^4. The limiting film thickness L_∞ for these curves are 93, 96 and 560 Å.

An attempt was made to fit the above computed curves with various types of simple growth equations. For the logarithmic-type curves produced by the opposing fields, $L(t)$ vs. log t and $L(t)$ vs. $\{1-\exp(-\alpha t)\}$ were tried unsuccessfully. The Nth root law $L(t) \sim t^{1/N}$ proved to be a moderately good fit, provided N could vary somewhat with film thickness. The parameter N has values between 1·2 and 13 for the different film thicknesses, concentrations, and electric fields in the above results. In general, the growth falls between parabolic and linear under these conditions for most film thicknesses and fields, with the notable exception of logarithmic-type growth under the opposing field, for which N is quite large. These logarithmic-type curves are qualitatively the same as much published experimental data(4, 5, 15–19) for low and intermediate temperatures.

For low temperatures, the space charge is not expected to be large. Figure 4 shows that the system of equations provides a good fit to intermediate temperature experimental data for growth of Cu_2O on Cu crystals in the small space charge limit. Also shown in the figure is the deviation of the growth curve for cases in which the space charge of ions becomes appreciable. The lower solid curve represents one of the experimental curves of YOUNG, CATHCART and GWATHMEY.(5) The external field needed to fit the data is $7{\cdot}84 \times 10^4$. Note that for this field and this film thickness range, small space charge denotes a value of 10^{16} or less. The curve for 10^{17} ions/cm^3 deviates slightly from the small space charge curve, and the curve for 10^{18} deviates completely from the small space charge curve starting at about 200 Å. The upper solid curve represents one of the experimental curves of RHODIN.(4) The external

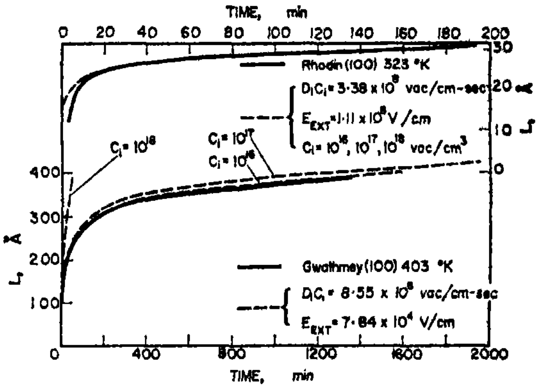

FIG. 4. Comparison of curves obtained for growth in a constant external field with experimental curves for oxidation of copper crystals.

field needed to fit this curve is $1{\cdot}11 \times 10^6$, and the film thickness range is about 30 Å. For this higher field and smaller film thickness, no deviation from the small space charge curve can be observed even for 10^{18} ions/cm^3. Therefore, it is concluded that an acceptable fit can be made to experimental data in the small space charge limit, assuming constant interfacial charge densities during growth.

The assumption of constant interfacial charge densities during growth at intermediate temperatures is reasonable for cases in which the transport of the electronic species occurs by tunnelling. This is discussed thoroughly in a subsequent treatment,(12) and so will not be repeated here. Note that in the small space charge limit, equation (10) is applicable to the diffusing species with E controlled by the *nondiffusing* species. This provides the basis of approximate solutions to the film growth problem, which constitute most of the subsequent paper.(12) Further correlation with low and intermediate temperature experimental data is deferred until then.

Equation (10) shows that for negligible space charge, the external or surface charge field magnitude must be greater than kT/qL for it to be effective for ionic transport with respect to the concentration gradient. For a film thickness of 1000 Å at 180°C, the field can be effective for values of the order of 4000 V/cm. For a film of 100 Å at 1000°C, the field must be of the order of 10^5 V/cm before it can be effective. An effect of electrical field on film growth has been observed(13) for the formation of SiO_2 on Si at 850°C with fields of the order of 10^4 V/cm. It would prove interesting to use this experimental technique to observe the effect of field on the growth of Cu_2O, since negative results(14) were obtained for growth of Cu_2O at 150°C in fields as large as $1{\cdot}55 \times 10^4$ V/cm using a different technique. The effect of the growth rate approaching zero under constant opposing fields noted in the above numerical computations was observed also in the experimental work(13) for the growth of SiO_2 on Si. Such growth curves are not strictly logarithmic, but can be called logarithmic-type since the growth rate becomes negligible in a time less than a few hours. It is interesting to note that growth in an aiding field always deviates from parabolic towards linear growth, so that only opposing fields yield growth curves which approximate low temperature experimental data.

4. CONCLUSIONS

1. A system of coupled diffusion equations rather than a single diffusion equation should be used to describe transport of charged species through homogeneous oxide films in the growth process.

2. The boundary conditions for the system of equations are related to the interfacial densities of the several species, which in turn are determined by interfacial reactions.

3. The steady-state approximation is valid for oxide film growth.

4. For time-dependent interfacial charge densities determined by the dynamic approach of the system to equilibrium, film growth tends to be parabolic in time and a potential nearly independent of film thickness is developed across the film which causes the rate constant to differ from its value for uncharged particles. The values of ϕ and ξ are determined by the parameters of the system.

5. For fixed interfacial charge densities or constant external fields, film growth shows Nth root and logarithmic-type behavior with limiting film thicknesses for large opposing fields.

6. Appreciable space charge with respect to interfacial charge results in a moderate change in growth rate, but has little effect on the type of growth law. The growth law is determined primarily by the variation of the surface charge density with film thickness.

7. High temperature experimental data of Benard and Talbot for oxidation of Cu monocrystals is in agreement with this analysis assuming time-independent bulk concentrations at the boundaries and time-dependent interfacial charge densities determined from the system parameters.

8. Intermediate temperature experimental data of Rhodin and of Young, Cathcart, and Gwathmey for growth of Cu_2O on Cu monocrystals can be reproduced with this analysis by assuming small space charge, time-independent bulk concentrations at the boundaries, and time-independent interfacial charge densities.

Acknowledgements—The author wishes to thank P. B. BAILEY and G. W. PETZNICK for programming the equations for numerical computation, and REGINA FROMHOLD for reducing the results to graphical form.

REFERENCES

1. Wagner C., (a) *Z. phys. Chem.* **B21**, 25 (1933); **B32**, 447 (1936); (b) *Diffusion and High Temperature Oxidation of Metals, Atom Movements* p. 158. American Society for Metals, Cleveland (1951).
2. (a) Hoar T. P. and Price L. E., *Trans. Faraday Soc.* **34**, 867 (1938). (b) Jost W., *Diffusion und Chemische Reaktion im festen Stoffen*, p. 149. Steinkopff, Dresden and Leipzig (1937).
3. Mott N. F., *Trans. Faraday Soc.* (a) **35**, 1175 (1939); (b) **39**, 481 (1939); (c) **43**, 431 (1947); (d) Cabrera N. and Mott N. F., *Rep. Progr. Phys.* **12**, 170 (1948–49).
4. Rhodin T. N., *J. Amer. chem. Soc.*, **72**, 5101 (1950).
5. Young F. W., Cathcart J. V. and Gwathmey A. T., *Acta Met.* **4**, 145 (1956).
6. (a) Kolodner I. I., *Communs. pure appl. Math.* **IX**, 1 (1956). (b) Ham F. S., *J. Phys. Chem. Solids* **6**, 335 (1958).
7. A preliminary report has been given: Fromhold A. T., Jr., *Bull. Amer. phys. Soc.*, **7**, 567 (1962).
8. Fromhold A. T., Jr., *J. chem. Phys.* **38**, 282 (1963).
9. Benard J. and Talbot J., *C.R. Acad. Sci., Paris* **225**, 411 (1948).
10. Gulbransen E. A. and Wysong W. S., *J. phys. Chem.* **51**, 1087 (1947).
11. Grimley T. B., *Oxidation of Metals, Chemistry of the Solid State*, 2nd ed., Chap. 14, p. 350. Butterworths, London (1955).
12. Fromhold A. T., Jr., *Kinetics of Oxide Film Growth on Metal Crystals—II. Homogeneous Field Approximations*, to be published.
13. Jorgensen P. J., *J. chem. Phys.* **37**, 874 (1962).
14. Uhlig H. H. and Brenner A. E., *Acta Met.* **3**, 108 (1955).
15. Cathcart J. V., Hall L. L. and Smith G. P., *Acta Met.* **5**, 245 (1957).
16. Vermilyea D. A., *Acta Met.* **6**, 166 (1958).
17. Uhlig H., Pickett J. and Macnairn J., *Acta Met.* **7**, 111 (1959).
18. Campbell W. E. and Thomas U. B., *Trans. Amer. electrochem. Soc.* **91**, 623 (1947).
19. (a) Smeltzer W. W. and Simnad M. T., *Acta Met.* **5**, 333 (1957); (b) Smeltzer W. W., *ibid.* **7**, 197 (1959).
20. Jost W., *Diffusion*, p. 47. Academic Press, New York (1952).

APPENDIX 1

Conditions for validity of steady-state solution

Choose a period of time T approximately 10 per cent of the time necessary for a monolayer of atoms to diffuse to the surface. For practical purposes the free boundary can be considered to be stationary during T, so that a separation of variables gives a solution valid during T. An iteration using a time increment $\Delta t \leqslant T$ would yield an arbitrarily close approximation to the true solution. The solution for charged species in the presence of a constant external field E neglecting space charge can be obtained from the zero field case using a transformation due to Jost.(20) The result can be shown to be:

$$C(x,t_{j+1}) = C(0,t_{j+1}) + \frac{(C(L,t_{j+1})-C(0,t_{j+1}))(1-\exp(E\mu x/D))}{1-\exp(E\mu L(t_{j+1})/D)} + \exp\left[\frac{\mu Ex}{2D}-\frac{\mu^2E^2\Delta t_{j+1}}{4D}\right]\sum_{n=1}^{\infty}A_n(t_j) \times \exp\left(-\frac{n^2\pi^2D\Delta t_{j+1}}{L(t_j)^2}\right)\sin\frac{n\pi x}{L(t_j)}, \quad (12)$$

where

$$A_n(t_j) = \frac{2}{L(t_{j-1})}\int_0^{L(t_j)}\exp\left(\frac{\mu Ex}{2D}\right) \times\left[C(x,t_j)-C(0,t_j) - \frac{(C(L,t_j)-C(0,t_j))(1-\exp(E\mu x/D))}{1-\exp(E\mu L(t_j)/D)}\right] \times\sin\frac{n\pi x}{L(t_{j-1})}\,\mathrm{d}x, \quad (13)$$

and the j^{th} time increment is Δt_j defined by

$$\Delta t_j = t_{j+1}-t_j. \quad (14)$$

The current is given by

$$J(x,t) = -D\frac{\partial C(x,t)}{\partial x}+\mu EC(x,t), \quad (15)$$

and film growth by

$$L(t)-L(0) = R\int_0^t J(\gamma',t)\,\mathrm{d}t. \quad (16)$$

The above equations also hold for $E = 0$, which is a reduction to Stefan's problem. In this case (13) can be cleared of integrals to yield a straightforward iterative scheme for the solution of Stefan's problem. (See Appendix 2.)

It can be seen from (12) that at any given point in the film *the concentration will decay to its steady-state value* in a time of the order of

$$\tau = \left[\frac{\mu^2E^2}{4D}+\frac{\pi^2D}{L(t)^2}\right]^{-1}. \quad (17)$$

Note that the approach to the steady-state is more rapid the greater the field, so that the steady-state is approached with a time constant as small or smaller than τ_0,

$$\tau_0 = \frac{L(t)^2}{\pi^2 D} \geqslant \tau. \tag{18}$$

The quantity (T/τ) gives a measure of the deviation from the steady-state of the defect concentration introduced by the moving boundary.

Consider two steady-state situations, one in which $L = L(t)$, the second in which $L = L(t+T)$, so that the difference in thickness is approximately 1/10 of a monolayer. Equations (12), (15), and (16) give the growth rate as

$$J(t) = \mu E \left[\frac{C(L(t),t) - C(0,t)\exp(E\mu L(t)/D)}{1-\exp(E\mu L(t)/D)}\right] \tag{19}$$

at $L(t)$, and the same at $L(t+T)$ with $L(t)$ replaced by $L(t+T)$. For a monolayer composed of 10^{15} atoms/cm^2,

$$T \geqslant \frac{10^{14}[1-\exp(E\mu L(t)/D)]}{\mu E[C(L(t),t) - C(0,t)\exp(E\mu L(t)/D)]}. \tag{20}$$

Taking a ratio,

$$T/\tau \geqslant \left[\frac{\mu^2E^2}{4D} + \frac{\pi^2 D}{L(t)^2}\right]\frac{10^{14}}{\mu E} \times \frac{1-\exp(E\mu L(t)/D)}{C(L,t) - C(0,t)\exp(E\mu L(t)/D)}. \tag{21}$$

For zero field this reduces to

$$\frac{T}{\tau} \geqslant \frac{10^{15}}{L(C(0,t) - C(L,t))}, \tag{22}$$

so that the steady-state approximation is valid for defect concentrations less than 10^{21}/cm^3 for a 10 Å film and 10^{20}/cm^3 for a 100 Å film. Therefore, unless the defect concentration rises to within an order of magnitude or so of the number of atoms/cm^3, no departure from the steady-state is expected for thin films. Note from (21) that in the high field limit, i.e.,

$$\frac{E\mu L(t)}{D} \gg 1, \tag{23}$$

then

$$\frac{T}{\tau} \simeq \frac{10^{15}E}{C} \geqslant \frac{10^{15}D}{\mu LC} \simeq \frac{10^{17}}{LC}. \tag{24}$$

A comparison with (22) shows that the field increases the tendency towards steady-state growth.

APPENDIX 2

Iterative scheme for solution of Stefan's problem

Equations (15) and (16) give,

$$\Delta L(t_{j+1}) = DR\,\Delta t_{j+1}\left(\frac{\partial C(x,t_j)}{\partial x}\right)_{x=\gamma'} \tag{25}$$

($E = 0$ throughout this discussion.)
Substituting $t_j = 0$ into equation (13) and integrating gives $A_n(0)$. Substituting equation (12) with t_{j+1} replaced by t_j into equation (13) and performing the integration yields $A_n(t_j)$. Both $A_n(0)$ and $A_n(t_j)$ thereby become free of integrals. Replacing t_{j+1} by t_j in equation (12), differentiating with respect to x, and substituting into equation (25) gives

$$\Delta L(t_{j+1}) = DR\,\Delta t_{j+1}\left[\frac{C(L(0),0) - C(0,0)}{L(t_{j-1})} + \sum_{n=1}^{\infty} A_n(t_{j-1})\exp\left(-\frac{n^2\pi^2 D\Delta t_j}{L(t_{j-1})^2}\right) \times \frac{n\pi}{L(t_{j-1})}\cos\frac{n\pi\gamma'}{L(t_{j-1})}\right]. \quad (t_j > 0) \tag{26}$$

(The ΔL is assumed to have at the time of its formation a defect concentration equal to the bulk defect concentration at the γ' interface.) The iterative procedure is as follows:

- (a) Substitute input parameters $t_0 = 0$, $L(0)$, $C(x,0)$, $C(0,t)$, and $C(L(t),t)$, (plus the constants R and D) into equation (25) with $j = 0$ and into the integrated expression for $A_n(0)$ to obtain $\Delta L(t_1)$ and $A_n(0)$. (Choose $\Delta t < T$, where T is defined in Appendix 1.) Then $L(t_1) = L(0) + \Delta L(t_1)$.
- (b) Compute $A_n(t_1)$ using the integrated expression for $A_n(t_j)$. Compute $\Delta L(t_2)$ using equation (26). Then $L(t_2) = L(t_1) + \Delta L(t_2)$.
- (c) Repeat (b) with j replaced by $j+1$ for each successive step.

It can be seen from these equations that if the steady-state is a good approximation, then

$$L(t) \sim t^{1/2}. \tag{27}$$

Thus the parabolic growth law is justified for the diffusion of uncharged defects in this limiting case.

J. Phys. Chem. Solids Pergamon Press 1963. Vol. 24, pp. 1093–1100. Printed in Great Britain.

SUPERCONDUCTIVITY OF SOME NEW Pt-METAL COMPOUNDS*

CH. J. RAUB, W. H. ZACHARIASEN,† T. H. GEBALLE‡ and B. T. MATTHIAS
University of California, San Diego, La Jolla, California

(*Received* 21 *March* 1963)

Abstract—Several new superconductors were discovered among compounds between Pt-metals and elements of the IV A, V A and VI A group of the periodic system. The position of the elements in the periodic system, the valence electron concentration and the crystallographic structure exhibit a strong influence on the superconducting behavior.

1. INTRODUCTION

AN INTERESTING way of investigating superconductivity is to observe how the superconducting properties of a given compound are changed when one element of the compound is replaced by a vertical or horizontal neighboring element in the periodic system. It is sometimes difficult to find extensive systems where this can be done because not too often do elements of one group show the same alloying behavior as their neighbors. A good series of alloys for this purpose are those of the Pt-metals with most of the elements of the IV A, V A and VI A groups of the periodic system. While the differences between the Pt-metals in their alloying behavior towards those elements are not too different, and many intermediate phases exist, the low temperature behavior of the Pt-metals themselves differs very much among themselves, e.g. Ru, Os, Ir are up to now the only superconductors. Pt and Pd are normal, and show a tendency to become ferromagnetic as indicated by the properties of dilute solutions of Co and Fe in them. This raises the question as to whether these differences in the low temperature behavior of the Pt-metals will also show up in their alloys and compounds.

The work done on the phase diagrams of the Pt-metals with the above-mentioned elements is either rather incomplete(1) or according to our experience, often not too reliable. Since most of the alloying elements are by themselves not superconducting above 0·1°K, occurrence of superconductivity in these alloys can be caused only by a superconducting intermediate phase. The procedure adopted was first to establish the occurrence of any superconducting phases by making three to four test samples whose stoichiometric concentrations were evenly spaced over the interesting concentration range. If any sign of superconductivity was detected, the problem of isolating the compound was attacked further by X-ray, metallographic and more detailed superconductivity investigations.

2. EXPERIMENTAL

Most of the compounds were prepared by heating weighed amounts of both elements up to 1200°C in heavy wall evacuated quartz tubes. This temperature was high enough to melt most of the samples, except some Rh–As and Rh–P alloys. By annealing for 3–4 days at temperatures between 1000 and 1200°C we were also able to get good equilibrium. Pd–Ge alloys were prepared by arc-melting in an argon atmosphere.

The elements used were from the following sources:

Ru —	Varlacoid Chem. Co.	99·8%
Rh —	Johnson Matthey and Co.	99·8%

---

* Research supported in part by the Air Force Office of Scientific Research and the National Science Foundation.

† University of Chicago, Chicago, Illinois.

‡ Bell Telephone Laboratories, Inc., Murray Hill, New Jersey.

Pd — Johnson Matthey and Co. 99·8%
Os — Varlacoid Chem. Co. 99·8%
Ir — Varlacoid Chem. Co. 99·8%
Pt — Johnson Matthey and Co. 99·999%
P — United Mineral and Chem. Co. 99·999%
As — ASAR Co. 99·999%
Sb — ASAR Co. 99·999%
Bi — ASAR Co. 99·999%
S — ASAR Co. 99·999%

Samples prepared were either cooled down slowly, or quenched in water. Sometimes it was necessary to anneal the alloys once more in the powdered form in order to obtain samples which gave sharp X-ray patterns.

The superconductivity measurements were done either with a ballistic method,⁽²⁾ or by the SCHAWLOW–DEVLIN resonance frequency shift technique.⁽³⁾ The latter worked for temperatures above 1·1°K as well as below.

The X-ray Debye–Scherrer patterns were obtained on a General Electric X-ray set XRD5. The powders used had a grain size of 40μ. In all cases they were obtained by careful smashing and grinding of the samples in a steel smasher or ceramic mortar, since all of the samples were brittle.

The covered 2θ range differed from sample to sample, it was normally between 2θ = 10 and 100°. This was found enough to allow a structure identification and/or determination.

RESULTS OF SUPERCONDUCTIVITY MEASUREMENTS (Tables 1, 2, 3)

The samples were checked down to 0·35°K, and by stating not superconducting we mean only to above 0·35°K.

Ru:

We checked Ru alloys with P, As, Sb, Bi at the concentrations Ru_2X and RuX. Since none showed superconductivity no phase evaluation was attempted. According to the available data⁽¹⁾ only RuS_2 and $RuTe_2$ are known. They are probably semiconductors.

Rh:

Rh_5Ge_3 is known to be superconducting at 2·1°K,⁽⁴⁾ and RhGe was found to become so at 0·96°K.⁽¹⁸⁾

In the Rh–As system we found two superconducting phases around the concentration 1:1.

RhAs $T_c = 0{\cdot}58°K$
$Rh_{1\cdot4-1\cdot6}As$ $T_c = 0{\cdot}56$ to below 0·3°K

Earlier an alloy of the concentration Rh_5P_4 was found to be superconducting.⁽¹³⁾ According to our

Table 1. *Superconducting compounds of the* Pt-*metals with the elements of the* IV A *group*

Compound	Transition temperature (°K)	Reference	Crystal structure				
			Type or crystal system	Lattice constants (Å)			Reference
Rh_5Ge_3	2·12	(4)	orthorhombic	$a = 5{\cdot}42$	$b = 10{\cdot}32$	$c = 3{\cdot}96$	(28)
RhGe	0·96	(18)	*B*31	$a = 5{\cdot}70$	$b = 6{\cdot}48$	$c = 3{\cdot}25$	(28)
$RhPb_2$	2·66	(25)	C16				(25)
PdSi	0·93	(18)	*B*31	$a = 6{\cdot}133$	$b = 5{\cdot}599$	$c = 3{\cdot}381$	(18)
Pd_2Sn	0·41	(40)	*C*37	$a = 8{\cdot}12$	$b = 5{\cdot}65$	$c = 4{\cdot}31$	(44)
Pd_3Sn_2	0·47–0·64	(40)	filled NiAs	$a = 4{\cdot}399$		$c = 5{\cdot}666$	(43)
PdSn	0·41	(40)	*B*31	$a = 3{\cdot}87$	$b = 6{\cdot}13$	$c = 6{\cdot}32$	(43)
$PdPb_2$	2·95	(25)	C16				(25)
IrGe	4·7	(4)	*B*31				(4)
Ir_3Ge_7	0·87	(40)					
PtSi	0·88	(18)	*B*31	$a = 5{\cdot}932$	$b = 5{\cdot}595$	$c = 3{\cdot}603$	(18)
PtGe	0·40	(18)	*B*31	$a = 6{\cdot}088$	$b = 5{\cdot}733$	$c = 3{\cdot}701$	(34)
$PtPb_4$	2·80	(25)	$D1_e$				(25)

Table 2. Superconducting compounds of the Pt-*metals with the elements of the* V A *group*

Compound	Transition temperature (°K)	Reference	Crystal structure				
			Type or crystal system	Lattice constant (Å)			Reference
Rh_2P	1·3		*C*1	$a = 5\cdot516$			(41)
$Rh_{1\cdot4-1\cdot6}As$	0·56 − <0·3	(40)	hexagonal	$a = 9\cdot15$		$c = 3\cdot53$	
RhAs	0·58	(40)	*B*31	$a = 5\cdot62$	$b = 3\cdot58$	$c = 6\cdot00$	(11)
RhBi	2·06	(26)	$B8_1$	$a = 4\cdot094$		$c = 5\cdot663$	(26)
$\beta RhBi_2$	3·2	(35)	orthorhombic	$a = 9\cdot027$	$b = 4\cdot24$	$c = 11\cdot522$	(36)
$\gamma RhBi_4$	2·7	(15)					
Pd_3P	0·75	(40)	DO_{11}	$a = 5\cdot18$	$b = 6\cdot00$	$c = 7\cdot46$	(7)
$Pd_{2\cdot3}P$ h.t.	1·00	(40)	rhombohedral	$a = 7\cdot28$		$\alpha = 110\cdot12°$	(40)
$Pd_{2\cdot3}P$ l.t.	0·70	(40)					
Pd_5As_2	0·46	(5)					
Pd_2As h.t.	1·70	(5)	*C*22	$a = 6\cdot65$		$c = 3\cdot58$	(5)
Pd_2As l.t.	0·6	(5)	hexagonal	$a = 9\cdot79$		$c = 6\cdot62$	(5)
PdSb	1·5	(4, 17)	$B8_1$				(4)
PdBi	3·7	(29)	orthorhombic	$a = 7\cdot203$	$b = 8\cdot707$	$c = 10\cdot662$	(30)
$\alpha PdBi_2$	1·7	(19,29)	monoclinic	$a = 12\cdot74$	$b = 4\cdot25$ $\beta = 102° 35'$	$c = 5\cdot665$	(19, 29)
$\beta PdBi_2$	4·2	(19, 29)	tetragonal	$a = 3\cdot362$		$c = 12\cdot983$	(19, 29)
PtSb	2·1	(17)	$B8_1$				(17)
PtBi	1·2/2·4	(17, 27)	$B8_1$	$a = 4\cdot31$		$c = 5\cdot49$	(27)
$\beta PtBi_2$	0·155	(42)	hexagonal	$a = 6\cdot44$		$c = 6\cdot25$	(27)

* Ross and Hume-Rothery(12) could not find this phase.

Table 3. Superconducting compounds of the Pt-*metals with the elements of the* VI A *group*

Compound	Transition temperature (°K)	Reference	Crystal structure		
			Type or crystal system	Lattice constant (Å)	Reference
$Rh_{17}S_{15}$	5·8	(13)	cubic	$a = 9\cdot911$	(37)
$RhSe_{1\cdot75}$	6·0	(31)	*C*2	$a = 6\cdot015$	(38)
α-$RhTe_2$	1·51	(13, 31)	*C*2	$a = 6\cdot441$	(39)
$Pd_{2\cdot2}S$	1·63	(40)	cubic	$a = 8\cdot93$	(32)
$Pd_{2\cdot50}Se$	2·3	(33)			
PdTe	2·3	(4)	$B8_1$		(4)
$PdTe_2$	1·53	(20)	*C*6		(20)

investigations the concentration of the superconducting phase is more likely Rh_3P ($T_c = 1{\cdot}3°K$).

None of the many Rh–Si, Rh–Sn and Rh–Pb compounds were investigated.

Pd:

Samples of the concentrations Pd_2Ge and Pd_5Ge_3 are not superconducting. We found a trace of a superconducting phase near $PdGe_{1\cdot5}$, which up to now we have not been able to isolate.

The superconducting phases in the system Pd–Sn are

Pd_2Sn	$T_c = 0{\cdot}41°K$
Pd_3Sn_2	$T_c = 0{\cdot}47–0{\cdot}64°K$
$PdSn$	$T_c = 0{\cdot}41°K$

The previously reported structure data(43, 44) of these phases were confirmed. Since no reliable information about the phase diagram is available, the presence of superconducting filaments in one or the other of these compounds, which themselves might be non-superconducting, cannot be excluded.

In the Pd–P system three superconducting phases were found, Pd_3P, and Pd_7P_3 in two temperature modifications, which were obtained by either a rapid quench from 750°C in a high-temperature modification or by annealing at 400°C in the low-temperature form.

Pd_3P shows a homogeneity range between $Pd_{3\cdot0}P$ and $Pd_{3\cdot2}P$. The transition temperature has a maximum of 0·75°K at the P-rich side of the homogeneity range, and drops down below 0·35°K at the Pd-side. Pd_3P is highly sensitive to impurities and, for instance, addition of 0·5 wt% Fe destroys superconductivity completely. More detailed investigations about the properties of Pd_3P are under way and will be published later.

Pd_7P_3 exists in a high and low temperature modification, both are superconducting:

Pd_7P_3 h.t.	$T_c = 1{\cdot}00°K$
Pd_7P_3 l.t.	$T_c = 0{\cdot}70°K$

While Pd_3As is not superconducting, Pd_5As_2 and the two forms of Pd_2As become so at:

	T_c(°K)
Pd_5As_2	0·46
Pd_2As h.t.	1·70
Pd_2As l.t.	0·60

An alloy of the composition Pd_5Sb_3 (quenched from 600°C) has been found to be not superconducting, so that the only superconducting compound in this system is PdSb.(4) $PdSb_2$ has been reported to be superconducting.(18) We rechecked alloys around this concentration and did not detect superconductivity. It is likely, that the erroneous superconductivity of $PdSb_2$ was caused by filaments of PdSb.

The compound $Pd_{2\cdot2}S$ (quenched from 750°C) becomes superconducting at 1·63°K. $Pd_{2\cdot8}S$ and PdS are not superconducting.

Os:

Besides the existence of OsP_2 no information about any other compounds was found. Judging from Ru it is rather unlikely that many phases are superconducting.

Ir:

Only IrGe ($T_c = 4{\cdot}7°K$)(17) is known to be superconducting. An alloy of the nominal composition Ir_3Ge_7 ($T_c = 0{\cdot}87°K$) shows some superconductivity. None of the alloys Ir_2X and IrX (S = P, As, Sb, Bi) is superconducting.

Pt:

Neither $Pt_{20}P_7$ nor Pt_2As_3 and $PtAs_2$ are superconductors above 0·35°K. A trace of a superconducting phase was found in an alloy of the composition PdP_2, but we could not isolate it.

STRUCTURE DETERMINATIONS (Table 2)

In the following we are dealing only with phases whose structures were up to the present unknown, or which are interesting in connection with superconductivity.

Rh–As:

$Rh_{1\cdot4-1\cdot6}As$ This phase shows a homogeneity range as found by QUESNEL and HEYDING.(10) Its structure is hexagonal of an unknown type. We determined:

	a (Å)	c (Å)
$Rh_{1\cdot6}As$	9·32	3·67
$Rh_{1\cdot4}As$	9·15	3·53

At $Rh_{1\cdot4}As$ there are weak lines corresponding also to a variant with $a = 9{\cdot}15$ Å $c = 5{\cdot}19$ Å, indicating stacking disorder in the structure. Ideal composition of the phase may be $Rh_{12}As_7$, with vacancies in the metal sides. On the other hand, we found that the diffraction pattern of an alloy

$Rh_{1\cdot7}As$—quenched from 750°C—showed two phases: The orthorhombic Rh_2As compound and the $Rh_{1\cdot6}As$ phase.

RhAs Orthorhombic Type B31 (MnP)
$a = 5{\cdot}65$ $b = 3{\cdot}58$ $c = 6{\cdot}00$ Å
HEYDING and CALVERT found:(11)
$a = 5{\cdot}62$ $b = 3{\cdot}58$ $c = 6{\cdot}00$ Å

Pd–P:

Pd_3P Orthorhombic Type Fe_3C (DO_{11})
Values at $Pd_{3\cdot0}P$

$a = 5{\cdot}18$ $b = 6{\cdot}00$ $c = 7{\cdot}46$ Å

(these values may be 0·3 per cent too high)

RUNDQVIST and GULLINAN reported for $Pd_{3\cdot0}P$(7)

$a = 5{\cdot}16_4$ $b = 5{\cdot}98_0$ $c = 7{\cdot}44_0$Å

According to our investigations the limit of homogeneity is $Pd_{3\cdot0}P$. It extends to the Pd rich end.

Pd_7P_3 (high temperature form)
This is the compound designated Pd_5P_2 by WIEHAGE *et al.*(8)
Rhombohedral unknown type
Hexagonal axes

$a = 11{\cdot}94$ Å $c = 7{\cdot}04$ Å

Rhombohedral

$a = 7{\cdot}28$ Å $\alpha = 110{\cdot}12^0$

The composition is probably Pd_7P_3 with two molecules in the rhombohedral unit cell. Density measurements confirmed the formula Pd_7P_3.
The diffraction pattern of the low temperature modification of Pd_7P_3 (transformation temperature between 400 and 700°C) has not yet been identified.

PdP_2 According to powder and single crystal investigations we found PdP_2 to crystallize monoclinic, space group

$a = 6{\cdot}207$ Å $b = 5{\cdot}857$ Å
$c = 5{\cdot}874$ Å $\beta = 111{\cdot}80^0$

4 molecules per unit cell

RUNDQVIST(9) found
$a = 6{\cdot}777$ Å $b = 5{\cdot}856$ Å
$c = 6{\cdot}206$ Å $\beta = 126{\cdot}42$
and a possible space group *C2/c* or *Cc*.

Pd–As:

Pd_3As The data of SCHUBERT(6) were confirmed:
It crystallizes tetragonal with the Fe_3P (DO_e) structure.
$a = 9{\cdot}986$ $c = 4{\cdot}83_0$ Å

Pd_5As_2 The pattern was not evaluated.

Pd_2As (above 480°C)
Hexagonal Type Fe_2P (C 22)
$a = 6{\cdot}65$ $c = 3{\cdot}58$ Å

Pd_2As (below 480°C)
Hexagonal unknown type*
$a = 9{\cdot}79$ $c = 6{\cdot}62$ Å

DISCUSSION

One of the interesting phenomena of finding superconductivity among compounds of the Pt-metals with the elements of the IV, V and VI group of the periodic system lies in the fact that it occurs nearly exclusively at concentrations of about A_2B or AB, without regard to the electronic structure of the platinum metal (Fig. 1).

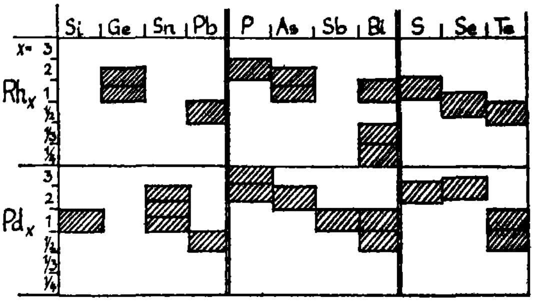

FIG. 1. Superconducting Rh- and Pd-phases.

Few superconducting Ru- or Os-compounds are known, and none were found recently. This may be explained by two facts: (1) the knowledge about the relevant phase diagrams is very uncertain, (2) little tendency of both metals exists to form compounds especially with elements of the VA group. ROSS and HUME-ROTHERY(12) explain this by the higher proportion of the *d*-type functions in the bonding orbitals of the VIII A group elements.

---

* *Note added in proof.* SCHUBERT *et al.*(45) found for Pd_2As (h.t.) $a = 6{\cdot}62$, $c = 3{\cdot}60$ Å.

In contrast to this, Rh which like Pd and Pt in its present state of purity is not superconducting above 0·1°K forms a much larger number of superconducting compounds than Ru or Os.

For the group IV A compounds of Rh the only known superconductors are Rh_5Ge_3 (T_c = 2·1°K),(4) RhGe(T_c = 0·96°K),(18) and $RhPb_2$ (T_c = 2·66°K).(25)

Compounds of Rh with P, As, Sb and Bi show the trend that going from P to Bi the concentration of superconducting phases shifts to the side of the non-metal, e.g., Rh_2P(13) vs. RhBi(14, 26) and $RhBi_4$.(15) In terms of electronic concentration *n* this means that with a decreasing number of valence electrons* superconductivity becomes more likely with increasing atomic number (Rh_2P $n = 7{\cdot}2$—$RhBi_4$ $n = 5{\cdot}8$). This once more confirms the observation that the superconducting critical temperature tends to drop if one approaches electron concentrations near eight. The superconducting compound with the highest electron concentration, thus far, is Pd_3P ($n = 8{\cdot}75$).

The $Rh_{1{\cdot}4}As$ phase is superconducting at 0·56°K. With small additions of Rh the transition temperature drops below 0·3°K. The same concentration effect was observed later for Pd_3P.

It is surprising that RhSb remains normal to 0·35°K while the analogous compounds RhAs and RhBi that bracket RhSb are superconducting with temperatures of 0·58°K and 2·06°K respectively. In addition, the MnP structure of RhSb appears, in other cases, to be favorable for the occurrence of superconductivity.(18) We are then left with no explanation for the lack of superconductivity in RhSb.

The same trend, as mentioned for the VA-alloys is found for the VI A group compounds: the concentration of the superconducting phases shifts with increasing metallic nature of the *B* element from S to Te, to the more chalcogenide rich side. The only known superconducting Rh–S compound is $Rh_{17}S_{15}$ (T_c = 5·8°K),(13) while $RhTe_2$(13, 31) but not RhTe(18) is superconducting.

In the IV A group, Pd alloys PdSi (T_c = 0·93°K), Pd_2Sn (T_c = 0·41°K), Pd_3Sn_2 (T_c = 0·47–0·64°K), PdSn (T_c = 0·41°K) and $PdPb_2$ (T_c = 2·95°K).(25) are superconductors. PdGe does not seem to be superconducting, and the few existing compounds do not yet permit any definite statements.

The phases between Pd and the VA group elements are an excellent example of the influence of the different alloying elements.

Let us consider first the properties of Pd_3P. Its superconductivity drops in a very small concentration range, as had been observed earlier only for nitrides and carbides.(16) No other phase crystallizing in the same type (Pd_3B, Pd_3Si) or forming at the same electronic concentration (Pd_3As, Pd_3Sb) is superconducting, and the same trend as shown for the Rh-compounds can be seen for the Pd-phases: Pd_3P (T_c = 0·75°K) PdSb (T_c = 1·5°K),(4, 17) β-$PdBi_2$ (T_c = 4·2°K).(19, 29) Again superconducting P-phases have a much higher Pt-metal concentration than the Bi-compounds.

This principle is valid, too, for the VI A group compounds. $Pd_{2{\cdot}2}S$ becomes superconducting at 1·63°K, the only superconducting Te-phases are PdTe (T_c = 2·3°K)(4) and $PdTe_2$ (T_c = 1·53°K).(20)

The superconducting Ir and Pt-phases are IrGe (T_c = 4·7°K),(4) Ir_3Ge_7 (T_c = 0·87°K), PtSi (T_c = 0·88°K),(18) PtGe (T_c = 0·40),(18) PtSb (T_c = 2·1°K)(17) and PtBi (T_c = 2·4, 1·2°K).(17, 27)

Various conclusions may be drawn from all this. The fact that compositions upon going from the less to the more metallic elements change always in the same characteristic way indicates a similar variation of the corresponding number of valence electrons. To assign the identical number of valence electrons to all elements in one column of the periodic system is, of course, the crudest approximation possible and it is interesting to see from our data in which way the refinement will have to go; namely, the more metallic the β-element the smaller its actual number of valence electrons that are essential for the occurrence of superconductivity.

On the other hand, the crystallographic structure, at a constant electronic concentration, is not without influence. It is known that f.c.c. phases are often more favorable to superconductivity than h.c.p. structures,(21, 22) but the effect of structure changes is normally less pronounced in more complicated structures, e.g., α-Hg rhombohedral $T_c = 4{\cdot}153°\text{K}$, and β-Hg tetragonal $T_c = 3{\cdot}949°\text{K}$.(23)

---

* Valence electrons: electrons outside a filled shell and for these compounds no connection with the chemical valence should be made.

We found two phases with high and low temperature modifications Pd_2As and Pd_7P_3 which showed a remarkable difference in the transition temperatures of both forms. The modifications of Pd_2As crystallize in a hexagonal lattice, but their transition temperatures differ nearly by a factor of three, which now and then shows that even a small structure change may have a great effect on superconductivity.

The difference in the superconductivity and magnetic behavior of the noble metals also shows up in their alloys. Pd is the most magnetic element (a high temperature-dependent susceptibility) and it, just like Pt, shows dilute ferromagnetism for solid solutions of Cr, Mn, Fe, Co and Ni.(24) With the possible exception of Ge, palladium forms superconducting alloys with all elements from Si to Pb, from P to Bi and from S to Te. This may be taken as an indication that even a small disturbance in the electron configuration of Pd will change the magnetic interaction into a superconducting one, while the elements Ru, Os, Ir, which do not show any of these peculiar magnetic properties, but are superconductors themselves form only a few superconducting phases with the elements of the IV A, V A and VI A group.

Acknowledgements—Our thanks to G. W. HULL JR., for the superconductivity measurements; and V. B. COMPTON, for many enlightening discussions. We want to thank, particularly, Mrs. S. HILLHOUSE for preparing the samples and the X-ray diffraction work.

REFERENCES

1. HANSEN M., *Constitution of Binary Alloys*, McGraw-Hill, New York (1958).
2. HARDY G. F. and HULM J. K., *Phys. Rev.* **93**, 1004 (1954).
3. SCHAWLOW A. L. and DEVLIN G. E., *Phys. Rev.* **113**, 120 (1959).
4. MATTHIAS B. T., *Phys. Rev.* **92**, 874 (1953).
5. RAUB CH.J. and WEBB G. W., *J. Less-Common Metals*, **5**, 271 (1963).
6. SCHUBERT K., BHAN S., BURKHARDT W., GOHLE R., MEISSNER H. G., PÖTZSCHKE M. and STOLZ E., *Naturwissenschaften* **47**, 303 (1960).
7. RUNDQVIST S., *Acta. Chem. Scand.* **15**, 451 (1961).
8. WIEHAGE G., WEIBKE F. and BILTZ W., *Z. anorg. Chem.* **228**, 357 (1936).
9. RUNDQVIST S., *Acta Chem. Scand.* **15**, 451 (1961).
10. QUESNEL T. C. and HEYDING R. D., *Canad. J. Chem.* **40**, 814 (1962).
11. HEYDING R. D. and CALBERT L. D., *Canad. J. Chem.* **39**, 955 (1961).
12. ROSS R. G. and HUME-ROTHERY W., *J. Less-Common Metals* **4**, 454 (1962).
13. MATTHIAS B. T., CORENZWIT E. and MILLER C. E. *Phys. Rev.* **93**, 1415 (1954).
14. ALEKSEEVSKII N. E., BRANDT N. B. and KOSTINA T. I. *Izv. Adad. Nauk. S.S.S.R. Ser. Fiz.* **16**, 233 (1952).
15. ALEKSEEVSKII N. E., ZHDANOV G. S. and ZHURAVLEV N. N., *Sov. Phys. J.E.T.P.* (English) Translation **1**, 99 (1955).
16. GIORGI A. L., SZKLARZ E. G., STORMS E. K., BOWMAN ALLEN L. and MATTHIAS B. T., *Phys. Rev.* **125**, 837 (1962).
17. MATTHIAS B. T., *Phys. Rev.* **90**, 487 (1953).
18. MATTHIAS B. T., GEBALLE T. H. and COMPTON V. B., *Rev. mod. Phys.* **35**, 1 (1963).
19. ZHURAVLEV N. N., *Zh. eksp. teor. fiz.* **32**, 1305 (1957).
20. GUGGENHEIM J., HULLIGER F. and MULLER J., *Helv. Phys. Acta.* **34**, 408 (1961).
21. GSCHNEIDNER K. A., JR. and MATTHIAS B. T., *Electrical and Magnetic Properties of the Rare Earth Metals, Their Alloys and Compounds; Rare Earth Research* (edited by KLEBER E. V.) p. 158. MacMillan, New York (1961).
22. GEBALLE T. H., MATTHIAS B. T., COMPTON V. B. CORENZWIT E. and HULL G. W., JR., *Phys. Rev.* **129**, 182 (1963).
23. SCHIRBER J. E. and SWENSON C. A., *Phys. Rev.* **123**, 1115 (1961).
24. BOZORTH R. M., DAVIS D. D. and WERNICK J. H., *Proc. of the International Conference on Magnetism and Crystallography* **1**, 112 (1961).
25. GENDRON M. F. and JONES R. E., *J. Phys. Chem. Solids* **23**, 405 (1962).
26. GLAGOLEVA V. P. and ZHDANOV G. S., *Zh. eksp. teor. fiz.* **25**, 248 (1953).
27. ZHURAVLEV N. N., ZHDANOV G. S. and ALEKSEEVSKII N. E., *Vest. Mosk. Univ., Ser. mat. mekhan. astron. fiz. khim.*, **14**, 117 (1959).
28. GELLER S., *Acta Cryst.* **8**, 15 (1955).
29. ALEKSEEVSKI N. E., ZHURAVLEV N. N. and LIFANOV I. I., *Zh. eksp. teor. fiz.* **27**, 125 (1954).
30. ZHURAVLEV N. N., *Sov. Phys. J.E.T.P.* (English Translation) **5**, 1064 (1957).
31. MATTHIAS B. T., *Phys. Rev.* **97**, 74 (1955).
32. GRONVOLD F. and ROST E., *Acta. Chem. Scand.* **10**, 1620 (1956).
33. MATTHIAS B. T. and GELLER S., *J. Phys. Chem. Solids* **4**, 318 (1958).
34. PFISTERER H. and SCHUBERT K., *Z. Metallk.* **41**, 358 (1950).

35. Alekseevskii N. E., Zhdanov G. S. and Zhuravlev N. N., *Sov. Phys. J.E.T.P.* (English Translation) **1**, 99 (1955).
36. Kuz'min R. N. and Zhdanov G. S., *Zh. eksp. teor. fiz.* **26**, 337 (1954).
37. Geller S., *Acta Cryst.* **15**, 1198 (1962).
38. Geller S. and Cetlin B. B., *Acta Cryst.* **8**, 272 (1955).
39. Geller S., *J. Amer. chem. Soc.* **77**, 2641 (1955).
40. Present investigations.
41. Zumbusch M., *Z. anorg. Chem.* **243**, 322 (1940).
42. Alekseevskii N. E. and Gaidukov Yu. P., *Zh. eksp. teor. fiz.* **25**, 383 (1953).
43. Nowotny H., Schubert K. and Dettinger U., *Z. Metallk.* **37**, 137 (1946).
44. Schubert K., Breimer H., Burkhardt W., Günzel E., Haufler R., Lukas H. L., Vetter H., Wegst J. and Wilkens M., *Naturwissenschaften* **44**, 229 (1957).
45. Schubert K., Frank F., Gohle R., Maldonado A., Meissner H. G., Raman A. and Rossteutscher W., *Naturwissenschaften* **50**, 41 (1963).

J. Phys. Chem. Solids Pergamon Press 1963. Vol. 24, pp. 1101–1106. Printed in Great Britain.

HOLE INJECTION INTO CdS FROM Cu_2S

P. N. KEATING

Associated Electrical Industries (Woolwich) Limited, West Road, Templefields, Harlow

(*Received* 28 *March* 1963; *revised* 28 *April* 1963)

Abstract—Diodes consisting of cuprous sulphide (Cu_2S) in contact with cadmium sulphide have been prepared by the evaporation of Cu_2S onto thin CdS plate crystals and current–voltage and electroluminescence measurements have been made on them. The forward characteristics are interpreted on the basis that up to a threshold voltage the electron current is primarily space-charge limited and the hole current is recombination limited in the CdS bulk; at the threshold voltage, the hole transit time becomes of the order of the hole lifetime and double injection currents occur, as predicted by Lampert; the Cu_2S–CdS barrier then mainly controls the current. On the basis of this theory, hole lifetimes lying between $1{\cdot}0$ and $2{\cdot}0 \times 10^{-8}$ sec have been deduced for six specimens. Long wavelength electroluminescence under forward bias has been observed which is linear in current, in agreement with theory for transitions taking place via a deep state.

INTRODUCTION

THE electrical properties of Cu_2S in contact with materials such as CdS and ZnS have become of increasing interest recently. BLEIL has shown[1] that copper is precipitated from the CdS lattice as cuprous sulphide even at concentrations as low as tens of parts per million; in view of the similarity between CdS and ZnS one might expect similar precipitation from the latter compound. Indeed, a number of workers[2, 3] have ascribed electroluminescence in ZnS to the possible presence of copper sulphide. There is a strong possibility that d.c. electroluminescence in ZnS is due either to hole injection or impact ionization at barriers between small Cu_2S precipitates and the bulk.

With this possibility in mind, it was decided to simulate such a system in a simple, planar form. Cadmium sulphide rather than the zinc compound, was chosen for the preliminary investigation which is reported here because more suitable crystals were available and because ohmic contacts to it are more easily prepared.

EXPERIMENTAL

The CdS used was in the form of thin plate crystals, about 20 mm² in area and 10–50μ thick, grown by the method of FOCHS and LUNN[4] from "pure" material. Cupric sulphide (CuS) was prepared by homogeneous precipitation from $Cu(SO_4)_2$ solution by thioacetamide. The Cu_2S was prepared by the thermal decomposition of the CuS followed by the melting of the Cu_2S sintered residue at 1160°C, in argon, to form ingots. Electrogravimetric analysis of one of the Cu_2S ingots indicated that it had the theoretical composition and the material was shown to be p-type by a thermal probe measurement. Ohmic contacts could be made to the Cu_2S by means of evaporated gold, after a slight forming process.

The specimens were prepared for measurement by the evaporation of (i) a Cu_2S dot, about 2 mm dia., onto one face of the CdS crystals, and (ii) a gold electrode of somewhat smaller area onto the Cu_2S. The specimen was then mounted on gallium supported by a copper plate, the gallium forming the ohmic electrode to the other face of the CdS crystal.

Preliminary measurements showed that irreversible changes were occurring at the higher current densities; therefore specimens were heated in air to about 250°C for 5 min. Apart from stabilizing the specimens, this treatment is likely to ensure that the gallium contacts are ohmic at the current densities used. Pressure contact to the gold electrode was made by a $0{\cdot}006$ in. dia. gold whisker.

The current–voltage characteristics of the specimens were measured at room temperature by means of a constant current source between 10^{-9} and 10^{-3} A, the upper limit being imposed by heat dissipation, and up to 100 V. The electroluminescence was measured by an EMI 9514 photomultiplier. The crystal thicknesses were measured by the observation of Edser–Butler fringes, with an error of less than 5 per cent.

SIMPLE SEMI-QUANTITATIVE CONSIDERATIONS

The combination of Cu_2S and CdS, with an ohmic contact to each, is effectively a diode with a p–n "junction", complicated by the presence of surface states in the junction and by the difference in energy gaps and work functions, etc., between the two materials. Thus at small voltages, currents through the diode will be largely diffusion currents limited by the barriers at the interface and, in this limit, the work of ANDERSON(5) is applicable to a large extent. However, the impedance of the CdS is not negligible and higher forward currents may be largely controlled by its bulk properties. If, in this region, the hole current is recombination limited in the bulk, the increasing voltage across the CdS bulk will result in a decreasing hole transit time until this time becomes of the order of the hole lifetime, when large double injection currents will occur.(6) The resulting large increase in bulk conductivity will allow most of any additional applied voltage to be developed across the junction so that the currents are again diffusion controlled.

The forward junction-controlled current density is of the form

$$J = \alpha \exp(\beta\phi_1)$$

provided $\beta\phi_1 > 1$ where α is only slightly voltage dependent,(5) β is a constant < 1, ϕ_1 is the dimensionless variable eV_1/kT and V_1 is the voltage across the junction. In the low current limit all the applied voltage V_0 will be developed across the junction and $V_1 = V_0$; the current is wholly diffusion controlled. In this region, a semi-logarithmic plot of J and V_0 will yield a straight line (region (a) in Fig. 1).

At somewhat higher currents, an increasing fraction of V_0 will be developed across the CdS bulk and the current will become increasingly bulk controlled. If space charge effects can be ignored, then

$$V_0 - V_1 = JR = V_2$$

where R is the CdS resistance/unit area. If $\phi_0 = eV_0/kT$ and $\phi_2 = eV_2/kT$, then ϕ_0 and ϕ_2 are proportional to V_0 and J, respectively, and

$$\frac{\mathrm{d}(\ln\phi_2)}{\mathrm{d}\phi_0} = \frac{\beta}{1+\beta\phi_2}$$

Region (a) of Fig. 1 is characterized by $\beta\phi_2 \ll 1$ and this is followed by region (b) where this is not valid and where $\beta\phi_2$ may become much larger than unity. In general, however, the electron current through the CdS will be space charge controlled to some extent and the current J will be a super-linear function of V_2. Provided that J varies more slowly than $\exp(\beta V_2)$, however, the region (b), characterized by a decreasing slope, will always exist. Only the detailed behavior will be different.

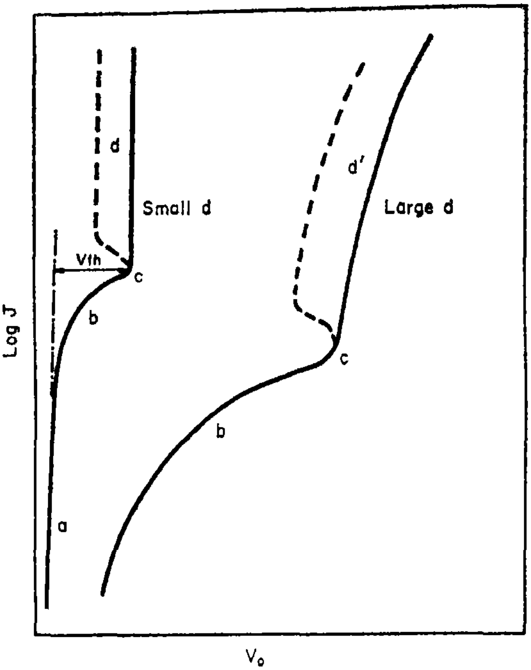

FIG. 1. Theoretical forward current–voltage characteristics. The dashed lines represent the case when a negative resistance region occurs.

As V_2 increases in this region, the hole transit time decreases. LAMPERT showed(6) that a steep increase in current will occur when the hole transit time is about twice the hole recombination lifetime, τ_p, due to the onset of double injection currents. Lampert's remarks on assumptions (1), (iv), (v), (vi) in his paper apply equally well here but the assumptions of volume controlled currents and negligible diffusion currents obviously need re-examination for this case. Lampert points out that these assumptions are reasonable providing the crystal thickness, d, is large compared with the ambipolar high lifetime diffusion length, L_a, in his notation. In the experiments described here, this requirement is not met since it is probable that $L_a \sim 100\mu$. However, the treatment of the voltage threshold involves the less stringent requirement that d is large compared with the *low* lifetime ambipolar diffusion length, which is of the order of a micron; this is satisfied in the experiments reported here. Thus, if we take V_2 to be the voltage used in Lamperts treatment, his results for the voltage threshold may be applied to the present case. Thus a sharp increase in current is to be expected when

$$V_2 = d^2/2\mu_p\tau_p = V_{\text{th}} \qquad (1)$$

where μ_p is the hole mobility. This is shown in Fig. 1 (point c). Lampert also showed that a negative resistance region may occur above this threshold under certain conditions. The requirement that $d \gg L_a$ is not, however, satisfied in the present experiments and, although, of course, the existence or the negative resistance region is not precluded, his treatment cannot be directly applied.

Above the threshold, the dynamic conductance of the CdS is relatively large as a result of the double injection and a large fraction of the additional applied voltage will be developed across the junction provided V_{th} is not too large compared with V_1 in the region of (c) i.e. provided d is not too large. Thus, in this case, the currents are again mainly diffusion controlled and a nearly exponential rise of current with additional applied voltage is to be expected (region d). If, however, V_{th} is large compared with V_1, then the fraction of the additional applied voltage which is developed across the junction may be small and the current will rise appreciably slower than exponentially. This will apply to the case of large d and is shown as region (d′) in Fig. 1.

On the basis of Lampert's model, which involves a deep recombination centre, the hole lifetime increases in this region, tending to become constant and approximately equal to the electron lifetime at high injection levels. In this case, the recombination radiation, or electroluminescence, will be proportional to the number of carriers and thus to the current. However, if the recombination is via shallow states only or between bands, the lifetimes will tend to become equal but will continuously decrease with increasing current. The recombination rate will tend to become proportional to the square of the carrier density (i.e. to the square of the current) at high injection levels.

The reverse characteristic is somewhat complex to treat, especially when avalanche breakdown and the possibility of hole injection from the gallium anode are included, and will not be considered in detail. However, as well as the possibility of avalanche breakdown electroluminescence the possibility of electroluminescence due to double injection cannot be discounted. This would have to occur at higher voltages since, in the reverse direction, large voltages are developed across the junction.

RESULTS AND DISCUSSIONS

The forward current–voltage characteristics of two of the six diodes measured are shown in Fig. 2 as semilogarithmic plots; the characteristics of the other specimens are very similar to one or the other of these. The qualitative agreement between these results and the simple theory above is good, although the quantitative agreement between these curves and the theoretical in region (b) is poor. The current rises more rapidly in this region than expected on the basis of negligible space charge effects, implying that the electron current in this region is largely space charge controlled. The negative resistance region, as suggested by Lampert, was seen in three of the six specimens, one of them being shown in Fig. 2.

According to the semiquantitative considerations above, the low-level hole lifetime can be deduced if the hole mobility, crystal thickness and threshold voltage are known. The absence of region (a) at the currents used prevents determination of V_1 and thus V_{th} but a lower limit is obtained for τ_p if V_{th} is taken as the applied voltage at which the kink (c) occurs. This should lead to a maximum error of less than 30 per cent since V_1 is unlikely to be as much as a volt. The hole mobility was not measured but a value of 15 cm^2 V^{-1} sec^{-1} was assumed, as a result of the work of Mort and Spear.[7] Values of τ_p, using equation (1), have been obtained for all six specimens and are presented in Table 1, together with the crystal thicknesses and values of V_{th}.

The values thus obtained all lie within the range $\tau_p = 1{\cdot}0-2{\cdot}0\times10^{-8}$ sec for values of d^2 ranging over more than an order of magnitude.

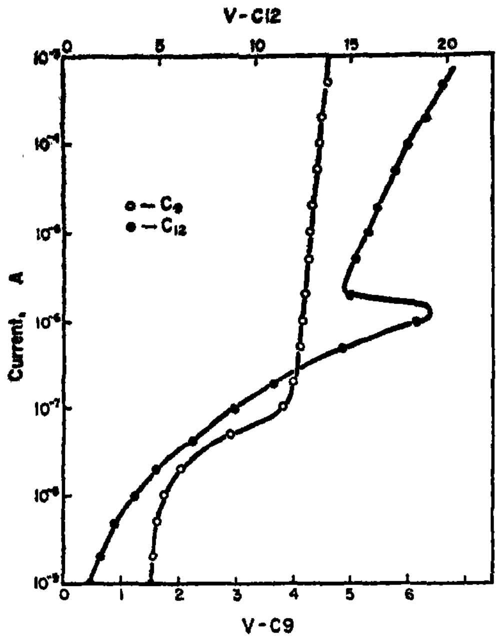

FIG. 2. Experimental current–voltage characteristics.
○ Speciman C9
● Specimen C12

Table 1. *Summary of experimental results*

Specimen no.	Thickness (μ)	V_{th} (V)	τ_p (sec)
C7	54	49	2×10^{-8}
C9	13	4·0	$1·4\times10^{-8}$
C10	15	4·3	$1·8\times10^{-8}$
C11	19	5·75	2×10^{-8}
C12	28	19	$1·4\times10^{-8}$
C13	14	6·25	$1·1\times10^{-8}$

They are about an order of magnitude lower than those obtained by MORT and SPEAR(7) but the lifetime observed here is that prevailing in the presence of negative space charge whilst the experiments of Mort and Spear were carried out under neutral conditions. However, to explain this change in lifetime (assuming the injected negative charge is given by *CV* and that it all enters the dominant recombination centre), one requires a hole capture cross-section of about 3×10^{-12} cm^2 which is very large and not very credible.

Electroluminescence could be detected in all specimens for forward currents greater than about 100μA (at about 4·4 V in C9) and in some specimens at reverse currents greater than about 0·5 mA. Quantitative measurements of relative output were carried out for specimen C9 under forward bias and the results are shown in Fig. 3. The light output is seen to be linear in current, as expected at a high injection level in the presence of recombination centres. This is consistent with the colour of the electroluminescence which was red. The emission was too weak for spectrographic measurement but measurements with filters indicated that all the emission visible to the photomultiplier was at wavelengths greater than 6000 Å and at least 90 per cent was above 6500 Å. Due to the geometry and refractive index of the CdS, it is probable that only a small fraction of the emitted light was actually measured by the photomultiplier but the quantum efficiency ($\sim 10^{-6}$) was within an order of magnitude of those observed in GaP *p–n* junctions at room temperature and at the same light level.

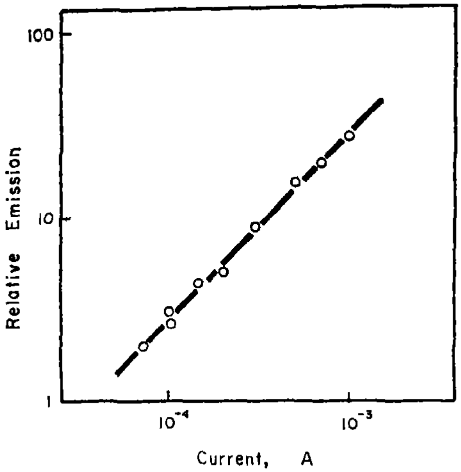

FIG. 3. Luminescence emission under forward bias.

It might be argued that the abrupt current increase was due to impact ionization. However, this argument requires that the "breakdown" voltage is either, (*a*), independent of *d* if the voltage is developed across a depletion layer or (b), linear in *d* (i.e. the field is constant) if it is developed across the bulk.(8) The d^2 dependence of V_{th} predicted by double injection theory is plainly shown in Fig. 4 although some scatter is present due to differences in lifetime. It might also be argued that the sharp increase in current corresponds to the trap filled limit discussed by LAMPERT(9) for one carrier injection since the trap filled limit voltage also varies as d^2.(9) However, a trap density of only $\sim 10^{14}$ cm^{-3} is necessary to explain the magnitude of the voltage, which is at least two orders of magnitude less than one expects. Furthermore, the negative resistance region cannot be explained on the basis of one-carrier injection and, in view of the large reservoir of holes in the Cu$_2$S anode and the relatively efficient electroluminescence, the absence of holes in the CdS is unlikely.

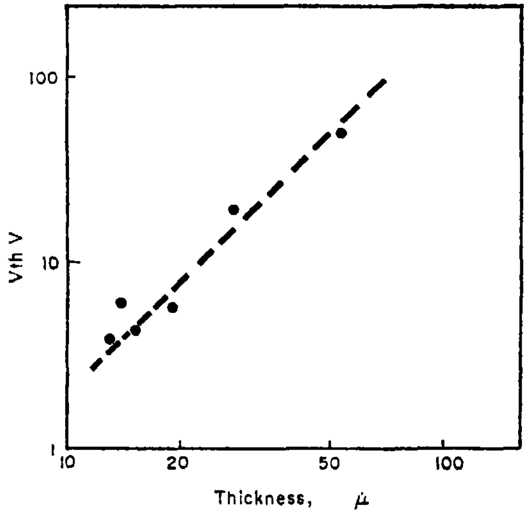

FIG. 4. The variation of threshold voltage with thickness.

The diodes all exhibited extensive rectification e.g. for C9 at $\sim$ 4·5 V the rectification ratio was $\gg 10^6$. Reverse characteristics were obtained for the four thinner specimens and all showed "soft breakdown". Two typical curves are shown in Fig. 5. In the case of the two thickest specimens, C7 and C12, the reverse voltages at 10^{-9} A were greater than 100 V. The reverse voltages increased with increasing thickness; this is consistent with both bulk impact ionization and double injection mechanisms of breakdown although the former is somewhat unlikely in view of the fact that most of the voltage is developed across the junction. The diodes gave an open circuit photovoltage of about 0·5 V when irradiated with high intensity tungsten light.

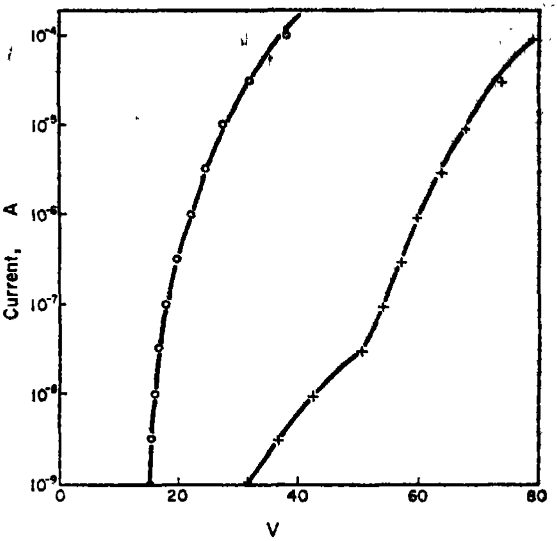

FIG. 5. Reverse current–voltage characteristics.
○ Specimen C9
+ Specimen C11

Previous observations(10–12) of electroluminescence in CdS, using a variety of electrode materials, are open to a similar double injection interpretation, as has been pointed out to some extent by SMITH(11) and LAMPERT.(6) For example, DIEMER(10) obtained a similar kink in the current voltage characteristics at about 10^3 V for a 200 μ gap and a value of $\tau_p \sim 1{\cdot}5 \times 10^{-8}$ sec can be computed from equation (1), with $\mu_p = 15$ cm^2 V^{-1} sec^{-1}. This is in remarkably good agreement with the results obtained here. This agreement may be fortuitous although it is possible that hole lifetimes in relatively pure CdS crystals vary only over a small range and that special treatment is necessary to change this lifetime appreciably. The values MORT and SPEAR obtained(7) for specimens from various sources under neutral conditions vary only over a small range as do those obtained here. The values obtained by SMITH(11) are appreciably larger but the crystals he used were specially selected and somewhat rare. SMITH(11) observed green electroluminescence in selected CdS crystals with a hole lifetime of $\tau_p \sim 10^{-6}$ sec, as measured by an independent method and estimated from his measurements. By applying equation (1) to his data, a low level lifetime of about 5×10^{-7} sec is obtained. He observed an abrupt decrease in voltage after about 900 V was applied across a 1 mm gap, probably due to the existence of a negative resistance region.

Smith also observed a linear relationship between current and electroluminescence, which is not expected since the radiating transition was either between bands or via only shallow states. No explanation is offered here. The quantum efficiency of Smith's luminescence was over an order of magnitude less than that observed in the present experiments.

The results obtained for CdS are not directly applicable to ZnS but it is of some value to speculate on the behaviour of this material in the light of these results. If a ZnS crystal of constant thickness, t, is divided into n equal parts by planes of a material which is a good source of holes and electrons, the voltage across the crystal necessary to allow V_{th} to be developed across each part is $\frac{t^2}{2n\tau_p\mu_p}$. Thus the larger n, the lower the voltage necessary for double injection currents. Small precipitates of cuprous (or argentous) sulphide will yield a similar result and may explain the beneficial effect of these materials on electroluminescence in ZnS and CdS.(3, 4, 13) PRESLAND and MARSHALL(14) have reported that ZnS:Cu:Cl phosphors exhibit unusual properties when quenched rapidly from about 1000°C to room temperature. For example, the electroluminescence disappears but can be made to return by the precipitation of copper onto them from solution.

CONCLUSIONS

Abrupt increases in current, accompanied by electroluminescence, have been observed in forward biassed Cu_2S–CdS combinations. The following evidence has been observed to support the hypothesis that the sharp increases in current, and thus the low voltage d.c. electroluminescence, is a direct result of double injection:

(a) Good qualitative agreement has been obtained between measured forward characteristics and those indicated by a simple theory largely based on the double injection theory of Lampert. Measurements on specimens ranging in thickness from 13 to 54 μ have produced consistent and credible values of the hole lifetime in CdS, derived on the basis of this theory. The threshold voltage shows a d^2 dependence, consistent with the double injection mechanism but inconsistent with impact ionization.

(b) Forward bias electroluminescence at high currrents was linear in current, as expected from the theory when the radiating transition involves a deep centre, which is consistent with the emission colour.

It is hoped to extend this work to thin ZnS crystals in the near future.

Acknowledgement—The author is indebted to Mr. B. LUNN for providing the crystals and to Mr. E. GRAY for carrying out the evaporation and for useful discussion. The author also wishes to thank Dr. J. FRANKS and Dr. P. D. FOCHS, for their advice and encouragement, and Dr. M. E. HAINE for permission to publish.

REFERENCES

1. BLEIL C., Private communication.
2. CUSANO A. *Luminescence of Organic and Inorganic Materials*, p. 494. Wiley, New York (1962).
3. ZALM P., *Philips res. Rep.* **11**, 353, 417 (1956).
4. FOCHS P. D. and LUNN B., to be published.
5. ANDERSON R. L., *Solid-State Electron.* **5**, 341 (1962).
6. LAMPERT M. A., *Phys. Rev.* **125**, 126 (1962).
7. MORT J. and SPEAR W. E., *Phys. Rev. Letters*, **8**, 314 (1962).
8. SCLAR N. and BURSTEIN E., *J. Phys. Chem. Solids*, **2**, 1 (1957).
9. LAMPERT M. A., *Phys. Rev.* **103**, 1648 (1956).
10. DIEMER G., *Philips res. Rep.* **9**, 109 (1954).
11. SMITH R. W., *Phys. Rev.* **105**, 900 (1957).
12. KOMIYA H., IBUKI S. and YAMASHITA H., *Luminescence of Organic and Inorganic Materials*, p. 523. Wiley, New York (1962).
13. LOZYKOWSKI H. and MECZYNSKA H., *Bull. Akad. Pollon.* **6**, 76 (1958).
14. PRESLAND M. J. and MARSHALL R., to be published.

J. Phys. Chem. Solids Pergamon Press 1963. Vol. 24, pp. 1107–1112. Printed in Great Britain.

THE OPTICAL PROPERTIES OF SINGLE CRYSTALS OF WSe_2 AND $MoTe_2$

R. F. FRINDT

Laboratory for the Physics and Chemistry of Solids,
Cavendish Laboratory, Cambridge, England

(*Received* 15 *February* 1963)

Abstract—Single crystals of tungsten diselenide and molybdenum ditelluride about 200–1000 Å thick have been prepared by cleavage. With such crystals, it is possible to make optical transmission measurements in wavelength regions where the absorption coefficient reaches 10^5–10^6 cm^{-1}. For tungsten diselenide, a strong absorption edge is observed at 7800 Å at room temperature, where the absorption coefficient rises to about 10^5 cm^{-1}, and a second edge is observed at 6000 Å. Strong absorption bands are observed on both edges. With molybdenum ditelluride, the first absorption edge is observed at 6600 Å at 77°K, and a second edge occurs at shorter wavelengths. Strong absorption bands have been observed on the first edge. The area of the crystal that gives rise to the absorption bands has been examined in the electron microscope, and dense dislocation networks are observed. For both compounds, the first absorption edge is attributed to direct transitions from a split valence band to the conduction band, and the second absorption edge to transitions from a lower valence band or at another value of the wave vector. The valence band splitting probably results from a spin–orbit interaction. The strong absorption bands are attributed to the formation of exciton states.

INTRODUCTION

A STUDY of the optical absorption spectrum can give information about the energy bands and excited states in a crystal. In the wavelength regions that are of interest for crystal band structure, the absorption coefficient can reach values of 10^6 cm^{-1}, so that crystals 1μ thick or less are required for transmission measurements. The absorption coefficient can be obtained from reflection measurements made on thicker crystals, however the analysis of the data obtained is more complex, and the properties of the crystal surface may influence the results in an unknown way.

Very thin crystals of solids having layer structures can be prepared by cleavage, so that the absorption coefficient can be determined by transmission measurements in wavelength regions where the absorption coefficient reaches 10^6 cm^{-1}.

Crystals of MoS_2, $MoSe_2$, $MoTe_2$ and WS_2, WSe_2, WTe_2 have the hexagonal layer structure of molybdenum disulphide (except perhaps WTe_2).(1) These crystals have remarkable cleaving properties, and absorb light strongly in the visible part of the spectrum. They also have an interesting trigonal coordination. With molybdenum disulphide, for example, the crystal is composed of sheets of molybdenum atoms, each atom surrounded by six sulphur atoms in the form of a trigonal prism.(2) The sheets are held together by weak bonds between the sulphur atoms, and these bonds are broken when the crystal is cleaved. The thickness of the sheet is 6·15 Å for molybdenum disulphide, 6·97 Å for molybdenum ditelluride and 6·48 Å for tungsten diselenide.(1) It has been shown that trigonal bonds can be formed from the d^4sp hybridization of atomic wave functions,(2) and the indications are that the bonding in the sheets is covalent. If the sulphur atoms in molybdenum disulphide are considered, it seems likely that there is sp^3 hybridization of the sulphur orbitals, resulting in a distorted tetrahedral configuration. The cleaving properties of the crystal and the relatively high electrical conductivity along the layers may be associated with the overlap of the sulphur orbitals that are directed away from the molybdenum atoms.

A detailed study of the optical properties and photoconductivity of single crystals of molybdenum disulphide has already been made.(3) The main absorption edge occurs at about 7000 Å at room temperature, and there is a second absorption edge at about 5000 Å. Structure is observed on both edges. This paper gives an account of an experimental investigation into the optical properties of tungsten diselenide and molybdenum ditelluride.

The absorption coefficient to the long wavelength side of the absorption edge can be increased by the presence of dislocations in a crystal.(4) Crystal strain can widen absorption bands.(5) Layer structures have a very high density of dislocations, probably introduced during the cleaving process. The defect structure and the optical properties of the same crystal are being studied in an attempt to establish a correlation between the two.

EXPERIMENTAL AND RESULTS

Small transparent crystals of layer structures of the molybdenum disulphide type suitable for optical studies or electron microscopy can be obtained by carefully cleaving a thick crystal, or by using a stripping technique with sticky tape.

The spectra of tungsten diselenide and molybdenum ditelluride were observed with the electric vector of the light perpendicular to the c-axis of the crystal ($E \perp c$). Percentage transmission measurements were made at room temperature using a Unicam SP500 spectrophotometer, modified for measurements on small crystals. The crystals were cooled to 77°K by direct immersion into liquid nitrogen, and the spectra were photographed using a Hilger E478 spectrograph with glass optics. A microscope objective was used to produce an image of the crystal on the slit of the spectrograph, giving a crystal magnification of × 100.

The crystal thicknesses and the absorption coefficients stated below are estimates based on measurements made on molybdenum disulphide crystals.(3) It seems reasonable to assume that the absorption coefficients for related trigonal solids are of the same order of magnitude.

(a) *The optical absorption of single crystals of tungsten diselenide*

When viewed with light from a tungsten lamp, crystals of tungsten diselenide a few tenths of a micron thick are a deep red colour in transmission. Crystals about 500 Å thick are orange, and crystals about 200 Å thick are grey.

The room temperature optical absorption of a crystal about $\frac{1}{10}$ mm² in area and about $0{\cdot}1\ \mu$ thick is shown in Fig. 1. In Fig. 1, $I_0/I = 100/T$, where T is the percentage transmission. Two strong absorption edges are observed, at about 7800 and 6000 Å, with a strong peak (A) on the first absorption edge. The absorption coefficient reaches a value of about $10^5\ \text{cm}^{-1}$ at the first edge. A photograph of the absorption spectrum of this crystal at 77°K is shown in Fig. 2. The band A shown in Figure 2(a) is seen to be very strong. The microdensitometer trace in Fig. 3 shows band A at 7265 ± 10 Å, and another small absorption band (A_2) at 7100 ± 10 Å.

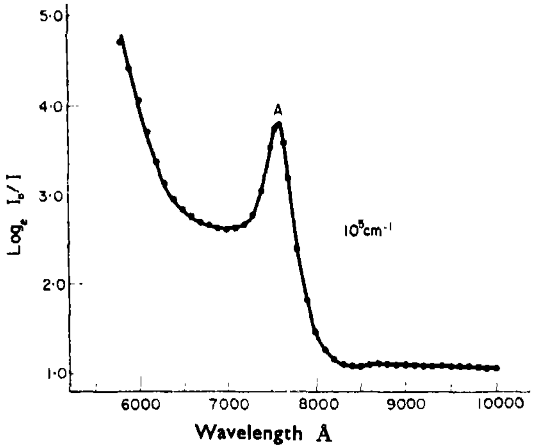

FIG. 1. Plot of absorption against wavelength for a WSe$_2$ crystal about $0{\cdot}1\ \mu$ thick at room temperature. The ratio $I_0/I = 100/T$, where T is percentage transmission. The absorption coefficient (in cm^{-1}) is based on measurements on MoS$_2$.(3)

The room temperature absorption of a thinner crystal, about $0{\cdot}05\ \mu$ thick, is shown in Fig. 4. It is seen that structure has been resolved on the second absorption edge (peaks B and C), and a broad peak D is observed at about 4000 Å. The absorption coefficient at peak C is about $7 \times 10^5\ \text{cm}^{-1}$. The peak locations are: A at 7640 ± 20 Å, B at 5650 ± 20 Å and C at 4800 Å. There were some cracks in the crystal, so that the peaks C and D do not show up as strongly as they would if the cracks were absent. When the crystal

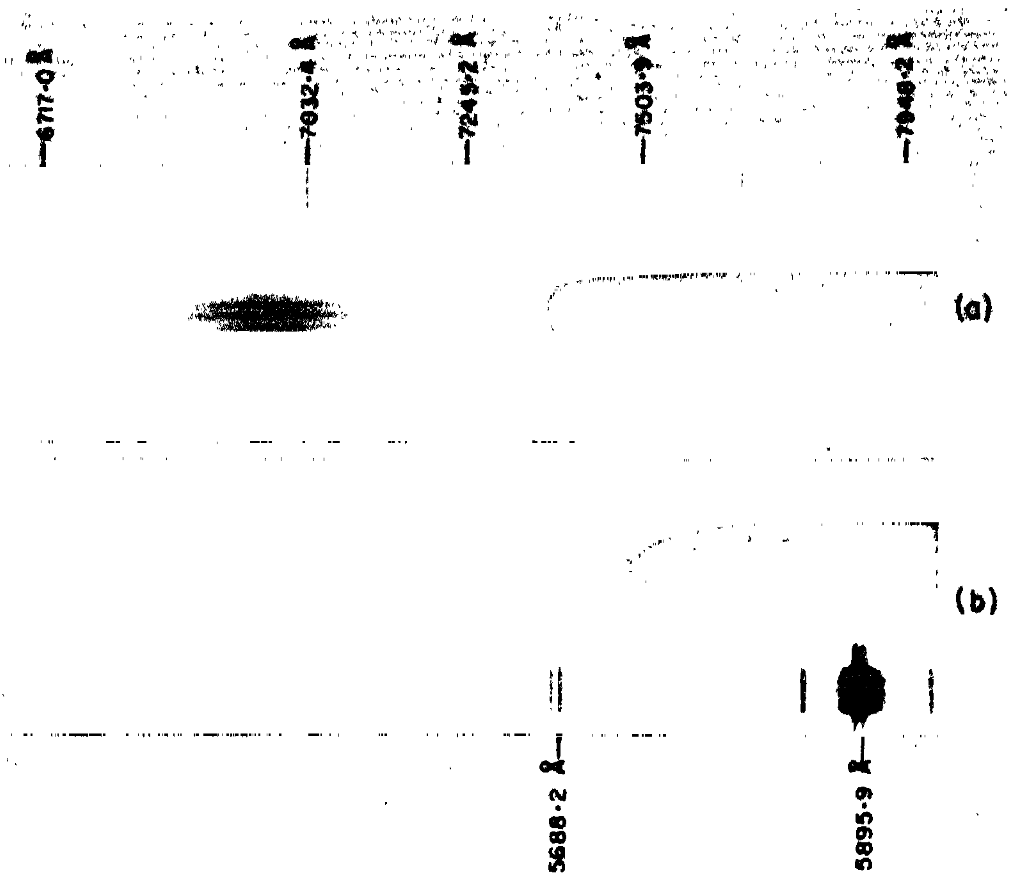

FIG. 2. Photograph of the absorption spectrum at 77°K for the same WSe_2 crystal as in Fig. 1. Figure 2(a) shows the band *A*, and Fig. 2(b) shows the second absorption edge.

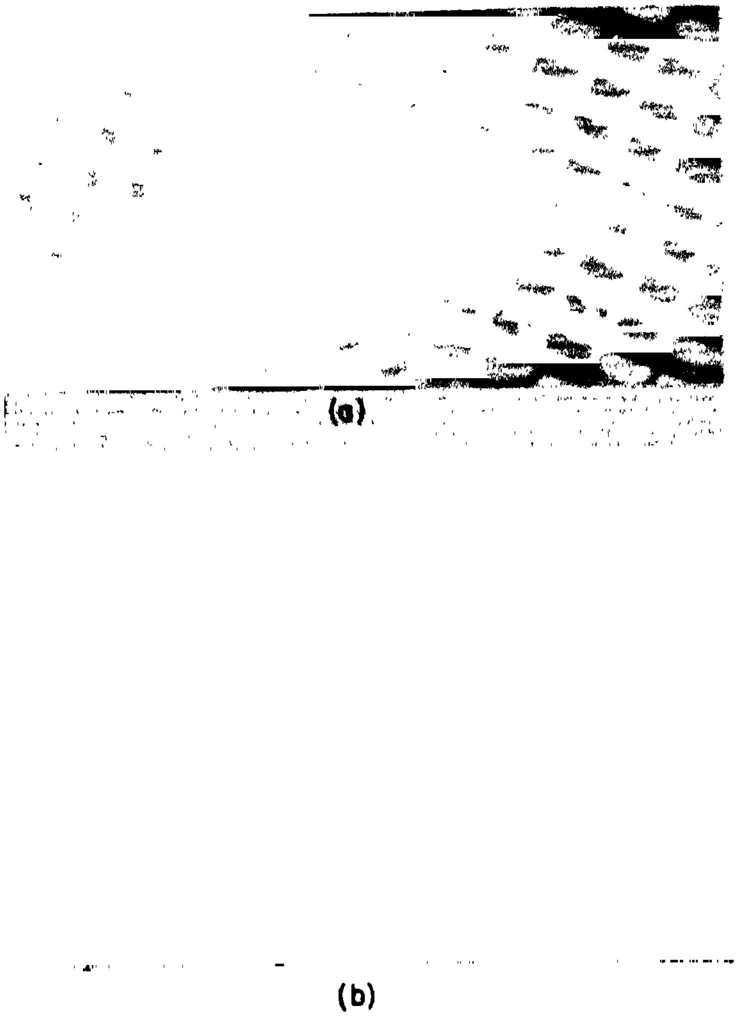

FIG. 7. Electron micrographs of the area of the $MoTe_2$ crystal that gave the spectrum in Fig. 6. (a) Hexagonal networks. Mag. ×100,000. (b) Moiré patterns. Mag. ×200,000.

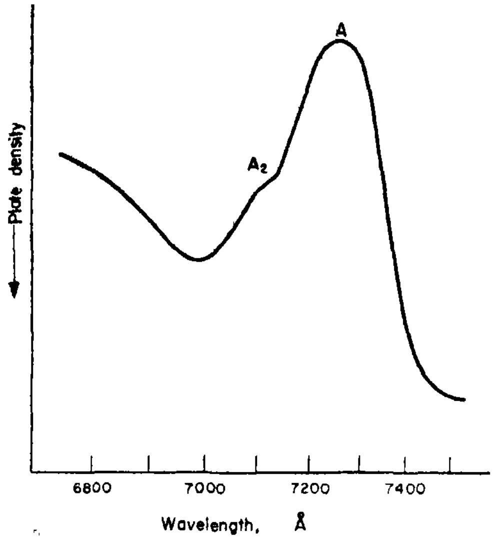

FIG. 3. *Microdensitometer trace of Fig. 2(a), showing* peaks A and A_2 for the WSe_2 crystal at 77°K.

is cooled to 77°K, peak B shifts to 5510 ± 10 Å, as shown by the microdensitometer trace in Fig. 5.

The absorption spectra were studied with the crystals stuck onto transparent sticky tape, so that the crystals may be strained, particularly at low temperatures. The crystals were prepared by means of a transport reaction with chemicals of purity better than 99·9%, and were kindly given to us by L. H. BRIXNER.[1]

(b) *The optical absorption and defect structure of a single crystal of molybdenum ditelluride*

The absorption spectrum of a molybdenum ditelluride crystal mounted on an electron microscope grid has been photographed at room temperature and 77°K. The crystal area selected by the spectrograph slit was about 1 μ long and 20 μ wide, and Fig. 6 shows the microdensitometer trace of the spectrum observed at 77°K. The peak positions in Fig. 6 are: A at 6465 ± 10 Å, A_2 at 6330 ± 10 Å and B at 5830 ± 20 Å. At room temperature, A is at 6720 ± 20 Å, A_2 is not resolved, and B is at 6030 ± 20 Å. The uncertainty in the peak location is caused by the width of the bands. A second absorption edge is observed at shorter wavelengths.

Without disturbing the crystal, the area that gave the spectrum in Fig. 6 was then studied in the electron microscope. Areas of parallel or hexagonal networks and moiré patterns were

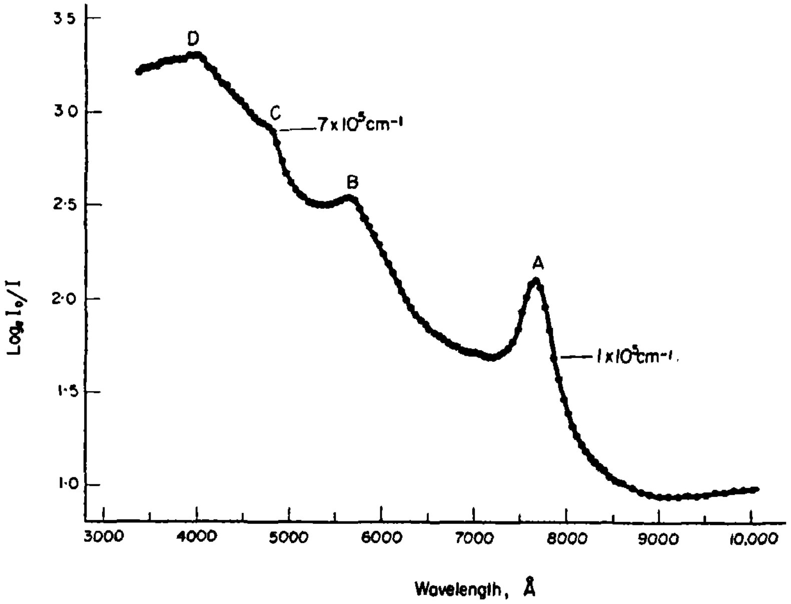

FIG. 4. Plot of absorption against wavelength for a WSe_2 crystal about 0·05 μ thick at room temperature. The absorption coefficients (in cm^{-1}) are based on measurements on MoS_2.[8]

observed, and representative electron micrographs of the area are shown in Fig. 7. The moiré patterns extended over an area of several square microns. The dislocation density is very high, varying from about $10^9/cm^2$ to $10^{11}/cm^2$. It is of interest that the length of Fig. 7(a) is about 1 μ, which is the width of the area that gave the absorption spectrum in Fig. 6.

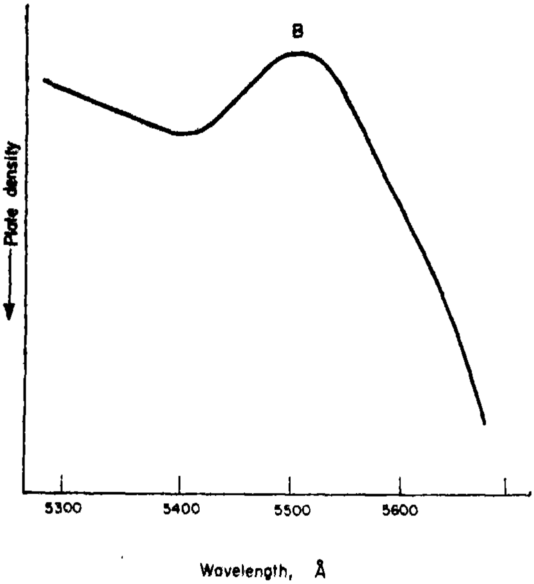

FIG. 5. Microdensitometer trace of absorption band B at 77°K, for the same WSe_2 crystal as in Fig. 4.

Parallel and hexagonal patterns and moiré fringes are also observed with tungsten diselenide crystals, and molybdenum disulphide crystals exhibit a very similar defect structure in the electron microscope. PASHLEY and PRESLAND(6) have shown that the hexagonal networks observed with molybdenum disulphide are caused by sets of dislocations on different slip planes in the crystal, and the same is probably true for molybdenum ditelluride and tungsten diselenide crystals. The moiré patterns probably result from shearing between successive crystal layers (see KAMIYA *et al.*(7)).

DISCUSSION

The properties of the layer structures MoS_2, $MoTe_2$ and WSe_2 are very similar, and the interpretation of the results presented here is based on the detailed quantitative measurements made on the absorption coefficient, oscillator strengths, refractive index and photoconductivity of single crystals of molybdenum disulphide.(3) The main absorption edge for tungsten diselenide crystals at room temperature occurs in the near infra-red wavelength region, at about 7800 Å, where the absorption coefficient reaches a value of about 10^5 cm^{-1}. At 6000 Å, a second absorption edge raises the absorption coefficient to about 10^6 cm^{-1}, and with very thin crystals, more structure is resolved to shorter wavelengths (Fig. 4). The absorption edges are attributed to direct transitions from the valence band to the conduction band, and the peaks A, B, and C are attributed to the formation of exciton levels below the conduction band.(3) At 77°K, the $n = 1$ and $n = 2$ exciton states are observed on the first absorption edge (peaks A and A_2 in Fig. 3).

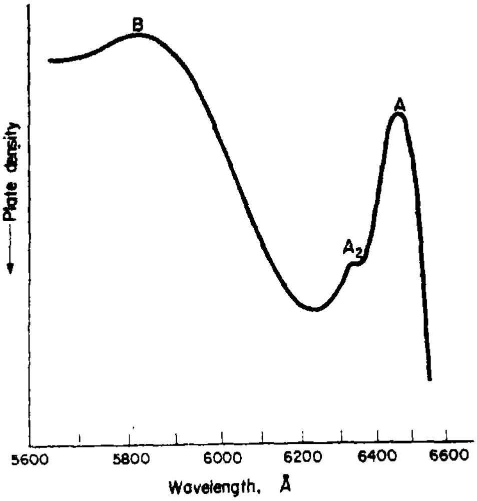

FIG. 6. Microdensitometer trace of the absorption spectrum for a $MoTe_2$ crystal about 0·05 μ thick at 77°K.

Similarly, exciton peaks A and A_2 are observed on the first absorption edge of the molybdenum ditelluride crystal (Fig. 6), and the exciton peak B is also observed. The absorption coefficient at peaks A and B is expected to be about 10^5 cm^{-1} or greater.

It is suggested that the separation of peaks A and B in tungsten diselenide and molybdenum ditelluride is caused by a spin-orbit splitting of the valence band, and that peak C observed with tungsten diselenide is a transition from a deeper level in the valence band, or a transition at another value of the wave vector. The corresponding structure in the molybdenum disulphide spectrum has been interpreted in a similar way.(3)

Some support for a spin–orbit interpretation of the *A–B* splitting can be obtained by considering the spin–orbit splittings for electron configurations of the free atoms. The splitting of atomic configurations can sometimes give the magnitude of the effect to be expected in solids (for example, see SAUM and HENSLEY(8) for a discussion of 2*a*–6*b* compounds, and BRAUNSTEIN(9) for 3–5 compounds). Table 1 gives the room temperature spin–orbit splittings for some relevant atomic *p* configurations (from BACHER and GOUDSMIT,(10) and SAUM and HENSLEY(8)).

Table 1. Atomic spin–orbit splittings for some p configurations

Electron configuration	Energy (eV)	Electron configuration	Energy (eV)
$4d^{10}5s^25p^1$(In)	0·273	$3s^23p^5$ (S^-)	0·065
$5d^{10}6s^26p^1$ (Tl)	0·966	$4s^24p^5$ (Se^-)	0·29
		$5s^25p^5$ (Te^-)	0·65

The splitting for the molybdenum atom would be expected to be somewhat less than the 0·273 eV for In, because of its lower atomic number, and the splitting of the tungsten atom would be less than 0·966 eV.

The room temperature splittings that have been observed in solids with trigonal configurations are given in Table 2. The splitting for $MoSe_2$ is expected to be about 0·198 eV.

Table 2. Valence band splittings in trigonal solids

Compound	Energy (eV)	Compound	Energy (eV)
MoS_2(3)	0·185	WS_2	—
$MoSe_2$	—	WSe_2	0·570
$MoTe_2$	0·210	WTe_2(?)	—

(The structure of WTe_2 is not certain.(1))

Assuming that we are concerned with the *p* wave functions in the solid, it is seen that the spin–orbit splitting is determined mainly by the molybdenum or tungsten atoms. By using simple ratios between the 5*p* and 6*p* atomic splittings and the $MoSe_2$ splitting, the spin–orbit separation for WSe_2 can be predicted to be 0·70 eV. Thus, the results show that the spin–orbit splittings of the molybdenum or tungsten atoms can give the magnitude of the valence band splitting to be expected in solids with the trigonal configuration.

In the case of WSe_2, the magnitude of the spin–orbit splitting is such that peak *B* lies on the second absorption edge leading to peak *C* (Fig. 4). This results in a spectrum which is somewhat different from the spectra for MoS_2 and $MoTe_2$.

Two factors which could affect the absorption spectra are crystal tension and the presence of impurities. Crystal tension would cause the bands *A* and *B* for tungsten diselenide to shift to longer wavelengths, but the change in the energy of the *A–B* splitting would not be large enough to affect the above discussion.(3) It has been shown that crystal impurities do not significantly affect the absorption spectra of natural crystals of molybdenum disulphide at high values of the absorption coefficient.(3) Therefore it is reasonable to assume that impurities in the tungsten diselenide and molybdenum ditelluride crystals will not appreciably affect the spectra that have been observed.

The width of band *A* in molybdenum ditelluride at 77°K is about 125 Å, or 0·04 eV. This width may be associated with the high density of dislocations in the crystal. Efforts are being made to obtain crystals that are relatively free from dislocations, in order to determine whether the band width changes significantly. It may be that wide absorption bands are a characteristic feature of exciton bands in layer structures, and further work on this is necessary. It seems that it may be possible to detect exciton diffusion in single crystals that are about 1000 Å thick. Another major problem in this field is the theoretical determination of the band structure for systems with the trigonal prism configuration.

Acknowledgements—The author would like to thank Dr. F. P. Bowden, F.R.S. for his interest in this work, Dr. A. D. Yoffe for many helpful discussions and Dr. L. H. Brixner for some tungsten diselenide crystals. Acknowledgement is also extended to the National Research Council of Canada for a Special Scholarship.

REFERENCES

1. Brixner L. H., *J. inorg. nucl. Chem.* **24**, 257 (1962).
2. Pauling L., *The Nature of the Chemical Bond*, 3rd ed. p. 175, Cornell University Press (1960).
3. Frindt R. F. and Yoffe A. D., *Proc. Roy. Soc.* **273**, 69 (1963).
4. Blakney R. M. and Dexter D. L., *Conference on Defects in Crystalline Solids, Bristol* 1955, p. 108. Physical Society, London (1955).
5. Chadderton L. T., Parsons R. B., Wardzynski W. and Yoffe A. D., *J. Phys. Chem. Solids* **23**, 416 (1961).
6. Pashley D. W. and Presland A. E. B., *Proc. Eur. Reg. Conf. on Electron Microscopy, Delft* 1960, Vol. 1, p. 417.
7. Kamiya Y., Ando K., Nonoyama M., and Uyeda R., *J. phys. Soc. Japan* **15**, (11), 2025 (1960).
8. Saum G. A. and Hensley E. B., *Phys. Rev.* **113**, 1019 (1959).
9. Braunstein R., *J. Phys. Chem. Solids* **23**, 1423 (1962).
10. Bacher R. F. and Goudsmit S., *Atomic Energy States*, McGraw-Hill, New York (1932).

J. Phys. Chem. Solids Pergamon Press 1963. Vol. 24, pp. 1113–1119. Printed in Great Britain.

SECOND HARMONIC GENERATION IN SOLIDS

P. L. KELLEY

Lincoln Laboratory,* Massachusetts Institute of Technology, Lexington 73, Massachusetts

(*Received* 18 *December* 1962; *revised* 12 *April* 1963)

Abstract—This paper is concerned with the relation in solids between second harmonic generation and electronic band structure. The second order response function is evaluated in the dipole approximation for two- and three-band transition schemes in a system with an idealized band structure. In addition, an estimate is made of the multipole terms which are of one order higher than the dipolar.

1. INTRODUCTION

A NUMBER of fruitful investigations$^{(1-5)}$ of the harmonic generation of light due to the interaction of solids with optical maser beams have been made recently. Early theories of harmonic generation dealt with: (1) a phenomenological description of electrons interacting with radiation,$^{(5)}$ and (2) localized electrons interacting with radiation using semiclassical radiation theory.$^{(6)}$

In a previous paper by the author,$^{(7)}$ that part of the electronic response of a solid which is proportional to the square of the classical electromagnetic field was derived using operator perturbation theory. The results were obtained in a form which was applicable to non-localized electrons such as Bloch electrons. The spatial dependence of the second harmonic wave within the solid was found. In addition, a three-band transition scheme was used to estimate the output of second harmonic power in the limit where both the first and second harmonic energies are near band gaps. This limit would most likely imply that the medium is absorbing to the second harmonic.

The present work is concerned primarily with describing the effect of electronic band structure on second harmonic generation. Direct transitions (those not involving phonons) which are allowed in the dipole approximation are described. It is found that two- and three-band schemes are allowed, with the two-band scheme including an intraband transition. The response function is then calculated for the two- and three-band transition schemes. In order to facilitate the calculations, a band structure is assumed in which the bands are parabolic and widely separated. In this idealized calculation, the two-band scheme does not exhibit any singular behavior near the band gap, while the three-band scheme may show for certain choices of the band parameters singular behavior but not necessarily at the band gap. Finally, an estimate is made of the term in the response function one order higher than the dipolar.

2. THE NONLINEAR RESPONSE FUNCTION

The quantity of interest in this paper is that part of the current induced in a solid which is proportional to the square of the external field. The second order nonlinear response function, α, relates the space and time Fourier transform of the current $J^{\epsilon}(\mathbf{q}\omega)$ to the product of the transformed vector potentials $A^{\mu}(\mathbf{q}'\omega')$ and $A^{\nu}(\mathbf{q}'', \omega'')$ in the following way:

$$J^{\epsilon}(\mathbf{q}, \omega) = \iiiint \mathrm{d}\omega' \mathrm{d}\omega'' \, \mathrm{d}\mathbf{q}' \mathrm{d}\mathbf{q}'' \times \alpha^{\epsilon\mu\nu}(\mathbf{q}, \mathbf{q}', \mathbf{q}'', \omega'+\omega'', \omega') \times A^{\mu}(\mathbf{q}', \omega') A^{\nu}(\mathbf{q}'', \omega'') \delta(\omega'+\omega''-\omega). \quad (1)$$

The response function, obtained in an earlier paper,(7) is given by

---

* Operated with support from the U.S. Army, Navy and Air Force.

$$\alpha^{\epsilon\mu\nu}(q, q', q'', \omega'+\omega'', \omega')$$

$$=\left\{\frac{v_c}{(2\pi)^3}\sum_{n}\exp[i(q+q'+q'')\cdot R_n]\right\}$$

$$\times\Gamma^{\epsilon\mu\nu}(q, q', q'', \omega'+\omega'', \omega'), \qquad (2)$$

where v_c is the volume of a unit cell, R_n is a lattice vector, and

$$\Gamma^{\epsilon\mu\nu}(q, q', q'', \omega'+\omega'', \omega')$$

$$= -\frac{e^3(2\pi)^3}{2m^3c^2V\hbar^2}\, Tr\rho(t_0)\, \{[(\eta(\mathscr{L}_0+\omega'+\omega'')\bar{p}^{\epsilon}(q)),$$

$$\delta_{\kappa,-q'-q''}\,\bar{P}(q'+q'')]\delta_{\mu\nu}\hbar$$

$$+2\hbar[(\eta(\mathscr{L}_0+\omega'')\,\bar{P}(q+q'')),\, \delta_{\kappa,-q'}\,\bar{p}^{\mu}\,(q')]\,\delta_{\epsilon\nu}$$

$$+\frac{1}{\pi}\,[(\eta(\mathscr{L}_0+\omega')\,[(\eta(\mathscr{L}_0+\omega'+\omega'')\,\bar{p}^{\epsilon}\,(q)),$$

$$\delta_{\kappa,-q'}\,\bar{p}^{\mu}\,(q')]),\ \delta_{\kappa,\,q''}\,\bar{p}^{\nu}\,(q'')]\}. \qquad (3)$$

In the above equation, $\rho(t_0)$ is the equilibrium one electron distribution operator, $\bar{p}(q)$ is the cellular transform of the momentum density operator

$$\bar{p}^{\mu}(q) = N\int_{\text{cell}} dr\,\exp(iq\cdot r)\,p^{\mu}(r), \qquad (4)$$

and $(\bar{P}q)$ is the transform of the mass density operator. $\eta(\omega)$ is given by $1/\omega+i\epsilon$ where $\epsilon\to 0^+$. The Liouville operator, $\mathscr{L}_0$, has been introduced and is defined by

$$\mathscr{L}_0A \equiv 1/\hbar\,[\mathscr{H}_0, A]; \qquad (5)$$

in addition, its analog κ, for the wave vector operator, is defined by

$$\kappa A \equiv [k, A]. \qquad (6)$$

Here, k is the wave vector operator defined in terms of Bloch states $\{n'k'\}$ by

$$k|n'k'\rangle = k'|n'k'\rangle. \qquad (7)$$

The response function may now be evaluated by writing the trace as a sum over the Bloch states of the solid.

The problem to be considered in the following calculations is that of frequency doubling. In this case, $\omega' = \omega'' = \omega_1$ and $\omega'+\omega'' = \omega_2 = 2\omega_1$. Here, ω_1 is the first harmonic frequency and ω_2 is the second harmonic frequency.

3. THE DIPOLE APPROXIMATION

In the preceding Section, the second order nonlinear response function has been given as a trace over the one-electron states of the solid. In this Section, the dipole approximation will be made and the response function will be evaluated for a simple model band structure. The aim here is to obtain a picture of the dipole transition schemes and give an order of magnitude estimate of the response function for the various processes.

The dipole approximation consists of making the approximation $\exp(iq\cdot r)\sim 1$ within the cellular integrals, under the assumption that $|q\cdot a| \ll 1$ (where a is a lattice spacing). Furthermore, the q's in the Kronecker deltas in equation (3) are set equal to zero. The last approximation constrains the interband transitions to be vertical. Although the transitions are not quite vertical, the error made in the vertical approximation is also of the order of $|q\cdot a|$. With these approximations in mind, equation (3) can be written explicitly in terms of matrix elements between Bloch states $\{nk\}$, $\{n'k'\}$ and $\{n''k''\}$ as

$$\Gamma^{\epsilon\mu\nu}(2\omega_1, \omega_1) = -\frac{e^3(2\pi)^2}{\hbar^2m^3c^2V}\sum_{\substack{k=k'=k''\\ n,n',n''}} f(\omega_n(k))$$

$$\times\left\{\frac{1}{\omega_{nn'}(k)+2\omega_1+i\epsilon}\,\frac{1}{\omega_{nn''}(k)+\omega_1+i\epsilon}\right.$$

$$\times\, p^{\epsilon}_{nn'}\,p^{\mu}_{n'n''}\,p^{\nu}_{n''n}(k)$$

$$-\frac{1}{\omega_{n'n''}(k)+2\omega_1+i\epsilon}\left(\frac{1}{\omega_{nn''}(k)+\omega_1+i\epsilon}\right.$$

$$\times\, p^{\mu}_{nn'}\,p^{\epsilon}_{n'n''}\,p^{\nu}_{n''n}(k)$$

$$\left.+\frac{1}{\omega_{n'n}(k)+\omega_1+i\epsilon}\,p^{\nu}_{nn'}\,p^{\epsilon}_{n'n''}\,p^{\mu}_{n''n}(k)\right)$$

$$+\frac{1}{\omega_{n''n}(k)+2\omega_1+i\epsilon}\,\frac{1}{\omega_{n'n}(k)+\omega_1+i\epsilon}$$

$$\left.\times\, p^{\nu}_{nn'}\,p^{\mu}_{n'n''}\,p^{\epsilon}_{n''n}(k)\right\}, \qquad (8)$$

where $\hbar\omega_{nn'}(k) = \langle nk|\mathscr{H}_0|nk\rangle - \langle n'k|\mathscr{H}_0|n'k\rangle$. Note that the solid considered for the dipole process cannot have inversion symmetry, since the states of such a system can be chosen to have definite parity (these are not the Bloch states) and the product of three dipole operators cannot connect states of the same parity. (See Appendix.)

The results can now be discussed in terms of transitions between energy bands. The three states $\{nk\}$, $\{n'k'\}$, and $\{n''k''\}$ may correspond to states in one, two, or three bands. If only one band were involved, expression (8) would vanish, since the four terms in (8) would cancel. Thus, the states must involve either two or three bands. The two-band scheme consists of two interband transitions and one intraband transition; the three-band scheme consists of three interband transitions.

The magnitude of Γ will be calculated for the two and three band schemes. The energy bands will be taken to be parabolic about $k = 0$ in wave vector space. Figure 1 represents the band structure of the idealized solid. The valence band (band 1) has energy versus wave vector dependence

$$\langle 1k|\mathscr{H}_0|1k\rangle = E_1(k) = -\frac{\hbar^2k^2}{2m_1}, \qquad (9)$$

while the conduction bands (bands 2 and 3) have the dependence

$$\langle 2k|\mathscr{H}_0|2k\rangle = E_2(k) = E_g + \frac{\hbar^2k^2}{2m_2}, \qquad (10)$$

and

$$\langle 3k|\mathscr{H}_0|3k\rangle = E_3(k) = E_g' + \frac{\hbar^2k^2}{2m_3}. \qquad (11)$$

Band 1 will be considered completely filled, while bands 2 and 3 are empty.

The transitions will be taken to be virtual (E_g, $E_g' > 2\hbar\omega_1$); in other words, none of the denominators in (8) are allowed to vanish. This implies that the energy of the radiation field is conserved but that there is mixing of the modes of the electromagnetic field by the solid.

The two-band calculation

First, the two-band scheme is considered. The interband transitions are taken between bands 1 and 2. The intraband momentum matrix element for a Bloch state $\{n, k\}$ is given by

$$\langle nk|p^\mu|nk\rangle = \frac{m}{\hbar}\frac{\partial E_n(k)}{\partial k^\mu}, \qquad (12)$$

and is, therefore, an odd function of k. On converting the sum over k in equation (8) into an integral, it is evident that only those terms in the remainder of the integrand (i.e. apart from the intraband matrix element) which are odd in k will contribute. Therefore, if the product of the two interband momentum matrix elements is expanded as a series in k, only the odd powers in k give a nonvanishing contribution. This expansion will be accomplished by means of a $k \cdot p$ perturbation calculation, where, for the sake of simplicity, only the term linear in k will be kept. This approximation is valid in the limit where the bands are far apart in energy. $k \cdot p$ perturbation theory contains

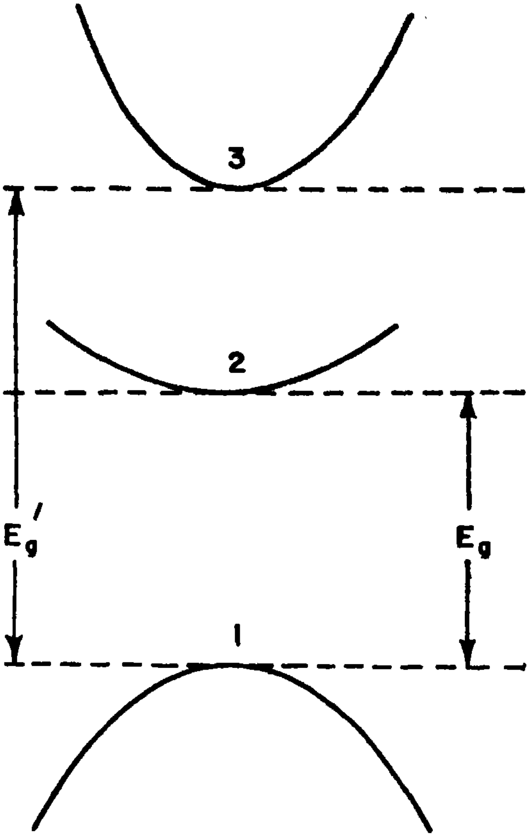

FIG. 1. Three-band model.

energy denominators and interband momentum matrix elements. The assumption made here is that the bands are far enough apart so that the denominators are large enough to make the series convergent. The linear part of the product of the interband matrix elements is found to be

$$(p_{12}^{\mu}(k)p_{21}^{\nu}(k))^{\text{linear}} = -(p_{12}^{\nu}(k)p_{21}^{\mu}(k))^{\text{linear}}$$
$$= \sum_{\delta} \hbar k^{\delta} \Delta_{12}^{\mu\nu\delta}, \qquad (13)$$

where

$$\Delta_{12}^{\mu\nu\delta} = \frac{1}{m}\sum_{j}\left\{\left(\frac{p_{1j}^{\mu}p_{j2}^{\delta}}{\hbar\omega_{j2}} - \frac{p_{1j}^{\delta}p_{j2}^{\mu}}{\hbar\omega_{1j}}\right)p_{21}^{\nu}\right.$$
$$\left. + p_{12}^{\mu}\left(\frac{p_{2j}^{\nu}p_{j1}^{\delta}}{\hbar\omega_{j1}} - \frac{p_{2j}^{\delta}p_{j1}^{\nu}}{\hbar\omega_{2j}}\right)\right\}. \qquad (14)$$

In the last expression, the matrix elements of p refer to the center of the zone. The sum over j is taken so that the ω_{ij}'s do not vanish. Note that if we were to include only bands 1 and 2 in the sum, then Δ would vanish. Other bands must be involved in the calculation of Δ. Substituting (9), (10), (12) and (13) into (8), the following is obtained in the spherical zone approximation:

$$\Gamma^{\epsilon\mu\nu}(2\omega_1, \omega_1) = \frac{2}{3}\left(\frac{e^3}{m^2c^2\hbar^3}\right)\frac{1}{\hbar\omega_1}(\Delta_{12}^{\epsilon\nu\mu} + \Delta_{12}^{\epsilon\mu\nu})$$
$$\times\left\{(a^-)^{3/2}\tan^{-1}\frac{p_M}{(a^-)^{1/2}} - (b^-)^{3/2}\tan^{-1}\frac{p_M}{(b^-)^{1/2}}\right.$$
$$\left. + (a^+)^{3/2}\tan^{-1}\frac{p_M}{(a^+)^{1/2}} - (b^+)^{3/2}\tan^{-1}\frac{p_M}{(b^+)^{1/2}}\right\}, \qquad (15)$$

where $p_M = \hbar k_M$, and k_M is the wave vector at the spherical Brillouin zone boundary. The a's and b's are defined by

$$a^{\pm} \equiv 2\mu_{12}(E_g \pm 2\hbar\omega_1), \qquad (16)$$

and

$$b^{\pm} \equiv 2\mu_{12}(E_g \pm \hbar\omega_1). \qquad (17)$$

The interband mass μ, introduced above, is defined by

$$\mu_{ij} = \frac{m_i m_j}{m_i + m_j}. \qquad (18)$$

The behavior of (15), as a function of ω_1, is not too transparent. However, it can be pointed out that (15) does not exhibit any strong singularities. If one goes to the limit of narrow bands, with $2\hbar\omega_1$ near enough to the band gap so that $E_g - 2\hbar\omega_1$ is small compared to the band width (in other words, $a^- \ll p_M^2 \ll a^+, b^{\pm}$), the inverse tangent functions can be expanded to obtain

$$\Gamma^{\epsilon\mu\nu}(2\omega_1, \omega_1) = \frac{2}{3}\left(\frac{e^3}{m^2c^2\hbar^3}\right)\frac{1}{\hbar\omega_1}$$
$$\times(\Delta_{12}^{\epsilon\mu\nu} + \Delta_{12}^{\epsilon\nu\mu})\frac{p_M^3}{3}. \qquad (19)$$

It should be mentioned that the two-band model places a restriction on the response tensor. PRICE(8) has shown that the third rank response tensor for a two-band process must be antisymmetric under the interchange of the two indices corresponding to the interband dipole matrix elements. This result may be obtained by applying Kramer's theorem to the interband elements. However, those crystals which have a nonvanishing third rank tensor are not necessarily constrained to be symmetric under the interchange of two arbitrary indices. Therefore, the two-band scheme will not be forbidden by crystal symmetry.

The three-band calculation

Next, the three-band calculation where all the momentum matrix elements are interband is treated. Since these matrix elements are complicated functions of k, it is advisable to make a simplifying assumption and replace the matrix by the band edge matrix element; in other words,

$$\langle nk|p^{\mu}|nk\rangle \simeq \langle n0|p^{\mu}|n'0\rangle = p_{nn'}^{\mu}. \qquad (20)$$

Here, it is assumed that symmetry will allow transitions between the band edges. For a particular symmetry type, this assumption must be tested by studying the transformation properties of the wave functions at the band edge. Substituting (9), (10), (11) and (16) into (8), the leading term in the three-band process gives:

$$\Gamma^{\epsilon\mu\nu}(2\omega_1, \omega_1) = 2\left(\frac{e^3}{m^3c^2\hbar^3}\right)(2\mu_{12})(2\mu_{13})$$
$$\times p_{12}^{\epsilon}p_{23}^{\mu}p_{31}^{\nu}$$

$$\times\frac{1}{a^- - c^-}\left\{(a^-)^{1/2}\tan^{-1}\frac{p_M}{(a^-)^{1/2}}-(c^-)^{1/2}\tan^{-1}\right.$$

$$\left.\times\frac{p_M}{(c^-)^{1/2}}\right\}, \tag{21}$$

where

$$c^- = 2\mu_{13}(E'_g-\hbar\omega_1). \tag{22}$$

Again assuming narrow bands, however, with $2\hbar\omega_1$ near E_g (i.e. $a^- \ll p_M^2 \ll c^-$), the inverse tangent functions can be expanded to obtain

$$\Gamma^{\epsilon\mu\nu}(2\omega_1,\omega_1) = \frac{e^3}{m^3c^2\hbar^3}(2\mu_{12})(2\mu_{13})$$

$$\times\, \overset{\epsilon}{p}_{12}\,\overset{\mu}{p}_{23}\,\overset{\nu}{p}_{31}$$

$$\times\,\frac{p_M}{\mu_{13}(E'_g-\hbar\omega_1)-\mu_{12}(E_g-2\hbar\omega_1)}. \tag{23}$$

Whether Γ has a singularity, and the position of this singularity, is determined by the gaps E_g and E'_g and by the interband masses μ_{12} and μ_{13}. The limit taken above constrains the second harmonic to be below both band gaps. This is in contrast to the previous(7) three-band model where $E'_g > 2\hbar\omega_1 > E_g$, in which case the medium will probably be absorbing to second harmonic radiation.

The ratio of the two-band to the three-band process can now be estimated as

$$\frac{\Gamma_{2\text{ Band}}}{\Gamma_{3\text{ Band}}} \sim \frac{\dfrac{p_M^2}{2\mu_{12}}}{E_g}. \tag{24}$$

Thus, it is seen that, under the assumption of bands narrow compared to the gap, the three band process will be dominant. It should be remembered, in considering the above results, that the amplitude of the second harmonic is proportional to Γ and local field corrections. These local field corrections are dependent on the dielectric tensor which usually shows a strong singularity near the band gap. Thus, it may well be that any dependence of the second harmonic on the difference between the band edge and the second harmonic frequency is due, in large measure, to the linear polarizability of the medium at the second harmonic frequency. The increased difficulty in phase matching will play an important role also, as the second harmonic approaches the band edge.

4. HIGHER ORDER EFFECTS

In solids with inversion symmetry the dipolar process vanishes and higher order processes must be considered. An order of magnitude estimate will be made of the term in Γ which is one order higher than the dipolar; this is that part of Γ which is linear in q. The linear term will then be compared with the dipolar term. Because of the complicated nature of the higher order processes only the first commutator in (3) will be evaluated here. The aim is to explicitly show for the simplified model used here that a typical term linear in q is of order qa or q/k_M smaller than the dipolar. The other terms in (3) should also be of order q/k_M smaller.

$$\{\Gamma^{\epsilon\mu\nu}(2\omega_1,\omega_1)\}^{(\text{linear in } q)} \approx \sum_{\delta}\frac{-e^3(2\pi)^3}{2m^3c^2V\hbar}$$

$$\times\, \overset{\delta}{q}_1 \sum_{\substack{k=k'\\ n,n'}} f(\omega_n(k))\,\delta_{\mu\nu}$$

$$\times\,\frac{1}{\omega_{nn'}(k)}\left\{\frac{1}{\omega_{nn'}(k)+2\omega_1}\overset{\epsilon}{p}_{nn'}\,\overset{\delta}{p}_{n'n}(k)\right.$$

$$\left.+\frac{1}{\omega_{n'n}(k)+2\omega_1}\overset{\delta}{p}_{nn'}\,\overset{\epsilon}{p}_{n'n}(k)\right\}, \tag{25}$$

where q_1 is the wave vector of the first harmonic. The matrix elements of the momentum operators will be taken between band 1 and band 2. As in (20), these matrix elements will be replaced by those at the band edge. Converting the sum in (25) to an integral, and carrying out the integration, the following is obtained

$$\{\Gamma^{\epsilon\mu\nu}(2\omega_1,\omega_1)\}^{(\text{linear in } q)} = \sum_{\delta}\frac{2\pi e^3}{m^3c^2\hbar^2}$$

$$\times\, \overset{\delta}{q}_1\, \delta^{\epsilon}_{\mu\nu}\, \overset{\delta}{p}_{12}\, p_{21}$$

$$\times\,\frac{\mu_{12}}{\hbar\omega_1}\left\{(a^+)^{1/2}\tan\frac{p_M}{(a^+)^{1/2}}+(a^-)^{1/2}\tan^{-1}\right.$$

$$\left.\times\frac{p_M}{(a^-)^{1/2}}-2(a)^{1/2}\tan^{-1}\frac{p_M}{(a)^{1/2}}\right\}. \tag{26}$$

Here, $a^{\pm}$ is defined by (16), and $a = 2\mu_{12}E_g$. Again going to the limit of narrow bands, but with $2\hbar\omega_1$ close to E_g (i.e. $a^- \ll p_M^2 \ll a, a^+$), equation (26) becomes

$$\{\Gamma^{\epsilon\mu\nu}(2\omega_1, \omega_1)\}^{(\text{linear in } q)} = \sum_{\delta} \frac{2\pi e^3}{m^3c^2\hbar^2}$$

$$\times\ q_1^{\delta}\,\delta_{\mu\nu}\,\frac{\mu_{12}}{\hbar\omega_1}\,p_{12}^{\epsilon}\,p_{12}^{\delta}\,p_M. \tag{27}$$

Comparing this result with the dipolar term, it is found that the ratio is approximately

$$\frac{\Gamma_{\text{linear in } q}}{\Gamma_{\text{dipolar}}} \approx q_1/k_M \approx 10^{-4}. \tag{28}$$

Thus, the second harmonic intensity, which is proportional to the square of Γ, is $\approx 10^{-8}$ smaller in crystals with inversion symmetry than in crystals without inversion symmetry.

5. CONCLUSIONS

The preceding has given an evaluation of the second harmonic response function for two- and three-band transition schemes in the dipole approximation, as well as an estimate of the response function for a two-band scheme for electromagnetic processes which are of higher order than the dipolar. The calculation has been carried out for a solid with highly idealized bands. This idealized model may be recognized as a first step toward the methods to be used in the calculation of the nonlinear response of an actual solid. The details of the calculation for a real solid would necessarily involve its symmetry properties and actual energy surfaces.

Acknowledgements—The author would like to thank Dr. W. H. KLEINER and Dr. A. L. MCWHORTER for their critical reading of this manuscript.

REFERENCES

1. FRANKEN P. A., HILL A. E., PETERS C. W. and WEINREICH G., *Phys. Rev. Letters* **7**, 118 (1961).
2. BASS M., FRANKEN P. A., HILL A. E., PETERS C. W. and WEINREICH G., *Phys. Rev. Letters* **8**, 18 (1962).
3. GIORDMAINE J. A., *Phys. Rev. Letters* **8**, 19 (1962).
4. MAKER P. D., TERHUNE R. W., NISENOFF M. and SAVAGE C. M., *Phys. Rev. Letters* **8**, 21 (1962).
5. LAX B., MAVROIDES J. G. and EDWARDS D. F., *Phys. Rev. Letters* **8**, 166 (1962).
6. ARMSTRONG J. A., BLOEMBERGEN N., DUCUING J. and PERSHAN P. S., *Phys. Rev.* **127**, 1918 (1962).
7. KELLEY P. L., *J. Phys. Chem. Solids* **26**, 607 (1963).
8. PRICE P. J., Private communication.

APPENDIX

It will now be shown that (3) vanishes for systems with inversion symmetry in the dipole approximation. This is most readily shown by introducing a complete orthonormal set of states defined in the following way:

$$\begin{aligned} |nk\pm\rangle &= \frac{1}{\sqrt{2}}\{|n,+k\rangle \pm |n,-k\rangle\},\ k_x < 0 \\ &\qquad\qquad k \neq 0,K \\ |n0+\rangle &= |n,0\rangle \qquad k = 0 \\ |nK+\rangle &= |n,K\rangle \qquad k = K \end{aligned} \tag{29}$$

$\{n,0\}$ and $\{n,K\}$, respectively, indicate states at $k = 0$ and symmetry points on the zone face. As is well known, these are energy eigenstates

$$\mathscr{H}_0|n,k\pm\rangle = \mathscr{E}_n(k)|n,k\pm\rangle. \tag{30}$$

It is easily shown for $k \neq 0$ that these are states of definite parity. If

$$\psi_n^{\pm}(k,r) = \exp(ik\cdot r)\,u_{nk}(r) = \langle r|nk\pm\rangle, \tag{31}$$

and the choice of phase $u_{nk}(-r) = u_{nk}^*(r)$ is made, then it can be shown that

$$\psi_{nk}^{\pm}(-r) = \pm\,\psi_{nk}^{\pm}(r). \tag{32}$$

The states at $k = 0,K$, namely $\{n,0\}$ and $\{n,K\}$, can also be chosen to have definite parity in systems with inversion symmetry; however, the + at $k = 0,K$ does not necessarily indicate parity +. In taking the trace in (3) if the sum is carried out over the states defined by (29), the following is obtained in the dipole approximation

$$\Gamma^{\epsilon\mu\nu}(2\omega_1,\omega_1) = \frac{-e^3(2\pi)}{\hbar^2m^3c^2V}\sum_{\substack{k=k'=k''\\ n,n',n'',\pm\\ k_x\leq 0}}$$

$$\times f(\omega_n(k))\left\{\frac{1}{\omega_{nn'}(k)+2\omega_1+i\epsilon}\,\frac{1}{\omega_{nn''}(k)+\omega_1+i\epsilon}\right.$$

$$\times\ \langle nk\pm|p^{\epsilon}|n'k\pm\rangle\langle n'k\pm|p^{\mu}|n''k\pm\rangle$$

$$\times\ \langle n''k\pm|p^{\epsilon}|nk\pm\rangle$$

$$-\ \frac{1}{\omega_{n'n''}(k)+2\omega_1+i\epsilon}$$

$$\times\left(\frac{1}{\omega_{nn''}(k)+\omega_1+i\epsilon}\langle nk\pm|\bar{p}^{\mu}|n'k\pm\rangle\right.$$

$$\times\ \langle n'k\pm|\bar{p}^{\epsilon}|n''k\pm\rangle\langle n''k\pm|\bar{p}^{\nu}|nk\pm\rangle$$

$$+\frac{1}{\omega_{n'n}(k)+\omega_1+i\epsilon}\langle nk\pm|\bar{p}^{\nu}|n'k\pm\rangle$$

$$\times\langle n'k\pm|\bar{p}^{\sigma}|n''k\pm\rangle\langle n''k\pm|\bar{p}^{\mu}|nk\pm\rangle\Big)$$

$$+\frac{1}{\omega_{n''n}(k)+2\omega_1+i\epsilon}\,\frac{1}{\omega_{n'n}(k)+\omega_1+i\epsilon}$$

$$\times\langle nk\pm|\bar{p}^{\nu}|n'k\pm\rangle\langle n'k\pm|\bar{p}^{\mu}|n''k\pm\rangle$$

$$\times\langle n''k\pm|\bar{p}^{\sigma}|nk\pm\rangle\Big\}. \qquad (33)$$

The operator $\bar{p}$ is nonvanishing only for states of opposite parity; hence an odd product of p's is nonvanishing only for states of opposite parity. Since the products of the p matrix elements have the same final as initial state, the product must vanish.

J. Phys. Chem. Solids Pergamon Press 1963. Vol. 24, pp. 1121–1129. Printed in Great Britain.

RESISTIVITY OF VACANCY–IMPURITY PAIRS*

JOSEPH M. KELLER

Institute for Atomic Research and Department of Physics, Iowa State University, Ames, Iowa,
and Brookhaven National Laboratory, Upton, New York

(*Received* 1 *March* 1963)

Abstract.—The contribution to electrical resistivity of impurity atoms adjacent to vacancies in metals is calculated. The calculation is based on the Born approximation, which allows separation of the effects of the individual imperfections from interference effects. Lattice relaxation is neglected. The resistivity due to Ag or Zn impurities adjacent to a vacancy in Au is related to the resistivity of the separate imperfections as $\rho_{\text{Ag+vac}} = \rho_{\text{Ag}} + \rho_{\text{vac}} - 0{\cdot}11\ (\rho_{\text{Ag}} \times \rho_{\text{vac}})^{1/2}$; $\rho_{\text{Zn+vac}} = \rho_{\text{Zn}} + \rho_{\text{vac}} + 0{\cdot}10\ (\rho_{\text{Zn}} \times \rho_{\text{vac}})^{1/2}$. Effects of anisotropy of the scattering are found to be almost completely removed if the vacancy–impurity pairs are randomly oriented along the several ⟨110⟩ directions.

INTRODUCTION

It is widely believed$^{(1)}$ that vacancies in a (non-transition) metal tend to associate with substitutional charged impurities. The present investigation seeks to determine the effect of such combined defects on electrical resistivity if the impurity and vacancy are on adjacent lattice sites.

Since past experience$^{(2, 3)}$ has shown that only in the case of interstitial atoms is the effect of lattice relaxation on electrical resistivity of major importance, we have ignored lattice relaxations in the present calculations. Cross sections for scattering by a vacancy–impurity pair have been calculated in Born approximation, which enables scattering by a pair to be resolved into scattering by the separate vacancy and impurity atom plus an interference. We believe that the familiar inadequacies of the Born approximation are satisfactorily compensated by adjusting the amplitudes of the separate scattering potentials to give the correct resistivities of the uncoupled defects. The problem then reduces to a treatment of the interference.

Each vacancy–impurity pair is an anisotropic scatterer, giving rise to a scattering potential that has only axial symmetry. The pairs are assumed to be oriented at random along the twelve ⟨110⟩ directions. In carrying out the calculations it will be necessary to average over these different directions, and the result will be largely to wash out the effects of anisotropy of the individual (pair) scatterers. In order to examine any remaining effect of anisotropy, we have used a more complicated Anzatz than is customary for the angular dependence of the solution to the Boltzmann equation. This correction turns out to be very small indeed.

METHOD OF CALCULATION

If $f(\boldsymbol{k})$ is the probability that a one-electron state of wave vector $\boldsymbol{k}$ is occupied, it is customary to write

$$\begin{aligned} f(\boldsymbol{k}) &= f_0(\boldsymbol{k}) - \Phi(\boldsymbol{k})\partial f_0/\partial\epsilon \\ &= f_0(\boldsymbol{k}) + \Phi(\boldsymbol{k}) f_0(\boldsymbol{k})[1-f_0(\boldsymbol{k})]/\mathrm{K}T \end{aligned} \tag{1}$$

where $\Phi(\boldsymbol{k})$ is a measure of the departure of $f(\boldsymbol{k})$ from the equilibrium Fermi distribution $f_0(\boldsymbol{k})$. Here ϵ is energy, K the Boltzmann constant, and T the temperature. Then the electric current density J is given by

$$\begin{aligned} J_i &= -(4\pi^3)^{-1}\, e \int \mathrm{d}^3k v_i f(\boldsymbol{k}) \\ &= \frac{1}{4\pi^3}\frac{e}{\hbar}\int \mathrm{d}^3k \frac{\partial\epsilon}{\partial k_i}\, \Phi(\boldsymbol{k})\, \frac{\partial f_0}{\partial\epsilon}, \end{aligned} \tag{2}$$

---

* This work was supported by the U.S. Atomic Energy Commission.

where e is the magnitude of the fundamental charge and $\boldsymbol{v}$ is the electron velocity.

The current is produced by an external electric field $\boldsymbol{E}$, which accelerates the electrons and alters their distribution. The change in distribution is opposed by some relaxation mechanism that produces the electrical resistivity—in the present case the concentration of s scatterers per unit volume, each with a partial scattering cross-section $I(\boldsymbol{k},\boldsymbol{k}')\,\mathrm{d}\omega_{k'}$ from state $\boldsymbol{k}$ to any state $\boldsymbol{k}'$ within an infinitesimal solid angle $\mathrm{d}\omega_{k'}$. The steady state distribution function $f(\boldsymbol{k})$, or $\Phi(\boldsymbol{k})$, is determined by a (linearized) Boltzmann equation of the form

$$\begin{aligned}
-(e/\hbar)\,(\boldsymbol{E}\cdot\mathrm{grad}_k)f_0(\boldsymbol{k})
&= s\int \mathrm{d}\omega_{k'}\{\boldsymbol{v}(\boldsymbol{k}')I(\boldsymbol{k}',\boldsymbol{k})f(\boldsymbol{k}')\,[1-f(\boldsymbol{k})] \\
&\qquad - \boldsymbol{v}(\boldsymbol{k})I(\boldsymbol{k},\boldsymbol{k}')f(\boldsymbol{k})\,[1-f(\boldsymbol{k}')]\} \\
&= (s/\mathrm{K}T)\int \mathrm{d}\omega_{k'}\,\boldsymbol{v}(\boldsymbol{k}')\,I(\boldsymbol{k}',\boldsymbol{k})\,f_0(\boldsymbol{k}')\,[1-f_0(\boldsymbol{k})] \\
&\qquad \times [\Phi(\boldsymbol{k}')-\Phi(\boldsymbol{k})]. \qquad (3)
\end{aligned}$$

To simplify the calculations, we are going to assume spherical energy contours in k-space. In fact, both this assumption and the elastic nature of scattering by fixed scattering centers have already been used in writing the Boltzmann equation in the form of equation (3).

From equation (3) it follows that

$$\begin{aligned}
(e/\hbar)\int \mathrm{d}^3k\Phi(\boldsymbol{k})\,(\boldsymbol{E}\cdot\mathrm{grad}_k)\,f_0(\boldsymbol{k}) \\
= (s/\mathrm{K}T)\int \mathrm{d}^3k\Phi(\boldsymbol{k})\int \mathrm{d}\omega_{k'}\,\boldsymbol{v}(\boldsymbol{k}') \\
\times\, I(\boldsymbol{k}',\boldsymbol{k})\,f_0(\boldsymbol{k})\,[1-f_0(\boldsymbol{k})]\int \Phi(\boldsymbol{k})-\Phi(\boldsymbol{k}')]. \quad (3a)
\end{aligned}$$

Now the expression for current density in equation (2) may be multiplied and divided by the two members of equation (3a), and the result somewhat simplified by use of the delta function nature of $\partial f_0/\partial\epsilon$. In this way one obtains the expression

$$J_i = \sum_j \sigma_{ij}E_j$$

where

$$\sigma_{ij} = (e^2/4\pi^3\hbar sP)\int \mathrm{d}\omega_k k_i\Phi(\boldsymbol{k})\int \mathrm{d}\omega_k k_j\Phi(\boldsymbol{k}) \qquad (4)$$

and

$$P \equiv \int \mathrm{d}\omega_k \int \mathrm{d}\omega_{k'}\Phi(\boldsymbol{k})\,I(\boldsymbol{k},\boldsymbol{k}')[\Phi(\boldsymbol{k})-\Phi(\boldsymbol{k}')]. \qquad (5)$$

All quantities in equations (4) and (5) are to be evaluated at the Fermi energy.

Expression (4) for the electrical conductivity has a valuable extremal property.(4) If the conductivity is calculated from equation (4), but using a function Φ that satisfies equation (3) only approximately, the resulting value for σ is smaller than the correct value by an amount of only second order in the error of Φ.

In f.c.c. crystals we may assume that impurity–vacancy pairs are oriented at random along the twelve $\langle 110\rangle$ directions. Since in a cubic crystal the conductivity tensor reduces to a scalar, the direction of the applied electric field is of no significance, and we choose it along a cubic axis designated as the z-axis. Because of the anisotropic nature of the scattering from an impurity–vacancy pair, one would expect Φ to be a somewhat complicated function of direction. But Φ must have 4-fold rotational symmetry about the z-axis, and must be odd to reflection in an xy plane. We shall approximate Φ as

$$\begin{aligned}
\Phi &= c_1P_1(\cos\theta)+c_3P_3(\cos\theta) \\
&= c_1\cos\theta + c_3(5\cos^3\theta - 3\cos\theta)/2 \qquad (6)
\end{aligned}$$

where θ is the angle between k and the z-axis. Then

$$\int \mathrm{d}\omega_k k_z\Phi(\boldsymbol{k}) = 4\pi kc_1/3. \qquad (7)$$

If c_3 is neglected, equation (4) is independent of the value of c_1. Otherwise the ratio c_3/c_1 may be determined to maximize the calculated value for σ.

The cross-section for scattering by a vacancy–impurity pair must be a complicated function of initial and final directions, the calculation of which would be surely difficult and probably unrewarding. Isolated vacancies and impurities each give rise to approximately spherically symmetric scattering potentials. The binding of impurities to vacancies must distort these separate potentials, and in fact the binding must be due to a combination of electron and lattice rearrangements. Nevertheless the effect of these distortions on scattering is probably small, and we shall here neglect it. We shall assume that a vacancy at $\boldsymbol{r}_1$

produces a scattering potential V_1 spherically symmetric about $\mathbf{r}_1$, and that an impurity atom at $\mathbf{r}_2$ produces its own scattering potential V_2 spherically symmetric about $\mathbf{r}_2$, independent of the presence of the vacancy. We are primarily concerned with the effects of interference produced by these two adjacent scattering centers on the scattering, and hence on electrical resistivity.

In first order perturbation theory (Born approximation), the scattering amplitude $A(\mathbf{k},\mathbf{k}')$ for scattering free electrons from an initial direction $\mathbf{k}$ to a final direction $\mathbf{k}'$ is given by$^{(5)}$

$$A(\mathbf{k},\mathbf{k}') = -(m/2\pi\hbar^2)\int \mathrm{d}^3r \exp[i(\mathbf{k}-\mathbf{k}')\cdot\mathbf{r}]V(\mathbf{r}).$$

For a sum of scattering potentials of the type we are assuming,

$$\begin{aligned}
&-(2\pi\hbar^2/m)\,A(\mathbf{k},\mathbf{k}')\\
&= \int \mathrm{d}^3r \exp[i(\mathbf{k}-\mathbf{k}')\cdot\mathbf{r}][V_1(\mathbf{r}-\mathbf{r}_1)+V_2(\mathbf{r}-\mathbf{r}_2)]\\
&= \exp[i(\mathbf{k}-\mathbf{k}')\cdot\mathbf{r}_1]\int \mathrm{d}^3r \exp[i(\mathbf{k}-\mathbf{k}')\cdot\mathbf{r}]V_1(r)\\
&+ \exp[i(\mathbf{k}-\mathbf{k}')\cdot\mathbf{r}_2]\int \mathrm{d}^3r \exp[i(\mathbf{k}-\mathbf{k}')\cdot\mathbf{r}]\;V_2(r)\\
&= -(2\pi\hbar^2/m)\Big[\exp[i(k-k')\cdot r_1][A_1(\mathbf{k},\mathbf{k}')]\\
&\qquad+\exp[i(\mathbf{k}-\mathbf{k}')\cdot r_2][A_2(\mathbf{k},\mathbf{k}')]\Big]
\end{aligned}$$

For spherically symmetric potentials, these last integrals are real, and we obtain

$$\begin{aligned}
I(\mathbf{k},\mathbf{k}') &= |A(\mathbf{k},\mathbf{k}')|^2\\
&= I_1(\mathbf{k},\mathbf{k}')+I_2(\mathbf{k},\mathbf{k}')+2\cos[(\mathbf{k}-\mathbf{k}')\\
&\qquad\cdot(\mathbf{r}_1-\mathbf{r}_2)]\,A_1(\mathbf{k},\mathbf{k}')\,A_2(\mathbf{k},\mathbf{k}'). \qquad (8)
\end{aligned}$$

I_1 and I_2 are the partial cross-sections corresponding to the individual potentials V_1 and V_2, and are isotropic—i.e., they depend on the angle between $\mathbf{k}$ and $\mathbf{k}'$ but not on the separate directions of $\mathbf{k}$ and $\mathbf{k}'$. Anisotropy of $I(\mathbf{k},\mathbf{k}')$ appears explicitly only in the cosine term. The simple form of equation (8) is not a general result but a consequence of the use of the Born approximation. For it is only in this approximation that scattering amplitude is a linear functional of potential.

The essential calculation is the evaluation of P, the integral over all directions of $\mathbf{k}$ and $\mathbf{k}'$ defined by equation (5). From the isotropic parts of the scattering cross-section $I(\mathbf{k},\mathbf{k}')$ one obtains

$$\begin{aligned}
&\int \mathrm{d}\omega_k \int \mathrm{d}\omega_{k'}\Phi(\mathbf{k})\,[I_1(\mathbf{k},\mathbf{k}')+I_2(\mathbf{k},\mathbf{k}')]\\
&\qquad\times\,[\Phi(\mathbf{k})-\Phi(\mathbf{k}')]\\
&= 8\pi^2\int \mathrm{d}\chi \sin\chi\{c_1^2[1-P_1(\cos\chi)]/3\\
&\qquad+c_3^2[1-P_3(\cos\chi)]/7\}\times[I_1(\chi)+I_2(\chi)] \qquad (9)
\end{aligned}$$

where χ represents the scattering angle.

The technique used to evaluate the interference terms is to introduce new vectors

$$\begin{aligned}
\mathbf{K} &= \mathbf{k}'-\mathbf{k},\\
\mathbf{L} &= \tfrac{1}{2}(\mathbf{k}'+\mathbf{k})
\end{aligned} \qquad (10)$$

The magnitudes of $\mathbf{k}$ and $\mathbf{k}'$ are each equal to the magnitude k at the Fermi surface, given by

$$k^2 = L^2+(K/2)^2. \qquad (11)$$

Vectors $\mathbf{K}$ and $\mathbf{L}$ are perpendicular. We choose as independent variables of integration the magnitude, polar angle θ_k and azimuth of $\mathbf{K}$, and an angle ϕ_L that measures the position of $\mathbf{L}$ as it rotates about $\mathbf{K}$. The angle ϕ_L is the angle between the $\mathbf{K}$–$\mathbf{L}$ plane and the plane containing $\mathbf{K}$ and the pole. Expressed in terms of these variables, the "volume element" is

$$\mathrm{d}\omega_k\mathrm{d}\omega_{k'} = K\mathrm{d}K\mathrm{d}\omega_k\mathrm{d}\phi_l/k^2.$$

The amplitudes A_1 and A_2 depend only on K; integration over the remaining variables is at worst tedious.

A random orientation of vacancy–impurity pairs implies that two thirds of them have their axes at an angle of 45° from the chosen electric field direction, and one third are orthogonal to the field direction. In evaluating the integrals, it is convenient in each case to measure the polar angle θ_k from the axis of the vacancy–impurity pair. Further details concerning the integrals over directions of $\mathbf{K}$ and $\mathbf{L}$ are relegated to the Appendix. The final results are contained in equations (A3) and (A17) through (A20). It is perhaps of interest to note that equation (A18) would have been obtained if one simply averaged the orientation of impurity–vacancy axes over all directions in space, instead of restricting the axes to the twelve $\langle 110 \rangle$ directions.

SCATTERING POTENTIALS AND AMPLITUDES

The scattering by a vacancy will be represented by a repulsive screened Coulomb potential of the form

$$V_{\text{vac}} = Z'e^2 \exp(-qr)/r, \tag{12}$$

where q is a reciprocal screening length given by

$$q^2 = (4/\pi)k/a_0$$

in terms of the wave number k at the Fermi level and the Bohr radius a_0. Equation (12) is the potential obtained by a linearized Thomas–Fermi approximation.(6) (In a theory including an effective mass, q^2 becomes multiplied by m^*/m.) The screened Coulomb potential was originally suggested by MOTT(7) to approximate the scattering by an impurity of valence different from that of the host metal. Subsequently, DEXTER(2) treated a vacancy as an impurity of valence zero.

The Born approximation to the scattering amplitude arising from the potential of equation (12) is given by

$$\begin{aligned} A_{\text{vac}} &= -(2Z'/a_0)(q^2+K^2)^{-1} \\ &= -B(\beta^2+z^2)^{-1} \end{aligned} \tag{13}$$

where

$$\begin{aligned} B &= Z'/2a_0k^2, \\ \beta^2 &= q^2/4k^2 \\ &= (12\pi^5)^{-1/3}\, a/a_0 \text{ for an f.c.c. crystal,} \\ z &= K/2k. \end{aligned} \tag{14}$$

The quantity z is equal to the sine of half the scattering angle; a is the cubic lattice spacing.

Equation (13) is admittedly only approximate. One reason why it is not entirely satisfactory is that the linearization of the Thomas–Fermi equation is not justified close to the center of the impurity (or vacancy).(8) Another limitation is that the potential obtained from the Thomas–Fermi approach lacks the long range tail obtained by partial wave analyses.(9) Finally, the Born approximation grossly exaggerates the scattering of any partial wave with a large phase shift. As mentioned earlier, we believe that these limitations are at least partially compensated by allowing the magnitude of B to be adjusted.

Similar criticisms are possible regarding our treatment of impurity scattering. For an impurity of valence different from that of the host metal (for example, Zn in Au) we shall again use equations (12) and (13). For an impurity whose valence equals that of the host (for example, Ag in Au), MOTT(7) suggested that the scattering is very closely that produced by a square well potential.

In spite of doubts as to the validity of Mott's argument,(10) the success of his calculations leads us to make a similar treatment. For a square potential barrier of energy V_0 over a sphere of radius r_0, the scattering amplitude in Born approximation is given by

$$\begin{aligned} A_{\text{imp}} &= -(2mV_0/\hbar^2K^3)\,[\sin(Kr_0) - Kr_0\cos(Kr_0)] \\ &= -Dz^{-3}[\sin(\alpha z) - \alpha z\cos(\alpha z)] \end{aligned} \tag{15}$$

where D and α are constants with the values

$$\begin{aligned} D &= mV_0/4\hbar^2K^3, \\ \alpha &= 2kr_0. \end{aligned} \tag{16}$$

If the volume occupied by the potential well is equated to an atomic volume, α takes on the value $(18\pi)^{1/3} = 3{\cdot}83832$.

RESISTIVITIES

For the evaluation of the quantity P, integrations over all variables except scattering angle have been performed and the results exhibited in the Appendix. The calculation must now be completed by inserting the scattering amplitudes into the relevant expressions, and carrying out the remaining integrations over z, the sine of half the scattering angle. With the notation used in the appendix,

$$\langle F,G \rangle \equiv \int \mathrm{d}\omega_k \int \mathrm{d}\omega_{k'} F(k)I(k,k')[G(k)-G(k')], \tag{17}$$

and with Φ as chosen in equation (6), P has the form

$$\begin{aligned} P = {} & \langle c_1P_1(\cos\theta)+c_3P_3(\cos\theta),\, c_1P_1(\cos\theta) \\ & \qquad + c_3P_3(\cos\theta)\rangle \\ = {} & c_1^2\langle P_1(\cos\theta), P_1(\cos\theta)\rangle + 2c_1c_3\langle P_1(\cos\theta), \\ & \qquad \times P_3(\cos\theta)\rangle \\ & + c_3^2\langle P_3(\cos\theta), P_3(\cos\theta)\rangle. \end{aligned} \tag{18}$$

We have further decomposed these bracket expressions into the parts contributed by the individual impurity and vacancy scattering centers and parts due to interference between the paired scatterers. Contributions from individual scattering centers are obtained from equation (9) or from equations (A8) and (A16). The integrals required for individual screened Coulomb potential scatterers are elementary; those arising from individual square potential barriers can be expressed in terms of elementary functions and cosine integrals. The former depend on the value of β, and for vacancies or impurities in Au, $\beta^2 = 0{\cdot}498$. The interference contributions based on equations (A17)–(A20) were all integrated numerically. The product KY that appears in these expressions was written in terms of z as

$$KY = z\eta$$

where

$$\eta = 2kY = \sqrt{2}\,(12\pi^2)^{1/3} = 6{\cdot}94505. \qquad (19)$$

Values of the several brackets are listed in Table 1.

From equations (4), (5) and (7) and Table 1, we see that the resistivity due to screened Coulomb scatterers alone is given by

$$\rho_{sC} = (36\pi^3\hbar s/e^2k^2)\,0{\cdot}289\,B^2, \qquad (20)$$

and that due to square barrier scatterers alone is given by

$$\rho_{sb} = (36\pi^3\hbar s/e^2k^2)16{\cdot}9\,D^2. \qquad (21)$$

As mentioned earlier, we make no attempt to evaluate B and D theoretically, but shall use equations (20) and (21) to express them in terms of resistivities of the individual scatterers.

The negative values of some of the interference terms in Table 1 indicate that if the scattering amplitudes of the two single scattering centers have the same sign (so that if the scattering centers were directly superimposed the amplitudes would add) the interference is actually destructive.

Results neglecting anisotropy

To the extent that a collection of anisotropic scatterers oriented more or less at random is equivalent to a collection of isotropic scatterers, we may neglect the coefficient c_3 in equation (6) for Φ. In this approximation, we obtain the following results with the help of Table 1.

Consider a silver impurity associated with a vacancy in gold. A silver ion in gold should repel electrons.[(7)] Likewise a vacancy, which is the lack of a positive ion, should also repel electrons. We find

$$\rho_{\mathrm{Ag+vac}} = \rho_{\mathrm{Ag}}+\rho_{\mathrm{vac}} - \frac{0{\cdot}236}{[(0{\cdot}289)(16{\cdot}9)]^{1/2}} \times (\rho_{\mathrm{Ag}}\times\rho_{\mathrm{vac}})^{1/2}$$

$$= \rho_{\mathrm{Ag}}+\rho_{\mathrm{vac}} - 0{\cdot}107\,(\rho_{\mathrm{Ag}}\times\rho_{\mathrm{vac}})^{1/2}. \qquad (22)$$

The resistivity due to a gold impurity associated with a vacancy in silver would differ from the above expression only in having a positive interference term.

For a divalent impurity such as zinc associated with a vacancy in gold (or silver) the impurity ion would attract electrons, and so give rise to a scattering amplitude of opposite sign to that of a vacancy. The result is

$$\rho_{\mathrm{Zn+vac}} = \rho_{\mathrm{Zn}}+\rho_{\mathrm{vac}}+(0{\cdot}0292/0{\cdot}289)(\rho_{\mathrm{Zn}}\times\rho_{\mathrm{vac}})^{1/2}$$

$$= \rho_{\mathrm{Zn}}+\rho_{\mathrm{vac}}+0{\cdot}101\,(\rho_{\mathrm{Zn}}\times\rho_{\mathrm{vac}})^{1/2}. \qquad (23)$$

Table 1. *Values of* $(4\pi)^{-2}\langle P_l(\cos\theta),\, P_{l'}(\cos\theta)\rangle$

l	l'	Individual screened Coulomb potential	Individual square barrier potential	Screened Coulomb–square barrier interference	Coulomb–Coulomb interference
1	1	$0{\cdot}289\ B^2$	$16{\cdot}9\ D^2$	$-0{\cdot}236\ BD$	$-0{\cdot}0292\ B_1B_2$
1	3	—	—	$0{\cdot}0144\ BD$	$-8{\cdot}57\times10^{-4}\ B_1B_2$
3	3	$0{\cdot}185\ B^2$	$14{\cdot}3\ D^2$	$0{\cdot}192\ BD$	$0{\cdot}0196\ B_1B_2$

It is a direct consequence of equation (8) that our results appear in the form of equation (22) and (23), and that the coefficient of the interference term lies between -2 and 2. The small value actually obtained for these coefficients is probably a rather general result that calls for some comment. Both the small values of the $\langle P_1(\cos\theta), P_1(\cos\theta)\rangle$ interference terms and their negative signs arise from the oscillating factor $\cos[\mathbf{K}\cdot(\mathbf{r}_1-\mathbf{r}_2)]$ in the expression (8) for scattering cross-section. Averaging the vector $\mathbf{r}_1-\mathbf{r}_2$ over the several directions of a vacancy–impurity pair results in the factor $\sin(KY)/KY = \sin(\eta z)/\eta z$ in equation (A18). The separation Y of two nearest neighbor ion sites is somewhat greater than the electron wave length at the Fermi surface ($\eta > 2\pi$). The resulting alternation in sign of the function $\sin(\eta z)/\eta z$, in averaging the scattering amplitudes over the scattering angle, is the factor responsible for the small size found for the interference. And combined with the relative importance of large angle scattering, this oscillation also accounts for the reversals in sign observed in Table 1.

Effect of anisotropy

If we do not throw away c_3 of equation (6), then we should determine it in accordance with the variation principle to maximize expression (4), or to minimize P/c_1^2 as given by equation (18). This quantity has for its minimum value

$$\langle P_1(\cos\theta), P_1(\cos\theta)\rangle - \frac{\langle P_1(\cos\theta), P_3(\cos\theta)\rangle^2}{\langle P_3(\cos\theta), P_3(\cos\theta)\rangle}.$$

If we evaluate the correction for the case of a silver impurity associated with a vacancy in gold, we find from Table 1 a correction

$$-(0{\cdot}0144\,BD)^2\,[0{\cdot}185\,B^2+0{\cdot}192\,BD+14{\cdot}3\,D^2]^{-1}.$$

By using the values of resistivities produced by the isolated imperfections to eliminate B and D, as before, the correction turns out to be

$$-(\rho_{\mathrm{Ag}}\times\rho_{\mathrm{vac}})^{1/2}[1{\cdot}51\times10^4\,(\rho_{\mathrm{vac}}/\rho_{\mathrm{Ag}})^{1/2}+2{\cdot}05\times10^3$$
$$+2{\cdot}00\times10^4\,(\rho_{\mathrm{Ag}}/\rho_{\mathrm{vac}})^{1/2}]^{-1}. \qquad (24)$$

This correction is less than 10^{-3} times the mean of the separated resistivities, and 100 times smaller than the isotropic interference correction. The anisotropic correction for a Zn impurity adjacent to a vacancy in Au appears to be still smaller by about a factor 3.

The extreme smallness of the quantity $\langle P_1(\cos\theta), P_3(\cos\theta)\rangle$ suggests that the actual value of this quantity is quite susceptible to details of the scattering. But it is highly improbable that a more careful treatment would increase the magnitude of the anisotropic correction to the point where it could be significant.

Acknowledgements—This problem was started, and a good deal of the work done while the writer was a summer visitor at the Brookhaven National Laboratory. The writer wishes to thank the Laboratory for its hospitality. He is indebted to Dr. G. J. Dienes for suggesting the problem. And he wishes to thank Mr. Sid Heller of Brookhaven and Mr. Robert Lilley of the Ames Laboratory for numerical evaluation of some of the integrals.

APPENDIX

We give here details of the integrals over directions of $\mathbf{K}$ and $\mathbf{L}$ necessary for evaluation of the quantity P defined by equation (5). All wave vectors will be expressed in units of k at the Fermi surface, and factors of k will be suppressed.

For each orientation of the vacancy–impurity axis we introduce primed coordinate axes rotated so that the z' axis is along the vacancy–impurity pair axis. For a pair oriented in the [101] direction we use

$$x = (z'+x')/\sqrt{2},$$
$$y = y',$$
$$z = (z'-x')/\sqrt{2}.$$

Then

$$\Phi = c_1\frac{k_{z'}-k_{x'}}{\sqrt{2}}+c_3\left\{\frac{5}{2}\left(\frac{k_{z'}-k_{x'}}{\sqrt{2}}\right)^3-\frac{3}{2}\frac{k_{z'}-k_{x'}}{\sqrt{2}}\right\}$$
$$= (c_1/\sqrt{2})(k_{z'}-k_{x'})+(c_3/16\sqrt{2})\,[-2(5k_{z'}^3-3k_{z'})$$
$$-9(5k_{z'}^2-1)k_{x'}+30k_{z'}(k_{x'}^2-k_{y'}^2)-5(k_{x'}^3-3k_{x'}k_{y'}^2)]. \qquad \text{(A1)}$$

Likewise, for a pair oriented along [110] we use

$$x = (z'+y')/\sqrt{2},$$
$$y = (z'-y')/\sqrt{2},$$
$$z = x',$$

and

$$\Phi = c_1k_{x'}+c_3(\tfrac{5}{2}k_{x'}^3-\tfrac{3}{2}k_{x'})$$
$$= c_1k_{x'}+\tfrac{1}{2}c_3[-3(5k_{z'}^2-1)k_{x'}+5(k_{x'}^3-3k_{x'}k_{y'}^2)]. \qquad \text{(A2)}$$

The different terms within each of the square brackets of equations (A1) and (A2) are orthogonal in azimuth.

With the bracket notation $\langle F,G\rangle \equiv \int \mathrm{d}\omega_k \int \mathrm{d}\omega_{k'}\, F(k)\, I(k,k')\, [G(k)-G(k')]$

$$= \tfrac{1}{2}\int \mathrm{d}\omega_k \int \mathrm{d}\omega_{k'}\, [F(k)-F(k')]\, I(k,k')\, [G(k)-G(k')], \tag{A3}$$

we find that

$$\begin{aligned}\langle P_1(\cos\theta), P_1(\cos\theta)\rangle &= \tfrac{2}{3}\langle k_{x'}, k_{x'}\rangle + \tfrac{1}{3}\langle k_{z'}, k_{z'}\rangle \\ &= \tfrac{1}{3}(\langle k_{x'}, k_{x'}\rangle + \langle k_{y'}, k_{y'}\rangle + \langle k_{z'}, k_{z'}\rangle),\end{aligned} \tag{A4}$$

$$\begin{aligned}\langle P_1(\cos\theta), P_3(\cos\theta)\rangle &= -1/24\,\langle k_{z'}, 5k_{z'}^3 - 3k_{z'}\rangle \\ &\quad + 1/16\,\langle k_{x'}, (5k_{z'}^2-1)\, k_{x'}\rangle.\end{aligned} \tag{A5}$$

$$\begin{aligned}\langle P_3(\cos\theta), P_3(\cos\theta)\rangle &= 1/192\,\langle 5k_{z'}^3 - 3k_{z'}, 5k_{z'}^3 - 3k_{z'}\rangle \\ &\quad + 39/256\,\langle 5k_{z'}^2 - 1)\, k_{x'}, (5k_{z'}^2-1)\, k_{z'}\rangle \\ &\quad + 75/64\,\langle k_{z'}\,(k_{x'}^2 - k_{y'}^2), k_{z'}\,(k_{x'}^2 - k_{y'}^2)\rangle \\ &\quad + 125/768\,\langle k_{x'}^3 - 3k_{x'}\, k_{y'}^2, k_{x'}^3 - 3k_{x'}\, k_{y'}^2\rangle.\end{aligned} \tag{A6}$$

In equations (A4)–(A6) the results obtained separately from equations (A1) and (A2) were combined with weights of 2/3 and 1/3 respectively, and use was made of the axial symmetry of I.

According to equations (10)

$$\begin{aligned}k &= L - \tfrac{1}{2}K, \\ k' &= L + \tfrac{1}{2}K.\end{aligned} \tag{A7}$$

We express the integrals in terms of another bracket notation:

$$\{H\} \equiv \int K\, \mathrm{d}K\, \mathrm{d}\omega_k\, \mathrm{d}\phi_L\, H(K,L)\, I(K,\theta_K).$$

All remaining calculations are carried out in primed coordinates, so we now drop the primes. Then

$$\langle P_1(\cos\theta), P_1(\cos\theta)\rangle = \tfrac{2}{3}\{z^2\}, \tag{A8}$$

where

$$z = K/2k.$$

$$\begin{aligned}\langle k_z, 5k_z^3 - 3k_z\rangle &= 2\{[15L_z^2 + 5(\tfrac{1}{2}K_z)^2 - 3]\, (\tfrac{1}{2}K_z)^2\} \\ &= \{(3z^2 - 5z^4)\, (3\cos^2\theta_k - 5\cos^4\theta_k)\}.\end{aligned} \tag{A9}$$

$$\begin{aligned}\langle k_x, (5k_z^2-1)\, k_x\rangle &= \tfrac{1}{4}\langle k_+ + k_-, (5k_z^2-1)\, (k_+ + k_-)\rangle \\ &= \tfrac{1}{2}\langle k_+, (5k_z^2-1)\, k_-\rangle \\ &= \tfrac{1}{2}\{(3z^2 - 5z^4)\, (1 - 6\cos^2\theta_k + 5\cos^4\theta_k)\}.\end{aligned} \tag{A10}$$

The symbols $k_\pm$ stand for $k_x \pm iky$.

$$\begin{aligned}&\langle 5k_z^3 - 3k_z, 5k_z^3 - 3k_z\rangle = \\ &\qquad \{\tfrac{1}{4}z^2(387\cos^2\theta_k - 990\cos^4\theta_k + 675\cos^6\theta_k) \\ &\qquad + \tfrac{1}{2}z^4(-495\cos^2\theta_k + 1350\cos^4\theta_k - 975\cos^6\theta_k) \\ &\qquad + \tfrac{1}{4}z^6(675\cos^2\theta_k - 1950\cos^4\theta_k + 1475\cos^6\theta_k)\}.\end{aligned} \tag{A11}$$

$$\langle (5k_z^2-1)\,k_z,\,(5k_z^2-1)\,k_z\rangle =$$
$$\{\tfrac{1}{8}z^2(43-273\cos^2\theta_k+905\cos^4\theta_k-675\cos^6\theta_k)$$
$$+\tfrac{1}{4}z^4(-55+405\cos^2\theta_k-1325\cos^4\theta_k+975\cos^6\theta_k)$$
$$+\tfrac{1}{8}z^6(75-625\cos^2\theta_k+2025\cos^4\theta_k-1475\cos^6\theta_k)\}. \quad \text{(A12)}$$

$$\langle k_z(k_x^2-k_y^2),\,k_z\,(k_x^2-k_y^2)\rangle =$$
$$\{\tfrac{1}{8}z^2(4+3\cos^2\theta_k-26\cos^4\theta_k+27\cos^6\theta_k)$$
$$+\tfrac{1}{4}z^4(-4-15\cos^2\theta_k+50\cos^4\theta_k-39\cos^6\theta_k)$$
$$+\tfrac{1}{8}z^6(4+35\cos^2\theta_k-90\cos^4\theta_k+59\cos^6\theta_k)\}. \quad \text{(A13)}$$

$$\langle k_x^3-3k_x\,k_y^2,\,k_x^3-3k_x\,k_y^2\rangle =$$
$$\{\tfrac{1}{8}z^2(27-9\cos^2\theta_k+9\cos^4\theta_k-27\cos^6\theta_k)$$
$$+\tfrac{1}{4}z^4(-39+45\cos^2\theta_k-45\cos^4\theta_k+39\cos^6\theta_k)$$
$$+\tfrac{1}{8}z^6(59-105\cos^2\theta_k+105\cos^4\theta_k-59\cos^6\theta_k)\}. \quad \text{(A14)}$$

From equations (A5), (A9) and (A10)

$$\langle P_1\,(\cos\theta),\,P_3\,(\cos\theta)\rangle =$$
$$1/96\{(3z^2-5z^4)\,(3-30\cos^2\theta_k+35\cos^4\theta_k)\}. \quad \text{(A15)}$$

And from equations (A6) and (A11)–(A14)

$$\langle P_3\,(\cos\theta),\,P_3\,(\cos\theta)\rangle =$$
$$\{1/2048\;z^2(4002-9090\cos^2\theta_k+25230\cos^4\theta_k-17550\cos^6\theta_k)$$
$$+5/512\;z^4(-497+1185\cos^2\theta_k-3495\cos^4\theta_k+2535\cos^6\theta_k)$$
$$+5/3072\;z^6(1975-4935\cos^2\theta_k+15345\cos^4\theta_k-11505\cos^6\theta_k)\}. \quad \text{(A16)}$$

For isotropic scattering, equations (A8) and (A16) reduce to equation (9), and the right hand member of equation (A15) becomes zero. For the interference terms, the integrations over ω_K and ϕ_L yield results of the form

$$\langle\;\;\rangle = 16\pi^2\int_0^2 K\,dK A_1(K)A_2(K)M(K,Y) \quad \text{(A17)}$$

where Y is the distance between the impurity atom and the center of the vacancy. The function M takes the following forms:

for $\langle P_1(\cos\theta),\,P_1(\cos\theta)\rangle$

$$M = \tfrac{2}{3}z^2u\sin(KY); \quad \text{(A18)}$$

for $\langle P_1(\cos\theta),\,P_3(\cos\theta)\rangle$

$$M = 1/12(3z^2-5z^4)[\sin(KY)(u-45u^3+105u^5)$$
$$+\cos(KY)\,(10u^2-105u^4)]: \quad \text{(A19)}$$

for $\langle P_3(\cos\theta),\,P_3(\cos\theta)\rangle$

$$M = 3/64\;z^2\,[\sin(KY)\,(27u+2520u^3-59505u^5+131625u^7)$$
$$+\cos(KY)\,(-235u^2+15630u^4-131625u^6)]$$
$$+5/32\;z^4\,[\sin(KY)\,(-17u-2280u^3+51795u^5-114075u^7)$$
$$+\cos(KY)\,(225u^2-13770u^4+114075u^6)]$$
$$+25/192\;z^6\,[\sin(KY)(11u+2136u^3-47169u^5+103545u^7)$$
$$+\cos(KY)\,(-219u^2+12654u^4-103545u^6)]. \quad \text{(A20)}$$

In these equations u stands for $(KY)^{-1}$.

Equations (A3)–(A16) are exact for any axially symmetric scatterers oriented at random along the 12 f.c.c. nearest-neighbor directions. Equations (A17)–(A20) depend on the Born approximation for treating interference between two spherically symmetric scatterers.

REFERENCES

1. Alfred L. C. R. and March N. H., *Phil. Mag.* **2**, 985 (1957); Flynn C. P., *Phys. Rev.* **125**, 881 (1962).
2. Dexter D. L., *Phys. Rev.* **87**, 768 (1952).
3. Overhauser A. W. and Gorman R. L., *Phys. Rev.* **102**, 676 (1956).
4. Ziman J. M., *Electrons and Phonons*, chap. VII. Oxford University Press, London (1960).
5. Mott N. F. and Massey H. S. W., *The Theory of Atomic Collisions*, 2nd ed., p. 117. Oxford University Press, London (1949).
6. Ziman J. M., *Electrons and Phonons*, section 6.3., Oxford University Press, London (1960).
7. Mott N. F., *Proc. Camb. phil. Soc.* **32**, 281 (1936); Mott N. F. and Jones H., *The Theory of the Properties of Metals and Alloys*, chap. VII, section 12. Dover, New York (1958).
8. Friedel J., *Advanc. Phys.* **3**, 446 (1954); Alfred L. C. R. and March N. H., *Phil. Mag.* **46**, 759 (1955).
9. Friedel J., *Phil. Mag.* **43**, 153 (1952); Kohn W. and Vosko S. H., *Phys. Rev.* **119**, 912 (1960).
10. Huang K., *Proc. phys. Soc., Lond.* **60A**, 161 (1948); Friedel J., *Canad. J. Phys.* **34**, 1190 (1956).

J. Phys. Chem. Solids Pergamon Press 1963. Vol. 24, pp. 1131–1139. Printed in Great Britain.

DISSOCIATION PRESSURES OF GaAs, GaP and InP AND THE NATURE OF III–V MELTS*

D. RICHMAN

RCA Laboratories, Princeton, N.J.

(*Received* 7 *March* 1963)

Abstract—Direct measurements of the dissociation pressures of GaAs, GaP and InP have been made as a function of temperature by the quartz Bourdon gauge technique. The pressures at the stoichiometric melting points were found to be: for GaAs, 1·00 ± 0·02 atm. at 1238°C; for GaP, 35 ± 10 atm. at 1467°C ± 3°C; and for InP, 21 ± 5 atm. at 1058°C ± 3°C. These data together with the phase diagram data for the III–V compounds indicate that the melts of these compounds are neither ideal nor regular solutions but show negative excess free energies which are dependent on composition and/or temperature. This result is interpreted as indicative of association of the group V species in these melts.

1. INTRODUCTION

REPORTS of the temperature dependence of the dissociation pressure of III–V compounds have been extant in the literature for several years.[1–6] However, for the compounds, GaAs[1, 6] and InP[1, 5] where more than one study has been carried out, large discrepancies in the reported values are found at temperatures below the melting points of these compounds. To clear up these discrepancies, it appeared appropriate to employ a direct measurement of the pressure, which had not been done previously. In addition, more accurate measurements over an extended temperature range are especially useful in testing thermodynamic theories of III–V systems.

Mass spectroscopic studies[2, 3] of the III–V compounds have established that these materials thermally dissociate at temperatures below their melting points, giving a vapor phase consisting almost completely of the more volatile Group V element. This fact makes the use of a quartz Bourdon gauge ideally suited for studying the dissociation pressures of GaAs, GaP and InP. By maintaining the gauge at a constant and sufficiently high temperature to prevent any condensation of the group V element and by varying the temperature of the sample, the dissociation pressure of the sample may be studied over an extended temperature range. In this paper the results of such a study on the compounds GaAs, GaP and InP are reported. These results are then combined with other experimental data and used to evaluate the applicability of regular solution theory to these systems. Conclusions concerning the nature of III–V melts are also presented.

2. EXPERIMENTAL

Standard Bourdon gauges of the spoon type were used for all measurements. Gauges of various sensitivity were obtained by varying the size and thickness of the spoon. A 10-in. quartz rod pointer was attached to the top of each spoon, and deflections of the spoon were detected by observing displacements of the pointer from a fixed reference with a low power telescope.

Calibration of the spoons was carried out in the temperature range, 25–800°C. In the range of pressures between 0 and 1 atm. the displacement of the pointer was a linear function of the pressure difference across the spoon for small pressure differences and, for all but the most sensitive gauge, independent of temperature.

---

* This research has been sponsored by the Electronic Research Directorate, Air Force Cambridge Research Laboratories, Office of Aerospace Research, under Contract No. AF 19(604)–6152.

During operation counterpressure was applied to the outside of the gauge through a side arm by dry air in the case of GaAs, or dry nitrogen for GaP and InP. For the GaAs study the balancing pressure was read with either an oil manometer, a mercury manometer or a universal vacuum (McLeod) gauge. A dial pressure gauge was used for the high pressures involved in the GaP and InP experiments. To take readings in all cases after equilibrium had been reached, the balancing pressure was brought to a value where the pointer deflection was in the linear range, but not necessarily completely to the null point. The balancing pressure was then changed, so that a second pointer deflection was obtained. Calibration curves were then used to correct the readings to zero pressure difference across the spoon, and the results of two or more such readings were averaged to obtain the dissociation pressure at each sample temperature.

As pointed out previously, two temperature zones were necessary for these experiments. This requirement was met by having two vertically mounted furnaces. The lower furnace which surrounded the sample had a 6-in. platinum wound core which was operable to 1500°C. A mullite sleeve inside the core was used to increase the thermal mass of the furnace. The upper furnace enclosed the gauge and pointer, and was kept at constant temperature in the range, 725–800°C range. Temperature control was obtained with saturable core reactor controllers operating from a regulated voltage, and with Pt–PtRh 13% thermocouples as the sensing elements. Temperature stability of at least ± 1°C over extended periods of time was obtained in this manner.

Since the temperature and pressure ranges to be covered were different for each of the three materials examined, different procedures were followed in handling each of them. These are described individually below.

A. GaAs

Previous work$^{(1, 4, 6)}$ has established that the dissociation pressure of GaAs at its melting point is in the neighborhood of one atmosphere. For measurements on this material three different gauges were used. The most sensitive gauge could reproducibly detect pressure differences of 0·1 torr. The other two gauges had sensitivities of 2 and 8 torr. With the most sensitive gauge, resonant oscillations were encountered at pressures above 420 torr, so that it was not possible to reach the melting point of GaAs with this gauge. However with the other two gauges it was possible to observe pressures at and above the melting point of the sample.

The samples used were high purity, polycrystalline GaAs prepared in these laboratories. These were cleaned prior to use by etching in aqua regia. After washing and drying, the pieces were placed in the quartz sample tube which was connected to the gauge by 6 in. of 10 mm bore quartz tubing. The entire system was then vacuum baked at 600°C before sealing off the sample and gauge. A typical charge of GaAs was 14 g. The volume of the cell and sample tube was estimated to be approximately 15 cm^3. Therefore, less than 1 per cent decomposition of the GaAs was required to give a pressure of 1 atm.

The temperature of the sample was determined by four thermocouples placed in dimples along the sample tube in contact with the solid GaAs. Readings of the dissociation pressure were taken during both heating and cooling. In addition to taking readings during the cooling cycle, after reaching the maximum temperature of each run a second procedure was used: This consisted of taking readings while heating the sample to a given temperature, cooling some 40°C, then taking readings from this point while heating to a new temperature higher than the first, and so proceeding to the highest temperature.

Equilibration times varied with the particular temperature. Near the melting point where equilibration was very rapid, a ½ to 1 hr interval in which there was no observable pressure change was taken as indicative of equilibrium. At lower temperatures times up to 16 hr on heating and 30 hr on cooling were used.

B. GaP

The melting point of GaP is greater than 1400°C. At these temperatures quartz is soft, and special care must be taken to enclose it to prevent its blowing out. The method of FISCHER$^{(7)}$ was most suitable for this work. A carbon block was machined to contain the quartz sample tube. This can be seen in the diagram of the apparatus in Fig. 1. The screw cap of the block was fitted over

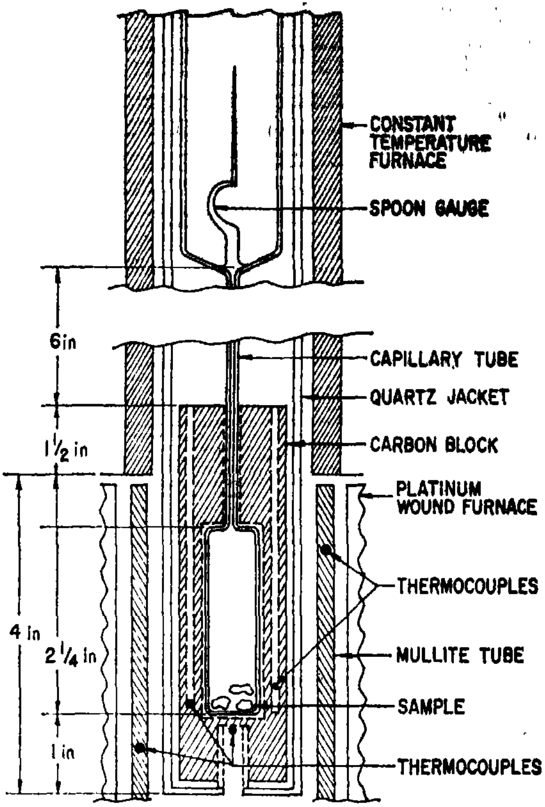

FIG. 1. Apparatus for the measurement of the dissociation pressure of GaP.

the capillary tube before sealing on the sample tube. The top of the screw cap extended into the cooler region of the furnace to provide mechanical support for the capillary to a point where the quartz was below its softening temperature. A quartz jacket surrounded the carbon block and gauge to prevent oxidation of the carbon at elevated temperature. A 2 mm capillary tube was used to connect the sample portion of the assembly to the spoon in order to minimize the volume of the sample space and to provide the greatest mechanical strength. The furnaces were arranged so that the thermal gradient between the isothermal sample region and the constant temperature spoon gauge was located along the capillary.

As seen in Fig. 1, five thermocouples surrounded the sample space while a sixth located nearer the furnace windings was used as the sensory element for the controller. Two of the five sample thermocouples were located in the mullite core of the furnace; two were enclosed in quartz tubes and placed in wells drilled in the walls of the carbon block, and the fifth was touching the outside wall of the quartz jacket in a well in the bottom center of the carbon block. These last three couples were arranged to cover the region of the block which contained the sample of GaP. The two couples in the mullite block being closer to the furnace windings gave readings higher than the three couples surrounded by the carbon block. As expected from the geometry, the top thermocouple in the mullite gave readings slightly lower than the bottom mullite couple. The three couples in more intimate contact with the carbon, gave readings which agreed with each other to ± 2°C. The bottom center couple was taken as the standard, since the two couples in the wells failed at temperatures above 1420°C, apparently due to attack by carbon. After the experiments were completed, the bottom thermocouple was calibrated against the melting point of nickel (1455°C).

Readings of pressure were taken only on heating since it was feared the quartz would rupture on slow cooling and destroy the gauge. The quartz spoon used in these experiments was sufficiently sensitive to allow pressures to be determined to ± 0·15 atm. The calibrated dial gauge used to read the pressures had a full scale deflection of 300 p.s.i., and was graduated in divisions of 2 p.s.i. Readings below 1 atm. were taken from the spoon deflection without waiting to assure that equilibrium had been established in order to prevent the sample tube from collapsing when held at these temperatures and pressures for extended periods of time. Once above 1 atm., readings were taken at a given sample temperature until no pressure change was observed for a period of 30–45 min.

The total volume of the sample chamber, spoon and connecting tube was estimated to be 6 cm³. Two grams of GaP were used for each run. There was a very slight increase in volume of the system during a run due to expansion of the quartz in the carbon block. This was minimized by having the block machined to fit tightly over the sample tube and filling the bottom and top of the block with powdered carbon. At the highest temperatures and pressures reached in these experiments the sample decomposition was less than 10 per cent. However, below the liquidus the pressure is not affected by such decomposition.

Two successful runs were carried out to temperatures within 10°C of the melting point of GaP.

C. InP

The lower melting point of InP (1058°C) allows the use of less elaborate sample containment than for GaP. In this case, a thick-walled quartz tube was used as the sample holder and two thermocouples were placed in contact with the sample tube 1 in. above and 1 in. below the sample. The sample temperature was taken as the average for the two couples. Up to 1055°C the thermocouples showed only a 3°C difference in their readings.

For InP, points were determined upon both heating and cooling. Equilibrium was assumed to have been reached when there was no observed pressure change on standing at constant temperature for 2 hr on heating and 6 hr on cooling.

Only one run was made. For this work, 26 g of high purity InP were sealed in a volume of 12cm³. The maximum degree of decomposition of the melt was calculated to be less than 1 per cent at the highest pressure reached. Pressure measurements were made to within 2°C of the InP melting point.

3. RESULTS

A. GaAs

The results for the three runs on GaAs are shown in Fig. 2. As seen in the figure, the results are extremely consistent at pressures above 4 mm Hg. Below this point there is some scatter in the results. This can be ascribed to non-equilibrium at the low temperature, perhaps coupled with some slight decomposition of the GaAs sample

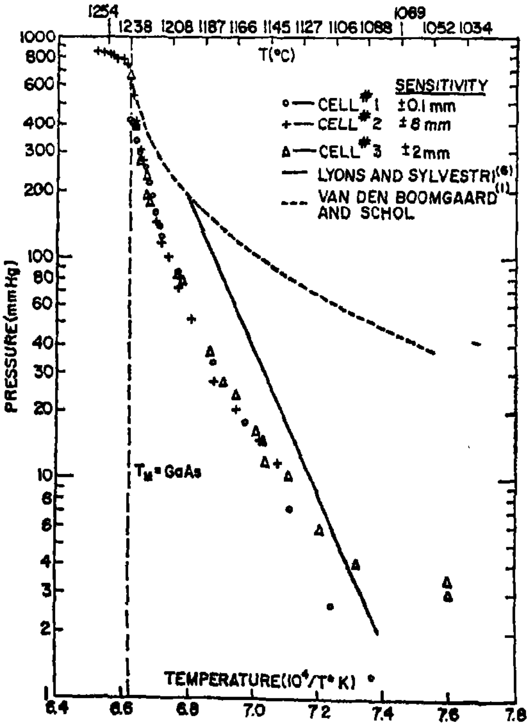

FIG. 2. Temperature dependence of the dissociation pressure of GaAs.

during sealing of the sample chamber. Such decomposition would lead to small residual arsenic pressures at low temperatures.

One of the three runs was carried well above the melting point of the sample. This is seen in the abrupt change in slope of the temperature–pressure curve. Further evidence of melting was obtained on examining the sample after the run. The sample, which was initially four pieces of polycrystalline GaAs, was recovered as a single monocrystal of GaAs. From the intersections of the curves above and below the melting point of GaAs, the melting point was found to be 1238°C and the dissociation pressure 740 torr. This represents a lower limit to the dissociation pressure, since the sample decomposition amounted to 1 per cent. At stoichiometry, the dissociation pressure would probably be 1 atm. This value is 10 per cent higher than that reported by VAN DEN BOOMGAARD and SCHOL,(1) whose work also show marked deviations from the present data at lower temperatures.

The reason for this deviation is not apparent; however, at low temperatures, melts of the III–V compounds are slow to equilibrate, and this may be the cause of the deviation. The present data are in reasonable agreement with the work of LYONS and SILVESTRI.(6) However, their points do not show the curvature predicted by theory and seen in these direct pressure measurements. This is probably due to the low sensitivity of the dew point technique at high temperatures. For purposes of comparison, the results of these two previous investigations are also included in Fig. 2. Extrapolation of the results of this investigation to low temperature shows them to be in excellent agreement with the data of DROWART and GOLDFINGER,(2) as seen in Fig. 5.

B. GaP

The data for two runs on GaP are shown in Fig. 3, and these show agreement within experimental error. It should be noted that the readings were taken only to 11 atm. (1455°C). To get the dissociation pressure at the stoichiometric melting point an extrapolation must be made. This extrapolation is discussed in the Appendix. The result shown in Fig. 4, 35 atm., is the value obtained for a melting point of 1467°C. If the melting point is varied by ± 3°C, the corresponding dissociation pressure will be varied by ± 10 atm.

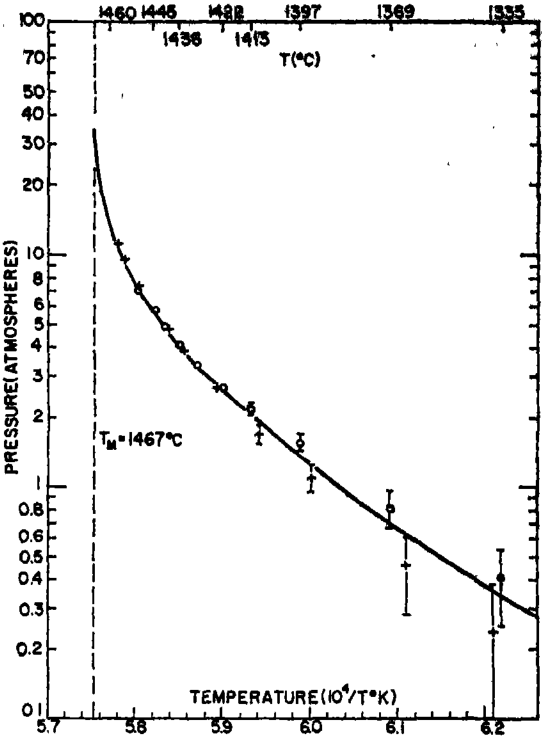

FIG. 3. Temperature dependence of the dissociation pressure of GaP.

MARINA *et al.*(8) have recently reported the dissociation pressure of GaP to be 13 atm. at a melting temperature of 1525°C. Their value of the melting point is high by about 60°C and their dissociation pressure too low. The value of 35 atm. obtained from the present work is in the range of earlier estimated values.(9)

C. InP

Figure 5 shows the results for the single run on InP. The highest temperature reached (1056°C) is below the stoichiometric melting point, and again an extrapolation is required to obtain the dissociation pressure at the melting point. The value obtained is 21 atm. at a melting point of 1058°C.

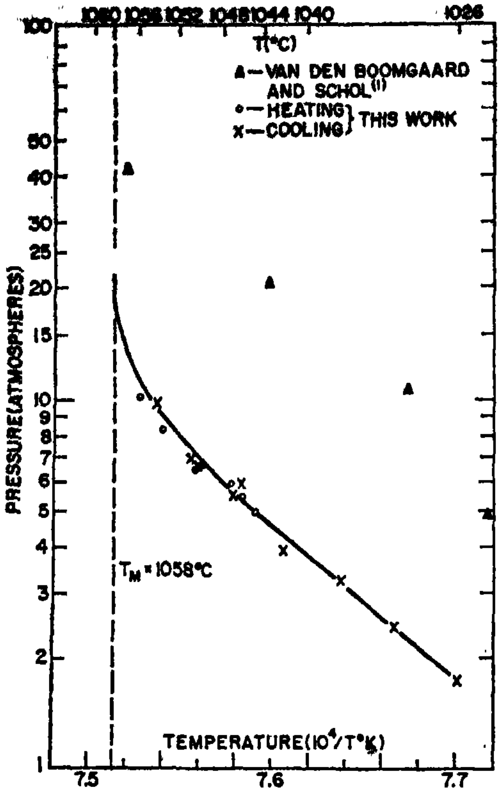

FIG. 4. Temperature dependence of the dissociation pressure of InP.

Here also the data of VAN DEN BOOMGAARD and SCHOL[1] is in marked disagreement with that of the present study both at low temperatures and near the melting point. Their value of 60 atm. for the dissociation pressure at the melting point is higher than the 21 atm. found in this work, as can be seen in Fig. 4. As in the case of GaAs, the results of the present study extrapolate smoothly into those reported by DROWART and GOLDFINGER.[2] The present results are also in reasonable agreement with the measurements of WEISER[5] in the intermediate temperature range, although a slight difference in the slope is evident. These results are shown in Fig. 5.

4. THE NATURE OF III–V MELTS

SCHOTTKY and BEVER[10] in their work on InSb and GaSb considered the melts of these compounds to be regular solutions. The entropy of the liquid is just that given by the ideal entropy of mixing, and the excess free energy of the melt over that of an ideal solution is given by

$$F_{\text{Excess}} = (W)(x)(1-x), \qquad (1)$$

where W is an interaction parameter independent of composition and x is the atom fraction of the Group V element in the melt. Using this assumption in an analysis of T–x diagrams given by WAGNER,[11] they concluded that GaSb melted to give a nearly ideal solution of the two components. On the other hand, InSb melted to give a solution which showed negative deviations from ideality.

More recently VIELAND[12] has presented a regular solution treatment covering the P–T as well as T–x diagrams for III–V compounds. In

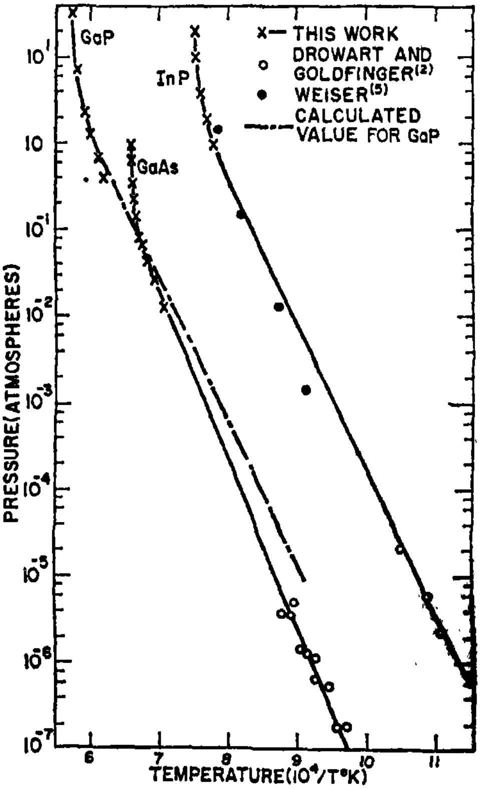

FIG. 5. Dissociation pressure of GaAs, GaP, and InP over an extended temperature range.

addition, HALL[13] has extended the T–x diagrams of these compounds to very low temperatures for compositions rich in the Group III element. Using these results together with the pressure data, it is now possible to consider the applicability of regular solution theory to the III–V systems.

From VIELAND,[12] neglecting terms in the difference in the heat capacities of solid and liquid phases, the relationship between W and the phase diagram is given by,

$$W=\frac{RT}{2(x-0\cdot5)^2}\left[\ln\frac{1}{4(x)(1-x)}-\frac{2\Delta S}{R}\left(\frac{T_m}{T}-1\right)\right] \quad (2)$$

where x is the atom fraction of group V element in the liquid, ΔS is the entropy of fusion of the III–V compound, and T_m is the melting point of the stoichiometric compound. Applying this to the phase diagram data of Hall and others,[14, 15] W was calculated for InSb, GaSb, InAs, GaAs, InP, and GaP over the composition range $2\times10^{-3} \leqslant x \leqslant 5\times10^{-1}$. Values of the entropy of fusion used in this calculation were taken from the literature[10] for the first two of the compounds above, and from measurements[16] made by a differential thermal analysis technique for all the others except GaP for which a value of 6·5 cal/g at. deg. was assumed. In the case of InSb, W was essentially independent of composition for $x \geqslant 0\cdot1$, in agreement with the results of SCHOTTKY and BEVER.[10] However, at lower concentrations W was a function of composition of the melt. This latter behavior was characteristic of all the compounds investigated even to more concentrated solutions than in the case of InSb. For all compounds W approached zero with decreasing concentration of Group V element in the melt, and in some cases was observed to change sign from negative to positive.

A second method for determining W, using both the composition vs. temperature and the pressure vs. temperature data, makes use of the relationship

$$P_4^{1/4}=P_{0,4}^{1/4}x\exp[W(1-x)^2/RT], \quad (3)$$

where P_4 is the pressure of tetratomic Group V series over a liquid containing x atom fraction of the Group V element, and $P_{0,4}$ is the pressure of the same species over pure liquid Group V element. In making this calculation, the data of HORIBA[17] were used to obtain values for the pressure of As_4 over liquid arsenic. Values for the As_2, As_4 equilibrium constant were taken from DROWART and GOLDFINGER.[9] Similar data for phosphorus were taken from FARR.[18] Values of W calculated for GaAs, InP and GaP from equation (3) were in good agreement with those obtained from equation (2).

The behavior at low temperature and low composition is contrary to the assumption that W is independent of composition as required by regular solution theory. Furthermore, the fact that W goes to zero at low concentration implies that the solutions tend to become more ideal. This strongly suggests that regular solution theory cannot be applied over the entire composition range of these solutions, although it does appear to be applicable in the region near stoichiometry.

It is perhaps more fruitful to look at these solutions as being non-ideal and consider the data from the relation,

$$P_4^{1/4}=P_{0,4}^{1/4}x\,\gamma \quad (4)$$

where γ is the activity coefficent of the Group V species in the melt. The results of such a calculation for GaAs, InP, and GaP are shown in Fig. 6.

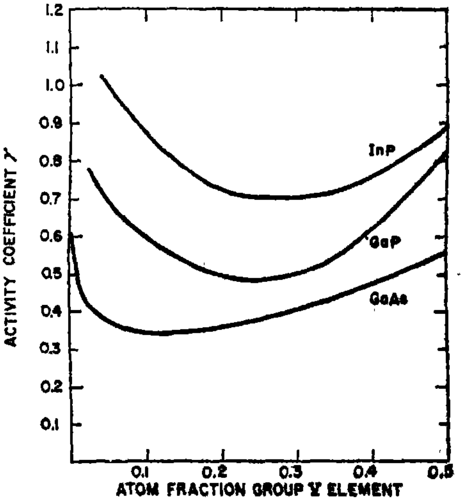

FIG. 6. Concentration dependence of the activity coefficient of Group V element in melts of GaAs, GaP and InP.

Since the data are taken along the three phase line, the temperature is not constant; however, the general shape of the curve is interesting. The pronounced minimum in the activity coefficient at an intermediate composition is reminiscent of the behavior observed in solutions of electrolytes in water. Such behavior is attributed to association of the electrolyte with increasing concentration, and perhaps the same type of behavior is occurring in the III–V systems.

The good agreement between the values of W calculated from the phase diagram alone and equation (2), and those calculated from the pressure data and equation (3), permits the calculation of γ for those compounds for which only the phase diagram data are available. This follows from equating equations (3) and (4), which yields,

$$\gamma = \exp[w(1-x)^2/RT] \tag{5}$$

Such calculations show that γ, for the remaining III–V compounds, has the same concentration dependence as that shown in Fig. 6. In particular, this procedure has been applied to the phase diagram data of GaP to extend the dissociation pressure curve below the region in which measurements were taken. Values of γ from equation (5) were used in equation (4) to calculate the partial pressure of P_4 over the melt, along the three-phase line. From this the total phosphorus pressure was determined. The result is shown in Fig. 5. It is of interest to note that below 1200°C the dissociation pressure of GaP is apparently higher than that of GaAs.

The low temperature ideal solution behavior is most unexpected. This result is consistent with the finding of Hall(13) that at low temperature the plots of ln $4(x)(1-x)$ vs. $(T_m/T)-1$ for all these systems are linear with almost identical slopes *corresponding to an entropy of fusion of* 9·5 ± 0·5 cal/g at. deg. This would be the entropy of fusion of these compounds melting to give a truly ideal solution. Experimental determination(10, 16) of the entropies of fusion of these compounds at their melting points gives values in the range 5·5 to 7·5 cal/g at. deg (which are comparable to the entropies of Ge and Si, 6·4 and 6·6 cal/g at. deg respectively). The difference between the lower measured values of the entropy of fusion and that given by the low temperature phase diagram indicates that the melt is not ideal, and is attributed to the amount of ordering in the stoichiometric melt.

The particular type of association occurring in the melt probably involves the formation of dimers and other species of the Group V element. This type of behavior would show a concentration dependence of the type observed. Clarification of this point would require experiments (1) in which the partial pressure of the Group V element was measured as a function of its concentration in a solution of a Group III metal at constant temperature, and (2) in which the temperature is varied but the composition held fixed.

5. CONCLUSIONS

The dissociation pressures of GaAs, InP, and GaP have been measured as a function of temperature. The pressures at the stoichiometric melting points were found to be: for GaAs, 1·00 ± 0·02 atm. at 1238°C; for InP, 21 ± 5 atm. at 1058 ± 3°C and for GaP, 35 ± 10 atm. at 1467 ± 3°C. These data, together with the phase diagram data for the III–V compounds, indicate that the melts of these compounds are neither ideal nor regular solutions but show negative excess free energies which are dependent on composition and/or temperature. The composition and temperature dependence of the activity coefficient of the Group V element in these solutions suggests that associated species of a Group V element are present in these melts.

Acknowledgements.—The author wishes to thank Mr. C. Yost for his assistance in the construction of the quartz Bourdon gauges used for these experiments, and Dr. J. Blanc for many helpful discussions.

REFERENCES

1. van den Boomgaard J. and Schol K., *Philips Res. Rep.* **12**, 127 (1957).
2. Drowart J. and Goldfinger P., *J. Chim. Phys.* **55**, 721 (1958).
3. Goldfinger P. and Jeunehomme M., *Joint Conference on Mass Spectrometry.* Sept., 1958, Pergamon Press, London (1959).
4. Folberth O. G., *J. Phys. Chem. Solids* **7**, 295 (1958).
5. Weiser K., *J. phys. Chem.* **61**, 513 (1957).
6. Lyons V. J. and Silvestri V. J., *J. phys. Chem.* **65**, 1275 (1961).
7. Fischer A. G., *J. electrochem. Soc.* **106**, 839 (1959).
8. Marina L. I., Nashel'shii A. Ya. and Yakobson S. V., *Zh. fiz. khim.* **36**, 1086 (1962).

9. Folberth O. G., *Halbleiterprobleme Band V*, Vieweg, Braunschweig (1960).
10. Schottky W. F. and Bever M. B., *Acta Met.* **6**, 320 (1958).
11. Wagner C., *Acta. Met.* **6**, 309 (1958).
12. Vieland L., *Acta. Met.* **11**, 137 (1963).
13. Hall R. N., *J. electrochem. Soc.* **109**, 208 C (1962).
14. Hansen M., *Constitution of Binary Alloys*, McGraw-Hill, New York (1958).
15. Rubenstein M., *J. electrochem. Soc.* **109**, 65C (1962).
16. Richman D. and Hockings E. F., to be published.
17. Horiba S., *Z. phys. Chem.* **106**, 295 (1923).
18. Farr T. D., *Chemical Engineering Report No.* **8**, Tennessee Valley Authority, Wilson Dam (1950).

APPENDIX

Extrapolation of the experimental data for InP *and* GaP.

At any temperature T the dissociation pressure in terms of the tetratomic species of a III–V solid in equilibrium with a liquid phase of atom fraction x of a Group V element is given by

$$P_4^{1/4} = P_{0,4}^{1/4}\, x\gamma \tag{A1}$$

where $P_{0,4}^{1/4}$ is the pressure of pure liquid Group V element, and γ is the activity coefficient of this element in the melt. Taking logarithms and differentiating with respect to $1/T$ yields

$$\frac{1}{4}\frac{\mathrm{d}\ln P_4}{\mathrm{d}1/T} = \frac{1}{4}\frac{\mathrm{d}\ln P_{0,4}}{\mathrm{d}1/T} + \frac{1}{x}\frac{\mathrm{d}x}{\mathrm{d}1/T} + \frac{\mathrm{d}\ln\gamma}{\mathrm{d}1/T} \tag{A2}$$

It follows from this expression that at the stoichiometric melting point the slope of the ln P vs. $1/T$ curve must become infinite, since from the phase diagram $\mathrm{d}x/\mathrm{d}1/T \rightarrow -\infty$ at that point when approaching from the gallium rich side (the case applicable here). Thus, to extrapolate the experimental curves it is only necessary to know the melting points of the compounds. The melting point of InP was established(14) to be 1058°C. The melting point of GaP was established by two methods. A differential thermal analysis measurement gave a value of 1470°C. A second value for the melting point was obtained by a slightly different extrapolation of the pressure-temperature data. Graphically taking the slope of the ln P vs. $1/T$ curve and plotting its reciprocal vs. $1/T$, the melting point can be found. At the melting point the reciprocal must be zero, and it must approach this value with a slope of $-\infty$. Applying this procedure, a value of 1465°C was obtained. These two values are in excellent agreement with that recently reported by Rubenstein.(15) For this work the stoichiometric melting temperature of GaP was taken to be 1467°C.

J. Phys. Chem. Solids Pergamon Press 1963. Vol. 24, pp. 1141–1143. Printed in Great Britain.

THE HYDROGEN ATOM POSITIONS IN FACE CENTERED CUBIC NICKEL HYDRIDE

E. O. WOLLAN, J. W. CABLE and W. C. KOEHLER
Oak Ridge National Laboratory, Oak Ridge, Tennessee

(*Received* 11 *April* 1963)

Abstract—Neutron diffraction observations on the nickel–nickel hydride system show that the hydrogen atoms occupy the octahedral sites of the face centered cubic lattice. The hydrogen to nickel atom ratio in the hydride phase was found to be 0·6 ± 0·1. In these respects nickel and palladium behave similarly. The systems differ, however, in the one important detail that the palladium hydride is stable at room temperature whereas the nickel hydride is unstable.

RECENTLY it was shown that nickel films could be electrolytically charged with hydrogen to concentrations as high as 0·7 hydrogen atoms per nickel atom.(1) Even though the resulting hydride is unstable a few physical properties have been reported. The X-ray diffraction studies(2, 3) showed that the face centered cubic structure was retained with a lattice spacing about 5·5 per cent larger than that of pure nickel. The saturation magnetization of the system falls to zero at a hydrogen to nickel atom ratio of 0·65 which indicates that the hydride is non-magnetic and that the electrons from the hydrogen atoms fill the nickel *d*-band.(4) This behavior is similar to that of palladium which also absorbs about 0·6 H/Pd and loses its magnetic moment in the process. Neutron diffraction studies by WORSHAM, WILKINSON and SHULL(5) have shown that the hydrogen atoms in palladium occupy the octahedral sites. It was considered of interest to determine their location in nickel.

The sample was prepared by the method reported by BARANOWSKI and SMAILOWSKI.(1) A 25 μ thick nickel foil was electrolytically loaded, cut into 1 × 5 cm strips, and sealed into a vanadium diffraction cell with an attached pressure gauge. Neutron diffraction patterns were obtained at room temperature as a function of time, and a portion of the data is shown in Fig. 1. Those reflections inside of the nickel reflections are from the hydride phase and correspond to a face centered cubic cell with a lattice spacing of 3·717 Å. In such a lattice there are two sites available to the hydrogen atoms; the tetrahedral sites with positions ± (1/4 1/4 1/4) f.c.c. and the octahedral sites at (1/2 0 0) f.c.c. For tetrahedral occupation the (200) reflection should be more intense than the (111) reflection. Inspection of Fig. 1 shows that this is not the case. On the other hand if the octahedral sites are occupied just the reverse is expected, and this is in accord with the observations. The intensity relationships of the (220) and (311) reflections also support the octahedral site model as will be shown later.

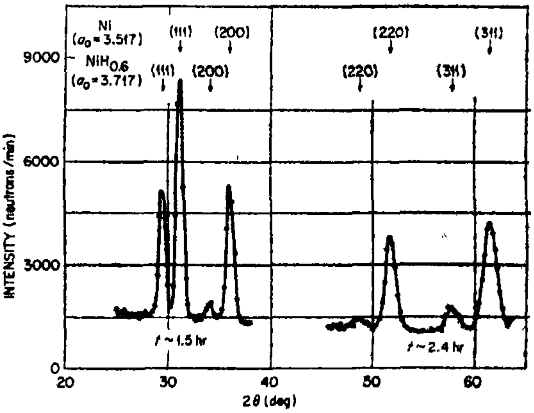

FIG. 1. Neutron diffraction patterns of the nickel–nickel hydride system.

The hydride is unstable at room temperature, decomposing into nickel and hydrogen gas. Consequently those reflections from the hydride phase disappear in time while those from pure nickel increase in intensity. This is illustrated in Fig. 2 in which the reduced pressure of the evolved hydrogen gas is shown on the left, and the intensities of the (111) reflections from the hydride and from nickel are shown on the right, both as functions of time after the cell was sealed. In the intensity plot the points are the experimental observations while the curves are calculated using the expressions

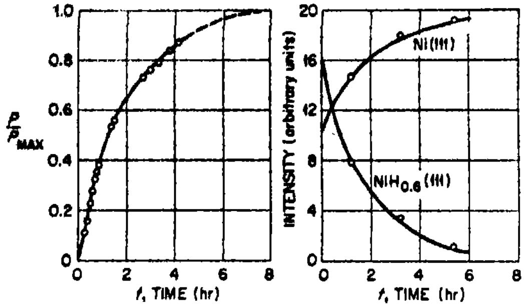

FIG. 2. The time dependence of the reduced hydrogen pressure and of the (111) intensities for the nickel–nickel hydride system.

$$P_{111}(\text{Ni}) \;= K\frac{b_{\text{Ni}}^2}{\sin\theta\sin 2\theta}\eta_{\text{Ni}}$$

$$P_{111}(\text{NiH}) = K\frac{(b_{\text{Ni}}-xb_{\text{H}})^2}{\sin\theta\sin 2\theta}(1-\eta_{\text{Ni}}).$$

Here, K is an instrumental constant, $b_{\text{Ni}} = 1{\cdot}03\times 10^{-12}$ cm, $b_{\text{H}} = -0{\cdot}38\times 10^{-12}$ cm, θ is the Bragg angle, η_{Ni} is the fraction of the nickel atoms in the nickel phase and x is the H/Ni ratio in the hydride phase. For sufficiently long times ($t > 6$ hr) η_{Ni} approaches unity and K may be determined from the intensity of the nickel (111) reflection. Then, assuming no preferred orientation effects, this constant can be used in the intensity expression for the (111) reflection of the hydride. At any given time η_{Ni} is determined from the total hydrogen content of the sample for various assumed x values. Notice that x and η_{Ni} enter the intensity expressions to different powers so that they are readily determined from the intensity and total hydrogen content. From the intensity of the (111) reflections in Fig. 1 an x value of $0{\cdot}6 \pm 0{\cdot}1$ was determined and this was used in calculating the curves of Fig. 2.

It was found that the instrumental constant K for the (111) reflection could not be applied to the other reflections, presumably because of preferred orientation effects. It was necessary then to calibrate each hydride reflection intensity to that of the corresponding reflection from the nickel phase. For intercomparison purposes the intensity curves of the various reflections were interpolated to a common time interval and intensity ratios taken to remove the instrumental constant. The results for $t = 3$ hr are compared with the calculated ratios in Table 1.

Table 1. *Comparison of calculated and observed intensity ratios for the nickel hydride–nickel system*

hkl	$\dfrac{P_{\text{NiH}}}{P_{\text{Ni}}}$(calc)*	$\dfrac{P_{\text{NiH}}}{P_{\text{Ni}}}$(obs)†
111	0·21	0·21
200	0·08	0·07
220	0·08	0·05
311	0·21	0·15

* An x value of 0·6 was used. The pressure at this time indicated a total hydrogen content of 0·066/Ni so that $\eta_{\text{Ni}} = 0{\cdot}89$.

† $t = 3$ hr.

The observed ratios of the higher angle reflections fall below the calculated values indicating that thermal effects are more pronounced in the hydride than in the metal. Thermal corrections have not been applied nor are the data sufficiently precise for the determination of individual thermal correction factors. Nevertheless the agreement is such as to establish the location of the hydrogen atoms in the octahedral sites.

These measurements were undertaken with the thought that they might have a significance with regard to the magnetic properties of nickel and palladium. It has been suggested by one of us⁽⁶⁾ that the difference in the magnetic properties of these two similar metals is associated with a difference in the occupation of the d-orbitals. In nickel which is ferromagnetic with a high Curie temperature ($T_c = 632$°K), the holes in the *d*-shell are assumed to occupy the *t*-orbitals which have strong overlap with near neighbor atoms. In palladium which does not appear to order magnetically even at very low temperatures it is assumed that the holes in the *d*-shell occupy the *e*-orbitals which have very small σ-overlaps with second near neighbor atoms. At the time these suggestions were made it was not known that nickel could be made to take up hydrogen by the electrolytic method and in so doing that the holes in the *d*-shell were filled in a fashion similar to that which has long been known to be the case for palladium. On this basis it was suggested that the ease of hydrogen uptake and the fact that the hydrogen atoms occupy the octahedral sites was some evidence for suggesting that the holes in palladium are in the *e*-orbitals which point towards and surround these sites.

A similar argument would then suggest that in nickel the hydrogen atoms would prefer the tetrahedral sites which are surrounded by the *t*-orbitals with which the holes are assumed to be associated. As pointed out, however, the octahedral holes are considerably larger than the tetrahedral holes, and this is undoubtedly the more important factor energetically. It is also to be recognized that the rather large change in volume (18 per cent) which accompanies the formation of the hydride could in itself significantly alter the energy relationships among the *d*-electrons. It would appear then that the assumptions relating to the orbital occupations in nickel and palladium are neither confirmed nor denied as a consequence of the observed structure of the hydrides and they must rest on other evidence. Pertinent to this, for example, are the properties of the hydrogenated and non-hydrogenated alloys dilute in various iron group constituents.(6) It may also be of significance that palladium hydride is stable at room temperature whereas nickel hydride is unstable.

Acknowledgement—The authors are indebted to Mr. R. B. QUINCY for the preparation of the samples used in this investigation.

REFERENCES

1. BARANOWSKI B. and SMIALOWSKI M., *J. Phys. Chem. Solids* **12**, 206 (1959).
2. JANKO A., *Naturwissenschaften* **47**, 225 (1960).
3. BONISZEWSKI T. and SMITH G. C., *J. Phys. Chem. Solids* **21**, 115 (1961).
4. BAUER H. J. and SCHMIDBAUER E., *Z. Phys.* **164**, 367 (1961).
5. WORSHAM J. E., WILKINSON M. K. and SHULL C. G., *J. Phys. Chem. Solids* **3**, 303 (1957).
6. WOLLAN E. O., *Phys. Rev.* **122**, 1710 (1961).

LETTER TO THE EDITOR

Energy and configuration of atoms in a simple model of an edge dislocation—

II. Morse potential

(*Received* 1 *March* 1963)

AN ATOMISTIC model of an edge dislocation has been described in the preceding publication(1) (Part 1). We give here further results obtained from it. We recall briefly that we have considered a two-dimensional edge dislocation in a plane close-packed lattice; such a dislocation has been realized and photographed by BRAGG and NYE in their bubble-raft experiment.(2) The atoms were allowed to interact with two-body central forces; only interactions between first neighbours were considered. We have reported previously the results obtained with the 6–12 inverse power potential. We have carried out similar calculations using a Morse potential to represent the metals copper, nickel, and silver; the energy of interaction between two atoms is given by:

$$e_{ij} = e_A\{-2\exp[-\alpha_A(r_{ij}-r_A)] + \exp[-2\alpha_A(r_{ij}-r_A)]\} \qquad (1)$$

The values of the specific constants e_A, r_A, α_A have been determined by GIRIFALCO and WEIZER(3) and are given in Table 1.

Table 1. *Parameters of the Morse potential for copper, nickel, and silver.*(3)

	α_A(Å^{-1})	r_A(Å)	e_A(eV)	$\alpha_A r_A$
Cu	1·3588	2·866	0·3323	3·894
Ni	1·4199	2·780	0·4205	3·947
Ag	1·3690	3·115	0·3323	4·264

In our calculation initial positions of the atoms have been deduced from elastic theory, considering an edge dislocation in an infinite lattice(4) and then the configuration corresponding to the minimum of the energy was found. The set was chosen large enough so that the positions of the atoms on the boundary were already those of minimum energy. There were 184 atoms in the set, arranged in 7 atomic layers around the dislocation core. The calculation was carried out numerically on an IBM 1620 electronic computer, the coordinates were corrected until none of the changes exceeded 10^{-4} of a, the atomic spacing in the perfect lattice.

The set considered is shown in Fig. 1; the atoms are numbered to permit identification. The energy of deformation $u-u_0$ of the atoms in the first and second layer around the centre of the dislocation expressed as fraction of the energy u_0 of an atom in a perfect lattice is given in Table 2. Let us recall that in a model where only interactions between nearest neighbours are considered, we have:

$$u_0 = ze_A \qquad (2)$$

z, the number of nearest neighbours, is equal to 6 in an hexagonal close-packed lattice. The values of u_0 given in Table 2 have been calculated from e_A as determined by GIRIFALCO.(8)

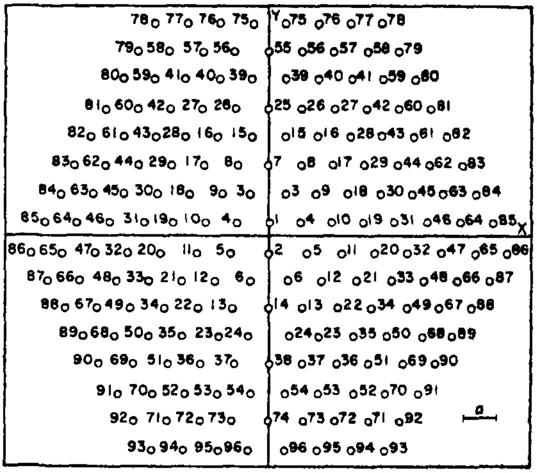

FIG. 1. Edge-dislocation in a closed-packed plane.

The energies in rows parallel to the x-axis are plotted against x in Fig. 2. The energy of fusion for copper, nickel, and silver is of the order of 0·04 of the energy of sublimation, or the energy per atom in a perfect lattice. There is a small region, comprising about 10 atoms, where the energy exceeds that of fusion; the energy of deformation falls off very rapidly with R, the distance from the dislocation core.

Table 2. Energy of deformation $u-u_0$ of atoms in the first and second layer around the dislocation core, expressed as fraction of the energy in a perfect lattice, u_0.

Number of the atom	Number of the layer	Cu $(u-u_0)/u_0$ $u_0 = 2{\cdot}057$ eV	Ni $(u-u_0)/u_0$ $u_0 = 2{\cdot}523$ eV	Ag $(u-u_0)/u_0$ $u_0 = 1{\cdot}994$ eV
1	0	0·229	0·233	0·236
2	0	0·052	0·054	0·082
3	1	0·015	0·017	0·018
4	1	0·114	0·118	0·132
5	1	0·068	0·069	0·080
6	1	0·014	0·023	0·028
7	2	0·006	0·007	0·008
8	2	0·007	0·008	0·009
9	2	0·010	0·011	0·013
10	2	0·042	0·045	0·053
11	2	0·020	0·021	0·024
12	2	0·016	0·015	0·018
13	2	0·009	0·008	0·010
14	2	0·010	0·010	0·012

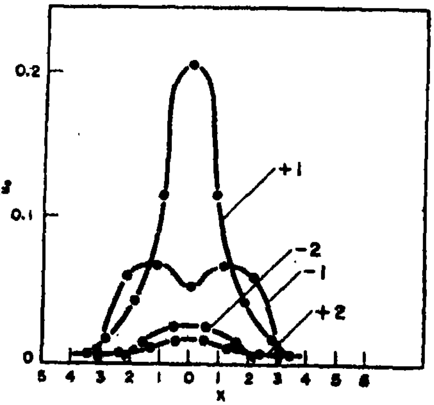

FIG. 2. Energy of atoms in the first (1) and second (2) row above (+) and below (—) the slip plane. Morse potential representing copper. The points on the curve represent the atoms.

The energies of deformation E_R in the array of 184 atoms as obtained by relaxation of the positions of atoms in regions of increasing size are given in Table 3 for copper, as well as the change in energy. Nearly the whole of the change in energy is due to the readjustment of the positions of the atoms in the first and second layer, the initial positions being those given by the elastic theory.

To bring about the degree of convergence obtained, about 20 iterations were required in the smaller regions and 12 in the final array; indeed, in the latter case the initial positions are very close to the final ones.

In Fig. 3 the energies of arrays of increasing size are plotted against ln R, R being the mean

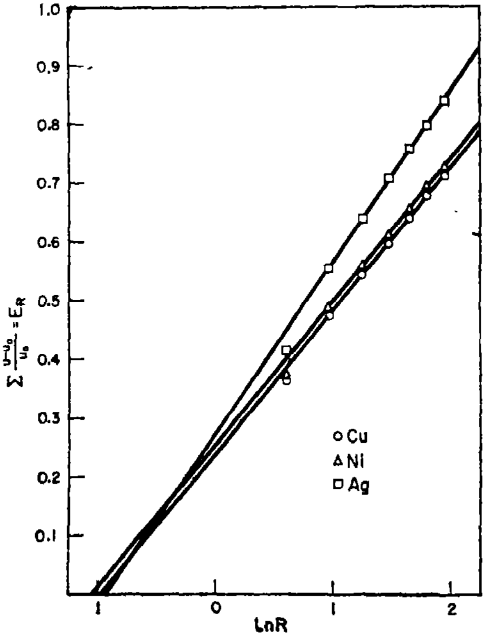

FIG. 3. Energy of deformation as a function of ln R for copper, nickel, and silver.

Table 3. Energy of deformation E_R in an array of 184 atoms when minimizing the energy in regions of increasing size. Morse potential representing copper.

Number of last layer added	$E_R = \sum \frac{u-u_0}{u_0}$	Change on minimization in percent of the final energy (%)
2	0·718	30
3	0·713	1·2
4	0·711	0·5
5	0·709	0·4
6	0·708	0·2
7	0·708	0·0

radius of the array, expressed in units of a; elastic theory gives a linear dependence of E_R, the energy of deformation, on ln R:

$$E_R = \frac{\mu a^2}{4\pi(1-\nu)} \ln R/R_d \tag{3}$$

In the expression (3) μ is the Lamé constant, ν the Poisson ratio, R_d a parameter, equal to the radius of the "bad" region in the core. At a distance of two atomic spacings from the centre, the variation of E_R with ln R is already linear. For copper, R_d comes out to be 0·37a. Using this value of R_d, the value of u_0 as quoted in Table 2, and from the variation of E_R with ln R, we find that the energy of the dislocation, in copper, is 9·2 eV at $R = 1$ cm. The energy of ten atoms in the centre (first layer), equal to 0·74 eV, is thus 8 per cent of the energy of deformation of a dislocation.

The general conclusions obtained from these calculations are similar to those obtained from the 6–12 inverse power potential:(1) in both cases there is only a limited number of atoms having an energy of the magnitude of that of fusion; the total energy of deformation $\Sigma\,(u-u_0)/u_0$ of the array of 184 atoms is equal to 0·708 for the Morse potential representing copper and 1·441 for the 6–12 inverse power potential. Indeed, the energy of deformation is primarily determined by the elastic constant μ and, if interatomic forces are central forces between first neighbours, by the second derivative of the potential with respect to r_{ij} at $r_{ij} = r_A$. For the inverse power potential, if e_{ij} is given by

$$e_{ij} = e_A\left[-2\left(\frac{r_{ij}}{r_A}\right)^{-n} + \left(\frac{r_{ij}}{r_A}\right)^{-2n}\right] \tag{4}$$

μ is proportional to n^2, for the Morse potential to $(\alpha_A r_A)^2$, with the same constant of proportionality. For Cu, Ni, Ag, $\alpha_A r_A$ is nearly equal to 4 (Table 1), and thus an inverse power 4–8 potential could be used to represent them. We have carried out calculations for inverse power n–$2n$ potentials with n ranging from 4 to 7. As expected, the results for the 4–8 potential are close to those obtained from the Morse potential. On increasing n, both the energy of deformation and the radius R_d of the bad region increase.

The initial positions of atoms, as obtained from elastic theory, do not depend in the model used on the exact form of the potential. The dislocation width, as calculated from elastic theory, equals 1·04 a.

The dislocation width, calculated from the final positions of the atoms equals 1·02 a, 1·04 a, 1·07 a for the Morse potentials representing Cu, Ni, Ag, respectively. For the inverse power potential, the width increases steadily from 1·10 a to 1·38 a when n increases from 4 to 7.

Acknowledgements—We are indebted to Mr A. Vosse, Mme L. Masui and Mme E. Provis for carrying out the numerical calculations.

Union Carbide European Research Associates,
95 *rue Gatti de Gamond*
Brussels 18, *Belgium*

A. Englert
H. Tompa

References

1. ENGLERT A. and TOMPA H., *J. Phys. Chem. Solids*, **21**, 306 (1961).
2. BRAGG W. L. and NYE J. F., *Proc. Roy. Soc.*, **A190**, 474 (1947).
3. GIRIFALCO L. A. and WEIZER V. G., *Phys. Rev.* **114**, 687 (1959).
4. HUNTINGTON H. B., DICKEY J. E. and THOMAS R., *Phys. Rev.* **100**, 1117 (1955).
5. Selected values of chem. therm. properties. *Nat. Bur. Stand.*, U.S. Gov. Print. Off., Wash. D.C. 1952.

BOOK REVIEWS

G. C. BOND: **Catalysis by Metals.** Academic Press, London and New York (1962). 519 pp. $15.50.

MUCH of our chemical technology is based on catalytic processes occurring on solids. The high degree of development of this technology is a tribute to the prowess of the catalytic chemist and to the success of the Edisonian approach. In contrast to these practical achievements, the basic understanding of catalytic processes is not far advanced. In this book, Professor Bond has addressed himself to the task of relating what *is* known about the physical chemistry of heterogeneous catalysis.

Since heterogeneous catalysis occurs through the intermediary of adsorbed entities, the author starts with a description of the properties of metals, and then considers at greater length the preparation and properties of the vacuum–metal interface. Next follows an outline of the qualitative behavior of adsorbed gases, and of the quantitative kinetics and energetics of surface processes. Roughly one third of this thick volume is devoted to this survey of the physics and chemistry of the adsorbed layer. The further chapters, which form the bulk of the book, deal with individual chemical processes such as, for example, the reactions of hydrogen, hydrogenation of olefins, synthesis and decomposition of ammonia, dehydrogenation and oxidation. In closing, Prof. Bond discusses the various relationships between the properties of the bulk metal and those of the surface layer.

The presentation throughout is chemical and descriptive—deductions from experiment are stated without going through the analysis in detail. In view of the vast subject matter covered this is almost inevitable. For the physicist or chemist primarily concerned with solid state phenomena, the elementary outline of the fundamentals will be superfluous. It should still be useful, however, in conveying an accurate impression of the level at which the subject matter is approached by workers in this field. Although the aim of the book is to present the basic facts of catalysis in relation to what is known about elementary surface processes, the author sometimes does not make full use of data on adsorption in the interpretation of more complex phenomena. The discussion of adsorption itself is not quite up to date; appreciable quantitative data have accumulated recently on the rates of atomic processes pertinent to catalysis. The physicist particularly would appreciate greater emphasis on these simple reactions. A more detailed discussion of the experimental methods might also be useful. These are relatively minor defects, however.

To appreciate the difficulty of writing such a book, it should be recalled that even in dealing with the simplest catalytic reaction occurring on metals, the heterogeneous recombination of hydrogen atoms, the experimental data are conflicting and the mechanism of the reaction is not yet clear. A real understanding of more complex processes is therefore not to be expected. Professor Bond does succeed in making this limitation on our knowledge clear, while presenting a wealth of descriptive material on catalytic reactions. He is to be particularly commended for putting into perspective the simple correlations of surface processes with electronic structure that have enjoyed a considerable but ill-founded popularity.

The book is lavishly provided with original tabular summaries of both qualitative and quantitative data; diagrams and graphs are similarly used to good advantage in presenting the material. Extensive references to original papers are carefully given in the text and make the transition to the current literature in the field of catalysis very simple. A complete index provides easy access to the material in the work. Throughout there is continuing evidence of careful preparation and execution.

The scientific foundations of catalysis may not yet be sufficiently developed to permit a definitive work on the physical chemistry of heterogeneous processes. However, *Catalysis by Metals* provides a very useful review. It will without doubt become a widely used reference of special appeal to the physical chemist, and by revealing the gaps in our knowledge should stimulate further work.

General Electric Company
Research Laboratory,
P.O. Box 1088,
Schenectady, New York

GERT EHRLICH

D. M. YOUNG and A. D. CROWELL: **Physical Adsorption of Gases.** Butterworths, London (1962). 436 pp. 70s.

PHYSICAL adsorption, the interaction between gases and solids through van der Waals forces, is a universal phenomenon whose deceptive simplicity has long challenged experimentalist and theoretician. At the same time, it is of great practical importance for determining the surface area of powders and in a variety of purification processes. The last book in English devoted entirely to this subject, BRUNAUER's *Physical Adsorption*, was written just 20 years ago. In the meantime, much work based on new techniques has been carried out both in experiment and theory; the rediscovery of adsorption pumping has led to a recent resurgence of practical interest in this field as well. This book by YOUNG and CROWELL, covering the literature from 1930 through 1960, is therefore very timely.

The authors devote the first 100 pages to a presentation of the forces responsible for physical adsorption, coupled with a discussion of the thermodynamics of these systems. Isotherms (plots of amount adsorbed as a function of pressure at constant temperature) in monolayer and multilayer adsorption are then analyzed and the procedures for deducing surface areas from such isotherms are explained (~ 140 pages). Experimental techniques involved in determining isotherms and in adsorption calorimetry are covered in separate chapters, totaling 50 pages. Discussions of adsorption on non-uniform surfaces, adsorption of gas mixtures, and on the electric and magnetic properties of adsorbed films round out the book.

As is clear from this sketch, *Physical Adsorption of Gases* touches only a limited portion of the subject—namely that which has been of traditional interest to the classical surface chemist, with particular emphasis on adsorption isotherms. Within this area, however, the presentation is complete. The literature is covered thoroughly, and derivations for important relations are given or at least sketched. Without any background, and merely with this book as a guide, it should be possible to plunge immediately into the current chemical literature.

This thoroughness is not wholly an advantage, however. To do justice to the vast number of original papers, the authors have had to adopt a style more suitable for a literature survey than a book. Although both YOUNG and CROWELL are active in the study of adsorption phenomena, their own scientific personality rarely emerges. The subject is largely presented in the form of brief summaries of the original papers, without extensive discussion by the authors, except insofar as this discussion is already in the literature. Nowhere is it made clear why anyone should be interested in physical adsorption; motivation and perspective are more apparent in some of the original papers than in this survey.

The arrangement of the book also assumes considerable prior interest in the subject on the part of the reader. For example, theories of van der Waals forces are presented in detail at the very start, before there is any extensive presentation of the facts which the theories are to explain.The choice of subject matter and emphasis is limited, reflecting the preoccupation of workers in physical adsorption during the decade 1945–55. Thus there is no consideration of the rates of adsorption and desorption, nucleation, surface migration, of energy exchange or the scattering of molecular beams at surfaces. These are subjects of considerable importance to the chemist as well as the physicist.

This criticism is really an expression of disappointment that the authors missed the opportunity to turn out a well rounded treatise in a field not yet overrun with books. Despite limitations on subject matter and style. "Physical Adsorption of Gases," even in its present form, constitutes an important reference and a reliable guide to an important segment of the literature. As such it deserves a place in the collection of every chemist and physicist working on surface phenomena, and should enjoy widespread use.

General Electric Company, GERT EHRLICH
Research Laboratory,
P.O. Box 1088,
Schenectady, New York

WILLIAM T. SIMPSON: **Theories of Electrons in Molecules.** Prentice–Hall, Englewood Cliffs, New Jersey (1962). v+183 pp. $9.00.

THE author of this remarkable and valuable little book states that it "is intended to fill in the gap between what is found in quantum chemistry books and what is found in the journals". The student of chemistry will find it rather more difficult than his casual journal-browsing, however, and the student of physics will find in it much to tax as well as to interest him. The contents are a terse but not cursory, formal but not non-physical, integrated account of the molecular orbital, valence bond, and independent systems approaches to electronic structure of molecules and molecular crystals. Of special interest to readers of the *Journal of Physics and Chemistry of Solids* should be the treatment of non-orthogonality in the valence bond method and the discussion of electrostatic contributions to electronic spectra of molecular crystals.

It is a measure of the significant original contributions SIMPSON himself has made to theories of electrons in molecules (although it detracts from the utility of his book) that he can present this penetrating discussion without citing many references. Current literature in this subject often seems preoccupied with attempts to merge alternative methods by calculations of higher and higher accuracy. That is not at all the emphasis of this book, which instead stresses and develops the special coherence in each of the different viewpoints.

This book is beautifully bound in carmine and black, with typography of high grade; it is the most attractive technical volume I have seen recently.

Department of Chemistry,
The Johns Hopkins University,
Baltimore 18, *Maryland*

ROBERT G. PARR

ERRATUM

N. B. GROVER and R. OREN: Majority-carrier mobility on germanium surfaces. *J. Phys. Chem. Solids* **24**, 693 (1963).

p. 696. Caption to Fig. 4 should have symbols, ⊙, △ and □ in the right hand column instead of bold symbols printed.

J. Phys. Chem. Solids Pergamon Press 1963. Vol. 24, pp. 1153–1158. Printed in Great Britain.

STRUCTURAL TRANSFORMATION OF ZIRCONIUM PHOSPHIDE*

K. S. IRANI and K. A. GINGERICH

The Pennsylvania State University, College of Chemistry and Physics, University Park, Pennsylvania

(*Received* 13 *November* 1962; *revised* 15 *April* 1963)

Abstract—Structural investigations have been made on the phosphides of zirconium, with reference to the phosphides of the transition metal family Ti, Zr, and Hf. For the hexagonal form of β-ZrP, the unit cell expansion as a function of temperature has been determined, using high temperature *x*-ray diffraction. The transformation from the hexagonal β-form to the f.c.c. α-form at elevated temperatures has been investigated. The unit cell dimensions of the hexagonal β-ZrP are found to increase linearly with temperature, until at a critical value in vacuum there is a slight decrease in phosphorus content and the cell suddenly collapses to the more stable cubic α-ZrP. The constancy of the hexagonal c/a value until its sudden fall to unity, for the cubic form, is indicative of a co-operative first order type of transformation. Mass spectrometric techniques have also been used to study this transformation. A structural model is given to explain this transition which is a function of both temperature and pressure, involving a slight stoichiometry change. The relative high temperature stabilities are TiP < ZrP < HfP.

INTRODUCTION

THE advantage of compound semiconductors over elemental semiconductors is that the former can be synthesized in a wide range of non-stoichiometric compositions, with resulting properties ranging from highly insulating refractories, through useful semiconductors, all the way to almost metallic behavior. In the present investigation of the structural and thermodynamic aspects of the Ti, Zr and Hf phosphides, the three monophosphides are found to be isomorphous, with the stability increasing from TiP to ZrP to HfP. The data for the ZrP high temperature structural transformation will be reported in detail herewith.

As early as 1908, GEWECKE[1] had reported the synthesis of ZrP_2. In the period 1938–40, BILTZ and co-workers have synthesized several metal phosphides (ranging from Mn and Fe to Ge, Rh, Ti[2] Zr,[3] U and Th). Their report on the Zr–P system showed the possible existence of ZrP_2, ZrP, and Zr_2P phases. In 1954, SCHÖNBERG[4] reporting on transition metal phosphides, gave a detailed X-ray structural analysis of TiP. The compound is hexagonal, having a superstructure of nickel arsenide, with the P atoms being at the center of Ti atom octahedra. The space group is D_{6h}^4–$P\,6_3/mmc$, with four molecules per unit cell. The position of the various atoms, layer by layer, can be denoted by $A_{Ti}B_PA_{Ti}C_PB_{Ti}A_PB_{Ti}C_P$. The compound ZrP was designated by the term β-ZrP. It was isomorphous with TiP. Schönberg also reported briefly a cubic form of $ZrP_{0.9}$ which he termed as α-ZrP.

EXPERIMENTAL

(*a*) *Synthesis*

The Faraday method was used for sample preparation. A weighed quantity of "reactor grade" Zr metal was placed in a tungsten boat at one end of a quartz tube and at the other end was placed the required quantity of 99·99% pure red phosphorus, and the whole tube was evacuated and sealed. This was heated in a double furnace arrangement whereby the P_2 end ("cold end") was maintained at a temperature varying from 300 to 400°C, and the Zr end ("hot end") was maintained between 700–950°C, depending on the composition required. The reaction was done for several days, and the product was ground and checked by X-ray diffraction to make sure that no free Zr metal lines existed.

---

* This work was supported under AEC Contract No. AT(30–1)–2541.

(*b*) *Analysis*

The gain in weight of the Zr metal during phosphidation was used to compute the formula of the product. Chemical analysis was also done by dissolving the phosphide in 20% HNO_4–5% HF solution, and then using standard gravimetrical methods.

(*c*) *X-ray diffraction*

The room temperature diffraction patterns were taken on a 114·6 mm diameter Straumanis type of camera using Cu Kα radiation. The low angle rings were used only for identification and indexing purposes, while the high angle reflections, where good α_1 and α_2 splitting was observable, were used for the accurate determination of the cell parameters. Suitable corrections for film shrinkage were applied.

For cell expansion and high temperature work, a Seeman high temperature X-ray camera and Cu Kα radiation was used. The sample was sealed in an evacuated quartz capillary, mounted in an evacuated chamber heated by Pt/Rh heater elements. Two thermocouples were located in close proximity to the radiated sample area—one for temperature control by an electronic controller unit to within 1°C at any set temperature; and another calibrated standard thermocouple for actual temperature measurement. This couple had been standardized in the camera, using standard transformations and melting points. The film mounting is of the regular symmetrical type, with six different exposures being recorded on the same strip of film. The first and last patterns were always made at room temperature to check that no change had taken place in the sample during heating. No internal standard was used, but the correction factor for each strip was determined by comparing the room temperature patterns of the same sample in this arrangement and in a standard 114·6 mm camera. This correction was then applied to the four other patterns taken at elevated temperatures on the same strip film. The maximum attainable temperature was 1300°C.

For checking phase transformations at temperatures higher than 1300°C, quenched samples were used. The substance was heated in a tungsten crucible by r.f. induction, while enclosed in a continuously evacuated quartz tube. The temperature was measured from a black body hole by an optical pyrometer. The sample, after quenching to room temperature, was analyzed by standard X-ray methods.

(*d*) *Electron diffraction*

Selective area diffraction and micrographs of the sample were taken on a Hitachi HU 11 type electron microscope. Aluminum evaporated on the grid served as the internal standard.

(*e*) *Mass spectrometry*

A 60° sector, 12 in. radius, first order directional focusing mass spectrometer, and a molybdenum Knudsen effusion cell, with an orifice diameter of 0·051 cm and an orifice/sample surface ratio of about 1/100 was used. A weighed quantity of the substance was placed in a tantalum liner and then inserted in the cell. Mass scanning was done by varying the magnetic field, keeping the energy of ionizing electrons constant at 55 eV. Heating up to 1000°C was done by radiation from tungsten ribbon filaments suspended around the cell. For higher temperatures electron bombardment was used. Temperatures were measured by a Pt/6% Rh vs. Pt/30% Rh thermocouple, located in the bottom of the cell, and previously calibrated vs. standards. In addition, an optical pyrometer, focused on a black body hole of the cell, was also used, after applying necessary emissivity and window corrections.

RESULTS AND DISCUSSIONS

A synthesized sample of β-ZrP showed, on analysis, a composition $ZrP_{0\cdot 99}$. The X-ray pattern indicated a hexagonal structure with the space group D^4_{6h}–$P6_3/mmc$. Density determination showed that $Z = 4$. The unit cell dimensions are "*a*" = 3·684 Å and "*c*" = 12·554 Å. This compares favorably with the values of "*a*" = 3·677 Å and "*c*" = 12·52 Å as reported by SCHÖNBERG,(4) who had determined the structure of β-ZrP as isomorphous with TiP. An indexed pattern is given in Table 1. The location of the Zr and P atoms in the various layers follows the arrangement $A_{Zr}B_PA_{Zr}C_PB_{Zr}A_PB_{Zr}C_P$. The 4 Zr atoms are located at 1/3, 2/3, 1/8; 1/3, 2/3, 3/8; 2/3, 1/3, 5/8; 2/3, 1/3, 7/8; while the phosphorus atoms are located at 2*P* in 2 (*a*) positions at 0, 0, 0 and 0, 0, 1/2 and 2*P* in 2 (*d*) positions at 1/3, 2/3, 3/4 and 2/3, 1/3, 1/4. The interatomic distances were calculated on the above model, and are given in Table 2. The cell expansion is indicated in Table 3 where unit cell dimensions are given at various temperatures. All readings except the last one, were made with the sample maintained at the respective temperature.

Table 1. *X-ray pattern of hexagonal β-*ZrP

d	I/I_1	*hkl*
3·20	30	010
3·13	15	004
3·10	30	011
2·85	15	012
2·523	100	013
2·226	50	014
1·963	40	015
1·837	80	110
1·583	40	114
1·558	40	008
1·487	25	023
1·420	10	024
0·9268	20	2, 0, 11
0·9213	20	220
0·8800	40	308
0·8662	40	313
0·8284	60	2, 1, 11
0·7944	80	228

Table 2. *Interatomic distances for hexagonal* β-ZrP (Å)

P–P along base plane	3·684
P–P between layers	3·791
Zr–Zr neighboring pairs	3·139
Zr–Zr adjacent columns between layers	3·791
Zr–P interlayer to base plane	2·643
P–Zr interlayer to interlayer	2·643

The variation of the unit cell dimensions "*a*","*c*", and volume, as a function of temperature, have been plotted in Figs 1 and 2. The "*a*" and "*c*" values are observed to increase almost linearly, until at 1425°C in vacuum the system transforms from hexagonal to f.c.c. structure.

The cubic or α-ZrP cell dimensions have been determined from a quenched sample, with an analyzed composition of $ZrP_{0\cdot93}$, having a cubic NaCl type of structure, Fm3m with Z = 4. The observed cell dimension is 5·242 Å, as compared to 5·27 Å reported by Schönberg,(4) who determined the structure of α-ZrP as of the NaCl type. An indexed pattern for α-ZrP is given in Table 4.

Table 3. *Unit cell dimensions of* ZrP *at elevated temperatures*

Temp. °C	"a" Å	"c" Å	c/a	Volume $Å^3$
25	3·684	12·554	3·408	147·5
235	3·697	12·569	3·400	148·8
437	3·702	12·589	3·401	149·4
640	3·709	12·609	3·400	150·3
792	3·714	12·629	3·400	150·9
955	3·718	12·649	3·402	151·5
1145	3·725	12·664	3·400	152·1
1245	3·729	12·669	3·397	152·6
*1425	5·242		1·000	144·04

* Cell dimensions for cubic form were determined at room temperature, using samples quenched from indicated temperature.

Table 4. *X-ray pattern for cubic α-*ZrP

d	I/I_1	*hkl*
2·998	30	111
2·602	70	200
1·847	100	220
1·579	40	311
1·513	40	222
1·311	30	400
1·217	30	331
1·173	100	420
1·069	100	422
1·007	40	511, 333
0·9262	40	440
0·8864	50	531
0·8741	100	600, 442
0·8304	80	620
0·8015	20	533
0·7928	80	622

The interatomic distances for the f.c.c. model are as follows: P–P distance equals Zr–Zr distance equals 3·708 Å; Zr–6P distance equals P–6 Zr distance equals 2·622 Å.

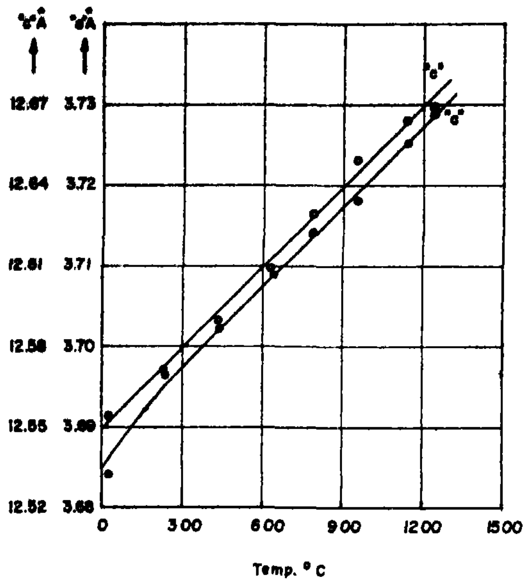

FIG. 1. Lattice parameter expansion as a function of temperature for β-ZrP.

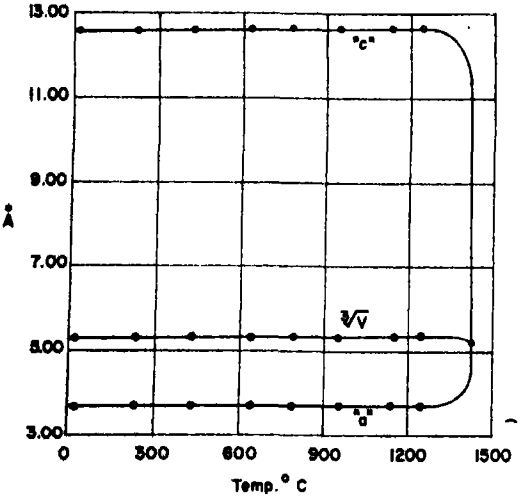

FIG. 2. Cell dimension vs. temperature for ZrP.

The distortion parameter (c/a) has been plotted as a function of temperature in Fig. 3. The constancy of c/a with temperature until transformation when there is a sudden decrease and the system reverts to cubic, is indicative of a first order type of transformation. The narrow range indicates a cooperative type of effect, so that once ordering begins, the whole process completes itself quite rapidly.

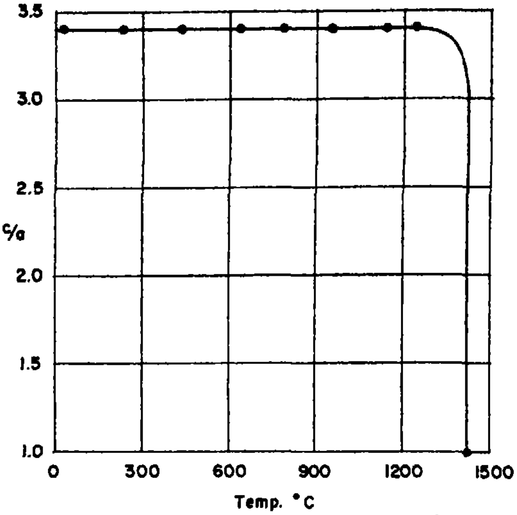

FIG. 3. Cell distortion vs. temperature for ZrP.

The mass spectrometric investigation reveals an increase in phosphorus evolution around 850°C. This may be due to the decomposition of the traces of di-phosphide to the mono-phosphide ($ZrP_2 \rightarrow ZrP$). Later, at 1425°C there is again an increase in phosphorus evolution corresponding to the $\beta \rightarrow \alpha$ transformation. The α sample was confirmed by X-ray analysis.

Also, a decomposition run was made in a continuously evacuated tube by r.f. heating. Here too, some phosphorus was evolved around 850°C corresponding to the $ZrP_2 \rightarrow ZrP$ decomposition. The change in phosphorus content at 1425°C is very slight, indicating that the change in composition from β-ZrP to α-ZrP was small. The heat treated sample on analysis by X-ray showed predominantly the α form, with traces of the β form still detectable. It was thought that during decomposition the stable α form would be formed on the outside surface of the grains while the core would have trapped some of the β form, which could not transform since there was no escape for the phosphorus. It was hoped that an electron diffraction pattern would give the surface pattern, differentiating it from the bulk pattern obtained by X-ray. The result was inconclusive, since the electron diffraction patterns indicated both the hexagonal and the cubic forms. However, the sample obtained from the mass spectrometer, after transformation, gave a pure α-pattern.

Attempts to determine ΔH by means of a differential thermal analysis run were unsuccessful, because of the immediate attack of Pt/Rh thermocouple wires by the phosphorus vapors.

From the mass spectrometric investigation it appears that the hexagonal β-form has a slight homogeneity range until it transforms at 1425°C to the α-cubic form. The change in phosphorus content during this transition is very slight, of the order of 1 at. per cent as estimated from the loss in weight of the sample. The α-form is quite stable to high temperatures in vacuum. To check that the $\beta \rightarrow \alpha$-form transformation is due to a change in stoichiometry and not just a temperature effect, some α-ZrP was analyzed by high temperature X-ray diffraction. Patterns taken up to 1200°C in vacuum still remained cubic and did not revert to hexagonal, confirming the compositional transformation.

The transition can be explained on the basis of the following model. The hexagonal β-ZrP can be considered as a superstructure of the nickel arsenide type. Taking the respective atomic radius as $r_P = 1{\cdot}10$ and $r_{Zr} = 1{\cdot}54$ we get a P/Zr ratio of 0·71. According to HAGG's rule,(5) a ratio greater than 0·59 indicates a complicated structure. In the case of β-ZrP, the large P atoms cause an expansion in the metal–metal distances causing a considerably weaker metallic bonding. However, between the layers there is strong metal to phosphorus bonding, probably ionic in character. This results in considerable stability of the compound. As the temperature is increased, there is a linear expansion of the unit cell, as shown in data of "*c*", "*a*", as well as volume given in Table 3 and Fig. 1. At a critical temperature, the bond expansion and the entropy contribution is of a sufficient magnitude to permit migration of the atoms, the loss of a few phosphorus atoms, and re-arrangement into a more stably packed configuration. In the present case this corresponds to the f.c.c. α-ZrP which has the rock salt structure with a few missing phosphorus atom vacancies, required to make the stoichiometric formula less than 1:1. It is evident that once the α-form is frozen in, a reversal to the β-form is impossible, except by reintroduction of phosphorus in the lattice, under pressure. At transformation $\Delta F = 0$, so that $\Delta H = T \cdot \Delta S$, and a measure of ΔH by D.T.A. would have helped in determining the change in entropy involved in the present structural rearrangement. This change from β-ZrP to α-ZrP does not affect the cation–anion distance appreciably, but the most significant change is the big decrease in Zr–Zr separation for the α-form as compared to the β-form, indicating that the cubic α-ZrP is more "metallic" in character. STROTZER *et al.*(3) in their plot of molecular volume vs. composition for the Zr–P system have shown a slight kink and change in slope in the region of $ZrP_{0{\cdot}95}$. Our X-ray results show that a change from β-ZrP to α-ZrP does in effect have a sudden volume shrinkage.

To confirm this compositional change from the hexagonal β-ZrP to the cubic α-ZrP, some α-substance was heated under an excess pressure of phosphorus (≃ 6 atm) at 900°C for over 48 hr. Under these conditions, some phosphorus atoms can be introduced into the expanded cubic lattice, re-arrangement takes place, and the equilibrium is shifted favouring the hexagonal structure, so that β-ZrP is now obtained. This confirms that the $\beta \rightarrow \alpha$ and the $\alpha \rightarrow \beta$ transformations are a function of both temperature and pressure, involving a change in composition.

One must realize the limited nature of the results of the present investigation. The system is sensitive to changes in temperature and pressure, involving changes in stoichiometry. Thus there are two phases of different composition α and β, the α form being stable in vacuum at temperatures above 1425°C, while the β form is stable at 900°C under excess phosphorus pressure. Under vacuum too, the β form has been observed to be stable up to 1425°C; at lower temperatures, it is possible that the rate of phosphorus loss under the experimental conditions employed, may be too slow to be observed. However, the co-operative type of effect, as well as the sudden evolution of phosphorus in the mass spectrometer at 1425°C, when the $\beta \rightarrow \alpha$ transformation occurs, seems to overrule the above doubt. A thorough study of the temperature pressure composition diagram for the Zr–P system is necessary.

Similar trends are to be expected for the Ti and Hf phosphides, as for Zr phosphides, since their similar outer electron configurations would result in similar bonding and structural properties. The respective stability as well as the $\beta \rightarrow \alpha$ transformation in each case is dependent on the ionic radii, mass etc., and is predicted to increase from Ti to Zr to Hf. In the case of hafnium phosphide, it has actually been found that the transformation from hexagonal to cubic does occur under vacuum at temperatures above 1600°C.

Acknowledgement—Thanks are due to Dr. J. Efimenko of the National Bureau of Standards, for help in the mass spectrometric investigation.

REFERENCES

1. Gewecke I., *Liebigs Ann. Chem.* **361**, 79 (1908).
2. Biltz W., Rink A. and Wiechmann F., *Z. anorg. Chem.* **238**, 395 (1938).
3. Strotzer E. F., Biltz W. and Meisel K., *Z. anorg. Chem.* **239**, 216 (1938).
4. Schönberg N., *Acta Chem Scand.* 8 226 (1954).
5. Hägg G. *Z phys Chem.* **B12** 33 (1931).

J. Phys. Chem. Solids Pergamon Press 1963. Vol. 24, pp. 1159–1164. Printed in Great Britain.

INFRARED LATTICE REFLECTION SPECTRA OF LiCl, LiBr, KF, RbF, AND CsF

MARVIN HASS

U.S. Naval Research Laboratory, Washington 25, D.C.

(*Received* 1 *February* 1963; *revised* 25 *April* 1963)

Abstract—The infrared lattice reflection spectra of LiCl, LiBr, KF, RbF and CsF have been measured in the spectral region from 95 to 1500 cm^{-1} and have been analysed by the Kramers–Krönig method. The following fundamental dispersion frequencies have been obtained: LiCl, 191 ± 2 cm^{-1}; LiBr, 159 ± 4 cm^{-1}; KF, 190 ± 2 cm^{-1}; RbF, 156 ± 2 cm^{-1}; CsF, 115(?) cm^{-1}. The effective charges and compressibilities have been computed with the aid of the Szigeti relations.

INTRODUCTION

THE appearance of a strong reflection band in the far infrared spectrum of the alkali halides has been known for many years and has been attributed to the optical branch of the lattice vibration spectrum of these compounds. The region of strong reflection is essentially bounded by the transverse and longitudinal frequencies for long wavelength vibrations.(1) The transmission and reflection spectra of many alkali halides were originally measured by BARNES.(2) In recent years these compounds and others have been remeasured and have been studied as a function of temperature.(3–7) However, no measurements have been reported of the heavier fluorides and heavier lithium salts. The lithium salts are of interest in that a small positive ion is combined with a large negative ion such that next-nearest neighbor interactions will be of greater importance than in the other alkali halides. Similarly, the fluorides are of interest as the positive ion polarizabilities are greater than the polarizability of the negative ion in contrast to the opposite situation in the other alkali halides. In this present investigation the lattice reflection spectra of LiCl, LiBr, KF, RbF, and CsF have been examined in the spectral region from 95 to 1500 cm^{-1} and have been analysed by the Kramers–Krönig method to determine the optical constants and fundamental dispersion frequencies. A sample of LiI was also examined, but it did not appear to give useful results.

EXPERIMENTAL

The reflection spectra were obtained using a Perkin–Elmer Model 210 grating monochromator for wavelengths greater than 35 μ and a CsBr prism spectrometer for wavelengths less than 35 μ. The experimental arrangement was similar to that described elsewhere.(7) The measurements were carried out in a room at a temperature of 21°C.

The crystals were grown by Semi-elements, Inc. and showed a well-defined cleavage plane except for CsF and LiI which may have been polycrystalline. The surfaces were ground and polished in a drybox and were polished again in the spectrometer drybox prior to being measured. In all cases this final step led to an increase in the observed reflectivity. The production of evaporated thin films was tried, but it was not possible to find a suitable protecting layer to prevent fogging of the film during transfer from the evaporator to the spectrometer.

RESULTS

The observed reflectivity of the lithium salts is shown in the top section of Fig. 1 and that of the fluorides in Fig. 2. The reflection spectrum of a sample of LiI is included in Fig. 1, but is not believed to be characteristic of the compound. In all cases (except LiI) the spectrum is that of a strong reflection band having a shoulder resolved on the high frequency side. In the case of KF, there appears to be a third shoulder present between the other two. It will be noted that the maximum reflectivities of LiCl and KF are above 80 per cent which is the case for many alkali halides. In

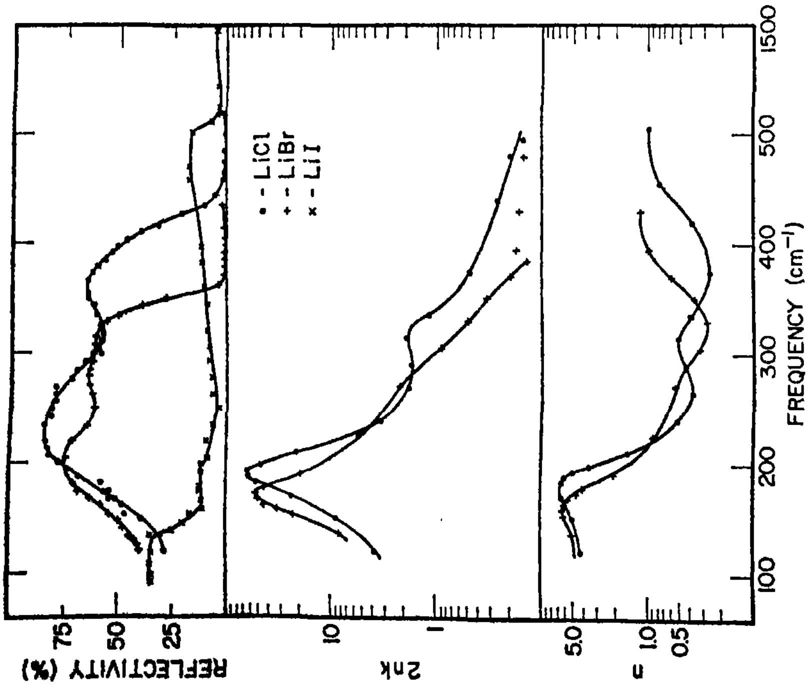

FIG. 1. The reflection spectra and optical constants of the lithium salts. The spectrum of LiI is believed to be poor and not representative of a good surface. The angle of incidence is 10°.

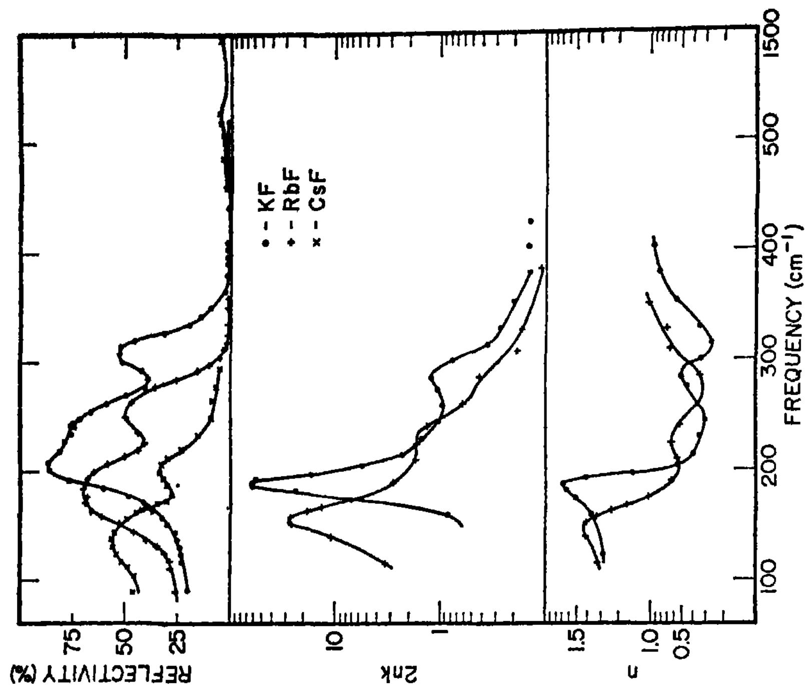

FIG. 2. The reflection spectra and optical constants of some alkali fluorides. The angle of incidence is 10°.

the rest of the compounds studied here, the maximum reflectivity is below 80 per cent. The failure to observe a higher reflectivity is probably due to some surface effect which is difficult to eliminate due to the highly hygroscopic nature of these crystals. In the case of LiI, the spectrum observed is quite different from what would be expected in the sequence: LiF, LiCl, and LiBr. For both LiI and CsF some small reflection bands can be seen around 600 cm^{-1}. It is quite probable that this is due to the imperfect surface.

In order to deduce the characteristic vibration frequencies the reflection data was subjected to a Kramers–Krönig analysis.(8,9) The results of such an analysis are shown in the bottom sections of Figs 1 and 2. Here the functions $2nk$ and n are given where n and k are the real and imaginary parts of the complex index of refraction N defined by the relation $N = n-ik$. The function $2nk$ is essentially the imaginary part of the complex dielectric constant, and the frequency corresponding to its maximum value (or more exactly the maximum value of $2nk\bar{\nu}$) is the dispersion frequency $\bar{\nu}_0$ for a single classical oscillator. The deduced frequencies are shown in Table 1.

The Kramers–Krönig analysis involves a knowledge of the reflectivity over the entire frequency range. In practice only that region of the spectrum in which the reflectivity is changing need be included. Since the reflectivity was not measured at sufficiently low frequencies so that the reflectivity became independent of frequency, it was necessary to estimate the missing region using experimental values of the static dielectric constant ϵ_0 as a first approximation. The resulting frequency $\bar{\nu}_0$ is not too sensitive to the selected value of ϵ_0. An even more important source of error lies in the possibility that the reflectivity is lowered due to surface effects. This type of error would be most serious in determining the magnitude of the optical constants. Additional calculations have been made which seem to show that the deduced value of $\bar{\nu}_0$ is not greatly affected. Consequently, where the reflectivity is less than 80 per cent, the numerical values of the optical constants should not be relied on, but the characteristic frequencies are probably satisfactory. However, in the case of CsF it was not possible to deduce a consistent set of optical constants. Consequently for CsF, $\bar{\nu}_0$ was estimated directly from the reflection spectra.

DISCUSSION

The dispersion frequency can be used in conjunction with the high and low frequency dielectric constants to calculate the following quantities: the longitudinal frequency $\bar{\nu}_l$ using the LYDDANE–SACHS–TELLER relation,(10) the effective charge e^* using a relation given by SZIGETI,(11) and the compressibility β_{calc} using another relation derived independently by SZIGETI(12) and ODELEVSKI.(13) These quantities are shown in Table 1.

The experimental value of the effective charge or distortion parameter e^*/e can be compared with those estimated from various theories of dielectric polarization. This is shown in Table 2 where e^*/e has been estimated in a number of ways. One set of estimates has been given by DICK and OVERHAUSER(14) in an article introducing the "shell" model which attempted to calculate e^*/e from the ionic polarizabilities subject to a number of assumptions. Two estimates for each compound

Table 1. *Characteristic frequencies and derived quantities*

Compound	$\bar{\nu}_0$ (cm^{-1})	ϵ_∞(a)	ϵ_0(b)	ϵ_0(c)	$\bar{\nu}_l$ (cm^{-1})	e^*/e(d)	β_{calc}(e)β_{obs}(f)
LiCl	191 ± 2	2·747	11·95	11·05	398	0·73	1·45
LiBr	159 ± 4	3·161	13·25	12·1	325	0·68	1·75
KF	190 ± 2	1·548	5·46	6·05	326	0·88	0·96
RbF	156 ± 2	1·926	6·48	5·91	286	0·95	0·94
CsF	115(?)(g)	2·158			220(?)(g)		

(a) Indices of refraction ($n^2 = \epsilon_\infty$) selected by TESSMAN J. R., KAHN A. H. and SHOCKLEY W., *Phys. Rev.* **92**, 890 (1953).
(b) HAUSSÜHL S., *Z. Naturf.* **12a**, 445 (1957).
(c) ERRERA J., *Z. Electrochem.* **36**, 818 (1930).
(d) Calculated using ϵ_0 data of HAUSSÜHL.
(e) Calculated using relations developed by SZIGETI(12) and ODELEVSKI(13) without next-nearest neighbor (overlap) interactions and using ϵ_0 data of HAUSSÜHL.
(f) Observed compressibilities from SPANGENBERG K. and HAUSSÜHL S., *Z. Krist.* **109**, 422 (1957).
(g) Estimated directly from reflection spectrum without analysis.

Table 2. Comparison of effective charges

Compound	e^*/e Obs.(a)	e^*/e Calc.(b)	e^*/e Calc.(c)	e^*/e_{extreme} Calc.(c)
LiCl	0·73	0·71	0·92	0·90
LiBr	0·68	0·66	0·91	0·90
KF	0·88	0·92	0·98	0·87
RbF	0·95	0·98	1·05	0·88

(a) Using SZIGETI(11) relation.
(b) Calculated using distortion polarizabilities of COCHRAN.(15)
(c) Calculated by DICK and OVERHAUSER.(14)

have been given by them and these differ in an assumption concerning the location of the exchange charge. It can be seen from Table 2 that their estimates for LiCl and LiBr are somewhat high and this is true of their other estimates for the alkali halides. On the other hand their estimates for KF and RbF bracket the experimental values. It will be noted that one of the estimates for RbF predicts that e^*/e might be greater than one and it was suggested that it would be of interest to determine e^*/e for this reason. Although the experimental value of e^*/e is less than one, it is greater than that of any other alkali halide. A convenient way of correlating the effective charges of the alkali halides has been given by COCHRAN(15) using a simple "shell" model calculation leading to an expression for e^*/e of the form

$$e^*/e = 1+d_+-d_-$$

where d_+ and d_- are parameters measuring the distortion polarizabilities of the positive and negative ions respectively. It can be readily seen that where $d_+ \approx d_-$, as in the heavy alkali fluorides, e^*/e will be close to unity. Although it is possible to estimate d_+ and d_- in terms of the model, COCHRAN has preferred to regard these as parameters to be determined by experiment. The parameters d_+ and d_- will vary for the same ion in different compounds. However, it has been found that $(d_- - d_+)/K$ for a particular material is an additive property of the ions involved, where K is the restoring force constant which can be obtained from the compressibility if next-nearest neighbor interactions are assumed small. It is of interest to see if the same parameters d/K given by COCHRAN can be used to predict e^*/e for the compounds studied in the present investigation. It can be seen from Table 2 that e^*/e can be predicted fairly well in this way. This is somewhat gratifying (and perhaps fortuitous) as it will be seen that next-nearest (overlap) neighbor interactions are of importance for the lithium halides. Consequently, the evaluation of K from the observed compressibility cannot be expected to yield exact results.

It can be readily seen from Table 1 that good agreement is obtained between the calculated and observed values of the compressibilities of the fluorides using the relation given by SZIGETI(12) and ODELEVSKI(13) (without next-nearest neighbor interactions). On the other hand the calculated compressibilities for the lithium halides are much higher than the observed values with $\beta_{\text{calc}}/\beta_{\text{obs}}$ being 1·45 for LiCl and 1·75 for LiBr. The deviation for the lithium halides is quite striking as $\beta_{\text{calc}}/\beta_{\text{obs}}$ for all of the other alkali halides range from 0·8 to 1·1.(3) Among the reasons which have been suggested for the deviation are the following: (1) presence of next-nearest neighbor interactions; (2) additional polarization mechanisms; (3) many-body interactions; (4) covalent bonding; and (5) anharmonicity. For most of the alkali halides the contributions from the various effects can be estimated to be about several per cent. The compressibility ratios have been calculated for the compounds studied in this investigation using various proposed relations and the results are shown in Table 3. The various formulae employed (except for that given by COCHRAN) have been compiled previously.(7) It can be seen from Table 3 that the compressibility of LiCl can be computed fairly well using the ODELEVSKI formula

Table 3. Comparison of compressibility relations

Compound	β_{calc}/β_{obs}(a)	β_{calc}/β_{obs}(b)	β_{calc}/β_{obs}(c)	β_{calc}/β_{obs}(d)	β_{calc}/β_{obs}(e)
LiCl	1·45	1·02	1·22	1·44	1·58
LiBr	1·75	1·18	1·38	1·73	1·82
KF	0·96	0·92	0·94	0·95	0·92
RbF	0·94	0·90	0·92	0·93	0·81

(a) Using SZIGETI relation(12) or ODELEVSKI relation(13) without next-nearest neighbor interaction term.
(b) Using ODELEVSKI relation(13) with next-nearest neighbor evaluation as explained in text.
(c) Calculated from distortion polarizabilities and force constant expression given by COCHRAN.(15)
(d) Using relation of DICK and OVERHAUSER.(14)
(e) Using LUNDQVIST relation.(16)

including interactions with next-nearest neighbors, but the agreement is not as good for LiBr. Such interactions are expected to be important for the heavier lithium halides which contain a large negative ion and a small positive ion. The magnitude of the correction term for this effect has been evaluated in a way which will be discussed shortly. It can also be seen from Table 3 that use of the relation given by COCHRAN which takes into account an additional polarization mechanism indicated by the "shell" model also decreases the discrepancy between the calculated and observed compressibilities of the lithium halides and such terms may also be of importance. On the other hand the correction terms obtained by DICK and OVERHAUSER are negligible and those proposed by LUNDQVIST(16) to take into account a three-body interaction lead to poorer agreement with experiment.

ODELEVSKI(13) showed that the inclusion of next-nearest neighbor interactions will decrease the calculated compressibility by a factor $1/(1+s)$ where s is given by the ratio

$$s = (\mathrm{d}^2 U_{aa}/\mathrm{d}r^2_{aa})/(\mathrm{d}^2 U_{ca}/r^2_{ca})$$

where U is the short-range interaction potential between ions and r_{aa} and r_{ca} refer to the anion–anion and cation–anion distances respectively. The major contributions to U arise from an overlap interaction and a van der Waals interaction which is small compared to the overlap interaction at the interionic distances under consideration and may be neglected. ODELEVSKI indicated that the experimental data was consistent with a correction term which was a function of $r_{aa}/2r_-$ where r_- is the ionic radius of the anion. This correction term will become important when the observed anion–anion distance differs from that predicted using the ionic radii (as for the heavy lithium halides). However, it is possible to evaluate s in a more quantitative manner using an expression for the potential energy given by PAULING(17) which gives excellent agreement for the nearest neighbor distances of the NaCl-type alkali halides (including the heavy lithium halides). Using this potential the ratios U_{aa}/U_{ca}(18) and U''_{aa}/U''_{ca} are readily found to be given by

$$s = \frac{U''_{aa}}{U''_{ca}} = \frac{1}{2}\frac{U_{aa}}{U_{ca}} = \frac{1}{2^{5\cdot5}}\left\{1\cdot25\left(\frac{2\rho}{1+\rho}\right)^8 + 0\cdot75\left(\frac{2}{1+\rho}\right)^8\right\}$$

which depends only on the radius ratio $\rho = r_+/r_-$. The treatment includes both anion–anion and cation–cation interactions. This result has been used in calculating the compressibility by the Odelevski formula given in Table 3.

The values of the dispersion frequencies and effective charges are useful in calculations of lattice vibration spectra such as those given recently by KARO and HARDY.(19) These calculations involve the effective charge as an input parameter. In the case of the lithium halides, the data presented here indicate that next-nearest neighbor interactions are of importance and it should be possible to estimate the amount of such interactions from the deviation of the Szigeti relation for the compressibility.(20) Next-nearest neighbor interactions have been included in a calculation given by DEMIDENKO and TOLPYGO for NaI.(21)

In conclusion, it may be pointed out that the data obtained in this investigation completes the list of known dispersion frequencies for the alkali halides with the exception of LiI.

SUMMARY

The infrared lattice dispersion frequencies of LiCl, LiBr, KF, RbF, and CsF have been obtained and have been employed to calculate the effective charges and compressibilities of these compounds with the aid of the Szigeti relations. The effective charges are in general agreement with those predicted from the ionic polarizabilities. The calculated compressibilities are in fair agreement with those observed experimentally provided some correction is made for next-nearest neighbor (overlap) interactions.

Acknowledgements—The author wishes to thank Dr. A. M. KARO for interesting discussions and a preprint of his work with Dr. J. R. HARDY. In addition, suggestions by Dr. R. F. WALLIS are gratefully acknowledged.

REFERENCES

1. BORN M. and HUANG K., *Dynamical Theory of Crystal Lattices*, p. 91. Oxford University Press, London (1954).
2. BARNES R. B., *Z. Physik* **75**, 723 (1932).
3. JONES G. O., MARTIN D. H., MAWER P. A. and PERRY C. H., *Proc. Roy. Soc.* **A261**, 10 (1961).
4. GENZEL L., HAPP H. and WEBER R., *Z. Physik* **154**, 13 (1959).
5. BELL E. E. and BROWN R. L., AFCRC-TN-260 Physics Department, Ohio State University (unpublished).
6. MITSUISHI A., YAMADA Y. and YOSHINAGA H., *J. opt. Soc. Amer.* **52**, 14 (1962).
7. HASS M., *Phys. Rev.* **117**, 1497 (1960); **119**, 633 (1960).
8. ROBINSON T. S. and PRICE W. C., *Proc. Phys. Soc.* **B66**, 969 (1953).
9. MOSS T. S., *Optical Properties of Semiconductors*, p. 24. Butterworths, London (1959).
10. LYDDANE R. H., SACHS R. G. and TELLER E., *Phys. Rev.* **59**, 673 (1941); BORN M. and HUANG K., *Dynamical Theory of Crystal Lattices*, p. 86. Oxford University Press, London (1954).
11. SZIGETI B., *Trans. Faraday Soc.* **45**, 155 (1949); BORN M. and HUANG K., *Dynamical Theory of Crystal Lattices*, p. 112. Oxford University Press, London (1954).
12. SZIGETI B., *Proc. Roy. Soc.* **A204**, 51 (1950).
13. ODELEVSKI V. I., *Izv. akad. nauk. S.S.S.R. Ser. Fiz.* **14**, 232 (1950).
14. DICK B. G. and OVERHAUSER A. W., *Phys. Rev.* **112**, 90 (1958).
15. COCHRAN W., *Phil. Mag.* **4**, 1082 (1959).
16. LUNDQVIST S. O., *Ark. Fys.* **9**, 435 (1955).
17. PAULING L. *The Nature of the Chemical Bond*, 3rd edition p. 523. Cornell University Press, Ithaca, New York (1960).
18. BORN M. and HUANG K., *Dynamical Theory of Crystal Lattices*, p. 32. Oxford University Press, London (1954).
19. KARO A. M. and HARDY J. R., *Phys. Rev.* **129**, 2024 (1963).
20. KARO A. M., private communication.
21. DEMIDENKO Z. A. and TOLPYGO K. B., *Fiz. Tverd Tela* **3**, 3435 (1961); [translation: *Sov. Phys. Solid-State* **3**, 2493 (1962).]

J. Phys. Chem. Solids Pergamon Press 1963. Vol. 24, pp. 1165–1174. Printed in Great Britain.

ANISOTROPIC SPIN-ORBIT INTERACTION IN PARAMAGNETIC RESONANCE

FRANK S. HAM

General Electric Research Laboratory, Schenectady, New York

(*Received* 5 *March* 1963)

Abstract—The part of the spin-orbit interaction due directly to crystalline electric fields or applied fields contributes to the *g*-tensor of a paramagnetic center a shift which, as Kneubühl has noted, may have a skew-symmetric part. We show (1) that in an applied electric field *g*-shifts from this source for centers lacking inversion symmetry are typically $\Delta g \lesssim 10^{-11}$ cm/kV, and thus negligible; (2) that these shifts are usually very much smaller (in cases where such shifts have been studied experimentally, by a factor of at least 10^5) than those produced by the applied field via an electron's electrostatic potential energy in the field, coupled with the unperturbed spin-orbit interaction due to the ion. We infer that crystalline fields (neglecting covalent effects) contribute to a skew-symmetric part of the *g*-tensor primarily through changes in the wave functions induced by the electrostatic potential energy, rather than through the field's contribution to the spin-orbit interaction. A skew-symmetric Δg arising from applied fields or crystalline fields is probably not larger than a few per cent of the corresponding symmetric change in *g*. A proposal due to Ludwig for distinguishing the skew-symmetric part of a *g*-tensor in an applied electric field is described.

I. INTRODUCTION

IN A RECENT letter KNEUBÜHL[1] has suggested that in calculating *g*-tensors and hyperfine interaction tensors for paramagnetic centers of low symmetry one should take into account the direct contribution of crystalline electric fields or applied fields to the spin-orbit interaction. In the general potential $V(\mathbf{r})$ the spin-orbit interaction of an electron takes the form[2]

$$\mathscr{H}_{\mathrm{SO}} = -\frac{e\hbar}{2m^2c^2}(\nabla V \times \mathbf{p}) \cdot \mathbf{S}, \qquad (1)$$

where $\mathbf{p}$ is the electron momentum, $\mathbf{S}$ $(= \frac{1}{2}\boldsymbol{\sigma})$ its spin (with $\hbar$ factored out), $-e$ its charge, and m its mass, while c is the speed of light. Kneubühl has shown that non-spherically symmetric contributions to $V(\mathbf{r})$ in (1) lead in appropriate symmetry to *g*-tensors and hyperfine interaction tensors having a skew-symmetric part.

An electric field also contributes to the *g*-tensor and other interaction tensors through the electrostatic potential energy,

$$\mathscr{H}_{\mathrm{P}} = e\boldsymbol{\mathscr{E}} \cdot \mathbf{r} \qquad (2)$$

(e.g. for a uniform field $\boldsymbol{\mathscr{E}}$), acting together with other terms in the Hamiltonian of the paramagnetic ion. Changes in the *g*-tensor arising in this way from an applied electric field have been studied experimentally for centers lacking inversion symmetry by LUDWIG and WOODBURY[3] and theoretically by HAM[4] in the case of transition metal impurities in silicon.

In this paper we shall show that the effects arising from applied electric fields or crystalline fields* via their direct contribution to the spin-orbit interaction (1) are usually very much smaller than those arising via the electrostatic potential energy (2). In tetrahedral symmetry, for example, the ratio of corresponding terms due to an applied field is typically no larger than $\Delta/mc^2 \lesssim 4 \times 10^{-6}$, where Δ is a crystal field splitting. Moreover, in any symmetry, the *g*-shift arising from the contribution of a uniform electric field to (1) will be shown to vanish to the accuracy of second-order perturbation theory for all states having no orbital degeneracy.†

The small size of the effects arising from electric fields via (1) does not, however, imply the conclusion that the skew-symmetric part of the various tensors is necessarily negligible. As we shall show, there is a second skew-symmetric contribution which should be appreciable even though $V(\mathbf{r})$ is approximated in (1) as being spherically symmetric. A method will be described whereby a skew-symmetric contribution to the g-tensor in an applied field might be distinguished experimentally by means of transitions induced by an alternating electric field.

---

* In discussing crystalline fields we shall ignore the effect of covalent bonding in spreading the electrons of a central paramagnetic ion onto neighboring ions. Thus by "crystalline field" we mean the electrostatic potential, at the central ion, due to the neighboring ions.

† *Note added in proof:* This last result has now been given also by Kneubühl. [F. K. KNEUBÜHL, *Phys. Letters* **4**, 208 (1963).]

In Section II we shall give a calculation which establishes under rather general conditions the order of magnitude of the shift in the g-tensor arising via (1) from an applied electric field and shows why this vanishes for a state with no orbital degeneracy. In Section III we shall examine two situations representative of transition metal ions at sites lacking inversion symmetry, to obtain the relative size of effects arising via interactions (1) and (2) in an applied field. In Section IV we show that a skew-symmetric part of the g-tensor can arise from interaction (2) as well as from (1), and in Section V we consider the effects of crystalline fields. The measurement of a skew-symmetric part of the g-tensor is considered in Section VI. Section VII concludes the paper with a discussion.

II. g-SHIFT FROM SPIN-ORBIT INTERACTION DUE TO AN APPLIED ELECTRIC FIELD

We wish to ascertain a typical value for the shift in the g-tensor arising from the contribution of an applied electric field $\boldsymbol{\mathscr{E}}$ to the spin-orbit interaction (1). Consider N electrons in a center of arbitrary symmetry. We denote* the ground state(s) of the unperturbed system by $|g\rangle$, excited states by $|n\rangle$. The ground state has spin degeneracy and may have orbital degeneracy as well.

Inserting $\nabla V = -\boldsymbol{\mathscr{E}}$ in (1) for the contribution of a uniform field $\boldsymbol{\mathscr{E}}$ to the spin-orbit interaction of each electron, we sum over N electrons and obtain from second order perturbation theory, using this and the orbital Zeeman interaction,

$$(e/2mc)\sum_{i}^{N}(\boldsymbol{\ell}_i\cdot\mathbf{H}) \tag{3}$$

($\boldsymbol{\ell}_i$ is the angular momentum operator $\boldsymbol{\ell}_i = \mathbf{r}_i\times\mathbf{p}_i$), the following contribution to the spin Hamiltonian(5) of the ground state

$$\langle g|\mathscr{H}_1|g'\rangle = \frac{e^2\hbar}{4m^3c^3}\sum_{n}\sum_{ij}^{N}\frac{\langle g|(\boldsymbol{\mathscr{E}}\times\mathbf{p}_i)\cdot\mathbf{S}_i|n\rangle\langle n|\boldsymbol{\ell}_j\cdot\mathbf{H}|g'\rangle+\langle g|\boldsymbol{\ell}_j\cdot\mathbf{H}|n\rangle\langle n|(\boldsymbol{\mathscr{E}}\times\mathbf{p}_i)\cdot\mathbf{S}_i|g'\rangle}{E_g-E_n}, \tag{4}$$

where the sum over n covers all excited states. Matrix elements of $\mathbf{p}_i$ may be expressed in terms of those of $\mathbf{r}_i$ by(6)

$$\langle a|\mathbf{p}_i|b\rangle = (im/\hbar)(E_a-E_b)\langle a|\mathbf{r}_i|b\rangle, \tag{5}$$

which follows from the commutation relation

$$\mathbf{p}_i = (im/\hbar)\,[\mathscr{H}_0, \mathbf{r}_i]. \tag{6}$$

Here $\mathscr{H}_0$ is the full unperturbed Hamiltonian (neglecting spin-orbit interaction),

$$\mathscr{H}_0 = \sum_{i}^{N}[(p_i^2/2m)+V(\mathbf{r}_i)]+\sum_{i\neq j}e^2/|\mathbf{r}_i-\mathbf{r}_j|, \tag{7}$$

and $|a\rangle$ and $|b\rangle$ in (5) must be eigenstates of $\mathscr{H}_0$. Substituting from (5) into (4), and carrying out the sum over n using the completeness relation

$$\sum_{n}|n\rangle\langle n| = 1-\sum_{g}|g\rangle\langle g|, \tag{8}$$

we find

$$\mathscr{H}_1 = \mathscr{H}_{1a}+\mathscr{H}_{1b}, \tag{9}$$

where

$$\langle g|\mathscr{H}_{1a}|g'\rangle = \frac{ie^2}{4m^2c^3}\langle g|\sum_{i}^{N}[(\boldsymbol{\mathscr{E}}\times\mathbf{r}_i)\cdot\mathbf{S}_i,\boldsymbol{\ell}_i\cdot\mathbf{H}]\,|g'\rangle \tag{10}$$

---

* We label the states here according to their orbital part only; the spin is treated as an operator without specifying any particular basis. All spin-orbit interactions, other interactions involving spin, and interactions with applied fields are treated by perturbation theory and are assumed weak compared with crystal field splittings of electrostatic origin; they are ignored in specifying the states of the unperturbed system.

$$\langle g|\mathscr{H}_{1b}|g'\rangle = \frac{ie^2}{4m^2c^3}\sum_{g''}\sum_{ij}^{N}\{\langle g|\boldsymbol{l}_j\cdot\boldsymbol{H}|g''\rangle \times \langle g''|(\boldsymbol{\mathscr{E}}\times\boldsymbol{r}_i)\cdot\boldsymbol{S}_i|g'\rangle - \langle g|(\boldsymbol{\mathscr{E}}\times\boldsymbol{r}_i)\cdot\boldsymbol{S}_i|g''\rangle\langle g''|\boldsymbol{l}_j\cdot\boldsymbol{H}|g'\rangle\}. \quad (11)$$

The commutator in (10) can be evaluated, to yield

$$\langle g|\mathscr{H}_{1a}|g'\rangle = -\frac{e\beta}{2mc^2}\langle g|\sum_i [(\boldsymbol{S}_i\cdot\boldsymbol{H})(\boldsymbol{\mathscr{E}}\cdot\boldsymbol{r}_i) - (\boldsymbol{\mathscr{E}}\cdot\boldsymbol{H})(\boldsymbol{S}_i\cdot\boldsymbol{r}_i)]|g'\rangle, \quad (12)$$

where $\beta = e\hbar/2mc$.

To estimate the magnitude of these terms in the spin Hamiltonian of the ground state, let us write

$$\mathscr{H}_1 = \beta\sum_{ijk} T_{ijk}S_iH_j\mathscr{E}_k. \quad (13)$$

Matrix elements of the tensor operator T_{ijk} are from (11) and (12) proportional to those of

$$\boldsymbol{d} = e\boldsymbol{r} \quad (14)$$

the dipole moment, among the ground state wave functions. These vanish for centers having inversion symmetry (take the origin for $\boldsymbol{r}$ at the center of symmetry). For centers lacking inversion symmetry $\boldsymbol{d}$ may have non-vanishing matrix elements. but since $\langle \boldsymbol{d}_i\rangle/e$ is at most the order of atomic dimensions for a paramagnetic ion, say $\langle g|\boldsymbol{d}_i|g'\rangle/e \lesssim 10^{-8}$ cm, we have for (13)

$$\langle g|T_{ijk}|g'\rangle \sim \frac{\langle g|\boldsymbol{d}_i|g'\rangle}{2mc^2} \lesssim 10^{-11}\ \text{cm/kV}. \quad (15)$$

The g-shift arising from an applied electric field via (1) is accordingly quite small.

The expression (12) for $\langle g|\mathscr{H}_{1a}|g'\rangle$ is not however invariant to the choice of the coordinate origin, to which $\boldsymbol{r}_i$ is referred. This difficulty arises because our calculation has not been gauge invariant. To restore gauge invariance we must replace $\boldsymbol{p}$ by $(\boldsymbol{p}+(e/c)\boldsymbol{A})$ in the spin-orbit interaction (1), where $\boldsymbol{A}$ is the vector potential of the applied magnetic field

$$\boldsymbol{A} = \tfrac{1}{2}(\boldsymbol{H}\times\boldsymbol{r}). \quad (16)$$

We thus must retain in our original Hamiltonian a small term,

$$\mathscr{H}'_{so} = -\frac{e^2\hbar}{4m^2c^3}[\nabla V\times(\boldsymbol{H}\times\boldsymbol{r})]\cdot\boldsymbol{S}, \quad (17)$$

which can usually be neglected, as it gives rise only to part of the small ($\Delta g \sim 10^{-5}$–10^{-4}) Breit–Margenau correction to the spin g-factor.[2,7] Inserting $\boldsymbol{\nabla}V = -\boldsymbol{\mathscr{E}}$ in (17) and taking matrix elements of this operator among the states $|g\rangle$, we find that the resulting contribution to the spin Hamiltonian of the ground state exactly cancels $\langle g|\mathscr{H}_{1a}|g'\rangle$. Hence we are left only with $\mathscr{H}_{1b}$ as given by (11). But if the ground state has no orbital degeneracy, then $\langle g|\boldsymbol{l}_j|g\rangle = 0$, and $\mathscr{H}_{1b}$ vanishes.

Accordingly, we have the result that to the accuracy of second-order perturbation theory, the contribution to the g-tensor of an applied electric field via the spin-orbit interaction vanishes identically for any state with no orbital degeneracy. Only states with orbital degeneracy have a non-vanishing g-shift from this source. This is given by $\mathscr{H}_{1b}$ in (11) and is small according to (15).

III. RELATIVE MAGNITUDE OF EFFECTS OF AN APPLIED ELECTRIC FIELD

To exhibit the relative magnitude of effects arising from an applied electric field via interactions (1) and (2), we consider two simple cases involving a transition metal ion at a site lacking inversion symmetry. The relative size of the effects in these cases is representative of more complicated configurations.[4]

First consider a single electron in the $3d$ shell of a transition metal ion at a site of tetrahedral symmetry. Assume the three-fold degenerate t_2 orbitals are lower by Δ in energy than the doubly degenerate e-orbitals.* The absence of inversion symmetry mixes odd parity wave functions into the orbitals derived from the free ion $3d$ functions[4] and thereby leads to the following non-vanishing matrix elements* of r

---

* This is the inverse of the order expected for tetrahedral symmetry when the point ion approximation to crystal field theory pertains. It agrees with the order found experimentally for interstitial transition metal ions in silicon.

$$\langle t_2x|z|t_2y\rangle = \langle t_2y|x|t_2z\rangle = \langle t_2z|y|t_2x\rangle = p/e, \tag{18a}$$

$$\begin{aligned}\langle e\theta|z|t_2z\rangle &= -2\langle e\theta|x|t_2x\rangle = -2\langle e\theta|y|t_2y\rangle \\ &= (2/\sqrt{3})\langle e\epsilon|x|t_2x\rangle \\ &= (-2/\sqrt{3})\langle e\epsilon|y|t_2y\rangle = t/e.\end{aligned} \tag{18b}$$

The parameters p and t hereby defined have the dimensions of an electric dipole moment. Matrix elements of the electron momentum p may be expressed in terms of those of r by means of (5).

The effect of an applied electric field $\mathscr{E}$ on the t_2 states via interaction (1) [and (17)] is given by $\mathscr{H}_{1b}$ in (11) of Section II. This does not vanish in this case, because of the orbital degeneracy of the t_2 states. Since matrix elements of p vanish among degenerate states, according to (5), there is no first order effect of $\mathscr{E}$ from(1) on the t_2 states. We define a parameter g_ℓ by

$$g_\ell = -\frac{1}{\hbar}\frac{\langle t_2i|\ell|t_2j\rangle}{\langle t_2i|\mathscr{L}|t_2j\rangle}, \tag{19}$$

which would be equal to unity for pure d states. Here $\mathscr{L}$ is an Hermitean vector operator[9] defined to have matrix elements only among the t_2 orbitals:

$$\begin{aligned}\langle t_2x|\mathscr{L}_z|t_2y\rangle = \langle t_2y|\mathscr{L}_x|t_2z\rangle &= \langle t_2z|\mathscr{L}_y|t_2x\rangle \\ &= -i.\end{aligned} \tag{20}$$

$\mathscr{L}$ behaves like an angular momentum for $\mathscr{L} = 1$, satisfying the commutation rules

$$[\mathscr{L}_x, \mathscr{L}_y] = i\mathscr{L}_z, \tag{21}$$

and those obtained from (21) by cyclic permutation. For a field $\mathscr{E}_z$ in the z (cubic) direction we find from (11) that we can write $\mathscr{H}_{1b}$ as

$$\begin{aligned}\mathscr{H}_{1b} = (p/2mc^2)\beta\mathscr{E}_z g_\ell\,\{2[&S_yH_x(\mathscr{L}_y^2-\mathscr{L}_z^2) \\ &+S_xH_y(\mathscr{L}_x^2-\mathscr{L}_z^2)] \\ -[(H_xS_x&+H_yS_y)(\mathscr{L}_x\mathscr{L}_y+\mathscr{L}_y\mathscr{L}_x) \\ &-S_xH_z(\mathscr{L}_y\mathscr{L}_z+\mathscr{L}_z\mathscr{L}_y) \\ -S_yH_z&(\mathscr{L}_x\mathscr{L}_z+\mathscr{L}_z\mathscr{L}_x)]\}.\end{aligned} \tag{22}$$

Turning to interaction (2), we find that it lifts the t_2 orbital degeneracy directly according to the term[4]

$$\mathscr{H}_{2a} = -p\mathscr{E}_z(\mathscr{L}_x\mathscr{L}_y+\mathscr{L}_y\mathscr{L}_x). \tag{23}$$

In addition, the spin-orbit interaction due to the ion potential (assumed spherically symmetric)

$$(\mathscr{H}_{SO})_I = -\frac{e\hbar}{2mc^2}\frac{1}{r}\frac{dV}{dr}(\ell\cdot S), \tag{24}$$

and the orbital Zeeman interaction contribute, via second order perturbation theory from coupling to the e orbitals, the terms

$$\mathscr{H}_{2b} = +\frac{\sqrt{3}\lambda' t}{\Delta}\mathscr{E}_z(\mathscr{L}_xS_y+\mathscr{L}_yS_x), \tag{25}$$

$$\mathscr{H}_{2c} = +\frac{\sqrt{3}g_\ell' t}{\Delta}\beta\mathscr{E}_z(\mathscr{L}_xH_y+\mathscr{L}_yH_x), \tag{26}$$

where λ' is defined by

$$\langle e\epsilon \pm \tfrac{1}{2}|(\mathscr{H}_{SO})_I|t_2z \pm \tfrac{1}{2}\rangle = \mp i\lambda', \tag{27}$$

and g_ℓ' by

$$\langle e\epsilon|\ell_z|t_2z\rangle = -2ig_\ell'\hbar. \tag{28}$$

In comparing the magnitude of effects produced by $\mathscr{E}_z$ via interactions (1) and (2), we should like to compare corresponding terms in the spin Hamiltonian arising from these sources. $\mathscr{H}_{1b}$ in (22) however has no precise counterpart among $\mathscr{H}_{2a}$, $\mathscr{H}_{2b}$, and $\mathscr{H}_{2c}$. While it could in principle thus be distinguished, it is most like $\mathscr{H}_{2c}$ in that these both contribute directly to a term of the form

$$T\beta\mathscr{E}_z(J_xH_y+J_yH_x) \tag{29}$$

in the spin Hamiltonian of levels into which the t_2 states are split by the ion's own spin-orbit interaction (24). In writing (29), we have defined the total effective angular momentum

$$J = \mathscr{L}+S. \tag{30}$$

In the present case ($\mathscr{L} = 1$, $S = \frac{1}{2}$) we obtain two levels corresponding to $J = \frac{1}{2}$ and $\frac{3}{2}$. The ratio of the coefficient of $\mathscr{H}_{1b}$ in (22) to that of $\mathscr{H}_{2c}$ in (26) is of order $\Delta/mc^2 \lesssim 4\times10^{-6}$, assuming that $g_\ell \cong g_\ell'$, $p \cong t$. Accordingly the effect of the applied electric field via (1) on the g-shift is very much smaller than its effect via (2). A similar conclusion holds for its effect on other interaction tensors, such as the hyperfine interaction.

---

* Our notation for the individual e and t_2 orbitals is adapted from that of GRIFFITH (Ref. 8, p. 226).

The dominant contribution of $\mathscr{E}_z$ to the g-shift in the present case actually arises not from $\mathscr{H}_{2c}$ but from $\mathscr{H}_{2a}$, which like the Zeeman interaction $\beta(2\boldsymbol{S}-g_\ell\boldsymbol{\mathscr{L}})\cdot\boldsymbol{H}$ has matrix elements between $J=\frac{1}{2}$ and $\frac{3}{2}$. Second order perturbation theory accordingly leads with these interactions to shifts in the g-tensors of both $J=\frac{1}{2}$ and $\frac{3}{2}$ with

$$|\Delta g| \sim \frac{(2+g_\ell)p\mathscr{E}_z}{|E(\frac{3}{2})-E(\frac{1}{2})|}. \tag{31}$$

$\mathscr{H}_{2b}$ of (25) contributes in similar fashion a shift smaller than (31) by a factor roughly λ'/Δ. Thus in this case the g-shift arising from (1) is in fact smaller than that from (2) by the ratio

$$\frac{|\Delta g_1|}{|\Delta g_2|} \sim \frac{|E(\frac{3}{2})-E(\frac{1}{2})|}{mc^2} \lesssim 10^{-7}. \tag{32}$$

A second case is provided if we lower the tetrahedral symmetry of the site by introducing a strong crystalline electric field $\mathscr{E}_0$ along the z cubic axis. The degeneracy of the t_2 states is thereby lifted: the resulting states and their energies are

$$\begin{aligned} |t_2\eta\rangle &= \frac{1}{\sqrt{2}}|t_2x\rangle - \frac{1}{\sqrt{2}}|t_2y\rangle \quad & E_\eta &= -p\mathscr{E}_0, \\ |t_2\xi\rangle &= \frac{1}{\sqrt{2}}|t_2x\rangle + \frac{1}{\sqrt{2}}|t_2y\rangle \quad & E_\xi &= +p\mathscr{E}_0, \\ |t_2z\rangle & & E_z &= 0, \end{aligned} \tag{33}$$

where ξ and η denote the directions [110] and [$\bar{1}$10], respectively. Taking $|t_2\eta\rangle$ to be the ground state, we assume that the energy splitting $\Delta E = |p\mathscr{E}_0|$ is larger than the spin-orbit interaction. The effect of interaction (1) on the ground state now vanishes, according to the result of Section II. For interaction (2) we obtain from third order perturbation theory

$$\begin{aligned} \mathscr{H}_2 = \frac{-2\lambda g_\ell\beta p}{(E_z-E_\eta)(E_\xi-E_\eta)} & [\mathscr{E}_\eta(H_\eta S_z+H_z S_\eta) \\ & -\mathscr{E}_\xi(H_\xi S_z+H_z S_\xi)] \\ & -\frac{2\lambda g_\ell\beta p}{(E_\xi-E_\eta)^2}\mathscr{E}_z S_z H_z. \end{aligned} \tag{34}$$

In deriving (34) we have used (18) and (19), neglecting possible changes in the matrix elements because of the lowered symmetry, and we have defined

$$\lambda = \frac{\langle t_2i|(\mathscr{H}_{so})_I|t_2j\rangle}{\langle t_2i|\boldsymbol{\mathscr{L}}\cdot\boldsymbol{S}|t_2j\rangle}. \tag{35}$$

We have considered a number of other configurations for transition metal ions in which an applied electric field leads to appreciable changes in the paramagnetic resonance spectrum.(4) In all of these the changes in the g-tensors (and in other tensors) due to interaction (2) overwhelmingly dominate those arising from the contribution of the applied field to the spin-orbit interaction (1). It appears to us that this conclusion is probably true for all paramagnetic centers in which effects of an applied electric field might be studied, and that in any case the effect of an applied field via (1) is probably too small to be observable.

IV. SKEW-SYMMETRIC PART OF g-TENSOR

KNEUBÜHL(1) concluded from (4) that his mechanism leads to a skew-symmetric part to the g-tensor when this is permitted by symmetry.* Our result in Section II that the entire g-shift from this source in an applied field vanishes for states with no orbital degeneracy weakens Kneubühl's conclusion as far as an applied field is concerned. But his conclusion should hold in the case of crystalline electric fields of low symmetry (which are not uniform, so that the considerations of Section II are not applicable in detail). However, even here his effect should be small (see Section V).

Our considerations for an applied field using interaction (2) have so far led only to a symmetric contribution to the g-tensor. In particular, we obtained (34) in a case in which a skew-symmetric part is allowed by symmetry. However, in arriving at (34) we have ignored the fact that g_ℓ and λ defined by (19) and (35) are not independent of i and j when the symmetry is lower than tetrahedral

---

* A skew-symmetric part to the g-tensor in an applied electric field is forbidden by symmetry (through terms linear in $\mathscr{E}$) for a site having tetrahedral symmetry. That a skew-symmetric part is allowed in the case of a site having symmetry C_{3v} has been noted by LUDWIG and HAM.(10)

We should have written the first bracket in (34) as

$$\frac{-2\beta}{(E_z-E_\eta)(E_\xi-E_\eta)}\{p_\eta\mathscr{E}_\eta[\lambda(z\xi)g_\ell(\xi\eta)S_\eta H_z \qquad (36)$$
$$+\lambda(\xi\eta)g_\ell(z\xi)S_zH_\eta]$$
$$+p_\xi\mathscr{E}_\xi[\lambda(z\eta)g_\ell(\xi\eta)S_\xi H_z+\lambda(\xi\eta)g_\ell(z\eta)S_zH_\xi]\},$$

where

$$\lambda(z\xi)=\frac{\langle t_2z|(\mathscr{H}_{\mathrm{so}})_I|t_2\xi\rangle}{\langle t_2z|\mathscr{L}\cdot S|t_2\xi\rangle},\ \text{etc.} \qquad (37)$$

There is no necessity that the ratio

$$R=\frac{\lambda(z\xi)g_\ell(\xi\eta)}{\lambda(\xi\eta)g_\ell(z\xi)}, \qquad (38)$$

for example, equal unity. Accordingly the coefficients of $S_\eta H_z$ and of S_zH_η in (36) may differ, as may those of $S_\xi H_z$ and S_zH_ξ, and the g-tensor defined by (36) then has a skew-symmetric part proportional to $(R-1)$.

The ratio R in (38) will differ from unity if the ratios $\lambda(z\xi)/\lambda(\xi\eta)$ and $g_l(z\xi)/g_l(\xi\eta)$ are not equal, that is if the anisotropy of the spin-orbit matrix elements is different from that of the orbital reduction factor g_l. Since the spin-orbit interaction (24) heavily weights the region of small r through the factor $(1/r)(\mathrm{d}V/\mathrm{d}r)$, these anisotropies will be different if the wave functions of the states $|t_2z\rangle$, $|t_2\xi\rangle$, and $|t_2\eta\rangle$ differ at all in their dependence on r. Such differences can arise from an anisotropic environment both through differing admixtures of wave functions on the central ion and through differences in covalent bonding in the various states with the wave functions of neighboring ions. We have not attempted a realistic estimate of departures of R from unity, but it seems plausible that departures of a few per cent can occur.* The skew-symmetric part of (36) is, however, then only a few per cent of the symmetric part of this contribution to the g-tensor.

V. EFFECTS OF CRYSTALLINE FIELDS

We have up to this point directed our attention at effects produced by an applied electric field. Since an applied field can be viewed as an increment in the existing crystalline electric fields at the site of the paramagnetic ion, our general conclusions hold for crystalline fields as well: that the electrostatic potential energy due to the crystalline field is ordinarily much the more important interaction in producing a change in the g-tensor or other interaction tensors than is the contribution of the crystal field to the spin-orbit interaction (1)†; that skew-symmetric contributions to the g-tensor (or other tensors) arise from the electrostatic potential energy, whenever symmetry permits, as a result of differences in the radial dependence of wave functions of the different states; and that these skew-symmetric contributions may be expected to be much larger than those arising from the crystal field through (1) but to be at most probably only a few per cent of the symmetric contribution to the change in the g-tensor from its value for a free electron.

Since crystalline fields are not uniform, we can *not* conclude, as we could in the case of a uniform applied field and no orbital degeneracy in Section II, that there is no g-shift to the accuracy of second order perturbation theory from the contribution of the crystalline field to (1). But such shifts should be much smaller than those arising via the electrostatic potential energy.

The presence of a skew-symmetric part in the g-tensor due to the effect of crystalline fields is not, of course, limited to sites lacking inversion symmetry. For the center of arbitrary symmetry considered in Section II (assume for simplicity a single electron and no orbital degeneracy), the g-shift for the ground state arising in second order from the perturbing effect of excited states is described by

$$\mathscr{H}=\frac{e}{mc}\sum_n\frac{\langle g|\boldsymbol{\ell}\cdot\boldsymbol{H}|n\rangle\langle n|(\mathscr{H}_{\mathrm{so}})_I|g\rangle}{(E_g-E_n)}. \qquad (39)$$

---

* KAMIMURA(11) has found that the anisotropy in the matrix elements of the spin-orbit interaction for Ni^{2+} and Cu^{3+} in $\mathrm{Al_2O_3}$ may be as much as 10–15 per cent.

† If covalent bonding with neighboring ions is important, the large potential gradient near the nuclei of these ions may contribute significantly to the matrix elements of the spin-orbit interaction. Our inferences from the effect of an applied electric field are then not applicable, and the crystalline field may, in this sense, contribute significantly to the spin-orbit interaction and, thereby, to the g-tensor. Under such conditions a skew-symmetric part of the g-tensor could perhaps be comparable with the symmetric part of the change in g from its free electron value.

The difference of the coefficients here of H_zS_y and H_yS_z, for example, is proportional to

$$\sum_n \frac{\langle g|l_z|n\rangle\langle n|\frac{1}{r}\frac{\mathrm{d}V}{\mathrm{d}r}l_y|g\rangle - \langle g|l_y|n\rangle\langle n|\frac{1}{r}\frac{\mathrm{d}V}{\mathrm{d}r}l_z|g\rangle}{(E_g-E_n)}. \tag{40}$$

This may be non-zero for the same reasons that R in (38) may differ from unity, if the center is not symmetric to the interchange of the y and z-axes, and if other symmetry conditions are appropriate.

VI. MEASUREMENT OF A SKEW-SYMMETRIC PART TO g-TENSOR

A skew-symmetric contribution to the g-tensor affects the observed paramagnetic resonance spectrum, but, as KNEUBÜHL has observed,(1) one cannot separate the symmetric and skew-symmetric parts of the g-tensor by means of the usual experiments. If we write the spin Hamiltonian in arbitrary symmetry for the interaction of a spin system with static applied magnetic and electric fields $\boldsymbol{H}$ and $\mathscr{E}$ as

$$\mathscr{H} = \beta\, \boldsymbol{S}\cdot\boldsymbol{K} \tag{41}$$

where the ith component of $\boldsymbol{K}$ is

$$K_i = \sum_j g_{ij}H_j + \sum_{jk} T_{ijk}H_j\mathscr{E}_k, \tag{42}$$

then the energy level spacing measures only $|\boldsymbol{K}|$, which is given by

$$K^2 = \sum_{ijl} g_{ij}g_{il}H_jH_l + \sum_{ijlk} (g_{ij}T_{ilk}+g_{il}T_{ijk})H_jH_l\mathscr{E}_k + 0(\mathscr{E}^2). \tag{43}$$

The coefficients in (43) being symmetric in indices j and l, there are therefore only six and eighteen independent parameters respectively which can be measured from the resonance frequency and its linear shift in an applied electric field. These would suffice to determine g_{ij} and T_{ijk} if it were true that $g_{ij} = g_{ji}$ and $T_{ijk} = T_{jik}$ (or if we wished to simulate the effects of the g- and T-tensors by symmetric tensors), but these do not determine uniquely the nine g_{ij} and twenty-seven T_{ijk} when a skew-symmetric part of the tensors is present.

Intensities of transitions between energy levels of (41) induced by an alternating magnetic field depend only on the symmetric combinations of the tensor coefficients appearing in (43) and thus provide no independent information.* However, using an alternating electric field to induce transitions between levels in a static magnetic field,(13) we find, as suggested by LÜDWIG,(14) that transition intensities determine other combinations of the T_{ijk} which now determine the symmetric and skew-symmetric parts of T_{ijk} independently. As an example, for a site of symmetry C_{3v}, if $\hat{\boldsymbol{c}}$ denotes the three-fold axis, and $\hat{\boldsymbol{a}}$, $\hat{\boldsymbol{b}}$ are mutually perpendicular vectors in the plane perpendicular to $\hat{\boldsymbol{c}}$, the spin Hamiltonian describing the linear effect of an applied electric field contains, among others, the terms(10)

$$\beta b_4[\mathscr{E}_a(S_cH_a+S_aH_c)+\mathscr{E}_b(S_cH_b+S_bH_c)] + \beta b_5[\mathscr{E}_a(S_cH_a-S_aH_c)+\mathscr{E}_b(S_cH_b-S_bH_c)] \tag{44}$$

Applying an alternating electric field along $\hat{\boldsymbol{a}}$, we find with static $\boldsymbol{H}$ along $\hat{\boldsymbol{a}}$ that the transition intensity depends on b_4 and b_5 through the combination $(b_4+b_5)^2H^2\mathscr{E}_a^2$, while with $\boldsymbol{H}$ along $\hat{\boldsymbol{c}}$ the intensity is proportional to $(b_4-b_5)^2H^2\mathscr{E}_a^2$. Thus b_4 and b_5 can be determined independently from these two intensity measurements.

VII. DISCUSSION

The calculations that we have given lead to values for the g-shift due to the contribution of an applied electric field to the spin-orbit interaction (1) which are small. Taking the electric dipole moment parameter $\langle \boldsymbol{d}\rangle$ of (14) or p and t of (18) to be the electron's charge times a length of at most an atomic dimension, say $\sim 10^{-8}$ cm, we found from (15) and (22) that the g-shift resulting from (1) is at most $\Delta g \sim \langle \boldsymbol{d}\rangle/2mc^2 \lesssim 10^{-11}$ cm/kV. This contrasts with shifts as large as 9×10^{-4} cm/kV which have been observed for transition metal ions in silicon(10) and which arise from the applied field via interaction (2).

Similar conclusions concerning the relative importance of (1) and (2) may be drawn for the effect of an applied electric field in changing other interaction tensors of interest in paramagnetic resonance, such as the hyperfine interaction, the nuclear quadrupole interaction, and the splitting of spin levels in zero magnetic field. Following Bloembergen's original suggestion(14) that such changes linear in $\mathscr{E}$ should be observable for paramagnetic centers lacking inversion symmetry, there has been particular interest in the last of these,(3, 4, 10, 15–17) which may be described by the terms

---

* This is true for linearly polarized alternating magnetic fields; independent information *can* be obtained using elliptical polarization. (See note added in proof at end of paper.)

$$\tfrac{1}{2}\sum_{ijk} R_{ijk}(S_iS_j+S_jS_i)\mathscr{E}_k$$

in the spin Hamiltonian (for $S > \frac{1}{2}$). The applied electric field makes a contribution via (1) to R_{ijk}, as we can see by replacing the orbital Zeeman interaction in the derivation of Section II by the spin-orbit interaction due to the ion potential [equation (24)]. But this contribution is not larger than $(\lambda/2mc^2)\langle \boldsymbol{d}\rangle$, where λ measures the strength of the ion's spin-orbit interaction, and this is $\lesssim 10^{-9}$ cm^{-1} (cm/kV) if $\lambda = 100$ cm^{-1}. Experimental values of R_{ijk} much larger than this have been found: LUDWIG and his coworkers(3, 10) obtained values of 40, 11, 1·0, and 0·04 [$\times 10^{-4}$ cm^{-1} (cm/kV)] for Mn$^+$, Cr^0, Fe^0, and Cr$^+$ respectively in silicon, while ROYCE and BLOEMBERGEN(15) and ARTMAN and MURPHY(16) found the value $R_{333} = 5{\cdot}9\times 10^{-6}$ cm^{-1} (cm/kV) for Cr^{3+} in ruby. These larger values can be accounted for easily using interaction (2), as these authors have shown,(4, 15, 16) so that, just as with the g-shift and as is evident from Section III, the contribution to R_{ijk} from (2) greatly exceeds that from (1).

The small effect of an applied field via (1) is a consequence primarily of the appearance of the relativistic energy mc^2 in the denominator of (1). The spin-orbit interaction is consequently very small except in the presence of a very large electric field, such as that inside the core of an ion due to the screened Coulomb potential of the nucleus. The spin-orbit interaction is accordingly a very insensitive probe for detecting relatively weak fields such as those that are applied in the laboratory or crystalline fields due to neighboring atoms. A much more sensitive probe of the environment is provided by the orbital energy of the electron via the electrostatic potential energy (2);* anisotropy thus detected is communicated to the spin via the ion's own large spin-orbit interaction. The resulting shift in the g-tensor and in other interaction tensors is, as we have seen, usually very much larger than that arising via (1). Shifts due to the direct effect of the applied field via (1) are probably in no case large enough to be observable.

To describe this conclusion in different words, we note that the shift in the g-tensor due to the perturbing effect of excited states is given by a sum of matrix elements like equation (39). A change in the electrostatic potential changes this sum in two ways, firstly by changing the spin-orbit operator $\mathscr{H}_{so}$ itself by changing ∇V in (1), and secondly by changing the wave functions and energies of the states used in forming the matrix elements. We have shown that the change in the g-tensor due to an applied electric field is very much greater via the second process (using the unperturbed spin-orbit operator) than via the first (using unperturbed wave functions). We have inferred that a similar conclusion holds for a change in the crystalline field.†

A second reason contributing to make the effect of an applied field via (2) so much larger than that of (1), particularly for some of the transition metal ions in silicon, is the vanishing of matrix elements of the electron momentum $\boldsymbol{p}$ among degenerate orbital states, according to (5), even when matrix elements of $\boldsymbol{r}$ are appreciable. The ions in which the largest effects of an applied field have been observed(3, 10) (interstitial Cr^0, Mn$^+$, and Fe$^+$ in Si) are those having orbital degeneracy in their ground state. This orbital degeneracy is lifted directly in an applied field by (2), as given by (23), and there is a correspondingly large g-shift. Matrix elements of the contribution of the applied field to (1) vanish among the degenerate states because of the vanishing matrix elements of p; the degeneracy is lifted in an applied field only by going to second order perturbation theory.

---

* The influence of an applied electric field is not limited to interactions (1) and (2). In particular the field may displace the ion and introduce local strains which, in the absence of inversion symmetry, contribute linearly in $\mathscr{E}$ to shifts in the interaction tensors.(4,10,14) Such shifts are not distinguishable experimentally from those produced by $\mathscr{E}$ via interaction (2) and may be of similar magnitude.

† Fields due to ions with which covalent bonding is strong may, however, contribute more significantly via the first process or, in second order, by the combined effect of both.

While it thus appears that we can usually ignore the contribution of applied fields or crystalline fields to the spin-orbit interaction (1), so that the resulting operator has spherical symmetry about the ion, matrix elements of (1) among states of a paramagnetic center may however still be appreciably anisotropic because of anisotropy of the wave functions of the states. KAMIMURA(11) has shown recently, for example, that anisotropy in the spin-orbit matrix elements, arising through the wave functions as a result principally of differences in the covalent bonding of different states, is very important for a consistent treatment of g-shifts, zero-field splitting, and trigonal crystal field splitting of various transition metal impurities in Al_2O_3. This anisotropy, together with a different anisotropy in the matrix elements of the orbital angular momentum, is responsible, as we have seen, for the skew-symmetric part of the g-tensor when symmetry allows this to be finite.

The skew-symmetric part of the shift in the g-tensor in an applied electric field (for a site of suitably low symmetry) which arises from (1) is of similar magnitude to the symmetric part of the shift from this source and is thereby, by our estimate above, negligible. In fact both parts vanish, to high accuracy, for a state with no orbital degeneracy. The skew-symmetric part arising from (2) will be a few per cent of the symmetric part from this same origin, if the ratio R in (38) can depart from unity by a few per cent, as seems quite likely. The skew-symmetric part of the shift in the g-tensor is thus in any case small, so that we should not make much of an error if we neglected it altogether in deducing the tensor coefficients T_{ijk} of (42) from the observed shifts in resonance frequency (i.e. if we assumed $T_{ijk} = T_{jik}$). Nevertheless, as a result of interaction (2) and a non-zero value for $(R-1)$, this skew-symmetric part may be large enough to contribute slightly to the observed shift. Unfortunately, the skew-symmetric and symmetric parts can not be distinguished by observations of the frequency shift alone, so that study of the skew-symmetric part would require accurate measurements of transition intensities in an alternating electric field or an alternating elliptically polarized magnetic field (see note added in proof below).

We infer from the results for an applied electric field that crystalline fields make very much greater changes in the g-tensor by changing the wave functions of the various states than by contributing to the spin-orbit interaction via ∇V in (1). The two effects may, however, be more nearly comparable if covalent bonding is strong. A skew-symmetric part of the g-tensor arises from crystalline fields of suitable low symmetry via the former process, but unless covalent effects are strong this part is probably not larger than a few per cent of the over-all shift in g from the free electron value.

Acknowledgement—We wish to thank G. W. LUDWIG for several stimulating discussions and for suggesting the method by which the skew-symmetric part of the tensor T_{ijk} might be distinguished experimentally.

REFERENCES

1. KNEUBÜHL F. K., *Phys. Letters* **2**, 163 (1962).
2. BETHE H. A. and SALPETER E. E., *Quantum Mechanics of One- and Two-Electron Atoms*, Springer, Berlin (1957).
3. LUDWIG G. W. and WOODBURY H. H., *Phys. Rev. Letters* **7**, 240 (1961).
4. HAM F. S., *Phys. Rev. Letters* **7**, 242 (1961).
5. PRYCE M. H. L., *Proc. phys. Soc., Lond.* **A63**, 25 (1950).
6. CONDON E. U. and SHORTLEY G. H., *The Theory of Atomic Spectra*, p. 109. University Press, Cambridge (1953).
7. PERL W., *Phys. Rev.* **91**, 852 (1953).
8. GRIFFITH J. S., *The Theory of Transition Metal Ions*, University Press, Cambridge (1961).
9. ABRAGAM A. and PRYCE M. H. L., *Proc. Roy. Soc. Lond.* **A205**, 135 (1951).
10. LUDWIG G. W. and HAM F. S., *Proceedings of the First International Conference on Paramagnetic Resonance*, Jerusalem (1962). p. 620. Academic Press, New York (1963).
11. KAMIMURA H., *Phys. Rev.* **128**, 1077 (1962).
12. LUDWIG G. W. and HAM F. S., *Phys. Rev. Letters* **8**, 210 (1962).
13. LUDWIG G. W., private communication.
14. BLOEMBERGEN N., *Science* **133**, 1363 (1961).
15. ROYCE E. B. and BLOEMBERGEN N., *Bull. Amer. phys. Soc.* **7**, 200 (1962); *Proceedings of the First International Conference on Paramagnetic Resonance*, Jerusalem (1962). Academic Press, New York (1963).

16. Artman J. O. and Murphy J. C., *Bull. Amer. phys. Soc.* **7**, 14, 196 (1962); *Proceedings of the First International Conference on Paramagnetic Resonance*, Jerusalem (1962). Academic Press, New York (1963).
17. Rado G. T., *Phys. Rev. Letters* 66, 90 (1961); *Phys. Rev.* **128**, 2546 (1962).

Note added in proof

Kneubühl (private communication) has pointed out that the skew-symmetric part of the g-tensor may be distinguished experimentally by means of measurements of transition intensities using an elliptically polarized alternating magnetic field.

J. Phys. Chem. Solids Pergamon Press 1963. Vol. 24, pp. 1175–1181. Printed in Great Britain.

THE ELECTRICAL PROPERTIES OF ALPHA FERRIC OXIDE—I.

THE IMPURE OXIDE

R. F. G. GARDNER, F. SWEETT and D. W. TANNER

Department of Scientific and Industrial Research, Warren Spring Laboratory, Stevenage, Hertfordshire

(*Received* 18 *December* 1962)

Abstract—Values are reported for the d.c. conductivity and Seebeck voltage of sintered polycrystalline specimens, prepared from various samples of alpha ferric oxide, in the temperature range 20–1350°C. High-purity samples show a non-linear relationship between the logarithm of the conductivity and the reciprocal of the absolute temperature. This is attributed to the presence of small amounts of ferrous iron (arising from oxygen loss by dissociation), whose influence is suppressed in impure samples. The latter show a linear relation between the logarithm of the conductivity and the reciprocal of the temperature.

The Seebeck voltage is very sensitive to the presence of foreign cations in amounts of 100–1000 p.p.m. Manganese and chromium provide trapping sites for negative carriers; magnesium and nickel create positive charge carriers.

It is concluded that conduction in ferric oxide is usually dominated either by the effects of impurities or, in highly pure ferric oxide, by deviation from stoichiometry towards metal-excess. An intrinsic process is believed to contribute to conduction above about 800°C.

INTRODUCTION

It has been reported(1–4) that alpha ferric oxide is a semiconductor in the temperature range 20–1350°C, with a d.c. conductivity (σ) varying exponentially with temperature according to the equation

$$\sigma = \sigma_0 \exp(-q/kT). \qquad (1)$$

Both *n*-type and *p*-type ferric oxide have been observed, as indicated by the sign of the Seebeck voltage. Morin(2) investigated the Hall effect and concluded that his results were spurious. The absence of a genuine Hall voltage was attributed to low carrier mobility.

The conductivity and Seebeck voltage of ferric oxide made *n*-type by the induced valency technique are reasonably well understood.(2, 5–7) Conduction in *p*-type ferric oxide and in apparently intrinsic material is less well explained.(2)

In all the above work little attention is paid to the effects of trace impurities. Their importance is demonstrated in the present work.

EXPERIMENTAL

(1) *Materials*

Six samples of ferric oxide powder were used to prepare specimens. Sample 1 was precipitated as a gel from a solution of laboratory reagent grade ferric nitrate by analytical reagent grade ammonium hydroxide. The gel was washed, dried, crushed, and roasted at 400°C for 15 hr. Sample 2 was prepared by the calcination to 450°C in the air of thin layers of finely divided ferrous oxalate, obtained by precipitation from a solution of analytical reagent ferrous sulphate. Sample 3 was a portion of steel rolling-mill scale which had been impregnated with potassium carbonate at 1100°C, and subsequently milled to a fine powder. Sample 4 was a commercial powder of high purity formed by the calcination of ferrous oxalate. A portion of sample 4 was milled in a stainless steel ball mill for 24 hr to give sample 5. Sample 6 was prepared by dissolving high-purity iron sponge in analytical reagent nitric acid, the nitrate solution being evaporated to dryness and the residue calcined overnight in air at 600°C.

Small amounts of cationic impurities were introduced into the high-purity sample 4 by making a paste of the powder with a dilute solution of the nitrate of the desired impurity. The paste was dried, crushed and fired for 15 hr. in air at 600°C. Ferric oxide does not sinter extensively below 800°C so that these doped samples did not require milling; they were gently crushed in an agate mortar before compacting.

The powder samples listed above were compacted at 26 tons/in^2 as rods (0·5 cm dia., 2·5 cm long) or rectangular pellets (0·5 cm × 0·3 cm × 1·5 cm) and were fired for 3–15 hr at 1250–1300°C. The specimens were allowed to cool in air, the temperature falling to 900°C in about 30 min. All firings were in air unless otherwise stated. Considerable shrinkage and extensive grain growth occurred during firing. The porosity of the fired specimens was ⩽10 per cent by volume. In no case was a second phase observed, either by X-ray diffraction analysis or by microscopic inspection of a polished section.

The oxides were analysed by emission spectroscopy, with an estimated accuracy of ± 10 per cent. The results given in Table 1 refer to the oxide samples; the analytical data in Table 2 refer to the fired specimens and were obtained after the electrical measurements were completed. In one case (copper) considerable loss of the added cation occurred during the firing.

(2) *Electrical measurements*

Electrical measurements were made on fired specimens in both rod and pellet form and showed good agreement. Current leads made contact with a rod via platinum discs sprung against the end faces. Thermocouples (Pt vs. 13% Rh–Pt) were spot-welded to the discs. Platinum wires were twisted round the rod as potential probes. Contact resistance was sometimes reduced (to about 10 Ω) by rubbing the end faces with a graphite pencil.

Current leads and thermocouples were embedded in the pellets during pressing. This method gave very satisfactory results and there was no evidence of contamination of either oxide or thermocouple after firing. The platinum leads of the thermocouples also served as potential probes.

Resistances were measured by both two- and four-probe techniques, the voltages being observed by means of a vibrating reed electrometer. The resistivity was calculated from the overall dimensions of the sample and the probe separation. Contact resistance showed ohmic behaviour; when this resistance was allowed for, or eliminated, two- and four-probe resistivities showed good agreement.

Table 1. Analyses of ferric oxide samples used for conductivity studies

Element	Sample 1	2	3	4	5	6	MORIN[2]
	parts per million of Fe_2O_3						
Al	800	100	700	3	400	≃ 300	190
Co	< 100	100	< 100	-	< 100	< 30	—
Cr	300	50	500	< 1	10,000	< 30	—
Cu	500	40	700	< 1	50	20	3
Mg	100	< 100	< 100	< 1	1000	< 100	300
Mn	1900	1600	10,000	< 2	670	10	800
Ni	40	260	320	≃ 1	800	< 10	—
Si	600	300	12,000	≃ 1	1200	100	280
Sn	< 100	< 100	200	-	500	—	—
Ti	< 100	100	< 100	-	< 100	—	—

Table 2. The effects of foreign cations on the electrical properties of ferric oxide

Cation	Concentration p.p.m.	At.%	σ 150°C Ω^{-1} cm^{-1}	q eV at 150°C	Seebeck voltage 150°C
Nil (Sample 4)			$1{\cdot}8 \times 10^{-4}$	0·68	*n*-type
Mn	80	0·018	$2{\cdot}0 \times 10^{-6}$	0·92	*n*-type
	280	0·041	$9{\cdot}3 \times 10^{-7}$	0·92	*n*-type
	460	0·067	$4{\cdot}9 \times 10^{-7}$	0·95	*n*-type
Cr	570	0·088	$4{\cdot}7 \times 10^{-5}$	0·86	*n*-type
Cu	30	0·004	$1{\cdot}6 \times 10^{-6}$	1·33	*n*-type
Mg	50	0·017	$2{\cdot}5 \times 10^{-5}$	0·71	*n*-type
	500	0·17	$1{\cdot}0 \times 10^{-2}$	0·45	*p*-type
Ni*	140	0·019	$5{\cdot}0 \times 10^{-6}$	0·81	*p*-type

* This sample was prepared by the oxidation of very pure iron carbonyl; nickel was the only impurity detected spectroscopically.

For measurement of the Seebeck voltage, the sample was placed in a temperature gradient in a furnace. Temperature differences along the sample of 2–20°C were used. The thermocouple voltages were measured to the nearest micro-volt on a potentiometer and the Seebeck voltage developed was measured between the platinum thermocouple leads on a vibrating reed electrometer. The Seebeck voltage in mV/°C was found by plotting the temperature difference against the voltage developed. The values are quoted relative to platinum. In a temperature gradient the predominant charge carriers diffuse towards the cold end of the sample. The sign of Seebeck voltages given in this paper is the sign of the probe which was at the lower temperature and is thus the sign of the predominant charge carrier.

All measurements were made in air, and all curves were obtained with rising temperature, unless otherwise stated. Good reproducibility was generally found on cooling; the changes occasionally observed were attributed to the effect of cooling rate on grain boundary composition. Measurements were made on several specimens of each of the samples. In view of the good reproducibility, and because the measurements were primarily exploratory, only one specimen of each doped sample listed in Table 2 was examined.

RESULTS AND DISCUSSION

(1) *Conductivity*

All previous workers(1–4) have reported linear plots of $\log_{10}\sigma$ vs. T^{-1} for sintered ferric oxide compacts. The present results for specimens from impure samples (nos. 1, 2, 3 and 5) shown in Fig. 1 are seen to agree fairly well with the earlier data. Apart from the deviation at lower temperatures shown by sample 3 the conductivity values of our specimens fell about a line of best fit (least squares criterion) given by

$$\sigma = 2{\cdot}7\times 10^{3}\exp(-0{\cdot}96/kT). \qquad (2)$$

The published values of the pre-exponential factor, $\sigma_0 \times 10^3\ \Omega^{-1}\ \text{cm}^{-1}$, and the activation energy q in eV are as follows: 40·8, 1·18(1); 21, 1·17(2); 12·6, 1·17(3); 0·74, 1·06(4). The agreement of past and present results is surprisingly good in view of the use of sintered compacts and the impurity of the materials. The available analytical data are summarized in Table 1.

Specimens of high-purity ferric oxide (from samples 4 and 6) fired above 1250°C invariably gave a non-linear conductivity plot in which three regions can be distinguished (Fig. 2). They are:

A. $q \simeq 0{\cdot}7$ eV; $T < 450$°C;
B. $q \simeq 0{\cdot}1$ eV; $450° < T < 800$°C;
C. $q \simeq 1{\cdot}0$ eV; $T > 800$°C.

The temperature limits are not precise. In region C the conductivity values are very closely similar to those for impure samples, as can be seen in Fig. 2. Carriers in this temperature range are thought to arise both from oxygen loss and by an intrinsic process. In regions A and B the conductivity is higher than for impure specimens. This is attributed to traces of ferrous iron arising from oxygen loss during firing. Evidence for this will be given in Part 2 of this paper: it will also be shown that in region B the conductivity changes are probably due to changes in mobility of the carriers, and that conduction in region A is dominated by effects at grain boundaries.

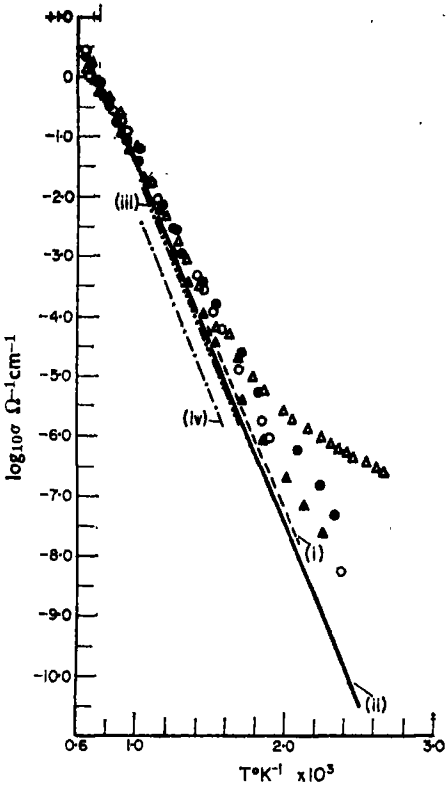

FIG. 1. The conductivity of impure ferric oxide as a function of temperature: ○, ▲, △, ● Specimens from samples 1, 2, 3 and 5; (i) Meyer and Neldel,(1) (ii) Morin,(2) (iii) Lessoff, Kersey and Horne,(3) (iv) Bevan, Shelton and Anderson.(4)

Sufficient ferrous iron should be formed (by oxygen loss(9)) during any normal firing schedule (firing temperature >1000°C) to make a ferric oxide compact appreciably conducting at room temperature ($Fe^{2+} > 10^{-4}$ at.% i.e. $\sigma_{20°C} > 10^{-4}$ Ω^{-1} cm^{-1}). However, the reported conductivities at room temperature are in the region of 10^{-13} Ω^{-1} cm^{-1}. Our results suggest two reasons for this discrepancy: first, the presence of foreign cations in amounts >100 p.p.m., and secondly the reoxidation at grain boundaries which occurs during cooling of a fired compact. Some evidence for grain boundary effects will be presented in Part 2.

We offer here three pieces of evidence relating to the effects of impurities. First, our finding that specimens from high-purity samples (nos. 4 and 6) gave non-linear conductivity plots (Fig. 2, curves i and ii) while specimens from impure samples (nos 1, 2, 3 together with Morin's samples) gave linear conductivity plots (Fig. 1), leads one to associate the linearity of the conductivity plot of a fired specimen with the presence of several cation impurities. Secondly, the effect of introducing several foreign cations into the high-purity sample (4) by milling (to give sample 5) is to alter the conductivity from curve ii, Fig. 2 (specimen of sample 4) to curve iii, Fig. 2 (specimen of sample 5); the latter curve is almost linear and is very close to curve iv, the line of best fit for specimens from impure samples. The impurities introduced by milling can be seen from Table 1. Thirdly, we examined the effects of introducing several common cation impurities singly into the high-purity oxide, sample 4. The results obtained with fired specimens are given in Fig. 3 (curves ii and iii) and are summarized in Table 2. Comparison with the results for high-purity specimens (Fig. 3, curve i, and Table 2) show the effects of foreign cations to be profound. Manganese, present in more than 80 p.p.m. lowers the conductivity and increases the activation energy. The ferrous content, as estimated from the conductivity values in region B of the curve, is little altered. Thus, manganese appears to affect the availability of carriers at lower temperatures but not the total number. This effect was also reported by JONKER(10) for 14,000 p.p.m. of manganese. Chromium behaves similarly to manganese. Copper, magnesium and nickel have a more radical effect. In small quantities (<0·02 at.%) they reduce the conductivity, presumably by elimination of the ferrous iron. Magnesium when added in larger amounts increases the conductivity by introducing p-type carriers. The behaviour of the Seebeck voltage suggests that copper and nickel can also introduce positive charge carriers.

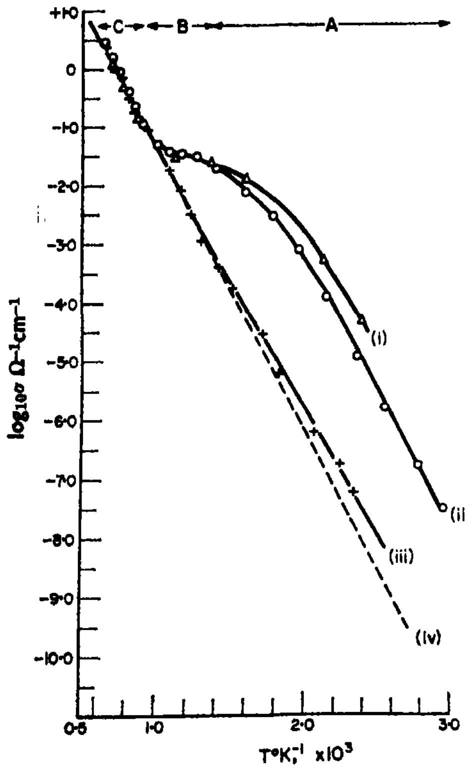

FIG. 2. The conductivity of high-purity ferric oxide specimens as a function of temperature (i) from sample 6, (ii) from sample 4, (iii) from sample 5, (iv) line of best fit for impure specimens.

These results lead one to suggest that the linearity of $\log_{10}\sigma$ vs. T^{-1} often reported for ferric oxide is a consequence of the presence of cation impurities and is probably not due to carrier formation by an intrinsic mechanism throughout the entire temperature range.

(2) *Seebeck voltage*

Although the published conductivity data for ferric oxide are reasonably consistent, the data for the Seebeck voltage show wide variation.(2, 3)

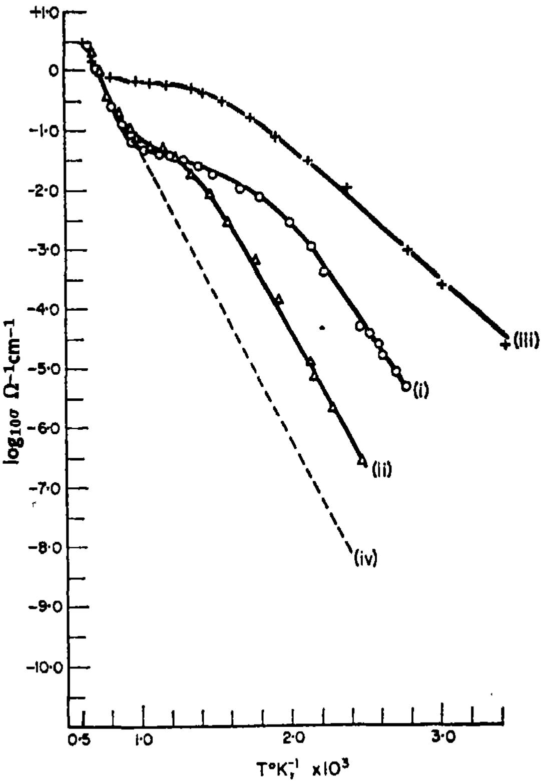

FIG. 3. The influence of foreign cations on the conductivity of high-purity ferric oxide as a function of temperature: (i) specimen of sample 4, (ii) + 280 p.p.m. Mn, (iii) + 500 p.p.m. Mg, (iv) line of best fit for impure specimens.

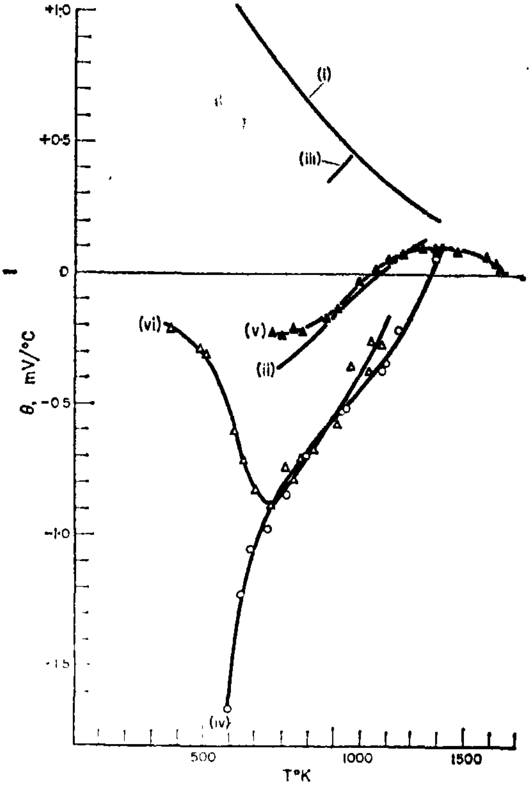

FIG. 4. The Seebeck voltage of impure ferric oxide as a function of temperature: (i) MORIN,[2] specimen fired in O_2, (ii) MORIN, specimen fired in $74N_2+2O_2$, (iii) LESSOFF, KERSEY and HORNE,[3] (iv)–(vi) specimens of samples 1, 2, 3.

(Figure 4, curves i–iii.) This has also been found in the present work with specimens from impure samples (Fig. 4, curves iv–vi). Such variations again suggest that conduction is not intrinsic at all temperatures in these samples despite the linear conductivity plots. The majority of samples is *n*-type at lower temperatures, as would be expected for an oxide showing deviations towards metal-excess. Conduction can also occur by positive carriers since some samples are *p*-type at all temperatures, and most *n*-type samples become *p*-type above 1000°K. At higher temperatures the Seebeck voltage again becomes negative; this is seen incipiently in Fig. 4 (curve v) and Fig. 5 (curves i, iii, iv and v), and will be more fully described in Part 2.

The presence of foreign cations is probably responsible for the wide variation of Seebeck voltage. The effects of foreign cations singly introduced in the high-purity ferric oxide, sample 4, can be seen from Fig. 5 and Table 2. Manganese increases the Seebeck voltage (Fig. 5, curve ii) which is consistent with the introduction of electron traps. Copper greatly reduces the Seebeck voltage (Fig. 5, curve vi), an effect which appears to be due to the suppression of negative carriers and the formation of positive carriers. A small amount of magnesium (50 p.p.m.) has little effect (Fig. 5, curve iii) although the conductivity is reduced as can be seen from Table 2; a larger amount of magnesium (500 p.p.m.) introduces predominating positive carriers (Fig. 5, curve iv). Nickel also introduces positive carriers (Fig. 5, curve v). These results lead one to expect that the p-type samples reported by MORIN(2) and LESSOFF(3) (Fig. 4, curves i and iii) contained a divalent impurity; indeed the analysis of Morin's material (quoted in Table 1 from Ref. 2) showed 300 p.p.m. of magnesium.

The Seebeck voltage for the specimen containing 500 p.p.m. of magnesium (Fig. 5, curve iv) is reasonably constant between 400°K and 1000°K, which indicates that the carrier concentration is constant in this temperature range. The Seebeck voltage is then given approximately by the equation(7)

$$\theta = \frac{k}{e}\log_e\frac{N_0}{p} \simeq 198 \cdot \log_{10}\frac{N_0}{p} \quad \mu V/°C \quad (3)$$

where k is Boltzmann's constant, e the electronic charge, and N_0 and p are the number of available states and the number of positive carriers per cm^3 respectively. Since p-carriers are identified as holes on oxygen ions (O^-, see Part II) N_0 is taken as the number of anions per cm^3, i.e. 6×10^{22} cm^{-3}. By substituting the observed value of θ in equation (3) the value of p is calculated to be 6×10^{19} cm^{-3} or 0·15 per cent of the cations; this is in excellent agreement with the analytical figure for magnesium content, 0·17 at.% (Table 2) and indicates that each Mg^{2+} introduces one positive carrier.

Since we can take the carrier concentration in this specimen as constant between 400 and 1000°K and equal to 6×10^{19} cm^{-3}, we can calculate hole mobilities from the conductivity values. The mobilities thus obtained at 300 and 600°K are $5{\cdot}6 \times 10^{-6}$ and $2{\cdot}1 \times 10^{-2}$ cm^2 V^{-1} sec^{-1} respectively; the activation energy for hole mobility in this sample is 0·46 eV. The mobilities of negative carriers at these temperatures in ferric oxide doped with 1·0 at.% of titanium are $1{\cdot}6 \times 10^{-2}$ and $5{\cdot}6 \times 10^{-2}$ cm^2 V^{-1} sec^{-1} (calculated from equation (5), given below). Thus in these samples below about 600°K the holes are less mobile than the electrons. At higher temperatures the holes become more mobile than the electrons, as indicated by the change of sign of the Seebeck voltage for high-purity specimens with increasing temperature (Fig. 5, curve i).

If the hole mobilities in the specimen containing 500 p.p.m. of magnesium are fitted to an equation for carrier movement by thermally-activated diffusion (of the type given in Ref. 7) one obtains:

$$\mu_p = \frac{91400}{T}\exp(-0{\cdot}46\ \text{eV}/kT) \quad (4)$$

This can be compared with the electron mobility equation for ferric oxide doped with 1·0 at.%

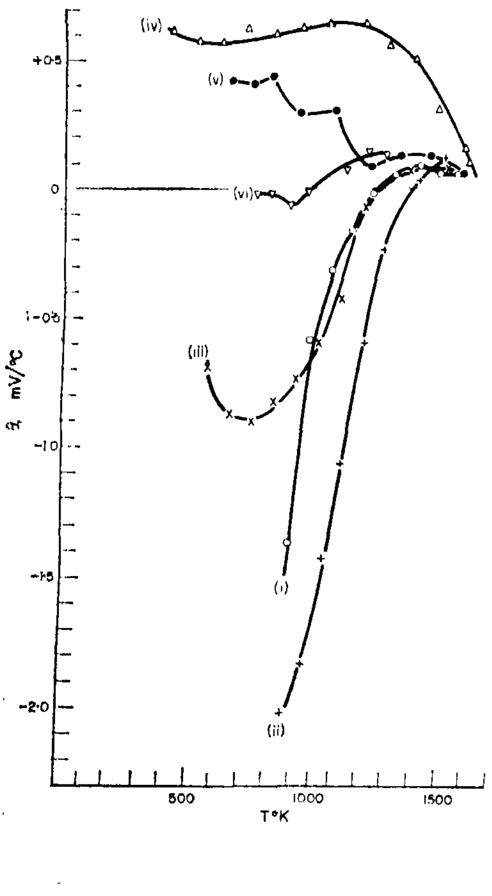

FIG. 5. The influence of impurities on the Seebeck voltage of high-purity ferric oxide as a function of temperature: (i) specimen of sample 4, (ii) +280 p.p.m. Mn, (iii) +50 p.p.m. Mg, (iv) +500 p.p.m. Mg, (v) +140 p.p.m. Ni (see Table 2), (vi) +30 p.p.m. Cu.

titanium, which is

$$\mu_n = \frac{232}{T}\exp(-0{\cdot}1\ \mathrm{eV}/kT) \tag{5}$$

In this equation the pre-exponential factor has been calculated from JONKER's conductivity data(7) using a value of 0·1 eV for the mobility activation energy.(2, 8)

(3) *The origins of the carriers*

We interpret the Seebeck voltage of ferric oxide as follows. A positive voltage at all temperatures is due to the presence of cation impurities, such as magnesium and nickel, which introduce positive carriers. We have been unable to prepare completely positive specimens by roasting high-purity material in oxygen. This is consistent with the thermodynamic data,(9) which indicate that small amounts of ferrous iron are formed in ferric oxide even when it is fired in oxygen at atmospheric pressure. Most of the ferrous iron formed during firing is "frozen in" on cooling and leads to *n*-type conduction at temperatures low enough for the intrinsic carriers to be negligible. The Seebeck voltage of *n*-type specimens is thus determined, below about 800°C, by the degree of non-stoichiometry introduced during firing, and by the nature and amounts of foreign cations; it is probably also influenced by the nature of the grain boundaries. Above 800°C (i.e. in region C of the conductivity plot, Fig. 2) both impure and high-purity samples show similar behaviour of conductivity and Seebeck voltage (e.g. compare curve v, Fig. 4 with curve i, Fig. 5). It is postulated that above this temperature carriers arise by two mechanisms:

(i) intrinsic: $Fe^{3+}+O^{2-} \rightarrow Fe^{2+}+O^{-}$ (6)

(ii) by oxygen loss:
lattice $\rightarrow 4xFe^{2+}+xO_2$ (gas) (7)

The electrons are believed to jump to neighbouring cations and the holes to neighbouring anions, processes requiring activation energies of ≃ 0·1 and ≃ 0·5 eV respectively. The rapid change of Seebeck voltage in pure samples above 800°K (e.g. Fig. 5, curve i) from a large negative value to a small positive maximum is attributed to the more rapid increase with temperature of the hole mobility than the electron mobility (as can be seen by comparing equations 4 and 5). At higher temperatures still (>1600°K) the number of *n*-carriers arising from oxygen loss outweighs the greater hole mobility and the Seebeck voltage becomes negative again.

The evidence for these processes will be discussed more fully in Part II. The question arises here, as to why specimens of high-purity show evidence of carriers arising from oxygen loss and "frozen in" during cooling while impure specimens do not. Two explanations can be suggested to account for this difference. The first is that conductivity changes of impure specimens below ≃ 1000°K are dominated by the influences of impurities on carrier mobility. Alternatively it is possible that in impure specimens carrier numbers rather than mobilities are changing with temperature. The role of cation impurities may then be to decrease the degree of non-stoichiometry at high temperatures, to provide traps for carriers arising from oxygen loss, or to accelerate the rate of equilibration (i.e. re-oxidation) during cooling of the specimen after firing. Further evidence is required to decide between these possibilities but the Seebeck voltage curves suggest that numbers rather than mobilities are altered by the presence of foreign cations.

Acknowledgements—We are indebted to Dr. G. H. JONKER (N.V. Philips' Laboratories, Eindhoven) and to Miss L. S. SOUTER (A.E.I. Research Laboratories, Harlow) for helpful discussions. This work forms part of the research programme of Warren Spring Laboratory, and is published by permission of the Director.

REFERENCES

1. MEYER W. and NELDEL H., *Z. tech. Phys.* **12**, 588 (1937).
2. MORIN F. J., *Phys. Rev.* **83**, 1005 (1951); **93**, 1195 (1954).
3. LESSOFF H., KERSEY Y. and HORNE R. A., *J. Chem. Phys.* **31**, 1141 (1959).
4. BEVAN D. J. M., SHELTON J. P. and ANDERSON J. S. *J. chem. Soc.* **1729** (1948).
5. VERWEY E. J., HAAYMAN P. W. and ROMEIJN F. C., *Chem. Weekblad.* **44**, 49 (1948).
6. VERWEY E. J., HAAYMAN P. W., ROMEIJN F. C. and VAN OOSTERHOUT G. W., *Philips Res. Rep.* **5**, 173 (1950).
7. JONKER G. H. and VAN HOUTEN S., *Halbleiterprobleme*, **6**, p. 118. Vieweg, Braunschweig (1961).
8. TANNER D. W., unpublished results.
9. SALMON O. N., *J. Phys. Chem.* **65**, 550 (1961).
10. JONKER G. H., *Proc. Conf. on Semiconductor Physics, Prague 1960*, p. 864. Academic Press, New York (1961).

J. Phys. Chem. Solids Pergamon Press 1963. Vol. 24, pp. 1183–1196. Printed in Great Britain.

THE ELECTRICAL PROPERTIES OF ALPHA FERRIC OXIDE—II.

FERRIC OXIDE OF HIGH PURITY

R. F. G. GARDNER, F. SWEETT and D. W. TANNER

Department of Scientific and Industrial Research, Warren Spring Laboratory, Stevenage, Hertfordshire

(*Received* 18 *December* 1962)

Abstract—Values are reported for the d.c. conductivity and Seebeck voltage of several specimens of high-purity polycrystalline alpha ferric oxide between 20°C and 1350°C. It is found that carriers arising from deviations in stoichiometry contribute to conduction in fired specimens. Below about 1000°C the carrier concentration is constant and equal to the concentration of quenched donors; above about 1000°C oxygen loss is equilibrated and the carrier concentration varies with temperature. The curve of $\log_{10}$ conductivity vs. reciprocal temperature accordingly shows two regions of activation energies about 0·1 and about 1·0 eV respectively. Below about 450°C oxidation at grain boundaries causes the activation energy to increase from about 0·1 to about 0·7 eV.

The positive Seebeck voltage observed above about 1000°C shows that positive carriers also contribute to conduction, and possible mechanisms for their formation are discussed. The most probable mechanism is thought to be the formation of both *n*- and *p*-carriers by transfer of an electron from an oxygen ion to a ferric ion. The thermal activation energy for this process of 1·8 eV (calculated by analysis of the activation energy for conduction) is reasonably close to the value of 1·9–2·5 eV calculated from spectral data.

A full conductivity scheme is described. Calculated values of the conductivity and Seebeck voltage are in close agreement with the experimental data. The scheme will also explain apparently conflicting observations in the literature on the effect of oxygen partial pressure on conductivity.

1. INTRODUCTION

ALPHA ferric oxide has been variously described as an intrinsic, and as a metal-excess oxide semiconductor. Conduction has been identified(1–6) as intrinsic for three reasons. First, WAGNER and KOCH(1) found that the conductivity at 1000°C was unaffected by changes in oxygen partial pressure between 0·21 atm and $3·6 \times 10^{-3}$ atm. Secondly, "pure" samples of ferric oxide have been found(2, 3) to give a linear plot of $\log_{10}$ conductivity vs. reciprocal temperature. Thirdly, the conductivity curves for titanium-doped ferric oxide approach that for "pure" ferric oxide at high temperatures.(2, 3)

Although it has been stated(7) with reference to conduction in pure ferric oxide that no appreciable deviation from stoichiometry occurs, such deviation has been demonstrated.(8) MEYER and NELDEL(9) showed that a slight metal excess (formed by hydrogen reduction) increased the conductivity, and BEVAN, SHELTON and ANDERSON(10) demonstrated that the conductivity between 400 and 700°C increased as oxygen partial pressure decreased from 0·21 atm to $1·3 \times 10^{-8}$ atm. It is on the basis of these findings that ferric oxide has been classified as a metal-excess oxide semiconductor.

MORIN(2, 6) while attributing conduction primarily to an intrinsic mechanism, recognized that carriers could arise by deviation from stoichiometry. He considered ferric oxide to be amphoteric, showing either a *p*-type or an *n*-type Seebeck voltage depending on the sintering atmosphere, and suggested that the carriers were Fe^{4+} and Fe^{2+} respectively. JONKER(11, 13) also reported a carrier contribution arising from oxygen loss during firing.

In Part 1 it was shown(12) that the linearity of the plot of $\log_{10}$ conductivity vs. reciprocal temperature for fired specimens of ferric oxide is probably due to the presence of cation impurities, and that ferric oxide shows a positive Seebeck voltage below about 1000°K, only when such impurities as Mg^{2+} and Ni^{2+} are present. These findings call in question earlier conclusions(2, 6) on the conduction mechanism.

In the present work the use of ferric oxide of high-purity has led us to conclude that carriers arising from deviations in stoichiometry play a significant part in the conduction process. Above about 1000°C, ferric oxide specimens equilibrate with the surrounding atmosphere and the number of carriers arising from oxygen-loss varies with temperature. Below about 1000°C equilibration is slow and donors are frozen into the lattice; hence their contribution to the carrier concentration is independent of temperature. We showed earlier(12) that the effects of carriers arising from non-stoichiometry are masked by the presence of cation impurities. In the present work we have found, from variation in the microstructure of the specimens, that below about 450°C, grain boundary oxidation also masks the effects of non-stoichiometry.

Although carriers arising from non-stoichiometry account for much of the electrical behaviour they do not explain the positive Seebeck voltage observed above about 1000°C. It is necessary to postulate a further source of carriers, and reasons are given for identifying this as the thermally-activated transition of an electron from an oxygen ion to a ferric ion, to form both *n*- and *p*-carriers. The negative carriers are thus identified as electrons on ferric ions, i.e. Fe^{2+}, as has been demonstrated(2, 11, 13) for titanium-doped samples; the positive carriers are thought to be holes on oxygen ions. We have found that when carriers from both sources are considered, a full conductivity scheme can be derived from earlier models(2, 6, 13) which explains in detail the observed electrical properties of high-purity ferric oxide.

2. EXPERIMENTAL DETAILS

Ferric oxide specimens for electrical measurements were prepared in one of two ways: (1) by oxidizing iron wire, and (2) by sintering ferric oxide powder compacts. For the first method platinum leads were spot-welded to short lengths of iron wire (0·25 mm dia.) which were subsequently converted to ferric oxide by prolonged roasting in air at 1000°C. In the preparation of the compacts current leads and thermocouples were embedded in the oxide powder compacts during pressing, and the compacts were subsequently fired as described earlier.(12) Resistivity and Seebeck voltage were measured by four-probe techniques.(12)

Two samples of high-purity ferric oxide were used to prepare compacts. Both were made by calcining ferrous oxalate in air, and gave X-ray diffraction patterns containing only lines due to alpha ferric oxide. They differed in that Sample 1 was prepared from thick layers (about 1 cm) of oxalate at about 650°C, and Sample 2 from thin layers (about 2 mm) at about 450°C; Sample 2 showed a lower ferrous iron content and smaller crystallite size. The properties of the samples and their spectrographic analyses are summarized in Table 1. Some four-probe resistance measurements were made on a synthetic single crystal of ferric oxide. The analysis of the crystal is also given in Table 1.

The ferric oxide samples and some fired specimens were analysed for ferrous iron. The oxide was dissolved by heating with constant boiling hydrochloric acid in a sealed Carius tube at 120–125°C. The acid was freshly distilled from ferrous chloride and was passed through a silver reductor immediately before use. The tube, sample and acid were thoroughly out-gassed, and the tube was filled with nitrogen before sealing. The ferrous iron was titrated with *N*/250 potassium dichromate. A blank run, in which standardized ferrous chloride solution replaced the sample, was made at the same time. The amount of ferrous iron consumed in the blank (typically 0·02 wt.%) was added to the ferrous content found for the sample, which generally ranged from 0·05 to 0·15 wt.%.

3 RESULTS AND DISCUSSIONS

In this Section the conductivity and Seebeck voltage of high-purity ferric oxide are reported and qualitative conclusions are drawn about the conduction mechanism. Below about 450°C the effects of grain boundaries complicate the behaviour of polycrystalline specimens. Behaviour at higher temperatures is free from these effects and provides more direct evidence for the conduction mechanism. Consideration of this behaviour has led to the development of the quantitative conduction scheme described in Section 4.

3.1 *Conductivity*

The conductivity curves for ferric oxide specimens of high purity, fired in air above 1000°C and slowly cooled, show three regions(12) of differing activation energy (e.g. curve (i) Fig. 1):

A. $q \simeq 0{\cdot}7$ eV; $T < 450°C$;
B. $q \simeq 0{\cdot}1$ eV; $450° < T < 800°C$;
C. $q \simeq 1{\cdot}0$ eV; $800°C < T$.

Table 1. ***Properties and analyses of Starting Materials***

	Oxide Samples		Iron wire	Single Crystal
	1	2		
Crystallite size (by X-ray diffraction line broadening), (microns)	0·1–1·0	0·07	—	
Ferrous iron content (wt.%)				
present method	≃ 0·08	< 0·02	—	
CLARK's method(14)	—	⩽ 0·005	—	
Analysis, p.p.m.				
Ag	—	< 1	< 1	—
Al	3	—	—	1400
B	—	—	—	< 30
Cr	< 1	—	—	1300
Cu	< 1	< 1	< 1	< 40
Mg	< 1	1	< 1	500
Mn	< 2	2	3	400
Nb	< 30*	< 30*	< 30*	< 100
Ni	≃ 1	2	2	400
Si	≃ 1	10	< 1	1800
Sn	< 5*	< 5*	< 5*	< 400
Ta	< 200*	< 200*	< 200*	< 800
Ti	< 10*	< 10*	< 10*	10
Zr	< 50*	< 50*	< 50*	< 200

* Lower limit of detection.

We have concluded first that in region A the value of q is greatly affected by oxidation at grain boundaries; secondly that the value of q in region B is that for n-carrier mobility, the carrier concentration remaining constant; and thirdly that in region C the activation energy is primarily determined by changes in carrier concentration.

3.1.1. *The effects of grain boundaries: Region A.* During firing of a ferric oxide specimen a slight metal-excess is formed by loss of oxygen. Reoxidation occurs on cooling, initially at grain boundaries. The extent of re-oxidation will depend on the rate of cooling and on the microstructure (porosity and grain size). We find a high value of q under conditions favouring re-oxidation; when re-oxidation is minimized, the region of high activation energy, A, is absent and region B ($q \simeq 0{\cdot}1$ eV) extends down to room temperature. We therefore consider the high q value in region A to be attributable to grain boundary oxidation.

This interpretation is supported by three pieces of evidence. First, the value of q is smaller for a rapidly cooled than for a slowly cooled polycrystalline compact (compare curves (i) and (ii) in Fig. 1). Secondly, the value of q is smaller for specimens of large grain size(15) than for those of small grain size—compare curves (i) and (iii) in Fig. 1 and the photomicrographs Figs 2(a) and (b). Thirdly, the combination of rapid quenching, adequate grain size and low open porosity, results in a conductivity curve showing only regions B and C (curve (iv), Fig. 1 and photomicrographs 2(c) and (d)). The reason for believing grain boundary effects to be absent from this specimen (oxidized iron wire) is that the curvature of curve (iv), Fig. 1, below 1000°K can be wholly accounted for by mobility changes (cf. Section 3.1.2); this is not possible for curves (i) and (ii) in Fig. 1.

The tendency of n-type oxides to adsorb oxygen at grain boundaries is well known and the resultant increase in resistance has been demonstrated by MORIN(2) and by SUCHET(16) using a.c. methods. Further evidence for an accompanying increase in the activation energy for conduction is provided by the increase of the temperature coefficient of resistivity(17) resulting from the deliberate introduction of porosity (and hence improved access of oxygen) into polycrystalline specimens of n-type ferric oxide. Since a complete explanation for the effects of grain boundary oxidation cannot be given at the present time further discussion will be primarily concerned with specimens in which the composition of the grain boundaries is believed to approximate to that within the grains.

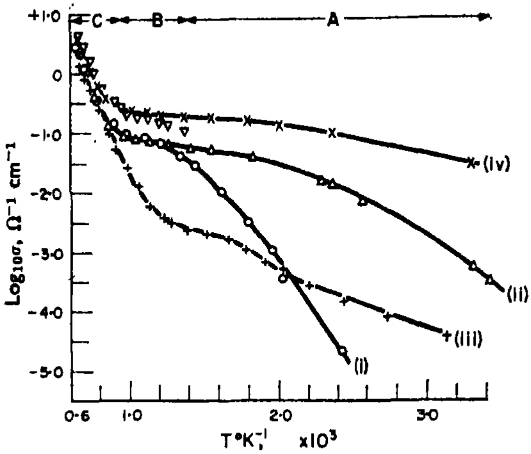

FIG. 1. The conductivity of ferric oxide specimens of high purity as a function of temperature: (i) compact of Sample 1 fired at 1300°C in oxygen and cooled to 900°C in about 30 min.; (ii) the same compact after quenching from 1300 to 20°C in about 10 sec; (iii) slowly cooled compact of Sample 1 in which large grains had grown; (iv) oxidized iron wire, quenched to 20°C in about 1 sec after 5 hr at 1300°C: ▽ Single crystal of ferric oxide grown from sodium tetraborate; four-probe resistivity along the (111) plane of a specimen quenched after 13 hr at 1300°C in air.

It has been argued that, apart from variation in composition, the very presence of grain boundaries can invalidate conclusions based on data obtained with polycrystalline specimens. In the present work, results obtained on polycrystalline specimens above 450°C are believed to be free from grain boundary effects. This is supported by preliminary measurements on a synthetic single crystal (Fig. 1,▽) which show that the conductivity is closely similar to that of polycrystalline specimens, both in absolute value and in temperature coefficient. This indicates that neither carrier mobility nor the activation energy for carrier formation is seriously affected above 450°C by the presence of grain boundaries. The analysis of the conduction mechanism given below is therefore believed to be of general validity.

3.1.2. *Quenched donors arising from oxygen loss: Region B.* Ferric oxide becomes oxygen-deficient at high temperatures in air.(8, 18) We find that the donor centres formed in this way are frozen into the lattice on cooling, in a manner analogous to that observed in NiO(19) and Cr_2O_3.(20) The carrier concentration in a fired specimen below about 800°C is thus fixed and equal to the concentration of quenched donors; hence the change in conductivity with temperature is due to changes of mobility. Region B of the conductivity curve corresponds to the temperature range of constant carrier concentration.

These conclusions are supported by the following evidence. The presence of excess metal in fired specimens was shown by analysis, ferrous iron contents of 0·05–0·15 wt.% being obtained; the excess metal gives rise to negative carriers, as indicated by the negative Seebeck voltage observed for these specimens below 1000°K (Fig. 5). There are two reasons for attributing the oxygen loss at high temperatures to genuine deviations from stoichiometry rather than to impurities such as carbon. First, ferric oxide specimens derived from different starting materials (ferrous oxalate, ferric nitrate, iron wire) gave closely similar conductivity curves (see Part 1, and Fig. 1). Secondly, the increase in oxygen deficiency with rising temperature(8) would lead one to predict that the conductivity in region B should increase with increasing firing temperatures; that this is the case can be seen from the results shown in Figs 3(B) and 4.

If the conductivity changes in region B are due only to changes of mobility they should obey an equation of the form:(13)

$$\sigma = N_d e \mu_n = N_d eA/T \exp(-\alpha/kT) \qquad (1)$$

where N_d = quenched donor concentration, e = the electronic charge, μ_n = n-carrier mobility, T = absolute temperature in degrees Kelvin, A is a temperature-independent constant, α is the activation energy for n-carrier mobility and k is Boltzmann's constant. Equation (1) requires that $\log_{10}(\sigma T)$ should be a linear function of T^{-1} in region B and this was found to be the case for the results shown in Fig. 4. Values of α were obtained from the gradients of plots of $\log_{10}(\sigma T)$ vs. T^{-1} and were used, together with

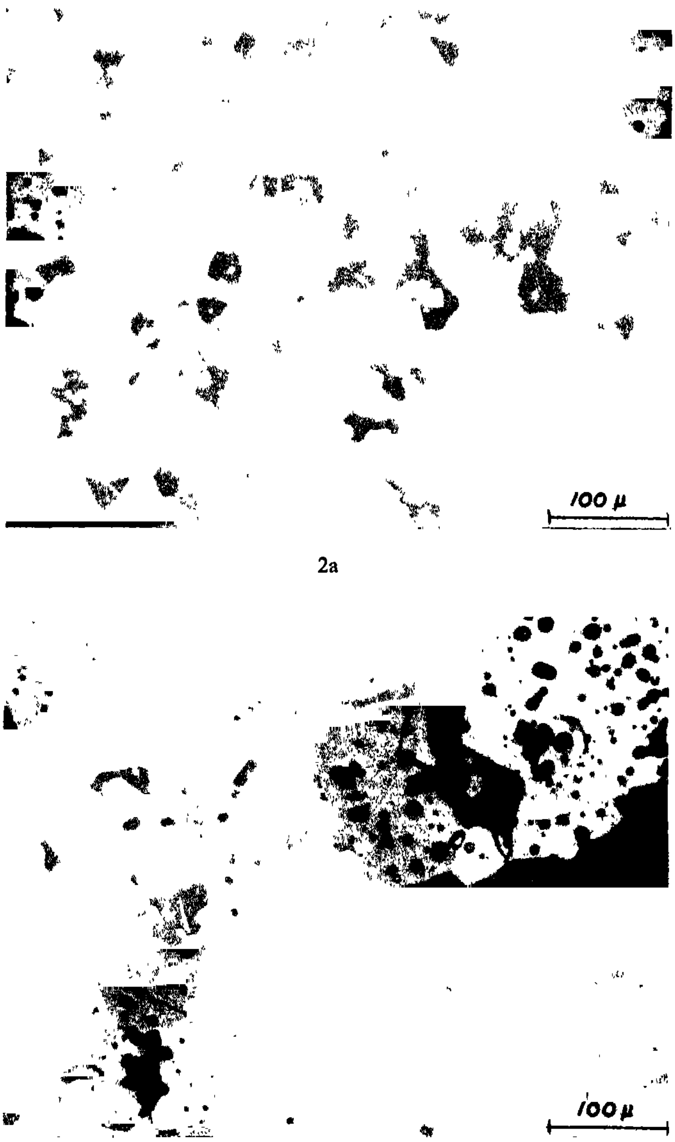

FIG. 2. Photomicrographs of ferric oxide specimens giving the curves shown in Fig. 1; (a) specimen giving curves (i) and (ii); average grain dia. 40μ; porosity, 12 vol.% on grain boundaries, 4% within grains; crossed Nicols: (b) specimen giving curve (iii); average grain dia. 130μ; porosity, 16 vol.% on grain boundaries, 11% within grains; crossed Nicols: (c) and (d) specimens giving curve (iv); average grain dia. 40μ; Nicols uncrossed (c), and crossed (d).

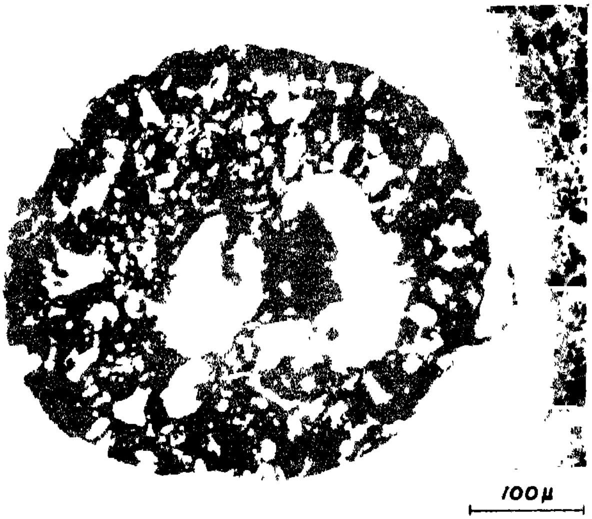

2c

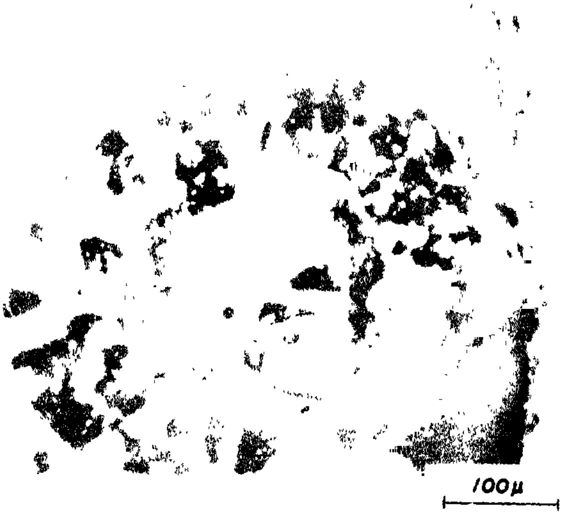

2d

values N_d calculated for the various firing temperatures from thermodynamic data,(8) to calculate values of A from the conductivities. Values of these constants are summarized in Table 2, and were used to obtain the solid curves shown in Fig. 4. It can be seen from Table 2 that the value of q in region B ($\simeq$ 0·1 eV) is comparable with the values of α; and from Fig. 4 that the mobility term in equation (1) adequately accounts for the temperature dependence of conductivity for non-stoichiometric ferric oxide below 1000°K.

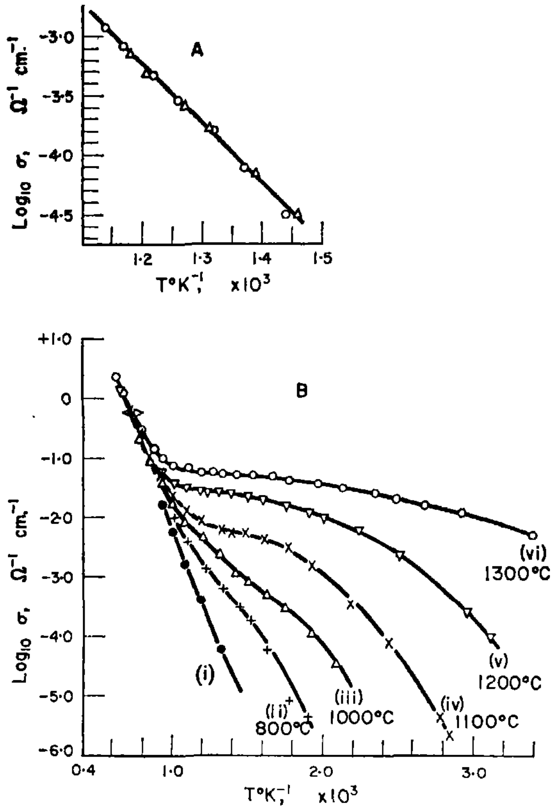

FIG. 3(A). The conductivity of an unfired compact of ferric oxide (Sample 2) between 400 and 600°C; temperature rising (○) and falling (△). 3(B). The influence of firing temperature on the conductivity of a compact of ferric oxide (Sample 2): (i) the unfired compact; (ii)–(vi) curves obtained for specimen quenched after 20 hr at the stated temperatures.

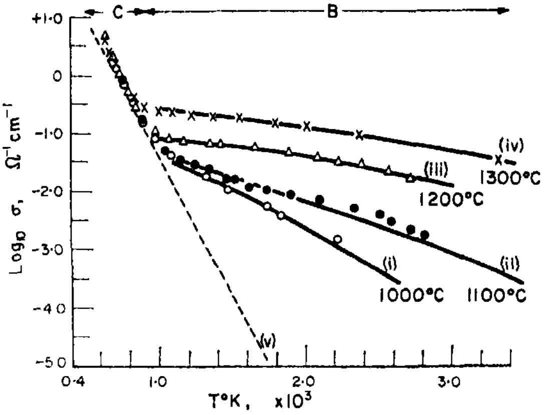

FIG. 4. The influence of firing temperature on the conductivity of ferric oxide from iron wire: specimen quenched after 5 hr at 1000°C (○); at 1100°C (●), at 1200°C (△) and at 1300°C (×);
— — — — impure specimens (best fit, see Ref. 12);
——— calculated from equation (1) using constants from Table 2.

The agreement between the experimental data and the calculated curves shown in Fig. 4 for oxidized iron wire justifies our assumption that re-oxidation during cooling was negligible. This was not the case for the oxide compact giving the curves shown in Fig. 3(B). Re-oxidation of this specimen during cooling is indicated by the more

Table 2. Conductivity constants for non-stoichiometric ferric oxide below about 800°C

Firing temperature (°C)	N_d* (cm^{-3}) calc	A* (cm^2 V^{-1} sec^{-1} °K)	α* (eV) exptl
1000	$4{\cdot}5\times10^{18}$	2270	0·31
1100	$1{\cdot}7\times10^{19}$	207	0·22
1200	$5{\cdot}5\times10^{19}$	44	0·13
1300	$1{\cdot}5\times10^{20}$	42	0·12
Fe_2O_3 +1·0 atom% Ti	4×10^{20}	232	0·10

* See equation (1).

pronounced curvature at lower temperatures and by the generally lower conductivities for a given firing temperature (cf. Fig. 4).

3.1.3. *Carrier formation at high temperatures: Region C.* We attribute the variation of conductivity with temperature in region C (800°C < T) primarily to changes in carrier concentration. Our results indicate that carriers are formed by a rapidly-equilibrated process common to all samples. Some of the carriers are negative and arise from loss of oxygen (as shown in Section 3.1.2), a process that probably equilibrates quite rapidly above 1000°C. Positive carriers also contribute to conduction in region C, as can be inferred from the positive Seebeck voltage in this temperature range.

We offer two reasons for believing that in region C carriers are formed by a rapidly-equilibrated process common to all samples. (a) Conductivity values for all specimens are very similar. This was shown for impure samples in Part 1 and can also be seen in Fig. 4 (compare curve (v) with the experimental points). The agreement between high-purity sintered compacts and oxidized wire can be seen in Fig. 1 by comparing curves (i)–(iii) with curve (iv); it is considered to be good in view of the very different cross-sectional areas—$\simeq 0{\cdot}05$ cm^2 and $\simeq 0{\cdot}001$ cm^2 respectively.

(b) Conductivity values in region C showed no polarization or time-dependence and were little affected by firing temperature. The small effect of firing temperature is most clearly seen in the results given in Fig. 4; the slight differences shown by the oxide compact (Fig. 3b) are attributed to sintering and grain growth (which occur at an appreciable rate in powder compacts above 1000°C).

Conduction in region C is mixed. Some negative carriers arise from oxygen loss, as was shown earlier. The presence of positive carriers is deduced from the Seebeck voltage.

3.2 *Seebeck voltage*

Values for the Seebeck voltage of ferric oxide specimens of high purity are shown as a function of temperature in Fig. 5, where the regions A, B and C are marked for reference to the fired specimens (curves (i) and (ii)). The behaviour of the Seebeck voltage of fired specimens is consistent with our earlier interpretation of these three temperature ranges. The Seebeck voltage in region A was found to be poorly reproducible from one specimen to another; this is reasonably attributed to grain boundary effects (see Section 3.1.1). Reproducibility as between specimens was generally better above 450°C. In region B the number of carriers is constant and equal to the number of quenched donors. This would lead one to expect a value of the Seebeck voltage independent of temperature;(13) the minima or inflections observed in the temperature range 600–900°K (Fig. 5, curves (i) and (ii)) are interpreted as indicating regions of constant carrier concentration.

In region C oxygen loss does not account for the positive carriers, whose presence is shown by the positive Seebeck voltage. Conduction is therefore mixed. The rapid decrease in Seebeck voltage observed in curve (i) (900–1200°K) and curve (ii) (1000–1300°K) in Fig. 5, and the subsequent change of sign from negative to positive are

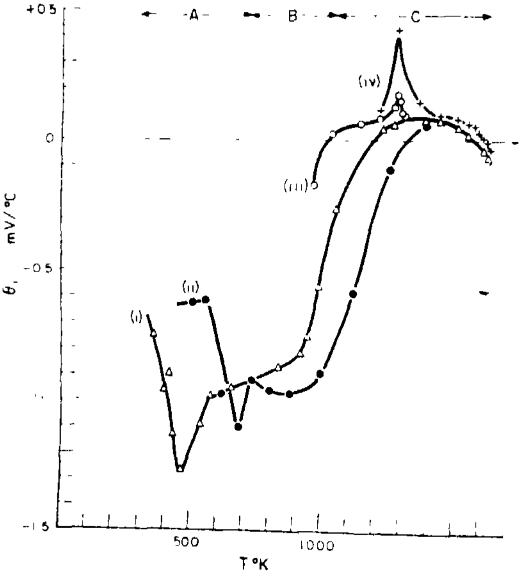

FIG. 5. The Seebeck voltage of high-purity ferric oxide as a function of temperature: (i) and (ii), fired specimens of Sample 1; (iii) and (iv) unfired specimens of Sample 2: (i) was obtained during slow cooling in air from 1364°C; (ii) was obtained with rising temperature for a specimen fired in oxygen at 1300°C; (iii) and (iv) were obtained for rising temperature.

attributed to an increase in the contribution of p-carriers to conduction, primarily due to an increase of p-carrier mobility (μ_p) over n-carrier mobility (μ_n). The further sign reversal from positive to negative between 1600° and 1640°K (Fig. 5, curves (i) and (iv)) is due to extensive loss of oxygen causing an increase in n-carrier concentration. It occurs at temperatures very close to that at which haematite decomposes to magnetite: 1653°K in air.

This interpretation is based on the following arguments. If carriers are present arising from oxygen loss (either quenched or equilibrated) then $p < n$ at all temperatures (p and n being respectively p-carrier and n-carrier concentrations); this is a necessary consequence of the requirements of electrical neutrality. A positive Seebeck voltage, then, implies that $\mu_p > n$. At lower temperatures in doped samples we found(12) that $\mu_p < \mu_n$; therefore the sign reversal at about 1100°K is attributed to mobility changes. There is evidence(12) that both μ_n and μ_p obey mobility equations of the form of the mobility term in equation (1); since the form of the equation does not predict a further change from $\mu_p > \mu_n$ to $\mu_p < \mu_n$ at higher temperatures, the second sign reversal, in the region of 1600°K, must be due to the n-carrier concentration exceeding that of p-carriers to an extent that outweighs the discrepancy in mobilities.

The above interpretation has further implications. First, when $n \simeq p$ the Seebeck voltage should change from negative to positive at a lower temperature and should show a higher positive value than when $n > p$. That this did in fact occur can be seen by comparing, in Fig. 5, curves (iii) and (iv) for unfired specimens, free from ferrous iron, with curves (i) and (ii) for fired specimens. Secondly, a specimen free from ferrous iron, maintained at a temperature where oxygen loss occurs at a detectable rate should show a value of the Seebeck voltage that becomes more negative with time. With an unfired compact of Sample 2 at 1300°K, it was found that the Seebeck voltage decreased from +0·17 mV/°C to a steady value of +0·09 mV/°C over a period of 2 hr.

4. A CONDUCTIVITY SCHEME FOR FERRIC OXIDE

Having drawn qualitative conclusions about the conduction mechanism it remains to place the conduction scheme on a quantitative basis.

4.1 *Nature and origin of the carriers*

It is generally accepted(2, 13) that in ferric oxide doped with titanium the negative carriers are electrons which move between ferric ions on equivalent lattice sites, in a manner analogous to that proposed(21) for magnetite. The donor centre in titanium-doped ferric oxide has been proposed as [Ti^{4+} Fe^{2+}].(11, 13) It is reasonable to identify the negative carriers in oxygen-deficient ferric oxide also as electrons on ferric ions. The nature of the donor centres is uncertain because it is not known whether non-stoichiometric ferric oxide contains oxygen vacancies or interstitial cations. If the former is the case the donor centres are probably ferrous ions associated with oxygen vacancies; if the latter, the centres may be ferrous ions on octahedral sites normally vacant, or on tetrahedral sites. It has been suggested(22) that ferrous ions on tetrahedral sites do not contribute to conduction; if this were so in haematite the ferrous content of a non-stoichiometric sample as determined by chemical analysis could exceed the value calculated from the conductivity.

Four possible origins of positive carriers in ferric oxide must be considered:

1. Ionic conduction.
2. Extrinsic processes.
3. Lattice disorder.
4. Electronic transition.

Ionic conduction is discounted for two reasons. First, the conductivity measurements showed no polarization effects. Second, the values of ionic mobilities, calculated from the diffusion coefficients for iron(23) and oxygen(24) by the Einstein relation, are so low that the maximum contribution available even if all the ions participated is 10^5 times smaller than the observed conductivity at 1300°C.

Extrinsic effects are discounted in the present specimens because of high purity of the material. They would appear to be unimportant at high temperatures even in impure specimens in view of the small influence of impurities on conductivity in region C (see Section 3.1.3).

Several types of lattice disorder are possible in ferric oxide, but only those involving oxygen vacancies are likely to lead to the formation of acceptor centres. Schottky disorder is a probable case, arising thus:

$$\text{Lattice} = 2\,\square_{\text{Fe}^{3+}} + 3\,\square_{\text{O}^{2-}} \qquad (2)$$

The cation vacancy ($\square_{Fe}{}^{3+}$) with three negative charges relative to the lattice could act as a donor centre, and the oxygen vacancy (with two positive charges) as an acceptor centre. The energy required for reaction (2), calculated from the activation energy for oxygen diffusion (by the method used by KINGERY(25) for alumina) is 6·4 eV, i.e. 1·07 eV per *n*–*p* pair. This value is comparable with the observed activation energy for conduction of about 1·0 eV in region C.

There are two objections to lattice disorder as a source of positive carriers. First, the conductivity values in region C were unaffected by the rate of cooling or heating. Second, attempts to quench acceptors into the lattice by rapid cooling of the specimens from the temperature region in which the Seebeck voltage is positive always resulted in a Seebeck voltage that was negative below 1000°K. This is not unambiguous evidence because of our earlier finding(12) that in doped samples below about 600°K *p*-carriers are less mobile than electrons. The ratio of mobilities is such that the concentration of *p*-carriers would have greatly to exceed that of the *n*-carriers for a specimen to show a positive Seebeck voltage.

Hole formation by an electronic transition is most likely to occur by one of the following processes:

$$Fe^{3+}+Fe^{3+} \rightarrow Fe^{2+}+Fe^{4+} \qquad (3)$$

or

$$Fe^{3+}+O^{2-} \rightarrow Fe^{2+}+O^{-} \qquad (4)$$

Neither process is free from objection. Holes on the cations (i.e. Fe^{4+}) may be expected to show low mobility with a positive temperature coefficient (as observed in *p*-type ferric oxide(12)) by analogy with electrons or cations (i.e. Fe^{2+}) but the calculated energy requirement(11) of 6·5 eV for process (3) seems prohibitively large. Hole formation by process (4) is indicated by two arguments. It is, presumably a necessary first step in the dissociative loss of oxygen. Furthermore, it has been postulated(26–29) as causing the intense absorption band at 25,000 cm^{-1} observed in the ferric oxide spectrum. This interpretation, based on spectroscopic data,(26) gives reasonable agreement between the thermal and optical values of the energy required for carrier formation. Thus the thermal value of 1·8 eV (obtained by analysis of the activation energy for conduction—see Section 4.3) can be compared with the optical value of 1·9–2·5 eV obtained from the position of the band edge in several spectra(2, 26–29) (see Fig. 6). The optical value for the energy of carrier formation usually exceeds the thermal value and the differences in the presence case are quite compatible with the energy of self-trapping of the carriers as indicated by the activation energies for carrier mobility (0·1–0·7 eV).

The main objection to identifying the positive carriers as holes in the 2*p* oxygen band is that such holes might be expected to have a low effective mass and high mobility whereas the carriers in *p*-type ferric oxide appear to have low mobility.(12) The argument for high mobility is based indirectly on the band width, which is believed to be 10–20 eV for the 2*p* band in oxides.(6, 30) No direct evidence exists as to the width of this band in ferric oxide. Since the absorption band at 25,000 cm^{-1} is thought to involve an oxygen 2*p* electron some measurements were made to determine its structure. The absorption spectra of several films of ferric oxide (0·04–0·15μ thick) showed the existence of two maxima at 25,500 cm^{-1} and 46,400 cm^{-1} (see Fig. 6) and subsidiary peaks at 19,200 31,700 and 39,000 cm^{-1}. A peak

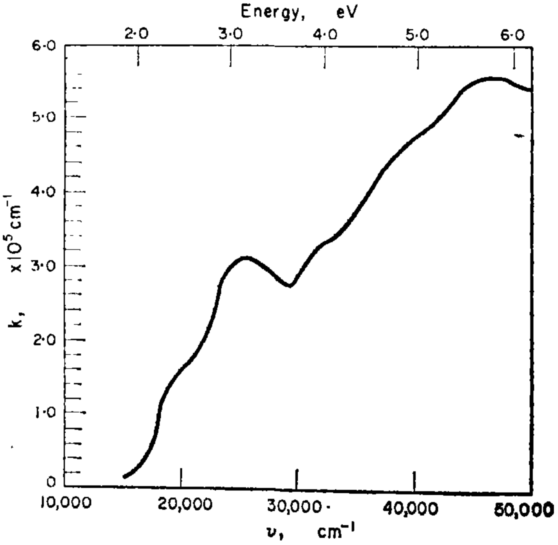

FIG. 6. The absorption spectrum of a film of ferric oxide (440 Å thick) on alumina.

(not shown) was also found at 11,800 cm^{-1}. The high values of the absorption coefficient indicate a charge transfer process as causing the bands at 25,500 and 46,400 cm^{-1}.

It can be seen from the spectrum shown in Fig. 6 that the width of the absorption band at 25,500 cm^{-1}, attributed(26) to process (4), would indicate an oxygen $2p$ band width of not more than 1–2 eV. In view of this and of the absence of contrary evidence as to the mobility of $2p$ holes the arguments in favour of process (4) are considered to outweigh the objections. Since the data for p-type ferric oxide indicate that the holes have a low mobility with a positive temperature coefficient the conduction scheme outlined below is based on the assumption of narrow bands for both holes and electrons, the density of states being given by the concentration of ions.

4.2 *Carrier concentrations*

The carrier concentration, N_d cm^{-3}, formed by oxygen loss can be calculated from the thermodynamic data obtained by SALMON.(8) The equation for the dissociation of ferric oxide given in that reference can be re-arranged to give

$$N_d = 3{\cdot}27\times10^{26}\cdot P_{O_2}^{-1/4}\cdot\exp(-2{\cdot}03/kT), \quad (5)$$

which for air becomes

$$N_d = 4{\cdot}79\times10^{26}\exp(-2{\cdot}03/kT) \quad (6)$$

In these equations P_{O_2} = oxygen partial pressure in atmospheres, k is in eV deg^{-1}, and it has been assumed that the mole fraction of haematite is equal to unity—this is justified for small deviations from stoichiometry.

Equation (6) gives the carrier concentration due to oxygen loss for specimens equilibrated with air. The actual value of N_d will depend on the history of the specimen and on the rate of equilibration; in quenched samples at lower temperatures it may exceed the value calculated from (6); it will probably also be influenced by cation impurities.

For carrier formation according to equation (4) we can write

$$np = K\exp(-E/kT) = N_c^2\exp(-E/kT) \quad (7)$$

where n and p are, respectively, the negative and positive carrier concentrations per cm^3. Following MORIN(2) and JONKER(13) we take K as N_c^2, where N_c is the number of cations per cm^3. E is the thermal energy required to transfer an electron from an oxygen ion to a ferric ion.

If carriers are formed both by oxygen loss and thermal excitation, charge neutrality must be maintained, according to the equation.

$$n-p = N_d \quad (8)$$

To calculate carrier concentrations from these equations we require a value for E. This is obtained from the activation energy for conduction, as described in the next Section.

4.3 *Analysis of the activation energy for conduction*

The experimental activation energy for conduction is given by:

$$q = \frac{-k\cdot d\log_e\sigma}{d(1/T)} \quad (9)$$

The interpretation of q depends on the conductivity scheme chosen.

In the present work there are three cases of interest:

Case 1. Intrinsic conduction, carriers arising only by thermal excitation according to equation (4);

Case 2. Carriers arising both by thermal excitation and by oxygen loss, which is assumed to be equilibrated (with air) at all temperatures;

Case 3. Above 1000°C carriers arise as in Case 2; below this temperature equilibration is slow and donors are frozen into the lattice; their concentration is taken as $N_d = 4\times10^{18}$ cm^{-3}.

Cases 1 and 3 are believed to correspond to stoichiometric and non-stoichiometric specimens respectively. Case 2 is unlikely to be valid at lower temperatures and is included to show the consequences of assuming equilibrated oxygen loss.

For all three cases

$$\sigma = ne\mu_n + pe\mu_p \quad (10)$$

Expressions for q have been obtained by combining equations (6)–(8) to give expressions for n and p in equation (10), followed by differentiation. They are as follows:

Case 1.

$$q = \frac{E}{2}+\frac{\alpha y+\beta}{y+1}-kT \quad (11)$$

Case 2.

$$q = \frac{2{\cdot}03\,(xy-x+1)}{(xy+x-1)(2x-1)} + \frac{E \cdot x(x-1)(y+1)}{(xy+x-1)(2x-1)} + \frac{\alpha xy+\beta(x-1)}{(xy+x-1)} - kT \qquad (12)$$

Case 3. Below 1000°C

$$q = \frac{E \cdot x(x-1)(y+1)}{(xy+x-1)(2x-1)} + \frac{\alpha xy+\beta(x-1)}{(xy+x-1)} - kT \qquad (13)$$

Above 1000°C, q is given by equation (12).

In these equations $y = \mu_n/\mu_p$ and $x = n/N_d$; both are functions of temperature: α and β are the activation energies in the mobility term in equation (1) for electron and hole mobility respectively.

It is clear from equations (12)–(14) that a value of E is most simply obtained from q under conditions where conduction is intrinsic. This condition was most closely approached by an unfired compact of oxide Sample 2. Values of σ for an unfired compact are shown in Fig. 3(A). There producibility of results for conditions of rising and falling temperature was taken as evidence that no carrier contribution was introduced by oxygen loss during the run. These results gave $q = 1{\cdot}0$ eV. Substitution of this value into equation (11), taking $\alpha = 0{\cdot}1$ eV, $\beta = 0{\cdot}69$ eV and $y = 9{\cdot}9$ at 500°C (see Section 4.4), gave $E = 1{\cdot}8$ eV. Thus equation (7) for intrinsic carrier formation becomes

$$np = 1{\cdot}56\times 10^{45} \exp(-1{\cdot}8/kT) \qquad (14)$$

The value of 1·8 eV for E obtained from conductivity measurements lies close to the values 1·9–2·5 eV obtained from optical data for the electronic transition shown in equation (4), as discussed earlier.

The carrier concentrations for the three cases listed above can now be calculated using equations (6), (8) and (14). The values are shown in Fig. 7(A); the reduction in p (relative to the intrinsic Case 1) by carrier formation due to oxygen loss can be clearly seen from these curves.

Values of q were also calculated taking $\alpha = 0{\cdot}1$ eV, $\beta = 0{\cdot}69$ eV, and using values of y from the mobility expressions in Section 4.4; they are plotted in Fig. 8(C). The curves illustrate two features of interest in the present models. The first concerns the effect of assuming equilibrated oxygen loss on the value of q for the intrinsic case (cf. curves *a–b* and *a–c*, Fig. 8(C); below 800°C the effect is negligible; between 800° and 1150°C q is lowered; and above 1150°C q rises towards the value for oxygen loss (2·03 eV). Secondly, *Case* 3 (curve *d–c*, Fig. 8(C)) shows that the temperature of the break in the conductivity curve between regions B and C (at about 800°C, cf curve (i), Fig. 1), when q rises from about 0·1 to about

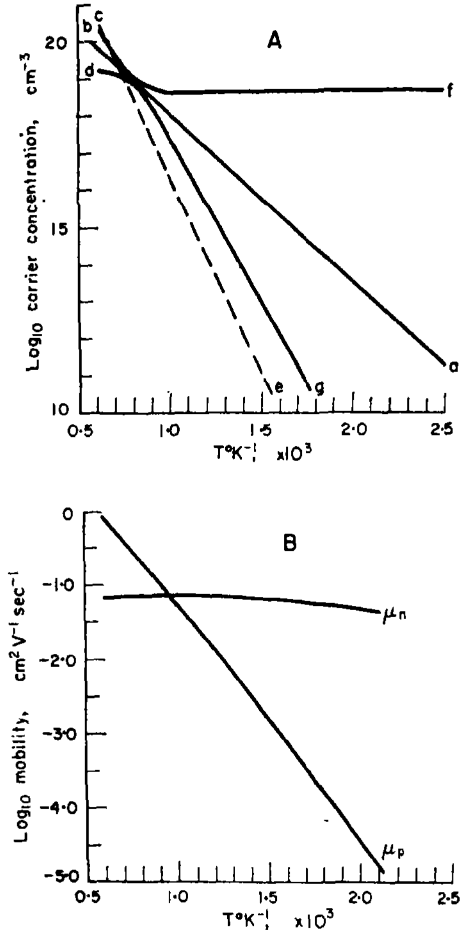

FIG. 7. Calculated values of carrier concentration (A) and mobility (B) for ferric oxide, as functions of temperature. (A): Values of n for Case 1 (a–b), Case 2 (a–c) and Case 3 (f–c); values of p for Case 1 (a–b), Case 2 (a–d) and Case 3 (g–d); values of N_d for Case 2 (e–c). (B): Values of μ_n and μ_p from equations (15) and (18).

1·0 eV, is not determined by the temperature at which equilibrium is frozen (assumed in the model to be 1000°C); it is rather the temperature at which the carrier contribution from the electronic transition becomes of comparable importance with the quenched donor contribution. This can also be seen from Fig. 7(A) and would explain the observed insensitivity of the break temperature in such curves as (i) and (ii), Fig. 1, to the rate of cooling. In this respect Fe_2O_3 differs from NiO(18) for which the break in the conductivity curve corresponds with the freezing of equilibrium and is very sensitive to cooling rate.

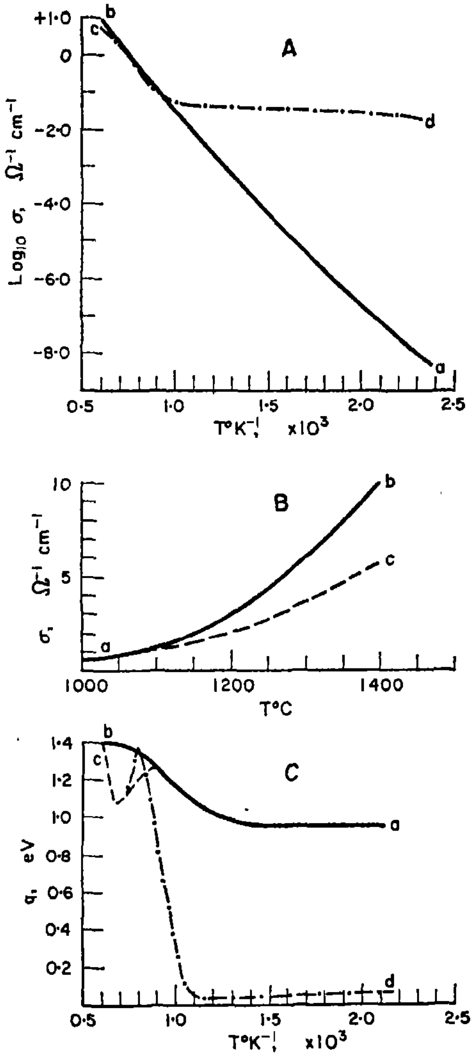

FIG. 8. Calculated values of σ (A) and (B) and q (C) in ferric oxide, as functions of temperature:
(A): Case 1, curve a–b; Case 2, curve a–c; Case 3, curve d–c.
(B) Case 1, curve a–b; Cases 2 and 3, curve a–c.
(C): Case 1, curve a–b; Case 2, curve a–c; Case 3, curve d–c.

4.4 *Carrier mobility*

To calculate the conductivity (σ) and Seebeck voltage (θ) of ferric oxide from the carrier concentrations obtained in the last Section we need mobility values for both electrons and holes. For n-carrier mobilities we have used the expression(12) derived for mobilities in ferric oxide containing 1·0 at.% titanium, viz:

$$\mu_n = \frac{232}{T}\exp(-0{\cdot}1/kT) \tag{15}$$

This assumption is probably an approximation. We found earlier (Section 3.1.2, Table 2) that A and α in equation (1) are functions of carrier concentration. Since the form of this function is unknown, this dependence has been neglected in the present calculations.

Values of μ_p were calculated from the ratio μ_n/μ_p at two temperatures at which $\theta = 0$: 1040°K for an unfired specimen, and 1624°K for an equilibrated specimen (curves (iii) and (iv), Fig. 5). Values of μ_n were calculated from equation (15).

At 1040°K: $n \simeq p$; $\mu_n = \mu_p = 0{\cdot}073$ cm^2 V^{-1} sec^{-1}.

At 1624°K: $\theta = 0$ but $n \neq p$ because of carriers arising from oxygen loss:

$$\sigma_n\,\theta_n = \sigma_p\,\theta_p \tag{16}$$

$$\frac{\mu_n}{\mu_p} = \frac{p\theta_p}{n\theta_n} \tag{17}$$

Values of n and p were calculated from the equations of Sections 4.2 and 4.3; from these values the position of the Fermi level, $E_F = -0{\cdot}70$ eV, was obtained. From this, approximate values of θ_p and θ_n were obtained (see Section 4.5). It was found that $\mu_p = 10{\cdot}75 \times \mu_n = 0{\cdot}75$ cm^2 V^{-1} sec^{-1}. Since it was earlier shown(12) that p-carriers probably obey a mobility equation of the form of equation (1), these values of μ_p were used to obtain the expression

$$\mu_p = \frac{1{\cdot}73\times 10^5}{T}\exp(-0{\cdot}69/kT) \qquad (18)$$

Values of μ_n and μ_p from equations (15) and (18) are shown in Fig. 7(B).

4.5 *Calculation of conductivity and Seebeck voltage*

Values of the conductivity for the three cases listed in Section 4.3 (intrinsic, oxygen equilibrated and quenched donors) were calculated from equation (10), using the carrier concentrations and mobilities shown in Fig. 7.

The results are shown in Figs 8(A) and (B). Two points should be noted. First, in the absence of quenched donors the conductivity below 1000°C is that for the intrinsic case, even if oxygen loss is equilibrated. Second, above 1000°C the consequence of oxygen loss is to reduce the conductivity relative to the intrinsic case; this can be seen more clearly in Fig. 8(B). Thus the model predicts that above 1000°C the conductivity should increase with increasing oxygen pressure, because electrons are replaced by more mobile holes.

The Seebeck voltage for mixed conduction is given by

$$\theta = \frac{\sigma_n\theta_n+\sigma_p\theta_p}{\sigma} \qquad (19)$$

where θ_n and θ_p are contributions from *n*- and *p*-carriers. The greatest part of θ_n comes from the energy difference between the Fermi level and the bottom of the conduction band; and of θ_p from the difference between the Fermi level and the top of the valence band. We have therefore neglected kinetic[13] and other[31] contributions and have calculated θ_n and θ_p from the equations[13]

$$\theta_n \simeq E_F/eT \qquad (20)$$

$$\theta_p \simeq (1{\cdot}8+E_F)/eT \qquad (21)$$

where E_F is the position of the Fermi level in eV relative to the bottom of the conduction band, $e = 1{\cdot}0$ and θ is given in V deg K^{-1}. The values of E_F were obtained from the equation.[32]

$$n = N_c\exp(E_F/kT) \qquad (22)$$

(where N_c is the number of cations per cm^3) and are shown in Fig. 9(A).

The calculated curves for the Seebeck voltage are shown in Fig. 9(B) for the three cases defined in Section 4.3. As was found for the conductivity, the influence of equilibrated oxygen loss is marked only at high temperatures; that of frozen donors is significant at lower temperatures. Comparison of Fig. 9(B) with Figs 7(A) and (B) makes it clear that the first sign reversal in curve d–c of Fig. 9(B), is primarily due to mobility changes, and the second to changes in carrier concentration (see Section 3.2).

4.6 *Comparison with experiment*

Calculated and experimental curves for conductivity are shown in Fig. 10(A), and for Seebeck voltage in Fig. 10(B). It can be seen from these curves that the assumptions of Case 3 (oxygen loss

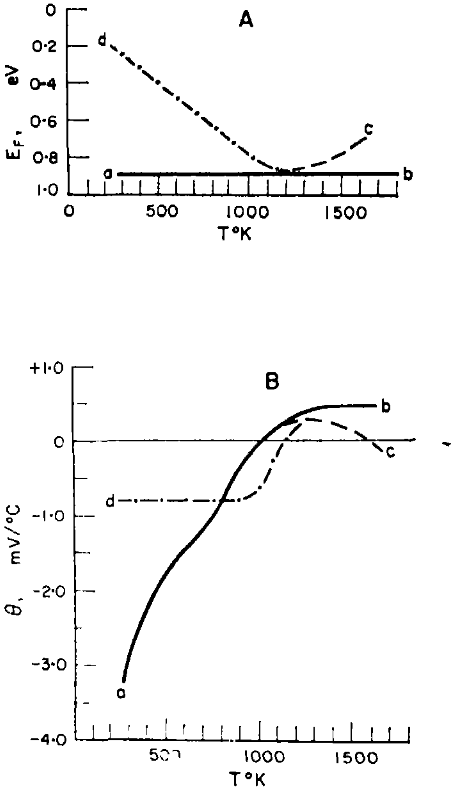

FIG. 9. Calculated values of the Fermi level (A) and the Seebeck voltage (B) for ferric oxide, as functions of temperature: Case 1, curves a–b; Case 2, curves a–c; Case 3, curves d–c.

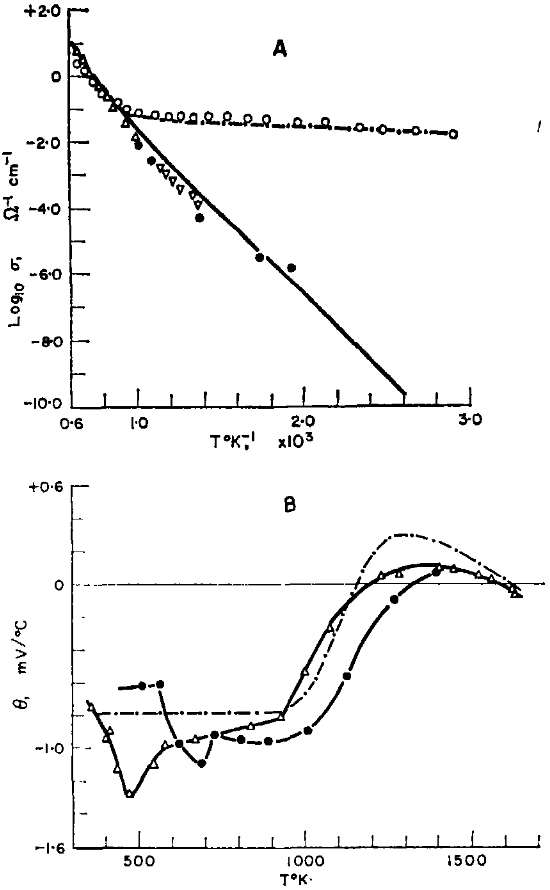

FIG. 10. Comparison of experimental and calculated values of conductivity (A) and Seebeck voltage (B) for ferric oxide, as functions of temperature:

A. ○ specimen of oxide Sample 2, fired in air at 1300°C and rapidly quenched:
△, ▽, ● unfired specimens of oxide Sample 2;
——— calculated for Case 1 and 2
—·—·—· calculated for Case 3
B. △, ● fired specimens (from Fig. 5)
—·—·—· calculated for Case 3.

equilibrated above 1000°C, quenched donors below 1000°C) account closely for the behaviour of fired compacts; and that the conductivity of unfired specimens most closely resembles intrinsic behaviour (Case 1). We conclude that the conductivity scheme for ferric oxide outlined above is substantially correct.

The scheme will also explain the apparently conflicting observations reported in the literature on the effects of oxygen partial pressure on the conductivity of ferric oxide. WAGNER and KOCH(1) reported that the conductivity of ferric oxide at 1000°C was constant over the range of oxygen partial pressure from 0·21 atm. to $3{\cdot}6\times10^{-3}$ atm. BEVAN, SHELTON and ANDERSON(10) found that between 400 and 700°C the conductivity increased with decreasing partial pressure of oxygen in the range 0·21 atm to $1{\cdot}3\times10^{-8}$ atm. In Table 3 it is possible to compare the experimental conductivity values given by these authors with values calculated from Case 2. It can be seen that the present scheme predicts only a small change (8 per cent) at 1000°C, and a more pronounced change (20 per cent) for the extremes of oxygen pressure at 700°C. The observed effect of oxygen partial pressure in the latter case(10) is much greater than the calculated; this is probably due to the oxide specimen being impure (which we infer(12) from the linearity of the conduction curve).

The insensitivity of σ to oxygen partial pressure at about 1000°C arises because changes in N_d are "buffered" by the contribution from the electronic transition. At lower temperatures this contribution is smaller and the effects of changes in N_d are more readily observed.

CONCLUSIONS

The conductivity and Seebeck voltage of ferric oxide of high purity can be quantitatively

Table 3. The effect of oxygen partial pressure on the conductivity of ferric oxide

Temperature (°C)	Oxygen partial pressure (atm)	$\sigma(\Omega^{-1}\,cm^{-1})$ exptl	calc
1000 (Ref. 1)	0·21	0·5	0·50
	$3{\cdot}6\times10^{-3}$	0·5	0·46
700 (Ref. 10)	0·21	0·00235	0·0160
	$1{\cdot}32\times10^{-6}$	0·0163	0·0167
	$1{\cdot}32\times10^{-8}$	0·0404	0·0200

explained by a conduction scheme which postulates that carriers arise both by oxygen loss at high temperatures and by an intrinsic electronic transition. This transition is believed to give rise to holes in the 2*p* oxygen band. The low mobility of these positive carriers indicates this band to be narrow, a conclusion that is supported by spectral data. The conduction scheme will explain the apparently conflicting observations reported in the literature on the effects of oxygen partial pressure on the conductivity of ferric oxide, and leads to the prediction that the conductivity should *increase* with increasing oxygen partial pressure at temperatures above about 1000°C.

Acknowledgements—We are greatly indebted to Dr. P. A. Albert (Westinghouse Research Laboratories, Pittsburgh, Pennsylvania) for the gift of the single crystal, and to Miss L. S. Souter (A.E.I. Research Laboratories, Harlow, Essex) for helpful discussion. Johnson, Matthey and Co., supplied the iron wire and the ferric oxide powders, and their spectrographic analyses.

This work forms part of the research programme of Warren Spring Laboratory and is published by permission of the Director.

REFERENCES

1. Wagner C. and Koch E., *Z. phys. Chem.* **B32,** 439 (1936).
2. Morin F. J., *Phys. Rev.* **83,** 1005 (1951); **93,** 1195 (1954).
3. Grunewald H., *Ann. Phys. Lpz.* **14,** 129 (1954).
4. Kittel C., *Solid State Physics*, 2nd ed. p. 349. Wiley, New York (1959).
5. Kingery W. D., *Introduction to Ceramics*, 1st ed., p. 667. Wiley, New York (1960).
6. Morin F. J., *Semiconductors, Amer. chem. Soc. Monograph* **140,** (edited by Hannay N. B.), p. 600. Reinhold, New York (1959).
7. Verwey E. J. W., Haaijman P. W., Romeijn F. C. and van Oosterhout G. W., *Philips res. Rep.* **5,** 173 (1950).
8. Salmon O. N., *J. phys. Chem.* **65,** 550 (1961).
9. Meyer W. and Neldel H., *Z. tech. Phys.* **12,** 588 (1937).
10. Bevan D. J. M., Shelton J. P. and Anderson J. S., *J. chem. Soc.* 1729 (1948).
11. Jonker G. H., *Proc. Conf. on Semiconductor Physics, Prague* 1960, p. 864. Academic Press, New York (1961).
12. Gardner R. F. G., Sweett F. and Tanner D. W., *J. Phys. Chem. Solids*, **24,** 1175 (1963).
13. Jonker G. H. and van Houten S., *Halbeiterprobleme* **6,** p. 118. Vieweg, Braunschweig (1961).
14. Clark L. J., *Analyt. Chem.* **34,** 348 (1962).
15. Gardner R. F. G. and Tanner D. W., *Nature, Lond.* **190,** 1161 (1961).
16. Suchet J., *J. Phys. Radium*, **18,** 10A (1957).
17. Haayman P. W., Haanstra H. B., van Oosterhout G. W. and Bol A., *Dutch Patent* 83982 (1957); *Chem. Abs.* **52,** 12630a (1958).
18. Richards R. G. and White J., *Trans. Brit. ceram. Soc.* **53,** 233 (1954).
19. Mitoff S. P., *J. chem. Phys.* **35,** 882 (1961).
20. Hagel W. C. and Seybolt A. U., *J. electrochem. Soc.* **108,** 1146 (1961).
21. Verwey E. J. W. and de Boer J. H., *Rec. Trav. chim. Pays-Bas* **55,** 531 (1936).
22. Verwey E. J. W., Haayman P. W. and Romeijn F. C., *J. chem. Phys.* **15,** 181 (1947).
23. Himmel L., Mehl R. F. and Birchenall C. E., *J. Metals* **5,** 827 (1953).
24. Kingery W. D., Hill D. C. and Nelson R. P., *J. Amer. ceram. Soc.* **43,** 473 (1960).
25. Oishi Y. and Kingery W. D., *J. chem. Phys.* **33,** 480 (1960).
26. Wickersheim K. A. and Lefever R. A., *J. chem. Phys.* **36,** 844 (1962).
27. Bailey P. C., *J. appl. Phys.* **31,** 39S (1960).
28. Clogston A. M., *J. appl. Phys.* **31,** 198 S (1960).
29. Vernon R. C., *J. appl. Phys.* **33,** 2140 (1962).
30. Mott N. F. and Gurney R. W., *Electronic Processes in Ionic Crystals*, 2nd ed. p. 74. Oxford University Press, London (1940).
31. Aronson S., Rulli J. E. and Schauer B. E., *J. chem. Phys.* **35,** 1382 (1961).
32. The analysis in this section follows the treatment for semiconductors given by Smith R. A., *Semiconductors*, p. 74. Cambridge University Press (1959).

J. Phys. Chem. Solids Pergamon Press 1963. Vol. 24, pp. 1197–1202. Printed in Great Britain.

THE PHASE DIAGRAM OF PLUTONIUM*

D. R. STEPHENS

University of California, Lawrence Radiation Laboratory, Livermore, California

(*Received* 18 *March* 1963)

Abstract—The pressure dependence of the phase transitions of plutonium, including melting, has been measured to 35 kbars. The phase transitions were detected by differential thermal analysis and by volume discontinuity. Three triple points were detected, the γ–δ–ϵ, γ–ϵ-liquid, and β–γ-liquid. The technique was not sufficiently sensitive to detect the δ–δ' transition, and thus the γ–δ–δ' triple point was not determined.

INTRODUCTION

PLUTONIUM is a very interesting element, not only due to its nuclear properties, but also due to its large number of polymorphic transitions. Thus, in spite of its hazardous nature, a great deal of work has been done on its physical properties. Several excellent reviews of the literature are available.(1, 2, 3) As a result of this previous work, the one-atmosphere phases are well known. Solid plutonium exists in six phases, designated α, β, γ, δ, δ', and ϵ. The transformation temperatures suggested by WILKINSON(1) are shown in Table 1. The crystal structures of the phases are known and have been summarized by ZACHARIASEN.(4)

Table 1. *One-atmosphere transition temperatures of plutonium*

Transition	Temperature, °C
α–β	119 ± 2
β–γ	206 ± 3
γ–δ	319 ± 5
δ–δ'	451 ± 9
δ'–ϵ	476 ± 5
ϵ-liquid	639·5 ± 2

The α–β transition has been studied at high pressure by two previous investigators. BRIDGMAN(5) studied the α–β transition to 7000 kg/cm^2 and also measured the room-temperature compressibility of Pu to 100,000 kg/cm^2. McWHAN *et al.*(6) measured the α–β transition to 18 kbar.† The object of the present work was to extend the study of plutonium phase transitions at high pressures to the other transitions, including melting.

EXPERIMENTAL METHOD

Most of the data were obtained by differential thermal analysis (DTA). Some data at lower pressures were obtained by volume discontinuity.

Differential thermal analysis (DTA)

Figure 1 shows the apparatus used for DTA runs. The high pressure die consisted of a tungsten carbide core and a hardened steel support ring. The die bore was 0·5005-in. to admit the 0·500-in. tungsten carbide piston. The sample assembly is similar to that used by BOYD and ENGLAND(7) and KENNEDY and NEWTON,(8) thus it will be only briefly described. A graphite furnace, insulated from the sample by boron nitride, was used to provide internal heat. The plutonium sample, 0·095 in. dia. by 0·125 in. long, was enclosed in a tantalum capsule which was in contact with the Chromel P and Alumel DTA thermocouple. Talc was used to insulate the furnace from the die and to act as the pressure transmitting medium. The talc cylinder was wrapped with lead foil to reduce

---

* Work performed under Contract No. W-7405-eng-48.

† 1 atm = 1·013 bar = 1·033 kg/cm^2. The kbar is now the standard unit for high pressure research.

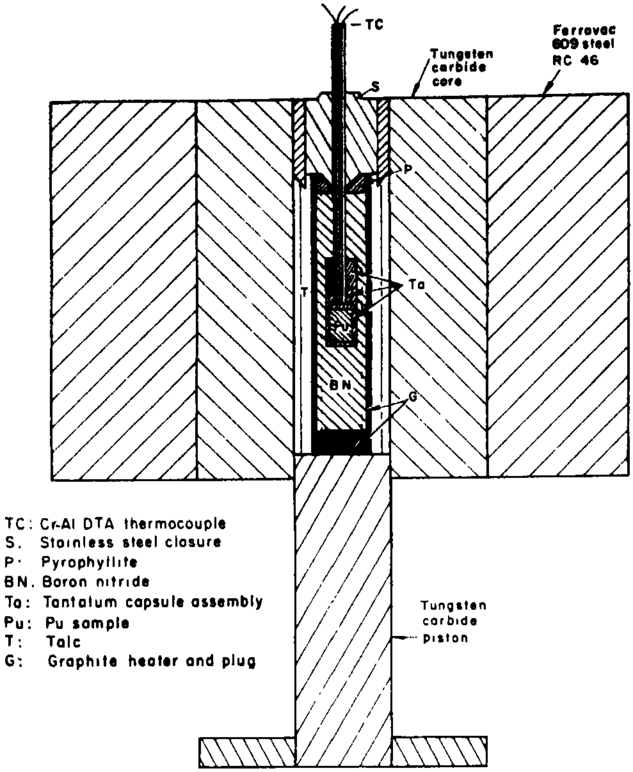

FIG. 1. High pressure apparatus for differential thermal analysis (DTA).

friction. Closure of the die was effected by a stainless steel power lead with a $\frac{1}{16}$-in. hole to admit the thermocouple and insulation. The power lead was insulated from the die with a pyrophyllite sleeve.

The thermocouple and DTA signals were recorded by a Brown X_1, X_2 double-pen recorder. The working parts of the press were contained in a glove box maintained under an argon atmosphere so that the plutonium and high pressure components were completely contained in an inert atmosphere. The assembly of the sample and components was also done in this box.

In taking data, the sample was kept at constant pressure while the temperature was raised smoothly until a transition was detected. Then the heat was discontinued. Actually, the pressure rises slightly during heating, but this effect was small and was easily corrected.

The next step was to determine any necessary corrections to the indicated pressure due to the heating cycle. A hysteresis loop at room temperature of piston displacement vs. pressure was obtained, using displacement gauges accurate to ± 0·0001 in. This established the friction, as described by BRIDGMAN,(9) and thus the true displacement vs. pressure was determined for the sample assemblies at room temperature. Essentially the friction was taken as one-half the difference in pressure at constant displacement of the ascending and descending loops. The "backlash" of the initial portion of the descending loop was neglected.

The displacement was measured at constant pressure for the sample assemblies undergoing the same heating cycle as for a run. The displacement for a given maximum temperature, such as 500°C, was noted for several pressures. Displacement vs. pressure curves were thus obtained for maximum temperatures of 100, 300, 500 and 700°C. These curves, corrected for friction, were compared with the true curve obtained at room temperature. It was assumed that the two curves should match and that if they did not, pressure corrections were necessary. It was found that the corrections were negligible. The effect of rapid internal heating was small, at least to 700°C. The expansion of the sample assembly showed up as effectively raising the pressure in the die.

Volume discontinuity

Figure 2 shows the die used for volume discontinuity measurements. The diameters of the samples were similar to those for DTA; the bore of the die was 0·105 in. The samples were not enclosed in any matrix for these runs. The die was made of Vascoloy Supreme steel, RC 48, with a Mo liner. Mo rings and wafers were used to contain the plutonium and to isolate it from the tungsten carbide piston. Thus only Mo was in contact with plutonium. The die was externally heated by a resistance winding. A plot of temperature vs. displacement was obtained on an X–Y recorder. The temperature was measured with a Chromel P and Alumel thermocouple, and the displacement with a linear differential transformer. A transition was noted as a break in the slope of the curve, not as a clean discontinuity, so that the actual magnitude of the volume change was not obtained. This apparatus was calibrated similarly to the DTA and was used only for lower pressure data.

Data reduction

The temperature quoted were not corrected for any pressure effect. The effects are not known at present for the pressure–temperature range covered in these experiments, but are probably small for Cr–Al thermocouples.(10, 11)

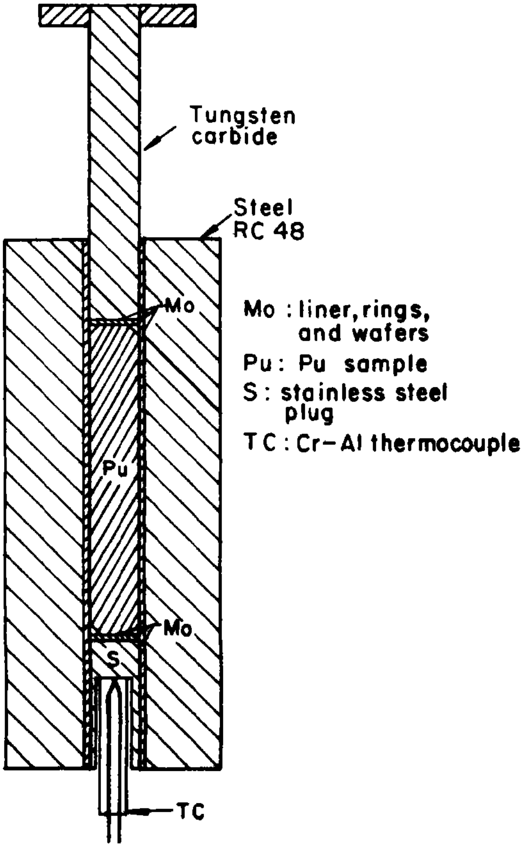

FIG. 2. High pressure apparatus for volume discontinuity.

One serious problem was encountered during data reduction. LEE and MARDON,[12] among others, have reported that the α–β and β–γ transitions are very sensitive to heating rates while the others are less affected. Our results also show this. The data for the α–β and β–γ transitions did not extrapolate to the correct temperatures at 1 atm, while the other transitions did. This phenomenon was due, at least in part, to the very rapid heating rates used. The rapid rates, about 7°C/sec, were necessary to obtain sharp DT signals.

During all runs an attempt was made to keep the heating rate constant for all transitions and to keep it as low as possible. No data were plotted for extremely fast heating rates. However, sufficient data were obtained on the effect of heating rate on the transitions at various pressures so that proper corrections could be made. These data, although rough, showed that the sensitivity of transition temperatures of the α–β and β–γ transitions decreases approximately linearly from its maximum effect at 1 atm to zero at 20 kbar. Above 20 kbar the transitions seemed unaffected by heating rate. This result was used to correct the temperatures in the following manner. The temperature correction to force the experimental data to fit the correct 1-atm values was decreased linearly from its maximum value at 1 atm to zero at 20 kbar. The errors introduced by this method are discussed later.

Samples

Plutonium samples of 99·85% purity, obtained from Dow Chemical Company at Rocky Flats, Colorado, and of 99·93% purity, obtained from Los Alamos Scientific Laboratory, were used in this work. Data obtained with both types agreed within experimental error.

RESULTS AND DISCUSSION

The experimentally derived phase diagram for plutonium is shown in Fig. 3. The results shown represent the data from seven DTA runs and two volume discontinuity runs. Data of BRIDGMAN[5] and MCWHAN *et al.*[6] are included for comparison. Our methods were not sensitive enough to detect the δ–δ' transition. No new phases were observed. The triple point data and initial slopes of the transitions are shown in Table 2, where some predicted values of LOASBY[13] are also shown for comparison.

The higher pressure data are believed to be accurate to ± 1 kbar and the lower pressure data to ± 0·2 kbar. The pressures could be read to

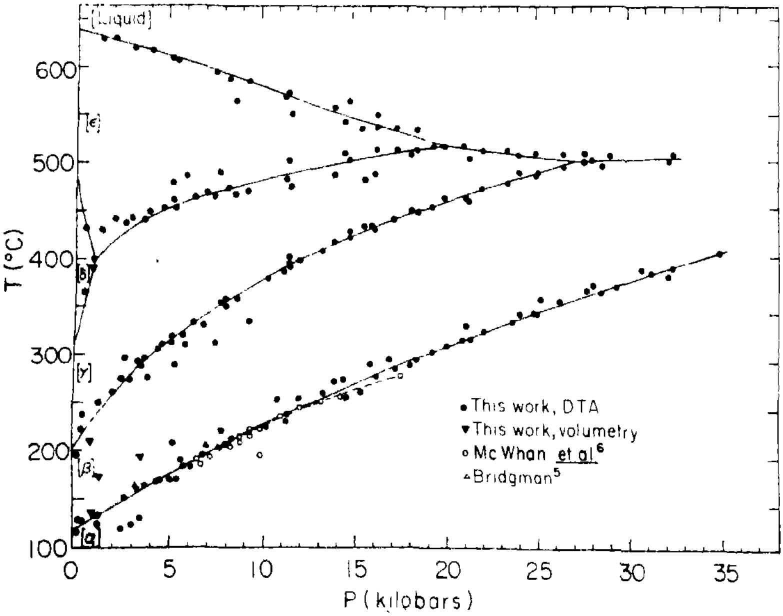

FIG. 3. The phase diagram of plutonium.

Table 2. Triple points and initial transition slopes

Triple point	Experimental values	Predicted by LOASBY(13)
γ–δ–ϵ	398 ± 10°C 0·9 ± 0·2 kbar	374°C 0·69 kbar
γ–ϵ-liquid	518 ± 10°C 19·5 ± 1 kbar	
β–γ-liquid	500 ± 10°C 27·0 ± 1 kbar	

	Initial slope of transition lines, °C/kbar	
Transition	Experimental slope	Predicted by LOASBY(13)
α–β	11·2	13·1
β–γ	27·3	38
γ–δ	88	95
δ–ϵ	−87	~ −190
ϵ-liquid	−4·4	−26

± 0·5 per cent and the reproducibility of the higher pressure data was within ± 0·5 kbar. However, due to the uncertainties of the actual degree of hydrostaticity of the talc and sample assembly, an error of ± 1 kbar seemed more realistic.

The temperatures were reproducible to ± 10°C. There seemed to be no corrosion or alloying of the Pu on the Ta capsule. The temperatures are believed accurate to ± 10°C with the exception of the β–γ transition, which is believed accurate to ± 20°C. The maximum temperature mentioned previously to correct the α–β transition data was 21°C, but the maximum correction for the β–γ transition was 53°C. If the correction taken was not truly linear, this could introduce a much larger error in the β–γ transition than indicated, hence an error of ± 20°C is assigned.

LOASBY(13) has predicted the initial slopes of the transitions and the location of several triple points. It may be seen that the predicted γ–δ–ϵ triple point agrees with the experimental values almost within experimental error. However, above 1 kbar the predictions break down, as β–γ–ϵ and β–ϵ-liquid triple points are predicted which did not occur experimentally. This is probably due to the assumption of the $\Delta V/\Delta H$ in the Clapeyron equation remaining constant to high pressures.

Data of previous investigators on the α–β transition seem to agree with the present work within the combined experimental error. BRIDGMAN's(5) data at 3100 and 7060 kg/cm^2 lie about 10°C above the equilibrium line in Fig. 3. The data of McWHAN *et al.*(6) agree well with the present work to 10 kbar but are about 14°C lower at 17·5 kbar.

The slope of the melting curve is negative until the β–γ-liquid triple point is obtained. From this point on the slope is positive. This is in qualitative agreement with the behavior of many other metals with a negative initial melting curve. Eventually a solid–solid–liquid triple point is met, after which the melting slope becomes positive. Examples of this include Bi,(14–16) Ga,(14, 17) Sb(8) and InSb.(18)

Some metastability of the α–β transition was noted, in agreement with the reports of many workers. The metastability seemed to decrease sharply with increasing pressure, however, as no such signals were detected over 10 kbar.

Acknowledgements—I wish to express sincere appreciation to Mr. EBEN LILLEY who assisted in the design and execution of this experiment and participated in all data runs. I would also like to thank Dr. WILLIAM RAMSEY for allowing us to use many experimental facilities and for critically reviewing the manuscript. The work was done under the auspices of the U.S. Atomic Energy Commission.

REFERENCES

1. WILKINSON W. D. (editor), *Plutonium and its Alloys.* Interscience, New York (1960).

2. Grison E., Lord W. B. H. and Fowler R. D. (editors), *Plutonium 1960*. Cleaver-Hume, London (1961).
3. Coffinberry A. S. and Miner W. H. (editors). *The Metal Plutonium*, University Press, Chicago (1961).
4. Zachariasen W. H., *The Metal Plutonium* (edited by Coffinberry A. S. and Miner W. M.), p. 99. University Press, Chicago (1961).
5. Bridgman P. W., *J. appl. Phys.* **30,** 214 (1959).
6. McWhan D., Montgomery P. W., Stromberg H. D. and Jura G., *J. phys. Chem.* (to be published Fall, 1963).
7. Boyd F. R. and England J. L., *J. geophys. Res.* **65,** 741 (1960).
8. Kennedy G. C. and Newton R. C., *Solids Under Pressure* (edited by Paul W. and Warschauer D. M.) p. 163. McGraw-Hill, New York (1963).
9. Bridgman P. W., *Proc. Amer. Acad. Arts Sci.* **74,** 21 (1940).
10. Birch F., *Rev. sci. Instrum.* **10,** 137 (1939).
11. Bundy F. P., *Progress in Very High Pressure Research*, p. 256. Wiley, New York (1960).
12. Lee J. A. and Mardon P. G., *The Metal Plutonium* (edited by Coffinberry A. S. and Miner W. H.) p. 99. University Press, Chicago (1961).
13. Loasby R. G., *Plutonium 1950* (edited by Grison E., Lord W. B. H. and Fowler R. D.) p. 97. Cleaver-Hume, London (1961).
14. Bridgman P. W., *Phys. Rev.* **48,** 893 (1935).
15. Butuzov V. P., *Sov. Phys. Cryst.* (English translation) **2,** 533 (1957).
16. Bundy F. P., *Phys. Rev.* **110,** 314 (1958).
17. Jayaraman A., Klement W., Jr., Newton R. C. and Kennedy G. C., *J. Phys. Chem. Solids* **24,** 7 (1963).
18. Jayaraman A., Newton R. C. and Kennedy G. C., *Nature, Lond.* **191,** 1288 (1961).

J. Phys. Chem. Solids Pergamon Press 1963. Vol. 24, pp. 1203–1206. Printed in Great Britain.

FERROMAGNETIC NUCLEAR RESONANCE IN COBALT NUCLEI IN STACKING FAULTS AND TWINS

LOUIS E. TOTH and S. FREDERICK RAVITZ

Department of Mineral Technology, University of California, Berkeley

(*Received* 14 *January* 1963)

Abstract—The ferromagnetic nuclear resonances in Co^{59} that occur intermediate in frequency between the resonance frequencies for the hexagonal and f.c.c. phases are identified as coming from nuclei in stacking faults and twins. A method is described whereby the resonance frequencies from nuclei in non-equivalent close-packed planes within a stacking fault can be calculated. The calculated frequencies are in good agreement with the experimental results. The experimental data indicate that intrinsic stacking faults are more prevalent than are extrinsic stacking faults and twins in cobalt.

THE ferromagnetic nuclear resonance in cobalt at room temperature occurs at 221·0 Mc/s for the hexagonal phase and at 213·1 Mc/s for the face-centered cubic phase. Additional resonances occur at 215·5, 217·0, 218·4, 221·0, and 223·0 Mc/s, as shown in Fig. 1. HARDY[(1)] has suggested that the resonances at 215 and 218 Mc/s originate from nuclei in stacking faults in the f.c.c. phase and that the resonance at 223 Mc/s is associated with the hexagonal phase. By cold-working or by alloying, we have prepared samples containing increased amounts of the hexagonal phase and have noted that the intensity of the resonance at 223 Mc/s has tended to increase, in agreement with Hardy's suggestion. Whether the intensity is proportional to the amount of hexagonal phase or is dependent in part on the cold-working or alloying has not yet been ascertained.

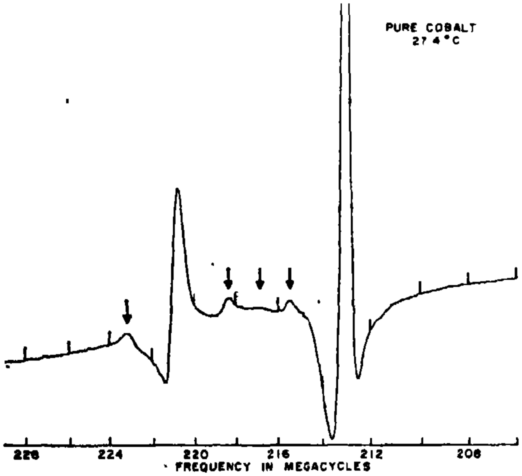

FIG. 1. Spectrum of Co^{59} showing the main f.c.c. and hexagonal resonances at 213·1 and 221·0 Mc/s, respectively, and the additional resonances, marked by arrows, at 223·0, 218·4, 217·0, and 215·5 Mc/s.

In this paper we shall discuss the types of stacking faults that exist in f.c.c. structures, calculate the relative changes in density that can be expected to occur at nuclear sites in these faults, and calculate the resonance frequencies expected from such sites.

Three simple operations can produce stacking faults in f.c.c. crystals: (a) slip along the ⟨112⟩ direction in the close-packed plane, (b) removing a close-packed plane and closing the gap, and (c) inserting a close-packed plane. The stacking sequence produced by operations (a) and (b) is $\text{BCABC}\overset{\downarrow}{\text{A}}\text{CABCAB}$ . . . (intrinsic fault), and that produced by (c) is $\text{ABCAB}\overset{\downarrow}{\text{A}}\text{CABCA}$ . . . (extrinsic fault). In addition, a third type of stacking fault, $\text{ABCAB}\overset{\downarrow}{\text{C}}\text{BACBA}$ . . ., can occur due to twinning.

Each of these stacking sequences contains close-packed atomic layers in the hexagonal order. As the hexagonal layers also form part of f.c.c. sequences, their c/a ratio can be expected to deviate from that of the pure hexagonal phase. The c/a ratio will in general differ according to the type of stacking fault. In the case of twinning, the hexagonal sequence, BCB, also forms part of two face-centered sequences:

$$\overbrace{\mathrm{A}\underbrace{\mathrm{BCB}}_{\text{hex}}\mathrm{A}}^{\text{f.c.c. f.c.c.}}$$

Operation (c) results in two adjacent hexagonal sequences which also form part of three f.c.c. sequences:

$$\overbrace{\mathrm{C}\underbrace{\mathrm{ABA}}_{\text{hex}}\underbrace{\mathrm{CA}}_{\text{hex}}\mathrm{B}}^{\text{f.c.c. f.c.c. f.c.c.}}$$

Operations (a) and (b) produce two overlapping hexagonal sequences which also form part of two f.c.c. sequences:

$$\overbrace{\mathrm{B}\underbrace{\mathrm{CAC}}_{\text{hex}}\mathrm{ABC}}^{\text{f.c.c. f.c.c.}}$$

The reason for the difference in the magnitude of the hyperfine fields in the cubic and the hexagonal phases has not yet been explained completely. GOSSARD(2) has estimated that a dipolar field in the hexagonal phase, resulting from deviations of the c/a ratio from the ideal 1·6330, could account for a third of the difference between the hyperfine fields. Other sources of the difference may be attributed to differences in the lattice constants of the two phases and to an orbital contribution to the magnetization.

We shall assume that the difference in the hyperfine fields is simply related to the differences in the c/a ratios of the two phases. As the interatomic distances in the close-packed planes are very nearly equal in the two phases (2·5010 kX for the f.c.c. and 2·5014 for the hexagonal(3)) this assumption is equivalent to relating the changes in hyperfine field to changes in the c-axis. To determine the resonance frequencies from nuclei in stacking faults we need to determine an "effective" c/a ratio for each atomic layer in the faulted area.

It is customary to estimate the energy of stacking faults in terms of next-nearest-planar violations.* We shall assume that the difference in the c/a ratio between the hexagonal and f.c.c. phases results from the formation of relatively weak next-nearest-planar bonds, directed along the c-axis in the hexagonal phase. These bonds reduce the c/a ratio from the ideal 1·6330 to 1·6237 at 293°K.(3) The interplanar bonding along the c-axis consists primarily of six nearest-neighbor bonds, originating from each atom and bonding nearest planes, and, in the hexagonal phase, two additional next-nearest-planar bonds.

Over small atomic displacements we assume that the movements follow Hooke's law. Let k be the equivalent force constant in the c-direction for each set of three bonds that connect an atom with its three nearest neighbors above or below the closest-packed plane. Let T be a tension representing the next-nearest-planar bond in the c-direction in the hexagonal phase; this bond reduces the c/a ratio. The face-centered-cubic closest-packed interplanar distance, z_1, is taken as the equilibrium or unstretched length of the nearest-neighbor bonds, and z_2 is the interplanar distance in the pure hexagonal phase. Diagrammatically, the interplanar bondings for the two phases and for the stacking faults are shown in Fig. 2. A stacking fault having two missing planes is also shown.

Analysis of the equivalent system for the hexagonal phase gives (z_1-z_2) in terms of T and k. For $N+1$ atomic layers the energy of the system, U, relative to the f.c.c. phase is

$$U = \tfrac{1}{2}Nk(z_1-z_2)^2-(N-1)T(2z_1-2z_2).$$

The equilibrium distance, z_2, for the hexagonal phase is found by differentiating with respect to (z_1-z_2):

$$\frac{\partial U}{\partial(z_1-z_2)} = 0 = Nk(z_1-z_2)-(N-1)(2T),$$

---

* These are commonly referred to as "next-nearest-neighbor violations" (see, for example, READ, *Dislocations in Crystals*, p. 94. McGraw-Hill, New York (1953)), but strictly speaking they are "next-nearest-planar" violations.

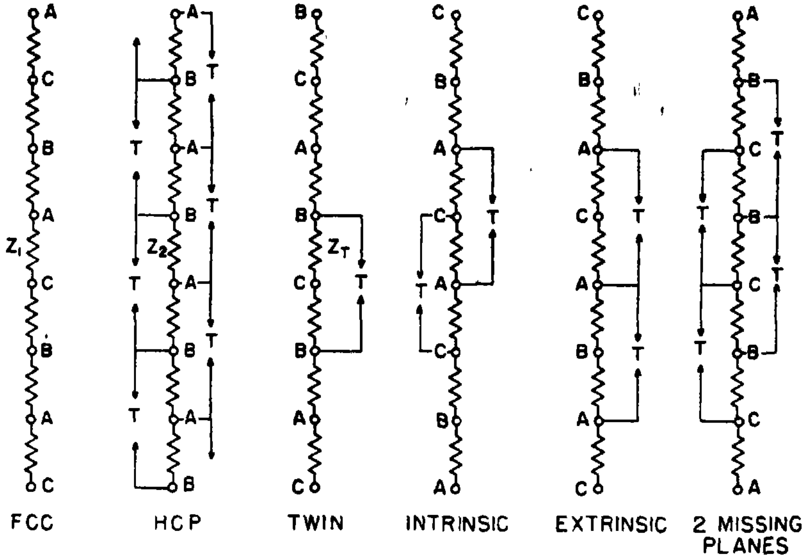

Fig. 2. Representation of stacking sequences in f.c.c. and hexagonal crystals and in stacking faults. z_1 is the separation of atomic planes in the f.c.c.; z_2 in the hexagonal; T represents the tension exerted by next-nearest-planar bonds.

which for large N reduces to

$$(z_1 - z_2) = 2T/k.$$

The distance z_T between atomic planes in a twin is determined similarly:

$$U = k(z_1 - z_T)^2 - T(2z_1 - 2z_T),$$

and

$$\frac{\partial U_T}{\partial(z_1 - z_T)} = 0 = 2k(z_1 - z_T) - 2T,$$

hence,

$$(z_1 - z_T) = T/k.$$

The results for the other types of stacking faults can be determined similarly. Having obtained the change in the planar spacing in terms of T and k for the various faults, we now find an effective change in spacing for a given atom layer by taking the arithmetical mean of the changes in the distances separating it from its neighboring close-packed planes. The interplanar spacings and the effective changes in spacing relative to the f.c.c.-hexagonal change are shown in Fig. 3, where Δ represents $2T/k$. The resonance frequencies from nuclei in stacking faults are then calculated by comparing the average change in interplanar separation for a given faulted plane with the change in spacing between the f.c.c. and hexagonal phases. The average change in interplanar spacing and the calculated and observed frequencies are shown in Table 1. The agreement between calculated and observed frequencies is good.

In addition, the number of planes having the same effective spacing in each type of stacking fault should indicate the relative intensity of the resonances caused by these planes. The number of such planes for each effective spacing may be seen from Fig. 3 and are tabulated in Table 1. As can be seen from Fig. 1, the intensities at 215 and 219 Mc/s are roughly equal and are considerably greater than that at 217. This indicates that intrinsic stacking faults are more abundant than the other types of faults or twins, and is in accord with the fact that electron microscope studies have revealed only one type of stacking fault.

No quantitative explanation for the resonance at 223·0 could be found. Any type of stacking fault in either the f.c.c. or the hexagonal phase would produce resonances that lie between the resonances for the pure phases.

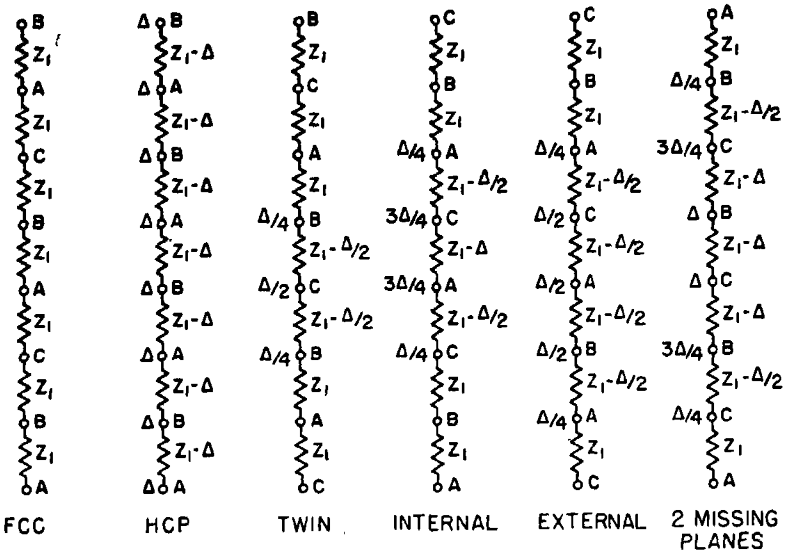

Fig. 3. Stacking sequences in f.c.c. and hexagonal crystals and in stacking faults, showing on the right of each sequence the interplanar separations and on the left the average change in interplanar separation compared to the f.c.c. (in units $\Delta = 2T/k$).

Table 1. *Predicted and observed resonance frequencies in cobalt*

Form	Average change in interplanar spacing (in units $2T/k = 1$)	Relative number of planes contributing	Predicted resonance frequency (Mc/s)	Observed frequency (Mc/s)
f.c.c.	0	—	—	213·1
Hexagonal	1	—	—	221·0
Twin	$\frac{1}{4}$	2	215·0	215·5
	$\frac{1}{2}$	1	217·0	217·0
Intrinsic stacking fault	$\frac{1}{4}$	2	215·0	215·5
	$\frac{3}{4}$	2	219·0	218·4
Extrinsic stacking fault	$\frac{1}{4}$	2	215·0	215·5
	$\frac{1}{2}$	3	217·0	217·0
Two missing planes	$\frac{1}{4}$	2	215·0	215·5
	$\frac{3}{4}$	2	219·0	218·4
	1	2	221·0	221·0*

* Coincides with hexagonal resonance.

Acknowledgements—We would like to thank Dr. R. C. La Force, Professors A. Portis and Jack Washburn, and Mr. Gene Day for their interesting and helpful discussions. We are indebted to the National Science Foundation, whose support made this work possible.

REFERENCES

1. Hardy W., *J. appl. Phys.* **32,** 122S (1961).
2. Gossard A. C., Ph.D. Thesis, University of California (1960).
3. Taylor A., *J. Inst. Metals* **77,** 585 (1950).

J. Phys. Chem. Solids Pergamon Press 1963. Vol. 24, pp. 1207–1212. Printed in Great Britain.

STUDIES OF THE ELECTRICAL PROPERTIES OF URANIUM OXIDES—I

ELECTRICAL CONDUCTIVITY OF α-U_3O_8

A. M. GEORGE and M. D. KARKHANAVALA
Chemistry Division, Atomic Energy Establishment, Trombay, Bombay

(*Received* 25 *February* 1963)

Abstract—The electrical conductivity of two grades of α-U_3O_8 (nuclear pure and pure) was studied as a function of temperature and partial pressure of oxygen in the ranges of 50–850°C and 150 to 10^{-2} mm of Hg. The log σ vs. $1/T$ plot (for $p_{O_2} = 150$ mm) shows two linear portions with a break at about 450°C. The temperature dependence of conductivity is represented by the equation $\sigma = \sigma_0 \exp(-\epsilon/2kT)$ with activation energies of $0{\cdot}64 \pm 0{\cdot}03$ eV and $1{\cdot}10 \pm 0{\cdot}02$ eV below and above the transition point respectively. In the high temperature region σ_0 could be regarded as constant with an average value of $138{\cdot}4$ (Ω-cm)$^{-1}$ for the nuclear pure material. The logarithm of conductivity varied linearly with log p_{O_2} and the average slope of the plots was found to be $-0{\cdot}170 \pm 0{\cdot}006$. The main features of conduction mechanism in the temperature range investigated are suggested.

INTRODUCTION

THE electrical conductivity of the oxides of uranium in the range UO_2 to $UO_{2{\cdot}5}$ has been widely investigated;[1] however no recent work has been reported on the oxides in the U_3O_8 region. The electrical conductivity of U_3O_8 was studied prior to 1931 and has been summarized by KATZ and RABINOWITCH.[2] LE BLANC and SACHSE[3, 4] studied the electrical conductivity of U_3O_8 as a function of temperature up to 500°C and indicated that the conductivity of U_3O_8 is not purely electronic in nature. WIEGAND[5] reported that the conductivity of U_3O_8 was $0{\cdot}05$ (Ω-cm)$^{-1}$ at 50° and $9{\cdot}35$ (Ω-cm)$^{-1}$ at 590°, while FRIEDERICH and SITTIG[6, 7] found that a U_3O_8 rod sintered in oxygen at 1000° had a specific resistivity of 40×10^6 (Ω-cm) at room temperature. Thus the early data on the electrical conductivity of U_3O_8 is highly conflicting, the reported values differing by a factor of about 10^6. The oxygen content of none of these samples has been specified and possibly the different O/U ratio of the samples might have complicated the results to a great extent. It has been reported[8] that U_3O_8 is a cation excess *n*-type semiconductor. However, it has not been established whether the conductivity is due to excess cations or anion vacancies present in the lattice. It was therefore decided to re-investigate the electrical conductivity of uranium oxides as close to the U_3O_8 composition as possible, as a function of temperature and partial pressure of oxygen.

EXPERIMENTAL

Two grades of U_3O_8 were used in the investigation. U_3O_8(I) was prepared by heating reprecipitated ammonium diuranate at 850°C for 20 hr in air. The ammonium diuranate was prepared from purified uranyl nitrate. The total impurities in the sample were spectroscopically estimated to be about 600 p.p.m. The powdered sample was reheated in air at 750°C for 18 hr.

U_3O_8(II) was prepared from nuclear purity UO_2 (supplied by the Metallurgy Division of this Establishment). The dioxide was oxidized in air at 750°C for 16 hr.

The powdered oxide so obtained was cold pressed in a circular die at 2400 kg/cm^2 without any binder. The pellets were sintered in air at 850°C for 8 hr and then annealed at 750°C for 24 hr. The pellets thus made were of 74–78 per cent theoretical density. From X-ray diffractometer patterns, it was confirmed that the phase was orthorhombic αU_3O_8.

The oxygen to uranium ratio of the sintered pellets was determined by the volumetric method.[9] The O/U ratio of a representative sample of U_3O_8(I) was 2·664 ± 0·003 and U_3O_8(II) was 2·665 ± 0·002.

A schematic diagram of the sample holder used for the measurements is given in Fig. 1. The pallet (1·0 cm dia. × 0·3 cm) was introduced between the two platinum foils (0·025 mm thick) each of which had a Pt and a Pt+ 10% Rh wire (0·03 mm dia.) spot welded on diametrically opposite edges. The pellet and the platinum foils were insulated from the steel sample holder by means of thoria discs (1·5 cm × 0·3 cm). This specimen assembly was introduced into a vertical resistance wound alumina tube furnace which could be evacuated.

The resistance of the specimen was measured by the fall of potential method using a Leeds and Northrup K–3 potentiometer. The thermocouple e.m.f. was also balanced on the potentiometer. While measuring the resistance, the Pt–Rh wires were used as current leads and Pt wires as potential probes. During all measurements current was less than 2 mA and temperature was controlled by an electronic controller to ± 1°C. The conductivity was measured while increasing and decreasing the temperature.

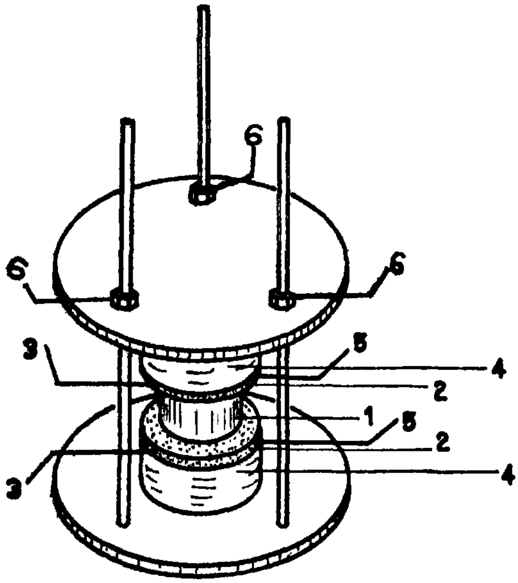

Fig. 1. Schematic view of sample holder
1. U_3O_8 pellet
2. 2 platinum foils
3. 3 Pt. lead wires
4. 4 thoria discs
5. 5 Pt+10% Rh lead wires
6. 6, 6 clamping nuts

To measure the conductivity of U_3O_8 as a function of the partial pressure of oxygen, the furnace tube was connected to a vacuum system and was evacuated to the required degree. The oxygen partial pressure was calculated from the total air pressure. Equilibrium between the sample and surroundings was reached within 30–70 min. at temperatures above 500°C. At lower temperatures (down to 400°C) the sample had to be kept for about 100–200 min to attain equilibrium, especially at low pressures of oxygen.

The measured conductivity was corrected for deviation from theoretical density using the Loeb formula[8]

$$\sigma_c = \sigma_m \left[1+\frac{P}{1-P^{2/3}}\right] \qquad (1)$$

where σ_m is the measured conductivity and P is the volume pore fraction of the specimen.

RESULTS

The temperature dependence of electrical conductivity of both the U_3O_8 samples in air at atmospheric pressure (p_{O_2} = 150 mm) is given in Fig. 2. The conductivity has a positive temperature coefficient. The close agreement between the readings on increasing and decreasing temperature cycles indicates that little hysteresis occurred and that throughout the temperature cycles equilibrium existed between the specimen and the surroundings. Two straight line regions are obtained with a discontinuity at about 450 ± 15°C. The variation of conductivity with temperature can be expressed by the relation

$$\sigma = \sigma_0 \exp(-\epsilon/2kT) \qquad (2)$$

where σ_0 accounts for the change in mobility of the charge carriers with temperature and ϵ is the activation energy for the conduction process and the other terms have their usual significance. The values of ϵ calculated from the slopes of the plot

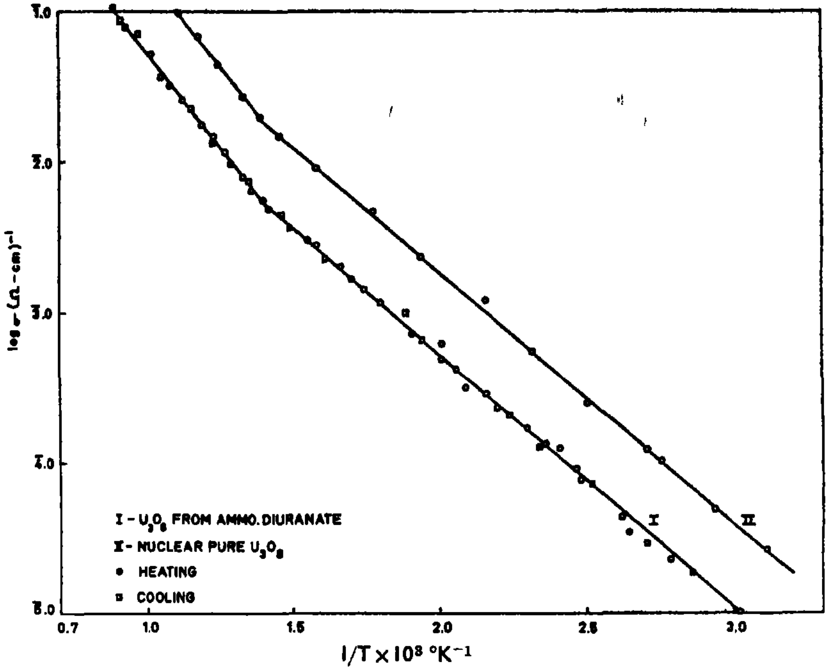

FIG. 2. Electrical conductivity of U_3O_8 I and II in air up to 850°C
○ Heating ☐ Cooling

log σ vs. $1/T$ are $0{\cdot}64 \pm 0{\cdot}03$ eV and $1{\cdot}10 \pm 0{\cdot}02$ eV for temperature ranges below and above 450 ± 15°C respectively. This latter value of 1·10 eV is in good agreement with the value of $1{\cdot}09 \pm 0{\cdot}01$ eV calculated from the data of LE BLANC and SACHSE.[2, 3] In the temperature range of 450–850° σ_0 has an average value of 18·34 $(\Omega\text{-cm})^{-1}$ for sample I and 138·4 for sample II; the small deviations in σ_0 noted for each sample are within the limits of experimental error. However, the value of σ_0 in the low temperature range showed large deviations in both cases.

The activation energies for conduction in the two temperature ranges, show little deviations for samples I and II. However, the conductivity values show a considerable increase for sample II. The observed decrease in the conductivity of the sample I (prepared from ammonium diuranate) might be due to the trapping of charge carriers by small amounts of impurities present in the sample, thereby decreasing the carrier concentration. This factor may also have contributed to the wide variation in the conductivity values reported by different workers.

The orthorhombic α-U_3O_8 phase exists in the composition range $UO_{2\cdot60}$ to $UO_{2\cdot67}$.[10] In the present experiments all the three samples used had an initial O/U ratio above 2·66 and since the temperature was restricted to 850° it is expected that in all cases the O/U ratio was above 2·65. The measurements were thus carried out on samples in the orthorhombic α-U_3O_8 phase very close to $UO_{2\cdot667}$.

The isothermal conductivity of both the U_3O_8 samples was also measured as a function of the partial pressure of oxygen at different temperatures. The oxygen pressures ranged from 150 to 10^{-2} mm of Hg. The results are shown in Fig. 3. Linear plots are obtained at all temperatures. The isothermal conductivity can be represented by the empirical relation

$$\sigma = cp_{O_2}^{-1/6} \tag{3}$$

where c is a constant. Figure 4 shows that the plot of log σ vs. $1/T$ at different oxygen partial pressures. Straight line plots were obtained over the entire temperature range (375 to 550°). The activation energy calculated from the slope is 1·1

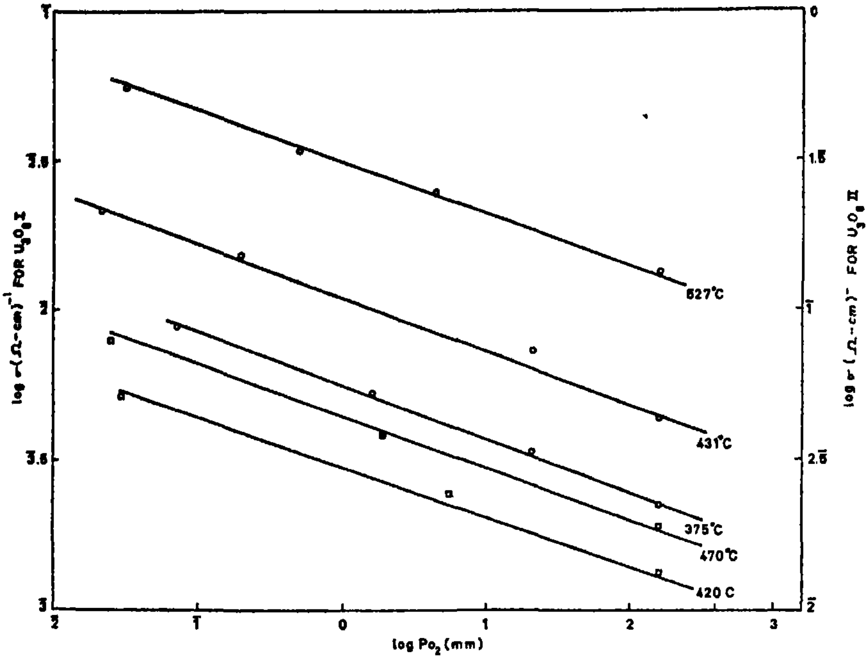

FIG. 3. Isothermal conductivity of U_3O_8 I ○ and II □ in the temperature range of 320–520°C.

eV corresponding to that of the high temperature conductivity in air.

DISCUSSION

I. *The discontinuity in the conductivity curve*

It is interesting that the discontinuity in the conductivity curve is observed only at atmospheric oxygen partial pressure and not at lower partial pressures.

HOEKSTRA *et al.*(11) in their high temperature X-ray study of U_3O_8 had observed an orthorhombic to hexagonal phase transition at about 400°C. From detailed considerations of the X-ray line intensities they had suggested that this was very likely to be a second-order transformation of the order–disorder type, and not a true first-order phase transition.

A break in the electrical conductivity is commonly attributed to either a phase transition or to a phase boundary. In the present case since the discontinuity is dependent on the environmental atmosphere, a first-order phase transformation can be ruled out. The discontinuity is therefore attributed to a second-order transformation as originally suggested by HOEKSTRA *et al.*(11) It is suggested that the oxygen lattice becomes ordered and apparently assumes hexagonal symmetry. Since the cation lattice in orthorhombic U_3O_8 already possesses an almost hexagonal symmetry,(12–14) the ordering of the anion lattice also to a hexagonal symmetry would lead to an X-ray diffraction pattern which could be indexed on the basis of hexagonal symmetry for the overall unit cell.

The postulate that the break is not due to a true phase transformation finds additional support from the fact that no heat effects are observed in the D.T.A. curve in that temperature region. This has been independently observed also by NOTZ, HUNTINGTON and BURKHARDT,(15)* who also attribute this transition to an order–disorder phenomena.

II. *Mechanism of conduction*

Since the conductivity increased with decrease in partial pressure of oxygen, α-U_3O_8 can be

---

* This work appeared as the present paper was being processed for publication.

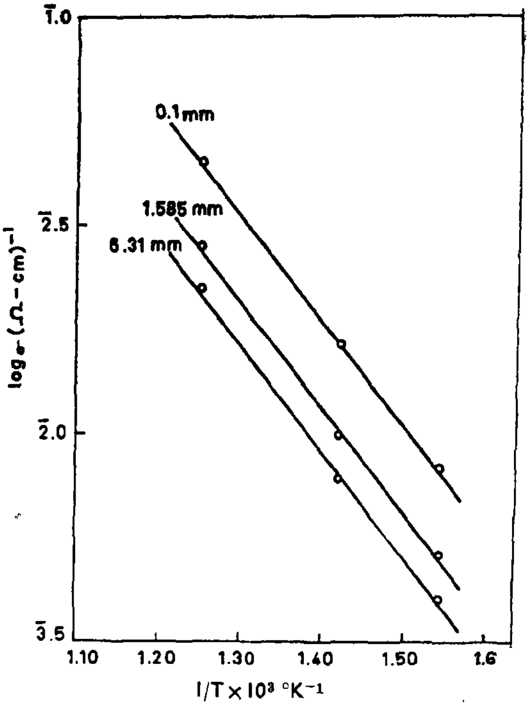

FIG. 4. Isobaric conductivity of U_3O_8I.

classified as a metal excess *n*-type semiconductor. The metal excess can be accounted for on the basis of cation interstitials or anion vacancies or both. Either of these give rise to an excess of positive charges and hence quasi-free electrons must be present to maintain electro-neutrality.

Compared to other metallic oxides like TiO_2(16) and ZnO(17) whose conductivities have been rigorously investigated, U_3O_8 shows a high degree of non-stoichiometry. From the work of BILTZ *et al.*(18) on the change of O/U ratio of the oxides of uranium with temperature it can be reasonably assumed that particularly in the temperature range 400–1000°C oxygen lattice vacancies are present. ZACHARIASEN(12) and GRONVOLD(13) who determined the structure of U_3O_8 by X-ray methods have also postulated a structure based on the existence of oxygen ion vacancies, though ANDERSON(14) from his neutron diffraction study has postulated a structure without any vacancies. If oxygen vacancies are assumed at least at higher temperatures these would contribute to the conductivity of the oxide. This assumption though questionable, finds additional support from the following considerations.

Taking into consideration the thermal energy available in the temperature range studied, the creation of a neutral anion lattice vacancy can be postulated:

$$O_1^{-2} = O\square_1^{v} + 2\theta + \tfrac{1}{2}O_2 \qquad (4)$$

where O_1^{-2} is an anion in the lattice. $O\square_1^{v}$ is a neutral anion vacancy formed and θ is the quasi-free electron. Applying the law of mass action to the above equation and approximating the activities to concentrations and partial pressures, the equilibrium constant for the reaction may be written

$$K = [\theta]^2 [O\square_1^{v}] p_{O_2}^{+1/2} \qquad (5)$$

This equation can be solved for $[\theta]$. Since the electro-neutrality of the sample is maintained according to

$$[\theta] = 2[O\square_1^{v}] \qquad (6)$$

hence substituting for $[O\square_1^{v}]$ in equation (5)

$$[\theta] = K' p_{O_2}^{-1/6} \qquad (7)$$

The electrical conductivity would be proportional to concentration of the charge-carriers and hence θ. Since the concentration of θ varies with the negative 1/6 power of the oxygen partial pressure, the electrical conductivity can also be expected to have the same dependence. The experimental results (Fig. 3) show that the electrical conductivity is proportional to $p_{O_2}^{-1/6}$. This lends strong support to the hypotheses that U_3O_8 is a *n*-type metal excess semiconductor with anion vacancies.

The temperature dependence of the constant K' in equation (7) is given by

$$K' = K_0' \exp(-E_f/2KT) \qquad (8)$$

where E_f is the activation energy for formation of an oxygen ion vacancy in the lattice.

The total conductivity of U_3O_8 can thus be expressed

$$\sigma = \sigma_0 \exp(-E_G/2KT) + K_0' \exp(-E_f/2KT) \cdot p_{O_2}^{-1/6} \qquad (9)$$

where E_G is the energy gap between the valence band and conduction band.

Acknowledgement—The authors thank Dr. JAGDISH SHANKAR, Head, Chemistry Division for his kind encouragement and interest in the work.

REFERENCES

1. BELLE J., *Uranium dioxide: Properties and Nuclear Applications*, U.S. AEC (1961).
2. KATZ, J. J. and RABINOWITCH E., *The Chemistry of Uranium*, National Nuclear Energy Series, Vol. 5 (1951).
3. LE BLANC M. and SACHSE H., *Ber. Verhandl. Sachs. Akad. Wiss.*, Leipzig **82**, 155 (1930).
4. LE BLANC M. and SACHSE H., *Z. Phys.* **32**, 887 (1931).
5. WEIGAND E., *Z. Phys.* **30**, 40 (1924).
6. FRIEDERICH E. and SITTIG L., *Z. anorg. Chem.* **145**, 127 (1925).
7. FRIEDERICH E., *Z. Phys.* **31**, 813 (1925).
8. WILLARDSON R. K., MOODY J. W. and GOERING H. L., *J. inorg. nucl. Chem.* **6**, 19 (1958).
9. NEUMANN L., *Coll. Trav. chim. Tchécosl.* **25**, 2235 (1960).
10. GRONVOLD F. and HERALDSEN H., *Nature, Lond.* **162**, 69 (1948).
11. HOEKSTRA H. R., SIEGEL S., FUCHS L. H. and KATZ J. J., *J. phys. Chem.*, **59**, 136 (1955).
12. ZACHARIASEN W. H., *Manhattan Project Report* CK-2667 and CC-2768 (1945).
13. GRONVOLD F., *Nature, Lond.* **162**, 70 (1948).
14. ANDERSON A. F., *Acta Cryst.* **11**, 612 (1958).
15. NOTZ K. J., HUNTINGTON C. W. and BURKHARDT W., *Ind. Eng. Chem. Proc. Des. Dev.* **1**, (3), 213 (1962).
16. EARLE M. D., *Phys. Rev.* **61**, 56 (1942).
17. BAUMBACH H. H. and WAGNER C., *Z. phys. Chem.* **B22**, 199 (1933).
18. BILTZ W. and MULLER H., *Z. anorg. Chem.* **163**, 295 (1927).

J. Phys. Chem. Solids Pergamon Press 1963. Vol. 24, pp. 1213–1216. Printed in Great Britain.

THE OPTICAL EFFECTIVE MASS AND ABSORPTION EDGE OF ELECTRONS IN SODIUM

J. N. HODGSON

Physics Department, The University, Keele, Staffordshire

(*Received* 29 *March* 1963)

Abstract—The optical constants of sodium have been measured by a reflection method in the wavelength range 0·65 to $2{\cdot}5 \times 10^{-4}$ cm. The values of dielectric constant in the infra-red give an optical effective mass $m^* = (1{\cdot}08 \pm 0{\cdot}01)m$. The variation of conductivity with wavelength indicates the onset of inter-band transitions at a photon energy of 1·2 eV. A comparison with the theoretical band structure suggests that these may be indirect transitions from the Fermi surface.

1. INTRODUCTION

THE experimental study of the physical properties of sodium is of special interest because accurate theoretical calculations of the band structure of this metal are now available, HAM.(1) The powerful low temperature methods of investigating band structure cannot easily be applied to sodium because of its low temperature phase transformation. A measurement of the optical constants of sodium is therefore valuable for the information it can give about the band structure, as well as for its intrinsic interest. The dielectric constant, $\epsilon = (n^2 - k^2)$, and conductivity, $\sigma = nk/\lambda$, as functions of wavelength, λ, or angular frequency, ω, will be used to describe the optical properties. The complex refractive index is $(n - ik)$ and the units of σ are such that $(\sigma/30)$ is the conductivity in Ω^{-1} cm^{-1}. IVES and BRIGGS(2) measured the optical constants of sodium for wavelengths between 0·25 and $0{\cdot}58 \times 10^{-4}$ cm. Their values for $\sigma(\lambda)$ show that the photon energies ($\hbar\omega$) in this spectral region are greater than the threshold energy ($\hbar\omega_1$) for inter-band transitions. To obtain information about the effective mass of electrons near the Fermi surface, one needs optical measurements at frequencies $\omega < \omega_1$. If the condition $\omega\tau \gg 1$, where τ is the relaxation time, can also be satisfied, the interpretation of the optical measurements is particularly simple. $\epsilon(\lambda)$ is then independent of τ and has values corresponding to a free electron gas without damping. $\sigma(\lambda)$ is proportional to $(1/\tau)$, according to simple theory; see Section 3. The value of τ depends on both bulk and surface relaxation processes, and may be only about half the value calculated from the bulk electrical conductivity. However, for the monovalent metals, the condition $\omega\tau \gg 1$ should be well satisfied for $\lambda \leqslant 5 \times 10^{-4}$ cm.

2. EXPERIMENTS

Because of the great affinity of sodium for oxygen, a sodium surface for reflection measurements must be protected from the air. The method used for the present work was suggested by the work of IVES and BRIGGS(3) on potassium, in which an internal metal–glass prism surface was used for reflection measurements. A film of sodium was deposited in vacuum on the base of a 75° isosceles prism of quartz glass. The free surface of the film was sealed from the air by a layer of vacuum grease. The prism to metal surface was used for reflection measurements. By this method, the optical measurements could be made with the prism in air without any oxidation of the film.

The sodium films were produced in a standard vacuum evaporation apparatus with a titanium getter which held the bell-jar pressure below 10^{-5} torr during evaporation. A piece of sodium (99·99%) was carefully cleaned from organic contamination, placed in a tantalum evaporating boat and the surrounding bell-jar was immediately evacuated. The small amount of oxide formed on the surface of the sodium should be retained in the boat because it is much less volatile than metallic sodium. The temperature of the evaporating boat was increased gradually until sodium vapour was coming off at the required rate. A magnetic shutter covering the prism base was then opened to allow a film to be deposited. A high rate of deposition ~ 500 Å per sec, was used to minimize the effects of residual gas contamination. The final thickness of the film, $\sim 10^{-4}$ cm, was more than adequate to make it opaque. The prism was kept at ~ 50°C during film deposition so that vacuum grease could be poured on immediately afterwards to seal the film. Sodium films made in this way were kept in the atmosphere for several days without deterioration.

The optical constants were measured for wavelengths between 0·65 and $2{\cdot}5\times10^{-4}$ cm by a modification of the Drude method, using an angle of incidence $\theta = 75°$. The optical apparatus and method were similar to those used in previous work, HODGSON.(4) If $r_p \exp(i\Delta_p)$ and $r_s \exp(i\Delta_s)$ are the complex reflection coefficients for p- and s-waves, then the measured quantities are $\Delta = (\Delta_p-\Delta_s)$ and $\psi = \tan^{-1}(r_p/r_s)$. Any strain double refraction in the prisms will cause spurious changes in the measured values of Δ and ψ. To check on this possibility, the values of Δ and ψ were measured for each prism before a sodium film was deposited. Theory predicts that in this case $\psi = 45°$ and

$$(1+\cos\Delta) = 2\sin^2\theta\tan^2\theta/(\tan^2\theta-1/n_0^2)$$

where n_0 is the refractive index of the prism material. The measured values of ψ and Δ for uncoated prisms agreed with these formulae within ±0·1°, showing that double refraction could be neglected.

The formulae for calculating ϵ and σ from Δ and ψ for prism–sodium surfaces, can be simplified because $(90°-2\psi) = \xi$ is a small angle, $< 2°$. The approximate formulae are:

$$\begin{aligned}\epsilon &= n^2-k^2\\ &= n_0^2[\tan^2\theta-2\sin^2\theta\tan^2\theta/(1+\cos\Delta)] \qquad (1)\end{aligned}$$

$$\begin{aligned}\sigma &= nk/\lambda\\ &= n_0^2\sin^2\theta\tan^2\theta\sin\Delta\sin\xi/\lambda(1+\cos\Delta)^2 \qquad (2)\end{aligned}$$

The experimental errors in ϵ and σ can be calculated from the estimated errors in Δ and ψ. Because σ is proportional to $\sin\xi$, its value is very sensitive to errors in ψ.

The modifications of these formulae to allow for the anomalous skin effect have been investigated by DINGLE(5) and COLLINS.(6) For the frequency region of interest here, Dingle found that the usual formulae for ϵ and σ as functions of θ, Δ and ψ are valid if $\omega \ll \omega_p$. ω_p is the plasma frequency defined by $[4\pi Ne^2/m(1+\epsilon_c)]^{1/2}$, where N is the number of electrons per cm^3 and ϵ_c is the ion core contribution to ϵ. For sodium $\epsilon_c \simeq 0{\cdot}1$ and the plasma wavelength $\lambda_p = 2\pi c/\omega \simeq 2{\cdot}0\times10^{-5}$ cm. Collins has derived formulae without the limitation $\omega \ll \omega_p$ and found that the usual formulae are incorrect for $\omega \sim \omega_p$. The corrections are very small, however, when $\omega \leqslant \omega_p/5$, i.e. $\lambda \geqslant 1{\cdot}0\times10^{-4}$ cm for sodium.

3. THEORY

The theoretical expression for the dielectric constant ϵ when $\omega < \omega_1$ and $\omega\tau \gg 1$ is:

$$\epsilon = 1+\epsilon_a-(Ne^2/\pi m^*c^2)\lambda^2 \qquad (3)$$

ϵ_a is the contribution to ϵ from inter-band transitions and ion core polarization. The optical effective mass m^* is defined by:—

$$m^*/m = (v_f^0S_e^0)/(v_fS_f) \qquad (4)$$

where v_f is the average velocity at the Fermi surface, S_f is the area of the F.S. and the quantities with superscript 0 refer to a spherical F.S. containing the same number of electrons; see COHEN.(7) HAM,(1) has calculated the energy bands and Fermi surfaces of the alkali metals. He finds for sodium that the F.S. is spherical and the Fermi energy differs inappreciably from the free electron value. Formula (4) therefore gives $(m^*/m) = 1{\cdot}00$ for sodium.

The conductivity σ for $\omega < \omega_1$ is determined by intra-band transitions of the valence electrons. These indirect transitions must be accompanied by scattering of electrons by phonons, imperfections or boundaries. If the relaxation time due to scattering is τ and $\omega\tau \gg 1$, then:

$$\sigma = (Ne^2/4\pi m^*c^3)(1/\tau)\lambda^2 \qquad (5)$$

The theory of the anomalous skin effect shows that the relaxation due to surface scattering depends on whether the electron scattering is specular or diffuse. One can assume for simplicity that a fraction p is specularly scattered and $(1-p)$ is diffusely scattered. The relaxation time for each set of electrons is given by an expression $(1/\tau) = (1/\tau_b + 1/\tau_s)$ where τ_b is the bulk relaxation time and τ_s is the surface relaxation time. For the fraction p, $\tau_s \gg \tau_b$ at room temperature and $1/\tau_s$ can be neglected. For the fraction $(1-p)$, τ_b and τ_s are of comparable magnitude. The average $(1/\tau)$ in equation (5) is given by:

$$(1/\tau) = (1/\tau_b)+(1-p)(1/\tau_s) \tag{6}$$

where τ_s is the surface relaxation time for diffusely scattered electrons; i.e.

$$(1/\tau_s) = \tfrac{3}{4}(v_f/c)\sqrt{(Ne^2\pi/m^*)} \tag{7}$$

where v_f is the electron velocity at the surface of the Fermi sphere. A simple derivation of (7) has been given by HOLSTEIN.(8)

The direct inter-band transitions of the lowest energy in sodium are due to electrons on the F.S. with k-vectors in the $\langle 110 \rangle$ or equivalent directions. The predicted energy for these transitions is about 2·0 eV. The possibility of indirect inter-band transitions should also be considered. The electrons just mentioned could make indirect transitions to the point N_1 in the second zone, requiring an energy of about 1·1 eV. These transitions could be assisted by bulk or surface relaxation effects.

4. DISCUSSION OF RESULTS

Previous determinations of the optical constants of sodium have been published by IVES and BRIGGS(2) and by DUNCAN and DUNCAN.(9) Ives and Briggs deposited a thin film of sodium on a glass plate in an evacuated glass bulb. They used reflection from the free surface of the film to measure optical constants. Duncan and Duncan poured liquid sodium into a container behind a glass plate. The optical constants were measured by reflection from the sodium–glass surface.

Experimental values of ϵ for $\lambda \leqslant 1{\cdot}0 \times 10^{-4}$ cm are shown in Fig. 1; the probable errors are about $\pm 0{\cdot}1$. The straight line represents equation (3) with $\epsilon_a = 0{\cdot}1$ and $m^* = m$, i.e.

$$\epsilon = 1{\cdot}1 - 2{\cdot}28 \times 10^9 \times \lambda^2 \tag{8}$$

Except for the slight dip near $\lambda = 0{\cdot}6 \times 10^{-4}$ cm in the present values and those of Duncan and Duncan, the points fall close to the theoretical line. The value of 0·1 for ϵ_a is approximate and equally good agreement could be obtained with any value between 0·0 and 0·2. In the present work, different films of sodium showed systematic differences in the values of ϵ amounting to one or two times the experimental error. The values of ϵ for $\lambda > 1{\cdot}0 \times 10^{-4}$ cm are shown in Fig. 2; the probable error is about ±1 per cent. The experimental values for $\lambda > 1{\cdot}5 \times 10^{-4}$ cm fall close to the line representing:

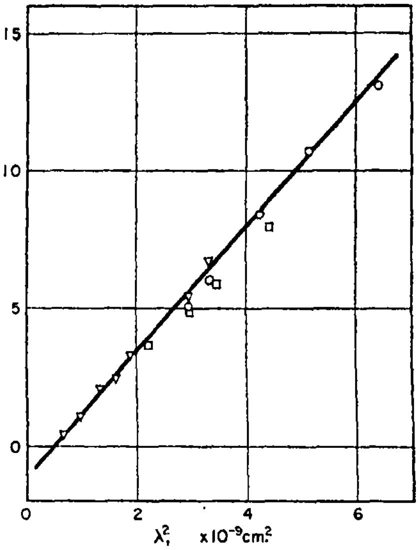

FIG. 1. Dielectric constant of sodium in the ultra-violet and visible. $\epsilon = n^2 - k^2$ = dielectric constant; λ = wavelength. Experimental points: □ DUNCAN and DUNCAN;(9) ▽ IVES and BRIGGS;(2) ○ HODGSON. Straight line: Formula (3) with $m^* = 1{\cdot}00$ m, $\epsilon_a = 0{\cdot}1$.

$$\epsilon = 1 - 2{\cdot}10 \times 10^9 \times \lambda^2 \tag{9}$$

The experimental error is too great to determine a non-zero value of ϵ_a. The coefficient of λ^2 corresponds to $m^* = 1{\cdot}08$ m, compared with the value $m^* = 1{\cdot}00$ m given by Ham's calculations. According to WOLFF,(10) such a difference cannot be due to electron correlation if the Fermi surface is spherical.

The experimental values of $\sigma(= nk/\lambda)$ plotted against wave number k $(= 1/\lambda)$ are shown in Fig. 3. The probable errors are about $\pm 0{\cdot}2 \times 10^3$ for $k \geqslant 1{\cdot}0 \times 10^4$ cm^{-1} and rise to $\pm 0{\cdot}6 \times 10^3$ for $k = 0{\cdot}4 \times 10^4$ cm^{-1}. The values of σ for $k \leqslant 1{\cdot}0 \times 10^4$ cm^{-1} are approximately proportional to k^{-s}

(i.e. λ^s) where $s \simeq 1{\cdot}8$. Other films gave values of σ up to 20 per cent different from those shown in Fig. 3 and for some $s \simeq 1{\cdot}6$. This may be compared with the theoretical λ^2 dependence of formula (5), assuming τ to be independent of λ. Experiments on films produced under rigidly controlled conditions and very high vacuum are needed to investigate the reasons for the scatter in the measured values of σ. Assuming $m^* = 1{\cdot}08$ m and using (5), (6) and (7), the theoretical expression for σ becomes:

$$\sigma = 5{\cdot}60\times 10^{10}\times[3{\cdot}11+1{\cdot}11(1-p)]\times \mathrm{k}^{-2} \quad (10)$$

The curve in Fig. 3 represents equation (10) with $p = 0$. The experimental value at $\mathrm{k} = 0{\cdot}41\times 10^4\,\mathrm{cm}^{-1}$ is $\sigma = 12{\cdot}6\times 10^3$, while (10) gives $10{\cdot}4\times 10^3$ for $p = 1$ and $14{\cdot}2\times 10^3$ for $p = 0$. This suggests an intermediate value of p for this film but the deviation of s from the theoretical value of 2, makes this interpretation uncertain.

The values of σ for all sodium films show a sharp rise above the power law curve for $\mathrm{k} > 1{\cdot}0\times 10^4\,\mathrm{cm}^{-1}$, i.e. $\hbar\omega > 1{\cdot}2$ eV. This suggests inter-band transitions with an energy gap of about 1·2 eV. This value is approximately equal to the indirect energy gap between the Fermi surface and point N_1, previously mentioned. The experimental values of σ also show a dip near $\mathrm{k} = 1{\cdot}6\times 10^4\,\mathrm{cm}^{-1}$, i.e. $\hbar\omega = 2{\cdot}0$ eV. This dip is pronounced in the values from Ives and Briggs but also appears in those from Duncan and Duncan which overlap satisfactorily with the present results. The dip may be evidence of direct transitions, expected to start at about this wave number.

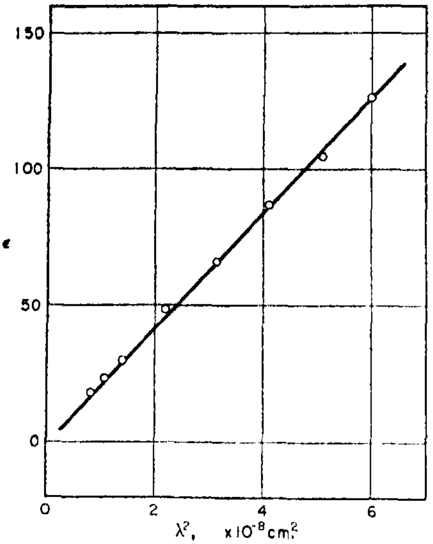

FIG. 2. Dielectric constant of sodium in the infra-red. $\epsilon = n^2-k^2$ = dielectric constant; λ = wavelength. Experimental points: O. Straight line: Formula (3) with $m^* = 1{\cdot}08$ m, $\epsilon_a = 0$.

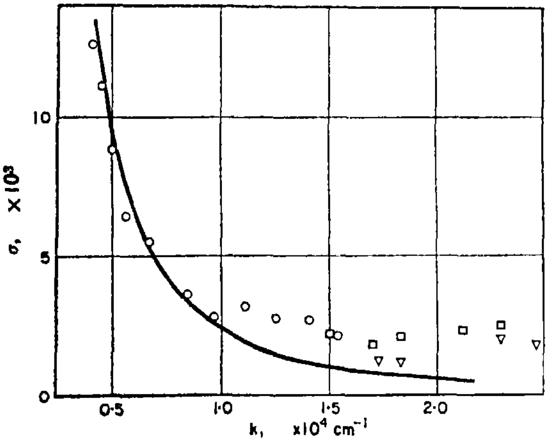

FIG. 3. Conductivity of sodium. $\sigma = nk/\lambda$ = conductivity; $\mathrm{k} = 1/\lambda$ = wave number. Experimental points: □ DUNCAN and DUNCAN;(9) ▽ IVES and BRIGGS;(2) O HODGSON. Theoretical curve: Formula (10) with $p = 0$.

REFERENCES

1. HAM F. S., *Phys. Rev.* **128,** 82, 2524 (1962).
2. IVES H. E. and BRIGGS H. B., *J. opt. Soc. Amer.* **27,** 181 (1937).
3. IVES H. E. and BRIGGS H. B., *J. opt. Soc. Amer.* **26,** 238 (1936).
4. HODGSON J. N., *Phil. Mag.* **4,** 183 (1959).
5. DINGLE R. B., *Physica* **19,** 729 (1953).
6. COLLINS J. G., *Appl. Sci. Res.* **B7,** 1 (1958).
7. COHEN M. H., *Phil. Mag.* **3,** 762 (1958).
8. HOLSTEIN T., *Phys. Rev.* **88,** 1427 (1952).
9. DUNCAN R. W. and DUNCAN R. C., *Phys. Rev.* **1,** 294 (1913).
10. WOLFF P. A., *Phys. Rev.* **116,** 544 (1959).

J. Phys. Chem. Solids Pergamon Press 1963. Vol. 24, pp. 1217–1221. **Printed in Great Britain.**

RADIOTRACER STUDIES OF GOLD ADSORPTION AND DESORPTION ON CLEAN MOLYBDENUM SURFACES*

EBERHARD von GOELER† **and EDGAR LÜSCHER**

University of Illinois, Urbana, Illinois

(*Received* 22 *March* 1963)

Abstract—The adsorption and desorption of gold on heat-cleaned surfaces of polycrystalline molybdenum was studied at a residual gas pressure of 2×10^{-9} torr. A radio-tracer method was used in a differential pumping system. The sticking coefficient was measured to be $s = 0{\cdot}99 \pm 0{\cdot}01$ at beam densities up to 10^{11} particles/cm^2 sec. The desorption probability per unit time was found to obey a relation $w = w_0 \exp(-E/kT)$ with $w_0 = 2 \cdot 10^{13}$ sec^{-1} and $E = 4{\cdot}2 \pm 0{\cdot}2$ eV.

INTRODUCTION

STUDIES of the interactions of single atoms or molecules with surfaces are necessary for an understanding of many surface phenomena. Radiotracer techniques can be used to advantage. The number of radioactive atoms present is small and permits the study of interactions with the clean surface. However, a considerable effort has to be made to avoid contaminating the surface with any material that might accompany the tracer.(2)

In the present paper we report on experiments designed to study by this method the adsorption and desorption of radioactive metal. isotopes on heat-cleaned surfaces of refractory metals. We quote results of measurements of the interaction of Au^{198} with a polycrystalline molybdenum substrate. An atomic beam of gold is produced in one vacuum system; this beam passes through a capillary into a second vacuum system where the beam hits the surface to be studied. The separation of the areas of beam production and surface interaction guarantees that the substrate remains clean throughout the course of the experiment.

APPARATUS

The apparatus consists of two complete ultrahigh vacuum systems connected by a capillary of such conductance that a pressure difference of two to three orders of magnitude can be maintained in the two parts. Each vacuum system is complete with fore pump, two-stage oil diffusion pump, copper trap, liquid nitrogen trap and experimental volume. The low pressure limit is 2×10^{-10} torr as measured with a Bayard–Alpert ion-gauge (WL 5966).

In Fig. 1, the apparatus is shown schematically. System 1 contains the equipment to produce the

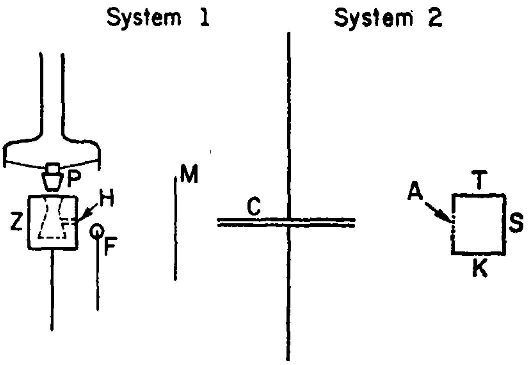

FIG. 1. Schematic view of the apparatus. Z: tantalum oven. F: filament for electron bombardment. H: hole through which the atomic beam leaves the oven. M: magnetically operated shutter. C: capilary. T: target. S: surface under study.

---

* This research was supported in part by the Air Force Office of Scientific Research under contract AF 18(603)49; it was also assisted by support extended to the Coordinated Science Laboratory, University of Illinois jointly by the Department of the Army (Signal Corps), Department of the Navy (Office of Naval Research), and the Department of the Air Force (Office of Scientific Research) under Signal Corps Contract DA-36-039-SC-85122.

† Present address: Deutsches Elektronen-Synchrotron, Hamburg (Germany).

atomic beam. It consists of a tantalum oven Z, of height and diameter 12·5 mm, that can be heated by electron bombardment from a filament F. The radioactive substance can be inserted through a hole in the top of the oven. The hole is closed by a tantalum plug P if a tungsten wire, from which the plug is suspended, is electrically heated to 2300°K. The atomic beam leaves the oven through a hole H of diameter 0·76 mm. It passes a magnetically operated shutter M and enters System 2 through a capillary C. The shutter, if closed, prevents the beam from continuing into the second system. The hole diameter of the capillary is 1 mm. The length is approximately 10 cm.

System 2 contains the target T. The target consists of the two parts shown in Fig. 2. One is a cubical box K made of molybdenum sheet. Its linear dimensions are 12·5 mm. The front face has a hole A of diameter 3 mm. The rear face is absent altogether. The second part is the surface under study, S. Its dimensions are 12 by 15 mm. It can be slid into the position of the rear face of the cubical box.

Both cube K and surface S are fastened to tungsten rods W, which in turn are held by nickel slugs Ni. The slugs fit loosely into the glass envelope of system 2 and can be slid back and forth by magnets. The atomic beam arriving from the capillary passes through the hole A into the cubical box, hits the surface S and is partly adsorbed, partly scattered to the inside of the box. After exposure to the beam the surface and the cubical box are moved in front of a scintillation counter where their activities are measured without removing them from the vacuum system.

The apparatus permits the measurement of the fraction of atoms which upon hitting a surface remain fixed. The method is to expose the target to the beam for a certain length of time and afterwards to count the number of atoms on both parts of the target. The sticking coefficient is given by the ratio between the number of atoms on the surface and the number of atoms on both surface and cube. Corrections have to be applied for the different counting geometries of the two parts.

Another quantity that can be measured with the present apparatus is the desorption rate as function of the surface temperature and structure. Further applications include studies of the dependence of the sticking coefficient upon the angle of incidence, upon the surface structure, and upon the surface cleanliness.

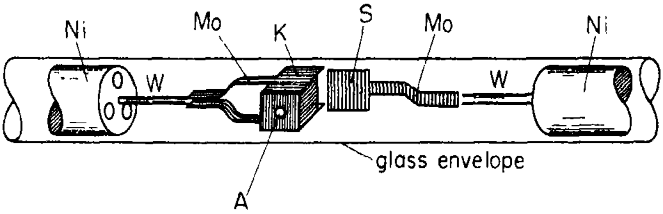

FIG. 2. Target assembly. The surface to be studied S and the cubical box K are fastened to tungsten rods W, which in turn are held by nickel slugs Ni.

EXPERIMENTAL PROCEDURES

The target foil and the cubical box were made from pure molybdenum sheet (0·125 mm thick, from A. D. Mackay, Inc., New York). After fabrication they were chemically polished until they had a mirror-like appearance. Next they were rinsed in acetone and distilled water. Then they were spotwelded to their supports in a hydrogen atmosphere. After installation in the vacuum system, all metal parts were outgassed for a few days at the highest permissible temperatures. In particular, the target and the oven were heated to 1800°K in ultrahigh vacuum for several days. After this treatment, the target showed signs of thermal etching. The tracer, Au^{198} (half-life 64·6 hr), was produced in the Argonne Pile CP–5 by irradiating Au^{197} (99·999% pure). The ratio of active gold atoms to inactive was of the order of 1 : 10^3.

When all of the parts of the apparatus had been thoroughly degassed the isotope was inserted. To do so helium was introduced through a break-off tip, a small hole was blown into the glass envelope of system 1, and the gold was dropped into the oven. After sealing and evacuation, the systems were twice baked for 10 hr at 450°C. Between the bake-outs, all metal parts were degassed either with an r.f.-heater or by electron bombardment. Prior to formation of the gold beam, the tantalum oven was kept at 1300°K for several hours. Then it was raised to the temperature of 1600°K. The magnetic shutter, however, remained closed for at least one more hour while the target was once again heated to 1800°K. At the end of this period, the pressure in system 1 was approximately 5×10^{-7} torr; in system 2, it was 2×10^{-9} torr or less.

Evaporation of the Au^{198} took place at a temperature between 1500°K and 1650°K, corresponding to a gold vapor pressure of between 10^{-5} and 10^{-3} torr. The total number of atoms, radioactive and stable, that passed through the capillary and hit the target surface at normal incidence, over an area of approximately 0·1 cm^2, was computed from the radioactivity count. It amounted to between 10^9 and 10^{12} per exposure. The maximal beam density obtained was 10^{11} cm^{-2} sec^{-1}. The oven temperature was kept constant during each run by electronically controlling the electron bombardment voltage and current. One measurement of the sticking coefficient took less than 10 min. One measurement of the desorption rate as function of the temperature took approximately half an hour. The total number of runs made in adsorption and desorption studies was 129. The agreement between the runs was within ± 5 per cent.

RESULTS AND DISCUSSION

The sticking coefficient at room temperature of gold on the cleaned surface of polycrystalline molybdenum was found to be

$$s = 0{\cdot}99 \pm 0{\cdot}01.$$

Multiple reflections can be excluded experimentally. No change was found between the sticking coefficient of the surface 15 min after cleaning and 24 hr after cleaning. Heating the ion-gauge grid and the resulting gas burst did not influence the sticking coefficient either. Removal of the liquid nitrogen from the cold trap and the resulting temporary increase in pressure to $4 \cdot 10^{-8}$ torr did not change the sticking coefficient. Upon switching off the diffusion pump, the pressure in system 2 dropped to 10^{-3} torr. After pumping back to 10^{-8} torr the sticking coefficient was measured again; it was now found to be $s = 0{\cdot}95 \pm 0{\cdot}01$. After flashing the surface, the value for the clean surface was reestablished.

The significant result of these measurements is that the sticking coefficient of gold on molybdenum is very high and that the surface conditions are in a first approximation not critical. A similar behavior was found by PTUSHINSKII(1) in experiments on the deposition of Ag on Mo. He found that the sticking coefficient in this case changed from $s = 1$ for the clean surface to $s = 0{\cdot}9$ for the surface in an ambient of 10^{-6} torr. For gold, the change is not as marked as for silver.

Some desorption rate measurements are shown in Fig. 3. In the graph, the abscissa represents the desorption temperature, as measured with a micro-optical pyrometer, but with appropriate emissivity corrections. The ordinate shows the fraction of Au^{198} atoms that remain on the molybdenum surface during 2 min of heating. The data were taken at a residual pressure of 2×10^{-9} torr. The same behavior was found for a surface exposed to 10^{-8} torr. After a surface had been exposed to a pressure of 10^{-3} torr the desorption took place at lower temperature than could be measured with the pyrometer. Heating for 2 min to 1070°K removed more than 90 per cent of the gold initially present.

The probability w per unit time of desorption from a homogeneous surface can be assumed in a first approximation to have a temperature dependence of the type

$$w = w_0 \exp(-E/kT).$$

The frequency factor w_0 and the desorption energy E are in this approximation assumed to be independent of the temperature T. The experimental data fit a relation of this kind, as is shown by the full-line curve in Fig. 3. This curve was obtained by using $w_0 = 2 \times 10^{13}$ sec^{-1} and $E = 4{\cdot}2$ eV. An idea of the accuracy of the measurement can be obtained by comparing the experimental points with the dotted line in Fig. 3. The dotted line is the result of using $w_0 = 1{\cdot}5 \times 10^9$ sec^{-1} and $E = 3{\cdot}0$ eV in the expression for the desorption probability. Another molybdenum foil used in these experiments showed a very similar behavior.

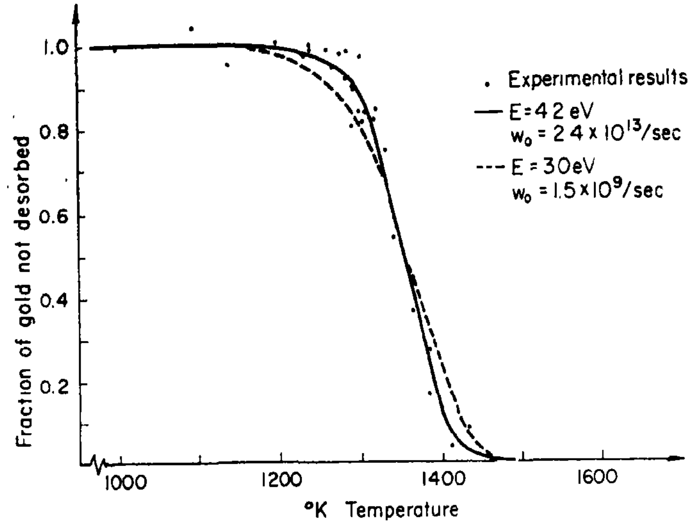

FIG. 3. Desorption of Au from a heat-cleaned polycrystalline Mo surface. Comparison of experimental results with two curves obtained by assuming the desorption probability w to have a temperature dependence $w = w_0 \exp(-Ekt)$.

The best desorption parameter values for it were $w_0 = 4 \times 10^{12}\,\text{sec}^{-1}$ and $E = 3{\cdot}9$ eV. The desorption energy of the "dirty" surface was estimated to be less than 1·5 eV.

The most serious error in the data is due to the fact that the apparatus did not permit precise temperature control during desorption. The foils were heated by a r.f. heater which gave temperature variations of ± 20° during the desorption periods. In addition, there were temperature gradients of the same magnitude across the substrate surface.

The value found for the binding energy E of gold on the clean molybdenum surface is high. It is of the same order as the sublimation energy of gold $E_S = 3{\cdot}6$ eV and molybdenum $E_S = 6{\cdot}7$ eV. No other gold binding energy E measurements are known to the authors. Comparisons with silver on molybdenum are reported in Table 1.

The desorption energies of silver are substantially lower than the gold value which compares with the highest desorption energies reported in the literature ($E = 6{\cdot}3$ eV for oxygen on tungsten and $E < 3$ eV for the alkali metals on tungsten(3)).

Table 1

	E	Authors
Au on Mo	4·2 eV	present paper
Ag on Mo	1·5 eV	PTUSHINSKII(1)
Ag on Mo	2·2 eV	VON GOELER(2)

The comparison of gold and silver desorption indicates that the electrostatic image force does not represent the major part of the surface binding force. The ionic radius of silver is smaller than that of gold. Therefore, in the image force picture, silver would be expected to be bound more tightly than gold. It is much more likely that the binding is by a metallic bond. The frequency factor is of a magnitude predicted for a two-dimensional ideal gas bound to the surface by a strong harmonic oscillator type force. For this model, $w_0 = kT/h = 2 \times 10^{13}\,\text{sec}^{-1}$ at 1000°K. It is interesting that the desorption is complete and that adsorption as well as desorption does not depend on the amount of adsorbed gold in the range indicated above. There is no sign of a binding state of higher energy and no diffusion of gold into the target.

Acknowledgements—The authors wish to thank DANIEL ALPERT, HANS FRAUENFELDER and R. NORMAN PEACOCK for helpful discussions. They are grateful for the assistance of the staff of the CP-5 reactor at Argonne National Laboratory where gold irradiations were performed.

REFERENCES

1. PTUSHINSKII I. G., *Sov. Phys. tech. Phys.* **3**, 1302 (1958).
2. VON GOELER E. and PEACOCK R. N., *J. chem. Phys.* **39**, 169 (1963)
3. EHRLICH G., *Structure and Properties of Thin Films*, (edited by NEUGEBAUER G. A., NEWKIRK J. G. and VERMILYEA D. A.,) p. 453. John Wiley, New York (1959).

J. Phys. Chem. Solids Pergamon Press 1963. Vol. 24, pp. 1223–1231. Printed in Great Britain.

ELECTRON AND NUCLEAR SPIN RESONANCE IN *n*-TYPE SILICON CARBIDE

G. E. G. HARDEMAN

Philips Research Laboratories, N.V. Philips' Gloeilampenfabrieken,
Eindhoven-Netherlands

(*Received* 7 *March* 1963)

Abstract—Some experiments are described of the electron nuclear double resonance in *n*-type silicon carbide at low temperatures. With this method the magnetic interaction between the bound donor electron and the ^{29}Si and ^{13}C nuclei is studied. Transitions of the lattice nuclei interacting with the donor electrons cause some change of the level of the electron spin resonance. By means of this effect (ENDOR), the nuclear magnetic resonance of the nuclei surrounding the donor centres was detected. The nuclear resonance frequency is shifted due to the bound donor electron, the shift being dependent on the position of the nucleus with respect to the centre.

By means of microwave radiation the nuclear polarization could be enhanced. The nuclear resonance was then observed of the majority of the nuclei of which the resonance frequency is not shifted.

By comparing the ^{29}Si and ^{13}C spin-lattice relaxation times with each other it is concluded that the donor impurities occupy carbon sites.

From the ENDOR spectra the extension of the bound donor electron around the impurity centre is estimated. Assuming a hydrogen-like envelope function a value of 5 Å was found for the orbital radius. This value is consistent with the observed effects of nuclear dynamic polarization and paramagnetic resonance.

1. INTRODUCTION

THE electron spin resonance of the impurity centres in silicon carbide was first observed by VAN WIERINGEN.(1) The investigations were extended by WOODBURY and LUDWIG(2) who also carried out some experiments on the electron nuclear double resonance (ENDOR). In this method which was introduced by FEHER(3) the e.s.r. signal is influenced when nuclear spin transitions are induced of nuclei which have a magnetic interaction with the electrons. Thus information regarding this interaction can be obtained. The data provided by WOODBURY and LUDWIG(2) are mainly concerned with *p*-type material. For *n*-type material only that ENDOR spectrum was obtained which originates from the interaction of the donor electron with the nuclear magnetic moment of the ^{14}N donor nuclei.

It is the purpose of this paper to present additional and more extensive data on ENDOR experiments with nitrogen doped SiC which allow some conclusions to be drawn about the extension of the wave function of the bound donor electron. Apart from the ENDOR the nuclear magnetic resonance of the ^{13}C and ^{29}Si nuclei could be detected by making use of nuclear dynamic polarization. In this way some nuclear relaxation effects could be studied leading to the conclusion that the nitrogen centres occupy carbon sites. In Section 2 a general outline of the various double resonance effects which can be expected in SiC is presented. After a short description of the experimental set up in Section 3 the results obtained with the various double and single resonance experiments are described and discussed in Section 4.

2. THE VARIOUS POSSIBILITIES FOR DOUBLE RESONANCE

The spin Hamiltonian of the combined electron nuclear spin system in nitrogen-doped SiC is given by:

$$\begin{aligned}\mathscr{H} = {} & g\mu_B \boldsymbol{H}\cdot\boldsymbol{S} - \gamma_d \hbar \boldsymbol{H}\cdot\boldsymbol{I}_d \\ & - \sum_k \gamma_{\mathrm{Si}} \hbar \boldsymbol{H}\cdot\boldsymbol{I}_k - \sum_l \gamma_c \hbar \boldsymbol{H}\cdot\boldsymbol{I}_l \\ & + A_d \boldsymbol{I}_d\cdot\boldsymbol{S} + \sum_k \{A_k \boldsymbol{I}_k\cdot\boldsymbol{S} + B_k(\boldsymbol{I}_k, \boldsymbol{S})\} \\ & + \sum_l \{A_l \boldsymbol{I}_l\cdot\boldsymbol{S} + B_l(\boldsymbol{I}_l, \boldsymbol{S})\}\end{aligned} \tag{1}$$

The first four terms give the interaction with the external magnetic field H, of the magnetic moments of the electron, the donor nucleus, the surrounding ^{29}Si and ^{13}C nuclei respectively. In this notation γ_d, γ_{Si} and γ_C represent the gyromagnetic ratios of the donor nuclei, the ^{29}Si and the ^{13}C nuclei respectively.

The fifth term is the hyperfine interaction between the electron and the donor nucleus. The last two terms represent the interaction between the electrons and the surrounding ^{29}Si nuclei with spin I_k and ^{13}C nuclei with spin I_l. The terms A_k and A_l are the scalar parts of this interaction. The terms $B_k(I_k,S)$ and $B_l(I_l,S)$ are the dipolar parts which can be given by:

$$B_\kappa(I_\kappa, S) = \frac{g\mu_B\hbar\gamma_I}{r_\kappa^3}\left\{I_\kappa\cdot S - \frac{3(S\cdot r_\kappa)(I_\kappa\cdot r_\kappa)}{r_\kappa^2}\right\} \qquad (2)$$

$$\kappa = k,l$$

where r_κ is the radius vector connecting the donor nucleus to the k^{th} or l^{th} lattice nucleus and γ_I the gyromagnetic ratio of either ^{29}Si or ^{13}C.

The term $A_d I_d \cdot S$ results in a threefold splitting of the e.s.r. line because of the spin-quantum-number $I_d = 1$ of the ^{14}N nucleus. The last two interaction terms cause no resolved splitting of the e.s.r. lines, but they can be determined in principle with the help of ENDOR.

Apart from causing e.s.r. line broadening the two last terms create the possibility of increasing the nuclear spin polarization of the lattice nuclei. In general one can distinguish two possibilities concerning the dynamic polarization.

a. Thermal motion of the electrons relative to the nuclei

This motion results in thermal fluctuations of the electron–nuclear interaction. Now the time-dependent operators A_κ and B_κ cause combined electron–nuclear spin flips resulting in extra relaxation transitions which were otherwise forbidden. If the e.s.r. is saturated, this extra relaxation causes a rearrangement of the occupation of the energy levels in such a way that the nuclear polarization is increased. Because the nuclear magnetic resonance signal is proportional to the nuclear polarization the n.m.r. signal is also increased by a factor p which is equal to the ratio of the enhanced polarization and the polarization at thermal equilibrium.

For the case that only A_κ fluctuates sufficiently we have the well known OVERHAUSER effect⁽⁴⁾ with the maximal p-value of $-\gamma_s/\gamma_I$ where γ_s is the (negative) gyromagnetic ratio of the electron.

If only the dipole coupling B_κ fluctuates sufficiently the theoretical enhancement factor will be $p = \frac{1}{2}\gamma_s/\gamma_I$.⁽⁵⁾

b. No thermal motion

In this limiting case the necessary double transitions cannot occur rapidly enough to obtain the above-mentioned effects. The thermal fluctuations at A_κ and B_κ are now contained only in the time variations of S caused by the electron spin relaxation. By causing single nuclear spin flips these remaining fluctuations are still the main source of the nuclear spin-lattice relaxation.

Nevertheless the nuclei can be polarized in a quite different way. This so-called solid state effect⁽⁶⁾ is based on the mixing of spin states by the dipolar interaction. Simultaneous electron-nuclear spin transitions can then be induced with an alternating magnetic field of frequency $\nu = \nu_S \pm \nu_I$, where ν_S and ν_I are the e.s.r. and the n.m.r. frequency respectively. For $\nu = \nu_S + \nu_I$ we obtain for the theoretical enhancement $p = -|\gamma_s/\gamma_I|$, while for $\nu = \nu_S - \nu_I$: $p = |\gamma_s/\gamma_I|$.

From the behaviour of the dynamic polarization one can conclude which of the two mentioned conditions are valid. In our case of a n-type semiconductor at low temperatures (lower than the value corresponding to the donor ionization energy) we can expect the following effects:

Low donor concentration N_d. Here the impurity centres are separated sufficiently to keep their bound donor electrons in stationary orbits, and the solid-state effect will be found.

Medium N_d. Now in a perceptible number of cases overlapping of the donor wave functions occurs, if the distance between two or more impurities becomes of the order of the orbital radii.

Then the corresponding electrons partly lose their localization around one donor nucleus. In these regions the electrons will probably occupy stationary orbits over two or more neighbouring centres at the same time. Then again the solid-state effect will occur. On the other hand the possibility cannot be excluded that thermally activated motion occurs which is confined to these regions. Then in principle an Overhauser effect is possible.

Higher N_d. The onset of impurity conduction is reached. The electrons then become mobile, i.e. different charge distributions can be realized with only a very small activation energy. This corresponds to more and more rapid fluctuations of A_κ and B_κ, and with increasing N_d the solid-state effect will eventually disappear because of too strong nuclear spin-lattice relaxation. Instead the Overhauser effect will become possible.

3. EXPERIMENTAL METHOD

The experiments on both ENDOR and nuclear dynamic polarization were carried out with the help of the double resonance cavity described elsewhere.(7) Only liquid helium temperatures were applied in order to obtain sufficiently large effects.

For the measurements of the n.m.r. of the polarized nuclei the coil surrounding the sample formed part of the tank circuit of a marginal oscillator for the detection of the resonance absorption. The n.m.r. signals were recorded as a function of the frequency of the oscillator while H was kept constant. The oscillator frequency could be swept with the help of a voltage dependent silicon capacitor.

The usual detection system with magnetic field modulation and a phase-sensitive amplifier was applied. Most recordings were made with the frequency scanning speed, field modulation amplitude and oscillator strength adjusted for maximal signal-to-noise ratio. Although no true representation of the n.m.r. line shape was obtained the signal strength could nevertheless be considered as proportional to the nuclear polarization.

For the ENDOR measurements the oscillator frequency has to be scanned over a much larger range owing to the large n.m.r. frequency shifts of the nuclei surrounding the centres. For this purpose another oscillator provided with a "Mullard" VC 101 frequency-linear tuning capacitor was employed. With a servo system the frequency was scanned over the range of 1 octave during a time that could be regulated between 15 and 1800 sec.

The e.s.r. spectrometer used in this work operates at X-band ($\nu \approx 9500$ Mc/s). It is a superheterodyne type with an intermediate frequency of 30 Mc/s. The e.s.r. signals were also obtained with the conventional method of audio-frequency modulation (60 c/s) of the external magnetic field and phase sensitive amplification of the signal appearing on the i.f. detector. The external magnetic field has a stability of better than $1:10^5$, which was necessary for the dynamic polarization and the ENDOR measurements.

4. RESULTS AND DISCUSSION

4.1 *Electron paramagnetic resonance*

It was shown by LELY and KRÖGER(8) that the nitrogen centres probably occupy carbon sites. The investigated crystals belonged to the 6H type, in which one can distinguish three non-equivalent carbon or silicon sites. From the e.s.r. spectrum at a frequency of 14 KMc/s WOODBURY and LUDWIG(2) showed that the impurity atoms are equally distributed over the three sites and that the spectra of the two sites coincide. In our case the applied frequency of 10 KMc/s was too low to resolve the small difference in g-factor between the sites.

Figure 1 shows e.s.r. recordings for three different donor concentrations N_d and $T = 4{\cdot}2$°K. The microwave bridge was adjusted for the detection of the real susceptibility. With the magnetic field modulation limited to a fraction of the e.s.r. line width the actual line shape was obtained from the phase-sensitive amplifier.(3)

The samples were taken from a series of batches with decreasing nitrogen content. The sample of Fig. 1(c) ($N_d = 1{\cdot}8\times10^{16}/\text{cm}^3$) was the last of the series of n-type crystals. For lower N_d the samples were p-type and showed a Boron acceptor spectrum. In fact Fig. 1(c) shows a superposition of a donor spectrum and a relatively small acceptor spectrum. This sample was probably inhomogeneous.

The main threefold splitting is due to the hyperfine interaction of the bound donor electron with the ^{14}N nuclei having spin quantum number $I = 1$. The spectra can be considered as a superposition of the contributions of single donors and clusters containing two or more donors. The position of the components of the cluster spectrum is determined by the average nuclear magnetic

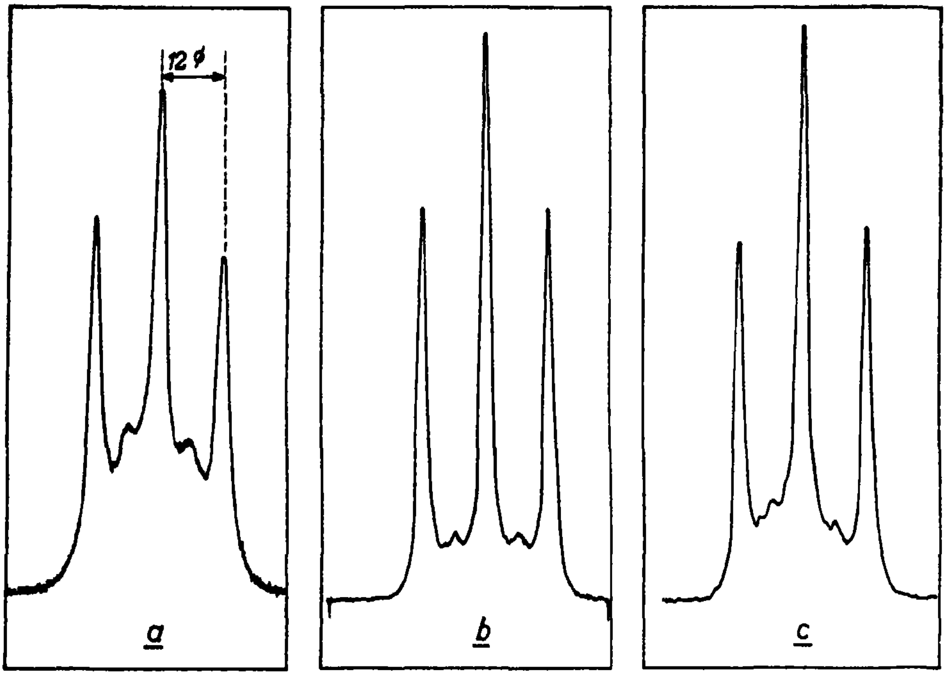

FIG. 1. The e.s.r. spectrum for $T = 4{\cdot}2°K$, $N_d = 1{\cdot}1 \times 10^{18}/cm^3$ (a), $N_d = 3{\cdot}1 \times 10^{17}/cm^3$ (b), $N_d = 1{\cdot}8 \times 10^{16}$ (c).

quantum number $\langle m_I \rangle$ of the n impurities belonging to it.$^{(9)}$ The $\langle m_I \rangle = \pm \frac{1}{2}$ peaks of the $n = 2$ clusters are clearly discernable between the main components.

Up to 77°K the shape of the spectra of Fig. 1 was independent of temperature. Figure 2 shows the derivative of the e.s.r. absorption spectra of a technically prepared sample with $N_d = 10^{19}/cm^3$ taken at $T = 77°K$ and $1{\cdot}2°K$. At the higher temperature the originally resolved ^{14}N hyperfine splitting is averaged out by thermal motion.

4.2 *Nuclear magnetic resonance with dynamic polarization*

Because of the small size of the samples (about $0{\cdot}04\ cm^3$) it was impossible to observe the n.m.r. without the help of dynamic polarization. Figure 3 shows the enhanced ^{29}Si resonance signal which is proportional to the polarization as a function of the external magnetic field H, for $N_d = 1{\cdot}1 \times 10^{18}/cm^3$ and $T = 4{\cdot}2°K$. Also plotted on the same field scale is the corresponding e.s.r. spectrum.

The result shows that the dynamic polarization is caused by the solid-state effect. Because the

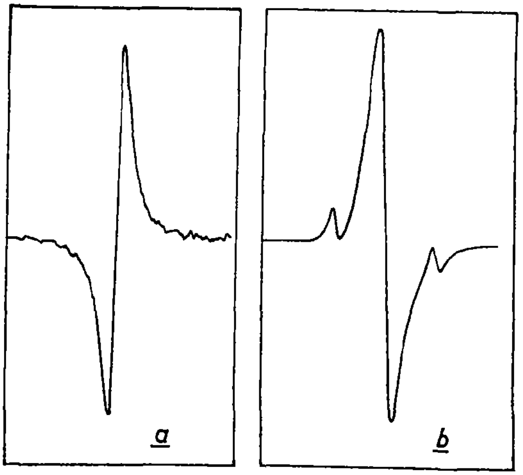

FIG. 2. The e.s.r. spectra of a sample with $N_d = 10^{19}/cm^3$ for $T = 77°K$ (a) and $T = 1{\cdot}2°K$ (b). The derivative of the e.s.r. absorption with respect to H was recorded as a function of H.

n.m.r. frequency is of the order of the e.s.r. line width the two transitions at $\nu_s \pm \nu_I$ cannot be induced separately and a differential effect occurs which is described elsewhere.(7) The same polarization has been found for the ^{13}C spin system.

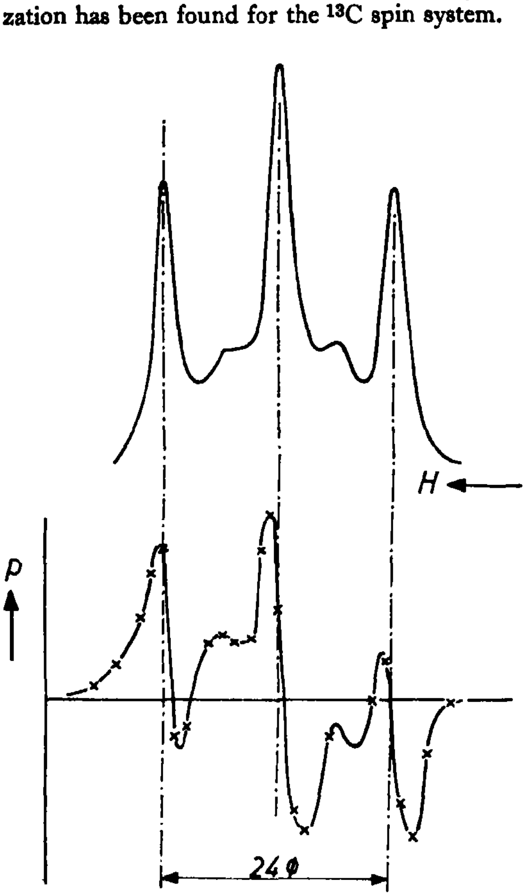

FIG. 3. Lower part: The enhanced n.m.r. signal of ^{29}Si plotted in arbitrary units as a function of *H*, for a constant frequency of 9526 Mc/s. With changing *H* the different conditions for the solid-state effect are traversed. Upper part: the e.s.r. spectrum recorded on the same field scale.

A similar experiment was carried out by COMBRISSON and SOLOMON(10) on *n*-type Si. For $N_d = 5 \times 10^{16}/\text{cm}^3$ they found a mixture of solid-state and Overhauser effect. This last effect was probably caused by photo-electrons generated by incidental radiation. In our case the samples were completely shielded by a brass vessel which was submerged in the liquid helium. During a separate series of experiments the SiC samples were deliberately illuminated with white light and with blue light corresponding to the bandgap energy. However, not a trace of Overhauser effect was found. Probably the lifetime of the photo-electrons was too short so that the necessary relaxation transitions were absent.

It is interesting to note that while in Si a phosphorus donor concentration $N_d \approx 10^{18}/\text{cm}^3$ leads to a pure Overhauser effect,(10) a comparable concentration of nitrogen donors in SiC yields a pure solid-state effect. It appears from our experiments that for the onset of an Overhauser effect in SiC nitrogen concentrations of at least a few times $10^{19}/\text{cm}^3$ are needed. This points to a linear extension of the nitrogen donor wave function in SiC which is smaller than that in Si by a factor of about 3. The more quantitative determination of the extension of the donor electron wave function in SiC, which will be given below on the basis of the ENDOR experiments, confirms this estimate.

It took a certain time for the nuclear polarization to be built up exponentially. Therefore the measuring points of Fig. 3 were taken after 10 min of microwave pumping while the nuclear polarization was initially made zero by means of saturation. Within the limited accuracy the polarization time t^* of the sample of Fig. 3 was about 10 min for the applied microwave power and not dependent on temperature.

The nuclear spin-lattice relaxation time t_1 could be determined with more accuracy. Again for the sample with $N_d = 1{\cdot}1 \times 10^{18}/\text{cm}^3$ the relaxation time t_1 of the ^{29}Si and ^{13}C spin system is plotted as a function of T in Fig. 4. The relaxation process can be described with the following well-known model.(11) Deviations of the nuclear polarization from the thermal equilibrium value are transported by nuclear spin diffusion to the paramagnetic centres where the nuclear spin-lattice relaxation is established by means of the electron-nuclear dipole interaction. Also by means of spin diffusion the dynamic polarization is transported from the centres and distributed over the total spin system.(7)

In principle the necessary condition for the dynamic polarization to be possible is that the polarization time has to be shorter than the relaxation time. The mechanism of nuclear spin diffusion is essentially not dependent on temperature. The observed constancy of t^* is consistent with this. On the other hand t_1 proves to be temperature dependent which shows that the limiting factor for the relaxation rate is determined by the electron-nuclear interaction.

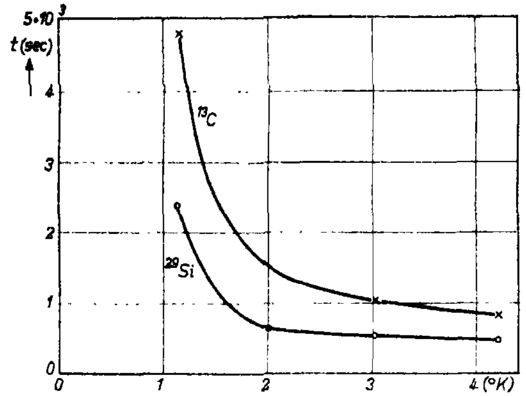

FIG. 4. The spin-lattice relaxation time t_1 of the ^{29}Si and ^{13}C nuclei as a function of temperature.

The transition probability W_{SI} of the nuclear spin-lattice relaxation of a nucleus interacting with an electron spin is given by:(12)

$$W_{SI} = \frac{1}{5}\cdot\frac{S(S+1)}{\tau}\cdot\left(\frac{H_s}{H}\right)^2 \tag{3}$$

where τ is the electron spin relaxation time and H_s the dipolar magnetic field-strength caused by the electron at the position of the nucleus. If the limitation by spin diffusion is neglected the rate equation for the occupation of the two nuclear spin levels N_+ and N_- is found by summing over the fraction of nuclei which are located around the donor centres.

$$\frac{\mathrm{d}}{\mathrm{d}t}N_+ = \frac{1}{5}\frac{S(S+1)}{\tau}\cdot H^{-2}\cdot\frac{N_d}{N}\sum_j N_j H_{sj}^2$$
$$\times\left\{-N_+\left(1-\frac{1}{2}\frac{h\nu_I}{kT}\right)+N_-\left(1+\frac{1}{2}\frac{h\nu_I}{kT}\right)\right\}, \tag{4a}$$

with a similar expression for the higher nuclear spin level. In these expressions N_j is the number of nuclei under consideration (for example silicon) in the j^{th} shell around the impurity and H_{sj} is the r.m.s. value of the electron field in the shell. The rate of change of the polarization by relaxation is now given by:

$$\frac{\mathrm{d}}{\mathrm{d}t}(N_+-N_-) = \frac{\mathrm{d}}{\mathrm{d}t}\Delta N = \text{constant}$$
$$\times \sum_j N_j H_{sj}^2(\Delta N_{th}-\Delta N) \tag{4b}$$

where ΔN_{th} is the thermal equilibrium value of ΔN. The natural abundance of the magnetic isotopes does not enter in this expression. The summation in (4) converges rapidly because H_{sj}^2 falls off rapidly with the distance to the impurity centre. Over the whole temperature range the relaxation time of the ^{13}C-nuclei appears to be longer than that of the ^{29}Si-nuclei. Because the first term of the summation in (4b) is predominant it can be concluded that the nearest neighbours of the impurity centres are silicon atoms, which confirms the conclusions of Ref. 8 that the nitrogen atoms occupy carbon sites.

At the cost of signal-to-noise ratio the r.f. voltage, magnetic field modulation and frequency scanning speed could be reduced sufficiently to obtain a more truthful representation of the n.m.r. line shape (Fig. 5). The linewidth proves to be about 200 c/sec for both resonances.

Nuclear dynamic polarization was also found in samples with smaller N_d value ($N_d \approx 10^{17}/\text{cm}^3$). Due to excessively large polarization- and relaxation times these samples were not investigated in detail. For instance with $N_d = 2\times 10^{17}/\text{cm}^3$ and $T = 4{\cdot}2$°K the following values were found: ^{29}Si : $t^* \approx 1$ hr, $t_1 \approx 3$ hr and ^{13}C : $t^* \approx 2$ hr, $t_1 \approx 5$ hr. Again only the solid-state effect was found with no influence from illumination of the samples.

No dynamic polarization was obtained in the sample with $N_d = 10^{19}/\text{cm}^3$. For $T = 77$°K we can expect the Overhauser effect (case 1). However the necessary saturation of the e.s.r. proved to be impossible owing to inadequate microwave power

4.3 *ENDOR*

The ENDOR frequencies are given by:

$$\nu = \nu_I \pm \{\tfrac{1}{2}a_\kappa+\tfrac{1}{2}b_\kappa(3\cos^2\theta_\kappa-1)\} = \nu_I \pm \Delta\nu_\kappa \tag{5}$$

where ν_I is the normal n.m.r. frequency of either ^{29}Si or ^{13}C and θ_κ the angle between $\boldsymbol{H}$ and $\boldsymbol{r}_\kappa$.

The term $\frac{1}{2}a_\kappa$ represents the frequency shift due to the scalar interaction. The term $\frac{1}{2}b_\kappa(3\cos^2\theta_\kappa - 1)$ gives the shift caused by the dipolar interaction.

As shown in Fig. 6 the ENDOR spectrum consists mainly of two broad and strong peaks resulting from the remote ^{29}Si and ^{13}C nuclei having a small interaction with the donor electron. The dips on the two peaks are associated with the nuclei with no interaction at all and thus occur at frequencies corresponding to the normal n.m.r. Quite similar signals from remote nuclei were found in n-type silicon.(3)

The resolved ENDOR signals from the more neighbouring nuclei proved to be very weak and were absent in the case of ^{13}C, which is probably due to the low ^{13}C abundance. After many repeated recordings the following reproducible peaks were found:

Table 1

Frequency shift $\Delta\nu_k$ with respect to ν_{Si} (Mc/s)	Orientation of H and strength $H\|c$-axis	 $H\|a$-axis
$\Delta\nu_1 = 1{\cdot}00$	absent	weak
$\Delta\nu_2 = 0{\cdot}62$	absent	weak
$\Delta\nu_3 = 0{\cdot}52$	clear	clear
$\Delta\nu_4 = 0{\cdot}34$	clear	clear
$\Delta\nu_5 = 0{\cdot}27$	weak	weak
$\Delta\nu_6 = 0{\cdot}13$	clear	weak

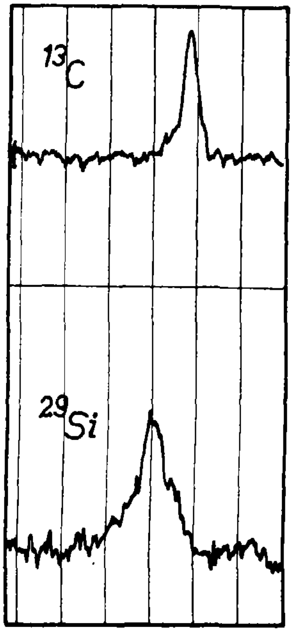

FIG. 5. The ^{29}Si and ^{13}C n.m.r. spectra recorded as a function of frequency. Frequency scale: 290 c/s per division for ^{29}Si and 580 c/s per division for the ^{13}C recording. Resonance frequency, 2·80 Mc/s and 3·64 Mc/s respectively.

It was not possible to follow the angular dependence of the shift $\Delta\nu_1$, which apparently contains an important dipolar contribution b_1^{*}. From the rather limited results given in Table 1 one cannot expect an unambiguous identification of the spectrum as in the case of n-type silicon.(3) Moreover much less is known about the band structure of silicon carbide than in the case of germanium or silicon. However, outside the central lattice cell we may tentatively assume a hydrogen-like distribution function for the electron around the impurity nucleus. The distribution function is then:

$$|\psi(r)|^2 = \text{const} \cdot \exp(-2r/r_0) \qquad \text{(6a)}$$

where r_0 is a measure for the extension of the wave function and r the separation from the donor nucleus. On the lattice points ($r = r_\kappa$) the value

---

[*] Because of the smallness of the available single crystals the sample had to be composed of 3 oriented pieces of the same batch. Small relative misalignments of the crystal axes can therefore be expected. For relatively high b_κ values this leads to ENDOR line splitting or broadening with subsequent loss of signal strength. One can expect this effect to be minimal for those orientations for which the dipolar contribution has an extreme value ($\theta_\kappa = 0°$ or $90°$).

of a_κ in (5) is given by:

$$a_\kappa = 8/3\,\gamma_I\,\mu_B\,|\psi(r_\kappa)|^2 \qquad (6b)$$

On the impurity nucleus ($r = 0$), where the function (6) is definitely no longer valid we have $|\psi(0)|^2 = 0{\cdot}7\times10^{24}/\mathrm{cm}^3$ from the known ^{14}N hyperfine coupling.(2) The experimental results of Table 1 combined with (5) and (6) give approximately the values of $|\psi(r_\kappa)|^2$ outside the central lattice cell. As the donor is most probably on a carbon site the next highest value of $|\psi(r_\kappa)|^2$ can be expected on the nearest Si neighbours occupying a tetrahedron around the impurity centre. Strong dipolar interaction can be expected there. In the case of As-doped silicon it was found that $\frac{1}{2}b =$ 0·55 Mc/s for the nearest neighbours.(3) In the SiC lattice the shorter interatomic distance yields a theoretical estimate of $\frac{1}{2}b_1$ equal to 1 Mc/s.

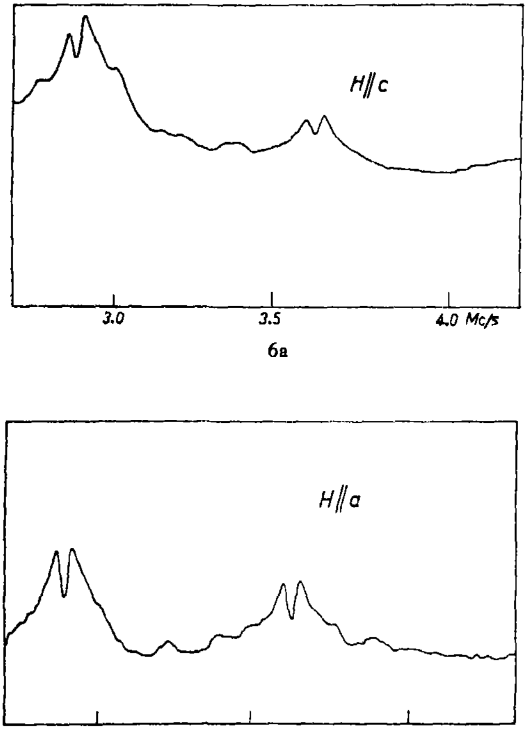

6a

6b

FIG. 6. The ENDOR spectra for $N_d = 2\times10^{17}/\mathrm{cm}^3$ and two different orientations of H, i.e. (a) parallel to the c-axis and (b) parallel to the a-axis.

For $H\|a$-axis two values of θ are realized for the nearest neighbours namely 90° and 35°. We now consider $\Delta\nu_1$ as the ENDOR frequency due to those two nearest neighbouring ^{29}Si for which $\theta = 90°$, because for the two others with $\theta = 35°$ the observed $\Delta\nu_1$ would lead to a very small and therefore unacceptable value of a_1. By substituting the measured value of $\Delta\nu_1$ into (5), taking $\theta = 90°$ and making use of the value for b_1 estimated above we derive for the nearest neighbours: $\frac{1}{2}a_1 =$ 2 Mc/s. In spite of the large signal to noise ratio no resolved hyperfine splitting due to these nearest neighbour—^{29}Si was found in the e.s.r. spectra for $H\|a$- and $\|c$-axis. This fact establishes an upper limit for a. The value of 2 Mc/s for $\frac{1}{2}a_1$ just being below this limit is therefore consistent with this observation.

Most of the next nearest Si neighbours are separated at a distance of 3·6 Å and 4·7 Å, both distances occurring in nearly equal amounts. There one can expect a much smaller dipolar contribution. The equally strong lines $\Delta\nu_3$ and $\Delta\nu_4$ are attributed to these nuclei, while the lines $\Delta\nu_2$ and $\Delta\nu_5$ may either result from anisotropy of the electron density distribution or from the remaining dipolar interaction. By using (5) and (6b) the function (6a) can now be fitted on the lines $\Delta\nu_3$ and $\Delta\nu_4$ (the dipolar contribution is thereby neglected). We obtain:

$$|\psi(r)|^2 = 3{\cdot}3\times10^{22}\cdot\exp(-2r/5{\cdot}0)\,\mathrm{cm}^{-3} \qquad (7)$$

(r in Å)

The value of 5·0 Å for r_0 is obviously less than one would obtain from the simple expression for the orbital radius: $r = \hbar^2\epsilon|e^2m^*$, which yields $r_0 = 8{\cdot}8$ Å for $\epsilon = 10$ and $m^* = 0{\cdot}6$ m. This is not astonishing as for this relatively deep donor centre the last expression for r_0 is a very bad approximation.

For $r = 1{\cdot}9$ Å (nearest Si neighbour) the empirical function (7) gives $\frac{1}{2}a_1 = 1{\cdot}04$ Mc/s compared with $\frac{1}{2}\alpha_1 = 2$ Mc/s as estimated above from $\Delta\nu_1$. The ENDOR peak $\Delta\nu_6$ corresponds to 7 Å (7) which is compatible with the next Si shell outside the 4·7 Å one. Altogether the electron extension as given by the expression (7) fits well with not only the ENDOR spectrum but also with the conclusions drawn from the e.s.r., dynamic polarization and n.m.r.

Acknowledgements—I am greatly indebted to Mr. G. B. GERRITSEN who took part in all this work. My thanks are also due to Dr. H. J. G MEYER with whom I had many stimulating discussions which ultimately led to this paper, and Mr. W. F. KNIPPENBERG who provided me with the samples.

REFERENCES

1. VAN WIERINGEN J. S., *Halbleiter und Phosphore.* p. 367. Vieweg, Braunschweig (1958).
2. WOODBURY H. H. and LUDWIG G. W., *Phys. Rev.* **124**, 1083 (1961).
3. FEHER G., *Phys. Rev.* **114**, 1219 (1959).
4. OVERHAUSER A. W., *Phys. Rev.* **92**, 411 (1953).
5. ABRAGAM A., *Phys. Rev.* **98**, 1729 (1955).
6. ABRAGAM A. and PROCTOR W. G., *C.R. Acad. Sci. Paris* **246**, 2253 (1958).
7. HARDEMAN G. E. G., *Philips Res. Rep.* **15**, 587 (1960).
8. LELY J. A. and KRÖGER F. A., *Halbleiter und Phosphore* p. 525. Vieweg, Braunschweig (1958).
9. SLICHTER C. P., *Phys. Rev.* **99**, 479 (1955).
10. COMBRISSON J. and SOLOMON I., *J. Phys. Radium* **20**, 683 (1959).
11. BLOEMBERGEN N., *Physica* **15**, 386 (1949).
12. ABRAGAM A., *The Principles of Nuclear Magnetism*, p. 380. Oxford University Press, London (1961).

J. Phys. Chem. Solids Pergamon Press 1963. Vol. 24, pp. 1233–1237. Printed in Great Britain.

PARAMAGNETISM OF POLYCRYSTALLINE NICKEL

SIGURDS ARAJS and R. V. COLVIN

Edgar C. Bain Laboratory for Fundamental Research,
United States Steel Corporation Research Center, Monroeville, Pennsylvania

(*Received* 12 *March* 1963; *revised* 10 *May* 1963)

Abstract—Because of appreciable discrepancies among past experimental studies of the paramagnetic behavior of nickel at elevated temperatures, we have carefully measured the magnetic susceptibility of two high purity nickel samples up to 1500°K. These measurements are in reasonable agreement with Fallot's (1944) studies. Phenomenologically, between 740 and 970°K the magnetic susceptibility follows the Curie–Weiss law, $\chi = C/(T-\theta_p)$, with $C = 5{\cdot}54_6 \times 10^{-3}$ cm^3 °K g^{-1} and $\theta_p = 654{\cdot}1$°K. At higher temperatures deviation from this law occurs which is describable by an additional temperature dependent contribution to the total susceptibility.

INTRODUCTION

RECENTLY we have started to investigate the magnetic properties of binary nickel-rich alloys in order to increase our knowledge of the origin of magnetism in transition metals. For the analysis of the alloying effects, one has to have reliable information on the magnetic behavior of pure nickel. One property of interest is the paramagnetic susceptibility. Although this quantity for nickel has been studied extensively in the past, we have found that available data not only show considerable scattering but also are mutually quite inconsistent, especially at elevated temperatures. Thus it was decided to review this problem and to measure carefully the magnetic susceptibility of nickel as a function of temperature above its ferromagnetic Curie point. The experimental results of this investigation are described in this paper.

EXPERIMENTAL CONSIDERATIONS

Two nickel samples (designated by 1 and 2) were used in this experiment. Sample 1 was made from high purity nickel by means of levitation melting.* The analysis of this metal, provided by the supplier, is given in Table 1. It was found that during the levitation melting considerable gas evolution occurred. Metallographic examination also revealed that this metal contained sizable amounts of inclusions. Therefore, it was necessary to purify this nickel by melting it together with about 0·02% carbon in a zirconia crucible. This procedure gave metal from which small levitation melts (dia. $\frac{3}{8}$ in., length $\frac{3}{4}$ in.) were easily made. Metallographic examination after the carbon treatment showed practically no inclusions present. The ratio $\rho(4{\cdot}2)/\rho(298)$, where $\rho(4{\cdot}2)$ and $\rho(298)$ are the electrical resistivities at 4·2 and 298°K, respectively, was found to be $3{\cdot}3 \times 10^{-3}$ for the purified nickel.

Table 1. *Partial analysis of nickel* (*sample* 1)

Impurities	Amount [p.p.m.]
Fe	10
Al	7
Si	5
Ca	2
Cu	2
Mg	2
Ag	< 1
Mn	< 1
As,Au,B,Ba,Be,Bi,Cd,Co, Cr,Cs,Ga,Ge,Hf,Hg,In,Ir, K,Li,Mo,Na,Nb,Os,P,Pb,Pt, Rb,Re,Rh,Ru,Sb,Se,Sn,Sr, Ta,Ti,Tl,V,W,Zn,Zr	Not detected

---

* Obtained from Johnson–Mathey Co.

This quantity is a reasonable value for high purity nickel.(1)

Sample 2 was prepared from electrolytic nickel.* A partial list of impurities according to the supplier is presented in Table 2. This nickel was melted in a vacuum of about 10^{-4} mm Hg using a magnesium oxide crucible and then was cast in a copper mold (dia. ½ in., length 6½ in.). The ratio of the electrical resistivity at 4·2 and 300°K of this material was found to be $33{\cdot}7 \times 10^{-3}$. The same nickel has been used to make nickel-rich nickel–niobium alloys whose electrical resistivities have been studied earlier.(2)

Table 2. Partial analysis of nickel (sample 2)

Impurities	Amount [w/o]
Fe	0·01
Cu	0·01
C	Trace
Co	Trace
S	Trace
Si	Trace

The nickel samples, whose susceptibilities were measured, were enclosed in silica capsules evacuated to 10^{-5} mm Hg. The magnetic susceptibility was determined with the Faraday method using essentially the apparatus described before(3) except for some improvements. The most important of them is the addition of a controller maintaining a stability of 1 part in 10^4 in the electric current in the solenoid. Another improvement is the replacement of the Mettler Type B-5 balance by a Sartorius Series 2500 semi-micro-balance capable of detecting weight changes of 0·01 mg. Third, a program controller, by means of which the furnace temperature can be varied in a predetermined manner, has been added.

The diamagnetic corrections of the quartz capsules, determined experimentally, were applied to the data to obtain the total magnetic susceptibilities of the nickel samples.

EXPERIMENTAL RESULTS AND DISCUSSION

Figure 1 shows in a conventional manner the measured inverse magnetic susceptibility per gram ($1/\chi$) of both nickel samples as a function of the absolute temperature (T). The susceptibility values were found to be independent of the magnetic field. The data clearly indicate that the susceptibilities of samples 1 and 2 are the same. Furthermore, we also found no hysteresis effects, i.e., the susceptibility of the samples at a particular temperature was independent of the previous thermal history.

Figure 1 also presents the susceptibility of most of the earlier studies(4–8) for which the numerical data have been published. The inconsistency of the various results especially at elevated temperatures and the scattering of the points are quite noticeable. Of all the above-mentioned studies our data agree in the most satisfactory way with the measurements of FALLOT.(8) The magnetic susceptibility of polycrystalline nickel has also been determined recently by NAKAGAWA.(9) Although he does not give numerical susceptibility data (and thus the comparison with our results is difficult) it appears from his $1/\chi$ vs. T plot that his results at high temperatures are somewhere between TERRY's(6) and those of SUCKSMITH and PEARCE.(7)

It is obvious from Figure 1 that the magnetic susceptibility of nickel does not obey the Curie–Weiss law

$$\chi = \frac{C}{T-\theta_p} \tag{1}$$

over the whole temperature range. The quantities C and θ are the Curie constant and the paramagnetic Curie temperature, respectively. However, according to our data, the Curie–Weiss law is phenomenologically applicable in the temperature range from about 740 to 970°K. Using the method of least squares we obtained from the susceptibility data on the sample 1 the quantities C and θ_p to be $5{\cdot}54_6 \times 10^{-3}$ cm^3 °K g^{-1} and 654·1°K, respectively. This value of C gives the paramagnetic moment of a nickel atom $\mu_p = 1{\cdot}61_3$ Bohr magnetons. The above-given values were obtained from the measured magnetic susceptibility data without correcting for the diamagnetism of nickel. This quantity is believed to be small and difficult to estimate exactly. FALLOT(8) quotes it to be $-0{\cdot}00307 \times 10^{-6}$ g^{-1} cm^3. For these reasons we, as usually done by other investigators, neglect this small contribution in our analysis of the data.

---

* Obtained from Williams and Co.

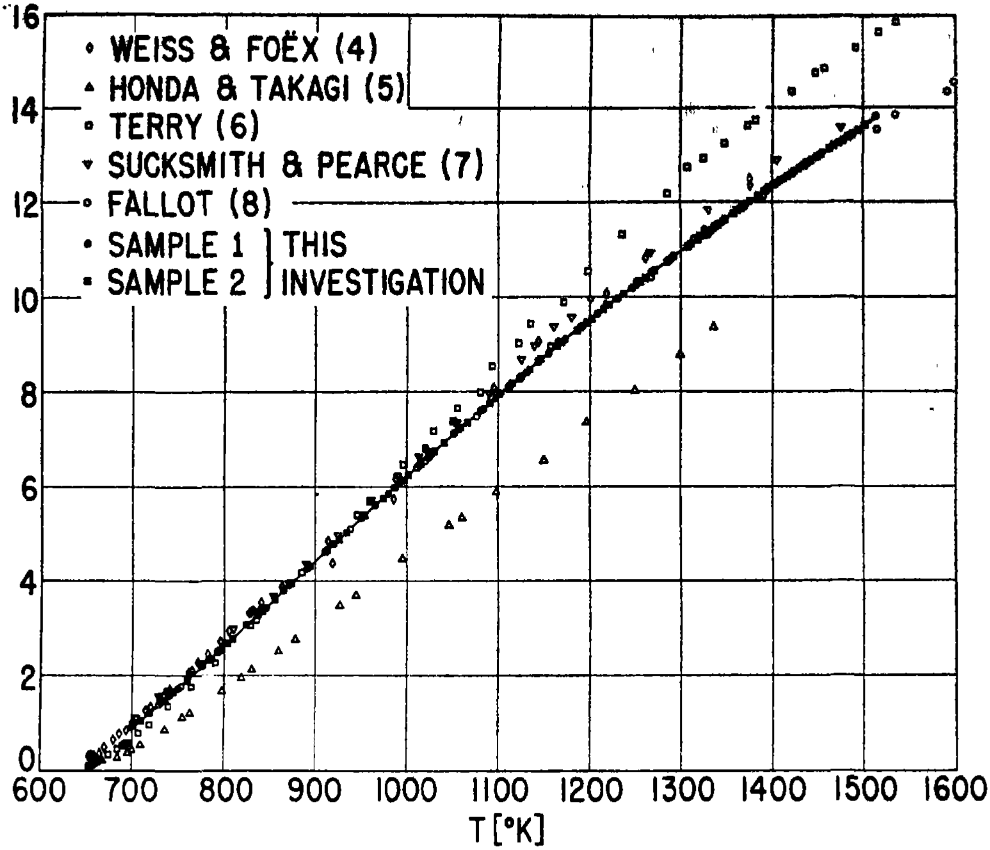

FIG. 1. Inverse magnetic susceptibility of nickel as a function of temperature.

The downward curvature in the $1/\chi$ vs. T plot of nickel at high temperature indicates a contribution to the susceptibility in addition to the Curie–Weiss term. It seems quite generally accepted(8, 10, 11) that the paramagnetic behavior of nickel and many nickel binary alloys can be represented by the equation

$$\chi = \frac{C}{T-\theta_p}+\chi_a, \qquad (2)$$

where χ_a is assumed to be independent of the temperature. Several values of χ_a for nickel have been given in the literature.(8, 11, 12) Since χ_a has a possible theoretical meaning (paramagnetic susceptibility of s-electrons, orbital contribution of d-electrons, influence of s–d exchange interactions, effect of s–d transfer)(13–16) a more accurate knowledge of it is of some importance. Our attempts to obtain χ_a completely independent of the temperature have been unsuccessful. That is, we found it impossible to fit our susceptibility data to equation (2) with χ_a as a constant over the whole temperature range.

Since it is convenient phenomenologically to use equation (2) for describing the magnetic susceptibility, we decided to consider χ_a as a function of temperature. This quantity is shown in Fig. 2. The points were obtained from the measured magnetic susceptibility values on the sample 1 using our values of C and θ as given above.

Finally, it may be remarked that we also tried to fit our experimental data to the equation

$$\chi = \alpha+\beta T+\gamma/T \qquad (3)$$

which has been used by KAUFMANN and STARR(17) for certain nickel–copper alloys. This, too, was found to be impossible.

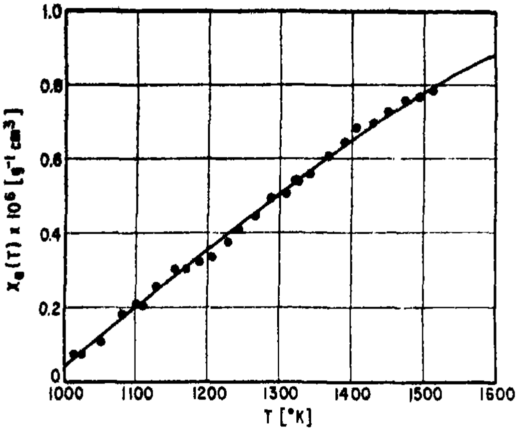

FIG. 2. χ_a of nickel (sample 1) as a function of temperature.

Recently it has been suggested by KOCH and ARROTT,(18) and by DANIELIAN(19) that it is more advantageous to plot $1/\chi T$ vs. $1/T$ instead of $1/\chi$ vs. T for analyzing the susceptibility data. This plot is particularly useful for obtaining the Curie constant and the interaction parameters based on the localized electron model. Figure 3 shows the magnetic susceptibility data of the sample 1 as the graph of $1/\chi T$ vs. $1/T$. The open points in this figure were calculted from FALLOTT's measurements,(8) made up to about 100°K above the melting point (m.p.) of nickel, in order to extend our plot at high temperatures. Moreover, it appears that even then one cannot reliably extrapolate the quantity $1/\chi T$ for $1/T = 0$ primarily because of the scattering of Fallot's points. An attempt was made to plot $1/(\chi-\chi_a)T$ vs. $1/T$ using various χ_a values. It was not possible to obtain a straight line, demonstrating, as already mentioned above, that the paramagnetic susceptibility of nickel does not follow equation (2).

Finally, it should be remarked that in spite of recent theoretical and experimental advances toward the understanding of the electronic structures of the transition elements(20, 21) no completely satisfactory theories of the paramagnetic behavior of the ferromagnetic transition metals exist at the present time.

Acknowledgements—The authors are grateful to the following members of this Laboratory: J. M. PECK and R. C. PECK for technical assistance, B. F. OLIVER and E. W. TROY for making the samples used in this investigation, and to D. S. MILLER for helpful comments. Stimulating discussion with ANTHONY ARROTT of the Ford Motor Company are greatly appreciated.

REFERENCES

1. WHITE G. K. and WOODS S. B., *Phil. Trans. Roy. Soc.* **251**, 273 (1959).
2. ARAJS S., *J. appl. Phys.* **32**, 97 (1961).

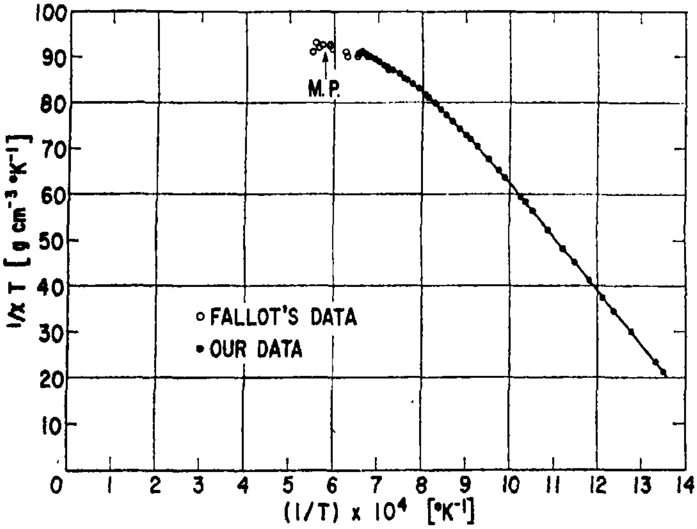

FIG. 3. Koch–Arrott–Danielian plot for nickel (sample 1).

3. Arajs S. and Miller D. S., *J. appl. Phys.* **31**, 986 (1960).
4. Weiss P. and Foëx C., *Arch. Sci. Natl.* **31**, 89 (1911).
5. Honda K. and Takagi H., *Sci. Rep. Tohoku Univ.* **1**, 229 (1911).
6. Terry E. M., *Phys. Rev.* **9**, 394 (1917).
7. Sucksmith W. and Pearce R. R., *Proc. Roy. Soc.* **A167**, 189 (1938).
8. Fallot M., *J. phys. Radium* **5**, 153 (1944).
9. Nakagawa Y., *J. phys. Soc. Japan* **11**, 855 (1956).
10. Néel L., *Ann. phys.* **5**, 232 (1936).
11. Volkov D. I. and Chechernikov V. I., *Izv. akad. nauk. S.S.S.R.* **21**, 1099 (1957).
12. Owe Berg T. G., *J. phys. Radium* **12**, 418 (1951).
13. Shimizu M., *J. phys. Soc. Japan* **16**, 1114 (1961).
14. Kubo R. and Obata Y., *J. phys. Soc. Japan* **11**, 547 (1956).
15. Vlasov K. B. and Vonsovskii S. V., *Fiz. met. metall.* **2**, 403 (1956).
16. Wohlfarth E. P., *Proc. Roy. Soc.* **A195**, 434 (1949).
17. Kaufmann A. R. and Starr C., *Phys. Rev.* **63**, 445 (1943).
18. Koch F. B. and Arrott A., *Bull. Amer. phys. Soc.* **7**, 263 (1962).
19. Danielian A., *Proc. phys. Soc. Lond.* **80**, 981 (1962).
20. Herring C., *J. appl. Phys.* **31**, 35 (1960).
21. Brooks H., *Electronic Structure and Alloy Chemistry of the Transition Elements*, p. 3 (edited by Beck P. A.) Interscience, New York (1963).

NOTICE

The International Conference on the PHYSICS of SEMICONDUCTORS will be held from July 20 to 24, 1964, in Paris under the auspices of the International Union of Pure and Applied Physics and la Société Française de Physique.

The general conference will be preceded and followed by specialized informal symposia on such subjects as Radiation Damage, Plasma Effects in Solids, and Transition Element Compounds.

Further information and details can be obtained from Prof. M. BALKANSKI, *Laboratoire de Physique, Ecole Normale Supérieure*, 24 *rue Lhomond, Paris* (5).

J. Phys. Chem. Solids Pergamon Press 1963. Vol. 24, pp. 1239–1250. Printed in Great Britain.

A COMPETITIVE ADSORPTION MODEL OF STEADY-STATE GROWTH OF A CRYSTAL FROM A LIGHTLY-DOPED MELT

P. J. HOLMES

Research Laboratory, Associated Electrical Industries Ltd., Aldermaston Court,
Aldermaston, Berks.*

(*Received* 7 *March* 1963; *revised* 13 *May* 1963)

Abstract—A model of the solid–liquid interface region of diamond-type crystals is postulated, in which conventional adsorption theory is used to derive an expression for the solute distribution in the growing crystal. It is found that there is a large variation with surface orientation of times available for approach to adsorption equilibrium at growth sites. Thus, on close-packed {111} planes, the proportion of solute adsorbed is not able to depart far from its initial value, while on most other orientations it can approach or attain equilibrium. The theory accounts, qualitatively, for the facet distribution coefficients, their independence of solute concentration over a wide range, and for the distribution coefficient in equilibrium crystals being at the equilibrium level, despite the facets on such crystals.

1. INTRODUCTION

THE statistical description of static and dynamic equilibria of a crystal in contact with a melt in terms of the relative rates of forward and reverse reactions has been given by JACKSON and CHALMERS,(1) and applied to semiconductor crystal growth by THURMOND.(2) The discovery of the facet effect,(3) whereby the distribution coefficient for solutes differs between {111} facets and other interfaces, showed that the atomic processes of solute incorporation into the solid could not be ignored, and thus it is necessary to examine them in more detail.

The growth processes may be considered as a series of consecutive reactions. If, in such a series there is a slowly-equilibrating process, it is only over a very long period of time that the equilibrium calculable in terms of initial and final energy states will appear. In a growing crystal the sites of the reactions are moving with the surface, and so the slower processes may never attain true equilibrium. The result of this freezing of non-equilibrium conditions is that the actual dynamic balances may approach those calculable from the faster reactions only. Adsorption at the interface, with a limited number of adsorption sites in a monatomic surface layer—generally identified with chemisorption—has been discussed by TRAINOR and BARTLETT,(4) but their treatment has a number of mathematical defects. We shall also consider the effect of the interface on free energy of atoms near the growing interface, i.e. physical adsorption. The range of this effect is still short compared with the thickness of the diffusion layer. Thus concentration variations are not confined (as in Trainor and Bartlett's theory) to the atomic layer in which growth is actually taking place, and no unreasonable discontinuity in solute content exists in the melt.

The rates of escape of atoms from differently oriented surfaces of the growing solid will also be discussed. The possibility that the growth rate dependence of this factor might be a significant feature in solute segregation in semiconductor crystals was first proposed by HALL,(5) in an endeavour to explain differences in growth rate variation of effective distribution coefficient on surfaces of different orientation.

---

* Now at Royal Aircraft Establishment, Farnborough, Hants.

2. TRANSITION RATES INVOLVED IN CRYSTAL GROWTH

We will use a scheme of energy levels as shown in Figs 1(a) and 1(b), the general form of the potential energy–distance curves being the same for both solute and solvent, though the barrier heights differ.

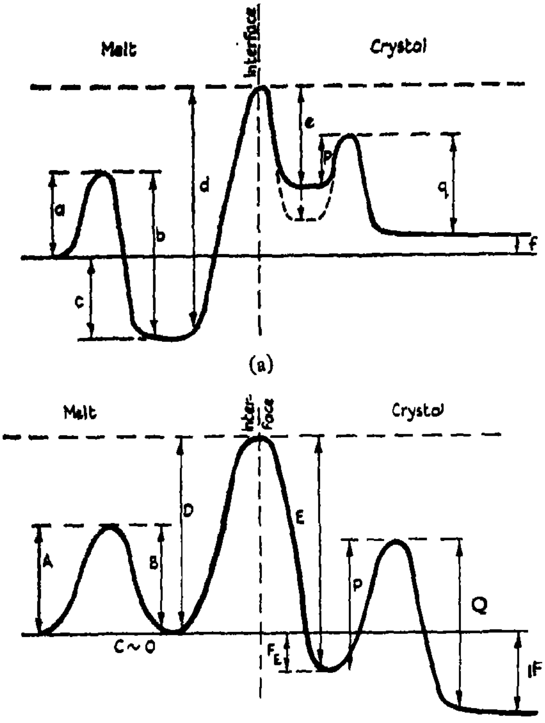

Fig. 1 (a). Activation energies for atomic movements (solute atoms). (b). Activation energies for atomic movements (solvent atoms).

All solutions will be considered to be ideal, and we will assume that the ranges of the forces involved are small compared with the thickness of the diffusion layer in the melt ahead of the growing interface. Thus, if we consider the rejection (or absorption) of solute in relation to the bulk melt, the analysis of BURTON *et al.*[(6)] still holds, and the macroscopic pile-up or depletion of solute ahead of the interface is considered in this paper to correspond to that given in the former analysis. We shall discuss the equilibrium at a uniform temperature between a solute concentration C_0 in the surface region of the melt just beyond the range of the exchange processes† and C_S in the crystal, related by BURTON's equation (14)

$$C_S = k^* C_0 \tag{1}$$

where k^* is the *interface* distribution coefficient. The *effective* distribution coefficient $k = C_S/C_L$ relative to the bulk liquid concentration C_L is given by BURTON's equation (15)

$$k = k^*/[k^* + (1-k^*)\, e^{-\Delta}] \tag{2}$$

where $\Delta = f\delta/D_l$ (f = growth rate, δ = "length of diffusion zone"). Since BURTON's work was unable to show any obvious difference between k^* and k_0 (the *equilibrium* distribution coefficient corresponding to the phase diagram) under his experimental conditions, these parameters have very frequently been equated in subsequent work. In fact, k^* can alter quite significantly under some circumstances, and thus can result in differences between the values of k measured under different conditions, over and above those due to the diffusion processes in the melt.

In a homogeneous phase the probability of an atom passing in a given direction over any barrier is given by the product of the probability of that atom being activated, the probability of an adjacent site being vacant, and a geometrical factor G to define the relevant direction of transitions and including any correlation effects of an atom jumping back into its previous position before it is otherwise refilled.

We shall consider the atomic motion across each barrier during the time t in which the interface advances one atomic layer. $t = 1/uv$, where v is the normal velocity of advance, and u is the number of atomic layers per cm.

The number of solute atoms crossing unit area of the barrier of height a in this time is

$$A_a = \gamma_a n_a \exp(-a/kT) \tag{3a}$$

where n_a is the number of atoms per unit area ready for activation, γ_a is given on the theory of absolute reaction rates by $G_a t/\tau_0 \exp(\Delta S_a/k)$. ΔS_a is the entropy of activation, which determines the partition function between unactivated and activated atoms, and $1/\tau_0$ is the effective frequency of atomic vibrations at temperature T ($1/\tau_{0_l}$, for the melt, $\sim kT/h$, and $1/\tau_{0S}$, for the solid, is a mean value of the atomic vibration frequencies, which will be expressed as $1/\tau_{0S} = \beta/\tau_{0_l}$).

---

† The range of this zone is of the order of $\sqrt{(D_l t,)}$ where D_l is the diffusion coefficient in the melt, and t is the mean time in which the surface advances by one atomic layer.

A similar scheme can be written for solvent atoms, using the corresponding capital letters for the activation energies

$$A_A = \gamma_A\, n_A \exp(-A/kT) \qquad (3A)$$

Putting x_a as the atom fraction of solute atoms,

$$A_a = \gamma_a x_a n_A \exp(-a/kT) \qquad (4a)$$

for dilute solutions.

Corresponding equations can be written for each of the other barriers.

Alternatively, we can write

$$A_a = \alpha_a x_a n_A \exp(-a'/kT), \text{ etc.}$$

where the α's are equal to the corresponding γ's divided by ($\exp\Delta S/k$), and the primed letters represent free energies of activation. In this form the A's are more easily comparable, since all the α's for solute and solvent entirely within one phase will be equal; at the interface they will differ.

It can be shown (see, for example Ref. 7, pp. 196–199) that the experimentally measured activation energy in condensed systems is usually very close to ΔH, the enthalpy change (heat of activation) for the activation process. The free energy of activation is thus

$$E' \sim E_{\exp} - T\Delta S_{\text{act}}$$

An important feature of our energy diagram is the distinction made between the potential energy of atoms in the surface layer and those in the bulk. Some such difference in escape probability was postulated by Hall.

An atom in the surface layer of a diamond or zinc-blende type semiconductor crystal is bound by one, two, or three covalent bonds, so each of the surface energy levels should be subdivided, as will be shown later. Release requires energy to break direct bonds, and possibly to overcome some degree of interaction with second-nearest neighbours, etc. The loss of the atom elevates those bulk atoms to which it was bonded to the status of surface atoms, so the entropy of activation is partly required for these atoms, and partly for the transition of the released atom from solid to melt. It is obvious that rates of the bulk-to-surface diffusion processes p and q must likewise be affected by this bulk-to-surface entropy increase.

By considering the balance of atomic movements near the interface, in terms of a frame of reference moving with the mean velocity of advance of the interface, we have for the solvent

$$n_A \frac{u_l}{u} + A_A - A_B = A_D - A_E$$
$$= n_E + A_P - A_Q = n_Q \qquad (5A)$$

and for the solute

$$n_A x_a \frac{u_l}{u} + A_a - A_b = A_d - A_e$$
$$= n_E x_e + A_p - A_q = n_Q x_q \qquad (5a)$$

where n_Q is the number of all atoms in one atomic layer of the crystal, n_A is that in one atomic layer of the liquid, and u and u_l are the corresponding layer densities. The significance of the terms other than the A's requires some comment. At all times there is a forward and reverse diffusive flow across the barriers ahead of and behind the interface, but since the frame of reference is moving with the interface, atoms are constantly being brought into the operative region of the melt and left behind in the bulk solid by means which do not involve any absolute atomic motion.

3. KINETICS WHEN ALL SURFACE SITES ARE ENERGETICALLY EQUIVALENT

3.1. *Solidification rate*

If there is no volume change on freezing, and there is no large vacancy concentration gradient between solid and bulk, the very dilute solution case of equation (5A) reduces to a single barrier problem, giving a result, at growth rate η, which is equivalent to Thurmond's growth rate equation (4.33).(2)

$$\frac{\eta}{k^F_A} = \frac{\Delta H^F_A}{RT^2_A}\Delta T \qquad (6)$$

but involving a "surface heat of fusion", instead of the bulk parameter ΔH^F_A. The meaning of this surface heat of fusion F_E and its difference from the equilibrium heat of fusion appearing in equation (6) (F in our notation) will be apparent from Fig. 1(b).

3.2. *Solute incorporation*

If we ignore solid diffusion except between the surface and the layer below, and assume one type of atom site to be completely dominant in processes d, e, and p, we have, when all surface sites are equivalent, and there are no vacancy gradients:

$$\frac{x_q}{x_a} = k^*,\ x_b = x_d,\ x_e = x_p,\ n_B = n_D,\ n_E = n_Q$$

Thus from (5a)

$$n_A \frac{1}{k^*}\left(\alpha_a \exp(-a'/kT) + \frac{u_l}{u}\right) - \alpha_b n_B \frac{x_b}{x_q} \exp(-b'/kT) = n_Q \tag{7}$$

$$\alpha_d n_B \frac{x_b}{x_q} \exp(-d'/kT) - \alpha_e n_Q \frac{x_e}{x_q} \exp(-e'/kT) = n_Q \tag{8}$$

$$n_Q \frac{x_e}{x_q} + \alpha_p n_Q \frac{x_e}{x_q} \exp\,(-p'/kT) - \alpha_q n_Q \exp(-q'kT) = n_Q \tag{9}$$

Whence

$$k^* = \frac{n_A\,[\alpha_a \exp(-a'/kT) + u/u_l]}{n_Q\left[1 + \dfrac{\alpha_b}{\alpha_d}\exp[(d'-b')/kT]\left\{1 + \dfrac{\alpha_e \exp[e'/kT(1+\alpha_q \exp(-q'/kT))]}{1+\alpha_p \exp(-p'/kT)}\right\}\right]} \tag{10}$$

For the equilibrium distribution coefficient, we drop all the 1's, and the u_l/u to get

$$k_0 = \frac{n_A}{n_Q}\frac{\alpha_d}{\alpha_e}\exp[(-a'+b'-d'+e'-p'+q')/kT]$$

$$= \frac{n_A}{n_Q}\frac{\alpha_d}{\alpha_e}\exp(-f'/kT)$$

Previous descriptions of segregation may be derived from equation (10) by making various simplifications. At all reasonable growth rates, we may neglect u_l/u in comparison with $\alpha_a \exp(-a'/kT)$.

1. BURTON *et al.*(6) put $k^* = k_0$ and derive the relation of k to k^* given by equation (2).

2. HALL(5) empirically puts $k = k^* = k_0 + (k_s - k_0)$ $\exp(-v_l/v)$ where k_s is an "interface distribution coefficient", and v_l is the growth velocity at which the relaxation time t_r for diffusion in the interface region equals the time for the interface to advance by one layer. This is given by

$$1/u \sim \sqrt{(D_S t_r)},$$

So,

$$v_l \sim \frac{1}{u}\cdot\frac{1}{t_r} = D_S u$$

Thus for $v_l \ll v$

$$k^* \simeq k_0 + \frac{k_s - k_0}{1 + D_S u/v} \sim \frac{\text{Constant } (k_s)}{1 + D_S u/v}$$

If we put $\alpha_e \exp(-e'/kT) \gg 1$ and $\alpha_e \exp(-p'kT) = 0$, equation (10) reduces to a form exactly comparable to this since $\alpha_q \exp(-q'/kT) \sim D_S u/v$. Hall's maximum growth rate for antimony in germanium was 8 in./hr. or $5{\cdot}6 \times 10^{-3}$ cm/sec. $v_l \sim D_S u = 3 \times 10^{-10} \cdot 3 \times 10^{7} \sim 10^{-2}$. So the approximation is probably just valid up to growth rates of this order. However, the effects of diffusion in the melt will set in before this rate is reached, according to equation (2).

3. THURMOND(2) derives (equation (4.38)).

$$k^* = \frac{k_0}{1 + \eta/k_B^r}$$

where η is the growth rate in atoms of all types per second and k_B^r is the rate of rejection of solute atoms from the growing crystal.

If we ignore diffusion in both solid and melt, equation (8) is the complete growth rate equation. Hence we can derive Thurmond's expression, giving a reduction of k^* with growth rate. The experimental observation of this relatively small effect on k^*/k_0 would normally be prevented by the tendency of k/k^* to increase with growth rate much more rapidly, so that k/k_0 increases with growth rate.

4. EFFECT OF ATOMIC STRUCTURE OF SURFACES

The theory of crystal growth from the melt has been considered so far in terms of addition of atoms to energetically equivalent surface sites. This corresponds to the "rough interface" described by JACKSON,(8) in which lateral extension of well-defined atomic layers does not play any part in the growth process. The alternative mode of growth, with a "smooth interface", is probably more applicable to many semiconductor crystal surfaces, since their entropy of melting is large.

The transitions represented in equation (5A) and (5a) by A_d, A_D, A_e, A_E, A_p, A_P, and A_q, A_Q, are generally the total of a number of sub-divisions corresponding to the differently-bonded atoms comprising the surface layer. In a material of diamond or zinc blende structure, it seems reasonable to regard most surface orientations as consisting of stepped layers of close-packed atoms in {111} planes, since complete close-packed layers are the most uniformly strongly bonded (three covalent bonds per atom) and therefore the most stable configuration.* So a surface profile consists of steps, as shown in Fig. 2, either monatomic or else consisting of alternating lengths of two different planes of {111} form. In addition there will be isolated atoms, singly bonded to these planes. By distinguishing between singly-bonded atoms forming part of the crystal, and atoms which are almost equally close to the surface but not bonded, we are implying that the interface is "sharp", and not "diffuse" as described by CAHN and HILLIARD.(9) However, the distinction made between the entropy of atoms in the liquid layer adjacent to the surface and those farther away acknowledges the possibility of some local ordering, and reconciles the two views.

The impact of an atom onto a surface will bring it roughly to a 1-, 2-, or 3-bonded site, i.e. $A_D = A_{D_1}+A_{D_2}+A_{D_3}$. (We will for simplicity consider these to be respectively synonymous with a site on a close-packed plane, a step edge, and a vacant space in a close-packed plane, and ignore the possibility of temporary surface bonds which differ from those required in the completed lattice). There will be a specific rate of release from each of these types of site, i.e.

$$A_E = A_{E_1}+A_{E_2}+A_{E_3}.$$

The energy and entropy changes involved in adding or removing one atom are determined not only by that atom alone, but also by the adjacent atoms whose bonding conditions are thereby changed. Thus the activation energies for loss of atoms may be greater than those for simply breaking 1, 2 or 3 bonds, because the other atoms may simultaneously require energy to raise them to a lower-bonded state. Likewise the entropy increase on loss of a surface atom is partly applied to the atom itself and partly to the newly exposed surface. The total of this and any other entropy changes occurring between bulk solid and bulk melt will be the entropy of melting. We are probably justified in considering that the entropy diagram in the interface region takes the form of one or two steps, rather than a barrier, since activation of an atom from the melt towards a site on the crystal surface must involve loss of some freedom of position, and a loss in entropy. This is to be contrasted with situations such as diffusion, in which there is an entropy of activation for diffusion in any direction, but no significant difference in entropy between initial and final states.

4.1. *Solvent atom transitions across a stepped crystal interface*

We can conveniently discuss the problem of escape of atoms from a crystal surface in terms of the ratio of the time during which a given atomic layer is exposed to the dwell times. The mean dwell time τ_j of the j-bonded solvent atoms on the surface will be

$$\tau_{0S} \exp(E_j'/kT)\dagger$$

We will now consider the meaning of growth velocities in terms of growth of atomic sheets (Fig. 2). If an interface is advancing with velocity v normal to itself, the velocity of advance normal to the close-packed planes is $v_{111} = v \sec \theta$ where θ is the angle of inclination. If we consider these layers to be nucleating and spreading singly at uniform rates, respectively $v_{111}u$ layers per second and v_y cm/sec normal to the growth steps along the close-packed plane, then a given point in any layer remains in the surface for $t = 1/v_{111}u$ sec before being covered over. This is the time during which addition or loss of 1- and 3-bonded atoms occurs.

---

* Similar arguments may be applied to other layer structures, with appropriate changes.

† It is possible that the presence of the surface will alter the frequency spectrum from that in the bulk of the crystal: if so, allowance should be made by using an appropriate τ_{0_S} here.

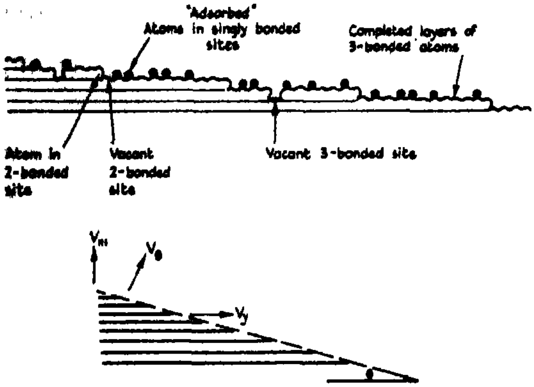

FIG. 2. Model used to describe layer growth in the diamond structure

$$v_y = v_{111} \cot \theta$$

$$v_{\theta} = v_{111} \cos \theta$$

Each atom spends time t exposed, and the growth steps pass over it in time $t_2 = (v_{111}/v_y)t = t \tan \theta$.

The actual rate of growth of layers, v_y, is controlled by the addition and loss of 2-bonded atoms at their edges. If the rate of addition is much greater than the rate of loss, the mean time for filling a site gives t_2, the time taken for the step to advance by one atomic row, and then $v_y = 1/ut_2$. If the rate of loss is comparable to the rate of addition (as it is when close to the melting point) t_2 is correspondingly larger. Thus t_2 is a more fundamental quantity than t, and v_y is approximately given by the simple velocity-undercooling relationship (6), with F_{E_2} substituted for ΔH_A^F. Any departure is due to the fact that a proportion of the growth sites may already be filled by 1-bonded atoms before the step reaches them.

The relation of t, t_2, v, v_y and v_{111} for any orientation on which layer growth operates is obvious from Fig. 2; the crystal morphology is determined by the extent to which v_y is arrested by the local temperature gradients. When the close-packed planes lie at a large angle to an isothermal, lateral growth of layers is slow: $v_y \sim v$ and $t_2 \sim t$. When the layers are nearly parallel to an isothermal, and can extend rapidly, $v_y = v_{111} \cot \theta$ (Fig. 2), and $t = t_2 \cot \theta$. Thus, on {111}, v_y must be very large to correspond to a finite normal growth rate, while only a fraction of a degree away it falls very rapidly. The relation of t_2, v_{111} and v_y is illustrated in Table 1, taking $u \sim 3 \times 10^7$ cm^{-1}.

Of the total number of solvent atoms activated sufficiently to surmount the energy barrier D and attach themselves to the crystal, the proportions going into the variously-bonded sites will be fixed by the relative numbers, n_j, and occupation factors, ϕ_j, of such sites. We will again consider the numbers of transitions corresponding to time t in which the reference plane advances by one

Table 1

		Orientation corresponding to		
t_2 (sec)	v_y (if t_2 remains constant) (cm/sec)	$v_{111} = 1$ mm/hr	$v_{111} = 1$ mm/min	$v_{111} = 1$ cm/sec
3×10^{-12}	10^4	$\theta = 0'\ 0{\cdot}001''$	$\theta = 0'\ 0{\cdot}036''$	$\theta - = 0'\ 2''$
3×10^{-10}	10^2	$0'\ 0{\cdot}1''$	$0'\ 3{\cdot}6''$	$0°\ 34'$
3×10^{-8}	1	$0'\ 10''$	$0°\ 6'$	$\sim 45°$
3×10^{-7}	10^{-1}	$1'\ 35''$	$0°\ 57'$	—
2×10^{-5}	$1{\cdot}6 \times 10^{-3}$	$0°\ 57'$	$\sim 45°$	—
10^{-4}	$2{\cdot}8 \times 10^{-4}$	$5°\ 43'$	—	—
10^{-3}	$2{\cdot}8 \times 10^{-5}$	$\sim 45°$	—	—

layer, because in a steady-state condition the final state in melt and solid must be the same as the initial state but with the interface advanced a distance $1/u$ cm in the direction of v_{111}, or $1/u \cos\theta$ in the direction of v.

In a square centimetre of surface, there are:

n_2 2-bonded atoms along step edges, and an equal number of 2-bonded addition sites.

n "smooth surface" sites, between step edges.

The effective values of n_1 and n_3 are obviously less than n, because each site may be

(a) occupied by a 3-bonded atom with
  (i) no other attached,
  (ii) a 1-bonded atom attached;
(b) unoccupied by a 3-bonded atom.

The symbols n_1 and n_3 will henceforth be taken to mean the effective values, which depend on the local values of the ϕ's, and are thus time-dependent.

There is no very reliable evidence as to what extent 1-layer, 2-layer, and larger steps occur, but we can discuss two limiting cases. When $\theta \sim 0$, it is very likely that the steps are mostly one monolayer high, though a few macroscopic steps may sometimes be visible. A low-index plane almost mid-way between two close-packed planes (e.g. close to {110}) is again likely to be smooth, corresponding to an atomic structure consisting entirely of monolayer steps. So for simplicity we will consider all surfaces up to this mid-way position to be made up of stepped monolayers parallel to one close-packed plane, and beyond these to be made up of monolayers parallel to the other. Field emission microscopy results from spherical surfaces illustrate these ideas in three dimensions,(10) and the relative values of n and n_2 may be derived by the method of MACKENZIE and NICHOLAS(11) for any crystal structure.

When solid diffusion, and physical adsorption in the melt, can be ignored, the expressions $A_D = A_D + A_{D_2} + A_{D_3}$, $A_E = A_{E_1} + A_{E_2} + A_{E_3}$ can be calculated for the variously bonded atoms using an approach similar to the derivation of adsorption isotherms.(12) Where the adsorption at any site is effectively independent of the occupation of adjacent sites, we suppose R_j atoms to be activated for adsorption into n_j sites of one type in unit time, and that they have a mean dwell time τ_j. If ϕ_{jt} is the instantaneous fractional coverage at an arbitrary time t, we have:

Number of atoms activated in time $\mathrm{d}t = R_j n_j \mathrm{d}t$

Number of atoms sticking in time $\mathrm{d}t = R_j n_j (1-\phi_{jt})\,\mathrm{d}t$

Number of atoms leaving in time $\mathrm{d}t = \dfrac{n_j \phi_{jt} \mathrm{d}t}{\tau_j}$

After time t, the total number stuck is thus:

$$n_j \phi_{jt} = \int_0^t \left[R_j n_j (1-\phi_{jt}) - \frac{n_j \phi_{jt}}{\tau_j} \right] \mathrm{d}t \qquad (11)$$

Figure 3 is a qualitative indication of the way in which the ϕ's vary during the history of a given site on the surface; if the growth steps are advancing uniformly, the site spends time t as a 1-bonded site, t_2 is the time taken for the growth step to pass the site, and a further time t is then spent in a 3-bonded state before the next layer covers it over. The inital values of the ϕ's are only zero in the case of ϕ_1, since as the steps advance they meet ϕ_{1t} atoms already in place, and leave behind completed layers with ϕ_3 initially very close to unity. In each case, however, the form of the curve will be a $[1-\exp(-y)]$ function, as in the simplest case where $\phi_{jt} = 0$ at $t = 0$ and $\mathrm{d}\phi_j/\mathrm{d}t \to 0$ as $t \to \infty$. Thus

$$\phi_{jt} = \frac{R_j}{R_j + 1/\tau_j} \left[1 - \exp\{-(R_j + 1/\tau_j)t\} \right]$$

$$\text{and } \left(\frac{\mathrm{d}\phi_j}{\mathrm{d}t}\right)_t = R_j \exp[-(R_j + 1/\tau_j)t]$$

For $\quad t \to \infty, \ \phi_{jt} \to \dfrac{R_j}{R_j + 1\tau_j}$ and $\dfrac{\mathrm{d}\phi_j}{\mathrm{d}t} \to 0$

For $\quad t \to 0, \ \phi_j \sim R_j t$ and $\dfrac{\mathrm{d}\phi_j}{\mathrm{d}t} = R_j$

The loss integral for 2-bonded sites during time t is

$$t/t_2 \int_0^{t_2} \frac{n_2}{\tau_2} \phi_2 \, \mathrm{d}t$$

(i.e. the number of atoms lost in the time t_2 during which each step advances $1/n$ cm, times the number of these unit distances advanced in time t). The addition term is derived similarly.

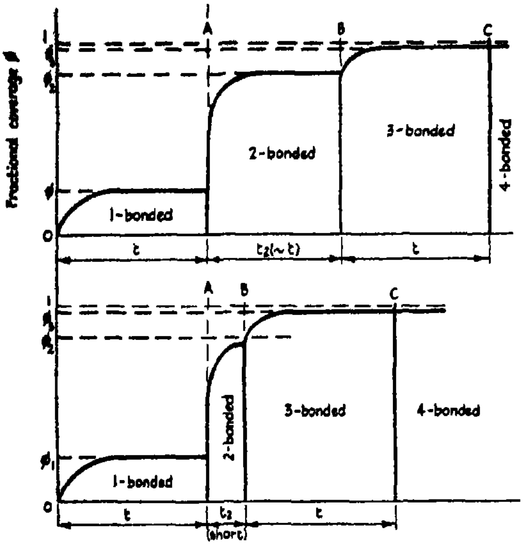

FIG. 3. Occupation history of a surface site during layer growth:

(upper) general site (lower) facet site

A Instant of arrival of step front
B Instant of passage of step front to next atomic row
C Instant of arrival of next step

The sum of the addition and loss integrals for all types of site over time t, $A_D - A_E$, equals n_Q, the number of atoms added per cm² of the given surface. Since for a given orientation t and t_2 and n and n_2 have fixed ratios, the growth rate for that orientation at any given temperature is unique, and the appropriate values of t and t_2 can be derived for insertion into the solute equations. When $t \to \infty$, the equilibrium (time-independent) values of n_j and ϕ_j appear, and other simplifications become permissible.

5. GROWTH OF SINGLE CRYSTALS OF SOLVENT FROM NEARLY PURE SOLUTIONS

It is not possible to grow a spherical crystal of a layer-structure material without careful control of heat flows, because the different rates of nucleation and net rates of accretion on different orientations at one temperature will liberate corresponding amounts of latent heat. Unless this heat can be dissipated and distributed rapidly and uniformly over the interface, a different steady-state interface temperature and normal growth rate will be attained for each orientation, resulting in a non-spherical crystal.

5.1. *Extent of facets on growing crystals*

The appearance of facets on growing crystals is a function of nucleation rates. Where 2-bonded steps are present in quantity on an extended area of a given orientation, there is no problem in maintaining the growth rate, but along each ⟨110⟩ zone there is a range of surfaces between $(\bar{1}11)$ and $(\bar{1}1\bar{1})$ where there are only 1- and 3-bonded step sites.(11) On {111} and {110} there are no steps of any sort, and entirely new layers must be nucleated for the growth front to advance. This requires the addition of a suitable sequence of 1- and 3-bonded atoms to build up a stable nucleus. The rate of formation of nuclei is low when the dwell time of singly-bonded atoms is very short, since adjacent sites are unlikely to be filled simultaneously. The normal growth velocity on these orientations will tend to be less than elsewhere, so they may lag behind an otherwise isothermal growth front. The consequent undercooling enhances the lateral extension of nuclei into complete layers, and facets thus develop. At a certain level of undercooling, the rate of peripheral addition will be so much greater than the rate of loss that almost any nucleus will generate a new layer. The facet can then keep pace with the development of the crystal. Unless the surface is strongly "poisoned" with solute, or the presence of the solute assists nucleation, the necessary undercooling for each type of plane will be independent of type of solute.

The majority of semiconductor crystals are grown in long ingots from the melt, either by pulling or by a zone-refining operation. This requires the growth rate, measured parallel to the growth direction, to be constant for all parts of the interface, so the growth rates normal to the interface at any point must be a function of orientation. If the axial growth rate is v_n, that in other directions is $v = v_n \cos\theta$ (Fig. 4). Thus if the growth direction is [111], v_{111} and t are constant and for any other orientation the normal growth rate is $v_\theta = v_{111} \cos\theta$. The local interface temperature and overall interface shape must adjust themselves to suit these impressed growth rate requirements.

In many of the semiconductor crystals in question the angular range covered by facets is about 7° from (111) on an otherwise curved interface.[13, 14] Thus at this angle and beyond, v_θ falls onto the curve $v_\theta = v_{111}\cos\theta$ and at smaller angles has a higher value.

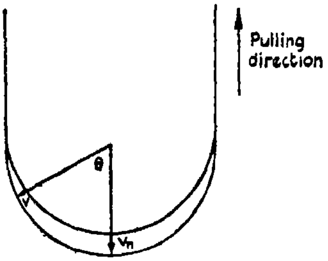

FIG. 4. Continuous growth of a pulled ingot in one direction

$$v = v_n \cos\theta$$

(growth velocity at all points, parallel to v_n, equals v_n).

In any form of growth from the melt, steady-state conditions can only be attained if the crystallization rate and rate of latent heat dissipation by conduction and convection are compatible. Otherwise the local interface temperature will rise and reduce the crystallization rate, and oscillatory conditions may appear.[15]

6. EFFECT OF SURFACE STRUCTURE ON ADDITION OF SOLUTE ATOMS*

Unless the rates of addition and loss of solute and solvent from a given type of site are exactly equal, there will be a net gain or loss of solute after the initial sticking, and the situation is then akin to the "poisoning" of a surface often found in catalysis.[9] If, however, $\tau_s \gg t$, the effective coverage frozen into the crystal is not very different from that produced by the initial attachment of melt atoms. The latter condition is applicable to layer growth close to {111}, with its very low values of t_2. So for growth at a finite rate, the ratio of distribution coefficients on and off a {111} facet is related to the ratio of initial and equilibrium solute coverages. The situation is qualitatively illustrated in Fig. 5, which will be discussed later. An equilibrium crystal, though faceted, grows with a very much larger value of t_2 than a facet on a crystal growing at a finite rate, so the distribution coefficient on the former is similar to that on the unfaceted portions of the latter.

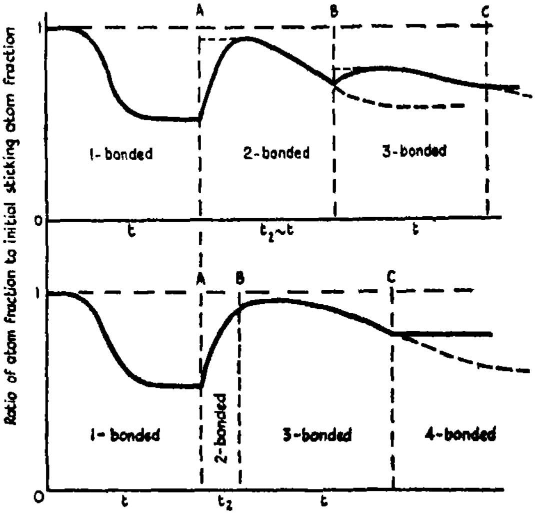

FIG. 5. Sketched curves showing atom fraction of solute as a function of time during layer growth: (above) general sites; (below) facet sites, for $\tau_s < \tau_v$. The relation of times t and t_2 to mean dwell times τ determines final atom fraction at C. If t is similar in the two cases, the level at C is principally dependent on t_2 especially if the equilibrium value of ϕ_1 is low. When $\tau_s > \tau_v$, atom fractions increase from their initial levels.

To derive k^* exactly, we must use equations corresponding to (7), (8) and (9). The situation is greatly simplified if diffusion within the solid can be ignored, i.e. if adsorption kinetics similar to those described above can be used to derive the steady-state value of x_{s_1} ϕ_1, etc. We then have:

---

* The subscript s will be used to denote parameters for the solute: v will be used for solvent parameters where it is particularly necessary to distinguish them.

	Solute	*Solvent*
Number of atoms activated in time dt	$R_{js}n_j\,\mathrm{d}t$	$R_{jv}n_j\,\mathrm{d}t$
Number of atoms sticking in time dt	$R_{js}n_j(1-\phi_{jt})\,\mathrm{d}t$	$R_{jv}n_j(1-\phi_{jt})\,\mathrm{d}t$
Number of atoms leaving in time dt	$\frac{n_j}{\tau_s}x_{s_{jt}}\phi_{jt}\,\mathrm{d}t$	$\frac{n_j}{\tau_v}(1-x_{e_{jt}})\phi_{jt}\,\mathrm{d}t$

where $x_{e_{jt}}$ is the instantaneous atom fraction of solute in the adsorbed layer. Hence the coverage of solute at time t is:

$$n_j\phi_{jt}x_{e_{jt}} = \int_0^t R_{js}n_j(1-\phi_{jt})\,\mathrm{d}t - \int_0^t \frac{n_j}{\tau_s}x_{e_{jt}}\phi_{jt}\mathrm{d}t \tag{12}$$

So

$$x_{e_{jt}}\left(\frac{\mathrm{d}\phi_j}{\mathrm{d}t}\right)+\phi_{jt}\left(\frac{\mathrm{d}x_{e_j}}{\mathrm{d}t}\right)_t = R_{js}(1-\phi_{jt}) - \frac{1}{\tau_s}x_{e_{jt}}\phi_{jt}$$

If ϕ_{jt} is primarily controlled by solvent atoms, $\mathrm{d}\phi_j/\mathrm{d}t$ is given by equation (11), and then:

$$x_{e_{jt}}\left[R_{jv}(1-\phi_{jt})-\left(\frac{1}{\tau_v}-\frac{1}{\tau_s}\right)\phi_{jt}\right] + \phi_{jt}\frac{\mathrm{d}x_{e_j}}{\mathrm{d}t} = R_{js}(1-\phi_{jt})$$

For

$$t\to\infty,\quad x_{e_{jt}}\to\frac{R_{js}}{R_{jv}}\cdot\frac{\tau_s}{\tau_v}$$

$$= x_a\exp[-(E_j'-D_j'+d_j'\quad{}_j')/kT]$$

While for t very small (e.g. t_2 near to close-packed orientations) $\phi_{jt}\sim 0$,

$$x_{e_{jt}}\to\frac{R_{js}}{R_{jv}} = x_a\exp[(D'-d')/kT]$$

and

$$\frac{dx_{ej}}{\mathrm{d}t} = 0$$

Thus the initial atom fraction of attached solute is altered in approaching equilibrium by a factor corresponding to the relative heats of desorption of solute and solvent. This is illustrated in Fig. 5.

6.1. *Effect of heavily adsorbed solutes*

When solute atoms are very heavily adsorbed on the growing surfaces, growth of the crystal will be seriously retarded, since unless the solute element crystallizes with a similar lattice structure to the solvent element, continuation of the latter will be impeded. Equation (12) still holds, but ϕ_j is now a function of both elements, and must be regarded as $(\phi_{j_s}+\phi_{j_v})$.

6.2. *Effects of diffusion in the solid*

If the growth rate is low, or diffusion of solute in the crystal is appreciable, the simple adsorption balance across the growing interface is altered, and the solute transport into the crystal is governed by the following relation, equivalent to equation (5a):

$$n_Ax_a\frac{u_l}{u}\frac{v}{v_{111}}+A_a-A_b = A_{d_1}+A_{d_2}+A_{d_3} - A_{e_1}-A_{e_2}-A_{e_3}$$

$$= A_{p_1}+A_{p_2}+A_{p_3}-A_{q_1}-A_{q_2}-A_{q_3}+n_3\phi_3x_{p_3}$$

$$= n_Qx_q \tag{13}$$

Since the value of each of these terms depends on the time available for approach to equilibrium, k^* (i.e. x_a/x_q) is growth-rate dependent. At very low growth rates (t large), k^* tends towards k_0, the equilibrium value. At high growth rates (t small, t_2 at its minimum value) k^* approaches unity, and if only one type of surface site is important, the expression reduces to the same form as equation (10).

6.3. *Equilibrium distribution coefficient*

This can be obtained by neglecting the $u_l/u \cos\theta$ and $n_3\phi_3 x_{p_3}$ in equation (13) and equating to zero. A detailed balancing system is then obtained for each type of site, where $A_{d_1} = A_{e_1}$, $A_{p_1} = A_{q_1}$, etc. The integrals are replaced by sums over any arbitrary time t, and the equilibrium values of the ϕ's and x's appear everywhere. The net result is thus identical with that for a single type of growth site, independent of intermediate atomic mechanism and thus of surface orientation.

6.4. *Orientation dependence*

Equation (13) gives an orientation dependence of k^*, because of the variation of the ratio t_2/t of the limits of integration of the A's, and of the ratio n/n_2. For a given value of t, the d_1 and e_1 integrals are proportional to n; the values of the d_2 and e_2 integrals will vary with orientation according to the values of t_2 and n_2. As θ increases, these increase very rapidly, so that only a very small angular range has to be traversed before t_2 becomes much greater than τ_{s_3} and the special conditions for close-packed planes cease to apply. It is not possible to separate the orientation and growth-rate dependences of k^* completely, but if $\tau_{s_3} > t_2$ for very small θ, at a given growth rate we can find a unique value k^*_{111} for close-packed planes, and a different value for planes more than a fraction of a degree away which varies very little with orientation. If, as in equilibrium growth, $\tau_{s_3} < t_2$ even for close-packed planes, only the latter value appears. The ratio of the two values can be shown to be almost independent of solute concentration in the bulk of the melt except at solute levels which are so high that equilibrium ϕ's are seriously affected, or so low that the statistical approach is inadequate in the surface region (e.g. at 10^{14} atoms per cm^3, there will be only about one solute atom per centimetre of step edge).(16)

If the nucleation kinetics are such that no facet forms, the portion of the crystal surface over which the special value k^*_{111} for rapid layer growth operates is very small, and lateral diffusion behind the interface will even out the solute concentration to a large extent.

For growth on $\{110\}$ planes, a 2-bonded process can operate at the ends of the individual zigzag rows of 3-bonded atoms which lie along $\langle 1\bar{1}0 \rangle$ directions, so the solute effects should be similar to those on $\{111\}$ planes. The absence of any reports of $\{110\}$ facets on diamond-type crystals grown from the melt prevents comparison of this prediction with experiment.

Solute segregation on all other planes of the diamond structure should follow the model for slow layer growth, except for $\{100\}$, which is a third unique case, since it is composed entirely of 2-bonded atoms. STRAUSS has shown that $\{100\}$ can give facets on compound materials such as InSb.(17) Since layer growth does not operate, the facet effect is here described by the ratio of the values of k^*_{100} given by equation (10) and k^* for surfaces other than $\{111\}$.

7. CONCLUSIONS

By using an atomistic model of the crystal surface it has been qualitatively shown that a close-packed facet on a growing crystal should have a different distribution coefficient from an equilibrium facet. In the former, addition takes place very rapidly at step edges, and the atom fraction of solute has no opportunity to equilibrate from its initial value before it becomes incorporated into the crystal. At zero growth rate, however, complete equilibration can take place, and on surfaces which are far from close-packed orientations, the step edges advance so slowly that a fair degree of equilibration can take place. Thus the dynamic distribution coefficient on random orientations is close to the equilibrium value, while that on layer orientations represents the initial sticking probability of solute atoms at step edges. The latter may result either in a smaller or a greater value for the distribution coefficient at a facet, according to whether the initial adsorption level of solute is smaller or greater than the equilibrium value. The majority of cases in which a facet effect has been reported give a higher solute level on the facet, so that there is a net desorption of solute elsewhere over longer periods. Gallium on germanium facets is an opposite case.

The numerical application of the above theory to practical systems is obviously complex. Since it involves time-dependent integrals of quantities which cannot be directly measured, any attempt to elucidate the relative importance of these quantities must involve very accurate measurements of distribution coefficient as a function of growth rate, surface orientation, and initial solute concentration. The survey made by TRUMBORE(18) shows how difficult it is to determine equilibrium distribution coefficients to the requisite accuracy, let alone the dynamic coefficients, which may, as explained elsewhere,(6, 16) be affected by mechanical and convective stirring. Careful experimental study of one or two systems should, however, give an idea of the validity of the atomistic approach used in this paper.

Acknowledgements—The author wishes to acknowledge many useful discussions with Mr. R. L. ROUSE, and thanks Dr. T. E. ALLIBONE, C.B.E., F.R.S., Director of the Laboratory, for permission to publish this paper.

REFERENCES

1. JACKSON K. A. and CHALMERS B., *Canad. J. Phys.* **34**, 473 (1956).
2. THURMOND C. D., *Semiconductors* (edited by HANNAY N. B.) Chap. 4. Reinhold, New York (1959).
3. HULME K. F., and MULLIN J. B., *Phil. Mag.* **4**, 1286 (1959), *J. Phys. Chem. Solids* **17**, 1 (1960).
4. TRAINOR A. and BARTLETT B. E., *Solid-State Electron.* **2**, 106 (1961).
5. HALL R. N., *Phys. Rev.* **88**, 139 (1952).
6. BURTON J. A., PRIM R. C. and SLICHTER W. P., *J. chem. Phys.* **21**, 1987 (1953); BURTON J. A., KOLB E. D., SLICHTER W. P. and STRUTHERS J. D. *J. chem. Phys.* **21**, 1991 (1953).
7. GLASSTONE S., LAIDLER K. J. and EYRING H., *The Theory of Rate Processes*. McGraw-Hill, New York and London (1941).
8. JACKSON K. A., *Growth and Perfection of Crystals* (edited by DOREMUS R. H., ROBERTS B. W. and TURNBULL D.) p. 319. John Wiley, New York (1958).
9. CAHN J. W. and HILLIARD J. E., *J. chem. Phys.* **28**, 258 (1958).
10. MOORE A. J. W., *J. Phys. Chem. Solids* **23**, 907 (1962).
11. MCKENZIE J. K. and NICHOLAS J. F., *J. Phys. Chem. Solids* **23**, 197 (1962).
12. e.g. GLASSTONE S., *Textbook of Physical Chemistry*, 2nd ed. pp. 1198–1200. Macmillan, London (1955).
13. DIKHOFF J. A. M., *Solid-State Electron.* **1**, 202 (1960).
14. STRAUSS A. J., *Massachusetts Institute of Technology, Lincoln Lab. Rep.: Solid-State Res.* 15th Apr. 1960, p. 28, 15th Oct. 1960, p. 34, etc.
15. MILEVSKII L. S., *Kristallografya* **6**, 249 (1961), English translation *Sov. Phys.-Crystallogr.* **6**, 193 (1961).
16. BANUS M. D. and GATOS H. C., *J. electrochem. Soc.* **109**, 829 (1962).
17. STRAUSS A. J., *Solid-State Electron.* **5**, 97 (1962).
18. TRUMBORE F. A., *Bell Syst. tech. J.* **31**, 205 (1960).

J. Phys. Chem. Solids Pergamon Press 1963. Vol. 24, pp. 1251–1262. Printed in Great Britain.

ORDERING AND DISORDERING PROCESSES IN Cu_3Au—III

LEONARD R. WEISBERG* and **S. L. QUIMBY**

Columbia University, New York, New York

(*Received* 3 *April* 1963)

Abstract—The isothermal change of Young's modulus with time is measured in a single crystal of Cu_3Au following a sudden change in temperature above and through the critical temperature, T_c, when the specimen is initially in one of various states of long and short range order. Short range ordering changes above and close to T_c are found to be completed within minutes. Evidence is adduced for the existence of a metastable short range order below T_c. When the specimen is quenched from above T_c to below, it is shown that the continual formation of new ordered nuclei is an important part of the ordering process. Equations are presented explaining the principal features of the ordering curves in terms of the relative contributions of nucleus formation and growth. When the specimen is heated from below T_c to above, it is deduced that the disorder diffuses from each domain boundary into the domains. Also, the initial disordering rate immediately above T_c is controlled by the existence of a metastable state of long range order.

1. INTRODUCTION

THE kinetics of ordering and disordering in Cu_3Au can be studied by observing the isothermal time variation of Young's elastic modulus of the specimen following a sudden change in temperature from an initial value T_i to a final stationary value T_f. The kinetic processes can be divided into four categories which depend on whether both T_i and T_f lie below T_c, both T_i and T_f lie above T_c, $T_i > T_c > T_f$, or $T_i < T_c < T_f$, where T_c is the critical temperature (389°C). The first of these, which corresponds to the kinetics of long range ordering and disordering, was the subject of a previous investigation.(1) The present research is a continuation of that described in Ref. 1, and includes the last three categories of ordering changes.(2)

Nearly all of the previous work on ordering kinetics in Cu_3Au have been concerned with the third category. Measurements of specific heat,(3) electrical resistivity,(4–6) and elasticity,(7) supplemented by X-ray examination of the internal structure of the material,(8) led to the hypothesis that the initial ordering process at T_f is the formation of small contiguous domains. Within each of the domains the order is in equilibrium for that temperature, but is characterized by one of four phases dependent upon which of the four sublattices is predominantly occupied by gold atoms. The subsequent ordering process is the coalescence of these antiphase domains to form larger domains of a single phase.

Measurements of elasticity by LORD,(9) resistivity by BURNS and QUIMBY,(10) and length by GROSS and QUIMBY,(11) confirmed this hypothesis and revealed details of the mechanism by which the domains are established. This is the occurrence, by statistical fluctuation, of stable nuclei of order in a disordered matrix, and the growth of these nuclei until their boundaries touch. In the present work, it is shown that, prior to the formation of stable nuclei, a new metastable state of short range order is formed. Further, critical experiments are described establishing that the role of nucleation in the ordering process is dominant below about 355°C. Simple equations are provided which indicate the relative importance of nucleation and growth at all temperatures, and explain the principal features of the curves of the time dependence of Young's modulus.

Categories two and four have been almost entirely neglected previously for Cu_3Au. Data is

---

* Present address: RCA Laboratories, Princeton, N.J.

presented here of disordering kinetics above T_c, and also of short range ordering both above and slightly below T_c. Evidence is provided that a metastable state of short range order can exist below T_c, and a metastable state of long range order can exist above T_c.

It is noteworthy that there is a considerable resemblance between the kinetics of ordering in Cu$_3$Au and that in other systems, such as Ni$_3$Fe,(12, 13) Cu$_3$Pd,(14) and Ni$_3$Mn,(15) For example, there is a strong similarity between Fig. 12 of IIDA(13) and Fig. 3 of this paper. It is suggested that the interpretation presented here for the ordering phenomena might be applicable to these other systems. One can further generalize the interpretation to apply, for example, to the solidification of a melt. One can consider an analogy to exist between a liquid and the disordered state, defects and wrong atoms, grains and domains, and a polycrystalline solid and an ordered structure of contiguous antiphase domains. Then the ordering theory presented in Section 2C can be considered as an alternative to those discussed by TURNBULL.(16) Also, in analogy to Bridgman single crystal growth, one might predict that long range ordered Cu$_3$Au can best be prepared by slowly lowering the crystal through a temperature gradient from above T_c to below T_c.

Young's modulus is employed here as an indicator of order, since at equilibrium, Young's modulus increases monotonically with increasing order. However, the exact relationship between Young's modulus and the degree of short or long range order has yet to be established. Therefore, the interpretation of the data offered subsequently is based on two principal features of the curves of the time variation of Young's modulus: the variation of the initial slopes with temperature, and the change of curvature with time at constant temperature. Evidence that these features of the data correspond to changes in order is provided by measurements of length in Cu$_3$Au by GROSS and QUIMBY.(11) In particular, there is a strong similarity between curves depicting the isothermal time variation of length and of Young's modulus, following a quench from 415°C to various temperatures below T_c.

The experimental procedure for this study was described in detail in Ref. 1. The same single crystal of Cu$_3$Au was used as before. Young's modulus E is measured in arbitrary units (a.u.), which are related to c.g.s. units by the formula $E_{\text{c.g.s.}} = 6{\cdot}790 \times 10^9 E_{\text{a.u.}}$. Measurements of Young's modulus can be made every 6 sec to a precision of ± 0·03 a.u. Now length, electrical resistivity, and the elastic moduli all *decrease* with increasing order. Hence, the Young's modulus, which is a reciprocal function of the elastic moduli, *increases* with increasing order. Therefore, to facilitate direct comparison with much data exhibited in the form of graphs in the literature, *increases* in Young's modulus are plotted *downward* in all of the graphs here shown.

2. RESULTS AND DISCUSSION

A. *Young's modulus at constant disorder*

The observed variation of Young's modulus at equilibrium order, E_e, above T_c is shown in Fig. 1, and is also tabulated in Table 1 in Ref. 1. It is found that in the range of 430 to 470°C, the variation of E_e is linear, with a temperature coefficient of $-0{\cdot}0995$ a.u./°C. When a specimen is quenched from an initial temperature T_i above T_c to a lower temperature T_f, the total change in

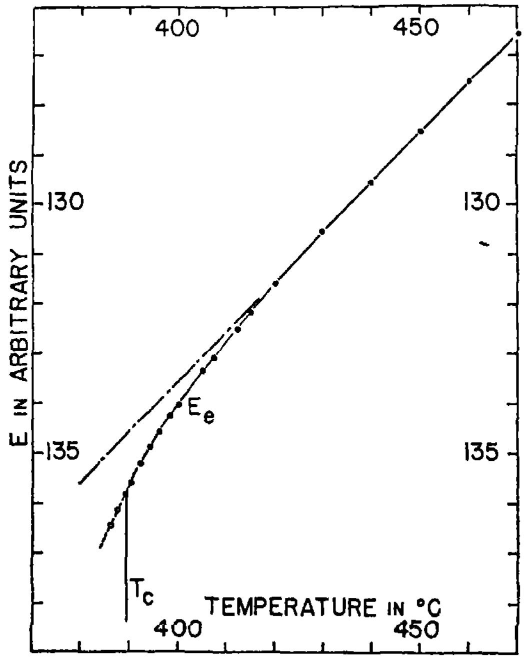

FIG. 1. The variation of equilibrium Young's modulus with temperature above T_c.

Young's modulus is due to both the changes in order and temperature. The quantity $E_{C.D.}$ is introduced to compensate for the temperature change so as to facilitate comparison of isothermal ordering curves measured at different temperatures. It is computed from the above temperature coefficient of E_e, and for a quench from 415°C, $E_{C.D.} = [132{\cdot}18+0{\cdot}0995\ (415-T_f)]$ a.u.

There is evidence that $E_{C.D.}$ is only an approximation to the temperature dependent part of E for a state of constant disorder. First, the temperature coefficient for constant disorder is greater than that for constant order, which has a temperature coefficient of only $-0{\cdot}0636$ a.u./°C, according to Ref. 1. This implies that at a low enough temperature, the values of $E_{C.D.}$ would intersect and pass beyond the curve for equilibrium long range order. Second, it was observed here that the initial value of E following a quench from 415 to 230°C was actually 2·7 a.u. *smaller* than the $E_{C.D.}$ value at 230°C, so that if shown in Fig. 4 for this temperature, the value of E-$E_{C.D.}$ would be negative. Finally, LORD(9) found that the temperature coefficient of E is nearly the same for ordered as for disordered specimens below 200°C. The same is true of the temperature coefficient of resistivity(5) and of the thermal expansion.(17)

B. *Kinetics of short range ordering*

Young's modulus at equilibrium varies linearly from 470 to 430°C. Below 430°C, as the temperature is lowered toward T_c, Young's modulus increases at an accelerated rate, as shown in Fig. 1. This non-linear increase is ascribed to the corresponding increase in equilibrium short range order which is revealed by measurements of the diffuse scattering of X-rays(8) and electrons(18) by the crystal.

Figure 2 depicts the isothermal change of E with time following a sudden change of temperature in the neighborhood of T_c (389°C). The solid circles represent observations made following, respectively, quenches from 405 to 400, 395 to 390, and 390 to 387°C. If the quenches were instantaneous, the initial points of these curves would lie on the dashed line above them. The open circles depict data obtained following sudden increases in temperature from 390 to 395, 395 to 400, and 400 to 405°C. In an instantaneous heating, each initial point would lie on the dashed line below the curve. It is thus evident that a measurable rate exists for the achievement of equilibrium short range order following a change in temperature above T_c, and that this rate increases rapidly as the ordering temperature is raised above T_c.

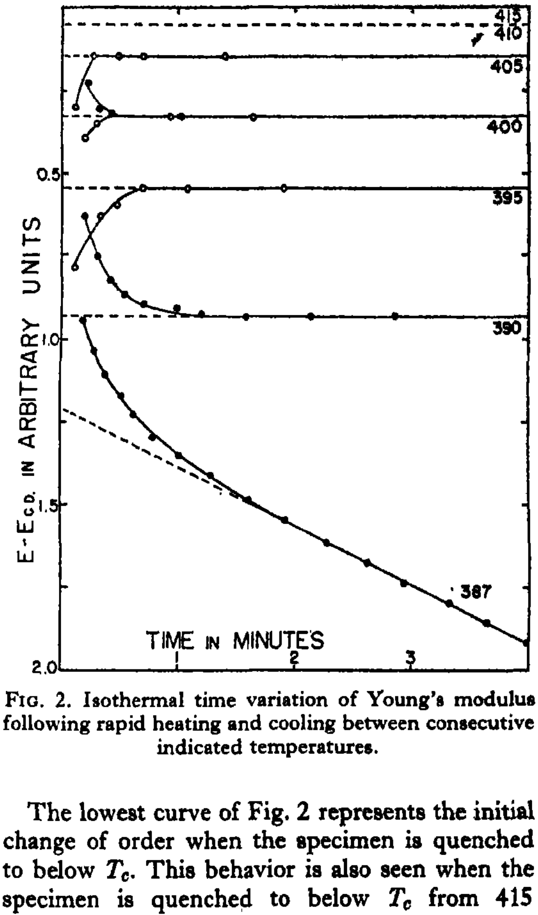

FIG. 2. Isothermal time variation of Young's modulus following rapid heating and cooling between consecutive indicated temperatures.

The lowest curve of Fig. 2 represents the initial change of order when the specimen is quenched to below T_c. This behavior is also seen when the specimen is quenched to below T_c from 415 instead of 390°C, as shown later in Fig. 5. The similarity of both the change in value of $(E-E_{C.D.})$ and the time duration of the change, between the 387°C curve and those above T_c, indicate that the ordering process is the same in both cases, viz. the establishment of a new state of short range order. Further corroboration of this viewpoint is provided by the observation that the terminal values of the initial rapid change in E below T_c (shown in Fig. 2 and later in Fig. 4) lie on a smooth extrapolation of the equilibrium curve above T_c. This is shown in Fig. 1, where the open circles mark such terminal values. This last behavior was also observed by Lord[9] but was given a different interpretation. It is concluded that there is no discontinuity of the short range order at T_c, so that a definite short range order persists at temperatures below T_c, which is in metastable equilibrium pending further ordering.

The kinetics of short range ordering seen here are in contrast with the findings of Damask, Fuhrman and Germagnoli.[10] They observed sizeable variations in the resistivity occurring during periods of 30 min and longer at temperatures as low as 390°C. However, there are several differences between the two investigations. First, the present measurements are performed on a single crystal of Cu_3Au rather than highly polycrystalline specimens. Second, the changes in temperature here are only about 5°C, rather than changes well in excess of 100°C. Finally, this study employs Young's modulus as the indicator of order instead of resistivity.

C. *Ordering in specimens quenched from above T_c to below T_c*

(i) *Isothermal ordering data.* The isothermal change of E with time following a quench from 415°C to the indicated temperature is shown in Figs 3, 4, and 5. These observations are in good accord with those of a similar nature reported by Lord[9] despite significant differences in the two specimens. The critical temperature of Lord's specimen was 386°C and the orientation of the cylinder axis nearly (100). Nevertheless, corresponding values of the quantity $(E-E_{C.D.})/(E_e-E_{C.D.})$ agree within 7 per cent over the entire range of temperature and time.

Inspection of Figs 3 and 5 reveals that above 355°C, ordering occurs in three distinct stages, separated by two inflection points. The first stage consists of a small rapid increase in E, and is completed within a few minutes. This stage can be discerned at temperatures at and above 370°C. The second stage is characterized by the upward convexity of the curves. The major increase in E occurs during this stage, and the ordering rate increases with decreasing temperature. The third state is characterized by an upward concavity of the curves, and by the slow rate of ordering.

At and below 355°C, only the second and third stages of ordering can be distinguished. Curves depicting the second stage below 355 differ in two respects from curves above 355°C: below 355°C the initial rate of ordering *decreases* with decreasing temperature, and the curves are concave upward. In this temperature range, the two stages are separated only by their marked differences in

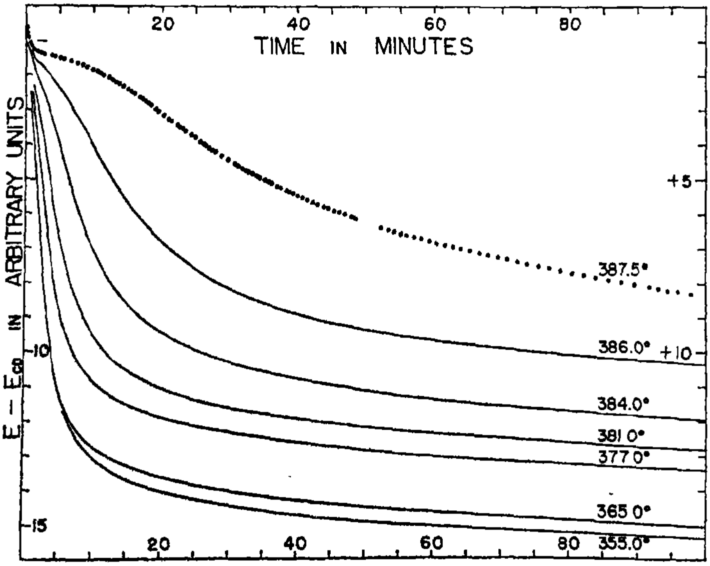

Fig. 3. Isothermal time variation of Young's modulus following a quench from 415°C to the indicated temperature.

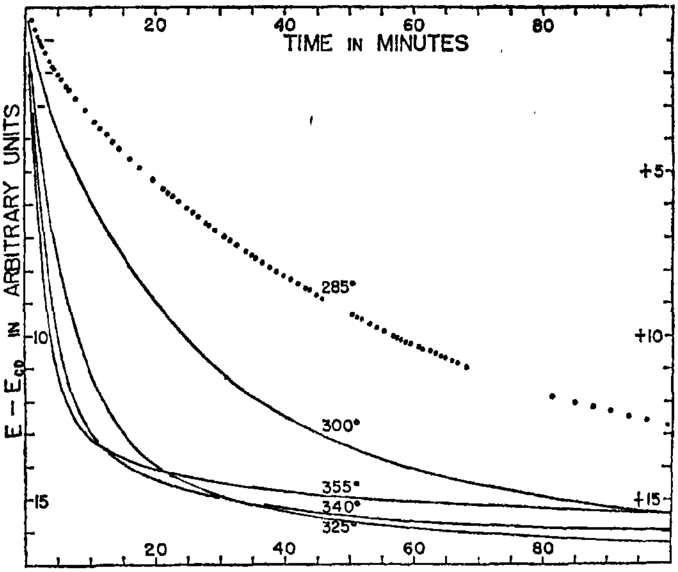

FIG. 4. Isothermal time variation of Young's modulus following a quench from 415°C to the indicated temperature.

ordering rates. Despite appearances, the shapes of the 285, 300, and 325°C curves are actually nearly identical, since by a suitable alteration of the time scales, the curves of $(E-E_{\text{C.D.}})/(E_e-E_{\text{C.D.}})$ can be accurately superimposed.

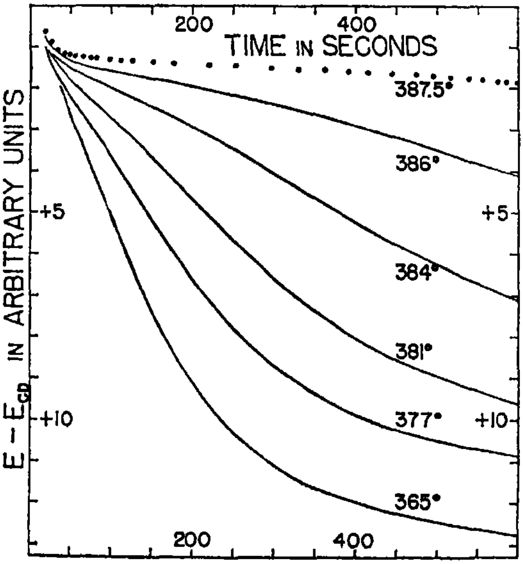

FIG. 5. The initial portions of curves similar to those of Fig. 3.

As discussed in the previous Section, the first stage of ordering corresponds to the establishment of a new metastable state of short range order. At temperatures between about 325 and 370°C, the rate of this process merges with that of the subsequent ordering process so that it can no longer be distinguished. Below 325°C, this first stage is mainly completed during the quench, so again it is not detected.

Consistent with the interpretation of Burns and Quimby,(10) the second stage is the process of nucleation and growth, and the third stage is the process of domain coalescence. The present research provides little additional information concerning the third stage of ordering, and it will not be discussed further. However, concerning the second stage of ordering, the question arises as to the relative contributions of the two processes of nucleation and growth.

(ii) *Role of Nucleation.* In the past, it has been considered,(9, 10) especially for temperatures below 355°C, that the process of nucleation is quite rapid, and is mainly completed in the earliest portions of the ordering, perhaps even during the quench process. Then the observed ordering curves are due either to the growth of isolated nuclei,(20) or the coalescence of contiguous nuclei.(10) Instead, it is here suggested that, at these temperatures, the dominant ordering process in the second stage of ordering is the continual formation of stable nuclei. Only at temperatures very close to T_c is the dominant ordering mechanism that of growth of isolated nuclei. Several critical experiments were carried out to test this suggestion, and also to illustrate clearly features of the nucleation process.

Consider two specimens of Cu_3Au having the same total amount of ordered material. In the first specimen, the order consists of many small nuclei, while in the second specimen, there are fewer larger nuclei. Concerning the subsequent ordering rates at a given temperature, if the dominant ordering process is either the growth of nuclei or their coalescence if they are contiguous, the ordering rates will be different in the two specimens (faster in the first). However, if the dominant ordering process is the formation of nuclei, the ordering rates should be identical, since the rate of nucleation should depend upon the total amount of disordered material, which would be the same in the two cases. Nucleation will be impaired only after about half of the second stage is completed, since the average distance between nuclei is then less than the minimum dimensions of a stable nucleus. This will obviously occur sooner when there are a greater number of smaller nuclei, rather than fewer larger nuclei.

To correspond to the above two specimens, the sample of Cu_3Au is given two different heat treatments before measuring the isothermal ordering. First, the sample is quenched from 415°C to the ordering temperature T_0. Next, the sample is quenched from 415°C to a temperature below T_0, held there for a given length of time, and then reheated to T_0. The sample then has smaller and more numerous nuclei than after the first treatment.

As discussed by Burns and Quimby,(10) the size of a stable nucleus below T_c increases as T_c is approached. During reheating, Young's modulus should decrease, in part due to the decrease in order within the nucleus, but mainly due to the dissolution of nuclei that are not stable at the higher temperature.(21) Observation of the latter effect would be further evidence of the importance of the nucleation process especially at low temperatures. If nucleation is completed during the initial quench, then upon quenching to a lower temperature and reheating, no such dissolution should be observed.

The results of such experiments are shown in Figs 6, 7, and 8. Figure 6 shows the isothermal time variation of E in a specimen quenched from 415 to 355°C, annealed there for times indicated by the numbers attached to the curves, and then reheated to 387°C. The curves labelled 387 and 355°C are the isothermal ordering curves for these temperatures, similar to those shown in Fig. 3. The value of $(E-E_{\text{C.D.}})$ at the initiation of a reheating is indicated by a solid circle on the 355° curve. As can be derived from Fig. 6, the 15 and 5 min curves afford conclusive evidence of the predicted dissolution of nuclei on heating, because here the observed decrease in E is greater than the difference in the equilibrium values of E, that is, greater than the decrease that would occur if the *entire medium* were in equilibrium at 355°C. Of further importance, suitable translation of the 387°C curve along the time axis reveals that the ordering rate for the 1 min curve is more rapid than that of the 387°C curve. This indicates the importance of nuclear growth at temperatures close to T_c.

Another feature revealed by Fig. 6 is that the number of surviving nuclei at 387°C produced during the first 5 min of anneal at 355°C is considerably greater than that produced during the

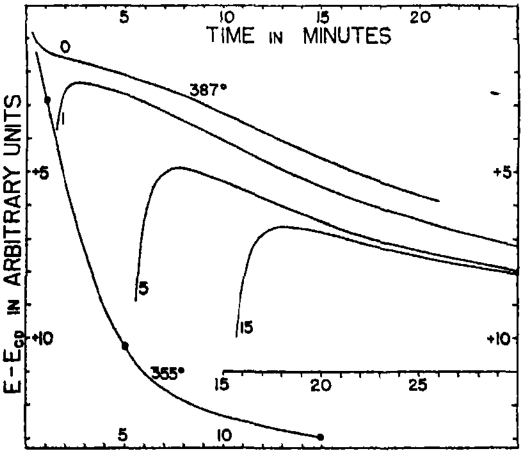

Fig. 6. Isothermal time variation of Young's modulus following a quench from 415 to 355°C, an anneal at 355°C for the indicated time, and a rapid heating to 387°C.

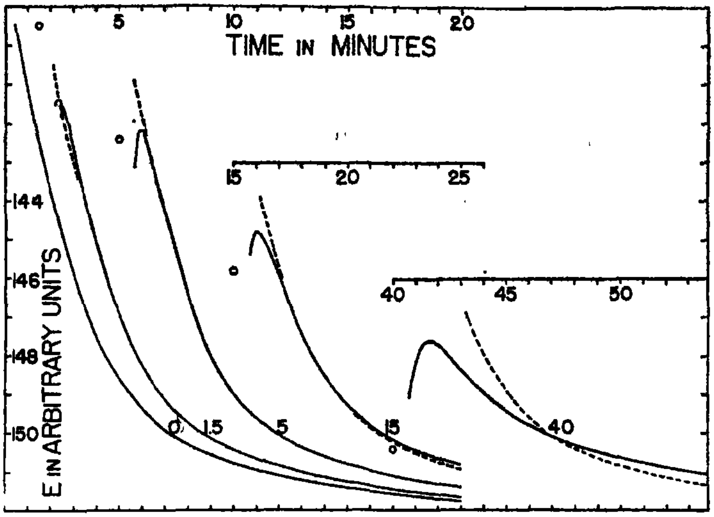

FIG. 7. Isothermal time variation of Young's modulus following a quench from 415 to 300°C, an anneal at 300°C for the indicated time, and a rapid heating to 355°C.

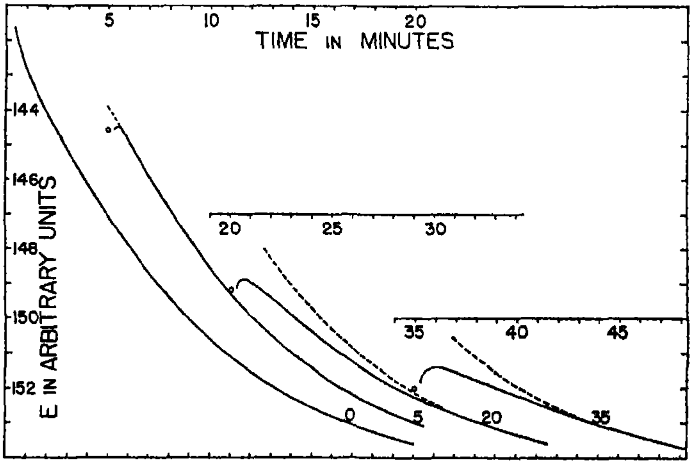

FIG. 8. Isothermal time variation of Young's modulus following a quench from 415 to 300°C, an anneal at 300°C for the indicated time, and a rapid heating to 325°C.

succeeding 10 min. This occurs because the process of nuclear growth is greatly inhibited after about 5 min at 355°C, since the nuclei then are becoming contiguous and the slow process of domain coalescence dominates.

Figure 7 shows the isothermal time variation of E in a specimen quenched from 415 to 300°C, annealed at 300°C for the time interval in minutes indicated by the numbers attached to the curves, and then heated suddenly to 355°C and held there. Accordingly, the curve labelled 0 is the isothermal ordering curve for a specimen quenched directly to 355°C. Each dashed curve, or its solid continuation, is obtained by translating the 0 min curve along the time axis. Ordinates of the circles are values of E at 300°C at the instant of heating minus the decrease due to the 55°C increase in temperature. The curves of Fig. 8 depict similarly the same phenomenon in a specimen also annealed at 300 but heated to 325°C. The curve labelled 0 is the isothermal ordering curve for a specimen quenched to 325°C.

It is first seen that nuclei still dissolve upon reheating, even at these lower temperatures. However, the principal feature of Figs 7 and 8 is that an anneal as long as 5 min at 300°C has practically no effect on the subsequent ordering rate at either 355 or 325°C, in contrast to the results of Fig. 6. Thus, it is concluded that the continual formation of new nuclei is the dominant ordering mechanism at these lower temperatures. As discussed previously, such ordering is not affected until roughly half of the ordering has occurred. This expected impairment can be seen in Fig. 7 for the 40 min curve, and in Fig. 8 for the 20 min and 35 min curves. Note that, in comparison, the ordering rate in Fig. 6 was *increased* by the presence of residual nuclei.

(iii) *Ordering theory*. The above experiments have indicated the importance of continual nucleus formation during the ordering process. Based on these results, it is possible to formulate a simple theory correlating the main ordering phenomena occurring in the second stage of ordering. It is first desirable to compute the fluctuation in free energy, ΔF, required to establish an ordered region of volume v in a disordered matrix.

In the calculations of Burns and Quimby,(10) a constant value of S, the long range order parameter, was assumed at all temperatures. However, Dienes(22) has subsequently shown that not all values of S will produce a decrease in the configurational free energy, so that actually ΔF must always be considered to be a function of both S and v. Present attempts to derive a more complete theory have revealed that the calculated values for the free energy fluctuation to form a stable nucleus are extraordinarily sensitive to the exact expression relating the configurational free energy to S. There is not yet available a physically acceptable expression relating these two quantities. Furthermore, it is questionable if the long range order parameter S should be used to describe the state of order in a small nucleus. Accordingly, it is unrewarding to discuss further such calculations, and instead, we proceed to a phenomenological description of the ordering process.

Consider a volume V_0 of specimen material initially disordered and held at a constant quench temperature below T_c. The quantity q denotes the number of nuclei formed per unit time per unit volume of disordered material. The quantity p denotes the increase in the linear dimensions of the nucleus per unit time. It can then be shown(11) that the volume V of ordered material at any time t is given by:

$$V = \int_{t_1=0}^{t_1=t} q(V_0 - V)[p(t-t_1) + v_0^{1/3}]^3 \mathrm{d}t_1 \qquad (1)$$

where v_0 is the minimum size of a stable nucleus, assumed cubical here for simplicity. The solution of this integral equation is of no interest in the absence of a reliable measure of V. However, it yields simple expressions for the initial time differential coefficients of V as follows:(23)

$$(\mathrm{d}V/\mathrm{d}t)_{t=0} = V_0 v_0 q \qquad (2)$$

and

$$(\mathrm{d}^2V/\mathrm{d}t^2)_{t=0} = V_0 v_0^{2/3} qp(3-y) \qquad (3)$$

where

$$y = v_0^{4/3}\, q/p \qquad (4)$$

All of the salient features of the second stage of ordering can be explained by these equations. The quantity y is a measure of the relative importance of the processes of nucleation and nuclear growth during the early stage of order. According to equation (3), the magnitude of y controls the sign of the second derivative. Therefore, at temperatures close to T_c where nuclear growth predominates, the second derivative would be expected to be positive since y would be small, and this is observed in Figs 3 and 5. At lower temperatures, nucleation predominates and the sign of the second derivative becomes negative, as observed in Fig. 4. Further, the temperature at which the second derivative becomes equal to zero must correspond to the temperature at which the initial ordering rate is a maximum, and this is seen to occur, at about 355°C. Also, if nucleation is the only ordering process, then the theoretical ordering curves would be exponential. At 300 and 285°C, the quantity $(E - E_{\mathrm{C.D.}})/(E_e - E_{\mathrm{C.D.}})$ does in fact vary exponentially with the time to 20 and 60 min respectively, although the question of the relation of Young's modulus to order remains.

According to equation (2), the initial ordering rate is controlled mainly by the value of q, and not by p. Physical insight as to why the initial ordering rate first increases and then decreases as the temperature is lowered is provided[(10)] by equation (5), relating q with the temperature T. Here

$$q = C\exp-(H-\Delta F_0)/kT \tag{5}$$

H is the activation energy for an ordering atomic interchange, ΔF_0 the free energy fluctuation to form a minimum stable nucleus, and C is a constant including the frequency factor for atomic interchange. According to BURNS and QUIMBY[(10)] the value of ΔF_0 decreases very rapidly with decreasing temperature directly below T_c so that the value of q first increases greatly. However, at lower temperatures, decreasing atomic mobility causes the nucleation rate to decrease.

When ΔF_0 becomes much smaller than H, the initial slope of the curves should vary exponentially with $1/T$. Therefore, the initial slopes of $(E-E_{\mathrm{C.D.}})/(E_e-E_{\mathrm{C.D.}})$ plotted semilogarithmically against $1/T$ should asymptotically approach a straight line having a slope of H/k. From such a plot, a very rough value of 40 kcal/g-atom is obtained for H, which is reasonable.

The magnitude of the quantities p and q can be estimated as follows, provided the observed slope of the curve for 355°C is accepted as an approximate measure of the rate of removal of disordered material. For this curve, the second derivative is zero so that $y = 3$. The value of L_0, which is the linear dimension of a minimum stable nucleus, is taken to be 8 interatomic distances from X-ray evidence.[(3)] The observed slope yields q from equation (2), and p is then computed with equation (4). The result is, $p = 8\times10^{-3}$ interatomic distances per second at 355°C; at this temperature one nucleus is formed per second in a cube 53 interatomic distances on an edge.

Finally, mention should be made of the recent study of ordering in Cu_3Au by E. NAGY, I. NAGY, and H. ELKHOLY.[(24, 25)] They were concerned almost entirely with the third stage of ordering, i.e. the process of domain coalescence, so that their experiments essentially begin where the present experiments cease. In particular, their temperature changes require at least 5 min to be accomplished, and their ordering changes occur during periods as long as 15 hr. In contrast, in the present study, temperature changes are accomplished in less than a minute, and the ordering changes considered are completed within an hour except at the lowest temperatures. In general, there is no contradiction between their model and the present model. Indeed, their conclusion that the "quasi-equilibrium" domain size increases with increasing temperature below T_c is a direct consequence of both the increase in initial nucleus size at higher temperatures, and the dominance of nucleus growth close to T_c. However, their conclusion that any heat treatment below T_c can never lead to a decrease in domain size is an overstatement, and is contradicted by the present Fig. 6.

D. *The kinetics of disordering above T_c.*

The curves of Fig. 9 show the isothermal variation of E with time in a specimen quenched from 415 to 375°C, annealed at 375°K for 15 min. and then heated to the indicated temperature. The domain boundaries are contiguous at the end of the anneal, and the value of E (147·83 a.u.) is exactly reproducible. Hence the curves describe the effect of temperature alone on the disordering process above T_c, namely the rapidity with which its rate increases with temperature; 1°C above T_c the rate is comparatively slow, 15°C above T_c it is extremely fast.[(26)] The following explanation of this phenomenon is suggested.

The isothermal curves of Fig. 10 show the variation of the quantity $[f(S)-f(0)]/kT$ with the long range order parameter S given by the Bragg–Williams theory of order.[(27)] Here $f(S)$ is the configurational free energy per atom in a lattice with order S. The equilibrium value of S on a given curve is that for which $\mathrm{d}f(S)/\mathrm{d}S$ is zero; the curve corresponding to T_c is that for which $[f(S)-f(0)]/kT$ and $\mathrm{d}f(S)/\mathrm{d}S$ are both zero at the same value of S. A range of temperatures immediately above T_c exists in which the curves have a minimum at a value of S different from zero, but this is not an absolute minimum since the latter occurs at $S = 0$ for all temperatures above T_c. The state of the material corresponding to a relative minimum is metastable pending the occurrence of a fluctuation in order, i.e. in free energy, sufficient to carry the free energy over the associated maximum. According to the Bragg-Williams theory, the pertinent range of temperature is only 8°C for a material whose critical temperature is 390°C. The minimum disappears at 398°C. It is suggested that when an ordered specimen is suddenly heated to a temperature immediately above T_c the material quickly reaches the metastable state appropriate to the new temperature; that the stability of this state is responsible for the observed slow disordering rate; and that the rapid increase in disordering rate as the temperature is raised follows the rapid decrease of the stability to zero.

The curves of Fig. 10 are, of course, quantitatively incorrect since they include only the configurational free energy; are based upon the

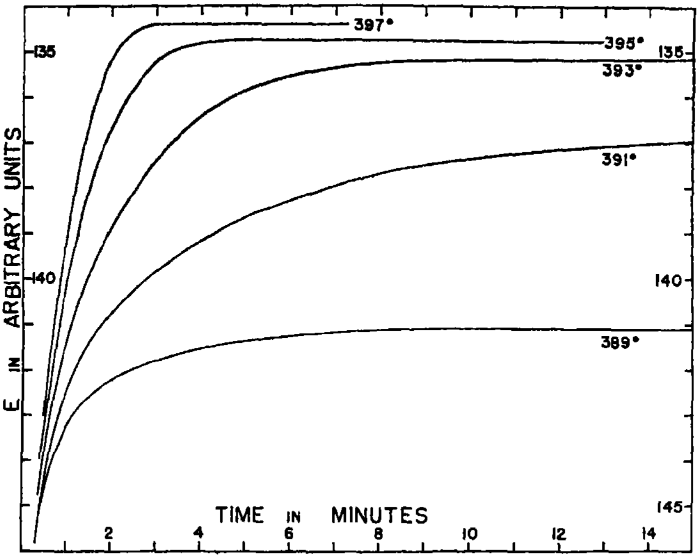

Fig. 9. Isothermal time variation of Young's modulus following a quench from 415 to 375°C, an anneal at 375°C for 15 min, and a rapid heating to the indicated temperature.

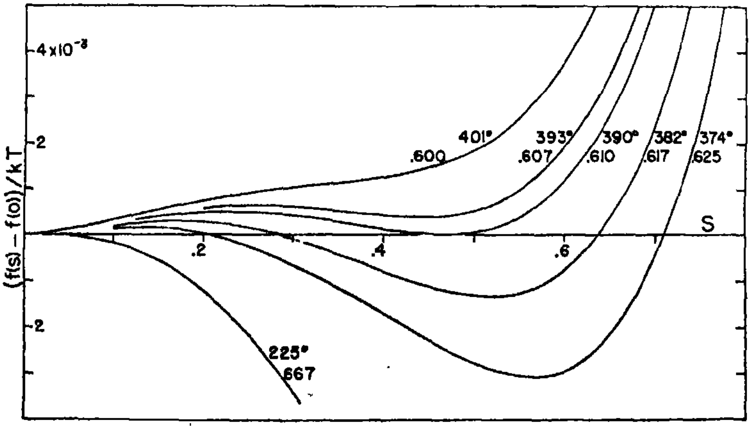

Fig. 10. The isothermal variation of configurational free energy per atom with order S at various temperatures according to Bragg and Williams. The numbers attached to the curves are values of V_1/kT, where V_1 is the Bragg and Williams ordering energy.

Bragg–Williams[27] evaluation of the configurational energy w per atom in terms of S, and lead to too low a value (0·46) of the equilibrium order at T_c. However, it can be argued that the correct isothermals, in which $f(S)$ now denotes the *total* free energy, must always possess minima in the region $[f(S)-f(0)]/kT$ negative, and the existence of a latent heat of disordering implies that at T_c the quantity $[f(S)-f(0)]/kT$ be zero at a value of S different from zero. These conditions alone are sufficient to establish the premise, and the suggestion here made remains plausible.

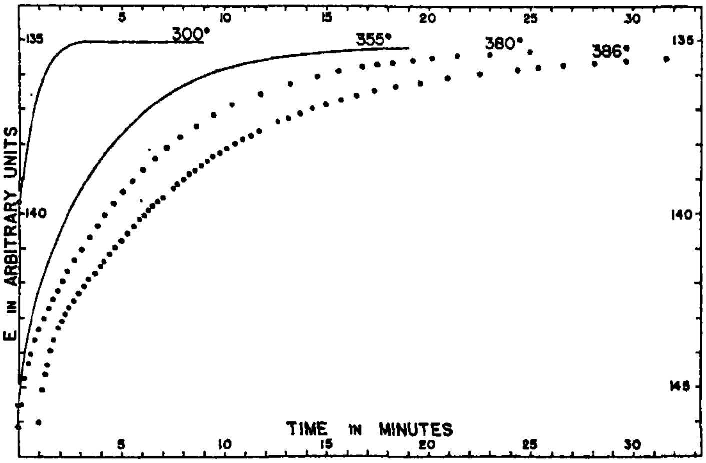

FIG. 11. Isothermal time variation of Young's modulus following a quench from 415°C to the indicated temperature, an anneal at that temperature for 2 hr, an anneal at 386°C for 2 min, and a rapid heating to 393°C. The abscissae of all points on the 386° curve are increased 1 min to separate this curve from the others.

The curves of Fig. 11 depict isothermal disordering in specimens quenched from 415°C to the indicated temperature, annealed there for 2 hr, then heated to 386°C and annealed for 2 min, and then heated to 393°C and held there. The anneal at 386°C establishes equilibrium order for that temperature within the domains, hence the initial states corresponding to the several curves differ only in respect to domain size, which decreases with decreasing quench temperature. The points indicated by open circles at $t = 0$ are obtained by extrapolation to 393 from the value of E at 386°C with the temperature coefficient 0·0639 a.u./°C.

The initial rapid decrease in E, discernable in the data for 386 and 380°C, indicates the relaxation of long range order within large domains from the stable equilibrium value at 386 to the metastable equilibrium value at 393°C. The subsequent disordering rate increases with increasing number of contiguous domains. This suggests that disorder diffuses from each domain boundary into the domain. This view is supported by the upward convexity of the curves for as diffusion proceeds, the area available for it diminishes and the disordering rate decreases. If the disordering process were the growth of nuclei of disorder within domains, the curves would be convex downward, initially at least, since then the area available for disordering would increase with nuclear size.

The data of Fig. 11, together with the 393°C curve of Fig. 9, yield a significant result. It is found that the five sets of values of the quantity $(E_t-E)/(E_t-E_f)$, regarded as a function of the time, can be superimposed exactly between $t = 2$ min and $t = t_1$ by suitable alteration of the time scale for each set. Here E_t is the value of E given by the open circles of Fig. 11, E_f the equilibrium value of E at 393°C, and $t_1 = 12$, 12, 10 and 3 min for the 386, 380, 355 and 300°C curves respectively, and 9 min for the 393°C curve of Fig. 9. Mathematically this means that an expression of the form $(E_t-E)/(E_t-E_f) = F(t, T_q)$ describes all the data, where T_q is the quench temperature, and furthermore that $F(t,T_q) = G[tg(T_q)]$; physically it indicates that a single process is operative, since it is unlikely that the same function $g(T_q)$ will characterize two different processes. A highly simplified example serves to illustrate, on the present hypothesis, the nature of the functions G and g.

Assume all domains to be cubes of edge d_i and volume $v_{0i} = d_i^3$, and let r denote the linear rate of diffusion of disorder from a domain boundary into the domain at 393°C. Then the volume v of domain material disordered in time t is given by the expression $v = v_{0i} - (d_i - 2rt)^3$, and the fraction of disordered material by the expression $(v/v_{0i}) = [6(rt/d_i) - 12(rt/d_i)^2 + 8(rt/d_i)^3]$. Thus $g(T_q) = r/d_i$ and G follows on equating the expression for v/v_{0i} to the fractional change in E. In fact, of course, all domains are not the same size, hence after a time a progressive decrease in the number of domains available for disordering commences. The several sets of data can no longer be superposed after the new process starts, and this occurs earlier the smaller the average initial domain size.

REFERENCES

1. Weisberg L. R. and Quimby S. L., *Phys. Rev.* **110**, 338 (1958).
2. Preliminary results of this investigation were previously presented: Weisberg L. R., *Bull. Amer. phys. Soc.* **1**, 146 (1956); Quimby S. L. and Weisberg L. R., *Bull. Amer. phys. Soc.* **1**, 146 (1956).
3. Sykes C. and Jones F. W., *Proc. Roy. Soc.* **A157**, 213 (1936).
4. Sykes C. and Evans H., *J. Inst. Metals* **58**, 225 (1936).
5. Jones F. W. and Sykes C., *Proc. Roy. Soc.* **A166**, 375 (1938).
6. Rhines F. N. and Newkirk J. B., *Trans. Amer. Soc. Metals* **45**, 1029 (1953).
7. Siegel S., *J. chem. Phys.* **8**, 860 (1940).
8. Various X-ray studies of Cu_3Au are described by: Owen E. A. and Sim G. McA., *Phil. Mag.* **38**, 342 (1947); Taylor C. A., Hinde R. M., and Lipson H., *Acta Cryst.* **4**, 261 (1951); Edmunds I. G. and Hinde R. M., *Proc. phys. Soc. Lond.* **65B**, 716 (1952); Keating D. T. and Warren B. E., *J. appl. Phys.* **22**, 286 (1951); Cowley J. M., *J. appl. Phys.* **21**, 24 (1950); *Phys. Rev.* **77**, 669 (1950).
9. Lord N. W., *J. chem. Phys.* **21**, 692 (1953).
10. Burns F. P. and Quimby S. L., *Phys. Rev.* **97**, 1567 (1955).
11. Gross W. and Quimby S. L., *Univ. Microfilms* (Ann Arbor, Mich.), L.C. Card No. MIC 59-3105; *Dissertation Abstr.* **20**, 1054 (1959).
12. Iida S., *J. phys. Soc. Japan* **7**, 373 (1952).
13. Iida S., *J. phys. Soc. Japan* **9**, 346 (1954).
14. Watanabe D., *J. phys. Soc. Japan* **14**, 436 (1959).
15. Marcinkowski M. J. and Brown N., *J. appl. Phys.* **32**, 375 (1961).
16. Turnbull D., *Solid State Physics*, Vol. 3 (edited by Seitz F. and Turnbull D.), p. 252. Academic Press, New York (1958).
17. Nix F. C. and MacNair D., *Phys. Rev.* **60**, 320 (1941).
18. Germer L. H., Haworth F. E. and Lander J. J., *Phys. Rev.* **61**, 614 (1942).
19. Damask A. C., Fuhrman Z. A. and Germagnoli E., *J. Phys. Chem. Solids* **19**, 265 (1961).
20. Feder R. and Nowick A. S., *Phys. Rev.* **98**, 1152 (A) (1955).
21. The removal by heating of precipitation hardening in metals, called "restoration", has a similar origin in the dissolution of nuclei. See, for example, Cottrell A. H., *Theoretical Structural Metallurgy* p. 246. Arnold, London (1951).
22. Dienes J., *Acta. Met.* **3**, 549 (1955).
23. If the nuclei are assumed disk-shaped and growing from the edge, the equations derived are unchanged, except in equation (3) the parenthesis becomes $(2-y)$ instead of $(3-y)$.
24. Nagy E. and Nagy I., *J. Phys. Chem. Solids* **23**, 1605 (1962).
25. Elkholy H. and Nagy E., *J. Phys. Chem. Solids* **23**, 1613 (1962).
26. The results of a similar investigation of the order-disorder transformation in well ordered specimens are given by Siegel S., *J. chem. Phys.* **8**, 860 (1940). He defines a rough measure of the relaxation time for disordering and finds that this decreases by a factor of 1/50 between 2 and 7°C above T_c.
27. Fowler R. H. and Guggenheim E. A., *Statistical Thermodynamics*, p. 601. Cambridge University Press, London (1939).

J. Phys. Chem. Solids Pergamon Press 1963. Vol. 24, pp. 1263–1270. Printed in Great Britain.

SPACE CHARGE INJECTION INTO IMPURITY SEMICONDUCTORS

G. G. ROBERTS and **R. H. TREDGOLD**

Physics Department, University College of North Wales, Bangor, Caernarvonshire

(*Received* 4 *March* 1963; *revised* 31 *May* 1963)

Abstract—An n-type semiconductor placed between two metal electrodes is considered. The ohmic contacts formed facilitate the injection of electrons into the semiconductor. A non-linear differential equation is obtained which relates the concentration of conduction electrons to the distance through the crystal. This equation is integrated exactly for the zero current case. For the current carrying case accurate numerical solutions are reported. The results are discussed in the light of apparent non-ohmic conductivity and theories of space charge limited currents.

INTRODUCTION

THE injection and extraction of carriers by the electrodes attached to a semiconductor can give rise to a net space charge in the crystal. In 1940, MOTT and GURNEY(1) indicated the possibility of achieving reasonably large space charge limited currents in insulators and, since then, solutions for various restricted ranges of interest have been reported. The majority of the studies are for the one carrier problem, all carriers having the same charge and mobility.(2, 3) The problem of space charge injection into a perfect insulator without deep traps or impurity centres but including diffusion has been considered by several workers.(4–8) WRIGHT(8) has pursued this problem by numerical means and has obtained actual current/voltage curves. He has not however considered the variation of current or voltage with thickness. ROSE and his co-workers(9–13) have also studied the problem involving effects dependent on both electrons and holes being simultaneously injected into an insulator from opposite contacts. In these cases a trap-free insulator was considered and the diffusive contribution to the current was neglected.

The problem of space charge conduction involving one type of carrier in an impurity semiconductor has been studied by MACDONALD.(14) He considered the case where the ionization energy, E, of the donor states is much less than kT and it is thus a good approximation to assume complete ionization. We have considered the converse case in which $E \gg kT$ and the degree of ionization is small. A brief account of certain preliminary results has already been published by us.(15)

In this paper we give a more complete account both of the methods employed and the results obtained.

THEORETICAL MODEL

The proposed model, shown schematically in Fig. 1, has two similar metal electrodes which furnish ohmic contacts to an n-type semiconductor with a single donor level. E_f, E_d, and E_c denote the energies of the Fermi level, donor level and the bottom of the conduction band respectively. The contribution of the valence band

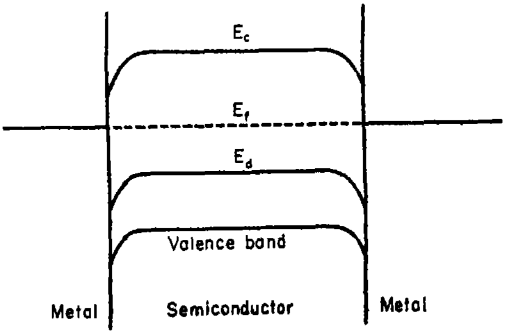

FIG. 1. Simplified energy band diagram for an n-type semiconductor with two injecting contacts.

is considered negligible and the existence of acceptor states is ignored. The validity of this latter approximation is discussed later in the paper.

When electronic equilibrium is established the Fermi levels in the system must, on thermodynamic considerations, be coincident. This involves a transfer of electrons from the metals into the semiconductor giving rise to local fields in the semiconductor which distort the energy levels as shown in Fig. 1. In the formation of the contacts the effect of surface states has been neglected.

The problem is treated in one-dimension and a one-carrier (electron) current is considered. A further limitation is that we shall be concerned with temperatures and energy levels for which Maxwell–Boltzmann statistics are a good approximation for the distribution of the carriers. This requires a small occupational density of the effective density of states in the conduction band and the energy gaps $(E_f - E_d)$ and $(E_c - E_f)$ must both be several times greater than kT at normal temperatures. These conditions are satisfied in many materials in which space charge limited currents have been reported.

BASIC EQUATIONS

The processes of current flow in a semiconducting system can be described by three equations—a current flow equation, the Poisson equation and an equation of state which relates the free electron density to the number of ionized donors in the donor level at any position in the semiconductor.

The total current density J is the sum of drift and diffusion current densities and is given by

$$J = \mu e n_E F + \mu k T\left(\frac{\mathrm{d}n_E}{\mathrm{d}x}\right) \tag{1}$$

where n_E is the concentration of conduction electrons, F is the electric field and μ is the electron mobility. The origin of x is taken at the centre of the crystal. Use has been made in equation (1) of the Einstein relationship thereby implying a diffusion constant independent of charge distribution.

For the model described in the preceding Section we may write the Poisson equation as

$$\frac{\mathrm{d}F}{\mathrm{d}x} = -\frac{4\pi e}{\kappa}(n_E - n_D) \tag{2}$$

where n_D is the concentration of ionized donors and κ is the dielectric constant. n_E and n_D will be functions of x.

In order to relate these quantities we make use of a statistical argument.

If W_{12} and W_{21} are the probabilities of transitions per unit time between the conduction band and the donor level and between the donor level and the conduction band respectively, then

$$W_{12} \cdot n_E \cdot n_D = W_{21}(A - n_E)(N_D - n_D) \tag{3}$$

where N_D is the concentration of donor states and A is an effective density of states in the conduction band.

In the preceding Section we indicated that, in our model, the conduction band is taken to be sufficiently empty so that $A \gg n_E$. Therefore equation (3) reduces to

$$n_D = \frac{N_D \cdot A}{(A + \beta n_E)} \tag{4}$$

where

$$\beta = \left(1 + \frac{W_{12}}{W_{21}}\right)$$

It is reasonable to assume that β is independent of n_E and n_D and is a function of temperature only. This assumption enables us to make use of the zero current case in finding an explicit value of β. Under these conditions, far into the crystal, we have charge neutrality.

Therefore $n_E = n_D$ and, taking into account that Maxwell–Boltzmann Statistics are applicable in our model, we may write

$$A \exp[(E_f - E_c)/kT] = N_D \exp[(E_d - E_f)/kT] \tag{5}$$

this gives

$$n_E = n_D = (AN_D)^{1/2} \exp[(E_d - E_c)/2kT] \tag{6}$$

Putting this value for n_E and n_D in equation (4) and using the approximation that $N_D \gg n_D$ gives

$$\beta = \exp[(E_c - E_d)/kT] \tag{7}$$

For a typical band gap in our model β is very large and the term A in the denominator of equation (4) may therefore be neglected. We now have the relation

$$n_D n_E = C \tag{8}$$

where

$$C = N_D A \exp[(E_d - E_c)/kT]$$

These fully justifiable assumptions therefore lead us to a Poisson equation of the form

$$\frac{\mathrm{d}F}{\mathrm{d}x} = -\frac{4\pi e}{\kappa}\left(n_E - \frac{C}{n_E}\right) \tag{9}$$

Somewhat similar treatments by PEKAR(16) and MACDONALD(14) have resulted in the same type of Poisson equation.

Eliminating F in equations (1) and (9), and dropping the suffix E, the concentration of electrons in the conduction band now being given by n, results in the following second order non-linear differential equation in n and x.

$$J\frac{\mathrm{d}n}{\mathrm{d}x} = \frac{4\pi e^2\mu}{\kappa}(n^3 - Cn) + \mu kT\left\{\left(\frac{\mathrm{d}n}{\mathrm{d}x}\right)^2 - n\frac{\mathrm{d}^2n}{\mathrm{d}x^2}\right\} \tag{10}$$

This equation may be reduced to the first order equation

$$\frac{\mathrm{d}Y}{\mathrm{d}Z} = -ae^{-Z}Y^{1/2} + b\sinh Z \tag{11}$$

where

$$Y = \left[\frac{\mathrm{d}n}{\mathrm{d}x}\Big/n\right]^2$$

and

$$Z = \log_e(C^{-1/2}n)$$

are the new variables and

$$a = \frac{2J}{C^{1/2}\mu kT}$$

and

$$b = \frac{16\pi e^2 C^{1/2}}{\kappa kT}$$

are constants for a particular model chosen.

ZERO CURRENT SOLUTION

In the equilibrium case, the diffusion of carriers away from the contacts is balanced by the drift of carriers towards the contacts and therefore $J = 0$. Accordingly, the constant a is also zero and equation (11) reduces to

$$\frac{\mathrm{d}Y}{\mathrm{d}Z} = b\sinh Z \tag{12}$$

As we are dealing with electrodes of the same work function we would expect a symmetrical distribution between the electron concentration in the absence of current, n_0, and x. At the centre of the semiconductor, where x has its origin, the electron concentration gradient will be zero. Thus $Y = 0$ at $x = 0$ and further let $Z = Z_1$ at this point.

Integrating equation (12) and making use of the above boundary condition gives

$$Y = b(\cosh Z - \cosh Z_1) \tag{13}$$

or

$$Y = \frac{b}{2}\left(C^{-\frac{1}{2}}n + \frac{C^{1/2}}{n} - 2\cosh Z_1\right)$$

This may be written in the form

$$Y = \frac{bC^{-1/2}}{2n}(n - n_1)(n - n_2) \tag{14}$$

where

$$n_1, n_2 = C^{1/2}e^{Z_1},\quad C^{1/2}e^{-Z_1}$$

Inspection of equation (9) will show that $C^{1/2}$ is the equilibrium concentration in an infinite slab of semiconductor. In the case of a finite slab we would expect the concentration of conduction electrons, at all points in the crystal, to be greater than this value and, therefore, for Z to be +ve everywhere. The electron concentration at the turning point will therefore be given by $C^{1/2}e.^{Z_1}$

At $x = 0$ let $n_1 = (C^{1/2} + \delta)$.
Then $n_2 = C^{1/2}(1 + \delta C^{-1/2})^{-1}$

or

$$\frac{n_2}{n_1} = (1 + \delta C^{-1/2})^{-2}$$

Equation (14) may be written

$$\frac{\mathrm{d}n}{\mathrm{d}x} = \pm w[n(n - n_1)(n - n_2)]^{1/2} \tag{15}$$

where

$$w = \left(\frac{bC^{-1/2}}{2}\right)^{1/2}$$

This equation may be integrated in terms of Jacobian Elliptic Functions using the boundary condition that $n = n_1$ when $x = 0$. The solution takes the form

$$\left(\frac{n_1-n_2}{n-n_2}\right)^{1/2} = cn\left\{\pm Bx\left|\frac{n_2}{n_1}\right.\right\} \qquad (16)$$

where $cn(p|q)$ is a Jacobian Elliptic Function of argument p and modulus $q^{1/2}$, as defined by MILNE THOMSON,(17) and where

$$B = \left(\frac{2\pi e^2 n_1}{\kappa kT}\right)^{1/2}$$

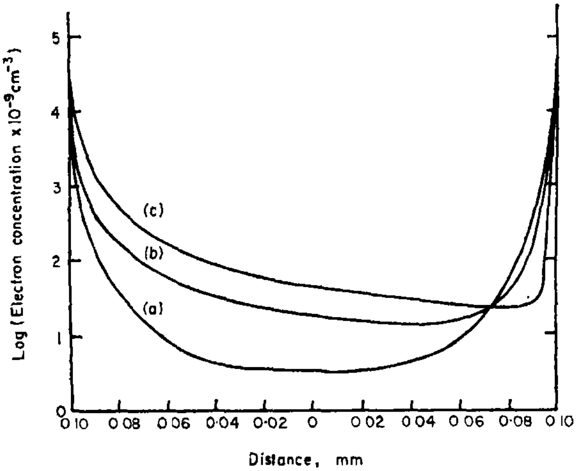

FIG. 2. Log electron concentration vs. distance. Curve (a) is the zero current solution. Curve (c) is the solution for the current carrying case with $J = 1{\cdot}41\cdot10^{-6}$ A cm^{-2}. Curve (b) is an interpolated solution for a current carrying case with $J = 0{\cdot}85\cdot10^{-6}$ A cm^{-2}.

The Fermi level must remain horizontal throughout the system and this will therefore determine the electron concentration at the contacts. Knowing the thickness of the crystal, one can then find the modulus of the elliptic function and hence trace the curve of n_0/x. A typical distribution is shown in Fig. 2. The log–linear plot tends to obscure the fact that the injected charge remains in thin surface layers of the crystal. The curves in Fig. 2, were plotted for the following values of the parameters.

$A = 10^{21}$ cm^{-3}
$N_D = 10^{18}$ cm^{-3}
$E_c - E_d = 1{\cdot}5$ eV
$T = 300$°K
$\chi = 10^3$
$\mu = 10^{-2}$ cm^2 V^{-1} sec^{-1}

These values are chosen to be of the right order for $BaTiO_3$ and $SrTiO_3$. The mobilities for these materials have not been measured but experimental information exists which shows that they are certainly less than 1 cm^2 V^{-1} sec^{-1}.

CURRENT SOLUTION

It appears to be very difficult, and perhaps impossible, to obtain an analytic solution of the equation (10) in terms of known functions. This equation has therefore been solved numerically, using an I.B.M. 7090 computer, for various values of thickness, band gaps and current. Computational details will be included in another Section.

Figure 2 includes a typical computed curve of the electron concentration vs. distance. The large concentration gradients emphasize the fact that near the contacts the diffusive contribution to the current is very important. The zero current boundary condition, that we have thermodynamic equilibrium across the contacts, is also used in this current carrying case. As this is the only boundary condition available an interpolation formula has been derived whereby, provided the zero current case as well as one particular current case for a certain thickness has been solved, the solution for any intermediate value of current may be obtained with reasonable accuracy.

Let n_1 be the solution for a particular current J and let n_0 be the corresponding zero current solution. Then a value of n for an intermediate value of current, say I, is expressed in terms of a power series in (n_1-n_0).

$$n = n_0+a_1(n_1-n_0)+a_2(n_1-n_0)^2+a_3(n_1-n_0)^3 \quad (17)$$

where a_1 and a_2 are constants which are independent of position x in the crystal but depend on the concentrations and concentration gradients at the contacts, and on J and I. a_1 satisfies the relationship

$$(1-a_1)ID_0\left[\frac{1}{(D_0-D_c)^2}+\frac{1}{(D_0-D_A)}\right]$$
$$= a_1(J-I)\left[\frac{D_c}{(D_0-D_c)^2}+\frac{D_A}{(D_0-D_A)^2}\right] \quad (18)$$

where D_0 is the modulus of the electron concentration gradient at the contacts in the zero current solution and D_c and D_A are the moduli of the electron concentration gradients at the cathode and anode respectively in the current carrying case. a_2 satisfies the equation

$$\left(a_1+\frac{2a_2N_0}{(1-a_1)}\right)(D_0-D_c)^2$$
$$= -ID_0+\frac{a_1}{(1-a_1)}D_c(J-I) \quad (19)$$

where N_0 is the electron concentration at the contacts in the zero current case.

The constant a_3 is added as a perturbation, its value being determined by the other two constants. Results have shown that, towards the centre of the crystal, the terms in (n_1-n_0) and $(n_1-n_0)^2$ are adequate for an accurate solution but that in the region of the contacts, where $(n_1-n_0)^3$ is appreciable, the term in $(n_1-n_0)^3$ is necessary. An example of an interpolated curve is given in Fig. 2.

Equation (1) may be rewritten in the form

$$\frac{Fe}{kT} = \frac{ae^{-Z}}{2} - Y^{1/2} \quad (20)$$

Hence the variation of electric field in the crystal may be found numerically by means of the Y/Z relations obtained in finding the n/x curves. The curves of F/x, for various values of current, may then be integrated to obtain a current-voltage relationship for the particular sets of parameters chosen. A typical J/V relation, for the same parameters as Fig. 2, is shown in Fig. 3. We find a non-ohmic relationship at high fields following an approximately ohmic behaviour at low electric fields. An investigation was made of the relationship between potential across the crystal and crystal thickness for a value of current on the non-ohmic part of the curve. A linear relationship was obtained as shown in Fig. 4. This indicates that we are not dealing with space charge limited currents which, on the simplest considerations (MOTT and GURNEY),(1) would be proportional to V^2/L^3.

DISCUSSION

It seems that although additional carriers are being injected at the cathode, producing a space charge, this is insufficient to dominate the potential distribution in the crystal. The current appears to be limited by the surface layer and not by the field due to the space charge. The fact that there is an intercept on the thickness axis in Fig. 4 is explained by our choice of variables which leads to "thick" surface layers where the material is flooded with electrons. Our results have shown that, as the surface layer is narrowed, this intercept gradually diminishes.

These predictions agree well with the experimental results obtained in barium titanate by BRANWOOD, HUGHES, HURD and TREDGOLD.(18) They showed that, in general, the current, for a given crystal at fixed temperature, may be reasonably accurately described by the equation

$$i = a\left(\frac{V}{L}\right)+b\left(\frac{V}{L}\right)^2 \quad (21)$$

where V is the applied potential, L the thickness of the crystal and a and b are characteristic of the bulk material and cathode respectively. Equation (21) indicates a nearly ohmic low field behaviour which is uninfluenced by the electrode material and a non-ohmic region where the cathode material and the resulting surface layer has a profound effect on the apparent conductivity. We note that equation (21) would lead to a linear relation between the voltage and the thickness even in the non-ohmic region.

Further experiments on photoconductive properties of barium titanate, carried out in this laboratory, are also consistent with this model.

It thus appears that the voltage current relationship for the type of material considered here may be divided into three regions.

(1) A low current ohmic region.

(2) An intermediate region which is dominated by injected space charge but in which the surface

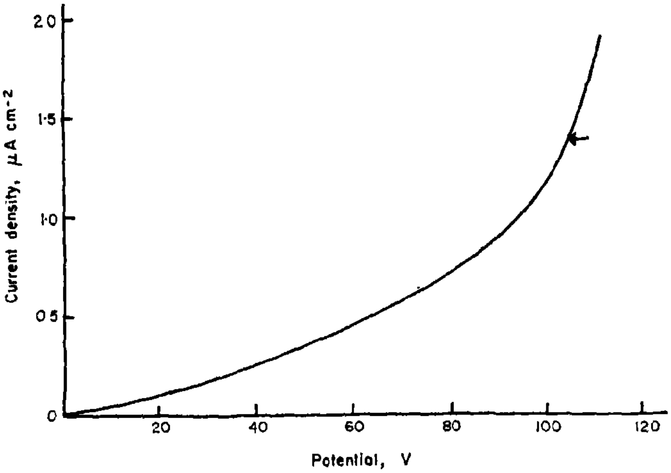

FIG. 3. Current–voltage relationship for crystal of thickness 0·2 mm. The arrow denotes the value of current chosen for Fig. 4.

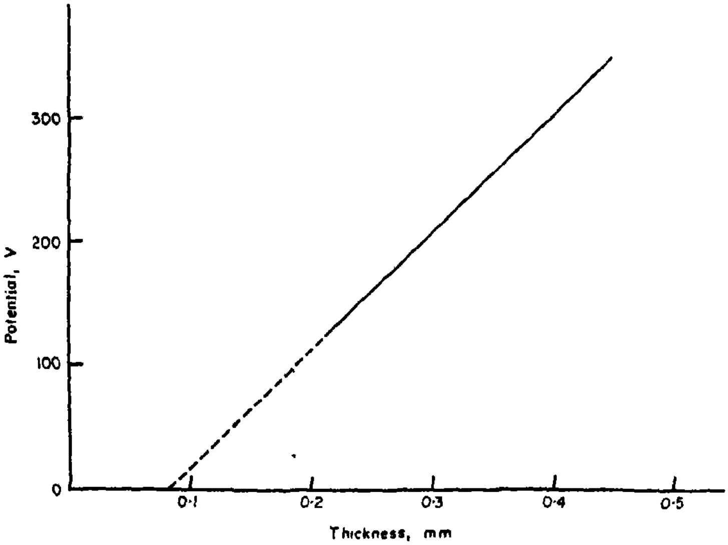

FIG. 4. Voltage–thickness relationship for a value of current $J = 1{\cdot}41 \cdot 10^{-6}$ A cm^{-2}.

conditions rather than the volume space charge limit the current.

(3) A region where a high enough field would probably inject sufficient space charge so that the volume charge would limit the current. It seems likely that, in many materials, breakdown occurs before this region is arrived at.

These results were obtained ignoring acceptor states. They provide a very good interpretation of the experimental results obtained with $BaTiO_3$. As these latter are difficult to explain in any other way it seems probable that the approximation of ignoring acceptors is, even if somewhat crude, partially correct. It is thus important to ask how plausible a model ignoring acceptors actually is. The important region to consider is near the surface where band bending takes place. The mean value of n_E here is about 10^{14} cm^{-3}. It is thus necessary to assume a smaller value for the concentration of acceptors. In a material like Ge this small value would be implausible. However in $BaTiO_3$ we have experimental evidence that conductivity is very weakly dependent on impurity concentration. We thus assume that impurities are largely compensated by ion vacancies. It also seems probable that the donor states are oxygen vacancies frozen in during crystal growth. In this case an *effective* acceptor concentration of less than 10^{14} cm^{-3} is not improbable.

Too much importance should not be attached to the actual numerical values of the parameters used here by way of illustration. We feel that the significance of this result is that a mechanism exists which allows the current to vary as V^2/L^2 in the high field region rather than V^2/L^3 as predicted by the simple theory which ignores diffusion and the existence of donors.

The more general problem including acceptors is now under study and it is hoped to publish the predictions of this model soon.

COMPUTATIONAL DETAILS

The first order differential equation (11) was solved numerically on an I.B.M. 7090 computer by means of the fourth order Runga–Kutta process. In this first stage the current J was specified at the start of the programme. The integration starts at a minimum value of n and is terminated when the electron concentration reaches values determined by the conditions pertaining at the contacts. The resulting relationship between dn/dx and n must then be integrated to obtain the n/x curve.

Making use of the zero current solution and the interpolation formula described in equation (17) the computer is then programmed to produce various n/x curves for intermediate values of current, i.e. $0 \rightarrow J$. This second stage has been designed to avoid a large amount of computational time. An alternative method would have been to select a value of electron concentration gradient at one of the contacts, which, upon integration, would provide a solution satisfying the necessary boundary condition at the other contact. However, the required value of dn/dx would have to be determined by the trial and error procedure used by MacDonald.(14)

The current flow equation (1), in conjunction with the n/x results of the second stage, is used to obtain the variation of electric field in the crystal for various values of current. A final numerical integration will then produce a J/V curve for the particular set of parameters chosen. Only a slight modification of the first stage is required to obtain a voltage-thickness relation for a particular value of current on the J/V curve. This consists in starting the integration at different minimum values of electron concentration and, as before, integrating up to specified values of the electron concentrations at the contacts.

The accuracy of our results is mainly dependent upon the increment or step size used in the Runga–Kutta process. A satisfactory value is determined by means of an approximate solution to equation (10) in the region where $dn/dx \simeq 0$. The interpolation formula has been shown to be very accurate and the inclusion of the term in a_3 has enabled us to extrapolate for higher values of currents with a fair amount of accuracy.

Acknowledgements—The authors are grateful to International Business Machines United Kingdom Ltd., for use of computational facilities under their Endowed Research Time Scheme. They also wish to thank Dr. J. R. MacDonald for helpful discussions. One of us (G.G.R.) held a Department of Scientific and Industrial Research studentship during the course of this work.

REFERENCES

1. Mott N. F. and Gurney R. F., *Electronic Processes in Ionic Crystals*, p. 127. Oxford University Press, London (1940).

2. ROSE A., *Phys. Rev.* **97**, 1538 (1955).
3. LAMPERT M. A., *Phys. Rev.* **103**, 1648 (1956).
4. FAN H. Y., *Phys. Rev.* **74**, 1505 (1948).
5. SKINNER S. M., *J. appl. Phys.* **26**, 498 (1955).
6. SUITS G. H., *J. appl. Phys.* **28**, 454 (1957).
7. ADIROVICH E. I., *Sov. Phys. Solid-State* **2**, 1228 (1961).
8. WRIGHT G. T., *Solid-State Electron.* **2**, 165 (1961).
9. PARMENTER R. H. and RUPPEL W., *J. appl. Phys.* **30**, 1548 (1959).
10. LAMPERT M. A., *R.C.A. Rev.* **20**, 682 (1959).
11. LAMPERT M. A. and ROSE A., *Phys. Rev.* **121**, 26 (1961).
12. LAMPERT M. A., *Phys. Rev.* **125**, 126 (1962).
13. LAMPERT M. A., *Proc. Inst. Radio Engrs.* **50**, 1781 (1962).
14. MACDONALD J. R., *Solid-State Electron.* **5**, 11 (1962).
15. ROBERTS G. G. and TREDGOLD R. H., *Phys. Letters* **2**, 6 (1962).
16. PEKAR S. I., *Zh. eksp. teor. fiz.* **10**, 1210 (1940).
17. MILNE-THOMSON L. M., *Jacobian Elliptic Function Tables*, Dover Publications, New York (1950).
18. BRANWOOD A., HUGHES O. H., HURD J. D. and TREDGOLD R. H., *Proc. phys. Soc. Lond.* **79**, 534 (1962).

J. Phys. Chem. Solids Pergamon Press 1963. Vol. 24, pp. 1271–1278 Printed in Great Britain.

THERMAL EXPANSION OF SILVER IODIDE

ARTHUR BIENENSTOCK* and **GORDON BURLEY**

National Bureau of Standards, Washington 25, D.C.

(*Received* 4 *April* 1963)

Abstract—The thermal expansion of silver iodide with the zincblende structure has been measured by X-ray diffraction techniques in the temperature range 4·2–300°K. Although dependent on sample preparation, it is negative to approximately 80°K, positive in the range 80–110°K, and then attains a constant negative high temperature value. This expansion is explained in terms of a model which shows the dependence of thermal expansion on structure and bonding. It is shown that the primary role of covalency, in its contribution to the low-temperature contraction, is to reduce the interaction between next-nearest neighbors. The particular form of the interatomic interaction appears to contribute primarily to the balance between modes with positive and negative Gruneisen factors. In the case of AgI, it is the large n in the nearest neighbor repulsive interaction, r^{-n}, which accounts for the negative high temperature limit. The positive thermal expansion at intermediate temperatures is the result of transverse optical modes with lower frequencies than transverse acoustic modes.

1. INTRODUCTION

AN APPARENTLY unusual and primarily negative thermal expansion over the large temperature range from 4·2 to 300°K has been found for cubic silver iodide. A negative thermal expansion for silver iodide was first reported by FIZEAU(1) in 1867. Using an interferometric technique, he obtained a value for the thermal expansion coefficient α of $-4{\cdot}1\times10^{-6}$ in the temperature range between 15° and 51°C. JONES and JELEN(2) in 1935, using a dilatometer, gave a value of $-1{\cdot}6\times10^{-6}$ for the value of the expansion coefficient between 20 and 60°C. COHEN and BREDÉE(3) reviewed the status of this field in 1937 and concluded that the Fizeau value was the more reliable. However, the exact phase relationship of the samples used is in doubt in both cases since no physical characterization was attempted.

Silver iodide has been shown to exist in both a wurtzite and a zincblende modification at room temperature.(4, 5) The latter is metastable over its entire range of existence.(6) All attempts to grow single crystals of this phase have thus far been unsuccessful. The two structures are related by a simple stacking difference and have a very small lattice energy difference.

A low temperature minimum of the lattice constant has been reported for several other materials with the zincblende-type, or the closely related diamond-type structure.(7–12) The minimum, and subsequent negative thermal expansion region, in all cases lies at a temperature below three-tenths of the value of the Debye characteristic temperature Θ. It was noted by GIBBONS(9) that in each of these cases the atoms have a fourfold coordination, they are open structures and have strongly covalent bonding.

In this paper we present the results of thermal expansion measurements in the range from 4·2 to 300°K for silver iodide, discuss the general relationship of bonding and coordination to thermal expansion, and attempt to relate these ideas to the specific case of the compound measured.

2. EXPERIMENTAL

The thermal expansion was measured on polycrystalline samples using powder X-ray diffraction techniques. The specimens were prepared by two different procedures, designed to yield an excess of the zincblende-type phase.(6) The first consisted of heating a quantity of the silver iodide powder to just above the melting point and immediately quenching it in cold water. The product was then crushed and ground. It yielded a mixture of the two phases, with about 90 per cent conversion to the zincblende-type. The second method involved pressing a pellet from the powder at about 3000 bars, then crushing and powdering this. By this procedure almost complete conversion was achieved.

---

* Present address: Div. Eng. and Appl. Physics, Harvard Univ., Cambridge, Mass.

An X-ray diffraction cryostat previously described(13, 14) was used for all measurements. This permitted data collection at any temperature between 4·2° and 300°K. The estimated accuracy of temperature measurement is ± 1·0°K. The cryostat was mounted on a horizontal G. E. diffractometer. The diffracted intensity was detected with a proportional counter and recorded on a strip chart. Copper $K\alpha$ radiation, filtered with a nickel foil was used. The polycrystalline sample was spread over a layer of vaseline on the planar surface of this X-ray cryostat. A small quantity of diamond dust was added over the silver iodide and the surface was smoothed. Because of its extremely small expansion in this temperature range, diamond served as a useful reference standard. The sample was cooled slowly to liquid nitrogen temperature, and then successively to liquid hydrogen and liquid helium temperatures. No phase transition was observed. A complete diffraction pattern was recorded at several temperatures. Careful measurement of the angular positions of several diffraction lines indicated an increase in unit cell dimensions at lower temperatures. This overall negative expansion appeared to be confined to the zincblende cubic phase.

Since a contraction is generally expected on cooling a solid, a series of careful lattice measurements between room temperature and 4·2°K was then undertaken to determine the thermal expansion behavior of cubic silver iodide in this region.

The sample was cooled to liquid helium temperature and a pattern obtained for the (642) reflection. At room temperature this occurs at a 2θ angle of 125·08°. No diffraction profiles could be resolved at larger 2θ angles. In addition, the (531) reflection at 89·02° 2θ and the (511) reflection at 76·00° 2θ were monitored for a check on the calculated lattice spacing. The temperature was raised in increments of about 20°K in the interval between 20 and 200°K and accurate values for the lattice spacing obtained for each temperature. The α and β components were adequately separated in all cases. The centroid of the diffraction profile was estimated to a corrected accuracy of 0·01° in 2θ with the aid of the diamond standard. This corresponds to an accuracy of five parts in 10^5 for the calculated lattice parameter. The parameter was obtained directly from the observed angles by use of the equation

$$a = \frac{\lambda}{2\sin\theta}(h^2+k^2+l^2)^{1/2}.$$

3. RESULTS

A thermal expansion which is negative over all but a small portion of the temperature range investigated was determined for both samples of silver iodide.

The results are shown in Fig. 1. The lattice constant of the cubic silver iodide prepared by quenching shows a minimum near 90°K, while that prepared under pressure has a minimum near 70°K. A small region of positive thermal expansion is associated with each minimum. On the low temperature side of these minima the lines are nearly parallel and the slopes essentially equal.

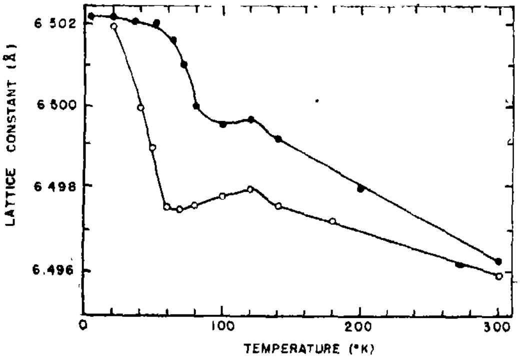

FIG. 1. Thermal expansion of zincblende cubic silver iodide in the temperature range from 4 to 300°K. Open circles represent data from specimen pressed at 3000 bars, solid circles data from specimen quenched from melt.

However, while the values of the lattice parameter at room temperature and at liquid hydrogen temperature are comparable, the slopes between 140 and 300°K appear to differ markedly. The calculated values for the coefficient of thermal expansion, α, defined as $1/l(\mathrm{d}l/\mathrm{d}T)_p$, for the upper linear part of the curves is $-1{\cdot}6\times10^{-6}(°\mathrm{K})^{-1}$ for the sample prepared under hydrostatic pressure and $-2{\cdot}8\times10^{-6}(^\circ\mathrm{K})^{-1}$ for that prepared by quenching from the melt. The former may be expected to be less disordered and exhibit a closer approach to equilibrium conditions. This value is thus to be preferred for the extrapolated room temperature thermal expansion coefficient of face-centered cubic silver iodide.

4. DISCUSSION

The measurements reported here show that the lattice spacing in cubic silver iodide at all temperatures depends on the method of preparation. This is presumably due to the presence of different concentrations of the more stable hexagonal phase, stacking faults, and defects. Despite these differences, there are characteristics of the thermal expansion which are independent of the method of sample preparation and which can be explained, tentatively, in detail.

In this Section an attempt is made to use the ideas of BARRON(15) to determine some of the effects of structure and bonding on thermal expansion. The Gruneisen factors,

$$\gamma_j = \frac{\mathrm{d}\ln\nu_j}{\mathrm{d}\ln V} \tag{1}$$

where ν_j the frequency of the jth mode and V the volume, are related, qualitatively, to the packing of atoms in simple structures, and the form of their interaction potential.

The formal theory of thermal expansion in the quasi-harmonic approximation has been discussed by BLACKMAN.(16) Gruneisen's temperature dependent constant, γ, is defined by the relationship

$$\gamma = \frac{V\alpha}{KC_v} = \frac{\sum\limits_j \gamma_j E(h\nu_j/kT)}{\sum\limits_j E(h\nu_j/kT)} \tag{2}$$

where α is the volume thermal expansion, K is the isothermal compressibility, and C_V is the specific heat. $E(h\nu_j/kT)$ is the heat capacity of the jth mode. For our purposes it is important to note that, at any given temperature, the contribution of each γ_j to γ is weighted by a factor which is roughly proportional to the population of that mode. We are concerned with the factors which determine the signs of the individual γ_j.

In each mode of the solid there are two conflicting tendencies. The first is the simple compressional, best illustrated by the longitudinal vibrations of a linear chain. The interatomic potential is quite asymmetric, with a much greater slope for interatomic distances smaller than those which minimize the potential than for interatomic distances which are larger. Thus, the effective spring constant can be decreased if the average interatomic distance is greater than that which minimizes the potential. The second type will be called shear, and is well represented in the transverse vibrations of a linear chain. All motion, since it is normal to the bond directions, tends to increase the interatomic distance. As BARRON(15) has pointed out, the effective spring constant will be reduced if the lattice contracts. The dominance of shear or compressional character in the volume dependence of the frequency of a given mode is quite dependent on structure, particularly for the transverse modes. To illustrate this dependence we examine a particular type of mode.

As we are primarily concerned with the phenomenon of negative thermal expansion, this mode is that which is most likely to have a negative Gruneisen factor. The same properties which tend to make the Gruneisen factor for this mode negative will tend to make the factors for modes of the same branch in the region of k-space around the mode negative. The smaller the factor for this mode, the smaller are the factors for the modes in the surrounding region.

In the discussion which follows, we assume that the forces between atoms are central. In this way, the dependence of the Gruneisen factor on structure can be analysed. We then remove the central force restriction and show the effects of forces which depend on the angle between the lines connecting an atom to its nearest neighbors.

The $[1\bar{1}0]$ polarizations of the (110) acoustic modes in the zincblende and cesium chloride structures, and the transverse (001) acoustic modes of the sodium chloride structure, are modes in which planes of atoms move, almost as a unit, perpendicular to the direction of all nearest-neighbor bonds which are not in the plane. If these planes moved entirely as units, the Gruneisen factors would have to be negative, as all bond lengths are either increased or remain constant. These, then, are the modes which are most likely to have negative Gruneisen factors. Calculations performed thus far(15–19) indicate that it is highly likely that all reasonable force models will lead to negative γ_j's for these modes in the zincblende structure, while the sign is quite dependent on the model in the sodium chloride structure. Since the signs must be negative if the planes move as a unit, it is the motion within the plane which alone could make a positive, compressional contribution. Here the two structures differ markedly. Within the {110} plane of the zincblende structure each atom has two nearest and two next-nearest neighbors. In the NaCl structure each atom has four nearest and four next-nearest neighbors. Thus, in the NaCl structure there are simply more nearest neighbors taking part in the smaller compressional motions within the plane than in the shear motions. We expect the compressional and shear motion approximately to cancel each other. Indeed, the calculations of BARRON(15) and GANESAN(17) both yield Gruneisen factors for these modes which are the smallest in magnitude of any calculated for the structure. Since these factors must be more positive for all other modes, we expect the Gruneisen constant to be positive for the sodium chloride structure at all temperatures on a structural basis alone. In the zincblende structure, the existence of fewer atoms within the plane, leading to smaller compressional contributions, implies that we may expect more negative Gruneisen factors.

We have considered, thus far, only the modes which are most likely to have negative γ_j's. For the zincblende and sodium chloride structures these modes involve the motion of the most densely packed planes. For other transverse modes, there are three changes. The out-of-plane bonds are no longer perpendicular to the direction of polarization. This tends to increase greatly the compressive contribution. Countering this tendency is the increase in out-of-plane bonds, contributing shear effects. In addition, the next-nearest neighbors begin to contribute compressively. Here again, the compressive contribution is smaller for the zincblende structure. There are the same number of next-nearest neighbors in both the sodium chloride and the zincblende structures, but these next-nearest neighbors are less likely to be in contact in the latter. The coordination numbers and distances about an atom of either type in these structures is shown in Table 1. Most compounds with the zincblende structure have bonds with appreciable covalent character and differ widely from the ideal anion–cation radius ratio for tetrahedral coordination. Thus we expect the γ_j modes to become progressively more positive, but this increase should be slower for the zincblende than the sodium chloride structure. The calculations cited indicate that the γ_j's do indeed become more positive. However, BLACKMAN's(18) calculation indicates that as long as the next-nearest neighbor forces are Coulombic, the transverse modes in the zincblende structure have, for a large range of nearest-neighbor interactions, negative Gruneisen factors. Since these transverse modes have lower velocities than the longitudinal, they dominate at low temperatures and yield negative thermal expansions. In sodium chloride, on the other hand, almost all the modes have positive γ's.

It has been assumed, thus far, that the nearest-neighbor bond energy is primarily determined by the interatomic separation. With increasing covalent character, however, this energy depends, to a greater degree, on the angles between the nearest neighbor bonds. This bond-angle dependent

Table 1. *Coordination spheres*

Type of Structure	Order	Neighbors		
		Number	Charge	Distance
NaCl	First	6	Opposite	$a/2$
	Second	12	Same	$(\sqrt{2}/2)a$
	Third	8	Opposite	$(\sqrt{3}/2)a$
ZnS (cubic)	First	4	Opposite	$(\sqrt{3}/4)a$
	Second	12	Same	$(\sqrt{2}/2)a$
	Third	12	Opposite	$(\sqrt{11}/4)a$

portion of the energy tends to make a positive contribution to the Gruneisen factor, as the angular change resulting from a unit displacement of an atom normal to a bond decreases with increasing interatomic separation. In addition, the force constant itself probably decreases with increasing separation at the equilibrium distance. The Gruneisen factors for the shear modes thus tend to become more positive with increasing angular dependence. In addition, the velocities of the shear modes, relative to the compressional modes, increase with increasing covalent character. The result of increasing covalency, then, is to make the Gruneisen constant more positive because the Gruneisen factors of the shear modes have become less negative and because they contribute less. This explains why NOVIKOVA(12) found, "... that the temperature at which α becomes negative increases, while the value of $\alpha_{\min}$ becomes increasingly small when passing from Ge to ZnSe; this result corresponds to the increase of the strength of the ionic components of the bonds. Similar results have been obtained for the isoelectronic series of α-Sn." It also explains Ganesan's positive Gruneisen factor for the transverse (100) modes in the sodium chloride structure. He included non-central forces in his calculation.

Within an isoelectronic sequence, the decrease of the low temperature Gruneisen constant with decreasing covalent character should continue up to the point where there is an effective anion contact. Silver iodide represents that limit. In the α-Sn sequence, the percentage of bond ionic character, as computed from PAULING's rule,(20) goes from zero for Sn, to 8 for InSb, to 11 for CdTe, and 15 per cent for AgI. Silver iodide is significantly more ionic than the other compounds in the sequence and is more ionic than all compounds, other than the cuprous halides, which crystallize with the zincblende structure. As expected, it has the largest magnitude negative low-temperature thermal expansion. To understand its high temperature behavior, we return to the results of Blackman for the central force model.

At high temperatures ($T \gtrsim \Theta_D$) there exists a temperature independent Gruneisen constant(21) which is just the average over all the modes of the γ_j. If one examines Blackman's(18) calculations for the long wavelength acoustic limit, one finds that for every direction of propagation, the average of the γ_j for the three modes is negative. Although Blackman states that "It seems, however, clear that the γ value is positive at high temperatures as contrasted with the negative values at low temperatures", the likelihood is that the acoustic modes make a negative contribution to the high temperature limit, γ_∞. The burden of making γ_∞ positive then lies with the optical modes. Even for the $[1\bar{1}0]$ polarization of the (110) optical mode in the zincblende structure, this positive γ is not unexpected. Although the shear motion is relatively unaltered compared to the corresponding transverse acoustical mode, the compressive motion has changed considerably. In the optical mode, the anions and cations are moving in opposite directions, greatly increasing the compressive component and the Gruneisen factor. The fact that there is much less variation of frequency with wave number in the optical branches than in the acoustic shows that this compressive interaction is the primary determinant of the frequency and will lead to a positive γ.

A thorough theoretical analysis of the expansion properties of silver iodide would require a knowledge of the interatomic potentials. With this knowledge, the frequencies of the normal modes and their volume dependence could be determined. Since silver iodide is partially covalent, we do not know these interatomic potentials. Moreover, since no success in preparing single crystals has been achieved, the elastic constant and Raman spectra cannot be determined. Hence, even the usual parameter fitting techniques are not open to us. In addition, as will be shown, even the sign of γ_∞ is quite sensitive to the choice of interatomic potential. Hence, we proceed with a "qualitative" calculation designed to show the delicate balance between the contributions of the acoustic and optical branches, as well as the possibility of predicting a negative γ_∞ with the quasi-harmonic approximation.

To do this we use BLACKMAN's(15) model in which a Coulomb potential between all neighbors and an r^{-n} repulsive potential between nearest neighbors forms the interatomic interaction. Combining the results of Blackman's calculations of the elastic constants with RAJAGOPAL and SRINIVASAN's(2) calculation of the mode frequency spectrum of cubic zinc sulfide, we find that the

Raman frequencies are given by the expressions

$$\omega^2_{\text{trans}} = \frac{e^2}{2}\left\{\frac{1{\cdot}681(n-1)r_0{}^{n-1}}{r^{n+2}} - \frac{4\pi}{3r^3}\right\}\left\{\frac{m_1+m_2}{m_1m_2}\right\}$$

$$\omega^2_{\text{long}} = \frac{e^2}{2}\left\{\frac{1{\cdot}681(n-1)r_0{}^{n-1}}{r^{n+2}} + \frac{8\pi}{3r^3}\right\}\left\{\frac{m_1+m_2}{m_1m_2}\right\} \tag{3}$$

where r is the nearest-neighbor separation and r_0 is the value for which the potential is minimized. m_1 and m_2 are anion and cation masses. These lead to the following expressions for the Gruneisen factors evaluated at $r = r_0$:

$$\gamma_{\text{trans}} = \frac{1}{6}\left(\frac{3{\cdot}782(n+2)(n-1)-9\pi}{3{\cdot}782(n-1)-3\pi}\right)$$

$$\gamma_{\text{long}} = \frac{1}{6}\left(\frac{1{\cdot}891(n+2)(n-1)+9\pi}{1{\cdot}891(n-1)+3\pi}\right) \tag{4}$$

To obtain an idea of the effect of n on the balance, we have assumed that the contribution of the acoustic modes to γ_∞ is the same as that which is obtained by taking the angular average of the contribution of the long wavelength modes. To calculate this average, the function

$$\tfrac{1}{3}\sum_{j=1}^{3N} \gamma_j$$

was calculated for the (100), (110), and (111) directions. These values were then fitted by the first three Kubic harmonics(22) appropriate to the symmetry type Γ, and the coefficient of the first term (s-like) was taken as the average. The contribution of the optical modes was taken to be the weighted average (2 transverse, 1 longitudinal) of the γ_j's computed from the Raman frequencies.

These derived Raman frequency values, for n equal to 6 and 11 are:

n	γ_{trans}	γ_{long}
6	2·165	0·919
11	2·720	1·612

From these, the following were then calculated:

n	Acoustic γ_∞	Optical γ_∞	γ_∞
6	−1·03	1·75	0·36
11	−2·73	2·35	−0·19

Here the value 11 for n was chosen because it is appropriate to an ionic model for silver iodide, while $n = 6$ is the value used by Blackman in his calculations. We see that for $n = 6$, the high temperature limit is positive, while for $n = 11$, it is negative. Thus, although no quantitative faith can be placed in this calculation, it seems likely that the negative γ_∞ can be explained on the basis of the large exponent for the repulsive interaction alone. The sensitivity of the balance is shown by the fact that the resulting γ_∞ for both values of n is small in magnitude compared to the contribution of the groups of modes themselves. The value of −0·19 should be compared with a γ_∞ of −0·136 which has been calculated for silver iodide using the thermal expansion results given here, the unpublished value of 9·890 × 10^{10} dyne cm^{-2} for the bulk modulus obtained by J. Wachtman on a sample of primarily zincblende cubic silver iodide, and the specific heat of 13·01 cal deg^{-1} mole^{-1} given by KELLEY(23) for a sample of unspecified phase composition. This shows, in addition to the crudeness of the calculation, the effect of covalency in making γ_∞ more positive. This is also illustrated by the fact that the observed γ_∞ of indium antimonide(9, 12) is positive. Approximately the same n value would be expected, with an ionic model, for this compound as for silver iodide. Because of the strong covalent bonding, however, the ionic model is not quite applicable to this compound.

We have already noted that AgI forms a limit of ionic character for the α-Sn isoelectronic sequence which explains its low temperature characteristics. In addition, it has the largest effective repulsive exponent, n, in the r^{-n} interaction. It is a consequence of these two facts that its thermal expansion is uniquely negative over such a large temperature range.

It is easy to form the misimpression that these results contradict those of BLACKMAN(16) who finds that $\gamma(2)$, where

$$\gamma(i) = \sum_{j=1}^{3n} \gamma_j\nu_j^i \Big/ \sum_{j=1}^{3n} \nu_j^i$$

is equal to $\frac{1}{6}(n+2)$. In this notation,

$$\gamma_0 = \gamma(-3)$$

$$\gamma_\infty = \gamma(0)$$

Because $\gamma(2)$ can be calculated easily for any given model, it has been used as an approximation to $\gamma(0)$. With this approximation, it would appear that γ_∞ should become more positive with increasing n. However, for this structure, the γ_j's for the low frequency modes are significantly less than those of the high frequency modes. $\gamma(i)$ is a quickly varying function of i, in the neighborhood of the origin. Therefore, the above replacement may have no validity. Further evidence for the failure of this approximation and the validity of the analysis given here is given by the decrease of $\gamma(-3)$ with increasing n noted by Blackman. This decrease in $\gamma(-3)$ would tend to decrease $\gamma(0)$ in an interpolation between $\gamma(2)$ and $\gamma(-3)$.

We have yet to explain the region of positive thermal expansion at intermediate temperatures. A clue to this behavior is contained in the calculation of RAJAGOPAL and SRINIVASANI.(21) In particular, we refer to their calculation which uses a long-range Coulomb interaction, plus parameters for additional nearest-neighbor and next-nearest neighbor interactions. While their ratio of ionic to covalent bonding is purposely too large for zinc sulfide, it may be close to being correct for silver iodide. The crucial result of their calculation (for our purposes) is the demonstration of a large number of transverse optical modes having lower frequencies than many of the transverse acoustic modes. It is these modes which have the largest γ_j's. For a short temperature range, the contributions of these modes and the longitudinal acoustic modes to the Gruneisen constant are sufficient to make that constant positive.

The temperature dependence of the thermal expansion can then be described as follows:

(1) The sign of the thermal-expansion coefficients is determined by the balance among all of the lattice modes occupied, some contributing positive and some negative tendencies. Since the relative populations, at least, are temperature dependent, the overall sign may change with temperature.

(2) The optical and longitudinal acoustical modes generally make positive contributions. The modes most likely to produce negative contributions are those transverse modes for which planes of atoms move almost in unison normal to the out of plane bonds. Since these modes are most populated at low temperatures, a negative thermal expansion usually occurs only at low temperatures, and the sign changes as the other modes become populated with rising temperature.

(3) The negative sign and the magnitudes of the contributions from these transverse acoustic modes depend upon a balance among several factors. Rapidly varying repulsive forces in the plane of the motion tend to produce a positive contribution. Hence, open structures with few in-plane neighbors like the diamond and zincblende structures are the most apt to show the negative coefficient. Covalency, by introducing non-central forces, makes the contribution more positive. Therefore, for a given structure type, the greatest tendency to negative thermal expansion is shown by the least covalent substances. The contribution from these transverse acoustic modes is increasingly negative with increasing n in the nearest-neighbor repulsive r^{-n} interaction.

(4) Silver iodide is unique because it represents extremes. The first is an extreme, except for the cuprous halides, of ionic character in a structure which is normally assumed by covalent compounds. Its radius ratio is just sufficiently different from the ideal so that the next-nearest neighbor interaction is slowly varying with distance. In addition, its exponent in the nearest neighbor interaction is the largest of any of the relatively ionic compounds known to have this structure.

(5) In silver iodide, these extreme tendencies cause the negative contribution due to the transverse acoustic modes to dominate even at high temperature, where all modes are populated. Hence the negative thermal expansion persists to high temperatures. At intermediate temperatures, the coefficient becomes positive as the result of the existence of a low lying group of optical modes whose positive contribution outweighs the negative contribution from the incompletely-occupied transverse acoustic modes.

As BLACKMAN(24) has suggested, one should not neglect the role of defects. It is possible that the lattice constant minimum of silver iodide is similar to that of the other compounds with the zincblende structure. That is, the Gruneisen constant is negative at low temperatures, but has a positive high temperature limit. Such a limit is not ruled out by the calculation discussed above, as the approximations are rather crude. The calculation does show, however, that whatever its sign, we may expect the limit of the Gruneisen constant to be small in magnitude.

Acknowledgements—The authors wish to express their appreciation to Mr. L. H. Bolz for obtaining the diffractometer patterns and to Mr. H. S. Peiser for a number of stimulating discussions which aided considerably in the development of the ideas presented here. They would also like to thank Dr. J. Wachtman for measuring the bulk modulus of silver iodide and for allowing us to use his results in advance of their publication.

A portion of this work was submitted by one of us (G.B.) in partial fulfillment of the requirements for a Ph.D. degree at Georgetown University (1962).

The project was financially supported by the National Science Foundation, Atmospheric Sciences Program, Grant No. 19648.

REFERENCES

1. Fizeau H., *Ann. Phys.* **208,** 2. Folge **132,** 292 (1867).
2. Jones G. and Jelen F. C., *J. Amer. chem. Soc.* **57,** 2532 (1935).
3. Cohen E. and Bredée H. L., *Z. phys. Chemie* **178A,** 184 (1937).
4. Wilsey R. B., *Phil. Mag.* **46,** 487 (1923).
5. Block R. and Moller H., *Z. phys. Chemie* **152A,** 245 (1931).
6. Burley G., Thesis, Georgetown University, 1962.
7. Adenstadt H., *Ann. Phys.* **26,** 69 (1936).
8. Erfling H. E. V., *Ann. Phys.* **41,** 467 (1942).
9. Gibbons D. F., *Phys. Rev.* **112,** 136 (1958).
10. Novikova S. I. and Strelkov P. G., *Fiz. tverd. tela* **1,** 1841 (1959); English translation *Sov. Phys. Solid-State,* **1,** 1687 (1960).
11. Novikova S. I., *Fiz. tverd. tela* **2,** 43 (1960); **2,** 1617 (1960); **2,** 2341 (1960); English translations *Sov. Phys. Solid-State,* **2,** 37 (1960); **2,** 1464 (1961); **2,** 2087 (1961).
12. Novikova S. I., *Fiz. tverd. tela* **3,** 178 (1961); English translation *Sov. Phys. Solid-State,* **3,** 129 (1961).
13. Black I. A., Bolz L. H., Brooks F. P., Mauer F. A. and Peiser H. S., *J. Res. Nat. Bur. Stand.* **61,** 367 (1958).
14. Mauer F. A. and Bolz L. H., *J. Res. Nat. Bur. Stand.* **65C,** 225 (1961).
15. Barron T. H. K., *Ann. Phys.* **1,** 77 (1957).
16. Blackman M., *Proc. phys. Soc. Lond.* **70,** 827 (1957).
17. Ganesan S., *Phil. Mag.* **7,** 197 (1962).
18. Blackman M., *Phil. Mag.* **3,** 831 (1958).
19. Barron T. H. K., *Phil. Mag.* **46,** 720 (1955).
20. Pauling L., *The Nature of the Chemical Bond,* 3rd ed. p. 98, Cornell University Press, Ithaca (1960).
21. Rajagopal A. K. and Srinivasan R., *Z. Phys.* **158,** 471 (1960).
22. Von der Lage F. C. and Bethe H., *Phys. Rev.* **71,** 612 (1947).
23. Kelley K. K., *U.S. Bur. Mines Bull.* 434 (1941).
24. Blackman M., private communication.

Note added in proof:

A negative thermal expansion for cubic silver iodide by dilatometric techniques has also been obtained by K. H. Lieser (*Z. phys. Chem.* **5,** 125 (1955)) over the range from 86 to 420°K. A constantly increasing value for the negative coefficient of expansion, from $-0{\cdot}7\times10^{-6}$ at 86°K to $-4{\cdot}0\times10^{-6}$ at 273°K and $-5{\cdot}7\times10^{-6}$ at 333°K, was reported. However, the data apparently indicate a limited region of positive thermal expansion similar to that reported here, since the mean lengths for 86 and 125°K are identical.

J. Phys. Chem. Solids Pergamon Press 1963. Vol. 24. pp. 1279–1284. Printed in Great Britain.

REARRANGEMENT OF A FLAT SURFACE WITHOUT ALTERING THE NUMBER OF BROKEN BONDS

J. F. NICHOLAS

Division of Tribophysics, C.S.I.R.O., University of Melbourne, Australia

(*Received* 16 *May* 1963)

Abstract—One property of an atomically-flat surface is that, for a given orientation, such a surface has the minimum possible number of missing inter-neighbour links. However, other near-flat surfaces may also possess this property and methods are described for constructing such rearranged surfaces. A criterion for judging whether or not a surface possesses the minimum number of missing bonds is given in terms of the facets that appear on the surface. A detailed argument is presented for face-centred cubic crystals with only nearest-neighbour bonds considered; then a brief outline is given for body-centred cubic crystals with nearest and next-nearest neighbours considered.

1. INTRODUCTION

DURING a study of the adsorption of hydrogen onto clean nickel surfaces, GERMER and MACRAE(1) found that the atoms on an atomically-flat (110) surface may be rearranged during the adsorption, but that no such effect occurs on a (100) or (111) surface. Since the rearrangement on the (110) surface is such as to destroy the flatness of the surface without altering the number of missing Ni–Ni nearest neighbours and since such a rearrangement is geometrically impossible on a (100) or (111) surface, Germer and MacRae have suggested that, in general, the only such "reconstructive rearrangements" that can occur during the adsorption of hydrogen are those which do not increase the number of missing nearest neighbours. It is, therefore, of interest to consider the general problem of how the atoms on an atomically-flat surface can be rearranged without changing the total number of broken bonds at the surface.

Although Germer and MacRae's experimental results provide a motive for considering this problem, the analysis given here is purely geometrical and must hold true irrespective of any physical assumptions. However, physical deductions can only be made from the analysis by introducing physical assumptions and these deductions will be valid only to the extent that the physical assumptions are valid. For instance, Germer and MacRae imply that, in the presence of hydrogen, the free energy of a nickel surface is determined by the number of broken nearest-neighbour bonds and, on this basis, the present analysis shows how flat surfaces can be rearranged without affecting the surface energy. The purpose of this paper is not to comment on this or other similar assumptions but simply to describe their geometrical consequences.

2. STATEMENT OF THE PROBLEM

The following definitions and restrictions will apply in all the succeeding argument, except that of Section 6.

(i). Only face-centred cubic crystals are considered.

(ii). *Neighbour* means nearest neighbour.

(iii). The link between two atoms will be referred to as a *bond* and will be specified by the vector u joining the centre of the atoms concerned. Since only bonds between neighbours are considered, u corresponds to one of the twelve vectors in the set $\frac{1}{2}\langle 110\rangle$.

(iv). An atom with one or more neighbours missing will be described as having some *broken bonds*; it will be said to be of type B_j if it has j broken bonds, i.e. if it has only 12-j neighbours.

(v). A *site* means a lattice point which is itself unoccupied, but which has at least one occupied lattice point as a neighbour. A site with j neighbouring atoms will be denoted by s_j.

(vi). A *flat surface* means an atomically-flat surface, i.e. one formed by dividing an infinite perfect crystal by a plane and then removing all atoms lying on one side of this plane. The orientation of such a surface will be specified by the Miller indices (hkl) of crystallographic planes parallel to the dividing plane, the axes of reference being so chosen that $h \geqslant k \geqslant l \geqslant 0$, i.e. that the pole lies on or within the unit stereographic triangle PQR in Fig. 1. Clearly such an ideal surface extends to infinity in all directions so that edge effects can be ignored.

(vii). A *rearranged surface* means a surface derived from a flat surface by moving, removing, or adding a number of atoms, the orientation of the new surface being defined as that of the parent flat surface. Any movement or addition of an atom is assumed to be to a lattice point.

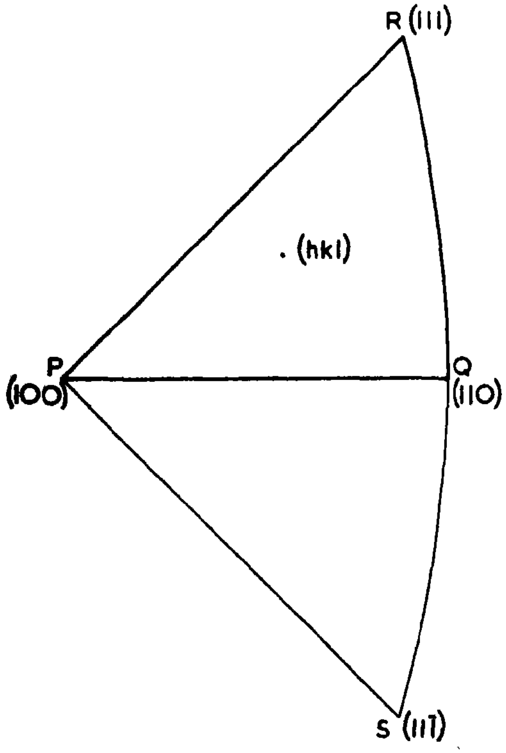

Fig. 1. Stereographic plot showing triangle PQR within which (hkl) is chosen to lie. For face-centred cubic crystals, surfaces of minimum $\Sigma n(u)$ consist of facets represented by P, R, and S.

(viii). An *allowable rearrangement* is one that does not increase the total number of broken bonds at the surface. It should be stressed that allowable must not be interpreted as meaning anything more than this; in particular, it does not mean "physically realizable".

Mackenzie, Moore and Nicholas(2) have derived a formula giving, for a flat surface, the number, $n(u)$, of atoms per unit area of surface having broken u-bonds. The present problem is to determine what rearrangements are possible without affecting $\sum\limits_{u} n(u)$, where the sum is taken over the twelve possible u.

In the paper quoted, it was pointed out that, by considering all the bonds with a particular vector, u_1 say, rows of atoms could be traced through the crystal by travelling continuously along a sequence of u_1-bonds and each such row of atoms would correspond to a lattice row parallel to u_1. In a semi-infinite crystal with a flat surface, it is now convenient to classify a row of atoms linked by u_1-bonds as

(a) negative, if it starts at a surface atom and then penetrates more and more deeply into the crystal; or

(b) neutral, if it lies parallel to the surface and therefore extends infinitely in both directions; or

(c) positive, if it starts infinitely deep in the crystal and terminates at a surface atom, this terminal atom having a broken u_1-bond.

This distinction and terminology corresponds to u_1 having a negative, zero, or positive component normal to the surface. For a given u_1, each atom in the crystal must lie on some row and all the rows must have the same character. Thus, there is a one–one correspondence between atoms with broken u_1-bonds and positive rows, and the density of atoms with broken u_1-bonds will be given by the density of the corresponding rows, i.e. by the number of lattice rows, parallel to u_1, that cut unit area of surface, the area being measured parallel to (hkl).

Any rearrangement of a flat surface will disturb some of the surface atoms, but since every positive row must still terminate somewhere, the total number of broken bonds cannot be decreased

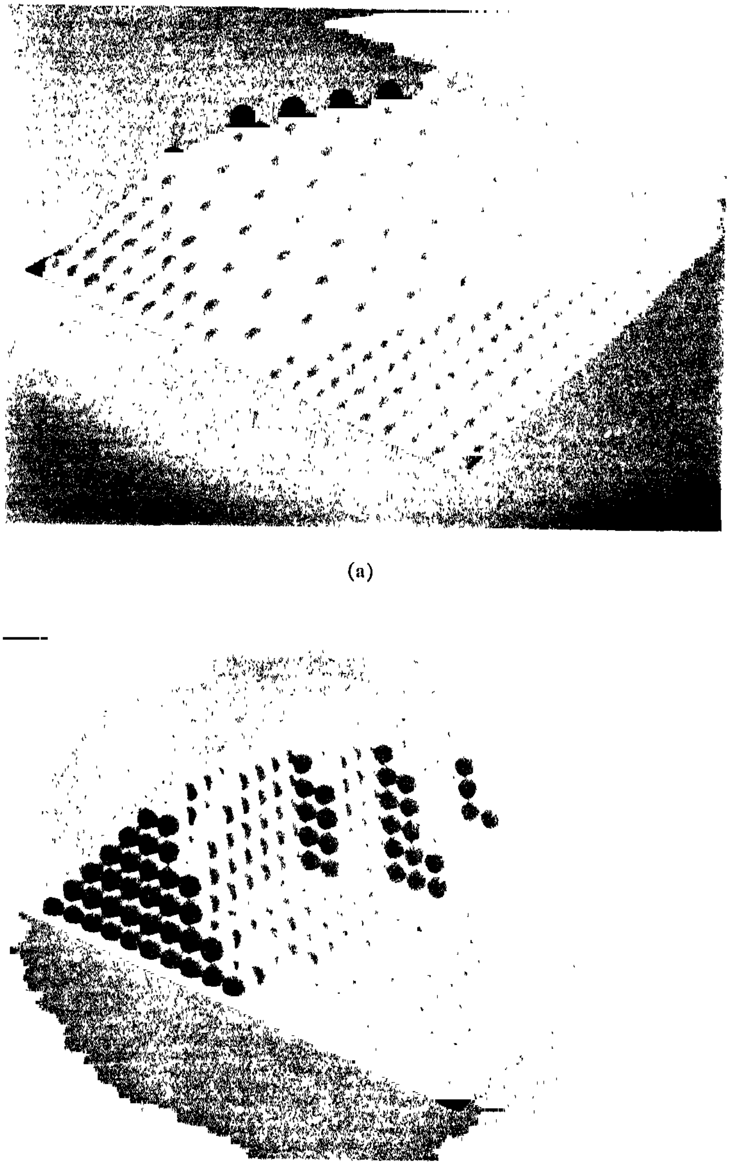

(a)

(b)

FIG. 2. Ball models of (531) surfaces in a face-centred cubic crystal, the black balls representing atoms in the outermost (531) plane. A flat (531) surface is shown in (a) and a rearranged surface of minimum $\Sigma n(u)$ is shown in (b). The facets of (100) are parallel to the layer of white balls in the foreground, and the facets of $(11\bar{1})$ are parallel to the plane of atoms bounding the model at the left. The other facets belong to (111) planes.

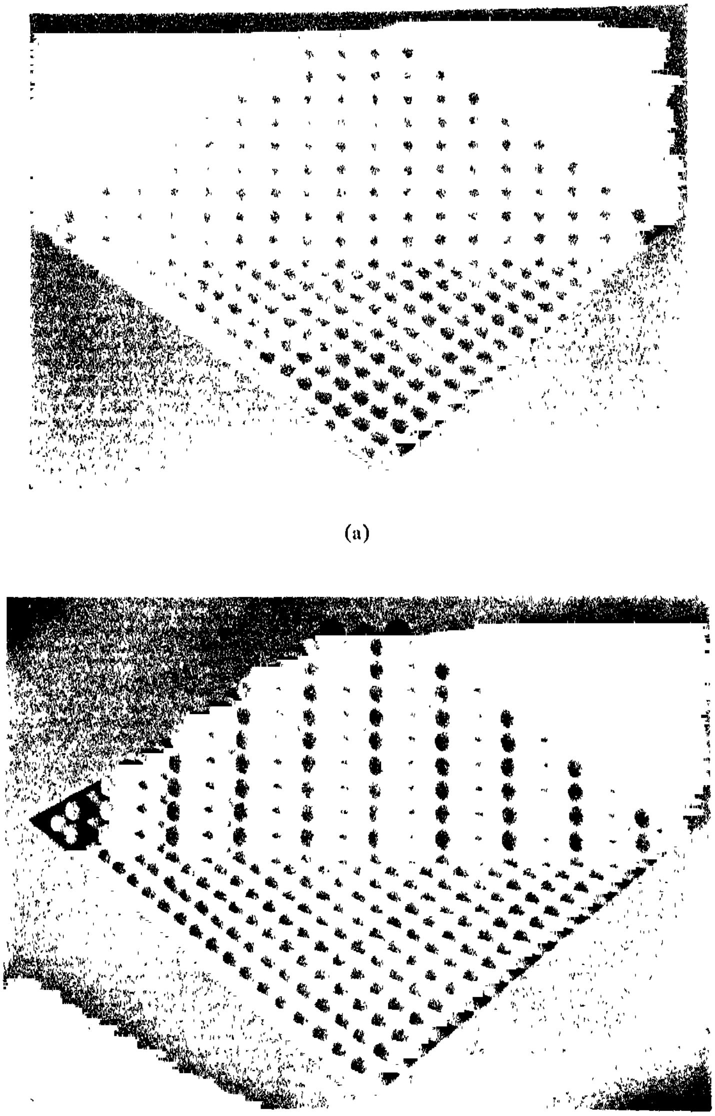

(a)

(b)

FIG. 3. Ball models of flat and rearranged (110) surfaces in a face-centred cubic crystal, the black balls representing the outermost plane of atoms. The layer of white balls in the foreground forms a (100) plane; the horizontal direction across the surface is [001] and the direction up the surface is [1$\bar{1}$0]. (a) A flat (110) surface. (b) The (2 × 1) surface of Germer and MacRae showing valleys formed from (111) facets on the left and (11$\bar{1}$) facets on the right. (c) An irregularly rearranged surface of minimum $\Sigma n(\boldsymbol{u})$. (d) The (1 × 2) surface of Germer and MacRae, which consists of horizontal (100) facets and vertical (010) facets; this is not an allowable rearrangement.

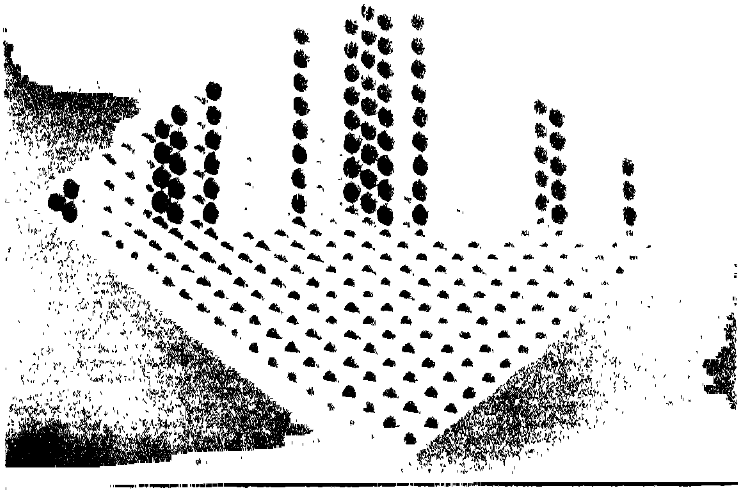

(c)

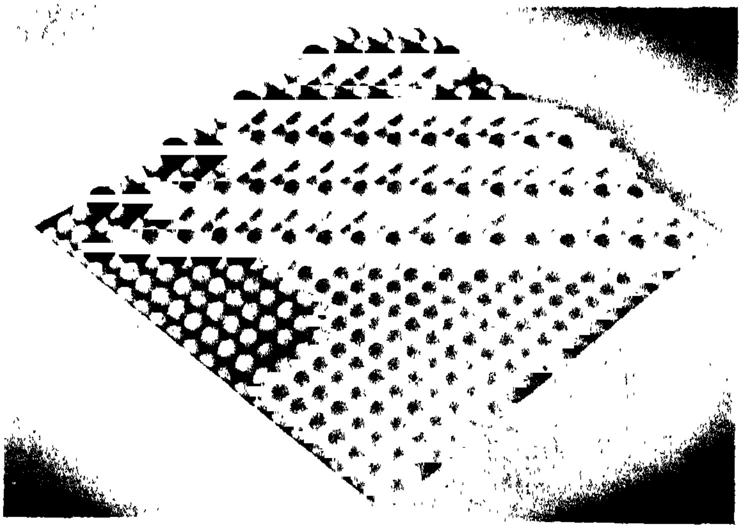

(d)

by rearrangement. However. if the rearrangement introduces a gap into any row (positive, negative, or neutral), then the corresponding $n(u)$ will be increased and so will the sum $\Sigma n(u)$. Thus, the problem can be reduced to that of determining how a flat surface can be rearranged without introducing gaps into *any* u-row.

3. ALLOWABLE REARRANGEMENTS

Rearrangements caused by the removal of atoms will be considered in detail first, since the effects of the other methods of rearrangement can be deduced from the effects of removal.

As a first step, consider the removal of atoms one at a time from a flat surface of such an orientation that $h > k > l$, i.e. such that the pole of the surface does not lie along *PR* or *RQ* in the stereographic triangle of Fig. 1. Then, since this restriction eliminates the possibility of neutral rows, each atom in the crystal will have six positive (and six negative) rows through it and, if the removal of an atom is not to create a gap in one of these, the atom must terminate all the positive rows, i.e. it must have 6 broken bonds and thus be of type B_6 [definition (iv)]. Therefore, the allowable rearrangements are those which can be described as the removal of a succession of B_6 atoms. The total number of B_6 atoms that can be removed in this way is not limited to the number existing in the flat surface, since the removal of one B_6 atom converts each neighbouring B_j atom into a B_{j+1} atom ($j = 0, 1, 2, ..., 5$) and, in this way, the supply of B_6 atoms can be augmented. In fact, quite extensive regions of rearranged surface can be built up. For example, Fig. 2(a) shows a flat (531) surface, while Fig. 2(b) shows one of the many possible rearranged surfaces that contain the same number of broken bonds.

The discussion can now be extended to cover the removal of a pair of atoms. If the pair are not neighbours, then they can be treated independently and the removal of the pair is allowable, if and only if the removal of each one separately is allowable, i.e. if and only if both are B_6 atoms. However, if the pair are neighbours joined by a bond u and if their removal is not to cause a gap in the u-row through them, then they must be the last and next-to-last atoms in that row. Considerations similar to those discussed in the previous paragraph show that, for an allowable removal, there must be five other positive rows terminating on each atom, i.e. the end atom must be of type B_6 and the other of type B_5. If this is so, then clearly they could have been removed successively. By extending this argument, it is relatively simple to show that the removal of any group of atoms is an allowable rearrangement if and only if the atoms can be ordered in such a way that they can be removed one by one without breaking a u-row at any stage.

To complete the discussion of rearrangement by removal of atoms, crystals containing neutral rows must be considered, i.e. crystals where the pole of the surface lies along *PR* or *RQ* (Fig. 1). Along *PR*, $k = l$ and any surface will have neutral rows parallel to $[01\bar{1}]$ and $[0\bar{1}1]$; along *RQ*, $h = k$ and any such surface will have neutral rows parallel to $[1\bar{1}0]$ and $[\bar{1}10]$. Excluding for the moment (100) and (111) surfaces, it is clear that, for any other surface in these sets, each atom must have five positive, five negative, and two neutral rows through it. Since the removal of any single atom must introduce a gap into each of the neutral rows through it, no such rearrangements are allowable; further, the same argument applies to the removal of any finite group of atoms. Thus, the only rearrangements that *could* be allowable would be those consisting of the removal of complete neutral rows of atoms. Such a removal *will* be allowable only if no gaps are created in other rows, i.e. if each atom terminates the five positive rows through it, i.e. if the row consists of B_5 atoms. As an example, consider the flat (110) surface shown in Fig. 3(a), where each line of dark balls corresponds to a neutral row of atoms parallel to $[1\bar{1}0]$. If each alternate row is removed, then the (2×1) structure of Germer and MacRae appears [Fig. 3(b)], but other allowable rearrangements, such as that shown in Fig. 3(c), are of course possible. The present arguments can say nothing about why, in the adsorption of hydrogen on nickel, the (2×1) structure is preferred over any other allowable rearrangement, or indeed why any rearrangement should occur.

The special cases of (100) and (111) surfaces must now be considered. On a (100) surface, each atom is of type B_4 and belongs to neutral rows parallel to [011] and $[01\bar{1}]$ while on a (111) surface, each atom is of type B_3 and belongs to neutral rows parallel to $[1\bar{1}0]$, $[10\bar{1}]$, and $[01\bar{1}]$.

Thus, since neutral rows must be removed as units, the only allowable way of rearranging either of these surfaces would be to remove a whole plane of atoms. However, such a removal simply reproduces the original surface in a slightly different position and therefore cannot be classed as a rearrangement. As mentioned previously, Germer and MacRae found that, for these surfaces, no change in structure occurred during adsorption.

In principle, the other methods of rearrangement could be ignored since a rearranged surface formed by addition or movement of atoms could be regarded as having been formed by the removal of atoms from a flat surface of the same orientation but differently located in space. However, it seems convenient to regard at least the addition of atoms as a distinct form of rearrangement. Then an argument, analogous to that given above, can be developed to show that isolated atoms can be added to s_6 sites [see definition (v)] to extend six positive rows simultaneously, or neutral rows of atoms can be added into a row of neighbouring s_5 sites when these occur. Rearrangements by the movement of atoms can then be regarded as removal followed by addition and such rearrangements will be allowable if and only if each stage is allowable in itself.

In summary, the position is:

(i). No allowable rearrangements can occur on (100) or (111) surfaces.

(ii). For surfaces along the zone between (100) and (111) or along the zone between (111) and (110), allowable rearrangements consist of the removal of projecting close-packed rows of atoms or the addition of such rows along troughs.

(iii). For all other surfaces, allowable rearrangements consist of the removal of B_6 atoms and/or the addition of atoms into s_6 sites.

4. FACETS ON A SURFACE

From a study of flat and rearranged surfaces, it is obvious that many of these can be described as consisting of facets of flat surfaces of other orientations. In this Section, a facet will be defined in such a way that any surface, except for a few pathological cases, can be completely described in terms of facets. This definition is then used to derive a criterion, based on facets, for determining whether or not a surface has minimum $\Sigma n(\boldsymbol{u})$.

Only facets of densely-packed planes will be considered, and a facet of (*hkl*) will be said to exist if either

(a) (*hkl*) belongs to {100} and there exist four atoms in a (*hkl*) plane, together with a site that is a neighbour of each atom,

or

(b) (*hkl*) belongs to (111) and there exist three atoms in a (*hkl*) plane, together with a site that is a neighbour of each atom but does not lie in the plane of the atoms.

In each case, the site must be on the side of the atoms that would be unoccupied if the atoms formed part of a flat (*hkl*) surface. Figure 4 shows the configurations of atoms and site necessary to define a facet.

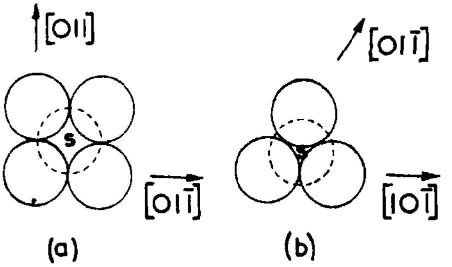

FIG. 4. Configurations of atoms (full circles) and sites (broken circles) necessary to define (a) a (100) facet, and (b) a (111) facet in a face-centred cubic crystal. In each case the site is assumed to be above the plane of atoms.

On this definition, any flat surface with $h \geqslant k \geqslant |l|$, i.e. with a pole within *PRS* in Fig. 1, can be regarded as constructed from facets of (100), (111), and (11$\bar{1}$), and no other facets can appear. Then it is relatively easy, but tedious, to show that "A surface has minimum $\Sigma n(\boldsymbol{u})$ if and only if it can be completely described in terms of facets of (100), (111), and (11$\bar{1}$)." The term "completely described" in this criterion is used to imply that every atom with a broken bond belongs to at least one facet and that it is impossible to find a facet of any other plane.

The surfaces shown in Figs 2 and 3 display facets and can be used to demonstrate the criterion just given. The rearranged surface in Fig. 2(b) shows large facets of (100), (111), and (11$\bar{1}$) and these can be extended into the flat surface at the right side of the figure. It is then easy to see how the whole of the flat surface in Fig. 2(a) can be made up from facets of these three planes. Similarly, the surfaces in Figs 3(a), (b), and (c) all consist of facets of (111) and (11$\bar{1}$), and all are surfaces of minimum $\Sigma n(\boldsymbol{u})$. However, Fig. 3(d), which represents another rearrangement of a (110) surface, the so-called (1 × 2) surface of Germer and MacRae, shows facets of (100) and (010) extending across the figure. Thus, the facet criterion says that this is not a surface of minimum $\Sigma n(\boldsymbol{u})$; in fact, the neutral rows parallel to [1$\bar{1}$0] contain gaps so that broken $\frac{1}{2}$[1$\bar{1}$0] and $\frac{1}{2}$[$\bar{1}$10] bonds occur.

In principle, surfaces could exist that were not completely describable in terms of facets, e.g. a surface could contain a feature such as a whisker only one atom across. However, in practice, such pathological surfaces are unlikely to exist and they are certainly not surfaces of minimum $\Sigma n(\boldsymbol{u})$.

In the terminology of this paper, all the surfaces shown in Figs 2 and 3 represent allowable rearrangements, with the exception of the surface in Fig. 3(d). However, it should be stressed again that to say that this (1 × 2) surface is not an allowable rearrangement does not imply that it cannot exist but just that, if it exists, it has more broken bonds per unit area than a flat (110) surface. In fact, GERMER and MACRAE[3] have found a surface of this type to exist on nickel in the presence of oxygen. They suggest that its existence is related to a strong interaction between oxygen and nickel atoms in contrast to the weak interaction between hydrogen and nickel.

5. TYPES OF ATOM ON REARRANGED SURFACES

In the earlier work,[2] the concentrations of different types of surface atom were determined for a flat surface. It should be noted that these concentrations are *not* necessarily preserved by an allowable rearrangement. For example, the surface shown in Fig. 3(a) contains B_1 and B_5 atoms in equal numbers, but the rearrangement shown in Fig. 3(b) has caused half of these atoms to be replaced by B_3 atoms. Thus, the ratio of concentrations $n(B_1):n(B_3):n(B_5)$ has changed from 1:0:1 to 1:2:1, but the average number of broken bonds per surface atom has remained at 3. Other allowable rearrangements simply correspond to different values for the relative concentration of B_3 atoms.

In contrast, an unallowed rearrangement *must* change the relative concentrations of atoms of different types. Thus, the change from the surface in Fig. 2 (a) to that in Fig. 2 (d) corresponds to a change in the ratio $n(B_1):n(B_3):n(B_5):n(B_7)$ from 1:0:1:0 to 1:2:0:1 and this last ratio corresponds to an average number of 3·5 broken bonds per surface atom. Since the number of surface atoms per unit area has not been altered by the rearrangement, this average number should be compared with the 3 for the flat surface. That is, $\Sigma n(\boldsymbol{u})$ has been increased by about 16 per cent.

6. APPLICATION TO BODY-CENTRED CUBIC CRYSTALS

Since, as yet, rearranged surfaces have been found only on nickel, the detailed argument above has been based on the face-centred cubic structure. However, it can easily be extended to cover any other structure in which there is only one class of atom, i.e. one in which all atoms are crystallographically and chemically identical. Structures containing more than one class of atom need a modified treatment that will not be investigated here. The discussion below shows how the argument needs to be modified for dealing with the body-centred cubic structure.

The basic definitions and restrictions listed in Section 2 need to be altered as follows:

(i). Only body-centred cubic crystals are considered.

(ii). *Neighbour* means nearest or next-nearest neighbour. This choice is made for convenience only.

(iii) *Bonds* are defined as before but $\boldsymbol{u}$ now corresponds to one of the eight vectors in the set $\frac{1}{2}\langle 111\rangle$ or one of the six in the set $\langle 100\rangle$.

(iv). B_j implies an atom with 14-j neighbours.

(v). is unaltered.

(vi). The stereographic triangle *PQR* is now part of Fig. 5.

(vii). and (viii). are unaltered.

Then the same argument as before shows that a rearrangement is allowable if and only if it introduces no gaps into any $\boldsymbol{u}$-row.

In this structure, neutral rows occur parallel to [1$\bar{1}\bar{1}$] and [$\bar{1}$11] when $h = k+l$, i.e. along the zone *QT* in Fig. 5, and parallel to [001] and [00$\bar{1}$]

when $l = 0$, i.e. along PQ. Thus, provided the pole does not lie along PQ or QT, an allowable rearrangement can be constructed by successively removing B_7 atoms and/or filling s_7 sites. If the pole lies along PQ, but not at (100) or (110), then rows of atoms, parallel to [001], can be removed from the surface if each atom is of type B_6 or can be added to the surface on a row of s_6 sites. Similarly, if the pole lies along QT but not at (110), rows of B_6 atoms parallel to $[1\bar{1}\bar{1}]$ can be removed or similar rows of atoms added to s_6 sites. For the (100) and (110) surfaces, non-parallel sets of neutral rows exist and no allowable rearrangements exist.

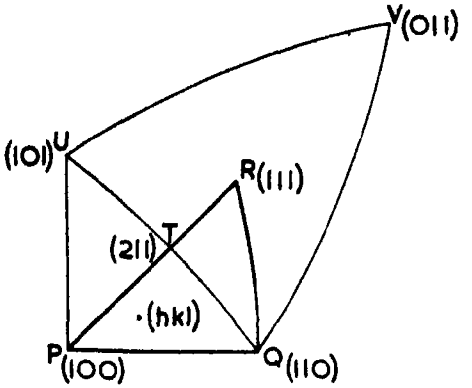

FIG. 5. Stereographic plot showing triangle PQR within which (hkl) is chosen to lie. For body-centred cubic crystals, if (hkl) lies within PQT, surfaces of minimum $\Sigma n(u)$ consist of facets represented by P, Q, and U but if (hkl) lies within QRT, the facets must be V, Q, and U.

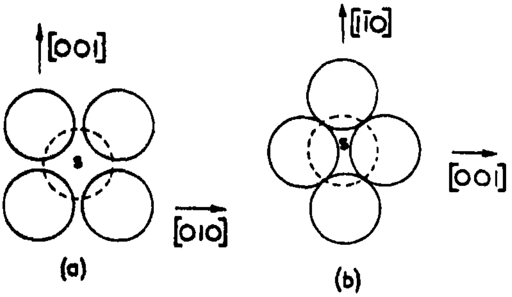

FIG. 6. Configurations of atoms and sites necessary to define (a) a (100) facet, and (b) a (110) facet in a body-centred cubic crystal. In (a), s is a nearest neighbour of each of the underlying atoms; in (b), s is a nearest neighbour of the atoms along [001] but only a next-nearest neighbour of those along $[1\bar{1}0]$.

A facet of (hkl) may be said to exist if (hkl) belongs to {100} or {110} and there exist four atoms in an (hkl) plane, together with a site that is a neighbour of each atom, the site being on that side of the atoms that would be unoccupied if the atoms formed part of a flat (hkl) surface. The necessary configurations of atoms and site are shown in Fig. 5. Then, a surface has minimum $\Sigma n(u)$ if and only if it can be completely described in terms of facets of (110), (101), and either (100) if $h > k+l$ or (011) if $h < k+l$. Completely described implies that facets of no other plane can occur and that every atom with a broken *nearest-neighbour* bond belongs to at least one facet. In actual fact, this criterion holds for any surface with a pole inside $PQVU$, (100) facets appearing on surfaces within PQU and (011) facets on those within QUV. It is less useful to consider these facets in the body-centred cubic structure than it is in the face-centred cubic, since the facet planes are less densely-packed and hence more difficult to identify.

REFERENCES

1. GERMER L. H. and MACRAE A. U., *J. chem. Phys.* **37**, 1382 (1962).
2. MACKENZIE J. K., MOORE A. J. W. and NICHOLAS J. F., *J. Phys. Chem. Solids* **23**, 185 (1962).
3. GERMER L. H. and MACRAE A. U., *J. appl. Phys.* **33**, 2923 (1962).

J. Phys. Chem. Solids Pergamon Press 1963. Vol. 24, pp. 1285–1289. Printed in Great Britain.

DIE "SANDWICH-METHODE"—EIN NEUES VERFAHREN ZUR HERSTELLUNG EPITAKTISCH GEWACHSENER HALBLEITERSCHICHTEN

ERHARD SIRTL

(*Received* 31 *May* 1963)

Forschungslaboratorium der Siemens und Halske, A.G.

Zusammenfassung—Die einfachste Ausführungsform des geschilderten Verfahrens wird durch zwei Plättchen verwirklicht, die auf einem Heizer übereinander geschichtet, einem Temperaturgefälle ausgesetzt sind. Bei Anwesenheit geeigneter gasförmiger Verbindungen lässt sich ein Stoffübergang zwischen den benachbarten Oberflächen nachweisen. Diese "Transportreaktion auf kurzem Wege" bietet verschiedene Vorteile auf dem Gebiet des Wachstums von homo- und hetero-Schichten aus der Gasphase. Sie vereinfacht oftmals — vor allem bei hohen Reaktionstemperaturen — die Erzeugung epitaktisch aufgebrachter Schichten mit gezielter oder sehr geringer Störstellenkonzentration.

Abstract—A standard model of the described method is realized by an arrangement of two wafers, piled up on a heater, which are subject to a thermal gradient. In the presence of suitable gaseous compounds a transport of solid material between the neighbouring surfaces can be observed. This "short-way-transport-reaction" shows several advantages in the case of vapor-grown homo- and hetero-layers. In many cases—especially at high temperatures—the production of epitaxial layers with defined or very low impurity concentrations is simplified.

1. EINLEITUNG

DIE Herstellung dünner, einkristalliner Halbleiterschichten auf epitaktischem Wege gewinnt immer mehr an Bedeutung. Eine besondere Stellung nehmen dabei solche Arbeitsmethoden ein, denen eine chemische Gasreaktion zugrunde liegt. Als man vor etwa 10 Jahren daran ging, das Aufwachsen einkristalliner Schichten aus der Gasphase näher zu studieren, bediente man sich hauptsächlich solcher Reaktionen, bei denen der abzuscheidende Festkörper in Form einer relativ leichtflüchtigen Verbindung vorliegt, die dann an einem auf höherer Temperatur befindlichen Kristallkeim durch einen Zerfalls- oder Reduktionsvorgang zersetzt wird (Pyrolyse). Dabei handelte es sich — chemisch gesehen — um ein Prinzip, das schon in den Zwanzigerjahren von VAN ARKEL und anderen(1) zum Zwecke der Herstellung hochreiner Metalle angewandt worden war.

Parallel zu diesen Arbeiten ist für die Reindarstellung halbleitender Stoffe ein neuer Reaktionstypus untersucht worden: Schon 1954 berichtete SCHÄFER(2) über einen Transport von Silizium im Temperaturgefälle $T_2 \overset{*}{\rightarrow} (T_1 T_2 > T_1)$ in einer halogenhaltigen Gasatmosphäre. Die Erschliessung und Systematisierung solcher Reaktionen, die eine Stoffwanderung an eine Stelle niedrigerer Temperatur bewirken, hat sich als äusserst fruchtbar erwiesen. So ist es heute möglich, neben den Elementhalbleitern Silizium und Germanium(3) eine ganze Reihe von Verbindungen vom Typ $A^{III}B^{V}$(4) und $A^{II}B^{VI}$(5) derart über die Gasphase zu transportieren. Daneben sind für eine Vielzahl anderer, technisch interessanter Stoffe ähnliche Transportbedingungen aufgefunden worden.(6)

Ein Vorteil der Anwendung derartiger Reaktionen auf Halbleiterstoffe ergibt sich vielfach dann, wenn ein Einsatz der erstgenannten Methodik — hauptsächlich bei Problemen der Epitaxie — auf grosse Schwierigkeiten stösst. Dies gilt für die Mehrzahl der obengenannten Verbindungshalbleiter, da die entsprechenden Metallhalogenide oder -chalkogenide meist einen sehr geringen Dampfdruck aufweisen. Die bisher bekanntgewordenen Verfahren lassen jedoch noch manche Wünsche offen. So ergeben sich beispielsweise folgende Probleme: Korrosion der Gefässwände durch hohe Temperatur und durch Wandabscheidung, mangelhafte Reproduzierbarkeit von Dotierungsprofilen, Schwierigkeiten bei gleichzeitiger Beschichtung mehrerer Scheibchen. Wir hatten es uns deshalb zur Aufgabe gemacht, eine Arbeitsmethode zu entwickeln, die imstande ist, die geschilderten Nachteile nach Möglichkeit zu vermeiden.

2. VORGESCHICHTE

Verschiedene Beobachtungen bei der epitaktischen Beschichtung von Silizium- und Germaniumscheiben nach der pyrolytischen Methode brachten uns vor etwa zwei Jahren dazu, die Wechselwirkung zwischen dem Scheibchen und seiner als Heizer dienenden Unterlage näher zu studieren. Es war — parallel zum Aufwachsvorgang auf der Scheibchenoberfläche — eindeutig ein Materialübergang von dem mit einer Halbleiterschicht überzogenen Heizer auf die Unterseite des daraufliegenden Scheibchens nachzuweisen. *Bild 1 zeigt einen stark vergrösserten Querschliff* eines doppelseitig polierten Siliziumscheibchens, das, auf einem mit feinkristallinem Silizium überzogenen Heizer liegend, einem Trichlorsilan–Wasserstoff-Gemisch ausgesetzt worden war. Das Resultat ist eine beidseitig epitaktische Aufwachsung von Silizium. Ein Parallelversuch mit einer inerten Heizeroberfläche (Bild 2) lässt erkennen, dass in diesem Falle eine Beschichtung der Unterseite des Scheibchens nicht eingetreten ist. Die gleichen Effekte konnten auch bei Verwendung von Gasgemischen aus Siliziumtetrachlorid oder Germaniumtetrachlorid und Wasserstoff beobachtet werden.

Die chemische Deutung dieses Vorganges ist nicht besonders schwierig, wenn man voraussetzt, dass die Umsetzung der Chlorsilane mit Wasserstoff über die Stufe des (gasförmigen) Dichlorids abläuft. So ergeben sich die Gleichungen

$$SiHCl_3 \rightarrow SiCl_2 + HCl \tag{1}$$

oder

$$SiCl_4 + H_2 \rightarrow SiCl_2 + 2HCl \tag{2}$$

und

$$SiCl_2 + H_2 \rightarrow Si + 2HCl \tag{3}$$

Die Umsetzung nach Gleichung (3) als Folgereaktion für die Gleichungen (1) oder (2) hat exothermen Charakter: Das bedeutet, dass im Reaktionsgasgemisch, das sich zwischen dem Heizer und der aufliegenden Scheibe befindet, durch die dort herrschende Temperaturdifferenz* ein Konzentrationsgefälle an $SiCl_2$ entsteht, das zur Auflösung von Silizium an der heisseren Stelle und dessen Abscheidung an der kälteren Stelle des Reaktionsraumes führt. Im freien Gasraum hingegen wird bei stetiger Frischgaszufuhr nach der Summenreaktion (1)+(2) oder (1)+(3) generell an heisseren Flächen Silizium abgeschieden. Dasselbe gilt sinngemäss für die Verhaltensweise des Germaniumtetrachlorids.

Die Klärung der Zusammenhänge im vorliegenden Fall war der Anlass für weitere Überlegungen, wie man eine derartige Versuchsanordnung — also eine Transportreaktion auf kurzem Wege — in verallgemeinerter Form zu einer neuen Beschichtungsmethode ausbauen könnte. Gewisse Vorteile waren von vornherein nicht zu übersehen: Der Transport findet in einem nahezu völlig von Halbleitermaterial umschlossenen Raum statt, seine Geschwindigkeit ist beträchtlich und der Ablauf der Reaktion ist relativ unempfindlich gegenüber der Zusammensetzung des Gases im übrigen Reaktionsraum. Den einfachsten Fall stellen zwei aufeinanderliegende Scheiben dar, die mit einem Heizer in Wärmekontakt stehen. Aus diesem Grunde haben wir die Arbeitsweise, die nachfolgend näher beschrieben werden soll, als "Sandwich-Methode" bezeichnet.

3. DIE SYSTEMATIK DER SANDWICH-METHODE

(a) *Technische Ausführungsformen*

In dem weiter oben beschriebenen, speziellen Fall liegt das als Substrat dienende Einkristallscheibchen mit seiner polierten Fläche auf einer feinkristallinen Halbleiterschicht. Es ruht also willkürlich auf drei (oder mehreren) Kristalliten, die zusammen mit der Oberflächenrauhigkeit einen mittleren Scheibenabstand ergeben. Der Stofftransport erfolgt hier wegen des kurzen Diffusionsweges trotz der relativ geringen Temperaturdifferenz sehr rasch. Das vorhergehende

---

* bedingt durch den gehemmten Wärmeübergang.

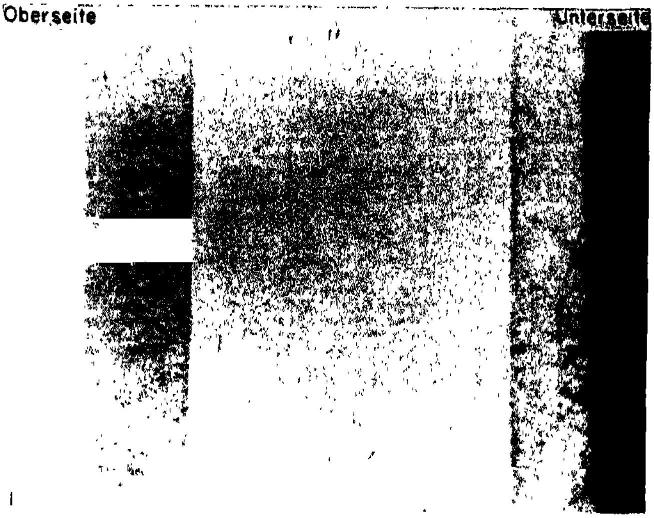

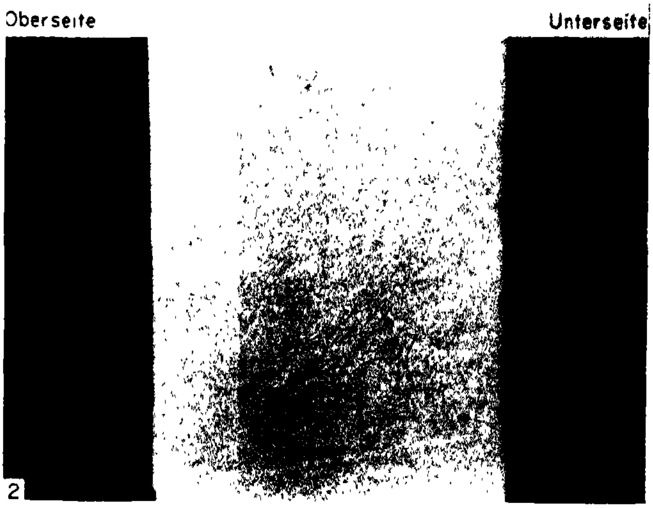

BILD 1. Querschliff eines beidseitig beschichteten Siliciumscheibchens (bei siliciertem Heizer), Cu-dekoriert, 200fach.

BILD 2. Querschliff eines auf der Oberseite beschichteten Siliciumscheibchens (bei inertem Heizer), Cu-dekoriert, 200fach.

4

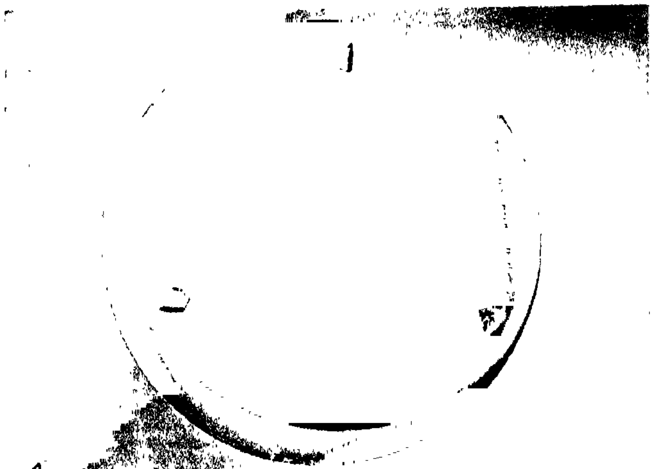

5

BILD 4. Übersichtsaufnahme einer nach der "Sandwich-Methode" beschichteten nach (111) orientierten Siliciumscheibe, 4fach. Gasgemisch $SiCl_4$–H_2.

BILD 5. Schrägschliff einer hochohmigen 10 μm dicken Silicium-Aufwachsschicht (100 Ω cm, *p*, auf 0,1 Ωcm, *n*), Cu-dekoriert, 100fach.

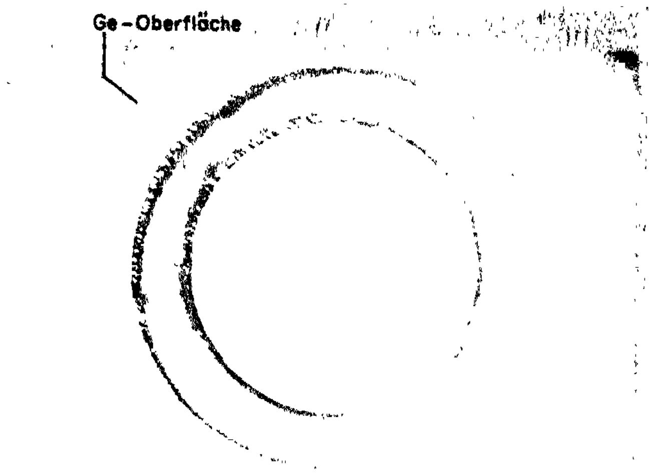

6

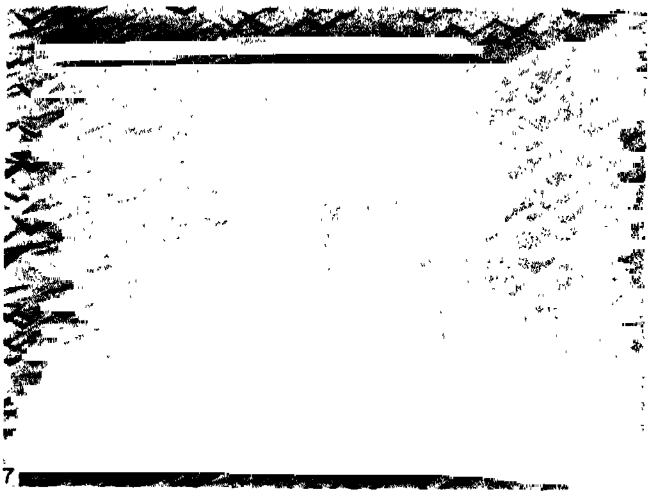

7

BILD 6. Übersichtsaufnahme einer 8 μm dicken GaAs-Aufwachsung auf einer nach (111) orientierten Germaniumscheibe, 13fach Gasgemisch : H_2O–H_2.

BILD 7. Typische Wachstumsform einer dickeren GaAs-Schicht auf Germanium (111), 200fach.

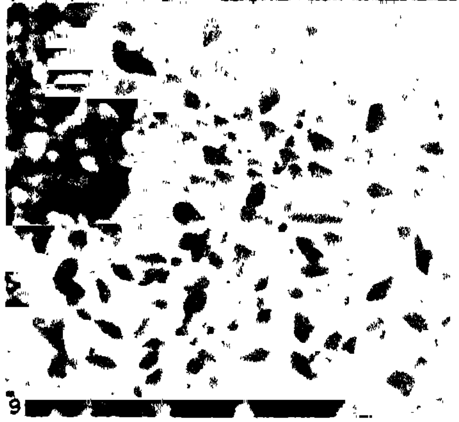

Bild 8. Aufwachstextur von SiC auf einem nach (0001) orientierten Plättchen der gleichen Substanz, 200fach. Gasgemisch : H_2O–H_2.

Bild 9. Aufwachstextur von ZnS auf einem GaP-Kristall unbekannter Orientierung, 500fach. Gasgemisch : I_2–H_2.

Aufbringen einer Halbleiterschicht mit definierten Eigenschaften auf den Heizer ist jedoch in vielen Fällen nicht möglich. Verwendet man deshalb zwei auf dem Heizer direkt übereinandergeschichtete Halbleiterscheiben, so muss die der "Substratscheibe" S zugekehrte Fläche der "Vorratsscheibe" V möglichst gleichmässig aufgerauht sein (Bild 3a).* Für sehr grossflächige Aufwachsungen hat es sich als günstig erwiesen, den Scheiben einen Abstand von etwa 100 μm zu geben. Der Abstandshalter *A* (Bild 3b) kann ringförmig ausgebildet sein oder aber auch in Form dünner Lamellen, z.B. für eine Dreipunktauflage, eingeschoben werden. Er muss entweder aus einer unter diesen Bedingungen inerten Substanz oder aber aus dem zu transportierenden Halbleiterstoff selbst bestehen. Öfters tritt auch das Problem auf, dass die Vorratssubstanz *V* in kompakter Form nur schwer erhältlich ist. In diesem Fall kann mit einer Anordnung gearbeitet werden, wie sie in Bild 3(c) gezeigt wird. Das zu transportierende Material ist in Pulverform von einem ringförmigen, auf dem Heizer aufliegenden, inerten Formkörper *A* umschlossen. Dieser Ring dient zugleich als Abstandshalter für die Substratscheibe *S*. Die sich einstellende Temperaturdifferenz liegt — je nach Versuchsanordnung — zwischen 20 und 100°C.

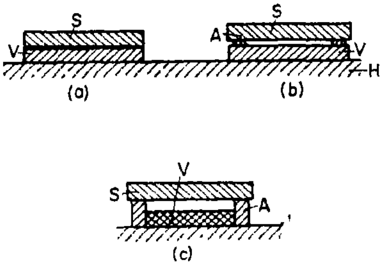

BILD 3.

(b) *Transportsysteme*

Als Transportmittel sind grundsätzlich alle Gassysteme einsetzbar, die mit dem zu transportierenden Stoff in reversibler Weise flüchtige Verbindungen bilden. Mit Vorteil wurden angewandt:

1. Die Elemente Chlor, Brom und Jod, auch JCl;
2. die Wasserstoffverbindungen HCl, HBr, HJ, H_2O und H_2S;
3. leichtflüchtige Halogenverbindungen des zu transportierenden Stoffes oder eines seiner Bestandteile, evtl. in Gegenwart von Wasserstoff.

Die genannten, den Transport auslösenden Stoffe werden mit Hilfe eines Trägergases strömend† an der "Sandwich-Anordnung" vorbeigeführt. Ihre Konzentration kann durch Veränderung ihres Partialdruckes in dem als Trägergas fungierenden Wasserstoff oder Inertgas optimal auf die Versuchsbedingungen eingestellt werden.

Kommt es darauf an, eine bestimmte Dotierungskonzentration möglichst quantitativ zu übertragen oder etwa gewisse Dotierstoffe fernzuhalten, so richtet sich die Auswahl des Transportmittels nach dem Verhalten des betreffenden Elementes im Reaktionsgleichgewicht. So lässt sich beispielsweise Aluminium (im Silizium) oder Zink (im Galliumarsenid) zwar im Jodsystem, aber nicht im Chlor–Wasserstoff-System, im Bereich der für die Epitaxie der Halbleitermatrix günstigen Temperaturen transportieren.

4. EXPERIMENTELLE BEISPIELE

(a) *Spezielle Dotierung*

Die Abmessung des Reaktionsraumes ist vorzüglich geeignet, in der Vorratssubstanz enthaltene Dotierstoffe möglichst quantitativ in die auf dem Substrat aufwachsende Schicht überzuführen. Ist die Transportreaktion mit Hilfe des der Apparatur zugeführten Gasgemisches erst einmal in Gang gekommen, wird der Austausch zwischen dem eigentlichen Reaktionsraum und dem freien Gasraum relativ gering.‡ Falls die chemische Gleichgewichtslage für den Einbau des Dotierstoffes nicht extrem ungünstig liegt, ist der Übertragungsfaktor nahezu gleich 1. Hält man demnach Vorratsscheibchen geeigneter Dotierung auf Lager, so ist es durch die automatische Ausschaltung des apparativ bedingten Einflusses möglich, unmittelbar Schichten mit gewünschten elektrischen Eigenschaften zu erzielen.

---

* In sämtlichen Bildern ist das Verhältnis der Dicke der Halbleiterscheibe zu deren Durchmesser aus Gründen der besseren Anschaulichkeit stark übertrieben.

† Für dünne Schichten genügt oftmals auch eine einmalige Füllung des Reaktionsgefässes.

‡ Das Ausmass des Austausches hängt natürlich von der Grösse des Scheibenabstands und von der Form des Abstandshalters ab.

Ein markantes Beispiel dafür ist die Erzielung einer hochohmigen, p-leitenden Siliciumaufwachsung. Derartige Schichten reproduzierbar herzustellen, ist uns bei Anwendung der pyrolytischen Methode bisher nicht gelungen. Die speziellen Verhältnisse, wie sie bei der Sandwich-Methode vorliegen, vermögen jedoch die von der Apparatur stammende, unerwünschte Donatorenkonzentration während des Transportvorganges so stark einzudämmen, dass man nunmehr in der Lage ist, Siliciumschichten mit einem spezifischen Widerstand bis herauf zu etwa 1000 Ω cm abzuscheiden. Bild 4 zeigt eine derartig präparierte Siliziumscheibe, die an drei Stellen mit Siliziumplättchen auf Abstand gehalten worden war. Bild 5 zeigt einen Schrägschliff durch eine solche Aufwachsschicht, deren Oberfläche vorher auf Stapelfehler geätzt wurde. Interessant ist die bei Anwendung dieses Verfahrens häufig gemachte Beobachtung, dass nur ein Teil der Stapelfehler sienen Ursprung in der Grenze der Aufwachsschicht hat.

(b) *Hetero-Aufwachsung*

Das epitaktische Aufbringen einer Halbleiterschicht auf einem Fremdmaterial ähnlicher Gitterstruktur und -dimension beansprucht aus zwei verschiedenen Gründen unser Interesse. Einerseits ist es günstig, für technologisch schwer zu handhabende Substanzen ein zugänglicheres Material als Keimkristall zu verwenden. Andererseits interessiert — wenn der als Substrat dienende Stoff ebenfalls ein Halbleiter ist — das Problem der sogenannten "hetero-junctions". Lässt sich eine solche Beschichtung nur mit Hilfe einer Transportreaktion realisieren, so ist es bei Anwendung der bisher bekanntgewordenen Methoden ziemlich schwierig, die chemischen Bedingungen so festzulegen, dass die Substratscheibe nicht angegriffen wird.

Hier bietet sich die "Sandwich-Methode" wiederum vorteilhaft an. Setzt man nämlich eine inerte Deckplatte auf die Oberseite der Substratscheibe, ist die genaue Einstellung der Reaktionstemperatur und des Partialdruckes der den Transport auslösenden Agentien keineswegs besonders kritisch. Lediglich die Forderung einer möglichst geringen Oberflächenrauhigkeit der Aufwachsschicht macht noch weitere Arbeit nötig. Als spezielles, recht aktuelles Beispiel hierzu haben wir die Aufwachsung von Galliumarsenid auf Germanium nach der Gleichung

$$2\ \mathrm{GaAs}\ (f) + \mathrm{H_2O}\ (g) \rightleftarrows \mathrm{Ga_2O}\ (g) + \mathrm{H_2} + \frac{2}{x}\mathrm{As}_x(g) \tag{4}$$

gewählt. Die ringförmig begrenzte Aufwachsschicht in Bild 6 wurde mit Hilfe eines Wasserdampf-Wasserstoff-Gemisches transportiert.* Interessanterweise wurde sowohl auf chemischem Wege, als auch mit Hilfe der Röntgenanalyse† gefunden, dass der Germaniumgrenzfläche immer die Galliumseite der (111)-Doppelschicht zugekehrt ist. Bild 7 zeigt die typische Oberflächenstruktur einer GaAs-Schicht, wie wir sie zu Beginn unserer Untersuchungen erhalten hatten. Inzwischen ist es gelungen, die Oberflächenrauhigkeit so zu vermindern, dass bei gleicher Vergrösserung praktisch keine Textur zu erkennen ist.

(c) *Einkristallschichten hochschmelzender Stoffe*

Eine weitere Anwendungsmöglichkeit unseres Verfahrens ist bei Substanzen gegeben, deren Herstellung in Form einkristalliner, kompakter Schichten bisher nicht möglich war. Dies gilt vor allem für solche Stoffe, bei denen sich Gasgleichgewichte, wie sie für den Transport im Temperaturgefälle geeignet sind, erst bei sehr hohen Temperaturen einstellen. Eines der Haupt-

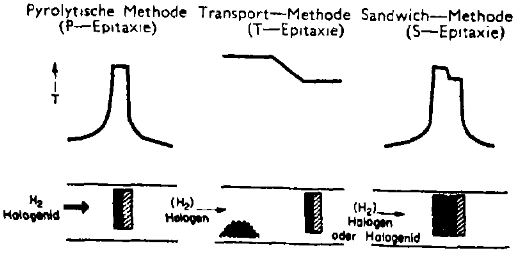
Pyrolytische Methode (P—Epitaxie)
Transport—Methode (T—Epitaxie)
Sandwich—Methode (S—Epitaxie)
T
H₂ Halogenid
(H₂) Halogen
(H₂) Halogen oder Halogenid

BILD 10.

---

* Eine Oxydhaut kann unter diesen Bedingungen auf der Germaniumoberfläche nicht existieren, da GeO_2 von H_2 vollständig reduziert wird.

† P. MECKE, *Naturwissenschaften* **50**, 399 (1963).

probleme liegt in diesem Fall darin, einen geeigneten Keimkristall zu finden, an dem sich die epitaktische Aufwachsung der reinen Substanz vollziehen kann. Auf den Bildern 8 und 9 sind Aufwachstexturen von Siliciumcarbid auf arteigenem Material sowie von Zinksulfid auf Galliumphosphid zu erkennen. Die Transportvorgänge dürften hier wohl durch die Gleichungen

$$\mathrm{SiC}(f)+2\mathrm{H_2O}(g) \rightleftarrows \mathrm{SiO}(g)+\mathrm{CO}+2\mathrm{H_2} \qquad (5)$$

und

$$\mathrm{ZnS}(f)+I_2(g) \rightleftarrows \mathrm{Zn}I_2(g)+S_2(g) \qquad (6)$$

wiedergegeben werden.

Diese Beispiele können nur als Anfänge bezeichnet werden. Eine systematische Untersuchung der Präparationsmöglichkeiten, die sich hier bieten, dürfte eine ganze Reihe interessanter stofflicher Eigenschaften solcher Schichten zutage fördern.

5. ZUSAMMENFASSENDE DISKUSSION

Abschliessend soll noch einmal die Eigenart der "Sandwich-Methode" umrissen und ein Vergleich mit schon bekannten Verfahren unternommen werden. In Abbildung 10 sind die für die einzelnen Verfahren charakteristischen Temperaturprofile in schematisierter Form nebeneinander gestellt. Man denke sich die zu beschichtende Kristallscheibe in einem Quarzrohr einseitig von Frischgas bespült (untere Bildreihe). Die dazugehörigen charakteristischen Temperaturprofile sind darüber aufgezeichnet. Während bei der *T*-Epitaxie* die Beheizung über die Gefässwände erfolgt, können bei der *P*- und *S*-Epitaxie* die Proben mittels Hochfrequenzinduktion oder Heiztisch auf höhere Temperaturen gebracht werden.

Folgende Vorteile ergeben sich unserer Ansicht nach bei Anwendung der Sandwich-Methode:

(a) Der wirksame Reaktionsraum ist vom übrigen Gasraum weitgehend abgetrennt und während des Wachstumsprozesses nur von der zu transportierenden Substanz umschlossen. Die Reinheit der aufgewachsenen Schicht ist also praktisch nur vom Reinheitsgrad des Vorratsscheibchens abhängig.

(b) Die Konzentration der transportbestimmenden Stoffe im freien Gasraum, sowie die Art ihrer chemischen Bindung ist keineswegs kritisch. Letzten Endes wird nur für die Aufrechterhaltung einer gewissen Gleichgewichtskonzentration des Transportmittels in der Randzone der Sandwich-Anordnung gesorgt. Die Strömungsgeschwindigkeit hat nur sehr geringen Einfluss auf die Transportgeschwindigkeit im Reaktionsraum.

(c) Die Gefässwände werden nicht aufgeheizt. Die Apparatur lässt sich deshalb relativ einfach gestalten und ist leicht zu bedienen.

(d) Die Eigenart der Methode gestattet es, mehrere Proben in einer Anlage gleichzeitig zu beschichten.

(e) Die Geschwindigkeit der einkristallinen Aufwachsung kann mehrere μm/min betragen.

Anerkennung—Meinen Mitarbeitern, Herrn Dr. Seiter und Herrn Doberstein möchte ich an dieser Stelle für ihren Beitrag zur Entwicklung dieser Methode meinen besonderen Dank aussprechen. Frau Rücker danke ich für die Herstellung der Schliffe und mikroskopischen Aufnahmen.

LITERATUR

1. Zusammenfassende Übersicht: van Arkel A. E., *Reine Metalle*, Springer, Berlin (1939).
2. Schäfer H., *IUPAC Colloquium*, Münster (1954).
3. Ruth R. P., Marinace J. C. und Dunlap W. C., *J. appl. Phys.* **31**, 995 (1960).
4. Antell G. R. und Effer D., *J. electrochem. Soc.* **106**, 509 (1959).
5. Nitsche R., *J. Phys. Chem. Solids* **17**, 163 (1960).
6. Schäfer H., *Chemische Transportreaktionen*, Verlag Chemie Weinheim (1962).

---

* Erläuterung siehe Bild 10.

J. Phys. Chem. Solids Pergamon Press 1963. Vol. 24, pp. 1291–1296. Printed in Great Britain.

ENERGY EXCHANGE BETWEEN GASES AND SOLIDS*

HENRY WISE

Chemical Physics Division, Stanford Research Institute, Menlo Park, California

(*Received* 19 *March* 1963; *revised* 12 *July* 1963)

Abstract—The accommodation coefficient for collisional energy exchange between a gas and a solid surface is examined in terms of a desorption process under non-isothermal conditions. A measure of the probability that a molecule will gain or lose energy on striking a surface is derived from the ratio of the rate of desorption at the temperature of the solid T_2 to the total rate of impingement of gas molecules with initial temperature T_1. The functional dependence of the accommodation coefficient on gas pressure and surface temperature is compared with experimental observations.

1. INTRODUCTION

AT LOW pressures the problem of heat transfer between solid surface and gas is governed by a factor which KNUDSEN(1) has named the coefficient of accommodation. This coefficient measures the fraction α of the energy difference between the gas and the surface which the gas carries away on leaving the surface. Thus one may define the accommodation coefficient as

$$\alpha = \frac{E_2^1 - E_1}{E_2 - E_1}$$

where E_1 and E_2^1 are the mean energies per molecule of the incident and re-emitted gas, E_2 that of the completely accommodated gas. Accordingly, the accommodation coefficient may be interpreted to represent the fractional mean energy taken up by the incident molecules relative to that needed to bring the gas into thermal equilibrium with the surface. Alternatively, one may assume that the fraction α of the incident molecules is trapped at the surface and subsequently emitted with a Maxwell distribution at the surface temperature, while the remainder of the gas $(1-\alpha)$ is unaffected by the collision and retains its original Maxwell energy distribution. The latter interpretation is employed in this paper. A similar interpretation was used by Maxwell in the derivation of the coefficient of slip.(2)

After the experimental work of ROBERTS(3) on the accommodation coefficient of helium and neon on tungsten, a series of theoretical papers appeared on this problem of heat transfer.(4–11) ZENER(12) attempted to account for the accommodation coefficient by considering a repulsive potential between the gas atoms and surface atoms. Subsequently, in the quantum mechanical treatment by DEVONSHIRE(13) the interaction potential between gas and solid was represented by a Morse potential function. By suitable choice of the parameters of the energy function and a "roughness" factor the theoretical results could be applied to the experimental measurements of ROBERTS.(3)

In the present analysis, the contribution of surface adsorption to the mechanism of heat transfer between a gas and solid will be considered. An encounter between a gas molecule and an atom in the surface of the solid may result in an elastic or inelastic collision. In the case of elastic collisions, no net exchange of energy is assumed to take place and the molecules are reflected from the surface with their initial thermal velocity. Ordinarily, however, because of the asymmetry in the surface layer and the ensuing force field, the collision is frequently inelastic. The impinging gas molecule remains adsorbed on the surface for a certain length of time before it re-evaporates into the gas phase.(14,15) Since the average life spent by a molecule in the adsorbed state is generally of a larger

---

* Sponsorship of this work by the Office of Naval Research, Department of the Navy, and Physical Sciences, Stanford Research Institute, is gratefully acknowledged.

magnitude than the time between molecular collisions(16) interchange of energy between the two phases may readily take place. The kinetic energy of an adsorbed molecule with a small number of internal degrees of freedom will therefore be accommodated to that of the surface atoms before desorption occurs. Accordingly, temperature accommodation between solid and gas may be governed by the time lag between condensation and evaporation of the molecules which in turn will depend on the intensity of the force field at the surface and on the temperature and nature of the gas and solid. Thus since α is defined in terms of the fraction of the theoretical energy carried away by the molecules from the surface, a measure of the probability that a molecule will gain or lose energy on striking a surface is found from the ratio of the rate of desorption of a gas at temperature T_2 to the total rate of impingement of gas molecules with initial temperature T_1.

2. THEORETICAL ANALYSIS

From these considerations, the problem may be treated as a rate process involving a reaction for a system composed of an atom or molecule and an adsorbing site on the surface. Based on the theory of absolute reaction rates(13) the process of desorption involves an activated state of the reactant in which a gas molecule attached to an adsorption center acquires the necessary configuration and energy of activation to evaporate from the condensed phase on the surface. The magnitude of the energy of activation for desorption E_d will therefore represent the sum of the activation energy for adsorption E_a and the heat of adsorption q.

In the derivation of the theoretical expression for the accommodation coefficient the following assumptions are made: (1) the energy barrier for desorption is independent of the presence of any condensed molecules on neighboring surface sites; (2) every adsorbed molecule occupies one active center on the surface for the case of a localized adsorbed layer; (3) the solid exhibits a uniform surface; (4) the gas obeys the ideal gas law; (5) the system has attained a steady state; (6) the residence time of the adsorbed molecule is sufficient to permit attainment of complete temperature equilibrium, and (7) reflected molecules which are not adsorbed exchange no energy with the surface. According to the theory of absolute reactions rates(17) the rate of desorption of a gas per square centimeter of surface is given by

$$v_d = \kappa C_a \frac{kT_2}{h} \frac{f_*}{f_a} \exp(-E_d/kT_2) \tag{1}$$

where κ represents the transmission coefficient; C_a the surface concentration of gas molecules in the adsorbed state; k Boltzmann's constant; h Planck's constant; T_2, the temperature of the surface; E_d the energy of activation for desorption of a single molecule at the absolute zero; f_a the complete partition function per unit area for the adsorbed state, and f_* that for the activated state from which the contribution of one degree of translational freedom across the potential-energy barrier has been excluded. Similarly the rate of impingement of gas molecules per square centimeter of surface(17) has been shown to be

$$v = C_{g_1} \cdot kT_1/(2\pi mkT_1)^{1/2} \tag{2}$$

where C_{g_1} identifies the concentration of gas molecules per cm³ at temperature T_1; and m the mass of the gas molecule under consideration.

Based on our definition for the accommodation coefficient one obtains

$$\begin{aligned}\alpha &\equiv v_d/v \\ &= \kappa \cdot \frac{C_a}{C_{g_1}} \cdot \frac{f_*}{f_a} \cdot \frac{T_2}{T_1} \cdot \frac{(2\pi mkT_1)^{1/2}}{h} \exp(-E_d/kT_2)\end{aligned} \tag{3}$$

A. *Mobile adsorbate-isothermal case*

It has been found experimentally that in physical adsorption, migration of the gas molecules over the solid surface takes place.(18,19) Based on the Freundlich adsorption isotherm an expression relating C_a to the gas pressure (C_g) may be derived. According to the postulate of the absolute rate theory, the gas molecules may be considered free to migrate in the adsorbed state as well as in the activate state. One may write therefore for adsorption equilibrium at any temperature

$$\begin{aligned}&C_g \frac{kT}{h} \frac{f_*}{F_g} \exp(-E_a/kT) \\ &\qquad = C_a \frac{kT}{h} \frac{f_*}{f_a} \exp(-E_d/kT)\end{aligned} \tag{4}$$

where F_g is the partition function per unit volume of adsorbing gas. Thus C_a may be evaluated, namely

$$C_a = C_g \frac{f_a}{F_g} \exp(q/kT) \qquad (5)$$

Substitution of equation (5) into (3) yields for the accommodation coefficient

$$\alpha = \kappa \frac{f_*}{F_g}\left(\frac{2\pi mkT}{h^2}\right)^{1/2} \exp(-E_a/kT) \qquad (6)$$

Since for a mobile surface layer the activated complex is essentially still in the gaseous state its partition functions f_* will contain vibrational and rotational contribution similar to that of the initial gas molecule. Hence the ratio of the partition function f_*/F_g reduces to the ratio of the translational terms. With two degrees of translational freedom in the activated state and three such degrees of freedom in the gas phase, the ratio of the partition function is equal to $(h^2/2\pi mkT)^{1/2}$. Therefore, for a mobile adsorbed layer under isothermal conditions

$$\alpha = \kappa \exp(-E_a/kT) \qquad (7)$$

B. *Mobile adsorbate; non-isothermal case*

From a practical standpoint the effect of the accommodation coefficient on heat transfer under non-isothermal conditions between the two phases is, of course, of greater importance. Under isothermal conditions the surface concentration of adsorbed molecules was related to the concentration in the gas phase by means of an adsorption isotherm. However when the gas reaching the surface is at a different temperature from that of the solid the steady condition is one of pseudo-equilibrium. A similar difficulty is encountered in the interpretation of experimental results on surface ionization,(20,21) electron affinity(22) and chemisorption(23) of gases. A hypothetical concentration of gas C_{g_2} at temperature T_2 may be postulated which is in equilibrium with the surface. Thus the pseudo-equilibrium concentration of gas molecules in the condensed phase is given by

$$C_a = C_{g_2} \frac{f_a}{F_g} \exp(q/kT_2) \qquad (8)$$

Substitution of (8) into equation (3) results in the following expression for α:

$$\alpha = \kappa \cdot \frac{C_{g_2}}{C_{g_1}} \cdot \frac{T_2}{T_1} \cdot \frac{f_*}{F_g} \cdot \left(\frac{2\pi m\,kT_1}{h^2}\right)^{1/2} \times \exp(-E_a/kT_2) \qquad (9)$$

As shown in Section A, the ratio of the partition functions f_*/F_g reduces to $(h^2/2\pi mkT_2)^{1/2}$ for a mobile adsorbed layer. Also for a gaseous system at constant pressure obeying the ideal gas law, the concentration of gas C_g is inversely proportional to the temperature. Consequently, equation (9) may be modified to read

$$\alpha = \kappa\left(\frac{T_1}{T_2}\right)^{1/2} \exp(-E_a/kT_2) \qquad (10)$$

which, of course, reduces to equation (7) as T_1 becomes equal to T_2, i.e., the isothermal case.†

For a polyatomic molecule adsorbed on the surface in a mobile layer the partition function of the activated state may differ from that of the free gas because of a decrease in the number of internal degrees of freedom. Thus if rotation about a number of principal axes is stopped in the activated state due to intermolecular forces, the ratio of the partition functions in equation (9) is no longer given by the ratio of the translational degrees of freedom only, but must include the contribution of the internal degrees of freedom to f_* and F_g. Thus

$$f_*/F_g = \left[\left(\frac{h^2}{2\pi mkT_2}\right) \cdot b_*\right] \Big/ \left[\left(\frac{h^2}{2\pi mkT_2}\right)^{3/2} \cdot b_g\right] \qquad (11)$$

where b_* and b_g represent the rotational and vibrational contributions of the internal degrees of freedom.

The vibrational part of the partition functions may be taken as unity. On the other hand, for a rigid non-linear, polyatomic molecule with three equal moments of inertia the ratio of the rotational partition functions with hindered rotation about two principal axes in the activated state will be given by

---

† Under these nonisothermal conditions an alternative expression for the ratio C_{g_2}/C_{g_1} may be sought in the assumption(23,24) that the gas collision rate with the surface equals the evaporation rate so that $C_{g_2}/C_{g_1} = (T_1/T_2)^{1/2}$. The accommodation coefficient then becomes $\alpha = \kappa \exp(-E_a/kT_2)$

$$(b_*/b_g)_r = \left[\left(\frac{8\pi^2 IkT_2}{h^2}\right)^{1/2}\cdot\sigma_g\right]\Big/\left[\left(\frac{8\pi^2 IkT_2}{h^2}\right)^{3/2}\cdot\sigma_*\right]$$

Therefore

$$f_*/F_g = \left(\frac{h^2}{2\pi mkT_2}\right)^{1/2}\cdot\frac{\sigma_g}{\sigma_*}\cdot\frac{h^2}{8\pi^2 IkT_2} \quad (13)$$

and

$$\alpha = \frac{\sigma_g}{\sigma_*}\left(\frac{T_1}{T_2}\right)^{1/2}\cdot\frac{h^2}{8\pi^2 IkT_2}\exp(-E_a/kT_2) \quad (14)$$

3. DISCUSSION

It is apparent that quantitative calculations of the accommodation coefficient are dependent upon reliable data for the energy of activation for adsorption in a given heterogeneous system. Unfortunately, such data are scanty, and calculations of surface rates can therefore be carried out only in an approximate manner. Nevertheless, the treatment proves useful as a semi-empirical approach in the evaluation of the contribution of surface adsorption to the accommodation coefficient. As a matter of fact, if this mechanism were to play the predominant role in the energy exchange between a gas and a solid, the equations presented will permit estimation of the activation energy for adsorption from experimental measurements of the accommodation coefficient (Table 1).

From a qualitative standpoint the expressions for the accommodation coefficient are in agreement with experimental observations on the parameters of interest to this problem of heat transfer. First, one may note the lack of dependence of α on the pressure of the gas, a fact which has been confirmed experimentally.(25–27)

Of special significance is the functional dependency of α on the gas temperature and surface temperature exhibited by the equation just derived. Let us consider first α as a function of the gas temperature T_1. For a mobile adsorbed layer the accommodation coefficient is expected to be proportional to the square root of the gas temperature. Experimental measurements(28) of the accommodation coefficient of monatomic gases have borne out the parabolic dependence of α on $\sqrt{T_1}$. It has also been found that for diatomic gases such as O_2 on Pt the proportionality between α and $(T_1)^{1/2}$ obtains.(29)

Table 1. *Energy of activation for adsorption as calculated by measurements of the thermal accommodation coefficient.**

Surface	Gas	E_a (cal/mole)	Reference
Pt	He	340	a
	A	350	a
	N_2	740	a
	O_2	900	b
	CO_2	760	b
W	He	400	a
	A	360	a
	N_2	800	a
	CO_2	900	b
	H_2	2400	c
Ni	CO_2	820	b

a Oliver R. N., Thesis, Calif. Inst. Techn., 1950.

b Farber M., private communication.

c Blodgett K. B. and Langmuir I., *Phys. Rev.* **40,** 78 (1932).

On the other hand, at constant gas temperature T_1, the accommodation coefficient goes through a maximum as the surface temperature is increased; thus for a monatomic gas this maximum occurs at $(T_2)_m = 2E_a/R$, while for polyatomic molecule $(T_2)_m = 2E_a/3R$, as can be shown by differentiation of α with respect to T_2. Such a conclusion has also been reached by Jackson(4) in his quantum-mechanical theory of energy exchanges between inert gas atoms and a solid surface. Recent experimental measurements have actually shown the existence of such a maximum(28,29) in the variation of α with surface temperature. Such behavior has been exhibited not only by polyatomic gases but also by monatomic noble gases. It suggests the existence of an energy barrier which may be due to some orientation effect whereby the presence of surface adsorbed gas causes some hindrance to the condensation process.

---

* In these calculations a mobile adsorbed layer was considered without change of the internal degrees of freedom upon adsorption.

With the assumption of a mobile adsorbate, the energy of activation for adsorption has been calculated from the maximum in the curves determined experimentally for the surface temperature coefficient of α (Table 1). Although the value for the activation energy does not vary greatly for the different gases and solid surfaces (except in the case of hydrogen on tungsten†), the absolute magnitude of α does not necessarily follow the same pattern since variations in the transmission coefficient are to be expected.

The present treatment is based on considerations of equilibrium between the adsorbate and the gas and therefore cannot be applied to the evaluation of α on bare surfaces. Under such conditions of energy exchange between a clean surface and a gas, the present theory would predict the accommodation coefficient to approach zero. It is well known from the experimental measurements by Roberts(3) and Mann(22) that α increases with time for a surface initially free of adsorbed gas. However, since even for a clean surface, the value of α extrapolated to zero time of contact between solid and gas has a finite value larger than zero,(3) it is to be realized that collisional energy transfer without adsorption makes some contribution to the over-all process of heat exchange in a heterogeneous system.

Another interesting consequence of this analysis applies to the average residence time τ of the gas molecule on the surface. From statistical considerations Frenkel(10) derived the following equation for τ as a function of surface temperature T and the heat of adsorption q:

$$\tau = \tau_0 \exp(q/kT) \qquad (15)$$

where τ_0 is postulated to be independent of T. If one defines τ in terms of the ratio of the concentration of gas molecules C_a adsorbed per unit area of surface to the rate of desorption v_d, one obtains with the aid of equation (1) for the residence time

$$\tau \equiv C_a/v_d = \frac{1}{\kappa} \cdot \frac{h}{kT} \frac{f_a}{f_*} \exp(E_d/kT) \qquad (16)$$

The ratio of the partition functions may be set equal to unity. Also for a system with negligible energy of adsorption, the parameter E_d will be approximately equal to the heat of adsorption q. Thus

$$\tau \simeq \frac{1}{\kappa} \cdot \frac{h}{kT} \cdot \exp(q/kT) \qquad (17)$$

Comparison of equations (17) and (15) indicates that τ_0 in Frenkel's expression is proportional to $h/(\kappa kT)$ and therefore dependent upon the surface temperature. A similar conclusion was drawn by Lennard-Jones and Devonshire(31) in a quantum-statistical treatment of this problem.

REFERENCES

1. Knudsen M., *Ann. Phys.* **34,** 593 (1911).
2. Jeans J., *The Dynamical Theory of Gases,* Dover, New York (1954).
3. Roberts J. K., *Some Problems in Adsorption,* Cambridge University Press, London (1939).
4. Jackson J. M., *Proc. Camb. phil. Soc.* **28,** 136 (1932).
5. Jackson J. M. and Mott N. F., *Proc. Roy. Soc.* **A137,** 703 (1932).
6. Jackson J. M. and Howarth A., *Proc. Roy. Soc.* **A152,** 515 (1935).
7. Landau L., *Phys. Z. Sowjetunion* **8,** 489 (1935).
8. Cabrera N. B., *Disc. Faraday Soc.* **28,** 16 (1959).
9. Zwanzig R. W., *J. chem. Phys.* **32,** 1173 (1960).
10. Goodman F. O. *J. Phys. Chem. Solids* **23,** 1269 (1962).
11. McCarroll B. and Ehrlich G., *J. chem. Phys.* **38,** 523 (1963).
12. Zener C., *Phys. Rev.* **40,** 335 (1932).
13. Devonshire A. F., *Proc. Roy. Soc.* **A158,** 269 (1937).
14. Frenkel J., *Z. Phys.* **26,** 117 (1924).
15. Langmuir I., *J. Amer. chem. Soc.* **54,** 2798 (1932).
16. Dewing J. and Robertson A. J. B., *Disc. Faraday Soc.* **17,** 102 (1954).
17. Glasstone S., Laidler K. J. and Eyring H., *The Theory of Rate Process,* McGraw-Hill, New York (1941).
18. Volmer M. and Estermann I., *Z. Phys.* **7,** 13 (1931).
19. Orr W. J. C., *Trans. Faraday Soc.* **35,** 1247 (1939).
20. Datz S. and Taylor E. H., *J. chem. Phys.* **25,** 389, 395 (1956).
21. Copley M. J. and Phipps T. E., *Phys. Rev.* **48,** 960 (1935).
22. McCollum K. J. and Mayer J. E., *J. chem. Phys.* **11,** 56 (1943).
23. Kisliuk P. *J. chem. Phys.* **30,** 174 (1959).
24. Pound G. M., Simnad M. T. and Yang L., *J. chem. Phys.* **22,** 1215 (1954).
25. Thomas L. B. and Brown R. E. *J. chem. Phys.* **18,** 1367 (1950).

---

† The value for H_2 on tungsten compares favorably with the heat of Van der Waals' adsorption.(30)

26. Rowley H. A. and Bonhoeffer K. F., *Z. phys. Chem.* **B21**, 84 (1933).
27. Mann W. B., *Proc. Roy. Soc.* **A146**, 776 (1934).
28. Oliver R. N., Thesis, Calif. Inst. Techn., Pasadena, Calif., 1950.
29. Farber, M., private communication.
30. Eley D. D. *J. Phys. Coll. Chem.* **55**, 1017 (1951).
31. Lennard-Jones J. E. and Devonshire A. F., *Proc. Roy. Soc.* **A156**, 6 (1936).

J. Phys. Chem. Solids Pergamon Press 1963. Vol. 24, pp. 1297–1300. Printed in Great Britain.

MEASUREMENTS ON THE DIELECTRIC CONSTANT OF IODINE SINGLE CRYSTALS IN VARIOUS CRYSTALLOGRAPHIC DIRECTIONS

M. SIMHONY

Department of Physics, The Hebrew University, Jerusalem, Israel

(*Received* 5 *June* 1963)

Abstract—Measurements at room temperature yield for the dielectric constant of iodine along the principal crystallographic directions: $\epsilon_a = 6$, $\epsilon_b = 3$ and $\epsilon_c = 40$. In the temperature range between 180–330°K these values change between 0·9–1·3 of their room temperature ones. The slope of $\epsilon(T)$ changes sign at a particular temperature, depending on the crystallographic direction: $\sim$ 260°K, $\sim$ 290°K, and $\sim$ 310°K in the direction of the *a*-, *b*- and *c*-crystal axes, respectively.

1. INTRODUCTION

IODINE forms molecular crystals that belong to the base-centered orthorhombic system.⁽¹⁾ Every lattice point has two molecules of I_2 with an interatomic distance of 2·7 Å. The unit cell shown in Fig. 1(a) contains 4 molecules and has the dimensions $a = 4{\cdot}792$, $b = 7{\cdot}271$ and $c = 9{\cdot}803$ Å. All molecules lie in the *a–c* planes of the crystal. (Fig. 1b).

The material studied were single crystal wafers, selected from commercial resublimated iodine (ACS specification). The large (≈ 1 cm^2) surfaces of the wafers grow parallel to the *a–c* crystal plane. In this plane one can determine an axis of easy bending (even in crystals 3 mm thick), and a perpendicular axis, around which the crystals are very fragile. X-ray investigation⁽²⁾ shows that the axis of easy bending is the *c*-crystal axis while the other one is the *a*-axis. By cutting, polishing and etching one can obtain samples with surfaces of $\sim 0{\cdot}1$ cm^2 perpendicular to the *a*- or to the *c*-crystal axis and having thicknesses of 0·2–2 mm.

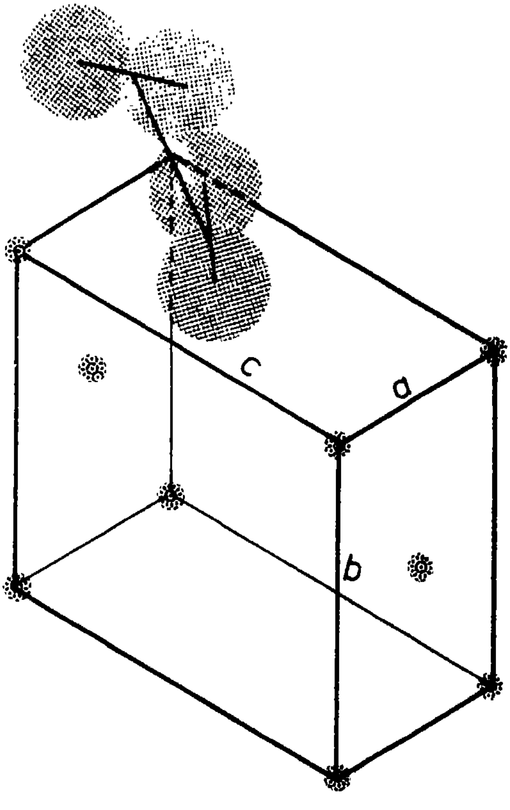

FIG. 1(a). The unit cell of the iodine crystal.

2. DIELECTRIC CONSTANT MEASUREMENTS AT ROOM TEMPERATURE

The jig (Fig. 2a) with crystals set between the platinum plates is placed in a mixture of two organic liquids of very low dielectric losses. The capacity of the jig C_m is measured by means of a Marconi type TF 329 Q-meter in ranges from 50 kc/s to 50 mc/s. Thereafter the crystals are

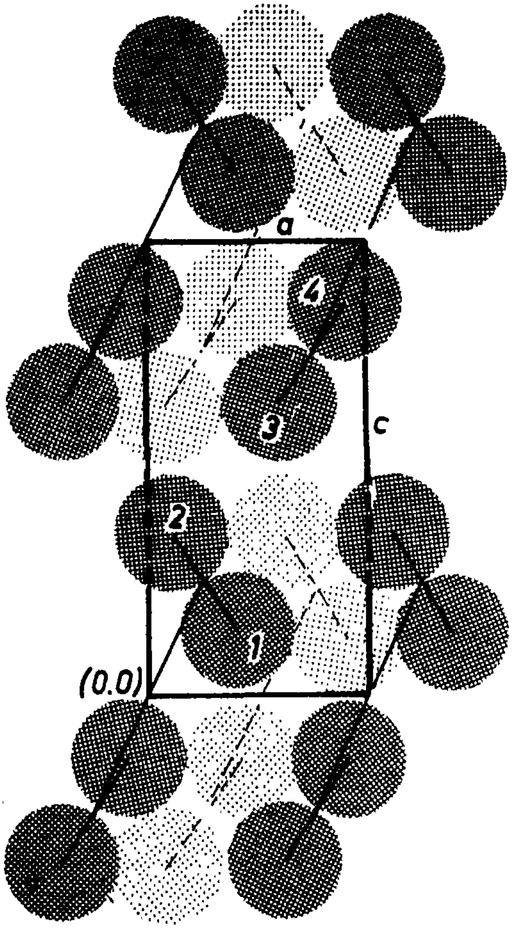

FIG. 1(b). Location of atoms in the a–c planes of the iodine crystal. Heavy circles stand for atoms with $b = 0$; the a and c coordinates of atoms numbered 1, 2, 3, 4 are (0·40; 0·13), (0·10; 0·37), (0·60; 0·63), (0·90; 0·87). Light circles represent atoms with $b = 1/2$.

removed without changing the distance between the plates and the capacity of the empty jig in the liquid C_L is measured.

The composition of the solution is changed to obtain a minimum deviation ΔC between the two measurements. The dielectric constant of the solution ϵ_L is determined by measuring the capacity of a capacitor in it. Plotting the values

$$\frac{\Delta C}{C_m} = \frac{C_L - C_m}{C_m} \text{ vs. } \epsilon_L$$

(e.g. Fig. 2b) we obtain the dielectric constant of the crystals given by the point where the line $\langle \Delta C/C_m \rangle$ crosses the ϵ_L coordinate axis.[3]

The values of the dielectric constant of iodine in various crystallographic directions obtained in this way are given in Table 1.

Table 1

Crystal axis direction	Dielectric constant
a	$6 \pm 0{\cdot}5$
b	$3 \pm 0{\cdot}3$
c	40 ± 2

3. TEMPERATURE DEPENDENCE OF THE DIELECTRIC CONSTANT OF IODINE

The crystals (thickness 0·2 mm, area 1–10 mm^2) are placed between two graphite electrodes of the jig (Fig. 3), being surrounded by a teflon spacer-ring (thickness 0·22 mm). The distance between

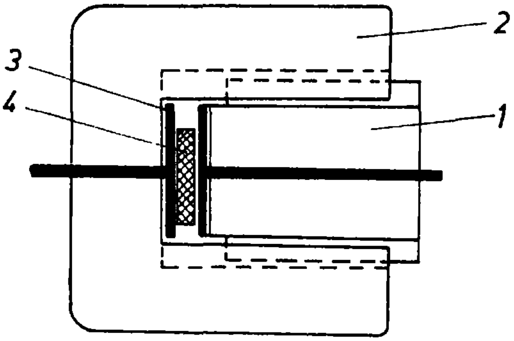

FIG. 2(a). The jig for dielectric-constant measurements. 1. Teflon slider. 2. Teflon frame. 3. Platinum electrodes. 4. Iodine crystal.

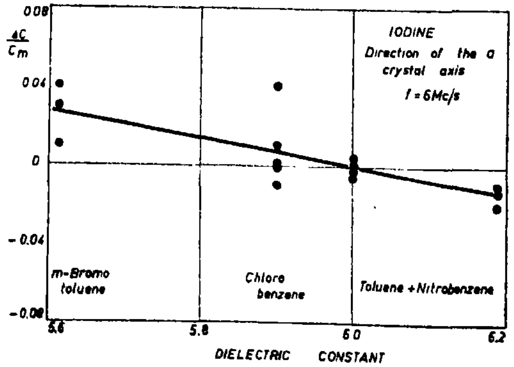

FIG. 2(b). Graphic construction for determination of ϵ_a.

the electrodes is slightly more than the crystal thickness, allowing them to expend independently of the thermal expansion of the jig. The jig is placed in a hermetically sealed Perspex box to prevent condensation of moisture. The long rod of the electrode may be put in various temperature baths (from liquid nitrogen to boiling water). The temperature of the crystals is measured by means of two copper–constantan thermocouples, whose junctions (protected from iodine vapour) are placed just on the surfaces of the electrodes. The other measured magnitudes are the capacities of the jig: when empty (C_1) and when filled with crystals (C_2). In both cases all parts and leads are identically placed. The measurements in the direction of the c axis of the crystal were made with a Marconi type TF 329 Q-meter in the 1·15 mc/s frequency range. For crystal sets (and temperature ranges) with small dielectric losses ($\mathrm{tg}\,\theta < 0{\cdot}01$) it was possible to observe capacity changes of $\sim 0{\cdot}02$ pF. The measurements in the a- and b-directions (and, for comparison, also one measurement in the c-direction) were made with a Brüel and Kjaer type 1506 deviation bridge in the 100 kc/s range. Capacity changes less than 0·01 pF could be observed even when $\mathrm{tg}\,\theta$ was $>0{\cdot}01$.

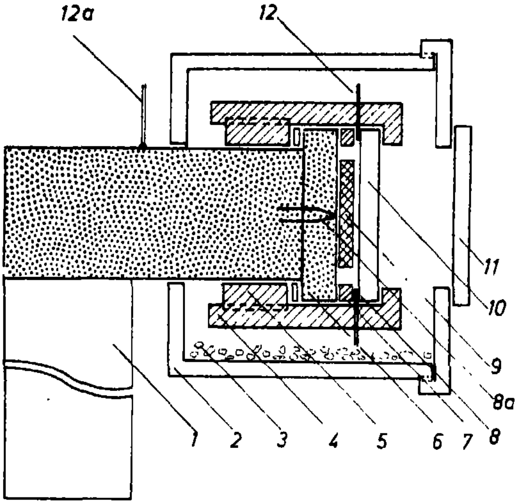

FIG. 3. The jig for measuring $\epsilon(T)$. 1. Heat conducting copper rod. 2. Perspex box. 3. Silica gel. 4. Teflon ring. 5. Teflon screw nut. 6. Graphite electrode. 7. Teflon spacer. 8, 8a. Thermocouples. 9. Iodine crystals. 10. Graphite or conducting glass electrode. 11. Window. 12, 12a. Electrode leads.

From the plots of C_1 and C_2 vs. T the plot of $\Delta C(T) = C_2(T) - C_1(T)$ can be drawn (Fig. 4). Since ΔC is proportional to the dielectric constant of iodine, the constant may be given by

$$\epsilon = \frac{\Delta C}{\Delta C_{300}} \cdot \epsilon_{300}$$

where ΔC_{300} and ϵ_{300} are the values of the corresponding quantities at 300°K (6, 3, 40 in the direction of the a, b, c-crystal axes, respectively).

The values of ΔC_{300} obtained for some sets of crystals are given in Table 2.

Plots of the averaged values of ϵ/ϵ_{300} against T in the three crystallographic directions are shown

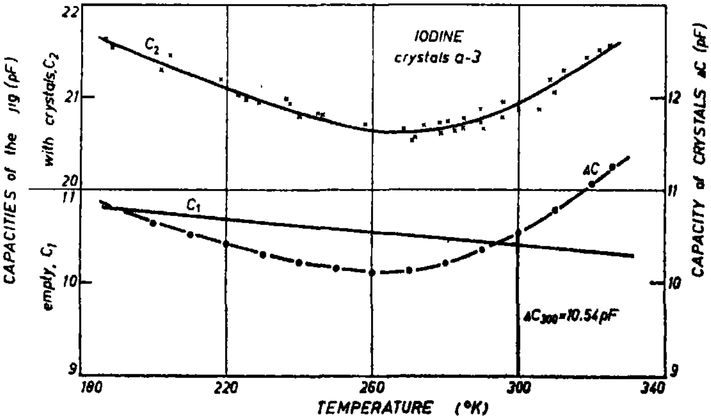

FIG. 4. The temperature dependence of the capacity of the jig and of the crystals.

in Fig. 5. It can be seen that the changes of ϵ with T between 180 and 330°K are quite small. No significantly larger changes were found down to liquid nitrogen temperatures. The extension to higher temperatures is limited by the high vapor pressure of iodine which causes sublimation and recrystallization of the iodine in the cell. The slope of $\epsilon(T)$ changes sign at a particular temperature depending on the crystallographic direction: $\sim$260°K, $\sim$290°K, and $\sim$310°K in the direction of the a-, b- and c-crystal axes respectively.

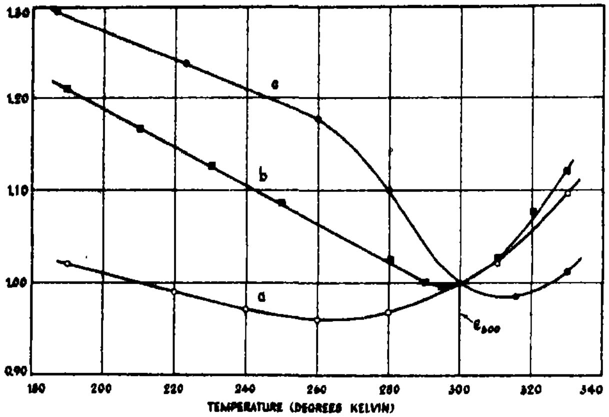

FIG. 5. Temperature dependence of the dielectric constant of iodine in the directions of the various crystal axes: a (circles), b (squares) and c (triangles).

Table 2

Set of crystals	Capacity of the jig (pF) at 300°K filled C_2	Capacity of the jig (pF) at 300°K empty C_1	ΔC_{300} (pF)
c–10	17·70	14·45	3·25
c–11	20·20	14·45	5·75
a– 2	20·56	10·60	9·96
a– 3	20·94	10·40	10·54
b– 3	13·86	11·40	2·46
b– 4	19·81	17·87	1·94
c–12	34·55	17·87	16·68

By replacing the thin graphite electrode of the jig with a conducting glass electrode it is possible to look for changes in the dielectric constant as a result of illuminating the crystal surfaces with highly absorbed light. The light source was a Mazda ME/D mercury lamp (with or without filters). In the b-direction no change in the capacity of the crystals under illumination was found over the entire temperature range. In the c-direction (crystals c-12) the changes ΔC_{ph} were less than 0·05 pF, which gives $\Delta\epsilon_{ph}/\epsilon = \Delta C_{ph}/C < 0{\cdot}003$. In the a-direction $\Delta C_{ph} < 0{\cdot}02$ pF and $\Delta\epsilon_{ph}/\epsilon < 0{\cdot}002$ was obtained.

Acknowledgements—The author wishes to thank Mr. Y. TEUCHER for his help in carrying out the room temperature measurements. Thanks are due to Professor A. MANY who has suggested the subject and helped throughout the whole work by important suggestions and useful discussions.

REFERENCES

1. SWANSON H. E. and FUYAT R. K., *NBS Circ.* 539, Vol. III 1953 (as quoted in ASTM Card Index 1958).
2. Carried out by Dr. Z. H. KALMAN.
3. WHITEHEAD S. and HACKETT W., *Proc. phys. Soc. Lond.* **51**, 173 (1939).

J. Phys. Chem. Solids Pergamon Press 1963. Vol. 24, pp. 1301–1304. Printed in Great Britain.

OPTICAL ABSORPTION IN CaO SINGLE CRYSTALS*

VICTOR L. NEELEY and JAMES C. KEMP

Department of Physics, University of Oregon, Eugene, Oregon

(*Received* 13 *May* 1963)

Abstract—The optical absorption of CaO single crystals has been measured in the range 14·5 μ–200 mμ. Absorption bands begin at approximately 250 mμ on the high energy side of the visible region and at 10 μ on the low energy side. $Ca(OH)_2$, which readily forms on the surface of these crystals when left standing, shows the strong (OH) stretching absorption at 2·755 μ. Surface effects also cause a weaker band at 260 mμ. Special precautions were necessary to eliminate these spurious absorptions. The forbidden band gap in CaO is definitely $\geqslant$ 6·0 eV.

INTRODUCTION

LITTLE if any experimental work on the optical and related properties of CaO single crystals has appeared in the literature, in spite of the importance of CaO in the alkaline earth oxide series. A principal reason for this has been the lack of sizeable single crystals.

Recently, work on electron spin resonance (e.s.r.) of several transition metal ions in CaO crystals has been initiated, CaO being in several respects an ideal host crystal for such studies.(1) *F*-centers and other defects have also been studied in CaO.(2)

Thermoluminescence, optical transmission, and other studies relevant to the band gap and band structure, carried out generally on thin polycrystalline layers or in powder, were reviewed by HANNAY;(3) an estimated lower limit for the band gap of 5.6 eV was mentioned.

Theoretical work on the band structure so far appears to have been nil. CALLAWAY(4) has discussed briefly band calculations in the alkaline earths, and refers to preliminary calculations in MgO and BaO.

EXPERIMENTAL PROCEDURE

The absorption spectra in the infrared region (15–2·5 μ) was done on a Beckman Model IR-7 recording spectrophotometer. The spectra through the region 2·5 μ–200 mμ were taken on Cary Models 14 and 15 recording spectrophotometers

The crystals were ultra pure CaO single crystals obtained commercially from Semi-Elements, Inc., Saxonburg, Pa. Typical crystals were some 0·05 cm^3 in volume. From these, cleaved thin samples with surface dimensions about 2·5 × 2·5 mm were prepared.

The purity of these crystals were checked by emission spectroscopy by the Oregon Metallurgical Corp., Albany, Oregon. Their results for CaO and some MgO crystals used for comparison purposes are shown in Table 1. The purity was further checked by e.p.r. techniques. The only paramagnetic ion detected was Mn^{2+} and its concentration was in agreement with the emission spectroscopy data.

A number of crystals having thicknesses from 1·5 to 0·15 mm were measured. The crystals were cleaved, then ground and polished to the desired thickness. Spectra from some MgO crystals treated in the same way were also taken for comparison purposes.

Calcium hydroxide forms rapidly on the surface of these crystals when left in the open. This surface coating can easily be seen after 6–8 hr. In order to eliminate the absorption and scattering due to the $Ca(OH)_2$ it was usually sufficient to grind and polish two crystals, one considerably thicker than the other, and immediately place one in each of the two beams of the dual beam spectrophotometer. The resulting spectrum was then due to pure CaO absorption. The small amount of residual (OH) could be made comparable in the two samples by

---

* Supported by the U.S. Air Force and by a Tektronix Foundation grant.

Table 1. *Impurities in wt per cent.*

	Al	Cu	Fe	Mg	Mn	Si	Ca
CaO	< 0·01	< 0·0005	0·01	< 0·01	< 0·005	0·1	
MgO	< 0·01	< 0·0005	0·01		< 0·005	0·1	0·1–0·01

treating them alike, and the spurious absorption and scattering was then cancelled out to first order in the spectrophotometer. The effectiveness of this method in removing the $Ca(OH)_2$ absorption could easily be checked by observing the intensity of the residual 2·755 μ(OH) stretching vibration peak.

Spectra were taken at 300, 77 and approximately 20°K. The latter measurement was made using liquid He; however, radiation through the optical ports of the dewar raised the sample temperature to approximately 20°K.

Because of the small size of the prepared crystals (approximately 2·5 mm on a side), most of the beam in the spectrophotometer had to be masked off. The result was a serious reduction in the optical density range that could be covered. Measurements at 300°K were carried out to 170 mμ; however, the optical density in CaO in the range 200–170 mμ remained consistently above any measurable value for the crystals used.

EXPERIMENTAL RESULTS AND DISCUSSION

The i.r. absorption spectra were taken in order to compare the single crystal CaO infrared absorption with older work done on thin polycrystalline films in which CaO and MgO infrared absorption peaks were found at 27·4 and 17·3 μ respectively.(5, 6) Also we wished to observe the (OH) stretching vibration from the $Ca(OH)_2$ surface layer, when present; this (OH) peak intensity was used to gauge the degree of surface contamination.

Figure 1 shows the i.r. absorption coefficient of pure CaO, CaO left in the open for approximately 24 hr and an MgO crystal for comparison. The CaO absorption occurs at a longer wavelength than MgO (curves A and B) in agreement with older work. The strong (OH) stretching absorption of the $Ca(OH)_2$ surface layer is seen at 2·755 μ in curve B.

Figure 2 shows the absorption coefficient in the u.v. region for the same types of crystals shown in Fig. 1. The absorption band at 260 mμ in curve C is due to surface effects but did not seem to grow at the same rate as the 2·755 μ band.

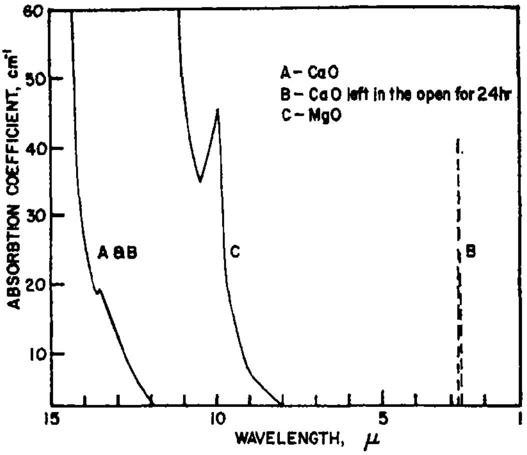

Fig. 1. I.R. absorption coefficient of single crystal CaO (A), CaO with $Ca(OH)_2$ surface layer (B), and MgO (C).

Our MgO spectra are in agreement with the work done by Clarke:(7) however, Clarke has shown that two small absorption bands which occur at 288 and 221 mμ in MgO may be removed by heating. These absorption bands are removed from curve D in order to more clearly show the difference in fundamental absorption between CaO and MgO. The absorption band at 182 mμ in MgO has been shown to be associated with impurities(7) and is not removed by heating. For CaO crystals used in the present work, no change in the spectra was observed after heating to 1100°C for several hours.

The exciton structure of other alkaline earth oxides, MgO, SrO, and BaO, has been thoroughly studied.(8, 9, 10) The separations between the usually observed two or three prominent exciton peaks, as well as the distance from the first strong exciton peak to the extrapolated band gap edge,

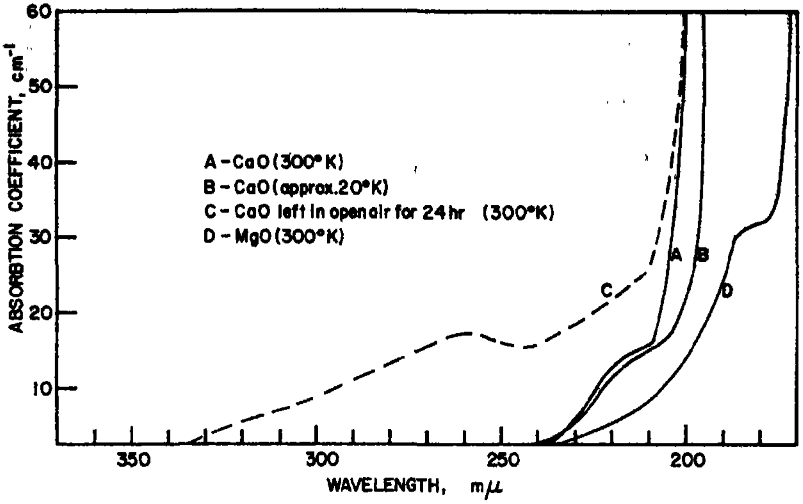

FIG. 2. Absorption coefficient of single crystal CaO at 300°K (A), single crystal CaO at approx. 20°K (B), CaO with $Ca(OH)_2$ surface layer (C) and MgO (D).

appear to follow the general trend of slowly decreasing separation as one progresses from MgO to BaO. The first strong exciton peak occurs at 7·6, 5·71 and 4·06 eV in MgO, SrO, and BaO respectively. These peaks generally show appreciable temperature narrowing.(8) In CaO, curves A and B, the band at 215 mμ shows no appreciable temperature narrowing and we believe it to be associated with an impurity or defect rather than with the exciton structure. Using DEXTER's(11) formula for impurity centers and assuming unity oscillator strength, approximately 2×10^{17} impurity centers per cm^3 would produce this band; this number is of the order of some of the impurity concentrations (Fe for example) listed in Table 1. On the other hand, the temperature shift of the strong absorption edge at 200 mμ indicate that the latter is more likely the edge of an exciton peak. Photoconductivity studies(12) in powdered CaO show a large photocurrent, independent of impurities, for excitation wavelengths shorter than 185 mμ (6·7 eV); this is consistent with our placing the first strong exciton peak at slightly beyond 200 mμ.

From the present work it can be stated that the forbidden band gap in CaO is definitely $\geqslant$ 6·0 eV. The mean separation between the first observed exciton peak and the extrapolated edge of interband absorption is slightly greater than 1 eV in the three other alkaline earth oxides.(8, 9, 10) Adding 1 eV to our assigned first exciton peak position would produce a band gap of 7·5 eV in CaO, which would agree qualitatively with the position of CaO in the series. Vacuum u.v. transmission studies covering the band gap transition have not to our knowledge been reported; these are expected to be more difficult in single CaO crystals than in MgO due to the surface preparation problems mentioned above.

Acknowledgement—We wish to acknowledge the able assistance of L. W. AGER in conducting many of the measurements and sample preparations.

REFERENCES

1. SHUSKUS A. J., *Phys. Rev.* **127,** 2022 (1962).
2. KEMP J. C. and NEELEY V. I., *J. Phys. Chem. Solids* **24,** 332 (1963).
3. HANNAY N. B., *Semiconductors*, pp. 569–76. Reinhold, New York (1959).
4. SEITZ F. and TURNBULL D. (editors), *Solid State Physics*, Vol. **7**, Academic Press, New York (1958).
5. TOLKSDORF S., *Z. phys. Chem.* **132,** 161 (1928).
6. PARODI M., *C.R. Acad. Sci. Paris* **204,** 1111 (1937).
7. CLARKE F. P., *Phil. Mag.* **2,** 607 (1957).
8. ZOLLWEG R. J., *Phys. Rev.* **97,** 228 (1955); *ibid.* **111,** 113 (1958).
9. SAUM G. A. and HENSLEY E. B., *Phys. Rev.* **113,** 1019 (1959).
10. REILING G. H. and HENSLEY E. B., *Phys. Rev.* **112,** 1106 (1958).
11. DEXTER D. L., *Phys. Rev.* **101,** 48 (1956).
12. JANIN J. and COTTON L., *C.R. Acad. Sci. Paris* **246,** 1536 (1958).

Note added in proof:

Optical transmission of thin CaO films over the vacuum n.v. range was recently reported by H. H. Glascock, Jr. and E. B. Hensley, *Phys. Rev.* **131**, 649 (1963). They give 7·7 eV for the band gap, which compares well with our estimate of 7·5 eV.

J. Phys. Chem. Solids Pergamon Press 1963. Vol. 24, pp. 1305–1308. Printed in Great Britain.

INTERACTION ENERGIES BETWEEN DEFECTS IN METALS

J. WORSTER and N. H. MARCH

Department of Physics, The University, Sheffield

(*Received* 24 *April* 1963)

Abstract—The predictions of perturbation theory regarding the interaction between charged impurities in metals are presented. The unperturbed conduction electrons are described by plane waves and the defects, treated as point charges, are screened to first order in the Hartree approximation. In the case of monovalent and divalent matrices, it is shown that at the nearest-neighbour distance the qualitative results are the same as would be predicted electrostatically. For trivalent matrices, the sign of the interaction is changed.

1. INTRODUCTION

IN TWO recent papers, CORLESS and MARCH(1, 2) have given a theory of the interaction between defects in metals using a perturbative treatment based on the Dirac density matrix,(3, 4) while, independently, BLANDIN, DÉPLANTÉ and FRIEDEL(5) have developed an essentially equivalent method. Indeed, some of the basic results of these theories are at least implicit in an early paper on electron–phonon interaction by BARDEEN(6) as well as in later work of NOZIÈRES and PINES.(7)

2. CALCULATION OF INTERACTION ENERGIES

Computations yielding the explicit numerical results predicted by the above mentioned theories have recently been carried out and it is the purpose of this note to report the main results for impurities in some monovalent, divalent, and trivalent metals.* In terms of the screened potential $V(\mathbf{r})$ due to unit excess positive charge embedded in the metal, the interaction energy between two impurity centres, distance a apart, and carrying excess charges Z_1 and Z_2 is given by (1, 2)

$$-Z_1 Z_2 V(a). \tag{1}$$

$V(a)$ may be obtained directly by solution of the equation, due to MARCH and MURRAY(8)

$$\nabla^2 V = \frac{2k_f^2}{\pi^2}\int \mathrm{d}\mathbf{r}_1 V(\mathbf{r}_1)\frac{j_1(2k_f|\mathbf{r}-\mathbf{r}_1|)}{|\mathbf{r}-\mathbf{r}_1|^2}, \tag{2}$$

where k_f is the magnitude of the Fermi wave vector, and

$$j_1(\rho) = \frac{\sin\rho - \rho\cos\rho}{\rho^2}, \tag{3}$$

or equivalently from the Fourier components of $V(\mathbf{r})$ given by(6, 8, 9)

$$V(\mathbf{k}) = \frac{-4\pi}{k^2 + \dfrac{k_f}{\pi}g\left(\dfrac{k}{2k_f}\right)} \tag{4}$$

where

$$g(x) = 2 + \frac{x^2-1}{x}\ln\left|\frac{1-x}{1+x}\right|. \tag{5}$$

Whereas some direct numerical solutions of (2) are already available,(4) the present results have been found by employing equation (4) as follows. We may write

$$rV(r) = -\frac{1}{\pi i}\int_{-\infty}^{\infty}\frac{x e^{2iRx}}{x^2 + \dfrac{1}{4\pi k_f}g(x)}\mathrm{d}x, \tag{6}$$

---

[*] Professor J. Friedel has kindly informed us that similar calculations have been carried out independently at Orsay by Drs Blandin and Déplanté, and are in agreement with our results.

where $R = k_f r$. Integrating

$$\frac{1}{\pi i}\frac{z e^{2iRz}}{z^2+\frac{1}{\pi k_f}\left[\frac{1}{2}+\frac{z^2-1}{4z}\ln\frac{1-z}{1+z}\right]}$$

round a semicircle in the upper half of the complex plane gives

$$-rV = \alpha e^{-2\beta R}+\frac{2}{\pi} Im \int_1^\infty dx$$

$$\times\left[\frac{x e^{2iRx}}{x^2+\frac{1}{4\pi k_f}g(x)}-\frac{x e^{2iR\,x}}{x^2+\frac{1}{4\pi k_f}\left[g(x)-i\pi\frac{(x^2-1)}{x}\right]}\right]$$

where $2\pi k_f\beta^3 = \beta+(1+\beta^2)\tan^{-1}\beta$ (7)

and

$$\alpha = \frac{4\pi k_f\beta^3}{4\pi k_f\beta^3-\beta+(1-\beta^2)\tan^{-1}\beta}.$$

The integrand is now expanded in powers of $1/\pi k_f$, and $g(x)$ is expanded in powers of $1/x$. The integral becomes

$$\sum_{n=1}^{\infty}\left(-\frac{1}{\pi k_f}\right)^n F_n(R) \tag{8}$$

where

$$F_n(R) = Re\frac{1}{2}\sum_{r=1}^{n}\binom{n}{r}\left(-\frac{i\pi}{4}\right)^r$$

$$\times\sum_{s=0}^{\infty} C_{s,n-r,r} I_{4n+1-3r+2s}(R),$$

$$I_t(R) = \int_1^\infty dx\, x^{-t}\, e^{2iRx}$$

$$C_{s,u,r} = \sum_{p=0}^{r}(-1)^p\binom{r}{p}C_{s-p,u,0}$$

and

$$\sum_{s=0}^{\infty} C_{s,u,0}x^s \equiv\left[\sum_{s=0}^{\infty}\frac{x^s}{(2s+1)(2s+3)}\right]^u$$

The series converges for $2\pi k_f > 1$, and is quite suitable for accurate computation.

3. DISCUSSION OF RESULTS

We show in Fig. 1 our results for $V(r)$ for an impurity in Cu and in Mg, and similar results are

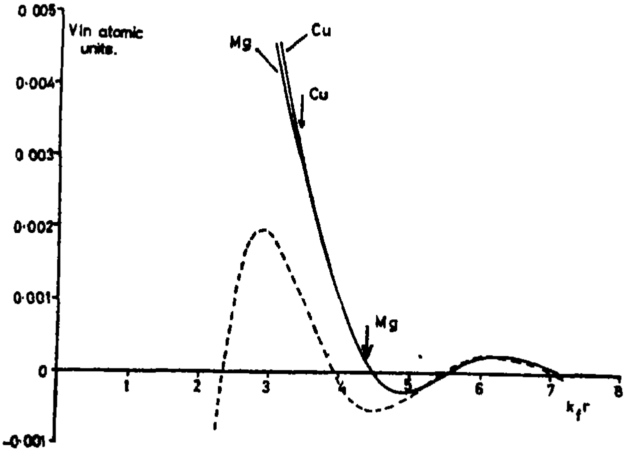

FIG. 1. Screened potential ($-V(r)$) round unit positive charge embedded in Cu and in Mg. Arrows indicate near-neighbour distance in the two cases. Broken line shows asymptotic form.

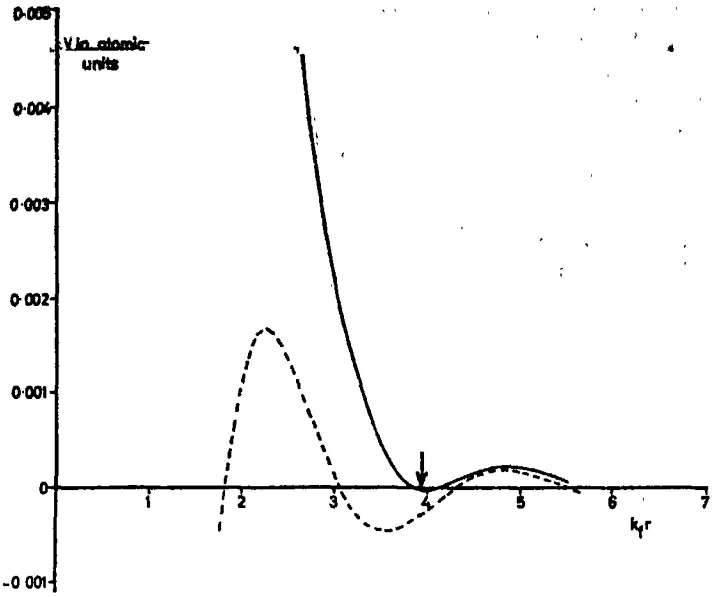

FIG. 2. Screened potential ($-V(r)$) round unit positive charge embedded in Al. Broken line shows asymptotic form.

plotted in Fig. 2 for Al as the matrix metal. For comparison, we have plotted also the asymptotic forms, given by

$$V(r) = -\frac{\pi}{k_f(1+2\pi k_f)^2}\frac{\cos 2k_f r}{r^3} \qquad (9)$$

It will be seen that, at the near-neighbour distances in the three metals, $V(a)$ has a sign determined electrostatically by the sign of the charge on the impurity centre for Cu and Mg, while the sign is changed for Al. This is different from the predictions using the asymptotic form, which would group Mg and Al together,(5) with Cu behaving differently.

Furthermore, the magnitudes of the interaction energies are very small at the near-neighbour distance for Mg and Al, whereas this is not so when the asymptotic form is used. Thus, for impurities in Mg and Al, interactions other than between near-neighbours may be the most important. In this connection, it may be of interest to observe that the first node in V disappears at $k_f = 0{\cdot}939$ and that it occurs actually at the nearest-neighbour distance of trivalent close-packed metals for $k_f = 0{\cdot}9325$.

We realize, of course, that the present form of the theory has a number of shortcomings:

(i) Relaxation effects are ignored.

(ii) Bloch wave effects are not properly accounted for although CORLESS and MARCH(2) have shown that equation (1) is still valid to a first approximation in a point-ion model.

(iii) Low order perturbation theory is not quantitatively accurate, and a phase shift in the oscillatory potential would be introduced by higher order terms. Unfortunately, the use of equation (1), if $V(a)$ is calculated to higher order in perturbation theory, is not rigorously justified.

(iv) Electron exchange and correlation effects have been neglected, and a Hartree treatment employed throughout. Preliminary calculations performed at Orsay(10) show that exchange, included without correlation, can cause significant changes, as also noted by CORLESS and MARCH.(1) Such a procedure, however, is known in other problems such as electronic specific heat and free electron diamagnetism to lead to non-physical results unless correlation effects are also accounted for.

While we feel that with the numerous approximations involved, it is unreasonable to suppose that the results presented here can be entirely quantitative, they point to the interest of further studies, both experimental and theoretical, of interaction energies between defects especially in multivalent matrices.

Acknowledgements—One of us (N.H.M.) wishes to thank Professor J. Friedel, both for communicating unpublished results, and for a fruitful correspondence over a long period on the present problem. We wish to acknowledge that this work was performed under contract with the United Kingdom Atomic Energy Authority, A.E.R.E., Harwell.

REFERENCES

1. Corless G. K. and March N. H., *Phil. Mag.* **6,** 1285 (1961).
2. Corless G. K. and March N. H., *Phil. Mag.* **7,** 1765 (1962).
3. March N. H. and Murray A. M., *Phys. Rev.* **120,** 830 (1960).
4. March N. H. and Murray A. M., *Proc. Roy. Soc.* **A261,** 119 (1961).
5. Blandin A., Déplanté J. L. and Friedel J., *Proc. Kyoto Conference on Crystal Lattice Defects, J. phys. Soc. Japan* **18,** Suppl. II, 85 (1963).
6. Bardeen J., *Phys. Rev.* **52,** 688 (1937).
7. Nozières P. and Pines D., *Phys. Rev.* **109,** 762 (1958).
8. Langer J. S. and Vosko S. H., *J. Phys. Chem. Solids* **12,** 196 (1960).
9. March N. H. and Murray A. M., *Proc. Roy. Soc.* **A266,** 559 (1962).
10. Friedel J., Private communication.

J. Phys. Chem. Solids Pergamon Press 1963. Vol. 24, pp. 1309–1323. Printed in Great Britain.

KINETICS OF OXIDE FILM GROWTH ON METAL CRYSTALS—II

HOMOGENEOUS FIELD APPROXIMATIONS*

A. T. FROMHOLD, JR.

Sandia Laboratory, Albuquerque, New Mexico

(*Received* 16 *January* 1963; *revised* 17 *May* 1963)

Abstract—Homogeneous field approximations yield simple equations relating film thickness $L(t)$ to time t of oxidation from coupled steady-state diffusion equations of I assuming equal ionic and electronic currents. High temperature parabolic equations are obtained with rate determined by transport of the low mobility species in the presence of the electric field created by the high mobility species; these parabolic equations have a modified rate constant k' due to a constant electrical potential difference ϕ across the film. Both k' and ϕ increase with (concentration) × (mobility) and ratio of boundary concentrations for the electronic species, and decrease for corresponding changes for the ionic species. For tunnelling or field emission of one species with rate determined by diffusion of the second species, the expression obtained is $[1 + \beta t = \exp(\alpha L(t)) - \alpha L(t)]$, with α and β determined from emission and diffusion parameters. This equation is based on the intermediate temperature approximation that the surface charge is essentially independent of $L(t)$ for tunnelling from the metal crystal through the film, to traps, and between traps in the oxide for film thicknesses less than some critical thickness L_{crit}: For limiting cases this equation reduces to *N*th root $[L(t) \propto t^{1/N}]$ and logarithmic $[L(t) \propto \log(1 + t/t_0)]$ laws. The final stage of growth occurs for $L(t) > L_{\text{crit}}$ and usually predominates at low temperatures; rate is controlled by tunnelling or field emission in a thickness dependent field ($E \propto 1/L(t)$) so that a limiting thickness L_∞ usually results, with $L_\infty - L_{\text{crit}}$ equal to several monolayers only. For this region of growth, a logarithmic law and an exponential law $[L(t) \propto 1 - \exp(-\nu t)]$ result for Fowler–Nordheim behavior of the current with field, a modified exponential law $[L(t) \propto 1 - \exp\{-(L(t)/L_\infty) - t/\tau\}]$ results for a linear dependence of tunnel current through the film on field, and a cubic law $[L(t) \propto t^{1/3}]$ results for a linear dependence of tunnel current between traps in the oxide on field. Application of this work is made to published experimental data for copper monocrystals at 1173°K and between 451 and 78°K.

1. INTRODUCTION

AN ANALYSIS[1] of oxide film kinetics using coupled diffusion equations has been presented in I. Growth rate was considered to be determined by diffusion of charged particles through planar homogeneous oxide films. The diffusion occurs in the presence of an electric field which is created by surface and space charge of diffusing species and modified by tunnelling or field emission of other species. Justification was presented for the steady-state approximation and fixed boundary values of the bulk concentrations during growth.

The primary purpose of the present work is to obtain simple approximate relations from the coupled equations of I to provide insight into the physics of film growth and to aid in ready interpretation of experimental data. The integration of the film growth equations is obtained by assuming small space charge magnitudes so the electric field can be treated as homogeneous through the film. The variation of the homogeneous field with film thickness at a given temperature then determines the growth law.

A derivation of parabolic growth equations applicable to high temperature oxidation is presented in Section 2. Derivations of logarithmic and *N*th root growth equations applicable to intermediate and low temperatures are given in Section 3. A discussion together with a comparison of the equations with published experimental data for copper monocrystals is given in Section 4. Conclusions are presented in Section 5.

---

* Work performed under the auspices of the United States Atomic Energy Commission.

2. PARABOLIC GROWTH EQUATIONS

The steady-state particle current J of a charged species through an oxide film in the presence of a homogeneous electric field E is given by equation (10) of I as

$$J(t) = \mu E \left[\frac{C(L(t),t) - C(0,t)\exp(E\mu L(t)/D)}{1-\exp(E\mu L(t)/D)}\right]. \quad (1)$$

The diffusion coefficient D and mobility μ of the species correspond to a direction in the oxide normal to the metal surface; $C(L(t), t)$ and $C(0,t)$ are the bulk concentrations of the species at the oxide–oxygen interface and the metal–oxide interface respectively. Note that conditions sufficient for parabolic growth

$$\frac{\mathrm{d}L(t)}{\mathrm{d}t} = \frac{k'}{L(t)}, \quad (2)$$

where k' is the rate constant independent of t and $L(t)$, are that the bulk concentrations at the interfaces and the potential difference $\phi = EL(t)$ across the film are independent of t and $L(t)$. It will be shown now that fixed bulk concentrations at the interfaces causes a constant potential difference to be established across the film.

The hypothesis is made that on the average the field produced at any given film thickness is such that the ionic and electronic charge currents are equal so that growth can continue. Equation (1) is applicable to each particle current for the case of a homogeneous field. The resulting equation for E is

$$\begin{aligned} &|Z_i|\Big[\mu_i C_i(L(0),0) - \mu_i C_i(0,0) \\ &\quad\times \exp\left(\frac{E\mu_i L(t)}{D_i}\right)\Big]\left[1-\exp\left(\frac{E\mu_e L(t)}{D_e}\right)\right] \\ &= |Z_e|\Big[\mu_e C_e(L(0),0) - \mu_e C_e(0,0) \\ &\quad\times \exp\left(\frac{E\mu_e L(t)}{D_e}\right)\Big]\left[1-\exp\left(\frac{E\mu_i L(t)}{D_i}\right)\right], \end{aligned} \quad (3)$$

where

i = subscript referring to the ionic species, and

e = subscript referring to the electronic species.

The Einstein relation $qD = \mu kT$ is applicable. The charge q per particle is $Z|e|$, where $|e|$ is the magnitude of the electronic charge; Z is positive for cations, anion vacancies and positive holes, but negative for cation vacancies, anions, and electrons.

Approximate solutions to equation (3) can be obtained readily for several limiting cases for which the two boundary concentrations for a given species are greatly different. In the low field limit defined by

$$|E| \lesssim \left|\frac{kT}{|e|L(t)}\right|, \quad (4)$$

one solution* exists for $E = 0$. For $E = 0$,

$$\frac{D_i}{D_e} = \left|\frac{Z_e}{Z_i}\right|\left(\frac{C_e(0,0) - C_e(L(0),0)}{C_i(0,0) - C_i(L(0),0)}\right). \quad (5)$$

Unless this equality is satisfied, then, a field must be created in the oxide film. For a field with magnitude much greater than $|(kT)/(|e|L(t))|$ (i.e., in the high field limit), equation (3) yields similar results for the eight combinations of positive or negative field and diffusion of cations, cation vacancies, anions, or anion vacancies together with the corresponding electronic species. For the case of positive field with transport of ions and electrons,

$$\begin{aligned} E &\simeq \frac{-kT}{Z_e|e|L(t)} \\ &\quad\times \log\left[\frac{|Z_e|\mu_e C_e(0,0)}{|Z_e|\mu_e C_e(L(0),0) - |Z_i|\mu_i C_i(0,0)}\right]. \end{aligned} \quad (6)$$

Therefore, the electrical potential difference $EL(t)$ established across the film is independent of $L(t)$ for fixed values of the bulk concentrations at the interfaces. The fact that a positive field is established in this case implies that $|\mu_e C_e(0,0)|$ is greater than the corresponding product for ions. The motion of ions and electrons occurs for a positive concentration gradient so that $C(0,0)$ is larger than $C(L(0),0)$. The extension to negative field and other species is given in Appendix 1.

The field given by equation (6) is established by the diffusing species in the approach of the system to equilibrium. Although film growth in this field is parabolic, the rate is modified from the rate for the corresponding case of diffusion of uncharged particles. For an ionic current, equation (1) gives

---

* *Note added in proof:* For other low field solutions, E is proportional to $1/L(t)$ as in the high field limit. This will be discussed subsequently in an analysis of the nonhomogeneous field case.

$$\frac{\mathrm{d}L(t)}{\mathrm{d}t} = \frac{RD_i \log g}{L(t)}\left[\frac{C_i(L(t),t)-gC_i(0,t)}{1-g}\right], \tag{7}$$

where

$$g = \exp\left(\frac{E\mu_i L(t)}{D_i}\right) = \exp\left(\frac{Z_i|e|EL(t)}{kT}\right). \tag{8}$$

The parameter R is the volume of oxide formed per particle of the ionic species which diffuses *to* the oxide–oxygen interface; this quantity is positive for cations and anion vacancies but negative for cation vacancies and anions. For diffusion of ions in zero field,

$$\frac{\mathrm{d}L(t)}{\mathrm{d}t} = \frac{-RD_i[C_i(L(t),t)-C_i(0,t)]}{L(t)}. \tag{9}$$

The ratio of the growth rate given by equation (7) to that given by equation (9) is denoted as ξ, so that

$$\xi = -\left[\frac{C_i(L(t),t)-gC_i(0,t)}{(1-g)\,\{C_i(L(t),t)-C_i(0,t)\}}\right]\log g. \tag{10}$$

The quantity ξ is therefore a measure of the effect of the field on the diffusion process, and has the value 1 for zero field. The determination of g permits ξ to be evaluated for known interfacial bulk concentrations; ξ is proportional to $\log g$ for large g. Thus the rate constant k' defined in equation (2) for the diffusion of charged particles is given by ξk, where k is the corresponding rate constant for diffusion of uncharged particles. The parameter ξ is called the *enhancement factor*, and it is significant that its value is determined by a combination of both electronic and ionic parameters. According to the above definition, the value of ξ is greater than 1 if ionic diffusion is slower than electronic diffusion in the absence of a field, and is less than 1 if ionic diffusion is more rapid than electronic diffusion in the absence of a field.

A limiting case of the above formulae illustrates clearly that the rate limiting process for growth is the transport of the low mobility species in the presence of the electric field due to the high mobility species. Assume that the magnitude of the mobility of the electronic species in the oxide is much greater than that of the ionic species. A large concentration gradient of electrons would then cause a rapid flow of electrons until the electric field created by the redistributed charge is nearly adequate to halt electron flow. For zero current flow, equation (1) gives

$$E = \frac{D}{\mu L(t)}\log\left(\frac{C(L(t),t)}{C(0,t)}\right). \tag{11}$$

In this case, D, μ, $C(L(t), t)$, and $C(0, t)$ refer to electrons. Substituting this value of the field into equation (8) gives

$$g = \left[\frac{C_e(L(t),t)}{C_e(0,t)}\right]^{Z_i/Z_e}. \tag{12}$$

For diffusion from the oxide–metal interface to the oxide–oxygen interface with large concentration differences across the film, equation (10) then reduces to

$$\xi = \log g = \frac{-Z_i}{Z_e}\log\frac{C_e(0,0)}{C_e(L(0),0)}. \tag{13}$$

This is a positive quantity greater than 1, so the field enhances the growth rate by this factor.

Equation (11) applied to electrons represents the maximum field which can be created by the redistribution of electrods with no interference from the ionic species. Equation (6) represents the field which is created by the electrons to aid the ionic diffusion and hinder the electronic diffusion such that the currents are equal. This field is less than the maximum field unless the smallest value of $|\mu_e C_e|$ is much greater than the largest value of $|\mu_i C_i|$ in the film.

The above derivation of the parabolic law emphasizes the large effect of the internal electric field on growth. Equation (13) can be used to illustrate that the transport of ions by the surface charge field can be as much as an order of magnitude greater than the transport of ions by the ionic concentration gradient. The case in which the diffusion process is modified by electron tunnelling or field emission is treated in the following Section.

3. LOGARITHMIC AND *N*th ROOT GROWTH EQUATIONS

(a) *Constant field approximation*

At intermediate and low temperatures the diffusion process for one of the two species may be very slow; the field created by the more rapidly diffusing species may then attain a value large enough to induce tunnelling or field emission of the first species. In such cases, the analysis of the preceding Section for which the field was found to vary as $1/L(t)$ is not applicable. In this Section it is shown that to a reasonable approximation E can be considered to be independent of $L(t)$ for a certain range of film thickness and temperature.

Denote the field emission or field-induced tunnel current as J_E. The following expressions[2, 3] are used for this current in the high and low field limits respectively:

$$J_E = \begin{cases} B\exp(-G/E) & (EL(t) \gg \phi_M) \quad (14) \\ KE\exp(-\chi L(t)). & (EL(t) \leqslant \phi_M) \quad (15) \end{cases}$$

The parameters B, G, K and χ are constants, and ϕ_M is the metal–oxide work function or the corresponding field emission parameter for ions. This current plus the thermionic emission current J_{TH} of the same species, given by Richardson's equation, must equal the diffusion current of the other species. This diffusion current is designated as J_{crit} and is given by equation (1); in the absence of a field it reduces to the diffusion current J_D for uncharged particles. The diffusion current creates the field E which cannot be greater than the value $E_{\max}$ given by equation (11).

Assume that some field E^* less than $E_{\max}$ is sufficient to give a J_E equal to $J_{\mathrm{crit}} - J_{TH}$. Then E will not rise above E^* because the additional current $J_E - J_{E^*}$ quickly reduces E to E^*. The value of E^* can be found for any $L(t)$ by equating $J_E + J_{TH}$ to J_{crit} and solving by an iterative procedure. The growth rate is given then by J_{crit}.

First consider the high field limit utilizing equation (14). Computations were performed for a specific example to illustrate the relations among the several currents and fields, and especially the temperature dependence. Figure 1 shows the variation of J_D, J_E, J_{TH}, and J_{crit} with temperature for two different film thicknesses. At low temperatures, J_{TH} is small, so most of the current to match J_{crit} is due to J_E. As temperature increases, J_{TH} becomes larger: J_E goes through a maximum and then decreases. Note that J_{crit} differs only by factors of 2 to 3 for a change in $L(t)$ from 30 to 55 Å; therefore, because J_E varies exponentially with E^*, E^* may change very slowly with $L(t)$, giving an approximately constant E^* during growth at any given temperature.

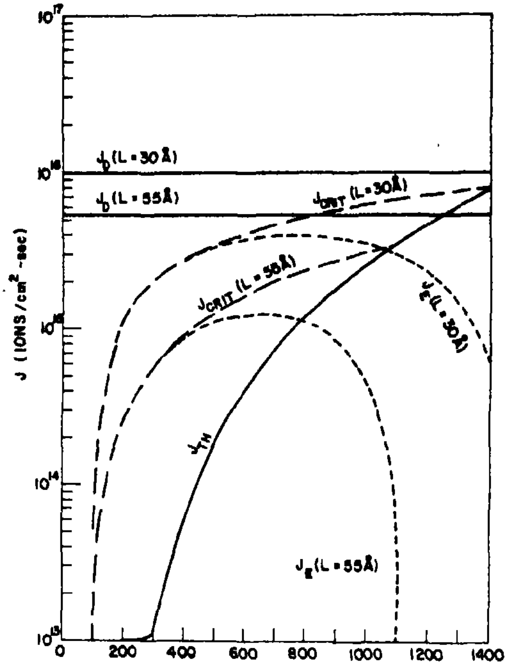

FIG. 1. Combination of thermionic and field emission currents to equal the field-modified diffusion current as a function of temperature for two film thicknesses.

A = $9 \cdot 70 \times 10^9$ electrons/cm^2-sec-°K^2 (Pre-exponential factor in Richardson's equation for thermionic emission.)
ϕ_M = $0 \cdot 112$ eV
B = $6 \cdot 00 \times 10^{16}$ electrons/cm^2-sec
G = $7 \cdot 50 \times 10^6$ V/cm
D = $3 \cdot 00 \times 10^{-9}$ cm^2/sec (Diffusion coefficient)
E_D = $0 \cdot 0$ eV (Activation energy for diffusion)
$C_i(0)$ = $1 \cdot 00 \times 10^{18}$ ions/cm^3
$C_i(L)$ = $1 \cdot 00 \times 10^{15}$ ions/cm^3.

Figure 2 shows the corresponding temperature variation of E^*, $E_{\max}$, L_{crit}, and L_∞ at the point $L = 30$ Å. The quantity L_{crit} is the thickness at which $E_{\max}$ is equal to E^*, and L_∞ is the limiting thickness to be discussed below. Note that E^* varies in the same manner as J_E with temperature, but has a much smaller range. Thus to a good approximation in the high field limit, $L(t)$ can be obtained by integrating equation (1) for constant

E for film thicknesses less than L_{crit}. This gives Nth root and logarithmic-type growth curves. The integrated expressions for $L(t)$ together with a comparison with experimental data will be presented later.

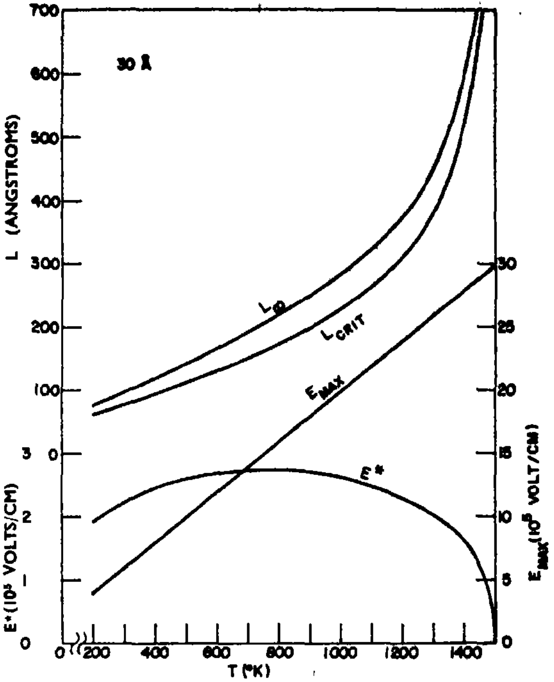

FIG. 2. Variation of the critical field, the maximum field, the critical film thickness, and the maximum film thickness with temperature for a 30 Å film.

Before examining the low field region, a brief examination of the case $L(t) > L_{\text{crit}}$ is appropriate. As soon as $L(t)$ reaches L_{crit}, the field E^* needed for $J_{E^*} = J_{\text{crit}} - J_{TH}$ becomes larger than the maximum field that can be created by the diffusing species. Provided J_{TH} is negligible, the growth between L_{crit} and L_∞ is determined entirely by the tunnel current produced by the field E_{max}. Since E_{max} is a function of $L(t)$, this growth region is outside the limits of validity of the constant field approximation. The film growth expression for this region in the high field limit is obtained by substituting equation (11) for E_{max} into equation (14) and integrating. This gives a logarithmic-type growth similar to that predicted from the first hypothesis of MOTT,[4a, b] except the limiting thickness now depends on temperature. Note from Fig. 2 that L_{crit} and L_∞ approach infinity as E^* approaches zero. This shows that the diffusion controlled parabolic equation is applicable at higher temperatures.

Consider next the low field region utilizing equation (15), in which J_E varies linearly with E and exponentially with $L(t)$. The validity of the constant field approximation for the high field limit discussed above rests primarily on the facts that J_E is independent of $L(t)$ and the decrease in J_{crit} with $L(t)$ can be compensated readily in J_E by a small change in E. Neither of these characteristics is inherent in equation (15); thus the constant field approximation can hold only if J_E and J_{crit} have the same functional dependence on $L(t)$. This is not the case, so the dependence of E^* on $L(t)$ is not simple and can be approximately constant over only a limited region of film thickness. The complicated dependence of E^* on $L(t)$ for this case precludes an integration of equation (1) to obtain a simple expression for $L(t)$.

In some instances tunnelling can occur between traps(5) in the oxide film instead of through the entire film. Such traps(5–7) can be lattice imperfections, positive holes, or ionic space charge. Equation (15) is applicable with $L(t)$ replaced by the average distance s between traps in the oxide. The number of continuous chains of traps N_T through the oxide should vary with temperature as $(N_T)_0 \exp(-E_T/kT)$ but should decrease inversely with $L(t)$. The parameter $(N_T)_0$ is a constant and E_T is the free energy for trap formation. Therefore the tunnel current should be given approximately by the expression,

$$J_E = \{K'E^* (N_T)_0 \exp(-\chi s) \exp(-E_T/kT)\}/L(t), \tag{16}$$

where K' is a constant. To the same degree of approximation, the expression for J_D can be used for J_{crit} and J_{TH} neglected for low temperatures. Equating J_E from equation (16) to J_D, E^* is found to be independent of $L(t)$ and depends exponentially on temperature,

$$E^* \propto \exp[(E_T - E_D)/kT]. \tag{17}$$

The approximations leading to this result are unrefined, but in lieu of a more accurate expression for J_E together with a numerical solution in the region $E_{\max} > E^*$, the assumption of a constant field seems to be the most generally valid approximation. An integration of the expression for film growth given by equation (1) will be presented now for the case of constant field ($E_{\max} > E^*$) and for the case in which the field is $E_{\max}$.

(b) *Integration of equations*

Equation (1) gives the current $(1/R)[\mathrm{d}L(t)/\mathrm{d}t]$ for the opposing homogeneous field $E = E^*$. The parameters D, μ, $C(0,0)$, and $C(L(0),0)$ refer to the diffusing species, i.e., the species which creates the field to induce tunnel or field emission current of the other species. Equation (1) can be integrated easily for both positive and negative concentration gradients by assuming:

(1) E^* is independent of $L(t)$.

(2) The interfacial bulk concentrations are time independent and much larger at one boundary than at the other.

The results can be expressed in the following form,

$$1+\beta t = \exp(\alpha L(t)) - \alpha L(t), \tag{18}$$

where $\alpha = |\mu E^*/D|$ and $L(0)$ is zero. For a positive concentration gradient, $\beta = |\alpha R \mu E^* C(L(0),0)|$; for a negative concentration gradient, $\beta = |\alpha R \mu E^* C(0,0)|$. Expansion of the exponential gives

$$t = \frac{1}{\beta} \sum_{n=2}^{\infty} \frac{[\alpha L(t)]^n}{n\,!}. \tag{19}$$

This implies that for $\alpha L(t)$ much less than 1, corresponding to $E^* \ll (q/kT)[1/L(t)]$, the simple parabolic law

$$L(t)^2 = 2RDCt \tag{20}$$

is valid, but for $\alpha L(t)$ of the order of 1, higher order terms must be considered. Approximate Nth root laws thus are obtained with N varying continuously from 2 to higher values depending on the dominant terms. For $\alpha L(t)$ much greater than 1, equation (18) reduces to the logarithmic law,

$$L(t) = \frac{1}{\alpha} \log(1+\beta t). \tag{21}$$

The above constant field equations with $E = E^*$ describe growth as long as $E_{\max}$ is greater than E^*. On the basis of equation (11), $E_{\max}$ decreases with increasing film thickness. Therefore, $E_{\max}$ will be greater than E^* for small film thicknesses, but at some critical thickness L_{crit}, depending on the temperature and ratio of boundary concentrations, $E_{\max}$ will equal E^*. Solving for this critical thickness and applying the Einstein relation,

$$\begin{aligned} L_{\text{crit}} &= \left| \frac{kT}{q} \frac{1}{E^*} \log \frac{C(L(t),t)}{C(0,t)} \right| \\ &= \frac{1}{\alpha} \left| \log \frac{C(L(t),t)}{C(0,t)} \right|. \end{aligned} \tag{22}$$

The mechanism responsible for the constant field determines the temperature dependence of E^* and hence of L_{crit}. The temperature dependence of L_{crit} in the high field limit is shown for a specific example in Fig. 2.

Note that αL_{crit} is always greater than 1, and can have values as large as 10. Therefore, the parabolic, Nth root, and logarithmic laws given respectively by equations (20), (19), and (21), are predicted for growth of the film from zero thickness to the value L_{crit}. Before L_{crit} is reached, the film passes sequentially through these regions, although the predominant growth on a time scale of hours may occur in a single region. For small E^*, equation (22) predicts a very large L_{crit}, so that growth can be parabolic over a large range of film thicknesses. A transition from the parabolic law of equation (20) to the enhanced parabolic law discussed in Section 2 (no tunnelling or field emission) takes place at some high temperature. Measurement of the temperature dependence of the parabolic rate constants above and below the transition temperature in principle can yield a value for the enhancement factor ξ.

The fact that there is no serious limitation on the magnitude of L_{crit} is important; logarithmic-type or limiting thickness growth for film thicknesses of several hundred angstroms is feasible. On the other hand, L_{crit} may be effectively zero at very low temperatures.

For $E_{\mathrm{max}} \leq E^*$, E is given by E_{max} and growth is limited by tunnel or field emission current in the presence of E_{max}. Integration of equations (14), (15), and (16) with equation (11) applied to the diffusing species for E_{max} gives:

$$L(t) = (\gamma/G)\log(1+GRBt/\gamma), \qquad (23)$$

$$t = [1/(\chi^2\gamma RK)]\,[\chi L(t)\exp\{\chi L(t)\} - \exp\{\chi L(t)\}+1], \qquad (24)$$

$$L(t)^3 = 3RK\gamma N_T t\exp(-\chi s), \qquad (25)$$

where γ defined as $(kT/q)\log[C(L)/C(0)]$ is determined by the diffusing species and $L(t) = L_{\mathrm{crit}}$ has been redefined as zero. Note that equation (23) has the form of the common logarithmic equation in time and equation (25) represents a cubic growth law in time. Equation (24) will be approximated below to give a better indication of the predicted growth law. If J_{TH} is nonzero, it must be added as a constant to the above equations before integration. The resulting equations can be integrated easily but the resulting expressions for $L(t)$ are long. Physically, J_{TH} gives a fixed contribution to the growth rate, so that for zero tunnel current, growth is linear but the rate constant is practically zero.

The limiting thickness nature of equations (23) and (24) becomes more clear by introducing L_∞ and E_∞, which are the quantities $L(t)$ and E in the limit in which growth rate as observed in the laboratory is zero. Then $(1/R)[\mathrm{d}L(t)/\mathrm{d}t]$ is given by $J_{E(\mathrm{max})} - J_{E(\infty)}$. Equation (14) gives

$$\frac{\mathrm{d}L(t)}{\mathrm{d}t} = RB\exp(-G\,L_\infty/\gamma) \times [\exp\{-G(L-L_\infty)/\gamma\}-1]. \qquad (26)$$

Since L_∞ is not much larger than L_{crit}, the exponential can be expanded. Integration, with L_{crit} redefined as zero, then gives

$$L(t) = L_\infty[1-\exp\{-(GRBt/\gamma) \times \exp(-GL_\infty/\gamma)\}]. \qquad (27)$$

Note that this expression has the common form $[1-\mathrm{e}^{-\nu t}]$; this shows that the logarithmic and exponential growth laws are not always distinguishable in the laboratory since equations (23) and (27) represent the same physical situation.

This same approximation can be applied to equation (15) to give a growth law which is easier to interpret than equation (24). The result is,

$$L(t) = L_\infty[1-\{\exp(-L(t)/L_\infty)\}\{\exp(-t/\tau)\}]. \quad (28)$$

where

$$\tau^{-1} = (RK\gamma/L_\infty^2)(1+\chi L_\infty)\exp(-\chi L_\infty). \qquad (29)$$

This is similar to the exponential law given in equation (27) but the rise time is shorter due to the factor in $L(t)$ which is additive to the normalized time.

Equations (23) through (29) are expected to give an increase in $L(t)$ over L_{crit} by only a few monolayers. Since the last stage of growth to L_{crit} is logarithmic, the transition into the final growth phase ($L(t) > L_{\mathrm{crit}}$) should be smooth.

4. DISCUSSION AND APPLICATION TO EXPERIMENTAL DATA FOR COPPER MONOCRYSTALS

(a) *High temperature growth*

Parabolic growth was found to be valid from numerical computations of I for the case in which transport of both species occurs entirely by diffusion. The approximate solutions given in Section 2 of this work confirm this conclusion in the limit of negligible space charge. Curves 1, 2, and 3 in Fig. 2. of I illustrate growth in the small space charge limit for oxidation of copper at 900°C; the numerical values obtained for ξ were

2·40, 3·35, and 3·55 respectively, and the corresponding values for ϕ were 0·222, 0·357, and 0·386 V. The approximate equations of Section 2 for the same values of the diffusion parameters give values for ξ of 2·34, 4·67, and 7·00 respectively, and the corresponding values of ϕ are 0·232, 0·464, and 0·695 V. Note that the numerical and approximate values of ξ and ϕ for curve 1 agree well, but that in proceeding to curves 2 and 3 the numerical values increase more slowly than the approximate values. In all three cases, however, the agreement is within a factor of 2 and the changes in values predicted by the approximate formulae are in the same direction as observed in the numerical solutions. Also the approximate formulae verify the generalizations of I for negligible space charge that:

(1) No changes should occur in ξ and ϕ for changes in the parameters D and C for either species as long as DC and $C(0)/C(L)$ for each species remain fixed,
(2) The values of ξ and ϕ increase with increasing values of DC and ratio of boundary concentrations for the electronic species and decrease for corresponding changes for the ionic species.

There are two reasons for the difference in the approximate and numerical values noted above. First, large current transients were present for the early growth stages in the numerical computations to create the field needed to give equal currents. Second, in the approximate formulae the assumption of equal currents is not completely consistent with the result that surface charge field varies as $1/L(t)$; the assumption of equal currents remains reasonably good, however, because a fraction of a monolayer change in the surface charge results in a relatively large change in the field.

Several derivations of the parabolic law have been given in the literature, but for the most part these derivations reduce to Fick's law for the diffusion of uncharged particles. Mott and Cabrera(4d) derived a parabolic law for thick films based on the assumption of equal electronic and ionic currents but neglected the coupling between the diffusion equations. The results, of course, indicate that rate is determined by diffusion of ions or electrons, whichever may diffuse less rapidly in zero field.

Wagner(8) recognized that transport occurs by charged particles, and in his general equations(9a) used essentially an enhanced mobility $\bar{\mu}$ defined as the reciprocal of $\mu_i^{-1}+\mu_e^{-1}$. For large electronic mobility, $\bar{\mu} \simeq \mu_i$, and the predicted rate is determined essentially by ionic diffusion in zero field. The assumption of charge neutrality implicit in the Wagner equations can be illustrated easily. Assume zero electronic current and solve the diffusion equation for E. Substitution of this value of E into the diffusion equation for the ionic current gives

$$J_i = -D_i\frac{\partial C_i}{\partial x}+\mu_i C_i\frac{D_e}{\mu_e C_e}\frac{\partial C_e}{\partial x}. \tag{30}$$

Assuming electrical neutrality for each point in the film, this equation reduces to the form

$$J_i = -D_i\frac{\partial}{\partial x}(C_i+C_e) = -D_i\frac{\partial C_{\text{atoms}}}{\partial x}. \tag{31}$$

This is Wagner's derivation(8g) under these conditions and is equivalent to Fick's law for the diffusion of uncharged particles. A replacement of concentrations by activities results in no essential change in the form of the equation or the underlying assumptions. The assumption of neutrality implies equal charge concentrations of oppositely charged species in each volume and surface element; the assumption of a homogeneous field implies that the volume charge is very small compared to surface charge, but implies nothing about the surface charge or about the relative bulk concentrations of oppositely charged species. This subtle distinction between charge neutrality for each volume and surface element, and over-all charge neutrality as determined by an integral of the charge density over both the volume and interfaces of the system, is the basis for the enhancement factor ξ obtained in this work. Charge neutrality in bulk oxide is not found experimentally; for example, measurements on Cu_2O show that the number of positive holes may be two or three orders of magnitude fewer than the number of copper ion vacancies.(10a)

Implicit in the work of Bardeen, Brattain and Shockley(11) is an enhancement factor of 2 for parabolic growth. This particular value of ξ can be obtained from equation (30) by applying the Einstein relation and assuming the concentrations of electrons and ions to be linear in position through the oxide. Then the total current J_i is twice the diffusion current in zero field. In general, ξ computed in the present work is different from 2 because of nonzero electronic current and nonlinear distributions of electronic and ionic concentrations in the film caused by the surface charge field.

Conductivity measurements on Cu_2O by WAGNER,(8) and more recently by others,(10) have shown that transport occurs by motion of positive holes and copper ion vacancies, the mobility of the holes being much greater than the mobility of the vacancies over the entire temperature range. For example, μ_{holes} is approximately 6 cm²/V-sec and μ_{vac} approximately 3×10^{-7} cm²/V-sec at 1000°C. Although the concentrations of the two species can differ by 2 or 3 orders of magnitude, D_eC_e is still much larger than D_iC_i for all temperatures in the range for which transport of both species occurs by diffusion. An enhanced parabolic growth therefore is expected. BENARD and TALBOT(12) oxidized single crystals of copper in air at 900°C, and found that the growth was approximately parabolic with different values of the rate constant applicable to different crystal faces. Parabolic curves chosen to fit these data yield values for the rate constant $\xi RD\{C(L)-C(0)\}$ as a function of the Cu face. For the (100) face, the value of $\xi D\Delta C$ is $7{\cdot}5 \times 10^{12}$ vac/cm-sec, considering the oxide to be CuO. Relative to this face, the values for the (123), (111) (211)–(110), and (210)–(221) faces are 0·88, 1·1 1·2, and 1·3 respectively.

Experimental results such as these have shown the rate constant to be anisotropic with crystal face. The present work does not clarify the nature of the anisotropy, because ξ becomes one more unknown factor in the rate constant. The factor ξ does depend on the metal–oxide work function, and it is well-known that the work function is anisotropic. Other sources of anisotropy are the atomic stacking and defect structure of the crystal face, which can affect ΔC, and an anisotropic D for non-cubic oxides, since the oxide film is epitaxially oriented with respect to the crystal face.

(b) *Intermediate and low temperature growth*

Several mechanisms have been proposed to justify or derive various forms of the logarithmic law since this type of growth is so common(13–17) at the lower temperatures of oxidation. Some of these mechanisms are electron tunnelling,(4a, b) nonlinear ion diffusion in a large surface charge field due to electrons,(4c, d) space charge,(7) variation of the boundary values of bulk concentration with film thickness,(18, 19) structure changes during growth,(20a) deactivation of the surface with increasing thickness,(21) and place-exchange.(22) None of these theoretical treatments has been successful in explaining large classes of experimental data, and several can be criticized on quite general grounds.

The electron tunnelling mechanism of MOTT(4a, b) appears to be limited to thicknesses less than about 50 Å and is temperature independent. Both of these are contrary to experimental data.(16, 17) The nonlinear ionic diffusion mechanism of MOTT(4c, d) (frequently referred to as the Mott–Cabrera theory) appears to violate equation (11) of this work for the maximum field which can be created by electronic surface charge, since the field given by equation (11) is too small for nonlinear ionic diffusion. On the basis of I, space charge effects are not expected to be the determining factor for the growth law; aside from this, the space charge model of UHLIG(7) and especially the mathematical treatment are subject to criticism. A large variation of boundary concentration with film thickness(18, 19) is incompatible with the strong driving force for mass transport provided by the large free energy of oxidation. The treatment of GRIMLEY and TRAPNELL(19) for this mechanism is not in agreement with equation (11) of this work for $E_{\max}$ and makes the questionable assumption that the equilibrium Boltzmann distribution is applicable to electrons in the growing oxide film. A change in structure with growth(20a) is quite possible; however, it would appear doubtful that this could affect growth systematically enough for different oxides to be the origin of logarithmic growth in so many metal–oxide systems. The deactivation of the surface with increasing coverage as conceived by LANDSBERG(21) is plausible in the adsorption or nucleation stage, but does not appear to be applicable to more than one monolayer. The place-exchange mechanism of ELEY and WILKINSON(22) would not be applicable to more than about 3 monolayers.

Whatever the merits of the above mechanisms, the constant field approximation for $L(t) < L_{\text{crit}}$ and the field emission and tunnelling mechanism for $L(t) > L_{\text{crit}}$ in this work appear to be simpler and more straightforward. In addition, the formulae are applied to experimental data for copper monocrystals and good agreement is found. A great many careful and well-chosen experiments are needed, however, before any one or several mechanisms can be said definitely to be responsible for logarithmic-type growth.

YOUNG, CATHCART and GWATHMEY[17] studied the oxidation of copper single crystals over the temperature region 70–178°C. Several *N*th root laws were observed as well as logarithmic-type laws. Application of equation (18) for the constant field approximation to these data produced curves in good agreement for most temperatures and crystal faces. Figures 3 through 7 illustrate the agreement between curves drawn to fit the data and curves computed using equation (18). The 70°C curves are shown in Fig. 3, and the agreement between experimental and computed curves is good for the (111) and (110) faces, but only fair for the (100) and (311) faces. At 106°C, Fig. 4 shows excellent agreement between computed and experimental curves for all four crystal faces.

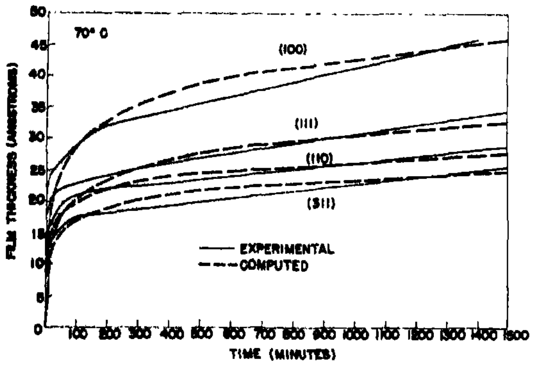

FIG. 3. Comparison of Cu_2O growth computations at 70°C with published experimental data.

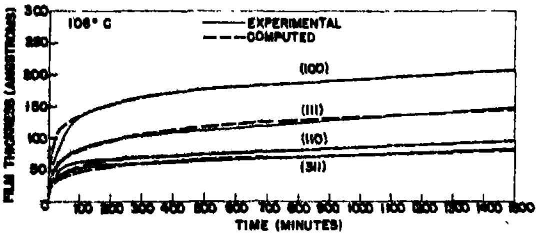

FIG. 4. Comparison of Cu_2O growth computations at 106°C with published experimental data.

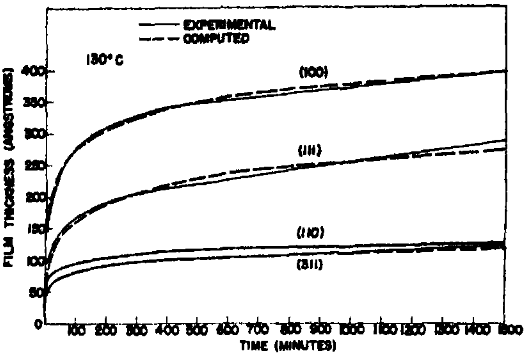

FIG. 5. Comparison of Cu_2O growth computations at 130°C with published experimental data.

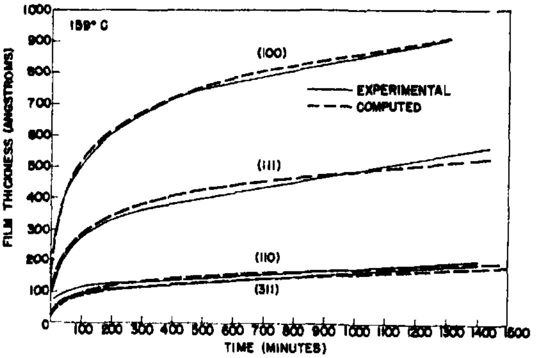

FIG. 6. Comparison of Cu_2O growth computations at 159°C with published experimental data.

Figure 5 for 130°C shows excellent agreement for the (100), (110), and (311) faces, but a small deviation for the (111) face. Note that Fig. 6 for 159°C shows about the same agreement as Fig. 5. At 178°C, Fig. 7 shows excellent agreement between the experimental and computed curves for all four crystal faces. The good agreement between computed and experimental curves would appear to be somewhat fortuitous in view of nucleation phenomena[23] usually associated with very thin films. This may be the reason the fit tends to be better for the thicker films associated with higher temperatures.

The set of values of $DC(L(0),0)$ obtained from this curve fitting procedure is given in Table 1; a decrease in DC with decreasing temperature and anisotropy with crystal face can be noted. The values are in the neighborhood of 10^7 vacancies/

Table 1. Values of DC in Cu_2O obtained by fitting data of Young, Cathcart, and Gwathmey with constant field approximation (units of 10^7 vacancies/cm-sec)

T(°C)	(100)	(111)	(110)	(311)
70	0·317	0·141	0·665	0·252
106	9·50	1·23	0·850	0·426
130	85·5	5·73	39·2	5·20
159	45·2	12·5	0·984	0·933
178	308·0	25·5	16·1	81·7

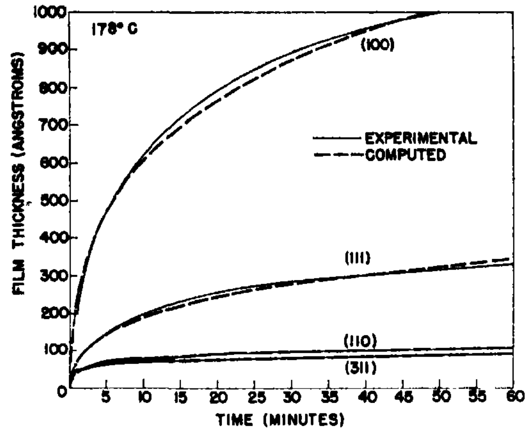

FIG. 7. Comparison of Cu_2O growth computations at 178°C with published experimental data.

cm-sec. The product DC may be expected to vary as

$$DC(L(0),0) = D_0C_0 \exp(-E_D/kT), \quad (32)$$

where E_D is the sum of the activation energy for vacancy diffusion and the free energy of formation of a vacancy at the reaction interface. Figure 8 shows that this relation gives a good fit to the data for the (111) face. The fit is not this good for the (100) face and is poor for the (110) and (311) faces. The values of E_D and D_0C_0 are given as a function of crystal face in Fig. 8. The Cu_2O plane parallel to the Cu face is taken from the structure work of LAWLESS and GWATHMEY.(24) The values of DC increase with crystal face in the order (311), (110), (111), and (100). This is the reverse of the sequence obtained from the data of BENARD and TALBOT(12) for the three faces common to both sets of measurements. Order of magnitude values of $D\Delta C$ extrapolated from the high temperature data of Benard and Talbot to the low temperature region on the basis of an activation energy of 20–40 kcal/mole,(9b, 20b) however, show reasonable agreement with the values given in Table 1. The values of E_D shown in Fig. 8 have an average of 21 kcal/mole, which agrees well with measured values(20b) for these temperatures. The values of E_D were similar for the (100) and (111) faces and

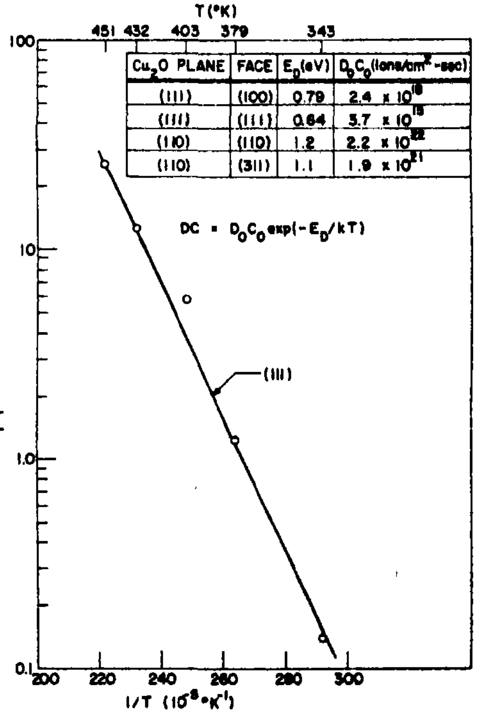

FIG. 8. Values of E_D and D_0C_0 for Cu_2O direction normal to the given Cu faces.

Table 2. Homogeneous field in Cu_2O obtained by fitting data of Young, Cathcart, and Gwathmey with constant field approximation (units of 10^4 V/cm)

T(°C)	(100)	(111)	(110)	(311)
70	47·5	64·7	103·0	103·0
106	12·4	13·4	23·8	24·9
130	7·84	7·94	28·6	24·6
159	2·32	3·94	9·05	10·4
178	1·16	3·11	21·8	40·0

for the (110) and (311) faces. This is interesting since these pairs of Cu faces have identical parallel Cu_2O planes, as noted in Fig. 8.

The corresponding values of E^* are given in Table 2; in general the value is about 10^5 V/cm, decreases with increasing temperature, and decreases with crystal face in the order (311), (110), (111), and (100). The values of E^* are less than the corresponding values of E_{max} in all cases, provided a ratio of $C(L)/C(0)$ of the order of 1000 is chosen. The relatively thick films together with the marked temperature dependence of E^* for these data indicate that the trap mechanism is probably applicable. Figure 9 shows the application of equation (17) to E^* for the (111) and (100) crystal faces. The fit for these two faces is much better than for the (110) and (311) faces. The agreement is particularly good for the (100) face. The single point in Fig. 9 for 323°K is taken from the data of RHODIN.$^{(16)}$ The values of $E_T - E_D$ are given for all faces in Fig. 9, and the average value is 0·35 eV. This signifies that the free energy for trap formation is of the order of 1·3 eV, since the average value for E_D is 0·93 eV.

RHODIN$^{(16)}$ observed logarithmic-type oxide growth on copper crystals between 78 and 298°K, with a transition to a cubic law at 323°K. Equation (18) for the constant field approximation gives an excellent fit to the 323°K curve for the (100) face; this is shown in the upper curve of Fig. 10. The value of $DC(L(0),0)$ is $33{\cdot}8 \times 10^7$ vacancies/cm-sec and the value of E^* is $1{\cdot}11 \times 10^6$ V/cm. Of course the cubic growth law given by equation (25) for $E = E_{max}$ with tunnelling between traps also could be applicable. Therefore it appears that tunnelling between traps occurs for temperatures of 323°K and above, but at 323°K it is uncertain whether $E = E^*$ or $E = E_{max}$. It is significant that the rate laws for $E = E^*$ and $E = E_{max}$ have a smooth transition.

The lower temperature data of RHODIN$^{(16)}$ cannot be fit with either the constant field approximation or a cubic law. Equation (28) for linear tunnelling through the film with $E = E_{max}$ does fit the lower temperature data quite well. Figure 10 shows the agreement for the (100) face for temperatures of 78, 195, 273 and 298°K. The corresponding

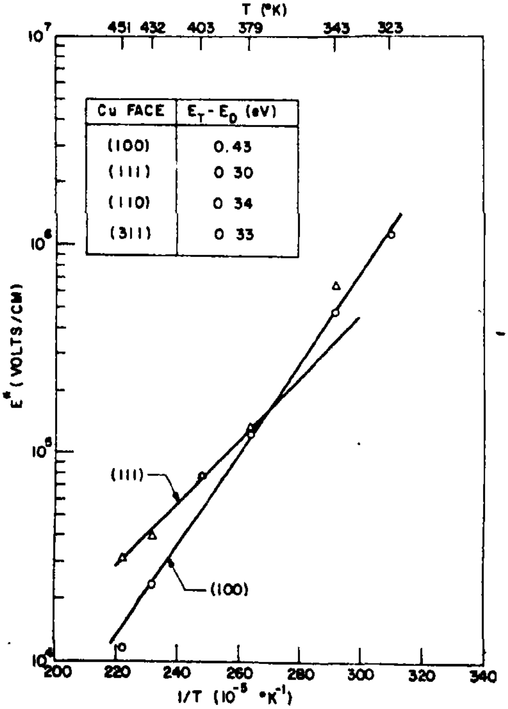

FIG. 9. Values of E_T-E_D for Cu_2O for the direction normal to the given Cu faces.

values of L_∞ are 4, 7, 11, and 15A, and the corresponding values of τ as defined in equation (29) are 13·0, 10·4, 13·0, and 7·82 min. These values may not be unique, however, because there are only a few data points for $L(t) < L_\infty/2$ and L_{crit} is considered to be zero. Tunnelling through the oxide film with a linear dependence on field seems most appropriate for these data because the range of film thicknesses (4–15 Å) is right for tunnelling, the temperature is low so that a small trap density is expected, ϕ_M is probably too large for a Fowler–Nordheim field dependence, and the maximum field at these low temperatures is probably less than E^* for most of the growth. This seems to be the type of logarithmic growth due to tunnelling envisaged by MOTT[4a, b] in his first hypothesis. The real difference between equation (28) and the work of MOTT[4a, b] is that for this case the tunnelling process is considered to be aided by a field; the aiding field is created by a second diffusing species, and therefore is temperature dependent. This causes the limiting film thickness to be temperature dependent.

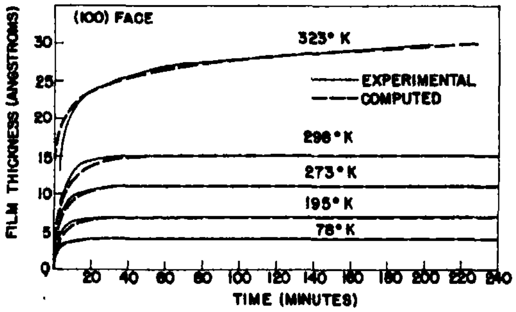

FIG. 10. Comparison of low temperature Cu_2O growth computations with published experimental data.

The same values of DC and E^* were used in the numerical computations for Fig. 4 of I as are used for the corresponding curves shown in Figs 5 and 10 obtained using the approximate equations. From this comparison, it can be seen that the exact equations and the approximate equations yield identical results in the small space charge limit.

In summary, this analysis of logarithmic-type growth, based on diffusion of one species with tunnelling or field emission of the second species in the field created by the diffusing species, is successful in fitting intermediate and low temperature experimental data for the oxidation of copper crystals. The tunnel current appears to vary linearly with field for both intermediate and low temperatures, which indicates a ϕ_M greater than kT. The tunnelling occurs from the metal crystal to the opposite surface of the oxide with $E = E_{\max}$ for temperatures below 323°K ($4\text{ Å} \leq L(t) \leq 15\text{ Å}$), and from the metal crystal to adjacent traps in the oxide and between traps with $E = E^*$ for temperatures between 343 and 451°K ($30\text{ Å} \leq L(t) \leq 1000\text{ Å}$).

5. CONCLUSIONS

(1). Coupled diffusion equations describing oxide film growth can be integrated for small space charge to yield simple relations between $L(t)$ and t for the following three limiting cases: (a) equal ionic and electronic diffusion currents with a thickness dependent surface charge, (b) constant surface charge because of tunnelling or field emission of one species, with rate controlled by diffusion of the second species in this field, and (c) rate controlled by tunnelling or field emission processes induced by a thickness-dependent field created by the diffusing species.

(2) In the high temperature limit, (1a) is applicable and the rate limiting step is interpreted to be transport of the low mobility species in the presence of the electric field created by the high mobility species. This field adjusts itself to such a value that diffusion of the low mobility species is aided and diffusion of the high mobility species is opposed in the right amount to yield equal charge currents of the two species. The field varies as $1/L(t)$ (i.e., ϕ is constant), and the resulting growth is parabolic with a modified rate constant. Both k' and ϕ increase in magnitude with increasing $D\Delta C$ and ratio of boundary concentrations for the electronic species, and decrease for corresponding changes for the ionic species.

(3) In the intermediate temperature limit, (1b) is applicable. For small ϕ_M ($\phi_M \leqslant 0{\cdot}01$ eV), Fowler–Nordheim behavior of the emission or tunnel current with field can account for a field which does not depend significantly on $L(t)$. For large ϕ_M ($\phi_M > 0{\cdot}01$ eV), a linear dependence of tunnel current on field combined with the assumption that tunnelling occurs between potential wells (traps) in the oxide accounts for a field which does

not vary greatly with $L(t)$. The following equation thus is derived for the relationship between $L(t)$ and t: $1+\beta t = \exp(\alpha L(t))-\alpha L(t)$, where $\alpha = |\mu E^*/D|$ and $\beta = |\alpha R\mu E^* C|$. Expansion of the exponential yields the simple parabolic law for small $\alpha L(t)$, Nth root laws for intermediate values of $\alpha L(t)$, and a logarithmic law for large values of $\alpha L(t)$.

(4) In the low temperature limit (as well as in the final growth stage of the intermediate temperature limit), (1c) is applicable. The field varies as $1/L(t)$ and represents the maximum field which can be created by the diffusing species. Integration then yields a logarithmic law $[L(t) \propto \log(1+t/t_0)]$ for Fowler–Nordheim behavior, a modified exponential relationship between $L(t)$ and t for linear tunnelling through the film, and a cubic law $[L(t) \propto t^{1/3}]$ for linear tunnelling between potential wells (traps) in the oxide. The introduction of L_∞ in the first two of these equations reduces them to the following forms: an exponential growth law $[L(t) \propto 1-e^{-\nu t}]$ for Fowler–Nordheim behavior, and a modified exponential law $[L(t) \propto 1-\exp\{-(L(t)/L_\infty)-t/\tau\}$ with short rise time for linear tunnelling through the film.

(5) The above equations provide a good fit to experimental data for copper monocrystals at high, intermediate, and low temperatures. The appropriate mechanisms are diffusion of both species yielding enhanced parabolic growth at 1173°K ($L(t) > 1000$ Å), linear tunnelling to traps in the film with constant field from 451 to 323°K ($1000\text{ Å} \geq L(t) \geq 30$ Å), and linear tunnelling through the film with a thickness dependent field from 298 to 78°K ($15\text{ Å} \geq L(t) \geq 4$ Å).

Acknowledgements—It is a pleasure for the author to acknowledge the aid and advice of ALBERT NARATH. In addition, the author wishes to express his appreciation to Professor HENRI S. SACK for stimulating discussions of the work.

REFERENCES

1. FROMHOLD A. T., Jr., *J. Phys. Chem. Solids* **24**, 1081 (1963).
2. FISHER J. C. and GIAEVER I., *J. appl. Phys.* **32**, 172 (1961).
3. STRATTON R., *J. Phys. Chem. Solids* **23**, 1177 (1962).
4. MOTT N. F., *Trans. Faraday Soc.* (a) **35**, 1175 (1939); (b) **39**, 481 (1939); (c) **43**, 431 (1947); (d) CABRERA N. and MOTT N. F., *Rep. Progr. Phys.* **12**, 170 (1948–49).
5. PENLEY J. C., *Phys. Rev.* **128**, 596 (1962).
6. GEPPERT D. V., *J. appl. Phys.* **33**, 2993 (1962).
7. UHLIG H. H., *Acta Met.* **4**, 541 (1956).
8. WAGNER C., *Z. phys. Chem.* (a) **B21**, 25 (1933); (b) **B32**, 447 (1936); (c) **B11**, 163 (1930); (d) **B22**, 181, 212 (1933); (e) **B40**, 197, 455 (1938); (f) **B37**, 148, 155 (1937); (g) *Diffusion and High Temperature Oxidation of Metals, Atom Movements.* p. 158. American Society for Metals, Cleveland (1951).
9. GRIMLEY T. B., *Oxidation of Metals, Chemistry of the Solid State.* 2nd ed. Chap. 14: (a) p. 343; (b) pp. 351, 352; (c) p. 350; (d) p. 336.
10. (a) TOTH R. S., KILKSON R. and TRIVICH D., *Phys. Rev.* **122**, 487 (1961); (b) O'KEEFE M. and MOORE W. J., *J. chem. Phys.* **35**, 1324 (1961).
11. BARDEEN J., BRATTAIN W. H. and SHOCKLEY W., *J. chem. Phys.* **14**, 717 (1946).
12. BENARD J. and TALBOT J., *C.R. Acad. Sci. Paris* **225**, 411 (1948).
13. CATHCART J. V., HALL L. L. and SMITH G. P., *Acta Met.* **5**, 245 (1957).
14. VERMILYEA D. A., *Acta Met.* **6**, 166 (1958).
15. UHLIG H., PICKETT J. and MACNAIRN J., *Acta Met.* **7**, 111 (1959).
16. RHODIN T. N., *J. Amer. chem. Soc.* (a) **72**, 5101 (1950); (b) **73**, 3143 (1951).
17. YOUNG F. W., CATHCART J. V. and GWATHMEY A. T., *Acta Met.* **4**, 145 (1956).
18. (a) HAMILTON O. H. and MILEY H. A., *Trans. electrochem. Soc.* **81**, 416 (1942); (b) MILEY H. A., *ibid.* **81**, 392, 396–398 (1942).
19. GRIMLEY T. B. and TRAPNELL B. M. W., *Proc. Roy. Soc.* **A234**, 405 (1956).
20. KUBASCHEWSKI O. and HOPKINS B. E., *Oxidation of Metals and Alloys.* (a) p. 66; (b) p. 46. Butterworths, London (1953).
21. LANDSBERG P. T., *J. chem. Phys.* **23**, 1079 (1955).
22. ELEY D. D. and WILKINSON P. R., *Proc. Roy. Soc.* **A254**, 340 (1960).
23. HARRIS W. W., BALL F. L. and GWATHMEY A. T., *Acta Met.* **5**, 574 (1957).
24. LAWLESS K. R. and GWATHMEY A. T., *Acta Met.* **4**, 162 (1956).

APPENDIX 1

Alternate expressions for E

(a) *Diffusion of cation vacancies and positive holes in positive field.* Equation (6) is applicable with Z_e replaced by $-Z_e$ and with the concentrations at the oxide–metal interface interchanged with the corresponding concentrations at the oxide–oxygen interface. Physically this gives no additional information. It accounts for the fact that a positive hole (cation vacancy) is of opposite charge from an electron (cation), and that diffusion is in opposite directions requiring concentration gradients of opposite sign. The fact that the field is positive for this case implies that $|\mu_e C_e(L(0),0)|$ is much larger than the corresponding quantity for cation vacancies. For both this situation and that of equation (6), the growth rate is enhanced compared to the rate for diffusion of uncharged particles.

(b) *Diffusion of cations and electrons in negative field.* Equation (6) is applicable with all electronic parameters replaced by ionic parameters and vice versa. The fact that the field is negative for this case implies that $|\mu_i C_i(0,0)|$ is greater than the corresponding product for electrons. The growth rate determined by ionic flow is less than for simple diffusion since the ions must flow against this opposing field.

(c) *Diffusion of cation vacancies and positive holes in negative field.* Equation (6) is applicable with Z_e replaced by $-Z_i$, μ_e replaced by μ_i and vice versa, $C_e(0,0)$ replaced by $C_i(L(0),0)$, $C_e(L(0),0)$ replaced by $C_i(0,0)$, and $C_i(0,0)$ replaced by $C_e(L(0),0)$. Again no additional information is obtained. The product $|\mu_i C_i(L(0),0)|$ is larger than the corresponding product for holes to give a negative field, and diffusion is from the oxide–oxygen interface to the metal–oxide interface. Vacancy diffusion again is retarded by the field.

(d) *Diffusion of anions or anion vacancies.* The above formulae are applicable. Diffusion of anions plus positive holes in positive (negative) field is formally equivalent to diffusion of cation vacancies plus positive holes in positive (negative) field. Diffusion of anion vacancies plus electrons in positive (negative) field is formally equivalent to diffusion of cations plus electrons in positive (negative) field.

J. Phys. Chem. Solids Pergamon Press 1963. Vol. 24 pp. 1325–1331. Printed in Great Britain.

THE INFLUENCE OF MANGANESE ON THE ELECTRICAL CONDUCTIVITY OF NICKEL FERRITE

D. ELWELL, R. PARKER and A. SHARKEY

Department of Physics, Portsmouth College of Technology

(*Received* 5 *April* 1963; *revised* 27 *May* 1963)

Abstract—Electrical resistivity measurements are reported for nickel ferrites with a Ni:Fe ratio ranging from 1:2 to 1:1·88 and with manganese content of up to 2%. Specimens were prepared at sintering temperatures between 1100 and 1250°C under oxygen pressures ranging from 3 to 456 cm of mercury. It is concluded that the large increase in resistivity resulting from the manganese impurity which was first reported by VAN UITERT(1) arises from the contribution of the impurity energy levels which lie approximately half way between those of Ni^{2+} and Fe^{2+}. The solubility limit for excess nickel in the ferrite lattice reported by PARKER and SMITH(2) is strikingly confirmed by the present results.

1. INTRODUCTION

NICKEL ferrite is a semiconducting substance which has a temperature dependence of resistivity described by the usual equations $\rho = \rho_\infty \exp(\epsilon/KT)$. Values of ρ_∞ and ϵ are very sensitive to the mode of preparation and according to the literature range generally between 10^{-3} and $10^{-1}\Omega$ cm and 0·15 and 0·45 eV, respectively. The reasons for this wide variation are fairly well established. Nickel ferrite is prepared by sintering the constituent oxides, carbonates or other volatile salts at an elevated temperature, usually above 1075°C. During the sintering process a certain amount of oxygen is lost from the material; except in samples which have deliberately been compacted loosely (PALADINO(3)) the oxygen loss can only be partially restored during the cooling cycle. In specimens produced by conventional techniques this irreversible loss of oxygen depends very critically upon the maximum temperature reached and the oxygen pressure applied during the firing process and upon the rate of cooling from the maximum temperature down to about 1000°C. If the fractional oxygen loss is denoted as δ, then 2δ Fe^{2+} ions per molecule are formed to preserve electrical neutrality, and the resulting ferrite may be described by the ionic formula $Ni_1^{2+}\ Fe_{2-2\delta}^{3+}\ Fe_{2\delta}^{2+}\ O_{4-\delta}^{2-}$. If δ is appreciable the conduction mechanism is determined by the activation energy of transfer of an electron from Fe^{2+} to Fe^{3+} ions in the crystal lattice (JONKER(4)) and this is approximately 0·18 eV. It is found that ferrites, in which a small stoichiometric excess of iron has replaced nickel in the spinel lattice, or which have been rapidly cooled from above 1250°C, have values of ϵ close to 0·18 eV and they exhibit marked *n*-type conductivity. LORD and PARKER(5) (to be referred to as I) have attempted to suppress the oxygen loss by sintering under oxygen pressures of up to 456 cm of mercury, but this pressure proved inadequate even at the lowest sintering temperature at which the ferrite forms completely. They were however able to demonstrate that the electron transfer $Fe^{2+} + Fe^{3+} \rightarrow Fe^{3+} + Fe^{2+}$ need not dominate the conduction process in nickel excess ferrites; curves were obtained of ϵ vs. oxygen pressure which contained a pronounced maximum, on the high pressure side of which the conductivity became *p*-type, corresponding to the transport of Ni^{3+} holes.

At about the same time it was established (PARKER and SMITH,(2) subsequently referred to as II) that the activation energy maximum in nickel excess ferrites could be greatly enhanced by quenching specimens from a temperature where the oxygen deficiency just converted all excess nickel ions to a valency two. In this way activation energies of nearly 0·7 eV could be obtained and it was concluded that in these materials the condition of intrinsic conduction was closely approached, i.e. where the current is carried by the activation of electrons from $Ni^{2+}+Fe^{3+}$ to $Ni^{3+}+Fe^{2+}$. Parker and Smith further concluded from the result of electrical measurements that excess nickel can dissolve in the nickel ferrite lattice up to a limit corresponding to a Ni:Fe ratio of $1·029 \pm 0·001:2$ and that the oxygen loss at about 1220°C corresponds to a value of δ of approximately 0·015.

VAN UITERT(1) has demonstrated that the addition of a small quantity of manganese or cobalt to otherwise stoichiometric or iron deficient nickel ferrite causes a large increase in the resistivity and this was subsequently confirmed by PARKER and LORD(6) who showed that this rise is due to an elevation of ϵ; under favourable conditions ϵ could be raised to nearly 0·7 eV, a value very close to the highest obtained in undoped nickel ferrite by the sintering technique described in II. Van Uitert suggested that the role of manganese in enhancing the resistivity of nickel ferrites arises from its ability to exist readily in at least two valence states in the solid state. The manganese was thus supposed to act as a buffer which suppresses the tendency of the ferrite to form both Ni^{3+} and Fe^{2+} ions. The present investigation was undertaken to test the validity of this suggestion. It is hoped to show in Section 3 that the results obtained are not only in full accord with van Uitert's qualitative hypothesis but that by combining the latter with the conclusions of I and II certain detailed features of the present results can be satisfactorily explained.

2. EXPERIMENTAL DETAILS

A range of nickel manganese ferrites was prepared with a cation composition as set out in Table 1, from spectroscopically pure NiO, Fe_2O_3 and MnO_2 with a total impurity content of less than 1 part in 10^5. From each composition specimens were prepared at sintering temperatures ranging from 1100 to 1250°C in 50°C intervals and at oxygen pressures of 3–456 cm of mercury. In order to preserve standard conditions the method of preparation of all specimens was identical to that described in I.

After surface grinding, the resistivity of each specimen was determined at various temperatures from 20 to 400°C and ϵ and ρ_∞ were evaluated from a plot of log ρ against the reciprocal of the absolute temperature. These results are summarized in Table 2; although no further considerations are based on the parameter ρ_∞ it has been included in the table to allow the evaluation of the actual resistivity in each case. The resistivity measurements could be made at various frequencies up to 5 Mc/s and in only a few specimens was appreciable dispersion observed as described by KOOPS.(7) In no case did this affect the accuracy of determining the value of ϵ by more than 0·02 eV. A possible error of similar magnitude arises from the variation in results obtained for specimens sintered apparently under identical conditions on different occasions. It will be noted that a maximum error in individual points of about 0·04 eV does not affect the general trend of the graphs in Figs 1–10.

Table 1. *Ferrite composition* $Ni_1Fe_xMn_yO_{2\delta}$

Code	*A*	*B*	*C*	*D*	*E*	*F*	*G*
X	1·98	1·96	1·94	1·92	1·88	1·99	1·93
Y	0·02	0·02	0·02	0·02	0·02	0·01	0·01

The thermo-electric power of the specimens was measured with nickel contacts at several temperatures. It was generally found that the power is negative, corresponding to *n*-type conduction (JONKER(4)) in the range in which the activation energy increases with oxygen pressure. It is *p*-type corresponding to hole conduction on the high oxygen pressure side of the activation energy maximum. The actual values of thermo-electric powers observed were reproducible to the order of magnitude only and did not follow any recognizable trend. This is probably due to imperfect thermal contact at the metal–ferrite interface with the apparatus available. It is now thought likely that similar results quoted by PARKER and LORD(6) may be in error even regarding the sign on account of possible oxide layer

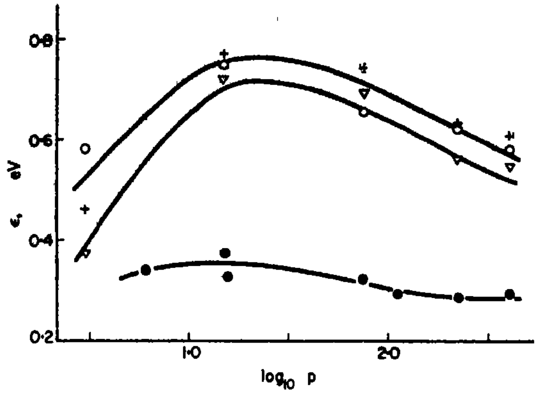

FIG. 1. Activation energy ε against logarithm of the oxygen-pressure (cm of mercury) during the sintering process. Sintering temperature 1100°C.

+ composition *D*
○ composition *E*
▽ composition *G*
● composition *H* corresponding to $NiO(Fe_2O_3)_{0\cdot95}$ (from I).

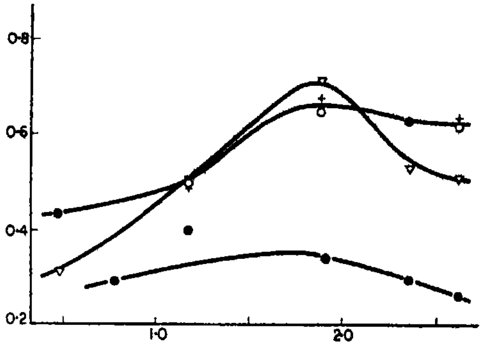

FIG. 2. Similar to Fig. 1 at 1150°C.

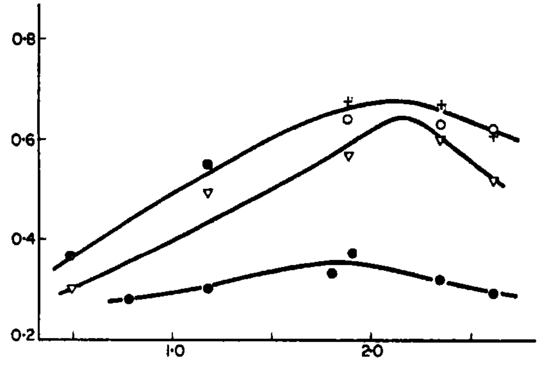

FIG. 3. Similar to Fig. 1 at 1200°C.

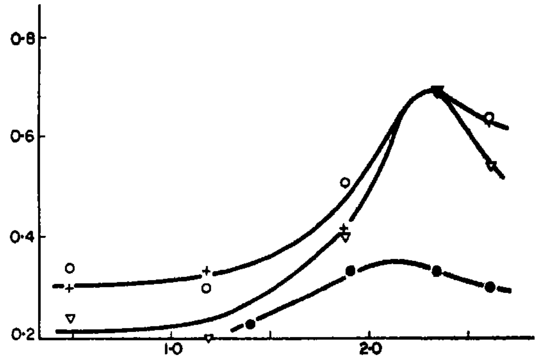

FIG. 4. Similar to Fig. 1 at 1250°C.

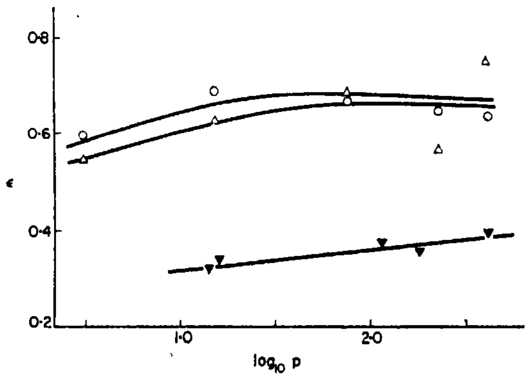

FIG. 5. Activation energy ε against oxygen pressure at 1100°C

○ composition *A*
△ composition *F*
● $NiFe_2O_4$ (according to I).

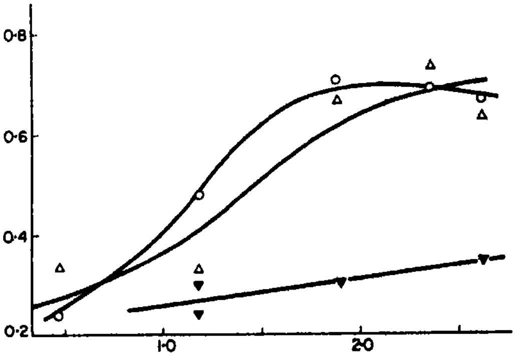

FIG. 6. Similar to Fig. 5 at 1150°C.

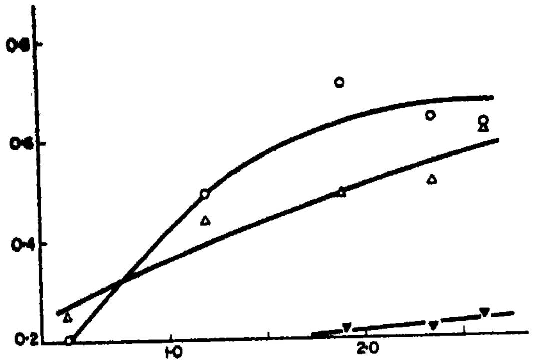

FIG. 7. Similar to Fig. 5 at 1200°C.

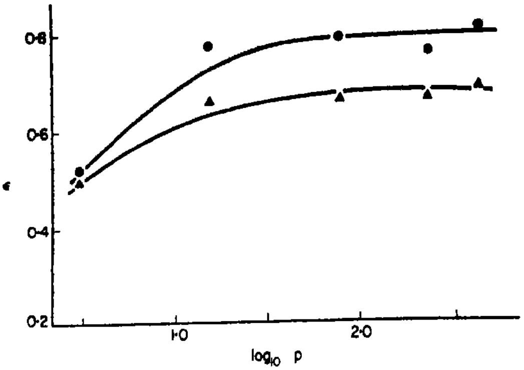

FIG. 8. Activation energy ε against oxygen pressure at 1100°C.
● composition *B*
▲ composition *C*

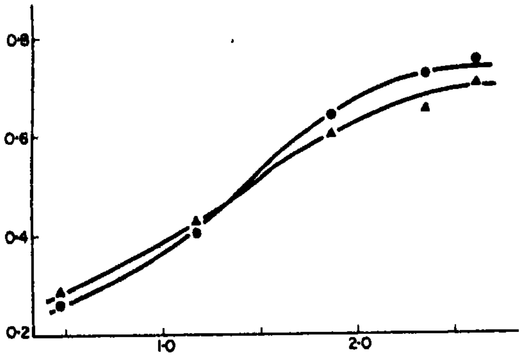

FIG. 9. Similar to Fig. 8 at 1150°C.

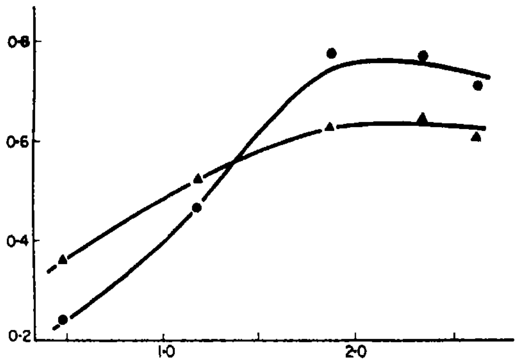

FIG. 10. Similar to Fig. 8 at 1200°C.

formation on the copper surfaces used in their experiments.

It is only possible to conclude from the present thermo-electric measurements that the electric current is carried predominantly by electrons below, and by positive holes above, the activation energy maximum in a material of given cation composition.

A number of X-ray powder diffraction photographs were taken and only the lines characteristic of the spinel structure could be detected. This is not an unexpected result since only NiO is likely to be present in reasonable abundance. All the prominent diffraction lines of cubic NiO coincide exactly with those of nickel ferrite. The spinel lattice parameter of a representative number of materials with and without manganese was determined with a back reflection camera and the results are summarized in Table 2. The accuracy of the measurements is approximately ±0·001 Å and within this limit the results are in good agreement with those of PALADINO(3) and other workers. The lattice parameter is not significantly dependent upon manganese impurity or nickel excess but it would appear to increase slightly with oxygen deficiency of the ferrites. This trend is only just outside the limits of the experimental error.

Saturation magnetization measurements were carried out on several otherwise identical nickel ferrites with and without 2% manganese content. The results are of considerable complexity and detailed discussion would not be appropriate

Table 2. Activation energy ϵ (eV) *and* $\rho\infty$ (x$10^3\Omega$-cm).

Firing temp. (°C)	Firing press. (cm of mercury)	Composition Code													
		A		*B*		*C*		*D*		*E*		*F*		*G*	
		ϵ	ρ_∞	ϵ	ρ_∞	ϵ	ρ_∞	ϵ	ρ_∞	ϵ	ρ_∞	ϵ	ρ_∞	ϵ	ρ_∞
1100	3	0·60	3·9	0·52	8·7	0·50	14	0·46	14	0·59	2·3	0·55	3·4	0·37	1·0
1150	3	0·24	46	0·26	26	0·29	8·0	0·43	16	0·44	17	0·34	3·2	0·31	1·0
1200	3	0·20	28	0·24	28	0·36	51	0·37	14	0·37	5·8	0·25	2·8	0·30	14
1250	3	—	—	—	—	—	—	0·30	32	0·34	1·0	0·20	2·1	0·24	1·7
1100	15	0·69	2·3	0·77	1·2	0·67	2·5	0·77	1·1	0·74	1·1	0·63	2·6	0·72	1·4
1150	15	0·48	4·3	0·40	1·4	0·43	7·1	0·49	2·2	0·50	1·5	0·34	14	0·50	35
1200	15	0·49	6·3	0·46	6·5	0·52	7·8	0·55	2·8	0·56	1·3	0·44	2·9	0·49	1·8
1250	15	0·49	0·60	0·31	11	0·25	22	0·33	8·1	0·30	21	0·32	6·9	0·20	40
1100	76	0·67	4·8	0·78	1·8	0·66	1·1	0·74	1·1	0·66	2·2	0·69	9·1	0·69	1·1
1150	76	0·71	27	0·64	0·34	0·61	9·1	0·68	1·9	0·65	1·3	0·67	4·7	0·71	0·28
1200	76	0·71	5·9	0·77	0·13	0·62	2·4	0·68	2·3	0·64	2·9	0·49	13	0·57	1·5
1250	76	0·48	2·7	0·73	0·58	0·66	0·14	0·41	15	0·51	5·1	0·29	2·0	0·40	35
1100	228	0·65	1·5	0·75	4·5	0·66	0·89	0·63	0·81	0·62	0·93	0·57	5·4	0·56	1·4
1150	228	0·70	5·9	0·72	8·5	0·65	8·7	0·63	0·05	0·65	0·36	0·74	0·17	0·53	0·16
1200	228	0·64	12	0·76	2·4	0·64	1·3	0·67	1·3	0·63	3·0	0·51	45	0·60	1·9
1250	228	0·50	5·2	0·72	1·0	0·65	1·4	0·69	1·3	0·68	1·7	0·55	5·5	0·68	1·5
1100	456	0·64	1·1	0·80	13	0·68	2·6	0·61	1·6	0·58	0·15	0·76	0·11	0·55	0·17
1150	456	0·67	1·9	0·75	5·1	0·70	0·40	0·64	0·17	0·61	0·85	0·64	6·3	0·51	2·1
1200	456	0·63	5·4	0·70	4·3	0·60	1·9	0·61	12	0·62	0·58	0·62	3·8	0·52	1·8
1250	456	—	—	—	—	—	—	0·63	1·3	0·64	0·76	0·59	1·3	0·54	2·0

in the present context. They are however consistent with a model of mainly Mn^{3+} ions situated on the octahedral sites of the spinel lattice and aligned parallel with the *B*-site sub-lattice magnetization.

Table 3

Material	Sintering temp (°C)	Oxygen pressure (cm Mercury)	Lattice parameter (Å)
$NiFe_2O_4$	1100	1	8·339
$NiFe_2O_4$	1100	456	8·339
$NiFe_2O_4$	1220	1	8·342
$NiO(Fe_2O_3)_{0·95}$	1100	1	8·341
$NiO(Fe_2O_3)_{0·95}$	1100	456	8·339
$NiO(Fe_2O_3)_{0·95}$	1175	15	8·340
$NiO(Fe_2O_3)_{0·95}$	1220	1	8·342
A	1100	456	8·343
A	1200	456	8·337
A	1250	15	8·342
E	1100	456	8·339
E	1250	3	8·344
E	1250	456	8·338

3. DISCUSSION

The results in Figs 1–4 are all for materials with nickel excess at or beyond the value of the solubility limit reported in II, even if it is assumed that manganese has replaced iron on the ferrite lattice. The activation energy curves for compositions *E* and *D* containing 2% Mn are identical within the limits of experimental error at all four sintering temperatures. Materials *G* and *H* differ from *E* only by the fact that they contain 1% and no manganese, respectively. It will be noted that the activation energy maximum shifts gradually towards higher oxygen pressures as the sintering temperature is increased, but does not depend upon the concentration of the manganese impurity. The latter appears to affect only the width of the peak. In the case of the manganese-free nickel excess ferrite the maximum value of $\epsilon \simeq 0{\cdot}7$ eV has not been obtained, presumably because the latter extends over too narrow a pressure range to be achieved by this mode of specimen preparation. As was shown in II activation energies closely approaching this value could be obtained by very careful control of sintering conditions at one atmosphere only. The manganese impurity thus broadens the transition region from *n*- to *p*-type conduction as a function of oxygen deficiency by an amount which increases with manganese concentration.

Somewhat similar considerations may now be applied to the results of materials which are less iron deficient. It has already been shown in I that in stoichiometric nickel ferrite the activation energy increases steadily with oxygen pressure; this presumably reflects the fact that the sintering pressures which have been attained so far are insufficient to prevent an irreversible loss of oxygen in the nickel ferrites formed. Figures 5, 6 and 7 illustrate these results and show similar curves for $NiFe_{2-x}Mn_xO_4$ with $x = 0{\cdot}01$ and $0{\cdot}02$. A description of the curves is similar to those of nickel excess ferrites with the only difference that the activation energy maximum would correspond to somewhat higher sintering pressures than have proved to be technically possible so far even at the lowest sintering temperature of 1100°C.

Figures 8, 9 and 10 show similar curves for ferrites with a nickel excess below the solubility limit. It would be expected that these results should be intermediate between those for stoichiometric ferrites and those with greater nickel excess. In fact the activation energy maxima appear to occur at the highest sintering pressure; a more detailed quantitative description can hardly be justified in view of the fact these materials exhibited the largest uncertainties with regard to dispersion and reproducibility, mentioned in the previous Section.

The contribution of manganese to the electrical properties of nickel ferrite can be conveniently described in terms of an energy level scheme proposed by JONKER[(4)] for cobalt ferrite. Following Jonker, we suggest that the electronic energy levels of nickel ferrite are represented by Fig. 11. q_1 denotes the activation energy necessary for an extra electron to move along a line of Fe^{3+} ions; q_2 is the corresponding energy for a positive hole along the divalent nickel ions. In a perfect nickel ferrite crystal the Fermi level would lie half way in the gap and the activation energy of transport would be $\Delta+q_1$ for electrons and $\Delta+q_2$ for holes. In a slightly oxygen deficient, but otherwise perfect nickel ferrite, the electrons released from the anion vacancies would fill some Fe^{2+} levels and the Fermi level would rise near to the Fe^{2+} level. The resistivity activation energy would then be approximately q_1. If, on the other hand, excess-nickel atoms are dissolved in the ferrite lattice with a concentration in excess of half the number of oxygen atoms lost, the Fermi level would fall close to the Ni^{2+} levels and hole conduction with an activation energy q_2 would take place. The variation of oxygen pressure in the sintering process may thus be regarded as a convenient device for moving the Fermi level across the forbidden energy gap. Although this movement will in practice be rather gradual on account of the inevitable imperfections and impurities in the crystal lattice it is sufficiently rapid that neither Jonker nor ourselves have been able to produce pure cobalt or nickel ferrite specimens for which the Fermi level may be regarded to lie half way in the gap.

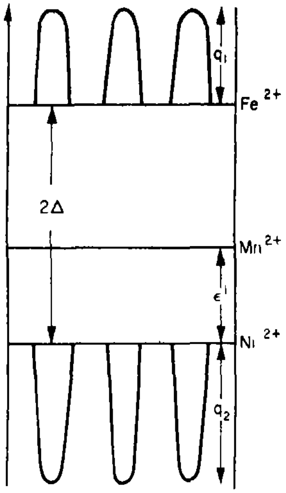

FIG. 11. Proposed energy level diagram following the notation of JONKER.[(4)]

We suggest that the introduction of a small manganese concentration introduces additional Mn levels into the energy gap. In the interest of simplicity and in accord with magnetic measurements the filled level is denoted as $Mn^{(2+)}$, although only the position of the level and not the valency of the ion, is relevant to the subsequent discussion. The upward movement of the Fermi level with decreasing oxygen pressure is then arrested at the $Mn^{(2+)}$ levels and until all these levels are filled the activation energy for electrical conduction would be approximately $q_1+2\Delta-\epsilon'$ for electrons and $q_2+\epsilon'$ for holes. ϵ' is the height of the $Mn^{(2+)}$ above the Ni^{2+} level (Fig. 11).

Unfortunately accurate numerical values cannot be assigned to the proposed energy level scheme since the actual oxygen loss under the various sintering conditions is not, at present, known. Without this information a determination of the electron and hole mobilities is not possible and these would be required for a calculation of the Fermi level from the resistivity data. All the results presented in the previous paragraph are however consistent with approximate values of 0·2 eV for q_1, 0·3 eV for q_2, 0·5 eV for 2Δ and 0·2 eV for ϵ'.

4. CONCLUSION

Electrical and magnetic measurements on nickel ferrites containing a small concentration of manganese suggest that Mn^{3+} replaces Fe^{3+} on the octahedral sites of the ferrite lattice and that excess nickel can dissolve in nickel ferrite to a limited extent of approximately 3% in good accord with an earlier estimate of 2·9% by Parker and Smith. Evidence is presented which indicates that the large increase in room temperature resistivity resulting from the manganese addition arises from the fact that Mn ions contribute energy levels which stabilize the position of the Fermi level in the energy gap between the Ni^{2+} and Fe^{2+} levels.

Acknowledgements—One of us (A. S.) is indebted to the Governors of the Portsmouth College of Technology for the award of a Research Studentship. Some of the graphs in Figs 1 to 7 are reproduced by kind permission of the Editor of *Nature*.

REFERENCES

1. VAN UITERT L. G., *J. chem. Phys.* **24,** 306 (1956).
2. PARKER R. and SMITH M. S., *J. Phys. Chem. Solids* **21,** 76 (1961).
3. PALADINO A. E., *J. Amer. ceram. Soc.* **42,** 168 (1959).
4. JONKER G. H., *J. Phys. Chem. Solids* **9,** 165 (1959).
5. LORD H. and PARKER R., *Nature, Lond.* **188,** 929 (1960).
6. PARKER R. and LORD H., *proc. phys. Soc. Lond.* **79,** 383 (1962).
7. KOOPS C. G., *Phys. Rev.* **83,** 121 (1951).

J. Phys. Chem. Solids Pergamon Press 1963. Vol. 24, pp. 1333–1339. Printed in Great Britain.

EFFET STARK EN SPECTROSCOPIE QUADRIPOLAIRE PURE

J. DUCHESNE, M. READ et P. CORNIL
Institut d'Astrophysique de l'Université de Liège, Cointe-Sclessin, Belgique

(*Received* 17 *April* 1963)

Abstract—The effect of electric fields of strengths up to about 50 kV/cm on the quadrupole lines of a series of halogenetad inorganic and organic compounds in the solid phase has been observed. In most cases, a doubling of the lines has been detected, and a general interpretation of this has been proposed. The shifts have been shown to vary linearly with the electric field, and a detailed analysis of the former, measured in structurally correlated molecules, has led to simple relationships being laid down between the Stark effect and the principal polarizabilities of the molecules involved.

Résumé—On a observé l'effet de champs électriques d'intensités s'élevant jusqu'à 50 kV/cm sur les raies quadripolaires d'une série de composés inorganiques et organiques en phase solide. Dans la plupart des cas, on a mis en évidence un dédoublement des raies, dont une interprétation générale a pu être proposée. Les déplacements en fréquence, qui varient linéairement avec le champ électrique, ont été mesurés dans les cas de molécules de structures apparentées. L'analyse détaillée de ce phénomène a conduit à l'établissement d'une relation simple entre l'effet Stark et les polarisabilités principales des molécules étudiées.

1. INTRODUCTION

DES recherches effectuées récemment par plusieurs auteurs$^{(1)}$ ont mis en évidence un effet d'élargissement des raies de RNQ lorsque les substances étudiées sont soumises à des champs électriques de l'ordre d'une vingtaine de kV/cm. Un tel effet, qui a été observé dans quelques cristaux ioniques tels que $KCl^{35}O_3$, $NaCl^{35}O_3$ et $NaBr^{81}O_3$ et dans quelques cristaux moléculaires comme le $pC_6H_4Cl_2^{35}$ avait d'ailleurs été prédit théoriquement par BLOEMBERGEN$^{(2)}$ et a déjà donné lieu à d' intéressantes tentatives préliminaires d'interprétation théorique. Il nous a paru toutefois qu'une connaissance complète du phénomène ne pourrait s'édifier que s'il était possible de résoudre la structure de la raie élargie d'une part et, ceci une fois obtenu, d'étendre l'analyse de l'effet à toute une série de molécules structuralement apparentées. Le but de cette note est donc de montrer qu'en faisant usage de champs électriques d'intensité plus élevée que celle des auteurs précités, on obtient la résolution espérée des raies quadripolaires et qu'à partir des mesures effectuées sur les composantes dans toute une série de cas, on peut mettre en évidence certains des facteurs importants qui régissent l'effet en cause.

2. DISPOSITIF EXPÉRIMENTAL

Les spectrographes radioélectriques utilisés dans notre laboratoire, inspirés des montages mis au point pour la première fois par DEHMELT et KRÜGER,$^{(3)}$ sont tels que l'échantillon est localisé dans une self qui forme une partie du circuit oscillant d'un oscillateur à superréaction. Les générateurs de fréquences à découpage extérieur opèrent à environ 1 per cent de la fréquence de l'oscillateur principal. L'oscillateur à superréaction est lui-même modulé en fréquence par un condensateur vibrant, ce qui permet l'enregistrement de la dérivée première des raise d'absorption après détection synchrone. Les domaines couverts par les deux spectrographes correspondent à des fréquences de l'ordre de 30–250 Mc/s qui permettent l'étude des transitions quadripolaires des atomes de Cl^{35}, de $Br^{79,81}$ et d'I^{127} lorsque ceux-ci sont introduits dans des liaisons pas trop ioniques.

Pour permettre l'étude de l'effet Stark, on introduit l'échantillon dans une cellule de verre de forme parallélipipédique (1 × 5 × 0,4 cm) sur les grandes faces de laquelle sont appliquées les électrodes. L'ensemble est introduit suivant l'axe de la self du spectrographe de telle sorte que la direction du champ électrique soit perpendiculaire à la direction du champ magnétique haute fréquence. Pour pouvoir effectuer des observations à basse température, on plonge la cellule et ses électrodes dans un dewar de forme appropriée, le tout étant introduit dans la self du circuit oscillant. Il est à noter qu'en vue d'éviter des perturbations de ce dernier, les électrodes sont isolées de leur alimentation par des bobines d'arrêt haute fréquence. Le générateur de tension dont nous avons fait usage est du type doubleur de tension et permet d'obtenir des champs électriques externes d'environ 50 kV/cm losqu'on tient compte de corrections dépendant du caractère inhomogène du milieu ainsi constitué. Pour assurer le meilleur coefficient de remplissage possible, au lieu d'utiliser une poudre cristalline de chaque échantillon considéré, on fondait l'échantillon dans sa cellule et on le soumettait ensuite à un refroidissement rapide suivi d'un recuit. Les mesures de fréquence ont été effectuées par interpolation sur les enregistrements à partir des harmoniques de découpage d'un générateur encadrant la raie quadripolaire.

3. STRUCTURE DES RAIES STARK

Parmi les différents essais auxquels nous avons procédé, c'est SnI_4^{127} qui nous a donné les résultats les plus favorables. La Fig. 1 représente l'évolution de l'intensité de l'une des deux raies quadripolaires de cette substance en fonction de l'intensité du champ électrique extérieur.

D'une manière générale, lorsqu'on soumet la raie de résonance quadripolaire d'une substance quelconque à des champs électriques d'intensités progressives s'élevant jusqu'à environ 50 kV/cm on s'aperçoit qu'au lieu d'un simple élargissement, comme l'avaient observé les auteurs antérieurs sur d'autres substances, on est en présence d'une véritable structure des raies de résonance qui se manifeste par deux maxima d'intensité, distribués symétriquement par rapport à la raie à champ nul, qui semblent séparés par une zone intermédiaire où l'absorption diminue et dont l'écartement s'accroît avec le champ d'une manière qui sera discutée dans la suite. Cette distribution remarquable peut s'interpréter facilement si l'on suppose une distribution au hasard des cristallites formant l'édifice de l'échantillon. Dans ce cas, en effet, on peut considérer que les liaisons contenant le noyau résonant sont distribuées spatialement de manière isotrope. Dans ces conditions, si l'on se réfère à un système d'axe triorthogonal oxyz tel que la direction oz soit perpendiculaire à la direction du champ magnétique excitateur, il est évident, puisque le champ électrique a également la direction oz, que l'intensité et le déplacement Stark seront maxima pour les liaisons dirigées suivant oz, si l'on admet que l'effet en cause est le plus élevé dans la direction de la liaison chimique. D' autre part, les liaisons situées dans le plan oxy donneront un déplacement Stark minimum et une intensité maximum pour la direction oy, tandis que l'effet sera nul dans la direction ox.

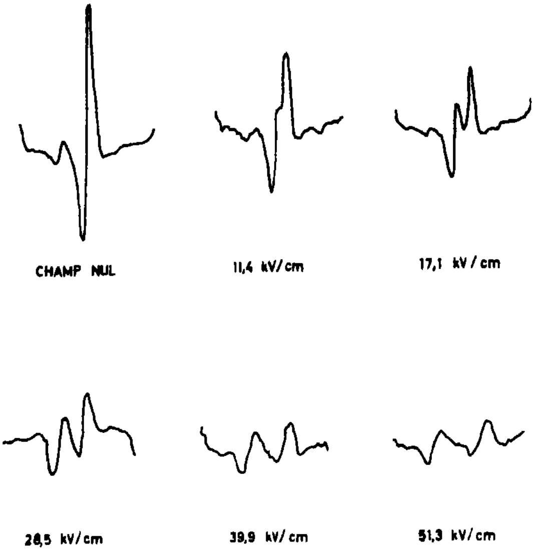

FIG. 1. Effet Stark sur la raie située à 209,133 Mc/s de I^{127} de SnI_4 à 77°K en fonction de l'intensité du champ électrique extérieur.

La situation se reproduit symétriquement pour les liaisons alignées en sens inverse. Cette image réduite à une distribution tridirectionnelle implique donc l'apparition de deux raies Stark correspondant au déplacement maximum, symétriquement disposées par rapport à la raie à champ nul et de deux autres raies, correspondant au déplacement minimum, également symétriques par rapport à la raie à champ nul.

Toutefois, en raison de la distribution isotropique, les liaisons ayant des positions intermédiaires doivent contribuer de manière intermédiaire à l'effet Stark et à l'intensité de sorte que la raie d'absorption soumise au champ électrique devrait présenter l'allure représentée dans la Fig. 2.

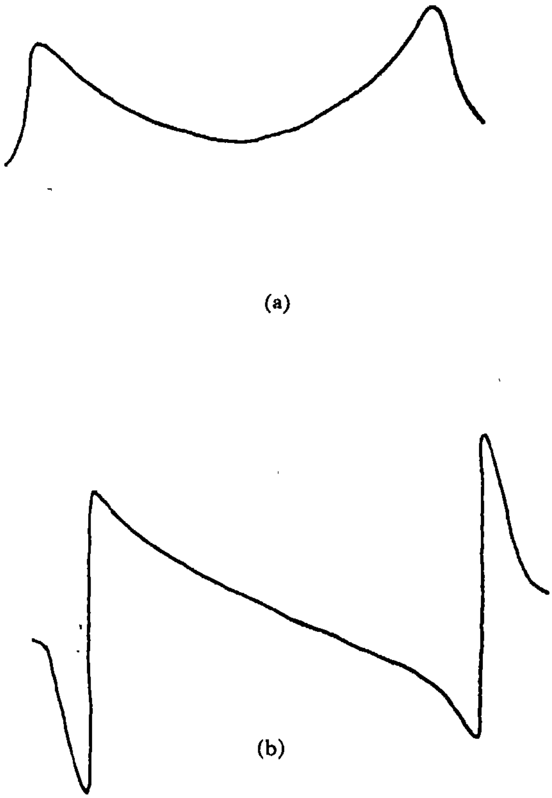

FIG. 2. (a) Allure de la courbe d'absorption théorique Stark dans le cas d'une poudre cristalline. (b) Allure de la dérivée premiere correspondante.

En comparant les Fig. 1 et 2, il semble bien que le modèle que nous proposons soit vérifié dans ses grandes lignes.

4. RÉSULTATS EXPÉRIMENTAUX

Il est à remarquer tout d'abord que, pour chaque substance utilisée, le champ électrique externe a été modifié en faisant usage de la formule ci-après de Lorentz, en vue de l'estimation du champ local: $E_{loc} = \epsilon + 2/3\ E$, où ϵ est la constante diélectrique de la substance.

Dans plusieurs cas nous avons été conduits, en l'absence de données expérimentales sur cette grandeur, à faire usage d'une valeur estimée, ce qui peut dans une mesure, probablement assez légère, affecter les résultats.

(a). *Evolution de l'effet Stark en fonction du champ électrique local*

L'évolution de l'effet Stark en fonction du champ électrique local a été observé pour Cl_2^{35}, Br_2^{81}, I_2^{127}, p-$C_6H_4Cl_2^{35}$, p-$C_6H_4Br_2^{79,81}$, p-$C_6H_4I_2^{127}$, SnI_4^{127}. En fait, la décomposition Stark que nous avons observée chez toutes ces molécules ne présente pas toujours le même degré de résolution qui caractérise SnI_4. C'est ainsi que pour Cl_2 et Br_2, l'on n'a observé qu'un élargissement de la raie quadripolaire, tandis que pour l'iode et les molécules aromatiques, la qualité des spectres obtenus était intermédiaire. A titre d'exemple, la Fig. 3 représente l'effet Stark de Cl_2 et de p-$C_6H_4Br_2$. Dans le graphique de la Fig. 4 sont représentés les effets Stark relatifs ($\Delta\nu/\nu_0$) en fonction du champ local. On constate que dans le domaine des champs électriques étudiés, la relation entre ces deux grandeurs est linéaire et que chacunes des droites extrapolées passe par l'origine. Que l'effet Stark en cause soit linéaire, ou tout au moins approximativement linéaire, était déjà en fait implicité dans la théorie de la distribution de l'effet que nous avons donnée au Paragraphe 3. S'il s'agissait d'un effet quadratique, il est clair qu'on aurait en fait une forte dissymétrie dans la distribution des intensités. On

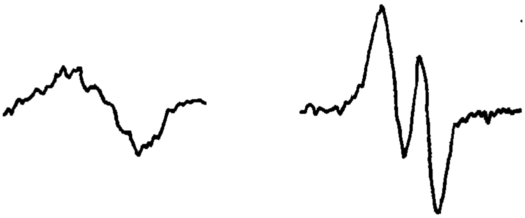

FIG. 3. Effet Stark à 77°K de Cl_2^{35} (à gauche) et de p-C_6H_4 $^{81}_{2}$ (à droite) dans des champs respectifs de 49,7 kV/cm et 54,7 kV/cm.

retrouve donc ainsi une nouvelle cohérence entre le modèle de départ et les observations.

(b). *Expression de l'effet Stark*

Les résultats résumés au Tableau 1 ont été obtenus à la température de 77°K et les colonnes 3, 4, 5 et 6 représentent respectivement les largeurs relatives des raies, l'effet Stark relatif par unité de champ électrique, les déplacements Stark absolus pour des champs locaux de 85 kV/cm et les constantes diélectriques des substances en cause, où les astérisques indiquent les valeurs qui ont été estimées. Il est à noter que la mesure du déplacement Stark ($\Delta\nu$) est effectuée à partir de la distance qui sépare les sommets extrêmes de la dérivée première de la courbe d'absorption. L'écart obtenu est alors divisé par deux pour les raisons que l'interprétation de la structure discutée plus haut impose et l'on doit encore en soustraire une demi largeur de raie correspondant à la raie à champ nul pour tenir compte implicitement des perturbations apportées à la postion des sommets de la courbe d'absorption proprement dite par le recouvrement des deux parties symé-

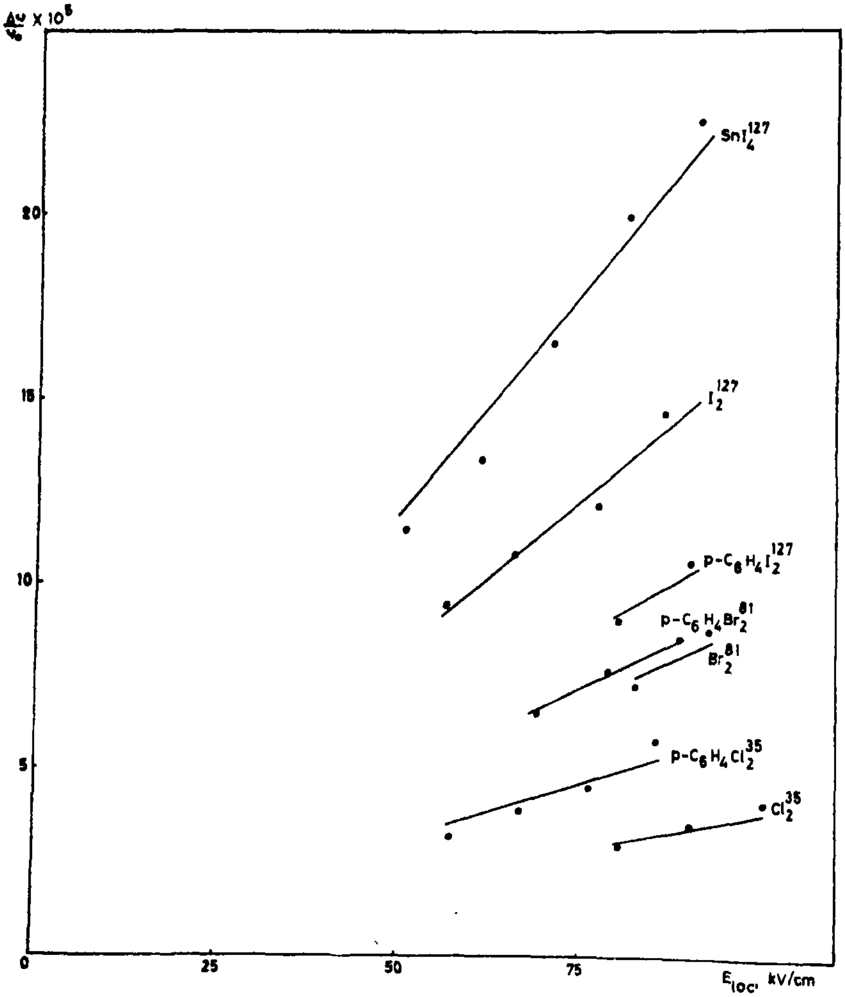

FIG. 4. Déplacement Stark relatif de différentes substances en fonction du champ interne.

triques de la raie totale. Cette façon de procéder présente notamment l'avantage de permettre l'estimation de l'effet en cause dans les cas (Cl_2, Br_2), où l'on n'a observé qu'un élargissement de la raie.

Tableau 1

Composé	77°K ν_0(Mc/s)	$\frac{\delta}{\nu_0} \times 10^5$	$\frac{\Delta\nu}{\nu_0 \cdot \Delta E} \times 10^{10}$ cm/V	$\Delta\nu$/Kc/s 85 kV/cm	$\epsilon^{(4)}$
Cl_2^{35}	54,2475	11	3,8	1,76	3,5*
Br_2^{81}	319,210	14	8,7	24,6	3,7*
I_2^{127}	334,39	14	16,4	46,4	4,0
p-$C_6H_4Cl_2^{35}$	34,7754	6	6,1	1,83	2,8
p-$C_6H_4Br_2^{79}$	271,125	8	9,7	22,1	2,9*
p-$C_6H_4Br_2^{81}$	226,49	9	9,7	18,5	2,9*
p-$C_6H_4I_2^{127}$	280,147	11	11,4	27,2	3,2
SnI_4^{127}	209,133	10	23,8	42,0	3,4

Dans tableau 1, l'on a omis d'inclure quelques résultats, de précision moins grande, en raison de la qualité des spectres relatifs aux molécules $C_6H_5Br^{79,81}$ et $C_6H_5I^{127}$. Toutefois, il est remarquable que, dans les limites des erreurs de mesure, le $\Delta\nu/\nu.\Delta E$ de ces substances est identique à celui qui caractérise respectivement le p-$C_6H_4Br_2^{79,81}$ et le p-$C_6H_4I_2^{127}$. Il est à noter en outre qu'aucune différence mesurable d'effet ne se manifeste lorsqu'on passe d'un isotope à l'autre, comme c'est le cas du paradibromobenzène.

5. INTERPRÉTATION DES RÉSULTATS

BLOEMBERGEN *et al.*(1) ont proposé que les contributions les plus importantes à l'effet Stark proviennent de la variation du caractère ionique et de l'hybridation des orbitales de liaisons dans lesquelles les moments quadripolaires sont impliqués. Toutefois, les relations que donnent ces auteurs paraissent d'une application difficile étant donné l'incertitude qui pèse sur la connaissance des taux d'hybridation caractérisant les atomes d'halogène dans les dérivés organiques. Dans la phase initiale du développement de cette question, il nous a donc paru qu'une méthode plus efficace consisterait peur-être à tenter de rattacher les effets Stark à des grandeurs expérimentales telles que les polarisabilités électroniques des atomes de halogènes eux-mêmes ou de la molécule tout entière dans laquelle ils sont introduits. Il faut d'ailleurs remarquer que de telles grandeurs doivent être étroitement liées aux variations, sous l'influence du champ, de l'état d'hybridation de ces atomes et du caractère ionique des liaisons correspondantes.

Dans une première tentative de classification, nous avons choisi comme paramètre variable la polarisabilité électronique de l'atome de halogène donnant lieu à la transition. Nous avons pu estimer celle-ci à partir de la connaissance du caractère ionique des liaisons correspondantes par interpolation linéaire entre les valeurs fournies dans la littérature pour les grandeurs caractéristiques de l'atome neutre et de l'ion négatif correspondant. Dans le cas de l'atome d'iode introduit dans les molécules p-$C_6H_4I_2$, I_2 et SnI_4, on déduit pour α_{e1} des valeurs comprises entre 51 et 57×10^{-25} cm^3, c'est-à-dire une variation d'environ 10 par cent. Or, les effets Stark correspondants, ainsi qu'on peut le voir d'après le Tableau 1, varient dans cette même série de composés, du simple au double, alors que l'on s'attendait plutôt à un effet proportionnel qui n'est en aucune façon réalisé dans l'exemple choisi. Dans ces considérations, la polarisabilité ionique a été estimée comme devant jouer un rôle négligeable. Devant cet échec de l'interprétation empirique des faits observés, il nous a paru qu'il fallait envisager non pas la déformation de l'atome lui-même, mais celle de l'édifice moléculaire tout entier. Comme l'effet Stark qui a été mesuré représente le déplacement maximum correspondant, selon la théorie proposée, à un alignement des liaisons halogénées suivant la direction du champ, c'est donc de la polarisabilité moléculaire suivant cette direction qu'il fallait faire usage.

Au Tableau 2 sont rassemblées les valeurs des polarisabilités principales des substances étudiées.(5,6)

Les valeurs accompagnées d'un astérisque ont été estimées par analogie avec les valeurs connues pour les dérivés correspondants monohalogénés en tenant compte de l'évolution habituelle de celles-ci en passant aux composés para.

Le graphique de la Fig. 5 exprime la dépendance de l'effet Stark vis-à-vis du grand axe de polarisabilité b_1.

Dans ces conditions, on remarque que la diffi-

Tableau 2

Substances	$b_1 \times 10^{15}$	$b_2 \times 10^{25}$	$b_3 \times 10^{25}$
Cl_2	66	36	36
Br_2	96	53	53
I_2	180	99	99
p-$C_6H_4Cl_2$	185*	151*	89*
p-$C_6H_4Br_2$	206*	168*	99*
p-$C_6H_4I_2$	234*	191*	113*
SnI_4	282	282	282

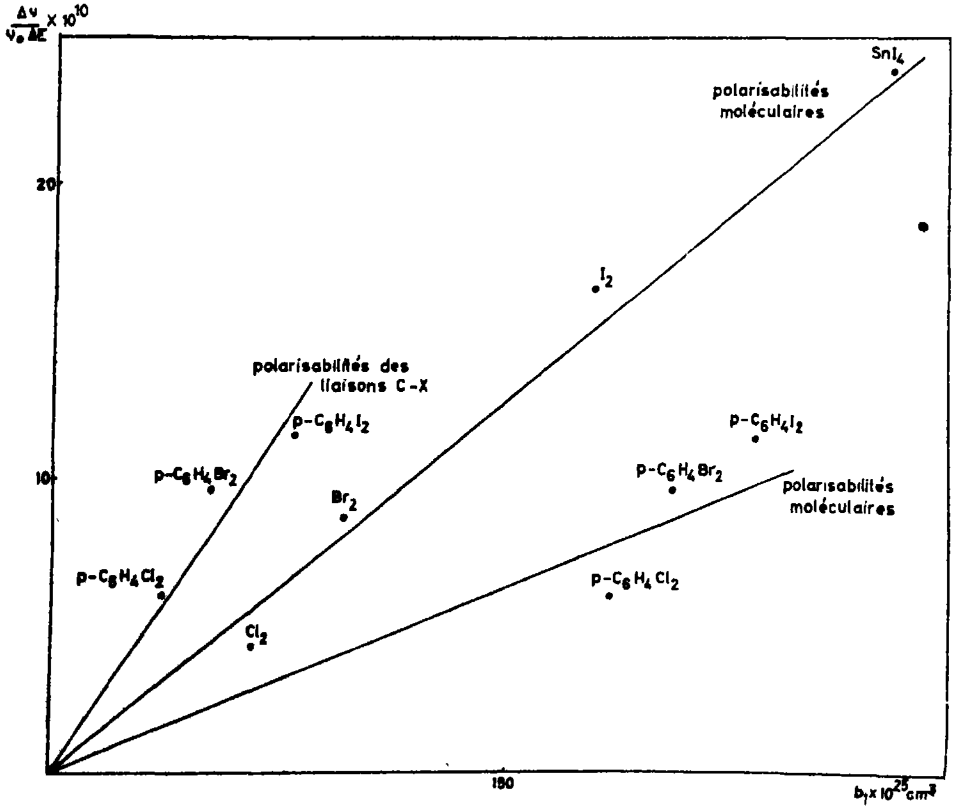

FIG. 5. Déplacement Stark relatif par unité de champ électrique en fonction de la polarisabilité principale suivant l'axe de la liaison.

culté principale recontrée lors de la tentative d'interpréter les faits sur la base de la polarisabilité atomique est remarquablement surmontée lorsqu'on considére la série des petites molécules Cl_2, Br_2, I_2 et SnI_4 où l'on trouve la relation de proportionnalité espérée entre les deux grandeurs physiques en cause.

Par contre, lorsqu'on considère la série des molécules aromatiques de grandes dimensions, on s'aperçoit que la relation reste approximativement proportionnelle, mais que la droite correspondante ne se superpose pas à la droite principale caractérisant les molécules de petites dimensions et qu'elle se trouve en fait en dessous de cette dernière. Il semble donc que la façon de procéder surestime les polarisabilités dans ces cas particuliers, ce à quoi il fallait s'attendre puisque les déformations électroniques subies par le noyau aromatique n'influencent le gradient de champ au noyau de halogène que d'une façon amortie.

C'est pourquoi nous avons tracé dans le même graphique une courbe exprimant les effets Stark en fonction de la polarisabilité des liaisons qui ont été calculées par SMITH et MORTENSEN.(5) On constate qu'une relation de proportionnalité se reproduit, mais que la droite correspondante se situe symétriquement par rapport à celle caractérisant les molécules de petites dimensions. On pourrait donc conclure que l'effet réel se manifeste par une influence qui est à mi-chemin entre les deux modéles.

6. CONCLUSIONS

Au terme de cette analyse, il semble bien que l'on puisse affirmer dès maintenant que l'étude de l'effet Stark en spectroscopie quadripolaire pure doive se révéler comme une méthode fructueuse pour l'étude de la polarisabilité des molécules en phase solide. Pour confirmer définitivement la validité du point de vue adopté ici, il conviendra non seulement de multiplier les observations dans des cas judicieusement choisis, mais aussi d'aborder le problème des monocristaux de manière à vérifier que les relations actuelles s'étendent à l'interprétation des effets Stark correspondant aux autres directions principales caractérisant l'anisotropie moléculaire. Des expériences dans ce sens sont actuellement en cours dans notre laboratoire.

RÉFÉRENCES

1. KUSHIDA T. et SAIKI K., *Phys. Rev. Letters* **7,** 9 (1961); ARMSTRONG J., BLOEMBERGEN N. et GILL D., *Phys. Rev. Letters* **7,** 11 (1961); BLOEMBERGEN N., *J. chem. Phys.* **35,** 1131 (1961); ARMSTRONG J., BLOEMBERGEN N. et GILL D., *J. chem. Phys.* **35,** 1132 (1961); BLOEMBERGEN N. et DIXON R. W., *Comptes Rendus de* 11ème *Colloque AMPERE Eindhoven* P. 39 (1962).
2. BLOEMBERGEN N., *Science,* **133,** 1363 (1961).
3. DEHMELT H. G., KRÜGER H., *Z. Phys.* **129,** 401 (1951).
4. *American Institute of Physics Handbook,* MCGRAW-HILL, New York (1957); *Handbook of Chemistry and Physics,* The Chemical Rubber Publishing Co., Cleveland (1961–1962).
5. SMITH R. P. et MORTENSEN E. M., *J. chem. Phys.* **32,** 508 (1960).
6. STUART H. A., *Molekülstruktur,* Springer, Berlin (1934).

J. Phys. Chem. Solids Pergamon Press 1963. Vol. 24, pp. 1341–1347. Printed in Great Britain.

STRUCTURAL EFFECTS OF IONIZING RADIATION IN FERROELECTRIC ROCHELLE SALT*

HENRI BOUTIN† and B. C. FRAZER‡
Brookhaven National Laboratory, Upton, New York

and

FRANCO JONA
IBM Research Center, Yorktown Heights, New York

(*Received* 11 *June* 1963)

Abstract—Neutron diffraction measurements of the intensity variation of certain sensitive Bragg reflections with radiation dosage, establish that the ferroelectric crystal structure of Rochelle salt is seriously affected by exposure to X-rays and γ-rays. Previously, the remarkable changes in the ferroelectric properties of this crystal had been ascribed almost entirely to macrostructural changes, leading to hindered domain mobility. Also, optical studies have thrown new light on the differences in radiation effects in crystals irradiated within and outside the ferroelectric temperature range. In the first case, crystals irradiated to the point where hysteresis loops are no longer observable not only continue to show domain patterns in polarized light within the normally ferroelectric region, as had already been reported, but also show domains at temperatures well outside of that range. On the other hand, crystals subjected to equivalent dosage at temperatures below the lower Curie point show no domains at all—even in the middle of the normal ferroelectric temperature range. It is suggested that there are two basic types of damage which must be considered. One of these involves local damage centers, distributed more or less uniformly throughout the volume of the crystal, and producing structural effects at the unit cell level similar to those produced by introduction of impurity ions in the lattice. In the other case, previously existing imperfections (such as dislocations, e.g., but perhaps also including domain walls) become greatly reinforced by collection of diffusing damage products. The latter type introduces macroscopic clamping effects which hinder domain mobility and tend to stabilize the crystallographic phase existing during irradiation.

INTRODUCTION

WHILE it has been known since the early observations of VIGNESS[1] in 1935 that Rochelle salt ($NaKC_4H_4O_6 \cdot 4H_2O$) is sensitive to ionizing radiation exposure, only in recent years have systematic studies been made on the striking changes induced in the ferroelectric properties of the crystal.[2–13] Crystals irradiated in the absence of an external field within the ferroelectric temperature range show progressive changes with radiation dosage in hysteresis loops, low-field dielectric constant vs. temperature curves, resonant frequencies, elastic constants, and various other properties. The hysteresis loops become distorted at low dosage, become split on continued irradiation, and finally degenerate into straight lines, as if the ferroelectric properties have disappeared entirely. The dielectric constant is depressed and the peaks at first shift toward one another, then coalesce into a single broad peak, and finally the temperature dependence curve flattens out, again as if the ferroelectric phase has been completely destroyed. Nevertheless, monoclinic twin patterns, characteristic of the ferroelectric domains, are still visible with polarized light long after the hysteresis loop has disappeared

---

* Work performed under the auspices of the U.S. Atomic Energy Commission.

† Guest Scientist from Picatinny Arsenal, Dover, New Jersey.

‡ At present a Guest Physicist at the Puerto Rico Nuclear Center, Mayaguez, P.R.

—thus indicating that the ferroelectric monoclinic symmetry is retained even after heavy radiation dosage. This latter observation has led various investigators to regard the effects of radiation as being primarily macrostructural in nature, rather than related to changes in the crystalline structure, that is, to involve mechanisms leading to locking of domains instead of tending to induce a reversion to the non-ferroelectric orthorhombic symmetry.

Crystals irradiated in the ferroelectric range under an a.c. field have shown somewhat different behavior. While distortions are produced in the hysteresis loops, and increases in coercive field are observed, the loops do not become split. The damage effects, at least for only moderate dosage, can be annealed out by heat treatment or by application of an a.c. field. Similar results are obtained with crystals irradiated above the upper Curie point.

It has been pointed out(4) that the effects of radiation in Rochelle salt are somewhat similar to those obtained when one introduces impurities into the lattice, as when crystals are doped with Mo, Cu, and B, or in the mixed crystal series (e.g., the partial replacement of K^+ by NH_4^+, Rb^+, or Tl^+). The ferroelectric properties are drastically affected in all of these cases at low concentration levels of the impurity ions. Some similarity to irradiated crystals is of course to be expected, since the trapped damage products will also act as impurities, and due to the large local strains, should have pronounced effects on the ferroelectric behavior at even lower concentrations than in the case of chemically impure crystals. It is known, however, that chemically introduced impurities can affect the crystal structure at the unit cell level, and, in fact, can completely eliminate the ferroelectric monoclinic phase on substitution of only small percentages of the impurity ions.

Despite the experimental fact that domains persist after heavy radiation dosage, and that a seemingly satisfactory explanation of the radiation effect is offered on the basis of hindered domain mobility, it seemed to us that possible crystal structural effects had not received adequate consideration. Partly this was because of what was mentioned above on chemical impurities, where definite structural changes are observed, but the major reason had to do with certain differences in the X-ray and neutron diffraction patterns of Rochelle salt.

CRYSTALLOGRAPHIC CONSIDERATIONS

In the non-ferroelectric/orthorhombic phases of Rochelle salt the space group symmetry is $P2_12_12$. In passing through the Curie point, the symmetry changes to monoclinic $P2_1$. The destruction of one set of the two-fold screw axes in this transition removes the condition that the $(0\,k\,0)$ reflections with k odd must be zero. (Here we are choosing the monoclinic axes in the same way the orthorhombic axes are usually labeled,(14) rather than adhering to the conventional crystallographic choice of b parallel to the remaining 2_1 axis.) These new reflections have never been observed in X-ray studies of the Rochelle salt structure,(14,15) and the prevailing view for sometime was that only the hydrogen positions were involved in the loss of orthorhombic symmetry. This assumption appeared to be supported at first by a neutron diffraction study of the structure,(16) but later work demonstrated conclusively that this is not the case.(17) The odd $(0\,k\,0)$ reflections, while rather weak, are easily observable with neutrons for both hydrogenous and deuterated crystals. If only the hydrogen positions were responsible for these reflections, then the odd $(0\,k\,0)$ neutron data collected from a deuterated sample should differ from data taken with an ordinary hydrogenous crystal by only a simple scale factor, but this is far from being true. Hence, at least some of the heavier atoms in the structure must deviate from their $P2_12_12$ positions, and even though the ferroelectric structure of Rochelle is very complex, and has never been completely solved(17) one would certainly expect from the drastic differences in the hydrogenous and deuterated neutron data that at least some of the odd $(0\,k\,0)$'s should be detectable in X-ray patterns.

These considerations led us to believe that hindered domain models for irradiated Rochelle salt fall short of providing a fundamental explanation of the nature of the radiation effects, and that the crystal structure itself must be affected. The persisting monoclinic twin patterns seemed to rule out a radiation induced phase transition, but there still could be significant alterations in the magnitudes or character of the ferroelectric atomic displacements. Neutron diffraction provided us with an especially convenient tool for investigating the truth of this hypothesis: by studying the odd $(0\,k\,0)$ intensities as functions of radiation dosage.

If any appreciable intensity changes could be observed, then there could be no doubt that important crystal structural changes were taking place.

SPECIMENS AND PROCEDURE

Specimens of both ordinary and deuterated Rochelle salt were prepared in rectangular plate form with the ferroelectric *a*-axis normal to the plate. The plates on which most of the neutron diffraction work was carried out were all about $1 \times 0{\cdot}5 \times 0{\cdot}2$ cm^3 in size. The optical studies were made using thinner specimens, about $1 \times 0{\cdot}5 \times 0{\cdot}07$ cm^3, which were carefully polished to good optical finishes. The deuterated samples were cut from a single large crystal supplied to us by Dr. S. Triebwasser of the IBM Research Center. The ordinary hydrogenous samples were cut from crystals grown from water solution of chemical-pure grade commercial stock. Representative samples were checked for normal behavior before irradiation by taking dielectric constant vs. temperature curves, and by observing hysteresis loops on an oscilloscope. Similar measurements were also made during the course of the irradiation experiments so as to be sure that the same effects were obtained as had been reported in the literature, and to observe whatever correspondence might exist between neutron intensity changes and changes in ferroelectric behavior.

Preliminary irradiation experiments were done using a copper target X-ray tube operated at 30 kV and 10 mA. All subsequent work was done using a Co^{60} γ-irradiation source at an estimated dosage rate of $2{\cdot}5 \times 10^5$ rep/hr. Except for some of the preliminary X-ray work, irradiations were made at 0°C and at liquid N_2 and dry ice temperature. With a crystal of suitable dimensions for neutron diffraction measurements it is likely that X-ray damage will be largely concentrated near the surface, while damage resulting from γ-irradiation should be distributed uniformly throughout the volume. It has been reported previously(8) that X-rays and γ-rays produce similar effects in Rochelle salt. While one would expect the energy dependent effects to be of secondary importance, nevertheless the X-ray experiments were done as a check before proceeding with the more extensive Co^{60} work. Substantially the same neutron diffraction effects were obtained in both cases, so it was deemed safe to assume that conclusions drawn on the basis of the Co^{60} experiments are applicable also to the case of X-irradiation.

No measurable damage effects were expected to result from radiation exposure of the samples in the neutron beam, since thermal neutron energies are quite low, and since the fast neutron and gamma contaminations in the beam are at very low flux levels. Nevertheless, a routine check experiment was carried out by exposing a deuterated sample in the neutron beam for a period of time longer than the accumulated experimental time expended in the collection of diffraction data. No changes were observed in the dielectric behavior of the sample or in the (050) intensity.

The neutron diffraction measurements of integrated intensities were made by the usual single crystal techniques. Several odd (0 *k* 0) reflections were examined using both hydrogenous and deuterated samples with the same general behavior noted in each case. The most complete data were collected using the (050) of the deuterated crystal, since this peak showed the largest peak-to-background ratio. While care was exercised to reproduce the same experimental conditions during each measurement, the (060) and (080) reflections, which undergo little or no change in intensity with irradiation, were measured along with the (050) as reference checks.

In the optical studies the domain patterns of the irradiated crystals were examined under polarized light over a temperature range of −30°C to +45°C. Each observation was checked by comparison with an unirradiated crystal.

OBSERVATIONS

A. *Neutron diffraction*

Typical results of the neutron diffraction measurements are shown in Figs 1 and 2. Deuterated specimens were used in both cases, with the irradiation performed at 0°C for the curve in Fig. 1, and liquid N_2 temperature in Fig. 2. Similar behavior was observed for the (070) reflection of the same crystals, and for other odd (0 *k* 0)'s in hydrogenous crystals. The intensity variation of the (050) reflection with dosage is plotted as a ratio of the (050) and the nearly constant (060) integrated intensities. The zero time points differ slightly in the two figures because of a somewhat stronger extinction effect for the (060) reflection for the crystal irradiated at 0°C. In both cases a marked dependence of the (050) intensity on irradiation time is observed, with an appreciably greater effect for the 0°C irradiation.

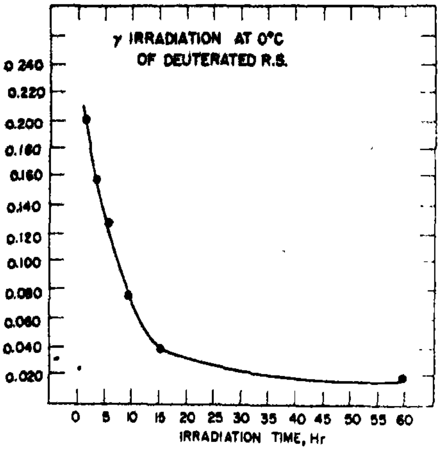

FIG. 1. Variation of the integrated intensity ratio (050)/(060) with γ-irradiation dosage for deuterated Rochelle salt. Irradiation temperature 0°C. Intensities measured at room temperature.

It was found that the (050) intensity of an irradiated crystal could be changed by applying a d.c. electric field. This is shown in Fig. 3. The (060) intensity remained unchanged. A virgin crystal failed to show a field dependence for its (050) reflection.

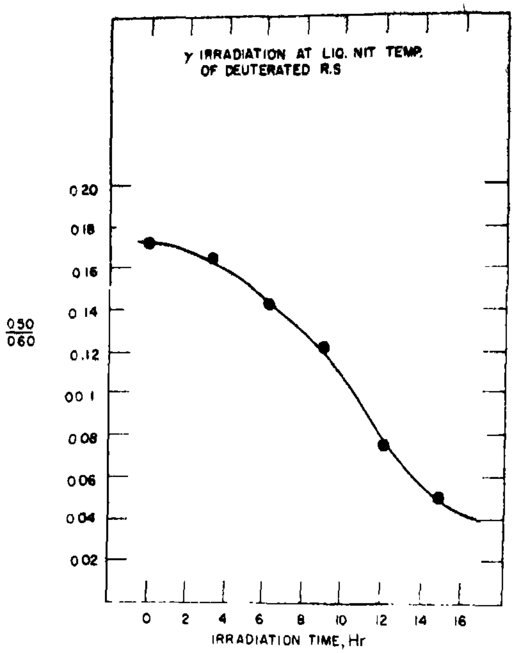

FIG. 2. Variation of the integrated intensity ratio (050)/(060) with γ-irradiation dosage for deuterated Rochelle salt. Irradiation temperature 77°K. Intensities measured at room temperature.

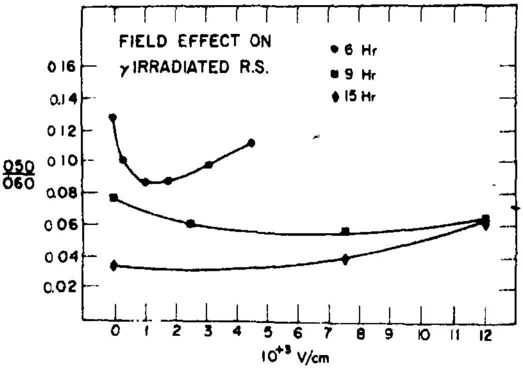

FIG. 3. D.C. field dependence of (050)/(060) intensity ratio for γ-irradiated deuterated Rochelle salt. Irradiation temperature 0°C.

In general, the observations of hysteresis loop behavior and changes in dielectric constant vs. temperature curves merely confirmed what had already been reported for crystals irradiated within the ferroelectric temperature range; however, it was of interest to compare the changes in ferroelectric properties with the neutron intensity changes for the same radiation dosage. Hysteresis loops of the 0°C irradiated crystals became distorted, but were not split into double loops, after about an hour of γ-irradiation. Observations of changes in the odd $(0\,k\,0)$ intensities were not statistically significant at this low dosage. After 3 hr double loops appeared and distinct decreases were observable in the odd $(0\,k\,0)$'s. After 9 hr of irradiation it was no longer possible to obtain a hysteresis loop, and the two dielectric constant peaks had coalesced into a single broad hump. At this dosage level the (050) intensity from a deuterated crystal had decreased to about one third of its initial value and its profile had become quite noticeably broadened. The broadening became more pronounced on continued irradiation, and for exposure times greater than 15 hr it became difficult to decide if a proper integrated intensity was being measured. Even after 60 hr of exposure, however, the counting rate was still definitely above background at the peak position.

B. *Optical*

Since the decreases in the neutron intensities for the odd (0 *k* 0) reflections clearly indicated an alteration in the ferroelectric crystal structure, optical studies were carried out to see what changes if any might be detectable in the domain structure.

The first experiment merely confirmed what had already been reported. A deuterated crystal that had been irradiated 27 hr at 0°C, well beyond the dosage required to eliminate hysteresis loops, was examined at room temperature with a polarizing microscope. While the crystal had turned slightly yellow as a result of irradiation, the optical transparency was quite good, and domains were clearly in evidence, as were also the dark lines, or sudares (as they have been called in Japan(9)). The only observation which might be considered new was that the domain pattern seemed to have a somewhat "faded" appearance, as compared to a virgin crystal. The pattern appeared to be similar to what one observed in an unirradiated crystal as the Curie point is approached, i.e., when the spontaneous strain is becoming small. This could have been an illusory effect, due simply to the yellow coloration of the crystal, but the visibility seemed sufficiently good to judge it as real.

A crystal irradiated 64 hr at 0°C also showed domains and an even higher density of sudares, but at this heavy dosage level the optical transparency had become too poor to draw any conclusions on "fading" of the domain pattern.

Next, the domain patterns were examined as a function of temperature, since the behavior of the dielectric constant(4,9,12) suggests that the ferroelectric temperature range shrinks with radiation exposure time, and this could offer an explanation for possible "fading" of the patterns. These studies led to unexpected but quite interesting results. Both the 27 hr and the 64 hr crystals showed domains over the entire range of measurement: −30° to +45°C. The temperature stage used did not permit us to go below −30°C, and we were afraid the crystal might decompose, or partially dehydrate, above 45°C. Thus, while dielectric constant measurements indicate a shrinkage of the ferroelectric range, the domain observations show that the monoclinic symmetry, characteristic of the ferroelectric phase, persists at temperatures well outside of the normal ferroelectric region.

Since crystals irradiated outside the ferroelectric temperature range are known to behave differently than crystals irradiated at a ferroelectric temperature, an investigation was made to see if this also applied to the domain structure. A deuterated crystal was irradiated 20 hr at dry ice temperature (−78°C). Before irradiation, this crystal showed normal domain behavior when examined under polarized light over a range of temperature that included the two Curie points. After irradiation *no domains* could be observed over the entire range of measurement (again −30° to +45°C). Thus, it appears that the crystallographic symmetry a Rochelle salt crystal normally possesses at the temperature at which it is irradiated, becomes the stable symmetry at all temperatures (or at least from −30°C up to decomposition).

DISCUSSION

Our original purpose in undertaking the present study was to investigate the possibility of structural effects of ionizing radiation on Rochelle salt, and clearly it has been established that very definite and non-trivial effects can be observed after only moderate dosage. The fact that the major portion of this work was carried out with γ-rays does little to limit the conclusions one may draw from the results. The preliminary work with X-rays demonstrated that, at least to a very good first approximation, the effects of X-rays and γ-rays are substantially the same. This agrees with conclusions reached previously by other investigators.(8)

Chynoweth has pointed out earlier in his paper on tri-glycine sulfate that X-ray dosages sufficient to produce large changes in ferroelectric properties of that crystal are small compared to those to which a crystal is commonly subjected in the course of an X-ray diffraction structure analysis, and he was led to imply that appreciable structural effects might result in this and other radiation-sensitive crystals during a crystallographic study. There can be little question now, at least in the case of Rochelle salt, that this is indeed true. The dosage rate in an X-ray diffraction beam ranges from about 10^5 to 10^6 R/min, and in a very short time will damage a crystal to the extent of those studied in the present paper. The results obtained in an X-ray diffraction study still may be very useful and significant, but in detail they cannot be characteristic of the fully polarized ferroelectric state.

The d.c. field measurements illustrated in Fig. 3 are interesting, but at the moment it appears that further work will be necessary before a very convincing argument can be developed to explain this behavior. It is worth noting that in the case of the 6 hr crystal, which shows a well-defined (050) intensity minimum, split hysteresis loops were still observable, whereas they were not observable for the 9 hr and 15 hr crystals.

The domain studies yielded some of the most interesting results of the investigation. It seems probable that the key to an explanation of these results must lie in clamping effects and the spontaneous strain. There should be two basic types of damage to consider in the crystal: one in which there are stable local damage centers distributed more or less homogeneously throughout the volume of the sample, and one in which previously existing imperfections (such as dislocations, e.g.) have become greatly reinforced by collection of diffusing damage products. With a modicum of faith, one can then argue that the latter type introduces macroscopic clamping effects which tend to stabilize the crystallographic phase existing during irradiation, and the distributed damage centers produce microscopic effects, or let us say effects at the unit cell level.

The clamping, which, depending upon the temperature of the crystal during irradiation, may be either orthorhombic or monoclinic, offers a logical explanation for hysteresis loop distortions in the lightly irradiated crystals. One would expect greater hindrance of domain mobility in the case of monoclinic clamping since the clamping of a given domain favors a particular polar direction. Also, a crystal irradiated in the ferroelectric temperature range has many more imperfections to trap damage products, since every domain wall can be considered as a sort of imperfection. In the case of orthorhombic clamping, a reasonable speculation is that before sufficient domain hindrance can be built up, the microscopic effects become dominant, and the loops never become truly split.

What can one say about the local damage centers and microscopic effects? Certainly the local strain in the vicinity of such a center must cause a much greater disturbance than a substitutional impurity such as Tl^+ or NH_4^+, and we already know that small percentages of these ions are sufficient to destroy the ferroelectric properties of Rochelle salt. Whatever the crystal chemical peculiarities of Rochelle salt are that normally cause the monoclinic phase to be stable over its limited temperature range, it seems logical to assume that the local damage centers tend to upset these stability conditions, and the crystal "wants" to stabilize its orthorhombic symmetry. If the crystal is orthorhombic while being irradiated, there is nothing to prevent this from happening, but if it is monoclinic this tendency must compete with the development of monoclinic clamping. The net result in the latter case is a decrease in the spontaneous strain within the normally ferroelectric region, but a "frozen-in" monoclinic strain outside of this region. This postulated strain behavior is illustrated in Fig. 4.

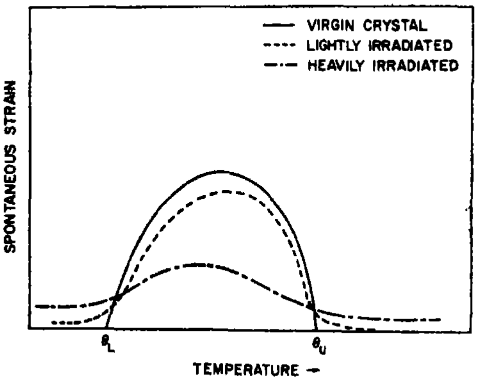

FIG. 4. Suggested changes in the spontaneous strain for a Rochelle salt crystal γ-irradiated within the ferroelectric temperature range.

The qualitative argument presented above would be very difficult to prove in a general theoretical treatment. It is consistent with both the neutron and optical observations reported in the present paper, and seems to offer an explanation for the dielectric behavior as well. Some additional experimental evidence in its favor appeared in the recent paper of KRUEGER *et al.*(13) Their measurements, including double-crystal X-ray rocking curves indicated an increase of crystal "perfection", i.e. decrease of spontaneous strain, for moderate radiation dosage.

Acknowledgements—The authors are indebted to Dr. G. J. Dienes of the Brookhaven National Laboratory for helpful discussions and encouragement during the course of this work.

REFERENCES

1. Vignes I., *Phys. Rev.* **48,** 198 (1935).
2. Zheludev I. S., Proskurnin M. A., Iurin V. A. and Baberkin A. S., *Dokl. akad. nauk. S.S.S.R.* **103,** 207 (1955).
3. Zheludev I. S. and Iurin V. A., *Izv. akad. nauk. S.S.S.R., Ser. fiz.* **20,** 211 (1956).
4. Iurin V. A., *Izv. akad. nauk S.S.S.R., Ser. fiz.* **21,** 329 (1957).
5. Eisner I., *Sov. Phys. Crystallogr.* **2,** 293 (1957).
6. Karmen K. N., *Sov. Phys. Solid State* **2,** 629 (1960). (English Translation.)
7. Quinn R. T., M.S. Thesis, U.S. Naval Postgraduate School (1960).
8. Toyoda K., Shimada A. and Tanaka T., *J. phys. Soc. Japan* **15,** 536 (1960).
9. Okada K., *J. phys. Soc. Japan* **15,** 363 (1960); *ibid.* **16,** 414 (1961); *ibid.* **16,** 1647 (1961).
10. Okada K., *Bull. Aichi Gakugei Univ., Okazaki* **X,** 9 (1961).
11. Moulton G. C. and Moulton W. G., *J. chem. Phys.* **35,** 208 (1961).
12. Toyoda K., Kawabata A. and Tanaka T., *Bull. Inst. chem. Res., Kyoto Univ.,* **39,** 189 (1961).
13. Krueger H. A. A., Cook W. R., Jr., Sartain C. C. and Yockey H. P., *J. appl. phys.* **34,** 218 (1963).
14. Beevers C. A. and Hughes W., *Proc. Roy. Soc.* **177,** 251 (1941).
15. Mazzi F., Jona F. and Pepinsky R., *Z. Kristallogr.* **198,** 359 (1957).
16. Frazer B. C., McKeown M. and Pepinsky R., *Phys. Rev.* **94,** 1435 (1954).
17. Frazer B. C., *J. phys. Soc. Japan* **17,** Suppl. B-II, 376 (1962).
18. Chynoweth A. G., *Phys. Rev.* **113,** 159 (1959).

J. Phys. Chem. Solids Pergamon Press 1963. Vol. 24, pp. 1349–1355. Printed in Great Britain.

OPTICAL MODES OF THE PEROVSKITE STRUCTURE*

R. I. JOSEPH and B. D. SILVERMAN

Raytheon Company, Research Division, Waltham, Massachusetts

(*Received* 13 *May* 1963)

Abstract—The optical modes of the perovskite structure are characterized by the displacements of five inequivalent sublattices. The motion of these sublattices is completely determined by seven sublattice couplings. Neglecting the three smallest couplings, three of the remaining couplings can be determined from the observed optical frequencies of $SrTiO_3$. These three couplings are then used to calculate the relative displacements of the sublattices. This is done as a function of a parameter Φ which is proportional to $T-T_c$. Two possible sets of solutions are found; one corresponds to a description of the ferroelectric mode as discussed by Slater, and the other to an alternate proposal of Last. It is found that the high frequency mode is a vibration of the oxygens against one another, while the two lower optical frequencies involve the motion of a fairly rigid oxygen framework. No suggestion is made as to which description (S or L) is the proper one for the ferroelectric mode, but it is shown that neither is *exactly* correct for $T \neq T_c$.

1. INTRODUCTION

It is now generally agreed that the interesting paraelectric properties of ferroelectric materials having the perovskite structure result from the temperature dependence of a low-lying transverse optical mode. Indeed, one can understand qualitatively, the origin of the Curie–Weiss behavior of the dielectric constant, nonlinear response, and electromechanical behavior in terms of a general Born–Von Kármán lattice dynamical approach.(1) A more detailed and quantitative understanding of these and other related phenomena has been frustrated however by our lack of knowledge concerning the actual ionic motions associated with the "soft ferroelectric mode" and other optical modes of the material. There have been attempts to calculate the optically active frequencies and assign the motions associated with these frequencies prior to the correct experimental observation and assignment of these frequencies. Rajagopal and Srinivasan(2) have obtained the infrared active frequencies of $SrTiO_3$ making use of the observed elastic constants to determine the couplings between the ions. Dvořák and Janovec(3) calculate these couplings using a procedure described by Fowler. The results of these investigations are illuminating, however, the frequencies obtained do not compare favorably with the observed frequencies,(4) and hence the displacements associated with the various modes are unreliable.

In this work the equations of motion are written in a manner similar to those appearing in the work previously mentioned; however, use is made of the observed frequencies to determine the displacements associated with each infrared active mode. Two possible sets of solutions are found; one corresponds to a description of the ferroelectric mode as discussed by Slater,(5) and the other to a proposal of Last.(6) The two solutions, however, exhibit one similar feature, namely the high frequency mode is a vibration of the oxygens against one another while the two lower frequencies involve the motion of a fairly rigid oxygen framework.

2. CALCULATION

The perovskite structure has five atoms in the unit cell and therefore a total of fifteen branches compose its spectrum. Three of these are of the acoustic type. Another three are of a torsional type and optically inactive. Of the nine remaining, six are transverse (doubly degenerate) optically active vibrations and three are optically inactive longitudinal vibrations. The long wavelength

---

* Work supported in part by the Electronics Research Directorate of the Air Force Cambridge Research Center, Air Research and Development Command.

optically active modes can be characterized by the relative motions of the five inequivalent rigid sublattices. Due to the cubic symmetry of the structure and the fact that three of the sublattices are composed of oxygen atoms, it is easily seen that if one restricts attention to vibrations along one of the cartesian axes (displacements are considered to be along the [100] direction), there are in general *seven* sublattice couplings. Since there are three observed optical frequencies ($SrTiO_3$),(4) one can choose three of the sublattice couplings different from zero and have a completely specified problem.* One can thus solve for these sublattice couplings and then for the relative motion of the sublattices for each mode.† This calculation has been carried out for the sublattices as labelled in Fig. 1 and for the following couplings:

k_1: O_2–Ti coupling,
k_2: O_2–O_3 and O_2–O_4 couplings,
k_3: Sr–O_3 and Sr–O_4 couplings.

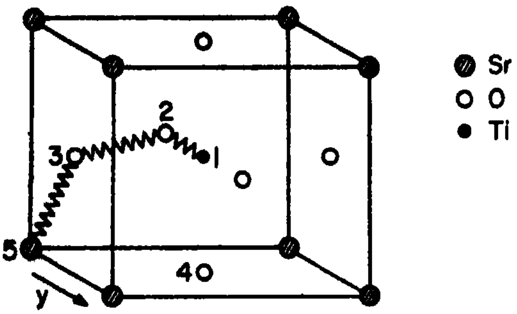

FIG. 1. Unit cell for the perovskite structure ($SrTiO_3$). The springs represent the couplings considered in the calculation. Displacements y are considered to be along the [100] direction.

We have chosen a coupling between oxygens, a strontium–oxygen coupling, and a titanium–oxygen coupling. Three of the couplings that have been neglected involve only nearest neighbor bond angle forces (no central forces). The remaining strontium–titanium coupling involves a central nearest neighbor interaction which can be shown to be small.(8)

The equations of motion can now be simply written down:

$$\begin{aligned} m_1\ddot{y}_1 &= -2k_1y_1+2k_1y_2 \\ m_2\ddot{y}_2 &= 2k_1y_1-(2k_1+8k_2)y_2+4k_2y_3+4k_2y_4 \\ m_3\ddot{y}_3 &= 4k_2y_2-(4k_2+4k_3)y_3+4k_3y_5 \\ m_4\ddot{y}_4 &= 4k_2y_2-(4k_2+4k_3)y_4+4k_3y_5 \\ m_5\ddot{y}_5 &= 4k_3y_3+4k_3y_4-8k_3y_5, \end{aligned} \tag{1}$$

where the m_i and y_i are the mass and displacement, respectively of the atom at site i. Since the atoms at sites 2, 3, and 4 are identical, we set $m_2 = m_3 = m_4 = m$. When $y_i = \bar{y}_i\, e^{i\omega t}$ is substituted into equation (1), the lefthand side of each of these equations is replaced by $-m_iy_i\omega^2$. The eigenfrequencies are now obtained by setting the determinant of the coefficients equal to zero. This 5×5 determinant is readily evaluated, with the result:

$$\begin{aligned} &\Omega[\Omega-4(k_2+k_3)]\,[\Omega^3-\Omega^2(\alpha k_1+\beta k_2+\gamma k_3) \\ &+\Omega(\delta k_1k_2+\epsilon k_1k_3+\nu k_2k_3)-\mu k_1k_2k_3] = 0, \end{aligned} \tag{2}$$

where we have written Ω for $m\omega^2$ and

$$\begin{aligned} \alpha &= 2(1+p) & \epsilon &= 8(1+p+2q+2pq) \\ \beta &= 12 & \nu &= 32(1+3q) \\ \gamma &= 4(1+2q) & \mu &= 64(p+q+3pq) \\ \delta &= 8(1+3p) \end{aligned}$$

$$p = m/m_1$$
$$q = m/m_5\ .$$

The solution represented by the first factor on the left-hand side of equation (2) corresponds to a uniform translation of all the atoms, that is, the acoustic mode mentioned previously. The solution represented by the second factor has a frequency given by $\omega^2 = 4/m\ (k_2+k_3)$. The corresponding displacements are given by: $y_1 = y_2 = y_5 = 0$, $y_3+y_4 = 0$. This is then the torsional mode discussed before. Finally, the three positive frequencies which one obtains from the third factor of equation (2) correspond to the measured

---

* The O_3–O_4 coupling only enters into the expression for the torsional frequency and therefore cannot be one of the three couplings chosen.

† These couplings implicitly include the effect of the local field, i.e. the sublattice coupling constants represent all effective harmonic contributions to the coupling.

transverse optical frequencies. The relative displacements corresponding to these solutions are:

$$\begin{aligned} y_2/y_1 &= -(p^{-1}\Omega-2k_1)/2k_1 \\ y_3/y_1 = y_4/y_1 &= -[2k_1+(y_2/y_1) \\ &\quad \times(\Omega-2k_1-8k_2)]/8k_2 \qquad (3) \\ y_5/y_1 &= -8k_3(y_3/y_1)/(q^{-1}\Omega-8k_3). \end{aligned}$$

Denote the three measured frequencies by Ω_1, Ω_2, and Ω_3 ($\Omega_1 > \Omega_2 > \Omega_3$). We now wish to find what values of k_1, k_2, and k_3 correspond to these frequencies. From equation (2) it is immediately observed that:

$$\begin{aligned} \Omega_1+\Omega_2+\Omega_3 &= \alpha k_1+\beta k_2+\gamma k_3 \\ \Omega_1\Omega_2+\Omega_1\Omega_3+\Omega_2\Omega_3 &= \delta k_1k_2+\epsilon k_1k_3+\nu k_2k_3 \qquad (4) \\ \Omega_1\Omega_2\Omega_3 &= \mu k_1k_2k_3. \end{aligned}$$

One can now solve this set of three nonlinear equations for k_1, k_2 and k_3 as a function of Ω_1, Ω_2 and Ω_3. After eliminating any two of the variables (say k_1 and k_2) it is found that one must solve a sixth degree equation for the third variable (say k_3). This must then be solved by numerical techniques.

We take for Ω_1, Ω_2 and Ω_3 the values for SrTiO$_3$ given in Refs 4. These measurements were made at room temperature. Since the interesting paraelectric properties of the perovskites result from the temperature dependence of the low-lying optical frequency, we shall study what effect this has on the couplings and hence the displacements. In order to do this we shall assume that the two high optical frequencies are temperature independent and remain at their given room temperature values. We introduce the temperature dependence of the low frequency mode through a parameter $\Phi \sim T-T_c$, T_c being the Curie temperature.(4) Thus we shall write that $\Omega_3 \sim \Phi$. The frequencies Ω_1, Ω_2 and Ω_3 are then given by:

$$\begin{aligned} 10^{-4}\Omega_1 &= 28{\cdot}2998 \\ 10^{-4}\Omega_2 &= 3{\cdot}0077 \\ 10^{-4}\Omega_3 &= 0{\cdot}94929\,\Phi. \end{aligned}$$

Both the Ω and k are given in units of rad^2 g sec^{-2}. At room temperature (300°K) Φ has the value 0·7656. The value of m has been taken as 16·0 times the mass of the proton in grams and p and q are given by 0·3340 and 0·1826, respectively.

3. RESULTS AND DISCUSSION

When the sixth degree equation resulting from the simplification of equation (4) is solved with the room temperature values for the frequencies, *only two* real solutions are found. As the parameter Φ is increased above the room temperature value, it is found that for $\Phi \gtrsim 0{\cdot}8$ no real solutions exist. That such a situation should arise is not too surprising, in that, having fixed two frequencies (Ω_1 and Ω_2) there is no a priori reason to expect to be able to find stable configurations as one arbitrarily varies the third frequency (Ω_3). When Φ is decreased, it is found that at $\Phi \approx 0{\cdot}7$ a second set of real solutions appear, and that at $\Phi \approx 0{\cdot}5$ a third set of real solutions appear. We shall concern ourselves here only with the two solutions which exist at room temperature. In Fig. 2 we plot our results for the three couplings

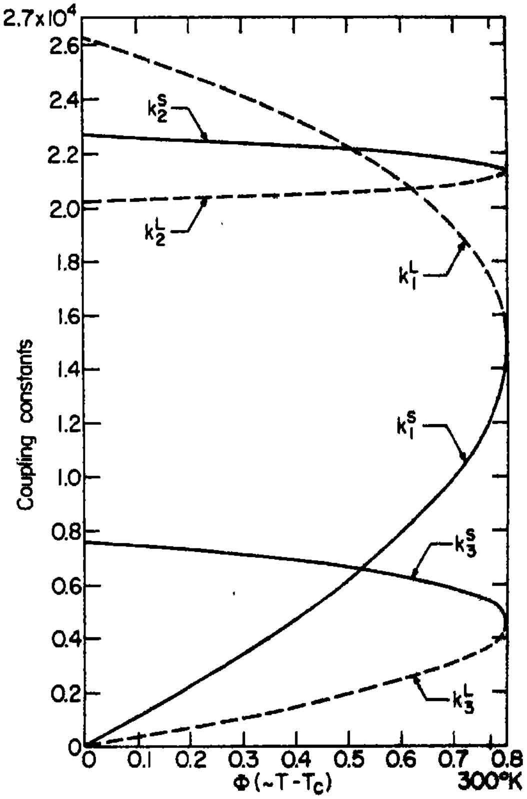

FIG. 2. The coupling constants, k_1, k_2 and k_3 in units of rad^2 g sec^{-2} as a function of the parameter $\Phi(\sim T-T_c)$ for the two solutions retained ("*S*" and "*L*").

k_1, k_2 and k_3 as a function of $\Phi(\sim T-T_c)$. We shall distinguish between the two solutions by superscripts "S" and "L"; the reason for this will become apparent when the atomic displacements are discussed.

The relative atomic displacements corresponding to the three optical frequencies can now be obtained. In Fig. 3, we plot the relative displacements, y_2/y_1, y_3/y_1, y_5/y_1, for both solutions which correspond to the low frequency "ferroelectric" mode. One can now see the reason for the labels "L" and "S". As $\Phi \rightarrow 0$ ($T \rightarrow T_c$), the displacements labelled "S" are:

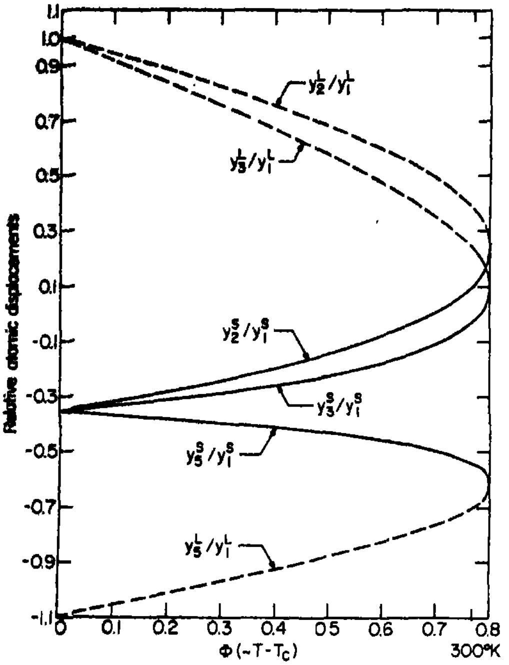

FIG. 3. The relative displacements y_2/y_1, y_3/y_1, and y_5/y_1 for the two solutions ("S" and "L") for the low optical frequency mode as a function of $\Phi(\sim T-T_c)$.

$$S: y_2 = y_3 = y_4 = y_5 \neq y_1,$$

that is, the titanium ion vibrates against all the remaining ions. This is just the description of the ferroelectric mode discussed by SLATER and others.(5) Similarly, for the "L" solution we find:

$$L: y_1 = y_2 = y_3 = y_4 \neq y_5,$$

that is, the strontium ion vibrates against all the remaining ions. This is a proposal for the ferroelectric mode considered by LAST.(6) Thus, both possibilities are seen to fall out of the calculation. When $\Phi \neq 0$, neither simple model is seen to be adequate. However, it should be noted that it is possible that neither solution (S or L) is the proper one at $T = T_c$. If one includes all seven couplings, alternate solutions may appear.

In Figs 4 and 5 we show the relative displacements y_2/y_1, y_3/y_1 and y_5/y_1 for the "Last" solution which correspond to the intermediate and high optical frequencies, respectively. Figures 6 and 7 show the relative displacements y_1/y_2, y_3/y_2 and y_5/y_2 for the "Slater" solution and for the same

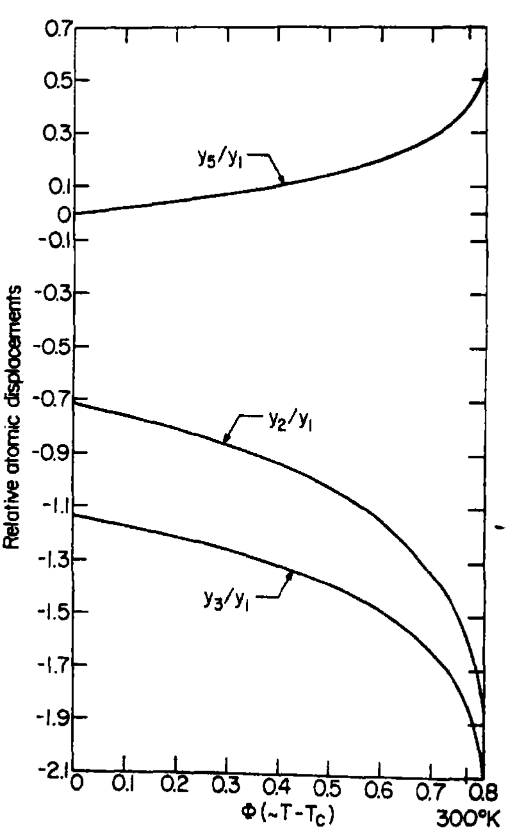

FIG. 4. The relative displacements y_2/y_1, y_3/y_1, and y_5/y_1 for the "Last" solution corresponding to the intermediate optical frequency mode as a function of $\Phi(\sim T-T_c)$.

two frequencies. The displacements of Figs 6 and 7 are relative to y_2 since $y_1 \rightarrow 0$ as $\Phi \rightarrow 0$. Note the breaks and changes in the scales of Figs 5 and 7.

We thus see that the high frequency mode is a vibration of the O_2 sublattice against the O_3 and O_4 sublattices which are rigidly fixed. This is in agreement with the assignment made by SPITZER(4) and in disagreement with the LAST(6) assignment. The two lower frequency motions essentially involve a fairly rigid motion of the entire oxygen framework (O_2, O_3 and O_4 sublattices). This is consistent with the observed ionic displacements from the cubic phase of ferroelectric materials of the perovskite structure as the material becomes polarized.(7) Since this indicates that oxygen-oxygen couplings are relatively strong, it is therefore reasonable that the highest frequency mode is a vibration between the oxygen sublattices. The two other modes involve little relative motion of the oxygen sublattices, so that it is again reasonable that their frequencies are both removed from the highest frequency, as has been observed.(4) That

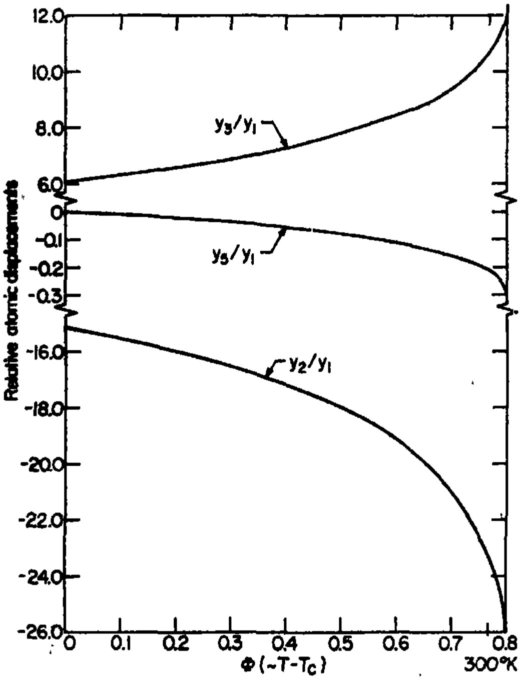

FIG. 5. The relative displacements y_2/y_1, y_3/y_1, and y_5/y_1 for the "Last" solution corresponding to the high optical frequency mode as a function of $\Phi(\sim T-T_c)$. Note the breaks and changes in the vertical scale.

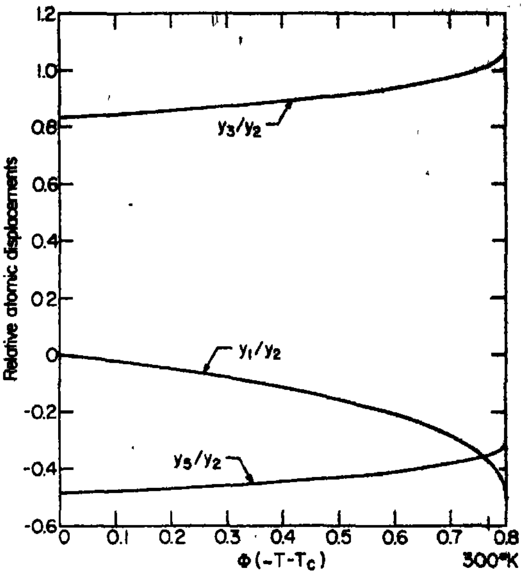

FIG. 6. The relative displacements y_1/y_2, y_3/y_2 and y_5/y_2 for the "Slater" solution corresponding to the intermediate optical frequency mode as a function of $\Phi(\sim T-T_c)$.

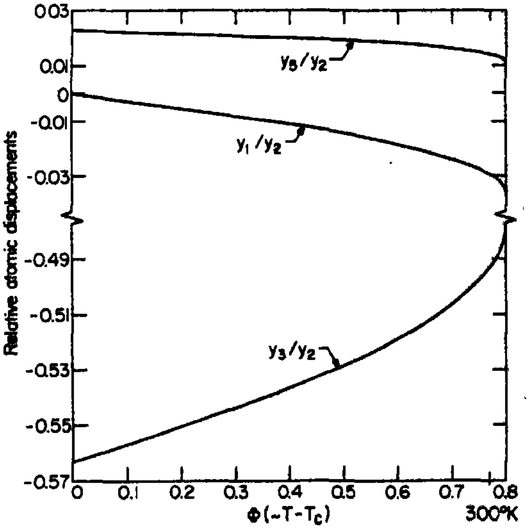

FIG. 7. The relative displacements y_1/y_2, y_3/y_2, and y_5/y_2 for the "Slater" solution corresponding to the high optical frequency mode as a function of $\Phi(\sim T-T_c)$. Note the breaks and changes in the vertical scale.

this high frequency is a common feature of the perovskite structure can be seen from reflectivity spectra.(6)

The torsional mode is infrared inactive. However, the torsional mode frequency has recently been measured by COWLEY(8) by means of inelastic neutron scattering. Cowley finds this frequency to be $5 \cdot 00 \times 10^{13}$ rad $\sec^{-1}$. Using the room temperature values of k_2 and k_3 from Fig. 2 ($\Phi = 0{\cdot}7656$) the torsional frequency is found to be $6 \cdot 09 \times 10^{13}$ rad $\sec^{-1}$ and $6 \cdot 35 \times 10^{13}$ rad $\sec^{-1}$ for the "Last" and "Slater" solutions, respectively. It is quite encouraging that the torsional frequency calculated on the basis of our simplified model falls in the right frequency range ($\omega_1 > \omega_T > \omega_2 > \omega_3$), and that it is within about 25 per cent of the measured value. With this additional piece of information, that is, the measured torsional frequency, one could consider an additional coupling. One then would have four equations in four unknowns (k_1, k_2, k_3 and k_4). Since the O_3–O_4 coupling enters only into the expression for the torsional frequency* it would be trivial to consider it as the fourth parameter, k_4. Then, all of our previous results concerning the optical modes are still true and the observed and calculated torsional frequency now exactly agree. The value of k_4 obtained in this way is negative, in agreement with what one expects.(3) Alternatively, the fourth parameter could be taken to be the bond angle coupling between the titanium and O_3 and O_4 oxygen atoms. Preliminary results for this case indicate that our conclusions concerning the high frequency mode are again obtained. The question now arises as to whether it is possible to find any additional experimental information which would enable us to uniquely determine the three neglected couplings. The three measured elastic constants in these materials immediately suggest themselves. Indeed, a procedure such as this was considered in Ref. 2. The elastic constants are however determined by the long wavelength acoustic motion of the lattice. This is motion in which each of the inequivalent sublattices is not rigid and hence, can be of little help in determining the sublattice couplings. We have calculated the elastic constants however using the initial three sublattice couplings obtained as springs between nearest neighbors. At room temperature the values obtained in this way are only about 20 per cent of the measured values.(9) This is not unreasonable, since the long range driving forces contribute most for the long wavelength optical modes. Couplings determined for these modes should therefore be smaller than the couplings for the acoustic modes. At the present time, we have no answer to the question of how to determine the additional couplings.

In conclusion then, the model considered here, although admittedly a simplification, enables one to make some simple, reasonable statements concerning the nature of the atomic displacements associated with the infrared active optical modes. The question of which solution, i.e., the "Last" or "Slater" one, represents the actual situation for the ferroelectric mode *cannot* be answered by the work presented here, although it does show that neither should be expected to exactly prevail at temperatures other than the Curie temperature.

Acknowledgement—The authors are greatly indebted to Miss W. M. DOHERTY for her help with the numerical calculations.

REFERENCES

1. COCHRAN W., *Advances in Physics*, **Vol. 9**, p. 387 (edited by MOTT N. F., Taylor and Francis, London (1960); ANDERSON P. W., *Fizika dielektrikov* (edited by SKANAVI G. I.) Akademicâ Nauk S.S.S.R. Fisicheskii Inst. im P. N. Lebedeva, Moscow (1960) in Russian; LANDAUER R., JURETSCHKE H. and SOROKIN P., unpublished manuscript; SILVERMAN B. D. and JOSEPH R. I., *Phys. Rev.* **129**, 2062 (1963); JOSEPH R. I. and SILVERMAN B. D., *Bull. Amer. phys. Soc.* **8**, 62 (1963), to be published in *Phys. Rev.*; SILVERMAN B. D. *Phys. Rev.* **131**, 2478 (1963).
2. RAJAGOPAL A. K. and SRINIVASAN R., *J. Phys. Chem. Solids* **23**, 633 (1962).
3. DVOŘÁK V. and JANOVEC V., *Czech. J. Phys.* **B12**, 461 (1962).
4. BARKER A. S., Jr., PhD. thesis, University of California, Berkeley, 1962 (unpublished); BARKER A. S., Jr. and TINKHAM M., *Phys. Rev.* **125**, 1527 (1962); SPITZER W. G., MILLER R. C., KLEINMAN D. A. and HOWARTH L. E., *Phys. Rev.* **126**, 1710 (1962); COWLEY R. A., *Phys. Rev. Letters* **9**, 159 (1962); LEFKOWITZ I., *Proc. phys. Soc.* **80**, 516 (1962).

---

* This fourth parameter is taken into account in the equations of motion by adding $-k_4y_3+k_4y_4$ and $+k_4y_3-k_4y_4$ to the right-hand sides of the third and fourth lines of equation (1), respectively. For the optical modes $y_3 = y_4$ so that k_4 drops out of the equations of motion. The torsional frequency is now given by $\omega^2 = 4/m(k_2+k_3+\frac{1}{2}k_4)$.

5. Slater J. C., *Phys. Rev.* **78**, 748 (1950); Devonshire A. F., *Phil. Mag.* **40**, 1040 (1949); Megaw, Helen D. *Acta Cryst.* **5**, 739 (1952).
6. Last J. T., *Phys. Rev.* **105**, 1740 (1957).
7. Shirane G., Pepinsky R. and Frazer B. C., *Phys. Rev.* **97**, 1179 (1955); Frazer B. C., Danner H. and Pepinsky R., *Phys. Rev.* **100**, 745 (1955); Evans H. T., Massachusetts Institute of Technology, Laboratory for Insulation Research. Technical Report No. 58 (1953).
8. Cowley R. A., private communication.
9. Bell R. O. and Rupprecht G., *Phys. Rev.* **129**, 90 (1963).

J. Phys. Chem. Solids Pergamon Press 1963. Vol. 24, pp. 1357–1361. Printed in Great Britain.

SECOND-ORDER EXCHANGE INTERACTIONS FROM SPIN WAVE RESONANCE

R. WEBER and P. E. TANNENWALD

Lincoln Laboratory,* Massachusetts Institute of Technology, Lexington 73, Massachusetts

(*Received* 5 *April* 1963)

Abstract—The temperature variation of the ferromagnetic exchange parameter D in the spin wave dispersion relation $E = Dk^2$ has been measured to high precision by the spin wave resonance method in a 81–19 permalloy film. D was found to vary as T to the $2{\cdot}5 \pm 0{\cdot}1$ power from 0 to 80°K in accordance with the theory of spin wave interactions; at higher temperatures D follows a 3/2 temperature variation. The effects of thermal expansion are shown to be negligible. The value of D at 0°K from s.w.r. is $0{\cdot}47 \times 10^{-28}$ erg cm² and from the Bloch law is $0{\cdot}41 \times 10^{-28}$ erg cm². On the assumption of a localized model, the respective exchange integral values are $J = 277\ k$ and $J = 244\ k$.

1. INTRODUCTION

SINCE the original description by BLOCH of the magnetization in terms of spin waves, experimenters(1) have attempted to make precise determinations of the temperature variation of the magnetization while theorists have tried to explain the observed deviations from the simple $T^{3/2}$ dependence which is generally regarded to hold at low temperatures, or interpret the deviations as evidence of inapplicability of the model. With the introduction of spin wave interactions into the Bloch localized electron spin wave model,(2) a term proportional to T^4 appears as a correction to the $T^{3/2}$ magnetization law. The origin of this term can be seen in a physical way from a semiclassical picture of spin wave interactions,(3) which predicts a temperature variation of the exchange parameter D (D is defined through the dispersion relation $E_k = Dk^2$, where E_k is the energy of excitation of a spin wave with wave vector k) proportional to $T^{5/2}$. When this is re-inserted into the first order Bloch law,

$$\frac{M}{M_0} = 1-A_0\left(\frac{T}{D}\right)^{3/2},$$

it leads to Dyson's expression

$$\frac{M}{M_0} = 1-A_0\left(\frac{T}{D}\right)^{3/2}-A_8T^4,$$

where structure-dependent terms have been omitted. It would be exceedingly difficult to determine the spin wave interaction term from magnetization data; however, it has proved to be possible to determine second-order exchange interactions from a measurement of the temperature variation of D itself by the spin wave resonance s.w.r. method.† There is no general agreement on the proper theoretical description of a ferromagnetic metal; however, in the spirit of HERRING and KITTEL,(5) there should be some validity in interpreting the present results in terms of the Bloch–Dyson model.

In the following Sections a brief description is given of the experimental apparatus and techniques, and a careful analysis is made of the data. Because of the small magnitude of the effect, the possible influence of thermal expansion on the exchange parameter must be especially considered.

---

* Operated with support from the U.S. Army, Navy and Air Force.

† Earlier results by this method on a 95 per cent Ni–5 per cent Fe film were *inconclusive because of* insufficient precision in the experimental techniques (Ref. 4.)

Secondary results are the determination of the exchange integral from s.w.r. and from the Bloch magnetization law, giving two values that are consistent.

2. EXPERIMENTAL PROCEDURE

In the spin wave resonance method,[6] the microwave absorption spectrum of a thin film is recorded as a function of the d.c. magnetic field which is perpendicular to the film plane. A given recording contains sufficient information to establish that the spin wave peaks selected obey the square-law dispersion relation, to obtain their separation in magnetic field, to compute the exchange constant (provided the film thickness is known), and to determine the value of the field for the main ferromagnetic resonance. In order to determine values of the saturation magnetization and the g-factor, it is necessary also to measure the magnetic field for resonance for the geometry in which the d.c. field is parallel to the surface of the film. To proceed this far, standard techniques are satisfactory. However, in order to study second-order exchange interactions, one must measure the change in separation between adjacent spin wave peaks. Since this involves the small change (10 per cent from 0 to 300°K, or 0·5 per cent from 0 to 80°K) in the difference ($\sim$500 Oe) between two large quantities ($\sim$ 11,000 Oe), special care in instrumentation is required.

To maintain the temperature constant to within ±0·1°K from 1·5 to 300°K for periods of at least 10 min, i.e., the time required to record a spectrum, a quadruple dewar system was designed and constructed. The X-band microwave cavity was enclosed in a copper dewar which had a heating element (10 W) wound on its outer surface. The amount of thermal contact between the cavity and the inner dewar was controlled, and largely determined, by the amount of helium exchange gas that was present in the dewar. The copper dewar was surrounded by a brass-bottomed stainless steel dewar, thermal contact being made by a fixed brass rod between the bottoms of the dewars and by the controlled atmosphere. The assembled temperature arm, in turn, fits into a standard glass double dewar system which could be placed in the 3¼ in. air gap of an electromagnet. By varying the vapor pressure above the cryogenic fluid surrounding the steel dewar, the pressures of the two exchange gases, and the thermal energy supplied by the heating element to the copper can, it was possible to control and stabilize the temperature satisfactorily over the entire range. The temperature itself was determined by a variety of means. Thermocouples were used over the entire scale, but in conjunction with a platinum resistor above about 40°K and germanium and carbon resistors below 20°K. The temperature-sensing elements were fastened to the copper X-band cavity directly across the thickness of the copper from the film.

A n.m.r. gaussmeter was modified so that as the d.c. magnetic field, from a 22-in. Varian electromagnet, was swept from high field ($\approx$15,000 Oe) to low field ($\approx$11,000 Oe) values in a period of approximately 6 min, a series of n.m.r. pips with a nominal spacing of 70 Oe, was superposed on the abscissa of the absorption recording. For well-defined spin wave peaks it was possible to obtain a precision of ±0·2 Oe in the determination of the absolute value of the magnetic field required for each resonance, while for the main peaks, due to their broadness, the precision was ±1·0 Oe.

In practice, with proper perpendicular orientation of the sample with respect to the d.c. magnetic field, once the temperature became sensibly constant for a minute or two, an absorption spectrum was recorded as a function of the field, at constant microwave frequency. From approximately 2 to 300°K more than 60 such recordings were made. For the parallel field case, because of the insensitivity of the resonance to temperature, 10 measurements were sufficient to obtain a smooth relationship between the magnetic field and temperature. The latter measurements were precise to ±1·0 Oe and were made in separate runs so as to avoid constant reorientation of the film in the d.c. magnetic field.

Additional errors of the same order of magnitude as those already mentioned above were introduced by small deviations from perfect orientation and by temperature fluctuations caused by turbulence in the cryogenic bath surrounding the temperature arm, especially above 100°K.

As is well-known to workers in the field, different evaporated magnetic films do not always have the same magnetic properties. These differences arise from many complex factors associated with the evaporation process, some of which are not well understood. The selection of the magnetic film sample in the present experiment was based on the following criteria: bulk values for the saturation magnetization and g-factor, and a large number of well-resolved spin wave peaks.

3. ANALYSIS OF DATA AND RESULTS

The permalloy film used was a 81 per cent Ni–19 per cent Fe film of 5,040 ± 100 Å thickness. At room temperature the exchange constant $A(D/\gamma\hbar = 2\,A/M)$ was found to have a numerical value of $0{\cdot}93\times10^{-6}$ erg/cm. Measurements of the perpendicular and parallel fields for the main resonance gave a magnetization $4\pi M$ of 10,400 ± 30 Oe at room temperature and a spectroscopic splitting factor $g = 2{\cdot}08 \pm 0{\cdot}01$ which was constant over the whole temperature range of the experiment. The probable error associated with $4\pi M$ and g is due to the uncertainty in calculating the exchange shift in $H\|$ and $H\perp$ (The exchange shift is the shift of the magnetic field for ferromagnetic resonance in a material with non-zero conductivity referred to the condition of zero conductivity, due to the effect of gradient of r.f. magnetization. See e.g., Ref. 17). The magnetic anisotropy in the plane of the film was less than 2 Oe at room temperature.

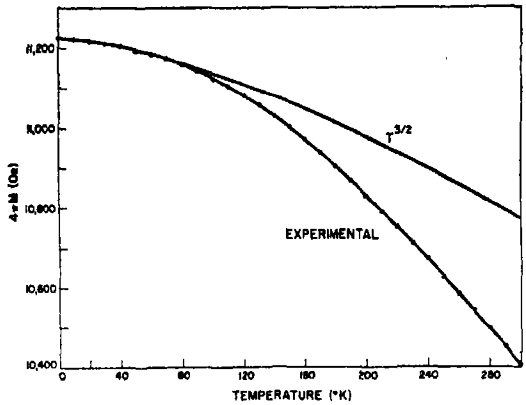

FIG. 1. Temperature dependence of saturation magnetization of an 81–19 permalloy film determined by ferromagnetic resonance measurements, compared with a $T^{3/2}$ relation. Slope is 1·5 ± 0·1 from 0 to 80°K.

The experimental dependence of the magnetization on the temperature from 0 to 300°K shown in Fig. 1 was obtained by fitting smooth curves to the perpendicular field data (more than 60 points) and to the parallel field data (10 points) from 2 to 300°K and substituting pairs of values into the appropriate ferromagnetic resonance expressions. From 0 to 80°K the curve thus derived can be accurately fitted by the expression $M = M_0\,[1-7{\cdot}76\times10^{-6}T^{3/2}]$. From approximately 90 to 300°K, the temperature dependence is 1·8 ± 0·1.

The data for the temperature dependence of the exchange parameter D were obtained in a similar fashion as those for the temperature dependence of the magnetization: that is, separate smooth curves were drawn for the magnetic field value for resonance as a function of temperature for two adjacent odd spin wave peaks from 3·2 to 300°K. Each curve was based on more than sixty pieces of data. The resultant spin wave peak separation, extrapolated to 0°K, is shown in Fig. 2. In a spin wave resonance experiment the magnetic field separation between odd peaks is given by

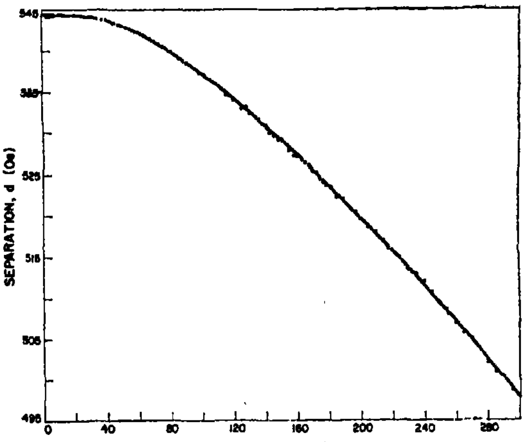

FIG. 2. Separation d of the sixth and seventh odd spin wave peaks (counted from the main resonance) as a function of temperature. The quantity d, which is proportional to D, is defined in text.

$$H_p - H_{p+2} = \frac{4D}{\gamma\hbar}\left(\frac{\pi}{L}\right)^2[p+1] \equiv d,$$

where L is the film thickness. Since the g-factor was found to be temperature independent, the separation of two spin wave peaks as a function of temperature is proportional to the temperature variation of the exchange parameter D. In order to obtain the power dependence of D on temperature, the data of Fig. 2 are displayed on a log–log plot in Fig. 3. There are two distinct regions in which a straight line fits the data well:

$$D = D_0(1-aT^{2.5\pm0.1}) \quad \text{for} \quad T < 80°\text{K}$$

$$D = D_1(1-bT^{1.5\pm0.1}) \quad \text{for} \quad T > 90°\text{K}.$$

4. DISCUSSION OF RESULTS

4.1 *Magnetization*

To what extent do the experimentally determined spin wave interactions, when substituted into the relation $\Delta M/M_0 \propto (T/D)^{3/2}$, correct the fit of the magnetization data shown in Fig. 1? The answer is that in the region where D varies as $T^{5/2}$, that is between 0 and 80°K, the correction is of insignificant magnitude, which is consistent with the fact that no correction is required over that range. Above 80°K, the discrepancy in Fig. 1 is reduced by only 20–25 per cent.

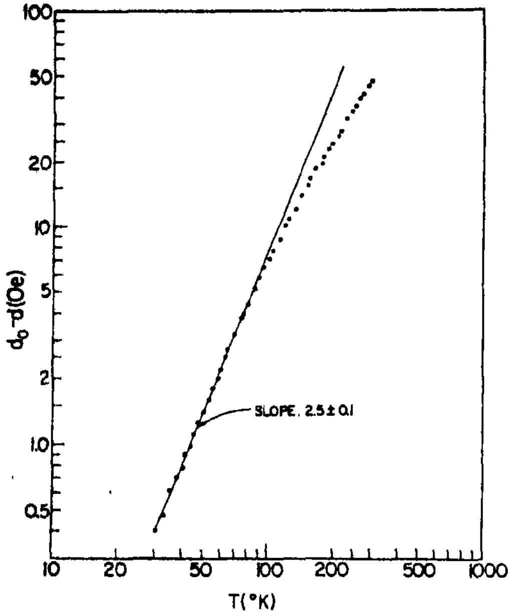

FIG. 3. Log–log plot of peak separation vs. temperature. In the low temperature region slope is 5/2, at higher temperatures it is 3/2.

4.2 *First-order exchange interactions*

The present s.w.r. data give $D = 0{\cdot}44\times10^{-28}$ erg cm² at room temperature and $D = 0{\cdot}47\times10^{-28}$ erg cm² at 0°K. An independent value of D, from measurements on the same sample, can be calculated from the $T^{3/2}$ coefficient in the Bloch law,

$$M = M_0\left[1-\frac{g\mu_B}{M_0}\zeta\left(\frac{3}{2}\right)\left(\frac{kT}{4\pi D}\right)^{3/2}\right],$$

where μ_B is the Bohr magneton, g is the spectroscopic splitting factor, and $\zeta(x)$ is the Riemann zeta function; the result, taken from the data of Fig. 1 between 0 and 80°K, is $D = 0{\cdot}41\times10^{-28}$ erg cm². The significance of this comparison is that the experimentally determined spin wave dispersion coefficient gives correct numerical results when inserted into the Bloch law, which is derived only from a statistical treatment of spin wave excitations.

If, further, a specific localized model is assumed, the exchange integral J can be calculated from the relation $D = \frac{1}{3}SJz\rho^2 = 2Ja^2S$ for a f.c.c. crystal, where S is the effective spin value, z is the number of nearest neighbors, ρ is the interatomic spacing and a is the lattice spacing. Then $J = 277\,k$ from s.w.r. near 0°K.

On some occasions in the past(7,8) the oversimplified viewpoint has been adopted that J could be calculated at a particular temperature by substituting measured values for D and S (i.e., $M/g\mu_B$) from the relation $D = \frac{1}{3}SJz\rho^2$. On this basis J is approximately independent of temperature because the most important numerical contribution to ΔD comes from the range where D varies as $T^{3/2}$ while S also has roughly a $T^{3/2}$ dependence. This explains the assertion in previous works that J is temperature independent in cobalt(7) and nickel.(8)

4.3 *Second-order exchange interactions*

Up to 80°K, the theoretically predicted (DYSON,(2) OGUCHI,(9) BROUT–ENGLERT,(10) KEFFER–LOUDON(3)) temperature variation of D due to spin wave interactions is verified experimentally. The experimental data lead to $D = D_0(1-15\times10^{-8}T^{5/2})$, while the theory gives the coefficient $0{\cdot}27\times10^{-8}$ from the expression

$$D = D_0\left[1-\pi\rho^2\frac{g\mu_B}{M_0}\zeta\left(\frac{5}{2}\right)\left(\frac{kT}{4\pi D_0}\right)^{5/2}\right].$$

A simple effective long-range exchange interaction $r \simeq 7{\cdot}5\rho$ would formally account for this discrepancy. However, such an effective parameter is inconsistent with the result of correlating J deduced from the Curie temperature and $J\rho^2$ from s.w.r. It is conceivable, though, that the apparent discrepancy could be reconciled through the introduction of a long-range interaction such as the Ruderman–Kittel–Yosida type.

The possible effects of thermal expansion must be examined since the experimentally measured quantity d is proportional to $D/L^2 \propto D/a^2$ and the theoretically desired quantity D is proportional to $J(a)a^2$. The coefficient of thermal expansion, β, of pure nickel between 0 and 80°K can be expressed as $\beta = 8\times 10^{-10}\ T^2$ from the data of Nix and MacNair.(11) Using β for pure nickel, the maximum fractional thermal expansion over the 80°K range where the $T^{5/2}$ relation holds is less than 3×10^{-5} compared with $\Delta d/d = 5\times 10^{-3}$ over the same range. Below the Curie temperature of nickel, β for high-nickel permalloy is smaller than β for nickel.(12)

The subject of the dependence of the exchange integral J on the lattice parameter, a, is complex and only qualitative arguments can be given. It is known that for Ni–Fe alloys of high nickel content the Curie temperature (and thus J) increases as a decreases.(13) The following argument leads to the conclusion that for 81–19 permalloy the inverse power dependence of J on a is small. The Curie temperature for 81–19 permalloy is slightly below the maximum occurring in nickel–iron alloys at about 70 per cent nickel.(14) This maximum apparently corresponds to the maximum of the Bethe–Slater exchange energy curve,(15) and consequently 81–19 permalloy falls near the peak of the Bethe–Slater curve on the side where the slope is negative and not too steep. Thus $D \propto J(a)a^2$ is probably not highly dependent on a. Irrespective of the above qualitative argument, since the experimentally determined $\Delta d/d$ is 5×10^{-3} between 0 and 80°K and $\Delta a/a$ is less than 3×10^{-5} over the same range, the $T^{5/2}$ spin wave interaction term is more than one order of magnitude larger than thermal expansion effects up to $n = 13$ in the proportionality $J \propto a^{\pm n}$. Of course, an attempt could be made to deduce the strain dependence of J directly by measuring s.w.r. in strained films. However, such experiments are difficult to carry out, especially at low temperatures.

Recently neutron scattering experiments at Harwell(16) have been carried out to measure the effective exchange interaction D as a function of temperature in nickel. The Harwell group can fit its data to a $T^{5/2}$ dependence over a range extending from 4°K to near the Curie temperature, but with quite a large uncertainty associated with the low temperature points. Comparison of the results with the present s.w.r. experiment is not conclusive because of the relative difficulty of obtaining accurate neutron scattering data at low temperatures—precisely the region where the spin wave interaction treatment is valid.

Acknowledgement—We wish to express our appreciation to Dr. H. J. Zeiger for many enlightening discussions, especially concerning the theoretical aspects of this problem.

REFERENCES

1. E.g., Pugh E. W. and Argyle B. E., *J. appl. Phys.* **33,** 1178 (1962) is the most recent one and includes references to earlier papers.
2. Dyson F. J., *Phys. Rev.* **102,** 1230 (1956).
3. Keffer F. and Loudon R., *J. appl. Phys.* **32,** 2S (1961).
4. Tannenwald P. E., *J. phys. Soc. Japan* **17,** Suppl. B-I, 592 (1962).
5. Herring C. and Kittel C., *Phys. Rev.* **31,** 869 (1951).
6. Seavey M. H., Jr. and Tannenwald P. E., *J. appl. Phys.* **30,** 227S (1959).
7. Tannenwald P. E. and Weber R., *Phys. Rev.* **121,** 715 (1961).
8. Nosé H., *J. phys. Soc. Japan* **16,** 2475 (1961).
9. Oguchi T., *Phys. Rev.* **117,** 117 (1960).
10. Brout R. and Englert F., *Bull. Amer. phys. Soc.* **II6,** 55 (1961).
11. Nix F. C. and MacNair D., *Phys. Rev.* **60,** 597 (1941).
12. Bozorth R. M., *Ferromagnetism*, p. 447, Van Nostrand, New York (1951).
13. Bozorth R. M., *Ferromagnetism*, p. 445, Van Nostrand, New York (1951).
14. Bozorth R. M., *Ferromagnetism*, p. 446, Van Nostrand, New York (1951).
15. Bozorth R. M., *Ferromagnetism*, p. 444, Van Nostrand, New York (1951).
16. Lowde R. D. Private communication.
17. Rado G. T. and Weertman J. R., *J. Phys. Chem. Solids* **11,** 315 (1959).

J. Phys. Chem. Solids Pergamon Press 1963. Vol. 24, pp. 1363–1367. Printed in Great Britain.

CONCENTRATION DEPENDENCE OF THE TRANSITION TEMPERATURE IN DILUTE SUPERCONDUCTING ALLOYS

LEWIS T. CLAIBORNE

Texas Instruments Incorporated, Dallas, Texas

(*Received* 1 *May* 1963; *revised* 14 *June* 1963)

Abstract—A semi-empirical formalism is developed to account for the detailed dependence of the superconducting transition temperature of dilute alloys on solute concentration. A mismatch of solute and solvent ion sizes causes small strain fields in the regions surrounding the solute ions. The precise change in transition temperature, ΔT_c, for a particular solute concentration, N_s, is derived by averaging the strain over the entire sample and reducing the strain field by a factor $\exp\{\alpha - \xi r_{\mathrm{eff}}^{-1}\}$, where α is a constant of order unity, ξ is the coherence distance, and r_{eff} is the total length of the strained region within ξ. The length, r_{eff}, is proportional to $N_s^{1/3}$. It is found that the strain is proportional to ΔR, the difference in ionic radii. Previously reported data on the effects produced by various solutes in tin, indium, and aluminum are explained in terms of this model.

1. INTRODUCTION

EXPERIMENTS have shown that the transition temperature, T_c, of an alloyed superconductor differs from the T_c of the solvent by an amount which depends on the concentration and nature of the solute. So far, the variation of T_c for sufficiently low density has been explained. In this paper an approximate theory for the effects of larger concentrations is developed by using a semi-empirical approach introduced by CLAIBORNE and EINSPRUCH(1) in their analysis of the temperature dependent ultrasonic absorption peaks in niobium–zirconium alloys. It was found necessary to consider the change in energy gap, $\Delta\epsilon_0$, due to a local strain field extending over distances, r_0, somewhat shorter than the coherence distance, ξ. The $\Delta\epsilon_0$ arising from a macroscopic strain $(\Delta L/L)$, with L a length greater than ξ, has been theoretically predicted by MOREL(2) and his values for $[\mathrm{d}\log\epsilon_0/\mathrm{d}\log L]$ are in good agreement with measured changes in the transition temperature, T_c, due to changes in volume, where T_c is proportional to ϵ_0. However, the $\Delta\epsilon_0$ due to localized strain must be greatly reduced because of the non-local nature of the electron-electron pairing interaction. CLAIBORNE and EINSPRUCH postulated that when $r_0 < \xi$, the magnitude of $\Delta\epsilon_0$, averaged over the region defined by ξ, must be reduced by the empirical factor $\chi(r_0) \equiv \exp\{\alpha - \xi r_0^{-1}\}$ where α is a constant of order unity. The form of the function $\chi(r_0)$ was suggested by the non-local nature of the superconducting state; its inclusion in the theory led to results consistent with experiment.

LYNTON *et al.*(3) and CHANIN *et al.*(4) have measured the change of the transition temperature, ΔT_c, as a function of solute concentration in the tin, indium and aluminum systems. With the exception of gallium in indium, it was found that for small solute concentrations ($\gtrsim 0{\cdot}1$ per cent) the transition temperature of each system decreased linearly, with slope $-2{\cdot}7\times10^{-6}$ (°K cm), as a function of the inverse of the electron mean-free path, l_e. PIPPARD(5) and ANDERSON(6) have discussed possible origins of this mean-free path effect. Following the notions of PIPPARD and ANDERSON, TSUNETO(7) has made a detailed calculation of the dependence of T_c on l_e and has found that indeed T_c should decrease linearly with l_e^{-1} until $h^{-1}\tau k_B T_c < 1$, where τ is the normal impurity-limited electron relaxation time, h is Planck's constant, and k_B is the Boltzmann constant. At this point there should be a rapid change in slope, then T_c should decrease logarithmically with l_e^{-1}. However, the data indicated that after the initial linear region (region a) the variation of

T_c with l_e^{-1} is strongly dependent on the particular solute involved (region *b*). As discussed by BARDEEN and SCHRIEFFER,(8) the solutes for which the valence is higher than that of the solvent ($\Delta Z > 0$) result in a strong increase in T_c with an increase in concentration, while those with ($\Delta Z < 0$) result in a strong decrease in T_c. In terms of charge density and density of states, the origin of this behavior is not clear.

2. DEVELOPMENT OF THEORY

It will be shown below that a consideration of the strain field about each solute ion which includes the empirical function $\chi(r_0)$, leads to a relation between the density of solute ions N_s and ΔT_c which agrees remarkably well with the available data in region *b*. First, however, some qualitative features of the experimental data should be pointed out. In Fig. 1, ΔT_c data for several solutes in indium are plotted vs. $\rho^{1/3}$ ($= N_s^{1/3}N_0^{-1/3}$) where N_0 is the number of indium ions per unit volume in the pure state (see Ref. 4).

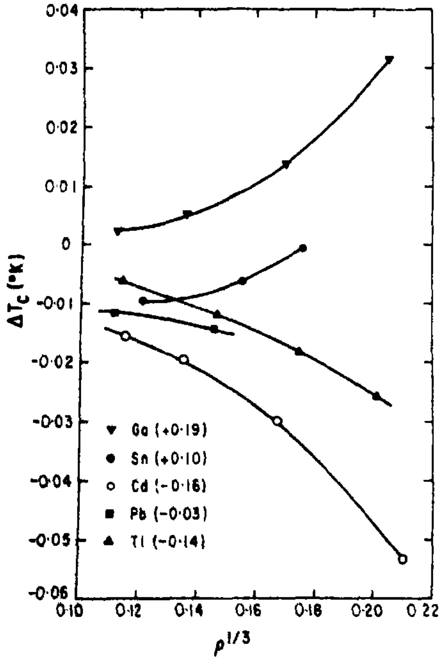

FIG. 1. ΔT_c(°K) vs. $\rho^{1/3}$ for various solutes in indium (data from Ref. 4). Symbols for the solutes are given in the figure. The numbers in parentheses are the values of ΔR in Angstrom units for the respective solutes (Ref. 10).

The ΔR values listed in Fig. 1 are defined by $\Delta R \equiv R_0 - R$, where R_0 is the radius of an indium ion and R is the radius of a solute ion. It can be seen that: (1) the absolute magnitude of the slope of ΔT_c is a rapidly increasing function of $\rho^{1/3}$; (2) the sign of ΔR seems to determine whether ΔT_c is an increasing or decreasing function of $\rho^{-1/3}$ in region *b*; and (3) the absolute magnitude of the change in ΔT_c for a given change in $\rho^{1/3}$ is approximately proportional to the absolute magnitude of ΔR. This suggests that ΔT_c depends on the mismatch between solute and solvent ion sizes rather than the difference in valence.*

Consider the highly idealized case of a one-dimensional solid solution which contains solute ions uniformly distributed at points x_i with separation $d \equiv N_s^{-1/3}$. Assume that any non-local effects are terminated at exactly $\pm\xi$ from the position of any solute ion and that the average strain associated with each solute ion extends to exactly $\pm r_0$ from each x_i. Consider first the low density limit $d > \xi + r_0$. This case is equivalent to the one which is assumed in Ref. 1. If $\chi(r_0)$ is a correct statement of the non-local effect of a strain field of short extent, then one would expect the observed change in T_c for a bulk sample to be

$$\Delta T_c = \left[\frac{\mathrm{d}\log T_c}{\mathrm{d}\log L}\right]\frac{T_c}{L}\Delta L, \tag{1}$$

where

$$\Delta L = \sum_{i=1}^{Ld^{-1}} \int_{x_i-B_i}^{x_i+B_i} \zeta_i(x-x_i)\,\mathrm{d}x \exp\{\alpha - \xi r_0^{-1}\}. \tag{2}$$

$\zeta_i(x-x_i)$ is the strain due to the presence of the ith solute ion, and the interval $[-B_i, B_i]$ is sufficiently large to include all non-zero values of $\zeta_i(x-x_i)$. The average strain about the ith solute ion is defined to be

$$\bar{\zeta} = (2B_i)^{-1} \int_{x_i-B_i}^{x_i+B_i} \zeta_i(x-x_i)\,\mathrm{d}x. \tag{3}$$

---

* Recently, Dr. W. DESORBO of the General Electric Research Laboratory has pointed out the correlation between the size of the solute atom and the transition temperature as well as the correlation with several other characteristics of the superconducting state [*Bull. Amer. phys. Soc.*, II, 7, 534 (1962) and *G.E. res. Lab. Rep.* No. 63-R1-(3249M) February 1963.

Equation (2) is equivalent to

$$\Delta L = \sum_{i=1}^{Ld^{-1}} 2r_0\zeta_i \exp\{\alpha - \xi r_0^{-1}\}, \tag{4}$$

where it is assumed that the exponential can be taken outside the integral. If $\zeta_i = \zeta$ for all i,

$$\Delta L = 2r_0\zeta L d^{-1} \exp\{\alpha - \xi r_0^{-1}\}. \tag{5}$$

The change in transition temperature is

$$\Delta T_c = \left[\frac{\mathrm{d}\log T_c}{\mathrm{d}\log L}\right] T_c\zeta(2r_0 d^{-1}) \exp\{\alpha - \xi r_0^{-1}\} \tag{6}$$

Thus, in the limit $d > \xi + r_0$, one would expect ΔT_c to be proportional to $N_s^{1/3}$. In view of the experimental observation that ΔT_c is proportional to ΔR, it will be postulated that $\zeta = a(\Delta R/R_0)$ where a is a constant.

It has long been recognized (cf. PIPPARD$^{(9)}$) that the interaction responsible for the superconducting state must involve only electrons contained within a shell in k-space defined by $\Delta k \sim [k_B T_c k_F E_F^{-1}]$, where the subscript F refers to the Fermi level. The coherence distance arises from a statement of the uncertainty principle, i.e., $\xi \sim \Delta k^{-1}$. The function $\chi(r_0)$ was introduced as an attempt to express the fact that any effect arising from an interaction over a distance shorter than ξ must be greatly reduced. If $d < \xi - r_0$ so that more than one solute ion is located within the interval $[-\xi + x_i,\ \xi + x_i]$, then the function χ must be modified to include the correlated effects of the additional strained regions within the interval. Now, the Cooper pair can be thought of as a wave packet spread over a distance 2ξ. The uncertainty principle requires that any attempt to localize a Cooper pair within one particular strained region ($2r_0 \ll 2\xi$) must fail. Therefore, it follows that the net effect of introducing additional strained regions within $\pm\xi$ of any x_i must not be a function of the exact coordinates of the strained regions but must be dependent only on the total extent of strain within 2ξ. On the basis of this qualitative argument it is asserted that $\chi(r_0)$ must go to $\chi(r_{\text{eff}})$ where r_{eff} is the sum of the distances over which each strained region extends within $\pm\xi$ of any solute ion.

The variation in T_c with $N_s^{1/3}$ for the bulk sample can be derived by considering r_{eff} as a function of $N_s^{1/3}$ for the interval $\pm\xi$ about any one of the solute ions. In the low density limit, $d > \xi + r_0$, for which equation (5) was derived, $r_{\text{eff}} = r_0$. When N_s is increased so that d goes from $(\xi + r_0)$ to $(\xi - r_0)$, r_{eff} increases from r_0 to $3r_0$. Similarly, when d goes from $(1/2)(\xi + r_0)$ to $(1/2)(\xi - r_0)$, r_{eff} increases from $3r_0$ to $5r_0$. In general, when $n^{-1}(\xi - r_0) > d > (n+1)^{-1}(\xi + r_0)$, n being a positive integer, $r_{\text{eff}} = (2n+1)r_0$; and when d goes from $n^{-1}(\xi + r_0)$ to $n^{-1}(\xi - r_0)$, r_{eff} goes from $(2n-1)r_0$ to $(2n+1)r_0$. In the limit that $\xi \gg r_0$ and $\xi d^{-1} \gg 1$, $r_{\text{eff}} \simeq (\xi d^{-1})r_0$, and $\chi(r_{\text{eff}}) \simeq \exp\{\alpha - d r_0^{-1}\}$. The relation between ΔT_c and N_s in this limit is

$$\Delta T_c = \left[\frac{\mathrm{d}\log T_c}{\mathrm{d}\log L}\right] T_c\zeta(2r_0)N_s^{1/3}\exp\{\alpha - (N_s^{1/3}r_0)^{-1}\}. \tag{7}$$

Note that in this limit ΔT_c is independent of ξ; but, for small n, $\chi(r_{\text{eff}})$ is strongly dependent on ξ. Unfortunately, in practice it would be essentially impossible to obtain the completely uniform distribution of solute ions necessary to observe the predicted variation of r_{eff} with N_s in the low density limit. However, region b of the experimental data should correspond to the limit $\xi d^{-1} \gg 1$, and equation (7) should be valid.

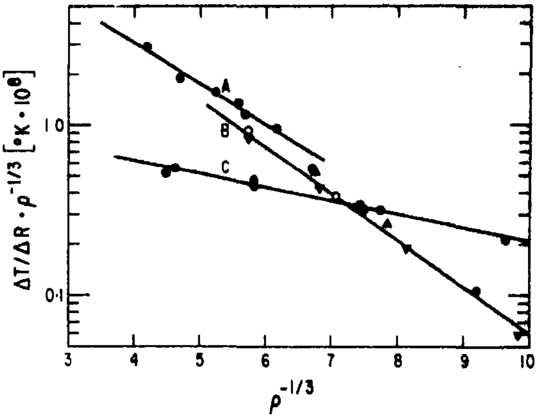

FIG. 2. Log $(\Delta T^*/\Delta R \cdot \rho^{-1/3})$ vs. $\rho^{-1/3}$ for the solvents (a) tin (b) indium, and (c) aluminum. The symbols used for Fig. 1 refer to the same solutes as seen on line (b).

3. COMPARISON OF THEORY AND DATA

In Fig. 2 $\log[\Delta T_c^*/(\Delta R) \cdot \rho^{-1/3}]$ is plotted vs. $\rho^{-1/3}$, where $\Delta T_c^* = \Delta T_c - \Delta T_c^0$ and ΔT_c^0 is the extrapolated ΔT_c at $N_s = 0$ ignoring the mean-free path effect in region a. From a consideration of

TSUNETO's calculation, ΔT_c^0 should be approximately equal to the ΔT_c at which $h^{-1}\tau k_B T_c$ becomes less than unity. It should be noted that the exponential term should dominate the logarithmic dependence of ΔT_c on l_e in region *b*. For any one solvent the log plot in Fig. 2 should give the same straight line for each solute, and the slope S should be $(N_0^{1/3} r_0)^{-1}$. The data plotted in Fig. 2 seem to indicate a common linear dependence on $\rho^{-1/3}$ for several solutes in each solvent. The slope seems to depend only on the particular solvent as one would expect.

There were only two cases out of the eighteen solutes in which the S and magnitude of ΔT_c determined from the data were significantly different from the S and magnitude of ΔT_c determined from Fig. 2, i.e., bismuth in indium and germanium in aluminum. LYNTON *et al.*[3] have pointed out that there will be a change in T_c with a change in density of states. This fact can be seen easily from the BCS relation $T_c \propto \epsilon_0 = k_B \Theta_D \exp\{-[n_F V(0)]^{-1}\}$ where $V(0)$ is the interaction constant for the formation of Cooper pairs. Undoubtedly, the correct expression for ΔT_c as a function of N_s must be a combination of Tsuneto's relation, Equation (7) and a term involving the explicit dependence on the density of states. It is possible, therefore, that the cases for which equation (7) is not valid are those cases for which the effect of the direct variation of the density of states becomes too large to be neglected. Another possible reason for the failure of equation (7) would be that the solid solution approximation is not valid for some solutes. Thus, we see that for the majority of cases equation (7) gives a reasonable approximation to the data.

The values of S determined from Fig. 2 are listed in the first column of Table 1. Calculated values of r_0 are listed in the second column. The ratios of the estimated r_0 to the nearest neighbor distance, A, are also given. Obviously, a ratio of r_0 to A which is less than unity is not meaningful. However, one would expect the perturbation introduced by the mismatch in ion sizes to extend over only a few nearest neighbor distances, thus, the order of magnitude of the values of r_0 are in fair agreement with this notion. In addition, one would expect the extent of the local strain fields to be greater in those materials which have a large modulus of elasticity. A comparison of the r_0 values with the moduli of elasticity reveals such a trend.

When N_s is sufficiently large so that $d \simeq 2r_0$, the strain field permeates the entire crystal. One would expect that an additional increase in concentration would only tend to increase the average strain; and, therefore, the variation of ΔT_c with $N_s^{1/3}$ should become approximately linear. For most of the solutes studied by CHANIN *et al.* and LYNTON *et al.* measurements were not taken at high enough concentrations for this change in behavior to be observed. However, for aluminum, which has the smallest S, the data for the solute Mg does seem to indicate a change from exponential to a much slower variation of ΔT_c with $N_s^{1/3}$ (see Fig. 3). If one attempts to determine α from the $N_s^{1/3}$ at which this change in slope occurs, one finds that $\alpha \sim 1{\cdot}5$. The strain $(a\Delta R/R_0)$ introduced by each impurity ion can be evaluated and is $\sim 0{\cdot}002$. These magnitudes are certainly not inconsistent with the model.

In conclusion, it should be pointed out that although a consideration of the non-local nature of the electron interaction led to the exponential factor $\chi(r)$, the final result (equation 7) is independent of ξ. Therefore any model which leads to an exponential dependence of ΔT_c on $N_s^{-1/3}$

Table 1

Solvent	s	r_0 (Å)	$r_0 A^{-1}$	E (10^{11} dyne cm^{-2})	μ (10^{11} dyne cm^{-2})
In	1·12	2·6	0·8	1·1*	
Sn	0·88	3·4	1·1	4·3*	1·7*
Al	0·11	21	7·3	7·1*	2·6*

* *Metals Handbook* (edited by LYMAN TAYLOR), 8th ed., Vol. I, p. 48, Amer. Soc. of Metals, Metals Park, Ohio (1961).

will achieve the same result. Conceptually, however, it seems logical to approach the problem from the standpoint of strain fields associated with impurity ions and to include the coherence effect. The important result of the present simplified model is the functional form of $\Delta T_c = aN_s^{1/3} \exp\{-bN_s^{-1/3}\}$. Certainly, the emphasis which should be placed on the actual detailed predictions for the constants a and b are debatable as would be the case with any such empirical model. However, the dependence of a on ΔR seems to be justified experimentally and gives weight to the strain field interpretation; the exponential dependence of ΔT_c on $N_s^{-1/3}$ seems to lend some weight to the form chosen for $\chi(r_0)$; finally, the variation of r_0 with the elastic properties of the solvent seems to give qualitative support for the simplified model.

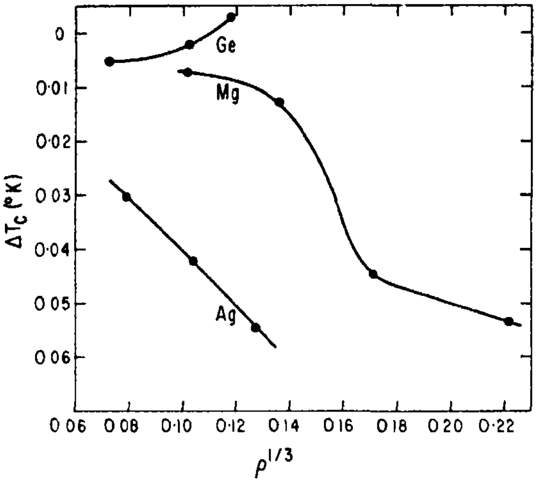

FIG. 3. ΔT_c(°K) vs. $\rho^{1/3}$ for Ag, Ge and Mg solutions in aluminum.

Acknowledgements—The author acknowledges with thanks the helpful discussions with Dr. NORMAN G. EINSPRUCH and Dr. ROBERT STRATTON.

REFERENCES

1. (a) CLAIBORNE L. T. and EINSPRUCH N. G., *Phys. Rev. Letters* **10**, 49 (1963); (b) CLAIBORNE L. T. and EINSPRUCH N. G., to be published, *Phys. Rev.*
2. MOREL P., *J. Phys. Chem. Solids* **10**, 277 (1959).
3. LYNTON E., SERIN B. and ZUCKER M., *J. Phys. Chem. Solids* **3**, 105 (1957).
4. CHANIN G., LYNTON E. and SERIN B., *Phys. Rev.* **114**, 719 (1959).
5. PIPPARD A. B., *J. Phys. Chem. Solids* **3**, 170 (1957).
6. ANDERSON P. W., *J. Phys. Chem. Solids* **11**, 26 (1959).
7. TSUNETO T., *Progr. theor. Phys.* **28**, 857 (1962).
8. BARDEEN J. and SCHRIEFFER J. R., *Progress in Low Temperature Physics* (edited by GORTER C. J.), Vol. 3, p. 170. North Holland, Amsterdam (1961).
9. PIPPARD A. B., *Proc. Roy. Soc.* **A216**, 547 (1953).
10. *Handbook of Physics and Chemistry* (edited by HODGMAN C. D.), 43rd ed., p. 2169. Chemical Rubber Publishing Co., Cleveland, Ohio (1961–1962).

J. Phys. Chem. Solids Pergamon Press 1963. Vol. 24, pp. 1369–1373. Printed in Great Britain.

THE SPECIFIC HEAT JUMP IN SUPERCONDUCTING LEAD*

C. A. SHIFFMAN, J. F. COCHRAN and M. GARBER

Center for Materials Science and Engineering, Massachusetts Institute of Technology, Cambridge Massachusetts

(*Received* 16 *April* 1963)

Abstract—We have measured the jump in the specific heat at the superconducting critical temperature of lead. We find $(\Delta C)_{T_c} = 57{\cdot}5 \pm 0{\cdot}6$ mJ-mole^{-1}-°K^{-1}, which is substantially higher than the previous calorimetric determination by Clement and Quinnell but which is in good agreement with the value obtained by Decker *et al.* from the temperature dependence of the critical field. Our result is relevant to the question of the energy dependence of the energy gap parameter $\Delta(\epsilon, T)$ in the BCS theory of superconductivity. We conclude that $\Delta(\epsilon, T)$ rises with ϵ, for small ϵ, in qualitative agreement with the calculations of Culler *et al.*

1. INTRODUCTION

As PART of a program to measure the thermodynamic properties of lead and mercury by calorimetric methods we have made a careful determination of the jump in the specific heat at the transition temperature of lead. The specific heat jump in lead has been observed previously by CLEMENT and QUINNELL$^{(1)}$ who measured C_n and C_s near T_c and derived ΔC by extrapolation. They found a value of 52·9 mJ-deg^{-1}-mole^{-1} which is in substantial disagreement with the value 58·1 derived by DECKER, MAPOTHER and SHAW$^{(2)}$ from magnetic measurements. The discrepancy is outside the stated ranges of error in the two experiments. Since Clement and Quinnell did not observe the transition directly it was decided to remeasure the specific heat in the neighborhood of the transition with a high resolution technique. In addition, KEESOM and VAN DER HOEVEN$^{(3)}$ recently found a substantial discrepancy below 4·2°K between the electronic specific heat, C_{es}, of lead and the predictions of the BARDEEN, COOPER, and SCHRIEFFER (BCS) theory.$^{(4)}$ Their result also disagrees with the extensive investigation of the critical field curve of lead by Decker *et al.* Resolution of the discrepancy between these measurements must await a precise determination of C_{es} over a wider range of temperatures than has heretofore been employed. However the jump in the specific heat can be used to check the result of Decker *et al.*, by means of the well known relation

$$(\Delta C)_{T_c} = \frac{VT_c}{4\pi}\left(\frac{dH_c}{dT}\right)^{2\dagger}_{T_c}.$$

The size of ΔC is also of interest because it can be used to study the energy dependence of the BCS gap parameter $\Delta(\epsilon, T)$. In the weak coupling approximation this dependence is ignored. This appears to be valid for metals like tin and aluminum where the agreement between theory and experiment is relatively good. In the case of lead, on the other hand, where the ratio of T_c to the Debye θ is five times as large as for tin, a higher order of approximation is required. Recently two

---

* This research was supported in part by the Advanced Research Projects Agency through contract No. SD90; and in part by the U.S. Army Signal Corps, The Air Force Office of Scientific Research, and The Office of Naval Research, through the Research Laboratory of Electronics, Massachusetts Institute of Technology.

† In what follows the subscript "T_c" will be dropped for convenience. Unless otherwise specified we will always refer to the jump at T_c.

solutions of the BCS integral equation have been published which take into account explicitly the energy dependence of Δ, the first by SWIHART[5] and the second by CULLER, FRIED, HUFF, and SCHRIEFFER.[6] These two calculations predict opposite signs for the initial variation of $\Delta(\epsilon, T)$ with energy. The sense of this variation can be determined experimentally from the size of ΔC, and we shall show that our measurement supports the theory of Culler *et al.*

TECHNIQUE AND ESTIMATE OF ERRORS

The steady warming method described by COCHRAN[7] was used to measure the specific heat with resolution comparable to the width of the transition. In this method the specimen is heated at a constant rate while the time intervals between successive nulls of a carbon resistance thermometer bridge are measured. The only modification to the apparatus described in Cochran's paper is the use of a phase-sensitive detector and magnetic-amplifier-driven relay to make a well defined mark on the strip chart record at the moment the bridge passes through null. With the elimination of human error in judging the location of the null on the chart the major source of random error was variation in the contact resistance of the bridge switches. With 1 Ω steps between nulls, corresponding to the desired temperature resolution, milli-ohm variations in the switches correspond to 2 per cent variations in ΔC. Only with careful wiping after each switch setting were the random errors kept small. The only important source of systematic error was the thermometer calibration. The corrections for the addenda and for the heat developed in the heater leads introduced negligible uncertainty by comparison. In order to calibrate the thermometer its resistance was measured as a function of bath pressure at about 20 points in the range between 1·9 and 4·2 degrees, and in addition the transition temperature of lead was used as a fixed point. For this purpose a small ellipsoid of pure lead was attached to the thermometer as a permanent part of the addenda. The transition was measured by a low frequency mutual inductance technique. This transition coincided with the center of the specific heat jump to within a millidegree even though the two specimens were taken from different batches of nominally 99·999% pure lead. (This suggests the use of lead as a practical secondary standard fixed point for the awkward region between 4 and 12 degrees.) T_0 was assigned the value 7·193°K taken from the gas thermometric measurements of FRANCK and MARTIN.[8] It was found by least squares analysis that the entire set of calibration points could be fitted to an expression of the form

$$\frac{1}{T} = A(\log R + C) + \frac{B}{(\log R + C)} - D$$

with an r.m.s. deviation of 1 to 2 millidegrees and an error at the lead point of less than a millidegree. In order to estimate the systematic error introduced by the choice of this form for $T(R)$ several other functions were tried and the values of dR/dT were compared. As a result of this study we estimate that absolute errors in the slope derived from the chosen equation were less than 1 per cent at the transition temperature of lead.

The specimen was cast in vacuum from 334 g of 99·999% pure lead. No attempt was made to grow a single crystal but since the melt was cooled slowly from one end to avoid a casting "pipe" it is quite likely that the crystalites were very large. The sharpness of the observed transition (< 0·006°K) was taken as evidence of sufficient purity for meaningful measurement of ΔC. The earth's magnetic field was compensated to within 0·01 G.

3. RESULTS

The specific heat in the neighborhood of the transition is shown in Fig. 1. The data displayed here are the result of some fifteen passes through the transition region made on two separate occasions and involving separate and independent thermometer calibrations. A systematic difference of 0·3 per cent between these runs has been removed in the figure by slipping one set of data over the other by a constant amount. For the sake of clarity some of the points have been omitted. Measuring intervals of 0·006°K were

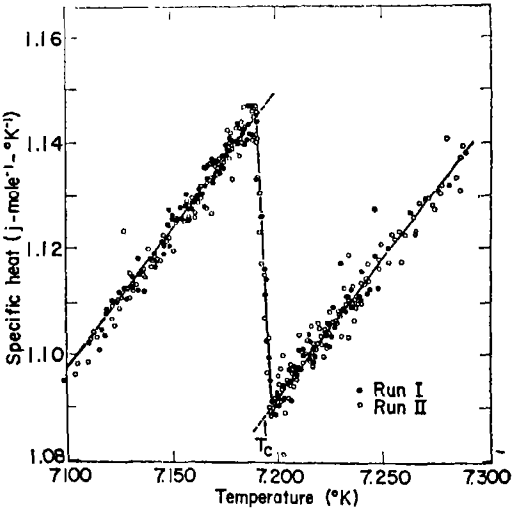

FIG. 1. The specific heat of lead vs. temperature near the transition temperature. The solid lines represent least-squares fits to the data on each side of the transition which have been extrapolated to obtain $(\Delta C)_{T_c}$.

used. ΔC was calculated separately for each run by fitting straight lines to the data in the 0·1 degree intervals on each side of the transition, extrapolating to the midpoint and subtracting. The two values of ΔC found in this way differed from each other by less than the probable error in each. The net result of the statistical analysis is $\Delta C = 57{\cdot}5 \pm 0{\cdot}6$ mJ-deg^{-1} mole^{-1}. This is in good agreement with the result of Decker *et al.* and in substantial disagreement with the estimate of Clement and Quinnell. The total specific heat is in good agreement with previous results. Near 7·5°K our measurements fall about 2 per cent below those of Keesom and VAN DEN ENDE(9) and lie about 3 per cent higher than the values given by Clement and Quinnell.

4. DISCUSSION

The excellent agreement between our measurement of ΔC and the value calculated from the critical field curve supports the thermodynamic consistency of the measurements of Decker *et al.* at temperatures near T_c. In particular, there can be no doubt that H_c rises above the value given by a parabolic law, at least near T_c. This is manifestly incompatible with a T^3 dependence for C_{es}, which is equivalent to the parabolic critical field curve. A much more complicated critical field curve than has heretofore been observed would be required to reconcile our result with the T^3 dependence observed at lower temperatures by Keesom and Van der Hoeven.

As we mentioned above, ΔC can be used to examine the energy dependence of the gap parameter in the BCS theory. According to Swihart the BCS expression for the specific heat jump, modified to allow for the energy dependence of Δ, is

$$(\Delta C)_{T_c} = \frac{3\gamma T_c}{\pi^2}\left[\frac{\Delta(0,0)}{kT_c}\right]^2\left[-\frac{d\delta^2}{dt}\right]_{t=1}\cdot I \qquad (1)$$

where

$$I = \int_0^\infty \frac{y^2 e^x dx}{(1+e^x)^2}$$

$$\delta = \Delta(0,T)/\Delta(0,0)$$

$$t = T/T_c$$

$$x = \epsilon/k\,T_c, \text{ and}$$

$$y = \Delta(\epsilon,0)\;\Delta(0,0).$$

$\Delta(\epsilon,\, T)$ has the usual definition in relation to the BCS energy parameter E,

$$E = [\epsilon^2+\Delta^2(\epsilon,T)]^{1/2} \qquad (2)$$

In the original BCS approximation Δ is not a function of ϵ, $y = 1$ and $I = \frac{1}{2}$. Using 4·18 for $2\Delta(0,0)/kT_c$(10,11) 3·06 mJ-mole^{-1}-°K^{-2} for γ(2), and the BCS value $(d\delta^2/dt)_{t=1} = -3{\cdot}03$ we obtain $\Delta C = 44{\cdot}0$ mJ-mole^{-1}-°K^{-1} for lead. This is compared with the various experimental results in Table 1. As a second approximation we take $y = 1+ax^2$, from which it follows that

$$I = \tfrac{1}{2}(1+2\pi^2 a/3), \qquad (3)$$

Table 1. Observed and calculated values of ΔC for Lead

Source	$(\Delta C)_{T_c}$(mJ-mole^{-1}-°K^{-1})	I
BCS Calculation	44·0	0·500
Clement and Quinnel (Calorimetric)	52·9	0·602
Decker *et al.* (Magnetic)	58·1	0·660
This work	57·7 ± 0·6	0·655
Culler *et al.* Calculation		
(a) using Debye $\theta = 96$°K	50·0	0·568
(b) using effective temperature from tunneling results	~60	~0·7
Swihart Calculation	42·3	0·481

neglecting terms of the order of x^4 and higher. Therefore the deviation of the specific heat jump from the BCS approximation has the same sign as a, from which we conclude that $a > 0$. That is, $\Delta(\epsilon, T)$ rises with ϵ at constant T, at least for small ϵ. At larger energies the effect of the exponential terms in I may be expected to dominate the integral, thereby obscuring any further variation of Δ with ϵ.

SWIHART[(5)] and CULLER *et al.*[(6)] have recently published two solutions of the BCS integral equation for Δ (ϵ, T) which involve more complicated interactions than the original theory. Swihart's solutions show an initial decrease of $\Delta(\epsilon, T)$ with ϵ. On the other hand the solutions of Culler *et al.* show an initial increase of Δ with ϵ in agreement with our observations. The degree of quantitative agreement can be estimated as follows. Near $\epsilon = 0$ the results of Culler *et al.* can be written as $\Delta(\epsilon)/\Delta/(0) = 1+A(\epsilon/k\theta)^2$, where θ is the Debye temperature. Equation (3) can then be rewritten

$$I = \tfrac{1}{2}\left[1+\frac{2\pi^2}{3}\left(\frac{T_c}{\theta}\right)^2 A\right] \qquad (3')$$

Taking $A \simeq 3{\cdot}62$ from Fig. 3 of their paper (using $C = 0{\cdot}5$ and $k = 0{\cdot}891$) and using 96°K for θ,[(12)] we find $I = 0{\cdot}568$ and $\Delta C = 50{\cdot}0$. About 40 per cent of the discrepancy between the observed and the BCS (weak coupling) value has been removed. The agreement can be improved by taking larger values for A in (3′), that is by assuming a stronger interaction. The value we have taken, however, corresponds to the strongest interaction which Culler *et al.* have used. As an alternative approach one can observe that the density of states vs. energy curve predicted by Culler *et al.* has peaks separated by about $k\theta$ and that a qualitatively similar structure has been deduced for the density of states of lead from tunneling experiments. However the observed structure corresponds to phonon energies of about $\frac{1}{2}k\theta$.[(13,14)] If we take this energy to be characteristic of the electron–phonon interaction rather than $k\theta$, then from (3′) we find $I \sim 0{\cdot}7$ and $\Delta C \sim 60$, in better agreement with experiment.[*]

It is a consequence of the general form of the dependence of Δ on ϵ that ΔC will always exceed the BCS value. The question arises then, to what extent do other superconductors reflect this. It has been known for some time that as a general rule the electronic specific heat lies above the BCS prediction near T_c. The extent of this is most simply characterized by the extent to which (ΔC) exceeds the BCS value. According to Equation (1) this is equivalent to comparing values of the integral I deduced from experimental values of ΔC, γ and $\Delta(0, 0)$ with $I_{\text{BCS}} = \frac{1}{2}$. We have done this for Al, Sn, In, V, and Pb for which direct measurements of ΔC and $\Delta(0, 0)$ have been made. Figure 2 is a plot of $I - I_{\text{BCS}}$ vs. T_c/θ for these metals, and also for mercury (using ΔC and γ derived from the critical field curve).[(15)] Within the limitations imposed by the uncertainty in the data we can draw three conclusions. First, the "well behaved" superconductors have essentially the same value of I. This observation is especially interesting in the case of indium and aluminum.

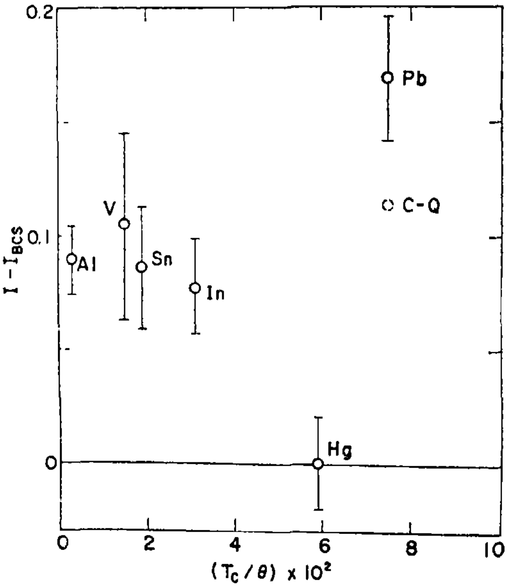

FIG. 2. The integral I of equation (1) derived from experimental measurements of $(\Delta C)_{T_c}$, γ and $\Delta(0, 0)$, minus the BCS value. The error bars are due to disagreements between various values of $\Delta(0, 0)$ and to the errors assigned to that quantity by the various investigators. The point labelled "C-Q" is from Clement and Quinnell's measurement of ΔC.

---

[*] Professor Schrieffer has informed us in conversation that he is in the process of making a more exact calculation of the electronic specific heat of lead.

Indium has a very large value of $\Delta C/\gamma T_c$, compared to tin, say, but it also has a very large $\Delta(0, 0)/kT_c$ which just compensates for this in the expression for I. For aluminum the reverse is true, $\Delta C/\gamma T_c$ is small, but so is $\Delta(0, 0)kT_c$. Secondly, this roughly constant value for I lies well above the BCS value. In terms of the previous discussion we can interpret this to mean that $\Delta(\epsilon, 0)$ rises with ϵ as a general rule amongst the pure soft superconductors. Finally, we see that mercury remains an anomalous case. It is quite possible that either γ or ΔC is in serious error, both of these quantities having been derived from the critical field curve. Calorimetric measurements are in progress to check this possibility.

REFERENCES

1. Clement J. R. and Quinnell E. H., *Phys. Rev.* **85**, 502 (1952).
2. Decker D. L., Mapother D. E. and Shaw R. W., *Phys. Rev.* **112**, 1888 (1958).
3. Keesom P. H. and Van der Hoeven Jr. B. J. C., *Phys. Letters* **3**, 360 (1963).
4. Bardeen J., Cooper L. N. and Schrieffer J. R., *Phys. Rev.* **108**, 1175 (1957); referred to as "BCS".
5. Swihart J. C., *IBM J. Res. Dev.* **6**, 14 (1962).
6. Culler G. J., Fried B. D., Huff, R. W. and Schrieffer J. R. *Phys. Rev. Letters* **8**, 399 (1962).
7. Cochran J. F., *Ann. Phys.* **19**, 186 (1962).
8. Franck J, P. and Martin D. L., *Canad. J. Phys.* **39**, 1320 (1961).
9. Keesom W. H. and Van den Ende J. H., *Proc. Acad. Sci. Amsterdam* **34**, 210 (1931).
10. Giaever I. and Megerle K., *Phys. Rev.* **122**, 1101 (1961).
11. Shapiro S., Smith P. H., Nicol J., Miles J. L. and Strong P. F., *IBM J. Res. Dev.* **6**, 34 (1962).
12. Horowitz M., Silvidi A. A., Malaker S. F. and Daunt J. G., *Phys. Rev.* **88**, 1182 (1952).
13. Giaever I., Hart H. R. and Megerle K., *Phys. Rev.* **126**, 941 (1962).
14. Rowell J. M., Chynoweth A. G. and Phillips J. C., *Phys. Rev. Letters* **9**, 59 (1962).
15. Finnemore D. K., Mapother D. E. and Shaw R. W., *Phys. Rev.* **118**, 127 (1960).

J. Phys. Chem. Solids Pergamon Press 1963. Vol. 24, pp. 1375–1377. Printed in Great Britain.

SEARCH FOR SUPERCONDUCTIVITY IN THE HYDRIDES OF LANTHANUM*

M. F. MERRIAM
University of California, San Diego; La Jolla, California
and
D. S. SCHREIBER†
University of California, Berkeley, California

(*Received* 20 *May* 1963)

Abstract—Metallic lanthanum hydride samples having atomic ratios H/La of 1·8, 1·96, 2·03, 2·11, 2·15 and 2·36 are not superconducting at 1·1°K. $LaH_{1\cdot 96}$ moreover is not superconducting at 0·33°K. Extensive n.m.r. measurements made previously by Schreiber on the same samples provide considerable information on their electronic structure. The lack of superconductivity is compatible with the density of states information obtained from the n.m.r. data, and is consistent with a split *d*-band model of the hydrides. It is also consistent with Matthias' empirical rules.

INTRODUCTION

SUPERCONDUCTIVITY in the lanthanum hydrogen system has been investigated by ZIEGLER and YOUNG,⁽¹⁾ by MATTHIAS,⁽²⁾ and by CHERRY *et al.*⁽³⁾ Ziegler and Young investigated a single sample, $LaH_{2\cdot 45}$ and found no superconductivity above 1·80°K. The lanthanum from which their sample was compounded had, however, a transition temperature of only 3·5°K, indicating substantial paramagnetic impurity. Matthias found no superconductivity in several transition metal hydrides, including some lanthanum hydrides. Cherry *et al.* examined only extremely dilute solutions.

Samples of LaH_x, with $x \leqslant 1{\cdot}95$ are two phase, consisting of cubic La metal and $LaH_{1\cdot 95}$. Structurally, the composition LaH_2 can be visualized as f.c. cubic La with all the tetrahedrally coordinated interstitial sites occupied by hydrogen (Fig. 1). Physically, however, LaH_2 should be regarded as an intermetallic compound with the CaF_2 structure, since little or no solubility of hydrogen occurs at hydrogen concentrations less than 1·95. The reason for departure from LaH_2 stoichiometry is not fully understood, but is sometimes ascribed to dissolved gaseous impurities.

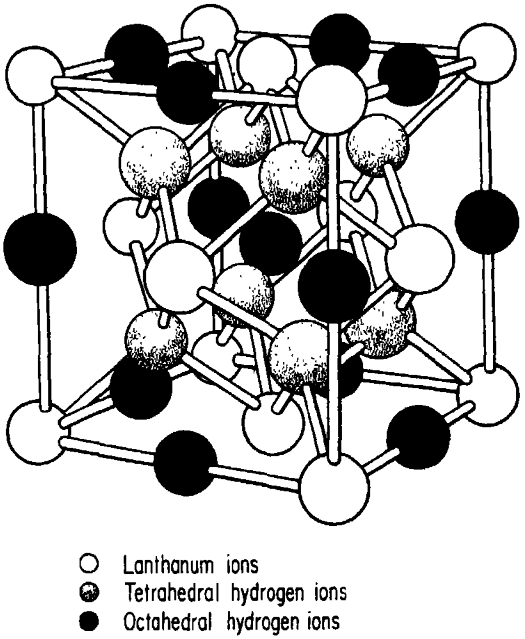

FIG. 1. Crystal structure of LaH_3.

---

* Research supported in part by the U.S. Air Force Office of Scientific Research and the National Science Foundation.

† Now at Northwestern University, Evanston, Illinois.

Furthermore, the n.m.r. work of SCHREIBER(4, 5) shows conclusively that the electronic structure of LaH_2 differs quite radically from that of La, though both are metallic. Compositions from LaH_2 to LaH_3 should be possible in principle, corresponding to various degrees of occupancy of the octahedrally coordinated interstitial sites in the face-centered cubic lattice. In practice the maximum hydrogen concentrations attainable correspond approximately to the formula $LaH_{2\cdot9}$. The hydrides with H/La less than about 2·4 are metallic; those with the lowest hydrogen concentration the most metallic. Compositions near LaH_3 are semiconducting. If superconductivity is present in any of the hydrides, it should be most pronounced in compositions with low hydrogen concentration, since the electron/atom ratio is highest in this case. There is also reason to believe, as we shall see below, that the density of electronic states at the Fermi surface increases with decreasing hydrogen concentration.

No superconductivity above 1·1°K was observed in any of the six samples investigated. The single phase sample with the lowest hydrogen concentration, $LaH_{1\cdot96}$, was measured to 0·33°K, also with negative results. We will show that this might have been predicted on the basis of Schreiber's n.m.r. work. From the point of view of MATTHIAS' rule,(6) superconductivity is marginal, since the number of valence electrons per atom is 1·5 or lower.

EXPERIMENTAL

The preparation and purity of the samples has been described previously.(4, 5) Each sample consisted of several grams of fine powder (0·1–10μ) enclosed in a pyrex tube under an atmosphere of argon–hydrogen. The tubes were opened to air for a few seconds in the course of replacing the argon–hydrogen with helium (the helium was used to insure thermal equilibrium at low temperature). The sample measured in the He^3 bath was open to the bath, but was handled so as to prevent deterioration prior to measurement. The characterization of the samples, i.e., the H/La atomic ratio cited, is based on known amounts of material reacted. The n.m.r. results leave little doubt that the samples are homogeneous.

The superconductivity checks to 1·1°K were made by monitoring the inductance, at 1 kc/s, of a coil containing the sample tube. In this method the onset of infinite conductivity results in perfect diamagnetism, excluding the measuring field from the volume of each grain and lowering the inductance of the coil. The particle size must be larger than the superconducting penetration depth unless the particles are in good electrical contact with each other. The validity of the superconductivity measurement was checked experimentally with a sample of dehydrided lanthanum powder (La metal + La_2O_3) having the same particle size distribution as the hydrides. A transition was observed at 5·0°K, approximately the expected temperature.

The single measurement to 0·33°K was made in a He^3 bath with the sample in one coil of a highly sensitive matched coil arrangement operated at 100 c/s.(7)

RESULTS AND DISCUSSION

As mentioned earlier, none of the hydrides became superconducting down to the lowest temperature reached (just below 1·1°K except for $LaH_{1\cdot96}$, for which it was 0·33°K). The samples included $LaH_{2\cdot36}$, $LaH_{2\cdot15}$, $LaH_{2\cdot11}$, $LaH_{2\cdot03}$ $LaH_{1\cdot96}$ and one sample which was approximately 10 at.% La and 90 at.% $LaH_{1\cdot95}$. The La transition was not observed in the two phase sample but this does not affect our confidence in the validity of the negative results on the other samples, since neither the percentage of La metal nor the extent of possible oxidation were accurately known. Furthermore, mixing a superconductor with a much larger amount of a nonsuperconducting metal would be expected to depress T_c.

It is possible to infer,(4, 5) from the temperature dependence of the spin-lattice relaxation time, that the density of states N_0 (E_f) at the Fermi energy in lanthanum dihydride is only about 25 per cent of its value in La metal. To explain this and other data on the hydrides the hypothesis has been put forward that the hydrogen ions constitute a periodic perturbation which results in a splitting of the 5d-band of La into two sub-bands, $5d_\gamma$, at lower energy, containing 4 electronic states/atom being separated by a finite gap from $5d_\epsilon$, the (unoccupied) sub-band at higher energy with 6 states/atom. This hypothetical band scheme, illustrated in Fig. 2, is similar to a split d-band hypothesis put forward earlier by MARTIN and

Rees(8) in connection with the zirconium hydrides. It can be seen by inspection (Fig. 2) that increasing the H/La ratio (i.e., putting more electrons into the $5d_\gamma$ sub-band) will rapidly decrease the density of states at the Fermi energy, to values well below the value for LaH_2. Thus T_c should decrease rapidly with increasing hydrogen concentration.

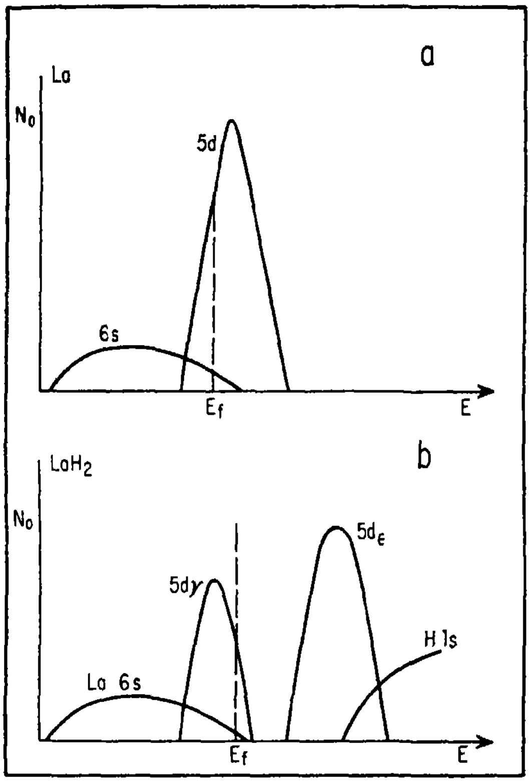

Fig. 2. Possible changes in the band scheme of La caused by alloying with hydrogen (schematic).

We can make a rough estimate of T_c for LaH_2 (or, more precisely, $LaH_{1\cdot 95}$) from the fact, mentioned above, that $N_0(E_f)$ for LaH_2 is about one quarter as large as for La, if we blindly apply the BCS formula:

$$T_c = \alpha\theta_D \exp[-(N_0V)^{-1}]$$

where θ_D is the Debye temperature, α is a constant of order unity and V is a parameter related to the strength of the attractive electron–phonon interaction. If V is assumed (for no particular reason) to be the same for La and LaH_2, and any variation in θ_D is neglected, then the ratio of T_c (La) to T_c (LaH_2) is about 20, leading to a predicted T_c of 0·25°K for LaH_2.

REFERENCES

1. Ziegler W. T. and Young R. A., *Phys. Rev.* **90,** 115 (1953).
2. Matthias B. T., unpublished.
3. Cherry W. H., Cody G. D., Gittleman J. I., Hanak J. J., McConville G. T. and Rosi F. D. unpublished report number WADD TR 60–919. p. 14–20. June (1961).
4. Schreiber D. S. and Cotts R. M., *Phys. Rev.* **131,** 1118 (1963).
5. Schreiber D. S., Thesis, Cornell University 1962.
6. Matthias B. T., *Progr. Low Temp. Phys.* Vol. **II,** (edited by C. J. Gorter) p. 138 North-Holland; Amsterdam (1957).
7. Hamilton D. C., unpublished. We are indebted to Mr. Hamilton for carrying out this measurement.
8. Martin S. L. and Rees A. L. G., *Trans. Faraday Soc.* **50,** 343 (1954).

LETTERS TO THE EDITOR

Evidence for hindered rotation of the BeF_4 ions in ferroelectric $(Glycine)_3$ BeF_4

(*Received* 22 *April* 1963; *revised* 28 *June* 1963)

HOSHINO, OKAYA and PEPINSKY(1) proposed an order–disorder type theory of the ferroelectric transition in $(glycine)_3SO_4$ (TGS), involving rearrangement of the glycine and associated rotation of the SO_4 ions. Various aspects of this theory have later been confirmed by critical X-ray scattering and proton magnetic resonance work both in TGS and in its isomorphs $(glycine)_3BeF_4$ (TGBe) and $(glycine)_3SeO_4$ (TGSe).[2–4] So far, however, rotation of the SO_4 ions (or of the BeF_4 or SeO_4 groups, respectively) has not been verified directly. The purpose of this note is to report the results of a F^{19} magnetic resonance absorption study in TGBe, bearing direct evidence for hindered rotation and "freezing in" of the BeF_4 ions in the ferroelectric phase.

Measurements have been made of the F^{19} magnetic resonance spectra from -175 up to $+100$°C both on a single crystal and on a powdered sample of TGBe. The angular dependence of the single crystal spectra showed marked anisotropy. On cooling below the Curie temperature (Tc), only a very small change in the line width and second moment at certain orientations could be detected in the single crystal spectra. No significant change was found in the powder spectra.

Some 50°C below Tc, however, a well defined line width transition, centered at 0°C, sets in (Fig. 1). The second moment of the powder spectra increases from 5 at 23°C to about 12·5 G^2 at -50°C. At still lower temperatures, below -130°C, a second line width transition occurs. The spectra become very broad, indicating a large intermolecular proton–fluorine contribution to the BeF_4 second moment.

The low temperature line width transition nearly exactly coincides with the onset of NH_3 motions as observed in the proton magnetic resonance spectra.(2,3) Thus this transition is evidently due to the averaging out of a part of the interionic fluorine–proton interactions due to hindered rotation of the NH_3 groups.

The high temperature line width transition (Fig. 1), on the other hand, occurs in a temperature region, *where no proton line width transition* was found and may thus be assigned to BeF_4 motion. Evidently it is due to the averaging out of the residual part of the interionic proton–fluorine interactions, as well as of the intraionic contribution to the BeF_4 second moment as a result of the onset of hindered rotation of the BeF_4 ions. Appreciable molecular disorder thus exists in the ferroelectric phase far below Tc.

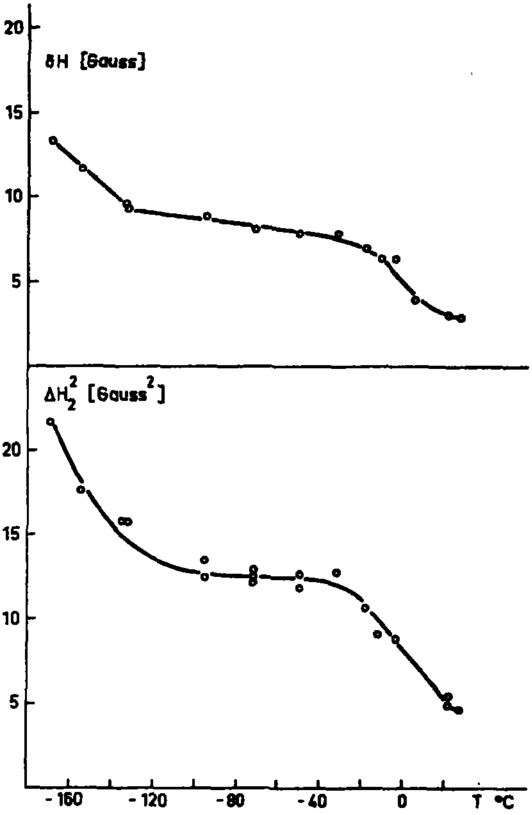

FIG. 1. Line width and second moment of the F^{19} magnetic resonance absorption in powdered TGBe as a function of temperature.

Though only a rough estimate of the characteristic frequency of molecular motion can be obtained from line width measurements, our data indicate, that the characteristic frequency of molecular motion may well lie in the 10^7 c/s region at Tc. Since magnetic resonance line width data are insensitive to any change in the frequency of molecular motion, that does not pass through a rather narrow frequency range (10^3–10^5 c/s), determined by the rigid lattice width, the absence of any drastic change in the F^{19} spectra on cooling below Tc can thus be well understood.(5)

Nuclear Institute, "J. Stefan" R. Blinc
Ljubljana, I. Zupančič
Yugoslavia

References

1. Hoshino S., Okaya I. and Pepinsky R., *Phys. Rev.* **115**, 323 (1959).
2. Hoshino S., *J. phys. Soc. Japan* **17**, 119 (1962).
3. Blinc R., Detoni S. and Pintar M., *Phys. Rev.* **124**, 1036 (1961).
4. Shibuya J. and Mitsui T., *J. phys. Soc. Japan* **16**, 379 (1961).
5. Miller S. R., Blinc R., Brenman M. and Waugh J. S., *Phys. Rev.* **126**, 528 (1962).

Interstitial mobility in NaCl*

(*Received* 26 *April* 1963; *revised* 10 *June* 1963)

The classical Born theory of ionic crystals, as developed by Mott and Littleton(1) (M.L.) for lattice imperfections, has been used recently to discuss the activation energies for ionic movement via vacancy mechanism, and the importance of the choice of repulsive potential in these calculations has been repeatedly stressed.(2–3) We have used this model, with both the Born–Mayer (B.M.) and the Born–Mayer–Verwey (B.M.V.) repulsive potential,(2) to calculate the activation energy for movement of interstitials in NaCl.

The total energy E_t of the imperfect crystal consists of contributions from Coulombic E_c, repulsive E_r, and polarization energy E_p of the lattice. It is convenient, in calculating these terms, to divide the crystal into four groups of ions; group O consisting of the mobile interstitial placed, in a symmetrical position (at which the origin of our co-ordinate system is chosen), at the cube centre configuration (c.c.c) or the face centre configuration (f.c.c). Group I, taken to be the nearest neighbours of group O, for the c.c.c. consists of 4 cations and 4 anions with a radial displacement of $\eta_1 \sqrt{(3)}\, r_0$ and $\xi_1 \sqrt{(3)}\, r_0$ respectively (from their normal sites) i.e. in the (111) direction, with r_0 as the anion–cation separation in perfect lattice. Similarly the group I for the f.c.c. consists of 2 cations and 2 anions radially displaced by $\eta_1 \sqrt{(2)}\, r_0$ and $\xi_1 \sqrt{(2)}\, r_0$ in the (110) direction. Group II now chosen to include all the nearest neighbours of group I, for the c.c.c. consists of 12 cations and 12 anions again with a radial displacement of $\eta_2 \sqrt{(11)}\, r_0$ and $\xi_2 \sqrt{(11)}\, r_0$ respectively. For the f.c.c. group II consists of (a) 4 cations and 4 anions (lying in the plane of groups O and I) with a radial displacement of $\eta_3 \sqrt{(10)}\, r_0$ and $\xi_3 \sqrt{(10)}\, r_0$ in the (1,3,0) direction and (b) 4 cations and 4 anions with a radial displacement of $\eta_2 \sqrt{(6)}\, r_0$ and $\xi_2 \sqrt{(6)}\, r_0$ in the (1,1,2) direction. The rest of the lattice, with the ions in their normal sites, is taken as group III.

For both configurations the Coulombic and repulsive energies (i.e. the sum of self energies of groups O to III and their mutual interaction) were calculated exactly. For charged interstitial the polarization energy contribution from groups II and III was calculated in the M.L. continuum approximation,(1) by attaching dipoles of moment $\{M_\pm r_0^3 F_i\}$ where F_i is the field at site i due to the interstitial and $M_\pm$ a non-dimensional constant involving the polarizabilities and the dielectric constant. The crystal symmetry simplifies this part of the calculation and the overall contribution from these groups depends only on the dielectric constant and a known lattice sum(4) of the type $\Sigma\, 1/r_i^4$. For the neutral interstitial however, F_i is taken to be the field due to the displacement dipoles of group I, and the individual terms are summed. In calculation of the polarization energy of group I the monopole field on these ions was calculated exactly, thus giving us the dipole moments on these ions. The interaction of these dipoles, amongst themselves and, with the previously assumed dipoles of groups II and III were also taken into account.

The long range displacement parameters η_2, ξ_2, η_3, ξ_3 were calculated in the M.L. continuum approximation and are found to be insensitive to the choice of repulsive potential; (for the neutral interstitial we have again used the numerical values of these long range displacements, since these gave us a lowering of the energy of the crystal for both c.c.c. and f.c.c.). The energy of the crystal thus obtained was minimized on an IBM 7090 computer with respect to η_1 and ξ_1 (in steps of 0·02). The minimum energy configuration $\bar{\eta}_1$, $\bar{\xi}_1$ and the various energy terms, for both types of repulsive potential, are given in Table 1, with the following choice of numerical values for the parameters that enter in the calculation.

---

* Work supported by the United States Atomic Energy Commission and the National Science Foundation.

Ionic radii (in Å): $r_+ = 0{\cdot}98$; $r_- = 1{\cdot}81$; $r_{\text{Cl}^\circ} = 1{\cdot}56$

Ionic polarizability ($\times 10^{24}$ cm^3): $\alpha_+ = 0{\cdot}26$; $\alpha_- = 2{\cdot}97$

B.M. potential $bc_{ij} \exp([r_i + r_j - r]/\rho)$: $b = 0{\cdot}229 \times 10^{-12}$ ergs; $\rho = 0{\cdot}345$ Å

Dielectric constant $= 5{\cdot}62$ and $r_0 = 2{\cdot}814$Å

We remark here that:

(1). The separation of the total energy of the crystal into its various components is artificial, since each term varies rapidly with η_1, ξ_1 where as the total energy E_t is a slowly varying function with a flat minimum.

(2). The effect of the harder B.M.V. potential is to give us a larger E_t for each configuration (and for the activation energy ΔE). In this connection it is important to note the indirect part played by the harder potential, in that it alters the crystal configuration, thus giving us a substantially higher Coulombic energy E_c. It is pertinent to mention that the close proximity of groups O and I ensure the corresponding $\bar{\eta}_1$ (for Cl$^-$ interstitial) and $\bar{\xi}_1$ (for Na$^+$ interstitial) to increase with increasing hardness of the cation–anion repulsive potential. In all other cases, where the hardness of repulsive interaction between groups O and I is unaltered, the $\bar{\eta}_1$, $\bar{\xi}_1$ values decrease, as expected, with increasing hardness.

Table 1. *The energy E* (*in* eV) *relative to the perfect lattice and the displacement parameters of cations* η *and anions* ξ *for cube centre* (c.c.) *and face centre* (f.c.) *configurations, calculated with the B.M.V. potential. The corresponding results with the B.M. potential are given in brackets and* ΔE (*in* eV) *is the activation energy for movement.*

Interstitial Configuration	Na$^+$ c.c.	Na$^+$ f.c.	Cl$^-$ c.c.	Cl$^-$ f.c.	Cl$^\circ$ c.c.	Cl$^\circ$ f.c.
E_r	2·99	3·38	7·57	9·15	4·94	5·59
	(2·81)	(4·01)	(6·56)	(7·09)	(5·11)	(5·22)
E_c	−2·90	−1·72	−3·98	−2·79	−0·70	−0·49
	(−4·08)	(−4·16)	(−4·72)	(−3·93)	(−1·15)	(−0·91)
E_p	−2·35	−2·66	−1·97	−2·58	−0·36	−0·35
	(−2·15)	(−3·06)	(−1·73)	(−2·32)	(−0·69)	(−0·78)
E_t	−2·26	−1·00	1·62	3·78	3·88	4·75
	(−3·42)	(−3·21)	(0·11)	(0·84)	(3·27)	(3·53)
ΔE	1·26		2·16		0·87	
	(0·21)		(0·73)		(0·26)	
$\bar{\eta}_1$	0·06	0·12	0·02	0·10	0·08	0·12
	(0·08)	(0·16)	(0·00)	(0·06)	(0·12)	(0·20)
$\bar{\xi}_1$	0·00	0·10	0·12	0·18	0·10	0·16
	(−0·02)	(0·00)	(0·14)	(0·22)	(0·12)	(0·20)
η_2 ξ_2	±0·005	±0·012	∓0·005	∓0·012	0·005	0·012
η_3 ξ_3		±0·006		∓0·006		0·006

(3). **Hatcher** and **Dienes**,(5) with a slightly different numerical values for the parameters (and by a different method, with $\eta_2 = \xi_2 = \eta_3 = \xi_3 = 0$), obtain a value of 0·5 eV for the activation energy of Cl°. A corresponding calculation gives us 0·35 eV. However, their calculation of the activation energy in a rigid non polarizable medium, appears to be overestimated by about 0·13 eV and taking this correction into account the agreement is fair. These authors in their calculations note that ΔE for Cl° is insensitive to the choice of $Cl°$–Cl^- interaction. The present calculation indicates that ΔE is sensitive to the hardness of the crystal, illustrating the importance of the choice of cation–anion repulsive interaction when their separation is less than r_0.

(4). M.L. by a method(1) different from above (and with a potential whose hardness lies between the B.M. and B.M.V.) obtained 0·47 eV for the activation energy of Na^+ interstitial, and as expected is within the extremum values quoted here. However, the energies of each configuration are vastly different and the discrepancy is not clear; these authors do not give the full details of the minimum energy configurations.

(5). Mobility of Cl^- interstitial was not known previously and the present calculation indicates a very low mobility for it. Here again we must note that the B.M. repulsive potential, for the interaction between the Cl^- interstitial and a Cl^- belonging to group I, may be inadequate.

(6). With the known values(2) for the energies to extract a cation and anion from a perfect lattice, and with a value of 7·88 eV for the cohesive energy, the energy of formation of a Schottky pair in NaCl with B.M. and B.M.V. potentials are 1·39 eV and 1·77 eV respectively. Using the present values for the Na^+ interstitial in the c.c.c., the energy of formation of Frenkel (cation) pair with the corresponding potentials are 1·36 eV and 2·63 eV respectively. Thus the B.M.V. potential favours the Schottky pair (this was also noted by M.L. with their values), and the B.M. potential predicts the cation Frenkel pair to be as favourable. The experimental evidence however is for Schottky pair with an energy of formation of about 2 eV, giving us yet another support to the validity of B.M.V. potential.

(7). It has been pointed out(6) that the Cl° interstitial and a Cl^- belonging to group I may tend to form a molecule, thus lowering the energy of the crystal, with a resulting favourable orientation in the (110) direction. In this connection we note that with the B.M. potential (which gives an activation energy of only 0·26 eV for Cl° in symmetrical position) the fact that the field in the (110) direction is larger than that in the (111) direction may lead to a favourable (110) orientation for the molecule. It is not clear, at this moment, what the corresponding results will be with the harder B.M.V. potential, which gives us a much larger value of 0·87 eV for the Cl° activation energy in the symmetrical position.

Solid State and Materials Programme,
Princeton University, K. Tharmalingam
Princeton, New Jersey

Acknowledgements—The author wishes to acknowledge the benefit of discussion with the members of the Princeton University Solid State and Materials Programme.

References

1. Mott N. F. and Littleton M. J., *Trans. Faraday Soc.* **34,** 485 (1938).
2. Guccione R. and Tosi M. P. and Asdente M., *J. Phys. Chem. Solids* **10,** 162 (1959).
3. Tharmalingam K. and Lidiard A. B., *Phil. Mag.* **6,** 1157 (1961).
4. Jones J. E. and Ingham A. E., *Proc. Roy. Soc.* **A107,** 636 (1925).
5. Hatcher R. D. and Dienes G. J., *Phys. Rev.* **124,** 726 (1961).
6. Dienes G. J., Hatcher R. D. and Smoluchowski R., *Bull. Amer. phys. Soc.* **8,** 89 (1963).

Optical spectra of several d¹-electron systems

(*Received* 21 *May* 1963)

Optical spectra of crystals containing d^1-electron ions are of considerable theoretical interest in that their transitions violate the usual selection rules. Furthermore, the development of crystal (ligand) field theory(1) is dependent on optical and electron paramagnetic resonance (e.p.r.) studies on simple d-electron systems. Thus far, spectra have only been observed[1,2] for a few transition ions that appear as d^1-ions in some complexes. In this Letter we report the spectra of Sc(III) $3d^1$, Y (III) $4d^1$, and La (III) $5d^1$ and suggest our experimental procedures can be extended so as to observe many transition ions in one-electron configurations.

Several single crystals of CaF_2 were grown containing 0·1 mole per cent of Sc^{3+}, Y^{3+}, La^{3+}, Ti^{3+}, V^{5+}, and Mo^{6+}. The dopant was added either as an oxide or fluoride. Except for Ti^{3+} ($3d^1$) these ions in their most stable valence state contain no d-electrons. The d-electrons are added by irradiating the crystals with $\sim 10^6$ rad of 2 MeV electrons from a Van de Graff generator.[3] In most cases the reduced valence of these ions is metastable for a period of several days. Prior to irradiation these crystals exhibit no optical absorptions between 180 mμ and 8 μ. After irradiation all materials show four characteristic absorption bands between 200 and 800 mμ. The absorption spectra for Y($4d^1$) and La($5d^1$) in CaF_2 are shown in Fig. 1. Also shown is the spectrum of Ti($3d^1$) which was not irradiated. Similar spectra are observed for these ions in SrF_2 and BaF_2. At this point we note that none of these materials exhibit color centers and that color centers previously reported[4] in CaF_2 are due to Y contamination.[5] We also report that several transition ions show intense cathodo- and thermoluminescence.

When a trivalent impurity substitutes for the cation in alkaline earth fluorides, some method of charge compensation must occur. The excess charge can be compensated by (1) an interstitial F^- ion along either a [100] or [111] direction, (2) a substitutional O^{2-} ion at an anion site, and (3) a substitutional monovalent ion along either a [100] or [111] direction. Every method of compensation produces an axial crystal field at the impurity. Tetra- and pentavalent impurities require a combination of these compensators. It is of interest to note that e.p.r. alone can not distinguish between compensators with the same spatial orientation. However, e.p.r. in conjunction with dielectric relaxation measurements can identify the compensator uniquely.[6]

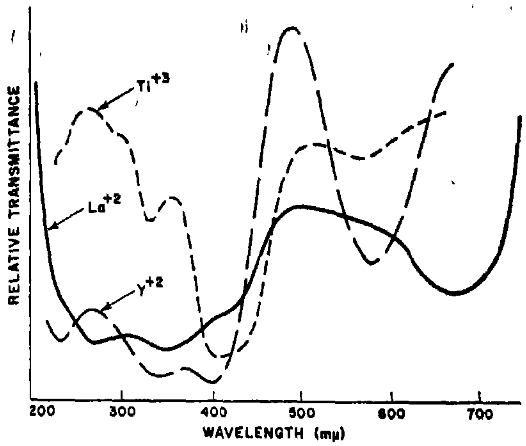

FIG. 1. Absorption spectra of Ti^{3+}, Y^{2+}, and La^{2+} in CaF_2 single crystals. The absorption bands are given in Table 1.

In the case of Y(III), several crystals were grown doped with Y_2O_3, YF_3, $NaYF_4$, and Y metal. For each method of charge compensation the spectra are nearly identical. These and other experimental results are shown in Table 1. For

Table 1. *Absorption bands of several* d^1-*electron systems.*

Ion	System	Host	Compensator		Absorption bands in mμ			
Ti	$3d^1$	CaF_2	O^{-2},	[111]	334	414	430	572
Sc	$3d^1$	CaF_2	O^{-2},	[111]	236	310	428	662
Y	$4d^1$	CaF_2	F^{-1},	[100]	234	346	402	582
Y	$4d^1$	CaF_2	O^{-2},	[111]	230	336	402	582
Y	$4d^1$	CaF_2	F^{-1},	[111]	236	336	402	582
Y	$4d^1$	CaF_2	Na^{+1},	[100]	232	349	402	582
Y	$4d^1$	SrF_2	F^{-1},	[100]	250	400	480	625
Y	$4d^1$	BaF_2	F^{-1},	[100]	270	460	550	670
La	$5d^1$	CaF_2	F^{-1},	[100]	271	351	421	678

each system the host lattice, compensator, and most probable orientation of the axial crystal field is given. Similar spectra are observed for V(V) and M_o(VI). JORGENSEN(2) has observed this type of spectra in a low symmetry, vanadyl complex.

The energy level diagram for a d^1-electron in a crystal with coordination number equal to eight is shown in Fig. 2. With axial distortion, caused by the charge compensator, the e-orbitals lie much lower than the t-orbitals; and one should expect three optical absorptions. Now, the fourth optical transition may be due either to the Jahn–Teller effect or a crystal field splitting of the ground state orbital doublet. This splitting may occur if the interaction of the charge compensator is sufficiently strong so as to distort the initial cubic symmetry at the impurity site. GRIFFITHS *et al.* have shown that the ground state orbitals, in low symmetry complexes, can be substantially split by strong crystal fields. For Fig. 2(d), where four Kramers doublets are separated by a large energy Δ from the ground state, only one e.p.r. should be observed. The g-value should be smaller than free-spin by a small orbital correction of the order λ/Δ (i.e., $g \sim 1{\cdot}99$) where λ is the spin-orbit coupling coefficient. Using a 23·4 Kmc/s spectrometer at 4·2°K, only one strong resonance was observed at $g = 1{\cdot}994 \pm 0{\cdot}005$ for several $CaF_2(Y)$ samples. The e.p.r. shows complex, hyperfine structure which is interpreted(9) as interaction between the 4d^1-electron and several fluorine nuclei.

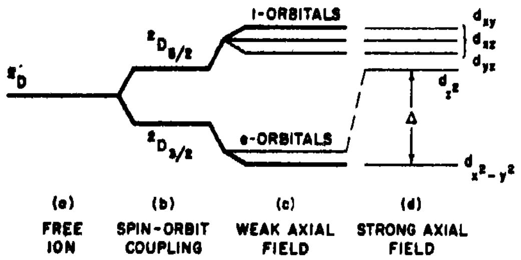

FIG. 2. Energy levels for a d^1-electron in CaF_2 single crystal. The spin–orbit and crystal field splittings are shown in (b) and (c). The level diagram shown in (d) is consistent with our experimental data.

The optical and e.p.r. data are consistent and indicate all orbital degeneracy is removed for d^1-electrons in compensated, alkaline earth fluorides. The data cannot indicate which orbital is the ground state, whether the excited orbitals are mixed, or the exact cause for the large splitting between the e-orbitals. The data does show the energy level diagram consists of five Kramers doublets, four of which lie an energy $\Delta \sim 16{,}000$ cm^{-1} above the ground state.

Acknowledgements—In addition to the assistance acknowledged thus far, the authors are indebted to R. M. HILTON for able experimental assistance and Dr. H. A. BOSTICK for several helpful discussions.

*Lincoln Laboratory,**
Massachusetts Institute of Technology, Lexington,
Massachusetts.
J. R. O'CONNOR

Physics Department,
Boston College,
Chestnut Hill,
Massachusetts
J. H. CHEN†

References

1. McCLURE D. S., *Solid-State Phys.* **9,** 399 (1959).
2. JØRGENSEN C. K., *Acta. Chem. Scand.* **11,** 73 (1957).
3. The authors gratefully acknowledge the help of Dr. K. A. WRIGHT at M.I.T. The reduction of Sm^{3+} to Sm^{2+} in CaF_2 has recently been published by O'CONNOR J. R. and BOSTICK W. A., *J. appl. Phys.* **33,** 1868 (1962).
4. PRZIBRAM K., *Irradiation Colours and Luminescence,* Pergamon Press, New York (1956).
5. O'CONNOR J. R. and CHEN J. H., *Phys. Rev.* **130,** 1790 (1963).
6. CHEN J. H., to be published.
7. GRIFFITHS J. H. E., OWEN J. and WARD I. M., *Proc. Roy. Soc.* **A219,** 526 (1953).
8. FROM W. H., to be published.

Electrical conductivity of sodium bromate crystals

(*Received* 9 *April* 1963; *Revised* 21 *June* 1963)

THE results of our investigations on the electrical conductivity of sodium bromate crystals in the temperature range 50–320°C are briefly reported here. A plot of the logarithm of the conductivity,

---

* Operated with support from the U.S. Army, Navy, and Air Force.

† Supported in part by the National Science Foundation.

σ, *vs.* the reciprocal of the absolute temperature $(1/T)$ has revealed three distinct regions (see Fig. 1) of differing slopes. A sharply enhanced conductivity sets in above 315°C. This appears anomolous since no phase transition is reported to occur for this crystal.(1,2) Our doubts regarding the melting point of sodium bromate received confirmation in the recent work by J. JACH(3) on its thermal decomposition, who reported a sudden increase in the rate of evolution of oxygen at 331°C. Our present results however indicate that an enhanced rate of decomposition may start early at 315°C as judged from the sudden increase in electrical conductivity.

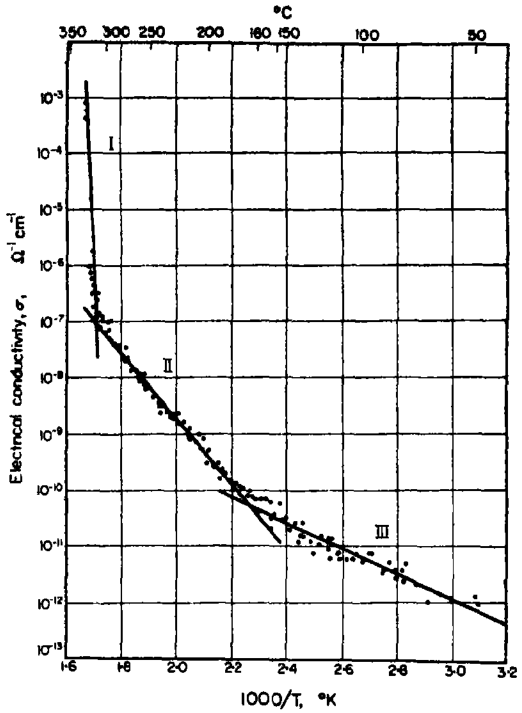

FIG. 1. Electrical conductivity of $NaBrO_3$ crystals. (Runs on several samples both while heating and cooling.)

The crystals employed in these measurements were grown from solution using material of chemical purity. Slow growth extending over a period of a few weeks produces crystals in tetrahedral form. Our attempts to modify the habit yielded plate like crystals by rapidly cooling hot saturated solutions. Samples for measurement were prepared in the form of plates triangular or square, by cutting the pyramidal crystals with a moistened thread. The surfaces of the crystals were polished on a wet chamoi leather and then painted with colloidal graphite. The samples thus prepared were mounted between the studs of a micrometer screw gauge; brass discs covered with aluminium foils served as electrodes. A general Radio 1230-A electrometer type direct current amplifier or a Philips GM 6020 vibrating reed type d.c. voltmeter was used to measure the resistance of the samples. Since the crystals show too high a resistivity ($\sim 10^{14}$ Ω cm) at low temperatures to permit an easy alternating current measurement, and since the factors against employing direct current methods do not appear to be so strong(4) we have carried out the present work with direct current voltages. The crystals were found to obey Ohm's law and effects of polarization were not felt. The conductivity changes over eight orders of magnitude in the temperature range 50–320°C. The readings taken on different samples both while heating and cooling were reproducible within the accuracy of the resistance measurement which is from 5 to 10 per cent. As a rule, the crystal in its mount is to be first heated at 250°C for 2 hr and annealed before measurements are made.

Conductivity data on four of the samples were plotted in Fig. 1. The regions II (298–182°C) and III (162–50°C) were made to fit into straight lines by the method of least squares (the lines are drawn in Fig. 1) giving slopes of 1·1 and 0·4 eV respectively. The electrical conductivity in the temperature range 182–298°C can be represented by $\sigma = 0{\cdot}0016 \exp(-1{\cdot}1\ \text{eV}/kT)\,\Omega^{-1}\,\text{cm}^{-1}$. One possible interpretation of the regions involves a tentative identification of region II as due to intrinsic conduction by positive ion vacancies analogous to that found in the halides of alkali metals.(5) It would appear then that the 0·4 eV energy of activation may provisionally be associated with jumps of positive ion vacancies which would be present in sufficient concentration as divalent metal ions of lead and iron are present in the samples to the extent of 5×10^{-5} mole fraction. A similar investigation(6) in this laboratory on $NaClO_3$ crystals gave a slope of the order of 0·38 eV in the low temperature region. Following the arguments in use for the ionic conductivity of alkali and silver halides(7) one may estimate the energy of formation of the defect responsible for electrical conduction in this crystal to be 1·4 eV.

JACH in Ref. 3 reported a sudden increase in the rate of evolution of oxygen between 331 and 339°C whereas a sharp enhancement of conductivity was observed for our samples above 315°C. When heated above 323°C our crystals were found to become powder* in the mount. This region I of high conductivity (310–323°C) may arise due to one or all of the following reasons: (i) presence of free oxygen produced by thermal decomposition in the ionic, atomic, or molecular form (ii) presence and motion of bromide ions which will be more mobile than the bromate ions (iii) motion of the bromide–bromate eutectic boundaries. The discrepancy about the temperature range of discontinuity may be partly due to the differences in the impurity content of our samples and those used by JACH. Perhaps the difference can also be partly accounted for by the fact that the electrical conductivity depends on the oxygen or bromide ions in the crystal while JACH's results correspond to the liberation of oxygen from the crystal.

Department of Physics, C. RAMASASTRY
Indian Institute of Technology, Y. V. G. S. MURTI
Madras 36

References

1. WYCKOFF R. W. G., *Crystal Structures*, Interscience, New York (1948).
2. *Structure Reports*, N.V.A. Oosthoek's Uitgevers Mij Utrecht.
3. JACH J., *J. Phys. Chem. Solids* **24**, 63 (1963).
4. DREYFUS R. W. and NOWICK A. S., *Phys. Rev.* **126**, 1369 (1962).
5. *Amer. Inst. Phys. Handb.* 5-185. Mcgraw-Hill, New York (1957).
6. SASTRY S. B. S. and RAMASASTRY C., unpublished work.
7. LIDIARD A. B., *Handb. Phys.* **20**, Springer-Verlag, Berlin (1956).

Two-dimensional antiferromagnetism in cupric formate tetrahydrate single crystal

(*Received* 17 *June* 1963)

FROM optical absorption measurements MOOKHERJI and CHHONKAR(1) showed that the behaviour of cupric formate tetrahydrate should be similar to that of cupric acetate monohydrate and from our unpublished susceptibility data on cupric formate tetrahydrate crystal in state of solution they suggested a value of -130 cm^{-1} for exchange integral. Also the mean moment value for the crystal powder of the salt ($\mu = 1{\cdot}67$ B.M.,(2) 1·64 B.M.,(3) at 288·7°K) is less than the spin-only value. Present measurements on magnetic anisotropy by the method of KRISHNAN and BANERJI(4) and the absolute susceptibility in a convenient crystal direction by a sensitive quartz microbalance(5) gave the mean magnetic moment as 1·69 B.M. at 300°K for the cupric formate tetrahydrate single crystal. This value is also lower than the spin-only value though higher than the powder values as reported by previous workers.(2,3) This low moment value also suggests that the magnetic behaviour is similar to cupric acetate monohydrate(6) and we must postulate some sort of exchange interaction between adjacent copper atoms. X-ray analysis(7) shows that cupric formate tetrahydrate is not a binuclear complex like cupric acetate monhydrate and we must rule out the possibility of any direct spin interaction between adjacent copper atom. Large Cu–Cu distance (5·8 and 6·2 Å) make us reject the chances of super exchange of Kramers type. To account for this low moment value MARTIN and WATERMAN(3) have suggested a super exchange in cupric formate tetrahydrate through the intermediary of formate group. The delocalized π-electron cloud arising from the overlapping of $2p_\pi$–(O)–$2p_\pi$–(C)–$2p_\pi$(O) atomic orbitals associated with the resonating $-\mathrm{O{-}CH = O/O = CH{-}O^-}$ anion system has been assumed to be the cause of the postulated superexchange.

The detailed crystal structure studies of single crystals of this salt is given by KIRIYMA, IBAMOTE and MATSUO(7) show that the crystal has a layer structure parallel to (001). In such layers one formate ion is coordinated to two copper atoms and each copper atom is surrounded by four oxygen atoms of four different formate ions in an approximately square configuration. There are two molecules linked with each cupric ion one above the layer and the other below it. These water molecules are sandwiched between these layers. In these layers Cu-Cu distance is 5·8 Å. Despite this large distance we can conceive of super exchange in these layers because of the part played by the formate ion. But in a direction perpendicular to this plane no such mechanism exists. Therefore we must expect two dimensional antiferromagnetism in (001) plane and paramagnetism in the direction perpendicular to this plane where large inter layer distance (6·2 Å) discounts the chances of any interlayer exchange.

---

* The aluminium foils were found to become part of the powder.

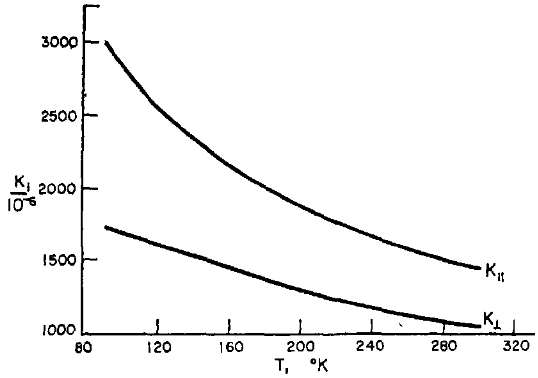

FIG. 1.

Our measurement on single crystals of cupric formate tetrahydrate show that the moment value in (001) plane are nearly isotropic $\approx 1{\cdot}60$, less than the spin-only value and nearer the moment value for cupric acetate monohydrate. The moment normal to (001) plane is $\approx 1{\cdot}87$, a value very nearly equal to that of other cupric salts.(8) These values also suggests that at least normal to (001) plane we should not think in terms of super exchange.

Our measurements of magnetic anisotropy show that the (001) plane is approximately isotropic (anisotropy in this plane is only $37{\cdot}2\times10^{-6}$ c.g.s. units as compared to about 400×10^{-6} c.g.s. units in a perpendicular plane). Also the angle between tetragonal axis and the *b*-plane is very small ($\approx 8°$). Therefore we can adopt without much approximation the expression for $K_{\perp}$ as given by BLEANEY and BOWERS.(9) Thus taking $g_{\perp} = 2$ and substituting our susceptibility value at 300°K we get exchange integral $J = -82$ cm^{-1}. This value of J corresponds to a critical temperature of 74°K. This explains why no maxima could be detected in the susceptibility versus temperature curve down to 80°K by MARTIN and WATERMAN(2) or by us. The value of J as suggested by MOOKHERJI and CHHONKAR(1) corresponds to a critical temperature 118°K. This value is evidently high and may be attributed to the fact that they utilized mean moment value and assumed an isotropic exchange integral. Recently HASEDA(10) has reported the existence of a maxima at 62°K which is in good agreement with our value. Further trend of our measurements with variation of magnetic susceptibilities of the crystal with temperature show that $K_{\perp}$ may reach a maxima at a temperature slightly below 80°K while $K_{\parallel}$ shows no such indication. These facts also go to suggest the existence of a two-dimensional antiferromagnetism.

Details will be published elsewhere.

Physical Laboratories,
University of Burdwan,
Burdwan, India

A. MOOKHERJI
S. C. MATHUR

References

1. MOOKHERJI A. and CHHONKAR N. S., *Ind. J. Phys.* **33**, 74 (1959).
2. AMIEL *C.R. Acad. Sci. Paris.* **207**, 1907 (1938).
3. MARTIN R. L. and WATERMAN H., *J. chem. Soc.* 1359 (1959).
4. KRISHNAN K. S. and BANERJI S., *Phil. Trans.* **234**, 265 (1935).
5. HEOGY D. and LAL R. B., *J. Sci. Ind. Res.* **21B**, 103 (1962).
6. MOOKHERJI A. and MATHUR S. C. In Press, *J. phys. Soc. Japan* (1963).
7. KIRIYAMA R., IBAMOTO H. and MATSUA K., *Acta Cryst.* **7**, 482 (1954).
8. MOOKHERJI A., *Ind. J. Phy.* **19**, 63 (1945).
9. BLEANEY B. and BOWERS K. D., *Proc. Roy. Soc.* **A214**, 451 (1952).
10. HASEDA T. and MIEDEMA A. R., *J. phys. Soc. Japan*, **17** suppl. (1962).

Compounds with the C33 tetradymite-type structure

(*Received* 5 *August* 1963)

ACCORDING to PEARSON(1) four compounds only have the rhombohedral/hexagonal C33 tetradymite-type structure, namely Bi_2Te_2S (tetradymite), Bi_2Te_3, Bi_2Se_3 and Sb_2Te_3. At an earlier date however, RAMSDELL(2) claimed the identification of a C33 type structure for As_2Se_3.

During studies in these laboratories of the two systems bismuth–tellurium and antimony–tellurium, it was shown that wide ranges of solid solution alloys with the C33 structure exist in both systems.(3) These alloys represent the solid solution of bismuth in Bi_2Te_3 and antimony in Sb_2Te_3 respectively. As an extension of these investigations, the systems bismuth–selenium and arsenic–selenium have been investigated to determine if similar ranges of solid solution exist. For completion a limited examination was also made of the antimony–selenium system, although Sb_2Se_3 itself is reported to have an orthorhombic structure, different from the C33 type.(4)

Little published information is available on the two systems bismuth–selenium and arsenic–selenium. SEMILETOV and PINSKER(5) report that in the bismuth–selenium system three intermediate phases exist—Bi_2Se_3 and Bi_8Se_4 which have the C33 structure, and BiSe which has the NaCl-type structure: the structure-cell dimensions of the alloys with the C33 structure increase with increasing Bi-content. The existence of an alloy BiSe with an NaCl-type structure is doubtful: SEMILETOV(6) claimed that BiTe also had this structure, but this claim was not substantiated in the later investigations of BROWN and LEWIS(3) referred to above. The limited information which is available on the arsenic–selenium system indicates that it is difficult, if not impossible, to prepare As_2Se_3 in a crystalline form.(7)

The various samples were prepared from calculated quantities of the pure elements by the thermal agitation technique described previously.(3) In most preparations the alloy was obtained essentially in the form of a coherent mass of fine crystals, which could be easily crushed and annealed before final X-ray examination. Conventional powder diffraction techniques were employed, using an 11·46 cm diameter camera and CuKα radiation.

The results obtained during the present study may be described as follows:

(a) *Bismuth–selenium system*

The diffraction patterns of three alloy preparations of compositions Bi_2Se_3, $Bi_{11}Se_9$ and Bi_2Se, showed that a range of solid solution alloys with the C33 structure exists in this system. These patterns indicated that the bismuth-rich limit of the solid solution range lies at some composition between 40 and 45 at.% Se. The selenium-rich limit was not examined in any great detail, but the limited experimental evidence obtained was consistent with the conclusion that it lies close to the composition Bi_2Se_3. The changes in the structure-cell dimensions between the approximate limiting compositions are shown in Table 1:

Table 1

Composition	a_{Hex}(Å)	c_{Hex}(Å)	a_R(Å)	$-\alpha$(°)
Bi_2Se_3	$4{\cdot}13_5 \pm 0{\cdot}01$	$28{\cdot}64 \pm 0{\cdot}01$	9·84	24·4
$Bi_{11}Se_9$	$4{\cdot}22_5 \pm 0{\cdot}01$	$28{\cdot}80 \pm 0{\cdot}01$	$9{\cdot}90_5$	24·8
Natural Bi_2Se_3 (8)	4·133	28·62	9·823	24·3

(b) *Arsenic–selenium system*

An alloy of composition As_2Se_3 was not obtained in a crystalline form. The product invariably had a glassy uniform appearance, was brittle, and did not fracture in the manner normally associated with compounds having the C33 structure. The diffraction pattern obtained from the product of a preparation at a temperature in excess of 250°C corresponded to that of a non-crystalline glass phase—probably a selenium glass. No change in constitution was effected after annealing a crushed sample for 28 days at 130–140°C. With temperatures of preparation below 250°C, appreciable quantities of free arsenic were observed in the sample. These results agree with the work of UPHOFF and HEALY(7) who reported in their investigation of the pseudo-binary system As_2Se_3–As_2Te_3 that all alloys except As_2Te_3 were amorphous.

(c) *Antimony–selenium system*

One alloy composition only was attempted, namely SbSe. Although incomplete reaction was achieved, the distribution of reflections observed in the diffraction pattern obtained from the resulting frit approximated to the distribution expected for the reported orthorhombic structure of Sb_2Se_3.

Thus it can be seen that under the conditions of preparation used in the present investigation there is a continuous range of solid solutions with the C33 structure in the bismuth–selenium system. This range extends from the composition Bi_2Se_3 to approximately $Bi_{11}Se_9$. No analogous solid solutions are formed in the systems arsenic–selenium and antimony–selenium.

The General Electric Company Limited,
Central Research Laboratories,
Hirst Research Centre,
Wembley, England

S. A. LANGSTON
B. LEWIS

References

1. PEARSON W. B., *Handbook of Lattice Spacings and Structures of Metals*, p. 250, Pergamon Press, London (1958).
2. RAMSDELL L. S. *Amer. Mineral.* **15**, 119 (1930).
3. ALLAN BROWN and LEWIS B., *J. Phys. Chem. Solids*, **23**, 1597 (1962).
4. TIDESWELL N. W., KRUSE F. H. and MCCULLOUGH D. J., *Acta. Cryst.* **10**, 99 (1957).
5. SEMILETOV S. A. and PINSKER Z. G., *Dokl. akad. nauk S.S.S.R.* **100**, 1079 (1955).
6. SEMILETOV S. A., *Trud inst. krist. akad. nauk. S.S.S.R.* **10**, 76 (1954).
7. UPHOFF H. L. and HEALY J. H., *J. appl. Phys.* **32**, 950 (1961).
8. *A.S.T.M. X-ray Powder Data File* (1962) Card No.: 12-732.

BOOK REVIEW

J. D. FAST: **Entropy.** Philips Technical Library, N. V. Philips Gloeilampenfabrieken, Eindhoven (1962). pp. vii + 313 57*s.* 6*d.*

THE present volume is, according to the preface, an expansion of an earlier book that discussed the basic principles needed to calculate the entropies of monatomic and diatomic gases. Solid-state problems are now discussed also, and the book amounts to an elementary text of thermodynamics, statistical mechanics and quantum mechanics. The scope is, therefore, so wide that the author's disclaimer of any attempt at rigor is hardly needed. Whether this has led to a compensating clarity of treatment is discussed below.

The first chapter, "The Concept of Entropy in Classical Thermodynamics," deals with the First and Second Laws. The concept of "heat" is undefined, and the equation

$$dU = dQ + dW$$

is said to be the "mathematical formulation of the First Law" and "at the same time, the defining equation for the internal energy." This is typical of older treatments and will only convince students that they are caught in a vicious circle. The formulation due to Born is much more satisfactory: the law of conservation of energy is stated for adiabatic processes, and heat is defined as the difference between the energy change and the work in non-adiabatic processes.

In Chapter II, the Boltzmann hypothesis for the entropy is introduced, and the most probable distribution of a collection of identical oscillators is shown to be plausible by a special method. The Boltzmann distribution is immediately rederived for a general system composed of independent sub-systems. Here the restrictions on the applicability of the final formulae could have been made more explicit.

Various equilibrium situations, mostly in condensed systems, are discussed in Chapter III, "Applications of the Concept of Entropy." This title would lead one to expect that the Second Law would be applied in its simplest form, without further preliminaries. Of course, it turns out that since the entropy is not very useful as a thermodynamic potential, the author is obliged to begin by defining the Helmholtz and Gibbs free energies, whereupon the discussion follows conventional lines.

In the remaining half of the book the statistical part of the first half is done again, but more carefully. An attempt is made to give the necessary quantum mechanical foundation, and the distribution laws are derived for fermions, bosons and classical particles. The canonical ensemble is briefly described, and the general formulae are written down relating thermodynamic functions to the partition function of a system. When these formulae are related to the earlier ones for systems of independent sub-systems, the factor $N!$ is put in, but neither here nor elsewhere are just the right words found to explain the simple underlying idea.

The last Sections of the book describe the calculation of entropies of simple gases from spectroscopic data.

One can share the author's enthusiasm for the elegance and power of statistical mechanics and thermodynamics, but not his impatience with the difficulty of acquiring a working knowledge of them. With his eye fixed on the results he knows so well, he neglects time and again to lay the groundwork needed for understanding the intermediate steps. For example, at the earliest possible place (Chapter II, Section 2.15), the heat capacity of N_2 is calculated at a number of temperatures in the harmonic oscillator-rigid rotator approximation. The computation uses the equipartition law for the translational and rotational contributions, but this law is not heard of until 175 pages later. Moreover, the results are compared, not with experiment, which might have been illuminating, but with "exact" values calculated from the observed spectra by a method described near the end of the last chapter.

The choice of subject matter is somewhat peculiar for a book aimed at practical calculations. The thermodynamics of chemical equilibrium is confined to 13 pages. Part of this is given to examples, and in the rest, partial molar quantities are mentioned but not defined, a number of ideas such as "standard state" are inserted as needed, and not more than a hint is given of deviations from ideal behavior in gaseous mixtures. The thermodynamics of solutions is omitted entirely, precluding a statistical derivation of Henry's law (but room is found for "Fuel Cells and Heat Pumps"). Although many pages are devoted to the details of numerical computation of thermodynamic functions of simple gases, their use in chemical equilibrium is only sketched, and but a single paragraph is allotted to the Debye solid.

"*Entropy*" cannot be recommended as a text for systematic study of the fields it purports to cover: illustrations, however numerous, cannot replace careful exposition of fundamentals, and this in turn is a lengthy task, if one wants to go from first principles to the boundaries of active research.

Argonne National Laboratory, LESTER GUTTMAN
Solid State Science Division,
Argonne,
Illinois

J. Phys. Chem. Solids Pergamon Press 1963. Vol. 24, pp. 1391–1404. Printed in Great Britain.

THE MICROSCOPIC KINETICS OF STEP MOTION IN GROWTH PROCESSES

W. W. MULLINS*
Carnegie Institute of Technology
and
J. P. HIRTH†
The Ohio State University

(*Received* 12 *July* 1963)

Abstract—Equations are developed which describe the motion of steps in diffusion controlled growth and dissolution processes. It is found that finite trains of steps break up in a pairwise fashion at the rear of step trains. Applications of the present model to cases of macroscopic step or facet formation by the coalescence of single steps are discussed.

1. INTRODUCTION

THE model(1) of a surface consisting of low index terraces separated by monatomic steps containing kinks has been extensively applied to kinetic processes including crystal growth,(2) evaporation,(3) electrodeposition,(4) oxidation,(5) etc. In general, these treatments have dealt with the dependence of the kinetic rate in question on step spacing, but have not considered in detail the time dependent change in step spacings as the process occurred.

FRANK(6) (see also CABRERA and VERMILYEA(7) and CHERNOV(8)) has developed a continuum kinematic theory of step motion based on LIGHTHILL and WHITHAM's(9) theory of traffic flow on highways. When the rate of say dissolution depends only on step density, Frank's theory describes the orientation profile as dissolution proceeds and hence describes the kinetics of change of step spacings. Frank's general formulation of the problem(10) includes solutions for cases where the dissolution rate depends on factors other than step density (e.g. time dependent impurity adsorption) but these cases, several of which have been described in the literature,(6,11,12) are difficult to analyze quantitatively. When q, the step flux at a point on a dissolving surface, is a function only of k, the step density at that point, Frank's theory predicts that (i) points of a given orientation (given k) will move in a straight line as dissolution proceeds, (ii) the straight line trajectory will be parallel to the normal of a polar diagram of the reciprocal dissolution rate at the same orientation, (iii) if a bunch of steps of spacing less than that on the surrounding surface forms, the bunch will develop a discontinuity at the leading edge if (d^2q/dk^2) is positive, at the trailing edge if (d^2q/dk^2) is negative, (iv) the average step density in a bunch decreases with time,(12) and (v) the discontinuities at the edges of the bunches move with a velocity $\Delta q/\Delta k$, where Δq and Δk are the change in q and k respectively, at the discontinuity.

The above conclusions are quite useful in predicting macroscopic changes in surface profiles as a function of time, particularly for continuous trains of steps. Indeed predictions (i) and (ii) above have been verified for two cases of crystal dissolution.(14,15) However, since the continuum kinematic theory characterizes all steps in a small bundle by the same density k and flux q, it cannot adequately describe any changes in step distribution that depend on large or qualitative differences in the behavior of adjacent step intervals. (The situation is very analogous to the inadequacy of continuous acoustical waves to account for the optical spectra of a crystal involving a contrary motion of adjacent atoms.)

---

* Professor of Metallurgy.

† Mershon Associate Professor of Metallurgy.

In this paper, step motion is described by a system of differential equations, each one corresponding to a step or to a step interval or terrace. The treatment agrees with the continuum kinematic theory to first order in cases where the steps may be described by a continuum model (i.e. q and k). There are however important discrepancies between continuum kinematic theory and the present theory when there are sharp differences between the behavior of alternate terraces such as occur in small finite trains and near the trailing end of a semi-infinite train.

2. EQUATIONS OF STEP MOTION AND GENERAL INTEGRALS

The model for a kinetic process progressing by step motion is depicted in Fig. 1. In the absence of such effects as impurity contamination, all of the processes (growth, etc.$^{(2-5)}$) mentioned above that are proposed to occur by a step mechanism are likely to be controlled by diffusion of atoms or molecules to or from the advancing steps. When this is so, the velocity v of a given step will increase monotonically with increasing distance ϵ to either adjacent step; when a continuum description applies this case corresponds to a negative (d^2q/dk^2) in Frank's formulation. We shall restrict ourselves to this case in this Section and Section 3, but shall examine other cases in Section 4.

We assume the velocity v of a given step λ depends only on the distance ϵ to the two adjacent steps and that this dependence can be expressed by the sum of a given function evaluated for the two distances.*

Thus for the case illustrated in Fig. 1, we have

$$\begin{aligned} v_1 &= f(\infty)+f(\epsilon_1) \\ v_2 &= f(\epsilon_1)+f(\epsilon_2) \\ &\cdot \\ &\cdot \\ &\cdot \\ v_i &= f(\epsilon_{i-1})+f(\epsilon_i) \qquad (1) \\ &\cdot \\ &\cdot \\ &\cdot \\ v_n &= f(\epsilon_{n-1})+f(\infty). \end{aligned}$$

We assume initially only that $f(\epsilon)$ is monotonic increasing with ϵ and is bounded by $f(\infty)$. The preceding assumptions are quite general and should describe a number of physical situations. They apply, for example, when the steps act as ideal line sources (sinks) at which a constant concentration of adsorbed† terrace atoms is maintained (on both sides).$^{(3)}$ This is certainly the case at equilibrium when the steps are not moving. It is an adequate approximation when the steps are moving slowly enough so that their net loss (gain) of atoms is small compared with the flux exchanged with the terrace at equilibrium; the latter condition should hold in the expected case that the fractional concentration of adsorbed atoms on terrace sites is small (see Appendix I).

Introducing the function $g(\epsilon) = f(\infty)-f(\epsilon)$, so that $g(\infty) = 0$, and noting that the time rate of change of step spacing is given by $\dot{\epsilon}_n = v_{n+1}-v_n$

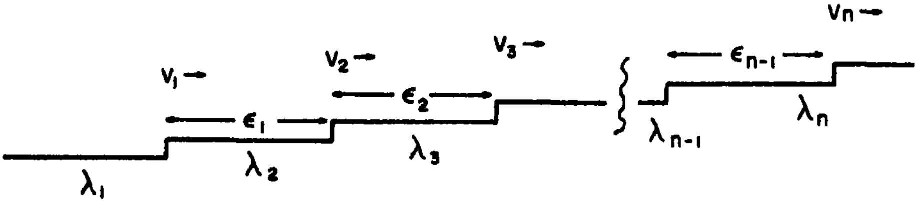

FIG. 1. Cross-section of a dissolving crystal surface showing steps λ separated by terraces of spacing ϵ and moving with velocity v.

---

* As shown in Fig. 1, λ_i is the name of a given step while ϵ_i is the spacing of the terrace ahead of the step λ_i.

† An adsorbed atom is an atom which is on a terrace but which is not adjacent to a step. Such an atom is bound to the terrace by only about half the condensation energy. As pertains to growth (or evaporation) processes as discussed here, the adsorbed atoms are the same element as those of the growing solid.

$= f(\epsilon_{n+1})-f(\epsilon_{n-1}) = g(\epsilon_{n-1})-g(\epsilon_{n+1})$, we rewrite the set of equations (1) as

$$\begin{aligned}\dot\epsilon_1 &= -g(\epsilon_2)\\ \dot\epsilon_2 &= g(\epsilon_1)-g(\epsilon_3)\\ \dot\epsilon_3 &= g(\epsilon_2)-g(\epsilon_4)\\ &\;\;\vdots\\ \dot\epsilon_{n-1} &= g(\epsilon_{n-2}).\end{aligned} \tag{2}$$

The monotone decreasing function $g(\epsilon)$ is also depicted in Fig. 2. If $g(\epsilon)$ becomes zero above some finite value ϵ_R we will speak of this value as the range of influence of steps on each other or simply as the range; otherwise the range is ∞. If n (the total number of steps) is even, an integral of equation (2) can be deduced immediately by summing over odd terraces.

Thus

$$\sum_{j=0}^{j=(n/2)-1} \dot\epsilon_{2j+1} = 0, \; (n \text{ even}), \tag{3}$$

so that

$$\sum_{j=0}^{j=(n/2)-1} \epsilon_{2j+1} = C, \; (n \text{ even}), \tag{4}$$

where C is a constant.

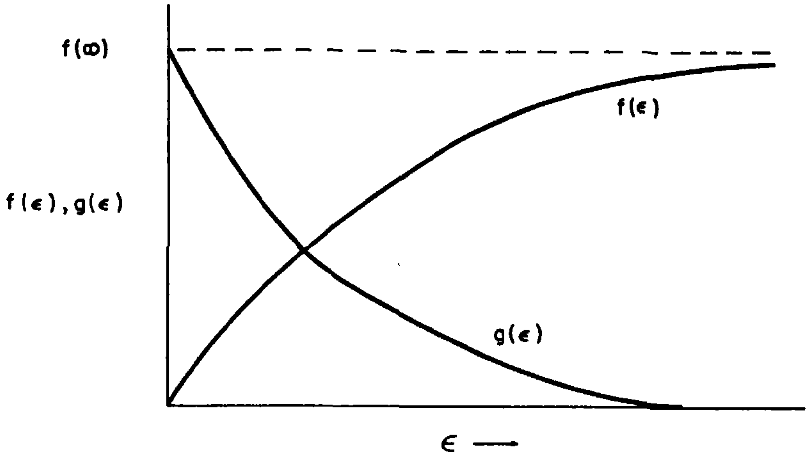

FIG. 2. The velocity functions $f(\epsilon)$ and $g(\epsilon)$.

A second integral, valid for any n, follows from multiplying the jth equation of equations (2) by $g(\epsilon_j)$ and adding; one obtains the second invariant condition

$$\sum_{j=1}^{j=n-1} g(\epsilon_j)\dot\epsilon_j = 0, \tag{5}$$

or

$$\sum_{j=1}^{j=n-1} G(\epsilon_j) = C', \tag{6}$$

where

$$G(\epsilon) = \int_0^\epsilon g(\epsilon)\,\mathrm{d}\epsilon$$

and C' is a constant. The function $G(\epsilon)$ is shown in Fig. 3; it must be monotonic increasing with ϵ. Also since $(\mathrm{d}^2G/\mathrm{d}\epsilon^2) = (\mathrm{d}g/\mathrm{d}\epsilon) \leqslant 0$, G is a convex function of ϵ. We assume that

$$G(\infty) = \int_0^\infty g(\epsilon)\,\mathrm{d}\epsilon$$

exists and therefore bounds $G(\epsilon)$. This is true for the functions $g(\epsilon)$ usually considered(3) as they decay at least exponentially for large ϵ.

3. BEHAVIOR OF SMALL STEP TRAINS

A. The case $n = 2$ comprises a pair of steps which according to equation (4) travel with a constant spacing $\epsilon_1 = C$. From equation (1) their velocity is less than that of a single step by the amount $f(\infty)-f(\epsilon_1) = g(\epsilon_1)$.

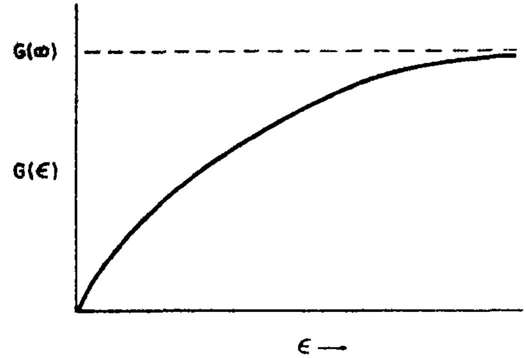

FIG. 3. The functions $G(\epsilon)$; $G(\infty) = \int_0^\infty g(t)\,dt$.

B. The case $n = 3$ comprises three steps separated by two terraces. Equations (6) and (2) reduce to $G(\epsilon_1)+G(\epsilon_2) = C'$, $\dot\epsilon_1 = -g(\epsilon_2)$, $\dot\epsilon_2 = +g(\epsilon_1)$. The latter equations show that ϵ_1 never increases and ϵ_2 never decreases. Integrating from initial value ϵ_1^0 of ϵ_1 at $t = 0$ to a final value ϵ_1^f at t we have†

$$t = \int_{\epsilon_1^0}^{\epsilon_1^f} \frac{d\epsilon_1}{\dot\epsilon_1} = \int_{\epsilon_1^f}^{\epsilon_1^0} d\epsilon_1/g(\epsilon_2)$$

$$= \int_{\epsilon_1^f}^{\epsilon_1^0} d\epsilon_1/g\{[G^{-1}(C'-G(\epsilon_1))]\}. \qquad (7)$$

In the limit $t = \infty$, the integral must be infinite. This is possible for a positive value ϵ_1^* of ϵ_1^f only if the denominator g in equation (7) equals zero for ϵ_1^* i.e., if the argument $G^{-1}[C'-G(\epsilon_1^*)] = \infty$ or $C'-G(\epsilon_1^*) = G(\infty)$; otherwise ϵ_1^f (the lower limit of integration) decreases to zero at or before $t = \infty$, the two steps coalesce to form a double height step and equation (7) no longer applies. Now as ϵ_1 and therefore $G(\epsilon_1)$ decrease toward zero, $C'-G(\epsilon_1)$ can clearly increase to $G(\infty)$, for some value ϵ_1^*, only if $C' > G(\infty)$. This condition is also sufficient since the initial value of $C'-G(\epsilon_1)$ cannot exceed $G(\infty)$, i.e., $C'-G(\epsilon_1^0) = G(\epsilon_2^0) \leqslant G(\infty)$. Therefore the necessary and sufficient condition for ϵ_1 to decrease to a finite limiting value (ϵ_1^*) as $t \to \infty$ is that‡

$$C' > G(\infty). \qquad (8)$$

Equation (8) will always hold, for example, if the first step starts out very far from a pair (which it will then overtake) i.e., $C' = G(\infty)+G(\epsilon_2^0) > G(\infty)$; furthermore the conservation of C' implies for this case that $\epsilon_2^0 = \epsilon_1^*$ since $C' = G(\epsilon_1^0) + G(\epsilon_2^0) = G(\infty)+G(\epsilon_2^0) = G(\epsilon_1^f)+G(\epsilon_2^f) = G(\epsilon_1^*) + G(\infty)$; the latter equality follows from the remark that when ϵ_1 has reached the constant value ϵ_1^*, $\dot\epsilon_1 = g(\epsilon_2)$ must be zero which requires that ϵ_2 either be ∞ or exceed the range ϵ_R, giving in either case $G(\epsilon_2^f) = G(\infty)$. Thus the faster moving single step joins the middle step of the pair and displaces the leading step which escapes forward; the initial and final pair have the same spacing.

For a typical case, that of evaporation(3) or crystal growth,(2)§

$$f(\epsilon) = A \tanh(\epsilon/\delta), \text{ and}$$

$$G(\infty) = A\delta \ln 2, \qquad (9)$$

where δ is the root mean square distance of surface diffusion of an adatom on a terrace,(2,3) $A = v_{\max}/2$, and $v_{\max}$ is the velocity of an isolated step determined by the diffusion parameters in the system in question. ϵ_1^* can be determined, when $C' > G(\infty)$, from the expression

$$G(\epsilon_1^*) = C'-G(\infty). \qquad (10)$$

ϵ_1^* values are computed for several cases in Table 1. It is seen that the step λ_1 always captures the step λ_2, and that the terminal spacing is either finite or zero. In every case in which equation (9) holds, $\epsilon_2^f = \infty$.

C. The case $n = 4$ comprises four steps separated by three terraces. Here equation (2) gives $-\dot\epsilon_1 = \dot\epsilon_3 = g(\epsilon_2)$ and $\dot\epsilon_2 = g(\epsilon_1)-g(\epsilon_3)$; the two integral invariants given by equations (4) and (6) are

---

† Since the function G is a monotone increasing function it has a unique inverse, G^{-1}.

‡ It is easy to see that the solution is symmetric about the values $\epsilon_1 = \epsilon_2$.

§ In the notation of the Appendix $A = \eta\sqrt{(ED)}$ and $\delta = 2\sqrt{(D/E)}$.

Table 1. Terminal step spacings ϵ_1^f for a train with $n = 3$. Collapse refers to the case when ϵ_1 reaches zero and the terrace collapses to a double height step.

Initial ledge spacing	C' (in units of $A\delta$)	ϵ_1^f
1. $\epsilon_1^0 = \epsilon_3^0 \ll \delta$	1	collapse
2. $\epsilon_1^0 = \epsilon_3^0 \gg \delta$	4	$\epsilon_1^0 - 0{\cdot}347\delta$
3. $\delta \gg \epsilon_1^0 \neq \epsilon_3^0 \ll \delta$	1	collapse
4. $\epsilon_1^0 \gg \delta \gg \epsilon_3^0$	$2/(1-\epsilon_3^0)$	$\epsilon_3^0 - \exp(-2\epsilon_1^0/\delta)$
5. $\epsilon_1^0 \ll \delta \ll \epsilon_3^0$	$2/(1-\epsilon_1^0)$	$\epsilon_1^0 - \exp(-2\epsilon_3^0/\delta)$
6. $\epsilon_1^0 \gg \epsilon_3^0 \gg \delta$	$4/[1+\exp(-2\epsilon_3^0/\delta)]$	$\epsilon_3^0 - 0{\cdot}5\{\exp(-2\epsilon_1^0/\delta)+\exp[(-2\epsilon_1^0+\epsilon_3^0)/\delta]\}$
7. $\epsilon_3^0 \gg \epsilon_1^0 \gg \delta$	$4/[1+\exp(-2\epsilon_1^0/\delta)]$	$\epsilon_1^0 - 0{\cdot}5\{\exp(-2\epsilon_3^0/\delta)+\exp[(-2\epsilon_3^0+\epsilon_1^0)/\delta]\}$

$\epsilon_1 + \epsilon_3 = C$ and $G(\epsilon_1)+G(\epsilon_2)+G(\epsilon_3) = C'$ respectively. The first equations show that ϵ_1 never increases and ϵ_3 never decreases. Also since $\dot{\epsilon}_2 = g(\epsilon_1) - g(C-\epsilon_1)$, ϵ_2 decreases if $\epsilon_1 > C/2$ and increases if $\epsilon_1 < C/2$; since ϵ_1 cannot decrease to a limiting value larger than $C/2$, as shown below, ϵ_2 must always end up by increasing.

Utilizing the expression $\dot{\epsilon}_1 = -g\{G^{-1}[C'-G(\epsilon_1) - G(C-\epsilon_1)]\}$ in a development analogous to equation (7), one easily finds for the present case that the critical condition for a positive limiting value ϵ_1^* of ϵ_1 (and therefore of $\epsilon_3 = C-\epsilon_1$) is that the equation

$$C' - [G(\epsilon_1)+G(C-\epsilon_1)] = G(\infty) \qquad (11)$$

have the solution $\epsilon_1 = \epsilon_1^* > 0$. Since the left hand side of equation (11) is simply $G(\epsilon_2)$, it cannot exceed $G(\infty)$ for any starting value ϵ_2^0. Furthermore, differentiation of the bracket and utilization of the monotone character of $g(\epsilon)$ shows the bracket to have its maximum value at $\epsilon_1 = C/2$ about which it is symmetric. Therefore as ϵ_1 decreases, the left hand side of equation (11) decreases if $\epsilon_1 > C/2$ and increases if $\epsilon_1 < C/2$. It follows immediately that ϵ_1^*, if it exists, must lie below $C/2$ and that the necessary and sufficient condition for its existence is that

$$C' > G(C)+G(\infty). \qquad (12)$$

Again, at the limiting value $\epsilon_1 = \epsilon_1^*$, the left hand side $G(\epsilon_2)$ of equation (11) must equal $G(\infty)$, that is, $\epsilon_2 \geqslant \epsilon_R$ corresponding to a split of the initial group of four steps into two pairs which do not interact; furthermore, since $\epsilon_1^* < C/2 < \epsilon_3^*$, the leading pair travels faster than and escapes the trailing pair. Additional conclusions are the following:

(a) Given ϵ_1^0 and ϵ_3^0, equation (12) shows that there is a minimum value of ϵ_2^0 below which ϵ_1 will go to zero and a double height step will form.

(b) If $\epsilon_1^0 = \epsilon_2^0 = \epsilon_3^0 = C/2$, ϵ_1^f is finite only if $3G(C/2) > G(C)+G(\infty)$, or, in the case of the special function of equation (9) if $\epsilon_1^0 \gtrsim 1{\cdot}1\,\delta$.

(c) For the special function of equation (9): If $\epsilon_1^0 \gg \delta$, $\epsilon_3^0 \gg \delta$, ϵ_1^f is finite for any ϵ_2^0 whereas if $\epsilon_1^0 \ll \delta$, $\epsilon_3^0 \ll \delta$, ϵ_1^f is finite only if $G(\epsilon_2) > G(\infty)$, i.e., $\epsilon_2 \gg \delta$.

In any case the four steps break up in a pairwise grouping, with the leading pair escaping the trailing pair, and the trailing pair approaching either a finite ϵ_1^f or collapsing to a double height step.

4. BEHAVIOR OF LARGE STEP TRAINS

A. *Some general conclusions*

Qualitatively the above results indicate that a finite evenly spaced train will start pairwise grouping from the rear and spreading from the front. To develop a consequence of this conclusion, which will be confirmed in detail below, we note that since $G(\epsilon)$ is convex,† the sum of the $G(\epsilon_i)$ for a group of terraces of non-uniform widths ϵ_i cannot exceed the value obtained when all widths are equal to the average width $\bar{\epsilon}$; it must be less than this value if the non-uniformly spaced steps are within the range of influence of each other. Thus, assuming that the steps are initially of equal width

---

† That is $d^2G/d\epsilon^2 \leqslant 0$ the equality holding only if $g(\epsilon)$ is zero corresponding to the case in which the steps are out of range (i.e., $\epsilon > \epsilon_R$).

$\epsilon_i^0 = \bar{\epsilon}^0$ and are within range we have

$$nG(\bar{\epsilon}) \geqslant G(\epsilon_1)+G(\epsilon_2) \ldots G(\epsilon_n) = C' = nG(\bar{\epsilon}^0) \tag{13}$$

the equality now holding only if $\epsilon_1 = \epsilon_2 \ldots \epsilon_n = \bar{\epsilon}^0$. Since, however, a non-uniform spacing (pairwise bunching) develops at the rear, equation (13) shows that the average spacing of the steps must increase, i.e., $\bar{\epsilon} > \bar{\epsilon}^0$. Furthermore, for the even train case, the sum and therefore the average of the odd widths is constant (C); therefore the increase in $\bar{\epsilon}$ must be entirely due to an increase in the average of the even terrace widths in this case. Additional conclusions for the even train case that follow from equation (4) are (i) that the spreading of odd pairs in front must offset their shrinkage toward the rear since the sum of the odd ledge widths remains fixed; (ii) the escape of the leading step from a long even train is impossible unless some terraces collapse; for example, the distance between the two leading steps cannot exceed C unless all other pairs have collapsed; (iii) the approach of a step from $-\infty$ to an odd train will displace the leading step to $+\infty$ according to equations (4) and (6), an example being the case $n = 3$ above.

B. *Phase velocity of a periodic disturbance—dispersion relations*

Consider an infinite train of steps whose spacing ϵ_n varies only slightly about some mean value $\bar{\epsilon}$; we do not necessarily assume, however, that ϵ_n varies slowly with n.

By expanding the function $g(\epsilon_n)$ about $\bar{\epsilon}$ and keeping only first order terms we may rewrite the nth member of equation (2) as the differential-difference equation

$$\begin{aligned} \dot{\epsilon}_n &= -g'(\bar{\epsilon})[(\epsilon_{n+1}-\bar{\epsilon})-(\epsilon_{n-1}-\bar{\epsilon})] \\ &= -g'(\bar{\epsilon})(\epsilon_{n+1}-\epsilon_{n-1}) \end{aligned} \tag{14}$$

where the prime denotes differentiation of g. Equation (14) would be exact if g were linear in the range of ϵ about $\bar{\epsilon}$ under consideration. Consider the traveling sinusoidal wave given by

$$\begin{aligned} \epsilon_n &= \bar{\epsilon}+\xi\, e^{i\omega t}\, e^{i\nu n} \\ &= \bar{\epsilon}+\xi\, e^{i\nu[n+(\omega/\nu)t]} \end{aligned} \tag{15}$$

where $\xi \ll \bar{\epsilon}$, and where $\nu = 2\pi/\Lambda$ is an adjusted wave number, Λ being the wave length expressed in units of $\bar{\epsilon}$. As written, the wave evidently has a phase velocity of $(\omega/\nu)\bar{\epsilon}$ toward smaller n (left). Substitution of equation (15) into equation (14) gives $i\omega = -g'(\bar{\epsilon})\,(e^{i\nu} - e^{-i\nu}) = -g'(\bar{\epsilon})2i \sin \nu$. Therefore the phase velocity v_w' of the wave with respect to the steps is given by

$$\begin{aligned} v_w' &= \frac{\omega}{\nu}\bar{\epsilon} = -2g'(\bar{\epsilon})\bar{\epsilon}\left(\frac{\sin \nu}{\nu}\right) \\ &= -2g'(\bar{\epsilon})\bar{\epsilon}\left[1-\frac{\nu^2}{3!}+\frac{\nu^4}{5!}-\ldots\right]. \end{aligned} \tag{16}$$

Using equation (1) and the definition of g, we find that the speed of the traveling wave to the right (larger n) with respect to the crystal is given by

$$\begin{aligned} v_w &= 2f(\bar{\epsilon})-2f'(\bar{\epsilon})\bar{\epsilon}\left(\frac{\sin \nu}{\nu}\right) \\ &= v(k)+k\frac{\mathrm{d}v}{\mathrm{d}k}\cdot\left(\frac{\sin \nu}{\nu}\right) \end{aligned} \tag{17}$$

where the second version is written in the notation of the continuum kinematic theory, $v(k) = 2f(\bar{\epsilon}) = 2f(1/k)$ being defined as the velocity of the steps as a function of their density $k = 1/\bar{\epsilon}$. For $\nu \ll 1$, representing a wave whose wavelength is many step spacings, $(\sin \nu/\nu) \simeq 1$ and equation (17) agrees with the expression $v_w = v+k(\mathrm{d}v/\mathrm{d}k)$ from the kinematic theory which evidently does not yield any dispersion; as ν increases however our expression shows an increasing dependence of v_w upon wavelength through the factor $(\sin \nu/\nu)$ which finally becomes zero for the pairwise grouping given by $\nu = \pi (\Lambda = 2)$; for this case $v_w = v$ which corresponds to the immediate conclusion from equation (2) that a train of steps whose alternate spacings are equal must move as a rigid unit. Figure 4 shows a plot of v_w' as a function of ν for a given value of $\bar{\epsilon}$. The dispersion relations (16) and (17), arising out of the present discrete treatment, are analogous to the dispersion relations for lattice waves arising out of the discrete treatment of atomic vibrations, relations that are entirely missed by the continuum approach of elasticity theory.

Neither the continuum kinematic theory nor the present modification of it including dispersion leads to a spontaneous growth of an initial spatial

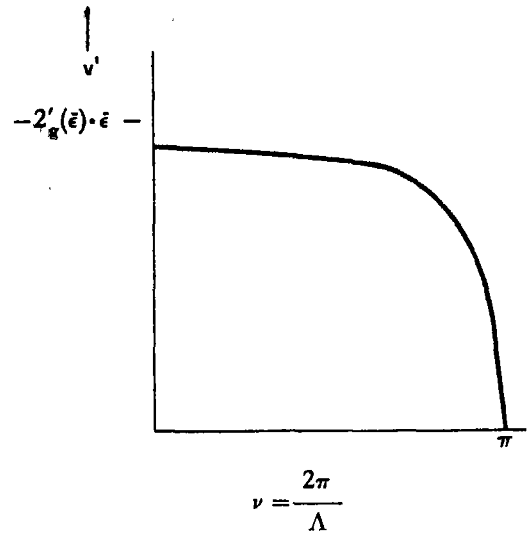

FIG. 4. Dispersion relation for a wave of nearly uniform spacing.

undulation in density in an infinite train; the Fourier components of the undulation are merely propagated with their appropriate velocities v_w with no change of amplitude. Furthermore, consideration of higher orders in the expansion leading to equation (14) does not modify this conclusion in any essential way; the higher order terms are easily seen to introduce non-linearities that have the effect of weakly coupling harmonic waves so that an initial sinusoidal wave becomes somewhat unsymmetric due to the growth of higher harmonics.

C. *Description of pairwise grouping by partial differential equations*

Since we wish to distinguish odd and even intervals the notation is changed from ϵ to u for odd terraces and to w for even terraces as shown in Fig. 5. The terrace widths are functions of terrace index and time $u(n, t)$, $w(n, t)$ according to equation (2). If u and w are taken to vary slowly with index, a supposition which still permits a drastic pairwise grouping, then equations (2) can be written

$$\dot{u}(n, t) = -(\mathrm{d}g/\mathrm{d}w)(\partial w/\partial n) = -p(w)(\partial w/\partial n). \quad (18)$$

and

$$\dot{w}(n, t) = -(\mathrm{d}g/\mathrm{d}u)(\partial u/\partial n) = -p(u)(\partial u/\partial n) \quad (19)$$

If the terrace width varies slowly for the entire train, $u(n, t) \cong w(n, t)$ and the above equations reduce to*

$$\dot{u} = -p(u)(\partial u/\partial n). \quad (20)$$

When applied to a small sinusoidal variation in spacing of wavelength long compared to the interstep spacing, equation (20) yields the result given by equation (16) or alternatively given by the continuum kinematic theory. Again, equation (20) may be applied directly to the front of a semi-infinite train, and results equivalent to FRANK's(6) result will obtain. However, at the back of the train both the u and w equations must be retained, a necessity not noted in the above kinematic treatments.(6–8)

We take the particular case, of a linear function for $g(\epsilon)$ of range ϵ_R, shown in Fig. 6 and given by

$$g(\epsilon) = (\epsilon_R - \epsilon)g(0)/\epsilon_R = c(\epsilon_R - \epsilon), \quad (21)$$

so that $p(\epsilon) = -c$ for $\epsilon < \epsilon_R$ and $p(\epsilon) = 0$ for $\epsilon > \epsilon_R$. Therefore, for $\epsilon < \epsilon_R$,

$$\dot{u} = c(\partial w/\partial n), \text{ and } \dot{w} = c(\partial u/\partial n) \quad (22)$$

yielding

$$\ddot{u} = c^2(\partial^2 u/\partial n^2) \text{ and } \ddot{w} = c^2(\partial^2 w/\partial n^2). \quad (23)$$

---

* Relating the expressions in equation (20) to FRANK's(6) q and k, we note that $u = k^{-1}$, $(\partial u/\partial n) = (\partial u/\partial x)(\partial x/\partial n) = (\partial u/\partial x)u$, so that equation (20) may be written $(p/k)(\partial k/\partial x) + (\partial k/\partial t) = 0$. This is equivalent to Frank's continuity equation where $p = k(\mathrm{d}q/\mathrm{d}k)$.

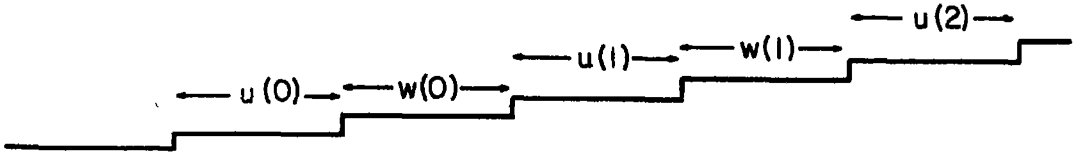

FIG. 5. Notation distinguishing odd terraces, u and even terraces, w.

Thus in the linear range of $g(\epsilon)$, and when u and w change slowly with n, each obeys the standard wave equation.

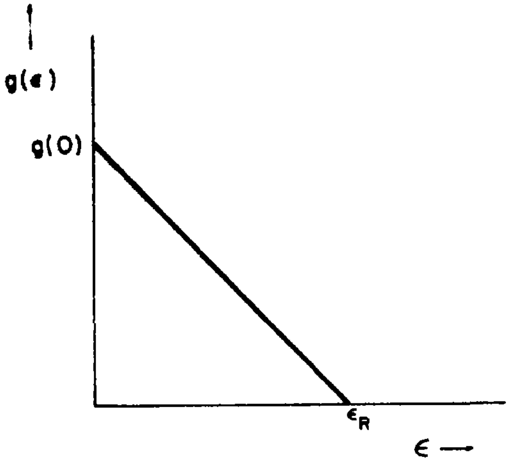

FIG. 6. Particular $g(\epsilon)$ for partial differential equation solution.

The solution of equations (23) for an initial condition of a semi-infinite step train of equal spacing $u = w = \epsilon_0$ proceeds by superposition of solutions to satisfy the boundary condition that applies to the rear, namely

$$(\partial u/\partial t)_{n=0} = -g[w(0,t)] = -c[\epsilon_R - w(0,t)]. \quad (24)$$

A solution that satisfies equation (22) (as may be verified by substitution) is given by the following superposition of traveling waves of strength $\phi(t)$

$$\begin{aligned} u(n,t) &= \epsilon_0 && \text{for } t < n/c \\ &= \epsilon_0 + \int_{n/c}^{t} \phi(t'-n/c)\mathrm{d}t' && \text{for } t > n/c \\ w(n,t) &= \epsilon_0 && \text{for } t < n/c \\ &= \epsilon_0 - \int_{n/c}^{t} \phi(t'-n/c)\mathrm{d}t' && \text{for } t > n/c \end{aligned} \quad (25)$$

where the form of ϕ may still be determined from the boundary condition. Substituting equation (25) into the boundary condition (24) we obtain

$$\phi(t) = -c\left[(\epsilon_R - \epsilon_0) + \int_0^t \phi(t')\mathrm{d}t'\right]. \quad (26)$$

Differentiating with respect to t, we find $\phi' = -c\phi$ so that the solution of equation (26) is

$$\phi(t) = c(\epsilon_0 - \epsilon_R)e^{-ct}. \quad (27)$$

Equation (27) determines ϕ as a function of its argument t. Substituting this function into equation (25) and carrying out the integrations we obtain for the final solution the expressions

$$\begin{aligned} u(n,t) &= \epsilon_0 && t < n/c \\ &= \epsilon_0 + (\epsilon_0 - \epsilon_R)[1 - \exp(n - ct)] && t > n/c \\ w(n,t) &= \epsilon_0 && t < n/c \\ &= \epsilon_0 - (\epsilon_0 - \epsilon_R)[1 - \exp(n - ct)] && t > n/c. \end{aligned} \quad (28)$$

Equations (28) show that the alteration of spacing propagates into the train like a wave with an index velocity of $c = -g'(\epsilon)$ and a front at $n = ct$.* The odd intervals (u) behind the wave front decrease with time and with increasing distance behind the front at any given time; the even intervals (w) behind the wave front increase with increasing time and with increasing distance behind the front at a given time. The limiting values of u and w for very long times are given immediately from equations (28) as

$$\begin{aligned} u(n,\infty) &= 2\epsilon_0 - \epsilon_R \\ w(n,\infty) &= \epsilon_R. \end{aligned} \quad (29)$$

This result shows the preceding description to be valid for all times only if $u(n,\infty) = 2\epsilon_0 - \epsilon_R \geqslant 0$ or

$$\epsilon_0 \geqslant \frac{\epsilon_R}{2} \quad (30)$$

which guarantees that the steps in a pair do not coalesce. Tentatively assuming this to be true, we see from equations (29) that the limiting arrangement is a pairwise grouping of steps in which the terminal spacing of steps within a pair (odd interval) is $2\epsilon_0-\epsilon_R$ and the terminal spacing between adjacent steps of two neighboring pairs (an even interval) is ϵ_R so that the pairs do not influence each other; the sum of consecutive even-odd intervals remains $2\epsilon_0 = (2\epsilon_0-\epsilon_R)+\epsilon_R$. The limiting speed v_p of the train of pairs is

---

* It is interesting to note that a finite time is required for the propagation of spacing alterations in spite of the fact that the velocity of a step is assumed to be instantaneously determined by the distance to the two neighboring steps. Note further that the velocity (LT^{-1}) of the wave with respect to the steps is approximately $c \cdot \epsilon_0$.

$$v_p = f(2\epsilon_0-\epsilon_R)+f(\epsilon_R) = 2c\epsilon_0 \tag{31}$$

The description of the front end of a train initially having the uniform spacing ϵ_0 requires the solution of only one equation since $u \simeq w$; namely,

$$\frac{\partial u}{\partial t} = c\frac{\partial u}{\partial n} \tag{32}$$

subject to the boundary condition

$$\left(\frac{\partial u}{\partial t}\right)_{n=0} = c[\epsilon_R-u(0, t)] \tag{33}$$

where the index n now starts at zero at the front interval of the train and increases going toward the rear. Proceeding in the same way as above, the solution is found to be

$$\begin{aligned} u(n, t) &= \epsilon_0 && t < n/c \\ &= \epsilon_0+(\epsilon_R-\epsilon_0)[1-\exp(n-ct)] && t > n/c \end{aligned} \tag{34}$$

Equation (34) again describes a wave like propagation of the alteration of interval spacing with an index velocity c and a front at $n = ct$. This time the alteration is evidently an elongation of all intervals behind the advancing wavefront to a terminal value of ϵ_R which places the steps just out of range. The terminal velocity v_s of this train of isolated steps is from equations (1) and (21)

$$v_s = f(\epsilon_R)+f(\epsilon_R) = 2c\epsilon_R. \tag{35}$$

The preceding results show that a finite equally spaced train will start pairwise grouping from the rear and spreading from the front. Thus under the assumed interaction, and still supposing $\epsilon_0 \geqslant \epsilon_R/2$, so that coalescence does not occur at the rear, and $\epsilon_0 < \epsilon_R$, so that interaction occurs, a finite train must break up into two groups; the paired group in the rear traveling at velocity v_p [equation (31)] and the group of isolated steps in the front traveling at the higher velocity v_s [equation (35)]; the two groups must continue to separate with the relative velocity

$$v = v_s-v_p = 2c(\epsilon_R-\epsilon_0). \tag{36}$$

We now drop the assumption that $\epsilon_0 \geqslant \epsilon_R/2$ and consider briefly the other extreme case in which $\epsilon_0 \ll \epsilon_R/2$. Equation (34) will still describe the essential features of spreading at the front end of the train, but the situation at the rear of the train will be considerably modified from that described in the preceding discussion due to the possibility of the coalescence of steps to form multiple steps. We characterize multiple steps by assuming (i) the original order of steps must be preserved because of the prohibitively high energy associated with any undercutting of one step beneath the one ahead of it which would produce an overhanging layer of crystal; (ii) the velocity of a multiple step (made of n monatomic steps) is determined by the assumption that the n-step represents the same boundary condition to the diffusion problem as a single step but must lose n-times more material to move the same distance, thus,

$$V(n) = \frac{1}{n}[f(\epsilon_-)+f(\epsilon_+)] \tag{37}$$

where ϵ_- and ϵ_+ are the distances to adjacent steps (single or multiple) on either side; and (iii) the stability of the n-step is determined purely kinematically by the requirement that if dissociated from the multiple step the last of the steps move faster and the first move slower than $V(n-1)$.

Under the preceding assumptions, it is clear that the last step of a semi-infinite equally, closely spaced train ($\epsilon_0 \ll \epsilon_R/2$) will sweep forward collecting steps until it is slowed down to the velocity of a single step in the train; thus assuming the spacing of the single steps ahead of the n-step is approximately unaltered,* the number of steps n it will collect is given by the equation

$$\frac{1}{n}[f(\infty)+f(\epsilon_0)] = 2f(\epsilon_0) \tag{38}$$

---

* This approximation should be fairly good for $\epsilon_0 \ll \epsilon_R/2$ since any given terrace ahead of the advancing multiple step will, according to equation (28), alternately tend to expand or contract depending on whether it is an even or odd number of terraces ahead of the advancing multiple step.

or

$$n \cong \frac{f(\infty)}{2f(\epsilon_0)}$$

the last approximation holding for large n. For the particular function given by equation (8), equation (38) becomes

$$n \cong \frac{\delta}{2\epsilon_0}. \qquad (39)$$

This multiple n-step should be kinematically stable at the rear of a semi-infinite train; in any finite train, however, spreading would always propagate backwards from the front end and cause the n-step to eventually dissociate.

In a large n-step, the diffusion of atoms from an interior step of the group out to the terrace may be a difficult step in which case equation (38) is an inadequate specification of the behavior of the multiple step.[*]

5. RECONSIDERATIONS OF THE CONTINUUM KINEMATIC THEORY

A. *General comparison with the present theory*

In view of the above results, it is clear that the step kinetics depend on the discrete dependence of v on ϵ_{odd} and ϵ_{even}, so that the kinematic theory[(6–8)] does not correctly describe the quantitative step kinetics in this case. For the above example the $q(k)$ curve would be as shown in Fig. 7. Thus for this case, as long as $k < k_R = 1/\epsilon_R$, the kinematic theory would predict that the entire step train would follow a trajectory of dy/dx equal to zero, and that the velocities of the discontinuities at the leading and trailing edges of the finite train would be equal. Contrary to this prediction, the above analysis shows that the train breaks up into two trains which have different limiting spacings and which continuously move apart with increasing time.

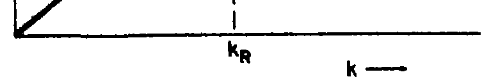

FIG. 7. $q(k)$ for the special case of $g(\epsilon)$ shown in Fig. 6; $k_R = (1/\epsilon_R)$.

Thus, the present treatment reproduces macroscopically the Frank conclusions (iii) and (iv) (see Section 1) that bunching will start at the rear of a step train, and that the average terrace spacing in the train will increase. In addition the present theory adds the conclusion that pairwise bunching occurs, and that only average even terrace widths increase. Further, clearly at the rear of a finite train, the step velocities and orientation trajectories depend explicitly on the values of ϵ_{odd} and ϵ_{even}. Therefore Frank's treatment, wherein v (and hence q) is supposed to be a function only of the average spacing $(\epsilon_{\text{odd}}+\epsilon_{\text{even}})/2$, would not, in general, give the correct quantitative time dependent charge in surface topography at the rear of a step train.

B. *The continuum kinematic theory condition for step pile-ups or macroscopic steps*

As noted in Section 2, our condition for divergent behavior of step trains is that $(d^2G/d\epsilon^2)$ is negative which requires that $(dv/d\epsilon)$ is positive. FRANK's[(6)] equivalent condition is that (d^2q/dk^2) is negative. Noting that $q = vk$, Frank's critical condition, (d^2q/dk^2) equals zero over a range of $\bar{k}$, becomes

$$\frac{dq}{dk} = v+k\frac{dv}{dk} = \text{const.} \qquad (40)$$

However, as shown by FRANK,[(6)] the wave velocity (dq/dk) equals v when (dq/dk) is constant, so that equation (40) reduces to the critical condition

$$\frac{dv}{dk} = 0, \qquad (41)$$

or noting that $k = (1/\epsilon)$,

$$\frac{dv}{d\epsilon} = 0 \qquad (42)$$

---

[*] It follows from a development similar to that presented in Appendix I that equation (38) will be valid as long as $(V/D) \ll (1/n^2 a_0)$, where D now refers to the surface diffusion coefficient on the step surface. Noting that $V \sim v_{\max}/n$, the above condition reduces to $(v_{\max}/D) \ll (1/n\, a_0)$, a condition which should be valid in most cases of growth or evaporation.

Also, if equation (42) is valid then Frank's condition, (d^2q/dk^2) = zero over a range of k, is valid. Thus Frank's critical condition and ours are identical, and can be stated: step trains will eventually diverge as described in Sections 2 and 3 if $(dv/d\epsilon)$ is positive, but pile-ups at the head of a step train will form if $(dv/d\epsilon)$ is negative.

Now conclusion (iv) of the kinematic theory (see Section 1) and the implication in the discussion(13) of Reference 6 [that steps can continue to move through step bunches without convergence even when (d^2q/dk^2) is positive] appear to be inconsistent both with the kinematic theory and with the present treatment. Clearly, the present formulation requires that when $(dv/d\epsilon)$ is negative, any step which has ahead of it a spacing ϵ greater than the spacing of the steps behind it will move with a lower velocity than the trailing steps, will thus cause a pile-up of steps behind it, and cause a macroscopic step bunch to form. No single steps will move through the bunch, and also the average step spacing in the bunch will decrease with time, contrary to the statements in References 6 and 13.

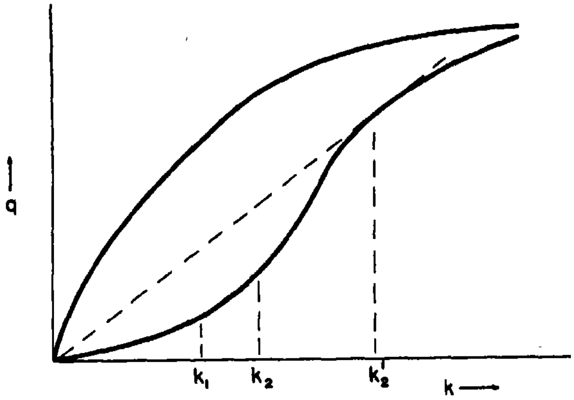

FIG. 8. $q(k)$ for a clean dissolving crystal and one contaminated by time dependent impurity adsorption.

We shall now show that this latter conclusion is indeed consistent with the kinematic theory. A typical $q(k)$ curve for a diffusion controlled process is shown in Fig. 8. Now if time dependent impurity adsorption, say, as proposed by FRANK,(6) hinders step motion, then the $q(k)$ curve will be changed as shown also in Fig. 8. A short range attraction between single steps would have a similar effect. Now a region of density k_2 with a local perturbation k_1, as shown in Fig. 8, would form a bunch with velocity(6)

$$v_b = \frac{q_1 - q_2}{k_1 - k_2}, \tag{43}$$

the steps ahead of the bunch would escape so that $k_1 \to 0$, $q_1 \to 0$, and k_2 would increase to a value k_2'. At this point the front of the bunch would move with a velocity according to equation (43) of $v_b = q_2'/k_2'$. Also the step velocity in the bunch would be $v = q_2'/k_2'$. Thus in agreement with the above conclusion, a step pile-up occurs, the average step density in the pile up increases to a limiting value k_2', and no single steps move through the step pile-up.

Therefore, any factor such as impurity adsorption or inter-step attraction which leads to a negative $(dv/d\epsilon)$ will lead to pile-up or macroscopic step formation, and the macroscopic step will completely block single steps.

6. SOME COMPARISONS WITH EXPERIMENT

As mentioned previously, there have been a number of experimental observations of growth (and dissolution or evaporation) steps and measurements of growth rates that confirm the mechanism invoked here of a diffusion controlled growth process (References 2–8, see also the review in Reference 19). There are not many data with which to compare our predictions for small groups of steps because most observations have dealt with continuous trains of steps. However in one instance, **VERMA**(20) has observed a set of pairs of steps which, for comparison with the present model, apparently are separated by a terrace of spacing greater than ϵ_R so that the terrace spacings are maintained at different constant values for each of the odd and even terrace sets.

There have been a number of observations of the formation of macroscopic steps under growth or evaporation conditions.(16–19) It seems likely, considering the environments in the experiments in question, that most of these steps formed because of impurity adsorption leading to a negative $(dv/d\epsilon)$ as discussed in Section 5B. Other conditions,(12) such as the formation of a stacking fault by the advancing step, could also have led to a negative $(dv/d\epsilon)$.

Finally, it is possible that in some instances macroscopic steps were formed by the mechanism leading to equation (39). Under low supersaturations or undersaturations the operation of step sources produces steps spaced such that $\epsilon_0 \geqslant \delta$.(2,3) The formation of a finite train by means of source termination in such a case will not produce a large macroscopic step according to equation (39). However, under high undersaturations or supersaturations, dislocation step sources produce steps spaced such that $\delta \gg \epsilon$ at the source. Termination of a source[*] under these conditions will produce a finite train that can produce a macroscopic step according to equation (39). As a possible example, suppose $2 \cdot 10^3$ steps spaced 10 atomic spacings a_0 apart, and $\delta = 2 \cdot 10^4 a_0$. According to equation (39) a macroscopic step would build up to a height of $\sim 10^3$ steps at which size spreading from the front would start to gradually decrease the step height. Further, according to equation (28), for the velocity function of equation (9), the spreading from the front will propagate backwards through the train at an index velocity $c = (dg/d\epsilon) = A/\delta$. Thus a time

$$\tau' = 10^3 \delta / A \tag{44}$$

will be required for the spreading to reach the macroscopic step. Using equation (A.7) for $A = v_{\max}/2$, taking $\delta = 2\sqrt{(D/E)}$, and noting that $c_0 E = J$, where J is the growth or evaporation flux, one can rewrite equation (44) as

$$\tau' = 10^3 c_r / [(c_s/c_0) - 1] J. \tag{45}$$

In a typical growth or evaporation experiment $(c_r/J) \sim 1$ sec, so that $\tau' \sim 10^3$ sec. Thus a ledge may form according to equation (39) and exist for a time appreciable compared to experimental observation time (where typically a macroscopic ledge would have an observation time of 10–10^2 sec). It is possible that this mechanism may explain results such as those of NEWKIRK(21) of McNUTT and MEHL,(22) and particularly those of LEMMLEIN and DUKOVA(23) who not only observed macroscopic steps formed around a dislocation spiral-source but also observed that a rapid change from high to low supersaturation produced larger macroscopic steps and vice versa in agreement with the predictions of the above postulations for finite train formation.

Acknowledgements—We are happy to acknowledge support of this research by the U.S. Army Research Office, Durham (W.W.M.), and by the U.S. Office of Naval Research (J.P.H.).

REFERENCES

1. KOSSEL W., *Nach. Ges. Wiss. Göttingen* **135**, (1927).
2. BURTON W. K., CABRERA N. and FRANK F. C., *Phil. Trans.* **243A**, 299 (1951).
3. HIRTH J. P. and POUND G. M., *J. chem. Phys.* **26**, 1216 (1957).
4. PRICE P. B., VERMILYEA D. A. and WEBB M. B., *Acta Met.* **6**, 524 (1958).
5. VERMILYEA D. A., *Acta Met.* **5**, 492 (1957).
6. FRANK F. C., *Growth and Perfection of Crystals*, p. 411 (edited by DOREMUS R. H., ROBERTS B. W. and TURNBULL D.). Wiley, New York (1958).
7. CABRERA N. and VERMILYEA D. A., *Growth and Perfection of Crystals*, p. 393 (edited by DOREMUS R. H., ROBERTS B. W. and TURNBULL D.) Wiley, New York (1958).
8. CHERNOV A. A., *Dokl. Akad. Nauk. S.S.S.R.* **117**, 983 (1957).
9. LIGHTHILL M. J. and WHITHAM G. B., *Proc. Roy. Soc.* **229A**, 281, 317 (1955).
10. FRANK F. C., unpublished research.

---

[*] A dislocation source may be terminated when the dislocation slips away or when, in evaporation or dissolution, the surface receding along a dislocation line reaches a dislocation node. An alternative method of producing a bunch that resembles a finite train involves a sudden change from a high to a low undersaturation (supersaturation) at a source: this results in a bunch of steps of small spacing, corresponding to the high supersaturation, behind which will be another train of much larger step spacing, corresponding to the low supersaturation.

11. IVES M. B. and HIRTH J. P., *J. chem. Phys.* **33**, 517 (1960).
12. HIRTH J. P., *ASM-AIME Symposium on Surfaces* (1962), to be published.
13. Discussion to *Growth and Perfection of Crystals* (edited by DOREMUS R. H., ROBERTS B. W. and TURNBULL D.). Wiley, New York (1958).
14. FRANK F. C. and IVES M. B., *J. appl. Phys.* **31**, 1996 (1960).
15. IVES M. B., *J. appl. Phys.* **32**, 1534 (1961).
16. MOORE A. J. W., *ASM-AIME Symposium on Surfaces* (1962), to be published.
17. FRASER M. J., CAPLAN D. and BURR A. A., *Acta, Met.* **8**, 647 (1960).
18. WALTER J. L. and DUNN C. G., *Acta Met.* **8**, 497 (1960).
19. HIRTH J. P. and POUND G. M., *Condensation and Evaporation—Nucleation and Growth Kinetics*. Pergamon, London (1963).
20. VERMA A. R., *Crystal Growth and Dislocations*, p. 68. Butterworths, London (1953).
21. NEWKIRK J. B., *Acta Met.* **4**, 316 (1956).
22. MCNUTT J. E. and MEHL R. F., *Trans. Amer. Soc. Metals* **50**, 1006 (1958).
23. LEMMLEIN G. G. and DUKOVA E. D., *Kristallografia* **1**, 477 (1956); DUKOVA E. D., *Sov. Phys. Cryst.* **6**, 357 (1961).

APPENDIX I

Conditions for the Validity of the Approximations to the Diffusion Problem Implied by equations* (1).

We first determine the conditions under which the motion of the step may be ignored in solving the diffusion problem, by considering the rigorous steady state solution for a single step. Choosing the step as the origin of coordinates, the following equation must be satisfied by $\Delta c = c - c_s$, where c is the concentration of adsorbed atoms and c_s is the value of c far from the step:

$$D\frac{\partial^2 \Delta c}{\partial x^2} + v\frac{\partial \Delta c}{\partial x} - E\Delta c = 0 \qquad \text{(A1)}$$

where D is the surface diffusion coefficient of adsorbed atoms, v the steady state velocity toward positive x of the step, and E the coefficient giving the net fraction of adsorbed atoms leaving the surface per unit time. Substituting $\Delta c = \text{const } e^{\alpha x}$ we obtain $D\alpha^2 + \alpha v - E = 0$ which has the two solutions

$$\alpha\pm = -\frac{v}{2D} \pm \sqrt{\left[\left(\frac{v}{2D}\right)^2 + \frac{E}{D}\right]}. \qquad \text{(A2)}$$

Therefore the general solution of equation (A1) is

$$\Delta c = a \exp(\alpha^+ x) + b \exp(\alpha^- x) \qquad \text{(A3)}$$

For positive x we must choose α^- and for negative x α^+ to assure that Δc becomes zero far from the step. Futhermore, at the step we assume the concentration is maintained at the value c_0 characteristic of a surface in equilibrium with its vapor. (Note $c_s = (p/p_e)c_0$ where p is the partial pressure of the vapor of the substance in question maintained above the solid and p_e is the value of p at equilibrium.) From the preceding boundary conditions the constants a and b in equation (A3) may be evaluated; the result is

$$\begin{aligned} \text{for} \quad x \geqslant 0 \quad c^+ &= c_s + (c_0 - c_s)\exp(\alpha^- x) \\ x \leqslant 0 \quad c^- &= c_s + (c_0 - c_s)\exp(\alpha^+ x). \end{aligned} \qquad \text{(A4)}$$

The velocity v of the step is determined by the flux of atoms out into the terrace which in turn is determined by the concentration gradients at the step. Since the advance of a unit length of step by a unit distance forward sweeps out a square within which the number of atoms changes by c_r (e.g., from $c_r + c_0$ to c_0) where c_r is the reticular concentration of atoms in the receding layer, we must have

$$v = \frac{D}{c_r}\left[-\left(\frac{\partial c^+}{\partial x}\right)_{x=0} + \left(\frac{\partial c^-}{\partial x}\right)_{x=0}\right]. \qquad \text{(A5)}$$

Substituting (A4) into (A5) we obtain

$$\begin{aligned} v &= \frac{D}{c_r}(c_0 - c_s)(\alpha^+ - \alpha^-) \\ &= \frac{D(c_0 - c_s)}{c_r} 2\sqrt{\left[\left(\frac{v}{2D}\right)^2 + \frac{E}{D}\right]}. \end{aligned}$$

Solving this expression for $v/2D$ and introducing the abbreviation

$$\eta = \frac{c_0 - c_s}{c_r}. \qquad \text{(A6)}$$

We have finally

$$\frac{v}{2D} = \eta\frac{\sqrt{(E/D)}}{\sqrt{(1-\eta^2)}}. \qquad \text{(A7)}$$

This expression for the velocity of the step clearly shows that the condition under which the motion of the step may be neglected in solving the diffusion problem is that $|\eta| = [(|c_0 - c_s|)/c_r] \ll 1$. In this case equation (A7) gives $v/2D \cong \eta\sqrt{(E/D)}$ which is precisely the result obtained from equation (A1) if the middle term corresponding to the motion is neglected. A sufficient condition for $\eta \ll 1$ is that $c_0/c_r \ll 1$ signifying that at equilibrium the adsorbed atoms occupy a small fraction of the possible surface sites. It is also possible, however, that $\eta \ll 1$ for $c_0 \cong c_r$ provided only that the undersaturation is small so that $c_s \cong c_0$. The largest possible value of η is unity for which the velocity becomes infinite according to equation (A7). Near this limit $c_0 \cong c_r$ so that the layer of adsorbed atoms and the original crystal layer are almost indistinguishable and the step (line of demarcation) can move extremely fast with very little shifting of atomic positions.

---

* These approximations are inherent in all of the kinetic treatments of growth and dissolution treated here[2-8] and elsewhere (see the review by HIRTH and POUND).[19]

Near the limit $\eta = 1$, the approximate width of the exponential tail of diffusing atoms is

$$-1/\alpha^- = \left\{\frac{v}{2D} + \sqrt{\left[\left(\frac{v}{2D}\right)^2 + E/D\right]}\right\}^{-1}$$

in the forward direction and

$$1/\alpha^+ = \left\{-\frac{v}{2D} + \sqrt{\left[\left(\frac{v}{2D}\right)^2 + E/D\right]}\right\}^{-1} \gg 1/\alpha^-$$

in the trailing direction. Thus the forward distribution is greatly foreshortened and the trailing distribution greatly elongated compared with the value of $(D/E)^{1/2}$ which they both have when $\eta \ll 1$. As a consequence, a given step exerts a much stronger influence on the motion of another step that trails it by a certain distance than on one which leads it by the same distance. For example, the leading member of a pair of steps separated by several times $-1/\alpha^-$ will travel with approximately the free velocity whereas the trailing member will travel much slower. This clearly accentuates the tendency, already present at $\eta \ll 1$, for a leading step to escape a group.

We next justify the use of the steady state rather than the rigorous time dependent solutions of the diffusion equation for steps interacting according to equation (9) when $\eta \ll 1$ by showing that a given step moves only a small fraction f of the interstep spacing ϵ_0 during the relaxation time τ required to establish the steady state. Now $\tau \cong (\epsilon_0)^2/D$ so that

$$f = \frac{v\tau}{\epsilon_0} = \frac{v}{D}\epsilon_0 = 4\eta\left(\frac{\epsilon_0}{\delta}\right)\tanh\left(\frac{\epsilon_0}{\delta}\right) \ll 1 \quad \text{(A8)}$$

where equation (9) and the definitions in the accompanying footnote have been used to substitute for v, and where the inequality is valid since the steps were assumed to interact so that $\epsilon_0 \gtrsim \delta$, and since $\eta \ll 1$ by hypothesis. If η is not small compared with unity, the time dependent solutions must be used and time lags will occur in the propagation of disturbances in step spacing over and above those we have found to arise from equations (1).

Finally, the assumption implied in equations (1) and used explicitly in the first part of this appendix that the concentration of diffusing atoms is maintained at the equilibrium value of c_0 at the step despite the motion of the step and the net loss of atoms it experiences is justifiable provided the net flux j_n of atoms lost by a moving isolated step is small compared with the equilibrium flux j_e exchanged between the step and the terrace at equilibrium. To an order of magnitude $j_e \cong [(c_0 a_0)/\tau'']$ where τ'' is the average jump time of a diffusing atom on the terrace; on the other hand $j_n \cong c_r v$ so that the ratio of fluxes is given by

$$j_n/j_e = \frac{c_r v \tau''}{c_0 a_0} \cong \frac{c_r v a_0}{c_0 D}$$

$$= 4\left(\frac{c_0 - c_s}{c_0}\right)\left(\frac{\eta}{\sqrt{(1-\eta^2)}}\right)\left(\frac{a_0}{\delta}\right) \quad \text{(A9)}$$

where we have used the expression $D \cong [(a_0)^2/\tau'']$ and have substituted for v/D from (A7) [using $\delta = 2\sqrt{(D/E)}$]. Now $[(c_0 - c_s)/c_0] < 1$ so that if η is not too close to unity

$$j_n/j_e < a_0/\delta. \quad \text{(A10)}$$

If, as is likely(19) (because the desorption free energy which determines E is generally large compared to the activational free energy for surface diffusion on a low index terrace), δ is many times a_0 so that $j_n/j_e \ll 1$, our approximation is upheld. In the case of evaporation, this simply means that the escape of an atom from a terrace into the vapor is the rate controlling step, diffusion on the terrace being much easier, so that a step easily maintains the equilibrium concentration c_0 on the adjacent element of terrace.

J. Phys. Chem. Solids Pergamon Press 1963. Vol. 24, pp. 1405–1418. Printed in Great Britain.

AN EXPERIMENTAL EQUATION OF STATE FOR SOLID XENON*

J. R. PACKARD† and C. A. SWENSON

Institute for Atomic Research and Department of Physics, Iowa State University, Ames, Iowa

(*Received* 8 *July* 1963)

Abstract—The pressure-volume-temperature relationship for solid xenon has been determined to 20 kbars pressure from 20 to 160°K. Approximate values for the zero pressure thermal expansion and bulk modulus are given, along with their pressure dependence. The extrapolated absolute zero P–V isotherm cannot be fitted by a theoretical curve based on a Lennard–Jones 6–12 potential, and the solid appears to be more compressible at high pressures than the theory would predict. The temperature-dependent contributions to the equation of state are small and cannot be determined with precision. The thermal pressure P^* is approximately independent of volume at constant temperature, although it appears to decrease slightly with decreasing volume. This implies that the bulk modulus tends to decrease with increasing temperature at constant volume. Various inconsistencies in the thermodynamic data and definitions of the Grueneisen constant are discussed. The only general conclusion which can be drawn is that for temperatures greater than θ_D the Grueneisen constant is apparently a linear function of the molar volume at constant temperature.

INTRODUCTION

THE heavier solidified inert gases (Ne, A, Kr, Xe) form perhaps the simplest system of solids, and, hence, afford one of the most fruitful systems for which a comparison of experimental and theoretical equations of state may be made. In theoretical work it is common to assume a Mie–Lennard–Jones type of interaction with the attractive energy varying as r^{-6} and the repulsive energy as r^{-m} where r is the atomic separation, and m is of the order of 12. Correlation or many-body effects are usually ignored. Recently, BERNARDES has summarized quite elegantly the type of calculations which lead to the volume dependence of the cohesive energy at absolute zero.(1, 2) These calculations are complicated by the rather large nuclear zero point motion effects for the lighter solids. The comparison of calculations of this type with experiment is difficult, since it is not obvious that the non-ideal gas values of the two constants for a potential of this type also should apply to the solid. They can be used, however, to obtain reasonable values for the molar volume and cohesive energy at absolute zero. If, on the other hand, these two experimental quantities are used to evaluate the L–J constants, and hence the shape of the P–V curve at absolute zero, satisfactory agreement is found between theory and experiment wherever the data exist.(3) It also is possible to calculate the cohesive energy more rigorously using a Hartree self-consistent field approach, neglecting correlation effects. Excellent agreement with experimental values of the cohesive energy are found.(4) These calculations have not been carried out so as to give the volume dependence of the cohesive energy, however. This type of calculation is perhaps much more satisfactory than one based on a L–J type of interaction in that no adjustable parameters are needed, and hence the success obtained gives some justification for neglecting many-body effects.

The calculation of the temperature and volume dependence of the thermodynamic functions is more difficult, and this has been done recently by HORTON and LEECH(5) for a number of different values of *m*. A comparison of their calculations with the experimental data for argon and krypton showed definite discrepancies which led them to believe that the Mie–Lennard–Jones type of interaction could not describe adequately the law of force between inert gas atoms in the solid, and that perhaps a modification of the type proposed by GUGGENHEIM and MCGLASHAN(6) would be necessary.

---

* Contribution No. 1323. Work was performed in the Ames Laboratory of the U.S. Atomic Energy Commission.

† Present address: The Minnesota Mining and Manufacturing Company, St. Paul, Minnesota.

The available thermodynamic data for these solidified inert gases are for zero pressure, with the exception of some P–V data given by STEWART.(7, 8) The pressure dependence of the thermodynamic functions may be obtained from a combination of the zero pressure heat capacity as a function of temperature and the equation of state $[V(T,P)]$ data. Solid xenon was chosen as the subject for our initial high pressure equation of state studies on inert gas solids for two basic reasons. First, no P–V data exist for this solid at any temperature. These data should be of considerable interest since the effects of zero point motion are so small for this solid that it is almost a "classical" solid. That is, the cohesive energy can be obtained approximately by summing over the two-body forces and ignoring kinetic energy (zero point motion) effects. If the basic theories of the binding in the solidified inert gases at absolute zero are correct, they should be most applicable for this solid where quantum effects are smallest. Secondly, the Debye temperature for solid xenon ($\theta_D = 50°\text{K}$) is only a fraction of its triple point temperature (161°K).(9) Hence, xenon should form a "classical" solid in another respect, since at temperatures above roughly 100°K its lattice vibrational modes should be fully excited, and the Law of Dulong and Petit should be obeyed. The available experimental high pressure techniques are crude, and it is important that the lattice vibrational energy make an appreciable contribution to the total energy of a solid if temperature effects on the equation of state are to be observed. The ratio of the triple point temperature to θ_D forms a useful criterion for this purpose, and indicates that solid xenon should show greater effects than any of the other inert gas solids.

The objective of the experiments which will be described below was to obtain P–V–T data for solid xenon for comparison with specific theories for both the P–V behavior at absolute zero and for the pressure dependence of the lattice vibrational properties. In addition, a realistic picture of the high pressure–high temperature equation of state of solids can be formed only if there exist data for a number of different solids which are obtained over a range of fairly high relative compressions and temperatures. The present data for solid xenon can be combined with those previously obtained for sodium(10) and with unpublished data for cesium metal(11) to form general guidelines for understanding the high temperature–high pressure behavior of solids.

EXPERIMENTAL DETAILS

The apparatus and general procedure which were used in these investigations have been described in some detail elsewhere.*(10) In principle, a solid sample of a plastic substance is placed in a cylinder, the ends of which are closed by pistons. The piston-cylinder-sample combination is mounted in the jaws of a press, the tension and compression members of which extend to a hydraulic ram at room temperature. When a force F is applied to the pistons, the pressure on the sample is given by F/A where A is the piston area. Roughly, a force of 10 tons produces a pressure of 25 kbars on a ¼ in. dia. sample. Friction forces are large, and must be compensated for by taking data at both increasing and decreasing pressure. The changes in length δL of the sample with applied force are measured by means of a dial indicator at room temperature which senses by means of quartz rods the relative motions of the pistons. The friction forces at low temperatures can be as great as 5 per cent of the maximum applied pressure, while the "press corrections" (cylinder dilation and piston compression) are of the order of 10 per cent of the observed changes in length for a compressible substance like xenon, and are known to a few percent. The changes in length of the sample with applied force, when corrected for friction and sample holder effects are then directly proportional to the changes in molar volume of the

---

* During the course of this work, a check of the cesium transition pressure at room temperature (22·5 kbars) was made, and it was found that the pressure scale used in previous measurements was in error by a uniform 3 per cent, the quoted pressures being too low. Hence, the earlier data should be corrected before being used.

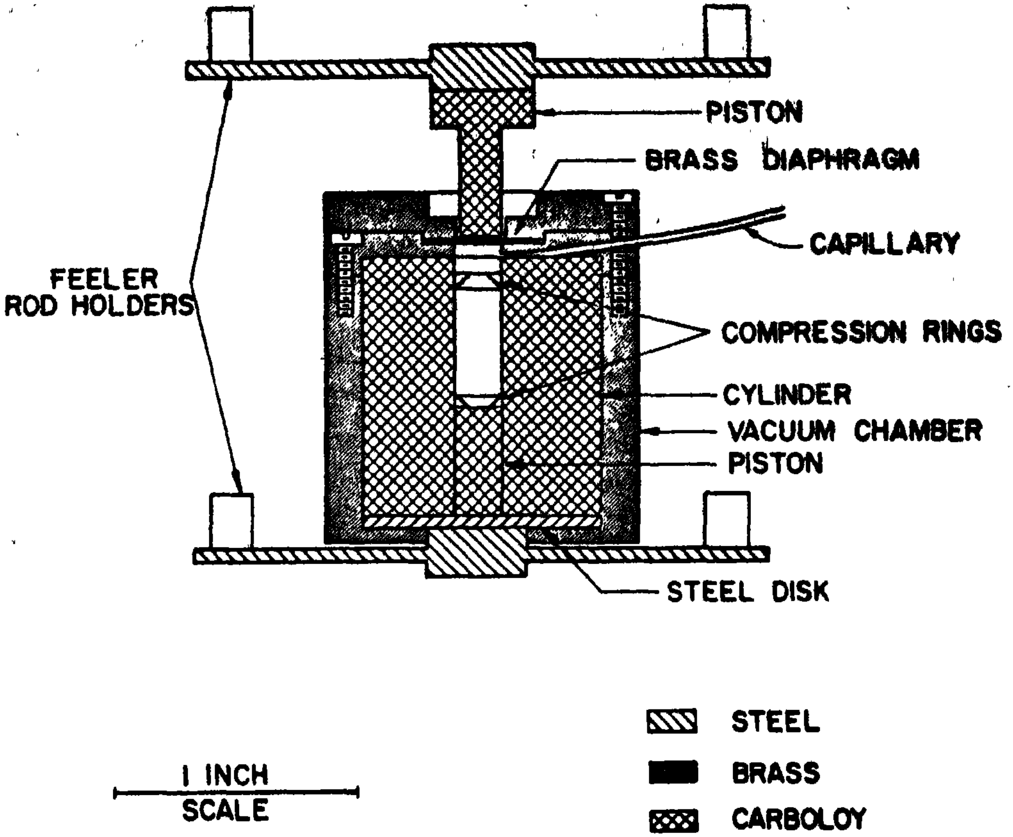

FIG. 1. The high pressure sample holder which was used for solid xenon. Not shown are the jaws of the press, and the connection of the capillary to a source of gas or vacuum at room temperature.

sample material with pressure. The press assembly was constructed so that its temperature could be maintained constant to within a few tenths of a degree for hours at a time at any temperature between 20°K and 200°C.

The above procedure is quite straightforward when the sample material is a solid at room temperature. Another approach is necessary for samples which solidify only at low temperatures. The type of sample holder which was used is shown in Fig. 1, and is similar to that described elsewhere.(7, 8) Earlier work by STEWART had shown that other solidified inert gases had small shear strengths at low temperatures,(7) and it was assumed that xenon also would satisfy the plasticity requirement. In Fig. 1, a sintered tungsten carbide cylinder has one end closed by a cylindrical rod of tungsten carbide, and is enclosed in a brass case. The end of the rod is supported by the thin steel disc at its base, and a vacuum tight seal is made by applying a thin layer of stopcock grease to all mating surfaces before the lower set of three screws are tightened. A thin brass disc (0·010 in. thick) was placed in the top of this assembly, and a second cap fastened into place to form a vacuum-tight sample holder assembly which could be evacuated (or filled with a liquid or a gas) through the capillary.

This assembly was then placed in the press, the capillary was attached to a valve system at room temperature, the sample holder was evacuated and isolated with a valve at room temperature, and it and the press were cooled to the boiling point of liquid xenon (165°K). At this time, a valve was opened at room temperature and approximately the correct amount of xenon gas necessary to produce a solid sample of length equal to the cylinder diameter was condensed as liquid into the sample holder. The press was cooled further to a temperature of about 150°K to solidify the liquid and force was applied to the upper piston to punch it through the brass diaphragm and to compact the sample. The small triangular extrusion rings shown in the cylinder in Fig. 1 prevented the extrusion of the sample during the experiment.

A serious difficulty in an experiment of this kind involves the determination of the length of the sample. It is difficult to meter precisely the amount of gas which is condensed, and it is not always certain that some solid is not formed in the capillary. The method which was used in these experiments was rather indirect, and subject to error, but was used for lack of a satisfactory substitute. The distance of the top of the diaphragm from the top of the bottom piston was known to some precision. A dial gauge reading was taken before the diaphragm was broken, and the motion of the piston was followed on the dial gauge as the sample was compacted after the breaking of the diaphragm. The length of the sample then could be calculated by subtracting the piston motion from the distance of the diaphragm from the bottom piston. It was not possible to obtain a zero pressure dial gauge reading due to friction effects, so in general the pressure on the sample was increased and then decreased during the compaction, and a dial gauge reading (corrected for friction) obtained at a standard 150°K and 1 kbar pressure. Hence, the length of the sample at 1 kbar and 150°K [$L_1(150°)$] was determined. This procedure was verified through the use of a similar procedure to determine the length of indium samples, which then could be measured at room temperature. The precision of the length measurement was of the order of 10^{-3} in. The zero pressure length of the sample was obtained by extrapolating the P–V isotherm at this pressure to zero pressure using the procedures outlined below.

The xenon gas which was used in these experiments was obtained from the Linde Corporation and was stated to be 99·99 per cent pure, or better. Every effort was made to insure that the samples were not contaminated, but it is believed that the results should not be sensitive to impurities of a few tenths of a percent or less, if they existed.

DATA ANALYSIS AND RESULTS

The data for solid xenon consisted of four series of "runs", each series involving a different sample. Two samples were measured in a 0·250 in. dia. cylinder, and two in a cylinder of twice the cross-sectional area, 0·354 in. dia. The maximum pressures used in each case were 20 kbars and 14 kbars, respectively. The sample lengths varied, but were generally of the same order of magnitude as the cylinder diameter. The dial gauge which was attached to the ends of the sample holder pistons by quartz rods (see Fig. 1) indicated changes in sample length due both to temperature and to pressure. The actual data for a given "run" were taken in the form of dial gauge readings as a function of increasing and decreasing pressure at constant temperature. These were corrected for friction and sample holder distortion so as to represent actual changes in sample length with pressure at constant temperature.(10) In the absence of dial gauge zero shifts due to a jarring of the apparatus, a direct comparison of the dial gauge readings for different runs on a given sample also gave the thermal expansion of the sample, since the thermal expansion of the sample holder was shown to be negligible.(10) The length of the sample at 1 kbar and 150°K was known, as was the corrected dial indicator reading at this point, so it was possible to use the dial indicator readings to obtain directly the length of the sample as a function of both temperature and pressure. In order to compare directly the data taken with the four samples, the length data for each sample were normalized by dividing by the length of the sample under our standard conditions 1 kbar and 150°K, to give $L(P,T)/L_1(150)$. If the molar volume at 1 kbar and 150°K is known (or can be determined as outlined below), these relative data can be converted directly into the desired P–V–T relationship, since the sample length is directly proportional to its volume (if the cylinder area remains constant).

The data for each sample have been converted to molar volumes in this way, and are given in Table 1. It must be emphasized that the molar volumes for each series of runs on a given sample

Table 1. *A summary of the experimental P–V isotherm data for solid xenon. The L and S designations refer to the* 0·354 in. *and* 0·250 in. dia. *sample holders, respectively. The molar volumes for a given series of runs* (*L*–1 *through L*–6, *for instance*) *differ from the actual measured and corrected length changes as a function of pressure and temperature only by a constant multiplicative factor. Hence scatter in these tabulations reflects true experimental scatter. The values of* V_0, B_0, *and the r.m.s. deviation were determined by at least squares fit to equation* (1), *as described in the text. The values in parentheses were obtained using all the data tabulated, while the others used only the data from the lowest pressure through* 8 kbars.

Pressure k bars	Run No.	Temperature, °K																
		0	20	30	40	64	77	77	77	90	90	100	115	130	150	150	150	160
		(Extrap.)	*L*–5	*S*–3	*L*–IV*	*L*–4	*L*–3	*L*–6	*S*–II	*S*–2	*L*–III*	*L*–2	*L*–II*	*L*–I*	*S*–1	*S*–1	*L*–1	*L*–V*†
0	(Extrap.)	34·70	34·69	35·07	35·05	35·75	35·97	35·92	35·90	36·59	36·32	36·65	37·10	37·56	38·43	38·19	38·16	38·63
		(35·01)	(34·75)	(35·12)	(35·16)	(35·71)	(35·99)	(35·92)	(36·54)	(36·45)	(36·37)	(36·58)	(37·21)	(37·71)	(38·31)	(38·68)	(38·17)	(38·88)
0·5	Molar volume cm³	—	—	—	—	—	35·36	35·33	—	—	35·63	35·93	36·23	36·60	—	—	37·20	37·37
1		33·86	33·87	—	34·05	34·64	34·86	34·77	—	—	35·00	35·31	35·55	35·92	36·36	36·36	36·36	36·54
2		33·16	33·16	33·27	33·27	33·72	33·94	33·88	33·87	34·16	34·05	34·25	34·45	34·72	35·11	35·04	35·12	35·16
3		32·56	32·53	32·63	32·60	33·00	33·16	33·11	33·11	33·35	33·24	33·44	33·54	33·75	34·10	34·13	34·15	34·12
4		31·98	31·99	32·05	32·00	32·36	32·52	32·48	32·49	32·69	32·56	32·78	32·83	33·05	33·30	33·35	33·37	33·32
5		31·45	31·49	31·53	31·47	31·82	31·95	31·91	31·91	32·09	31·99	32·19	32·20	32·38	32·63	32·66	32·67	32·64
6		31·00	31·03	31·06	31·02	31·33	31·47	31·41	31·40	31·59	31·48	31·66	31·67	31·82	32·05	32·12	32·08	32·04
7		30·58	30·60	30·65	30·61	30·88	30·98	30·95	30·96	31·14	31·02	31·18	31·17	31·32	31·53	31·59	31·55	31·52
8		30·20	30·23	30·29	30·21	30·47	30·55	30·52	30·54	30·73	30·60	30·75	30·74	30·87	31·10	31·13	31·08	31·06
10		29·50	29·55	29·60	29·54	29·74	29·82	29·77	29·84	29·96	29·85	29·98	30·01	30·11	30·39	30·35	30·25	30·27
12		28·96	28·95	29·00	28·97	29·12	29·19	29·15	29·23	29·33	29·24	29·32	29·37	29·48	29·60	29·67	29·56	29·62
14		28·47	—	28·53	—	—	28·63	—	28·73	28·78	—	28·75	—	—	29·02	29·11	28·94	—
16		28·03	—	28·06	—	—	—	—	28·27	28·27	—	—	—	—	28·48	28·62	—	—
18		27·63	—	27·65	—	—	—	—	27·85	27·85	—	—	—	—	28·04	28·15	—	—
20		27·27	—	27·26	—	—	—	—	27·49	27·44	—	—	—	—	27·65	27·80	—	—
B_0	(kbars)	38·8	38·7	31·3	31·6	27·7	28·2	27·6	27·9	21·3	23·5	22·5	19·3	17·9	13·8	15·8	22·5	13·2
		(29·4)	(36·6)	(30·1)	(28·5)	(28·6)	(27·7)	(27·9)	(18·1)	(23·7)	(22·5)	(24·3)	(17·5)	(15·8)	(14·9)	(11·6)	(24·3)	(10·9)
ξ		−1·25	−1·41	−2·89	−2·57	−2·82	−2·24	−2·50	−2·49	−4·18	−3·4	−3·4	−3·8	−3·9	−5·2	−4·5	−3·4	−5·1
		(−3·54)	(−1·90)	(−3·14)	(−3·47)	(−2·51)	(−2·40)	(−2·38)	(−5·67)	(−3·26)	(−3·7)	(−2·8)	(−4·7)	(−4·9)	(−4·7)	(−6·7)	(−2·8)	(−6·8)
r.m.s.	(kbars)	0·024	0·010	0·024	0·017	0·012	0·022	0·013	0·013	0·011	0·012	0·019	0·011	0·022	0·021	0·022	0·019	0·014
Dev.		(0·076)	(0·022)	(0·037)	(0·037)	(0·015)	(0·022)	(0·017)	(0·045)	(0·031)	(0·035)	(0·026)	(0·024)	(0·031)	(0·084)	(0·070)	(0·026)	(0·034)

* The measured changes in length in the L–V run were adjusted by a constant factor to compensate for an apparent dial indicator shift.

† The initial sample length in the LI thru LIV series was adjusted (by 3%) to give agreement with the other runs at 12 kbars.

($L1$ through $L6$, for instance) are directly proportional to the length of the sample as measured experimentally, with the only adjustable parameter being the conversion factor between $L_1(150)$ and the molar volume. Hence, one could read "sample length in arbitrary units" for "molar volume in cm^3" in the captions.

There was a difficulty, however, in that a comparison of the data for the LI through LV series with the other series showed a consistently different behavior which could be explained if the initial length determination for this sample were in error by three per cent. Hence, the length of this sample was determined by forcing the data obtained on it to agree with the other three series at 12 kbars. It also was evident that the dial indicator had been jarred between LIV and LV, so an arbitrary additive adjustment was made to the data taken for this run. It is perhaps worth noting that the relative precision in the determination of the length of the sample should be comparable with the relative precision with which the total changes in length with pressure can be determined, or of the order of 0·3 per cent. The precision of the data given in Table 1 is limited by the sensitivity of the length determination (2×10^{-4} in.) for the smaller molar volumes (± 0·3 cm^3 for the L series, ± 0·05 cm^3 for the S series), while for the larger molar volumes it is limited by the pressure determination (± 0·03 kbars for the L series, ± 0·06 kbars for the S series). This implies that in the low pressure region near the triple point a scatter of the data in excess of 0·1 cm^3/mole would not be excessive. An inspection of the data given in Table 1 shows that they are consistent to within these limitations.

The difficulties involved in an absolute determination of the densities of the samples which were used in these experiments have been commented upon. It is, however, important for theoretical comparisons that the final results be expressed in terms of molar volumes. The zero pressure lattice constants of solid xenon have been determined by X-ray measurements for temperatures below about 120°K.(12, 13, 14) Our data do not extend to zero pressure, so a direct comparison is not possible. However, earlier work has shown that most P–V data may be fitted by a relationship given by BIRCH;(15)

$$P = (3B_0/2)(y^7-y^5)[1-\xi(y^2-1)], \quad (1)$$

where B_0 is the bulk modulus at $P = 0$, ξ is an adjustable constant, and $y = (V_0/V)^{1/3}$, where V_0 is the volume at $P = 0$. In this case, $V_0/V = L(T,P = 0)/L(T,P)$. Out data for $L(T,P)$ were fitted to this expression using a least squares program and an IBM 7074 computer. In this program, B_0 and ξ were taken as adjustable parameters and an extrapolated value of $L(T,P = 0)$ was selected by an iterative process.*

The results of this extrapolation are given in Table 1. In practice, two least squares fits were made to the data. The first involved only the data up to and including 8 kbars, while the second included all the data. The values of $V_0(T,P = 0)$, B_0 and ξ, as well as the r.m.s. deviation of the experimental pressures from equation (1) are given for both extrapolations in Table 1. The less reliable "all data" results are given in parentheses. Except for two of the high pressure runs, the r.m.s. deviations are within our expected experimental precision. Considerable scatter is evident in the temperature dependence of both B_0 and ξ as given in Table 1.

If the resulting normalized values of $L(T,P = 0)/L_1(150)$ are fitted to the X-ray data at one point and a conversion factor calculated, the shape of the resulting $V_0(T)$ curve is uniquely determined, and should agree with the X-ray data for other temperatures. This fit was made at 77°K and a comparison of our extrapolated zero pressure data with the X-ray data of EATWELL and SMITH(13) (dashed line) and SEARS and KLUG(14) (open circles) is shown in Fig. 2. Our precision is much less than that of the X-ray determinations, but the agreement as to shape is gratifying and gives some justification for our extrapolation. SEARS and KLUG mention an unexplained discrepancy which appears to exist between their

---

* Equation (1) was rewritten as $P = P_0+[A(y^7-y^5)-C(y^7-y^5)(y^2-1)]$, where $A = 3B_0/2$ and $C = 3B_0\xi 2$. A value of $L(T,P = 0)$ was assumed for a given run, and a least squares fit of the data to the above equation was made with P_0, A and C as the adjustable parameters. P_0 is now the pressure at which the sample length is equal to the assumed value $L(T,P = 0)$ if an incorrect choice of the initial length was made. If the magnitude of P_0 were greater than a certain value (about 0·01 kbars), the zero pressure length of the sample was corrected by the computer using the value of A, and the least squares fit was rerun. This process continued until a satisfactory value of the zero pressure length was found for which $P_0 = 0$.

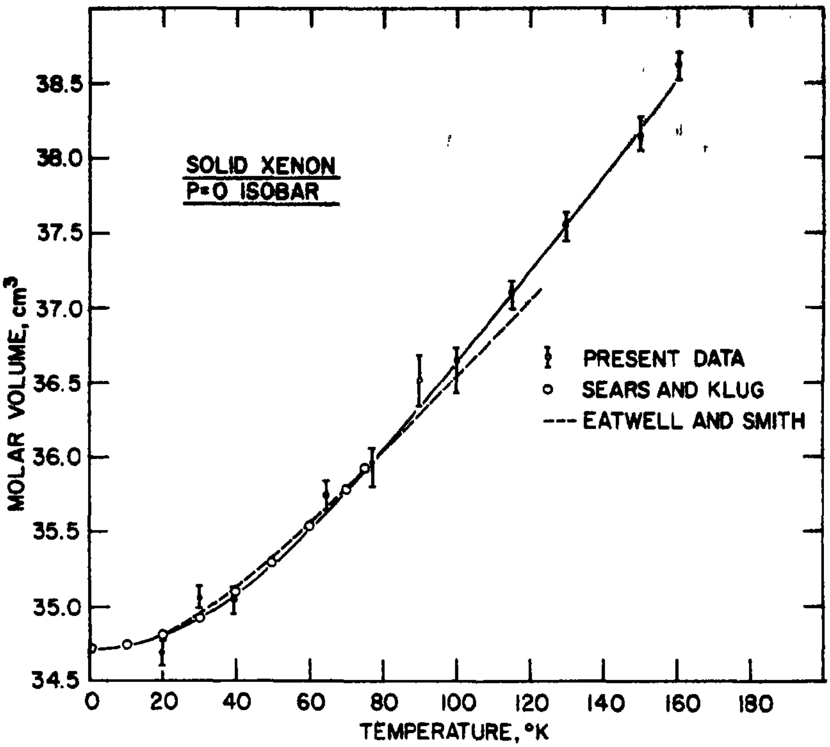

FIG. 2. The molar volume of solid xenon as a function of temperature at zero pressure.

data and those of Eatwell and Smith. Indeed, our data appear to agree better with an extrapolation of Sears and Klug's data than with an extrapolation of Eatwell and Smith's data.

The same least squares program gave calculated values of the bulk modulus $B = -(\partial P/\partial \ln V)_T$ as a function of volume, using the best values of B_0, ξ and V_0. These calculations indicated that B was independent of temperature at constant volume to within a few per cent, although (as will be discussed later) this conclusion cannot be strictly true. Figure 3 gives a summary of these calculations for various volumes, together with error bars which indicate the scatter from run to run at constant volume, and the differences obtained in the two least squares fits.

The first column of molar volumes in Table 1 was obtained by a smoothed, visual extrapolation to absolute zero of the composite data (plotted as isobars). This, then represents the best average which can be made using the low temperature data from various samples to obtain a curve which can be compared with theoretical predictions.

DISCUSSION

The equation of state at absolute zero

The theoretical treatment of the properties of the inert gas solids at absolute zero has in general involved only two body forces as given by the Mie–Lennard-Jones potential. More specifically, the 6–12 form of this potential has been commonly used although HORTON and LEECH[5] have investigated the effects of varying the exponent in the repulsive term. This type of potential can be expressed in reduced form as;

$$V(r) = 4\epsilon[(\sigma/r)^{12}-(\sigma/r)^{6}], \qquad (4)$$

where ϵ and σ are a characteristic energy and length, respectively. The effects of zero point motion are appreciable for these solids, and its importance can be expressed qualitatively in terms of a quantum parameter, introduced by

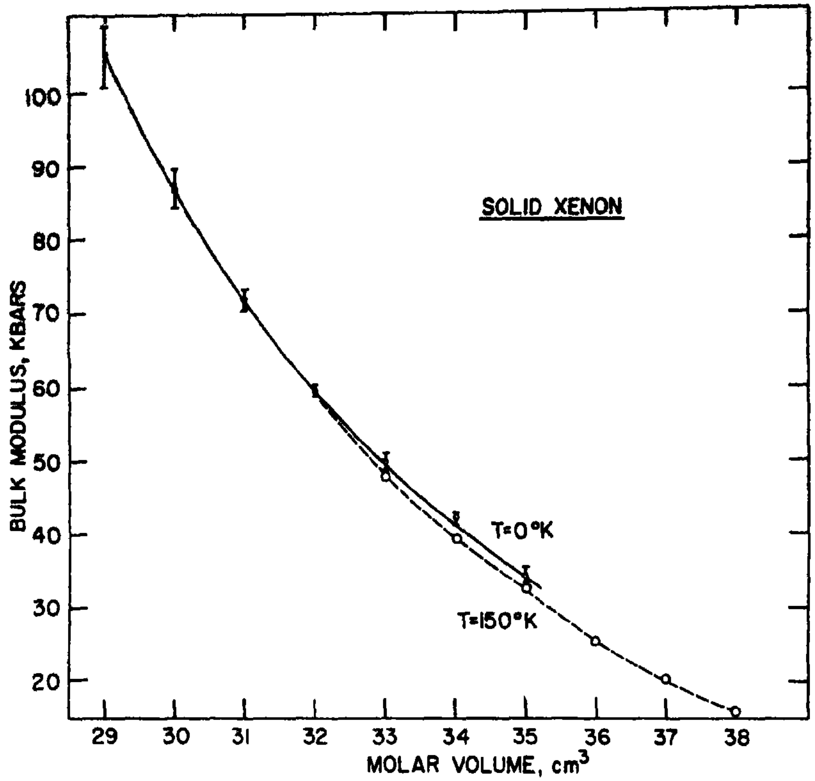

FIG. 3. The bulk modulus for solid xenon as a function of volume at both absolute zero and high temperatures (150°K).

de Boer, $\lambda = \hbar^2/2m\epsilon\sigma^2$. Here, m is the mass of the atom, and ϵ and σ are the coefficients in equation (2). BERNARDES recently has given an explicit relationship for the thermodynamic properties at absolute zero of the heavier inert gas solids, expressed as a law of corresponding states involving a power series in λ.⁽²⁾ In such a relationship, it is convenient to measure energies in units of ϵ, length in units of σ, and, hence, pressures in units of ϵ/σ^3. Quantum effects are small for solid xenon ($\lambda = 7 \times 10^{-3}$), and for this solid Bernardes' relationships in terms of these reduced units become:

$$E_{coh}/N_0\epsilon = E^*_{coh} = 8{\cdot}61(1-5{\cdot}34\lambda+16\lambda^2) = 0{\cdot}829 \tag{3a}$$

$$V_0/N_0\sigma^3 = V^*_0 = 0{\cdot}916(1+2{\cdot}02\lambda+5\lambda^2) = 0{\cdot}929 \tag{3b}$$

$$B_0(\sigma^3/\epsilon) = B^*_0 = 75(1-9{\cdot}4\lambda+28\lambda^2) = 70{\cdot}05 \tag{3c}$$

$$P(V)(\sigma^3/\epsilon) = P^* = 24{\cdot}3V^{*-5}-28{\cdot}9V^{*-3} + 114\lambda V^{*-10/3} \tag{3d}$$

$$\doteq 24{\cdot}3V^{*-5}-28{\cdot}1V^{*-3}.$$

Here, V_0 and B_0 are the molar volume and bulk modulus at absolute zero and zero pressure, and equation (3d) gives the P–V relationship at absolute zero.

Various procedures are possible for the comparison of theory and experiment. In general, it is not obvious that the values of ϵ and σ as determined from non-ideal gas data will be applicable. It is more systematic to use values of these parameters which have been obtained in a fashion similar to that in which they will be used. Hence, we choose to use the experimental value of the cohesive energy at absolute zero (3830 ± 50 cal/mole)(16) and the molar volume at absolute zero (34·72 cm^3)(14) to calculate values of $\epsilon(= 3{\cdot}21(\pm\ 0{\cdot}04)\times 10^{-14}$ ergs) and $\sigma(= 3{\cdot}96\times 10^{-8}$ cm) which then can be used to analyze our experimental P–V relationship. These values of ϵ and σ agree well with those given by BERNARDES(2) and BOATO and CASANOVA,(17) but differ slightly from the non-ideal gas values. The limitations on this type of approach have been discussed by BOATO and CASANOVA.(17)

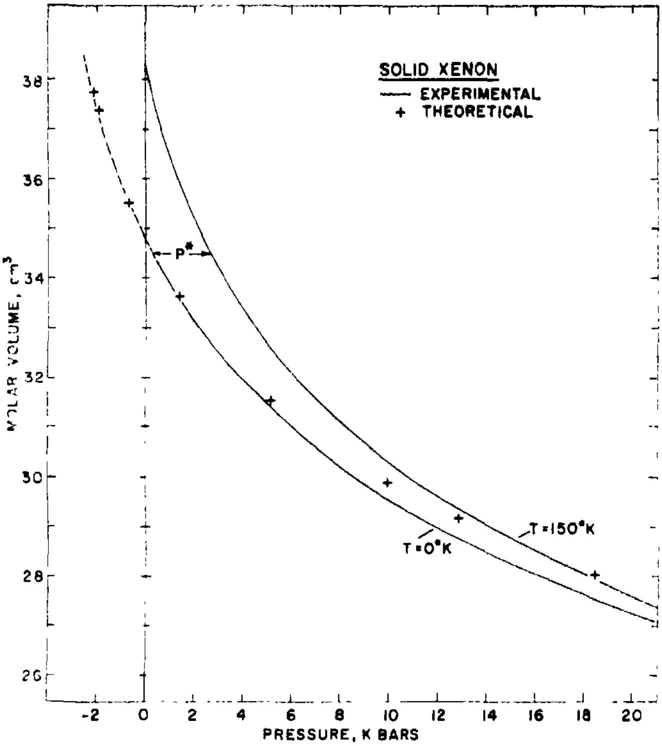

FIG. 4. Experimental P–V isotherms for solid xenon at both absolute zero (extrapolated) and 150°K. A theoretical isotherm for absolute zero also is given. The extrapolation of the experimental isotherm to negative pressures (needed for thermal pressure determinations) was obtained using equation (1) with $B_0 = 36$ kbars and $\xi_0 = -2$.

The conversion factor for the pressure units becomes $\epsilon/\sigma^3 = 0{\cdot}517$ ($\pm$ 0·005) kbars, and for the volume units, $N_0\sigma^3 = 37{\cdot}37$ cm^3, where N_0 is Avogadro's number. These can be used with equation (3d) to predict the shape of the pressure-volume relationship at absolute zero. This is shown in Fig. 4, where the experimental isotherm (solid line) is compared with the theoretical (crosses). The agreement is not good except at low pressures. The zero pressure bulk modulus calculated from equation (3c), $B_0 = 36{\cdot}2$ ($\pm$ 0·5) kbars is in excellent agreement with the experimental value, 36 ($\pm$ 1) kbars.*

This is indicated also in the close agreement between the extrapolations to negative pressures as obtained using equation (3d) and the Birch function (Fig. 4). Horton and Leech have commented on the indication from the thermodynamic data that perhaps the Lennard–Jones type of potential, summed over all neighbors, gave too large an attractive force.(5) Our data indicate too large a repulsive term; the solid actually being too compressible at high pressures. The reason for this is not known.

---

* The Birch function does not appear to fit these extrapolated $T = 0$ data extremely well. The compressibility data (Fig. 3) imply that $B_0 = 36(\pm 1)$ kbars is preferable to the Birch value given in Table 1. Care must be exercised in using the Birch function to extrapolate these data either to negative pressures or to pressures greater than 20 kbars.

Temperature-dependent contributions to the equation of state

The basic temperature-dependent contributions to the equations of state of the solidified inert gases involve the lattice vibrations. It is customary to consider the contributions of the ground state and the excited states as being independent; that is, the Helmholtz Free Energy of the solid is written as:

$$F(T,V) = U_0(V)+F^*(T,V). \tag{4}$$

Here, $U_0(V)$ is the cohesive energy at absolute zero, and F^* is the phonon contribution to the free energy. Now the pressure, entropy, and internal energy are given as:

$$P(T,V) = -(\partial F/\partial V)_T = -\mathrm{d}U_0/\mathrm{d}V-(\partial F^*/\partial V)_T$$
$$= P_0(V)+P^*(T,V), \tag{5}$$

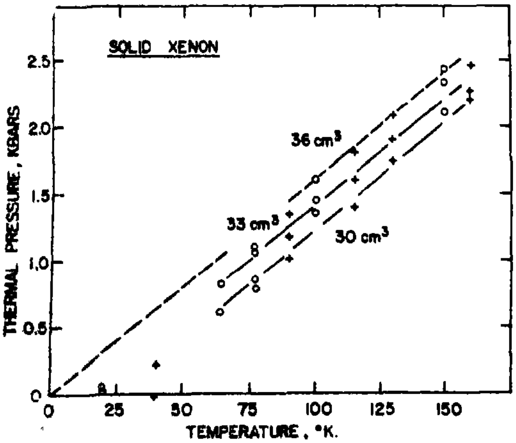

FIG. 5. The temperature dependence of the thermal pressure P^* for solid xenon for three selected molar volumes.

$$S(T,V) = -(\partial F/\partial T)_V = -(\partial F^*/\partial T)_V, \tag{6}$$

$$U(T,V) = -T^2(\partial(F/T)/\partial T)_V = U_0(V) + U^*(T,V). \tag{7}$$

The asterisks here signify quantities which approach zero as the temperature approaches zero. The thermal pressure P^* is obtained easily from our measurements, as is illustrated in Fig. 4 where the isotherms for both absolute zero and 150°K are plotted. The thermal pressure is given by the separation at constant volume of the isotherm for a given temperature from the isotherm at absolute zero. For volumes greater than those of the solid at zero pressure at absolute zero, the $P_0(V)$ curve must be extrapolated to a negative pressure at that volume, as is indicated in Fig. 4. The volume dependences of all of the thermodynamic functions are contained in $P^*(T,V)$, since:

$$(\partial S/\partial V)_T = (\partial P/\partial T)_V = (\partial P^*/\partial T)_V, \tag{8}$$

and

$$(\partial U^*/\partial V)_T = T(\partial P^*/\partial T)_V-P^*. \tag{9}$$

Hence, it only is necessary to know $P^*(T,V)$ to obtain changes in the entropy, lattice vibrational energy, and, hence, free energy, with pressure.

Figure 5 shows the thermal pressure for solid xenon as a function of temperature at constant volume as obtained for several of the runs and 3 molar volumes. The points were derived from the data given in Table 1 with no smoothing. The precision of each point is of the order of $\pm$ 0·1 kbars. The pressure at 30 cm³/mole is roughly 10 kbars. The dominant features exhibited in Fig. 5 and common to a detailed analysis are, first, that above 100°K $(\partial P^*/\partial T)_V = 16 \pm 1$ bars/°K, independent of volume, and, second, that $(\partial P^*/\partial V)_T$ is quite small and is always positive. A temperature-dependent contribution to the bulk modulus can be calculated as $B^* = -V(\partial P^*/\partial V)_T$. Above 100°K, this contribution is independent of temperature and volume within experimental error and is given by $B^* = -1{\cdot}5 \pm 0{\cdot}7$ kbars. At zero pressure and 150°K, this represents roughly 10 per cent of the observed bulk modulus, but it rapidly becomes less important as the molar volume is decreased (Fig. 3). This conclusion is not at variance with the values of the bulk modulus as obtained from the isothermal Birch equation least squares analysis because of the scatter which was observed. It is to some extent an amazing conclusion that as the thermal energy is added to the solid at constant volume, the solid becomes more compressible.

The volume dependence of the thermodynamic functions are best discussed in terms of the Mie–Grueneisen equation of state. Two possible approaches are contained in the following definitions of "Grueneisen" constants⁽³⁾

$$\gamma_c(T,V) = \beta B_0 V/C_v = (V/C_v)(\partial P^*/\partial T)_V, \quad (10)$$

and

$$\gamma_u(T,V) = P^* V/U^*. \quad (11)$$

These two expressions give identical values of γ which are independent of temperature only if the lattice properties of the solid can be described in terms of a characteristic temperature θ which is dependent on volume only. In this case,

$$\gamma = -\mathrm{d}\ \ln\theta/\mathrm{d}\ \ln V.$$

Both of these expressions involve a knowledge of the zero pressure thermodynamic properties of the solid. The zero pressure thermal properties from 20°K to the triple point can be obtained from the heat capacity measurements of CLUSIUS and RICCOBONI.⁽⁹⁾ A summary of their data is given in the third column in Table 2. The temperature dependence of both the entropy and the enthalpy as calculated from these data are given in the next columns. The temperature dependence of the enthalpy involves two contributions; the first is due to the phonon energy and the second is due to an increase of the lattice potential energy as the lattice expands. This latter contribution can be estimated from the variation of the cohesive energy with volume, or the area under the extrapolation of the $P_0(V)$ curve to negative pressures shown in Fig. 4. The values of U^* (the phonon energy) as calculated in this manner are given in Table 2 also. While these are true phonon energies, it is not legitimate to compare directly the tabulated values of U^* for different temperatures, since because of thermal expansions they refer to different molar volumes.

Zero pressure values of the thermal pressure (as derived from Table 1), the bulk modulus [as obtained from Fig. 3 and $V_0(T)$] and the thermal expansion are included in Table 2. The thermal expansion data below 75°K are those given by SEARS and KLUG,⁽¹⁴⁾ while the two sets of values given above 75°K are due, first, to the data in Fig. 2, and, second, to the thermodynamic relationship $\beta B = (\partial P^*/\partial T)_V = 16$ bars (see Fig. 5). The agreement between these two sets of data is not spectacular, but is satisfactory and gives an indication of the precision of the individual determinations since the latter relationship is merely a geometrical requirement for consistency.

The data in Table 2 can be used to calculate $\gamma_u = 2{\cdot}9\ (\pm\ 0{\cdot}1)$, roughly independent of temperature at zero pressure. This is in agreement with the low temperature values of γ suggested by BERNARDES⁽²⁾ and HORTON and LEECH.⁽⁵⁾ The

Table 2. *A summary of the smoothed zero pressure thermodynamic properties of solid xenon. The sources of the data are given in the text.*

T (°K)	$V_0(T)$ (cm³/mole)	C_p (cal/mole-deg)	S (cal/mole-deg)	H (cal/mole)	U^* (cal/mole)	P^* (kbars)	B_T (kbars) (Fig. 3)	β (10^{-4} °K⁻¹) (Fig. 2)	(Eq. 1)
0	34·72	0	0	0	0	0	36(±2)	0	—
20	34·80	4·07	2·88	38	38	0·1(±0·1)	35(±2)	$2{\cdot}8^{2}$	—
50	35·31	6·00	7·60	196	194	0·65(±0·1)	32(±2)	$6{\cdot}2^{7}$	—
75	35·94	6·39	10·11	352	337	1·16(±0·1)	27(±2)	7·7	—
100	36·63	6·74	12·00	514	477	1·65(±0·1)	23(±2)	7·0(±0·7)	8·2(±0·5)
125	37·41	7·30	13·57	691	621	2·06(±0·1)	19(±2)	8·4(±0·8)	8·8(±0·5)
150	38·20	8·02	14·97	886	774	2·47(±0·1)	15^{5}(±2)	10·3(±1·0)	9·0(±0·5)

values of γ_c show a considerable variation from 2·0 at 20°K to a maximum of 3·2 at 75°K to 2·1 at 150°K, all at zero pressure. One of the problems involved in attaching any significance to these deviations concerns a lack of information about the value of C_v. However, since its θ_D is of the order of 50°K, solid xenon should be essentially a classical solid above 75°K with a value of C_v close to 6 cal/mole-deg. If one attempts to calculate C_v from C_p and the data in Table 2, using the relationship

$$C_v = C_p/(1+\beta\gamma_c T), \qquad (12)$$

it is found that a value of $\gamma_c = 2{\cdot}3$ (± 0·1) is necessary to give the classical value above 75°K.

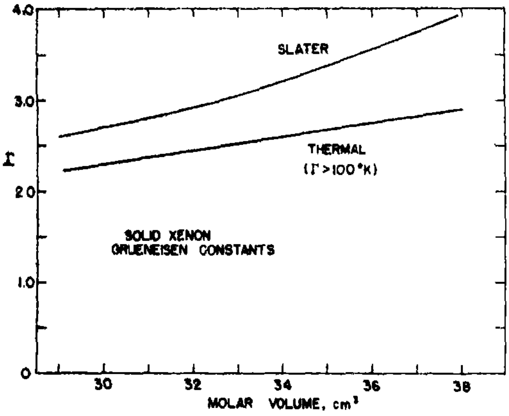

FIG. 6. The volume dependence of the Grueneisen constants for solid xenon.

This is close to the low temperature value γ_c found by BEAUMONT *et al.*, for solid krypton.(18) Thus, there is a discrepancy between the values of γ_u and γ_c, and, indeed, an apparent thermodynamic inconsistency involving most likely the values of β and B given in Table 2. It is difficult to know how much importance to attach to this discrepancy. If there is a significant contribution to the specific heat and thermal expansion due to vacancy formation, such discrepancies should be expected to appear. These effects have been observed for both argon and krypton,(18) and could, by analogy, be serious for solid xenon. The only data which are at all pertinent to effects such as these for solid xenon are the activation energies for self-diffusion in liquid and solid xenon which have been determined by YEN and NORBERG, using n.m.r. techniques.(19)

An interesting question involves the volume dependence of the Grueneisen constant. For temperatures well above θ_D, both C_v and U^* should be independent of molar volume, and C_v should be independent of temperature. An inspection of the U^* values in Table 2 shows that above 100°K, $\Delta U^*/\Delta T = 5{\cdot}90$ cal/mole-deg, even though the molar volume has increased by 5 per cent in this interval. Experimentally, we find that both P^* and $(\partial P^*/\partial T)_V$ are, to a first approximation, independent of molar volume at constant temperature. Hence, one can conclude from the definitions of both γ_u and γ_c [equations (10) and (11)] that these constants should be roughly proportional to the molar volume for solid xenon. This is indicated schematically in Fig. 6. Another demonstration of this fact can be seen in Fig. 5. If U^* is independent of volume at constant temperature, then, from equation (9), $T(\partial P^*/\partial T)_V = P^*$, and P^* should be linear in the temperature at constant volume. Indeed, this is what is observed for $V = 36$ cm³/mole (Fig. 5). θ decreases at smaller molar volumes, and some (small) dependence of U^* on V is observed at constant temperature.

A Grueneisen constant also can be defined for an isotropic solid in terms of the shape of the P–V isotherm. A relationship given by SLATER(20) can be written as:

$$\gamma_{SL} = 0{\cdot}50(\partial B/\partial P) - 1/6, \qquad (13)$$

where B is the bulk modulus. A more complex definition of a similar γ has been proposed by DUGDALE and MACDONALD(21) which in general gives smaller values than the above relationship.(10) The values of B given in Fig. 3 were plotted as a function of pressure and $(\partial B/\partial P)$ was determined from this plot by graphical differentiation. The resulting values of γ_{SL} are shown also in Fig. 6. While the magnitudes of the two γ's differ slightly the volume dependence is roughly the same. This is in contrast with the results for sodium, and implies that the shape of the frequency spectrum for solid xenon is not affected appreciably by volume changes.(10)

A Debye temperature θ_D can be defined from the experimental values of the entropy listed in Table 2 and the tabulated Debye functions.(22) The results of such a calculation are shown in

Fig. 7 as the $P = 0$ line. If now, changes in entropy are calculated from an integration of equation (8), the variation of θ_D with volume at constant temperature can be determined. It is interesting to note that the temperature dependence of θ_D at zero pressure disappears when the values are corrected to the value of the molar volume at absolute zero and zero pressure. The values of θ_D for smaller molar volumes are included merely for information purposes. It is difficult to place more than qualitative significance in calculations of this type, since the heat capacity data only extend down to slightly below $\theta_D/2$ (approximately). Similar data for argon and krypton,(18, 23) as well as theoretical calculations(5) indicate that θ_D for solid xenon should rise considerably at low temperatures to a value near 65°K.

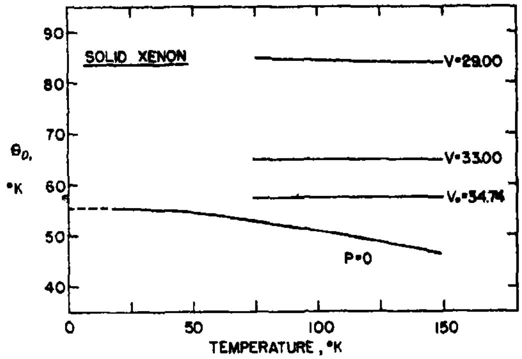

FIG. 7. The temperature dependence of the Debye temperature θ_D for solid xenon. θ_D is defined here from the Debye entropy function.

CONCLUSIONS

The present work should be regarded as a first effort, and cannot pretend to give more than semi-quantitative experimental data for comparison with theory, except at very low temperatures. To be really useful, high pressure P–V–T data must be at least an order of magnitude more precise than the present data. Zero pressure thermodynamic data, however, such as specific heat, thermal expansion, and possibly compressibility, should be easier to obtain and again are lacking for xenon in the detail which is needed. The discrepancies in the X-ray data are not understood, and these data do not extend to sufficiently high temperatures. Bulk thermal expansion measurements would be extremely useful for comparison with the X-ray data since (as for argon)(18) one should observe quite large contributions due to vacancy formation. These effects also appear in the specific heats for argon and krypton at high temperatures,(18) and a useful comparison could be made with data such as the n.m.r. determinations of the activation energy for self-diffusion as determined for solid xenon by YEN and NORBERG.(19) Heat capacity data at lower temperatures are needed for comparison with theoretical predictions of low temperature θ_D's. Indeed, no specific heat measurements have been made for the heavier inert gas solids which extend down into the true T^3 region, which is, unfortunately, well below 1°K. Unusual effects have been found for solid helium at these temperatures at small molar volumes, and these might also appear for the other inert gas solids.(24) The interrelationship of these various zero pressure thermodynamic properties is expressed in the definition of γ_c [equation (10)], and in the need for thermal expansion and compressibility data to correct high temperature C_p data to C_v [equation (12)].

One possible solution to these difficulties of obtaining data for comparison with theory would be to measure C_v directly as a function of temperature at constant volume, as has been done for solid helium.(24, 25) These experiments would be most interesting, but also quite difficult for the heavier inert gas solids (such as krypton and xenon) due to the large molar volume and, hence the small specific heats/cm^3 in the classical ($T > \theta_D$) region where the heat capacity of the high pressure bomb would be large. Certainly, the present work should serve as a guide in planning such experiments.

Most of the above comments apply to all of the heavier inert gas solids, and echo comments of BEAUMONT *et al.*(18) It would appear that experimental work on this class of solids, where theoretical calculations of the thermodynamic properties are the most feasible, has been neglected due to obvious (and hidden) experimental difficulties.

REFERENCES

1. BERNARDES N., *Phys. Rev.* **112,** 1534 (1958).
2. BERNARDES N., *Phys. Rev.* **120,** 807 (1960). This paper contains several misprints (see Ref. 3 below).

3. Bernardes N. and Swenson C. A., *Solids under Pressure* (edited by Warschauer D. and Paul W.) p. 101. McGraw-Hill, New York (1963).
4. Nosanow L. H. and Shaw G. L., *Phys. Rev.* **128,** 546 (1962).
5. Horton G. K. and Leech J. W., *On the Statistical Mechanics of the Ideal Inert Gas Solids,* to be published. The authors are indebted to Dr. Leech for a preprint of this paper.
6. Guggenheim F. A. and McGlashan M. L., *Proc. Roy. Soc.* **A255,** 456 (1960).
7. Stewart J. W., *Phys. Rev.* **97,** 578 (1955).
8. Stewart J. W., *J. Phys. Chem. Solids* **1,** 146 (1956).
9. Clusius K. and Riccoboni L., *Z. phys. Chem.* **B38,** 81 (1938).
10. Beecroft R. I. and Swenson C. A., *J. Phys. Chem. Solids* **18,** 329 (1961).
11. Monfort C. R., Packard J. R. and Swenson C. A., unpublished results, Iowa State University.
12. Cheesman G. H. and Soane C. M., *Proc. phys. Soc. Lond.* **B70,** 700 (1957). More recent data (see Ref. 13, 14 below) cast doubt on the reliability of these data, which are expressed in terms of X units, not angstroms, as was stated in Ref. 13.
13. Eatwell A. J. and Smith B. L., *Phil. Mag.* **6,** 461 (1961).
14. Sears D. R. and Klug H. P., *J. chem. Phys.* **37,** 3002 (1962).
15. Birch F., *J. geophys. Res.* 227 (1952).
16. Dobbs E. R. and Jones G. O. in *Reports on Progress in Physics,* p. 516, vol. XX. The Physical Society, London (1957).
17. Boato G. and Casanova G., *Physica* **27,** 571 (1961).
18. Beaumont R. H., Chihara H. and Morrison J. A., *Proc. phys. Soc. Lond.* **78,** 1462 (1961).
19. Yen W. M. and Norberg R. E., *Nuclear Magnetic Resonance of* Xe^{129} *in Solid and Liquid Xenon,* to be published. The authors are grateful to Prof. Norberg for furnishing a preprint of this paper prior to publication.

20 Slater J. C., *Introduction to Chemical Physics,* p. 239. McGraw-Hill, New York (1939).

21. Dugdale J. S. and MacDonald D. K. C., *Phys. Rev.* **89,** 832 (1953).
22. See, for instance, Jahnke-Emde-Losch, *Tables of Higher Functions,* 6th ed. (revised by F. Losch) McGraw-Hill, New York (1960).
23. Flubacher P., Leadbetter A. J. and Morrison J. A., *Proc. phys. Soc. Lond.* **78,** 1449 (1961).
24. Heltemes E. C. and Swenson C. A., *Phys. Rev.* **128,** 1512 (1962).
25. Dugdale J. S. and Simon F. E., *Proc. Roy. Soc.* **A218,** 291 (1953).

J. Phys. Chem. Solids Pergamon Press 1963. Vol. 24, pp. 1419–1434. Printed in Great Britain.

PREPARATION, ELECTRICAL CONDUCTIVITY AND TETRAGONAL DISTORTION OF SOME MANGANITE-SYSTEMS

M. ROSENBERG, P. NICOLAU, R. MANAILA and P. PAUSESCU

Institute of Physics of the Academy of the R.P.R., Bucharest, Rumania

(*Received* 28 *May* 1963)

Abstract—The preparation of the tetragonal spinels in the series (1) $Cu_xMn_{3-x}O_4$ ($0 \leqslant x \leqslant 0{,}2$), (2) $Zn_{1+x}Mn_{2-x}O_4$ ($0 \leqslant x \leqslant 0{,}2$), (3) $Mg_xMn_{3-x}O_4$ ($0 \leqslant x \leqslant 1$) and (4) $Zn_xMn_{3-x}O_4$ ($0 \leqslant x \leqslant 1$) is described.

Studies of the crystal symmetry as a function of composition and of electrical conductivity as a function of composition and temperature, are reported. All the compositions exhibit a thermal hysteresis of the electrical conductivity in the range of the tetragonal to cubic transition.

Analysis of crystal-chemical and electrical properties leads to the probable cation distribution formulae for each system.

The electrical conductivity involves the *hopping* mechanism of electrons between octahedral-site Mn^{3+} and Mn^{4+} ions.

In the systems (1) and (2) the presence of Cu^{2+} and Zn^{2+} ions in the octahedral positions together with the equivalent distorting power of the octahedral Cu^{2+} and Mn^{3+} ions has been established.

1. INTRODUCTION

AMINOFF,(1) MASON(2) and BERTAUT(3) have pointed to the existence of a tetragonal distortion of the crystalline lattice with $c/a > 1$ for oxide compounds with a spinel structure Mn_3O_4, $ZnMn_2O_4$, $CuFe_2O_4$. This distortion is due to the presence of Mn^{3+} or Cu^{2+} ions in the octahedral sites of the spinel lattice.(4,5)

This distortion was also made evident by means of X-rays, for systems formed of solid solutions of cubic and tetragonal spinels.(6–11) In $CuCr_2O_4$, the opposite distortion ($c/a < 1$) was discovered,(30) and solid solutions of tetragonal spinels with $c/a > 1$ and $c/a < 1$ were then studied.(12)

X-ray measurements allowed to follow the variation of the c/a ratio with temperature and the transition from the tetragonal phase to the cubic phase that occurs at temperatures depending on the nature, on the concentration and on the distribution of the cations in the octahedral and tetrahedral sites of the spinel lattice.(3,9, 12–14)

For Mn_3O_4, $ZnMn_2O_4$(15) and for the system $Co_xMn_{3-x}O_4$,(9) it has been possible to show that in the tetragonal–cubic transition range of temperature, a thermal hysteresis of the electric resistance is noticed, and thermodifferential analysis indicates the existence of an endothermal process.(9,16)

The explanation of the mechanism of tetragonal distortion for compounds containing ions of the transition metals followed two different paths. GOODENOUGH and LOEB(4) attribute the tetragonal distortion to the tendency of the Mn^{3+} and Cu^{2+} ions placed in the octahedral sites of the spinel lattice, to form coplanar square covalent bonds.

DUNITZ and ORGEL(5) explain the mechanism of distortion, based on the general theory of the crystalline field. The 3d orbitals of a cation of the iron group placed in an octahedral crystalline field undergo a splitting into a lower triplet and a higher doublet. Due to the Jahn–Teller effect,(17) the doublet states cannot be degenerated, so that in the case of orbital degeneracy the elementary octahedron is deformed, acquiring axial symmetry ($c/a > 1$). A similar phenomenon also occurs in the case of the ions of this type placed in the tetrahedral sites of the spinel lattice, however, with an opposite distortion ($c/a < 1$).

An analysis of the electronic configuration of the cations in the 3d transition series points to the Cu^{2+} and Mn^{3+} ions in octahedral coordination, as having the states of doublet degenerated, wherefrom their distortioned quality also results.

The variation of distortion with the concentration of the distorting ions and with temperature is generally treated as an order–disorder phenomenon. Bulk tetragonal distortion appears whenever the concentration of the distorting cations is sufficient to allow the formation of ordered chains of a cooperative distortion and the temperature is sufficiently low to prevent this order from being disturbed.(17–19) A more satisfactory view was presented by KANAMORI(20) who showed that Jahn–Teller stabilization is dynamical above the transition, static below. This view is supported in (31).

The results of the researches carried out so far seem to confirm the character of first-order phase transformation of the tetragonal–cubic transition. They likewise agree satisfactorily with theory, with respect to the variation of the c/a ratio with temperature and with the concentration of the distorting ions in the octahedral sites of the spinel lattice.(9,20)

However, the influence of the non-distorting ions in the octahedral sites, as well as the influence of distortion and its variation with temperature on electrical conduction in these compounds have only been investigated to a small extent.

The comparison of the results obtained through X-ray analysis and measurement of electrical conductivity allows valuable information to be obtained on the distribution of cations in spinel compounds and consequently the elimination of the models which do not simultaneously fulfill the requirements imposed from both structural and electrical conduction considerations.

Likewise, the effects caused by the presence of two strongly distorting ions in the lattice of tetragonal spinels have not, so far been investigated.

The researches carried out by the authors aimed to:

(a) Study the crystalline structure and the electric conduction of spinel structure oxydic systems containing two types of distorting ions.

(b) Investigate the influence of the Zn^{2+} and Mg^{2+} ions placed in the tetrahedral sites on the distortion of the spinel lattice.

(c) Investigate the influence of the non-distorting Zn^{2+} ions placed in the octahedral sites of the spinel lattice, on tetragonal distortion.

(d) Study electrical conduction before, during and after the tetragonal–cubic transition.

(e) Investigate the influence of the ions introduced in octahedral sites on electrical conduction in the tetragonal spinel lattices.

In view of realizing these aims, 18 oxide compounds were prepared, grouped in 4 systems: $Cu_xMn_{3-x}O_4$ with $0 \leqslant x \leqslant 0{\cdot}2$; $Zn_{1+x}Mn_{2-x}O_4$ with $0 \leqslant x \leqslant 0{\cdot}2$; $Mg_xMn_{3-x}O_4$ with $0 \leqslant x \leqslant 1$ and $Zn_xMn_{3-x}O_4$ with $0 \leqslant x \leqslant 1$.

The values of the compound parameter x were limited in view of obtaining pure tetragonal phases without any interference of other phases which could, through their presence, have distorted the experimental results.

2. EXPERIMENTAL

2.1. *Synthesis*

The oxide samples were prepared by firing the co-precipitated oxalates at 400°C. The powders thus obtained consisted of a mixture of superior oxides.(22) For the X-ray structural analysis and the electrical measurements in the 20–100°C range, pellets were pressed and then sintered in air at a temperature ranging between 900 and 1250°C, then rapidly cooled to room temperature. After sintering, the samples were chemically analyzed, the concentration of the metallic ions and of the active oxygen being determined.

For electrical measurements at high temperature, samples were prepared by sintering a drop of oxide mixture with a greater proportion of binder, on two 0·1 mm diameter platinum wires. After sintering, the wires were cut off in such a way as to leave one on each part of the sample, to play the part of metal electrodes.

The X-ray analysis made on both types of sample yielded the same results.

The temperature and duration of the sintering treatment were so chosen for each system that the compounds obtained should present a single phase of the tetragonal spinel type.

Silver electrodes were deposited by evaporation in vacuum on the pellet-type samples on which electrical measurements were carried out at temperatures between 20 and 100°C.

2.2. *X-ray structural analysis*

The compounds of the systems shown were analyzed by X-ray diffraction with the aim to determine with accuracy the lattice parameters.

The CrKα radiation, filtered through a vanadium filter, was used. The choice of a soft radiation was necessary in order to have only a small number of diffraction lines and thus to index them more readily. The Debye–Scherrer method was used, the substance in fine powder form being introduced into 0·5 mm Lindemann glass capillaries. A 57·6 mm diameter chamber with circular diaphragms was used in view of obtaining a reduced time of exposure.

The measurement of the diffraction rings was made with a Kirem coincidence ruler capable of reading 1/100 mm. After applying the film contraction correction, the determination of the *a* and *c* lattice parameters was made by means of the graphic method of successive approximations suggested by LIPSON and WILSON(21) which requires the measurement of several lines at various angles. An accuracy of $\pm 7 \times 10^{-4}$ Å was thus reached for determining the lattice parameters.

2.3. *Electrical conductivity*

The dependence of the electrical resistance on temperature was measured in the temperature ranges 20–100°C and 700–1300°C.

The measurements in the 20–100°C range were made in a Höppler-type thermostat on the pellet-type samples fixed in a device ensuring the electrical contact through pressure.

For the high temperature measurements, the samples fixed on a quartz stand were placed in a tubular furnace, the temperature being measured by means of a Pt–PtRh thermocouple. The quartz support on which the samples were placed consisted of a 15 mm diameter 800 mm long tube on which 40 mm long quartz cross-bars had been fixed. Platinum wire conductors on which the samples situated in the central region of the tube were fixed, were then stretched on the cross-bars. The Pt–PtRh thermocouple was also placed in the same manner.

The electrical resistance was measured by means of a Wheatstone bridge.

From the variation of resistivity with temperature on portions corresponding to rather large temperature intervals, the conclusion was reached that resistivity varies according to an exponential law and consequently an activation energy of the conduction process can be defined.

The electrical measurements at temperatures within the 20–100°C range allow to determine the resistivity at room temperature (ρ_{20}) and the activation energy of the conduction process (ΔE).

At high temperatures, besides the determination of the activation energy ($\Delta E'$) the variation of resistance was also studied in the domain of transition from the tetragonal phase, stable at room temperature, to the cubic phase, stable at high temperatures.

To establish the tetragonal–cubic transition temperature, the exploration of the hysteresis cycles obtained was effected by travelling through cycles whose maximum temperature was gradually increased up to the maximum cycle. For temperatures lower than the transition temperature the variation of resistance with temperature is reversible, while beyond this temperature larger and larger cycles appear, tending at the limit towards the maximum cycle. This phenomenon indicates the existence of a temperature range in which the transition occurs, the width of this range being dependent on the compound. The lower limit of this interval has been chosen as the transition temperature (T_t).

The carrier sign was determined by means of a thermoelectric sounder, all the samples presenting a *p*-type conduction.

3. RESULTS OBTAINED AND THEIR DISCUSSION

The main results obtained are shown in Figs 1–27 where the values of the active oxygen concentration (per cent active O), the tetragonal–cubic transition temperature (T_t), the activation energies at room temperature (ΔE) and at the tetragonal cubic transition temperature ($\Delta E'$), the resistivity at 20°C (ρ_{20}) and the axial ratio (c/a) at room temperature are plotted as functions of composition or temperature.

3.1. *The* $Cu_xMn_{3-x}O_4$ *system*

It has been shown in a previous study of this system(28) that in order to obtain tetragonal monophasic compounds, the compound parameter x should be limited to the value $x \leqslant 0{\cdot}25$ since for greater values of x a second phase, having a monoclinic structure (crednerite) is obtained besides the main phase.

The results obtained for the dependence of the c/a ratio and of the electrical resistivity on the composition and temperature can be interpreted by assuming that the Cu^{2+} ions are placed in the octahedral sites of the spinel lattice according to the formula $Mn^{2+}(Cu^{2+}_{x}Mn^{4+}_{x}Mn^{3+}_{2-2x})\,O_4$. There is a whole series of structural arguments pointing to the preference of the Cu^{2+} ions for placing themselves in the octahedral sites of the spinel lattice, viz.:

(a) The Cu^{2+} ions have quite a strong tendency to place themselves in octahedral sites, a fact made evident by cation distribution X-ray analysis on Cu ferrite.(3,12) At room temperature $CuFe_2O_4$ is an almost inverse spinel (91 per cent inverse). Moreover, Cu^{2+} and Mn^{3+} have, according to Refs 5 and 26 the same ratio of energetic stabilization in the octahedral and in the tetrahedral sites (3/2).

(b) It is only the placing of the Cu^{2+} ions on the octahedral sites of the spinel lattice that can explain the slow decrease of the axial ratio (Fig. 1), the Cu^{2+} producing, in this case, a tetragonal distortion with $c/a > 1$ equivalent to the one produced by Mn^{3+}. Cu^{2+} localized tetrahedrally, producing the opposite distortion ($c/a < 1$), would on the contrary result in the tetragonal distortion decreasing rapidly with the increase of the Cu^{2+} content. This is what happens for $CuFe_2O_4$ where the increase in temperature causes the migration of the Cu^{2+} ions on tetrahedral sites, producing a very steep decrease of tetragonal distortion.(12)

The slow decrease of the axial ratio in the system $Cu_xMn_{3-x}O_4$ can be better justified by formula $Mn^{2+}(Cu^{2+}_{x}Mn^{4+}_{x}Mn^{3+}_{2-2x})O_4$ than by formula $Mn^{2+}_{1-x}Mn^{3+}_{x}(Cu^{2+}_{x}Mn^{3+}_{2-x})O_4$ which assumes the appearance of the Mn^{3+} ions in the tetrahedral sites of the spinel lattice. These ions would produce an opposite distortion ($c/a < 1$) and in this case the axial ratio would decrease rapidly with the increase of the Cu content. This fact can be seen in AOKI's paper(9) in the case of system $Co_xMn_{3-x}O_4$ for which a rapid decrease of tetragonal distortion was found by cation distribution X-ray analysis.

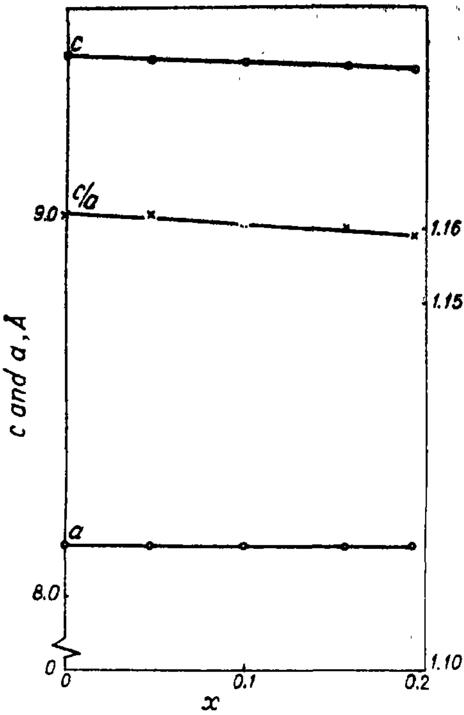

FIG. 1. Unit cell dimensions vs. composition for the system $Cu_xMn_{3-x}O_4$.

Considering formula

$$Mn^{2+}(Cu^{2+}_{x}Mn^{4+}_{x}\,Mn^{3+}_{2-2x})O_4$$

as valid, one can see that the only non-distorting ions in the octahedral sublattice are the Mn^{4+} ions.

In Fig. 1, the variation of the axial ratio with the proportion of non-distorting ions is presented, in the case of system $Cu_xMn_{3-x}O_4$.

In Fig. 2, the variation of the transition temperature with the proportion of Cu^{2+} ions is shown. It can be seen that T_t decreases linearly as the proportion of non-distorting Mn^{4+} ions increases, according to the formula suggested above.

The shape of the hysteresis cycles is but little changed (Fig. 3), the temperature range in which the transition occurs increasing, this being one more argument in favour of the hypothesis which places the Cu^{2+} ions with an effect similar to the

Mn^{3+} ions, in the octahedral sites of the spinel lattice, the only change occurring being the slow decrease of the proportion of distorting ions.

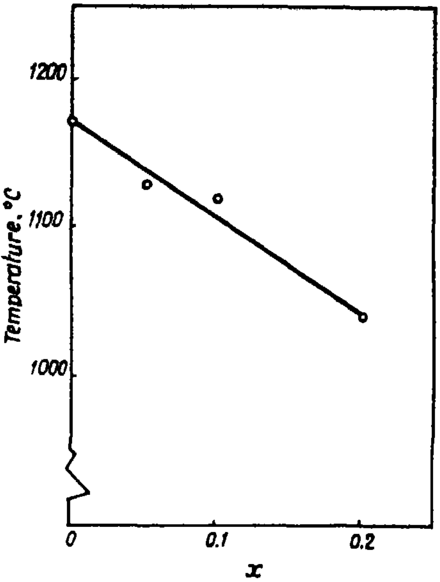

FIG. 2. Transition temperature vs. composition for the system $Cu_xMn_{3-x}O_4$.

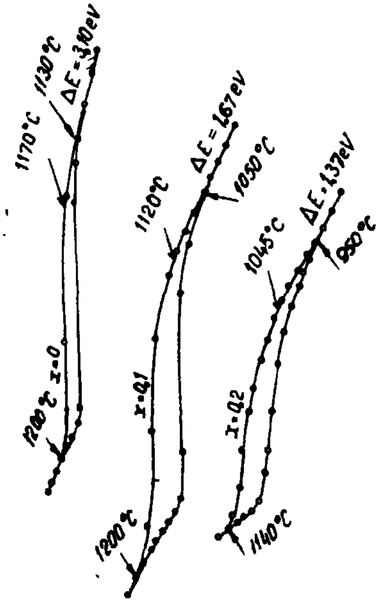

FIG. 3. Thermal hysteresis cycles of the electrical resistance ($\log R$ vs. $1/T \times 10^3$) for the system $Cu_xMn_{3-x}O_4$. Characteristic temperatures are indicated with arrows.

The most conclusive argument in favour of the suggested formula is, however, the way in which the electrical parameters ρ_{20}, ΔE and $\Delta E'$ vary with the composition (Figs 4–6). Indeed, these quantities which have, initially, high values (for $x = 0$, i.e. for Mn_3O_4, $\rho_{20} = 1 \cdot 2 \times 10^8$, $\Delta E = 1 \cdot 19$, $\Delta E' = 3 \cdot 10$), decrease very rapidly with the increase of the proportion of Cu^{2+}, a fact that can only be explained by the mechanism of electrical conduction for the oxides with a spinel structure suggested by VERWEY,(25) through the appearance in the octahedral sites of the spinel lattice, of two types of ions of the same metal, but at different valencies, the electrical conduction taking place by jumps of the electrons between two neighboring ions which thus change their valence. This process probably occurs in the way described by YAMASHITA and KUROSAWA,(28) i.e. through jumps caused by the interaction of the autolocalized holes with the lattice vibrations, leading to an

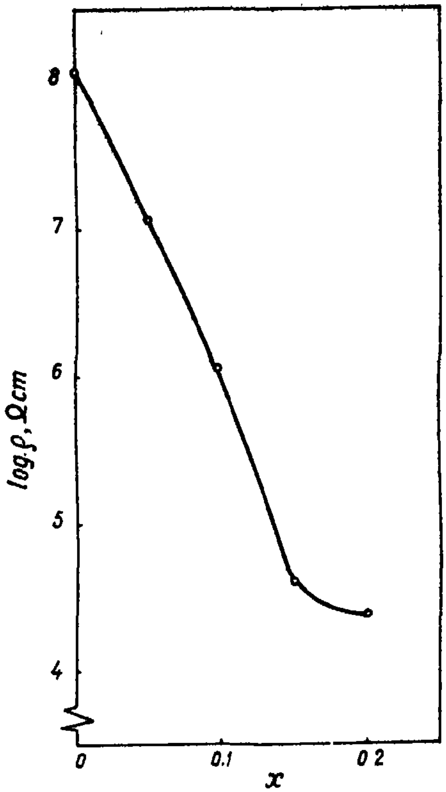

FIG. 4. Log $\rho_{20°C}$ vs. composition for the system $Cu_xMn_{3-x}O_4$.

exponential dependence of mobility and, indirectly, of electrical conductivity, on temperature.

Since the analysis of active oxygen only shows very small deviations from stoichiometry (Fig. 7), the only way in which the steep change of resistivity can be explained is the appearance of the Mn^{4+} ions in the octahedral sites of the spinel lattice, occuring concomitantly with the increase of the proportion of Cu^{2+} ions, the electronic jumps between the Mn^{3+} and the Mn^{4+} ions thus becoming possible according to the formula $Mn^{2+}(Cu_x^{2+}Mn_x^{4+}Mn_{2-2x}^{3+})O_4$. Arguments in favour of this formula are also the recently published results on the system $N_{1-x}Mn_{2+x}O_4$.(29)

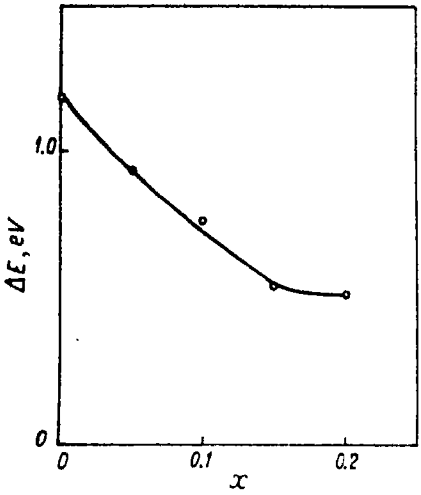

FIG. 5. Activation energy ΔE vs. composition for the system $Cu_xMn_{3-x}O_4$ (temperature range: 20–100°C).

3.2 *The system* $Zn_{1+x}Mn_{2-x}O_4$

As it has been shown,(4) Zn^{2+} has a powerful tendency to place itself tetrahedrally. It was of course endeavored to see whether it can be made to enter in the octahedral sublattice in the case where the tetrahedral sublattice is completely occupied. With this in mind, it was endeavored to obtain monophasic compounds in the system $Zn_{1+x}Mn_{2-x}O_4$.

The X-ray analysis made evident, in the $x < 0{\cdot}2$ domain, the existence of a single tetragonal spinel phase, a fact which is an argument in favor of the placing of the Zn^{2+} ions on the octahedral sites, according to the formula

$$Zn^{2+}(Zn_x^{2+}Mn_x^{4+}Mn_{2-2x}^{3+})O_4.$$

The variation of the transition temperature, of resistivity, of activation energy, of active oxygen content and of the shape of the hysteresis cycles with the composition is presented in Figs 8–14.

It can be seen that the transition temperature decreases with the increase of the zinc content. Likewise, ρ_{20}, ΔE and $\Delta E'$ present a continuous decrease, a fact which can be interpreted in the sense of the discussion in paragraph 3.1, assuming the structural formula $Zn^{2+}(Zn_x^{2+}Mn_x^{4+}Mn_{2-2x}^{3+})O_4$ as valid.

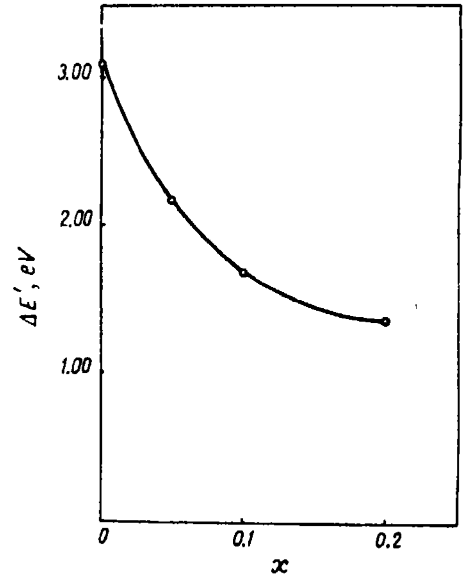

FIG. 6. Activation energy $\Delta E'$ vs. composition for the system $Cu_xMn_{3-x}O_4$ (below the transition temperature).

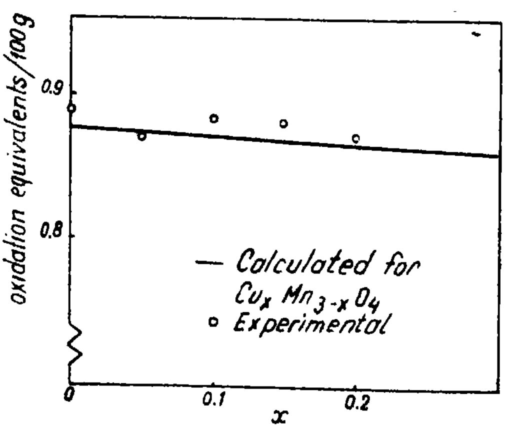

FIG. 7. Oxidizing power vs. composition for the system $Cu_xMn_{3-x}O_4$.

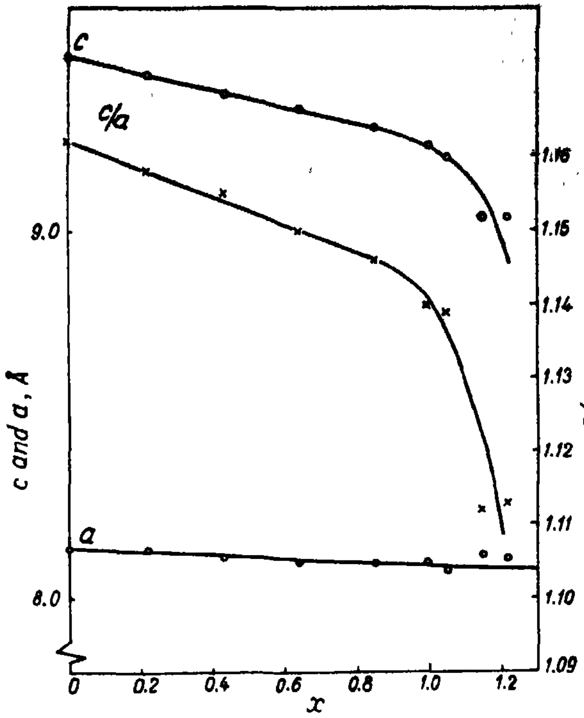

FIG. 8. Unit cell dimensions vs. composition for the systems $Zn_xMn_{3-x}O_4$, and $Zn_{1+x}Mn_{2-x}O_4$ where $x \leq 1$.

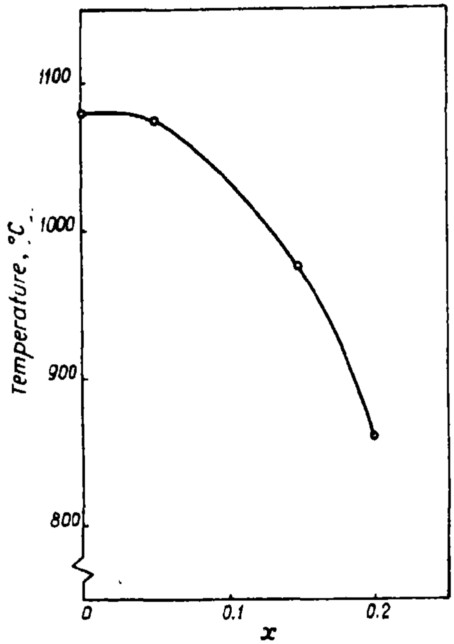

FIG. 9. Transition temperatures vs. composition for the system $Zn_{1+x}Mn_{2-x}O_4$.

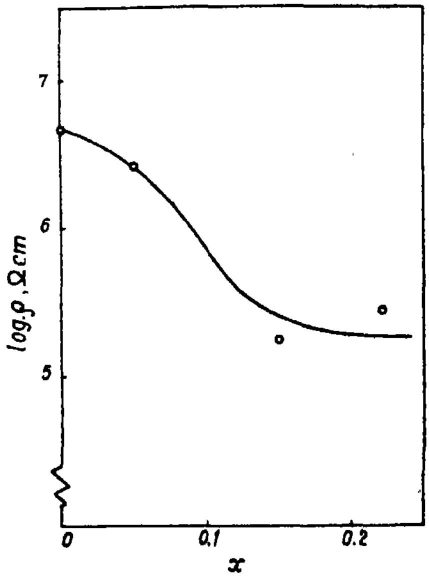

FIG. 10. Log $\rho_{20°C}$ vs. composition for the system $Zn_{1+x}Mn_{2-x}O_4$.

Indeed, in this case, the octahedral sublattice of the spinel lattice presents a variation with composition similar to that of the system $Cu_xMn_{3-x}O_4$ the Zn^{2+} ion having now replaced the Cu^{2+} ion. The decrease of resistivity and of the activation energies is less rapid in this case than in 3·1, because the system starts with $ZnMn_2O_4$ for which the values of these quantities are much smaller than those for Mn_3O_4 in the case of the system mentioned.

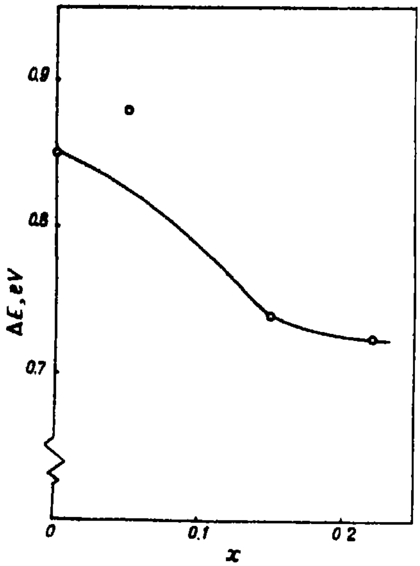

FIG. 11. Activation energy ΔE vs. composition for the system $Zn_{1+x}Mn_{2-x}O_4$ (temperature range: 20–100°C).

3.3. *The systems* $Zn_xMn_{3-x}O_4$ *and* $Mg_xMn_{3-x}O_4$

The cations Zn^{2+}, Mg^{2+} have the tendency to place themselves on the tetrahedral sites of the spinel lattice where the former forms covalent bonds and the latter forms ionic bonds with the oxygen.(4, 8)

One notices in Fig. 15 a slight decrease of the *c/a* ratio with the Mg concentration going from 1·162 (Mn_3O_4) to 1·150 ($MgMn_2O_4$). The decrease of the axial ratio is due to the fact that at the treatment temperature of 1200°C a fraction of the Mg^{2+} ions is probably on the octahedral sites, thus reducing the proportion of distorting Mn^{3+} ions.(24)

The system $Zn_xMn_{3-x}O_4$ having the structural formula $Zn_x^{2+}Mn_{1-x}^{2+}(Mn_2^{3+})O_4$ presents a more pronounced decrease of tetragonal distortion (Fig. 8), reaching down to $c/a = 1{\cdot}144$ for $ZnMn_2O_4$. This decrease is explained by the fact that Zn^{2+} tetrahedrally placed weakens the octahedral bonds which cause distortion, in accord with Goodenough's theory.

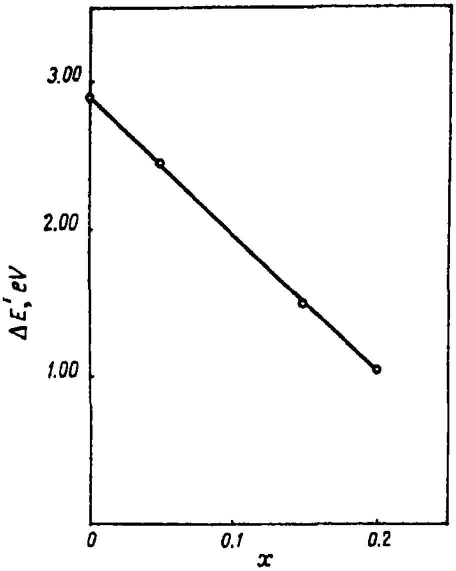

FIG. 12. Activation energy $\Delta E'$ vs. composition for the system $Zn_{1+x}Mn_{2-x}O_4$ (below the transition temperature).

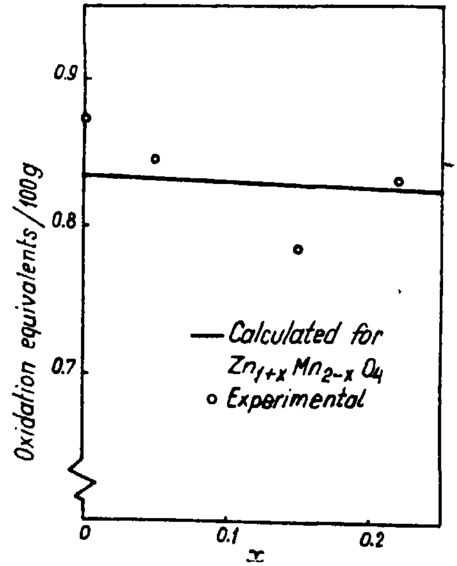

FIG. 13. Oxidizing power vs. composition for the system $Zn_{1+x}Mn_{2-x}O_4$.

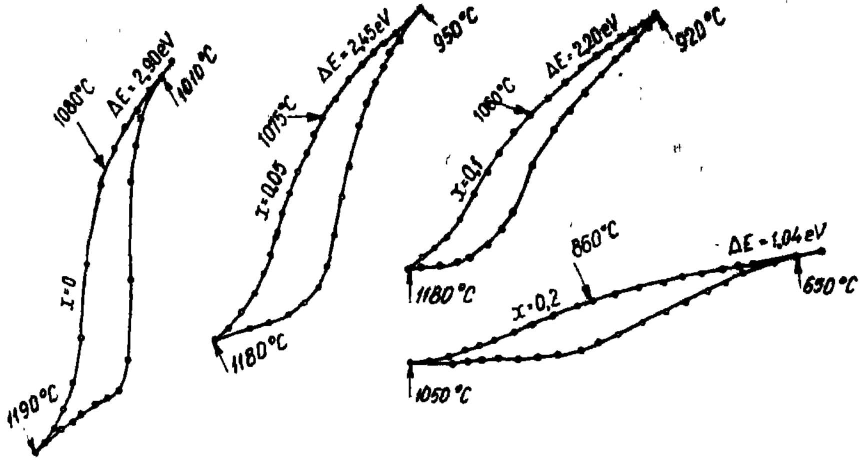

FIG. 14. Thermal hysteresis cycles of the electrical resistance (log R vs. $1/T\times 10^3$) for the system $Zn_{1+x}Mn_{2-x}O_4$. Characteristic temperatures are indicated with arrows.

The tetragonal–cubic transition temperature for the system $Mg_xMn_{3-x}O_4$ decreases linearly with the composition parameter (Fig. 16), while for the system $Zn_xMn_{3-x}O_4$ this temperature presents a more irregular variation (Fig. 22).

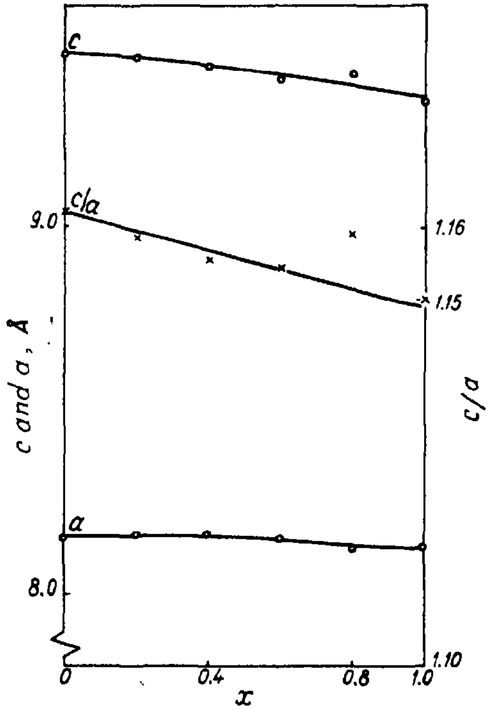

FIG. 15. Unit cell dimensions vs. composition for the system $Mg_xMn_{3-x}O_4$.

For these two systems the shape of the hysteresis cycles is about the same for all the compounds (Figs 17 and 23), the tetragonal–cubic transition generally occurring within a narrow temperature range, as for Mn_3O_4, excepting the last composition of each system $Mg_xMn_{3-x}O_4$ and $Zn_xMn_{3-x}O_4$ where the temperature range in which the transition occurs is much larger. Probably in these compounds a fraction of the Mg^{2+} and Zn^{2+} ions migrate to the octahedral sites of the spinel lattice.

The quantities ρ_{20}, ΔE and $\Delta E'$ (Figs 18, 19, 20 and 24, 25, 26 respectively) generally have very high values which continue along both systems at about the level for Mn_3O_4, a fact which indicates in general a steady octahedral sublattice for both systems, i.e. the octahedral sublattice at Mn_3O_4 formed of only Mn^{3+} ions. For the system $Mg_xMn_{3-x}O_4$ a slight decrease of the electrical parameters can be noticed, probably due to the migration of the Mg^{2+} ions in the octahedral sublattice and to the forming of the Mn^{4+} ions to maintain electrical neutrality, a fact which can improve electrical conduction. For the system $Zn_xMn_{3-x}O_4$ only the compound $ZnMn_2O_4$ presents much smaller values of the electrical parameters than the other compounds of the system, on account, probably of the same phenomenon.

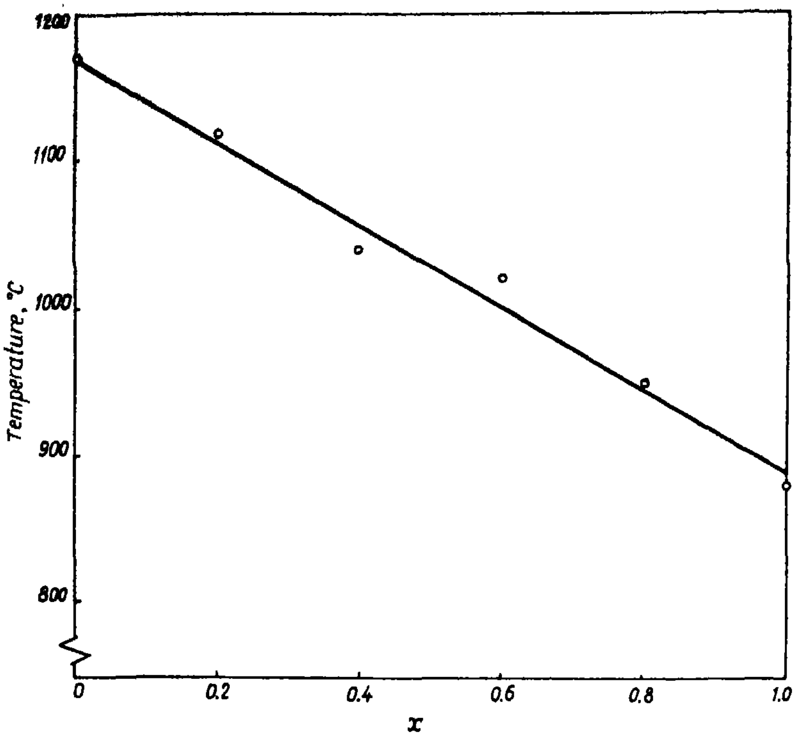

FIG. 16. Transition temperature vs. composition for the system $Mg_xMn_{3-x}O_4$.

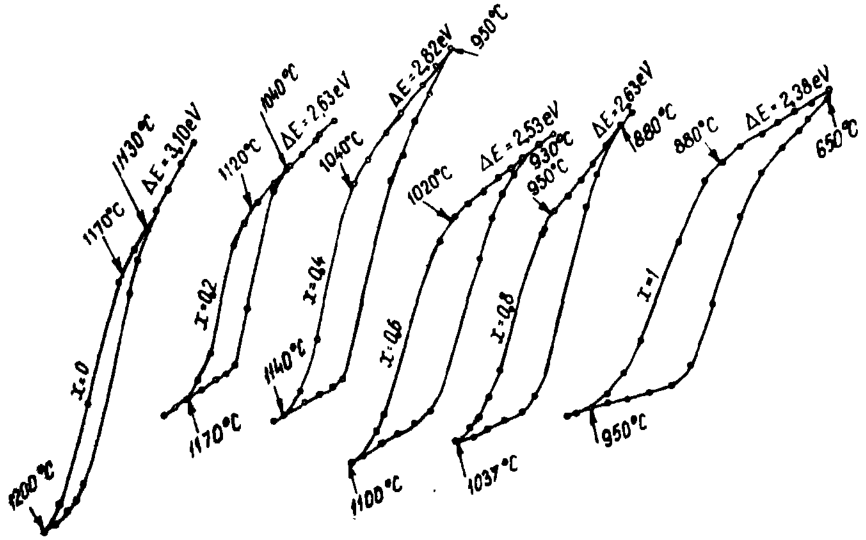

FIG. 17. Thermal hysteresis cycles of the electrical resistance (log R vs. $1/T \times 10^3$) for the system $Mg_xMn_{3-x}O_4$. Characteristic temperatures are indicated with arrows.

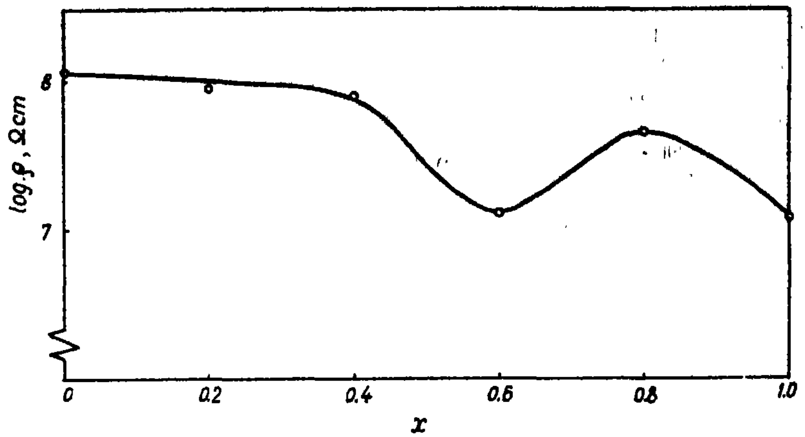

FIG. 18. Log $\rho_{20^\circ C}$ vs. composition for the system $Mg_xMn_{3-x}O_4$.

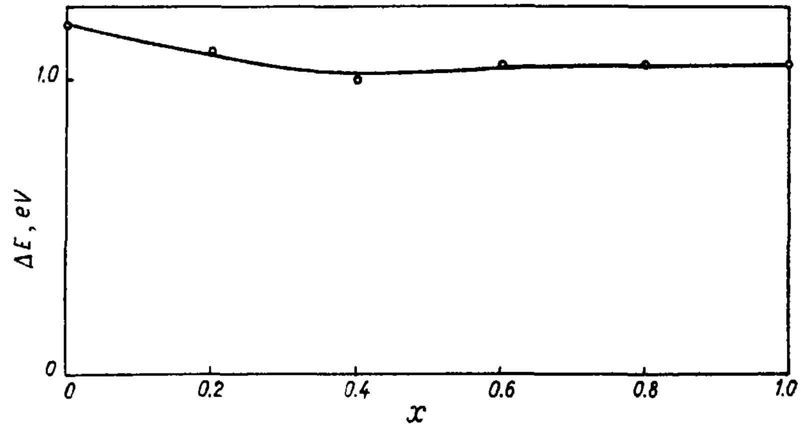

FIG. 19. Activation energy ΔE vs. composition for the system $Mg_xMn_{3-x}O_4$ (temperature range: 20–100°C).

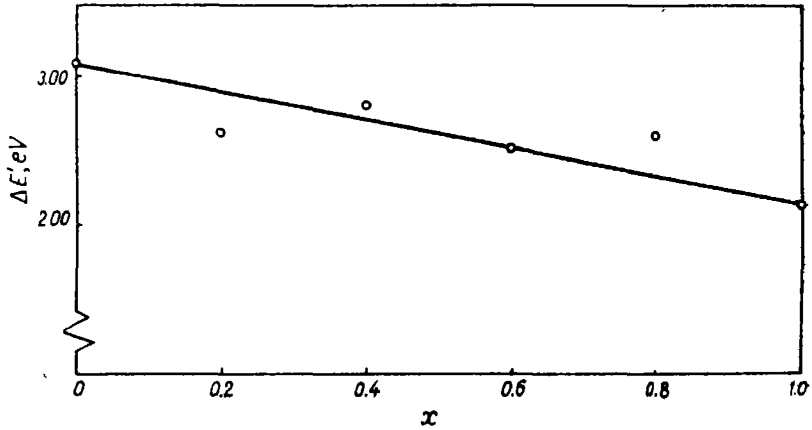

FIG. 20. Activation energy $\Delta E'$ vs. composition for the system $Mg_xMn_{3-x}O_4$ (below the transition temperature).

The content of active oxygen in the samples of these systems generally presents deviations from stoichiometry (Figs 21 and 27), a fact which probably also explains the more irregular variations of the electrical resistivity and activation energy.

4. CONCLUSIONS

All the spinel compounds studied in the systems $Cu_xMn_{3-x}O_4$ (1), $Zn_{1+x}Mn_{2-x}O_4$ (2), $Mg_xMn_{3-x}O_4$ (3), $Zn_xMn_{3-x}O_4$ (4), present at room temperature a tetragonal distortion of the crystalline lattice.

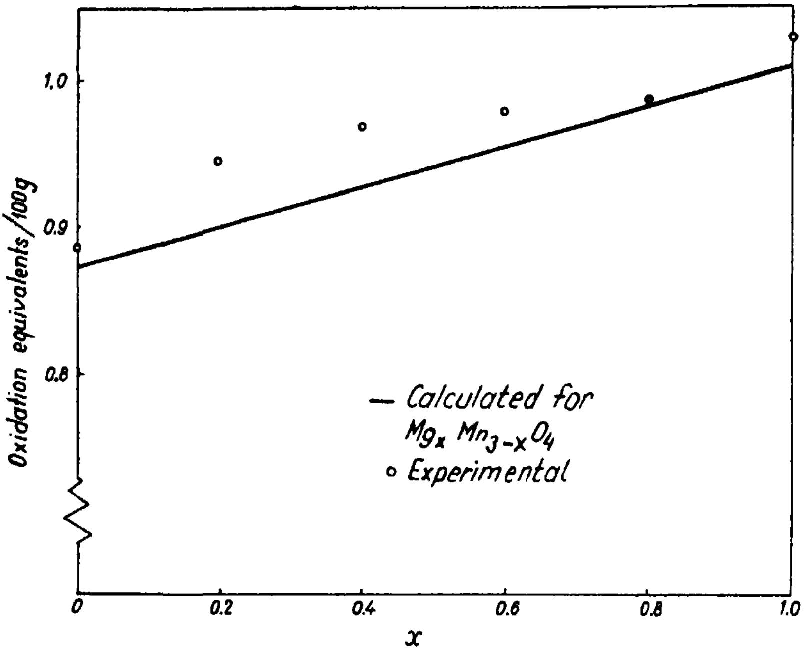

Fig. 21. Oxidizing power vs. composition for the system $Mg_xMn_{3-x}O_4$.

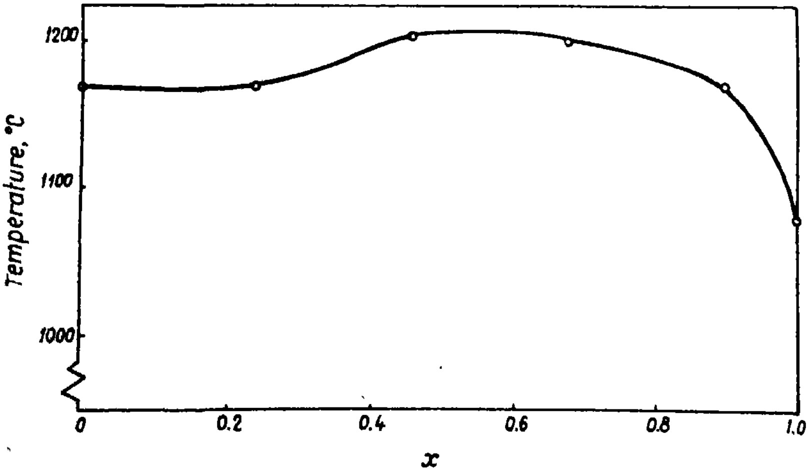

Fig. 22. Transition temperature vs. composition for the system $Zn_xMn_{3-x}O_4$.

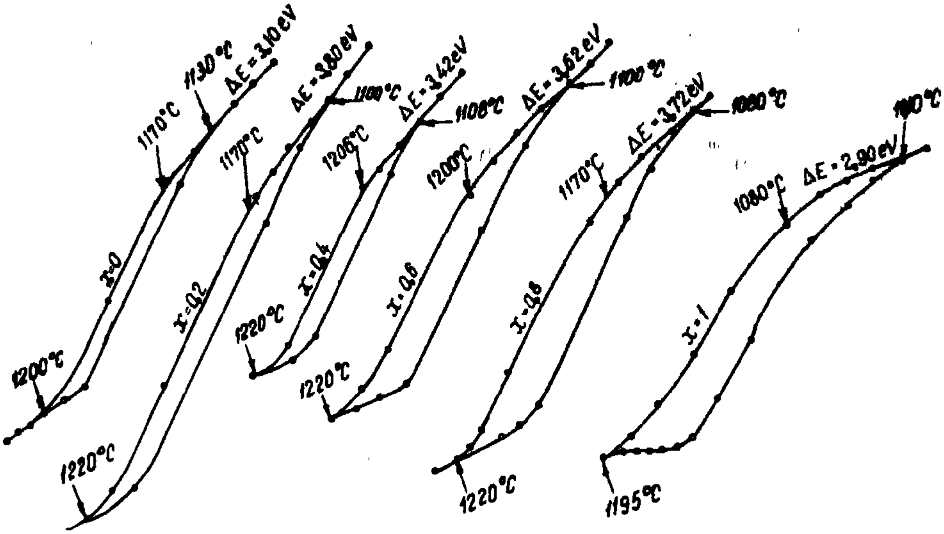

FIG. 23. Thermal hysteresis cycles of the electrical resistance (log R vs. $1/T \times 10^3$) for the system $Zn_xMn_{3-x}O_4$. Characteristic temperatures are indicated with arrows.

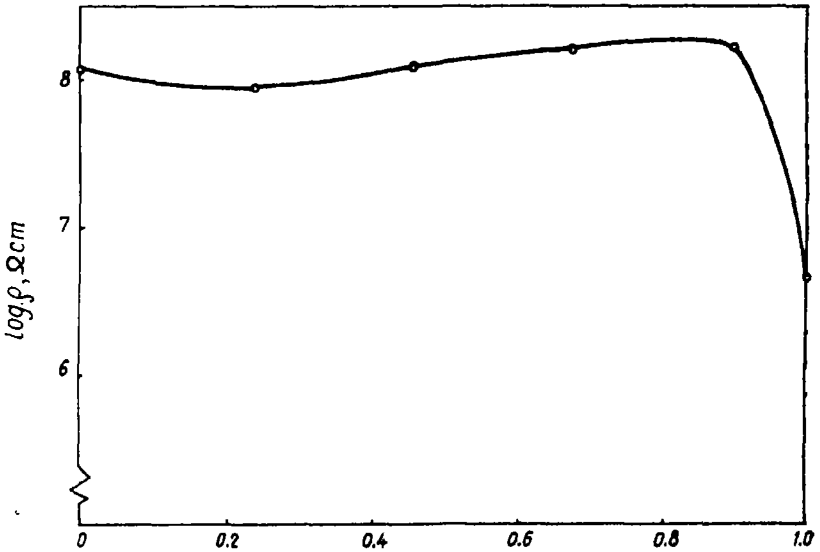

FIG. 24. Log $\rho_{20°C}$ vs. composition for the system Zn

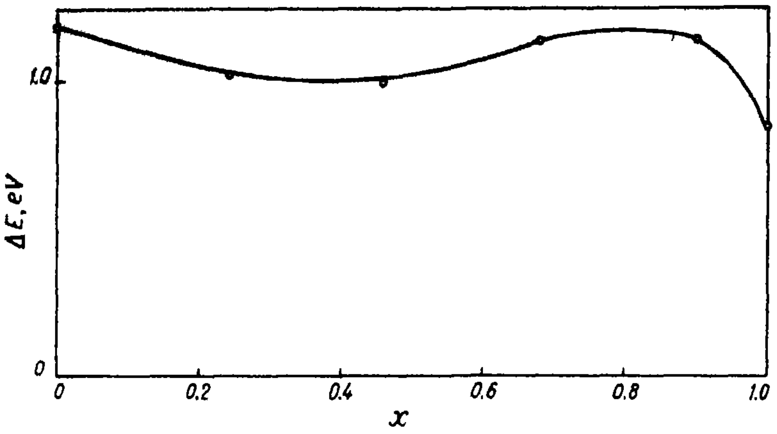

FIG. 25. Activation energy ΔE vs. composition for the system $Zn_xMn_{3-x}O_4$ (temperature range: 20–100°C).

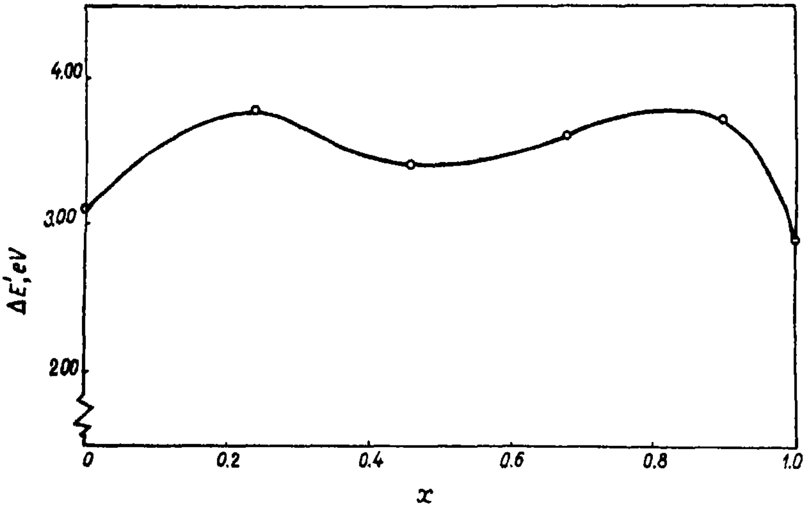

FIG. 26. Activation energy $\Delta E'$ vs. composition for the system $Zn_xMn_{3-x}O_4$ (below the transition temperature).

In the system (1) the Cu^{2+} ions place themselves on the octahedral sites of the spinel lattice, contributing to the distortion by a quantity equivalent to Mn^{3+}, the structural formulae of this system being $Mn^{2+}(Cu_x^{2+}Mn_x^{4+}Mn_{2-2x}^{3+})O_4$.

In system (2) compositions were obtained where the Zn^{2+} ion placed itself octahedrally, the structural formula of the system being probably $Zn_t^{2+}Mn_t^{2+}(Zn_u^{2+}Mn_u^{4+}Mn_{2-2u}^{3+})O_4$ where $u+t = x+1$ and t approach 1.

All the compounds studied show in the variation of electrical resistance with temperature a thermal hysteresis in the range of transition from the tetragonal to the cubic structure. The more the percentage of non-distorting ions in the octahedral sublattice increases, the more deformed the hysteresis cycles and the larger the temperature range in which they extend.

The dependence of the transition temperature on the percentage of non-distorting ions is linear,

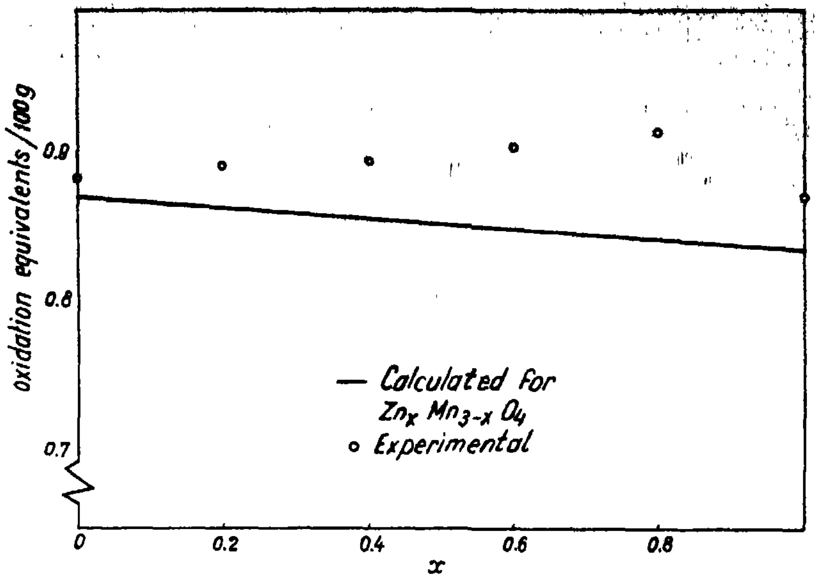

Fig. 27. Oxidizing power vs. composition for the system $Zn_xMn_{3-x}O_4$.

in agreement with the predictions of Wojtowicz's theory, a fact bringing an extra argument for considering the tetragonal-cubic transition as a phase transformation of the 1st order.

From the resistivity and activation energy measurements it has been possible to show that, at least qualitatively, the electrical properties of the compounds studied can be interpreted by means of Verwey's hypothesis on the mechanism of electrical conduction in the oxide compounds with a spinel structure. The gradual increase of the quantity of Mn^{4+} in the octahedral sublattice for the compounds of systems (1) and (2), causes the decrease of resistivity and activation energy, since the possibility of transition between ions of the same type but of different valencies, located in the equivalent sites of the spinel lattice (the octahedral ones) thus increases.

In exchange, in systems (3) and (4), resistivity and activation energy are less sensitive to the gradual replacement of the Mn^{2+} through Zn^{2+} or Mg^{2+} ions in the tetrahedral sublattice.

From the dependence of electrical conduction on temperature, a confirmation is obtained of the structural formulae suggested for the compounds studied in agreement with the results reached on basis of the X-ray-structural analysis.

Acknowledgements—Finally, the Authors wish to thank A. Cormos and E. Vǎrzaru for the chemical analysis and preparations carried out, and likewise Gh. Anghelea for effecting the technological operations and some of the measurements.

REFERENCES

1. Aminoff G., *Z. Krist.* **64**, 475 (1962).
2. Mason B., *Amer. Mineralogist* **32**, 426 (1947); *Geol. Fören Stock Förn* **65**, 97 (1943).
3. Bertaut E. F., *J. Phys. Radium* **12**, 252 (1951).
4. Goodenough J. B. and Loeb A. L., *Phys. Rev.* **98**, 391 (1955).
5. Dunitz J. D. and Orgel E., *J. Phys. Chem. Solids* **3**, 20, 318 (1957).
6. Wickham D. G. and Croft W. J., *J. Phys. Chem. Solids* **7**, 106 (1958).
7. Sinha A. P. B., Sanjana N. R. and Biswas A. B., *Acta Cryst.* **10**, 439 (1957).
8. O'Keeffe M., *J. Phys. Chem. Solids* **21**, 172 (1961).
9. Aoki I., *J. phys. Soc. Japan* **17**, 53 (1962).
10. Bongers P. F., Thesis, Leiden (1957).
11. Miyahara S., Muramori K. and Tokuda N., *J. phys. Soc. Japan* **16**, 1490 (1961).
12. Ohnishi H. and Teranishi S., *J. phys. Soc. Japan* **16**, 35 (1961).
13. Mc Murdie H. F., Sullivan B. M. and Maurer P. A., *J. Nat. Bur. Stand.* **45**, 35 (1952).
14. McMurdie H. F. and Golovato E., *J. Research Nat. Bur. Standards* **41**, 489 (1948).
15. Romeijn F. C., *Philips res. Rep.* **8**, 327 (1953).

16. Blazec A., Cihar V., Caslavska V., and Caslavsky J., *Coll. Czech. Chem.* **25**, 2419 (1959).
17. Jahn H. A. and Teller E., *Proc. Roy. Soc.* **A161**, 220 (1937).
18. Finch G. I., Sinha K. P. and Sinha A. P. B., *Proc. Roy. Soc.* **A242**, 28 (1957).
19. Wojtowicz P. J., *Phys. Rev.* **116**, 32 (1959).
20. Kanamori J. J., *J. appl. Phys.* (Japan) **S31**, 14 S (1960).
21. Lipson H. and Wilson A. J. C., *J. Sci. Instrum.* **18**, 144 (1941).
22. Landolt–Börnstein, *Zahlenwerte und Functionen* Vol. I, p. 4. (Kristalle) Springer, Berlin (1955).
23. Rosenberg M., Nicolau P., Mănaila R. and Păusescu P., *Stud. Cercet. Fiz.* **13**, 651 (1962).
24. Irani K. S., Sinha A. P. B. and Biswas A. B., *J. Phys. Chem. Solids* **23**, 711 (1962).
25. Verwey E. J. W., *Semiconducting Materials*, Butler, London (1951).
26. McClure D. S., *J. Phys. Chem. Solids* **3**, 318 (1957).
27. Miller A., *J. appl. Phys.* **30**, 249 S (1959).
28. Yamashita J. J. and Kurosawa T., *J. Phys. Chem. Solids* **5**, 43 (1959).
29. Larson E. G., Arnott R. J. and Wickham D. G. *J. Phys. Chem. Solids* **23**, 1771 (1962).
30. Bertaut E. F. and Delorme C., *Compt. Rend. acad. Sci.*, Paris **249**, 726 (1959).
31. Goodenough J. B., Wold A., Arnott R. J. and Menyuk N., *Phys. Rev.* **124**, 373 (1961).

J. Phys. Chem. Solids Pergamon Press 1963. Vol. 24, pp. 1435–1450. Printed in Great Britain.

THE THERMODYNAMICS AND HINDERED ROTATION OF OCCLUDED CO IN THE β-QUINOL CLATHRATE*

G. L. STEPAKOFF† and L. V. COULTER

Department of Chemistry, Boston University

(*Received* 24 *May* 1963)

Abstract—The heat capacities of four β-quinol clathrates of CO, $y\mathrm{CO}\cdot 3\mathrm{C_6H_4(OH)_2}$, having compositions in the $y = 0{\cdot}4$–$0{\cdot}8$ range, have been measured from 15° to 300°K in an adiabatically operated calorimeter.

At 298·15°K, the molar heat capacity and entropy of clathrated CO are 9·76 and 20·94 cal deg^{-1} mole^{-1}, respectively. The pressure isotherm constant for the reaction $\mathrm{CO}(g) \leftrightharpoons \mathrm{CO}_{(\beta\text{-quinol},\, s)}$, is $p(1-y)/y = K_{25°\mathrm{C}} = 8{\cdot}9$ atm.

The heat capacity in the 15–40°K range is interpreted in terms of a three-dimensional harmonic oscillator ($\nu = 104{\cdot}3$ cm^{-1}) for the vibrational motion of CO in the cavity and a two-dimensional hindered rotator with $V_0 = 745$ cal mole^{-1}.

At 298·15°K, the thermodynamic properties are correlated by the use of the classical cell model for the rattling motion of CO corrected for the effect of hindered rotation. Agreement between calculated and observed properties is obtained for $Z\bar{\epsilon}(/k)^{1/2} = 390$ and $\bar{\sigma} = 3{\cdot}22$ Å for the interaction parameters of the cavity wall, and $V_0 = 2867$ cal mole^{-1} for the potential hindering the rotation of occluded CO.

The apparent increase of potential with temperature perhaps results from increased alignment of the CO molecules with the cavity walls.

INTRODUCTION

In a preliminary communication⁽¹⁾ the molar heat capacities of CO and N_2 in their respective β-quinol clathrates have been given graphically for the 15–100°K range, and an interpretation of the data has been offered in each case based on a model consisting of a three-dimensional isotropic harmonic oscillator for the rattling or vibrational motion of CO in the host cavity and a two dimensional harmonic oscillator for the librational motion. For clathrated CO the librational frequency was found to be 43·1 cm^{-1} and the barrier restricting the rotation was calculated to be 691 cal mole^{-1}.

This paper now presents the complete results of the measurements of the heat capacities of four β-quinol clathrates of CO of various compositions for the 15–300°K range from which the molar heat capacity and entropy of clathrated CO have been obtained. In addition, an interpretation of these data and the vapor pressures of β-quinol clathrates of CO at 25°C is given in terms of the van der Waals⁽²⁾ theory for the vibrational motion of CO enclosed in the host cavity, and the properties of a two-dimensional hindered rotator for which the appropriate partition function and statistical thermodynamic equations have been derived.

EXPERIMENTAL

The clathrates of CO employed in this work were prepared under isothermal conditions by subjecting a slurry of doubly vacuum sublimed Eastman hydroquinone (99·99 per cent by CeIV ion titration)⁽³⁾ in *n*-propyl alcohol to a predetermined constant pressure of CO gas (Matheson, 99·5 per cent) in a thermostated high pressure autoclave. The slurry was agitated by rocking the bomb for several days at 25·0 ± 0·1°C to insure synthesis of homogeneous samples. Following the conversion of the α-hydroquinone to the β-quinol clathrate

---

* Supported in part by a grant from the National Science Foundation.

† Present address: Manlabs, Inc., Cambridge, Mass.

of CO by the net reaction: 3 α-quinol$_{(s)}$ + yCO$_{(g)}$ = 3 β-quinol · yCO$_{(s)}$, where y is the fraction of cavities filled or number of moles of gas occluded, the mother liquor was filtered from the clathrate crystals *in situ* under the prevailing equilibrium pressure and the clathrate partially dried by circulating CO at the same pressure through the bed of crystals for about 1 hr in order to avoid reversal of the above reaction. The product was then quickly removed from the reaction vessel and placed on a high vacuum line to remove last traces of solvent. Infra-red spectra and X-ray powder diagrams confirmed the presence of the β-structure. Prior to calorimetric use, the samples were stored in a vacuum desiccator maintained below 25°C. The gas content of the clathrates was determined by fusion of a weighed amount of sample in a calibrated vacuum manifold provided with a constant volume manometer for pressure observations. Pressures of the order of 0·5–0·8 atm were measured to ± 0·005 cm with a Gaertner cathetometer.

During the course of the preparation of the clathrates, the pressures for the equilibrium: $CO_{(g)} \rightleftharpoons CO_{(\beta\text{-quinol},\, s)}$ were also observed and were used to calculate the 25°C pressure isotherm constant $K_{25°C} = P_{(CO)}(1-y)/y$.(2)

Strictly speaking, the observed pressures must be regarded as tentative equilibrium pressures since in all cases the "equilibrium" preparations were approached from only one direction and, accordingly, cannot yet be regarded as true equilibrium preparations until a more rigorous equilibrium study is completed.

The heat capacities of four CO clathrates, having 46·0, 62·6, 75·7 and 81·0 per cent of the cavities filled, were measured from 15 to 300°K in an adiabatically operated calorimeter and cryostat which have been described previously.(4) The ice point was taken as 298·15°K and one defined calorie was taken as 4·1840 abs J.

RESULTS AND DISCUSSION

The pressure isotherm constant at 25·0°C, calculated as the slope of the plot of $P_{(obs)}$ vs. $y/1-y$ at low pressures (Fig. 1), was found to be 8·9 ± 0·3 atm. The three phase pressure at y = 0·34 was calculated to be 4·6 atm, assuming the validity of the van der Waals theory for the composition of the clathrate for the three-phase equilibrium.(2)

Although the dependence of P, or fugacity, on $y/1-y$ deviates from linearity above ~10 atm, these deviations cannot yet be properly attributed to the breakdown of the isotherm function or the effect of pressure on the stability of the β-quinol lattice, since the systems were not rigorously tested for equilibrium.

The experimental heat capacities of the clathrates of CO are given in Tables 1–4. No discontinuities were found in the 15–300°K range. From 15 to 120°K, the heat capacity of each clathrate is curved substantially towards the T axis while above 120°K, C_p is almost linearly dependent on temperature. Since the heat capacity of enclosed gas is obtained from the difference of large numbers, the measurements of heat capacities in temperature regions of interest were often repeated to insure reproducible results. The average deviations of the data from a smooth curve amounted to about ± 0·1–0·2 per cent above 90°K and increased to about ± 0·5 per cent below 50°K.

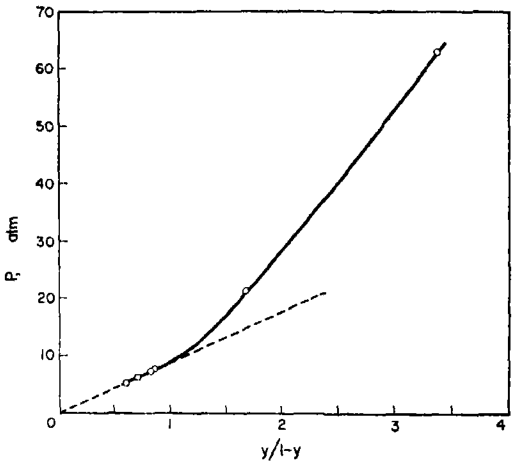

FIG. 1. Equilibrium pressure isotherm for $CO_{(g)} \rightleftharpoons CO_{(\beta\text{-quinol},\, s)}$. Lower left segment of dotted line—region of instability of clathrate relative to α-quinol and CO gas. Complete dotted line—apparent low pressure limiting slope.

Two of the samples lost a small amount of CO presumably during the soldering operations on the loading port of the calorimeter. This was evidenced as a small anomaly near the triple point of carbon monoxide (~66°K). Sample 3 with a final y value of 0·757 had an initial value of 0·771 before loading the calorimeter while the y value of

Table 1. *Experimental heat capacity of carbon monoxide clathrate No.* 1: $3C_6H_4(OH)_2 \cdot 0{\cdot}460$ CO *in cal deg*$^{-1}$ 3 *moles β-quinol*$^{-1}$ (0·1113 *moles of clathrate in the calorimeter*)

Series I

T°K	C_p
57·54	27·62
61·03	28·92
64·41	30·10
67·71	31·22
70·94	32·26
75·19	33·66
80·12	35·18
84·63	36·49
89·08	37·76
93·63	39·00
98·14	40·16
102·32	41·36
108·29	42·99
114·15	44·71
118·56	45·97
123·29	47·34
128·34	48·80
133·36	50·23
138·39	51·66
143·62	53·13
148·90	54·69
154·27	56·38
159·71	57·97
165·04	59·62
170·45	61·19
175·65	62·86
181·06	64·54
183·64	65·42
188·97	66·98
194·72	68·70
200·68	70·65
206·53	72·48
212·28	74·37
217·94	76·05
223·65	78·05
229·45	80·00
235·15	81·88
240·93	83·78
246·78	85·70
252·50	87·61

Series II

T°K	C_p
242·09	84·18
247·62	86·05
253·39	87·96
259·20	89·81
264·87	91·68
270·64	93·67
276·50	95·78
282·44	97·64
288·50	99·74

Series III

T°K	C_p
13·28	1·91
14·96	3·14
16·37	4·26
18·79	6·17
21·46	8·29
23·46	9·79
25·29	11·01
26·90	12·04
28·74	13·10
31·02	14·49
33·48	16·00
35·89	17·44
38·21	18·77
40·44	19·98
43·20	21·43
46·72	23·07
50·65	24·80
54·74	26·53
59·23	28·26
64·27	30·06

Series IV

T°K	C_p
15·26	3·41
16·76	4·58
18·66	6·11
21·00	7·96
23·29	9·67
25·69	11·31
28·48	12·95
31·57	14·88
34·54	16·66
37·83	18·55
41·31	20·38
44·67	22·10
48·55	23·89
52·85	25·70

Series V

T°K	C_p
273·93	94·82
279·84	96·80
285·62	98·76
291·49	100·76
297·75	103·04

sample 4 went from 0·816 to 0·810. When more care was taken to keep the calorimeter cool during soldering operations, subsequent samples did not undergo any decomposition. The heat capacity data have been corrected for the presence of solid and gaseous CO as well as for the heat effect associated with the sublimation of the CO. These corrections did not exceed 0·2 per cent below 50°K and 0·1 per cent above 70°K. The molar heat capacity of the enclosed CO in the clathrate was obtained from the slope of the heat capacity-composition isotherms, i.e., plots of the heat capacity of 3-β quinol. yCO against y, for selected temperatures. With few exceptions the points fell on a straight line for each temperature in the 15–300°K range with the deviations falling within the range of the experimental uncertainties of the observed values for C_p. Values of the molar heat capacity of the clathrated CO obtained in this manner for selected temperatures are given in Table 5 along with smoothed values for the same temperatures. The dependence of the heat capacity on temperature is illustrated in Fig. 2.

The heat capacity of 3 moles of β-quinol at selected temperatures is also listed in Table 5 and has been determined from the $y = 0$ intercepts of the heat capacity-composition isotherms for selected temperatures.

The entropy of each of the CO clathrates at 298·15°K was evaluated in the usual fashion by

Table 2. Experimental heat capacity of carbon monoxide clathrate No. 2. $3C_6H_4(OH)_2 \cdot 0{\cdot}626\ CO$ in cal deg^{-1} 3 moles β-quinol^{-1} (0·1230 moles of clathrate in the calorimeter)

Series I

T°K	C_p
59·16	29·41
62·03	30·50
65·11	31·62
68·39	32·75
71·94	33·85
75·55	34·98
79·22	36·13
83·04	37·40
87·32	38·67
91·95	39·99
96·40	41·21
100·93	42·42
105·62	43·84
110·28	45·11
115·07	46·59
120·13	48·07
125·32	49·58
130·54	50·97
135·78	52·56
141·03	53·88
146·31	55·56
151·61	57·16

Series II

T°K	C_p
149·47	56·46
154·66	58·20
160·07	59·75
165·52	61·47
170·86	62·86
176·26	64·62
181·71	66·27
187·22	67·83
192·77	69·68

Series III

T°K	C_p
54·97	27·80
57·91	29·06
60·94	30·10

Series IV

T°K	C_p
15·02	3·37
16·03	4·29
17·20	5·18
19·18	6·84
21·46	8·77
23·57	10·37

Series V

T°K	C_p
13·93	2·67
15·64	3·90
17·06	5·10

Series V—contd.

T°K	C_p
19·11	6·81
21·60	8·80
23·74	10·52
25·83	11·94
28·32	13·50
30·96	15·16
33·42	16·77
35·88	18·33
38·34	19·67
40·97	21·18
43·80	22·73
46·73	24·14
49·74	25·55
52·79	26·91
55·96	28·17
59·32	29·45
62·85	30·81
66·60	32·14

Series VI

T°K	C_p
19·07	6·71
21·58	8·75
23·92	10·57
26·62	12·44
29·52	14·26
32·07	15·84
34·53	17·46
40·11	20·74
43·01	22·31
45·99	23·78
49·17	25·29
52·58	26·80

Series VII

T°K	C_p
190·16	68·94
195·79	70·63
201·93	72·70
207·88	74·51
213·86	76·40
219·71	78·26
225·60	80·18
231·92	82·28
238·47	84·46
244·99	86·58
251·35	88·74
257·54	90·87
263·62	92·82
269·71	94·81
275·99	97·06
282·35	99·27
288·60	101·07
294·57	103·30
299·98	105·77

Series VIII

T°K	C_p
210·70	75·36
221·31	78·74
227·74	80·90
234·03	82·97
240·20	85·16

Series IX

T°K	C_p
58·36	29·13
61·17	30·17
64·08	31·31
67·17	32·34

Series X

T°K	C_p
187·93	68·03
193·69	70·02
199·87	71·91
206·24	73·89
213·70	76·52
219·72	78·51
225·80	80·40

Series XI

T°K	C_p
178·16	65·22
183·42	66·92
189·02	68·63
194·88	70·35
200·84	72·24
206·84	74·30
212·87	76·10
219·11	78·08
225·37	80·13
231·56	82·35
237·69	84·31
243·88	86·36
250·15	88·31
256·32	90·36

Series XII

T°K	C_p
188·14	68·25
193·78	70·03
199·65	71·86
205·72	73·65
211·99	75·77
218·14	77·75
224·42	79·78
230·97	82·14
237·39	84·13
243·69	86·20
249·87	88·39
256·13	90·14

Table 3. *Experimental heat capacity of carbon monoxide clathrate No.* 3. $3C_6H_4(OH)_2 \cdot 0.757$ CO *in cal deg*$^{-1}$ 3 *moles* β-*quinol*$^{-1}$ (0·1275 *moles of clathrate in the calorimeter*)

Series I

T°K	C_p
53·91	28·31
56·67	29·38
59·24	30·44
61·82	31·43
64·57	32·43
67·81	33·71
71·55	34·91
75·35	35·99
79·21	37·28
83·32	38·60
87·68	40·06
92·29	41·34
97·13	42·65
102·00	44·07
106·74	45·42
111·63	46·87
116·92	48·47
122·31	49·97
127·53	51·55
133·34	53·30
139·40	55·08
144·94	56·61

Series II

T°K	C_p
143·22	56·17
148·75	57·91
154·67	59·53
160·33	61·09
165·80	62·82
171·55	64·59
177·30	66·38
182·90	68·15
188·71	69·93
194·73	71·67
202·70	74·22
208·49	76·13
211·92	76·99
217·79	78·86

Series III

T°K	C_p
215·60	78·15
221·33	79·93
227·28	81·90
236·43	84·93

Series IV

T°K	C_p
226·17	81·81
232·07	83·71
237·97	85·53

Series V

T°K	C_p
235·74	85·09
242·03	87·18
248·22	89·22
254·29	91·08
260·63	93·32
266·92	95·35
273·02	97·48
279·23	99·46
285·52	101·60
291·91	103·92

Series VI

T°K	C_p
54·72	28·60
58·27	29·99
62·06	31·66
65·80	32·98
69·50	34·19
73·23	35·34
76·82	36·37
80·23	37·89
85·02	39·18
89·05	40·51
93·48	41·59
98·33	43·05
103·27	44·44
105·89	45·12
110·85	46·67
115·95	48·13
121·18	49·70
128·37	51·77
134·09	53·23
139·95	55·22
145·62	56·75
151·17	58·46
156·92	60·28
162·69	61·94
168·34	63·62
174·07	65·43
179·85	67·25
188·18	70·02
194·12	71·75
199·95	73·57
205·97	75·49

Series VII

T°K	C_p
14·91	3·51
16·31	4·70
18·33	6·39
20·69	8·36
22·50	9·91
24·16	11·13
25·88	12·38
28·13	13·90
30·95	15·78
34·28	17·97
37·47	19·95
40·83	21·85
44·51	23·86
48·18	25·61
51·94	27·53
55·77	29·05
59·44	30·52

Series VIII

T°K	C_p
16·32	4·71
18·22	6·30
20·41	8·15
22·33	9·74
24·26	11·23
26·89	13·04
30·04	15·20
33·31	17·32
36·83	19·56
40·45	21·67
44·63	23·84
49·13	26·14

Series IX

T°K	C_p
54·94	28·65
58·45	30·13
62·06	31·47
65·99	33·02
70·00	34·47
74·05	35·70

Series X

T°K	C_p
280·60	99·97
286·55	102·03
292·26	103·99
298·47	106·30

Table 4. Experimental heat capacity of carbon monoxide clathrate No. 4. $3C_6H_4(OH)_2 \cdot 0{\cdot}810\,CO$ *in cal deg*$^{-1}$ *3 moles β-quinol*$^{-1}$ (0·1355 *moles of clathrate in the calorimeter*)

T°K	C_p
Series I	
56·16	29·53
59·07	30·80
61·95	31·95
64·87	33·06
67·69	34·05
70·58	34·92
74·16	36·05
78·74	37·51
83·80	39·27
88·99	40·92
94·09	42·25
99·13	43·71
104·14	45·11
109·82	46·78
115·82	48·53
121·20	50·13
126·43	51·64
132·13	53·27
138·28	54·77
143·98	56·57
149·21	58·22
Series II	
147·41	57·72
152·64	59·26
Series II (continued)	
157·96	60·76
163·40	62·48
168·69	63·97
174·16	65·67
179·85	67·52
185·52	69·24
191·07	70·93
196·51	72·70
202·18	74·70
208·09	76·61
213·88	78·14
219·88	80·26
226·38	82·37
232·81	84·22
238·82	86·25
Series III	
239·21	86·74
245·07	88·55
251·14	90·52
257·07	92·76
263·22	94·83
269·57	96·77
275·91	98·64
Series III (continued)	
282·27	101·20
288·54	103·17
294·37	105·44
299·77	107·29
Series IV	
52·99	28·20
56·05	29·51
59·06	30·77
62·06	31·98
64·90	33·08
67·82	34·09
70·78	35·10
73·76	35·94
Series V	
14·35	3·25
15·62	4·06
16·75	5·05
18·75	6·77
21·25	8·96
23·34	10·79
25·37	12·24

the graphical integration of C_p-log T plots from 14·79°K to 298·15°K and from 0 to 14·79°K by extrapolating the heat capacity data with the function:

$$C_p = 3[3(240/T)_D + 3(81{\cdot}7/T)_E] + y[3(140/T)_E + 2(62/T)_E]$$

which represents C_p for $3C_6H_4(OH)_2 \cdot yCO$ over the 15–60°K range to within ±1 per cent. The terms in the first bracket consist of three Debye and three Einstein functions per mole of β-quinol whereas the second bracketed expression applies to the y moles of guest CO with which are associated one three-dimensional Einstein function for the vibrational or "rattling" heat capacity and one two-dimensional function for the librational motion.

The molar entropy of clathrated CO at 298·15°K obtained from an entropy-composition isotherm at this temperature was found to be 20·94 ± 0·20 cal deg^{-1} mole^{-1}, assuming the validity of the third law of thermodynamics for these clathrate systems. From the $y = 0$ intercept of the same isotherm, the entropy of three moles of β-quinol at 298·15°K was

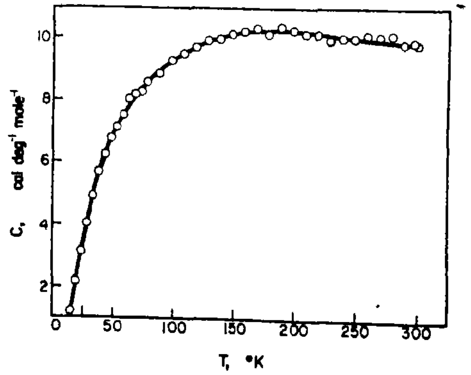

FIG. 2. Molar heat capacity of occluded CO in the β-quinol clathrate.

Table 5. Smooth values of the heat capacity of the CO clathrates in cal deg^{-1} 3 moles β-quinol^{-1} at selected temperatures

T°K	C			
	$y = 0{\cdot}460$	0·626	0·757	0·810
15	3·20	3·40	3·56	3·65
20	7·17	7·54	7·79	7·90
25	10·82	11·37	11·56	11·96
30	13·91	14·56	15·17	15·32*
35	16·94	17·76	18·40	18·65*
40	19·75	20·68	21·41	21·70*
45	22·27	23·30	24·41	24·42*
50	24·53	25·66	26·55	26·87
55	26·63	27·83	28·70	29·05
60	28·55	29·74	30·78	31·15
65	30·31	31·59	32·70	33·10
70	31·96	33·25	34·35	34·80
75	33·48	34·82	35·94	36·30
80	35·15	36·38	37·52	37·89
90	37·98	39·43	40·63	41·06
100	40·72	42·20	43·52	44·08
110	43·49	45·12	46·42	47·00
120	46·52	48·02	49·33	49·88
130	49·39	50·91	52·27	52·68
140	52·14	53·73	55·14	55·52
150	55·02	56·66	58·18	58·44
160	58·05	59·74	61·08	61·38
170	61·06	62·74	64·12	64·38
180	64·26	65·73	67·37	67·53
190	67·30	68·80	70·40	70·63
200	70·42	72·04	73·45	74·00
210	73·62	75·24	76·58	77·14
220	76·90	78·44	79·76	80·26
230	80·19	81·71	83·04	83·50
240	83·51	84·94	86·59	86·73
250	86·82	88·30	89·78	90·23
260	90·08	91·63	93·10	93·75
270	93·44	95·03	96·42	96·91
280	96·88	98·40	99·86	100·28
290	100·24	101·88	103·22	103·86
298·15	103·20	104·84	106·21	106·72
300	103·86	105·48	106·84	107·37

*Interpolated values.

found to be 100·28 cal deg^{-1} to be compared with 100·4 and 99·8 cal deg^{-1}, reported by PARSONAGE and STAVELEY(5) for the entropy of 3 moles of β-quinol based on the heat capacities of the clathrates of methane, and argon respectively.

The heat capacity of clathrated CO *at low temperatures*

It is assumed that the heat capacity of clathrated molecules at low temperatures is composed of two contributions which, to a rough approximation, are taken to be separable.(6) These contributions consist of the three-dimensional oscillations of the center of mass or so called rattling motion, and the two-dimensional librations of the molecular axis in a hindering potential of the form, $V = (V_0/2)(1-\cos 2\theta)$. It has been found previously(1) that these contributions, to the harmonic oscillator approximation, accounted for the heat capacity from 15 to 80°K if the rattling frequency was taken as 97·3 cm^{-1} and the librational frequency as 43·1 cm^{-1}, corresponding to a barrier $V_0 = 691$ cal mole^{-1} restricting the rotation.

The proper analysis of the heat capacity data should take into consideration the anharmonicity of the rattling motion as well as the hindered rotational behavior of the guest CO molecules which previously has been approximated as a librational motion with the associated heat capacity of a two-dimensional harmonic oscillator.(1) For the latter motion we now introduce the more realistic two-dimensional hindered rotator model and associated equations for use in the calculation of its contributions to the thermodynamic properties of clathrated guest diatomic molecules.

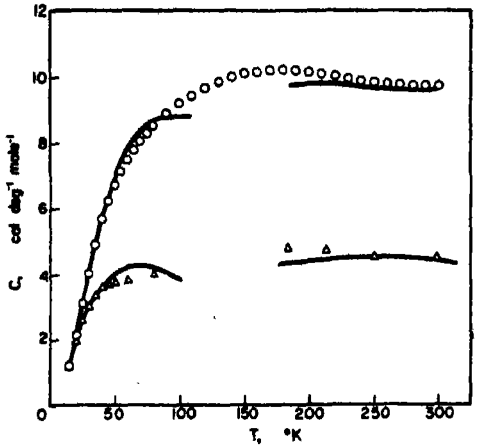

FIG. 3. Comparison of smoothed molar heat capacity of occluded CO in the β-quinol clathrate with the calculated heat capacity.

(a) Upper left curve: $C_{\text{total}} = C_{3^\circ\text{H.O.}}(\nu = 104{\cdot}3\ \text{cm}^{-1}) + C_{2^\circ\text{h.r.}}(V_0 = 745\ \text{cal mole}^{-1})$.

(b) Upper right curve: $C_{\text{total}} = C_{CCM} + C_{2^\circ\text{h.r.}}(V_0 = 2867\ \text{cal mole}^{-1})$.

(c) Lower left curve: $C_{2^\circ\text{h.r.}}$ with $V_0 = 745$ cal mole^{-1}.

(d) Lower right curve: $C_{2^\circ\text{h.r.}}$ with $V_0 = 2867$ cal mole^{-1}.

O—Smoothed experimental heat capacity; △—lower left: $C_{\text{exp}} - C_{3^\circ\text{H.O.}(\nu=104\cdot3\text{cm}^{-1})} = C_{\text{rot}}$; △—lower right: $C_{\text{rot}} = C_{\text{exp}} - C_{CCM}$ (heat capacity of CO according to classical cell model with $\Lambda/k = 3906°$ and $(V^*/V)^2 = 0{\cdot}95$).

The partition function of the two-dimensional hindered rotator has been obtained by an approximation method analogous to the procedure first used by PITZER and GWINN(7) for the one-dimensional case, the internally restricted rotation of co-axial tops, and later by HILL(8) for similar type problems of localized adsorption.

The approximation consists of writing the partition function for the hindered rotator in the form $Q_{hr} = Q_f\, q_{qmo}/q_c$, where Q_f is the classical phase integral for the rigid rotator in the potential field, and q_{qmo} and q_c are partition functions for a quantum mechanical and a classical harmonic oscillator, respectively, in two dimensions. The derivations of the partition function and thermodynamic functions are given in the appendix and result in functions for the two-dimensional hindered rotator which are sums of contributions of a two-dimensional harmonic oscillator with a frequency $\nu = (1/\pi c)(V_0/2I)^{1/2}$ plus functions expressed in terms of probability integrals in the form extensively studied by MILLER and GORDON:(9)

$$F(X) = \exp(-X)^2 \int_0^X \exp(y^2)\, dy$$

where $X = (V_0/kT)^{1/2}$ in our case.

Thus for the heat capacity of the two dimensional hindered rotator:

$$C_{2^\circ\text{h.r}} = \frac{R}{2}\left[\frac{X^3}{F(X)} - 1\right] - \frac{RX}{4F(X)}[1 + X/F(X)] + C_{qmo} \qquad (1)$$

where C_{qmo} is the heat capacity for a two-dimensional harmonic oscillator. Although this equation presumably takes into account the effect of hindered rotational motion of guest diatomic molecules over the entire temperature range of concern, an accurate calculation of the contribution of the rattling motion to the heat capacity is somewhat less certain.

At low temperatures we assume again that the vibrational motion of the CO molecule in the host cavity may be described as a three-dimensional isotropic harmonic oscillator. On this basis, with $\nu = 104{\cdot}3$ cm^{-1} for the rattling vibration and a barrier, $V_0 = 745$ cal mole^{-1}, hindering the rotational motion, the heat capacity is well accounted for in the 15–40°K range as indicated in Fig. 3.

In comparison with the previous analysis,$^{(1)}$ the frequency of the rattling motion has been increased by 7 cm^{-1} and the barrier increased by 54 cal $mole^{-1}$.

It is to be noted, however, that this analysis accounts for the heat capacity only up to 40°K whereas the previous analysis,$^{(1)}$ based in part on the harmonic oscillator approximation for the librational motion, accounted for the heat capacity from 15° to ~90°K.

It may be that the latter correlation of the heat capacity to as high a temperature as 90°K by the use of the harmonic oscillator approximation was fortuitous since presumably the hindered rotator model, which approaches the harmonic oscillator model at low temperatures, should be more appropriate at higher temperatures where libration becomes free rotation to an increasing extent with increasing temperature. Accordingly, assuming the validity of equation (1), it would appear that this semiempirical analysis is an overly simplified approximation which fails to take into account complexities that become significant above the vicinity of ~40°K.

Table 6. The partial molal heat capacity of clathrated CO *and the heat capacity of three moles of β-quinol at selected temperatures*

T°K	C_{CO}(obs.) (cal deg^{-1} $mole^{-1}$)	C_{CO} (smoothed) (cal deg^{-1} $mole^{-1}$)	C_P (cal deg^{-1} 3 $moles^{-1}$)
15	1·20	1·20	2·66
20	2·15	2·15	6·18
25	3·11	3·11	9·39
30	4·04	4·04	12·06
35	4·90	4·90	14·69
40	5·68	5·68	17·16
45	6·23	6·23	19·40
50	6·72	6·72	21·44
55	7·10	7·13	23·34
60	7·48	7·48	25·07
65	8·01	7·79	26·61
70	8·16	8·06	28·18
75	8·22	8·30	29·66
80	8·52	8·52	31·06
90	8·90	8·90	33·90
100	9·23	9·20	36·47
110	9·43	9·44	39·21
120	9·65	9·67	42·03
130	9·87	9·86	44·76
140	9·90	10·01	47·58
150	10·06	10·12	50·40
160	10·15	10·18	53·39
170	10·23	10·22	56·36
180	10·05	10·23	59·58
190	10·26	10·22	62·52
200	10·17	10·17	65·76
210	10·04	10·12	69·00
220	10·01	10·03	72·24
230	9·85	9·97	75·58
240	9·89	9·92	78·85
250	9·89	9·86	82·21
260	10·09	9·84	85·41
270	9·93	9·80	88·86
280	9·98	9·79	92·22
290	9·74	9·78	95·79
298·15	9·78	9·76	98·72
300	9·75	9·76	99·42

The thermodynamic properties of clathrated CO *at* 25°C

Consideration of the high molar heat capacity (~ 10 cal deg^{-1} mole^{-1}) of occluded CO in the range 100–300°K compels one to abandon the assumption of free rotation of CO for which the combined rotational and vibrational heat capacity of CO in the host cavity would not exceed $\sim 4R$. It is in fact necessary to assume that the barrier restricting rotation in the high temperature region is substantially larger than the barrier of 745 cal mole^{-1} found in the low temperature region since the heat capacity associated with a restricted rotator of the latter nature has already fallen to $\sim 2{\cdot}3$ cal mole^{-1} at 300°K, and in this sense is essentially a free rotator at 300°K. Accordingly, since we are dealing with hindered rotation, the assumption of separability of the rotational and rattling motions is, strictly speaking, not valid, a possibility anticipated by VAN DER WAALS.(6)

For the present, we propose an interpretation of the heat capacity and entropy data for clathrated CO, and the pressure isotherm constant, based on the classical equations of VAN DER WAALS(2) for the thermodynamic properties of clathrates of monatomic, or freely rotating polyatomic, molecules corrected for restricted rotation by the use of the equations presented in the appendix for the two-dimensional hindered rotator. Thus, for the total molar heat capacity of clathrated CO:

$$C = C_{CCM} + C_{2^{\circ}\mathrm{h.r}} \tag{2}$$

where the last term is given by equation (1) and C_{CCM} is the molar heat capacity of the occluded molecule according to the classical cell model:(2)

$$\begin{aligned} C_{CCM} &= \\ R[1{\cdot}5 &+ (\Lambda/kT)^2(V^*/V)^4(1/g^2)[(V^*/V)^4 g g_{11} \\ &+ 4gg_{mm} - (V^*/V)^4 g_1^2 - 4g_m^2 \\ &- 4(V^*/V)^2 g g_{1m} + 4(V^*/V)^2 g_1 g_m]; \end{aligned} \tag{3}$$

$$\Lambda = Z\bar{\epsilon}^{1/2}\epsilon_{\mathrm{CO}}^{1/2};\ V^* = [(\bar{\sigma}+\sigma_{\mathrm{CO}})/2]^3\ ;\ V = 2^{-1/2}a^3,$$

(with a, the cavity radius $= 3{\cdot}95$ Å(2)); and the "g functions" are complicated integrals dependent on the dimensionless parameters Λ/kT and V^*/V. ϵ_{CO} and σ_{CO} are the characteristic energy parameters of the familiar Lennard–Jones expression for pure CO, and $\bar{\epsilon}$ and $\bar{\sigma}$ are the average corresponding parameters for the Z atoms comprising the cavity wall.

Application of equation (2) to determine $C_{2^{\circ}\mathrm{h.r.}}$ and, accordingly, the barrier restricting the rotation of guest CO molecules, depends on a knowledge of the parameters Λ/kT and V^*/V and hence on $Z\bar{\epsilon}^{1/2}$ and $\bar{\sigma}$ for the lattice as well as ϵ_{CO} and σ_{CO} for the guest CO molecule. Although values for the latter based on second virial coefficient data are available(10) it is necessary to assign values to $Z\bar{\epsilon}^{1/2}$ and $\bar{\sigma}$ which will not only account for the heat capacity but the other thermodynamic properties as well.

In order to facilitate the determination of the appropriate set of the dimensionless parameters, Λ/kT and V^*/V, the "g functions" which are dependent on these parameters have been calculated with an IBM 7090 computer at closely spaced intervals of Λ/kT and V^*/V over a range of values that encompasses those for the usual guest molecules of clathrate systems. In turn, the parts of each of the thermodynamic functions dependent on the same dimensionless parameters have been computed for the same selected values of the parameters. The resulting values of the "g functions" which we have obtained are in good agreement with the previously published tables(11) limited to a narrower range of Λ/kT and V^*V.

Application of equation (2) for the heat capacity and the corresponding equations for the entropy and the equilibrium pressure of formation of the CO clathrate then involves an iterative procedure in which the assignments are made for Λ/kT and V^*/V and the hindering potential V_0 which will account for the experimental values for the heat capacity, entropy and the pressure isotherm constant. For the best correlation of the observed data, we find $(V^*/V)^2 = 0{\cdot}95$ and $\Lambda/k = 3906°$ from which we obtain $Z(\bar{\epsilon}/k)^{1/2} = 390$ and $\bar{\sigma} = 3{\cdot}22$ Å for the lattice cavity parameters based on the use of $\epsilon_{\mathrm{CO}}/k = 100{\cdot}2°$ and $\sigma_{\mathrm{CO}} = 3{\cdot}763$ Å for the interaction parameters for CO.(10) For the barrier restricting rotation we obtain $V_0 = 2867$ cal mole^{-1} which is approximately four times the barrier indicated by the heat capacity data at low temperatures. However, in view of the naive model assumed and the semiempirical approaches used in determining the barriers, the conclusion that the barrier is dependent on temperature is admittedly tentative.

Table 7. Comparison of the observed and calculated thermodynamic properties of CO in the β-quinol clathrate at 25°C*

Property	Observed	Calculated
$K = p(1-y)/y$ atm	8·9	8·89
C cal deg^{-1} mole^{-1}	9·76	9·64
S cal deg^{-1} mole^{-1}	20·94	19·83

* Based on $Z(\bar{\epsilon}/k)^{1/2} = 390$; $\bar{\sigma} = 3{\cdot}22$ Å; $V_0 = 2867$ cal mole^{-1}.

For the proposed "best" assignment the calculated properties are given in the final column in Table 7 for comparison with the observed properties listed in the second column. Although very good agreement exists for the pressure isotherm constant and the heat capacity at 25°C, the calculated entropy is ~5 per cent too low.

To some extent the direct contrasting of the "low" and "high" temperature barriers restricting the rotation of guest CO is probably not justified since the basis for the calculation of the contribution to the vibrational heat capacity is different in the two cases and C_{rot} is accordingly obtained by two different procedures. Nevertheless, it appears quite likely for the following reasons that the barrier indicated for the "high temperature region" is significantly larger than the barrier restricting rotation in the "low temperature region".

The interpretation of the data at 25°C leading to a barrier of ~2·9 kcal is in qualitative agreement with the spectroscopic observations of BALL and MCKEAN(12) who have observed strong absorption for the β-quinol clathrate of CO at 2133 cm^{-1} in the region of the forbidden Q branch of CO with quite uncertain indications of P and R branches. It is difficult to reconcile the "low temperature" barrier of 745 cal mole^{-1} with the spectroscopic data at room temperature since for this low barrier more pronounced P and R branches would be expected. Moreover, it is only possible to account for the rather large heat capacity of clathrated CO in the vicinity of 300°K by the use of a large barrier unless we assume that drastic modification of the host lattice is occurring for which there is no evidence.

The low value obtained for the barrier restricting the rotation of clathrated CO in the region of low temperatures is consistent with the values found by a variety of methods for the barriers for other diatomic molecules in their respective clathrates. Magnetic data(13,14) indicate barriers of 127 cal mole^{-1} for O_2(13) and ~420 cal mole^{-1} for NO;(14) pure quadrupole resonance spectra(15) and heat capacity data(1) for clathrated N_2 indicate 960 and 511 cal mole^{-1}, respectively, for V_0 at low temperatures. With the exception of the higher value for the barrier for N_2, based on the temperature dependence of the pure quadrupole resonance spectrum of N_2 in the β-quinol clathrate of N_2,(15) the barriers restricting rotation of these molecules, and CO, in the corresponding clathrates increase more or less regularly as indicated in Fig. 4 with increasing $\bar{\sigma}$, the collision diameter, which is a measure of "snugness of fit" of the guest molecule in the cavity. Alternatively, for this group of diatomic molecules, including CO, the restricting barrier increases with increasing quadrupole moment in a regular manner as shown graphically on the left side of Fig. 4. Accordingly, a barrier of ~1 kcal, or less, restricting the rotation of CO in the clathrate at low temperatures would appear to be quite reasonable in comparison with the barriers for other diatomic molecules in their β-quinol clathrates at low temperature.

The apparent increase of the restricting barrier with increasing temperature is also plausible from a theoretical point of view and has been anticipated by VAN DER WAALS.(6) For the excited vibrational states of the occluded CO in the host cavity, the probability density will be larger near the cavity wall in comparison with the ground state. Hence with increasing temperature an increasing fraction of CO molecules will be aligned along the host cavity wall and accordingly be subjected to higher barriers restricting rotation than is characteristic of the ground state.

In view of the apparent dependence of the restricting barrier on temperature as well as the uncertainty associated with the extent of anharmonicity of the vibrational motion of the guest molecules in the cavities, an accurate interpretation of the dependence of the heat capacity on temperature in the intermediate range is precluded at this time. Nevertheless, we find that the apparent barrier of 2867 cal mole^{-1} accounts fairly well for the heat capacity of clathrated CO, down to 250°K as illustrated in Fig. 3, below which the calculated rotational heat capacity is too small by ~6 and 10 per cent at 200 and 180°K, respectively.

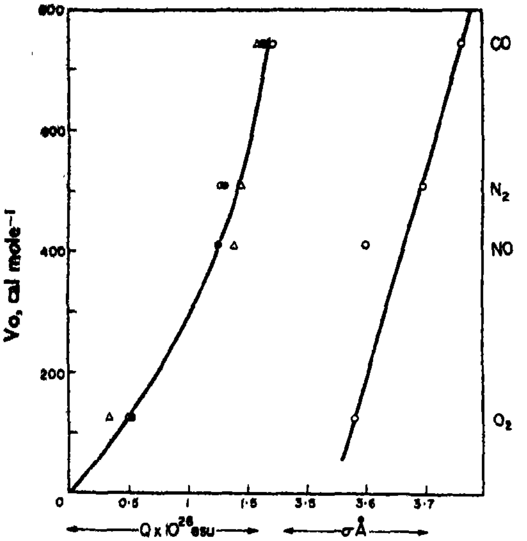

FIG. 4. Dependence of barrier restricting rotation of diatomic molecules in β-quinol clathrates on (a) quadrupole moment, Q-left; (b) collision diameter, σ-right. Quadrupole moments: △—GORDY W., SMITH W. V. and TRAMBARULO R., *Microwave Spectroscopy*, p. 345. Wiley, New York (1953); O-JANSEN L. and DEWETTE F. W., *Physica* 21, 83 (1955); ● HILL R. M. and SMITH W. V., *Phys. Rev.* 82, 451 (1951); Collision diameters—Ref. 10. V_0 data: CO—this research; N$_2$—Ref. 1; NO (approx.)—Ref. 14; O$_2$—Ref. 13.

As an alternative to the calculation of the vibrational heat capacity, C_{CCM}, according to the classical cell model, *it is of interest to note that the model* employed to account for the heat capacity at low temperatures, but with a different assignment for the vibrational frequency and potential restricting the rotation of CO, accounts accurately for the heat capacity and entropy of the occluded CO at 25°C and holds reasonably well for the heat capacity down to ~120°K. For a vibrational frequency, $\nu = 74$ cm^{-1} for the three dimensional isotropic harmonic oscillatory motion of CO in the cavity and a restricting barrier of 2027 cal mole^{-1}, the calculated heat capacity and entropy are 9·78 cal deg^{-1} mole^{-1} and 20·97 cal deg^{-1} mole^{-1}, respectively, at 25°C, essentially in exact agreement with the observed values. Hence by this approximation as well, the barrier restricting rotation in the high temperature region appears to be in the vicinity of 2 kcal mole^{-1}.

Acknowledgements—The authors wish to thank the Computation Center, Massachusetts Institute of Technology, for an allocation of time on the IBM 7090 computer for the calculation of the "*g* functions" for the classical cell model. The authors also thank Mr. G. ROPER for his assistance with the measurements.

REFERENCES

1. COULTER L. V., STEPAKOFF G. L. and ROPER G. C., *J. Phys. Chem. Solids* **24,** 171 (1963).
2. VAN DER WAALS J. H., *Trans. Faraday Soc.* **52,** 184 (1956); VAN DER WAALS J. H. and PLATTEEUW J. C., *Advanc. chem. Phys.* **2,** 1 (1959). Also see PARSONAGE N. G. and STAVELEY L. A. K., *Mol. Phys.* **2,** 212 (1959) for the equations for C and S.
3. FURMAN N. H. and WALLACE J. H., JR., *J. Amer. chem. Soc.* **52,** 1443 (1930).
4. COULTER L. V., SINCLAIR J. R., COLE A. and ROPER G. C., *J. Amer. chem. Soc.* **81,** 2986 (1959).
5. PARSONAGE N. G. and STAVELEY L. A. K., *Mol. Phys.* **3,** 59 (1960).
6. VAN DER WAALS J. H., *J. Phys. Chem. Solids* **18,** 82 (1961).
7. PITZER K. S. and GWINN W. D., *J. chem. Phys.* **10,** 428 (1942).
8. HILL T. L., *J. chem. Phys.* **16,** 181 (1948); *Introduction to Statistical Thermodynamics*, p. 172. Addison-Wesley, Reading, Mass. (1960).
9. MILLER W. L. and GORDON A. R., *J. phys. Chem.* **35,** 2788 (1931).
10. HIRSCHFELDER J. O., CURTIS C. F. and BIRD R. B., *Molecular Theory of Gases and Liquids*, p. 1111. Wiley, New York (1954).
11. LENNARD-JONES J. E. and DEVONSHIRE A. F., *Proc. Roy. Soc.* **A163,** 53 (1937); **165,** 1 (1938); PRIGOGINE I. and GARIKIAN G., *J. Chim. Phys.* **45,** 273 (1948); WENTORF R. H., JR., BUEHLER R. J., HIRSCHFELDER J. O. and CURTISS C. F., *J. chem. Phys.* **18,** 1494 (1950).
12. BALL D. F. and MCKEAN D. C., *Spectrochim. Acta* **18,** 933 (1962).

13. MEYER H., O'BRIEN M. C. M. and VAN VLECK J. H., *Proc. Roy. Soc.* **A243**, 414 (1957).
14. VAN VLECK J. H., *J. Phys. Chem. Solids* **20**, 241 (1961).
15. MEYER H. and SCOTT T. A., *J. Phys. Chem. Solids* **11**, 215 (1959).
16. STERNE T. E., *Proc. Roy. Soc., Lond.* **A130**, 551 (1931); FLAMMER C., *Spheroidal Wave Functions*, Stanford University Press (1957); STRATTON J. A., MORSE P. M., CHU L. J., LITTLE D. C. and CORBATO F. J., *Spheroidal Wave Functions*, Technology Press, Cambridge, Mass. (1956).

APPENDIX

The two-dimensional hindered rotator

The rigorous formulation of the equations for the hindered rotational properties of a clathrated diatomic molecule (or a diatomic molecule in its condensed state) necessitates the summation over the eigen values of the spheroidal wave function.(16) Since this would be a sizable task even with high speed computers, it was considered adequate to utilize the approximation technique for the construction of the quantum mechanical partition function for the hindered rotator as described by PITZER and GWINN.(7) This technique has also been used by HILL(8) for the problem of localized adsorption and hindered rotation on an adsorbing surface.

The approximation consists in writing the partition function for the hindered rotator in the form:

$$Q_{\text{h.r.}} = Q_f \frac{q_{qmo}}{q_c} \tag{A1}$$

where Q_f is the classical phase integral for the rigid rotator in the potential field, and q_{qmo} and q_c are partition functions for a quantum mechanical and a classical harmonic oscillator, respectively (in two dimensions, in this case). Thus, as summarized by HILL,(8) in the limit as $V_0/kT \to \infty$, Q_f must approach a classical oscillator, q_c, so that $Q_{\text{h.r.}}$ approaches q_{qmo}. On the other hand, as $V_0/kT \to 0$, q_{qmo} approaches q_c so that $Q_{\text{h.r.}}$ becomes Q_f. In order to formulate Q_f in this case, it is assumed that one can employ the axially symmetrical function,

$$V = (1/2)V_0(1-\cos 2\theta)$$

as discussed by MEYER, O'BRIEN and VAN VLECK.(13) Thus, the positions of $\theta = 0$ and $\theta = \pi$ are positions of equal minimum potential energy, which is in accord with the relative orientation of the diatomic molecule with respect to the oxygen hexagons of the cavity.(15) Thus the classical Hamiltonian for rotation becomes:

$$H = \frac{p_\theta^2}{2I} + \frac{p_\phi^2}{2I\sin^2\theta} + (1/2)V_0(1-\cos 2\theta) \tag{A2}$$

The classical integral can be written as:

$$Q_f = \frac{1}{2h^2}\int_0^{2\pi}\int_0^{\pi}\int_{-\infty}^{\infty}\int_{-\infty}^{\infty} \exp(-H/kT)\,\mathrm{d}p_\theta \mathrm{d}p_\phi \mathrm{d}\theta \mathrm{d}\phi \tag{A3}$$

Substitution of (2) into (3) and integration over the momenta and ϕ yields:

$$Q_f = \frac{2\pi^2 IkT}{h^2}\int_0^{\pi} \exp\{-V_0/kT(1-\cos 2\theta)\}\sin\theta\,\mathrm{d}\theta \tag{A4}$$

The factor 2 in the denominator of (3) arises from the fact that there are two positions of equal minimum potential energy in the cavity. By use of the following transformations:

$$(1/2)(1-\cos 2\theta) = 1-\cos^2\theta$$

$$z = \cos\theta$$

$$V_0/kT = X^2$$

(4) becomes:

$$Q_f = \frac{2\pi^2 IkT}{h^2}\exp(-X^2)\int_{-1}^{1}\exp(X^2 z^2)\,\mathrm{d}z \tag{A5}$$

which can be further simplified by defining the new variable $y = Xz$ and redefining the limit of integration. Thus:

$$Q_f = \frac{4\pi^2 IkT}{h^2}\frac{\exp(-X^2)}{X}\int_0^{X}\exp(y^2)\,\mathrm{d}y \tag{A6}$$

In order to investigate the limiting properties of (6) as V_0/kT approaches infinity, use is made of the relation between the barrier V_0 and the librational frequency, $(1/\pi)(V_0/2I)^{1/2}$. Thus, if one defines the term $[(2\pi^2 IkT)/h^2]$ as B, then:

$$V_0/kT = B(h\nu/kT)^2 \text{ or } B = X^2 q_c \quad \text{(A7)}$$

Substitution of (7) into (6) gives:

$$Q_f = 2Xq_c F(X) \quad \text{(A8)}$$

$$F(X) = \exp(-X^2)\int_0^X \exp(y^2)\,\mathrm{d}y \quad \text{(A9)}$$

The $F(X)$ function has been studied extensively by MILLER and GORDON(9) and its limiting properties and numerical integration have been given by these workers. The relations of immediate use here are the following:

$$\lim_{X\to\infty} XF(X) = 1/2 \quad \text{(A10)}$$

$$\frac{\mathrm{d}F(X)}{\mathrm{d}X} = 1-2XF(X) \quad \text{(A11)}$$

Thus, when the limit of (A8) is taken as $X \to \infty$, $Q_f = q_c$ which justifies the correct asymptotic behavior of Q_f. If (A8) is substituted into (A1), one has finally:

$$Q_{\text{h.r.}} = 2XF(X)q_{qmo} \quad \text{(A12)}$$

From equation (A11) and the usual statistical mechanical relations, the following relations for the thermodynamic functions are obtained:

$$F = -RT(\ln X + \ln F(X) + \ln 2) + F_{qmo} \quad \text{(A13)}$$

$$U = -RT[1/2 + (1/2)X/F(X) - X^2] + U_{qmo} \quad \text{(A14)}$$

$$S = -R[1/2 + (1/2)X/F(X) - X^2] + R[\ln X + \ln F(X) + \ln 2] + S_{qmo} \quad \text{(A15)}$$

$$C = (1/2)R[X^3/F(X) - 1] - [(1/4)RX/F(X)][1 + X/F(X)] + C_{qmo} \quad \text{(A16)}$$

Values of the function $F(X)$ for selected values of X, taken from the extensive listing of MILLER and GORDON,(9) are given in the second column of Table A-1. In columns 3 and 4 the heat capacity and entropy functions in equations (A16) and (A15), exclusive of the harmonic oscillator contributions, are tabulated for selected values of X, where $X = (V_0/RT)^{1/2}$. It is seen that for small X, the function $C(X)$ approaches $-R$ cal deg^{-1} mole^{-1} so that equation (16) approaches R, the value for free rotation. On the other hand, for large X, the function $C(X)$ vanishes so that the major contribution to the heat capacity arises from the quantum mechanical oscillator. The function $C(X)$ has a maximum in the vicinity of $X = 2{\cdot}4$. Since the harmonic oscillator term for intermediate values of X has almost attained its limiting value (liberational frequencies for clathrated molecules are known to lie in the 20–60 cm^{-1} range) the total hindered rotational heat capacity can rise above the $2R$ value for the classical oscillator for appropriate values of V_0 and I.

It is noted with interest that below the maximum of the heat capacity curve, equation (A16) is in quantitative agreement with the heat capacity calculated by multiplying PITZER's(7) tables by 2. However, above the maximum (which is of the order of 4·3 cal deg^{-1} mole^{-1}) the rotational heat capacity curve defined by equation (16) falls to R faster than the Pitzer function, for the given value of V_0 and I. (See Fig. 5.)

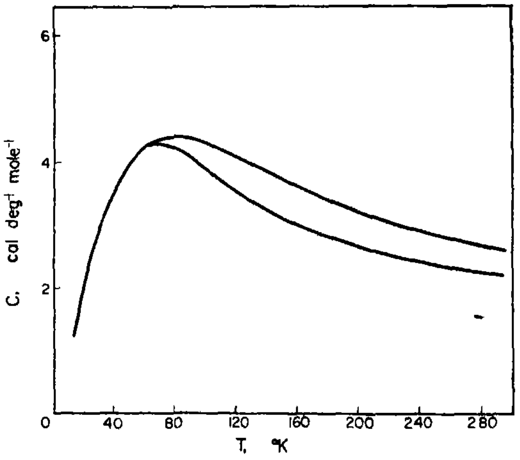

FIG. 5. Comparison of the two-dimensional hindered rotator heat capacity function with 2x Pitzer's function.
$V_0 = 745$ cal mole^{-1}
$I = 14{\cdot}55 \times 10^{-40}$ g cm^2
Upper curve: Pitzer's function.
Lower curve: Two-dimensional hindered rotator.

It is found that the entropy decrease from free rotation calculated from equation (15) is of the order of one e.u. greater than that calculated from twice the value of Pitzer's tables, for barriers and

Table A-1. *The heat capacity and entropy functions of the hindered rotator* $C(X) = C_{\text{h.r.}} - C_{2^\circ qmo}$ *and* $S(X) = S_{\text{h.r.}} - S_{2^\circ qmo}$ where $X = (V_0/kT)^{1/2}$.

X	$F(X)$*	$C(X)$†	$S(X)$‡
0·00	0·000000	−1·987	−∞
0·20	0·194751	−1·987	−7·006
0·40	0·359943	−1·982	−4·254
0·60	0·474763	−1·963	−2·652
0·80	0·532101	−1·907	−1·536
1·00	0·538080	−1·786	−0·6799
1·20	0·507273	−1·564	−0·0916
1·40	0·456507	−1·217	+0·3420
1·60	0·399940	−0·7562	0·6086
1·80	0·346773	−0·2480	0·7280
2·00	0·301340	+0·2033	0·7317
2·20	0·264511	0·5053	0·6615
2·40	0·235313	0·6320	0·5594
2·60	0·212165	0·6221	0·4586
2·80	0·193551	0·5410	0·3718
3·00	0·178271	0·4417	0·3042
3·20	0·165462	0·3534	0·2532
3·40	0·154524	0·2850	0·2146
3·60	0·145042	0·2340	0·1849
3·80	0·136721	0·1970	0·1616
4·00	0·129348	0·1690	0·1429
4·20	0·122761	0·1473	0·1276
4·40	0·116835	0·1302	0·1146
4·60	0·111472	0·1161	0·1041
4·80	0·106593	0·1044	0·0941
5·00	0·102134	0·0946	0·0865
5·50	0·092493	0·0754	0·0703
6·00	0·084543	0·0620	0·0581
6·50	0·077868	0·0519	0·0488
7·00	0·072181	0·0449	0·0424
8·00	0·063000	0·0332	0·0317
10·00	0·050254	0·0217	0·0199

* Ref. 9.

† $C(X) = 0{\cdot}9935[X^2/F(X)-1]-0{\cdot}49675[X/F(X)][1+(X/F(X)]$

‡ $S(X) = -0{\cdot}9935[1+X/F(X)-2X^2]+4{\cdot}576[\log_{10}XF(X)+0{\cdot}3010]$.

moments of inertia relevant to clathrated diatomic molecules.

For the theoretical equilibrium pressure for the reaction $X_2(g) \rightleftharpoons X_{2(\beta\text{-quinol, } s)}$ VAN DER WAALS[(2)] assumed free rotation of guest molecules in the lattice cavities and obtained:

$$P_T = \frac{kT}{2\pi a^3}\,\frac{\exp\{W_{(0)}/kT\}}{g}\,\frac{y}{1-y} = K_T y/1-y \quad \text{(A17)}$$

where $a = 3{\cdot}95$ Å, the average radius of the cavity; g is a complicated integral dependent on the dimensionless parameters Λ/kT and $V^*/V, W_{(0)}$ is the potential energy of the guest molecule at $r = 0$ the center of the cavity; and y is the fraction of host cavities filled by the guest molecules. On taking into account the restricted rotational behavior of diatomic molecules in the host cavities equation (17) becomes

$$P_T = 2\frac{X}{F(X)}\,\frac{q_{co}}{q_{qmo}}K_T\frac{y}{1-y} \quad \text{(A18)}$$

Note added in proof

STAVELEY [*Advanc. Chem. Series*: *Nonstoichiometric Compounds* 39, 218 (1963)] has estimated $V_0 \sim 1200$ cal mole^{-1} based on unpublished data of Grey and

Staveley. To some extent the difference between the barrier estimated by Staveley and that obtained in this research may result from a lack of agreement with respect to the experimental heat capacity data or the assignment of parameters employed in the calculation of C_{CCM} according to equation (2). However, it is to be noted that Staveley's estimate which has been made with the use of the tables of PITZER and GWINN(7) is expected to be less than the "high temperature" barrier reported in this work since $C_{2}{}^{\circ}{}_{\text{h.r.}}$, calculated by equation (1), is less than $2 \times C_{1}{}^{\circ}{}_{\text{h.r.}}$ (where $C_{1}{}^{\circ}{}_{\text{h.r.}}$ is given by PITZER and GWINN(7)) above 80°K as indicated in Fig. 5 for CO.

J. Phys. Chem. Solids Pergamon Press 1963. Vol. 24, pp. 1451–1466. Printed in Great Britain.

ON THE THEORY OF ACCOMMODATION COEFFICIENTS—III

CLASSICAL PERTURBATION THEORY FOR THE THERMAL ACCOMMODATION OF LIGHT GASES

F. O. GOODMAN*

Royal Aircraft Establishment, Farnborough, Hants., England

(*Received* 22 *April* 1963)

Abstract—A new classical theory of thermal energy exchange between gases and solid surfaces is proposed. A perturbation method is used and, because of the inherent errors in this method, the theory is restricted to light gases and small thermal accommodation coefficients. Realistic interaction potentials of the Morse type between the gas atoms and the solid surfaces are used; detailed consideration is given to finding the best possible values of the relevant interaction parameters for the systems considered. The experimental data with which the theory is compared are for the interaction systems He/Ni, He/W, He/Pt, Ne/Fe and Ne/W; it is shown that in each of these cases adequate *quantitative* agreement of the theory with experiment is obtained.

1. INTRODUCTION

PAPERS I(1) and II(2) of this series were published under the general heading "The dynamics of simple cubic lattices". In view of the intended content of this and subsequent papers it seems natural to continue numbering in sequence, but to change the general heading to "On the theory of accommodation coefficients". The first of the author's papers cited above will be referred to hereafter simply as I.

The thermal accommodation coefficient (hereafter abbreviated to "*ac*", or simply to "α") is a measure of the efficiency of energy exchange between a gas and a solid surface in contact with the gas. The meaning and importance of α have been discussed adequately before (see for example Ref. 3), but it may not be out of place to give here a brief discussion of the differences between the theoretical definition used in this paper and the experimental definition of α. In any experimental set-up, α is usually defined as follows: Let T_2 be the temperature of the solid surface and let T_1 be either the temperature or an "average temperature" of the gas atoms impinging on this surface. Similarly, let T_3 be an "average temperature" of gas atoms reflected from this surface. Then α is defined by $T_1-T_3 = \alpha(T_1-T_2)$; this definition involves two "averaging" procedures, and these are over the initial and final gas velocity distributions to obtain T_1 and T_3. From the point of view of the theoretical calculations in this paper, we shall concern ourselves with just one impinging gas atom to which we assign an "effective initial gas temperature" T_1 and an "effective final gas temperature" T_3. Our solid surface will always be initially at 0°K, and the theoretical α which we shall compare with the corresponding experimental ones is defined by $T_1-T_3 = \alpha T_1$.

Several of the definitions and results of I will be used in this paper, and it is unnecessary to discuss them all in detail here. For example, a detailed description of the three-dimensional ("*n*-dimensional" will hereafter be abbreviated to "*nD*") semi-infinite lattice to be used in this paper is given in I, as is the derivation of its "velocity response function" $\dot{X}_3(t)$ which we shall abbreviate to $\dot{X}(t)$. This lattice is an artificial one with nearest-neighbour only central and non-central forces; the motions of this lattice in the x, y and z directions are independent of one another.

---

*Present address: Department of Natural Philosophy, University of Aberdeen.

In I we were concerned with some *qualitative* aspects of the accommodation of He, Ne, A, Kr and Xe on W. In this paper we shall attempt to give a *quantitative* discussion of the accommodation of the two lightest of these gases, He and Ne, on several metals and we shall show that agreement with experiment is possible using a simple classical model. The theory will apply only to clean surface conditions, the effects of surface impurities on the lattice motion(2) and on the values(3) of α being by now well-known. The hope is that the experimental data we use are in fact clean-surface values of α; it is of course very difficult to judge this for any particular data in the literature. Most experimental data so far obtained have probably been dirty-surface data; this problem is discussed more fully by WACHMAN.(3)

The experimental data we have chosen to use are those of RAINES(4) for He/Ni, EGGLETON and TOMPKINS(5) for Ne/Fe, THOMAS and SCHOFIELD(6, 7) for He/W and Ne/W and that for He/Pt cited in Table 1 of Ref. 3. In some of these cases it has been claimed that DEVONSHIRE's quantum theory(8) gives agreement with experiment; the validity of these claims will be discussed later.

A brief survey of previous types of theory would perhaps be desirable at this point; for more detailed discussions the reader is referred to the survey by GILBEY(9) and again to that by WACHMAN.(3)

(i). *Classical hard spheres*

The first theory of *acs* was of this type and was published by BAULE(10) some 50 years ago; both the solid (lattice) and the beam of gas atoms are assumed to be composed of hard spheres. Although useful for rough calculations, this type of theory clearly cannot be expected to yield quantitative agreement with experiment.

(ii). *Continuum theories*

LANDAU(11) in 1935 proposed a theory in which the solid was treated as a continuum and a classical perturbation method was used. He considered a perturbation by a purely repulsive exponential field between the gas atoms and the solid which may be represented by

$$v(z) = Ae^{-2az} \qquad (1.1)$$

However, this theory is probably not valid for any experimental conditions; reasons for this are explained on p. 276 of Ref. 8. In any case, the theory disagrees with experiment.

(iii). *The quantum theory*

The quantum theory of *acs* is due to DEVONSHIRE,(8) and is based on a first order perturbation approach. The interaction potential used was of the Morse type which includes an attractive potential well and is the form of potential we shall use in this paper (see (2.2) and Fig. 2a). Before continuing further, it is necessary to point out that it is shown in Section 4 that a proper consideration of the relevant parameters yields a value of the Morse a of about 1·6 A^{-1} for the systems to be considered. The method used is the well-known(12) "combination-rule" method for determining the interaction parameters for unlike atoms (e.g., for Ne/W) from the corresponding parameters for like atoms (e.g., for Ne/Ne and W/W)

It may seem at first sight that DEVONSHIRE's theory has had some success,(4, 7, 8) but bearing in mind the value $a \approx 1{\cdot}6$ A^{-1} discussed above there are important objections which cannot be overlooked:

(a) Using this "realistic" value of a it seems possible to make the quantum theory agree with some of the experimental data on *acs* which clearly pertain to dirty-surface conditions; these values of α are far higher than those we nowadays believe to be correct. Although the value $a = 1{\cdot}6$ A^{-1} has not been used before, an example of this agreement with high values of α is DEVONSHIRE's(8) fit of data for He/W in which he takes $a = 2$ A^{-1} and $D = 0$. These values of α seem to range from $\alpha \approx 0{\cdot}025$ at 100°K to $\alpha \approx 0{\cdot}055$ at 300°K; they should be compared with the corresponding modern(6, 7) values of $\alpha < 0{\cdot}02$ from 100°K to 300°K.

(b) When the quantum theory is used in conjunction with what are considered to be "clean-surface" values of α, then values of a much smaller than 1·6 A^{-1} are obtained. These much smaller values of a will be recognized in this paper as "unrealistic" values. Examples of this are the value $a \approx 0{\cdot}75$ A^{-1} for He/Ni used by RAINES(4) and the values $a \approx 0{\cdot}7$ and $0{\cdot}8$ A^{-1} respectively for He/W and Ne/W used by one of THOMAS' co-workers.(7)

An example of an unrealistic value of a being used to fit dirty-surface data is afforded by the value $a \approx 0\cdot7\,\text{A}^{-1}$ for Ne/W used by DEVONSHIRE;(8) from 100°K to 300°K these values of α all seem to be about 0·075 and should be compared with the corresponding modern(7) values of $\alpha \approx 0\cdot05$ at 100°K falling to $\alpha \approx 0\cdot04$ at 300°K.

The reasons for this unsatisfactory situation regarding Devonshire's theory are not clear; the answer may be that the previous calculations are incorrect. The author, having done no calculations whatever using this theory, is in no position to judge this matter. It is significant, however, that GILBEY(13) has been unable to reproduce the numerical results of the above authors in most cases, and has been unable as yet to get a satisfactory agreement with experiment.

(iv). *Classical lattice theories*

These are the theories of CABRERA,(14) ZWANZIG(15) and the author;(1) both $1D$(14, 15, 1) and $3D$(1) lattice models are used. Of the models used in these theories the one which at first sight seems most realistic is the $3D$ "trapping model" developed in I. However, in all cases the theoretical *acs* are far higher than the experimental ones. HURLBUT(16) suggests that a reason for this may be that experimental results are derived from a condition in which all incident angles are possible; in his opinion it seems physically plausible that at oblique incidence, conditions are less favourable for the transfer of energy than in the head-on collisions used throughout the theory. In the author's opinion, the most serious approximation was the impulsive nature of the interaction potential used (see Fig. 6 of I). This impulse is very efficient at transferring energy and is unlike any realistic interaction potential. The impulse was in the "attractive" part of the potential, and we shall show in this paper that when a more realistic potential is considered the attractive part in fact contributes very little to the energy transfer. If any part of a real interaction is impulsive, then it will be in the repulsive part for very small separations of gas atom and solid. Thus the trapping model is almost the opposite of what is to be expected in nature.

In fact, the collisions of gas atoms with solid surfaces are in general "slow" or "languid". This means that in general the "collision times" are considerably larger than the inverse "natural frequencies" of the solids. This was pointed out by ZWANZIG,(15) and from this he concluded that for a sufficiently slow collision the energy of compression (of the solid) is dissipated as fast as it is produced and in general high *acs* result. This conclusion was a direct result of his use of a $1D$ lattice model; when a $3D$ lattice model is used the opposite conclusion is reached. That is, for sufficiently slow collisions the energy of compression is not dissipated at all and the collision is effectively conservative. This is due to the fact that a $3D$ lattice is capable of remaining in equilibrium under the action of a slowly-varying force, whereas a $1D$ lattice is not. In fact it is shown in I that the equilibrium displacement $y(t)$ of a surface atom of our $3D$ lattice model under the action of a slowly-varying force $f(t)$ is given by

$$(3D\ \text{case}) \qquad y(t) \approx 0\cdot34\, f(t)/\kappa \qquad (1.2)$$

where κ is the lattice spring-constant. It follows that for a sufficiently slowly-varying force the velocity of the surface atom $\dot{y}(t)$ is given by

$$(3D\ \text{case}) \qquad \dot{y}(t) \approx 0 \qquad (1.3)$$

and very little energy is transferred to the lattice. The $1D$ lattice has no such equilibrium position, and in fact will "give away" indefinitely under the action of a constant force f_0, the constant velocity of its surface atom being given by

$$(1D\ \text{case}) \qquad \dot{y}(t) \approx f_0/(\kappa m)^{1/2} \qquad (1.4)$$

where m is the mass of a lattice atom. Thus a slowly-varying force is very efficient at transferring energy to a $1D$ lattice.

(v). *The present theory*

It is the purpose of this paper to show that when a realistic interaction potential function (a Morse potential) is used it is possible to get adequate *quantitative* agreement with experiment for He and Ne (with a proper consideration of the relevant Morse parameters) using a simple classical perturbation theory. The approximation used is the "adiabatic approximation" and is similar to that used by LANDAU(11) and more recently in a closely related context by RAPP(17) and TURNER and RAPP.(18) Briefly, the method is as follows: To a first approximation the lattice is assumed to be at rest during the entire interaction. Using this "rigid-lattice" approximation the force on the lattice due to a gas atom first approaching and then receding from the lattice may be expressed as a known function of time. In the second approximation this force is allowed to operate on the free lattice and the resulting energy uptake of the lattice is calculated and is assumed to be the same as the energy lost by the gas atom in an actual collision.

A major difference between this and the previous perturbation theories[8, 11] should be made clear: in the previous theories the energy transfer to each normal mode of the solid is calculated first and then the integration over normal modes is performed; in this theory the integration over normal modes is done first (see I) to obtain the velocity response function $\dot{X}(t)$ and then the energy transfer to the lattice as a whole is calculated using $\dot{X}(t)$.

Several assumptions are involved in using this perturbation theory. For example, it will be valid only for a "small" α and "small" ratio of mass of gas atom to mass of solid atom, μ; a reasonable guess at the criteria for validity of the theory might be

$$\alpha \ll 1 \tag{1.5a}$$

and

$$\mu \ll 1. \tag{1.5b}$$

Roughly speaking, these conditions arise because in the first approximation (a) the gas atom is assumed to lose no energy at all during its collision with the solid and (b) the surface atom is assumed to be at rest during the collision; these two assumptions are not independent of one another.

However, it is possible to discover quite accurately the error involved for each particular case by performing the detailed calculation of the interaction without use of the perturbation method. Because of the simplicity of the perturbation method compared with the far more complex "exact" method, this will be done in a few cases only (i.e., one "check" may be done for each set of experimental data to determine the accuracy to be expected). The results of these checks are in Table 4.

A useful result which comes naturally from the theory is an estimate of the relative quantitative effects on the values of α of the attractive and repulsive forces due to a realistic potential. It is clear that one effect of the attractive force is that a gas atom will accelerate as it approaches the solid and decelerate as it leaves the solid while it is in this part of the interaction potential; the opposite is true for the repulsive part of the potential. What is not yet clear is just what fraction of the energy transfer between a gas atom and a solid is due to the attractive forces and what fraction is due to the repulsive forces. An attempt to investigate this question will be made in this paper.

Apart from the introduction of a realistic potential function, the approximations we shall make regarding the lattice model, the gas atom flux and the detailed collision kinetics are the same as those listed on p. 1288 of I, and it seems unnecessary to repeat the list in this paper.

2. DESCRIPTION OF THE MODEL

We consider a gas atom moving perpendicularly on to the surface of our $3D$ semi-infinite lattice and impinging directly on to a surface atom (hereafter this atom may be referred to simply as "the surface atom"). The lattice is assumed to be initially stationary; this is illustrated in Fig. 1.

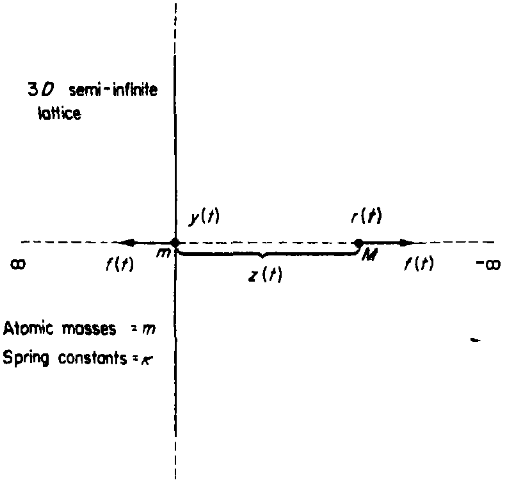

FIG. 1. The collision of a gas atom with a solid surface.

$y(t)$ is the displacement of the surface atom from its initial equilibrium position, M is the mass of the gas atom and $r(t)$ is its distance from the initial position of the surface atom. Distances from this position are measured so that $r(-\infty) = -\infty$. κ, m and θ are respectively the spring constants, atomic masses and Debye temperature of the lattice.

A relative coordinate $z(t)$ is defined by

$$z(t) = y(t) - r(t) \qquad (2.1)$$

and the gas atom is assumed to interact with the surface atom via a Morse potential function:

$$v(z) = D(e^{-2az} - 2e^{-az}). \qquad (2.2)$$

This function is shown in Fig. 2(a). The entire interaction of the gas atom with the solid is assumed to be via these two atoms only; the mutual force f of Fig. 1 is therefore given by

$$f(z) = -(\partial v/\partial z) = 2aD(e^{-2az} - e^{-az}). \qquad (2.3)$$

Dimensionless variables are introduced as follows:

$$\tau = 2\omega_0 t \qquad (2.4)$$

where ω_0 is the "natural frequency" of the lattice given by

$$\omega_0 = (\kappa/m)^{1/2} \qquad (2.5)$$

$$Y(\tau) = ay(t) \qquad (2.6)$$

$$R(\tau) = ar(t) \qquad (2.7)$$

$$u(\tau) = az(t) \qquad (2.8)$$

$$F(\tau) = (a/\kappa)f(t) \qquad (2.9)$$

$$\mu = M/m \qquad (2.10)$$

$$V = (a^2/\kappa)v \qquad (2.11)$$

$$B = (a^2/\kappa)D. \qquad (2.12)$$

In terms of these variables our basic equations (2.1) to (2.3) become

$$u(\tau) = Y(\tau) - R(\tau) \qquad (2.13)$$

$$V(u) = B(e^{-2u} - 2e^{-u}) \qquad (2.14)$$

and

$$F(u) = 2B(e^{-2u} - e^{-u}). \qquad (2.15)$$

To a first order in our perturbation procedure, we assume that

$$Y(\tau) = 0, \qquad (2.16)$$

which implies that the motion of the gas atom is as though it were interacting with an immovable surface atom. We let $\tau = 0$ be the time of closest approach of the gas atom to the solid surface, and let τ_0 be a time well before the interaction has become significant (thus we may take $\tau_0 = -\infty$); we use the notation that a subscript 0 refers to the time τ_0. At time τ_0 the gas atom is at $u = \infty$ and is approaching the lattice at a positive speed $-\dot{u}_0$. It interacts with the (rigid) surface atom via the potential (2.14) and therefore its motion is described by the equation

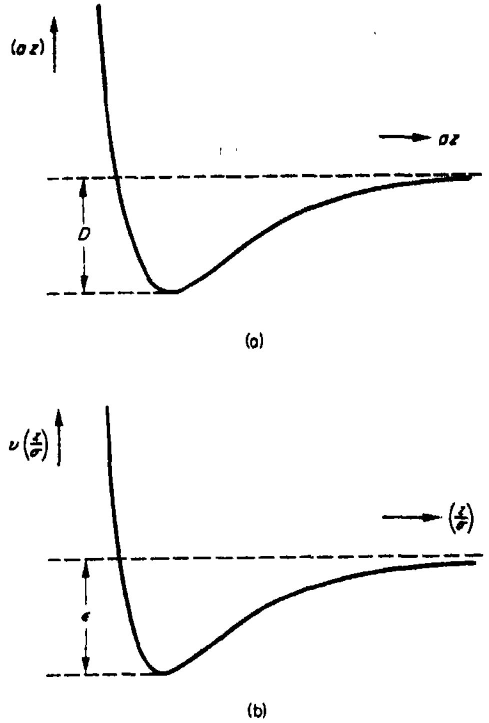

FIG. 2. (a) The Morse and (b) Lennard-Jones 6–12 potentials drawn with $D = \epsilon$ and $a\sigma = 55/12$ to satisfy (A1.1).

$$E(\tau) = E_0 - V[u(\tau)] \qquad (2.17)$$

in which $E(\tau)$ is the kinetic energy of the gas atom at time τ and E_0 is its initial kinetic energy. The kinetic energy $E(\tau)$ is related to the velocity $\dot{u}(\tau)$ in the new units by the expression

$$E(\tau) = 2\mu\dot{u}(\tau)^2. \qquad (2.18)$$

It follows from (2.14), (2.17) and (2.18) that

$$(\dot{u}\tau)^2/\dot{u}_0^2 = 1 - [e^{-2u(\tau)} - 2e^{-u(\tau)}]/\rho, \qquad (2.19)$$

where ρ is defined as the ratio of the initial kinetic energy of the gas atom to the potential well depth:

$$\rho = E_0/B = 2\mu\dot{u}_0^2/B. \qquad (2.20)$$

By direct substitution into (2.19) we may show that its solution is

$$u(\tau) = \ln[(1+\rho)^{1/2}\cosh(\dot{u}_0\tau)-1]-\ln\rho. \tag{2.21a}$$

For later use, we may solve this equation for τ to display τ as a function of u:

$$\tau(u) = \pm\frac{1}{\dot{u}_0}\ln\left[\frac{(1+\rho e^u)}{(1+\rho)^{1/2}}+\left\{\frac{(1+\rho e^u)^2}{(1+\rho)}-1\right\}^{1/2}\right]. \tag{2.21b}$$

The force as a function of time is obtained by combining (2.15) with (2.21a) and using (2.20):

$$F(\tau) = 2E_0(C^2-C)/\rho \tag{2.22a}$$

where C is given by

$$C = \rho/[(1+\rho)^{1/2}\cosh(\dot{u}_0\tau)-1]. \tag{2.22b}$$

To a second order we calculate the energy uptake by the free lattice by assuming that the true gas atom/surface atom interaction is completely described by the force function in (2.22). Using the assumption that the gas atom interacts with only the one surface atom (whose motion is $Y(\tau)$), this energy uptake W is given by

$$W = \int_{-\infty}^{\infty} F(\tau)\dot{Y}(\tau)\,\mathrm{d}\tau. \tag{2.23}$$

It is shown in I that $\dot{Y}(\tau)$ may be written in terms of the velocity response function of the lattice, $\dot{X}(\tau)$, as follows:

$$\dot{Y}(\tau) = \frac{1}{4}\int_0^{\infty} F(\tau-s)\dot{X}(s)\,\mathrm{d}s. \tag{2.24}$$

The function $\dot{X}(\tau)$ is shown for completeness in Fig. 3. The lattice is in all cases assumed to be initially at rest:

$$Y_0 = \dot{Y}_0 = 0. \tag{2.25}$$

α is defined in this model (solid initially at 0°K) as the ratio of the energy uptake by the lattice to the initial kinetic energy of the gas atom; by combining (2.23) and (2.24) we obtain

$$\alpha = \frac{W}{E_0} = \frac{1}{4E_0}\int_{-\infty}^{\infty}\int_0^{\infty} F(\tau)F(\tau-s)\dot{X}(s)\,\mathrm{d}s\mathrm{d}\tau. \tag{2.26}$$

3. CALCULATION OF ACCOMMODATION COEFFICIENTS

Let us consider the introduction of finite limits into the integral (2.26) in order to assist numerical calculations.

(i). *The integration over s in equation* (2.26)

The lattice velocity response function $\dot{X}(\tau)$ is derived[1] using a very special lattice model; it represents the subsequent velocity of a surface atom of the lattice model to a unit velocity of this

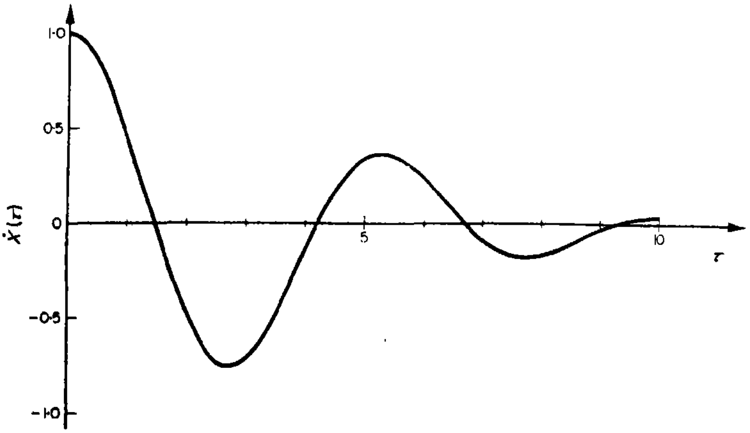

Fig. 3. The 3*D* lattice velocity response function $\dot{X}(\tau)$.

atom applied at $\tau = 0$. $\check{X}(\tau)$ probably gives a reasonable quantitative representation of the motion of a real lattice surface atom for small τ: for large τ the qualitative form of $\check{X}(\tau)$—(oscillatory motion damped as $\tau^{-3/2}$)—is probably reasonably correct, but it is clear that it cannot agree quantitatively with a real lattice for more than the first one or two of its cycles. We may therefore make the approximation that

$$\check{X}(\tau) = 0 \text{ for } \tau > 10, \qquad (3.1)$$

and it is difficult to see how one can do better than this without knowledge of the quantitative long-time behaviour of a real lattice.

Another justification of the approximation (3.1) is the fact that the oscillations of $\check{X}(\tau)$ for $\tau > 10$ are relatively much smaller than those for smaller times. Large surface atom oscillations are much more efficient at transferring energy to (and from) the lattice than are small ones. Roughly speaking, it follows from (2.23) and (2.24) that the efficiency of energy transfer of a particular oscillation (for the same value of the force) is proportional to the "size" of that oscillation. The maximum value of $\check{X}(\tau)$ for $\tau > 10$ is of the order of 5 per cent of the value (unity) of $\check{X}(0)$, so that (3.1) is a sensible approximation.

(ii). *The integration over τ in equation* (2.26)

Let us now consider the details of an actual collision process with reference to Fig. 2. At time τ_0 the gas atom is at $u = \infty$ well over to the right of Fig. 2 and is travelling to the left with a speed $-\dot{u}_0$. The initial part of the interaction will be entirely conservative and no energy will be transferred to the lattice; this is because during this initial part of the interaction the lattice is effectively at rest and in equilibrium under the action of the slowly-varying force $F(\tau)$ due to the approaching gas atom. We may recall at this point the results (1.2) and (1.3) which in our new units become

$$Y(\tau) \approx 0{\cdot}34F(\tau) \qquad (3.2a)$$

and

$$\dot{Y}(\tau) \approx 0. \qquad (3.2b)$$

Similar arguments apply to the slowly-varying force in the final part of the interaction when the gas atom is receding.

A value u_1 of u, corresponding via (2.21) to times $\tau_1 < 0$ and $\tau_2 = -\tau_1$, is chosen so that the interaction for $\tau < \tau_1$ and $\tau > \tau_2$ is likely to be effectively conservative. The integration over τ is performed between times τ_1 and τ_2 (i.e., for $u \leqslant u_1$) and this is sufficient provided that the interaction is indeed conservative outside this range (i.e., for $u > u_1$). This will be so provided that u_1 has been chosen sufficiently large and it is essential to check that this has been done for each case.

Using the work of this section the integral in (2.26) may be approximated by

$$\alpha = \frac{1}{4E_0} \int_{-\tau_2}^{\tau_2} \int_{0}^{10} F(\tau)F(\tau - s)\check{X}(s)\, \mathrm{d}s\mathrm{d}\tau. \qquad (3.3)$$

The integrand is known for all values of s and τ and therefore the integral may be evaluated as it stands. That u_1 (and hence τ_2) have been chosen sufficiently large is easily checked. Values of α are calculated using our chosen value of u_1 and two or three larger values. If all the results agree to the desired accuracy, our originally chosen value is large enough; but if the results disagree, a new value of u_1, larger than the first, is chosen. This checking procedure is repeated until the desired agreement is obtained.

Using this procedure the relative effects of the attractive and repulsive forces between a gas atom and a solid can be estimated by comparing the values of α obtained for several values of $u_1 > 0$ with that obtained for $u_1 = 0$. (The potential minimum for the Morse potential (2.14) is at $u = 0$.)

All the theoretical values of α presented in this paper have been calculated numerically using the method described above on the "Mercury" computer at the Royal Aircraft Establishment, Farnborough.

4. VALUES OF THE PARAMETERS OF THE THEORY

(a). *The interaction parameters derived from the literature*

The values of the interaction parameters (e.g., the Morse a and D) for the systems inert gases/metals have not yet received proper consideration. Some data are available on pairwise interaction of like inert gas atoms and on pairwise interaction of some like metal atoms; but nearly all these data are for model interaction potentials other than the Morse potential (e.g., the various Lennard-Jones m–n potentials). Of these others we shall in this paper consider only the Lennard-Jones 6–12 potential, which we shall write as follows:

$$v(x) = 4\epsilon(\sigma^{12}/x^{12} - \sigma^{6}/x^{6}). \qquad (4.1)$$

This potential is shown in Fig. 2(b) and its similarity to the Morse potential (Fig. 2(a)) when the relations stated in the caption to Fig. 2 are obeyed should be noted.

Our reason for considering the "6–12" potential (4.1) in this paper is that there are many data on the inert gases for this potential, whereas there is a lack of the corresponding Morse data; for example, the author has been unable to find any Morse data for He. It is shown in Appendix 1 how an estimate of the Morse parameters may be made from a knowledge of the corresponding 6–12 parameters. Apart from He and Ne, we shall also consider the rare gases A, Kr and Xe since it is easier to estimate parameters for He from those for Ne, A, Kr and Xe than from those for Ne only.

Intermolecular potential parameters are derived(12) from many experimental sources, e.g., virial coefficients, viscosity, diffusion and solid-state data. The Morse and 6–12 parameters for the interaction of like atoms of W, Fe, Ni and the above rare gases which are in the author's opinion the best "average" values obtainable from the literature at the present time are presented in Table 1; as yet there are no data for Pt. The Morse parameters for He/He are those estimated in Appendix 1 of this paper. Also included in Table 1 are values of $55D/12\epsilon a\sigma$ which, theoretically, should be approximately unity in all cases (see Appendix 1).

To obtain(12) the interaction parameters for unlike atoms (e.g., for the systems He/Pt, Ne/W, etc.) we consider possible "combination rules" which may be written in an obvious notation:

$$\sigma_{12} = \tfrac{1}{2}(\sigma_{11} + \sigma_{22}). \qquad (4.2)$$

$$a_{12}^{-1} = \tfrac{1}{2}(a_{11}^{-1} + a_{22}^{-1}) \qquad (4.3)$$

$$D_{12} = (D_{11}D_{22})^{1/2} \qquad (4.4)$$

$$\epsilon_{12} = (\epsilon_{11}\epsilon_{22})^{1/2} \qquad (4.5)$$

These rules are reasonable provided that the 1/1 parameters do not differ greatly from the 2/2 parameters. We may expect therefore to be able to estimate σ_{12} and a_{12} for the rare gas/metal interactions, but not D_{12} and ϵ_{12}. Using rule (4.3) as a guide in conjunction with column 5 of Table 1 we have estimated the "mixed" values of the Morse a_{12} shown in column 2 of Table 4. In estimating the value for He/Pt it has been assumed that the Morse a for Pt/Pt is 1·4 A^{-1}; this is a reasonable assumption since (see Table 1) each of the other three metals has this same value of a.

Table 1. *Literature values of some intermolecular potential parameters for pairwise interaction of like atoms of some rare gases and metals*

Like atom pair	Lennard-Jones 6–12 parameters σ (A)	ϵ (kcal mole^{-1})	References	Morse parameters a (A^{-1})	D (kcal mole^{-1})	References	$\frac{55D}{12\epsilon a\sigma}$
He/He	2·56	0·0203	12, 19	1·95*	0·0221*	Appendix 1 of this paper	1·00*
Ne/Ne	2·78	0·0687	12, 20–22	1·84	0·0875	31	1·14
A/A	3·42	0·240	12, 20–26	1·48	0·288	31	1·09
Kr/Kr	3·62	0·339	12, 22 24–29	1·28	0·364	31	1·06
Xe/Xe	4·01	0·449	12, 22, 24 27, 28, 30	1·26	0·547	31	1·11
W/W				1·41	22·9	32	
Ni/Ni				1·42	9·68	32	
Fe/Fe				1·39	9·61	32	

* These values are estimated in this paper and are not literature values.

It is noteworthy that, correct to two figures, all the mixed values of a are $1{\cdot}6\ \text{A}^{-1}$; this value is thought to be the best value of the Morse a which can be derived from the literature for the mixed interaction systems considered.

Very little can be said about the values of D_{12} from the combination rule (4.4) in view of the great differences between D_{11} and D_{22}, evident in Table 1. Also, the author knows of no reliable experimental data for D_{12} for the systems considered. However, there are some data(33) on the heats of adsorption ΔH of A, Kr and Xe on W, and these are included here for completeness:

$$\begin{aligned} &\text{A/W}-\Delta H \approx 1{\cdot}9\ \text{kcal mole}^{-1} \\ &\text{Kr/W}-\Delta H < 4{\cdot}5\ \text{kcal mole}^{-1} \qquad (4.6) \\ &\text{Xe/W}-\Delta H \approx 8 \text{ or } 9\ \text{kcal mole}^{-1}. \end{aligned}$$

But it is not yet clear how heats of adsorption are related to potential well depths.

(b) *The parameters θ, μ, ρ and $\dot{u}_0$*

It is necessary to make an estimate of the natural lattice frequency ω_0. Although our lattice model is not a Debye model, we assume that the Debye temperature θ of the lattice may be related to ω_0; this relationship is somewhat arbitrary. In this paper we shall assume (as in Ref. 1 for the $3D$ lattice and Ref. 15 for the $1D$ lattice) that

$$\omega_0 \approx k\theta/2\hbar \qquad (4.7)$$

where k is Boltzmann's constant and $\hbar$ is Planck's constant h divided by 2π. The values of Debye θ we shall take for W, Ni, Fe and Pt are shown in Table 2.

If the initial velocity of the gas atom in ordinary units is V_0, it follows from (2.1), (2.4), (2.6), (2.8) and (2.25) that

$$V_0 = -2\omega_0\dot{u}_0/a. \qquad (4.8)$$

An "effective gas temperature" T is introduced as in Ref. 15 and in I; the definition used in this paper will be different from that used in the work just cited, however. We are considering thermal accommodation; it therefore seems more reasonable to define our effective gas temperature to be the temperature of a Maxwellian flux of monatomic gas atoms which results in an average energy per atom brought to the solid surface equal to the initial kinetic energy of our single gas atom. Our assumption that the gas atom moves perpendicularly on to the solid surface in all cases means that our flux of gas atoms is essentially $1D$. The average energy per atom brought to a fixed surface by such a flux at temperature T is kT and therefore we shall use the relation

$$T = MV_0^2/2k. \qquad (4.9)$$

For given M and V_0, this value of T is half that obtained in Refs 1 and 15.

It follows from (4.7) to (4.9) that

$$\dot{u}_0 \approx -9{\cdot}8(a/\theta)(T/M)^{1/2}\text{A deg}^{1/2}(\text{a.m.u.})^{1/2}. \qquad (4.10)$$

Using (4.9) with the definition (2.20) of ρ it follows that

$$\rho = \tfrac{1}{2}MV_0^2/D = kT/D, \qquad (4.11)$$

That is,

$$\rho \approx T/500D\ \text{kcal mole}^{-1}\ \text{deg}^{-1}. \qquad (4.12)$$

Because of the new definition of the effective gas temperature T, for given T and D this value of ρ is twice that obtained in Refs 1 and 15.

Relations (2.10), (4.10) and (4.12) enable us to evaluate μ, $\dot{u}_0$ and ρ for any given experiment and knowledge of these three parameters enables us to calculate α from the work of Sections 2 and 3 above.

5. COMPARISON OF THE THEORY WITH EXPERIMENTAL DATA

The experimental data on the variation of α with temperature for the systems He/Ni(4),

Table 2. Values of Debye θ for the metals

Metal	W	Ni	Fe	Pt
θ°K	330	320	400	230
References	34 (p. 379) 35 (p. 143)	35 (p. 143)	35 (p. 143) 36 (p. 44)	34 (p. 380) 35 (p. 143)

He/W(7) and Ne/W(7) are shown as dots in Figs 4 to 6; for He/Pt and Ne/Fe, we have no temperature-dependent data. The value of α given for He/Pt (cited in Ref. 3) at presumably about 300°K and that given(8) for Ne/Fe at about 300°K are shown in column 2 of Table 3.

The values of a estimated from the literature (see column 2 of Table 4) have been used in conjunction with the theory to choose suitable values of D to fit the experimental data as well as possible. These values of D are listed in the third column of Table 4, and the corresponding fits are shown as

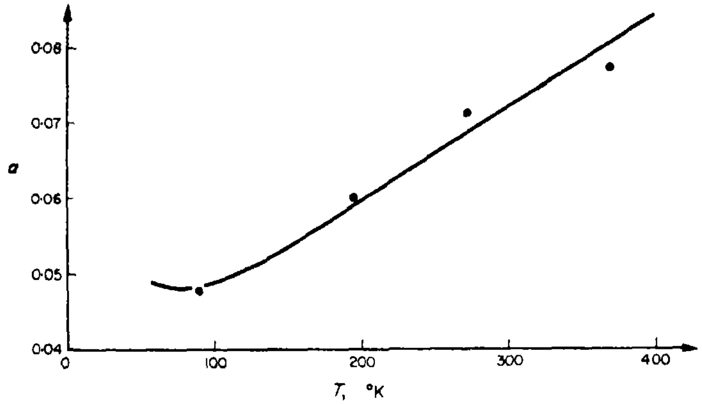

FIG. 4. Comparison of the theory with experimental data for He/Ni.
The theoretical line is for $a = 1{\cdot}6\ \text{A}^{-1}$ and $D = 0{\cdot}13$ kcal mole^{-1}

Table 3. Comparison of the theory with experimental data for He/Pt *and* Ne/Fe

System	Experimental value of α	Theoretical fit with the estimated value of a		Theoretical fits with other values of a			
		a (A^{-1})	D (kcal mole^{-1})	a (A^{-1})	D (kcal mole^{-1})	a (A^{-1})	D (kcal mole^{-1})
He/Pt	0·038	1·6	0·10	1·5	0·12	1·7	0·08
Ne/Fe	0·053 to 0·056	1·6	0·37	1·5	0·43	1·7	0·32

Table 4. Theoretical fit of the experimental data

System	Theoretical fit of experimental data with values of a estimated from the literature		Theoretical best-fit of experimental data		Check values of the percentage over-estimate of α due to the perturbation method
	a (A^{-1})	D (kcal mole^{-1})	a (A^{-1})	D (kcal mole^{-1})	
He/Ni	1·6	0·13	1·6	0·13	7
He/W	1·6	0·10 or 0·11	1·5	0·13	2
He/Pt	1·6	0·10	—	—	3
Ne/Fe	1·6	0·37	—	—	12
Ne/W	1·6	0·44 or 0·45	1·7	0·40	6

the full curves in Figs 4–6. For He/Pt and Ne/Fe the values of D shown in Table 4 are those for which the theory fits exactly the experimental values of α.

For the data on He/W and Ne/W (Figs 5 and 6) it is possible to choose a slightly different pair of values of a and D which, in each case, gives a "best-fit". These best-fits are shown as the broken curves in Figs 5 and 6, and are perhaps a little better than those obtained with the values of a estimated in Section 4; the differences in a between these estimated values and the best-fit values are in both cases quite small (about 7 per cent). The best-fit for He/Ni is that obtained with the value of a estimated in Section 4. These best-fit values of a and D are shown in columns 4 and 5 of Table 4.

The best-fit procedure is possible only if we have values of α as a function of T; this was pointed out by EGGLETON and TOMPKINS.(5) Hence we cannot obtain better fits for He/Pt or Ne/Fe: for each of these cases two other pairs of

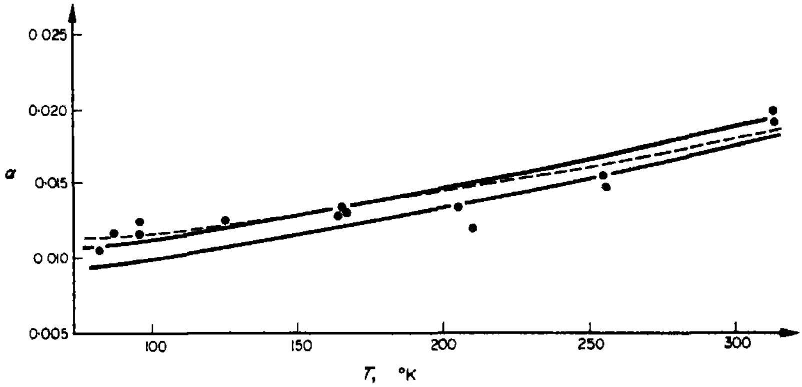

FIG. 5. Comparison of the theory with experimental data for He/W.

The theoretical curves are for
(upper full curve) $a = 1{\cdot}6\ \text{A}^{-1}$ and $D = 0{\cdot}11$ kcal mole^{-1}.
(lower full curve) $a = 1{\cdot}6\ \text{A}^{-1}$ and $D = 0{\cdot}10$ kcal mole^{-1}.
(broken curve) $a = 1{\cdot}5\ \text{A}^{-1}$ and $D = 0{\cdot}13$ kcal mole^{-1}.

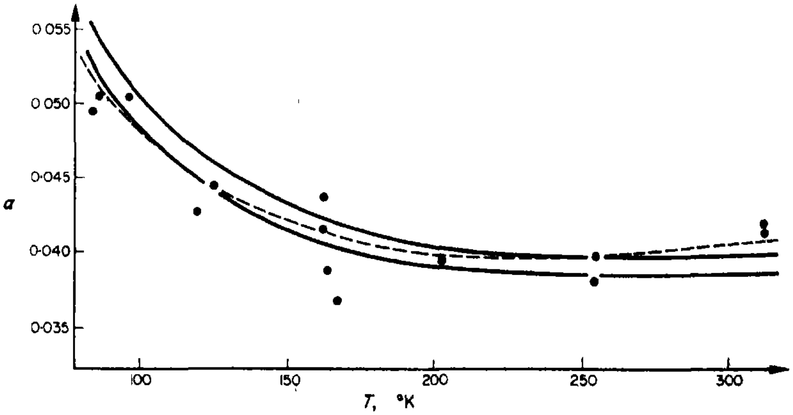

FIG. 6. Comparison of the theory with experimental data for Ne/W.

The theoretical curves are for
(upper full curve) $a = 1{\cdot}6\ \text{A}^{-1}$ and $D = 0{\cdot}45$ kcal mole^{-1}.
(lower full curve) $a = 1{\cdot}6\ \text{A}^{-1}$ and $D = 0{\cdot}44$ kcal mole^{-1}.
(broken curve) $a = 1{\cdot}7\ \text{A}^{-1}$ and $D = 0{\cdot}40$ kcal mole^{-1}.

values of a and D, which from the theory yield the experimental value of α, have been chosen; these are shown in columns 5 to 8 of Table 3.

For each set of experimental data one value of α has been obtained by calculating the interaction without use of the perturbation approximation, but by use of a step-by-step procedure. In all cases we find that the perturbation method overestimates the energy transfer to the lattice. In other words use of the perturbation method results in values of α which are too high; the reasons for this are given in Section 6. The percentage error found by comparing the "exact" method with the perturbation method for the one *ac* from each set of data is shown in Table 4. No corrections for this error will be made in this paper, however.

Some idea of the slowness or languidness of an interaction may be obtained by considering the time spent by the gas atom (a) in the repulsive part only of the potential field and (b) in both the attractive and repulsive parts of this field. It is reasonable to call these two times (a) the "repulsion time" τ_r and (b) the "interaction time" τ_i. For the Morse potential (2.14) τ_r is the total time spent in the region $u < 0$ and it follows from (2.21b) that

$$\tau_r = -(2/\dot{u}_0)\ln[(1+\rho)^{1/2}+\rho^{1/2}]. \qquad (5.1)$$

τ_i may be defined as the total time spent in the region $u < u_i$ where u_i is suitably chosen. It is reasonable to choose u_i so that from (2.14)

$$\text{and} \qquad \left.\begin{aligned} u_i &> 0 \\ V(u_i) &\approx 0{\cdot}1B, \end{aligned}\right\} \qquad (5.2)$$

and this results in a value

$$u_i \approx 3{\cdot}0. \qquad (5.3)$$

Using (2.21b) and (5.3) τ_i may then be calculated for any particular case. The values of τ_r and τ_i for each case at 300°K are shown in Table 5 and may be compared with the time scale of the lattice velocity response function $\bar{X}(\tau)$ shown in Fig. 3. (Note that these times are in units of $1/[2\omega_0]$.)

In order to show how, in a particular case, the theoretical *acs* vary with the choice of a and D, we have calculated *acs* for the case of He/Fe (for which we have no experimental data). This has been done for the 9 possible combinations of $a = 1{\cdot}2$, $1{\cdot}6$ and $2{\cdot}0$ A^{-1} and $D = 0{\cdot}05$, $0{\cdot}10$ and $0{\cdot}15$ kcal mole^{-1} between 100°K and 300°K, and the results are shown in Fig. 7.

The relative effects of the attractive and repulsive forces on the *acs* may be estimated by calculating α as a function of $u_1 \geqslant 0$. For each set of experimental data α has been calculated at 300°K for $u_1 = 0, 1, 2$ and 3 and the results of these calculations are presented in Table 5. Also in Table 5 is shown the value of u_1 finally chosen in each case for the other calculations presented in this paper.

6. DISCUSSION OF THE RESULTS AND CONCLUSIONS

The agreement of the theory with experiment using the values of a estimated from the literature is remarkably good. Also, the values of the potential well-depth D derived from these values of a are reasonable (see Table 4). The best-fit values of the parameters for He/W and Ne/W are hardly significantly different from these values; for He/Ni, the estimated value of a gives the best fit (see Fig. 4). The best-fit values of a for He/W and Ne/W turn out to be 1·5 and 1·7 A^{-1} respectively. Because a He atom is smaller than a Ne atom we

Table 5. *Some more results of the analysis*

System	Values of the repulsion and interaction times at 300°K		Theoretical *acs* as a function of u_1 at 300°K. Best-fit parameters (see Table 4) are used where possible				Final value of u_1 chosen for the calculations	The mass-ratio	Hard-spheres value of α
	τ_r	τ_i	$u_1 = 0$	$u_1 = 1$	$u_1 = 2$	$u_1 = 3$		μ	$\frac{4\mu}{(1+\mu)^2}$
He/Ni	7	21	0·073	0·072	0·072	0·072	2	0·0681	0·239
He/W	8	23	0·018	0·018	0·018	0·018	1	0·0217	0·0833
He/Pt	6	15	0·037	0·038	0·038	0·038	2	0·0205	0·0788
Ne/Fe	14	49	0·051	0·053	0·054	0·055	2	0·362	0·781
Ne/W	11	38	0·039	0·040	0·040	0·041	2	0·110	0·356

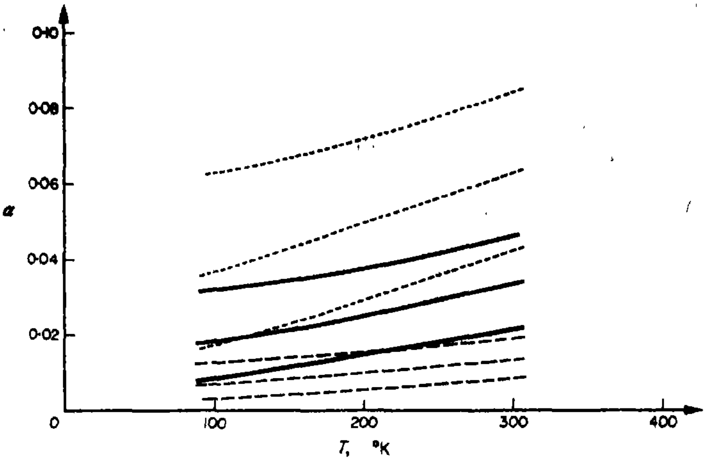

FIG. 7. α as a function of a and D for He/Fe.

.... $a = 2{\cdot}0\ \text{A}^{-1}$
———— $a = 1{\cdot}6\ \text{A}^{-1}$
– – – – $a = 1{\cdot}2\ \text{A}^{-1}$

upper curve in each case is for $D = 0{\cdot}15$ kcal mole^{-1}.
middle curve in each case is for $D = 0{\cdot}10$ kcal mole^{-1}.
lower curve in each case is for $D = 0{\cdot}05$ kcal mole^{-1}.

might expect the value of a for He/W to be a little larger than that for Ne/W; the best-fit values are the other way round. However, the small differences between the fits obtained using

(a). $a = 1{\cdot}6\ \text{A}^{-1}$ for both He/W and Ne/W and
(b). $a = 1{\cdot}5\ \text{A}^{-1}$ for He/W and $1{\cdot}7\ \text{A}^{-1}$ for Ne/W

are perhaps not significant owing to the spread of the relevant experimental points (see Figs 5 and 6). The best-fit for He/W (see Fig. 5) is considered better then the others shown because its gradient $(\partial\alpha/\partial T)$ gives a better agreement with the trend of the experimental points. The best-fit for Ne/W (see Fig. 6) is considered better than the others shown because it clearly displays the minimum in α vs. T which seems to be apparent from the experimental points.

In Section 5 we discussed the errors due to use of the perturbation method; in all cases considered this method over-estimates the energy transfer from the gas atom to the solid. The reason for this is that the maximum repulsive force between the gas atom and the surface atom is over-estimated. $u(0)$ is the distance of closest approach of the atoms and it is assumed that the gas atom reaches a maximum height $V[u(0)]$ in the potential field equal to its initial kinetic energy E_0 (it does not matter that $u(0)$ is in fact negative). At $u(0)$ the repulsive force reaches a maximum and it is easy to show that this maximum value is

$$F[u(0)] = 2B[1+\rho+(1+\rho)^{1/2}]. \qquad (6.1)$$

However, in any real collision the gas atom will have lost some if its energy to the lattice before it reaches its position of closest approach to the surface atom and will not quite reach the height $V[u(0)]$ equal to E_0 in the potential field. Hence the corresponding maximum repulsive force will be smaller than that given by (6.1) and the energy transfer to the lattice, which is mainly due to the large repulsive forces, is smaller than that calculated.

Considering the assumptions involved in the perturbation method, we should expect it to be reasonably valid when conditions (1.5) are obeyed. Taking into account the values of α (see Table 3 and Figs 4–6) and the values of μ (see Table 5), we should expect the perturbation method to be best for He/W and He/Pt and worst for Ne/Fe; this is what is found in practice by comparing our results with those obtained using the "exact" method. On the basis of this comparison displayed in Table 4 we conclude that the perturbation method is very good for He/W and He/Pt, good for He/Ni and Ne/W and relatively poor for Ne/Fe.

On comparing the repulsion times τ_r and the interaction times τ_i in Table 5 with the time-scale of the lattice velocity response function $\dot{X}(\tau)$ (see Fig. 3) it becomes clear that we are dealing with collisions which are rather slow, or languid; this is especially true of the attractive part of the interaction. Since in all cases it turns out that $\tau_i \approx 3\tau_r$, we should expect that the effect of the attractive part of the interaction on the energy transfer will be much less than that of the repulsive part. In fact the attractive part has a negligible effect on the values of the *acs*, as is shown by the values of α as a function of u_1 in Table 5. In all cases the errors involved in ignoring the attractive part of the interaction altogether (i.e., taking $u_1 = 0$) are less than the errors inherent in the perturbation method (see Table 4).

However, the attractive forces are very important in accelerating and decelerating the gas atom, especially if the well-depth is comparable with, or greater than, the initial kinetic energy of the gas atom (i.e., $\rho \approx 1$ or $\rho < 1$). In these cases the gas atom enters the repulsive part of the interaction with a velocity considerably greater than its initial velocity; the maximum repulsive force experienced by the gas atom is therefore larger than it would be in absence of the attractive forces. The point is not that the attractive forces can be ignored, but that they play very little direct part in the mechanism of energy transfer in the systems considered here. In other words, the attractive parts of these interactions are themselves effectively conservative, but lead to the repulsive part of the interaction being more dissipative.

In any real situation, the head-on-collisions assumed to occur in this theory will be rare; each gas atom is far more likely to interact strongly with two or more surface atoms. Also, each gas atom will interact with solid atoms other than those nearest to it on the surface. We are not able to comment on the effect of the assumption that a head-on collision always occurs. Assuming that this is so, however, it is possible to estimate the effect of the interactions of the gas atom with solid atoms other than that hit head-on. We have shown that the effect on α of the attractive forces between a gas atom and the surface atom directly hit is small; this is because the force between the two atoms in the attractive part of the interaction is slowly-varying. The interactions of the gas atom with these *other* solid atoms will always be through the attractive part of the potential, and the attractive forces involved will be smaller and even more slowly-varying because of the much larger distances involved. We conclude that for the systems studied in this paper the interactions of a gas atom with solid atoms other than that directly hit (in the head-on approximation) will contribute very little to the energy exchange between a gas atom and a solid; these interactions will be conservative.

However, the interactions of the gas atom with these other solid atoms will indirectly modify the energy transfer in the same way as do the attractive forces between the gas atom and the solid atom directly hit. This effect is automatically taken into account in the theory by the use of the parameters a and D, which may be considered from this point of view to be "effective interaction parameters".

The theory predicts that, in general, α will have a minimum when expressed as a function of T; this theoretical minimum shows itself clearly in Figs 4 and 6, and would be to the left in Figs 5 and 7. The only set of experimental data displaying such a minimum is that for Ne/W in Fig. 6, and it is not clear just how significant is this minimum. It may be as well at this point to give a discussion of the occurrence of a minimum:

(i). When T is sufficiently small, the initial kinetic energy of the gas atom is much smaller than the potential well-depth ($\rho \ll 1$). This means that as the gas atom enters the repulsive part of the interaction it has a kinetic energy much larger than that which it had initially; in fact its kinetic energy is approximately equal to the well-depth and is effectively independent of T. The gas atom will lose a certain amount, W, of energy to the solid and this amount of energy will also be effectively independent of T. It follows that in this regime of small T

$$\alpha(\text{small } T) = W/E_0 \approx T'/T, \tag{6.2}$$

where T' is a constant. Thus for $T \ll T'$, $\alpha > 1$, and this merely means that the gas atom is "trapped"; this can occur because although the gas atom may lose to the solid only a small fraction of the energy it has on entering the repulsive part of the interaction, this fraction may still be more than its initial kinetic energy.

(ii). When T is sufficiently large ($\rho \gg 1$), the collision will be effectively that of two hard spheres of mass ratio μ; the resulting *ac* is given (for $\mu < 0{\cdot}84$) by[1]

$$\alpha(\text{large } T) \approx 4\mu/(1+\mu)^2. \tag{6.3}$$

Theoretical values of this "high-temperature limit" of α are shown in Table 5 for the systems considered in this paper. The theoretical values of α for these systems are in all cases less than those given by (6.3), and it follows that according to the theory, for these systems $\alpha(T)$ has a minimum.

A rough estimate of the value of T, $T_{\min}$, at which this minimum occurs may be made for each case by making the plausible assumption that it will occur when the initial kinetic energy of the gas atom is approximately equal to the well-depth. This yields the conditions $\rho \approx 1$ and using (4.12) we obtain

$$T_{\min} \approx 500\ D \text{ deg kcal}^{-1} \text{ mole.} \tag{6.4}$$

By using the values of D in Table 4 in conjunction with (6.4) we obtain the following rough estimates of $T_{\min}$ for the two types of system considered:

$$(\text{He/metal systems})\,T_{\min} \approx 60^\circ\text{K} \tag{6.5a}$$

$$(\text{Ne/metal systems})\,T_{\min} \approx 200^\circ\text{K}. \tag{6.5b}$$

It may be significant that (6.5b) agrees quite well with the temperature at which the *minimum* appears to occur in the experimental points for Ne/W (see Fig. 6).

In view of the arguments presented above and the agreement of the theory with the available experimental data, we conclude that Table 4 contains what are perhaps the best values to date of the effective Morse interaction parameters a and D for the gas/metal systems considered. We have already mentioned that Table 1 contains what are in the author's opinion the best Lennard-Jones 6–12 and Morse parameters which are available from the literature for the interaction of pairs of the like atoms considered. In transforming from 6–12 to Morse parameters, and vice versa, it is clear from Table 1 that the empirical rule (A1.1) can serve as a useful guide. The similarity of the two potential functions when (A1.1) is satisfied is clear from Fig. 2; the range of validity of this rule is as yet uncertain, however. In conclusion we may mention that it follows from this work that the 6–12 values of σ_{12} used for the gas/metal interactions in I are an order of magnitude too small.

Acknowledgements—The author wishes to acknowledge many valuable discussions with Dr. R. O. Davies. The author is indebted also to Prof. L. B. Thomas for permission to use the unpublished experimental data.

REFERENCES

1. Goodman F. O., *J. Phys. Chem. Solids* **23**, 1269 (1962).
2. Goodman F. O., *J. Phys. Chem. Solids* **23**, 1491 (1962).
3. Wachman H. Y., *Amer. Rocket Soc. Journal* **32**, 2 (1962).
4. Raines B., *Phys. Rev.* **56**, 691 (1939).
5. Eggleton A. E. J. and Tompkins F. C., *Trans. Faraday Soc.* **48**, 738 (1952).
6. Thomas L. B. and Schofield E. B., *J. chem. Phys.* **23**, 861 (1955).
7. Thomas L. B., Private communication (1961).
8. Devonshire A. F., *Proc. Roy. Soc.* **A158**, 269 (1937).
9. Gilbey D. M., *J. Phys. Chem. Solids* **23**, 1453 (1962).
10. Baule B., *Ann. Phys.* **44**, 145 (1914).
11. Landau L., *Phys. Z. Sowietunion* **8**, 489 (1935).
12. Hirschfelder J. O., Curtiss C. F. and Bird R. B., *Molecular theory of gases and liquids*. Wiley, New York (1954). See p. 168 for combination rules and p. 1110 for Lennard-Jones 6–12 parameters.
13. Gilbey D. M., Private communication (1963).
14. Cabrera N. B., *Disc. Faraday Soc.* **28**, 16 (1959).
15. Zwanzig R. W., *J. chem. Phys.* **32**, 1173 (1960).
16. Hurlbut F. C., *Univ. Calif. Engrs Proj. Rep.* HE-150-208 (1962).
17. Rapp D., *J. chem. Phys.* **32**, 735 (1960).
18. Turner R. E. and Rapp D., *J. chem. Phys.* **35**, 1076 (1961).
19. de Boer J. and Michels A., *Physica* **5**, 945 (1938).
20. Lennard-Jones J. E., *Physica* **4**, 941 (1937).
21. Corner J., *Trans. Faraday Soc.* **44**, 914 (1948).
22. Bernardes N., *Phys. Rev.* **112**, 1534 (1958).
23. Srivastava I. S., *Indian J. Phys.* **34**, 539 (1960).
24. Whalley E. and Schneider W. G., *J. chem. Phys.* **23**, 1644 (1955).
25. Bahadur J. and Madan M. P., *Proc. Nat. Inst. Sci. India* **A26**, 64 (1960).
26. Zucker I. J., *J. chem. Phys.* **25**, 915 (1956).
27. de Boer J., *Physica* **4**, 139 (1948).
28. Mason E. A. and Rice W. E., *J. chem. Phys.* **22**, 522 (1954).
29. Beattie J. A., Brierley J. S. and Barriault R. J., *J. chem. Phys.* **20**, 1615 (1952).
30. Beattie J. A., Barriault R. J. and Brierley J. S., *J. chem. Phys.* **19**, 1222 (1951).
31. Konowalow D. D. and Hirschfelder J. O., *Phys. Fluids* **4**, 629 (1961).
32. Girifalco L. A. and Weizer V. G., *Phys. Rev.* **114**, 689 (1959).
33. Ehrlich G., *Molecular processes at the gas-solid interface. Structure and properties of thin films*, p. 433. Wiley, New York (1959).
34. Blackman M., *Handb. Phys.* **7** (**1**), 325 (1955).

35. Wilson A. H., *The theory of metals*, Cambridge University Press (1953).
36. Born M. and Huang K., *Dynamical theory of crystal lattices*, Clarendon Press, Oxford (1954).

APPENDIX 1

A relation between the Morse parameters and the Lennard-Jones 6–12 parameters. Morse parameters for He.

It is well-known$^{(12)}$ that for a given set of experimental data on virial coefficients, viscosities, etc., fairly good agreement with experiment may usually be obtained with quite different intermolecular potential functions. One feature which these different potential functions seem to have in common is that the area contained within the potential well is approximately the same (see p. 207 of Ref. 12). The area contained within the Lennard-Jones 6–12 well is $(24\epsilon\sigma/55)$ and that contained within the Morse well is $2D/a$. Thus the empirical rule of equality of these areas gives

$$55D/12\epsilon a\sigma = 1. \qquad \text{(A1.1)}$$

The quantity on the L.H.S. of this relation is tabulated in Table 1 for those cases for which there are sufficient data. It is evident that the agreement with the rule (A1.1) is remarkably good. To proceed further, we assume that this rule holds for He, and we choose values of a and D for He which satisfy (A1.1) and fit in with all the trends evident from Table 1. The values finally chosen and quoted in Table 1 are

$$(\text{for He/He})\left\{\begin{aligned} a &= 1{\cdot}95\ \text{A}^{-1} \\ D &= 0{\cdot}0221\ \text{kcal mole}^{-1} \end{aligned}\right\}. \qquad \text{(A1.2)}$$

J. Phys. Chem. Solids Pergamon Press 1963. Vol. 24, pp. 1467–1474. Printed in Great Britain.

SPIN AND COMBINED RESONANCE ON ACCEPTOR CENTRES IN Ge AND Si TYPE CRYSTALS—I

PARAMAGNETIC RESONANCE IN STRAINED AND UNSTRAINED CRYSTALS

G. L. BIR, E. I. BUTIKOV and G. E. PIKUS

Institute of Semiconductors, Academy of Science U.S.S.R., Leningrad, U.S.S.R.

(*Received* 22 *November* 1962)

Abstract—A theory of paramagnetic resonance on acceptor centres in deformed and non-deformed Ge and Si type crystals is developed. The splitting of the ground state under the action of the deformation and magnetic field is determined and the probability of transitions between levels is estimated. Using the effective mass approximation, estimates are made of the deformation potential constant and the *g*-factor.

1. INTRODUCTION

UNTIL recently electron-spin resonance has not been observed on shallow acceptor centres in Ge and Si under ordinary conditions. In 1960 FEHER, HENSEL and GERE(1) established that resonance can occur in homogeneously deformed crystals. At this stage the present authors suggested observing the resonance in deformed *p*-Ge and *p*-Si on free holes and evaluated the resonance frequencies and transition probability as a function of the direction of deformation.(2, 3) As was then pointed out,(3) the formulae are applicable to resonance of bound holes. But this resonance differs in a number of respects and it is with this topic that the present paper is concerned.

2. THE HAMILTONIAN FOR THE IMPURITY CENTRE

In the analysis of various effects on shallow impurity centres, the effective mass approximation is usually employed. Here the potential is written as the coulomb potential in a medium with dielectric permeability ϵ_0: $V(r) = -e^2/\epsilon_0 r$. This approximation holds for sufficiently great distances from the acceptor ion and good results are obtained for shallow acceptors with large radii. Here in the effective mass approximation the ionization energy E_i is independent of the type of acceptor species, which is more or less the case for Ge. But in Si the ionization energy of the acceptors is essentially dependent on the type of impurity and it increases with increasing Z of the acceptor atom.

Therefore, in this paper, in considering bound holes, we avail ourselves of the more general matrix method based solely on considerations of symmetry.

As regards the effective mass approximation, we use it solely to express the constants in the Hamiltonian of the impurity centre in terms of known parameters of the free carriers.

From certain theoretical papers(4, 5) and experimental data,(1) the ground state of shallow acceptor centres in Ge and Si is four-fold degenerate and the corresponding wave functions Ψ_i transform according to the same representation Γ_8 as the eigen-functions of the free holes near the band extremum. The point is that only functions which transform according to this representation remain finite in the effective mass approximation at the point $r = 0$ where the potential energy $V(r)$ is a minimum whereas all the other functions vanish at this point.

In the following we shall be interested in the effect on an acceptor centre of deformations, and of magnetic and electric field. If the energy associated with these perturbations is small compared with the distance from the ground state to the nearest excited level, i.e. if in practice it is small compared with the ionization energy of the acceptor, we can confine our consideration to the ground state. Here the operator H' for the acceptor centre becomes a 4×4 matrix, the explicit form of which depends solely on the symmetry of the crystal and the representation according to which the wave functions are transformed. In the effective mass approximation, the field created by the impurity centre has spherical symmetry and the symmetry of the impurity centre is determined by the Bloch wave functions and, consequently, coincides with the symmetry of the crystal $T_d \times I$, i.e. with the symmetry of the group of the wave vector $G_{\boldsymbol{k}_0}$ at the point $\Gamma(\boldsymbol{k}_0 = 0)$. The wave functions of the impurity centre in the effective mass approximation transform according to the same representation as the functions of the free holes. In point of fact, in Ge and Si, the impurity ion is at one of two equivalent nodes of the elementary cell. Therefore the field near this ion and, more particularly, the fields associated with the deformation of the crystal by this ion,(6) have symmetry T_d and not $T_d \times I$. However, this difference in symmetry does not affect the form of the matrices H'_H and H'_ϵ, which define the influence of the magnetic field and deformation on the ground state of the acceptor.

In the presence of uniform deformation ϵ, which we will describe by the tensor deformation $\epsilon_{\alpha\beta}$, and of a uniform magnetic field $\vec{H}$, the energy matrix H' which defines the displacement of the ground state of the acceptor, is:*

$$H' = H'_H + H'_\epsilon \tag{1}$$

where

$$\begin{aligned} H'_H = \mu_0\{g'_1(J_xH_x+J_yH_y+J_zH_z) \\ +g'_2(J_x^3H_x+J_y^3H_y+J_z^3H_z)\}, \end{aligned} \tag{2}$$

$$\begin{aligned} H'_\epsilon = a\epsilon I + b'\{(J_x^2-\tfrac{5}{4}I)\epsilon_{xx}+(J_y^2-\tfrac{5}{4}I)\epsilon_{yy} \\ +(J_z^2-\tfrac{5}{4}I)\epsilon_{zz}\}+(2d'/\sqrt{3})\{[J_xJ_y]\epsilon_{xy} \\ +[J_xJ_z]\epsilon_{xz}+[J_yJ_z]\epsilon_{yz}\} \end{aligned} \tag{3}$$

Here J_α are matrices of the operator of the angular momentum with $j = \frac{3}{2}$ in the representation,(7) $[A_i, B_j] \equiv \frac{1}{2}(A_iB_j+A_jB_i)$, I is the unit matrix, $\epsilon = Sp\tilde{\epsilon} = \epsilon_{xx}+\epsilon_{yy}+\epsilon_{zz}$, μ_0 is the Bohr magneton, $\mu_0 = e\hbar/2mc$, and a', b' and d' are deformation potential constants of the impurity centre which are analagous to the constants a, b and d for free holes.(8)

In the following, by the effective mass approximation, we express a', b' and d' in terms of a, b and d and also establish the relationship between g'_1 and g'_2 with the corresponding constants for free holes.†

It need only be pointed out that the term Γ_8^- for the free holes occurs as a result of spin-orbit splitting of the term $\Gamma_{15}^- \times D_{1/2}$. For free holes the coefficient g_2 therefore vanishes in the approximation of weak spin-orbital interaction and, apparently, is much less than g_1. For a shallow acceptor centre spin-orbit splitting of the valence band Δ is usually greater than or of the order of the ionization energy E_i. Therefore it mixes the functions which correspond to the various single group representations, and the term Γ^8 of the impurity centre descends from different terms: Γ_{15}, Γ_{25} and Γ_{12}. In consequence, the coefficients g'_1 and g'_2 of equation (3) can in principle be of the same order even if $g_2 = 0$. For example, if the term Γ_8 derives solely from Γ_{12}, then in a magnetic field two-fold degeneracy should be preserved: if $H = H_z$ for this term, $(H'_H)_{11} = (H'_H)_{33} = -(H'_H)_{22} = -(H'_H)_{44}$, which corresponds to $g'_2 = -4/7g'_1$. However, as shown by calculations which follow, the main contribution to Ψ_i for Ge and Si arises from functions which originate from the representation Γ_{15} and, therefore, g'_2 is usually much less than g'_1 for the impurity centre also.

Using the matrices (2) and (3) we can calculate the spectrum under various conditions and also the transition probability in alternating fields which are defined by matrices which are no different from (2) and (3) except that constant fields have to be replaced by alternating fields. This latter rule holds of course only in those cases when we can ignore the space dispersion, i.e. when the wavelength $\lambda = 2\pi/q$ of the corresponding field is large compared with the radius r_0 of the impurity centre. For an electrical as well as a magnetic field, the condition $2qr_0 \lesssim 1$ is fulfilled for all the possible frequencies ω of the external fields up to $\omega_t = E_t/\hbar$. For analysis of transitions due to long-wave acoustic oscillations, this method is only applicable up to frequencies

---

* Here we ignore the very slight interaction with the spin of the nucleus of the ion itself and other adjacent atoms.

† For free holes the expression of equation (3) coincides with that of LUTTINGER(7) if we replace $g'_1 \to 2k$, $g'_2 \to 2q$.

$$\omega \lesssim \omega_{\max} = \frac{c}{2r_0}, \tag{4}$$

where c is the velocity of sound. According to SCHECHTER,(5) r_0 is equal to 44 Å for Ge and 17 Å for Si. Correspondingly, if $c = c_t$, where c_t is the velocity of transverse acoustic waves, $\omega_{\max}$ is equal to $0{\cdot}6\times 10^{12}\,\mathrm{sec}^{-1}(\hbar\omega = 0{\cdot}4\times 10^{-3}\text{ eV})$ for Ge and to $2{\cdot}6\times 10^{12}\,\mathrm{sec}^{-1}(\hbar\omega = 1{\cdot}7\times 10^{-3}\text{ eV})$ for Si. For higher frequencies we have to consider spatial dispersion, and therefore it is necessary to have more detailed knowledge of the wave functions. As a rule the transition probability decreases rapidly if $\omega > \omega_{\max}$. Thus, if $\Psi \sim e^{-r/r_0}$, the transition probability is proportional to $[1+(\omega/2\omega_{\max})^2]^{-4}$.

3. THE UNSTRAINED CRYSTAL

We will confine ourselves to the case where the magnetic field is in the direction of the principal axis (e.g. along the axis $z-(001)$). In such a field, as is seen from equation (3), the ground state is split into four non-equidistant levels with the energies

$$\begin{aligned} E_{1,4} &= E_0 \pm \mu_0 H(\tfrac{3}{2}g_2' + 27/8\, g_2'), \\ E_{2,3} &= E_0 \pm \mu_0 H(\tfrac{1}{2}g_1' + \tfrac{1}{8}g_2'). \end{aligned} \tag{5}$$

It can be shown without difficulty that the alternating magnetic field $\bar{h}(t) = 2\bar{h}_0 \cos \omega t$ causes transitions between levels $1 \rightleftarrows 2$ and $3 \rightleftarrows 4$ at the frequency $\omega_{12} = \omega_{34} = \mu_0 H/\hbar(g_1' + 13/4\, g_2')$, between the levels $2 \rightleftarrows 3$ at the frequency $\omega_{23} = \mu_0 H/\hbar(g_1' + \tfrac{1}{4}g_2')$, and between the levels $1 \rightleftarrows 4$ at the frequency $\omega_{14} = 3\mu_0 H/\hbar(g_1' + 9/4\, g_2')$. Here the corresponding matrix elements of the operator $H'h$, which define the probability of these transitions, are:

$$\begin{aligned} |(H_h')_{12}|^2 &= |(H'_h)_{34}|^2 = \tfrac{3}{4}\mu_0^2 h_\perp^2 (g_1' + 7/4\, g_2')^2, \\ |(H_h')_{23}|^2 &= \mu_0^2 h^2 (g_1' + 5/2\, g_2')^2, \\ |(H_h')_{14}|^2 &= 9/16(\mu_0^2 h_\perp^2 g_2'^2), \end{aligned} \tag{6}$$

where $h_\perp^2 = h_x^2 + h_y^2$. If $g_2' = 0$ all four levels are equidistant and the frequency of the transitions is $\omega = (\mu_0 H/\hbar)g_1'$. It is obvious that the corresponding formulae (5) and (6) for $g_2' = 0$ hold good for any orientation of the magnetic field H.

4. THE SPECTRUM OF A STRAINED CRYSTAL

Equation (1) holds true only when the splitting of the ground state in deformation is considerably less than E_t. If, however, the deformations are large and the splitting of the valence band Δ_ϵ is much greater than E_t, then the g-factor for bound holes will be the same as the g-factor of free holes in the lower of the split off bands.

In the event of comparatively small deformations when the splitting of the zones Δ_ϵ is much less than E_t, the splitting of the impurity level is analogous to that of the band edge zone of the free holes(8) and has the form

$$\Delta_\epsilon = 2\sqrt{E_\epsilon} = 2\sqrt{\{(b'^2/2)[(\epsilon_{xx}-\epsilon_{yy})^2 + (\epsilon_{xx}-\epsilon_{zz})^2 + (\epsilon_{yy}-\epsilon_{zz})^2] + d'^2(\epsilon_{xy}^2 + \epsilon_{xz}^2 + \epsilon_{yz}^2)\}}$$

Each of the levels split by deformation remains two-fold degenerate. In the magnetic field this degeneration is removed. If the splitting in the magnetic field is considerably less than the splitting Δ_ϵ associated with the deformation, then, in analogy with the case of free holes,(2, 3) the resonance frequency and g-factor are appreciably dependent on the direction and sign of deformation. Using equations (2) and (3) we get for the splitting of the levels in the magnetic field in a deformed crystal:

$$\Delta E_l = \hbar\omega_{s(l)} = \mu_0(\bar{H}\tilde{g}_l^2\bar{H})^{1/2} = \mu_0 \sum_{\alpha,\beta} H_\alpha g_{\alpha\beta} H_\beta \tag{7}$$

where the components of the tensor $\{g_{1,2}^2\}_{\alpha\beta}$ are:

$$\begin{aligned} \{g_{1,2}^2\}_{xx} = \frac{1}{E_\epsilon}\{[\pm\sqrt{E_\epsilon}(g_1' + 13/4\, g_2') \\ + b'(\epsilon - 3\epsilon_{xx})(g_1' + 7/4\, g_2')]^2 \\ + 3d'^2(\epsilon_{xy}^2 + \epsilon_{xz}^2)(g_1' + 9/4\, g_2')(g_1' + \tfrac{1}{4}g_2')\}, \end{aligned} \tag{8}$$

$$\begin{aligned} \{g_{1,2}\}_{xy} = (\sqrt{(3)}d'/E_\epsilon)\{\sqrt{(3)}d'\epsilon_{xz}\epsilon_{yz}(g_1' + 9/4\, g_2')^2 \\ + \epsilon_{xy}(g_1' + 7/4\, g_2')[\pm 2\sqrt{(E_\epsilon)}(g_1' + 7/4\, g_2') \\ + b'(\epsilon - 3\epsilon_{zz})(g_1' + 13/4\, g_2')]\} \end{aligned} \tag{9}$$

The remaining components $\tilde{g}_{1,2}^2$ are obtained by cyclical permutation of the subscripts. Here the upper sign corresponds to the lower of the split levels ($l = 1$), whilst the lower sign corresponds to the upper level ($l = 2$).

In the case of deformations along the axes (001) and (111) the g-factor has two components, viz. $g_\parallel$ and $g_\perp$, and the splitting of the levels in the magnetic field is:

$$\Delta E = \mu_0\sqrt{(g_\parallel^2 H_\parallel^2 + g_\perp^2 H_\perp^2)} \tag{10}$$

In equation (10) the subscript "$\parallel$" corresponds to the direction of deformation. The magnitude of $g_\parallel$ and $g_\perp$ from (7–9), as a function of g_1' and g_2' for deformations in the principal directions, is given in Table 1.

Table 1. *Values of the g-factors for deformation along the principal axes*

Deformation	along (100)		along (111)	
	$b'\epsilon_{xx} > 0$	$b'\epsilon_{xx} < 0$	$d'\epsilon_{xy} > 0$	$d'\epsilon_{xy} < 0$
$g_\parallel$	$g_1' + \frac{1}{4}g_2'$	$3[g_1' + 9/4\, g_2')$	$g_1' + 13/4\, g_2'$	$3(g_1'^2 + 23/6\, g_1' g_2' + 187/48\, g_2'^2)^{1/2}$
$g_\perp$	$2g_1' + 5g_2'$	$3/2\, g_2'$	$2g_1' + 7/2\, g_2'$	0

As stated above, spin resonance has been measured by FEHER, HENSEL and GERE.(1) They found that in deformation along the principal axes the variation of the resonance frequency with the direction of the magnetic field is governed by equation (10). In their paper(1) they show the values of the g-factor for various acceptors in Si with deformation in the (001) direction.

Using their data it is possible to determine $g_\parallel$ and $g_\perp$ for each of the acceptors and to calculate g_1' and g_2' for them on the basis of Table 1. However, this calculation requires knowledge of the sign of the constants b' and d' as well as the sign of the ratio $g_\parallel/g_\perp$. Depending on the selection of the signs of b' and $g_\parallel/g_\perp$, four sets of constants can be obtained from this data.

If the values of $g_\parallel$ and $g_\perp$ were known for deformation along (111), it would be possible to make an unambiguous selection. No such data are given by FEHER *et al.*,(1) but they indicate that $g_\parallel$ and $g_\perp$ are practically the same in value for this direction as for deformation along (100). It will be seen from Table 1 that this can occur only if $b'\epsilon_{xx} > 0$ and $d'\epsilon_{xy} > 0$, i.e. if $b' < 0$ and $d' < 0$, $g_\perp/g_\parallel > 0$ and $g_2' \ll g_1'$. The last inequality also follows from the estimates given below in the effective mass approximation. The values of g_1' and g_2' which correspond to this choice of signs, are given in Table 2. Heae the sign of g_1' cannot of course be determined, but from estimates using the effective mass approximation, it follows that it should not differ from the sign of g_1. Therefore, in accordance with Ref. 9, we assume that for Si, $g_1' < 0$.

4. THE DEPENDENCE OF THE g-FACTOR FROM THE DEFORMATION

Equations (7–9), which define the g-factor in the case in question, only hold good for deformations such that $\hbar\omega_{cn} \ll \Delta_\epsilon \ll E_t$. This implies that the g-factor for the impurity centre will depend on the deformation and that the relative corrections to the g-factor will be of the order of Δ_ϵ/E_t and $\hbar\omega_{cn}/\Delta_\epsilon$.

Under the experimental conditions of FEHER *et al.*,(1) the first corrections are considerably greater than the second. Corrections proportional to the deformation can be calculated by including

Table 2. *Values of* g_1' *and* g_2' *for various acceptors in* Si (*for* $b < 0$ *and* $g_\perp/g_\parallel < 0$)

	B	Al	Ga	In
g_1'	−1·21	−1·19	−1·14	−1·00
g_2'	0·002	0·047	0·051	0·087

in $\hat{H}'$ the term $\hat{H}'_{\epsilon H}$ which can be written as

$$\begin{aligned}\hat{H}'_{\epsilon H} = &-(\mu_0 g_1/E_t)\{a\epsilon[\rho_1(\bar{J}\bar{H})+\rho_2(\bar{J}^3\bar{H})]\\ &+b\epsilon_{zz}[\rho_3(V_y H_y - V_x H_x)+\rho_4(\bar{J}\bar{H}-3J_z H_z)\\ &+\rho_5(\bar{J}^3\bar{H}-3J_z^3 H_z)]\ldots+d\epsilon_{xy}[\rho_6(V_x H_y - V_y H_x)\\ &+\rho_7(J_x H_y + J_y H_x)+\rho_8(J_x^3 H_y + J_y^3 H_x)\\ &+\rho_9 J_z(J_x J_y)H_x]+\ldots\} \qquad (11)\end{aligned}$$

where $V_x = [J_x(J_y^2 - J_z^2)]$ and so on.

The terms which are omitted in equation (11) for the sake of simplicity, are obtained by cyclical permutation of coordinates. In hydrostatic deformation, all the terms in equation (11), except the first two, vanish. The coefficients ρ_1 and ρ_2 of these terms are considerably less than the rest since in hydrostatic compression no change in symmetry occurs and the variation of the g-factor can be related solely to the influence of neighbouring bands. It is of the order of $a\epsilon/E_g$ and, consequently, $p_1 \sim p_2 \sim E_t/E_g$, where E_g is the energy gap.

Equation (11) permits calculation of the variation of the g-factor. Thus, in deformation along (001) for $\rho_1 = \rho_2 = 0$:

if $b'\epsilon_{zz} > 0$

$$\begin{aligned}\delta g_{\parallel} &= g_1(2\sqrt{(E_\epsilon)}/E_t)(\rho_4+\tfrac{1}{4}\rho_5),\\ \delta g_{\perp} &= -g_1(2\sqrt{(E_\epsilon)}/E_t)(\rho_4+5/2\ \rho_5-\tfrac{3}{4}\rho_3); \qquad (12)\end{aligned}$$

if $b'\epsilon_{zz} < 0$

$$\begin{aligned}\delta g_{\parallel} &= g_1(2\sqrt{(E_\epsilon)}/E_t)(3\rho_4+27/4\ \rho_5),\\ \delta g_{\perp} &= -g_1(2\sqrt{(E_\epsilon)}/E_t)\tfrac{3}{4}(\rho_5+\rho_3). \qquad (13)\end{aligned}$$

In the following we shall estimate the coefficients appearing in (12) and (13) using the effective mass approximation, and we shall compare the calculated value with observation.

6. THE TRANSITION PROBABILITY IN A STRAINED CRYSTAL

First we must point out that an alternating magnetic field can also cause transitions between levels which have split under deformation without a constant magnetic field. The corresponding resonance frequency ω is equal to $\Delta_\epsilon/\hbar$, where Δ_ϵ is determined by equation (7). The operator H'_h which causes these transitions, differs, as it did above, from (3) only in the substitution of $\bar{h}(t) = 2\bar{h}_0 \cos \omega t$ for $\bar{H}$.

For analysis of the transition probability, it is necessary to plot eigen-functions which diagonalize H'_ϵ. Since each of the split states is degenerate, the corresponding transition probabilities need to be averaged with respect to the initial state and summed with respect to the final state. The corresponding "averaged" value of the matrix element of the operator $(\bar{J}\bar{h})$ which defines the transition probability if $g_2 \approx 0$, is

$$|(\bar{J}\bar{h})_{\mathrm{I,II}}|^2 = \mu_0^2 g_1'^2(\bar{h}\tilde{\alpha}\bar{h}) \qquad (14)$$

where

$$\begin{aligned}\alpha_{xx} &= \frac{1}{4E_\epsilon}\{d'^2(\epsilon_{xy}^2+\epsilon_{xz}^2+\epsilon_{yz}^2)\\ &\quad+3[b'^2(\epsilon_{yy}-\epsilon_{zz})^2+d'^2\epsilon_{yz}^2]\},\\ \alpha_{xy} &= -\frac{1}{4E_\epsilon}\{3d'^2\epsilon_{xz}\epsilon_{yz}+\sqrt{(3)}b'd'\epsilon_{xy}(\epsilon-3\epsilon_{zz})\} \qquad (15)\end{aligned}$$

The rest of the components $\tilde{\alpha}$ are obtained by cyclical permutation of the subscripts. For example, for tension along the principal axes (100) or (111):

$$|(\bar{J}\bar{h})_{\mathrm{I,II}}|^2 = \tfrac{3}{4}\mu_0^2 g_1'^2 h_\perp^2 \qquad (16)$$

The transition probability between levels which have split in the magnetic field, as in the case of free holes,(2, 3) is proportional to the square of the modulus of the matrix element $|(H'_h)_{1,2}|^2$:

$$|(H'_h)_{1,2}|^2 = \frac{\mu_0^2}{4}\frac{(\bar{H}\tilde{g}^2\bar{H})(\bar{h}\tilde{g}^2\bar{h})-(\bar{H}\tilde{g}^2\bar{h})^2}{(\bar{H}\tilde{g}^2\bar{H})}, \qquad (16a)$$

where the components $\{g^2\}_{\alpha,\beta}$ are determined from (8) or (9). In the case of deformation along the principal axes, from (16) and (10) we have:

$$|(H'_h)_{1,2}|^2 = \mu_0^2\frac{g_\parallel^2[\bar{H}\times\bar{h}]_\perp^2+g_\perp^2[\bar{H}\times\bar{h}]_\parallel^2}{g_\parallel^2 H_\parallel^2+g_\perp^2 H_\perp^2}, \qquad (17)$$

where $g_\parallel$ and $g_\perp$ for each case are given in Table 1.

7. ANALYSIS OF THE WAVE FUNCTIONS AND PARAMETERS OF THE IMPURITY CENTRE IN THE EFFECTIVE MASS APPROXIMATION

In the effective mass approximation the wave function of the impurity electron or hole Ψ is represented as a product of fast-changing (with the period of the elementary cell) Bloch functions ϕ_i of free carriers at the bottom of the zone with the smooth functions $f(x)$:

$$\Psi_i = \sum_s \phi_s f_s^i \tag{18}$$

Here the subscript i indicates the number of the degenerate function Ψ_i, the maximum value of i being equal to the "degeneration multiple" of the impurity centre, but summation in equation (18) is performed with respect to all the degenerate functions ϕ_s and the maximum value of s is determined by the degree of degeneracy of the band at the point of the extremum.

The functions f satisfy the equation

$$\{\hat{D}(\hat{k}) + V(r)\}f = Ef \tag{19}$$

where $\hat{D}(\hat{k})$ is determined from equation (13) of Ref. 8, and $V(r) = -e^2/\epsilon_0 r$. If the wave functions ϕ_i of the free carriers transform according to the representation Γ_ϕ, whilst the "total" function of the acceptor centre transforms according to Γ_Ψ, then the smooth functions f_s^i must transform according to the irreducible representations appearing in the product

$$\Gamma_f = \Gamma_\Psi^* \times \Gamma_\phi \tag{20}$$

The functions f_s^i which effect irreducible representations of a cubic group, can be expanded into harmonic polynomials of different degree l. Amongst the functions constructed in this way, the lowest energy corresponds to those which are finite at zero, where $V(r)$ is minimal, i.e. to those which contain polynomials with $l = 0$ and, consequently, which transform according to the identity representation. It will be seen from equation (20) that an identity representation is contained in Γ_f only if the representations Γ_{Ψ} and Γ_ϕ coincide. Wave functions of the ground state of a small impurity centre therefore transform according to the same representation as the wave functions of free holes at the extremum point and the degeneracy factor of the ground state is equal to that of the zone at this point, i.e. in p-Ge and p-Si the functions Ψ_i in the effective mass approximation, and also ϕ_s, transform according to Γ_8^- and therefore the smooth functions f must transform according to the following representations:

$$\Gamma_8^- \times \Gamma_8^- = 2\Gamma_{15}^+ + 2\Gamma_{25}^+ + \Gamma_{12}^+ + \Gamma_2^+ + \Gamma_1^+ \tag{21}$$

But since equation (19) is not solved exactly, these functions are determined by the variational method. Variational calculations for the ground and excited states of acceptor centres in Ge and Si have been performed by KOHN and SCHECHTER.(4, 5)*

Knowing the functions f_s, we can evaluate the corresponding matrices H' for the acceptor centre by using the matrices $\hat{H}$ for free holes.

In fact,

$$H'_{ij} = \sum_{s,t} \int f_s^{i*} H_{st} f_t^j \,\mathrm{d}t = \sum_{s,t} H_{st} \int f_s^{i*} f_t^i \,\mathrm{d}t \tag{22}$$

The last equality in equation (22) holds only if $\hat{H}$ is a multiplicative operator, as occurs for the operators $\hat{H}_\epsilon$, $H_{\bar{H}}$ and $H_{\epsilon\bar{H}}$. In evaluating H'_ϵ and H'_H the resulting matrices can be written in the form of (2) and (3) respectively, and the constants a', b', d', g'_1 and g'_2 can be determined in this way. Here a' is always equal to a since in the approximation (18) the impurity level is shifted together with the band-edge in hydrostatic compression.

Tables 3 and 4 show the resulting constants b', d', g'_1 and g'_2 as calculated by the functions f_s^i for values of the parameters given by SCHECHTER.(5) Estimated values of these constants are given in the Tables.

It will be seen from Table 3 that the constants b' and d' of deformation potential for an acceptor centre can differ considerably from the corresponding constants for free holes. In the paper of KLEINER and ROTH,(11) these constants are determined from the shift of the absorption lines in strained crystals, all these constants here being assumed identical for free and bounded holes. It will be seen from Table 3 that this untenable assumption can lead to substantial errors in experimental determination of the constants b and d.

It follows from Table 4 that $g'_2 \neq 0$ for bound holes, even if $g_2 = 0$ for free holes. However, in all cases $|g'_2|$ is much less than $|g'_1|$, the ratio g'_2/g'_1 is negative, which agrees with the experimental data in Table 1.

The values of g'_1 and g'_2 calculated from the data of Ref. 9, are also in satisfactory agreement with

---

* For p-Ge they were performed by E. I. BUTIKOV (Diploma paper, Leningrad State University, 1962) with regard to the latter data concerning the constants A, B and D.(10)

The results are practically the same as those of SCHECHTER.(5) The published data(5) is therefore employed.

Table 3. *Constants of the deformation potential for acceptor centres of* Ge *and* Si

					Numerical values in eV			
			b'/b	d'/d	$b^{(12,13)}$	$d^{(12,13)}$	b'	d'
	Ge		0·56	0·61	−2	−7	−1·1	−4·3
$\Delta = \infty$	Si		0·77	0·82			−1·08	−2·5
	Si	$B < 0$	0·84	0·93	−1·4	−3·1	−1·17	−2·9
$\Delta = 0$		$B > 0$	0·73	0·75			−1·02	−2·3

Table 4. *Values of* g_1' *and* g_2' *for acceptor centres in* Ge *and* Si

				Numerical estimates of			
		g_1'	g_2'	g_1	g_2	g_1'	g_2'
	Ge	$0{\cdot}86\,g_1+0{\cdot}23\,g_2$	$-0{\cdot}04\,g_1+0{\cdot}78\,g_2$	6·58	≈ 0	5·66	−0·26
$\Delta = \infty$	Si	$0{\cdot}97\,g_1+0{\cdot}15\,g_2$	$-0{\cdot}025\,g_1+0{\cdot}89\,g_2$	−0·78	≈ 0	−0·76	0·02

experiments. We mention that these estimates are a further confirmation of the fact that, for Si, b is negative and, consequently, B is also negative.* In fact, the ratio $g_\parallel/g_\perp$ would otherwise be of the order of $2g_1'/g_2' \approx 10^2$ for $\epsilon_{zz} < 0$, whereas in experiment, as will be seen from Table 1, it does not exceed 0·63. Conversely, the theoretical value of $g_\parallel/g_\perp$ for $b < 0$, equal to 0·47, is close to the experimental value for B which, according to Table 1, is equal to 0·50. For the rest of the acceptors the agreement is less than that for least fulfilment of the conditions under which the effective mass approximation is applicable for ions with large Z. However, even the maximal value $g_\parallel/g_\perp$ for In, equal to 0·63, does not differ greatly from the calculated value.

By using the wave functions f_s^i we can also estimate the constants ρ_i in (11) for the variation of the g-factor in deformation.

The matrix $H'_{\epsilon\bar{H}}$ for an acceptor centre can be evaluated to a second approximation in perturbation theory by taking into account the terms H_ϵ and $H_{\bar{H}}$ for free holes:(3, 8)

$$(H'_{\epsilon\bar{H}})_{ij} = \sum_n{}' \frac{(H_{\bar{H}})_{in}(H_\epsilon)_{nj}+(H_\epsilon)_{in}(H_{\bar{H}})_{nj}}{E_0-E_n} \tag{23}$$

Here the summation is performed with respect to all the excited states of the acceptor centre, including, in principle, the region of the continuous spectrum. It will be seen from equation (23) that by virtue of the orthogonality of the functions of the ground ($n = 0$, $i = 1,\ldots 4$) and excited ($n \geqslant 1$) states, the term in H_ϵ which is equal to $\hat{I}a\epsilon$, where $\hat{I}$ is a unity matrix, makes no contribution to $H_{\epsilon H}$ and, consequently, ρ_1 and ρ_2 are zero in this approximation as they should be.

To estimate the rest of the constants, we substitute $-\bar{E}$ for E_0-E_n in equation (23) and put $\bar{E} = E_i$, where E_i is the ionization energy. By definition we get:

$$(H'_{\epsilon\bar{H}})_{ij} = -\frac{1}{E_i}\{(H_{\bar{H}}H_\epsilon+H_\epsilon H_{\bar{H}})_{ij} - \sum_s [(H_{\bar{H}})_{is}(H_\epsilon)_{sj}+(H_\epsilon)_{is}(H_{\bar{H}})_{sj}]\}, \tag{24}$$

where summation is performed with respect to the degenerate functions (s) of the ground state.

But since according to (22)

$$(H')_{ij} \equiv \sum_{s,t} \langle f_s^i|H_{st}|f_t^j\rangle,$$

while $(H'_{\bar{H}}H'_\epsilon)_{ij}$, according to the rules of matrix multiplication, is equal to the sum $\sum_s (H'_{\bar{H}})_{is}(H'_\epsilon)_{sj}$, equation (24) can be written as

$$(H'_{\epsilon\bar{H}})_{ij} = -\frac{1}{E_i}\{(H_{\bar{H}}H_\epsilon+H_\epsilon H_{\bar{H}})_{ij} - [(H'_\epsilon H'_{\bar{H}})_{ij}+(H'_\epsilon H'_{\bar{H}})_{ij}]\} \tag{25}$$

where the second term is the product of the matrices H', while the first is a matrix element from the product

$$(H_{\bar{H}}H_\epsilon)_{ij} \equiv \sum_{s,t} \langle f_s^i|(H_{\bar{H}}H_\epsilon)_{st}|f_t^j\rangle.$$

---

* This indicates that the calculations of the constants A, B and D in Ref. (12), the authors of which obtained a contradictory result, are apparently erroneous. Measurements of quantum cyclotron resonance which have recently been published,(9) confirm that the constants B and D are negative both for Ge and for Si.

Table 5. The variation of the g-factor of an acceptor centre during deformation (for $\epsilon = \epsilon_{zz}$)

	ρ_3	ρ_4	ρ_5	$\delta g_\parallel/g_1 \cdot \Delta\epsilon/E_t$		$\delta g_\perp/g_1 \cdot \Delta\epsilon/E_t$	
				$b'\epsilon_{zz} > 0$	$b'\epsilon_{zz} < 0$	$b'\epsilon_{zz} > 0$	$b'\epsilon_{zz} < 0$
Ge	−0·33	0·65	−0·16	0·61	0·85	−0·5	−0·005
Si	0·16	0·26	−0·22	0·22	−0·70	0·35	−0·02

Having evaluated the matrix elements from (25), we can, by comparing them with (11), find the constants ρ_i which determine the variation of the g-factor during the specified deformation.

If we use the variational functions of SCHECHTER,(5) the analysis produces values of ρ_3, ρ_4 and ρ_5 which are shown in Table 5. This Table also gives values of $\delta g_\parallel$ and $\delta g_\perp$ from equations (12) and (13) for $\epsilon = \epsilon_{zz}$. Here it is assumed that $g_2 = 0$, $g_2' = 0$ and that $\Delta \to \infty$.

If we substitute values of b, g_1 and E_t according to the Tables, then for Si if $b'\epsilon_{zz} > 0$, we get

$$\frac{\delta g_\perp}{\epsilon_{zz}} = -0{\cdot}7; \qquad \frac{bg_\perp}{E_t} = -20.$$

(In equations (12–13) $g_\perp$ everywhere represents its absolute value.) According to data in Ref. 1, the experimental value $\delta g/T_{zz} = -7{\cdot}1\times 10^{-11}\,\mathrm{cm^2/dyne}$ (if $T_{zz} < 0$). Since the relative extension in the z-direction $\epsilon_{zz}' = \epsilon_{zz} - \frac{1}{2}(\epsilon_{xx}+\epsilon_{yy}) = (S_{11}-S_{12})T_{zz} = 0{\cdot}982\times 10^{-12}\,T_{zz}$, the experimental value of $\delta g/\epsilon_{zz}'$ is equal to -70. It will be seen that the theoretical estimates provide the correct sign of this coefficient, but a considerably too low absolute value. Of course, it is difficult to expect exact agreement here, because of the error in the effective mass approximation itself, the variational method for analysing the wave functions for $\Delta = \infty$, and the inadequately reliable value of the constant b. Apparently, however, the main cause is that we considerably reduce the quantity δg by putting $E_n - E_0 = E_t$ in equation (23).

The point is that in Si and Ge the excited states of the acceptor are close to the ground state. Thus, according to SCHECHTER,(5) the distance to the nearest level Γ_6 in Si is $\frac{1}{6}E_t$, to Γ_7 it is $\frac{1}{6}E_t$ and to Γ_8 it is $\frac{1}{4}E_t$. According to the selection rules, all these levels make a contribution to (23). Therefore, apparently, it is not correct to put $E_n - E_0 \sim E_t$ in equation (23). To obtain satisfactory agreement with experiment, it is necessary to put $\bar{E} \sim \frac{1}{3}E_t$, i.e. $\bar{E}$ is approximately double the distance to the nearest level $E_1 - E_0$.

REFERENCES

1. FEHER G., HENSEL J. C. and GERE E. A., *Phys. Rev. Letters* **5**, 309 (1960); *Proc. Intern. Conf Semicond., Prague*, 1960, p. 579. Prague (1961).
2. PIKUS G. E. and BIR G. L., *Proc. Intern. Conf. Semicond., Prague*, 1960, p. 89. Prague (1961).
3. PIKUS G. E. and BIR G. L., *F.T.T.* **3**, 3050 (1961); *Phys. Rev. Letters* **6**, W3, 103 (1961).
4. KOHN W., Solid State Physics, Vol **5**, (edited by SEITZ F. and TURNBULL D.) p. 257, Academic Press, New York (1957); KOHN W. and SCHECHTER D., *Phys. Rev.* **99**, 1903 (1955).
5. SCHECHTER D., *J. Phys. Chem. Solids* **23**, 237 (1962).
6. WEINRICH G., *J. Phys. Chem. Solids* **8**, 216 (1959).
7. LUTTINGER J. M., *Phys. Rev.* **102**, 1030 (1956).
8. PIKUS G. E. and BIR G. L., *F.T.J.* **1**, 1642 (1959).
9. SICKLER T. T., LEISER H. T. and HELLER T. S., *Phys. Rev.* **127**, 1077 (1962).
10. LEVINGER B. W. and FRANKL D. R., *J. Phys. Chem. Solids* **20**, 281 (1961).
11. KLEINER W. H. and ROTH L., *Phys. Rev. Letters* **2**, 334 (1959).
12. KLEIMAN L. K. and PHILIPS J. C., *Phys. Rev.* **118**, 1953 (1960).

J. Phys. Chem. Solids Pergamon Press 1963, Vol. 24, pp. 1475–1486. Printed in Great Britain.

SPIN AND COMBINED RESONANCE ON ACCEPTOR CENTRES IN Ge AND Si TYPE CRYSTALS—II

THE EFFECT OF THE ELECTRICAL FIELD AND RELAXATION TIME

G. L. BIR, E. I. BUTIKOV and G. E. PIKUS

Institute of Semiconductors, Academy of Science U.S.S.R., Leningrad, U.S.S.R.

(*Received* 22 *November* 1962)

Abstract—The splitting of the ground state under the action of an electric field is determined and the transition probability in the electric field is calculated. The relaxation time in strained and unstrained crystals is also computed.

1. THE HAMILTONIAN OF THE IMPURITY CENTRE IN AN ELECTRIC FIELD

FOR analysis of the effects due to the electric field, we use the matrix method. If the field distortion near the impurity ion is not considered, i.e. for symmetry $T_d \times I$, the only terms which can appear in $\hat{\mathbf{H}}'$ are quadratic in the electric field and the corresponding matrix $\mathbf{H}'_{E^2}$ is similar to the matrix $\mathbf{H}'_\epsilon$:

$$\mathbf{H}'_{E^2} = -(p_0^2/E_i)\{\alpha E^2\hat{I}+\beta[J_x^2E_x^2+J_y^2E_y^2+J_z^2E_z^2-(5/4)\hat{I}E^2]+(2/\sqrt{3})\delta([J_xJ_y]E_xE_y+[J_yJ_z]\,E_yE_z+[J_xJ_z]\,E_xE_z)\} \tag{1}$$

where $p_0 = e\bar{r}$ is the dipole moment, $\bar{r}$ being the mean radius of the ground state, defined by the equation

$$\bar{r} = \left(\int \Psi^* r^2\Psi\, d\tau\right)^{1/2}, \tag{2}$$

where Ψ is the corresponding wave function and α, β and δ are dimensionless constants of the order of unity which we shall estimate using the effective mass approximation.

Consideration of the local fields of ions reduces the symmetry to T_d, and causes terms to appear in $\hat{\mathbf{H}}'$ which are linear in $\mathbf{E}$ as well as terms which contain products of the components of $\mathbf{E}$ and $\mathbf{H}$:

$$\mathbf{H}'_{\bar{E}} = (2p\chi/\sqrt{3})\{E_x[J_yJ_z]+E_y(J_xJ_z)+E_x(J_xJ_y)\} \tag{3}$$

$$\mathbf{H}'_{\bar{E}\bar{H}} = (p\mu_0/E_i)\{\gamma_1(J_x[E_yH_z]+J_y[E_zH_x]+J_z[E_xH_y])+\gamma_2(J_x^3[E_yH_z]+J_y^3[E_zH_x]+J_z^3[E_xH_y])+(2/\sqrt{3})\,\gamma_3(\bar{V}[\bar{E}\times\bar{H}])\} \tag{4}$$

Here $V_x = [J_x(J_y^2-J_z^2)]$ and so on, $[A_iB_j] = \frac{1}{2}(A_iB_j+A_jB_i)$, whilst $p = ea_B$, where a_B is the Bohr radius. We have selected dimensional factors in equations (3) and (4) such that the dimensionless constants χ and γ_i are not very small.

In the following we make numerical estimates of these constants. We mention that the sign of these constants will be different depending on the particular sub-lattice in which the impurity ion occurs. This implies that there are always centres in the crystal with negative as well as positive values of χ and γ_i. For deep levels, where the electron is localized near the ions, the effect of the electric field is very substantial and the displacement of the lines caused by it is detected directly in experiments.(1, 2) For shallow centres the terms which are linear in the field are non-zero only to the extent that departures from the effective mass approximation are appreciable. Therefore the coefficients in equations (3) and (4) will be considerably less for them than for deep levels, and, in the presence of sufficiently strong fields the contribution of the terms which are quadratic with respect to the field becomes the more noticeable.

Note that terms should also be included in $\hat{\mathbf{H}}'$

which contain the products of E_t and ϵ_{ij}. However, since these terms, as distinct from (4), do not lead to total removal of degeneracy, it follows that even in the case when the splitting due to the deformation greatly exceeds the splitting in the magnetic field, the contribution from these terms will always be small compared with the terms included in (3) and (4). Using the matrices (1), (3) and (4) we can compute the splitting due to constant electric fields as well as the probability of transition in alternating electric fields.

2. SPLITTING OF THE TERMS IN THE ELECTRIC FIELD IN AN UNSTRAINED CRYSTAL

In a non-deformed crystal the electric field, like the deformation, can cause partial removal of degeneracy. From a comparison of (1), (3) with (2.I),* it will be seen that the splitting in the electric field is determined by the equation:

$$\Delta_{E^2,E} = 2\{(p_0^4/E_t^2)\,[\beta^2E^4+(\delta^2-3\beta^2) \times (E_x^2E_y^2+E_x^2E_z^2+E_y^2E_z^2)]+p^2\chi E^2\}^{1/2} \tag{5}$$

It is seen that for sufficiently weak fields when the linear terms predominate:

$$\Delta_E = 2p\chi E \tag{6}$$

Transitions between these split-off levels may be caused by electric fields as well as by magnetic fields. The corresponding transition probabilities are determined by equations which differ from (14.I) and (15.I) in the substitution of:

$(p_0^2\beta/E_t)E_x^2$ for $b'\epsilon_{xx}$, $(p_0^2\delta/E_t)\ E_xE_y+p\chi E_z$ for $d'\epsilon_{xy}$ and so on. (7)

Then, for example, for weak fields in (14.I)

$$\alpha_{xx} = \tfrac{1}{4}(1+3E_x^2/E^2), \quad \alpha_{xy} = -\tfrac{3}{4}(E_xE_y/E^2) \tag{8}$$

3. DISPLACEMENT OF THE TERMS IN A STRAINED CRYSTAL

The displacement of the terms in a deformed lattice in the presence of a field which is associated with the terms $\mathbf{H}_{E^2}'$ and $\mathbf{H}_E'$ can be calculated without difficulty if in equations (8.I) and (9.I) which determine the g-factors, we add to $b'\epsilon_{ii}$ and $d'\epsilon_{ij}$ terms which are analogous to (7) and if we then expand the resulting expressions into a series in $\Delta_E/\sqrt{(E_\epsilon)}$. Since here the electric field only changes the g-factor, it is clear that the corresponding additional splitting $\Delta\omega$ is approximately equal to $\omega(\Delta_E/\Delta_\epsilon)$. For example, for deformation along the (001) axis, the frequency change due to the terms $\mathbf{H}_{E^2}'$ for the lower two levels is determined by the equation

$$\frac{\Delta\omega_{E^2}}{\omega} = -\sqrt{3}\,\frac{p_0^2}{E_t\Delta_\epsilon}\,\frac{g_1'+(7/4)g_2'}{g_\parallel^2H_\parallel^2+g_\perp^2H_\perp^2} \times \{g_\perp[\sqrt{3}\beta(E_x^2-E_y^2)\,(H_x^2-H_y^2) +4\gamma\delta E_xE_yH_xH_y]+2g_\parallel\delta E_zH_z\,(E_xH_x+E_yH_y)\}, \tag{9}$$

where $\gamma \equiv b'\epsilon_{zz}/|b'\epsilon_{zz}| = \pm 1$.
Analogously, the contribution due to $\mathbf{H}'_E$ is

$$\frac{\Delta\omega_E}{\omega} = -2\sqrt{3}\,\frac{p\chi}{\Delta_\epsilon}\,\frac{g_1'+(7/4)g_2'}{g_\parallel^2H_\parallel^2+g_\perp^2H_\perp^2} \times [2g_\perp E_zH_xH_y+g_\parallel H_z(H_xE_y+H_yE_x)] \tag{10}$$

The splitting associated with the terms $\mathbf{H}_{\bar{E}\bar{H}}'$ is in general less than (10) since their contribution to $\hbar\Delta\omega$ is of the order of $\hbar\omega(\Delta_E/E_t)$, i.e. it is Δ_ϵ/E_t times smaller than $\mathbf{H}_E'$. But possibly their contribution is more noteworthy insofar as in certain directions of the magnetic field $\Delta\omega_E$ vanishes according to (10). The contribution from these terms can be taken into account without difficulty by adding to $g_{1,2}H_x$ in (8.I) and (9.I) the term $(p/E_t)\ \beta_{1,2}(H_yE_z+H_zE_y)$. For deformation along (001) the corresponding contribution to $\Delta\omega$ is

$$\frac{\Delta\omega}{\omega} = \frac{p}{2E_t} \times \frac{(g_\parallel\beta_\parallel+g_\perp\beta_\perp)H_z(E_xH_y+E_yH_x)+2g_\perp\beta_\perp H_xH_yE_z}{g_\parallel^2H_\parallel^2+g_\perp^2H_\perp^2} \tag{11}$$

where $\beta_\parallel$ and $\beta_\perp$ are determined by equations which differ from those in Table 1.I by the substitution of β_t for g_t.

The contribution from the third term is calculated in the usual way in the first approximation of perturbation theory. Using the eigenfunctions

---

* Here and throughout I denotes Part I of this article.

$\mathbf{H}'_\epsilon$ we find that if $\epsilon = \epsilon_{zz}$, the corresponding shift $\Delta\omega$ is:

$$\frac{\Delta\omega}{\omega} = \frac{\sqrt{3}\, g_\perp \beta_8 p}{E_t(g_\parallel^2 H_\parallel^2 + g_\perp^2 H_\perp^2)} \times [2E_z H_x H_y - H_z(E_x H_y + E_y H_x)] \tag{12}$$

It will be seen from equations (9–12) that by selecting a certain orientation of the fields $\bar{E}$ and $\bar{H}$, we can in principle isolate each of these shifts. The contributions from $\mathbf{H}'_{E^2}$ and $\mathbf{H}'_{\bar{E}}$ further differ in the dependence on the deformation, whilst that from $\mathbf{H}'_{E^2}$ differs in the non-linear dependence on the field.

4. COMBINED RESONANCE IN AN UNSTRAINED CRYSTAL

Transitions between spin levels due to a variable (alternating) electric field is called *combined resonance*. The term was introduced by RASHBA who first called attention to the possibility of such an effect$^{(4)}$ and who then, together with SHEKA, evolved a detailed theory of combined resonance for free carriers in CdS, InSb and other crystals.$^{(5)}$ The transition probability due to a variable electric field $\bar{e}(t) = 2\bar{e}\cos\omega t$ is determined by a matrix element of the operator $\mathbf{H}'_e$ which differs from (3) in the substitution of $\bar{e}$ for $\bar{E}$, or correspondingly of the operator $\mathbf{H}'_{\bar{e}\bar{H}}$, analogous to (4). Terms which are quadratic with respect to e, similar to $\mathbf{H}'_{E^2}$ (equation 1), can also cause transitions at the frequency $\omega = \frac{1}{2}(\Delta E/\hbar)$, where ΔE is the distance between the respective levels. However, for small amplitude of the alternating field, the probability of such transitions is insignificant and we shall not consider them in detail. Note only that the corresponding matrix elements differ from the foregoing elements of the matrix $\mathbf{H}'_e$ by a substitution analogous to (7).

In an undeformed crystal, according to (3), if $H = H_z$, transitions between the levels 1–2 and 3–4 can be caused only by the transverse component of the electric field and the corresponding matrix elements are:

$$|(H'_{\bar{e}})_{1,2}|^2 = |(H'_{\bar{e}})_{3,4}|^2 = P^2\chi^2 e_\perp^2 \tag{13}$$

Conversely, transitions forbidden in a magnetic field between the levels 1–3 and 2–4 are caused only by the longitudinal field and

$$|(\mathbf{H}'_{\bar{e}})_{1,3}|^2 = |\mathbf{H}'_e)_{2,4}|^2 = p^2\chi^2 e_\parallel^2 \tag{14}$$

Comparing (13) and (6,I) we see that the ratio of the intensity of combined and paramagnetic resonance for transitions 1–2 or 3–4 is

$$\frac{w^e_{1,2}}{w^h_{1,2}} \approx \frac{4}{3}\frac{p^2\chi^2}{\mu_0^2(g'_1 + 7/4\, g'_2)^2}\frac{e_\perp^2}{h_\perp^2}$$

If $e \approx h/\sqrt{(\epsilon_0)}$, where ϵ_0 is the dielectric permeability, and $g'_2 \ll g'_1$

$$\frac{w^e_{1,2}}{w^h_{1,2}} \approx \frac{16}{3\bar{\alpha}^2}\frac{\chi^2}{g_1'^2\epsilon_0} = 10^6\frac{\chi^2}{g_1'^2\epsilon_0} \tag{15}$$

where $1/\bar{\alpha} = \hbar c/e^2 = 137$.

As regards transitions associated with $\mathbf{H}'_{\bar{e}\bar{H}}$, the probability of which is proportional to $e^2\mu_0^2H^2/E_t^2$, their intensity is much less than (13) in a non-deformed crystal and we will not consider them here.

5. COMBINED RESONANCE IN A STRAINED CRYSTAL

In a deformed crystal in the absence of a magnetic field the electric field can cause transitions between split-off levels at the spacing Δ_ϵ. This transition can be regarded as an "optical" transition. The corresponding matrix element of the operator $\mathbf{H}'_{\bar{e}}$, averaged with respect to the initial degenerate state and added with respect to the final state, is

$$|(\mathbf{H}'_{\bar{e}})_{\mathrm{I,II}}|^2 = p^2\chi^2[e^2 - (d'^2/E_\epsilon) \times (e_x\epsilon_{yz} + e_y\epsilon_{xz} + e_z\epsilon_{xy})^2] \tag{16}$$

Such transitions, unlike transitions due to the magnetic field, the probability of which is determined by equations (14.I) and (15.I), are therefore possible only in the presence of shear deformations. Thus, in tension along the axis (111).

$$|(\mathbf{H}_{\bar{e}})_{\mathrm{I,II}}|^2 = p^2\chi^2 e_\perp^2 \tag{17}$$

As will be seen from equations (14.I) and (15.I) the ratio of the intensity of the transitions due to the electric and magnetic fields is in this case defined by equation (15) also.

In a magnetic field the electric field causes transitions between the split levels 1–2 and 3–4.

The electric field also causes transitions between more distant levels, e.g. 1–3 and 2–4; this is in fact the optical transition mentioned above. As regards "spin" transitions 1–2 and 3–4, transitions associated with $\mathbf{H}'_{\bar{\epsilon}}$ in a deformed crystal are possible only in the second approximation of perturbation theory and therefore the corresponding matrix elements here are an order of magnitude $\hbar\omega_0/\Delta\epsilon$ times smaller than in undeformed crystals.

To calculate the probability of these transitions, it is necessary to construct from $\mathbf{H}'_{\bar{\epsilon}}$ and $\mathbf{H}'_{\bar{H}}$ the operator $\mathbf{H}'_{\bar{\epsilon}}$ in the second approximation of perturbation theory, which includes terms proportional to e and H, after which it is necessary to evaluate the corresponding matrix element. If $\epsilon = \epsilon_{zz}$ the computations give:

$$|(\mathbf{H}'_{\bar{\epsilon}})_{1,2}|^2 = \frac{3\mu_0^2 p^2\chi^2(g_1'+7/4\,g_2')^2}{\Delta_\epsilon^2(g_\parallel^2H_\parallel^2+g_\perp^2H_\perp^2)} \times \{g_\perp^2H_\perp^2(e_xH_y+e_yH_x)^2 + g_\perp^2e_z^2(H_x^2-H_y^2)^2+g_\parallel^2H_z^2H_\perp^2e_z^2 - 4g_\parallel g_\perp H_xH_yH_ze_z(H_xe_y+H_ye_x)\} \tag{18}$$

Hence it will be seen that $(\mathbf{H}'_{\bar{\epsilon}})_{1,2} = 0$ if $H = H_z$. If $H = H_\perp$

$$|(\mathbf{H}'_{\bar{\epsilon}})_{1,2}|^2 = 3\,\frac{\mu_0p^2\chi^2}{\Delta_\epsilon^2}(g_1'+7/4\,g_2')^2 \times [(e_xH_y+e_yH_x)^2 + (e_z^2/H_\perp^2)(H_x^2-H_y^2)^2] \tag{19}$$

Consequently, for example if $H = H_x$ and $e = e_z$, the intensity ratio of combined and paramagnetic resonance here is (if $e = h/\sqrt{\epsilon_0}$)

$$\frac{w^e_{1,2}}{w^e_{1,2}} = g\,\frac{\chi^2p^2H^2}{\epsilon_0\Delta_\epsilon^2} = \frac{27}{16}\left(\frac{\hbar\omega_0}{\Delta_\epsilon}\right)^2\left(\frac{w^e_{1,2}}{w^h_{1,2}}\right)_0, \tag{20}$$

where $(w^e_{1,2}/w^h_{1,2})_0$ is the ratio of the probabilities in an undeformed crystal from equation (15), i.e. this ratio decreases roughly $(\hbar\omega_0/\Delta_\epsilon)^2$ times.

Transitions in an electric field can be associated also with the operator $\mathbf{H}'_{\bar{e}\bar{H}}$. It should be pointed out that although the matrix elements of this operator are already non-zero in the first approximation of perturbation theory, however, owing to the small magnitude of the coefficients in (4), the ratio $|\mathbf{H}'_{\bar{e}\bar{H}}/\mathbf{H}'_{\bar{\epsilon}}|^2$ in the deformed crystals is of order $(\Delta\epsilon/E_t)^2$, i.e. it is in general very small. Of course in calculating the transition probability it is necessary to sum the matrix elements of all the terms in $\mathbf{H}'_{\bar{\epsilon}}$ and $\mathbf{H}'_{\bar{e}\bar{H}}$, and not the probabilities themselves. However, in order to avoid cumbersome calculations, we will consider each of the terms in (4) separately, bearing in mind that with appropriate orientations of the magnetic and electric fields we can in general separate the transitions associated with these terms. Furthermore, transitions which are associated with the operator $\mathbf{H}'_{\bar{\epsilon}}$, differ in the dependence of the matrix element on the magnitude of deformation.

Since the structure of the first two terms in (4) is similar to that of the operator $\mathbf{H}'_{\bar{h}}$ defined by equation (2.I), the probabilities for the transitions caused by these terms are calculated in a similar manner. Since $|\gamma_2|$ is apparently much less than $|\gamma_1|$, just as $|g_2| \ll |g_1|$, the term with γ_2 can generally be neglected. The transition probabilities associated with the first term in (4) differ from (14.I) only in the substitution of $(p/E_t)\gamma_1\,[E_yH_z]$ for g_1H_x and so on (if $g_2 = 0$).

As distinct from (18), if $\epsilon = \epsilon_{zz}$, transitions are also possible here for $H = H_z$. The corresponding matrix element is (if $b'\epsilon_{zz} < 0$):

$$|(\mathbf{H}^{(1)}_{\bar{e}\bar{H}})_{1,2}|^2 = \frac{1}{4}\,\frac{p^2\mu_0^2\gamma_1^2}{E_t^2}\,e_\perp^2H_z^2 \tag{21}$$

In a perpendicular magnetic field

$$|(\mathbf{H}^{(1)}_{\bar{e}\bar{H}})_{1,2}|^2 = \frac{\gamma_1^2p^2\mu_0^2}{16E_t^2} \times [(e_xH_y+e_yH_x)^2 + (4e_z^2/H_\perp^2)(H_x^2-H_y^2)^2] \tag{22}$$

For deformation along (001) the last term in (4) gives a transition probability proportional to:

$$|(\mathbf{H}^{(3)}_{\bar{e}\bar{H}})_{1,2}|^2 = \frac{3}{4}\,\frac{p^2\mu_0^2\gamma_3^2}{E_t^2}\,\frac{1}{g_\parallel^2H_z^2+g_\perp^2H_\perp^2} \times \{g_\parallel^2H_z^2\,[\bar{e}\times\bar{H}]_\perp^2 + g_\perp^2(H_x[e\times H]_y+H_y[\bar{e}\times\bar{H}]_x)^2\} \tag{23}$$

Here transitions are also possible for $H = H_z$ if the electric field, as is the case in (13), has the component $e_\perp$, where if $H = H_\perp$ transitions are possible only if e_z is non-zero:

$$|(\mathbf{H}^{(2)}_{\epsilon\bar{H}})_{1,2}|^2 = \frac{3}{4}\frac{p^2\mu_0^2\gamma_3^2}{E_t^2}\frac{e_z^2(H_x^2-H_y^2)^2}{H_\perp^2} \tag{24}$$

It will be seen that if $H_x^2 = H_y^2$ this matrix element vanishes, whereas (22) and (19) are finite here if only $e_\perp$ is not perpendicular to $H_\perp$.

It will be seen from (23, 24) that the ratio of the intensity of the combined resonance associated with $H_{\epsilon\bar{H}}$ to the intensity of the resonance in a non-deformed crystal (equation 15) is of the order of $(\hbar\omega/E_t)^2$, i.e. it is very small.

6. NUMERICAL ESTIMATES

First let us evaluate the constants in (1–4). As regards the constants α, β and δ, they can be estimated by analyzing the matrix $\mathbf{H}'_{E^2}$ in an analogous way to $\mathbf{H}'_{\epsilon\bar{H}}$ in (I). This matrix is the matrix of the operator $\hat{\mathbf{H}}_{\bar{E}} = e(Er)$, which is constructed on the eigenfunctions Ψ_t. If the field E is so small that $eE\bar{r} \ll E_t$, it can be calculated in the effective mass approximation solely with the smooth functions f_s^i. In the first approximation the corresponding matrix elements vanish since these functions correspond to symmetry $T_d \times I$ and the matrices of any odd operator on them are zero. By virtue of the latter condition, the matrix elements in the second approximation as distinct from (I.25) are

$$(\mathbf{H}_{E^2})_{ij} = \frac{e^2}{\bar{E}}\langle i|(\bar{r}\bar{E})^2|j\rangle \approx \frac{3e^2}{E_t}\langle i|(\bar{r}\bar{E})^2|j\rangle \tag{25}$$

Here in analogy with (24.I) we have replaced E_0-E_n by $\bar{E}$, it here being assumed in accordance with the estimates of paper I that $\bar{E} \sim \frac{1}{3}E_t$ but not that $\bar{E} \approx E_t$ as in (I.25).

Using the functions f_s^i we have calculated the mean radius $\bar{r}$ defined by equation (2) and computed the coefficients α, β and δ in (1) for Ge and Si in the approximation $\Delta \to \infty$. The results of these calculations are given in Table 1.

As regards the coefficient χ in (3), it vanishes in the effective mass approximation. For deep levels in Si, according to the data of HAM,[2] the coefficient p/e, which in our notation corresponds to the quantity $p/e\chi\sqrt{3} = a_B\chi\sqrt{3}$, is equal to $0{\cdot}3\times10^{-8}$ cm and, consequently, for these levels $\chi = 0{\cdot}33$, i.e. it is in fact close to unity. For shallow centres a departure of the ion field from cubic symmetry can be expected to affect distances a_0 of the order of a lattice constant and therefore δ is proportional to $\int|\Psi|^2\,d\tau$ across this region and consequently it is $(\bar{r}/\sqrt{3}\,a_0)^3$ times less than for deep levels, $\bar{r}$ being the mean radius of the impurity centre.* (In fact, if $\Psi \sim e^{r/r_0}$, then $\bar{r} \sim \sqrt{3}\,r_0$.) The corresponding estimates of the constants χ for Ge and Si are given in Table 2. This Table gives order of magnitude estimates of the constants γ_1 and γ_3. Here we have assumed in accordance with the foregoing that $\mu_0\gamma_1/E_t \approx \chi g_1\mu_0/\bar{E}$ and consequently for $\bar{E} \approx \frac{1}{3}E_t$, $\gamma_1/\chi = 3g_1$, γ_3/χ is apparently of the same order, whilst γ_2/χ is of the order of g_2, i.e. it is considerably less.

Availing ourselves of this data, we first estimate the intensity ratio of combined and paramagnetic resonance.

According to (15) the ratio $\overset{\epsilon}{w}_{1,2}/\overset{h}{w}_{1,2}$ is 5×10^{-5} for Ge and 1·5 for Si, i.e. in Si the combined resonance is approximately the same in intensity as the paramagnetic.

In deformed crystals combined resonance decreases greatly in intensity. Thus for $\epsilon \sim 3\times10^{-4}$ the ratio $(\Delta_\epsilon/\hbar\omega_0)^2$, which defines this decrease (equation 20), is 3×10^2. The terms associated with $\mathbf{H}'_{\epsilon H}$ apparently produces still less effect since the probability of such transitions is $(\hbar\omega_0/E_t) \sim 10^{-6}$

Table 1. *The value of $\bar{r}$ and the coefficients α, β and δ for acceptor centres in* Ge *and* Si. (*For $\bar{E} \sim \frac{1}{3}E_t$.*)

	r (Å)	α	β*	δ*
Ge	91	1	−0·3	−0·36
Si	34·4	1	−0·2	−0·42

*The signs of β and δ coincide with those of the constants B and D which in accordance with our estimates are assumed to be negative. This sign of constant B and D was confirmed by recent experiment, HENSEL and FEHER.[15]

---

* May be this estimate of χ and γ is very reduced.

Table 2. Estimates of the constants, χ, γ_1 *and* γ_3 *for acceptors in* Ge *and* Si.

	$(a_0/\sqrt{3}\bar{r})^3$	χ	$\gamma_1 \approx \gamma_3$
Ge	2×10^{-3}	$0\cdot7\times10^{-3}$	2×10^{-2}
Si	3×10^{-2}	1×10^{-2}	2×10^{-2}

times less than the transitions probability in an undeformed crystal.

Using the data of Tables 1 and 2, we can also estimate the magnitude of the splittings due to a constant electric field. In an undeformed crystal the splitting associated with the quadratic terms is:

$$\Delta E_I \approx \frac{2p_0^2\beta E^2}{E_i} \approx \begin{cases} 5\times10^{-11}\,E^2\,(\mathrm{Ge}) & (\Delta E \text{ in eV} \\ 1\cdot5\times10^{-12}\,E^2\,(\mathrm{Si}) & E \text{ in V/cm}) \end{cases} \tag{26}$$

From Table 2 the splitting due to the linear terms is

$$\Delta E_{II} \approx 2p\chi E \approx \begin{cases} 10^{-11}\,E\,(\mathrm{Ge}) & (\Delta E \text{ in eV} \\ 10^{-10}\,E\,(\mathrm{Si}) & E \text{ in V/cm}) \end{cases} \tag{27}$$

Consequently, the splitting due to the quadratic term becomes predominant if $E > E_0$, where

$$E_0 = \frac{E_i p\chi}{p_0^2\beta} \tag{28}$$

The values of E_0 for Ge and Si are given in Table 3.

For investigation of paramagnetic resonance on shallow acceptors in Ge and Si it is impossible to employ very strong electric fields since they cause ionization of the acceptors. Table 3 gives the maximum possible fields $E_{\max}$ above which low-temperature "breakdown" (experimentally) commences.(6, 7) The data for silicon(6) refers to Si with B doping; for other acceptors with a greater ionization energy the value of $E_{\max}$ is of course higher. Furthermore $E_{\max}$ can be increased slightly by increasing the concentration of the admixture. It will be seen from Table 3 that in both Si and Ge, fields can be attained in excess of E_0 for which the effects that are quadratic with respect to E are predominant. It is possible that in the presence of variable fields of large amplitude combined resonance can occur which is associated with these quadratic terms. Table 3 gives the approximate values of the splitting ΔE_{II} for $E_z = E_{\max}$. It will be seen that these splittings are too small for them to be observed directly.

However it may be possible to observe displacement of terms in a magnetic field which in order of magnitude is

$$\Delta\omega/\omega_0 \approx \Delta E/\hbar\omega_0 \tag{29}$$

It will be seen that if $E = E_{\max}$ and $\omega_0 = 5\cdot6\times10^{10}$ 1/sec, then $\Delta\omega/\omega_0$ is of the order of 10^{-4} in Ge and 10^{-3} in Si.

Apparently, to observe such a shift, it is necessary for the displacement $\Delta\omega_{E^2}$ to be greater than, or of the order of 0·1, of the width of the line $\Delta\tilde{\omega}$.

The displacement $\Delta\omega$ of the terms in a deformed crystal is of the order of magnitude of

$$\Delta\omega/\omega = \Delta E/\Delta_\epsilon \tag{30}$$

Although $\Delta\omega$ is much less in absolute magnitude than in (29), it is apparently easier to observe. Table 3 shows values of $\Delta\omega_{E^2}/\omega$ for $\epsilon = \epsilon_{zz} = 3\times10^{-4}$, $H = H_x$, $E_x = E_{\max}$ and $b'\epsilon_{zz} > 0$.

Table 3

	E_0 (V/cm)	$E_{\max}$ (for $p = 10^{16}$ cm^{-3}), (V/cm)	ΔE (for $E = E_{\max}$), (eV)	$\Delta\omega_E/\omega$ (for $\epsilon_{zz} = 3\times10^{-4}$)	$\Delta\omega_{E^2}/\omega$ (for $\epsilon_{zz} = 3\times10^{-4}$)
Ge	0·2	20	2×10^{-8}	2×10^{-5}	2×10^{-4}
Si	70	200	6×10^{-8}	$0\cdot8\times10^{-4}$	2×10^{-4}

If the quadratic effect occurs, it is possible that in Si we can also isolate the linear displacement in the field $\Delta\omega_E$, since according to the data of Table 3, if $E = E_{\max}$, it is always just 3 times less. These calculations are of course only approximate since the estimates of the constants in Tables 1 and 2 and, more particularly of γ, are very approximate.

7. THE WIDTH OF THE SPIN RESONANCE LINE IN UNSTRAINED AND STRAINED CRYSTALS

As stated above, spin resonance is not observed in undeformed crystals. The cause of this is the great width of the line in such crystals.

Kohn was the first to discuss the causes of such broadening of the line.(8) He indicated that the broadening may be connected with local deformations which lead to splitting of the ground state and a corresponding change in the g-factor. The magnitude of the local deformations due to dislocations can be evaluated if it is assumed that the deformations ϵ decrease linearly with distance, whilst near the dislocation itself $\epsilon_0 \sim 1$. Therefore $\bar{\epsilon} \approx \epsilon_0 a_0 N^{1/2}$, where N is the density of the dislocation per 1 cm^2, while a_0 is a lattice constant, i.e. $\bar{\epsilon} \approx 3\times 10^{-8} N^{1/2}$. It is obvious that for observation of resonance it is necessary for the splitting due to these deformations to be much less than the splitting due to the magnetic field. Since $\Delta_\epsilon \approx 2\bar{b}\bar{\epsilon}$, where $\bar{b} = 3$–7 eV, it follows that $\Delta_\epsilon \approx 3\times 10^{-7} N^{1/2}$ eV, whereas $\hbar\omega_{\mathrm{cn}} = 3{\cdot}7\times 10^{-5}$ eV (for $\omega = 5{\cdot}6\times 10^{10}\ \mathrm{sec}^{-1}$). Therefore, for Δ_ϵ to be roughly 10 times less than $\hbar\omega_{\mathrm{cn}}$, it is necessary for the dislocation density N to be less than 10^2 cm^{-2}. Studies are being made on how to grow Ge and Si crystals with this or even a considerably lower dislocation density. But even in good conventionally produced crystals the dislocation density is much higher (from 10^3 to 10^5 cm^{-3}).

In the paper of Feher *et al.*,(9) no data are given concerning the dislocation density in the crystals which they used, but it is quite probable that the cause of line-broadening in these specimens is the local deformations. It is obvious that in highly deformed specimens, when the homogeneous deformation ϵ is much greater than $\bar{\epsilon}$, the relative broadening of the lines is approximately $\bar{\epsilon}/\epsilon$, i.e. it decreases compared with an undeformed specimen by a factor of $\hbar\omega/\Delta_\epsilon$. For the specimen investigated by Feher,(9) if $T = 300$ kg/cm^2 ($\epsilon'_{zz} = 3\times 10^{-4}$), then $\Delta\omega/\omega = 3\times 10^{-2}$. Therefore, if the broadening of the lines is in fact caused by local deformations as suggested by Feher *et al.*(9) then $\bar{\epsilon} = 10^{-8}$ and consequently $N = 10^5$ cm^{-2}, which is quite possible.

Apparently, if the production process is particularly careful, it is possible to make crystals with sufficiently small internal stresses so that the line-width is determined by other factors.

In this connexion it is worthwhile to ascertain the line-broadening associated with lattice vibration, in order to elucidate the possibility of resonance and estimate the possible width of the lines in deformed crystals.

For an analysis of the transition probability due to acoustic modes of the lattice, we must evaluate the matrix elements of the operator $\mathbf{H}_\epsilon$, defined by (3.I), and put the deformation ϵ_f due to the oscillation of the lattice in place of ϵ. These matrix elements $(\mathbf{H}'_{\epsilon_f})_{ij}$ have to be taken between eigenfunctions which diagonalize the operators H'_ϵ and H'_H (for $\epsilon \neq 0$).

The transition probability is

$$w_{ij} = \frac{2\pi}{\hbar}\int \langle\langle |(\mathbf{H}'_{\epsilon_f})_{ij}|^2 \rangle\rangle\, \delta(\epsilon_i - \epsilon_j \pm \hbar\omega_q)\, \mathrm{d}q^3, \tag{31}$$

where $\langle\langle (H'_{\epsilon_f})_{ij} \rangle\rangle$ is a matrix element averaged with respect to the wave functions of the phonons.

We are interested in transitions from a lower level to a higher level, i.e. transitions which are associated with absorption of phonons. Correspondingly

$$\langle\langle a_q^2 \rangle\rangle = \frac{\hbar\bar{n}_q}{2\rho\omega_q} = \frac{\hbar}{2\rho\omega_q}\left(\exp\left[\frac{\hbar\omega_q}{kT}\right] - 1\right)^{-1}, \tag{32}$$

where ρ is the density and a_q is an operator for phonon absorption with the wave vector q.

Performing the integration with respect to ω_q in (31) we find that for each polarization ν

$$w_{ij}^{\nu} = \frac{\overline{n_\omega}\omega^3}{8\hbar\rho C_\nu^5}\int |\tilde{\mathbf{H}}_{ij}|^2\, \mathrm{d}\Omega_q, \tag{33}$$

where $\hbar\omega = \epsilon_j - \epsilon_i$, c_ν is the appropriate velocity of sound, while $\tilde{\mathbf{H}}_{ij}$ is an element of the matrix $\mathbf{H}'(\epsilon'_\nu)$ which differs from (3.I) in the replacement of ϵ

by ϵ'_ν, where ϵ'_ν is

$$(\epsilon'_\nu)_{\alpha\beta} = \frac{i}{2q}(q_\alpha e_\beta + q_\beta e_\alpha),$$

and here $\bar{e}$ is a polarization vector.

In an undeformed crystal, owing to the fact that the ground state is degenerate, phonon transitions between spin levels are resolved. Here the reciprocal lifetime is equal to the sum of the transition probabilities in all possible states

$$\frac{1}{\tau_i} = \sum_{j,\nu} w^\nu_{ij} \tag{34}$$

In the case where the magnetic field is directed along the principal axis (001) and where $g'_2 = 0$, and all four levels are equally spaced, the use of equations (31)–(34) for the lowest level gives the following value of $1/\tau_0$:*

$$\frac{1}{\tau_0} = \frac{3}{10}\frac{kT\omega_0^2}{\pi\hbar^2\rho C_t^5}(d'^2+2b'^2)\left(1+\frac{2}{3}\frac{C_t^5}{C_l^5}\right), \tag{35}$$

where C_l and C_t are the velocity of longitudinal and transverse sound, whilst ω_0 is the frequency of spin resonance, definable by the distance to the nearest level and equal to $\hbar\omega_0 = \mu_0 g'_1 H$ according to (I.5). If $\hbar\omega_0 \ll kT$ the relaxation time is the same for all levels, but, of course, in the general case this is not so.

In a deformed crystal phonon transitions between nearest levels which are split in a magnetic field, are forbidden in the first approximation and only allowed in the second. Correspondingly the relaxation time increases by a factor of $(\Delta_\epsilon/\hbar\omega_0)$.

For analysis of the transitions probability in the second approximation of perturbation theory, it is necessary to form that sub-matrix $\mathbf{H}'_\epsilon$ for the two lower levels of the second approximation which contains the products of terms proportional to $(\epsilon_f)_{\alpha\beta}$ and H_i from $\mathbf{H}'_{\epsilon_f}$ and $\mathbf{H}'_{\bar{H}}$. The equation $\hat{\mathbf{H}}'\Psi = E\Psi$ in a representation in which $\mathbf{H}_\epsilon$ is diagonal, can be written as

$$\begin{aligned}(\mathbf{H}'_{\mathrm{I,I}}-E)\Psi_{\mathrm{I}}+\mathbf{H}'_{\mathrm{I,II}}\Psi_{\mathrm{II}} &= 0,\\ (\mathbf{H}'_{\mathrm{II,II}}-E)\Psi_{\mathrm{II}}+\mathbf{H}'_{\mathrm{II,I}}\Psi_{\mathrm{I}} &= 0,\end{aligned} \tag{36}$$

where Ψ_{I} and Ψ_{II} are columns from two functions which correspond at $H = 0$ to the same energy $E_{\mathrm{I,II}} = \pm\,\Delta_\epsilon/2$, whilst $\mathbf{H}'_{\mathrm{I,I}}$ and $\mathbf{H}'_{\mathrm{I,II}}$ are corresponding 2×2 matrices. Eliminating Ψ_{II} from these equations the equation for Ψ_{I} is:

$$\{(\mathbf{H}'_{\mathrm{I,I}}-E)-\mathbf{H}'_{\mathrm{I,II}}(\mathbf{H}'_{\mathrm{II,II}}-E)^{-1}\mathbf{H}'^{+}_{\mathrm{I,II}}\}\Psi_{\mathrm{I}} = 0 \tag{37}$$

Since to a first approximation phonon transitions are forbidden, off-diagonal matrix elements which cause transitions associated with $\mathbf{H}'_{\epsilon_f}$, are contained only in the second term in (37). Here, if Ψ_{I} corresponds to the lower of the two levels which are split by deformation, then in the zero approximation $\mathbf{H}_{\mathrm{I,I}} = -\sqrt{(E_\epsilon)}\hat{I}$, while $\mathbf{H}_{\mathrm{II,II}} = \sqrt{(\mathbf{E}_\epsilon)}\hat{I}$, i.e. $\mathbf{H}_{\mathrm{II,II}}-E = 2\sqrt{(E_\epsilon)}\hat{I} = -\Delta_\epsilon\hat{I}$, where I is the identity matrix and, consequently, to a first approximation

$$\mathbf{H}'' = -\frac{\mathbf{H}'_{\mathrm{I,II}},\mathbf{H}'^{+}_{\mathrm{I,II}}}{\Delta_\epsilon} \tag{38}$$

Here $\mathbf{H}_{\mathrm{I,II}}$ and $\mathbf{H}_{\mathrm{II,I}} = \mathbf{H}^*_{\mathrm{I,II}}$ are "non-diagonal" sub-matrices 2×2 of matrices $\mathbf{H}'_H$ and $\mathbf{H}_{\epsilon_f}$ in the corresponding representation.

We can construct $\mathbf{H}''$ by multiplying these matrices, it here being necessary to leave in (38) terms which are linear with respect to $\bar{H}$ and ϵ_f. By constructing this matrix $\mathbf{H}''$, we can then find the matrix element $\mathbf{H}''_{ij}$ between the eigenfunctions $\mathbf{H}'\bar{H}$ and calculate the probability of transition.

In our analysis we confine ourselves for the sake of simplicity, to the case where the deformation is directed along the principal axis (001). The relaxation time τ_1

$$\begin{aligned}\frac{1}{\tau_1} = \frac{1}{\tau_0}\frac{1}{2\Delta_\epsilon^2}&\frac{(g'_1+7/4\,g'_2)^2}{(g_\parallel^2H_\parallel^2+g_\perp^2H_\perp^2)(d'^2+2b'^2)}\\ &\times[g_\parallel^2H_\perp^2H_z^2(d'^2+3b'^2)+2g_\perp^2\,d'^2H_\perp^4\\ &\quad+4g_\perp^2H_x^2H_y^2(3b'^2-d'^2)],\end{aligned} \tag{39}$$

where τ_0 is the relaxation time in an undeformed crystal, whilst $g_\parallel$ and $g_\perp$ are defined by Table (I.I). Thus, for example, if $b'\epsilon < 0$, $H = H_x$ and $g'_2 \approx 0$

$$\frac{1}{\tau_1} = \frac{1}{4}\frac{1}{\tau_0}\left(\frac{\hbar\omega_0}{4\Delta_\epsilon}\right)\frac{d'^2}{d'^2+2b'^2} \tag{40}$$

Besides transitions to the nearest level, transitions may also occur to higher levels which have been separated as a result of deformation. These transitions are resolved to a first approximation in perturbation theory, but if $\Delta_\epsilon \gg kT$ their probability is very low owing to the smallness of $\bar{\mathbf{n}}_\omega$.

---

* The spin relaxation time in acceptor centres in Ge and Si has already been calculated by KANE,(10) but he used imprecise expressions for the electron–phonon interaction operator and his final formulae do not agree with (35).

Furthermore, for these transitions, the condition (4.I) may be unfulfilled and then if $\omega < \omega_{\max}$ the corresponding relaxation time will rapidly grow, roughly in proportion to $(\Delta_\epsilon/2\hbar\omega_{\max})^8$.

If $\omega < \omega_{\max}$ the transition probability can be analyzed without difficulty, it only being necessary to evaluate the matrix $\mathbf{H}'(\epsilon_f)$ in the corresponding representation. In deformation along the principal axis (001) the relaxation time associated with these transitions is (if $\omega < \omega_{\max}$):

$$\frac{1}{\tau_2} = \frac{1}{\tau_0}\,\frac{d'^2+b'^2}{2(d'^2+2b'^2)}\left(\frac{\Delta_\epsilon}{\hbar\omega_0}\right)^2\left(\frac{\Delta_\epsilon}{kT}\right) \times\left(\exp\left[\frac{\Delta_\epsilon}{kT}\right]-1\right)^{-1} \tag{41}$$

It is seen that if the ratio of Δ_ϵ to kT is not very large, this time can be comparable with τ_0 since $\Delta_\epsilon \gg \hbar\omega_0$.*

It is necessary to point out that the splitting of a line owing to interaction with lattice oscillations can be connected not only with transitions between levels due to *off-diagonal* elements $\mathbf{H}'_{\epsilon f}$, but also with fluctuations of spacing between levels owing to deformation of the lattice during oscillation. These fluctuations are proportional to the difference $(\mathbf{H}'_{\epsilon f})_{ii}-(\mathbf{H}'_{\epsilon f})_{jj}$ between the *diagonal* elements, taken in the appropriate representation:

$$\overline{(\Delta E_{ij}{}^2)}_{\omega,\nu} = \frac{\hbar}{2\rho\omega}(\bar{n}_\omega+\tfrac{1}{2})\int [H'_{ii}(\epsilon'_{f,q_\nu}) - H'_{jj}(\epsilon'_{f},q_\nu)]^2\,\delta(\omega-\omega_0)\,\mathrm{d}^3q; \tag{42}$$

if $\hbar\omega_0 \ll kT$

$$\overline{(\Delta E_{ij}^2)}_{\omega,\nu} = \frac{kT\omega^2}{16\pi^3\rho C_\nu^5}\int [H_i(\epsilon'_{f,q_\nu}) - H'_{jj}(\epsilon'_{f},\,q_\nu)]^2\,\mathrm{d}\Omega q \tag{43}$$

In an undeformed crystal the sum $\sum_\nu(\Delta E^2_{12})_{\omega,\nu}$ for $H = H_z$ is:

$$\overline{(\Delta E^2_{1,2})}_\omega = \frac{3}{10}\,\frac{kT}{\pi^2}\,\frac{\omega^2 b'^2}{\rho C_t^5}\left(1+\frac{2}{3}\,\frac{C_t^5}{C_l^5}\right) \tag{44}$$

To calculate the mean square fluctuation $\overline{\Delta\omega} = \overline{(\Delta E^2_{1,2})}^{1/2}/\hbar$, it is necessary to integrate (44) over all the possible frequencies ω. In the solution of a similar problem concerning the broadening of the optical absorption lines soluble in an adiabatic representation, LAX and BURSTEIN[11] integrated $\overline{(\Delta E^2)}_\omega$ up to the frequency $\omega_{\max}$ defined by equation (4.I), since for these transitions the transition frequency $\omega_0 \gg \omega_{\max}$. But in the present case $\omega_0 \ll \omega_{\max}$. It is clear that for frequencies $\omega \gg \omega_0$ the adiabatic approximation is unacceptable and the contribution of these frequencies to $\Delta\omega$ must fall sharply. Therefore, the *upper limit of integration must here not exceed* ω_0, and to obtain the upper estimate $\overline{\Delta\omega}$ we integrate (44) with respect to ω_0. We then get

$$\overline{\Delta\omega} \leqslant \overline{\Delta\omega_{\max}} = \frac{1}{\tau_0}(\omega_0\tau_0)^{1/2}\left[\frac{b'^2}{3\pi(d'^2+2b'^2)}\right]^{1/2} \tag{45}$$

where $1/\tau_0$ is defined by equation (35).

Since $\omega_0\tau_0$ must be large in the conditions where resonance occurs, it will be seen that the width of the lines can be determined here by equation (45). In a deformed crystal the difference $(\mathbf{H}'_{\epsilon f})_{11}-(\mathbf{H}'_{\epsilon f})_{22}$ between diagonal terms for states which are split in the magnetic field are non-zero only in the second approximation of perturbation theory. Therefore, here, as previously, it is first necessary to evaluate the matrix $\mathbf{H}''$ from equation (38) and then to find the difference $\mathbf{H}''_{11}(\epsilon_f)-\mathbf{H}''_{22}(\epsilon_f)$ in the representation where $\mathbf{H}'_H$ is diagonal, after which $\overline{(\Delta E^2_{1,2})}_\omega$ is determined from equation (43). If, as above, we put ω_0 for the upper limit of integration, then for the case when the deformation is directed along the principal axis for $g_2 = 0$ and $b'\epsilon_{zz} > 0$, we get:

$$\overline{\Delta\omega} \leqslant \overline{\Delta\omega_{\max 1}} = \frac{1}{\tau_1}(\omega_0\tau_1)^{1/2}\left(\frac{2}{3\pi}\right)^{1/2} \times\left\{\frac{d'^2H_z^2H_\perp^2+4d'^2H_\perp^4-16(d'^2-3b'^2)H_x^2H_y^2}{\frac{1}{4}(d'^2+3b'^2)(H_z^2H_\perp^2)+2d'^2H_\perp^4-4(d'^2-3b'^2)H_x^2H_y^2}\right\}^{1/2} \tag{46}$$

---

* Recently LUDWIG and WOODBURY[16] have investigated the strain dependence of relaxation time τ. It is followed from their data that $\lg\tau \sim \epsilon/kT$. This result is in agreement with equation (41).

Thus, if $H = H_x$,

$$\overline{\Delta\omega_1} \leqslant \overline{\Delta\omega_{\max 1}} = \frac{2}{\sqrt{(3\pi)}}\frac{1}{\tau_1}(\omega_0\tau_1)^{1/2}, \quad (47)$$

where τ_1 is the relaxation time in a deformed crystal, determined correspondingly by equation (39) or (40). It will be seen from (39) and (46) that under deformation the term $\Delta\bar{\omega}$ decreases in proportion to $\hbar\omega_0/\Delta_\epsilon$, i.e. it decreases considerably more slowly than τ_1, which decreases as $(\hbar\omega_0/\Delta_\epsilon)^2$. Here under conditions where resonance is observed, $\omega_0\tau_1$ must be large and consequently $\Delta\bar{\omega}_{\max}$ is here greater than $1/\tau_1$.

We have estimated the relaxation time and magnitude of $\Delta\omega_{\max}$ in undeformed (for $H = H_z$) and deformed (for $b'\epsilon_{zz} > 0$ and $H = H_x$) crystals Ge and Si. These estimates are given in Table 4. This table also contains the initial parameters. The deformation potential constants are taken from Ref. 15 and listed in Table (3.I).

From Table 4 it will first be seen that the calculated width of the lines in *p*-Ge and *p*-Si associated with lattice oscillations is much greater than the theoretical width as calculated for semiconductors with non-degenerate bands.(12, 13) Therefore, even though the conditions for observation of resonance in *p*-Ge and *p*-Si are the most unfavorable, this broadening ought not to lead to the disappearance of resonance since in the experiments of FEHER *et al.*(9) resonance is distinctly observed at $\Delta\omega/\omega = 3\times10^{-2}$, i.e. for wider lines. The calculated value of $1/\omega_0\tau$ and $\Delta\bar{\omega}_{\max}/\omega_0$ for deformed crystals is considerably greater than the values observed experimentally,(9) also shown in Table 4. Since $\Delta\bar{\omega}$ does not exceed $\Delta\bar{\omega}_{\max}$ in any case, this indicates that the cause of the experimentally observed broadening of the lines is not lattice oscillations but rather the local deformations. It needs to be borne in mind that besides the deformations associated with dislocations, broadening of the lines can also be caused by deformation due to neighbouring impurity centres. These deformations are of the order of $\bar{\epsilon} \approx \epsilon_0 a^3/\bar{r}^3 = \epsilon_0 (N_i/N_a)$,(14) where $\bar{r}$ is the mean distance to the nearest centres, a is the radius of the atom, N_i is the concentration of the impurity centres (the admixture) and N_a is the concentration of the atoms of the basic substance.

*Table 4. Widths of the spin resonance lines in interaction with acoustic oscillations.**

	ρ	C_l	C_t	$\epsilon = 0$			$\epsilon'_{zz} = 3\times10^{-4}$				$\epsilon'_{zz} = 9\times10^{-4}$			
	(g/cm³)	(10⁻⁶ cm/sec)		$\frac{1}{\omega_0\tau_0}$	$\frac{\Delta\omega_{\max}}{\omega_0}$	experimental $\Delta\omega/\omega$	$\frac{1}{\omega_0\tau_1}$	$\frac{1}{\omega_0\tau_2}$	$\frac{\Delta\omega_{\max}}{\omega}$	experimental $\Delta\omega/\omega$	$\frac{1}{\omega_0\tau_1}$	$\frac{1}{\omega_0\tau_2}$	$\frac{\Delta\omega_{\max}}{\omega}$	experimental $\Delta\omega/\omega$
Ge	5·36	0·57	0·36	2×10^{-3}	5×10^{-3}	$\gtrsim 1$	10^{-6}	2×10^{-4}	6×10^{-4}	—	10^{-7}	10^{-9}	2×10^{-4}	—
Si	2·33	0·89	0·53	2×10^{-4}	$7·5\times10^{-3}$	$\gtrsim 1$	10^{-7}	2×10^{-4}	2×10^{-4}	3×10^{-2}	10^{-8}	6×10^{-5}	6×10^{-5}	2×10^{-2}

* The analysis is carried out for $\omega_0 = 5·65\times10^{10}$ 1/sec, $T = 1·3$°K. In the estimate of τ_2 in Ge the spatial dispersion is taken into account.

Deformation ϵ_0 near the centre is of order $\Delta a/a$, where Δa is the difference between the radius of the impurity and that of the basic atom. The corresponding broadening of the line $\Delta_\epsilon \approx \bar{b}\epsilon_0 \; N_i/N$; if $\bar{b} \approx 5$ eV, $\epsilon_0 \approx 0{\cdot}2$ and $N \approx 5\times 10^{22}$ cm^{-3}, then $\Delta_\epsilon = 2\times 10^{-23} N_i$ and $\bar{\epsilon} \approx 0{\cdot}4\times 10^{-23} N_i$. The concentration of the impurities N_i is in any case not less than the concentration of acceptors, which in Feher's experiments exceeded 10^{17} cm^{-3}, but sometimes it can be considerably greater owing to the presence of a neutral impurity, e.g. oxygen. If $N_i \approx 10^{17}$ cm^{-3}, then $\Delta_\epsilon \approx 2\times 10^{-6}$ eV, i.e. $\Delta\omega/\omega$ is approximately 5×10^{-2}. The corresponding broadening in the deformed crystal for $\epsilon_{zz}' = 3\times 10^{-4}$ is $\Delta\omega/\omega = \epsilon/\epsilon_{zz}' \approx 10^{-3}$. This broadening is less than in FEHER's experiments,(9) but it will be seen from these estimates that it is at least an order of magnitude greater than the line width to be expected from Table 4. Therefore, for observation of broadening due to lattice oscillations, the concentration of impurities needs to be reduced at least to 10^{15} cm^{-3}.

8. LINE BROADENING DUE TO ELECTRIC FIELD OF THE IONS

As shown below, considerable broadening of the lines can also be caused by the local electric fields produced by compensating impurities.

Since an electric field of the ions causes displacement of the levels in undeformed and deformed crystals, it also leads to broadening of the lines. The mean electric field created by an ion is

$$E \approx \frac{e}{\epsilon_0 \bar{r}^2} \approx \frac{e}{\epsilon_0} N_i^{2/3} \tag{48}$$

where $\bar{r}$ is the mean distance between ions, N_i is their concentration, and ϵ_0 is the dielectric permeability.

Consequently, the corresponding broadening of a line according to (26) is

$$\Delta\omega = \frac{2p_0^2\beta e^2}{\hbar E_i \epsilon_0^2} N_i^{4/3} \tag{49}$$

If $\omega = 5{\cdot}6\times 10^{10}$ c/sec

$$\Delta\omega/\omega = \begin{cases} 10^{-22} N_i^{4/3} \text{ (Se)} \\ 5\times 10^{-24} N_i^{4/3} \text{ (Si)} \end{cases} \tag{50}$$

At low temperatures the concentration of the ions in Ge and Si is practically equal to the concentration of the compensating impurities. For an impurity concentration of approximately 10^{17} cm^{-3} and a compensation of the order of $0{\cdot}1$, $\Delta\omega/\omega$ according to (50) is $0{\cdot}2$ in Ge and 10^{-3} in Si, i.e. with this concentration ($N_i \approx 10^{15}$ cm^{-3}), resonance will apparently not be observable in *p*-Ge, but the broadening of the lines in *p*-Si will be of the same order as that due to acoustic vibrations.

In a deformed crystal the quantity $\Delta\omega$ decreases linearly with the deformation, whereas $1/\tau_1$ and $1/\tau_2$ decrease quadratically, and in order that this broadening should be less than that associated with acoustic oscillation, the degree of compensation must be considerably less in Si also. Therefore, for occurrence of narrow paramagnetic resonance lines, it is not enough to have crystals without mechanical deformation, a small concentration of donor impurities also needs to be present. However, we can expect to observe resonance on undeformed specimens in crystals with a low dislocation density, no internal stresses, but with a small concentration of compensating impurities. Note that if the width of the lines in a deformed crystal is in fact determined by the local deformations and the internal fields, then it must depend appreciably on the orientation of the magnetic field. Thus, for deformation ϵ along the *z*-axis and $\Delta_{\bar{\epsilon}} \gg \hbar\omega_0, \Delta_{\bar{\epsilon}}$, where $\bar{\epsilon}$ is the mean magnitude of the local deformations, the broadening of the lines $\Delta\omega_{\bar{\epsilon}}/\omega$ is

$$\begin{aligned} \frac{\Delta\omega_{\bar{\epsilon}}}{\omega} = -\frac{\sqrt{3}}{\Delta_\epsilon} \frac{g_1'+7/4\, g_2'}{g_\parallel^2 H_\parallel^2 + g_\perp^2 H_\perp^2} & \\ \times \{g_\perp[\sqrt{3}b'(\bar{\epsilon}_{xx}-\bar{\epsilon}_{yy})(H_x^2-H_y^2) & \\ +[\gamma d'\bar{\epsilon}_{xy}H_xH_y]+2g_\parallel d' & \\ \times(\bar{\epsilon}_{xz}H_xH_z+\bar{\epsilon}_{yz}H_yH_z)\}, & \end{aligned} \tag{51}$$

where $\gamma \equiv b'\epsilon_{zz}/|b'\epsilon_{zz}|$ and ϵ_{ij} = local deformation.

It will be seen from equation (51) that if $\epsilon = \epsilon_{zz}$ and $H = H_z$, $\Delta\omega_{\bar{\epsilon}}$ vanishes, just like $1/\tau_2$ defined by equation (39) and $\Delta\omega_{1\max}$ (equation 46).

Here the broadening associated with the electric field (equation 11) and (equation 12) also vanishes, which implies that $\Delta\omega$ must be determined either by the quantity $1/\tau_2$, or by other causes which are still unknown, or by the terms which are quadratic with respect to $\bar{\epsilon}$. In the latter case the quantity $\Delta\omega$ for $H = H_z$ must be $\bar{\epsilon}/\epsilon_{zz}$ times less than when $H = H_{\perp}$, i.e. $(\Delta\omega/\omega)_{H-H_z}$ must be of the order of $(\Delta\omega/\omega)^2_{H-H_{\perp}}$. Here with increasing deformation the quantity $(\Delta\omega)_{H-H_{\perp}}$ must decrease in proportion to $1/\epsilon_{zz}$, but $(\Delta\omega)_{H-H_z}$ must decrease in proportion to $1/\epsilon^2_{zz}$. Therefore a study of the dependence of the width of a line on the orientation of the magnetic field and magnitude of deformation can help in establishing the causes of broadening of the resonance lines in *p*-Ge and *p*-Si.

Acknowledgement—In conclusion the authors wish to thank E. I. Rashba for his useful advice in discussing the paper.

REFERENCES

1. Ludwig G. W. and Woodbury H. H., *Phys. Rev. Letters* **7**, 240 (1961).
2. Ham F. S., *Phys. Rev. Letters* **7**, 242 (1961).
3. Pikus G. E. and Bir G. L., *F.T.T.* **1**, 1642 (1959).
4. Rashba E'. I., *F.T.T.* **2**, 1225 (1960).
5. Rashba E'. I. and Sheka V. I., *F.T.T.* **3**, 1735, 1863, 2369 (1961).
6. Sohm G. C., *J. Phys. Chem. Solids* **18**, 181 (1961).
7. Zavaritskaya E'. I., *Zh. exsp. teor. fiz.* **36**, 1342 (1959); *F.T.T.* **3**, 1887 (1961).
8. Kohn W., *Solid State Physics*, Vol. 5, p. 257 (edited by Seitz F. and Turnbull D.). Academic Press, New York (1957).
9. Feher G., Hensel J. C. and Gere E. A., *Phys. Rev. Letters* **5**, 309 (1960).
10. Kane E. O., *Phys. Rev.* **119**, 40 (1960).
11. Lax M. and Burstein E., *Phys. Rev.* **100**, 592 (1955).
12. Roth L., *Phys. Rev.* **118**, 1534 (1960).
13. Hasegawa H., *Phys. Rev.* **118**, 1523 (1960).
14. Kleiner W. H. and Roth L. M., *Phys. Rev. Letters* **2**, 334 (1959).
15. Hensel T. C. and Feher T., *Phys. Rev.* **129**, 1071 (1963).
16. Ludwig T. W. and Woodbury H. H., *Solid State Physics*, Vol. 13, p. 262 (edited by Seitz F. and Turnbull D. Academic Press, New York (1962).

J. Phys. Chem. Solids Pergamon Press 1963. Vol. 24, pp. 1487–1494. Printed in Great Britain.

ANISOTROPIC FREE CARRIER VOIGT EFFECT IN CUBIC SEMICONDUCTORS

S. TEITLER

U.S. Naval Research Laboratory, Washington, D.C.

(*Received* 27 *May* 1963; *revised* 30 *August* 1963)

Abstract—The free carrier Voigt effect is calculated for cubic semiconductors with free carriers having anisotropic effective masses using a Drude–Zener model. Particular attention is paid to the nature of the approximation involved in only keeping terms to the square of the magnetic field for evaluating the phase shift. Application is made to the case of mass ellipsoids in the [111]-directions and the orientational dependence of the Voigt effect for a typical sample of *n*-type Ge is presented for a configuration and conditions of experimental interest, namely, for a thin sample coinciding with the [100]-plane. It is shown that the infrared Voigt effect has limited application in that for realistic samples of Ge and other prospective materials, the Voigt effect will be rather small for usual working frequencies and available magnetic fields. Another interesting but less feasible experiment is noted in which, for certain magnetic field directions, with incident radiation polarized either parallel or perpendicular to the magnetic field, there occurs, in principle, a component of transmitted radiation respectively perpendicular or parallel to the magnetic field. Unfortunately this effect is not discernible for the typical sample of Ge under the experimental conditions considered.

1. INTRODUCTION AND THEORY

THE VOIGT effect,(1) i.e. magnetic birefringence, has provided a useful tool in the study of free carriers with isotropic effective masses in cubic semiconductors.(2–4) CARDONA(5) has pointed out that because of its anisotropic nature, the Voigt effect may play a significant role in the study of cubic semiconductors in which the free carriers have anisotropic effective masses. Recently WEBSTER and DONOVAN(6) have extended the analysis of the use of the Voigt effect in such cases. In the present note, we consider the general experimental expectations and evaluate them by considering a typical experimental configuration for a sample of *n*-type Ge which has a conduction band with equivalent ellipsoids along the [111]-directions. It is shown that the Voigt effect has limited application in that it will usually be quite small for materials of interest for available magnetic fields and usual observing frequencies. Also an interesting, but less feasible experiment is noted and evaluated, in which, for certain magnetic field directions, with incident radiation polarized either parallel or perpendicular to the magnetic field, there occurs, in principle, a component of transmitted radiation respectively perpendicular or parallel to the magnetic field.

Using a Drude-Zener model, assuming a time dependence given by $e^{i\omega t}$ and taking samples whose geometry is such that depolarization effects are negligible, we may write the equations of motion in the form

$$\mathbf{v} = \mathbf{m}^{-1}\cdot q\mathbf{E}_0/(\nu+i\omega)+\mathbf{m}^{-1}\cdot q\mathbf{v}\times\mathbf{B}/c(\nu+i\omega) \tag{1.1}$$

Here ν is equal to the reciprocal of the scattering time which, for convenience has been taken as isotropic. In our actual experiment conditions, we shall consider a frequency region and material parameters such that ν may be neglected. The charge of the carriers is q, and $\mathbf{B}$ is the magnetic induction. Here and throughout we use unrationalized c.g.s. units.

We may, without loss of generality, assume we have chosen a Cartesian coordinate system (1,2,3) such that $\mathbf{B}$ is the 3-direction. Solving for $\mathbf{v}$, we find

$$\mathbf{v} = \boldsymbol{\mu}\cdot\mathbf{E}_0 \tag{1.2}$$

where $\boldsymbol{\mu}$ is the mobility tensor to be identified as follows. We define

$$m^{-1}/(\nu+i\omega) \equiv \boldsymbol{a} \equiv \begin{pmatrix} a_{11} & a_{12} & a_{13} \\ a_{21} & a_{22} & a_{23} \\ a_{31} & a_{32} & a_{33} \end{pmatrix} \quad (1.3)$$

Then keeping only terms that contribute to order B^2 we find for any given ellipsoid

$$\mu = q \left(\begin{array}{lll} \begin{array}{l} \{a_{11} \\ \quad + a_{11}(a_{12}^2 - a_{11}a_{22})B^2q^2/c^2\} \end{array} & \begin{array}{l} \{a_{12} \\ \quad -(a_{12}^2 - a_{11}a_{22})Bq/c \\ \quad + a_{12}^2(a_{12} - a_{11}a_{22})B^2q^2/c^2\} \end{array} & \begin{array}{l} \{a_{13} \\ \quad -(a_{13}a_{12} - a_{11}a_{23})Bq/c \\ \quad + a_{13}(a_{12}^2 - a_{11}a_{22})B^2q^2/c^2\} \end{array} \\ \begin{array}{l} \{a_{12} \\ \quad + (a_{12}^2 - a_{11}a_{22})Bq/c \\ \quad + a_{12}(a_{12}^2 - a_{11}a_{22})B^2q^2/c^2\} \end{array} & \begin{array}{l} \{a_{22} \\ \quad + a_{22}(a_{12}^2 - a_{11}a_{22})B^2q^2/c^2\} \end{array} & \begin{array}{l} \{a_{23} \\ \quad -(a_{22}a_{13} - a_{23}a_{12})Bq/c \\ \quad + a_{23}(a_{12}^2 - a_{11}a_{22})B^2q^2/c^2\} \end{array} \\ \begin{array}{l} \{a_{13} \\ \quad + (a_{12}a_{13} - a_{11}a_{23})Bq/c \\ \quad + a_{13}(a_{12}^2 - a_{11}a_{22})B^2q^2/c^2\} \end{array} & \begin{array}{l} \{a_{23} \\ \quad + (a_{22}a_{13} - a_{12}a_{23})Bq/c \\ \quad + a_{23}(a_{12}^2 - a_{11}a_{22})B^2q^2/c^2\} \end{array} & \begin{array}{l} \{a_{33} \\ \quad + 2a_{13}a_{23}a_{12}B^2q^2/c^2 \\ \quad - a_{13}a_{22}B^2q^2/c^2 \\ \quad - a_{23}a_{11}B^2q^2/c^2\} \end{array} \end{array} \right) \quad (1.4)$$

Here we have used the fact that for ellipsoids $a_{ij} = a_{ji}$. We also specify for convenience in evaluating the Voigt phase shift, that in the frequency region of interest, the non-magnetic contribution to the index of refraction is much larger than the magnetic contribution. For work in a limited frequency region, this provides a weak restriction on the carrier concentration in that the plasma frequency must not be too close to the working frequency. This, in turn implies that the non-magnetic free carrier contribution to the index of refraction is considerably smaller than the host-lattice contribution.

Our procedure is to find the components of $\boldsymbol{a}$ for all the ellipsoids in the coordinate systems of interest. The coordinate systems are such that 3-axis is in the direction of the magnetic induction in the plane of the sample and the other two axes are respectively parallel and perpendicular to the plane of the sample. Then we are able to evaluate μ for the various ellipsoids. The total conductivity tensor is obtained by multiplying the mobility for each ellipsoid by the density and charge of the carriers in that ellipsoid and the summing over the ellipsoids.

Once we have the total conductivity tensor $\boldsymbol{S}$, we may insert the current density into Maxwell's equations and apply the so-called Voigt condition. This latter is based on the fact that, in the Voigt configuration, the electric displacement field in the direction of propagation is vanishing. For a cubic semiconductor this provides a relationship between the electric field and current in the direction of propagation which is called the Voigt condition. Thus if we choose the x-direction to coincide with the direction of propagation and write the spatial dependence of the fields in the form $e^{-i\omega nx/c}$, where n is the index of refraction, we find

$$E_1 = -[4\pi S_{12}E_2 + 4\pi S_{13}E_3]/(i\omega\epsilon_0 + 4\pi S_{11}) \quad (1.5)$$

where the S_{ij} are the components of the total conductivity tensor obtained by the procedure indicated above and ϵ_0 is the static dielectric constant of the host lattice. We then have only two independent components of current, namely

$$\left. \begin{array}{l} J_2 = \sum_{22} E_2 + \sum_{23} E_3 \\ J_3 = \sum_{32} E_2 + \sum_{33} E_3 \end{array} \right\} \quad (1.6)$$

where

$$\begin{aligned}\textstyle\sum_{22} &= S_{22}-(S_{21}S_{12})/(S_{11}+i\omega\epsilon_0/4\pi)\\ \textstyle\sum_{23} &= S_{23}-(S_{21}S_{13})/(S_{11}+i\omega\epsilon_0/4\pi)\\ \textstyle\sum_{32} &= S_{32}-(S_{31}S_{12})/(S_{11}+i\omega\epsilon_0/4\pi)\\ \textstyle\sum_{33} &= S_{33}-(S_{31}S_{13})/(S_{11}+i\omega\epsilon_0/4\pi)\end{aligned} \tag{1.7}$$

The Voigt condition then provides extra terms in the conductivity components in the directions transverse to the direction of propagation which are second order in the carrier concentration and are frequently called the plasma corrections.

There are only two independent component wave equations which may be written in the form

$$\begin{aligned}n^2E_2 &= \mathscr{A}E_2+\mathscr{B}E_3\\ n^2E_3 &= \mathscr{C}E_2+\mathscr{D}E_3\end{aligned} \tag{1.8}$$

where

$$\begin{aligned}\mathscr{A} &= \epsilon_0+(4\pi\textstyle\sum_{22})/i\omega\\ \mathscr{B} &= 4\pi\textstyle\sum_{23}/i\omega\\ \mathscr{C} &= 4\pi\textstyle\sum_{32}/i\omega\\ \mathscr{D} &= \epsilon_0+(4\pi\textstyle\sum_{33})/i\omega\end{aligned} \tag{1.9}$$

Equations (1.8) are equivalent to a set given by Webster and Donovan. However Webster and Donovan do not explicitly mention the plasma correction terms arising because of the Voigt condition. It should be noted that such plasma corrections played an essential role in the iterative procedure used by TEITLER, *et al.*(3) for relating Voigt and Faraday effects in materials having isotropic masses. Indeed, the iterative procedure was only necessary when plasma corrections were non-negligible. It seems that Webster and Donvan, by not considering plasma corrections explicitly, have been unduly pessimistic about the use of an iterative procedure (when it is necessary) in the anisotropic mass case. We distinguish two cases, namely those when plasma corrections are negligible and secondly those when they are not. We refer to these as the "pure" and "impure" limits respectively.

The determinantal condition on equation (1.8) leads to an equation for the index of refraction

$$2n^2 = \mathscr{A}+\mathscr{D}\pm\sqrt{[(\mathscr{A}-\mathscr{D})^2+4\mathscr{B}\mathscr{C}]} \tag{1.10}$$

This means, in general, that there are two types of waves propagating in the sample. It will turn out for our problems that $\mathscr{A}-\mathscr{D}$ is negative semi-definite so we may have two types of waves as follows. The type II wave, corresponding to a plane wave polarized in the 2-direction when the anisotropy vanishes, has index of refraction determined by

$$2n^2 = \mathscr{A}+\mathscr{D}-\gamma \tag{1.11a}$$

The type III wave, corresponding to a plane wave polarized in the 3-direction when the anisotropy vanishes, has index of refraction determined by

$$2n_{\rm II}^2 = \mathscr{A}+\mathscr{D}+\gamma \tag{1.11b}$$

where

$$\gamma = \sqrt{[(\mathscr{A}-\mathscr{D})^2+4\mathscr{B}\mathscr{C}]} \tag{1.12}$$

When $\mathscr{B}$ and $\mathscr{C}$ vanish we have the usual Voigt case with two linearly polarized beams, one perpendicular and one parallel to the magnetic induction. More generally, the ratio of the 3- to the 2-component for the type II wave is

$$r_{\rm II} = -\mathscr{B}/(\mathscr{A}-n_{\rm II}^2) \tag{1.13a}$$

For the type III wave, the ratio of the 2- to the 3-component is

$$r_{\rm III} = -\mathscr{C}/(\mathscr{D}-n_{\rm III}^2) \tag{1.13b}$$

We note that when $\mathscr{B} = \mathscr{C}$, we may write

$$r_{\rm II} = -r_{\rm III} = r \tag{1.14}$$

It is the case when equation (1.14) holds that is of interest to us and we shall, for simplicity, restrict our attention to it.

Let us consider the situation when the incident radiation makes an angle φ with the magnetic induction so that at the incident surface (where we set $x = 0$), we have

$$E_1 = 0,\ E_2 = E^0\sin\phi\, e^{i\omega t},\ E_3 = E^0\cos\phi\, e^{i\omega t} \tag{1.15}$$

This must be resolved into waves of type II and III in such a way that the ratio of the amplitudes of their components is given by equations (1.14). We have

Type II

$$E_2 = E^0\frac{\sin\phi+r\cos\phi}{1+r^2}e^{i(\omega t-\omega n_{\rm II}x/c)}$$

$$E_3 = E^0\frac{r[\sin\phi+r\cos\phi]}{1+r^2}e^{i(\omega t-\omega n_{\rm II}x/c)} \tag{1.16a}$$

Type III

$$E_2 = -E^0 r \frac{[\cos\phi - r\sin\phi]}{1+r^2} e^{i(\omega t - \omega n_{\mathrm{III}} x/c)}$$

$$E_3 = E^0 \frac{[\cos\phi - r\sin\phi]}{1+r^2} e^{i(\omega t - \omega n_{\mathrm{III}} x/c)} \qquad (1.16b)$$

In general, r will be complex. We write it in the form $r = r_0\, e^{i\chi}$. Then for general ϕ each of the components, equations (1.16a, b), may be considered to be made up of two contributions out of phase by an amount χ. These may be combined to give single in-phase waves for each component of the two types of waves. In general, however, the two components belonging to each type will not only differ in amplitude but also then be out of phase so that both types of waves will be elliptically polarized. Of course we do not measure the waves in the crystal but only their combination once they leave the sample. It is simplest to consider the contributions of the two waves at the back of the sample in terms of their components. Thus we would combine the two 2-components of the type II and type III waves respectively, (each of which had previously been formulated as a single in-phase component), into a single in-phase component, and similarly for the 3-components. The result will in general be linearly polarized components in the 2- and 3-directions combined effect will be elliptically polarized radiation.

In the experimental situation of interest, we shall be working in a frequency region where dissipative effects may be neglected. This will have the simplifying effect of making r real. Then inside the crystal both type II and type III waves would be linearly polarized. From equations (1.16) we see they are at right angles to one another although *not* (when $r \neq 0$) along the axes respectively perpendicular and parallel to the magnetic induction.

As in the more general case above, we again want the combination of the type II and III waves at the back of the sample as the wave that is actually measured. Setting $x = d$ at the back surface, we obtain for the total 2-component.

$$E_{2b} = \frac{E^0 e^{i\omega t}}{1+r^2} e^{-i\omega n_{\mathrm{II}} d/c} \{\sin\phi + r\cos\phi$$
$$- r[\cos\phi - r\sin\phi]\, e^{-i\Delta}\} \qquad (1.17)$$

where we have defined

$$\Delta \equiv \omega(n_{\mathrm{III}} - n_{\mathrm{II}})\, d/c) \qquad (1.18)$$

Defining

$$A_2 = \frac{E^0}{1+r^2}\{[(1+r^2\cos\Delta)\sin\phi + r(1-\cos\Delta)\cos\phi]^2 + r^2\sin^2\Delta(\cos\phi - r\sin\phi)^2\}^{1/2} \qquad (1.19)$$

and

$$\tan\zeta_2 = \frac{r\sin\Delta(\cos\phi - r\sin\phi)}{(1+r^2\cos\Delta)\sin\phi + r(1-\cos\Delta)\cos\phi} \qquad (1.20)$$

we may rewrite equation (1.17) in the form

$$E_{2b} = A_2\, e^{i\omega t}\, e^{-i\omega n_{\mathrm{II}} d/c}\, e^{i\zeta_2} \qquad (1.21)$$

Similarly we have for the combined 3-component

$$E_{3b} = A_3\, e^{i\omega t}\, e^{-i\omega n_{\mathrm{III}} d/c}\, e^{i\zeta_3} \qquad (1.22)$$

where

$$A_3 = \frac{E^0}{1+r^2}\{[(1+r^2\cos\Delta)\cos\phi + r\sin\phi(\cos\Delta - 1)]^2 + r^2\sin^2\Delta(\sin\phi + r\cos\phi)^2\}^{1/2} \qquad (1.23)$$

and

$$\tan\zeta_3 = \frac{r\sin\Delta\,(\sin\phi + r\cos\phi)}{(1+r^2\cos\Delta)\cos\phi + r\sin\phi(\cos\Delta - 1)} \qquad (1.24)$$

We consider two cases of particular interest. The first is the usual Voigt experiment in which the incident linearly polarized light makes an angle of 45° with the magnetic induction direction. Then $\sin\varphi$ and $\cos\varphi$ are both equal to $\sqrt{(2)}/2$ and the incident beam has equal components in the 2- and

3-directions respectively. For the exiting beam, the 2- and 3-components will in general have differing amplitudes and phases corresponding to elliptically polarized light with its major axis rotated away from the orientation of the incident radiation. However, if we consider the situation when Δ is quite small so that its trigonometric functions may be expanded to lowest order, i.e. neglecting terms of order Δ^2, then both A_2 and A_3 may be approximated by $(\sqrt{(2)}/2)E^0$ and the major axis of the exiting ellipse makes an angle of 45° with the magnetic induction, independent of the magnetic induction direction. The neglect of terms to order Δ^2 in the A's is further enhanced by the fact that the coefficient of the Δ^2 term is a function of r which is always less than one and may be quite small. To sum up, when ω, $\boldsymbol{B}$ and d are chosen so that terms to order Δ^2 are negligible, the standard experimental procedure for measuring the Voigt effect$^{(3)}$ is applicable in all directions subject, of course, to the conditions that equation (1.14) is valid and r is real. Actually and unfortunately, the conditions for the neglect of Δ^2 terms will be the only easily realizable ones for the example of n-type Ge to be considered in the next Section.

However, even when the Δ^2 terms are sufficiently small that the major axis essentially makes an angle of 45° with the magnetic induction direction the phase difference between the two components of the exiting radiation, namely δ, is *not* given by Δ, but rather by

$$\delta = \Delta - \zeta_3 + \zeta_2 \qquad (1.25a)$$

$$\simeq \Delta\left[\frac{1-r^2}{1+r^2}\right], \ |\Delta| \ll 1 \qquad (1.25b)$$

It is noteworthy that when $\mathscr{B} = \mathscr{C}$ is non-vanishing, there are two opposite contributions, namely one in Δ which tends to increase δ and one in the difference of the ζ's which tends to cancel the first contribution. Indeed for the example discussed in the next Section, the plot of δ as a function of magnetic induction direction is the same when we take $\mathscr{B}$ into account or neglect it. Thus to a large extent, the non-vanishing of $\mathscr{B}$ has no effect on the phase shift.

Perhaps a more interesting situation than the usual Voigt experiment is the case when the incident radiation is polarized along either the axis perpendicular or parallel to the magnetic induction. Again we consider the case when equation (1.14) is valid and r is real. Suppose, for example, that $\sin\phi = 1$, $\cos\phi = 0$, i.e., the incident radiation is polarized along the axis perpendicular to the magnetic induction, the 2-direction. Then the exiting wave has a component in the 3-direction.

$$(E_{3b})_{\phi=\pi/2} = \frac{E^0 r}{1+r^2}\, e^{i(\omega t - \omega n_{\mathrm{III}} d/c)}[e^{i\Delta}-1] \qquad (1.26a)$$

$$\simeq \frac{E^0 r}{1+r^2}\, e^{i(\omega t - \omega n_{\mathrm{III}} d/c)}[i\Delta], \ |\Delta| \ll 1 \qquad (1.26b)$$

Unfortunately, $(E_{3b})_{\phi=\pi/2}$ will be very small when the approximation equation (1.26b) is valid. The ratio of its intensity to the initial intensity is

$$\left(\frac{I_{3b}}{I_0}\right)_{\phi=\pi/2} = \frac{r^2}{(1+r^2)^2}\Delta^2 \qquad (1.27)$$

Thus for Δ of the order of 0·1 we are already working with considerably less than one percent of the incident radiation since the factor $r^2/(1+r^2)^2$ is less than one. This is then a marginal experiment when Δ is small particularly in view of the imperfect polarizers available and possible sample absorption of the component of interest. Nevertheless, if one had sufficiently high magnetic induction or other parameters such that equation (1.26a) had to be used without approximation, we would be able to see this effect. Clearly concomitant with the rise in the 3-component, there is a matching attenuation in the 2-component. Equally straightforward is the fact that a similar result holds if the incident radiation is parallel to the magnetic induction and the observation for the rise in transmission is made perpendicular to the magnetic field. We turn now to our example.

2. *n*-TYPE Ge

The conduction band in n-type Ge has equivalent ellipsoids along the [111]-directions. The most practical choices of experimental situation are such that the plane of the sample contains as many symmetry axes as possible. As our working example we choose a sample cut in the [100]-plane. The experimental situation would then be, radiation propagating along the [100]-direction and

$\boldsymbol{B}$ in the [100]-plane. Consistent with our discussion in the first Section, we choose coordinate axes in such a way that the 1-axis coincides with the direction of propagation, the 2–3 plane is the plane of the sample, and the 3-axis coincides with the magnetic induction direction.

For the case of [111]-ellipsoids with sample plane coinciding with the [100]-plane and radiation propagating in the [100]-direction we find for the conductivity tensor

$$S^{[100]} = \frac{Nq^2}{3\alpha}\begin{pmatrix} \begin{matrix}\{1+2K \\ \quad -3K(1+2K)(2+K)G^2\}\end{matrix} & 3K(2+K)G & 0 \\ -3K(2+K)G & \begin{matrix}\{1+2K-3K(1+2K)(2+K)G^2 \\ -3K(1-K)^2\,(\sin^2 2\theta)G^2\}\end{matrix} & (3/2)K(1-K)^2\,(\sin 4\theta)G^2 \\ 0 & (3/2)K(1-K)^2\,(\sin 4\theta)G^2 & \begin{matrix}\{1+2K-6K(1-K)^2G^2 \\ 3+K(1-K)^2\,(\sin^2 2\theta)G^2\end{matrix} \end{pmatrix} \tag{2.1}$$

where

$K = m_L/m_T$
m_L = longitudinal effective mass
m_T = transverse effective mass
$\alpha = m_L(\nu+i\omega)$
θ = angle between the [001]-direction and the magnetic induction
N = total density of free carriers
$G = qB/3\alpha c$

We may identify the quantities in Section 1 for this case. Keeping terms only to second order in the magnetic induction, we find,

$$\begin{aligned} \mathscr{A}^{[100]} &= \epsilon_0+(4\pi Nq^2/3\alpha i\omega)\{1+2K-3K(1+2K)(2+K)G^2-3K(1-K)^2\,(\sin^2 2\theta)G^2\} \\ &\quad +(4\pi/i\omega)^2(Nq^2/3\alpha)^2[3K(2+K)G]^2/[\epsilon_0+(4\pi Nq^2/3\alpha i\omega)(1+2K)] \\ \mathscr{B}^{[100]} &= \mathscr{C}^{[100]} = (2\pi Nq^2/3\alpha i\omega)[3K(1-K)^2\,(\sin 4\theta)G^2] \\ \mathscr{D}^{[100]} &= \epsilon_0+(4\pi/i\omega)(Nq^2/3\alpha)\{1+2K-6K(1-K)^2G^2+3K(1-K)^2\,(\sin^2 2\theta)G^2\} \end{aligned} \tag{2.2}$$

In the limit of no dissipation i.e. when $\nu \to 0$, $\alpha \to im_L\omega$ and all the quantities in equations (2.2) are real. Since we also have $\mathscr{B}^{[100]} = \mathscr{C}^{[100]}$, this corresponds to the case discussed at length in the first Section.

We now turn to an experimentally realizable situation. Consider a plane sample of n-type Ge with an intrinsic concentration of $10^{18}/\text{cm}^3$ cut in the [100]-plane. We suppose the experiment to be performed at a wavelength of 20μ at a magnetic induction of 80 kgauss. The material is supposed sufficiently good that in this frequency range $\nu/\omega \ll 1$ so we deal with the no dissipation case. We use the material constants for Ge given by DRESSELHAUS, *et al.*(7) These are

$$\begin{aligned} m_L &= 1{\cdot}58m_0 \\ m_T &= 0{\cdot}082m_0 \end{aligned} \tag{2.3}$$

Thus if we consider an average cyclotron frequency $\omega_c = (1+2k)|q|B/3m_Lc$ we find $\omega_c^2/\omega^2 \ll 1$. Further if we define an average plasma frequency by means of $\omega_p^2 = 4\pi q^2N(1+2K)/3m_L\epsilon_0$, we also have $\omega_c^2/(\omega^2-\omega_p^2) \ll 1$ so that the B^2 approximation used above is appropriate to the present experimental case.

In Fig. 1 we plot r as a function of θ for the given sample at 80 kgauss. The carrier concentration and magnetic induction only enter the evaluation of r through the plasma corrections. This sample with $10^{18}/\text{cm}^3$, corresponds to the impure limit and plasma corrections are important. For n-type Ge with carrier concentration less than $10^{17}/\text{cm}^3$, plasma corrections are unimportant and that material corresponds to the pure limit. As we see r never gets as large as 0·3. Since r enters the formulae at lowest order as r^2, this means the effects dependent on it will be reasonably small for n-type Ge.

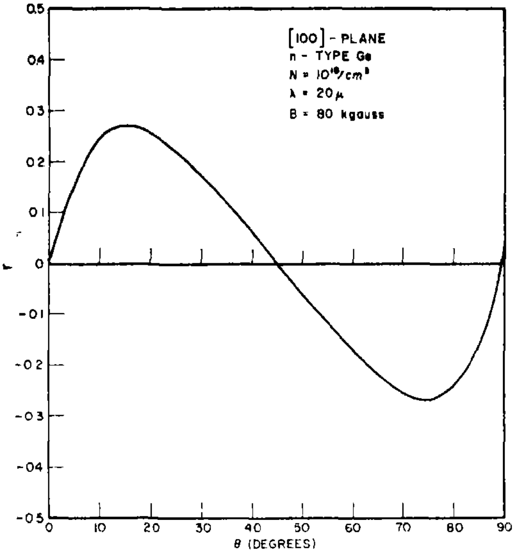

FIG. 1. *Orientational dependence of r given in equation (1.14), for the non-dissipative case when r is real.* The sample plane coincides with the [100]-plane and the radiation propagates parallel to the [100]-axis. The abscissa θ represents the angle the magnetic induction makes with the [001]-axis.

In Fig. 2 we plot the expected Voigt phase shift, δ, as a function of θ for a sample of thickness 10^{-2} cm measured at the wavelength 20μ and magnetic induction 80 kgauss. The thickness is chosen to make the sample sufficiently transparent to perform the experiment which, for the material considered,(8) is about 10^{-2} cm. The results are not large shifts being of the order of 0·2 radian or less so that they are measurable, but not easily measurable. However the shifts are sufficiently small throughout that we do not have to worry about rotation of the major axis of the ellipse particularly since r is also small.

If we had performed the Voigt experiment without knowledge of the effective masses but knowing the carrier concentration (e.g. from the Hall effect), then we could have used such a curve to obtain both the longitudinal and transverse effective masses. It might be noted that in setting up an actual experiment, it could be advantageous to use samples of lower concentration so that a greater thickness could be employed and plasma corrections would not be necessary. Lower concentration material also has the advantage that the possibility of dealing with good material, i.e. such that $\nu/\omega \ll 1$ may be enhanced. However, the Voigt phase shift measured will not be significantly altered from our present value since one trades carrier concentration for thickness.

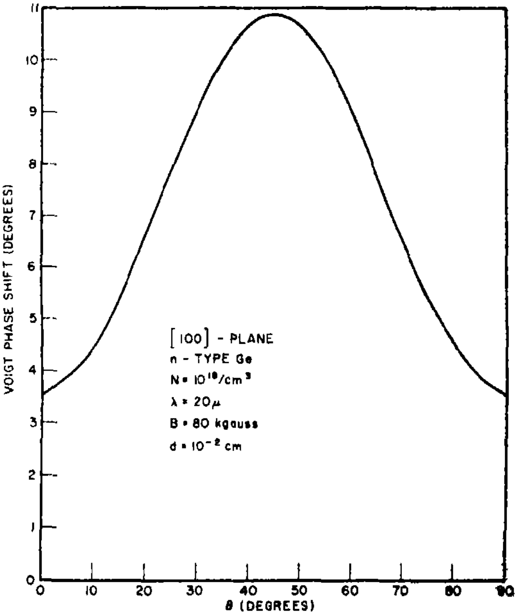

FIG. 2. Orientational dependence of the free carrier Voigt phase shift when the sample plane coincides with the [100]-plane and the radiation propagates parallel to the [100]-axis. The abscissa θ represents the angle the magnetic induction makes with the [001]-axis.

As is apparent from the relatively small Voigt phase shift even at 80 kgauss for the typical sample of Ge considered, the method has severe limitations as a general tool. Unless magnetic induction significantly greater than 80 kgauss can be routinely used or techniques for measuring phase shifts considerably improved, it will probably only find limited use since many of the materials of possible interest may have heavy effective masses without large anisotropy.

Even more difficult is the experiment in which a transmission observation is made in direction perpendicular to the direction of incident polarization which is parallel or perpendicular to the magnetic induction. With both Δ small and r^2 a small fraction when it does not vanish, it will not be detectable for the present experimental situation. However, with an appropriate material and considerably higher magnetic induction, perhaps this interesting manifestation of the anisotropy of the effective masses may eventually be observed.

REFERENCES

1. See e.g. Voigt W., *Electro- and Magneto-Optics*, Teubner, Leipzig (1907).
2. Teitler S. and Palik E. D., *Phys. Rev. Letters* **5**, 546 (1960).
3. Teitler S., Palik E. D. and Wallis R. F., *Phys. Rev.* **123**, 1631 (1961).
4. Palik E. D. Teitler S. and Wallis R. F., *J. appl. Phys.* **32**, 2132 (1961).
5. Cardona M., *Helv. Phys. Acta* **34**, 796 (1961).
6. Webster J. and Donovan B., *Phys. Letters* **2**, 330 (1962).
7. Dresselhaus G., Kip A. F. and Kittel C. *Phys. Rev.* **98**, 368 (1955).
8. See e.g. Fan H. Y., Spitzer W. and Collins R. J., *Phys. Rev.* **101**, 566 (1956).

J. Phys. Chem. Solids Pergamon Press 1963. Vol. 24, pp. 1495–1502. Printed in Great Britain.

OVERLAP FUNCTIONS IN PLANAR CRYSTALS

V. HALPERN

Mathematical Institute, Oxford

(*Received* 19 *August* 1963)

Abstract—The overlap function $F^2 = |\int u_{\boldsymbol{k}}^*(\boldsymbol{r})u_{\boldsymbol{k}'}(\boldsymbol{r})d\boldsymbol{r}|^2$ is evaluated for several values of $\boldsymbol{k}$ and a wide mesh of points $\boldsymbol{k}'$, where $u_{\boldsymbol{k}}$ is the modulating part of the Bloch wave function for a π-electron in the valence or conduction band, in planar boron nitride and graphite. It is found that for boron nitride, if $u_{\boldsymbol{k}}$ and $u_{\boldsymbol{k}'}$ are in the same band and $|\boldsymbol{k}-\boldsymbol{k}'|$ is less than a quarter of the radius of the Brillouin zone, then F^2 usually lies between 0·9 and 1. In graphite, however, F^2 behaves more erratically because the top of the valence band is degenerate with the bottom of the conduction band; a theoretical analysis of this behaviour is also presented.

1. INTRODUCTION

It is well known that in a perfect crystal, if the single-electron approximation is used, the electronic eigenfunctions corresponding to molecular orbitals can be written in the Bloch form

$$\psi_{n,\boldsymbol{k}}(\boldsymbol{r}) = \exp(i\boldsymbol{k}\cdot\boldsymbol{r})u_{n,\boldsymbol{k}}(\boldsymbol{r}) \tag{1}$$

where n numbers the band, $\boldsymbol{k}$, the reduced wave vector, identifies the molecular orbital being considered, and $u_{n,\boldsymbol{k}}(\boldsymbol{r})$ has the same translational symmetry as the crystal lattice. The integral

$$I_n^{n'}(\boldsymbol{k},\boldsymbol{k}') = \int u^*_{n,\boldsymbol{k}}(\boldsymbol{r})u_{n',\boldsymbol{k}'}(\boldsymbol{r})\,d\boldsymbol{r}, \tag{2}$$

where the volume of integration is one unit cell, is then of interest in certain contexts,(1) and especially in connection with the inter-band Auger effect.(2) It has been studied by a number of approximate methods,(1) including first-order $\boldsymbol{k}\cdot\boldsymbol{p}$ perturbation theory,(3) and also on the basis of a one-dimensional Kronig–Penney band model.(4) However, no previous attempt appears to have been made to study this integral using wave functions obtained from eigenvalue calculations on a real crystal. This is not too surprising, since such wave functions are usually complicated, of unknown accuracy, and only available at a few points of special symmetry in reciprocal space. However, approximate L.C.A.O. wave functions of a simple analytical form have been found at all points in reciprocal space for the valence and conduction bands of graphite(5) and planar boron nitride,(6) when these crystals are regarded as containing a single isolated plane of atoms. It was therefore thought of interest to evaluate $I(\boldsymbol{k},\boldsymbol{k}')$ for these substances, and to compare its behaviour with the previous predictions. There are often considerable differences between the results of quantum mechanical calculations in two or three dimensions and those in one dimension. This, and the probable effects of the presence of two different atoms in a unit cell, suggested that our results might well differ from those of Beattie and Landsberg.(4)

2. THE BAND STRUCTURE OF GRAPHITE AND PLANAR BORON NITRIDE

In this Section, we summarize the results obtained by Coulson and Taylor.(5,6)

Both graphite and planar boron nitride contain, in addition to the core electrons, σ and π electrons which to a first approximation can be treated as independent. In that case, it is the π electrons which give rise to the highest valence band and lowest conduction band, and these are the only ones we consider. It is to be expected that the presence of the σ electrons will cause some modification to the bottom of the valence and the top of the conduction bands, but their effects on the parts of the bands nearest to the energy gap should be small. It is these regions that are of most interest in practice. In boron nitride there is an appreciable energy gap, but in graphite the gap vanishes and the valence and conduction bands touch. In both substances, the adjacent band extrema are not at $\boldsymbol{k} = 0$, but lie at the edge of the first Brillouin zone; this is not the case in most semiconductors having the diamond or zincblende structures.

The graphite or planar boron nitride lattice, regarded as a two-dimensional array of unit cells, is as shown in Fig. 1. The unit cell is a rhombus of side a, with angles of 120° and 60° at its vertices, as shown in Fig. 2. We take the x-axis parallel to the long diagonal and the y-axis parallel to the short diagonal of the rhombus, and assume that the crystal contains N unit cells, with respect to which the usual Born–von Karman cyclic boundary conditions are applied.

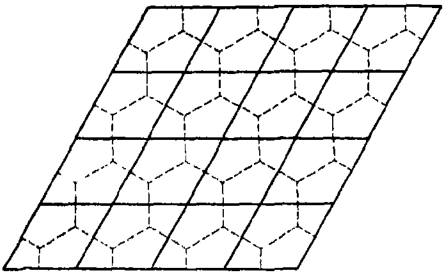

FIG. 1. The graphite lattice.

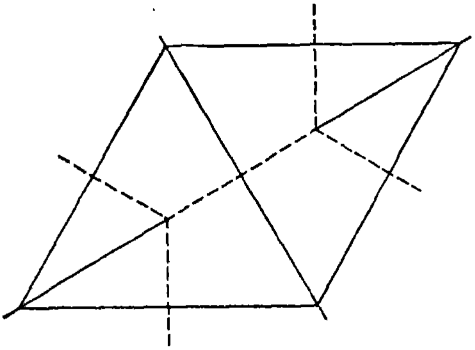

FIG. 2. The unit cell for graphite.

All the unit cells can be obtained from any given one through translations by the vectors $\boldsymbol{R}_n = n_1\boldsymbol{a}_1 + n_2\boldsymbol{a}_2$ where $n_j = 0, \pm 1, \pm 2$, etc. and the $\boldsymbol{a}_j$ are the basis translational vectors. With our system of coordinates, we can take $\boldsymbol{a}_1 = a(\sqrt{[3]}/2, -1/2)$ and $\boldsymbol{a}_2 = a(\sqrt{[3]}/2, 1/2)$. It is convenient to define also a vector $\boldsymbol{h} = 1/6(\boldsymbol{a}_1 + \boldsymbol{a}_2)$ equal to half the distance between the two atoms in the same unit cell.

In reciprocal space, $\boldsymbol{k} = 1/a(\xi, \eta)$ and we write $\zeta = 2/\sqrt{[3]}\xi$; all coordinates in reciprocal space are henceforth expressed in terms of ζ and η. The first Brillouin zone is the hexagon formed by the perpendicular bisectors of the joins of (0, 0) to $(\pm\pi, \pm 2\pi)$ and $(\pm 2\pi, 0)$. Adjacent band extrema lie at $(\pm\pi, \pm 2\pi/3)$, and the bottom of the valence band and the top of the conduction band lie at (0, 0).

Figure 2 shows that there are two atoms in each unit cell. We call the corresponding $2p\pi$ atomic orbitals $\psi(\boldsymbol{r}+\boldsymbol{h})$ and $\phi(\boldsymbol{r}-\boldsymbol{h})$, where $\boldsymbol{r}$ is measured from the centre of the cell. Let

$$S = \int \psi(\boldsymbol{r}+\boldsymbol{h})\phi(\boldsymbol{r}-\boldsymbol{h})\,\mathrm{d}\boldsymbol{r},$$

and let $E_{\boldsymbol{k}}$, the energy of the state $\boldsymbol{k}$ measured from the centre of the gap, be expressed in the form $Z\gamma$, where γ is a convenient unit of energy defined by Coulson and Taylor. In addition, let $f = 1 + 2\exp(i\zeta)\cos\frac{1}{2}\eta$, and let $g^2 = ff^* = 3 + 2\cos\eta + 4\cos\zeta\cos\frac{1}{2}\eta$. Then the molecular orbitals $\psi_{\boldsymbol{k}}$ are given by

$$\psi_{\boldsymbol{k}} = \frac{1}{N_{\boldsymbol{k}}}\sum_n \exp(ik\cdot\boldsymbol{R}_n)(\psi(\boldsymbol{r}-\boldsymbol{R}_n+\boldsymbol{h})$$

$$+c_{\boldsymbol{k}}\phi(\boldsymbol{r}-\boldsymbol{R}_n-\boldsymbol{h}))$$

where $c_{\boldsymbol{k}} = (1 - ZS/Z - t)f = qf$ say, and $N_{\boldsymbol{k}}^2 = 1 + g^2(2qS + q^2)$. For planar boron nitride,

$$Z = \frac{-g^2S \pm (g^2 + t^2(1 - g^2S^2))^{1/2}}{1 - g^2S^2},$$

and $t = -1$ according to Coulson and Taylor.

For graphite, $t = 0$, so that $Z = \pm g/(1 + gS)$ and $q = \pm 1/g$; in this homonuclear case, $\phi(\boldsymbol{r}) = \psi(\boldsymbol{r}) =$ the $2p\pi$ orbital for a carbon atom.

In each case, the + sign corresponds to the valence band and the − sign to the conduction band. It should be noted that, unless $t = 0$, $c_{\boldsymbol{k}} = 0$ at $(\pi, 2\pi/3)$, while, if $t = 0$, $c_{\boldsymbol{k}}$ has an essential singularity there since the two bands are then degenerate at this point.

For both substances, S lies between 0·2 and 0·25 for Slater orbitals(7), although slightly larger values may be appropriate for self-consistent-field orbitals.

Method of calculation

Let $\boldsymbol{l} = \boldsymbol{k} - \boldsymbol{k}'$. If $\boldsymbol{k}$ and $\boldsymbol{k}'$ are both in the first Brillouin zone, then

$$\int u_{\boldsymbol{k}}^*(\boldsymbol{r})u_{\boldsymbol{k}'}(\boldsymbol{r})\,\mathrm{d}\boldsymbol{r} = \int \exp(i\boldsymbol{l}\cdot\boldsymbol{r})\psi_{\boldsymbol{k}}(\boldsymbol{r})\psi_{\boldsymbol{k}'}(\boldsymbol{r})\,\mathrm{d}\boldsymbol{r}.$$

Now if $\boldsymbol{K}$ is a basis vector of the reciprocal lattice, $\psi_{\boldsymbol{K}+\boldsymbol{k}} = \psi_{\boldsymbol{k}}$, so that $\psi_{\boldsymbol{k}}$ is periodic in $\boldsymbol{k}$. But $u_{\boldsymbol{K}+\boldsymbol{k}}(\boldsymbol{r}) = \exp(-i\boldsymbol{K}\cdot\boldsymbol{r})u_{\boldsymbol{k}}(\boldsymbol{r})$, so that $u_{\boldsymbol{k}}$ is not periodic in $\boldsymbol{k}$. It was therefore decided to take for the fundamental form for $I(\boldsymbol{k}, \boldsymbol{k}')$ in equation (2)

$$\int \exp(i\boldsymbol{l}\cdot\boldsymbol{r})\psi_{\boldsymbol{k}}^*(\boldsymbol{r})\psi_{\boldsymbol{k}'}(\boldsymbol{r})\,\mathrm{d}\boldsymbol{r}.$$

This distinction is important for planar crystals, where the adjacent band extrema lie at the edge of the first Brillouin zone, but not for tetrahedral crystals where the relevant extrema are usually at the centre of the zone.

We write

$$F_j^2 = \left|\int \exp(i\boldsymbol{l}\cdot\boldsymbol{r})\psi_{\boldsymbol{k}}^*(\boldsymbol{r})\psi_{\boldsymbol{k}'}(\boldsymbol{r})\,\mathrm{d}\boldsymbol{r}\right|^2,$$

where $j = 1$ corresponds to both $\psi_{\boldsymbol{k}}$ and $\psi_{\boldsymbol{k}'}$ being in the conduction band;

$j = 2$ corresponds to $\psi_{\boldsymbol{k}}$ in the conduction band and $\psi_{\boldsymbol{k}'}$ in the valence band;

$j = 3$ corresponds to $\psi_{\boldsymbol{k}}$ in the valence band and $\psi_{\boldsymbol{k}'}$ in the conduction band; and

$j = 4$ corresponds to both $\psi_{\boldsymbol{k}}$ and $\psi_{\boldsymbol{k}'}$ being in the valence band.

The values of F_j^2 were found for seven different values of $\boldsymbol{k}$, shown in Fig. 3, and for $\boldsymbol{l} = (l_1, l_2)$ with l_1 and l_2 lying between $\pi/2$ and $-\pi/2$. Figure 3 also shows the contours of constant g, which are lines of constant energy.

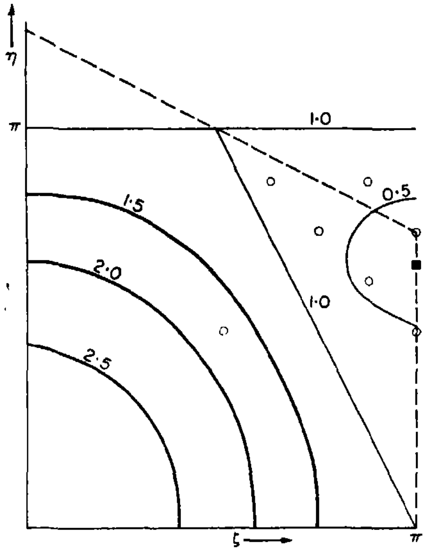

FIG. 3. $g(\boldsymbol{k})$ as a function of ζ and η. The full lines are the contours $g = 0{\cdot}5$, $1{\cdot}0$, $1{\cdot}5$, $2{\cdot}0$, and $2{\cdot}5$; $g = 3$ at $(0, 0)$ and $g = 0$ at $(\pi, 2\pi/3)$, the band edge, which is marked by a black square. It should be noted that $g(\pm\zeta, \pm\eta) = g(\zeta, \eta)$. The broken lines mark the edge of the first Brillouin zone, and the circles indicate the values of $\boldsymbol{k}$ for which the F_j^2 were evaluated.

The integrals of form

$$\int \exp(i\boldsymbol{l}\cdot\boldsymbol{r})\phi(\boldsymbol{r}+\boldsymbol{h})\phi(\boldsymbol{r}-\boldsymbol{h})\,\mathrm{d}\boldsymbol{r}$$

were evaluated by expanding $\exp(i\boldsymbol{l}\cdot\boldsymbol{r})$ in powers of $\boldsymbol{l}\cdot\boldsymbol{r}$ and integrating term by term, using SLATER(7) orbitals and bipolar coordinates. This led to a rapidly convergent double series for the integral in powers of $\boldsymbol{l}\cdot\boldsymbol{h}$ and $\boldsymbol{l}\times\boldsymbol{h}$. Integrals between orbitals not centred about the same or neighbouring atoms were ignored, as in Refs 5 and 6.

3. OVERLAP FUNCTIONS IN PLANAR BORON NITRIDE

The results of the calculations on planar boron nitride are shown in Figs 4–6 and in Table 1. In Fig. 4, the contours $F_1^2 = 0{\cdot}9$ and $0{\cdot}8$ are plotted as functions of $\boldsymbol{l}$ for two typical points, $\boldsymbol{k} = (7\pi/8, 5\pi/8)$ and $\boldsymbol{k} = (5\pi/8, 7\pi/8)$, in reciprocal space, and in Fig. 5 the contours $F_2^2 = 0{\cdot}1$ and $0{\cdot}2$ are plotted similarly. The first of these points is much closer than the second to the band extrema both in energy and in reciprocal space. It will be observed that F_1^2 seems to depend more on $|\boldsymbol{l}|$ than on the direction of $\boldsymbol{l}$. This result was quite generally true for planar boron nitride, although directional effects increase somewhat as $\boldsymbol{k}$ approaches the band extremum $(\pi, 2\pi/3)$. Fig. 6

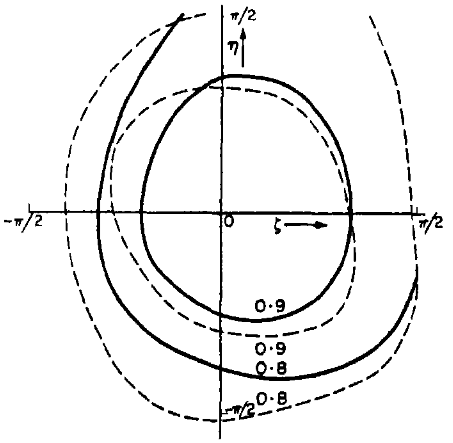

FIG. 4. Contour diagrams of F_1^2 for planar boron nitride. The contours $F_1^2 = 0{\cdot}9$ and $F_1^2 = 0{\cdot}8$ are plotted as functions of $\boldsymbol{l} = \boldsymbol{k}-\boldsymbol{k}'$ for $\boldsymbol{k} = (7\pi/8, 5\pi/8)$ (full lines) and $\boldsymbol{k} = (5\pi/8, 7\pi/8)$ (broken lines).

shows the variation of F_1^2 and F_2^2 along the line $l = (\zeta, 0)$ for three different values of k; similar results were found for other lines through the point $l = 0$, and for the other values of k.

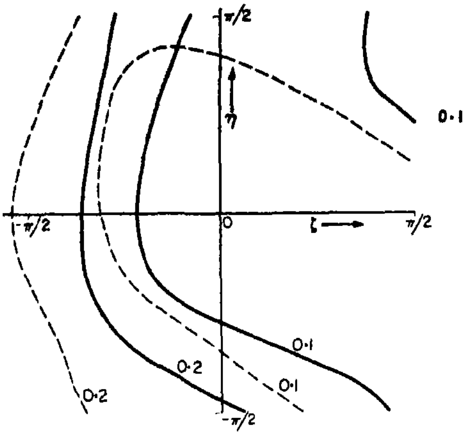

FIG. 5. Contour diagrams of F_2^2 for planar boron nitride. The contours $F_2^2 = 0{\cdot}1$ and $F_2^2 = 0{\cdot}2$ are plotted as functions of l for $k = (7\pi/8,\ 5\pi/8)$ (full lines) and $k = (5\pi/8,\ 7\pi/8)$ (broken lines).

The behaviour of F_4^2 is similar to that of F_1^2, except that at almost all points F_4^2 is slightly greater than F_1^2, the difference between these two quantities tending to increase in a somewhat irregular way as $|l|$ increases. This suggests that u_k for the valence band varies less rapidly with k than does u_k for the conduction band, as is to be expected. Table 1 contains the mean value of each F_j^2 for $l = (\pm\ \pi/4, 0)$ and $(0, \pm\ \pi/4)$ for all the seven values of k for which calculations were carried out. F_3^2 behaves in a similar manner to F_2^2, although the difference in magnitude between these quantities is often 0·02 or more, i.e. 10 per cent or more.

Since $F_3^2+F_4^2 \leqslant 1$, while generally $F_4^2 > F_1^2$, $F_1^2+F_2^2$ tends to be somewhat less than unity, unlike the results found by BEATTIE and LANDSBERG.$^{(4)}$ Whether the difference is due to the error

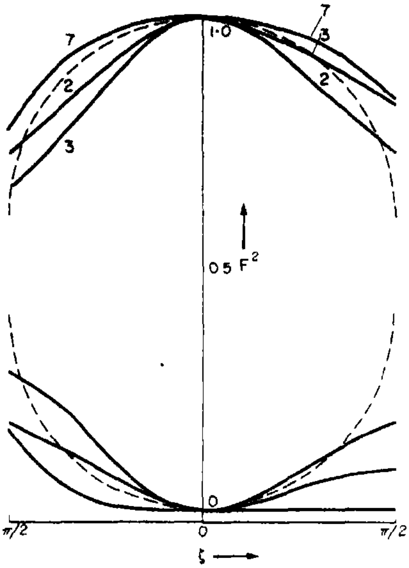

FIG. 6. F_1^2 (upper curves) and F_2^2 (lower curves) for boron nitride as functions of $l = (\zeta, 0)$ for $k = (\pi, 3\pi/4)$, $(7\pi/8, 5\pi/8)$, and $(\pi/2, \pi/2)$, numbered 2, 3, and 7 respectively. The broken lines are arcs of circles centred at $F^2 = 0{\cdot}6$ and $0{\cdot}4$, passing through these values at $\zeta = \pm\ \pi/2$, and touching the ζ-axis at $F^2 = 1$ and 0 respectively.

Table 1. *The mean value of* F_j^2, *averaged over the points* $l = (\pi/4,\ 0),\ (-\pi/4,\ 0),\ (0,\ \pi/4)$ *and* $(0,\ -\pi/4)$.

		Planar boron nitride					Graphite			
Index No.	k	g	F_1^2	F_2^2	F_3^2	F_4^2	F_1^2	F_2^2	F_3^2	F_4^2
1	$(\pi, \pi/2)$	0·4142	0·909	0·073	0·073	0·917				
2	$(\pi, 3\pi/4)$	0·2346	0·904	0·077	0·078	0·913	For these values of k, the deviation of F_j^2 from its mean value exceeds 0·15.			
3	$(7\pi/8, 5\pi/8)$	0·4260	0·908	0·074	0·074	0·917				
4	$(7\pi/8, 7\pi/8)$	0·6567	0·992	0·058	0·058	0·933				
5	$(3\pi/4, 3\pi/4)$	0·7095	0·922	0·058	0·058	0·933				
6	$(5\pi/8, 7\pi/8)$	0·9239	0·931	0·047	0·047	0·944	0·882	0·100	0·100	0·892
7	$(\pi/2, \pi/2)$	1·7321	0·965	0·010	0·010	0·980	0·972	0·008	0·008	0·981

in our wave functions or to the difference between a Kronig-Penney chain and a planar crystal is not known. It should be noted that in this heteronuclear case all the F_j^2 are continuous functions of $\boldsymbol{k}$ and $\boldsymbol{k}'$, in contrast to the results found for the linear chain.(4)

4. OVERLAP FUNCTIONS IN GRAPHITE

The results for graphite differ markedly from those obtained for boron nitride because of the essential singularity in the wave functions for the valence and conduction band levels at $(\pi, 2\pi/3)$, where on our model the two bands touch and the wave functions are degenerate. It is found that on passing through this point of reciprocal space in certain directions the valence and conduction bands switch over, so that F_1^2 on one side is continuous with F_2^2 on the other. This behaviour is clearly shown in Fig. 12 and a theoretical explanation of it is presented in the next Section. Because of this singularity, the behaviour of F_j^2 in the region for which $\boldsymbol{k}'$ is near $(\pi, 2\pi/3)$ is very erratic, and the overlap functions depend strongly on the direction of $\boldsymbol{l}$ relative to the line joining $\boldsymbol{k}' = \boldsymbol{k}$ to the point of degeneracy. For this reason, it is not practicable to draw a contour map for $\boldsymbol{k} = (7\pi/8, 5\pi/8)$; however, $\boldsymbol{k} = (5\pi/8, 7\pi/8)$ is sufficiently far from the band edge for reasonable contour maps of F_1^2 and F_2^2 to be drawn. These are shown in Figs 7 and 8 and should be contrasted with the corresponding results for boron nitride shown in Figs 4 and 5. Table 1 contains the mean value of each F_j^2 for $\boldsymbol{l} = (\pm\,\pi/4, 0)$ and $(0, \pm\,\pi/4)$ for those values of $\boldsymbol{k}$ where the maximum deviation from the mean is less than 0·1. F_1^2 and F_4^2 tend to be smaller than for boron nitride unless $\boldsymbol{k}$ is very far from the band edge; this is because $u_{\boldsymbol{k}}$ tends to vary rapidly near the point of degeneracy. This behaviour is also exhibited in Figs 9 and 10, in which the variation of F_1^2 and F_2^2 along the line $\boldsymbol{l} = (\zeta, 0)$ is plotted, and should be contrasted with the corresponding results for boron nitride shown in Fig. 6. Finally, in order to show quite clearly what is happening, Figs 11 and 12 show for planar boron nitride and graphite respectively the values of F_1^2 and F_2^2 along the line $\boldsymbol{k}' = (\pi, M'\pi/8)$ for four different values of $\boldsymbol{k}$; the band edge lies at $M' = 5\frac{1}{2}$ on this line.

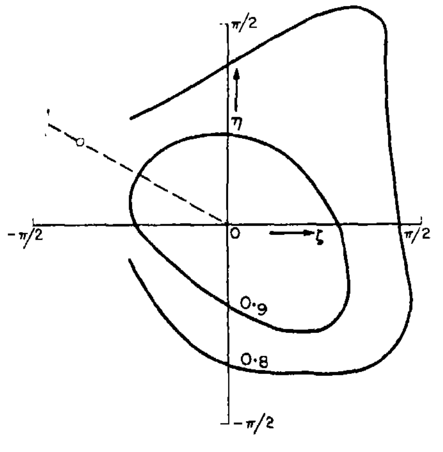

FIG. 7. Contour diagram of F_1^2 for graphite, The contours $F_1^2 = 0{\cdot}9$ and $F_1^2 = 0{\cdot}8$ are plotted as functions of $\boldsymbol{l}$ for $\boldsymbol{k} = (5\pi/8, 7\pi/8)$. The broken line is the join of $\boldsymbol{k}' = \boldsymbol{k}$ to $\boldsymbol{k}' = (\pi, 2\pi/3)$, the band edge, which is marked by a circle.

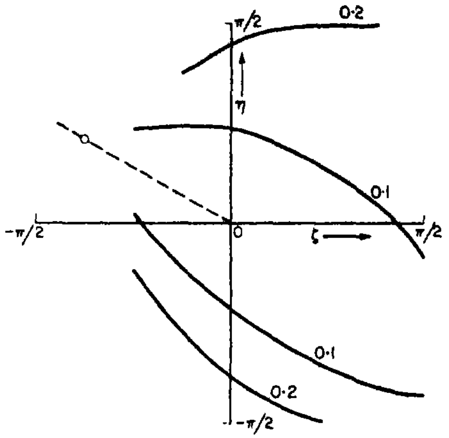

FIG. 8. Contour diagram of F_2^2 for graphite. The contours $F_2^2 = 0{\cdot}1$ and $F_2^2 = 0{\cdot}2$ are plotted as functions of $\boldsymbol{l}$ for $\boldsymbol{k} = (5\pi/8, 7\pi/8)$. The broken line is the join of $\boldsymbol{k}' = \boldsymbol{k}$ to $\boldsymbol{k}' = (\pi, 2\pi/3)$, the band edge, which is marked by a circle.

5. THEORETICAL CONSIDERATIONS

In this Section, we apply the methods of the usual L.C.A.O. theory for diatomic molecules to the functions $u_{\boldsymbol{k}}$, which are the periodic parts of the molecular orbitals in the crystal.

The Schrödinger equation for a molecular orbital ψ_k is

$$(-\hbar^2/2m)\nabla^2\psi_k + V\psi_k = E_k\psi_k. \qquad (3)$$

Consider now a crystal, the unit cell of which contains one A atom and one B atom, and assume that we can write $V = V^A + V^B$, where V^A and V^B are periodic potentials concentrated chiefly in the regions of the A and B atoms respectively. We assume in addition that V is a local potential, so that

$$V(\mathbf{r})\exp(i\mathbf{k}\cdot\mathbf{r})u_k(\mathbf{r}) = \exp(i\mathbf{k}\cdot\mathbf{r})V(\mathbf{r})u_k(\mathbf{r}).$$

Then, since

$$\nabla[\exp(i\mathbf{k}\cdot\mathbf{r})u_k(\mathbf{r})] = \exp(i\mathbf{k}\cdot\mathbf{r})(\nabla + i\mathbf{k})u_k(\mathbf{r}),$$

the substitution of equation (1) into equation (3) leads to

$$T_k u_k(\mathbf{r}) + V(\mathbf{r})u_k(\mathbf{r}) = E_k u_k(\mathbf{r}),$$

where

$$T_k = (-\hbar^2/2m)(\nabla + i\mathbf{k})^2.$$

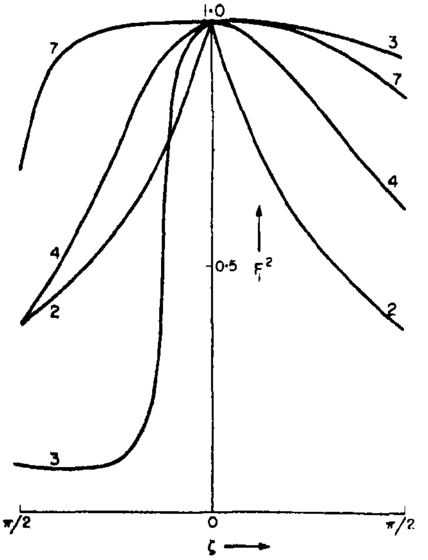

FIG. 9. F_1^2 for graphite as a function of $\mathbf{l} = (\zeta, 0)$ for $\mathbf{k} = (\pi, 3\pi/4)$, $(7\pi/8, 5\pi/8)$, $(7\pi/8, 7\pi/8)$, and $(\pi/2, \pi/2)$, numbered 2, 3, 4, and 7 respectively.

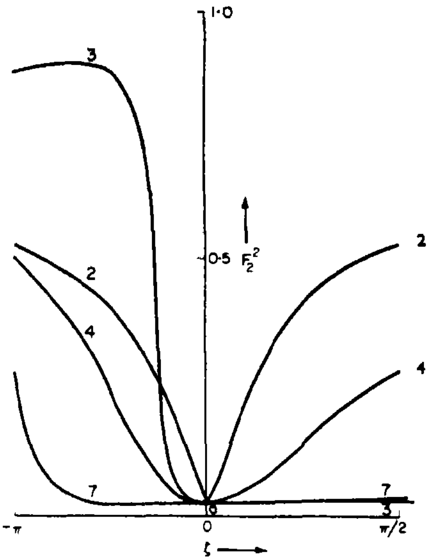

FIG. 10. F_2^2 for graphite as a function of $\mathbf{l} = (\zeta, 0)$ for $\mathbf{k} = (\pi, 3\pi/4)$, $(7\pi/8, 5\pi/8)$, $(7\pi/8, 7\pi/8)$ and $(\pi/2, \pi/2)$, numbered, 2, 3, 4 and 7 respectively.

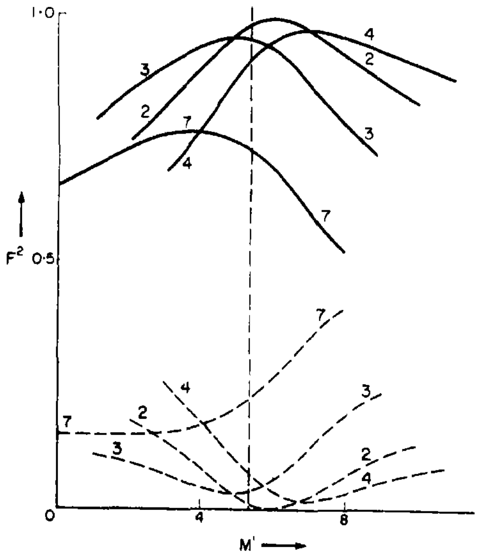

FIG. 11. F_1^2 (full line) and F_2^2 (broken line) for planar boron nitride as functions of $\mathbf{k}' = (\pi, M'\pi/8)$ for $\mathbf{k} = (\pi, 3\pi/4)$, $(7\pi/8, 5\pi/8)$, $(7\pi/8, 7\pi/8)$ and $(\pi/2, \pi/2)$, numbered 2, 3, 4, and 7 respectively. The vertical broken line marks the band edge.

Suppose now that the functions u_k^A and u_k^B satisfy the same periodicity conditions as u_k and are such that

$$(T_k+V^A)u_k^A = E_k^A u_k^A$$

and

$$(T_k+V^B)u_k^B = E_k^B u_k^B,$$

and that neither E_k^A nor E_k^B is degenerate or quasi-degenerate.

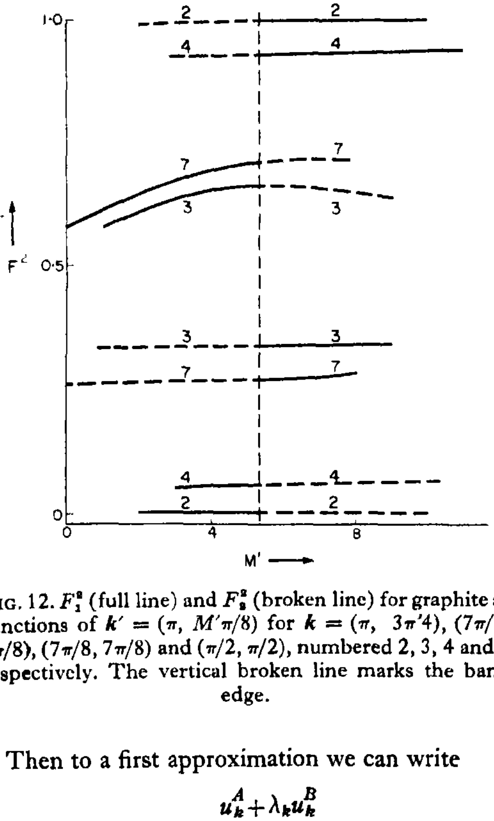

FIG. 12. F_1^2 (full line) and F_2^2 (broken line) for graphite as functions of $\boldsymbol{k}' = (\pi, M'\pi/8)$ for $\boldsymbol{k} = (\pi, 3\pi'4)$, $(7\pi/8, 5\pi/8)$, $(7\pi/8, 7\pi/8)$ and $(\pi/2, \pi/2)$, numbered 2, 3, 4 and 7 respectively. The vertical broken line marks the band edge.

Then to a first approximation we can write

$$u_k = \frac{u_k^A+\lambda_k u_k^B}{(1+\lambda_k S_k+\lambda_k^* S_k^*+\lambda_k\lambda_k^*)^{1/2}}$$

where

$$S_k = \int u_k^{A*} u_k^B \, dr$$

and λ_k is such as to minimize

$$E_k = \int u_k^*(T_k+V)u_k \, dr.$$

Let

$$\beta_k = \tfrac{1}{2}\int (u_k^{A*} V^A u_k^B + u_k^{B*} V^B u_k^A)\, dr.$$

Then for a homonuclear substance, in which atoms A and B are the same, $\lambda_k = \pm 1$. The sign of β_k determines which of these has the lower energy. However if for some value of $\boldsymbol{k}$ ($\boldsymbol{k} = \boldsymbol{k}_0$ say) $\beta = 0$, then λ is indeterminate at $\boldsymbol{k}_0$ and there are two degenerate states there. If β_k takes both positive and negative values in the neighbourhood of $\boldsymbol{k}_0$, then even if u_k^A and λ are continuous functions of $\boldsymbol{k}$ in this region, u_k (valence) will be a discontinuous function of λ and so of $\boldsymbol{k}$. Thus in certain directions there will be a switch of valence and conduction band wave functions on opposite sides of $\boldsymbol{k}_0$, as is observed in graphite.

For a heteronuclear substance, however, where in general E_k^A and E_k^B differ, the two different values of λ_k will everywhere correspond to states differing by a finite energy, and so no degeneracy will occur. Even if, for some value of $\boldsymbol{k}$, λ_k becomes infinite, $1/\lambda_k$ will be a continuous function of $\boldsymbol{k}$ at this point. Hence, as the energies are distinct and are continuous functions of λ_k or $1/\lambda_k$, u_k (valence) will also be a continuous function of one of these, and so in general no switching of functions is to be expected; this is what happens in planar boron nitride.

6. CONCLUSIONS

The wave functions used in this work probably differ considerably from the exact ones, so that the quantitative results obtained may not be too reliable; however, the qualitative results are expected to be reasonably accurate. Thus it seems probable that for planar compounds in which the valence and conduction bands are separated by a finite energy gap the usual approximation of $F_1^2 = 1$ should involve an error of no more than 10 per cent provided that $|\boldsymbol{k}-\boldsymbol{k}'|$ is less than one quarter of the radius of the first Brillouin zone. A similar result was found on the one-dimensional Kronig–Penney model,$^{(4)}$ and so it seems quite probable that it is also true in three dimensions, i.e. for non-degenerate bands in tetrahedral semiconductors. It is difficult to generalize the results for F_2^2 to such crystals, since they usually have several valence and several conduction bands fairly close together in energy, in contrast to the planar compounds which do not. Thus no reliable conclusions can be drawn about the range in which $\boldsymbol{k}\cdot\boldsymbol{p}$ perturbation theory is likely to be valid. Finally, the results for graphite suggest that, even for small $|\boldsymbol{k}-\boldsymbol{k}'|$, $F_1^2 = 1$ may not be a very good approximation for degenerate bands near the point of degeneracy.

Acknowledgements—The author's thanks are due to Professor C. A. Coulson for his valuable help and guidance, and to Professor P. T. Landsberg and Mr. C. J. Hearn of University College, Cardiff, for several valuable discussions, as well as to D.S.I.R. for providing a research studentship during the tenure of which this work was carried out.

REFERENCES

1. Hachenberg O. and Brauer W., *Advanc. Electron.* **11,** 413 (1959).
2. Beattie A. R. and Landsberg P. T., *Proc. Roy. Soc.* **A249,** 16 (1959).
3. Antoncik E. and Landsberg P. T., *Proc. phys. Soc. Lond.* (in press).
4. Beattie A. R. and Landsberg P. T., *Proc. Roy. Soc.* **A258,** 486 (1960).
5. Coulson C. A. and Taylor R., *Proc. phys. Soc. Lond.* **A65,** 815 (1952).
6. Coulson C. A. and Taylor R., *Proc. phys. Soc.* **A65,** 834 (1952).
7. Slater J. C., *Phys. Rev.* **36,** 57 (1930).

J. Phys. Chem. Solids Pergamon Press 1963. Vol. 24, pp. 1503–1510. Printed in Great Britain.

CALCIUM TUNGSTATE—III

TRIVALENT RARE EARTH SUBSTITUTION

K. NASSAU and G. M. LOIACONO

Bell Telephone Laboratories, Incorporated, Murray Hill, New Jersey

(*Received* 30 *July* 1963)

Abstract—The charge compensation of trivalent rare earths in the divalent Ca site of calcium tungstate was studied by the determination of distribution coefficients. The behavior of neodymium was investigated in the presence of all the alkali metal ions and niobium, and all the other rare earths in the presence of sodium.

The distribution coefficient of Nd is found to vary with the concentration of Nd itself, as well as with the concentration of charge compensating ions present. Several separate mechanisms including vacancy formation are inferred, and are confirmed by paramagnetic resonance results.

In the next paper a theory covering this data is presented.

Columnar growth has been observed and can be caused by either CaO or WO_3 excess in the melt.

1. INTRODUCTION

THE rise in importance of the optical maser technology is providing an intensified impetus for the study of substitution in ionic crystals. Growth from the melt is particularly useful in this aspect, as it provides in the distribution coefficient, a measure of the relative energy of different substitution and charge compensation arrangements. A combination of such determinations with evidence from other physical measurements can provide detailed insight into the substitution and charge compensation mechanisms in action. In this paper distribution coefficient data and supporting evidence from paramagnetic resonance experiments are presented for rare earth doped calcium tungstate. The next paper presents a theoretical interpretation of coupled substitution covering the $CaWO_4$:Nd^{3+} and $CaWO_4$:Nd^{3+}:Na^+ systems.

The general background to the growth and properties of calcium tungstate has been presented in two previous papers,(1, 2) hereafter referred to as I and II respectively. In the present work, attention is focused in part on the system $CaWO_4$:Nd:Na, since this provides one of the best available solid-state optical maser materials,(3) being the only one to operate continuously at room temperature.(4)

Yttrium and the trivalent rare earths provide a particularly favorable situation for substitution in calcium sites. They are, in fact, related to Ca^{2+} by GOLDSCHMIDT'S diagonal rule(5) for favorable isostructural replacement. The same is true for Na^+ and Nb^{5+} in the Ca^{2+} and W^{6+} sites respectively; these have been found to be particularly suitable for charge compensation of the excess positive charge of Nd^{3+} in a Ca^{2+} site. Also studied was the effect of the other alkali metal ions on Nd^{3+}, as well as the effect of Na^+ on all the trivalent rare earth ions.

2. EXPERIMENTAL

Conditions used for the Czochralski growth of $CaWO_4$ were described in I. Concentrations are expressed as atom %, being the number of ions per hundred Ca^{2+} or W^{6+} sites present in the structure or based on the total of $Ca^{2+}+Nd^{3+}+Na^+$ or $W^{6+}+Nb^{5+}$ in the melt. The calcium tungstate was Sylvania Luminescent Grade No. 2402, except in the lowest concentration experiments, where material purified by a preliminary pulling was used. Rare earths were generally 99·9% grade, Na_2WO_4 was Fischer Scientific Co. ACS grade dried at 120°C, and WO_3 Amend Drug and Chemical Co. CP grade. Compounds such as $Nd_2(WO_4)_3$ were prepared by grinding stoichiometric amounts of the components together, firing overnight at 1000°C, or just below the melting point when it was lower than 1000°C, regrinding and refiring.

Distribution coefficients are calculated from X-ray fluorescent or emission spectroscopic analyses as the ratio of concentration of a species in the solid to that in the melt, both concentrations being expressed in identical units. Pulling rates were 0·5–1 in. per hr, and it is assumed that the observed distribution coefficients represent a good approximation of the equilibrium values as discussed in I.

3. SITE SUBSTITUTION CONSIDERATIONS

In Tables 1 and 2 are summarized the possible substituents and substitution arrangements in $CaWO_4$ which are of relevance to the present work, based on both *a priori* and experimental conclusions. In these tabulations Nd^{3+} is used as a typical trivalent rare earth ion, and Na^+ is representative of one of the alkali metal ions. Ca^{2+} can also be replaced by Sr^{2+}, Ba^{2+} and Pb^{2+}, and W^{6+} by Mo^{6+}. A vacancy is indicated by ϕ.

Since the scheelite structure is very compact, interstitial ions are eliminated from consideration. Vacancies in the W^{6+} site are expected to be insignificant in number compared to Ca^{2+} vacancies on the basis that a much larger energy would be associated with a discrepancy of six charges than with two charges at one lattice site. Free mobile electrons do not occur, the resistivity of pure and doped $CaWO_4$ both being over 10^{10} Ω-cm. The possibility of electrons being trapped at some type of center can also be eliminated as a process occurring during growth, since trapped electrons were observed to disappear on heating up to room temperature.(6)

There is no definite knowledge as to the nature of the species present in the melt; in view of its good electrical conductivity ionic species are clearly present. In the pseudo-chemical reactions listed in Table 2, oxides are written as the components for convenience. In view of the volatility of WO_3, Na_2O, etc. these materials are best added as sintered $Nd_2(WO_4)_3$, Na_2WO_4, etc. to avoid losses on addition. Even so, there may be a slow loss of sodium and perhaps other volatile components from the melt with time.

Equation (a) of Table 2 represents the formation of stoichiometric $CaWO_4$. The vacancy pair formation of equation (*b*) corresponds to a Schottky defect. This occurs not only when excess WO_3 is added, but will accompany equation (*a*) at all times due to the appreciable value of the entropy term in $\Delta F = \Delta H - T\Delta S$ at the high temperature of 1850°K.(7) Excess WO_3 or CaO are both readily soluble in $CaWO_4$ in small amounts and permit satisfactory growth despite the resultant nonstoichiometry in the melt (however see Section 7).

Reduction of tungsten to lower valency states, e.g., as in equation (*c*) occurs on gentle reduction by hydrogen, giving the typical blue or black colors of the lower valence states of tungsten. Reoxidation takes place at 1000°C in oxygen in a few minutes, demonstrating the ready mobility of oxgyen in $CaWO_4$, and providing at the much higher growing temperature a sea of mobile oxygen ions.

In equations (*d*), (*e*), and (*f*) are represented the substitutions of Nd^{3+}, Na^+ and Nb^{5+}, one at a time. Evidence for the nature of (*d*) is the existence of the compound $Nd_2(WO_4)_3$, corresponding to $x = 1/3$ (see I). This compound does not have the scheelite structure, but the volume per equivalent unit is almost the same (78·7 Å^3 per WO_4 in $Eu_2(WO_4)_3$(8) as against 78·1 Å^3 per WO_4 in $CaWO_4$) and it appears likely that it is a distortion of the scheelite structure permitted by ordering of the vacancies. In the cases of (*e*) and (*f*), lack of color eliminates the possibility of reduced tungsten. In the absence of any other species, and in view of the consideration previously discussed, the compensations shown are the only likely ones, and are made credible by the ready mobility of oxygen.

The coupled substitutions of (*g*) and (*h*) rest on similar evidence. Compounds of the type $NaNd(WO_4)_2$, corresponding to $x = \frac{1}{2}$ in equation (*g*) have the scheelite structure and form a complete range of solid solutions with $CaWO_4$, corresponding to the range $0 < x < 0{\cdot}5$. In addition, changes in the distribution coefficient and other properties described below confirm these compensation mechanisms. Depending on the relative energies involved, the single processes (*d*) and (*e*) or (*f*) may also occur simultaneously with (*g*) or (*h*) respectively.

4. ALKALI METAL ION COMPENSATION OF Nd^{3+}

The distribution coefficient of Nd^{3+}, k_{Nd}, in

$CaWO_4$ was studied as it is affected by the addition of various alkali metal ions to the melt.(9) For comparison purposes, all the data shown in Fig. 1 refer to crystals grown from melts containing between 1 and 2 at. % Nd^{3+}. It is to be noted that the effect is a gradual one, and saturation in the case of Na^+ is not reached until more than 15 Na^+ ions are present for each Nd^{3+} ion.

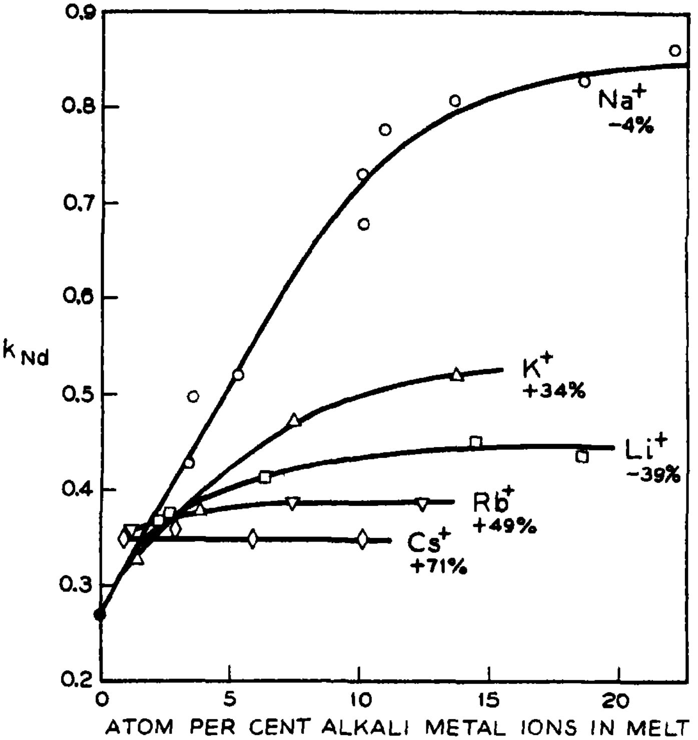

FIG. 1. Variation of the distribution coefficient of neodymium k_{Nd} with the concentration of alkali metal ions in $CaWO_4$ melt.

The numbers adjacent to the alkali metal symbols represent the per cent misfit of these ions in the Ca^{2+} site (Pauling ionic radius = 0·99 Å). It appears that the magnitude of the effect depends on the misfit and is independent of the sign.

A clarification of this behavior results from the examination of the K^+ case in Fig. 2, which shows the crystal concentrations $[Nd]_c$ and $[K]_c$ as they vary with the melt concentration $[K]_m$. It can be seen that approximately $5K^+$ are needed for every Nd^{3+} in the melt to produce one K^+ for each Nd^{3+} in the crystal. A similar study has not been possible on Na^+ compensation, since it has proved difficult to obtain accurate sodium analyses. However, the variation of k_{Nd} as it depends on both the Nd^{3+} and Na^+ concentration is shown in Fig. 3. For a complete representation, the equivalent surface for k_{Na} would also be required. It is significant that even in the absence of sodium, Fig. 3 shows the distribution coefficient of neodymium to vary with the melt neodymium concentration at low concentrations. A full explanation of this behavior appears to be possible on the basis of vacancy formation and is presented in the next paper.

5. NIOBIUM COMPENSATION OF Nd^{3+}

In Fig. 4 the crystal concentrations ($[Nd]_c$ and $[Nb]_c$) and distribution coefficients (k_{Nd} and k_{Nb}) for neodymium and niobium are shown together with the ratio $[Nd]_c/[Nb]_c$ as a function of niobium

Table 1. Possible substituents in the scheelite structure showing net charge on site and ionic radius in Å.

Calcium site		Tungsten site		Oxygen site	
$[Ca]^{2+}$	0·99	$\{W\}^{6+}$	0·62	$(O)^{2-}$	1·40
$[Nd]^{3+}$	1·04	$\{Nb\}^{5+}$	0·69	$(\phi)^{\circ}$	—
$[Na]^{+}$	0·95				
$[\phi]^{\circ}$	—				

melt concentration $[Nb]_m$ in the presence of a fixed neodymium melt concentration $[Nd]_m$.

It appears from the curves that the use of 1: 1 Nd/Nb melt ratio produces approximately 1: 1 Nd/Nb crystal ratio. This implies that the energies involved in equations (*d*) and (*f*) of Table 2 are approximately equal or that there is a strong chemical affinity between Nd^{3+} and Nb^{5+}, neither of which appears to be the case with the alkali metal ion compensation described above.

The $CaWO_4$: Nd^{3+}: Nb^{5+} system displays some of the characteristics of a buffer system, in that it tries to approximate equation (*h*) of Table 2 even at unfavorable melt concentrations. Thus, when $[Nb]_m$ is 0·5 with $[Nd]_m/[Nb]_m = 2{\cdot}2$, k_{Nd} is low and k_{Nb} is high, resulting in a $[Nd]_c/[Nb]_c$ ratio of 1·10. When $[Nb]_m$ is 2·1, with $[Nd]_m/[Nb]_m = 0{\cdot}55$, k_{Nd} rises and k_{Nb} falls so that the $[Nd]_c/[Nb]_c$ ratio is now 0·82.

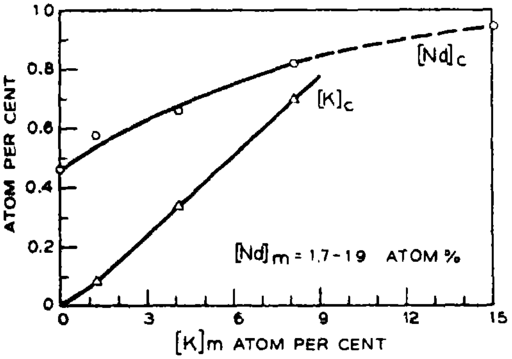

FIG. 2. Crystal concentrations in the system $CaWO_4$: Nd :K (see text for symbols).

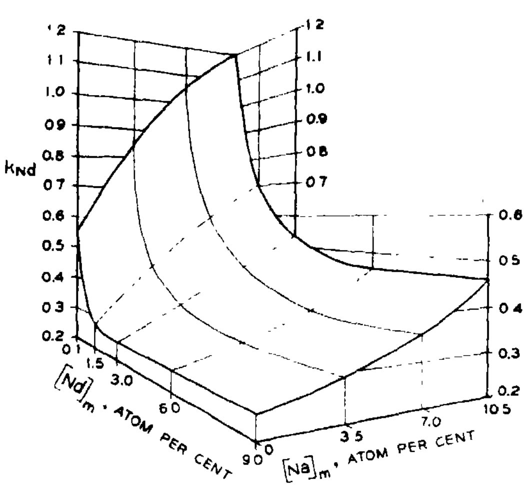

FIG. 3. The distribution coefficient of neodymium in the system $CaWO_4$:Nd:Na.

Table 2. Electrically neutral combinations of the substituents of Table 1 in the scheelite structure.

(*a*)	$CaO + WO_3 \rightarrow [Ca]\{W\}(O_4)$
(*b*)	$(1-x)CaWO_4 + xWO_3 \rightarrow [Ca_{1-x}\phi_x]\{W\}(O_{4-x}\phi_x)$
(*c*)	$CaWO_4 + xH_2 - xH_2O \rightarrow [Ca]\{W^{6+}_{1-2x}W^{5+}_{2x}\}(O_{4-x}\phi_x)$ etc.
(*d*)	$(1-3x)CaWO_4 + xNd_2O_3 + 3xWO_3 \rightarrow [Ca_{1-3x}Nd_{2x}\phi_x]\{W\}(O_4)$
(*e*)	$(1-2x)CaWO_4 + xNa_2O + 2xWO_3 \rightarrow [Ca_{1-2x}Na_{2x}]\{W\}(O_{4-x}\phi_x)$
(*f*)	$(1-2x)CaWO_4 + xNb_2O_5 + 2xCaO \rightarrow [Ca]\{W_{1-2x}Nb_{2x}\}(O_{4-x}\phi_x)$
(*g*)	$(2-4x)CaWO_4 + xNd_2O_3 + xNa_2O + 4xWO_3 \rightarrow 2[Ca_{1-2x}Nd_xNa_x]\{W\}(O_4)$
(*h*)	$(2-2x)CaWO_4 + xNd_2O_3 + xNb_2O_5 \rightarrow 2[Ca_{1-x}Nd_x]\{W_{1-x}Nb_x\}(O_4)$

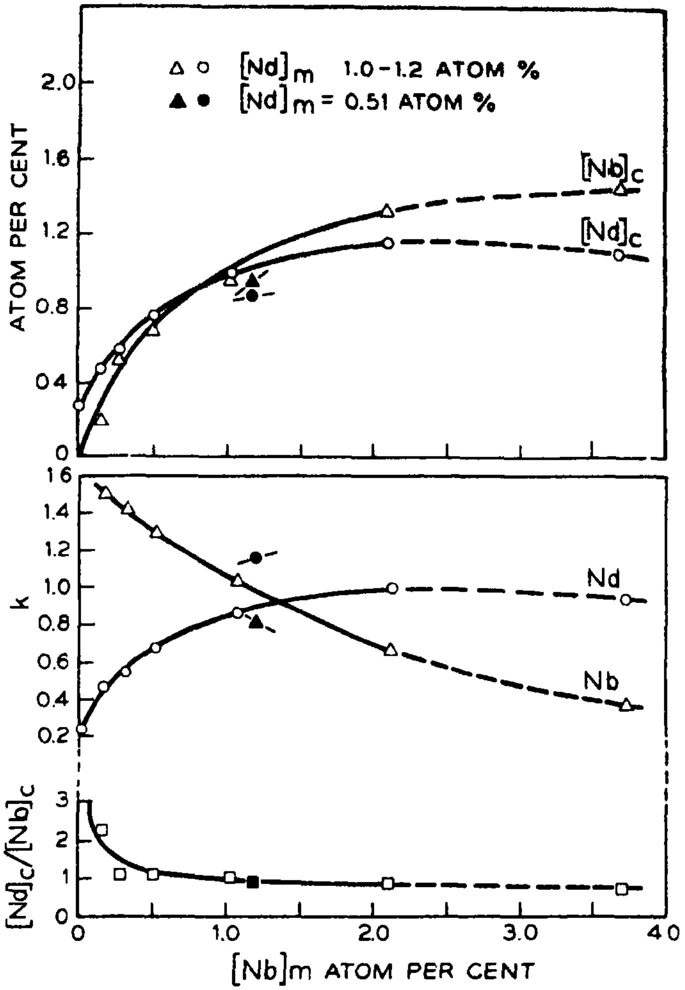

FIG. 4. The system $CaWO_4$:Nd:Nb (see text for symbols).

6. SODIUM COMPENSATION OF TRIVALENT RARE EARTHS

In paper I, Table 3, approximate distribution coefficients were given for most of the rare earths in the presence of one Na^+ per rare earth ion, and for some of these also in the absence of sodium. Further study has shown that these data were only approximations, in that flux-grown Na *r.e.*$(WO_4)_2$ is now known to always contain some excess Na_2WO_4, and some of the $CaWO_4$ used at that time also contained small but variable amounts of sodium.

In Fig. 5 is shown the detailed variation of *k* for the various rare earths as well as for yttrium and thorium at the 1–2 at. % level in calcium tungstate with sodium addition. Except for the ion that has the strongest tendency towards the divalent state (Eu), the behavior is roughly similar. Differences in intercept and saturation probably originate in small differences in the equilibrium constants for the appropriate form of equation (*d*) of Table 2. Spectroscopic evidence shows that both di- and trivalent species are present in the cases of Eu, and Yb. In the case of Eu there is an increase in the fraction of Eu^{3+} present as the sodium concentration is increased. The same may be true in the case of Yb, but this was not investigated. No obvious systematic differences which could be

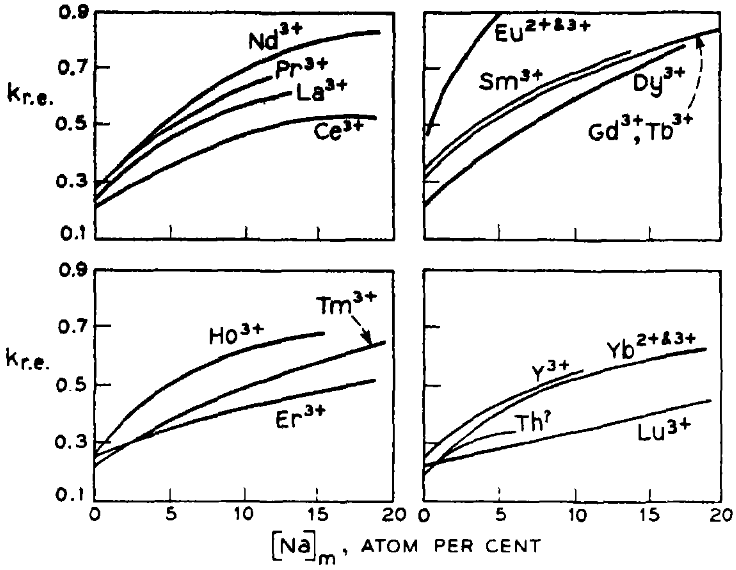

FIG. 5. Variation of the distribution coefficient of the rare earths, Y, and Th in the presence of sodium $[\mathrm{Na}]_m$ in $CaWO_4$ melt.

assigned to sequential filling of the 4*f* shell are apparent.

7. COLUMNAR GROWTH

If anywhere from 70 to 95 per cent of a quantity of $CaWO_4$ melt is pulled, a point is reached beyond which clear crystal can no longer be grown. Microscopic examination(10) gives an appearance similar to that observed for columnar growth due to constitutional supercooling in metals.(11) It was not possible to correlate the severity of this phenomenon with impurity analyses in the starting material,(10) which led to the possibility that deviations from stoichiometry might be at fault.

It was, in fact, found that as little as 1 wt.% CaO (10 at.%) added to $CaWO_4$ caused columnar growth to occur; however, about 10 wt.% WO_3 (10 at.%) produced a similar result. These two cases are easily distinguished, since with excess WO_3 the solidified melt has a green coloration, while with excess CaO it becomes brown. An examination of equation (*b*) of Table 2 shows that Schottky defect formation will use up WO_3, i.e., produce excess CaO in a stoichiometric $CaWO_4$ melt. Excess CaO in the starting material will intensify this effect, as would volatilization of WO_3. It would, therefore, seem desirable to add 2 or 3 wt.% excess WO_3 during normal crystal growth, since with approximately stoichiometric material, prolonged growth should then be possible.

8. EVIDENCE FOR THE NATURE OF SUBSTITUTION IN $CaWO_4$

A series of paramagnetic resonance experiments by MIMS and KLEIN(12, 13) provide supporting evidence for the nature of the substitution of trivalent rare earths in $CaWO_4$, and the changes produced by coupled substitution. Cerium was used in these experiments, since the single unpaired electron gives one line without hyperfine structure.

A typical paramagnetic resonance spectrum is presented in Fig. 6, corresponding to 0·1% Ce added in the form of $Ce_2(WO_4)_3$ without any charge compensation addition. Orientation experiments show that the central line A does not shift with rotation of the crystal about the *c*-axis; the pairs of lines *B* and *C* do shift, and are related as shown, the two *B*'s interchanging positions every 180°, and the *C*'s similarly. These eight "anomalous" lines correspond to only two *g*-tensors. At the lowest concentrations (< 0·01% Ce) line *A* predominates; as the concentration is increased, the relative intensities change, *A* decreasing and

B and *C* increasing. This same change is produced by adding Y^{3+}, being an ion of about the same size and charge as Ce^{3+} but having no unpaired $4f$ electrons. Lastly, the addition of Na^+ eliminates the anomalous lines, leaving only the single line *A*. It is possible to relate these observations to the various mechanisms listed in Table 2.

In the presence of Na^+, charge compensation occurs by a $Ce^{3+}Na^+$ combination replacing two Ca^{2+} ions (equation (*g*), Table 2). The presence of a single line independent of rotation about the *c*-axis leaves three possibilities: (i) the Na^+ is always in the *c*-axis direction from the Ce^{3+}, the nearest Ca^{2+} site it could occupy being 11·37 Å away; (ii) the Na^+ is always in one of the immediately adjacent Ca^{2+} sites, at 3·86 Å or perhaps at 5·24 Å, but since it is nonmagnetic and a good size fit (Pauling ionic radii $Ca^{2+} = 0{\cdot}99$, $Na^+ = 0{\cdot}95$ Å), does not disturb the electric and magnetic environment of the Ce^{3+}; or (iii) the Na^+ is more or less randomly distributed over all Ca^{2+} sites, most of the time being far enough away so that its influence is not felt. The uniform occurrence of case (i) is clearly unlikely; (ii) would produce some distortion due to the not quite perfect fit, which is not consistent with the single line, leaving (iii) as the reasonable explanation. In this last case, some (i) and (ii) would also occur; minor lines observed at very low levels may well correspond to these cases or to other arrangements in small amounts.

The change with the concentration of the rare earth itself in the absence of Na can now be viewed as a change from isolated Ce^{3+} ions with a single line predominating at the lower concentrations of 0·01 % to predominately Ce^{3+}–vacancy combinations in two adjacent Ca^{2+} sites with the second Ce^{3+} somewhat further away (at random) (equation (*d*), Table 2) at 1 %. Apparently, at the lowest concentrations, the vacancy and the rare earth ions need not be closely associated; this is the region where Schottky defects and rare earth concentrations are comparable in magnitude. Since the addition of Y^{3+} produces the same effect as adding more Ce^{3+}, a specific magnetic interaction is not present, as is also shown by the absence of dipole-dipole splitting, which eliminates Ce^{3+}–vacancy–Ce^{3+} combinations as well as Ce^{3+}–Ce^{3+}.

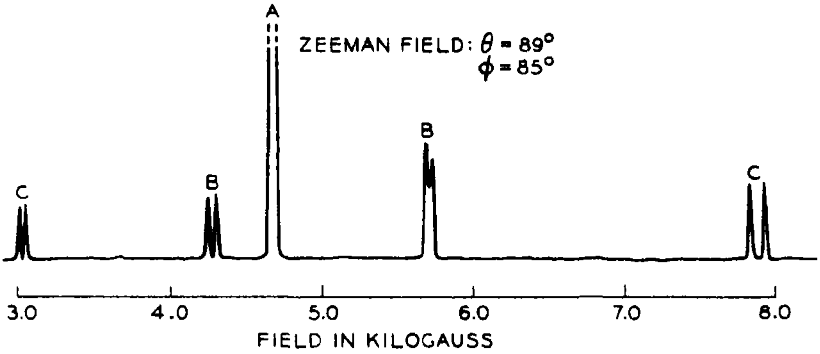

FIG. 6. Paramagnetic resonance spectrum of $CaWO_4$ containing 0·1 at. % cerium.

On a more speculative basis, it is tempting to identify the eight anomalous lines with the four nearest neighbor Ca^{2+} sites around each of the two types Ca^{2+} sites, viewing the net effect of the vacancy as a fractional change in position or charge of the connecting oxygens. The two types of Ca^{2+} sites, related by the body centering of the scheelite lattice, are not equivalent in the presence of a vacancy.

Related, but not as clearcut changes are also observed in the optical spectra.$^{(10)}$

Acknowledgements—The authors wish to thank J. E. KESSLER and E. K. JAYCOX for the many analyses and W. B. MIMS for the use of paramagnetic resonance results and for helpful discussion.

REFERENCES

1. NASSAU K. and BROYER A. M., Calcium Tungstate: Growth, Perfection and Substitution, *J. appl. Phys.* **33**, 3064 (1962).

2. LEVINSTEIN H. J., LOIACONO G. M. and NASSAU K., Calcium Tungstate: II. *Observations of Dislocations*, submitted to *J. appl. Phys.*
3. JOHNSON L. F. and NASSAU K., *Proc. Inst. Radio Engrs.* **49**, 1704 (1961).
4. JOHNSON L. F., BOYD G. D., NASSAU K. and SODEN R. R., *Phys. Rev.* **126**, 1406 (1962).
5. GOLDSCHMIDT V. M., quoted in EITEL W., *The Physical Chemistry of the Silicates*, University of Chicago Press, 3rd English Ed., p. 74 (1954).
6. HAHN D. and LERTES K., *Z. Phys.* **169**, 331 (1962).
7. VAN BUREN H. G., *Imperfections in Crystals*, p. 36, 512, North-Holland, Amsterdam (1960).
8. MACDONALD R. E., VOGEL M. J. and BROOKMAN J. W., *IBM J.* **6**, 363 (1962).
9. NASSAU K., The data of a part of this section will appear in *Proceedings of the 3rd International Symposium on Quantum Electronics*, February 11–15, 1963, Paris, France.
10. NASSAU K., *Proceedings of the Brooklyn Polytechnic Institute Symposium on Optical Masers*, April 16–18, 1963 (in press).
11. HURLE D. T. J., *Solid-State Electron.* **3**, 37 (1961).
12. MIMS W. B., private communication.
13. KLEIN M. P. and MIMS W. B., presented at American Physical Society Meeting, Stanford University, December 1962. Abstract, see *Bull. Amer. Phys. Soc.*, Ser. II, **7**, 625 (1962).

Note added in proof

On the basis of the analogy of certain paramagnetic resonance results between Fe^{3+} and Nd^{3+} in $CaWO_4$, KEDZIE and KESTIGIAN (*Appl. Phys. Letters* **3**, 86–87, 1963) concluded that Nd^{3+} may also enter the W-site. In view of the large discrepancies in both the ionic sizes and charges involved, a much higher energy would be associated with such an arrangement, and a negligible occurrence would be expected for this arrangement compared with substitution in the Ca-site with or without charge compensation. Yet another contraindication is the existence of the compound $Nd_2(WO_4)_3$, corresponding to complete substitution with vacancy compensation. This has a monoclinic structure with $a = 7{\cdot}75$ Å, $b = 11{\cdot}59$, $c = 11{\cdot}50$ and $\beta = 109{\cdot}7°$. This structure is the same as that of $Eu_2(WO_4)_3$ determined by TEMPLETON and ZALKIN (*Acta Cryst.* **16**, 762–766, 1963), which can be described as $CaWO_4$ with two Eu^{3+} and one vacancy in every three Ca-sites; the vacancies are ordered and distortion exists, particularly in the WO_4^{2-} tetrahedron.

J. Phys. Chem. Solids Pergamon Press 1963. Vol. 24, pp. 1511–1517. Printed in Great Britain.

CALCIUM TUNGSTATE—IV

THE THEORY OF COUPLED SUBSTITUTION

K. NASSAU

Bell Telephone Laboratories, Incorporated, Murray Hill, New Jersey

(*Received* 30 *July* 1963)

Abstract—A theory is developed for the coupled substitution e.g., of Nd^{3+} and Na^+ in Ca^{2+} sites in the scheelite ($CaWO_4$) lattice. Allowance is made for Schottky defect formation.

The results fit the $CaWO_4$: Nd system up to 2% Nd, the $CaWO_4$: Nd : Na system up to 15% Na and 5% Nd, and the $CaWO_4$: Nd : K system up to 8% K and 2% Nd.

Equilibrium constants resulting from the theory give the vacancy concentrations in O and Ca sites as 0·054% each and the free energy of formation of a pair of vacancies as 55 kcal or 2·4 eV, all in pure $CaWO_4$ in air at the melting point.

Energies are also obtained for the various other substitution arrangements. For exactly balanced substitution of one Na^+ for each Nd^{3+} in the crystal, it is necessary to use 4·05 Na for each Nd in the melt. This also results in the minimum number of vacancies in the crystal.

1. INTRODUCTION

IN THE third paper of this series,(1) hereafter referred to as III, experimental data were presented for the distribution coefficient, k, of various rare earths in the Czochralski growth of calcium tungstate crystals from the melt. It was found that at very low melt concentrations, the magnitude of k varies with the concentration of the rare earth itself, as well as at all concentrations with the concentration of mono- or penta-valent ions which are able to compensate the excess positive charge of, e.g., a Nd^{3+} in a Ca^{2+} site.

In the field of geochemistry such charge compensating substitutions are well known and have been termed coupled replacement or coupled diadochy,(2) or compensatory solid solution.(3) The designation "coupled substitution" is used here as being simple and descriptive.

In this paper derivations are presented for the substitution of trivalent ions, and for the coupled substitution of trivalent and monovalent ions, in $CaWO_4$. The equations obtained give a satisfactory description of the variation of the distribution coefficient of Nd^{3+} with both Nd^{3+} and Na^+ concentration, as well as information on vacancy behavior in the scheelite lattice.

In view of the general similarity of the trivalent rare earths, and of the various scheelite structured compounds, the qualitative aspects of this development are also expected to apply to combinations other than $CaWO_4$: Nd and $CaWO_4$: Nd : Na.

2. THEORY OF $CaWO_4 : Nd^{3+}$ SUBSTITUTION

In this and the following Section Nd^{3+} is used as representing a typical trivalent rare earth ion, and Na^+ as a typical monovalent alkali metal ion. A series of assumptions and approximations are made which will be discussed in Section 4.

In the system $CaWO_4 : Nd^{3+}$, two processes are taken to be at work. The first, the formation of Schottky defects (equation (b) of III) by the simultaneous creation of one oxygen vacancy plus one calcium vacancy, can be written as

$$WO_{3\,\mathrm{melt}}+(1-x)CaO_{\mathrm{melt}}\rightarrow[Ca_{1-x}\varphi_x]\{W\}(O_{4-x}\varphi_x)$$

crystal or in the conventional manner

$$\rightarrow \varphi_{Ca}+\varphi_O \tag{1}$$

Here φ indicates a vacancy, the subscripts indicate the crystal lattice site, and x is very small. Writing the law of mass action and using square brackets for activities (thermodynamically effective concentrations):

$$[\varphi_{Ca}][\varphi_O] = k_1 \tag{2}$$

Here k_1 is the equilibrium constant for equation

(1). The activities of the other components of (1) remain essentially constant and can be taken as unity for convenience. The second process is the entry of Nd^{3+} into a Ca^{2+} site with the formation of one calcium vacancy for every two Nd^{3+} ions (equation (d) of III), which can be written

$$2\mathrm{Nd}_m \to 2\mathrm{Nd}_c + \varphi_{\mathrm{Ca}} \tag{3}$$

Here the subscript m indicates the melt. The crystal concentration $[\mathrm{Nd}]_c$ is taken to be identical with $[\mathrm{Nd}_{\mathrm{Ca}}]$. The law of mass action applied to (3) gives the equilibrium constant k_2 as

$$\frac{[\mathrm{Nd}]_c^2[\varphi_{\mathrm{Ca}}]}{[\mathrm{Nd}]_m^2} = k_2 \tag{4}$$

Since electrical neutrality must be preserved in the crystal, and using $'$ and $''$ for the concentrations originating from equations (1) and (3),

$$[\varphi_{\mathrm{Ca}}]' = [\varphi_{\mathrm{O}}]' \tag{5}$$

and

$$[\varphi_{\mathrm{Ca}}]'' = \tfrac{1}{2}[\mathrm{Nd}]_c'' \tag{6}$$

Adding (5) and (6) and taking the total calcium vacancies $[\varphi_{\mathrm{Ca}}] = [\varphi_{\mathrm{Ca}}]' + [\varphi_{\mathrm{Ca}}]''$ yields the over-all electrical neutrality condition for the crystal phase

$$[\varphi_{\mathrm{Ca}}] = [\varphi_{\mathrm{O}}] + \tfrac{1}{2}[\mathrm{Nd}]_c \tag{7}$$

The distribution coefficient for Nd is given by

$$K_{\mathrm{Nd}} = \frac{[\mathrm{Nd}]_c}{[\mathrm{Nd}]_m} \tag{8}$$

Using (8) on (4) and (7) to eliminate $[\mathrm{Nd}]_c$

$$K_{\mathrm{Nd}}^2[\varphi_{\mathrm{Ca}}] = k_2 \tag{9}$$

and

$$[\varphi_{\mathrm{Ca}}] = [\varphi_{\mathrm{O}}] + \tfrac{1}{2}K_{\mathrm{Nd}}[\mathrm{Nd}]_m \tag{10}$$

Using (2) on (10) to eliminate $[\varphi_{\mathrm{O}}]$

$$[\varphi_{\mathrm{Ca}}] = \frac{k_1}{[\varphi_{\mathrm{Ca}}]} + \tfrac{1}{2}K_{\mathrm{Nd}}[\mathrm{Nd}]_m \tag{11}$$

Using (9) on (11) to eliminate $[\varphi_{\mathrm{Ca}}]$ and rearranging

$$[\mathrm{Nd}]_m = \frac{2k_2}{K_{\mathrm{Nd}}^3} - \frac{2k_1K_{\mathrm{Nd}}}{k_2} \tag{12}$$

At very low Nd concentration, as $(\mathrm{Nd})_m \to 0$

$$\frac{2k_2}{K_{\mathrm{Nd}}^3} = \frac{2k_1K_{\mathrm{Nd}}}{k_2}$$

The intercept on the K_{Nd} axis is then given by

$$[\mathrm{Nd}]_m \overset{\mathrm{Lim}}{\to} 0\; K_{\mathrm{Nd}} = 4\sqrt{\left(\frac{k_2^2}{k_1}\right)} \tag{13}$$

The limiting slope is obtained from the differential of (12):

$$\frac{\mathrm{d}[\mathrm{Nd}]_m}{\mathrm{d}K_{\mathrm{Nd}}} = -\frac{6k_2}{K_{\mathrm{Nd}}^2} - \frac{2k_1}{k_2}$$

by using (13) and inverting to give

$$[\mathrm{Nd}]_m \overset{\mathrm{Lim}}{\to} 0\; \frac{\mathrm{d}K_{\mathrm{Nd}}}{\mathrm{d}[\mathrm{Nd}]_m} = -\frac{k_2}{8k_1} \tag{14}$$

3. THEORY OF $\mathrm{CaWO_4}$: Nd^{3+} : Na^+ COUPLED SUBSTITUTION

Here equations (1–6), (8) and (9) still apply. When sodium is now added, in addition to the process of (1) and (3), Na^+ also enters into Ca^{2+} sites with one oxygen vacancy for every two Na^+ (equation (e) of III)

$$2\mathrm{Na}_m \to 2\mathrm{Na}_c + \varphi_{\mathrm{O}} \tag{15}$$

The law of mass action equation gives the equilibrium constant k_3 as

$$\frac{[\mathrm{Na}]_c^2[\varphi_{\mathrm{O}}]}{[\mathrm{Na}]_m^2} = k_3 \tag{16}$$

For electrical neutrality using $'''$ for concentrations originating from equation (15)

$$\tfrac{1}{2}[\mathrm{Na}]_c''' = [\varphi_{\mathrm{O}}]''' \tag{17}$$

Adding (17) to (5) and (6) and clearing as before

$$[\varphi_{\mathrm{Ca}}] + \tfrac{1}{2}[\mathrm{Na}]_c = [\varphi_{\mathrm{O}}] + \tfrac{1}{2}[\mathrm{Nd}]_c \tag{18}$$

The distribution coefficient for Na is given by

$$K_{\mathrm{Na}} = \frac{[\mathrm{Na}]_c}{[\mathrm{Na}]_m} \tag{19}$$

Using (8) and (19) on (18) and (16) to eliminate $[\mathrm{Nd}]_c$ and $[\mathrm{Na}]_c$

$$[\varphi_{\mathrm{Ca}}] + \tfrac{1}{2}K_{\mathrm{Na}}[\mathrm{Na}]_m = [\varphi_{\mathrm{O}}] + \tfrac{1}{2}K_{\mathrm{Nd}}[\mathrm{Nd}]_m \tag{20}$$

and

$$K_{\mathrm{Na}}^2[\varphi_{\mathrm{O}}] = k_3 \tag{21}$$

Using (2) on (20) and (21) to eliminate $[\varphi_{\mathrm{O}}]$

$$[\varphi_{\mathrm{Ca}}] + \tfrac{1}{2}K_{\mathrm{Na}}[\mathrm{Na}]_m = \frac{k_1}{[\varphi_{\mathrm{Ca}}]} + \tfrac{1}{2}K_{\mathrm{Nd}}[\mathrm{Nd}]_m \tag{22}$$

and

$$\frac{K_{\mathrm{Na}}^2 k_1}{[\varphi_{\mathrm{Ca}}]} = k_3 \tag{23}$$

Using (9) on (22) and (23) to eliminate $[\varphi_{\mathrm{Ca}}]$

$$\frac{k_2}{K_{\mathrm{Nd}}^2} + \tfrac{1}{2}K_{\mathrm{Na}}[\mathrm{Na}]_m = \frac{k_1 K_{\mathrm{Nd}}^2}{k_2} + \tfrac{1}{2}K_{\mathrm{Nd}}[\mathrm{Nd}]_m \tag{24}$$

and

$$K_{\mathrm{Na}} = \frac{1}{K_{\mathrm{Nd}}}\sqrt{\left(\frac{k_2 k_3}{k_1}\right)} \tag{25}$$

Eliminating K_{Na} from (24) and (25) and rearranging

$$[\mathrm{Nd}]_m = \frac{2k_2}{K_{\mathrm{Nd}}^3} - \frac{2k_1 K_{\mathrm{Nd}}}{k_2} + \frac{[\mathrm{Na}]_m}{K_{\mathrm{Nd}}^2}\sqrt{\left(\frac{k_2 k_3}{k_1}\right)} \tag{26}$$

For the sake of completeness the equation corresponding to equation (26) for the $\mathrm{CaWO_4}$: $\mathrm{Nd^{+3}}$: $\mathrm{Na^+}$ system written in terms of the sodium parameters becomes

$$[\mathrm{Na}]_m = \frac{2k_3}{K_{\mathrm{Na}}^3} - \frac{2k_1 K_{\mathrm{Na}}}{k_3} + \frac{[\mathrm{Nd}]_m}{K_{\mathrm{Na}}^2}\sqrt{\left(\frac{k_2 k_3}{k_1}\right)} \tag{27}$$

Again, if a pentavalent ion such as $\mathrm{Nb^{5+}}$ in a $\mathrm{W^{6+}}$ site is used to compensate the excess charge of $\mathrm{Nd^{3+}}$ in a $\mathrm{Ca^{2+}}$ site, the equations would be quite analogous and $[\mathrm{Nb}]_m$ for $[\mathrm{Na}]_m$ would be the only substitution needed in equations (26) and (27).

4. ASSUMPTIONS

In view of the large number of assumptions made in arriving at a workable theory, a separate discussion of these appears in order. The final confirmation of such assumptions must inevitably rest on the adequacy of the description thus obtained.

The evidence for a close approach to equilibrium conditions at the rather high pulling rates of 0·5–1 in. per hour have been discussed in a previous paper.[4] At these high growth rates, the possibility of diffusion in the crystal having an effect on the concentrations can be ignored. The evidence for the vacancy compensation of a trivalent rare earth in $\mathrm{Ca^{2+}}$ sites, the nature of $\mathrm{Na^+}$ charge compensation, and the improbability of $\mathrm{W^{6+}}$ vacancies or free or trapped electrons have been discussed in III. The paramagnetic resonance results quoted in III indicate that, except for vacancies, clustering does not appear to take place. The various substitution processes can thus be treated as occurring separately with some assurance.

More serious assumptions made are those concerning the nature of the species in the melt. Particularly, it is assumed that the solutions are ideal, i.e., that the concentrations as determined from analyses are identical to the activities or that the activity coefficients are all equal to unity for the added species, and constant for the components of $\mathrm{CaWO_4}$ itself. The $\mathrm{CaWO_4}$ is assumed to be stoichiometric; at very low concentration of $\mathrm{Na^+}$ and $\mathrm{Nd^{3+}}$, where nonstoichiometry might produce significant deviations, pulled $\mathrm{CaWO_4}$ crystal was used in place of the usual raw material. Deviations from ideal solution behavior are, of course, expected at high concentrations.

It is also assumed in the calculations that the various additives do not change the melting point. The qualitative check of Table 1 shows some changes, although, as a percentage of the absolute temperature, the differences appear to be tolerable. All growth occurred in air.

Table 1. *Approximate solidification points*

Pure $\mathrm{CaWO_4}$	1850°K
$\mathrm{CaWO_4}$ + 4 % Nd + 10 % Nd	1850°K
$\mathrm{CaWO_4}$ + 1 % Nd + 18 % K	1815°K
$\mathrm{CaWO_4}$ + 5 % Nd + 5 % Na	1805°K

5. DETERMINATION OF EQUILIBRIUM CONSTANTS

For the purpose of application of the results of Sections 2 and 3, concentrations must be expressed as atom fractions. Equations (13) and (14) were used to fit the K_{Nd} vs. $[\mathrm{Nd}]_m$ data for $[\mathrm{Na}]_m \to 0$ shown in Fig. 1, giving

$$k_1 = 2{\cdot}9 \times 10^{-7}$$

$$k_2 = 1{\cdot}8 \times 10^{-4}.$$

Using these equilibrium constants, curve A of Fig. 1 was constructed, giving a satisfactory fit up to $[\mathrm{Nd}]_m = 2$ at. %.

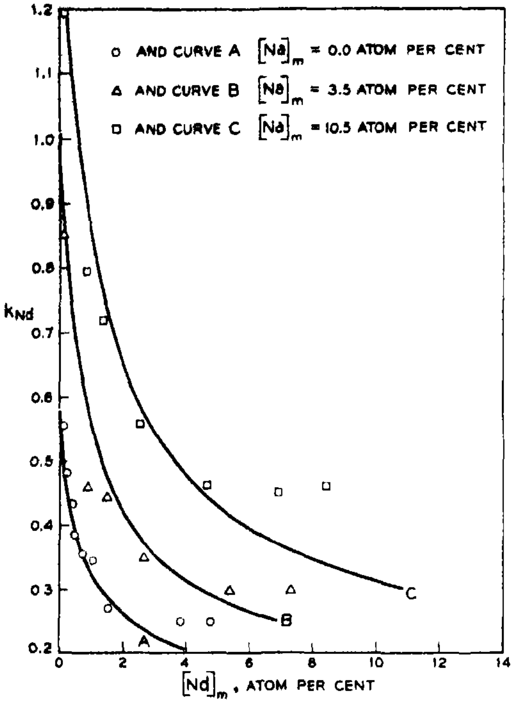

FIG. 1. Variation of K_{Nd} with neodymium concentration $[Nd]_m$ at various sodium concentrations $[Na]_m$ in the melt. Points are experimental, lines are theoretical.

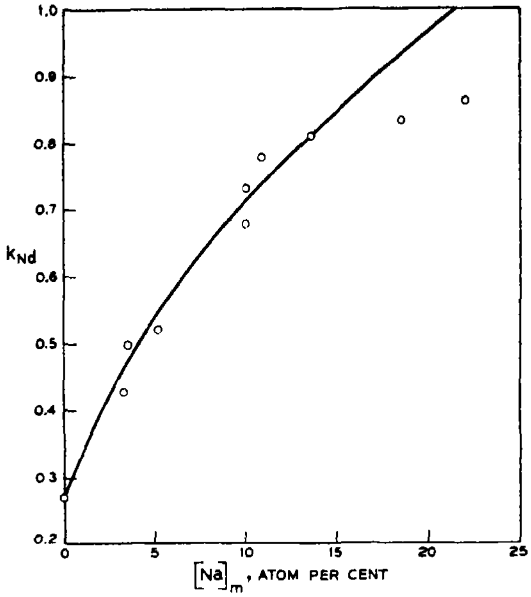

FIG. 2. Variation of K_{Nd} with sodium concentration $[Na]_m$ at fixed neodymium concentration of 1·5 atomic per cent in melt. Points are experimental, line is theoretical.

Using k_1 and k_2, k_3 is now obtained by fitting the curve of Fig. 2 to the experimental points of K_{Nd} against $[Na]_m$ at $[Nd]_m = 1{\cdot}5$ at. % by the use of equation (26). This gives a satisfactory fit up to $[Na_m] = 15$ per cent for

$$k_3 = 1{\cdot}1\times10^{-5}$$

The accuracy of the equilibrium constants is estimated to be ±5 per cent.

By the use of the values of k_1, k_2, and k_3 thus obtained, curves B and C of Fig. 1 were constructed for $[Na]_m = 3{\cdot}5$ and 10·5 per cent respectively. The fit up to 5 at. % in both curves is quite satisfactory. It appears that the high temperature of the melting point is a major factor in the system being so close to ideal at such high concentrations. The various assumptions outlined in the previous section are confirmed by the fit of the equations; it seems unlikely that the agreement would be fortuitous.

Using the equilibrium constants, and expressing concentrations as fractions, equations (26) and (27) now become

$$[Nd]_m = \frac{0{\cdot}00036}{K_{Nd}^3} - 0{\cdot}00322\,K_{Nd} + \frac{0{\cdot}083[Na]_m}{K_{Nd}^2} \tag{28}$$

and

$$[Na]_m = \frac{0{\cdot}000022}{K_{Na}^3} - 0{\cdot}0528K_{Na} + \frac{0{\cdot}083[Nd]_m}{K_{Na}^2} \tag{29}$$

6. DISCUSSION

(a) *Distribution coefficients*

Using the values of the equilibrium constants it is now possible to plot the variation of K_{Nd} and K_{Na} over the field in which the equations apply. This is shown in Fig. 3. From this plot, the contours for constant crystal concentrations of $[Nd]_c$ and $[Na]_c$ shown in Fig. 4 were determined. The locus of intersections gives the compositions where exact charge compensation occurs along the

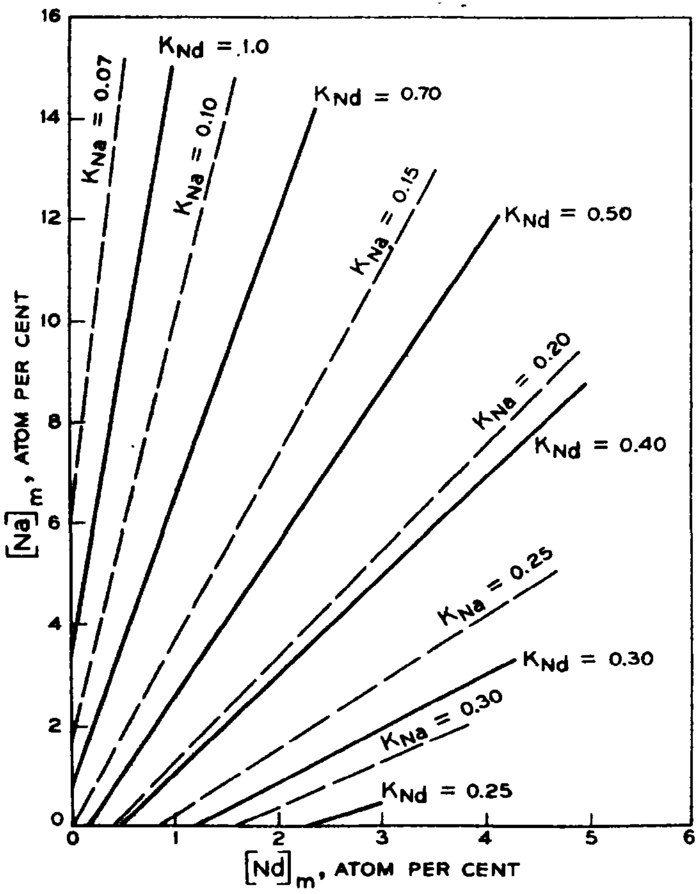

FIG. 3. Theoretical distribution coefficients of sodium K_{Na} and neodymium K_{Nd} in area where theory is valid.

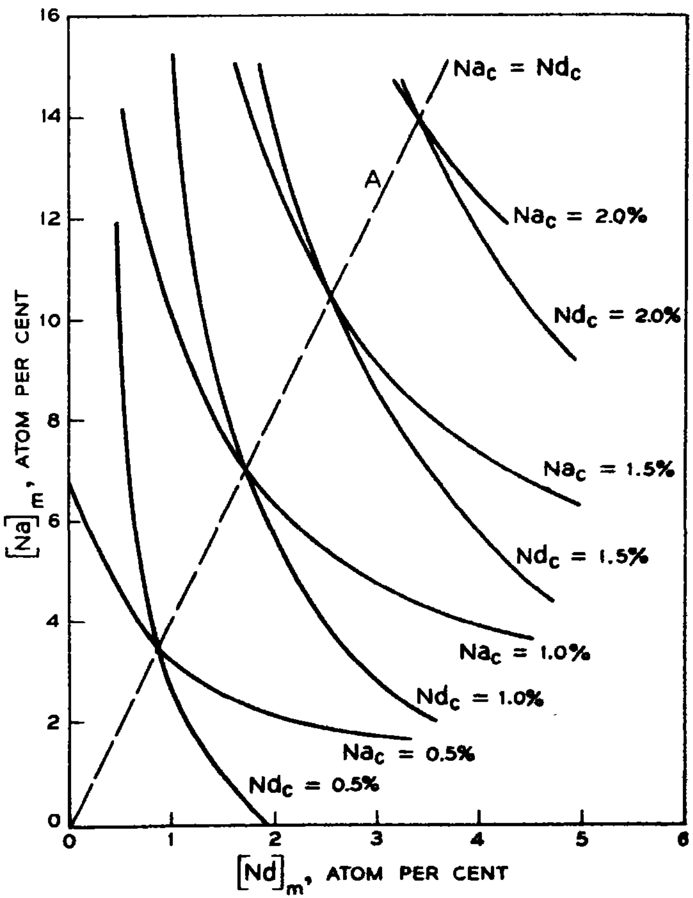

FIG. 4. Lines of constant crystal concentration of sodium $[Na]_c$ and neodymium $[Nd]_c$ in area where theory is valid. Line A gives condition for $[Na]_c = [Nd]_c$.

line A. Along this line $K_{Nd} = 0{\cdot}58$ and $K_{Na} = 0{\cdot}143$. From equation (18) it follows that this is also the condition for equal quantities of oxygen and calcium vacancies $\varphi_O = \varphi_{Ca}$ and from (2) that this corresponds to the minimum number of total vacancies.

It is interesting that the concentration for minimum laser threshold was empirically found to be 3–4 at. % Nd at 15 at. % Na,(5) bracketing the above ratio of 4·05 : 1.

(b) *Vacancy concentrations*

The equilibrium constant k_1 for the formation of Schottky defects permits a determination of the concentration of vacancies in pure $CaWO_4$ as formed in air at the melting point. This is given by $\varphi_{Ca} = \varphi_O = \sqrt{k_1} = 0{\cdot}054$ per cent. This figure may be compared to the value of 0·043 per cent for LiF at its melting point of 1115°K.(6)

For any given melt composition the crystal concentrations and calcium vacancies can now be calculated. From (23), (2) and (9)

$$\varphi_{Ca} = \frac{k_1 K_{Na}^2}{k_3} = \frac{k_2}{K_{Nd}^2} \tag{32}$$

and

$$\varphi_O = \frac{k_3}{K_{Na}^2} = \frac{k_1 K_{Nd}^2}{k_2} \tag{33}$$

Anywhere along line A of Fig. 4, $\varphi_O = \varphi_{Ca} = 0{\cdot}054$ per cent. Other values can be visualized from two typical examples: Anywhere along the line $K_{Nd} = 0{\cdot}25$ of Fig. 3, $\varphi_O = 0{\cdot}010$ per cent and $\varphi_{Ca} = 0{\cdot}24$ per cent; along the line $K_{Na} = 0{\cdot}07$ of Fig. 3, $\varphi_O = 0{\cdot}13$ per cent and $\varphi_{Ca} = 0{\cdot}022$ per cent.

(c) *Energy values*

The following development is aimed at obtaining approximate energies for the various processes occurring. All the assumptions of Section III are implied, and are confirmed by the good fit of the theoretical curves to the experimental data.

Following an argument similar to that of SWALIN,(7) obtaining the equilibrium number of vacancies by taking $(\delta F/\delta n) = 0$ where F is the free energy of formation of n vacancies in N lattice sites,

$$\frac{n}{N} = \exp\left(\frac{\Delta S_V}{R}\right)\exp\left(\frac{-\Delta H}{RT}\right)$$

or

$$\Delta H - T\Delta S_V = -RT \log n/N \tag{34}$$

Here ΔS_V is the change in vibrational, nuclear spin and other entropy terms except that of mixing, ΔH is the enthalpy and R the gas constant. If the configurational (mixing) ΔS_c is now added

$$\Delta F^0 = \Delta H - T\Delta S_V - T\Delta S_c$$

or

$$\Delta F^0 = RT[(2n'+2)\log n' + (1-2n')\log(1-2n')] \tag{35}$$

for the case under consideration where $n' = \varphi_O = \varphi_{Ca} = 0{\cdot}00054$.

This gives the value of 55 kcal, or 2·4 eV, for the free energy of formation of one mole of vacancy pairs at the melting point in air. This may be compared with the heat of formation of a vacancy pair in LiF of 2·68 eV(6) or a single vacancy of Pt of 1·3 eV(7)

Since the equilibrium constants k_2 and k_3 are valid at infinite dilution, it is possible to obtain the free energy of formation of equations (3) and (15) from $\Delta F_2^0 = -RT \ln k_2$ and $\Delta F_3^0 = -RT \ln k_3$ as 32 and 42 kcal (1·4 and 1·8 eV) per mole vacancy formed. These are the free energies involved in the replacement of two Ca^{2+} ions by two Nd^{3+} or Na^+ ions with the formation of one Ca or O vacancy respectively, the transfer occurring from an infinitely dilute solution to an infinitely dilute crystal at the melting point in air. By combining these figures with the vacancy formation energy, one obtains for the balanced substitution

$$Na_m + Nd_m \rightarrow Na_c^+ + Nd_c^{3+}$$

the free energy

$$\Delta F^0 = \frac{32+42-55}{2} = 9{\cdot}5 \text{ kcal } (0{\cdot}4 \text{ eV}).$$

This is the free energy involved in the replacement of 2 moles Ca^{2+} ions in the calcium tungstate lattice at the melting point by 1 mole each of Na^+ and Nd^{3+} ions, the transfer occurring from an infinitely dilute solution to an infinitely dilute crystal.

The accuracy of these free energies is estimated to be ±3 per cent except for the value of 9·5 above which is ±10 per cent.

(d) *Other compensating systems*

The limited data for the K^+ compensation of Nd^{3+} in $CaWO_4$ (Fig. 2 of III) gives a good agreement for the $[Nd]_c$ (or the equivalent K_{Nd} data) up to about 8 at. % Na in the presence of 1·7 at. % Nd when $k_3 = 3{\cdot}0 \times 10^{-6}$. This corresponds to 7·8 K^+ per Nd^{3+} for exact charge compensation at the lower concentrations where the solution is close to ideal. At this ratio $K_{Nd} = 0{\cdot}58$ and $K_K = 0{\cdot}075$. The fit to the $[K]_c$ data is not as good; this was expected since analytical data on the alkali metals in $CaWO_4$ have been difficult to obtain with any degree of accuracy particularly at low concentrations. The ΔF^0 for the vacancy compensation of K^+ is then 47 kcal, and 12 kcal for the coupled $Nd^{3+} : K^+$ compensation determined as in Section 6(c) (2·0 and 0·5 eV).

Data for the other alkali metal ions are too incomplete at the lowest concentrations for the determination of k_3; the range of applicability to these ions is expected to be even more restricted as the ionic size misfit becomes larger. The application of the theory to the case of niobium compensation (Fig. 4 of III) is being further investigated in detail.

Acknowledgements—The author wishes to thank G. M. LOIACONO for experimental assistance and C. D. THURMOND and F. A. TRUMBORE for helpful discussions.

REFERENCES

1. NASSAU K. and LOIACONO G. M., *J. Phys. Chem. Solids* **23**, 1505 (1963).
2. EITE W., *The Physical Chemistry of the Silicates*, 3rd English Ed., p. 75. U. of Chicago Press (1954).
3. SMITH F. G., *Physical Geochemistry* p. 42, Addison-Wesley, Reading, Mass. (1963).
4. NASSAU K. and BROYER A. M., *J. appl. Phys.* **33**, 3064–3073 (1962).
5. NASSAU K., *Proceedings of the Brooklyn Polytechnic Institute Symposium on Optical Masers*, April 16–18. Brooklyn, New York (1963).
6. HAVEN Y., *Rec. Trav. Chim.* **69**, 1259 (1950).
7. SWALIN A. A., *Thermodynamics of Solids*, p. 218–227. Wiley, New York (1962).

J. Phys. Chem. Solids Pergamon Press 1963. Vol. 24, pp. 1519–1524. Printed in Great Britain.

X-RAY DIFFRACTION AT ULTRA-HIGH PRESSURES

N. B. OWEN, P. L. SMITH, J. E. MARTIN and A. J. WRIGHT

Basic Physics Division, National Physical Laboratory, Teddington, Middlesex

(*Received* 6 *May* 1963; *revised* 4 *September* 1963)

Abstract—Apparatus is described which was designed to obtain X-ray diffraction patterns from materials subjected to very high pressures. Miniature Bridgman anvils of diamond are used to squeeze the sample without the conventional form of annular gasket. Load is applied either directly by means of a helical compression spring or through a hydraulic intensifier with a load magnification of about 20. Models to fit two standard X-ray cameras of 5·73 and 11·46 cm diameter have been made and both can oscillate about the vertical axis in the usual manner. One model has been designed to oscillate through an included angle of 300° and has provision for heating the test sample to 250°C. X-ray diffraction patterns have been obtained at pressures exceeding a nominal 200 kb.

The results of work on cadmium sulphide and cadmium telluride up to pressures of 200 kb obtained with this apparatus are given. Cadmium sulphide in the wurtzite form is found to transform to the rock salt structure under pressure while cadmium telluride transforms from the zinc-blende structure first to the rock salt structure and then to a diatomic analogue to the β-tin structure.

INTRODUCTION

SEVERAL types of apparatus have been designed over the last few years to obtain X-ray diffraction patterns of materials whilst under high pressures.(1–5) This apparatus is in general based on one of two designs, either a piston and cylinder arrangement or a pair of opposed anvils, but in either case the choice of materials for the high pressure cell is severely restricted because there are few materials with adequate mechanical strength which are sufficiently transparent to X-rays. Suitable materials include diamond, sapphire, beryllium and carbon, and of these diamond is by far the strongest.

A piston and cylinder arrangement affords a more uniform pressure than opposed anvils but with the small size necessary for X-ray work the frictional losses at the piston are high and effective gasketing of the pressure cell is difficult to achieve. In addition there is extra scatter and a loss of intensity of the X-ray beam. The maximum pressure realized with cylinders of materials suitable for X-ray diffraction work, including miniature diamond cells,(3,4) does not exceed about 30 kb. On the other hand much higher pressures can be obtained from opposed anvils. The small specimen size is advantageous because the volume of highly stressed anvil material is small and hence much higher pressures can be supported than with anvils of conventional size. Anvils of single crystal sapphire have been used to pressures exceeding 30 kb(3,6) and of diamond to pressures exceeding 60 kb.(5)

Apparatus

Because of the superiority of anvils for generating very high pressures they have been used in apparatus developed at N.P.L. Two models have been made, one to fit a Hilger and Watts single crystal camera of 5·73 cm film diameter and one to fit a Unicam camera of 11·46 cm dia. Photographs of these are shown in Figs 1 and 2 respectively and a sectional drawing of Fig. 2 is shown in Fig. 3. The instrument designed for the Hilger and Watts camera can accommodate a rotation about its vertical axis of 120 degrees and that for the Unicam camera 300 degrees.

The sample is squeezed between a pair of miniature diamond Bridgman anvils and a finely collimated X-ray beam directed through it perpendicular to the axis of the anvils. The sample is in the form of a very thin wafer held between the anvils without the conventional annular gasket. The anvils are modified Rockwell hardness indentors with a

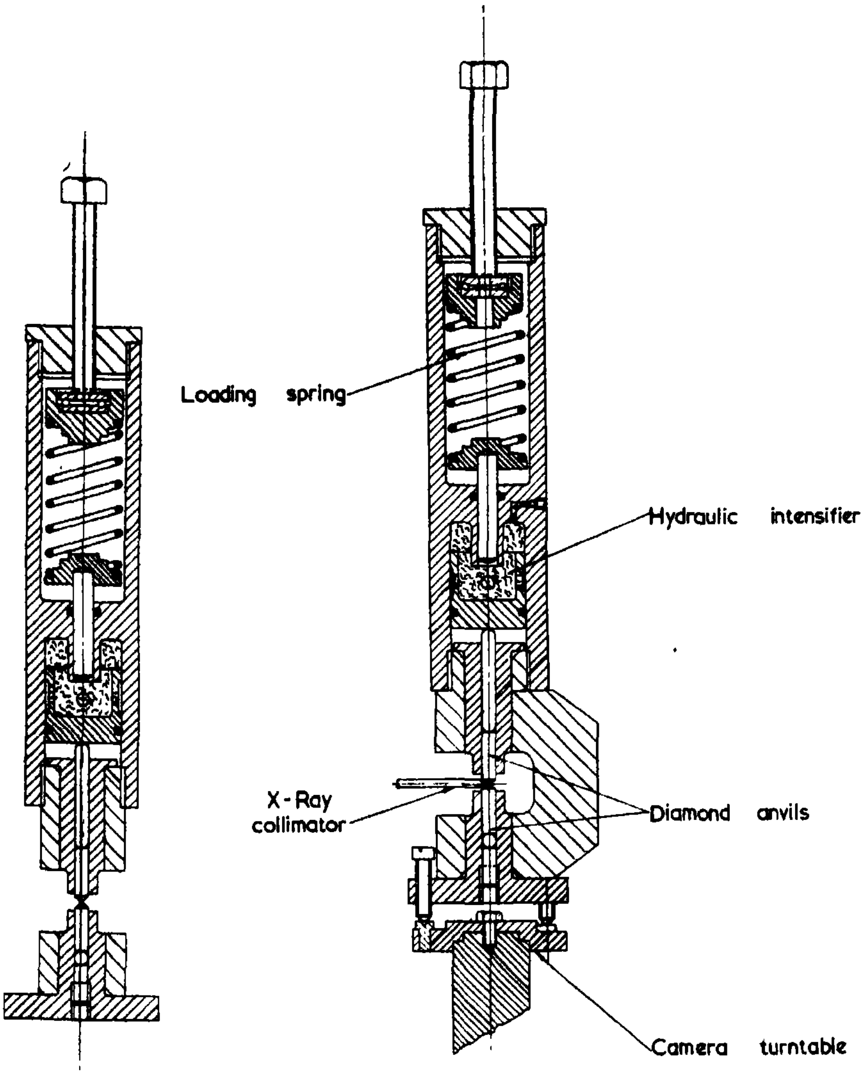

FIG. 3. High pressure X-ray apparatus for 11·46 cm camera.

small flat polished on the diamond tip as in Fig. 4(a). Flats of 0·005–0·030 in. dia. are normally used. To ensure complete coverage of the sample they are used in pairs with the lower anvil 0·005 in. larger in diameter than the upper anvil. The included cone angle is 120°. These anvils are accurately located in a steel frame and load is applied to the upper anvil by means of a piston. This piston can be loaded directly through a sliding rod to about 250 lb by a helical compression spring. Alternatively, by suitably positioning the sliding rod to introduce a hydraulic intensifier, the spring load can be magnified from 15 to 20 times. To allow for a further variation in load, the spring holders are made to accommodate springs of different sizes and stiffnesses. This feature, in conjunction with the intensifier, extends the load range from a few pounds to over 1000 lb, which when applied to a 0·020 in. dia. anvil gives a nominal pressure of over 200 kb. The spring is

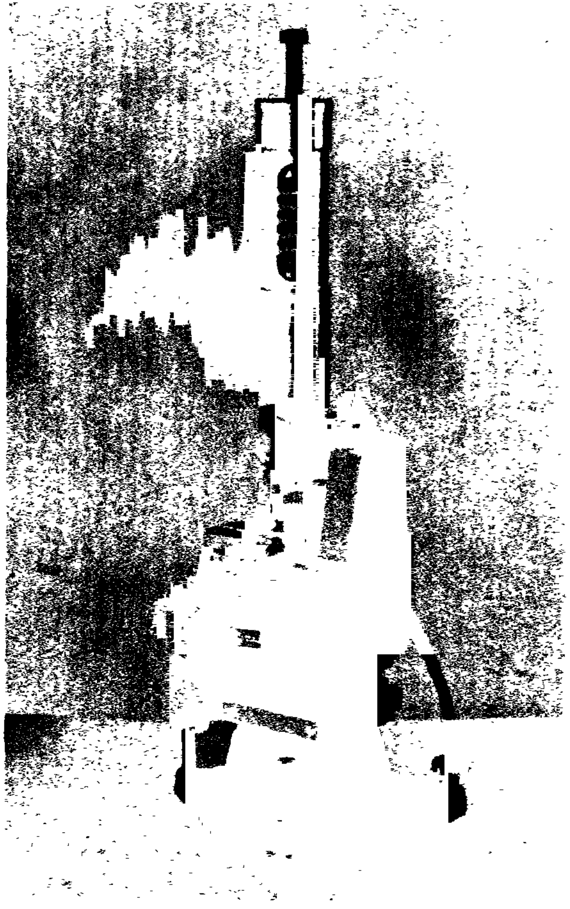

FIG. 1. X-ray high pressure apparatus for 5·73 cm camera.

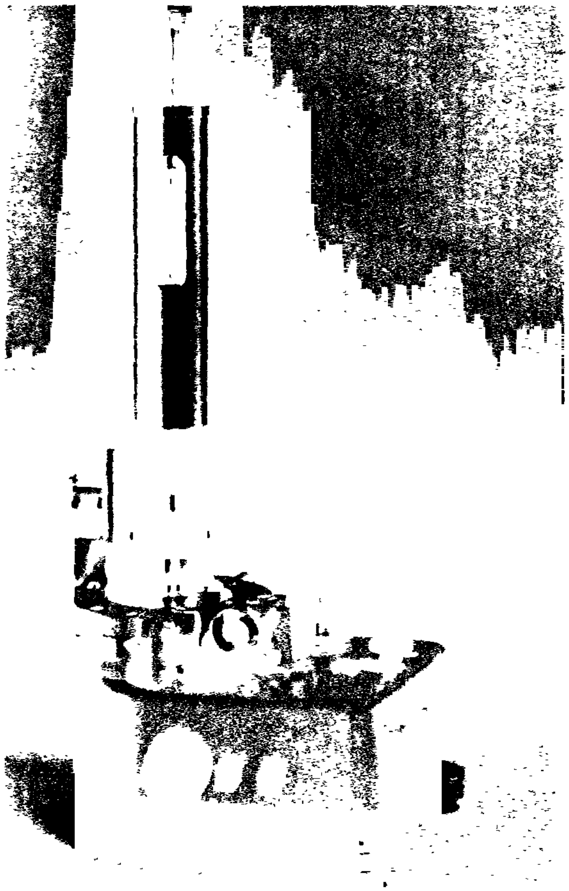

FIG. 2. X-ray high pressure apparatus for 11·46 cm camera.

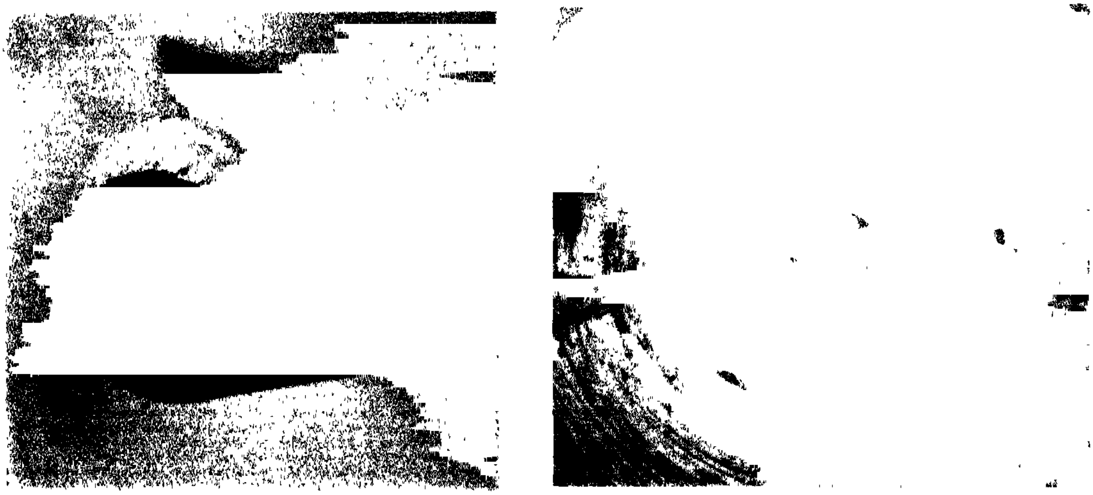

(4a) (4b)

FIG. 4. Diamond tipped anvils, (a) unused and (b) broken.

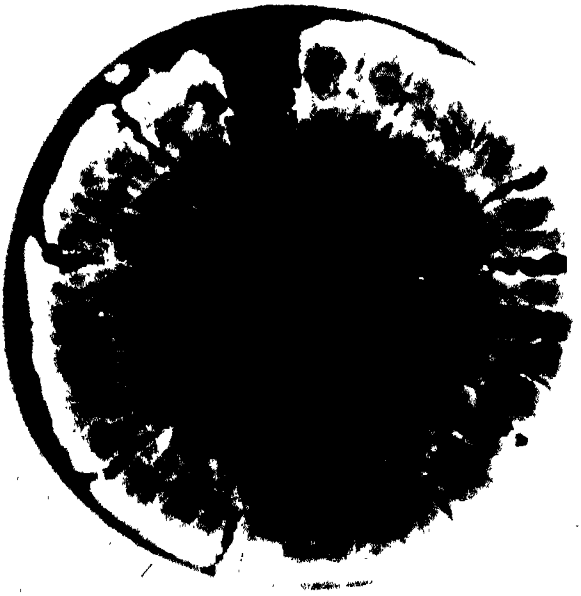

FIG. 5. Appearance of cadmium sulphide after release of pressure. × 150.

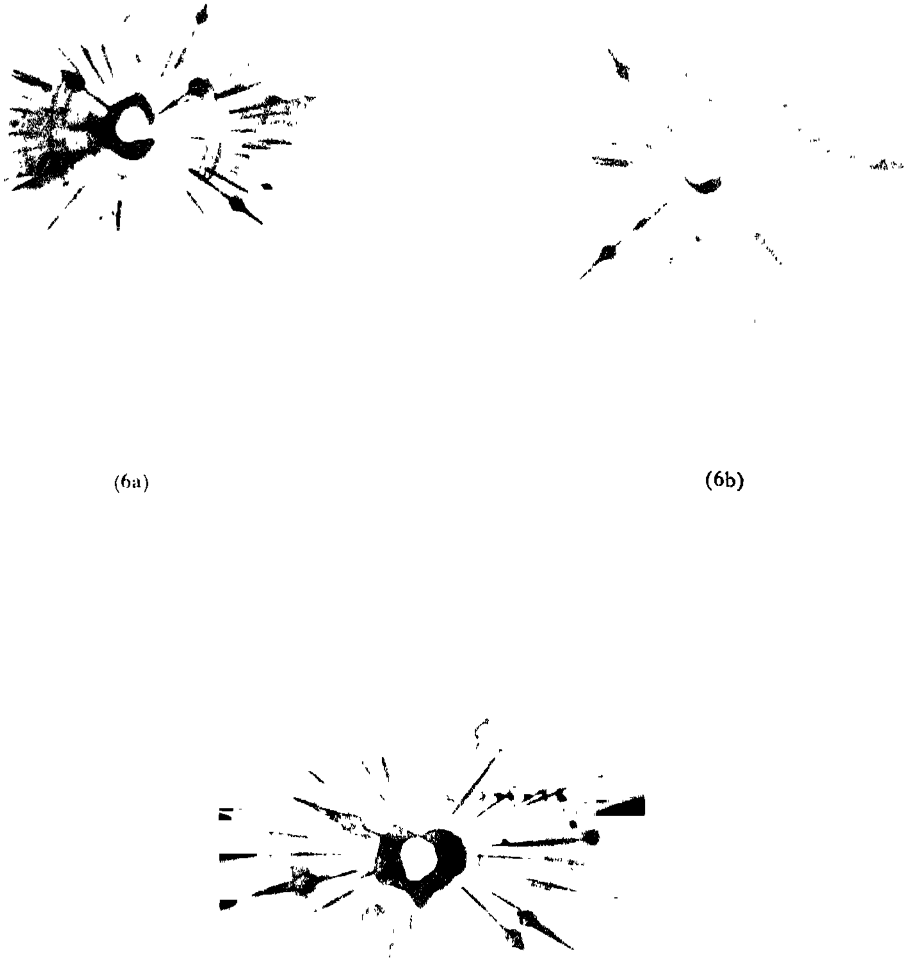

(6a)

(6b)

(6c)

FIG. 6. X-ray diffraction patterns of cadmium sulphide under pressure, (a) phase 1 at 8 kb, (b) phases 1 and 2 at 25 kb and (c) phase 2 at 190 kb.

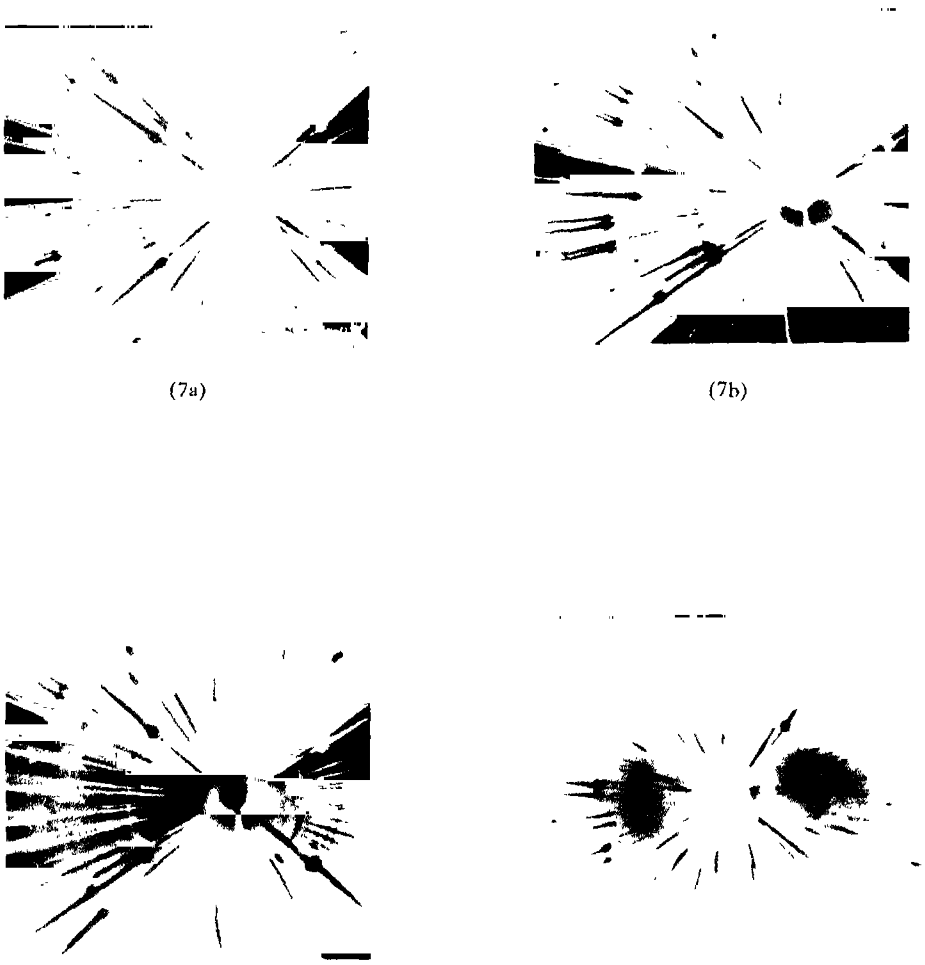

(7a) (7b)

(7c) (7d)

FIG. 7. X-ray diffraction patterns of cadmium telluride under pressure, (a) phase 1 at 10 kb, (b) phases 1 and 2 at 45 kb, (c) phases 1, 2 and 3 at 90 kb and (d) phase 3 at 200 kb.

compressed by a screw and the load is determined by measuring the spring deflection. To reduce the friction a small thrust race is fitted between the screw and the spring adaptor.

The high pressure apparatus is mounted on the camera on a small turntable attached to the camera spindle and it stands freely on a conventional cone, vee groove and plane kinematic mounting accurately positioned relative to the rotational axis of the camera. This enables the high pressure unit to be easily and precisely repositioned after its removal for mounting the sample and setting the pressure. The three feet of the mounting are threaded to allow the height to be adjusted. So far the standard cameras have been used as bought without structural alteration to support the weight of the high pressure unit, but since both pressure units weigh considerably more than the normal X-ray specimen and goniometer it is anticipated that the thrust bearings may require modification.

Provision has been made on the model shown in Fig. 2 for adding heating coils to both anvil guides and a temperature of 250°C is readily achieved.

Method of use

Several materials have been examined over a range of nominal pressures exceeding 100 kb; they include potassium iodide, indium antimonide,(7,8) tin,(8) cadmium, gallium antimonide, cadmium telluride and cadmium sulphide. The results of the work on the last two compounds are given below.

To set up the apparatus the pressure unit is first mounted on the camera and aligned in the usual way. It is then removed and the lower (and larger) diamond anvil is withdrawn. The material to be examined is finely powdered and pre-pressed between two metal anvils into a wafer about 0·005 in. thick, a fragment of which is stuck onto the larger of the two diamond anvils with Canada balsam. This anvil is then replaced in the apparatus and the spring compressed to give the desired pressure, its deflection being measured with a cathetometer. The surplus material extruded from the sample is carefully removed to avoid diffraction patterns being obtained from any unpressurized material. The unit is then replaced on the camera and final alignment adjustments made. An alternative method of sample preparation was also tried in which wafers were cut from large single crystals but, because of difficulties associated with the preferred orientation of the crystal, this method was discarded in favour of that described above. The first X-ray diffraction pattern is usually obtained at a very low pressure. The load is then increased by steps and a new exposure taken after each increase.

The pressures quoted are nominal pressures, assuming that the ram load is applied to the full diameter of the smaller anvil. The object so far has been the determination of structures rather than precise transition pressures because it is known from preliminary work that severe pressure gradients occur across the sample. Indeed, the peak pressure can be of the order of two to three times the nominal pressure. Figure 5 shows a sample of cadmium sulphide after it had been subjected to pressure. Evidence of a pressure gradient is provided by the concentric circular zones of varying darkness and under the microscope these zones are coloured and range from dark red in the centre to a light orange at the edge. The accurate determination of the pressure is a complex problem since several factors influence the magnitude of the pressure gradients. Among these are:

(1) the type and thickness of the sample material, e.g. whether it is a material with a low shear strength or one which is 'gritty'.

(2) the surface finish and parallelism of the anvil faces and

(3) the maintenance of the parallelism of the loading faces under the high loads involved.

No attempt has yet been made to select special diamonds for this work and those used so far are supplied as commercial grade Rockwell indentors. Accordingly their quality is an unknown factor and could be the main reason for the variation in the failure load experienced with different anvils. Most anvils will support a load of 500 lb on a flat diameter of 0·015 in. and occasionally this can be increased to 750 lb or more. When the diamonds fail the mode of failure is not dissimilar to that of tungsten carbide in that the loading face remains virtually intact whilst the bevelled faces crack or flake off as shown in Fig. 4(b).

RESULTS

Measurements of electrical resistance as a function of pressure on group IV elements and several of the III–V and II–VI compounds show a sudden transition to metallic conduction.(9,10) For germanium and silicon and most of the III–V compounds this resistance change is now known to be the result of the collapse under pressure of the somewhat open diamond or zinc blende lattice to a more closely packed structure.(11) Using the apparatus described above it was decided to determine the structure of the two compounds cadmium sulphide and cadmium telluride under pressure. These were chosen because cadmium sulphide at zero pressure can have the wurtzite structure as well as the zinc blende structure and it seemed worthwhile to study the collapse of the former structure. In addition, two transitions below 100 kb had been observed in cadmium telluride(10) and it seemed of interest to determine the structure of both new phases.

Accordingly a series of X-ray exposures was made using MoKα radiation with both of the devices described above. The apparatus shown in Fig. 1 was used for cadmium sulphide and that shown in Fig. 2 for cadmium telluride.

Cadmium sulphide

The powder diffraction lines for wurtzite-type CdS at a nominal pressure of 8 kb are seen in Fig. 6(a). The derived spacings are in close agreement with the accepted value of 4·136 a.u. for *a* and 6·71 a.u. for *c*. Figure 6(b) shows the diffraction pattern of CdS under a nominal pressure of 25 kb and new lines can be seen indicating the presence of a new phase. This phase undoubtedly corresponds to the transition observed both optically and electrically by Edwards and Drickamer.(10,12)

There is, however, an ambiguity to be resolved before the structure can be stated definitely. The spacings and corresponding planes could indicate either a zinc blende or a sodium chloride lattice with identical lattice constants. In order therefore to assign a structure it is necessary to calculate the expected intensities and compare the calculated values with those observed.

Table 1 gives the observed spacings, corresponding planes and observed intensities together with the calculated intensities for the rock salt and zinc blende structures. It is apparent from the agreement that the new phase has in fact the NaCl structure.

The mean a_0 value obtained from the above spacings is 5·42 a.u., corresponding to a density of 6·10 g/cm^3. Within experimental error, no change could be detected in the spacings of the wurtzite phase between 0 and 25 kb so that the density of this phase at 25 kb must be taken as approximately equal to the density at atmospheric pressure, which is 4·82 g/cm^3. Using these values, the volume contraction on transition is found to be approximately 21 per cent. When zinc blende structures collapse under pressure a similar value of $\Delta V/V_0$ is found (e.g. −21 per cent for InSb).

The pressure was raised to a nominal 200 kb to see if any new phase was formed. At this pressure all the lines arising from the wurtzite structure had disappeared and only lines due to the high pressure structure remained. The lines are shown in Fig. 6(c). The value of a_0 was 5·42 a.u. at 40 kb and 5·20 a.u. at 200 kb, corresponding to a decrease in volume of 12 per cent.

Rooymans(13) has recently published data on rock-salt structure CdS, giving an a_0 value of 5·30 a.u. in fair agreement with our figure when the experimental difficulties are considered.

Cadmium telluride

Figure 7(a) shows the pattern obtained when the sample is under a nominal pressure of 10 kb. Only lines due to the zinc blende phase are seen and a

Table 1. *Spacings, planes and observed and calculated intensities*

d	*hkl*	Observed *I*	Calc *I* (NaCl)	Calc *I* (ZnS)
3·15	111	medium	55	100
2·71	200	strong	100	22
1·90	220	medium	77	57
1·63	311	medium-weak	32	46
1·56	222	medium-weak	28	7
1·35	400	weak	13	10
1·21	420	medium-weak	35	5

cell constant of 6·52 a.u., in close agreement with the accepted value, is obtained from them. Upon increasing the pressure to a nominal 40 kb, however, new lines appear and are shown in Fig. 7(b). The formation of this new phase must correspond to the fall in electrical resistance observed by Samara and Drickamer(10) at about 30 kb. The structure which may be assigned to the new lines is found to be the NaCl structure with an a_0 value of 5·92 a.u. The spacings observed could indicate the presence of the cesium chloride structure, but both density and intensity calculations rule out this alternative. If the high pressure phase has the NaCl structure then the calculated density is 7·66 g/cm^3 while if the CsCl structure is correct the density would be 5·53 g/cm^3. Since the zero pressure density is 5·83 g/cm^3, it is clear that the NaCl structure is the more probable. Similarly, a structure factor calculation shows that for the CsCl form the intensity ratio of the first two lines is approximately 6 : 1, while for the NaCl structure it is about 3 : 2. It can be seen from Fig. 7(b) that the latter figures in fact apply and hence it would appear correct to assign the rock salt structure to the second phase of CdTe. It is not possible to estimate the intensities of the higher order lines because of the coincidence or close proximity of lines due to the ZnS phase. That the lines reported are true NaCl phase lines, however, is evident not only from the way they may be indexed but also from the fact that their intensities do not decrease as the pressure is raised i.e. as the fraction of ZnS phase present decreases.

The table below gives the planes and spacings for the NaCl phase of CdTe at 40 kb. Planes of the order of $h^2+k^2+l^2 \neq 4n$, normally found for the NaCl structure, are absent because of the nearly equal scattering powers of cadmium and tellurium.

d	*hkl*
2·94	200
2·09	220
1·71	222
1·50	400
1·32	420
1·22	422
1·04	440

a_0 = 5·92 a.u. $(\Delta V)_{1-2}/V_1$ = −24 per cent

The fractional volume change quoted is referred to the volume at atmospheric pressure since no volume change in the ZnS phase was detectable before the transition.

Figure 7(c) shows the lines observed at a nominal pressure of 100 kb. Here, still further lines are apparent, denoting the presence of a third phase. The formation of this phase must correspond to the sharp drop in electrical resistance observed by Samara and Drickamer(10) at this pressure. Because of the difficulty in indexing the third phase lines, due to occasional overlapping with lines arising from phases one and two, the pressure was increased to a nominal 200 kb, using the apparatus shown in Fig. 1. Here only phase III lines appear and these are shown in Fig. 7(d). Only three lines remain visible and their spacings and intensities are consistent with a diatomic analogue of the white tin structure. Having identified the lines arising from phase III, the pattern observed at 100 kb was used for measurement. The lattice constants derived from these spacings are a = 5·86 a.u., c = 2·94 a.u. giving c/a = 0·501. At 200 kb a has decreased to 5·62 a.u. but c remains nearly constant at 2·96 a.u. In common with other "white tin" structures,(8) c/a for CdTe is found to increase with pressure and is 0·526 at 200 kb.

The lines observed at 100 kb give the following planes and spacings:

d	*hkl*	*I* observed
2·92	200	Strong
2·63	101	Strong
1·96	211	Medium-strong

a = 5·86 a.u. c = 2·94 a.u.

DISCUSSION OF RESULTS

The common feature in the behaviour of these two compounds is the appearance of the NaCl structure at the comparatively low pressure of 30 kb. At this pressure the electrical resistivity is not "metallic" and is about 10^{-1} Ω-cm for CdS and 4 Ω-cm for CdTe. The similarity ceases here, however, since the resistivity of CdS rises steadily with pressure (reminiscent of the behaviour of n-InSb and n-InAs) but with no sign of a further phase change, while CdTe maintains a nearly constant resistance with pressure before a second transition to the "white tin" structure at around 90 kb. The resistivity in this phase is now metallic, like the high pressure phases of the III–V compounds.

It is worth remarking that both in the III–V series of compounds and in the cadmium sulphide studied here, the NaCl structure appears when the atom of higher valency is the lighter of the two, emphasizing the importance of the relative atomic radii in determining whether the NaCl or white tin structures are first adopted under pressure.

The "*iso*-row" compounds InSb, CdTe, AgI, together with tin, show, not surprisingly, systematic behaviour as the ionic character of the compound increases.

	Low pressure structure	High pressure structure	Transition Pressure	$\Delta V/V$
Sn	Diamond	'White tin'	0	21%
InSb	Zinc blende	'White tin'	25 kb	18%
CdTe	Zinc blende	NaCl → 'White tin'	30 → 90 kb	24–3%
AgI[14]	Zinc blende	NaCl	3·5 kb	18%

Jamieson(11) points out that for *iso*-row III–V compounds the relationship $P\Delta V = \Delta E/2$, where P is the transition pressure and ΔE the semiconductor gap energy, is obeyed surprisingly well. It is obeyed less well for CdTe, but the agreement is better than for III–V compounds formed from different rows of the periodic table. The figures are $-P\Delta V = 0{\cdot}6$ eV/atom, $\Delta E/2 = 0{\cdot}75$ eV/atom.

The same relation could not be expected to hold in the case of CdS, since the transition here is not to a genuine 'metallic' state. The figures are $\Delta E/2 = 1{\cdot}2$ eV/atom, $-P\Delta V = 0{\cdot}10$ eV/atom, confirming the view that the behaviour of CdS under pressure is quite different from that of other II–VI compounds.

Musgrave(15) has also shown that the relation $P^2_{\text{crit}} = 2/9(c_{11}+2c_{12})n\Delta E$ where $\frac{1}{3}(c_{11}+2c_{12})$ is the bulk constant and ΔE the gap energy per unit volume, gives a transition pressure for the III–V compounds about 40 kb greater than those observed experimentally. It is interesting to note that this relation applied to CdTe gives a transition pressure of 140 kb, some 50 kb above the observed transition. Using the $P\Delta V = \Delta E/2$ relation to predict the transition pressure, the value obtained would be about 115 kb. The good agreement with experiment obtained using each of these expressions shows that the energy gap is one of the more important factors governing the transition pressure of the zinc-blende structure semiconductors.

Acknowledgements—We are grateful to Mr. M. J. P. Musgrave for many stimulating discussions and to Mr. B. K. Taylor and his staff for the construction of the apparatus. This work forms part of the research programme of the National Physical Laboratory and is published by permission of the Director.

REFERENCES

1. Lawson A. W. and Riley N. A., *Rev. Sci. Instrum.* **20**, 11 (1949).
2. Lawson A. W. and Ting-Yuan Tang, *Rev. Sci. Instrum.* **21**, 815 (1950).
3. Jamieson J. C., Lawson A. W. and Nachtrieb N. D., *Rev. Sci. Instrum.* **30**, 11 (1959).
4. Kasper J. S., Hilliard J. E., Cahn J. W. and Phillips V. A., *G.E.C. Res. Lab. Rep.* No. 60-RL-2422M (1960).
5. Piermarini G. J. and Wier C. E., *N.B.S. J. Res.* **66A**, 4 (1962).
6. NPL. Unpublished.
7. Smith P. L. and Martin J. E., *Nature, Lond.* **196**, 4856 (1962).
8. NPL To be published.
9. Minomura S. and Drickamer H. G., *J. Phys. Chem. Solids* **23**, 451 (1962).
10. Samara G. A. and Drickamer H. G., *J. Phys. Chem. Solids* **23**, 457 (1962).
11. Jamieson J. C., *Science* **139**, 845, No. 3557 (1963).
12. Edwards A. L. and Drickamer H. G., *Phys. Rev.* **122**, 1149 (1961).
13. Rooymans C. J. M., *Phys. Letters* **4**, 186 (1963).
14. Jacobs R. B., *Phys. Rev.* **54**, 325 (1938).
15. Musgrave M. J. P., *The Physics and Chemistry of High Pressures*, p. 117. The Society of Chemical Industry, London (1963).

J. Phys. Chem. Solids Pergamon Press 1963. Vol. 24, pp. 1525–1530. Printed in Great Britain.

DIFFUSION OF LEAD IN LEAD SULPHIDE AT 700°C*

M. S. SELTZER† and J. B. WAGNER, Jr.‡

Hammond Metallurgical Laboratory, Yale University, New Haven, Connecticut

(*Received* 4 *June* 1963; *revised* 8 *July* 1963)

Abstract—The diffusion of Pb^{210} into single crystals of lead sulfide, undoped or containing 2×10^{19} bismuth/cm^3, has been studied as a function of stoichiometry at 700°C. While it is clear that lead vacancies which act as acceptor centers are the atomic defects responsible for the observed diffusion in the sulfur excess region of the homogeneity range for PbS, the nature of the donor defects is still uncertain. It is suggested that singly ionized sulfur vacancies $V_S^{\bullet}$ are the primary donor defects in PbS, but that there is also an appreciable concentration of doubly ionized interstitial lead, $Pb_i^{\bullet\bullet}$.

INTRODUCTION

STUDIES of the point defect disorder in lead sulfide are of particular interest because the homogeneity range of PbS includes compositions on either side of the stoichiometric ratio 1:1.(1) Recently SIMKOVICH and WAGNER(2) studied the self-diffusion of Pb^{210} in PbS single crystals as a function of sulfur pressure and foreign atom concentration. From a study of diffusion in undoped crystals heated under controlled sulfur atmospheres, it was found that diffusion in specimens with excess sulfur (p-type) and in specimens with excess lead (n-type) was faster than in undoped crystals of the stoichiometric composition ($n = p$).

Higher diffusion coefficients were also obtained from specimens doped with Bi_2S_3 or Ag_2S compared with diffusivities from undoped PbS in experiments carried out under a given sulfur partial pressure. These results were interpreted in terms of Frenkel disorder on the lead sublattice being the predominant point defect disorder in lead sulfide. Excess sulfur is thus thought to enter PbS under the formation of lead vacancies whereas excess lead is introduced as an interstitial species. The high diffusion coefficients found upon doping PbS with the donor impurity, bismuth or the acceptor, silver are then attributed to an increase in the concentration of lead vacancies (acceptors) in the first case and to a rise in the interstitial lead (donor) concentration in the second case.

The work of Simkovich and Wagner on undoped PbS included only one composition on either side of the stoichiometric compound, and so information concerning the dependence of D^*_{Pb} on sulfur partial pressure could not be obtained. Since such information can aid in determining the degree of ionization of the defects responsible for diffusion, and to investigate further the point defect disorder for PbS, the present authors have studied the diffusion of Pb^{210} into single crystals of PbS, undoped and doped with 2×10^{19} bismuth atoms per cm^3, over the entire homogeneity range of the compound at 700°C.

THEORY

The reactions for the establishment of equilibrium between compounds, such as PbS, and their gas phases may be formulated in various ways. For example, using the atomic notation of KRÖGER and VINK,(3) the incorporation of excess sulfur into PbS may take place according to one of the following reactions.

$$\tfrac{1}{2}S_2(g) = V_{Pb} + S_S \qquad 1(a)$$

$$\tfrac{1}{2}S_2(g) = V'_{Pb} + \dot{h} + S_S \qquad 1(b)$$

$$\tfrac{1}{2}S_2(g) = V''_{Pb} + 2\dot{h} + S_S \qquad 1(c)$$

---

* This work was supported by the Office of Naval Research.

† Present address: Battelle Memorial Institute, Columbus, Ohio. Based on a thesis submitted in partial fulfillment of the requirements for the degree of Doctor of Engineering at Yale University.

‡ Present address: Department of Materials Science, Northwestern University, Evanston, Ill.

where V_{Pb} is a lead vacancy, $\dot{h}$ is an electron hole, S_S is a sulfur atom on a normal site, $S_2(g)$ is a gaseous sulfur molecule and the primes refer to negative charge remaining on the acceptor center. Application of the ideal mass action law to equation 1 gives:

$$[V_{Pb}] = K_1 p_{S_2}^{1/2} \qquad 2(a)$$

$$[V'_{Pb}][\dot{h}] = K_2 p_{S_2}^{1/2} \qquad 2(b)$$

$$[V''_{Pb}][\dot{h}]^2 = K_3 p_{S_2}^{1/2} \qquad 2(c)$$

where K_1, K_2 and K_3 are constants which depend only on temperature. Assuming that the concentrations of vacancies and holes are equal in equation 2(b) and that each vacancy gives rise to two electron holes in equation 2(c), one obtains:

$$[V_{Pb}] \propto p_{S_2}^{1/2} \qquad 3(a)$$

$$[\dot{h}] = [V'_{Pb}] \propto p_{S_2}^{1/4} \qquad 3(b)$$

$$[\dot{h}] = 2[V''_{Pb}] \propto p_{S_2}^{1/6} \qquad 3(c)$$

It can be shown in a similar manner that the concentration of lead interstitials, Pb_i, sulfur vacancies, V_S, and quasi-free electrons, e', may vary in one of the following ways:

$$a[V_S] = b[\mathrm{Pb}_i] \propto p_{S_2}^{-1/2} \qquad 4(a)$$

or

$$c[e'] = d[V_S^{\bullet}] = i[\mathrm{Pb}_i^{\bullet}] \propto p_{S_2}^{-1/4} \qquad 4(b)$$

or

$$f[e'] = g[V_S^{\bullet\bullet}] = j[\mathrm{Pb}_i^{\bullet\bullet}] \propto p_{S_2}^{-1/6} \qquad 4(c)$$

Where a, b, c, etc. are constants, and the heavy dots refer to positive charge remaining on the donor centers.

The work of BLOEM[4] on controlled conductivity in lead sulfide single crystals, pure and doped with bismuth or silver showed that:

(a) the concentration of electrons and holes in PbS is proportional to $p_{S_2}^{\pm 1/4}$ for sulfur partial pressures not too close to those corresponding to the stoichiometric composition, thus indicating that singly ionized atomic defects predominate in PbS.

(b) the equilibrium constant relating the two dominant atomic defect species (K_S for Schottky defects and K_F for Frenkel defects) is less than the intrinsic constant, K_I, where:

$$K_S = [V_S^{\bullet}][V'_{Pb}] \qquad 5(a)$$

$$K_F = [\mathrm{Pb}_i^{\bullet}][V'_{Pb}] \qquad 5(b)$$

and

$$K_I = [\dot{h}][e'] \qquad 5(c)$$

(Bloem assumed Schottky defects predominated in lead sulfide, but his results can be explained equally well by assuming a Frenkel defect model. The work of SIMKOVICH and WAGNER[2] showed that the correct model involves Frenkel defects.)

(c) doping PbS with the donor impurity bismuth moves the equivalence point ($p = n$) to higher sulfur pressures while addition of the acceptor, silver, lowers the sulfur pressure at which the equivalence point is reached, and

(d) regions of "controlled valency" where $[e'] = [\mathrm{Bi}_{Pb}^{\bullet}]$ or $[\dot{h}] = [\mathrm{Ag}'_{Pb}]$ and "controlled imperfection" where the concentration of the predominant atomic defect is approximately equal to the concentration of added foreign ions, could be obtained from measurements of conductivity on PbS–Bi and PbS–Ag, where 10^{18} foreign atoms per cm^3 were added to the pure material. Here $\mathrm{Bi}_{Pb}^{\bullet}$ are singly ionized donors, and Ag'_{Pb} are singly ionized acceptors, both introduced substitutionally on lead sites.

Bloem used the method of KRÖGER and VINK[3] for the relations between imperfections in compounds to construct high temperature isotherms of defect concentration versus partial pressure of sulfur from his experimental data which was obtained at room temperature. Then, by taking into account the changes which occur in carrier concentration during the cooling process, Bloem was able to give a self-consistent explanation of his results.

Using Bloem's data we have constructed isotherms for 700°C of PbS and PbS with 2×10^{19} Bi/cm^3 (see Figs 1 and 2). It is assumed that (1) Frenkel disorder predominates, (2) all bismuth enters lead sulfide as $\mathrm{Bi}_{Pb}^{\bullet}$ and (3) no association between atomic defects occurs. The validity of these assumptions will be examined below.

Figure 1 is divided into three regions, in each of which two different terms dominate the electroneutrality condition. In regions I and III the atomic defect concentrations vary with 0, ±¼ or ±½ power of the sulfur partial pressure; in region

II all atomic defects vary according to $p_{S_2}^{\pm 1/2}$. Also included in Fig. 1 are the homogeneity limits for single phase lead sulfide, as determined by BLOEM.(4) Figure 2 on the other hand is divided into two regions. Region I is that of "controlled imperfection" in which the bismuth concentration is equal to the concentration of lead vacancies, V'_{Pb}, while region II is that of "controlled valency", where $[\mathrm{Bi}^{\cdot}_{\mathrm{Pb}}] \cong [e']$ are the predominant defects.

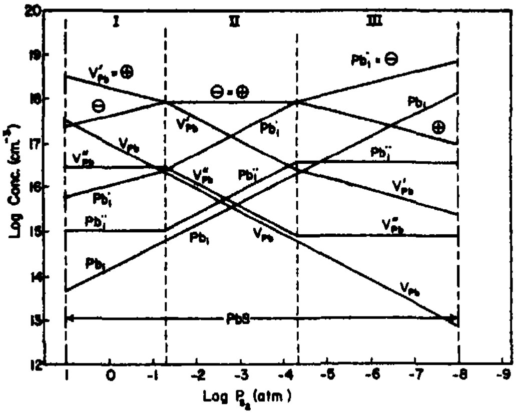

FIG. 1. Schematic diagram of high temperature equilibrium for undoped PbS (700°C).

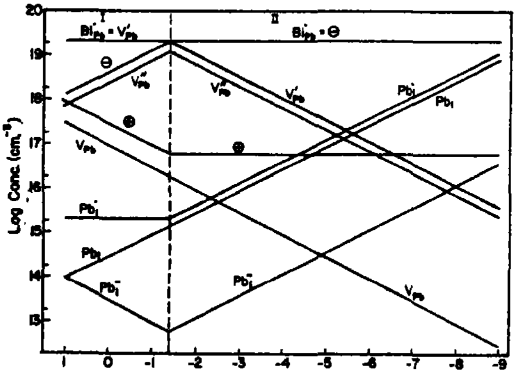

FIG. 2. Schematic diagram of high temperature equilibrium for PbS with 2×10^{19} bismuth atoms per cm^3 (1000°K).

Now the self diffusion coefficient for lead in PbS is directly proportional to the concentration of defects responsible for the observed diffusion.(5) Therefore information concerning the diffusion mechanisms and degree of ionization of the defects involved in diffusion can be obtained in principle from diffusion studies as a function of stoichiometry.

EXPERIMENTAL PROCEDURE

Most of the experimental procedures employed are described elsewhere.(2,6) In the present study single crystals were grown by the Bridgman technique in evacuated quartz vessels, using a lowering rate of 1 cm/hr. The methods described by BLOEM(4) were employed to obtain crystals of controlled stoichiometry. With two stage furnaces for high sulfur pressures and H_2/H_2S gas trains for lower pressures it is possible to obtain all sulfur pressures which can be maintained over single phase PbS at 700°C.(1)

In order to prepare crystals of a desired composition for subsequent diffusion anneals, specimens of PbS, undoped, and doped with 1/20 mole per cent Bi_2S_3 were heated at 700°C under well-defined sulfur partial pressures. Diffusion anneals were carried out on specimens plated with Pb^{210}, under conditions identical with those employed in the pre-diffusion anneal.* Typical penetration curves for Pb^{210} in PbS and PbS–Bi at 700°C are shown in Fig. 3.

RESULTS AND DISCUSSION

The results of this study are plotted in Figs 4 and 5 as log D (cm^2/sec) versus log p_{S_2} (atm), where D is the diffusion coefficient. For the case of diffusion of lead in undoped PbS, a minimum is observed at the sulfur pressure approximately equal to that required to obtain stoichiometric PbS at 700°C. This indicates that the same diffusion mechanism does not predominate over the entire homogeneity range for this compound.

The experimental data in Fig. 4 for sulfur pressures greater than $2{\cdot}5 \times 10^{-4}$ atm. are best fit by the contour for $[V'_{\mathrm{Pb}}]$ in Fig. 1. The slopes of the straight lines drawn through the experimental points for sulfur pressures greater than 0·001 atm. are 1/4 and 1/2, in accordance with the theoretical values for V'_{Pb} in regions I and II of Fig. 1. The sharp change in slope of the experimental data is placed at $4{\cdot}1 \times 10^{-2}$ atm., as predicted in Fig. 1. Thus it would appear that diffusion of lead through *p*-type lead sulfide, containing an excess of sulphur, occurs primarily by jumps into singly ionized lead vacancies, V'_{Pb}, in the lead sublattice. Some contribution to the total diffusion may occur from V_{Pb} and V''_{Pb} centers whose concentrations are a factor of fifty less than that of V'_{Pb} in the region of 0·1 to 0·001 atm.

---

* Tabular values of the annealing data may be obtained on request.

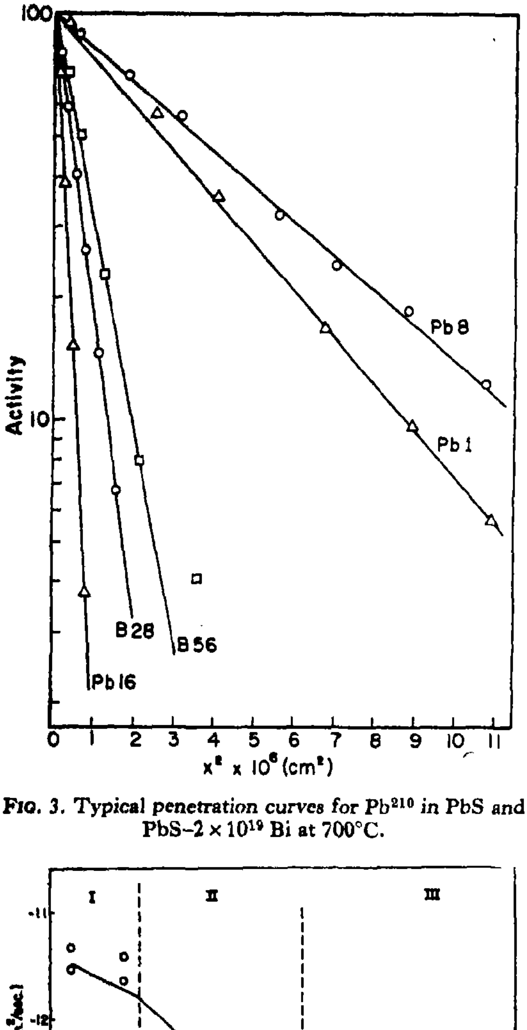

FIG. 3. Typical penetration curves for Pb^{210} in PbS and PbS-2×10^{19} Bi at 700°C.

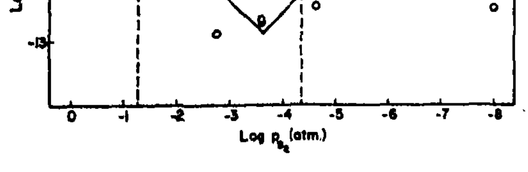

FIG. 4. Pressure variation for diffusion of Pb^{210} in PbS at 700°C.

Comparison of the results for diffusion of Pb^{210} in PbS at low sulfur pressures (*n*-type, excess lead) with the plots in Fig. 1 leads to the conclusion that the observed increase in diffusion at low sulfur pressures is due to the predominance of interstitial diffusion in PbS containing an excess of lead. The data for diffusion of lead in lead sulfide annealed under sulfur pressures less than $2\cdot5\times10^{-4}$ atm. can best be fit by the contour for Pb_i in Fig. 1. The concentration of this species increases with the ½ power of p_{S_2} in region II of Fig. 1, and is independent of sulfur pressure in region III of this figure. The change in slope occurs around $4\cdot6\times10^{-5}$ atm. Such a contour has been constructed through the experimental data in Fig. 4.

It is surprising that the greatest contribution to the total diffusion in lead sulfide with excess lead comes from doubly ionized lead donors, $\text{Pb}_i^{\cdot\cdot}$, whose concentration according to Fig. 1 is less than those of Pb_i and $\text{Pb}_i^{\cdot}$ by a factor of 50–100 in this region of the homogeneity range. The doubly charged lead interstitial is smaller than Pb_i and $\text{Pb}_i^{\cdot}$ however, and the lower energy required for this species to move from one equilibrium position to another may explain the apparent large influence of $\text{Pb}_i^{\cdot\cdot}$.

Another possible explanation for this result is that the lines given in Fig. 1 for Pb_i, $\text{Pb}_i^{\cdot}$ and $\text{Pb}_i^{\cdot\cdot}$ are indeed due to the respective sulfur vacancy centers, V_S, $V_S^{\cdot}$ and $V_S^{\cdot\cdot}$ as assumed by Bloem, and that lead interstitials are a "minority" donor defect in lead sulfide. In this case $\text{Pb}_i^{\cdot\cdot}$ may be the only interstitial species which exists in appreciable quantities in PbS. This concept of sulfur vacancies acting as the predominate donor defects in PbS, with lead interstitials existing at some lower, but substantial concentration, is discussed further below.

From the Kröger–Vink diagram of Fig. 2, for PbS with 2×10^{19} Bi/cm^3 at 700°C one would expect lead diffusion to be independent of sulfur pressure in region I (controlled vacancies) and to decrease according to the ½ power of the sulfur pressure in region II (controlled valency), if diffusion occurs by jumps into singly ionized lead vacancies. At the lowest sulfur pressures an increase in diffusion due to the increasing lead interstitial concentration might be expected. From comparison of Figs 1 and 2 one would also expect diffusivities for Pb^{210} in bismuth doped crystals to be approximately an order of magnitude greater then in undoped PbS, when both crystals are annealed under sulfur pressures greater than 10^{-3} atm. The experimental diffusion coefficients for Pb^{210} in PbS with 2×10^{19} bismuth atoms per cm^3 are plotted in Fig. 5. The results can best be explained in terms of two regions, one at high sulfur pressures, in which diffusivities decrease with 1/4 power of the sulfur pressure, and another at low sulfur pressures in which D_{Pb}^{*210} is almost independent of p_{S_2}. Diffusion coefficients for PbS–Bi are greater than those for undoped PbS at sulfur pressures near the *p–n* equivalence point, and almost equal to those for undoped PbS at the extremes of the homogeneity range.

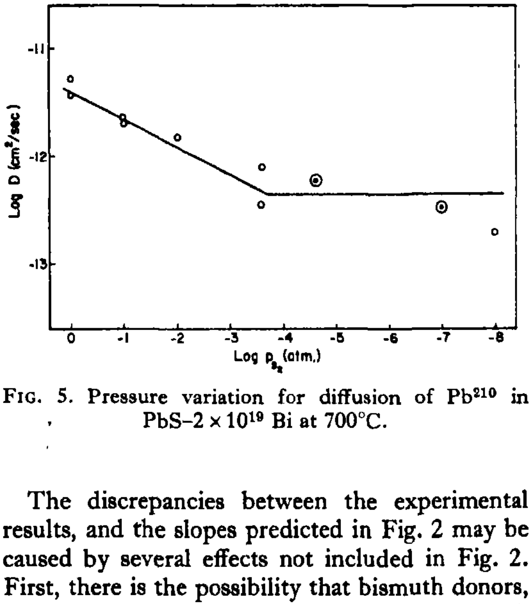

FIG. 5. Pressure variation for diffusion of Pb^{210} in PbS–2×10^{19} Bi at 700°C.

The discrepancies between the experimental results, and the slopes predicted in Fig. 2 may be caused by several effects not included in Fig. 2. First, there is the possibility that bismuth donors, $\mathrm{Bi}_{\mathrm{Pb}}^{\bullet}$ have asociated with acceptor centers, such as V_{Pb}' to form $(\mathrm{Bi}_{\mathrm{Pb}}^{\bullet}, V_{\mathrm{Pb}}')$ pairs, thus lowering the concentration of unassociated lead vacancies available for diffusion. This effect would be particularly important in region I of Fig. 2, where $\mathrm{Bi}_{\mathrm{Pb}}^{\bullet} \simeq V_{\mathrm{Pb}}'$, and would explain the absence of a noticeable difference between diffusion of Pb^{210} in PbS and in PbS–Bi at high sulfur pressures.

Secondly, we have not considered the possibility that, for the high concentration of bismuth used in this study, a large portion exists as unionized $\mathrm{Bi}_{\mathrm{Pb}}$. In constructing Fig. 2 it was assumed that:

$$[\mathrm{Bi}_{\mathrm{Pb}}^{\bullet}] = [\mathrm{Bi}]_{\mathrm{Total}} \qquad 7(a)$$

a better equation might be:

$$[\mathrm{Bi}_{\mathrm{Pb}}^{\bullet}]+[\mathrm{Bi}_{\mathrm{Pb}}]+[\mathrm{Bi}_{\mathrm{Pb}}^{\bullet}, V_{\mathrm{Pb}}'] = [\mathrm{Bi}]_{\mathrm{Total}} \qquad 7(b)$$

In this case, a region in the homogeneity range might be found in which $[\mathrm{Bi}_{\mathrm{Pb}}] \simeq [\mathrm{Bi}]_{\mathrm{Total}}$ predominates in equation 7(b) and $[\mathrm{Bi}_{\mathrm{Pb}}^{\bullet}] = [V_{\mathrm{Pb}}']$ dominates the electroneutrality relation. In this range $[V_{\mathrm{Pb}}']$ decreases monotonically with decreasing $p_{S_2}^{1/4}$ (see Ref. 3, p. 382). This pressure dependence corresponds to that found experimentally above 10^{-4} atm. for Pb^{210} in PbS–2×10^{19} Bi.

Finally we return to the point concerning the *predominate donor defects in* PbS. No *influence* of interstitial lead is observed in the pressure dependence for Pb^{210} in PbS–Bi, even at the lowest sulfur pressures obtainable. Instead, the experimental diffusion coefficients are best represented as being independent of sulfur pressure below 10^{-4} atm. The defect most likely responsible for this behavior is the neutral vacancy pair $(V_{\mathrm{Pb}}', V_{S}^{\bullet})$, whose concentration is independent of sulfur pressure, and concentration of dopant at a given temperature. Such vacancy pairs may be expected to exist in substantial quantity only if there is a high concentration of $V_S^{\bullet}$ available, thus supporting the view that sulfur vacancies are the predominate donor defects in PbS. Results to be published$^{(7)}$ for diffusion of S^{35} in PbS and PbS–2×10^{19} Bi/cm^3 show that D_S^{*35} is independent of bismuth concentration and sulfur partial pressure, below 10^{-4} atm., again indicating the presence of neutral $(V_{\mathrm{Pb}}', V_S^{\bullet})$ pairs.

From the ideal mass action law one expects the concentration of $(V_{\mathrm{Pb}}', V_S^{\bullet})$ centers to be independent of foreign atom concentration. Therefore lead should diffuse primarily via these centers in undoped, *n*-type PbS, rather than by the interstitial mechanism proposed above. Indeed the pressure independent region found in undoped crystals at sulfur pressures below 10^{-4} atm. might be attributed to diffusion through $(V_{\mathrm{Pb}}', V_S^{\bullet})$ pairs. The minimum observed in this study near the stoichiometric composition at 700°C, and in the investigation by SIMKOVICH and WAGNER$^{(2)}$ over a range of temperatures, cannot however be explained in terms of neutral vacancy pairs acting as the sole vehicle for diffusion of lead. It must be concluded that there is a sizable contribution to the total diffusion from the movement of lead by an interstitial mechanism in undoped *n*-type lead sulfide.

CONCLUSIONS

The results of this study have led to the following conclusions:

(1) The predominant mechanism for self-diffusion of lead in PbS at 700°C undergoes a transformation near the stoichiometric composition. Diffusion in *p*-type crystals containing an excess of sulfur occurs primarily by jumps into singly ionized lead vacancies, V'_{Pb}. The predominate mode for diffusion of lead in *n*-type lead sulfide involves an interstitial mechanism in which doubly ionized donors $Pb_i^{\cdot\cdot}$ are the diffusing species.

(2) The observed dependence of diffusion of Pb^{210} on sulfur partial pressure at 700°C in PbS containing 2×10^{19} bismuth atoms/cm^3 is best described in terms of simple lead vacancy diffusion predominating above 10^{-4} atm. sulfur pressure with diffusion through neutral vacancy pairs (V'_{Pb}, $V_S^{\cdot}$) predominating below 10^{-4} atm.

(3) To obtain a detailed quantitative understanding of the observed dependence of Pb diffusion on sulfur partial pressure contributions to the total diffusion from other atomic defects ionized and un-ionized, associated and unassociated must be considered.

(4) While it is clear that lead vacancies which act as acceptor centers are the atomic defects responsible for the observed *p*-type conductivity in lead sulfide, the situation for *n*-type material is less clear. It is suggested that singly ionized sulfur vacancies $V_S^{\cdot}$, are the primary donor defect in PbS, but that an appreciable concentration of $Pb_i^{\cdot\cdot}$ also exists.

Acknowledgements—The authors wish to thank Dr. H. J. Vink, Dr. F. A. Kröger, Dr. J. Bloem and Dr. W. Albers for several helpful discussions with one of us (M.S.S.) during his stay at the Philips Research Laboratories, Eindhoven, Netherlands.

REFERENCES

1. Bloem J. and Kröger F. A., *Z. phys. Chem.* **7,** 1 (1956).
2. Simkovich G. and Wagner J. B., Jr., *J. chem. Phys.* **38,** 1368 (1963).
3. Kröger F. A. and Vink H. J., *Solid-State Physics* Vol, **3,** (edited by Seitz F. and Turnbull D.) 307. Academic Press, New York (1956).
4. Bloem J., *Philips res. Rep.* **11,** 273 (1956).
5. Kittel C., *Introduction to Solid State Physics* p. 310. Wiley, New York (1953).
6. Seltzer M. S. and Wagner J. B., Jr. *J. chem. Phys.* **36,** 130 (1962).
7. Seltzer M. S., Thesis, Yale University (1962).

J. Phys. Chem. Solids Pergamon Press 1963. Vol. 24, pp. 1531–1534. Printed in Great Britain.

FERRIMAGNETISM OF MANGANESE FERRITE–CHROMITE*

T. R. McGUIRE
IBM Research Center, Yorktown Heights, New York
and
S. J. PICKART
U.S. Naval Ordnance Laboratory, White Oak, Silver Spring, Maryland
and Brookhaven National Laboratory, Upton, New York

(*Received* 15 *July*, 1963)

Abstract—A study of manganese ferrite–chromite by means of magnetic moment, electronic resonance, and neutron diffraction measurements shows clearly that a compensation composition exists when about half the iron is replaced by chromium, and that spiral spin configurations form when just over three-fourths the iron has been replaced. In the regions where these transitions take place, microwave resonance absorption curves become very broad and the effective *g* factor shifts to very large values. For the higher chromium compositions, there are discrepancies between the magnetic moment measurements and sublattice values from neutron diffraction, probably connected with the occurrence of spirals.

INTRODUCTION

THE manganese ferrite–chromite system ($MnFe_{2-t}Cr_tO_3$) exhibits a complex magnetic behavior with apparent discrepancies between moment values and the Néel model. These compounds have the spinel crystal structure with an almost normal distribution of ions: divalent manganese ions on the *A* or tetrahedral sites and trivalent chromium and iron on the *B* or octahedral sites. The complexity of behavior is illustrated in the magnetic moment measurements of GORTER,(1) which show an initial decrease in moment equivalent to about minus three Bohr magnetons for each chromium atom added. Further, it has been established by CORLISS and HASTINGS(2) from neutron diffraction studies and based in part on the theoretical work of KAPLAN *et al.*,(3) that manganese chromite is composed of spiral sublattices. This paper reports magnetization, neutron diffraction and microwave resonance measurements which were carried out to determine in detail when the spiral structure first occurs and, in addition, which sublattice has the dominant or higher moment at various compositions.

In the Néel model for ferrimagnetics having the spinel lattice, the spins on the *A* and *B* sites are antiparallel, but each sublattice has a parallel spin system. Several explanations have been proposed for the anomalously low moments which are found in all the chromites.(4) They include multi-spin axis arrangements as envisaged in the YAFFET–KITTEL theory,(5) an antiparallel *B* site arrangement of spins,(1,4) and pin quenching mechanisms.(6) The first two of these has been considered for $MnFe_{2-t}Cr_tO_4$ by GORTER,(1) while PICKART and NATHANS(7) have pointed out that spin quenching of iron ions to a value of $1\mu_B$ for each chromium present would also fit the data. There is no strong experimental evidence to support any one of these models over the other two.

Manganese chromite, as mentioned previously, appears to satisfy a more complex arrangement than was considered in the Yaffet and Kittel theory. KAPLAN *et al.*(3) showed that triangular arrangements are in general not stable in cubic spinels (no distortions have been reported for the

---

* Work done in part under auspices of A.E.C.

$MnFe_{2-t}Cr_tO_4$ system); a lower energy state is that of a spiral arrangement of spins. In terms of this model the neutron diffraction data of Corliss and Hastings lead to a spiral structure of three sublattices, one containing the *A* sites and the other two the *B* sites. On each of these sublattices the spins lie on cones with the axis of the *A* cones antiparallel to the *B* cones. The axial components give rise to the magnetization and fundamental reflections, while the transverse components give rise to superlattice reflections. It is primarily the observation of superlattice peaks that identify long range spiral structures in this present investigation.

EXPERIMENTAL RESULTS

The samples were prepared in a partial pressure of oxygen to maintain divalent manganese. Since chromium is strongly trivalent, no unusual difficulty is encountered in forming spinel solid solutions.

Magnetization measurements were made by a force method in fields up to 24,000 gauss. Specimens for compositions $t = 0{\cdot}75$, 0·85, 1·08, 1·25, 1·5, 1·6, 1·7, 1·8, 1·9 and 2·0 were measured at 77°K and 4·2°K. The 4·2°K results of this work are plotted in Fig. 1 which also shows the points measured by GORTER.(1) It will be noticed that the values 0·75 and 0·85 fill in a rather wide gap in the data as do the compositions $t = 1{\cdot}5$ through 2·0. The three points marked with X refer to $t = 0{\cdot}75$, 1·25 and 1·50 in $Mn_{0\cdot8}Zn_{0\cdot2}Fe_{2-t}Cr_tO_4$ where 0·2-zinc replaces manganese. The significance of the Zn substitutions, which bears on the placement of the compensation point where *A* and *B* sublattice moments become equal in value, will be discussed later.

From Fig. 2 it appears that large shifts in g_{eff} take place at the lower temperatures in the region of $t = 1$ and $t = 1{\cdot}6$. We identify the first as a compensation point and the latter as the beginning of spirals, as will be seen from the neutron diffraction data. Corresponding to the large g_{eff}, the half widths of the resonant absorption curves broaden greatly. It is of interest that for $t = 1{\cdot}6$ g_{eff} shows very little change from room temperature to 77°K evidently because the spirals do not occur until temperatures below 77°K.

The results of the neutron diffraction measurements are given in Fig. 3 and Table 1. For cases intermediate between $t = 1{\cdot}5$ and 2·0 we assume the manganese atoms are on *A* sites, since both these compositions were previously reported to be completely normal.(2,7) The sublattice moments were determined in two ways: by calculating the nuclear contribution to the diffraction data and

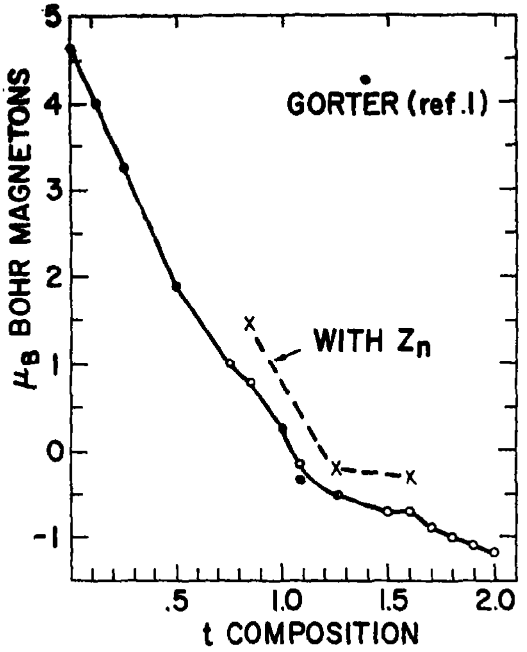

FIG. 1. Magnetic moments at 4·2°K of $MnFe_{2-t}Cr_tO_4$ (circles) and $Mn_{0\cdot8}Zn_{0\cdot2}Fe_{2-t}O_4$ (X's). Filled circles are taken from GORTER,(1) open circles and X's refer to present work.

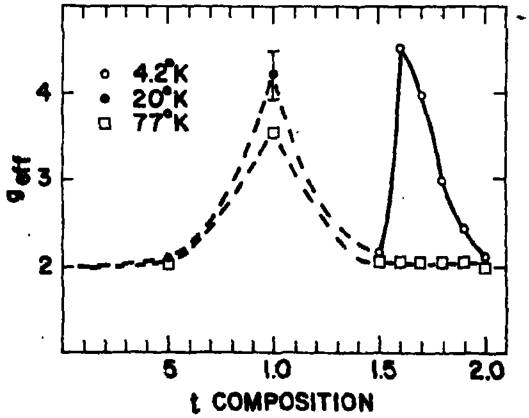

FIG. 2. g_{eff} from microwave resonance absorption at 9600 mc/s at various temperatures.

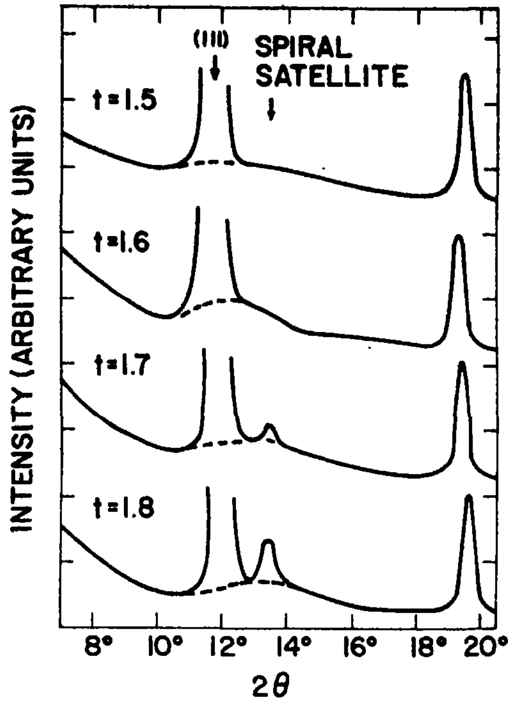

FIG. 3. Low angle neutron diffraction patterns of $MnFe_{2-t}Cr_tO_4$ showing the development of $MnCr_2O_4$ type spiral structure.

then subtracting it from the observed data, and by subtracting the room temperature data from the low temperature data, since the Curie points are below room temperature. The scale factor was obtained from high-angle peaks (511, 333 and 440) where the magnetic contribution is negligible. The magnetic intensities thus obtained were fitted with a model of antiparallel *A* and *B* site moments, whose magnitudes are given in the table. From the data, we note the appearance at $t = 1{\cdot}6$ to $1{\cdot}7$ of the (111) satellite peak similar to that found by Corliss and Hastings in $MnCr_2O_4$. The peak shows short-range order at $t = 1{\cdot}6$ with some long-range order superimposed at $t = 1{\cdot}7$. Coincident with the beginning of long-range order, there is a sudden decrease in the *B* sublattice moment, an effect which is observed in the magnetic moment measurement as only a very small inflection in the moment-composition plot.

Table 1

Composition vs. sublattice moments for $MnFe_{2-t}Cr_tO_4$

t composition	M_A Bohr magnetons	M_B
1·0*a*	4·6	4·3
1·5*a*	4·5	5·2
1·6	4·1	5·2
1·7	3·9	3·9
1·8	3·9	3·8
2·0*b*	3·56	2·40

a from Ref. 7, *b* from Ref. 2.

DISCUSSION

As chromium is first added to $MnFe_2O_4$ it goes on *B* sites with a negative contribution. Whether this is due to antiparallel chromium on *B* sites or an inhomogeneous structure with angles or spirals is not known from work reported here or from previous investigations.

The moments of the samples of composition $t = 0{\cdot}75$ and $0{\cdot}85$ fit on a smooth curve between $t = 0{\cdot}5$ and 1 and go through a compensation composition in the region of $t = 1{\cdot}05$. That a compensation occurs is also in agreement with information from Zn substitutions and microwave resonance absorption. Since zinc is nonmagnetic and is known to go on *A* sites, it will increase the measured moment when the *B* sublattice is dominant, as occurs at $t = 0{\cdot}75$ (see Fig. 1). Similarly, when the total moment of the sample is decreased, it means that the *A* lattice dominates. Such a decrease is found for $t = 1{\cdot}25$ and $1{\cdot}5$. Thus, the substitutions at $t = 0{\cdot}75$ and $1{\cdot}25$ bracket the compensation compositions. As was noted above g_{eff} becomes very large in this region which is a consequence of the A and B sublattices becoming equal in value. The behavior of the effective *g* value depends on small orbital angular momentum contributions from Mn^{2+}, Fe^{3+} and Cr^{3+} as governed by the relation(8)

$$g_{\text{eff}} = \sum_i g_i S_i / \sum_i S_i$$

where *S* is the spin value and *g* the spectroscopic splitting factor for the individual ions. In this system where the *g* factors for the ions are all very close to two, the increase in g_{eff} would be a typical behavior. The large half-widths in a compensation region are a consequence of anisotropy effects.(8,9) As a final consideration, it is noted from Table 1 that at $t = 1$ the neutron diffraction data are not inconsistent with a compensation when the assigned errors are taken into account.

For the remainder of the compositions from $t = 1{\cdot}1$ to $t = 2$, the magnetic moments follow a smooth curve with the possible exception of a very small dip at $t = 1{\cdot}6$, where the first indications of a superlattice of the $MnCr_2O_4$ type appear. Since, as already discussed, we are in a region of compositions where the A sublattice is dominant, it is apparent that the sublattice moments in Table 1 cannot be completely correct. The exact origin of the disagreement at $t = 1{\cdot}5$ and $1{\cdot}6$ is not clear; however, there may be short-range effects of the spiral structure on such a small scale as to create an extremely diffuse peak so that all the intensities are not counted properly.

In the theory of ferrimagnetic spirals, the pitch angle (which gives the ferromagnetic component per sublattice) depends on the exchange energy ratio J_{AA}/J_{AB} and J_{BB}/J_{AB}. By introducing iron on B sites in $MnCr_2O_4$, we are changing both J_{BB} and J_{AB}, thereby changing the cone angle. In addition, the random distribution of Fe^{3+} ions creates the possibility that a Cr^{3+} could have a large number of Fe^{3+} neighbors which might interrupt the spiral. It is probably safe to conclude that the magnetic structure of these spinels is inhomogeneous, consisting of structures ranging from antiparallel chromiums to spiral clusters, including short-range ordered states.

Acknowledgement—We wish to thank Dr. M. W. Shafer for preparing the samples, Dr. P. E. Seiden for his help in obtaining the microwave resonance absorption data, and Mr. H. L. Lilienthal for his assistance in the magnetic moment measurements.

REFERENCES

1. Gorter E. W., *Philips res. Rep.* **9**, 295 (1954).
2. Hastings J. M. and Corliss L. M., *Phys. Rev.* **126**, 556 (1962).
3. Kaplan T. A., Dwight K., Lyons D. and Menyuk N., *J. appl. Phys.* **32**, 13S (1961); *Phys. Rev.* **126**, 540 (1962).
4. McGuire T. R. and Greenwald S., *Proceedings of the International Conference on Solid State Physics*, Brussels (1958) Academic Press Inc., New York, Vol. 3, p. 50 (1960).
5. Yaffet Y. and Kittel C., *Phys. Rev.* **87**, 290 (1952).
6. Baltzer P. K. and Wojtowicz P. J., *J. appl. Phys.* **30**, 27S (1959).
7. Pickart S. J. and Nathans R., *Phys. Rev.* **116**, 317 (1959).
8. Wangsness R. K., *Phys. Rev.* **91**, 1085 (1953).
9. Schloemann E. and Zeender J. R., *J. appl. Phys.* **29**, 341 (1958).

J. Phys. Chem. Solids Pergamon Press 1963. Vol. 24, pp. 1535–1538. Printed in Great Britain.

THE USE OF CO–CO_2 ATMOSPHERES FOR THE PREPARATION AND FREE ENERGY DETERMINATIONS OF SEVERAL OXIDE SYSTEMS

W. KUNNMANN, D. B. ROGERS and A. WOLD*
Lincoln Laboratory,† Massachusetts Institute of Technology, Lexington, Massachusetts.

(*Received* 28 *May* 1963; *revised* 25 *June* 1963)

Abstract—A number of transition metal oxide systems have been prepared that require controlled CO–CO_2 atmospheres for attaining certain desired valencies. In addition standard free energies for numerous mixed oxides are determined by a direct evaluation of the equilibrium atmospheres.

INTRODUCTION

THE substitution of unusual or unstable valencies into different chemical structures is sometimes difficult to achieve by standard preparative techniques. This paper deals with the preparation of a number of transition metal oxide systems that require controlled atmospheres for attaining certain desired valencies. Successful valency stabilizations are achieved in otherwise difficult chemical syntheses by the regulation of CO–CO_2 atmospheres to maintain a desired oxygen equilibrium pressure. This technique has been reported by several workers.(1–3) However, its versatility is demonstrated in this paper and applied to a number of different chemical systems.

The absence of thermodynamic data for many mixed oxide systems necessitates an empirical approach to the determination of the proper CO–CO_2 ratio for the synthesis of a given mixed oxide. Fortunately, there usually exists a rather broad atmospheric range in which the materials are stable and this stability region can be found by trial and error. For the synthesis of these oxides it is possible to determine the equilibrium atmosphere under which the material begins to undergo decomposition at various temperatures. It is readily shown that such a formalization of the equilibrium atmospheres provides a direct evaluation of standard free energies for numerous mixed oxides. Free energy changes for many of the simple oxides have been determined in this manner. However, little thermodynamic data for mixed oxides exist. A knowledge of such data is required for an understanding of the relative stability and chemistry of the materials. The technique is illustrated in this paper by application to several vanadite and chromite spinels.

EXPERIMENTAL

The apparatus used both for syntheses and for equilibrium determinations was similar to that employed by EMMETT and SCHULTZ,(4) the major difference being the substitution of a commercially available flowmeter and gas-mixer system. For both gases, the flowmeters were carefully calibrated with respect to each other and were checked by a precision wet-test flowmeter. The reactions were carried out in a small platinum boat provided with a magnetic pulling device, which enabled the sample to be removed completely from the hot zone of the furnace, and quenched in a stream of nitrogen.

The compounds that have been prepared in the present investigation are reported in Table 1. The mixed oxides were prepared by grinding together equivalent quantities of the component oxides in their most stable valency state, and then heating to an appropriate temperature under the CO:CO_2

---

* Present Address, Brown University, Providence, R.I.

† Operated with support from the U.S. Army, Navy and Air Force.

Table 1. Mixed oxides prepared under CO–CO_2 atmospheres with experimental conditions imposed.

Compound*	CO/CO_2	T°C	% of theoretical[6, 7] reducing power
$FeAl_2O_4$	2·50	1050	
FeV_2O_4	4·50	1100	99·95
CoV_2O_4	0·25	1000	99·5
Fe_2VO_4	0·33	1100	99·8
Fe_2TiO_4	2·00	1100	
Fe_2MoO_4	2·00	1150	100·6
$FeTiO_3$	0·33	1000	
$FeWO_4$	2·00	1150	
$LiVO_2$	0·50	700	
$LiFeO_2$	Pure CO_2	750	
MoO_2	1·00	650	99·8

* Analyzed composition.

ratio required for valency adjustment. In the case of compounds containing vanadium, the relatively unstable V_2O_3 was used as a starting material in order to avoid volatilization of V_2O_5 at the reaction temperatures. For syntheses of the chromites premixing of the oxides was obtained by the precursor technique of WHIPPLE and WOLD[5] in lieu of grinding operations. Where possible, all starting materials were either spectroscopic grade or purified reagent grade. Carbon monoxide and carbon dioxide gases used were of the Matheson "purified" type.

With the premixed oxides in the exterior (cool) part of the silica firing tube, a trial ratio of $CO:CO_2$ was established, and the furnace brought up to temperature. When the desired temperature had been obtained, the sample was placed in the hot zone by means of the magnetic pulling device, allowed to remain there for several hours, and then quenched in a stream of nitrogen to room temperature. The product was then examined by X-ray diffraction and, if necessary, the procedure was repeated under different $CO:CO_2$ ratios until the desired phase was obtained. All the compounds reported in Table 1 were subjected to chemical analyses by standard procedures and found to correspond to the formulae as written. Total reducing power values are given for a number of the compounds listed. Reducing power is the number of reduction equivalents per gram of sample employed in reducing a standard oxidant (e.g. $KMnO_4$). The reducing power values reported in Table 1 were performed by the method of WICKHAM and WHIPPLE[6] and discussed by NADALIN and BROZDA.[7]

Stability investigations were carried out for the compounds $FeCr_2O_4$, $CoCr_2O_4$, $NiCr_2O_4$, FeV_2O_4, and CoV_2O_4. These materials were specifically chosen since it was believed that initial reduction would lead to a direct collapse of the spinel phase to metal and the corresponding Cr_2O_3 or V_2O_3 phase. The presence of other magnetic phases in the reduction products of these materials has never been observed and the existence of such phases is highly unlikely. X-ray diffraction patterns of the products have verified the formation of corundum and free metal phases. They have been further substantiated by the highly magnetic character of the resultant metal. Carefully characterized compounds were placed in a silica boat and subjected to increasing ratios of $CO:CO_2$ until the reduction products first appeared to be magnetic. This technique was standardized utilizing nickel powder and alundum mixtures and found to be capable of detecting the presence of 0·4% by weight of nickel. The $CO:CO_2$ ratios were then bracketed successively until an equilibrium ratio was established. These observations appear consistent with the following equation as it proceeds to the right

$$CO(g)+AM_2O_4(s) = A(s)+M_2O_3(s)+CO_2(g) \tag{1}$$

Table 2. Equilibrium ratios observed for the reduction

$CO(g)+AM_2O_4(s) = A(s)+M_2O_3(s)+CO_2(g)$

T(°K)	1380	1320	1234	1154	1073
$FeCr_2O_4$	240/16	225/18	222/18		217/13
$CoCr_2O_4$	176/36	175/31	250/24	240/14	400/10
$NiCr_2O_4$	13/180	14/177		30/180	48/180
FeV_2O_4	217/12		225/11	225/11	220/13
CoV_2O_4	103/180	83/176	76/175	33/179	20/175

Equilibrium ratios determined in this manner are given in Table 2.

DISCUSSION

The data of Table 1 indicate both the effectiveness and the general versatility of CO–CO_2 atmospheres as a means of stabilizing unusual valency states. The technique appears to be particularly useful for the syntheses of compounds containing Fe^{2+}. The more common techniques usually employ non-stoichiometric FeO or metallic iron as a starting material and both of these often lead to poor product stoichiometry. In the case of FeV_2O_4 it has been pointed out previously⁽⁸⁾ that direct reaction of the component oxides in sealed, evacuated silica tubes usually results in the formation of an undesirable corundum phase. This difficulty is eliminated by the present technique. The use of CO–CO_2 atmospheres in the synthesis of compounds containing lithium offers the additional advantage of reducing the sublimation tendency of Li_2O at the reaction temperatures. Other techniques for the preparation of lithium iron oxide and lithium vanadium oxide resulted in the volatilization of lithium oxide as substantiated by analysis of vanadium and X-ray diffraction studies. Where a loss of lithium occurs there is the formation of an additional phase.

Under the equilibrium conditions indicated by equation (1), it can be shown⁽⁹⁾ that the standard change of free energy is given by

$$\Delta F^0_{(I)} = \Delta F^0_{CO} - \Delta F^0_{CO_2} + RT \ln \alpha,$$

where α is the ratio of CO to CO_2. Since the quantities ΔF^0_{CO} and $\Delta F^0_{CO_2}$ are well known, $\Delta F^0_{(I)}$ is readily determined by experimentally finding α. The standard free energy of formation for the compounds AM_2O_4 from the elements is then given by the equation

$$\Delta F^0_{AM_2O_4} = \Delta F^0_{M_2O_3} - \Delta F^0_{(I)}.$$

Calculated values of $\Delta F^0_{(I)}$ are given in Table 3.

Frequently, values of free energy changes for reactions of the type

$$AM_2O_4(s) \rightarrow AO(s)+M_2O_3(s) \qquad (2)$$

are of greater value to the chemist than those of Reaction 1. These may be determined, with recourse to tabulated data for the simple oxides, from the equation

$$\Delta F^0_{(II)} = \Delta F^0_{AO} + \Delta F^0_{M_2O_3} - \Delta F^0_{AM_2O_4}.$$

In Fig. 1 are plotted values of $\Delta F_{(II)}/T$ as functions of $1/T$ for the spinels $CoCr_2O_4$, $NiCr_2O_4$, and CoV_2O_4. Ideally the slopes of these curves should be proportional to the enthalpy of the reaction as given by the Gibbs–Helmholtz equation. In reality such methods rarely give accurate heats of formation and recourse to entropy measurements is usually required. As an order of magnitude, however, enthalpy values obtained from such slopes are useful. Comparison of enthalpy values for a series of compounds undergoing similar reactions rather than their free energies can be made if it is assumed that the entropy contributions to the free energies are relatively constant. It is interesting, therefore, that CoV_2O_4 has a negative slope (Fig. 1) and from the enthalpy point of view appears to be unstable relative to its component oxides. If trends are consistent from the chromite to the vanadite series, it appears probable from these data that

Table 3. Standard free energy changes for the reaction:* $AM_2O_4(s) \rightarrow A(s) + M_2O_3(s) + \frac{1}{2} O_2(g)$.

T (°K)	1380	1320	1234	1154	1073
$FeCr_2O_4$	+46·20 ± 0·25	+46·65 ± 0·25	+47·95 ± 0·25		+51·15 ± 0·25
$CoCr_2O_4$	+43·15 ± 0·25	+44·55 ± 0·25	+47·55 ± 0·25	+50·00 ± 0·25	+53·0 ± 0·50
$NiCr_2O_4$	+31·60 ± 0·25	+33·40 ± 0·25		+39·35 ± 0·25	+42·35 ± 0·25
FeV_2O_4	+46·70 ± 0·25	+47·00 ± 0·25	+49·20 ± 0·25	+50·40 ± 0·25	+51·20 ± 0·25
CoV_2O_4	+37·25 ± 0·25	+38·05 ± 0·25	+39·70 ± 0·25	+39·50 ± 0·25	+40·50 ± 0·25

* All values in Kcal/formula wt.

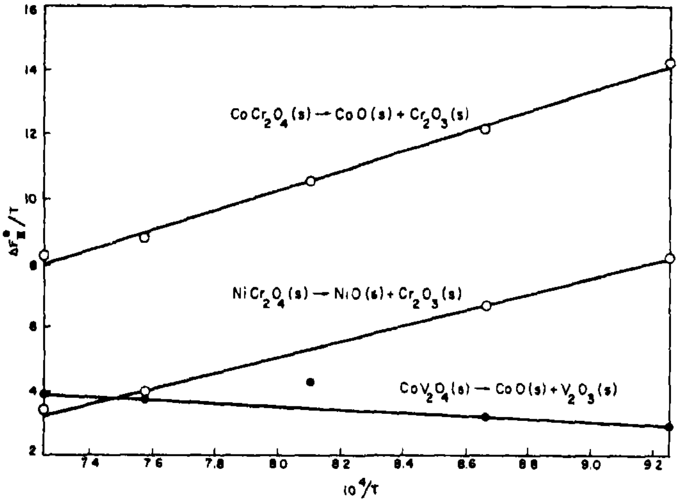

FIG. 1. Dependence of $\Delta F^0_{(II)}/T$ on reciprocal temperature.

NiV_2O_4 would undergo spontaneous decomposition to the oxides. Unsuccessful attempts to prepare NiV_2O_4 have been previously reported.(10, 11)

From the thermodynamic data for $FeCr_2O_4$,(12) a value for $(\Delta F/T)$ was calculated and found to lie on the extrapolated plot of $(\Delta F)/T$ vs. $10^4/T$ for data reported in this paper.

Acknowledgement—The authors would like to thank Mr. E. DELANEY who assisted in performing the analytical work.

REFERENCES

1. BURDESE A., *Ann. Chim. (Rome)* **47,** 827 (1957).
2. VEANAR H. J., KORTRIGHT J. M. and LANGENHEIM R. H., *J. chem. Phys.* **22,** 1196 (1954).
3. SMILTENS J., *J. chem. Phys.* **20,** 990 (1952).
4. EMMETT P. H. and SCHULTZ J. F., *J. Amer. chem. Soc.* **52,** 1782 (1930).
5. WHIPPLE E. and WOLD A., *J. inorg. nucl. Chem.* **24,** 23 (1962).
6. WICKHAM D. G. and WHIPPLE E., *Talanta* **10,** 314 (1963).
7. NADALIN R. J. and BROZDA W. B., *Analyt. Chem. Acta.* **28,** 282 (1963).
8. WOLD A., ROGERS D. B., ARNOTT R. J. and MENYUK N., *J. appl. Phys.* **33,** 1208 (1962).
9. WALL F. T., *Chemical Thermodynamics*, Chap. 8, 10, Freeman, New York (1958).
10. BLASSE G. and GORTER E. W., *J. phys. Soc. Japan* **17,** Suppl. **B-I,** 176 (1962).
11. ROGERS D. B., ARNOTT R. J., WOLD A. and GOODENOUGH J. B., *J. Phys. Chem. Solids* **24,** 347 (1963).
12. *Selected Values of Chemical Thermodynamic Properties, Nat. Bur. Stand.* (1952).

J. Phys. Chem. Solids Pergamon Press 1963. Vol. 24, pp. 1539–1542. Printed in Great Britain.

TEMPERATURE DEPENDENCE OF HALL MOBILITY AND μ_H/μ_D FOR Si

JEAN MESSIER and JORGE MERLO FLORES*

Service d'Electronique Physique, Centre d'Etudes Nucléaires de Saclay, France

(*Received* 19 *April* 1963; *revised* 8 *July* 1963)

Abstract—The temperature dependence of the Hall mobilities has been determined as $6{\cdot}4\times10^9\ T^{-2{\cdot}91}$ and $2{\cdot}4\times10^8\ T^{-2{\cdot}06}$ for holes and electrons respectively. Using for the drift mobilities the expression found by LUDWIG and WATTERS, $2{\cdot}3\times10^9\ T^{-2{\cdot}7}$ and $2{\cdot}1\times10^9\ T^{-2{\cdot}5}$ for holes and electrons, we have calculated the temperature dependence of $\mu_H/\mu_D = r$, and found it coherent with the observed variation of the Hall coefficient. At 300°K, for holes $\mu_H = 398$ cm^2 $(V_s)^{-1}$ and $r_p = 0{\cdot}84$ and for electrons $\mu_H = 1880$ cm^2 $(V_s)^{-1}$ and $r_n = 1{\cdot}31$.

1. INTRODUCTION

THE determination of the density carrier in Si through measurements of Hall coefficient, $R_H = hV/BI$,† implies knowing the value of the ratio $\mu_H/\mu_D = r$. There exists a certain dispersion in the results obtained by other investigators (1, ..., 15) for the values of the drift mobility, μ_D, Hall mobility, $\mu_H = R_{H\sigma}$, and consequently $\mu_H/\mu_D = r$. We have determined, by using high purity, floating zone refined Si, the temperature dependence of the Hall mobility. Using the results of LUDWIG and WATTERS(1) (from here on we shall refer to their paper as 1) for the values of the drift mobilities, μ_D, we have calculated the temperature dependence of the ratio μ_H/μ_D, and compared it with that of R_H.

2. EXPERIMENTAL TECHNIQUES

The facilities in the laboratory allow us to measure Hall effect and resistivity between 320 and 100°K, the temperature homogeneity of the studied sample being 0·1°.

The magnetic field is generated by a Varian electromagnet which allows to work with fields up to 10,000 G. The measurements of the magnetic field were done with the usual nuclear resonance equipment. The samples were normally measured in a 5,000 G field in the direction of the crystal axis (111). The linearity of the results as a function of the magnetic field was verified in several instances.

The Si samples can be measured in vacuum or in an inert atmosphere. When the contact resistance in the sample was sufficiently low, we used an opposition bridge for the measurements, otherwise, a VIBRON electrometric voltmeter.

The Si samples were cut with an ultra-sonic drill in the shape shown in Fig. 1. The dimensions were chosen so as to reduce as much as possible the effects of geometry and injection of minority carrier by the contacts.

During the measurements, the electric field E in the Si was never superior to 400 mV/cm and the linearity of the Hall effect as a function of E was in all cases verified.

The sparking technique(16) was used for the formation of the contacts, with Au–Sb for Si–*n* and Al for Si–*p*. To make sure that the irregularity of the contacts did not affect the measurements, an electrical analogy for the sample was made. It was verified that the influence of the current injecting contacts completely disappeared before reaching the nearest pair of arms.

In Si–*p* and Si–*n* samples a certain dispersion in the results is observed when the abrased surface is attacked either with NO_3H or FH. This dispersion is caused by the formation of an oxygen surface layer and was of 8, 4 and 3·5 per cent, for samples 0·5, 1 and 2 mm thick respectively. A direct relation can be found between the dispersion values and the surface–volume ratio. We have used for our measurements samples 2 mm thick which had been attacked with FH.

---

* On leave of absence from the Comision Nacional de Energia Atomica, Argentina.

† h: sample thickness; I: total current; B: magnetic field; V: Hall tension.

The homogeneity of the Si crystals used was below 1 per cent for the *p*-type Si, while for the *n*-type a gradual variation not superior to 9 per cent, was observed along the sample, in this later case a convenient average value for the Hall voltage measured on the two pairs of arms was determined. The precision for the resistivity measurements amounted to 6 per cent and for the mobility 3 per cent. The reproducibility of the results for the same sample was below 1 per cent.

Si-*p*

We have used *p*-type, floating zone refined Si with resistivities of approximately 1,000; 5,000; and 8,000 Ω cm. The Hall mobility results between 100 and 320°K are shown in Fig. 2, curve 1, they follow the law: $\mu_H = (6{\cdot}4 \pm 0{\cdot}15) \times 10^9\ T^{-2{\cdot}91}$.

In Table 1 are shown the results obtained by different authors for the Hall mobility and drift mobility at 300°K, and the coefficient α in the expression $\mu = AT^{-\alpha}$.

There is a good agreement between the mobility values of Refs 2, 4, 5, 6, 7 and 8 and our results. We can find no explanation for the difference with the value given by Ref. 3. Nothing can be said with respect to coefficient α since there is a large dispersion in the results.

Using the results of (1) for the drift mobility of holes we have calculated the absolute value and the temperature dependence of the ratio $r_p = \mu_H/\mu_D$. This ratio can be approximately represented between 300 and 150°K by the $2{\cdot}8\ T^{-0{\cdot}21}$ law. In Fig. 2, curve 2 are represented the experimental

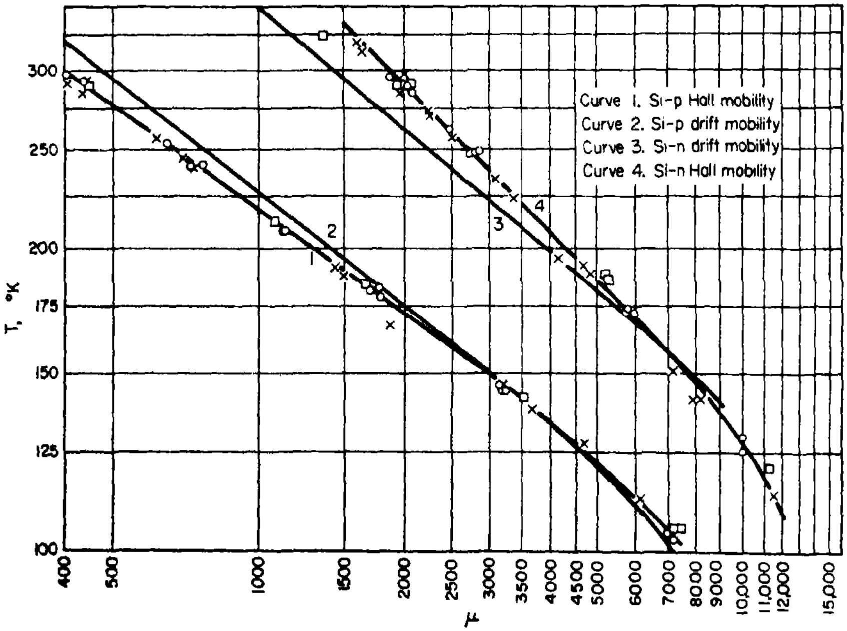

FIG. 2. Curve 1: $\mu_{Hp} = f(T)$, ⊙ 1440 Ω-cm Si-*p*
× 7700 Ω-cm Si-*p* (authors)
⊡ 6200 Ω-cm Si-*p*.
Curve 2: $\mu_{Dp} = f(T)$, Ref. (1)
Curve 3: $\mu_{Dn} = f(T)$, Ref. (1)
Curve 4: $\mu_{Hn} = f(T)$, ⊙ 900 Ω-cm Si-*n*
× 800 Ω-cm Si-*n* (authors)
⊡ 1400 Ω-cm Si-*n*.

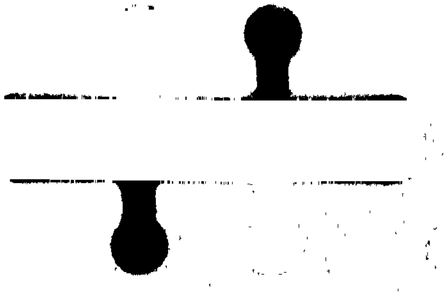

FIG. 1. Photograph of a Si sample (dimensions of the body: 16 × 3 mm).

Table 1. Si–*p*

Reference	(3)	(2)	(4)	(5)	(6)	(7)	(1)	(13)	(8)	Authors
$T = 300°\text{K}$ μ_H	619	350	350	404	375	370			399	398
$T = 300°\text{K}$ μ_D				356			475	495	504	
α_H	2·7		2·36			2·9				2·9
(Ω-cm) α_D	5000	33	50	110	85	115	180		1000	8000

results of (1), with their highest resistivity Si–*n* sample. In Fig. 3, curve 1, the value of r_p is shown as a function of T. If the carrier density were constant with T, then the variation of R_H with T should be equal to the variation of r_p. In Fig. 3, curve 2, we have plotted the variation of R_H with temperature, normalized to the value of r_p at 300°K. Our results for the temperature dependence of r_p agree, as can be seen in Fig. 3, with the Hall coefficient variation observed by LONG⁽⁶⁾ for samples of 35 Ω-cm. The difference between curves 1 and 2 can be explained by a small variation in the carrier density as a function of the temperature ($1\text{–}2\times 10^{11}$ for a $\Delta T = 200°$). It can be rightly supposed that this effect is due to a change in the charge state of the dislocations, or other crystal imperfections and which will be more noticeable in a high resistivity sample than on a low resistivity one as can be seen for the sample of 35 Ω-cm of Long. It is on account of this that we can conclude that our results for μ_H and those of μ_D obtained by (1) are coherent and curve 1 represents the correct variation of r_p with the T.

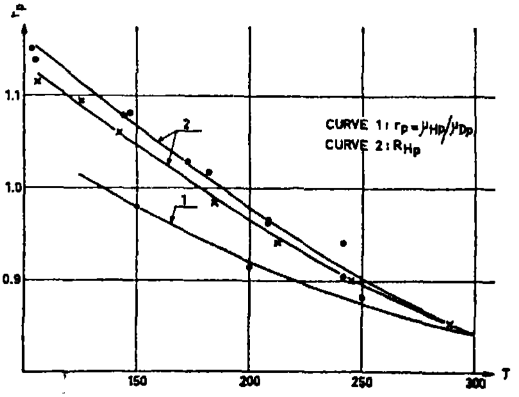

FIG. 3. Curve 1: $r_p = f(T)$ (authors).
● R_H values for 35 Ω-cm Si–*p* obtained by LONG.⁽⁶⁾
Curve 2: $R_H = f(T)$, × 6200 Ω-cm Si–*p* (authors)
○ 1400 Ω-cm Si–*p*.

Si–*n*

We have used Si–*n* of a resistivity superior to 500 Ω-cm purified by floating-zone. The Hall mobility results between 100 and 320°K, are shown in Fig. 2, curve 4. Between 150 and 300°K they follow the law $\mu_H = (2{\cdot}4 \pm 0{\cdot}04)\times 10^8\, T^{-2{\cdot}06}$. For temperatures lower than 170°K the measured Hall mobilities are smaller than the values given by the above law.

In Table 2 are given the results of μ_H and μ_D at 300°K, together with the value of α, from the $\mu = AT^{-\alpha}$ law.

Our value of μ_H at 300°K is slightly higher than those given by Refs 4, 8, 5 and 9. This could be explained by the fact that we have used a higher

Table 2. Si–*n*

Reference	(3)	(4)	(5)	(9)	(8)	(1)	(13)	Authors
$T = 300°\text{K}$ μ_H	1345	1740	1830	1770	1810			1880
$T = 300°\text{K}$ μ_D			1590		1345	1335	1485	
α_H	2	2·04						2·06
α_D						2·5		
ρ(Ω-cm)	1800	27	94	27	300	120		800

resistivity Si, however we cannot explain the low value obtained at the same temperature by Putley and Mitchell,(3) although they have also worked with high resistivity Si. The coefficient α is also slightly higher, although a better agreement is found for this case than for the Si–p.

Using as drift mobility value that given by Ludwig for their higher resistivity samples, we have calculated the variation of r_n with temperature. In Fig. 2, curve 3, are shown the results of Ludwig for the drift mobility of electrons. In Fig. 4, curve 1, are represented the calculated values of r_n, which between 300°K and 150°K approximately follow the $0{\cdot}11\ T^{0{\cdot}44}$ law.

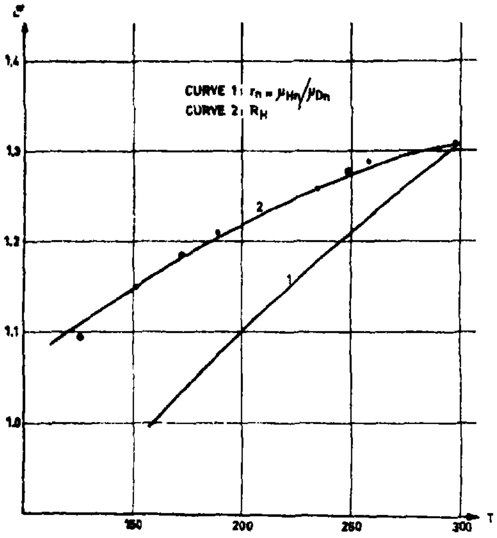

Fig. 4. Curve 1: $r_p = f(T)$ (authors)
Curve 2: $R_H = f(T)$ ● 900 Ω-cm Si–n (authors)
○ 800 Ω-cm Si–n.

In Fig. 4, curve 2, is given the variation of R_H with T, normalized at 300°K for the corresponding value of r_n. The decrease of R_H with T can only be explained if r_n is temperature dependent. The difference in Fig. 4, between curves 1 and 2 may be related to an effective diminution with T of the carrier density. Nevertheless, if we accept curve 1 as correct, curve 2 implies a 10 per cent variation in the carrier density for a temperature change from 300 to 170°K, variation which is approximately independent from the resistivity of the sample.

It seems that a carrier density variation with T that could be caused by levels due to lattice imperfection would lead to a smaller relative variation in the low resistivity crystals, a fact which is contrary to our experimental results. It is on account of this that a more likely value of α for the electrons drift mobility would be 2·4 instead of 2·5.

REFERENCES

1. Ludwig G. W. and Watters R. L., *Phys. Rev.* **101,** 6, 1699 (1956).
2. Klein C. A. and Straub W. D., *Bull. Amer. phys. Soc.* **4,** Ser. 2, 28 (1959).
3. Putley E. H. and Mitchell W. H., *Proc. phys. Soc. Lond.* **72,** 464 (1958).
4. Morin F. J. and Maita J. P., *Phys. Rev.* **96,** 1, 28 (1954).
5. Debye P. P. and Kohane T., *Phys. Rev.* **101,** 6, 1699 (1956).
6. Long D., *Phys. Rev.* **107,** 3, 672 (1957).
7. Long D. and Myers J., *Phys. Rev.* **109,** 4, 1098 (1958).
8. Cronmeyer D. C., *Phys. Rev.* **105,** 2, 522 (1957).
9. Krag W. E., *Phys. Rev.* **118,** 2, 435 (1960).
10. Lee P. A., *Semiconductors and Phosphors*, p. 380, Interscience, New York (1958).
11. Conwell E. M., *Proc. Inst. Radio Engrs.* **46,** 1281 (1958).
12. Long D. and Myers J., *Butt. Amer. phys. Soc.* **4,3,** Ser. 2, 145 (1959).
13. Prince M., *Phys. Rev.* **93,** 1204 (1954).
14. Atkins K. R., Donovan R. and Walmsley R. H., *Phys. Rev.* **118,** 2, 411 (1960).
15. Lax B. and Mavroides J. G., *Phys. Rev.* **100,** 6, 1650 (1955).
16. Merlo Flores J. *Rev. sci. Instrum.* (To be published.)

J. Phys. Chem. Solids Pergamon Press 1963. Vol. 24, pp. 1543–1555. Printed in Great Britain.

BAND PARAMETERS OF SEMICONDUCTORS WITH ZINCBLENDE, WURTZITE, AND GERMANIUM STRUCTURE

MANUEL CARDONA
RCA Laboratories, Princeton, New Jersey

(*Received* 10 *June* 1963)

Abstract—The $\boldsymbol{k} \cdot \boldsymbol{p}$ method is used for calculating the band parameters of semiconductors with germanium, zincblende, and wurtzite structure at $\boldsymbol{k} = 0$ and at the L and X points of the zincblende structure. At $\boldsymbol{k} = 0$, the interaction between the highest valence band and the two lowest conduction bands is considered. The energy gaps between these states are obtained from reflectivity measurements. The wave functions of a polar material are obtained from the wave functions of the iso-electronic non-polar material by the application of an antisymmetric perturbing potential. The matrix elements of $\boldsymbol{p}$ between two given states of the non-polar material are assumed to be the same for all materials. The band parameters of the wurtzite materials are obtained by the application of a small hexagonal crystal-field to the corresponding zincblende-type compound. It is possible by this method to account for the existing experimental data and to predict the band parameters of many materials for which they have not been measured. It is suggested that the absolute valence band maximum in several II–VI compounds may not be at the center of the Brillouin zone.

1. INTRODUCTION

THE $\boldsymbol{k} \cdot \boldsymbol{p}$ method(1, 2) has been very helpful for interpreting the effective masses and g-factors(3) of semiconductors with germanium and zincblende structure. By applying first and second order perturbation theory to the $\boldsymbol{k} \cdot \boldsymbol{p}$ ($\boldsymbol{k}$ is the crystal momentum, $\boldsymbol{p}$ the linear momentum operator) term in the Hamiltonian, one can show that the inverse effective mass parameters are functions of squares of matrix elements of $\boldsymbol{p}$ divided by energy gaps. The magnitude of the various matrix elements of $\boldsymbol{p}$ between two given states seems to be approximately the same for all compounds of this family and differences in the corresponding band parameters are due only to differences in energy gaps.(4) The temperature dependence of the band parameters also indicates that the matrix elements of $\boldsymbol{p}$ are temperature independent.(5, 6) These matrix elements do not vary much from one pair of states to another, provided they are not zero due to symmetry.(7)

For future reference we show in Fig. 1 the band structure of germanium calculated by BASSANI and YOSHIMINE(8) neglecting the spin–orbit interaction. The states have been labelled according to the standard notation, with the subindices c and v

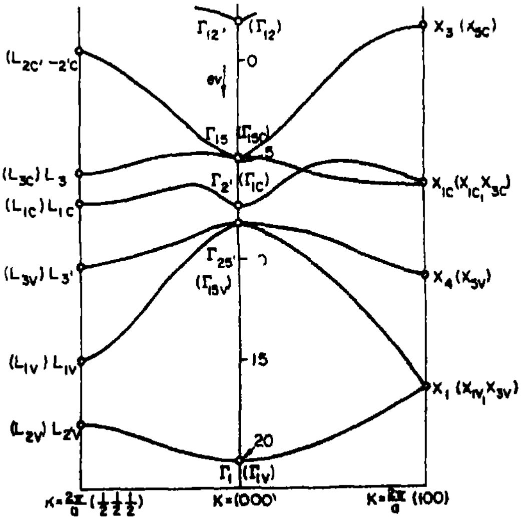

FIG. 1. Band structure of germanium according to BASSANI and YOSHIMINE(8). The L_1 state, which according to this calculation lies above the $\Gamma_2{}'$ state, is actually known to be below $\Gamma_2{}'$.

added to distinguish between conduction and valence band states when two states of the same symmetry exist within the energy range of Fig. 1. We have indicated in brackets the symmetry of the corresponding states in zincblende-type materials. In semiconductors with germanium structure, the parameters of the $\Gamma_{2'}$ minimum (lowest conduction band minimum in germanium and maybe gray tin) are determined almost exclusively by the $\boldsymbol{k}\cdot\boldsymbol{p}$ interaction between this state and the $\Gamma_{25'}$ state (top of the valence band). The parameters at the $\Gamma_{25'}$ state are largely determined by the interaction with $\Gamma_{2'}$, which is responsible for the light hole mass and the mass at the lower valence band split by spin–orbit interaction, and the interaction with Γ_{15c}, which determines the heavy hole mass.(1) The $\boldsymbol{k}\cdot\boldsymbol{p}$ interaction with the $\Gamma_{12'}$ conduction band produces a small correction on the $\Gamma_{25'}$ band parameters.

Braunstein and Kane(9) extended the approach described above to the III–V compounds. They calculated the light hole and split-off hole masses by taking into account only the $\boldsymbol{k}\cdot\boldsymbol{p}$ interaction between the valence band (Γ_{15v} for the zincblende structure) and the Γ_{1c} conduction band. They used the value of the magnitude square of the matrix element of $\boldsymbol{p}$ between these states calculated from the measured electron effective masses at Γ_{1c} assuming they are only determined by the interaction with Γ_{15c} and neglecting the interaction of the Γ_{1c} with the Γ_{15c} band. While this interaction vanishes in the germanium structure for parity reasons, it becomes appreciable in the zincblende structure due to the lack of inversion symmetry. If one neglects the Γ_{15c}–Γ_{1c} interaction, one obtains, from the fit of the experimental electron effective masses, a value of $|\langle\Gamma_{15v}|\boldsymbol{p}|\Gamma_{1c}\rangle|^2$ lower than the value found for germanium. Also the decrease in the Γ_{15v}–Γ_{1c} interaction, due to the mixing of the $\Gamma_{25'}$ and the Γ_{15} states when the inversion symmetry is lifted, gives for zincblende-type compounds a value of $|\langle\Gamma_{15v}|\boldsymbol{p}|\Gamma_{1c}\rangle|^2$ lower than for the germanium-type materials.

In this paper, we shall give a method for calculating band parameters which takes into account the $\boldsymbol{k}\cdot\boldsymbol{p}$ interaction of the Γ_{15c} band with Γ_{15v} and Γ_{1c}, provided the $E(\Gamma_{15c})$–$E(\Gamma_{15v})$ gap is known. This approach is based on the assumption that the energy bands of a zincblende-type compound can be obtained from the bands of the isoelectronic germanium-type material by the action of a purely antisymmetric perturbing potential.(7, 10) The $E(\Gamma_{15c})$–$E(\Gamma_{15v})$ gaps of most of these materials are known from optical reflectivity measurements.(7, 11–14) This approach yields only a small correction to the light hole and split-off hole masses of the III–V compounds calculated by Braunstein and Kane,(9) but is essential for calculating these masses in the II–VI compounds because of the larger $\Gamma_{25'}$–Γ_{15} mixing. The treatment of the Γ_{15c}–Γ_{15v} interaction also yields an estimate of the heavy hole masses in these materials.

This approach can be extended to wurtzite-type compounds if one assumes that their band structure is obtained from the band structure of the corresponding zincblende-type material by the application of a small hexagonal perturbing crystal field.(15) Since the unit cell of wurtzite has twice as many atoms as that of zincblende, the Brillouin zone of materials crystallized in that structure occupies only one-half of the volume of the Brillouin zone of the same material crystallized in the zincblende structure. Hence at $\boldsymbol{k} = 0$ there are twice as many energy eigenstates for wurtzite as for zincblende. The interaction with the extra states contributes to the band parameters of the top valence band and it is possible to extract from the experimental effective masses the values of the matrix elements corresponding to this interaction.

During the last few years a considerable amount of information has become available about the energy gaps of semiconductors with germanium, zincblende and wurtzite structure at points other than $\boldsymbol{k} = 0$. (See Table 1 and references.) Hence it has become possible to extend the $\boldsymbol{k}\cdot\boldsymbol{p}$ approach for calculating band parameters to points other than $\boldsymbol{k} = 0$. In this paper we describe the application of this approach to states at the L and X points of the Brillouin zone.

2. EFFECT OF AN ANTISYMMETRIC PERTURBING POTENTIAL ON THE BAND STRUCTURE OF A GERMANIUM-TYPE MATERIAL

The effect of an antisymmetric potential on the band structure of a germanium-type material has been discussed by Callaway.(16) The antisymmetric potential combines levels of opposite parity at a given point of the Brillouin zone. By this method, one can derive the band structure of

Table 1. *Experimental and estimated values of the various energy gaps relevant for the determination of band parameters at low temperatures (liquid nitrogen or helium) unless otherwise indicated.*

	$\Gamma_{25'}-\Gamma_{2'}$ or $\Gamma_{15v}-\Gamma_{1c}$ (E_0)	$\Gamma_{25'}-\Gamma_{15}$ or $\Gamma_{15v}-\Gamma_{15c}$	Δ_0	$L_{3'}-L_{1c}$ or $L_{3v}-L_{1c}$	$\Lambda_3-\Lambda_1$	Δ_1	$L_{3'}-L_3$ or $L_{3v}-L_{3c}$	X_4-X_{1c} or $X_{5v}-X_{1c}$
Si	3·6(a)	3·43(c)	0·044(a)		3·7(o)		5·5(x, y)	4·4(c)
Ge	0·89(b)	3·05(j, o)	0·29(t)	2·0(u)	2·20(c)	0·18(c)	5·9(x, y)	4·49(c)
α-Sn	0·08(c)	2·9(c)			1·32(c)	0·47(c)	4·4(c, y)	3·5(c)
GaP	2·70(d)	3·76(c)	0·127(α)		3·7(a)		7·0(x, y)	5·3(x, y)
InP	1·34(e)	4·1(p)			3·24(c)	0·14(c)	6·9(r, y)	5·0(c, y)
GaAs	1·55(f)	4·2(q)	0·35(f)	2·6(v)	2·99(q)	0·24(q)	6·6(x, y)	5·12(q)
InAs	0·45(c)	3·9(p)	0·41(e)		2·57(q)	0·28(q)	6·4(x, y)	4·83(q)
AlSb	1·8(d)	4·3(a)	0·75(e)		2·88(c)	0·40(c)	6·5(a)	4·5(a)
GaSb	0·81(b)	3·74(q)			2·08(q)	0·47(q)	5·7(q)	4·33(q)
InSb	0·24(g)	3.45(q)			1·87(q)	0·58(q)	5·4(q)	4·20(q)
ZnO	3·44(h)	5·3(r)	0·0087(h)					
ZnS	3·94(i)	5·7(p)	0·10(i)		5·7(a)		9·5(p, y)	7·0(p, y)
ZnSe	2·80(j)	7·6(a)	0·43(c)		4·85(c)	0·35(w)	9·1(w, y)	6·4(w, y)
ZnTe	2·38(k)	4·82(k)	0·91(k)	3·48(k)	3·71(k)	0·57(k)	6·9(k, y)	5·4(k)
CdS	2·58(l)	6·1(p)	0·068(l)		5·2(p)		9·5(p, y)	7·1(p, y)
CdSe	1·84(m)	6·1(p)	0·43(m)		4·9(p)	0·28(p)	9·5(p, y)	7·6(p, y)
CdTe	1·59(k)	5·20(k)	0·81(k)	3·20(k)	3·44(k)	0·57(k)	6·76(k, y)	5.49(k)
HgSe	0·2(n)	5·2(a)			2·91(c)	0·31(c)	8·3(z)	5·7(z)
HgTe	?	4·10(k)		2·0(k)	2·21(k)	0·69(c)	7·5(z)	4·95(k)

(*a*) See Section 3.
(*b*) Lax B., Roth L. M. and Zwerdling S. *J. Phys. Chem. Solids* **8**, 311 (1959).
(*c*) See Ref. 7.
(*d*) Ehrenreich H., *J. appl. Phys. Suppl.* **32**, 2155 (1961).
(*e*) See Ref. 9.
(*f*) Sturge M., *Phys. Rev.* **127**, 768 (1962).
(*g*) Zwerdling S., Kleiner W. H. and Theriault J. P., *J. appl. Phys.* Suppl. **32**, 2118 (1961).
(*h*) See Ref. 20.
(*i*) Piper W. W., Johnson P. D. and Marple D. T. F., *J. Phys. Chem. Solids* **8**, 457 (1959).
(*j*) Cardona M. and Harbeke G., *J. appl. Phys.* **34**, 813 (1963).
(*k*) See Ref. 14.
(*l*) See Ref. 18.
(*m*) See Ref. 19.
(*n*) Wright G. B., Strauss A. J. and Harman T. C., *Phys. Rev.* **125**, 1534 (1962).
(*o*) Tauc J. and Abraham A., *J. Phys. Chem. Solids* **20** 190 (1961).
(*p*) See Ref. 12.
(*q*) See Ref. 13.
(*r*) Cardona M., unpublished work.
(*s*) Zwerdling S., Button K. J., Lax B. and Roth L. M., *Phys. Rev. Letters* **4**, 173 (1960).
(*t*) Hobden M. V., *J. Phys. Chem. Solids* **23**, 821 (1962).
(*u*) See Ref. 29.
(*v*) See Ref. 28.
(*w*) Aven M., Marple D. T. F. and Segall B., *J. appl. Phys.* Suppl. **32**, 2261 (1961).
(*x*) Ehrenreich H., Philipp H. R., and Phillips J. C. *Phys. Rev. Letters* **8**, 59 (1952).
(*y*) Measured at room temperature.
(*z*) Scouler W. J. and Wright G. B., *Bull. Amer. phys. Soc.* Sec. II, **8**, 246 (1963).
(α) Hodby J. W., *Proc. Phys. Soc. Lond.* **82**, 324 (1963).

a zincblende-type material with its two atoms belonging to the same row in the periodic table, from the band structure af the isoelectronic group IV material. The same approach can be extended to materials whose two atoms belong to different rows of the periodic table; one must take for the band structure of the corresponding group IV material the average of the band structures of the two group IV materials belonging to the two rows of the elements in the compound.(7)

At the Γ point, the $\Gamma_{25'}$ level of the germanium structure interacts with the Γ_{15} level via the antisymmetric potential giving the Γ_{15v} and Γ_{15c} zincblende levels. Neglecting the interaction with other Γ_{15} and $\Gamma_{25'}$ levels, one can write the following Hamiltonian for the interaction between Γ_{15} and $\Gamma_{25'}$:

$$H = \begin{Vmatrix} E(\Gamma_{15}) & V \\ V^* & 0 \end{Vmatrix} \tag{1}$$

where V is the matrix element of the perturbing potential between $\Gamma_{25'}$ and Γ_{15}. We have taken the origin of energies to be the unperturbed $\Gamma_{25'}$ state. Diagonalizing equation (1) we obtain:

$$\begin{aligned} E_p(\Gamma_{15c}) &= \frac{E(\Gamma_{15})}{2} + \left[\left(\frac{E(\Gamma_{15})}{2}\right)^2 + V^2\right]^{1/2} \\ E_p(\Gamma_{15v}) &= \frac{E(\Gamma_{15})}{2} - \left[\left(\frac{E(\Gamma_{15})}{2}\right)^2 + V^2\right]^{1/2} \end{aligned} \tag{2}$$

(we use the subindex p for wave functions and energies of zincblende-type compounds and no subindex for germanium-type materials). Equation (1) also yields the perturbed wave functions:

$$\begin{aligned} \psi_p(\Gamma_{15c}) &= a\psi(\Gamma_{15}) - b\psi(\Gamma_{25'}) \\ \psi_p(\Gamma_{15v}) &= b\psi(\Gamma_{15}) + a\psi(\Gamma_{25'}) \end{aligned} \tag{3}$$

with

$$\begin{aligned} a &= \frac{1}{\sqrt{2}}\left[\frac{E_p(\Gamma_{15c}) - E_p(\Gamma_{15v}) + E(\Gamma_{15})}{E_p(\Gamma_{15c}) - E_p(\Gamma_{15v})}\right]^{1/2} \\ b &= \frac{1}{\sqrt{2}}\left[\frac{E_p(\Gamma_{15c}) - E_p(\Gamma_{15v}) - E(\Gamma_{15})}{E_p(\Gamma_{15c}) - E_p(\Gamma_{15v})}\right]^{1/2} \end{aligned} \tag{4}$$

Equations (4) give the coefficients a and b if we know the gaps $E_p(\Gamma_{15c})$–$E_p(\Gamma_{15v})$ and $E(\Gamma_{15})$–$E(\Gamma_{25'})$ of the polar and the corresponding nonpolar compound.

The $\Gamma_{2'}$ conduction band level interacts with the Γ_{1c} and Γ_{1v} levels via the antisymmetric potential. Both levels are more than 10 eV away from the $\Gamma_{2'}$ level and therefore the admixture of Γ_1 wave function produced on the $\Gamma_{2'}$ level by the antisymmetric potential is likely to be much smaller than the corresponding effect on the $\Gamma_{25'}$–Γ_{15} levels. Since no experimental information is available about the position of the Γ_1 levels, we shall assume that the polar potential does not appreciably mix $\Gamma_{2'}$ and Γ_1 levels. The possible effect of this mixing will be discussed in Section 3.

At the L point the antisymmetric potential mixes the L_1 and $L_{1'}$ states. Since all the $L_{1'}$ states are very far away in energy from the L_{1c} state, we assume that we have no admixture of the L_{1c} with $L_{1'}$ states. The L_3 and $L_{3'}$ states are strongly mixed by the antisymmetric potential giving L_{3c} and L_{3v}. The admixture coefficients can be obtained from equation (4) replacing $E_p(\Gamma_{15c})$–$E_p(\Gamma_{15v})$ by $E_p(L_{3c})$–$E_p(L_{3v})$ and $E(\Gamma_{15})$ by $E(L_3)$–$E(L_{3'})$.

At the X point the antisymmetric potential splits the X_1 germanium states into X_1 and X_3 and mixes the X_4 and X_3 states giving the X_5 levels of the zincblende structure. Only the position of the X_{5v}, X_{1c} and X_{3c} levels is known experimentally at the X point. However, due to the large X_4–X_3 gap in germanium (~ 13 eV) no large mixing of these states by the antisymmetric potential is expected to occur.

3. Γ_{1c} CONDUCTION BAND PARAMETERS

If we neglect the interaction of Γ_{1c} with Γ_{15c}, the electron effective mass at $\Gamma_{2'}$ or Γ_{1c} is given by:(2)

$$\frac{m}{m^*(\Gamma_{2'})} = 1 + P^2/3\left(\frac{2}{E_0} + \frac{1}{E_0 + \Delta_0}\right) \tag{5}$$

where $P^2 = (2/3m)|\langle\Gamma_{2'}|p|\Gamma_{25'}\rangle|^2$, E_0 is the $E(\Gamma_{2'})$–$E(\Gamma_{25'})$ energy gap, and Δ_0 the spin–orbit splitting at $\Gamma_{25'}$.

For diamond-type materials, there is no interaction of $\Gamma_{2'}$ with Γ_{15}. In polar materials this interaction increases the effective mass at Γ_{1c}, since the Γ_{15c} state is normally above Γ_{1c}. Using the wave functions for the polar material derived in Section 2, we can calculate the term contributed to equation (5) by the Γ_{15c} interaction:

$$-\frac{2|\langle\psi(\Gamma_{2'})|p|a\psi_c(\Gamma_{15})-b\psi_v(\Gamma_{25'})\rangle|^2}{3m[E_p(\Gamma_{15c})-E_p(\Gamma_{1c})]} \tag{6}$$

$$=P^2\frac{E_p(\Gamma_{15c})-E_p(\Gamma_{15v})+E(\Gamma_{15})-E(\Gamma_{25'})}{2[E_p(\Gamma_{15c})-E_p(\Gamma_{15v})][(E_p(\Gamma_{15c})-E_p(\Gamma_{1c})]}$$

P is obtained from the matrix element of p between the $\Gamma_{25'}$ and the $\Gamma_{2'}$ states in the corresponding non-polar compound. The interaction of Γ_{1c} with Γ_{15v} is also weakened, in polar materials, by the admixture of $\Gamma_{25'}$ and Γ_{15} wave functions at Γ_{15v}. The resulting effective mass at Γ_{1c} is given by:

$$\frac{m}{m^*(\Gamma_{1c})} = 1+\frac{P^2}{2[E_p(\Gamma_{15c})-E_p(\Gamma_{15v})]}$$
$$\times\left[\frac{E_p(\Gamma_{15c})-E_p(\Gamma_{15v})+E(\Gamma_{15})-E(\Gamma_{25'})}{3}\right.$$
$$\times\left(\frac{2}{E_{0p}}+\frac{1}{E_{0p}+\Delta_0}\right) \tag{7}$$
$$\left.-\frac{E_p(\Gamma_{15c})-E_p(\Gamma_{15v})-E(\Gamma_{15})+E(\Gamma_{25'})}{E_p(\Gamma_{15c})-E_p(\Gamma_{15v})-E_{op}}\right]$$

In equation (7) we have neglected the spin–orbit splitting of the Γ_{15c} state since it is always much smaller than the energy difference between this state and Γ_{1c}.

If we neglect the $\Gamma_{25'}$–Γ_{15} mixing we obtain the following expression for the effective g-factor at $\Gamma_{2'}$ or $\Gamma_{1c}^{(3)}$:

$$g^*(\Gamma_{2'}) = 2\left(1-\frac{P^2\Delta_0}{3E_0(E_0+\Delta_0)}\right) \tag{8}$$

In polar materials not only the spin–orbit splitting at Γ_{15v} contributes to $g^*(\Gamma_{1c})$, but also the splitting at Γ_{15c}. This last contribution, however, is quite small since the energy gap $E_p(\Gamma_{15c})$-$E_p(\Gamma_{1c})$ is much larger than $E_p(\Gamma_{1c})$-$E_p(\Gamma_{15v})$ and the contribution to g^* is inversely proportional to the square of these gaps. The contribution of Γ_{15c} to $g^*(\Gamma_{1c})$ can be estimated by assuming that the spin–orbit splitting at Γ_{15c} is the same as at Γ_{15v}. The expression for g^* becomes:

$$g^*(\Gamma_{1c}) = 2\left\{1-\frac{P^2\Delta_0}{6[E_p(\Gamma_{15c})-E_p(\Gamma_{15v})]}\right.$$
$$\times\left[\frac{E_p(\Gamma_{15c})-E_p(\Gamma_{15v})+E(\Gamma_{15})-E(\Gamma_{25'})}{E_0(E_0+\Delta)}\right.$$
$$\left.\left.+\frac{E_p(L_{15c})-E_p(\Gamma_{15v})-E(\Gamma_{15})+E(\Gamma_{25'})}{[E_p(\Gamma_{15c})-E_p(\Gamma_{1c})]^2}\right]\right\} \tag{9}$$

Table 1 lists all energy gaps required for the evaluation of equations (7) and (9) at low temperatures (liquid nitrogen or helium depending on the availability of data; this difference in temperature is not significant for the evaluation of band parameters). For energy gaps which have not been measured at low temperatures, their low temperature values have been estimated from the room temperature gaps and the known temperature coefficients of these gaps in other materials of the family.(7, 13, 14)

The gaps preceded by the ~ sign have not been observed experimentally; they have been estimated from the general trend followed by the corresponding gaps of the nearest compounds in the family. The E_0 gap of silicon has not been directly observed. We have estimated $E_0 \approx 3{\cdot}4$ eV in silicon by extrapolating the direct gap observed in the germanium–silicon alloys up to 10% silicon concentrations.(17) Another estimate of this gap has been obtained by calculating, from the values of E_0 in GaP and ZnS, E_0 for the hypothetical ordered GeSi compound. This compound should have approximately the average gaps of germanium and silicon and hence, from the values of E_0 for germanium and GeSi we estimate $E_0 \approx 3{\cdot}8$ eV for silicon. In Table 1 we have listed the average of these two estimates ($E_0 = 3{\cdot}6$ eV).

In the calculations of $m^*(\Gamma_{1c})$ and $g^*(\Gamma_{1c})$ we have used the values of Δ_0 given in Table 1. When no experimental value of Δ_0 is available, we use for Δ_0 three-halves of the spin–orbit splitting at L_{1c}, listed under Δ_1 in Table 1.(7) If neither the value of Δ_0 nor that of Δ_1 has been obtained experimentally, we use the values of Δ_0 estimated from atomic data.(7, 9)

In Table 2 we list the estimated values of $m^*(\Gamma_{1c})$ and $g^*(\Gamma_{1c})$. We have taken $P^2 = 23$ eV for group IV and III–V materials since this value gives the best agreement between experimental and calculated data.

For the II–VI compounds good effective mass determinations are not very numerous. The best known electron masses seem to be those of CdTe, CdSe and CdS. Two of these materials (CdS and CdSe) have wurtzite structure, but, as we shall see in the next Section, the band parameters at Γ_{1c} are the same for zincblende and wurtzite-type materials. In order to obtain good agreement with the experimental values in these materials we have taken $P^2 = 21$ eV. This lower value of P^2 is probably due to some admixture of Γ_1 wave function of the non-polar material in the Γ_{1c} state of the zincblende.

4. VALENCE BAND PARAMETERS AT THE Γ POINT

(a) III–V *Compounds*

In these materials the shape of the valence band around $\boldsymbol{k} = 0$ is given by:(1)

$$\frac{2m}{\hbar^2}E = Ak^2 \pm [B^2k^4 + C^2(k_x^2k_y^2 + k_y^2k_z^2 + k_z^2k_x^2)]^{1/2}$$
$$\frac{2m}{\hbar^2}E = A'k^2 - \Delta_0 \qquad (10)$$

where

$$\begin{aligned} A &= \tfrac{1}{3}(F+2G+2M)+1 \\ B &= \tfrac{1}{3}(F+2G-M) \\ C^2 &= \tfrac{1}{3}[(F-G+M)^2-(F+2G-M)^2] \\ A' &= \frac{1}{3}\left[\frac{E_0F}{E_0+\Delta_0}+2G+2M\right]+1 \end{aligned} \qquad (11)$$

F represents the interaction between Γ_{15v} and Γ_{1c}, M the interaction between Γ_{15v} and Γ_{15c} and G the interaction between Γ_{15v} and Γ_{12}. All other interactions, including those yielding linear terms in(2) $\boldsymbol{k}$, have been neglected. F can be obtained from P by the method of Section 3:

$$F = -\frac{P^2[E_p(\Gamma_{15c})-E_p(\Gamma_{15v})+E(\Gamma_{15})-E(\Gamma_{25'})]}{2E_{0p}[E_p(\Gamma_{15c})-E_p(\Gamma_{15v})]} \qquad (12)$$

and likewise:

$$M = -\frac{Q^2[E(\Gamma_{15})-E(\Gamma_{25'})]^2}{[E_p(\Gamma_{15c})-E_p(\Gamma_{15v})]^3}, \qquad (13)$$

We shall take $Q^2 = 15{\cdot}5$ eV, calculated from the value of M in germanium.(2) G is 1·6 in germanium.(2) The $E(\Gamma_{12'})$–$E(\Gamma_{25'})$ gap is about 12 eV in germanium.(1, 8) The gaps of the materials of this family (with the exception of diamond) differ from the corresponding gaps in germanium by no more than 4 eV. In order to calculate the small correction due to the $E(\Gamma_{12})$–$E(\Gamma_{15v})$ interaction, we assume that the corresponding gap is the same for all materials. The value of G in any compound will thus be the value for germanium (1·6) decreased by the admixture of $\Gamma_{25'}$ and Γ_{15} states in Γ_{15v}:

$$G = -1{\cdot}6\frac{E_p(\Gamma_{15c})-E_p(\Gamma_{15v})+E(\Gamma_{15})-E(\Gamma_{25'})}{2[E_p(\Gamma_{15c})-E_p(\Gamma_{15v})]} \qquad (14)$$

Table 2 lists the values of A, B and C^2 that we have calculated by using equations (11)–(14). It also lists the values of the split-off hole effective masses m_{sh}^* and the average heavy and light hole masses m_{hh}^* and m_{lh}^* obtained by averaging equation (8) over all possible directions of $\boldsymbol{k}$:

$$\begin{aligned} \frac{1}{m_{lh}^*} &\approx -A-B\left(1+\frac{C^2}{10B^2}\right) \\ \frac{1}{m_{hh}^*} &\approx -A+B\left(1+\frac{C^2}{10B^2}\right) \\ \frac{1}{m_{sh}^*} &= -A' \end{aligned} \qquad (15)$$

The agreement of the calculated m_{lh}^* and m_{sh}^* with the few available experimental data is quite good, somewhat better than for the estimates of Braunstein and Kane,(9) as expected. The calculated m_{hh}^* does not agree so well with the experimental values for the III–V compounds. These experimental values, however, are not very reliable since all available determinations are only indirect and not very sensitive to the value of m_{hh}^*. The accuracy of our estimate of m_{hh}^* is not very good either: m_{hh}^* is obtained as the difference of two large terms almost equal in magnitude (see equation (15)).

(b) II–VI *Compounds*

The amount of experimental information available about the valence band of II–VI compounds is very small. Only the transverse masses of the top valence band at Γ (Γ_9 double group representation) in CdS and CdSe (wurtzite structure) and the transverse mass of the second highest Γ band (Γ_7 double group representation) in CdSe are known with a certain degree of reliability.(18, 19) It is possible to derive the band parameters of the wurtzite-type materials if we assume that their band structure can be obtained from the band structure of the zincblende-type materials by the application of a small hexagonal crystal-field.(15) In most of the materials which can crystallize in the wurtzite structure (ZnS, ZnSe, CdS, CdSe), the spin–orbit splitting of the Γ valence band is larger than the crystal-field splitting ($\sim$ 0·02 eV). In ZnO, however, the spin–orbit splitting is smaller than the crystal-field splitting.(20)

When going from the zincblende to the wurtzite structure, the size of the unit cell doubles and hence the size of the Brillouin zone is divided by two. As a result the number of $\boldsymbol{k} = 0$ states is doubled: a Γ_6 (doubly degenerate point group representation) and two Γ_3 (non-degenerate) states are added to the valence states at Γ. These new states do not interact with Γ_1 via $\boldsymbol{k}\cdot\boldsymbol{p}$ and hence do not affect the conduction band parameters of Γ_{1c}. Since the crystal field splitting of the other (Γ_{15v} and Γ_{15c}) states interacting with Γ_{1c} is very small,(12) the band parameters at Γ_{1c} must be nearly the same for the zincblende and the wurtzite structures. This conclusion explains the lack of anisotropy in the experimentally observed $m^*(\Gamma_{1c})$ of CdS and CdSe.(18, 19) Linear terms in $\boldsymbol{k}$, allowed by symmetry at Γ_{1c} in wurtzite-type materials, are too small to be of any significance.(21)

A Γ_6 state is known to exist about 1 eV below the Γ_9 (double group) top valence band state. The two highest valence band states at Γ (Γ_9 and Γ_7 double group representations) belong to the Γ_5 and Γ_1 point group representation. Since Γ_6 interacts with Γ_5 via the transverse component of $\mathbf{p}$, it is expected that the presence of Γ_6 will affect the transverse masses at Γ_9, Γ_7 and the lower Γ_7 valence band. This effect will be absent in zincblende-type materials.

Let us neglect for a moment the Γ_6–Γ_5 interaction. For crystal-field splittings much smaller than the spin–orbit splitting, the lowest Γ_{15v} band, split off by spin–orbit interaction, has the same parameters in wurtzite as in zincblende-type materials (see equation (15)). The effective masses of the two higher Γ_{15v} bands, split now by the crystal field, are found as the solution of a 4×4 $\boldsymbol{k}\cdot\boldsymbol{p}$ secular equation. The problem is analogous to the problem of a group IV semiconductor under the action of a uniaxial stress in the (111) direction.(22) The highest of these bands (Γ_9 symmetry in wurtzite) has the masses:

$$\begin{aligned} \frac{m}{m^*_{\perp}(\Gamma_9)} &= -1-\frac{F}{2}-\frac{G}{2}-\frac{5M}{6} \\ \frac{m}{m^*_{\parallel}(\Gamma_9)} &= -1-\frac{M}{3}-G \end{aligned} \qquad (16)$$

where $m_{\parallel}$ is the mass in the direction of the hexagonal axis and $m_{\perp}$ perpendicular to it. The masses at the lower (Γ_7) valence band, split from Γ_{15v} by the crystal field, are:

$$\begin{aligned} \frac{m}{m^*_{\perp}(\Gamma_7)} &= -1-\frac{F}{6}-\frac{M}{2}-\frac{5}{6}G \\ \frac{m}{m^*_{\parallel}(\Gamma_7)} &= -1-\frac{2F}{3}-\frac{G}{3}-M. \end{aligned} \qquad (17)$$

It can be easily shown that the effect of the Γ_6–Γ_5 interaction is to add to F in the expressions of m^* (equations (15)–(17)) a positive term W. The longitudinal masses are not affected by this interaction. $W = 3{\cdot}9$ can be calculated from the experimental values of $m^*_{\perp}(\Gamma_7)$ and $m^*_{\perp}(\Gamma_9)$ for CdSe. Since both $m^*_{\perp}(\Gamma_7)$ and $m^*_{\perp}(\Gamma_9)$ can be fitted within the experimental accuracy with this value of W (see Table 2), we conclude that any possible contribution of the core d-electrons,(14) which lie about 10 eV below Γ_9, is negligible.

Let us now treat the case of a spin–orbit splitting much smaller than the crystal-field splitting (ZnO). We shall again first assume $W = 0$. For a finite W, we must add it to F in the expressions of the transverse masses. The orbital wave functions which diagonalize the Hamiltonian are:

$$\psi_1 = \tfrac{1}{2}X\left(1+\frac{i}{\sqrt{3}}\right)+\tfrac{1}{2}Y\left(-1+\frac{i}{\sqrt{3}}\right)-\frac{i}{\sqrt{3}}Z$$

$$\psi_{-1} = \tfrac{1}{2}X\left(1-\frac{i}{\sqrt{3}}\right)+\tfrac{1}{2}Y\left(-1-\frac{i}{\sqrt{3}}\right)+\frac{i}{\sqrt{3}}Z$$

$$\psi_0 = \frac{1}{\sqrt{3}}(X+Y+Z)$$

where X, Y and Z are the orbital wave functions

Table 2. Estimated values of the band parameters at $\Gamma_{2'}$ and $\Gamma_{25'}$ (germanium structure), Γ_{1c} and Γ_{15v} (zincblende structure) and the equivalent points for the wurtzite structure (Γ_1 for the conduction band, Γ_9, Γ_7, and Γ_7 for the valence band). The effective masses are given in units of the free electron mass.

	$m^*(\Gamma_2')$ or $m^*(\Gamma_{1c})$ calc.	$m^*(\Gamma_2')$ or $m^*(\Gamma_{1c})$ exp.	$g^*(\Gamma_2')$ or $g^*(\Gamma_{1c})$ calc.	$g^*(\Gamma_2')$ or $g^*(\Gamma_{1c})$ exp.	A calc.	B calc.	C^2 calc.	$m^*(\Gamma_9)$ or m^*_{lh} calc.	$m^*(\Gamma_9)$ or m^*_{lh} exp.	$m^*(\Gamma_7)$ or m^*_{hh} calc.	$m^*(\Gamma_7)$ or m^*_{hh} exp.	$m^*(\Gamma_7)$ or m^*_{sh} calc.	$m^*(\Gamma_7)$ or m^*_{sh} exp.
Si	0·13		1·95		−5·2	−1·7	20	0·12	0·16(a)	0·44	0·52(a)	0·19	
Ge	0·040	0·041(a)	−2·22		−12·1	−8·0	96	0·047	0·045(a)	0·35	0·35(a)	0·10	
α-Sn	0·0050		−172		−99	−95	1160	0·0051		0·25	~0·2(c)	0·075	
GaP	0·13		1·76		−4·7	−2·6	9	0·13		0·56		0·22	
InP	0·072	0·073(d)	0·60		−6·3	−5·3	0	0·086		1·0	0·4(e)	0·18	
GaAs	0·084	0·07(d)	0·32		−5·5	−4·5	−1	0·10	0·12(d)	1·0	0·68(d)	0·21	0·20(d)
InAs	0·026	0·026(f)	−12		−16·5	−15·2	12	0·031	0·025	0·82	0·41(d)	0·11	0·083(d)
AlSb	0·11		0·4		−4·8	−4	−5	0·12		1·1	0·9(e)	0·27	
GaSb	0·046	0·047(e)	−6·1	−6·5(p)	−10·2	−8·6	16	0·053	0·06(d)	0·71	0·3(e)	0·16	
InSb	0·0152	0·0155(g)	−44	−48(h)	−31·5	−29·3	113	0·016	0·012(e)	0·53	0·25(d)	0·12	

Table 2—continued

ZnO	0·25	0·32$^{(i)}$	1·99					0·67 ∥ 0·63 ⊥		0·67 ∥ 0·63 ⊥ ⊥		0·25 ∥ 2 ⊥
ZnS(cubic)	0·39		1·82		−1·81	−1·93	−4·3	0·76 ⊥		10		0·56
ZnS(hex.)	0·39		1·82					−1·9 ∥ 0·67 ⊥		0·32 ∥ 1·1 ⊥		0·85 ∥ 0·55 ⊥
ZnSe	0·21	∼0·1$^{(j)}$	1·46		−1·71	−2·39	4·5	0·25		−1·9		0·67
ZnTe	0·17		0·4		−1·2	−2·38	−0·2	0·16		1		0·42
CdS	0·18	0·20$^{(k)}$	1·89	1·78$^{(k)}$				2·5 ∥ 0·56 ⊥	∼5 ∥$^{(k)}$ 0 7 ⊥$^{(k)}$	0·24 ∥ 1·2 ⊥		0·77 ∥ 0·43 ⊥
CdSe	0·13	0·13$^{(l, m)}$	0·84	0·70$^{(m)}$				2·5 ∥ 0·42 ⊥	0·45 ⊥$^{(l)}$	0·18 ∥ 0·94 ⊥	0·9$^{(l)}$ ⊥	0·71 ∥ 0·40 ⊥
CdTe	0·11	0·11$^{(n)}$	−0·40		−3·9	−4·0	−14	0·13		5		0·37
HgSe	0·016	0·018$^{(o)}$	−34		−27·8	−27·9	−72	0·018		5		0·11

(*a*) See Ref. 1.

(*b*) Roth L. M., Lax B. and Zwerdling S., *Phys. Rev.* **114**, 90 (1959).

(*c*) See Ref. 7.

(*d*) Ehrenreich H., *J. appl. Phys.* Suppl. **32**, 2155 (1961), other references given in this paper.

(*e*) See Ref. 9.

(*f*) See Ref. 5.

(*g*) See Ref. 6.

(*h*) Zwerdling S., Kleiner W. H. and Theriault J. P., *J. appl. Phys.* Suppl. **32**, 2118 (1961).

(*i*) Hutson A. R., *J. appl. Phys.* Suppl. **32**, 2287 (1961).

(*j*) Aven M., Marple D. T. F. and Segall B., *J. appl. Phys.* Suppl. **32**, 2261 (1961).

(*k*) See Ref. 18.

(*l*) See Ref. 19.

(*m*) Hopfield J. J., *J. appl. Phys.* Suppl. **32**, 2277 (1961).

(*n*) Marple D. T. F., *Phys. Rev.* **129**, 2466 (1963).

(*o*) Wright G. B., Strauss A. J. and Harman T. C., *Phys. Rev.* **125**, 1534 (1962).

(*p*) Johnson E. J., Filinski I. and Fan H. Y., *Proceedings of the International Conference on the Physics of Semiconductors* July 1962, Exeter, England, p. 375. The Institute of Physics and the Physical Society, London (1962).

in the absence of crystal field splitting, which transform like the coordinates x, y and z. In the tight binding limit equation (18) represents angular momentum wave functions for $l = 1$ and magnetic quantum number equal to 1, -1 and 0, in the direction of the hexagonal axis.

When the spin–orbit interaction is applied, the wave functions which diagonalize the $\boldsymbol{k}\cdot\boldsymbol{p}$ Hamiltonian, including spin–orbit coupling, are:

$$\begin{matrix} \psi_{1\uparrow}, & \psi_{-1\downarrow} \\ \psi_{1\downarrow}, & \psi_{-1\uparrow} \\ \psi_{0\uparrow}, & \psi_{0\downarrow} \end{matrix} \qquad (19)$$

where ↑ and ↓ represent spin eigenfunctions referred to the hexagonal axis. Each pair of functions in equation (19) defines a doubly degenerate valence band. The two upper bands have the same effective masses:

$$\begin{aligned} \frac{1}{m_{\parallel}} &= -1-G-M \\ \frac{1}{m_{\perp}} &= -1-\frac{F}{2}-\frac{M}{2}-\frac{G}{2} \end{aligned} \qquad (20)$$

and the lower ψ_0 band has the masses:

$$\begin{aligned} \frac{1}{m_{\parallel}} &= -1-F \\ \frac{1}{m_{\perp}} &= -1-G-M \end{aligned} \qquad (21)$$

We have listed in Table 2 the valence band parameters for the II–VI compounds, calculated with the rules discussed above. We have calculated zincblende parameters for ZnS, ZnSe, ZnTe, CdTe and HgSe and wurtzite parameters for ZnO, ZnS, CdS and CdSe. We have estimated W in these materials from the value of W in CdSe, by making the reasonable assumption that W is proportional to F. A salient feature of the calculated zincblende parameters is that m_{hh}^* is very large, and even negative for ZnSe. m_{hh}^* is only an average mass and actually the heavy hole mass in the (100) direction is also negative for ZnS, CdTe and HgSe. The small contribution to M of the d-electrons, which we have neglected, is likely to make this mass even more negative and may be also negative in ZnTe. This effect is due to the decrease in the Γ_{15v}–Γ_{15c} interaction produced by the $\Gamma_{25'}$–Γ_{15} admixture. When this interaction becomes very small, the -1 term in the expression for some inverse masses can become dominant and the corresponding bands are curved upwards like free electron bands. Under these conditions the highest valence band maximum does not occur at the Γ point, as shown in Fig. 2. There is considerable experimental data in the literature which can be explained using this model for the valence band. Indirect transitions have been reported to occur below the direct exciton gap in ZnTe,(24) CdTe(25) and ZnO.(26) These transitions would occur, in our model, between the highest valence band off $\boldsymbol{k} = 0$ and the lowest conduction band at $\boldsymbol{k} = 0$. In HgSe and HgTe the existence of a valence band off $\boldsymbol{k} = 0$ overlapping the conduction band, has been postulated in order to explain the variation of the Hall constant with temperature.(27) The overlapping valence band may well be the highest maximum off $\boldsymbol{k} = 0$ as shown in Fig. 2. While this estimate of the heavy masses is rather crude and other interactions which we have

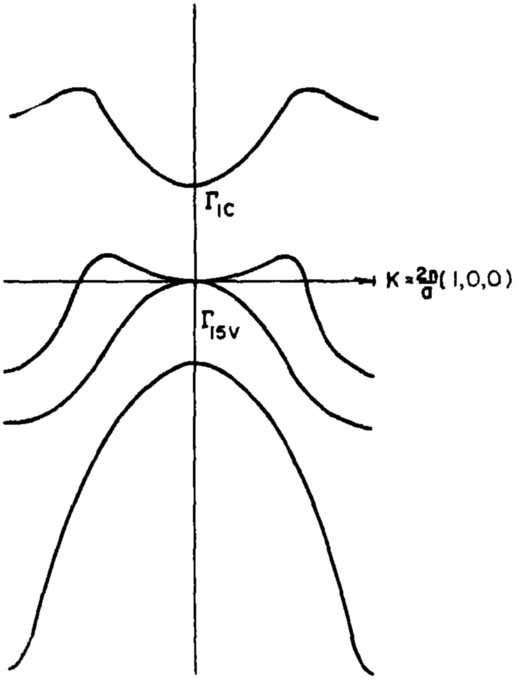

FIG. 2. Sketch of the band structure proposed in Section IV(b) for the II–VI compounds.

neglected may appreciably change this estimate, it indicates clearly the possibility of large negative hole masses at the top of the valence band. These comments must be considered speculative at present; more accurate calculations, based on a direct computation of the matrix elements of p for the calculated wave functions of the material, are needed. We expect them to yield negative heavy hole masses for some, if not all the II–VI compounds.

We have not been able to apply this type of approach to the I–VII compounds with zincblende and wurtzite structure. While the various band gaps required are known experimentally, the values of F and M are probably strongly modified by the admixture of d-electrons of the metal in the Γ_{15v} top valence band. No experimental information on effective masses is available for these materials.

5. BAND PARAMETERS AT Γ_{15c}

The same type of analysis applies to Γ_{15c} of the zincblende structure. Equations (10), (11) and (15) hold provided the proper values of F, M and G are used. In group IV materials F (Γ_{15c}) is determined by the interaction with the very remote Γ_1 bands. Since we have no experimental information about these bands, it is reasonable to take $F(\Gamma_{15c}) = 0$. In polar compounds, the interaction with the lowest conduction band (Γ_{1c}) contributes the following term to F (Γ_{15c}):

$$F(\Gamma_{15c}) = \frac{E_p(\Gamma_{15c})-E_p(\Gamma_{15v})-E(\Gamma_{15})+E(\Gamma_{25'})}{[E_p(\Gamma_{15c})-E_p(\Gamma_{15v})-E_{0p}][E_p(\Gamma_{15c})-E_p(\Gamma_{15v})]}P^2 \tag{22}$$

$M(\Gamma_{15c})$ has the same magnitude as $M(\Gamma_{15v})$ but opposite sign. In group IV materials, $G(\Gamma_{15c}) = 0$ since all interacting bands (Γ_{12}) are very far away in energy. In polar materials $G(\Gamma_{15c})$ is determined by the interaction with the Γ_{12} conduction band. $G(\Gamma_{15c}) \approx 0{\cdot}3$ eV for the II–VI compounds. The correction due to the d-electrons in the II–VI compounds $M_d(\Gamma_{15c})$ and $G_d(\Gamma_{15c})$ can be estimated to be the same as for the Γ_{15v} bands.

6. BAND PARAMETERS AT L

The $L_{3'}$–L_3 gap of the germanium structure (L_{3c}–L_{3v} in zincblende) is known in many semiconductors of the family we are considering (see Table 1). The $L_{3'}$–L_{1c} (or L_{3v}–L_{1c}) gap is known for CdTe, ZnTe, HgTe(14) and GaAs.(28) It is also known to be 2·0 eV from band calculations in germanium.(29) In all these materials L_{3v}–L_{1c} is only slightly smaller ($\sim 0{\cdot}3$ eV) than the Λ_3–Λ_1 gap obtained from reflectivity measurements in almost all materials of this family (see Table 1). We can estimate the L_{3v}–L_{1c} gap in those materials for which it is not known by assuming it is 0·3 eV smaller than the Λ_3–Λ_1 gap. The method described in the previous Sections can now be used to determine the band parameters at L_{3c}, L_{1c} and L_{3v}. The longitudinal masses at L_{3c} and L_{3v} are given only by the interaction between these two states and possibly (for II–VI compounds) some contribution from d-states. The calculation of these masses is equivalent to the calculation of M in Section 4. No experimental data are available for determining the square of the matrix elements for the L_{3c}–L_{3v} interaction. One can reasonably assume that it is the same as for the Γ_{15v}–Γ_{15c} interaction (15·5 eV). Similarly to what happens at Γ_{15v}, the curvature at L_{3v}, which is downwards for group IV and III–V materials, becomes upwards in some II–VI compounds.

The transverse mass at L_{1c} is given almost entirely by the interaction with L_{3c} and L_{3v}. The square of the matrix element for the transitions is also 23 eV(7) (in Ref. 7 we found 25 eV for this square matrix element since we used the Λ_3–Λ_1 gap instead of the L_3–L_1 gap). $m^*_\perp(L_{1c})$ is given by equation (7) with Γ_{15c}, Γ_{15v}, $\Gamma_{25'}$ and E_{0p} replaced by L_{3c}, L_{3v}, $L_{3'}$ and $E(L_1)-(L_{3v})$.

The longitudinal mass at L_{1c} is determined by the interaction with other L_1 or $L_{1'}$ states which are very far in energy. Hence this mass must be close to the free electron mass.

The transverse mass at L_{3v} is determined by the interaction with L_1, L_2 and other L_3 states. It can only be qualitatively estimated from the interaction with L_{1c} and L_{3c} since the interaction with L_{1v}, which cannot be easily estimated, contributes significantly to $m_\perp(L_{3v})$.

The longitudinal effective g-factor at L_1 can also be estimated by this method.(30)

7. BAND PARAMETERS AT X

The only energy gap at X known experimentally for the materials under consideration is the X_4–X_{1c} gap (see Fig. 1). The splitting at $X_{1c}(X_1$–$X_3)$ is also known for several polar materials. The X_4–X_{1c} gap determines the transverse effective mass at X_{1c}. No corrections due to the admixture of X_4 and X_3 wave functions in polar materials can be made since no information about the position of X_3 is available. It has been shown in Section 2, however, that this correction is quite small, due to the large gaps involved. The square matrix element for the X_4–X_{1c} interaction can be estimated from the value of the transverse mass at the lowest conduction band minimum in silicon.(11) This minimum occurs in the (111) direction near X but somewhat inside the Brillouin zone. At this point the matrix elements and the energy denominators are likely to be close to the corresponding values at X. The square matrix element for the X_4–X_{1c} interaction obtained by this procedure, is 19 eV. The electron effective masses have been determined in two materials which are likely to have the lowest conduction band minimum at the X point(31): AlSb and GaP.(32) From the values of the average masses determined from the Faraday rotation and with the reasonable assumption $m^*_\parallel(X_1) \approx 1$ (like in silicon), one obtains(33) $m^*_\perp(X_1) = 0{\cdot}22$ for GaP and $m^*_\perp(X_1) = 0{\cdot}25$ for AlSb. The values of $m(^*_\perp X_1)$ estimated by the method described above are 0·22 for GaP and 0·19 for AlSb. This fact lends further support to the hypothesis that these two materials have (100) lowest conduction band minima: both the Γ_{1c} and the L_{1c} minima have much smaller transverse masses.

REFERENCES

1. Dresselhaus G., Kip A. F. and Kittel C., *Phys. Rev.* **98**, 368 (1955).
2. Kane E. O., *J. Phys. Chem. Solids* **1**, 82 (1956); *ibid.* **1**, 249 (1957).
3. Roth L. M., *Lincoln Lab. quart. progr. Rep.* November 1 p. 45 (1957).
4. Ehrenreich H., *J. appl. Phys. Suppl.*, **32**, 2155 (1961).
5. Cardona M., *Phys. Rev.* **121**, 752 (1961).
6. Smith S. D., Pidgeon C. R. and Prosser V., *Proceedings of the International Conference on the Physics of Semiconductors* July 1962, Exeter, England, p. 301. The Institute of Physics and the Physical Society, London (1962).
7. Cardona M. and Greenaway D. L., *Phys. Rev.* **125**, 1291 (1962).
8. Bassani F. and Yoshimine M., *Phys. Rev.* **130**, 20 (1963).
9. Braunstein R. and Kane E. O., *J. Phys. Chem. Solids* **23**, 1423 (1962).
10. Herman F., *J. Electron.* **1**, 103 (1955).
11. Ehrenreich H., Phillips J. C. and Philipp H. R., *Phys. Rev. Letters* **8**, 59 (1952).
12. Cardona M., *Phys. Rev.* **129**, 1068 (1963).
13. Greenaway D. L. and Cardona M., *Proceedings of the International Conference on the Physics of Semiconductors* July 1962, Exeter, England, p. 666. The Institute of Physics and the Physical Society, London (1962).
14. Cardona M. and Greenaway D. L., *Phys. Rev.* **131**, 98 (1963).
15. Birman J. L., *Phys. Rev.* **115**, 1493 (1959).
16. Callaway J., *J. Electron.* **2**, 330 (1957).
17. Braunstein R., Herman F. and Moore A., *Phys. Rev.* **109**, 395 (1958).
18. Hopfield J. J. and Thomas D. G., *Phys. Rev.* **122**, 35 (1961).
19. Dimmock J. O. and Wheeler R. G., *Phys. Rev.* **125**, 1805 (1962); *J. appl. Phys. Suppl.* **32**, 2271 (1961).
20. Thomas D. G., *J. Phys. Chem. Solids* **15**, 86 (1960).
21. Hopfield J. J., *J. appl. Phys. Suppl.* **32**, 2277 (1961).
22. Phillips J. C., *Phys. Rev.*, to be published.
23. Pikus G. E. and Bir G. L., *Phys. Rev.* Letters **6**, 103 (1961).
24. Aten A. C., Van Doorn C. Z. and Vink A. T., *International Conference on the Physics of Semiconductors* July 1962, Exeter, England, p. 696. The Institute of Physics and the Physical Society, London (1962).
25. Davis D. W. and Shilliday T. S., *Phys. Rev.* **118**, 1020 (1960).
26. Hutson A. R., *J. appl. Phys. Suppl.* **32**, 2287 (1961).
27. Harman T. C. and Strauss A. J., *J. appl. Phys. Suppl.* **32**, 2265 (1961).
28. Greenaway D. L., *Phys. Rev. Letters* **9**, 97 (1962).
29. Brust D., Phillips J. C. and Bassani F., *Phys. Rev. Letters* **9**, 94 (1960).
30. Roth L. M., *Lincoln Lab. quart. progr. Rep.*, Jan. 15, p. 45 (1959).
31. Paul W., *J. appl. Phys. Suppl.* **32**, 2082 (1961).
32. Moss T. S., Walton A. K. and Ellis B., *International Conference on the Physic of Semiconductors*, July 1962, Exeter, England, p. 295. The Institute of Physics and the Physical Society, London (1962).
33. Moss T. S., *J. appl. Phys.* **30**, 951 (1959).
34. Groves S. and Paul W., *Phys. Rev. Letters* **11**, 194 (1963).
35. Bagguley D. M. S., Robinson M. L. A. and Stradling R. A., *Phys. Rev. Letters* **6**, 143 (1963).
36. Baer W. S. and Dexter R. N., *Bull. Amer. phys. Soc.* Ser. II, **8**, 516 (1963).
37. Sawamoto K., *J. phys. Soc. Japan* **18**, 1224 (1963).

Note added in proof

GROVES and PAUL(34) have recently reinterpreted the existing data for α-Sn in terms of a negative E_0 gap ($E_0 \approx -0{\cdot}2$ eV). Accordingly the band parameters listed for this material in Table 2 should be recalculated for this value of E_0 if this interpretation is correct.

BAGGULEY *et al.*(35) have determined the valence band parameters of InSb by cyclotron resonance. They obtain $m^*_{lh} = 0{\cdot}021 \pm 0{\cdot}005$ and $m^*_{hh} = 0{\cdot}4$, in good agreement with our calculations. Cyclotron resonance measurements have also been reported for n(36) and p(37) type CdS. For n-type material $m^*_\perp(\Gamma_1) = 0{\cdot}175$ and $m^*_\parallel(\Gamma_1) = 0{\cdot}156$. While these values agree well with the estimate in this paper, the anisotropy of $m^*(\Gamma_1)$ is larger than expected. For p-type material $[m^*(\Gamma_9)m^*_\parallel(\Gamma_9)]^{1/2} = 1{\cdot}87$(37) was obtained, in reasonable agreement with our estimates.

J. Phys. Chem. Solids Pergamon Press 1963. Vol. 24, pp. 1557–1565. Printed in Great Britain.

POLARISATION DYNAMIQUE DU SODIUM METALLIQUE EN CHAMP FAIBLE A LA TEMPERATURE DE L'HELIUM LIQUIDE

D. JEROME et G. GALLERON

Service de Physique du Solide et de Résonance Magnétique, Centre d'Etudes Nucléaires de Saclay, France

(*Received* 26 *April* 1963)

Résumé—Nous augmentons la polarisation des spins nucléaires de ^{23}Na par effet Overhauser à la température de 1,5°K. Dans le champ magnétique statique appliqué (2,88 G) l'énergie Zeeman nucléaire est du même ordre que l'énergie dipolaire entre spins nucléaires. La théorie(6) montre que le mélange de ces deux énergies produit une diminution de l'augmentation Overhauser, effectivement observée expérimentalement.

La méthode de détection particulièrement sensible (détection déclenchée) et une raie de résonance électronique étroite, donc aisément saturable, nous permettent de mesurer avec précision et très directement le temps de relaxation nucléaire dans divers champs appliqués ainsi que l'absorption d'énergie des spins nucléaires.

Abstract—Nuclear spins of ^{23}Na have been dynamically polarized by Overhauser effect in a 2·88 G applied magnetic field. At temperature of liquid helium a wide electronic resonance line permits good saturation by the radiofrequency field. When the static magnetic field has about the same value as the nuclear local field, ABRAGAM's theory(6) predicts a decrease of nuclear polarization enhancement in fairly good agreement with experimental results. The use of a trigger detection method to observe the Overhauser effect provides a very direct measurement of the nuclear spin–lattice relaxation time and of the nuclear spin absorption in low fields.

1. INTRODUCTION

DANS les métaux alcalins, le couplage prédominant entre les spins $\mathbf{S}$ des électrons de conduction et les spins $\mathbf{I}$ des noyaux est de la forme scalaire(1, 2)

$$\hbar\mathscr{H} = -\frac{8\pi}{3}\gamma_e\gamma_n\hbar^2\mathbf{I}\cdot\mathbf{S}\delta(r_I) \qquad (1)$$

γ_e et γ_n étant respectivement les rapports gyromagnétiques électroniques et nucléaires. $\delta(r_I)$ est la fonction de Dirac centrée sur un noyau. C'est ce couplage qui est essentiellement responsable de la relaxation des noyaux de sodium.

La saturation de la résonance des électrons de conduction produit une augmentation de la polarisation nucléaire $\langle I_z\rangle/I_0$. Cet effet a été prévu par OVERHAUSER.(2)

A l'équilibre thermique avec le réseau, l'aimantation nucléaire est donnée par la formule de Langevin :

$$I_0 = I\frac{\sum m\exp\left(-m\dfrac{\gamma_n\hbar H_0}{kT}\right)}{\sum\exp\left(-m\dfrac{\gamma_n\hbar H_0}{kT}\right)}$$

qui devient, lorsque $\gamma_n\hbar H_0 \ll kT$,

$$I_0 = \frac{\gamma_n\hbar H_0 I(I+1)}{3kT} \qquad (2)$$

Dans notre cas H_0, le champ appliqué, vaut 2,88 G, correspondant à une fréquence de résonance électronique de 8050 kc/s.

Lorsque la relaxation est due uniquement à l'interaction (1) des spins nucléaires avec les spins des électrons de conduction, et si l'on sature la résonance électronique, l'aimantation nucléaire prend une valeur au plus égale à γ_e/γ_n fois l'aimantation à l'équilibre thermique.(2, 3)

Les expériences de Carver et Slichter(4) ont permis de mesurer l'augmentation de la polarisation nucléaire par effet Overhauser à la température ambiante. L'augmentation de la polarisation des noyaux de ^{23}Na dans un champ appliqué de 44,2 G était observée directement par l'augmentation du signal de résonance nucléaire mais demeurait limitée par la faible saturation de la raie électronique, large de 12 G, et par l'existence d'autres causes de relaxations nucléaires.

Dans notre cas, les expériences de résonance et de saturation électronique sont effectuées sur des particules de sodium métallique qui se forment spontanément dans l'hydrure de sodium NaH. Le caractère métallique est bien mis en évidence par les observations expérimentales que nous décrivons dans la partie 3. Une raie de résonance électronique étroite à 1,5°K permet une importante saturation par le champ radiofréquence (8 Mc/s).

La méthode de détection que nous utilisons est différente de celle employée par Carver et Slichter. Elle a été proposée par Overhauser(2) et utilisée par Ryter(5) sur le lithium.

La fréquence de résonance des électrons vaut

$$\omega_e = \gamma_e(H_0+H_n) \tag{3}$$

H_0 est le champ extérieur appliqué, et H_n le champ nucléaire moyen "vu" par les électrons. La formule (1) conduit à la valeur

$$H_n = \frac{8\pi}{3}\langle|\Phi(0)|^2\rangle_F \gamma_n\hbar\langle I_z\rangle \tag{4}$$

$\langle|\Phi(0)|^2\rangle_F$ est la moyenne sur les fonctions d'onde au niveau de Fermi de la valeur à l'emplacement d'un noyau de la fonction $\Phi(r)$ normalisée dans le volume atomique.

L'impossibilité d'observer la résonance nucléaire en bas champ nécessite l'emploi d'une méthode de détection déclenchée (trigger-detection) décrite plus en détail dans la partie 3.

Le déplacement $\gamma_e H_n$ de la fréquence de résonance électronique nous renseigne sur l'intensité de l'aimantation nucléaire. Nous pourrons ainsi mesurer très directement le temps de relaxation spin-réseau ^{23}Na dans des champs appliqués qui sont de l'ordre du champ local nucléaire (1 G).

De plus, irradiant les spins nucléaires par un champ oscillant, nous obtiendrons la variation de la puissance absorbée par les spins nucléaires en fonction de la fréquence, pour des fréquences proches de la fréquence de Larmor ou de ses harmoniques.

Enfin, les expériences se prêteront bien à une vérification de la théorie de l'effet Overhauser en champ faible établie avec rigueur par Abragam(6) et présentée d'une manière plus phénoménologique par Solomon.(7)

2. THEORIE

Relaxation nucléaire

Le système des spins nucléaires possède un hamiltonien de la forme

$$\mathscr{H}_{\mathrm{I}} = Z_{\mathrm{I}} + \mathscr{H}_{\mathrm{II}} + \mathscr{H}_{\mathrm{ex}} \tag{5}$$

$$Z_{\mathrm{I}} = -\gamma_n\hbar H_0 \sum_i I_{zi} \tag{6}$$

$$\begin{aligned} \mathscr{H}_{\mathrm{II}} &= \sum_{j<k} \frac{\gamma_n^2\hbar^2}{R_{jk}^3}\left\{\boldsymbol{I}_j\cdot\boldsymbol{I}_k - 3(\boldsymbol{I}_j\cdot\boldsymbol{n}_{jk})(\boldsymbol{I}_k\cdot\boldsymbol{n}_{jk})\right\} \\ \mathscr{H}_{\mathrm{ex}} &= \sum_{j<k} A_{jk}\boldsymbol{I}_j\cdot\boldsymbol{I}_k \end{aligned} \tag{7}$$

$\boldsymbol{n}_{jk} = \boldsymbol{R}_{jk}/R_{jk}$ vecteur unitaire décrivant la position relative des deux spins nucléaires.

Le troisième terme qui représente les interactions d'échange est supposé négligeable par rapport à l'hamiltonien Zeeman et à l'hamiltonien dipolaire. Dans des champs appliqués de l'ordre de grandeur du champ local nucléaire, nous ne devons pas négliger $\mathscr{H}_{\mathrm{II}}$ devant Z_{I}. Si l'on fait l'hypothèse de l'existence d'une température de spin dans le système nucléaire(8, 9) on peut montrer que, moyennant certaines hypothèses, on peut définir un temps de relaxation par la formule suivante :

$$\frac{\partial\langle\mathscr{H}_{\mathrm{I}}\rangle}{\partial t} = -\frac{\langle\mathscr{H}_{\mathrm{I}}\rangle - \langle\mathscr{H}_{\mathrm{I}}\rangle_0}{T_1} \tag{8}$$

dans laquelle les variations sont dues uniquement à la relaxation. $\langle\mathscr{H}_{\mathrm{I}}\rangle$ représente la valeur moyenne de l'énergie définie à partir de la matrice densité

$$\rho = \frac{\exp\left(-\dfrac{\mathscr{H}_{\mathrm{I}}}{kT}\right)}{tr\exp\left(-\dfrac{\mathscr{H}_{\mathrm{I}}}{kT}\right)}$$

et

$$\langle \mathscr{H}_{\mathrm{I}} \rangle = tr\{\rho \mathscr{H}_{\mathrm{I}}\}$$

$\langle \mathscr{H}_{\mathrm{I}} \rangle_0$ est la valeur moyenne à l'équilibre thermique.

Considérés indépendamment, les deux hamiltoniens (6) et (7) évolueraient vers leur valeur à l'équilibre thermique suivant les lois exponentielles.(10)

$$\frac{\partial \langle \mathscr{Z}_{\mathrm{I}} \rangle}{\partial t} = -\frac{\langle \mathscr{Z}_{\mathrm{I}} \rangle - \langle \mathscr{Z}_{\mathrm{I}} \rangle_0}{T_{1\infty}} \tag{9}$$

$$\frac{\partial \langle \mathscr{H}_{\mathrm{II}} \rangle}{\partial t} = -\delta \frac{\langle \mathscr{H}_{\mathrm{II}} \rangle - \langle \mathscr{H}_{\mathrm{II}} \rangle_0}{T_{1\infty}} \tag{10}$$

Le temps de relaxation des spins nucléaires en champ élevé, $\mathscr{T}_{1\infty}$, est indépendant du champ appliqué et inversement proportionnel à la température. δ prend la valeur 2 lorsque les champs internes "vus" par les noyaux proches voisins sont totalement non corrélés, et 3 dans le cas contraire pour une interaction dipolaire.(10, 11)

Le résultat du calcul de REDFIELD,(10) et de HEBEL et SLICHTER(25) donne, pour la valeur du temps de relaxation;

$$\frac{1}{T_1} = \frac{1}{T_{1\infty}} \frac{H_0^2 + \delta H_{\mathrm{L}}^2}{H_0^2 + H_{\mathrm{L}}^2} \tag{11}$$

H_L est un champ local mesurant l'interaction entre les spins nucléaires et donné par :

$$H_{\mathrm{L}}^2 = H_0^2 \frac{tr\mathscr{H}_{\mathrm{II}}^2}{trZ_{\mathrm{I}}^2}$$

On trouve $H_{\mathrm{L}} = (5/3)\overline{\Delta H^2}$ où $\overline{\Delta H^2}$ est le second moment de Van Vleck calculé pour une poudre et qui vaut 0,63 G^2 dans le sodium métallique.

Effet Overhauser

La saturation de la raie de résonance électronique en champ élevé produit une augmentation du signal de résonance nucléaire de

$$A_\infty = \frac{\langle I_z \rangle}{I_0}.$$

Dans un champ magnétique appliqué faible, les énergies Zeeman et dipolaire sont du même ordre mais la saturation de la raie de résonance électronique n'affecte que l'énergie Zeeman. Le calcul(8) montre que, dans ce cas, l'augmentation de la polarisation $\langle I_z \rangle / I_0$ devient :

$$\frac{\langle I_z \rangle}{I_0} = \frac{H_0^2}{H_0^2 + H_{\mathrm{L}}^2} \frac{T_1}{T_{1\infty}} A_\infty. \tag{12}$$

Dans l'hypothèse d'un couplage purement scalaire tel que (1)

$$A_\infty = 1 - \frac{\gamma_e}{\gamma_n} s$$

$$s = \frac{S_0 - \langle S_z \rangle}{S_0}$$

$\langle S_z \rangle$ est la valeur moyenne de l'aimantation électronique, S_0 est sa valeur à l'équilibre thermique, s est le facteur de saturation de la raie électronique.

Avec une forme de raie électronique de Lorentz et des temps de relaxation

$$\tau_1 = \tau_2 = \tau = 15 \cdot 10^{-7} \text{s à } 4{,}2^\circ\text{K}$$

$$s = \frac{\gamma_e^2 H_1^2 \tau^2}{1 + \gamma_e^2 H_1^2 \tau^2} \tag{13}$$

(4), (12), (13) montrent que $1/H_n$ reste proportionnel à $1/H_1^2$, inverse de la puissance radiofréquence électronique

Absorption d'énergie par les spins nucléaires(12, 13)

Les spins nucléaires sont irradiés par un champ oscillant à la fréquence ν, d'amplitude H_A. La puissance absorbée pour une fréquence ν par les spins à la température T_I est $A(\nu)$ (14)

$$A(\nu) = \frac{\pi^2}{2kT_I} \nu^2 f(\nu) H_A^2 \tag{14}$$

$f(\nu)$ est une fonction de distribution construite à partir des éléments de matrice du moment magnétique total entre deux états $|k\rangle$ et $|l\rangle$ du système total d'énergies respectives E_k et E_l.(14, 15)

$$f(\nu)\Delta\nu = \sum_{\nu-(\Delta\nu/2)}^{\nu+(\Delta\nu/2)} |M_{kl}|^2$$

$$\nu - \frac{\Delta\nu}{2} < E_k - E_l < \nu + \frac{\Delta\nu}{2}.$$

L'absorption d'énergie correspond à une variation de température du système nucléaire. C'est cette variation de température qui, par l'intermédiaire de l'interaction (1), produit un déplacement de la fréquence de résonance électronique. La théorie de VAN VLECK(15) prévoit un pic d'absorption à la fréquence de Larmor des spins nucléaires, et d'autres d'intensités plus faibles pour les harmoniques de cette fréquence, et dans le cas où les énergies Zeeman et dipolaire sont seules importantes, CHENG(16) a trouvé, pour la raie à la fréquence de Larmor et celle à la fréquence double, des valeurs quadratiques moyennes de la largeur très voisines.

Pour faire une mesure des seconds moments de le raie de Larmor et de la raie à fréquence double, il est nécessaire de calculer $f(\nu) = A(\nu)/\nu^2$ en séparant dans $A(\nu)$ les contributions provenant de chacune des raies.

Le mode de détection ne nous permet pas d'observer l'absorption due à un champ oscillant parallèle au champ statique. En effet le champ audiofréquence oscillant produit une modulation du champ statique, donc de la fréquence de résonance électronique.

3. EXPERIMENTATION

Les expériences sont effectuées sur une poudre microcristalline d'hydrure de sodium contenant environ 1 % de métal. A 3300 G et à basse température on obtient une raie nucléaire de métal dont le second moment vaut 0,62 G^2 de forme typiquement gaussienne en accord avec la valeur 0,63 G^2 théorique. La fréquence de la raie de résonance des noyaux de métal est déplacée par rapport à celle des noyaux du sodium constituant le réseau de NaH d'une quantité correspondant à un déplacement relatif de $(1{,}1 \pm 0{,}05)10^{-3}$ en accord avec la valeur du déplacement de KNIGHT $1{,}13 \times 10^{-3}$.(17)

Alors qu'à 9200 Mc/s la raie de résonance électronique présente une forme asymétrique typique des particules conductrices(18) plus grandes que l'épaisseur de peau,(19) à 8 Mc/s la forme de raie électronique est bien symétrique (Fig. 1). La taille des particules est donc de l'ordre de 1 à 10 μ.

L'appareillage comprend essentiellement:(20)

(1). Un spectromètre à bobines croisées et fréquence fixe de 8.050 kc/s qui sert à saturer et à observer la résonance électronique. Un système de compensation électrique permet de choisir le mode d'observation du signal (absorption ou dispersion);

(2). Des bobines en position de Helmholtz qui produisent le champ appliqué;

(3). Un circuit audiofréquence qui permet la saturation de l'aimantation nucléaire.

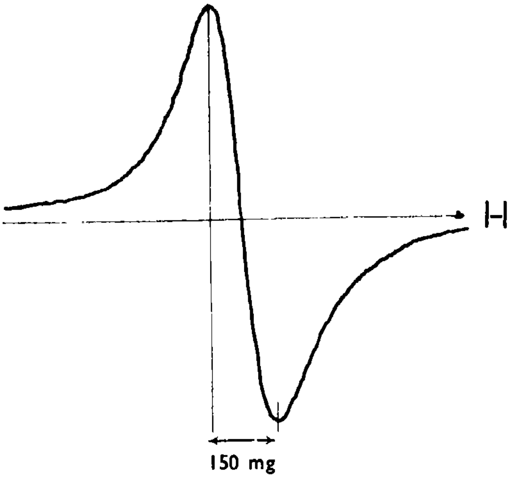

FIG. 1. Forme du signal de résonance électronique enregistré dans le mode absorption après une détection synchrone.

Nous observons, à l'aide d'une modulation à 20 c/s du champ statique appliqué et d'un dispositif de détection synchrone, le centre de la raie de résonance électronique dans le mode absorption. Par irradiation à une fréquence voisine de la fréquence de Larmor des noyaux, l'aimantation nucléaire est détruite de même que le champ H_n qui lui est proportionnel. Cette variation du champ "vu" par les électrons est compensée par l'application simultanée d'un champ statique produit dans des bobines de Helmholtz auxiliaires étalonnées avec précision. Nous ajustons la grandeur du champ statique auxiliaire de manière que les électrons "voient" le même champ total appliqué qu'auparavant sans destruction de l'aimantation nucléaire. Nous nous assurons que le champ auxiliaire a la valeur correcte lorsque l'enregistreur ne dévie pas lors de l'application simultanée du champ d'audiofréquence et du champ statique auxiliaire. Le facteur de saturation $s = (S_0 - \langle S_z \rangle)/S_0$ de la raie électronique ne varie pas pendant les diverses phases de l'opération.

L'augmentation Overhauser A qui lui est proportionnelle reste constante. La mesure du champ H_n par cette méthode a donc un sens.

En faisant varier la fréquence du champ de saturation nucléaire cette méthode permet d'obtenir la variation de la puissance absorbée par les spins nucléaires.

(4). Pour mesurer le temps de relaxation nucléaire $T_1(H)$ dans un champ appliqué H qui peut être différent du champ d'étude H_0, un dispositif approprié fournit une impulsion carrée de champ statique de durée déterminée τ.

En suivant la Fig. 2:

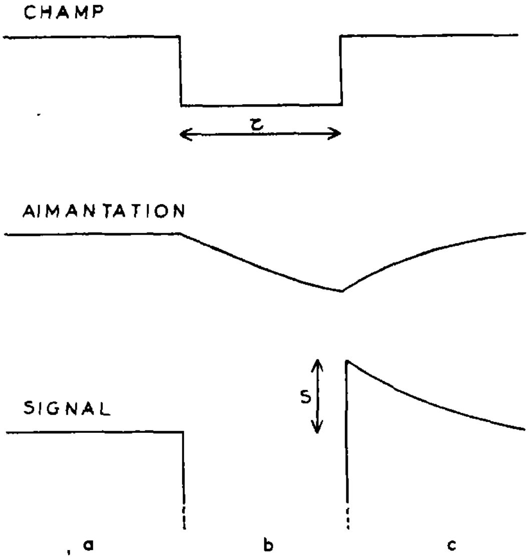

FIG. 2. Principe de la méthode de mesure des temps de relaxation nucléaire dans des champs appliqués qui sont de l'ordre du champ local nucléaire.

(a). L'aimantation nucléaire $\langle I_z \rangle$ prend sa valeur augmentée dans le champ $H_0 = 2{,}88$ G lors de la saturation électronique.

(b). Le champ appliqué devient H, la saturation de la raie électronique cesse. $\langle I_z(t) \rangle$ relaxe avec le temps de relaxation $T_1(H)$ vers sa valeur d'équilibre dans le champ H, négligeable comparée à $\langle I_z \rangle$ augmentée dans le champ H_0.

(c). Au bout du temps τ, le champ appliqué redevient H_0 et l'aimantation tend vers la valeur qu'elle avait en (a) avec le temps de relaxation $T_1(2{,}88)$.

L'observation à l'oscillographe de la différence des signaux aux temps τ et 0 en fonction de τ permet de mesurer $T_1(H)$.

4. RESULTATS ET DISCUSSION

D'après la théorie d'ELLIOTT(21) la largeur de raie électronique varie comme $1/T$ de 300°K à 4,2°K, ce qui est sensiblement vérifié.

Le temps de relaxation électronique de $1{,}1 \times 10^{-8}$ sec à 300°K a une variation proportionnelle à la température à partir de 4,2°K.

Par contre, au-dessous de 4°K, la raie cesse de se rétrécir. L'augmentation maximum en champ élevé A_∞ est inférieure à γ_e/γ_n que prévoit la seule interaction scalaire (1).(18) Déjà observée dans l'hydrure de lithium irradié,(22) cette réduction est due à un mécanisme de relaxation nucléaire(23) autre que (1) des noyaux métalliques.

Dans un champ de 3300 G, à 1,5°K, on peut constater une dispersion des temps de relaxation électronique créant ainsi une dispersion des facteurs de saturation (13) suivant les différents grains (Ryter, communication particulière).

Dans ces conditions, à cause de cette distribution, les déplacements étant petits par rapport à la largeur de raie, le déplacement observé n'est qu'une moyenne de déplacements des différents grains. La variation de $1/H_n$ cesse d'être rectiligne en fonction de $1/H_1^2$ (Fig 3) Pour obtenir la valeur maximum du déplacement Overhauser, nous extrapolons la courbe par sa tangente vers les puissances infinies.

$$H_n = 36{,}7 \pm 3{,}5 \text{ mG}.$$

Si nous supposons pour $f(\nu)$ une forme gaussienne qui, comme nous pourrons le vérifier, est une bonne approximation

$$A(\nu) \propto \nu^2 \exp - \frac{(\nu-\nu_0)^2}{2\overline{\Delta\nu_0^2}}$$

$\overline{\Delta\nu_0^2}$ est le second moment de VAN VLECK(15) pour une poudre. $\overline{\Delta\nu^2}$, tiré de l'évaluation de la largeur à mi-hauteur de la courbe, vaut, en gauss (Figs 4 et 5):

$$\overline{\Delta H^2} = \left[\frac{\Delta H_{1/2}}{2{,}36}\right]^2 \tag{15}$$

$$\overline{\Delta H^2} = 0{,}59 \pm 0{,}05 \text{ G}^2$$

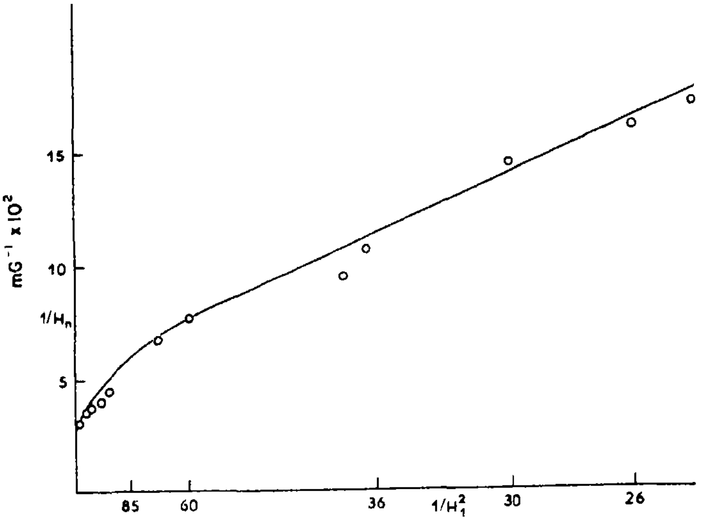

FIG. 3. Variation de l'inverse du champ nucléaire moyen produit par les noyaux en fonction de l'inverse de la puissance radiofréquence électronique. Des valeurs en milligauss du champ tournant H_1 sont portées en abscisses.

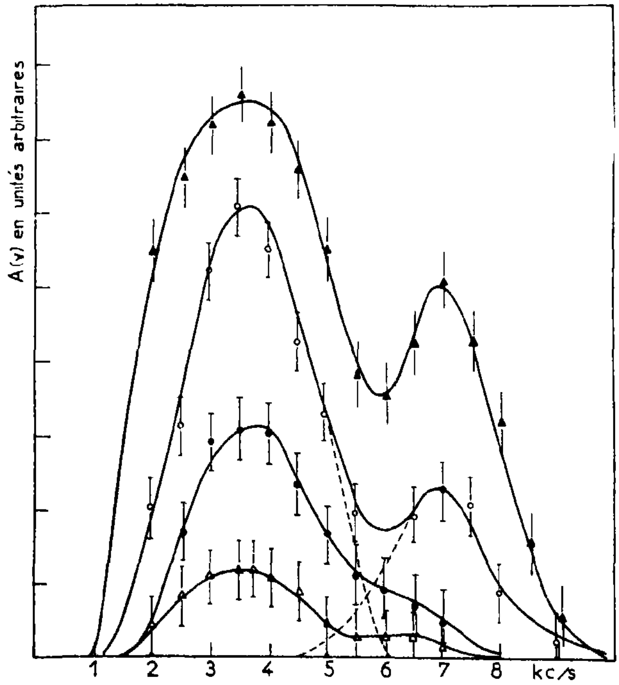

FIG. 4. Variation de l'absorption d'énergie par les spins nucléaires en fonction de la fréquence du champ audiofréquence H_A pour diverses valeurs de son intensité

▲ $H_A = 23$ mG ○ $H_A = 10$ mG
● $H_A = 5$ mG △ $H_A = 2{,}5$ mG

Pour $H_A = 10$ mG les contributions de l'absorption près de la fréquence de Larmor, et de sa première harmonique, sont séparées.

en bon accord avec les résultats d'ANDERSON(12) et la valeur théorique de 0,63 G^2.

Nous observons distinctement, d'après la Fig. 4, que, pour des puissances audiofréquences croissantes, la raie $2\nu_0$ se sature moins rapidement que la raie ν_0.

On vérifie bien la loi (11) de variation de T_1T en fonction du champ appliqué (Fig. 6)

$$A\ 3300\ \mathrm{G} \qquad T_1T = 5{,}08 \pm 0{,}15\ \mathrm{sec}$$

$$A\ 2{,}88\ \mathrm{G} \qquad T_1T = 4{,}5\ \pm 0{,}12\ \mathrm{sec}$$

Ces deux valeurs déterminent le facteur de corrélation δ de la loi (11) qui peut s'écrire

$$T_1T = (T_1T)_\infty \frac{H^2+(5/3)\overline{\Delta H^2}}{H^2+\delta(5/3)\overline{\Delta H^2}} \qquad (16)$$

$$\overline{\Delta H^2} = 0{,}63\ \mathrm{G}^2$$

$$\delta = 2{,}15 \pm 0{,}06$$

δ est le rapport des temps de relaxation en champ élevé et en champ nul pour une température donnée du réseau. Cette valeur expérimentale est en très bon accord avec l'estimation théorique obtenue par WOLFF:(24) 2,1 pour le sodium.

D'après la formule (12) l'augmentation en champ faible est réduite par le facteur

$$\frac{H_0^2}{H_0^2+H_\mathrm{L}^2}\,\frac{T_1(H_0)}{T_{1\infty}}.$$

Avec la détermination de $T_1(2{,}88)$ et $H_\mathrm{L}^2 = \frac{5}{3}\,\overline{\Delta H^2}$ ce facteur est égal à 0,78 ± 0,03.

A 3370 G et à la température de 1,57°K, RYTER trouve, pour le déplacement augmenté extrapolé à saturation électronique infinie(23)

$$H_n \doteq 64 \pm 3\ \mathrm{G}$$

Le déplacement naturel sans effet Overhauser de la raie de résonance électronique mesuré par RYTER vaut, à 1,57°K, d'après la Réf. 18.

$$H_{n0} = 29 \pm 1\ \mathrm{mG}$$

L'augmentation en champs élevés :

$$A_{H\text{élevés}} = \frac{H_n}{H_{n0}} = 2.200$$

A 2,88 G :

$$H_n = 36{,}7 \pm 3{,}5\ \mathrm{mG}$$

et

$$H_{n0} = (25 \pm 2)\ 10^{-3}\ \mathrm{mG}$$

L'augmentation en champs faibles :

$$A_{(\text{faibles})} = \frac{H_n}{H_{n0}} = 1465.$$

Nous trouvons donc un rapport des augmentations en champs faibles et en champs élevés qui vaut 0,60 ± 0,30. L'accord avec la valeur 0,78 déterminée à partir de $T_1(2{,}88)$ et de la formule (12) est médiocre. Cela provient de l'incertitude sur la valeur du champ nucléaire H_n augmenté, qui est probablement sous-estimé en champs faibles. Il faudrait, pour justifier la validité de l'extrapola-

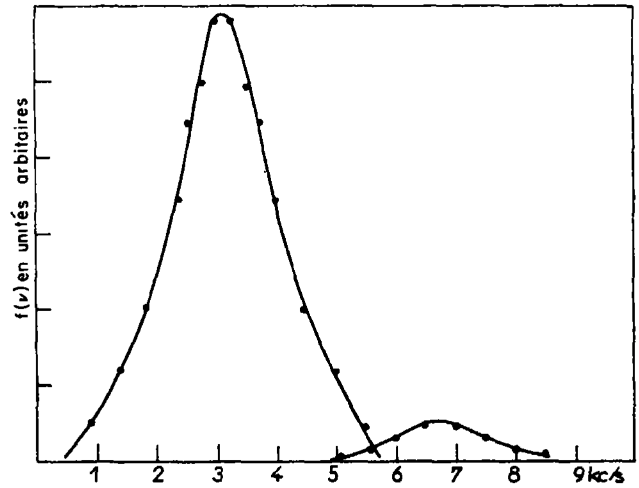

FIG. 5. Forme de la courbe $f(\nu)$ proportionnelle à $A(\nu)/\nu^2$ pour $H_A = 10$ mG.

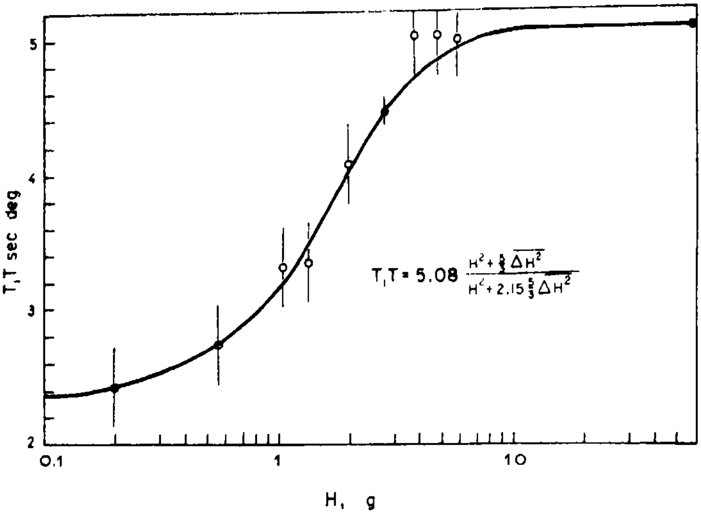

Fig. 6. Variation du temps de relaxation nucléaire de ^{23}Na en fonction du champ magnétique à la température de 1,5°K. La courbe est tracée pour la valeur $\delta = 2{,}15$ déterminée à l'aide des valeurs des temps de relaxation dans un champ appliqué de 2,88 G, et dans un champ appliqué grand par rapport au champ local nucléaire $\overline{\Delta H^2} = 0{,}63$ G^2.

tion de la courbe $1/H_n(1/H_1^2)$ (Fig 3) pour une puissance infinie, obtenir des résultats de mesure à des puissances de radiofréquence difficiles à obtenir à basse température.

5. CONCLUSION

Les résultats expérimentaux obtenus pour la relaxation nucléaire confirment une fois de plus l'hypothèse de la température de spin. Ils sont assez proches des résultats de Redfield et Anderson(26) qui utilisaient un coefficient de corrélation $\delta = 2{,}28$ au lieu de 2,15.

La variation de l'absorption d'énergie des spins nucléaires en fonction de la fréquence d'irradiation met clairement en évidence le satellite d'absorption de Van Vleck. La précision n'est toutefois pas suffisante pour permettre une étude quantitative sérieuse dans une région de champs appliqués où la théorie est délicate.

Compte tenu de la sous-estimation de la valeur du champ nucléaire augmenté, l'accord de la valeur expérimentale de la réduction de l'augmentation Overhauser en champs faibles avec la valeur théorique 20 pour cent de la formule d'Abragam(6) peut être considéré comme assez satisfaisant.

Remerciements—Nous exprimons ici toute la reconnaissance et les remerciements que nous tenons à adresser à tous nos camarades de l'équipe de résonance magnétique du laboratoire de Saclay, et plus particulièrement à Monsieur le Professeur Abragam qui nous a suggéré cette étude et a constamment dirigé avec bienveillance nos travaux. Les suggestions de Messieurs J. Winter, Ch. Ryter et I. Solomon nous ont été fort précieuses et nous les en remercions.

REFERENCES

1. Holcomb D. F. et Norberg R. E., *Phys. Rev.* **98**, 1074 (1955).
2. Overhauser A. W., *Phys. Rev.* **92**, 411 (1953).
3. Kittel C., *Phys. Rev.* **95**, 589 (1954).
4. Carver T. R. et Slichter C. P., *Phys. Rev.* **102**, 975 (1956).
5. Ryter Ch., *Phys. Rev. Letters* **3**, 338 (1959); **5**, 10 (1960).
6. Abragam A., *C.R. Acad. Sci. Paris* **254**, 3848 (1962).
7. Solomon I., *Comptes rendus du* 11*ème Colloque Ampère, Eindhoven* 1962. North Holland, Amsterdam (1963).
8. Abragam A., *Principles of Nuclear Magnetism*, Oxford University Press, London (1961).
9. Abragam A. et Proctor W., *Phys. Rev.* **109**, 1441 (1958).
10. Redfield A. G., *I.B.M. Journal* 1957,
11. Solomon I., *Phys. Rev.* **127**, 78 (1962).
12. Anderson A. C., *Phys. Rev.* **115**, 863 (1959).

13. ANDERSON A. C., *Phys. Rev.* **125,** 1517 (1962).
14. BROLER L. J., *Physica* **10,** 801 (1943).
15. VAN VLECK J. H., *Phys. Rev.* **74,** 1168 (1948).
16. CHENG H., *Phys. Rev.* **124,** 1359 (1961).
17. KNIGHT W. D., *Solid-State Phys.* **2,** 93 (1956), et communication particulière.
18. RYTER Ch., *Phys. Letters,* **4,** 69 (1963).
19. DYSON F. J., *Phys. Rev.* **98,** 349 (1955).
20. JEROME D., *Thèse 3e cycle,* Université de Paris, Faculté des Sciences d'Orsay.
21. ELLIOTT R. J., *Phys. Rev.* **96,** 226 (1954).
22. SCHUMACHER R. T. et HALL J. L., *Phys. Rev.* **125,** 428 (1962).
23. RYTER Ch. (à paraître).
24. WOLFF P. A., *Phys. Rev.* **129,** 84 (1963).
25. HEBEL L. C. et SLICHTER C. P., *Phys. Rev.* **113,** 1504 (1959).
26. REDFIELD A. G. et ANDERSON A. C., *Phys. Rev.* **116,** 583 (1959).

J. Phys. Chem. Solids Pergamon Press 1963. Vol. 24, pp. 1567–1575. Printed in Great Britain.

Z-BANDS IN KCl*

M. KLEEFSTRA

Compagnie Générale de T.S.F., Paris

(*Received* 20 *May* 1963)

Abstract—The oscillator strength of the *F*-centre has been chemically determined as $f = 0{\cdot}93 \pm 0{\cdot}11$. From the transformation of *F*- into Z_1- and Z_2-centres, the values of *f* of the latter were estimated to be: $0{\cdot}9 \pm 0{\cdot}2$. The ratio of the electron capture cross-sections in the formation of Z_1- and *F*-centres respectively was found to be 0·15. Under irradiation with visible light, a stationary state $F \rightleftarrows Z_1$ is established, which depends on the wave-length of the light. From the thermal decomposition of Z_1- into *F*- and Z_2- centres, which has an activation energy of 1·7 eV, it was concluded that Z_1- and Z_2-centres are formed from the same type of Sr centres. The dichroism Z_1–Z_4 was found to be analogous to the *F*–*M* dichroism. These results are explained by a scheme where a Z_1-centre is a combination of a *F*-centre with a complex of a Sr-atom and a *K*-vacancy, and where a Z_2-centre is represented as a Z_1-centre which has lost a cation–anion vacancy pair. The mobility of the anion vacancy left by optical ionization of a *F*-centre is attributed to the gain in polarization energy due to the relaxation of the lattice.

1. INTRODUCTION

COLOUR centres in KCl are considered(1) as combinations of electrons or holes with lattice defects, such as vacant sites, vacancy pairs or impurity centres. In pure KCl, *F*-, *M*-, *N*- and *R*-centres occur which are characterized by their absorption bands. KCl contaminated with divalent impurities shows in addition Z_1, Z_2, Z_3 and Z_4 absorption bands. The structure of most of the colour centres is still a subject of discussion. Only the structure of the *F*-centre, proposed by SCHOTTKY and DE BOER,(1) is generally accepted. It consists of an anion vacancy having captured an electron. The *M*-centre is very probably a combination of two *F*-centres (VAN DOORN(2)).

In all work on colour centres, the number of colour centres is calculated by Smakula's formula: $n_0 f = 1{\cdot}06 \times 10^{16} k_m H$, where n_0 is the chemical number of colour centres, *f* their oscillator strength, k_m the extinction coefficient at the maximum and *H* the half-way width. Since the values given by various authors for the oscillator strength of the *F*-centre, differ considerably, we first redetermined this quantity; then experiments were done on the transformation between *F* and other centres.

After the experiments of PICK(4) who was the first to obtain the *Z*-bands, CAMAGNI and CHIAROTTI,(5–6) COLE and FRIAUF(7) and WEST and COMPTON,(18) have investigated the nature of *Z*-centres. In order to get a deeper insight into these centres, our experiments were done on crystals containing a relatively large variety of numbers of impurity centres and *F*-centres.

We shall use the nomenclature proposed by KRÖGER *et al.*,(8) in which normal lattice sites are neutral and defects can be charged or neutral; e.g. a normal K^+ ion is considered as neutral but an anion vacancy (V_{Cl}^+) and a *F*-centre (V_{Cl}) are, respectively, positively charged and neutral. Thus we have:

V_K	vacant K-site
V_{Cl}^+	vacant Cl-site
$(V_K V_{\mathrm{Cl}})$	vacancy pair
Sr_K^+	Sr^{2+} ion occupying a K-site
$(\mathrm{Sr}_K V_K)$	pair of a vacant K-site and a Sr_K^+
e	electron in the conduction band
$h\nu$	light quantum

2. EXPERIMENTAL

All the crystals were grown by means of KYROUPOULOS's technique(9) and pieces of 7×7×15 mm were coloured additively by heating them in K vapour. From these crystals, samples

---

[*] Part of the contents of a thesis by M. Kleefstra entitled "Recherches sur les centres colorés en KCl contaminé par Sr" (Groningen 1961).

were cleaved and heated for 2 min at 450°C before measuring their absorption spectra. The latter were measured then at liquid air temperature, with a band width of 0·01 eV and an accuracy of about 5 per cent in the percentage transmission. Experiments with polarized light were carried out by using Polaroid HN32 or a nicol. The stoichiometric excess of K was determined after dissolving the crystals in 0·000054 HCl by measurement of the pH and comparison with a calibration curve. The amount of Sr was determined in a flame photometer.

3. OSCILLATOR STRENGTHS AND NUMBERS OF DEFECTS

The "optical" numbers of *F*-centres were calculated by means of Smakula's formula and the oscillator strength was obtained by dividing the optical number by the chemical number. The results are given in Table 1.

As a mean value, $f = 0{\cdot}93 \pm 0{\cdot}11$ was obtained, which is in accordance with the recent value of DOYLE(10) i.e. $f = 0{\cdot}91 \pm 0{\cdot}12$.

When *F*-centres are transformed into Z_1- or Z_2-centres, the integrated absorption does not change more than 10 per cent, which indicates that the oscillator strengths of Z_1- and Z_2-centres are within about 20 per cent equal to the oscillator strength of *F*-centres. In the following Sections, the optical numbers of *F*-, Z_1- and Z_2-centres will be used

The number of vacant lattice sites in stoichiometric KCl in thermal equilibrium at 600°C, can be estimated as $n(V_K^-) = 1{\cdot}4 \times 10^{17}$.(11) It is quite probable that this amount is still present at room temperature in quickly cooled crystals (cf. Ref. 12).

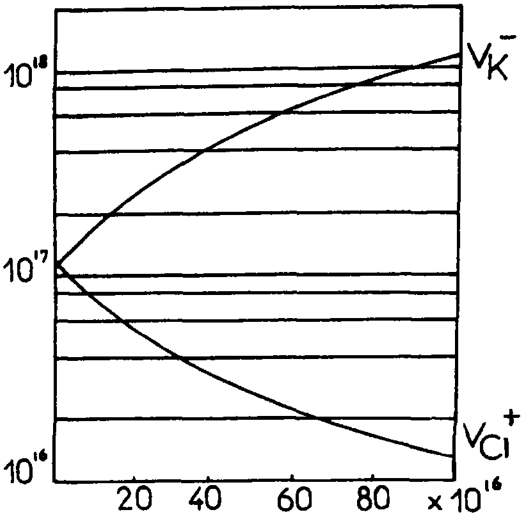

FIG. 1. Numbers of vacant sites pro cm³ at 600°C as a function of the Sr concentration.

In KCl contaminated with Sr at 600°C, an equilibrium exists between V_K^-, V_{Cl}^+ and Sr_K^+. The amount of Sr_K^+ determines the amounts of V_K^- and V_{Cl}^+ as is shown in Fig. 1. At room temperature the numbers $n(V_K^-)$, $n(V_{Cl}^+)$ and $n(Sr_K^+)$ are determined by the amount of Sr

Table 1. Determination of the oscillator strength of the F-centre. The "optical" numbers are the averages of 2 or 3 measurements, the "chemical" numbers were obtained by a single measurement.

Crystal	Number in 10^{16}/cm³		f
	chemical	optical	
56–12–13	32	33	1·03
56–12–13	30	33	1·10
56–8–16	36	30	0·83
56–8–16	39	30	0·77
56–8–3	18	17·5	0·97
56–8–3	17	17·5	1·03
56–9–18	67	59	0·88
56–9–18	67	59	0·88

present and by the temperature from which the equilibrium has been frozen in, i.e. 600°C in this case. Little is known about the way these defects are present at room temperature. The existence of $\mathrm{Sr_K}V_\mathrm{K}$ complexes is proved by their dielectric relaxation;(13) since the $(V_\mathrm{K}V_\mathrm{Cl})$ complexes have an association energy higher than the $(\mathrm{Sr_K}V_\mathrm{K})$ pair has,(20) it seems reasonable to assume that the $(V_\mathrm{K}V_\mathrm{Cl})$ complexes are completely associated.

Myake and Susuki(14) have shown that a precipitation in quantities of some thousands of $CaCl_2$ units may occur in NaCl. Similarly it is very plausible to suppose that in KCl crystals, strongly contaminated by Sr, only $20\cdot10^{16}$ atoms of Sr are atomically dispersed and that the remaining Sr is in a precipitated form. This will be shown in Section 5.

4. ELECTRON-CAPTURE CROSS-SECTIONS

For reasons given in the Discussion, we represent a Z_1-centre by $(\mathrm{Sr_K}V_\mathrm{K}V_\mathrm{Cl})$. On irradiating in the F-band, a light quantum absorbed by a F-centre puts an electron into the conduction band (cf. 1). This electron will be captured either by a $(\mathrm{Sr_K}V_\mathrm{K})$ pair, or by a $(V_\mathrm{K}V_\mathrm{Cl})$ pair. It may be assumed that in the first case a Z_1-centre is formed according to (2a) and 2b). Schematically:

$$V_\mathrm{Cl}+h\nu \rightarrow V_\mathrm{Cl}^{+}+e$$

$$(\mathrm{Sr_K}V_\mathrm{K}) + e + V_\mathrm{Cl}^{+} \rightarrow (\mathrm{Sr_K}V_\mathrm{K}V_\mathrm{Cl}) \qquad (1)$$

$$(V_\mathrm{K}V_\mathrm{Cl}) + e \rightarrow V_\mathrm{Cl} + V_\mathrm{K}^{-} \qquad (2a)$$

$$V_\mathrm{K}^{-} + V_\mathrm{Cl}^{+} \rightarrow (V_\mathrm{K}V_\mathrm{Cl}) \qquad (2b)$$

As the F- and Z_1-bands partially overlap, there is also a small absorption in the Z_1-band which can produce a ionization of Z_1-centres.(7)

The latter process will be discussed in Section 5; in the present Section we only consider the transformation of F-centres into Z_1-centres under the influence of quanta absorbed by the F-centres. If a_F/aZ_1 is the proportion of quanta absorbed by equal numbers of F- and Z_1-centres respectively, q the total number of absorbed quanta, σ the ratio of electron-capture cross-sections in the reactions (1) and (2), $n(\mathrm{Sr_K}V_\mathrm{K})$ and $n(V_\mathrm{K}V_\mathrm{Cl})$ the numbers of pairs and $n_0(\mathrm{Sr_K}V_\mathrm{K})$... the numbers of pairs at $q = 0$, we have:

$$\frac{dn(Z_1)}{dq} = \frac{\sigma n(\mathrm{Sr_K}V_\mathrm{K})}{n(V_\mathrm{K}V_\mathrm{Cl})+\sigma n(\mathrm{Sr_K}V_\mathrm{K})} \cdot \frac{n(F)\cdot a_F}{n(F)\cdot a_F+n(Z_1)\cdot a_{Z_1}}$$

As $n(V_\mathrm{K}V_\mathrm{Cl})$ does not change during this reaction, we have:

$$\frac{dn(Z_1)}{dq} = \frac{\sigma\{n_0(\mathrm{Sr_K}V_\mathrm{K})-n(Z_1)\}}{n_0(V_\mathrm{K}V_\mathrm{Cl})+\sigma\{n_0(\mathrm{Sr_K}V_\mathrm{K})-n(Z_1)\}} \cdot \frac{n(F)\cdot a_F}{n(F)a_F+n(Z_1)a_{Z_1}}$$

For the beginning of the reaction $(q = 0\ n(Z_1) = 0)$, we find:

$$\left\{\frac{dn(Z_1)}{dq}\right\}_0 = \frac{\sigma n_0(\mathrm{Sr_K}V_\mathrm{K})}{n_0(V_\mathrm{K}V_\mathrm{Cl})+\sigma n_0(\mathrm{Sr_K}V_\mathrm{K})}$$

Crystals with different concentrations of F-centres and Sr impurities, have been irradiated, with known amounts of quanta, at 25°C. During the irradiation, almost all quanta were absorbed; losses by reflection and transmission were less than 10 per cent. The results are shown in Fig. 2. It can be seen that

$$\left\{\frac{dn(Z_1)}{dq}\right\}_0$$

is approximately the same for the 4 samples (0·4, 0·25, 0·25 and 0·35 respectively) and is thus independent of the concentrations of F-centres and Sr impurities. The fact that there is no dependence between

$$\left\{\frac{dn(Z_1)}{dq}\right\}_0$$

and the Sr concentrations suggests that in all samples the number of atomically dispersed Sr atoms $n_0(\mathrm{Sr_K}V_\mathrm{K})$ is the same. In Section 5, it will be shown that $n_0(\mathrm{Sr_K}V_\mathrm{K}) = 20\cdot10^{16}/\mathrm{cm}^3$. This makes (cf. Fig. 1) $n_0(V_\mathrm{K}V_\mathrm{Cl}) = 7\cdot10^{16}/\mathrm{cm}^3$, which gives $\sigma \simeq 0{\cdot}15$. This value will be discussed in Section 8.

Camagni and Chiarotti(5) found $\sigma \simeq 1$, but they used only low F-centre concentrations, $3\cdot10^{16}/\mathrm{cm}^3$, and assumed that $n(\mathrm{Sr_K^+}) = 2\cdot10^{16}$

and $n(V_{\text{Cl}}^{+}) = 1 \cdot 10^{17}$ defects were able to form Z_1- and F-centres. In the case of high F-centre concentrations, $n(Z_1)$ approaches $20 \cdot 10^{16}/\text{cm}^3$; therefore their assumptions are not valid. Their value of

$$\left\{\frac{\mathrm{d}n(Z_1)}{\mathrm{d}q}\right\}_0 = 0{\cdot}2$$

however, agrees reasonably with our value.

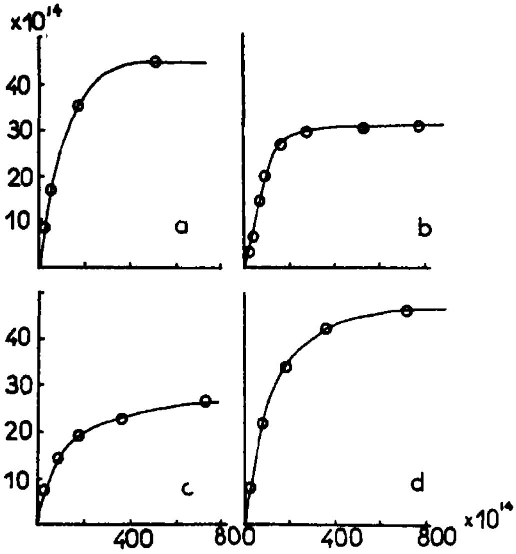

FIG. 2. Absolute numbers of Z_1-centres per cm² vs. number of absorbed quanta per cm².
(a) Thickness 0·94 mm 87×10^{14} F-centres
(b) Thickness 1·14 mm 70×10^{14} F-centres
(c) Thickness 0·18 mm 183×10^{14} F-centres
(d) Thickness 0·32 mm 180×10^{14} F-centres
(a) and (b) contained 400×10^{16} at Sr/cm³
(c) and (d) contained 50×10^{16} at Sr/cm³.

5. STATIONARY STATE $F \rightleftarrows Z_1$

A complete conversion of F- into Z_1-centres by irradiation was found to be impossible, even for small F-centre concentrations and large Sr concentrations. Therefore it must be assumed that the reaction $Z_1 \rightarrow F$ can also take place. Similar to the reaction $F \rightarrow Z_1$ discussed in Section 4, the reverse reaction can be represented as follows:

$$(\text{Sr}_{\text{K}}V_{\text{K}}V_{\text{Cl}}) + h\nu \rightarrow (\text{Sr}_{\text{K}}V_{\text{K}}) + V_{\text{Cl}}^{+} + e \qquad (1)$$

$$(\text{Sr}_{\text{K}}V_{\text{K}}) + e + V_{\text{Cl}}^{+} \rightarrow (\text{Sr}_{\text{K}}V_{\text{K}}V_{\text{Cl}}) \qquad (2)$$

$$(V_{\text{K}}V_{\text{Cl}}) + e \rightarrow V_{\text{Cl}}^{+}V_{\text{K}}^{-} \qquad (2a)$$

$$V_{\text{K}}^{-} + V_{\text{Cl}}^{+} \rightarrow (V_{\text{K}}V_{\text{Cl}}) \qquad (2b)$$

For the rate of transformation $Z_1 \rightarrow F$, we thus obtain:

$$\frac{\mathrm{d}n(F)}{\mathrm{d}q} = \frac{n(V_{\text{K}}V_{\text{Cl}})}{n(V_{\text{K}}V_{\text{Cl}}) + \sigma n(\text{Sr}_{\text{K}}V_{\text{K}})} \cdot \frac{\eta n(Z_1)a_{Z_1}}{n(Z_1)a_{Z_1} + n(F)a_F} \qquad (3)$$

in which η is the probability that an electron is released from a Z_1-centre by the absorption of a light quantum. Other reactions which occur simultaneously, such as the formation of M- and Z_1-centres, were found to proceed much slower than the transformations $F \rightarrow Z_1$ and $Z_1 \rightarrow F$, and have been neglected here. A stationary state is obtained when

$$\frac{\mathrm{d}n(Z_1)}{\mathrm{d}q} = \frac{\mathrm{d}n(F)}{\mathrm{d}q},$$

from which condition the following relation is derived:

$$\eta \cdot n(V_{\text{K}}V_{\text{Cl}}) \cdot n(Z_1) \cdot a_{Z_1} = n(\text{Sr}_{\text{K}}V_{\text{K}}) \cdot n(F) \cdot a_F \cdot \sigma \qquad (4)$$

or:

$$\frac{n(Z_1)}{n(F)} = \frac{a_F}{a_{Z_1}} \cdot \frac{\sigma}{\eta} \cdot \frac{n_0(\text{Sr}_{\text{K}}V_{\text{K}}) - n(Z_1)}{n_0(V_{\text{K}}V_{\text{Cl}})} \qquad (5)$$

For the light used to irradiate the F band ($h\nu = 2{\cdot}27$ eV), the ratio $a_F/a_{Z_1} = 2{\cdot}3$.

As σ/η is constant, the maximum number of Z_1-centres that can be obtained will approach $n_0(\text{Sr}_{\text{K}}V_{\text{K}})$ for high F-centre concentrations. Crystals, with Sr concentrations ranging from 22 to $400 \cdot 10^{16}/\text{cm}^3$ and with different F-centre concentrations (6 to $100 \cdot 10^{16}$), have been irradiated until the stationary state was reached. The values for $n(Z_1)$ showed no dependence on the Sr concentrations. The results are given in Fig. 3 and Table 1. As is shown in Fig. 3, the measurements can be represented by the drawn curve, which obeys the formula:

$$\frac{n(Z_1)}{n(F)\{20 \times 10^{16} - n(Z_1)\}} = 0{\cdot}065 \times 10^{16}$$

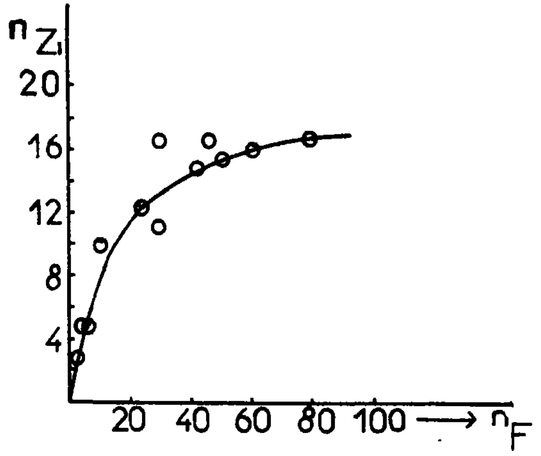

FIG. 3. Number of Z_1-centres in the stationary state, as a function of the number of F-centres in the stationary state, both in $10^{16}/\mathrm{cm}^3$.

A comparison with equation (5), in the form:

$$\frac{n(Z_1)}{n(F)\{n_0(\mathrm{Sr_K}V_\mathrm{K})-n(Z_1)\}} = \frac{a_F}{a_{Z_1}}\cdot\frac{\sigma}{\eta}\cdot\frac{1}{n_0(V_\mathrm{K}V_\mathrm{Cl})},$$

then, leads to the assumption that, in all samples, $20\times10^{16}(\mathrm{Sr_K}V_\mathrm{K})$ pairs are present and that the rest of the strontium is somehow precipitated. With $a_F/a_{Z_1} = 2{\cdot}3$ and $\sigma = 0{\cdot}15$, we calculate, from

$$\frac{a_F}{a_{Z_1}}\cdot\frac{\sigma}{\eta}\cdot\frac{1}{n_0(V_\mathrm{K}V_\mathrm{Cl})} = 0{\cdot}065\times10^{16},$$

the value $\eta \simeq 1$, which is valid for 2·27 eV light.

In Fig. 4 the dependence of the ratio $n(Z_1)/n(F)$ on a_F/a_{Z_1}, that is on the wavelength of the light used for the irradiation, is shown.

6. THERMAL DECOMPOSITION OF Z_1- CENTRES

The Z_1-band is not very stable, even at room temperature, and decomposes at 50°C at an appreciable rate into Z_2- and F-centres. Z_2-centres can also be obtained directly from F-centres by thermal decomposition. The thermal equilibrium $F \rightleftarrows Z_2$ was studied by CAMAGNI.[6] We studied the thermal decomposition of Z_1-centres at 50°C, because the thermal reactions $F \rightarrow Z_2$ and $Z_2 \rightarrow F$ are still very slow at this temperature (cf. Ref. 6). The results of the measurements are given in Fig. 5.

It is possible to estimate, for the reaction

$$\left(Z_1 \begin{smallmatrix}\nearrow F\\ \searrow Z_2\end{smallmatrix}\right)$$

an average activation energy by determining the reaction speed as a function of temperature. The

Table 2. *Defects in additively coloured* KCl *containing* Sr. *In the columns* Sr, *F and* Z_2, *the numbers before irradiation are given; in the* 4 *next columns the numbers afer irradiation are given; in all cases in* $10^{16}/\mathrm{cm}^3$.

Crystal	Sr	F	Z_2	F	Z_1	M	Z_4
57-2-12a	400	9	0	4·5	4·8		
57-2-12b	400	6	0	3·4	2·7		
56-8-15	22	19	0	14	7	1·4	0
56-8-6	25	13	0	6	5	0·4	0·2
56-8-7	27	25	0	11	6	1·3	0·5
56-8-16	30	30	0	16	7	1·8	0
56-9-18	27	59	0	46	17	4·8	0
56-8-29	49	43		24	12	2·1	0
56-12-20	64	33	0		11		
56-12-21	65	29		12	10	1·1	0·6
56-8-30	67	54	0	30	17	3·1	2·5
56-9-21	70	66	12	51	16	3·2	0
56-12-12	80	56			14		
56-12-10	84	66	4	43	15	2·4	0
56-9-24	77	70	9	61	16	4·7	0
56-12-8	80	102			17		

reaction speed, for a given sample, was taken as $dn(Z_1)/dt$ for $t = 0$ and its logarithm is plotted vs. the reciprocal absolute temperature in Fig. 6. In this way the activation energy is found to be $E_a = 1{\cdot}7 \pm 0{\cdot}2$ eV.

Z_2-centres are also formed optically by irradiation in the F-band at 110°C. At this temperature the thermal reaction $F \rightarrow Z_1$ is slow, compared with the optical reaction. From Fig. 7 it is seen that in the optical formation at 110°C, the rate of

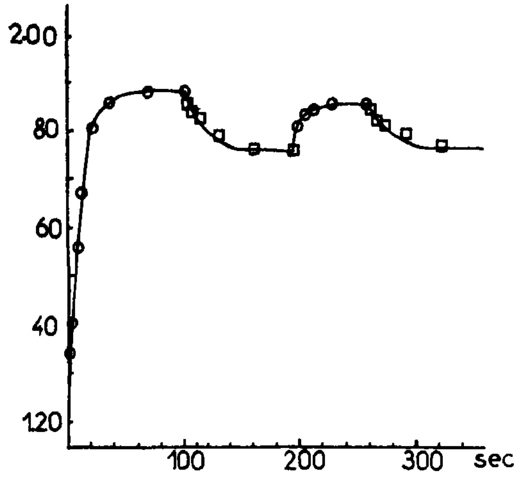

FIG. 4. Extinction coefficient for the Z_1-band vs. irradiation time.

□ 1·95 eV light

○ 2·27 eV light.

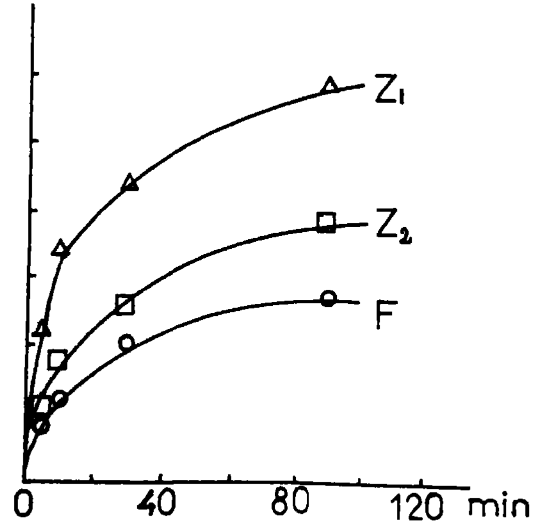

FIG. 5. Thermal destruction of Z_1-centres at 50°C. The decrease of the number of Z_1-centres and the increase of the numbers of Z_2- and F-centres are shown.

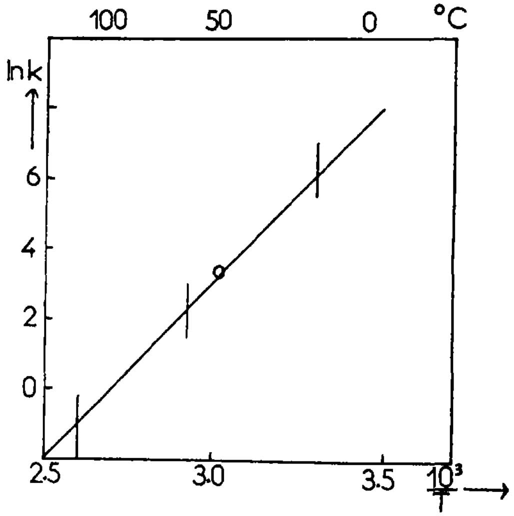

FIG. 6. Determination of the average activation energy in the thermal decomposition of Z_1-centres.

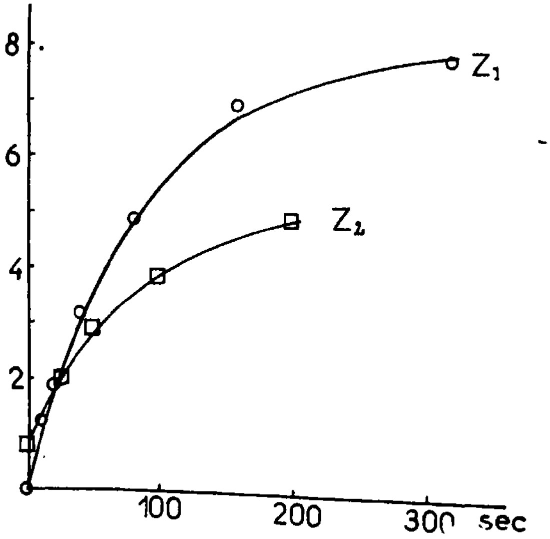

FIG. 7. Growth of Z_1-centres at 20°C compared with growth of Z_2-centres at 110°C.

formation of Z_2-centres and the ultimate yield are smaller than the rate of formation and yield for the optical transformation $F \rightarrow Z_1$ at 20°C. This makes it probable that in the optical formation of Z_2-centres, from F-centres at 110°C, first Z_1-centres are formed and that subsequently these Z_1-centres are transformed into Z_2- and F-centres by thermal decomposition, which at 110°C is very fast. This means that the same kind of Sr centres are responsible for the formation of either Z_1- or Z_2-centres.

7. DICHROISM

KANZAKI(15) and VAN DOORN and HAVEN(16) have shown that dichroism can only occur in the F-band when the M-band is present. In the pure F-band no dichroism can be introduced at all. Likewise we have found that no dichroism can be introduced in the Z_1- or Z_2-band in the absence of the Z_4-band. The irradiation with [001] or [011] polarized light, at 20°C and −180°C, produced only bleaching, but there was no polarizing effect.

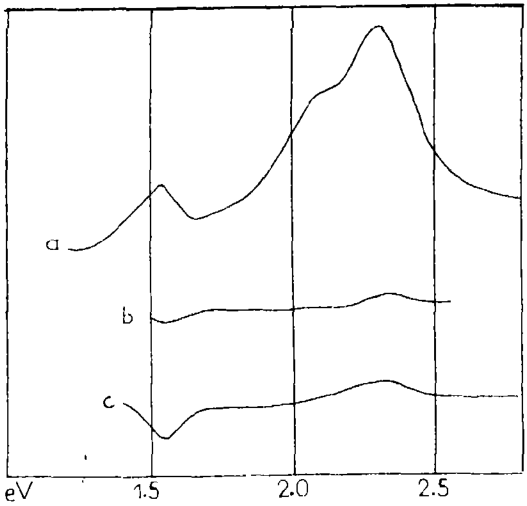

FIG. 8. (a) Absorption spectrum
(b) Dichroitic spectrum [010]–[001]
(c) Dichroitic spectrum [011]–[0$\bar{1}$1].

The Z_1-band can be polarized however, in the presence of the Z_4-band, just as the F-band can be polarized in the presence of the M-band. We did not succeed in obtaining an appreciable Z_4-band beside the Z_2-band: therefore a possible Z_2–Z_4 dichroism could not be detected.

At −180°C, in the interval 1·8–3·0 eV, we irradiated crystals containing Z_4-, M-, Z_1- and F-centres with [0$\bar{1}$1] and [001] polarized light. The absorption for [0$\bar{1}$1] decreased in the F- and Z_1-bands and increased in the M- and Z_4-bands. The total absorption and two dichroitic spectra are given in Fig. 8. The dichroitic spectra are obtained by plotting the difference in absorption-coefficients for the two directions of polarization as a function of wavelength. It appears that the [0$\bar{1}$1] dichroism is about 3 times as strong as the [001] dichroism. These experiments on the dichroism of the Z_1-band indicate that the mechanisms of the F–M dichroism on the one hand and the Z_1–Z_4 dichroism on the other hand, might be similar.

8. DISCUSSION

If we consider only the structure elements which probably have concentrations in excess of $10^{16}/\text{cm}^3$, the following models can be used *a priori* to explain the reaction $F \rightleftarrows Z_1$:

$$
\begin{array}{lll}
V_{\text{Cl}}+h\nu \rightarrow V_{\text{Cl}}^{+}+e & \text{Sr}_{\text{K}}^{+}+e \rightarrow \text{Sr}_{\text{K}} & \text{(i)} \\
\text{id.} & (\text{Sr}_{\text{K}}V_{\text{K}})+e \rightarrow (\text{Sr}_{\text{K}}V_{\text{K}})^{-} & \text{(ii)} \\
\text{id.} & (\text{Sr}_{\text{K}}V_{\text{K}})+e \rightarrow \text{Sr}_{\text{K}}+V_{\text{K}}^{-} & \text{(iii)} \\
 & V_{\text{K}}^{-}+V_{\text{Cl}}^{+} \rightarrow (V_{\text{K}}V_{\text{Cl}}) & \\
\text{id.} & (\text{Sr}_{\text{K}}V_{\text{K}})+e+V_{\text{Cl}}^{+} \rightarrow (\text{Sr}_{\text{K}}V_{\text{K}}V_{\text{Cl}}) & \\
 & & \text{(iv)}
\end{array}
$$

PICK(4) proposed (ii) and SEITZ(17) (i) and (iii), but we think that (iv) is the most probable model, for the following reasons:

(a) As we shall see later on, Sr_{K} seems to be the most probable model for the Z_2-centre. This excludes (i) and (iii) for the formation of Z_1-centres.

(b) It was found by CAMAGNI and CHIAROTTI(5) and confirmed by us that irradiation by X-rays of KCl crystals containing Sr but no F-centres, does not produce Z-centres. This makes (i) and (ii) rather unlikely because X-ray irradiation produces electrons in the conduction band.

(c) The thermal decomposition of Z_1-centres favours model (iv). The optical ionization of a Z_1-centre removes the electron and cannot lead to the formation of Z_2-centres; this applies to the models (i), (ii), (iii) and (iv); but the thermal agitation in (iv) can remove either an electron with a V_{Cl}^{+}, by which process a F-centre is formed, or a $(V_{\mathrm{K}}V_{\mathrm{Cl}})$ pair resulting in formation of a Z_2-centre.

(d) It can be understood from mechanism (iv) that the cross-section for the formation of Z_1-centres by electron-capture is smaller than that for the formation of F-centres, because in the second of the two reactions concerned:

$$(V_{\mathrm{K}}V_{\mathrm{Cl}})+e \rightarrow V_{\mathrm{Cl}}+V_{\mathrm{K}}^{-} \qquad (1)$$

$$(\mathrm{Sr_K}V_{\mathrm{Cl}})+e+V_{\mathrm{Cl}}^{+} \rightarrow (\mathrm{Sr_K}V_{\mathrm{K}}V_{\mathrm{Cl}}) \qquad (2)$$

the $(\mathrm{Sr_K}V_{\mathrm{K}})^{-}$ pair may lose its captured electron before the complex is stabilized by the association with V_{Cl}^{+}.

The formation of Z_1-centres is, in model (iv), similar to the formation of M-centres, according to the mechanism put forward by VAN DOORN.(2)

Formation of M-centres

$$V_{\mathrm{Cl}}+h\nu \rightarrow V_{\mathrm{Cl}}^{+}+e$$

$$V_{\mathrm{Cl}}+e \rightarrow V_{\mathrm{Cl}}^{-}$$

F'-centre unstable at 20°C and reacting according to either

$$V_{\mathrm{Cl}}^{-} \rightarrow V_{\mathrm{Cl}}+e \text{ or } V_{\mathrm{Cl}}^{-}+V_{\mathrm{Cl}}^{+} \rightarrow (V_{\mathrm{Cl}}V_{\mathrm{Cl}}) = M\text{-centre}$$

Formation of Z_1-centres

$$V_{\mathrm{Cl}}+h\nu \rightarrow V_{\mathrm{Cl}}^{+}+e$$

$$(\mathrm{Sr_K}V_{\mathrm{K}})+e \rightarrow (\mathrm{Sr_K}V_{\mathrm{K}})^{-}$$

centre unstable at 20°C and reacting according to either

$$(\mathrm{Sr_K}V_{\mathrm{K}})^{-} \rightarrow (\mathrm{Sr_K}V_{\mathrm{K}})+e$$

$$\text{or} \quad (\mathrm{Sr_K}V_{\mathrm{K}})^{-}+V_{\mathrm{Cl}}^{+} \rightarrow (\mathrm{Sr_K}V_{\mathrm{K}}V_{\mathrm{Cl}}) = Z_1\text{-centre}$$

The mobility of the V_{Cl}^{+}, left after the optical ionization of the F-centre, is in fact much larger than the mobility of an ordinary $V_{\mathrm{Cl}}{}^{+}$, because the relaxation of the lattice around the ionized F-centre makes an activation energy available. According to the Frank Condon principle, the optical excitation takes place so rapidly that the neighbouring ions do not move. For the complete ionization, the electron takes about 0·6 eV from the lattice (cf. 19). But after the removing of the electron, the ions adjacent to the vacancy are displaced over about 10 per cent of the lattice distance. The polarization energy, thus gained, is about 2 eV, which is larger than the activation energy for diffusion, and thus makes the V_{Cl}^{+} very mobile.

The Z_4–Z_1 dichroism is very analogous to the M–F dichroism; therefore it is convenient to consider a Z_1-centre as a F-centre adjacent to a $(\mathrm{Sr_K}V_{\mathrm{K}})$ pair, and a Z_4-centre as a M-centre adjacent to a $(\mathrm{Sr_K}V_{\mathrm{K}})$ pair. The $\mathrm{Sr_K}V_{\mathrm{K}}$ pair shifts the absorption maximum of the F- and M-centres about 0·1 eV towards the infrared.

We think that Pick's model of the Z_2-centre $\mathrm{Sr_K}$ is the best to account for:

(i) the impossibility to polarize either the luminescence(3) or the absorption of the Z_2-centre

(ii) the observation that the wavelength of absorption maximum of the Z_2-centre is more dependent on the character of the foreign ions (Ca, Sr, Ba) than the wavelength of the absorption maximum of the Z_1-centre.(4)

Moreover, the thermal decomposition of Z_1-centres is best explained by using Pick's model for the Z_2-centre. In our opinion, this decomposition consists in either the dissociation of an electron or that of a $(V_{\mathrm{K}}V_{\mathrm{Cl}})$ complex, for which we found an activation energy of about 1·7 eV. With Seitz's model, in the case of Z_2-centre formation, there is an attraction of a $(V_{\mathrm{K}}V_{\mathrm{Cl}})$ complex, for which the activation energy of diffusion has been calculated to be only 0·4 eV.

Acknowledgement—The author is much indebted to Prof. Dr. E. H. WIEBENGA for advice and stimulating discussions.

REFERENCES

1. SEITZ F., *Rev. mod. Phys.* **26,** 7 (1954).
2. VAN DOORN C. Z., *Phys. Rev. Letters* **4,** 236 (1960).
3. DALE COMPTON W., *Phys. Rev. Letters* **7,** 57 (1961).
4. PICK H., *Ann. Phys.* **35,** 73 (1939).
5. CAMPAGNI P. and CHIAROTTI G., *Nuovo Cim.* **11,** 1 (1954).
6. CAMPAGNI P., *Nuovo Cim. suppl.* **9,** 372 (1958).
7. COLE G. R. and FRIAUF R. J., *Phys. Rev.* **105,** 1564 (1957).
8. KRÖGER F. A., STIELTJES F. M. and VINK H. J., *Philips res. Rep.* **14,** 557 (1959).
9. KYROUPOULOS Z., *Z. anorg. Chem.* **154,** 308 (1926).

10. Doyle W. T., *Phys. Rev.* **111,** 1072 (1958).
11. Wagner C. and Hantelmann P., *J. chem. Phys.* **18,** 72 (1950).
12. Nowick A. S., *Phys. Rev.* **111,** 16 (1958).
13. Morrison J. A. and Rudham R., *J. Phys. Chem. Solids* **6,** 402 (1958).
14. Myake H. and Suzuki K., *Acta Cryst.* **7,** 514 (1954).
15. Kanzaki H., *Phys. Rev.* **110,** 1063 (1958).
16. Van Doorn C. Z. and Haven Y., *Philips res. Rep.* **11,** 497 (1956).
17. Seitz F., *Phys. Rev.* **83,** 134 (1951).
18. West E. J. and Dale Compton W., *Phys. Rev.* **108,** 576 (1957).
19. Mott N. F. and Gurney R. W., *Electronic processes in ionic crystals,* Oxford University Press, London (1953).
20. Fumi F. G. and Tosi M. P., *Disc. Faraday Soc.* **23,** 92 (1957).

J. Phys. Chem. Solids Pergamon Press 1963. Vol. 24, pp. 1577–1583. Printed in Great Britain.

ELECTRON MOBILITIES IN ORGANIC SEMICONDUCTORS

SIVERT H. GLARUM

Bell Telephone Laboratories, Incorporated, Murray Hill, New Jersey

(*Received* 10 *May* 1963; *revised* 14 *June* 1963)

Abstract—The calculation of electron mobilities in organic molecular crystals is considered in terms of band and hopping models. It is concluded that, within the limits of the tight-binding approximation employed, maximum mobilities of 10–30 cm^2/V-sec exist for such systems.

1. INTRODUCTION

IN RECENT years there has been a growing interest in the investigation of semiconduction in organic materials. As examples, one might cite numerous studies of anthracene and the charge-transfer complexes.(1–3) Many of the interesting properties exhibited by inorganic semiconductors stem from the high mobilities of their charge carriers. To assess the potential of organics as semiconductor materials it is necessary to know what their mobility characteristics may be. For anthracene, mobilities of order 1 cm^2/V-sec have been reported.(2) In the case of the charge-transfer complexes no mobilities have yet been directly measured, although indications are that they are less than 0·01 cm^2/V-sec. A basic unsettled question concerning organic semiconductors involves the mechanism of charge transport. There has been a strong temptation among workers in the field to discuss their results in terms of a band picture, implying that carriers travel in a wavelike fashion through the lattice. An alternative model visualizes carriers hopping randomly from molecule to molecule.

It is the purpose of this discussion to investigate the mobility of charge carriers in organic molecular lattices in terms of established semiconductor theory. Although numerous theoretical discussions of semiconductor mobilities have appeared in the past decade, it remains to be demonstrated how these ideas apply to organic systems. Specific interest centers on the distinction between the two proposed transport mechanisms, the dependence of the mobility on such factors as temperature and lattice anisotropy, and the magnitudes of the mobilities to be expected in organic semiconductors. Because of our almost total lack of information concerning the parameters needed in mobility calculations, it is necessary to resort to a model oversimplified by certain approximations. We believe, however, that these approximations do not materially affect our basic conclusions.

2. ONE ELECTRON WAVE FUNCTIONS

Consider a region of a molecular crystal containing a few excess electrons. The sources of these charges do not concern us, although we assume that they are far enough removed from the region under consideration to exercise a negligible influence on the behavior of the electrons. The charge density is assumed to be sufficiently small that electron–electron interactions are also unimportant. If the molecules of the lattice were widely separated, the excess charges would, in a one-electron approximation, occupy orbitals localized on specific molecules of the system. In real lattices the orbitals on adjacent molecules overlap, thereby modifying these isolated molecular ion states. In inorganic lattices this interaction can be quite large, and the grip of the lattice on the electrons may be considerably diminished. In organic lattices, however, the energy states of the system are only very slightly perturbed by overlap effects, the overlap being considerably smaller, and the electron wave functions are still strongly centered upon the molecular cores. (Murrell finds, for instance, that the overlap between adjacent molecules in the anthracene lattice is of order 10^{-3}.(4))

The problem of finding states for excess electrons is then considerably simplified, for one may employ a tight-binding approximation in which delocalized crystal orbitals are given by a Bloch sum of localized molecular orbitals, i.e.,

$$\phi_k = N^{-1/2} \sum_j^N \sum_l^M \exp(i\boldsymbol{kj})\, \lambda_{kl}\, \chi_{jl}, \tag{1}$$

χ_{jl} being a one-electron function centered on the l^{th} molecule in the j^{th} unit cell. Components of the wavevector $\boldsymbol{k}$ range over an interval of 2π in reciprocal lattice space. The coefficients λ_{kl} are readily found from the secular equations

$$\sum_l \sum_u \exp(-i\boldsymbol{ku})\, [H_{0l}^{ul'} - \epsilon_k S_{0l}^{ul'}]\, \lambda_{kl} = 0, \tag{2}$$

where

$$\begin{aligned} \epsilon_k &= \langle \phi_k | \boldsymbol{H}^0 | \phi_k \rangle / \langle \phi_k | \phi_k \rangle \\ H_{0l}^{ul'} &= \langle \chi_{j+u,l'} | \boldsymbol{H}^0 | \chi_{jl} \rangle \\ S_{0l}^{ul'} &= \langle \chi_{j+u,l'} | \chi_{jl} \rangle, \end{aligned} \tag{3}$$

$\boldsymbol{H}^0$ being a one-electron, rigid-lattice Hamiltonian operator. Upon evaluation of the various matrix elements, it is a trivial matter to solve the secular determinant and find the energy eigenvalues, which fall into bands centered about the localized site energies H_{0l}^{0l}.

Le Blanc has carried out this calculation for the anthracene lattice, and found the over-all bandwidth to be 0·015 eV.(5) For the charge-transfer complexes no equivalent calculations have yet been reported. Qualitative considerations suggest, however, that the bandwidth should be of the same magnitude as the energy for complex formation (0·05–0·5 eV), provided the stability of the complex is due in fair measure to electronic delocalization effects.

The narrowness of these bands when compared with the energy differences between the various orbital energy levels of the isolated negative ions supports the use of the tight-binding approximation. (In the advent of an orbital degeneracy or near degeneracy, the preceding expressions require minor modifications.) It is to be emphasized that, although the band description is a legitimate one under the above assumed conditions, it is not necessarily correct for a nonrigid lattice. Lattice vibrations limit the lifetime of an electron in a delocalized state through electron–lattice interactions. One expects these interactions to be particularly strong when the tight-binding approximation is applicable, for then the electron wavefunctions are closely tied to the molecular cores. If the lifetimes of carriers in delocalized states become so short that mean free paths are of the order of a lattice spacing, the band concept breaks down, and it is more appropriate to choose the localized one-electron functions as zero-order eigenfunctions. In the following Section we consider the calculation of lifetimes of electrons in localized and delocalized states.

3. THE RELAXATION TIME

The major difficulty in mobility theory lies in the calculation of a relaxation time, i.e., the lifetime of a carrier in a zero-order eigenstate. For defect-free crystals scattering occurs through the vibrational modulations of electron energies. When charge motion through the lattice is sufficiently fast, carriers respond rapidly to motions of the lattice, and the intermolecular matrix elements $H_{jl}^{j'l'}$ and $S_{jl}^{j'\,'}$ may be expressed as functions of relative molecular coordinates. This condition is satisfied when the one-electron energy bands are wider than the phonon energy bands. If the converse is true, the lattice instead can follow the charge carriers, and as these slow carriers migrate through the lattice they carry a lattice distortion with them. In the following paragraphs we consider the lifetimes of fast electrons in the delocalized or band representation, and the lifetimes of slow electrons in the localized or hopping representation.

A. *Delocalized representation*

The calculation of relaxation times requires a knowledge of the electron wavefunctions, lattice vibrational functions, and electron-lattice interaction terms. At present there is almost a total absence of information concerning these parameters for organic lattices, and, for heuristic purposes, we consider a hypothetical lattice of translationally equivalent molecules, trusting that its properties will bear at least a qualitative resemblance to those of real systems.

For this lattice the appropriate one-electron wave-functions are

$$\phi_k = N^{-1/2} \sum_j^N \exp(i\boldsymbol{kj})\, \chi_j, \tag{4}$$

with energies

$$\epsilon_{\boldsymbol{k}} = \sum_{\boldsymbol{u}} \beta_{\boldsymbol{u}}^0 \exp(i\boldsymbol{ku})$$
$$\beta_{\boldsymbol{u}}^0 = \langle \chi_{j+\boldsymbol{u}} | H^0 | \chi_j \rangle. \tag{5}$$

The lattice vibrational eigenfunctions are represented by the product of $3N$ harmonic oscillator functions,

$$\Phi_v = \prod_{q}^{N} \prod_{p}^{3} \psi_{qp}. \tag{6}$$

The frequencies of the three polarization components of mode q are assumed to be equal and given by

$$\omega_q^2 = \tfrac{1}{2} \sum_{u} \omega_u^2 \sin^2(\boldsymbol{q}\boldsymbol{u}/2), \tag{7}$$

the frequency ω_u depending on the force constant between molecules j and $j+u$.

The displacement of molecule j from its rigid lattice positions is, in terms of the normal coordinates Q_q of the lattice modes,

$$\boldsymbol{r}_j = N^{-1/2} \sum_{q} \exp(-ijq) Q_q. \tag{8}$$

To introduce an electron-lattice interaction, it is necessary to express the β_u as functions of the various $\boldsymbol{r}_j$. We consider here only those terms for which $\boldsymbol{u} \neq 0$, and assume that

$$\begin{aligned} \langle \chi_{j+u} | \boldsymbol{H} | \chi_j \rangle &= \beta_{\boldsymbol{u}}^0 \exp[-(\boldsymbol{r}_{j+u} - \boldsymbol{r}_u)\boldsymbol{u}/\lambda_u] \\ &\simeq \beta_{\boldsymbol{u}}^0 [1 - N^{-1/2} \sum_{q} \exp(-i\boldsymbol{j}\boldsymbol{q}) [\exp(-i\boldsymbol{u}\boldsymbol{q} - 1)] \\ &\quad \times \boldsymbol{u} \boldsymbol{Q}_q / \lambda_u]. \end{aligned} \tag{9}$$

The expansion to terms linear in Q_q is equivalent to the neglect of multiphonon scattering processes. In the tight-binding approximation one expects the dependence of the intermolecular resonance energies β_u to parallel that of the molecular overlap, hence the assumed exponential dependence upon relative intermolecular displacements. As λ measures the decay of the tail of the molecular wavefunction, λ should correspond to several tenths of an Ångstrom. Consideration of the vibrational dependence of the localized site energy β_0 would lead to further scattering. In nonpolar lattices this contribution is probably not the dominant one when the band approximation is valid. In polar lattices, however, it may be necessary to include these additional scattering terms.

Scattering theory requires the evaluation of the elements $\langle \Phi_{v'} \phi_{k'} | H | \phi_k \Phi_v \rangle$. Upon combination of equations (4) and (9) one finds that these elements vanish unless one component of mode q gains or loses one phonon, q being given by

$$\boldsymbol{k} - \boldsymbol{k}' - \boldsymbol{q} = \boldsymbol{K}, \tag{10}$$

where $\boldsymbol{K}$ is an arbitrary reciprocal lattice vector. When $\hbar\omega_q \ll kT$, one finds

$$\begin{aligned} \sum_{p} |\langle \Phi_{v'} \phi_{\boldsymbol{k}'} | H | \phi_{\boldsymbol{k}} \Phi_v \rangle|^2 &= \frac{4kT}{NM} \\ &\times \frac{\{\sum_{u} (\beta_u^0/\lambda_u) \cos[(\boldsymbol{k}+\boldsymbol{k}')\boldsymbol{u}/2] \sin[(\boldsymbol{k}-\boldsymbol{k}')\boldsymbol{u}/2]\boldsymbol{u}\}^2}{\sum_{u} \omega_u^2 \sin^2[(\boldsymbol{k}-\boldsymbol{k}')\boldsymbol{u}/2]} \\ &= 2kT\, \hbar\omega_0 \gamma(\boldsymbol{k},\boldsymbol{k}')/N, \end{aligned} \tag{11}$$

M being the molecular mass and ω_0 being the Debye frequency for acoustic waves.

The complex dependence of the dimensionless electron-lattice interaction parameter $\gamma(\boldsymbol{k},\boldsymbol{k}')$ upon $\boldsymbol{k}$ and $\boldsymbol{k}'$ makes it difficult to proceed without certain approximations. When the lattice is isotropic in those directions for which electron motion occurs, and when only states near band edges are populated, $\gamma(\boldsymbol{k},\boldsymbol{k}')$ is independent of $\boldsymbol{k}$ and $\boldsymbol{k}'$. As, however, $\gamma(\boldsymbol{k},\boldsymbol{k}')$ is a relatively slowly varying function of its variables, the mean value of $\gamma(\boldsymbol{k},\boldsymbol{k}')$ on constant energy surfaces throughout the band does not differ greatly from its value at the band edges. For analytical simplicity we therefore approximate γ to be constant.

The relaxation time is then given by[6]

$$1/\tau_k = (8\pi\omega_0 kT\gamma/V_0)(\partial V(\epsilon_k)/\partial\epsilon_k) \tag{12}$$

V_0 being the volume of a zone in the reciprocal lattice, and $(\partial V/\partial\epsilon_k)\mathrm{d}\epsilon$ being the volume enclosed in a constant energy shell of width $\mathrm{d}\epsilon$. As this result is based upon first order time-dependent perturbation theory, equation (12) is only rigorously correct when the bandwidth is much larger than both $\hbar/\tau$ and $\hbar\omega_0$.

B. *Localized representation*

In the foregoing Section we have assumed as an initial approximation that electronic and lattice motions are separable. In more refined calculations the purely electronic waves are replaced by electron–phonon wavepackets in which charge carriers are accompanied by lattice distortions.(7–10) These distortions may materially reduce the bandwidth when electronic and lattice waves have comparable velocities. In polar crystals there appears to be a rapid but continuous decrease in the bandwidth due to a coulombic interaction with optical lattice modes. For nonpolar lattices a shorter range interaction with acoustic modes is possible and Toyozawa has suggested that the bandwidth may decrease discontinuously to an extremely small value.(10)

In either situation, the ultimate effect of electron–lattice interactions in narrow-band semiconductors is to reduce the bandwidth to a point where scattering introduces an uncertainty in the energy of an electron–phonon wavepacket comparable to the bandwidth.(11) Bloch functions are then no longer useful, and it is more appropriate to employ as a basis set localized electron–phonon functions.

In the localized representation the relaxation time corresponds to the time a carrier sits on a particular lattice site before hopping to an adjacent site. When this time is long compared with the periods of lattice vibrations, any interaction between the lattice and the electron tends to distort the lattice about the occupied site. We assume that the term in the Hamiltonian representing this interaction is of the form

$$\boldsymbol{H}_{\text{int}} = N^{-1/2} \sum_{q} \exp(-i\boldsymbol{qj})\,\boldsymbol{A}_q\,\boldsymbol{Q}_q, \tag{13}$$

$\boldsymbol{j}$ indicating the lattice site occupied by the electron, and the vectors $\boldsymbol{A}_q$ depending upon the details of the interaction. YAMASHITA and KUROSAWA have treated the case of polar lattices where the interaction is with the polarization of optical lattice modes.(7) Even in nonpolar lattices, however, a local distortion of the lattice by a charge carrier may occur. Retaining the more general form of $\boldsymbol{H}_{\text{int}}$, one may follow the calculation of Yamashita and Kurosawa.

The lattice vibration normal coordinates are replaced by the displaced harmonic oscillator coordinates

$$\boldsymbol{Q}_{q'} = \boldsymbol{Q}_q + (M^2\omega_q^4 N)^{-1/2} \exp(i\boldsymbol{jq})\boldsymbol{A}_{q'}^*, \tag{14}$$

and it is assumed that all lattice modes have approximately the same frequency, ω_0. It then follows that the probability of electron transfer from site $\boldsymbol{j}$ to site $\boldsymbol{j}+\boldsymbol{u}$ in some short time t is

$$P(j,j+u;\ t) = (2\pi\beta_u^2/\hbar^2\omega_0)\exp[-\gamma_u(2S+1)] \times I_0\{2\gamma_u[S(S+1)]^{1/2}\}\,t = t/\tau_u \tag{15}$$

where

$$NM\hbar\omega_0^3\gamma_u = \sum_q (1-\cos \boldsymbol{uq})\,\boldsymbol{A}_q\boldsymbol{A}_q^*$$

$$1/S = \exp(\hbar\omega_0/kT)-1. \tag{16}$$

Here γ again plays the role of a dimensionless electron–lattice interaction parameter, although it should be remembered that in the two models considered γ is a different analytical function. It should also be noted that the above expressions are only correct when the conditions for slow localized electrons are satisfied ($\omega_0\tau \gg 1$ and $\hbar\omega_0 \gg \beta$).

4. MOBILITIES

In the band representation the drift mobility measured parallel to an electric field applied along the x-axis of a crystal is

$$\mu = (e/kT)\,\langle v_x^2\tau\rangle, \tag{17}$$

provided carrier densities are sufficiently low that Boltzmann statistics apply. The brackets indicate an average in reciprocal lattice space employing the Boltzmann exponential term as a weighting factor, and v_x is the x component of the carrier velocity. Generally a numerical integration is required. For analytical purposes, however, we set

$$v_x = (\alpha/\hbar)\,(\partial\epsilon/\partial k_x) \simeq (\alpha/\hbar)\,(J^2-\epsilon^2)^{1/2}$$

$$-J \leqslant \epsilon \leqslant J, \tag{18}$$

$2J$ being the bandwidth, and α the lattice period in the x-direction. To further simplify our analysis we consider the limiting cases in which the bandwidth is either much smaller or much larger than kT. In the former case energy levels of the band are thermally degenerate and one finds

$$\mu = \frac{e\alpha^2}{\hbar}\,\frac{1}{6\pi\gamma}\,\frac{J^3}{\hbar\omega_0(kT)^2}. \tag{19}$$

The factor $e\alpha^2/\hbar$ has the dimensions of mobility and corresponds to 1–2 cm²/V-sec for typical intermolecular separations.

For broad bands the calculation is sensitive to the form of $\partial V/\partial \epsilon$. In the case of an isotropic three-dimensional semiconductor

$$\partial V/\partial \epsilon = 2\pi(2/J)^{3/2}\epsilon^{1/2}, \tag{20}$$

and one obtains the conventional expression

$$\mu = \frac{e\alpha^2}{\hbar}\frac{1}{4\pi\gamma}\frac{J}{\hbar\omega_0}\left(\frac{2\pi J}{kT}\right)^{3/2}, \tag{21}$$

J being proportional to a reciprocal effective mass, and γ being proportional to the square of the deformation potential. The effects of lattice anisotropy can be simulated by assuming

$$V(\epsilon) \propto (\epsilon/J)^{n/2}, \tag{22}$$

n corresponding to the effective isotropic dimensions for the scattering process. The qualitative effect of anisotropy is to replace the factor $(2\pi J/kT)^{3/2}$ in equation (21) by $(2\pi J/kT)^{n/2}$.

Two conditions which must be satisfied for the band model under consideration to be valid are

$$\begin{aligned} J &\gg \hbar\omega_0 \\ J\tau &\gg \hbar. \end{aligned} \tag{23}$$

These imply that, in the narrow band case,

$$\mu \gg \frac{e\alpha^2}{\hbar}\frac{\hbar\omega_0}{kT}. \tag{24}$$

As the energies $\hbar\omega_0$ and kT are usually of the same magnitude, one finds the band description to be appropriate only when mobilities are greater than about 1 cm²/V-sec.

In the hopping model the mobility is given by

$$\mu = e\alpha^2/kT\tau, \tag{25}$$

or, from equation (15)

$$\begin{aligned}\mu = \frac{e\alpha^2}{\hbar}\frac{2\pi\beta^2}{kT\,\hbar\omega_0}\exp[-\gamma(2S+1)] \\ \times I_0\{2\gamma[S(S+1)]^{1/2}\}.\end{aligned} \tag{26}$$

In the particular limit

$$\gamma S = \gamma\, kT/\hbar\omega_0 \gg 1, \tag{27}$$

expansion of the Bessel function I_0 yields

$$\begin{aligned}\mu = \frac{e\alpha^2}{\hbar}\left(\frac{\pi}{\gamma}\right)^{1/2}\frac{\beta^2}{(\hbar\omega_0)^{1/2}(kT)^{3/2}} \\ \times \exp(-\gamma\hbar\omega_0/4kT).\end{aligned} \tag{8}$$

A condition for the validity of this model is $\omega_0\tau \gg 1$, or

$$\mu \ll \frac{e\alpha^2}{\hbar}\frac{\hbar\omega_0}{kT}. \tag{29}$$

This result is complementary to equation (24), and indicates the hopping model to apply only when the mobility is less than about 1 cm²/V-sec.

5. DISCUSSION

Any estimate of the mobility characteristics of organic semiconductors hinges on the evaluation of the electron-lattice interaction parameter γ. Although a rigorous calculation of this term appears formidable, one can make reasonable guesses as to its magnitude. Thus in the band representation one finds that equation (11)

$$\gamma \simeq (J/\hbar\omega_0)^2(\hbar/M\omega_0\lambda^2) = (J/\hbar\omega_0)^2(x^2/\lambda^2), \tag{30}$$

x being a measure of the amplitude of zero point molecular vibrations. Typically $x \simeq 0{\cdot}1$ Å and $\lambda \simeq 0{\cdot}2$ Å. As the band model requires $J \gg \hbar\omega_0$, γ should be of order unity or greater. In the hopping model γ depends upon the nature of the electron–lattice interaction. For polar crystals the results of Yamashita and Kurosawa may be used, and one estimates $\gamma \gtrsim 10$. In nonpolar lattices the interactions are of shorter range, and the use of macroscopic dielectric parameters to evaluate these interactions is of dubious value. If, however, the principal effect is the displacement of only those molecules immediately surrounding a charged lattice site, then one obtains from equations (8), (14) and (16)

$$\gamma \simeq \sum(\Delta r)^2/x^2, \tag{31}$$

Δr being the displacement of an adjacent molecule from its rigid lattice position. Assuming, on intuitive grounds, that Δr is several tenths of an Angstrom, one again concludes that $\gamma \gtrsim 1$.

One problem which we wish to consider is the distinction between the two transport mechanisms, wavelike motion and hopping. The inequalities derived in the preceding Section suggest that the magnitude of the mobility is a useful criterion. When the mobility is greater than about 1 cm^2/V-sec the band representation applies, and when less than this value the hopping model is most suitable. Another often assumed distinction is based on the temperature dependence of the mobility. In the band model we have found that $\mu \propto T^{-n}$ where $n < 2$ when only single acoustic phonon scattering processes are considered. The exact value of n is a rather sensitive function of anisotropy and bandwidth. For the hopping model the temperature dependence is more complicated. When electron–lattice interactions are large, the mobility increases rapidly with increasing temperature. If, however, $\gamma < 10$ one finds the mobility to be either insensitive to thermal changes or to decrease with increasing temperature. The criterion of a positive mobility temperature coefficient as an indication of the hopping process does not appear to be generally valid, except possibly for polar lattices. Then, under the limits for which equation (28) is valid, one can find hopping activation energies of order 0·1 eV.

It is tempting to apply our results to a real lattice, namely anthracene, even though the model considered is not strictly equivalent. From equation (19), using the experimental mobility value of 1 cm^2/V-sec, LeBlanc's calculated bandwidth of 0·015 eV, and assuming $\hbar\omega_0 \simeq 0{\cdot}01$ eV, one finds $\gamma \simeq 10^{-2}$. In view of our estimates, this value appears to be at least one order of magnitude too low. For the hopping model, on the other hand, equation (26) yields $\gamma \simeq 10^{-1}$ in somewhat better agreement with our calculations. Considerably better agreement could be obtained in both cases if the true bandwidth were several times larger. In view, however, of the magnitude of the mobility, it would seem that the true behavior lies in the transition region between hopping and wave motion.

For the charge-transfer complexes it is believed that mobilities are much less than 1 cm^2/V-sec, so that the hopping model is clearly appropriate. For such small mobilities equation (26) implies either that $\beta \ll kT$ or $\gamma S \gg 1$. Since the stability of these complexes is presumably based upon large β values, the former condition seems unlikely, and one therefore concludes that the mobility should increase rapidly with increasing temperature. Many highly conducting charge-transfer complexes are paramagnetic, and it has been suggested that the spin density corresponds to the carrier density. If so, differences in activation energies for conduction and paramagnetism should correspond to the mobility activation energy. In many cases this difference is of order 0·1 eV. For the iodine complexes with pyrene and perylene, however, there is essentially no difference implying a temperature-independent mobility. This is difficult to explain satisfactorily on the basis of our analysis. Either our results are inappropriate because of high carrier densities and our neglect of electron–electron correlations, or the spin densities do not reflect the true carrier densities, or the scattering process is different from that envisioned.

Finally one asks, under optimum conditions, what may be expected from organic semiconductors in the way of high carrier mobilities. Most favorable conditions arise when bands are wide and the lattice is isotropic. Even then, however, it is difficult to conceive of situations where the mobility exceeds 10–30 cm^2/V-sec, provided the tight-binding approximation holds.

One objection to this conclusion might be that our arguments have assumed a simple lattice of translationally equivalent molecules rather than a real lattice structure. In the latter case it is possible to find configurations which give much smaller effective masses at band edges, and therefore a mobility higher than that to be expected for a simple lattice. In organic molecular lattices, however, these advantages are small, for the deformation potential is inversely proportional to the effective mass. This effect, combined with the effects of lattice anisotropy suggest that little is to be gained in seeking favorable lattice structures. It should also be remembered that in our band model we have ignored multiphonon processes, vibrational modulations of localized site energies, defect and impurity scattering, and librational lattice modes—all factors which may be important, and which will further reduce the mobility below that calculated. Unless, therefore, it can be shown that bandwidths in the electron-volt region may occur in organic crystals, so that the tight-binding approximation is no longer adequate, our conclusions stand as to the magnitudes of electron mobilities in organic semiconductors.

REFERENCES

1. Akamatu H., Inokuchi H. and Matsumaga Y., *Bull. chem. Soc. Japan* **29**, 213 (1956); Eley D. D., Inokuchi H. and Willis M. R., *Disc. Faraday Soc.* **28**, 54 (1959); Kallman H. and Pope M., *J. chem. Phys.* **32**, 300 (1960); Kepler R. G., Bierstedt P. E. and Merrifield R. E., *Phys. Rev. Letters* **5**, 503 (1960); Labes M. M., Sehr R. and Bose M., *J. chem. Phys.* **33**, 868 (1960); see also references cited in these papers.
2. Kepler R. G., *Phys. Rev.* **119**, 1226 (1960); LeBlanc O. H., *J. chem. Phys.* **33**, 626 (1960).
3. Kommandeur J. and Hall F. R., *J. chem. Phys.* **34**, 129 (1961); Singer L. S. and Kommandeur J. *J. chem. Phys.* **34**, 133 (1961).
4. Murrell J. N., *Mol. Phys.* **4**, 205 (1961).
5. LeBlanc O. H., *J. chem. Phys.* **35**, 1275 (1961).
6. Radcliffe J. M., *Proc. phys. Soc. Lond.* **68A**, 675 (1955).
7. Yamashita J. and Kurosawa T., *J. phys. Chem. Solids* **5**, 34 (1958); *J. phys. Soc. Japan* **15**, 802 (1960); Kurosawa T., *J. phys. Soc. Japan* **15**, 1211 (1960).
8. Sewell G. L., *Phil. Mag.* **3**, 1361 (1958).
9. Holstein T., *Ann. Phys.* **8**, 325 (1959); *Ann. Phys.* **8**, 343 (1959).
10. Toyozawa Y., *Progr. theor. Phys.* **26**, 29 (1961); *J. appl. Phys.* **33**, 340 (1962).
11. Frohlich H. and Sewell G. L., *Proc. phys. Soc. Lond.* **74**, 643 (1959).

J. Phys. Chem. Solids Pergamon Press 1963. Vol. 24, pp. 1585–1591. Printed in Great Britain.

THE DENDRITIC GROWTH OF InSb

R. G. SEIDENSTICKER* and D. R. HAMILTON

Westinghouse Research Laboratories, Pittsburgh 35, Pennsylvania

(*Received* 24 *June* 1963)

Abstract—The limiting $\langle 2\bar{1}\bar{1} \rangle$ and $\langle \bar{2}11 \rangle$ growth velocities have been measured as a function of melt undercooling for InSb dendrites containing two twin planes. From analysis of the data using a layer flow model, it is found that the kinetic rate constant for the interface is greater than 3 cm/sec°C and that the effective interfacial energy is small, of the order of or less than 50 ergs/cm^2. It is shown that InSb freezing kinetics are probably slower than those of Ge. The envelope of decanted solid–liquid interfaces is asymmetric, an effect probably related to the anisotropy of kinetics induced by the polarity of the lattice; there is also a tendency for preferential formation of "Sb" facets. Experiments on growth from non-stoichiometric melts are reported, as well as the negative results of attempts to grow continuous dendrites in directions other than $\langle 2\bar{1}\bar{1} \rangle$ or $\langle \bar{2}11 \rangle$. Comparisons are made with the dendritic growth of Ge.

1. INTRODUCTION

IN PREVIOUS papers(1–3) we have reported studies of the freezing processes at the solid–liquid interfaces of Ge dendrites, pulled continuously from undercooled melts. The fastest pull velocity at which continuous growth could be obtained was a reproducible function of melt undercooling, and was related to the growth velocity at the interface. Representative interfaces were obtained by decanting, and many of these were found to be paraboloids which could be characterized by an average tip radius. Data on the velocity, radii and melt undercooling were analyzed to obtain estimates of the interfacial energy, σ, and the kinetic rate constant, μ_f. These enter the problem because the local melting point on any curved interface is depressed below that of a plane according to the Gibbs–Thompson relationship, and because an interface must depart an amount—v/μ_f from its local melting point in order to freeze at the velocity v. For Ge it was concluded that the effective interfacial energy was $45 \lesssim \sigma \lesssim 90$ ergs/cm^2, and the rate constant $\mu_f \gtrsim 3$ cm/°C-sec.

In this paper we present the results of similar work on the III–V compound, InSb, undertaken to determine if differences between the growth of Ge and InSb might be ascribed to the latter's polar character. To this end, we sought kinetic and morphological effects, prepared specimens in off-stoichiometric melts, and attempted to duplicate the $\langle 110 \rangle$ and $\langle 321 \rangle$ growth reported by ALBON and OWEN.(4) The literature on the growth of InSb has been primarily concerned with "facet segregation" and the occasional twinning that occur in Czochralski crystals. InSb exhibits facets on the more noble *B*, or Sb {111} faces, so there is a preference for twinning on these planes(5,6) rather than on In planes. "Facet segregation" describes anomalous segregation coefficients observed on such low index planes, but will not concern us further. HURLE *et al.*(7) show that excess In or Sb can give rise to constitutional undercooling in Czochralski crystals, but HULME and MULLIN,(8) in a review of the literature, report that there is no conclusive evidence that off-stoichiometry in the melt has any marked influence on the electrical properties of the grown crystals, at least in the absence of gross segregation on cell boundaries.

2. EXPERIMENTAL APPARATUS AND PROCEDURES

InSb dendrites were grown from a well shielded, isothermal crucible, with a cavity 10 cm in height above the melt which reduced any temperature

---

* This work was supported in part by the Aeronautical Systems Division, Wright–Patterson Air Force Base.

gradients in the solid stem at the liquid surface, ensuring that the heat from freezing flowed through the undercooled melt.(2) Since InSb melts at $T_m = 525°\text{C}$, the cavity had to be illuminated through ports in the heat shields. The furnace was operated in vacuum during initial heating, or in pre-purified hydrogen while growing dendrites; an air lock was provided so samples could be removed without cooling the crucible. Despite the use of pure hydrogen and high purity InSb, difficulty was experienced with the formation of a surface scum. This was alleviated to some extent by melting the InSb in a separate crucible with a small hole in the bottom. Most of the liquid InSb would run from this crucible into the main crucible while the scum remained behind. The separate crucible was then removed and growth started.

The presence of residual scum may have induced some of the difficulties experienced in initiating or seeding new dendritic growth. There were frequent changes in twin plane spacing during seeding, with degeneration of the existing structure or nucleation of new twin lamella. Furthermore, the joint between the seed and the new growth was often found to be structurally weak, even when the twin structure was continuous, so that samples would break off when the air lock was used. These problems were partially overcome by either striking an arc between the seed and the melt while starting growth(9) or by "splash seeding." In the latter, the melt was undercooled below the melting point by an amount ΔT, the seed was brought as close to the surface as feasible, and the melt then disturbed so that waves splashed the seed allowing growth to start. This was particularly useful when the expected growth velocity was high, for the pulling mechanism could be started upwards from rest, which was not so when the seed was plunged downwards into the melt. In spite of these techniques, the yield of data on limiting growth velocity as a function of melt undercooling, $v(\Delta T)$, was much lower than experienced with Ge.

Experiments using the decanting apparatus(10) were less productive than in Ge, because of poor seeding, and also because InSb has lower resistance to shock. Even when the decanting velocity was reduced below 100 cm/sec, at best only one in five specimens survived, and these were useful only if the twin spacing had not changed. Two principal radii were measured on photographs of the survivors taken in silhouette perpendicular and parallel to the twin structure. These radii, $\rho_\perp$ and $\rho_\parallel$, were used to compute an average radius, characteristic of the tip curvature,(2)

$$2/\rho_{\text{av}} = 1/\rho_\perp + 1/\rho_\parallel$$

The thermal constants used in computations are shown in Table 1. The electrical conductivity of the liquid lies between 9 and 10×10^3 Ω/cm.(11) The thermal conductivity of the liquid, k_l, was obtained from the latter figure and the Weidemann–Franz ratio. The thermal diffusivity of the liquid, α, was calculated, using the classical specific heat of the liquid, $c = 7R/2$. Although the liquid vapor interfacial tensions are known,(12) there are no published data on the solid–liquid interfacial energies. A rough estimate may be

Table 1. *A collection of the physical parameters of* InSb.

Quantity			Reference
T_m	798°K	equilibrium melting point	14, 18, 19
k_s	0·0179 cal/C-cm-sec	conductivity of solid at T_m	20
k_l	0·0467 cal/C-cm-sec	conductivity of liquid at T_m	see text
L	288 cal/cm^3	latent heat of fusion	19, 21, 22
c	0·192 cal/cm^3-°C	specific heat of the liquid $= 7R/2$ cals/mole-C°	
α	0·244 cm^2/sec	$= k_l/c_l$	
σ		average interfacial energy	see text
ρ_s	5·75 g/cm^3	density of solid at T_m	22
ρ_l	6·45 g/cm^3	density of liquid at T_m	22

made by assuming that the bonding is entirely covalent, and that the interfacial energy is proportional to the product of the latent heat of fusion per bond and the number of bonds per unit area. The latter is inversely proportional to the square of the lattice parameter, a_0, so

$$\sigma = AL/a_0^2$$

where A is a constant for both the diamond and the zinc blende structures. Comparing Ge and InSb one finds

$$\sigma_{\mathrm{Ge}} = \sigma_{\mathrm{InSb}} \left(\frac{L}{a_0^2}\right)_{\mathrm{Ge}} \left(\frac{a_0^2}{L}\right)_{\mathrm{InSb}} = 2{\cdot}33\ \sigma_{\mathrm{InSb}}$$

whence

$$\sigma_{\mathrm{InSb}} \sim 85\ \mathrm{ergs/cm^2}.$$

3. EXPERIMENTAL RESULTS

Because of the difficulty in obtaining data, we restricted the investigation to two families of dendrites, with twin spacings of $d = 9{\cdot}5$ and $19{\cdot}5\ \mu$. The results for $v(\Delta T)$ are shown in Figs 1 and 2, respectively. Note that in Fig. 1 there are two sets of points, corresponding to data taken with the seed oriented in two positions, 180° apart, i.e., $\langle 2\bar{1}\bar{1}\rangle$ and $\langle \bar{2}11\rangle$. In Ge, two twin dendrites have six-fold growth symmetry, so $\langle 2\bar{1}\bar{1}\rangle$ and $\langle \bar{2}11\rangle$ directions are equivalent; this may not be true for InSb.

In Fig. 3 is shown the decanted tip of a $d = 9{\cdot}5\ \mu$ specimen. This resembles the analogous Ge tip, but there are important differences. Although the envelope normal to the twin structure is parabolic and has a characteristic radius $\rho_\perp$, (as in the Ge dendrites) its axis does not lie in the plane of the twins. Alternatively, if the twin lamella were taken to divide the crystal in half, then each half crystal may be characterized by half a parabola with a characteristic radius. These radii may also be identified by their association with the facet systems which develop in a region analogous to the transition region[(2)] in Ge dendrites. In InSb, the larger radius was always associated with facets which were equilateral triangles with a corner pointing in the direction of growth, while the smaller radius, for the other

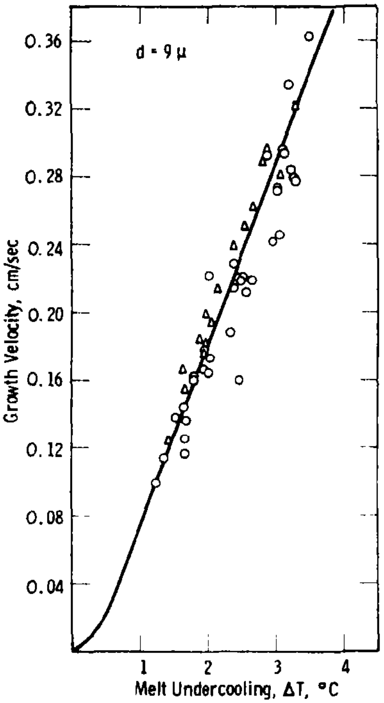

FIG. 1. The limiting growth velocity of a family of InSb dendrites, twin spacing $d = 9{\cdot}5\ \mu$, is plotted as a function of melt undercooling. The data has been taken in two different seed orientations, $\langle 2\bar{1}\bar{1}\rangle$ and $\langle \bar{2}11\rangle$. The two sets of data points suggest there may be a difference between these.

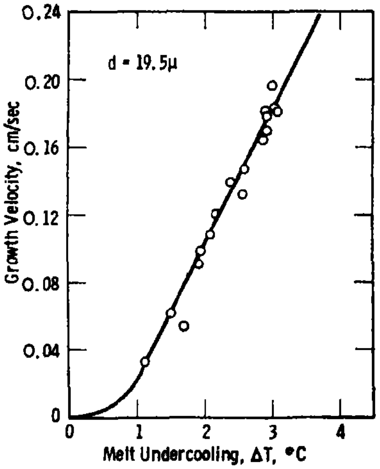

FIG. 2. The growth velocity and undercooling are shown for a group of dendrites with $d = 19{\cdot}5\ \mu$. These dendrites, like their counterparts in Ge, had interfaces largely bounded by low index $\{111\}$ and $\{\bar{1}\bar{1}\bar{1}\}$ planes, that is, they were "end form" specimens.

half of the crystal, was accompanied by triangular facets which pointed in the reverse direction. The former were in general larger and more sharply defined, developed earlier, and were associated with Sb {111} facets.

Measurements on the silhouette of decanted tips about the twin planes show that this curve was not parabolic, and that the radius in the twin planes ($\rho_{\parallel}$) was sharper at the tip than elsewhere. It may be shown that the thermal gradients in the solid should fall to $1/e$ of their value at the tip in distances of the order of $\rho_{\parallel}$. The radius $\rho_{\parallel}$ should therefore be defined at the tip, and we have chosen to use the average value of this parameter over an axial distance $z = 5\rho_{\parallel}$. At distances $\sim 20\rho_{\parallel}$, the dendrites were roughly 20 per cent wider than expected from the parabola defined by this choice of $\rho_{\parallel}$.

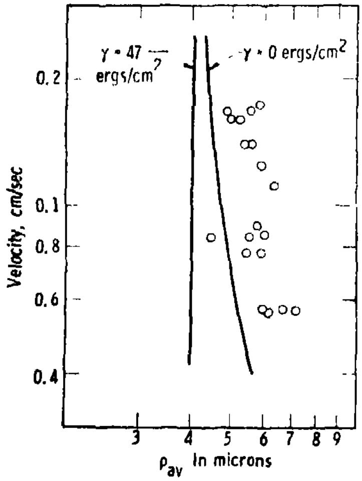

FIG. 4. Theory and the data of Fig. 1 were used to compute an average radius, using the kinetic rate constant μ_l and the interfacial energy σ as free parameters. The best fit of the experimental data occurs when $50 > \sigma \gtrsim$ ergs/cm^2 and $\mu_f \gtrsim 3$ cm/°C-sec.

Specimens of the $d = 19{\cdot}5\,\mu$ family were found to be end form crystals(2) with tips bounded by well developed $\{111\}$ and $\{\bar{1}\bar{1}\bar{1}\}$ planes, except for a region of sharp curvature about the twin lamella.

Experiments on growth in directions other than $\langle 2\bar{1}\bar{1}\rangle$ and $\langle \bar{2}11\rangle$ were unsuccessful. We are indebted to ALBON and OWEN(4) for supplying us with all their specimens, but even using these as seeds, we were unable to obtain propagation in any other direction.

Dendrites $d = 9{\cdot}5\,\mu$ were grown from melts containing one, three and six per cent excess In or Sb. Within the experimental error, these all grew at the same velocity, for given undercooling, as those prepared from nominally stoichiometric melts.

JOHN(13) found evidence for the inclusion of spherical pockets the In or Sb rich eutectic(14) resulting from the solidification of what FAUST and JOHN(15) have called the *H*-arm structure of these dendrites. If InSb freezes in stoichiometrc ratio then these inclusions would be expected in off-stoichiometric melts. The liquid trapped by the *H*-arms rejects the excess component until a droplet of eutectic composition remains, which then freezes as a spherical inclusion.

4. THEORY AND DISCUSSION

The equation appropriate to the analysis of the results is

$$-\frac{v\rho}{2\alpha}\exp(v\rho/2\alpha)\,E_i\left(-\frac{v\rho}{2\alpha}\right) = \frac{c}{L}\,\frac{\Delta T - v/\mu_f}{1+\dfrac{(Nk_l+Mk_s)T_m\sigma}{v\rho^2 L^2}} \tag{1}$$

where L is the specific latent heat, k_s the thermal conductivity of the solid and N and M constants derived by TEMPKIN(16) in his treatment of the non-isothermal paraboloid. Equation (1) assumes that there is a source of layers at the tip of the dendrite, the re-entrant corners at the twins,(1) and that μ_f is the average value of the rate constant taken over this source and over the layers advancing on the interface. The velocity in this equation is the velocity of the interface relative to the liquid, which was taken to be at rest in Tempkin's derivation. In the present experiments, the interface is stationary, and both solid and liquid are in motion. The flux condition on mass at the interface is

$$v_l\rho_l = v_s\rho_s \tag{2}$$

where v_s is the component of the solid velocity normal to the interface, which is equal to the pull velocity on the axis. v_l is the normal component of

FIG. 3. This is a photograph of a very asymmetric decanted InSb interface, $d = 9{\cdot}5\ \mu$, taken in the direction of the twin structure. The envelope about the interface is asymmetric with respect to the trace of the central twin (bright horizontal line), and the blunter half is associated with the Sb or $\{111\}$ face. The trace of the first facet may be seen.

the liquid velocity towards the interface, and ρ_s and ρ_l are the respective densities of the two phases. For Ge and most metals,

$$\left|\frac{\rho_s-\rho_l}{\rho_l}\right| \lesssim 0{\cdot}05,$$

so it is legitimate to take the limiting pull velocity as the growth velocity, i.e., $v_s = v_l = -V_{\text{growth}}$. However, for InSb,

$$\left|\frac{\rho_s-\rho_l}{\rho_l}\right| = 0{\cdot}11$$

Thus the axial growth velocity with respect to the liquid, $-v_l$, is, from equation (2), $-0{\cdot}893$ times the pull velocity. This effect is caused entirely by the expansion that occurs on freezing. In the following, the data are plotted against experimental pull velocities, but the computations have been made relative to the liquid and converted to pull velocity.

We have used this equation and the function $v(\Delta T)$ to compute values of radii, using μ_f and σ as free parameters. The results are plotted in Fig. 4 with the observed values of ρ_{av}. It is concluded that the rate constant for the interface was large, $\mu_f > 3$ cm/sec-°C, so that the temperature, v/μ_f, driving the average interfacial kinetics, was very small relative to ΔT. The best fits of the InSb data occur with the interfacial energy small, in keeping with the results on Ge and the estimate made earlier. The interface was thus very nearly isothermal. Because of the complicated envelope of the tip, the most one can claim with certainty is that the surface energy appropriate to this data is $50 > \sigma \gtrsim 0$ ergs/cm^2.

Since the $d = 19{\cdot}5\ \mu$ decanted tips were all found to be end form, analysis based on a paraboloidal interface is not applicable. The pyramidal morphology of the tip is undoubtedly the result of effects like those in Ge at similar twin spacings.$^{(2)}$

Since we are unable to determine absolute kinetic rate constants from either these or the Ge experiments, a comparison of rates must be made by other means. This should be done in such a way as to eliminate differences in thermal parameters and in v, ρ, and ΔT. Equation (1) may be differentiated to eliminate ΔT.

$$-\frac{\partial}{\partial v}(\Delta T - v/\mu_F) = -\frac{\partial \Delta T}{\partial v}+\frac{1}{\mu_f}$$
$$=\frac{L}{2k_l}\left[\rho[E_i(-x)+xE_i(-x)+1] + \frac{Nk_l+Mk_s}{v\rho L^2}T_m\sigma\right] \qquad (2)$$

where $x = v\rho/2\alpha$. The slope $\partial T/\partial v$, appears, but it is easily measured and is a constant for undercoolings greater than about a degree. The term in σ is of the order of 0·01 of $L\rho(E_i+xE+1)/2k_l$ and may be neglected. If one compares Ge and InSb at the same velocity and radius, then to a good approximation one may write, for $\rho_{\text{Ge}} \approx \rho_{\text{InSb}}$

$$\left(\frac{\partial \Delta T}{\partial v}-\frac{1}{\mu_f}\right)_{\text{Ge}} \Bigg/ \left(\frac{\partial \Delta T}{\partial v}-\frac{1}{\mu_f}\right)_{\text{InSb}}$$
$$= \left(\frac{L}{k_l}\right)_{\text{Ge}} \left(\frac{k_l}{L}\right)_{\text{InSb}}$$

The radii of the $d = 9{\cdot}5\ \mu$ InSb and the $d = 9{\cdot}0\ \mu$ Ge dendrites are equal, and the Ge data may readily be interpolated to $d = 9{\cdot}5\ \mu$, so the rate constants may be compared at equal radii or equal twin spacing. In both instances it is concluded that the average rate constant for InSb is somewhat smaller than that of Ge. It should be emphasized that this result is just outside the root mean square deviations in the respective radii, but it does confirm the expectation that a polar compound will grow more slowly than an element under equivalent circumstances.

The asymmetry of the decanted interfaces can be ascribed to a polarity of either interfacial energy or rate constant. If we characterize the halves of the interface by the character of the (111) or $(\bar{1}\bar{1}\bar{1})$ planes on either side of the twin structure, then near the tip the Sb or (111) half has a larger radius and thus either a higher average surface energy or faster kinetics than the In or $(\bar{1}\bar{1}\bar{1})$ half. In view of the occurrence of macroscopic facets only at Sb{111} poles in Czochralski crystals, in which the Gibbs–Thompson correction is small, it is concluded that the anisotropy in dendrite morphology is more likely caused by an anisotropy of kinetics rather than of interfacial energy. Although it may be shown that the relative surface populations of A- or B-bonds on dendritic interface is dependent on position, so that in certain areas one type may predominate over the other, it is not at all clear how to relate such information to the average kinetics and the radii, and needless to say, the situation cannot be treated mathematically with sufficient precision. A plausible explanation is that it is easier to grow on, or to complete, the more noble Sb half than the reverse In half of the interface.

There is no convenient explanation of the absence of growth direction other than $\langle 2\bar{1}\bar{1}\rangle$ and $\langle\bar{2}11\rangle$ in our experiments, except the differences in externally imposed thermal gradients between the present equipment and that of Albon and Owen.(4) Since our apparatus was designed for low gradients, ~ 1/4°C/cm, it is presumed that thermal fields imposed in Albon and Owen's crucible were sufficient to induce the alternate dendritic growth directions. Thermal gradients do influence the preferred mode of solidification,(17) and it is plausible they should also influence the selection among alternative dendritic growth directions.

The results of the experiments with non-stoichiometric melts must be considered in light of the phase diagram.(14) Since the segregation coefficient for excess of either component is zero, a considerable increase in the interfacial concentration of the excess component would be expected during crystal growth, but the amount of resultant constitutional undercooling would be small because the liquidus slope about the InSb composition is zero for low initial concentrations. The results indicate that even 6 per cent excess component did not lead to a measurable constitutional contribution to undercooling for dendrites. It is known that constitutional undercooling may exist with planar interfaces(7) but it should be remembered that the paraboloid is the most efficient geometry for diffusion, whether it be heat, impurities, or excess component. Excess component could effect kinetics, if, for example, the supply of that component were in any way rate determining. The relative population of associated pairs will be increased. This population(23) might play a part kinetics. The magnitude of the kinetic departure from the melting point, $v/\mu_f \ll \Delta T$, and the above effects, if present, were not detectable. The invariance of $v(\Delta T)$ suggests that there were no marked changes in interface morphology with deviations from stoichiometry. In short, deviations from stoichiometry did not affect the growth appreciably.

5. CONCLUSIONS

These experiments show that the general character of dendritic growth of InSb is similar to that of Ge. The twin plane spacing dominates the tip morphology and the transition from paraboloidal to fully faceted "end form" tips occurs at about the same twin spacing as in Ge. The polar nature of the InSb lattice does not have much influence on this or on the dependence of growth velocity on melt supercooling. Polar effects do appear in the details of the tip morphology, for the more noble Sb side of the interface is blunter than the In half, on the opposite side of the twin lamella. It is probable that Sb freezing kinetics are faster than In kinetics, although the average for the entire interface is lower than for Ge. The experiments indicate that the constant for this, $\mu_f \gtrsim 3$ cm/°C-sec, and that the effective interfacial energy $50 < \sigma \lesssim 0$ ergs/cm^2. Deviations from stoichiometry in the melt do not have a marked influence on growth, and growth directions other than $\langle 2\bar{1}\bar{1}\rangle$ and $\langle\bar{2}11\rangle$ do not occur in melts with gradients < 1/4°C/cm.

Acknowledgements—The authors acknowledge the assistance of B. F. Westwood, who grew the dendrites, and N. R. Anderson, who performed the microscopic work.

REFERENCES

1. Hamilton D. R. and Seidensticker R. G., *J. appl. Phys.* **31**, 1165 (1960).
2. Hamilton D. R. and Seidensticker R. G., *J. appl. Phys.* **34**, 1450 (1963).
3. Seidensticker R. G. and Hamilton D. R., *J. appl. Phys.* **34**, 3113 (1963).
4. Albon N. and Owen A., *J. Phys. Chem. Solids* **24**, 899 (1963).
5. Mullin J. B., *Electrochem. Soc. Mtg. Abstr.* **9**, 176 (1960).
6. Mueller R. K. and Jackobson R. L., *J. appl. Phys.* **32**, 550, 1406 (1961).
7. Hurle D. T. J., Jones O. and Mullin J. B., *Solid-State Electron.* **3**, 317 (1961).
8. Hulme K. F. and Mullin J. B., *Solid-state Electron.* **5**, 226 (1962).
9. Bennett A. I., *U.S. Patent* 3,058,915; *see also* Lever R. F., Powers J. K., Richards J. L., Sirgo H. V., *J. appl. Phys.* **31**, 1334 (1960).

10. Bennett A. I., Fekete J. M., Hamilton D. R. and O'Hara S., *Rev. sci. Instrum.* **33,** 999 (1962).
11. Hamilton D. R. and Seidensticker R. G., *J. appl. Phys.* **34,** 2697 (1963; Busch G. and Vogt O. *Helv. Phys. Acta* **27,** 241 (1954).
    Blum A. I., Mokrovski N. P. and Regel P. A. *Izv. akad. nauk. S.S.S.R. Ser. fiz.* **16,** 139 (1952).
12. Lazavev V. B. and Pugachevich P. P., *Proc. Acad. Sci. U.S.S.R. phys. Chem.* **134,** 823 (1960); Lazavev V. B. and Slovokhotova N. A., *Dokl. akad. nauk. S.S.S.R.* **146,** 822 (1962).
13. John H. F., private communication.
14. Liu T. S. and Peretti E. A., *Trans. Amer. Soc. Metals* **44,** 539 (1952).
15. Faust J. W., Jr. and John H. F., *J. electrochem. Soc.* **108,** 860 (1961).
16. Tempkin D. E., *Dokl. akad. nauk. S.S.S.R.* **132,** 1307 (1960).
17. Tiller W. A., *Trans. Amer. Inst. min. (metall.) Engrs.* **206,** 847 (1957) and the references therein.
18. Bednar J. and Smirous K., *Czech. J. appl. Phys.* **5,** 546 (1955).
19. Nachtrieb N. H. and Clement N., *J. phys. Chem.* **62,** 876 (1958).
20. Bowers R., Ure R., Jr., Bauerle J. E. and Cornish A. J., *J. appl. Phys.* **30,** 930 (1959).
21. Schottky W. F. and Bever M. B., *Acta Met.* **6,** 320 (1958).
22. Mokrovski N. P. and Regel A. R., *Z. tekh. fiz. S.S.S.R.* **22,** 1281 (1952).
23. Faust J. W., Jr. and John H. F., *J. Phys. Chem. Solids* **23,** 1119 (1962).

J. Phys. Chem. Solids Pergamon Press 1963. Vol. 24, pp. 1593–1599. Printed in Great Britain.

IMPURITY STATES ASSOCIATED WITH SUBSIDIARY ENERGY-BAND MINIMA*

HARVEY KAPLAN

Department of Physics, Syracuse University, Syracuse, New York

(*Received* 12 *June* 1963)

Abstract—Two results have been established concerning the existence of localized electronic states associated with a point impurity in a substance having a spherical energy band, $E(\mathbf{k}) = \varepsilon_0 + \varepsilon_1 \times \cos k + \varepsilon_2 \cos 2k$, where $k = |\mathbf{k}|$, with a subsidiary minimum at $k = 0$. The 1st result is a generalization of Slater and Koster's result, that in 1 dimension an energy band with a subsidiary minimum has no localized states associated with this minimum if the impurity potential is of the δ-function type; i.e., it has only 1 matrix element between Wannier functions, a diagonal one referring to 1 site. We show that this result also holds for a spherical band in 3 dimensions. Our 2nd result is that, for the Coulomb-impurity potential screened by the static dielectric constant, and the above spherical band, there are hydrogen-like localized states built out of states near the subsidiary minimum, even when all powers of k in $E(k)$ are taken into account in the equation for the envelope function. The deviation of the impurity potential from slow variation causes a long lifetime for decay of the localized state into conduction states of the same energy. For a typical shallow impurity state, the lifetime is $\simeq 10^{-8}$–10^{-9} sec.

RECENTLY the existence of discrete localized electronic states, arising because of a localized impurity, and coincident in energy with states in an energy band has been invoked in order to explain a number of observations in semiconductors.(1) These states are of two slightly different types.

The first type is associated with the valence band systems in silicon and germanium. Spin–orbit coupling causes a partial breakdown of what would otherwise be a sixfold degeneracy at $\mathbf{k} = 0$ into two- and four-fold degeneracies, the four-fold degenerate band having the higher energy. If the perturbation potential caused by a localized impurity such as a type III or type V substitutional atom is sufficiently weak (i.e. its matrix elements are not comparable in size to the spin–orbit splitting at $\mathbf{k} = 0$), and it varies slowly over distances of unit cell dimensions, so that effective mass theory holds, one can imagine that the two-fold and the four-fold degenerate bands separately give rise to hydrogen-like localized states. In this case a localized state arising from the two-fold degenerate band will have the same energy as some continuum state of the four-fold degenerate band.

A second, similar situation arises when one considers the conduction band of germanium, which has four absolute minima at the ends of the [1,1,1] axes in the Brillouin zone, and a subsidiary minimum at $\mathbf{k} = 0$. As above, one may suspect that localized states arise composed of Bloch states with $\mathbf{k}$-vectors near the subsidiary minimum, in addition to the localized states that arise from Bloch states near the absolute minima. The weak point in such speculations is that the usual effective mass theory, upon which they are based (a form of perturbation theory) ignores the existence of possible continuum states degenerate with the localized state that is created. Although a slowly varying potential has very small matrix elements between states with widely different $\mathbf{k}$ values, a small or vanishing unperturbed energy difference between these states may cause appreciable mixings of these types of unperturbed states in any state describing the perturbed system. As an example of such mixing we may mention that for a strongly localized impurity potential perturbing a monatomic one-dimensional solid having an energy band with a subsidiary minimum,

---

* Work supported in part by the U.S. Air Force Office of Scientific Research.

Slater and Koster(2) have shown that no completely localized state exists associated with the subsidiary minimum regardless of the strength of the localized impurity potential. The purpose of this paper is to show that if certain restrictions of the effective mass approximation are removed, allowing one to effectively include interactions of all Bloch waves in an energy band, and if, in addition, the effective potential caused by the localized impurity is still slowly varying, rigorously localized states exist associated with a subsidiary minimum of the band. The remainder of the perturbation potential is estimated to be responsible for a lifetime long compared to a typical lifetime caused by the electron lattice interaction.

Let us first review some aspects of Slater and Koster's one-dimensional calculation. They consider an infinite one-dimensional monatomic crystal which contains a localized impurity. The wave function $\psi(x)$ for the perturbed problem is expanded as a linear combination of Wannier functions $\phi_n(x-pa)$ for the different bands defined by the unperturbed, periodic Hamiltonian. Thus,

$$\psi(x) = \sum_{p,n} U_n(p)\phi_n(x-pa)$$

where p is an integer, n is the band index, and a is the lattice spacing. The sum over p extends from $-\infty$ to $+\infty$. The simple case is treated in which the bands are decoupled, i.e. the impurity potential energy has no interband matrix element between Wannier functions, and further, for any one band only one matrix element of the perturbation is non-zero:

$$\int \phi(x-qa)V(x)\phi(x-pa) = V_0\delta_{q0}\delta_{p0}$$

We consider a simple energy band having a subsidiary minimum in $E(k)$ defined by the unperturbed problem. The equations defining the amplitudes $U(p)$ for the unperturbed problem are taken to be

$$\begin{aligned} 0 = (-E+\varepsilon_0)U(p)&+\varepsilon_1[U(p+1)+U(p-1)] \\ &+\varepsilon_2[U(p+2)+U(p-2)], \\ p &= \ldots, -1,0,1,\ldots, \end{aligned} \tag{1}$$

where $\varepsilon_l = \int \phi(x)H_0(x)\phi(x-la)\,dx$. Only enough terms l have been kept so that the subsidiary minimum can occur in $E(k)$. The solutions of this problem are

$$U(p) = \exp(ikpa)$$

and

$$E(k) = \epsilon_0+2\varepsilon_1\cos k+2\varepsilon_2\cos 2k. \tag{2}$$

If $\varepsilon_1 > 0$ and $4\varepsilon_2 < -\varepsilon_1$, $E(k)$ exhibits a subsidiary minimum as shown in Fig. 1.

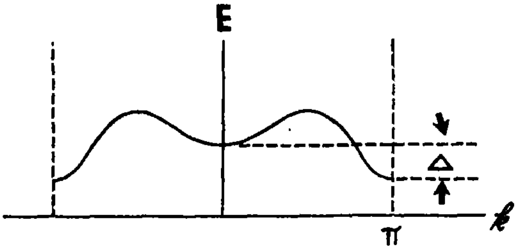

Fig. 1. $E(k)$ for an energy band having a subsidiary minimum at $k = 0$.

The perturbed problem has solutions that are either symmetric, $U(p) = U(-p)$ or antisymmetric $U(p) = -U(-p)$, in p, and because of the simple nature of the impurity energy V_{pq} it only effects the symmetric solutions. The equations for the perturbed problem are the same as for the unperturbed problem except for $p = 0, \pm 1$. By making use of the remaining unperturbed equations and the boundary condition that the wave function $U(p)$ must not become indefinitely large as p gets large we find that we may write $U(p) = A\exp(-\gamma p)+B\cos(kp-\alpha)$ for $p > 0$, when we are in the energy range Δ in Fig. 1, in which localized states associated with the subsidiary minimum would be expected to occur. Here $k = k_1$ and $i\gamma = k_2$ are given, for E fixed, by the two solution for k of the dispersion relation, equation (2). The coefficients A and B are now determined by the homogeneous equations

$$\begin{aligned} U(1)-U(-1) &= 0, \\ V_0U(0)+\varepsilon_2[U(2)-U(-2)] &= 0, \end{aligned} \tag{3}$$

where in these equations $U(-p)$ means $U(p)$ for $p>0$ evaluated formally for negative values of p. The existence of a localized solution requires $B = 0$, and it is easy to show that no such solutions exist in the energy range Δ.

Let us now consider a three-dimensional problem analogous to Slater and Koster's one-dimensional model. We consider an infinite three-dimensional crystal with one substitutional localized impurity. We assume that there is an energy band of the pure infinite crystal which is far from other bands and has a subsidiary minimum, and that there are no matrix elements of the impurity potential energy between states from different bands. The Schrodinger equation in the Wannier representation cannot be solved exactly in this case and it is more convenient to work with the "summation equation" form of the difference equations for the Wannier function amplitudes as derived by Slater and Koster. The summation equation is

$$U_i = \sum_{jk} G_{ij} V_{jk} U_k. \tag{4}$$

Here, $U_i\,(= U(\boldsymbol{R}))$ is the amplitude of the Wannier function centered at lattice point $\boldsymbol{R}_i$. $V_{jk} = \int \phi^*(\boldsymbol{r}-\boldsymbol{R}_j)\, V(\boldsymbol{r})\phi(\boldsymbol{r}-\boldsymbol{R}_k)\, \mathrm{d}^3\boldsymbol{r}$ is the matrix element of the impurity potential energy between Wannier functions on sites $\boldsymbol{R}_j$ and $\boldsymbol{R}_k$, and G_{ij} is the Green's function defined by the unperturbed periodic potential problem:

$$G_{ij} = \frac{1}{N^3} \sum_{\boldsymbol{k}\text{ in B.Z.}} \frac{\exp\left[i\boldsymbol{k}\cdot(\boldsymbol{R}_i-\boldsymbol{R}_j)\right]}{E-E(\boldsymbol{k})}$$

$$\cong \frac{1}{(2\pi)^3} \int_{\text{B.Z.}} \frac{\exp\left[i\boldsymbol{k}\cdot(\boldsymbol{R}_i-\boldsymbol{R}_j)\right] \mathrm{d}^3\boldsymbol{k}}{E-E(\boldsymbol{k})}, \tag{5}$$

where $E(\boldsymbol{k}) = \Sigma_m\, \varepsilon_m \exp(-i\boldsymbol{k}\cdot\boldsymbol{R}_m)$.

We will now study a model which approximates our problem but for which analytic answers can be obtained. We consider a spherical band ($E(k)$ only where $k = |\boldsymbol{k}|$) and also consider the Brillouin zone to be spherical. A typical form for E might be $E(k) = \varepsilon_1 \cos k + \varepsilon_2 \cos 2k$ and $k_{\max} = \pi$ would be the radius of the zone. We keep two terms in $E(k)$ in order that there be a subsidiary minimum, and will evaluate the Green's function for an energy below the subsidiary minimum, but above the bottom of the band. Because we are only interested in a qualitative question, namely the admixture of continuum and bound components of states lying within an unperturbed energy band but below a subsidiary minimum, we may further approximate $E(k)$ by $E(k) = 2\alpha k^2 - \beta k^4$ where both α and β are greater than zero, thus ensuring the existence of a subsidiary minimum. We are particularly interested here in the case of the very localized impurity potential.

$$V_{ij} = V_0 \delta(\boldsymbol{R}_i, 0)\delta(\boldsymbol{R}_j, 0). \tag{6}$$

In order to study this case we must have a finite value for G_{00}. In the case that no subsidiary minimum exists and $E(k)$ may be satisfactorily approximated by $E(k) = 2\alpha k^2$ it is necessary to treat seriously the existence of a high wave number cutoff (the Brillouin zone boundary) in the integral for G_{00}. Failure to do so leads to an infinite value for G_{00}. However, in the case we are treating such a cutoff is not necessary to avoid a divergence of G_{00}, and for mathematical simplicity, we extend the range of the integration in $\boldsymbol{k}$ space to include all of $\boldsymbol{k}$ space. In this way we find

$$G^0_{ij} \propto \int_{\text{all }\boldsymbol{k}} \frac{\exp\left[i\boldsymbol{k}\cdot(\boldsymbol{R}_i-\boldsymbol{R}_j)\right]}{E-2\alpha k^2+\beta k^4}\, \mathrm{d}^3\boldsymbol{k} = \left[4\pi\beta(b^2+c^2)\right]^{-1}$$

$$\times \left\{ \frac{\cos b|\boldsymbol{R}_i-\boldsymbol{R}_j| - \exp\left[-c|\boldsymbol{R}_i-\boldsymbol{R}_j|\right]}{|\boldsymbol{R}_i-\boldsymbol{R}_j|} \right\}, \tag{7}$$

where b^2 and $-c^2$ are solutions of $E-2\alpha k^2+\beta k^4 = 0$. We may of course add to this result any solution of the homogeneous equation, i.e. the Schrodinger equation in the Wannier function representation for the periodic potential problem *with energy E*. We may usefully consider such solutions to be $\exp\left[i\boldsymbol{k}\cdot(\boldsymbol{R}_i-\boldsymbol{R}_j)\right]$ where $E(\boldsymbol{k}) = E$. We thus consider Green's functions of the form

$$G_{ij} = G^0_{ij} + K(\boldsymbol{k}) \exp\left[i\boldsymbol{k}\cdot(\boldsymbol{R}_i-\boldsymbol{R}_j)\right], \tag{8}$$

which give rise to solutions of a perturbed problem resembling as closely as possible unperturbed Bloch states. If the impurity potential is of the form (6) then the equation (5) gives rise to the eigenvalue condition

$$1 = V_0 G_{00}$$

or

$$\frac{1}{V_0} = \frac{c}{4\pi\beta(b^2+c^2)} + K(\boldsymbol{k}). \tag{9}$$

We see that for any energy that would give rise to a discrete level associated with the subsidiary minimum we may choose $K(\boldsymbol{k})$ to satisfy equation

(9). Thus we see that no completely bound state can exist for a very localized potential. Even if equation (9) could be solved with $K(\mathbf{k}) = 0$, the resultant solution (for a single energy) would contain almost equal portions of localized and continuum parts. We have thus extended Slater and Koster's result for the absence of localized levels associated with a subsidiary minimum of an energy band and a strongly localized impurity potential to a three dimensional case.

Let us now for comparison examine the case of a Coulomb impurity potential screened by the static dielectric constant. The main point of our work is to show that this potential gives rise, for a spherical band, rigorously in the limit that the potential is slowly varying, and approximately in other cases, to bound states which are coincident in energy with continuum states of the perturbed problem. For this purpose it is convenient to write the Schrodinger equation in the Bloch representation:

$$\sum_{\substack{n'\\ \mathbf{k}'}} (n\mathbf{k}|H_0+U|n'\mathbf{k}')A_{n'}(\mathbf{k}') = EA_n(\mathbf{k}). \qquad (10)$$

Here $U(\mathbf{r}) = e^2/\epsilon r$ (ϵ is the static dielectric constant) and $H_0 = (-\hbar^2/2m)\nabla^2+V(\mathbf{r})$ where $V(\mathbf{r})$ is the periodic potential. $U(\mathbf{r})$ is, of course, an approximate impurity potential energy which has been justified for semiconductors by many workers using recent many-body theory.[3] Following Kohn[4] we now write these equations in a form which separates the isolated band (subscript 0) under discussion from all other bands:

$$\begin{aligned}(E_0(\mathbf{k})-E)A_0(\mathbf{k})+\sum_{\mathbf{k}'}(0\mathbf{k}|U|0\mathbf{k}')A_0(\mathbf{k}')+\sum_{\substack{n'\neq 0\\ \mathbf{k}'}}(0\mathbf{k}|U|n'\mathbf{k}')A_{n'}(\mathbf{k}') &= 0,\\ (E_n(\mathbf{k})-E)A_n(\mathbf{k})+\sum_{\mathbf{k}'}(n\mathbf{k}|U|0\mathbf{k}')A_0(\mathbf{k}')+\sum_{\substack{n'\neq 0\\ \mathbf{k}'}}(n\mathbf{k}|U|n'\mathbf{k}')A_{n'}(\mathbf{k}') &= 0, \quad n\neq 0, \qquad (11)\end{aligned}$$

where $A_n(\mathbf{k})$ is the amplitude of the Bloch function with wave vector $\mathbf{k}$ in band n. Here we have used the fact that

$$(n\mathbf{k}|H_0|n'\mathbf{k}') = E_n(\mathbf{k})\delta_{nn'}\delta_{\mathbf{k}\mathbf{k}'}.$$

The matrix elements of the perturbation are given by

$$(n\mathbf{k}|U|n'\mathbf{k}') = -\sum_{\nu} C^{\nu}_{n\mathbf{k};n'\mathbf{k}'}\left(\frac{e^2}{2\pi^2\epsilon|\mathbf{K}_\nu+\mathbf{k}'-\mathbf{k}|^2}\right), \qquad (12)$$

where $\mathbf{K}_\nu$ is a reciprocal lattice vector and $C_{n\mathbf{k};n'\mathbf{k}'}$ is the νth coefficient in the Fourier expansion of the product of the periodic parts of the Bloch functions $\psi_{n\mathbf{k}}(\mathbf{r})$ and $\psi_{n'\mathbf{k}'}(\mathbf{r})$. In particular $C^{0}_{n\mathbf{k};n'\mathbf{k}} = \delta_{nn'}$.

The Coulomb potential is slowly varying except in the cell containing the impurity atom. In the familiar situation of a band with no subsidiary minimum it is assumed that only Bloch functions with wave vectors near the minimum will contribute appreciably to any bound impurity state wave functions. Thus all terms in equation (12) with $\mathbf{K}_\nu \neq 0$ are neglected, and all interband terms are at first neglected because the impurity potential matrix elements are much smaller than typical interband energies. Furthermore $E(\mathbf{k})$ is approximated by $E_0+(\alpha/2)(\mathbf{k}-\mathbf{k}_0)^2$, an expression valid near the band minimum $\mathbf{k}_0$. The restriction that $\mathbf{k}$ lie within the Brillouin zone is then lifted and the usual slowly varying hydrogen atom type envelope functions result, together with a hydrogen atom energy spectrum, for the bound levels. Finally one can check that the envelope functions only involve small $\mathbf{k}$ values, thus establishing the consistency of the solution.

When a subsidiary minimum exists it is not clear that all $\mathbf{K}_\nu \neq 0$ can be neglected. Let us nevertheless make the same assumptions for the subsidiary minimum problem as were made in the case in which there is only an absolute minimum and examine the justification later. We neglect all $\mathbf{K}_\nu \neq 0$, and interband effects, and we extend the range of $\mathbf{k}$ out of the Brillouin zone into all reciprocal space. However we now use an $E(\mathbf{k})$ that allows a subsidiary minimum. In addition we assume a spherical band in order that we can solve the equations for the envelope function. The impurity equation in $\mathbf{k}$ space then becomes

$$(E(\boldsymbol{k})-E)A_0(\boldsymbol{k})$$

$$-\frac{1}{2\pi}\int \frac{e^2}{\epsilon|\boldsymbol{k}-\boldsymbol{k}'|^2}A_0(\boldsymbol{k}')\,\mathrm{d}^3k' = 0, \qquad (13)$$

where the sum over $\boldsymbol{k}'$ in (11) has been changed to an integral. We take $E(\boldsymbol{k}) = \varepsilon_0+\varepsilon_1\cos k+\varepsilon_2\cos 2k$ where the conditions $\varepsilon_1+4\varepsilon_2<0$ and $\varepsilon_1>0$ establish a subsidiary minimum at $k = 0$ and an absolute minimum at $k = \pi$. Here k is the magnitude of $\boldsymbol{k}$.

If we now return the problem to "real" space by multiplying by $\exp(i\boldsymbol{k}\cdot\boldsymbol{r})$ and integrating over reciprocal space, we find the following equation for the envelope function $X(\boldsymbol{r})$

$$[\cos([-\nabla^2]^{1/2})+\delta\cos(2[-\nabla^2]^{1/2})-\eta/r]$$
$$\times\chi(\boldsymbol{r}) = -\varepsilon\chi(\boldsymbol{r}) \qquad (14)$$

where $\delta = \varepsilon_2/\varepsilon_1$, $\eta = e^2/\epsilon\varepsilon_1$, and $\varepsilon = (E-\varepsilon_0)/\varepsilon_1$. Here we understand the cos terms to mean their power series. Because the Hamiltonian is spherically symmetric we can write

$$\chi(\boldsymbol{r}) = R(r)Y_l^m(\theta,\phi),$$

We then find that

$$\nabla^2\chi = \left[O_rR-\frac{l(l+1)}{r^2}R\right]Y_l^m(\theta,\phi),$$

where

$$O_r = \frac{1}{r^2}\frac{\mathrm{d}}{\mathrm{d}r}\left(r^2\frac{\mathrm{d}}{\mathrm{d}r}\right).$$

Similarly,

$$(\nabla^2)^n\chi = \left(O_r-\frac{l(l+1)}{r^2}\right)^n R(r)Y_l^m(\theta,\phi).$$

Let us first treat the case $l = 0$. We let $R(r) = F(r)/r$ and find that the equation for F becomes

$$\sum_{n=0}^{\infty}\frac{F^{2n}}{2(n)!}+\delta\sum_{n=0}^{\infty}\frac{2^{2n}F^{2n}}{(2n)!}-\frac{\eta}{r}F = -\varepsilon F, \qquad (15)$$

where

$$F^{2n} = \frac{\mathrm{d}^{2n}F}{\mathrm{d}r^{2n}}.$$

This equation is a generalization of the confluent hypergeometric equation,(5) and it is thus not surprising that when we try a solution of the form $R(r) = \exp(-\alpha r)$ the resulting equations for α,

$$\cosh\alpha+\delta\cosh 2\alpha+\varepsilon = 0, \qquad \text{(a)}$$
$$-\sinh\alpha-2\delta\sinh 2\alpha-\eta = 0, \qquad \text{(b)} \qquad (16)$$

have a solution with α real. These equations arise when the coefficients of the different powers of r are set equal to zero. Equation (16a) gives the energy when α is known and equation (16b) gives α in terms of the parameters of the problem, including the strength of the impurity potential. Equation (16b) has two solutions for α, one real and positive, and the other of the form $\alpha = i\pi+\gamma$, where γ is positive. These solutions correspond to bound states splitting off from the band at $k = 0$ and $k = \pi$ respectively.

For α or γ small the equations may be solved approximately yielding the usual effective mass results:

$$\alpha = -\frac{\eta}{1+4\delta}, \quad \varepsilon_\alpha = -\delta-1+\frac{\eta^2}{2|1+4\delta|};$$

$$\gamma = \frac{-\eta}{-1+4\delta}, \quad \varepsilon_\gamma = -\delta+1+\frac{\eta^2}{2|-1+4\delta|}. \qquad (17)$$

It can be seen that for the form of $E(k)$ that we used $\alpha>\gamma$ no matter what the values of η and δ, but that equality of these quantities is approached when δ becomes large. Bound states of higher energy for $l = 0$ can undoubtedly be constructed. For $l \neq 0$ it is not possible to solve the differential equation exactly. However, for large r all contributions from $l(l+1)/r^2$ in equation (14) are negligible so that the *asymptotic* solution $\exp(-\alpha r)$, where α has a positive real part, is again possible.

Our result shows that, to the extent that the potential energy in the equation for the envelope function can be assumed to be Coulomb-like, bound impurity states of the effective mass type may be associated with a subsidiary minimum in a spherical band. In contrast with the case of the localized impurity, it is not true that all states with energies in the unperturbed band region contain admixtures of continuum states. It is reasonable to expect that this result does not depend critically on the use of a spherical band but we have not studied this point in detail.

Of great interest is the possible effect of a deviation of the potential that should be inserted in the envelope equation from the Coulomb form. In this connection we remember that there are two effects to consider: the neglect of $\boldsymbol{K}_\nu \neq 0$ and the extension of the Brillouin zone to all of $\boldsymbol{k}$ space. These effects are indeed connected. Consider first the effect of the extension of the band to all reciprocal space on the term $1/|\boldsymbol{k}'-\boldsymbol{k}|^2$. If the band were not extended we would be omitting high $\boldsymbol{k}-\boldsymbol{k}'$, thus putting a bottom on the potential well. This should not matter as long as no bound states lie near the bottom of the well. Now consider the term proportional to $1/|\boldsymbol{k}-\boldsymbol{k}'-\boldsymbol{K}_\nu|^2$. The coefficient of this term, $C^\nu_{0\boldsymbol{k};0\boldsymbol{k}'}$, is not likely to be greater than unity but can be counted on to be of order unity until ν gets large, in which case no large contributions are expected anyway. We will neglect the $\boldsymbol{k}$ and $\boldsymbol{k}'$ dependencies of $C^\nu_{0\boldsymbol{k};0\boldsymbol{k}'}$ and set this coefficient equal to unity. We are thus led to terms in the potential energy of the form

$$\int_{\text{B.Z.}} \frac{\exp[i(\boldsymbol{k}-\boldsymbol{k}')\cdot\boldsymbol{r}]}{|\boldsymbol{k}-\boldsymbol{k}'-\boldsymbol{K}_\nu|^2}\,\mathrm{d}^3\boldsymbol{k}. \tag{18}$$

If we extend the boundary of the Brillouin zone to infinity this term gives

$$\exp(i\boldsymbol{K}_\nu\cdot\boldsymbol{r})\int \frac{\exp[i(\boldsymbol{k}-\boldsymbol{k}'-\boldsymbol{K}_\nu)\cdot\boldsymbol{r}]}{|\boldsymbol{k}-\boldsymbol{k}'+\boldsymbol{K}_\nu|^2}\,\mathrm{d}^3(\boldsymbol{k}-\boldsymbol{k}'-\boldsymbol{K}_\nu)$$

$$\propto \frac{\exp(i\boldsymbol{K}_\nu\cdot\boldsymbol{r})}{r}.$$

Including both $\boldsymbol{K}_\nu$ and $-\boldsymbol{K}_\nu$, we get a contribution to the potential of the form

$$V \propto \frac{\cos \boldsymbol{K}_\nu\cdot\boldsymbol{r}}{r}. \tag{19}$$

Terms such as equation (19) are *smaller* than the $1/r$ we have been using. If the zone is not extended to infinity, the integrals become very hard to do, and it is questionable whether the approximations of the problem warrant such a calculation. This discussion shows that it is not easy to find the proper potential to use in the envelope function equation when the real potential (for low lying states) in the Schrodinger equation is the Coulomb potential. However, it is also indicated that the Coulomb potential is surely of the right order of magnitude and it is a bit surprising that bound states coincident in energy with continuum states exist for this potential. Perhaps there is a mathematical connection with the fact that the Klein–Gordon equation, in which the kinetic energy can also be thought of as a series in powers of the Laplacian operator, has bound solutions for the hydrogen atom.

A change in the potential from the Coulomb form will probably change the wave functions enough to cause bound states coincident in energy with continuum states to no longer be eigenstates of the impurity problem, but if so the lifetimes of these states will probably be long. An estimate was made of the lifetime of a bound state of the form $u_0(\boldsymbol{r})\exp(-\alpha r)$ with respect to decay into continuum states of the same energy, using a potential of the form (19) summed over the smallest reciprocal lattice vectors and a spherical band of the form used above. The result for the width ΔE of the bound state is

$$\Delta E \cong 3^{(11/2)}4^{-2}5^{-3}\pi^{-2}(B\mathscr{B})^2\left(\frac{e^2\alpha}{2\epsilon}\right)$$

$$\times(\alpha a)\left[\frac{e^2\alpha}{2\epsilon}\frac{1}{|2\varepsilon_2-\varepsilon_1|}\right], \tag{20}$$

where B and $\mathscr{B}$ arise from expansions of products of the periodic parts of two Bloch functions from the same band in terms of a Fourier series in reciprocal lattice vectors,(6) and are of order of unity; a is the Bohr radius, and all other symbols have been defined earlier. Here $e^2\alpha/2\epsilon$ is the energy of a shallow impurity and we see that ΔE is smaller than this by two factors, the first being the ratio of the impurity energy to an energy of the order of a band width, and the second the ratio of the Bohr radius to the impurity orbit radius. Equation (20) gives a lifetime for a typical shallow impurity of 10^{-8}–10^{-9} sec.

In summary, we may say that impurity levels with very long lifetimes are associated with subsidiary minima for a Coulomb impurity potential, although no such levels exist for a very localized impurity potential. It would be interesting to know how slowly the impurity potential must vary in order that localized impurity levels be associated with subsidiary minima.

REFERENCES

1. Zwerdling S., Button K. J., Lax B. and Roth L. M., *Phys. Rev. Letters* **4**, 173 (1960); Bate R. T., *Bull. Amer. phys. Soc.* II **7**, 214 (1962); Bate R. T., *J. appl. Phys.* **33**, 26 (1962).
2. Koster G. F. and Slater J. C. *Phys. Rev.* **95**, 1167 (1954).
3. Klein A., *Phys. Rev.* **115**, 1136 (1959); Kohn W. *ibid.* **110**, 857 (1958).
4. Kohn W., *Solid State Physics* (edited by Seitz F. and Turnbull D.) Vol. **5**, p. 258, Academic Press, New York (1957).
5. All solutions of equation (15) can be found by making a Laplace transform.
6. See equation (12) and the discussion following it.

J. Phys. Chem. Solids Pergamon Press 1963. Vol. 24, pp. 1601–1607. Printed in Great Britain.

SUR LA POLARISATION DE SPIN DES ELECTRONS DE CONDUCTIBILITE DANS LES METAUX FERROMAGNETIQUES

E. DANIEL
Institut de Physique, Strasbourg

et

J. FRIEDEL
(Faculté des Sciences, Orsay, S. & O.)

(*Received* 12 *July* 1963)

Resume—Les électrons de conductibilité d'un métal ferromagnétique peuvent être polarisés par le couplage d'échange *s–d*. Si l'on attribue à cette polarisation de spin le champ magnétique effectif mesuré au noyau d'un atome non magnétique dissous, un calcul simple montre qu'on peut observer un champ local de signe contraire à celui de la polarisation globale des électrons dan la matrice. La comparaison de la théorie aux quelques résultats expérimentaux connus indique que la polarisation est positive dans le fer pur, comme on s'y attend pour une polarisation d'échange *s–d*.

Abstract—*s–d* exchange coupling may polarize the conduction electrons in a ferromagnetic metal. If the effective magnetic field measured at the nucleus of a non-magnetic atom dissolved in the metal is ascribed to this spin polarization, then a simple theory shows that the observed local field may have a sign opposite to that of the overall spin polarization in the matrix. According to this calculation experimental results indicate a positive spin polarization in pure iron as expected for an *s–d* exchange polarization. This is likely to be true also for cobalt and nickel.

1. INTRODUCTION

LE CHAMP magnétique effectif mesuré aux noyaux d'un métal ferromagnétique provient en partie de la polarisation de spin des couches internes et en partie de celle des électrons de conductibilité par interaction d'échange avec les couches d incomplètes.(1,2) On pouvait penser isoler la contribution des électrons de conductibilité, en grandeur et en signe, en mesurant le champ effectif au noyau d'un atome non magnétique dissous dans le métal ferromagnétique. On s'attend à observer une tendance à l'alignement des spins des électrons de conductibilité sur ceux des couches d magnétiques, c'est à dire une polarisation positive. En fait, dans plusieurs cas où le signe du champ effectif a pu être déduit de l'étude de l'effet Mössbauer par exemple ou de l'asymétrie de l'émission β des noyaux polarisés, les mesures ont donné un champ local négatif aux noyaux des atomes dissous.(3,4)

Le cas le plus sûr semble celui de Sn^{119} dissous, pour lequel le champ local vaut—88 kOe dans Fe, -26 kOe dans Co, mais $+16$ kOe dans Ni. KOGAN *et al.*(4) ont trouvé des champs négatifs également pour Re^{186}, Ir^{192} et In^{114} dissous dans le fer. Par contre, le champ serait positif sur Sb dissous dans Fe, avec la valeur 280 kOe; son signe ne semble pas avoir été déterminé pour Al (17 kOe) et Cu (213 kOe) dans Fe. Enfin, le champ mesuré sur l'or dissous dans le fer est exceptionnellement élevé, supérieur à 10^6 Oe; mais les expérimentateurs ne sont pas unanimes sur son signe.(3)

Si l'on admet que les électrons de conductibilité de l'alliage sont seuls responsables du champ local observé au noyau de l'atome dissous, on peut être tenté d'attribuer le champ négatif observé sur Sn dans Fe, par exemple, à une polarisation négative des électrons de conductibilité dans le fer, c'est à dire à un excès d'électrons de spin antiparallèles aux spins des couches *d* par rapport aux électrons de spins parallèles. En réalité, une polarisation positive des électrons de conductibilité de la matrice ferromagnétique peut donner lieu à un champ effectif négatif au noyau d'un atome non magnétique dissous. En effet, le couplage *s–d* est supprimé dans le volume de cet atome et, de plus, celui-ci introduit un potentiel perturbateur qui altère localement la polarisation de la bande de conductibilité, de façon à faire écran à la charge ionique correspondant à la différence de valence entre l'atome dissous et la matrice. Dans ces conditions, il n'est pas surprenant que le champ effectif mesuré sur l'atome dissous diffère en grandeur de la contribution des électrons de conductibilité au champ effectif sur les noyaux de la matrice ferromagnétique. Il peut même être de signe contraire; c'est ce que montre le calcul que nous développons ci-dessous sur un schéma simple. D'après ce calcul, le champ négatif observé sur Sn dissous dans Fe correspond à une polarisation positive des électrons de conductibilité dans le fer. A partir de la valeur mesurée du champ sur Sn, nous calculons la contribution des électrons de conductibilité au moment ferromagnétique du fer pur. Il est bien évident que des résultats vraiment quantitatifs ne peuvent pas être basés sur un schéma aussi sommaire que celui que nous utilisons, mais la valeur obtenue: 0,1 μ_B par atome, semble très raisonnable.

Nous considérons à part le cas du nickel, qui nécessite un schéma différent; les données magnétiques ne permettent guère de savoir à quel modèle donner la préférence pour le cobalt, mais il est très vraisemblable que la polarisation des électrons de conductibilité y soit positive, comme dans le fer.

2. POLARISATION DE SPIN DANS LE MÉTAL PUR

Dans un métal ferromagnétique pur, l'interaction d'échange *s–d* entre les électrons de conductibilité et les couches d magnétiques tend à stabiliser l'une des directions de spin des électrons de conductibilité par rapport à l'autre, relativement à la direction de l'aimantation. Ceci conduit à considérer deux demi-bandes de conductibilité, décalées l'une par rapport à l'autre de l'énergie d'échange 2ϵ et remplies jusqu'au même niveau de Fermi E_F (Fig. 1). Pour les besoins du calcul, nous admettrons dans la suite que les électrons de chaque demi-bande se comportent approximativement comme des électrons libres, avec des fonctions d'ondes de Bloch de la forme:

$$\phi_k(\mathbf{r}) = \phi_0(\mathbf{r}) \exp(i\mathbf{k}\mathbf{r}) \tag{1}$$

où la fonction périodique $\phi_0(\mathbf{r})$ ne dépend pas du vecteur d'onde $\mathbf{k}$. Dans ces conditions, l'énergie d'un électron de vecteur d'onde $\mathbf{k}$ vaut:[*]

$$E(\mathbf{k}) = \frac{k^2}{2} \pm \epsilon \tag{2}$$

le signe à prendre devant ϵ étant − ou +, selon que l'orientation du spin est positive ↑ ou négative ↓ .

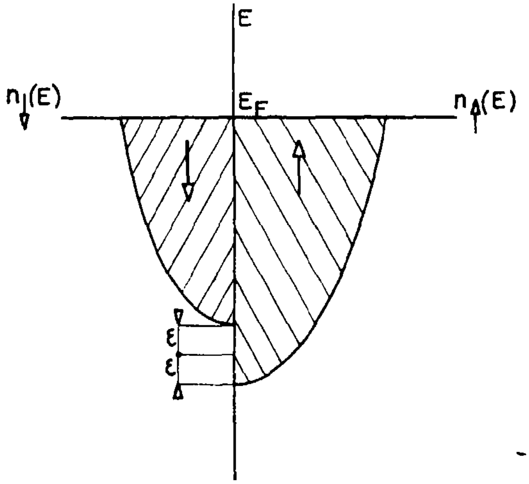

FIG. 1. Polarisation de spin des électrons de conductibilité d'un métal ferromagnétique. ↑ direction du spin des couches *d*.

Soit $k_{F\uparrow}$ et $k_{F\downarrow}$ les modules des vecteurs d'ondes au niveau de Fermi dans les deux demi-bandes. La densité des états par unité de volume du métal et par unité d'énergie étant $k/(2\pi^2)$ dans chaque demi-bande, l'excès d'électrons de spin ↑ sur le nombre d'électrons de spin ↓ par unité de volume du métal vaut:

---

[*] Sauf mention du contraire, les formules sont écrites dans le système d'unités atomiques de Hartree, où $e = m = \hbar = 1$.

$$\delta n = \frac{1}{2\pi^2}\int_0^{k_{F\uparrow}} k^2\,\mathrm{d}k - \frac{1}{2\pi^2}\int_0^{k_{F\downarrow}} k^2\,\mathrm{d}k$$

$$= \frac{k_{F\uparrow}^3 - k_{F\downarrow}^3}{6\pi^2} \simeq \frac{k_F\epsilon}{\pi^2} \qquad (3)$$

avec $k_F^2 = 2E_F \cdot k_F$ définirait le niveau de Fermi en l'absence de polarisation de spin; d'autre part, l'énergie d'échange est beaucoup plus petite que l'énergie de Fermi: $\epsilon \ll k_F^2$.

3. STRUCTURE ELECTRONIQUE DE L'ALLIAGE

En général, l'addition de petites quantités d'éléments non magnétiques, en particulier d'étain, au fer diminue le moment magnétique de celui-ci de 2,2 μ_B par atome dissous, sans changement du point de Curie.(5) On peut donc admettre, en première approximation qu'un atome d'étain se substitue à une atome de fer sans affecter les atomes de fer voisins. Pour le nickel, au contraire, la diminution du moment moyen de l'alliage correspond quantitativement au remplissage de la bande d par les électrons de valence de l'élément dissous.(5,6) Le modèle d'alliage que nous utilisons ci-dessous s'applique en principe au fer, peut être aussi au cobalt, mais pas au nickel, pour lequel nous introduirons un autre schéma plus loin.

Soit C le nombre d'électrons de conductibilité par atome du métal ferromagnétique M dans lequel on a dissous en très petite quantité un élément X non magnétique de valence $V = C+Z$. Nous supposons la solution solide parfaite de façon à pouvoir considérer isolément chaque atome dissous. Nous décrivons la présence d'un atome X substitué à un atome M par un potentiel perturbateur qui sera particulièrement important si Z est élevé. Ce potentiel produit une polarisation électrostatique des électrons de conductibilité autour de l'atome X, dont ils écrantent l'excès de charge Z. D'autre part, l'absence de couche magnétique dans l'atome X supprime le couplage d'échange dans le volume occupé par cet atome.

Le schéma sur lequel nous basons notre calcul repose sur les approximations suivantes:

—les électrons de conductibilité du métal M pur sont assimilés à des électrons libres dont la fonction d'onde est modulée par la fonction de bas de bande $\phi_0(1)$;

—la perturbation due à l'atome dissous X est représentée par un puits de potentiel de rayon a et de profondeur $k_0^2/2$.

Nous avons fixé la valeur de a par la condition $k_F\,a = 2$, ce qui correspond à une valeur légèrement supérieure au rayon atomique de M si on suppose que celui-ci contient un électron de conductibilité par atome. k_0 est déterminé par la condition que la charge électronique attirée par le puits de potentiel neutralise exactement l'excès Z de charge ionique de X sur M.(7) Avec $C = 1$ et $V = 4$, on a $Z = 3$ pour FeSn. Le produit k_0a croît de façon monotone avec Z et vaut 2,31 pour $Z = 3$. En fait, nous calculons k_0a en effectuant la correction de Harrison pour l'effet de taille, telle qu'elle a été utilisée avec succès par BLATT(8) pour le calcul des résistivités résiduelles des métaux nobles. L'étain, par exemple, avec un rayon atomique de 1,86 Å, dilate le réseau du fer, dont le rayon atomique vaut seulement 1,40 Å, et, par conséquent, repousse le fond continu de charge positive. Dans ces conditions, la charge d'écran à fournir par les électrons de conductibilité prend une valeur effective $Z' < Z$. Calculé suivant l'approximation de l'élasticité classique, le rayon d'équilibre de l'étain dissous dans le fer vaut 1,58 Å, ce qui correspond à une charge d'écran effective.

$$Z' = Z - \frac{\delta v}{v} = 2{,}56$$

v désignant le volume atomique du fer et δv celui de l'étain dissous. Cette charge d'écran effective est obtenue avec une profondeur du puits de potentiel définie par $k_0a = 2{,}18$.

Jusqu'ici, n'avons pas tenu compte de la polarisation de spin de la bande de conductibilité, ou, si l'on préfère, nous avons supposé l'alliage non aimanté. Imaginons maintenant que l'aimantation s'établisse. L'interaction d'échange *s–d* décale les deux demi-bandes de conductibilité de $\pm\epsilon$ par rapport au bas de bande "initial", le niveau de Fermi restant sensiblement le même pour ϵ petit ($\epsilon \ll k_F^2$). Nous sommes alors conduits au schéma suivant (Fig. 2): l'atome X agit sur les électrons de conductibilité par un puits de potentiel de rayon

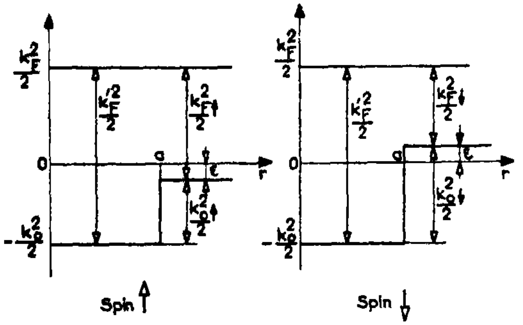

FIG. 2. Potential agissant sur les électrons de conductibilité, selon leur spin, dans la sphère atomique de l'atome dissous. a = rayon de la sphère atomique.

a et dont le fond se situe à$(k_F'^2/2)$ au-dessous du niveau de Fermi. La profondeur effective de ce puits de potentiel n'est pas la même pour les deux directions de spin à cause du décalage des deux demi-bandes de conductibilité; elle vaut $(k_0^2/2)-\epsilon$ pour les électrons de spin ↑, mais $k_0^2/2+\epsilon$ pour les électrons de spin ↓. On a d'ailleurs:

$$k_F'^2 = k_F^2+k_0^2 \tag{4}$$

4. POLARISATION DE SPIN AU NOYAU D'ATOME DISSOUS

Il est déjà possible de se rendre compte, qualitativement, sur ce schéma pourquoi la polarisation locale de spin mesurée au noyau de l'atome X dissous peut être de signe contraire à la polarisation globale des électrons de conductibilité dans la matrice M. En effet, si celle-ci est positive, par exemple, c'est à dire s'il y a moins d'électrons de spin ↓ que d'électrons de spin ↑, le potentiel de l'atome X devient plus attractif pour les électrons de spin ↓ que pour ceux de spin ↑, à cause de la suppression de l'interaction d'échange dans le volume de cet atome. La densité locale de spin au noyau X, pris pour origine des coordonnées:

$$\begin{aligned}\delta\rho(0) &= \rho_\uparrow(0)-\rho_\downarrow(0)\\ &= \sum_{k\uparrow}\left|\psi_{k\uparrow}(0)\right|^2-\sum_{k\downarrow}\left|\psi_{k\downarrow}(0)\right|^2\end{aligned} \tag{5}$$

peut devenir négative si l'amplitude à l'origine $\psi_{k\downarrow}(0)$ des fonctions d'ondes de spin ↓ dans l'alliage est suffisamment plus grande, en moyenne, que celle des électrons de spin ↑. Ceci a des chances de se produire quand le potentiel de l'atome X est assez fort pour lier des électrons (ce qui est le cas pour Fe Sn); en effet, les états liés de spin ↓ sont alors plus fortement liés que ceux de spin ↑. Compte tenu de la complexité de la structure électronique réelle des alliages des métaux de transition, il va de soi qu'un calcul de la polarisation de spin basé sur un schéma aussi simple que celui que nous adoptons ici peut prétendre, tout au plus, à une estimation d'ordre de grandeur. Le calcul qui suit n'est destiné qu'à rendre plausible l'explication proposée ci-dessus. Les résultats en confirment simplement la vraisemblance.

Nous précisons maintenant la structure des fonctions d'ondes ψ_k de la formule (5), qui décrivent les électrons de conductibilité de chaque direction de spin dans l'alliage. Supposons la fonction de bas de bande ϕ_0 de la formule (1) calculée par la méthode de Wigner–Seitz dans la sphère atomique de la matrice M; dans le volume occupé par l'élément X dans l'alliage, on doit lui substituer la fonction $u(r)$ que l'on calculerait par la même méthode avec la potentiel atomique de l'atome X dissous. Au voisinage du noyau, $u(r)$ se comporte comme la fonction d'onde vraie d'un électron de valence de X. Le puits de potentiel n'agit que sur la partie e^{ikr} des fonctions de Bloch (1) et a pour effet de les remplacer dans l'alliage par des fonctions d'ondes diffusées. Les fonctions d'ondes ψ_k s'obtiennent en multipliant les fonctions d'ondes diffusées par $u(r)$ pour $r < a$ et par $\phi_0(r)$ pour $r > a$. Il est commode d'analyser les fonctions d'ondes diffusées en composantes sphériques. Seules les composantes s contribuent à la densité au noyau; celle-ci vaut, pour chaque direction de spin:(9)

$$\rho'(0) = \frac{2a^3}{3\pi}|u(0)|^2\int\limits_0^{k_F}\frac{k^2\,\mathrm{d}k}{1-(k_0^2/k'^2)\sin^2 k'a} \tag{6}$$

où $k'^2 = k_0^2+k^2$, pourvu que $u(r)$ soit normalisée dans la sphère de rayon a. De la formule (6), on déduit la densité de spin au noyau X dûe aux électrons de la bande de conductibilité de l'alliage:

$$\delta\rho'(0) = \rho'_\uparrow(0)-\rho'_\downarrow(0) = -2\epsilon\frac{\partial\rho'(0)}{\partial(k_0^2/2)}, \tag{7}$$

la dérivée étant prise pour une valeur constante de k_F'.

A ceci s'ajoute la contribution des électrons éventuellement liés dans un état s par le puits de potentiel. La fonction $u(r)$ étant approximativement constante dans la majeure partie du volume atomique (mais pas au voisinage du noyau), la densité à l'origine d'un état s lié vaut:

$$\rho''(0) = \frac{2}{3}|u(0)|^2 \frac{(\mu a)^2}{1-(\mathrm{tg}\,\mu a/\mu a)}, \qquad (8)$$

où: $\lambda^2+\mu^2 = k_0^2$ et: $\lambda a = -(\mu a/\mathrm{tg}\,\mu a)$, l'énergie de liaison étant $\lambda^2/2$. La fonction d'onde normalisée $\psi_s(r)$ du premier état s lié du puits de potentiel a en effet pour densité à l'origine:

$$|\psi_s(0)|^2 = \frac{1}{2\pi a^3}\frac{(\mu a)^2}{1-(\mathrm{tg}\,\mu a/\mu a)}$$

Aux deux demi-bandes de conductibilité polarisées correspondent deux profondeurs différentes du puits de potentiel et, par conséquent, des énergies de liaison et des densités à l'origine différentes pour les états liés. La densité de spin au noyau X dûe à ces électrons liés est:

$$\delta\rho''(0) = \rho''_{\uparrow}(0)-\rho''_{\downarrow}(0) = -2\epsilon\frac{\partial\rho''(0)}{\partial(k_0^2/2)} \qquad (9)$$

La densité totale de spin électronique (5) au noyau de l'atome X est la somme des densités (8) et (9):

$$\delta\rho(0) = \delta\rho'(0)+\delta\rho''(0). \qquad (10)$$

Elle n'a pas nécessairement le signe de la polarisation globale δn définie par (3), des électrons de conductibilité dans la matrice M.

5. CHAMP EFFECTIF AU NOYAU

Le champ effectif H_{eff} créé par les électrons de conductibilité au noyau de l'atome X peut se déduire, par analogie, de la formule qui donne le déplacement de Knight $(\Delta H)/H$ dans un métal ordinaire:(10)

$$\frac{\Delta H}{H} = \frac{8\pi}{3}\chi_A|\psi_F(0)|^2 = \frac{a_s\chi_A\xi}{2g_N\mu_B} \qquad (11)$$

Dans cette formule, χ_A désigne la susceptibilité de spin, par atome, des électrons de conductibilité et $|\psi_F(0)|^2$ la densité au noyau des électrons du niveau de Fermi, calculée avec une fonction ψ_F normalisée dans le volume atomique;

$$a_s = \frac{16\pi}{3}g_N\mu_B|\psi_A(0)|^2$$

est la constante de couplage hyperfin de l'atome X, g_N le facteur g nucléaire de X, μ_B le magnéton de Bohr et ψ_A la fonction d'onde d'un électron de valence. ξ est le facteur de Knight:

$$\xi = \frac{|\psi_F(0)|^2}{|\psi_A(0)|^2}$$

La formule (11) du déplacement de Knight peut encore s'écrire:

$$\Delta H = \frac{a_s\xi}{2g_N\mu_B}\eta_A \qquad (12)$$

où η_A désigne l'aimantation par atome de métal résultant de l'orientation des électrons de conductibilité par le champ H appliqué.

Dans le cas de l'alliage MX, η_A apparaît spontanément du fait de la polarisation des électrons de conductibilité par les couches d:

$$\eta_A = \mu_B\delta n = \frac{4\pi a^3}{3}\frac{\mu_B k_F\epsilon}{\pi^2} = \frac{4a^3}{3\pi}\mu_B k_F\epsilon, \qquad (13)$$

d'après (3).

La fonction $u(r)$ étant normalisée dans la sphère atomique, on peut prendre, en première approximation:

$$\psi_A(0) \simeq u(0)$$

pour le calcul du champ local sur le noyau X. On a alors:

$$\frac{\eta_A}{\mu_B}\xi = \frac{\delta\rho(0)}{|u(0)|^2}$$

dans la formule (12), ce qui conduit à l'expression suivante du champ effectif H_{eff} au noyau X dissous:

$$H_{\mathrm{eff}} \simeq \frac{a_s}{2g_N}\frac{\delta\rho(0)}{|u(0)|^2} \qquad (14)$$

6. COMPARAISON AUX RESULTATS EXPERIMENTAUX

Nous avons calculé numériquement la polarisation de spin au noyau X en fonction de la charge d'écran Z, qu'on peut supposer corrigée pour l'effet de taille, en prenant $k_F a = 2$. (cf. 3). Le puits de potentiel possède un état s lié pour $k_0 a > \pi/2$, c'est à dire quant Z dépasse une valeur voisine de 1,2. Les résultats sont illustrés par la Fig. 3, où sont portées, en fonction de Z, les quantités f', f'' et $f = f' + f''$ définies par:

$$\delta\rho' = \frac{4\epsilon a^2}{3\pi}|u(0)|^2 f' \quad \text{et} \quad \delta\rho'' = \frac{4\epsilon a^2}{3\pi}|u(0)|^2 f'' \qquad (15)$$

f' représente la contribution des états étendus de la bande de conductibilité de l'alliage, f'' celle des états liés du puits de potentiel. Chacun de ces termes est discontinu pour $k_0 a = \pi/2$ (apparition de l'état lié), f'' étant nul pour $k_0 a < \pi/2$, mais la somme $f' = f''$ est continue.

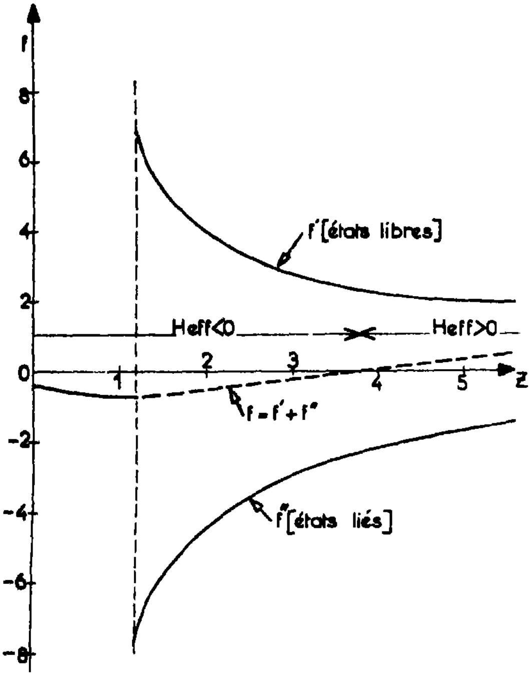

FIG. 3. Polarisation de spin au noyau de l'atome dissous. (f'' = pour $Z \lesssim 1,2$).

Si l'on ne tenait pas compte du renforcement, local de densité électronique à l'origine lié à la localisation de la charge d'écran, le diagramme de la Fig. 3 se réduirait à la droite d'ordonnée $f = 2$, correspondant à un champ H_{eff} positif. L'analyse détaillée de la formation de l'écran montre au contraire que le champ local doit être négatif tant que la charge d'écran ne dépasse pas une valeur de l'ordre de 3 à 4. (Il est bien évident que la valeur exacte de cette charge dépend de la valeur choisie pour le produit $k_F a$ et de la précision avec laquelle le schéma extrêmement simplifié que nous avons utilisé représente la réalité.) Conformément à des résultats expérimentaux qui avaient surpris certains auteurs, notre calcul prédit que, dans le fer par exemple, le champ effectif mesuré au noyau d'un atome dissous doit être négatif dans la plupart des cas. C'est bien ce qui est observé sur Sn($Z' \simeq 2,5$), In, Ir et Re ($Z' \simeq 0$ à 1). Pour Sb($Z' \simeq 3,4$)H_{eff} pourrait être positif, mais les résultats expérimentaux ne semblent pas très sûrs eux-mêmes.

Il nous faut insister sur le fait que le schéma utilisé ci-dessus ne fait intervenir que les électrons de conductibilité de l'alliage; il suppose que les couches internes du soluté ne sont pas polarisées. Il a des chances d'être valable surtout quand Z est assez grand pour que l'effet d'écran soit l'essentiel. D'autres effets peuvent être prépondérants lorsque la différence du nombre d'électrons de conductibilité entre la matrice et le soluté n'est pas bien définie. Ceci semble être le cas, en particulier, pour l'or dissous dans le fer. Les valeurs très élevées du champ effectif mesuré aux noyaux d'or sont probablement liés à la présence de la couche 5 d de l'or, peu profonde, qui peut se combiner à la couche magnétique 3 d du fer et polariser ses propres couches internes.

Dans l'étain, la couche 4 d est probablement assez profonde pour que notre schéma représente raisonnablement la réalité.

Avec un spin $I = \frac{1}{2}$ et un moment nucléaire $\mu = -1{,}046\,\mu_N$(11) Sn^{119} a un facteur $g_N \simeq 2$. Si l'on prend $a \simeq 3$ unités atomiques et, pour la constante de couplage hyperfin corrigée d'après KNIGHT,(10) la valeur $a_s \simeq 0{,}5$ cm^{-1}, on obtient, d'après (14) et (15) pour valeur du champ effectif en oersteds:

$$H_{\text{eff}} \simeq 0{,}8\ 10^6\,\epsilon f,$$

à condition d'exprimer l'énergie ϵ du couplage s–d en électron-volts par atomes. Avec $f \simeq 0{,}3$, d'après le graphique de la Fig. (3), on obtient la valeur expérimentale—88 kOe pour $\epsilon \simeq 0{,}4$ eV, ce qui semble d'un ordre de grandeur acceptable. En effet, ceci correspond, d'après (13) à une contribution des électrons de conductibilité au moment ferromagnétique du fer: $\eta_A = 0{,}12\,\mu_B$ par atome, ce qui est une valeur tout à fait raisonnable.

Il est possible que le modèle précédent s'applique encore au cobalt comme solvant, au lieu du fer, bien que les données magnétiques sur les alliages de cobalt ne permettent pas de l'affirmer.(5) S'il est valable, il associe encore une polarisation positive des électrons de conductibilité au champ effectif négatif mesuré sur l'étain dissous dans le cobalt.

Comme on l'a vu plus haut (3) le schéma précédent n'est certainement pas applicable au nickel, que nous allons considérer séparément.

7. CAS DU NICKEL

Alors que les atomes non magnétiques dissous dans le fer ont généralement un écran assez localisé pour ne pas perturber beaucoup les atomes de fer voisins, il n'en va pas de même pour le nickel. Les mesures magnétiques indiquent clairement que dans celui-ci les quatre électrons supplémentaires introduits avec un atome d'étain vont remplir la bande $3d$ incomplète de la matrice.(5,6) Comme cette bande ne contient que 0,6 trous par atome, chaque atome dissous supprime le couplage s–d dans une sphère de rayon R relativement grand autour de l'impureté (Fig. 4). Si b désigne le rayon atomique du nickel, on a approximativement, dans le cas de Ni Sn:

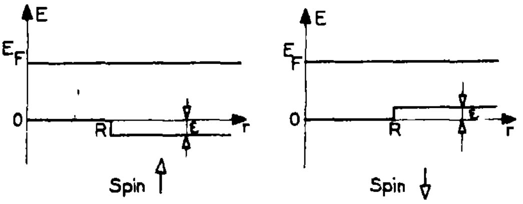

FIG. 4. Polarisation de spin des électrons de conductibilité dans Ni Sn.

$$\frac{R}{b} = \left(\frac{4}{0{,}6}\right)^{1/3}$$

en négligeant les effets de taille, qui ne modifient guère le résultat. Le puits de potentiel a maintenant une profondeur pratiquement nulle, puisque les électrons de conductibilité ne participent pratiquement pas à l'écran. Dans ces conditions, la fonction f du paragraphe précédent se réduit à:

$$f = \frac{\sin 2k_F R}{2}$$

Pour la valeur de R indiquée ci-dessus, on a:

$$k_F R = 1{,}92(0{,}6)^{1/3}\left(\frac{4}{0{,}6}\right)^{1/3} = 3{,}05$$

donc: $f \simeq -0{,}1$, valeur négative alors que H_{eff} est positif, mais relativement petit: 16 kOe. Ce désaccord apparent peut tenir à la simplification extrême du schéma. Il suffit d'augmenter la valeur de R de 5% seulement pour obtenir un champ positif et du bon ordre de grandeur.

BIBLIOGRAPHIE

1. MARSHALL W., *Phys. Rev.* **110,** 1280 (1958).
2. FREEMAN A. J. and WATSON R. E., *The Mössbauer Effect, Proceedings of the Second International Conference on the Mössbauer Effect,* Saclay (1961). p. 117. Wiley, New York (1962).
3. On trouvera des tableaux détaillés des principaux résultats expérimentaux dans les articles suivants: (a) L. Meyer-Shützmeister: *The Mössbauer Effect, Proceedings of the Second International Conference on the Mössbauer Effect,* Saclay (1961). p. 190. Wiley, New York (1962). (b) W. Marshall and C. E. Johnson, *J. Phys. Radium* **23,** 733 (1962).
4. KOGAN A. V., KUL'KOV V. D., NIKITIN L. P., REINOV N. M., STEL'MAKH N. F. and SCHOTT M., Sov. Phys. *J. exp. theor. phys.* **16,** 586 (1963); *J. exp. theor. phys. U.S.S.R.* **43,** 828 (1962).
5. HOSELITZ K., *Ferromagnetic properties of Metals and Alloys.* Clarendon Press, Oxford (1952).
6. BOZORTH R. M., *Ferromagnetism.* Van Nostrand, New York (1951).
7. FRIEDEL J., *Advanc. Phys.* **3,** 446 (1954); *Nuovo Cim.* Suppl. **7,** 287 (1958).
8. BLATT F. J., *Phys. Rev.* **108,** 285 (1957).
9. DANIEL E., *J. Phys. Chem. Solids* **10,** 174 (1959); *J. Phys. Radium* **20,** 769 (1959).
10. KNIGHT W., *Solid-State Physics* (edited by SEITZ F. and TURNBULL D.). Vol. **2,** p. 93. Academic Press, New York (1956).
11. SMITH K. F., *Progr. nucl. Phys.* **6,** 52 (1957).

J. Phys. Chem. Solids Pergamon Press 1963. Vol. 24, pp. 1609–1615. Printed in Great Britain.

THE TRAPPING OF PHOTOCARRIERS IN ANTHRACENE BY ANTHRAQUINONE, ANTHRONE AND NAPHTHACENE*

D. C. HOESTEREY and G. M. LETSON

Research Laboratories, Eastman Kodak Company, Rochester 4, N.Y.

(*Received* 11 *April* 1963; *revised* 1 *July* 1963)

Abstract—The trapping of electrons and holes in anthracene crystals doped with anthraquinone, anthrone, or naphthacene has been observed when these impurities are present in concentrations of 10 p.p.m. or less. Anthraquinone and anthrone are more effective at trapping electrons than holes, probably as a consequence of their high electron affinities. Naphthacene acts as a hole trap located 0·43 eV above the hole band and having a capture cross-section exceeding 10^{-15} cm^2. The behavior of the hole photocurrent in naphthacene-doped anthracene is indirect support for the hypothesis that the holes move in a band whose energy width is comparable to 1/80 eV.

INTRODUCTION

THE work of NORTHRUP[1] and KEPLER[2] suggests that small amounts of chemical impurities play an important role in the photoconduction of anthracene. To obtain a more quantitative measure of the effects of impurities, we have studied the bulk, transient photocurrents in anthracene crystals intentionally doped with either anthraquinone, anthrone, or naphthacene.

The experimental approach was to find a way of preparing anthracene so that the trapping lifetimes for holes and electrons in single crystals were in the 200-μsec range. Single crystals were then grown from a starting material prepared by these techniques but also containing a known amount of impurity, and any degradation in the lifetimes was then ascribed to trapping by the impurity.

EXPERIMENTAL EQUIPMENT

The experimental equipment is similar to that described by KEPLER[2] and is discussed in detail elsewhere.[3] A single crystal section is the dielectric of a condenser, the front and rear electrodes of which are a Nesa-coated, quartz plate and a metal block, respectively. This condenser is in series with a high voltage supply and a load resistor. The photocurrents are measured as the voltage drop across the resistor when the crystal is illuminated through the transparent electrode by a short, 0·2 μsec, high intensity flash from an air-spark. The trapping lifetime is determined from the time-dependence of the decay of the photocurrent following the exposure. Except for two cases, the photocurrents decayed exponentially with time for times less than the transit time of a carrier through the crystal. This exponential decay could be observed over the entire measurable range of the photocurrent, i.e., from the initial maximum photocurrent to 5 per cent of the maximum. The trapping lifetime is the time constant of the exponential decay. We call this process *deep trapping*, implying that, once trapped, a carrier has a negligible probability of being thermally ejected from the trap to contribute again to the photocurrent during the time of the measurement. This decrease of current cannot be due to recombination since the photocarriers in anthracene come predominantly from the illuminated surface and therefore the holes and electrons are separated by their motion in the crystal and cannot recombine.

PREPARATION OF THE CRYSTAL

The starting material, Eastman Organic Anthracene H-480, was synthesized from cyclized *o*-

---

*Presented in part at the Organic Crystal Symposium, Ottawa, Canada, 11 October 1962.

benzoylbenzoic acid by a two-step reduction. It is free from the contaminants commonly found in anthracene derived from coal tar, e.g., carbazole, phenanthrene, naphthacene, etc. The H-480 was further purified with two treatments. First, the toluene adsorbed to this material during the final step of the synthesis was removed by heating the H-480 to 120°C in a vacuum of about 10^{-4} mm of Hg. Second, the material was zone-refined in an apparatus similar to that described by BENYON and SAUNDERS.(4)

Because the density of anthracene increases by about 25 per cent upon freezing, the Pyrex zone-refining tube was oriented vertically and the molten zones entered at the top of the charge to be refined. Qualitative observations of the changes in the fluorescence and the optical absorption of the refined material indicated that most impurities have a distribution coefficient(5) less than unity. Consequently, only the top one-third of the zone-refined charge was used. In most cases the refining consisted of thirty zone-passes where the zone width was 5 per cent of the charge length and the rate of zone travel was 8 cm/hr.

The anthracene was handled in air but under yellow safelights to prevent any photo-oxidation.(6) After they had been loaded, both the zone-refining and the crystal-growing tubes were pumped for at least 2 hr at a pressure of less than 10^{-4} mm of Hg on a liquid-nitrogen-trapped vacuum system and then filled with helium to a pressure of $\frac{1}{2}$ atm before being sealed.

Single crystals were grown by the Bridgman technique. The growing rate was 1·2 mm/hr and the temperature profile in the furnace is shown in Fig. 1. The crystal-growing tube is similar to that proposed by SHERWOOD and THOMSON.(7)

Sections, 1–2 mm thick, were cleaved from the single-crystal ingots, polished on a felt soaked in xylene, and then washed in spectro-grade benzene. Only photocurrents moving perpendicular to the *ab*-crystal plane have been studied in detail.

In crystals grown with the preceding treatment, the hole and electron lifetimes never exceeded 250 μsec. Frequently, minute traces of a yellow deposit were found at the last-frozen end of the crystal. It was thought that some material from the air was being adsorbed to the anthracene when it was transferred between the zone-refining and the crystal-growing tubes and then reacting with the anthracene during the crystal growth. Therefore, following SLOANE,(8) the crystal-growing tube was modified by the addition of a separate zone-refining section. With this combination-tube configuration, anthracene which had been previously purified was loaded into the zone-refining section, the combination tube containing a helium atmosphere was sealed, and the anthracene was zoned with 20 passes. The top 3 g of this zoned charge were melted into the growing tube which was then sealed and removed from the zoning section. In crystals grown by this method the carrier lifetimes were increased to about 2,000 μsec.

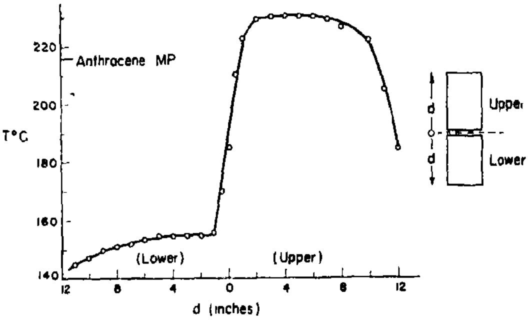

FIG. 1. The temperature profile in the furnace during the growth of anthracene crystals.

Because the effect of doping was observable in crystals grown without resorting to the combination tube, this technique was used only to prepare undoped, long-lifetime crystals.

At doping levels greater than 20 p.p.m., the impurities were added as solids to the zone-refined material as the crystal-growing tube was loaded. At a level of 10 p.p.m., the appropriate amount of impurity was dissolved in spectro-grade benzene, and 1 cm^3 of this solution was allowed to dry on the inside wall of the crystal-growing tube before the anthracene was added. The anthraquinone and naphthacene were Eastman Organic 304 and 4785, respectively. The anthrone was obtained during the anthracene synthesis.

RESULTS AND DISCUSSION

The results are summarized in Table 1. The lifetimes for crystals grown in the combination tube were not derived from an exponential decay of the photocurrent, since to get a significant

Table 1. *Carrier lifetimes in doped anthracene*

Treatment		Impurity and concentration	τ_n (μsec-electrons)	τ_P (μsec-holes)
1. H-480 untreated			50	20
2. Combination tube (50 zones)		None intentionally	>2000	>2000
3. 30 zones only	*T*	None intentionally	125	130
	B		250	220
4. 30 zones only	*T*	Anthraquinone	$<\frac{1}{2}$	15
	B	10^3 p.p.m.	6	45
5. 30 zones only	*T*	Anthraquinone	8	40
	B	10 p.p.m.	16	75
6. 30 zones only	*T*	Anthrone	2	35
	B	10^3 p.p.m.	4	76
7. 30 zones only	*T*	Anthrone	15	80
	B	10 p.p.m.	110	160
8. [illegible] zones only		Naphthacene 40 p.p.m.	17	-
9. 30 zones only		Naphthacene 10 p.p.m.	80	-

T—top, last-frozen, part of the crystal.
B—bottom, first-frozen, part of the crystal.

photocurrent decay without transit of the carriers through the crystal, it was necessary to use low biasing fields, 200 V/cm, and the currents showed space-charge effects,(9,10) where the lifetime cannot be uniquely determined from the current decay. The currents decayed to one-half their initial value in 2,000 μsec, which represents a lower limit of the lifetime.

The omission of the hole lifetime data for the naphthacene-doped crystals will be explained later.

A. *Anthraquinone and anthrone*

The concentrations of anthraquinone and anthrone given in Table 1 are the initial additions. The actual impurity content of the individual crystal sections was not determined.

Entries 4 through 7 in Table 1 show three features. First, since the lifetimes are shorter at the last-frozen end of the ingot, the distribution coefficient of these compounds in anthracene is less than unity. Second, a degradation of the carrier lifetime is observed at some point in the ingot when the initial impurity concentration is 10 p.p.m. Finally, these impurities are more effective at trapping electrons than holes.

The last phenomenon may be a manifestation of the higher electron affinity of these compounds relative to anthracene.(11) It does not seem unreasonable that the qualitative trapping properties of an impurity should be a reflection of its electron affinity relative to that of the host since the weak crystalline fields in organic solids should not significantly perturb those electronic processes which determine the electron-donating or electron-accepting properties of the free molecules.

At doping levels intermediate between those in the table, the lifetimes generally decreased with increasing impurity content although at each concentration there was some variation. One uncertainty is that we do not know what fraction of these impurities has changed chemical structure during the crystal growing. We suspect that the anthrone does not come through unaltered since the lifetimes in the anthrone-doped crystals varied by a factor of three at each doping level. Also, there was a visible collection of a black impurity on the top of these doped crystals. The anthrone data in Table 1 are the longest lifetimes observed with this impurity. A chemical change in anthrone is not unexpected since it is heated to 70°C above its melting point for at least two days during crystal growth. We certainly can say, however, that the photocarrier lifetimes are noticeably degraded when crystals are grown from a starting material containing either anthraquinone or anthrone at a level of 10 p.p.m. of added impurity.

B. *Naphthacene*

Because the optical absorption of naphthacene is at longer wavelengths than that of anthracene, the naphthacene content of the crystal sections could be determined by conventional spectrophotometric methods. Crystal sections weighing about 0·06 g were dissolved in 10 cm^3 of spectro-grade benzene, and the optical absorption of the naphthacene was measured with a General Electric Recording Spectrophotometer. The naphthacene content was determined by comparing this absorption with that of naphthacene–benzene solutions of known concentrations. The limit of detectability was 6 p.p.m. Figure 2 shows the distribution of naphthacene in an anthracene crystal initially doped at 100 p.p.m. These data can be approximated by the normal freezing equation(10) with a distribution coefficient of 0·01. The saturation solubility of naphthacene in solid anthracene appears to be 100 p.p.m.

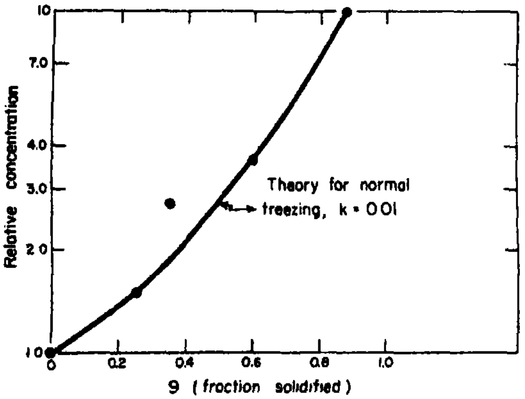

FIG. 2. The distribution of naphthacene in anthracene single crystals. The points were determined experimentally, and the solid curve is a plot of the equation of normal freezing for $k = 0{\cdot}01$.

In crystals initially doped with 10 p.p.m. of naphthacene, the impurity content could be measured only near the last-frozen end. The concentration at other points was determined from the concentration near the last-frozen end, the equation of normal freezing, and the distribution coefficient of 0·01.

Naphthacene is an electron trap. If we know the trapping lifetime, τ_c; the density of trapping centers, N_t; and the thermal velocity of the electrons, v, the capture cross-section, σ, can be computed from

$$\sigma = \frac{1}{N_t \tau_c v}$$

If it is assumed that all the naphthacene molecules are equally effective as traps, and if the thermal velocity is 10^5 cm/sec as computed by LE BLANC,(11) the capture cross-section for electrons is 3×10^{-17} cm^2.

The hole response in the naphthacene-doped crystals is significantly different from that found in the other crystals. Carrier transit is observed at times of the order of 1000 μsec, Fig. 3(b), where in undoped crystals of the same thickness (in the same electric field) the hole transit time is about 30 μsec, Fig. 3(a). There is no evidence of deep hole-trapping. This suggests that naphthacene is a shallow hole-trap and that the drift mobility is reduced by multiple trapping. Further evidence in support of this contention is derived from the temperature variation of the drift mobility, Fig. 4. For crystals containing more than 5 p.p.m. of naphthacene, the drift mobility varies as

$$\mu^* = \mu_0 \exp(-B/T)$$

where μ_0 and B are constants and T is the absolute temperature. The slope of these curves corresponds to an activation energy of 0·43 eV. At lower impurity concentrations, the exponential behavior is observed only at lower temperatures, whereas at higher temperatures,† the drift mobility is almost independent of T and approaches the value for the undoped crystals. With the lower dopings, the activation energy is again 0·43 eV in the exponential region. (The temperature range, 22–90°C, was limited at high temperatures by the condenser assembly which was designed for use at low temperatures and the low mobility at room temperature made it impractical to go to lower temperatures because the photocurrents became indistinguishable from the amplifier noise.)

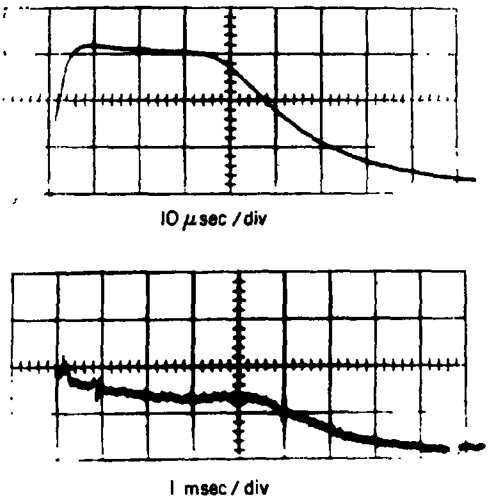

FIG. 3. The transient photocurrent for holes in anthracene crystals at room temperature. In (a) the crystal was undoped; in (b) the crystal contained 5 p.p.m. of naphthacene.

The interpretation of these data is straightforward in terms of the band model for hole conduction. With multiple (or shallow) trapping, the effective mobility, μ,* is reduced from the microscopic mobility, μ_0, according to(12)

$$\mu^* = \frac{\mu_0 \tau_c}{\tau_c + \tau_r} \qquad (1)$$

where τ_c is the trapping lifetime and τ_r is the trap release time, i.e., the average time a carrier resides in a trap.

SHOCKLEY and READ(13) have shown that

$$\frac{\tau_c}{\tau_r} = \frac{N_c}{N_t} \exp(-E_t/kT) \qquad (2)$$

where N_c is the effective density of states in the carrier band of interest and N_t is the density of trapping sites. E_t is the energy separation between the trap and the carrier band, and k is the Boltzmann constant. At low temperatures, $\tau_c \ll \tau_r$, μ^* will vary exponentially as $-1/T$. At high T, τ_c exceeds τ_r and the effective drift mobility approaches, and has the temperature-dependence, of the microscopic mobility. For a given E_t, N_t is the dominant factor in determining the temperature at which μ^* approaches μ_0. Decreasing N_t decreases the temperature at which this transition occurs. Also, in the temperature region where $\tau_c \ll \tau_r$, μ^* is inversely proportional to the trap concentration.

From the data in Fig. 4, E_t = 0·43 eV and the mobilities vary approximately as the reciprocal of the impurity content.

Since the width of the hole band in anthracene appears to be about 1/80 eV(14) wide, N_c should

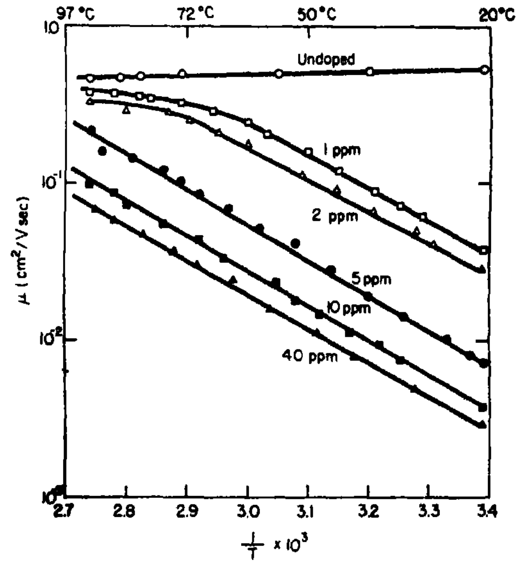

FIG. 4. The temperature-dependence of the drift mobility in undoped and naphthacene-doped anthracene crystals.

---

† In these experiments the condenser was mounted at the bottom of a quartz tube. A thermocouple was embedded in the rear condenser plate near the crystal. The temperature of the crystal was raised by surrounding the quartz tube with boiling water until the crystal temperature was about 95°C. The hot water was removed, and the transient photoconductivity was measured as the crystal cooled.

be approximately equal to the density of anthracene molecules. Thus, the coefficient N_c/N_t should be the reciprocal of the impurity concentration. Using equations (1) and (2), the measured impurity concentration, and the experimentally determined trap depth, the calculated reduction in the drift mobility from the value in the undoped crystals agrees closely with the observed reduction (Table 2).

Table 2.

Impurity concentration (p.p.m.)	$\mu^*/\mu_0 \times 10^2$ at 300°K Experimental	Calculated
1	7·1	6·3
2	5·0	3·1
5	1·3	1·3
10	0·71	0·63
40	0·54	0·16

A concentration of 40 p.p.m. is close to the saturation concentration and all of the naphthacene molecules might not be equally effective as traps. This may be the cause of the discrepancy between the experimental and the calculated mobility ratios.

The Shockley–Read treatment of trapping is based on a free-carrier (band) approximation. Since the photoconductive behavior of holes in naphthacene-doped anthracene is in apparent agreement with this theory, we believe that these experiments are indirect confirmation that the motion of holes above room temperature is describable in terms of the band approximation with a narrow hole band.

With multiple trapping τ_c can be measured from the behavior of the photocurrent immediately following exposure. To see this, assume the following: (1) A density of holes p_0 is instantaneously generated near the illuminated surface of the crystal. (2) The density of traps, N_t, is larger than p_0 so that complete trap-filling is impossible. (3) $\tau_c \ll \tau_r$ and the holes come into thermal equilibrium with the traps instantaneously. (4) Recombination is neglected and thus $p+p_t = p_0$, where p and p_t are the densities of free and trapped holes, respectively. The differential equation for the density of free carriers is then

$$\frac{dp}{dt} = \frac{-p}{\tau_c}+\frac{p_t}{\tau_r}$$

The solution is

$$p = \frac{p_0\tau^*}{\tau_r}\left[1+\frac{\tau_r}{\tau_c}\exp(-t/\tau^*)\right]$$

where

$$\frac{1}{\tau^*} = \frac{1}{\tau_c}+\frac{1}{\tau_r}$$

The current from the motion of the injected holes starts at an initial maximum, i_m, and decays exponentially to a steady-state value, i_{ss}, with a time constant of τ^*. When $\tau_c < \tau_r$, $\tau^* = \tau_c$, and the ratio i_{ss}/i_m

$$\frac{i_{ss}}{i_m} = \frac{\tau_c}{\tau_r} = \frac{N_c}{N_t}\exp(-E_t/kT)$$

In naphthacene-doped anthracene the aforementioned current behavior is observed. However, the time constant of the photo-current decay is that of our measuring equipment, 5 μsec. Therefore $\tau_c < 5$ μsec and the hole-capture cross section must exceed 10^{-15} cm^2.

NORTHRUP and SIMPSON$^{(1)}$ report that the d.c. photoconductivity of naphthacene-doped anthracene decreases with increasing naphthacene content. This could be a consequence of either a decreased mobility resulting from multiple trapping or a decreased quantum efficiency for carrier generation. The latter cause cannot be excluded since traces of naphthacene compete effectively with the anthracene host for degrading radiant energy absorbed by the anthracene.$^{(15)}$

With the transient technique, there are two ways of estimating the quantum efficiency for carrier generation. If, as with the electrons, there is deep trapping, the number of moving carriers can be computed from the initial current and the drift velocity, provided the drift mobility is known. Without deep trapping, i.e., there is transit, the number of moving carriers is equal to the time-integral of the photocurrent. Using the latter method in the naphthacene-doped crystals, the number of mobile holes per exposing flash was not only independent of naphthacene content and temperature, Fig. 5, but it was also equal to the number created in undoped crystals. The number of mobile carriers per absorbed photon is about 10^{-4} for holes and 10^{-5} for electrons. (These data were obtained at low light-intensities where space-charge effects were negligible.) Also, the naphthacene-doped crystals, like the undoped crystals, showed an increase in hole current and a decrease in electron current when the illuminated surface was covered with a thin layer of a Lewis acid.(16) No photocurrents were observed for energy absorbed by the naphthacene.

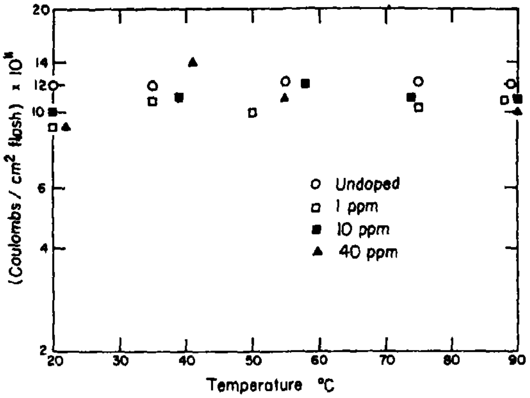

Fig. 5. The number of holes moving through the volume of undoped and naphthacene-doped anthracene crystals as a function of temperature and impurity content.

It is somewhat surprising that the quantum efficiency for hole generation is independent of the naphthacene content, since the ratio of the anthracene fluorescence to the naphthacene fluorescence* varied from 3/1 at 1 p.p.m. to 1/4 at 40 p.p.m.

CONCLUSION

The trapping of photoholes and photoelectrons, in anthracene by the impurities anthraquinone, anthrone, and naphthacene is measurable in crystals grown from a starting material containing any of these impurities at a concentration of 10 p.p.m. Anthraquinone and anthrone are more effective in trapping electrons than in trapping holes; this probably is due to their large electron affinities. Naphthacene adds hole traps with a capture cross-section greater than 10^{-15} cm^2. The traps are located 0·43 eV above the hold band. The hole mobility in naphthacene-doped crystals varies with both temperature and impurity content, as predicted by the simple theory of multiple trapping if it is assumed that: (1) each naphthacene molecule is a hole trap; and (2) the effective density of states in the hole band equals the density of anthracene molecules. The generation of holes and electrons is independent of the naphthacene content.

Acknowledgements—The authors wish to thank R. S. Van Heyningen, F. Urbach and F. Grum for many helpful and stimulating discussions.

REFERENCES

1. Northrup D. O. and Simpson O., *Proc. Roy. Soc.* **244A**, 377 (1958).
2. Kepler R. G., *Phys. Rev.* **119**, 1226 (1961).
3. Hoesterey D. C., *Rev. sci. Instrum.* (to be published).
4. Benyon J. H. and Saunders R. A., *Brit. J. appl. Phys.* **11**, 128 (1960).
5. Pfann W. G., *Solid State Physics, Advances in Research and Applications*, Vol. **4** (edited by Seitz F. and Turnbull D.), Chap. 5, Academic Press, New York (1957).
6. Bree A. and Lyons Lee E., *J. chem. Soc.* 5179 (1960).
7. Sherwood J. N. and Thomson S. J., *J. sci. Instrum.* **37**, 242 (1960).
8. In Heine E. *Du Pont Mag.* **55**, 2–5, May–June (1961).
9. Many A., Semhony H., Weizz S. Z. and Levinson J., *J. Phys. Chem. Solids* **22**, 285 (1962).
10. Silver M., Sevicord M. and Jarnagin R., *J. Phys. Chem. Solids* **23**, 419 (1962).
11. In Andrews L. J., *Chem. Revs.* **54**, 713 (1961).
12. Bube R. H., *Photoconductivity In Solids*, p. 68. John Wiley, New York (1960).
13. Shockley W. and Read W. T., Jr. *Phys. Rev.* **87**, 835 (1952).
14. Le Blanc O. H. Jr., *J. chem. Phys.* **33**, 626 (1960).
15. Bowen E. J. and Mikiewizc E., *Nature, Lond.* **159**, 106 (1947).
16. Hoesterey D. C., *J. chem. Phys.* **36**, 557 (1962).

---

* These data were determined by F. Grum on a modified Beckman DK-2R Spectrophotometer with an exciting wavelength of 365 mμ.

J. Phys. Chem. Solids Pergamon Press 1963. Vol. 24, pp. 1617–1624. Printed in Great Britain.

DILATATION ET POUVOIR THERMOELECTRIQUE DU PLUTONIUM α A BASSE TEMPERATURE

R. LALLEMENT

Centre d'études nucléaires de Fontenay-Aux-Roses (Seine) France

(*Received* 22 *February* 1963; *revised* 21 *June* 1963)

Résumé—Des mesures de dilatation et de pouvoir thermoélectrique ont été faites sur le plutonium en phase α à basse température. Le pouvoir thermoélectrique présente une anomalie à 50°K environ, la dilatation présente un minimum vers cette même température. Ces anomalies sont attribuées à une transition magnétique. Utilisant les idées principales de Rocher, nous montrons qu'il faut supposer que la température de Néel du plutonium s'abaisse quand la pression augmente pour expliquer l'anomalie de dilatation.

Abstract—We have measured the dilatation and the thermoelectric power of plutonium at low temperature. The thermoelectric power is anomalous around 50°K. The dilatation has a minimum around the same temperature. These anomalous properties are assumed to be induced by a magnetic transition. Using Rocher's main ideas we show that it is necessary to suppose that the Néel temperature of plutonium decreases when pressure increases to explain the anomalous dilatation.

INTRODUCTION

Les principales propriétés physiques du Plutonium ont été présentées en détail à la Conférence de Grenoble en 1960.

A basse température, la résistivité a une allure remarquable, la chaleur spécifique, la dilatation thermique présentent des anomalies. Cependant la susceptibilité magnétique est pratiquement constante.(1, 2) Ces résultats sont présentés sur la Fig. 1.

Pour expliquer l'allure de la résistivité en fonction de la température, une structure de bandes analogue à celle proposée pour l'uranium et les métaux de transition a été avancée par plusieurs auteurs.(1, 17) Un autre type de solution invoque une transition ordre–désordre atomique ou magnétique.(18) Cette dernière hypothèse doit être conciliée avec l'absence d'anomalie de susceptibilité magnétique. Ces deux solutions sont actuellement toujours proposées, la cohérence interne de la seconde est un peu renforcée par la théorie avancée par Rocher(3) pour justifier l'existence d'une transition magnétique sans anomalie de susceptibilité magnétique.

Nous avons mesuré le pouvoir thermoélectrique et la dilatation du plutonium alpha pour tenter de choisir entre ces deux solutions.

TECHNIQUES EXPERIMENTALES

Nous avons mesuré le pouvoir thermoélectrique et la dilatation. Dans les deux types de mesures, nous avons refroidi les échantillons jusqu'à des températures voisines de 4°K. Le plutonium étant manipulé en boîte à gants, ceci posait un petit problème que nous avons résolu de la manière suivante : la boîte à gants est remplie d'hélium gazeux. Un tube de mesures est fixé au fond de la boîte. Les échantillons, fixés sur des supports convenables (avec les fils de thermocouple, les amenées de courant. . .) sont introduits dans ce tube, qui plonge à l'intérieur du cryostat à hélium liquide.

Le tube de mesures est formé de deux parois concentriques entre lesquelles nous pouvons soit faire le vide, soit introduire de l'hélium gazeux. Nous réalisons ainsi soit un bon isolement thermique, soit un refroidissement énergique des échantillons. Une fuite réglable permet en outre de se placer dans des situations intermédiaires. Il

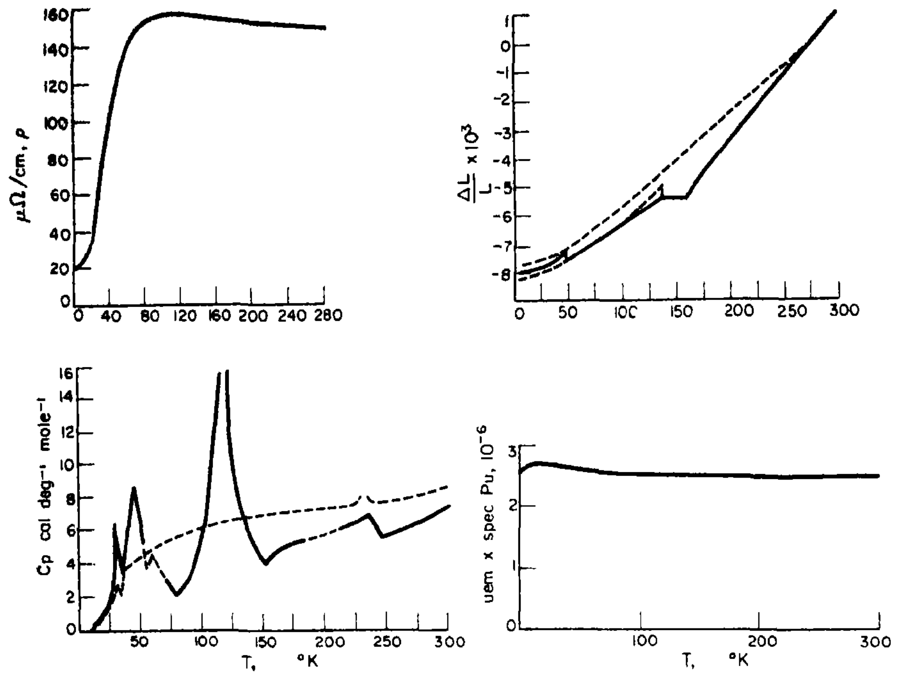

FIG. 1. Résistivité, dilatation, chaleur spécifique et susceptibilité magnétique du plutonium d'après les résultats publiés dans *Plutonium 1960*.

est relativement facile d'obtenir ainsi toute température entre 4 et 70°K.

Les températures ont été mesurées avec un thermocouple constitué d'un alliage Argent–Or, Or–Cobalt.[4] Ce thermocouple a encore une sensibilité de 5 μV par degré absolu à 4°K. Nous avons fait un étalonnage de contrôle pour plusieurs températures fixes:

hélium liquide	4,2°K
azote liquide	77°K
fusion du sulfure de carbone	−108°C, 6
fusion du tétrachlorure de carbone	− 22°C, 6
fusion du chloroforme	− 63°C, 5

Nous avons pu corriger ainsi les tables publiées pour ce thermocouple.[4] Nous estimons que l'erreur commise sur la mesure de la température est inférieure à 0,5°K.

Mesure du pouvoir thermoélectrique, Erreurs

Le pouvoir thermoélectrique a été mesuré par la technique différentielle déjà utilisée pour les mesures faites à haute température sur le plutonium.[5] Cette méthode a l'avantage de ne pas nécessiter la mesure des différences de températures toujours petites existant entre les deux extrémités de l'échantillon. Le porte échantillon est extrêmement simple : le cylindre de plutonium de 5 cm de long et 6 mm de diamètre est serré entre deux blocs de cuivre dans un cylindre de plexiglass. Une résistance chauffante est enroulée autour du bloc de cuivre supérieur. Le tout est fixé à l'extrémité d'une tige fine d'acier inoxydable. Les thermocouples sont fixés dans deux trous percés dans l'échantillon. Ces trous sont remplis d'un amalgame d'argent qui durcit en quelques heures, donnant ainsi un excellent contact thermique et électrique, ainsi qu'une fixation solide.

D'après POWELL,[4] il est difficile, avec le thermocouple utilisé, d'éviter la présence de différences de potentiel parasites de l'ordre de 2 à 3 μV. En général, les différences de potentiel mesurées sont supérieures à 100 μV. Nous estimons que dans ces conditions l'erreur commise sur la valeur du pouvoir thermoélectrique est de l'ordre de quelques pour cent. Il n'en est pas ainsi aux basses températures (entre 4 et 30°K) où les différences de potentiel mesurées deviennent faibles. L'erreur pourrait atteindre alors 50%.

Le pouvoir thermoélectrique S du métal de référence, l'alliage Argent–Or est trés peu différent de celui du cuivre et se confond avec lui pour des températures inférieures à 40°K.(4) Or il apparaît que le pouvoir thermoélectrique du cuivre est mal connu à basse température et que des traces d'impuretés peuvent le faire varier beaucoup.(6) Nous avons donc décidé de mesurer S par rapport au plomb(7) et de prendre ces valeurs mesurées comme référence.

Mesure des dilatations, Erreurs

Pour mesurer les dilatations nous avons utilisé des jauges de contraintes. Une jauge de contrainte est essentiellement un fil résistant collé sur le corps à étudier. La colle transmet les déformations du corps au fil dont les dimensions varient. La variation correspondante de résistance est liée à l'allongement du corps par la relation :

$$\frac{\mathrm{d}R}{R} = K\frac{\mathrm{d}l}{l} \qquad (1)$$

(K est le facteur de jauge, voisin de 2 pour les jauges utilisées).

Quand la température varie, la résistivité de la jauge change, ainsi que la dilatation relative de la jauge et du métal étudié.

$$\frac{\mathrm{d}R}{R} = K\left(\frac{\mathrm{d}lg}{lg}-\frac{\mathrm{d}lm}{lm}\right)+\alpha_g t \qquad (2)$$

Les notations sont les suivantes :

$\frac{\mathrm{d}R}{R}$ = variation relative, entre 0°C et t, de la résistance de la jauge.

t = température.

$\frac{\mathrm{d}lg}{lg}$ = allongement relatif entre 0°C et t, du métal dont la jauge est faite.

$\frac{\mathrm{d}lm}{lm}$ = allongement relatif du métal étudié.

α_g = coefficient de température de la résistance du métal dont la jauge est faite.

K, $(\mathrm{d}lg/lg)$ sont mal connus. Nous avons éliminé ces coefficients douteux en prenant deux métaux de référence, le plomb et le fer, pour lesquels nous avons mesuré soigneusement les variations de résistance $(\mathrm{d}R/R)_1$, et $(\mathrm{d}R/R)_2$ avec la température et dont les allongements sont connus.(8) Nous mesurons ensuite $(\mathrm{d}R/R)_x$ pour le métal étudié. De la formule (2) nous tirons alors :

$$\frac{\dfrac{\mathrm{d}lx}{lx}-\dfrac{\mathrm{d}l_1}{l_1}}{\dfrac{\mathrm{d}l_2}{l_2}-\dfrac{\mathrm{d}l_1}{l_1}} = \frac{\left(\dfrac{\mathrm{d}R}{R}\right)_x-\left(\dfrac{\mathrm{d}R}{R}\right)_1}{\left(\dfrac{\mathrm{d}R}{R}\right)_2-\left(\dfrac{\mathrm{d}R}{R}\right)_1} \text{ d'où } \frac{\mathrm{d}l_x}{l_x}$$

La Fig. 2 représente les résultats de nos mesures sur l'argent. La précision est bonne jusque vers 77°K environ. Elle devient médiocre aux températures inférieures. Dans le domaine de température 4–77°K, nous avons une erreur probablement systématique d'environ 10 à 15%. La méthode utilisée est donc inapte aux mesures absolues en dessous de 77°K. Nous considérerons les résultats obtenus entre 4 et 77°K comme des indications semi-quantitatives seulement.

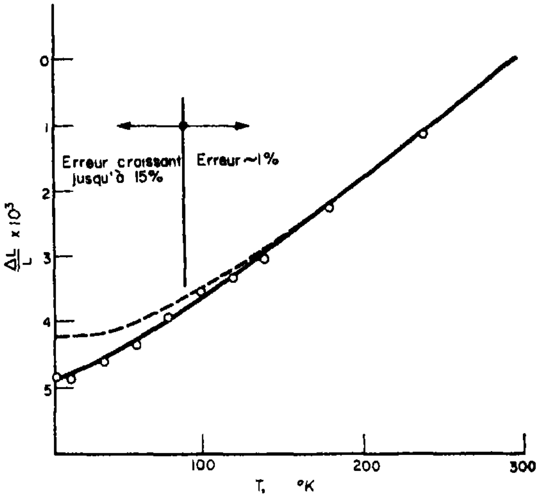

Fig. 2. Résultats des mesures de dilatation de l'argent:
—en trait pleins nos mesures
—en tirets les mesures de Nix et McNair(8) prises comme référence.

RESULTATS EXPERIMENTAUX

Pouvoir thermoélectrique

Les résultats obtenus sont présentés sur la Fig. 3. Les mesures faites par Meaden y figurent aussi. L'allure générale des deux courbes est la même. Les différences de valeur absolue du pouvoir thermoélectrique doivent probablement être attribuées aux différences de pureté des métaux d'origines française et anglaise. Nos valeurs de S à 300°K concordent avec les premières valeurs présentées par les chercheurs anglais.(9) Nos mesures montrent que S devient faiblement négatif vers 17°K. La courbe de la Fig. 3 présente un léger maximum vers 60°K et un minimum vers 80°K. Cependant, nous n'attachons pas de signification particulière à ce minimum. En effet, les mesures nous ont vite amenés à constater l'importance du temps passé par l'échantillon dans l'hélium liquide sur l'allure des courbes $S(T)$.

Après ces opérations, nous constatons (Fig. 4, courbes 3 et 4) un accroissement ΔS très net du pouvoir thermoélectrique, d'autant plus grand que le maintien à 4°K a été plus long. ΔS diminue quand la température croît, et finalement les valeurs de S redeviennent identiques aux valeurs initiales. Des mesures ultérieures entre 80°K et 300°K redonnent la courbe initiale (Fig. 3, courbe 1).

On sait maintenant(10) que le plutonium s'auto-irradie à basse température. Les mesures d'ELLIOTT et OLSEN(10) semblent montrer que la température de revenu des défauts d'auto-irradiation est voisine de 50°K. Nous avons voulu attribuer l'accroissement à ces défauts. A partir de cette hypothèse, nous avons pensé que le maximum observé vers 65°K était dû au séjour à des températures inférieures à la température de revenu des défauts. Les températures entre 50 et 77°K peuvent être atteintes à partir d'azote bouillant sous pression réduite. Les mesures dans ce domaine de température ont donné la courbe 2 de la Fig. 4 qui prolonge la partie linéaire observée entre 80 et 300°K. L'influence du temps de séjour à des températures inférieures à 50°K semble donc très nette.

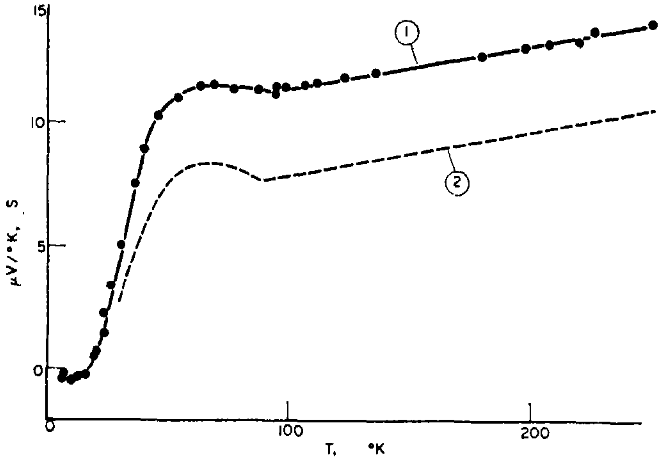

FIG. 3. Pouvoir thermoélectrique du plutonium:
(1) nos mesures
(2) les mesures de MEADEN(9) (réf. 9)

La courbe de la Fig. 3 est relative à un chauffage de 4 à 80°K modérément lent, d'une heure environ. Mais, l'allure des courbes change nettement (Fig. 4) après les opérations suivantes.

(a). maintien dans l'hélium liquide de 2 à 4 hr.

(b). après chaque maintien, chauffage rapide jusqu'à 77°K, et mesure de S à partir de 77°K.

(L'opération (b) nous permet d'éviter les mesures dans le domaine de températures où S varie très vite, où les erreurs sur la valeur de S sont importantes, où il est assez délicat d'obtenir une température stable assez longtemps pour que l'on puisse considérer que l'équilibre thermique est atteint dans l'échantillon).

Nous avons alors mesuré l'accroissement de S dans l'hélium liquide en fonction du temps. Mais, après 4, 8, 12 h à 4°K, nous n'avons constaté

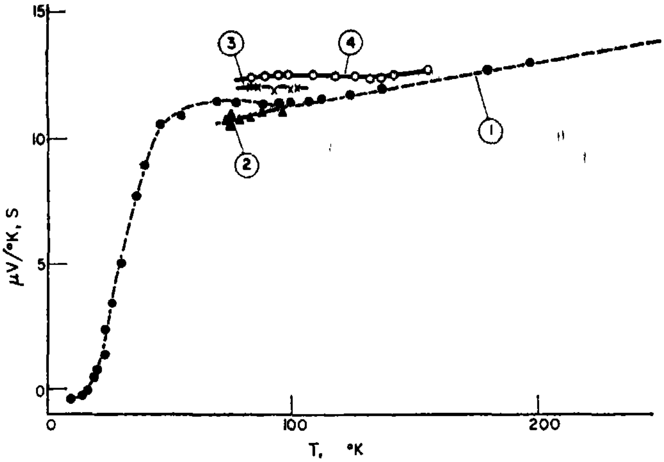

FIG. 4. Influence d'une court maintien dans l'hélium liquide sur le pouvoir thermoélectrique:

courbe (1) en tirets, les résultats obtenus normalement.

courbe (2) en trait plein les résultats obtenus à partir de températures voisines de 60°K, dans l'azote bouillant sous pression réduite.

courbe (3) résultats obtenus après 3 h de maintien à 4°K.

courbe (4) résultats obtenus après 4 h de maintien à 4°K.

aucun accroissement notable. Ce résultat pose donc des problèmes : il faut supposer, ce qui est étonnant, l'influence des défauts plus forte vers 70°K que vers 4°K. D'autre part, le nombre des défauts produits après 4 h à 4°K est très faible. En admettant les estimations d'Elliott et Olsen, la concentration de défauts serait de l'ordre de 10^{-5}. Nous noterons simplement que la région de température où l'influence des défauts est très forte, est voisine de la température de la transition magnétique, que suivant Rocher, nous supposons dans le plutonium.

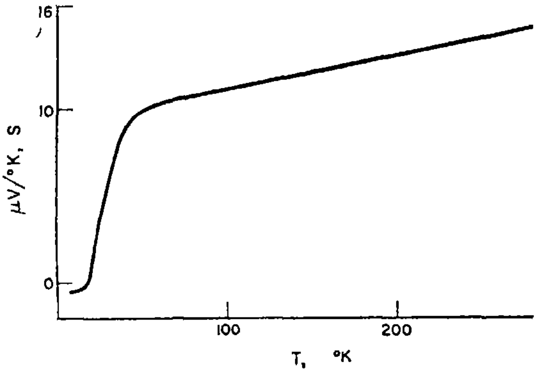

FIG. 5. Pouvoir thermoélectrique "idéal" du plutonium.

Dilatation

Nos résultats relatifs à la dilatation du plutonium sont présentés sur la Fig. 6 ainsi que les résultats obtenus par Sandenaw. Il n'est pas tellement facile de comparer les résultats, car les résultats américains dépendent des cycles de température subis par l'échantillon. Dans nos expériences, l'échantillon a été refroidi rapidement jusqu'à 77°K, puis 4,2°K, ensuite chauffé

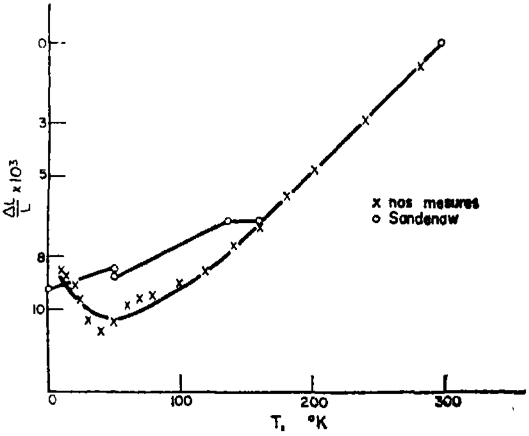

FIG. 6. Résultats des mesures de dilatation.

jusqu'à 77°K en 8 h environ d'une part, d'autre part refroidi rapidement jusqu'à 77°K et chauffé jusqu'à 300°K en 8 h environ. En supposant que les cyclages pendant pendant deux jours entre 48 et 77°K pratiqués par Sandenaw n'ont aucune influence, nos cycles de température sont intermédiaires entre les cycles trés lents et rapides de Sandenaw.

Pour nous, la dilatation du plutonium est très régulière jusque vers 50°K, température au-dessous de laquelle le coefficient de dilatation s'annule et devient négatif. C'est précisément dans la zone des températures où la précision est médiocre que nous constatons l'existence d'une anomalie. Des mesures plus précises, en particulier la mesure des paramètres aux Rayons X, sont infiniment souhaitables. Cependant, l'indication qu'un minimum de dilatation est possible est très intéressante.

INTERPRETATION DES RESULTATS

Les théories sur la structure électronique du plutonium alpha sont au moins de deux types :

> l'une, développée par Smoluchowski(17), déjà proposée par Lee,(1) suppose une structure à deux bandes, (l'une, étroite de caractère *f* l'autre, de caractère *d*) se chevauchant au niveau de Fermi ; l'autre, proposée par Rocher suppose l'existence de niveaux liés virtuels 5*f* au niveau de Fermi, donnant lieu à des moments magnétiques localisés sur chaque atome, couplés antiferromagnétiquement à très basse température. Dans l'état actuel de nos connaissances, ces deux modéles sont également satisfaisants.
>
> Les anomalies que nous avons trouvées dans la dilatation et le pouvoir thermoélectrique ne permettent sans doute pas de choisir entre ces deux modèles. Notre propos sera uniquement de montrer que ces anomalies peuvent s'expliquer par l'hypothèse d'un ordre magnétique, dans le cadre des théories de Rocher que nous allons brièvement exposer.

Résumé de la thèse de Rocher

D'aprés Rocher, dans le plutonium les états 5*f* commencent à se stabiliser par rapport aux états 6*d* et 7*s*. La couche 5*f* se resserre sur le noyau et les intéractions entre couches *f* centrées sur des ions voisins deviennent faibles. Les fonctions 5*f* sont très localisées dans l'espace et l'on peut s'attendre à l'existence de niveaux liés virtuels 5*f* chaque fois que le potentiel ionique n'est pas assez attractif pour que les électrons 5*f* occupent des états liés. Les niveaux *f* tombent alors dans le continuum des états étendus et s'élargissent en énergie par des résonances avec ces états. Nous obtenons une situation analogue à celle introduite pour les impuretés de transition dans un métal noble par Blandin et Friedel.(11)

Les niveaux liés virtuels se recouvrent peu d'un atome à l'autre. Le calcul montre que la largeur de ces niveaux est de 10^{-1} à 1 eV. Les corrélations entre électrons sont trop faibles pour séparer ces niveaux en 14 niveaux d'énergie distincte. Rocher suppose donc que l'échange découple les états 5*f* en deux niveaux pouvant contenir chacun sept électrons d'une même direction de spin. Il y a peu d'électrons 5*f* pour le plutonium (deux à trois) et la largeur du niveau est grande par rapport à l'énergie d'échange. Les calculs prédisent dans ce cas un découplage partiel des niveaux. La différence de population des niveaux de spins opposés est faible et prise égale à 0,3 électrons ; deux à trois électrons sont placés dans la couche *f*. Trois à quatre électrons presque libres sont supposés occuper une bande de conductibilité de caractère sd ; deux électrons sont placés dans une bande d. La structure de bandes finale est présentée sur la Fig. 7.

La structure de bandes proposée donne à chaque atome un moment magnétique de 0,3 μB. Rocher suppose le couplage magnétique entre ces moments suffisant pour donner un ordre magnétique à basse température.

Les propriétés physiques dans ce schéma

La bande étroite 5*f* au niveau de Fermi rend bien compte de la forte résistivité. L'ordre magnétique explique la décroissance brutale en dessous de 100°K. La légère décroissance au dessus de 100°K est attribuée à l'existence d'un ordre local.

La susceptibilité magnétique ne peut présenter d'anomalies notables étant donnés le petit nombre de magnétons portés par chaque atome et la forte susceptibilité de Pauli, surtout si l'on suppose la transition quelque peu étalée en températures.

Le pouvoir thermoélectrique mesuré est positif,

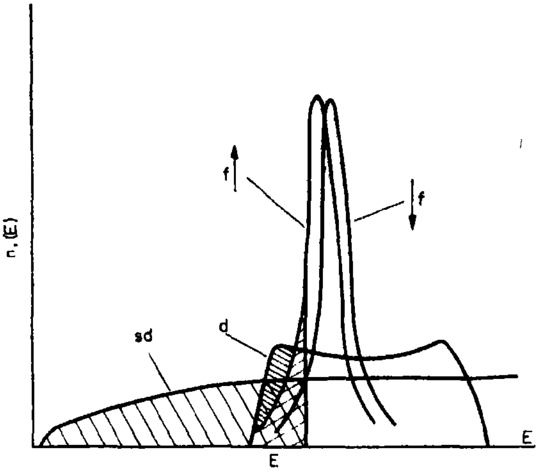

FIG. 7. Structure de bandes proposée par Rocher.

fort et présente un changement de pente vers 50°K. Dans une structure de bandes comme celle proposée par Rocher on s'attend à un pouvoir thermoélectrique fort. D'autre part, la théorie(12) prévoit dans le cas d'une transition ordre-désordre un changement de pente du pouvoir thermoélectrique en fonction de la température au point de transition. C'est ce que nous avons observé vers 50°K dans nos mesures. Il ne semble pas possible d'exploiter plus ce résultat, les calculs théoriques étant faits pour des structures ferromagnétiques ou antiferromagnétiques simples et ne pouvant donc pas être appliqués à la structure complexe du plutonium alpha. Les mesures de pouvoir thermoélectrique sont donc en accord avec les hypothèses de Rocher:—ordre magnétique à basse température.—bande 5*f* étroite au niveau de Fermi.

Nous lierons la contraction observée à des températures inférieures à 50°K à l'établissement d'un ordre magnétique. Nous suivrons les calculs faits par Rocher : soit Tc la température de transition, V le volume, la dépendance en volume de l'énergie Em liée aux couplages magnétiques est :

$$\frac{\delta Em}{Em\delta V} = \frac{\delta Tc}{Tc\delta V} = \frac{C}{V}$$

Si Tc diminue quand P augmente C est une constante positive. C tient compte de la loi de variation de Tc en fonction de P et de la compressibilité X du plutonium.

La suite du calcul conduit Rocher à un coefficient de dilatation lié à l'aimantation :

$$\alpha = -1{,}5\, C K \frac{X}{V_0}$$

(K est la constante de Boltzmann et V_0 le volume pour un ordre magnétique parfait).

Nos mesures donnent une valeur de α de l'ordre de 40–60 10^{-6}/°K. Nous ne connaissons pas C. Mais nous notons qu'une constante C positive est nécessaire pour expliquer un coefficient α négatif, c'est-à-dire que nous devons supposer que la température du point de transition diminue quand la pression augmente. Ce point serait très intéressant à vérifier.

CONCLUSION

Nous avons présenté des mesures de pouvoir thermoélectrique et de dilatation. Le pouvoir thermoélectrique présente un coude marqué vers 50°K ; un minimum de dilatation est probable vers 50°K mais mériterait un examen plus soigné, peut être aux rayons X.

Ces anomalies peuvent s'expliquer, dans le cadre des théories de Rocher, par l'apparition d'un ordre magnétique vers 50°K. La preuve formelle de l'existence de cet ordre reste encore à faire. Nous ne pouvons terminer sans faire un rapprochement : l'uranium présente lui aussi un minimum de dilatation vers 40°K.(15) Tout récemment.(16) BARRETT a signalé après étude de l'uranium à basse température par diffraction de neutrons qu'un ordre magnétique existait probablement dans ce métal. On peut se demander si un ordre magnétique à basse température n'est pas une règle générale pour les actinides comme pour les lanthanides.

Remerciements—L'auteur tient à remercier Monsieur le Professeur J. FRIEDEL pour ses précieux conseils et Monsieur P. COSTA du Centre d'Etudes Nucléaires de Fontenay-aux-Roses pour de nombreuses discussions fructueuses.

BIBLIOGRAPHIE

1. *Plutonium 1960*, Chap. 2. Cleaver Hume Press, London (1960).
2. SANDENAW, T. H., *J. Phys. Chem. Solids* **23**, 1241 (1962).

3. Rocher Y. A., *Advanc. Phys.* **2**, 43 (1962).
4. Powell R. L. *et al.*, *Cryogenics Mars* (1961).
5. Costa P., *J. Mat. Nucl.* **5**, 56 (1960).
6. Gold A. W., McDonald D. K. C. et Pearson W. B., *Phil. Mag.* **5**, 56 (1960).
7. Christian J. W. *et al.*, *Proc. Roy. Soc.* **A245**, 213 (1958).
8. Nix F. C. et Macnair D., *Phys. Rev.* **60**, 597 (1941); *Phys. Rev.* **61**, 74 (1942).
9. Waldron M. B., et Lee J. A., *2ème Conférence de Genève* 1958, **15**, 71.
10. Olsen C. E. et Elliott R. O., *J. Phys. Chem. Solids* **23**, 1225 (1962).
11. Friedel J. et Blandin A., *J. Phys. Radium* **19**, 573 (1958). Anderson P. W., *Phys. Rev.* **124**, 41 (1961).
12. Rocher Y. A., *Advanc Phys.* **2**, 43 (1962) (annexe). Beal M. T., *J. Phys. Chem. Solids* **18**, 150 (1961).
13. Mott N. F. and Jones H., *Theory of the Properties of Metals and Alloys*, Dover, New York (1936).
14. Lee J. A., Mendelsohn K. et Wigley D. A., *Phys. Letters* 325, 15 Juillet (1962).
15. Schuch A. F. et Laquer H. L., *Phys. Rev.* **86**, 803 (1952).
16. Barrett C. S., *Phys. Rev. Letters Abstr.* Décembre (1962).
17. Smoluchowski R., *Phys. Rev.* **125**, 1577 (1962).
18. Rocher Y. A. et Friedel J., *J. Phys. Chem. Solids* **18**, 196 (1961).

J. Phys. Chem. Solids Pergamon Press 1963. Vol. 24, pp. 1625–1631. Printed in Great Britain.

PRESSURE EFFECT ON COLOR CENTERS IN RbF, RbCl, RbBr and CsI*

HANS KNOF and WILLIAM G. MAISCH

Institute for Molecular Physics, University of Maryland, College Park, Maryland

(*Received* 29 *July* 1963)

Abstract—The absorption spectra of the *F* and *M* centers in RbF, RbCl, RbBr and CsI have been investigated as a function of pressure. In addition to the *F* and *M* bands, the No 3 band and some other unidentified bands have been observed. These experiments were conducted at room temperature with both electrolytically and additively colored crystals. Frequency shifts were observed under pressures up to 10,000 atm for the absorption spectra of RbCl and RbBr and up to 50,000 atm for the absorption spectra of RbF and CsI. In RbF a phase transition appears at 33,000 atm. The pressure dependence of the frequency shift in the rubidium halides is similar to that in the potassium halides.

INTRODUCTION

DURING the last ten years there have been investigations of the effect of pressure on the spectra of trapped-electron centers in alkali halide crystals.(1–6) Some of these experiments were run under pressures up to 166,000 atm. It was found that with increasing pressure the absorption bands shift to higher frequencies as long as no phase transition occurs. Extensive studies of KCl have been published. A plot of log ν_m vs. log a gives a straight line for the *F* centers in KCl and various other salts (ν_m = frequency of maximum absorption, a = lattice parameter). In colored KCl the shift in frequency of the absorption band is strongest for the *F* band, gradually weaker for the *N*, *M* and R_2 bands.

At the phase transition, which transforms crystals with a f.c.c. lattice into a s.c. lattice,(7) the frequencies of the absorption bands change discontinuously. The discontinuous shift can occur towards higher or lower frequencies, depending on the color center and the alkali halide. In Table 1 previously measured shifts at the phase transition are listed for most of the potassium halides. Some measurements already exist of the effect of pressure on color centers in several rubidium halides above the transition point. In this paper optical measurements on RbCl and RbBr below the phase transition are described. In addition, the *F* center in RbF and the *F* and *M* centers in CsI are investigated and the phase transition of RbF is determined.

Table 1. *Frequency shift* $\Delta\tilde{\nu}$ *of the F and M bands at the phase transition.* + *sign indicates a shift to higher frequencies.*

$\Delta\tilde{\nu}$(cm^{-1})	KCl	KBr	KI
F	+680	−420	−2320
M	+50	−250	−860

EXPERIMENTAL PROCEDURE

Two different types of high pressure optical cells, both developed by DRICKAMER and coworkers(8, 9) were used to cover the pressure range from 1 to 50,000 atm. In the cell used in the low pressure range from 1 to 10,000 atm, the pressure is hydrostatic. A 12·7 mm diameter piston in the high pressure end of this cell is linked mechanically to a 76·2 mm diameter piston in the hydraulic

---

* This research was supported in part by the United States Air Force under Contract No. AF 49(638)-627 monitored by the AF Office of Scientific Research of the Air Research and Development Command.

press which forms the low pressure end of the cell. The oil pressure behind the large piston is generated by a hand pump. Two sapphires 12·7 mm long and 12·7 mm in diameter are used as windows. The effective aperture of the windows is 6 mm and the maximum path length available for the crystals is about 5 mm. Freon 11 was used as the pressure transmitting liquid. The crystals were held in the optical path by a clamp which screwed to one of the window mounts. The crystals remained clear below the transition pressure but clouded as the transition took place. The spectra were observed with increasing pressure only, and those above the transition region were inferior in quality to those below. Although these crystals tend to regain most of their transparency at pressures sufficiently higher than the transition pressure, such pressures could not be achieved in this apparatus.

At higher pressures, the "liquid" cell described above cannot be used. A "solid" cell, in which solid samples are embedded in a disk of sodium chloride, is used up to pressures of 50,000 atm. The sodium chloride flows under pressure above 5000 atm without cracking and transmits the pressure from a piston to the sample. Sodium chloride is used also as the windows in this cell, and is extruded from single crystals into the window openings at 20,000 atm. The diameter of each window opening increases in a series of steps from the center of the cell (sample compartment) from 0·7 mm to 6·1 mm. The sample compartment itself is 5 mm high and 3·175 mm in diameter, permitting a maximum sample thickness of 2·5 mm. In operation, this cell is placed in a small hydraulic press designed to fit in the optical path of the spectrometer. The pressure is generated in the same manner as described above, the ratio of the press/cell piston diameters in this case being 11·43 mm/3·175 mm. The design of this cell permits the pressure to be raised and lowered repeatedly, but measurements are made only after an increase in pressure to insure consistent results.

Neither of the cells described above fills the entire slit with light, i.e., the *f*-number of each cell is larger than that of the instrument. Since the *f*-number of the liquid cell is much less than the *f*-number of the solid cell, more strongly absorbing crystals could be studied in the former cell.

High pressure cells of the above types were calibrated originally by Drickamer by means of a manganin gauge (liquid cell) and various solid-solid phase transitions (solid cell). These calibrations were checked by means of frequency shifts observed in both laboratories and found to be still applicable. The phase transition undergone by many of the alkali halides studied served as a further check of the calibration.

The absorption spectra were observed with a single beam spectrophotometer, the Beckman IR3. This instrument had a quartz-tungsten lamp as the light source, two LiF prisms as the dispersing elements, and an RCA 931A photomultiplier as the detector. The sample optics were modified to accommodate the high pressure equipment between the exit slit and the detector. All spectra were recorded directly as percentage transmission by the use of a tape recorded slit program which took into account the various background effects, including those of the uncolored crystal and the cell.

The single crystals used in these experiments were obtained from the Harshaw Chemical Company. The CsI crystals were colored electrolytically at a temperature of 470°C and under an applied voltage of 100 V/cm. Each crystal was fused on one side to a flat strip of nickel, which served as the anode, and a hot pointed platinum wire, the cathode, was driven into the other side. Electrolysis was completed in one minute and the crystals were then quenched in air. The rubidium halide crystals were colored additively in a Pyrex tube in potassium vapor at 550°C for 2 to 3 days. The tube was cooled in air and the crystal stored in the dark. Subsequent handling of the crystals was done under weak illumination, and, in the case of RbF, under a stream of dry nitrogen.

RESULTS AND DISCUSSION

The results of the measurements for RbCl and RbBr are plotted in Figs 1 and 2. In the pressure region below the phase transition the frequency shift of the *F* band vs. pressure can be represented with sufficient accuracy by a straight line. In both figures, the frequencies measured previously in the pressure range from 10,000 to 50,000 atm(6) are extrapolated to lower frequencies into the region of the phase transition.

RbCl

The absorption of the F center in RbCl was studied by JACOBS(2) at pressures up to 5000 atm. This experiment was repeated and extended to 7500 atm, i.e., up to the point where the phase transition was first observed. The frequencies observed in this experiment agree very well with those found by Jacobs. The frequency increases with increasing pressure and changes discontinuously at the phase transition by 2250 cm^{-1} from 16,700 cm^{-1} to 19,250 cm^{-1} (Fig. 1). The change of frequency (E) of the F center with lattice parameter (a) is defined by the quantity n_F,(2) where

$$n_F = -\frac{\partial \ln E}{\partial \ln a}$$

The quantities n_F for several crystals are listed in Table 3. In the case of RbCl, this quantity is greater below the transition than above.

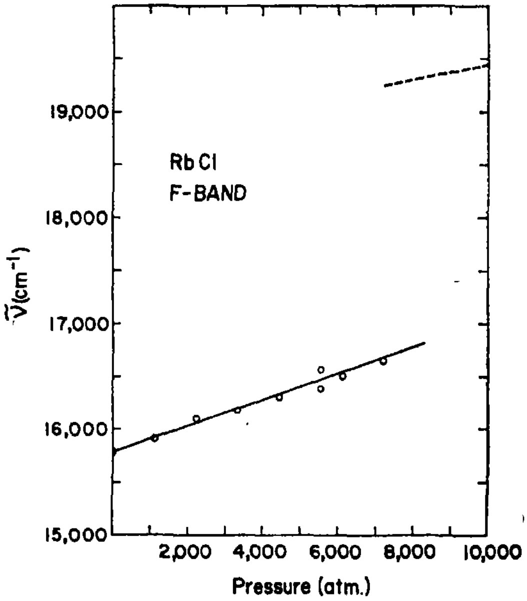

FIG. 1. F band in RbCl. The measured values (o) below the phase transition lie approximately on a straight line. The dashed line above the phase transition (see Ref. 6) is extrapolated from measurements at higher pressures.

RbBr

The effect of pressure on the frequency of the F band in RbBr is plotted in Fig. 2. The behavior in RbBr is similar to that in RbCl. At the phase transition the frequency changes discontinuously by 1500 cm^{-1} from 15,300 cm^{-1} to 16,800 cm^{-1}. This is considerably smaller than the corresponding jump in RbCl. The values of n_F for RbCl are listed in Table 3.

Absorption curves for various pressures are plotted in Fig. 3. The first three curves, at 1, 2200 and 4450 atm were all observed below the transition pressure. These curves are plotted to the same scale and show a slight decrease in intensity with increasing pressure. The half-width of the band is approximately 2800 cm^{-1} and remains constant.

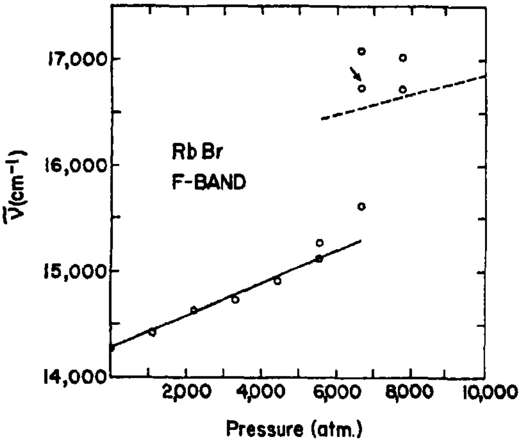

FIG. 2. F band in RbBr. The measured values (o) below the phase transition lie approximately on a straight line. The dashed line is extrapolated from measurements at higher pressures (see Ref. 6). The frequency at the phase transition corresponding to the s.c. lattice is marked by an arrow.

The bottom two curves in Fig. 3, at 6700 atm and 8900 atm, were observed in the region of the phase transition and just above the transition, respectively. Each of these curves is taken from a different experiment and is plotted to a scale different from that of the other and from that of the first three curves. Nevertheless, the general change in intensity which occurs as the crystal goes through the phase transition is fairly well represented. At 6700 atm, the crystal has become almost opaque due to the break-up of the lattice. In fact, the sample now consists of crystallites of both phases which scatter the light at their interfaces. Two *F* bands, F_f and F_b, are observed in the spectrum, the former belonging to the f.c.c. structure and the latter to the s.c. structure. B and F_b increases in intensity with time at the expense of band F_f until, after about twenty minutes at room temperature, only band F_b remains.

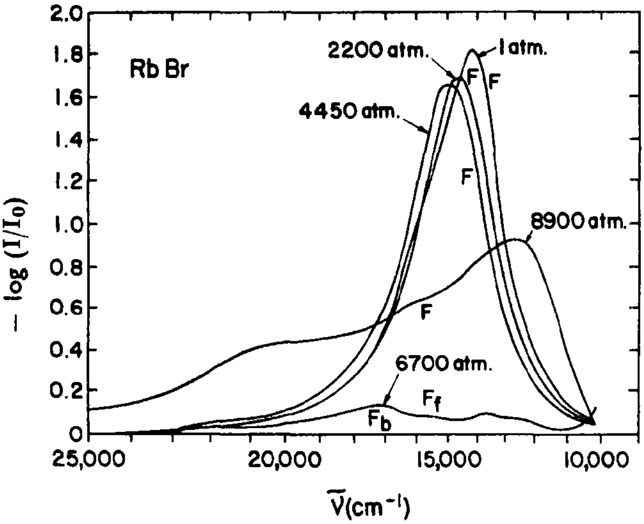

FIG. 3. Absorption curves of color centers in RbBr at different pressures. The location of the *F* band is marked by *F*. The absorption curve at the phase transition shows simultaneously one *F* band in f.c.c. structure, F_f, and one in s.c. structure, F_b.

In the absorption spectrum at 8900 atm, there appear two bands in addition to the *F* band. The band at 20,500 cm^{-1}, the No. 3 band, has been observed previously in the spectra of KI, RbBr and RbI.(3, 6) The values of $n_{\text{No. 3}}$ and n_M are about the same, and it has been suggested that the No. 3 band has its origin in the *M* center.(6) The band at 12,600 cm^{-1} is located about 2000 cm^{-1} higher than the *M* band observed at one atmosphere, and its intensity is greater than that of the *M* band by a factor of two to three. MINOMURA and DRICKAMER(5) observed a similar increase in the intensity of the *M* band in KCl, KBr and KI as these crystals changed from the f.c.c. to the s.c. structure. Therefore, the band at 12,600 cm^{-1} in RbBr can be identified as the *M* band.

RbF

The absorption of the *F* center in RbF was studied as a function of pressure up to 33,000 atm. As can be seen in Fig. 4, the increase in frequency with pressure is less at higher pressures than at lower pressures. At 33,000 atm (an average of increasing and decreasing pressure readings), the crystal became opaque and cleared up only after the pressure was increased by several thousand atmospheres. The low frequency tail of an absorption band, presumably the *F* band, was observed on the high frequency side of the original *F* band at these higher pressures. Unfortunately, the absorption band itself was out of the measurable range. Since the discontinuous jump of the *F* band toward higher frequencies in the various crystals increases in the order iodide, bromide, chloride, a very large change in the position of the *F* band in the fluoride is to be expected. Accordingly, this behavior of RbF at 33,000 atm is attributed to a change in phase. The reduction of transmission by RbF in the transition region is similar to that of the other alkali halides which undergo the phase transformation from the NaCl type to the CsCl type structure under pressure. Optical investigations of pure KCl and KBr in the region of the phase transition showed that, with both increasing and decreasing pressure, the transmission of the crystals was diminished over a range of 6000–10,000 atm.(10) The onset of opacity with increasing pressure was 3000 atm above that observed with decreasing pressure, and the transmission minima were separated by 10,000–12,000 atm. This onset of opacity indicates the beginning of the phase transformation. In the present experiment with RbF, the regions of diminished transmission were 8000–10,000 atm wide, and the pressures where transmission first began to fall off were separated by 6000–7000 atm. From these figures, the averages of two observations made in each direction, the transition pressure is calculated to be (33,000 ± 4000) atm.

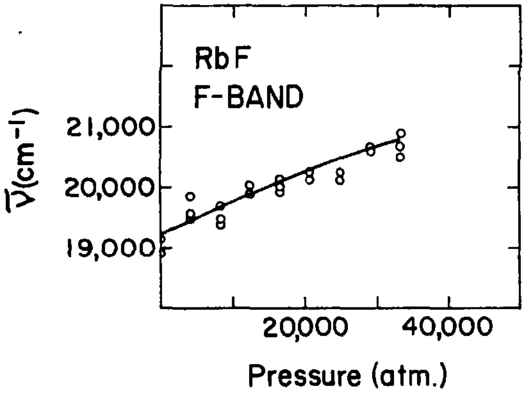

FIG 4. F band in RbF. Measurements (o) up to the phase transition.

PIERMARINI and WEIR(11) have studied the X-ray diffraction patterns of RbF at high pressure and have concluded that the f.c.c. structure is converted to the s.c. structure between 9 and 15 kbar. The authors have since stated that these figures may be somewhat unreliable.* It is very difficult to calibrate their apparatus accurately, so that the measured pressures are uncertain. Furthermore, the reported pressures were observed with decreasing pressure, indicating that the true transition pressure was higher. There is also some uncertainty in the transition pressure reported in the present work. The transition pressures of the other alkali halides observed in the same apparatus are several thousand atmospheres higher than those observed by BRIDGMAN.(7) However, if internal consistency in the pressure apparatus is assumed, the transition in RbF occurred at least 12,000 atmospheres above the transition pressures of the potassium halides, or between 30,000 and 33,000 atm.

CsI

The absorption of the F and M centers in CsI were studied at pressures up to 50,000 atm. Since this crystal has the s.c. structure at one atmosphere, no phase change, and, therefore, no discontinuities in the absorption bands are to be expected. This, indeed, is the case, as can be seen in Fig. 5, where the F and M band frequencies are plotted as a function of pressure. $\nu_m(F)$ increases with pressure but at a decreasing rate at higher pressures. $\nu_m(M)$ is constant to within the limits of the experiment. In previous investigations of the M band in other crystals,(4, 5) a shift to higher frequencies, amounting to about 25 per cent of the F band frequency shift, has always been observed.

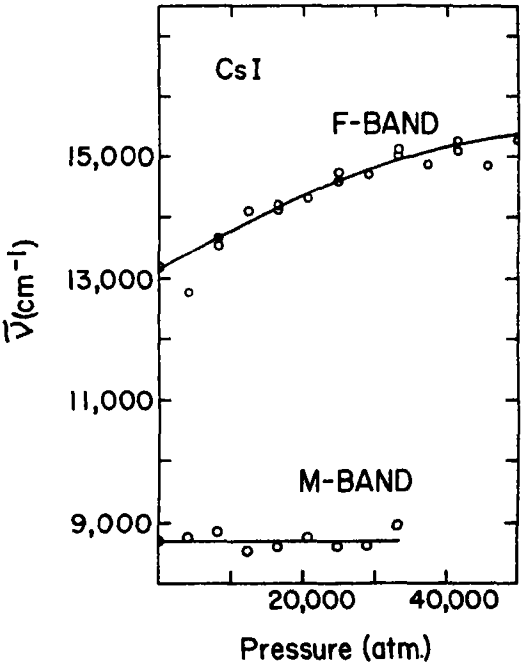

FIG. 5. F and M band in CsI. The frequency of the M band is independent of pressure and the intensity becomes zero at 35,000 atm.

---

* Personal communication.

The intensity of the M band in CsI decreases with increasing pressure and disappears completely at 35,000 atm. This also differs from previous observations on other crystals.$^{(5)}$

SUMMARY

The discontinuous shift in frequency of the F center at the phase transition is given in Table 2 for crystals of the rubidium halides. This frequency jump is positive for all the rubidium halides but decreases going from the fluoride to the iodide. The general trend is the same for F bands in the potassium halides. The latter show an even faster decrease and the frequency jumps for KBr and KI become negative. The M bands in the potassium halides shift in the same direction as the F bands, although the shifts are much smaller.

Table 2. Frequency shift $\Delta\bar{\nu}$ of the F band at the phase transition. All shifts are towards higher frequencies. (a) Ref. 6.

$\Delta\bar{\nu}$(cm^{-1})	RbF	RbCl	RbBr	RbI(a)
F	+	2250	1500	20

The pressure dependence of the F bands can be visualized by a plot of logarithm of the frequency vs. logarithm of the lattice constant. This gives straight lines for most of the alkali halides.$^{(3-6)}$ The lattice parameters were calculated from BRIDGMAN's density data.$^{(7)}$ Fig. 6 shows the lines for RbCl and RbBr below the phase transition; a similar line is drawn for CsI which has the s.c. structure. The slopes, n_F, for those crystals are listed in Table 3. The values of RbF and RbI at atmospheric pressure are contained in Fig. 6. They deviate from the slope at one atmosphere for the f.c.c. structure (drawn as dashed line with $n_F = 1{\cdot}89$). The corresponding slope for the sodium and potassium halides is $n_F = 1{\cdot}84$.

Table 3. Slope $n_F = -\partial \ln E(\bar{\nu})/\partial \ln a(\text{Å})$ of the F band for several crystals.

	RbCl	RbBr	CsI
n_F	4·77	3·79	1·94

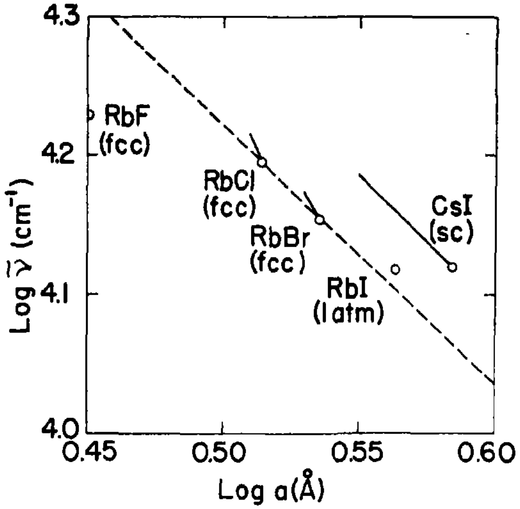

FIG. 6. F bands in RbCl, RbBr and CsI.

The particle-in-the-box-model would give a slope $n_F = 2$, since the energy of the particle is inversely proportional to the square of the box diameter, i.e., to the lattice parameter.$^{(1)}$ This model fails to explain the pressure dependence of the F band for most of the crystals. The deviation of this model is largest for the fluorides and small alkali atoms. It becomes less pronounced going from the fluorides to the iodides and from sodium to cesium where we have the largest cations and anions. The pressure dependence of CsI, with $n_F = 1{\cdot}94$, agrees well with that predicted by the particle-in-the-box-model.

New bands can appear in some crystals under pressure. Of these, the origin of the No. 3 band has not been positively identified.$^{(6)}$ It was observed in KI, RbBr and RbI, but not in KCl, KBr, CsCl, CsBr and CsI.

REFERENCES

1. BURNSTEIN E., OBERLY J. J. and DAVISSON J. W., *Phys. Rev.* **85**, 729 (1952).
2. JACOBS I. S., *Phys. Rev.* **93**, 993 (1954).
3. MAISCH W. G. and DRICKAMER H. G., *J. Phys. Chem. Solids* **5**, 328 (1958).

4. EPPLER R. A. and DRICKAMER H. G., *J. phys. Chem.* **32**, 1418 (1960).
5. MINOMURA S. and DRICKAMER H. G., *J. phys. Chem.* **33**, 290 (1960).
6. ECKERLE K. L. and MAISCH W. G., to be published.
7. BRIDGMAN P. W., *Proc. Amer. Acad. Arts Sci.* **76**, 1 (1945).
8. FISHMAN E. and DRICKAMER H. G., *Analyt. Chem.* **28**, 804 (1956).
9. FITCH R. A., SLYKHOUSE T. E. and DRICKAMER H. G., *J. opt. Soc. Amer.* **47**, 1015 (1957).
10. SLYKHOUSE T. E. and DRICKAMER H. G., in *Propriétés Optiques et Acoustiques des Fluides Comprimés et Actions Intermoléculaires*, p. 163–169, C.N.R.S., Paris (1959).
11. PIERMARINI G. I. and WEIR C. E., *J. chem. Phys.* **37**, 1887 (1962).

J. Phys. Chem. Solids Pergamon Press 1963. Vol. 24, pp. 1633-1637. Printed in Great Britain.

SURFACE SELF-DIFFUSION OF IODIDE IONS IN THIN FILMS

H. J. ARNIKAR and O. P. MEHTA

Department of Chemistry, University of Poona, Poona-7, India

(*Revised* 22 *July* 1963)

Abstract—A method is described for measuring the surface self-diffusion coefficient of labelled ions on solid surfaces. This consists in depositing the given ions to mono or multilayer thickness on one half of a metal foil and the labelled species of the same ions on the other half of the foil and to the same thickness. After the self-diffusion had occurred between the two halves at constant temperature for a definite time, the distribution of the radioactivity is measured on the initially inactive side as a function of distance from the line of contact.

This has been applied for obtaining D^* values for I^- ions in mono and multi (~ 100) layers adsorbed on Cu and Al in the temperature range 145–255°C. Corresponding data for the energy of activation and typical autoradiographs are also presented.

1. INTRODUCTION

FIRST revealed by the classical experiments of VOLMER and ESTERMANN on the rate of the growth of mercury crystals from vapour,(1) the occurrence of surface mobility in adsorbed layers has since been well established.(2–5) Diffusion rates in these surface layers have been measured chiefly by changes in the thermionic and photoelectric emission characteristics,(5–8) and sometimes by methods based on mass transfer.(9,16) It is only recently that radioactive tracers have been employed in these measurements.(10–12) We describe here results of our work on the surface self-diffusion of labelled iodide ions in mono- and multilayers adsorbed on copper and aluminium in the temperature range 145–255°C.

2. EXPERIMENTAL

The surface of sheets of electrolytically pure copper and aluminium of thickness 0·1 mm were polished mechanically and chemically following the procedure of SIEJKA and CAMPBELL.(13) Circular coupons of diameter 16 mm were punched out of these sheets. Sixty ml of 10^{-3} M, KI solution labelled with I-131 to known specific activity were taken in a polythene container. A series of adsorbent coupons were fixed vertically supported on perspex platforms and kept fully immersed in the solution. The system was maintained at constant temperature in an automatically regulated thermostat and was subjected to gentle stirring by slow rotation of 4–5 rev/min.

The period of adsorption was varied from 0·5 sec to 100 hr in each series of experiments. At different intervals of time the sample was removed, dipped 20 times in each of the three vessels containing distilled water, once in alcohol and finally dried by air from a blower. The coupon was then placed in a numbered aluminium planchette and the activity was measured on both the faces of the sample. Two samples were run simultaneously for each period and for the final activity the mean of the countings of the four faces was taken. The corrections due to decay, scattering and self-absorption of activity, were applied to the experimental data.

The activity-time curves are characteristically stepwise in nature (cf. Fig. 1) consisting alternately of steady rises and constant plateaux. The specific activity being known, the total number of adsorbed iodide ions at any given instant is readily found from the activity measured at that instant. A comparison of this figure (x) corresponding to the first plateau with the apparent number of adsorbent atoms ($y_{\text{app.}}$) computed on the basis of known interatomic distance from X-ray data(14) in the (100) planes of these metals, shows the ratio ($x/y_{\text{app.}}$) to vary between 1·2 and 1·5. It is, however, reasonable to assume that the first plateau corresponds to the completion of the unimolecular adsorption (i.e. $x/y_{\text{real}} = 1$) and the observed value of 1·2–1·5 may therefore be taken as the surface roughness factor. We have used the value of 1·5 for this factor in all our computations of the thickness of the adsorbed layers.

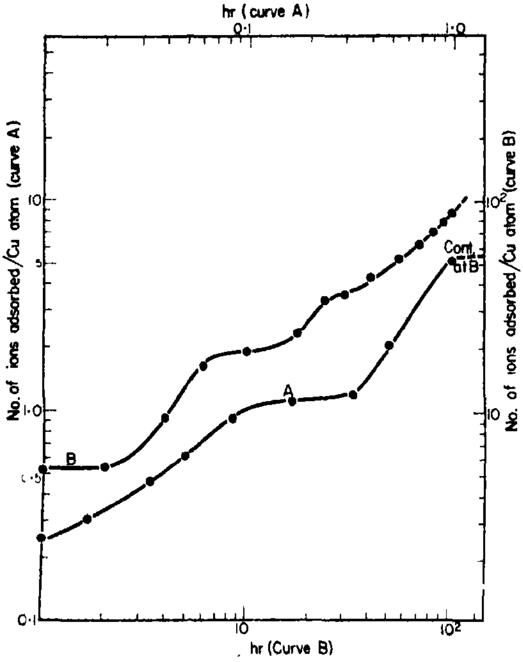

FIG. 1. Time-rate of adsorption of $I^-(10^{-3}M)$ ions on copper at 25°C.

Results on a detailed study of a variation of the thickness of the layer with time on the varying conditions of concentration have been reported earlier.(15) On the basis of these results it is possible to restrict the adsorption to any desired nominal thickness within certain limits by letting the adsorption to proceed for the required duration.

In the present experiments half the length of the adsorbent surface (8×1 cm) was covered with iodide ions to mono- or multilayer of definite thickness by adsorption over a calculated period from a 10^{-3} molar solution of potassium iodide labelled with I^{131} to a known specific activity. The other half of the adsorbent surface was similarly covered to the same thickness but with unlabelled iodide ions. It was ensured that the two halves just overlapped (by about a mm) all along the line of contact. The specimen was next placed in an electric furnace of constant temperature for a definite period of the order of 48 hr. In the end it was cut into a series of strips of 2 mm length on either side of the boundary line and the activity on each of them was measured with a thin end-window G.M. counter and scaler under conditions of constant geometry. Some of the uncut specimens were used for autoradiography to reveal the surface diffusion of the labelled ions.

The diffusion in the above experiments corresponds to the movement of the "front" of the labelled into that of the unlabelled, but otherwise identical, species of same concentration and vice-versa, the two bands being initially contiguous along the boundary line $x = 0$. The conditions of the experiment are further such that at the end of the diffusion there is no change in the concentration of either species (active or inactive) at the extreme ends $x = \pm a$, where a is the half-length of the foil. The boundary conditions for this one-dimensional diffusion can be stated in terms of the concentrations of the active species, thus:

$$\left.\begin{aligned} C &= C_0 \text{ for } x \leqslant 0 \\ C &= 0 \quad \text{for } x > 0 \end{aligned}\right\} \text{ at } t = 0$$

and

$$\left.\begin{aligned} C &= C_0 \text{ at } x = -a \\ C &= 0 \quad \text{at } x = +a \end{aligned}\right\} \text{for all values of } t > 0$$

It can be shown that the basic integral of FICK's second law reduces under these conditions to

$$D = \frac{S^2\pi}{b^2C_0^2t}$$

where D is the surface diffusion coefficient, S the total activity that has traversed the boundary line of width b in time t, and C_0 the initial amount of activity per unit area on the labelled side. As the diffusion is measured under conditions of zero concentration gradient for the total iodide ions (labelled + unlabelled), the result gives the surface self-diffusion coefficient ($D = D^*$).

3. RESULTS AND DISCUSSION

Figure 2 shows typical autoradiographs of the surface migration of the "front" of the active half

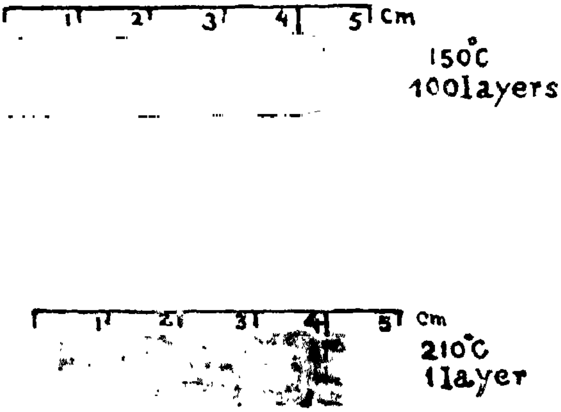

FIG. 2. Autoradiographs representing the surface self-diffusion of I⁻ in its mono- and multilayers adsorbed on copper. The initial boundary line between the labelled and unlabelled halves was at 4 cm from the left.

of the iodide film for several millimeters beyond the initial boundary line. A plot of the activity as a function of distance is roughly Gaussian in the initially unlabelled half (Fig. 3). This shows that the surface migration of adatoms is related to a two-dimensional Brownian movement by

$$D^* = \overline{(\Delta x)^2}/2t$$

where $\overline{(\Delta x)^2}$ is the mean square of displacement in time t.

In Table 1 are presented data for the surface self-diffusion of iodide ions in mono and multi (nominally 100) layers adsorbed on copper and aluminium for different temperatures in the range 145–255°C. Corresponding energies of activation (E) are calculated from the slope of the linear plot of log D^*_- vs. $1/T$ (Fig. 4).

Results show that surface diffusion of iodide ions on these metals becomes measurable above 100°C and that the observed D^* values are distinctly

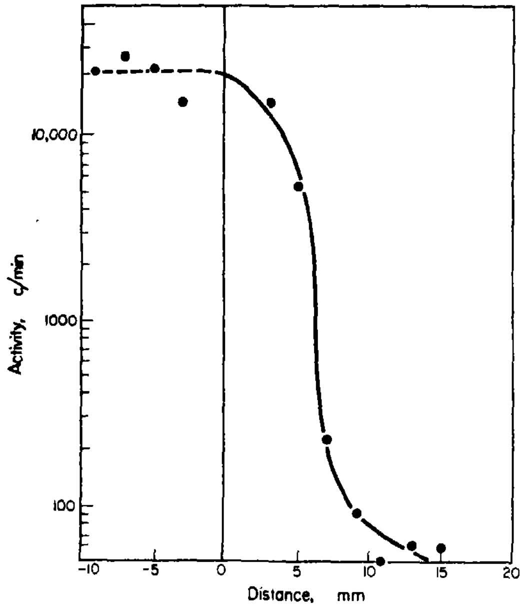

FIG. 3. Surface self-diffusion of iodide ions from the labelled half (left) to the unlabelled half (right) in the adsorbed layers on copper. Time 48hr, Temperature: 210°C.

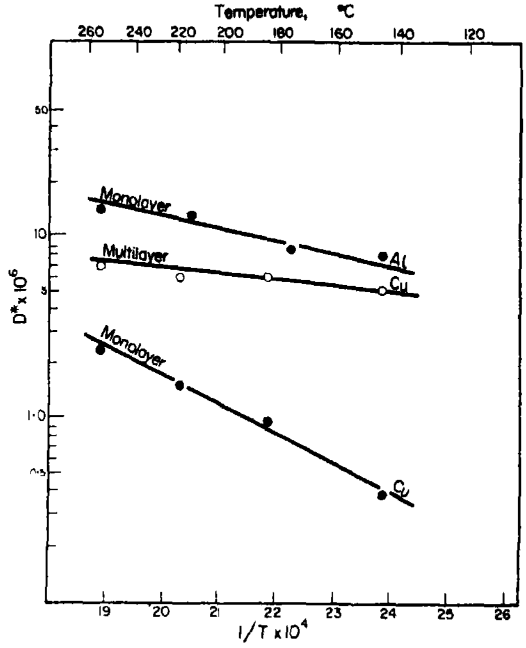

FIG. 4. Variation of surface self-diffusion coefficient with temperature.

Table 1. *Surface self-diffusion coefficient of* I⁻ *ions adsorbed on* Cu *and* Al, $D^* \times 10^6$ cm² sec⁻¹.

Layer thickness (nominal)	Copper		Aluminium
	mono	multi (~100)	mono
Temp. (°C)			
145	0·4	5·2	7·8
175	—	—	8·4
185	1·0	6·0	—
215	—	—	12·9
218	1·5	6·0	—
255	2·4	6·9	14·2
E (k cal/mole)	9·6	1·8	3·1

higher than for bulk diffusion at these temperatures. This is similar to the results reported earlier for the surface diffusion of polonium on silver,(4) thorium on tungsten(3) and the surface self-diffusion of silver(10,11) and copper.(12) These results have been explained on the "vacancy" mechanism of diffusion according to which

$$D_s > D_g > D_v$$

where the subscripts refer to surface, grain-boundary and volume diffusion. The corresponding energies of activation are in the order(3)

$$E_s < E_g < E_v$$

The "monolayer" in the present study may actually be between about 0·8–1·2 layers thick in clear distinction from a thick multilayer of 100–200 layers. Though only the labelled I^- ions are followed in the present study, it is apparent that the corresponding cations of the original adsorbate phase (KI aq.) are also present in the adsorbed layers. We have no knowledge of its exact composition and structure. We make the simplifying assumption that the "monolayer" is spread uniformly over the surface and not collected into "multilayered islands" for the reason that self-diffusion could be observed in cases where the initial layer corresponded to a minimum thickness of a monolayer, while in layers even slightly less than the "monolayer" (i.e. 0·7–0·8), no self-diffusion could be observed whether by autoradiography or by activity scanning. It is, therefore, presumed in the "monolayer" there is a continuity of the structure, though the possibility of local islands slightly thicker than the "monolayer" cannot be excluded, as the layer thickness could vary up to about 1·5. However, the self-diffusion characteristics in this "monolayer" are shown to be different from those in distinctly thick "multilayers" (100–200).

Results of Table 1 further show that at all temperatures studied the rate of diffusion is less in mono than in multi (~100) layers. The energy of activation is accordingly less for the latter. The possibility of a greater mobility of adatoms in the subsequent than in the first layer in contact with the substratum metal has been both envisaged in theory and actually observed in the surface diffusion of alkali metals and of thorium on tungsten.(3) TAYLOR and LANGMUIR(17) postulated a decrease in the heat of sorption with increasing layer thickness, which equals in the limit the heat of vaporization of the adsorbate in the liquid state.

It may further be noted that diffusion in multilayers approximates more nearly to self-diffusion than in the first layer where the substratum is different from the diffusing species. The energy barrier of the vacancies is therefore higher in mono than for diffusion in thicker layers where the substratum and the diffusion species are identical.

According to LANGMUIR,(18) the force (F) responsible for the surface migration is the resultant of two forces, one due to lateral concentration gradient of the adatoms and the other due to lateral dipole repulsion between each adatom and its "electrical image". This leads to expressions of the type:(19)

$$D = D_0\left(\frac{2F}{NkT}-1\right)$$

and

$$F = K(E_0-E)N$$

for the diffusion coefficient (D) and energy of activation (E) as functions of surface concentration (N) of adatoms, D_0 and E_0 being the limiting values when $N \simeq 0$. An increase of D and decrease of E with rising concentration, as observed, is to be expected on this theory.

Acknowledgement—One of us (O.P.M.) is grateful to the Council of Scientific and Industrial Research, New Delhi, for the award of a Research Fellowship.

REFERENCES

1. VOLMER M. and ESTERMANN J., *Z. Phys.* **7,** 13 (1921).
2. VOLMER M. and ADHIKAR I. G., *Z. Phys.* **35,** 170 (1925); *Z. phys. Chem.* **119,** 46 (1926).
3. BARRER R. M., *Diffusion in and Through Solids,* pp. 328, 346, 363, 371. The Cambridge Series of Physical Chemistry (1951).
4. SCHWARTZ K., *Z. phys. Chem.* **168A,** 241 (1934).
5. BECKER J. A., *Trans. Amer. electrochem. Soc.* **55,** 153 (1929); *Phys. Rev.* **28,** 341 (1926); *ibid.* **34,** 1323 (1929).
6. BRATTAIN W. and BECKER J. A., *Phys. Rev.* **43,** 428 (1933).
7. LANGMUIR I. and TAYLOR J. B., *Phys. Rev.* **40,** 463 (1932).
8. BOSWORTH R. C., *Proc. Roy. Soc.* **150A,** 58 (1935); *ibid.* **154A,** 112 (1936).

9. GOMER R., *Structures and properties of Solid Surfaces*, p. 76, University of Chicago Press (1953).
10. NICKERSON R. A. and PARKER E. R., *Trans. Amer. Soc. Metals* **42**, 376 (1950).
11. WINEGRAD W. C. and CHALMERS B., *Canad. J. Phys.* **30**, 422 (1952).
12. HACKERMANN N. and SIMPSON N. H., *Trans. Faraday Soc.* **52**, 628 (1956).
13. SIEJKA J. and CAMPBELL I. G., *Neukleonika* p. 119. Special Number (1958).
14. WYCKOFF R. W. G., *Crystal Structures* Vol. I, p. 5. Interscience, New York (1948).
15. ARNIKAR H. J. and MEHTA O. P., *J. Sci. Ind. Res.* **20B**, 209 (1961).
16. BLAKELY J. M. and MYKURA H., *Acta Met.* **9**, 23, 595 (1961).
17. TAYLOR J. B. and LANGMUIR I., *Phys. Rev.* **44**, 423 (1933).
18. LANGMUIR I., *J. Amer. chem. Soc.* **54**, 1252 (1932).
19. TOPPING J., *Proc. Roy. Soc.* **114A**, 67 (1927).

J. Phys. Chem. Solids Pergamon Press 1963. Vol. 24, pp. 1639–1643. Printed in Great Britain.

HEAT CAPACITY OF Ni–Pd ALLOYS

C. A. MACKLIET and A. I. SCHINDLER

U.S. Naval Research Laboratory, Washington 25, D.C.

(*Received* 3 *June* 1963)

Abstract—Heat capacity measurements in the liquid helium temperature range have been made for pure palladium and for alloys of palladium containing approximately 20, 40, 60 and 80 at. % nickel. Calculated electronic specific heat coefficients (γ-values) are 9·38, 10·66, 8·54, 7·82 and 7·52 mJ/mole°K^2, respectively. Calculated Debye temperatures are 272, 295, 305, 330·5, and 388°K, respectively. The implications of the present results are discussed in regard to other work on Ni–Pd alloys and in regard to the band structure of this system.

INTRODUCTION

HEAT capacity measurements in the liquid helium temperature range have been made for a series of Ni–Pd alloys in order to help clarify the band structure of this system. WOHLFARTH[1] has noted that data on intrinsic magnetization and susceptibility indicate that Ni and Pd each have approximately 0·6 holes/atom in the *d*-band (and an equal number of electrons in the *s*-band). On the basis of this observation, plus the fact that these alloys are single phase and of the same structure (f.c.c.) for all compositions, he has tentatively made the simplifying assumption that Ni–Pd alloys of all compositions have 0·6 holes/atom in the *d*-band—although, of course, the number of holes having parallel and anti-parallel spins must be chosen to agree with the observed magnetization data. Several investigators[1,6–9] have interpreted experimental results by using this model, along with some assumed band shape. Since conflicting band shapes have been employed, it seems useful to obtain the information that heat capacity data can supply.

EXPERIMENTAL

Specimen geometry, apparatus, and procedures used in the present investigation were generally similar to those frequently used by other workers. Cylindrical specimens, roughly 1 in. long by 1 in. dia., were cast from high purity nickel and palladium. Specimen masses varied from 1·32 to 1·68 moles. Spectrographic analyses of the specimens indicated about 0·05 per cent impurities; carbon content was 0·01 per cent or less. Each specimen was surface ground on both ends and annealed in vacuum for 6–18 hr at about 250°C below the solidus temperature.

The specimen holder consisted of two distinct parts held firmly against opposite ends of the specimen. An Allen–Bradley carbon composition resistor (with the insulation ground off) was cemented into one end-piece for use as a thermometer; a flat heater coil of manganin wire was cemented into the other piece. (GE 7031 cement was used.) The specimen-holder assembly was suspended by nylon threads from a nichrome wire stand which in turn rested on a cover plate at the bottom of the specimen chamber. Heater leads of fine superconducting niobium wire and thermometer leads of fine manganin wire were run to glass–metal seals (soldered in the cover plate) and then into the helium bath.

Access to the specimen chamber was provided by the cover plate which was sealed to the chamber with replaceable "gold O-rings". A separate, toroidal chamber around the middle of the specimen chamber was used for vapor pressure measurements. Each chamber could be evacuated or filled with helium as desired.

Heat capacity measurements were made in the usual manner: heater power was applied for some period of time and the change in specimen temperature was determined. Power levels (of about 2–20 μW) were measured with a K-3 potentiometer and associated circuitry. Time intervals (of about 40–240 sec) were measured with an electric timer. Resistance (and thereby temperature) measurements were made by connecting the carbon resistor as one arm of a high-sensitivity resistance bridge; temperature excursions (i.e., ΔT's) ranged from approximately 4·5 to 27 millidegrees. Temperatures ranged from about 1·5 to 4·2°K. Heat capacities for each specimen were usually determined at 40–50 values of the temperature.

The probable random errors in the calculated values of the power level and of the time interval may be straightforwardly estimated as roughly $\frac{1}{8}$ per cent and $\frac{1}{10}$ per cent, respectively. The probable random errors in ΔT and in T are not easily determined but may be conservatively estimated as perhaps 1 to 2 per cent and $\frac{1}{2}$ to 2 per cent, respectively, depending upon the magnitudes of ΔT and T. These estimates are in satisfactory agreement with the scatter of the points on the C/T vs. T^2 plots.

It might finally be mentioned that helium exchange gas was used in cooling the specimen-assembly to helium temperatures and that residual gas in the specimen chamber was then found to be the main factor limiting thermal isolation. However, thermal isolation could be significantly improved by (a) raising the bath temperature, (b) pumping away more residual gas, and (c) cooling the bath to trap helium on the walls. The use of such a procedure yielded heating curves which had small initial and final temperature drift and, generally, insignificant temperature overshoot. Although the heater and the thermometer were at opposite ends of the specimen, significant temperature overshoot occurred if the above manipulation of the bath temperature was omitted.

RESULTS

Heat capacities in the liquid helium temperature range were measured for nickel–palladium alloys having the compositions given in Table 1. (The heat capacity of the specimen holder was equal to roughly 10 per cent of the total.) Plots of C/T vs. T^2 yielded good straight lines, although significant scatter of the data points for each specimen was evident. Curve fitting [to the equation $C = \gamma T + 1{\cdot}945 \cdot 10^6 (T/\Theta)^3$] and error analysis were carried out on a computer. Table 1 lists the Debye temperature, Θ, the electronic specific heat coefficient, γ, and the statistical errors in each.

Table 1 *Specific heat of* Ni–Pd *Alloys.*

Composition (at.%)	Θ(°K)	γ(mJ/mole deg^2)
100 Pd	272 ± 3	$9{\cdot}38^5 \pm 0{\cdot}03^5$
18·91 Ni 81·09 Pd	295 ± 3·5	10·66 ± 0·03
39·65 Ni 60·35 Pd	305 ± 4	8·54 ± 0·03
59·63 Ni 40·37 Pd	330·5 ± 4·5	$7{\cdot}82^5 \pm 0{\cdot}02^5$
79·84 Ni 20·16 Pd	388 ± 8	$7{\cdot}52^5 \pm 0{\cdot}02^5$

DISCUSSION

The results of the present investigation will be considered first in connection with other work on Ni–Pd alloys. WOHLFARTH,(1) on the one hand, has employed the simple model given in the Introduction. By assuming inverted, parabolic *d*-bands, and by applying the collective electron theory of ferromagnetism, he was able to interpret data on magnetization, susceptibility, and Curie temperature. His work also yielded a predicted composition-dependence of the electronic specific heat coefficient, γ; this curve appears as the full line in Fig. 1. [It may be noted that Wohlfarth calculated a relative variation, i.e., γ(alloy) ÷ γ(Ni). The

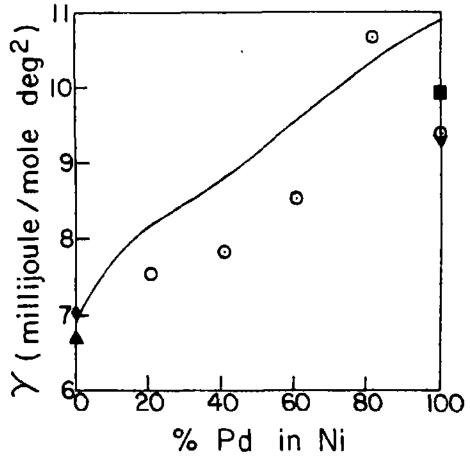

FIG. 1. Specific heat of Ni–Pd alloys. ○ present investigation. ▲, ▼, ■, ◆ Refs. 2–5 respectively. —— WOHLFARTH's calculation.(1)

curve shown has been arbitrarily normalized to the average of the two experimental values of γ(Ni).] The experimental results of the present investigation (○) and those of other workers(2–5) (▲, ▼, ■, ◆) are also shown. Although the general trend of Wohlfarth's curve is correct, there is no indication of a maximum in γ for an intermediate composition—in contrast to the experimental results. It might finally be mentioned that Wohlfarth's treatment made no allowance for the composition-dependence of the lattice parameter of these alloys. His assumptions of a constant number of d-electrons per atom and a composition-independent Fermi energy may not be entirely consistent. However, the effect of lattice expansion does not seem readily calculable in the general case, although for free electrons it may be shown that the γ vs. composition curve should be multiplied by a factor $(1+\alpha)^2$, where $\alpha = [d(\text{alloy})-d(\text{Ni})]\div d(\text{Ni})$, and d is the lattice parameter. If a qualitatively similar correction were applicable in this case, then the agreement between theory and experiment would be even poorer, since $\alpha \approx 0{\cdot}1$ for Pd.

The electronic transport properties of Ni–Pd alloys have been investigated by SCHINDLER *et al.*(6–8) (residual and temperature-dependent resistivity) and by DREESEN and PUGH(9) (residual resistivity and Hall coefficients). All of these workers adopted the simplifying assumptions discussed in the Introduction. But a parabolic band (as used by Wohlfarth) did not seem appropriate for fitting their data, and, in fact, these investigators employed an exponential d-band: $n(E) \propto \exp(\text{const}\cdot E)$. Such a dependence corresponds to $n(E) \propto q^1$, i.e., the density of states at a given energy level is proportional to the *first* power of the total number of states (per atom) having higher energies in the band. [For an inverted, parabolic band, $n(E) \propto q^{1/3}$.] The γ vs. composition curve to be expected for exponential bands may be obtained as follows. If the usual direct proportionality is assumed between γ and $n(E_f)$, and if contributions from the spin-up and spin-down halves of the d-band are considered, then $\gamma(\text{alloy}) \propto [n_d^{\uparrow}(E_f)+n_d^{\downarrow}(E_f)]+n_s(E_f)$, where the last term is the contribution from both halves of the s-band and is essentially independent of composition. Since $n_d(E) \propto q^1$ in this case, $n_d^{\uparrow}+n_d^{\downarrow} \propto q^{\uparrow}+q^{\downarrow}$ which is assumed to equal $0{\cdot}6$, independent of composition. Thus, for exponential bands and for Ni–Pd alloys subject to the above assumptions, γ would be independent of composition—a conclusion not supported by the present investigation. (Expansion of the lattice with increased Pd content does not seem relevant in this treatment.)

Brief consideration will be given to the relatively poor agreement between the results of the present investigation and some of the implications of the above work on these alloys. The most immediate problem seems to concern band shape. Although WOHLFARTH(1) (using parabolic bands) and OVERHAUSER and SCHINDLER(7) (using exponential bands) obtained reasonable agreement between theory and experiment, their calculations are only moderately sensitive to band shape and do not rule out $n(E)$ dependences different from the ones they used. DREESEN and PUGH,(9) however, apparently could not obtain a satisfactory fit to their data without assuming an exponential, or nearly exponential, band. But it is difficult to determine the significance of this result because of one feature of their treatment. One of their basic equations was Pugh's 4-band generalization of Sondheimer's solution of the Boltzmann transport equation. This solution is apparently for the case of two overlapping parabolic bands, and its use with the assumption of non-parabolic (exponential) bands would seem to require more detailed investigation.

In summary, it appears that, even for a presumably very simple alloy system such as Ni–Pd, no reasonably simple band picture is adequate for describing a variety of properties with more than qualitative accuracy, if that. But most band calculations for transition elements, and for Ni in particular, yield a peak in the d-band density of states curve near the upper edge of the band. Since the occupied regions of the band most likely include this peak in the case of Ni–Pd alloys, it would seem unlikely that a simple, monotonic $n_d(E)$ curve could yield detailed agreement with experiment.

It is of interest to attempt a rough estimate of $n_d(E)$, the d-band density of states curve (for one direction of spin), for Ni–Pd alloys by using the present specific heat data. A procedure suited to non-ferromagnetic alloys has, for example, been carried out by HOARE and YATES(3) for Ag–Pd alloys. However, Ni–Pd alloys containing greater than about 3 at. per cent Ni are ferromagnetic. The two halves of the d-band will be filled to different levels (so as to yield the observed net magnetization) and the d-band contribution to γ will therefore be the sum of two unequal contributions whose relative sizes are not known. The following means of separating these two contributions and obtaining $n_d(E)$ has been employed: (a) the γ(Ag–Pd) data mentioned above are used to determine the upper part of the $n_d(E)$ curve; (b) magnetization data⁽¹¹⁾ are used to determine the levels of filling of each half-band for any composition; (c) the present specific heat data are then used to determine a portion of the $n_d(E)$ curve at lower energies. A more detailed discussion follows.

Since Ag–Pd alloys are paramagnetic, the two half-bands are equally filled and γ yields $n_d(E_f)$ directly if a suitable correction is first made for the s-band contribution to γ. Since adding silver to palladium gradually fills the d-band in a known manner (each Ag atom presumably contributes one electron to the d-band), the number, q, of vacant states per atom in a half-d-band may be easily calculated from the composition. Thus, the γ(Ag–Pd) data yield $n_d(q)$, in the range q = 0[60Ag40Pd] to $q = 0{\cdot}3$ [pure Pd]. [γ(Ag) was subtracted from γ(Ag–Pd) in order to remove the contribution of the s-electrons.] The resultant $n_d(q)$ curve is assumed to characterize the upper part of a half-d-band for pure Pd and for Ni–Pd alloys as well.

Saturation magnetization data for Ni–Pd alloys,⁽¹¹⁾ along with the previously-discussed assumption that $q^{\uparrow}+q^{\downarrow} = 0{\cdot}6$ for all compositions, may then be used to determine $q^{\uparrow}$ and $q^{\downarrow}$ (i.e., the filling of each half-band) for any composition. Since one half-band is filled to a level that lies in the previously-determined upper part of the band, the density-of-states contribution for that half-band may be obtained. Subtracting both this value and the assumed s-band contribution, γ(Ag), (in appropriate units) from an observed γ-value yields the density-of-states contribution of the other half-band. Since the level of filling of this band is known—and falls in a region of lower energy (with respect to the top of the band)—it is possible in the present case to obtain $n(q)$ for $q = 0{\cdot}49$ to $0{\cdot}6$. The $n(q)$ data in the $q = 0$ to $0{\cdot}3$ range (Ag–Pd alloys) and in the $q = 0{\cdot}49$ to $0{\cdot}6$ range (Ni–Pd alloys and pure Ni) indicate that a maximum must occur for $q \gtrsim 0{\cdot}49$. Although the

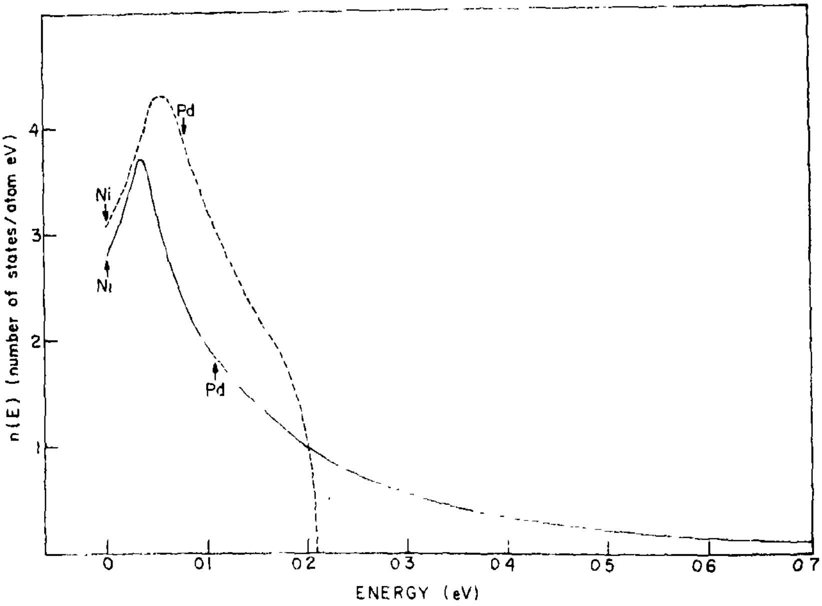

FIG. 2. d-band density-of-states curve. —— present calculation for Ni–Pd alloys. – · – – FLETCHER's curve⁽¹⁰⁾ for Ni.

position and magnitude of this maximum can be estimated only roughly, it is possible to draw a smooth and reasonable curve in the $q = 0{\cdot}3$ to $0{\cdot}49$ region. (Moderate changes in this interpolated portion of the curve will hardly change the qualitative nature of the overall results.) The final transition from $n(q)$ to $n(E)$ is straightforward and the results appear as the solid line in Fig. 2. The dashed line is FLETCHER's calculation(10) for the *d*-band in Ni. (Since the above procedure yields only changes in energy, it is necessary to choose an energy-zero for the curve calculated above. This was done by arbitrarily making the Fermi level for Ni agree with that of Fletcher's curve. The level of filling of the bands appropriate to pure palladium is also indicated in the two cases.) An examination of Fig. 2 suggests that the peak in the present γ(Ni–Pd) data is probably due to a peak in the *d*-band density-of-states curve.

In all of the calculated density-of-states curves, as well as the one experimentally determined here, there is a clear indication of a maximum appearing in the energy interval between the Fermi energy of nickel and the top of the *d*-band. It is appropriate to inquire into the reason for the lack of any effect of this maximum upon the electrical resistivity measurements of the Ni–Pd system made earlier by SCHINDLER *et al.*,(6–8) and by DREESEN and PUGH.(9) The electrical resistivity for the Ni–Pd system can be considered equivalent to a parallel network of spin-up and spin-down electrons:

$$1/\rho = 1/\rho^{\uparrow}+1/\rho^{\downarrow}. \qquad (1)$$

Assuming only *s*-band conduction, the resistivity contribution of, say, the spin-up half-band is

$$\rho^{\uparrow} = \rho^{\uparrow}_{ss}+\rho^{\uparrow}_{sd}, \qquad (2)$$

with a similar expression for the other half-band. Using the Born approximation, each of these terms can be shown to be proportional to the appropriate density of states, evaluated at the Fermi energy:

$$\rho^{\uparrow}_{si} \propto n^{\uparrow}_{i}\left|\int \psi_i^{*}\Delta V\psi_s \,d\tau\right|^2 \equiv n^{\uparrow}_{i}U^{\uparrow}_{si}, \qquad i = s \text{ or } d, \qquad (3)$$

where the ψ's are the appropriate wave functions and ΔV is the perturbation on the electron potential giving rise to transitions between electronic states. Equations (1), (2) and (3), yield for the resistivity:

$$\rho \propto (n_sU_{ss}+n_d^{\downarrow}U_{sd}^{\downarrow})\bigg/\left[1+\frac{n_sU_{ss}+n_d^{\downarrow}U_{sd}^{\downarrow}}{n_sU_{ss}+n_d^{\uparrow}U_{sd}^{\uparrow}}\right]. \qquad (4)$$

Since the exchange splitting in the *s*-band is small, the spin-up and spin-down values of n_s and U_{ss} are essentially equal and do not have to be identified. In pure nickel, the spin-up portion of the *d*-band is filled to some level on the low energy side of the density of states maximum, while the other half of the *d*-band is completely filled. As palladium is alloyed with nickel, the Fermi level of the spin-up portion of the *d*-band shifts to a region of the *d*-band with higher values of $n_d^{\uparrow}$. At the same time, unoccupied states appear in the top of spin-down portion of the *d*-band, where $n_d^{\downarrow}$ is rather small. Since $n_d^{\uparrow}$ is near the maximum of the density-of-states curve, it is clear that $n_d^{\downarrow} < n_d^{\uparrow}$. Consequently, equation (4) becomes

$$\rho \propto n_sU_{ss}+n_d^{\downarrow}U_{ss}^{\downarrow}. \qquad (5)$$

Therefore, because the contributions to the resistivity of the spin-up and spin-down portions of the *d*-band are added in parallel, the measured resistivity will be dominated by that portion of the *d*-band with the smaller value of the density of states, i.e., the resistivity will not be sensitive to the shape of the density-of-states curve in the neighborhood of the maximum.

Acknowledgements—The authors wish to thank J. R. CLEMENT for valuable advice and assistance during the early phases of this work.

REFERENCES

1. WOHLFARTH E. P., *J. Phys. Chem. Solids* **1,** 35 (1956).
2. WALLING J. C. and BUNN P. B., *Proc. phys. Soc., Lond.* **74,** 417 (1959).
3. HOARE F. E. and YATES B., *Proc. Roy. Soc.* **240,** 42 (1957).
4. RAYNE J. A., *Phys. Rev.* **107,** 669 (1957).
5. RAYNE J. A. and KEMP W. R. G., *Phil. Mag.* **1,** 918 (1956).
6. SCHINDLER A. I., SMITH R. J. and SALKOVITZ E. I., *J. Phys. Chem. Solids* **1,** 39 (1956).
7. OVERHAUSER A. W. and SCHINDLER A. I., *J. appl. Phys.* **28,** 544 (1957).
8. SCHINDLER A. I., SMITH R. J. and SALKOVITZ E. I., *Phys. Rev.* **108,** 921 (1957).
9. DREESEN J. A. and PUGH E. M., *Phys. Rev.* **120,** 1218 (1960).
10. FLETCHER G. C., *Proc. phys. Soc. Lond.*, **A65,** 192 (1952).
11. SADRON C., *Ann. Phys.* **17,** 371 (1932); WENT J. J., *Physica* **17,** 98 (1951).

J. Phys. Chem. Solids Pergamon Press 1963. Vol. 24, pp. 1645–1649. Printed in Great Britain.

STUDY OF THE BANDS OF UNIFORM BIREFRINGENCE IN FAULTED ZnS

JOSEPH SINGER*

General Telephone and Electronics Laboratories, Inc., Bayside 60, New York

(*Received* 23 *May* 1963)

Abstract—Several vapor phase grown hexagonal ZnS crystals, faulted as synthesized and also by heating perfect specimens, have been scanned with a 10 μ beam X-ray oscillation camera. Structure and birefringence of many individual bands have been compared; some bands were wide enough to permit several adjoining exposures. Structural changes within bands were as abrupt as those occurring across band boundaries; there was other evidence of heterogeneity in bands which were too narrow for direct exploration. Heterogeneity within bands directly refutes simple models for the birefringence. Additional refutation derives from the establishment (in another report) of a *two*-parameter model for the disorder in ZnS; even if there were any homogeneously scattering regions they could not be characterized by a single faulting parameter. Thus the value of the birefringence of a band is *not* a simple measure of the degree of disorder, nor of relative amounts of hexagonal and cubic sequences, as has sometimes been assumed.

1. INTRODUCTION

Bands of uniform birefringence parallel to the close-packed planes are a striking characteristic of vapor phase grown hexagonal ZnS crystals viewed between crossed polarizers (Fig. 1). These bands range widely in size, although most often they are of the order of microns. They are of uniform color and are more or less sharply separated by thin black lines; the latter can be seen in direct light to mark very small steps in the crystal. Similar banding may be seen in the crystallites of ZnS powders which have been processed to be electroluminescent. The banding is well known to be closely associated with faulting and it has been tempting to correlate structure to the value of birefringence. Although no quantitative work has been done on the question of such a correlation, it has sometimes been assumed to exist⁽¹⁾ and has even been taken for granted in work on electroluminescence.⁽²⁾ The present work has demonstrated that there is no correlation between the value of birefringence and any practicable faulting parameter such as "α, the fraction of planes out of sequence".⁽³⁾ Reasons why a simple relation of this type cannot exist have been established; an alternate model for the birefringence has not been achieved however.

2. EXPERIMENTAL

Several crystals with c_0 elongation were selected from batches grown in this Laboratory.⁽⁴⁾ They have been studied by an X-ray microbeam technique which permitted oscillation diagrams to be made from selected regions down to 10 μ in extent (along c_0), with the ability to move the beam along the crystal in steps as small as 2 μ.

The micro-camera is shown in Figs 2 and 3. The fine micrometer beneath the goniometer provides the fine control of beam location along the rotation axis. Correlation was made, within 2 μ, between positions of the 10 μ beam on the crystal and birefringence readings taken on a polarizing microscope at 200 ×.

Retardation was measured by a rotation compensator, and thickness by focusing; absolute values of birefringence are taken to be correct to ± 10 per cent, the error being that of the thickness measurement. However, relative values along the same crystal are as precise as the retardation measurement alone, $\pm \sim 1$ per cent, and where the color is the same, the birefringence may be taken as exactly the same.

Observations of X-ray structure were made on the $(10 \cdot l)$ *REL* row, which is typical of the fault sensitive rows whose index is $H-K = 3n \pm 1$.⁽⁵⁾

---

* Present address: Lewis Research Center, NASA, Cleveland 35, Ohio.

The oscillations were set to bring in this row between (10·1) and $(10\cdot\bar{1})$, thus including the region where the (10·1) of the cubic structure appears. A typical diagram, taken with a conventional camera, is shown in Fig. 4. Comparisons of structure were based on visual estimates of relative amounts of coherent and diffuse scattering; densitometry of the microbeam diagrams was impractical. Since analysis of the general nature of the faulted structure(6) has shown that a single faulting parameter is inapplicable, there was no way to apply any more quantitative measurements of the faulting to the question of correlation with birefringence (see Discussion).

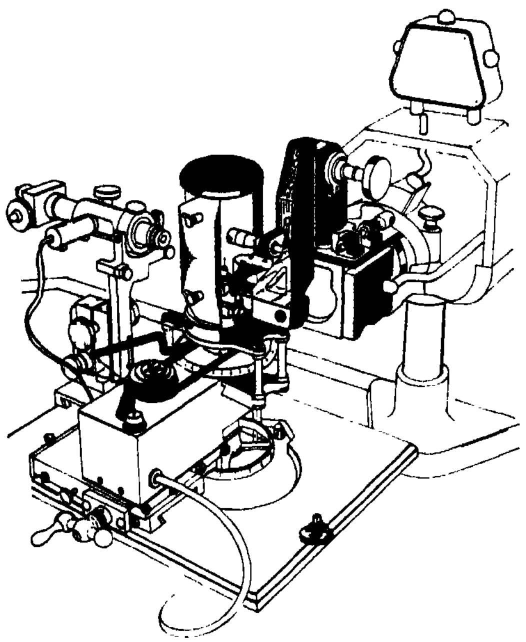

FIG. 2. Micro-beam oscillation camera, overall view.

3. RESULTS

A. Crystals as synthesized ranged widely in structural types. It was soon discovered that very few crystals occurred with a wide range of birefringence and at the same time with only $2L$ and $3L$ sequences. None the less it was possible to obtain some information bearing on the questions at hand from crystals faulted as synthesized. Some information was obtained also with perfect hexagonal crystals which were heated.

A notable feature of the micro-beam diagrams was the sharpness of the hexagonal maxima against the diffuse scattering in the $(10\cdot l)$ row, as contrasted to the blending observed with normal sized beams.

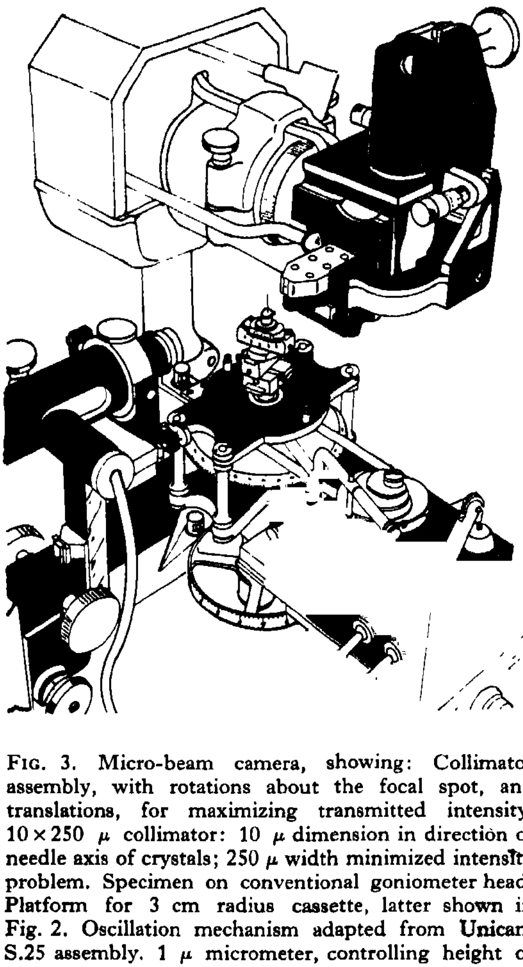

FIG. 3. Micro-beam camera, showing: Collimator assembly, with rotations about the focal spot, and translations, for maximizing transmitted intensity. 10×250 μ collimator: 10 μ dimension in direction of needle axis of crystals; 250 μ width minimized intensity problem. Specimen on conventional goniometer head. Platform for 3 cm radius cassette, latter shown in Fig. 2. Oscillation mechanism adapted from Unicam S.25 assembly. 1 μ micrometer, controlling height of crystal. Entire assembly containing sample mount and oscillation mechanism can be moved as a unit to the center of the maximized beam.

B. Crystal No. 1 was a mixture of $2L$ and $6L$ sequences, the latter having been found to be the *ABCACB* type for which the (10·0) is extinguished; this allowed any $2L$ to be readily identified by its (10·0) intensity. Table 1 contains

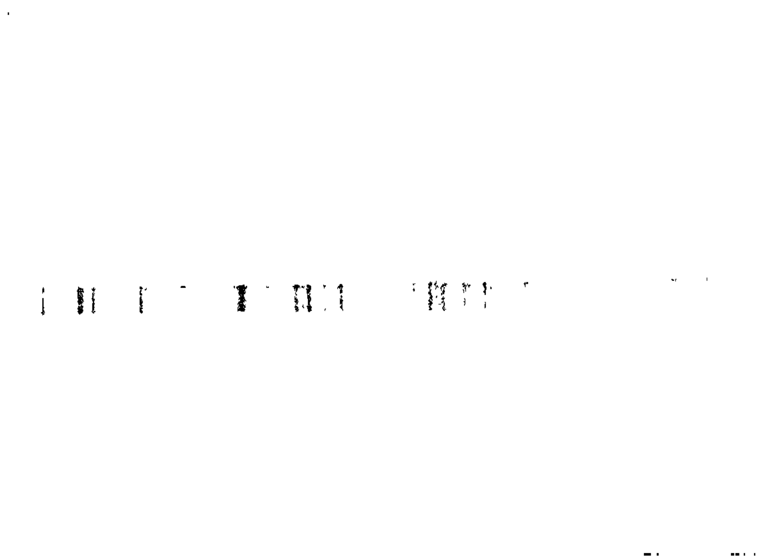

FIG. 1. Birefringent banding in ZnS. Photographed between crossed polaroids; crystal about 50 μ wide.

FIG. 4. Typical intensity distribution, (10·1)–(10·$\bar{1}$), with a moderately faulted ZnS crystal; conventional oscillation camera. Note scattering from highly faulted cubic phase in vicinity of (10·1)$_{3L}$–(111).

Table 1. ***Birefringence band observations on 6L and 2L mixed polytype crystal.***

Band (retardation color, width, and birefringence)	Description of 10 μ X-ray oscillation diagram
1st green. 70 μ. $\Delta n = 0\cdot050$	Six contiguous positions show increasing amount of coherent $2L$ on background of lightly faulted $6L$ and some extensively faulted $2L$. All $6L$ abruptly disappears upon entry into 1st blue.
1st blue. Contains color discontinuity Part A; mixed green and blue, 28 μ	Principally coherent $2L$, with some faulted $2L$ at beginning. Second 10 μ shows $6L$, $2L$ mixed structure like end of 1st green.
Part B; pure blue, 12 μ. $\Delta n = 0\cdot014$.	Abrupt return to pure $2L$, very slightly faulted. No. $6L$ of any type until entry into 2nd green.
2nd green. 60 μ. $\Delta n = 0\cdot050$	Abrupt appearance of extensively faulted $6L$; $2L$ continuing mainly coherent. Amount of faulted $6L$ increases near end.
3rd green. 120 μ. $\Delta n = 0\cdot050$ (separated from 2nd green)	Traces of extensively faulted $2L$. Largely a slightly variable mixture of coherent and faulted $6L$. Sudden disappearance of coherent $6L$ upon entry into 2nd blue.
2nd blue. 40 μ. $\Delta n = 0\cdot014$	$6L$ continues only in faulted form. Some coherent $2L$ commences near end.
Only red. 10 μ. $\Delta n = 0\cdot021$ (not contiguous to other explored bands).	Single diagram shows $2L$ and $6L$ sharp maxima on background of extensively faulted $6L$.

descriptions of the observed structures and associated birefringences. The following may be noted:

1. The broad sections of green retardation color with the unexpectedly high Δn of 0·050 are repeated along the crystal as if they constitute a "background" structure in which bands have formed.
2. All bands large enough to allow more than one 10 μ oscillation diagram show variations in structure. It is perhaps particularly noteworthy that this is true even of the green bands with $\Delta n = 0\cdot050$.
3. Unfaulted $2L$ in the first blue band of 12 μ width is found with $\Delta n = 0\cdot014$, whereas Wurtzite's birefringence is supposed to be 0·024.
4. Abrupt change in color occurs between parts *A* and *B* of the first blue band with an abrupt change in structure but with no well-defined line such as marks other band borders.
5. Part *B* of the first blue band and the second blue band, both with $\Delta n = 0\cdot014$, have quite different structures.

C. Crystal No. 2 (no tabulation presented) consisted of a section of $2L$ material more or less faulted, with the rest fundamentally a $30L$ polytype. Two bands in the $2L$ section, and one in the $30L$ section, were of the same retardation color, corresponding to $\Delta n = 0\cdot019$. The two bands in the $2L$ section gave much the same oscillation diagrams, these being, of course, altogether different from that obtained in the band in the $30L$ region.

D. Crystal No. 3 was initially pure unfaulted $2L$ with $\Delta n = 0\cdot028$, except for one lightly faulted 20 μ band with $\Delta n = 0\cdot020$. The 0·028 value was one of a number of anomalously high birefringences ranging to 0·050 found with pure $2L$ material; any bands occurring in such crystals had birefringences below 0·024.

After this initial study, Crystal No. 3 was heated to 400°C for 10 min. The entire crystal became banded, Δn ranging from 0·015 to 0·020 (in bands >5 μ). The few bands wide enough to allow 10 μ beam oscillation diagrams to be taken in them disclosed moderately faulted $2L$ structures only, differing slightly in the intensity of the incoherent scattering. Here too, as with the usual crystal faulted at synthesis, the coherent hexagonal maxima were very sharply defined against the diffuse scattering.

Crystal No. 3 was finally heated to 530°C for 10 min. The range of birefringence produced thereby was found to be 0·0085–0·020; the microbeam diffraction diagrams were analogous to those from the 400°C treatment but for a slightly larger range in the intensity of the distributions of the incoherent scattering.

E. An additional perfect $2L$ crystal, No. 4, was heated directly to 530°C. This specimen banded only in its middle third, the birefringences ranging from 0·011 to 0·020. The X-ray scattering distributions were plainly closer to those obtained with the 530°C treatment of Crystal No. 3 than with the 400°C heating. Reheating Crystal No. 4 to 530°C produced no further changes in the banding.

4. DISCUSSION

A. The results contain ample refutation of the assumption of a simple correlation between the birefringence and structure of a band; i.e.:

(1) Uniformly birefringent bands have been observed to contain changes in structure.

(2) Band boundaries may always mark a change in structure, but changes within bands may be as abrupt.

(3) The same birefringence may occur in bands of differing structures.

(4) The $6L$ sequence *ABCACB* is "2/3 cubic" in terms of single layer lamelae, yet no relation can be discerned between this fact and the birefringences observed in Crystal No. 1 (Table 1).

B. Although the bands in crystals with only $2L$ and $3L$ sequences were too narrow to allow much direct exploration with the 10 μ beam, evidence of another type has been accumulated on the existence of heterogeneity in these crystals which bears indirectly on the birefringence structure correlation, as follows:

(1) The sharpness of hexagonal maxima against the diffuse scattering indicates separately diffracting domains (resolved by the X-ray diffraction process) of alternately coherent and disordered material.

(2) This sharpness may be maintained against variations in diffuse scattering intensity, further indicating independent scattering by the several types of domains.

(3) In separately reported work$^{(6)}$ the departure from fit between calculated and observed X-ray scattering by faulted ZnS has been attributed to such micro-heterogeneity.

The aforementioned calculated distributions were based on the two-parameter model of disorder of JAGODZINSKI;$^{(7)}$ this model has been shown to correctly describe the structure of faulted ZnS.$^{(6)}$ The requirement of *two* independent disorder parameters constitutes an additional problem for a model of birefringence, even if an entirely homogeneous structure were to be considered; that is, the simplification inherent in the one-parameter model, whereby planes are either in coherent hexagonal or coherent cubic sequences only, is lacking.

The analysis in this other report$^{(6)}$ made use of the above heat treated crystals Nos. 3 and 4. It appeared that the less the range of birefringence, the less the range of heterogeneity in the $2L$–$3L$ crystals, and that these ranges could be controlled by the range of temperature at which fault nuclei were activated. This offered an explanation of the heterogeneity prevailing in most synthetic crystals; it could be attributed to the large temperature range through the cubic region of the post-synthesis cooling.

5. SUMMARY AND CONCLUSIONS

(1) A micro-diffraction technique has shown that the uniformly birefringent bands in faulted ZnS are not uniform in structure.

(2) The range of birefringence in ZnS crystals which contain only $2L$ and $3L$ sequences does loosely indicate the range of heterogeneity, although no simple correlation could be established between structure and birefringence even in these cases.

(3) The usual synthetic hexagonal ZnS crystal contains transformation faults, produced during the post-synthesis cooling, superimposed upon whatever growth faults and polytypism had been incorporated during synthesis.

(4) The heterogeneity in the usual synthetic hexagonal ZnS crystal is a result primarily of the nature of transformation disordering; this heterogeneity is largely microscopic in scale and cannot be detected by looking for differences in diffraction patterns taken along the crystal. Reference has been made to associated work wherein it has been shown that a two-parameter model of disorder is required for the observed scattering from homogeneous domains.

(5) Heterogeneity, and the requirement of two independent fault parameters for any homogeneous scattering, constitute serious obstacles to the employment of birefringence in ZnS as a measure of structure. A model for the banding of birefringence in this substance continues to be lacking.

Acknowledgements—It is a pleasure to acknowledge the advice and support of Dr. J. L. BIRMAN throughout this work. The assistance of W. S. ROMITO is deeply appreciated. The successful development of the micro-camera is owed to R. ADLER and A. PIORKOW.

REFERENCES

1. SHORT M. A., STEWARD E. G. and TOMLINSON E. B., *Nature, Lond.* **177**, 240 (1956).
2. BAUM F. J. and DARNELL F. J., *J. electrochem. Soc.* **109**, 165 (1962).
3. WILSON A. J. C., *Proc. Roy. Soc.* **A180**, 277 (1942).
4. SAMELSON H., *J. appl. Phys.* **32**, 309 (1961).
5. WILSON A. J. C., *X-ray Optics*, Methuen, London (1949).
6. SINGER J., *Acta Cryst.* **16**, 601 (1963).
7. JAGODZINSKI H., *Acta Cryst.* **2**, 208, 298 (1949).

J. Phys. Chem. Solids Pergamon Press 1963. Vol. 24, pp. 1651–1655. Printed in Great Britain.

CRYSTALLOGRAPHIC AND MAGNETIC PROPERTIES OF THE SYSTEMS LITHIUM FERRITE–ALUMINATE AND LITHIUM FERRITE–GALLATE

J. A. SCHULKES and G. BLASSE

Philips Research Laboratories, N. V. Philips' Gloeilampenfabrieken, Eindhoven, Netherlands

(*Received* 17 *June* 1963)

Abstract—Measurements of the saturation magnetization σ against temperature have been carried out for the systems $Li_{0\cdot5}Fe_{2\cdot5-a}Al_aO_4$ and $Li_{0\cdot5}Fe_{2\cdot5-a}Ga_aO_4$ ($0 < a < 2\cdot5$), which have an ordered spinel structure. From the σ–T curves the saturation moments were obtained, and from these it was possible to calculate the trivalent cation distribution, since X-ray diffraction shows that the Li^+ ions are always on octahedral sites. For small values of a Al^{3+} is substituted mainly on octahedral sites, whereas Ga^{3+} mainly enters the tetrahedral sites. It is argued that in spinels a certain preference for tetrahedral sites exists which increases in the sequence Al^{3+}, Fe^{3+}, Ga^{3+}. All Néel's anomalous σ–T curves have been found in the system $Li_{0\cdot5}Fe_{2\cdot5-a}Al_aO_4$.

INTRODUCTION

THE crystallographic and magnetic properties of systems of the type $Li_{0\cdot5}Fe_{2\cdot5-a}Me^{3+}_aO_4$ are very interesting. Lithium ferrite itself is an inverse spinel $Fe[Li_{0\cdot5}Fe_{1\cdot5}]^*O_4$ with a 1:3 order of Li^+ and Fe^{3+} ions in the octahedral sublattice.(1) GORTER(2) reported the system $Li_{0\cdot5}Fe_{2\cdot5-a}Cr_aO_4$ ($0 \leqslant a \leqslant 2$) in which for the first time the *N*-type anomalous magnetization vs. temperature curve was found,(3) which has a compensation point as was predicted by NÉEL.(4) The present paper deals with the systems $Li_{0\cdot5}Fe_{2\cdot5-a}Al_aO_4$ and $Li_{0\cdot5}Fe_{2\cdot5-a}Ga_aO_4$. Magnetic properties of some compositions $Li_{0\cdot5}Fe_{2\cdot5-a}Al_aO_4$ have been reported by CARTER, MILES and WELCH(5) but these data are incomplete. The crystallographic properties of this system have been reported by STRICKLER and ROY(6) who paid special attention to the phase diagram. Our main interest was in the cation distribution and the anomalous magnetization vs. temperature curves.

EXPERIMENTAL

Materials with composition $Li_{0\cdot5}Fe_{2\cdot5-a}Al_aO_4$ and $Li_{0\cdot5}Fe_{2\cdot5-a}Ga_aO_4$ ($0 \leqslant a \leqslant 2\cdot5$) were prepared from high purity Li_2CO_3, Fe_2O_3, Ga_2O_3 and hydrated alumina (33·7%Al). These compounds were milled in the desired proportion in an agate ball-mill under ethanol. After drying, the mixture was prefired for 2 hr at 750°C in an atmosphere consisting of an 80–20 mixture of oxygen and carbon dioxide. The prefired products were ball-milled again. After drying they were heated for 4 hr in oxygen, the materials containing aluminium at 1150°C and subsequently at 1350°C, those containing gallium at 1150°C.

X-ray diagrams of the samples were obtained on a Philips X-ray diffractometer, using CoKα-radiation ($\lambda = 1\cdot7892$ Å).

Some of the samples were analyzed for their Fe^{2+} content by J. Visser of this laboratory; no Fe^{2+} was found. The Li^+ content of the materials containing aluminium, which were sintered at relatively high temperatures for a compound containing lithium, were checked by spectrochemical analysis.

Saturation magnetizations were measured against temperature for all materials with Curie temperature above 100°K, using the ponderomoter method described by RATHENAU and SNOEK.(7) These measurements were carried out in fields up to 21,000 Oe, which is high enough to saturate the samples completely. For the materials containing aluminium, measurements of the saturation magnetization were carried out at liquid-hydrogen temperature, also using a ballistic method. The saturation moments at 0°K and the Curie temperatures were obtained from the saturation magnetization vs. temperature curves by extrapolation.

---

* Octahedral site cations are given between brackets.

RESULTS

The X-ray diagrams of the materials containing aluminium which were sintered at 1150°C showed two spinel phases, those of the materials sintered at 1350°C only one though the composition $Li_{0\cdot5}Al_{1\cdot7}Fe_{0\cdot8}O_4$ showed a slight indication of a second spinel phase. The materials containing gallium appeared to be pure spinels after sintering at 1150°C. Besides the spinel reflections, all X-ray diagrams showed the same superstructure reflections as have been found for $Li_{0\cdot5}Fe_{2\cdot5}O_4$.

The analysis of the lithium content yielded satisfactory results. A representative example is given: $Li_{0\cdot5}Al_{1\cdot2}Fe_{1\cdot3}O_4$, theoretical 2·0% Li, experimental $1{\cdot}9 \pm 0{\cdot}1\%$ Li. Sintering at 1350°C of the samples sintered already at 1150°C did not change the lithium content.

The saturation moments for both systems are plotted in Fig. 1. The three straight lines in this figure correspond to the calculated value of the moment, assuming that all Al^{3+} (or Ga^{3+}) ions are introduced in $Li_{0\cdot5}Fe_{2\cdot5}O_4$

(a). on tetrahedral sites
(b). on octahedral sites
(c). distributed statistically among the two sites. For this calculation we used the NÉEL hypothesis,(4) that the magnetic moments of the ferric ions on tetrahedral and octahedral sites are aligned antiparallel.

There is fair agreement between the saturation moments reported by CARTER, MILES and WELCH(5) for some aluminium substituted lithium ferrites and those given in the present paper. Only the moment given by them for the composition $Li_{0\cdot5}Fe_{1\cdot5}AlO_4$, viz. 0·13 μ_B, is much lower than ours (0·55 μ_B).

In Fig. 2 the σ–T curves for the system $Li_{0\cdot5}Fe_{2\cdot5-a}Al_aO_4$ are presented on a reduced temperature scale. As can be seen, all anomalous curves predicted by NÉEL(4) have been found. For increasing values of a the normal curve (Q-type) of $Li_{0\cdot5}Fe_{2\cdot5}O_4$ changes into the anomalous curve with a maximum (P-type), and for still higher Al^{3+} content into the anomalous curve with a compensation point (N-type). For the system $Li_{0\cdot5}Fe_{2\cdot5-a}Ga_aO_4$ no anomalous curves have been found. When Ga^{3+} is substituted, the Q-type curve of $Li_{0\cdot5}Fe_{2\cdot5}O_4$ changes into a nearly straight line.

The lattice parameters for both systems are plotted in Fig. 3. The straight lines following Vegard's rule are also given.

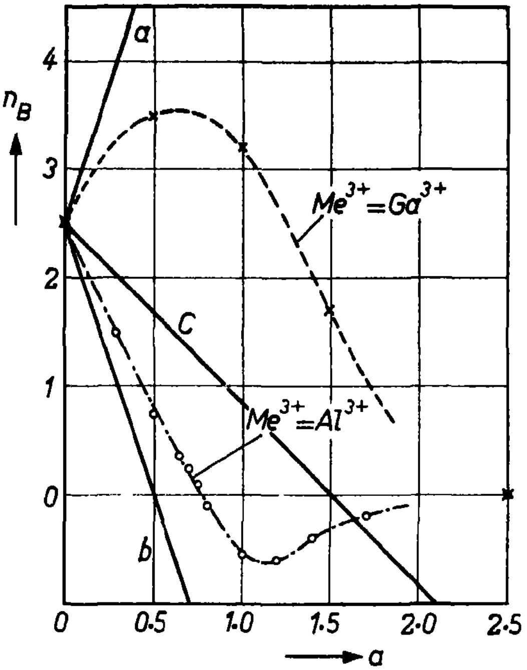

FIG. 1. Saturation moments in $\mu_B(n_B)$ for the systems $Li_{0\cdot5}Fe_{2\cdot5-a}Me_aO_4$($Me^{3+}$ = Al^{3+} or Ga^{3+}). The full lines give the moments calculated for
(a) all Me^{3+} ions on tetrahedral sites
(b) all Me^{3+} ions on octahedral sites
(c) statistical distribution of Me^{3+} ions among the two sites.

DISCUSSION OF THE RESULTS

A. *Crystal chemical properties*

From the X-ray diagrams it follows that $Li_{0\cdot5}Fe_{2\cdot5}O_4$ and $Li_{0\cdot5}Ga_{2\cdot5}O_4$ are completely miscible. $Li_{0\cdot5}Fe_{2\cdot5}O_4$ and $Li_{0\cdot5}Al_{2\cdot5}O_4$ are completely miscible at 1350°C but at 1150°C there is a broad miscibility gap. This is in accordance with the data of STRICKLER and ROY (Fig. 4 of Ref. 6). They found complete miscibility above about 1200°C. Below 1180°C they found a miscibility gap. Although the samples containing aluminium

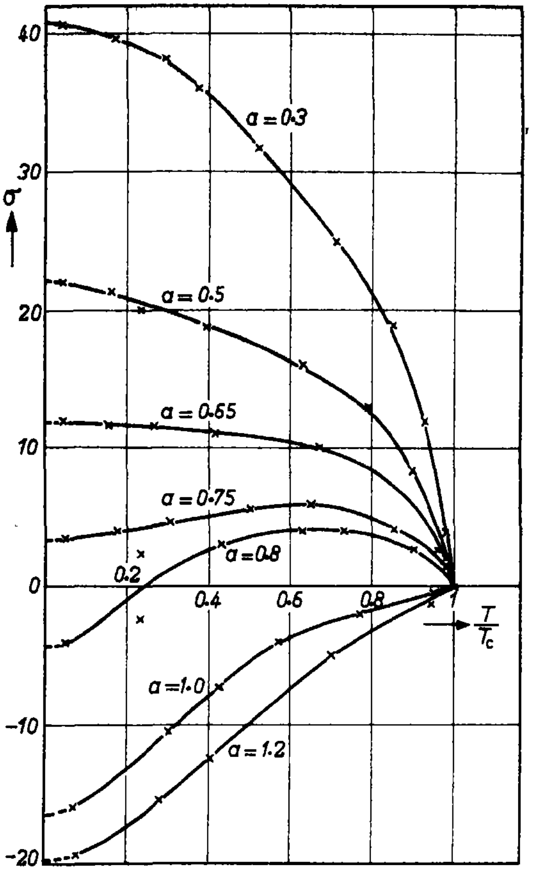

FIG. 2. Saturation magnetization per gram (σ) vs. reduced temperature T/T_c for the system $Li_{0.5}Fe_{2.5-a}Al_aO_4$.

were cooled slowly (2–3°/min), the spinel phase obtained did not separate into two phases. As has been reported earlier(8) separation occurs only after annealing the samples for a long time. Our cooling rate was apparently too high for separation. The difference in miscibility between the two systems can be ascribed to the difference between the ionic radii of the trivalent metal ions. The Fe^{3+} and Ga^{3+} radii are about equal, whereas the Al^{3+} ion is much smaller (values according to AHRENS(9) Fe^{3+} 0·64 Å, Ga^{3+} 0·62 Å, Al^{3+} 0·51 Å).

Chemical analysis showed that the high temperature treatment had no influence on the chemical composition, as has been reported before.(8)

The X-ray diagrams of all samples showed the superstructure reflections of lithium ferrite. Since these reflections were strong and sharp and their intensity remained about constant in both systems, it is concluded that in all samples the lithium ions are exclusively on the octahedral sites. Calculations of the lithium ion distribution among tetrahedral and octahedral sites from the intensity of the X-ray reflections were not carried out, since our conclusion from the superstructure reflections is of the same accuracy, the intensity and sharpness of these reflections decreasing strongly if the ratio of monovalent and trivalent ions on octahedral sites deviates from 1:3. The long-range order does not seem to be influenced by introducing more than one kind of trivalent ion.

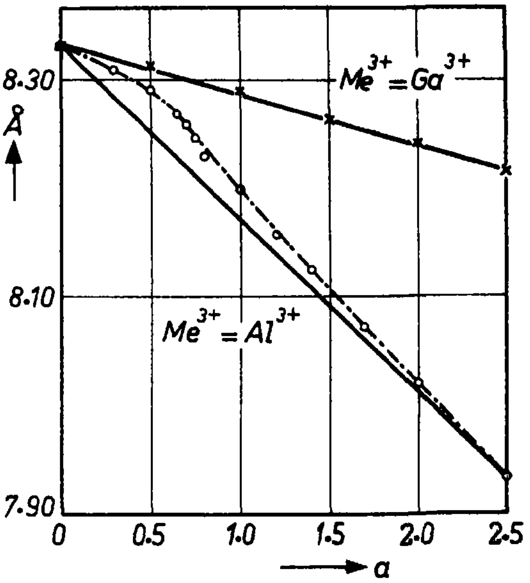

FIG. 3. Lattice parameters in Å for the systems $Li_{0.5}Fe_{2.5-a}Me_aO_4(Me^{3+} = Al^{3+}$ or $Ga^{3+})$. The full lines are straight lines between the values for $a = 0$ and $a = 2{\cdot}5$.

The distribution of the trivalent metal ions can be deduced from the saturation moments. It is not known at which values of a the Néel hypothesis of antiparallel alignment of octahedral and tetrahedral sub-lattice magnetization breaks down. However, we can be certain that it is still valid for $a = 0{\cdot}5$ in the system $Li_{0.5}Fe_{2.5-a}Ga_aO_4$ and up to $a = 1$ in the system $Li_{0.5}Fe_{2.5-a}Al_aO_a$. From the saturation moment of $Li_{0.5}Fe_2Ga_{0.5}O_4$ the distribution $Fe_{0.65}Ga_{0.35}[Li_{0.5}Fe_{1.35}Ga_{0.15}]$ was calculated. For the system $Li_{0.5}Fe_{2.5-a}Al_aO_4$ the calculated amount of Al^{3+} ions in tetrahedral sites in the region $0 \leqslant a \leqslant 1$ is given in Fig. 4. From these calculations it is concluded that the Al^{3+} ions enter mainly the octahedral sites, while the Ga^{3+} ions for the greater part enter the tetrahedral sites. This is immediately seen from Fig. 1, where the experimental saturation moments for the ferrite–aluminate system lie between the lines calculated for statistical distribution and for Al^{3+} substitution exclusively on octahedral sites, while those for the ferrite–gallate system lie between the lines calculated for statistical distribution and Ga^{3+} substitution exclusively on tetrahedral sites. This behaviour is completely analogous with that found in the systems $NiFe_{2-a}Al_aO_4$(2,10) and $NiFe_{2-a}Ga_aO_4$.(10)

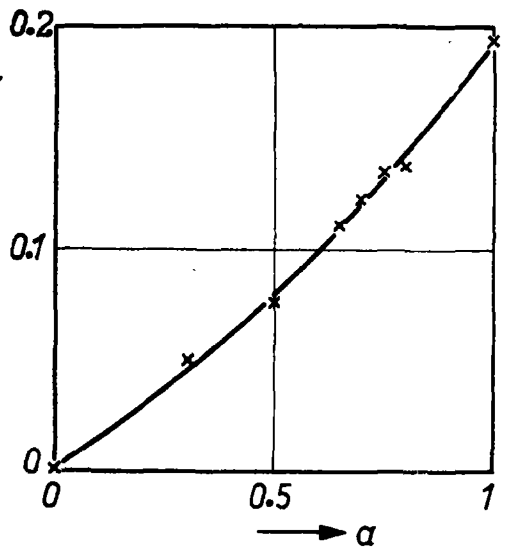

FIG. 4. Amount of Al^{3+} ions on tetrahedral sites (x) in the system $Li_{0\cdot5}Fe_{2\cdot5-a}Al_aO_4$ ($0 < a < 1$), calculated from saturation moments.

The two present systems form a proper case for studying the so-called preference energies of Al^{3+}, Fe^{3+} and Ga^{3+} in the spinel structure. There are many factors which determine the cation distribution in spinels.(11) Very important is the Madelung energy, which depends strongly on the oxygen parameter u.(17) From Fig. 7 in GORTER's paper(11) it is seen that the Madelung energy is practically independent of u in the case where the ionic charge on tetrahedral sites q_A equals 3. Neglecting the influence of the trivalent metal distribution on the lattice parameter (which is expected to be small; however, see below), we conclude that the trivalent metal ion distribution in these systems is independent of the Madelung energy. The distribution is assumed to be independent also of the repulsive energy and of ordering- and polarization energies, the Li^+ ions being on octahedral sites in all cases. The distribution found experimentally is ascribed to a certain site preference of the trivalent ions. This preference cannot be explained by crystal field theory,(12) the Al^{3+} ion having noble-gas configuration and the Fe^{3+} and Ga^{3+} ions having half and completely filled d-shells respectively. There must therefore be another origin of this preference for tetrahedral sites, which increases in the sequence Al^{3+}, Fe^{3+}, Ga^{3+}. It is possible to make this statement, since all other energies governing the cation distribution do not influence it in this case. The influence of these energies can be important in other cases, e.g. the distribution in the spinels $MgMe_2^{3+}O_4$. For $Me^{3+} = Al^{3+}$ one finds a normal spinel,(13) for $Me^{3+} = Fe^{3+}$ a nearly inverse spinel(14,22) and for $Me^{3+} = Ga^{3+}$ a statistically distributed spinel.(15) For these compounds the energy terms determining the cation distribution are all different, owing to the presence of the Mg^{2+} ions on different sites.

It is noteworthy that the site preference of the Al^{3+}, Fe^{3+} and Ga^{3+} ions in the spinel structure differs from that in the garnet structure. It has been found by GILLEO and GELLER,(16) that the tetrahedral site preference in the latter structure increases in the sequence Fe^{3+}, Ga^{3+}, Al^{3+}; the difference between Ga^{3+} and Al^{3+} is not very large. The sequence found in the spinel structure is the one expected, if the bonding is considered to be partly covalent.(17,18)

Finally, we turn to the lattice parameters. From Fig. 3 it is seen that in the system $Li_{0\cdot5}Fe_{2\cdot5-a}Ga_aO_4$ Vegard's rule holds, whereas in the system $Li_{0\cdot5}Fe_{2\cdot5-a}Al_aO_4$ a positive deviation is found. This agrees with the data reported by STRICKLER and ROY.(6) Although the ratio of tetrahedral to octahedral Fe–O distance differs from the analogous Al–O ratio (0·94 and 0·91 respectively, reported by GELLER(19) for the garnet structure), this small difference cannot explain the relatively large deviation (about 0·03 Å). It seems more probable that anion–anion contact occurs in the spinels containing aluminium as has been pointed out by GORTER.(11) Calculations of the lattice parameters, performed in the same way as in(11) and using the calculated distribution (Fig. 4), give some evidence for this explanation, since the calculated parameter decreases more rapidly upon Al^{3+} substitution than the experimental one. The positive deviation from Vegard's rule does not affect our arguments in deducing the sequence of tetrahedral site preference for the trivalent ions, because a larger lattice parameter only means a relatively smaller Madelung energy.

B. *Magnetic properties*

Figure 2 shows the σ–T curves found in the system $\mathrm{Li}_{0\cdot5}\mathrm{Fe}_{2\cdot5-a}\mathrm{Al}_a\mathrm{O}_4$. Anomalous σ–T curves occur in the region $0{\cdot}7 < a < 0{\cdot}9$ in the sequence P, L, N, as has been reported earlier.(20,5) Because of the weak negative magnetic interaction between octahedral ferric ions in spinels, as has been found for $\mathrm{Zn[Fe_2]O_4}$,(21) one expects β, the ratio between octahedral–octahedral (BB) and tetrahedral–octahedral (AB) interaction, to be small and negative for this system. From the simple extension of Néel's theory given in(20) a sequence N, L, P follows for this case. This discrepancy between theory and experiment cannot be explained. An investigation into the shape of σ–T curves in other ferrimagnetic spinels containing lithium is at present in progress.

Acknowledgements—Thanks are due to Dr. E. W. GORTER for discussions on this subject and to Mr. D. J. SCHIPPER, who prepared the compounds containing gallium.

REFERENCES

1. BRAUN P. B., *Nature, Lond.* **170**, 1123 (1952).
2. GORTER E. W., *Philips res. Rep.* **9**, 403 (1954).
3. GORTER E. W. and SCHULKES J. A., *Phys. Rev.* **90**, 487 (1953).
4. NÉEL L., *Ann. Phys. Paris*, **3**, 137 (1948).
5. CARTER A. E., MILES P. A. and WELCH A. J. E., *Proc. Inst. Elec. Engrs* **104B**, Suppl. **5**, 141 (1957).
6. STRICKLER D. W. and ROY R., *J. Amer. ceram. Soc.* **44**, 225 (1961).
7. RATHENAU G. W. and SNOEK J. L., *Philips res. Rep.* **1**, 239 (1946).
8. GORTER E. W., *Advanc. Phys.* **6**, 336 (1957).
9. AHRENS L. H., *Geochim. Cosmochim. Acta* **2**, 155 (1952).
10. MAXWELL L. R. and PICKART S. J., *Phys. Rev.* **92**, 1120 (1953).
11. GORTER E. W., *Philips res. Rep.* **9**, 295 (1954).
12. DUNITZ J. D. and ORGEL L. E., *J. Phys. Chem. Solids* **3**, 318 (1957).
13. BACON G. E., *Acta Cryst.* **5**, 684 (1952).
14. GORTER E. W., *Philips res. Rep.* **9**, 321 (1954).
15. HUBER M., *C. R. Acad. Sci. Paris* **244**, 2524 (1957).
16. GILLEO M. A. and GELLER S., *Phys. Rev.* **110**, 73 (1958).
17. VERWEY E. J. W. and HEILMANN E. L., *J. chem. Phys.* **15**, 174 (1947).
18. GOODENOUGH J. B. and LOEB A. L., *Phys. Rev.* **98**, 391 (1955).
19. GELLER S., *J. chem. Phys.* **33**, 676 (1960).
20. BLASSE G. and GORTER E. W., *J. phys. Soc. Japan*, **17**, Suppl. **B-I**, 176 (1962).
21. ARROTT A. and GOLDMAN J. E., *Bull. Amer. phys. Soc.* **20** (1), 62 (1955).
22. PAUTHENET R. and BOCHIROL L., *J. Phys. Radium* **12**, 249 (1951).

J. Phys. Chem. Solids Pergamon Press 1963. Vol. 24, pp. 1657–1661. Printed in Great Britain.

APPLICATION OF THE UNCERTAINTY PRINCIPLE TO ELECTRON SCATTERING BY PHONONS IN SOLIDS

T. N. MORGAN

IBM, Thomas J. Watson Research Center, Yorktown Heights, N.Y.

(*Received* 29 *May* 1963; *revised* 17 *July* 1963)

Abstract—The contribution of the uncertainty principle to the scattering rates of electrons by phonons in non-polar semiconductors is derived and applied to the hot electron problem. It is shown to modify all of the transport integrals to a certain extent and to remove a singularity appearing in the expression for the mobility when expanded in powers of the electric field. This singularity results from the occurrence of an abrupt threshold for the emission by an electron of an optical phonon. The contribution to the mobility of the term in question and its dependence on the energy uncertainty are calculated for conduction in *n*-type germanium.

1. INTRODUCTION

THE scattering rate of electrons in solids with the emission or absorption of phonons depends upon the density of final states available for the transition. Thus in non-polar semiconductors the rate of scattering of electrons by phonons is found proportional to the square root of the energy of the final state.(1) Such a steep rise in transition probability introduces singularities into the transport coefficients if they are expanded in powers of the applied electric field (hot electron effect), as the higher order coefficients contain derivatives with respect to energy of the scattering rate. In Section 2 of this paper we introduce by a physical argument the uncertainty principle and show how this modifies the transition probabilities. In Section 3 we calculate the transport coefficients in question,(2) and in Section 4 apply the results to germanium.

2. UNCERTAINTY BROADENING

An electron which exists in a given state a time less than τ before being scattered cannot have its energy specified within the limits, $\Delta\epsilon = \hbar/\tau$. Thus all spectral lines have their natural line widths and all edges of continuous spectra are somewhat diffuse. To determine what the effect of this broadening is on the optical and acoustical phonon scattering thresholds, we extend the theory of natural line widths to transitions within a continuum.

For a transition between two states (say in an atomic system) the distribution of quanta in the emitted line is well known and is given by(3)

$$P(\epsilon-\epsilon_0)d\epsilon = \frac{\hbar}{2\pi\tau}\frac{d\epsilon}{(\epsilon-\epsilon_0)^2+(\hbar/2\tau)^2} \qquad (1)$$

where ϵ is the emitted energy, ϵ_0 is the spacing of the two states, and $1/\tau$ is the transition probability. When both initial and final states have finite lifetimes, τ_1 and τ_2, the transition probability, $1/\tau$, is replaced by the sum, $1/\tau = 1/\tau_1+1/\tau_2$.

In order to apply this result to a continuum of states, we consider the following problem. Electrons are distributed in energy according to the probability function, $f_0(\epsilon)$. We wish to calculate the transition probability associated with the energy, $\epsilon_1 = y+\hbar\omega$, for emission of a phonon of well-defined energy, $\hbar\omega$.

In the absence of uncertainty broadening this transition probability is proportional to the density of final states, $\propto\sqrt{y}$. Because of the uncertainty effects, energy is not necessarily conserved exactly, and the final states are distributed over a range of energies according to the probability $P(\epsilon-y)$ from (1). That this same distribution applies to transitions within a continuum follows (in the absence of a rigorous density matrix solution) from the treatment of Ref. 3. The only change needed appears in the energy of the final state which becomes the sum of a fixed radiation energy, $\hbar\omega$, and a variable electron energy, ϵ. Thus the density of final states becomes an average weighted by the factor $P(\epsilon-y)$ and integrated over all energy. This gives a transition probability proportional to $F(y)$ where:

$$F(y) = \frac{a}{\pi}\int_0^{\infty} \frac{\sqrt{x}\,\mathrm{d}x}{(x-y)^2+a^2} \qquad (2)$$

and $a = \hbar/2\tau$ is assumed constant.

This integral can be evaluated by contour integration (see Appendix A) to yield:

$$F(y) = \{[(y^2+a^2)^{1/2}+y]/2\}^{1/2} \qquad (3)$$

The function $F(y)$, becomes $\sqrt{y}$ for positive y and vanishes for negative y as $a \to 0$, and has a first derivative which is well behaved at $y = 0$:

$$F'(y) = \tfrac{1}{2}F(y)/(y^2+a^2)^{1/2} \qquad (4)$$

Figure 1 shows $F(y)$ and $\sqrt{y}$ for values of y near zero.

The factor $1/\tau$ occurring in the parameter, a, is taken as the sum of the scattering rates for the initial and final states, $\epsilon \approx 0$ and $\epsilon = \hbar\omega$, where this correction is most important. Elastic, as well as inelastic, scattering is included following KOHN and LUTTINGER(4) who show that for transport calculations elastic impurity scattering can be considered to broaden the levels as described by (1). However, inelastic scattering alone is sufficient to remove the singularity in $\tau'(x)$ and the transport coefficients.

3. TRANSPORT COEFFICIENTS (MOBILITY)

To apply this result to transport in a semiconductor, assumed isotropic, we write the scattering rate of electrons by phonons as:

$$1/\tau(x) = W\{F(x)+B[F(x+x_0)+\exp(x_0)F(x-x_0)]\} \qquad (5)$$

where the energy, x, is measured in units of kT, $x_0 = \hbar\omega_0/kT$ is the optical phonon energy, and the coefficients, W and B are functions of the temperature but not of energy, see Section 4. We make the usual expansion of the distribution function:

$$f(v) = f_0(x)+vP_1(\cos\theta)f_1(x) + v^2P_2(\cos\theta)f_2(x)+\dots \qquad (6)$$

and solve the Boltzmann equation in terms of these coefficients.

We shall consider the lowest order contribution of the $f_2(x)$ term to the mobility μ. This is shown in Appendix B to be:

$$\delta\mu = \frac{-8ekT}{15m^2}\int_0^{\infty}\tau(x)[x^{5/2}f_2(x)]'\,\mathrm{d}x\Big/\int_0^{\infty}\sqrt{x}f_0(x)\,\mathrm{d}x \qquad (7)$$

which can be written to lowest order:

$$\delta\mu = \frac{32}{45\sqrt{\pi}}\frac{e^3E^2}{m^2kT}\int_0^{\infty}\tau(x)\{x^{5/2}\tau(x)[\tau(x)e^{-x}]'\}'\,\mathrm{d}x. \qquad (8)$$

Here $f_0(x)$ has been replaced by its equilibrium value, Ae^{-x}.

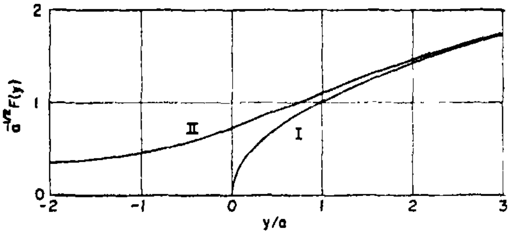

FIG. 1. The function $F(y)$ representing the effective density of final states: I, without uncertainty, $F(y) = \sqrt{y}$; *II, with uncertainty broadening, see equation (3).*

Without the uncertainty correction the integrand of (8) includes a term in $(x-x_0)^{-3/2}$ which is not integrable. If uncertainty is included through (5), $\tau'(x)$ has no singularities and the integral in (8) can be integrated by parts once to become:

$$I_2 = W^3\int_0^{\infty} x^{5/2}\tau^5(x)[1/\tau(x)]' \times\{[1/\tau(x)]'+1/\tau(x)\}\,\mathrm{e}^{-x}\,\mathrm{d}x. \qquad (9)$$

Here the explicit dependence of $\tau(x)$ on W has been eliminated from I_2. This integral, (9), can be evaluated numerically to give a part of the field dependence of the mobility. Examples are given in Section 4.

The remaining contribution to μ of order E^2 arises through the field dependence of $f_0(x)$ and is discussed in a separate article.(5)

The singularity appearing in (8) in the absence of uncertainty is shown in Appendix B to occur only if μ is expanded in powers of E. Thus, though the mobility is well defined for small fields, it cannot be expanded beyond the lowest order in E. Uncertainty broadening re-establishes the validity of such an expansion in agreement with the experimentally observed low-field dependence.(6)

$$\mu = \mu_0(1+\beta E^2). \tag{10}$$

4. RESULTS APPLIED TO GERMANIUM

If we wish to determine the current flowing in a crystal of a particular semiconductor when we apply an electric field, E, we might derive equations (B1) through (B6) of Appendix B, select appropriate values for the scattering constants in equation (5), and compute the first few terms for the mobility expressed as a power series in E^2, equation (10). All of the integrals will be finite, as we have shown above, and will depend to a greater or lesser degree on the amount of energy uncertainty which the scattering introduces.

In order to demonstrate the extent of this dependence in n-type germanium we have varied the scattering strength, and hence the uncertainty, and with the aid of an IBM 7090 computer have evaluated the transport integrals which contribute to μ_0 and β. In this Section we report some of these results for the integral, I_2, which determined the $f_2(x)$ contribution to β and is most strongly influenced by uncertainty. For comparison we also show results for the integral, I_1, determining μ_0.

The following set of parameters has been used. The optical phonon energy

$$x_0 = \hbar\omega_0/kT = 436/T$$

is chosen as 1·00 corresponding to $T = 436$. The value of 436°K for the characteristic optical phonon temperature is known from neutron spectroscopy.(7) The coefficient B can be written as

$$B = \frac{0{\cdot}55x_0}{2(\exp x_0-1)}$$

where the factor, 0·55, representing the relative strength of optical to acoustical phonon scattering is deduced from low-field mobility and warm electron experiments.(8) For the scattering strength parameter, W, written, $W = W_1x_0^{-3/2}$, we should choose,(8)

$$W_1 \approx 3{\cdot}52{\cdot}10^{12}\ \text{sec}^{-1}.$$

However, we have varied W_1 from 2^{-10} to 2 times this value to demonstrate the effects of changing the uncertainty. No ionized impurity scattering is included.

The function $F(y)$ differs appreciably from $\sqrt{y}$ only when y is small in comparison with the uncertainty, a. From equation (5) we see that this occurs, for small a, only when the energy is near $x = 0$ or $x = x_0$. By considering the leading terms in these energy regions we find that I_2 is approximately linear in $\ln(1/a)$ if a is appropriately large or small. Thus I_2 diverges logarithmically as $a \rightarrow 0$ (as indicated by the dashed lines in Fig. 2) and approaches

$$\frac{\mathrm{d}I_2}{\mathrm{d}\ln(1/a)} = \frac{1}{4}$$

as W_1 (and a) become large.

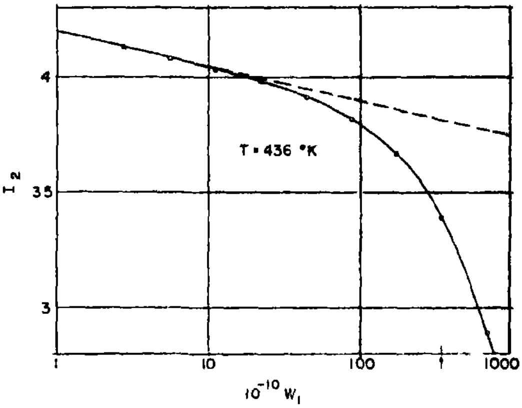

FIG. 2. The transport integral, I_2 vs. scattering strength for $x_0 = 1{\cdot}0$, $T = 436$°K. The assymptote for small values of W_1 is indicated by a dashed line, and the value of W_1 (in sec^{-1}) for electrons in germanium is marked by an arrow.

The uncertainties, a, differ in general for the optical and accoustical phonon scattering processes and have been calculated in a self-consistent way for the chosen scattering strengths, W_1. As an example we list those obtained for Ge, $W_1 = 3{\cdot}52\times 10^{12}\,\mathrm{sec}^{-1}$.

Optical: $x_0 = 1{\cdot}00$, $a = 5{\cdot}02\times 10^{-2}$.
Acoustical: $x_0 = 1{\cdot}00$, $a = 2{\cdot}04\times 10^{-2}$.

By examining the curve in Fig. 2 near $W_1 = 3{\cdot}52\times 10^{+12}$, appropriate for germanium, we see that the introduction of the uncertainty correction not only eliminates the infinite contribution produced by the optical phonon emission threshold but also makes an appreciable reduction in the contribution to I_2 produced by low energy electrons near $x = 0$. This latter effect is most pronounced at low temperatures.

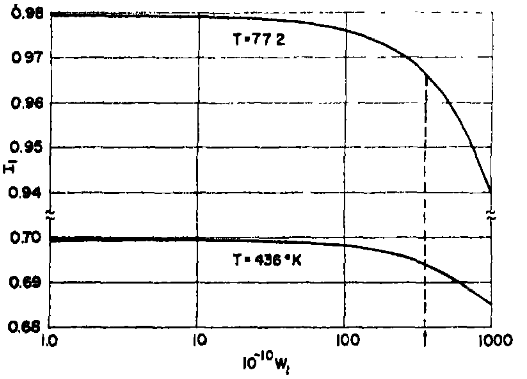

FIG. 3. The mobility integral, I_1, vs. scattering strength for two temperatures: $x_0 = 1{\cdot}00$, $T = 436$°K below and $x_0 = 5{\cdot}65$, $T = 77{\cdot}2$°K above. The value of W_1 (in sec^{-1}) for electrons in germanium is marked by an arrow.

Similar but much smaller effects appear in the other transport integrals. For comparison the integral,

$$I_1 = W\int_0^\infty x^{3/2}\tau(x)\,\mathrm{e}^{-x}\,\mathrm{d}x,$$

which determines the mobility to lowest order (derivable from equation (B5)), is plotted against W_1 in Fig. 3. The decrease in I_1 with increasing W_1 arises principally from the region near $x = 0$ and hence will become less pronounced when impurity scattering is present.

The integrals, I_1 and I_2 determine the coefficients of equation (10) according to the relations:

$$\mu_0 = \frac{4}{3\sqrt{\pi}}\frac{e}{mW}I_1$$

and

$$\beta = \beta_0+\tfrac{4}{5}\gamma I_2/I_1$$

where

$$\gamma = \frac{2e^2}{3mkTW^2}$$

and the remaining coefficient, β_0, is calculated from the solution of the differential-difference equation for $f_0(x)$, in Ref. 5.

Thus, though the values of these integrals for electrons in germanium are those calculated for $W_1 \approx 3{\cdot}52\cdot 10^{12}\,\mathrm{sec}^{-1}$, the contribution of the energy uncertainty to conductivity in another material can be estimated from the figures by choosing a value of W_1 which gives the correct magnitude of the uncertainty, a, for the dominant scattering process.

APPENDIX A

We wish to evaluate the integral:

$$F(y) = \frac{a}{\pi}\int_0^\infty \frac{\sqrt{x}\,\mathrm{d}x}{(x-y)^2+a^2} \tag{A1}$$

where the parameter, a, is a constant. This can be rewritten as the real part of the integral along the entire real axis:

$$F(y) = \frac{a}{\pi}Re\int_{-\infty}^\infty \frac{\sqrt{z}\,\mathrm{d}z}{(z-y)^2+a^2}. \tag{A2}$$

By completing the contour around the positive half plane we find that all other integrals vanish leaving:

$$\int_{-\infty}^\infty \frac{\sqrt{z}\,\mathrm{d}z}{(z-y)^2+a^2} = 2\pi i\sqrt{(y+ia)}/2ia. \tag{A3}$$

On taking the real part of (A3) we obtain the desired result:

$$F(y) = \{[(y^2+a^2)^{1/2}+y]/2\}^{1/2} \tag{A4}$$

APPENDIX B

The contribution of $f_2(x)$ to mobility

Using the expansion of the distribution function, (6), we make the relaxation time approximation (except for $f_0(x)$),

$$\frac{\partial f(v)}{\partial t_{\mathrm{scatt}}} = -\frac{f(v)-f_0(x)}{\tau(x)} \tag{B1}$$

and obtain the usual solutions:

$$f_1(x) = -\frac{eE\tau(x)}{kT}\left\{f_0'(x)+\frac{4}{5}\frac{kT}{m}x^{-3/2}[x^{5/2}f_2(x)]'\right\} \tag{B2}$$

$$f_2(x) = -\frac{2eE\tau(x)}{3kT}f_1'(x)+0(E^4). \tag{B3}$$

It is sufficient in this discussion to express $f_0(x)$ as:

$$f_0(x) = Ae^{-x}+0(E^2). \tag{B4}$$

Thus as the drift velocity is given by:

$$\bar{v} = \frac{2kT}{3m}\int\limits_0^\infty x^{3/2}f_1(x)\,\mathrm{d}x\Big/\int\limits_0^\infty x^{1/2}f_0(x)\,\mathrm{d}x, \tag{B5}$$

the desired term is:

$$\delta\mu = -\frac{8ekT}{15m^2}\int\limits_0^\infty \tau(x)[x^{5/2}f_2(x)]'\mathrm{d}x\Big/\int\limits_0^\infty \sqrt{x}f_0(x)\,\mathrm{d}x. \tag{B6}$$

That the mobility itself does not diverge can be seen from the expression for drift velocity derivable for isotropic, elastic scattering from a kinetic argument:(9)

$$\bar{v} = Cv_T\int\limits_0^\infty \mathrm{d}x\sqrt{(x)}\,\frac{f_0(x)}{\tau(x)}\int\limits_{-1}^1$$

$$\times\frac{\mathrm{d}w}{2}\int\limits_0^\infty \mathrm{d}t(\sqrt{(x)}w+\alpha t)\exp\left[-\int\limits_0^t\frac{\mathrm{d}s}{\tau(x')}\right] \tag{B7}$$

where:

$$v_T = \left(\frac{2kT}{m}\right)^{1/2}, \quad w = \cos\theta, \quad \alpha = eE/mv_T,$$

$$x' = x+2\sqrt{(x)}w\alpha s+\alpha^2s^2,$$

and the normalizing factor, C, is given by:

$$C^{-1} = \int\limits_0^\infty \mathrm{d}x\sqrt{x}\frac{f_0(x)}{\tau(x)}\int\limits_{-1}^1\frac{\mathrm{d}w}{2}\int\limits_0^\infty\exp\left[-\int\limits_0^t\frac{\mathrm{d}s}{\tau(x')}\right]\mathrm{d}t$$

This expression generates the velocity distribution at time, 0, by summing over all electrons last scattered (isotropically) at time, $-t$, $0 < t < \infty$, and tracing their motion in the presence of the electric field, E. The energy, $x'(s)$, is the energy at time, 0, of an electron scattered at time, $-s$, into a state of energy, x, and direction cosine, w, relative to the electric field. As (B7) omits energy relaxation effects, the function $f_0(x)$ should be chosen to generate the desired (equilibrium) energy distribution at time, $t = 0$. However, our qualitative purposes are served equally well by the equilibrium distribution, $f_0(x) = Ae^{-x}$.

Inspection of the integrals occurring in (B7) reveals that the mobility is finite for a scattering rate, $1/\tau(x)$, which is finite for all x and nonvanishing for large x. However, if an attempt is made to expand (B7) in (odd) powers of the electric field, difficulties are encountered, after the first term, for a scattering rate containing a term in $(x-x_0)^{1/2}$. The same derivatives of $\tau(x)$ shown in (8) appear when the exponential is expanded in powers of E. Thus, although the mobility is well defined, it cannot be expanded beyond the lowest order in the field unless some broadening effect "softens" the optical phonon emission threshold.

REFERENCES

1. See, for example, Herring C., *B.S.T.J.* **34,** 237 (1955).
2. An analysis similar to this has been made of the effects of collision broadening on the magnetic properties of metals by Dingle R. B., *Proc. Roy. Soc.* **A211,** 517 (1952).
3. See Heitler W., *Quantum Theory of Radiation,* 2nd ed., Chap. III, Sec. 12, Oxford University Press, London (1944).
4. Kohn W. and Luttinger J., *Phys. Rev.* **108,** 590 (1957), equation 103 ff.
5. Morgan T. N. To be published. See also Ref. 8.
6. See, for example, the review by Gunn J. B., *Progr. Semiconductors* **2,** 211 (1957).
7. Brockhouse B. N. and Iyengar P. K., *Phys. Rev.* **111,** 747 (1958).
8. Morgan T. N. and Kelly C. E., *Proc. Int. Conf. on Semiconductor Phys.* **70,** Prague (1960).
9. See Chambers R. G., *Proc. phys. Soc. Lond.* **A65,** 458 (1952).

J. Phys. Chem. Solids Pergamon Press 1963. Vol. 24, pp. 1663–1665. Printed in Great Britain.

THE MAGNETIC MOMENT DISTRIBUTION IN Cu_2MnAl

G. P. FELCHER,* J. W. CABLE and M. K. WILKINSON

Oak Ridge National Laboratory, Oak Ridge, Tennessee

(*Received* 20 *June* 1963)

Abstract—Saturation magnetization and neutron diffraction measurements were made on an ordered Cu_2MnAl sample in order to determine the distribution of magnetic moments in this ferromagnetic alloy. The magnetization measurements were made by the ballistic method in fields up to 5 kOe and at sample temperatures of 298 and 77°K. The magnetic moments obtained at these temperatures were 3·2 and 3·7 μ_B per molecule. The neutron diffraction data were obtained at 298°K using a magnetic field of 12 kOe to separate the magnetic and nuclear scattering. The nuclear scattering showed a long range order parameter $S = 0{\cdot}98$, while the magnetic scattering revealed that within 0·1 μ_B the entire moment of the molecule could be attributed to the manganese atom.

THE Heusler alloy Cu_2MnAl is strongly ferromagnetic but the type of interaction responsible for this ferromagnetism is not known. The crystal structure of the ordered alloy may be described as a rocksalt type array of manganese and aluminum atoms in which the tetrahedral sites are filled with copper atoms.(1) In this structure the manganese atoms are so widely separated that direct Mn-Mn exchange probably cannot account for the high observed Curie temperatures so that an indirect exchange mechanism must be considered. This could be either a conduction band mechanism or a superexchange mechanism involving the overlapping wave functions of the copper and aluminum atoms. In the latter situation it is reasonable that magnetic moments associated with transient *d*-orbital vacancies might appear on the copper atoms. This experiment represents an attempt to detect such moments by neutron diffraction techniques in order to better understand the nature of the ferromagnetic interactions in this material.

The alloy was prepared by arc melting and was subsequently filed to 100 mesh particle size and heat treated for 6 months at 110°C to enhance the development of long range atomic order. Chemical analysis showed that the stoichiometry was correct within 0·3 at.% for each constituent while X-ray patterns revealed only a single phase system. Saturation moments of 3·2 and 3·7 μ_B/molecule were measured at 298 and 77°K, respectively.†

The crystal structure of the ordered alloy is cubic with the Cu atoms at (0 0 0, 1/2 1/2 1/2) f.c.c., the Mn atoms at (3/4 3/4 3/4) f.c.c., and the Al atoms at (1/4 1/4 1/4) f.c.c.(1) The allowed reflections are then those with all odd or all even indices and are of three types:

$$F_{\text{odd}} = b_{\text{Mn}} - b_{\text{Al}}$$

$$F_{\text{even}} = \begin{matrix} b_{\text{Mn}} + b_{\text{Al}} - 2b_{\text{Cu}} & h+k+l = 4n+2 \\ b_{\text{Mn}} + b_{\text{Al}} + 2b_{\text{Cu}} & h+k+l = 4n \end{matrix}$$

The first two types are superlattice reflections for which the intensities depend on the degree of long range order. The last type corresponds to normal lattice reflections with intensities independent of the degree of order.

Neutron powder diffraction data were obtained at room temperature both in the absence of a magnetic field and with 12 kOe applied parallel to the scattering vector so as to extinguish the magnetic neutron scattering. The nuclear scattering, as represented by the data with an applied field, is shown in the lower part of Fig. 1. The intensities of the nuclear reflections correspond to a highly ordered alloy as illustrated in Table 1. Here, the observed intensities have been reduced to absolute values by means of an internal calibration with the (220) normal lattice reflection. They agree within 5 per cent with the calculated values for a perfectly ordered alloy which corresponds to a long range order parameter of about 0·98 for this sample.*

---

* International Atomic Energy Agency Fellow from C.I.S.E., Milan, Italy. Present Address: Centro di Studi Nucleari Della Casaccia, Rome, Italy.

† These moments are about 15 per cent higher than those reported by HEUSLER (*Ann. Phys.* **19**, 155 (1934)), who estimates that the saturation moment at 0°K for the perfectly ordered alloy should be 20 per cent higher than his measurement.

Table 1. *A comparison of the calculated and observed intensities from* Cu_2MnAl.

hkl	Nuclear		Magnetic	
	F^2(obs)*	F^2(calc)†	F^2(obs)	F^2(calc‡)
111	0·55	0·52	0·30	0·31
200	2·40	2·56	0·29	0·27
220	(2·43)	2·43	0·14	0·16
311	0·49	0·52	0·12	0·11
222	2·44	2·56	0·09	0·10

* Normalized to the (220) normal lattice reflection.

† For complete long range order and $b_{Cu} = 0{\cdot}79$, $b_{Mn} = -0{\cdot}37$, $b_{Al} = 0{\cdot}35$.

‡ Assuming 3·2 μ_B/Mn and the calculated Mn^{2+} form factor.

The magnetic scattering, obtained by subtraction of the 12 kOe data from the zero field data, is shown in the upper part of Fig. 1 and each reflection is seen to have a sizeable ferromagnetic component. The intensities were converted to absolute values by taking magnetic to nuclear intensity ratios and are compared with calculated values in Table 1. These calculated values† are based on the assumption that all of the measured moment of 3·2 μ_B per molecule (room temperature value) resides on the Mn atoms and that the charge distribution may be represented by the Hartree–Fock

---

* This description of the degree of order with a single long range order parameter assumes that the misplaced atoms are equally distributed among the "wrong" sites.

† The assumption of an equal distribution of the misplaced atoms introduces an uncertainty of about 4 per cent into these calculated intensities. This is the same magnitude as the statistical errors in the measurements and does not alter the conclusions.

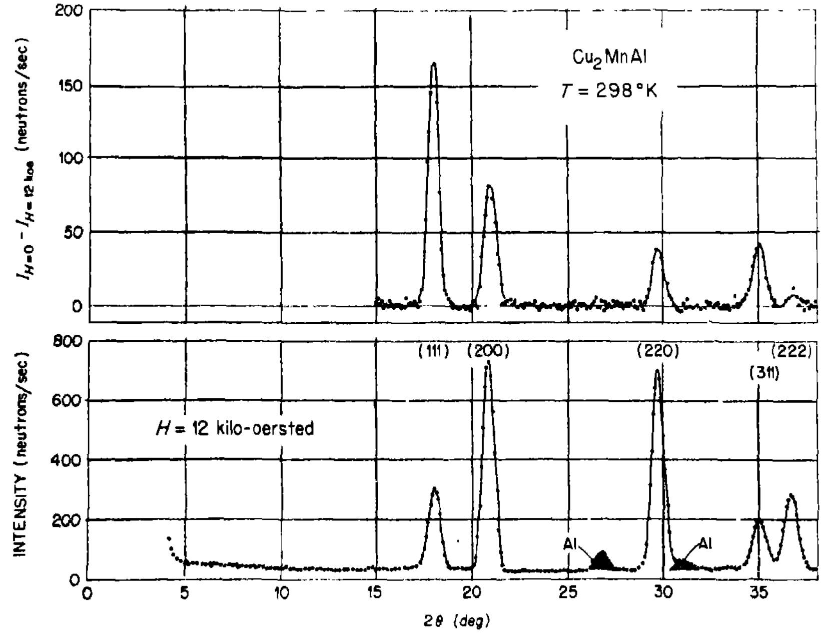

FIG. 1. Neutron diffraction patterns of Cu_2MnAl. The lower curve depicts the nuclear scattering and the upper curve represents the magnetic scattering. The cross hatched peaks are from the Al sample holder.

Mn^{2+} form factor.(2) Comparison of the two columns shows that this provides an adequate representation of the observations. If there were moments on the copper atoms then discrepancies should be observed. In particular the (200) intensity which is proportional to $(p_{Mn}-2p_{Cu})^2$ should exhibit a departure just opposite to that of the (220) for which the intensity is proportional to $(p_{Mn}+2p_{Cu})^2$. Such an opposite variation is present but the differences are the same magnitude as the statistical errors. It can therefore only be concluded that any copper moment present is less than $0{\cdot}1\ \mu_B$ per copper atom.

In summary, saturation magnetization and neutron diffraction measurements have been made on a Cu_2MnAl sample with a known amount of long range order. For this sample with a long range order parameter of about 0·98 a saturation moment of $3{\cdot}7\ \mu_B$ per molecule was measured at 77°K. The room temperature neutron data show that within $0{\cdot}1\ \mu_B$ per atom the entire moment may be attributed to the manganese atoms. This result could be taken as support for the conduction electron mechanism since any polarization of the conduction band might easily escape detection in a diffraction experiment due to a rapid form factor fall off. However, the superexchange mechanism must not be ruled out because the magnitudes and life times of the transient moments to be associated with the intermediary atoms are not known and small values (i.e. $<0{\cdot}1\ \mu_B$ or $<10^{-13}$ sec) for either of these quantities would render the diffraction technique insensitive. Apparently a more sensitive experimental technique would be required to establish the presence and magnitude of magnetic moments on the copper atoms in this alloy.

REFERENCES

1. Bradley A. J. and Rodgers J. W., *Proc. Roy. Soc.* **144A**, 340 (1934).
2. Watson R. E. and Freeman A. J., *Acta Cryst.* **14**, 27 (1961).

J. Phys. Chem. Solids Pergamon Press 1963. Vol. 24, pp. 1667–1669. Printed in Great Britain.

d-BAND TRANSITIONS IN SOLIDS

W. C. WALKER

University of California, Santa Barbara, Goleta, California

(*Received* 12 *June* 1963; *revised* 29 *July* 1963)

Abstract—The significance of measurements of *d*-band transitions in solids is discussed and qualitative criteria necessary for direct observation of *d*-band transitions are established. Data on the positions of far ultraviolet absorption edges in In, Sn, Pb, and Bi are presented and the evidence for their assignment to *d*-band transitions is discussed.

INTRODUCTION

ABSORPTION edges in the far ultraviolet have been observed for thin films of several metals and semimetals.(1) On the basis of known atomic energy levels(2) and other criteria discussed below, they have been assigned to transitions of electrons from filled *d*-bands to the Fermi surface. Similar edges also appear in reflection spectra of certain semiconductors as small but distinct humps.(3) The condition for the appearance of these edges in a given material, which is related to a favorable spacing of the electron-plasma oscillation and the various interband transitions, is specified in detail below.

Positive identification of these absorption edges can be of importance in improving band structure calculations. For example, in the recent band calculations for copper by SEGALL, the position of the *d*-band with respect to the higher levels was the single largest uncertainty involved.(4) It was found that the relative position of the *d*-band is dependent on the crystal potential used, so that experimental values for a specific *d*-band transition could serve as a sensitive check on the accuracy of this potential. Although the techniques of this paper cannot be used to clarify the situation in copper, it is reasonable to expect that the general conclusions reached by Segall regarding the sensitivity of the *d*-band position to the crystal potential will remain valid for those materials displaying *d*-band edges.

Experimentally the position of the *d*-band edges can be obtained directly from thin film studies, in favorable cases, or indirectly by detailed analysis of reflection data. Structure in reflection spectra interpreted as *d*-band edges, has been observed in several semiconductors by PHILIPP and EHRENREICH.(3) Unfortunately, the raw reflection data do not lend themselves to an accurate determination of the edge and the accuracy of the dispersion analysis yielding the imaginary part, ϵ_2, of the dielectric constant above 15 eV is low due to the small value of the reflectivity in this region. By contrast, the edges observed in transmission can be made very sharp by the proper choice of film thickness and yield good values for the transition energy. The relative insensitivity of the *d*-band edges to crystalline perfection removes in part the usual objection to the use of thin films for obtaining fundamental solid-state information.

EXPERIMENTAL RESULTS

Far ultraviolet edges have been observed in In, Sn, Pb, and Bi. Three of these materials (In, Sn, Bi) were measured several years ago by WALKER, RUSTGI and WEISSLER.(5, 6) Measurements on In have been repeated and in addition those for Pb have been obtained. An improved version of the technique described in the above papers was used for these recent measurements. The room temperature transmission spectra of self-supported evaporated foils of the order of 1000 Å thick were obtained for In and Pb. Results for In were identical, within experimental error, to the earlier ones and firmly establish the absorption edge at 16·3 eV. The transmission data of a Pb film approximately 1000 Å thick are shown in

Fig. 1. An absorption edge having a "half width", i.e. the energy region over which the transmission decreases to one half its original value, of the order of 0·1 eV was observed at 17·7 eV. The absorption edges measured up to the present are given in Table 1. Atomic *d*-shell transitions for atoms stripped to the *d*-shell are also shown for comparison. The term values were taken from Moore[(2)] for those transitions satisfying the atomic selection rules. Similar edges should be observed in Ga, Sb and possibly Zn provided the *d*-band is sufficiently well separated from the conduction band.

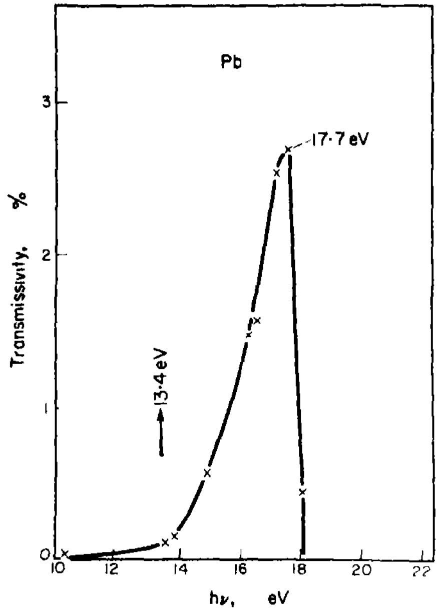

Fig. 1. Transmission spectrum of Pb film. The *d*-band transition at 17·7 eV is indicated by the arrow. Vertical arrow indicates the free electron plasma frequency.

Table 1. *d-band energy gaps and associated atomic transitions.*

Element	*Ed* (eV)	Atomic transition (eV)
In	16·3	$4d^{10} \rightarrow 4d^{9}5p$ (24·7)
Sn	24·3	$4d^{10} \rightarrow 4d^{9}5p$ (33·2)
Sb	—	$4d^{10} \rightarrow 4d^{9}5p$ (42·7)
Pb	17·7	$5d^{10} \rightarrow 5d^{9}6p$ (27·2)
Bi	24·0	$5d^{10} \rightarrow 5d^{9}6p$ (34·0)
Zn	—	$3d^{10} \rightarrow 3d^{9}4p$ (17·4)

DISCUSSION

The absorption edges in Table 1 are believed due to transitions from the filled *d*-band to the Fermi level. Similar transitions in semiconductors to states near the bottom of the conduction band would be expected and indeed seem to appear in reflection spectra.[(3)] Detailed assignment of these edges on the basis of band calculations cannot yet be given. Indeed the usefulness of these data may be, as mentioned previously, in establishing a fixed point for band calculations. The indirect evidence for the specific assignment given can be summarized as follows:

(1). The edges are in the region expected for *d*-band transitions.

(2). The strength of the absorption, corresponding to an absorption coefficient of 10^5 cm^{-1}, is of the order expected.

(3). Reflection humps observed by Philips[(3)] in InAs and InSb agree reasonably well with the transmission edge in metallic indium as would be expected if the *d*-band location is not greatly shifted in forming the compound.

(4). The relative order of the edges for adjacent elements is, as can be seen in Table 1, that expected on the basis of atomic data. For example in Sb and Te which both show increased transparency due to plasma transmission, no edges are observed below 30 eV in agreement with expectations from atomic data.

(5). No absorption edges are found for metals such as Al which lack *d*-electrons.[(5)]

These arguments give strong evidence for the proposed interpretation of these absorption edges.

The criteria which a material must satisfy to show these edges distinctly can now be easily stated and used as a guide to further measurements. First, the material must be transparent enough in the region adjacent to the edge to allow films of reasonable uniformity to be used. This condition requires that the electron plasma oscillation be a well defined mode of excitation. In addition it must have a frequency greater than that corresponding to the region where the oscillator strength for conduction intra-band transitions is exhausted. For semiconductors, this should be altered to require the exhaustion of the oscillator strengths for valence to conduction band transitions. A further condition is that the plasma frequency fall between the conduction or valence band transition region and the *d*-band edge with a spacing of the order of 1 eV between each region. A comparison of unpublished reflection data for bulk In(7) with the transmission spectrum shows that these conditions are satisfied to a high order. Several solids adjacent in the periodic table to those included in the present paper should also satisfy these criteria. Zinc in particular presents an interesting transition case, since it is well known that copper, the element preceding it, certainly does not satisfy the above criteria due to the proximity of the *d*-band transition, plasma frequency, and conduction band transitions.

Acknowledgements—The author is grateful to Mr. ABDUL AL KEZWEENY for making the measurements on In and Pb and to the National Aeronautics and Space Administration for its continued support of this research.

REFERENCES

1. WALKER W. C. and WEISSLER G. L., *J. Quant. Spectrosc. Radiat. Transf.* **2,** 613 (1962).
2. MOORE C. E., Atomic Energy Levels, *NBS Circ.* No. 467, vols. **I, II, III** (1949, 1952, 1958).
3. PHILIPP H. R. and EHRENREICH H., *Phys. Rev. Letters* **8,** 92 (1962).
4. SEGALL B., *Phys. Rev.* **125,** 109 (1962).
5. WALKER W. C., RUSTGI O. P. and WEISSLER G. L., *J. Opt. Soc. Amer.* **49,** 471 (1959).
6. RUSTGI O. P., WALKER W. C. and WEISSLER G. L. **51,** 1357 (1961).
7. KEZWEENY A. Al, Unpublished Thesis, Physics Department, University of California, Santa Barbara.

J. Phys. Chem. Solids Pergamon Press 1963. Vol. 24, pp. 1671–1673. Printed in Great Britain.

THE INFLUENCE OF VACANCIES ON THE REDUCTION OF SILVER IONS IN SILVER DOPED ALKALI HALIDES

W. GOMES

Rijksuniversiteit, Laboratorium voor Kristallografie en Studie van Vaste Stoffen,
Rozier 6, Ghent, Belgium

(*Received* 9 *May* 1963)

Abstract—Hydrogen treatment of alkali halide crystals doped with silver halide leads to a partial reduction of the silver ions. The fact that the reaction is incomplete appears not to be due to a chemical equilibrium but to a factor inherent in the crystal.

Experiments with alkali halides, doped with Ag^+ and divalent ions, show that the concentration of metallic silver formed is determined by the anion vacancy concentration. This fact is interpreted in terms of the agglomeration of silver atoms and vacancies.

INTRODUCTION

WHEN an alkali halide crystal doped with silver halide is heated in hydrogen, a coloured zone containing metallic silver develops from the surface. The colouration is caused by the presence of silver colloids. We studied the kinetics of this zone reduction by following the penetration depth x of the reaction zone as a function of different variables.(1) It was found that the relation between x and the duration t of hydrogen treatment could be written as:

$$x = (2kt)^{1/2} \tag{1}$$

where k is the rate constant.

From the exponential temperature dependence of k, the activation energy E of the process was derived.

(0·8 eV for $K_{1-\delta}Ag_{\delta}Cl$, 0·4 eV for $K_{1-\delta}Ag_{\delta}Br$).

It also appeared that k was directly proportional to the hydrogen pressure p_{H_2}.

These results led to the assumption that the reduction of Ag^+ ions is caused by hydrogen molecules which dissolve and diffuse into the crystals. For k we proposed the expression:

$$k = \frac{2D_{H_2} \times C \times p_{H_2}}{n_{Ag^0}} \tag{2}$$

where D_{H_2} and C are respectively the diffusion and solubility coefficients of H_2 in the alkali halide and n_{Ag^0} the number of silver atoms formed per cm³.

A peculiar fact is that, in the range of temperature and Ag^+ concentration investigated, only part of the Ag^+ ions present in the reaction zone were reduced. This problem will be considered here in detail.

EXPERIMENTAL

1. We obtained information about the silver metal concentration by two methods, namely by polarographic analysis and by measuring the absorption coefficient at the wavelength corresponding to the maximum of the colloid band.

Both methods present some disadvantages. By polarography we obtain the Ag^0 concentration by subtracting the Ag^+ concentration in the reduced material from that in the unreduced material. The accuracy is therefore small in cases where the per cent of reduced silver is small. As for the optical method, we must take into account that the metallic silver is not present entirely in colloidal form, that various sizes of colloid particles are present and that the height of the absorption maximum depends on the peak wavelength.

2. We could establish that the Ag^0 concentration is constant in the reaction zone, except for a small region near the surface where the concentration is greater. So, during the process we have

to consider a progressing zone of constant Ag^0 concentration, independent of x and t.

This Ag^0 concentration also appears to be independent of p_{H_2} in the considered pressure range (0·1–1 atm.)

These facts are in agreement with the formulation of the penetration kinetics, since in (2) containing n_{Ag^0}, k is time independent by definition and directly proportional to p_{H_2}.

The possible influence of the initial Ag^+ concentration on the concentration of Ag^0 formed has not been thoroughly investigated, since different crystals have to be compared here and structure sensitivity has then to be taken into account. The penetration depth of the reaction zone appears to be practically the same in two $K_{1-\delta}Ag_\delta Cl$ crystals having an initial Ag^+ concentration differing by an order of magnitude. This indicates again, according to (2), that n_{Ag^0} is independent of the initial Ag^+ concentration.

As the concentration of the reactants (Ag^+, H_2) has, as a first approximation, no influence on the concentration of Ag^0 formed, we must reject the idea of an equilibrium in the reaction $2Ag^+ + H_2 \rightleftharpoons 2Ag^0 + 2H^+$ as a possible interpretation of the partial reduction of the Ag^+ ions present in the reaction zone.

With increasing temperature, an increase of the Ag^0 concentration has been observed.

3. The influence of the vacancy concentration on the concentration of Ag^0 formed has been studied. This was done by comparing a KCl crystal doped with Ag^+ ions only and crystals which also contain divalent ions.

Positive divalent ions were incorporated by adding a mixture of AgCl and $SrCl_2$ to the KCl melt. Sr^{2+} was chosen because of its electronegativity, i.e. in order to avoid reduction of the divalent impurity by hydrogen, and also because the ionic radius of Sr^{2+} is similar to that of K^+.

In spite of this, the crystal of KCl+AgCl+$SrCl_2$ was opaque. It was however possible to obtain completely clear specimens by heating them in air to the same temperature as used for the hydrogen treatments (540°), followed by rapid cooling. Tests on $K_{1-\delta}Ag_\delta Cl$ crystals showed that this preliminary treatment had no influence on the subsequent behaviour with regard to hydrogen. No analysis of the Sr^{2+} ions incorporated in the crystals was made. From data of KELTING and WITT(2) for the distribution of Sr^{2+} between solid and molten KCl, we estimate that the ionic fraction of Sr^{2+} was about 2×10^{-3}.

Negative divalent ions were incorporated by adding Ag_2O in the KCl melt instead of AgCl. Since nothing is certain about eventual chemical reactions accompanying the introduction of Ag_2O in the melt, the O^{2-} concentration cannot be simply deduced from the amount of Ag^+ incorporated in the crystal.

The experimental data on hydrogen treated specimens are listed in Table 1. All hydrogen treatments were carried out at atmospheric pressure and at 540°C, which is, in nominally pure KCl, approximately the temperature of transition between the extrinsic and intrinsic regions.

The ionic fraction of Ag^+ for the three crystals was of the order of 10^{-4}.

The analytical and optical results (3rd and 5th column respectively) clearly show that the Ag^0 concentration increases with increasing anion vacancy concentration.

In the last column, the corresponding values of the rate constant of penetration are tabled. It can be seen that k decreases with increasing Ag^0

Table 1.

Crystal	Initial Ag^+ concentration (p.p.m.)	Ag^0 concentration (p.p.m.)	λ_m(mμ)	Mean absorption coeff. at λ_m (cm^{-1})	k(cm^2 sec^{-1})
KCl+AgCl+$SrCl_2$	190	<5	435	0·6	$4{\cdot}6 \times 10^{-6}$
KCl+AgCl	90	15	460	6	$5{\cdot}3 \times 10^{-7}$
KCl+Ag_2O	110	60	445	20	$5{\cdot}7 \times 10^{-8}$

concentration which is qualitatively in agreement with equation (2).

DISCUSSION

1. The role of the anion vacancies can be interpreted as follows. The formation of silver particles, with dimensions of the order of 10 mμ to 1 μ (observed by electron microscopy) is equivalent to the agglomeration of point defects; for this we propose the following reaction equation:

$$n(\mathrm{Ag}^0|\square^+)+n\square^- \rightarrow (\mathrm{Ag}^0)_n|(\square^+)(\square^-)_n \qquad (3)$$

The symbol at the right represents the silver particle, contained in the space created by the agglomeration of vacancies. This equation shows that an anion vacancy is needed for each silver atom. If we accept that separate silver atoms on cation sites are not stable, equation (3) accounts for the experimentally stated influence of anion vacancies on the reaction: we assume that the number of silver atoms that can be formed is equal to the number of anion vacancies originally present.

This supposition is moreover supported by the fact that the concentration of Ag^0 formed is of the same order of magnitude as the vacancy equilibrium concentration at a given temperature (see e.g. Table 1 : $\mathrm{K}_{1-\delta}\,\mathrm{Ag}_\delta\,\mathrm{Cl}$ at 540°C : 15 p.p.m. of Ag^0, thus $n_{\mathrm{Ag}^0} = 1{\cdot}7\times10^{17}\ \mathrm{cm}^{-3}$).

Possibly, a direct method for determining the vacancy concentration is available here.

2. With these assumptions, the incomplete reduction of Ag^+ ions in the reaction zones can be attributed to the fact that the Ag^+ concentration is always greater than the anion vacancy concentration in the present range of concentration and temperature.

In a crystal with very low Ag^+ concentration, complete reduction should be possible. This has been verified for a $\mathrm{K}_{1-\delta}\,\mathrm{Ag}\delta\,\mathrm{Cl}$ crystal with 0·0003 mol% of AgCl.

3. Our assumptions imply that the vacancies which have been annihilated by agglomeration are not replaced by new ones. Considering the relatively low values of the diffusion coefficients of vacancies, we suppose that, on warming up a crystal with dimensions of the order of 1 cm to treatment temperature, the vacancies necessary to reach the equilibrium concentration come from the dislocations, where they are formed by the climb mechanism.

As the reduced silver forms a precipitate along the dislocations⁽³⁾, the latter should be blocked and no new vacancies should be formed.

From then on, vacancies can only be furnished from the crystal surface, so that they will not be able to follow the penetration of the zone, as the diffusion coefficients for anion vacancies ($\simeq 10^{-11}\ \mathrm{cm}^2\,\mathrm{sec}^{-1}$ at the temperatures considered) is several orders of magnitude smaller than that of hydrogen molecules ($\simeq 10^{-4}\ \mathrm{cm}^2\,\mathrm{sec}^{-1}$ in KBr⁽⁴⁾).

This also means that the Cl^- ions, corresponding to the reduced Ag^+ ions, will not be able to escape from the crystal (in the form of HCl). Nevertheless, it was impossible to detect HCl in the treated crystals by infrared spectroscopy, probably because the concentration is too small, or because the H^+ ions do not form HCl molecules in the lattice.

Anion vacancies will diffuse only into a small region just below the surface. This might be the reason why the Ag^0 concentration was found to be greater in this region than in the rest of the zone, and why in powdered material very large Ag^0 concentrations (several hundred p.p.m.) have been obtained.

4. The relation between the equilibrium vacancy concentration and the concentration of Ag^0 formed also explains why the latter increases with temperature.

We notice here that, since n_{Ag^0} rises with temperature, the activation energy E associated with the temperature dependence of k (*see* equation 2) is not simply the sum of Q, the dissolution energy and U, the activation energy for diffusion of H_2 in the lattice.

As n_{Ag^0} stands in the denominator of the expression for k, we have that $Q+U > E$.

Acknowledgements.—This work is part of a research programme sponsored by I.R.S.I.A. (Brussels) to which we express our gratitude. We thank Prof. W. DEKEYSER for many helpful discussions.

REFERENCES

1. GOMES W., *Trans. Faraday Soc.* **59**, 1648 (1963).
2. KELTING H. and WITT H., *Z. Physik* **126**, 697 (1949).
3. VAN DER VORST W. and DEKEYSER W., *Phil. Mag.* **1**, 882 (1956).
4. HILSCH R., *Ann. Phys.* **29**, 407 (1937).

J. Phys. Chem. Solids Pergamon Press 1963. Vol. 24, pp. 1675–1677. Printed in Great Britain.

BOUND STATES IN THE SPIN WAVE PROBLEM*

NOBUYUKI FUKUDA† and MICHAEL WORTIS‡

Department of Physics, University of California, Berkeley

(*Received* 8 *July* 1963)

Abstract—The existence of bound states of two spin waves in the Heisenberg model has been demonstrated(1, 2) previously. In the present note we exhibit an alternative derivation based directly on the Schroedinger equation and not involving the introduction of any fictitious interactions.

RECENTLY HANUS(2) and one of the present authors(2) have shown that, contrary to a conjecture by DYSON,(3) there exist bound states of two spin waves in the Heisenberg ferromagnet provided that the total momentum of the bound pair is sufficiently large. Hanus restricted his treatment to spin $S = \frac{1}{2}$. Like certain previous authors,(4) he introduced a fictitious hard core potential to insure that his final results should not be influenced by his inclusion in the calculation of the in principle undefined amplitude, $U(\mathbf{R}_i, \mathbf{R}_i)$, for finding two spin waves on the same lattice site. In Ref. (2), on the other hand, introduction of the two-particle Green's function allowed all spins to be treated on an equal footing. The purpose of the present note is to show that the same generality may be had by working, as Hanus did, simply in terms of the two-particle wave functions but without the introduction of any fictitious interaction. We emphasize that the present formulation forms a complete parallel with that of Ref. (2), differing only in that it focuses on construction of the wave function rather than the Green's function. No new results are derived. We feel that this work is justified first by the insight which it affords into the S-dependence of the structure of the spin wave dynamics and second by the accessibility of its straightforward basis on the Schroedinger equation.

Consider the Heisenberg Hamiltonian,

$$H = \mu \sum_i S_i^z - \tfrac{1}{2} \sum_{i,j} J(i,j)\, \mathbf{S}_i \cdot \mathbf{S}_j, \tag{1}$$

with nearest neighbor exchange coupling,

$$J(i,j) = J(j,i) = \begin{cases} J, & i \text{ and } j \text{ nearest neighbours} \\ 0, & \text{otherwise.} \end{cases} \tag{2}$$

We assume for definiteness that μ and J are positive and that the lattice is simple cubic and periodic. The spin deviation number operator,

$$n = NS + \sum_i S_i^z, \tag{3}$$

commutes with the Hamiltonian. The Heisenberg ground state, $|0\rangle$, is characterized by $n = 0$. The normalized energy eigenstates, Ψ, of the $n = 2$, two spin-wave, subspace may be written as

$$\Psi = \sum_{i,j} U(i,j) S_i^+ S_j^+ |0\rangle, \qquad U(i,j) = U(j,i). \tag{4}$$

Note that for $S = \frac{1}{2}, U(i,i)$ is not defined. The normalized two-particle wave functions are given in terms of the amplitudes $U(i,j)$ by

$$\psi(i,j) = 4S\left(1 - \frac{\delta(i,j)}{2S}\right)^{1/2} U(i,j). \tag{5}$$

The amplitudes are to be determined from the Schroedinger equation,

$$\sum_{i,j} U(i,j)\, [S_i^+ S_j^+, H]\, |0\rangle = -\omega \sum_{i,j} U(i,j) S_i^+ S_j^+ |0\rangle, \tag{6}$$

---

* Research supported in part by the Air Force Office of Scientific Research, Grant No. AF-AFOSR-130-63.

† On leave of absence from the Tokyo University of Education.

‡ Fellow of the Miller Institute for Basic Research in Science.

where ω is the excitation energy $(E_\psi - E_0)$. The eigenvalue equation following from (6) is

$$[\omega - 2\mu - 4SJd]\, U(i,j) = -S \sum [J(l,j) U(l,i) + J(l,i)\, U(l,j)] + J(i,j)\, [\tfrac{1}{2}(U(i,i) + U(j,j)) - U(i,j)], \tag{7}$$

where d is the lattice dimensionality. For $S > \frac{1}{2}$ no comment is necessary; however, for $S = \frac{1}{2}$ we must notice that the $i = j$ component of (7) does *not* follow from (6). In fact it is easy to verify that the components $U(l, l)$ entirely cancel out of (7) for $i \neq j$. Thus the Schroedinger equation leaves $U(l, l)$ totally undetermined. The physics of this situation is simply that for $S = \frac{1}{2}$ the Hamiltonian (1) cannot propagate two spin deviations onto the same site: physical states with two units of spin flipped at a single site do not exist. The set of equations (7) with $i \neq j$ is complete for the determination of the $S = \frac{1}{2}$ problem. It will be convenient, however, to be able to take transforms of (7) without special attention for $i = j$; therefore, for $S = \frac{1}{2}$ we choose to let the $i = j$ component of (7) *define* the unphysical and previously undetermined $U(i, i)$ in terms of the physical $U(i, j)$, $i \neq j$. This definition can have no effect on the physical $U(i, j)$'s and by (5) is not reflected in the wave function. All components of equation (7) now hold for arbitrary S.

We now introduce sum and difference coordinates,

$$2\boldsymbol{R} = \boldsymbol{R}_i + \boldsymbol{R}_j \quad \text{and} \quad \boldsymbol{r} = \boldsymbol{R}_i - \boldsymbol{R}_j \tag{8}$$

and the transform,

$$U(i,j) = \frac{1}{N} \sum_{\boldsymbol{K}} \exp(i\boldsymbol{K} \cdot \boldsymbol{R})\, U_{\boldsymbol{K}}(\boldsymbol{r}), \qquad U_{\boldsymbol{K}}(\boldsymbol{r}) = U_{\boldsymbol{K}}(-\boldsymbol{r}), \tag{9}$$

where the summation runs over the first Brillouin zone. Equation (7) then takes the form,

$$(\omega - 2\mu - 4SJd) U_{\boldsymbol{K}}(\boldsymbol{r}) + 2SJ \sum_{\boldsymbol{\delta}} \cos \frac{\boldsymbol{K}}{2} \cdot \delta \times [U_{\boldsymbol{K}}(\boldsymbol{r} + \delta) + U_{\boldsymbol{K}}(\boldsymbol{r} - \delta)] = J(\boldsymbol{r}) \left[\cos \frac{\boldsymbol{K}}{2} \cdot \boldsymbol{r} U_{\boldsymbol{K}}(0) - U_{\boldsymbol{K}}(\boldsymbol{r})\right], \tag{10}$$

with the periodicity condition $U_{\boldsymbol{K}}(\boldsymbol{r}) = \exp(i\boldsymbol{K}/2 \cdot L\boldsymbol{\delta})\, U_{\boldsymbol{K}}(\boldsymbol{r} + L\boldsymbol{\delta})$, where the sum is over the d Cartesian unit lattice vectors, $\boldsymbol{\delta}$, and L is the linear dimension of the crystal, $L^3 = N$. The right-hand side of (10) expresses the interaction, only at nearest neighbour separation, of two otherwise free spin deviations. A further transform,

$$U_{\boldsymbol{K}}(\boldsymbol{r}) = \frac{1}{N} \sum_{\boldsymbol{k}} \exp(i\boldsymbol{k} \cdot \boldsymbol{r})\, U_{\boldsymbol{K}}(\boldsymbol{k}), \qquad U_{\boldsymbol{K}}(\boldsymbol{k}) = U_K(-\boldsymbol{k}), \tag{11}$$

where $\boldsymbol{k}$ ranges over a first Brillouin zone slightly modified$^{(2)}$ so as to incorporate the periodicity, reduces (10) to

$$(\omega - \epsilon_{\boldsymbol{K}}(\boldsymbol{k})) U_{\boldsymbol{K}}(\boldsymbol{k}) = \frac{1}{N} \sum_{\boldsymbol{k}} V_{\boldsymbol{K}}(\boldsymbol{k}, \boldsymbol{k}')\, U_{\boldsymbol{K}}(\boldsymbol{k}'), \tag{12}$$

where the interaction is

$$V_{\boldsymbol{K}}(\boldsymbol{k}, \boldsymbol{k}') = 2J \sum_{\gamma=1}^{d} \cos k_\gamma \left(\cos \frac{K_\gamma}{2} - \cos k'_\gamma\right), \tag{13}$$

and

$$\epsilon_{\boldsymbol{K}}(\boldsymbol{k}) = 2\mu + 4SJ \sum_{\gamma=1}^{d} \left(1 - \cos \frac{K_\gamma}{2} - \cos k_\gamma\right) \tag{14}$$

is the energy of two free spin waves with relative and total momenta $\boldsymbol{k}$ and $\boldsymbol{K}$ respectively. The summation index, γ, refers to the d Cartesian components of the indicated vectors.

Bound state energies lie outside the spectrum of (14). The corresponding wave functions have no "free particle" components. If we define

$$U_{\boldsymbol{K}}^{\gamma} = \frac{1}{N} \sum_{\boldsymbol{k}} \left(\cos \frac{K_\gamma}{2} + \cos k_\gamma\right) U_{\boldsymbol{K}}(\boldsymbol{k}), \tag{15}$$

then

$$2SU_{\boldsymbol{K}}^{\gamma'} = \sum_{\gamma} U_{\boldsymbol{K}}^{\gamma} B_{\boldsymbol{K}}(\gamma, \gamma'), \tag{16}$$

where

$$B_{\boldsymbol{K}}(\gamma, \gamma') = \frac{4SJ}{N} \sum_{\boldsymbol{k}} \frac{\cos k_\gamma (\cos K'_\gamma/2 + \cos k'_\gamma)}{\omega - \epsilon_{\boldsymbol{K}}(\boldsymbol{k})}. \tag{17}$$

Thus, the secular equation determining* the bound state energies, ω, is

$$\det\left[2S\delta(\gamma,\gamma') - B_{K}(\gamma,\gamma')\right] = 0. \tag{18}$$

The identical condition was obtained and analyzed in Ref. 2. It was shown there that bound states exist for arbitrary spin and dimensionality. For three dimensions there is always a domain of sufficiently small K's for which bound states are absent.

The bound state wave functions are determined from the eigenvectors of (16) by equations (5), (9), (11), and

$$U_{K}(\boldsymbol{k}) = \frac{2J}{(\omega - \epsilon_{K}(\boldsymbol{k}))} \sum_{\gamma} \cos k_{\gamma}\, U_{K}. \tag{19}$$

Equation (10) with the right-hand side set equal to zero holds for all $\boldsymbol{r}$ greater than nearest neighbor and can serve to give a rough idea of the asymptotic† behavior of the wave function for large relative coordinate. When $K\gamma \approx \pi$, so $\cos K/2 \cdot \boldsymbol{\delta}$ is small, the wave function is sharply localized at nearest neighbor separation. On the other hand when there is a bound state with zero binding energy relative to the continuum,

$$2\left[\sum_{\boldsymbol{\delta}} \cos \frac{K}{2}\cdot\delta\right] U_{K}(\boldsymbol{r}) = \sum_{\boldsymbol{\delta}} \cos \frac{K}{2}\cdot\delta \times \left[U_{K}(\boldsymbol{r}+\boldsymbol{\delta}) + U_{K}(\boldsymbol{r}-\boldsymbol{\delta})\right], \tag{20}$$

which suggests that the wave function is quite spread out at threshold.

The methods suggested herein are easily generalized to the $n > 2$, many-spin-wave subspaces. In particular it is easy to show that equations of motion for the physical amplitudes never involve amplitudes for states with "overly occupied" sites. Of course, explicit diagonalization like (15)–(18) cannot be attained for $n > 2$, unless other constants of the motion in addition to the total momentum can be found.

REFERENCES

1. Hanus J. G., *Quart. Progr. Rep.* Solid State and Molecular Theory Group (M.I.T.), **43,** 96; **44,** 38; **46,** 137 (1962). In the first paper Hanus' treatment of the fictitious hard core introduces spurious dynamical effects. This error is subsequently rectified.
2. Wortis M., *On the Bound States of Two Spin Waves in the Heisenberg Ferromagnet,* submitted to *Phys. Rev.*
3. Dyson F. J., *Phys. Rev.* **102,** 1217 (1956).
4. Van Kranendonk J., *Physica* **21,** 749 (1955). Morita T. *Progr. theor. Phys.* (*Kyoto*) **20,** 614, 728 (1958).

---

* For logical completeness one must check for $S = \frac{1}{2}$ that no solutions of (18) correspond to eigenvectors which are projected to zero by (5), i.e., for which $U(i,j) = 0$ for $i \neq j$. Equation (7) shows that such an eigenvector can only occur when $\omega = 2\mu + 4SJd$, which is well within the continuum.

† Note that the periodicity condition on (10) makes $U_{K}(0) = \pm U_{K}(L\boldsymbol{\delta})$, so the asymptotic region must be defined as $1 \ll |\boldsymbol{r}| \ll L$.

J. Phys. Chem. Solids Pergamon Press 1963. Vol. 24, pp. 1679–1681. Printed in Great Britain.

ANTIFERROMAGNETIC STRUCTURE OF EuTe*

G. WILL

U.S. Army Electronics Research and Development Laboratory, Fort Monmouth, New Jersey
and Brookhaven National Laboratory, Upton, New York

S. J. PICKART and H. A. ALPERIN

U.S. Naval Ordnance Laboratory, Silver Spring, Maryland and
Brookhaven National Laboratory, Upton, New York

and

R. NATHANS

Brookhaven National Laboratory, Upton, New York

(*Received* 5 *August* 1963)

Abstract—EuTe has been shown by neutron diffraction to undergo at 7·8°K a transition to antiferromagnetism. The antiferromagnetic ordering is of the second kind with the spins lying within the (111) planes. The temperature dependence of the magnetic scattering was analyzed by adding a biquadratic exchange interaction to the usual bilinear term.

INTRODUCTION

THE chalcogenides of divalent europium, EuO, EuS, EuSe, and EuTe, comprise an isomorphous series crystallizing in the simple NaCl structure, and have attained considerable attention for the study of the Heisenberg model of ferromagnetism. EuO, EuS, and EuSe become ferromagnetic(1–3) with transition temperatures of 77, 18 and 7°K respectively, while EuTe exhibits no spontaneous moment down to 1·6°K. The dependence of susceptibility on temperature, however, suggests that EuTe may be antiferromagnetic at liquid helium temperatures.(2, 3) We have, therefore, undertaken a neutron diffraction study of EuTe to establish the magnetic type of ordering.

The study was performed on a powdered sample kindly provided by Dr. Shafer of the IBM Research Center. The sample was studied in transmission using a flat aluminum cell of 1·5 by 1·5 in. and 0·4 mm effective thickness, because of the high absorption cross section ($\sigma = 1{,}600$ barns) for Eu at 1·055 Å. This arrangement yielded about 80 counts/min for the (111) reflection.

MAGNETIC ORDERING

The neutron diffraction pattern of EuTe at liquid helium temperature is shown in Fig. 1. Based on a crystallographic unit cell $a_0 = 6{\cdot}56$ Å

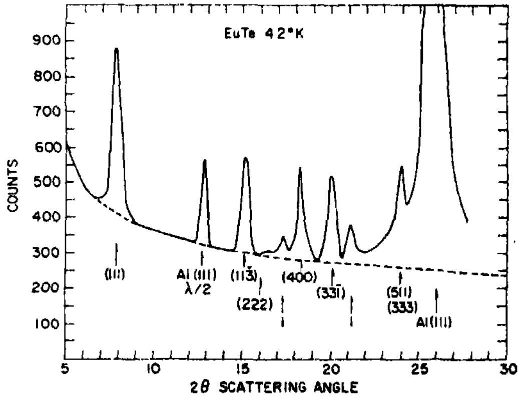

FIG. 1. Neutron diffraction pattern of EuTe taken below the Néel point. Scanning rate 1°/hr, wavelength, $\lambda = 1{\cdot}055$ Å.

---

* Work performed under the auspices of the U.S. Atomic Energy Commission.

(derived from the low temperature neutron diffraction pattern), we observe only one nuclear peak, (400); (222) is a difference peak and is too weak to be observed. (All indices are based on the doubled magnetic cell.) In addition we observe aluminum peaks from the sample holder and some peaks (*i*) resulting from unidentified impurities in the sample due to a slow decomposition of EuTe in air.

Additional peaks with all odd indices which do not appear at room temperature are observed at 4·2°K because of an ordering of the magnetic moments. The extinction rule observed by these magnetic peaks, (*hkl*) all even forbidden, indicates ordering of the second kind(4) if one assumes a uniaxial model. This is the same ordering present in MnO, CoO, and NiO. Each Eu ion is surrounded by six parallel and six antiparallel nearest neighbors at distances $\frac{1}{2}a_0\sqrt{2}$ along the face diagonals, and by six antiparallel next nearest neighbors across Te ions along the *a*-axes at a distance of a_0. The unit cell is then doubled in all three directions, giving superlattice peaks at lower angles than the nuclear peaks of the chemical unit cell.

It is convenient to sub-divide the magnetic unit cell into four sublattices shifted by 0; $\frac{1}{2}a_0+\frac{1}{2}b_0+c_0$; $\frac{1}{2}a_0+b_0+\frac{1}{2}c_0$; and $a_0+\frac{1}{2}b_0+\frac{1}{2}c_0$ from the origin. Combining all four sublattices with their proper phase shifts imposes further extinctions and leaves

$$\begin{array}{llllll} (111) & (11\bar{3}) & (33\bar{1}) & (333) & (511) & \text{allowed} \\ (111) & (113) & (331) & (\bar{3}33) & \left.\begin{array}{l}(511)\\(5\bar{1}1)\end{array}\right\} & \text{forbidden} \\ & (1\bar{1}3) & (\bar{3}31) & & & \end{array}$$

In this type of ordering the spins are parallel within (111) planes, which are stacked together in an alternating antiparallel sequence along the [111] direction.

ORIENTATION OF THE MOMENTS

The magnetic scattering from the unpaired electron spins is described in the standard notation by(5)

$$F_{h(\mathrm{mag})} = \sum_{x} (q)p \exp(2\pi i(h\cdot x))$$

with

$$p = \frac{e^2\gamma}{m\cdot c^2} S\cdot f \text{ and } q = \epsilon(\epsilon\cdot K) - K,$$

or $q^2 = \sin^2\alpha$, where α is the angle the magnetization vector K makes with the scattering vector ϵ.

The intensity of the magnetic scattering will therefore depend on the orientation of the moments in the lattice, and by comparing the intensity $P_{h(\mathrm{mag})}$ scattered from two different planes the angle alpha can be determined. The (111) and (11$\bar{3}$) reflections have been chosen because they are free from impurity contributions and are most sensitive to alpha. With

$$q^2_{(111)} = \sin^2\alpha$$

and

$$q^2_{(11\bar{3})} = \tfrac{2}{3} - \tfrac{5}{33} \times (\sin^2\alpha - 2\cos^2\alpha)$$

and with

$$P_{h(\mathrm{mag})} = \text{const.}\frac{\exp(-\mu t \sec\theta)}{\sin^2 2\theta} jF^2_{h\mathrm{mag}} \exp(-2W)$$

we derived from two independent runs values of $\sin\alpha = 1{\cdot}02$ and $0{\cdot}99$ respectively. The form factor values *f* were taken from Reference 6, and the variation of the Debye temperature $W = B(\sin\theta/\lambda)^2$ between (111) and (11$\bar{3}$) at 4·2°K was considered negligible. From this result it is concluded that the spins lie within the (111) planes. Based on powder diffraction data no conclusions can be drawn about the direction of the spins within the (111) planes, nor about a possible multispin axis structure.

NÉEL TEMPERATURE

By measuring the magnetic scattering from the (111) planes as a function of temperature (Fig. 2), the Néel temperature of transition from paramagnetic disorder to antiferromagnetic ordering has been determined. A heater wired around the sample was used to keep the sample at various temperatures, which were determined by a carbon

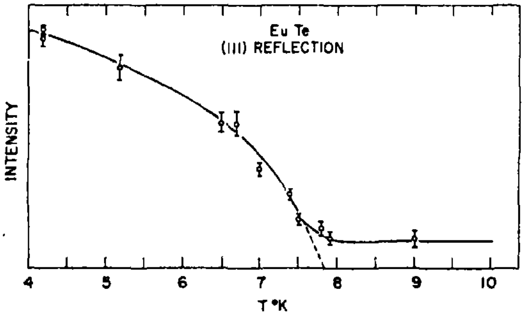

FIG. 2. Temperature dependence of the (111) magnetic reflection for EuTe, indicating a Néel point of 7·8°K.

resistance thermometer with a variation of about 100–200 Ω per degree in the temperature range studied. Each point in the Figure represents the average of about 30 min of counting, after allowing sufficient time for thermal equilibrium. The temperature dependence indicates the Néel point is 7·8°K, with an accuracy of about ± 0·5°.

The intensity variation does not however follow a Brillouin temperature dependence, as is indicated in Fig. 3 for the (111) reflection, if the moment is taken as $S = 7/2$. An explanation for this discrepancy may be sought in the biquadratic exchange interaction recently proposed by HARRIS and OWEN[(8)] and applied to the temperature dependence of the sublattice magnetization in MnO and NiO by RODBELL *et al.*[(9)] According to these authors, in addition to the usual bilinear term in the Hamiltonian there exist a biquadratic contribution of the form

$$J(S^a \cdot S^b) - j(S^a \cdot S^b)^2,$$

which may not always be negligibly small. In the case of EuTe an analysis of the observed temperature variation including a biquadratic term results in the agreement depicted in Fig. 3 for $(2j_1+j_2)/J_2 = 0{\cdot}016$, where j_1 and j_2 are the biquadratic exchange interactions for first and second nearest neighbors respectively.

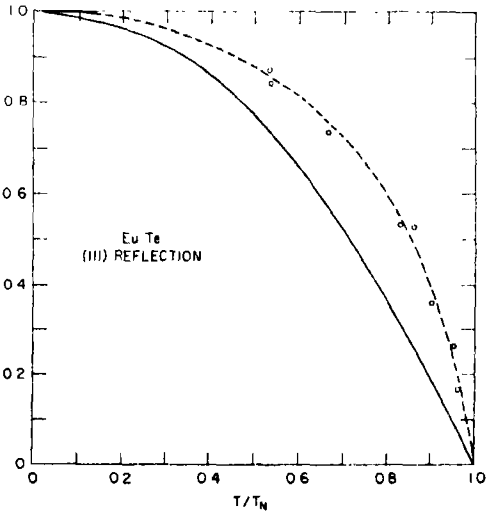

FIG. 3. Magnetic scattering from (111) planes of EuTe compared with a Brillouin dependence for $S = 7/2$. (Solid curve). The dashed curve is calculated including biquadratic exchange. The observed intensities (circles) are normalized at 4·2°K.

CONCLUSION

An analysis of the magnetic behavior of the Eu chalcogenides has been presented[(3, 7)] on the basis of molecular field theory. According to this analysis, the magnetic properties of this isostructural series result from a positive near-neighbor direct exchange interaction, J_1, decreasing with distance, combined with a negative next-nearest-neighbor superexchange interaction, J_2. Our results confirm this model. EuTe is found to undergo at $T_{N_2} = 7{\cdot}8°$K a transformation into an antiferromagnetic ordering of the second kind, which leads, with

$$\theta = T_c = \tfrac{2}{3}S(S+1)\,[12J_1+6J_2]$$

$$T_{N_2} = \tfrac{2}{3}S(S+1)\,[-6J_2]$$

to a negative superexchange interaction of $J_2 = -(0{\cdot}12 \pm 0{\cdot}01)$°K. From the asymptotic (antiferromagnetic) Curie temperature T_c, reported[(2, 3)] to range between −4 to −7·5°K, a direct exchange interaction in the order of $J_1 = (0{\cdot}025 \pm 0{\cdot}025)$°K is derived. Thus, in the case of EuTe, the negative next-nearest superexchange interaction is about five times larger than the direct exchange interaction and causes antiferromagnetism.

REFERENCES

1. MATTHIAS B. T., BOZORTH R. M. and VAN VLECK J. H., *Phys. Rev. Letters* **7**, 160 (1961).
2. MCGUIRE T. R., ARGYLE B. E., SHAFER M. W. and SMART J. S., *Appl. Phys. Letters* **1**, 17 (1962).
3. VAN HOUTEN S., *Phys. Letters* **2**, 215 (1962); ENZ U., FAST J. F., VAN HOUTEN S. and SMIT J., *Philips res. Rep.* **17**, 451 (1962).
4. SMART J. S., *Phys. Rev.* **86**, 968 (1952).
5. BACON G. E., *Neutron Diffraction*, Clarendon Press, Oxford (1962).
6. BLUME M., FREEMAN A. J., and WATSON R. E. *J. chem. Phys.* **37**, 1245 (1962).
7. MCGUIRE T. R., ARGYLE B. E., SHAFER M. W. and SMART J. S., *J. appl. Phys.* **34**, 1345 (1963).
8. HARRIS E. A. and OWEN J., *Phys. Rev. Letters* **11**, 9 (1963).
9. RODBELL D. S., JACOBS I. S., OWEN J. and HARRIS E. A., *Phys. Rev. Letters* **11**, 10 (1963).

J. Phys. Chem. Solids Pergamon Press 1963. Vol. 24, pp. 1683–1685. Printed in Great Britain.

A STUDY OF HYPERFINE INTERACTION IN CATIONS OF DIBENZENECHROMIUM AND DITOLUENECHROMIUM

YU. S. KARIMOV, V. M. CHIBRIKIN and I. F. SHCHEGOLEV

Institute for Physical Problems, Institute of Chemical Physics, Academy of Science, U.S.S.R.

(*Received* 12 *January* 1963)

Abstract—The magnetic susceptibility of iodides of dibenzene-chromium (DBC) and ditoluene-chromium (DTC) is measured in the temperature range from 1·3 to 295°K. Using the method of nuclear magnetic resonance, a study is made of the hyperfine interaction between non-coupled electronic spin and protons in cations DBC and DTC. It has been discovered that there is an axial-symmetric anisotropic part in the hyperfine interaction as well as an isotropic part. The values and signs of constants characterizing these two parts are determined. The nature of the spin density distribution in the molecule is discussed.

INTRODUCTION

THE rapid development of electronic paramagnetic spectroscopy in recent years has led to the publication of many papers dealing with the magnetic properties and electron structure of organic stable free radicals (see, for example, INGRAM[1]). However, this class of paramagnetic compounds still largely remains outside the field of vision of physicists, even though the study of their properties can be of considerable interest from the point of view of the physics of magnetic phenomena and in view of certain anomalies which have recently been discovered in these compounds. In effect, the magnetic susceptibility of some free radicals at sufficiently low temperatures begins to depend in a very complex manner on temperature, whilst in the spectrum of electron paramagnetic resonance a line appears which corresponds to forbidden transitions with $g = 4$;[2] the origin of the intensive undisplaced line which has been detected in the spectrum of proton resonance of diphenylpicrylhydrazil also remains obscure.[3,4]

In this paper, using the method of nuclear magnetic resonance, a study is made of hyperfine interaction between uncoupled electron spin and protons in molecules of the cations of dibenzene-chromium (DBC) and ditoluenechromium (DTC) and their magnetic susceptibility is measured over a wide range of temperatures.

Dibenzenechromium and its derivatives belong to the metal-aromatic class of compounds in which the metal atom is directly coupled with the whole system of π-electrons of the benzene rings. A molecule of DBC is illustrated in Fig. 1; the molecule of DTC is different in that one of the hydrogen atoms in each ring is replaced by a CH_3 group.

All the measurements were taken on iodides of DBC and DTC. The values of the isotropic coupling constants between the spin and protons in these compounds had already been measured[5]

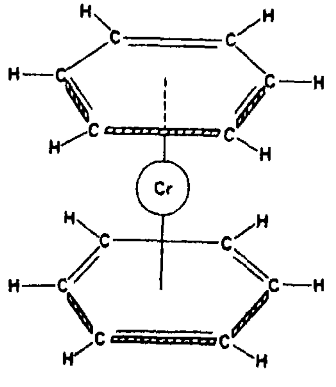

FIG. 1.

from the observable unpaired splitting of the spectra of electron paramagnetic resonance. The study of hyperfine interaction by nuclear magnetic resonance has made it possible to determine the signs of these constants as well as their values. A strong anisotropic hyperfine interaction has been discovered and the parameters characterizing it have been determined. These findings make it necessary, in particular, to revise certain conclusions concerning the nature of the distribution of spin density in these molecules.[5]

RESULTS

The variation of the magnetic susceptibility of paramagnetic compounds with temperature in the range 1·3–295°K reveals no anomalies and it is excellently described by the Curie–Weiss law $X = c/(T-\theta)$, where $\theta = -4{\cdot}6° \pm 0{\cdot}2°K$ for DBC iodide, and $\theta = -2{\cdot}0° \pm 0{\cdot}2°K$ for DTC iodide. In both cases the value of the constant c corresponds closely to the presence of one electron spin on a molecule, which testifies to the insignificance of the impurities.

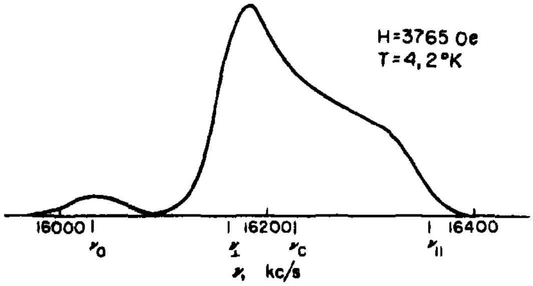

FIG. 2.

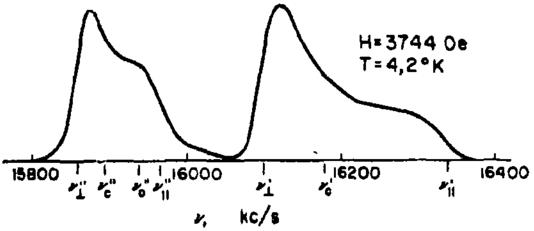

FIG. 3.

Nuclear magnetic resonance was studied at liquid helium temperatures when the paramagnetic shifts of the lines become large enough to be measured well. The typical shape of proton absorption spectra is shown in Figs 2 and 3. For the DBC cation there is one asymmetrical line shifted towards greater frequencies in relation to that frequency ν_0 which the protons have in diamagnetic compounds. The weak non-shifted line (less than 5 per cent of total intensity) can be explained by the presence of protons in the insulation of the conductor of the r.f. coil and at the walls of the glass ampoule with the specimen; the presence of a small amount of diamagnetic impurity in the specimen itself is not excluded either.

For the DTC cation there are two asymmetrical absorption lines. One of them, shifted towards greater frequencies, is due to the protons of the benzene rings, as in the case of the DBC cation. The other line, shifted towards lower frequencies, is to be ascribed to the protons of the CH_3 group.

The observable form of the lines is typical for a polycrystalline specimen in the case when there is an axial-symmetric anisotropic part in the hyperfine interaction as well as an isotropic part. The displacement of the centre of gravity of the lines is determined here by the isotropic coupling constant a:

$$\nu_c = \nu_0 + aXH/hN, \tag{1}$$

where X is the specific magnetic susceptibility, and N is the number of unpaired spins per 1 g of matter. The anisotropic coupling constant b determines how the resonant frequencies are shifted relative to the centre of gravity with parallel and perpendicular orientation of the axis of symmetry relative to the external field:

$$\begin{aligned} \nu_\parallel &= \nu_c + 2bXH/hN, \\ \nu_\perp &= \nu_c - bXH/hN. \end{aligned} \tag{2}$$

The measurements show that the shifts $\nu_c - \nu_0$ of the centre of gravity of the lines and the differences $\nu_\parallel - \nu_\perp$ which characterize their width, in accordance with formulae (1) and (2), are in fact proportional to the quantities $\chi(T)$ and H. These measurements result in the following values for the coupling constants:

$$a_{\mathrm{DBC}} = +3{\cdot}15 \pm 0{\cdot}15 \text{ Oe};$$
$$b_{\mathrm{DBC}} = +1{\cdot}05 \pm 0{\cdot}05 \text{ Oe};$$
$$a'_{\mathrm{DTC}} = +4{\cdot}0 \pm 0{\cdot}4 \text{ Oe};$$
$$b'_{\mathrm{DTC}} = +1{\cdot}3 \pm 0{\cdot}15 \text{ Oe};$$
$$a''_{\mathrm{DTC}} = -0{\cdot}75 \pm 0{\cdot}08 \text{ Oe};$$
$$b''_{\mathrm{DTC}} = +0{\cdot}6 \pm 0{\cdot}06 \text{ Oe}.$$

The constants a' and b' are attributed to the protons of the benzene rings, a'' and b''—to the protons of the CH_3 groups.

DISCUSSION

Certain difficulties arise in interpreting these results. The observable axial-symmetry of the anisotropic hyperfine interaction can apparently only be explained by the presence of notable dipole–dipole interaction between the protons and the unpaired electron, localized on the chromium atom, either in the *s*-orbital, or in any orbital the dimensions of which are small compared with the distance between the chromium atom and the protons. In particular, the quantities b' and b'' are inversely proportional to the cubes of the distances from the chromium nucleus to the corresponding protons (3·0 Å and 3·9 Å respectively). Assuming further that the anisotropic part of the hyperfine interaction is due to dipole–dipole interaction between the protons and one single point electron at the nucleus of the chromium atom, the calculated value of the constant b is 1·05 Oe, which agrees well with its measured value. Hence the spin density on the chromium atom must be close to +1.

The isotropic part of the hyperfine interaction is due to the contact interaction of the non-coupled spin with the protons. The values of the constants a and a' agree well with the values obtained by VETCHINKIN *et al.*(5) But their sign is at variance with the assumption which was made in that paper concerning the nature of the spin density distribution. Assuming that the isotropic hyperfine interaction is due to the presence of the unpaired spin on $2p_z$ orbitals of the carbon atoms of the benzene rings,(6) it is necessary to ascribe to the carbon atoms the negative spin density $\rho_c = -0{\cdot}14$. Here we shall have to assume that the spin density on the chromium atom ρ_{Cr} is 2·61, since the sum of the spin densities in the molecule must be unity.

Such a large spin density on the chromium itself seems improbable. Moreover, it ill agrees with the measurements of the constants of the anisotropic hyperfine interaction, the sign and the magnitude of which, as we have seen, is well explained by assuming one unpaired spin on the atomic orbit of the chromium.

Furthermore, if the isotropic part of the hyperfine interaction were due solely to the presence of unpaired spin density on the carbon atoms of the benzene rings, the constants a' and a'' ought to be close to each other in absolute value.(7, 8) But their measured values differ from each other by a factor of approximately 6.

Such divergence between the measured and theoretically predicted values of the isotropic coupling constants, equally like the need to ascribe to the chromium atom the anomolously large spin density, ill agreeing with the observable magnitude of the anisotropy of the hyperfine interaction, could of course be explained simply by the fact that the calculations performed by MCCONNELL(6) for the fragment C–H and by MCLACHLAN(7) and CHESNUT(8) for the fragment C–CH_3, are quite inapplicable to our case. It would, however, seem to be more probable that the isotropic part of the hyperfine interaction between the unpaired spin, localized mainly on the chromium atom, and the protons of the benzene rings is determined by the presence of hyperconjugation between the atomic orbits of the chromium and hydrogen, which ensures the rise of sufficient spin density directly on the protons of the ring. Here to the carbon atoms of the benzene rings must be ascribed the small spin density $\rho_c \approx 0{\cdot}025$ necessary for explaining the negative shift of the proton line associated with the CH_3 group. This gives for the spin density on the chromium atom $\rho_{\mathrm{Cr}} \approx 1{\cdot}3$.

Acknowledgements—In conclusion we wish to express our sincere thanks to academician P. L. KAPITZA and corresponding member V. V. VOEVODSKII for their attention to the paper and to A. S. BOROVIK-ROMANOV for his comments and kind provision of magnetic weights.

REFERENCES

1. INGRAM D. J. E., "*Free Radicals*" *as studied by Electron Spin Resonance.* Butterworth, London (1958).
2. RHODES R. S., BURGESS J. H. and EDELSTEIN A. S., *Phys. Rev. Letters* **6**, 462 (1961).
3. KARIMOV YU. S. and SHCHEGOLEV I. F., *Zh. eksp. teor. fiz.* **40**, 3 (1961).
4. HERVÉ J., REIMANN R. and SPENCE R. D., *Bull. du Groupement Ampere du IX Coll.*, p. 396. 12–16 September (1960).
5. VETCHINKIN S. I., SOLODOVNIKOV S. P. and CHIBRIKIN V. M., *Opt. Spectrosc.* (*Opt. spektrosk.*), **8**, 137 (1960).
6. MCCONNELL H. M., *J. chem. Phys.* **28**, 107 (1958).
7. MCLACHLAN A. D., *Molec. Phys.* **1**, 2331 (1958).
8. CHESNUT D. B., *J. chem. Phys.* **29**, 43 (1958).

J. Phys. Chem. Solids Pergamon Press 1963. Vol. 24, pp. 1687–1691. Printed in Great Britain.

OPTICAL ABSORPTION OF COLOR CENTERS IN LITHIUM FLUORIDE CONTAINING MAGNESIUM ADDITIVE

F. PILCHER,* D. SCHINKE† and R. J. FRIAUF

University of Kansas, Lawrence, Kansas

(*Received* 8 *April* 1963; *revised* 18 *June* 1963)

Abstract—A new absorption band appears when LiF containing small amounts of magnesium is irradiated by gamma rays. This band is very broad, extending from the *F*-band out to 600 mμ, and is somewhat unstable thermally at room temperature. It appears when the magnesium ions are precipitated as well as when they are dispersed, although the behavior is slightly different in the two cases. An interpretation in terms of F_2^- molecules stabilized by proximity of magnesium ions is given. When LiF containing magnesium is irradiated by neutrons at 350°C, a band peaking near 225 mμ is observed in place of the *F*-band. This band is similar to a band previously reported at 222 mμ by several workers, but these experiments are the first to show that its occurrence is definitely associated with the presence of magnesium. *It is tentatively suggested that this band may be a Z-band, analogous* to *Z*-bands in, e.g., KCl:Sr.

INTRODUCTION

A NUMBER of absorption bands associated with excess Sr^{2+} have been found in the system KCl:Sr. Different models of configurations responsible for these bands, termed *Z*-bands, have been proposed; it has not yet been possible, however, to decide among these various models by experimental means.(1) The theoretical problem of computing energy levels for these impurity atoms is extraordinarily difficult because of the large numbers of orbital electrons involved. One might hope that the theoretical problems would be somewhat less intractable in LiF containing Mg because of the smaller number of orbital electrons.

Previous to this investigation no direct evidence of *Z*-centers in LiF containing Mg had been obtained, but a number of unusual features had been observed. DELBECQ and PRINGSHEIM, working with supposedly pure LiF made in 1952 or earlier by the Harshaw Chemical Company, bleached the *F*-band in its own light. The *F*-band disappeared and in its place a narrow band peaking at 222 mμ was formed.(2) This band was especially strong in crystals in which the *F*-band had been originally formed at 350°C. The 222 mμ band was observed under similar circumstances by KATO, who also used Harshaw crystals.(3) This behavior has no counterpart in other alkali halides, and this suggests that it may be due to an otherwise undetected impurity.

When LiF was irradiated at liquid nitrogen temperature, it contained in addition a band peaking at 340 mμ with half width 1·2 eV, but this band disappeared when the crystal was warmed to room temperature. Recently DELBECQ, HAYES and YUSTER have investigated this band and found that it is caused by F_2^- molecules.(4) Analogous species found in other alkali halides can be formed in large concentration only in the presence of small quantities of impurities such as Pb^{2+}, Ag^+, or NO_2^-. The F_2^- band can be formed in apparently pure LiF, however, and this further suggests the presence of small amounts of impurities.

W. G. JOHNSTON has found that Harshaw LiF crystals manufactured in 1957 contained 75 p.p.m. Mg but that those made in 1960 contained only 3 p.p.m. Mg(5) This makes one further suspect that the 222 band observed in 1952 was due to an impurity. He found furthermore that if LiF containing Mg was heated above 200°C and then cooled rapidly from 200 to 100°C the Mg was atomically dispersed. But if the crystal was cooled very slowly within this range, the Mg precipitated into colloidal aggregates. Not much over 100 p.p.m. Mg could be dispersed under any kind of treatment; the rest was precipitated.

---

* Present address: Illinois College, Jacksonville, Illinois.

† Present address: Central Methodist College, Fayette, Missouri.

EXPERIMENTAL METHODS

In the present investigation the authors used LiF prepared from reagent grade chemicals and used Harshaw crystals ordered in 1961 only as controls. To one batch of laboratory-prepared LiF, 1·00% by weight of MgF_2 was added; to another batch, 0·25% MgF_2 was added. Crystals were grown in air from a platinum crucible by withdrawing from the melt on a platinum wire. On the basis of an assumed segregation factor upon freezing of 10, it is estimated that the heavily-doped crystals contain nominally 400 p.p.m. Mg and that the lightly-doped crystals contain nominally 100 p.p.m. Mg. The crystals were cleaved into pieces about 1 mm thick and were then subjected to various heat treatments. Some of the cleaved crystals were heated to 300°C for 2 hr and quenched in quiet air in an effort to disperse as much magnesium as possible. Others were annealed for as long as 24 hr at 150°C and cooled slowly in an effort to precipitate most of the magnesium.

After heat treatment the crystals were irradiated for several hours near room temperature in a Co^{60} gamma ray source to a total dose of approximately 300,000 r. Neutron irradiations of approximately 5×10^{12} n/cm^2 at room temperature and 5×10^{13} n/cm^2 at 350° were performed in a 10 kW training reactor. The samples were held at the high temperature by means of a small electric resistance furnace built to fit inside a 4 in. square cross section hole obtained by removing a graphite stringer from the thermal column of the reactor.

Optical absorption measurements were made at room temperature with a Beckman DK spectrophotometer. Spectra are shown from 210 to 600 mμ in Figs 1–4; no additional bands were observed in the region of 600–2800 mμ. A few spectra obtained at liquid nitrogen temperature showed slightly sharper bands but did not reveal any additional structure. For optical bleaching the crystals were illuminated with a mercury vapor mineral-light filtered by two Corning 9863 red–violet filters, which transmitted the bright line at 254 mμ but excluded the visible radiations.

EXPERIMENTAL RESULTS

Immediately after gamma irradiation the Harshaw crystals showed a strong *F*-band and a very weak absorption band near 450 mμ as illustrated in Fig. 1. One of these crystals was kept several months in the dark at room temperature without any decrease in intensity of either band. The *F*-band in another Harshaw crystal was bleached optically for 60 hr with filtered mineralight. The 450 mμ band disappeared completely, and the *F*-band was steadily diminished to one third of its original height during this process, but no trace of the 222 mμ band observed by DELBECQ and PRINGSHEIM appeared at any stage of the bleaching.

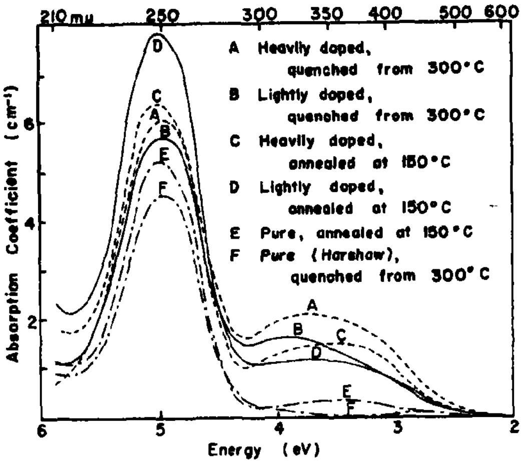

FIG. 1. Absorption spectra of a number of LiF crystals *immediately after gamma irradiation* at room temperature.

The doped crystals exhibited a very different behavior. As illustrated in Fig. 2 a heavily-doped (~400 p.p.m. Mg) crystal which had been quenched from 300°C to disperse the magnesium showed after irradiation a broad band peaking near 320 mμ in addition to the *F*-band. The short wavelength end was hidden under the *F*-band, and the long wavelength tail extended to 600 mμ. After a few days in the dark the 320 mμ band had decreased somewhat in intensity, and the *F*-band was also somewhat reduced. Irradiating with the filtered mineralight greatly increased the rate of disappearance of both bands, but no new bands appeared during any stage of the bleaching.

A heavily-doped crystal which was annealed at 150°C prior to irradiation showed a slightly different behavior, illustrated in Fig. 3. It, too, showed a broad band extending from the *F*-band to 600 mμ, but the peak fell near 350 mμ instead of near 320 mμ as in the quenched crystal. This band was even more unstable thermally than that in the quenched crystal, disappearing almost completely after a week in the dark at room temperature and reducing the intensity of the *F*-band somewhat in the process. The 350 mμ band also bleached readily under irradiation by the mineralight, but, as for the quenched crystal, no new bands appeared while the bleaching was taking place. A lightly-doped (~100 p.p.m. Mg) annealed crystal showed a 350 mμ band which was initially somewhat weaker and which had largely disappeared after a week in the dark.

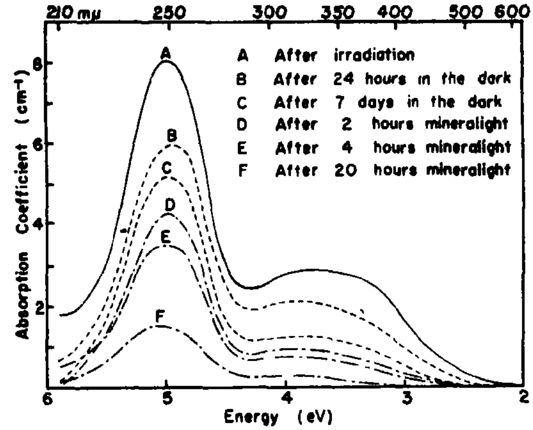

FIG. 2. Absorption spectra of a heavily-doped crystal quenched from 300°C. The gamma irradiation and all subsequent treatments were performed at room temperature.

Johnston's data indicate that even by rapid quenching not all of the magnesium in a heavily-doped crystal should be dispersed.(5) And the absorption spectra of the heavily-doped quenched crystal, Fig. 2, do show features of both quenched and annealed lightly-doped crystals. The peak of the broad band is broadened, suggesting that there are two overlapping unresolved peaks near 320 and 350 mμ, respectively. And the long wavelength end bleaches more rapidly than the region near 320 mμ, both when kept in the dark and when irradiated with the mineralight.

Magnesium certainly increases the intensity of the 320 and 350 bands, but it is possible that some other impurity either was present in the reagent grade chemicals used to prepare the LiF or else was inadvertently introduced during preparation. Crystals made from the same batch of LiF but to which no impurity was intentionally added were also examined. A crystal which was quenched from 300°C prior to irradiation showed immediately after irradiation a very weak band, which seemed to resemble in shape and in almost total bleaching after a week the 350 mμ band in the annealed crystal. But any magnesium in this crystal would almost certainly be dispersed, and would hence be expected to produce a 320 mμ band resembling that in the doped, quenched crystals. There is no doubt, however, that the pure crystal contains much less magnesium than the intentionally doped ones.

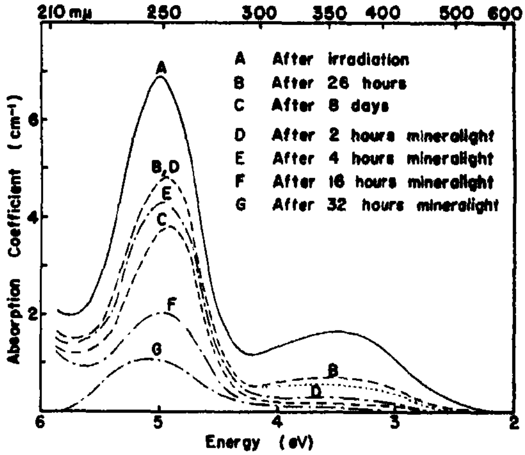

FIG. 3. Absorption spectra of a heavily-doped crystal annealed at 150°C. The gamma irradiation and all subsequent treatments were performed at room temperature. The optical and thermal bleaching experiments were carried out with two different samples.

Room temperature neutron irradiation of two pure crystals produced only the *F*- and *M*-bands, as for room temperature gamma irradiation. The results from neutron irradiation at 350°C are shown in Fig. 4. The Harshaw crystal and the undoped laboratory-made crystal show a normal *F*-band with no other bands present. The two doped crystals, however, show a new band peaking near 225 mμ, with a suggestion of a weaker *F*-band appearing as a long wavelength shoulder. A second neutron irradiation under similar conditions with a different set of samples has given entirely similar results.

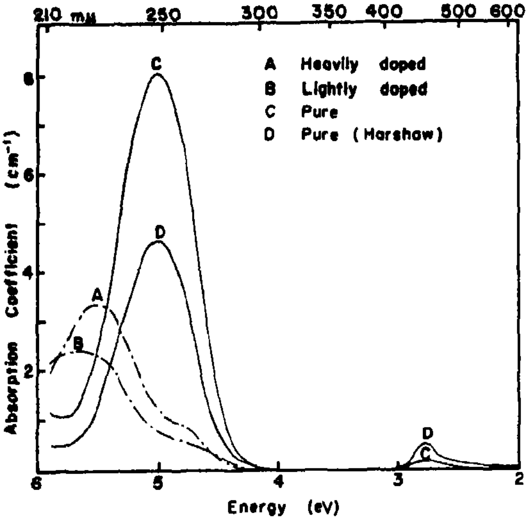

FIG. 4. Absorption spectra of a number of LiF crystals immediately after neutron irradiation at 350°C. The absorption spectra were measured at room temperature.

DISCUSSION

The 350 and 320 mμ bands both resemble in shape the F_2^- band observed by DELBECQ, HAYES and YUSTER in pure LiF at low temperature,[4] but differ in being moderately stable at room temperature. The authors suggest that these bands are caused by F_2^- molecules stabilized by the presence of magnesium, perhaps in the manner suggested by HAYES.[6] Two observations tend to confirm this. (i) The shape of the bands resembles the shape of the F_2^- absorption band described by DELBECQ, HAYES and YUSTER.[4] (ii) The fact that the *F*-band bleaches somewhat as the broad band bleaches in the dark suggests that the latter is a hole band. After the holes are released thermally, they annihilate with *F*-centers, bleaching a band otherwise stable at room temperature.

The F_2^- molecule may be stabilized either by the presence nearby of an isolated magnesium ion or by a cluster of precipitated ions. Both neighborhoods may perturb the basic F_2^- wave function and energy levels in such a way as to increase the thermal stability of the configuration. But these neighborhoods are different from each other and perturb the F_2^- wave function in different ways. Thus, near a magnesium cluster the energy of transition and the stability against thermal decay are both somewhat lower than near an isolated magnesium ion. Further study with polarized bleaching and paramagnetic resonance would help to test the hypotheses presented here.

The 222 mμ band observed after bleaching by DELBECQ and PRINGSHEIM[2] and KATO[3] is not found in any of our crystals irradiated at room temperature. It is highly probable, however, that the prominent band observed near 225 mμ in the doped crystals following the high temperature irradiation is the same band. This conclusion seems even more reasonable in view of the fact that both previous groups[2,3] found high temperature irradiation to enhance the subsequent production of the 222 mμ band by bleaching.

The results presented here show definite evidence for the first time that the 222 mμ band is associated with the presence of magnesium in the crystal. It is therefore our very tentative suggestion that this band represents a genuine electron-excess *Z*-band. Possibly holes are trapped more readily than electrons near magnesium ions, thus leading to the production of hole centers at temperatures for which these are stable but of electron centers at higher temperatures. This behavior might account for our failure to produce this band in crystals irradiated and bleached at room temperature. Much further study will be needed to establish the nature of the center giving rise to this band, and such work will soon be underway at The University of Kansas.

Acknowledgements—The authors would like to express their appreciation to the Atomic Energy Commission ~~for~~ providing a research contract that supported some of this work. One of the authors (D.S.) would like to thank the National Science Foundation for the grant of an Undergraduate Research Fellowship. The gamma irradiations were made possible by the cooperation of Profs. E. Zeller, E. Angino, and the Radiation Biophysics group at The University of Kansas, and the neutron irradiations were performed by Mr. D. Elliott under the direction of Prof. R. Mesler at the Nuclear Reactor Center. The assistance of Messrs. R. Mellott and H. Breedlove in carrying out some of the experimental work is also gratefully acknowledged.

REFERENCES

1. Pick H., *Z. Phys.* **114**, 127 (1939); Seitz F., *Phys. Rev.* **83**, 134 (1951); *Rev. mod. Phys.* **26**, 7 (1954); Kleefstra M., Thesis, Groningen (1961).
2. Delbecq C. J. and Pringsheim P., *J. chem. Phys.* **21**, 794 (1953).
3. Kato R., *Bull. Inst. chem. Research, Kyoto Univ.* **39**, 153 (1961).
4. Delbecq C. J., Hayes W. and Yuster P. H., *Phys. Rev.* **121**, 1043 (1961).
5. Johnston W. G., *J. appl. Phys.* **33**, 2050 (1962).
6. Hayes W., *J. appl. Phys.* **33**, 329 (1962).

LETTERS TO THE EDITOR

Conductance of strontium-doped potassium chloride crystals

(*Received* 11 *March* 1963; *revised* 30 *July* 1963)

AN ANALYSIS of recent measurements⁽¹⁾ of the ionic conductance of potassium chloride doped with strontium chloride revealed two unexpected features. Firstly, the values of ζ (where $-\zeta$ is the free energy of association of divalent strontium cations with cation vacancies to form complexes) showed a pronounced temperature dependence, varying from 0·43 to 0·20 eV over the temperature range 300–900°K. Such a strong variation with temperature is unexpected on the simple association model as the (vibrational) entropy change on forming the complex should be small. Secondly, the plots of $c/(\xi-1/\xi)$, where c is the concentration of divalent impurity added and ξ the ratio of the molar fraction of cation vacancies (x_1) in the doped crystal to the molar fraction (x_0) in the undoped crystal at the same temperature, showed a pronounced curvature at low concentrations whereas the simple association theory predicts that such plots should be linear. Such a curvature can be understood in terms of LIDIARD's theory⁽²⁾ of non-nearest neighbour interactions between defects; however it was pointed out⁽¹⁾ that such an analysis is very sensitive to the values of c and in view of doubts about the precision of the method used for the strontium analyses, a quantitative reconciliation of the data with the Lidiard theory was not attempted.

A new series of measurements of the specific conductance (σ) of KCl doped with $SrCl_2$ is in good agreement with the previous measurements as far as the primary data, $\sigma(c)$, are concerned and an analysis of the defect interactions can therefore be performed with somewhat greater confidence than before. The apparatus and experimental procedure were the same as those described previously.⁽¹⁾

The conductance of five crystals doped with strontium chloride was determined as a function of temperature. The results were reproducible on thermal cycling indicating complete solution of the $SrCl_2$ during the annealing procedure. The concentration of $SrCl_2$ in the five crystals expressed as the molar ratio $SrCl_2$: KCl, is given in Table 1. These values were determined (using the actual cleave from the conductance measurements) by the X-ray fluorescence technique. A calibration curve for the instrument (a Philips X-ray Diffractometer, type PW1051) was established using standard samples of known $SrCl_2$ content.

Table 1. Sr^{2+} *concentration in the* $KCl+SrCl_2$ *mixed crystals.*

Run	Mole ratio in melt × 10⁵	Mole ratio × 10⁵ by analysis	Mole ratio × 10⁵ effective
12	20	14·4	6·5
15	50	31·0	28·0
16	50	41·8	38·8
17	100	94·0	91·0
11	200	117·0	114·0

Plots of log σT vs. T^{-1} were slightly curved (concave downwards) indicating association between the Sr^{2+} impurity ions and the cation vacancies. One would therefore expect the conductivity–concentration isotherms to be parabolic, intersecting the σ axis at σ_0 the conductance of the pure salt, the amount of curvature decreasing as the temperature increases. Typical plots of $\sigma-\sigma_0$ against c are shown in Fig. 1: at high

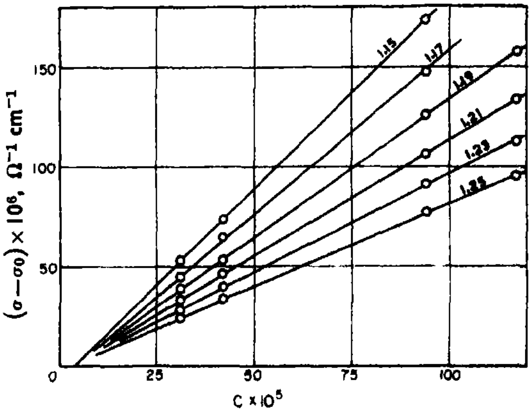

FIG. 1. Plot of the excess specific conductance $\sigma-\sigma_0$ due to doping against c, the concentration of added strontium chloride. The numbers on the isotherms are the values of $10^3/T$°K.

temperatures one would expect these to be almost linear but it is clear that the best straight lines do not intersect the origin but cut the concentration axis at a point c_0. For temperatures above 870°K, c_0 appeared to increase with T, but below this temperature it was substantially constant at $3{\cdot}0\times10^{-5}$. Furthermore, the points for run 12, the lowest concentration, require an additional displacement to bring them on to the lines through the other four points. The mean value for this additional displacement is $4{\cdot}9\times10^{-5}$. The final concentrations obtained in this way are also given in Table 1.

It thus appears that not all the Sr^{2+} produce the equivalent number of mobile cation vacancies when crystals are grown in evacuated silica vessels from A.R. materials which have been thoroughly outgassed and then exposed to a mixture of HCl and dry N_2 at temperatures up to 500°C. Despite the absence of an absorption band at 204 mμ in these crystals they must nevertheless contain OH^- in a form which is capable of complexing with the Sr^{2+} ions in such a way as to provide charge compensation without the production of cation vacancies. Similar conclusions have been arrived at by LÜTY *et al.* by doping KCl with KOH and $CaCl_2$.(3) This same effect was in fact evident in the results obtained previously(1) for the same system but there was then felt to be insufficient justification for the mechanism proposed. Consequently, the best line was drawn through the origin, and the concentration for the crystal containing least Sr^{2+} determined by interpolation. In any case, the correction exerts only a small effect on the slopes of the lines and hence on the mobility parameters. These were obtained in the manner described previously.(1) The concentration of vacancies in the undoped KCl (x_0) is given

$$\log_{10} x_0 = 1{\cdot}676{-}5{\cdot}700\times10^3\,T^{-1} \qquad (1)$$

and the mobility of the cation vacancies (u_1) by

$$\log_{10} u_1T = 3{\cdot}191{-}3{\cdot}820\times10^3\,T^{-1} \qquad (2)$$

The activation energy for cation vacancy conduction (0·76 eV) is in good agreement with other modern determinations: GRÜNDIG(4) (0·77 eV); PIERCE(5) (0·76 eV) and KOBAYASHI and TOMIKI.(6) (The latter authors do not quote a numerical value but one of ~0·75 eV may be deduced from their graph.)

The activation energy for anion conduction (Δh_2), however, presents difficulties. If we assume that the experimental activation energy from diffusion measurements, E, may be written as $E = \frac{1}{2}h+\Delta h_2$ where h is the energy required to form a Schottky defect pair ($h = 2{\cdot}28$ eV from equation (1)) then the diffusion data give 1·46 eV (from $E = 2{\cdot}60$ eV(7)) and 0·86 eV (from $E = 2{\cdot}0$ eV(8)). These values differ quite widely from each other and bracket the calculated value of $\Delta h_2 = 1{\cdot}18$ eV.(9) If the value of Δh_2 is comparable with that for Δh_1, then curvature of the conductance plot log σT vs. T^{-1} ought to be obtained. Only a slight curvature was observed by ALLNATT and JACOBS(1) who obtained 1·77 eV for Δh_2 by a subtraction procedure. A similar analysis of the new data yields 1·87 eV but Harshaw and SO_4^{2-}-doped crystals show hardly any curvature. The values found from conductance measurements are in fair agreement with the diffusion value of EWLES and JAIN(10) (1·86 eV), a value calculated from Kerkhoff's transport number data(11) (1·9 eV) and the activation energy for the diffusion of F-centers(12) (2·0 eV). However, structure-sensitivity in the anion vacancy mobility is evident and successful anion-doping experiments are required to resolve this difficulty.

The values of ζ are plotted in Fig. 2 which also shows a recalculation of the data of ALLNATT and JACOBS(1) allowing for complexing of Sr^{2+} with OH^- ions. The variation with temperature of ζ is confirmed. The interaction energy between two point defects of effective charge $+e$ and $-e$ would be expected at large separations to approach

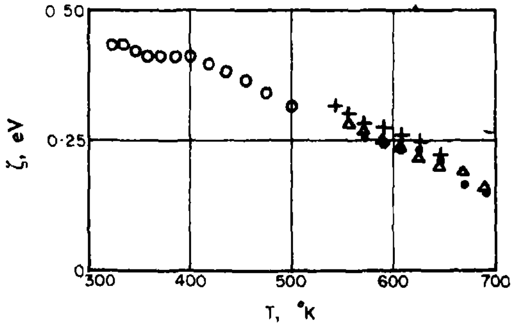

FIG. 2. The dependence of ζ on temperature.
○ run 12; + run 15; ○ run 16;
△ ALLNATT and JACOBS,(1) recalculated.

the value given by the simple Coulombic formula $-e^2/\kappa\epsilon_0 r$, where κ is the dielectric constant of the medium and ϵ_0 the permittivity of free space. However, the use of the Born–Mayer model for an ionic crystal yields values(13, 14) for ζ which are substantially less than those calculated from Coulombic interactions alone. This is due to the fact that while polarization of the medium between the defects would increase the interaction energy, polarization of the material around the defects will decrease it. The dielectric constant of ionic crystals is known to increase at high temperatures and this effect ought, therefore, to be taken into account in making theoretical estimates of ζ. There do not appear to have been any measurements of κ in the temperature range of interest. However, HAVINGA's equation(15) predicts that κ varies only from 4·68 at 300°K to 5·32 at 700°K. This change is much too small to account for the variation in ζ if ζ varies approximately as κ^{-1}. While it is a contributory feature, the temperature-dependence of κ cannot account for the whole of that of ζ which thus casts doubt on the validity of the simple association model. Measurements at low concentrations are needed to provide quantitative estimates of the importance of non-nearest neighbour interactions and in such experiments hydroxide-free material must be used. There is independent evidence of the importance of non-nearest neighbour interactions in the work of WATKINS(16) (e.s.r.) and DREYFUS(17) (dielectric relaxation).

Acknowledgements—This work was performed during the receipt from the D.S.I.R. of a maintenance grant by one of us (J.N.M.). We are indebted to The Chemical Society for an apparatus grant which has defrayed part of the cost of the research.

Department of Chemistry,
Imperial College,
London, S.W.7
P. W. M. JACOBS

R.I.A.S.,
7212 *Bellona Avenue,*
Baltimore 12, *Maryland*
J. N. MAYCOCK

References

1. ALLNATT A. R. and JACOBS P. W. M., *Trans Faraday Soc.* **58,** 116 (1962).
2. LIDIARD A. B., *Handb. Phys.* **20,** 246 (1957).
3. FRITZ B., LÜTY F. and ANGER J., *Z. Phys.* **174,** 240 (1963).
4. GRÜNDIG H., *Z. Phys.* **158,** 577 (1960).
5. PIERCE C. B., *Phys. Rev.* **123,** 744 (1961).
6. KOBAYASHI K. and TOMIKI T., *J. phys. Soc. Japan* **15,** 1982 (1960).
7. BARR L. W., HOODLESS I. M., MORRISON J. A. and RUDHAM R., *Trans. Faraday Soc.* **56,** 697 (1960).
8. LAURENT J-F. and BERNARD J., *J. Phys. Chem. Solids* **3,** 7 (1957).
9. GUCCIONE R., TOSI M. P. and ASDENTE M., *J. Phys. Chem. Solids* **10,** 162 (1959).
10. EWLES J. and JAIN S. C., *Proc. Roy. Soc.* **A243,** 353 (1957).
11. KERKOFF F., *Z. Phys.* **130,** 449 (1951).
12. MIZUNO H. and MIYAMOTO S., *Physica* **27,** 800 (1961).
13. BASSANI F. and FUMI F. G., *Nuovo Cim.* **11,** 274 (1954).
14. TOSI M. P. and AIROLDI G., *Nuovo Cim.* **8,** 584 (1958).
15. HAVINGA E. E., *J. Phys. Chem. Solids* **18,** 253 (1961).
16. WATKINS G. D., *Phys. Rev.* **113,** 79 (1959).
17. DREYFUS R. W., *Phys. Rev.* **121,** 1675 (1961).

Pressure and high current effects on a graphite contact

(*Received* 15 *August*, 1963)

IT WAS reported earlier(1) that if condensers were charged to certain voltages and discharged through a column of graphite powder, the electrical resistance of the powder decreased irreversibly.

This technique was called flash sintering, and a development of it has recently been published by BUNDY.(2)

The powder was prepared by grinding block graphite and it was found that this process caused the thermo-electric power of the graphite to change from small negative to large positive values. Powdering the block material probably increases the number of defects located on the surface of the particles. These defects, however, do not appear to present a barrier to current flow from one particle to the next. The activation energies calculated from log conductivity vs. $1/T$ plots for block and powdered material closely agreed. The decrease of electrical resistance observed on flash sintering was interpreted in terms of an increase in the contact area between particles brought about by a melting or flow process. The present note reports on some preliminary results obtained when the more simple system of two graphite surfaces in contact was investigated.

The graphite rod (Johnson Matthey spectrographic electrode) was machined to form a pointed cone which rested on a flat surface of another rod. Two potential probes measured the voltage drop across the contact when a small monitoring current passed through it. The contact was first loaded and then this load was reduced. Without breaking the contact the resistance was then measured for increasing and decreasing load. A number of cycles were carried out and the results of four such cycles are shown in Fig. 1. The effect of loading on the resistance can be expressed as

$$RW^{+0\cdot 38} = \text{constant}$$

where R is the resistance of the contact in milliohms and W is the load in grams.

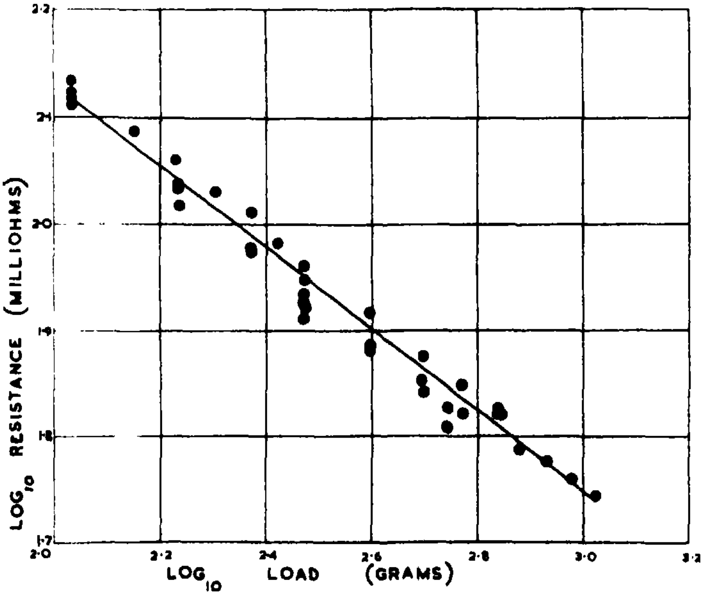

FIG. 1. Contact resistance vs. load. (Four cycles of increasing and decreasing load.)

It has been shown(3) that for elastic deformation the electrical resistance of a contact should vary inversely as the cube root of the load and inversely as the square root of the load if the surface deforms plastically. The load resistance behaviour of the graphite contact in this work suggests that elastic deformation has taken place.

The graphite surfaces were brought together under a variety of loads to give a range of resistances. A discharge of the same voltage from a bank of condensers was released through each of them and the change in resistance measured. Figure 2 shows the changes observed on passing a discharge of 1200 V through contacts made in this way when the capacitance of the circuit was 10, 40, 80 and 120 μF respectively. The circuit parameters were chosen in such a way that the change in value of the contact resistance did not affect the overall resistance to more than 2 per cent. For discharges of the same voltage then, the current through each contact could be said to be the same and its duration proportional to the capacitance of the circuit. It can be seen that the effect of increasing the time for which the current passes is mainly to cause the resistance at which the first change occurs to drop to lower values. This effect is of limited extent, however, because the curves for 80 and 120 μF coincide. For values of capacitance below 80 μF, the graph showed a curvature at the lower initial resistance region which tended to increase as the capacitance decreased. Above 80 μF, however, there was little

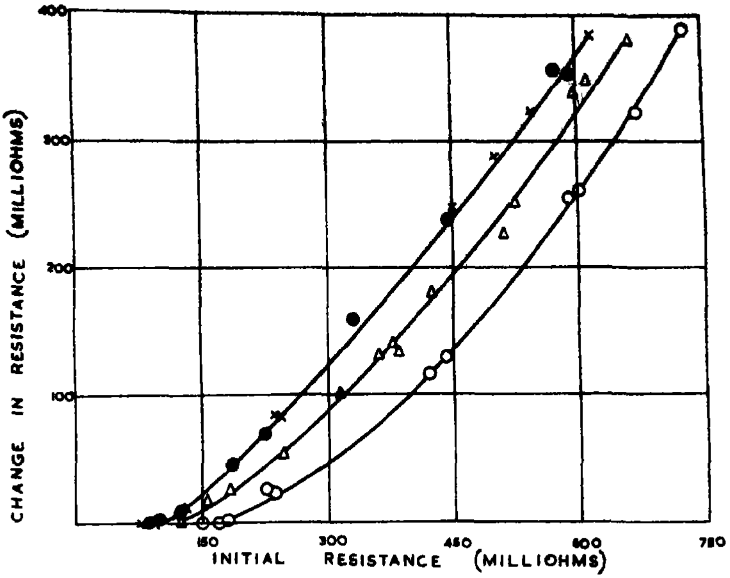

FIG. 2. Decrease in resistance for a range of contact resistances subjected to the same peak current discharge.

○ 80 μF
△ 40 μF
× 80 μF
● 120 μF

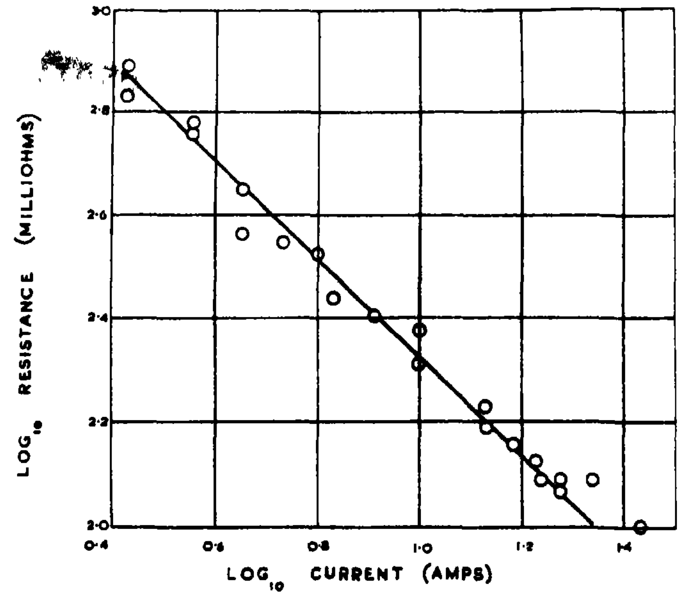

FIG. 3. Peak current vs. critical resistance at constant capacity.

curvature. All the graphs showed a straight line region. The slopes of all the straight lines tended to unity. The resistance at which the first change was observed is called the "critical resistance", and the manner in which the critical resistance depended upon the peak current of the discharge at a constant capacity was then investigated. The value of the capacitance chosen was 120 μF since this value should be outside the capacitance dependent region. The results are shown in Fig. 3. The peak current is the ohmic current given by dividing the voltage in the condensers by the total circuit resistance. The relationship is linear with a slope of -1 and can be expressed thus:

$$R_c I_c = K$$

where R_c and I_c are the critical resistance and critical current respectively and K is a constant.

The relationship between peak current and critical resistance $R_c I_c = K$ is the same relationship which Bowden and Williamson(4) found for gold contacts. K can be taken to represent the maximum voltage which may exist across the contact without decrease of resistance. The plots of Fig. 2 show some curvature which increases as the capacity or time constant of the circuit decreases. This curvature might represent the onset of some flow process by which the contact area is increased. If the contact resistance is reduced by such a flow process this will require a certain time to take place and unless the time constant is greater than a certain minimum value the process will not be complete. The overlap of the 80 and 120 μF plots and their small amount of curvature suggests that at the time constants determined by these capacitances the flow process for each initial resistance is almost complete. If the action of the current discharge was to dispel an impurity film then the decrease of resistance might be accounted for in this way. However, previous work(1) suggested that such films where they exist in graphite do not contribute significantly to the contact resistance. This is not surprising since it is difficult to envisage a mechanism whereby a film could be built up on graphite surface of such an extent as to cause insulation. Adsorbed water which has been shown to exist in graphite(4) even when present on metals, does not contribute to the electrical resistance(5) and even on metals any film which is less than 5 Å thick will permit conduction by the tunnel effect.

If the decrease in contact resistance on the application of load to a graphite contact was due to slip resulting in an increased contact area, this must be reversible since in the present work the original resistance was recovered when the load was removed. There may, however, be a load beyond which graphite deforms plastically. In this respect the results of current discharges may be relevant. The decrease of resistance observed in the latter experiments was permanent. By the creation of a high transient temperature in the contact, sufficient mobility could be imparted to the crystal layers to cause them to slip permanently. This movement of layers would be similar to a recrystallization phenomena. X-ray diffraction photographs taken of material removed from the graphite surfaces after pressure and high current discharge experiments showed no evidence of this but electron microscopy might be more relevant in this respect. Recrystallization in the present work would be on a small scale and confined to the surface.

Isotopes Laboratory,
University of St. Andrews,
Queen's College,
Dundee

J. C. Orr

References

1. Lewis F. A., Orr J. C. and Ubbelohde A. R., *Proc. phys. Soc. Lond.* **70,** 928 (1957).
2. Bundy F. P., *J. chem. Phys.* **38,** 618, 631 (1963).
3. Bowden F. P. and Tabor D., *Proc. Roy. Soc.* **A169** 391 (1938).
4. Savage R., *N.Y. Acad. Sci.* **53,** 862 (1951).
5. Bowden F. P. *The Friction and Lubrication of Solids,* University Press, Oxford (1945).

SOLID STATE COMMUNICATIONS

A new international medium for the rapid publication of short Communications in the solid state sciences.

SOLID STATE COMMUNICATIONS is basically the letters section of the Journal of Physics and Chemistry of Solids (Harvey Brooks, Editor-in-Chief) which is now being issued separately in order to achieve true letter speed of publication. Communications, not normally to exceed 1,200 words, will be published in English, French or German.

SOLID STATE COMMUNICATIONS will appear once a month, *starting June*, 1963, and it is expected that the publication time of a Communication will be from four to six weeks. To ensure the rapid distribution of the journal to areas where surface mailing time exceeds one week, copies will be airmailed ***at no extra cost to the subscriber.***

SOLID STATE COMMUNICATIONS has a truly international Board of Editors, and each Editor has full authority to accept or reject contributions on the basis of *originality, scientific merit and timeliness.*

Board of Editors

Pierre Aigrain, *Paris, Chairman*

S. Amelinckx, *Mol-Donk*
E. F. Bertaut, *Grenoble*
P. G. Bordoni, *Rome*
B. N. Brockhouse, *Hamilton, Ont.*
G. Busch, *Zürich*
P. G. De Gennes, *Orsay, S.-et-O.*
H. H. Jensen, *Copenhagen*
G. Liebfried, *Aachen*
E. M. Lifshitz, *Moscow*
W. M. Lomer, *Harwell, Didcot, Berks.*
W. Low, *Jerusalem*
S. Lundquist, *Gothenburg*
G. G. MacFarlane, *Great Malvern, Worcs.*
E. Mollwo, *Erlangen*
T. Muto, *Tokyo*
F. R. N. Nabarro, *Johannesburg*
G. W. Rathenau, *Amsterdam*
H. Suhl, *La Jolla, Calif.*
J. Tauc, *Prague*
A. R. Verma
G. S. Zhdanov, *Moscow*

Elias Burstein, *Philadelphia, Pa., Secretary*

Annual subscription rates: "A" for libraries, governments and research institutions, £10 ($30.00); "B", for private individuals who place their order direct with the publisher, £5 ($15.00); "C", for subscribers to the Journal of Physics and Chemistry of Solids,* £2 10*s*. ($7.50).
* *Gratis during* 1963. (Copies will be mailed automatically without application.)

Specimen issues and further information from the publishers:

PERGAMON PRESS
HEADINGTON HILL HALL, OXFORD
122 EAST 55TH STREET, NEW YORK 22

A NEW FREE BIBLIOGRAPHIC SERVICE AND SPECIAL PROCUREMENT CENTRE

The Documentation & Procurement Centre

DIVISION OF MAXWELL SCIENTIFIC INTERNATIONAL INC.

This unique service provides you—free of charge and in a systematic, comprehensive and objective way—with rapid and up-to-the-minute details of every significant new publication issued—or about to be issued—throughout the world. The information, which will be sent to you in the form of a regular weekly service, is classified in 204 different subject-categories and will thus assist you in keeping up with new developments in your specialized field.

The Documentation & Procurement Centre helps you in your task of dealing with the mass of published information, and simplifies your record keeping by:

- ★ giving new book information on standardized, easy-to-store-and-refer-to IBM-type cards (one card per title gives full bibliographical details plus descriptive information of contents).
- ★ providing a fast, reliable and economical channel for ordering books and journals from more than 1,000 participating publishers throughout the world.

The service is absolutely without cost. The expense of both the information service and the ordering service is borne entirely by the MSI Documentation Service in the interest of greater dissemination of news about forthcoming publications and fast, simpler order-processing through centralization and automation.

Use this coupon now to obtain a complete description of this revolutionary concept and its wide range of time-saving advantages to you.

THE DOCUMENTATION & PROCUREMENT CENTRE

MAXWELL SCIENTIFIC INTERNATIONAL INC.
122 East 55th Street, New York 22, N.Y.

NEW YORK - OXFORD - PARIS - LONDON

GENTLEMEN:

Please rush me complete information about the bibliographic service you have been instituting in co-operation with over 1,000 scientific and scholarly book publishers throughout the world.

Name.............................. *Institution*..............................

Full address..

....

....

PCS/2

NOTES FOR CONTRIBUTORS

I. GENERAL

1. Submission of a paper to *The Journal of Physics and Chemistry of Solids* will be taken to imply that it represents original research not previously published (except in the form of an abstract or preliminary report), that it is not being considered for publication elsewhere, and that if accepted it will not be published elsewhere in the same form, in any language, without the consent of the editor-in-chief. It should deal with original research work in the field of the physics and chemistry of solids.

2. Papers should be submitted to the appropriate regional editor (all English-language papers to be sent to the U.S. editor).

3. Papers will be published as quickly as possible after acceptance, and, subject to space being available, should appear in the issue next following, if this is due for publication not earlier than three months after the acceptance date. Short communications under the heading of "Letters to the Editor" will receive priority for publication, and will be published in the issue following receipt, if accepted not later than the beginning of the month preceding publication.

II. SCRIPT REQUIREMENTS

1. Papers submitted should be concise and written in a readily understandable style. Scripts should be typed and double spaced and submitted in duplicate to facilitate refereeing.

It will be appreciated if authors clearly indicate any special characters used. An abstract not exceeding 200 words, should be provided in the language of the paper. French and German papers should be submitted with English abstract and titles, but if this is not possible the abstract will be translated by the publishers. To conserve space, authors are requested to mark less important parts of the paper, such as details of experimental technique, methods, mathematical derivations, etc. for printing in small type. The technical description of methods should be given in detail only when such methods are new. Authors will receive proofs for correction when their papers are first set; further proofs will be sent only when the amount of alteration makes it advisable.

2. **Illustrations** should not be included in the typescript of the paper, and legends should be typed on a separate sheet. Line drawings which require redrawing should include all relevant details and clear instructions for the draughtsman. If figures are already well drawn it may be possible to reproduce them direct from the originals, or from good photo-prints if these can be provided. It is not possible to reproduce from prints with weak lines. Illustrations for reproduction should normally be about twice the final size required. The lettering should be sufficiently large and bold to permit this reduction. Photographs should only be included where they are essential.

3. **Tables and figures** should be so constructed as to be intelligible without reference to the text. Every table and column should be provided with an explanatory heading. Units of measure must always be clearly indicated. The same data should not be published in both tables and figures. The following standard symbols should be used on line drawings since they are easily available to the printers: ○, ●, +, ×, □, ■, △, ▲, ◇, ◆, ▽, ▼.

4. References are indicated in the text by superior numbers in parentheses, and the full reference should be given in a list at the end of the paper in the following form:

1. Hill R., *J. Iron St. Inst.* **158**, 177 (1948).
2. Pearson C., *The Extrusion of Metals*, p. 137. Chapman and Hall, London (1944).

Abbreviations of journal titles should follow those given for *Physics Abstracts*. It is particularly requested that authors' initials, and appropriate volume and page numbers, should be given in every case.

Footnotes, as distinct from literature references should be indicated by the following symbols—*,†, ‡,‡‡, commencing anew on each page; they should *not* be included in the numbered reference system.

5. Due to the international character of the journal no rigid rules concerning notation and spelling will be observed, but each paper should be consistent within itself as to symbols and units.

THE JOURNAL OF PHYSICS AND CHEMISTRY OF SOLIDS

VOLUME 24 No. 12 1963 DECEMBER

W. W. Mullins and J. P. Hirth: The microscopic kinetics of step motion in growth processes . 1391
J. R. Packard and C. A. Swenson: An experimental equation of state for solid xenon . . 1405
M. Rosenberg, P. Nicolau, R. Manaila and P. Pausescu: Preparation, electrical conductivity and tetragonal distortion of some manganite-systems 1419
G. L. Stepakoff and L. V. Coulter: The thermodynamics and hindered rotation of occluded CO in the β-quinol clathrate 1435
F. O. Goodman: On the theory of accommodation coefficients—III Classical perturbation theory for the thermal accommodation of light gases 1451
G. L. Bir, E. I. Butikov and G. E. Pikus: Spin and combined resonance on acceptor centres in Ge and Si type crystals—I Paramagnetic resonance in strained and unstrained crystals . . 1467
G. L. Bir, E. I. Butikov and G. E. Pikus: Spin and combined resonance on acceptor centres in Ge and Si type crystals—II The effect of the electrical field and relaxation time . . . 1475
S. Teitler: Anisotropic free carrier Voigt effect in cubic semiconductors 1487
V. Halpern: Overlap functions in planar crystals 1495
K. Nassau and G. M. Loiacono: Calcium tungstate—III Trivalent rare earth substitution . 1503
K. Nassau: Calcium tungstate—IV The theory of coupled substitution 1511
N. B. Owen, P. L. Smith, J. E. Martin and A. J. Wright: X-ray diffraction at ultra-high pressures 1519
M. S. Seltzer and J. B. Wagner, Jr: Diffusion of lead in lead sulphide at 700°C . . . 1525
T. R. McGuire and S. J. Pickart: Ferrimagnetism of manganese ferrite–chromite . . . 1531
W. Kunnmann, D. B. Rogers and A. Wold: The use of CO–CO_2 atmospheres for the preparation and free energy determinations of several oxide systems 1535
Jean Messier and Jorge Merlo Flores: Temperature dependence of Hall mobility and μ_H/μ_D for Si 1539
Manuel Cardona: Band parameters of semiconductors with zincblende, wurtzite, and germanium structure 1543
D. Jerome et G. Galleron: Polarisation dynamique du sodium métallique en champ faible à la température de l'helium liquide 1557
M. Kleefstra: Z-bands in KCl 1567
Sivert H. Glarum: Electron mobilities in organic semiconductors 1577
R. G. Seidensticker and D. R. Hamilton: The dendritic growth of InSb 1585
Harvey Kaplan: Impurity states associated with subsidiary energy-band minima . . . 1593
E. Daniel et J. Friedel: Sur la polarisation de spin des electrons de conductibilité dans les métaux ferromagnétiques 1601
D. C. Hoesterey and G. M. Letson: The trapping of photocarriers in anthracene by anthraquinone, anthrone and naphthacene 1609
R. Lallement: Dilatation et pouvoir thermoélectrique du plutonium α à basse température . 1617
Hans Knof and William G. Maisch: Pressure effect on color centers in RbF, RbCl, RbBr and CsI 1625
H. J. Arnikar and O. P. Mehta: Surface self-diffusion of iodide ions in thin films . . . 1633
C. A. Mackliet and A. I. Schindler: Heat capacity of Ni–Pd alloys 1639
Joseph Singer: Study of the bands of uniform birefringence in faulted ZnS 1645
J. A. Schulkes and G. Blasse: Crystallographic and magnetic properties of the systems lithium ferrite–aluminate and lithium ferrite–gallate 1651
T. N. Morgan: Application of the uncertainty principle to electron scattering by phonons in solids 1657
G. P. Felcher, J. W. Cable and M. K. Wilkinson: The magnetic moment distribution in Cu_2MnAl 1663
W. C. Walker: d-band transitions in solids 1667
W. Gomes: The influence of vacancies on the reduction of silver ions in silver doped alkali halides 1671
Nobuyuki Fukuda and Michael Wortis: Bound states in the spin wave problem . . . 1675
G. Will, S. J. Pickart, H. A. Alperin and R. Nathans: Antiferromagnetic structure of EuTe . 1679
Yu. S. Karimov, V. M. Chibrikin and I. F. Shchegolev: A study of hyperfine interaction in cations of dibenzenechromium and ditoluenechromium 1683
F. Pilcher, D. Schinke and R. J. Friauf: Optical absorption of color centers in lithium fluoride containing magnesium additive 1687
Letters to the Editor:
  P. W. M. Jacobs and J. N. Maycock: Conductance of strontium-doped potassium chloride crystals 1693
  J. C. Orr: Pressure and high current effects on a graphite contact 1695

PRINTED BY J. W. ARROWSMITH LTD., BRISTOL, ENGLAND